SCHOLARLY PUBLICATIONS

A CURRENT AWARENESS BULLETIN
OF RESEARCH OUTPUT

@DTU

(125th Edition)

MAY 2023

BY: CENTRAL LIBRARY

DELHI TECHNOLOGICAL UNIVERSITY
(FORMERLY *DELHI COLLEGE OF ENGINEERING)*
GOVT. OF N.C.T. OF DELHI
SHAHBAD DAULATPUR, MAIN BAWANA ROAD
DELHI 110042

PREFACE

This is the **One Hundred Twenty Fifth** Issue of Current Awareness Bulletin started by Delhi Technological University, Central Library. The aim of the bulletin is to compile, preserve and disseminate information published by the faculty, students and alumni for mutual benefits. The bulletin also aims to propagate the intellectual contribution of Delhi Technological University (DTU) as a whole to the academia.

The bulletin contains information resources available in the internet in the form of articles, reports, presentations published in international journals, websites, etc. by the faculty and students of DTU. The publications of faculty and student which are not covered in this bulletin may be because of the reason that the full text either was not accessible or could not be searched by the search engine used by the library for this purpose.

The learned faculty and students are requested to provide their uncovered publications to the library either through email or in CD, etc. to make the bulletin more comprehensive.

This issue contains the information published during **May, 2023**. The arrangement of the contents is alphabetical. The full text of the article which is either subscribed by the university or available in the web is provided in this bulletin.

Central Library

CONTENTS

1. A Cocktail of Natural Compounds Holds Promise for New Immunotherapeutic Potential in Head and Neck Cancer, ***6.Sunil Kumar*** and ***3.Asmita Das***, Biotechnology, DTU

2. A Comparative Study of Text Summarization using Gensim, NLTK, Spacy, and Sumy Libraries, ***3.Abhilasha Sharma***, ***8.Raghav Aggarwal*** and ***8.Raghav Alawadhi***, Software Engineering, DTU

3. A Comprehensive Review of Sensor-based Sign Language Recognition Models, ***8.Manas Taneja***, ***8.Navya Singla***, ***8.Neha Goyal*** and ***3.Rajni Jindal***, CSE, DTU

4. A Latch-Based Sense Amplifier with improved performance for single ended SRAM application, ***6.Bhawna Rawat*** and ***3.Poornima Mittal***, Electronics, DTU

5. A Non-invasive Optical Method for Anaemia Detection, ***6.Paritosh Chamola*** and ***3.Poornima Mittal***, Electronics, DTU

6. A Novel approach to Handle Imbalanced Dataset in Machine Learning, ***8.Taj Sapra***, ***8.Shubhama*** and ***3.Shweta Meena***, Software Engineering, DTU

7. A novel locally connected recurrent neural network for identification of nonlinear dynamical system, ***6.Shobana. R***, Rajesh Kumar & ***3.Bhavnesh Jaint***, Electrical, DTU

8. A novel passive micromixer model computational analysis with twist and bend, ***6.Md Gulam Mustafa***, ***3.Mohammad Zunaid*** & ***3.Samsher Gautam***, Mechanical, DTU

9. A review of vision-based indoor HAR: state-of-the-art, challenges, and future prospects, ***3.Geetanjali Bhola*** and ***3.Dinesh Kumar Vishwakarma***, IT, DTU

10. A robust model for improving the quality of underwater images using enhancement techniques, ***8.Nishant Singh*** and ***3.Aruna Bhat***, CSE, DTU

11. A Systematic Literature Review: Approach Toward Blockchain Future Research Trends, ***7.Himanshu Nandanwar*** and ***3.Rahul katarya***, CSE, DTU

12. Adaptive-Optimal Control for Reconfigurable Robots, ***8.Adya Maheshwari***, ***8.Aaditya Rautela***, ***3.Madan Mohan Rayguru*** and ***3.Sudarshan K. Valluru***, Electrical, DTU

13. AI And Its Application in CAD, ***8.Mohit Saini***, Mechanical, DTU

14. Algorithm based determination of the Planck's constant, Smita Korpal, ***8.Anmol Aggarwal***, Ajay Kumar Arora, Jyoti Anand, Maya Verma & Divya Haridas, CSE, DTU

15. An In-Silico Comparison Of Ginsenoside's Anticancer Activity Against The Son Of Sevenless Homolog 1, ***7.Anjali Sinha***, ***7.Bharmjeet*** and ***3.Dr. Asmita Das***, Biotechnology, DTU

16. An Intelligent System for Bearing Fault Identification based on Gramian Multi-Resolution Dynamic Mode Decomposition, ***7.Sonalika Bhandari***, ***3.Sachin Taran*** and ***3.Varun Sangwan***, Electronics, DTU

17. Ancient Indian Script Transliteration Using GANs, ***8.Anshumani Sharma***, ***8.Ayushi Verma***, ***8.Chetan Shahra*** and ***3.S. Indu*** Electronics, DTU

18. Audio Based Music Genre Classification using Convolutional Neural Networks Sequential Model, ***8.Simran Pasrija***, ***8.Shubham Sahu*** and ***3.Shweta Meena***, Software Engineering, DTU

19. Blockchain-based distributed application for multimedia system using Hyperledger Fabric, ***6.Pratima Sharma***, ***3.Rajni Jindal*** and ***7.Malaya Dutta Borah***, CSE, DTU

20. Carbon nanotubes modified conductive ink for application to paper-based electrochemical biosensor for pathogenic DNA detection, ***7.Niharika Gupta***, ***3.D. Kumar***, ***3.Asmita Das***, Seema Sood and ***3.Bansi D. Malhotra***, Biotechnology and Applied Chemistry, DTU

21. Carboxymethylated gum tragacanth crosslinked poly(sodium acrylate)hydrogel: Fabrication, characterization, rheology and drug-delivery application, ***6.Meenakshi Tanwar***, ***3.Rajinder K Gupta*** and ***3.Archna Rani***, Applied Chemistry, DTU

22. CNTFET BASED M-DMTGDI (CMDMTGDI) DESIGN AND ITS LEAKAGE ANALYSIS, ***6.1.NEETIKA YADAV***, ***3.NEETA PANDEY*** AND ***3.DEVA NAND***, ELECTRONICS, DTU

23. Comparative Analysis of Different Profiles of Riblets on an Airfoil using Large Eddy Simulations, ***8.Aryan Tyagi***, ***8.Aakash Ghosh*** & ***3.Rajkumar Singh***, Mechanical, DTU

24. Comparison of the Heat Transfer Capability of Various Nanofluids in a Flat Plate Solar Collector, ***8.Utkarsh Verma***, ***8.Shivraj Yadav*** and ***6.Gaurav Kumar***, Mechanical, DTU

25. Crocin: A Potent Secondary Metabolite As BACE1 Inhibitor In Alzheimer's Disease, ***7.Murali Mohan Mishra*** and ***3.Pravir Kumar***, Biotechnology, DTU

26. Cross-Domain Learning for Pulmonary Nodule Detection using Gestalt Principle of Similarity, ***3.Seba Susan***, ***8.Dhaarna Sethi*** and ***8.1.Kriti Arora***, IT, DTU

27. Cyber Attack Detection in IoT using Deep Learning Techniques, ***8.Kartik Tomar***, ***8.Krishi Bisht***, ***8.Kshitiz Joshi*** and ***3.Rahul Katarya***, CSE, DTU

28. Damage identification in Concrete under impact loading at varying temperatures using voltage relations technique: An experimental and numerical study, ***6.Indrajeet Singh***, ***3.Nirendra Dev*** and ***3.Shilpa Pal***, Civil, DTU

29. Deep Siamese Network with Handcrafted Feature Extraction for Hyperspectral Image Classification, ***6.Pallavi Ranjan*** and ***3.Ashish Girdhar***, CSE, DTU

30. Denoising of Palm Leaf Manuscripts Using Gaussian Filter and Conservative Smoothing, ***8.Mayank Singh*** and ***3.S. Indu***, Electronics, DTU

31. Density functional characterization of electronic and optical properties of strontium titanate under doping and strain for optoelectronic applications, ***6.Ashish Raturi***, ***3.Poornima Mittal*** and Sudhanshu Choudhary, Electronics, DTU

32. Design & Validation of ANN based Reinforcement Learning Control Algorithm for Coupled Tank System, ***8.Digant Rastogi***, ***8.Manika Jain***, ***3.Madan M. Rayguru*** and ***3.Sudarshan K. Valluru***, Electrical, DTU

33. Development and Validation of Hindu Gratitude Scale (HGS-15): A Rnas Perspective, ***3.Naval Garg***, USME, DTU

34. Effect of Intermetallic Compounds on Mechanical and Microstructural Properties of Dissimilar Alloys Al-7Si/AZ91D, Husain Mehdi, ***6.Sumit Jain***, Velaphi Msomi, Sipokazi Mabuwa and Chandrabhanu Malla, Mechanical, DTU

35. Effective Brain Tumor Segmentation for MRI Image Analysis using Dual Attention Network based YOLACT++, ***8.Neil Roy***, Sandip Kumar Roy and Preeta Sharan, CSE, DTU

36. Efficient photosensitive light harvesting dye sensitized solar cell using hibiscus and rhodamine dyes, Geetam Richhariya, ***3.Anil Kumar***, Akash Kumar Shukla, Kailash Nath Shukla and Issara Chanakaewsomboon, Mechanical and Environment, DTU

37. End-of-life solar photovoltaic panel waste management in India: forecasting and environmental impact assessment, ***8.A. Sharma***, ***3.P. Mahajan*** and ***3.R. Garg***, Electrical, DTU

38. Estimation of Respiratory Rate from a Corrupted PPG Signal using Time-Frequency Spectrogram, Pankaj, Ashish Kumar, Rama Komaragiri and ***3.Manjeet Kumar***, Electronics, DTU

39. Estimations of Wind-Generated Effects on a Regular Tower of Varying Cross-Sectional Shape, ***6.Abhishek Prakash Paswan***, ***8.Bhagya Jayant***, ***8.Ark Rukhaiyar***, ***8.Kunal Dahiya***, ***3.Ritu Raj*** and ***8.Rahul Kumar Meena***, Civil, DTU

40. Experimental Investigation of Modern Control Algorithms for Power Quality Improvement for Single-Phase Grid-Connected Photo-Voltaic System, ***3.Prakash Chittora***, ***3.Alka Singh***, ***3.Madhusudan Singh*** and ***6.Hemant Saxena***, Electrical, DTU

41. Extractive Text Summarization, ***8.Abhishek Kumar*** & ***3.Garima Chhikara***, CSE, DTU

42. Fake News Detection using Attention Based Model, ***8.Khushi Jain***, ***8.Harsh Bansal***, ***8.Gaurav Saxena*** and ***3.Rohit Kumar***, Electronics, DTU

43. Finding the Network of Unsocial Elements, ***3.Rajesh Kumar Yadav***, ***8.Archit Gupta*** and ***8.Areeshaa Parveen***, CSE, DTU

44. Forest Fire Detection using Convolutional Neural Network Model, ***8.Shubham Sah***, ***8.Suneet Prakash*** and ***3.Shweta Meena***, Software, DTU

45. FPGA IMPLEMENTATION OF A HIGH THROUGHPUT LOW POWER ADVANCED ENCRYPTION STANDARD (AES-128) CIPHER, ***7.Jaideep Kala***, ***3.Jeebananda Panda*** and ***3.Lavi Tanwar***, Electronics, DTU

46. Gate Engineered Ferroelectric Junctionless BioFET for Label-Free Detection of Biomolecules, ***7.Snehlata yadav***, ***3.Sonam Rewari*** and ***3.Rajeshwari Pandey***, Electronics, DTU

47. Helping Local Businesses by using IoT Embedded Systems, ***3.Dr. Ajai Kumar Gautam***, ***8.Ritvick A. Lohani***, ***8.Sudeep Saurabh*** & ***8.Swapnil Gour***, Electronics, DTU

48. Hexagonal lattice twin core photonic crystal fiber based chemical sensor, ***6.Vishal Chaudhary*** and ***3.Sonal Singh***, Electroncis, DTU

49. Hybrid deep learning with improved Salp swarm optimization based multi-class grape disease classification model, Shtwai Alsubai, Ashit Kumar Dutta, Ahmed Hussein Alkhayyat, Mustafa Musa Jaber, Ali Hashim Abbas and ***7.1.Anil Kumar***, CSE, DTU

50. Image flare removal using Deep Convolutional Generative Adversarial Networks, ***8.Ishan Prakash*** and ***8.Aryan***, Electrical and Electronics, DTU

51. INDUSTRY 4.0 AND THE SMART FACTORY: A REVIEW OF EMERGING TECHNOLOGIES AND APPLICATIONS, ***8.Ravi Prakash***, ***8.Somnath Pal*** and ***3.Ashok Kumar Madan***, Mechanical, DTU

52. INDUSTRY 4.0 –The Industry Internet of Things (Computer aided manufacturing), ***3.A.k Madan***, ***8.Mohit Raj*** and ***8.Saksham Agrawal***, Mechanical and Production and Industrial Engineering, DTU

53. In-silico approach to DNA codon optimization of Zaire Ebola Virus Genes for Vaccine Development, ***7.Ruchi Tirkey***, ***8.Soniya*** & ***3.Yasha Hasija***, Biotechnology, DTU

54. INTEGRATION OF DIMENSIONING AND TOLERANCING INTO CAD SYSTEMS: A SYSTEMATIC APPROACH USING TTRS, ***3.AK Madan***, ***8.Arko Sardar***, ***8.Ankush Kapoor*** and ***8.Badal Singh***, Mechanical, DTU

55. Interpolative AMBTC based Reversible Data Hiding In Encrypted Images using Rhombus Mean, ***8.Sezal Mittal***, ***8.Sanya Goyal***, ***8.Shruti Aggarwal*** and ***3.Rajeev Kumar***, CSE, DTU

56. Light-Weight Deep Learning Model for Human Action Recognition in Videos, ***6.Rahul Kumar*** and ***3.Shailender Kumar***, CSE, DTU

57. Machine Learning Aided Techniques for Constraints Elimination in Optimal Power Flow Problem, ***8.Chaitanya Agarwal***, ***8.Kabir*** and ***3.Vinod Kumar Yadav***, Electrical, DTU

58. MACHINE LEARNING APPROACHES TO MANUFACTURING, ***3.AK Madan***, ***8.Rohin Verma***, ***8.Rudansh Singh*** and ***8.Ritik Kamboj***, Mechanical, DTU

59. Mitigating YouTube Recommendation Polarity using BERT and K-Means Clustering, ***8.Zoheb Ahmad***, ***8.Danish Quasim***, Shreeya Garg and ***3.Vinod Kumar***, Software and CSE, DTU

60. MonkeyPox, Measles and ChickenPox Detection through Image-Processing using Residual Neural Network (ResNet), ***3.Kapil Sharma***, ***8.Kishlay***, ***8.Mayank Mittal*** and ***3.Vinod Kumar***, CSE, DTU

61. Next-LSTM: A novel LSTM-based Image Captioning technique, ***3.Priya Singh***, ***8.Chandan Kumar*** and ***8.Ayush Kumar***, DTU

62. Optimal Control Strategies to Cope with Unemployment During the Covid-19 Pandemic, ***6.Charu Arora*** and ***3.Sudhakar Yadav***, Applied Mathematics, DTU

63. Optimization of PV array with PID controller and MPPT(P&O), Shilpa Saxena, V.K Tayal, H.P Singh and ***3.Vinod Kumar Yadav***, Electrical, DTU

64. Optimized Pair Trading Strategy using Unsupervised Machine Learning, ***8.Vanshika Gupta***, ***8.Vineet Kumar***, ***8.Yuvraj*** and ***3.Manoj Kumar***, CSE, DTU

65. PERFORMANCE EVALUATION OF BISMUTH TELLURIDE SEMICONDUCTOR BASED PARABOLIC DISH CONCENTRATED SOLAR THERMOELECTRIC GENERATOR IN REALISTIC METEOROLOGICAL CONDITIONS OF CENTRAL INDIA, Sanjeev Kumar Bhukesh, ***3.Anil Kumar*** and Suresh Kumar Gawre, Mechanical, DTU

66. Performance evaluation of indirect type domestic hybrid solar dryer for tomato drying: Thermal, embodied, economical and quality analysis, Mukul Sharma, Deepali Atheaya and ***3.Anil Kumar***, Mechanical and Environment, DTU

67. Phytochemical-Based Synthesis of Silver Nanoparticle: Mechanism and Potential Applications, ***8.Ritu***, ***8.Krishan Kumar Verma***, ***3.Asmita Das*** and ***3.Prakash Chandra***, Biotechnology, DTU

68. Plant Disease Detection And Prevention Using Deep Learning, ***3.Prashant Giridhar Shambharkar*** and ***7.Saurabh Sharma***, CSE, DTU

69. Potential application of novel graphene/diamane interface in silicon-based heterojunction with intrinsic thin layer solar cell, ***6.Naima***, ***3.Pawan K. Tyagi*** and ***3.Vinod Singh***, Applied Physics, DTU

70. Power Quality Disturbances Detection and Classification Based on Deep Convolution Auto-encoder Networks, PORAS KHETARPAL, ***6.1.NEELU NAGPAL***, MOHAMMED AL-NUMAY, PIERLUIGI SIANO, YOGENDRA ARYA and NEELAM KASSARWANI, Electrical, DTU

71. Pre-training meets Clustering: A Hybrid Extractive Multi-Document Summarization Model, ***6.Akanksha Karotia*** and ***3.Seba Susan***, IT, DTU

72. Prospects and Challenges with Legal Informatics and Legal Metrology Framework in the Context of Industry 6.0, ***8.S. Chourasia***, S. M. Pandey and A. K. Keshri, Mechanical, DTU

73. Psyche.ly: Personality Detection for Hindi Text-based Dataset, ***8.Rijul Chauhan***, ***8.Prakhar Mehta***, ***8.Nikhil Chauhan*** and ***3.Garima Chhikara***, CSE, DTU

74. Radius of Uniformly Convex g-Spirallikeness of Combination of Derivatives of Bessel Functions, Stanislawa Kanas and ***6.Kamaljeet Gangania***, Applied Mathematics, DTU

75. RECENT FINDINGS ON PLASTIC WASTE POLLUTION AND BIOTRANSFORMATION, ***7.Tushar Agarwal*** and ***3.Jai Gopal Sharma***, Biotechnology, DTU

76. Review on advancement in solar and waste heat based thermoelectric generator, Sanjeev Kumar Bhukesh, Suresh Kumar Gawre, and ***3.Anil Kumar***, Mechanical and Environment, DTU

77. Review on Ultrasound-Image Analysis of Fetus Using Deep Learning, ***6.Lavendra Gautam*** and ***3.Gull Kaur***, CSE, DTU

78. REVIEW PAPER ON AIR GAUGING FOR INDUSTRY 4.0, ***8.Aditya Mudgal***, ***8.Anmol Sharma*** and ***3.AK Madan***, Mechanical, DTU

79. Review—Magneto-Electrochemical based Biosensors Devices for Recognition of Tumour Vesicles from Blood Plasma, Anusuiya Bora, ***8.Rashi Sharma***, Ishi Gupta, Mahika Singh, Nilabha Mukherjea, Yuvraj Ranjan Bartaria, Utkarsh Chadha, Preetam Bhardwaj, Srinivasan Latha and Arghya Chakravorty, Biotechnology, DTU

80. RGB-D Dataset: The Impact of Yoga and Gym Exercise for Human Activity Recognition, ***8.Vishal Sharma***, ***8.Bhavana Sharma*** and ***3.Jeebananda Panda***, Electronics, DTU

81. Scenario of Offshore Wind Power Generation in India, Anubhav Singh, Dharmraj Meena, ***6.1.Shanti Lal Meena*** and Shiv Lal, Mechanical, DTU

82. SIMULATION AND PERFORMANCE ANALYSIS OF A MULTIFUNCTIONAL OFF-BOARD EV CHARGER WITH SOLAR PV INTEGRATION AND IMPROVED POWER QUALITY USING MATLAB/SIMULINK, ***8.Sohail Ahmad***, ***8.Tarun, Tushar***, ***8.Vishal Kumar*** and ***3.Aniruddha B Bhattacharya***, Electrical, DTU

83. Simulation of an Elevator Controller with Weight Sensing Mechanism using VHDL, ***8.Rahul Sharma***, ***8.Saarthak Shakargaye***, ***3.Rohit Kumar*** and ***3.Sachin Taran***, Electronics, DTU

84. Simulation of reservoir outflows using regression tree and support vector machine, ***6.Vijay Kaushik*** and ***7.Noopur Awasthi***, Civil, DTU

85. Software Testing using Genetic Algorithms-A review, ***8.Ishaan Rajora***, ***8.Lakshay Sandhu***, ***8.Mohammad Yamin Bhat*** and ***3.Rohit Beniwal***, CSE, DTU

86. Spectroscopic studies of Pr3+ doped red-emitting BaO–ZnO– Li2O–P2O5 glasses for luminescent devices applications, ***6.Kartika Maheshwari***, ***6.Ravita***, ***6.Aman Prasad***, ***6.Yasha Tayal*** and ***3.A.S. Rao***, Applied Physics, DTU

87. Speed Control of Three-Phase Induction Motor Using PI, Fuzzy and ANFIS Controllers, ***8.Naman Gogia***, ***8.Rishabh Prasad*** and ***8.Ritik Arora***, Electrical, DTU

88. Statistical and cosmological analysis of Weyl-type f(Q; T) models using Pantheon+ dataset, Gaurav N. Gadbail, ***6.Harshita***, Amine Bouali, and P.K. Sahoo, Applied Mathematics, DTU

89. Steerable Pyramid-based Multi-Scale Fusion Algorithm for Single Image Dehazing, ***7.Paulami Purkayastha***, ***3.M. S. Choudhary*** and ***3.Manjeet Kumar***, Electronics, DTU

90. Stilbostemin C as a Potential Candidate for Therapeutic Targeting of Rab3b Protein in Countering Alzheimers, ***7.Sanya Madaan*** and ***3.Pravir Kumar***, Biotechnology, DTU

91. Study of SXR and HXR transitions with intensity spectra of W LXIX, ***6.Richa Paijwar***, ***3.Rinku Sharma*** and Alok Kumar Singh Jha, Applied Physics, DTU

92. SUSPENSION GEOMETRY OPTIMISATION FOR OFF-ROAD VEHICLES USING ARTIFICIAL NEURAL NETWORK AND PARTICLE SWARM OPTIMISATION, ***8.Satwik Dudeja***, ***8.Satwik Gupta*** and ***8.Shaswat Garg***, Mechanical, DTU

93. Third Harmonic Injected Nearest Level Control of Nine-Level Grid-Tied PV-CHB Converter, Sanjay Upreti, Bhim Singh and ***3.Narendra Kumar***, Electrical, DTU

94. TransFAS: Transformer-based network for Face Anti-Spoofing using Token Guided Inspection, ***8.Dipra Chaudhry***, ***8.Harshit Goel*** and ***3.Dr Bindu Verma***, IT, DTU

95. Transfer Learning Approach to Multilabel Biomedical Literature Classification using Transformer Models, ***8.Pahalage Dona Thushari***, ***8.Sakina Niazi*** and ***3.Shweta Meena***, Software Engineering, DTU

96. Transition metal induced-magnetization in zigzag SiCNTs, ***3.Anurag Chauhan***, ***3.Kapil Sharma*** and Sudhanshu Choudhary, IT, DTU

97. TRIBOLOGICAL ANALYSIS OF NANOPARTICLES IN LUBRICANTS USING FOUR BALL TESTER, ***8.Shaurya Tarun***, ***8.Siamjoyful Keishing*** and ***8.Subhash Sharma***, Mechanical, DTU

98. Tunable LSPR in Asymmetric Plasmonic Bowtie Nanostructures, ***6.Kirti Dalal*** and ***3.Yashna Sharma***, Electronics, DTU

99. Underwater Image Enhancement using Convolutional Block Attention Module, ***8.Nishant Singh*** and ***3.Aruna Bhat***, CSE, DTU

100. Underwater Image Restoration Using Color Correction and Empirical Mode Decomposition, ***6.Amarendra Kumar Mishra***, ***3.Mahipal Singh Choudhry*** and ***3.Manjeet Kumar***, Electronics, DTU

101. Variation-Tolerant Sense Amplifier Using Decoupling Transistors for Enhanced SRAM Read Performance, ***8.Ayush Dahiya***, ***3.Poornima Mittal*** and ***3.Rajesh Rohilla***, Electronics, DTU

102. Word spotting and character recognition of handwritten Hindi scripts by Integral Histogram of Oriented Displacement (IHOD) descriptor, ***6.Enock Osoro Omayio***, ***3.Sreedevi Indu*** and ***3.Jeebananda Panda***, Electronics, DTU

1. *Vice Chancellor*
2. *Pro Vice Chancellor*
3. *Faculty*
4. *Teaching-cum-Research Fellow*
5. *Asst. Librarian*
6. *Research Scholar*
7. *PG Scholar*
8. *Undergraduate Student*

1.1. *Ex Vice chancellor*
2.1. *Ex Pro Vice Chancellor*
3.1. *Ex Faculty*
4.1. *Alumni*
5.1 *Others*
6.1. *Ex Research Scholar*
7.1. *Ex PG Scholar*
8.1. *Ex Undergraduate Student*

Chinese Journal of Integrative Medicine
Available online at link.springer.com/journal/11655
Journal homepage: www.cjim.cn/zxyjhen/zxyjhen/ch/index.aspx
E-mail: cjim_en@cjim.cn

Original Article

A Cocktail of Natural Compounds Holds Promise for New Immunotherapeutic Potential in Head and Neck Cancer

Sunil Kumar and Asmita Das

ABSTRACT **Objective**: To obtain detailed understanding on the gene regulation of natural compounds in altering prognosis of head and neck squamous cell carcinomas (HNSC). **Methods**: Gene expression data of HNSC samples and peripheral blood mononuclear cells (PBMCs) of HNSC patients were collected from Gene Expression Omnibus (GEO). Differential gene expression analysis of GEO datasets were achieved by the GEO2R tool. Common differentially expressed gerres (DEGs) were screened by comparing DEGs of HNSC with those of PBMCs. The combination was further analyzed for regulating pathways and biological processes that were affected. **Results**: Totally 110 DEGs were retrieved and identified to be involved in biological processes related to tumor regulation. Then 102 natural compounds were screened for a combination such that the expression of all 110 commonly DEGs was altered. A combination of salidroside, ginsenoside Rd, oridonin, britanin, and scutellarein was chosen. A multifaceted, multi-dimensional tumor regression was showed by altering autophagy, apoptosis, inhibiting cell proliferation, angiogenesis, metastasis and inflammatory cytokines production. **Conclusions**: This study has helped develop a unique combination of natural compounds that will markedly reduce the propensity of development of drug resistance in tumors and immune evasion by tumors. The result is crucial to developing a combinatorial natural therapeutic cocktail with accentuated immunotherapeutic potential.

KEYWORDS natural compounds, chemopreventive, gene expression, head and neck cancer, immunomodulator, salidroside, ginsenoside Rd, oridonin, britanin, scutellarein

The genetic variability across different cancer types has impeded the identification of therapeutic targets and the drug design and development against tumors.[1] The most commonly used cancer therapies include surgery, radiation, and chemotherapy, which can be used in isolation or different combinations.[2] However, these techniques have been associated with a high morbidity rate and a significant decline in quality of life.[3] Head and neck squamous cell carcinomas (HNSC) could affect different head and neck areas, including the tongue, pharynx, larynx, nasal cavity, and salivary glands.[4] It is the sixth most common cancer globally, with over 880,000 new cases diagnosed and over 450,000 patients dying yearly.[5] HNSC, with complex pathophysiology and pathogenesis, makes it difficult to determine the optimal treatment strategy.[6]

Additionally, despite monotherapy's specificity and efficiency, cancer cells' molecular flexibility renders ideal lethal effects challenging.[7] HNSC has a poor prognosis due to many patients' high likelihood of recurrence or metastasis following radiation or chemotherapy.[8] This high metastatic rate of HNSC is because of the tumor cell's interactions with the surrounding tissues and immune cells that will form the tumor microenvironment (TME).[9] Host immune cells can recognize and eliminate the tumor cells, but an evasion of immunosurveillance generates an environment that accommodates the progression and survival of tumor cells.[10] Cancer-associated stromal fibroblasts, T cells, B cells, neutrophils, macrophages, myeloid-derived suppressor cells (MDSC), natural killer (NK) cells, and mast cells are all part of the TME.[11] These numerous cell subsets penetrate tumors and interact with cells one another through multiple networks.[12] Tumors progress if they can evade and/or suppress antitumor immune responses.[13] Tumors frequently elude the immune system of their hosts by inhibiting cytotoxic T-cell activity or activating

©The Chinese Journal of Integrated Traditional and Western Medicine Press and Springer-Verlag GmbH Germany, part of Springer Nature 2023
Department of Biotechnology, Delhi Technological University, Delhi (110042), India
Correspondence to: Dr. Asmita Das, E-mail: asmita1710@gmail.com, asmitadas1710@dce.ac.in
DOI: https://doi.org/10.1007/s11655-023-3694-0

and increasing immunosuppressive cell populations.[14]

Efforts to increase the efficacy of cancer treatment have primarily failed in recent decades, underlining the need for novel techniques such as complementary and alternative medicine.[15] Numerous natural herbal substances have caught the interest of academics and physicians due to their potential to prevent or improve the treatment of chronic diseases, including cancer.[16] Natural chemicals and combinations thereof may be a potential source of synergistic cancer treatments since they can interact with multiple biological targets involved in tumor growth, drug resistance, and metastasis.[17] Through their multitargeting action, natural chemicals may enhance the efficacy of already available cancer treatments or diminish treatment resistance.[18] Cancer treatment tries to eliminate or destroy tumor cells while sparing normal ones. The majority of natural substances are less poisonous, less expensive, have fewer side effects, and have been carefully researched for their carcinogenic potential.[19] Due to the adverse effects and drug resistance associated with conventional therapy, it was evident that natural substances can act as anticancer agents or adjuvants in chemotherapy.[20]

Cancer chemoprevention reverses, suppresses, or prevents cancer initiation, propagation, or advancement using natural or synthetic medications.[21] To be effective in people, a chemopreventive medicine must have an acceptable safety profile and be efficacious at a low enough dose to avoid severe side effects.[22] Natural dietary interventions such as fruits and vegetables show tremendous promise for chemopreventive research due to their potential to prevent and reduce cancer.[23] The chemical diversity of natural chemicals suggests a range of cancer chemoprevention techniques. Chemoprevention appears to be a rational and appealing strategy, as indicated by the success of several recent clinical trials aimed at cancer prevention in high-risk populations.[21]

Combination therapy combines two or more therapeutic drugs and is a crucial component of cancer treatment.[24] In comparison to monotherapy, the combination of anticancer drugs is more effective because it targets important pathways in a synergistic or additive.[25] This method might reduce drug resistance while providing therapeutic anticancer benefits, such as inhibiting mitotically active cells, reducing cancer stem cell populations, and triggering death.[26] Most metastatic tumors still have poor 5-year survival rates, and creating a new anticancer medicine is expensive and time-consuming.[27] As a result, new techniques are being investigated that target survival pathways and give efficient and effective results at a low cost.[28] In TME, the expression of many genes is regulated, affecting cancer prognosis. Thus, designing combinatorial therapy required evidence to reverse those gene regulations and be free of side effects due to concomitant undesirable gene regulation. In this study, the different combinations of natural compounds have been studied for the treatment of HNSC through various computational approaches.

METHODS

Data Collection

Gene expression data of HNSC samples and peripheral blood mononuclear cells (PBMCs) of HNSC patients were collected from Gene Expression Omnibus (GEO)[29] with accession Nos. GSE83519 and GSE39400,[30] respectively. In GSE83519, 22 HNSC tumors and 22 paired normal samples were studied from the same patients. In GSE39400, there are 28 samples of peripheral blood cells of HNSC patients who underwent surgery by means of expression profiling, with a controlled group of 11 patients who underwent surgery in the head and neck region for non-HNSC reasons. RNA was extracted from PBMCs using RNA-bee (Campro Scientific bv., Veenendaal, Netherlands). Microarrays agilent low RNA input fluorescent linear amplification kit and 4 × 44K whole human genome arrays were used for microarray hybridization (Agilent Technologies, Amstelveen, Netherlands).

GSE85871[31] contains gene expression profiles of MCF7 cells cultured in minimum essential medium/ Earle's balanced salt solution (MEM/EBSS, Hyclone), 10% fetal bovine serum, 1 mmol/L sodium pyruvate, and 100 mg/mL streptomycin in an incubator containing 5% CO_2 at 37 ℃ with 102 different molecules in Chinese medicines (CMs), and vehicle control (dimethyl sulfoxide, DMSO). Concentration and duration of compound administration may influence the gene expression patterns. According to the CMap database, the concentration of natural compounds was set to a single dosage of 10 μmol/L for 12 h, an internationally accepted concentration for high-throughput screening.[32] Two biological replicates for each group and the data set included profiles for 212 samples. RNA was isolated

from MCF7 cells using TRIzol after pre-treatment (Life Technologies, Carlsbad, US) and analyzed with Affymetrix Human Genome U133A 2.0 (Santa Clara, US) for gene expression patterns.

Differential Gene Expression Analysis

Differential gene expression analysis of GEO datasets of GSE83519 and GSE39400 were achieved by the GEO2R tool, an R-based tool that provides different high-throughput genetic data analysis packages.[33] Annotated gene tables and graphs were provided to help normalize the data, remove the data error, and visualize differentially expressed genes (DEGs).

Data normalization and differential gene expression analysis of the GSE83519 dataset was achieved with a cut-off of adjusted (adj.) *P*-value ⩽ 0.05, logFC value ⩾1 for differentially upregulated genes and logFC value ⩽−1 for differentially downregulated genes. Differential gene expression analysis of the GSE39400 dataset was also achieved by GEO2R with a cut-off adj. *P*-value ⩽0.05, logFC value >0 for upregulated genes and logFC value <0 for downregulated genes.

Enrichment Analysis

Enrichment analysis of selected upregulated and downregulated genes were achieved by the FunRich tool,[34] a standalone tool used for the functional enrichment analysis of genes. Results can be depicted in various forms like doughnut, Venn, pie, bar etc., and it can handle irrespective of the organism's verity of gene/protein datasets. Users can search either against the default background database or customized database for functional enrichment analysis in biological processes, pathways, etc.

Common Differential Gene Analysis

Common upregulated and downregulated differential genes were selected from the HNSC patient's tumor samples and PBMCs of HNSC patients by comparing their list of DEGs in Microsoft Excel. The set of differential genes from datasets GSE83519 and GSE39400 were compared by using conditional formatting > highlight cells rule > duplicate values.

Differential Gene Expression of Natural Compounds

GEO dataset GSE85871 was analyzed by GEO2R for 102 different natural compounds. Two replicates for each compound were considered a test set and compared with the vehicle control set in which only DMSO was present one by one, and the differential expression profile for all genes was collected. The expression of common upregulated genes was matched with the expression profile of natural compounds in Microsoft Excel and selected compounds that alter the maximum number of gene expressions. Similarly, it was achieved for common downregulated genes.

Screening of Natural Compounds

Natural compounds were screened on the bases of their regulation of common DEGs. The compound which regulates the maximum number of genes from common DEGs was selected first. Then the second compound was selected based on whether it can alter the expression of the maximum number of genes from the remaining ones (which remain unaltered by the first compound). Similarly, the remaining compounds were screened.

Analysis of Selected Combination of Natural Compounds

The selected combination of natural compounds was analyzed with the help of a Venn diagram of genes regulated by selected compounds and Enrichment analysis of the shared genes by the FunRich tool. Different biological processes and pathways regulated by these compounds were also analyzed from the literature (retrieved from PubMed, Google Scholar, SCOPUS, and others).

RESULTS

Differential Gene Expression Analysis

The normalization plot and volcano plot of GSE83519 and GSE39400 are shown in Appendix 1. In dataset of GSE83519, a total of 1,094 genes were found to be differentially upregulated, these genes had high expression in the HNSC tumor sample as compared to the respective normal sample of the same patient, and 889 genes were found to be differentially downregulated; these genes had low expression in the HNSC tumor as compared to the respective normal sample. GSE83519 dataset contains the tumor microenvironment samples, which include not only tumor cells but also other cell mediators like immune cells, fibroblast, blood vessels etc., so when immune cell comes in contact with this tumor microenvironment, they may alter their gene expression profile; therefore

the expression data of PBMCs need to be analyses individually, so we can identify the DEGs in PBMCs, because it is beneficial to target immune cell for the tumor regression along with only targeting tumor cells.

In dataset of GSE39400, a total of 737 genes were found to be upregulated, these genes had high expression in the PBMCs which were retrieved from HNSC patients after surgery as compared to the PBMCs retrieved from patients who got head and neck surgery for a non-HNSC reason, while 1,954 genes were found to be downregulated. These DEGs are mainly present in PBMCs, including dendritic cells, lymphocytes, and monocytes. Therefore they might alter these immune cells' function and help tumor cells escape the immune system. Thus these genes can be further analyzed to screen immunological biomarkers for HNSC.

Screening of Common DEGs

DEGs of HNSC tumors were compared with the DEGs of PBMCs so that common DEGs could be screened. Therefore, 1,094 upregulated DEGs of HNSC were compared with 737 upregulated DEGs of PBMCs and found 46 common genes. These 46 DEGs were upregulated in HNSC tumor samples and PBMCs of HNSC patients. PBMCs may infiltrate the tumor and affect tumor progression. The influence of the tumor microenvironment alters the expression of these genes in the tumor-infiltrating lymphocytes. These genes might be involved in the alteration of gene regulation in the subset of the immune cells in the vicinity of the tumor in HNSC patients due to the complex interplay of cells in the tumor microenvironment. Similarly, 889 downregulated DEGs of HNSC tumor samples were compared with 1,954 downregulated DEGs of PBMCs of HNSC patients, and 64 genes were common in both. The list of common upregulated and downregulated genes with their adj. *P*-value and logFC in HNSC tumor samples and PBMCs of HNSC patients are shown in Appendices 2 and 3. There were 110 common DEGs in HNSC samples and PBMCs, out of which 46 common upregulated genes (Appendix 4).

Enrichment analysis of these 110 DEGs was achieved and found that 46 common upregulated genes were mainly involved in biological processes like signal transduction, cell migration, RNA metabolism, anti-apoptosis, regulation of cell cycle, regulation of gene expression, cell communication, energy pathways, transport, protein metabolism, immune response, cell growth and/or maintenance. These biological processes might help in tumor progression because processes like suppression of apoptosis, cell migration, cell cycle regulation, cell growth and/or maintenance directly support tumor growth. Biological processes like immune response, signal transduction, cell communication, etc., could play an essential role in the tumor microenvironment for tumor progression. Therefore, the overexpression of these genes enhances these biological processes in the tumor microenvironment, which could help in tumor progression. Sixty-four common downregulated genes were mainly involved in biological processes like CGMP-mediated signaling, ribosome biogenesis and assembly, immune response, regulation of signal transduction, RNA metabolism, transcription, DNA repair, signal transduction, cell communication, transport, protein metabolism, energy pathways, metabolism, apoptosis. These biological processes are also linked with tumor progression or regression; therefore, downregulation of these genes could help tumor progression. So those drugs should be screened, which alter the expression of these genes to restore normal expression levels such that normal biological processes are restored. Enrichment analysis of 46 upregulated and 64 downregulated genes are shown in Figure 1.

Differential Expression Analysis of Natural Compounds

The expression profiles of 102 natural compounds already known for their antitumor activity were analyzed with GEO2R, and DEGs were studied. These DEGs were those whose expression were altered after the treatment with a particular natural compound. So, the list of differential genes was made of all the 102 natural compounds with their logFC values. The list of 110 common DEGs (46 upregulated genes and 64 downregulated genes) was compared with the natural compounds' DEGs. The natural compounds were sorted based on their ability to reverse the expression of the maximum number of genes. The list of natural compounds with respective No. of genes whose expression were reversed by that natural compound is shown in Appendix 5.

Combination of Natural Compounds

A combination of natural compounds was selected that alter the expression of the maximum number of genes out of 110 common DEGs. Therefore,

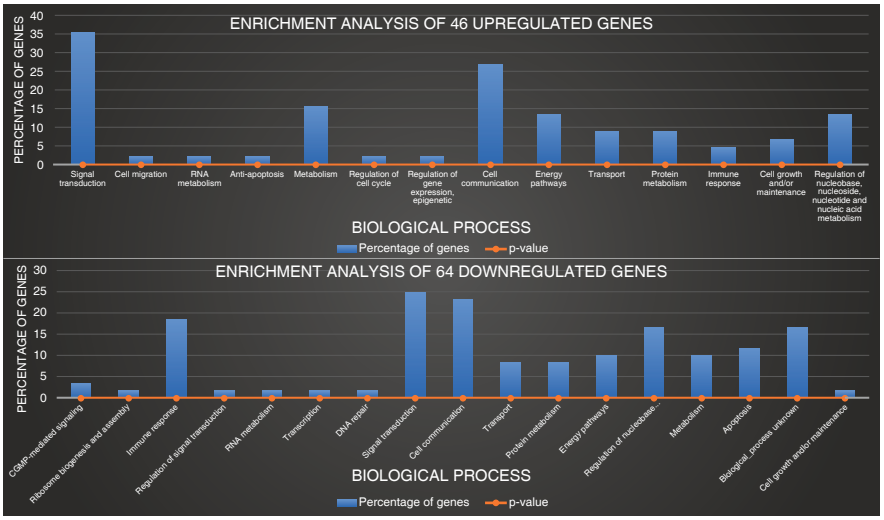


Figure 1. Enrichment Analysis of 46 Common Upregulated Genes and 64 Common Downregulated Genes with Respect to Biological Processes

we first selected that natural compound, which altered the expression of the maximum number of genes, salidroside. Salidroside altered the expression of 66 genes from 110 common DEGs. Then the remaining 44 commonly altered genes were studied for their susceptibility to restorative regulation by other such natural compounds that impacted the expression of the maximum number of the gene. Therefore, ginsenoside Rd was found to regulate the expression of 20 genes. Oridonin was found to regulate 12 genes out of the 24 common DEGs. Britanin was found to regulate 6 genes, and Scutellarein regulated 4 genes. Therefore, these 5 compounds together resulted in the regulation of 108 genes out of 110 common DEGs, restoring the gene expression to that in normal matched tissues. Two genes, GPR15 and CYP2U1, were not suitably regulated by our combination of natural compounds. Appendix 6 shows the screening process of natural compounds for targeting 110 common DEGs.

A combination of 5 compounds was selected and further checked for their combined effect on these common 110 DEGs. Therefore, the expression of these 110 DEGs was compared with the expression of the individual compounds. Salidroside, ginsenoside Rd, oridonin, britanin, and scutellarein individually regulated 66, 60, 58, 52, 62 genes. The gene expression regulation of common upregulated genes by different selected natural compounds separately is listed in Appendix 7. This data analysis showed that many genes were regulated more efficiently in combination rather than isolation; therefore, these compounds might show synergistic effects. The alteration of expression of genes by more than one compound is also beneficial to preventing drug resistance and toxic side effects due to alternative engagement of redundant pathways. The expression of different genes in PBMCs and regulated by the different compounds are shown in the Appendix 8. Venn diagram shows that all the 5 compounds regulated 11 genes, i.e., ZAP70, HFE, TRPM6, RPAIN, PAX9, PCNX2, TRAM2, ARHGEF5, ERN1, SAFB2, and SLC4A10. Twenty-five genes were regulated by any 4 compounds, 24 genes were regulated by any 3 compounds, 23 genes were regulated by any 2 compounds, 25 were regulated only 1 compound out of these 5 compounds (Figure 2).

Enrichment analysis of these 11 compounds was achieved and found that these compounds were involved in biological processes like transport, immune response, signal transduction, and regulation of nucleic acid metabolism. These biological processes are related to cancer progression and the immune system. Therefore, synergistic targeting of these genes would be beneficial for efficient combating HNSC tumors. All the selected compounds were efficient at targeting the expression of these 11 genes that effected the above-mentioned biological processes.

Compound Analysis from Literature

Natural compounds are multitargeting compounds, so targeting genes that positively impact cancer regression may result in undesirable side effects. Hence, to test the synergistic potential for targeting of the selected natural compounds, their mechanisms of

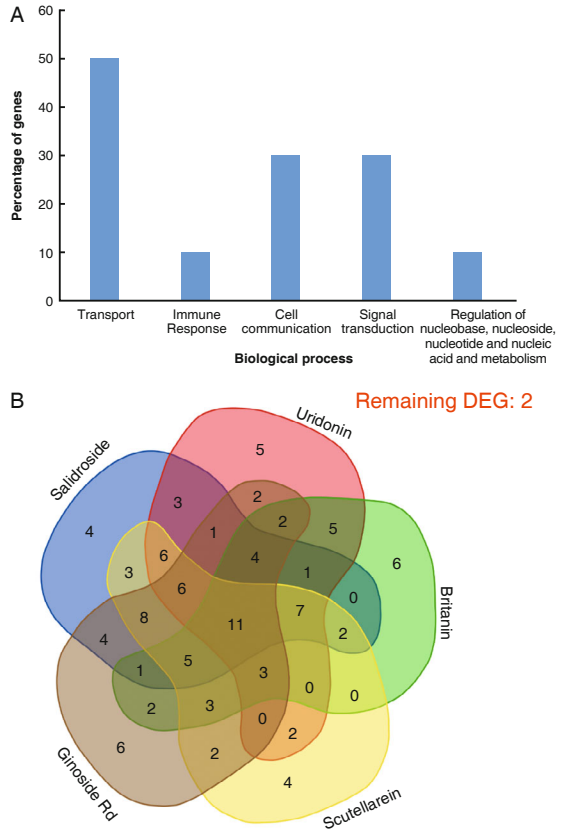


Figure 2. Enrichment Analysis of 11 Genes (A) and Gene Regulation of 110 Common DEGs (B) Regulated by Five Identified Natural Compounds

action were retrieved from the literature and congruence analysis was done. The drug combination of natural compounds must ideally target diverse pathways that converge to result in effective tumor regression.

Salidroside induced autophagy via phosphoinositide 3-kinase/protein kinase B/mammalian target of rapamycin (PI3K/Akt/mTOR) signaling. mTOR is highly upregulated in tumor cells, hence inhibiting autophagy. PI3K/Akt plays an essential role in the regulation of mTOR. Salidroside regulates the PI3K/Akt pathway, decreasing anti-apoptotic factors and increasing pro-apoptotic factors, thus inducing caspase-dependent and mitochondria-mediated apoptotic cell death.[35] Salidroside inhibits proliferation, migration, and invasion of tumor cells by inhibiting reactive oxygen species (ROS), which regulates Src, and downregulates HSP70 via Akt/ERK signaling.[36] Salidroside also reduces the pro-inflammatory cytokine secretion via activating IkB α /NF- κ B pathway and induces apoptosis via p53 and caspase signaling.[37]

Oridonin inhibits angiogenesis via the hypoxic inducible factor 1 α /vascular endothelial growth factor (HIF-1 α /VEGF) pathway and shows anti-migratory, anti-invasive and anti-adhesive properties.[38] Oridonin also inhibits the proliferation and migration of tumor cells via targeting transient receptor potential melastatin 7 (TRPM7) through the inactivation of ERK/AKT signaling.[38] Oridonin induces phagocytosis via activating ERK, which activates NF- κ B.[39]

Ginsenoside Rd reduces metastasis via miR-18a-mediated downregulation of SMAD2.[40] Ginsenoside Rd increases the expression of miR-144-5p, which inhibits the expression of Toll-like receptor 2 (TLR2) hence reducing the proliferation and metastasis of tumor cells.[41] Ginsenoside Rd inhibits VEGF-induced migration, tube formation, and proliferation and suppresses VEGF-induced regulation of Akt/mTOR signaling pathways, inducing apoptosis and inhibiting cell proliferation.[42] Ginsenoside Rd inhibits proliferation, and metastasis mainly reverses epithelial-mesenchymal transition (EMT) via STAT3/JAK2 signaling and STAT3 is the direct target of ginsenoside Rd.[43]

Britanin inhibits NF-kB via downregulation of IKK1/1KK2, controlling tumor cell proliferation and angiogenesis.[44] Britanin shows an anti-inflammatory response via inhibiting NF- κ B signaling.[45] Britanin downregulates cMyc and HIF1 α via upstream effectors like mTOR, reducing the expression of specific proteins, including programmed cell death 1 ligand 1 (PD-L1), leading to the inhibition of angiogenesis and cell proliferation.[46] Britanin induces apoptosis and autophagy via activating AMPK signaling regulated by ROS.[47]

Scutellarin inhibits glutamic-pyruvic transaminase (ALS) and aspartate transaminas (AST) hence regulating the immune system against tumor cells.[48,49] Scutellarin inhibits monocyte chemoattractant protein-1 (MCP1), thus inhibiting cell migration and reducing inflammation.[50] Scutellarin downregulates intercellular cell adhesion molecule 1 (ICAM-1) and inhibits the activation of NF- κ B hence inhibiting adhesion and showing an anti-inflammatory effect.[51] Scutellarin induces vasodilation via eNOS/NO/PKG pathways.[52]

As shown in Figure 3, these compounds regulate many different pathways and can target more than one process. So, our drug combination offers a highly potent multifaceted antitumor and immunomodulatory role and helps in the regression of HNSC cancer. The biological

network of the compounds is shown in Figure 4, which shows the key genes regulated by these compounds.

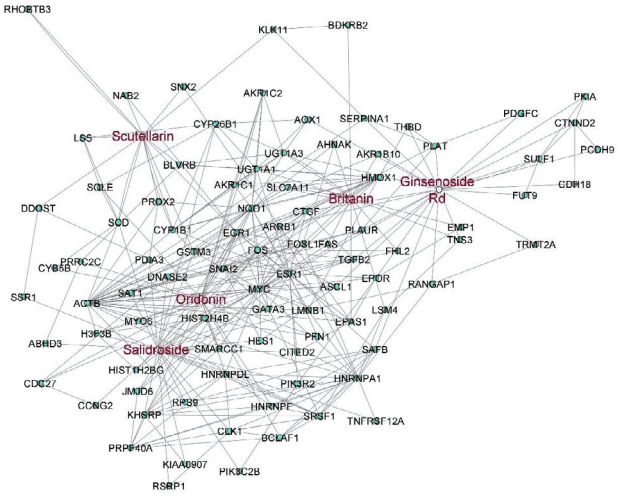


Figure 3. Different Biological Processes and Genes Regulated by Different Natural Compounds Where Different Signs Were Used for Inhibiting, Stimulating, and Activating Genes and Biological Processes

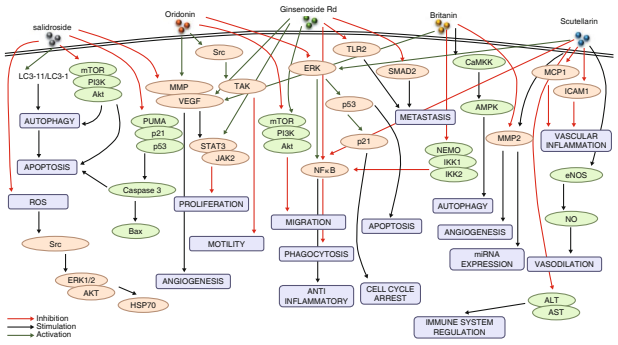


Figure 4. Biological Network of Selected Compounds with Their Regulating Genes

DISCUSSION

Tumor cells change their gene morphology quickly when exposed to single target drugs to find a way to escape the drug effect. So, the problem of drug resistance can be minimized by using a combination of natural compounds because they target multiple pathways, and tumor progression can be effectively reversed. Natural compounds are multitargeting; therefore, they can simultaneously target multiple pathways and many biological processes, helping in tumor regression. Natural compounds are more cost-effective as compared to synthetic compounds. As the cases of HNSC cancer increase in developing countries due to poor lifestyles, it is necessary to find cost-effective drugs for them. So, this study aimed to find a combination of natural compounds that can help in HNSC tumor regression with minimal side effects.

A combination of salidroside, ginsenoside Rd, oridonin, britanin, and scutellarein was chosen such that they can alter the expression of 108 genes out of the selected 110 genes. Salidroside is widely found in *Rhodiola* plants. *Rhodiola sacinehalnsis*, *Rhodiola rosea*, *Rhodibetic tibetica* and large *Rhodiola*. *Ligustrum lucidum*, in the leaves of *Salix triandra* L. and Willow bark, *Vaccinium vitisidaea* L leaves of *Oleaceae*, *Veroniceae* of Veronica minor. Salidroside was found to induce autophagy, inducing caspase-dependent and mitochondria-mediated apoptotic cell death, and inhibiting proliferation, migration, and invasion of tumor cells via PI3K/Akt/mTOR signaling, IkB α /NF- κ B signaling.[35-37] Salidroside is generally deemed safe and effective. In the experimental conditions, salidroside at doses of 0.5, 0.25, and 0.125 g/kg in Sprague-Dawley rats did not cause maternal or embryonic toxicity, nor did it have teratogenic consequences.[53] Genotoxicity testing is critical in drug risk assessment. Salidroside is not genotoxic at a clinical dose of 150 mg/60 kg per day) in humans, according to the Ames test, reverse mutation, chromosomal abnormalities, and mice micronucleus studies.[54] Another study of 60 breast cancer patients found no clinical adverse effects when an effective dose of salidroside (600 mg/kg daily) was given throughout the therapy procedure.[55] The lack of negative effects in pre-clinical and clinical trials suggests salidroside is a safe common clinical medication.

Ginsenoside Rd is mainly found in plants like *P. ginseng*, *Panax notoginseng*, *P. quinquefolius*, *Panax japonicas*, etc. Ginsenoside Rd reduces metastasis, proliferation, migration, inducing apoptosis, reverses EMT via different signaling pathways like Akt/mTOR signaling, STAT3/JAK2 signaling, miR-18a-mediated downregulation of SMAD2.[40-43] Many studies show that ginsenoside Rd has no significant side effects.[56,57]

Oridonin is primarily found in plants like *Rabdosia rubescens*, *Isodon japonicus* Hara, *Isodon trichocarpus*, *Isodon enanderianus*, and *I. lophanthoides*. Oridonin inhibits angiogenesis, migration, invasion and adhesion, proliferation, and phagocytosis properties via HIF-1 α / VEGF, ERK/Akt, ERK/NF κ B signaling.[38,39] Oridonin reduces the side effects of various other cancer drugs when used in combination.[58] Oridonin shows anticancer properties with very low side effects.[59]

Table 1. Plant Sources, Biological Process Regulated, Pathways Regulated and Toxicity of Selected Natural Compounds

Natural compound	Source of origin	Biological process regulated	Biological pathways regulated	Side effects & toxicity
Salidroside	*Rum lucidum* *Salix triandra* L. Willow bark *Vaccinium vitisidaea* L *Oleaceae veroniceae* of Veronica minor	Induces autophagy Induces caspase-dependent and mitochondria-mediated apoptotic cell death Inhibits proliferation Inhibits migration Inhibits invasion of tumor cells	PI3K/Akt/mTOR signaling IkB α /NF- κ b signaling	Salidroside is generally deemed safe and effective[53-55]
Ginsenoside Rd	*Panax ginseng* *Panax notoginseng* *Panax quinquefolius* *Panax japonicas*	Reduces metastasis Inhibits proliferation Inhibits migration Induces apoptosis Reverses emt	Akt/mTOR signaling STAT3/JAK2 signaling miR-18a-mediated downregulation of SMAD2	Ginsenoside Rd have no major side effect[56,57]
Oridonin	*Rabdosia rubescens* *Isodon japonicus* Hara *Isodon trichocarpus* *Isodon enanderianus* *Isodon lophanthoide*	Inhibits angiogenesis Inhibits migration Inhibits invasion Inhibits adhesion Proliferation Phagocytosis properties	HIF-1 α /VEGF signaling ERK/AKT signaling ERK/NF κ B signaling	Very low side effects[59]
Britanin	*Inula linearіifolia* Turcz. (asteraceae) *Inula japonica* *Inula britannica*.	Induces apoptosis Autophagy Inhibits cell proliferation Angiogenesis	IKK1/1KK2 signaling NF- κ B signaling AMPK signaling	Tolerable side effects at low dose administration *in vivo*[60]
Scutellarein	*Scutellaria lateriflora* *Asplenium belangeri* *Mexican oregano* Sweet orange *Scutellaria barbata*	Inhibits cell migration Inhibits adhesion Reduces inflammation Induces vasodilation	eNOS/NO/PKG signaling NF- κ B signaling	No side effects were observed in various studies[61]

Britanin is mainly found in plants like *Inula linearіifolia* Turcz. (Asteraceae), *Inula japonica*, *Inula britannica*. Britanin induces apoptosis and autophagy and inhibits cell proliferation and angiogenesis via regulating different pathways like IKK1/1KK2, NF- κ B, and AMPK signaling.[44,45,47] Britanin shows tolerable side effects at low-dose administration *in vivo*.[60] Scutellarein is found primarily in plants like *Scutellaria lateriflora*, *Asplenium belangeri*, *Mexican oregano*, sweet orange, *Scutellaria barbata*.

Scutellarein inhibits cell migration, adhesion, reducing inflammation, induces vasodilation via regulating different pathways like eNOS/NO/PKG, NF- κ B.[48,49,52] No side effects were absorbed when treated with scutellarein in various studies[61] as shown in Table 1. As this combination was further analyzed, it was found that many biological processes were regulated by more than one compound via different pathways; therefore, it might not be easy for tumor cells to escape this regression mechanism. Further, tumor cells cannot gain drug resistance easily against them.

Immunotherapy is typically associated with side effects that often deter the use of such treatment strategies. Our combination of natural compounds holds a better immunotherapeutic potential without the commonly associated side effects typically seen with chemical immunomodulatory drugs.

In conclusion, our studies showed a multifaceted, multi-dimensional tumor regression by altering autophagy, apoptosis, inhibiting cell proliferation, angiogenesis, metastasis and inflammatory cytokines production. It has helped develop a unique combination of natural compounds that will markedly reduce the propensity of development of drug resistance in tumors and immune evasion by the tumors. Our study has opened a new dimension for developing a combinatorial natural compound cocktail as a potential immunomodulatory drug alternative. Thus, we propose that such a combination could be further analyzed in *in vitro* and *in vivo* studies to develop better treatment for HNSC tumor patients.

Author Contributions

Project conceived and designed by Das A; Data collection, results validation and manuscript written by Kumar S and Das A. Both authors read the manuscript carefully and agreed to submit.

Conflict of Interest

The authors declare that is no conflict of Interest.

Electronic Supplementary Material: Supplementary material is available in the online version of this article at https://doi.org/10.1007/s11655-023-3694-0.

REFERENCES

1. Fisher R, Pusztai L, Swanton C. Cancer heterogeneity: implications for targeted therapeutics. Br J Cancer 2013;108:479.
2. Wadhawan A, Chatterjee M, Singh G. Present scenario of bioconjugates in cancer therapy: a review. Int J Mol Sci 2019;20:5243.
3. Miller KD, Siegel RL, Lin CC, Mariotto AB, Kramer JL, Rowland JH, et al. Cancer treatment and survivorship statistics, 2016. CA Cancer J Clin 2016;66:271-289.
4. Johnson DE, Burtness B, Leemans CR, Lui VWY, Bauman JE, Grandis JR. Head and neck squamous cell carcinoma. Nat Rev Dis Prim 2020;6:1-22.
5. Bray F, Ferlay J, Soerjomataram I, Siegel RL, Torre LA, Jemal A. Global cancer statistics 2018: GLOBOCAN estimates of incidence and mortality worldwide for 36 cancers in 185 countries. CA Cancer J Clin 2018;68:394-424.
6. Pisani P, Airoldi M, Allais A, Valletti PA, Battista M, Benazzo M, et al. Metastatic disease in head & neck oncology. Acta Otorhinolaryngol Ital 2020;40(Suppl 1):S1.
7. Zhong L, Li Y, Xiong L, Wang W, Wu M, Yuan T, et al. Small molecules in targeted cancer therapy: advances, challenges, and future perspectives. Signal Transduct Target Ther 2021;6:1-48.
8. Economopoulou P, de Bree R, Kotsantis I, Psyrri A. Diagnostic tumor markers in head and neck squamous cell carcinoma (HNSCC) in the clinical setting. Front Oncol 2019;9:827.
9. Young MRI. Protective mechanisms of head and neck squamous cell carcinomas from immune assault. Head Neck 2006;28:462-470.
10. Beatty GL, Gladney WL. Immune escape mechanisms as a guide for cancer immunotherapy. Clin Cancer Res 2015;21:687.
11. Chen SMY, Krinsky AL, Woolaver RA, Wang X, Chen Z, Wang JH. Tumor immune microenvironment in head and neck cancers. Mol Carcinog 2020;59:766.
12. Baghban R, Roshangar L, Jahanban-Esfahlan R, Seidi K, Ebrahimi-Kalan A, Jaymand M, et al. Tumor microenvironment complexity and therapeutic implications at a glance. Cell Commun Signal 2020;18:1-19.
13. Vinay DS, Ryan EP, Pawelec G, Talib WH, Stagg J, Elkord E, et al. Immune evasion in cancer: mechanistic basis and therapeutic strategies. Semin Cancer Biol 2015;35:S185-S198.
14. Waldman AD, Fritz JM, Lenardo MJ. A guide to cancer immunotherapy: from T cell basic science to clinical practice. Nat Rev Immunol 2020;20:651-668.
15. Buckner CA, Lafrenie RM, Dénommée JA, Caswell JM, Want DA. Complementary and alternative medicine use in patients before and after a cancer diagnosis. Curr Oncol 2018;25:e275.
16. Atanasov AG, Zotchev SB, Dirsch VM, Orhan IE, Banach M, Rollinger JM, et al. Natural products in drug discovery: advances and opportunities. Nat Rev Drug Discov 2021;20:200-216.
17. Sharifi-Rad J, Ozleyen A, Tumer TB, Adetunji CO, Omari N El, Balahbib A, et al. Natural products and synthetic analogs as a source of antitumor drugs. Biomolecules 2019;9:679.
18. Ramsay RR, Popovic-Nikolic MR, Nikolic K, Uliassi E, Bolognesi ML. A perspective on multi-target drug discovery and design for complex diseases. Clin Transl Med 2018;7:1-14.
19. Karimi A, Majlesi M, Rafieian-Kopaei M. Herbal *versus* synthetic drugs; beliefs and facts. J Nephropharmacology 2015;4:27.
20. Huang M, Lu JJ, Ding J. Natural products in cancer therapy: past, present and future. Nat Products Bioprospect 2021;11:5-13.
21. Steward WP, Brown K. Cancer chemoprevention: a rapidly evolving field. Br J Cancer 2013;109:1-7.
22. Mohan Shankar G, Swetha M, Keerthana CK, Rayginia TP, Anto RJ. Cancer chemoprevention: a strategic approach using phytochemicals. Front Pharmacol 2022;12:4044.
23. Kotecha R, Takami A, Espinoza JL. Dietary phytochemicals and cancer chemoprevention: a review of the clinical evidence. Oncotarget 2016;7:52517.
24. Mokhtari RB, Homayouni TS, Baluch N, Morgatskaya E, Kumar S, Das B, et al. Combination therapy in combating cancer. Oncotarget 2017;8:38022-38043.
25. Ayoub NM. Editorial: novel combination therapies for the treatment of solid cancers. Front Oncol 2021;11:2377.
26. Li Y, Wang Z, Ajani JA, Song S. Drug resistance and cancer stem cells. Cell Commun Signal 2021;19:1-11.
27. Eccles SA, Welch DR. Metastasis: recent discoveries and novel treatment strategies. Lancet 2007;369:1742.
28. Yang L, Shi P, Zhao G, Xu J, Peng W, Zhang J, et al. Targeting cancer stem cell pathways for cancer therapy. Signal Transduct Target Ther 2020;5:1-35.
29. Barrett T, Wilhite SE, Ledoux P, Evangelista C, Kim IF, Tomashevsky M, et al. NCBI GEO: archive for functional genomics data sets—update. Nucleic Acids Res 2012;41:D991-D995.
30. Braakhuis B, Graveland A, Dijk F, Ylstra B, van Wieringen W, Leemans C, et al. Expression signature in peripheral blood cells for molecular diagnosis of head and neck squamous cell carcinoma. Oral Dis 2013;19:452-455.
31. Lv C, Wu X, Wang X, Su J, Zeng H, Zhao J, et al. The gene expression profiles in response to 102 traditional Chinese medicine (TCM) components: a general template for research on TCMs. Sci Rep 2017;7:352.
32. Qu XA, Rajpal DK. Applications of Connectivity Map in drug discovery and development. Drug Discov Today 2012;17:1289-1298.
33. Smyth GK. Linear models and empirical bayes methods for assessing differential expression in microarray experiments. Stat Appl Genet Mol Biol 2004;3:1-25.

34. Pathan M, Keerthikumar S, Ang CS, Gangoda L, Quek CYJ, Williamson NA, et al. FunRich: an open access standalone functional enrichment and interaction network analysis tool. Proteomics 2015;15:2597-601.
35. Rong L, Li Z, Leng X, Li H, Ma Y, Chen Y, et al. Salidroside induces apoptosis and protective autophagy in human gastric cancer AGS cells through the PI3K/Akt/mTOR pathway. Biomed Pharmacother 2020;122:109726.
36. Qi Z, Tang T, Sheng L, Ma Y, Liu Y, Yan L, et al. Salidroside inhibits the proliferation and migration of gastric cancer cells via suppression of Src-associated signaling pathway activation and heat shock protein 70 expression. Mol Med Rep 2018;18:147.
37. Kong YH, Xu SP. Salidroside prevents skin carcinogenesis induced by DMBA/TPA in a mouse model through suppression of inflammation and promotion of apoptosis. Oncol Rep 2018;39:2513-2526.
38. Li C, Wang Q, Shen S, Wei X, Li G. Oridonin inhibits vegf-a-associated angiogenesis and epithelial-mesenchymal transition of breast cancer *in vitro* and *in vivo*. Oncol Lett 2018;16:2289-2298.
39. Liu YQ, You S, Tashiro SI, Onodera S, Ikejima T. Activation of phosphoinositide 3-kinase, protein kinase C, and extracellular signal-regulated kinase is required for oridonin-enhanced phagocytosis of apoptotic bodies in human macrophage-like U937 cells. J Pharmacol Sci 2005;98:361-371.
40. Wang P, Du X, Xiong M, Cui J, Yang Q, Wang W, et al. Ginsenoside Rd attenuates breast cancer metastasis implicating derepressing microRNA-18a-regulated Smad2 expression. Sci Reports 2016 61 2016;6:1-14.
41. Liu GM, Lu TC, Sun ML, Jia WY, Ji X, Luo YG. Ginsenoside Rd inhibits glioblastoma cell proliferation by up-regulating the expression of miR-144-5p. Biol Pharm Bull 2020;43:1534-1541.
42. Zhang E, Shi H, Yang L, Wu X, Wang Z. Ginsenoside Rd regulates the Akt/mTOR/p70S6K signaling cascade and suppresses angiogenesis and breast tumor growth. Oncol Rep 2017;38:359-367.
43. Yang L, Zhang XY, Li K, Li AP, Yang WD, Yang R, et al. Protopanaxadiol inhibits epithelial-mesenchymal transition of hepatocellular carcinoma by targeting STAT3 pathway. Cell Death Dis 2019;10:1-13.
44. Xia L, Tan S, Zhou Y, Lin J, Wang H, Oyang L, et al. Role of the NF κ B-signaling pathway in cancer. Oncotargets Ther 2018;11:2063.
45. Park HH, Kim SG, Park YN, Lee J, Lee YJ, Park NY, et al. Suppressive effects of britanin, a sesquiterpene compound isolated from *Inulae flos*, on mast cell-mediated inflammatory responses. Am J Chin Med 2014;42:935-947.
46. Bailly C. Anticancer targets and signaling pathways activated by britannin and related pseudoguaianolide sesquiterpene lactones. Biomedicines 2021;9:1325.
47. Cui YQ, Liu YJ, Zhang F. The suppressive effects of Britannin (Bri) on human liver cancer through inducing apoptosis and autophagy via AMPK activation regulated by ROS. Biochem Biophys Res Commun 2018;497:916-923.
48. Zhao LY, Yang DD, Ma XK, Liu MM, Wu DH, Zhang XP, et al. The prognostic value of aspartate aminotransferase to lymphocyte ratio and systemic immune-inflammation index for overall survival of hepatocellular carcinoma patients treated with palliative treatments. J Cancer 2019;10:2299.
49. Xiong LL, Du RL, Xue LL, Jiang Y, Huang J, Chen L, et al. Anti-colorectal cancer effects of scutellarin revealed by genomic and proteomic analysis. Chin Med (UK) 2020;15:1-15.
50. Yuan Y, Rangarajan P, Kan EM, Wu Y, Wu C, Ling EA. Scutellarin regulates the Notch pathway and affects the migration and morphological transformation of activated microglia in experimentally induced cerebral ischemia in rats and in activated BV-2 microglia. J Neuroinflammation 2015;12:1-21.
51. Luo P, Tan ZH, Zhang ZF, Zhang H, Liu XF, Mo ZJ. Scutellarin isolated from *Erigeron multiradiatus* inhibits high glucose-mediated vascular inflammation. J Pharm Soc Jap 2008;128:1293-1299.
52. Chen YJ, Chen C, Li MY, Li QQ, Zhang XJ, Huang R, et al. Scutellarin reduces cerebral ischemia reperfusion injury involving in vascular endothelium protection and PKG signal. Nat Products Bioprospect 2021;11:659.
53. Zhong Z, Han J, Zhang J, Xiao Q, Hu J, Chen L. Pharmacological activities, mechanisms of action, and safety of salidroside in the central nervous system. Drug Des Devel Ther 2018;12:1479.
54. Zhu J, Wan X, Zhu Y, Ma X, Zheng Y, Zhang T. Evaluation of salidroside *in vitro* and *in vivo* genotoxicity. Drug Chem Toxicol 2010;33:220-226.
55. Zhang H, Shen WS, Gao CH, Deng LC, Shen D. Protective effects of salidroside on epirubicin-induced early left ventricular regional systolic dysfunction in patients with breast cancer. Drugs R D 2012;12:101-106.
56. Zeng X, Deng Y, Feng Y, Liu Y, Yang L, Huang Y, et al. Pharmacokinetics and safety of ginsenoside Rd following a single or multiple intravenous dose in healthy Chinese volunteers. J Clin Pharmacol 2010;50:285-292.
57. Zhang G, Xia F, Zhang Y, Zhang X, Cao Y, Wang L, et al. Ginsenoside Rd Is Efficacious against acute ischemic stroke by suppressing microglial proteasome-mediated Inflammation. Mol Neurobiol 2016;53:2529-2540.
58. Kazantseva L, Becerra J, Santos-Ruiz L. Oridonin enhances antitumor effects of doxorubicin in human osteosarcoma cells. Pharmacol Reports 2022;74:248-256.
59. Zhou GB, Kang H, Wang L, Gao L, Liu P, Xie J, et al. Oridonin, a diterpenoid extracted from medicinal herbs, targets AML1-ETO fusion protein and shows potent antitumor activity with low adverse effects on t(8;21) leukemia *in vitro* and *in vivo*. Blood 2007;109:3441-3450.
60. Li K, Zhou Y, Chen Y, Zhou L, Liang J. A novel natural product, britanin, inhibits tumor growth of pancreatic cancer by suppressing nuclear factor- κ B activation. Cancer Chemother Pharmacol 2020;85:699-709.
61. Wang L, Ma Q. Clinical benefits and pharmacology of scutellarin: a comprehensive review. Pharmacol Ther 2018;190:105-127.

(Accepted September 5, 2022)
Edited by YUAN Lin

A Comparative Study of Text Summarization using Gensim, NLTK, Spacy, and Sumy Libraries

Abhilasha Sharma
Software Engineering
Delhi Technological University
Delhi, India

Raghav Aggarwal
Software Engineering
Delhi Technological University
Delhi, India

Raghav Alawadhi
Software Engineering
Delhi Technological University
Delhi, India

***Abstract*— The exponential increase of textual information on the internet has led to a considerable expansion of digital content. However, this abundance of information makes it challenging to extract valuable insights due to the sheer volume of content. Text summarization has become an essential tool to address this issue by providing a condensed version of the selected content. This research paper introduces an Auto Text Summarizer Application is introduced which is developed in Python. The application can accept a web page URL or textual input as its source, which is then processed to generate a summary using the Extractive Text Summarization technique. The application utilizes four distinct Python libraries including Natural Language Toolkit (NLTK), Spacy, Gensim, and Sumy, and Flask framework is employed to present the summarized content on the front-end. The back-end of the application involves the use of the Beautiful Soup library to scrape web page content or read the provided text data. The results obtained by each of these libraries are compared based on the reading time required for the summarized content, while also computing Rouge Score, F1 Score and Precision. The development of the Text Summarizer Application is a valuable addition to the Natural Language Processing domain, as it provides a means for summarizing large volume of textual data in an efficient and effective manner. Furthermore, the use of Python libraries and frameworks makes this application scalable and easy to use, while also providing accurate and reliable results.**

Keywords: Machine Learning, Text Summarizer, NLTK, Spacy, Gensim, Sumy.

I. INTRODUCTION

The ability to summarize large amounts of text data found online has become increasingly important, highlighting the significance of text summarization tools. It allows for the extraction of valuable information from text sources that would otherwise be too time-consuming and challenging to read. Python, being a versatile and popular programming language, provides various libraries and frameworks that can be utilized for text summarization.

The objective of this study is to present a text summarization tool that can automatically generate a summary of a given text by allowing the user to input a web page URL or text samples directly. The application utilizes the Extractive Text Summarization technique to generate a concise and effective summary of the input data by identifying and displaying the most significant sentences that correspond to the relevant keywords of the document. The output is then displayed in the form of a summarized text on the front end of the web application.

The project utilizes four different Python libraries, namely Gensim, NLTP, Spacy, and Sumy, to compare their summarization techniques and determine the best performing one. To summarize the text, the content of a web page is retrieved (if the input is an http URL) using the Beautiful Soup library or simply reading of text provided, and after that, pre-processing is carried out on the content, followed by summarization using the suitable library. Python's Flask framework is utilized to present and display the final summarized content at the front end.

The four Python Libraries used are -

1. **NLTK:** NLTK stands for Natural Language Toolkit. It is a widely utilized Python library that performs various Natural Language Processing (NLP) tasks. NLTK offers several functionalities for analyzing text, which includes Part-of-Speech Tagging, Tokenization, as well as Stemming. NLTK also comprises of a module for text summarization, which uses a statistical approach to extract important sentences from the text. This approach involves calculating the frequency of different words in the text and then selecting those sentences that contain the most frequent words.
2. **Spacy**: Spacy is also a popular NLP library in Python. Spacy provides a comprehensive set of features for processing text, including tasks including Named Entity Recognition, Tokenization, and Part-of-Speech Tagging. Additionally, it incorporates a text summarization module that utilizes a graph-based technique to extract significant sentences from the input text. This method entails constructing a sentence graph of the input text and utilizing the PageRank algorithm to determine the sentences with greatest significance to generate summaries.
3. **Gensim**: Gensim is a topic modelling library used mainly for document similarity analysis. It provides various algorithms for the process of text summarization, including TextRank and Latent Semantic Analysis (LSA). TextRank is a graph-based approach that is somewhat similar to the approach used by Spacy. In contrast, the LSA approach uses a mathematical technique called Singular Value Decomposition to identify the most important sentences within the text.

4. **Sumy**: Sumy is another Python library which is designed specifically for text summarization. It provides various algorithms for summarization, including TextRank, LexRank, and Luhn. TextRank and LexRank are graph-based approaches similar to the approaches used by Spacy and Gensim. Luhn is a heuristic method that chooses sentences on the basis of their relevance to the text topic, in contrast to other summarization techniques.

II. Literature Review

Text summarization is a huge challenge that has existed for a significant amount of time in the domains of information retrieval and natural language processing (NLP). It revolves around producing a brief and cohesive summary of a lengthier text, while also ensuring that the essential information is retained. The field of text summarization offers numerous applications, including but are not limited to news article summarization, document summarization, social media summarization, email summarization, meeting minutes summarization, and scientific paper summarization. With the advent of the internet and the explosion of digital data and due to the exponential growth of the available data, the task of text summarization has gained significant importance to assist individuals in comprehending and utilizing the vast amounts of data present.

There has been significant research on text summarization in the fields of natural language processing (NLP) and information retrieval. Researchers have explored various approaches, including extractive, abstractive summarization, as well as hybrid approaches. The first one is Extractive Summarization, a method used in text summarization which involves choosing crucial phrases or sentences from the original text. Secondly, Abstractive Summarization, which is a technique that generates new sentences that capture the essential meaning of the source text in a condensed form. And lastly, Hybrid methods combine elements of both extractive and abstractive summarization techniques.

Text summarization with the help of Deep Learning techniques has become more prevalent in recent years [1]. For instance, models based on neural networks like the encoder-decoder architecture have demonstrated efficacy in abstractive summarization. Transformer models like BERT and GPT [2] have also been employed in text summarization, yielding encouraging outcomes. In addition to deep learning approaches, there are also many traditional machine learning and NLP techniques that have been used for text summarization, such as graph-based methods, clustering algorithms, and feature-based methods [3]. Some of the most used libraries and tools for text summarization include NLTK, Spacy, Gensim, Sumy, and TextBlob [4]. Overall, there is a vast body of literature on text summarization, and the field continues to evolve as new techniques and approaches are developed [5].

III. Proposed Methodology

Proposed Methodology for the text summarizer project using the Python libraries Gensim, NLTK, Spacy, and Sumy:

1. **Data Collection**: The first step in the text summarization process is to gather data from web pages by collecting URLs of web pages to be summarized. To accomplish this, Python libraries like Requests and Beautiful Soup are used to scrape web pages and extract the text.

2. **Pre-processing**: After the data is collected, the next step is to preprocess it in order to prepare it for summarization. This involves carrying out tasks such as tokenization, stop word removal, stemming, and lemmatization using libraries such as NLTK, Spacy, and Gensim.

3. **Summarization**: The Gensim, NLTK, Spacy, and Sumy libraries will be utilized to generate summaries, utilizing their various summarization techniques, such as extractive summarization and abstractive summarization. Various techniques will be experimented with to determine the optimal method for the given data.

4. **Evaluation**: Different evaluation metrics, including but not limited to Rouge, F1 score, and precision, will be employed to measure the effectiveness of the text summarizer. The results obtained using different summarization techniques and libraries will be compared.

5. **User Interface**: A user interface for the text summarizer will be created using Flask. Upon inputting the URL of the web page to be summarized, the summarizer will generate a summary, along with the corresponding performance metrics.

6. **Optimization**: The aim is to optimize the summarization process for better performance, including increasing the efficiency of the program and the quality of the summaries. Various techniques, models, and algorithms will be experimented with to enhance the efficiency of the text summarizer.

Overall, the proposed methodology will allow us to build an effective text summarizer using Python libraries and provide an interface that is easy to use for the user. The steps of the proposed methodology are shown in Fig-1.

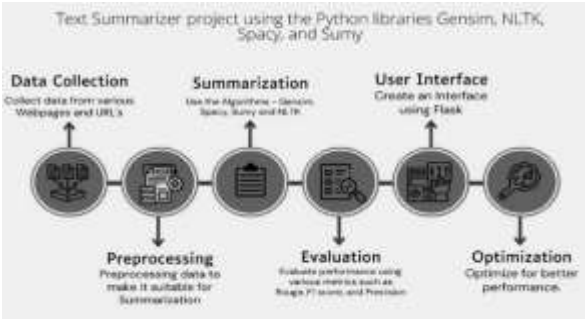


Fig-1: Proposed Methodology Steps

IV. Result and Analysis

Result analysis is the process of evaluating and comparing the performance of different methods used in the text summarization project. In the project, four different Python libraries, namely Gensim, NLTK, Spacy, and Sumy have been used to implement various summarization techniques [6].

The four libraries used in this project were compared based on their performance in generating summaries for given text input [7]. The evaluation was based on two criteria: the quality of the summary produced and the time taken for the summarization process [8].

To analyze the performance of these libraries, various metrics such as Rouge, F1 score, and precision have been used. Although Rouge metric determines the similarity between the reference and the summary produced, whereas, the Precision metrics as well as F1 score measure the correctness of the generated summary [13].

Table-1: Metrics Scores

Library	Rouge	F1 Score	Precision
Gensim	0.39	0.53	0.77
NLTK	0.35	0.64	0.49
Spacy	0.37	0.49	0.71
Sumy	0.44	0.71	0.67

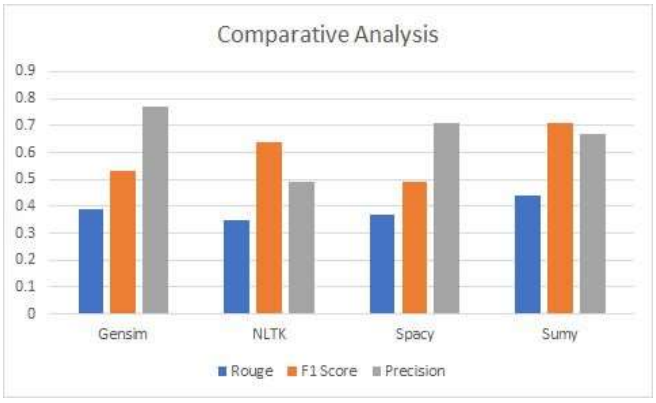


Fig-2: Comparative Analysis

The analysis represents that the NLTK library performed well in terms of F1 score and precision, while the Gensim library performed well in terms of Rouge score. However, the Sumy library had the highest overall performance in terms of all three metrics [19-22].

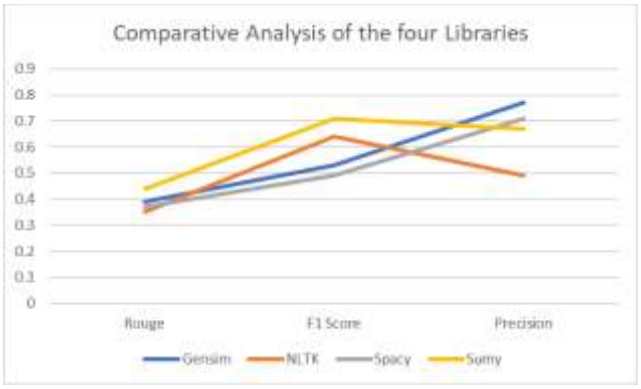


Fig-3: Comparative Analysis of the four Libraries

The performance of each Python library has also been assessed by comparing the summaries they generated to the original text and evaluating their ability to capture the most significant information while minimizing irrelevant details. Many metrics including Rouge score, F1 score, as well as Precision were used to evaluate the quality of the generated summaries [14-17]. On the basis of these metrics, it was found that Gensim and Spacy produced the highest quality summaries, while NLTP and Sumy produced summaries that were less coherent and less representative of the original text.

The second metric used to evaluate the performance of these libraries was the time taken to generate the summary. The time taken by each of these libraries to generate a summary for a given text input was measured and the results were compared. It was found that NLTP was the fastest among the four, followed by Gensim and Spacy, while Sumy was the slowest [18]. Overall, the results of the experiments suggest that Gensim and Spacy are the most effective libraries for generating high-quality summaries, while NLTP is the fastest library. Sumy, on the other hand, produced summaries that were less representative of the original text and were slower to generate.

Table-2: Comparative Analysis based on Quality and Time

Library	Quality of Summary	Time Taken
Gensim	High	Moderate
NLTK	Low to Moderate	Fast
Spacy	High	Moderate
Sumy	Low to Moderate	Slow

It should be acknowledged that the efficiency of the libraries discussed above could differ based on the particular input data and use cases. Therefore, additional testing and evaluation may be required to identify the optimal library for a specific task [23-27]. The performance of the summarization libraries was evaluated on various types of data, including news articles and academic articles. The analysis showed that the performance of these libraries varies depending on the type of data, and that different libraries performed better on different types of data.

Overall, the result analysis showed that the summarization methods implemented using the Python libraries were effective for the generation of accurate as well as informative summaries. The performance of the libraries varies depending on the type of data and the specific metrics used for evaluation [28]. Therefore, the choice of the most suitable method and library for a particular task depends a lot on the specific requirements and task constraints.

V. FUTURE WORK

The study conducted in this research examined the effectiveness of different text summarization techniques in creating web page summaries. Although the findings show potential, there are still areas that require further improvement in enhancing the system's performance. Some potential avenues for future research are discussed below:

1. **Integrating Deep Learning Techniques**: To further improve the text summarization process, deep learning techniques like Neural Networks can be integrated to capture complex relationships between sentences and words in the text.

2. **Improving the User Interface**: To enhance the user experience, the user interface of the text summarization system can be improved by adding various features. For instance, the system can summarize multiple web pages, customize summarization parameters, and provide a more interactive visualization of the summary.

3. **Enhancing the Evaluation Metrics**: There are several ways to enhance the evaluation metrics for text summarization. One approach is to use human evaluation, where human annotators rate the system generated summary's quality. Another approach is to use more advanced metrics, such as the ROUGE-L metric. Possible ways to achieve this are by incorporating semantic similarity metrics or designing new metrics that evaluate the coherence and fluency of the summary.

4. **Evaluating the System on Other Languages**: Evaluating the text summarization system's performance on web pages in languages other than English would be an interesting area for future research. It would require developing language-specific models and evaluating their effectiveness on text in those languages. This could help in the development of more comprehensive as well as accurate text summarization systems which are capable of processing content in multiple languages. This will enable a broader understanding of the system's capabilities and limitations, and provide insights into potential modifications that may be necessary to accommodate different languages.

Overall, the future work outlined above provides exciting directions for improving the text summarization system developed in this research and expanding its applications to various domains.

VI. CONCLUSION

With the abundance of text data available on the internet, text summarization has become a crucial area to help people quickly and effectively extract the most important information from large volumes of text. The report discusses the development of an Auto Text Summarizer Application that processes selected data elements, performs text summarization, and presents the output as summarized text content on the front end of the web application. The application was implemented using four different Python libraries, and different summarization libraries were evaluated and compared based on various metrics, such as 'Rouge,' 'F1 score,' and 'precision.'

The application is based on the Extractive Text Summarization technique, which selects important keywords and phrases to create a condensed summary of textual data. It has a simple and intuitive interface and can be applied across various domains, including news articles, academic papers, blog posts, and search marketing. Overall, the text summarizer application provides an efficient and effective solution for summarizing textual data.

REFERENCES

[1] H. P. Luhn, "The automatic creation of literature abstracts," IBM Journal of Research and Development, vol. 2, no. 2, pp. 159–165, 1958.

[2] D. R. Radev, "SUMMONS: Stanford University multi-document summarization system," in Proceedings of the 2000 ANLP-NAACL Workshop on Summarization, 2000, pp. 21–30.

[3] E. Filatova and V. Hatzivassiloglou, "A formal model for information selection in multi-sentence text extraction," in Proceedings of the 40th Annual Meeting of the Association for Computational Linguistics, 2002, pp. 111–118.

[4] P. Goyal, S. Chavan, and K. H. Kothari, "A comparative study of text summarization techniques," International Journal of Advanced Research in Computer Science and Software Engineering, vol. 3, no. 2, pp. 53–58, 2013.

[5] A. Nenkova and K. McKeown, "Automatic summarization," Foundations and Trends® in Information Retrieval, vol. 2, no. 2-3, pp. 113–195, 2008.

[6] D. Cer, D. Jurafsky, and C. Manning, "The best of both worlds: combining recent advances in neural machine translation," in Proceedings of the 55th Annual Meeting of the Association for Computational Linguistics (Volume 1: Long Papers), 2017, pp. 76–85.

[7] S. Banerjee and A. Lavie, "METEOR: An automatic metric for MT evaluation with high levels of correlation with human judgments," in Proceedings of the ACL Workshop on Intrinsic and Extrinsic Evaluation Measures for Machine Translation and/or Summarization, 2005, pp. 65–72.

[8] J. H. Martin, C. D. Potts, and D. Jurafsky, "Scoring sentence extraction for summarization: the importance of syntactic parsing and inference," in Proceedings of the Workshop on Text Summarization Branches Out (WAS 2004), 2004, pp. 43–50.

[9] H. Poonawala, "Text summarization: a survey," Journal of Computer Science, vol. 7, no. 10, pp. 1520–1527, 2011.

[10] P. W. Foltz, K. K. Laham, and T. K. Landauer, "Automated essay scoring: applications to educational technology," in Automated Essay Scoring: A Cross-disciplinary Perspective, 2003, pp. 129–159.

[11] M. Verspoor, K. E. Crouch, and T. Baldwin, "A preliminary evaluation of text mining to improve evidence-based diagnosis," Studies in Health Technology and Informatics, vol. 107, pp. 1214–1218, 2004.

[12] M. A. Al-Muhaideb and W. F. Al-Khowaiter, "Text summarization techniques: a brief survey," Journal of King Saud University - Computer and Information Sciences, vol. 23, no. 1, pp. 29-37, 2011.

[13] P. Erjavec, "Text Summarization: A Brief Survey of Techniques," Artificial Intelligence and Applications, vol. 2, no. 1, pp. 45-50, 2011.

[14] S. Das, S. Bandyopadhyay, and A. Gelbukh, "Recent approaches to extractive document summarization: A review," Intelligent Data Analysis, vol. 21, no. 1, pp. 35-63, 2017.

[15] D. D. D. Costa, T. de Lima Bandeira, and A. O. de Salles, "An overview of automatic text summarization," Procedia Computer Science, vol. 55, pp. 1203-1212, 2015.

[16] M. Hasan and V. Ng, "Automatic keyphrase extraction: A survey of the state of the art," Proceedings of the Association for Computational Linguistics, vol. 52, pp. 126-139, 2014.

[17] A. Garg and J. Kaur, "A systematic literature review of text summarization," Information Processing & Management, vol. 56, no. 3, pp. 102082, 2019.

[18] R. Barzilay and M. Lapata, "Modeling Local Coherence: An Entity-Based Approach," in Proceedings of the 43rd Annual Meeting of the Association for Computational Linguistics (ACL), 2005, pp. 141-148.

[19] D. Dang and H. Croft, "A Query-Focused Multi-Document Summarization," in Proceedings of the 22nd International Conference on Computational Linguistics (COLING), 2008, pp. 193-200.

[20] S. M. Kim, O. Medelyan, and M. W. K. Lawless, "SemEval-2014 Task 3: Multilingual Semantic Textual Similarity," in Proceedings of the 8th International Workshop on Semantic Evaluation (SemEval), 2014, pp. 81-91.

[21] K. Kripalani and N. Majumder, "Improving Text Summarization by Learning Sentence Weight through Distribution of Words," in Proceedings of the 11th International Conference on Natural Language Processing (ICON), 2014, pp. 1-6.

[22] S. Narayan, S. Bhatia, and S. Srinivasan, "Document Summarization Using Submodular Functions," in Proceedings of the 49th Annual Meeting of the Association for Computational Linguistics (ACL), 2011, pp. 612-621.

[23] Y. Nenkova, "Automatic text summarization," Foundations and Trends in Information Retrieval, vol. 5, no. 2-3, pp. 103-233, 2011.

[24] M. Nishikawa, K. Saito, and M. Inaba, "Summarization of Scientific Papers Based on Citation Contexts," in Proceedings of the 15th International Conference on Knowledge-Based Intelligent Information and Engineering Systems (KES), 2011, pp. 268-277.

[25] T. R. Pudota and P. Bhattacharya, "Query-Based Multi-Document Summarization Using Markov Random Fields," in Proceedings of the 10th International Conference on Natural Language Processing (ICON), 2013, pp. 1-10.

[26] L. Turchi, F. Zanzotto, and E. Cabrio, "Joint Segmentation and Labeling of Multi-Party Dialogue for Text Summarization," in Proceedings of the 14th Conference of the European Chapter of the Association for Computational Linguistics (EACL), 2014, pp. 78-83.

[27] M. Wan, J. Yang, and J. Xiao, "Adaptive Local Modeling for Extractive Document Summarization," in Proceedings of the 23rd International Conference on Computational Linguistics (COLING), 2010, pp. 1212-1220.

[28] X. Wan, J. Yang, and J. Xiao, "Single Document Summarization with Supervised Learning," in Proceedings of the 15th ACM SIGKDD International Conference on Knowledge Discovery and Data Mining (KDD), 2009, pp. 929-938.

A Comprehensive Review of Sensor-based Sign Language Recognition Models

Manas Taneja*, Navya Singla*, Neha Goyal*, Rajni Jindal*

** Department of Computer Science and Engineering, Delhi Technological University, Rohini, Delhi, India - 110042*

***Abstract* - Sign language is a visual language used by millions of people worldwide who are deaf or hard of hearing. Sign language recognition (SLR) has been an active research area in the field of human-computer interaction for several decades. Sign Language, which is a combination of hand and facial gestures, is used as a method of articulation by this community. However, not everyone knows these gesture languages. Thus, deafness and loss in hearing capabilities impacts their ability to communicate, which further leads to social isolation. SLR is essential to build an inclusive society. SLR helps to automate the conversion of SL to text or voice. With the availability of low-cost sensors and advancements in machine learning techniques, there has been a growing interest in using sensor data for SLR. Sensor-based SLR (SSLR) has the potential to improve the accuracy and robustness of the recognition system and enable the development of portable and wearable SLR devices. This review paper provides a comprehensive overview of the existing techniques for SLR using sensor data. The paper discusses the data acquisition, preprocessing, feature extraction, selection, and machine learning models used in SSLR. The review paper also highlights the challenges and limitations of the existing techniques and provides insights into future research directions and opportunities.**

Keywords - Sign Language Recognition, Human Computer Interaction, Sensor-based, Feature Extraction, Machine Learning

I. INTRODUCTION

A. *Overview*

Sign languages are visual languages used by the deaf and hard-of-hearing communities to communicate with each other. Unlike spoken languages, sign languages use a combination of hand gestures, facial expressions, and body movements to convey meaning [1]. There are over 300 different sign languages used worldwide, each with its own grammar, syntax, and vocabulary. SLR is a field of research that aims to develop computer systems capable of recognizing sign language gestures in real-time. The goal of SLR is to facilitate communication between deaf and hearing individuals and provide greater accessibility to information and services for the deaf community.

One of the main challenges in SLR is the variability [2,3] and complexity [4,5] of sign language gestures. Sign language gestures can vary in speed [6], direction [7], and orientation [8], and can be affected by environmental factors such as lighting [9] and background [3,5,10]. To address these challenges, researchers have explored the use of sensor data for SLR.

SSLR involves using sensors such as accelerometers [11], gyroscopes [12,13], gloves [14,15], and flex sensors [14,16] to capture the movement and orientation of the hands and fingers during sign language gestures. The data captured by the sensors is then processed and analyzed using machine learning algorithms to recognize the sign language gestures.SSLR has shown promising results in improving the accuracy and robustness of SLR systems. It could enable portable and wearable devices, making sign language communication more convenient.

This review paper provides a comprehensive overview of the existing techniques for SLR using sensor data. The paper discusses the data acquisition, preprocessing, feature extraction, selection, and machine learning models used in SSLR. The paper also highlights the challenges and limitations of the existing techniques and provides insights into future research directions and opportunities.

B. *Motivation*

The motivation for this review paper on SLR using sensor data stems from the need to improve the accessibility of communication for the deaf and hard-of-hearing communities. Traditional SLR systems have relied on video-based approaches, which can be limited by factors such as lighting and background noise [17,18]. By contrast, SSLR has the potential to improve the accuracy and robustness of SLR systems, making communication more accessible and convenient for the deaf and hard-of-hearing communities [14]. Moreover, the availability of low-cost sensors [19] and advancements in machine learning techniques have opened up new possibilities for SSLR. This paper reviews SLR techniques using sensor data, noting strengths, limitations, and future research potential. Overall, the motivation for this review paper is to contribute to the ongoing efforts to improve the accessibility of communication for the deaf and hard-of-hearing communities. By providing a critical analysis of the existing techniques and identifying future research opportunities, this review paper aims to advance the field of SLR and pave the way for the development of more effective and efficient SLR systems.

C. Background

SLR using sensor data is a research field that aims to develop algorithms and systems capable of interpreting and recognizing sign language gestures using data from different sensors such as accelerometers, gyroscopes, and flex sensors. The process typically involves collecting data from sensors attached to the user's hand or body as they perform sign language gestures. This data is then processed and analyzed using machine learning algorithms to recognize and interpret the gestures. Using numerous sensors, SSLR collects data on gestures. The recognition model is used to draw conclusions after data analysis. To recognize hand gestures, various types of sensors are attached to the hands. Data is recorded and analyzed every time the hand is moved. Gloves with sensors that can detect finger and hand bending and orientation are used in this approach. Gloves with sensors measure the tension and pressure between fingers. The most well-known sensor-glove technologies include smart gloves [14,20], data gloves [21,22], and CyberGlove [23]. Data gloves are excessively costly and painful to wear, which restricts their appeal, even if systems based on them achieve higher performance than other methods [24]. Sensors can be embedded in wearable devices such as gloves, wrist bands, or rings to combat this.

The remainder of this paper is organized as follows. Section II includes a brief review of the datasets used to test and train SSLR models. Section III gives an overview of the sensor technologies used in SSLR. Section IV, V and VI present a review of the different techniques of data preprocessing, feature extraction and dimensionality reduction used. The commonly used machine learning models in SSLR are reviewed in Section VII. Finally, we summarize the applications, main challenges and future scope in CSLR in sections VIII, IX and X respectively, and conclude the work in Section XI.

II. Datasets

There are several datasets that are commonly used in SSLR research. Here are some examples:

1) RWTH-BOSTON-50 Sign Language Corpus: This dataset contains recordings of 50 different sign language gestures performed by 20 different signers using data gloves. The dataset includes sensor data, video data, and annotations [25,26].
2) Chalearn LAP IsoGD Dataset: This dataset contains videos of isolated gestures performed by multiple signers using data gloves and Kinect sensors.
3) BVC3DSL: BVC3DSL is a 3D Indian sign language motion capture dataset consisting of 700 classes, each with 50 sign videos captured from five different signers.
4) HDM05: This is a motion capture dataset that contains over three hours of well-documented and systematically recorded motion capture data in both C3D and ASF/AMC data formats. This dataset includes nearly 2337 sequences and 130 motion classes performed by five actors.
5) American Sign Language Lexicon Video Dataset: This dataset contains recordings of 1,000 different sign language gestures performed by 9 different signers using a Kinect camera. The dataset includes video data and annotations.

These datasets are widely used in research on SSLR and have contributed to the development of new techniques and algorithms for SLR. It is important to note that there are other datasets available as well, and the choice of dataset depends on the specific research objectives.

III. Sensor Technologies

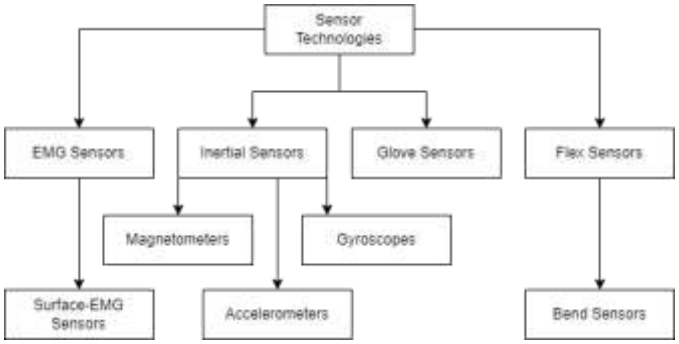


Fig 1: A summary of different sensor technologies.

SLR using sensor data is an active area of research, and there are several existing techniques that have been developed and evaluated. These techniques can be broadly categorized into two types: glove-based and accelerometer/gyroscope-based [12,27].

Data glove-based techniques involve the use of gloves equipped with flex sensors, which capture the movements of the hand and fingers during sign language gestures [28,29]. These movements are then used to classify the sign language gesture. Exo-gloves [30,31] are another type of glove used for sign recognition. These gloves use external sensors attached to the glove to capture hand movements. The sensors can be in the form of cameras, markers, or other types of sensors. Cyber gloves [24,32] are similar to data gloves but use more advanced sensors such as fiber optic sensors or magnetic sensors. These gloves are more accurate and can capture a wider range of hand and finger movements. Smart gloves [14,33] are gloves that have integrated electronics and sensors that allow for wireless communication and data transmission. These gloves are often used for remote SLR, where the user's hand

movements are captured and transmitted in real-time to a remote location for interpretation [34].

Accelerometer and gyroscope-based techniques [12,13,16] involve the use of sensors such as accelerometers and gyroscopes, which are attached to the wrist, forearm, or upper arm. These sensors capture the movements of the arm and hand during sign language gestures.

Each of these techniques has its advantages and disadvantages. Data glove-based techniques are highly accurate in recognizing hand and finger movements, but they may be less robust to variations in sign language gestures and may require the use of specialized equipment [35,36]. Accelerometer/gyroscope-based techniques are less intrusive and can be used in everyday situations, but they may be less accurate in recognizing hand and finger movements [37]. In terms of accuracy, accelerometer and gyroscope-based techniques generally outperform data glove-based techniques [36,38]. However, data glove-based techniques may be more suitable for certain applications where high accuracy is required, such as in the recognition of complex sign language gestures [39]. In terms of speed, data glove-based techniques tend to be faster as they can capture hand and finger movements in real-time [40]. Accelerometer-based techniques may have a slight delay due to the time required to capture and process sensor data [41]. In terms of robustness, accelerometer-based techniques may be more robust to variations in sign language gestures, as they can capture movements from the entire arm and hand. Data glove-based techniques may be more susceptible to errors caused by variations in hand and finger movements [42].

In conclusion, there are several existing techniques for SLR using sensor data, each with its advantages and disadvantages. The choice of technique depends on the specific application requirements and the trade-offs between accuracy, speed, and robustness. It is important for researchers to continue to develop and evaluate new techniques to improve the accessibility and convenience of SLR systems for the deaf and hard-of-hearing communities.

IV. Data Preprocessing

Sensor data preprocessing involves cleaning, filtering, and processing sensor data before it is used in a recognition system. The preprocessing step is critical as it can improve the accuracy and reliability of the recognition system. Here are some of the commonly used techniques for sensor data preprocessing:

1. Noise Removal: Sensor data can contain noise, which can reduce the accuracy of the recognition system. Noise removal techniques such as mean filtering, median filtering, and wavelet filtering can be used to remove noise from the sensor data [43–45].

2. Signal Amplification: In some cases, the sensor signal may be weak, making it difficult to detect small changes in the signal. Signal amplification techniques such as gain adjustment, signal averaging, and signal resampling can be used to improve the quality of the sensor signal [46,47].

V. Feature Extraction And Selection

Feature extraction involves the process of extracting meaningful information from the raw sensor data obtained from the gloves or other sensors. The extracted features are then used to represent the sign language gestures, which are later used for classification. Several feature extraction techniques have been proposed in the literature, such as statistical features, time-domain features, frequency-domain features, and wavelet-based features [48–50]. Each of these techniques has its advantages and limitations, and the selection of the most appropriate technique depends on the specific application scenario. A method for extracting features in Brazilian Sign Language that uses the RGB-D sensor to obtain position, intensity, and depth data has been presented [51,52]. Numerous algorithms for analysis of 3D image are presented in [53] including 3D image acquisition and hand segmentation. [54] proposes a SLR technique for the American sign language alphabet based on a neural network that extracts geometrical features from hands.

In addition to feature extraction, feature selection is also an important step in SSLR. Feature selection involves selecting a subset of relevant features from the feature space that best represent the sign language gestures. This reduces the computational complexity and improves the accuracy of the classification algorithm. Several feature selection techniques have been proposed, such as filter methods, wrapper methods, and embedded methods [55].

The suitability of each feature extraction and selection technique depends on the specific application scenario. For example, statistical features are commonly used for recognizing static signs, while time-domain features are more suitable for recognizing dynamic signs [38,56]. Frequency-domain features are suitable for capturing the frequency content of the sensor data [57], while wavelet-based features are useful for capturing the temporal and frequency content simultaneously [58]. Similarly, the selection of the most appropriate feature selection technique depends on the specific application scenario, such as the size of the dataset, the number of features, and the classification algorithm used. Several studies have compared the different feature extraction and selection techniques in terms of their accuracy and robustness [59]. [60] examines two classification methods, namely Simplification of Support Vector Machine (SimpSVM) and Relevance Vector Machine (RVM), and demonstrate that both SimpSVM and RVM perform well, with SimpSVM exhibiting superior predictive performance compared to

RVM for sign recognition. Furthermore, the authors found that the prediction behaviors of both methods were similar in terms of accuracy, data amount, feature number, and sign discrimination.

VI. Dimensionality Reduction

In some cases, the sensor data may have too many features to be used effectively by the machine learning model. Dimensionality reduction is a common technique used in SSLR to reduce the number of features or variables needed for accurate recognition while maintaining a high recognition rate. The reduction in dimensionality helps to reduce the computational complexity of the recognition system, making it more efficient and effective.

There are several methods used for dimensionality reduction in SLR, including principal component analysis (PCA), linear discriminant analysis (LDA), and manifold learning techniques such as t-distributed stochastic neighbor embedding (t-SNE) and locally linear embedding (LLE). PCA [61,62] is a popular technique used for dimensionality reduction in SLR. It involves identifying the most important features that capture the majority of the variation in the data and projecting the data onto a lower-dimensional space. LDA [61] is another technique commonly used for dimensionality reduction in SLR. It aims to find a linear transformation of the data that maximizes the separation between different classes of signs. Manifold learning techniques such as t-SNE [63] and LLE [64] are also used for dimensionality reduction in SLR. These techniques aim to retain the structure of the data in the lower-dimensional space, allowing for a better representation of the data and improved recognition performance. Methods for efficient dimensionality reduction of dynamic signs, and classification for nearest neighbor in sign gesture space search are described in a study by [52]. [65] propose to reduce the dimensionality of the expanded vector through the use of stepwise regression. [65,66] presents enhanced gesture-based human-computer interaction through a compressive sensing reduction scheme of very large and efficient depth feature descriptors.

VII. Machine Learning Models for SSLR

SSLR is a challenging task that requires advanced machine learning techniques. Here is an overview of different machine learning models that have been used for SLR:

1. Hidden Markov Models (HMMs): HMMs have been used extensively for SLR due to their ability to model temporal dependencies. HMMs are generative models that assume the underlying state of the system is hidden and can only be inferred from the observed data. HMMs have been used in conjunction with features such as hand shape, hand location, and motion trajectories [67,68]. However, their accuracy may be limited if the data has complex patterns, and they may require extensive hyperparameter tuning [67–69]. HMMs can be computationally efficient, but their training time can be slow compared to some other models [70].

2. Support Vector Machines (SVMs): SVMs are a popular machine learning model that has been used for SLR [41,71]. SVMs are a discriminative model that tries to find the best separating hyperplane between different classes of data. SVMs have been used in conjunction with hand-crafted features such as Histograms of Oriented Gradients (HOG) and Scale-Invariant Feature Transform (SIFT) [72]. However, their performance can be limited by the choice of kernel function and the selection of hyperparameters. SVMs are generally faster to train than HMMs, but their prediction time can be slower.

3. Deep Neural Networks (DNNs): DNNs are a powerful class of models that have been used for a wide range of machine learning tasks, including SLR [67–69,73]. DNNs consist of multiple layers of interconnected neurons that are trained using backpropagation. DNNs have been used to automatically learn features from raw data such as depth images, RGB images, and skeleton data. They are capable of handling large datasets. However, they can be computationally expensive and require large amounts of training data and computational resources.

4. Convolutional Neural Networks (CNNs): CNNs are a type of DNN that have been used for SLR. CNNs have been used to automatically learn features from images and videos. CNNs have been used in conjunction with hand-crafted features such as motion history images and optical flow. CNNs are a type of DNN that have been successful in image and video recognition tasks, including SLR [71,74]. They can automatically learn spatial features from images and videos, and they can handle large datasets. They are, nevertheless, computationally costly and may need substantial hyperparameter adjustment.

5. Recurrent Neural Networks (RNNs): RNNs are DNNs that are used to represent temporal dependencies. RNNs have been used for SLR by processing the sequence of hand gestures [75]. RNNs have been used in conjunction with hand-crafted features such as joint angles and velocity. They are capable of processing sequences of data and can handle varying-length input sequences. However, they can suffer from vanishing and exploding gradient problems [76] and may require specialized architectures such as LSTM and GRU.

6. Long Short-Term Memory (LSTM) Networks: LSTM networks are a type of RNN that have been specifically designed to model long-term dependencies. LSTM networks have been used for SLR by processing the sequence of hand gestures [77,78]. LSTM networks have been used in conjunction with hand-crafted features such as

joint angles and velocity. However, they can be computationally expensive and may require extensive hyperparameter tuning.

7. Generative Adversarial Networks (GANs): GANs are a type of deep learning model that consists of two neural networks that are trained in an adversarial manner. GANs have been used for SLR by generating synthetic sign language data that can be used to augment the training data [79,80]. GANs have been used in conjunction with CNNs and RNNs. They can be computationally expensive to train, but they can produce high-quality synthetic data. However, their robustness can be limited if the synthetic data is too dissimilar from the real data.

In terms of accuracy, DNNs, CNNs, and RNNs have shown state-of-the-art performance in many SLR tasks. SVMs and HMMs can also achieve high accuracy if appropriately trained and tuned. In terms of speed, SVMs can be faster to train and predict than some of the deep learning models such as DNNs, CNNs, and RNNs. However, the training and prediction times of deep learning models can be improved using parallel processing and hardware accelerators such as GPUs. In terms of robustness, models such as HMMs and SVMs can be less susceptible to overfitting and can perform well on small and noisy datasets. Deep learning models such as DNNs, CNNs, and RNNs require large amounts of data and can be prone to overfitting if not regularized properly.

These are some of the machine learning models that have been used for SSLR. Table 2 presents information like datasets used, features, machine learning models, input modalities and results about the models proposed for SSLR in the recent years. The choice of model depends on the characteristics of the data and the specific requirements of the application.

Table 1: A Survey of Major Works in Sensor-Based Sign Language Recognition

S. No	Ref	Year	Feature	Classification	Dataset	Input Modality	Sensors used	Results (%)
1	[81]	2018	PCA	KNN	ASL, 10 numbers	Static, Isolated	Flex Sensors	85%
2	[82]	2017	LDA	KNN, DT, SVM	ASL, 36 gestures	Static/Dynamic, Isolated	MEMS sensors	80%
3	[83]	2019	Statistic Methods	SVM, DTW	8 gestures	Static/Dynamic, Isolated	Pressure Sensors	95.28% (exp) and 86.20% (inexp)
4	[84]	2019	PCANet	Linear SVM	ASL fingerspelling Dataset	Static, Isolated	Microsoft Kinect Sensor	89%
5	[85]	2017	-	HMM and BLSTM-NN	7500 Indian Sign Language (ISL) gestures consisting of 50 different sign-words	Dynamic	Microsoft Kinect, Leap Motion	97.85% and 94.55%
6	[86]	2021	Zernike moments, Hu moments, Fourier Descriptors	HMM	A dataset containing 33 isolated signs	Isolated and continuous	Microsoft Kinect, Leap Motion	95.18% and 93.87%
7	[87]	2020	finger direction patterns detected by Leap Motion Controller.	Threshold and ANN	Sign Language gestures of numbers 0-9	Isolated	Leap Motion	98%
8	[88]	2019	-	Neural Network	ASL, 5 numbers	Isolated, Static	IMU, Magnetic Field Sensors	99.2%

S. No	Ref	Year	Feature	Classification	Dataset	Input Modality	Sensors used	Results (%)
9	[89]	2019	Statistic Methods	Modified KNN, HMM	ArSL, 40 sentences	Continuous	DG5-V hand data glove	96.70%

VIII. Applications

SSLR has numerous applications in various fields, including:

1. Communication accessibility: One of the most significant applications of SLR is to enable communication between deaf and hearing individuals. By recognizing sign language, SLR can provide deaf individuals with access to real-time communication with non-signers, allowing them to participate in daily conversations, meetings, or other social interactions. SLR can also be used to translate sign language into text or speech, making it accessible to non-signers.

2. Education and training: SLR can be used to develop interactive sign language learning systems for both deaf and hearing individuals. For example, an SLR system can provide real-time feedback to learners to help them improve their sign language skills. SLR can also be used to evaluate sign language proficiency in learners, providing a more objective and accurate assessment of their skills [90].

3. Human-robot interaction: SLR can enable robots to recognize and understand sign language, allowing for natural and intuitive human-robot interaction. This can have numerous applications, such as in service robots for deaf individuals, where the robot can understand sign language commands or provide sign language feedback to the user [91].

4. Assistive technology: SLR can be integrated into assistive devices, such as smart gloves or wearable sensors, to provide real-time translation of sign language into text or speech. This can allow deaf individuals to communicate with non-signers more easily and can also facilitate access to education, healthcare, and other services [92].

5. Video surveillance: SLR can be used in video surveillance to detect and recognize sign language gestures, which can be useful in security and safety applications [93,94]. For example, an SLR system can detect a sign language gesture for "help" and alert security personnel to a potential emergency.

6. Gaming and entertainment: SLR can be used in gaming and entertainment applications to control avatars or characters in virtual environments using sign language. This can provide a more immersive and inclusive gaming experience for deaf players [95].

7. Medical and rehabilitation: SLR can be used in medical and rehabilitation applications to monitor and analyze the movements of patients during physical therapy or rehabilitation exercises [96].

SSLR applications are numerous, and they may have a substantial influence on the lives of deaf people and the larger society through promoting accessibility and inclusion.

IX. Challenges

SSLR presents a number of issues owing to the complexity of sign language, which includes non-manual components such as facial emotions and body language, as well as sign language heterogeneity across signers. Some of the challenges faced in SSLR are:

1. Sensor selection: Different sensors can be used for SLR, such as cameras, gloves, or accelerometers. However, the choice of sensor depends on the specific requirements of the SLR system, such as accuracy, speed, cost, and ease of use. Some challenges in sensor selection for SLR include selecting the best sensor for a particular task, balancing cost and performance, and dealing with sensor limitations [97].

2. Data collection and annotation: Collecting and annotating sign language data can be challenging because sign language involves complex and subtle movements, and different signers may use different variations of signs. Some challenges in data collection and annotation include obtaining high-quality data, dealing with variability among signers, and ensuring proper annotation of the data.

3. Recognition of non-manual components: Sign language involves not only hand gestures but also facial expressions and body language, which are crucial for conveying meaning. Recognizing these non-manual components is challenging because they are often subtle and context-dependent. Some challenges in recognizing non-manual components of sign language include identifying which non-manual components to recognize, capturing subtle movements, and dealing with context-dependent variations.

4. Variability among signers: Sign language can vary widely among different signers, depending on their regional or cultural background, age, gender, or proficiency level [98]. This variability can make it difficult to train a generalizable SLR system that works well for all signers.

Some challenges in dealing with variability among signers include creating a diverse dataset that captures this variability, developing algorithms that can handle variability, and ensuring that the SLR system is accessible to all signers.

5. Real-time recognition: SLR systems must operate in real-time to enable natural communication between signers and non-signers. Achieving real-time performance requires efficient algorithms and hardware optimization [13]. Some challenges in achieving real-time recognition include designing efficient algorithms that can handle the complexity of sign language, optimizing hardware for performance, and minimizing latency.

6. Gesture segmentation and recognition: SLR systems must accurately segment and recognize individual signs from continuous sign streams [84]. This task is challenging because signs can overlap or blend into each other, and some signs may have multiple meanings depending on the context. Some challenges in gesture segmentation and recognition include developing algorithms that can handle continuous sign streams, dealing with sign overlaps, and resolving ambiguity in sign meanings.

7. Handling noisy or incomplete data: Sensors can produce noisy or incomplete data due to environmental factors such as lighting conditions or occlusions. SLR systems must be able to handle such noisy or incomplete data and still provide accurate recognition results [63]. Some challenges in handling noisy or incomplete data include developing algorithms that can handle missing or noisy data, ensuring robustness to environmental factors, and improving sensor quality.

X. SSLR: Promises and Future Directions

The use of sensors, such as gloves or cameras, can automate the process of sign language interpretation and make it more widely accessible. This technology could also be used to create more advanced and interactive communication devices that can be used in a variety of settings, such as in education, healthcare, and public services.

Furthermore, SSLR technology could be combined with other emerging technologies, such as augmented reality and virtual reality, to create even more immersive and interactive communication experiences. Some of the promising areas of research for the future include:

1. Federated Learning: SSLR in federated learning [99,100] has the potential to revolutionize the way sign language is recognized and interpreted [99]. The combination of sensor-based technology and federated learning has several benefits that can greatly enhance the accuracy and privacy of SLR systems. One major advantage of federated learning is that it enables the training of models on distributed data without sharing the data itself. This is particularly important in the context of SLR, where users' privacy must be protected. Federated learning can ensure that users' data remains on their devices, and only model updates are sent to a central server for aggregation. This approach can greatly enhance the privacy and security of SLR systems. In addition, the use of sensors in SLR can improve the accuracy of the recognition process by capturing more precise and detailed information about the signer's movements. By combining sensor data from multiple users in a federated learning framework, the model can learn from a larger and more diverse dataset, which can lead to improved accuracy and robustness. Furthermore, the use of federated learning in SLR can enable the development of more personalized and adaptive models that can better accommodate individual differences in signing styles and variations in sign language across different cultures and regions.

2. Augmented and Virtual Reality: SSLR in augmented reality (AR) and virtual reality (VR) has the potential to create more immersive and interactive communication experiences for individuals who use sign language. In AR, SSLR can enable the creation of real-time, interactive sign language interpretation that can be overlaid on top of the real world. For example, an AR headset could recognize sign language gestures and display corresponding text or images to aid communication. This technology could also be used to create educational and training tools for sign language learners. In VR, SSLR can enable more natural and intuitive communication in virtual environments. By recognizing sign language gestures, VR systems can create more immersive and interactive virtual worlds that are accessible to individuals who use sign language. This technology could also be used to create more inclusive gaming and entertainment experiences. Moreover, the use of sensors in AR/VR systems can improve the accuracy and responsiveness of SLR.

3. Evolutionary Computing: SSLR in evolutionary computing has the potential to enhance the performance and efficiency of SLR systems. Evolutionary computing is a subfield of artificial intelligence that uses principles of natural selection and evolution to optimize complex systems. In the context of SLR, evolutionary computing can be used to optimize the design and parameters of SLR systems based on sensor data. One potential application of evolutionary computing in SLR is the optimization of feature extraction algorithms. Feature extraction is the process of extracting relevant information from sensor data that can be used to recognize sign language gestures. Evolutionary computing can be used to automatically generate and optimize feature extraction algorithms that are tailored to specific sensor modalities and sign language styles. Another potential application of evolutionary computing in SLR is the optimization of machine learning models. Machine learning models are trained on sensor data

to recognize sign language gestures, but the performance of these models can be greatly influenced by the choice of algorithms, hyperparameters, and training data. Evolutionary computing can be used to automatically generate and optimize these parameters to improve the accuracy and efficiency of SLR models.

In conclusion, SSLR is a rapidly evolving field with a bright future. Potential future directions include multi-modal sensor fusion, continual learning, context-aware SLR, real-time feedback and interaction, privacy-preserving SLR, and application-specific SLR.

XI. Conclusion

SSLR is a rapidly evolving field that has seen significant progress in recent years. This review paper has discussed the challenges, techniques, and models used in SSLR and compared the accuracy, speed, and robustness of different machine learning models.

One of the main challenges in SSLR is the variations in sign language across different individuals, dialects, and cultures, as well as environmental factors such as lighting, background noise, and camera placement. Feature extraction is a critical step in SSLR, and several techniques have been developed to extract meaningful features from the sensor data, including hand shape, hand motion, and facial expressions. Furthermore, various machine learning models have been applied to SLR, including HMM, SVMs, DNN, CNN, RNN, LSTM, and GAN, each with varying degrees of success. Finally, the choice of machine learning model for SSLR depends on several factors, including the characteristics of the data, the resources available, and the specific requirements of the application. These key findings provide a useful insight into the current state-of-the-art in SLR, and can guide future research in this area towards more accurate and efficient SLR systems. There are several recommendations for future research which will pave the way for more accurate and efficient SLR systems. One of the key areas is to develop robust and accurate feature extraction techniques that can handle variations in sign language and environmental factors. Additionally, more comparative studies are needed to evaluate the performance of different machine learning models in different scenarios and for different applications. Another crucial area is to develop SLR systems that can recognize sign language from multiple individuals and gestures that are not part of the standard sign language, and also adapt to individual users. Finally, researchers need to focus on developing SLR systems that can operate in real-world environments, such as noisy or low-light conditions, and in low-power or low-resource devices. In conclusion, SSLR is a promising field that has the potential to improve communication and accessibility for the hearing-impaired community. Continued research and development in this field can lead to more accurate, robust, and practical SLR systems that can have broad applications in human-computer interaction, VR, AR, and robotics.

XII. Acknowledgment

We want to extend our heartfelt appreciation to everyone who helped us complete this research work successfully. We would like to express our gratitude to Prof. Rajni Jindal, our supervisor, for her invaluable advice and assistance. We are also appreciative of the authors' significant contributions to the field of sign language recognition in the form of the research articles used in our study. Additionally, we would like to thank Delhi Technological University for giving us the tools and resources we needed to complete this study. The university's assistance has been crucial in enabling us to accomplish our research goals. We would like to express our gratitude to our family and friends for their constant support and inspiration.

XIII. Authors

First Author – Manas Taneja, Bachelor of Technology, Delhi Technological University.
Second Author – Navya Singla, Bachelor of Technology, Delhi Technological University.
Third Author – Neha Goyal, Bachelor of Technology, Delhi Technological University.
Fourth Author – Rajni Jindal, Professor, Delhi Technological University.

Correspondence Author – Manas Taneja, Bachelor of Technology, Delhi Technological University.

References

[1] K.P. Kour, L. Mathew, Literature Survey on Hand Gesture Techniques for Sign Language Recognition, International Journal of Technical Research and Science. 2 (2017) 431–434.
[2] R. Rastgoo, K. Kiani, S. Escalera, Sign Language Recognition: A Deep Survey, Expert Syst. Appl. 164 (2021) 113794. https://doi.org/10.1016/j.eswa.2020.113794.
[3] M. Mukushev, A. Ubingazhibov, A. Kydyrbekova, A. Imashev, V. Kimmelman, A. Sandygulova, FluentSigners-50: A signer independent benchmark dataset for sign language processing, PLoS One. 17 (2022) e0273649. https://doi.org/10.1371/journal.pone.0273649.
[4] P. Patel, N. Patel, Vision Based Real-time Recognition of Hand Gestures for Indian Sign Language using Histogram of Oriented Gradients Features, Ijngc. (2019) 92–102. https://doi.org/10.47164/ijngc.v10i2.158.
[5] R. Rastgoo, K. Kiani, S. Escalera, Hand pose aware multimodal isolated sign language recognition, Multimed. Tools Appl. 80 (2021) 127–163. https://doi.org/10.1007/s11042-020-09700-0.
[6] Z. Zhou, V.W.L. Tam, E.Y. Lam, SignBERT: A BERT-Based Deep Learning Framework for Continuous Sign Language Recognition, IEEE Access. 9 (2021) 161669–161682. https://doi.org/10.1109/ACCESS.2021.3132668.
[7] S. Villameriel, B. Costello, M. Giezen, M. Carreiras, Cross-modal and cross-language activation in bilinguals reveals lexical competition even when words or signs are unheard or unseen, Proc. Natl. Acad. Sci. U. S. A. 119 (2022) e2203906119. https://doi.org/10.1073/pnas.2203906119.

[8] J. Ma, W. Gao, J. Wu, C. Wang, A continuous Chinese sign language recognition system, in: Proceedings Fourth IEEE International Conference on Automatic Face and Gesture Recognition (Cat. No. PR00580), 2000: pp. 428–433. https://doi.org/10.1109/AFGR.2000.840670.
[9] H. Park, Y. Lee, J. Ko, Enabling Real-time Sign Language Translation on Mobile Platforms with On-board Depth Cameras, Proc. ACM Interact. Mob. Wearable Ubiquitous Technol. 5 (2021) 1–30. https://doi.org/10.1145/3463498.
[10] S. Nadgeri, D.A. Kumar, Survey of Sign Language Recognition System, (2018). https://doi.org/10.2139/ssrn.3262581.
[11] R. Gupta, N. Jha, Real-Time Continuous Sign Language Classification using Ensemble of Windows, in: 2020 6th International Conference on Advanced Computing and Communication Systems (ICACCS), 2020: pp. 73–78. https://doi.org/10.1109/ICACCS48705.2020.9074319.
[12] S. Sharma, R. Gupta, A. Kumar, On the Use of Multi-Modal Sensing in Sign Language Classification, in: 2019 6th International Conference on Signal Processing and Integrated Networks (SPIN), 2019: pp. 495–500. https://doi.org/10.1109/SPIN.2019.8711702.
[13] Y. Yu, X. Chen, S. Cao, X. Zhang, X. Chen, Exploration of Chinese Sign Language Recognition Using Wearable Sensors Based on Deep Belief Net, IEEE J Biomed Health Inform. 24 (2020) 1310–1320. https://doi.org/10.1109/JBHI.2019.2941535.
[14] N. Saleh, M. Farghaly, E. Elshaaer, A. Mousa, Smart glove-based gestures recognition system for Arabic sign language, in: 2020 International Conference on Innovative Trends in Communication and Computer Engineering (ITCE), 2020: pp. 303–307. https://doi.org/10.1109/ITCE48509.2020.9047820.
[15] P.V. Naresh, R. Visalakshi, B. Satyanarayana, A Study on Sign Language Recognition-A Literature Survey, in: ICDSMLA 2019, Springer Singapore, 2020: pp. 745–752. https://doi.org/10.1007/978-981-15-1420-3_80.
[16] A. Suri, S.K. Singh, R. Sharma, P. Sharma, N. Garg, R. Upadhyaya, Development of Sign Language using Flex Sensors, in: 2020 International Conference on Smart Electronics and Communication (ICOSEC), 2020: pp. 102–106. https://doi.org/10.1109/ICOSEC49089.2020.9215392.
[17] S. Katoch, V. Singh, U.S. Tiwary, Indian Sign Language recognition system using SURF with SVM and CNN, Array. 14 (2022) 100141. https://doi.org/10.1016/j.array.2022.100141.
[18] J.J. Raval, R. Gajjar, Real-time Sign Language Recognition using Computer Vision, in: 2021 3rd International Conference on Signal Processing and Communication (ICPSC), 2021: pp. 542–546. https://doi.org/10.1109/ICSPC51351.2021.9451709.
[19] Y. Wang, Z. Hao, X. Dang, Z. Zhang, M. Li, UltrasonicGS: A Highly Robust Gesture and Sign Language Recognition Method Based on Ultrasonic Signals, Sensors . 23 (2023). https://doi.org/10.3390/s23041790.
[20] P.N. Ghuse, N. Ghuse, Sign Language Recognition using Smart Glove, International Journal for Research in Applied Science and Engineering Technology. 9 (2021) 328–333. https://doi.org/10.22214/ijraset.2021.36347.
[21] A.Z. Shukor, M.F. Miskon, M.H. Jamaluddin, F.B. Ali@Ibrahim, M.F. Asyraf, M.B.B. Bahar, A New Data Glove Approach for Malaysian Sign Language Detection, Procedia Comput. Sci. 76 (2015) 60–67. https://doi.org/10.1016/j.procs.2015.12.276.
[22] K.-W. Kim, M.-S. Lee, B.-R. Soon, M.-H. Ryu, J.-N. Kim, Recognition of sign language with an inertial sensor-based data glove, Technol. Health Care. 24 Suppl 1 (2015) S223–30. https://doi.org/10.3233/THC-151078.
[23] K. Kudrinko, E. Flavin, X. Zhu, Q. Li, Wearable Sensor-Based Sign Language Recognition: A Comprehensive Review, IEEE Rev. Biomed. Eng. 14 (2021) 82–97. https://doi.org/10.1109/RBME.2020.3019769.
[24] H.-D. Yang, Sign language recognition with the Kinect sensor based on conditional random fields, Sensors . 15 (2014) 135–147. https://doi.org/10.3390/s150100135.
[25] K.M. Lim, A.W.C. Tan, C.P. Lee, S.C. Tan, Isolated sign language recognition using Convolutional Neural Network hand modelling and Hand Energy Image, Multimed. Tools Appl. 78 (2019) 19917–19944. https://doi.org/10.1007/s11042-019-7263-7.
[26] S. Fakhfakh, Y. Ben Jemaa, Shape Trajectory Analysis Based on HOG Descriptor for Isolated Word Sign Language Recognition, in: Advanced Information Networking and Applications, Springer International Publishing, 2022: pp. 46–54. https://doi.org/10.1007/978-3-030-99619-2_5.
[27] S.A. Khomami, S. Shamekhi, Persian sign language recognition using IMU and surface EMG sensors, Measurement. 168 (2021) 108471. https://doi.org/10.1016/j.measurement.2020.108471.
[28] Y. Pan, W. Wang, P. Zhang, Y. Liang, F. Li, H. Wang, Artificial Intelligence Hand Spatial Position Predictor Based on Data Gloves and Jetson Xavier NX, in: 2022 Global Conference on Robotics, Artificial Intelligence and Information Technology (GCRAIT), 2022: pp. 232–236. https://doi.org/10.1109/GCRAIT55928.2022.00056.
[29] N. Tubaiz, T. Shanableh, K. Assaleh, Glove-Based Continuous Arabic Sign Language Recognition in User-Dependent Mode, IEEE Transactions on Human-Machine Systems. 45 (2015) 526–533. https://doi.org/10.1109/THMS.2015.2406692.
[30] M. Caeiro-Rodríguez, I. Otero-González, F.A. Mikic-Fonte, M. Llamas-Nistal, A Systematic Review of Commercial Smart Gloves: Current Status and Applications, Sensors . 21 (2021). https://doi.org/10.3390/s21082667.
[31] X. Chen, L. Gong, L. Wei, S.-C. Yeh, L. Da Xu, L. Zheng, Z. Zou, A Wearable Hand Rehabilitation System With Soft Gloves, IEEE Trans. Ind. Inf. 17 (2021) 943–952. https://doi.org/10.1109/TII.2020.3010369.
[32] Z. Sun, A Survey on Dynamic Sign Language Recognition, in: Advances in Computer, Communication and Computational Sciences, Springer Singapore, 2021: pp. 1015–1022. https://doi.org/10.1007/978-981-15-4409-5_89.
[33] M.S. Amin, M.T. Amin, M.Y. Latif, A.A. Jathol, N. Ahmed, M.I.N. Tarar, Alphabetical Gesture Recognition of American Sign Language using E-Voice Smart Glove, in: 2020 IEEE 23rd International Multitopic Conference (INMIC), 2020: pp. 1–6. https://doi.org/10.1109/INMIC50486.2020.9318185.
[34] P.M. Sathya, P. Velrajkumar, P. Lavanya, L. Ramesh, C. Senthilpari, Raspberry Pi Processor-based i-Gloves for Mute Community and Home Automation System, in: 2022 8th International Conference on Smart Structures and Systems (ICSSS), 2022: pp. 01–05. https://doi.org/10.1109/ICSSS54381.2022.9782194.
[35] N. Saquib, A. Rahman, Application of machine learning techniques for real-time sign language detection using wearable sensors, in: Proceedings of the 11th ACM Multimedia Systems Conference, Association for Computing Machinery, New York, NY, USA, 2020: pp. 178–189. https://doi.org/10.1145/3339825.3391869.
[36] P. Paudyal, J. Lee, A. Banerjee, S.K.S. Gupta, A Comparison of Techniques for Sign Language Alphabet Recognition Using Armband Wearables, ACM Trans. Interact. Intell. Syst. 9 (2019) 1–26. https://doi.org/10.1145/3150974.
[37] R.K. Athota, D. Sumathi, Human activity recognition based on hybrid learning algorithm for wearable sensor data, Measurement: Sensors. 24 (2022) 100512. https://doi.org/10.1016/j.measen.2022.100512.
[38] A. Qaroush, S. Yassin, A. Al-Nubani, A. Alqam, Smart, comfortable wearable system for recognizing Arabic Sign Language in real-time using IMUs and features-based fusion, Expert Syst. Appl. 184 (2021) 115448. https://doi.org/10.1016/j.eswa.2021.115448.
[39] S. Patil, S. Joshi, H.B. Kulkarni, P. Hagawane, P. Shinde, Marathi Sign Language Hand Gesture Recognition Using Accelerometer and 3D Printed Gloves, in: 2022 14th International Conference on Computational Intelligence and Communication Networks (CICN), 2022: pp. 72–77. https://doi.org/10.1109/CICN56167.2022.10008290.
[40] H. Liu, Z. Zhang, Z. Jiao, Z. Zhang, M. Li, C. Jiang, Y. Zhu, S.-C. Zhu, A Reconfigurable Data Glove for Reconstructing Physical and Virtual Grasps, arXiv [cs.RO]. (2023). http://arxiv.org/abs/2301.05821.
[41] Y. Na, H. Yang, J. Woo, Classification of the Korean Sign Language Alphabet Using an Accelerometer with a Support Vector Machine, Journal of Sensors. 2021 (2021). https://doi.org/10.1155/2021/9304925.
[42] Y. Liu, F. Jiang, M. Gowda, Finger Gesture Tracking for Interactive Applications: A Pilot Study with Sign Languages, Proc. ACM Interact. Mob. Wearable Ubiquitous Technol. 4 (2020) 1–21. https://doi.org/10.1145/3414117.
[43] G. Latif, N. Mohammad, J. Alghazo, R. AlKhalaf, R. AlKhalaf, ArASL: Arabic Alphabets Sign Language Dataset, Data Brief. 23 (2019) 103777. https://doi.org/10.1016/j.dib.2019.103777.
[44] V. More, S. Sangamnerkar, V. Thakare, D. Mane, R. Dolas, Sign

language recognition using image processing, JournalNX. (2021) 85–87. https://www.neliti.com/publications/342497/sign-language-recognition-using-image-processing.
[45] R. Saif, M. Ahmad, S.Z.H. Naqvi, S. Aziz, M.U. Khan, M. Faraz, Multi-Channel EMG Signal analysis for Italian Sign Language Interpretation, in: 2022 International Conference on Emerging Trends in Smart Technologies (ICETST), 2022: pp. 1–5. https://doi.org/10.1109/ICETST55735.2022.9922949.
[46] G.L. Sukruth, V.K. Bp, M.R. Tejas, K. Rithvik, Enhancing Collaborative Interaction with the Augmentation of Sign Language for the Vocally Challenged, Journal of Advanced …. 1 (2023) 2010. https://doi.org/10.14569/IJACSA.2023.0140199.
[47] F. Hamid Yousuf, A. Bushnaf Alwarfalli, I. Ighneiwa, Arabic Sign Language Recognition System by Using Surface Intelligent EMG Signal, in: The 7th International Conference on Engineering & MIS 2021, Association for Computing Machinery, New York, NY, USA, 2021: pp. 1–6. https://doi.org/10.1145/3492547.3492606.
[48] S.K. Singh, A. Chaturvedi, A reliable and efficient machine learning pipeline for american sign language gesture recognition using EMG sensors, Multimed. Tools Appl. (2022). https://doi.org/10.1007/s11042-022-14117-y.
[49] X. Jiang, S.C. Satapathy, L. Yang, S.-H. Wang, Y.-D. Zhang, A Survey on Artificial Intelligence in Chinese Sign Language Recognition, Arab. J. Sci. Eng. 45 (2020) 9859–9894. https://doi.org/10.1007/s13369-020-04758-2.
[50] P. Pranav, R. Katarya, Optimal Sign language recognition employing multi-layer CNN, in: 2022 4th International Conference on Advances in Computing, Communication Control and Networking (ICAC3N), 2022: pp. 288–293. https://doi.org/10.1109/ICAC3N56670.2022.10074397.
[51] S.G.M. Almeida, F. Guimarães, J.A. Ramírez, Feature extraction in Brazilian Sign Language Recognition based on phonological structure and using RGB-D sensors, Expert Syst. Appl. (2014). https://doi.org/10.1016/j.eswa.2014.05.024.
[52] S. Sclaroff, M. Betke, G. Kollios, J. Alon, V. Athitsos, R. Li, J. Magee, T.-P. Tian, Tracking, analysis, and recognition of human gestures in video, in: Eighth International Conference on Document Analysis and Recognition (ICDAR'05), 2005: pp. 806–810 Vol. 2. https://doi.org/10.1109/ICDAR.2005.243.
[53] A. Boukdir, M. Benaddy, A. Ellahyani, O.E. Meslouhi, M. Kardouchi, 3D gesture segmentation for word-level Arabic sign language using large-scale RGB video sequences and autoencoder convolutional networks, J. VLSI Signal Process. Syst. Signal Image Video Technol. 16 (2022) 2055–2062. https://doi.org/10.1007/s11760-022-02167-6.
[54] H. Kolivand, S. Joudaki, M.S. Sunar, D. Tully, A new framework for sign language alphabet hand posture recognition using geometrical features through artificial neural network (part 1), Neural Comput. Appl. 33 (2020) 4945–4963. https://doi.org/10.1007/s00521-020-05279-7.
[55] M. Al-Qurishi, T. Khalid, R. Souissi, Deep Learning for Sign Language Recognition: Current Techniques, Benchmarks, and Open Issues, IEEE Access. 9 (2021) 126917–126951. https://doi.org/10.1109/ACCESS.2021.3110912.
[56] R. Gupta, A. Kumar, Indian sign language recognition using wearable sensors and multi-label classification, Comput. Electr. Eng. 90 (2021) 106898. https://doi.org/10.1016/j.compeleceng.2020.106898.
[57] Z. Zhang, Z. Su, G. Yang, Real-Time Chinese Sign Language Recognition Based on Artificial Neural Networks, in: 2019 IEEE International Conference on Robotics and Biomimetics (ROBIO), 2019: pp. 1413–1417. https://doi.org/10.1109/ROBIO49542.2019.8961641.
[58] J. Peguda, V.S.S. Santosh, Y. Vijayalata, A.D.R. N, V. Mounish, Speech to Sign Language Translation for Indian Languages, in: 2022 8th International Conference on Advanced Computing and Communication Systems (ICACCS), 2022: pp. 1131–1135. https://doi.org/10.1109/ICACCS54159.2022.9784996.
[59] C. Nyaga, R. Wario, A Review of Sign Language Hand Gesture Recognition Algorithms, Advances in Artificial Intelligence, Software and Systems Engineering. (2021) 207–216. https://doi.org/10.1007/978-3-030-51328-3_30.
[60] P.Q. Thang, N.D. Dung, N.T. Thuy, A Comparison of SimpSVM and RVM for Sign Language Recognition, in: Proceedings of the 2017 International Conference on Machine Learning and Soft Computing, Association for Computing Machinery, New York, NY, USA, 2017: pp. 98–104. https://doi.org/10.1145/3036290.3036322.
[61] S. Jiang, B. Lv, W. Guo, C. Zhang, H. Wang, X. Sheng, P.B. Shull, Feasibility of Wrist-Worn, Real-Time Hand, and Surface Gesture Recognition via sEMG and IMU Sensing, IEEE Trans. Ind. Inf. 14 (2018) 3376–3385. https://doi.org/10.1109/TII.2017.2779814.
[62] S.Z. Gurbuz, A.C. Gurbuz, E.A. Malaia, D.J. Griffin, C. Crawford, M.M. Rahman, E. Kurtoglu, R. Aksu, T. Macks, R. Mdrafi, American sign language recognition using RF sensing, IEEE Sens. J. (2020) 1–1. https://doi.org/10.1109/jsen.2020.3022376.
[63] F. Wen, Z. Zhang, T. He, C. Lee, AI enabled sign language recognition and VR space bidirectional communication using triboelectric smart glove, Nat. Commun. 12 (2021) 5378. https://doi.org/10.1038/s41467-021-25637-w.
[64] H. He, H. Chu, R. Pan, L. Ye, K. Zhang, W. Chen, P. Zhang, S. Lan, Overview of Electromagnetic Representation and Interpretation of Sign Language Semantics, in: 2022 IEEE MTT-S International Wireless Symposium (IWS), 2022: pp. 1–3. https://doi.org/10.1109/IWS55252.2022.9977943.
[65] T. Shanableh, K. Assaleh, Feature modeling using polynomial classifiers and stepwise regression, Neurocomputing. 73 (2010) 1752–1759. https://doi.org/10.1016/j.neucom.2009.11.045.
[66] T. Mantecón, A. Mantecón, C.R. del-Blanco, F. Jaureguizar, N. García, Enhanced gesture-based human-computer interaction through a Compressive Sensing reduction scheme of very large and efficient depth feature descriptors, in: 2015 12th IEEE International Conference on Advanced Video and Signal Based Surveillance (AVSS), 2015: pp. 1–6. https://doi.org/10.1109/AVSS.2015.7301804.
[67] M. Maebatake, I. Suzuki, M. Nishida, Y. Horiuchi, S. Kuroiwa, Sign Language Recognition Based on Position and Movement Using Multi-Stream HMM, in: 2008 Second International Symposium on Universal Communication, 2008: pp. 478–481. https://doi.org/10.1109/ISUC.2008.56.
[68] X. Zhang, X. Chen, Y. Li, V. Lantz, K. Wang, J. Yang, A Framework for Hand Gesture Recognition Based on Accelerometer and EMG Sensors, IEEE Transactions on Systems, Man, and Cybernetics - Part A: Systems and Humans. 41 (2011) 1064–1076. https://doi.org/10.1109/TSMCA.2011.2116004.
[69] S. Shahriar, A. Siddiquee, T. Islam, A. Ghosh, R. Chakraborty, A.I. Khan, C. Shahnaz, S.A. Fattah, Real-Time American Sign Language Recognition Using Skin Segmentation and Image Category Classification with Convolutional Neural Network and Deep Learning, in: TENCON 2018 - 2018 IEEE Region 10 Conference, 2018: pp. 1168–1171. https://doi.org/10.1109/TENCON.2018.8650524.
[70] P. Sharma, R.S. Anand, A comprehensive evaluation of deep models and optimizers for Indian sign language recognition, Graphics and Visual Computing. 5 (2021) 200032. https://doi.org/10.1016/j.gvc.2021.200032.
[71] L. Ji, J. Liu, S. Shimamoto, Recognition of Japanese Sign Language by Sensor-Based Data Glove Employing Machine Learning, in: 2022 IEEE 4th Global Conference on Life Sciences and Technologies (LifeTech), ieeexplore.ieee.org, 2022: pp. 256–258. https://doi.org/10.1109/LifeTech53646.2022.9754851.
[72] R.H. Abiyev, M. Arslan, J.B. Idoko, Sign language translation using deep convolutional neural networks, KSII Transactions on Internet and. (2020). https://www.koreascience.or.kr/article/JAKO202011161036129.page.
[73] S.A. Mehdi, Y.N. Khan, Sign language recognition using sensor gloves, in: Proceedings of the 9th International Conference on Neural Information Processing, 2002. ICONIP '02., 2002: pp. 2204–2206 vol.5. https://doi.org/10.1109/ICONIP.2002.1201884.
[74] A.I. Nadaf, S.A. Pardeshi, Decision Tree-Based Classification of sEMG and Accelerometer Data of Sign Language, in: Advances in Communication, Devices and Networking, Springer Nature Singapore, 2023: pp. 87–97. https://doi.org/10.1007/978-981-19-2004-2_8.
[75] G. Fang, W. Gao, A SRN/HMM system for signer-independent continuous sign language recognition, in: Proceedings of Fifth IEEE International Conference on Automatic Face Gesture Recognition, 2002: pp. 312–317. https://doi.org/10.1109/AFGR.2002.1004172.
[76] Y. Bengio, P. Simard, P. Frasconi, Learning long-term dependencies with gradient descent is difficult, IEEE Trans. Neural Netw. 5 (1994)

157–166. https://doi.org/10.1109/72.279181.
[77] A. Mittal, P. Kumar, P.P. Roy, R. Balasubramanian, B.B. Chaudhuri, A Modified LSTM Model for Continuous Sign Language Recognition Using Leap Motion, IEEE Sensors Journal. 19 (2019) 7056–7063. https://doi.org/10.1109/jsen.2019.2909837.
[78] S. Mhatre, S. Joshi, H.B. Kulkarni, Sign Language Detection using LSTM, in: 2022 IEEE International Conference on Current Development in Engineering and Technology (CCET), ieeexplore.ieee.org, 2022: pp. 1–6. https://doi.org/10.1109/CCET56606.2022.10080705.
[79] I. Papastratis, K. Dimitropoulos, P. Daras, Continuous Sign Language Recognition through a Context-Aware Generative Adversarial Network, Sensors . 21 (2021). https://doi.org/10.3390/s21072437.
[80] S. Krishna, J. Ukey, Gan based indian sign language synthesis, Proceedings of the Twelfth Indian Conference on. (2021). https://dl.acm.org/doi/abs/10.1145/3490035.3490301.
[81] P.D. Rosero-Montalvo, P. Godoy-Trujillo, E. Flores-Bosmediano, J. Carrascal-García, S. Otero-Potosi, H. Benitez-Pereira, D.H. Peluffo-Ordóñez, Sign Language Recognition Based on Intelligent Glove Using Machine Learning Techniques, in: 2018 IEEE Third Ecuador Technical Chapters Meeting (ETCM), 2018: pp. 1–5. https://doi.org/10.1109/ETCM.2018.8580268.
[82] N. Siddiqui, R.H.M. Chan, A wearable hand gesture recognition device based on acoustic measurements at wrist, in: 2017 39th Annual International Conference of the IEEE Engineering in Medicine and Biology Society (EMBC), 2017: pp. 4443–4446. https://doi.org/10.1109/EMBC.2017.8037842.
[83] Y. Zhang, B. Liu, Z. Liu, Recognizing Hand Gestures With Pressure-Sensor-Based Motion Sensing, IEEE Trans. Biomed. Circuits Syst. 13 (2019) 1425–1436. https://doi.org/10.1109/TBCAS.2019.2940030.
[84] W. Aly, S. Aly, S. Almotairi, User-Independent American Sign Language Alphabet Recognition Based on Depth Image and PCANet Features, IEEE Access. 7 (2019) 123138–123150. https://doi.org/10.1109/ACCESS.2019.2938829.
[85] A multimodal framework for sensor based sign language recognition, Neurocomputing. 259 (2017) 21–38. https://doi.org/10.1016/j.neucom.2016.08.132.
[86] M. Jebali, A. Dakhli, M. Jemni, Vision-based continuous sign language recognition using multimodal sensor fusion, Evolving Systems. 12 (2021) 1031–1044. https://doi.org/10.1007/s12530-020-09365-y.
[87] M.I. Rusydi, S. Syafii, R. Hadelina, E. Kimin, A.W. Setiawan, A. Rusydi, Recognition of sign language hand gestures using leap motion sensor based on threshold and ANN models, Bulletin of Electrical Engineering and Informatics. 9 (2020) 473–483. https://doi.org/10.11591/eei.v9i2.1194.
[88] P. Meier, K. Rohrmann, M. Sandner, M. Prochaska, Application of magnetic field sensors for hand gesture recognition with neural networks, in: 2019 IEEE 1st Global Conference on Life Sciences and Technologies (LifeTech), 2019: pp. 200–203. https://doi.org/10.1109/LifeTech.2019.8884006.
[89] M. Hassan, K. Assaleh, T. Shanableh, Multiple Proposals for Continuous Arabic Sign Language Recognition, Sensing and Imaging. 20 (2019) 4. https://doi.org/10.1007/s11220-019-0225-3.
[90] Z. Liu, L. Pang, X. Qi, MEN: Mutual Enhancement Networks for Sign Language Recognition and Education, IEEE Trans Neural Netw Learn Syst. PP (2022). https://doi.org/10.1109/TNNLS.2022.3174031.
[91] D. Ryumin, D. Ivanko, A. Axyonov, I. Kagirov, A. Karpov, M. Zelezny, Human-Robot Interaction with Smart Shopping Trolley Using Sign Language: Data Collection, in: 2019 IEEE International Conference on Pervasive Computing and Communications Workshops (PerCom Workshops), 2019: pp. 949–954. https://doi.org/10.1109/PERCOMW.2019.8730886.
[92] E.P. da Silva, P.D.P. Costa, K.M.O. Kumada, J.M. De Martino, SILFA: Sign Language Facial Action Database for the Development of Assistive Technologies for the Deaf, in: 2020 15th IEEE International Conference on Automatic Face and Gesture Recognition (FG 2020), 2020: pp. 688–692. https://doi.org/10.1109/FG47880.2020.00059.
[93] V. Gomathi, Indian Sign Language Recognition through Hybrid ConvNet-LSTM Networks, EMITTER International Journal of Engineering. (2021). http://emitter.pens.ac.id/index.php/emitter/article/view/613.
[94] D. Bragg, O. Koller, N. Caselli, W. Thies, Exploring collection of sign language datasets: Privacy, participation, and model performance, Proceedings of the 22nd. (2020). https://dl.acm.org/doi/abs/10.1145/3373625.3417024.
[95] D. Bragg, N. Caselli, J.W. Gallagher, M. Goldberg, C.J. Oka, W. Thies, ASL Sea Battle: Gamifying Sign Language Data Collection, in: Proceedings of the 2021 CHI Conference on Human Factors in Computing Systems, Association for Computing Machinery, New York, NY, USA, 2021: pp. 1–13. https://doi.org/10.1145/3411764.3445416.
[96] X. Jiang, Y.-D. Zhang, Chinese Sign Language Fingerspelling via Six-Layer Convolutional Neural Network with Leaky Rectified Linear Units for Therapy and Rehabilitation, Journal of Medical Imaging and Health Informatics. 9 (2019) 2031–2090. https://doi.org/10.1166/jmihi.2019.2804.
[97] M.S. Amin, S.T.H. Rizvi, M.M. Hossain, A Comparative Review on Applications of Different Sensors for Sign Language Recognition, J. Imaging Sci. Technol. 8 (2022). https://doi.org/10.3390/jimaging8040098.
[98] O.M. Sincan, J.C.S. Jacques, S. Escalera, H.Y. Keles, ChaLearn LAP large scale signer independent isolated sign language recognition challenge: Design, results and future research, in: 2021 IEEE/CVF Conference on Computer Vision and Pattern Recognition Workshops (CVPRW), IEEE, 2021: pp. 3472–3481. https://doi.org/10.1109/cvprw53098.2021.00386.
[99] R. Presotto, G. Civitarese, C. Bettini, FedCLAR: Federated Clustering for Personalized Sensor-Based Human Activity Recognition, in: 2022 IEEE International Conference on Pervasive Computing and Communications (PerCom), 2022: pp. 227–236. https://doi.org/10.1109/PerCom53586.2022.9762352.
[100] B. McMahan, E. Moore, D. Ramage, Communication-efficient learning of deep networks from decentralized data, Artif. Intell. (2017). http://proceedings.mlr.press/v54/mcmahan17a?ref=https://githubhelp.com.

Physica Scripta

ACCEPTED MANUSCRIPT

A latch-based sense amplifier with improved performance for single ended SRAM application

To cite this article before publication: Bhawna Rawat *et al* 2023 *Phys. Scr.* in press https://doi.org/10.1088/1402-4896/acd6c2

Manuscript version: Accepted Manuscript

Accepted Manuscript is "the version of the article accepted for publication including all changes made as a result of the peer review process, and which may also include the addition to the article by IOP Publishing of a header, an article ID, a cover sheet and/or an 'Accepted Manuscript' watermark, but excluding any other editing, typesetting or other changes made by IOP Publishing and/or its licensors"

This Accepted Manuscript is **© 2023 IOP Publishing Ltd**.

During the embargo period (the 12 month period from the publication of the Version of Record of this article), the Accepted Manuscript is fully protected by copyright and cannot be reused or reposted elsewhere.

As the Version of Record of this article is going to be / has been published on a subscription basis, this Accepted Manuscript will be available for reuse under a CC BY-NC-ND 3.0 licence after the 12 month embargo period.

After the embargo period, everyone is permitted to use copy and redistribute this article for non-commercial purposes only, provided that they adhere to all the terms of the licence https://creativecommons.org/licences/by-nc-nd/3.0

Although reasonable endeavours have been taken to obtain all necessary permissions from third parties to include their copyrighted content within this article, their full citation and copyright line may not be present in this Accepted Manuscript version. Before using any content from this article, please refer to the Version of Record on IOPscience once published for full citation and copyright details, as permissions may be required. All third party content is fully copyright protected, unless specifically stated otherwise in the figure caption in the Version of Record.

View the article online for updates and enhancements.

This content was downloaded from IP address 14.139.251.98 on 24/05/2023 at 05:32

A Latch-Based Sense Amplifier with improved performance for single ended SRAM application

Bhawna Rawat[1], Poornima Mittal[1*]

[1]Department of Electronics and Communication Engineering, Delhi Technological University, Delhi, India

bhawnarawat12@gmail.com, poornimamittal@dtu.ac.in

*Corresponding author: poornimamittal@dtu.ac.in

The growing processing load and decreasing technology node has augmented the need for single ended memory. Consequently, generating requirement for a single ended sense amplifier for ease of integration with single ended memory. Therefore, this paper presents a single bitline based latch type sense amplifier. It is designed at feature size of 32 nm and its performance is evaluated at 1 V supply, with the environment temperature at 27 ºC. It is analyzed for its output waveform, delay, variability tolerance, and area occupancy. The ON current for the proposed sense amplifier is 1.2 uA, while the OFF current is 10 nA. The ON current for proposed sense amplifier is is 0.18, 0.43, and 0.88 times higher than SA-2, SA-5, and SA-6 respectively. While, its OFF current is lowest with the exception of SA-3 at 9 nA. Also, the delay for the proposed sense amplifier is minimal at 0.77 ns in comparison to other topologies. The SA-1, SA-2, SA-5, and SA-6 are 3.9, 2.8, 3.7, and 0.3 times slower than SA-P, thereby deeming its operation faster than others. The reliability for the proposed circuit is evaluated using process corner analysis for all performance parameters.

Keywords : single ended, sense amplifier, fast sensing, lower variability

1. INTRODUCTION

The growing dependence of contemporary world on artificial intelligence and hyper-personalized devices has augmented the need for larger and faster memory. Also, the growing demand for sleek and portable personalized devices has fueled the need for devices with low power appetite and high packaging density. A major component of these system-on-chips (SoC) is cache memory, formed by static random access memory (SRAM) bit cells and its supporting peripheral circuitry. The increase in size of data, processing load, and round the clock connectivity, has increased the size of SRAM memory integrated in a SoC. Resulting in more area occupancy, and higher power requirements, thereby limiting its performance. The conventional differential 6T SRAM cell had been the go-to industry standard for a very long time. But, its inherent read-write conflict and poor performance at scaled technology node has motivated researchers to resolve its bottlenecks and design alternative bit cells. The most conventional mechanism to resolve the inherent read-write conflict for the bit cell, is to isolate its read and write port. A 6T cell with similar configuration was reported by Suarna and Mikie [1] in 2019. In this cell, the read and write port are single ended i.e. they are performed via a single bitline. Recently, single bitline based read ports have been gaining popularity. This is a consequence to two primary reasons – first, it allows easy isolation between the read and write port without any significant impact on the area of the bit cell, and second, use of a single bitline for a port reduces its activity factor, thereby lowering its dynamic power consumption.

Additional to the bit cell, a cache memory also comprises of write drivers, pre-charge circuit, and sense amplifier (SA). Amongst this peripheral circuitry, the SA is the most crucial component as the read operation for the cache is depends on it. In the array arrangement of the cache, each column culminates in an SA (as illustrated in Fig. 1 (a)). Conventionally, SA detects a small differential voltage on the bitline, to produce a full swing data output [2-3]. Therefore, it is highly critical for performance of cache memory. It helps in determining the operational frequency, power consumption, and minimum operating point, for cache memory [4-5]. The essential performance parameters for SA includes - minimum differential input voltage, sensing delay, and power consumption [6-7]. Over the years various SA designs have been reported by researchers. These different SA topologies reported in literature can be categorized into either voltage mode or current mode. The latter is quickly able to amplify a small differential signal at the bitlines to a full swing voltage output [8-9]. But, its higher transistor count and larger area occupancy makes it economically unfeasible. An area efficient SA topology is the latch based voltage mode SA. They are also popular owing to their high speed sensing mechanism and low power consumption [10-11]. Conventionally, both the topologies were differential in nature. But, as single ended bit cells are gaining popularity, it is crucial to inspect and design a single ended SA topology. Additional to the topology constraints, lower feature size is another constraint that is a pivotal design challenge that SA designers have to resolve, to shrink the diverging gap amongst timing and power constraints [12-13]. Process corner is another concern that majorly impacts the SA performance in nanometer domain [14-15]. Researchers have also reported that aging in SA results in degradation of speed [16], and off-set voltage related problems [17-18]. In traditional SA designs, the voltage latch based SA offers a three times better offset tolerance, for the same area footprint making it a better alternative [18]. Different existing SA topologies are studied in this paper to propose a modified SA topology with improved performance. Based on the learnings from the pre-existing SA designs, a voltage mode SA, with single ended design is proposed. The proposed SA is characterized by low input voltage, low power requirement, faster sensing, and improved reliability. The rest of the paper is categorized into the following five sections, with the ongoing introduction. The pre-existing SA topologies and their functionality is elaborated in section II. The proposed SA design is explained in section III. The simulations results are graphically presented and compared in section IV. The findings of the paper are summed up in section V.

Accepted Manuscript

2. SCHEMATIC REVIEW OF THE EXISTING SA TOPOLOGIES

The increasing popularity of single ended memory is a direct consequence of the rising demand for low power devices. Consequently generating the need for single ended SA topology. Over the years, different SA topologies have been reported in literature. These different topologies can be pre-dominantly categorized as voltage based or current based SAs. Amongst the two SA topologies the voltage based SA has low transistor count, and low power consumption. While, the current mode SA is quickly able to amplify a small differential signal at the bitlines to a full swing voltage output [8-9]. But, its higher transistor count and larger area occupancy makes it economically unfeasible. Therefore, owing to its area efficiency voltage mode SA are more popular. Other merits that add to the qualities of voltage mode SA are high speed sensing mechanism and low power consumption [10-11]. Another sensing topology that is deemed reliable for single ended SRAM is the inverter based sensing topology [19]. But, it results in substantial delay and incurs high energy overhead [20]. Consequently, to enable low bitline swing based sensing, a symmetrical single-ended SA topology was introduced by Lin et al. [21]. But, its dependence on an additional voltage reference generator adds to the additional peripheral circuitry [22] resulting in large area overhead and high energy requirement [23-24]. To eliminate the requirement for an additional reference voltage generator, a few asymmetrical differential SA have been reported [25-26]. But, they are susceptible to local variations, global variation, and require a substantially large differential voltage to generate feasible output [27]. Some of the popular SA topologies reported in literature are as follows -

The most common and conventional design for an SA (SA-1) [28-29] is depicted in Fig. 1 (b). This topology is composed of a mutually coupled inverter pair (M1-M3 and M2-M4). The cross coupled nature of the inverter pair helps reduce the delay for the circuit. The core for the SA is accessed via transistors M5 and M6. The M7 transistor at the bottom acts as the current driver for the circuit and ensures a high drive current through the topology during the sensing operation. This SA is enabled only after a detectable voltage difference is created between the bit lines. The essential aspect of this SA topology is that during the evaluation phase it decouples the input and output node via transistors M5 and M6. Therefore, it achieves higher speed while maintaining lower energy consumption. But, a major limitation for this topology is that, the use of pass-gate transistors reduces the available input voltage, thereby poorly impacting its noise margin [30].

An alternative SA (SA-2) that removes the pass transistor gate from the input node for the SA topology was reported in [31]. The optimal functioning of this SA is dependent on the positive feedback of the cross coupled inverter pair. The schematic diagram for SA-2 is depicted in Fig. 1(c). Alike, the previous SA topology the sensing operation for SA-2 is initialed by setting the SAE signal high. This topology is differential in nature and therefore, depending on the polarity of input differential voltage, the output of the SA is determined. The disadvantage of this topology is that, its input and output node are the same, therefore it cannot be directly connected to the memory bit lines. If it is directly connected the delay and power for the circuit will increase significantly. It may also poorly impact the stability of the cells connected to the SA.

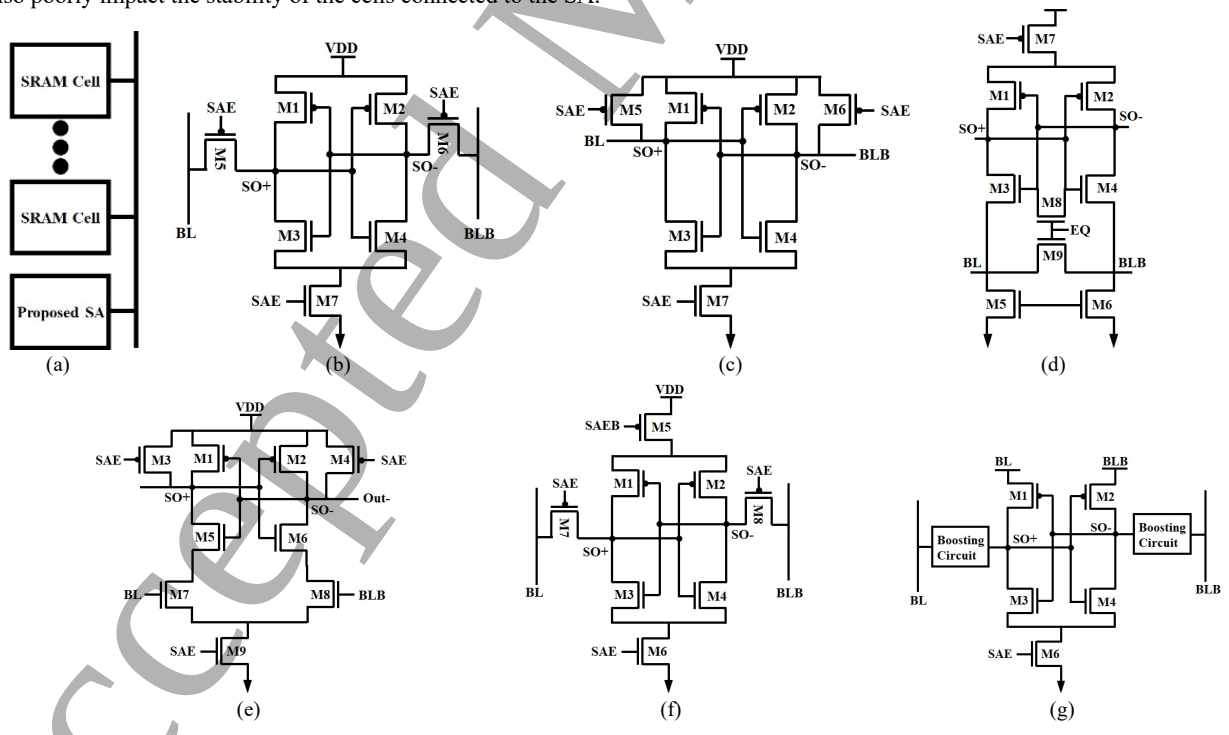


Fig. 1 (a) Column representation and placement of SA in the SRAM array, schematic diagram for (b) SA-1, (c) SA-2, (d) SA-3, (e) SA-4, (f) SA-5, and (g) SA-6

An alternative to isolate the input and output nodes for a SA topology (SA-3) was reported in [32]. The schematic diagram for SA-3 is presented in Fig. 1(d). In this SA, the sensing operation begins by turning the M7 transistor ON. The utility of M8 and M9

Accepted Manuscript

transistor is to maintain the BL and BLB at equal potential; they are ON only during the pre-charge phase. This also forces the output nodes (SO+ and SO-) of SA-3 to equal potential. The utility of the M7 transistor is to ensure high drive current through the circuit. A major advantage of this topology is that its speed is independent of the bit-line capacitance. As the sensing node impedance is very small, the read discharge current from the memory can be directly injected into the sense amplifier [33]. This SA topology has demonstrated commendable performance for higher operational voltages (V_{DD}). But, as the operational voltage for devices is decreasing, its performance is also declining.

Another SA topology (SA-4) that isolates the input and output node was reported in literature by Kobayashi et al. [34]. The schematic diagram for SA-4 is depicted in Fig. 1(e). It combines the strong positive feedback of cross-coupled inverter pair with high resistive input to resolve the problem encountered by SA-2. Therefore, this SA does not require decoupling at its input because of a high-impedance input differential stage [35-37]. The enable signal (SAE) starts the operation by activating M7. Immediately, current begins to flow and pulls down the source terminal of M5 and M6. Successively, the input transistor pair M5, M6 starts to discharge the cross-coupled invertors. When the output voltage reaches V_{DD}-V_{TH} level, strong positive feedback enhances the output voltage difference.

A similar path based SA topology (SA-5) was reported in [38] is depicted in Fig. 1(f). The SA-5 is composed of a cross coupled inverter pair formed by transistors (M1-M3 and M2-M4). The M5 and M6 transistors work as sleep transistors and are utilized to lower the static power dissipation for the SA; while transistors M7 and M8 are used to access the SA. The enable (SAE) signal is used to activate the topology. Initially, the SAE signal is low and the PMOS transistors (M7 and M8) are ON and the differential voltage between BL-BLB gets transferred to the internal nodes of the SA. Then, the SAE signal is turned high and the access transistors are cut off, thereby activating the SA-5. The inverter core then amplifies the voltage difference to develop the output values. Only when the SAE signal is high, the V_{DD} and the ground rail are connected with the inner core of the topology, thereby enabling it to function correctly. This also ensures that SA-5 works only when it's required and does not detect each time a voltage difference is generated on the bitline pair.

Another SA topology (SA-6) was reported by Patel et al. [39] in 2018. This circuit utilizes a sample latch boost based SA scheme. The schematic diagram for SA-6 is depicted in Fig. 1(g). Apart from using the boosting circuit to improve the performance of the SA, the other fundamental difference between SA-1 and SA-6 is that of the supply voltage. SA-1 is driven using V_{DD} while the pull up network of the inverter core for SA-6 circuit is designed with a bitline based supply. SA-2 was initially designed for 65 nm technology node. Lowering the technology node poorly impacts its performance. But, the aspect ratio for the circuit is maintained to not bias it unfairly. The output swing, and delay performance for the SA-6 is fairly good, but its major drawback is the increased area footprint, that makes it economically unfeasible.

3. ARCHITECTURE OF THE PROPOSED SENSE AMPLIFIER

The growing popularity of single ended memory cells has created the need for designing a single ended sense amplifier. To cater to the same, a single ended sense amplifier (SA-P) is proposed in this paper. The circuit configuration for SA-P is depicted in Fig. 2(a). It can be observed that the core for SA-P is formed by a combination of two inverters (M1-M3 and M2-M4), connected in a back-to-back configuration via an NMOS transistor M5. The utility of M5 is to convert the back-to-back inverter configuration into a cascaded inverter configuration. This is enabled by enable bar signal (ENB); when ENB is high the back-to-back configuration is effective (as depicted in Fig. 2(b). Whereas, when ENB is low the cascaded inverter configuration is effective, the same is depicted in Fig. 2(c). Additional to the inverter configuration, there is an NMOS transistor M6 in the SA-P topology. The utility of M6 is to increase the drive current through the circuit and also turn the SA-P ON or OFF. This M6 transistor is controlled via enable signal (EN). Thus, when SA-P is functional the EN signal is high and when it is low the SA-P is OFF. Additionally, the input to the circuit is provided at the Data In node and the output for the SA is read at the Data Out node. The functioning of SA-P during the ON and OFF state is explained in the subsequent sub-sections. The layout design for SA-P is depicted in Fig. 2(d).

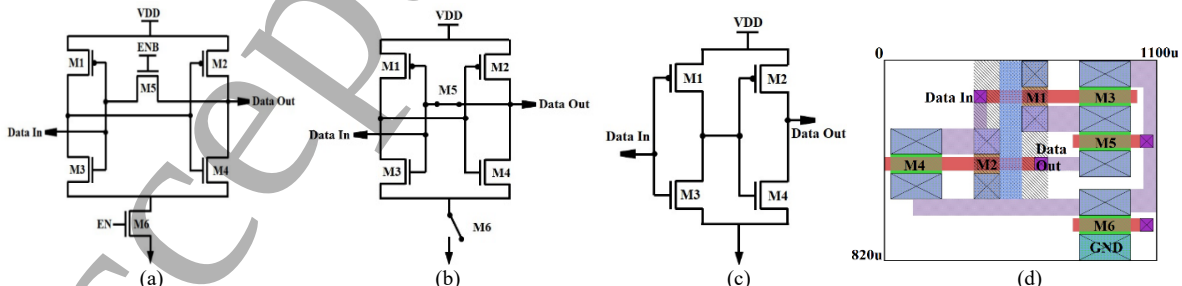


Fig. 2 Circuit diagram for (a) proposed SA, (b) equivalent circuit for proposed SA during the OFF state, (c) equivalent circuit for proposed SA during the ON state, and (d) layout design for proposed SA

OFF State

Accepted Manuscript

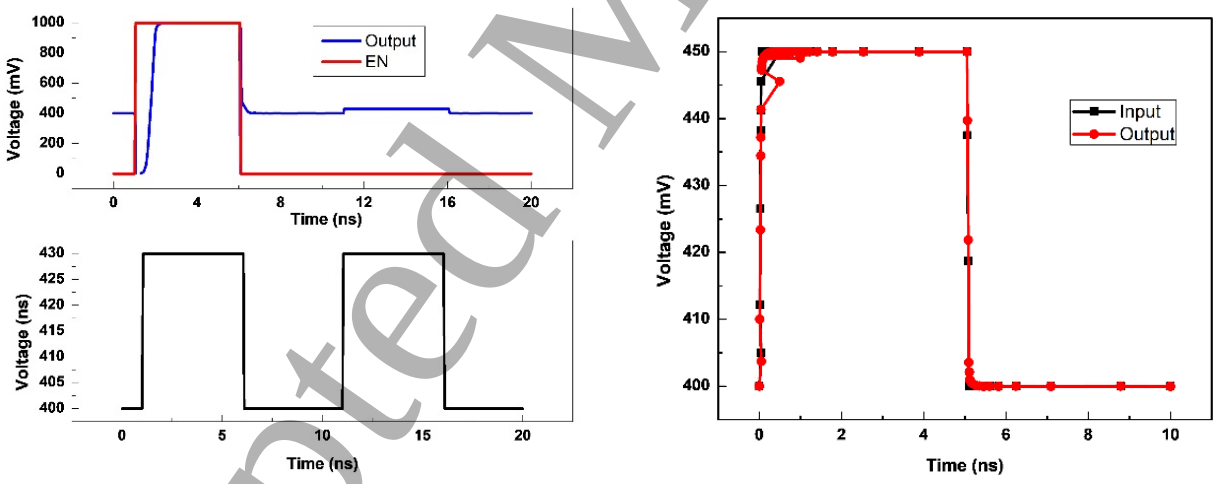
In a conventional SRAM array, the number of SAs required is dependent on the number of columns in the array; as SA is common to a column. This SA is utilized only when a particular cell in a column is to perform a read operation, otherwise the SA is maintained in OFF state. The OFF state circuit configuration of SA-P is depicted in Fig. 2(b). During this state the core of the SA is maintained in a cascaded inverter configuration (to ensure that the input fluctuations do not impact the SA output) and the M6 transistor is also non-conducting, to ensure minimal current flow through the circuit; as the source terminals for M3 and M4 are in floating condition.

ON State

During the read operation, an SA is operational, so the EN signal is high. The ON state circuit configuration for SA-P is depicted in Fig. 2(c). During this state, a small variation at the data input for the SA-P causes the left inverter (M1-M3) to drive the right inverter (M2-M4) to develop a full voltage swing at the data output node. The M6 transistor in this state is in conduction mode and results in a high current flow through SA-P.

4. RESULT AND ANALYSIS

The proposed SA is designed for 32 nm feature size using CMOS Predictive Technology Models and simulated at 1 V V_{DD}, with environment temperature maintained at 27 ºC. During the OFF mode, the mutually coupled inverter core for the proposed SA is biased at the meta-stability point. Whereas, during the read operation (ON mode), the bitline from the SRAM bit cell discharges, resulting in change in the Data In voltage for the SA. During the read operation, the EN signal is high (ENB is low), thus a small change in the input voltage gets amplified to yield the correct output at the data out terminal. The circuit simulation for read timing analysis of SA-P for different input, output, and enable signals configurations are depicted in Fig. 3(a). The three different signal configurations depicted in Fig. 3(a) are as follows-for the first cycle, the EN signal is high along with the input signal. Therefore a full swing output is achieved. During the next cycle the EN signal is low and so is the input signal, consequently no variation is observed at the output. In the next cycle, the EN signal is low but the input signal is high. This particular condition corresponds to a situation when a SA is disabled and input voltage is registered due to bitline fluctuations. This particular case is very crucial as for a conventional SA the possibility of registering a false read output is high during this condition. But it can be inferred form Fig. 3(a), that even under this condition the SA-P topology performs reasonably, as no output is registered, only a small fluctuation from the nominal value is observed.



(a) (b)

Fig. 3 The read circuit simulation results for the proposed sense amplifier when (a) SAE is high and (b) SAE is low.

The simulation results for the proposed SA during OFF state is represented in the Fig. 3(b). During the OFF state, the EN signal is low; this disables the M6 transistor, resulting in the drain node of the inverter core to be in a high impedance state. Additionally, the M5 transistor is ON, thereby enabling the mutual feedback connection between the inverter pair. As a consequence, even when the data input detects a slight variation in the input voltage, it would not translate into a full swing output voltage, as is depicted in Fig. 3(b). This establishes the integrity of the proposed SA during ON as well as OFF state.

A. Current analysis

The data input to the SA is a bitline common to a column in the SRAM array. Therefore, at a given instant of time, there is always some input to the SA. To ensure that the input to SA does not result in an erroneous read output, the SA is controlled via EN and ENB control signals. The former helps in faster operation, while the latter reduces static power dissipation for the SA topology. Low value of OFF current for the proposed SA is achieved via sleep transistor M6. The utility of EN and ENB is to ensure appropriate functioning of the SA topology.

Accepted Manuscript

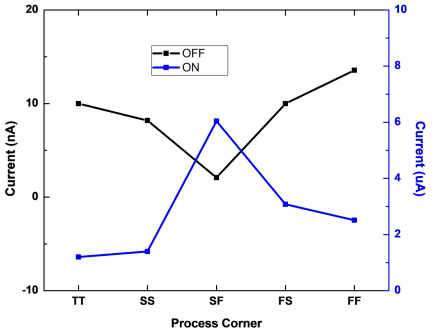


Fig. 4 Sensing current (ON) and leakage current (OFF) values for SA-P at different process corners.

Table 1. ON and OFF current values obtained for the different SA topologies at the different process corners

Sense Amplifier	ON current (uA)					OFF Current (nA)				
	TT	SS	SF	FS	FF	TT	SS	SF	FS	FF
SA-1	1.6	1.85	4.8	3.36	2.89	18	16.34	11.54	17.84	22.78
SA-2	1.9	2.89	3.68	3.98	4.1	14.73	13.76	9.89	12.96	15.79
SA-3	6.8	5.78	5.87	6.3	6.34	9	18.6	17.36	20.29	25.68
SA-4	5.68	4.58	6.23	5.12	4.98	19.4	6.98	4.25	8.89	11.87
SA-5	2.3	7	7.02	9.26	9.3	12	9.8	16.1	9.78	16
SA-6	3.02	1.8	2.1	5.2	5.8	23.64	21.6	22.7	25.6	25.6
SA-P	1.6	1.4	4.04	3.08	2.51	10	8.2	2.08	10	13

When the SA is not operational, M6 is OFF and disconnects the V_{DD} from the ground terminal. The output levels for the SA depends on the voltage level, but those voltage levels are attained via current flow in the inverter core topology. The higher the current flow, the faster the switching between levels [40]. Therefore, ideally for an SA, sensing current is expected to be high, whereas the OFF state current is expected to be as low as possible. The OFF current for the proposed SA is found to be as low as 10 nA. While, during ON state, M6 increases the drive current in the circuit, causing the ON current to be 1.2 uA

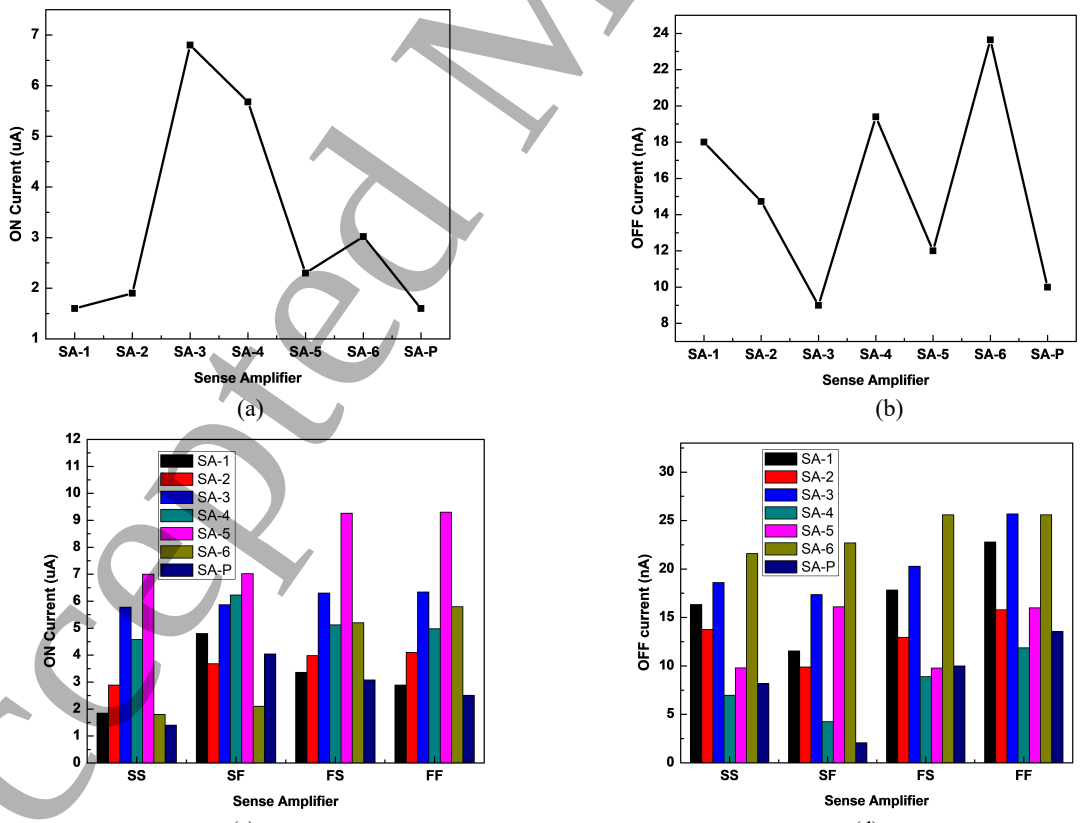


Fig. 5 Graphical comparison for (a) ON current, (b) OFF current, (c) ON current at different process corners and (d) OFF current at different process corners for all SAs at different process corners.

Accepted Manuscript

. The ON and OFF performance of SA-P is compared against the pre-existing SA topologies in Fig. 5(a), and (b) respectively, while the values are tabulated in Table 1. The highest ON current amongst the different SAs is obtained for SA-3 at 6.8 uA, closely followed by SA-4 at 5.68 uA. Therefore, in comparison to SA-P the SA-3 and SA-4 topologies register 0.76 and 0.71 times higher ON current respectively. Whereas, the ON current for SA-P is 0.18, 0.43, and 0.88 times higher than SA-2, SA-5, and SA-6 respectively. The ON current values obtained for SA-1 and SA-P are identical. Whereas, in terms of OFF current, the lowest value is obtained for SA-3 at 9 nA, closely followed by SA-P at 10 nA. Another SA topology that has low OFF current value is SA-5 at 12 nA. All the other SAs- SA-1, SA-2, SA-4, and SA-6, have a comparatively higher OFF current values, that are 0.8, 0.4, 0.94, and 1.364 times higher than SA-P. Therefore, in terms of ON and OFF current the SA-3 has the best performance followed by SA-P. The SA-3 topology has an edge over the SA-P circuit because the former is current based, whereas the latter is voltage based.

When a circuit is fabricated, there are possibilities of variation in performance of the circuit due to fabrication imperfections [41]. Therefore, the ON and OFF current performance for all the SA topologies are also calculated for the different process corners (slow-slow (SS), slow-fast (SF), fast-slow (FS), and fast-fast (FF)) and compared in Fig. 5(c) and (d) respectively. This is done to ensure that the variation (calculated as the difference between the maximum and minimum current values) in performance of the SA is within bounds. The variation in performance of SA-P is 2.64 uA, while for SA-1, SA-2, SA-3, SA-4, SA-5, and SA-6 are 2.95, 1.21, 0.56, 1.65, 2.3, and 4 uA respectively. The variations in ON current for SA-P is within bounds and would not have any drastic implication on ITS SA performance. It can be inferred from the aforementioned data that the current based SAs - SA-3 and SA-4 are more resilient to process variation than voltage mode SAs. Whereas, for the OFF current values, the variation in SA-1, SA-2, SA-3, SA-4, SA-5, SA-6, and SA-P are 11.2, 5.9, 8.3, 7.6, 6.3, 4, and 11.4 nA respectively. It may be observed that the SA-P registers a slightly higher variation in performance due to global variation (process corners), but the variation is within reasonable bounds to not have any drastic impact on its performance.

B. Delay Analysis

A conventional SA requires a large differential voltage for performing a successful Read operation and the time required to attain the appropriate differential input voltage, limits the operational speed for the SA topology. The proposed SA rectifies the same using a symmetrical single ended topology. The operational delay for SA is defined as the difference between the time when the input signal is applied and the time when the output attains 90% of its value. In the SA-P topology the M6 transistor is added primarily to increase drive current, consequently reducing its delay. Therefore, the delay performance for the proposed SA is analyzed for two different topologies – with and without the M6 topology. The delay results for the proposed SA with and without M6 transistor are compared in Fig. 6. As can be inferred from the results at the typical corner, the M6 transistor helps improve the delay performance for SA-P. If the M6 transistor is removed, the drive current through the internal core of the SA topology decreases, thereby increasing the delay for the circuit.

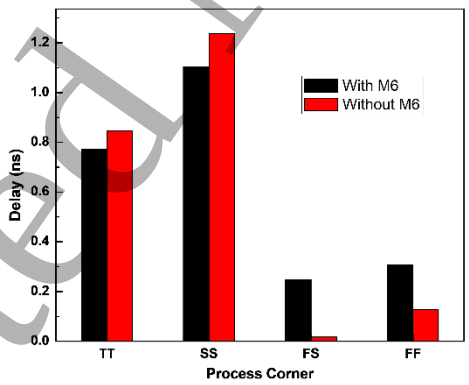
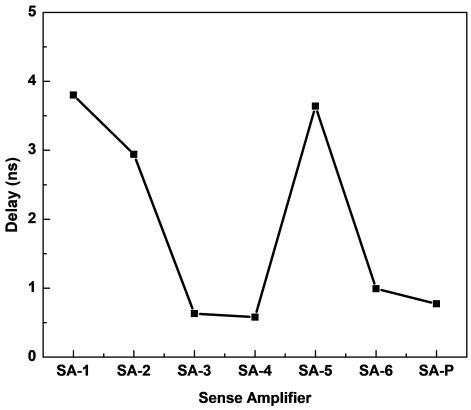


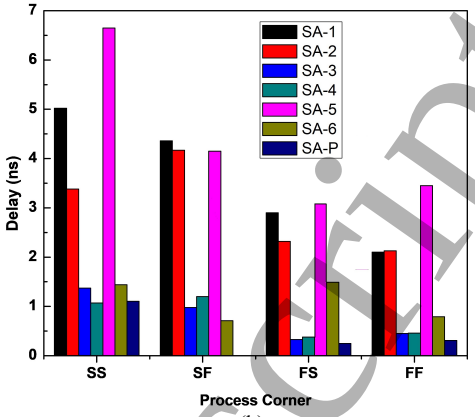
Fig. 6 Delay analysis for the proposed SA topology with respect to different process corners with and without the use of the bottom drive transistor.

The delay recorded for the proposed SA at the typical corner is of 0.77 ns. While, the delay recorded for the other SA topologies – SA-1, SA-2, SA-3, SA-4, SA-5, and SA-6 is 3.8, 2.94, 0.63, 0.58, 3.64, and 0.99 ns respectively. Delay for an SA should be as minimum as possible. This increases the operating speed for the memory. The delay performance for all SA designs topologies are compared in Fig.7 (a) and tabulated in Table 2. It can be inferred from Fig. 7(a) that SA-3 and SA-4 are 0.2 and 0.3 times faster than SA-P. While, the other SAs – SA-1, SA-2, SA-5, and SA-6 are 3.9, 2.8, 3.7, and 0.3 times slower than SA-P. Thus, amongst the voltage mode SAs the SA-P is better than others. The performance for each digital circuit is subject to variation due to global variations caused during the circuit fabrication. Consequentially, the delay performance of SA-P at process corners is analyzed and compared with pre-existing SAs in Fig. 7(b). The best performance amongst all the corners is obtained at the FS corners; here the performance for the PMOS is fast while the NMOS is made slower. This results in bridging the gap between the mobility difference for PMOS and NMOS, thereby improving the performance for the SA at FS corner. A general observation, from the figure is that, worst performance for all the SAs is observed at the SS corner, due to poor performance for both PMOS and NMOS transistors. Whereas, best performance for all SAs is observed at FS corner, as the performance parity between NMOS and PMOS is bridged at this corner.

Accepted Manuscript



(a)



(b)

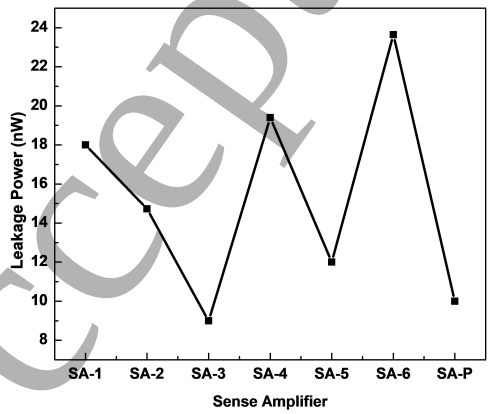
Fig. 7 Graphical comparison for sensing delay (a) at TT corner, and (b) all process corners for the different SA topologies at all the process corners.

Table 2. Delay values (in ns) obtained for the different SA at the different process corners

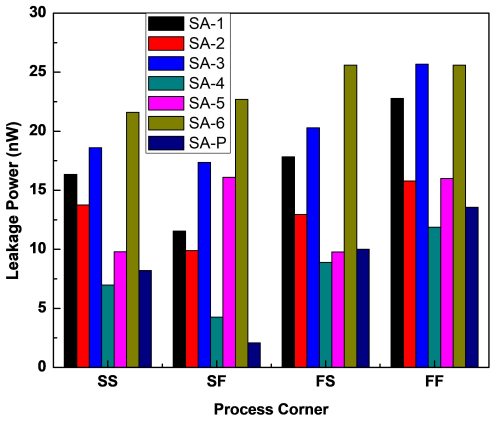
Sense Amplifier	TT	SS	SF	FS	FF
SA-1	3.8	5.02	4.36	29	2.1
SA-2	2.94	3.38	4.17	2.32	2.13
SA-3	0.63	1.37	0.98	0.33	0.45
SA-4	0.58	1.07	1.2	0.38	0.46
SA-5	3.64	6.65	4.15	3.17	3.45
SA-6	0.99	1.44	0.71	1.49	0.79
SA-P	0.773	1.104	0.11	0.248	0.308

C. Leakage Power Analysis

An SA is dependent on high amplification of small deflection in the input voltage, the proposed SA is biased at the trip point (meta-stability point for the inverter). Consequently, it is expected that the ON and OFF current for the SA will have a significant difference. Thus, the read current for the SA should be high, while the OFF current (leakage current) should be very low (as explained previously). But, at scaled technology node, maintaining low leakage current is a challenge. Typically, the leakage current for a latch based SA topology is low. The leakage performance of SA-P is compared against the topologies explained in section II. The leakage power values obtained for all the SAs are compared in Fig. 8(a). The SA topology with the highest leakage power dissipation is the SA-6 topology at 23.64 nW, which is 1.36 times greater than SA-P. The high value of leakage power dissipation for the SA-6 topology is caused by the additional boosting circuitry that adds to the leakage current sources in the circuit. The lowest leakage power is observed for SA-3 at 9 nW, closely followed by SA-P at 10 nW. While, the leakage power values of the other SA topologies – SA-1, SA-2, SA-4, and SA-5 are 18, 14.73, 19.4, and 12 nW respectively. These values are 0.8, 0.47, 0.94, and 0.2 times larger than the value obtained for the SA-P topology. The lower leakage power value for SA-P is an implication on the disconnection of the feedback connection and the bottom sleep NMOS transistor. The design for SA-P is optimized to have the least leakage power dissipation at all corners. Thereby, ensuring its performance reliability.



(a)



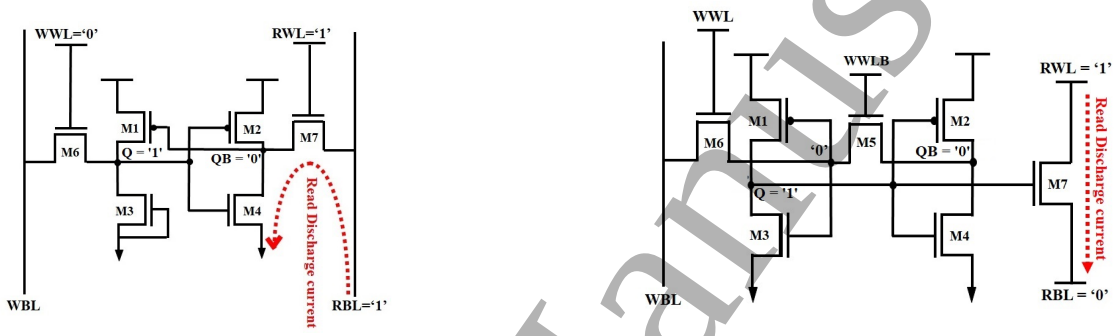
(b)

Fig. 8 Graphical comparison for leakage power at (a) TT corner and (b) all process corners for the different sense amplifier topologies'

Accepted Manuscript

5. PERFROMANCE OF SA-P WITH A SINGLE ENDED SRAM BIT CELLS

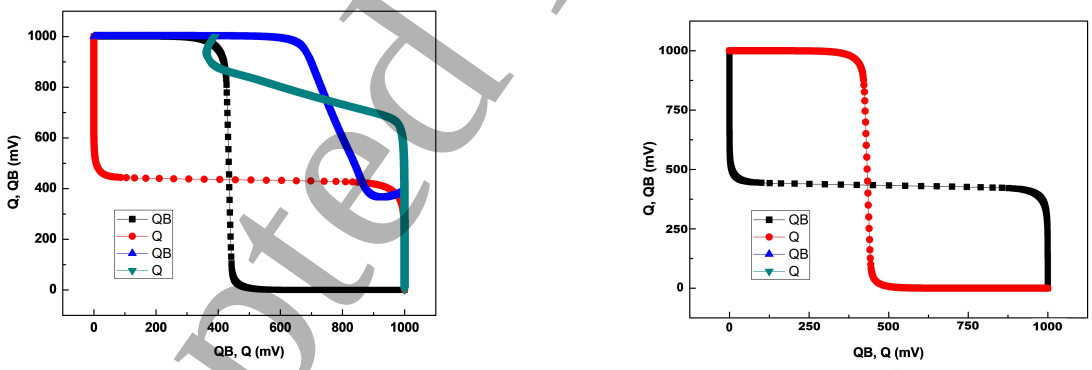
The performance of the proposed SA is validated and analyzed against other pre-existing SA topologies in the previous section. As the proposed SA is designed for a single ended SRAM cell, it is also essential to evaluate its performance in combination with SRAM cells. Thus, performance of the proposed SA is analyzed with two different single ended bit cell – 6T cell and 7T cell. The single ended cell 6T cell was reported by Suarna and Mikie [1] in 2019, while the 7T cell was reported by Rawat and Mittal [12] in 2022. The schematic design highlighting the read discharge current path for 6T and 7T cell are depicted in Fig. 9(a) and (b) respectively. The cells are designed to isolate read-write port for the cell. But the read port design for both the cells is different, the 6T cell is conventional in design, while the 7T cell has read SNM free configuration. The read port for the 6T bit cell is formed by the ACR transistor connected between the QB data node and the read bitline (RBL) signal. The read operation is controlled by the read wordline (RWL) signal. While, the read port for the 7T cell is formed by the M7 transistor, and the control signals RWL and RBL; the data node Q controls the conduction mode of M7. Thus, the read port for the 7T cell is only operational when '1' is stored at Q. The major difference between the read port for 6T and 7T is that the read port for 6T cell allows the read discharge current to pass through the data node for the bit cell (as depicted in Fig. 9(a)), this makes the cell vulnerable to read disturbance.



(a) (b)

Fig. 9 (a) Schematic diagram, (b) Hold butterfly, and (c) read butterfly curve for the single ended 6T SRAM bit cell

Whereas, the read port for the 7T cell is designed to exclude the data storage node from the read discharge current path (depicted in Fig. 9(b)). Due to the read port design of the 7T cell, the variation of bitline voltage due to sensing operation has no impact on its stability. Therefore, the read SNM is as high as the hold SNM and error due to read disturbance is never observed.



(a) (b)

Fig. 10 Butterfly curve for read and hold operation of the single ended (a) 6T and (7T) SRAM bit cell

Both the cells are analyzed for hold and read stability in terms of static noise margin (SNM). The SNM for a bit cell is defined as the maximum noise a bit cell can withstand before an error is registered by the cell [42]. The conventional method to determine the SNM for the bit cell is the butterfly curve [43]. The read and hold butterfly curves obtained for the 6T and 7T cell are represented in Fig. 10(a), and (b) respectively. The SNM for the operation is measured as the side of the largest square that can be accommodated inside the smaller lobe of the butterfly curve [44]. The hold SNM and read SNM values obtained for the 6T cell are 427 and 230 mV respectively. While, for the 7T SRAM bit cell the read and hold butterfly curves are overlapping, therefore resulting in identical values for hold and read SNM values at 420 mV. The same may also be inferred from Fig. 10(b). Therefore, it may be concluded that for a single ended read operation, a read free SNM port is more reliable for the cell. Therefore, SA-P topology will also have better results when integrated with a single ended cell with read SNM free port.

Accepted Manuscript

6. LIMITATIONS OF SA-P

A key factor in the optimal functioning of the proposed SA is that the input signal should be biased around $V_{DD}/2$. This enables the inverter to operate in the metastable state thereby, ensuring the inverter cascaded circuit to act as an SA. The proposed SA utilized the advantage of high gain that may be achieved by biasing the cascaded inverter pair at the meta-stability point. But, the trouble with doing so is that, if due to noise or leakage the biasing for the input varies, the SA-P design may end up yielding an erroneous data output. This bottleneck for SA-P may be resolved by using an EN check for the read operation, i.e. every time the SA output is being read, and there should be a check if the EN signal was high or not. This was also the motivation factor for adding the M6 transistor into the SA-P design. But, for additional safety check for a practical application, an EN flag could be created to ensure, a double check for erroneous read outputs. The proposed SA is designed for single ended topology and when implemented with a single ended read SNM free bit cell, will make a commendable match.

7. CONCLUSION

A single ended voltage based latch type sense amplifier is proposed in this paper for 32 nm feature size. The performance of the newly designed sense amplifier topology is compared and analyzed against pre-existing sense amplifier designs in terms of sensing current, leakage current, delay, impact of process variation and leakage power. The ON current recorded for the proposed sense amplifier is 1.2 uA, which is 0.18, 0.43, and 0.88 times higher than SA-2, SA-5, and SA-6 respectively. While, its OFF current value is 10 nA. The only SA-2 topology that has OFF current lower than SA-P is SA-3 at 9 nA. Thus, it may be concluded that there is a high degree of isolation between the ON and OFF current for SA-P. A fairly low value for OFF current also suggests that the leakage power consumption for the proposed topology is low; this is an essential performance parameter for circuits designed at lower technology node. Also, the operational delay for SA-P is minimal at 0.77 ns, while, SA-1, SA-2, SA-5, and SA-6 are 3.9, 2.8, 3.7, and 0.3 times slower than SA-P. Thereby, deeming its operation faster than others. Also, the aforementioned performance are strengthened by the low degree of variation in performance for the design with global variation. Thereby, validating the reliability of the design.

Statements and Declarations
Funding Not Applicable
Conflicts of interest/Competing interests Not Applicable
Availability of data and material All data generated or analyzed during this study are included in this published article
Code availability Not Applicable

REFERENCE

[1] Surana N and Mekie J 2019 Energy Efficient Single-Ended 6-T SRAM for Multimedia Applications *IEEE Transactions on Circuits and Systems II: Express Briefs* 66(6) 1023–1027.
[2] Lai YC and Huang SY 2008 A resilient and Power-Efficient Automatic-Power Down Sense Amplifier for SRAM Design *IEEE Transactions on circuits and Systems II: Express briefs* 55(10) 1031-1035.
[3] Divya, Mittal P, Rawat B and Kumar B 2022 Design and Performance Analysis of High-Performance Low Power Voltage Mode Sense Amplifier for Static RAM *International Journal of Advances in Electrical and Electronic Engineering* 19(2) 145-154.
[4] Zhang K, Hose K, De V and Senyk B 2020 The scaling of data sensing schemes for high speed cache design in sub-0.18 μ/m technologies *Symposium VLSI Circuits Digital Technical Papers* USA. 226–227.
[5] Divya and Mittal P 2022 A low-power high-performance voltage sense amplifier for static RAM and comparison with existing current/voltage sense amplifiers *International Journal of Information Technology* 14 323-331.
[6] Houle R 2007 Simple statistical analysis techniques to determine minimum sense amp set times *Proceedings IEEE Custom Integration Circuits Conference* 37–40.
[7] Ayush, Mittal P and Rohilla R 2022 Comparative Analysis of Current Sense Amplifiers Architectures for SRAM at 45 nm Technology Node *International Conference on Advances in Data-driven Computing and Intelligent Systems* BITS Pilani, India, 23-25 Sep.
[8] Seevinck E, Beer PJV, and Ontrop H 1991 Current-mode techniques for high-speed VLSI circuits with application to current SA for CMOS SRAM's *IEEE Journal Solid-State Circuits* 26(5) 525–536.
[9] Singh R and Baht N 2004 An offset compensation technique for latch type sense amplifiers in high-speed low-power SRAMs *IEEE Transactions VLSI System Transaction Briefs* 12(6) 652–657.
[10] Sarpeshkar R, Wyatt JL, Lu NC and Gerber PD 1991 Mismatch sensitivity of a simultaneously latched CMOS sense amplifier *IEEE Journal Solid-State Circuits* 26(10) 1413–1422.
[11] Wicht B, Nirschl T and Schmitt-Landsiedel D 2004 Yield and speed optimization of a latch-type voltage sense amplifier *IEEE Journal Solid-State Circuits* 39(7) 1148–1158.
[12] Yang BD and Kim LS 2005 A low-power SRAM using hierarchical bit line and local sense amplifier *IEEE Journal Solid-State Circuits* 40(6) 1366–1376.
[13] Shin JL, Petrick B, Singh M and Leon A 2005 Design and implementation of an embedded 512-KB level-2 cache subsystem *IEEE Journal Solid-State Circuit* 40(9) 1815–1820.
[14] Dounavi HM, Sfikas Y, Tsiatouhas Y 2009 Periodic Monitoring of BTI Induced Aging in SRAM Sense Amplifiers *IEEE Transaction On Device And Materials Reliability* 19(1) 64-72.

Accepted Manuscript

[15] Rawat B and Mittal P 2022 A comprehensive analysis of different 7T SRAM topologies to design a 1R1W bit interleaving enabled and half select free cell for 32 nm technology node *Proceedings of the Royal Society A: Mathematical, Physical and Engineering Sciences* 478 20210745-20210771.

[16] Agbo I, Taouil M, Kraak D, Hamdioui S, Ku¨kner H, Weckx P, Raghavan P and Catthoor F 2017 Integral impact of BTI, PVT variation, and workload on SRAM sense amplifier *IEEE Transaction Very Large Scale Integration (VLSI) System* 25(4) 1444–1454.

[17] Kraak D, Taouil M, Agbo I, Hamdioui S, Weckx P, Cosemans S, and Catthoor F 2017 Impact and mitigation of sense amplifier aging degradation using realistic workloads *IEEE Transaction Very Large Scale Integration (VLSI) System* 25(12) 3464–3472.

[18] Kraak D, Agbo I, Taouil M, Weckx P, Cosemans S, Catthoor F, Hamdioui S and Dehaene W 2017 Mitigation of sense amplifier degradation using input switching *Proceedings Design Automation Test Europe Conference (DATE)* 858–863.

[19] Jeong H, Kim T, Son T, Kim G and Jung SO 2014 Trip-Point Bit-Line Precharge Sensing Scheme for Single-Ended SRAM *IEEE Transactions on Very Large Scale Integration (VLSI) Systems* 23(7) 1370-1374.

[20] Wang Y, Chen J, Pu Y and Ha Y 2020 Energy-efficient arbitrary precision multi-bit multiplication with bi-serial in/near memory computing *Proceedings IEEE International Symposium Circuits System (ISCAS)* 1–5.

[21] Lin Z, Zhan H, Li X, Peng C, Lu W, Wu X and Chen J 2020 In-memory computing with double word lines and three read ports for four operands *IEEE Transaction Very Large Scale Integration (VLSI) System* 28(5) 1316–1320.

[22] Yin S, Jiang Z, Seo JS, and Seok M 2020 XNOR-SRAM: In-memory computing SRAM macro for binary/ternary deep neural networks *IEEE Journal Solid-State Circuits* 55(6) 1733–1743.

[23] Dong Q, Jeloka S, Saligane M, Kim Y, Kawaminami M, Harada A, Miyoshi S, Blaauw D and Sylvester D 2018 A 4+ 2T SRAM for searching and in-memory computing With 0.3-V VDDmin *IEEE Journal Solid-State Circuits* 53(4) 1006–1015.

[24] Reniwal BS, Bhatia P and Vishvakarma SK 2017 Design and investigation of variability aware sense amplifier for low power, high speed SRAM *Microelectronics Journal* 59 22–32.

[25] Kulkarni JP, Keane J, Koo KH, Nalam S, Guo Z, Karl E and Zhang 2017 5.6 Mb/mm2 1R1W 8T SRAM arrays operating down to 560 mV utilizing small-signal sensing with charge shared bitline and asymmetric sense amplifier in 14 nm FinFET CMOS technology *IEEE Journal Solid-State Circuits* 52(1) 229–239.

[26] Agrawal A, Jaiswal A, Lee C and Roy K 2018 X-SRAM: Enabling in-memory Boolean computations in CMOS static random access memories *IEEE Transaction Circuits System I Regular Papers* 65(12) 4219–4232.

[27] Chen J, Zhao W, Wang Y and Ha Y 2021 Analysis and Design of Reconfigurable Sense Amplifier for Compute SRAM With High-Speed Compute and Normal Read Access *IEEE Transaction on Circuits and Systems II: Express Briefs* 68(12) 3503-3507.

[28] Pileggi L, Keskin G, Xin L, Ken M and Proesel J 2008 Mismatch analysis and statistical design at 65 nm and below *Custom Integrated Circuits Conference* 9-12.

[29] Seki T, Itoh E, Furukawa C, Maeno I, Ozawa T, Sano H and Suzuki N 1993 A 6-ns 1-Mb CMOS SRAM with latched sense amplifier *IEEE Journal Solid-State Circuits* 28, 478-483.

[30] Wicht B, Nirschl T and Landsiedel DS 2004 Yield and speed optimization of a latch-type voltage sense amplifier. *IEEE Journal Solid-State Circuits* 39 1148-58.

[31] Hill JM and Lachman J 2001 A 900 MHz 2.25 MB cache with on-chip CPU—now in Cu SOI. *IEEE International Solid-State Circuits Conference Digital Technical Papers*, 176–177, 444.

[32] Blalock TN and Jaeger RC 1991 A High Speed Clamped Bit-line Current Mode Sense Amplifier *IEEE Journal of Solid-State Circuits* 26(4) 542-548.

[33] Zhu J, Bai N and Wu J 2013 A Review of Sense Amplifiers for Static Random Access Memory *IETE Technical Review* 30(1) 72-81.

[34] Kobayashi T, Nogami K, Shirotori T and Fujimoto Y 1993 A current controlled latch sense amplifier and a static power-saving input buffer for low-power architecture *IEEE Journal on. Solid-State Circuits* 28(4) 523–527.

[35] Wicht B, Nirschl T, Landsiedel DS, 2003 A yield-optimized latch-type SRAM sense amplifier. Proceedings of. 29th European Solid-State Circuits Conference 409-412.

[36] Nikolic VG, Oklobdzija V, Stojanovic J, Wenyan C, Shing JK and Leung MKT 2000 Improved sense-amplifier-based flip-flop: Design and measurements *IEEE Journal on Solid-State Circuits* 35 876-884.

[37] Wong KL and Yang CK 2004 Offset compensation in comparators with minimum input-referred supply noise IEEE Journal on Solid-State Circuits 39 837-840.

[38] Sasaki K, Ishibashi K, Yamanaka T, Shimohigashi K, Moriwaki N and Honjo S 1990 A 23 ns 4 Mb CMOS SRAM with 0.5 uA standby current," in IEEE International Solid-State Circuits Conference 130-131.

[39] Patel D and Sachdev M 2018 0.23-V Sample-Boost-Latch Based Offset Tolerant Sense Amplifier *IEEE Solid State Circuit Letters* 1(1), 6-9

[40] Ohbayashi S, Yabuuchi M, Nii K, Tsukamoto Y, Imaoka S, Oda Y, Yoshihara T, Igarashi M, Takeuchi M, Kawashima H, Yamaguchi Y, Tsukamoto K, Inuishi M, Makino H, Ishibashi K and Shinohara H 2007 A 65-nm SOC embedded 6 T-SRAM designed for manufacturability with read and write operation stabilizing circuits *IEEE Journal Solid-State Circuits* 42(4) 820–829.

[41] Rawat B and Mittal P 2021 A 32 nm single ended single port 7T SRAM for low power utilization *Semiconductor Science and Technology* 36(9), 095006-095022.

[42] Singh J, Mohanty SP and Pradhan DK, 2013, Robust SRAM designs and analysis. New York: Springer.

[43] Rawat B and Mittal P 2021 Single Bit Line Accessed High Performance Ultra Low Voltage operating 7-T SRAM Cell with Improved Read Stability *International Journal of circuit theory and applications* 49(5) 1435-1449.

[44] Rawat B and Mittal P A reliable and temperature variation tolerant 7T SRAM cell with single bitline configuration for low voltage application *Circuits, Systems, and Signal Processing* 41 2779-2801.

Accepted Manuscript

Physica Scripta

ACCEPTED MANUSCRIPT

A non-invasive optical method for anaemia detection

To cite this article before publication: Paritosh Chamola *et al* 2023 *Phys. Scr.* in press https://doi.org/10.1088/1402-4896/acd5b8

Manuscript version: Accepted Manuscript

Accepted Manuscript is "the version of the article accepted for publication including all changes made as a result of the peer review process, and which may also include the addition to the article by IOP Publishing of a header, an article ID, a cover sheet and/or an 'Accepted Manuscript' watermark, but excluding any other editing, typesetting or other changes made by IOP Publishing and/or its licensors"

This Accepted Manuscript is **© 2023 IOP Publishing Ltd**.

During the embargo period (the 12 month period from the publication of the Version of Record of this article), the Accepted Manuscript is fully protected by copyright and cannot be reused or reposted elsewhere.

As the Version of Record of this article is going to be / has been published on a subscription basis, this Accepted Manuscript will be available for reuse under a CC BY-NC-ND 3.0 licence after the 12 month embargo period.

After the embargo period, everyone is permitted to use copy and redistribute this article for non-commercial purposes only, provided that they adhere to all the terms of the licence https://creativecommons.org/licences/by-nc-nd/3.0

Although reasonable endeavours have been taken to obtain all necessary permissions from third parties to include their copyrighted content within this article, their full citation and copyright line may not be present in this Accepted Manuscript version. Before using any content from this article, please refer to the Version of Record on IOPscience once published for full citation and copyright details, as permissions may be required. All third party content is fully copyright protected, unless specifically stated otherwise in the figure caption in the Version of Record.

View the article online for updates and enhancements.

This content was downloaded from IP address 14.139.251.98 on 18/05/2023 at 06:06

A Non-invasive Optical Method for Anaemia Detection

Paritosh Chamola[1, a], Poornima Mittal[1, b, *]

[1]*Department of Electronics and Communication Engineering, Delhi Technological University, Delhi, 110042, India*

E-mail address: [a]paritoshchamola@gmail.com, [b]poornimamittal@dtu.ac.in

*Corresponding Author: poornimamittal@dtu.ac.in

Abstract

The latest non-invasive biomedical electronic sensors are capable of providing continuous reliable information, for instance oxygenation level of blood, level of glucose etc. These biomedical sensors are in general based on the electro-chemical or spectral properties of the substances. The absorption of blood in infrared and visible range is prominently determined by haemoglobin. The coefficient of absorption for blood is different at different wavelengths. This optical absorption characteristic of the blood yields the vital information on the composition of the blood. Haemoglobin is primarily used to measure the status of anaemia, in developing countries like India and other African countries numerous people with greater health needs don't have access to proper diagnostic facilities. Therefore, an introduction of portable, low cost and non-invasive Haemoglobin detector will give a vast opportunity for screening the population suffering with anaemia. The present article purposes a non-invasive method of haemoglobin detection comprising of an organic photovoltaic cell and three LED's sources i.e., blue, green and red which are used with their respective radiation spectral range of 450-495 nm, 495-570 nm and 620-750 nm to illuminate an area of the skin on finger, this transmitted light after interacting with tissues is detected by an arrangement of Coumarin 30 : C_{60}/NN'-QA/ZnPc active layer based organic solar cell. Thus, the approach provide in this article presents a simple, biocompatible and flexible means for assessing blood haemoglobin level by utilizing an multi spectral optical processing method. The method developed herein could further be integrated to wearable electronic devices.

Keywords: Organic solar cell, Biomedical, Anaemia, Haemoglobin, Photovoltaic

1. Introduction

The scattering of light is in general used in the domain of soft, condensed, biological material applications. In the domain of biomedical applications scattering of light presents promising aspects of non-invasive monitoring and imaging of various medical conditions [1]. Blood is an important and attractive fluid of biological nature which could be used for applications requiring scattering of sunlight. The RBCs remain the main constituent of the human blood and is almost 45% of the blood by volume. These RBCs contain an extremely dense solution of haemoglobin. This haemoglobin is the primary component for the absorption and scattering of the blue, green and UV spectrum of visible light spectrum [2]. The different techniques of light scattering have been already utilized for the measurement of the various RBC properties [3-6]. For instance, the light scattering has been utilised for the measurement of changes in the shape of the RBCs in case of sickle cell anaemia [6], malaria [3], monitoring fluctuations in the membrane of the RBCs [3, 4] for studying the dynamics and metabolic characteristic of the RBCs [7, 8]. Anaemia is a grave complication indicating deficiency of iron and can lead to death. Much (>50%) of the childbearing women in economically developing nations suffers from anaemia. Further, In India, anaemia is a prevalent health problem and according to WHO, 52% population in India is anaemic.

The non-invasive technologies which are capable of monitoring patients health continuously and with reliability are expected to considerably improve the quality of life and will also create new and innovative opportunities in medicine. The major benefits associated with the use of non-invasive technologies are simplified medical practices, increased patient comfort, cost effectiveness, immediate and reliable measurement of information and monitoring, environment friendly techniques as there are no disposable

Accepted Manuscript

biohazardous waste produced. The, frequent monitoring made possible by the non-invasive character and reliability has a potential to revolutionize the treatment practises, especially in case of chronic disease. A perfect example for continuous measuring and monitoring could be found in insulin delivery and glucose monitoring which have saved and improved millions of lives worldwide in last ten years [9-11].

The absorption by blood in IR and visible region is dominated by various haemoglobin derivatives [12, 13]. The haemoglobin is the primary constituent of human red blood cells. Further, the presence of haemoglobin in blood is an extremely important parameter to evaluate the medical condition, physiological status and oxygen transportation capability of any individual which is used to diagnose the condition of anaemia. Anaemia presents a condition of low haemoglobin level. The existing invasive systems are capable of measuring haemoglobin [14] via spectrophotometric methods. The present invasive methods also involve high cost and huge size specifically designed and optimized laboratory optical equipment which are not of portable nature.

Presently, the used invasive methods for determining the haemoglobin, blood sample is taken from patient and then analysed. This method causes patient discomfort while collecting the blood sample moreover, in this method there is a significant delay in-between the sample collection and sample analysis thus, not allowing a real time or continues monitoring of the patient. In comparison to the present method of measuring haemoglobin a non-invasive method presented in this article allows for pain free, immediate and reliable measurement without any infection risk. Further, a low-cost and portable but invasive method of haemoglobin detection known as Haemoglobin colour scale method is also used wherein, the patient's blood is matched with the scale, but this particular method suffers from high variability and inaccuracy.

The solar cell made with semiconductors of organic nature are an attractive alternate to their inorganic counterparts primarily due to their flexibility and low cost of fabrication. The organic semiconductor materials have been reported with the photoconductive properties. P. Peumans *et al.* in 2000 demonstrated a high-speed multilayer photodetector [15]. A transparent photodiode for detecting polarized light is reported by H. Tanaka *et al.* in 2006 [16]. In this article a portable device is presented to detect the deficiency of haemoglobin in blood by a non-invasive, easy to use, environment friendly and reliable method.

The main rationale for the use of our proposed method is that it can increase testing at low cost by providing on the spot results without any requirement of large setup, further as this method does not require any blood to be drawn out from the body and is completely reliant on the optical properties of the haemoglobin and that of the organic solar cell it is accurate, without any risk of infection and is highly reliable as the physical conditions cannot tamper with it. The method is also environment friendly as it creates no biohazardous waste i.e., no chemical reagents or syringes are required and is also reusable.

2. Device design requirements

To address the vital need to increase access to health services in underdeveloped areas the practical features which are essentially required in a haemoglobin detection device for its clinical utility are:

- It should be portable, reliable and accurate with low margin of error, replaceable and inexpensive.
- Should not require biohazardous chemicals and should be low or free on maintenance.
- Easy to use, especially in remote and resource poor settings where laboratory facilities aren't available.
- Allow anaemia detection irrespective of patient gender, age, pregnancy etc.

Thus, objective of this research article is to design and develop an inexpensive, portable, accurate, easy to use and environment friendly haemoglobin detection device by utilizing the optical properties to the haemoglobin pigment to determine the health of the RBCs and to diagnose diseases such as anaemia, sickle cell anaemia, low iron content, malaria, thalassemia.

Colour can be defined as the perception of the incident sunlight on the retina of the human eye. The visible spectrum extends from violet colour at 380 nm to the colour red at 750 nm as shown in Table I. In visible

Accepted Manuscript

spectrum different components of colour display dissimilar ranges of reflectance. The wavelength range for colour red in visible spectrum exists from 620-740 nm.

Table I. Spectrum of the visible light

Colour	Wavelength (nm)
Red	620 - 750
Orange	590 – 620
Yellow	570 – 590
Green	495 – 570
Blue	450 - 495
Violet	380 - 450

The Haemoglobin pigment remains one of the primary chromophores of the skin which is prominent in red blood cells (RBCs). The Haemoglobin also comprises of optical characteristics [17-21] which when methodologically used can detect anaemia. The reflection of wavelengths at and above 600 nm by the haemoglobin pigment (oxy-haemoglobin) validates and explain the red colour appearance of the red blood cells under visible spectrum [22]. Hence, from this information about haemoglobin it can be hypothesized that the organic photodiodes sensitive to the colours could extract the information about the health of any patient's blood sample.

3. Basic method and organic solar cell architecture

The simulations which are based on computer are proved to be an important and effective instrument to examine the photovoltaic cells and reproduce their results under the given environmental conditions. These simulations are crucial as they help to produce the output results of a photovoltaic device exactly and assists in estimating the device performance. Further, these simulations aid in determining the optimum conditions for enhanced performance and also provide a detail account of the photovoltaic cell performance. This research article utilises the industry standard Silvaco Atlas 2D numerical device simulation software. The Silvaco Atlas accuracy in simulation results arise by combination of multiple models of propagation and accurate ray tracing. Moreover, the Silvaco software have both the integrated spectrum AM 1.5 and AM 1.0 which corresponding to real outdoor solar conditions. The Silvaco also permits the user to define own materials. The Silvaco Atlas being an industry level standard device simulator, the simulators based on analytical models are established methods to envisage the performance of a device before it is realized physically. The Silvaco Atlas software utilizes the basic mathematical charge transport equations so as to comprehend the performance and behaviour of the photovoltaic device.

In a solar cell the process of photovoltaic carrier generation begins instantly whenever the device is illum innated by solar spectrum. Generally, the solar spectrum is utilised for modelling the optical propagation for calculating performance of the solar cell. The spectrums in Silvaco Atlas device simulator are capable of representing the real and practical environmental conditions under the natural sunlight. The Table II presents the simulation parameters used for photovoltaic solar cell simulation performed in this article [23-26].

Table II. Simulation parameters for the solar cell.

Parameter (Unit)	Coumarin 30 : C_{60}	NN'-QA	ZnPc
Hole mobility ($cm^2 V^{-1} s^{-1}$)	1.5×10^{-4}	1×10^{-3}	1.619×10^{-6}
Electron mobility ($cm^2 V^{-1} s^{-1}$)	1×10^{-5}	1×10^{-4}	1×10^{-7}
Bandgap (eV)	2.2	2.1	1.97
Dielectric permittivity	3.2	4.4	5.4
Electron affinity (eV)	2.6	3.5	3.1

Accepted Manuscript

In this article a vertically stacked Coumarin 30 : C_{60}/NN'-QA/ZnPc based three-layer organic semiconductor solar cell sensitive individually to red, green and blue light is simulated via Silvaco Atlas 2D device simulator [27-29]. This organic solar cell acts as a photodetector detecting the light transmitted through the skin tissues and hence is an extremely important component in the purposed method. Each layer of the organic solar cell presented a satisfactory spectral selectivity. This spectral selectivity is utilised herein for the application of organic photovoltaic cell as a Haemoglobin detector. The Fig. 1 presents the architecture of the multilayer organic solar cell used.

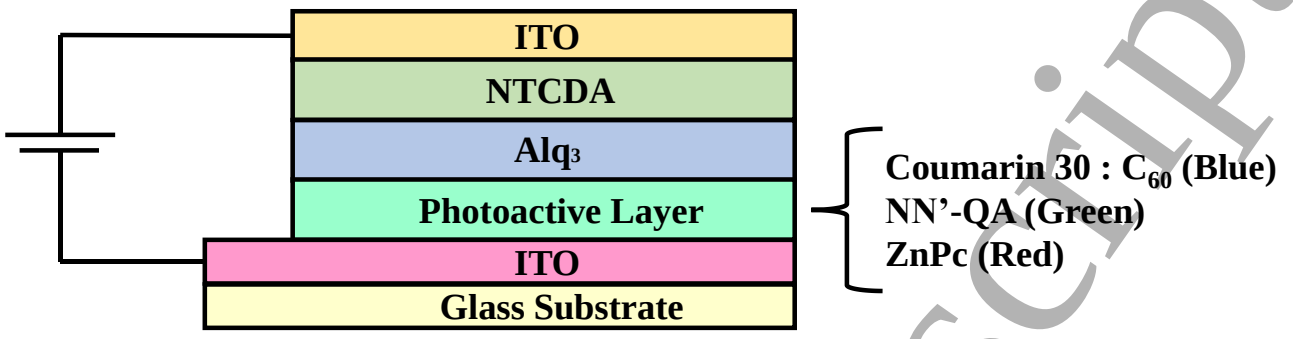


Fig. 1. Architecture of simulated photovoltaic cell.

When incoming light is incident on top of organic solar cell the blue light component is absorbed by Coumarin 30 : C_{60} layer of the photoactive layer. Thereafter, the green and red light components of the incident light are absorbed by the middle NN'-dimethylquinacridone (NN'-QA) and bottom-last Zinc phthalocyanine (ZnPc) layer of the solar cell respectively. The mentioned materials are semiconductors of organic in nature. The Table III summarises the complete structure of the solar cell utilised.

Table III. Thickness of the constituent layers of the simulated solar cell.

Material Layers	Thickness
Glass	700 μm
ITO	0.15 μm
Coumarin 30 : C_{60}	0.08 μm
NN'-QA	0.2 μm
ZnPc	0.25 μm
Alq_3	0.05 μm
NTCDA	0.3 μm
ITO	0.02 μm

The photosensitive part for the blue colour is composed of a Coumarin 30 and Fullerene (Coumarin 30 : C_{60}). The Coumarin-Fullerene (60) material are very attractive because of their range of absorption and photostability [30-34]. The Coumarin and its derivatives are generally used in signalling applications in the sophisticated sensors, photophysical structures [35, 36] and biosensors [37]. For, the green colour the photosensitive part contains a layer of N,N'-dimethylquinacridone (NN'-QA). The electron affinity for NN'-QA is reported to be at 3.5 eV. Similarly, Zinc Phthalocyanine (ZnPc) ($C_{32}H_{16}N_8Zn$) is used as a photosensitive part for the red colour due to its easy synthesis and non-toxic character it remains as a propitious contender for photovoltaic cell applications. Phthalocyanine (Pc) is a self-organised crystalline liquid with a bandgap of 1.97 eV and is an active part in all the organic photovoltaic cells. It is also chemically and physically very durable [38]. The various kinds of Phthalocyanines are used in variety of device application including photovoltaic cells [39, 40] and medical photodynamic healing therapy [41]. The layer of Alq_3 (tris(8-hydroxyquinoline) aluminum) make available the transportation of electrons possible. The deposited layer of NTCDA (naphthalene tetracarboxylic anhydride) over Alq_3 layer helps in preventing electrical short [42] caused because of the counter ITO electrode layer.

4. Validation of organic solar cell constituent materials

Accepted Manuscript

The device simulators have demonstrated their important role in picturing the concept and optimising the performance of devices before they are actually physically realised. In this section individual structures of the multilayer photovoltaic devices are simulated and their current-voltage measurement plots obtained with Sivaco Atlas device simulator are compared with the experimentally obtained and reported data [43].

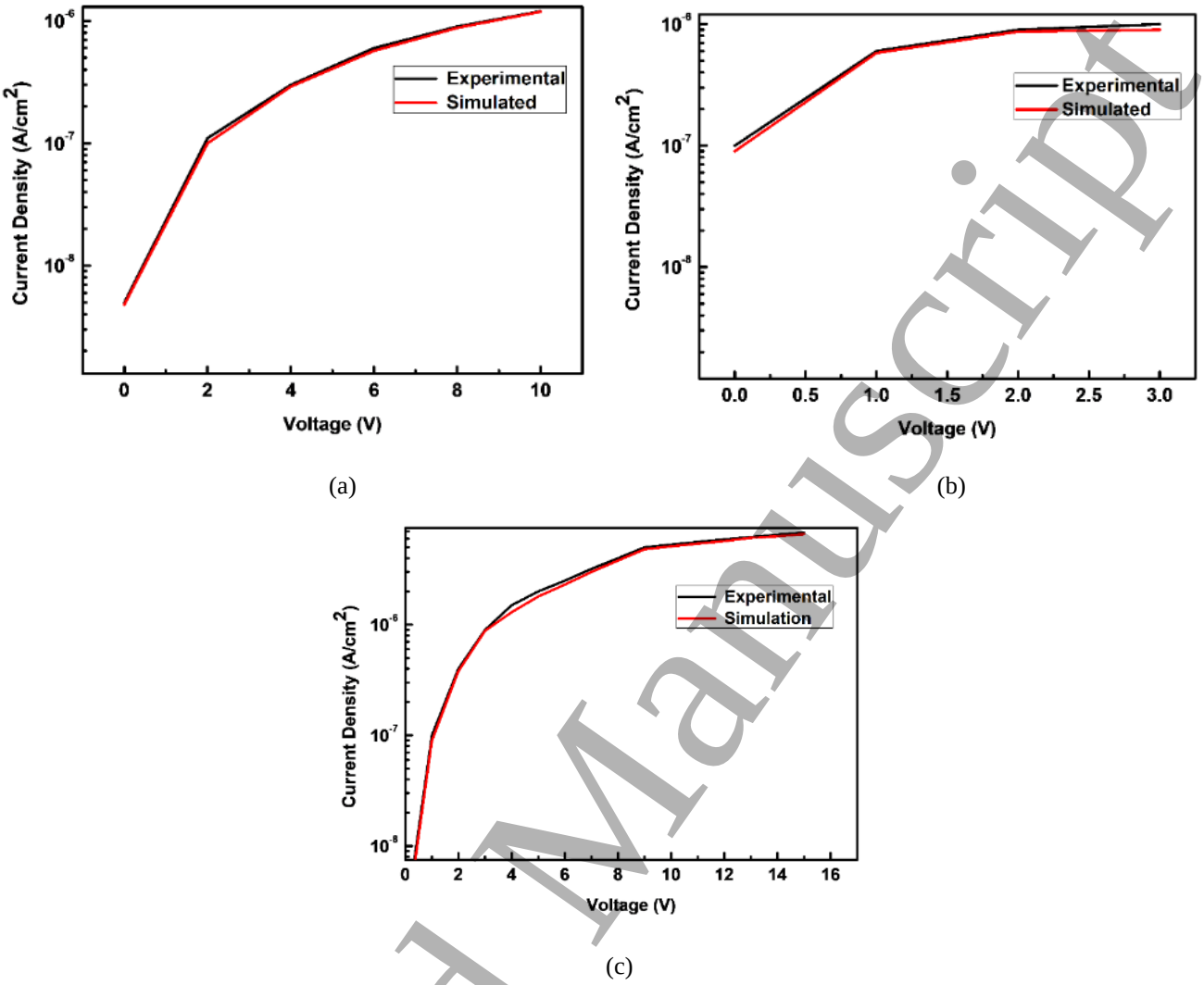


Fig. 2. The current voltage characteristic plots of (a) Coumarin 30 : C_{60} (b) NN'-QA (c) ZnPc organic photovoltaic cell (black colour curve presents the experimental photo-current and red colour curve presents simulated photo-current).

The Fig. 2 presents photo-current characteristic of the blue, green and red colour photosensitive organic solar cells. In all the three plots photocurrent density rises with the increase in voltage applied. The close agreement between the simulated (presented with the red colour curve) and experimentally reported (presented with black colour curve) data allow us for the further analysis of purposed organic photovoltaic device structure for design, development and application in non-invasive haemoglobin detection.

5. Optical properties of haemoglobin and organic solar cell

There are various reported articles on the absorption characteristics of the haemoglobin [44-47]. The absorption spectrum of oxy-haemoglobin is represented in Fig. 3 [48]. The human blood's optical characteristics are prominently determined by optical property of the haemoglobin. The coefficients of absorption of haemoglobin are presented in the Fig. 3 for oxygenated haemoglobin. Further from Fig. 3 it can be observed that for oxygenated haemoglobin the peak absorptions are present at 274, 344, 415, 542, and 577 nm. Oxygenated haemoglobin or oxyhaemoglobin is oxygen bound to haemoglobin present in the RBCs. One molecule of haemoglobin pigment binds to the four molecules of oxygen to form oxyhaemoglobin. It's the primary function of oxyhaemoglobin to transport oxygen to different tissues of the body and hence is an extremely important human physiological parameter. In condition of anaemia the oxygen affinity of haemoglobin pigment reduced i.e., anaemia compromises the oxygen transport machinery of the patient's

Accepted Manuscript

body. This leads to the low oxygen level in RBCs which creates condition of hypoxia in the tissues which could be life threatening. Therefore, in this article the method purposed to detect anaemia is adapted in accordance with the optical properties of oxyhaemoglobin, the method utilises the optical properties of haemoglobin primarily the absorption spectrum to detect condition of anaemia.

The haemoglobin not combined to oxygen is referred as deoxygenated haemoglobin. As oxyhaemoglobin is the haemoglobin combined with the oxygen and anaemia presents a condition of low oxygen combined to haemoglobin the detection of oxyhaemoglobin in blood indicates an anaemia free patient. Therefore, the proposed method is based on detecting oxyhaemoglobin will furnish the accurate diagnosis. Moreover, as this method detects anaemia based on oxyhaemoglobin i.e., the organic solar cell absorbs the transmitted wavelengths and produce a photosensitivity corresponding to an anaemia free patient. Any major deviation in the value of photosensitivity in itself will mean the patient to be anaemic i.e., lack of oxygen bounded to the haemoglobin or presence/detection of deoxyhaemoglobin (purple-blue colour).

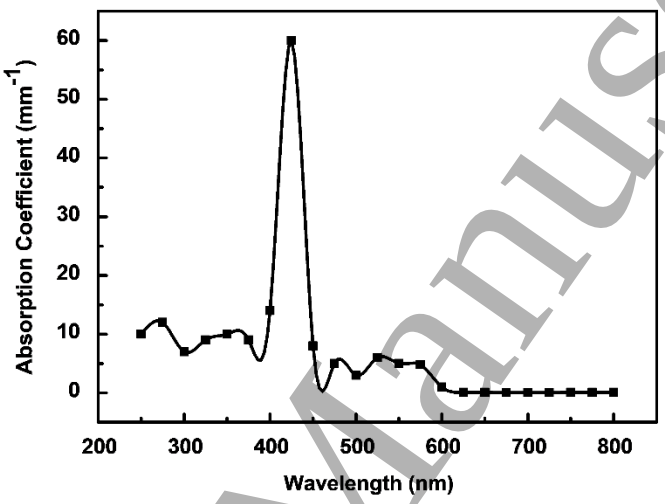
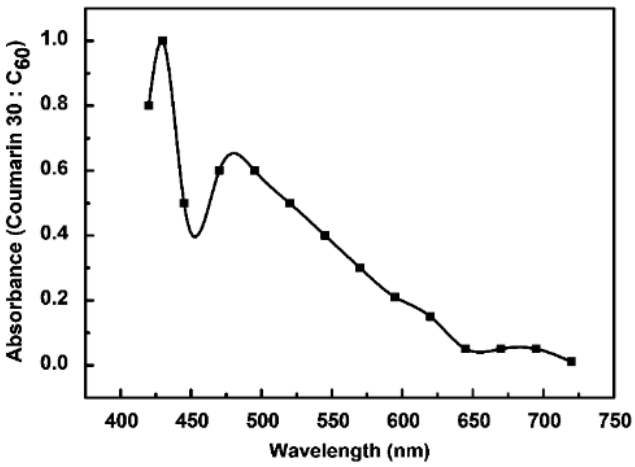


Fig. 3. Absorption coefficient of oxygenated haemoglobin.

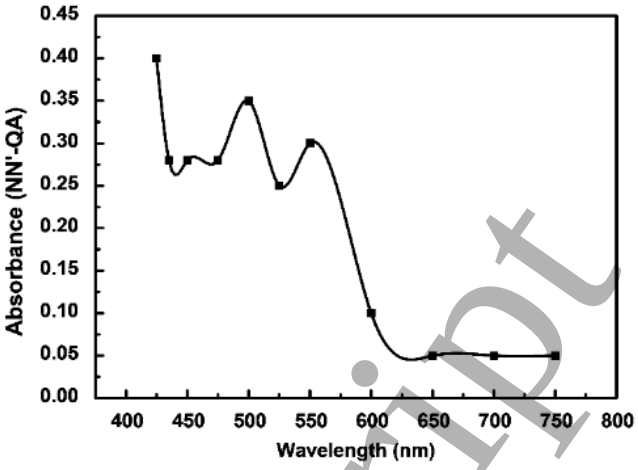
Fig. 3. presents the plot of absorption coefficient as a function of wavelength. From the plot it can be noticed that absorption coefficients are of high magnitude in the wavelength range of 250 to 600 nm, with a spike in magnitude around 425 nm, and this magnitude of absorption coefficients start to decrease from 600 nm and remains almost constant in the wavelength range of 600 to 800 nm. Thus, it can be inferred from the plot presented in Fig. 3. that the oxygenated haemoglobin has higher light absorption for wavelengths below 600 nm and lower absorption for wavelength ranges above 600 nm. As presented in Table I the wavelength range for blue colour is from 425 - 495 nm, for green colour it's from 500 - 540 and for red colour it's from 615 - 700 nm. Thus, from the Fig. 3. it can be concluded that oxygenated Haemoglobin absorbs the blue and green colour wavelength spectrum efficiently and let pass or transmits the red colour wavelengths.

The Haemoglobin, capable of absorbing wavelength ranges from 250 nm to ~ 600 nm absorbs Soret band (as observed from the Fig. 3 between 390 nm to 410 nm) and transmits (does not absorb) wavelength ranges beyond ~600 nm i.e., wavelengths corresponding to red colour in visible spectrum. Our proposed method is based on the detection of these wavelengths (620 nm to 750 nm) transmitted through the skin/blood by organic solar cell. Therefore, though Soret band (390-410 nm) is an important peak to detect heme, the iron containing molecule which combines with globin proteins to form haemoglobin. The wavelengths corresponding to the Soret band (390 nm to 410 nm) would not be transmitted through the skin/blood but will be absorbed by the haemoglobin present in RBCs. Hence, there will be no detection on the organic solar cell. Thus, inclusion or focusing on the Soret band in our method will not yield the required results.

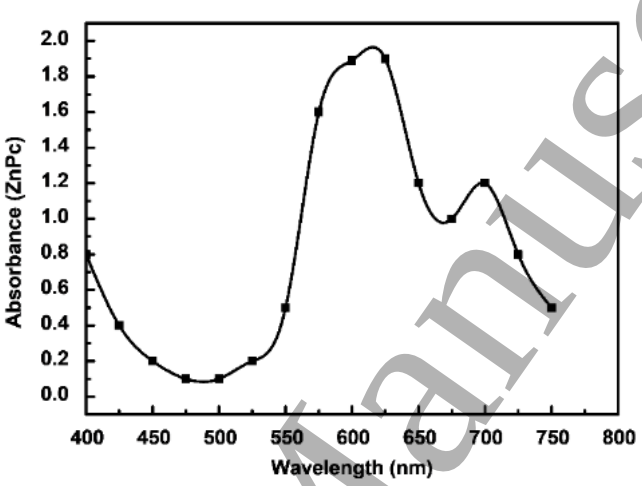
Accepted Manuscript



(a)



(b)



(c)

Fig. 4. (a) Coumarin 30 : C_{60} (b) NN'-QA (c) ZnPc photodetectors individual (single structure) optical absorption spectrum in the wavelength range of 400 to 750 nm. The Coumarin 30 : C_{60}, NN'-QA and ZnPc are blue, green and red colour photodetectors respectively.

The Fig. 4 (a) represents the optical absorption spectrum of blue (Coumarin 30 : C_{60}), green (NN'-QA) and red (ZnPc) colour photodetectors. From the Fig. 4 (a) it can be noticed that blue colour photodetector has absorption spikes around 420 nm and 540 nm. For green colour photodetector the absorption spikes are at 500 and 540 nm. Therefore, it can also be observed from Fig. 4 (a) and 4 (b) that both of the photodetectors blue and green transmitted the wavelengths longer than 600 nm i.e., wavelengths corresponding to the red colour. Similarly, as observed from Fig. 4 (c) the red colour photodetector has the absorption spikes at 610 nm and 700 nm. The observations from Fig. 4 further establishes and consolidate the fact that Coumarin 30 : C_{60}, NN'-QA and ZnPc absorb the blue, green and red colour lights respectively.

6. Sensing Concept

The thought or idea of using colour of haemoglobin for anaemia detection goes as back as to 1900. Tallquist proved the theory that blood colour could indicate condition of anaemia reliably. In the method the scale includes a card with six colour shades on it representing haemoglobin levels. The blood sample of the patient after pricking is matched immediately against the one of the prearranged shades of red colour on the scale, indicating if the patient is anaemic or not. Modern technology further perfected this method [49-52]. Apart from being an invasive technique the primary sources of error in utilisation of these currently available Haemoglobin colour scale are (i) colours of produced scales vary between different manufactures (ii) absorbent paper also show variation and are somewhat unusable due to: uneven spreading of blood leading to colour dilution, also due to excessive blood absorption the paper becomes damp and translucent (iii) proper natural or artificial lighting is required. The, purposed method in this article also uses the similar idea of using

Accepted Manuscript

the red colour of blood's haemoglobin to detect the anaemia which overcomes the limitation of haemoglobin colour scale method and is also non-invasive.

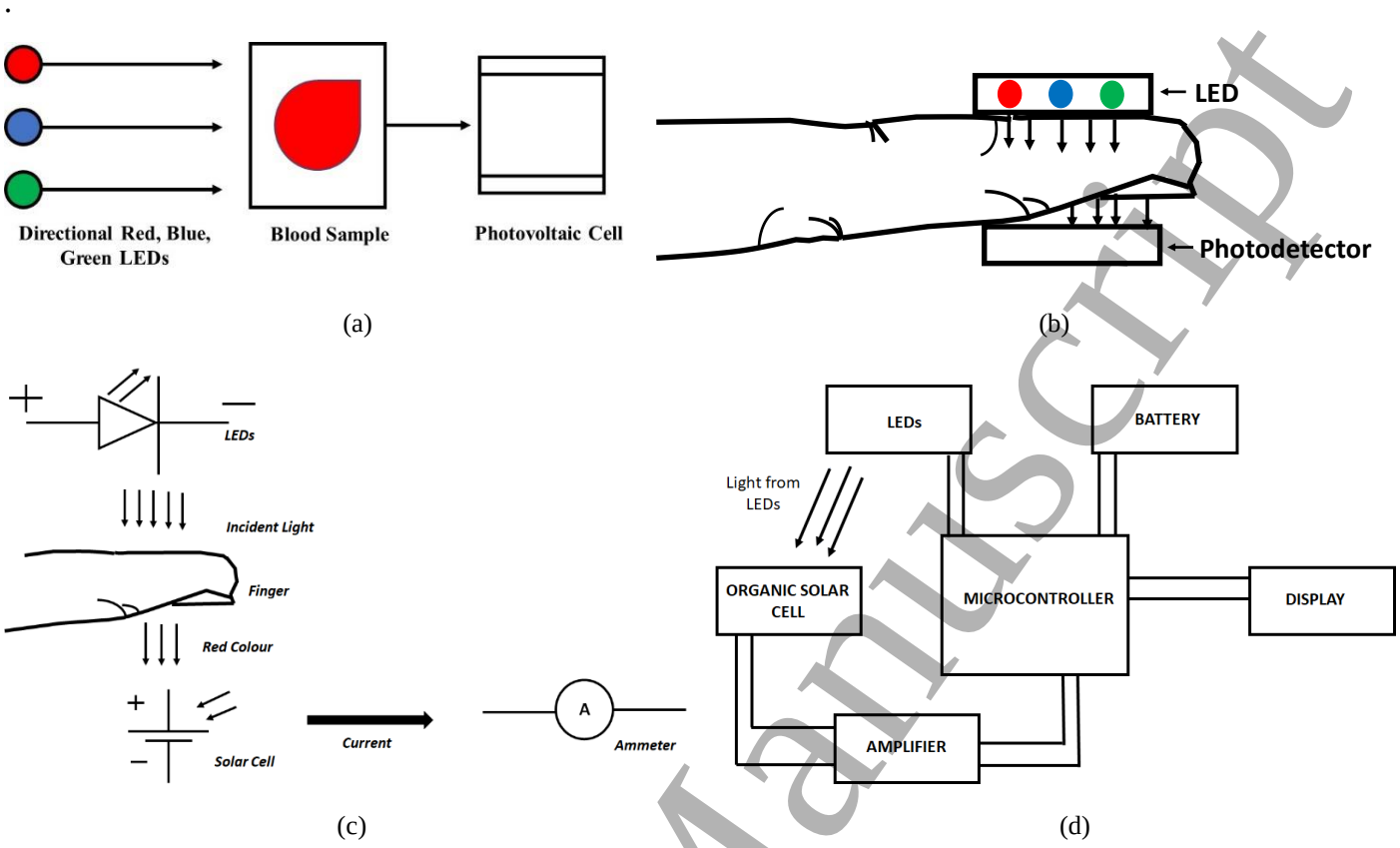


Fig. 5. (a) The schematic representation of sensing concept. (b) organic photodetector-based haemoglobin detection device used on a finger. (c) The basic circuit design and (d) block diagram of device proposed.

The sensing method proposed in this article is illustrated in the Fig. 5 (a) and Fig. 5 (b) presents the organic photovoltaic cell receiving the wavelengths of light transmitted through the finger. The proposed method consists of three directional LED sources which are utilised to pass through the finger or through the specimen of the blood. The appropriate wavelengths of light passed through or transmitted through finger's area are selected for detection of the haemoglobin. The Fig. 5 (c) present the basic circuit design of the proposed device and Fig. 5 (d) represent the block diagram of the device proposed which could be achieved through a microprocessor. A battery is connected which provides the power required for the LEDs and microprocessor to operate. The LEDs project light at the organic solar cell (OSC), the patient's finger is to be inserted in-between the LEDs and the OSC. The OSC generates the current as per the wavelengths of light detected by it, as this current is in microamperes (μA), its amplified and sent to the microprocessor, which displays the output.

The purposed measurement method presented in this article is of non-invasive nature and is based on the radiation of light emitted by LEDs in the wavelength rage of 450–750 nm through skin area. The method takes advantage of the absorption of light by the RBC of the human. The different colour wavelengths after passing through the finger get absorbed in accordance with the absorption character of the blood's components. Then the transmitted light is then detected by non-invasive organic photovoltaic device to produce a photosensitivity. The obtained value of photosensitivity detects the haemoglobin and determines if the patient suffers from anaemia.

The major advantages associated with the proposed non-invasive technology in comparison to other technologies are lower production cost, portability, high reliability, accuracy, and immediate and continuous measurement. Further, it does not require any large setup or trained manpower, the input power required to operate it is significantly lower. It provides higher patient comfort; the data is of digital nature hence history

Accepted Manuscript

can be stored. Moreover, it could be integrated to the wearable electronic devices. Thus, proving beneficial for increasing testing and reducing hospital costs. On the other hand, the drawbacks associated are that to use this method the patient should be still and the skin surface on which the device is used should be contamination free so that nothing may interfere with the measurements.

7. Evaluation of the photosensitivity to detect anaemia

The negatives of present finger-prick technique used to determine the anaemia are complications, invasiveness and errors while reporting especially in case of younger women as haemoglobin concentration in blood capillaries are higher in comparison to the venous blood [53] and finger piercing also causes an alteration in the fluids as the pressure on fingertip increases concentration of plasma in the blood capillary thus falsifying the reading.

The Fig. 6 presents the characteristic spectral photo-response of the tandem multilayer organic photovoltaic cell. The three monochromatic lights of blue, green and red colour are irradiated from the three Light Emitting Diodes of blue, green and red colour onto the blue colour sensitive side of the photovoltaic device. The resultant photo-response curves of the blue, green and red colour sensitive film layers have their spikes at the wavelengths of 420 nm, 510 nm, and 650 nm respectively. Thus, from this obtained photo-response curves it is firmly evident that the separation of colours occurs in the purposed multilayer organic photovoltaic device. Further, from this finding it could be established that the different value of photosensitivity (A/W) are related to different colours in their wavelength range. It is also very well known that the spectrum of wavelength for blue colour is form 425-540 nm, the wavelength spectrum for green colour is known to be from 500 to 540 nm and similarly the wavelength spectrum for red colour is from 615-700 nm.

The photosensitivity, represents the current generated in Amperes per Watt of incoming sunlight incident on the surface of the solar cell. Photosensitivity can give the current produced by the organic photovoltaic cell according to the formula given in equation (1).

$$I_p = \text{Area} \times \text{Sensitivity} \times \text{Intensity} \quad (1)$$

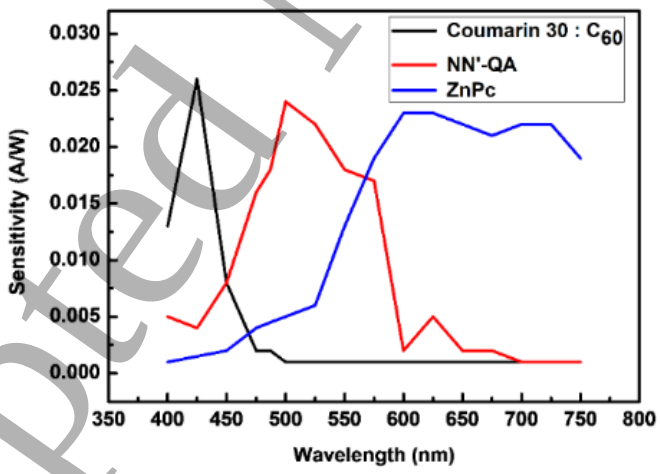


Fig. 6. Photosensitivity as a function of wavelength for organic photovoltaic cell.

The Fig. 7 represents the comparison in-between the sensitivity or the output current produced for the single structure red colour photo-detector and the complete multilayer photovoltaic device. In the Fig. 7 it could be observed that the single structure has an undesirable output current signal with-in the blue and green colour ranges, while the multilayer photovoltaic device has a highly reduced blue and green colour current signal as the top layer of the solar cell acts as blue colour filter and the middle layer act as a green colour filter, absorbing the blue and green colour respectively. Thus, from the Fig. 7 it could be confirmed that individual or stand-alone structure of the ZnPc material film does not possess an exceptional characteristic for the separation of colour. Hence, the use of multilayer structure arranged in blue, green and red from top to bottom layer is required for the excellent separation characteristic of colours. Also, from the Fig. 7 it could be observed that

Accepted Manuscript

the sensitivity for the multilayer structure is around 0.020 A/W for the wavelengths range of 600 nm and above.

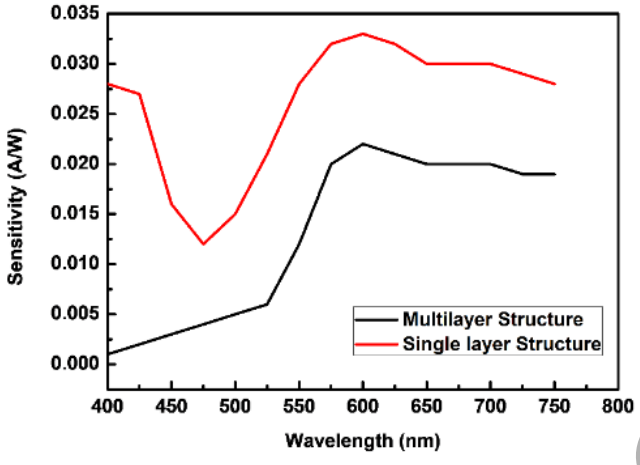


Fig. 7. Photosensitivity as a function of wavelength for single layer (red colour curve) and multilayer structure (black colour curve).

Hence, from the combination of Fig. 6 and the photosensitivity results obtained in Fig. 7 it can be further established that when a skin area is exposed to the three LEDs of different wavelengths for instance red, blue and green the blue and green colour should be completely absorbed by the skin i.e., the blood should completely absorb the both blue and green colours and should only let pass the red colour, this only red colour wavelengths (spectrum of red light 615-750 nm) which is able to passes through the patient's blood sample should strike the stacked organic photovoltaic cell wherein they should get absorbed completely producing an photosensitivity of 0.02 A/W or a current of 1 μA (considering device area to be 1cm^2 and intensity as 50 μW/cm^2).

The red colour light absorbed by the photodetector is direct evidence to the presence of Haemoglobin and denotes absence of anaemia. Hence, ultimately proving and stablishing the fact that the sample of blood under consideration is completely healthy and the person is anaemia free. If the photo sensitivity deviates from the value of 0.02 A/W it means that the organic photovoltaic cell used as a detector has absorbed some other light colour i.e., blue or green indicating that the blood sample isn't completely healthy and has a lower count of red blood cells (anaemia), iron deficiency which are required to be treated. Therefore, the haemoglobin concentrations which could be detected through this technology are in the range of 18 to 12 g dl^{-1}, 18 g dl^{-1} to 14 g dl^{-1} for males and 16 g dl^{-1} to 12 g dl^{-1} which are the normal Hb levels for males/females, and if the patient haemoglobin concentration is less than the mentioned normal haemoglobin concentration the patient is suffering from anaemia.

Conclusion

In this research article a Coumarin 30 : C_{60}/NN'-QA/ZnPc based multilayer organic photovoltaic solar cell is presented wherein three organic photodetector layers individually sensitive towards the blue, green and red colour lights are arranged in a stack one above the other. The output produced from the purposed multilayer photovoltaic device represented an excellent selectivity of the spectrum and also demonstrated separation of the colours in the photovoltaic cell. This excellent capability to separate the colours makes this organic photovoltaic cell to be further utilised as a photodetector to realise a haemoglobin detector device by combining it with blue, green and red colour LEDs. The photodetector detects the haemoglobin present in RBC due to the optical property of haemoglobin not to absorb or to reflect the red colour. This transmitted red colour wavelengths are absorbed by the ZnPc layer of the multilayer structure producing a photosensitivity of 0.02 A/W. This purposed method being low-cost and non-invasive would be an extremely useful device for checking anaemia anywhere and will be vital primarily for children and women suspected to be anaemic. It's an extremely portable device with minimal requirement of training and provides immediate results. Moreover, the use of optical properties of haemoglobin proves this proposed methodology to be extremely reliable and

Accepted Manuscript

easy to use which is capable of reducing mortality primarily in the world's most marginalized and poor populations.

Declarations

Data availability statement

All data is contained within the article itself.

References

[1] Ninck M, Untenberger M, Gisler T. Diffusing-wave spectroscopy with dynamic contrast variation: disen tangling the effects of blood flow and extravascular tissue shearing on signals from deep tissue. Biomed Opt Express. 2010; 1:1502–1513.

[2] Meinke MC, Friebel M, Helfmann J. Optical properties of flowing blood cells. In: Tuchin VV, editor. Advanced Optical Flow Cytometry: Methods and Disease Diagnoses. Wiley-VCH Verlag GmbH & Co.KGaA; 2011. p. 95–132

[3] Park YK, Diez-Silva M, Fu D, Popescu G, Choi W, Barman I, et al. Static and dynamic light scattering of healthy and malaria-parasite invaded red blood cells. J Biomed Opt. 2010; 15:020506

[4] Park YK, Best-Popescu CA, Dasari RR, Popescu G. Light scattering of human red blood cells during metabolic remodeling of the membrane. J Biomed Opt. 2011; 16:011013.

[5] Lim J, Ding H, Mir M, Zhu R, Tangella K, Popescu G. Born approximation model for light scattering by red blood cells. Biomed Opt Express. 2011; 2:2784–2791.

[6] Kim Y, Higgins JM, Dasari RR, Suresh S, Park YK. Anisotropic light scattering of individual sickle red blood cells. J Biomed Opt. 2012; 17:040501

[7] Park YK, Best CA, Auth T, Gov NS, Safran SA, Popescu G, et al. Metabolic remodeling of the human red blood cell membrane. Proc Natl Acad Sci USA. 2010; 107:1289–1294.

[8] Turlier H, Fedosov DA, Audoly BA, Auth T, Gov NS, Sykes C, et al. Equilibrium physics breakdown reveals the active nature of red blood cell membrane fluctuations. Nat Phys. 2016; 12:513–519.

[9] Arafa H Aly *et al* "Theoretical study of hybrid multifunctional one-dimensional photonic crystal as a flexible blood sugar sensor" 2020 *Phys. Scr.* **95** 035510.

[10] R. Hovorka, Closed-loop insulin delivery: from bench to clinical practice, Nat. Rev. Endocrinol. 7 (2011) 385 Review Article.

[11] Abdulkarem H M Almawgani *et al* "Detection of glucose concentration using a surface plasmon resonance biosensor based on barium titanate layers and molybdenum disulphide sheets" 2022 *Phys. Scr.* **97** 065501

[12] Roberts V C, 1982, Photoplethysmography –fundamental aspects of the optical blood in motion, *Trans. Inst. Meas. Control* **4**, pp. 101-6

[13] Roggan A, Friebel M, Dörschel K, Hahn A, Müller G 1999 Optical properties of circulating human blood, *J. Biomed. Opt.* **4**, pp. 36-46

[14] I. Fine and A. Finarov, "Probe for use in non-invasive measurements of blood related parameters," ed: Google Patents, 2006.

[15] P. Peumans, V. Bulovic, and S. R. Forrest: Appl. Phys. Lett. 76 (2000) 3855.

[16] H. Tanaka, T. Yasuda, K. Fujita, and T. Tsutsui: Adv. Mater. 18 (2006) 2230.

[17] Symon D'Oyly Cotton, Ela Claridge, "Developing a Predictive Model of Human Skin Colouring", Proceedings of SPIE Medical Imaging, Vol. 2708, pp. 814 – 825, 1996.

[18] Norimichi Tsumura, Hideaki Haneishi, and Yoichi Miyake, "Independent Component Analysis of Skin Colour Image", Journal of Society of America, Vol. 16, Issue 9, pp. 2169-2176, 1999.

[19] Symon Cotton, Ela Claridge and Per Hall, "A Skin Imaging Method Based on a Colour Formation Model and its Application to the Diagnosis of Pigmented Skin Lesions", Proceedings of Medical Image Understanding and Analysis, Oxford: BMVA, pp.49-52, 1999.

Accepted Manuscript

[20] Ela Claridge, Symon Cotton, Per Hall, and Marc Moncrieff4, *"*From Colour to Tissue Histology: Physics Based Interpretation of Images of Pigmented Skin Lesions*"*, MICCAI 2002, LNCS 2488, pp. 730–738,2002.

[21] Norimichi Tsumura, Hideaki Haneishi and Yoichi Miyake, *"*Independent Component Analysis of Skin Color Images*"*, The Sixth Color Imaging Conference: Color Science, Systems, and Applications, 1999.

[22] Nielsen, K. P., Zhao, L., Stamnes, J. J., Stamnes, K., & Moan, J., "The Optics of Human Skin : Aspects Important for Human Health,", (1), 35-46, 2008.

[23] Maria Joao Brites, Celia Santos, Susana Nascimento, Barbara Gigante, Heinrich Luftmann, Aleksandre Fedorov and Mario N. Berberan-Santos, "Synthesis and fluorescence properties of [60] and [70]fullerene–coumarin dyads: Efficient dipole–dipole resonance energy transfer from coumarin to fullerene" New J. Chem., 2006, 30, 1036–1045.

[24] Dong-Seok Leem, Kwang-Hee Lee, Kyung-Bae Park, Seon-Jeong Lim, Kyu-Sik Kim, Yong Wan Jin, and Sangyoon Lee, "Low dark current small molecule organic photodetectors with selective response to green light", Applied Physics Letters 103, 043305 (2013).

[25] S. senthilarasu, S. velumani, R. sathyamoorthy, A. subbarayan, J. A. ascencio, G. canizal, P. J. Sebastian, J. A. Chavez, R. perez, "Characterization of zinc phthalocyanine (ZnPc) for photovoltaic applications", Appl. Phys. A 77, 383–389 (2003)

[26] R. M. L. Kitaneh, M. M. Abu-Samreh, S. M. Musameh, S. M. Hraibat, A.M. Saleh, "Dielectric characterization of semiconducting ZnPc films sandwiched between Gold or Aluminum electrodes", Appl Phys A (2014) 114:1267–1275.

[27] ATLAS. ATLAS User's Manual Device Simulation Software. Silvaco International Ltd. Santa Clara 2014.

[28] S. Negi, P. Mittal and B. Kumar, "Analytical Modelling and Parameters Extraction of Multilayered OLED", IET Circuits, Devices and Systems, Vol. 13, Issue 8, 1255-1261.

[29] Paritosh Chamola and Poornima Mittal "Flexible organic solar cell to power modern cardiac pacemakers: Versatile for all age groups, skin types and genders" 2023 *Phys. Scr.* **98** 035018.

[30] R. M. Christie and C. Lui, Dyes Pigm., 1999, 42, 85–93.

[31] R. M. Christie and C. Lui, Dyes Pigm., 2000, 47, 79–89.

[32] S. R. Trenor, A. R. Shultz, B. J. Love and T. E. Long, Chem. Rev., 2004, 104, 3059–3077.

[33] B. Kovac and I. Novak, Spectrochim. Acta, Part A, 2002, 58, 1483–1488.

[34] X. Zhou, J. Blochwitz-Nimoth, M. Pfeiffer, B. Maenning, J. Drechsel, A. Werner and K. Leo, Synth. Met., 2003, 138, 193–196.

[35] K. Hara, K. Sayama, Y. Ohga, A. Shinpo, S. Suga and H. Arakawa, Chem. Commun., 2001, 569–570.

[36] K. Hara, Y. Tachibana, Y. Ohga, A. Shinpo, S. Suga, K. Sayama, H. Sugihara and H. Arakawa, Sol. Energy Mater. Sol. Cells, 2003, 77, 89–103.

[37] C. Jiao, C. Niu, L. Chen, G. Shen and R. Yu, Sens. Actuators, B, 2003, 94, 176–183.

[38] S. senthilarasu, S. velumani, R. sathyamoorthy, A. subbarayan, J. A. ascencio, G. canizal, P. J. Sebastian, J. A. Chavez, R. perez, "Characterization of zinc phthalocyanine (ZnPc) for photovoltaic applications", Appl. Phys. A 77, 383–389 (2003)

[39] P.A. Lane, J. Rostalski, C. Giebeler, S.J. Martin, D.D.C. Bradley, D. Meissner: Sol. Energy Mater. Sol. Cells **63**, 3 (2000).

[40] D. Wrobel, A. Boguta: J. Photochem. Photobiol. A: Chem. **6045**, 1 (2002)

[41] K. Oda, S.-I. Ogura, I. Okura: J. Photochem. Photobiol. B: Biol. **59**, 20 (2000)

[42] K. Suemori, T. Miyata, M. Yokoyama, and M. Hiramoto: Appl. Phys. Lett. 85 (2004) 6269.

[43] Hokuto Seo, Satoshi Aihara, Toshihisa Watabe, Hiroshi Ohtake, Toshikatsu Sakai, Misao Kubota, Norifumi Egami, Takahiro Hiramatsu, Tokiyoshi Matsuda, Mamoru Furuta, and Takashi Hirao, "A 128 × 96 Pixel Stack-Type Color Image Sensor: Stack of Individual Blue-, Green-, and Red-Sensitive Organic Photoconductive Films Integrated with a ZnO Thin Film Transistor Readout Circuit" Japanese Journal of Applied Physics 50 (2011) 024103.

Accepted Manuscript

[44] Friebel, M. and Meinke, M. (2005) Determination of the complex refractive index of highly concentrated hemoglobin solutions using transmittance and reflectance measurements. *J. Biomed. Opt.*, **10**, 064019

[45] Assendelft, O. (1970) *Spectrophotometry of Hemoglobin Derivates*, Royal Vangorcum.

[46] Prahl, S. (2009) Tabulated data from Various Surces Compiled by S. Prahl, *http://omlc.ogi.edu/spectra/* (accessed 2009).

[47] Alexander Nahmad-Rohen *et al* "On the effective refractive index of blood" 2016 *Phys. Scr.* **91** 015503

[48] Anderson, R. R., & Parrish, J. A., "The Optics of Human Skin", *Journal of Investigative Dermatology*, *77*(1), 13-19, 1981.

[49] Stott G, Lewis SM. A simple and reliable method for estimating haernoglobin. *Bulletin of the World Health Organization*, 1995;**73**:369-73.

[50] Miinster M et al. Field evaluation of a novel haemoglobin measuring device designed for use in rural setting. *South African Medical Journal*, 1997;**87**:1522-26

[51] Beales PE. Anaemia in malaria control: a practical approach. *Annals of Tropical Medicine & Parasitology*, 1997;**91**:713-8.

[52] Lewis SM, Stott GJ, Wynn KJ. An inexpensive and reliable new haemoglobin colour scale for assessing anaemia. *Journal of Clinical Pathology*, 1998;**51**:21-4.

[53] Patel AJ, Wesley R, Leitman SF, Bryant BJ. Capillary versus venous haemoglobin determination in the assessment of healthy blood donors. Vox Sang 2013; **104**: 317-23.

Accepted Manuscript

Accepted Manuscript

2023 IEEE 8th International Conference for Convergence in Technology (I2CT)
Pune, India. Apr 7-9, 2023

A Novel approach to Handle Imbalanced Dataset in Machine Learning

Taj Sapra
Department of Software Engineering
Delhi Technological University
Delhi, India
tajsapra 2k19se132@dtu.ac.in

Shubhama
Department of Software Engineering
Delhi Technological University
Delhi, India
shubham 2k19se120@dtu.ac.in

Shweta Meena
Department of Softtware Engineering
Delhi Technological Uiversity
Delhi, India
shwetameena@dtu.ac.in

2023 IEEE 8th International Conference for Convergence in Technology (I2CT) | 979-8-3503-3401-2/23/$31.00 ©2023 IEEE | DOI: 10.1109/I2CT57861.2023.10126309

***Abstract*— The world has seen an exponential rise in machine learning and artificial intelligence since the 1990s. We apply machine learning models to solve various real life problems like regression and clasˇ sification. However, class imbalance is a very common issue faced for classification problems in machine learning. In this study, we propose new greedy resampling techniques to solve the problem of class imbalance. We shall also compare the results of these techˇ niques with the Synthetic Minority Over-sampling Technique (SMOTE).**

Keywords*— *Class Imbalance, Machine Learning, Greedy Algorithm, SMOTE, COVID-19, Credit Card Fraud Detection

I. INTRODUCTION

Classification is one the biggest application of machine learning, which has found it's use in various fields like medicine, fraud detection, sentiment analysis [1][2][3]. Machine learning classifiers depend on the pattern in the training dataset. The problem of class imbalance is very frequent for classification tasks in machine learning. Class imbalance can occur not only because of a bad dataset but also because of rest classification techniques. Due to this, the count of data points for 1 class is very high as compared to all other classes. Various techniques have been suggested to solve this problem such as: data re-sampling [4], cost sensitive training [5], ensemble techniques.

SMOTE [6] is one of the most commonly used data re-sampling techniques which is used to over-sample the minority classes. In this study, we propose new greedy techniques that have provided us better classification results on a covid symptom detection dataset released by the Government of Israel [7]. These techniques can be used for any other field as well. We shall also discuss the short comings of SMOTE.

For this paper, we have considered two types of datasets, the first one has categorical inputs, and the second one has continuous inputs. For dataset with categorical input, we have developed five new techniques for handling imbalanced datasets namely: Greedy Duplicate Array Removal Method (GDARM), Greedy Duplicate Array Removal Method with Multiplier (GDARMM), Greedy Duplicate Array Removal Method with Multiplier for 3 or more classes (GDARMM2.0), Greedy Duplicate Array Removal Method Cost Sensitive (GDARMCS) and Greedy Duplicate Array Removal Method Model Prediction Oversampling (GDARMPO).

For dataset with continuous input, we have developed three new techniques for handling imbalanced data sets namely: Greedy Similar Array Removal Method(GSARM), Greedy Similar Array Removal Method Prediction Oversampling(GSARMPO) and Greedy Similar Array Removal Method Model Prediction Oversampling with cleaner(GDARMPO2)

II. RELATED WORK

For credit card fraud detection, SMOTE has already been used by researchers[8] to tackle class imbalance in datasets. However the dataset size increased to almost double the initial size. If the dataset contained more than two classes with multiple minority classes, the multiplication factor would have been higher than 2. SMOTE has its own disadvantages because of which outliers can be introduced to the final dataset. which can change the decision boundary drastically from what it should be. This problem regarding SMOTE was pointed out [9] and new variants of SMOTE were suggested. However oversampling does increase the size of the dataset. Also if the new points generated by the new versions of SMOTE are very close to each other they wont be conveying any new information for the model to learn causing repeated learning.

Random Under sampling has also been used by various researchers in compariˇ son to SMOTE [10]. This can not only lead to varying results near the decision boundary but can in the worst case remove a huge part of data from the majority class and can eventually form a new decision boundary that may be correct on this new dataset but may give poor results on the original dataset.

III. ALGORITHMS AND EXPRESSIONS

In this section we shall discuss the developed algorithms and how they perform a refined greedy undersampling to perform better than SMOTE.

Algorithm 1 GDARM

```
pos ← [ ]
neg ← [ ]
fdata ← [ ]
for i in odata:
    if i belongs to minority class:
        add i to fdata
    else:
        if i in fdata:
            remove i
        else
            add i to fdata
```


Authorized licensed use limited to: DELHI TECHNICAL UNIV. Downloaded on May 29,2023 at 05:55:12 UTC from IEEE Xplore. Restrictions apply.

Algorithm 2 GDARM

```
pos ← [ ]
neg ← [ ]
fdata ← [ ]
for i in odata:
    if i belongs to minority class:
        add i to fdata m times ▷ m is an integer passed by the user
    else:
        add i to fdata if i not in fdata
```

Algorithm 3 GDARMM2.0

```
pos ← [ ]                          ▷ Minority Class 1
oth ⇐ []                           ▷ Minority Class 2
neg ← [ ]
fdata ← [ ]
for i in odata:
    if i belongs to minority class1:
        add i to fdata m[0] times
    else if i belongs to minority class 2:
        add i to fdata m[1] times
    else:
        if i in fdata:
            remove i
        else
            add i to fdata
```

Algorithm 4 GDARMPO

```
model1.fit(X1, Y1) ▷ model1 is the 1st model trained on 2*k points, where k is the count of data points of minority class
N ewP red ⇐ [...] ▷ We create sample test cases for prediction i model1
for i in NewPred
    if i belongs to minority class:
        add i to fdata
for i in odata
    add i to fdata
fdata=GDARM(fdata) ▷ GDARM is defined in Algorithm 1
model2.fit(fdata) ▷ The new data points added to the dataset creates an indirect parameter transfer learning from model1 to model2
```

Algorithm 5 GDARMCS

```
fdata=GDARM(odata) ▷ The GDARM function is modified by applying a limiter on the points being removed
model=KNNClassifier(weights="distance") ▷ The new data after partial GDARM is still imbalanced but is in a better condition.
```

Algorithm 6 GSARM

```
Define a compare Function that compares two datapoints
The function returns a score in the range [0,1] which represents the similarity of 2 data points
Now define an extractor function.
fdata ← [ ]
for i in dataset:
    flag=1
    update th depending on how many points were skipped previously
    for j in fdata:
        if(similarity(j,i)⩾th): ▷ th is threshold, a is from odata
            flag=0
            continue
    if flag==1:
        fdata.append(i)
Apply classification models on fdata after splitting it into training and testing sets
```

Algorithm 7 GSARMPO

```
Use a model on a small subset of dataset to manufacture new samples
If generated samples belong to minority class append it fdata
Add the original data samples to fdata
fdata=GSARM(fdata) ▷ GSARM is defined as algorithm 6
```

Algorithm 8 GSARMPO2.0

```
model1.fit(X1, Y1) ▷ model1 is the 1st model trained on 2*k points, where k is the count of data points of minority class
N ewP red ⇐ [...] ▷ We create sample test cases for prediction i model1
for i in NewPred
    if i belongs to minority class:
        add i to fdata
for i in odata:
    add i to fdata
fdata=GSARM(fdata) ▷ GSARM is defined as algorithm 6
Apply classification models as model2
```

IV. RESULTS

The types of data for which tthis study is useful discussed in this section with resulta interpretation.

A. Categorical Input Data

Table 1 and 2 in section 4 displays accuracy of various models on the dataset and values of many accuracy metrices. The values of both the table clearly show that our algorithms perform far better than SMOTE to tackle class imbalance. Even after creating copies of the minority class, SMOTE does not give satisfactory results on minority cloaks. Meanwhile our new methods perform far better results on not only the minority but on majority class as well by reducing repeated learning on the same data points.

B. Continuous Input Data

Table 3 and 4 in section 4 displays accuracy of various models on the dataset and values of many accuracy metrices. From Table 3, one might think that SMOTE has a better

Authorized licensed use limited to: DELHI TECHNICAL UNIV. Downloaded on May 29,2023 at 05:55:12 UTC from IEEE Xplore. Restrictions apply.

accuracy than other algorithms however when we look at other performance metrics, we can clearly see that the proposed algorithms are better performing ones. For finding how good the model actually is, we must see how it performs on all classes. We know that specificity reflect the model's performance on negative class(majority in this case), and other metrics like sensitivity and precision reflect the model's performance on the positive class(minority in this case). From Table 2, it can be observed that the greedy methods perform better on minority class. Most accuracy metrics like Sensi˘ tivity, AUC-ROC, MCC and f1 score also show improvements as compared to SMOTE.

V. TABLES

The answers to the research questions formulated in Section I are addressed in this section to achieve the objective of this study.

TABLE I. MODELWISE ACCURACY COMPARISON

Method	Decision Tree	Random Forest	SVC	Logistic Regression	MLP (hidden_dense:[100,])	KNN
SMOTE	0.861, 0.861	0.862, 0.861	0.792, 0.792	0.799, 0.799	0.891, 0.86	0.837, 0.838
GDARM	0.913, 0.904	0.912, 0.909	0.902,0.896	0.735, 0.739	0.909, 0.909	0.906, 0.908
GDARMM	0.894,0.893	0.893, 0.896	0.892,0.894	0.81, 0.809	0.892, 0.891	0.885, 0.886
GDARMM2.0	0.823,0.82	0.826, 0.812	0.812, 0.814	0.65, 0.654	0.82, 0.82	0.80, 0.80
GDARMCS	-N/A-	-N/A-	0.942, 0.938	0.87, 0.871	-N/A-	0.946, 0.946
GDARMPO	0.96, 0.961	0.96, 0.96	0.96, 0.96	0.954, 0.954	0.956,0.959	0.959, 0.958

Hidden layers of MLP=[100,] -N/A- means not applicable Values in the table belong to the range [0,1]

TABLE II. ACCRUACY METRICS

Method	**SMOTE**	**GDARM**	**GDARMM**	**GDARMMCS**	**GDARMPO**
SENSITIVITY	0.714	0.942	0.914	0.896	0.973
SPECIFICITY	0.8734	0.865	0.873	0.89	0.851
PRECISION	0.849	0.874	0.879	0.515	0.977
F1	0.776	0.907	0.896	0.6524	0.975
AUC	0.792	0.903	0.893	0.893	0.9124
MCC	0.5956	0.8094	0.782	0.627	0.8155
UNIQUE POINT %	0.7214	0.74	0.745	0.7365	0.127
ACC POSITIVE	0.7144	0.9422	0.8738	0.8907	0.9731
ACC NEGATIVE	0.8734	0.8635	0.9138	0.8968	0.8741

TABLE III. MODELIWISE ACCURACY COMPARISON

Methods	Decision Tree	Random Forest	SVC	MLP (hidden_dense:[100,])	KNN	ADA BOOST
SMOTE	1,1	1,1	0.979, 0.98	0.915, 0.915	0.99, 0.99	0.983, 0.983
GSARM	1	1,1	0.826, 0.811	0.8, 0.76	0.934,0.9054	0.9365,0.9256
GSARMPO	1, 0.9635	1, 0.987	0.722, 0.72	0.757, 0.734	0.88, 0.822	0.927, 0.9198
GSARMPO 2.0	1, 0.955	1, 0.984	0.74, 0.73	0.76, 0.75	0.876, 0.827	0.928, 0.931

Hidden layers of MLP=[100,] Values in the table belong to the range [0,1]

TABLE IV. PERFORMANCE METRICS FOR ADABOOST CLASSIFIER

Method	SMOTE	GSARM	GSARMPO	GSARMPO2.0
SENSITIVITY	0.2	0.73	0.9035	0.929
SPECIFICITY	0.999	0.971	0.911	0.932
PRECISION	0.837	0.856		0.91
F1	0.328	0.7878	0.9	0.92
AUC	0.6018	0.85	0.907	0.931
MCC	0.409	0.7466	0.8141	0.859
ORIGINAL MINORITY ACCURACY	0.257	0.725	0.6857	0.724

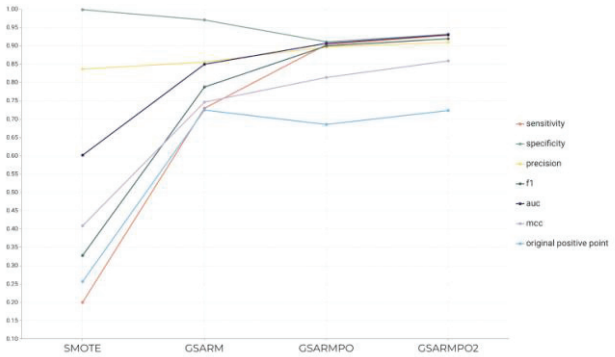


Fig. 1. Performance analysis of proposed imbalanced dataset techniques with SMOTE

VI. METHODS

To handle the class imbalance problem, we can either over sample the minority class or under sample the majority class. This helps in making the count of both the classes similar. There are 2 ways to solve this problem. We can either increase the count of minority class or decrease the count of majority class by removing points.

A. Problem with SMOTE

SMOTE is a method of oversampling data points. Now this leads to repeated learning. The same data is being learnt again and again and no improvement is being made on the general performance of classifier. This is a classic case of

Authorized licensed use limited to: DELHI TECHNICAL UNIV. Downloaded on May 29,2023 at 05:55:12 UTC from IEEE Xplore. Restrictions apply.

overfitting. Consider figure 1. Here we can see that the data set indicates a sine type function. Now if we make copies of any single point, that point will have a stronger impact on weights during training. This repeated point will try to bring the function's graph towards itself, hence changing the expected shape of the graph. This will lead to overfitting on training data. SMOTE algorithm faces this problem as it simply creates copies of all data points in the minority class. There is another problem with SMOTE. Consider a dataset having 5 output classes with data distributed as follows: (1000000, 1000, 50000, 49000, 500). SMOTE will try to make copies of all minority classes till they have 1000000 samples resulting in a total dataset size of 5000000. This can lead to wastage of resources(time and computing power) even on simplest of models.

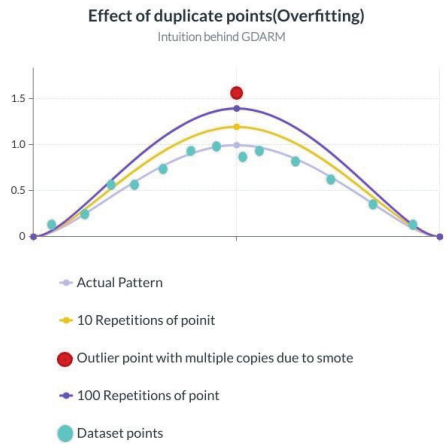


Fig. 2. Effect of repeated learning

B. Categorical Input Data

1) GDARM

This method reduces the size of majority classes by deleting duplicate data points till the size of major and minor classes are similar/same. Consider a data point as an array of size k+1, where k is the number of features of the data. Create a 2 dimensional array where current data point(1 dimensional array) will be added if it already exists in the 2 dimensional array. This method has a disadvantage that it can lead to decrease in a lot of data depending upon the size of minority class.

2) GDARMM

This method is a hybrid of oversampling and undersampling. If the count of minority class is too low, we can create copies of it to a small extent like 2 times/ 3 times. After that, we can apply GDARM on the majority class to remove duplicates. Due to the increase in size of minority class initially, this helps in overcoming a problem of GDARM. For multi-class classification GDARMM2.0 can be used as the value of multiplier can vary from class to class.

3) GDARMCS

This technique is a hybrid of undersampling along with cost sensitive training. This method applies GDARM partially by placing a stopper on the count of the duplicate arrays that can be removed from the minority class. This technique is valid for data where repetition of data points matter in the dataset. This method is suitable only for data sets where the count of samples of majority class is way higher than the count of samples of minority class.

4) GDARMPO

This is a two phase technique which involves the usage of 2 models. This technique also has an application when resources are limited. Let's consider a dataset having 2 output classes. Let us say there are 5500 points(5000 for class A and 500 for class B) For each data point there are 4 features, f1(int:can vary from 1-100), f2(int: can vary from 1-10), f3(bool:1/0), f4(bool:1/0). We take 500 points of B and 500 random points of class A. We train a model on these 1000 points. Now we can make sample test cases for predictions by varying values of one feature at a time and keeping the rest constant. In this case that can result in 100*10*2*2(4000 cases if we consider only integers for features a and b). If out of these 4000 points, let us assume 2000 belong to each class. Out of these 500 have already been considered in the original dataset and hence we can increase 1500 data points. After getting the predictions, we can add the data points created by us belonging to the minor class to the original dataset. This will help in oversampling the minor class by some amount without creating duplicates. Now GDARM can be applied on the majority class. Figure 2 shows the decision boundaries of the 2 models with original and newly added points.

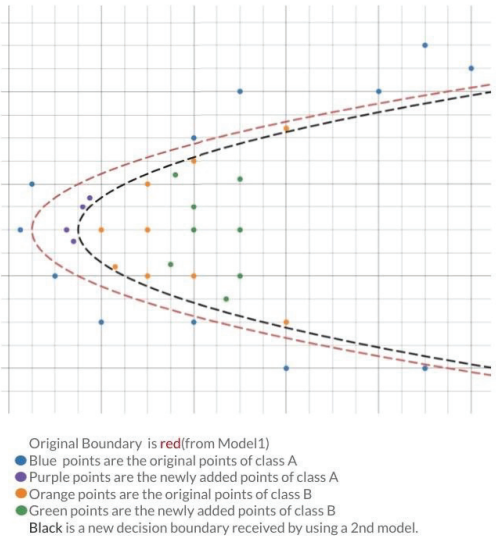


Fig. 3. Parameter transfer learning in GDARMPO

C. Continuous Input Data

1) GSARM

We need to reduce the size of majority class but we need to make sure that we don't reduce the spectrum of the dataset. We also need to make sure that we do not change the decision boundary by reducing the dataset size. Hence we should find similarity of points. If there are 2 points that are very similar, then we can ignore one of them as the decision boundary will be affected similarly by both of them. Now the similarity between 2 data samples, can be computed as: points gained divided by maximum points possible. Here points are awarded depending on how similar are 2 points feature wise. Lets say 1st feature has more importance, hence they can have higher points. Now to normalize the score, we

Authorized licensed use limited to: DELHI TECHNICAL UNIV. Downloaded on May 29,2023 at 05:55:12 UTC from IEEE Xplore. Restrictions apply.

have to divide it by the maximum possible points that can be scored. For comparing any 2 decimal values, we have not used Euclidean distance. Instead we have used a modified version of the Euclidean distance that helps us to normalise the score from any range to [0,1]. After the similarity is found out, the process is repeated for all points that are currently in fdata(initially empty). If there is no point with similarity(with respect to the current point) more than the threshold, we append the current point into final data.

$$\text{Similarity} = (\text{Points gained})/(\text{Maximum points that can be gained}) \quad (1)$$

2) GSARMPO

This technique is a 2 stage method to handle class Imbalance. We have disˇ cussed a similar technique for categorical data in our previous paper. In the first stage, we use a model(any ml model) on a small subset of data. After that we can generate new data points for the minority class by applying nested for loops within the feature ranges. We use the model we train in stage 1 to preˇ dict the class of these new data points. Then we will use data points predicted as minority to oversample our original data. Stage 2 includes application on GSARM on the final data(original+new data samples of minority class). This method helps in increasing the data set size in comparison to the original GSARM method.

3) GSARMPO 2.0

In GSARMPO, we added new points belonging to minority class. However in these new additions, there may be some noisy points that get eventually added in fdata. Hence a cleaner can be used to prevent that. Now while appending the new data samples of minority class, we can use something very similar to the comparing function we built in GSARM. If for any newly generated data point, there exists at least some k data points belonging to the original minority class, then we can assume that it is not a noisy point. here k is a hyper-parameter and can be set accordingly. This helps in increasing accuracies of the 2nd stage model(Final Model) in GSARMPO.

4) Statistical Analysis of the results

The values of various accuracy metrices were used to perform the Wilcoxon test to compare every new algorithm with SMOTE. This was done to make sure that there was a significant improvement in the performance of the variants when compared to SMOTE.

5) What if undersampling reduces dataset drastically?

Those cases are already handled in some of the algorithms like GDARMPO, GSARMPO and GSARMPO2.0. There are new points added before training and predicting. However if that is still less, advances in Deep Learning proˇ vide us with a method to solve this problem. Generative Adversarial Networks (GANs)[11] help us to generate new data that is similar to any sample of dataset. This will help us maintain a decent size dataset even after undersamˇ pling for training purposes. If all these options are not available, one may have to resort to re-sample the minority class to increase its sample count.

VII. CONCLUSION AND FUTURE WORK

Classification problems very often face the challenge of class imbalance not only in some specific tasks like credit card detection or medical related tasks but also in the case of one vs all type of problems. If we consider a data set containing 10 output classes, one vs all will lead to a 1:9 ratio for each class assuming that all classes have same/similar count of points in the original data set. It is also not wise to simply create copies of the data points belonging to minority class as it will not only lead to overfitting but will also be a wastage of resources like time and computing power. The results clearly depict that SMOTE can often lead to poor performance on not only the minority class but also the majority class. The approaches introduced in this paper are performing better in almost every aspect in comparison to SMOTE. The relative performance of the techniques introduced in this paper can vary depending on training data.

REFERENCES

[1] Y. Iwatate, I. Hoshino, H. Yokota, F. Ishige, M. Itami, Y. Mori, S. Chiba et al. "Radiogenomics for predicting p53 status, PD-L1 expression, and prognosis with machine learning in pancreatic cancer", *British Journal of Cancer,* vol. 123, no. 8, pp. 1253-1261, 2020. https://doi.org/10.1038/s41416-020-0997-1

[2] E. Ileberi, Y. Sun, Z. Wang, "A machine learning based credit card fraud detection using the ga algorithm for feature selection", *Journal of Big Data*, vol. 9, 2022. https://doi.org/10.1186/s40537-022-00573-8

[3] A. A. Enguang, M. Muhammat, Y. Zhao, K. Ubul, "Context aware semantic adaptation network for cross domain implicit sentiment classification", *Scientific Reports*, vol. 11, 2021. https://doi.org/10.1038/ s41598-021-01385-1

[4] V. Rasche, R. Proksa, R. Sinkus, P. Bornert, H. Eggers, "Resampling of data between arbitrary grids using convolution interpolation", *IEEE transactions on medical imaging*, vol. *18*, no. 5, pp.385-392, 1999. https://doi.org/10.1109/42.774166

[5] F. Feng, K-C. Li, J. Shen, Q. Zhou, X. Yang, "Using cost-sensitive learning and feature selection algorithms to improve the performance of imbalanced classification", *IEEE Access,* vol. 8, 2020. https://doi.org/10.1109/ ACCESS.2020.2987364

[6] S. Wang, Y. Dai, J. Shen, J. Xuan, "Research on Expansion and Classification of Imbalanced Data Based on SMOTE Algorithm", Scienific reports, vol. 11, no. 1, pp. 1-11, 2021. https://doi.org/10.1038/s41598-021-03430-5

[7] https://data.gov.il/dataset/covid-19: Government of israel dataset page

[8] E-N. Abd, E.E. Hemdan, A. El-Sayed, "An efficient fraud detection framework with credit card imbalanced data in financial services", *Multimedia Tools and Applications*, (2022). https://doi.org/10.1007/ s11042-022-13434-6

[9] F. Feng, K.C. Li, E. Yang, Q. Zhou, L. Han, A. Hussain, M. Cai, "A novel oversampling and feature selection hybrid algorithm for imbalanced data classification", *Multimedia Tools and Applications*, vol. 82, no. 3, pp. 3231-3267. https://doi.org/10.1007/s11042-022-13240-0

[10] D.T. Dehkordy, A. Rasoolzadegan, "A new machine learning-based method for android malware detection on imbalanced dataset", *Mutimedia Tools and Applications*, vol. 80, 2023. https://doi.org/10.1007/ s11042-021-10647-z

[11] I.J. Goodfellow, J. Pouget-Abadie, M. Mirza, B. Xu, D. Warde-Farley, S. Ozair, A. Courville, Y. Bengio, "Generative Adversarial Networks", arXiv, 2014. https://doi.org/10.48550/ARXIV.1406.2661. https://arxiv.org/abs/1406.2661

[12] https://www.kaggle.com/datasets/nyashachizampeni/hit400-credit-cardfraud-dataset

Authorized licensed use limited to: DELHI TECHNICAL UNIV. Downloaded on May 29,2023 at 05:55:12 UTC from IEEE Xplore. Restrictions apply.

2023 10th International Conference on Signal Processing and Integrated Networks (SPIN) | 978-1-6654-9099-3/23/$31.00 ©2023 IEEE | DOI: 10.1109/SPIN57001.2023.10117315

A novel locally connected recurrent neural network for identification of nonlinear dynamical system

Shobana. R
Dept. of Electrical Engineering
Delhi Technological University
New Delhi, India
shobanaramasubramanian@gmail.com

Rajesh Kumar
Dept. of Electrical Engineering
National Institute of technology
Kurukshetra-136119, India
rajeshmahindru23@gmail.com,
rajeshmahindru23@nitkkr.ac.in

Bhavnesh Jaint
Dept. of Electrical Engineering
Delhi Technological University
New Delhi, India
bhavneshjaint@dtu.ac.in

***Abstract*—In this work, a novel Locally Connected Recurrent Neural Network structure (LLCRNN) is designed for the identification of nonlinear systems. The structure is an extension of a local recurrent neural network with better dynamic extraction capability. The weights are updated using the offline mode of the gradient descent algorithm. The proposed structure is found to give better identification as compared to other considered neural network structures such as Feed Forward Neural Network (FFNN) and Local Recurrent Neural Network structure (LRNN). The efficiency of the proposed structure is proved against the selected structures.**

***Keywords*— RNN, LRNN, identification, ANN, dynamical systems, PRNN**

I. INTRODUCTION

Nonlinear systems are ones whose outputs are not proportional to the inputs at any instant in time. They infer properties such as uncertainty, varied temporal patterns, and time-varying parameters over time. With most real-world applications being highly nonlinear, an appropriate physical model that depicts the system's behavior is always required for future prediction. System identification is one such approach to derive the necessary physical model with the available input-output measurements. Black-box models have been widely used identification methods when more insight regarding the system under observation is required without any information regarding the system. On one side, black-box methods such as the ARIMA models are available for accurate learning and identification of the system. But fail to map the nonlinear data present in the observed model. Neural networks, on the other hand, can successfully approximate any nonlinear input-output relationship and give a better identification model without requiring any differential equation [1]. In this context, neural networks are classified into two categories: Feed Forward Neural Networks (FFNN) and Recurrent Neural Networks (RNN). FFNN is successfully applied to many applications of prediction, classification, and regression problems [2]. They are networks with static mappings. Unless they are provided with tapped delay lines, FFNN cannot be made dynamic and they cannot retain their past information. RNNs are more robust than FFNNs. They possess dynamic mappings by nature. This helps them in retaining their past information without externally supplying the memory connections. RNN can be developed as a Partial Recurrent Neural Network (PRNN) or a Fully Recurrent Neural Network (FRNN) type. FRNN has self-feedback connections with every hidden neuron connected to other neurons in the layer [2]. FRNNs are very capable networks for accurate identification but are quite complex and possess a large number of trainable weights due to their structure. Many forms of PRNN such as Elman and Jordan are also widely used in place of FRNN to extract the dynamics of the system under observation. In Elman and Jordan, an additional context layer is introduced and the inputs to the context layer are from self-hidden units or the output layer respectively. One another type of PRNN is the Local Recurrent Neural Network (LRNN). These structures have self-feedback hidden connections connected to themselves and not with other hidden neurons in the layer [4]. They have the advantage of the structure is simple with few possible weights and shorter training time yet as efficient as FRNN and other structures of PRNN. RNNs are found to relatively give good analysis and prediction for time series data [5]. Time series are generally characterized by past input and output samples. RNN being a dynamic structure is found to easily capture the deterministic nature of the system under the influence of external input such as noise. The author in [7] has proposed a structure for diagonal neural network and has proved the efficiency of a dynamic network against the static networks. The authors of [8] have proposed a deep learning hybrid structure for diagonal neural network. The weights are updated using lyapunov stability and hybrid algorithm based

978-1-6654-9099-3/23/$31.00 ©2023 IEEE

Authorized licensed use limited to: DELHI TECHNICAL UNIV. Downloaded on May 15,2023 at 09:57:56 UTC from IEEE Xplore. Restrictions apply.

on kohonen map. Many papers in literature also cite the applications of local recurrent networks in wide application [9], [10], [11], [12]. In this paper, a novel partial recurrent structure named locally connected recurrent neural network structure (LLCRNN) is proposed for the identification of nonlinear systems. The main idea is to propose a better structure with simplicity and robustness than existing recurrent structures in the literature. The weights are updated using an offline gradient descent algorithm. Series-parallel mode of identification is considered. The rest of the paper is organized as follows: Section II explains the problem statement and the main objective to carry out this work. Section III elaborates on the structure of the proposed identification neural model. Section IV explains the weight update equations using the gradient descent algorithm. The proposed structure is applied to one example and the simulation results are included in section V. Section VI briefs the conclusion and efficiency of the proposed structure over the existing local recurrent network and feed-forward network.

II. PROBLEM STATEMENT

Let us consider a plant with the following input-output relationship:

$$y_p(k) = f[y_p(k), y_p(k-1), \ldots, y_p(k-n), r(k-1) \ldots, r(k-m)] \quad (1)$$

Here, f(.) is the nonlinear mapping function. In this study, a neural network is considered for approximation. n and m are the orders of the plant. The plant uses the series-parallel type of identification. When LLCRNN is considered as an identifier, the input-output mapping is as below:

$$y_{llcrnn}(k) = \tilde{f}[y_p(k), y_p(k-1), \ldots, y_p(k-n), r(k-1) \ldots, r(k-m)] \quad (2)$$

Where, $y_{llcrnn}(k)$ denotes the output of the proposed structure. $\tilde{f}$ is the nonlinear function. The plant becomes completely identifiable when the newly identified function $\tilde{f} = f$. The main objective of the work is to achieve$\tilde{f} = f$, by keeping the identification error as low as possible.

$$\lim_{k\to\infty}(y_p(k) - y_{llcrnn}(k)) \quad (3)$$

The weights are continuously updated by the gradient descent back propagation algorithm.

III. MATHEMATICAL FORMULATION OF THE PROPOSED STRUCTURE

The proposed structure LLCRNN has one hidden and an output layer with an additional trainable weight between the input and output layers. A series-parallel identification structure is used to design the new model. The structure is supplied with one external input r(k) and one delayed input of the plant y_p(k-1). The number of inputs required for this proposed structure is minimum, due to their self-recurrent loops. The input signals are passed to the hidden layer through weight links w_x(k). The hidden layer receives the weighted sum of signals from both the input layer and its self-recurrent neurons. A tangent hyperbolic activation function is used as a nonlinear function. The weighted sum of signals from the hidden layer is sent to the output layer via weights w_o(k). The signals from the input layer are multiplied by weight w_α(k), before reaching the output layer. This additional layer is found to make the structure more robust to incoming external noises getting added to the system.

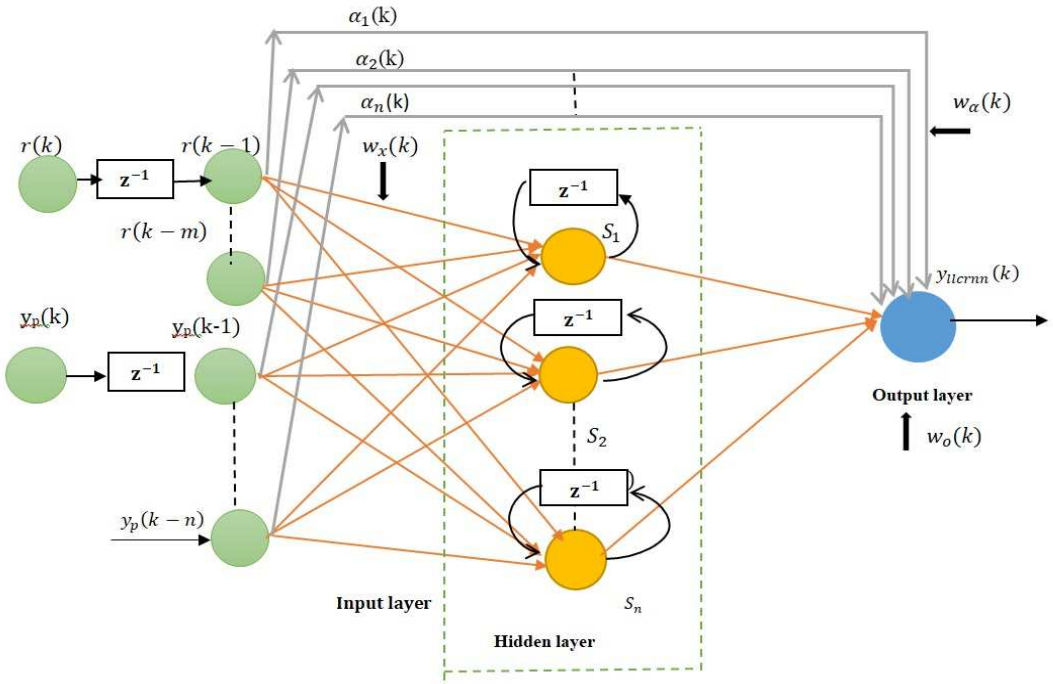


Fig.1 Proposed LLCRNN structure

Authorized licensed use limited to: DELHI TECHNICAL UNIV. Downloaded on May 15,2023 at 09:57:56 UTC from IEEE Xplore. Restrictions apply.

Fig 1 shows the proposed structure. The hidden layer output, $S_i(k)$ is computed as follows:

$$S_i(k) = g_1\left(\sum_{i=1}^{m} X(k-i)w_x(k) + b_x(k)w_b(k) + P_i(k)\right) \quad (4)$$

where X(k-i)=[r(k),y_p(k-1)] denotes the input vector. $P_i(k)$ denotes the self-recurrent neurons of the hidden layer.

The output of the network is computed as follows:

$$y_{llcrnn}(k) = g_2\left(\sum_{i=1}^{m} S_i(k)w_o(k) + b_o(k)w_o(k) + X(k)w_\alpha\right) \quad (5)$$

where w_α denotes the weights acting across the input and output layer.

IV. LEARNING ALGORITHM

The weights are updated offline through a gradient descent back propagation algorithm at every iteration. A cost function is defined at the beginning of the training and the training is carried out until the cost function is found to reach the minimum value. Here, Mean square error (MSE) is chosen as the cost function. The trainable weights are [w_x, w_o, w_α].

Mathematically the cost function is given as

$$E(k) = \frac{1}{2}\left[y_p(k) - y_{llcrnn}(k)\right]^2 \quad (6)$$

Using the chain rule, all the weights [w_x, w_o, w_α] are updated at every iteration and the stochastic descent algorithm is applied to update the new weights using the formula:

$$w_{x,o,\alpha}(new) = w_{x,o,\alpha}(old) + \beta\frac{\delta E}{\delta w_{x,o,\propto}} \quad (7)$$

where $\frac{\delta E}{\delta w_{x,o,\propto}}$ indicates the weight updation derivative of [w_x, w_o, w_α] and β is the learning rate. It is kept close between 0 and 1.

V. SIMULATION RESULTS

Consider a nonlinear plant with a differential equation given by [4]:

$$y_p(k) = \frac{y_p(k-1)}{1+y_p(k-2)^2} + r^3(k-1) \quad (8)$$

The output of the plant depends on past inputs and outputs. They can be expressed in series-parallel identification mode as:

$$y_p(k) = f[y_p(k-1), y_p(k-2), r(k-1)] \quad (9)$$

The LLCRNN as an identifier will also take the form as below:

$$y_{llcrnn}(k) = f1\left[y_p(k-1), r(k-1)\right] \quad (10)$$

The LRNN and FFNN when used as an identifier take the form as below:

$$y_{lrnn}(k) = f2[y_p(k-1), r(k-1), y_p(k-2)\ ] \quad (11)$$

$$y_{ffnn}(k) = f3[y_p(k-1), r(k-1), y_p(k-2)] \quad (12)$$

Here, f1, f2, f3 are the nonlinear mapping functions. The performance of the LLCRNN is compared with the local recurrent neural network and feed forward recurrent network in terms of MSE, MAE, and RMSE. The proposed structure though seems complex in terms of addition of extra additional weights as compared to FFNN and LRNN, the ability of those structures to learn more complex problems that change highly with time is comparatively high. The reason being that FFNN are static structures with no memory. FFNN networks cannot retain past information that is very necessary for any dynamic system. Similarly though LRNN are dynamic structures yet to capture more complex behaviour, more temporal connections are required. The proposed structure has an additional link between input and output that makes the structure more adaptable to new changes and is found to give better efficiency compared to other structures with lesser inputs and computation time. The number of dependent past information required for successful training are also very less in LLCRNN as compared to FFNN and LRNN. The FFNN uses more hidden neurons to achieve the same training result. Figure 2 shows the comparison of MSE obtained for various structures. Figure 3 shows the comparison of MAE obtained for various structures. Figure 4 shows the comparison of responses obtained for various structures. Table 1 gives the comparison of the proposed structure with other selected structures. It can be seen from the table that the proposed structure though has more trainable parameter compared to FFNN but has better prediction accuracy as compared to LRNN and FFNN. The structure takes minimum inputs and fewer hidden neurons as compared to FFNN and LRNN. When the trainable weights w_α are made zero, then the structure itself reduces to LRNN.

Authorized licensed use limited to: DELHI TECHNICAL UNIV. Downloaded on May 15,2023 at 09:57:56 UTC from IEEE Xplore. Restrictions apply.

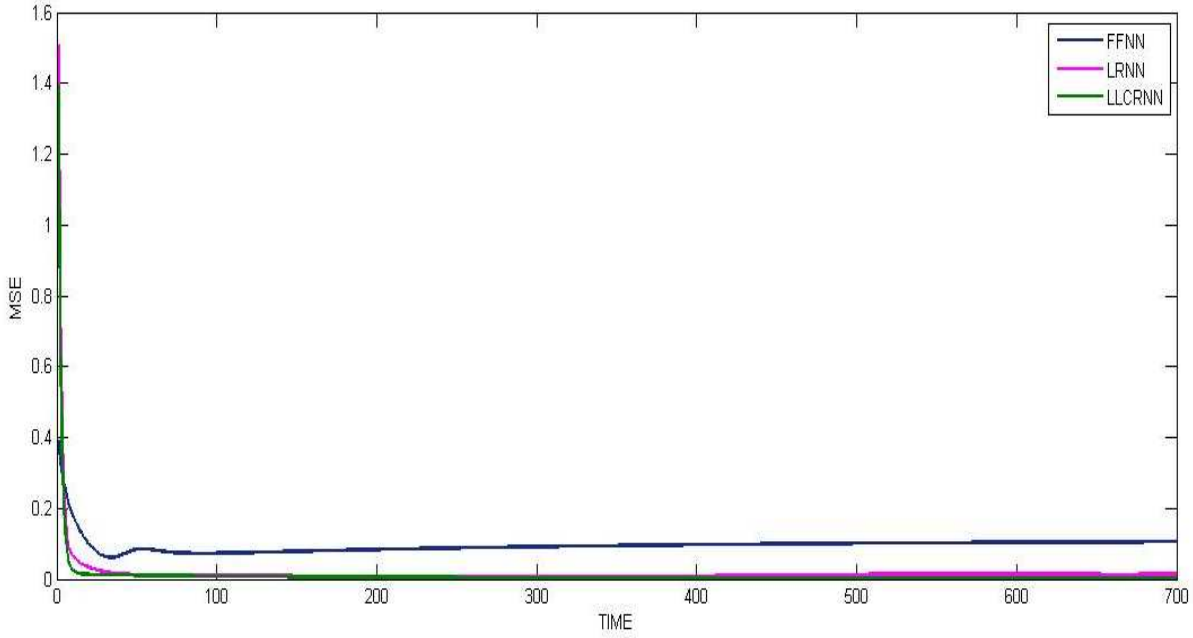


Fig 2 Comparison of MSE plots of various structures

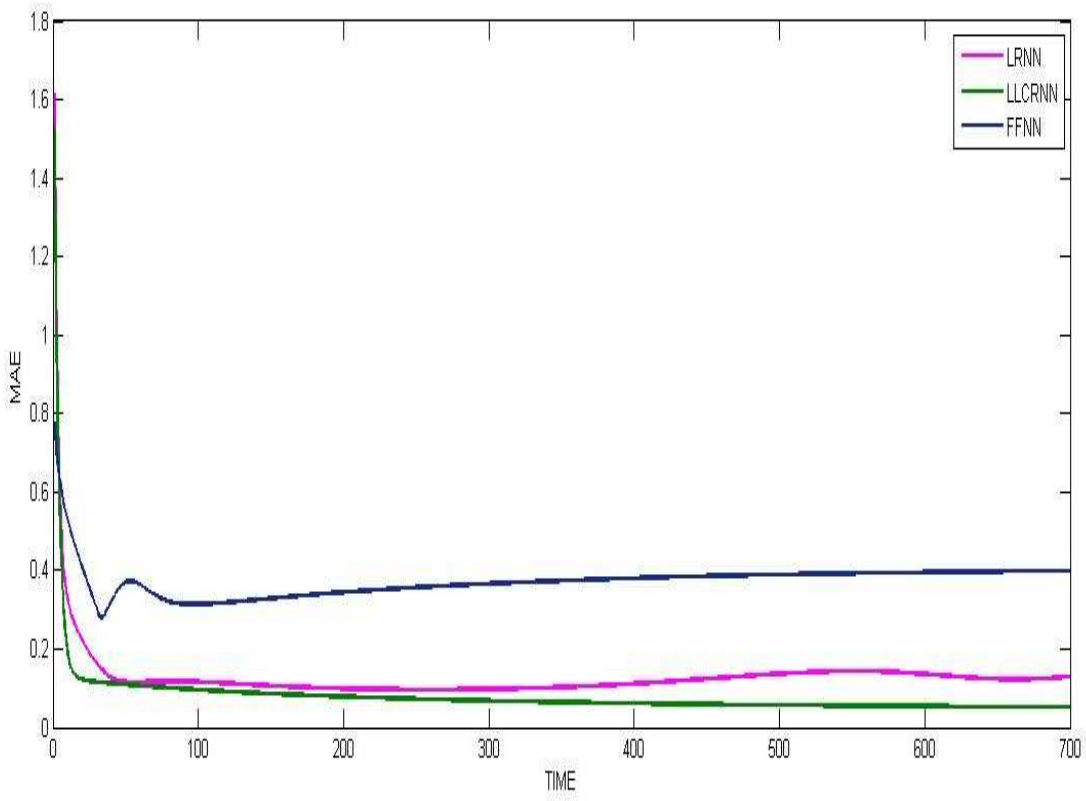


Fig 3 Comparison of MAE plots of various structures

Authorized licensed use limited to: DELHI TECHNICAL UNIV. Downloaded on May 15,2023 at 09:57:56 UTC from IEEE Xplore. Restrictions apply.

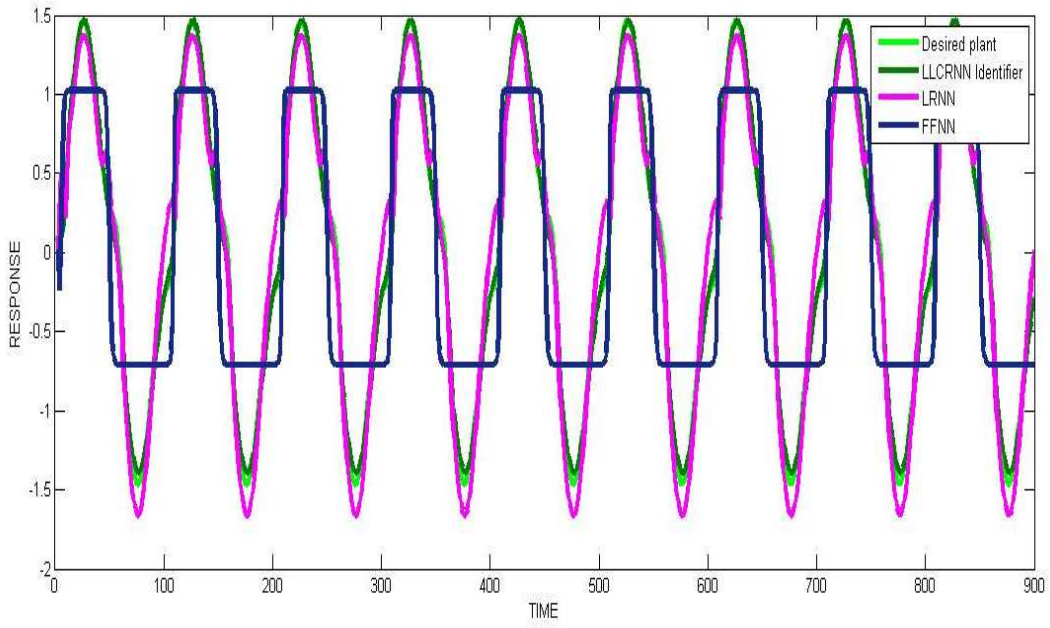


Fig 4 Comparison of performance of proposed structure at the end of training

Table 1 Comparison of performance of proposed structure with other neural structures

Structure	No of Samples	No of hidden neurons	No of Inputs considered	MSE	MAE	RMSE
LLCRNN	900	3	2	0.0014	0.0448	0.0369
LRNN	900	3	3	0.3001	0.1895	0.1734
FFNN	900	4	3	0.1051	0.3986	0.3282

VI. CONCLUSION

In this paper, we have proposed a novel recurrent structure named locally connected recurrent neural network structure (LLCRNN) for the identification of nonlinear systems. The identification structure proposed is quite simple with fewer tunable parameters. The additional links made the structure more adaptable to changing dynamics of the system even with a simple learning algorithm. The proposed structure MSE and RMSE as low as 0.0014 and 0.0369 respectively as compared to LRNN and FFNN. Also FFNN being the static network has high MAE and RMSE characteristics. It can be concluded that memory structures models dynamic systems efficiently than static networks.

VII. FUTURE WORKS

Many studies still needs to be carried out in the field of dynamics extraction in future studies. One research field would be use of hybrid learning rate during weight update process. Another would be use of optimisation based algorithm for training the network such as PSO to achieve global stability and to make learning more effective. An approach to select optimal number of hidden neurons for real-time problems needs be reviewed in future works.

REFERENCES

1. Quaranta, Giuseppe, Walter Lacarbonara, and Sami F. Masri. "A review on computational intelligence for identification of nonlinear dynamical systems." Nonlinear Dynamics 99.2 (2020): 1709-1761.
2. Chen, S. A. B. S., and Stephen A. Billings. "Neural networks for nonlinear dynamic system modelling and identification." International journal of control 56.2 (1992): 319-346.
3. Kumpati, S. Narendra, and Parthasarathy Kannan. "Identification and control of dynamical systems using neural networks." IEEE Transactions on neural networks 1.1 (1990): 4-27.
4. Thammano, Arit, and Phongthep Ruxpakawong. "Nonlinear dynamic system identification using recurrent

Authorized licensed use limited to: DELHI TECHNICAL UNIV. Downloaded on May 15,2023 at 09:57:56 UTC from IEEE Xplore. Restrictions apply.

connection weight." Memetic Computing 2.4 (2010): 273-282.
5. Coban, Ramazan. "A context layered locally recurrent neural network for dynamic system identification." Engineering Applications of Artificial Intelligence 26.1 (2013): 241-250.
6. Kumar, Rajesh, Smriti Srivastava, and J. R. P. Gupta. "Diagonal recurrent neural network based adaptive control of nonlinear dynamical systems using lyapunov stability criterion." ISA transactions 67 (2017): 407-427.

7. Kumar, Rajesh, et al. "Comparative study of neural networks for dynamic nonlinear systems identification." Soft Computing 23.1 (2019): 101-114.
8. El-Nagar, Ahmad M., Ahmad M. Zaki, F. A. S. Soliman, and Mohammad El-Bardini. "Hybrid deep learning diagonal recurrent neural network controller for nonlinear systems." Neural Computing and Applications (2022): 1-20.
9. Banakar, Ahmad, and Mohammad Fazle Azeem. "Local recurrent sigmoidal–wavelet neurons in feed-forward neural network for forecasting of dynamic systems: Theory." Applied Soft Computing 12, no. 3 (2012): 1187-1200.
10. Elsheikh, Ammar H., Swellam W. Sharshir, Mohamed Abd Elaziz, A. E. Kabeel, Wang Guilan, and Zhang Haiou. "Modeling of solar energy systems using artificial neural network: A comprehensive review." Solar Energy 180 (2019): 622-639.
11. Noël, Jean-Philippe, and Gaëtan Kerschen. "Nonlinear system identification in structural dynamics: 10 more years of progress." Mechanical Systems and Signal Processing 83 (2017): 2-35.
12. Kroll, Andreas, and Horst Schulte. "Benchmark problems for nonlinear system identification and control using soft computing methods: Need and overview." Applied Soft Computing 25 (2014): 496-513.

Authorized licensed use limited to: DELHI TECHNICAL UNIV. Downloaded on May 15,2023 at 09:57:56 UTC from IEEE Xplore. Restrictions apply.

Journal of Physics: Conference Series

PAPER • OPEN ACCESS

A novel passive micromixer model computational analysis with twist and bend

To cite this article: Md Gulam Mustafa *et al* 2023 *J. Phys.: Conf. Ser.* **2484** 012041

View the article online for updates and enhancements.

You may also like

- Micromixers—a review
Nam-Trung Nguyen and Zhigang Wu
- A novel application of dielectric stack actuators: a pumping micromixer
Susana Solano-Arana, Florian Klug, Holger Mößinger et al.
- Volume-preserving strategies to improve the mixing efficiency of serpentine micromixers
Sajad Razavi Bazaz, Amir Hossein Hazeri, Omid Rouhi et al.



This content was downloaded from IP address 14.139.251.98 on 18/05/2023 at 06:04

A novel passive micromixer model computational analysis with twist and bend

Md Gulam Mustafa[1], Mohammad Zunaid[1] and Samsher Gautam[1]

[1]Department of mechanical Engineering, Delhi Technological University, Delhi, India

E-mail: gm09mes31@gmail.com

Abstract. A dynamic mixing model for a microfluidic platform that uses bending and twisting characteristic is proposed in this work. The action of twisting and bending on mixing efficient in the microchannel is tested using Navier-Stokes equations. Micromixers being broadly applied in micro total analysis systems (μTAS). Passive micromixers are largely preferred from their heftiness, serenity of amalgamation and cost effective. However rapid mixing in this model is difficult but can be achieved with a twist in the model and offset. From the past study, we know that with a high Reynolds number mixing efficiency effectively improved. Chaotic advection allows the micromixer model to generate secondary flow which led to a drop in high-pressure drop in the model.

1. Introduction

Microfluidic systems have newly been popularized as a fundamental and constructive affair in different areas such as industry, chemistry, biomedical, and many other. One of the pivotal components of these whole systems is the micromixer structure, the main goal is to make agent mixing highly effective and quick [1]. However, the small feature size reduces the Reynolds number, which limits the mixing of fluid to diffusion. However, mixing of fluid is important in many operations, and the effectiveness of the mixing process may have a direct implication on the performance of the entire structure. Although numerous strategies and procedure have been put out to address this issue, additional research is still required.

The micromixers can be parted into passive and active varieties, depending on whether or not external pressures are used to produce correct mixing. Regarding the passive macromixing, the design and implementation of microchannels, such as Y- [2] and T-type [3] flows, multi-laminating, split-and-recombine raza [4, 5], chaotic [6, 7], jet colliding, spiral [8, 9] etc. can be used. On other way, techniques for active mixing include time-pulsing flow [10], which is the result of a periodic change in electrical or pumping fields, and acoustic fluid shaking [11], ultrasound [12, 13], etc. can be signed. A fluid motion was induced (ultrasonically) can be utilized in analytical instrument, for synthesizing chemical for medicinal value. The 3D twisted micromixer promoted by [14] for Re ~ 6–70 which utilized secondary motion for better mixing. [15] Use finite element analysis for mixing process in a zig-zag microchannel and focal point is the impact of flow recirculation's at high Reynold (Re) on mixing. [16, 17] heft out a review on sinusoidal walls passive micromixers showing analysis of both procedures using CFD and experimental. The aspect of the side walls was shown to be a crucial factor influencing the Dean build and separating vortices' mixing effectiveness.[18] a detailed review to show the need for microdevices, in various field, further stated that model with sharpness and smallness chaotic flow increases. Raza et

Content from this work may be used under the terms of the Creative Commons Attribution 3.0 licence. Any further distribution of this work must maintain attribution to the author(s) and the title of the work, journal citation and DOI.
Published under licence by IOP Publishing Ltd

al [19] introduced multi objective optimization in their model and on similar pattern heuristic algorithms [20, 21] can be implemented.

There are instances when the usual behaviour of the fluid flow is altered by the employment of external forces for mixing, which results in the anomaly of active mixing. the use of outside forces in blending, which results in the phenomena of active mixing, can induce modifications in the fluid flow's usual behaviour [22, 23]. There is good amount of enthusiasm in employing microfluidic equipment's in experimental electronics and medical research as a result of their advancement [24]. These devices have a high surface to volume ratio, excellent control system, and the capability to alter samples throughout the procedure, all of which reduce the expense of samples (reactants) in the process. As a result, using these devices with lab equipment minimizes the amount of time and space needed for analysis. Feature of microfluidic are surface-to-volume ratio higher, to have substantially faster analysis times than milli-scale ones. To supply an unceasing flow of one liquid phase or many liquid phases through microchannels, continuous-flow microfluidics needs an external delivery system. As specimen preparation and disclosure are necessary for a range of biological and chemical experiments, mixing and separation are crucial procedures in the majority of lab-on-a-chip platforms [25]. [26] gave an overview of cooling technique in MCHS in various fractal, [27] analysed ejector refrigeration using numerical computation.

2. Methodology

The current problem work is shown schematically in figure 1, which is a proposed hybrid T model with twisting and bending (TTM). The inlet cross-section of the TTM is 100x200 µm and length of 3000 µm. We have varied the twisting for 30^0, 50^0, and 70^0 of bending with four twists.

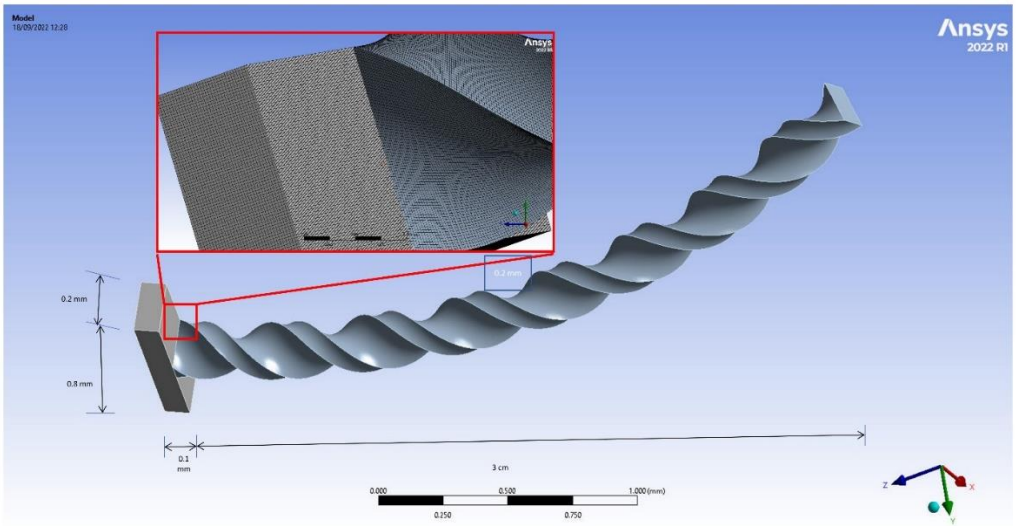


Figure 1. Geometry with 4 Twist and 30^0 bend with 3.25M element mesh (Insert).

2.1. Governing Equations

Fluid mixing and flow dynamics is evaluated by applying the unsteady continuity and Navier-Stokes equations in the microchannel, ANSYS Fluent 2022 computational fluid dynamics (CFD) software program used in analysis of this work. Following is an example of how to describe the unstable continuity and Navier-Stokes equations:

Fluids with multi-component, the bulk motion is represented by utilizing one value of velocity and pressure, & equations is defined for every component regarding the conservation of mass. With the use of the following transient advection-diffusion model, mixing analysis was carried out [18] specified for concentration field:

$$\frac{\partial C_i}{\partial t} + \left(\underset{V}{\rightarrow}.\underset{\nabla}{\rightarrow}\right) C_i = \alpha \nabla^2 C_i \tag{1}$$

In this study we used two akin fluids having the similar viscosity, ν, and fluid density, ρ. The kinematic viscosity (ν) & diffusion coefficient (α), were set to $10^{-6}m^2s^{-1}$ and $2*10^{-09}m^2s^{-1}$, respectively [24]. In order to study mixing, working fluids properties is of water and a water dye. The water dye mass fraction was calculated using equation (3) both in time and space.

Table 1. Nomenclature.

$\underset{V}{\rightarrow}$	Fluid Velocity	ρ	Density
ν	Kinematic Viscosity	C_i	Concentration
μ	Viscosity		

The computational domain was discretized using hexahedral cells. The grid lines were perfectly matched with the channel's shape in the streamwise direction to capture the sinusoidal walls. The mixing index (MI) was tested for grid sensitivity to estimate the final value of element needed for spatial resolution. We used five set of element systems i.e., 3076794, 2060740, 1056088, and 500072 to test grid sensitivity. In comparison to a finer grid, the grid with 3076794 nodes was determined to have a relative inaccuracy in the mixing index of less than 0.5%, making it suitable for study.

The advection variables in the governing eqs. were discretized with the help of a second-order upwind differencing technique [20]. The convergence behaviour was considerably enhanced using multigrid approaches. The residual value of 10-6 for the normalized root mean square served as the convergence criteria. A periodic solution—one that does not appreciably differ from one cycle to the next—was computed for the pulsatile flows over a long enough length of time.

A variance-based methodology was used to assess the micromixer's mixing effectiveness. [24] applied an evaluating factor has been applied to explain the variations in mass flowrate between the channel sides and the centre. The mathematical formula below can be used to numerically express the fluctuation of the mass fraction of the fluid mixture on a cross sectional plane perpendicular to the direction of flow:

$$\sigma = \sqrt{\sum_{i=1}^{N} \frac{(C_i - \mu)^2}{N} \left(\frac{V_i}{V_{mean}}\right)} \tag{2}$$

The MI is finally expressed as follows for any plane which is cross sectional and parallel to the axial direction:

$$MI = 1 - \frac{\sqrt{\sum_{i=1}^{N}((C_i - \mu)^2)/N(V_i/V_{mean})}}{\mu} \tag{3}$$

It was determined that the variance would be at its highest for completely undiffuse fluids and at its lowest for fully mixed fluids. A higher MI value (nearly 1) denotes better mixing performance. To take the temporal dependence into consideration of equations (4) & (5), the MI was moderated across 4 values at intervals of one quarter cycle.

2.2. Computational approach validation and analysis

It's very imperative to validate the numerical technique before beginning the actual research. Figure 2 shows the result comparison with [28] and my problem for bend angle 300, and is a great deal similar to one another. After

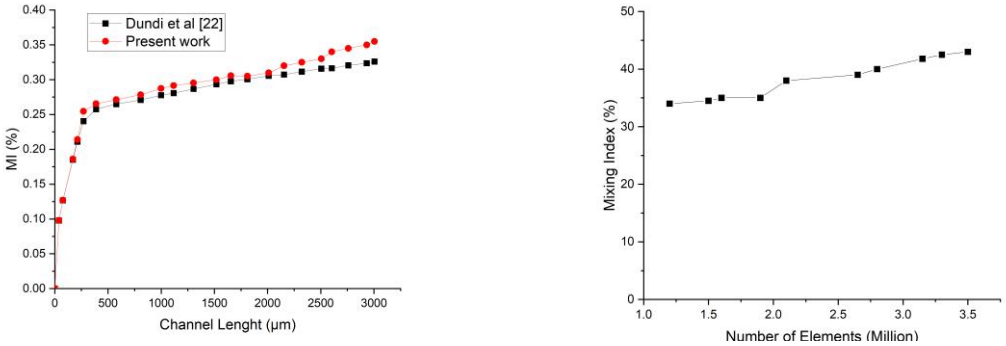


Figure 2. (a) Comparison of current work with [28] (b) grid sensitivity

going through rigorous testing for grid validation, the results show the good accuracy with 3.1 million elements, which is thus selected for all simulation and is acceptable result with little or no variation in result with further increased in element shown in Figure 2 (b).

3. Results and discussions

3.1. Variation of Re effect of MI

Figure 2 shows mixing performance at various Re for present model for bend angle 30^0, 50^0 and 70^0. Further we can say by seeing the result that it's better from ST (for TTM). For this effect to be study, we took Re from 10 to 550. From this figure we came to conclusion that with increase in Re, MI also increases.

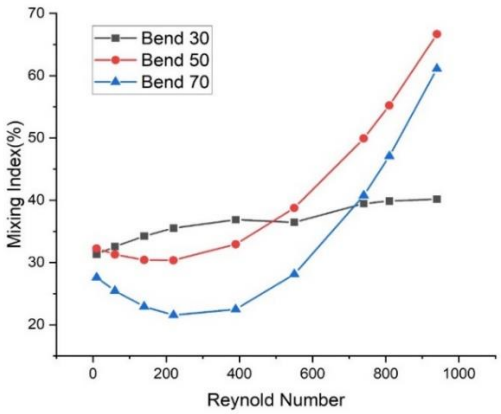


Figure 3. Mixing index for TTM at different Re at bend angle 30^0, 50^0 and 70^0 for 4 twists.

As already discussed, TTM gives better MI than ST shown in Figure 3, the pressure drops (ΔP) for model is also less. This increase in MI is due to chaotic advection induced by twisting and bending, which is secondary flow, which can be described from Fig 4 which is a velocity contour. We coupled pressure and velocity using the SIMPLEC algorithm [21]. By use of second-order backward Euler techniwue, the discretization in time for transient computation was carried out.

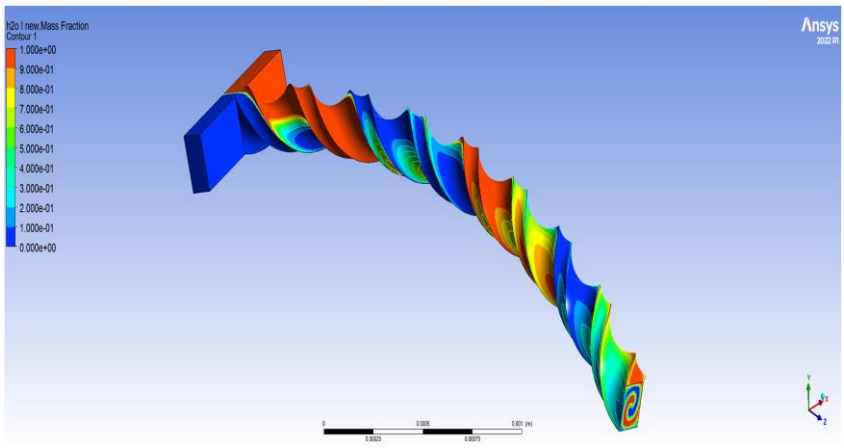


Figure 4. Mass fraction of water and dye of TTM at bend angle 30^0 with 4 twists for Re 550 (at wall-fluid).

3.2. Effect of bend with twist

For this we varied the twisting from 1 to 3 with bending, which is shown in the Figure 3. With number of twisting, Mi increases. This kind of microchannel creates a secondary flow driven by centrifugal force, which drives an accelerated pressure decrease in the microchannel. Chaotic advection is formed in micromixers by bending or folding the mixing channel. Along the mixing channel, the mixing performance of offset entrances T shape mixers, basic T shape mixers, and offset entrances T-micromixers maintaining bend shape were all assessed. Figure 4 shows the mass fraction of the water with dye for my model TTM bend angle of 30^0 with 4 twists for Re 550.

4. Conclusions

From the above numerical results, the MI of the TTM was discussed, some of the valuable conclusions reached. From the simulation, we conclude that the MI of the micromixer increased with number of bend angle and by increasing Re above 1, chaotic convection phenomenon occurred the model channel, which have a vast impact on the mixing efficiency, especially in the micromixer. Re has a specific rule that governs how it affects the micromixer's mixing performance, and the micromixer's structure affects how much Re has an impact. Therefore, to enhance the functionality of the micromixer in issues of this nature, we should focus on improving the microchannel framework. Additionally, the performance of the micromixer after the change in Re complies with the general principle. The mixing performance of the micromixer can be further improved by changing Re. We can thus point out the following finding

a) TTM model gives better results than ST by inclusion of chaotic advection mechanisms. Up to 35% where is increase in MI from ST
b) ΔP is slightly more in TTM than in ST
c) With the number of twisting, MI increases

References

[1] Lee CY, Fu LM 2018 Recent advances and applications of micromixers. *Sensors and Actuators, B: Chemical* **259** 677–702
[2] Baheri Islami S, Khezerloo M 2017 Enhancement of mixing performance of non-newtonian fluids using curving and grooving of microchannels. *Journal of Applied Fluid Mechanics* **10** 127–141
[3] Shi H, Zhao Y and Liu Z 2020 Numerical investigation of the secondary flow effect of lateral structure of micromixing channel on laminar flow. *Sens Actuators B Chem*; **321** Epub ahead

of print 15 October 2020 DOI: 10.1016/j.snb.2020.128503
[4] Raza W, Hossain S and Kim KY 2018 Effective mixing in a short serpentine split-and-recombination micromixer. *Sens Actuators B Chem* **258** 381–392
[5] Chen X, Li T, Zeng H, et al.2016 Numerical and experimental investigation on micromixers with serpentine microchannels. *Int J Heat Mass Transf* **98** 131–140
[6] Deval J, Tabeling P and Ho CM 2002 A dielectrophoretic chaotic mixer *Proceedings of the IEEE Micro Electro Mechanical Systems (MEMS)* 36–39
[7] Prakash R, Zunaid M and Samsher 2021 Simulation analysis of mixing quality in T-junction micromixer with bend mixing channel In: *Materials Today: Proceedings Elsevier Ltd* pp. 3833–3838
[8] Tokas S, Zunaid M and Ansari MA 2021 Non-Newtonian fluid mixing in a Three-Dimensional spiral passive micromixer In: *Materials Today: Proceedings Elsevier Ltd* 3947–3952
[9] Mehrdel P, Karimi S, Farré-Lladós J, et al.2018 Novel variable radius spiral-shaped micromixer: From numerical analysis to experimental validation. *Micromachines (Basel)* **9** Epub ahead of print 2018 DOI: 10.3390/mi9110552
[10] Balasubramaniam L, Arayanarakool R, Marshall SD, et al. 2017 Impact of cross-sectional geometry on mixing performance of spiral microfluidic channels characterized by swirling strength of Dean-vortices *Journal of Micromechanics and Microengineering* **27** Epub ahead of print 2017 DOI: 10.1088/1361-6439/aa7fc8
[11] Lim E, Lee L, Yeo LY, et al. Acoustically-Driven Micromixing : Effect of Transducer Geometry 1
[12] Moroney RM, White RM and Howe RT Ultrasonically induced microtransport 1991 *Proceedings IEEE Micro Electro Mechanical Systems* 277–282
[13] Yang Z, Matsumoto S, Goto H, et al. 2001 Ultrasonic micromixer for microfluidic systems *Sens Actuators A Phys* **93** 266–272
[14] Liu M 2011 Computational study of convective–diffusive mixing in a microchannel mixer *Chem Eng Sci* **66** 2211–2223
[15] Mengeaud V, Josserand J and Girault HH 2002 Mixing Processes in a Zigzag Microchannel: Finite Element Simulations and Optical Study *Anal Chem* 2002 **74** 4279–4286
[16] Khosravi Parsa M, Hormozi F 2014 Jafari D Mixing enhancement in a passive micromixer with convergent-divergent sinusoidal microchannels and different ratio of amplitude to wave length. *Comput Fluids* **105** 82–90
[17] Bird RB 2002 Transport phenomena *Appl Mech Rev* **55** R1–R4
[18] Bayareh M, Ashani MN and Usefian A 2020 Active and passive micromixers: A comprehensive review *Chemical Engineering and Processing - Process Intensification* 2020 **147** 107771
[19] Raza W, Ma SB and Kim KY 2018 Multi-objective optimizations of a serpentine micromixer with crossing channels at low and high Reynolds numbers *Micromachines (Basel)* **9** Epub ahead of print 2018 DOI: 10.3390/mi9030110
[20] Singh RK, Gangwar S, Singh DK, et al.2021 Multi-objective optimization of magnetic abrasive finishing by desirability function with genetic algorithm *International Journal of Engineering, Science and Technology* **13** 1–9
[21] Tayyab M, Ahmad S, Akhtar MJ, et al.2022 Prediction of mechanical properties for acrylonitrile-butadiene-styrene parts manufactured by fused deposition modelling using artificial neural network and genetic algorithm. https://doi.org/101080/0951192X20222104462 Epub ahead of print 2022. DOI: 10.1080/0951192X.2022.2104462
[22] van Doormaal JP, Raithby GD 1984 enhancements of the simple method for predicting incompressible fluid flows *Numerical Heat Transfer* **7** 147–163
[23] Glasgow I and Aubry N 2003 Enhancement of microfluidic mixing using time pulsing *Lab Chip* **3** 114–120
[24] Samiei E, Tabrizian M and Hoorfar M A 2016 review of digital microfluidics as portable platforms for lab-on a-chip applications. *Lab Chip* **16** 2376–2396

[25] Nguyen NT, Hejazian M, Ooi CH, et al.2017 Recent advances and future perspectives on microfluidic liquid handling *Micromachines* **8** Epub ahead of print 12 June 2017 DOI: 10.3390/mi8060186
[26] Sadique H, Murtaza Q and Samsher 2022 Heat transfer augmentation in microchannel heat sink using secondary flows: A review. *Int J Heat Mass Transf*; **194** Epub ahead of print 15 September 2022 DOI: 10.1016/J.IJHEATMASSTRANSFER.2022.123063
[27] Mishra RS, Dwivedi A and Ahmad S 2017 A thermodynamic analysis of ejector type vapour refrigeration system using eco-friendly refrigerants *International Journal of Research in Engineering and Innovation (IJREI)* **1** 40–48
[28] Dundi TM, Raju VRK and Chandramohan VP 2021 Numerical evaluation of swirl effect on liquid mixing in a passive T-micromixer. *Australian Journal of Mechanical Engineering* **19** 363–377

Multimedia Tools and Applications
https://doi.org/10.1007/s11042-023-15443-5

A review of vision-based indoor HAR: state-of-the-art, challenges, and future prospects

Geetanjali Bhola[1] · **Dinesh Kumar Vishwakarma**[1]

Received: 28 December 2021 / Revised: 10 February 2023 / Accepted: 18 April 2023
© The Author(s), under exclusive licence to Springer Science+Business Media, LLC, part of Springer Nature 2023

Abstract
With the advent of technology, we are getting more comfortable with the use of gadgets, cameras, etc., and find Artificial Intelligence as an integral part of most of the tasks we perform throughout the day. In such a scenario, the use of cameras and vision-based sensors comes as an escape from many real-time problems and challenges. One major application of these vision-based systems is Indoor Human Activity Recognition (HAR) which serves in a variety of scenarios ranging from smart homes, elderly care, assisted living, and human behavior pattern analysis for identifying any abnormal behavior to abnormal activity recognition like falling, slipping, domestic violence, etc. The effect of HAR in real time has made the area of indoor activity recognition a more explored zone by the industrial segment to attract users with their products in multiple domains. Hence, considering these aspects of HAR, this work proposes a detailed survey on indoor HAR. Through this work, we have highlighted the recent methodologies and their performance in the field of indoor activity recognition. We have also discussed- the challenges, detailed study of approaches with real-world applications of indoor-HAR, datasets available for indoor activity, and their technical details in this work. We have proposed a taxonomy for indoor HAR and highlighted the state-of-the-art and future prospects by mentioning the research gaps and the shortcomings of recent surveys with respect to our work.

Keywords Human activity recognition · Assistive technology · Assisted living · Elderly care · Indoor activity · Patient care · Real-time HAR

1 Introduction

Human activity recognition has been studied, reviewed, and discussed in some of the previous works [13, 15, 24, 47, 85, 105, 132, 160, 175, 190, 216]. Human activity recognition has been under constant limelight in the area of video analysis technology due to the rising needs from many key areas like entertainment environments,

✉ Dinesh Kumar Vishwakarma
dvishwakarma@gmail.com

[1] Biometric Research Laboratory, Department of Information Technology, Delhi Technological University, Bawana Road, Delhi 11042, India

human-computer interaction (HCI), surveillance environments, and healthcare systems. Its application in the surveillance environment involves the detection of abnormal activities or dangerous behaviors which can alert the related authorities. Similarly, in an entertainment environment, activity recognition can be used to improve human-computer interaction (HCI), for e.g., by embedding AR (augmented reality) features in real-time applications [27]. Furthermore, activity recognition can help in the automatic recognition of patient's actions to facilitate the rehabilitation processes in a healthcare system. Applications in the area of human interaction [61], pedestrian traffic [93], home abnormal activity [63], human gestures [33], ballet activity [29], tennis activity [108, 203], sports activity [133, 163] simple actions [1, 25, 60, 91, 113, 125, 145, 166–168, 187] and healthcare applications [2, 20, 64, 71–74, 77, 78, 81, 114, 118, 120, 124, 129, 131] are a few examples of HAR.

Indoor-HAR, which can be considered as one of the emerging areas of HAR, deals with the recognition of activities limited to an indoor environment like homes, gyms, sports clubs, hospitals, schools, corridors, parking lots, etc. The area of Indoor-HAR is different in terms of the challenges and applications it has. For example, we can relate activities like walking, moping, and wandering to a school's corridor. Whereas jumping, weight lifting, running, etc. can be a part of gym activities. Activities inside a house, hospital, sports complex, gym, or any closed environment can be limited compared to outdoor activities. These activities can be basic ones like walking, sitting, sleeping, studying, cooking, moping, drinking water, etc. or complex ones like "taking medication" which can involve a series of simple activities like "opening the pill box", and "drinking water". Similarly, another complex activity can be "praying" which can further involve activities like "sitting" or "standing", "holding a book(studying)", "ringing a bell" or "lighting a candle" or "lamp".

Certain activities may be simple but the pose of the person performing the activity and the orientation may make them complex for the machine to recognize. An activity like "drinking water" while sitting, standing or walking may generate different recognition rates. Also, a few activities may have certain similarities while performing due to which the results can be incorrect. For e.g., jumping and dancing/doing aerobics may have similar movements which may be ambiguous for the system.

In order to recognize activities limited to some indoor environments, we cannot use conventional deep learning methods as there are different challenges involved, based on the environment. As in the case of indoor HAR, the activity set differs from one environment to the other, one model cannot fit in every scenario.

In other words, the use of one type of HAR model meant for general may not be suitable for a specific indoor environment. So, indoor HAR is a different track that requires the problem of activity recognition to be considered differently as per its application area involved. Through this survey, we have tried to introduce Indoor-HAR as a new and emerging area of research. Through indoor HAR, concepts like smart homes, ADL(Activities of Daily Living), automated patient care, and elderly care can be strengthened and practically have a lot of research potential to be looked into. In this survey, we have discussed recent developments in the field of indoor HAR, different approaches, datasets, the use of indoor HAR for human behavior analysis, and the real-time application of indoor HAR.

The main contributions of this work are as follows:

- It outlines the comparison of previous surveys in indoor HAR, which includes its merits and shortcomings.
- Deliberates the latest and important developments recently reported covering both the general aspects of HAR and the specific vision-based indoor-HAR systems.

- Elaborates the scope and wide application area of indoor HAR, discussing various existing and suggested research works which can help in real-life situations
- Proposes a taxonomy for indoor-HAR on the basis of input methodology, datasets, and challenges which one by one explores the role of each of these parameters and how are they connected to HAR and indoor-HAR.
- Highlights the HAR and specifically indoor HAR datasets which includes the technical details like dimensionality, fps, number of activities etc.
- The methodology included for indoor HAR is highlighted which includes the use of handcrafted features and automatic feature learning in HAR
- Summarises the detailed findings of various state-of-art, challenges and hurdles involved at different levels of processing and at different stages of research for any indoor-HAR system.

The steps involved in HAR are shown in Fig. 1. Depending on the nature of the data, it can be vision-based or sensor-based.

Previously, there have been some surveys [6, 24, 34, 84, 141] in the field of HAR which have been summarised below in Table 1.

The ultimate aim of this work is to bridge the gap between existing parameters and the real-time applications of indoor HAR. With this survey, we wish to enhance the usability of existing works for more practical and real-time scenarios.

The area of indoor-HAR is vast and can have a variety of scope for future work. Some of the application areas are discussed here.

The sections are explained as follows: section 2 gives the literature review, and section 3 discusses the input methodology for the various research techniques, which are RFID/sensor-based and vision based. Section 4 discusses datasets; section 5 discusses the approaches and human body representation. Section 6 discusses the challenges and section 7 gives conclusions and future scope.

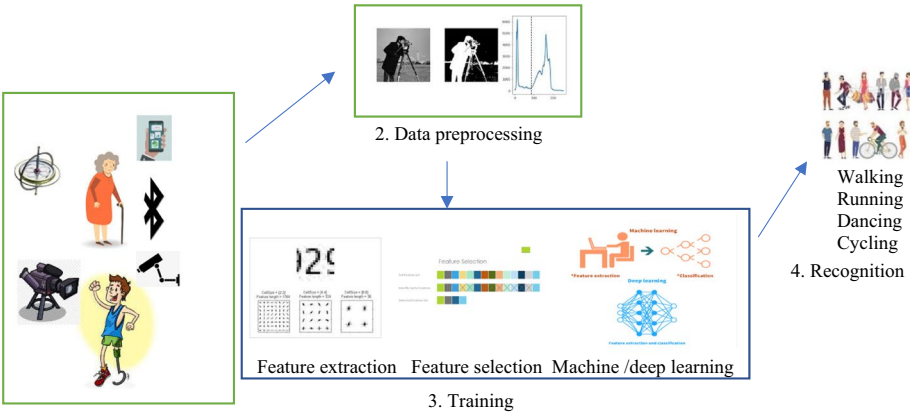


Fig. 1 Steps for HAR i) data collection ii) data pre-processing iii) training iv) recognition

Table 1 Recent surveys in the field of HAR

Ref.	Year	Merits	Shortcomings
[34]	2016	Comprehensive state-of-art survey for different phases of HAR	No detail about real-time feasibility is covered.
[141]	2020	Covers sensor-based and vision-based HAR; Discusses datasets, methods involved in data processing and feature engineering, future direction	Sensor and vision-based methods are discussed in one paper and an overall conclusion on the suitability for real-time application is not discussed.
[24]	2020	Provides an up-to-date analysis of vision-based HAR-related literature and recent progress in the field. Highlights the challenges and future prospects	Gives overall broader picture of different aspects related to HAR and not specific to one domain
[84]	2021	An in-depth and comprehensive survey on HAR with recently developed deep learning methods	Requirement of lot of labelled data; non-existence of universal activity recognition model with multimodal signals and data.
[6]	2021	Surveys two distinct domains of IoT and DL and their amalgamation for indoor HAR and position/ tracking system	IoT has challenges like security, connectivity and compatibility which have not been covered [181]
[177]	2022	Reviews the different modalities in HAR	Only modalities have been discussed. Other components are not reviewed in detail.
Our work	–	Talks specifically of indoor-HAR with a vision-based scenario in particular. Proposed indoor-HAR taxonomy based on different parameters associated Lists datasets explicitly for indoor HAR	Role of sensor-based indoor HAR is not covered in detail

2 Related work

The area of HAR has been popular for many years now and a lot has been achieved in this area. This section will discuss various applications of Indoor-HAR and their related work and the recent research that has been done in that area involving both vision-based and sensor-based input.

2.1 Elderly care system

There is a need for extra care for the elderly and people with special needs as their number is increasing and there is a shortage of care staff. During recent times of COVID-19, we came across many instances where family members were not there to look after the elderly and they died in isolation. Some countries also faced a dire shortage of nurses and caretakers. This is a consistent problem where the elderly lives alone. The monitoring is difficult. Wearable sensors are not very efficient in the case of old people as they tend to forget to wear them. Sometimes, the uneasiness caused while wearing them can cause hurdles in totally depending on such sensors for their activity monitoring. Also, the statistics cannot be as impactful as watching a person doing some activity. In such cases, a vision-based HAR can provide a solution for the challenges and problems related to wearable sensors. Vision-based methods deploy a camera for recognising the activities of a person. Different research works based in the same field are [69, 106]. Recent work includes [153] which proposes unsupervised HAR with skeletal Graph Laplacian Invariance.

The daily activities can be detected and a pattern can be observed which can help in understanding their needs better. Apart from regular monitoring, systems for special alerts can be designed which can help in situations like falls, slipping, painful walking or limping and some abnormal activity with respect to the environment. The risk of falling is one of the most prevalent problems faced by elderly individuals. A study published by the World Health Organization [198] estimates that between 28% and 35% of people over 65 years old suffer at least one fall each year, and this figure increases to 42% for people over 70 years old. According to the World Health Organization, falls represent greater than 50% of elderly hospitalizations and approximately 40% of the non-natural mortalities for this segment of the population. A model which is trained for the detection of "fall" [72, 176, 206, 211] might be used for alerting the neighbors or other members of the house about the same. In the survey [212], vision-based fall detection systems were discussed. Vision-based approaches of fall detection were divided into four categories, namely individual single RGB cameras, infrared cameras, depth cameras, and 3D-based methods using camera arrays. Other works based on fall detections are [67, 87, 149, 207]. Figure 2 gives an idea of how a vision-based system can be used for monitoring the elderly [35].

2.2 Patient care system

Vision sensors(cameras) can be deployed to monitor a patient who may need constant observation or is going under treatment or needs post-recovery care. Apart from vital signs which are monitored for such patients, a vision-based system may be helpful in case or abnormalities or medical emergencies. Capturing the visual cues, facial gestures or

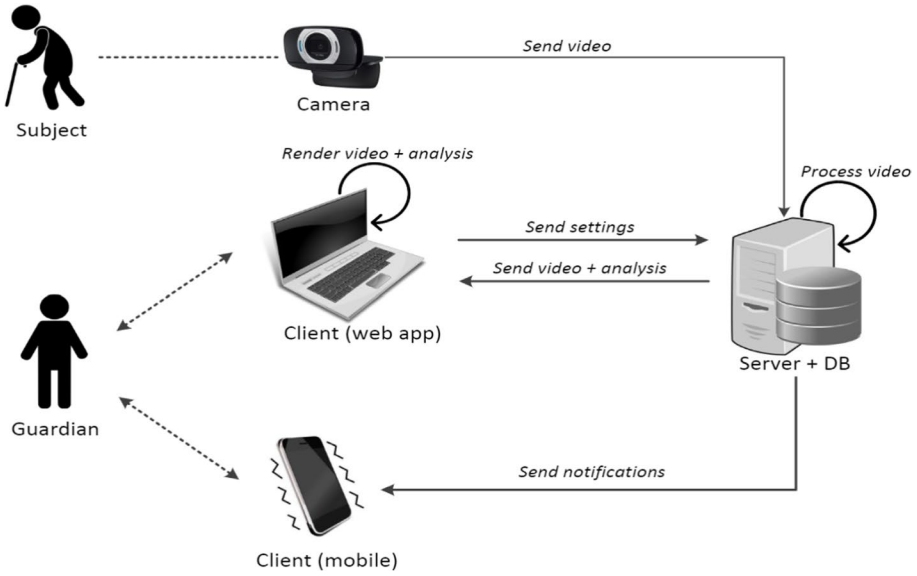


Fig. 2 Elderly monitoring vision-based system [35]

detection of motion or activity of such patients can help in alerting the concerned team which can be significant in the recovery of a patient.

2.3 Physical fitness

Intelligent systems have been built over the years which have been designed to benefit us in our fitness domain. Multiple wearable fitness trackers have boomed the market over the years. These trackers have sensors that record our data and instruct us about better workouts, balanced eating, and sensible living. Research on pose estimation directs naturally to human activity recognition [48, 157]. Smartphones have also given a new shape to the fitness model. The ubiquity of smartphones together with their ever-growing computing, networking, and sensing powers have been changing the landscape of people's daily life [76, 191].

Wearable sensors and smartphones have opened a pool of options in the fitness domain for research but these methods may suffer from problems like interference, the privacy of data, unease of wearing the sensors, and skin irritation [197]. Vision-based systems can be effective as they offer an unobtrusive solution for the monitoring and diagnosis of the person. Google's on-device, real-time body pose tracking with MediaPipe BlazePose is a great research example that is making use of human body pose and can be used to build fitness and yoga trackers [82]. Figure 3 shows the screenshots of the real-time results captured from the same.

2.4 Abnormal human activity recognition

Abnormal activity means any irregularity in the set of activities belonging to an environment. When we talk of abnormal activities in an indoor environment, we mean any activity

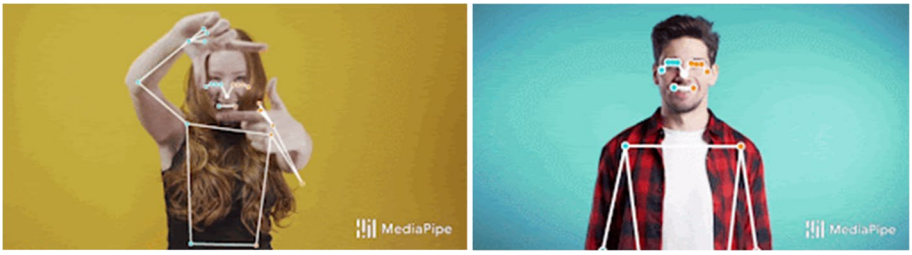


Fig. 3 Google's real-time pose estimation in fitness domain [82]

which can be a matter of concern or may require immediate attention [17]. We come across cases of domestic violence, child sexual and physical abuse, and even physical abuse of the elderly at home. Researchers have also worked on providing a solution to this problem [185]. As per the reports [49], worldwide, approximately 20% of women and 5–10% of men are sexually abused in their childhood. In India, 2 out of every 3 children are physically abused and every second child is a victim of emotional abuse. In general, these malpractices are never done in the open, and thus saving such children is an essential step toward building a healthy and happy future. Indoor activity recognition may be vision-based or wi-fi signal based. Systems are built for accurately detecting abnormal activities on commercial-off-the-shelf (COTS) IEEE 802.11 devices [55, 215]. This system makes use of IoT and wi-fi signals for any abnormal indoor activity recognition.

2.5 Human abnormal behavior analysis

Our society suffers from a lack of awareness about mental health. It is taboo to talk about mental health issues. Another useful application for indoor HAR can be for analyzing human behavior by studying the pattern of indoor activities. A sick person may have a different activity pattern than a healthy person. He may be less active and may not be performing his activities like on usual days. This can also help in detecting any mental illness like depression where a person may repeat an activity or may skip his daily activities. Research like this may be helpful for situations like the onset of depression.

Recent works involve the use of smartphone data collection of the sensory sequence which is collected from people performing their daily tasks. Later, the cycle detection algorithm helps in segmenting the data sequence for activity [41].

Indoor-HAR taxonomy In the present era, human activity recognition [12, 34, 56, 65, 188, 189] in videos has become a prominent research area in the field of computer vision. Videos are used in daily living applications such as patient monitoring, object tracking, threat detection, security, and surveillance. In general, all HAR algorithms are categorized on various aspects from how the data acquisition is performed to what activities are considered. Figure 4 shows different facets of indoor HAR.

The taxonomy is based on parameters like the approach, data type, data sets, 2D or 3D representation of the input, etc. This survey also discusses the challenges and problems at different levels of HAR recognition for indoor activities. The survey covers the parameters shown in the figure and throws light on them one by one w.r.t the existing work in that field and the characteristics of the same.

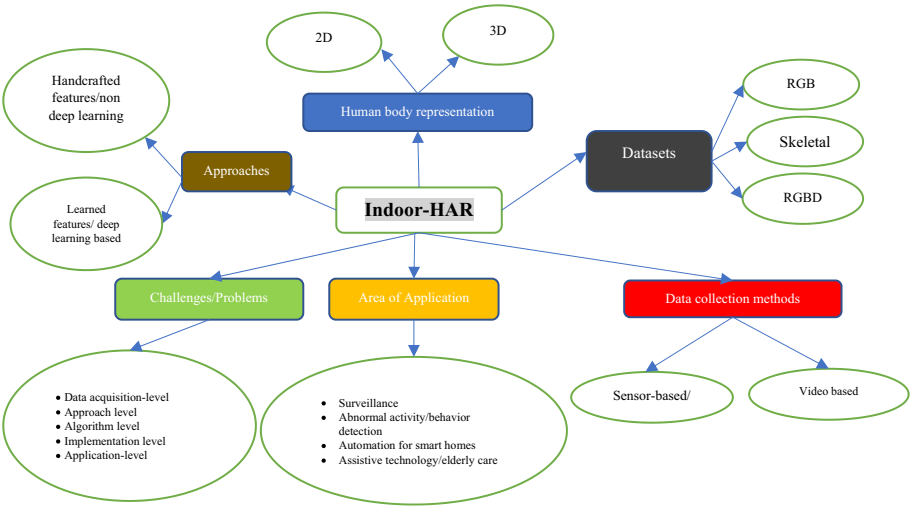


Fig. 4 Taxonomy of Indoor-HAR

3 Input methods: vision-based and sensor-based

Specifically, indoor HAR methods are classified into two main groups, which are sensor-based/RFID-based HAR and vision-based HAR, based on the generated data type. [97, 202] talks about another category called multimodal where sensor data, as well as visual data, are used to detect human activities.

Sensor technology has grown in multiple perspectives, including computational power, size, accuracy, and manufacturing costs. This has widened the band of portable devices which are making use of this technology to record data for activity recognition. Examples are wristbands, smartphones, etc. This growth and development of sensor technology have also fostered techniques for pervasive human tracking, silhouette tracking, detection of uncertain events [90, 98, 208], human motion observation, and emotion recognition in real environments [3, 99, 192].

Human tracking and activity recognition problems require feature extraction and pattern recognition techniques based on specific input data from innovative sensors (i.e., motion sensors and video cameras) [4, 5, 100, 152, 204]. Motion sensors-based activity recognition is based on classifying sensory data using one or more sensor devices. [39], proposed a complete review about the state-of-the-art activity classification methods using data from one or more accelerometers. In [102], the classification approaches are based on RFs features which classify five daily routine activities from Bluetooth accelerometer placed at breast of the human body, using a 319-dimensional feature vector. In [22], fast FFT and decision tree classifier algorithms are proposed to detect physical activity using biaxial accelerometers attached to different parts of the human body. However, these motion sensors-based approaches are not feasible methods for recognition due to the discomfort of the users to wear electronic sensors in their daily life. Also, combining multiple sensors for improvement in recognition performance causes a high computation load.

Recently, there has been a tremendous increase in the number of applications using closed-circuit television (CCTV) for monitoring and security purposes due to the evolution in CCTV technology which has resulted in better video quality, more straightforward

setup, lower cost, and secure communication. Although each type of sensor aims at specific services and applications, sensors generally collect raw data from their target ubiquitously, and general knowledge is acquired by analyzing the collected data. Human activity recognition or HAR, allows machines to analyze and comprehend several human activities from input data sources, such as sensors, and multimedia content. HAR is applied in surveillance systems which can be for home [21, 147], for mass crowd-monitoring [38, 95] and for detecting humans under distress using UAVs [134], behavior analysis, gesture recognition, patient monitoring systems, ambient assisted living (AAL), and a variety of healthcare systems that involve direct interaction or indirect interaction between human and smart devices. HAR for elderly care has been a key area of work [37, 101, 109]. Various opportunities can be provided by these sensor technologies which can improve the robustness of the data through which human activities can be detected and also provide services based on sensed information from real-time environments, such as cyber-physical-social systems [205]; there is also a type of magnetic sensors when embedded in a smartphone can track the positioning [19]. The above points can be summarised in Fig. 5. Table 2 lists recent works in sensor-based input and vision-based input with the technique used.

3.1 Vision-based input

With the ever-developing field of HAR, there is also a need of a more practical way of fetching the data. This is where vision-based HAR proves efficient as compared to sensor-based HAR. The sensor-based HAR involves the placement of sensors as per the activity which is difficult to plan whereas vision-based HAR is a compatible approach for real-time videos which are the most common source of input and data considering the increase of CCTVs and cameras. The vision-based HAR is an important research area of computer vision. Vision-based HAR helps us identify the activity being performed in the video/image. The task is cumbersome due to the challenges involved like cluttered background, shape variation of the objects/people involved, illumination differences, placement of camera(s), viewpoint, stationery or moving camera etc. These challenges are further dependent on the category of activity being considered. There are four major categories of activities: gestures, action, interaction, and group activity represented in Fig. 6. Indoor HAR can include activities from these categories.

[93] discusses components of an automated, "smart video" system to track pedestrians and detect situations where people may be in peril, as well as suspicious motion or

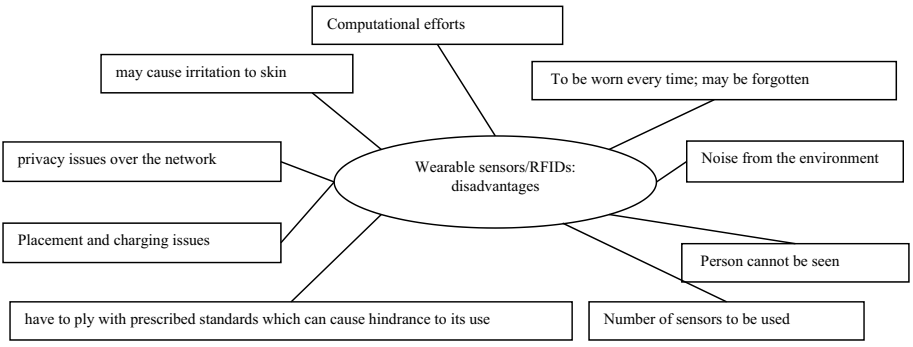


Fig. 5 Disadvantages of wearable sensors/RFIDs

Table 2 Recent work with sensor-based and vision-based inputs

Ref.	Year	Key contributions	Input type	Advantages	Disadvantages	Dataset used	Technique
[32]	2021	comprehensive dataset intended to evaluate passive Human Activity Recognition (HAR) and localization techniques with measurements obtained from synchronized Radio-Frequency (RF) devices and vision-based sensors	Sensor, Vision	Captures transitioning of activities too. Like walking to falling	Spectrograms may differ in most realistic scenarios as the human motions might not be restricted to a single aspect angle with respect to the radar. It could be due to the shadowing of some part of the human body if captured at a different angle	Gathered during experiment	ML techniques
[28]	2021	integrated system prototype that provides an efficient technological tool to caregivers operating promptly and ensures efficient performance throughout the entire healthcare system process	Sensor	Takes care of situations where the elderly are to be monitored every time without the use of expensive cameras etc	Sensor placements	Wireless Sensor Data Mining (WISDN) dataset in Jennifer R. Kwapisz et al. t. [153].	Localization using CNN
[214]	2021	Joint tracking and activity recognition in indoor environment using radar sensors	Radar sensors	Placement of sensors even in sensitive areas is not a privacy concern	Boundary error Data representation Imbalanced dataset Loss function	Collect own dataset using the setup uses K-fold method as dataset is limited	Deep learning
[146]	2021	(HAR) based on Radio Frequency energy harvesting (RFEH) as the harvested voltage signals of different human activities exhibit distinctive patterns.	Radio frequency	Accuracy and computational efficiency	Interference from other wifi devices Complex activities and variety of ways in which one may perform them.	Gathered dataset performance of the system by applying the four light-weight classifiers and calculating their accuracies on the collected datasets	Machine learning classifiers

Table 2 (continued)

Ref.	Year	Key contributions	Input type	Advantages	Disadvantages	Dataset used	Technique
[51]	2021	HAR for indoor using channel information of wifi signals	Wifi signals	Cost-effective as wifi devices are mostly already installed.	Interference in signal	Collected own data set	CNN
[182]	2021	Smart-home, smart-gym fitness tracker solution using a single mm-wave radar point cloud data	Radar sensors	The privacy of the user is intact. contactless, accurate, real-time fitness tracker system for indoor fitness activities, capable of running on edge devices for applications in IoT-connected healthcare	Interference/noise has not been commented upon	Data set collected from radar sensors	Deep learning
[170]	2021	Combination of acceleration audio and wifi round trip time localization to recognize indoor activities.	Wifi round trip audio acceleration	Audio related to activity gives another useful feature in recognition. Accuracy is consistent upon 12 activities	Limited activities, Maybe not suitable if activities with similar audio are tested, technology used is relatively new and hardware is not ubiquitous	Dataset created and model trained again and again for new activities	ML
[7]	2021	Gives a mathematical representation for human body as clusters of different points	Radio frequency	Time variant features and properties explored while representing human as cluster of scattered points	Signa based, stationary objects	CSI and IMU data were used as collected	ML

Table 2 (continued)

Ref.	Year	Key contributions	Input type	Advantages	Disadvantages	Dataset used	Technique
[83]	2015	online activity recognition system, which explores WiFi ambient signals for received signal strength indicator (RSSI) fingerprint of different activities.	Wifi signal data	Simple use. Fine average accuracy	context between persons and motions, context between locations and motions, and even context between emotions and motions can be explored as the current scenario is simple	Data collected using set up/ wifi	ML
[186]	2018	Uses video camera and radar sensors fusion for predicting activities	Radar sensors, video camera	Fusion of radar and video with deep learning gives good accuracy	Computation can be worked upon	Accuracy checked on Standard data set	DL
[148]	2019	robust approach for human activity recognition which uses the open source library *OpenPose* to extract anatomical key points from RGB images.	Camera vision based	Good accuracy on standard datasets. Good approach for independent living for elderly	OpenPose can be difficult to use	Standard dataset	RNN with LSTM

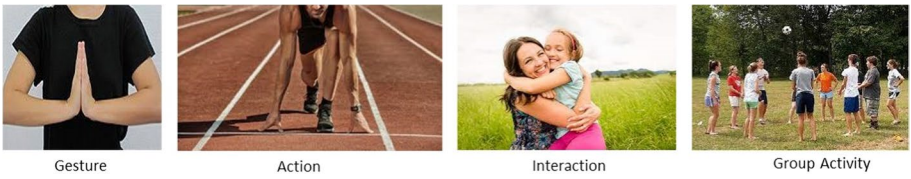


Fig. 6 Categories of Activities

activities at or near critical transportation assets. Activity recognition through Gait is the process of identifying an activity by the manner in which they walk. The identification of human activities in a video, such as a person walking, running, jumping, jogging, etc. is an important activity in video surveillance. Gupta et al. [86], contribute to the use of a Model-based approach for activity recognition with the help of the movement of the legs only.

Researchers have also worked on an efficient depth video-based HAR system that monitors the activities of elder people 24 hours a day and provides them an intelligent living space which comforts their life at home.

HAR is also influenced by culture of people. This was established in the work [139] which proposed that daily life activities, such as eating and sleeping, are deeply influenced by a person's culture, hence generating differences in the way a same activity is performed by individuals belonging to different cultures and that by taking cultural information into account we can improve the performance of systems for the automated recognition of human activities. They proposed four different solutions to the problem and used a Naive Bayes model to associate cultural information with semantic information extracted from still images. They used a dataset of images of individuals lying on the floor, sleeping on a futon and sleeping on a bed. Vision based HAR has further processing steps which will be discussed in later sections.

4 Datasets: RGB, RGB-D

There has been a lot of research based on RGB images [11, 50, 94] in the past decades. Computer vision and RGB images are closely associated with each other. RGB images give the information about the appearance of objects in the frame. The information about only the colours is a little less though as with this limited information it is a cumbersome task to partition the foreground and background having similar colours and textures. Additionally, the object appearance described by RGB images is not sturdy against common variations, such as changing illumination conditions, which hinders the usage of RGB based vision algorithms in real. While a lot of work has been going on to design sophisticated algorithms, research is parallelly going for finding a new type of representation that can better represent the scene information. Due to its complementary nature of the depth information and the visual (RGB) information, RGB-D image/video is an emerging data representation that is able to help solve fundamental problems. Meanwhile, it has been proved that combining RGB and depth information in high-level tasks (i.e., image/video classification) can dramatically improve classification accuracy [179, 180]. Table 3 shows examples of some of the RGB datasets for activity recognition whereas Table 4 lists datasets available for indoor activity recognition.

These datasets divided into two categories based on the modalities in which they are recorded such as RGB and RGB-D. Before 2010, a large number of RGB video dataset was

Table 3 RGB DATASETS

Name of the Dataset	Year	Purpose	Quality/ Format/ Source of preparation	FPS/Remarks	Action Types/Activities covered
FineGym [70]	2020	It provides temporal annotations at both action and sub-action levels with a three-level semantic hierarchy	RGB videos of gymnasts. 303 Competition records ~708 hours	High-quality videos 720P or 1080P	gymnasium videos dataset
HACS [213]	2019	source for spatiotemporal feature learning	HACS clips includes: 1.55 M 2-sec clips on 504 K videos. HACS segment includes: 140 K complete segments on 50 K videos	RGB videos of 200 actions category	504 K untrimmed videos and 1.5 M annotated clips were sampled from them. HACS Segments contains 139 K action segments densely annotated in 50 K untrimmed videos spanning 200 action categories
20BN-Something-Something Dataset V2 [158]	2017	Large collection of labeled video clips that show humans performing pre-defined basic actions with everyday objects	Quality is 100px. FPS = 12	RGB-labeled videos of sub-activities	220,847 videos, with 168,913 in the training set, 24,777 in the validation set and 27,157 in the test set. There are 174 labels
Kinetics [110]	2017	high-quality dataset for human action recognition in videos	RGB High-quality video dataset of 650,000 video clips;	Covers 400/600/700 activities lasting 10 seconds Dataset contains URLs of the videos.	500,000 video clips covering 600 human action classes with at least 600 video clips for each action class
Watch-n-Patch [199]	2015	focus on modelling human activities, comprising multiple actions in a completely unsupervised setting	RGB-D dataset	Videos capturing daily activities. Kinect sensor used for skeleton data ground truth annotations.	seven subjects perform daily activities in eight offices and five kitchens with complex background
Penn Action [96]	2013	human joint annotations for each sequence	RGB frames within 640×480	15 different actions	2326 video sequences of 15 different actions
UCF101 [173]	2012	UCF101 is one of the largest datasets of human actions	101 action categories are grouped into 25 groups containing 4–7 videos each	RGB videos	classified into 101 categories consisting of 13,320 video clips

Table 3 (continued)

Name of the Dataset	Year	Purpose	Quality/ Format/ Source of preparation	FPS/Remarks	Action Types/Activities covered
HMDB51 [169]	2011	realistic videos from various sources, including movies and web videos	Youtube, Google	RGB videos	51 action categories such as "jump", "kiss" and "laugh", with each category containing at least 101 clips, 6849 video clips
Kth [162]	2004	most standard datasets and first datasets for activity recognition, which contains six actions:	25 individuals participated as actors	RGB videos	walk, jog, run, box, hand-wave, and hand clap

Table 4 Indoor Activities Datasets

Name of the dataset	Indoor activities covered	Source of preparation	Format/Resolution/ Quality
Toyota Smarthome [53]	Consists of common daily life activities of 18 subjects;	Actors senior people of age 60–80 years old	7 Kinect v1 camera; 3 modalities: RGB, Depth and 3D skeleton; Resolution 640×480
STAIR Actions [174]	100 everyday human action categories. Each category contains around 900 to 1800 trimmed video clips.	Clips taken from Youtube and crowd-source workers	RGB videos and clips; 109,478 total videos; 100 categories
MPII Human Pose dataset [143]	25 K imagesof everyday human activities containing over 40 Kpeople with annotated body joints.	Image dataset extracted from Youtube	Every day human activities;410totalactivities;Labelled dataset;coversaseparateclassforhomeactivities
MoVi [80]	everyday actions and sports movements, and one self-chosen movement	60 female and 30 male actors with their 20 predefined activities	Captured using optical motion capture system, video cameras, inertial measurement units IMU); dataset contains 9 hours of motion capture data, 17 hours of video data from 4 different points of view (including one hand-held camera), and 6.6 hours of IMU data
HomeActionGenome [88]	Large-scale Multiview video database	Dataset prepared with actors using synchronized multi-view cameras including egocentric view.	30 hours of video; 70 daily activities; 453 classes of atomic actions; multiple modalities dataset
ActivityNet [9]	The largest benchmark for temporal activity containing 200 different types of activities and a total of 849 hours of videos collected from YouTube	Dataset relied on crowd and Amazon mechanical turk was used	203 classes of activities; average of 137 untrimmed videos per class and 1.41 activity instances per video; total of 849 hours video.
MSRDailyActivity3D [68]	There are 16 activity types: drink, eat, read a book, call cellphone, write on paper, use a laptop, use a vacuum cleaner, cheer up, sit still, toss paper, play games, lay down on the sofa, walk, play guitar, stand up, sit down	Daily activities captured by Kinect device.	Total activity samples is 320
GTEA (Georgia Tech Egocentric Activity) [192]	contains seven types of daily activities such as making sandwiches, tea, or coffee,	performed by four different people, thus a total of 28 videos.	Seven activities by 4 people 28total videos; 20 fine-grained instances for every video

Table 4 (continued)

Name of the dataset	Indoor activities covered	Source of preparation	Format/Resolution/ Quality
CAD-120 [36]	sequences of humans performing activities in the kitchen, living room and office environment etc.	Depth videos recorded using Kinect sensor; 4 people in different environments	RGB-D videos
Florence3D [140]	activities like wave, drink from a bottle, answer phone, clap, tight lace, sit down, stand up, read watch, bow	10 subjects performed all activities 2/3 times; Kinect was used	Total 215 activity samples; depth dataset
UT-Kinect (UTKinect-Action3D Dataset) [184]	activities like walk, sit down, stand up, pick up, carry, throw, push, pull, wave hands, clap hands.	10 subjects performed 10 activities	3 channels used: RGB, depth and skeleton joint locations; 30fps;
PKU-MMD [130]	Number of activities covered in 2 phases	51 actions performed by 66 subjects using Kinect V2 sensor.	4 modalities-RGB,Depth, Infrared radiation and skeleton; videos containing 30fps; dataset contains 2 phases, phases #1 contains 51 action categories, performed by 66 distinct subjects in 3 camera views

available [40]. After the advancement of low-cost depth sensors, e.g., Microsoft Kinect, there has been a drastic increase in the 3D dataset, and multi-modal videos dataset [13, 119, 132]. Due to low cost and lightweight sensors datasets are recorded with multiple modalities such as depth frames, accelerometer, IR sensors frames, acoustical data, and skeleton data information. The RGB-D datasets have multiple modalities which reduces the loss of information in 3D videos as compared to traditional RGB datasets at the cost of increased complexities. Table 3 shows a few of the existing datasets for activity recognition including examples of multi-modal datasets as well.

The challenges and concerns which might exist for performing HAR on such complex datasets are- occlusion, cluttered background, localization of activity, noise removal, etc. The use of depth sensor like Microsoft Kinect for creating RGB-D datasets may also pose practical problems like sensor placement and orientation. At the beginning, Kinect was as an Xbox accessory, enabling players to interact with the Xbox 360 through body language or voice instead of the usage of an intermediary device, such as a controller. Later on, due to its capability of providing accurate depth information with relatively low cost, the usage of Kinect goes beyond gaming, and is extended to the computer vision field. This device equipped with intelligent algorithms is contributing to various applications, such as 3D-simultaneous localization and mapping (SLAM) [89, 117] people tracking [151], object recognition [30] and human activity analysis [42, 128] etc.

5 Approaches of HAR

Activity recognition systems classify and recognise various activities for which they have been trained. Since, the data and variety of data is always better for such systems, the features from this data are again crucial and significant part of the HAR process. This leads to two types of approaches for the feature extraction- handcrafted features (machine learning), automated feature learning (deep learning) method. Traditionally, the researchers used the manual extraction of features from data (handcrafted features) [31, 116] for training the machine learning models. However, with the development of deep neural networks [112], models tend to automatically learn features. With great success of CNNs on image classification tasks, CNNs were applied to recognize human activities in videos. Well known approaches for action recognition in RGB videos based on CNNs are presented in [107, 123, 171, 194, 196]. With the introduction of cost inexpensive RGB-D sensors, researchers shift their attention, towards other vision cues like depth and skeletal data along with RGB data. One of the advantages of depth data and skeletal data, as compared to traditional RGB data is that they are less sensitive to changes in lighting conditions. Furthermore, the availability of well-known and diverse RGB-D datasets like MSR Action 3D [58], UTD-MHAD [43], Berkeley MHAD [150], CAD-60 [178], SBU Kinect interaction [150], and many more, encouraged extensive research for human activity recognition using multiple vision cues. However, the two approaches are efficient in their own respect. Table 5 lists a few of the recent works using the two above-mentioned approaches.

The results of HAR models for activity recognition also vary with how the human body is represented. Based on the category of representation of a Human body, its representation can be classified into 2D and 3D representation methods. 2D methods take into account spatial information, contour, shape, and skeletal information. 3D representation on the other hand talks of skeletal joints in terms of depth together with other characteristics such as spatial and temporal components related to the frame.

Table 5 Handcrafted and automated feature in HAR

Ref.	Year	Approach	Objective	Dataset used	Performance measures
[159]	2021	Automatically learned features	A neural network (NN) based approach for the classification and evaluation of human activities has been explored together with long short-term memory (LSTM)	KARD, CAD-60, MSR DAILY ACTIVITY 3D	Precision, Recall on KARD: 100% Precision, recall on CAD-60:100% Accuracy on MSR daily 95.6%
[8]	2021	Handcrafted features	Recognition of significant joints using features from spatial and temporal event feeds.	Real-time event Video dataset	10–15% memory usage over 532 MB of digitised real-time event data with 0.5431 sec processing time
[137]	2021	Automatically learned features	The work proposed a novel deep-learning framework to solve the HAR effect on overall accuracy. The framework is a location-based CNN-LSTM hybrid model.	DHA dataset with CNN-LSTM approach shows best accuracy	Acc. Of 96.75%
[172]	2021	Automatically learned features	a deep bottleneck multimodal feature fusion (D-BMFF) framework that fused three different modalities of RGB, RGB-D(depth) and 3D coordinates information for activity classification	Four RGB-D datasets: UT Kinect, CAD-60, Florence 3D, and SBU Interaction	The ARR on UT Kinect, CAD-60, Florence 3D, SBU Interaction are 99%, 98.50%, 98.10%, and 97.75% respectively
[209]	2021	Automatically learned features	approach for human activity recognition using ensemble learning of multiple convolutional neural network (CNN) models		Ensemble of CNN models gives accuracy of 94%
[26]	2021	Automatically learned features	deep learning-based method for human activity recognition problem. The method uses convolutional neural networks to automatically extract features from raw sensor data and classify six basic human activities	Diabetes dataset	Different activities covered with approximately 90% accuracy using CNN,Random forest, SVM

Table 5 (continued)

Ref.	Year	Approach	Objective	Dataset used	Performance measures
[135]	2021	Automatically learned features	a deep learning architecture that leverages the feature extraction capability of the convolutional neural networks and the construction of the temporal sequences of recurrent neural networks to improve existing classification results		Accuracy increased from 30% to 35% due to transfer learning
[57]	2021	Automatically learned features, handcrafted features	framework to extract handcrafted high-level motion features and in-depth features by CNN in parallel to recognize human action. SIFT is used as a handcrafted feature to encode high-level motion features from the maximum number of input video frames. The combination of deep and handcrafted features preserves more extended temporal information from entire video frames present in action video with minimal computational power	UCF and KTH	89.5%; CNN combined with SIFT gives a lesser vector dimension for the model making it computationally efficient.

Table 5 (continued)

Ref.	Year	Approach	Objective	Dataset used	Performance measures
[92]	2020	Automatically learned features	propose a deep learning multi-channel architecture using a combination of convolutional neural network (CNN) and Bidirectional long short-term memory (BLSTM). The advantage of this model is that the CNN layers perform direct mapping and abstract representation of raw sensor inputs for feature extraction at different resolutions. The BLSTM layer takes full advantage of the forward and backward sequences to improve the extracted features for activity recognition significantly.	WISDM dataset	For 5 sec: 98.6±0.682 For 10 sec: 99.1±0.455 For 15 sec: 92.6±0.431 For 20 sec: 82.7±0.513
[144]	2020	Automatically learned features, Hand-crafted features	aims in capturing the motion information of the whole video by producing a dynamic image corresponding to the input video; use two parallel ResNet-101 architectures to produce the dynamic images for the RGB video and depth video separately	MSR Action 3D Dataset and proposed dataset on which many existing algorithms were tested.	MSR Action 3D: approx. 90%; proposed dataset had 54.94% with processing and 50.12% without processing.
[59]	2020	Automatically learned features	a deep view-invariant human action recognition framework, which is a novel integration of two important action cues: motion and shape temporal dynamics (STD)	NUCLA multi-view dataset, UWA3D-II Activity dataset and NTU RGB-D Activity dataset	NUCLA- 87.3% UWA3D-II –85.2% NTU RGBD- 79.4%
[23]	2020	Automatically learned features, hand-crafted features	combines a traditional classifier based handcrafted feature extractor and a deep learning-based method in order to replace the artisanal feature extraction method with a new one.	MSR Daily Activity 3D Dataset	99.92%: pretrained CNN+ SVM 98.77% precision; 99.79- recall; F-measure: 99.28

Table 5 (continued)

Ref.	Year	Approach	Objective	Dataset used	Performance measures
[10]	2020	Automatically learned features	a Lightweight Deep Learning Model for HAR requiring less computational power, making it suitable to be deployed on edge devices. The performance of proposed model is tested on the participant's six daily activities data	RNN-LSTM trained on WISDM	RNN-LSTM- 99% Accuracy for jogging, walking; min 81% accuracy for upstair activity
[75]	2020	Handcrafted features	approach for activity recognition combining RGB data and skeleton analysis using Kinect sensors	CAD-60, CAD-120, OAD Dataset internally aquired	CAD-60: precision,recall Skeleton 95.0 95.0; RGB (20 sectors) 92.5 89.4; Score-level fusion 98.8 98.3 CAD-120: precision,recall Skeleton 77.6 73.;1 RGB (20 sectors) 61.1 59.3 Score-level fusion 85.4 83.3 OAD: precision,recall Skeleton 80.6 80.5; RGB (20 sectors) 85.8 85.9; Score-level fusion 90.6 90.4

Table 5 (continued)

Ref.	Year	Approach	Objective	Dataset used	Performance measures
[183]	2019	Automatically learned features, hand-crafted features	a novel approach to recognize human actions by considering both deep spatial features and handcrafted spatiotemporal features. Firstly, the deep spatial features by employing a state-of-the-art deep convolutional network, namely Inception-Resnet-v2 are extracted. Secondly, they introduced a novel handcrafted feature descriptor, namely Weber's law based Volume Local Gradient Ternary Pattern (WVLGTP), which brings out the spatiotemporal features. It also considers the shape information by using gradient operation	KTH, UT Interaction, Hollywood2, UCF101, UT INTERACTION	On KTH dataset, proposed method (Inception-resnet-v2 with WVLGTP) shows 96.5% accuracy; On UT interaction, it is 97.6%; ON Hollywood2, accuracy is 70.3%; On UCF-101, it is 94.9%;
[191]	2019	Automatically learned features	designs a smartphone inertial accelerometer-based architecture for HAR. When the participants perform typical daily activities, the smartphone collects the sensory data sequence, extracts the high-efficiency features from the original data, and then obtains the user's physical behaviour data through multiple three-axis accelerometers	UCI HAR dataset, Pamap2 dataset	UCI HAR dataset: CNN, LSTM, BLSTM, MLP, SVM Average acc 0.9100 0.8586 0.8952 0.8272 0.8407 Respectively. Pamap2 dataset: CNN, LSTM, BLSTM, MLP, SVM average acc 0.9321 0.8914 0.8941 0.8683 0.9050 respectively.
[46]	2019	Automatically learned features, hand-crafted features	A fusion of handcrafted features with automatically learned features by a deep algorithm for HAR using smartphones	A public dataset and proposed dataset	On proposed algorithm, Maximum Full a Posterior (MFAP) accuracy is 98.85%

Table 5 (continued)

Ref.	Year	Approach	Objective	Dataset used	Performance measures
[45]	2018	Handcrafted features	An argument is proposed that feature embedding from deep neural networks may convey complementary information and propose a novel knowledge distilling strategy to improve its performance. More specifically, an efficient shallow network, i.e., single-layer feedforward neural network (SLFN), with handcrafted features is utilized to assist a deep long short-term memory (LSTM) network.	Proposed dataset readied as per the protocols.	97.7%
[138]	2018	Automatically learned features, hand crafted features	a new deep learning network for action recognition that integrates quaternion spatial-temporal convolutional neural network (QST-CNN) and Long Short-Term Memory network (LSTM), called QST-CNN-LSTM	Weizmann, UCF sports, UCF11	On Weizmann: QST-CNN-LSTM −96.34% recognition accuracy, 3D CNN, Gray-CNN, and 3Channel-CNN were 90.12%, 86.46%, and 76.00%, respectively
[14]	2018	Automatically learned features	a robust position-independent HAR system for smartphone using a deep CNN model	New dataset	98%
[18]	2017	Automatically learned features, handcrafted features	Uses RGB-D data for recognition of the action using multimodal fusion by using scene flow as early fusion and integrating the modalities' data in a late fusion fashion	Montalbano II, MSR Daily Activity 3D	DT and MMDT accuracy on MSR Daily Activity 3D is 63.125%, 78.13%; DT and MMDT accuracy on Montalbano is 83.5% and 85.66%
[136]	2017	Handcrafted features	The method tries state-of-art classifiers and explains the role of feature selection for activity recognition in smartphones	State-of-the-art classifiers: Bayes classifier, kNN, MLP, SVM, MLM and MLM-NN	MLM and SVM achieved accuracy of more than 99.2% in the original data set and 98.1% using new feature selection method

The skeleton is a high-level presentation that can be used to describe human activity in a very precise way and is adapted to the challenge of activity analysis, pose estimation, and action recognition. However, skeleton data include the coordinates of the human body's key joints over time. This is an important factor for the motion presentation of each action. Body pose is an important indicator of human actions. Human body pose is a type of high-level semantic feature that has shown effect in recognizing human actions with discriminative geometric relations with body joints. Recent researches focus on either 2D or 3D modeling of these body joints. Most of the latest research in the field of automated HAR in fact based on skeleton data and uses depth devices such as Kinect to obtain three-dimensional (3D) skeleton information directly from the camera. Although these researches achieve high accuracy but are strictly device dependent and cannot be used for videos other than from specific cameras.

The 2D representation approach is effective for applications where precise pose recovery is not needed or possible [154]. The low-resolution image or single viewpoint can also be a reason for 2D representation methods. Example surveillance camera positioning. 3D approaches are suitable for a scenario involving a high level of discrimination between various unconstrained and complex human movements (Table 6).

6 Challenges in indoor HAR

Human activity recognition is an active and pervasive field for researchers not only from the areas of Computer Science, Electrical Engineering, and Informatics but also from many interdisciplinary backgrounds. This is because this field involves many challenges. From capturing data to the recognition process, all steps involve a thoughtful procedure that can be helpful in devising an appropriate way of recognizing the targeted activities. The environment for regular activities can be constrained and noisy.

The hardware involved has to be carefully thought out. One has to take into consideration real-world hardware implementation, efficient and resource-constraint computation, novel physics-based sensing, and socio-economical and human factor-related challenges.

The activities for which the model is to be built, also help in deciding the approach ahead. The indoor activities performed in controlled and static background conditions may not require a great deal of complex pre-processing steps whereas localization and denoising become an integral part of the process involving activities performed with complex backgrounds and multiple objects in a single frame. Choosing features is again a challenge for building a good model. Traditionally, machine learning used handcrafted features but with the popular and successful implementation of convolution neural network models, the deep learning approach has gained momentum and is a preferred choice for researchers. Thus, broadly talking of the levels of challenges in the pipeline for HAR we can categorize them as Application-level challenges, Data acquisition-level challenges, Approach level challenges, Algorithm level challenges, and Implementation level challenges. These are represented in Fig. 7 below.

6.1 Application-level challenges

The application area of indoor HAR is a big factor to study the challenges involved. The general application areas of HAR are surveillance, elderly care [176, 210], assisted living [185], smart homes, abnormal activity recognition [115, 131, 215], sports [164], etc. The

Table 6 2D and 3D representation approach

Ref.	Year	2D/3D	Objective	Model Used/Remarks
[104]	2020	2D,3D	Better presentation of the human body using different features and the exploitation of the RNN structure for activities.	Training using human skeleton features; Recognition using GRU + RNN
[62]	2019	2D	2d representation of the human body using skeleton key points and contour key points for human shape information	depth differential silhouettes (DDS) between two consecutive frames, and it is represented by the histogram of oriented gradients (HOG) format; multi-fused features + Accumulated HMM
[79]	2019	2D	2D skeletal data is extracted from videos obtained from a normal camera for activity recognition. Uses OpenPose library to find appearance and motion features using 2D positions of human skeletal joints	Comparisons of KNN, SVM, LDA, NB, and BPNN used for fall, walk, and sitting activities and comparison with state-of-the-art for the proposed work with normalized skeleton data
[121]	2018	2D	an approach based on a deep neural network architecture for 2D pose-based action recognition tasks	The use of pose features and global features for multi-modal action recognition made the system perform better than the P-CNN and JDD which are recent pose-based approaches.
[200]	2018	3D,2D	first method to capture the 3D total motion of a target person from a monocular view input	POFs are predicted by a Fully Convolutional Network, along with the joint confidence maps
[52]	2018	2D,3D	Motion information gathered from skeleton joint sequences and use of ConvNets based approach for activity recognition by combining multiple vision cues	Combination of multiple cues by means of decision level fusion.
[103]	2017	3D	multi-fused features for online human activity recognition (HAR) system that recognizes human activities from continuous sequences of depth map	Combining spatio-temporal features and depth silhouettes give a better idea of the activity. Forward spotting scheme was also proposed to differentiate between activity and non-activity.
[102]	2016	3D	spatiotemporal features approach to detect, track, and recognize human silhouettes using a sequence of RGB-D images	Use of spatiotemporal data from depth images is a good feature that increased the accuracy as it can be used for storing data in case of sequential activities.
[126]	2015	3D	A deep structured model, which decomposes an activity instance into temporal parts using the CNN	The temporal feature helps in considering large variations within activities and sub-segments of the activities are taken into account for better results of the deep learning model; CNN with back propogation

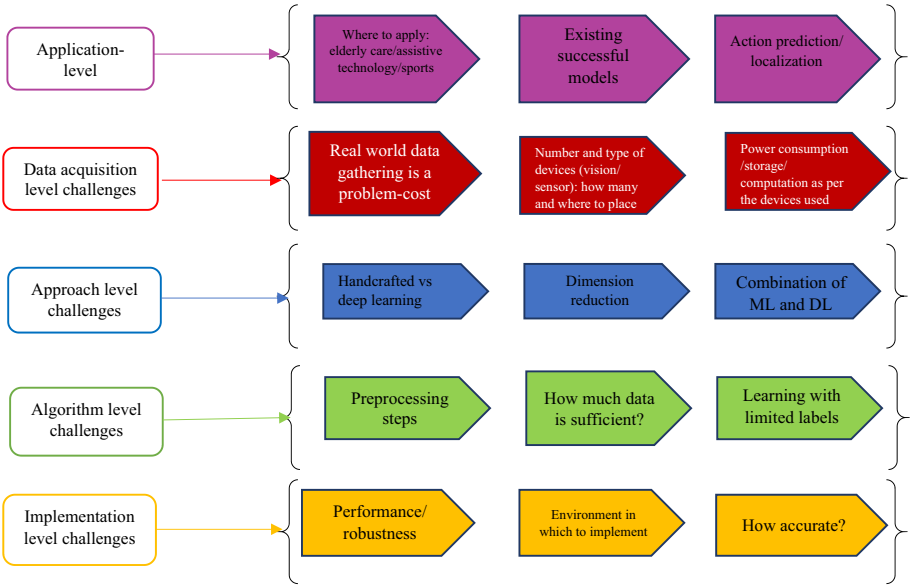


Fig. 7 Various levels of challenges and factors involved in Indoor HAR

challenges vary according to the area of application. Application of the model will help in deciding the steps ahead for building a system that considers the challenges which exist in that research problem.

6.2 Data acquisition level challenges

As previously discussed, the data for indoor HAR which can be a video or an image from the video can be either captured using vision-based methods or sensor-based methods. Some studies have combined the image/video under the sensors category for the sake of simplicity. This survey has considered vision-based input but also discussed current research in both the sensor-based and vision-based input fields.

6.2.1 Real-world data gathering

The data captured from whichever medium may have noise due to the environment from which the data has been extracted. For example, speech data from a kitchen activity will have background noise. Similarly, the images or video captured from cameras placed indoors in the living room can have noise in the form of dust particles, low visibility [122, 155] etc. Due to this noise the accuracy of the model may suffer.

6.2.2 Number and type of devices single camera or multiple cameras

The other problem is the choice of device to capture the data. Data can be captured from a static camera installed in the region of the activity or it can be collected using types of sensors (wearable, ambient) as discussed in section 2. In both cases the number and location

of the sensor/camera matter. The data may lose its worth if it loses the critical features which are important for recognizing a particular activity. The capturing devices should be thoughtfully placed. The application for which it is being used will also matter together with the choice of sensor. Like, if the monitoring of the elderly is to be done using a wearable sensor, then one sensor is sufficient on the wrist. On the other hand, if the camera-based sensor is to be used then we may need two cameras or even more to detect and capture the whole activity being done.

6.2.3 Power consumption/storage/computation/Privacy

With the increase in application areas of activity monitoring, CCTVs have gained popularity in various segments involving AAL [54] elderly care [165]. But the challenge is the increasing demand of power, storage and computation which are essential pillars to the success of a model for activity recognition. These factors cannot be overlooked and thus reduction in terms of these parameters play as a gamechanger for the model.

Apart from storage and power consumption, privacy of data and person are also very important. The elderly person may feel uncomfortable being monitored by someone for his daily activities in case of a camera. While using wearable sensors, other issues related to networking may cause a concern.

6.3 Approach level challenges

The recognition and analysis by a model require knowing in depth of the features which can prove efficient. Knowledge of feature dimension and interpretability is also a key aspect to create a powerful yet computationally light model.

6.3.1 Handcrafted vs. deep learning

The impressive classification performance of the deep learning methods is making it popular among the researchers. However, it is known that they typically require a large training sample to achieve that accuracy. Meanwhile, handcrafted (HC) features have been implemented for decades and still serve as a powerful tool when combined with machine learning classifiers. Researchers are still exploring the best technique to suit their problem [16, 127]. Table 5 listed some of the latest research works using either or both of these approaches.

6.3.2 Dimension reduction

Another important challenge is to reduce the size of the feature so that the computation is easy to process. Also, a non-contributing feature should not be part of the process. Researchers have been working on this aspect for a better solution to the problem. Table 7 lists some of the recent works in the dimensionality reduction area for deep learning and machine learning techniques.

6.3.3 Combination of automatically-calculated and handcrafted features

Researchers have been trying to combine handcrafted features (machine learning) and automatically-calculated (deep learning) features to design such systems which can be accurate and robust. Table 5 lists a few of the recent works which have combined both types of

Table 7 Few of the recent works for dimensionality reduction

Ref.	Year	Area	Objective	Method used/Remarks
[161]	2021	Deep learning	proposes a hybrid approach to analyse and recognize human activity on the same dataset using deep learning methods on a cloud-based platform and principal component analysis is applied to the dataset to get the most important features.	561 features to 48 using 50 PCA components; CNN used further
[142]	2021	Sensor data	proposed a dimensionality reduction technique called fast feature dimensionality reduction technique (FFDRT)[reduces the number of features to 561 to 66]	Input features: 6000×561; output: 6000×66; classification algorithm used: KNN, random forest, deep learning
[201]	2019	CNN	a network intrusion detection model based on a convolutional neural network-IDS (CNN-IDS). Redundant and irrelevant features in the network traffic data are first removed using different dimensionality reduction methods. Features of the dimensionality reduction data are automatically extracted using CNN, and more effective information for identifying intrusion is extracted by supervised learning.	CNN-IDS, DNN, RNN
[156]	2017	Deep learning, hand-crafted features	investigates a particular approach to combine hand-crafted features and deep learning to (i) achieve an early fusion of off-the-shelf handcrafted global image features and (ii) reduce the overall number of dimensions to combine both worlds. This method allows for fast image retrieval in domains, where training data is sparse.	Reduction in processing time; handcrafted and deep learning;
[66]	2016	Machine learning	to deal with HAR modeling involving a significant number of variables in order to identify relevant parameters from data and thus maximize the classification accuracy while minimizing the number of features using data mining techniques	Dimensionality reduction models: Pristine, PCA with KNN, C5.0 as recognition models
[44]	2016	Sensor data	introduce the framework of a manifold elastic net that encodes the local geometry to find an aligned coordinate system for data representation.	PCA for dimensionality reduction
[195]	2016	Deep learning	to investigate the dimensionality reduction ability of the auto-encoder, and see if it has some kind of good property that might accumulate when being stacked and thus contribute to the success of deep learning.	Auto-encoders for dimensionality reduction
[193]	2014	Neural network	a dimensionality reduction method by manifold learning, which iteratively explores data relations and uses the relation to pursue the manifold structure.	Autoencoder used for dimensionality reduction; deep autoencoders used for complex datasets

Table 8 Summary of Proposed Taxonomy in terms of Components

Components of Vision-based indoor HAR	Remarks/Challenges
Types of Input • Camera • Depth (camera) sensor	Pros: No dependence on wearing/ placement of sensors; No battery issues. Cons: Camera cost/ Installation angles/ number of cameras/ sensors to be deployed/ application for which used
Body Representation • 2D • 3D	Human body 2D representation low computation and storage requirement; Relies on edges and shape; 3D considers depth; requires depth sensors like Kinect
Modalities • 2D • 3D • Skeleton based	*2D* relies of visual RGB content only; *3D* has a depth channel; gives better results; *Skeleton-based attaches* information of standard key-points of human body; Pose estimation and activity becomes clear.
Solutions • Handcrafted features (Global feature-based, local feature-based) Approaches: Space-time trajectory, Space-time features, Shape-based, motion-based, LBP, fuzzy logic, etc. • Learned feature representation/ Deep learning based > Spatio-temporal network > Multiple stream network > Deep Generative Network > Temporal coherency network	*Handcrafted Solutions* Popular methods: HMM, BOW, HOG, Bayesian network, etc. Pros: Works well for lesser data; Cons: challenges like lighting, and occlusion may impact the system's accuracy to greater lengths. *Deep Learning Solutions:* Popular methods: CNN, LSTM, CNN-3D, RNN,etc. Pros: Appropriate for sequential processing; temporal data with spatial data can help in increasing the accuracy; Cons: requires large amounts of data. Costly set up required
Challenges • Application level • Data acquisition level • Approach level • Algorithm level • Implementation level	*Where* to apply; *What* application area is involved; *How* to acquire the data; *Which* approach is suitable; *Which* algorithm is to be chosen; *Robustness, performance measures, etc.*

features for HAR models. This is a challenging task to choose the appropriate techniques and compare them with other models.

6.4 Algorithm-level challenges

This challenge talks about the concerns like pre-processing steps to be included, the data volume to be taken, and learning with limited labels. These concerns and issues are correlated and overlap with the issues discussed above. For a better HAR performance, data pre-processing is a crucial step in machine learning and deep learning algorithm. Data

pre-processing includes data cleaning, normalization, transformation, feature extraction, and selection [111].

An important issue in HAR is whether to use training data from a general population (subject-independent), or personalized training data from the target user (subject-dependent). Past research has shown better results with personalized data but a collection of end-user data for training is not a practical option. Thus, the subject-independent approach is more common. [164] introduce a novel approach that uses nearest-neighbor similarity to identify examples from a subject-independent training set that are most similar to sample data obtained from the target user and uses these examples to generate a personalized model for the user.

6.5 Implementation-level challenges

Implementation of the model finally gives us an idea of how the system behaves in real-time. This arises because of the challenges like low lighting conditions, occlusions, etc. Overall, the requirement is for a robust and reliable system. These challenges also include network issues which may cause real-time glitches in HAR. The accuracy and time to execute, both are important aspects of a real-time system. If the system takes too long to process then the lag decreases the real-time effect thus making the system inefficient. If the system accuracy is less but the speed of processing is good then the system is unreliable. So, both concerns should be addressed equally.

7 Conclusion and future work

In this survey, we have reviewed recent trends in the field of indoor human activity recognition. We have proposed a taxonomy for indoor HAR. The review is conducted on the state-of-the-art HAR input methodology, approaches, datasets, and human body representation methods. The datasets which have been used in various recent research have alsso been listed. The survey lists various challenges associated with indoor HAR at various levels. Indoor-HAR can provide smart solutions for elderly care, patient care systems, physical fitness systems, abnormal human behavior detection, and analysis, etc. We can monitor our indoor activities to observe the change in activity patterns before the onset of any disease or major illness. These can help in situations where these changes go unnoticed because we tend to ignore certain changes in the body. Such systems can generate data and help us observe physical changes. The cases of child abuse during the pandemic had increased. Such systems can help in such situations too for detecting any abnormal behavior, fall detection, domestic violence, child abuse, etc. Table 8 summarises the survey in terms of the individual components of the proposed taxonomy. Indoor-HAR is a vast area with many key and challenging applications.

Data availability Data sharing not applicable to this article as no datasets were generated or analysed during the current study.

References

1. "(4) (PDF) Human Activity Recognition from Video: modeling, feature selection and classification architecture." (n.d.) https://www.researchgate.net/publication/237448747_Human_Activity_Recognition_from_Video_modeling_feature_selection_and_classification_architecture. Accessed 19 Aug 2021

2. "(4) (PDF) Real time detection, tracking and recognition of medication intake." (n.d.) https://www.researchgate.net/publication/242772663_Real_time_detection_tracking_and_recognition_of_medication_intake. Accessed 19 Aug 2021
3. "(8) (PDF) Dense RGB-D Map-Based Human Tracking and Activity Recognition using Skin Joints Features and Self-Organizing Map." (n.d.) https://www.researchgate.net/publication/326175323_Dense_RGB-D_Map-Based_Human_Tracking_and_Activity_Recognition_using_Skin_Joints_Features_and_Self-Organizing_Map. Accessed 28 Aug 2021
4. "(8) Development of a life logging system via depth imaging-based human activity recognition for smart homes | Request PDF." (n.d.) https://www.researchgate.net/publication/292224847_Development_of_a_life_logging_system_via_depth_imaging-based_human_activity_recognition_for_smart_homes Accessed 28 Aug 2021
5. "(8) Human activity recognition using the labeled depth body parts information of depth silhouettes | Request PDF." (n.d.) https://www.researchgate.net/publication/329877194_Human_activity_recognition_using_the_labeled_depth_body_parts_information_of_depth_silhouettes. Accessed 28 Aug 2021
6. Abdel-Basset M, Chang V, Hawash H, Chakrabortty RK, Ryan M (2021) Deep learning approaches for human-centered IoT applications in smart indoor environments: a contemporary survey. Ann Oper Res 2021:1–49. https://doi.org/10.1007/S10479-021-04164-3
7. Abdelgawwad A, Mallofre AC, Patzold M (2021) A Trajectory-Driven 3D Channel Model for Human Activity Recognition. IEEE Access 9:103393–103406. https://doi.org/10.1109/ACCESS.2021.3098951
8. Abdul Lateef Haroon PS, Premachand DR (2021) Human Activity Recognition using Machine Learning Approach. J Robot Control (JRC) 2(5):395–399. https://doi.org/10.18196/JRC.25113
9. "Activity Net." (n.d.) http://activity-net.org/. Accessed 23 Nov 2021
10. Agarwal P, Alam M (2020) A Lightweight Deep Learning Model for Human Activity Recognition on Edge Devices. Procedia Comput Sci 167:2364–2373. https://doi.org/10.1016/J.PROCS.2020.03.289
11. Aggarwal JK, Cai Q (1999) Human Motion Analysis: A Review. Comput Vis Image Underst 73(3):428–440. https://doi.org/10.1006/CVIU.1998.0744
12. Aggarwal JK, Ryoo MS (2011) Human activity analysis. ACM Comput Surv (CSUR) 43(3):43. https://doi.org/10.1145/1922649.1922653
13. Aggarwal JK, Xia L (2014) Human activity recognition from 3D data: A review. Pattern Recogn Lett 48:70–80. https://doi.org/10.1016/J.PATREC.2014.04.011
14. Almaslukh B, Artoli AM, Al-Muhtadi J (2018) A robust deep learning approach for position-independent smartphone-based human activity recognition. Sensors 18(11):1–17. https://doi.org/10.3390/s18113726
15. Amirbandi EJ, Shamsipour G (2016) Exploring methods and systems for vision-based human activity recognition. 2016 1st conference on swarm intelligence and evolutionary computation (CSIEC), Bam, Iran, 2016, pp 160–164. https://doi.org/10.1109/CSIEC.2016.7482122
16. Antipov G, Berrani SA, Ruchaud N, Dugelay JL (Oct. 2015) Learned vs hand-crafted features for pedestrian gender recognition. MM 2015 - Proceedings of the 2015 ACM Multimedia Conference, pp. 1263–1266. https://doi.org/10.1145/2733373.2806332
17. Arifoglu D, Bouchachia A (2019) Detection of abnormal behaviour for dementia sufferers using convolutional neural networks. Artificial Intelligence in Medicine 94:88–95. https://doi.org/10.1016/J.ARTMED.2019.01.005
18. Asadi-Aghbolaghi M, Bertiche H, Roig V, Kasaei S, Escalera S (2017) Action Recognition from RGB-D data: comparison and fusion of spatio-temporal handcrafted features and deep strategies. pp. 3179–3188
19. Ashraf I, Zikria YB, Hur S, Bashir AK, Alhussain T, Park Y (2021) Localizing pedestrians in indoor environments using magnetic field data with term frequency paradigm and deep neural networks. Int J Mach Learn Cybern 12:3203–3219. https://doi.org/10.1007/S13042-021-01279-8
20. Ayase R, Higashi T, Takayama S, Sagawa S, Ashida N (2008) A method for supporting at-home fitness exercise guidance and at-home nursing care for the elders, Video-based simple measurement system. *2008 10th IEEE Intl. Conf. on e-Health Networking, Applications and Service, HEALTHCOM 2008*, pp. 182–186. https://doi.org/10.1109/HEALTH.2008.4600133
21. Babiker M, Khalifa OO, Htike KK, Hassan A, Zaharadeen M (Mar. 2018) Automated daily human activity recognition for video surveillance using neural network. *2017 IEEE International Conference on Smart Instrumentation, Measurement and Applications, ICSIMA 2017*, vol. 2017-November, pp. 1–5. https://doi.org/10.1109/ICSIMA.2017.8312024
22. Bao L, Intille SS (2004) Activity Recognition from User-Annotated Acceleration Data. Lecture Notes in Computer Science (including subseries Lecture Notes in Artificial Intelligence and Lecture Notes in Bioinformatics), vol. 3001, pp. 1–17. https://doi.org/10.1007/978-3-540-24646-6_1

23. Basly H, Ouarda W, Sayadi FE, Ouni B, Alimi AM (Jun. 2020) CNN-SVM Learning Approach Based Human Activity Recognition. *Lecture Notes in Computer Science (including subseries Lecture Notes in Artificial Intelligence and Lecture Notes in Bioinformatics)*, vol. 12119 LNCS, pp. 271–281. https://doi.org/10.1007/978-3-030-51935-3_29.
24. Beddiar DR, Nini B, Sabokrou M, Hadid A (2020) Vision-based human activity recognition: a survey. Multimed Tools Appl 79(41–42):30509–30555. https://doi.org/10.1007/S11042-020-09004-3
25. Ben-Arie J, Wang Z, Pandit P, Rajaram S (2002) Human activity recognition using multidimensional indexing. IEEE Trans Pattern Anal Mach Intell 24(8):1091–1104. https://doi.org/10.1109/TPAMI.2002.1023805
26. Bhat O, Khan DA (2021) Evaluation of deep learning model for human activity recognition. Evol Syst 1:1–10. https://doi.org/10.1007/S12530-021-09373-6
27. Bhola G, Kathuria A, Kumar D, Das C (May 2020) Real-time Pedestrian Tracking based on Deep Features. *Proceedings of the International Conference on Intelligent Computing and Control Systems, ICICCS 2020*, pp. 1101–1106, https://doi.org/10.1109/ICICCS48265.2020.9121061
28. Bibbo L (n.d.) AN INTEGRATED SYSTEM FOR INDOOR PEOPLE LOCALIZATION, TRACKING, AND MONITORING Localization and tracking of people in indoor environment View project. [Online]. Available: www.scientific-publications.net. Accessed Oct. 17, 2021
29. Blank M, Gorelick L, Shechtman E, Irani M, Basri R (n.d.) Actions as Space-Time Shapes
30. Bo L, Ren X, Fox D (2013). Unsupervised feature learning for RGB-D based object recognition. Experimental Robotics. 88. https://doi.org/10.1007/978-3-319-00065-7_27
31. Bobick AF, Davis JW (2001) The recognition of human movement using temporal templates. IEEE Trans Pattern Anal Mach Intell 23(3):257–267. https://doi.org/10.1109/34.910878
32. Bocus MJ et al (Oct. 2021) OPERAnet: A Multimodal Activity Recognition Dataset Acquired from Radio Frequency and Vision-based Sensors. [Online]. Available: https://arxiv.org/abs/2110.04239v1. Accessed 17 Oct 2021
33. Brand M, Oliver N, Pentland A (1997) Coupled hidden Markov models for complex action recognition. *Proceedings of the IEEE Computer Society Conference on Computer Vision and Pattern Recognition*, pp. 994–999, https://doi.org/10.1109/CVPR.1997.609450
34. Bux A, Angelov P, Habib Z (2017) Vision Based Human Activity Recognition: A Review. Adv Intell Syst Comput 513:341–371. https://doi.org/10.1007/978-3-319-46562-3_23
35. Buzzelli M, Albé A, Ciocca G (2020) A Vision-Based System for Monitoring Elderly People at Home. Appl Sci 10:374. https://doi.org/10.3390/app10010374
36. "CAD-120 Dataset | Papers With Code." (n.d.) https://paperswithcode.com/dataset/cad-120. Accessed 23 Nov 2021
37. Capela NA, Lemaire ED, Baddour N (2015) Feature Selection for Wearable Smartphone-Based Human Activity Recognition with Able bodied, Elderly, and Stroke Patients. PLoS One 10(4):e0124414. https://doi.org/10.1371/JOURNAL.PONE.0124414
38. Cardone G, Cirri A, Corradi A, Foschini L, Ianniello R, Montanari R (2014) Crowdsensing in Urban areas for city-scale mass gathering management: Geofencing and activity recognition. IEEE Sensors J 14(12):4185–4195. https://doi.org/10.1109/JSEN.2014.2344023
39. Casale P, Pujol O, Radeva P (2011) Human activity recognition from accelerometer data using a wearable device. *Lecture Notes in Computer Science (including subseries Lecture Notes in Artificial Intelligence and Lecture Notes in Bioinformatics)*, vol. 6669 LNCS, pp. 289–296. https://doi.org/10.1007/978-3-642-21257-4_36
40. Chaquet JM, Carmona EJ, Fernández-Caballero A (2013) A survey of video datasets for human action and activity recognition. Comput Vis Image Underst 117(6):633–659. https://doi.org/10.1016/J.CVIU.2013.01.013
41. Chen Y, Shen C (2017) Performance analysis of smartphone-sensor behavior for human activity recognition. IEEE Access 5:3095–3110. https://doi.org/10.1109/ACCESS.2017.2676168
42. Chen L, Wei H, Ferryman J (2013) A survey of human motion analysis using depth imagery. Pattern Recogn Lett 34(15):1995–2006. https://doi.org/10.1016/J.PATREC.2013.02.006
43. Chen C, Jafari R, Kehtarnavaz N (Dec. 2015) UTD-MHAD: A multimodal dataset for human action recognition utilizing a depth camera and a wearable inertial sensor. *Proceedings - International Conference on Image Processing, ICIP*, vol. 2015-December, pp. 168–172. https://doi.org/10.1109/ICIP.2015.7350781
44. Chen YL, Wu X, Li T, Cheng J, Ou Y, Xu M (2016) Dimensionality reduction of data sequences for human activity recognition. Neurocomputing 210:294–302. https://doi.org/10.1016/J.NEUCOM.2015.11.126
45. Chen Z, Zhang L, Cao Z, Guo J (2018) Distilling the Knowledge from Handcrafted Features for Human Activity Recognition. IEEE Trans Industr Inform 14(10):4334–4342. https://doi.org/10.1109/TII.2018.2789925

46. Chen Z, Xiang S, Ding J, Li X (2020) Smartphone sensor-based human activity recognition using feature fusion and maximum full a posteriori. IEEE Trans Instrum Meas 69(7):3992–4001. https://doi.org/10.1109/TIM.2019.2945467
47. Cheng G, Wan Y, Saudagar AN, Namuduri K, Buckles BP (Jan. 2015) Advances in Human Action Recognition: A Survey. [Onlisssne]. Available: https://arxiv.org/abs/1501.05964v1. Accessed 19 Aug 2021
48. Cheng X, He M, Duan W (Apr. 2018) Machine vision based physical fitness measurement with human posture recognition and skeletal data smoothing. *Proceedings of the 2017 International Conference on Orange Technologies, ICOT 2017*, vol. 2018-January, pp. 7–10. https://doi.org/10.1109/ICOT.2017.8336075
49. "Child maltreatment." (n.d.) https://www.who.int/en/news-room/fact-sheets/detail/child-maltreatment. Accessed 09 Nov 2021
50. Chua CS, Guan H, Ho YK (2002) Model-based 3D hand posture estimation from a single 2D image. Image Vis Comput 20(3):191–202. https://doi.org/10.1016/S0262-8856(01)00094-4
51. Chung YY (2021) Design and Implementation of CNN-Based Human Activity Recognition System using WiFi Signals. J Adv Navig Technol 25(4):299–304. https://doi.org/10.12673/JANT.2021.25.4.299
52. "Combining CNN streams of RGB-D and skeletal data for human activity recognition | Elsevier Enhanced Reader." (n.d.) https://reader.elsevier.com/reader/sd/pii/S0167865518301636?token=783B2B6816D52EBDE82954EF671CD3D613E82F9615D667D214FBAE255C11798716F7DDC0FDCCC7E62D77F1BE4C2CBBEC&originRegion=eu-west-1&originCreation=20210925093934. Accessed 25 Sep 2021
53. Dai R et al (2022) Toyota smarthome untrimmed: real-world untrimmed videos for activity detection. IEEE Trans Pattern Anal Mach Intell 45:2533–2550. https://doi.org/10.1109/TPAMI.2022.3169976
54. Damaševičius R, Vasiljevas M, Šalkevičius J, Woźniak M (2016) Human activity recognition in AAL environments using random projections. Comput Math Methods Med 2016:1–17. https://doi.org/10.1155/2016/4073584
55. Dang X, Huang Y, Hao Z, Si X (2018) PCA-Kalman: device-free indoor human behavior detection with commodity Wi-Fi. EURASIP J Wirel Commun Netw 2018(1):1–17. https://doi.org/10.1186/S13638-018-1230-2/FIGURES/15
56. Das Dawn D, Shaikh SH (2015) A comprehensive survey of human action recognition with spatio-temporal interest point (STIP) detector. Vis Comput 32(3):289–306. https://doi.org/10.1007/S00371-015-1066-2
57. Dash SCB, Mishra SR, Srujan Raju K, Narasimha Prasad LV (2021) Human action recognition using a hybrid deep learning heuristic. Soft Comput 25(20):13079–13092. https://doi.org/10.1007/S00500-021-06149-7
58. Wang J, Liu Z, Wu Y, Yuan J (2012) Mining action let ensemble for action recognition with depth cameras, IEEE Conf Comput Vis Pattern Recognit (CVPR 2012), Providence, Rhode Island, June 16–21
59. Dhiman C, Vishwakarma DK (2020) View-Invariant Deep Architecture for Human Action Recognition Using Two-Stream Motion and Shape Temporal Dynamics. IEEE Trans Image Process 29:3835–3844. https://doi.org/10.1109/TIP.2020.2965299
60. Dollár P, Rabaud V, Cottrell G, Belongie S (2005) Behavior recognition via sparse spatio-temporal features. *Proceedings - 2nd Joint IEEE International Workshop on Visual Surveillance and Performance Evaluation of Tracking and Surveillance, VS-PETS*, vol. 2005, pp. 65–72. https://doi.org/10.1109/VSPETS.2005.1570899
61. Du Y, Chen F, Xu W (2007) Human interaction representation and recognition through motion decomposition. IEEE Signal Process Lett 14(12):952–955. https://doi.org/10.1109/LSP.2007.908035
62. Duan H, Lin K, Jin S, Liu W, Qian C, Ouyang W TRB: A Novel Triplet Representation for Understanding 2D Human Body
63. Duong TV, Bui HH, Phung DQ, Venkatesh S (2005) Activity Recognition and Abnormality Detection with the Switching Hidden Semi-Markov Model
64. Duong TV, Phung DQ, Bui HH, Venkatesh S (n.d.) Human Behavior Recognition with Generic Exponential Family Duration Modeling in the Hidden Semi-Markov Model
65. Edwards M, Deng J, Xie X (2016) From pose to activity: Surveying datasets and introducing CONVERSE. Comput Vis Image Underst 144:73–105. https://doi.org/10.1016/J.CVIU.2015.10.010
66. El S, el Moudden I, Rabat I, Ouzir MM, Benyacoub B, el Bernoussi S (2016) Mining Human Activity Using Dimensionality Reduction and Pattern Recognition. Contemp Eng Sci 9(21):1031–1041. https://doi.org/10.12988/ces.2016.67119
67. Espinosa R, Ponce H, Gutiérrez S, Martínez-Villaseñor L, Brieva J, Moya-Albor E (2019) A vision-based approach for fall detection using multiple cameras and convolutional neural networks: A case

study using the UP-Fall detection dataset. Comput Biol Med 115:103520. https://doi.org/10.1016/J.COMPBIOMED.2019.103520
68. Fathi A, Ren X, Rehg JM (2011) Learning to recognize objects in egocentric activities. *Proceedings of the IEEE Computer Society Conference on Computer Vision and Pattern Recognition*, pp. 3281–3288. https://doi.org/10.1109/CVPR.2011.5995444
69. Feng W et al (2014) Fall detection for elderly person care in a vision-based home surveillance environment using a monocular camera. SIViP 8:1129–1138. https://doi.org/10.1007/s11760-014-0645-4
70. "FineGym: A Hierarchical Video Dataset for Fine-grained Action Understanding." (n.d.) https://sdolivia.github.io/FineGym/ Accessed 26 Aug 2021
71. Foroughi H, Rezvanian A, Paziraee A (2008) Robust fall detection using human shape and multi-class support vector machine. *Proceedings - 6th Indian Conference on Computer Vision, Graphics and Image Processing, ICVGIP 2008*, pp. 413–420, https://doi.org/10.1109/ICVGIP.2008.49
72. Foroughi H, Aski BS, Pourreza H (2008) Intelligent video surveillance for monitoring fall detection of elderly in home environments. *Proceedings of 11th International Conference on Computer and Information Technology, ICCIT 2008*, pp. 219–224. https://doi.org/10.1109/ICCITECHN.2008.4803020
73. Foroughi H, Yazdi HS, Pourreza H, Javidi M (2008) An eigenspace-based approach for human fall detection using integrated time motion image and multi-class support vector machine. Proceedings - 2008 IEEE 4th International Conference on Intelligent Computer Communication and Processing, ICCP 2008. 83–90. https://doi.org/10.1109/ICCP.2008.4648358
74. Foroughi H, Naseri A, Saberi A, Sadoghi Yazdi H (2008) An eigenspace-based approach for human fall detection using integrated time motion image and neural network. 2008 9th international conference on signal processing, Beijing, China, 2008, pp. 1499–1503. https://doi.org/10.1109/ICOSP.2008.4697417
75. Franco A, Magnani A, Maio D (2020) A multimodal approach for human activity recognition based on skeleton and RGB data. Pattern Recogn Lett 131:293–299. https://doi.org/10.1016/J.PATREC.2020.01.010
76. Fu B, Kirchbuchner F, Kuijper A, Braun A, Gangatharan DV (2018) Fitness Activity Recognition on Smartphones Using Doppler Measurements. Informatics 5:24. https://doi.org/10.3390/INFORMATICS5020024
77. Gao J, Hauptmann AG, Bharucha A, Wactlar HD (2004) Dining activity analysis using a hidden Markov model. Proceedings of the 17th international conference on pattern recognition 2004, Cambridge, UK, 2:915–918. https://doi.org/10.1109/ICPR.2004.1334408
78. Ghali A, Cunningham AS, Pridmore TP (2003) Object and event recognition for stroke rehabilitation. Vis Commun Image Process 5150:980–989. https://doi.org/10.1117/12.503470
79. Ghazal S, Khan US, Saleem MM, Rashid N, Iqbal J (2019) Human activity recognition using 2D skeleton data and supervised machine learning. IET Image Process 13(13):2572–2578. https://doi.org/10.1049/IET-IPR.2019.0030
80. Ghorbani S et al (2021) MoVi: A large multi-purpose human motion and video dataset. PLoS One 16(6). https://doi.org/10.1371/JOURNAL.PONE.0253157
81. Goffredo M, Schmid M, Conforto S, Carli M, Neri A, D'Alessio T (2009) Markerless human motion analysis in Gauss-Laguerre transform domain: An application to sit-to-stand in young and elderly people. IEEE Trans Inf Technol Biomed 13(2):207–216. https://doi.org/10.1109/TITB.2008.2007960
82. "Google AI Blog: On-device, Real-time Body Pose Tracking with MediaPipe BlazePose." (n.d.) https://ai.googleblog.com/2020/08/on-device-real-time-body-pose-tracking.html. Accessed 14 Dec 2021
83. Gu Y, Ren F, Li J (2016) PAWS: Passive Human Activity Recognition Based on WiFi Ambient Signals. IEEE Internet Things J 3(5):796–805. https://doi.org/10.1109/JIOT.2015.2511805
84. Gu F, Chung MH, Chignell M, Valaee S, Zhou B, Liu X (2021) A Survey on Deep Learning for Human Activity Recognition. ACM Computing Surveys (CSUR) 54(8). https://doi.org/10.1145/3472290
85. Guo G, Lai A (2014) A survey on still image based human action recognition. Pattern Recogn 47(10):3343–3361. https://doi.org/10.1016/J.PATCOG.2014.04.018
86. Gupta JP, Singh N, Dixit P, Semwal VB, Dubey SR (2013) Human Activity Recognition Using Gait Pattern. Int J Comput Vis Image Process 3(3):31–53. https://doi.org/10.4018/IJCVIP.2013070103
87. Harrou F, Zerrouki N, Sun Y, Houacine A (2017) Vision-based fall detection system for improving safety of elderly people. IEEE Instrum Meas Mag 20(6):49–55. https://doi.org/10.1109/MIM.2017.8121952
88. "Home Action Genome." (n.d.) https://homeactiongenome.org/. Accessed 29 Jan 2023
89. Hu G, Huang S, Zhao L, Alempijevic A, Dissanayake G (2012) A robust RGB-D SLAM algorithm. *IEEE International Conference on Intelligent Robots and Systems*, pp. 1714–1719. https://doi.org/10.1109/IROS.2012.6386103

90. Xu F, Fujimura K (2003) Human detection using depth and gray images. Proceedings - IEEE conference on advanced video and signal based surveillance, AVSS 2003:115–121. https://doi.org/10.1109/AVSS.2003.1217910
91. Huo F, Hendriks E, Paclik P, Oomes AHJ (2009) Markerless human motion capture and pose recognition. *2009 10th International Workshop on Image Analysis for Multimedia Interactive Services, WIAMIS 2009*, pp. 13–16. https://doi.org/10.1109/WIAMIS.2009.5031420
92. Ihianle IK, Nwajana AO, Ebenuwa SH, Otuka RI, Owa K, Orisatoki MO (2020) A deep learning approach for human activities recognition from multimodal sensing devices. IEEE Access 8:179028–179038. https://doi.org/10.1109/ACCESS.2020.3027979
93. "II. DESCRIPTION OF WORK". (n.d.)
94. Schreier H, Orteu JJ, Sutton MA (2009) Image correlation for shape, motion and deformation measurements: basic concepts, theory and applications. Image correlation for shape, motion and deformation measurements: basic concepts,theory and applications, pp. 1–321. https://doi.org/10.1007/978-0-387-78747-3/COVER
95. Incel OD, Ozgovde A (2018) ARService: A Smartphone based Crowd-Sourced Data Collection and Activity Recognition Framework. Procedia Comput Sci 130:1019–1024. https://doi.org/10.1016/J.PROCS.2018.04.142
96. "Introducing the Penn Action Dataset | Penn Action." (n.d.) http://dreamdragon.github.io/PennAction/. Accessed 26 Aug 2021
97. Islam MM, Iqbal T (Oct. 2020) HAMLET: A hierarchical multimodal attention-based human activity recognition algorithm. *IEEE International Conference on Intelligent Robots and Systems*, pp. 10285–10292. https://doi.org/10.1109/IROS45743.2020.9340987
98. Jalal A, Kim Y (Oct. 2014) Dense depth maps-based human pose tracking and recognition in dynamic scenes using ridge data. *11th IEEE International Conference on Advanced Video and Signal-Based Surveillance, AVSS 2014*, pp. 119–124. https://doi.org/10.1109/AVSS.2014.6918654
99. Jalal A, Uddin I (2007) Security architecture for third generation (3G) using GMHS cellular network. *Proceedings - 3rd International Conference on Emerging Technologies, ICET 2007*, pp. 74–79. https://doi.org/10.1109/ICET.2007.4516319.
100. Jalal A, Lee S, Kim JT, Kim T-S (2012) Human Activity Recognition via the Features of Labeled Depth Body Parts. *Lecture Notes in Computer Science (including subseries Lecture Notes in Artificial Intelligence and Lecture Notes in Bioinformatics)*, vol. 7251 LNCS, pp. 246–249. https://doi.org/10.1007/978-3-642-30779-9_36
101. Jalal A, Kamal S, Kim D (2014) A Depth Video Sensor-Based Life-Logging Human Activity Recognition System for Elderly Care in Smart Indoor Environments. Sensors 14(7):11735–11759. https://doi.org/10.3390/S140711735
102. Jalal A, Kamal S, Kim D (2016) Human Depth Sensors-Based Activity Recognition Using Spatiotemporal Features and Hidden Markov Model for Smart Environments. J Comput Netw Commun 2016:1–11. https://doi.org/10.1155/2016/8087545
103. Jalal A, Kim YH, Kim YJ, Kamal S, Kim D (2017) Robust human activity recognition from depth video using spatiotemporal multi-fused features. Pattern Recogn 61:295–308. https://doi.org/10.1016/J.PATCOG.2016.08.003
104. Jaouedi N, Perales FJ, Buades JM, Boujnah N, Bouhlel MS (2020) Prediction of Human Activities Based on a New Structure of Skeleton Features and Deep Learning Model. Sensors 20:4944. https://doi.org/10.3390/s20174944
105. Kang S-M, Wildes R (2016) Review of Action Recognition and Detection Methods. *undefined*
106. Kareem I, Ali SF, Sheharyar A (Nov. 2020) Using Skeleton based Optimized Residual Neural Network Architecture of Deep Learning for Human Fall Detection. *Proceedings - 2020 23rd IEEE International Multi-Topic Conference, INMIC 2020*. https://doi.org/10.1109/INMIC50486.2020.9318061
107. Karpathy A, Toderici G, Shetty S, Leung T, Sukthankar R, Li FF (Sep. 2014) Large-scale video classification with convolutional neural networks. *Proceedings of the IEEE Computer Society Conference on Computer Vision and Pattern Recognition*, pp. 1725–1732. https://doi.org/10.1109/CVPR.2014.223
108. Ke Y, Sukthankar R, Hebert M (2007) Spatio-temporal shape and flow correlation for action recognition. *Proceedings of the IEEE Computer Society Conference on Computer Vision and Pattern Recognition*, https://doi.org/10.1109/CVPR.2007.383512
109. Khan ZA, Sohn W (2011) Abnormal human activity recognition system based on R-transform and kernel discriminant technique for elderly home care. IEEE Trans Consum Electron 57(4):1843–1850. https://doi.org/10.1109/TCE.2011.6131162
110. "Kinetics | DeepMind." (n.d.) https://deepmind.com/research/open-source/kinetics. Accessed 26 Aug 2021

111. Kotsiantis S, Kanellopoulos D, Pintelas P (2007) Data Preprocessing for Supervised Leaning. *undefined*
112. Krizhevsky A, Sutskever I, Hinton GE (2012) ImageNet Classification with Deep Convolutional Neural Networks. Adv Neural Inf Process Syst 25 [Online]. Available: http://code.google.com/p/cuda-convnet/. Accessed 06 Oct 2021
113. Kumari S, Mitra SK (2011) Human action recognition using DFT. *Proceedings - 2011 3rd National Conference on Computer Vision, Pattern Recognition, Image Processing and Graphics, NCVPRIPG 2011*, pp. 239–242, https://doi.org/10.1109/NCVPRIPG.2011.58
114. Kuo Y-M, Lee J-S, Chung P-C (2010) A visual context-awareness-based sleeping-respiration measurement system. IEEE Trans Inf Technol Biomed 14(2):255–265. https://doi.org/10.1109/TITB.2009.2036168
115. Lahiri D, Dhiman C, Vishwakarma DK (Apr. 2018) Abnormal human action recognition using average energy images. *2017 Conference on Information and Communication Technology, CICT 2017*, vol. 2018-April, pp. 1–5. https://doi.org/10.1109/INFOCOMTECH.2017.8340622
116. Laptev I, Marszałek M, Schmid C, Rozenfeld B (2008) Learning realistic human actions from movies. *26th IEEE Conference on Computer Vision and Pattern Recognition, CVPR*. https://doi.org/10.1109/CVPR.2008.4587756
117. Lee TK, Lim S, Lee S, An S, Oh SY (2012) Indoor mapping using planes extracted from noisy RGB-D sensors. *IEEE International Conference on Intelligent Robots and Systems*, pp. 1727–1733. https://doi.org/10.1109/IROS.2012.6385909
118. Leu A, Ristic-Durrant D, Graser A (2011) A robust markerless vision-based human gait analysis system. *SACI 2011 - 6th IEEE International Symposium on Applied Computational Intelligence and Informatics, Proceedings*, pp. 415–420. https://doi.org/10.1109/SACI.2011.5873039
119. Li W, Zhang Z, Liu Z (2010) Action recognition based on a bag of 3D points. IEEE computer society conference on computer vision and pattern recognition - workshops, CVPRW 2010, pp. 9–14. https://doi.org/10.1109/CVPRW.2010.5543273
120. Li YR, Miaou SG, Hung CK, Sese JT (2011) A gait analysis system using two cameras with orthogonal view. *2011 International Conference on Multimedia Technology, ICMT 2011*, pp. 2841–2844. https://doi.org/10.1109/ICMT.2011.6002046
121. Li C, Tong R, Tang M (2018) Modelling Human Body Pose for Action Recognition Using Deep Neural Networks. Arab J Sci Eng 43(12):7777–7788. https://doi.org/10.1007/S13369-018-3189-Z
122. Li X, Dong W, Shi G (2018) Sparsity-Based Denoising of Photographic Images: From Model-Based to Data-Driven. Adv Comput Vis Pattern Recognit:37–62. https://doi.org/10.1007/978-3-319-96029-6_2
123. Liangliang W, Lianzheng G, Ruifeng L, Yajun F (2017) Three-stream CNNs for action recognition. Pattern Recogn Lett 92:33–40. https://doi.org/10.1016/J.PATREC.2017.04.004
124. Liao TY, Miaou SG, Li YR (2010) A vision-based walking posture analysis system without markers. *ICSPS 2010 - Proceedings of the 2010 2nd International Conference on Signal Processing Systems*, vol. 3. https://doi.org/10.1109/ICSPS.2010.5555656
125. Lin C-H, Hsu F-S, Lin W-Y (2010) Recognizing Human Actions Using NWFE-Based Histogram Vectors. EURASIP J Adv Signal Process 2010(1):1–15. https://doi.org/10.1155/2010/453064
126. Lin L, Wang K, Zuo W, Wang M, Luo J, Zhang L (Dec. 2015) A Deep Structured Model with Radius-Margin Bound for 3D Human Activity Recognition. [Online]. Available: http://arxiv.org/abs/1512.01642. Accessed 28 Sep 2021
127. Lin W, Hasenstab K, Moura Cunha G, Schwartzman A (2020) Comparison of handcrafted features and convolutional neural networks for liver MR image adequacy assessment. Sci Rep 10(1):1–11. https://doi.org/10.1038/s41598-020-77264-y
128. Liu L, Shao L (n.d.) Learning Discriminative Representations from RGB-D Video Data
129. Liu C-D, Chung P, Chung Y, Thonnat M (2007) Understanding of human behaviors from videos in nursing care monitoring systems. *undefined*
130. Liu C, Hu Y, Li Y, Song S, Liu J (Mar. 2017) PKU-MMD: A Large Scale Benchmark for Continuous Multi-Modal Human Action Understanding. [Online]. Available: http://arxiv.org/abs/1703.07475. Accessed 23 Nov 2021
131. Lühr S, Venkatesh S, West G, Bui HH (n.d.) Explicit State Duration HMM for Abnormality Detection in Sequences of Human Activity
132. Lun R, Zhao W (2015) A survey of applications and human motion recognition with Microsoft Kinect. Int J Pattern Recognit Artif Intell 29(5). https://doi.org/10.1142/S0218001415550083
133. Luo Y, der Wu T, Hwang JN (2003) Object-based analysis and interpretation of human motion in sports video sequences by dynamic bayesian networks. Comput Vis Image Underst 92(2–3):196–216. https://doi.org/10.1016/J.CVIU.2003.08.001

134. Lygouras E, Santavas N, Taitzoglou A, Tarchanidis K, Mitropoulos A, Gasteratos A (2019) Unsupervised human detection with an embedded vision system on a fully autonomous uav for search and rescue operations. Sensors 19(16):3542. https://doi.org/10.3390/S19163542
135. Manjarres J, Lan G, Gorlatova M, Hassan M, Pardo M (2022) Deep learning for detecting human activities from piezoelectric-based kinetic energy signals. IEEE Internet Things J 9(10):7545–7558. https://doi.org/10.1109/JIOT.2021.3093245
136. Marinho LB, de Souza Junior AH, Filho PPR (2016) A New Approach to Human Activity Recognition Using Machine Learning Techniques. Adv Intell Syst Comput 557:529–538. https://doi.org/10.1007/978-3-319-53480-0_52
137. Mekruksavanich S, Promsakon C, Jitpattanakul A (2021) Location-based daily human activity recognition using hybrid deep learning network. JCSSE 2021 - 18th international joint conference on computer science and software engineering: cybernetics for human beings. https://doi.org/10.1109/JCSSE53117.2021.9493807
138. Meng B, Liu X, Wang X (2018) Human action recognition based on quaternion spatial-temporal convolutional neural network and LSTM in RGB videos. Multimed Tools Appl 77(20):26901–26918. https://doi.org/10.1007/S11042-018-5893-9
139. Menicatti R, Bruno B, Sgorbissa A (2017) Modelling the influence of cultural information on vision-based human home activity recognition. 2017 14th international conference on ubiquitous robots and ambient intelligence, URAI 2017, pp. 32–38. https://doi.org/10.1109/URAI.2017.7992880
140. Seidenari L, Varano V, Berretti S, Del Bimbo A, Pala P (2013) Recognizing actions from depth cameras as weakly aligned multi-part bag-of-poses", 3rd International Workshop on Human Activity Understanding from 3D data (HAU3D'13), in conjunction with CVPR 2013, Portland, Oregon
141. Minh Dang L, Min K, Wang H, Jalil Piran M, Hee Lee C, Moon H (2020) Sensor-based and vision-based human activity recognition: A comprehensive survey. Pattern Recogn 108:107561. https://doi.org/10.1016/J.PATCOG.2020.107561
142. Mohammed Hashim BA, Amutha R (2020) Human activity recognition based on smartphone using fast feature dimensionality reduction technique. J Ambient Intell Humaniz Comput (JAIHC) 12(2):2365–2374. https://doi.org/10.1007/S12652-020-02351-X
143. Zhang L, Halber M, Rusinkiewicz S (2019) Accelerating large-kernel convolution using summed-area tables. arXiv preprint arXiv:1906.11367
144. Mukherjee S, Anvitha L, Lahari TM (2020) Human activity recognition in RGB-D videos by dynamic images. Multimed Tools Appl 79(27):19787–19801. https://doi.org/10.1007/S11042-020-08747-3
145. Natarajan P, Nevatia R (2008) Online, real-time tracking and recognition of human actions (2008) IEEE workshop on motion and video computing. WMVC 2008. https://doi.org/10.1109/WMVC.2008.4544064
146. Ni T, Chen Y, Song K, Xu W (2021) A simple and fast human activity recognition system using radio frequency energy harvesting. UbiComp/ISWC 2021 - adjunct proceedings of the 2021 ACM international joint conference on pervasive and ubiquitous computing and proceedings of the 2021. ACM International Symposium on Wearable Computers, pp. 666–671. https://doi.org/10.1145/3460418.3480399
147. Niu W, Long J, Han D, Wang YF (2004) Human activity detection and recognition for video surveillance. *2004 IEEE International Conference on Multimedia and Expo (ICME)*, vol. 1, pp. 719–722. https://doi.org/10.1109/ICME.2004.1394293
148. Noori FM, Wallace B, Uddin MdZ, Torresen J (Jun. 2019) A Robust Human Activity Recognition Approach Using OpenPose, Motion Features, and Deep Recurrent Neural Network. *Lecture Notes in Computer Science (including subseries Lecture Notes in Artificial Intelligence and Lecture Notes in Bioinformatics)*, vol. 11482 LNCS, pp. 299–310. https://doi.org/10.1007/978-3-030-20205-7_25
149. Núñez-Marcos A, Azkune G, Arganda-Carreras I (2017) Vision-based fall detection with convolutional neural networks. Wirel Commun Mob Comput 2017. https://doi.org/10.1155/2017/9474806
150. Ofli F, Chaudhry R, Kurillo G, Vidal R, Bajcsy R (2013) Berkeley MHAD: a comprehensive multimodal human action database. Proceedings of IEEE workshop on applications of computer vision, pp. 53–60. https://doi.org/10.1109/WACV.2013.6474999
151. Oikonomidis I, Kyriazis N, Argyros A (2011) Efficient model-based 3D tracking of hand articulations using Kinect pp. 101.1–101.11. https://doi.org/10.5244/C.25.101
152. Okeyo G, Chen L, Wang H (2013) An agent-mediated ontology-based approach for composite activity recognition in smart homes. J Univ Comput Sci 19(17):2577–2597. https://doi.org/10.3217/JUCS-019-17-2577
153. Paoletti G, Cavazza J, Beyan C, del Bue A (Apr. 2022) Unsupervised Human Action Recognition with Skeletal Graph Laplacian and Self-Supervised Viewpoints Invariance. https://doi.org/10.48550/arxiv.2204.10312

154. Perez-Sala X, Escalera S, Angulo C (2012) Survey on 2D and 3D human pose recovery. Front Artif Intell Appl 248:101–110. https://doi.org/10.3233/978-1-61499-139-7-101
155. Perry S (2018) Image and Video Noise: An Industry Perspective. Adv Comput Vis Pattern Recognit:207–234. https://doi.org/10.1007/978-3-319-96029-6_8
156. Petscharnig S, Lux M, Chatzichristofis S (Jun. 2017) Dimensionality reduction for image features using deep learning and autoencoders. *ACM International Conference Proceeding Series*, vol. Part F130150. https://doi.org/10.1145/3095713.3095737
157. Pham HH, Salmane H, Khoudour L, Crouzil A, Zegers P, Velastin SA (2019) A Unified Deep Framework for Joint 3D Pose Estimation and Action Recognition from a Single RGB Camera. Sensors (Switzerland) 20(7) [Online]. Available: https://arxiv.org/abs/1907.06968v1. Accessed 30 Oct 2021
158. "Prepare the 20BN-something-something Dataset V2 — gluoncv 0.11.0 documentation." (n.d.) https://cv.gluon.ai/build/examples_datasets/somethingsomethingv2.html. Accessed 26 Aug 2021
159. Rahman M, Das T (2021) Human activity recognition using deep learning-based approach. Lecture Notes in Networks and Systems 204:813–830. https://doi.org/10.1007/978-981-16-1089-9_63/COVER
160. Ramanathan M, Yau WY, Teoh EK (2014) Human action recognition with video data: Research and evaluation challenges. IEEE Trans Hum Mach Syst 44(5):650–663. https://doi.org/10.1109/THMS.2014.2325871
161. Ray S, Alshouiliy K, Agrawal DP (2020) Dimensionality Reduction for Human Activity Recognition Using Google Colab. Information 12(1):6. https://doi.org/10.3390/INFO12010006
162. Kang SM, Wildes RP (2016) Review of action recognition and detection methods. arXiv preprint arXiv:1610.06906
163. "Recognizing Non-rigid Human Actions Using Joints Tracking in Space-time | Proceedings of the International Conference on Information Technology: Coding and Computing (ITCC'04) Volume 2 - Volume 2." (n.d.) https://dl.acm.org/doi/abs/10.5555/977403.978309. Accessed 19 Aug 2021
164. Sani S, Wiratunga N, Massie S, Cooper K (2017) kNN Sampling for Personalised Human Activity Recognition. *Lecture Notes in Computer Science (including subseries Lecture Notes in Artificial Intelligence and Lecture Notes in Bioinformatics)*, vol. 10339 LNAI, pp. 330–344. https://doi.org/10.1007/978-3-319-61030-6_23
165. Schrader L et al (2020) Advanced sensing and human activity recognition in early intervention and rehabilitation of elderly people. J Popul Ageing 13(2):139–165. https://doi.org/10.1007/S12062-020-09260-Z
166. Schüldt C, Laptev I, Caputo B (2004) Recognizing human actions: A local SVM approach. Proc - Int Conf Pattern Recog 3:32–36. https://doi.org/10.1109/ICPR.2004.1334462
167. Scovanner P, Ali S, Shah M (2007) A 3-dimensional sift descriptor and its application to action recognition. Proceedings of the ACM International Multimedia Conference and Exhibition, pp. 357–360. https://doi.org/10.1145/1291233.1291311
168. Sempena S, Maulidevi NU, Aryan PR (2011) Human action recognition using Dynamic Time Warping. *Proceedings of the 2011 International Conference on Electrical Engineering and Informatics, ICEEI 2011*, https://doi.org/10.1109/ICEEI.2011.6021605
169. Wang L, Qiao Y, Tang X (2015) Action recognition with trajectory-pooled deep-convolutional descriptors. In Proceedings of the IEEE conference on computer vision and pattern recognition pp. 4305–4314
170. Seshan A (n.d.) Enabling High-Accuracy Human Activity Recognition with Fine-Grained Indoor Localization
171. Simonyan K, Zisserman A (2014) Two-stream convolutional networks for action recognition in videos. Adv Neural Inf Process Syst vol. 1, pp. 568–576. Available: https://arxiv.org/abs/1406.2199v2. Accessed 7 May 2023
172. Singh T, Vishwakarma DK (2021) A deep multimodal network based on bottleneck layer features fusion for action recognition. Multimed Tools Appl 2021:1–21. https://doi.org/10.1007/S11042-021-11415-9
173. Soomro K, Zamir AR, Shah M (Dec. 2012) UCF101: A Dataset of 101 Human Actions Classes From Videos in The Wild. [Online]. Available: https://arxiv.org/abs/1212.0402v1. Accessed 26 Aug 2021
174. Yoshikawa Y, Lin J, Takeuchi A (2018) Stair actions: a video dataset of everyday home actions. arXiv preprint arXiv:1804.04326.
175. Subetha T, Chitrakala S (Jul. 2016) A survey on human activity recognition from videos. *2016 International Conference on Information Communication and Embedded Systems, ICICES 2016*, https://doi.org/10.1109/ICICES.2016.7518920
176. Sumiya T, Matsubara Y, Nakano M, Sugaya M (2015) A Mobile Robot for Fall Detection for Elderly-Care. Procedia Comput Sci 60(1):870–880. https://doi.org/10.1016/J.PROCS.2015.08.250

177. Sun Z, Ke Q, Rahmani H, Bennamoun M, Wang G, Liu J (2022) Human Action Recognition From Various Data Modalities: A Review. IEEE Trans Pattern Anal Mach Intell 45:1–20. https://doi.org/10.1109/TPAMI.2022.3183112
178. Sung J, Ponce C, Selman B, Saxena A (Jul. 2011) Unstructured Human Activity Detection from RGBD Images. *Proc IEEE Int Conf Robot Autom*, pp. 842–849. https://doi.org/10.1109/icra.2012.6224591
179. Tao D, Jin L, Yang Z, Li X (2013) Rank preserving sparse learning for kinect based scene classification. IEEE Trans Cybern 43(5):1406–1417. https://doi.org/10.1109/TCYB.2013.2264285
180. Tao D, Cheng J, Lin X, Yu J (2015) Local structure preserving discriminative projections for RGB-D sensor-based scene classification. Inf Sci (N Y) 320:383–394. https://doi.org/10.1016/J.INS.2015.03.031
181. "Three Major Challenges Facing IoT - IEEE Internet of Things." (n.d.) https://iot.ieee.org/newsletter/march-2017/three-major-challenges-facing-iot.html/. Accessed 20 Dec 2021
182. Tiwari G, Bajaj P, Gupta S (2021) mmFiT: Contactless Fitness Tracker Using mmWave Radar and Edge Computing Enabled Deep Learning. IEEE Internet Things J (Y). https://doi.org/10.36227/TECHRXIV.16574588.V1
183. Uddin MA, Lee Y-K (2019) Feature Fusion of Deep Spatial Features and Handcrafted Spatiotemporal Features for Human Action Recognition. Sensors 19(7):1599. https://doi.org/10.3390/S19071599
184. "UTKinect-Action3D Dataset." (n.d.) http://cvrc.ece.utexas.edu/KinectDatasets/HOJ3D.html. Accessed 23 Nov 2021
185. Vallathan G, John A, Thirumalai C, Mohan S, Srivastava G, Lin JC-W (2020) Suspicious activity detection using deep learning in secure assisted living IoT environments. J Supercomput 77(4):3242–3260. https://doi.org/10.1007/S11227-020-03387-8
186. Vandersmissen B, Knudde N, Jalalvand A, Couckuyt I, Dhaene T, de Neve W (2020) Indoor human activity recognition using high-dimensional sensors and deep neural networks. Neural Comput Appl 32(16):12295–12309. https://doi.org/10.1007/S00521-019-04408-1/TABLES/8
187. Veeraraghavan A, Roy-Chowdhury AK, Chellappa R (2005) Matching shape sequences in video with applications in human movement analysis. IEEE Trans Pattern Anal Mach Intell 27(12):1896–1909. https://doi.org/10.1109/TPAMI.2005.246
188. Vishwakarma S, Agrawal A (2012) A survey on activity recognition and behavior understanding in video surveillance. Vis Comput 29(10):983–1009. https://doi.org/10.1007/S00371-012-0752-6
189. Vishwakarma S, Agrawal A (2013) A survey on activity recognition and behavior understanding in video surveillance. Vis Comput 29(10):983–1009. https://doi.org/10.1007/S00371-012-0752-6/EMAIL/CORRESPONDENT/C1/NEW
190. Vrigkas M, Nikou C, Kakadiaris IA (2015) A Review of Human Activity Recognition Methods. Front Robot AI 2(NOV):28. https://doi.org/10.3389/FROBT.2015.00028
191. Wan S, Qi L, Xu X, Tong C, Gu Z (2019) Deep Learning Models for Real-time Human Activity Recognition with Smartphones. Mob Netw Appl 25(2):743–755. https://doi.org/10.1007/S11036-019-01445-X
192. Wang J, Liu Z, Wu Y, Yuan J (2012) Mining actionlet ensemble for action recognition with depth cameras. *Proceedings of the IEEE Computer Society Conference on Computer Vision and Pattern Recognition*, pp. 1290–1297. https://doi.org/10.1109/CVPR.2012.6247813
193. Wang W, Huang Y, Wang Y, Wang L (2014) Generalized Autoencoder: A Neural Network Framework for Dimensionality Reduction. pp. 490–497.
194. Wang L, Qiao Y, Tang X (May 2015) Action Recognition with Trajectory-Pooled Deep-Convolutional Descriptors. *Proceedings of the IEEE Computer Society Conference on Computer Vision and Pattern Recognition*, vol. 07–12-June-2015, pp. 4305–4314. https://doi.org/10.1109/cvpr.2015.7299059
195. Wang Y, Yao H, Zhao S (2016) Auto-encoder based dimensionality reduction. Neurocomputing 184:232–242. https://doi.org/10.1016/J.NEUCOM.2015.08.104
196. Wang P, Cao Y, Shen C, Liu L, Shen HT (n.d.) TEMPORAL PYRAMID POOLING CNN FOR ACTION RECOGNITION 1 Temporal Pyramid Pooling Based Convolutional Neural Network for Action Recognition
197. "Wearable Health Device Dermatitis: A Case of Acrylate-Related Contact Allergy | MDedge Dermatology." (n.d.) https://www.mdedge.com/dermatology/article/143798/contact-dermatitis/wearable-health-device-dermatitis-case-acrylate. Accessed 30 Oct 2021
198. WHO global report on falls prevention in older age." https://www.who.int/publications/i/item/9789241563536. Accessed 7 May 2023

199. Wu C, Zhang J, Sener O, Selman B, Savarese S, Saxena A (2016) Watch-n-Patch: Unsupervised Learning of Actions and Relations. IEEE Trans Pattern Anal Mach Intell 40(2):467–481 [Online]. Available: https://arxiv.org/abs/1603.03541v1. Accessed 26 Aug 2021
200. Xiang D, Joo H, Sheikh Y (Dec. 2018) Monocular Total Capture: Posing Face, Body, and Hands in the Wild. *Proceedings of the IEEE Computer Society Conference on Computer Vision and Pattern Recognition*, vol. 2019-June, pp. 10957–10966. [Online]. Available: https://arxiv.org/abs/1812.01598v1. Accessed 25 Sep 2021
201. Xiao Y, Xing C, Zhang T, Zhao Z (2019) An Intrusion Detection Model Based on Feature Reduction and Convolutional Neural Networks. IEEE Access 7:42210–42219. https://doi.org/10.1109/ACCESS.2019.2904620
202. Yadav SK, Tiwari K, Pandey HM, Akbar SA (2021) A review of multimodal human activity recognition with special emphasis on classification, applications, challenges and future directions. Knowl Based Syst 223:106970. https://doi.org/10.1016/J.KNOSYS.2021.106970
203. "Yamato-HumanAction". (n.d.)
204. Yang X, Tian Y (2014) Super Normal Vector for Activity Recognition Using Depth Sequences. pp. 804–811
205. Yang W, Liu X, Zhang L, Yang LT (2013) Big data real-time processing based on storm. *Proceedings - 12th IEEE International Conference on Trust, Security and Privacy in Computing and Communications, TrustCom 2013*, pp. 1784–1787. https://doi.org/10.1109/TRUSTCOM.2013.247
206. Yang L, Ren Y, Zhang W (2016) 3D depth image analysis for indoor fall detection of elderly people. Digital Commun Netw 2(1):24–34. https://doi.org/10.1016/J.DCAN.2015.12.001
207. Yu M, Gong L, Kollias S (Nov. 2017) Computer vision based fall detection by a convolutional neural network. *ICMI 2017 - Proceedings of the 19th ACM International Conference on Multimodal Interaction*, vol. 2017-January, pp. 416–420. https://doi.org/10.1145/3136755.3136802
208. Zanfir M, Leordeanu M, Sminchisescu C (2013) The Moving Pose: An Efficient 3D Kinematics Descriptor for Low-Latency Action Recognition and Detection. https://doi.org/10.1109/ICCV.2013.342
209. Zehra N, Azeem SH, Farhan M (Mar. 2021) Human activity recognition through ensemble learning of multiple convolutional neural networks. *2021 55th Annual Conference on Information Sciences and Systems, CISS 2021*. https://doi.org/10.1109/CISS50987.2021.9400290
210. Zhan K, Faux S, Ramos F (2015) Multi-scale Conditional Random Fields for first-person activity recognition on elders and disabled patients. Pervasive Mob Comput 16(PB):251–267. https://doi.org/10.1016/j.pmcj.2014.11.004
211. Zhang C, Tian Y, Capezuti E (2012) Privacy Preserving Automatic Fall Detection for Elderly Using RGBD Cameras. *Lecture Notes in Computer Science (including subseries Lecture Notes in Artificial Intelligence and Lecture Notes in Bioinformatics)*, vol. 7382 LNCS, no. PART 1, pp. 625–633. https://doi.org/10.1007/978-3-642-31522-0_95
212. Zhang Z, Conly C, Athitsos V (Jul. 2015) A survey on vision-based fall detection. *8th ACM International Conference on PErvasive Technologies Related to Assistive Environments, PETRA 2015 – Proceedings*. https://doi.org/10.1145/2769493.2769540
213. Zhao H, Torralba A, Torresani L, Yan Z (Oct. 2019) HACS: Human action clips and segments dataset for recognition and temporal localization. *Proceedings of the IEEE International Conference on Computer Vision*, vol. 2019-October, pp. 8667–8677
214. Zhu S (2021) Multiple Target Tracking and Human Activity Recognition based on The IR-UWB Radar Sensor Networks. [Online]. Available: https://repository.tudelft.nl/islandora/object/uuid%3A8a0a66cc-7d94-4149-aa56-4213a588b86d. Accessed 17 Oct 2021
215. Zhu D, Pang N, Li G, Liu S (Jun. 2017) NotiFi: A ubiquitous WiFi-based abnormal activity detection system. *Proceedings of the International Joint Conference on Neural Networks*, vol. 2017-May, pp. 1766–1773. https://doi.org/10.1109/IJCNN.2017.7966064
216. Ziaeefard M, Bergevin R (2015) Semantic human activity recognition: A literature review. Pattern Recogn 48(8):2329–2345. https://doi.org/10.1016/J.PATCOG.2015.03.006

Publisher's note Springer Nature remains neutral with regard to jurisdictional claims in published maps and institutional affiliations.

Springer Nature or its licensor (e.g. a society or other partner) holds exclusive rights to this article under a publishing agreement with the author(s) or other rightsholder(s); author self-archiving of the accepted manuscript version of this article is solely governed by the terms of such publishing agreement and applicable law.

Multimedia Tools and Applications
https://doi.org/10.1007/s11042-023-15617-1

A robust model for improving the quality of underwater images using enhancement techniques

Nishant Singh[1] · **Aruna Bhat**[2]

Received: 1 April 2022 / Revised: 24 March 2023 / Accepted: 22 April 2023
© The Author(s), under exclusive licence to Springer Science+Business Media, LLC, part of Springer Nature 2023

Abstract
Underwater image enhancement is an important research field that is now being addressed across the world. The primary reason for this is that water scatters and absorbs light, resulting in images with extremely low contrast and color cast. Hence, in order to overcome this issue with underwater images, we designed a simple and effective method. This method is split into two parts. The first section focuses on boosting contrast, while the second on improving color. To begin with, under the RGB colour model, contrast enhancement equalizes the G and B channels. Each R, G, and B channel's histogram is then redistributed using effective parameters connected with the intensity distribution in the input image and the wavelength attenuation of various colors underwater. The noise is subsequently reduced using a bilateral filtering technique, which only keeps important facts in an underwater image but also increases local information. In the second section, the color is enhanced by increasing the L component and modifying the 'a' and 'b' components of the CIE lab color space. Experiment findings show that the suggested method outperforms alternative strategies. Our enhanced results stand out for their brilliant color, greater contrast, and enhanced features. When compared to other approaches, the values of entropy, mean square error (MSE), peak signal to noise ratio (PSNR), underwater color image quality evaluation (UCIQE), and underwater image quality measures are 7.88, 920.20, 18.92, 0.596, and 2.734, respectively. This technique improves image quality by increasing entropy, PSNR, and UCIQE values while lowering MSE. It is an entirely algorithm-based technique that is independent by image datasets. The images used to evaluate the results come from a variety of datasets, and their enhanced performance confirms their robustness. Because of its single image-based approach, our method is very compelling in terms of processing speed. Comprehensive findings on a variety of underwater image datasets demonstrate that our approach outperforms the vast majority of them. For these reasons, the Comparative Universal Stretching approach is better than others.

Keywords Underwater image enhancement · Contrast Improvement · Color Improvement · Comparative Universal Stretching (CUS)

✉ Aruna Bhat
aruna.bhat@dtu.ac.in

Extended author information available on the last page of the article

1 Introduction

Underwater image enhancement for clear images and real videos is very important for applications like underwater robots, marine ecology, underwater biological recognition, underwater archaeology and many more [34]. However, with respect to images in the natural environment, the images are visible very poor and more complex in the ocean. There are primarily two reasons for this: the first is light absorption, reflection, and scattering; the second is the underwater atmosphere, including the existence of noise and water turbidity. If we assume crystal clear water with a very high attenuation lever, even though the beam of light is absorbed and scattered. When the light is travelling to the camera, the beam of light is deviated and reflected many number of times by the particles that are present in underwater [1]. One basic property of water is that the higher the wavelength of light, the quicker the light disappears. Due to this property, in comparison to green and blue, red light is more affected. Hence the images are appeared blue tone in underwater [7].

Underwater images get affected by poor visibility of light which significantly fades while travelling in the water, thus impacting the result in terms of haziness and poor contrast. The visibility of light gets affected under water by the distance travelled i.e., around twenty meter in case of clear water and approximately five meters or less in case of cloudy water. Scattering and absorption affects the travelling of light in water. In scattering the direction of light path is changed while in absorption light energy is reduced. Hence scattering and absorption influence overall performance of underwater imaging system.

Underwater image restoration and enhancement algorithms are two types of underwater image clarity approaches. The aim of underwater image restoration techniques is to discover a way to reverse the physical degradation process and repair the deteriorated underwater image to a cleaner underwater image. Underwater image enhancement algorithms, which are based on current image enhancement techniques, either emphasize the region of interest or minimize the non region of interest by altering the pixels of the actual image to increase the clarity of underwater images. It is due to the fact that they do not take into account the underwater optical imaging method, enhancement methods are simple and effective.

In general, underwater image enhancement and restoration are mainly done by two types of techniques: one is based on the physical based method used by the restoration technique and second is based on the image based method used by the enhancement technique [8, 27]. The physical based method improves underwater images by taking into account the basic physics of light transmission through the water. Zhao et al. enhance underwater images by obtaining the natural optical attribute of water, from the background color of the image [12]. Haziness occurs in images due to the scattering and absorption of light inside water, as well as color cast, and a very similar process occurs in a normal environment due to fogginess. Dark Channel Prior (DCP) [9] is one of the core dehazing methods that have been commonly used in the improvement of underwater images [10, 11]. The Wavelength compensation and image dehazing (WCID) [3] algorithm not only compensates for the attenuation divergence along with the transmission path but also controls the feasible occurrence of artificial light. It retains the color cast while also increasing the clarity of underwater images. WCID has some drawbacks also, like it needs high computing resources and too much computing time.

In comparison to physical based methods, image based methods are more efficient and also simpler because we have to focus on the image instead of the capturing mechanism [24]. Color equalization techniques are commonly employed to address the color casting issue in underwater images. In which the blue and green color is highly dominant due to their wavelength property in the water medium. For this reason, the

underwater images are generally blue toned in nature. Iqbal et al. developed an unsupervised color improvement method (UCM) [25], also offered an integrated color model (ICM) [23]. These methods not only increase the color cast, but also the contrast of underwater images. It used RGB color mode histogram stretching and then HSI color model saturation-intensity stretching. UCM is different from ICM as they modify both green and red channels depending on the hypothesis of Von Kries. It stretches either one or both sides, depending on the characteristics of the RGB channel. Whereas in the output of these two models, there is no such fruitful difference, even though there is still blue and green illumination present [21]. Due to this, there is some noise in the enhanced images. However, instead of considering the peculiarities of distinct channels, the Rayleigh distribution is used to stretch each one [35].

Considering the numerous advantages of the mentioned enhancement techniques, there are certain limitations in underwater image color correction. These techniques in [30] conduct the piece wise stretching process for color correction, without paying attention to the attenuation adjustment of underwater images. The author in [13], first converts the color channel of every input image into lower, middle, and upper color channels based on the total pixel intensity of each color channel, and then designs dedicated fractions to compensate for the loss of the middle and lower color channels due to light attenuation at different wavelengths. As a result, in the underwater imaging environment, we adaptively split every color channel into a foreground image and a background image based on the fact that the region nearer the source of light is brighter than the region distant from the light source. The background-stretched and foreground-stretched images for each color channel are incorporated depending on the best possible threshold point to enhance the contrast of the output image. But the enhancement achieved by using these techniques is not that accurate.

Unlike these algorithms, we thus suggest a novel approach, namely comparative universal stretching (CUS) based on contrast and color improvement. The contrast improvement is mainly based on the GB channel equalization and stretching of the histogram in RGB color space. It calculates the tensile range factor using original image distribution features as well as light absorption of different wavelengths in water. Once the image is extended in RGB color space, the bilateral filter is used, which is a non iterative and simple method. This bilateral filter is used to efficiently confine the fine details of an image by smoothing the edges. After performing contrast improvement on the original image, we have to perform color improvement on the resultant image. The resultant image is the output of the contrast improvement method. This approach preserves image details while also increasing visibility. The importance of this model with respect to ICM, DCP and UCM models is represented by having the highest entropy [4], PSNR and UCIQE [36] and a lower value in Q-MOS [15] and MSE [16]. As, it is a single image based system [20], it is independent from the datasets, which provide the robustness of the system. To justify their robustness, we applied our model to eight different datasets and evaluated the images. On the basis of result evaluation, we can easily conclude that the images enhanced using our comparative universal stretching method in the UIEB, RUIE, EUVP, UFO-120, and U45 datasets are above average, while those in the LSUI, Underwater MOT, and DUO datasets are below average. The detailed explanation is given in Sect. 4.

In Sect. 2 we briefly discuss the correlated processing work, which has been used to enhance the images, and in Sect. 3 we elaborate in detailed on the proposed work. Section 4 contains the evaluation of the results. In last, give the conclusion in Sect. 5.

2 Related work

2.1 Underwater model

Various well-defined image hazing models [29, 31] are generally used to estimate the transmission equation of the scattered background light in an underwater scene. The equation is given below:

$$I_\lambda(x) = J_\lambda(x)t_\lambda(x) + (1 - t_\lambda(x))B_\lambda \tag{1}$$

where λ is the light wavelength that belongs to red, green and blue. x is the underwater image $I_\lambda(x)$ pixel point. $J_\lambda(x)$ denotes the light at sight location$x$. $t_\lambda(x)$ denotes the residual energy ratio (RER). RER is the ratio of reflection in underwater from location x to back to camera. Uniform background light is represented by B_λ. $J_\lambda(x)t_\lambda(x)$ represents the straight attenuation of scene radiant $J_\lambda(x)$ in underwater [28]. The RER $t_\lambda(x)$ is depends upon the λ as well as the site camera distance$d(x)$,which shows the overall effects of color change which has been suffered by the wavelength of light in underwater distance $d(x)$ and light scattering. Therefore $t_\lambda(x)$ can be defined as:

$$t_\lambda(x) = NRER(\lambda)^{d(x)} \tag{2}$$

where NRER is normalized RER, which defines the proportion of residual energy ratio to original energy for a minimum single unit of distance transmitted. As we know, the green & blue light have a higher frequency because of their shorter wavelengths, and therefore they attenuate extremely lower as a comparison to the red light. For this reason, as we move deep inside the sea, the images appear as blue toned images. The values of the light wavelength of NRER (λ) are defined as follows:

$$NRER(\lambda) = \begin{cases} 0.83 \sim 0.90 \;\; if \;\lambda = 590 \sim 750 \;\mu m \,(Red) \\ 0.90 \sim 0.95 \;\; if \;\lambda = 490 \sim 590 \;\mu m \,(Green) \\ 0.95 \sim 0.99 \;\; if \;\lambda = 400 \sim 490 \;\mu m \,(Blue) \end{cases} \tag{3}$$

We are using these values to predict the range of RGB channels in the CUS model.

2.2 Histogram stretching

The underwater images have very low visibility and contrast because of the very low range of histograms and relatively concentrated distribution. To overcome this problem, we use histogram stretching, which gives us a fair distribution of pixels in the image channels across the dynamic range. This improves the visibility and contrast in the image. Contrast stretching function is given as in Eq. (4). [21, 23][17, 18]

$$p_0 = (p_i - a) + \frac{c - d}{b - a} + d \tag{4}$$

where p_i is the intensity value of the input pixel, p_o is the intensity value of the output pixel. The min & max intensity values of the actual image and the desired output image is represented by a, b & c, d, respectively. $c\&d$ are constant in a global stretching and are frequently fixed to 255&0 respectively; $a\&b$ are chosen at 0.2%&99.8% in the original image's entire histogram.

3 Proposed work

Generally our suggested model is consists of three basic steps: contrast improvement, color improvement, and quality evaluation as shown in Fig. 1.

In contrast improvement, first of all, we are doing RGB channel decomposition. After that, we perform color equalization on green and blue channels. Then we determine the adaptive stretching range. After that, we perform comparative universal stretching on the image. Finally, while keeping the information of the needed colorful underwater image, we use a bilateral filter to eliminate the noise created by the aforesaid transformation [28]. This will not only diminish the color cast result because of the light absorption and scattering, but also reduce the effect of the low contrast. Once we performed all the steps in contrast improvement, we got the resultant image. After that, we performed color improvement on the resultant image [37]. In color improvement, first of all, we change the image into CIELAB color model. We extend L parameter of the image using basic global histogram stretching and correct the a & b parameters in CIE Lab color model. The adaptive stretching of L, a, b improves the image's brightness and saturation, resulting in a more vibrant color. After performing contrast improvement and color improvement, to estimate the quality of our designed model, we use a few quality evaluation parameters. Now we are going to elaborate in detail on contrast improvement and color improvement.

3.1 Contrast improvement

Figure 2 shows the sequence used in contrast improvement.

3.1.1 Color equalization on GB channel

Imagesare rarely color balanced appropriately when taken underwater. We begin colorequalization for the underwater image after RGB channel decomposition. According to Von Kries hypothesis [25, 23] modified color values in RGB components, keeping the leading

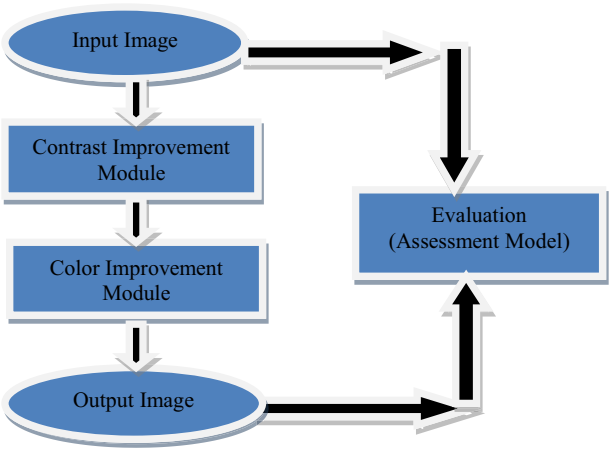


Fig. 1 Comparative Universal Stretching (CUS) Model

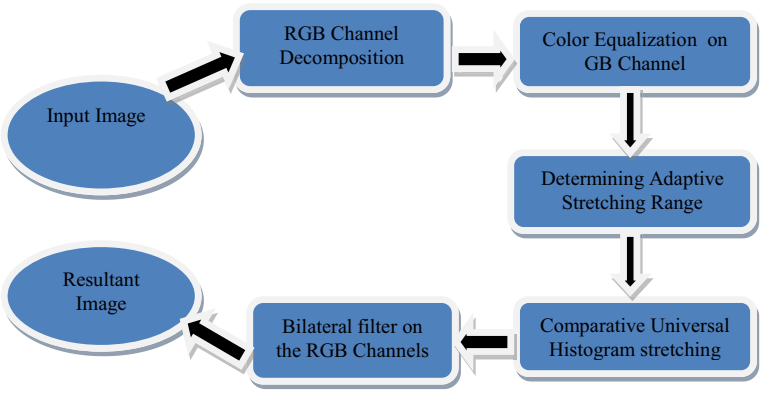


Fig. 2 Sequence used in contrast improvement

color cast channelconstant. As per UCM model, if one channel's average is very low, the channelmust increase with a larger multiplier, resulting in incorrect image colorprocessing. Whereas motivated by the Gray World Assumption Theory (GWAT)[2], in a perfect image, the mean value of any colorobject is always gray. Hence, we improve the green and blue channelswith the help of the following assumptions,

$$\left(\mathrm{R_{avg}} + \mathrm{G_{avg}} + \mathrm{B_{avg}}\right)/3 = 0.5 \tag{5}$$

where$\mathrm{R_{avg}}$, $\mathrm{G_{avg}}$, $\mathrm{B_{avg}}$ and are the normalizedmean values of the recovered RGB channels. and are the normalizedmean values of the recovered RGB channels.

$$\begin{aligned} \mathrm{R_{avg}} &= \frac{1}{255*MN}\sum_{i=1}^{M}\sum_{j=1}^{N} I_g(i,\, j),\ \theta_g = \frac{0.5}{\mathrm{G_{avg}}} \\ \mathrm{B_{avg}} &= \frac{1}{255*MN}\sum_{i=1}^{M}\sum_{j=1}^{N} I_b(i,\, j),\ \theta_b = \frac{0.5}{\mathrm{B_{avg}}} \end{aligned} \tag{6}$$

Pixel values can vary between 0 and 256. Everyvalue denotes a color code. The calculation on these large numerical values mayget more difficult when processing the image as it is, i.e., by taking thesimple mean value. It can be minimized by normalizing the numbers to the range between0 to 1. As a result, the numbers would be minimal and the calculation would beeasy as well as quicker. Pixel values vary between 0 to 256; apart from 0, therange is 255. Hence, dividing all the numbers by 255 (i.e., the standarddeviation), will convert them to a range of 0 to 1. That is the reason fortaking the normalized mean value instead of the simple mean value in Eq.(6).

With the help of GWAT, we improve the *G* & *B* channel.The *R* channelis not taken into attention here since the red light in water is difficult tocorrect with basic color equalization. If we consider the red light, then itbrings red over saturation. Theabove equation is defined for computing channels color equalization coefficient i.e. θ_g & θ_b ,respectively. The underwater image size is given by M * N. Depends upon thecolor equalization coefficients θ_g & θ_b,the intensity of the *G* channel and *B* channel is modified by changing θ_g and θ_b respectively. After this, we now have to perform comparativeuniversal stretching for image channels.

3.1.2 Comparative universal stretching (CUS)

The overall histogram stretching method typically employs the same values for each R, G, B channel of an image, neglecting the histogram allocation features of individual channels and images. If predefined values for example $(0, 255)$ have been used in (4), some color channels either over or under stretched, causing destruction to the input image's features. Due to the transmission principle of light in underwater, to repair the distorted images, we must use the contrast improvement approach. Based on the following observation in underwater images, the RGB channel's histogram distribution requirements are as follows: The histogram of red light in most underwater images is decided in the band [50, 150], whereas in G & B channel have values in [70, 210]. Due to this the histogram stretching is sensitive to channels. We rewrite the comparative universal stretching in Eq. (7) to distinguish it with global histogram stretching in Eq. (4).

$$p_{out} = \left(p_{in} - I_{min}\right)\left(\frac{O_{max} - O_{min}}{I_{max} - I_{min}}\right) + O_{min} \tag{7}$$

where p_{in} is the input pixel, p_{out} is the output pixel. I_{min} and I_{max} are the adaptive parameters before the stretching images. O_{min} and O_{max} are the adaptive parameters after the stretching images. After this, we'll go through how to calculate the stretching range (I_{min}, I_{max}) and the desired range (O_{min}, O_{max}).

3.1.3 Determining adaptive stretching range

If we consider the histogram distribution of different underwater images, it is seen that, histogram distribution in RGB channel is comparable to variant of the Rayleigh distribution described as (8), and that is an ongoing probability proportion for positive valued random variables.

$$RayleighDistribution = \frac{x}{a^2} e^{-x^2/2a^2}, x \geq 0, a > 0 \tag{8}$$

In Eq. (8), the distribution's scaling parameter a is the mode, which is the highest in $R, G\&B$ channel histogram. It is worth noting that, when a channel's allocation follows a regular pattern, its midpoint and mode are almost identical. In the histogram stretching, we use the mode result as a borderline to determine the minimum intensity level as the left and maximum intensity level as the right of the original image.

Because underwater images are impacted by a variety of causes, stretching ranges between 0.1% and 99.9% of the histogram are commonly used to decrease the impact of certain high pixels in comparative universal stretching. If the histogram is not regularly distributed, the procedure of removing the same quantity of pixels from both ends in histogram is not appropriate. To compute the I_{min} and I_{max} for each RGB channel, we partition the top and the bottom portion of the intensity values, as shown in Eq. (9).

$$\begin{aligned} I_{min} &= S.sort[S.sort.index(a) * 0.1\%] \\ I_{max} &= S.sort[-(S.length - S.sort.index(a)) * 0.1\%] \end{aligned} \tag{9}$$

where S is the group of image pixel values for each $R, G\&B$ channel, $S.sort$ is the increasing sorted data set, $S.sort.index(a)$ is the index number of the mode in the histogram

distribution, and $S.sort[x]$ is the value at index x of the positive sorted data set. To implement the unique approach, we extract pixels values in the lowest 0.1% of the left side and the largest 0.1% of the right side from histogram distribution using Eq. (9). The RGB channels and different images of the Rayleigh distribution, the I_{min} and I_{max} are both channel and image sensitive.

Global histogram stretching of [0, 255] range typically results in excessive blue and green light in underwater images. We dynamically decide the highest (Omax) and lowest (Omin) intensity level values by each RGB channel to obtain a perfect intended band of stretching.

We begin by calculating the Rayleigh distribution's standard deviation values σ_λ, as shown in Eq. (10).

$$\sigma_\lambda = \sqrt{\frac{4-\pi}{2}} a_\lambda = 0.655 a_\lambda, \lambda \epsilon \{R, G, B\} \tag{10}$$

where a denotes the channel mode, λ belongs to RGB Channels. After that, we establish the required range's minimum value $O_{\lambda\,min,}$ as shown in Eq. (11)

$$O_{\lambda min} = a_\lambda - \beta_\lambda * \sigma_\lambda, 0 \le O_{\lambda min} \le I_{\lambda min} \tag{11}$$

Here β_λ is drived from Eq. (11) and substitute σ_λ from Eq. (10)

$$\beta_\lambda = \frac{a_\lambda - O_{\lambda min}}{\sigma_\lambda}, \frac{a_\lambda - I_{min}}{\sigma_\lambda} \le \beta_\lambda \le \frac{a_\lambda}{\sigma_\lambda} \tag{12}$$

In the right side of Eq. (12), we get $\beta_\lambda \ge 0$, as $a \ge I_{min}$.

Now, substitute the value of σ_λ in the right side in Eq. (12), we obtain $\beta_\lambda \le 1.526$.

Now describe $\beta_\lambda \in Z$, it must have a unique solution that is $\beta_\lambda = 1$. Hence Eq. (11) is rewritten in the form of Eq. (13) as shown below:

$$O_{\lambda min} = a_\lambda - \sigma_\lambda \tag{13}$$

Because of the varying degrees of depletion of the various bands of light in underwater, we should study individual R, G, B channel to compute optimum parameters of the required range. Based on the simple fuzzy image method (1), the image dehazing function $J_\lambda(x)$ is improved as shown in Eq. (14)

$$J_\lambda(x) = \frac{I_\lambda(x) - (1 - t_\lambda(x))B_\lambda}{k t_\lambda(x)} \tag{14}$$

where the red and the green–blue channel have experienced values of 1.1 and 0.9, respectively. When maximizing the recovered image $J_\lambda(x)$, as shown in Eq. (15), the maximum value of the required range Omax is obtained.

$$Max\big(J_\lambda(x)\big) = Max\Big(\frac{I_\lambda(x) - \big(1 - t_\lambda(x)\big)B_\lambda}{k t_\lambda(x)}\Big) \tag{15}$$

B_λ is 0, when $J_\lambda(x)$ reaches its maximum value. Then, for each color channel Omax is defined as shown in Eq. (16).

$$O_{\lambda max} = \frac{I_\lambda}{k t_\lambda} = \frac{a_\lambda + \mu_\lambda * \sigma_\lambda}{k * t_\lambda}, I_{\lambda max} \le O_{\lambda max} \le 255 \tag{16}$$

$t_\lambda(x)$ is calculated with the help of Eq. (2), where $NRER(\lambda)$ values are 0.83, 0.95 and 0.97 for the RGB channels, respectively (also look at Eq. (3)). Due the estimated path between the camera and the site, $d(x)$ is fixed to 3.

The coefficient μ_λ fulfils the inequality as shown in Eq. (17), depending on the overall range value of $O_{\lambda max}$.

$$\mu_\lambda = \frac{(O_{\lambda max} * k * t_\lambda) - a_\lambda}{\sigma_\lambda}$$

$$\frac{k * t_\lambda * I_\lambda}{\sigma_\lambda} \leq \mu_\lambda + 1.526 \leq \frac{k * t_\lambda * 255}{\sigma_\lambda} \tag{17}$$

In Eq. (17), in the integer field μ_λ has either no solution or specific solutions. We take the mean of all solutions when μ_λ are many solutions. When there are no solutions of μ_λ, $O_{\lambda max}$ is set to 255. These adaptive parameters, which are derived from the histogram distributions from several channels, may substantially enhance the contrast of stretched images while also reducing noise and preserving features.

3.2 Color improvement

Figure 3 shows the sequence used in color improvement.

3.2.1 CIELAB color model

The human eye is capable of seeing large numbers of colors. However, it does not always differentiate between colors properly. Based on our viewing position and illumination, we may see two slightly different colors as the same or detect distinctions in things of equal color. These create challenges when we try to enhance the color component. To enhance the color of underwater images every time, we need strategies to define a color's qualities and identify the quantitative difference between shades. CIELAB, generally CIE L*a*b*, is a three dimensional color space that is device independent and enables for exact analysis and measurement of all observable colors via three color variables. In this color space,

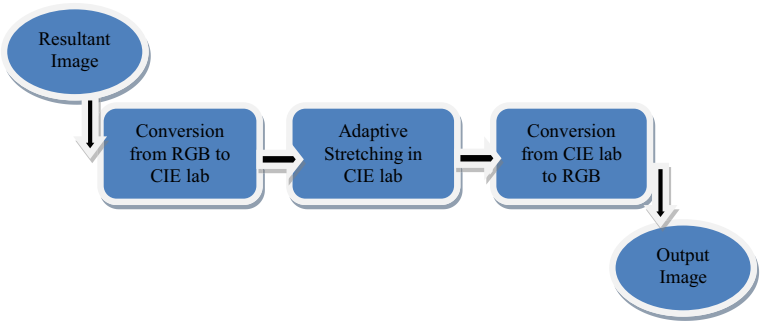


Fig. 3 Sequence used in color improvement

numerical changes between values generally correlate to the degree of difference in colors that humans perceive.

Each of the three variables used by the CIELAB color space to measure objective color and calculate color differences is given by L*, a*, and b*. L* signifies brightness within a range of 0 to 100. Whereas a* & b* signify chromaticity without numerical boundaries. (–ve) a* represents green, (+ve) a* represents red, (-ve) b* represents blue, and (+ve) b* represents yellow. The CIELAB color space plots a color's location in a chart that comprises an unlimited range of different colors, including colors outside the visible spectrum, by measurements of its L*, a*, and b* values. We may utilize formulas to quantify the difference between distinct colors with the values on the L* a* b* chart, which is referred to as Delta (Δ). To compute L*, for example, reduce the L* value of the standard color from the L* value of the sample. L*a*b* values can also be used to transform to a different color scale. Because of these various qualities of the CIE Lab color model, it is chosen over other models.

3.2.2 Adaptive stretching in CIE lab

Now, resultant image will be color corrected after the contrast enhancement in the RGB color space. To enhance color quality, the image is transformed further into CIELAB color space in this step. The 'L' parameter is similar to image lightness in CIE-Lab color model, provides the darkest assessment at L = 0 whereas the brightest assessment at L = 100. The color channel will show true neutral gray values when 'a' and 'b' are both zero. As a result, the output color successions in 'a', 'b' parameters are updated to obtain proper color improvement, while the intensity of the full image is tuned using 'L' component.

The 'L' component is used in conjunction with linear slide stretching, as described in Eq. (8), which lies within 0.1% to 99.9% is stretched to [0 to 100]. The minimum and maximum 0.1% of the image's value is adjusted to 0 & 100, respectively.

'a', 'b' have values ranging [128, 127], where 0 represents the median. An S-model curve is used to define the extending of 'a' and 'b' parameters as shown in Eq. (18).

$$P_{\gamma} = I_{\gamma} * \left(\varphi^{1-\left|\frac{I_{\gamma}}{128}\right|} \right), \gamma \epsilon \{a, b\} \tag{18}$$

where I_{γ} is the input pixels, P_{γ} is the output pixels. γ represents the 'a', 'b' parameters. φ is the ideally suitable value which is 1.3. The stretching coefficient in Eq. (18) is an exponential function, in which case if the value is close to 0, the more it will be stretched.

The importance of contrast and color in an image's clarity and visibility cannot be overstated. As a result, the background and foreground objects in an image are easily distinguished. The channels are assembled and turned into an RGB color model once the stretching process in $L, a\&b$ elements in CIE Lab has been completed. As the observed and viewable final output image, a contrast improved and color improved result can be formed.

4 Result evaluation and analysis

Our designed technique, which includes saturation equalization, sharpness improvement and contrast improvement is quantitatively and qualitatively correlate to other standard enhancement techniques. He [9] utilized image haze reduction with DCP and is taken as

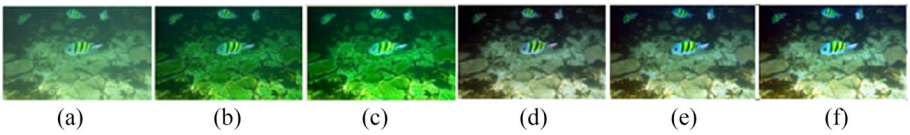


Fig. 4 Represents the (**a**) Input Image and enhanced images using methods (**b**) Bianco Prior (**c**) Dark Channel Prior (**d**) New Optical Model (**e**) Unsupervised Color Correction Method (**f**) Our proposed method

a comparison with our proposed work since it is a traditional approach for dehazing and underwater images are frequently termed haze images. ICM and UCM [23, 25] are the other comparison techniques since they are the most efficient imaging models and have the best similarities to the suggested approach in the context of histogram modification. Because the Rayleigh distribution method failed to run out in [17, 18, 21], we only provide the UCM images in the comparative outcomes because the ICM has comparable outcomes to the UCM. Bianoc Prior (BP) [2] and New Optical Model (NOM) [32] are also compared with our approaches, as they are also based on the single image enhancement system. In our designed technique, as shown in Fig. 4, appears to provide an improved visual image than the other way. UCM and NOM models produces a general sense of fish that has simple changes that do not boost image quality or reduce the brightness and visibility. The BP and DCP oversaturates the color because the image's blue and green colors are dominating in nature, which causes noise and decreases the overall visual effect. As the fisher is more distinguished from the background, the color saturation and the contrast of the image created by our approach improves, and a smaller amount blue green lighting is preserved.

The x-axis in the histogram in input as well as in output images lies from 0 to 255 as shown in the other part of Fig. 5. In (a) and (b) part the gray level values of histogram distributions are relatively dense, which helps to explain why two vibrant pictures have poor contrast and visibility. The gray level values in (c) & (d) spread as comparison to (a) & (b) but not as good with respect to (e) & (f) The gray level values of histogram distribution in (e) & (f) are dispersed

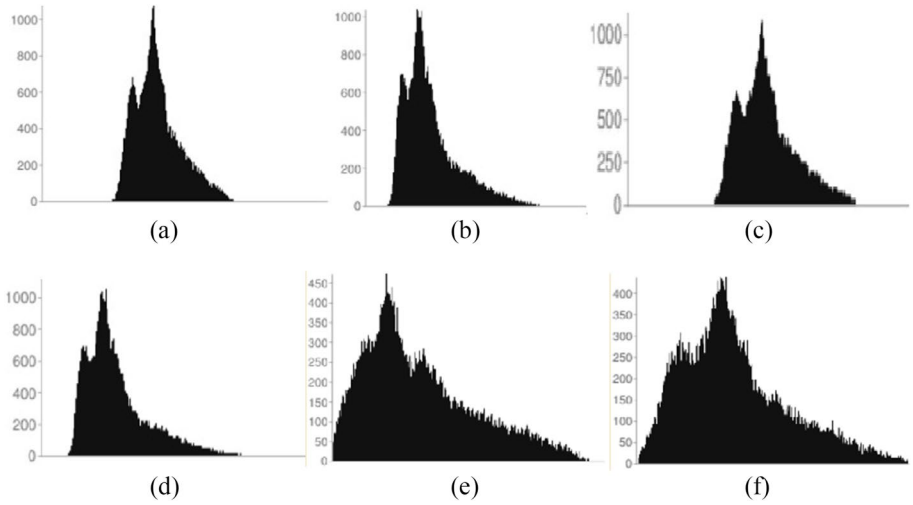


Fig. 5 Represents the histogram distribution of (**a**) Input Image (**b**) Bianco Prior (**c**) Dark Channel Prior (**d**) New Optical Model (**e**) Unsupervised Color Correction Method (**f**) Our proposed method

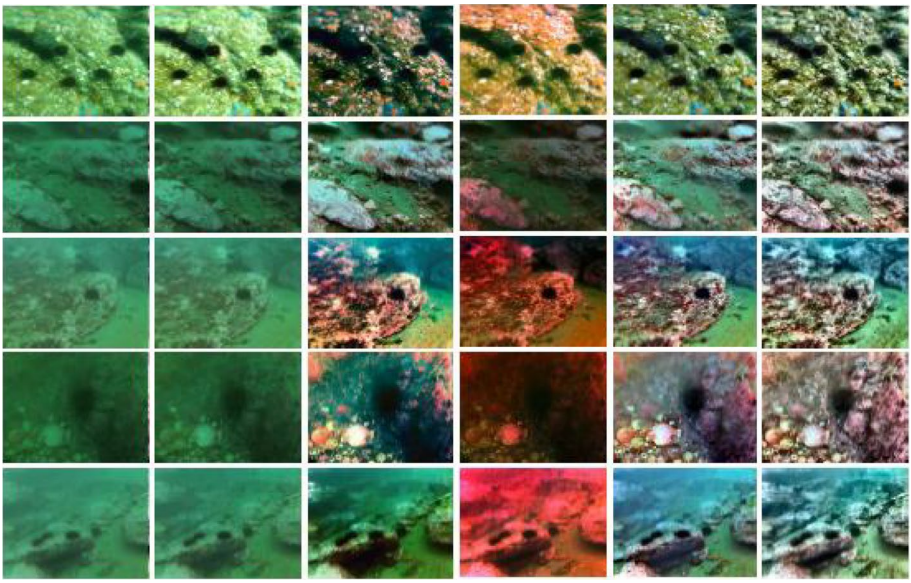


Fig. 6 (**a**) Input Image (**b**) Bianco Prior (**c**) Dark Channel Prior (**d**) New Optical Model (**e**) Unsupervised Color Correction Method (**f**) Our proposed method

throughout the x-axis, but according to GWAT [33], because of the accurate histogram stretching, the histogram of the improved image as shown in (f) has a better distribution.

Various approaches used for image improvement attains the outcome as giving in Fig. 6. Input images are from the Real World Underwater Image Enhancement (RUIE) Data Set. Clearly, the images are not enhanced by BP and NOM as shown in Fig. 6 (b) & Fig. 6 (d). In Fig. 6 (c) & Fig. 6 (e), the top two images of the DCP and UCM oversaturates image color when image's blue & green color gets too intense, resulting in enhanced images that are less realistic than those produced by our technique as shown in Fig. 6 (d) (top two images). The UCM's output underwater images have considerable noise; however our technique successfully reduces the noise while preserving image features as represented in the below three images in Fig. 6 (e) and Fig. 6 (f), respectively.

We use objective metrics like entropy, mean square error (MSE), peak signal to noise ratio (PSNR) [16], High-Dynamic Range Visual Difference Predictor2 (HDR-VDP2) [15] and underwater color image quality evaluation (UCIQE) [36] to perform quantitative analysis. The amount of information is represented by entropy, which is understood as the mean unpredictability of the information source. The more information there is, the greater the entropy value. MSE and PSNR are standard image quality evaluation measures that primarily measure image noise deterioration. The HDR-VDP2 predicts both the presence of artefacts and the overall quality of images using a pretty complex model of human perception. It generates a QMOS value ranging from 0 (best) to 100 (worst) to represent image quality. The UCIQE, which is an appropriate analytical predictor of hue, brightness, and contrast, is a relatively new non reference metrics for the evaluation of color image quality. However, MSE, PSNR and Q-MOS are full reference metrics that take an actual image as a reference. They can be used to show how the created image compares to the original in terms of observed loss in quality and increase in noise. The comparative outcomes with following evaluation models

are given in Table 1. We compared our Comparative Universal Stretching model with Bianco Prior [32], Dark Channel Prior [9], New Optical Model [33], Integrated Color Model [23], and Unsupervised Color Correction Method [25]. In the assessments, our method comparative universal stretching gets the highest outcomes while in Unsupervised Color Correction gets the second highest outcomes. The Bianco Prior and Dark Channel Prior methods are based on the underwater image restoration method. The New Optical and Integrated Color Models are based on the underwater image enhancement method. The Comparative Universal stretching is also uses fusion based approach in underwater image enhancement method.

It keeps the most details and information, provides excellent visibility, overall quality and reduces noise. The greatest UCIQE score indicates that our approach can properly balance the improved underwater images' chroma, saturation, and contrast. In all four approaches, the DCP delivers the lowest results, which is constant with the viewing experience of low brightness and poor visibility. This implies that basic haze elimination with the DCP to underwater enhancement should not be employed straight forward. The UCM and ICM technique generate images having visible noise, resulting in a high MSE and low PSNR value.

Figure 7 represents the underwater images and their corresponding enhanced images from eight different datasets having Underwater Test Dataset (U45) [5] in Fig. 7(a), Enhancing Underwater Visual Perception (EUVP) [14] in Fig. 7(b), Underwater Image Enhanced Benchmark dataset (UIEB) [26] in Fig. 7(c), Large-scale Underwater Image (LSUI) dataset [38] in Fig. 7(d), UFO-120 dataset [6] in Fig. 7(e), Real-world Underwater Image Enhancement (RUIE) dataset [39] in Fig. 7(f), Underwater MOT dataset [19] in Fig. 7(g) and dataset for Underwater object detection (DUO) [22] in Fig. 7(h). The size of the input images is of 1360 * 1024. Table 2, represents the evaluation metrics in the form of MSE, PSNR, UCIQE and UIQM values of four enhanced images of each eight datasets which have been shown in Fig. 7.

Tables 3, 4, 5, 6, 7, 8, 9 and Table 10 represents the quantitative analysis of all eight datasets in detail. In each table, ten random test sample images have been chosen to compute evaluation metrics. In these tables, the bold values given in RMSE, PSNR, UCIQE, and UIQM represent the average values of the sample images for each dataset. The chosen images are totally different from all the above images, which have been used in Fig. 7. On the basis of the RMSE evaluation parameter, the top two results have been seen in the UIEB dataset, i.e., 731.326, and the RUIE dataset, i.e., 818.134, whereas the bottom two results have been seen in the LSUI dataset, i.e., 1093.794, and the Underwater MOT dataset, i.e., 1232.432. With the PSNR evaluation parameter, the top two results have been seen in the UIEB dataset, i.e., 18.366, and the EUVP dataset, i.e., 17.353, whereas the bottom two results have been seen in the LSUI dataset, i.e., 15.878, and the DUO dataset, i.e., 16.493. With the UCIQE evaluation parameter, the top two results have been seen in the UIEB dataset, i.e., 0.513, and the RUIE dataset, i.e., 0.486, whereas the bottom two results have been seen in the LSUI dataset, i.e.,

Table 1 Evaluation of various methods based on entropy, MSE, PSNR, HDR-VDP2 and UCIQE

Methods	ENTROPY	MSE	PSNR	HDR-VDP2	UCIQE	UIQM
Bianco Prior [32]	5.432	3201.665	12.641	55.896	0.401	0.114
Dark Channel Prior [9]	6.172	3116.789	13.361	53.688	0.419	1.396
New Optical Model [33]	6.554	2224.367	15.512	48.369	0.453	1.327
Integrated Color Model [23]	7.224	1440.126	16.582	42.657	0.485	2.236
Unsupervised Color Correction Method [25]	7.567	1355.568	16.973	38.666	0.528	2.668
Comparative Universal Stretching	7.887	920.205	18.924	33.695	0.596	2.734

Table 2 Evaluation Metrics of our proposed method on various datasets using MSE, PSNR, UCIQE and UIQM

Dataset	Images	RMSE	PSNR	UCIQE	UIQM
U45	Figure 7 (a) (i)	1389.985	17.369	0.489	2.123
	Figure 7 (a) (ii)	1458.398	16.254	0.456	1.965
	Figure 7 (a) (iii)	1187.325	17.321	0.496	1.587
	Figure 7 (a) (iv)	1255.985	15.323	0.532	2.321
EUVP	Figure 7 (b) (i)	1026.987	16.548	0.498	2.541
	Figure 7 (b) (ii)	826.698	17.896	0.562	2.365
	Figure 7 (b) (iii)	855.258	17.549	0.554	2.897
	Figure 7 (b) (iv)	812.987	18.369	0.589	3.168
UIEB	Figure 7 (c) (i)	750.357	19.398	0.599	3.245
	Figure 7 (c) (ii)	712.987	19.687	0.601	3.112
	Figure 7 (c) (iii)	650.325	18.368	0.532	2.987
	Figure 7 (c) (iv)	623.245	19.967	0.491	2.645
LSUI	Figure 7 (d) (i)	1055.325	15.359	0.402	1.987
	Figure 7 (d) (ii)	1032.357	16.356	0.425	2.665
	Figure 7 (d) (iii)	1652.365	16.245	0.489	1.986
	Figure 7 (d) (iv)	984.325	17.554	0.487	1.889
UFO-120	Figure 7 (e) (i)	820.125	15.748	0.523	2.568
	Figure 7 (e) (ii)	850.256	15.356	0.432	2.325
	Figure 7 (e) (iii)	1052.658	16.958	0.489	2.578
	Figure 7 (e) (iv)	981.854	17.698	0.502	2.222
RUIE	Figure 7 (f) (i)	752.995	19.689	0.569	3.568
	Figure 7 (f) (ii)	715.658	19.584	0.635	3.115
	Figure 7 (f) (iii)	655.358	19.284	0.555	2.998
	Figure 7 (f) (iv)	620.356	19.657	0.489	2.897
Underwater MOT	Figure 7 (g) (i)	1110.879	16.358	0.502	3.589
	Figure 7 (g) (ii)	1204.689	16.325	0.565	3.456
	Figure 7 (g) (iii)	1002.359	18.658	0.486	2.154
	Figure 7 (g) (iv)	995.987	17.658	0.466	2.753
DUO	Figure 7 (h) (i)	1056.337	16.526	0.416	3.129
	Figure 7 (h) (ii)	985.401	15.469	0.337	2.101
	Figure 7 (h) (iii)	1054.159	16.334	0.499	3.825
	Figure 7 (h) (iv)	9987.232	17.567	0.562	2.219

0.415, and the Underwater MOT dataset, i.e., 0.398. With the UIQM evaluation parameter, the top two results have been seen in the RUIE dataset, i.e., 2.750, and the UFO-120 dataset, i.e., 2.632, whereas the bottom two results have been seen in the LSUI dataset, i.e., 2.420, and the Underwater MOT dataset, i.e., 1.935.

If the RMSE value is lower, then the image quality is better, whereas if the PSNR, UCIQE, and UIQM values are higher, the image is better. If the average value of any dataset in the test samples is less than 1000 in RMSE and greater than 16.700, 0.450, and 2.500 in PSNR, UCIQE, and UIQM, respectively, we consider our method to be above average for the datasets; otherwise, we consider our method to be below average for the datasets. Using these qualitative and quantitative analyses, we can easily conclude that the images enhanced using our comparative universal stretching method in the UIEB, RUIE, EUVP, UFO-120, and U45 datasets are above average, while those in

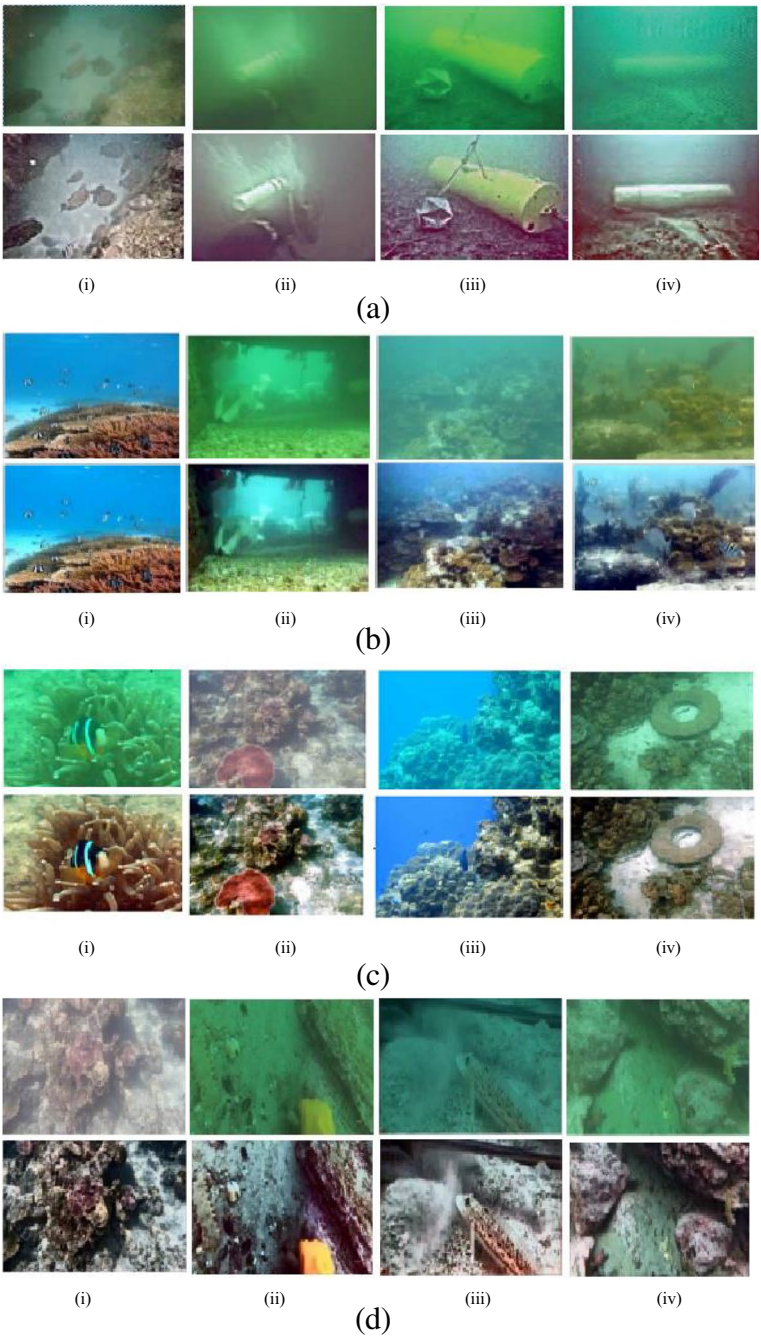
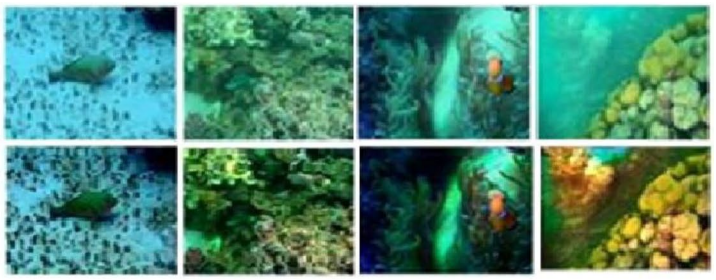
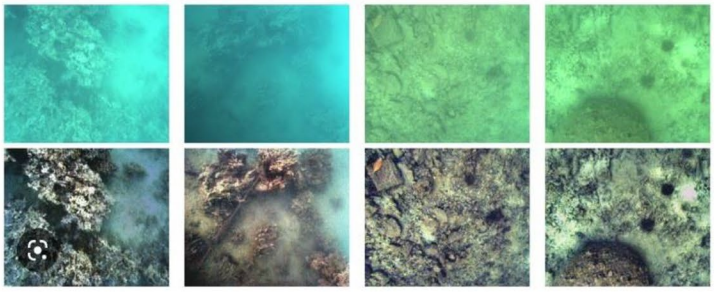


Fig. 7 (**a**) U45 datasets input and enhanced images (**b**) EUVP datasets input and enhanced images (**c**) UIEB datasets input and enhanced images (**d**) LSUI datasets input and enhanced images (**e**) UFO-120 datasets input and enhanced images (**f**) RUIE datasets input and enhanced images (**g**) Underwater MOT datasets input and enhanced images (**h**) DUO datasets input and enhanced images.



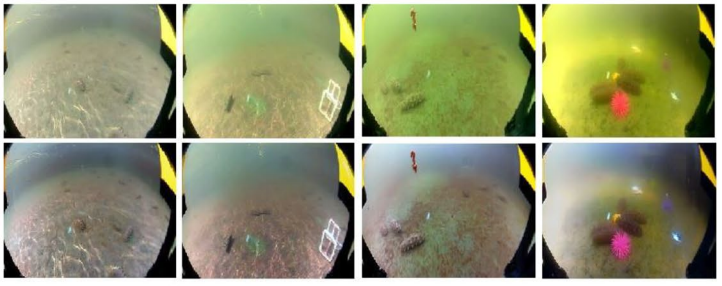
(i) (ii) (iii) (iv)

(e)



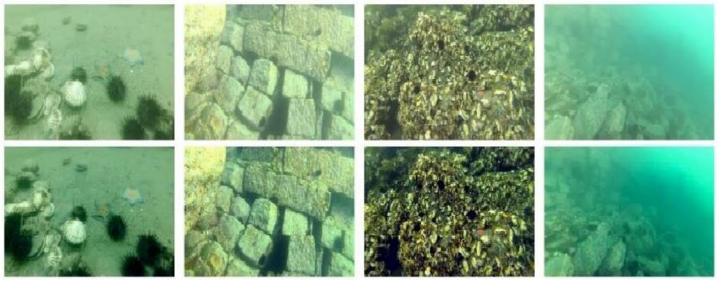
(i) (ii) (iii) (iv)

(f)



(i) (ii) (iii) (iv)

(g)



(i) (ii) (iii) (iv)

(h)

Fig. 7 (continued)

Table 3 Evaluation Metrics of our proposed method on U45 dataset using MSE, PSNR, UCIQE and UIQM

Dataset	Images	RMSE	PSNR	UCIQE	UIQM
U45	Sample Image 1	1040.709	17.441	0.436	2.302
	Sample Image 2	905.390	17.435	0.441	3.589
	Sample Image 3	989.783	17.000	0.478	1.666
	Sample Image 4	822.131	16.255	0.423	1.863
	Sample Image 5	1071.325	16.235	0.456	2.365
	Sample Image 6	1074.658	17.321	0.569	3.265
	Sample Image 7	1018.698	17.256	0.444	1.325
	Sample Image 8	979.258	17.369	0.565	2.325
	Sample Image 9	1085.147	16.357	0.462	2.654
	Sample Image 10	906.963	17.238	0.423	3.698
	Sample Image Average	**989.406**	**16.991**	**0.470**	**2.505**

Table 4 Evaluation Metrics of our proposed method on EUVP dataset using MSE, PSNR, UCIQE and UIQM

Dataset	Images	RMSE	PSNR	UCIQE	UIQM
EUVP	Sample Image 1	842.026	15.749	0.419	1.864
	Sample Image 2	872.154	17.275	0.418	2.137
	Sample Image 3	830.644	15.534	0.430	1.661
	Sample Image 4	872.253	15.822	0.422	2.247
	Sample Image 5	1022.762	17.987	0.445	2.156
	Sample Image 6	922.121	18.654	0.556	3.654
	Sample Image 7	913.356	18.123	0.456	2.355
	Sample Image 8	1184.800	18.357	0.564	2.658
	Sample Image 9	1045.131	18.456	0.598	3.325
	Sample Image 10	1134.175	17.569	0.444	2.298
	Sample Image Average	**963.942**	**17.353**	**0.475**	**2.436**

Table 5 Evaluation Metrics of our proposed method on UIEB dataset using MSE, PSNR, UCIQE and UIQM

Dataset	Images	RMSE	PSNR	UCIQE	UIQM
UIEB	Sample Image 1	606.608	16.095	0.465	1.887
	Sample Image 2	662.074	17.776	0.459	2.107
	Sample Image 3	767.527	16.592	0.401	1.888
	Sample Image 4	727.181	17.663	0.410	1.904
	Sample Image 5	798.359	18.862	0.625	2.632
	Sample Image 6	780.157	18.426	0.588	2.231
	Sample Image 7	759.153	19.842	0.564	3.214
	Sample Image 8	684.953	19.874	0.489	3.278
	Sample Image 9	763.759	18.896	0.525	3.865
	Sample Image 10	763.486	19.632	0.608	2.536
	Sample Image Average	**731.326**	**18.366**	**0.513**	**2.554**

Table 6 Evaluation Metrics of our proposed method on LSUI dataset using MSE, PSNR, UCIQE and UIQM

Dataset	Images	RMSE	PSNR	UCIQE	UIQM
LSUI	Sample Image 1	1043.574	15.366	0.441	1.827
	Sample Image 2	1020.682	15.576	0.405	2.333
	Sample Image 3	1252.697	15.006	0.467	1.921
	Sample Image 4	979.576	16.699	0.439	1.790
	Sample Image 5	1163.800	16.933	0.307	2.787
	Sample Image 6	1255.143	17.116	0.369	2.636
	Sample Image 7	908.869	15.056	0.309	2.462
	Sample Image 8	1006.861	15.025	0.476	2.095
	Sample Image 9	1241.307	16.407	0.471	3.168
	Sample Image 10	915.795	15.664	0.404	3.221
	Sample Image Average	**1093.794**	**15.878**	**0.415**	**2.420**

Table 7 Evaluation Metrics of our proposed method on UFO-120 dataset using MSE, PSNR, UCIQE and UIQM

Dataset	Images	RMSE	PSNR	UCIQE	UIQM
UFO-120	Sample Image 1	820.711	16.779	0.414	1.613
	Sample Image 2	818.224	16.771	0.496	1.737
	Sample Image 3	816.678	15.337	0.500	2.449
	Sample Image 4	847.085	15.109	0.427	2.058
	Sample Image 5	1060.826	17.567	0.472	2.905
	Sample Image 6	976.274	17.779	0.487	2.202
	Sample Image 7	1113.448	16.119	0.452	3.934
	Sample Image 8	1150.686	18.752	0.420	3.876
	Sample Image 9	1169.523	15.155	0.467	3.182
	Sample Image 10	1128.895	15.343	0.428	2.584
	Sample Image Average	**991.216**	**16.584**	**0.454**	**2.623**

Table 8 Evaluation Metrics of our proposed method on RUIE dataset using MSE, PSNR, UCIQE and UIQM

Dataset	Images	RMSE	PSNR	UCIQE	UIQM
RUIE	Sample Image 1	706.448	15.604	0.446	1.755
	Sample Image 2	663.923	17.641	0.410	2.306
	Sample Image 3	697.657	16.949	0.500	2.194
	Sample Image 4	705.228	15.570	0.414	2.064
	Sample Image 5	979.839	17.907	0.423	3.228
	Sample Image 6	864.686	18.933	0.579	2.655
	Sample Image 7	997.312	16.036	0.503	3.550
	Sample Image 8	833.470	17.422	0.493	3.846
	Sample Image 9	914.562	17.945	0.502	3.725
	Sample Image 10	818.213	17.041	0.586	2.180
	Sample Image Average	**818.134**	**17.105**	**0.486**	**2.750**

Table 9 Evaluation Metrics of our proposed method on Underwater MOT dataset using MSE, PSNR, UCIQE and UIQM

Dataset	Images	RMSE	PSNR	UCIQE	UIQM
Underwater MOT	Sample Image 1	1099.793	15.898	0.490	1.987
	Sample Image 2	1253.287	15.166	0.464	1.601
	Sample Image 3	1033.680	17.286	0.405	1.543
	Sample Image 4	1129.493	17.313	0.415	2.484
	Sample Image 5	1287.365	17.687	0.352	1.957
	Sample Image 6	1343.265	15.572	0.342	1.938
	Sample Image 7	1338.458	15.521	0.380	1.929
	Sample Image 8	1254.369	17.355	0.435	2.018
	Sample Image 9	1303.245	18.895	0.375	2.058
	Sample Image 10	1281.365	17.529	0.323	1.837
	Sample Image Average	**1232.432**	**16.822**	**0.398**	**1.935**

the LSUI, Underwater MOT, and DUO datasets are below average. Hence, the overall results of our proposed method are better in these datasets compared to other methods.

To prove the robustness of our approach, we took input images from different datasets and then performed our technique to improve the underwater images. In most of the datasets, our designed technique gives the best results, whereas in some datasets the results are below average. But the overall performance of our approach is above average. To summaries, the research suggests that our technique is better to commonly used underwater image enhancement methods in producing high-quality underwater images.

5 Conclusion and discussion

In this research, we analyzed challenges with water images and videos and current underwater image improvement methods, and successfully suggested a novel image enhancement approach called CUS for a variety of underwater images. Various underwater image enhancement algorithms and methods have been used to improve the

Table 10 Evaluation Metrics of our proposed method on DUO dataset using MSE, PSNR, UCIQE and UIQM

Dataset	Images	RMSE	PSNR	UCIQE	UIQM
DUO	Sample Image 1	1045.142	16.548	0.401	3.287
	Sample Image 2	1037.716	16.674	0.441	2.129
	Sample Image 3	960.472	15.987	0.353	2.019
	Sample Image 4	1013.565	16.542	0.441	3.187
	Sample Image 5	924.647	17.341	0.493	2.070
	Sample Image 6	1074.894	16.993	0.437	3.182
	Sample Image 7	813.642	17.086	0.412	2.183
	Sample Image 8	1069.631	16.224	0.338	2.087
	Sample Image 9	969.763	15.074	0.493	2.999
	Sample Image 10	1047.834	16.461	0.431	2.529
	Sample Image Average	**995.731**	**16.493**	**0.424**	**2.567**

images but they are mostly dataset-specific. We worked not only on the color component but also on the contrast component. This fusion-based enhancement approach is a single image-based system which not only improves the result over other standard methods but also works well on various datasets that's why it is also dataset independent. This dataset-independent approach provides robustness to our model which makes it superior in comparison to other methods. Our suggested model initially conducts contrast improvement using a basic histogram stretching with adaptive characteristics obtained in the RGB color space that considers both the raw image's histogram distribution parameter and underwater propagation capabilities of distinct light channels. The CIE Lab color model is then used to perform adaptive stretching for color improvement. After that our proposed technique is compared to other standard dehazing model DCP, as well as other enhancement models like UCM and ICM. These enhancement models also use histogram stretching in HSI/HSV and R-G-B color space. Qualitative and quantitative findings show that our technique is more successful at increasing visibility, improving details, and reducing artefacts and noise from images. Other underwater image datasets can also benefit from the incorporation of histogram restructuring in RGB and CIE Lab color models. Hence, it shows that our system is highly robust in nature, which provides a fruitful output for different datasets.

In addition, our system enhances the visibility of blurry and low light images. Even though our method outperforms the competition, it has some shortcomings. On one side, our method may have over enhanced regions for underwater images taken in artificial light. While on other side, the process of choosing the CIE lab color space may increase the algorithm's complexity. As a result, we will investigate and solve these issues in future work. The following aspects should also be considered in future research.

1) Developing underwater image enhancement systems that is more robust and computationally efficient. The proposed image enhancement approach should be capable of adapting to various underwater environments and developing an effective enhancement strategy for various types of underwater applications. We may conclude from this research that only a few of the techniques can increase the quality of all underwater images.
2) Creating a suitable underwater image dataset. There are currently no publicly accessible underwater image datasets, such as pairings of hazed and clear images, background lights of underwater images, depth maps, transmission maps, etc.
3) Providing a relationship between low level image processing and high level classification & detection. Existing underwater image enhancement approaches concentrate on increasing image intuitive effects while ignoring whether the improved images may improve the precision of high level characteristics analysis like target recognition and classification.
4) Designing an efficient underwater image quality evaluation measure. Although several image quality evaluation measures have been published, only a few in numbers are applicable to underwater images. Here, the commonly used UIQM and UCIQE, which is motivated by human vision structure properties to evaluate underwater color images, failed to give a valid evaluation of quality of underwater image. Their assessment prefers overly-enhanced colored images, which contradicts subjective preferences for naturalness. Future work must be given to the sensible combination of both objective and subjective evaluation, as well as the continuous improvement of non-reference evaluation models.

Funding Any agency does not fund this study.

Data availability The manuscript does not have any associated data which was generated.

Declarations

Conflict of interest All the authors of this paper declare that he/she has no conflict of interest.

Ethical approval This article does not contain any studies with human participants or animals performed by any of the authors.

References

1. Bhat A, Tyagi A, Verdhan A, Verma V (2021) Fast Under Water Image Enhancement for Real Time Applications. In 2021 6th International Conference for Convergence in Technology (I2CT) 1–8
2. Carlevaris-Bianco N, Mohan A, Eustice RM (2010) Initial results in underwater single image dehazing. In Oceans 2010 Mts/IEEE Seattle 1–8
3. Chen BH, Tseng YS, Yin JL (2020) Gaussian-adaptive bilateral filter. IEEE Signal Process Lett 27:1670–1674
4. Daway HG, Daway EG (2019) Underwater image enhancement using colour restoration based on YCbCr colour model. In IOP Conference Series: Materials Science and Engineering 571(1):012125
5. Drews PL, Nascimento ER, Botelho SS, Campos MFM (2016) Underwater depth estimation and image restoration based on single images. IEEE Comput Graphics Appl 36(2):24–35
6. Fu X, Fan Z, Ling M, Huang Y, Ding X (2017) Two-step approach for single underwater image enhancement. In: 2017 International Symposium on Intelligent Signal Processing and Communication Systems (ISPACS) 789–94
7. Fu Z, Fu X, Huang Y, Ding X (2022) Twice mixing: a rank learning based quality assessment approach for underwater image enhancement. Signal Processing: Image Communication 102:116622
8. Galdran A, Pardo D, Picón A, Alvarez-Gila A (2015) Automatic red-channel underwater image restoration. J Vis Commun Image Represent 26:132–145
9. Ghani ASA, Isa NAM (2014) Underwater image quality enhancement through Rayleigh-stretching and averaging image planes. International Journal of Naval Architecture and Ocean Engineering 6(4):840–866
10. Ghani ASA, Isa NAM (2015) Underwater image quality enhancement through integrated color model with Rayleigh distribution. Appl Soft Comput 27:219–230
11. Ghani ASA, Isa NAM (2015) Enhancement of low quality underwater image through integrated global and local contrast correction. Appl Soft Comput 37:332–344
12. Ghani ASA, Aris RSNAR, Zain MLM (2016) Unsupervised contrast correction for underwater image quality enhancement through integrated-intensity stretched-Rayleigh histograms. Journal of Telecommunication Electronic and Computer Engineering (JTEC) 8(3):1–7
13. Gupta S, Mohan N, Kumar M (2021) A study on source device attribution using still images. Archives of Computational Methods in Engineering 28(4):2209–2223
14. Han R, Guan Y, Yu Z, Liu P, Zheng H (2020) Underwater Image Enhancement Based on a Spiral Generative Adversarial Framework. IEEE Access 8:218838–218852
15. He K, Sun J, Tang X (2010) Single image haze removal using dark channel prior. IEEE Trans Pattern Anal Mach Intell 33(12):2341–2353
16. Iqbal K, Odetayo M, James A, Salam RA, Talib AZH (2010) Enhancing the low quality images using Unsupervised Color Improvement Method. In IEEE International Conference on Systems, Man and Cybernetics 1703–1709
17. Islam MJ, Luo P, Sattar J (2020) Simultaneous enhancement and super-resolution of underwater imagery for improved visual perception. arXiv preprint arXiv:2002.01155
18. Islam MJ, Xia Y, Sattar J (2020) Fast underwater image enhancement for improved visual perception. IEEE Robotics and Automation Letters 5(2):3227–3234
19. Lai Y, Zhou Z, Su B, Xuanyuan Z (2022) Single underwater image enhancement based on differential attenuation compensation. Frontiers in Marine Science 2216
20. Lee Z, Shang S, Hu C, Du K, Weidemann A, Hou W, Lin J, Lin G (2015) Secchi disk depth: A new theory and mechanistic model for underwater visibility. Remote Sens Environ 169:139–149
21. Li CY, Guo JC, Cong RM, Pang YW, Wang B (2016) Underwater image enhancement by dehazing with minimum information loss and histogram distribution prior. IEEE Trans Image Process 25(12):5664–5677

22. Li Y, Lu H, Li J, Li X, Li Y, Serikawa S (2016) Underwater image de-scattering and classification by deep neural network. Comput Electr Eng 54:68–77
23. Li C, Guo J, Guo C (2018) Emerging from water: Underwater image color correction based on weakly supervised color transfer. IEEE Signal Process Lett 25(3):323–327
24. Li C, Guo C, Ren W, Cong R, Hou J, Kwong S, Tao D (2019) An underwater image enhancement benchmark dataset and beyond. IEEE Trans Image Process 29:4376–4389
25. Liu C, Li H, Wang S, Zhu M, Wang D, Fan X, Wang Z (2021) A dataset and benchmark of underwater object detection for robot picking. IEEE International Conference on Multimedia & Expo Workshops (ICMEW) 1–6
26. Liu R, Fan X, Zhu M, Hou M, Luo Z (2020) Real-world underwater enhancement: Challenges, benchmarks, and solutions under natural light. IEEE Trans Circuits Syst Video Technol 30(12):4861–4875
27. Middleton WEK (1957) Vision through the atmosphere. In geophysik ii/geophysics ii Springer, Berlin, Heidelberg, pp 254–287
28. Narwaria M, Mantiuk R, Da Silva MP, Le Callet P (2015) HDR-VDP-2.2: a calibrated method for objective quality prediction of high-dynamic range and standard images. Journal of Electronic Imaging 24(1):010501
29. Peng L, Zhu C, Bian L (2021) U-shape Transformer for Underwater Image Enhancement. arXiv preprint arXiv:2111.11843
30. Schettini R, Corchs S (2010) Underwater image processing: state of the art of restoration and image enhancement methods. EURASIP Journal on Advances in Signal Processing 1–14
31. Shen L, Zhao Y, Peng Q, Chan JCW, Kong SG (2018) An iterative image dehazing method with polarization. IEEE Trans Multimedia 21(5):1093–1107
32. Singh N, Bhat A (2021) A Detailed Understanding of Underwater Image Enhancement using Deep Learning. In 5th International Conference on Information Systems and Computer Networks (ISCON) 1–6
33. Soni OK, Kumare JS (2020) A survey on underwater images enhancement techniques. In IEEE 9th International Conference on Communication Systems and Network Technologies (CSNT) 333–338
34. Tamou AB, Benzinou A, Nasreddine K, Ballihi L (2018) Underwater live fish recognition by deep learning. In International Conference on Image and Signal Processing, Springer, Cham 275–283
35. Ulutas G, Ustubioglu B (2021) Underwater image enhancement using contrast limited adaptive histogram equalization and layered difference representation. Multimedia Tools and Applications 80(10):15067–15091
36. Wen H, Tian Y, Huang T, Gao W (2013) Single underwater image enhancement with a new optical model. In 2013 IEEE International Symposium on Circuits and Systems (ISCAS) 753–756
37. Yang M, Sowmya A (2015) An underwater color image quality evaluation metric. IEEE Trans Image Process 24(12):6062–6071
38. Zhang W, Pan X, Xie X, Li L, Wang Z, Han C (2021) Color correction and adaptive contrast enhancement for underwater image enhancement. Comput Electr Eng 91:106981
39. Zhao X, Jin T, Qu S (2015) Deriving inherent optical properties from background color and underwater image enhancement. Ocean Eng 94:163–172

Publisher's note Springer Nature remains neutral with regard to jurisdictional claims in published maps and institutional affiliations.

Springer Nature or its licensor (e.g. a society or other partner) holds exclusive rights to this article under a publishing agreement with the author(s) or other rightsholder(s); author self-archiving of the accepted manuscript version of this article is solely governed by the terms of such publishing agreement and applicable law.

Authors and Affiliations

Nishant Singh[1] · Aruna Bhat[2]

[1] Department of Computer Science & Engineering, Delhi Technological University, Delhi 110042, Delhi, India

[2] Department of Computer Science & Engineering, Delhi Technological University, Delhi 110042, Delhi, India

2023 International Conference on Device Intelligence, Computing and Communication Technologies, (DICCT) | 978-1-6654-7491-7/23/$31.00 ©2023 IEEE | DOI: 10.1109/DICCT56244.2023.10110088

A Systematic Literature Review: Approach Toward Blockchain Future Research Trends

Himanshu Nandanwar
Computer science and engineering
Delhi Technological University
Delhi, India
himanshunandanwar9cm0@gmail.com

Rahul katarya
Computer science and engineering
Delhi Technological University
Delhi, India
rahulkatarya@dtu.ac.in

***Abstract*—A decentralised peer-to-peer technology called blockchain offers security services based on the following four core ideas: authentication, confidentiality, integrity, and authorisation. The purpose of this paper is to provide an overview of the blockchain's mechanism, architecture, and various components. It also compares different blockchain types based on various parameters and their applicability. This paper also emphasises the general security of blockchain. We evaluate the blockchain in particular to create thorough categories for blockchain security risks, examine actual attacks by bugs against the blockchain, and list recently created security measures for the technology. This paper also demonstrates the significance of various blockchain applications in the fields of healthcare, IoT, smart grid, governance, defence, and military. Overall, this paper provides an overview of various blockchain applications, their characteristics, challenges, and potential future.**

***Index Terms*—Blockchain, Distributed ledger, Bitcoin, Security privacy, Blockchain application.**

I. Introduction

Blockchain technology makes it possible to send digital assets directly between users, as opposed to more conventional means [1]. Bitcoin and Blockchain Technology were first presented by Satoshi Nakamoto in 2008, describing how a digital application might incorporate a cryptology-based decentralised, distributed public ledger[2][3]. In essence, a blockchain is a collection of blocks that employs a public ledger to keep every committed transaction[4]. The chain continues to grow as new blocks are added to it. Blockchain uses a number of important technologies, such as distributed consensus algorithms, cryptographic hashes, and digital signatures, to work in a decentralised environment. Because all transactions are decentralised, there is no need for middlemen to check or verify any of them[5]. Decentralization, transparency, immutability, and auditability are some of the major features of blockchain [6]. Blockchain technology aims to provide a decentralised ecosystem in which data and transactions are controlled by no third entity. A paradigm shifter, blockchain has sparked new concepts for safely exchanging data and information. By utilizing shared and dispersed networks, With the help of cutting-edge technology, a chain of blocks is created that securely stores all committed transactions.[7,8]. This is achieved through a number of core technologies, including thedigital signatures, distributed consensus techniques, and cryptographic hash functions. Because all transactions are decentralised, no intermediaries are required to examine and validate them [5].

As a data storage medium, blockchain technology employs an encrypted database and a peer-to-peer network. It is a technology made to create a special system of value exchange. The technique depends on encryption technology (public and private keys) to establish ownership and is dependent on the consistency of a distributed system packed with consensus methods.The academic community has paid close attention to how quickly blockchain technology is becoming practical. Blockchain research is becoming more popular among academics.Many people studied the technical features, functional aspects, and potential challenges of the blockchain. However, there is still a great deal to discover about blockchain technology and information systems. With the development of blockchain technology, researchers have begun to use purely descriptive research to highlight more specific blockchain results. The majority of the research concerns found have been centred on blockchain-based service offerings and technology implementation. There is a clear upward trend in the study of the adoption, business, and absorption of blockchain technology, which reflects the constant traits of technological innovation and information systems research. The remainder of the paper is divided as follows: The history of blockchain is covered in Section 2 along with its types and traits. Section 3 includes a systematic literature review on various applications of Blockchain technology.A few unresolved issues and potential directions for future research are covered in Section 4. Finally, we provide our conclusion in Section 5.

II. BACKGROUND OF BLOCKCHAIN TECHNOLOGY

The virtual money Blockchain technology serves as the foundation for bitcoin. A distributed database called the blockchain maintains copies of all completed transactions and other shared digital events. The great majority of system users confirm each transaction. Every transaction is captured in the record.the mostly used cryptocurrency and a prime example of a blockchain is Bitcoin 2008 saw the publication of the first white paper on Bitcoin:a Peer-to-Peer electronic cash system created by "Satoshi Nakamoto" or some other

Authorized licensed use limited to: DELHI TECHNICAL UNIV. Downloaded on May 04,2023 at 06:34:43 UTC from IEEE Xplore. Restrictions apply.

person or group.Blockchain technology is used to spread an immutable digital ledger of transactions across the network. Any item of value, including vehicles, real estate, and other goods, can have a transaction recorded for it on the blockchain. There are three different types of networks, as shown in figure 1,2, and 3:

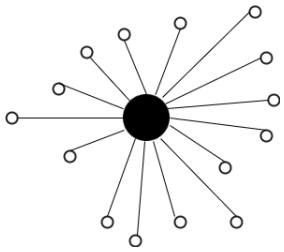


Fig. 1. Generic Architecture of Centralized System in blockchain

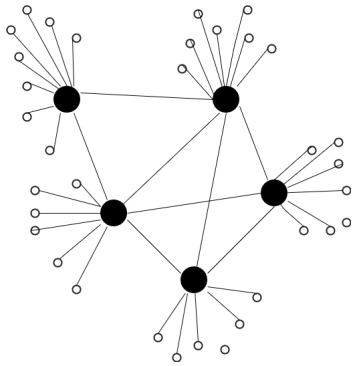


Fig. 2. Generic Architecture of Decentralized System in blockchain

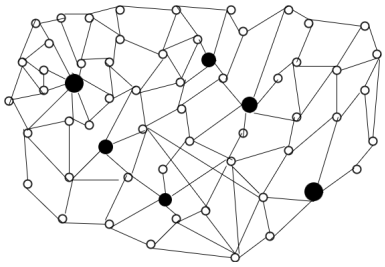


Fig. 3. Generic Architecture of Distributed System in blockchain

- Centralized network: Central network owner is responsible for all tasks in a centralized network. It acts as a single point contact for message passing. Users face two issues while using a centralized network. One is as there is a single central owner. If the owner node is down, then the whole network information passing system fails; the second reason is the increased access time issue because of only one copy stored with the owner.
- Decentralized network: multiple central owners are present in decentralized networks. This network solves the main issues caused by centralized networks. As there are multiple central owner nodes copy of each message is also stored at multiple central owners, which indeed reduces access time also, single point failure problem is answered by a decentralized system because even though one of the central owners fails whole message passing is not affected because remaining central owner nodes have one copy of stored information.
- Distributed network: this employs a completely decentralized network concept. This distributed network provides access to everyone, and copies of messages are maintained at every node due to this, access time is also reduced.

A. How does Blockchain Mechanism work?

A popular Blockchain application is Bitcoin. A cryptocurrency called bitcoin is utilised for online trading of digital assets. Bitcoin doesn't rely on third parties' trust but instead uses cryptographic evidence to allowtwo entities to carry out online transactions. A digital signature is used to record each transaction. Distributed Database:- There is no central server or system used by the blockchain process to store data. Thousands of computers or other devices connected to the blockchain throughout the world are where the data is spread out.The data in this system can be notarized because it is accessible to the public and is present on every node. A node is a computer that is a part of the Blockchain Network.

Figure 4 depicts how the Blockchain Mechanism works.

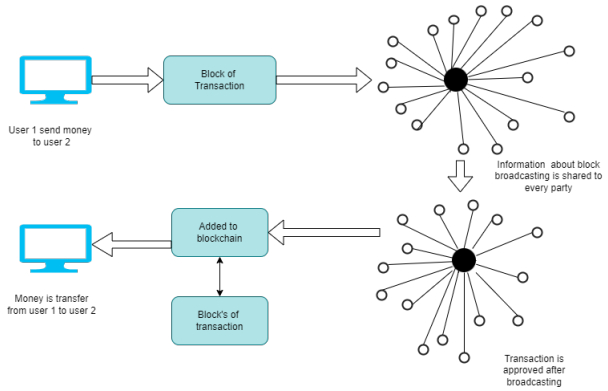


Fig. 4. Blockchain Mechanism

B. Components of Blockchain

Blockchain is a distributed ledger method that may be used to securely record node information, making data changes impossible. In other words, it is a decentralised computing system that serves as a data exchange platform, allowing different authoritative domains to engage in logical decision-making. In this context, the term "decentralised" or "distributed" refers to the fact that each node has an equal priority and distributes its resources among itself. As the name implies, information (i.e. transactions) will be recorded as blocks of data on a blockchain. Each node can view the block but cannot modify it. If any block value is changed, the block is deleted from the network, and its hash value is updated. The most recent

Authorized licensed use limited to: DELHI TECHNICAL UNIV. Downloaded on May 04,2023 at 06:34:43 UTC from IEEE Xplore. Restrictions apply.

blockchain is sent to each node in the blockchain network in an average of 12.6 seconds. The fundamental technology of Bitcoin is the blockchain network. The figure 5 depicts the architecture of the blockchain.

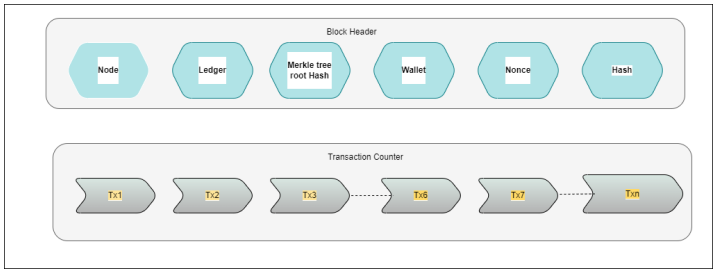


Fig. 5. Architecture of Blockchain

C. Types of Blockchain:-

The figure 6 shows the diagram of different types of Blockchains.

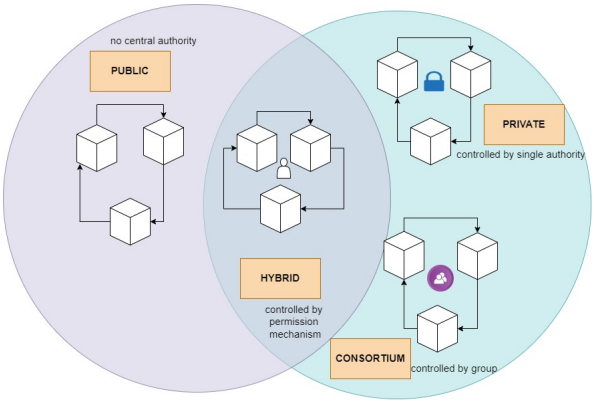


Fig. 6. Different type of Blockchain and its relation

- Public blockchain:- distributed ledger system with no restrictions and no permits is known as a public blockchain. Anyone with an internet connection can join the network as an authorised node and the blockchain network by registering on a platform.The public blockchain allows any node or user to access both recent and historical data, confirm transactions, and mine by completing the proof-of-work for each incoming block.
- Private blockchain:- A restricted or permissioned blockchain known as a private blockchain can only be used within a closed network. Private blockchains are widely used in corporations or organisations where only a small number of people are permitted to join a blockchain network.
- Hybrid blockchain:- The advantages of both public and private blockchains are combined in a hybrid blockchain. It uses both the private permission-based and public permissionless parts of a blockchain.Users can manage who has access to what data stored on the blockchain by utilising a hybrid network.
- Consortium blockchain:- In a consortium blockchain, a network of blockchains is controlled by a number of different organisations in a semi-decentralized fashion. Contrary to what we would say in the case of a private enterprise run by a single corporation, this is not the case. In this kind of blockchain, numerous organisations may participate as nodes, mining or exchanging data. Financial institutions, governmental bodies, and other businesses frequently use consortium blockchain.

III. Literature Review

The idea of using blockchain technology to support the well-known cryptocurrency Bitcoin was first put out [9]. However, in recent years, blockchain has become more widely used in numerous innovative areas other than cryptocurrencies [10,11], including healthcare [11], intelligent transportation [12], and the Internet of Things (IoT) [13]. In fact, this technology impacts a wide range of businesses [14], from straightforward personal amusement to handling delicate and important issues facing governments and nations. We present a succinct analysis of nine key survey studies from 2020 to 2022 that focus on the deployment of blockchain technology in contemporary applications in this part. Table 1 summarizes the previously analyzed survey articles. We discovered that the bulk of these survey papers focused on a small number of application domains per article and did not go into adequate detail on the challenges and difficulties faced in the disciplines under examination.

A. Blockchain in Finance

The financial and business sectors have made extensive use of blockchain technology.It can be used for settling financial transactions, trade financing, insurance, real-time money transfers, cross-border payments, and other things[24]. Bitcoin was the first non-central bank backed by a decentralised cryptocurrency and payment system. The banking system, which is the cornerstone of traditional banking, has the drawbacks of costing money, taking time, and being less secure[25]. These constraints may be eliminated by recreating this payment system with blockchain.

B. Blockchain in healthcare

Despite the importance of sharing medical data, some health systems require patients to give clinicians their medical information on paper or electronically on specific storage devices. This technique of transferring medical records is ineffective since it is cumbersome, risky, and information-deficient. According to [26], healthcare interoperability should be divided into three levels: basic, structural, and semantic. The adoption of blockchain technology may be able to overcome this interoperability problem[27]. Indeed, using blockchain technology, patient medical data will be shared with the required rights via smart contracts that govern operations such as changing viewing privileges or creating new records[28].

Authorized licensed use limited to: DELHI TECHNICAL UNIV. Downloaded on May 04,2023 at 06:34:43 UTC from IEEE Xplore. Restrictions apply.

TABLE I
A SYSTEMATIC LITERATURE REVIEW OF RECENT APPLICATION OF BLOCKCHAIN .

Reference	Year of Publication	Different applications/ areas of Blockchain	Description	Drawback
[15]	2022	Blockchain technology for IoT systems	An overview of IoT systems' future research goals, blockchain applications, trends, problems, and solutions.	The researchers concentrated their research on one blockchain application (in the field of IoT systems).
[16]	2022	Blockchain technology for smart grids and energy trade	An examination of blockchain prospects in smart grids in light of cyber security and the safety of energy data perspectives.	The authors ignored other potential challenges linked with implementing blockchain technology and concentrated primarily on security concerns.
[17]	2022	blockchain technology for Manufacturing supply chain and logistics	A thorough explanation of how blockchain technology may be utilised to address supply chain and logistics issues.	The authors focused on a single use of blockchain technology (in the field of manufacturing, supply chain and logistics).
[18]	2021	The Evolution of Blockchain	thorough review and analysis of blockchain technology development frameworks, architecture, and security challenges	adoption of a broad strategy for implementing blockchain technology; no specific application industries were mentioned.
[19]	2021	Methodologies for Utilization Of blockchain	a description of blockchain and its applications in smart grid, smart healthcare, and smart financial institutions	Only a few blockchain technology challenges and applications were explored.
[20]	2021	The use of blockchain in transportation systems	an analysis of how blockchain technology may be used to boost the safety and effectiveness of transportation operations.	Only one use of blockchain technology was considered, and only a few issues were fixed.
[21]	2020	Multimedia protection via blockchain	The taxonomic classification for developing blockchain-based multimedia copyright protection that integrates technical and application information.	There hasn't been enough detail provided about the probable difficulties and problems linked with this topic.
[22]	2020	Smart systems based on the blockchain	A detailed examination of the applications of blockchain technology for protecting and trusting smart systems.	Not much information is supplied about the application fields and related issues.
[23]	2020	Blockchain with industry 4.0	a detailed examination of blockchain's structures, methodologies, applications, and difficulties in Industry 4.0	Several issues and difficulties are investigated, including system integration, throughput and scalability, privacy, and security.

C. Blockchain in information system

A collection of various data types that ensures the achievement of a business goal is known as an information system. There is no independent IT business model for information systems. Contrarily, successful deployment depends on integration with data and business processes[29]. Businesses may benefit from blockchain's wide range of applications and advantages by integrating it into their information systems. Through interconnected networks and blockchain transaction ledgers, blockchain provides a common interface for engaged agents to communicate with one another, ensuring the authenticity of each involved party[30]. Furthermore, it reduces the possibility that third-party agents will obtain important information. Interoperability helps the marketing and acceptance of blockchain by providing all parties involved with a single platform to exchange data.

D. Blockchain in Wireless network

All wireless applications, including mobile handsets, broadband internet connections, and vehicle internet, require a radio spectrum. Large portions of the licensed spectrum are underutilized, and both of these issues plague the outdated spectrum management system. Blockchain technology can potentially be employed in spectrum management for various applications, such as spectrum sensing, secondary spectrum trading platforms, and regulatory enforcement[31]. Collaborative sensing combines the sensing results of multiple secondary sensors or users and can ensure the effectiveness of spectrum sensing findings[32]. It is anticipated that active blockchain storing of user geolocation data and details about unused frequency bands will improve spectrum access and use effectiveness. To improve the energy efficiency and sensing precision of cognitive wireless networks, a secure blockchain-based spectrum sensing method is presented. The system can adjust the number of nodes participating in cooperative sensing in real-time in response to environmental changes[33]. The system keeps track of each node's energy usage, sensing capabilities, trust value, and other things. This study combined the spectrum of the sensing approach with blockchain technology and a reputation system. Before the cooperative node may request access to a frequency band, its availability must be validated. If the fusion centre does not answer, a proposal request will be issued[34].

E. Blockchain in the Internet of Things

The networking of smart devices for data collecting and wise decision-making is known as the Internet of Things (IoT) [35,36,37]. Nevertheless, IoT is vulnerable to privacy and security issues, as there are no built-in security measures. The Internet of Things' dispersed and centralised architecture presents serious problems [38,39,40]. The contribution in [41] may be considered an all-purpose solution applicable to any IoT industry. Researchers devised a system that would let

Authorized licensed use limited to: DELHI TECHNICAL UNIV. Downloaded on May 04,2023 at 06:34:43 UTC from IEEE Xplore. Restrictions apply.

sensors trade data for bitcoin. A transaction is transmitted to the sensor's public key whenever a user requests data from a sensor after finding it in a sensor repository. In response, the sensor will then submit a transaction with data to the client. The approach shown here is a development of the one in [42].

Another fascinating option is the Enigma framework [43]. The use of blockchain in IoT applications also offers high levels of security that guard against unwanted data access.

F. Blockchain in Smart Grid

A smart grid is an electrical network based on digital communications that allow data and electricity to move in both directions. Control and communication technologies are integrated into modern smart grids. Traditional centralized ways of managing smart grids face significant challenges[44]. By incorporating blockchain technology into a smart grid, the best data and cash flow for energy trading may be gained[45].

Despite the fact that implementing blockchain technology in smart grids seems promising, as previously shown, there are still impediments to fully embracing this new technology[46]. Re-architecting present grid networks, for example, or adding blockchain into the smart grid would necessitate major infrastructure investments, discouraging grid operators from incorporating blockchains into their grid architecture[47].

G. Blockchain in Governmental Services

The capacity of blockchain technology to enable direct contact between governmental entities, people, and enterprises is one of its key benefits. Blockchain technology has the ability to change how governments interact with citizens and with one another as a result. Blockchain technology has the ability to change how governments interact with citizens and with one another as a result. This could prompt governmental organisations to reevaluate their functions in delivering public services[48]. Researchers should conduct additional research to compile a list of these implications to reduce unanticipated outcomes while applying this technology in the public sector. And last, research on how the government views blockchain technology may speed up implementation[49].

IV. Future research and open challenges

In this part, we investigate and highlight current challenges with blockchain technology. The following is a list of some of the looming challenges associated with the fusion and integration of numerous related technologies:

- Privacy:-Public blockchain ledgers process data securely and authentically, yet any readers can access the information that has been collected. This may create concerns about invasion of privacy.
- Scalability:-It is one of the key problems with the blockchain system because the blockchain has very few transactions per second compared to other platforms like Facebook.
- Side chain:- also known as a side channel. It helps in the faster execution of transactions between the parties.
- Security:- As blockchain is based on a decentralized network, it may get affected by the abuse and misuse of transaction information. Security concerns vary with the type of blockchain.
- Smart contract vulnerabilities and deterministic execution:- while implementing the user agreement between the parties, it is important to develop a smart contract in a bug-free manner, and it must be secure against different attack vulnerabilities.
- Performance Suitability:- If there are numerous entities in a scattered setting and the data source cannot be trusted, blockchain is a viable option. A simple database is a better choice if performance is essential. Determining the structure of blockchain is therefore crucial before using it in any application.

V. Conclusion

We described Blockchain in this study as a sort of database used to store data in a distributed system. The blockchain has received acclaim and endorsement for its peer-to-peer architecture and decentralised nature. However, many analysts believe that bitcoin protects blockchains. On the other hand, Blockchain offers uses that go well beyond bitcoin. First, we addressed the fundamentals of blockchain technology, including blockchain architecture. This article provides an overview of blockchain technology and its working principles. An overview of the blockchain literature is provided in this essay.In this article, we look at new research on how blockchain technology is being used in modern industries like finance, healthcare, information systems, wireless networks, the internet of things, smart grids, government services, and military and defense. Finally, in this essay, we highlight some blockchain-related characteristics that have the potential to alter how transactions are now carried out completely. Additionally, upcoming studies and unresolved issues with blockchain technology are addressed.

References

[1] Aste, Tomaso, Paolo Tasca, and Tiziana Di Matteo. "Blockchain technologies: The foreseeable impact on society and industry." (2017).

[2] Xu, Min, Xingtong Chen, and Gang Kou. "A systematic review of blockchain." Financial Innovation 5, no. 1 (2019): 1-14.

[3] Nakamoto, Satoshi. "Bitcoin: A peer-to-peer electronic cash system." Decentralized Business Review (2008): 21260.

[4] Salah, Khaled, M. Habib Ur Rehman, Nishara Nizamuddin, and Ala Al-Fuqaha. "Blockchain for AI: Review and open research challenges." IEEE Access 7 (2019): 10127-10149.

[5] Litke, Antonios, Dimosthenis Anagnostopoulos, and Theodora Varvarigou. "Blockchains for supply chain management: Architectural elements and challenges towards a global scale deployment." Logistics 3, no. 1 (2019): 5.

[6] Kouhizadeh, Mahtab, and Joseph Sarkis. "Blockchain practices, potentials, and perspectives in greening supply chains." Sustainability 10, no. 10 (2018): 3652.

[7] Salah, Khaled, M. Habib Ur Rehman, Nishara Nizamuddin, and Ala Al-Fuqaha. "Blockchain for AI: Review and open research challenges." IEEE Access 7 (2019): 10127-10149.

[8] Lahami, Mariam, Afef Jmal Maâlej, Moez Krichen, and Mohamed Amin Hammami. "A Comprehensive Review of Testing Blockchain Oriented Software." ENASE (2022): 355-362.

[9] Schilling, Linda, and Harald Uhlig. "Some simple bitcoin economics." Journal of Monetary Economics 106 (2019): 16-26.

Authorized licensed use limited to: DELHI TECHNICAL UNIV. Downloaded on May 04,2023 at 06:34:43 UTC from IEEE Xplore. Restrictions apply.

[10] Ravishankar, C. V., and K. S. Kavitha. "Blockchain Applications that are Transforming the Society." In Convergence of Internet of Things and Blockchain Technologies, pp. 23-39. Springer, Cham, 2022.
[11] Zaabar, Bessem, Omar Cheikhrouhou, Faisal Jamil, Meryem Ammi, and Mohamed Abid. "HealthBlock: A secure blockchain-based healthcare data management system." Computer Networks 200 (2021): 108500.
[12] Jamil, Faisal, Omar Cheikhrouhou, Harun Jamil, Anis Koubaa, Abdelouahid Derhab, and Mohamed Amine Ferrag. "PetroBlock: A blockchain-based payment mechanism for fueling smart vehicles." Applied Sciences 11, no. 7 (2021): 3055.
[13] Frikha, Tarek, Faten Chaabane, Nadhir Aouinti, Omar Cheikhrouhou, Nader Ben Amor, and Abdelfateh Kerrouche. "Implementation of blockchain consensus algorithm on embedded architecture." Security and Communication Networks 2021 (2021).
[14] Al-Jaroodi, Jameela, and Nader Mohamed. "Blockchain in industries: A survey." IEEE Access 7 (2019): 36500-36515.
[15] Abdelmaboud, Abdelzahir, Abdelmuttlib Ibrahim Abdalla Ahmed, Mohammed Abaker, Taiseer Abdalla Elfadil Eisa, Hashim Albasheer, Sara Abdelwahab Ghorashi, and Faten Khalid Karim. "Blockchain for IoT Applications: Taxonomy, Platforms, Recent Advances, Challenges and Future Research Directions." Electronics 11, no. 4 (2022): 630.
[16] Hasan, Mohammad Kamrul, Ali Alkhalifah, Shayla Islam, Nissrein Babiker, A. K. M. Habib, Azana Hafizah Mohd Aman, and Md Hossain. "Blockchain technology on smart grid, energy trading, and big data: security issues, challenges, and recommendations." Wireless Communications and Mobile Computing 2022 (2022).
[17] Raja Santhi, Abirami, and Padmakumar Muthuswamy. "Influence of blockchain technology in manufacturing supply chain and logistics." Logistics 6, no. 1 (2022): 15.
[18] Bhutta, Muhammad Nasir Mumtaz, Amir A. Khwaja, Adnan Nadeem, Hafiz Farooq Ahmad, Muhammad Khurram Khan, Moataz A. Hanif, Houbing Song, Majed Alshamari, and Yue Cao. "A survey on blockchain technology: evolution, architecture and security." IEEE Access 9 (2021): 61048-61073.
[19] Guru, Divya, Supraja Perumal, and Vijayakumar Varadarajan. "Approaches towards blockchain innovation: a survey and future directions." Electronics 10, no. 10 (2021): 1219.
[20] Khoshavi, Navid, Gabrielle Tristani, and Arman Sargolzaei. "Blockchain applications to improve operation and security of transportation systems: A survey." Electronics 10, no. 5 (2021): 629.
[21] Qureshi, Amna, and David Megías Jiménez. "Blockchain-based multimedia content protection: Review and open challenges." Applied Sciences 11, no. 1 (2020): 1.
[22] Rawat, D. B., V. Chaudhary, and R. Doku. "Blockchain technology: Emerging applications and use cases for secure and trustworthy smart systems. J. Cybersecurity Priv. 1 (1), 4–18 (2020)."
[23] Zuo, Yanjun. "Making smart manufacturing smarter–a survey on blockchain technology in Industry 4.0." Enterprise Information Systems 15, no. 10 (2021): 1323-1353.
[24] Zhang, Li, Yongping Xie, Yang Zheng, Wei Xue, Xianrong Zheng, and Xiaobo Xu. "The challenges and countermeasures of blockchain in finance and economics." Systems Research and Behavioral Science 37, no. 4 (2020): 691-698.
[25] Tapscott, Alex, and Don Tapscott. "How blockchain is changing finance." Harvard Business Review 1, no. 9 (2017): 2-5.
[26] Lumpkin, John, Simon P. Cohn, and Jeffrey S. Blair. "Uniform data standards for patient medical record information." National Committee on Vital and Health Statistics 53 (2003).
[27] Jabbar, Rateb, Noora Fetais, Moez Krichen, and Kamel Barkaoui. "Blockchain technology for healthcare: Enhancing shared electronic health record interoperability and integrity." In 2020 IEEE International Conference on Informatics, IoT, and Enabling Technologies (ICIoT), pp. 310-317. IEEE, 2020.
[28] Zhuang, Yan, Lincoln R. Sheets, Yin-Wu Chen, Zon-Yin Shae, Jeffrey JP Tsai, and Chi-Ren Shyu. "A patient-centric health information exchange framework using blockchain technology." IEEE journal of biomedical and health informatics 24, no. 8 (2020): 2169-2176.
[29] Marakas, George M., and James A. O'Brien. Introduction to information systems. New York: McGraw-Hill/Irwin, 2013.
[30] Fullana, Olga, and Javier Ruiz. "Accounting information systems in the blockchain era." International Journal of Intellectual Property Management 11, no. 1 (2021): 63-80.
[31] Jabbar, Rateb, Eya Dhib, Ahmed ben Said, Moez Krichen, Noora Fetais, Esmat Zaidan, and Kamel Barkaoui. "Blockchain Technology for Intelligent Transportation Systems: A Systematic Literature Review." IEEE Access (2022).
[32] Jabbar, Rateb, Noora Fetais, Mohamed Kharbeche, Moez Krichen, Kamel Barkaoui, and Mohammed Shinoy. "Blockchain for the Internet of vehicles: How to use blockchain to secure vehicle-to-everything (V2X) communication and payment?." IEEE Sensors Journal 21, no. 14 (2021): 15807-15823.
[33] Leyton-Brown, Kevin, Paul Milgrom, and Ilya Segal. "Economics and computer science of a radio spectrum reallocation." Proceedings of the National Academy of Sciences 114, no. 28 (2017): 7202-7209.
[34] Pei, Yiyang, Shisheng Hu, Feng Zhong, Dusit Niyato, and Ying-Chang Liang. "Blockchain-enabled dynamic spectrum access: cooperative spectrum sensing, access and mining." In 2019 IEEE Global Communications Conference (GLOBECOM), pp. 1-6. IEEE, 2019.
[35] Mukhtar, Hamid, Saeed Rubaiee, Moez Krichen, and Roobaea Alroobaea. "An IoT framework for screening of COVID-19 using real-time data from wearable sensors." International Journal of Environmental Research and Public Health 18, no. 8 (2021): 4022.
[36] Krichen, Moez, and Roobaea Alroobaea. "A new model-based framework for testing security of iot systems in smart cities using attack trees and price timed automata." In 14th international conference on evaluation of novel approaches to software engineering, pp. 570-577. SCITEPRESS-Science and Technology Publications, 2019.
[37] Jabbar, Rateb, Mohammed Shinoy, Mohamed Kharbeche, Khalifa Al-Khalifa, Moez Krichen, and Kamel Barkaoui. "Urban traffic monitoring and modeling system: An iot solution for enhancing road safety." In 2019 international conference on internet of things, embedded systems and communications (iintec), pp. 13-18. IEEE, 2019.
[38] Bhandari, Khadak Singh, In-Ho Ra, and Gihwan Cho. "Multi-topology based QoS-differentiation in RPL for internet of things applications." IEEE Access 8 (2020): 96686-96705.
[39] Bhandari, Khadak Singh, and GI Hwan Cho. "An energy efficient routing approach for cloud-assisted green industrial IoT networks." Sustainability 12, no. 18 (2020): 7358.
[40] Bhandari, Khadak Singh, and Gi Hwan Cho. "Resource oriented topology construction to ensure high reliability in IoT based smart city networks." International Journal of System Assurance Engineering and Management 11, no. 4 (2020): 798-805.
[41] Wörner, Dominic, and Thomas von Bomhard. "When your sensor earns money: exchanging data for cash with Bitcoin." In Proceedings of the 2014 ACM International Joint Conference on Pervasive and Ubiquitous Computing: Adjunct Publication, pp. 295-298. 2014.
[42] Zhang, Yu, and Jiangtao Wen. "An IoT electric business model based on the protocol of bitcoin." In 2015 18th international conference on intelligence in next generation networks, pp. 184-191. IEEE, 2015.
[43] Shrobe, Howard, David L. Shrier, and Alex Pentland. "Enigma: Decentralized computation platform with guaranteed privacy." (2018): 425-454.
[44] Zidi, Salah, Alaeddine Mihoub, Saeed Mian Qaisar, Moez Krichen, and QasemMuhammedHaija. "Theft detection dataset for benchmarking and machine learning ng based classification in a smart grid environment." Journal of King Saud University-Computer and Information Sciences (2022).
[45] Fang, Xi, Satyajayant Misra, Guoliang Xue, and Dejun Yang. "Smart grid—The new and improved power grid: A survey." IEEE communications surveys tutorials 14, no. 4 (2011): 944-980.
[46] Farhangi, Hassan. "The path of the smart grid." IEEE power and energy magazine 8, no. 1 (2009): 18-28.
[47] Gungor, Vehbi C., Dilan Sahin, Taskin Kocak, Salih Ergut, Concettina Buccella, Carlo Cecati, and Gerhard P. Hancke. "Smart grid technologies: Communication technologies and standards." IEEE transactions on Industrial informatics 7, no. 4 (2011): 529-539.
[48] Molnar, Andreea, Marijn Janssen, and Vishanth Weerakkody. "E-government theories and challenges: findings from a plenary expert panel." In Proceedings of the 16th Annual International Conference on Digital Government Research, pp. 160-166. 2015.
[49] Atzori, Marcella. "Blockchain technology and decentralized governance: Is the state still necessary?." Available at SSRN 2709713 (2015).

Authorized licensed use limited to: DELHI TECHNICAL UNIV. Downloaded on May 04,2023 at 06:34:43 UTC from IEEE Xplore. Restrictions apply.

Adaptive-Optimal Control for Reconfigurable Robots

2023 International Conference on Device Intelligence, Computing and Communication Technologies, (DICCT) | 978-1-6654-7491-7/23/$31.00 ©2023 IEEE | DOI: 10.1109/DICCT56244.2023.10110043

Adya Maheshwari
Department of Electrical Engineering
Delhi Technological University
New Delhi, India
adya.maheshwari@gmail.com

Aaditya Rautela
Department of Electrical Engineering
Delhi Technological University
New Delhi, India
aadityarautela@gmail.com

Madan Mohan Rayguru
Control of Dynamical Systems and Computation Laboratory
Department of Electrical Engineering
Delhi Technological University
New Delhi, India
mmrayguru@dtu.ac.in

Sudarshan K. Valluru
Control of Dynamical Systems and Computation Laboratory
Department of Electrical Engineering
Delhi Technological University
New Delhi, India
sudarshan_valluru@dce.ac.in

***Abstract*—Reconfigurable robots refer to the robotic systems which have the ability to transform their morphological structure to adapt to changes in their surroundings. A specialized control system based upon the dynamic characteristics is required to be modelled so that a vast range of operations can be performed by the reconfigurable robots. Reinforcement learning based technique is therefore considered as a suitable mechanism for carrying out adaptive optimal control for the robotic systems. In this paper, an attempt has been made to model the adaptive optimal control mechanism for a single-link manipulator: a reconfigurable robotic system. The system has been modelled for a dynamic environment. The loss and reward plots are obtained from the simulation of the robotic system by deploying reinforcement learning based techniques with the given controlled input**

Keywords— Reinforcement learning, reconfigurable robots, adaptive-optimal control, value iteration, single-link manipulator

I. INTRODUCTION

Over time, robotic systems have evolved from simple mechanical machines that were performing monotonous tasks to sophisticated autonomous systems. In the past few years, researchers have been aiming to inculcate scalability and adaptability functionalities to the robotic systems so that they are capable of performing intricate tasks such as medical surgeries and space exploration [1], [2].

Reconfigurable robots, also referred to as modular robots are the systems that are designed to be adaptable and versa- tile. They possess the ability to change their morphological structure in response to the changes in the environment. Such robotic systems are constituted by a number of modules, each of which can be added or removed with ease. Due to the modularity and scalability of the reconfigurable robots, they can be deployed for a wide range of applications, from manufacturing, cleaning and healthcare units to search operation purposes. PANTHERA [3] and hTetro [4] are some of the examples for such reconfigurable robotic systems.

The movement control of reconfigurable robotic systems is an arduous task due to the complexity of the system dynamics that are taken into consideration for the multiple robotic configurations. The process of determining the optimal path for the movement of a robotic system in a given environment with the pre-defined constraints is referred to as large-scale motion planning and control. The literature review reveals that the past optimization has been attempted through Genetic Algorithm and Particle Swarm Optimization techniques [5], [6], [7]. The instant problem pertains to large-scale motion planning and control and this requires adaptability of manipulators. Therefore, an attempt has been made to incorporate the reinforcement learning based technique to carry out adaptive optimal control for a single-link robotic manipulator system powered by a dc motor.

A. Reinforcement Learning

Reinforcement learning (RL) is a type of machine learning technique which is utilized for decision-making purposes. It is used to train agents in an environment while aiming at maximization of reward signal. The idea behind RL based technique is that the agent interacts with the environment and performs actions based upon the current state of the model. The feedback on the quality of the action is gauged by the agent by providing suitable rewards or penalties [8]. Over time, the decision-making ability of the agent in the environment increases with the feedback thus provided to the system.

As the actions of the agent are dependent upon the current state of the system, such systems fall under the category of Markov Decision Processes - i.e., given present states ofthe input, the past states do not matter. Markov Decision Process is a five-tuple mathematical formulation consisting of the parameters - set space of the system, actions performed by the agent, state transitional probabilities, discount factor (γ) and the reward function (R).

Authorized licensed use limited to: DELHI TECHNICAL UNIV. Downloaded on May 04,2023 at 06:32:09 UTC from IEEE Xplore. Restrictions apply.

B. Dynamic Programming

Dynamic programming seeks to determine the optimal configuration of the robotic system for a given task or environment, in an iterative manner by updating estimates of the valueas well as the best possible action for each configuration. In case of reconfigurable robots, dynamic programming can be deployed to find the optimal configuration of the given modules pertaining to a particular task in the defined environment. Further, in order to utilize dynamic programming for reconfigurable robotic systems, the environment should be fully observable and the dynamics for the robot should be expressible mathematically. In dynamic programming, Bellman equation plays a key role as it is used to define the optimal function for the model, i.e., the value function. On evaluating the parameters by the Bellman equation in an iterative manner, the value function for a given robotic systemcan be determined [8].

The Bellman equation that is used to determine the optimal value function (V^{π}) for the model, provided the policy π, is given by (1).

$$V^{\pi}(s) = E\left[R(s0) + \gamma\left(R(s1) + \gamma R(s2) + \ldots\right)|\pi_{s0=s}\right] \quad (1)$$

C. Value Iteration

Value iteration refers to the procedure of computing the numerical values of the states for Markov decision processes, given that the transition probabilities and rewards for each state is known. [9] It refers to the algorithm that is deployed for finding out the value of V*, where, V* refers to the optimal value function. [10] The value iteration mechanism is governed by the Bellman Equation described in (1) as it initializes the estimate of the value function and improves the estimate repeatedly. Through the Bellman equation, the value for the total expected payoff is obtained for starting an action in state '*s*' with policy π [11]. Value iteration is a sought-after technique that is relatively simple and can be used to find the optimal solution for the given Markov Decision Process based problem. The value iteration mechanism has been mentioned in Algorithm 1.

Algorithm 1 Value Iteration

Require: V(s)
Ensure: $\Delta V \leftarrow 0$
for $s \in S$ **do**
  while $N < max_iter$ or $\Delta V > \epsilon$ **do**
    $V \leftarrow V(s)$
    $V(s) \leftarrow \max_u \sum_0^n p(s', r|s, u)\left[r + \gamma V(s)\right]$
    $\Delta V \leftarrow \max\left(\Delta V, |V - V(s)|\right)$
  end while
  $\pi(s) \leftarrow \arg\max_u \sum_p (s', r|s, u)\left[r + \gamma V(s)\right]$
end for
$optimalpolicy \leftarrow \pi(s)$

D. Neural Networks

Neural Networks refer to computational networks that provide output by mimicking the action of a human brain [12]. Similar to the neurons in the human brain, the Artificial Neural Networks consist of interconnected nodes with weights assigned to them [13]. The representation of a neuron in such a network with weight vector *w* with bias unit *b* is given by (2):

$$z = w^T x + b \quad (2)$$

In this paper, the Artificial Neural Network based model has been utilized as a basis of a function approximator to train upon the policy thus obtained from the process of value iteration for a given state of the reconfigurable robotic system.

II. Implementation

Robotic manipulators are multifunctional and reprogrammable mechanical devices that can be deployed to perform tasks that are involving programmed motion control. Manipulators consist of a number of jointed segments in continuation so as to form an arm-like mechanism. They are composed of an assembly of links and joints where links are referred to as the rigid sections that form the mechanism of the robotic system whereas the joints are the point of connection of two given links. The jointed segments enable the arm-like structure to get a hold of objects and also move them up to certain degrees of freedom [14]. To perform robotic operations, one end of the manipulator system is kept fixed whereas the other is movable.

For the present work, adaptive-optimal control is attempted for a single-link manipulator system that refers to a robotic system consisting of a flexible link. This is connected to a motor shaft at one end and the other end is movable and free to rotate [15]. The second-order dynamics for a single-link manipulator system [16] that is powered by dc motor are given by (3) and (4).

$$\dot{x}_1 = x_2 \quad (3)$$

$$\dot{x}_2 = \frac{-N}{M}\sin x_1 - \frac{B}{M}x_2 + \frac{1}{RM}u - \frac{K_b}{RM}x_2 \quad (4)$$

Here, in (3) and (4), x_1 and x_2 correspond to the position and velocity for the robotic manipulator system. The Table 1 showcases the parameter values for the single-link manipulator system. Further, the contour plot showcasing the reward values with regard to the controlled input is depicted by Fig. 1.

TABLE I. Parameters for the single-link manipulator

S. No.	Parameter	Value	Units
1.	M	1.514	kg m^2
2.	N	1.9782	kg m^2/sec^2
3.	B	16.251	N m sec/rad
4.	R	5.0	Ohm
5.	K_b	0.90	V sec/rad

Authorized licensed use limited to: DELHI TECHNICAL UNIV. Downloaded on May 04,2023 at 06:32:09 UTC from IEEE Xplore. Restrictions apply.

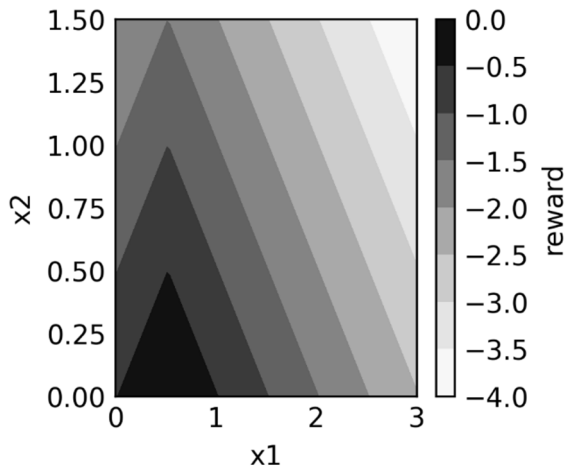


Fig. 1. Contour plot for rewards corresponding to different states

For simulation purposes, the control mechanism has been achieved with the help of Python programming language. Various libraries viz. NumPy, Matplotlib and TensorFlow framework have also been incorporated. The target values for x_1 and x_2 are set to $\pi/6$ and 0 respectively. The reward for the model has been specified by taking negative of the absolute (abs) values for both the parameters with regard to the set target values and is therefore, given by (5) where, x_i refers to the specified controlled input for the given system. Further, the loss plot corresponding to the specified reward function has been shown in Fig. 2.

$$-\text{abs}(x_1 - x_i) - \text{abs}(x_2) \quad (5)$$

With the aforementioned initialized parameters, the value iteration process is carried out so as to obtain the optimal policy and the corresponding values for the given state space. For the given set of values, the Artificial Neural Network based model, acting as a function approximator for the robotic system of the single-link manipulator is utilized for training on the policy thus obtained from the value iteration mechanism which provides us with the parameters to plot the loss curve for the system in Fig. 2. In order to obtain the rewards plot, the state is randomly initialized and the policy evaluation process is thus carried out in an iterative manner.

The Keras-based neural network model utilized for the robotic manipulator system is a three layer network with the input layer sizes as 50 × 50 × 1. The simulation has been performed by taking into consideration a random initial state and the model has been trained to perform iterations up to the convergence for the required controlled input state. The loss is calculated on the basis of the mean squared error by taking into consideration the desired output value and the initialized random state. The activation functions deployed in the neural network include softplus for the input and hidden layers and the tanh function for the output layer so as to limit the output between -1 and 1. Further, the Adam optimizer has been utilized to carry out the optimization for the given model.

Fig. 3 represents the plot of actions with respect to theepisode lengths that have been taken as 200 for training upon the robotic system. Using (5) for the instant model and considering the value of x_i as $\pi/6$, the reward plot, as shown in Fig. 4 has been obtained. The Fig. 3 and Fig. 4 indicate that the system is converging towards the required stable state.

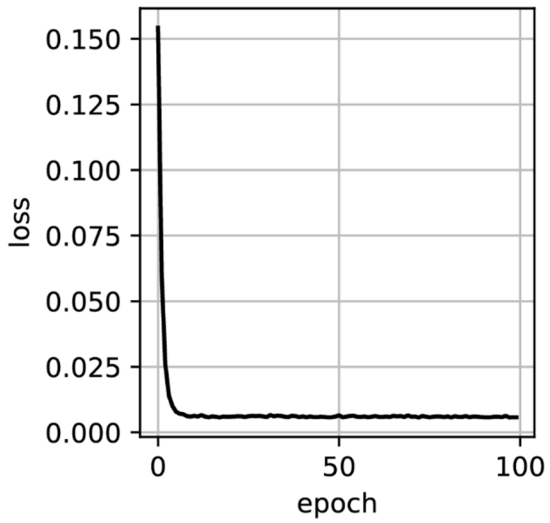


Fig. 2. Training loss curve for the neural network

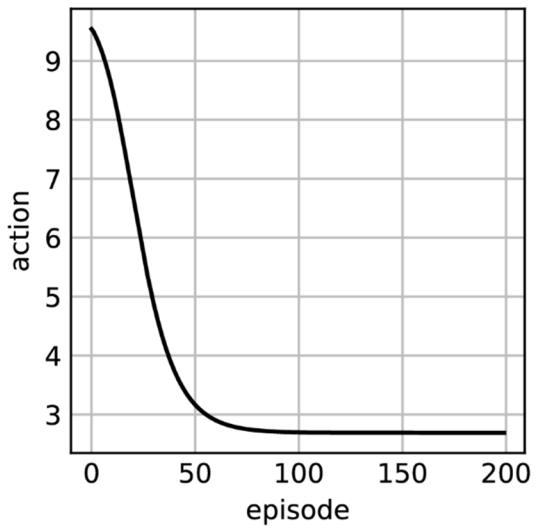


Fig. 3. Control signal plot obtained by neural network

Authorized licensed use limited to: DELHI TECHNICAL UNIV. Downloaded on May 04,2023 at 06:32:09 UTC from IEEE Xplore. Restrictions apply.

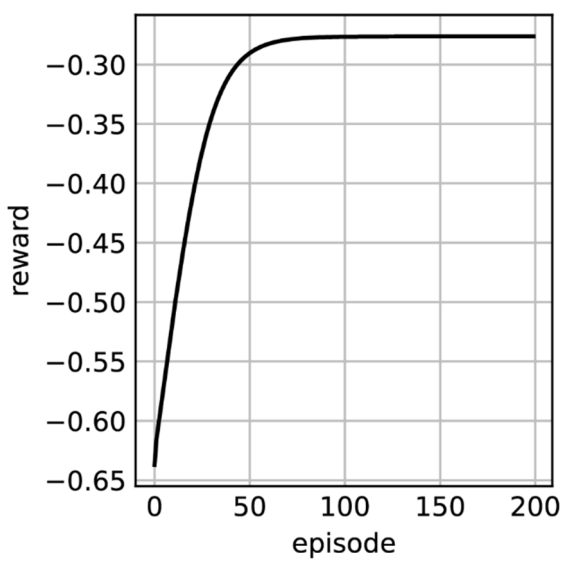


Fig. 4. Reward plot

III. Conclusion

Movement of reconfigurable robots requires robust algorithms and effective control strategies. Reinforcement learning based technique by using the value iteration algorithm have been successfully implemented for achieving the optimization for the single-link manipulator based reconfigurable robotic system. Upon performing value iteration up to 200 episodes and using the neural network as function approximator for the given system, the reward attains the value -0.295612 after the 52nd episode for the input set state of π /6. The feedback in the form of rewards has been successfully utilized to train the system in a dynamic environment. Thus, for the stable manipulator system, the flexible link control has been accomplished with the specified controlled input parameters.

References

[1] B. Salemi, M. Moll and W. -m. Shen, "SUPERBOT: A Deployable, Multi-Functional, and Modular Self-Reconfigurable Robotic System," 2006 IEEE/RSJ International Conference on Intelligent Robots and Systems, Beijing, China, 2006, pp. 3636-3641.

[2] X. Cai, S. K. H. Win, H. Bhardwaj and S. Foong, "Modeling, Control and Implementation of Adaptive Reconfigurable ROtary Wings (AR- ROWs)," in IEEE/ASME Transactions on Mechatronics, 2023.

[3] M. M. Rayguru, M. R. Elara, A. A. Hayat, B. Ramalingam and S. Roy, "Modeling and Control of PANTHERA Self-Reconfigurable Pavement Sweeping Robot under Actuator Constraints," 2021 IEEE/RSJ International Conference on Intelligent Robots and Systems (IROS), Prague, Czech Republic, 2021, pp. 2742-2748

[4] R. Parween, L. T. L. Clarissa, M. Y. Naing, N. A. F. B. M. Fuad and M. R. Elara, "Modeling and Analysis of the Cleaning System of a Reconfigurable Tiling Robot," in IEEE Access, vol. 8, pp. 137770- 137782, 2020

[5] K. P. Cheng, R. E. Mohan, N. H. Khanh Nhan and A. V. Le, "Multi-Objective Genetic Algorithm-Based Autonomous Path Planning for Hinged-Tetro Reconfigurable Tiling Robot," in IEEE Access, vol. 8, pp. 121267-121284, 2020.

[6] S. M. B. P. Samarakoon, M. A. V. J. Muthugala and M. R. Elara, "Online Complete Coverage Path Planning of a Reconfigurable Robot using Glasius Bio-inspired Neural Network and Genetic Algorithm," 2022 IEEE/RSJ International Conference on Intelligent Robots and Systems (IROS), Kyoto, Japan, 2022, pp. 5744-5751.

[7] Y. Yamada, "Dynamic reconfiguration of reconfigurable manufacturing systems using particle swarm optimization," Proceedings 2006 IEEE International Conference on Robotics and Automation, 2006. ICRA 2006., Orlando, FL, USA, 2006, pp. 1444-1449.

[8] F. L. Lewis, D. Vrabie and K. G. Vamvoudakis, "Reinforcement Learn-ing and Feedback Control: Using Natural Decision Methods to Design Optimal Adaptive Controllers," in IEEE Control Systems Magazine, vol. 32, no. 6, pp. 76-105, Dec. 2012.

[9] H. Jiang, T. An, B. Ma, Y. Li and B. Dong, "Value Iteration-based Decentralized Fuzzy Optimal Control of Modular Reconfigurable Robots via Adaptive Dynamic Programming," 2022 5th International Con- ference on Robotics, Control and Automation Engineering (RCAE), Changchun, China, 2022, pp. 186-190.

[10] M. M. Noel, B. J. Pandian, "Control of a nonlinear liquid level system using a new artificial neural network based reinforcement learning approach," Applied Soft Computing, Volume 23, 2014, pp. 444-451.

[11] R. S. Sutton and A. G. Barto, "Reinforcement Learning: An Introduc- tion," The MIT Press: 2nd edition, 2018

[12] S. K. Valluru and T. N. Rao, "Introduction to Neural Networks, Fuzzy Logic and Genetic Algorithms," Jaico Publishing House, Mumbai, 2011.

[13] N. Rahuja and S. K. Valluru, "A Deep Neural Network Approach to Automatic Multi-Class Classification of Electrocardiogram Signals," 2021 International Conference on Intelligent Technologies (CONIT), Hubli, India, 2021, pp. 1-4.

[14] Y. Li, S.Tong and T. Li, "Adaptive fuzzy output feedback control for a single-link flexible robot manipulator driven DC motor via backstep- ping," Nonlinear Analysis: Real World Applications. 14. pp. 483–494, 2013

[15] J. J. E. Slotine and W.Li, "Applied nonlinear control," Vol. 199, No. 1, pp. 705, NJ: Englewood Cliffs, Prentice Hall, 2019

[16] M. M. Rayguru and I.N. Kar "Contraction Theory Approach to Dis-turbance Observer Based Filtered Backstepping Design." Journal of Dynamic Systems Measurement and Control, 2019.

Authorized licensed use limited to: DELHI TECHNICAL UNIV. Downloaded on May 04,2023 at 06:32:09 UTC from IEEE Xplore. Restrictions apply.

International Journal of Advances in Engineering and Management (IJAEM)
Volume 5, Issue 4 April 2023, pp: 1874-1879 www.ijaem.net ISSN: 2395-5252

AI And Its Application in CAD

Mohit Saini
Department of Mechanical Engineering, Delhi Technological University, Rohini, India

Date of Submission: 20-04-2023 Date of Acceptance: 30-04-2023

ABSTRACT— Computer Aided Design (CAD) is on the brink of another revolution with primary drivers in the form of AI and Machine Learning involving the use of Deep Learning (DL). This paper reviews the various real-life applications of AI integrated with CAD like Computer-Aided Teaching, CAD in extended reality, architectural design and aircraft component manufacturing while also discussing the different ideologies and methodologies used for the same. The paper also discusses the prospects of AI integrated with CAD. AI is often integrated within CAD for automated decision -making (ADM), where AI algorithms are implemented for data collection, processing, modelling, and utilization in support of automated decisions. The feedback is evaluated for the improvement of the decision-making process.

Keywords—CAD, AI, DL

I. INTRODUCTION

The major goal of the branch of computer science known as artificial intelligence is to show that a computer system may exhibit intelligence that is strikingly close to human intellect. Learning, prediction, vision, speech recognition, decision-making, translation, social intelligence, motion, and manipulation are just a few examples of what it is capable of learning. In other words, the intelligence displayed by the machines is also referred to as machine intelligence.

In the mid-1980s AI(Artificial Intelligence) was introduced, with this new technology the problem solving abilities of CAD software were enhanced significantly. The purpose of AI is to learn and replicate human problem-solving capabilities. AI software, unlike procedural programming software (such as Fortran, C, C++, or Java), models non-numerical cognitive processes of pattern matching and decision-making [1]. The competence of professionals who can conduct activities involving synthesis, diagnosis, planning, interpretation, and execution of design tasks is captured by AI. As a result, AI software's language is not procedural; rather, it is based on rules that specify how decisions should be made.

Currently, CAD software's main purpose is to automate a design's analytical phases. To ensure that parts and assemblies perform as intended and adhere to design criteria, CAD software is used to construct computer models of the parts, fit them together, and model their performance. Because expert design assessments evaluate whether modifications should be made, the analytical steps of a design process are iterative (design synthesis). Because AI-based solutions incorporate the knowledge and experience of professionals, design synthesis can be carried out without the need for a separate design review and synthesis.

II. HOW CAD AND AI ARE MERGED

MBR (Model-Based Reasoning) is the process through which CAD can be merged with AI. It analyzes qualitatively and quantitively in order to predict the interaction of the design components. MBR is model-based and extracts knowledge from past behavior.

Model-based reasoning tries to solve a problem with a diverse set of approaches and multiple loosely connected techniques. It is mostly applied in the areas of monitoring, control and diagnosis. For diagnostic applications of the model it usually consists of the following elements: (a) replicate and predict the normal behavior of the system, (b) record the relations between internal model components and predicted observations, (c) on detection of an abnormal observation, use the relation between the internal model components and predicted observations to identify contradicting model assumptions, and (d) in the presence of multiple elements, apply a measurement strategy to reduce the number of elements [2].

III. ARTIFICIAL INTELLIGENCE IN CAD

The term “Artificial Intelligence” was used to describe a machines ability to replicate human intelligence through learning and reasoning. Recently, the companies have been able to set up an intelligent CAD environment by incorporating AI into their systems. Integrating AI into the CAD

International Journal of Advances in Engineering and Management (IJAEM)
Volume 5, Issue 4 April 2023, pp: 1874-1879 www.ijaem.net ISSN: 2395-5252

system will reduce the lead time significantly and constructs a knowledge-based design environment. In hospitals, AI-based CAD is being implemented in a clinical practice along with a Picture Archiving and Communication System (PACS) to improve workflow [3]. AI integrated with a variety of technology is currently in great demand with respect to green manufacturing and sustainable development. [4].

Fig.1 shows how a traditional CAD system can be converted into an intelligent CAD system. Model-based Reasoning (MBR) is the process of merging AI into an CAD system .By using the quantitative and qualitative analysis, it predicts the interaction that could exist between different parts of the design [5].

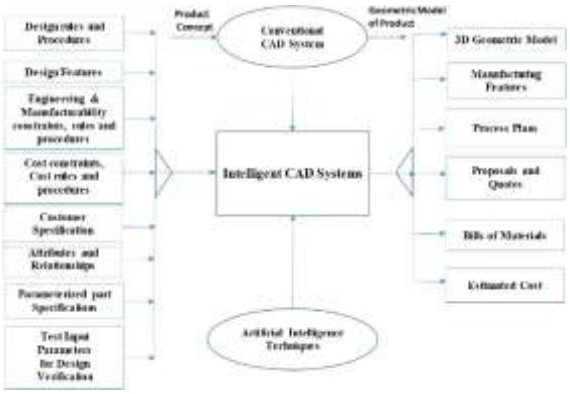


Fig1.-CAD into Intelligent CAD [6]

Some examples of AI integrated CAD software are-

- SOLIDWORKS-The owners of the software (Dassault Systems Company) introduced xDesign that uses AI as a tool to draw and extrude in engineering design works. In SOLIWORKS xDesign, operators can deploy different solutions to their design challenges instantaneously through cloud collaboration that are generated by AI tool. The operator first creates the model and specifies the constraints. After the required specifications are defined, SOLIDWORKS xDesign will generate the part instantly with the help of AI integrated within its system based on the defined constraints. [7].

- NETVIBES One Part- NETVIBES One Part is another example of an AI enabled design software introduced by Dassault Systems Company. The utility offers a simple application for reusing previously used components to save time. Operators can access 2D/3D related components in NETVIBES One Part with just a few clicks. [8].

- Artificial intelligence (AI) denoiser-Artificial intelligence Denoiser is an AI tool developed by NVIDIA that employs AI and machine learning to give users interactive feedback instantly so they can make better decisions. [9]. It creates noise-free images quickly using GPU-accelerated AI. The quickest and simplest picture visual rendering tool currently available is called AI Denoiser. [10].

- Generative Design-It is a space filling generative design technology (GDT) which combines a computer program and CAD for the creation of an innovative and original design.

IV. APPLICATIONS

Currently CAD consists of an array of engineering functions from simple drawings to 3D models. CAD integrated with AI makes the designing part a bit easier as AI takes the lead in integrating the engineering aspects as well as predict and perform tasks with its own intelligence. This is suitable for all designs-new design, innovative design or routine design. Here are some of the applications:

1. AI IN COMPUTER AIDED ART TEACHING

The most important part of the intelligent teaching is to test the learning effect of the learners and give suggestions accordingly in order to realize the intelligence of the learning system. The main functions are-

- Knowledge points are divided according to the teaching content and a database of learning elements is established

- The learning effect is evaluated based on the learning situation and the learning guidance and

International Journal of Advances in Engineering and Management (IJAEM)
Volume 5, Issue 4 April 2023, pp: 1874-1879 www.ijaem.net ISSN: 2395-5252

learning suggestions are further given in accordance to the learning effect.

- Different teaching content is chosen for different students and a collection of students response information in time is done, analyzed, and processed and the student's performance is judged off it.

- The intelligent teaching model mainly comprises of Knowledge base, Student Model, Teacher Model, and intelligent interface

Knowledge base comprises of Static and Dynamic Knowledge. Static Knowledge means the professional knowledge, assessment knowledge and teaching goals, process, and strategies. Professional Knowledge is the core of the knowledge base and it describes the teaching content and relationship between them. AI methods are used to convert the above knowledge into one that could be understood by the computers-this is called Knowledge Representation.

Dynamic knowledge is temporary knowledge generated during the operation of the system, which is the precondition for the further operation of the system, including the intermediate data obtained in the inference process, the intermediate result of the problem, and the record of theproblem-solving process. A good knowledge representation method can not only organize domain knowledge reasonably and effectively, but also provide information query for the system, but also help students establish clear conceptual relationships, establish knowledge structures, and improve problem-solving capabilities [11].

The Reasoning Mechanism is divided into 3 parts namely Forward Reasoning, Backward Reasoning and Two-way Reasoning.

Forward Reasoning is data driven as each production has a set of conditions on the left and a set of actions on the right. When the conditions are met, the production is activated and the actions are executed.

Backward Reasoning is goal driven and reverse of the forward reasoning. The basic principle is to set a target state and check whether the data base is currently there.

Two-Way Reasoning is also called mixed reasoning as it combines the strength of forward and backward reasoning as well as overcomes the shortcomings of both.

The inference engine comprises of 3 parts namely scheduler, executor and consistency coordinator. The inference model adopts different strategies in accordance to different knowledge bases. Scheduler oversees the whole reasoning process so that it can proceed in a set manner.

The executor acts on the actions selected by the scheduler and is also responsible for accessing the knowledge from the knowledge base and the information from the global blackboard.
The consistency of results is usually used in reverse reasoning.

2. AIRCRAFT COMPONENT DESIGNING

The application is based mainly on the development of a KBM(Knowledge-Based System) for the determination of manufacturing processes for some selective airframe components. The system enables the engineers to design the strongest yet the lightest wing possible at least cost.

The representation of the knowledge regarding material selection, manufacturing procedures, stiffener types and materials, fasteners and fundamental part configuration must be in a suitable manner in order for the KBS to operate effectively.. Domain knowledge is typically represented in the following ways: a KBS acts as a set of regulations. The frames used to define the items that appear within the rules are frequently combined with the rules themselves.

Knowledge-Based Engineering (KBE) can be considered as a subset of KBS and AI related technologies with its primary focus on the automation of CAD geometry creation, engineering analysis and support information generation. [12].

The system must function inside an integrated design environment in order to be helpful and show its functioning. One of the most crucial elements in building system acceptance and credibility will be system integration. Without the proper interface automation techniques, the system's intended functionality will not be visible. Figure 1 shows the suggested integrated design environment in which the KBS will be operational. Many different existing tools and codes will be implemented within the environment in order to perform the required product and process modelling and design trades. The success of the KBS is closely linked to the integrated design environment and without it the success would be restricted. [13].

International Journal of Advances in Engineering and Management (IJAEM)
Volume 5, Issue 4 April 2023, pp: 1874-1879 www.ijaem.net ISSN: 2395-5252

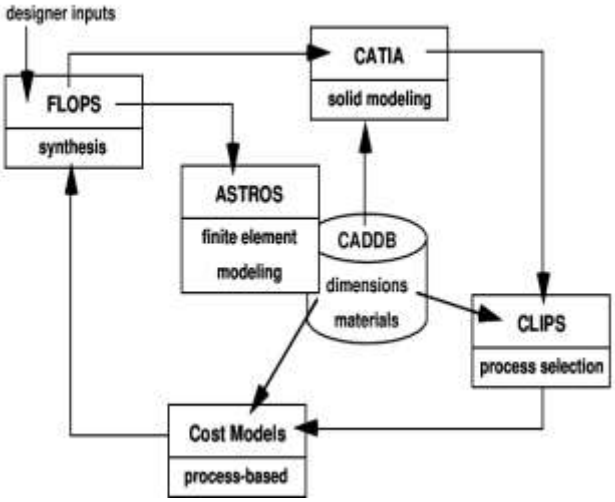


Fig.2-Integrated Design Environment [14]

3.EXTENDED REALITY (VR,AR AND MR)

Virtual Reality(VR) is a type of virtual simulation that enables the users the experience a virtual world of the system generated by a computer stimulation. VR is based on two characteristics- Immersion and Interaction.

Currently, VR is upgraded to use a variety of sensors (eye recognition, voice, gestures, and brain waves) and multi-dimensional information environment interaction, combined with interaction in the real world [15]. VR allows students to have a better understanding of the subject matter, especially when a visual representation of the real process is required [16]. In the health sector, virtual reality technology is being used to support procedural training, diagnosis, and to give virtual therapy in times of emergency [17]. In the health sector, virtual reality technology is being used to support procedural training, diagnosis, and to give virtual therapy in times of emergency [18].

AR also referred to as Augmented Reality. Its main goal is to have some sort of interaction between the virtual world on screen and the real world. Lai et al. (2020) [19], introduced a worker-centered system comprised of multi-modal AR instructions backed by a deep learning network for tool recognition to reduce time and error in an assembly operation. Their research states that the dataset was created using CAD tool models and displayed in a two-dimensional setting without the use of actual tool images.

At the University of Washington, Phillip Dunston and his team have presented the initial concept of AR CAD that can support construction and design [20]. In order to give good intuitive interaction with models created, the report claims that the AR CAD system integrates the AR helper viewer into regular CAD. [20]. The AR CAD system consists of computers for CAD modeling, running and viewing AR and head-mounted display with a camera attached to it.

MR also referred to as Mixed Reality is a step further in the development of VR. It's based on introducing the reality into the virtual world. MR will improve the sense of understanding for better understanding as it utilizes both virtual and real objects. Mixed Reality has 3 main features-

- Combination of virtual and reality
- In virtual 3D
- Real-time operation

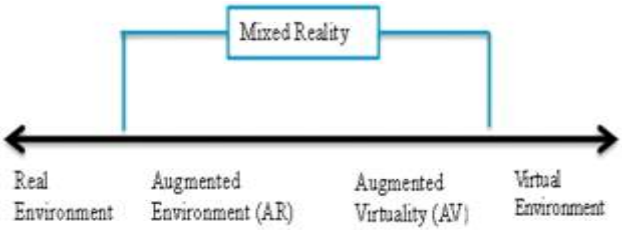


Fig.3-Relationship between VR, AR and MR [21]

International Journal of Advances in Engineering and Management (IJAEM)
Volume 5, Issue 4 April 2023, pp: 1874-1879 www.ijaem.net ISSN: 2395-5252

4. AI AIDED ARCHITECTURAL DESIGN

Numerous artificial intelligence approaches are distinguishable in design process varying from low-autonomy to swarm intelligence and neural networks which are capable of achieving high levels of autonomy.

There are 2 main models of AI- Subsymbolic System and Symbolic System. The Subsymbolic systems give their creators a higher level of control since they are created in a form of algorithms whose parameters need to be analyzed strictly in hierarchical way making them less autonomous.

Symbolic System is a set of autonomous design processes that work in a non-hierarchical way. However, this system offers a high freedom of choice in the achieved result having different levels of computation.

Evolutionary Algorithms- They are a set of algorithms inspired by some basic biological phenomenon such as reproduction, mutation, recombination, and selection. Genetic algorithms (Mitchell, 1996) are the most popular variety of multi-criteria optimization techniques in the field of evolutionary computing. Consequently, they are developing the topic that architects, designers, and artists are interested in. Since the middle of the 1990s, the potential applications of evolutionary algorithms in the field of architectural design have been researched as a means of producing answers to issues whose structures could not be easily grasped.

Swarm Intelligence- From a mathematical perspective, it is an emergent behavior that develops from a straightforward set of rules and is created by self-moving entities without the aid of outside coordination. Due to the availability of numerous design software tools based on the boids library, virtual control of swarm behavior and its potential applications became a significant topic in modern generative design.

The development of automated design systems enhanced conceptual thought's potential and involvement in the design process. Soon one can expect digital artificial intelligence aided designer's assistant, which concept can
be based on the existing system, taking a primitive forms nowadays, which learn our behavior and patterns of thinking- recently introduced personal assistants such as Siri or Alex, help us find best possible way to solve our problem or suggest other solutions on their own [22].

V. FUTURE PROSPECT AND CHALLENGES

AI embedded with CAD makes the automation process much easier and more effective for the engineers. As discussed above, AI has already found applications in major sectors and will continue to thrive in the future because of the principle it works upon. AI will play a major role not only in design but also other fields as technology continues to grow. However, designs are based on human's subjective thoughts and emotions which can never be replaced by AI completely no matter how much it goes on to develop.

Although AI is bound to make huge strides in design, it will still require the human thoughts and emotions to produce the best and most effective designs.

VI. CONCLUSION

This paper was successfully able to review different applications of AI integrated with CAD along with their methodologies/principles involved. Additionally, various integrated software was discussed, as well as how AI and CAD are combined. Prospects for AI in design are promising because the field has already started off on the right foot and will only get stronger from here, the only problem being that they can never completely replace human thoughts and emotions.

REFERENCES

[1]. https://www.indiacadworks.com/blog/applications-of-artificial-intelligence-in-cad-technology/
[2]. https://www.sciencedirect.com/topics/computer-science/model-based-reasoning
[3]. M.I. Fazal, M.E. Patel, J. Tye, Y. Gupta The past, present and future role of artificial intelligence in imaging Eur. J. Radiol., 105 (2018), pp. 246-250
[4]. R. Cioffi, M. Travaglioni, G. Piscitelli, A. Petrillo, F. De Felice Artificial intelligence and machine learning applications in smart production: progress, trends, and directions Sustainability, 12 (2) (2020), p. 492
[5]. S. Khan, M.J. Awan A generative design technique for exploring shape variations Adv. Eng. Inf., 38 (2018), pp. 712-724
[6]. X.F. Zha Artificial intelligence and integrated intelligent systems in product design and development Intelligent Knowledge-Based

Systems, Springer, Boston, MA (2005), pp. 1067-1123

[7]. B. Duan Analysis on the value of 3D printing in jewelry design based on artificial intelligence Journal of Physics: Conference Series, vol. 1744, IOP Publishing (2021, February), Article 42132

[8]. M. P. Dimitrov and S. I. Antonov, "APPLICATION OF ARTIFICIAL INTELLIGENCE AND MA- CHINE LEARNING IN CAD/CAM SYSTEMS," pp. 531–553.

[9]. G. Soares, J.M. Pereira Lift: an Educational Interactive Stochastic Ray Tracing Framework with AI-Accelerated Denoiser (2021)

[10]. M. P. Dimitrov and S. I. Antonov, "APPLICATION OF ARTIFICIAL INTELLIGENCE AND MA- CHINE LEARNING IN CAD/CAM SYSTEMS," pp. 531–553.

[11]. http://cad-journal.net/files/vol_18/CAD_18(S4)_2021_118-129.pdf

[12]. Warburton, L. M. and Glatfelter, J. W., "Development and Utilization of a KnowledgeBased (KB) Environment on a Production Helicopter Program", presented at the American Helicopter Society Vertical Lift Aircraft Design Conference, San Francisco, CA, January 1995.

[13]. https://smartech.gatech.edu/bitstream/handle/1853/6415/ICES-95-B6-3.pdf

[14]. https://www.researchgate.net/figure/Integrated-Design-Environment-The-system-executive-scripts-will-be-coded-using-the_fig1_27523276

[15]. N.K. Sankaran, H.J. Nisar, J. Zhang, K. Formella, J. Amos, L.T. Barker, …, T. Kesavadas Efficacy study on interactive mixed reality (IMR) software with sepsis prevention medical education 2019 IEEE Conference on Virtual Reality and 3D User Interfaces (VR), IEEE (2019, March), pp. 664-670

[16]. Jun Luo, Hongjie Zhu Teaching Reform and Exploration of PLC Programmable Control Technology Course [J] vol. 10, Western China Quality Education (2016), pp. 37-39

[17]. Y.M. Tang, G.W.Y. Ng, N.H. Chia, E.H.K. So, C.H. Wu, W.H. IpApplication of virtual reality (VR) technology for medical practitioners in type and screen (T&S) training J. Comput. Assist. Learn., 37 (2) (2021), pp. 359-369

[18]. C.G. Oh, K. Lee, M. Oh Integrating the first person view and the third person view using a connected VR-MR system for pilot training J. Aviat. Aerosp. Edu. Res., 30 (1) (2021), pp. 21-40

[19]. Z.H. Lai, W. Tao, M.C. Leu, Z. Yin Smart augmented reality instructional system for mechanical assembly towards worker-centered intelligent manufacturing J. Manuf. Syst., 55 (2020), pp. 69-81

[20]. P.E.C.T. Team Augmented Reality Computer-Aided Drawing (AR-CAD). 1–6 (2007).

[21]. https://ars.els-cdn.com/content/image/1-s2.0-S2590123022001487-gr4_lrg.jpg

[22]. Jan Cudzik1 , Kacper Radziszewski2 1,2Gdansk University of Technology

[23]. Make sure to remove all placeholder and explanatory text from the template when you add your own text. This text should not be here in the final version

Physics Education

PAPER

Algorithm based determination of the Planck's constant

To cite this article: Smita Korpal *et al* 2023 *Phys. Educ.* **58** 045003

View the article online for updates and enhancements.

This content was downloaded from IP address 14.139.251.98 on 29/05/2023 at 06:55

PAPER

Phys. Educ. **58** (2023) 045003 (8pp) iopscience.org/ped

Algorithm based determination of the Planck's constant

Smita Korpal[1], Anmol Aggarwal[2], Ajay Kumar Arora[1], Jyoti Anand[1], Maya Verma[3] and Divya Haridas[1,*]

[1] Keshav Mahavidyalaya, University of Delhi, New Delhi 110034, India
[2] Delhi Technological University, New Delhi 110042, India
[3] Hansraj College, University of Delhi, Delhi 110007, India

E-mail: divyaharidas@keshav.du.ac.in

Abstract

In this paper we report a novel method for determining the Planck's constant experimentally. We have determined the Planck's constant using light emitting diodes (LEDs) of four different colours (Red, Green, Yellow and Blue) with the aid of a python programming. The LEDs were not provided with a specific wavelength value, and they could have any arbitrary wavelength in their respective colour bands. We determined the wavelengths of the LED lights using a Python program and calculated the value of the Planck's constant using them. The value obtained was compared with the Planck's constant value determined using a traditional method being followed in undergraduate labs and its actual value. The relative error while reporting the value of Planck's constant using traditional method was around 18% which was reduced to 6% by using the method reported in the present study.

Keywords: Planck's constant, LEDs, Python programming

1. Introduction

The advent of quantum physics brought a revolution to the understanding of physics. According to this branch of physics, energy and many physical quantities are quantized in terms of Planck's constant. Many branches of physics gradually emerged which made Planck's constant (h) an important universal constant [1]. It is named after the German theoretical physicist, 'Max Planck' who initially derived the Planck's constant in an attempt to explain the black body radiation. Later, when Albert Einstein explained the photoelectric effect using the Planck's constant, many physicists started making efforts to measure the Planck's constant experimentally [1]. Millikan was one of the pioneers to give experimental value of 'h' with his photoelectric effect experiment. The use of Planck's constant in numerous domains of Physics emphasizes its importance for learners to accurately determine its value experimentally. Several experiments were designed to obtain the accurate value of Planck's constant [1] and a continuous endeavour is going onto achieve this accuracy experimentally. Nevertheless, this makes the study of the experiment to determine

* Author to whom any correspondence should be addressed.

 © 2023 IOP Publishing Ltd

Table 1. Associated wavelengths of the LEDs [13].

Colour of the LED	Wavelength (minimum) (nm)	Wavelength (maximum) (nm)
Red	676	732
Orange	645	696
Yellow	611	663
Green	493	578
Blue	419	536

the Planck's constant as one of the vital experiments taught at undergraduate level owing to its contribution in the growth of Physics and exploring many new areas.

There are numerous methods to determine the Planck's constant [2–13]. In the undergraduate laboratories the Planck's constant is experimentally calculated using light emitting diode (LEDs) of different colours. LED with features like being compact, cheap, easily available, with little or no maintenance and easily replaceable makes it more popular choice for studying this experiment at undergraduate level to determine '*h*'. First the turn on voltage of the LEDs is determined using their respective *I*–*V* curves. Then a graph is plotted between turn on voltage on the *y*-axis and the inverse of their respective wavelengths on the *x*-axis. The slope of the second plot is computed to calculate the value of Planck's constant.

The LEDs used for this experiment are usually of normal quality which can be easily procured from local market. Hence, standard wavelength value is unknown for these LEDs and the wavelength is estimated from a predetermined set of wavelength range for the colours emitted by the respective LEDs, as reported by C. Cziproket al. [13]. The range of wavelength of different colours emitted by LED is presented in table 1.

Calculating the value of Planck's constant using the wavelengths as mentioned in table 1 bears a huge drawback of estimating the exact value of wavelength emitted by the LEDs. One can randomly choose any value of wavelength for LED of a specific colour from the respective ranges mentioned in table 1. This can increase the error in determining the value of the Planck's constant experimentally. So it is of utmost importance that the accurate wavelength of the light emitted by the LEDs must be known before starting the experiment. Zhou *et al* calculated the Planck's constant using five LEDs which are provided with nominal wavelength values where the actual peak wavelength could be within ± 5 nm from the nominal wavelength [12]. The reported values of Planck's constant varied from 5.77×10^{-34} to 7.67×10^{-34} for the five LEDs. The emission spectrum width accounts for this observed variation in the value of '*h*'. Hence, Zhou *et al* have suggested refraining from using such nominal wavelength values for calculating the Planck's constant [12]. Instead, one should measure the wavelength of light emitted by the respective LEDs in the experiment to accurately determine the Planck's constant.

Mosiori *et al* and Eagan [4, 14] used a spectrophotometer to find the wavelength of the light being emitted by the LEDs and used these values to experimentally find the Planck's constant. Nieves *et al* [10] used a monochromator to determine the respective wavelengths of the light emitted by the LEDs. But such devices are quite expensive to be made available at the undergraduate laboratories. Even when Nieves *et al* [10] used a monochromator and Eagan [14] used a spectrophotometer for determining the wavelength of light emitted by the LEDs and determined the Planck's constant using these values, they reported a relative error of 10% and 6.7% respectively.

In the present study, initially we performed the experiment using the existing method which are usually used in undergraduate laboratories. For this, simple LEDs of four different colours were chosen which are readily available in any local market. The value of Planck's constant was evaluated with a relative error of 18%. To improve the results, we have determined the wavelength of the light emitted by the respective LEDs using a digital spectrometer. Planck's constant was reported with a relative error of 8%. The error is now reduced below 10% but to get this result we need

a digital spectrometer which is not readily available in introductory physics lab. So in the present study we proposed to use our algorithm to find the values of wavelength emitted by the respective LEDs. It was observed that using those values of wavelength we were able to find the value of Planck's constant with a relative error of 6%.

2. Experimental setup

Our experimental setup for determining the Planck's constant through LEDs is very simple. We use a digital voltmeter for measuring the potential, an ammeter to measure the respective current, a DC power supply with variable voltage (0–32 V), four LEDs (Red, Green, Blue and Yellow), a breadboard (for easily connecting the LEDs in the circuit) and some connecting wires. Figure 1 shows the schematic of the circuit diagram for the experimental setup.

The LEDs were used on the basis of the colour of the emitted light but did not have any predefined wavelength. These types of LEDs are quite cheap and easily available.

3. Formula used

LED is essentially a semiconductor P–N junction diode which emits photons when an external potential is applied across its two junctions in forward bias mode. The electrons from the conduction band of the n type material flow across the junction to the conduction band of the p type material. These excited electrons recombine with a hole (in the valence band of the p type material) to emit photons with energy approximately equal to the band gap energy. If V_{o} is the minimum voltage required for the emission of light we can write

$$eV_{\mathrm{o}} = h\nu + NR \tag{1}$$

where NR is the energy lost in non-radiative recombination which is usually very less than $h\nu$. So, NR can be neglected in the above equation and we can write

$$eV_{\mathrm{o}} = h\nu. \tag{2}$$

The energy of the photon emitted by the LED is given as $h\nu$,

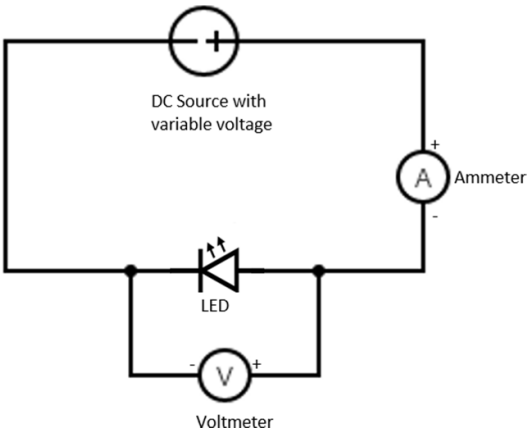


Figure 1. Circuit diagram of the experiment.

$$E = h\nu = h\frac{c}{\lambda} \tag{3}$$

where ν is the frequency of the electromagnetic wave, c is the speed of light ($=2.9979 \times 10^8$ m s^{-1}) and λ is the wavelength of the radiation emitted by the LED.

Equating both the equations (2) and (3), we can write

$$eV_o = h\frac{c}{\lambda}. \tag{4}$$

Hence Planck's constant can be evaluated from equation (4).

4. Experimental procedure

The experiment was performed in a dark room, so that even the smallest glow in the LED lights can be detected by a naked eye.

1. Make the connections as shown in figure 1. A variable power supply can be used or a rheostat can be used as a potential divider across a fixed supply of 5 V DC to change the voltage across the LED in required small steps.
2. Connect the first LED in the circuit.
3. Increase the input voltage from zero volt in small steps. The voltmeter will measure the voltage (V) across the LED and the ammeter will measure the current (I) flowing in the circuit.
4. Note down the reading of the voltage and current.

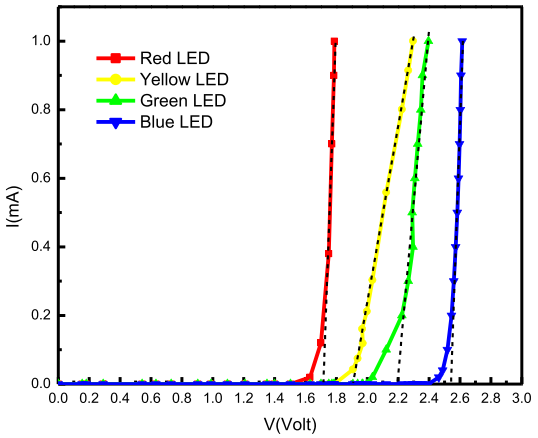


Figure 2. Plot of *I*–*V* characteristics for the four LEDs.

5. Draw a graph with the voltage (in volt) along the *x*-axis and current (in mA) along the *y*-axis.
6. Note down the turn on voltage V_o by extrapolating the linear portion of the curve. The turn on voltage or threshold voltage is the minimum voltage at which the LED begins to glow. Note the colour of the light emitted.
7. Repeat steps 3, 4, 5 and 6 for LED of different colour and note down their respective turn on voltage for the respective LED.

Figure 2 shows the *I*–*V* curve for the four different colours of LEDs. The linear portion of the curve was extrapolated to find its intercept on the *x*-axis, which gives the turn on voltage (V_o) for the respective LEDs [15]. Even though the experiment is done in a complete dark room but we have avoided finding turn on voltage just by looking at the diode. This may cause error as it would be difficult to find the voltage at which LED just begins to glow. Ten different LEDs of each colour were used to perform the experiment to find the turn on voltage.

Table 2 gives the turn on voltage for each LED.

The respective wavelengths selected for the LEDs are listed in table 3. These values have been obtained from the practical books used in undergraduate lab classes that mention the maximum wavelength of light emitted by various LEDs. The maximum wavelength corresponds to the turn on voltage V_o.

Table 2. Turn on voltage for the LEDs.

Colour of the LED	Turn on voltage V_o (V)[4]
Red	1.71 ± 0.02
Yellow	1.90 ± 0.19
Green	2.19 ± 0.03
Blue	2.54 ± 0.02

Table 3. Wavelength of the light emitted by the LEDs.

Colour of the LED	Wavelength used (nm)
Red	695
Yellow	590
Green	570
Blue	472

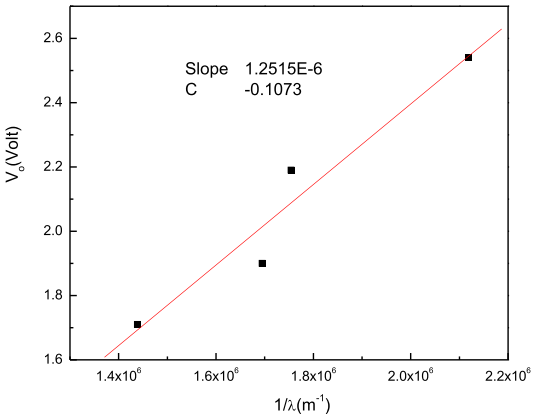


Figure 3. Plot of $(1/\lambda)$ and the respective turn on voltage for the LEDs.

After the calculation of turn on voltages and the wavelengths of the respective LEDs, a best fit graph was drawn between the inverse of wavelengths $(1/\lambda)$ and their respective turn on voltage (V_o) for the four LEDs as shown in figure 3. The method of linear regression determines the parameters of the straight line, which better covers the experimental points.

The slope of the above graph is equal to hc/e, where c is the speed of light and e is the charge of an electron.

[4] value taken from spreadsheet.

Table 4. Wavelength of the light emitted by the LEDs.

Colour of the LED	Wavelength (nm)
Red	639.12
Yellow	588.63
Green	536.72
Blue	457.10

Then, Planck's constant h is calculated using equation (5)

$$h = \frac{e}{c} \times slope \tag{5}$$

where,

$$e = 1.6022 \times 10^{-19}\mathrm{C}$$

$$c = 2.998 \times 10^{8}\,\mathrm{m\,s^{-1}}.$$

We obtained the value[5] of slope as 1.2515×10^{-6} Vm with an error of 0.2237×10^{-6} Vm leading to the value of $h = 6.688\ (\pm 1.196) \times 10^{-34}$ J s corresponding to a relative error of 18%. The result for h is to be compared with the handbook value 6.626×10^{-34} J s.

Since the values of wavelength mentioned in table 3 are general values so it was decided to find the wavelength of the light emitted by the LEDs used in the present study using spectrometer. USB4000 spectrometer was used to get the spectra of all four LEDs. The transmittance spectra of Red LED, Yellow LED, Green LED and blue LED are given in the supplementary material for reference.

The wavelengths of the emitted light of the respective LEDs as determined by the spectrometer are mentioned in the table 4. When the relative intensity is maximum, the excitation current flowing through the LED corresponds to the forward voltage V_f [10]. This applied voltage corresponds precisely with the excitation energy of the gap of the LED, which thus emits light with a characteristic wavelength. The forward voltage is related to the energy gap by $E_g = eV_f$ [10]. Since $E_g = h\nu$ and $h\nu = eV_o$ (from equation (2)) so forward voltage V_f is considered for turn on voltage/cut off potential.

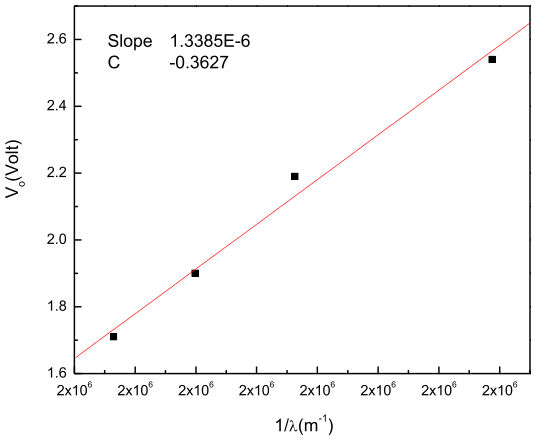


Figure 4. Plot of $(1/\lambda)$ and the respective turn on voltage for the LEDs.

Now again a best fit graph was drawn between the inverse of wavelengths $(1/\lambda)$ and their respective turn on voltage (V_o) for the four LEDs as shown in figure 4.

The value[6] of slope obtained from the figure 4 is 1.3385×10^{-6} V m with an error of 1.04172×10^{-7} V m leading to the value of $h = 7.154\ (\pm 0.556) \times 10^{-34}$ J s corresponding to a relative error of 8% Indelicato *et al* had also used a digital spectrometer to record the emission spectrum of four different coloured LEDs. It was reported that the value of Planck's constant varied up to 10% when the centroid of the wavelength distribution was used or a peak (maximum intensity) in the wavelength distribution was used [16]. This probably explains the relative error of 8% in our study when we used the spectrometer to get the value of wavelength emitted by the LEDs.

The error is now reduced below 10% but to get this result we need a digital spectrometer which is not readily available in introductory physics lab. So in the present study we proposed to use our algorithm to find the values of wavelength emitted by the respective LEDs. Hence, a python program based on the proposed algorithm was used to evaluate the accurate value of the respective wavelengths of light being emitted by the LEDs.

[5] value taken from spreadsheet for convenience.

[6] value taken from spreadsheet for convenience.

5. The algorithm to calculate the wavelength

The following algorithm uses the RGB values from the digital image of the LEDs as an argument and determines their wavelength. The algorithm which was implemented in Python 3 is as follows: -

i. START.
ii. Call the function 'sector' with R, G and B values as the arguments.
iii. Print the value returned by sector. The returned value is the wavelength of light being emitted/reflected from the source/object.
iv. STOP.

The algorithm of the function sector:

i. Receive the arguments in the variables R, G and B.
ii. If R = G or G = B or R = B return 'Sector cannot be determined'.
iii. Identify the highest, second largest and lowest value among R, G and B.
iv. Select a sector from the six sectors based on highest and second highest values in RGB triplet.
v. Assign values to the variables sign1, sign2, sign3, sR, sG, sB, first, last, mid and base for the sector selected in 'step 4'. These values are assigned on the basis of the behaviour of the RGB colour model in the selected sector. The value for the base variable is a wavelength of light whose RGB value is known.
vi. Alter the values of the variables R, G and B according to their effect in the selected sector.
vii. Divide R, G and B by 255.
viii. If mid-last <10 return 'No Wavelength', else go to 'step 9'.
ix. Return a function call to 'RGB_to_wavelength' with the arguments R, G, B. sign1, sign2, sign3, sR, sG, sB and base.

The algorithm of the function RGB_to_wavelength:

i. Receive the arguments in the variables R, G, B. sign1, sign2, sign3, sR, sG, sB and base.
ii. Multiply sign1, sR and R and assign this to the variable *R*_eff, multiply sign2, sG and G and assign it to the variable *G*_eff and multiply sign3, sB and B and assign it to the variable *B*_eff.
iii. Add *R*_eff, *G*_eff and *B*_eff and assign it to the variable total_eff.
iv. Return the sum of the variables total_eff and base.

Essential conditions for the proposed algorithm

- There should be a highest, a second highest and a lowest value in an RGB triplet being fed to the function 'sector'.
- There should be a difference of at least ten in the second highest and lowest value of the RGB triplet.

As the light being reflected by an object contains many wavelengths it becomes important to identify the most dominant, second dominant and all the other wavelengths in the order of decreasing dominance to find what exactly will be the colour perceived of the object. The same is also required while calculating the wavelength of that light which is reflected from an object using the RGB values of its digital image. So, the first condition is applied. The second condition is used to minimize duplicate values, because if the values of any two RGB triplets are very close to each other, then our program might return very similar results for some of them.

To determine the wavelength of the light being emitted by the LEDs, the LEDs were first brightly lit in a dark room and their images were captured using a simple mobile phone camera. The mobile phone camera that was used to obtain the images of the LEDs is a simple camera without the use of any effects or filters. They were then transferred to a computer system, and the RGB values of their pixels were found using Microsoft Paint software. The above-mentioned algorithm was then used to find their respective wavelengths. The mobile phone camera has no role in actually calculating the wavelengths of the respective LEDs. Although a better camera will allow us to capture better data for the algorithm, but our algorithm is not entirely dependent upon

Table 5. Wavelengths of LED lights determined using the computer algorithm.

Colour of the LED	$\lambda 1$ (nm)	$\lambda 2$ (nm)	$\lambda 3$ (nm)	$\lambda 4$ (nm)	$\lambda 5$ (nm)	$\lambda 6$ (nm)	$\lambda 7$ (nm)	$\lambda 8$ (nm)	$\lambda 9$ (nm)	$\lambda 10$ (nm)	Mean λ (nm)	Standard Deviation (nm)
Red	667.6	665.4	667.9	666.1	670.2	665.5	668.3	669.0	666.9	665.8	667.3	1.6
Yellow	584.9	584.9	584.9	584.9	584.9	584.9	584.9	584.9	584.9	584.9	585.0	0.4
Green	528.2	530.1	526.8	525.9	532.6	527.2	526.1	526.6	533.5	529.0	528.6	2.7
Blue	453.9	455.4	453.9	451.6	453.4	451.6	455.2	455.3	451.4	454.9	453.6	1.6

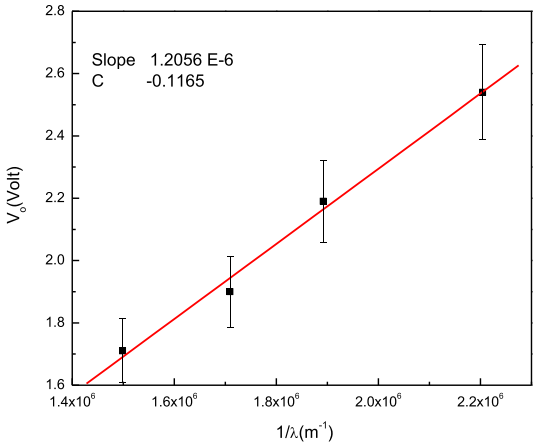


Figure 5. Plot of $(1/\lambda)$ determined by the python program versus the respective turn on voltage for the LEDs.

the camera and hence it can be used with the images obtained using any digital camera.

Ten different sets of wavelength readings for each coloured LED were taken. The calculated wavelengths for the respective LEDs are presented in table 5. The mean value of wavelength for each LED along with standard deviation is also given in table 5.

The mean wavelengths presented in table 5 were used further to calculate the Planck's constant.

Figure 5 shows the variation between the turn on voltage and $(1/\lambda)$, where the wavelength has been determined from python programming as mentioned above. For each measurement the error is shown by the corresponding error bars.

The value[7] of slope obtained from the figure 5 is 1.2056×10^{-6} Volt meter with an error of 7.49405×10^{-8} Volt meter leading to the value of $h = 6.443\ (\pm 0.399) \times 10^{-34}$ J s corresponding to a relative error of 6%. This value was compared with the standard value of Planck's constant which is 6.62607×10^{-34} J s. Hence, the Planck's constant was determined with accuracy by this method. Though we are still unable to find the accurate value of Planck's constant with a relative error less than 5%, this may be due to issues such as the non consideration of energy lost due to non radiative recombination and other issues as reported by Zollman and Bearden [15]. However, we are still able to find an accurate value of Planck's constant in comparison to the one which is currently been done in physics laboratory class.

[7] value taken from spreadsheet for convenience.

6. Conclusion

In the present study, the value of Planck's constant is determined by using LEDs of four different colours with the aid of python program. This work deploys normal LEDs easily available in local market. Initially an approximate value of wavelength of light emitted by respective LED is taken and the value of Planck's constant is calculated and reported with a relative error of 18%. However, the error was reduced to 8% when the wavelength of the light emitted by the respective LEDs is obtained from a digital spectrometer. Since a digital spectrometer is not readily available in introductory physics lab so we proposed an algorithm to find the value of wavelength. The mean value of ten wavelengths calculated from the python programming were used to calculate Planck's constant. The Planck's constant using the proposed method was reported with a relative error of 6%. Though, we are still unable to find the accurate value of Planck's constant with a relative error less than 5%. However, we are able to find an accurate value of Planck's

constant in comparison to the method which is currently been done in physics laboratory class. The above method of using python programming can be readily incorporated in undergraduate labs as it does not require expensive devices such as a monochromator or a spectrometer. Also, any LED that is available in the local market whose wavelength is not predetermined can be used easily. Hence, this method is simple, accurate and cost effective to determine the Planck's constant, the speed of light or the charge of an electron experimentally at the Undergraduate level for better understanding.

Data availability statement

All data that support the findings of this study are included within the article (and any supplementary files).

ORCID iDs

Anmol Aggarwal https://orcid.org/0000-0003-3666-8873
Maya Verma https://orcid.org/0000-0002-0296-3631
Divya Haridas https://orcid.org/0000-0003-3392-2055

Received 17 September 2022, in final form 14 April 2023
Accepted for publication 5 May 2023
https://doi.org/10.1088/1361-6552/acd31c

References

[1] Steiner R 2013 History and progress on accurate measurements of the Planck constant *Rep. Prog. Phys.* **76** 016101
[2] Bileska M 2020 Measuring Planck's constant using light emitting diodes *J. Phys. Astron.* **8** 198–212
[3] Pili U and Violanda R 2019 Smartphone-based measurement of the Planck's constant with light emitting diodes *Phys. Educ.* **54** 023007
[4] Mosiori C O, Oeba D A and Shikambe R 2017 Determination of Planck's constant using light emitting diodes *Path Sci.* **3** 2007–12
[5] Nemoto K 2004 Experiment for measuring Planck's constant using eight colored LEDs *Proc. of the Int. Conf. on Physics Education in Cultural Contexts* (*Cheongwon, South Korea, 13 – 17 August 2001)* pp 409–15
[6] Checchetti A and Fantini A 2015 Experimental determination of Planck's constant using light emitting diodes (LEDs) and photoelectric effect *World J. Chem. Educ.* **3** 87–92
[7] O'Connor P J and O'Connor L R 1974 Measuring Planck's constant using a light emitting diode *Phys. Teach.* **12** 423–5
[8] Jewett J W Jr 1991 Get the LED out *Phys. Teach.* **29** 530–4
[9] Holcomb D F 1997 Apparatus for LED measurement of Planck's constant *Phys. Teach.* **35** 261
[10] Nieves L, Spavieri G, Fernandez B and Guevara R A 1997 Measuring the Planck constant with LED's *Phys. Teach.* **35** 108–9
[11] Garver W P 2006 The photoelectric effect using LEDs as light sources *Phys. Teach.* **44** 272–5
[12] Zhou F and Cloninger T 2008 Computer-based experiment for determining Planck's constant using LEDs *Phys. Teach.* **46** 413–5
[13] Cziprok C and Popescu F F 2016 Using the Vee heuristic in laboratory classroom for teaching and learning physics of photonic devices *Roman. Rep. Phys.* **68** 879–90
[14] Eagan R 2011 *Experimental Determination of Planck's Constant* (University Park, PA: The Pennsylvania State University)
[15] Zollman D and Bearden I 2020 Determining Planck's constant with LEDs—what could possibly go wrong? vol 55 pp 1–4
[16] Indelicato V, La Rocca P, Riggi F, Santagati G and Zappala G 2013 Analysis of LED data for the measurement of Planck's constant in the undergraduate laboratory vol 34 pp 819–30

2023 6th International Conference on Information Systems and Computer Networks (ISCON)
GLA University, Mathura, India. Mar 3-4, 2023

2023 6th International Conference on Information Systems and Computer Networks (ISCON) | 979-8-3503-4696-1/23/$31.00 ©2023 IEEE | DOI: 10.1109/ISCON57294.2023.10112037

An In-Silico Comparison Of Ginsenoside's Anticancer Activity Against The Son Of Sevenless Homolog 1.

Anjali Sinha
Department of Biotechnology
Delhi Technological University
Delhi, 110042
anjalisinha.official@gmail.com

Bharmjeet
Department of Biotechnology
Delhi Technological University
Delhi, 110042
bharmjeetsingh1@gmail.com

Dr. Asmita Das
Department of Biotechnology
Delhi Technological University
Delhi, 110042
asmitadas1710@dce.ac.in

***Abstract* - The roots of *Panax notoginseng* (Sanqi) or ginseng contain bioactive saponins called ginsenosides. Ginseng has been extensively studied for its therapeutic potential, and ginsenosides, are involved in modulating multiple bioactivities in cancer. Ginsenosides have been extensively researched and emphasized in cancer chemoprevention and therapy. However, its mechanism of action is not well known. According to research, ginsenosides interact with many proteins involved in the epidermal growth factor receptor (EGFR) signaling pathway. This pathway includes various proteins that transduce the signals to the nucleus and is responsible for cell proliferation, survival, angiogenesis, and differentiation. In our study, we tried to elucidate the role of ginsenosides in inhibiting SOS protein homolog 1 - KRAS interaction and hence EGFR signaling. The anticancer activity of ginsenoside compounds was studied using various bioinformatics software, tools, and web servers, as well as the molecular docking process. The current in silico study takes into account 20 ginsenosides and employs dock scores; Rc has the lowest energy score of -11.56 kcal/mol but the lowest applicability score for individuals, whereas F1, Rh2+, compound K, and Rh1 have higher dock scores of -8.93, -8.88, -8.44, and -8.38 respectively, but higher applicability scores ascertained from admetSAR. This suggests that we can use only F1, Rh2+, compound K, and Rh1 for druggability purposes.**

Keywords- Ginsenoside, Molecular docking, Cancer, admetSAR, SOS1

I. INTRODUCTION

Cancer continues to be a disease of concern, with the second-highest mortality rate after CVDs. Even though cancer cases are rising globally, no viable medication that can stop the spread of cancer is available as of now. Surgical resection, radiotherapy, chemotherapy, and immunotherapy are some of the treatment options available today [1], but each one has its disadvantages and advantages. Therefore, it is crucial to create innovative medicines that may specifically kill cancer cells without endangering healthy cells.

The therapeutic value of natural products in the management of many ailments has long been acknowledged. For millennia, East Asian nations have utilized ginseng roots extensively as a natural tonic [2]. Ginsenosides, the main active components, have a range of pharmacological effects, including anti-inflammatory, antioxidant, and anticancer properties [3]. The anticancer action of ginsenosides incorporates approximately 14 criteria, which are now the hallmarks of the disease [4]. Fig. 1 summarizes comprehensive information about the anticancer effects of ginsenosides.

Previous studies have explored the potential of ginsenosides as a therapeutic intervention for different cancer types.

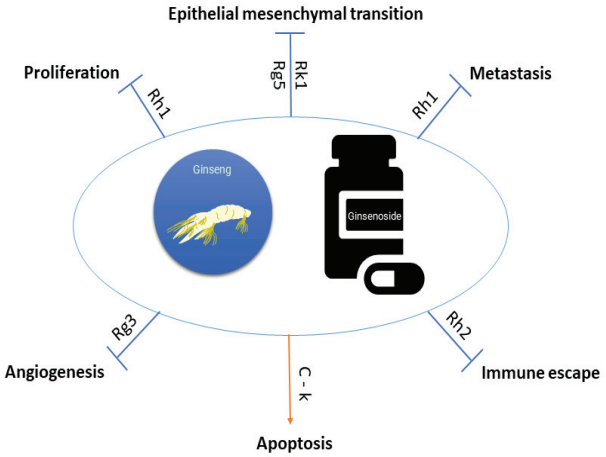


Fig. 1. The anticancer effects of ginsenosides

These studies have sought to determine the effectiveness and safety of ginsenosides as a cancer therapy option and to gain a better understanding of their mechanisms of action in cancer cells. Past investigations have shown that ginsenoside Rg5 can inhibit the growth of breast cancer cells in vivo by inducing apoptosis and autophagy and blocking the PI3K/Akt signaling pathway [5]. Ginsenoside Rh4 has been discovered to be extremely successful in treating colorectal cancer with little toxicity and few side effects. It does this by switching on the ROS/JNK/p53 pathway, which in turn sets off apoptosis and autophagic cell death, thus inhibiting the growth of colorectal tumors [6]. In both in vivo and in vitro experiments in hepatocellular carcinoma, ginsenoside Rg3 therapy dramatically reduces the expression of EGF, EGFR, phosphorylated ERK1/2, and HIF-1[7]. Ginsenoside Rg3 has been discovered to have inhibitory effects on the migration and invasion of nasopharyngeal cancer [8]. The involvement of ginsenosides in the intricate process of tumor progression

Authorized licensed use limited to: DELHI TECHNICAL UNIV. Downloaded on May 11,2023 at 10:12:24 UTC from IEEE Xplore. Restrictions apply.

encompasses multiple aspects such as proliferation, apoptosis, migration, angiogenesis, and immunogenicity of the tumor [9]. Several research has looked at how ginsenosides affect the EGFR signaling pathway and have found that 20(S)-protopanaxadiol (PPD), a significant active compound found in *Panax ginseng*, was observed to decrease EGFR phosphorylation and suppress the activation of downstream pathways. Inducing apoptosis and stopping the cell cycle in the G0/1 phase has the effect of decreasing cell growth [10]. We are aware of no other studies that have used ginsenoside to target SOS protein in the EGFR signaling pathway.

It is worth noting that EGFR is dysregulated or overexpressed in a variety of solid tumors, rendering it a promising target for anticancer therapy. EGFR signaling leads to cell proliferation and migration [11]**.** Upon binding to a ligand, EGFR undergoes dimerization, and subsequently by transferring the phosphate group from ATP, the tyrosine residue gets phosphorylated. This phosphorylated tyrosine acts as a docking site for various proteins, which in turn activate downstream signaling pathways [12].

Here we have compared the binding affinities of different ginsenosides with the SOS1 homolog protein, which is a mediator in signal transduction from GRB2 to Ras protein. Our results could help further research to discover a potent anticancer drug.

II. METHODOLOGY

A. *Data collection*

A list of all ginsenoside compounds was curated through literature that had potential anti-tumor activity. These compounds were then screened for their ability to directly or indirectly affect cell proliferation at the target site via a literature review. The SDF structures for all these compounds were downloaded from the PubChem database. The SOS1 homolog structure was also downloaded from the PDB database (PDB Id - 7UKS).

B. *Preparation of target and ligand*

For carrying out the docking of oncoprotein and shortlisted compounds, the oncoprotein SOS (target) was prepared using BIOVIA Discovery Studio. It was done by removing heteroatoms, water molecules, and ligand groups from the PDB structure of the target. The structure was then saved in PDB format. The SDF structures of ligands (drugs) were also converted to MOL2 format using BIOVIA Discovery Studio.

C. *Molecular docking using SwissDock*

The SOS1 PDB file was uploaded in the target section of SwissDock (http://www.swissdock.ch/)-'submit docking' section. The structure and aspect ratio of the uploaded structure was checked by Swiss Dock and accepted within a few minutes. The MOL2 file of each ligand was uploaded in the ligand section of SwissDock- 'submit docking' section, one after the other, and SwissDock checked the topology of the structures uploaded. Docking was then started. The results for free energy estimates of each docking were obtained via email which was then retrieved via Chimera for future analysis. Compounds with a free binding energy of -8.33 kcal/mol or less were considered and ranked.

D. *admetSAR*

The SMILES of the molecule were uploaded in the draw molecule section of admetSAR (http://lmmd.ecust.edu.cn/admetsar2/) - click 'PREDICT'. The uploaded molecules were checked for ADME/T (absorption, distribution, metabolism, excretion, and toxicity) by admetSAR. The results for the "applicability domain" were checked. The results of each molecule were checked individually.

III. RESULT & DISCUSSION

The well-being of individuals all over the world is seriously threatened by cancer. It is critical to make use of contemporary pharmacology and multidisciplinary approaches to advance our knowledge of the mechanisms underlying cancer metabolism. Doing so will aid in the creation of new therapies and offer new information on the diagnosis, prevention, and management of cancer, along with its associated complications. In our research, we aimed to target the SOS1 protein with ginsenosides shown in fig. 2.

Swissdock is an online serice built on EADock DSS that provides results in the form of CHARMM energies following local or blind docking and enables estimation of interactions among target proteins and small compounds such as drugs, inhibitors, ligands, etc. It is designed on an Ajax/HTML interface with an integrated S3DB database containing manually selected complexes, allowing users to construct, submit and receive predicted target-ligand complexes with ease.

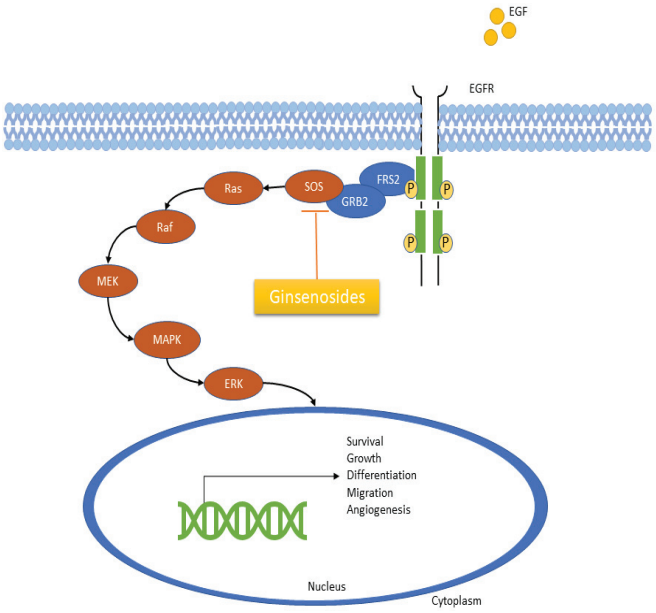


Fig. 2. Inhibition of EGFR pathway by inhibiting SOS 1 homolog.

It operates similarly to Molegro Virtual Docker, AutoDock Vina, and AutoDock in that it enables the selection and grouping of the lowest energy sites for product standardization [13]. SwissDock calculations are utilized for two-step SBVS (structure-based virtual screening) techniques, with the primary docking utilizing a rapid engine and the subsequent docking

Authorized licensed use limited to: DELHI TECHNICAL UNIV. Downloaded on May 11,2023 at 10:12:24 UTC from IEEE Xplore. Restrictions apply.

using exhaustive methods [14]. These computations are dependent on Vital-IT clustering. Out of hundreds of ginsenosides, only 20 compounds passed our binding energy criteria, which should be less than -8.33 kcal/mol. Rc with the lowest ΔG value i.e. -11.56 kcal/mol gave the best results. MRTX0902 a potential inhibitor of SOS-KRAS interaction [15] was taken as control whose estimated ΔG value is -8.33 kcal/mol. Interactions of SOS protein's amino acid are shown in fig. 3.

admetSAR provides the opportunity to predict ADME/T characteristics. Around 50 ADMET endpoints can be predicted by admetSAR using QSAR models. The outcomes suggest that only 4 compounds out of 20 can be used for medication use, given in table 1.

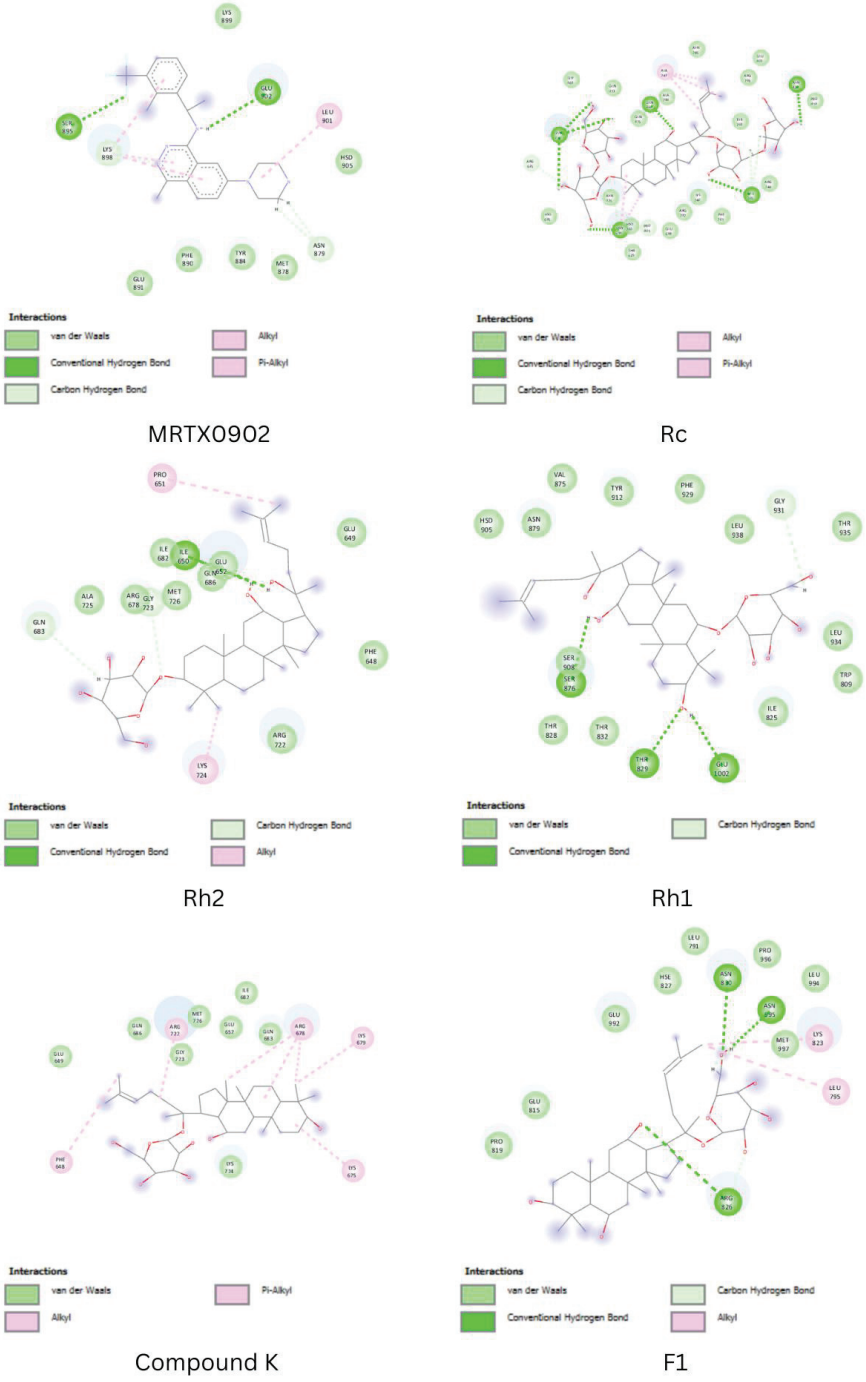


Fig. 3. Target ligand interactions. MRTX0902 is control

Authorized licensed use limited to: DELHI TECHNICAL UNIV. Downloaded on May 11,2023 at 10:12:24 UTC from IEEE Xplore. Restrictions apply.

IV. CONCLUSIONS

Phytochemicals are proven to be potent anticancerous agents. Ginsenosides have been extensively studied for their therapeutic potential in cancer. This work focused on the role of ginsenosides in inhibiting SOS protein homolog 1 – KRAS interaction and hence EGFR signaling. Using various bioinformatics software tools and web servers as well as the molecular docking process, we compared the anticancer activity of 20 different ginsenosides. The results suggest that ginsenosides, F1, Rh2, Compound K, and Rh1 are the most promising candidates for drugability purposes. These *in silico* studies provide valuable insights into the ginsenosides' potential as a therapeutic agent in cancer treatment. Further research should focus on validating these findings and determining the efficacy of ginsenosides in preclinical and clinical studies.

TABLE I. GINSENOSIDES WITH THEIR ESTIMATED ΔG AND RELATIVE TOXICITY

Ginsenoside	**Formula**	**Estimated ΔG (kcal/mol)**	**Applicability domain**
Rc	C53H90O22	-11.56	WARNING
Ra3	C59H100O27	-10.64	WARNING
Ra2	C58H98O26	-10.47	WARNING
Rb1	C54H92O23	-10.41	WARNING
Rb2	C53H90O22	-10.41	WARNING
Ra1	C58H98O26	-10.17	WARNING
F2	C42H72O13	-9.98	WARNING
Re	C48H82O18	-9.98	WARNING
Rd	C48H82O18	-9.52	WARNING
Rg1	C42H72O14	-9.49	WARNING
Rg2	C42H72O13	-9.49	WARNING
R1	C47H80O18	-9.44	WARNING
Rf	C42H72O14	-9.36	WARNING
Ro	C48H76O19	-9.33	WARNING
Rg3+	C42H72O13	-9.23	WARNING
R2	C43H72O15	-9.14	WARNING
F1	C36H62O9	-8.93	IN DOMAIN
Rh2	C36H62O8	-8.88	IN DOMAIN
Compound K	C36H62O8	-8.44	IN DOMAIN
Rh1	C36H62O9	-8.38	IN DOMAIN

ACKNOWLEDGMENTS

We acknowledge the Department of Biotechnology, DTU, New Delhi, for providing all the necessary facilities.

REFERENCES

[1] M. Najafi, J. Majidpoor, H. Toolee, and K. Mortezaee, "The current knowledge concerning solid cancer and therapy," J Biochem Mol Toxicol, vol. 35, no. 11, p. e22900, Nov. 2021, doi: 10.1002/JBT.22900.

[2] H. Hong, D. Baatar, and S. G. Hwang, "Anticancer Activities of Ginsenosides, the Main Active Components of Ginseng," Evidence-based Complementary and Alternative Medicine, vol. 2021, 2021, doi: 10.1155/2021/8858006.

[3] M. Sun, Y. Ye, L. Xiao, X. Duan, Y. Zhang, and H. Zhang, "Anticancer effects of ginsenoside Rg3 (Review)," Int J Mol Med, vol. 39, no. 3, pp. 507–518, Mar. 2017, doi: 10.3892/ijmm.2017.2857.

[4] D. Hanahan, "Hallmarks of Cancer: New Dimensions," Cancer Discov, vol. 12, no. 1, pp. 31–46, Jan. 2022, doi: 10.1158/2159-8290.CD-21-1059.

[5] Y. Liu and D. Fan, "Ginsenoside Rg5 induces apoptosis and autophagy via the inhibition of the PI3K/Akt pathway against breast cancer in a mouse model," Food Funct, vol. 9, no. 11, pp. 5513–5527, Nov. 2018, doi: 10.1039/C8FO01122B.

[6] Q. Wu et al., "Ginsenoside Rh4 induces apoptosis and autophagic cell death through activation of the ROS/JNK/p53 pathway in colorectal cancer cells," Biochem Pharmacol, vol. 148, pp. 64–74, Feb. 2018, doi: 10.1016/J.BCP.2017.12.004.

[7] X. Li, J. Tsauo, C. Geng, H. Zhao, X. Lei, and X. Li, "Ginsenoside Rg3 Decreases NHE1 Expression via Inhibiting EGF-EGFR-ERK1/2-HIF-1α Pathway in Hepatocellular Carcinoma: A Novel Antitumor Mechanism," https://doi.org/10.1142/S0192415X18500969, vol. 46, no. 8, pp. 1915–1931, Jan. 2019, doi: 10.1142/S0192415X18500969.

[8] D. Wang et al., "Ginsenoside Rg3 Inhibits Migration and Invasion of Nasopharyngeal Carcinoma Cells and Suppresses Epithelial Mesenchymal Transition," Biomed Res Int, vol. 2019, 2019, doi: 10.1155/2019/8407683.

[9] Z. Jiang et al., "Ginsenoside Rg3 attenuates cisplatin resistance in lung cancer by downregulating PD-L1 and resuming immune," Biomed Pharmacother, vol. 96, pp. 378–383, Dec. 2017, doi: 10.1016/J.BIOPHA.2017.09.129.

[10] B. Peng et al., "Ginsenoside 20(S)-protopanaxadiol inhibits triple-negative breast cancer metastasis in vivo by targeting EGFR-mediated MAPK pathway," Pharmacol Res, vol. 142, pp. 1–13, Apr. 2019, doi: 10.1016/J.PHRS.2019.02.003.

[11] E. Levantini, G. Maroni, M. del Re, and D. G. Tenen, "EGFR signaling pathway as therapeutic target in human cancers," Semin Cancer Biol, vol. 85, pp. 253–275, Oct. 2022, doi: 10.1016/J.SEMCANCER.2022.04.002.

[12] Y. Liang et al., "Cucurbitacin IIb induces apoptosis and cell cycle arrest through regulating EGFR/MAPK pathway," Environ Toxicol Pharmacol, vol. 81, p. 103542, Jan. 2021, doi: 10.1016/J.ETAP.2020.103542.

[13] G. Bitencourt-Ferreira and W. F. de Azevedo, "Docking with SwissDock," 2019, pp. 189–202. doi: 10.1007/978-1-4939-9752-7_12.

[14] A. Daina and V. Zoete, "Application of the SwissDrugDesign Online Resources in Virtual Screening," Int J Mol Sci, vol. 20, no. 18, p. 4612, Sep. 2019, doi: 10.3390/ijms20184612.

[15] J. M. Ketcham et al., "Design and Discovery of MRTX0902, a Potent, Selective, Brain-Penetrant, and Orally Bioavailable Inhibitor of the SOS1:KRAS Protein–Protein Interaction," J Med Chem, vol. 65, no. 14, pp. 9678–9690, Jul. 2022, doi: 10.1021/acs.jmedchem.2c00741.

Authorized licensed use limited to: DELHI TECHNICAL UNIV. Downloaded on May 11,2023 at 10:12:24 UTC from IEEE Xplore. Restrictions apply.

2023 10th International Conference on Signal Processing and Integrated Networks (SPIN) | 978-1-6654-9099-3/23/$31.00 ©2023 IEEE | DOI: 10.1109/SPIN57001.2023.10117292

An Intelligent System for Bearing Fault Identification based on Gramian Multi-Resolution Dynamic Mode Decomposition

Sonalika Bhandari
Department of Electronics and Communication Engineering
Delhi Technological University
Delhi, India
sonalikabhandari288@gmail.com

Sachin Taran
Department of Electronics and Communication Engineering
Delhi Technological University
Delhi, India
taransachin2@gmail.com

Varun Sangwan
Department of Electronics and Communication Engineering
Delhi Technological University
Delhi, India
sangwan.varun@gmail.com

***Abstract*— This work introduces a single sensor intelligent end-to-end framework for fault detection based on Gramian-multi-resolution dynamic mode decomposition (GMrDMD). Vibration signals are transformed using gram matrix followed by spatial temporal decomposition based on multi-resolution dynamic mode decomposition (MrDMD). The gram matrix converts the 1D data into time evolving snapshot matrix which retains the relation of signal with time. This forms the input to the MrDMD framework which decomposes the system dynamics into hierarchically evolving fast and slow modes capable of isolating the transient fault characteristics. To handle sensor and environmental noise a robust total least square DMD algorithm is applied at each level of MrDMD. The resultant mode matrix is color coded and fed as image to a convolutional neural network (CNN) for classification. The performance of the designed method is verified on University of Ottawa dataset which contains five type of fault vibration signal under four different time varying rotational speed condition. The results demonstrate that of the proposed data driven method is effectively able to distinguish between different fault characteristics with an accuracy of 96.83%.**

Keywords—Fault detection, DMD, Gram matrix, Convolutional neural network, Vibration signal.

I. INTRODUCTION

The foundation of industry 4.0 revolves around automation and remote condition monitoring of systems. The industrial sector inhabits some of the most complex machines which work under stochastic conditions. These machines require time to time quality check but physical inspection-based methods are not scalable. Hence the shortcoming gave rise to a broad field of intelligent machine health monitoring and prognostics. The aerospace and atomic energy are the earliest industries [1] to adopt fault monitoring systems.

Today, with the technological advancement in sensing devices, network connectivity and high-speed processors all large-scale industrial setups include early fault monitoring and warning systems. Machines are made of multiple rotating parts that house a crucial rolling element called ball bearing, which comprises of equally-spaced balls between two concentric circular races. These elements in any system are critically exposed to different stress profile, load and speed which cause non-deterministic abrasion and limit their life cycle. The early warning of faults in ball bearing elements at lower severity of abrasion saves huge resources and industrial down-time avoiding machine strip down. So, bearing fault detection is hour of need and several algorithms have been proposed for the same.

The earliest works for fault identification with varying speed condition [2] focused on order tracking based on resampling using the changing speed signal. It involves an extra sensor i.e., tachometer and additional multiple resampling needs to be performed. An improved order tracking method using virtual multichannel signals based on variational mode decomposition (VMD) has been proposed in [3] with a primary target of improving performance for detecting compound faults. Another work in [4] proposes a deep learning (DL) based speed normalization-based auto encoder method to normalize the effect of speed using speed accounting function. The effectiveness of the method is only studied for determining healthy and faulty state with 97% accuracy. The research in [5] uses a tachometer free approach which focuses on optimizing the ridge detection using time-frequency ridge estimation method but with the application of this method classification of fault requires manual efforts and domain knowledge. A DL based speed fusion network is proposed in [6] it uses multihead self-attention modules to improve accuracy for distinguishing between healthy, inner and outer race fault but details about network performance for ball and combined fault is not mentioned. Work in [7] discusses time frequency-based method improved using sparse and low rank decomposition based on robust principle component analysis for noise removal. Presently, DL architectures are being used rigorously to address variable working condition, work in [8] develops a condense sense network with emphasis on non-linear fitting functions to improve accuracy by 9% but limits the real time application due to computational complexity. To address the existing algorithms gap in terms of algorithmic complexity, sensor requirement and accuracy this work proposes Gramian-multi-resolution dynamic mode decomposition (GMrDMD).

Prominent spectrum analysis methods [9] like fast Fourier transform, short time Fourier transform, Hilbert transform and envelop detection worked best in case of datasets acquired from test-bench with constant operating conditions with less or no ambient noise. Still they are not

978-1-6654-9099-3/23/$31.00 ©2023 IEEE

Authorized licensed use limited to: DELHI TECHNICAL UNIV. Downloaded on May 15,2023 at 09:58:33 UTC from IEEE Xplore. Restrictions apply.

suitable for classifying fault type as inner cage fault, outer cage fault, ball fault or combined fault. This led to the further development of time-frequency based multi-resolution analysis [10]. It focused more on identification of fault type using wavelet transform and scalogram but these methods require lot of manual parameter selection and are unable to work for signals collected under varying rotational speed. Owing to the non-deterministic and stochastic variation of characteristic frequency lead to methods like order tracking [4] but it deploys a greater number of sensors to track the speed and collect reference signal hence making it cost inefficient. Latest work focuses on adaptive data driven methods like empirical mode decomposition (EMD) [11] which has been used to decompose the raw vibration signal based into intrinsic mode functions (IMF). These modes represent signal as high and low frequency components. This method suffered from mode aliasing, as a result different adaptive decomposition were proposed like local mean decompositions which outperformed EMD but it was less efficient in space-time complexity. Another advancement introduced VMD [12] which proved extremely efficient for mechanical fault analysis. VMD is based on segmentation of spectrum as result initial selection of parameters is challenging.

Basic problem with mode decomposition methods [13] is that they lack physical interpretation of the extracted intrinsic mode functions or product functions. These problems led to the development of dynamic mode decomposition stemming from fluid mechanics [14] it has strong mathematical and physical significance originating from Koopman spectrum analysis [15]. Multiple variations of standard dynamic mode decomposition (DMD) has been worked upon to fit into different applications. Work in [16] used approximate entropy of the decomposed DMD modes for fault diagnosis. Work proposed in [17] lays the foundation of application of DMD and its advantages over other signal processing methods; it describes a rank truncation method to extract dominant DMD modes. Another efficient algorithm periodic low rank DMD is proposed in [18] to preserve amplitude and energy of transient features from faulty signals. The extension of standard DMD used in this work is called multi-resolution DMD (MrDMD) [19] which is capable of extracting transient events using recursive application of DMD.

This work extends the MrDMD framework for the application of early bearing fault identification using only univariate time-series accelerometer signal. The proposed work is a novel attempt at increasing the spatial resolution of vibration signal using gram matrix transformation while preserving the temporal characteristics. This work introduced GMrDMD based on spatial temporal decomposition of gram matrix using multi-resolution dynamic mode decomposition. The resultant mode matrix is colour coded to perform fault classification using convolutional neural network. The proposed approach is verified using experimental simulation of the data provided under varying rotational speed by University of Ottawa [20].

The structure of the work is as follows: section 2 discusses the proposed GMrDMD method for fault identification. Section 3 introduces the dataset and discusses the results. Finally section 4 lists the conclusions drawn from the work.

II. Proposed Methodology

This section is divided into three stages namely signal preprocessing, feature generation and classification. Fig. 1 shows the flowchart of the proposed method.

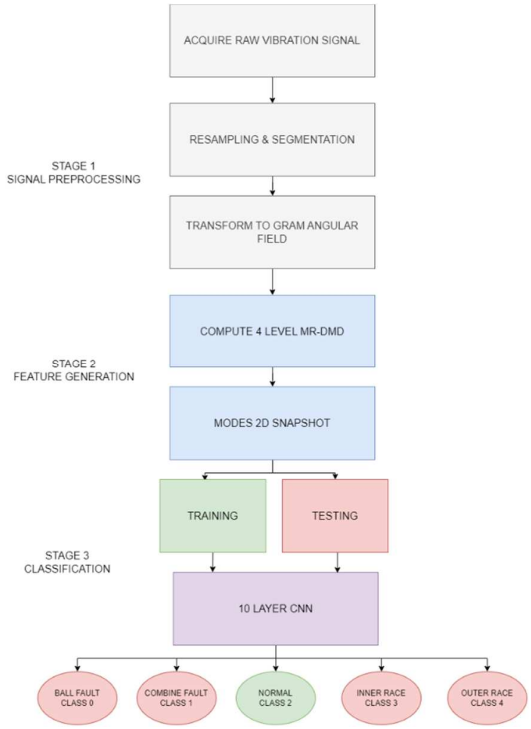


Fig. 1. Flowchart of the proposed methodology

A. Signal Preprocessing

The raw signal is originally sampled at 200 kHz for duration of 10s. For efficient resource utilization the signal is resampled at 100 kHz and segmented without overlapping. The purpose of segmentation is to subdivide a large signal into small sections which have similar properties. The segment size varies according to the occurrence of the frequency region of interest in a signal. Then each sub-signal is transformed into a gram angular field which preserves the temporal relation of the original segment while separating inference signal.

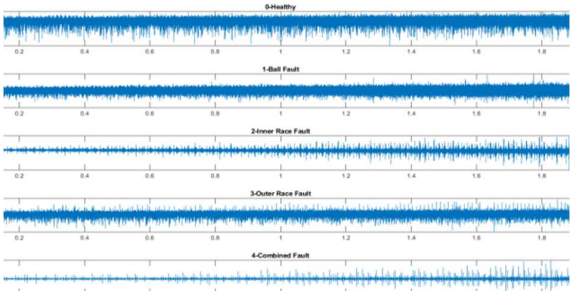


Fig. 2. Raw vibration signals under increasing speed condition

Authorized licensed use limited to: DELHI TECHNICAL UNIV. Downloaded on May 15,2023 at 09:58:33 UTC from IEEE Xplore. Restrictions apply.

Fig. 2 shows the raw signals under increasing rotational speed. It can be observed that no significant information can be understood based on the raw signals except that the amplitude is increasing with time. To further analyze the signal FFT of the input signal is plotted as shown in Fig. 3. It can be seen from the frequency spectrum that majority information is present below 50 kHz. Hence resampling of original vibration signal at 100 kHz is performed. The resampled signal is segmented into 500 sub signals such that each sub-signal has fault characteristics.

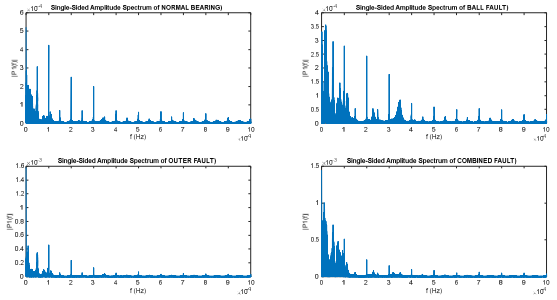


Fig. 3. Frequency spectrum of orignal signals shown in Fig. 2

1) Gram Based Transformation

In case of varying speed, it is important to preserve the temporal relation between sample points. Gram matrix is an ancient representation that calculates complete inner product space of vectors. The extension of this to gram angular field was first proposed in 2015 [21], as a transformation of 1D time series signal to a 2D representation using polar coordinates. Since then, gram angular field has shown excellent results with ECG, ECoG for activity tracking, financial market tracking, fault monitoring etc. Let V be a given time series sensor data that is first rescaled to have a maximum value 1 and minimum value -1 using (1). Then the scaled signal is transformed into polar space where the angular value is determined by taking trigonometric inverse of amplitude and the radius is calculated as the time stamp divided by number of samples as shown in (2) [21].

$$v' = \frac{(v - V_{max}) + (v - V_{min})}{V_{max} - V_{min}} \tag{1}$$

$$f(v') = \begin{cases} cos^{-1}(v), & -1 \le v \le 1 \\ t/N, & t \in N \end{cases} \tag{2}$$

$$G = [\cos \emptyset_i - \cos \emptyset_j] \tag{3}$$

Finally, the polar representation is used to calculate the G matrix (3) whose leading diagonal represent original signal and remaining columns from top left to right represent the preserved the temporal correlation between signal. This transformation method is bijective and invertible as followed from mathematical principle of inverse trigonometric operations.

B. Feature Generation

1) Multi-Resolution DMD

The basic idea of DMD is to form dynamic system matrix using Koopman frequency analysis [14]. The eigenvectors of this matrix form coherent spatial-temporal modes while eigenvalues depict how each mode evolves in time. The advantage of DMD is that it produces non-orthogonal single frequency modes which are used in diagnostics. Usually, DMD decompose a multivariate time signal but mechanical vibration signals are 1D time-series. The algorithm of proposed standard DMD is presented in [22] transforms mechanical signal into a m x n shift-stack Hankel matrix as shown in (4). Considering V_1, $V_2 \ldots V_n$ as snapshots V' can be written as (5).

$$V' = \begin{bmatrix} v_1 & v_2 & \cdots & v_n \\ \cdots & \cdots & \cdots & \cdots \\ v_m & v_{m+1} & \cdots & v_{m+n-1} \end{bmatrix} \tag{4}$$

$$V' = [V_1\, V_2\, V_3 \ldots\ldots V_n] \tag{5}$$

This V' matrix is now rearranged in the form of two snapshot matrix X (6) and Y (7).

$$X = [V_1\, V_2\, V_3 \ldots\ldots V_{n-1}] \tag{6}$$

$$Y = [V_2\, V_3\, V_4 \ldots\ldots V_n] \tag{7}$$

The crux is to find A matrix such that Y = AX, the algorithm applied to find A can be found in [17]. Thus, evolution of X to Y is found using eigenvalues of A. This approach suffers from noise bias effect hence an improved framework total least square DMD (tlsDMD) [22] is used for countering the effect of noise. The tlsDMD aims to find a total least square solution for estimating error in both the matrix X and Y. The problem of noise tolerance is solved using tlsDMD and multi resolution DMD approach has been adopted to handle the problem of extracting transient events. The recursive nature of MrDMD pulls time-frequency information in a principled manner. The slowest varying modes are extracted for each time bin. The obtained time frequency representation is as shown in Fig. 4, where sampling window at each level is divided into half and slow varying modes are selected at each level for reconstructing the original signal without initial conditions as shown in (8) [19] where l is the level of decomposition and M_1, M_2 ... are number of slow modes selected at each level ω is the frequency corresponding to the eigenvector φ.

$$V(t) = \left\{ \sum_{\substack{d=1 \\ l=1}}^{M_1} \varphi_d e^{(\omega_d t)} + \cdots + \sum_{\substack{d=1 \\ l=4}}^{M_2} \varphi_d e^{(\omega_d t)} \right\} \tag{8}$$

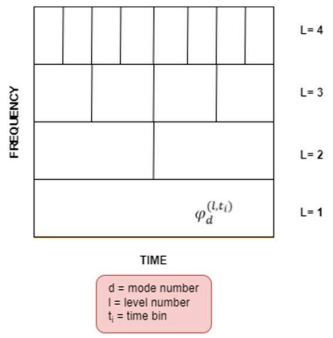


Fig. 4. Time frequency representation generated using MrDMD

After completion of signal processing we get an NxN gram matrix on which a four-level multi-resolution tlsDMD is applied. This step gives two matrices namely mode and dynamic whose significance can be understood from Koopman theory [15]. At each level of decomposition, the time axis is sampled into 2^L sub-parts,

Authorized licensed use limited to: DELHI TECHNICAL UNIV. Downloaded on May 15,2023 at 09:58:33 UTC from IEEE Xplore. Restrictions apply.

where L represents the level of decomposition and tlsDMD is performed on each sub part to calculate the modes. The mathematical process of calculating modes matrix is already discussed in [22]. These modes are typically Eigen vectors corresponding to individual frequencies of the original gram matrix. Hence the collection of the entire modes into a snapshot is able to isolate the behavior corresponding to all frequencies of original matrix. This snapshot is used as input for classification using a CNN. Fig. 5 shows the mode snapshot for the five classes under four types of varying rotational speed.

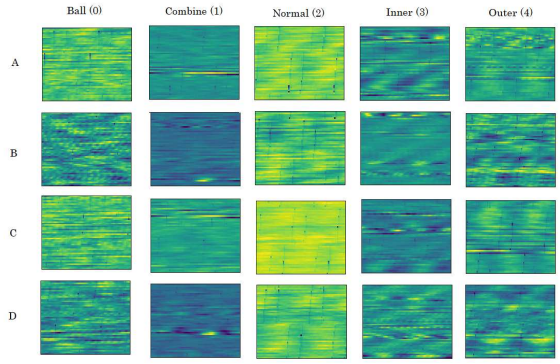


Fig. 5. Mode snapshots generated for 5 classes under four speeds

C. Classification

The next step after generating mode snapshot is to perform classification, in this work we used a 10 layer CNN inspired from GoogleNet architecture [8]. A CNN consists of three basic layers namely convolutional layer which strides kernel of a specified size over the input image to get a convolved output of kernel function with input image followed by pooling layer and activation layer. The proposed structure uses 4 inception blocks with dimension reduction as shown in Fig. 6 with different kernel sizes of (5x5, 3x3 and 1x1) each with a single stride. The main advantage of the structure is that it gives the network an idea about the spatial resolution of the input. After each inception block filter output concatenation is performed along the depth.

Since fault characteristic require non-linear classification, hence relu is used as activation function for the proposed CNN. We have also used drop out layer with 0.2 dropping fraction which ensures that our network avoids over fitting on the training data. Fig. 7 shows the basic block diagram of the used CNN model for fault classification.

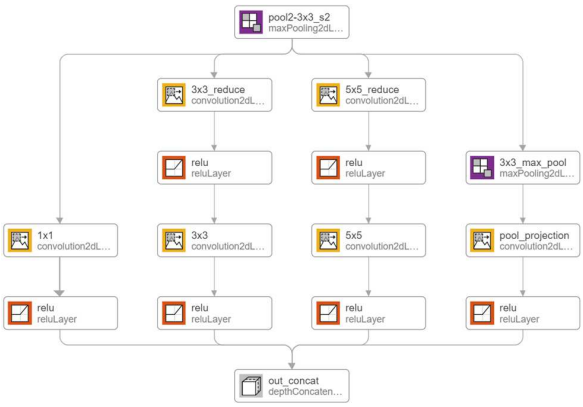


Fig. 6. Inception module used in CNN

III. Experimental Results

This section firstly describes the used dataset followed by an overview of the considered performance metrics. Lastly the results and discussion section cover the comparison of the proposed work with other relevant deep learning-based methods from literature. All the experiments are carried on Intel i5 9th gen processor with 8 GB RAM.

A. Dataset

The proposed data driven fault classification method is validated using time-varying rotational speed dataset from the University of Ottawa, version 2 published in 2019 [20]. The data from university of Ottawa consists of vibration signals under four time-varying rotational speeds as mentioned in Table I. The vibration data is collected for ER16K rolling element using ICP accelerometer. The experimental setup for recording signals is shown in Fig. 8. The recorded signal length is of 10s, and has a sampling frequency of 200 kHz and for each speed condition three trials are conducted.

When the ball element of the bearing interacts with a fault region it produces a fault frequency proportional to rotational speed in Hz. This data contains vibration signals for five faults type namely ball (class-0), combined (class-1), healthy (class-2), inner raceway (class-3) and outer raceway fault (class-4).

TABLE I. Various Speed Condition Of Dataset

Speed Condition	Speed Value (in Hz)
A- Increasing	14.1 to 23.8
B- Decreasing	28.9 to 13.7
C- Increasing - Decreasing	Increased: 14.7 to 25.3 Decreased: 25.3 to 21
D- Decreasing - Increasing	Decreased: 24.2 to 14.8 Increased: 14.8 to 20.6

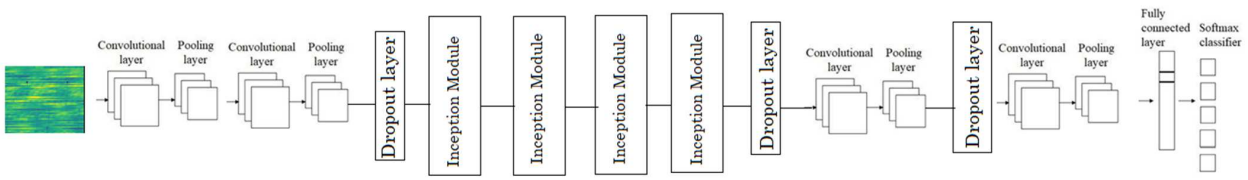


Fig. 7. Proposed 10 layer CNN network

Authorized licensed use limited to: DELHI TECHNICAL UNIV. Downloaded on May 15,2023 at 09:58:33 UTC from IEEE Xplore. Restrictions apply.

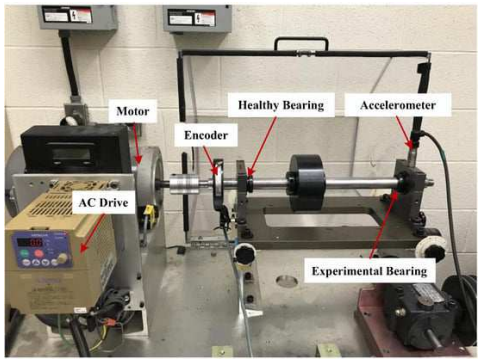


Fig. 8. Experimental setup to record vibration data [20]

B. Performance Metrics

To evaluate the proposed GMrDMD method widely used accuracy metric and confusion plot is considered. Accuracy is the ratio of total correct classified sample to the total number of samples. It evaluates an overall average performance without considering class wise categorization. Accuracy is insightful only for a balanced class problem. Since in our dataset we have equal samples for each class accuracy gives a good idea about model performance. Another metric to understand the micro-level performance is confusion metric it gives a holistic analysis of each class. It helps in understanding which classes are closer to each other causing confusion and wrong prediction in the model.

C. Results and Discussion

The data of trial 1 is divided into 5 datasets which are individually used for training and testing. Table II summarizes the experimental data setup for trial 1 (T1) where 80% data is used for training and 20% for testing. The remaining two trials T2 and T3 are only used as testing data for the model. The D5 dataset is most crucial for our experiment as it captures all types of speed variation.

TABLE II. EXPERIMENTAL SETUP OF DATA

Data (T1)	Symbol	Total Sample	Train	Test
A	D1	2500	2000	500
B	D2	2500	2000	500
C	D3	2500	2000	500
D	D4	2500	2000	500
(A+B+C+D)	D5	10000	8000	2000

The 500 sub signals from each class were used to generate the mode snapshots according to the methodology discussed in previous section. The snapshots obtained after GMrDMD are augmented for scale and rotational invariance. These were now given as input to a 10-layer CNN inspired from GoogleNet architecture. The CNN structure uses multiple kernel sizes of which gives network a perspective about spatial resolution of the image. A summary of accuracy obtained using the model is mention in Table III. The model shows best performance for increasing speed with an average accuracy of 98.2% while, the average accuracy for all four-speed condition is 94.8%. Fig. 9 shows the confusion matrix on dataset D5 it can be seen that class 0 corresponding to ball fault has maximum misclassification with a false detection rate of 4.8% while the class 3 corresponding to inner raceway fault has the lowest false detection rate of 0.9%. Also, it should be noted that the model raises a fault warning for 2.7% times when in reality the roller bearing is not faulty. This category of false alarm is of concern and further improvement is possible in this direction. The plot of model training accuracy and loss for dataset D5 is shown in Fig. 10.

TABLE III. SUMMARY OF ACCURACY OBTAINED ON DATASET

Trial Accuracy	Dataset				
	D1	D2	D3	D4	D5
T1	98.67	96.81	97.17	97.43	94
T2	98.41	96.46	98.31	96.71	96.12
T3	97.52	96.9	96.48	97.24	94.28
Mean	98.2	96.72	97.32	97.12	94.8

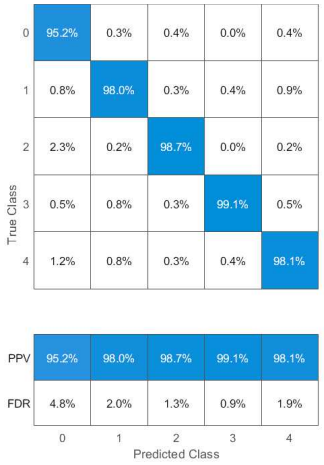


Fig. 9. Plot of accuracy for three trials of each dataset

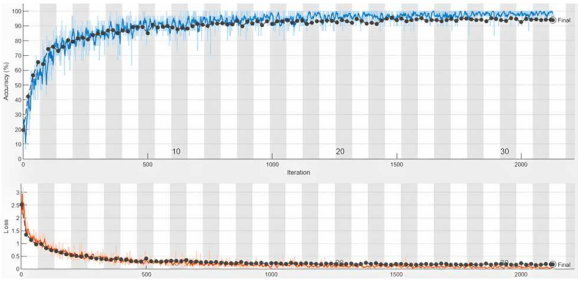


Fig. 10. Plot of accuracy for three trials of each dataset

We also tested the generated feature set with other state of art DL architectures the results for the same is summarized in Table IV along with other similar work done on the same dataset for fault identification. Most of the discussed work uses a standard train-test split size of 80:20. A VMD based transfer learning method [23] using Hilbert spectrum images with DenseNet is able to achieve 92% accuracy. Similar method proposed in [24] is also using IMF of VMD as an input to a deep belief network is achieving an accuracy of 93.17%. The other works proposed in [25] considers subset of fault types using a feature set based on wavelet packet transform. Research in [26] uses local mean decomposition-based data driven method to identify three classes viz. inner raceway, outer raceway and normal condition, the method achieved an accuracy of 95.88% with random forest classifier.

Authorized licensed use limited to: DELHI TECHNICAL UNIV. Downloaded on May 15,2023 at 09:58:33 UTC from IEEE Xplore. Restrictions apply.

TABLE IV. COMPARISON WITH RELATED WORK

Method	Features	Class	Average Accuracy (%)
Proposed-CNN	GMrDMD modes	3	98.89
Proposed-CNN		5	96.83
Proposed-AlexNet			84
Proposed-DenseNet			93.62
Proposed-GoogleNet			93.4
VMD-DenseNet [23]	Hilbert Spectrum	5	92
AVMD-DBM-ELM [24]	IMFs Data driven	5	93.17
WPT-MWSVD+SVM [25]	Wavelet packet	3	87.8
HPO-RF [26]	Local mean decomposition	3	95.88

IV. CONCLUSION

This work explored gram matrix-based transformation followed by multi-resolution DMD on the vibration signal recorded under varying rotational speeds. An advantage of the proposed GMrDMD method is that it requires only a single sensor data for distinguishing four major fault types and healthy bearing. This is possible because of the increased spatial resolution and preserved temporal relation generated by the gram-based transformation. The input gets decomposed into two matrices viz. dynamics and modes which describe the non-linear system. Further, it isolates transient events as multiscale spatiotemporal modes, which is essential for fault identification. Since the method preserves the variation of univariate signal with respect to time, hence it can be seen as a great input for mode decomposition. Lastly, inception module-based 10-layer CNN architecture is used for classification which benefits from spatial resolution of multiple size kernels. The average accuracy for five class problems is 96.83% which is significantly higher than the state-of-the-art DenseNet or GoogleNet. The observation can be supported with the fact that optimal model depth varies for different problem statements. The future scope for the problem includes improvisation of the false alarm rate and testing of the GMrDMD method for lower fault severity and maximum noise robustness.

REFERENCES

[1] Isermann, R. (1997). Supervision, fault-detection and fault-diagnosis methods—an introduction. *Control engineering practice*, *5*(5), 639-652.

[2] Wang, Y., Peter, W. T., Tang, B., Qin, Y., Deng, L., Huang, T., & Xu, G. (2019). Order spectrogram visualization for rolling bearing fault detection under speed variation conditions. Mechanical Systems and Signal Processing, 122, 580-596.

[3] G. Tang, Y. Wang, Y. Huang, N. Liu and J. He, "Compound Bearing Fault Detection Under Varying Speed Conditions With Virtual Multichannel Signals in Angle Domain," in IEEE Transactions on Instrumentation and Measurement, vol. 69, no. 8, pp. 5535-5545, Aug. 2020, doi: 10.1109/TIM.2020.2965634.

[4] Rao, M., Zuo, M. J., & Tian, Z. (2023). A speed normalized autoencoder for rotating machinery fault detection under varying speed conditions. Mechanical Systems and Signal Processing, 189, 110109.

[5] Hu, Y., Tu, X., Li, F., Li, H., & Meng, G. (2017). An adaptive and tacholess order analysis method based on enhanced empirical wavelet transform for fault detection of bearings with varying speeds. Journal of Sound and Vibration, 409, 241-255.

[6] Chi, F., Yang, X., Shao, S., & Zhang, Q. (2022). Bearing Fault Diagnosis for Time-Varying System Using Vibration–Speed Fusion Network Based on Self-Attention and Sparse Feature Extraction. Machines, 10(10), 948.

[7] Wang, R., Fang, H., Yu, L., Yu, L., & Chen, J. (2022). Sparse and low-rank decomposition of the time–frequency representation for bearing fault diagnosis under variable speed conditions. ISA transactions, 128, 579-598.

[8] Wang, Y., Ding, X., Liu, R., & Shao, Y. (2021). Conditionsensenet: A deep interpolatory convnet for bearing intelligent diagnosis under variational working conditions. IEEE Transactions on Industrial Informatics, 18(10), 6558-6568.

[9] D. Neupane and J. Seok, "Bearing Fault Detection and Diagnosis Using Case Western Reserve University Dataset With Deep Learning Approaches: A Review," in IEEE Access, vol. 8, pp. 93155-93178, 2020, doi: 10.1109/ACCESS.2020.2990528.

[10] G. Yu, "A Concentrated Time–Frequency Analysis Tool for Bearing Fault Diagnosis," in IEEE Transactions on Instrumentation and Measurement, vol. 69, no. 2, pp. 371-381, Feb. 2020, doi: 10.1109/TIM.2019.2901514.

[11] Singh, D. S., & Zhao, Q. (2016). Pseudo-fault signal assisted EMD for fault detection and isolation in rotating machines. Mechanical Systems and Signal Processing, 81, 202-218.

[12] Jiang, F., Zhu, Z., & Li, W. (2018). An improved VMD with empirical mode decomposition and its application in incipient fault detection of rolling bearing. IEEE Access, 6, 44483-44493.

[13] Jiang, F., Zhu, Z., & Li, W. (2018). An improved VMD with empirical mode dadecomposition methods and their applications in signal analysis for machinery fault diagnosis: a review with examples. IEEE access, 5, 24301-24331.

[14] Schmid, P. J. (2010). Dynamic mode decomposition of numerical and experimental data. Journal of fluid mechanics, 656, 5-28.

[15] Williams, M. O., Kevrekidis, I. G., & Rowley, C. W. (2015). A data–driven approximation of the koopman operator: Extending dynamic mode decomposition. Journal of Nonlinear Science, 25, 1307-1346.

[16] Dang, Z., Lv, Y., Li, Y., & Wei, G. (2019). A fault diagnosis method for one-dimensional vibration signal based on multiresolution tlsDMD and approximate entropy. Shock and Vibration, 2019, 1-32.

[17] Dang, Z., Lv, Y., Li, Y., & Wei, G. (2018). Improved dynamic mode decomposition and its application to fault diagnosis of rolling bearing. Sensors, 18(6), 1972.

[18] Zhang, Q., Lv, Y., Yuan, R., Li, Z., & Li, H. (2022). A local transient feature extraction method via periodic low rank dynamic mode decomposition for bearing incipient fault diagnosis. Measurement, 203, 111973.

[19] Kutz, J. N., Fu, X., & Brunton, S. L. (2016). Multiresolution dynamic mode decomposition. SIAM Journal on Applied Dynamical Systems, 15(2), 713-735.

[20] Huang, H., & Baddour, N. (2018). Bearing vibration data collected under time-varying rotational speed conditions. Data in brief, 21, 1745-1749.

[21] D. Neupane and J. Seok, "Bearing Fault Detection and Diagnosis Using Case Western Reserve University Dataset With Deep Learning Approaches: A Review," in IEEE Access, vol. 8, pp. 93155-93178, 2020, doi: 10.1109/ACCESS.2020.2990528.

[22] Kutz, J. N., Brunton, S. L., Brunton, B. W., & Proctor, J. L. (2016). Dynamic mode decomposition: data-driven modeling of complex systems. Society for Industrial and Applied Mathematics.

[23] Lin, S. L. (2021). Intelligent fault diagnosis and forecast of time-varying bearing based on deep learning VMD-DenseNet. Sensors, 21(22), 7467.

[24] Lei, X., Lu, N., Chen, C., & Wang, C. (2022). An AVMD-DBN-ELM Model for Bearing Fault Diagnosis. Sensors, 22(23), 9369.

[25] Zhu, H., He, Z., Wei, J., Wang, J., & Zhou, H. (2021). Bearing fault feature extraction and fault diagnosis method based on feature fusion. Sensors, 21(7), 2524.

[26] Ma, J., & Liu, F. (2022). Bearing Fault Diagnosis with Variable Speed Based on Fractional Hierarchical Range Entropy and Hunter–Prey Optimization Algorithm–Optimized Random Forest. Machines, 10(9), 763.

Authorized licensed use limited to: DELHI TECHNICAL UNIV. Downloaded on May 15,2023 at 09:58:33 UTC from IEEE Xplore. Restrictions apply.

2023 10th International Conference on Signal Processing and Integrated Networks (SPIN) | 978-1-6654-9099-3/23/$31.00 ©2023 IEEE | DOI: 10.1109/SPIN57001.2023.10116237

Ancient Indian Script Transliteration Using GANs

Anshumani Sharma
Department of Electronics and Communication Engineering
Delhi Technological University
Delhi, India
anshumani2001@gmail.com

Ayushi Verma
Department of Electronics and Communication Engineering
Delhi Technological University
Delhi, India
ayushiverma0721@gmail.com

Chetan Shahra
Department of Electronics and Communication Engineering
Delhi Technological University
Delhi, India
shahrachetan@gmail.com

S. Indu
Department of Electronics and Communication Engineering
Delhi Technological University
Delhi, India
s.indu@dtu.ac.in

***Abstract*—This study aims to investigate the application of Generative Adversarial Networks (GANs) for transliterating ancient Indian script characters into present day devanagari script characters. The ancient scripts Nandinagari and Sharda are known for their ornate and complex forms, making it a challenge to read and understand for modern readers. The goal of this research is to use GANs to train a model that can convert ancient Indian script images like Nandinagari and Sharda to present day Devanagari script images, which can be useful for preserving and digitizing ancient texts, and making them more accessible to modern readers. The study will evaluate the ability of Generative Adversarial Networks to accurately recognize and transliterate ancient script characters, and will provide insights into the potential of this approach for preserving cultural heritage and digitizing and transliterating historical texts to modern scripts.**

Keywords— Generative Adversarial Networks, Discriminator, Generator, Script, Transliteration, pix2pix

I. INTRODUCTION

The motivation behind this research is to explore the capabilities of Generative Adversarial Networks (GANs) in recognizing and converting ancient script characters into modern script characters. Ancient scripts such as Nandinagari and Sharda are known for their intricate and complex forms, making them challenging to read and understand for modern readers. As a result, preserving and digitizing ancient texts written in these scripts becomes a daunting task. To address this problem, this research aims to use GANs that can transliterate ancient script images to modern script images. The goal is to provide a valuable tool for preserving and digitizing ancient texts, making them more accessible to modern readers, and promoting the study and understanding of ancient cultures and civilizations. This can be especially important for historical documents, manuscripts, and inscriptions, which may be difficult to read and understand for present day readers.

Furthermore, GANs have shown to be effective in other image-to-image translation tasks[3,6], and this research aims to apply this technique to the field of language transliteration. The use of GANs for recognizing and converting ancient script characters can also have a wide range of potential applications in areas such as archaeology, history, and library science[14].

To summarize, this research aims to investigate the potential of Generative Adversarial Networks for recognizing and transliterating ancient script characters, currently done for Nandinagari and Sharda indian scripts, into present day understandable script characters.This study is a pioneering effort in this field and the results can pave the way for more research in this area.

II. RELATED WORK

A. Improving Adversarial Neural Machine Translation for Morphologically Rich Language

This research[1] explores the use of a modified Generative Adversarial Networks (GAN) model for neural machine translation (NMT) in order to improve the performance of translations in languages with rich morphological systems. The proposed model employs the use of morphological word embeddings as input to the GAN, rather than traditional word embeddings, with the goal of providing more context and enhancing the representation of words. Additionally, this model aims to address the issue of data sparsity during training. In contrast to previous studies, which typically utilized a single reference translation during training, this research expands upon this by incorporating multiple references into the discriminator. This allows for the GAN model to have access to more context information on the morphology of words used in various languages.

The study conducts experiments on several language pairs, including French-English, Czech-English, Finnish-Turkish, Finnish-English, Turkish-English, German-English, Turkish-Czech and Chinese-English pair translations.

B. Recognizing English Cursive Using Generative Adversarial Networks

The paper[2] presents a study on using Generative Adversarial Networks (GANs) for recognizing English cursive handwriting. The authors of the paper explain that traditional machine learning techniques like SVMs and CNNs have been widely used for handwriting recognition, but have limitations when it comes to recognizing cursive writing.

To address this challenge, the authors propose using GANs for handwriting recognition. The GAN is trained on a dataset of English cursive handwriting, and is able to generate new samples of cursive writing that are similar to the training dataset. The authors then use this model for recognizing cursive writing by comparing the generated samples with the input handwriting.

The authors evaluate their model using a dataset of English cursive handwriting and report that their GAN model achieved an accuracy of 82.59%, which is a significant

Authorized licensed use limited to: DELHI TECHNICAL UNIV. Downloaded on May 15,2023 at 09:51:44 UTC from IEEE Xplore. Restrictions apply.

improvement over traditional handwriting recognition methods.

The authors also note that the use of GANs for handwriting recognition is a relatively new area of research, and there are currently few studies on using GANs for this task. However, they highlight that their study shows the potential of GANs for recognizing cursive writing, and suggest that further research in this area could lead to even better performance.

In conclusion, the paper presents a study on using GANs for recognizing English cursive handwriting. The authors proposed a GAN model that achieved a high accuracy of 96.5% and showed the potential of GANs for recognizing cursive writing. The paper highlights the need for more research in this area to improve the recognition accuracy and efficiency.

C. Image-to-Image Translation with Conditional Adversarial Networks

The approach [4] for image-to-image translation described in this paper uses conditional generative adversarial networks (cGANs). Given a set of related picture pairings, the authors suggest a framework that can learn how to transfer an input image to a desired output image.

The proposed method is based on the cGAN architecture, which is an extension of the traditional GAN architecture that allows for control over the generated data by providing additional information, known as the conditioning variable. In this case, the generator employs the input picture and the intended output image as the conditioning variables to create the translated output.

The cycle consistency loss, which the authors suggest, is a novel loss function that helps guarantee that the output is consistent with the input picture. This loss function is based on the hypothesis that, when the generator's output is fed back into it, it should be somewhat close to the original input picture. Label-to-image, day-to-night, and edges-to-images are a few of the image-to-image translation tasks that the authors use to test the suggested technique, and show that it produces high-quality results that are comparable to or better than those produced by existing methods. Additionally, they show that a variety of image-to-image translation challenges may be solved using the suggested method.

Overall, the paper provides a strong contribution to the field of image-to-image translation and GANs. The authors provide a novel cGAN architecture and loss function that may efficiently learn the mapping between input and output pictures and yield excellent results.. The experiments in the paper's results show how well the suggested approach works and how many different image-to-image translation problems it may be used for.

D. Comparison with previous approaches

Most of the previous works on transliteration focus on methods other than GANs such as optical character recognition (OCR), machine learning, or knowledge distillation for this task. For example, the paper “TextKD-GAN: Text Generation using Knowledge Distillation and Generative Adversarial Networks” proposes a text generation model using knowledge distillation and GANs, however it does not deal with ancient scripts specifically.[11]

Some papers with different approaches for similar tasks include “Recognition of Brahmi Words by Using Deep Convolutional Neural Network”[12] which does pre-processing of input images including binarization and resizing. Convolutional Neural Networks are implemented on the input images with layers including Convolutional layer, sub sampling layer, classification layer, back propagation. The study implemented a deep convolutional neural network (DCNN) architecture consisting of six layers to recognize Brahmi words. Two layers were assigned for both convolution and pooling, and the remaining two layers were used for classification. To classify the Brahmi words, the dataset was divided into three subsets: 3/4 of the total 6,475 data points were allocated for training, 1/4 for validation, and 536 for testing. [12]

In 2017, a paper titled "Optical Character Recognition for Brahmi Script Using Geometric Method" presented an approach for identifying Brahmi characters. This approach utilized geometric features, including corner points, bifurcation points, ending points, intersection points, circles, and lines, for feature extraction. The paper also established classification rules to accurately identify Brahmi characters based on these extracted features. The method uses a combination of horizontal projection profile, vertical projection profile, connected component analysis, and contour tracing for segmentation etc.[13]

The limitation in both these papers, however, is that these did not include conversion of ancient scripts to modern scripts. These studies need labeled data for recognition of characters, however, in our study, labeling of each character of ancient script for the dataset is not required, direct mapping of source and target pairs is done.

Our proposed approach uses a dataset of 988 pairs of source and target images, focused more on conversion and transliteration task compared to other papers and achieved a FID score of 57.68, indicating high similarity between the generated and real images, and hence an indicator of good quality of generated images. It can be useful for various applications such as digitizing historical documents, preserving cultural heritage, and making historical texts more accessible.

III. METHODOLOGY

The methodology used in our study is based on the Pix2Pix[4] architecture of Generative Adversarial Networks (GANs). Pix2Pix is a kind of GAN made for image-to-image translation problems, where the objective is to produce a new picture from an input image.

The first step in the methodology is to gather a dataset of ancient script characters images. The dataset used in this research consists of two subsets, one containing images of ancient Nandinagari script characters and the other containing images of ancient Sharda script characters. Each image in the dataset is of dimensions 256 x 256 pixels, providing a high-resolution representation of the ancient script characters.

The next step is to preprocess the dataset by removing noise and improving the quality of the images. The Pix2Pix

Authorized licensed use limited to: DELHI TECHNICAL UNIV. Downloaded on May 15,2023 at 09:51:44 UTC from IEEE Xplore. Restrictions apply.

architecture is then implemented using the TensorFlow and Keras libraries. Two essential parts of this architecture are a generator network and a discriminator network. The generator network is represented by the function G(x), which converts input picture x into output image y (y=G(x)). The generator aims to learn how to produce visuals that resemble the actual appearance of contemporary script characters. The discriminator network, on the other hand, is taught to differentiate between the produced pictures and the genuine images.[8] A function D(x) that converts an input picture x to a scalar value, or probability that the input is a real image, serves as the discriminator's representation.

The discriminator and generator networks are trained concurrently. The following objective function (Eqn. 1) is minimized by the generator network during training to increase the likelihood that the discriminator network will make a mistake[9].

$$\min G(x) \{-\log D(G(x))\} \quad (1)$$

while the discriminator network is trained to minimize the following objective function (Eqn 2)[9]:

$$\min D(x) \{-\log D(x) - \log(1-D(G(x)))\} \quad (2)$$

The generator and discriminator networks engage in an adversarial interaction during training, with the discriminator attempting to accurately recognize the produced pictures as fake while the generator attempts to produce images that are as realistic as possible. Through this competition, the discriminator network improves its ability to recognize fake pictures, and the generator network learns how to create better images.[5]

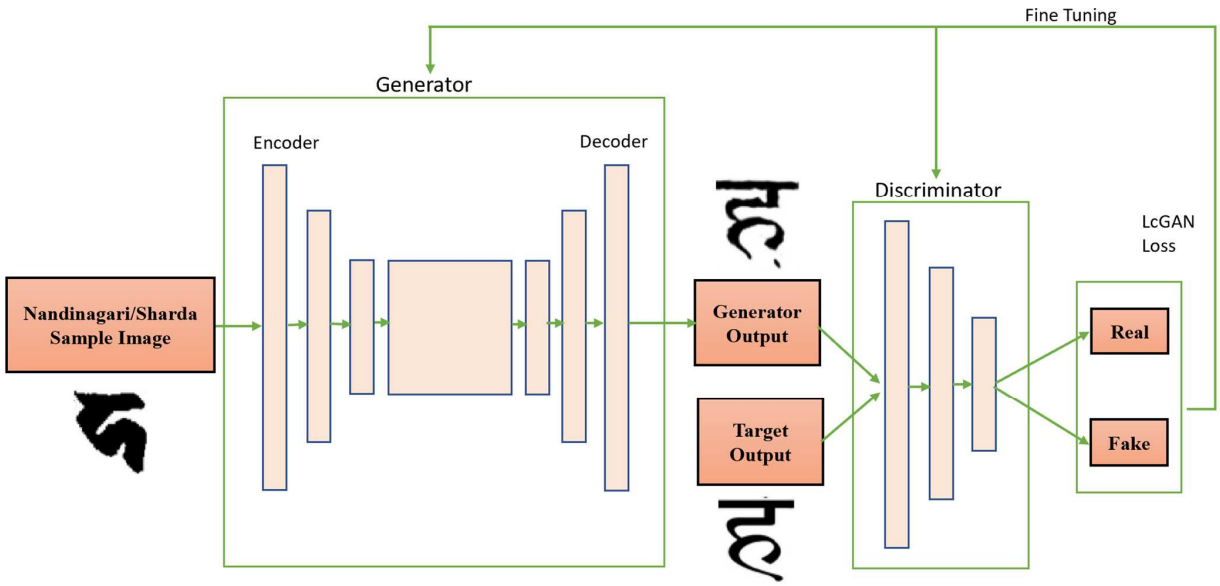


Fig. 1. Architecture for Script Transliteration using GAN

Using an input picture of ancient script characters, the generator network may be used to create new images of modern script characters when the training is over. The quality of the produced pictures is then assessed by comparing them to actual images of modern script characters. In order to translate ancient script to modern script, this procedure aims to create images that are comparable to true modern script characters.

IV. EXPERIMENT

A. Dataset

The dataset used for training our GAN model is a collection of 988 pairs of source and target images. The source images are ancient script characters, and the target images are modern script characters. The dataset is divided into two subsets: one containing images of ancient Nandinagari script characters and the other containing images of ancient Sharda script characters.

The first subset contains 381 pairs of images, where the source images are ancient Nandinagari script characters and the target images are modern Devanagari script characters. The Nandinagari script is an ancient script used in India, primarily in the western and southern regions of the country. It is known for its ornate and complex forms, making it a challenge to read and understand for modern readers. This subset of data is prepared manually using handwritten image pairs of characters of both the scripts.

The second subset contains 607 pairs of images, where the source images are ancient Sharda script characters and the target images are modern Devanagari script characters. The Sharda script is an ancient script that was used in the northern regions of India and is known for its elegant and simplified forms. The source characters in this subset of data are extracted from ancient script while the target characters are typed manually. These images were preprocessed to remove noise and improve the quality.

TABLE I. DATASET DESCRIPTION

Subset		Number of Pairs
Source	Target	
Nandinagari	Devanagari	381
Sharda	Devanagari	607

The target images in both subsets are modern Devanagari script characters, which are the standard script used in modern

Authorized licensed use limited to: DELHI TECHNICAL UNIV. Downloaded on May 15,2023 at 09:51:44 UTC from IEEE Xplore. Restrictions apply.

Indian languages such as Hindi and Marathi. Each image in the dataset is of dimensions 256 x 256 pixels, providing a high-resolution representation of the ancient script characters. The dataset is balanced and diverse, providing a good representation of the ancient scripts and their variations.

B. Training

After acquiring and preparing the dataset, we set up the generator and discriminator networks. The generator network's purpose is to create new images of modern script characters using input images of ancient script characters. The generator network is represented by G(x), which maps the input image x to an output image y, denoted by y=G(x). The discriminator network's goal is to distinguish between the generated images and actual images of modern script characters. The discriminator network is represented by D(x) which takes an input image x and produces a scalar value indicating the probability of the image being real.

The generator and discriminator networks are trained simultaneously in a process where the generator network is trying to generate images that can fool the discriminator network by reducing the function -logD(G(x)) and the discriminator network is trying to identify the generated images as fake by minimizing the function -logD(x) - log(1-D(G(x)))[4]. This creates a competition in which the generator network is driven to create better images and the discriminator network is pushed to enhance its ability to spot fake images. Through this competition, the generator network learns to produce highly realistic images and the discriminator network learns to become more adept at identifying fake images.

The model was trained for 100 epochs and after each epoch, the performance of the model was evaluated.

The figures (Fig 2 a-d) of the source images, target images, and output images after 1st, 10th, 50th, and 100th epochs provide a clear visual representation of the model's performance over time. At the 1st epoch, the output images are not very similar to the target images and contain a lot of noise. However, after the 10th epoch, the output images are starting to look more similar to the target images. At the 50th epoch, the output images are almost identical to the target images, with fewer noise and more clearly defined features.. Finally, at the 100th epoch, the output images are almost perfect replicas of the target images. This indicates that the model has learned to recognize the ancient script characters and convert them into modern script characters with high accuracy. The images suggest that the model has been trained well and its performance increases over time.



(a): After 1st Epoch



(b): After 10th Epoch



(c): After 50th Epoch



(d): After 100th Epoch

Fig. 2. Performance of the model
(Source, Generated Output, Real Output)

C. Examples

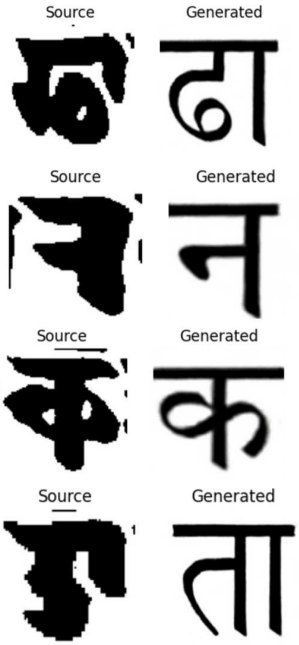


Fig. 3. Generated images on Example Characters

D. Analysis

The FID values are a measure of the similarity between the images generated by GAN and the real images in the dataset.

Authorized licensed use limited to: DELHI TECHNICAL UNIV. Downloaded on May 15,2023 at 09:51:44 UTC from IEEE Xplore. Restrictions apply.

Low values of FID score indicates increased similarity of the generated images to the real images.[10]

TABLE II. FID SCORES

S.No.	Number of Iterations	FID Scores
1	3035	96.92415
2	6070	94.86575
3	9105	91.11341
4	12140	92.36248
5	15175	90.37993
6	18210	88.74278
7	21245	76.12847
8	24280	78.89884
9	27315	71.08202
10	30350	66.71451
11	33385	63.83123
12	36420	71.64861
13	39455	65.97386
14	42490	60.49965
15	45525	59.24905
16	48560	64.03234
17	51595	61.87271
18	54630	60.33724
19	57665	58.37979
20	60700	57.68799

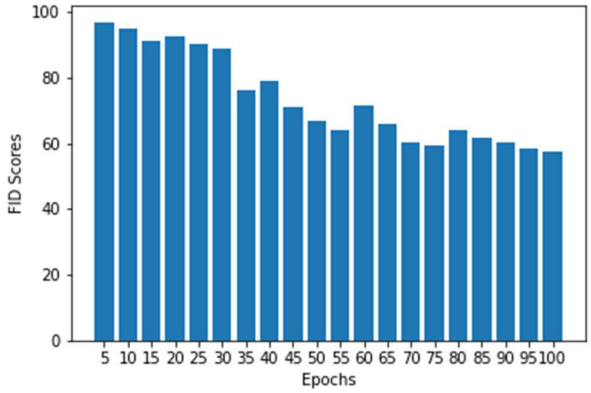


Fig. 4. FID Values vs Epochs

We can see that the FID scores decrease as the number of training epochs increases, indicating that the similarity between the generated images and the real images increase as the model is trained for more epochs. The FID score starts at 96.92 for 3035 iterations (5 epochs) and gradually decreases to 57.69 for 60,700 iterations(100 epochs). This suggests that the model's performance improves as it is trained for more epochs. The FID score reaches its lowest value at 60,700 iterations, indicating that the model has reached its best performance at this point. The FID score of 57.69 is a good score, indicating that the generated images are close to the real images.

During the training process of the Pix2Pix GAN model, three main losses were monitored: the generator loss, the discriminator-fake loss, and the discriminator-real loss. The generator loss is a measure of how well the generator network is able to produce images that can confuse the discriminator network. The discriminator-fake loss is a measure of how well the discriminator network identifies fake images generated by the generator network. The discriminator-real loss is a measure of how well the discriminator network identifies real images from the dataset.[7]

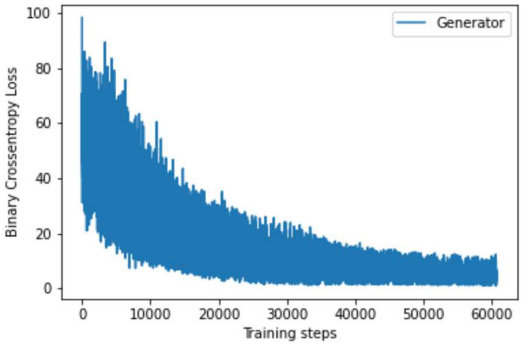


Fig. 5. Binary Cross entropy Loss (Generator) vs Training Steps Plot

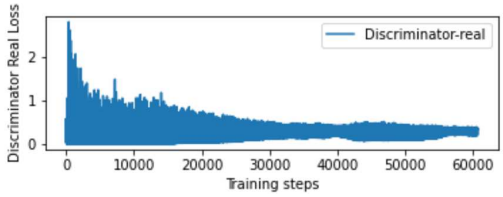


Fig. 6. Discriminator-real Loss vs Training steps Plot

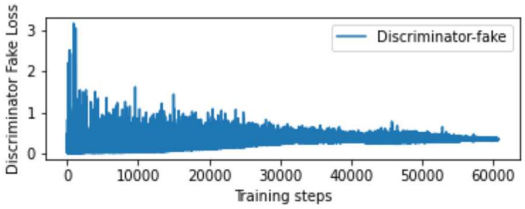


Fig. 7. Discriminator-fake Loss vs Training steps Plot

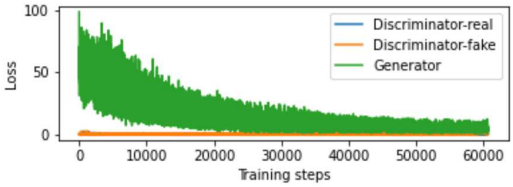


Fig. 8. Collective Loss (GAN Loss) vs Training steps Plot

It's observed that all three losses decreased with each iteration, indicating that the model's performance improved as it was trained for more iterations. The decrease in the generator loss suggests that the generator network was able to produce better images as it was trained for more iterations. Similarly, the decrease in the discriminator-fake loss suggests that the discriminator network became more adept at identifying fake images as it was trained for more iterations. The decrease in the discriminator-real loss suggests that the discriminator network was able to identify real images with greater accuracy as it was trained for more iterations.This means that the generator network was producing more realistic images and the discriminator network was becoming better at identifying both real and fake images, which is the goal of training GANs.

Overall, the decrease in the generator loss, the discriminator-fake loss, and the discriminator-real loss indicates that the Pix2Pix GAN model was able to improve its performance as it was trained for more iterations, which is as expected.

Authorized licensed use limited to: DELHI TECHNICAL UNIV. Downloaded on May 15,2023 at 09:51:44 UTC from IEEE Xplore. Restrictions apply.

V. CONCLUSION

This research has explored the use of Pix2Pix GAN architecture for recognizing ancient script characters and converting them into modern script characters. The dataset used in this research consisted of 988 pairs of source and target images, and the model was trained for 100 epochs. The results of the study showed that the model was able to improve its performance as it was trained for more epochs, as indicated by the decrease in the generator loss, the discriminator-fake loss, and the discriminator-real loss. Furthermore, the FID score reached its lowest value at 100 epochs, indicating that the model has reached its best performance at this point.

The FID scores were used to evaluate the performance of the GAN and the results show that the model is able to generate images that are very similar to the real images. This research demonstrates the potential of GANs to recognize historical script characters and convert them into modern script characters. The proposed model can be useful for various applications such as digitizing historical documents, preserving cultural heritage, and making historical texts more accessible.

It's worth noting that this research is not without limitations, further research could be done to improve the quality of the generated images, test the model on a larger dataset, and apply the model to other script characters. The proposed model can be further enhanced by incorporating other computer vision techniques such as optical character recognition (OCR) and text recognition.

ACKNOWLEDGMENT

We would like to express our heartfelt gratitude to Professor Santanu Chaudhary, Director, IIT Jodhpur for introducing us to this research project and for his guidance and support throughout the entire process. His invaluable insights, suggestions, and constant encouragement have been instrumental in the successful completion of this study.

We would also like to express our sincere gratitude to Prof. S. Indu and Dr. Kritikant Sharma for their guidance, support and supervision during the course of this research. Prof. S. Indu has been an invaluable mentor, providing the necessary guidance and knowledge to successfully conduct this research. Her expertise in the field has been instrumental in shaping our understanding of the subject and her encouragement and support have been greatly appreciated. Dr. Kritikant Sharma provided us with initial transliterated versions of the ancient palm leaf manuscripts which helped us to create our dataset. His expertise in the field of ancient Indian scripts was invaluable in our research.

We are truly grateful to have had the opportunity to work with such an amazing team of supervisors and we are confident that the knowledge and experience gained during this research will be of great value to us in our future endeavors.

REFERENCES

[1] C. Mi, L. Xie and Y. Zhang, "Improving Adversarial Neural Machine Translation for Morphologically Rich Language," in IEEE Transactions on Emerging Topics in Computational Intelligence, vol. 4, no. 4, pp. 417-426, Aug. 2020, doi: 10.1109/TETCI.2019.2960546.

[2] X. Yu and J. Saniie, "Recognizing English Cursive Using Generative Adversarial Networks," 2020 IEEE International Conference on Electro Information Technology (EIT), 2020, pp. 293-296, doi: 10.1109/EIT48999.2020.9208298.

[3] A. Rashid, A. Do-Omri, Q. Haidar, M. Liu, and Rezagholizadeh, "Bilingual-GAN: A Step Towards Parallel Text Generation." Available: https://arxiv.org/pdf/1904.04742.pdf

[4] Isola, P., Zhu, J. Y., Zhou, T., & Efros, A. A. (2016, October). Image-to-image translation with conditional adversarial networks. In Proceedings of the IEEE conference on computer vision and pattern recognition (pp. 1125-1134).

[5] C. Ledig et al., "Photo-Realistic Single Image Super-Resolution Using a Generative Adversarial Network," 2017 IEEE Conference on Computer Vision and Pattern Recognition (CVPR), Honolulu, HI, USA, 2017, pp. 105-114, doi: 10.1109/CVPR.2017.19.

[6] J. -Y. Zhu, T. Park, P. Isola and A. A. Efros, "Unpaired Image-to-Image Translation Using Cycle-Consistent Adversarial Networks," 2017 IEEE International Conference on Computer Vision (ICCV), Venice, Italy, 2017, pp. 2242-2251, doi: 10.1109/ICCV.2017.244.

[7] Goodfellow, Ian & Pouget-Abadie, Jean & Mirza, Mehdi & Xu, Bing & Warde-Farley, David & Ozair, Sherjil & Courville, Aaron & Bengio, Y.. (2014). Generative Adversarial Networks. Advances in Neural Information Processing Systems. 3. 10.1145/3422622.

[8] T. Kim, M. Cha, H. Kim, J. K. Lee, and J. Kim, "Learning to Discover Cross-Domain Relations with Generative Adversarial Networks," arXiv:1703.05192 [cs], May 2017, Available: https://arxiv.org/abs/1703.05192

[9] Z. Liu, T. Yuan, Y. Lin and B. Zeng, "Recent Advances of Generative Adversarial Networks," 2022 IEEE 2nd International Conference on Electronic Technology, Communication and Information (ICETCI), Changchun, China, 2022, pp. 558-562, doi: 10.1109/ICETCI55101.2022.9832194.

[10] T. Salimans, I. Goodfellow, W. Zaremba, V. Cheung, A. Radford, and X. Chen, "Improved Techniques for Training GANs," arXiv.org, 2016. https://arxiv.org/abs/1606.03498

[11] M. A. Haidar and M. Rezagholizadeh, "TextKD-GAN: Text Generation using KnowledgeDistillation and Generative Adversarial Networks," arXiv:1905.01976 [cs], Apr. 2019, Accessed: Mar. 09, 2023. [Online]. Available: https://arxiv.org/abs/1905.01976

[12] Gautam, Neha & Chai, Soo See & Jose, Jais. (2020). Recognition of Brahmi Words by Using Deep Convolutional Neural Network. 10.20944/preprints202005.0455.v1.

[13] Gautam, Neha and Soo See Chai. "Optical Character Recognition for Brahmi Script Using Geometric Method." Journal of Telecommunication, Electronic and Computer Engineering 9 (2017): 131-136.

[14] S. R. Rahmayanti, C. Fatichah and N. Suciati, "Sketch Generation From Real Object Images Using Generative Adversarial Network and Deep Reinforcement Learning," 2021 13th International Conference on Information & Communication Technology and System (ICTS), Surabaya, Indonesia, 2021, pp. 134-139, doi: 10.1109/ICTS52701.2021.9608634.

Authorized licensed use limited to: DELHI TECHNICAL UNIV. Downloaded on May 15,2023 at 09:51:44 UTC from IEEE Xplore. Restrictions apply.

2023 IEEE 8th International Conference for Convergence in Technology (I2CT)
Pune, India. Apr 7-9, 2023

Audio Based Music Genre Classification using Convolutional Neural Networks Sequential Model

Simran Pasrija
Department of Software Engineering
Delhi Technological University
Delhi, India
simranpasrija_2k19se128@dtu.ac.in

Shubham Sahu
Department of Software Engineering
Delhi Technological University
Delhi, India
shubhamsahu_2k19se122@dtu.ac.in

Shweta Meena
Department of Software Engineering
Delhi Technological University
Delhi, India
shwetameena@dtu.ac.in

2023 IEEE 8th International Conference for Convergence in Technology (I2CT) | 979-8-3503-3401-2/23/$31.00 ©2023 IEEE | DOI: 10.1109/I2CT57861.2023.10126446

***Abstract*— Music recommendation system has high demand in the modern world, and these types of systems recommend music according to music genres. The music combines lyrics and beautiful sounds, and lyrics can be in any language. Thus, sound plays an essential role in defining the genres of all music written in different. Therefore, the recognition of music genres is a challenging task. However, various studies have been found in this area that performed well. However, the performance of the system can be further increased. Thus, the proposed research aims to identify the music genres with good performance. This study used GTZAN Dataset, which is a publicly available dataset. This dataset has ten classes and around 1000 samples for each category. This system used the Convolutional neural network (CNN) model to recognize the performance of the music genres recognition system. The CNN model has ten layers, eight dense and two dropout layers. The achieved accuracy by the proposed model is 98.30%.**

Keywords—Convolutional Neural Network, Feature Extraction, GTZAN Dataset, Music Genres Recognition,

I. INTRODUCTION

Various recommendation systems, such as movie and music recommendation systems, are available and are very famous in the modern world [1] [2]. These recommendation systems help suggest movies and music according to the user's priority. Moreover, the recommendation system depends on the genres of the music. Music is a combination of lyrics and soulful sound. Lyrics can be written in different type of languages so; it can say that genres can be recognize of music if you know the specific language. However, music does not have any language thus same type of music can be used with two different types of lyrics. Thus, the genres recognition by using sound is a complex task but important task as people is listening the music of different language. Various studies can be found in the area of music genre recommendation systems [3]. Hence, recognizing the genres of music play a very important role in suggesting a piece of good music to a user according to the requirement. Various studies have been found in this area, which performed well [4]. However, the performance of the system can be further increased. Thus, this study focuses on recognizing the genres of music with good performance.

To build a recognition system, two-part always play a crucial role: dataset and methodology. Dataset feed to the method during training and testing time which helps to train the model and calculate the system's performance. Similarly, the training process is done by methodology, which means whatever happens between the input and output is a part of the methodology.

The dataset can be of two types: personal and public, which means the dataset is not available on any online platform, and researchers create it only for their own work, which is called a personal (private) dataset. Nevertheless, the public dataset is available freely online for research work. This dataset is better than a private dataset for performance comparison as the transparency in the performance is most important. Zuhair and Hassani [5] worked on music genres recognition system and used their own dataset. Furthermore, Yang and Zhang [6] used GTZAN and the extended ballroom Dataset, a publicly available dataset. Similarly, Cheng, et al. [7], Yu, et al. [8], Ndou, et al. [9], and Allamy and Koerich [10] also used the GTZAN dataset.

Machine Learning (ML) and Deep Learning (DL) approaches can be used for the recognition part. Chillara, et al. [11] used where ML and DL based approaches were considered to recognize the Music genres. This study used the Convolutional Neural Network (CNN), Convolutional Recurrent Neural Network (CRNN), Convolutional Neural Network- Recurrent Neural Network (CNN-RNN) model, Logistic Regression (LR), and simple Artificial Neural Network (ANN) for the recognition part. Similarly, Ghildiyal, et al. [12] ANN, Support Vector Machine (SVM), Multi-Layer Perceptron (MLP), Decision Tree, and CNN to recognize the music genres. Another study was also used where ML and DL based approaches were considered to recognize the Music genres [11].

This article completed in five sections where one section talk about introduction of the study and second section has details of previous published study, that is called literature. Methodology to recognize the music genres is discussed in section three and the outcome of methodology is presented in section four. In the last, conclusion of the study along with limitation and future work is discussed in section five.

II. LITERATURE

Toshniwal, et al. [13] used Visual Geometry Group (VGG)-16 deep learning architecture to recognize the Music genres and achieved 88.5% accuracy, whereas this study used the GTZAN dataset. Similarly, Deep Neural Network (DNN) and CNN were also used to recognize the genres of music and achieved 92% and 90% recognition rates, respectively. However, this study used its own (private) dataset, 880 samples from eight Kurdish music genres [5]. Sugianto and Suyanto [14] also tried to solve the issue using Melspectrogram and CNN, where a voting scheme made the final decision. Archived accuracy by this model was 71.87% and 63.49%, where a voting classifier and a single method

Authorized licensed use limited to: DELHI TECHNICAL UNIV. Downloaded on May 29,2023 at 05:53:58 UTC from IEEE Xplore. Restrictions apply.

were used, respectively. In the same year (2019), another study was also used where ML and DL based approaches were considered to recognize the Music genres [11]. However, this study used its own dataset. This study used the CNN, CRNN, CNN-RNN model, LR, and simple ANN to recognize the genres and achieved 88.54%, 53.5%, 56.4%, 60.892%, 64.0625% accuracy, respectively. Another study also tried to acknowledge music genres where deep-learning architectures were used for classification [15].

GTZAN and the extended ballroom Dataset were used in this study. Deep learning architectures such as CNN got 88% and 92%, AlexNet showed 81.4% and 88.8%, VGG-11 achieved 86.8% and 88.7%, and ResNet-18 presented 86.8% and 87.6% accuracy without and with RNN, respectively where GTZAN Dataset was considered. CNN got 92.2% and 92.5%, AlexNet showed 83.5% and 92.0%, VGG-11 achieved 82.3% and 93.4%, and ResNet-18 presented 93.1% and 93.38% accuracy without and with RNN, respectively where the extended ballroom dataset was used. Another study also used the GTZAN dataset and CNN to recognize the music genres and achieved 90.7% accuracy [6].

Cheng, et al. [7] considered Mel-Frequency Cepstral Coefficients (MFCC) for features extraction and a combination of CNN and RNN for classifying extraction features. Archived accuracy by approach was 43%, whereas the GTZAN dataset was used for training and testing. Similarly, Yu, et al. [8] used Short Time Fourier Transform (STFT) for features extraction and a combination of Bidirectional RNN (BRNN) and Parallelized CNN attention (PCNNA) for the classification. This study achieved 90% and 92.7% accuracy, respectively, where GTZAN and Extended Ballroom datasets were considered. Another study also used CNN and K-Nearest Neighbor (KNN) to recognize the music genres and achieved 72.40% and 92.69% accuracy using the GTZAN dataset [9].

Allamy and Koerich [10] also used CNN and performed with 80.93% accuracy where the GTZAN dataset was used. Moreover, deep learning architecture, such as Resnet34, Resnet50, Alexnet, and VGG16, also applied to recognize music genres and achieved 79.00%, 75.90%, 71.30%, and 76.93%, respectively [16]. This study also used the GTZAN dataset. Another study focused on ML, and DL approaches, such as ANN, SVM, MLP, Decision Tree, and CNN, showed 70%, 68.9%, 68.7%, 74.3%, and 91% accuracy, respectively, where the GTZAN dataset was used [12]. Cheng, et al. [17] also used the GTZAN dataset and CNN and achieved accuracy by this model was 84%.

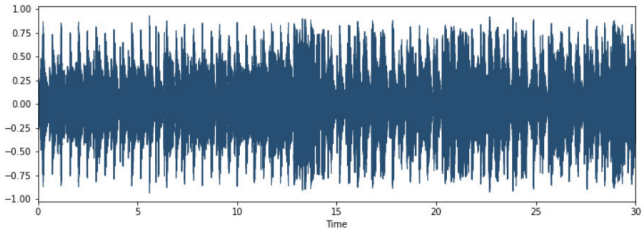
At the conclusion of the session, most studies used the GTZAN dataset, and the DL approach performed well.

III. Research Methodology

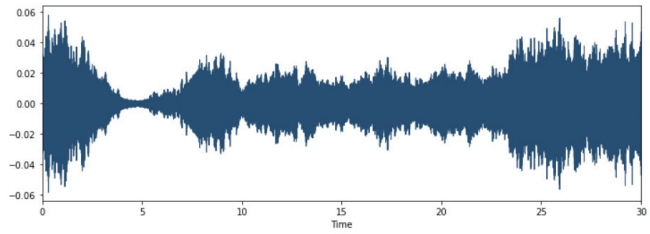
The methodology of the proposed study is divided into two parts: dataset and method.

A. Dataset

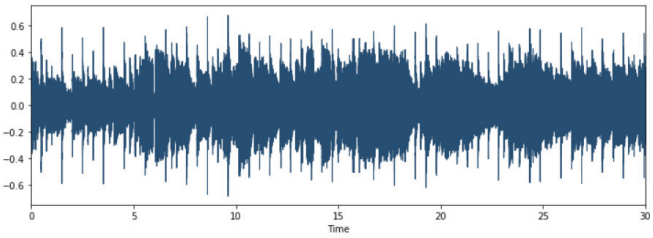
This study used a GTZAN dataset [18], as already discussed in the literature. This dataset has audio samples of 30 sec, and all samples are divided into ten classes, each representing a genre. The dataset has 1000, 1000, 1000, 1000, 1000, 999, 998, 998, 998, 997 sample classes, subtypes Blues, Classical, Country, Disco, Hip-hop, Jazz, Metal, Pop, Reggae, and Rock, so the total number of samples in this dataset is one thousand.



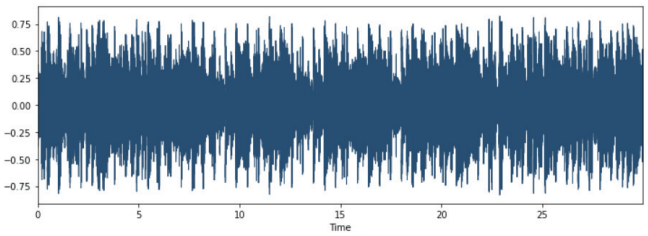
Wave plot of Blue genre



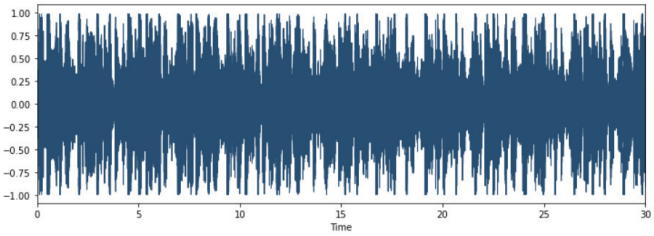
Wave plot of Classical genre



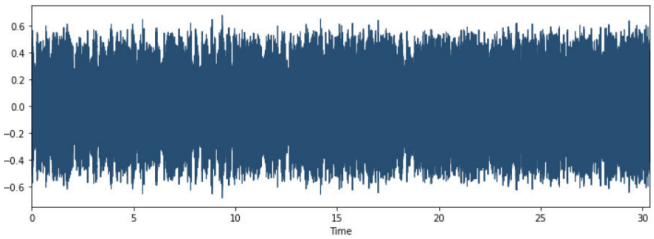
Wave plot of Country genre



Wave plot of Disco genre

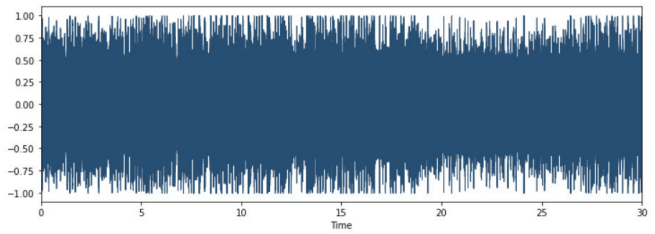


Wave plot of Hip-Hop genre

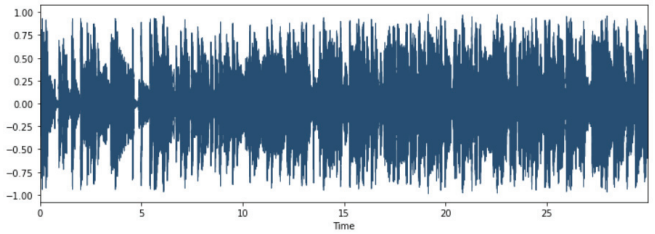


Wave plot of Jazz genre

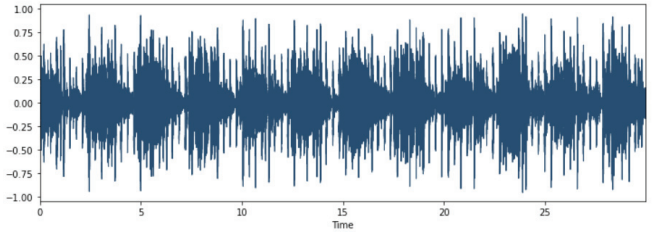
Authorized licensed use limited to: DELHI TECHNICAL UNIV. Downloaded on May 29,2023 at 05:53:58 UTC from IEEE Xplore. Restrictions apply.



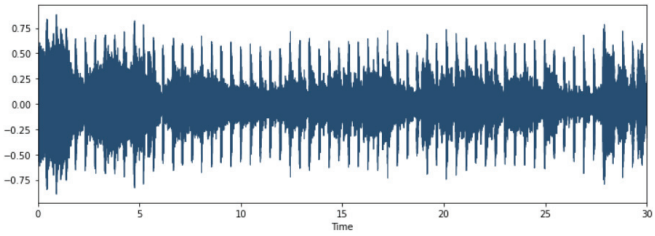
Wave plot of Metal genre



Wave plot of Pop genre



Wave plot of Reggae genre



Wave plot of Rock genre

Fig. 1. Wave plot of all genres, which is a part of dataset

Figure I represents the wave plots for all genres of the dataset. As can see that amplitude, frequency of each genre has different that's the reason, waves of the plot are also different to each other. As can see the plot of Jazz and Metal genre, waves are quite dense although, max and min value of both genres is different. Similarly, waves of Reggae has lowest density. As compare to density of Reggae's wave, Rock's wave has better density but not too good. Classical, Country also has different type of wave so, it can recognize easily. However, the waves of Blue, Disco, and Hip-Hop are very similar to each other so, it will be tough to recognize it. All these three genres represents a loud music thus, the wave are similar to each other.

B. Method

This section is divided into input, feature extraction, and classification.

a) Input: All samples of the dataset are considered input samples. The Audio file is in Waveform Audio (.WAV) file format. All the input samples are in equal length which is 30 sec and uniform format (.WAV) hence, converting the samples in uniform size and format is not required here.

b) Feature extraction: Feature extraction is essential in extracting useful information from input. This critical information will help in classification. First, convert the Audio file into a floating point time series to extract the features from Audio samples. After that, it is converted into amplitude which stands for the change of air pressure in the Audio, and another one presents the number of channels in the Audio. This study focuses on the amplitude features to recognize the music genres..

c) Classification: Classification is performed to take final decision so, it can understand that this is very important part as the performance of the system depend on this step. This study used CNN for the classification task. Ten Layer CNN architecture was used, where eight Dense layers and two dropout layers were considered.

Dense layer works for the classification part, where neurons are essential. Neurons help to take the information, and all neurons are connected to each other to share the knowledge of other neurons of the next layer. Dropout [19] is also used in this architecture which helps to reduce the overfitting issue. This study used two dropout layers, with a 0.5 probability of each dropout layer.

Layer (type)	Output Shape	Param #
dense (Dense)	(None, 512)	30208
dropout (Dropout)	(None, 512)	0
dense_1 (Dense)	(None, 256)	131328
dropout_1 (Dropout)	(None, 256)	0
dense_2 (Dense)	(None, 128)	32896
dense_3 (Dense)	(None, 128)	16512
dense_4 (Dense)	(None, 64)	8256
dense_5 (Dense)	(None, 64)	4160
dense_6 (Dense)	(None, 64)	4160
dense_7 (Dense)	(None, 10)	650

Total params: 228,170
Trainable params: 228,170
Non-trainable params: 0

Fig. 2. *Architeture of CNN model*

The architecture of the CNN model considered the GTZAN dataset as input. The input feed to dense layer where "Relu" activation function and 512 nodes is used. Relu activation function used to reduce the vanishing gradient issue in deep network. Apart from vanishing gradient problem, overfitting is also a considerable issue in deep network which is overcome by dropout layer where the probability value is 0.5. Similarly, output of first Dense layer is considered as input of second and in second layer, tanh activation function, 256 nodes and 0.5 probability value of dropout is used. the tanh activation function results in higher values of gradient during training and higher updates in the weights of the network. Furthermore, tanh activation function, and 128 nodes is used in third layer where input of third layer was the output of second layer. samples parameter of dense layer was used for fourth layer. For fifth, six, and

Authorized licensed use limited to: DELHI TECHNICAL UNIV. Downloaded on May 29,2023 at 05:53:58 UTC from IEEE Xplore. Restrictions apply.

seventh layer, relu activation function, and 64 nodes are used where these layers are sequentially connected to each other. The last layer considered a classification layer thus, softmax activation function is conserved along with ten node value as last layer node values represents the number of classes of the model. This study has ten number of classes. The architecture of the CNN model is mentioned in Figure II where parameters of each layer and overall number of parameters is also mentioned.

IV. Result

The performance of the system is calculated by recognition rate (accuracy), which is the ratio of correctly recognized samples and the total number of samples, and multiplication of 100 to convert into rate (%). Similarly, other parameters also used to check the performance of the system such as Precision, Recall, F1-Score and support.

Precision represents the positive recognition rate that's means, the ratio of correctly recognize samples of true class, and all samples. Similarly, ration of correctly recognize samples of true class and total number of samples of true class called recall. F1-score represents the harmonic mean of precision and recall and this is important parameter to measure the performance. In the last, support parameter used which represents the number of correctly recognize samples.

	precision	recall	f1-score	support
0	0.99	0.99	0.99	312
1	0.99	0.99	0.99	314
2	0.97	0.97	0.97	315
3	0.98	0.98	0.98	291
4	0.99	0.98	0.99	285
5	0.97	0.99	0.98	275
6	1.00	0.98	0.99	317
7	0.98	0.99	0.99	287
8	0.99	0.98	0.98	290
9	0.98	0.97	0.98	311
accuracy			0.98	2997
macro avg	0.98	0.98	0.98	2997
weighted avg	0.98	0.98	0.98	2997

Fig. 3. Performance evaluation of the proposed system

The proposed model achieved 98.30%. Apart from that, the performance of the system is also calculated by precision, recall, f1-score, and support. Usually, these things are calculated when the binary problem is resolved, but this study has a ten-class problem. So, it is checked by the macro average. The precision, recall, f1-score, and support performance value is 98%, 98%, 98%, and 2997, respectively. Details are mentioned in Figure III.

Apart from these performance parameters, one more parameter is used to check the performance, which is the confusion matrix. The confusion matrix is a part recognition rate, and it helps to find out how many samples were recognized correctly and how many sales were confused with which class. The Confusion Matrix of this study is presented in Figure IV.

	blues	classical	country	disco	hiphop	jazz	metal	pop	reggae	rock
blues	310	0	1	0	0	0	0	0	1	0
classical	0	310	0	0	0	4	0	0	0	0
country	2	1	307	1	0	2	0	1	1	0
disco	0	0	2	286	2	0	0	0	1	0
hiphop	0	0	1	1	280	1	0	2	0	0
jazz	0	3	1	0	0	271	0	0	0	0
metal	0	0	0	0	0	0	311	0	1	5
pop	0	0	0	2	0	0	0	285	0	0
reggae	1	0	0	1	1	2	0	2	283	0
rock	1	0	4	1	0	0	1	1	0	303

Fig. 4. Confusion matrix of the proposed system

The performance of this study is also compared to other studies that focus on the recognition of Music genres and use the GTZAN dataset. Ndou, et al. [9] and Toshniwal, et al. [13] studies were considered for the comparison. Ndou, et al. [9] considered CNN and KNN to recognize the music genres and achieved 72.40% and 92.69% accuracy using the GTZAN dataset. Similarly, Toshniwal, et al. [13] used VGG-16 deep learning architecture to recognize the Music genres and achieved 88.5% accuracy. Although, the proposed CNN architecture achieved 98.30% which is better the previous studies. The comparison of the proposed research with previous studies mentioned in Table 1.

TABLE I. Comparison with previous studies (highlighted test represents the highest study)

Study	Performance
Ndou, et al. [9]	72.40%
	92.69%
Toshniwal, et al. [13]	88.5%
Proposed study	**98.30%**

V. Limitation

This study has few limitations also as this study is worked on only ten classes if apart from the earlier mentioned ten class, this study cannot recognize the other genres. Apart from that, input sample size was 30 sec so, if the music length more than 30 sec so, this study cannot provide suitable output. In the last, this when the input samples used in this system so, music clip should be without noise as this study did not consider any noise removal technique.

VI. Conclusion

Music genres are a modern-day problem that helps to create a list according to the mood of the user. The primary focus of this study is to recognize the music genres with reasonable accuracy. This study used the GTZAN dataset, which has ten classes and 1000, 1000, 1000, 1000, 1000, 999, 998, 998, 998, 997 samples of blues, jazz, metal, pop, reggae, disco, classical, hip-hop, rock, country category, respectively. Training and testing dataset ratio was 68-32% so, around 315 samples of each class were using for the testing. This study used a combination of eight Dense layers and two dropout layers to introduce the proposed CNN model.

Authorized licensed use limited to: DELHI TECHNICAL UNIV. Downloaded on May 29,2023 at 05:53:58 UTC from IEEE Xplore. Restrictions apply.

This study achieved 98.30% accuracy, which is better than the previous studies, and the comparison is made in Table I. This study only used a customized CNN model, although predefined CNN models, such as AlexNet, VGG, etc., can also be used. Apart from that, another dataset with more samples and classes can also be used.

REFERENCES

[1] M. Goyani, and N. Chaurasiya, "A review of movie recommendation system: Limitations Survey and Challenges," *ELCVIA: electronic letters on computer vision and image analysis*, vol. 19, no. 3, pp. 0018-37, 2020.

[2] M.S. Fathollahi, and F. Razzazi, "Music similarity measurement and recommendation system using convolutional neural networks," *International Journal of Multimedia Information Retrieval*, vol. 10, pp. 43-53, 2021.

[3] R. M. Pereira, Y. M. G. Costa, R. L. Aguiar, A. S. Britto, "Representation Learning vs. Handcrafted Features for Music Genre Classification," 2019 *International Joint Conference on Neural Networks (IJCNN)*, 2019, pp. 1-8, IEEE.

[4] Y. Zhuang, Y. Chen, and J. Zheng, "Music genre classification with transformer classifier," in *Proceedings of the 2020 4th International Conference on Digital Signal Processing*, 2020, pp. 1-5, IEEE.

[5] A. Zuhair and H. Hassani, "Comparing the accuracy of deep neural networks (DNN) and convolutional neural network (CNN) in music genre recognition (MGR): experiments on Kurdish music," *arXiv preprint arXiv:2111.11063*, 2021.

[6] H. Yang and W.-Q. Zhang, "Music Genre Classification Using Duplicated Convolutional Layers in Neural Networks," in Interspeech, 2019, pp. 3382-3386, IEEE.

[7] Y.-H. Cheng, P.-C. Chang, D.-M. Nguyen, and C.-N. Kuo, "Automatic Music Genre Classification Based on CRNN," *Engineering Letters*, vol. 29, no. 1, 2020.

[8] Y. Yu, S. Luo, S. Liu, H. Qiao, Y. Liu, and L. Feng, "Deep attention based music genre classification," *Neurocomputing*, vol. 372, pp. 84-91, 2020.

[9] N. Ndou, R. Ajoodha, and A. Jadhav, "Music genre classification: A review of deep-learning and traditional machine-learning approaches," in 2021 *IEEE International IOT, Electronics and Mechatronics Conference (IEMTRONICS)*, 2021, pp. 1-6, IEEE.

[10] S. Allamy and A. L. Koerich, "1D CNN architectures for music genre classification," in 2021 *IEEE Symposium Series on Computational Intelligence (SSCI)*, 2021, pp. 01-07: IEEE.

[11] S. Chillara, A. Kavitha, S. A. Neginhal, S. Haldia, and K. Vidyullatha, "Music genre classification using machine learning algorithms: a comparison," *Int Res J Eng Technol*, vol. 6, no. 5, pp. 851-858, 2019.

[12] A. Ghildiyal, K. Singh, and S. Sharma, "Music genre classification using machine learning," in *2020 4th international conference on electronics, communication and aerospace technology (ICECA)*, 2020, pp. 1368-1372: IEEE.

[13] T. Toshniwal, P. Tandon, and P. Nithyakani, "Music Genre Recognition Using Short Time Fourier Transform and CNN," in *2022 International Conference on Computer Communication and Informatics (ICCCI)*, 2022, pp. 1-4: IEEE

[14] S. Sugianto and S. Suyanto, "Voting-based music genre classification using melspectogram and convolutional neural network," in *2019 International Seminar on Research of Information Technology and Intelligent Systems (ISRITI)*, 2019, pp. 330-333: IEEE.

[15] R. Yang, L. Feng, H. Wang, and S. Luo, "Parallel recurrent convolutional neural networks-based music genre classification method for mobile devices," *IEEE Access*, vol. 8, pp. 19629-19637, 2020.

[16] J. Mehta, D. Gandhi, G. Thakur, and P. Kanani, "Music genre classification using transfer learning on log-based mel spectrogram," in *2021 5th International Conference on Computing Methodologies and Communication (ICCMC)*, 2021, pp. 1101-1107: IEEE.

[17] Y.-H. Cheng, P.-C. Chang, and C.-N. Kuo, "Convolutional neural networks approach for music genre classification," in *2020 International Symposium on Computer, Consumer and Control (IS3C)*, 2020, pp. 399-403: IEEE.

[18] B. L. Sturm, "The GTZAN dataset: Its contents, its faults, their effects on evaluation, and its future use," *J arXiv preprint arXiv:1312.6632*, 2013.

[19] N. Srivastava, G. Hinton, and R. Salakhutdinov, "Dropout: a simple way to prevent neural networks from overfitting," *The Journal of Machine Learning Research*, vol. 15, no. 1, pp. 1929-1958, 2014.

Authorized licensed use limited to: DELHI TECHNICAL UNIV. Downloaded on May 29,2023 at 05:53:58 UTC from IEEE Xplore. Restrictions apply.

Multimedia Tools and Applications
https://doi.org/10.1007/s11042-023-15690-6

Blockchain-based distributed application for multimedia system using Hyperledger Fabric

Pratima Sharma[1] · **Rajni Jindal**[1] · **Malaya Dutta Borah**[2]

Received: 29 November 2021 / Revised: 24 February 2022 / Accepted: 23 April 2023
© The Author(s), under exclusive licence to Springer Science+Business Media, LLC, part of Springer Nature 2023

Abstract
Over the past few years, blockchain technology has acquired good faith as a modern, secure distributed network in the form of a ledger to conduct and store records of transactions. Blockchain is an evolving technological innovation that can offer solutions to real-world problems of various domains such as cloud computing, the Internet of Things, supply chain, and multimedia. In multimedia, there is an increased requirement for security due to various threats, including replicating digital data without any information loss and manipulating the same without any detection. Moreover, the security of personal multimedia systems is perceived as one of the fundamental human rights concerns. Therefore, this paper proposed a blockchain-based distributed application to secure personal multimedia data such as images, text, videos, etc. The proposed work maintains personal multimedia data's security, privacy, and integrity to meet multimedia security requirements and address the above issues. The blockchain architecture is developed on Hyperledger Fabric, a permissioned blockchain structure using Hyperledger Composer, and stores multimedia data by utilizing SWARM decentralized storage system. The proposed architecture provides a cross-platform, low-cost, and energy-efficient blockchain prototype to manage and secure personal multimedia data. Many experimental tests are conducted to evaluate the performance of the proposed work based on various parameters such as transaction latency, asset latency, throughput, power consumption, upload, and download time for multimedia data. Finally, the proposed work's robustness, feasibility, and reliability are proved by comparing it with the existing works. Results and discussion show that the proposed scheme is more efficient than the existing schemes.

Keywords Blockchain · Multimedia data · Hyperledger · Energy efficient

✉ Pratima Sharma
pratimasharma1114@gmail.com

[1] Department of Computer Science and Engineering, Delhi Technological University, Delhi, India

[2] Department of Computer Science and Engineering, National Institute of Technology Silchar, Silchar, Assam, India

Published online: 15 May 2023

1 Introduction

A multimedia is a form of communication that combines different content forms such as text, audio, images, or video into a single presentation [11]. Due to the advances in multimedia technologies, image capturing, recording of audio and video content has become very common for everyone with the help of smartphones. As the utility and usage of the Internet have grown considerably, a massive amount of personal multimedia data is being generated and used every day. Conventionally, the personal multimedia data are managed by the cloud storage providers, which are generally designed using centralized architecture and rely on trusted third parties for data processing. However, such centralized architecture may suffer from a single point of failure. The cloud storage providers may manipulate the data without users' knowledge, creating privacy and security issues [8]. One of the best-known examples of security breaches is the unauthorized and illegal access of celebrity pictures from iCloud. A collection of 500 private pictures of various celebrities were leaked on social networks such as Imgur and Reddit due to the security issues of iCloud API [10]. Hence, multimedia data security is a major concern as users fear that their data can be copied and misused through unauthorized and illegal channels. Moreover, the existing multimedia mobile applications process personal multimedia data such as images, videos, audio, and scanned personal documents in the centralized data controller [13]. Due to the involvement of a centralized data controller, data security faces some severe challenges in mobile applications. This is due to the complexity of the mobile application ecosystem: it depends not only on application development methods but also on the centralized servers. Because of this, the assessment of an application's privacy and security characteristics is difficult. For example, Photosquared photo application suffers from massive identity theft, malware, or phishing attacks, resulting in the leakage of thousands of users' photos from an unsecured S3 bucket of Photosquared application [25]. Therefore, decentralized methods are required to handle these issues by providing architecture with traceable and immutable logs. Also, the identification of roles and corresponding access control [23] should be used to protect personal multimedia data.

Blockchain technology provides a robust distributed ledger that was proposed by Nakamoto [22]. It is used in the transactions of cryptocurrencies for validation or verification purposes, such as Bitcoin and Ether. A blockchain network offers shared resources without a single failure point [26]. Therefore, it removes the central point bottleneck. In a blockchain network, a transaction stores the user's information in a block to connect to a ledger and transmit some information to other nodes, i.e., users. Blockchain technology is an economic model that combines peer-to-peer networks and uses a distributed algorithm to solve the database's synchronization problems [28]. Blockchain includes Merkle root, parent block hash, present block hash, timestamp, and other information. Here, a consensus mechanism determines how a block is added to the blockchain network [33]. A blockchain network cannot be forked, and developers from worldwide are continuing their works to extend it.

Many researchers have already developed many blockchain-based multimedia systems. Although many studies are proposed to use blockchain to manage multimedia data, there is still a requirement for better utilization of blockchain technology in the multimedia system to provide secure storage of personal multimedia data and maintain authentication, authorization, and integrity features. Many blockchain-based multimedia systems are already developed by many researchers [3, 6, 32]. For example, in [3], the authors proposed a distributed ledger-based system to ensure the integrity of the video archives. The designed

architecture utilizes the hierarchical attention autoencoder technique to compute the hashes of minutes to hour-long video or audio streams. The authors also deployed the deep neural network with blockchain technology to auto train the audio-video signatures that are sensitive to tampering to maintain the integrity of the video audio streams. However, this scheme faces access control-related issues. Vishwa et al. designed a blockchain-based media transaction framework to ensure tamper-proof features [32]. The designed architecture utilizes the watermarking technique to generate cryptographic and image hash for the multimedia data to preserve the original content. The cryptographic hash is stored as a transaction log in the blockchain network, and the image hash utilizes to identify the edited or tampered media data. Reference [6] suggested a signature-based image authentication technique using blockchain technology. The signature of the image is stored in the blockchain network to ensure security. The main issue of this scheme is that it considers only images multimedia data and ensures only authentication features. In addition, there are some critical issues in multimedia systems, such as privacy, integrity, and access control.

Furthermore, most of the existing blockchain techniques utilize the Ethereum platform with a Proof of Work mining algorithm that requires intensive computational work thus consumes a lot of energy [3, 28, 33]. Therefore, this paper proposes a blockchain-based Distributed application (Dapp) to improve the security and privacy of personal multimedia data using Hyperledger Fabric. The proposed application utilizes the Hyperledger Fabric framework to provide an energy-efficient system without using any mining process and cryptocurrency. The proposed application is developed over Hyperledger Fabric and Composer blockchain framework using standard programming languages that allow users to access services and act as nodes of the blockchain ledger. The front-end part of the proposed application provides the user interface. Here, the application users use a unique ID to access stored multimedia data. As personal multimedia data is rapidly growing with the excessive use of smartphones and social networks, it is difficult to save all multimedia data on the ledger. Due to the limited capacity of the blockchain nodes, this paper uses SWARM, decentralized storage, and a shared document system, which supports high integrity and durability in data storage [31]. In the proposed scheme, the SWARM framework assigns a unique hash to the uploaded multimedia file, and the generated unique hash is saved on the blockchain. Thus, the proposed scheme allows the collection of large-scale multimedia data with excellent usability. Here, to improve data security, only authorized users can access their respective multimedia files.

1.1 Motivation of the work

In multimedia, there is an increased requirement for security due to various threats, including replication of digital data without any information loss and manipulations of the same without any detection [25]. As the utility and usage of the Internet have grown considerably, multimedia documents are easily copied through unauthorized and illegal channels [23]. Therefore, the users fear the threat that their data can be copied easily. Cloud storage provider offers services to store users' multimedia data, but it relies on trusted third parties for data processing. Cloud server reveals customer privacy to commercial benefit [13]. Cloud providers may release users' data for scientific research advertising without the customer's consent to increase their profits. Existing multimedia systems incorporated the data controller to process personal user data. Due to the involvement of a centralized data controller, data security faces some serious challenges. Enforcing proper security measures on multimedia information has therefore become vital. Thus, there is a requirement to develop

a secure blockchain-based distributed application for managing personal multimedia that does not involve trusted parties and is completely decentralized [26]. Therefore, a flexible, fault-tolerant, and safe blockchain-based application is needed to meet multimedia security requirements. To address the above issues, we design a secure personal multimedia data management architecture focused on blockchain technology, where multimedia data is encoded to control access, ensure integrity checking and use storage techniques for storing the multimedia data.

1.2 Contributions

The principal contributions of the work are defined as follows.

1) In this paper, a blockchain-based distributed application has been proposed to protect large-scale personal multimedia data using the energy-efficient Hyperledger Fabric framework. The proposed architecture provides a complete distributed approach to generate key-related information and provide security features without involving any centralized authority using the blockchain structure.
2) The proposed scheme implements cryptographic algorithms to store multimedia data securely. It provides confidentiality by using encryption technique to encode multimedia data. The integrity feature is achieved using the blockchain-based Merkle root concept. The proposed scheme also maintains the access control feature, thus ensuring privacy-preserving features.
3) The proposed work utilizes the SWARM decentralized storage system to store the multimedia files such as images, videos, documents, etc., in a distributed manner. The SWARM system returns the unique hash to the user for the stored data utilized by the user for access purposes. Thus, it reduces the processing overload.
4) Various experimental tests are conducted to evaluate the performance of the proposed work using the parameters such as transaction latency, throughput, access time, upload, and download time for multimedia data. The proposed work also compared with the state-of-art techniques to measure its reliability and feasibility. The results and discussion prove that the proposed scheme is very effective.

The rest of the paper is organized as follows. Some related works are discussed in Section 2. The background details of the proposed work are described in Section 3. The proposed scheme is discussed in Section 4. Section 5 presents the proposed architecture smart contract functions. Section 6 deals with the results and discussion. Finally, the conclusions and future work are presented in Section 7.

2 Related work

This section presents the review work related to the conventional multimedia system architecture based on blockchain. Many studies have discussed the advantages of using blockchain in multimedia systems [4, 12]. For example, in [4], the authors present blockchain technology's ability to solve media problems such as plagiarism, copyright, and unauthorized distribution. Similarly, in reference [12], the authors explore the security aspect of blockchain technology in multimedia applications. They also identify multimedia data's authentication, privacy, and trust features with the convergence of blockchain with the IoT

domain. Han et al. [9] propose an auditable access control model using blockchain technology for the IoT environment. The proposed model controls the private data access in IoT by jointly managing the access control policy and the access records using the smart contracts. Shi et al. [30] design a blockchain-based architecture for multimedia sharing in vehicular adhoc networks. It uses cryptographic algorithms to hide the identity of the users, vehicles, and roadside units. Kumar et al. [16] propose a blockchain-based peer-to-peer network to provide image and video sharing platforms. The proposed network uses the perceptual hash to detect the tampered images and videos but lacks the access control feature. In reference [20], the authors utilize the data aggregation scheme to manage big multimedia data and personal multimedia data and improve the system performance using the batch verification technique. The designed scheme includes a certificateless batch verification approach to tackle the key escrow problem of multimedia terminals. The proposed scheme avoids the bilinear pairing technique to provide a lightweight environment to collect multimedia documents. However, this scheme is deficient from the advantages of blockchain technology to provide a more secure system for multimedia data. Many researchers have proposed advanced schemes to improve multimedia systems' security, performance, and efficiency [15, 18, 19, 24]. Khan et al. [15] present a blockchain-based architecture for multimedia forensics investigations. The proposed architecture collects, analyses, and interprets the digital evidence to perform different operations in forensics. In reference [18], the authors developed a blockchain-based architecture to manage multimedia data using a decentralized storage system. The designed architecture uses decentralized identifiers to manage the copyright owners' identity and provides a multi-level capability-based access control method for the multimedia data. The designed work only focuses on the multimedia data generated by well-known applications such as Netflix, Amazon Prime, etc., with the help of maintaining copyright information on blockchain technology. This scheme lacks the management of personal multimedia data generated by individuals using smartphones. Nandakumar et al. [24] present a decentralized architecture to provide multimedia integrity protection without involving trusted third parties. The presented work ensures multimedia data safety using sanitizable signatures by recording on the blockchain network. It utilizes smart contract functionality with the chameleon hash function and Merkle tree to ensure the integrity verification process of multimedia data, thus increasing the system's complexity.

Furthermore, in reference [19], the authors ensure sharing and privacy protection model for communicating multimedia data using blockchain technology. The proposed scheme designs a security-proof layer for encrypting and decrypting multimedia data. However, this work lacks the implementation of an access control mechanism. In [7], the authors develop a novel integrity verification method for video multimedia data using blockchain technology. The designed work integrates hash-based message authentication code and elliptic curve cryptography techniques to verify the integrity of video data. It bifurcates the video data into the same size segments and creates a chronological chain to create a database. The verification method recalculates the hash of the video segments and compares them with the hash store on the blockchain structure. This scheme only focuses on the integrity feature of the video data without providing authentication, authorization, and access control features. In reference [14], the authors propose the blockchain-based architecture to summarize video data to remote IoT devices using the secured channel. The proposed system allows users to summarize videos considering humans and objects as parameters. The cryptographic hash is calculated and stored in the blockchain structure for each video summarized block. It uses the cumulus blockchain technique to protect the integrity of the video data. The proposed scheme only considers the video multimedia data. In [17],

the authors design a cross blockchain-based architecture for Secure Service Discovery (SDD) for the Internet of Multimedia Things (IoMT). The proposed system resists the tampering and eavesdropping in the propagation of encrypted location information between different applications using cross-blockchain-based fog computing technique. It ensures the trust propagation process between multiple parallel blockchain systems. Table 1 summarize the strength and weakness of the existing techniques.

3 Preliminaries

This section briefly explains the essential components of the proposed blockchain-based architecture to secure multimedia data.

3.1 Blockchain technology

Blockchain technology is a list of records, called blocks, connected using cryptographic algorithms. Each block holds the cryptographic hash value, previous block hash, a timestamp, and Merkle root for the transaction data. The block hash value is derived from the previous block hash and contains the previous block hash information to form a chain. Therefore, the blockchain is resistant to manipulation attacks because once the data is recorded, the data in any block cannot be changed without altering all the subsequent blocks. The timestamp value is used to get the block hash and proved the transaction data existed within the block. The Merkle tree utilizes cryptographic hash functions to create the binary tree structure by combining the leaf nodes to form intermediate nodes and the root node. The blockchain transaction data is divided into multiple chunks stored at the bottom of the tree structure as leaf nodes, and then intermediate nodes are created by combining the hash values of the child nodes. Finally, the Merkle root combines its two child nodes and forms the tree's top root node. Merkle root helps validate the data stored in leaf nodes as hash values and considers all transactions signatures that are part of the block in the blockchain network. Blockchain is a peer-to-peer network that uses a distributed ledger shared with the network participants. Moreover, the consensus algorithm ensures the security of the blockchain network by allowing multiple untrustworthy nodes to agree on a single data block. Smart contracts are programs deployed on the blockchain network to establish the contractual rules among the network participants [29]. As a result, blockchain technology provides high-security features for its application scenario [27], such as a multimedia system. The most significant aspect of blockchain technology is decentralization. It indicates that the central authority does not manage blockchain transactions. This remarkable property has several intriguing advantages, including reducing the chance of a single point of failure problem due to a breakdown of centralized authority, minimizing operations expenses, and increasing reliability.

3.2 Hyperledger Fabric

Hyperledger Fabric [1] is developed by IBM as a distributed ledger solution under the Linux Foundation. It provides a permissioned blockchain platform with modular architecture features. Because Hyperledger is private and requires permission to access, businesses can segregate information, and transactions execute in less time as the number of nodes on the network is reduced. The Fabric is a highly modular distributed ledger

Table 1 Strength and weakness of related works

Reference	Findings	Technique used	Features	Limitations
[15]	Propose a blockchain-based architecture for digital multimedia forensics investigation.	Hyperledger sawtooth with Practical Byzantine Fault Tolerance (PBFT) algorithm.	Provide integrity, prevention, and preservation mechanism.	Specially designed for forensics investigations.
[18]	Propose a blockchain-based multimedia data management architecture.	Multi-level capability-based access control and smart contracts.	Ensure identity management scheme with the access control mechanism.	Utilizes the on-chain workflow, which increases the blockchain complexity.
[24]	Design a novel signature scheme to sign the multimedia content during creation time using blockchain technology.	Chameleon hash function and Merkle tree.	Provide integrity checking of multimedia content.	System complexity is high.
[19]	Combine multi-technology with blockchain to preserve multimedia data.	Elgamal signature scheme and secure multi-party computation based shamir secret sharing.	Ensure authentication scheme with data access protection.	Lacks details of integrity checking feature.
[7]	Propose a novel video integrity verification scheme using blockchain technology.	Elliptic curve cryptography with hash and message authentication code.	Attain integrity and authenticity verification features.	Consider only video multimedia data.
[14]	Design a video summarization system to allow secure transmission using blockchain technology.	Cumulus blockchain and X-mean clustering.	Provide integrity checking feature.	Consider only video multimedia data.
[17]	Suggest a novel privacy-preserving service discovery process with parallel blockchain networks.	Location-based service database, chaotic system, and generalized Arnold transform with cross-blockchain.	Achieve privacy-preserving features.	Involvement of complex functions increases the computational overhead.
Proposed work	Propose a blockchain-based distributed architecture to protect large-scale personal multimedia data using the energy-efficient Hyperledger Fabric framework.	Hyperledger Fabric, and composer with SWARM storage system.	Maintain security, privacy, access control, and integrity features.	Lacks the scalability details for handling increasing multimedia data.

technology that provides a foundation for developing blockchain-based products, solutions, and applications using plug-and-play components. The main features of this framework are faster transactions, streamlining data sharing, and updated smart contract technology. Hyperledger Fabric supports membership based on permission; all network participants must have known identities to participate in the blockchain network. The main advantage of using the Hyperledger Fabric is employing a PBFT consensus algorithm [21]. The proposed architecture is implemented using the Hyperledger Fabric framework that bounds the data protection regulations to maintain multimedia data and provide access control features. The proposed Fabric architecture contains pre-defined parties for maintaining the personal multimedia data without any centralized authority. The fabric has various components, as explained below:

Membership Service Provider (MSP): The MSP is responsible for all the cryptographic techniques such as identity management, generation and verification of the signature, issuing and validating user certificates, and maintaining authentication features in the proposed architecture. The Fabric certificate authority API of Hyperledger Fabric is responsible for providing an interface for MSP. It also provides flexibility to the participating organizations to deploy an external certificate authority. The configuration of the MSP needs to be specified locally at each peer and orderer to enable the signing process. The MSP is also set up on the channels to allow peer, orderer, and client identity verification and respective signature validation.

Consensus Algorithm: The consensus algorithm is the core part of the blockchain network, which validates and updates the transactions in the ledger. It implements the procedure through which all the blockchain network nodes reach a common agreement about the present state of the distributed ledger. In this way, the consensus mechanism attains reliability and maintains trust between unknown nodes in a distributed blockchain network. The proposed architecture deploys a PBFT [21] consensus algorithm that does not need the mining process to attain consensus in the blockchain network. The consensus mechanism's functionality depends on the smart contract layer determining which transactions will be added and rejecting invalid transactions.

Couch database: Hyperledger Fabric architecture supports two databases, LevelDB and CouchDB. LevelDB uses a key-value pair-based method to store chaincode data and maintains key, key-range, and composite queries. LevelDB acts as a default state database of the peer nodes of Hyperledger Fabric. CouchDB [1] is an on-chain database that stores the information in JSON format rather than key-value pairs. In the proposed architecture, CouchDB improves security and protects personal multimedia data.

Hyperledger Composer: Hyperledger Composer [5] is a collection of tools that model and design the business network of the blockchain network. It provides an easy and quick approach for business owners and developers to design smart contracts and blockchain applications. Hyperledger composer defines the business network with smart contract functions in the proposed architecture. It also creates the access control rules in ACL files, defines the assets, and defines queries to query the state database.

Chaincode: Chaincodes are the smart contracts that define the network transactions rules and are currently written in Java language that is instanced by the valid users of the channel peers. These self-executing codes include the application logic for personal multimedia transactions such as authentication, uploading multimedia data, accessing processes, and checking the integrity of uploaded multimedia data. The smart contract functions are executed for each user request to grant permission and provide access to the services of the proposed architecture.

SWARM Storage System: SWARM is a distributed storage system that stores the user documents in a peer-to-peer blockchain network [31]. SWARM supports data-streaming, and storage services in which participants share bandwidth and storage space to provide the necessary infrastructure for the services. It collectively stores the encrypted data of users in a distributed way. In the proposed scheme, storage nodes are dependent on SWARM, and its framework is maintained and controlled by the blockchain network. The SWARM storage system divides the large multimedia files into multiple chunks and distributes them in the peer-to-peer network. SWARM utilizes a method of addressing the content in which location is extracted from the document's contents.

4 Proposed work

The proposed architecture is shown in Fig. 1. The designed framework utilizes Hyperledger Fabric, Hyperledger Composer, Chaincode, CouchDB, Angular 4, Composer Rest Server, SWARM storage, and Fabric Client. Hyperledger Fabric is a permissioned blockchain network that provides distributed ledger solutions with the help of smart contracts called chain codes which can be written in Go, Java, and Node.js to provide basic functionalities to the users. Hyperledger Fabric provides a fast (10 K transactions per second) and energy-efficient (no mining or no cryptocurrency) [5] blockchain solution for the proposed architecture. Hyperledger Composer models and develops the business logic for the blockchain network by creating smart contract functions for decentralized applications. Angular

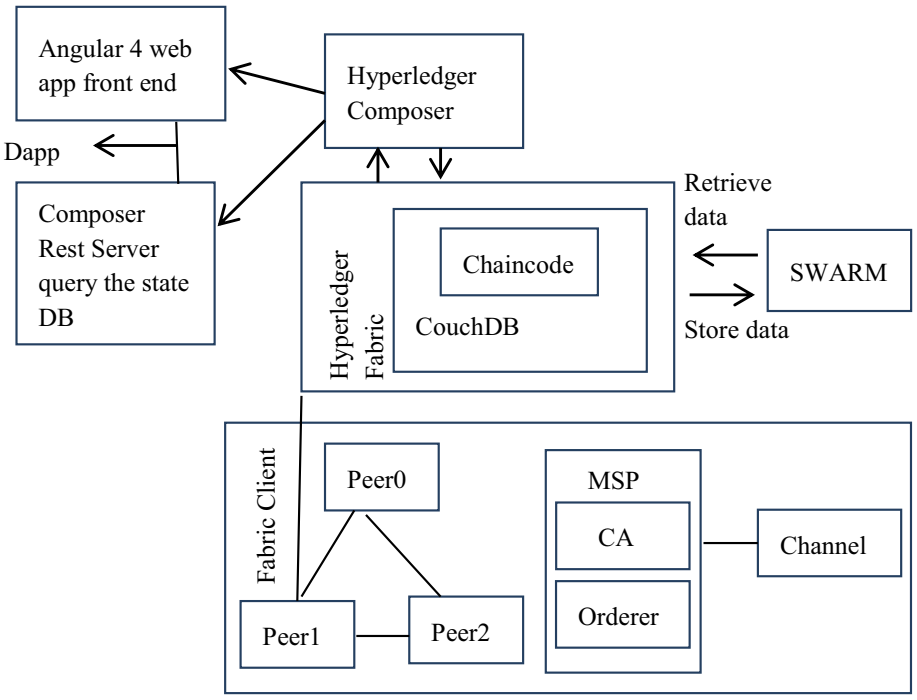


Fig. 1 Proposed architecture

4 is used for creating the front-end part of the decentralized application that communicates with the Composer Rest Server to visualize the CouchDB, the state database. The Angular framework provides the interaction between the Dapp admin to the user interface. The Dapp processes the user requests to the Hyperledger Fabric network using a REST API called Composer Rest Server. The Composer Rest Server retrieves the present state of the CouchDB database, and the Angular framework uses the GET calls to the Composer Rest Server to retrieve the data from the database. The proposed architecture deploys two solutions (1) implements an on-chain database using CouchDB to provide a secure network of Hyperledger Fabric, (2) uses an off-chain database using SWARM decentralized storage system to store the personal multimedia data in the distributed manner securely. The proposed architecture user interactions or requests are recorded in the form of transactions of the blockchain network that are only visible to the related users and secured via cryptography. The proposed application combines with an identity management scheme in which the ledger acts as a supreme indicator to verify the user identity using the transactions history stored in a blockchain ledger. Each transaction is identified using a unique hash value that ensures the integrity of the personal multimedia data. If the records have been tampered with, it produces a different hash value that will not match the previous hash value.

Furthermore, the proposed architecture incorporates three peer nodes in an organization with one anchor peer node as a validating node and an ordering node Kafka using the single public channel to register the network users. The proposed scheme configured multiple peer nodes to access the CouchDB database and SWARM decentralized storage system. It also involves a single ordering node, certificate authority, MSP, and chain codes to connect to the blockchain network. Further, the network can be extended to include multiple peer nodes and organizations configured in different machines to provide scalability features. It has ledgers and corresponding smart contracts that access the ledger to provide users with functionality. The proposed Hyperledger Fabric network is developed for a single organization having three peer nodes that use the docker containers on the local computer. But in a real-world scenario, each peer node belongs to separate IP networks or cloud systems. The proposed work designs the single channel so that the composer communicates with peer nodes using the channel. The organization contains three peer nodes denoted as $Peer_0$, $Peer_1$, and $Peer_2$, and each peer node holds a copy of the ledger and smart contracts, as shown in Fig. 2. The proposed application requests a transaction T to peer nodes $Peer_0$, $Peer_1$, and $Peer_2$ using channel C. During the execution of each transaction, and the chaincode will be installed to the peer nodes. The proposed application communicates with peer nodes and executes chaincode to query or update the ledger. The designed framework stores the transactions as blocks with hash values in the blockchain structure that defines the history of changes requested by the different users. The block in the ledger denotes the multimedia data Meta detail of a user u that contains transaction workload as $W_t(u)$, previous transaction hash as $W_p(u)$, and current transaction hash as $W_c(u)$. Thus, the total workload of the block is calculated as $W_{tot}(u)$:

$$W_{tot}(u) = W_t(u) + W_p(u) + W_c(u)$$

The proposed architecture measures the energy efficiency of the model in terms of power consumed by the nodes for transferring the data in the blockchain network. Thus, the proposed architecture utilizes the power consumption concept to calculate the power consumed by each node while transferring data or transaction-related information from one end to another end. When a node transfers the data from one end to another, it consumes

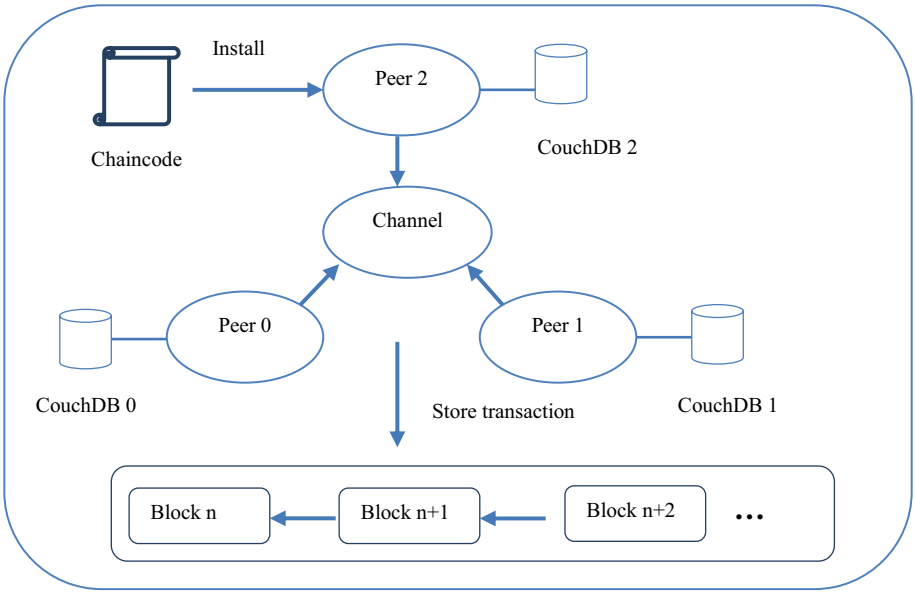


Fig. 2 Node structure of the proposed blockchain network

P_s amount of power, whereas receiving the data from another node consumes P_r amount of power. The Dapp admin is responsible for tracking the power consumption of each node required to transfer the transaction or data to the network nodes as it is different for each node. Table 2 shows the details of notations used in this paper.

$$Total_{powerconsumption} P_t = P_s + P_r$$

5 Smart contract functions

This section presents all the functions of the smart contract. In the proposed scheme, the smart contract mainly executes all the important tasks based on the received information. The smart contract in the proposed scheme comprises various functions: (1) User registration function (2) Add record function (3) Access control function (4) Integrity checking function (5) Power consumption calculation function. There are the following main algorithms or functions:

5.1 User registration function

Figure 3 shows the user registration process of the proposed architecture. The designed system allows users to register in the distributed application using the general sign-up process. Users can be individuals willing to store their data on the decentralized application securely. The developed architecture registers the user and, in response, provides login credentials such as email ID and password. The proposed work maintains the user details on the CouchDB database shared during the registration process. The Composer Rest

Table 2 Notations and descriptions

Notations	Descriptions
C	Channel of the Hyperledger Fabric
u	User
$W_t(u)$	Transaction workload
$W_p(u)$	Hash of the previous transaction
$W_c(u)$	Hash of the current transaction
$W_{tot}(u)$	Total workload of the block
P_t	Total power consumption of each node
P_s	Amount of power consumed for sharing the data
P_r	Amount of power consumed for receiving the data
PK_u	Public key of the user
SK_u	Secret key of the user
$User_{details}$	Personal details of the user such as username, address, and contact details
$User_{credentails}()$	Function to generate login credentials for the user
$User_{email}$	Email ID credential of the user
$User_{password}$	Password of the user
$Hash_{pass}$	SHA-256 generated hash of the password
F_{hash}	SHA-256 generated hash of multimedia file
CT	Generated cipher text
$Swarm_{hash}$	File hash value returned by SWARM storage system
F	Multimedia file
F_{ID}	Unique identifier of the file
$TransID$	Transaction identity
$Access_{request}()$	Function to send a data access requests to the Dapp
$Retrieve_{Details}()$	Function to retrieve user details from the blockchain
$Verify()$	Function to match the user public key with the file identifier
$Access()$	Function to request ciphertext from the blockchain network
$Fetch()$	Function to fetch the ciphertext from the SWARM storage system
$Send()$	Function to send the ciphertext to the user
$Decrypt()$	Function to decrypt the ciphertext
$Integrity_{check}()$	Function to send the integrity checking request to the Dapp
$RECALCULATE_Hash()$	Function to recalculate the hash of the decrypted file for integrity checking process

Server uses Rest API to visualize and query the values stored in the on-chain database, i.e., CouchDB for the deployed blockchain business network. Moreover, the network admin is responsible for adding user nodes in the blockchain network after the validation from the consensus nodes. The users will be included in the proposed system with the help of their username and password credentials. The designed application also generated public-private key pairs PK_u and SK_u for each user during the registration process. The user will utilize the generated private key to encrypt and decrypt the personal multimedia file, whereas the public key will be used as a user's address. The proposed architecture uses the SHA-256 hashing algorithm to store the user password in the hash format in the Hyperledger Fabric blockchain network to provide a more secure environment for the user. The following algorithm presents the sequential steps required for the registration process.

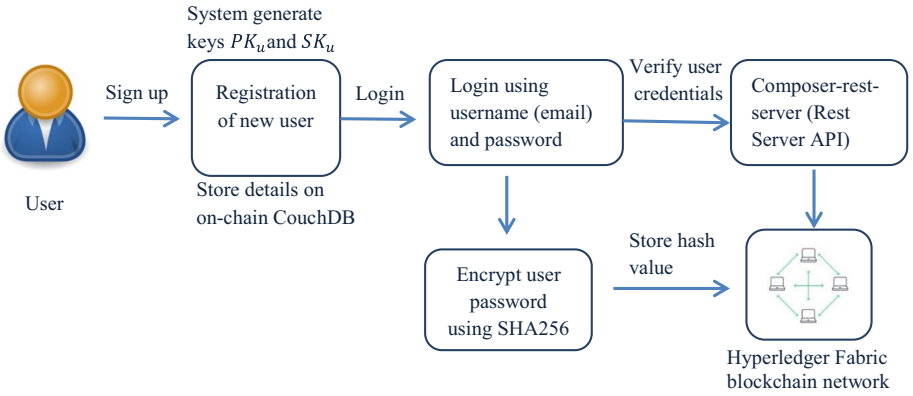


Fig. 3 User registration process

Algorithm 1 User registration function

Input: User details $User_{details}$
Output: Login credentials $User_{email}$, $User_{password}$

1. User u $(User_{details})$ $\xrightarrow{request}$ Dapp
2. for each user Dapp
3. GENERATE PK_u and SK_u
4. STORE $User_{details}$ →CouchDB
5. GENERATE $User_{credentials}(User_{email}, User_{password})$
6. COMPUTE $Hash_{pass} \leftarrow SHA256(User_{password})$
7. SAVE $Hash_{pass}$ → Network
8. end for

5.2 Add record function

Figure 4 presents the multimedia file upload process in the proposed architecture. The distributed application allows users to login into the system using a shared email ID and password. The application verifies the login details using the CouchDB database of the blockchain network. After the verification process, the user executes the proposed

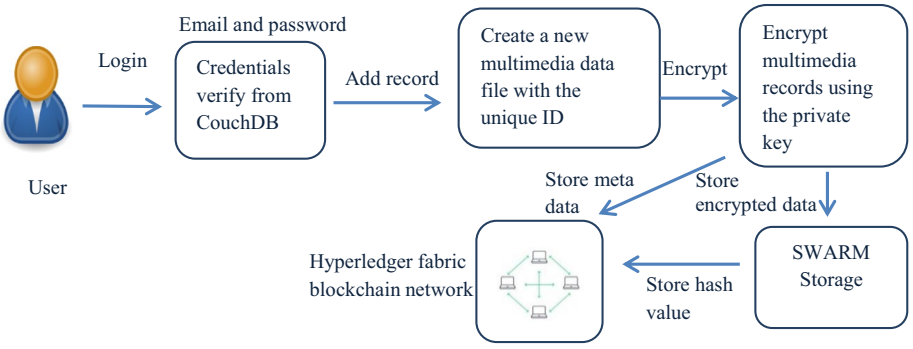


Fig. 4 Add multimedia file process

architecture add record smart contract function using the add data option available on the application's portal. The user creates the Meta details for the multimedia data, such as file unique identifierF_{ID} and file hash F_{hash}using SHA256 hash algorithms and stores the details on the user portal. Once the Meta details are saved, the user encrypt the personal multimedia file using Advanced Encryption Standard (AES) encryption algorithm with the help of private key SK_u. The encryption algorithm converts the multimedia plaintext into ciphertext CT. Then, the encoded ciphertext is uploaded on the SWARM decentralized storage system, and the returned hash is stored on the Hyperledger Fabric blockchain network. The below algorithm provides the stepwise details of the uploading process.

Algorithm 2 Add record function $Add_{record}(PK_u, F)$

Input: User and file details PK_u, F Output: Transaction ID $TransID$
1. for each file 2. CALCULATE hash for each $F_{hash} = SHA256(F)$ 3. ENCRYPT file using AES $CT \leftarrow Encrypt(F, SK_u)$ 4. STORE file and user details on blockchain $(PK_u,\ F_{ID}, F_{hash})$ 5. UPLOAD CT to Swarm 6. STORE Swarm hash $Swarm_{hash}$ on blockchain 7. RETURN $TransID$ 8. end for

5.3 Access record function

Figure 5 presents the steps required to access the personal multimedia file stored on the proposed blockchain network. Users login into the proposed system with the help of provided credentials. After the successful login, the user requests the multimedia file with file identifier and hash values to the proposed system. The system verifies the user details with the file details from the values stored in the blockchain network. After the verification process, the user allows access to the data from the SWARM storage system. SWARM storage system generates the composite encrypted data and sends the encrypted file to the user. The user receives the encrypted multimedia file and uses the AES decryption algorithm to decrypt the received file using a private key. The following algorithm shows the steps required to access the multimedia data stored on the blockchain network.

Algorithm 3 Accessing file $Access_{Request}(PK_u, F_{ID})$

Input: User and file details PK_u, F_{ID} Output: File F
1. User REQUEST for file $Access_{Request}(PK_u, F_{ID})$ 2. Dapp RETREIVE user file details from blockchain $Retrieve_{Details}(PK_u, F_{ID})$ 3. if $(Verify(PK_u, F_{ID}) == True)$ 4. Dapp REQUEST ciphertext from blockchain $Access(PK_u, F_{ID})$ 5. Blockchain FETCH the requested File from SWARM $Fetch(PK_u, F_{ID})$ 6. Dapp SEND retrieved ciphertext to user $Send(CT)$ 7. User DECRYPT ciphertext $F \leftarrow Decrypt(CT, SK_u)$ 8. else 9. Access request is DECLINED.

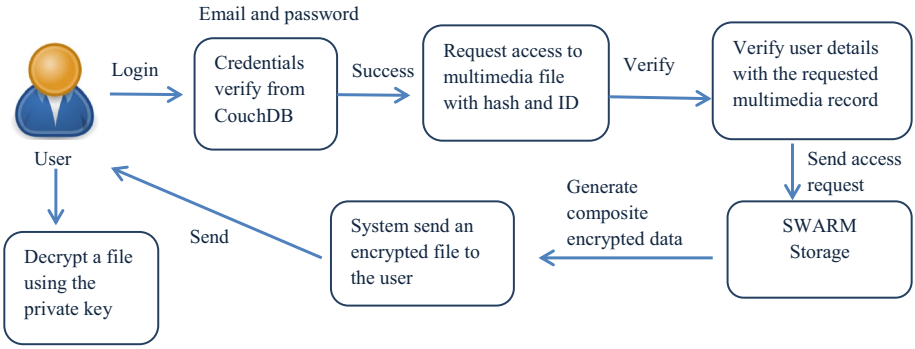


Fig. 5 Multimedia access file process

5.4 Integrity checking function

The proposed architecture allows users to check the integrity of the stored multimedia files, as shown in Fig. 6. The user can initiate the integrity check request to the distributed applications. The application verifies the user and multimedia file details from the blockchain network. After the verification process, the user fetches the ciphertext from the SWARM decentralized storage system using the $Swarm_{hash}$ and performs the decryption process to recalculate the hash of the decrypted file. Then, the user compares the recalculated hash value with the hash value retrieved from the blockchain network. If hash values match, then the multimedia's integrity is maintained; otherwise, the integrity is compromised. The below algorithm defines the steps required for integrity checking.

Algorithm 4 Integrity check $Integrity_{Check}(F_{ID})$

Input: File identifier F_{ID} Output: True/False
1. User sends REQUEST for integrity checking $Integrity_{Check}(F_{ID})$ 2. Blockchain RETURN F_{hash} 3. User FETCH ciphertext from SWARM and DECRYPT $F \leftarrow Decrypt(CT, SK_u)$ 4. User RECALCULATE $RECALCULATE_Hash(F)$ 5. if $F_{hash} == RECALCULATE_Hash(F)$ 6. Integrity is VERIFIED 7. else 8. Integrity is NOT VERIFIED

5.5 Power consumption calculation function

The proposed architecture provides an energy-efficient model using the node-wise power consumption concept. The power consumption measures the processing time required by the node to process the received transaction or data element and send it to another network node. This function automatically calculates the power consumed by the network node after the successful commitment of each transaction. It keeps a record of transferring and receiving data or transactions and node details involved in the transaction and calculates the value of P_s and P_r as these values are different for each node. A maximum of 1000

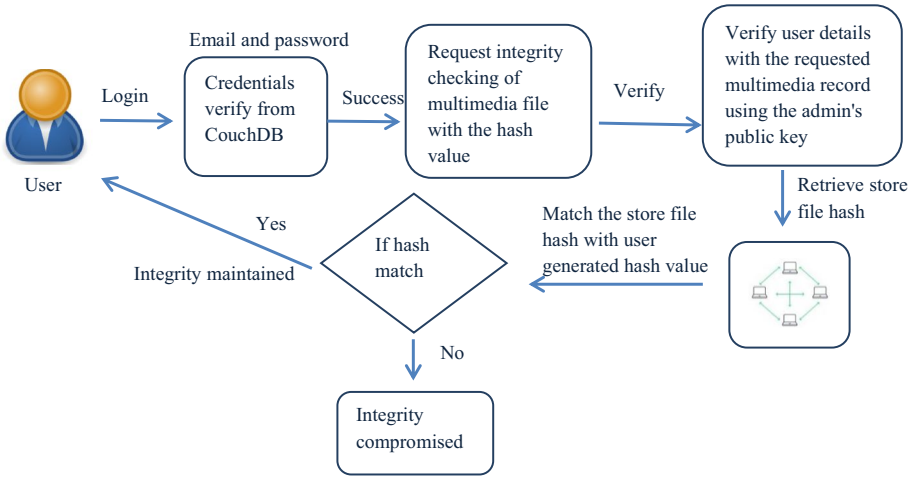


Fig. 6 Integrity checking process

rounds is monitored with a checkpoint of 100 transactions to calculate the total power consumption of each node as depicted in below algorithm 5.

Algorithm 5 Power calculation $Calculate_{power}(PK_u, windowsize)$

Input: Node Details PK_u, Window size Output: Total Power Consumed P_t
1. for each Node n 2. for each transaction T 3. CALCULATE Ps and P_r power parameters 4. end for 5. CALCULATE total power, $P_t = \sum_1^{windowsize} P_s + P_r$ 6. end for

6 Results and discussion

This section analyses the performance of the proposed application and compares it with the state of art techniques.

6.1 Performance evaluation

Various experiments are performed on the proposed architecture to measure the performance parameters such as transaction latency, throughput, access time, upload, and download time for multimedia data. The transactions of the proposed work are defined for the smart contract functions such as register, add a record, access request, and integrity check. Firstly, the experiment is conducted to measure the latency of transaction sets, as shown in Fig. 7. The latency measures the time required to commit the transactions and make them available to the other network nodes. The following equation used to calculate the transaction latency:

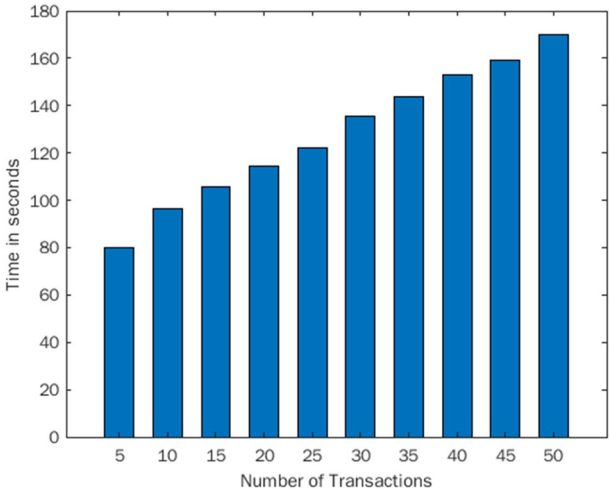


Fig. 7 Transaction latency of the proposed architecture

$$T_l(n) = T_c(n) - T_s(n)$$

In the above equation, $T_l(n)$ denotes the transaction latency, $T_c(n)$ represents the node confirmation time, and $T_s(n)$ denotes the transaction submission time. Many sets of transactions were carried out on the Hyperledger blockchain network. In each set, the number of transactions ranges from 5 to 50. It is analyzed from Fig. 7 that the initial 5 transactions required an average of 80 s to confirm across the blockchain network, and the final 50 transactions set took an average of 70 s.

The performance analysis of the proposed architecture is further extended to the BLOCKBENCH environment [2] to analyze the transaction latency for a large number of transactions ranging from 50 to 500. BLOCKBENCH provides an evaluation framework to analyze the private blockchain networks. It is combined with the proposed architecture via APIs to measure the overall performance in terms of latency and throughput

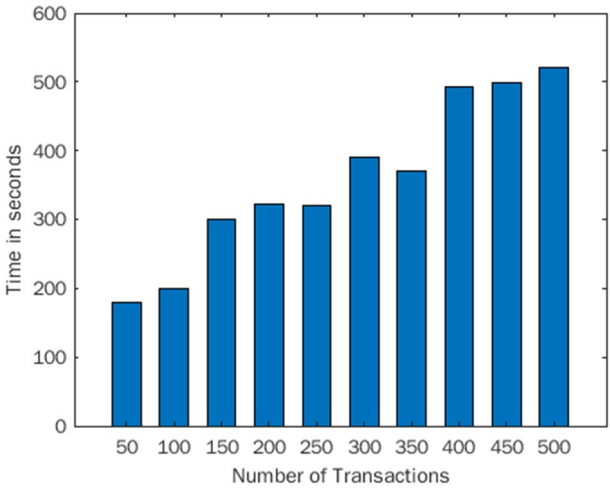


Fig. 8 Transaction latency of the proposed architecture using BLOCKBENCH simulation

for a large number of transactions. As shown in Fig. 8, we have extended the transaction latency analysis of the proposed architecture using the BLOCKBENCH environment for transactions ranging from 50 to 500. It is observed that an average of 520 s was required to execute 500 transactions in the BLOCKBENCH environment, and transaction latency showed the increment curve. Furthermore, to perform comparative latency analysis, the proposed architecture deploys in three organization structures with one peer node, two peer nodes, and three peer nodes using BLOCKBENCH. The comparative analysis of transaction latency for three different organization structures is shown in Fig. 9. The transactions for all structures range from 5 to 50, and average latency is calculated for different structures one after another. It is observed that the time required to execute the transactions increases with an increase in peer nodes and an increase in the number of transactions. For ten sets of transactions, an organization with 1 peer takes 45 s, an organization with 2 peers takes 72 s, and an organization with 3 peers takes 80 s for the initial 5 transactions set. Similarly, for 50 transactions set, an organization with 1 peer takes 135 s, an organization with 2 peers takes an average of 89 s, and an organization with 3 peers takes an average of 99 s. Therefore, it shows that the increment in the number of peer nodes increases the transaction latency time of the organization.

Secondly, the proposed blockchain network performance is analyzed based on transaction throughput. The throughput denotes the rate at which the blockchain network confirms the transactions in a definite time. Consider there are n nodes in the Hyperledger blockchain network, $T_t(n)$ denotes the throughput of the transaction, $T_{comm}(n)$ represents the total number of confirmed transactions of the network, and $T_{tot}(n)$ symbolizes the total time:

$$T_t(n) = T_{comm}(n)/T_{tot}(n)$$

Figure 10 represents the throughput in terms of Transactions Per Minute (TPM) for the set of transactions. The experiment is carried out to determine the throughput of the proposed system—the initial set of 5 transactions required around 4 TPM in the blockchain network. Similarly, the final set of 150 transactions took approximately 32 TPM.

The throughput analysis is further extended using BLOCKBENCH environment for a large number of transactions ranging from 50 to 500. As shown in Fig. 11, the initial set of 50 transactions requires the throughput at the rate of 27 transactions per minute, whereas the last

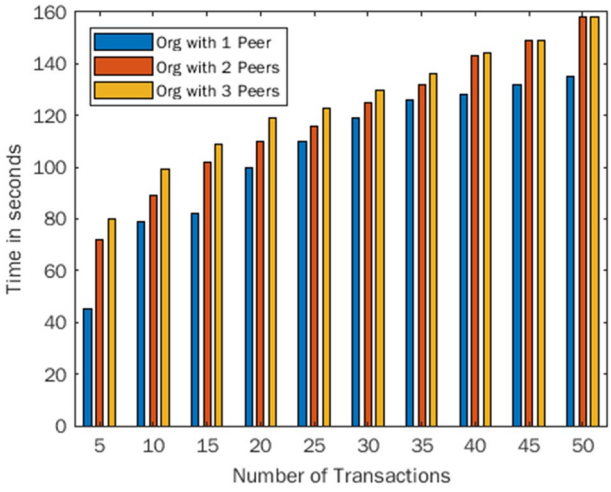


Fig. 9 Comparative analysis of organization wise transaction latency of the proposed architecture

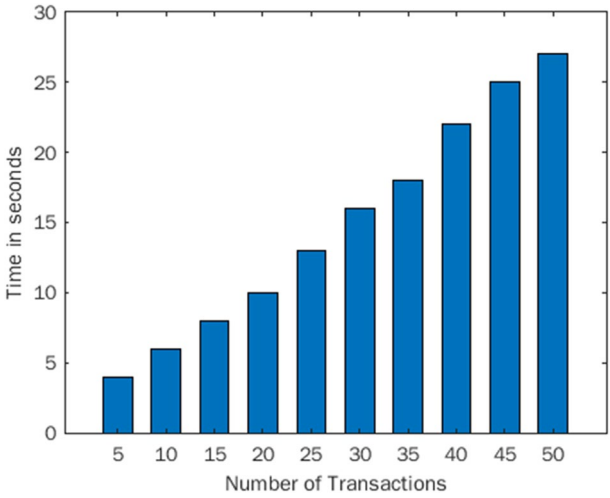


Fig. 10 Throughput of the proposed architecture

set of 500 transactions needs a rate of 85 transactions per minute to commit in the proposed architecture. Thus, the throughput rate increases by increasing the number of transactions in the proposed architecture. Similarly, the throughput of the proposed architecture is analyzed for different organization structures with a different number of peer nodes. The transaction throughput of the proposed architecture for the organization with 1 peer node, 2 peer nodes, and 3 peer nodes is calculated in Transactions Per Minute. The comparative analysis of transaction throughput of the proposed architecture for different structures is shown in Fig. 12. It is observed that the rate of throughput for the organization with 1 peer is higher than the organization structure with 2 and 3 peer nodes.

The asset in the proposed architecture denotes the Meta details of multimedia data such as images, videos, audios, scanned documents, files, etc. The asset latency measures the time required by the blockchain network to load the asset details on the CouchDB database successfully. For n number of nodes in the blockchain network, $A_l(n)$ denotes the asset latency, $T_r(n)$ represents the response time, and $T_s(n)$ denotes the submission time in a millisecond, then.

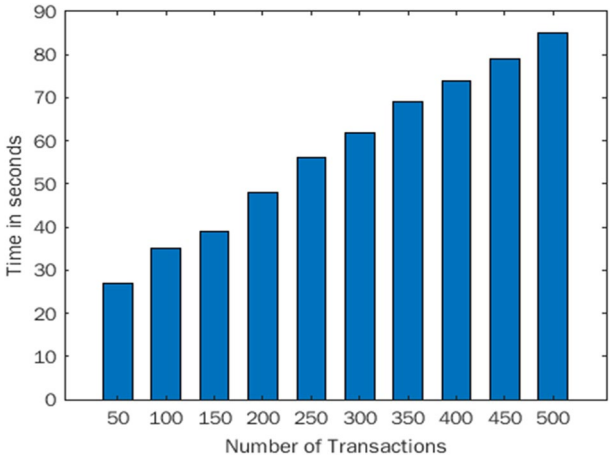


Fig. 11 Throughput of the proposed architecture using BLOCKBENCH simulation

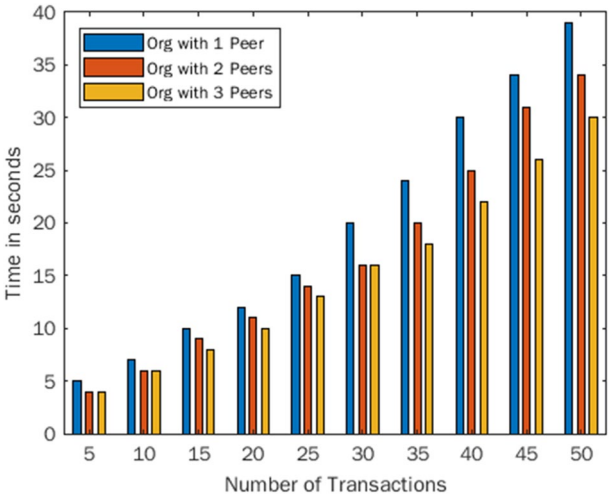


Fig. 12 Comparative analysis of organization wise throughput of the proposed architecture

$$A_l(n) = T_r(n) - T_s(n)$$

Figure 13 shows the asset latency time required by the blockchain network. It is observed that the asset size of 154 K bytes required around an average of 2.6 s, and 1000 K bytes size took around an average of 2.7 s.

The proposed system is capable of processing and uploading large size multimedia files and achieves scalability and efficiency features. The efficiency of the proposed architecture is measured by analyzing the time required to upload and download the different-sized multimedia files. This experiment analyses the processing time for different multimedia data such as images, video, and scanned documents or PDFs to measure the performance of the SWARM storage system. Figure 14 presents the upload and downloads time required for the multimedia image file to store on SWARM in the proposed blockchain network. The results are considered for executing the transactions concurrently from multiple users. For a 100 MB file, the proposed system requires

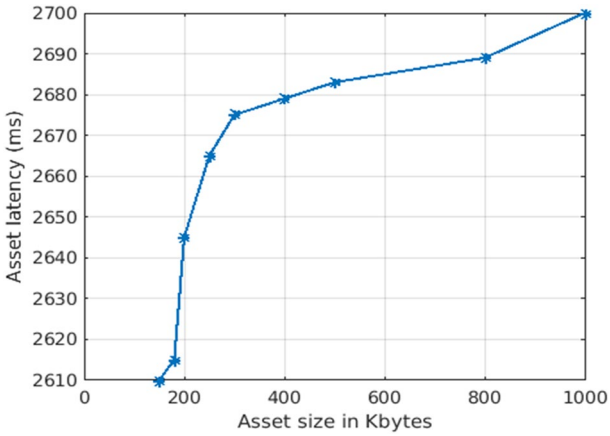


Fig. 13 Asset latency of the proposed architecture

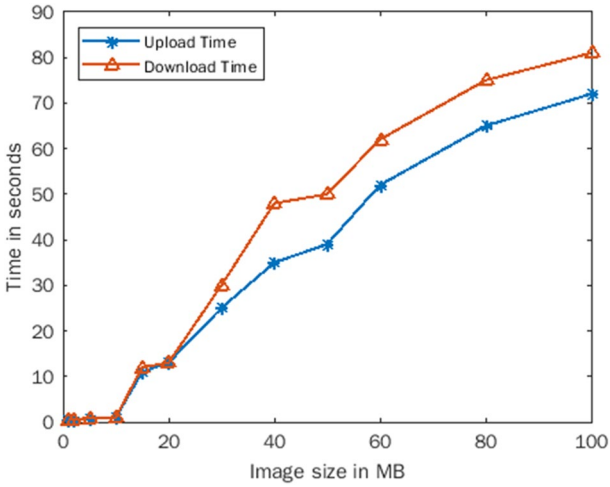


Fig. 14 Uploading and downloading time comparison of image data in SWARM

72 s to upload the file on the SWARM storage system, whereas downloading requires approximately 81 s. Similarly, the processing time of video data is analyzed in Fig. 15. It is observed that the proposed system needs around 69 s for the uploading process, whereas downloading needs approximately 70 s. In contrast, the multimedia 100 MB documents require 70 s for uploading and 115 s for downloading from the SWARM storage system, as shown in Fig. 16. Thus, it is concluded that the proposed architecture handles extensive data at low processing or latency.

Figure 17 presents the power consumption required by nodes varying the number of transactions. It is observed that the proposed architecture deployment using Hyperledger Fabric requires less power as compared to the Ethereum platform. The reason for high power consumption is that using the Proof of Work consensus algorithm in the Ethereum platform requires more energy to process network transactions. In contrast, the Hyperledger fabric deployment does not include any mining algorithm thus requires less power to process the transaction.

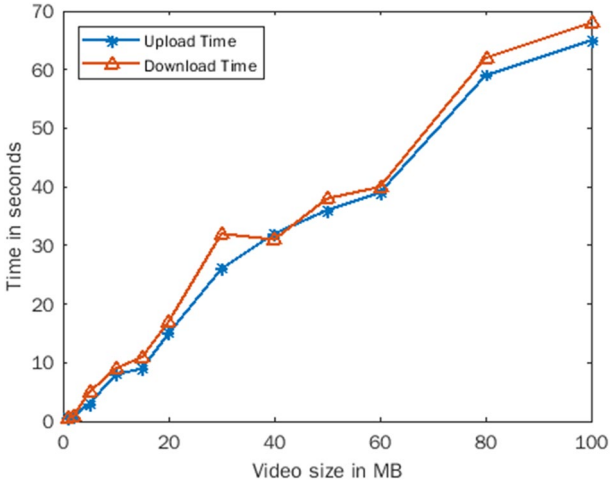


Fig. 15 Uploading and downloading time comparison of video data in SWARM

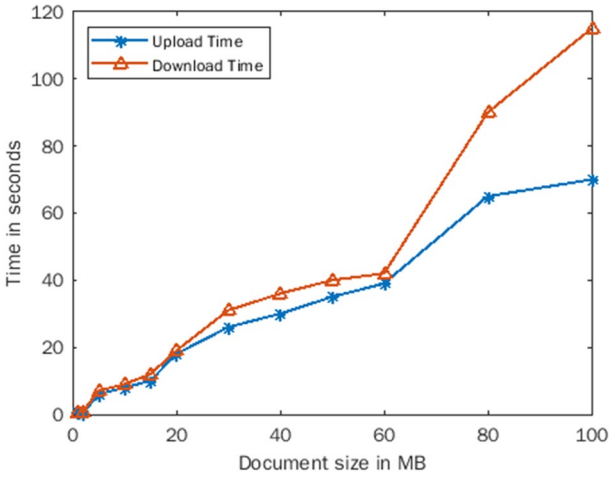


Fig. 16 Uploading and downloading time comparison of the document in SWARM

6.2 Comparative analysis

This section compares the proposed work with related works such as blockchain-based multimedia sharing [30], mobile multimedia security [20], and image and video data security [16]. The proposed work's different aspects such as time cost, computing overhead, and storage efficiency fare evaluated and compared with the related works. The proposed architecture average time cost for the execution of transactions is evaluated and compared with the blockchain-based multimedia sharing system [30]. The computing overhead of the encryption and decryption process of the proposed work are analyzed and compared with the mobile multimedia security [20]. Also, the storage performance of the SWARM is compared with the InterPlanetary File System (IPFS) storage system used in the image and video data security system [16]. The performance of the proposed work is evaluated using different parameters such as time cost, computing overhead, and time for storing

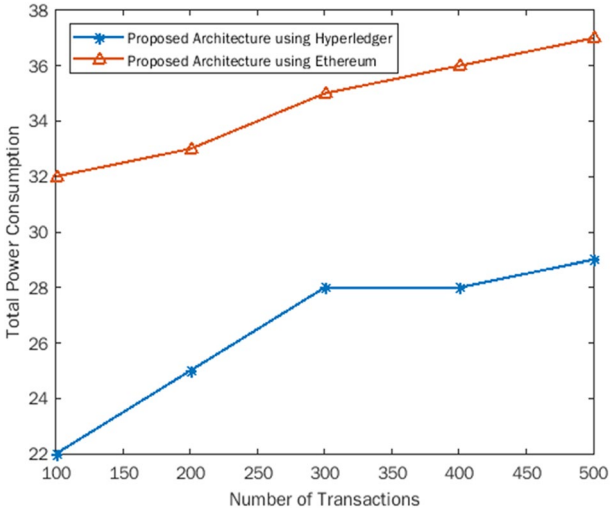


Fig. 17 Total power consumption comparison between proposed architecture with Hyperledger and Ethereum

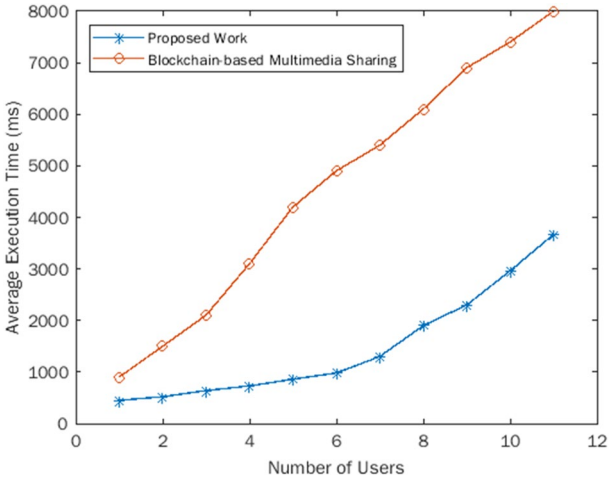


Fig. 18 Average execution time comparison between proposed work and literature [30]

multimedia data on the decentralized storage system. First, the proposed work is compared with the literature [30] based on the time cost parameter required by the transactions by varying the number of users and size of the multimedia data. Next, the literature [20] encryption and decryption process computing overhead compared with the proposed scheme. Last, the proposed work storage performance is compared with the related work [16]. This comparative analysis evaluates the proposed work's performance, robustness, and efficiency compared to the existing works.

The blockchain-based multimedia sharing system utilizes the privacy-preserving approach to share data in vehicular social networks. The experimental evaluation of the system uses the average execution time for analyzing system performance. As shown in Figs. 18 and 19, the proposed work efficiency is evaluated using the time cost parameter required for executing the number of transactions and compared with the related work [30]. First, the average execution time is evaluated for executing the transaction by varying the number of users and then compared with the blockchain-based multimedia sharing work.

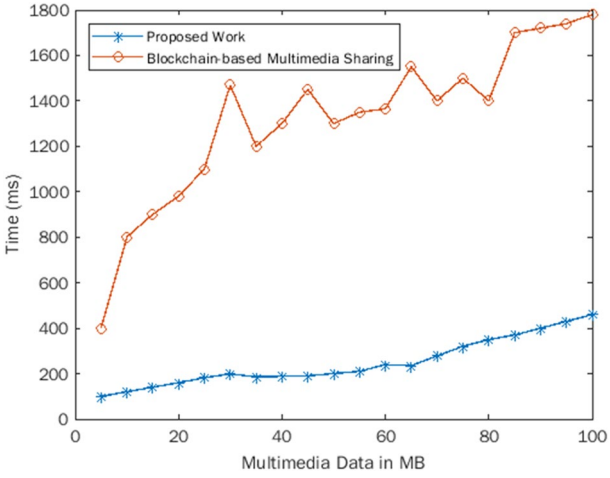


Fig. 19 Time cost comparison between proposed work and literature [30]

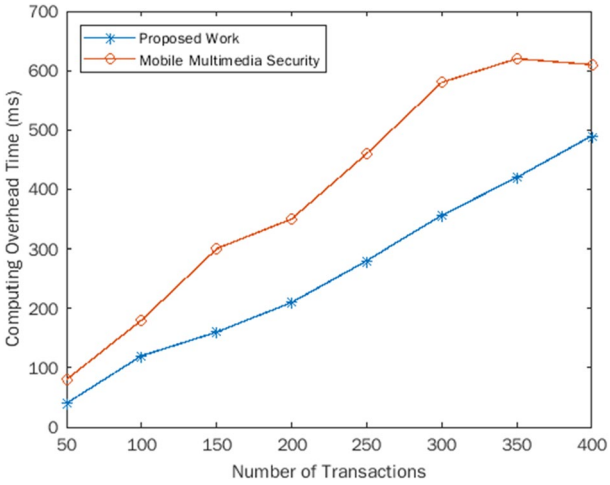


Fig. 20 Encryption computing overhead comparison between proposed work and literature [20]

It is observed that the proposed architecture requires less time for executing the transactions initiated by the users randomly as compared to the existing work. The existing work requires a two-step process for executing the authentication transaction for roadside units and vehicles, thus requiring more execution time than the proposed work. Also, the proposed architecture directly executes the transaction as per the user request because it only allows the validated user to initiate the transaction. Thus, it executes faster. Next, the performance is evaluated based on the time required for sharing multimedia data. As shown in Fig. 19, the proposed work requires less time for sharing the different size multimedia files than the existing work [30]. The existing work required the extra overhead for validating and verifying the entities involved in the sharing process as compared to the proposed work.

As shown in Figs. 20 and 21, the proposed work performance is analyzed based on computing overhead involved in the encryption and decryption process and compared with the

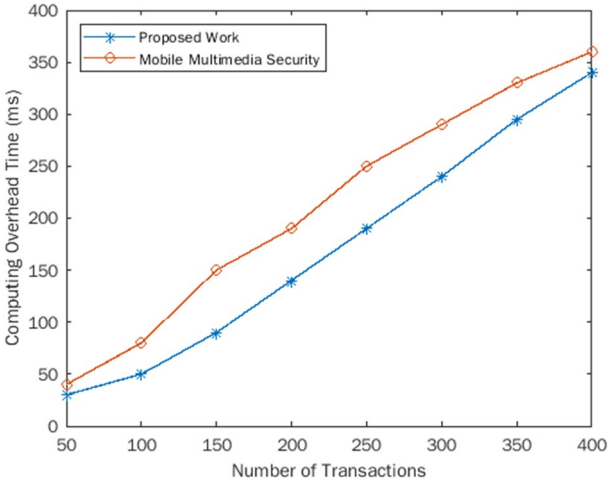


Fig. 21 Decryption computing overhead comparison between proposed work and literature [20]

existing work [20]. The mobile multimedia security system involves the aggregation area creation phase for the encryption and decryption process. During this phase, the involved entities first verify the correctness of the message requested by the other entities and then generate the ciphertext or plaintext with corresponding signatures. Thus, the existing work required a lot of computing overhead time for generating the ciphertext during the encryption and decryption process. Whereas the proposed work generates the keys during the key generation process, the same keys are utilized to encrypt the multimedia files and decrypt them during the access process. As depicted in Figs. 20 and 21, the proposed work involves less computing overhead time than the literature [20]. Therefore, the proposed work provides a more robust solution for handling multimedia data than the existing work.

The computation time required for uploading the multimedia documents on the decentralized storage is considered for comparing the proposed work storage performance with the existing work [16]. As shown in Fig. 22, the storage performance of the proposed work is compared with the existing work. The uploading time is evaluated for uploading the different-sized multimedia files on the storage system. It is observed that the proposed work requires less computation time to upload the multimedia data on the SWARM storage system than the existing work [16]. The existing work utilizes the IPFS storage system for uploading multimedia files that require more time than the SWARM system.

7 Conclusion and future work

This work designed a permissioned blockchain architecture-based application to secure personal multimedia data using Hyperledger Fabric and Composer. The proposed architecture provides a tamper-proof blockchain structure to handle multimedia data using the SWARM storage system, preserves data security, ensures access control, and maintains integrity. Moreover, the proposed work ensures the users' ownership of their multimedia files by including a no-incentive method for the blockchain mining process with the help of the Hyperledger Fabric framework to provide an energy-efficient environment. The architecture ensures multimedia data security using encryption techniques and access control methods. Also, the working prototype of the architecture provides a tamper-resistant

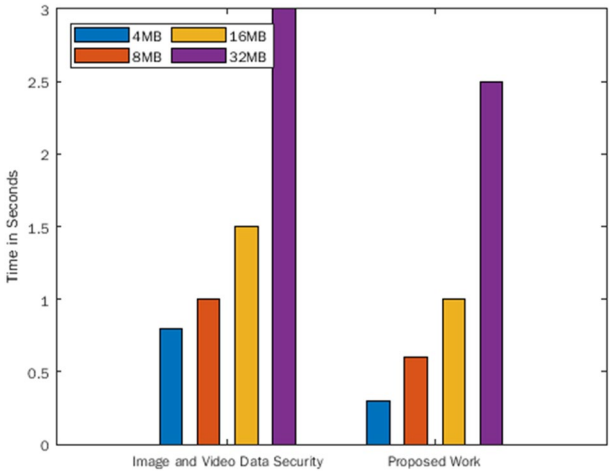


Fig. 22 Comparison of uploading time between proposed system and literature [16]

mechanism as multimedia file information will be stored as hash values in the application for each transaction. The performance evaluation of the proposed architecture is measured based on various parameters such as transaction latency, throughput, asset latency, upload and download time, and power consumption for multimedia data. For future work, we plan to refine this architecture prototype with rigorous simulations in terms of scalability to handle the increasing growth of personal multimedia data. The proposed work may be further enhanced to include the Internet of Things devices for collecting the multimedia data.

Data availability Data sharing is not applicable to this article as no datasets were generated or analyzed during the current work.

Declarations

Conflict of interest The authors declare that they have no conflict of interest.

References

1. Androulaki E, Barger A, Bortnikov V, Cachin C, Christidis K, De Caro A et al (2018) Hyperledger fabric: a distributed operating system for permissioned blockchains. In: Proceedings of the Thirteenth EuroSys Conference. ACM, pp 1–15
2. Anh Dinh TT, Wang J, Chen G, Liu R, Chin Ooi B, Tan KL (2017) BLOCKBENCH: a framework for analyzing private blockchains. In: Proceedings of the ACM International Conference on Management of Data (SIGMOD '17). Association for Computing Machinery, New York, pp 1085–1100. https://doi.org/10.1145/3035918.3064033
3. Bui T, Thereaux O, Cooper D, Collomosse J, Bell M, Green A, Keller JR (2020) Tamper-proofing video with hierarchical attention autoencoder hashing on blockchain. IEEE Trans Multimedia. https://doi.org/10.1109/tmm.2020.2967640
4. Cho S, Jeong C (2019) A blockchain for media: survey. In: Proceedings of the International Conference on Electronics, Information, and Communication (ICEIC), pp 1–2. https://doi.org/10.23919/ELINFOCOM.2019.8706434
5. Dhillon V, Metcalf D, Hooper M (2017) The hyperledger project. In: Blockchain-enabled applications. Springer, pp 139–149
6. Dobre RA, Preda RO, Oprea CC, Pirnog I (2018) Authentication of JPEG Images on the Blockchain. In: Proceedings of the International Conference on Control, Artificial Intelligence, Robotics & Optimization (ICCAIRO), pp 211–215. https://doi.org/10.1109/ICCAIRO.2018.00042
7. Ghimire S, Choi JY, Lee B (2020) Using blockchain for improved video integrity verification. IEEE Trans Multimed 22(1):108–121. https://doi.org/10.1109/TMM.2019.2925961
8. Gupta BB, Yamaguchi S, Agrawal DP (2018) Advances in security and privacy of Multimedia Big Data in Mobile and Cloud Computing. Multimedia Tools and Applications 77:9203–9208. https://doi.org/10.1007/s11042-017-5301-x
9. Han D, Zhu Y, Li D, Liang W, Souri A, Li KC (2022) A blockchain-based auditable access control system for private data in service-centric IoT environments. IEEE Trans Industr Inf 18(5):3530-3540. https://doi.org/10.1109/TII.2021.3114621
10. iCloud leaks of celebrity photos, Wikipedia [Online] Available: https://en.wikipedia.org/wiki/ICloud_leaks_of_celebrity_photos
11. Jain R (2009) Multimedia data. In: Liu L, Özsu MT (eds) Encyclopedia of database systems. Springer, Boston. https://doi.org/10.1007/978-0-387-39940-9_1008
12. Jan MA, Cai J, Gao X-C, Khan F, Mastorakis S, Usman M, Alazab M, Watters P (2021) Security and blockchain convergence with internet of Multimedia Things: current trends, research challenges, and future directions. J Netw Comput Appl 175
13. Keepsafe photo vault : Hide Private Photos and Videos, [Online] Available: https://keepsafe.en.softonic.com/android

14. Khan G, Jabeen S, Khan MZ, Khan MUG, Iqbal R (2020) Blockchain-enabled deep semantic video-to-video summarization for IoT devices. Comput Electr Eng 81. https://doi.org/10.1016/j.compeleceng.2019.106524
15. Khan A, Uddin M, Shaikh AA, Laghari AA, Rajput AE (2021) MF-ledger: blockchain hyperledger sawtooth-enabled novel and secure multimedia chain of custody forensic investigation architecture. IEEE Access 9:103637–103650. https://doi.org/10.1109/ACCESS.2021.3099037
16. Kumar R, Tripathi R, Marchang N, Srivastava G, Gadekallu TR, Xiong NN (2021) A secured distributed detection system based on IPFS and blockchain for industrial image and video data security. J Parallel Distrib Comput 152:128–143
17. Liang H, Wu J, Zheng X, Zhang M, Li J, Jolfaei A (2020) Fog-based secure service discovery for internet of multimedia things: a cross-blockchain approach. ACM Trans Multimed Comput Commun Appl 16(3s):1-23. https://doi.org/10.1145/3415151
18. Liu Y, Lu Q, Zhu C, Yu Q (2021) A blockchain-based platform architecture for multimedia data management. Multimed Tools Appl. https://doi.org/10.1007/s11042-021-10558-z
19. Liu J, Fan K, Li H, Yang Y (2021) A blockchain-based privacy preservation scheme in multimedia network. Multimed Tools Appl. https://doi.org/10.1007/s11042-021-10513-y
20. Ma S, Zhang T, Wu A, Zhao X (2019) Lightweight and privacy-preserving data aggregation for mobile multimedia security. IEEE Access 7:114131–114140. https://doi.org/10.1109/ACCESS.2019.2935513
21. Mingxiao D, Xiaofeng M, Zhe Z, Xiangwei W, Qijun C (2017) A review on consensus algorithm of blockchain. In: Proceedings of the IEEE International Conference on Systems, Man, and Cybernetics (SMC), pp 2567–2572
22. Nakamoto S (2008) Bitcoin: a peer-to-peer electronic cash system, Available: http://www.bitcoin.org/bitcoin.pdf . Accessed on 15 June 2021
23. Namasudra S (2020) Fast and secure data accessing by using DNA computing for the cloud environment. IEEE Trans Serv Comput. https://doi.org/10.1109/TSC.2020.3046471
24. Nandakumar K, Ratha N, Pankanti S (2019) Proving multimedia integrity using sanitizable signatures recorded on blockchain. In: Proceedings of the ACM workshop on information hiding and multimedia security, pp 151–160. https://doi.org/10.1145/3335203.3335729
25. Photosquared data leak exposes user's photos and information, [Online], Available: https://www.infosecurity-magazine.com/news/photosquared-app-leaks-data/
26. Sharma P, Jindal R, Borah MD (2020) Blockchain technology for cloud storage: a systematic literature review. ACM Comput Surv 53:1–32
27. Sharma P, Jindal R, Borah MD (2021) A review of blockchain-based applications and challenges. Wirel Pers Commun:1–43
28. Sharma P, Jindal R, Borah MD (2021) Blockchain-based decentralized architecture for cloud storage system. J Inform Secur Appl 62:1–15
29. Sharma P, Jindal R, Borah MD (2022) A review of smart contract-based platform, applications, and challenges. Cluster Comput:1–27
30. Shi K, Zhu L, Zhang C, Xu L, Gao F, (2020) Blockchain-based multimedia sharing in vehicular social networks with privacy protection. Multimed Tools Appl 79:8085–8105. https://doi.org/10.1007/s11042-019-08284-8
31. Trón V, fischer Á, Johnson N, Nagy DA, Felföldi Z (2020) Swarm documentation release 0.5. White Paper. [Online] Available. https://Swarmguide.readthedocs.io/_/downloads/en/latest/pdf/
32. Vishwa A, Hussain FK (2018) A Blockchain-based approach for multimedia privacy protection and provenance. In: Proceedings of the IEEE Symposium Series on Computational Intelligence (SSCI), pp 1941–1945. https://doi.org/10.1109/SSCI.2018.8628636
33. Zhang S, Lee J-H (2020) Analysis of the main consensus protocols of blockchain. ICT Express 6(2):93–97

Publisher's note Springer Nature remains neutral with regard to jurisdictional claims in published maps and institutional affiliations.

Springer Nature or its licensor (e.g. a society or other partner) holds exclusive rights to this article under a publishing agreement with the author(s) or other rightsholder(s); author self-archiving of the accepted manuscript version of this article is solely governed by the terms of such publishing agreement and applicable law.

Check for updates

View Article Online
View Journal

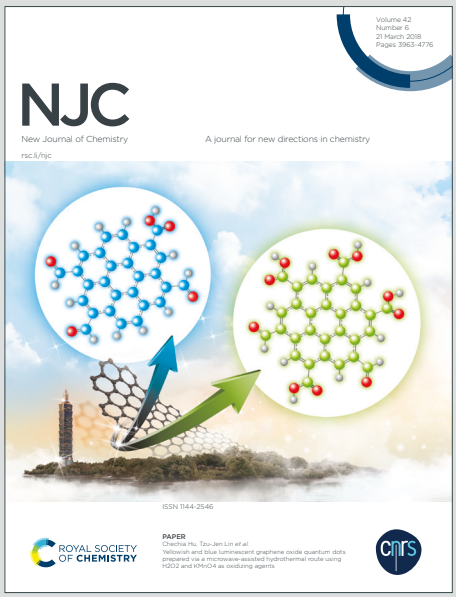
NJC

New Journal of Chemistry

A journal for new directions in chemistry

Accepted Manuscript

This article can be cited before page numbers have been issued, to do this please use: N. Gupta, D. Kumar, A. Das, S. Sood and B. D. Malhotra, *New J. Chem.*, 2023, DOI: 10.1039/D3NJ01557B.



This is an Accepted Manuscript, which has been through the Royal Society of Chemistry peer review process and has been accepted for publication.

Accepted Manuscripts are published online shortly after acceptance, before technical editing, formatting and proof reading. Using this free service, authors can make their results available to the community, in citable form, before we publish the edited article. We will replace this Accepted Manuscript with the edited and formatted Advance Article as soon as it is available.

You can find more information about Accepted Manuscripts in the Information for Authors.

Please note that technical editing may introduce minor changes to the text and/or graphics, which may alter content. The journal's standard Terms & Conditions and the Ethical guidelines still apply. In no event shall the Royal Society of Chemistry be held responsible for any errors or omissions in this Accepted Manuscript or any consequences arising from the use of any information it contains.

View Article Online
DOI: 10.1039/D3NJ01557B

Carbon nanotubes modified conductive ink for application to paper-based electrochemical biosensor for pathogenic DNA detection

Niharika Gupta[1], D. Kumar[2], Asmita Das[1], Seema Sood[3], Bansi D. Malhotra[1,*]

[1]Department of Biotechnology, Delhi Technological University, Delhi 110042, INDIA

[2]Department of Applied Chemistry, Delhi Technological University, Delhi 110042, INDIA

[3]Department of Microbiology, All India Institute of Medical Sciences (AIIMS), New Delhi 110016, India

*Corresponding Author: bansi.malhotra@gmail.com

Published on 09 May 2023. Downloaded on 5/22/2023 6:14:26 AM.

New Journal of Chemistry Accepted Manuscript

View Article Online
DOI: 10.1039/D3NJ01557B

Published on 09 May 2023. Downloaded on 5/22/2023 6:14:26 AM.

Abstract

We report results of the studies relating to the development of a conductive ink–coated paper-based, electrochemical DNA hybridization assay for detection of *porA* pseudogene of *Neisseria gonorrhoeae* (gonococcal DNA), the causative agent of gonorrhoea. Briefly, a conductive and highly homogenous ink was prepared by dispersing carboxylated MWCNTs (cMWCNTs) in a stable emulsion consisting of terpineol as solvent, carboxymethyl cellulose (CMC) as binder and polysorbate 80 (PS80) as the stabilizing agent. This cMWCNT-based ink was coated onto paper substrates to obtain the cMWCNT@paper electrodes with a mean (± standard deviation, SD) resistivity of 1.066 (± 0.33) Ω.cm. Further, a magnetic beads (MBs)-mediated hybridization assay comprising of specific 5'-biotinylated capture DNA probe (C) and 3'-methylene blue (MetB)-tagged detector DNA probe (D) was designed. These probes hybridized specifically with a *porA* target DNA sequence (T) forming a sandwich hybridization complex (C-T-D) at the MB surface. Thus formed C-T-D/Av/MB samples with different T concentrations were drop cast and adsorbed onto the cMWCNT@paper for electrochemical detection. The linear detection range and sensitivity of the electrochemical biosensing assay were found to be 100 fM–100 nM and 5.09 µA. $(\log[\text{concentration}])^{-1}$, respectively. The biosensing assay was further shown to detect the target genomic gonococcal DNA in a mixture consisting of different DNA and protein interferents indicating its clinical viability. The results of rheological studies reveal that this thixotropic cMWCNT ink can be utilized for screen printing. These studies demonstrate the utilization of a conductive ink formulation for the fabrication of paper-based electrochemical sensing electrodes having high potential for cost-effective batch production and application in PoC clinical diagnostics.

Keywords: Carbon nanotubes, conductive ink, paper-based devices, DNA biosensor, *Neisseria gonorrhoeae*

New Journal of Chemistry Accepted Manuscript

View Article Online
DOI: 10.1039/D3NJ01557B

Published on 09 May 2023. Downloaded on 5/22/2023 6:14:26 AM.

1. Introduction

The field of paper diagnostics has recently aroused much interest. Paper-based devices for application to medical diagnostics have come a long way from the traditional dipstick and lateral flow assays and are being gradually transformed into microfluidic platforms for simultaneous detection of multiple analytes.[1-3] These devices can be used for detection of various analytes ranging from cancer biomarkers to DNA amplification products and bulky proteins.[1, 4-7] Features such as high surface-to-volume ratio, capillary flow, high adsorption capacity, biocompatibility and ease of disposability have led to the application of paper as an efficient and cost-effective substrate for clinical diagnostics. Optical transduction via nanoparticles and other agents such as dyes is one of the most prominent choices for application to biosensing, (intracellular) parameter monitoring, cellular imaging, etc.[8-13] And likewise, most commercial paper-based diagnostic devices aid in visual detection of the target analyte via colour change/formation. However, with increasing emphasis on the development of cost-effective and sensitive point-of care (PoC) devices, there is increased interest in the development of electrochemical paper-based diagnostics.

Electrochemical paper biosensors are quantitative in nature, which, coupled with high sensitivity, may prove highly advantageous toward developing a low-cost diagnostic device.[14] However, the poor conductivity of paper is currently one of the major bottlenecks for paper-based electrochemical devices.[7] This may perhaps be addressed by using conductive nanomaterials onto a desired paper matrix via dip coating, *in situ* growth/polymerization, and direct drop casting.[7] While these methods have succeeded in terms of conductive paper fabrication, many of these methods are not scalable. Also, the coating of nanomaterials can be non-uniform and uncontrollable due to nature of the synthesis and fabrication method. For example, *in situ* growth of nanomaterials, though efficient, is difficult to control. This may eventually lead to batch-to-

New Journal of Chemistry Accepted Manuscript

View Article Online
DOI: 10.1039/D3NJ01557B

Published on 09 May 2023. Downloaded on 5/22/2023 6:14:26 AM.

batch variation and subsequently, low sensitivity. Additionally, the same properties that render a paper substrate advantageous for biosensing appear to hinder the electrochemical applications of paper-based biosensors. For example, the high degree of capillary flow allows the buffer to easily flow through the paper matrix leading to lower signal-to-noise ratio. And the paper substrate may be prone to high non-specific adsorption resulting in poor sensitivity. At the same time, complete blocking of the pores in the paper matrix may render it unsuitable for interaction with the buffer that contains the target analyte and redox probes required for electrochemical analysis. Leaching of nanomaterials is another issue that is presently hindering the development of paper-based electrochemical biosensors.

The conductive inks have been projected to be a promising option toward the fabrication of paper-based electrochemical biosensors. The conductive inks comprise of conductive nanomaterials and binders that impart enhanced conductivity and allow them to bind strongly to the target substrate (in this case, paper), respectively.[15, 16] The wettability of these inks can be modified using additives and their coating may allow tuning of the capillary flow at the paper surface.[17] Different printing techniques are available that can be used to coat these inks on paper substrates, such as inkjet printing, screen printing, flexographic printing, etc.[18-20] Conductive, printable inks have found prominent applications in the field of flexible and printed electronics.[15-17] There are only a few reports on conductive ink-coated paper electrodes for electrochemical detection of different analytes.[16, 19] Traditionally silver nanoparticles (Ag NPs) have been used extensively as conductive fillers in screen printable inks for printable electronics applications. However, Ag NPs are not suitable for electroanalytical applications as they get easily oxidized on repeated electrochemical cycles. Thus, carbon nanomaterials such as graphene, carbon nanotubes (CNTs), etc. have aroused increased interest for development of conductive, screen-printing inks.

New Journal of Chemistry Accepted Manuscript

View Article Online
DOI: 10.1039/D3NJ01557B

Published on 09 May 2023. Downloaded on 5/22/2023 6:14:26 AM.

Carbon nanomaterials have been found to have electroanalytical applications due to their high surface-to-volume ratio, chemical inertness, high conductivity, and a wide potential window in different buffers.[18] Multiwalled CNTs (MWCNTs) have these interesting characteristics with the added advantage of lower relative costs and have found extensive applications in printed pseudo capacitors and biosensors.[18, 20] Most studies on carbon nanomaterial-based conductive inks have focused on application of graphene or composites of MWCNTs as conductive filler[21-24]. There are a few studies on development of conductive inks using only MWCNTs. Besides this, conductive inks are largely being explored for applications in supercapacitors, batteries, flexible electronics, etc.[23-26] This work pertains to the formulation of an MWCNT-based conductive ink towards the fabrication of paper-based electrodes. These electrodes have further been utilized as biosensing substrates for the detection of *Neisseria gonorrhoeae*.

N. gonorrhoeae is the causative agent of the sexually transmitted infection (STI) gonorrhea, which is presently one of the most prominent bacterial STIs over the world. According to a recent study, about 87 M cases of gonorrhoea were found worldwide among individuals aged 15-49 in 2016.[27] And it has been associated with many health problems in men, women and children including high HIV infection risk, preterm birth, infertility, neonatal ophthalmia, etc.[28] Additionally, this STI remains highly under-reported and under-diagnosed in both high-income and low-income economies, which has hampered the efforts towards the world-wide decrease of this STI. Thus, a simple, cost-effective device that can be used for mass screening can significantly transform gonorrheal diagnostics and may aid in achieving the WHO goal of reducing the incidence of this disease by 90% by 2030.[29]

There have been some few reports on DNA-based electrochemical biosensors for the detection of *opa* gene (and its PCR amplicons) of *N. gonorrhoeae.*[30-32] However, *opa* gene is highly

New Journal of Chemistry Accepted Manuscript

View Article Online
DOI: 10.1039/D3NJ01557B

polymorphic and is also present in other commensal (harmless) *Neisseria* species, that may lead to cross reactivity and false positive results. On the other hand, *porA* pseudogene is a non-functional gene in *N. gonorrhoeae that* has a highly conserved sequence and is not present in any of the commensal *Neisseria* species. Thus, this pseudogene can perhaps act as a promising detection target for *N. gonorrhoeae*.

In this work, we first formulated a carboxylated MWCNT (cMWCNT)-based conductive ink, which was subsequently utilized to fabricate paper-based biosensing electrodes. Oligonucleotide probes (one capture and one detector) specific to *N. gonorrhoeae porA* pseudogene were designed. Further, to impart specificity to the biosensing assay, a magnetic bead (MB)-based sandwich hybridization assay was designed, wherein the capture probe (CP) was immobilized onto the MBs to specifically bind to the target sequence in a complex matrix. The detector probe (DP) was allowed to bind thereafter to form a capture-target-detector (C-T-D) sandwich hybridization complex at the MB surface. This assembly was thereafter drop cast onto the paper electrodes for electrochemical analysis. To the best of our knowledge, there is no report on the fabrication of a conductive ink-coated, paper-based biosensor for the detection of gonorrhoeal *porA* pseudogene.

Published on 09 May 2023. Downloaded on 5/22/2023 6:14:26 AM.
New Journal of Chemistry Accepted Manuscript

View Article Online
DOI: 10.1039/D3NJ01557B

Published on 09 May 2023. Downloaded on 5/22/2023 6:14:26 AM.

2. Materials and Methods

2.1 Materials and Reagents

Carboxylated multi-walled carbon nanotubes (cMWCNT) and polysorbate 80 (PS80) were obtained from SRL Pvt. Ltd. (India). Carboxymethyl cellulose (CMC; high viscosity) and terpineol were procured from Central Drug House (P) Ltd. (CDH, India). All reagents were of analytical grade and were used without purification. Carboxylated magnetic beads (Dynabeads™ MyOne™ Carboxylic Acid; MBs) were purchased from Thermo Fisher Scientific. The oligonucleotide probes used in these studies were purchased from IDT (USA). The sequences of the oligonucleotide probes were self-designed (**Table 1**). All electrochemical studies were performed in phosphate buffered saline (PBS, 0.1 M) of pH 7 supplemented with 5 mM ferro-ferricyanide as the redox probes. PBS (pH 7) was prepared by first mixing 39 mL of monobasic sodium phosphate (NaH_2PO_4, 0.2M, Fisher Scientific) and 61 mL of dibasic sodium phosphate ($Na_2HPO_4.2H_2O$, 0.2M, Fisher Scientific), and thereafter diluting the resulting mixture to 200 mL with autoclaved MilliQ water. Sodium chloride (NaCl, 0.9%, Fisher Scientific) was added to this mixture to constitute the final buffer.

Table 1. DNA sequences of the biosensor oligonucleotide probes.

Biosensor Probes		
Probe type and name	**Sequence**	**Melting temperature (T_m; °C)**
Capture Probe (CP)	5'Biotin-CCT GCT ACT TTC ACG CTG GA 3'	62
Detector Probe (DP)	5'AAG TAA TCA GAT GAA ACC AGT TC-Met Blue 3'	62

New Journal of Chemistry Accepted Manuscript

View Article Online
DOI: 10.1039/D3NJ01557B

Target strand (T)	5'GAA CTG GTT TCA TCT GAT TAC TTT CCA GCG TGA AAG TAG CAG G 3'	65
Non-complementary probe (NC)	5'TTG ATT GAG CGT CAT AGA TCG GAC GGC ACT AGT CAG TAC TCG A 3'	63

2.2 Conductive Ink formulation

A conductive ink consists of four major components: i) solvent, ii) binder for proper adhesion to the desired substrate, iii) rheology modifier for appropriate flow properties according to the application, and iv) conductive filler that imparts conductivity. For ink formulation, CMC (1.5% w/v) was first dissolved in distilled water and was then mixed with terpineol and PS80 in the optimized ratio 2:1:1 (water: terpineol: PS80) (**Figure 1(A)**). The resulting emulsion was stirred vigorously using a magnetic stirrer (~500 rpm, 2 h). Subsequently, cMWCNTs (1 % w/v) were added to the desired emulsion with vigorous stirring (~1000 rpm, 1 h). The resulting conductive emulsion was probe ultrasonicated in an ice bath at a pulse of 0.5 s and 70 % amplitude for 15 min. The ultrasonication was paused every 5 minutes to avoid overheating of the sample. The resulting conductive ink was stored in a closed container at low temperature (4 – 10 °C) to prevent evaporation of the solvent.

2.3 Design of biosensor oligonucleotide probes

The oligonucleotide probes were self-designed using open access software. In brief, the oligonucleotide probes specific to gonococcal *porA* pseudogene were selected using NCBI Nucleotide database and NCBI Primer-BLAST. For this purpose, the gonococcal *porA* pseudogene sequences from different strains of *N. gonorrhoeae* were aligned using Clustal Omega to confirm homology. Thereafter, the same sequence was aligned with the *porA*

Published on 09 May 2023. Downloaded on 5/22/2023 6:14:26 AM.
New Journal of Chemistry Accepted Manuscript

View Article Online
DOI: 10.1039/D3NJ01557B

Published on 09 May 2023. Downloaded on 5/22/2023 6:14:26 AM.

pseudogene sequences from different strains of *N. meningitidis* to determine a sequence conserved only to *N. gonorrhoeae*. The selected capture (C) and detector (D) biosensor probes (**Table 1**) along with complementary target sequence (T) and non-complementary sequence (NC) were purchased from IDT, USA.

2.4 Fabrication of ink-coated paper bioelectrodes

For fabrication of the flexible paper electrodes, drawing paper (ivory paper, 200-300 gsm) was first cut into pieces of size 2 × 2 cm^2. The choice of paper type was made based on the higher mechanical strength and lower porosity in relation to the traditionally used filter paper. Thereafter, 75 µL of the conductive ink was drop cast and coated uniformly over the paper using a paint brush (Faber Castell). The paper electrodes were annealed within the temperature range of 80–130 °C for a period of 5–15 min to optimize the annealing temperature and time and determine their effect on the conductivity. The coating process was repeated to determine the optimum number of coats (n) to obtain appreciable conductivity while maintaining adhesion on the paper substrate. The obtained cMWCNT@paper electrodes were cut into pieces of size 1 × 1 cm^2 each and assessed for conductivity. After optimization of the number of coats, annealing temperature and time, cMWCNT@paper electrodes were fabricated for electrochemical studies (2 × 1 cm^2) and stored in dry, dark conditions till further use.

2.5 Electrochemical magnetic DNA hybridization assay

DNA complementary base pairing is currently a prominent method for DNA-based biosensors. In this study, a capture (CP) and a detector probe (DP) were designed to hybridize with the target DNA (T) at two adjacent sites. To enhance the specificity and the sensitivity of the assay, the CP was labeled with biotin at the 5' end and the DP was labelled with methylene blue (MetB)

New Journal of Chemistry Accepted Manuscript

View Article Online
DOI: 10.1039/D3NJ01557B

at the 3' end. Further, an MB-based assay was designed for specific detection of gonorrhoeal DNA. The primary role of MB was sample enrichment: to isolate the target DNA from a mixture of interferents. The MetB labelling on the DP resulted in the amplification of the redox signal at the electrode surface.

For the electrochemical DNA assay, avidin (Av) was first immobilized onto the carboxylated MBs via EDC/NHS-mediated covalent bond formation (detailed protocol given in the **Supplementary Information**). Thereafter, the biotinylated CP (1800 pmol/mg beads) was immobilized onto the Av/MBs via affinity interactions. Different concentrations of the T strand were then added to the C/Av/MB probes and incubated at 60 °C for 15 min with tilt rotation. This was followed by addition of the DP and incubation at 60 °C for 15 min with tilt rotation. This resulted in the formation of a sandwich hybridization complex at the MB surface. Washing with double distilled water (3-5×) was conducted after every modification step to remove non-specifically bound and unbound probes. Thus formed C-T-D/Av/MB complexes were redispersed in 30 µL deionized water and drop cast onto the cMWCNT@paper electrodes (1 × 1 cm^2). These modified electrodes were dried at 60 °C for 15 min and analyzed for electrochemical response via cyclic voltammetry (CV). The CV studies were conducted in PBS buffer supplemented with ferro-ferricyanide as the redox couple (**Section 2.1**) at scan rate of 50 mV s^{-1} unless otherwise specified.

2.6 Real sample analysis

In order to check the applicability of the designed electrochemical biosensing assay in clinical settings, DNA from *N. gonorrhoeae* bacterial culture was first extracted using commercial QIAGEN DNA extraction kits. Thereafter, the DNA samples were diluted to different concentrations and denatured by incubation at 95 °C for 5 min. This was followed by

Published on 09 May 2023. Downloaded on 5/22/2023 6:14:26 AM.
New Journal of Chemistry Accepted Manuscript

View Article Online
DOI: 10.1039/D3NJ01557B

ultrasonication in a water bath for 10 min. These steps facilitated the de-hybridization and shortening of the DNA molecules, respectively. Thereafter, the procedure as described in **Section 2.5** was repeated to determine the concentration of the gonococcal DNA sequences in the samples. The results were compared to those obtained by using the synthetic T probe.

Clinical samples (cervical/urethral swabs) are known to consist of a large amount of human DNA and DNA from non-pathogenic commensal bacteria that may significantly interfere with the detection of pathogenic DNA. Protein contamination can also occur sometimes during DNA extraction (especially when crude extraction methods are used, e. g. the boiling method). To determine the effect of interfering DNA and proteins on the detection of gonococcal DNA, non-gonococcal DNA from different bacteria was extracted and mixed with the gonococcal DNA in the ratio of 50:1. The response of the electrochemical biosensing assay was then recorded to these DNA mixtures using the aforementioned procedure.

Published on 09 May 2023. Downloaded on 5/22/2023 6:14:26 AM.

New Journal of Chemistry Accepted Manuscript

View Article Online
DOI: 10.1039/D3NJ01557B

Published on 09 May 2023. Downloaded on 5/22/2023 6:14:26 AM.

3. Results and discussion

3.1 Characterization and optimization studies

Figures S1(A) and S1(B) show the XRD spectrum and the TEM image of the cMWCNT used in this study. The XRD spectrum reveals a sharp, high intensity peak at 26.2° corresponding to the (002) reflection plane of the crystalline carbon nanotubes. The smaller peaks are also observed centred at about 43.4° and 54.2° corresponding to the exposed (100) and (004) planes of the carbon nanotubes. The average diameter of the nanotubes, as seen in the TEM image, has been found to be 117.12 nm.

3.1.1 SEM and Contact Angle Studies

The cMWCNT-based conductive ink was formulated by dispersing cMWCNT in an emulsion of CMC (dispersed in water) and terpineol stabilized by PS80. **Figure 1(A)** depicts the various steps followed in the formulation of the conductive ink and subsequent coating on paper substrates. The SEM analysis was conducted to analyse the surface morphology of the cMWCNT@paper electrodes and further modifications with MBs (**Figures 1(B-G)**). The SEM micrographs of bare paper (**Figure 1(B)** and **(C)**) show the rough surface of paper consisting of cellulose fibres. An additive/modifying agent can also be seen in the image (**Figure 1(C)**) that probably has been used to bleach or modify the porosity of cellulose fibres. In contrast, the coating of MWCNT ink appears smooth and evenly distributed along the paper surface indicating the homogeneity of the ink formulation (**Figure 1(D)**). The inset of **Figure 1(D)** shows the optical photograph of the cMWCNT@paper electrode. cMWCNTs can be seen protruding out of the ink matrix held together by CMC and residual PS80 remaining after annealing (**Figure 1(E)**). For comparison, we modified the paper with cMWCNTs dispersed in PS80 via dip coating (3×) and

New Journal of Chemistry Accepted Manuscript

View Article Online
DOI: 10.1039/D3NJ01557B

analysed by SEM (**Figure S2**) (dip coating was utilized because the dispersion was not viscous enough to be coated/printed). cMWCNTs are visible and scattered over the paper surface. Cellulose fibres are visible beneath the cMWCNTs. This is in contrast with the MWCNT@paper as shown in **Figure 1(D)**. Further, **Figure 1(F)** shows the impregnation of the ink matrix by Av/MBs (5 mg beads were adsorbed on 1 × 1 cm^2 ink-coated paper). On further magnification, spherical Av/MBs can be clearly seen on the cMWCNT@paper electrodes (**Figure 1(G)**). It appears that the Av/MBs have covered the surface evenly without any aggregation in a particular area.

The wettability of the cMWCNT ink coating on the paper substrate was assessed by contact angle measurements (**Figure 1(H) & (I)**). The contact angle of the paper used in the study (ivory drawing paper, 250-300 gsm) was found to be 98.3 ± 7.29° (mean ± error) (**Figure 1(H)**), which decreased to 47.97 ± 1.48° for the cMWCNT@paper electrode (3 ink coats, 75 µL for one coat) (**Figure 1(I)**). The observed high contact angle of the bare paper indicates the presence of additional modifying agents in the paper matrix, as indicated by the SEM studies. Further, the decrease in the contact angle after ink coating may be due to the presence of CMC in the ink, which is hydrophilic in nature. The presence of a low surface tension solvent (terpineol) and PS80 perhaps contributes to the observed lower contact angle of the ink.[33]

Published on 09 May 2023. Downloaded on 5/22/2023 6:14:26 AM.

New Journal of Chemistry Accepted Manuscript

View Article Online
DOI: 10.1039/D3NJ01557B

Published on 09 May 2023. Downloaded on 5/22/2023 6:14:26 AM

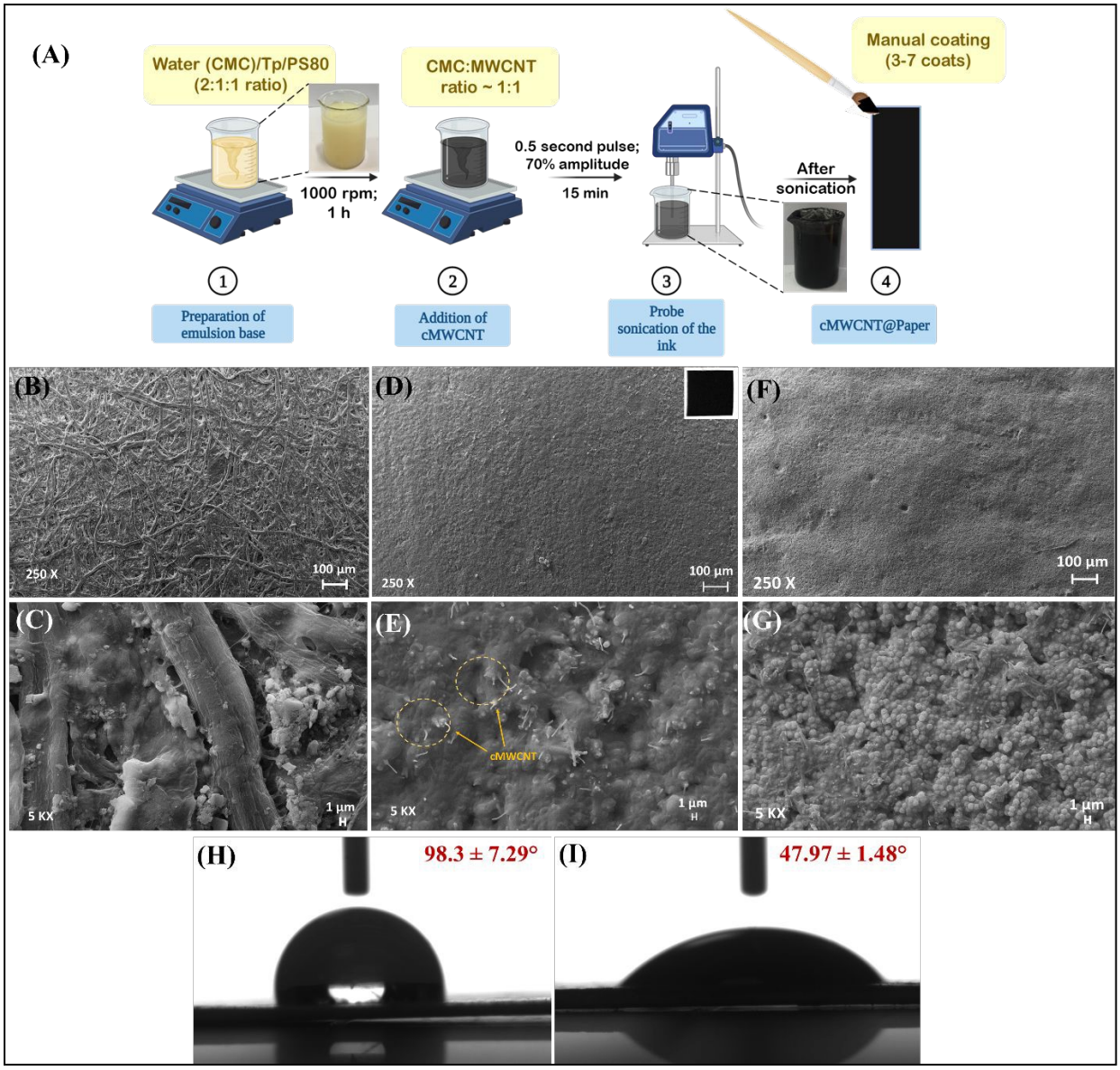


Figure 1. **(A)** Schematic depicting the preparation of the conductive ink and subsequent fabrication of the cMWCNT@paper electrodes. SEM micrographs of **(B)**, **(C)** bare paper; **(D), (E)** cMWCNT ink-coated paper (cMWCNT@Paper) (inset of **(D)** shows the photograph of the cMWCNT@paper electrode (2 × 2 cm^2)) ; and **(E), (F)** Avidin-modified MB/cMWCNT@Paper electrode. Contact angle measurements for **(H)** bare paper, and **(I)** cMWCNT@Paper electrode.

New Journal of Chemistry Accepted Manuscript

View Article Online
DOI: 10.1039/D3NJ01557B

Published on 09 May 2023. Downloaded on 5/22/2023 6:14:26 AM

3.1.2 Conductivity studies

The effect of annealing temperature, annealing time and the number of ink coatings (*n*) on the conductivity of the cMWCNT@paper electrodes was investigated. First, the paper substrates (2 × 2 cm^2) were coated thrice (75 µL per coat) and annealed within the temperature range, 80 °C-130 °C (**Figure 2(A)**). The resistivities of the annealed cMWCNT@paper electrodes were subsequently determined. It was found that the resistivity decreased with annealing temperature and time, with the minimum value at 120 °C and annealing time of 10 min. Keeping the annealing time fixed at 10 min, it was seen that the resistivity decreased till 120 °C after which there was only a slight (non-significant) change (**Figure 2(B)**). Hence, 120 °C for 10 min was considered as the optimum annealing temperature and time, respectively, for further studies. This decrease in resistivity with annealing temperature and time is attributed to the evaporation and degradation of terpineol and PS80 at temperatures > 100 °C. Additionally, the mean (± SD) resistivity of the cMWCNT@paper at *n* = 7 decreased to 1.066 (± 0.31) Ω.cm from 9.89 (± 1.2) Ω.cm at *n* = 1(**Figure 2(C)**). The corresponding conductivity (*n* = 7) was found to be 1.48 S cm^{-1}. The resistivity was not measured beyond seven coatings as MWCNTs leached out when the cMWCNT@paper electrode was immersed in aqueous solution. The following equations were utilized to determine the resistivity of the cMWCNT@paper electrodes:

$$\rho = \frac{\rho o}{G'} \qquad \text{(Eq. 1)}$$

where ρ is the final resistivity corrected for the thickness of coating, ρ_o is the resistivity given by the following equation:

$$\rho_o = \left(\frac{V}{I} \times 2\pi S\right) \qquad \text{(Eq. 2)}$$

New Journal of Chemistry Accepted Manuscript

View Article Online
DOI: 10.1039/D3NJ01557B

Published on 09 May 2023. Downloaded on 5/22/2023 6:14:26 AM.

where V is the potential, I is the current and S is the distance between the probes of the conductivity meter (0.2 cm), and G′ is the error introduced when the thickness of the conductive layer, t << S and is given by:

$$G' = \frac{2S}{t} \ln 2 \qquad \text{(Eq. 3)}$$

The decrease in resistivity with *n* may be assigned to higher loading of cMWCNTs on to the paper that perhaps created a highly inter-networked matrix. **Table 2** compares the resistivities of some MWCNT-based screen-printing inks with the present work. **Section S2** presents a video that shows use of the cMWCNT@paper electrodes to complete a circuit and light a red LED, demonstrating their conductivity.

Another important factor in determining the application of paper-based biosensors is scalability in the fabrication process. Printing of the prepared cMWCNT conductive ink via an established printing technology may potentially ensure scalability of the fabrication of the paper electrodes. Hence, the prepared cMWCNT ink was analysed for rheology (flow behaviour) to determine whether it can be used for screen printing. The flow behaviour of the cMWCNT ink was analysed at different shear rates (0.1–1000 s^{-1}) using a parallel plate of 40 mm in diameter. It was found that the apparent viscosity of the ink decreased with the increase in shear rate, indicating a shear thinning and thixotropic behaviour (**Figure 2(D)**), with initial apparent viscosity of 22 Pa·s, which is an ideal condition for screen printing. The presence of CMC may account for the high initial viscosity; however, the carbon nanomaterials are also known to increase the viscosity of inks. Thus, while both CMC and cMWCNT can together contribute to the high initial viscosity, the shear thinning behaviour of the ink is, perhaps, mostly due to CMC, which is a well-known rheology modifier and a thixotropic agent. These results indicate the suitability of the formulated

New Journal of Chemistry Accepted Manuscript

View Article Online
DOI: 10.1039/D3NJ01557B

Published on 09 May 2023. Downloaded on 5/22/2023 6:14:26 AM

ink for screen printing suggesting that the formulated ink can be used for the batch production of low cost, screen-printed electrodes (SPEs).

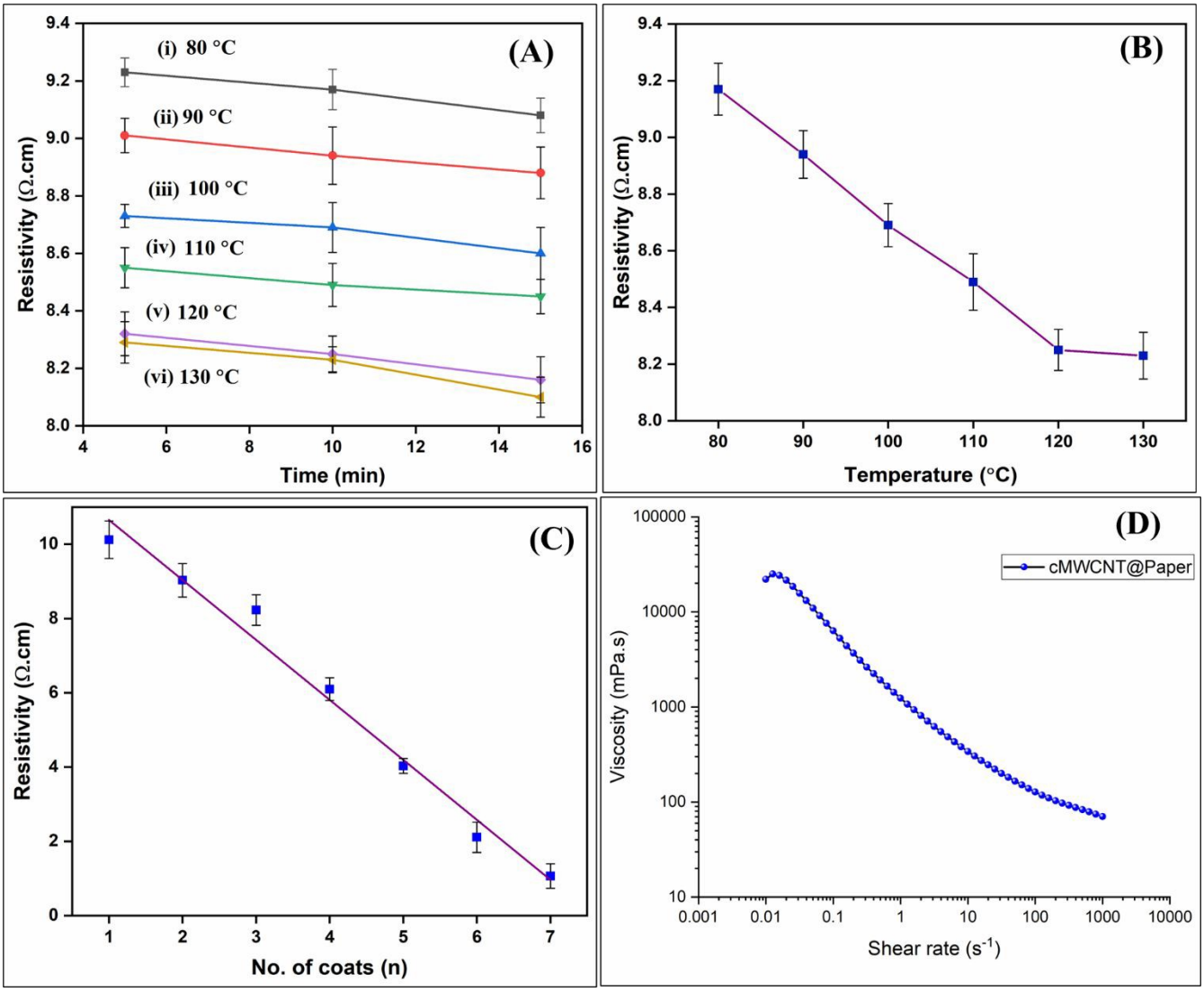


Figure 2(A) the change in resistivity of the cMWCNT@paper electrodes with annealing temperature and time, **(B)** the corresponding curve depicting the relationship between the resistivity of the cMWCNT@paper electrodes with temperature at fixed annealing time of 10 min., **(C)** the change in the resistivity of the cMWCNT@paper electrodes with number of coats of the conductive ink, and (D) change in the viscosity of the cMWCNT ink with shear rate displaying shear thinning behaviour.

New Journal of Chemistry Accepted Manuscript

View Article Online
DOI: 10.1039/D3NJ01557B

Published on 09 May 2023. Downloaded on 5/22/2023 6:14:26 AM.

Table 2. Comparison among different MWCNT-based ink formulations.

S. No.	*Nanomaterial*	*Binder*	*Resistivity*	*Applications*	*Reference*
1.	MWCNT			All-in-one fabric-based supercapacitors	[25]
2.	MWCNT/PEDOT:PSS	PEDOT:PSS	51.31 ± 0.25 Ω sq^{-1}	Flexible heating	[21]
3.	Graphene/MWCNT/Carbon black	Water-based acrylic resins	4 Ω sq^{-1}	Electrothermal films	[22]
4.	dihydroxyphenyl-functionalized multi-walled carbon nanotubes (MWNT-f-OH)/carbon black/graphite	waterborne acrylic resins	up to 29 Ω sq^{-1}	Electrochemiluminescent devices	[34]
5.	Functionalized MWCNT	Hydroxyethyl cellulose	--	Humidity sensing	[35]
6.	MWCNT	PVP	0.5–13 Ω sq^{-1}	Patch antennas	[26]
7.	**Carboxyl-functionalized MWCNT**	**Carboxymethyl cellulose**	**1.066 ± 0.31 Ω sq^{-1}**	**DNA Biosensor**	**Present work**

3.1.3 Raman and XPS analyses

The Raman and XPS analyses were conducted to verify the presence of cMWCNT in the formulated conductive ink. For this purpose, the ink was dried at 120 °C overnight and then kept at 350 °C for 2 h to degrade the residual CMC. The obtained dried ink powder was analysed via Raman and XPS studies. The Raman spectrum of the dried ink reveals the two characteristic bands of graphitic carbon-containing materials—the G band and the D band (**Figure 3(A)**). The G band seen at 1582.53 cm^{-1} is a first order Raman process corresponding to the tangential mode vibrations of the C atoms. The presence of a single, sharp graphitic peak at ~1582 cm^{-1} indicates the multiwalled nature of the carbon nanotubes (and the large diameter). The D and 2D (G') bands observed at 1353.69 cm^{-1} and 2705.54 cm^{-1}, respectively, are assigned to the double resonance

New Journal of Chemistry Accepted Manuscript

View Article Online
DOI: 10.1039/D3NJ01557B

Published on 09 May 2023. Downloaded on 5/22/2023 6:14:26 AM.

Raman processes. The D band indicates the presence of disorder induced by amorphous carbon, structural defects, etc., while the 2D (G') band is an overtone of the D band that is dispersive in nature (its frequency is dependent on the excitation laser wavelength). Together with the G band, the G' is due the Raman signature of materials consisting of the graphitic sp^2 carbon. The I_D/I_G ratio is known to indicate the degree of defects, that may either be already present or induced by some physicochemical interaction, in the MWCNT structure. The I_D/I_G ratio was found to be 0.66 for the dried ink powder indicating the presence of less defects in the chemical structure.

The XPS studies were conducted to investigate the surface elemental composition of the as prepared conductive ink. **Figure 3(B)** shows the survey scan spectra consisting of the major peaks are attributed to the C 1s (284.5 eV) and O1s (530.5 eV) confirming the presence of cMWCNTs in the dried ink. The deconvoluted spectra for the C1s in **Figure 3(C)** exhibits five characteristic peaks and O1s (**Figure 3(D)**) shows four characteristic peaks. The C1s main peak located at 284.5eV (C=C) corresponds to the sp^2 hybridization. The peak observed at 285.1eV is attributed to the sp^3 hybridization of C-C bonds. The peaks seen at 286.3 eV, 287.2 eV and 289.6 eV are assigned to the epoxy/hydroxy (-C–O), carbonyl groups (C=O) and carboxyl groups (O–C=O) of the cMWCNT, respectively. In case of O 1s, the deconvoluted peak at 530.5eV and 531.3 eV corresponds to the oxygen double bonded to the carbon (O=C) and single bonded to carbon (C-O), respectively. The peak at the 533.5eV corresponds to the oxygen atoms in carboxyl group and those at 534.5eV indicates the presence of oxygen in water at the surface.[36-39] These results clearly reveal the presence of the cMWCNTs in the intact form in the as-prepared dried ink.

New Journal of Chemistry Accepted Manuscript

View Article Online
DOI: 10.1039/D3NJ01557B

Published on 09 May 2023. Downloaded on 5/22/2023 6:14:26 AM.

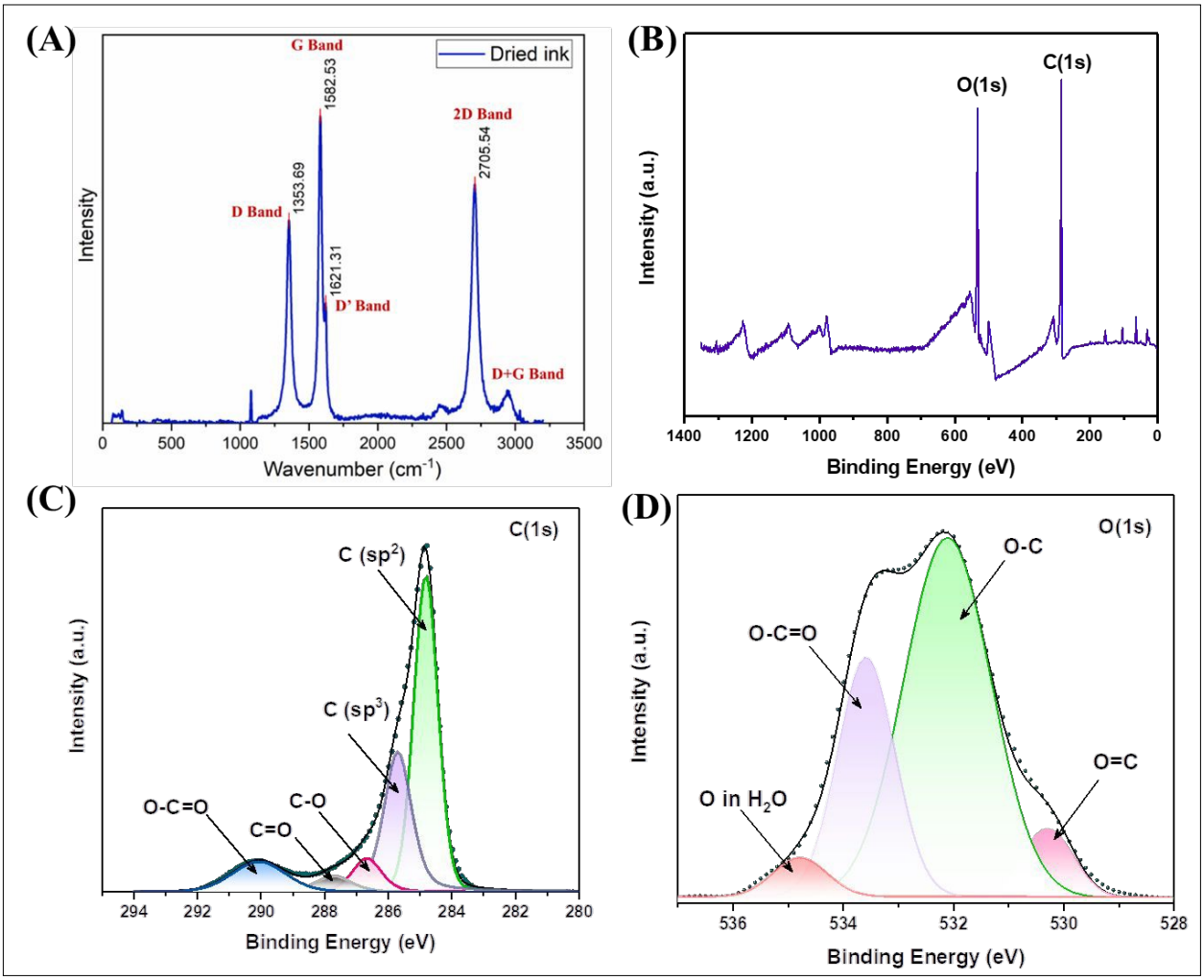


Figure 3(A). Raman spectrum, **(B)** XPS survey scan, and deconvoluted peaks of **(C)** C(1s), and **(D)** O(1s).

3.2 Electrochemical characterization studies

The continuous use stability is an essential consideration for a biosensing electrode. In this regard, the electrochemical response of a biosensing electrode should be stable enough to disallow any significant fluctuations with time provided there are no changes in the system (e. g., buffer composition). The cMWCNT@paper electrodes were analysed for continuous use stability in terms of their electrochemical response via cyclic voltammetry (CV). **Figure 4(A)** shows the electrochemical response of the same electrode in the first and the 20th CV scan. There is no

New Journal of Chemistry Accepted Manuscript

View Article Online
DOI: 10.1039/D3NJ01557B

Published on 09 May 2023. Downloaded on 5/22/2023 6:14:26 AM.

significant change in the peak current of both the scans indicating the stability of the cMWCNT@paper biosensing electrodes. It may be noted that the electrodes take about 20 minutes to stabilize (time taken by a biosensing electrode to be in dynamic equilibrium with the surrounding buffer to yield a stable response). The swelling nature of CMC present in the ink matrix may partially account for the stabilization time of the electrode. However, the eventual (and continued) stability of the electrode response suggests that the hydrophilic nature of the CMC perhaps does not interfere with the electrochemical response of the electrodes.

Batch reproducibility is another important consideration for paper-based electrodes. To assess the batch reproducibility of the fabricated cMWCNT@paper electrodes, 10 electrodes were randomly selected from different batches and analysed via CV (**Figure 4(B)**). The current density (J) of a working electrode in an electrochemical system is given by,

$$J = I/A \qquad \text{(Eq. 4)}$$

where I is the current and A is the surface area. Since the surface area of the electrodes used in the study for electrochemical analysis was 1 cm^2, the J and I values were equivalent. The peak J value of the cMWCNT@paper electrode was found to be 27.03 ± 0.38 μA cm^{-2} (mean ± SD). This indicates that despite the manual nature of the coating process, the ink coatings on the electrodes are uniform enough to obtain similar electrochemical response. This further suggests that the cMWCNTs are homogenously dispersed in the ink leading up to a stable, similar electrochemical response across different batches of electrodes.

The change in the electrochemical response of the cMWCNT@paper electrodes after adsorption of the unmodified and modified MBs was recorded. As shown in **Figure 4(C)**, the electrochemical peak response of the MB/cMWCNT@paper is slightly lower than that of the

New Journal of Chemistry Accepted Manuscript

View Article Online
DOI: 10.1039/D3NJ01557B

cMWCNT@paper electrode. This may be attributed to the repulsion of the negatively charged redox probes by the carboxylated MBs. The electrochemical response was found to be further decreased significantly for the Av/MB/cMWCNT@paper and CP/Av/MB/cMWCNT@paper electrodes due to the insulating nature of Av, which is a bulky glycoprotein, and DNA molecules. This also confirms, indirectly, the modification of MBs with avidin and subsequent immobilization of CP onto the Av/MBs via biotin-avidin interactions.

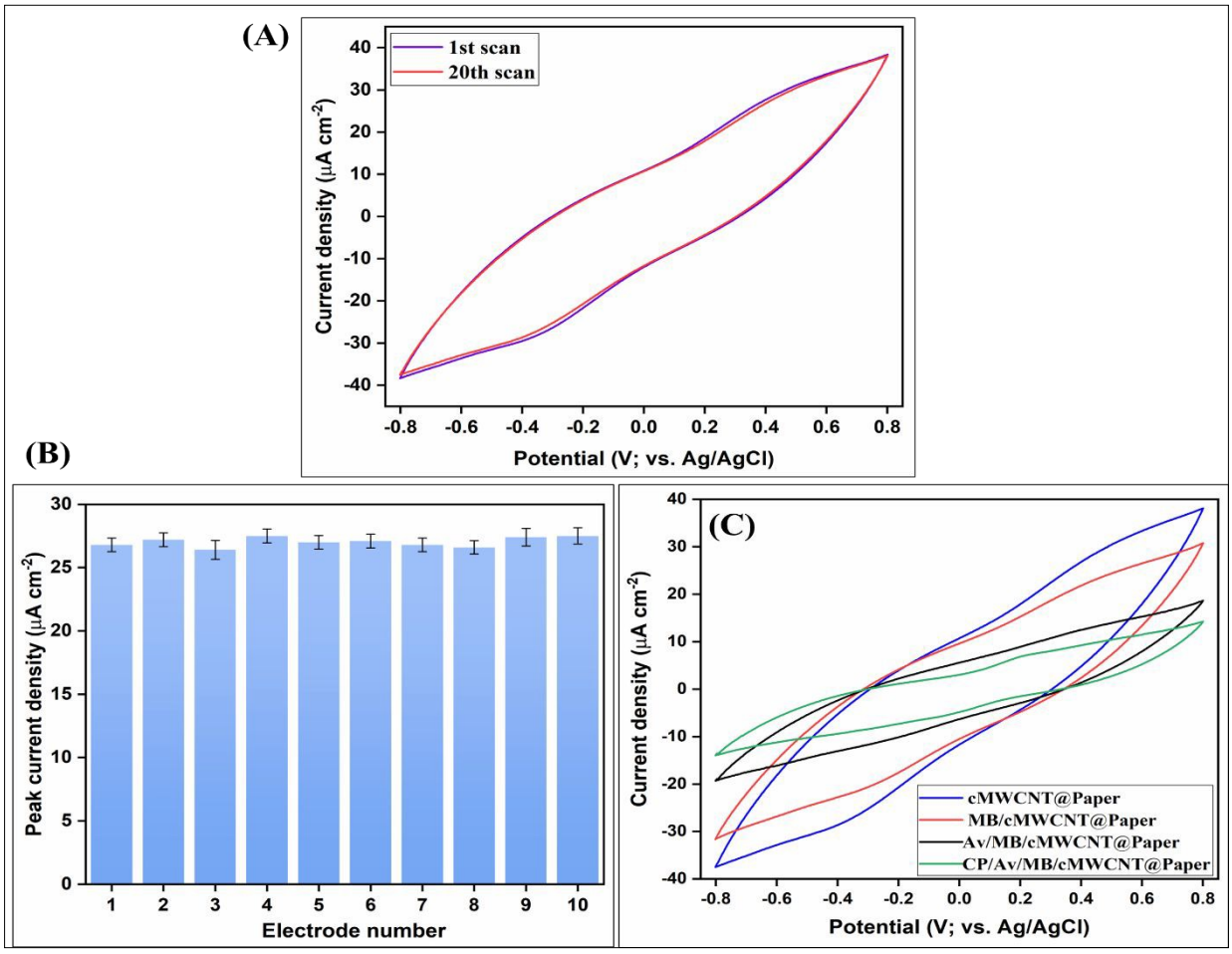


Figure 4. (A) Current density vs. potential scans of the cMWCNT@paper showing continuous use stability, **(B)** Peak current density (J) of different cMWCNT@paper electrodes indicating batch reproducibility, and **(C)** Change in the current density curves of the cMWCNT@paper electrodes after modification with MBs and modified MBs.

Published on 09 May 2023. Downloaded on 5/22/2023 6:14:26 AM.

New Journal of Chemistry Accepted Manuscript

View Article Online
DOI: 10.1039/D3NJ01557B

Published on 09 May 2023. Downloaded on 5/22/2023 6:14:26 AM.

3.3 Electrochemical response studies

An electrochemical MB-assisted sandwich hybridization assay was designed for the detection of gonorrhoeal *porA* pseudogene (**Figures 5(A)** and **(B)**). Prior to the response studies, the amount of MB required to yield a significant response at the cMWCNT@paper electrodes was optimized (**Figure S3**). A response time analysis was also conducted to determine the minimum time required for saturation of the CV response after drop casting of the C-T-D/Av/MB assembly. It was found that the response of the C-T-D/Av/MB/cMWCNT@paper electrode(s) saturated after 20 min for 1 pM target concentration (**Figure S4(A)**). Thereafter, the response was recorded after 20 min of immersion of the C-T-D/Av/MB/cMWCNT@paper electrodes in the buffer for biosensing measurements. For the electrochemical response studies, 0.5 mg MBs were adsorbed on the cMWCNT@paper electrodes for every concentration of the target DNA. Since temperature is an important factor controlling the DNA hybridization process, the annealing (DNA hybridization) was allowed to occur at 60 °C for 10 min. The temperature was selected in respect to the melting temperature of the oligonucleotide probes; normally the ideal annealing temperature is within ± 5 °C of the melting temperature of a particular DNA sequence. **Figure 5(C)** shows the CV response of the cMWCNT@paper with change in the concentration of the target DNA sequence within the range 100 fM–100 nM. The corresponding calibration curve was plotted between the net change in current density (ΔJ) and the concentration of the target DNA sequence, wherein the ΔJ values were calculated as:

$$\Delta J = J_c - J_0 \qquad \text{(Eq. 5)}$$

where J_c is the peak current density for a particular concentration of target DNA, and J_0 is the peak current density of the CP/Av/MB/cMWCNT@paper electrode (blank). As shown in Figure 5(D),

New Journal of Chemistry Accepted Manuscript

View Article Online
DOI: 10.1039/D3NJ01557B

a linear correlation was found between ΔJ and the log of concentration of the target DNA, given by the equation:

$$\Delta J = 5.09 \times \log[\text{concentration}] + 12.59, R^2 = 0.98 \qquad \text{(Eq. 6)}$$

The observed increase in the current density can be attributed to the participation of MetB, attached at 3' end of DP, in the electron transfer process at the electrode surface. In fact, the redox peak of MetB is visible in the CV scans at higher concentrations of the target DNA sequence (**Figure 5(C)**). The detection limit and sensitivity of the biosensing assay were found to be 0.13 pM and 5.09 μA.(log[concentration])$^{-1}$, respectively. Further, to ascertain the clinical applicability of the electrochemical biosensing assay, the response of the biosensing electrode was recorded against genomic DNA isolated from *N. gonorrhoeae*. The protocol followed was the same as that for the response studies with one minor modification—the genomic DNA was subjected to denaturation by heating at 95 °C for 10 min followed by shearing by ultrasonication for 10 min. **Figure 5(E)** compares the response of the biosensing electrode to the genomic DNA and the same concentration of synthetic target DNA strand used in the response studies. The recovery rate was found to be 98-99% for the genomic samples for three different concentrations.

DNA isolated from clinical specimens consists of a small amount of pathogenic DNA mixed with human DNA and DNA from other commensal bacteria. In some cases, proteins or other cellular components may also be mixed (in case DNA is isolated by boiling method) that can act as interferents. **Figure 5(F)** shows the results relating to the studies conducted to determine the effect of DNA/protein interferents on the biosensing assay response. The peak response of the biosensing electrode to gonorrhoeal genomic DNA was recorded in the presence of DNA from different bacterial species including *Neisseria meningitidis* (NM), *Chlamydia trachomatis* (Ch),

Published on 09 May 2023. Downloaded on 5/22/2023 6:14:26 AM.
New Journal of Chemistry Accepted Manuscript

View Article Online
DOI: 10.1039/D3NJ01557B

Published on 09 May 2023. Downloaded on 5/22/2023 6:14:26 AM.

Streptococcus aureus (SA), *Ureaplasma urealyticum* (U), *Enterococcus faecalis* (EF), and a cocktail of all these bacterial DNA (M). The response in the presence of excess of BSA alone and along with non-gonorrhoeal DNA was also recorded. For this study, a fixed quantity of gonorrhoeal genomic DNA (1 pM) was mixed with either 50× concentration of DNA of other bacteria or BSA (as a protein interferent). No significant difference was found in the peak response of the C-T-D/Av/MB/cMWCNT@paper biosensing electrodes in the presence of the interfering DNA and proteins, indicating not only the specificity of the designed probes but also the significance of sample enrichment via MBs before biosensing. **Table 3** summarizes the results of the recent studies involving fabrication of paper-based electrochemical biosensors (printed either by inhouse prepared or commercial ink) for the detection of pathogenic DNA, and compares it to the present work. The storage stability of the cMWCNT@paper electrodes was also analysed by recording their CV response for 7-90 days, wherein the electrodes were stored at room temperature in dark, dry conditions (**Figure S4(B)**). The value of current density of the bioelectrode did not change significantly until 30 days (99.7% of response on 7 days). Thereafter, the response fell to 97.78% and 94.8% of initial response at 60 and 90 days, respectively, indicating excellent storage stability of the fabricated cMWCNT@paper electrodes. This further eliminates the need of special storage conditions for the electrodes.

New Journal of Chemistry Accepted Manuscript

View Article Online
DOI: 10.1039/D3NJ01557B

Published on 09 May 2023. Downloaded on 5/22/2023 6:14:26 AM.

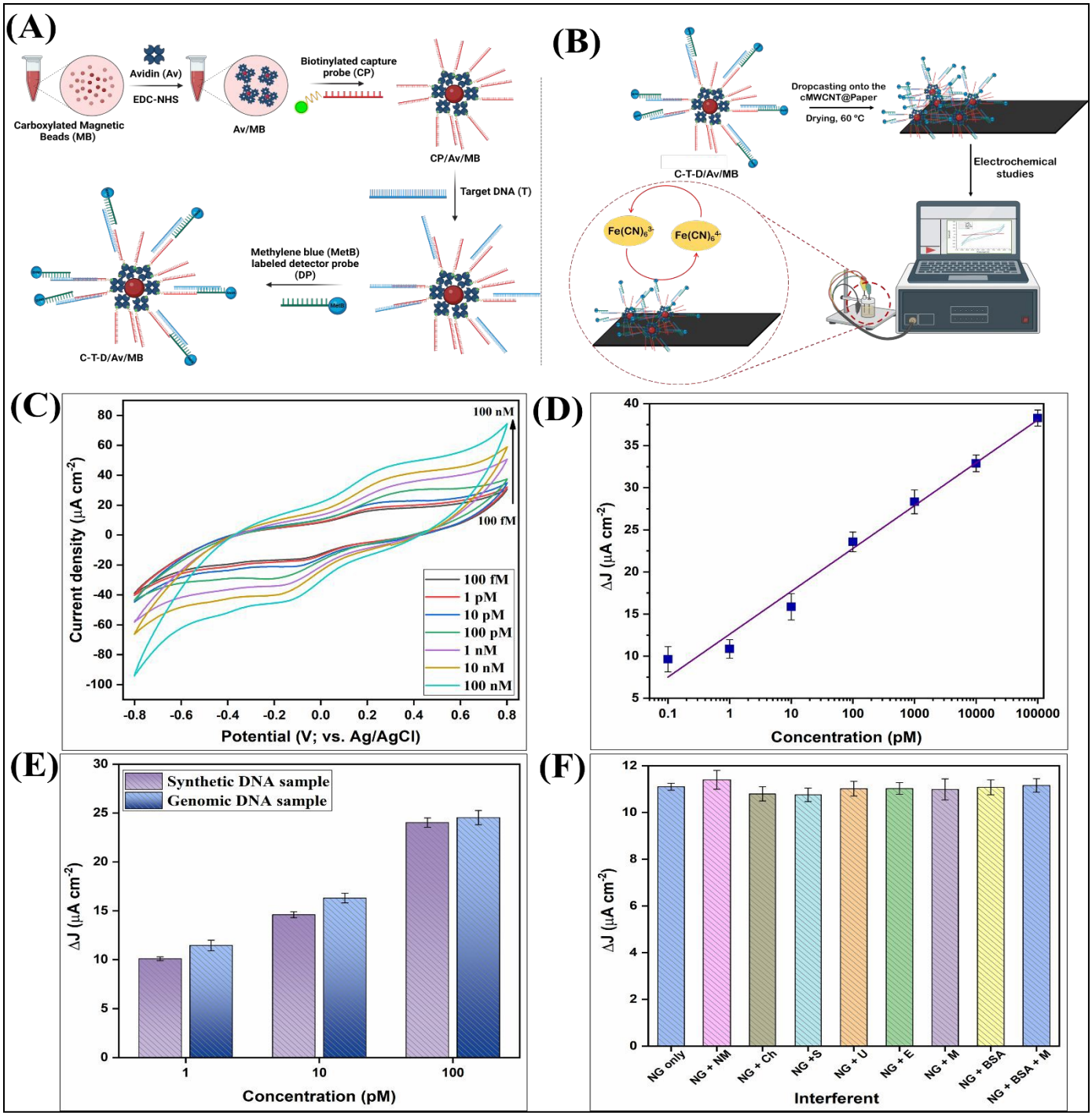


Figure 5 Schematic displaying the **(A)** steps involved in the magnetic bead-assisted sandwich hybridization assay, **(B)** subsequent drop casting on the cMWCNT@paper electrodes for electrochemical analysis. **(C)** Current density vs. potential curves of the cMWCNT@paper electrodes with increasing concentration of the C-T-D hybridization complex, **(D)** the corresponding calibration curve showing a linear correlation between the change in peak current density (ΔJ) and the log of target sequence concentration, **(E)** comparison between the ΔJ values obtained for synthetic target DNA sequence and gonorrhoeal genomic DNA in different

New Journal of Chemistry Accepted Manuscript

View Article Online
DOI: 10.1039/D3NJ01557B

Published on 09 May 2023. Downloaded on 5/22/2023 6:14:26 AM.

concentrations, and **(F)** the ΔJ response of the electrochemical biosensing electrodes to genomic DNA mixed with non-gonorrheal DNA and proteins.

Table 3. Table comparing the recent studies on paper based electrochemical biosensors for pathogenic DNA detection

S. No.	Ink formulation/ Nanomaterial	Target pathogen	Linear range	Sensitivity (LOD)	Reference
1.	Graphene oxide-modified carbon ink screen printed on paper	*Orientia tsutsugamushi* (single stranded DNA)	0.05×10^2 pg μL^{-1} to 6.3×10^2 pg μL^{-1}	1228.4 $\mu A\ cm^{-2}\ ng^{-1}$ (20 pg μL^{-1})	40
2.	Ni-Au/CNT/PVA (vacuum filtration and drop casting)	HIV DNA	10 nM–1 μM	-- (0.13 nM)	41
3.	Graphene nanosheets	-- (dsDNA)	0.2-5 pg mL^{-1}	0.00656 mA $pg^{-1}\ cm^{-2}$	42
4.	Carbon graphene ink (commercial)	Hepatitis B virus	50 pM-100 nM	-- (1.45 pM)	43
5.	Ag nanoprisms electrodeposited on graphene quantum dots (GQDs)	*Leishmania infantum*	1 zM - 1 nM	1 zM (LOQ*)	44
6.	**cMWCNT**	***Neisseria gonorrhoeae***	**100 fM-100 nM**	**5.09 μA (log[concentration])$^{-1}$ (0.13 pM)**	**Present work**

4. Conclusions

We have fabricated a conductive ink-coated paper biosensing electrode for magnetic bead assisted electrochemical detection of *porA*, a pseudogene specifically present in *N. gonorrhoeae*. The conductive ink consists of cMWCNTs homogenously dispersed in an emulsion consisting of terpineol and CMC dispersed in distilled water stabilized by PS 80. The ink-coated paper electrodes have displayed excellent continuous use stability and batch reproducibility, despite manual coating of the paper substrates by the cMWCNT ink. The electrochemical DNA biosensing assay has been shown to be highly sensitive and specific to the *porA* gene sequence in a wide linear

New Journal of Chemistry Accepted Manuscript

View Article Online
DOI: 10.1039/D3NJ01557B

Published on 09 May 2023. Downloaded on 5/22/2023 6:14:26 AM.

range spanning 10^5 orders of magnitude. The biosensing assay has been used to detect genomic gonorrhoeal DNA with excellent recovery. The addition of magnetic beads has imparted high selectivity to the biosensing assay as it was shown to detect gonorrhoeal genomic DNA even in the presence of other non-gonorrhoeal DNA present in concentrations as high as 50 times that of gonorrhoeal DNA. Further, the formulated ink has been shown to be thixotropic, which signifies its ability to be screen printed. This study demonstrates the fabrication of efficient paper-based electrodes for electrochemical biosensing using a highly homogenous, conductive ink. Further studies should focus on modifications in the conductive ink formulation for conductivity enhancement and adherence to different substrates. It should be interesting to investigate the effect of different conductive ink formulations on the electrochemical performance of the resulting electrodes.

Acknowledgments

NG acknowledges the Vice Chancellor, Delhi Technological University (DTU), Delhi. NG also thanks Dr. Suveen Kumar, DST-INSPIRE Faculty, Department of Chemistry, Delhi University, Delhi, India, and Dr. Shine Augustine, Postdoctoral Fellow, Sungkyunkwan University, Suwon, South Korea, for help in XPS and Raman spectroscopic analyses. The Central Research Facility (CRF), IIT Delhi, New Delhi (Hauz Khas and Sonipat campus) is acknowledged for the SEM and XPS analyses.

Credit Author Statement

BDM, NG: Conceptualization; NG: Investigation, Formal Analysis, Writing-original draft; DK, AD, BDM: Writing-review and editing, Supervision, Project Administration; SS: Resources, Writing-review and editing

New Journal of Chemistry Accepted Manuscript

View Article Online
DOI: 10.1039/D3NJ01557B

Published on 09 May 2023. Downloaded on 5/22/2023 6:14:26 AM.

Conflict of Interest

The authors declare no conflict of interest.

References

1. T. Pinheiro, A. C. Marques, P. Carvalho, R. Martins and E. Fortunato, *ACS Appl. Mater. Interfaces*, 2021, **13**, 3576-3590.

2. J. P. Devadhasan and J. Kim, *Sens. Actuators B Chem.*, 2018, **273**, 18-24.

3. H. Li and A. J. Steckl, *Anal. Chem.*, 2019, **91**, 352-371.

4. Q. H. Nguyen and M. I. Kim, *Trends Analyt. Chem.*, 2020, **132**, 116038.

5. K. Ratajczak and M. Stobiecka, *Carbohydr. Polym.*, 2020, **229**, 115463.

6. S. Khaliliazar, A. Toldrà, G. Chondrogiannis and M. M. Hamedi, *Anal. Chem.*, 2021, **93**, 14187-14195.

7. S. Kumar, S. Kumar, S. Srivastava, B. K. Yadav, S. H. Lee, J. G. Sharma, D. C. Doval and B. D. Malhotra, *Biosens. Bioelectron.*, 2015, **73**, 114-122.

8. H. Yan, F. Huo, Y. Yue, J. Chao and C. Yin, *Journal of the American Chemical Society*, 2020, **143**, 318-325.

9. Y. Huang, Y. Zhang, F. Huo, J. Chao, F. Cheng and C. Yin, *Journal of the American Chemical Society*, 2020.

10. X. Chen, X. Zhang and F.-G. Wu, *Chinese Chemical Letters*, 2021, **32**, 3048-3052.

11. B. Feng, Y. Zhu, J. Wu, X. Huang, R. Song, L. Huang, X. Feng and W. Zeng, *Chinese Chemical Letters*, 2021, **32**, 3057-3060.

12. J. Li, M. Zhang, L. Yang, Y. Han, X. Luo, X. Qian and Y. Yang, *Chinese Chemical Letters*, 2021, **32**, 3865-3869.

13. H. Yan, Y. Wang, F. Huo and C. Yin, *Journal of the American Chemical Society*, 2023, **145**, 3229-3237.

14. E. Solhi, M. Hasanzadeh and P. Babaie, *Anal. Methods*, 2020, **12**, 1398-1414.

15. B. Yao, J. Zhang, T. Kou, Y. Song, T. Liu and Y. Li, *Adv. Sci.*, 2017, **4**, 1700107.

New Journal of Chemistry Accepted Manuscript

View Article Online
DOI: 10.1039/D3NJ01557B

Published on 09 May 2023. Downloaded on 5/22/2023 6:14:26 AM.

16. C. Zhao, J. Wang, Z.-q. Zhang, Z. Sun and Z. Maimaitimin, *ChemElectroChem*, 2022, **9**, e202200948.

17. T. S. Tran, N. K. Dutta and N. R. Choudhury, *Adv. Colloid Interface Sci.*, 2018, **261**, 41-61.

18. J. R. Camargo, L. O. Orzari, D. A. G. Araujo, P. R. de Oliveira, C. Kalinke, D. P. Rocha, A. L. dos Santos, R. M. Takeuchi, R. A. A. Munoz and J. A. Bonacin, *Microchem. J.*, 2021, **164**, 105998.

19. W. T. Fonseca, K. R. Castro, T. R. de Oliveira and R. C. Faria, *Electroanalysis*, 2021, **33**, 1520-1527.

20. M. Mass, L. S. Veiga, O. Garate, G. Longinotti, A. Moya, E. Ramón, R. Villa, G. Ybarra and G. Gabriel, *Nanomater.*, 2021, **11**, 1645.

21. A. S. Pillai, A. Chandran and S. K. Peethambharan, *Appl. Mater. Today*, 2021, **23**, 100987.

22. Y. Liao, Y. Tian, X. Ma, M. Zhao, J. Qian and X. Wang, *ACS Appl. Mater. Interfaces*, 2020, **12**, 48077-48083.

23. W. Yang and C. Wang, *Journal of Materials Chemistry C*, 2016, **4**, 7193-7207.

24. Y. Htwe and M. Mariatti, *Journal of the Taiwan Institute of Chemical Engineers*, 2021, **125**, 402-412.

25. L. Jiang, H. Hong, J. Hu and X. Yan, *ACS Appl. Mater. Interfaces*, 2022, **14**, 12214-12222.

26. H. Menon, R. Aiswarya and K. P. Surendran, *RSC Adv.*, 2017, **7**, 44076-44081.

27. J. Whelan, V. Abbing-Karahagopian, L. Serino and M. Unemo, *BMC Infect. Dis.*, 2021, **21**, 1-23.

28. J. Whelan, J. Eeuwijk, E. Bunge and E. Beck, *Infect. Dis. Ther.*, 2021, **10**, 1887-1905.

29. W. H. Organization, *Global health sector strategy on sexually transmitted infections 2016-2021: toward ending STIs*, World Health Organization, 2016.

30. R. Verma, S. Sood, R. Singh, G. Sumana, M. Bala, V. K. Sharma, J. C. Samantaray, R. M. Pandey and B. D. Malhotra, *Diagn. Microbiol. Infect. Dis.*, 2014, **78**, 16-23.

31. R. Singh, R. Verma, A. Kaushik, G. Sumana, S. Sood, R. K. Gupta and B. Malhotra, *Biosens. Bioelectron.*, 2011, **26**, 2967-2974.

32. A. Soni, C. M. Pandey, S. Solanki and G. Sumana, *RSC Adv.*, 2015, **5**, 45767-45774.

33. R. P. Tortorich, H. Shamkhalichenar and J.-W. Choi, *Appl. Sci.*, 2018, **8**, 288.

New Journal of Chemistry Accepted Manuscript

View Article Online
DOI: 10.1039/D3NJ01557B

Published on 09 May 2023. Downloaded on 5/22/2023 6:14:26 AM

34. Y. Liao, R. Zhang, H. Wang, S. Ye, Y. Zhou, T. Ma, J. Zhu, L. D. Pfefferle and J. Qian, *RSC Adv.*, 2019, **9**, 15184-15189.

35. V. S. Turkani, D. Maddipatla, B. B. Narakathu, T. S. Saeed, S. O. Obare, B. J. Bazuin and M. Z. Atashbar, *Nanoscale Adv.*, 2019, **1**, 2311-2322.

36. F. G. Pacheco, A. A. Cotta, H. F. Gorgulho, A. P. Santos, W. A. Macedo and C. A. Furtado, *Appl. Surf. Sci.*, 2015, **357**, 1015-1023.

37. S. Augustine, P. Kumar and B. D. Malhotra, *ACS Appl. Bio Mater.*, 2019, **2**, 5366-5378.

38. V. Duc Chinh, G. Speranza, C. Migliaresi, N. Van Chuc, V. Minh Tan and N.-T. Phuong, *Sci. Rep.*, 2019, **9**, 1-9.

39. G. Stando, S. Han, B. Kumanek, D. Łukowiec and D. Janas, *Sci. Rep.*, 2022, **12**, 1-13.

40. D. Kala, T. K. Sharma, S. Gupta, V. Verma, A. Thakur, A. Kaushal, A. V. Trukhanov and S. V. Trukhanov, *Sensors*, 2021, **21**, 4366.

41. Q. Lu, T. Su, Z. Shang, D. Jin, Y. Shu, Q. Xu and X. Hu, *Biosens. Bioelectron.*, 2021, **184**, 113229.

42. J. Mohanraj, D. Durgalakshmi, R. A. Rakkesh, S. Balakumar, S. Rajendran and H. Karimi-Maleh, *J. Colloid Interface Sci.*, 2020, **566**, 463-472.

43. C. Srisomwat, P. Teengam, N. Chuaypen, P. Tangkijvanich, T. Vilaivan and O. Chailapakul, *Sens. Actuators B Chem.*, 2020, **316**, 128077.

44. F. Farshchi, A. Saadati and M. Hasanzadeh, *Anal. Methods*, 2020, **12**, 4759-4768.

New Journal of Chemistry Accepted Manuscript

Indian Journal of Chemical Technology
Vol. 30, May 2023, pp. 308-319
DOI: 10.56042/ijct.v30i3.70100

Carboxymethylated gum tragacanth crosslinked poly(sodium acrylate)hydrogel: Fabrication, characterization, rheology and drug-delivery application

Meenakshi Tanwar, Rajinder K Gupta* & Archna Rani*
Department of Applied Chemistry, Delhi Technological University, Delhi 110 042, India
E-mail:rkg67ap@yahoo.com,

Received 5 January 2023; accepted 16 February 2023

This study aimed to synthesize Carboxymethylated Gum Tragacanth (CMGT) from the Gum Tragacanth (GT). Modified gum's potential as a drug delivery carrier has been explored by synthesizing CMGT based hydrogels. The viscoelastic characteristics of the fabricated hydrogel have been examined by Rheological analysis. SEM studies have been conducted to examine the surface morphology and TGA is used to perform the thermal analysis. XRD, FTIR, and solid state ^{13}C NMR have been used to examine the structural features of the GT, CMGT, sodium acrylate based hydrogel (SAH) and carboxymethylated gum tragacanth co-polymerized with sodium acrylate based hydrogel (CMGT-co-SAH). The anti-inflammatory drug, Aceclofenac Sodium(AFS) loaded onto the hydrogel has been used as a model drug. The AFS follows the Fickian mechanism of diffusion and the results are best fitted in Higuchi and Korsmeyer–Peppas models.

Keywords: *Astragalus gummifer*, Carboxymethylation, Drug-delivery, Hydrogel, Polysaccharides

An excellent way to increase the drug's effectiveness is to deliver it using any reliable carrier in medical science. In this modern period, natural gum polysaccharides are explored as the main component in pharmaceutical formulations[1–3]. Recently, the potential of Gum Tragacanth has been explored in cosmetics, pharmaceuticals, bio and food industries[4,5]. The GT obtained from *Astragalus gummifer* is considered GRAS (Generally Recognized As Safe)[6]. GT is a heterogeneous, anionic and naturally available polysaccharide. The presence of arabinogalactan in GT was confirmed by acid hydrolysis[7]. In traditional local medications, GT act as a demulcent for gastrointestinal problems and sore throats. It may additionally have analgesic properties[8]. The property of the GT can be enhanced through chemical modifications, as previously reported in the literature. The reported modification methods of GT are graft-copolymerization[9] and carboxymethylation[10]. However, carboxy-methylation is most widely favoured as it is cheap, quickly processed and produces versatile products with better water retention properties and strength[11] compared to natural ones[12]. In the current study, GT was carboxymethylated to synthesize CMGTand the potential of CMGT in drug delivery was further investigated by synthesizing CMGT based hydrogel.

The three-dimensional network structure of a hydrogel has been created by the chemical cross-linking of polysaccharides with suitable monomer by using a suitable initiator and multifunctional cross-linker. In the past few years, the hydrogel has increasingly been utilized as a carrier in drug delivery application to produce sustained and controlled drug release because of its 3Dweb structure and excellent swelling property[13,14].

The swell ability of the hydrogel can be enhanced by using sodium acrylate (SA) content in the graft polymerization[15]. Ganguly *et al*. also observed the same swellability of the hydrogel based on psyllium gum copolymerized with acrylic acid and sodium acrylate[16]. The application of CMGT in the preparation of superabsorbent hydrogel has been reported by Mohammad B *et al.*[17]. Previous literature reveals that CMGT based hydrogel and their application in drug delivery is still to be explored. In this study, we have synthesized and characterized the novel AFS loaded hydrogel based on graft co-polymerization of SA onto the CMGT backbone. The various formulations of CMGT-co-SAH were synthesized by varying the amount of KPS as initiator and MBA as cross-linker, and their swelling Index (SI) was assessed. Also, by changing the temperature, i.e., 27, 37 and 47°C, SI and network parameters of the hydrogel were determined. Modification of the GT to CMGT and their graft copolymerization with SA was confirmed by XRD, FTIR, TGA, SEM and C^{13}-NMR. Rheological analysis

of the SAH, which is considered as control hydrogel and CMGT-co-SAH were done to determine the gel characteristics. Further, the drug release behaviour of the CMGT-co-SAH was evaluated by using a model drug, AFS by applying different kinetic models such as Hixon-Crowell, Higuchi, Korsmeyer-Peppas, Zero-order and First-order kinetic model to analyse the drug release profile.

Experimental Section

Materials

GT(purchased from local market, New Delhi), Sodium monochloroacetate (SMCA, CDH, New Delhi), N,N′-methylenebis-acrylamide (MBA, CDH, New Delhi),Sodium hydroxide (NaOH, Fischer Scientific, Mumbai), Acrylic acid (AA, CDH, New Delhi), Potassium per sulphate (KPS, Fischer Scientific, Mumbai), Iso propyl alcohol(Fischer Scientific, Mumbai), methanol (Fischer Scientific, Mumbai), AFS was gifted from Unicure India Pvt. Ltd. and all the solutions were prepared in milli-Q grade distilled water.

Synthesis of Carboxymethylated Gum Tragacanth (CMGT)

The CMGT was synthesized using a previously described method[12] with slight modifications in the procedure. Derivatization of the polysaccharides chain follows Williamson's synthesis reaction. For 0.2 degrees of substitution (0.2 DOS chosen for good swelling properties), the required amount of GT was weighed and mixed continuously for 15 min in distilled water. Then (0.00775 moles) of NaOH was added to the homogeneous solution of GT. After 30 min of stirring, SMCA (0.00123 moles) was gradually added. The solution was stirred at magnetic stirrer for 3 h at 70°C to make it homogeneous. Once the CMGT solution was cooled, the precipitates of CMGT were filtered, washed at least three times with isopropyl alcohol (80%), and oven dried at 45 °C.

Estimation of Degree of Substitution (DOS) on GT

DOS of CMGT was determined by back titration[18]. CMGT (1 g) was dispersed in the required volume of HCl and Isopropyl alcohol was added as a solvent. The stirring of the solution with a glass rod was carried out for 15 min to avoid the formation of lumps. The solution was left undisturbed for 20 min. Afterwards, distilled water was added and subjected to magnetic stirring for a few minutes. Post sedimentation, water was decanted. The sediment was filtered. Multiple washing was done with distilled water to free it from excess acid. A silver nitrate test was performed to check the presence of acid in the filtrate. Finally, the residue was divided into two accurately weighed parts. One part of the residue was dispersed in 0.1 N NaOH and subjected to magnetic stirring for 30 min before back titrating with 0.1 N HCl. The dried content was calculated after drying the other part of the residue.

Equations (1 and 2) were used to calculate DOS[19].

$$\mathrm{DOS} = \frac{0.162\mathrm{A}}{1-0.058\mathrm{A}} \quad \ldots (1)$$

Where

$$\mathrm{A} = \frac{(mL\ of\ NaOH \times N1)-(mL\ of\ HCl \times N2)}{g\ of\ the\ dried\ sample} \quad \ldots (2)$$

N1 and N2 represent the normalities of NaOH and HCl, and A represents (milliequivalents of NaOH /g of sample).

Synthesis of CMGT-co-SAH

CMGT-co-SAH was synthesized by taking required amount of CMGT with DOS (0.2) (0.33% w/v) in distilled water. 7.2 mL of acrylic acid (AA) was neutralized using 13 mL of 8.07 mol/L NaOH solution and added to CMGT solution. At room temperature, KPS (0.0061 mol/L) and MBA (0.017 mol/L) were added to the aqueous reaction with continuous stirring for 2 h on a magnetic stirrer. The polymerization procedure was carried out in a water bath at 60°C for 2 h. The synthesized hydrogel was washed with an organic/aqueous solvent to remove the soluble components. It was then dried in the hot air oven at 45°C, till constant weight. Reaction contents were optimized by varying the amount of reactants; KPS0.0061 mol/L to 0.01223 mol/L and MBA0.010 mol/L to 0.021 mol/L (Table 1). Optimal formulation of hydrogel (i.e., CMGT-co-SAH-4) was selected for further characterization based on the highest swelling Index among various compositions(CMGT-co-SAH-1 to 11).

Characterization and analysis

Swelling studies

Effect of cross-linker, initiator and the temperature on hydrogel's network was analyzed by the swelling equilibrium method in buffer solution of *p*H 7.4. The oven dried and weighed discs of hydrogel were dipped in the solvent. After a fixed interval, the hydrogel discs were removed from the swelling medium, extra fluid was tapped with tissue paper, and weighed again until the constant weight was obtained.

Table 1 — Different formulation of CMGT-co-SAH and their swelling Index.

Formulation	Polymer(CMGT)(g)	Monomer(AAc)(g)	NaOH (mol/l)	Initiator(KPS) (mol/L)	Cross-linker (MBA)(mol/L)	Swelling Index g/g of gel) (After 24 h)
CMGT-co-SAH-1	0.1	7.2	8.07	0.0061	0.01	22.28±0.27
CMGT-co-SAH-2	0.1	7.2	8.07	0.0061	0.012	23.29±0.17
CMGT-co-SAH-3	0.1	7.2	8.07	0.0061	0.015	28.95±0.02
CMGT-co-SAH-4	0.1	7.2	8.07	0.0061	0.017	33.13±0.04
CMGT-co-SAH-5	0.1	7.2	8.07	0.0061	0.019	27.13±0.08
CMGT-co-SAH-6	0.1	7.2	8.07	0.0061	0.021	25.74±0.25
CMGT-co-SAH-7	0.1	7.2	8.07	0.0074	0.01	26.92±0.56
CMGT-co-SAH-8	0.1	7.2	8.07	0.0074	0.012	30.45±0.04
CMGT-co-SAH-9	0.1	7.2	8.07	0.0086	0.01	30.25±0.19
CMGT-co-SAH-10	0.1	7.2	8.07	0.0086	0.015	27.67±0.02
CMGT-co-SAH-11	0.1	7.2	8.07	0.0098	0.01	26.26±0.50

These studies were done in triplicate. Equation 3 was used to calculate the swelling index (SI)[20].

$$SI\% = \frac{Ws-Wi}{Wi} \times 100 \quad \ldots (3)$$

Wi represents the dried hydrogel disc's weight, whereas *Ws* represents the swollen hydrogel disc's weight at a certain period.

Rheological analysis

Steady rheological behaviour

The rheological characteristics of CMGT-co-SAH and SAH were assessed in the swollen state in PBS buffer of pH 7.4 at room temperature using an Anton Paar Modular Compact Rheometer 302 (MCR). The shear rate ranged from 0.001 to 1 s^{-1} with a PP-25 i.e., parallel plate having a diameter of 25 mm and along with 2.5 mm of the inter-platen gap. The results from the plot, shear vs. shear rate, were fitted to Power Law (PL) model to acquire the required parameters.

$$\text{PL model: } \tau = K\gamma^n \quad \ldots (4)$$

The shear stress (τ) in (Pa), consistency coefficient (K) in (Pa.s), shear rate (γ) in (s^{-1}), and fluidity index (n) are all represented in the equation (4)[21].

Amplitude sweep

The test for amplitude sweep was done on SAH and CMGT-co-SAH in an oscillatory condition at a frequency of 10 $rads^{-1}$ to optimize suitable parameters for further dynamic testing. The amplitude sweep test is conducted in a fixed strain % of 0.001 % to 10 %. The test may reveal the linear viscoelastic region (LVR), which may be used to examine sample characteristics.

Frequency sweep

Low and high frequencies (1-100 rad s^{-1}) and (100-1000 rad s^{-1}) respectively, were used in the frequency sweep test. For CMGT-co-SAH and SAH, the loss (G″) and storage (G′) moduli are plotted against (ω) angular frequency at room temperature.

SEM

Morphology of four samples (GT, CMGT, SAH and CMGT-co-SAH) was compared by using JEOL JSM-6610LV Scanning Electron Microscope and all samples were coated with gold for analysis. SEM was operated at 20 kV accelerating voltage and 1,000x magnifications[22].

FTIR

FTIR of CMGT-co-SAH were compared with GT, CMGT and SAH. The FTIR analysis of samples was done between range 4000 to 650 cm^{-1} on Perkin-Elmer model 2000 FT-IR spectrometer[23].

^{13}C NMR

Solid state^{13}C-NMR was done for four samples, i.e., GT, CMGT, SAH and CMGT-co-SAH with 200 mg of samples at 9T of magnetic field on a Bruker Avance 500 WB solid state NMR spectrometer using 4mm of the probe[24].

XRD

The samples (GT, CMGT, SAH and CMGT-co-SAH) X-Ray Diffract gram we rerecorded by diffracting angle from 10° to 80° at 2°/min with 40 KV generator voltage using Expert Pro MRD, Panalytical, X-Ray diffractometer[25].

TGA

The samples (GT, CMGT, SAH and CMGT-co-SAH) were thermally tested with a consistent heating rate of 10°C/min from 25 to 800°C in N_2 atmosphere, using a PerkinElmer TGA, 4000[26].

Analysis of network parameters of CMGT-co-SAH

The AFS amount released from the hydrogel matrix is determined by the hydrogel's swelling,

which is directly related to the network parameters like Molecular weight of the segments between two neighbouring crosslinks of the network hydrogel ($\overline{Mc}$), the volume fraction of the swollen hydrogel (ϕ), mesh size (ξ), Flory Huggins interaction parameter (χ) and crosslink density (ρ). These parameters were calculated by Flory-Rehner equation given in equation 5[27].

$$\overline{Mc} = -D_H + \mathrm{V}m + \phi^{\frac{1}{3}} [\ln(1-\phi) + \phi + \chi\phi^2]^{-1} \quad \ldots (5)$$

Here, ϕ represents the swollen hydrogel's volume fraction, Vm represents the molar volume of the swelling agent, which determine the amount of solvent absorbed by the hydrogel and the Flory Huggins interaction parameter is represented by χ. ϕ, for swollen hydrogel, was calculated using equation (6).

$$\phi = \left[\left(\frac{D_H}{D_S}\right)\left(\frac{\mathrm{Ws}-\mathrm{Wi}}{\mathrm{Wi}}\right) + 1\right]^{-1} \quad \ldots (6)$$

Here, D_S and D_H are the densities of the solvent (g/cm^3) and hydrogel, respectively. Wi and Ws are the weight of initial and swollen state of the hydrogel.

The Flory Huggins interaction parameter (χ) was determined by using the equation (7)

$$\chi = \left(\phi\left({}^{1}/_{1-\phi}\right) + \mathrm{Z}\ln(1-\phi) + \mathrm{Z}\phi\right)[2\phi - \phi 2\mathrm{Z} - \phi 2\mathrm{T} - 1 d\phi/dT - 1 - 1 \quad \ldots (7)$$

where

$Z = \left[\left(\frac{\phi^{\frac{2}{3}}}{3} - \frac{2}{3}\right)\left(\phi^{\frac{1}{3}} - \frac{2\phi}{3}\right)\right]^{-1}$ and $d\phi/dT$ is the slope calculated by plotting a graph between temperature in °C and volume fraction ( ). 24 h swelling of hydrogel was determined at 27°, 37° and 47°C in buffer of pH 7.4. Mesh size and Crosslink density were determined by using the given equation (8,9)[28,29].

$$\rho = \frac{D_H}{\overline{Mc}} \quad \ldots (8)$$

$$\xi = \left[\left(\frac{71}{1000}\right)(\phi)^{-\frac{1}{3}}\right](\overline{Mc})^{\frac{1}{2}} \quad \ldots (9)$$

Drug loading and release profile

The AFS loading and release profile of CMGT-co-SAH was determined in *p*H 7.4 buffer solution at 37°C. The swelling equilibrium approach was used to load the drug into the hydrogel[30]. For 24 hours, the hydrogel was immersed in a drug solution with a fixed concentration (1.25 mg/mL). The drug-loaded hydrogel was immersed in a buffer solution of *p*H 7.4 in a beaker and placed in a water bath shaker, set at 80 rpm and 37°C, to analyze the release profile of hydrogel. After an interval of time, 1ml of the drug containing solution was taken out and replaced by a fresh buffer solution. The process was continued for 24 h. The withdrawn samples were analyzed by a UV -visible spectrometer at 274 nm. The amount of AFS was measured by comparing the absorbance value from the calibration curve. The experiment was conducted in triplicates and drug release kinetics was analyzed by applying various drug release models. The Encapsulation Efficiency (EE)was observed using the formula, given in equation 10[31].

$$\%\ \text{of EE} = \left(\frac{\text{Actual loading}}{\text{Theoretical loading}}\right) \times 100 \quad \ldots (10)$$

Kinetic models for Drug release profile

To determine the drug release profile of AFS loaded CMGT-co-SAH, Higuchi, Hixon-Crowell, Korsmeyer-Peppas, First-order and Zero-order kinetic models were employed[20,32]. Mathematical equations of the models have been given in Table 2.

Hemo-compatibility studies

The hemolytic potential of hydrogel was determined by an *in vitro* hemolytic index. The blood sample was collected from healthy human in EDTA

Table 2 — Mathematical expression of kinetic models.

Models	Mathematical equation	Parameter
Zero Order	$F_t = K_o t$	F_t=Amount of drug release in time *t* K_o= Zero-order constant
First Order	$(1 - F_t) = K_1 t$	K_1= First order constant
Higuchi	$F_t = K_H t^{1/2}$	K_H= Higuchi constant
Hixon-Crowell	$W_o{}^{1/3}$-$W_t{}^{1/3} = K_{HC} t$	W_o=Initial amount of drug present in hydrogel W_t=Amount of drug release at time t K_{HC}= Hixon-crowell constant
Korsmeyer-Peppas	$\frac{M_t}{M_\infty} = K_{KP} t^n$	$\frac{M_t}{M_\infty}$=Amount of drug release in time *t* K_{KP}=Rate constant n= Release exponent

treated tubes and centrifuged for 5 min, at 3000 rpm. Supernatant of blood plasma was discarded, and separated RBCs were, washed in 1× PBS (*p*H 7.4), further resuspended in 1×PBS. For use in experiments this stock solution was diluted to 4% v/v in 1×PBS.Triton X-100 was used as the positive control (0.1%w/v) and 1×PBS (pH 7.4) act as negative control[33].

The hemolysis in % was calculated by using equation 11:

$$\text{Hemolysis in \%} = \left(\frac{A_{CMGT-co-SAH} - A_{1xPBS}}{A_{triton\ X-100} - A_{1xPBS}}\right) \times 100 \quad \ldots (11)$$

Hemolysis in % was evaluated on average of two replicates[34].

Results and Discussion

Swelling studies

CMGT-co-SAH formulations 1-11 were synthesized by varying concentrations of KPS and MBA where monomer and polysaccharides concentrations were not changed. Their swelling index was determined. The formulation which is having maximum SI has been used to determine the effect of change in temperature on swelling of the hydrogel.

Effect of cross-linker on hydrogel's swelling

The effect of cross-linker's concentration was observed in samples (CMGT-co-SAH-1 to 6 listed in Table 1, shown in Fig. 1(a). Swelling Index increases when the cross-linker concentration increases from 0.01mol/L to 0.017 mol/L due to a rise in cross-linked density beyond which the swelling index decreases. This may be due to the occurrence of rigid structure, beyond cross-linker concentration of 0.017 mL/L which causes a reduction in polymer stretching.

Effect of initiator on hydrogel's swelling

According to Fig. 1(b), as the initiator concentration increases, the anionic radical increases. Anionic radical will increase macro-radicals in the parent chain, which raises the swelling Index to

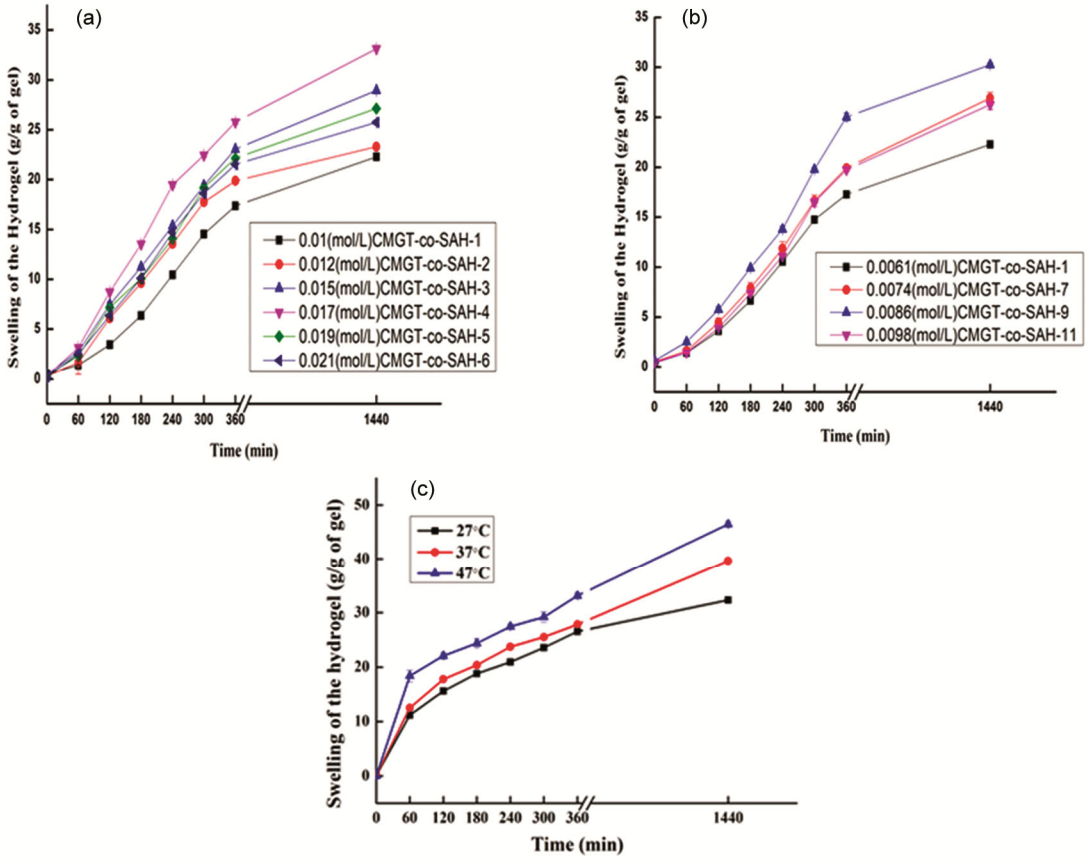


Fig. 1 — (a) Effect of cross-linker on hydrogel's swelling; (b) Effect of initiator on hydrogel's swelling and (c) Effect of temperature on hydrogel's swelling.

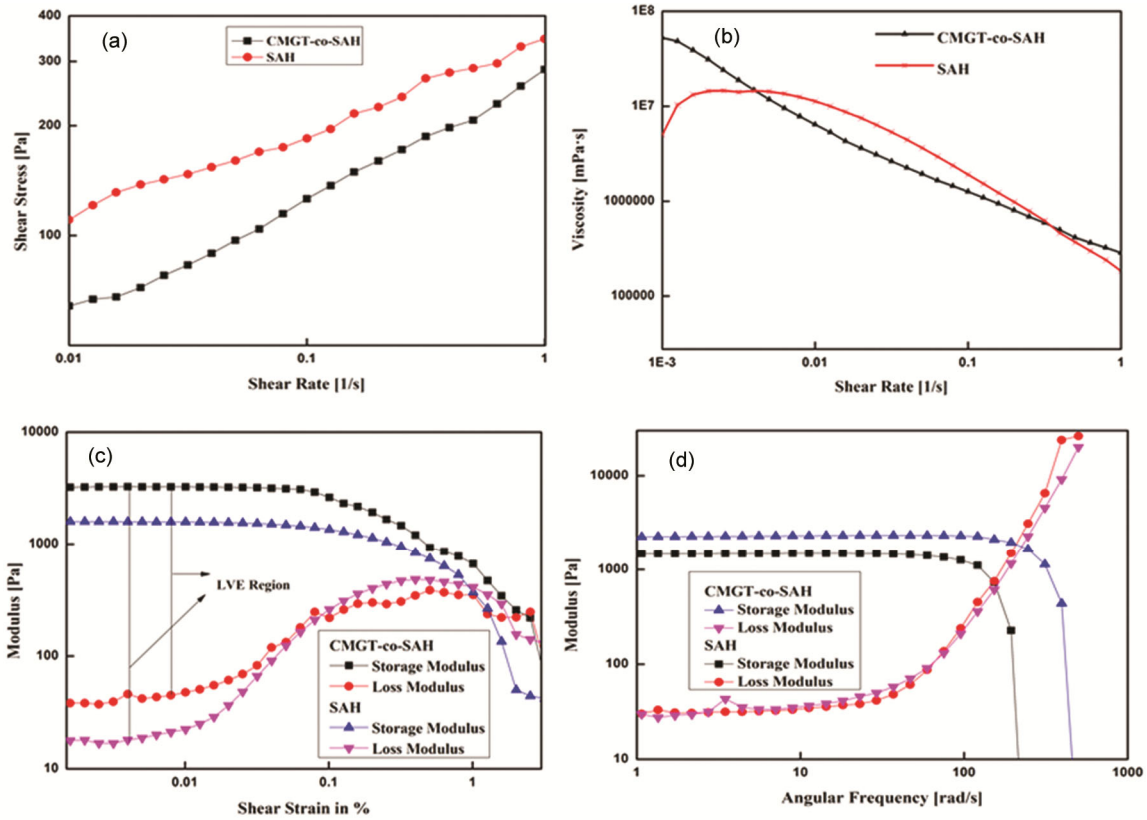


Fig. 2 — (a) Shear rate versus Shear stress graph for CMGT-co-SAH and SAH; (b) Viscosity profile of CMGT-co-SAH and SAH with varying shear rate; (c) Amplitude sweep with LVE and (d) frequency sweep graphs.

30.25±0.19 g/g (CMGT-co-SAH-1, 7, 9 and 11) listed in table 1 (where cross-linker concentration is constant). Further, with increase in the concentration of initiator beyond 0.0086 mol/L, swelling index decreases due to termination of the chain through the biomolecular collision.

Effect of temperature on hydrogel's swelling

The SI (g/g of gel) at 27°, 37° and 47° was found to be 32.30±0.12, 39.63±0.30, 46.47±0.54 respectively. It was observed from results that as the temperature increases, hydrogel's swelling increases (Fig.1(c)) due to increase in movement of the segments of the polymerized chains. This confirms that the rate of absorption/diffusion of solvent molecules by CMGT-co-SAH is temperature dependant.

Rheological analysis

The gel strength and rigidity of the swollen hydrogel were determined by using rheological analysis. From Fig. 2(a), in which the graph was plotted against shear stress and shear rate, for both hydrogels (CMGT-co-SAH and SAH), it was observed that the shear stress is directly proportional to shear rate. For data (shear rate vs. shear stress graph), the PL model was fitted to calculate the consistency coefficient (K) and fluidity index(N).The value of R^2 obtained from the PL model indicates that both the hydrogels have high consistency and correlated with reported results in the previous literature[35]. The value of 'n' shows flow characteristics, when obtained results of shear rate versus shear stress was fitted to the PL model. The value of 'n' in Table 3 is more for CMGT-co-SAH than SAH, representing the intermolecular interaction of the monomer and the CMGT. The value of n for both hydrogel is less than one, which means pseudo-plastic behaviour of the hydrogel. This behaviour was also determined by the shear viscosity test, Fig. 2(b). The hydrogel showed a steady decrease in shear-dependent viscosity with an increase in shear rate,

Table 3 — Parameters according to Power law model in steady rheological behaviour (shear stress vs. shear rate).

	Power law model		
Hydrogel	K	N	R^2
SAH	11.70	0.23	0.9907
CMGT-co-SAH	11.35	0.33	0.9946

which might indicate the time-dependent rupturing of the hydrogel matrix's intrinsic bonding, thus representing the shear thinning behaviour of hydrogel.

Amplitude sweep

The whole strain was divided into two regions. One is the Linear Viscoelastic Region (LVR), a shear region, which is not affected by applied stress. The other area is non-linear and it was observed from Fig. 2(c) that the G' and G" values change when the strain exceeds 0.01%. Above this LVR, the storage and the loss modulus dropped due to rupturing of the hydro gel matrix. By increasing the stress %, intermolecular interaction deformed, reducing the moduli values. Samples act as viscoelastic solid when G'>G". Below 0.01% strain, the shape of CMGT-co-SAH&SAH was retained. Above 0.01% strain, intermolecular chains start to disentangle. The yield strain of CMGT-co-SAH is more than SAH due to the addition of CMGT, which shows intermolecular interaction of CMGT and SA. Similar properties were observed by Ganguly et al. in psyllium grafted with poly acrylic acid and sodium acrylate hydrogel[16]. The viscoelastic sweep should be analyzed within the LVE range[35].

Frequency sweep

For this analysis, the frequency ranged from 1 to 1000 rads^{-1}. Storage and loss moduli were plotted against (ω) i.e., angular frequency Fig. 2(d). The graph shows viscoelastic solid behaviour, where the loss modulus is dominant at high frequencies and the storage modulus is prominent at low frequencies. Therefore the structure of the hydrogel is stable at low frequency and deformed at high frequency. CMGT-co-SAH has a greater storage modulus than SAH because there may be crosslinking between SA and CMGT. It shifts the cross-over point toward a higher frequency[16,36].

Scanning Electron Micrograph (SEM)

The surface morphology of GT, CMGT, SAH and CMGT-co-SAH has been analyzed by SEMs, which are represented in Fig. 3. It has been observed from the SEMs that GTand SAH have a smooth and homogeneous morphology, whereas CMGT and CMGT-co-SAH have structural heterogeneity and porous morphology. The change in surface morphology of the CMGT and its hydrogel is due to the cross-linked networks confirmed by SEMs taken at 1000x magnification[6,37].

FTIR Analysis

Peaks observed from FTIR spectra were compared with previously published literature as given in Fig. 4 (a). A broad absorption band at 3311 cm^{-1} was observed in GT, representing an overlapped peak indicating H-bond due to -OH groups of polysaccharides. Absorption bands at 1720 cm^{-1} in GT represent a stretch of acidic and ester carbonyl groups and at 1602 cm^{-1} represent C-O and COO^{-} groups of D-Glacturonic acid. The peak at 1247 cm^{-1} represents the esteric skeleton group. Stretch at 1029cm^{-1} corresponds to C-O and C-C group present in GT's pyranose rings[12].

The broad absorption band at 3329 cm^{-1} in CMGT and GT, but band intensity is lower in CMGT than GT, suggests that carboxymethylation may reduce the number of –OH groups. A band at 1600 cm^{-1}representsthe extension vibration of the COO^{-} groups, which confirms the carboxymethylation process. Other absorption bands at 1244 cm^{-1} and

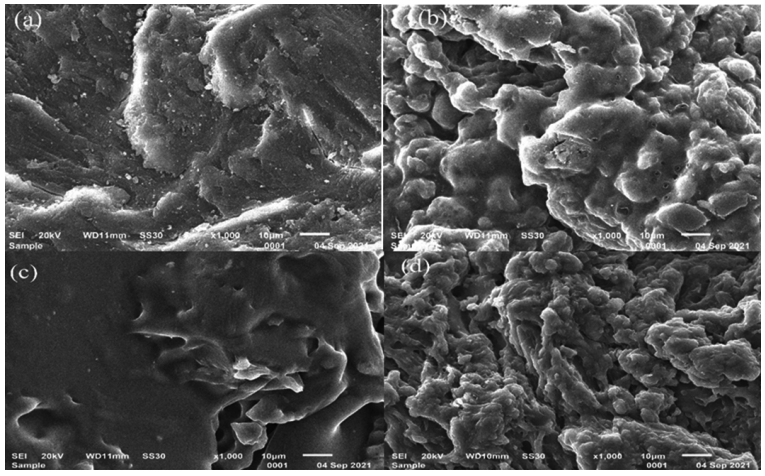


Fig. 3 — SEM at (1000x) for (a) GT; (b) CMGT; (c) SAH and (d) CMGT-co-SAH.

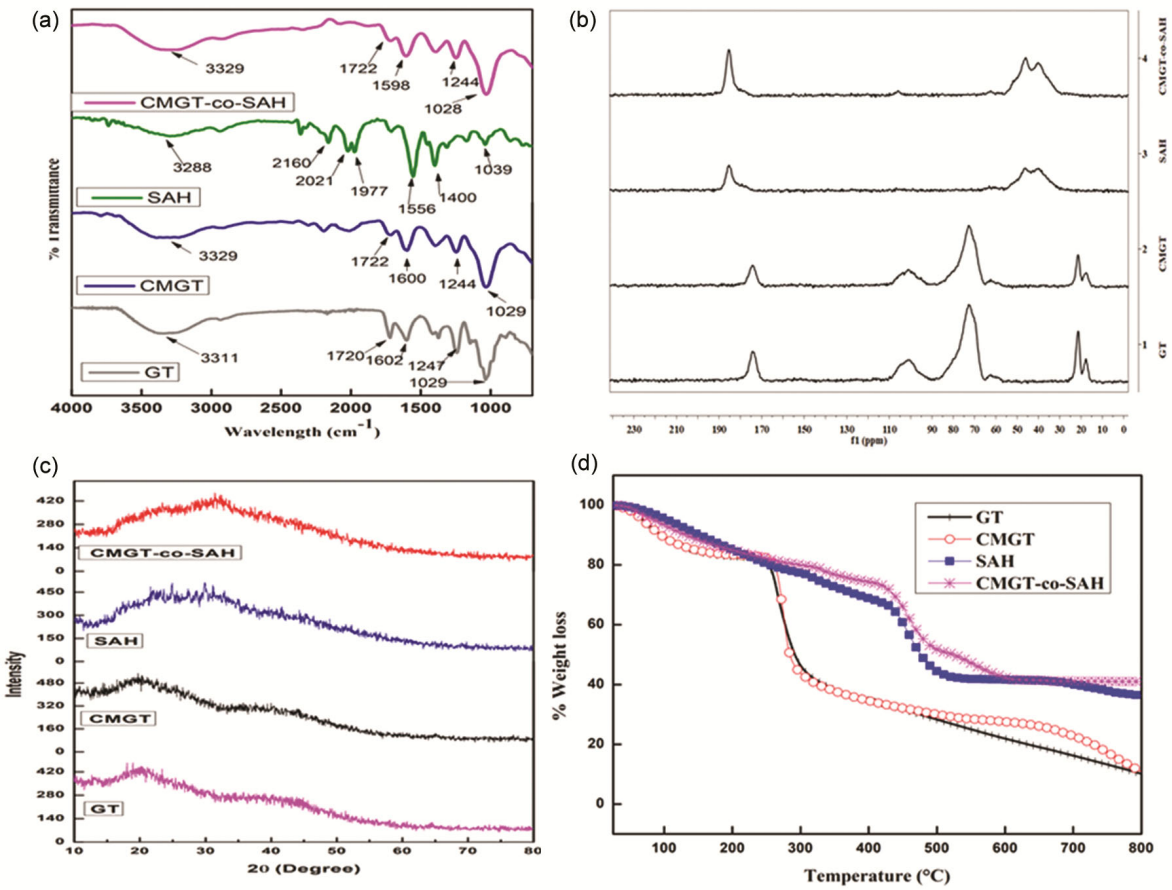


Fig. 4 — (a) FTIR; (b) ^{13}C-NMR; (c)XRD and (d) TGA spectra of GT, CMGT, SAH and CMGT-co-SAH.

1029 cm^{-1} are corresponding to the similar vibrations of GT as explained above[38].

SAH's FTIR spectrum represents absorption bands at 1556 cm^{-1}and 1400 cm^{-1}due to the bending vibrations of the CH_2 group of sodium acrylate parts[39].

In the CMGT-co-SAH's spectrum, the absorption band at 3329 cm^{-1} corresponds to the acidic -OH group overlapped with the amide -NH group. Absorption bands at 1722 cm^{-1} represent the stretch of acidic and ester carbonyl groups and at 1606 cm^{-1} are due to the amide carbonyl group. Absorptions at 1244 cm^{-1} and 1028 cm^{-1} are assigned as of CMGT. A little shift in absorptions confirms the crosslinking of CMGT with sodium acrylate[37].

^{13}C-NMR studies

The result of solid-state ^{13}C-NMR spectra of GT, CMGT, SAH and CMGT-co-SAH are shown in Fig. 4(b). At 174.24 ppm, characteristic peaks have been identified in GT due to the -COOH group of galacturonic acid in the GT[32].At 100.59 ppm (represents anomeric carbon of polysaccharides), at 72.56 ppm (due to C attached to-OH group of polymeric chain), 17-22 ppm (assigned to -CH_3 and -CH_2 group of polysaccharides). NMR spectrum of CMGT represents characteristic peaks at 174.26 ppm (carbonyl carbon of CMGT), at 101.04 ppm (anomeric carbon of polysaccharides). This peak shifted to a higher ppm value than GT may be due to carboxymethylation. Peak at 72.71 ppm due to –C-OH group, peak intensity lower down as compared to GT, confirms carboxymethylation. In SAH, characteristic peaks from 40-47 ppm and 185.51 ppm assigned to -CH and -COOH group, respectively. In CMGT-co-SAH, characteristics peaks from 40-47 ppm assigned to -CH of sodium acrylate and little shift in frequency confirmed crosslinking of CMGT with SA. At 106.05 ppm small intensity peak was identified, representing anomeric carbon of polysaccharides. At 185.38 ppm (-COOH of SA and CMGT, a shift in frequency due to crosslinking of CMGT with SA)[6,32].

XRD studies

Figure 4(c) represents the crystallinity/amorphous characteristics of the samples, analyzed by XRD. The GT showed a broad diffraction peak at ≈20°, indicating that it is an amorphous polysaccharide, and there is little shift in the 2θ value due to carboxymethylation. The diffraction pattern of SAH and CMGT-co-SAH show the amorphous nature. The shift in the diffraction peak of CMGT-co-SAH was observed, may be due to cross-linking of CMGT and SA[40,41].

TGA

Figure 4(d) represents the thermal degradation of GT, CMGT, SAH and CMGT-co-SAH. GT demonstrates two-step weight loss, with an initial loss of around 18% between 39 - 234°C due to the loss of moisture from the gum. The decomposition of GT's highly branched heterogeneous structure results in a 72 % weight loss from temperature 234°C to 800°C, with a residual weight of about 10%.

CMGT decomposes in three stages, 35-240°C,the range shows 16% loss due to humidity. The second stage ranges from 240-620°C due to decomposition of polysaccharide rings, breaking of C-O-C bond in CMGT chain and elimination of CO_2, which is around 74%. 620-800°C range shows weight losses due to breakdown of CMGT backbone and 10% were residual weight.

Thermal decomposition of SAH occurs in four stages, 30-299°C, 299-427°C, 427-548°C, 672-800°C and were about 23%, 11%, 25% and 5% respectively. The first stage weight loss was result of loss of moisture. The second stage of weight loss was due to carboxyl group decomposition of the SAH and the last two stages show the breakage of cross-linking in SAH network. 36% is the residual weight at 800°C.

CMGT-co-SAH decomposed in four stages 44-322°C, 322-411°C, 411-521°C, and 521-629°C. The first stage shows 21% loss due to moisture content. The second stage of 6% loss represents the decomposition of polysaccharide rings along with the elimination of CO_2. The latter two stages represent breakage of the CMGT backbone and SA chain with 23% and 9% weight loss respectively. The residual weight at 800°C was 41%. From the decomposition of all samples, it was concluded that modified gum and its hydrogel were more thermally stable than GT and SAH[17,42].

Network parameters of hydrogel

The network parameters like (Molecular weight of the segments between two neighbouring crosslinks ($\bar{M}_c$), the volume fraction of the hydrogel in the swollen state (ϕ), mesh size (ξ), Flory Huggins interaction parameter (χ) and crosslink density (ρ)) of CMGT-co-SAH were determined as a function of temperature and given in Table 4. When a hydrogel is immersed in a liquid for swelling, it expands until the osmotic forces that aid in the polymer's dissolution is counterbalanced by the elastic forces caused by stretched polymer chains. High $\bar{M}_c$ value shows that the network is highly elastic and expands quickly when exposed to a liquid solvent[27]. As the temperature increases, $\bar{M}_c$ and ξ of the hydrogel network increases along with that ρ and χ decreases[43].

AFS release studies

The encapsulation efficiency of the loaded hydrogel found out to be 63.8% and the release studies of AFS from AFS-loaded-CMGT-co-SAH were determined in a buffer solution of *p*H 7.4, AFS is soluble in buffer of *p*H 7.4 therefore 7.4 *p*H buffer was selected for release study. Also, the swelling of the hydrogel is maximum in *p*H 7.4 buffer. Here, the two factors, the solubility of the drug and swelling of the hydrogel are responsible for the diffusion of the drug. Generally, the release/swelling of drug/ hydrogelis co-related with the cross-linked matrix of monomer and polysaccharides, nature of the solvent, density and composition of the hydrogel[28]. The rate was reasonably rapid during the early phases of drug release from the hydrogel, as shown in Fig. 5(a). After that, it demonstrated controlled and sustained release. The rate of drug release decreases with an instant of time. It was observed from the release data that 52.2% of the loaded drug was released from the matrix in early time interval. It might be because the drug on the surface of the polymer matrix releases faster than the drug integrated into the polymeric matrix, allowing for controlled drug delivery from the hydrogel. The results reveals that the release of the drug from the hydrogel is related to the swelling of the hydrogel and follows the Fickian mechanism[44]. The kinetics were further investigated by fitting the obtained drug release data to several mathematical models. Fig. 5(b) and Table 5, shows that the highest correlation coefficient(R^2)value was found in the Korsmeyer-Peppas model, representing drug release from a polymeric system. The measured 'n' value is 0.4176 given in table 5, less than 0.5 and corresponds to the Fickian mechanism of drug release[45], in which the driving force is a chemical gradient and the release

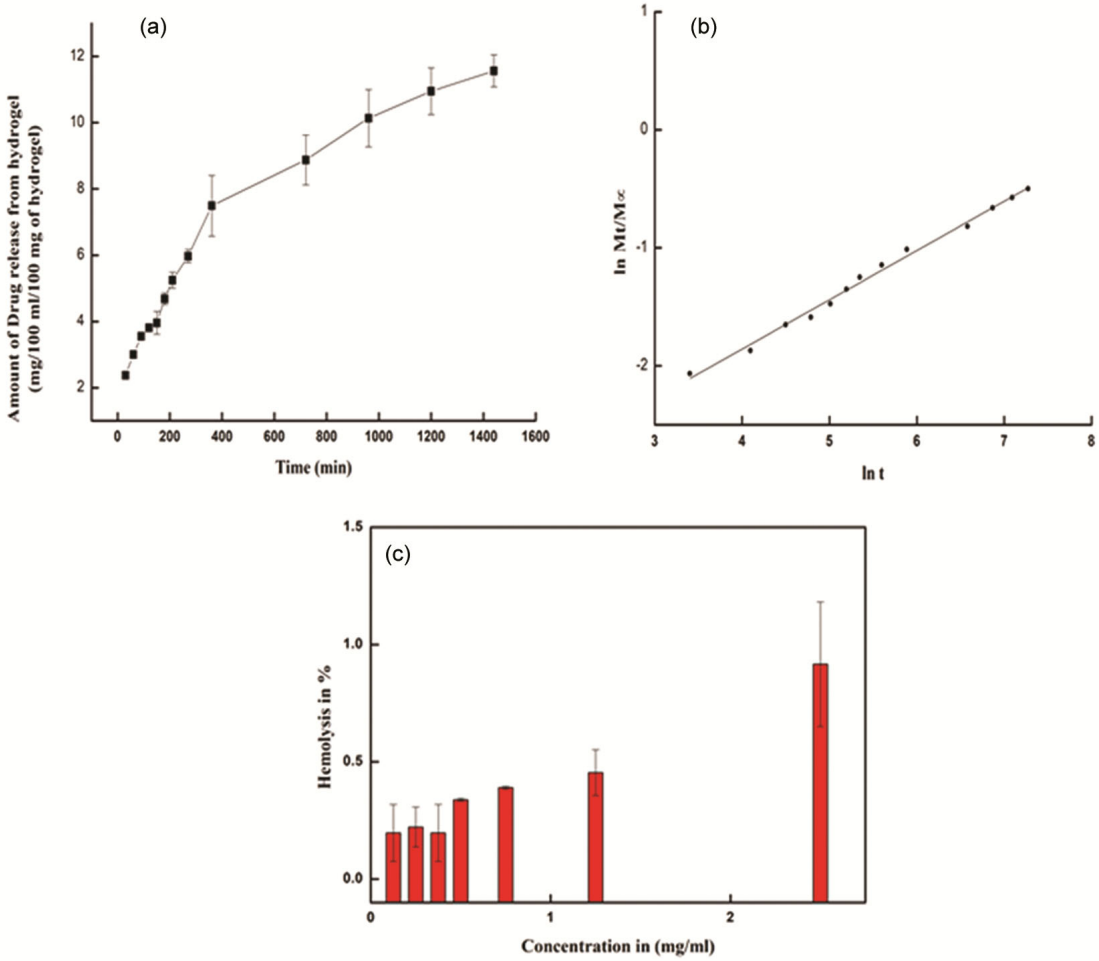


Fig. 5 — (a) Release profile of AFS from CMGT-co-SAH; (b) Graph between $ln\frac{M_t}{M_\infty}$ and *ln*t for determination of the rate constant and rate exponent and (c) Hemo-compatability studies.

Table 4—Network parameters of CMGT-co-SAH as a function of temperature.

Temperature (°C)	Φ	X	$\bar{M}_c$(g/mol)	ρ (mol/cm^3)	ξ (nm)
27	0.042079	0.217329772	8458	8.3578	18.773
37	0.034604	0.239979899	12807	5.5194	24.657
47	0.028767	0.261771407	19100	3.7010	32.024

Table 5 — Different models to study drug release kinetics of AFS from CMGT-co-SAH

Models	R^2	K	N
Zero-order	0.9344	K_o (min^{-1}) 0.03251±0.0024	
First-order	0.9292	K_1 (min^{-1}) 0.11515±0.0040	
Hixon-Crowell	0.9344	K_{HC}($min^{-1/2}$) 0.002±1.55	
Higuchi	0.9919	K_H($min^{-1/3}$) 1.48271±0.038	
Korsmeyer-Peppas	0.9933	K_{KP}(min^{-n}) 0.029348±0.005	0.4176

mechanism is diffusion-controlled[31]. The Higuchi model also supports the fickian diffusion of the drug from the hydrogel polymeric matrix.

Hemo-compatibility studies

Hemolytic potential of CMGT-co-SAH was evaluated (Table 6) and results was plotted shown in Fig. 5(c). The evaluated results show that % hemolysis is less than 1 at every concentration. In general, the sample shows %hemolysis less 5 is highly hemo-compatible and may be good for pharmaceutical application[46].

Table 6 — Hemocompatibility studies result.

CMGT-co-SAH Concentration(mg/mL)	Haemolysis in %	Remarks
0.125	0.1965±0.12	Highly hemocompatible
0.25	0.2223±0.08	Highly hemocompatible
0.375	0.1965±0.12	Highly hemocompatible
0.5	0.3381±0.006	Highly hemocompatible
0.75	0.3895±0.006	Highly hemocompatible
1.25	0.4539±0.09	Highly hemocompatible
2.5	0.9164±0.26	Highly hemocompatible

The results obtained from Hemolysis test show that CMGT-co-SAH is highly hemocompatible shown in Fig. 5(c) and Table 6 and all the reactants used to synthesize CMGT-co-SAH previously been reported as safe and non-toxic to the environment. Recently, cytocompatibilities of GT and Acrylic acid based hydrogel by MTT assay was confirmed by Sayadnia *et al.*[41]. Khan and Anwar have proven that carboxymethylation does not have any cytotoxic effects[47]. N,N′-methylenebis(acrylamide) used in the synthesis of CMGT-co-SAH is also safe for drug delivery[48].

Conclusion

The current investigation focused on the structural modification of natural gum into its carboxymethylated derivative and the subsequent fabrication of CMGT-co-SA Hydrogel by graft copolymerization technique. The synthesized CMGT-co-SAH shows more stability than SAH, revealed by characterization performed by using an optimum formulation (CMGT-co-SAH-4).The investigation reveals that cross-linker and initiator concentration affect the swelling of the hydrogel. Molecular weight and mesh size between two neighbouring crosslinks increase with the increase in temperature. The elasticity of SAH was less than CMGT-co-SAH as (G'/G") was raised with the addition of CMGT to the hydrogel. The hemolysis test result confirms the hemocompatible nature of the hydrogel. The drug release from the hydrogel loaded with the non-steroidal anti-inflammatory drug, aceclofenac sodium follows the Fickian diffusion mechanism. It is best fitted in Korsmeyer-Peppas and Higuchi models. Thus it can be concluded that synthesized hydrogel is suitable for the controlled release of drug molecules.

Acknowledgements

The authors would like to acknowledge Dr. Santosh Yadav (Institute of Genomics and Integrative Biology, Mall road, New Delhi-110007) for carrying out Hemolysis test for the synthesized CMGT-co-SAH, Tata Institute of Fundamental Re-search Hyderabad, Gopanpally, Hyderabad-500107, Telangana, India for ^{13}C-NMR spectroscopy. The authors are also thankful to Vice Chancellor, DTU for providing financial assistance and research facility and to Dr. Manish Jain (Delhi Technological University) for helpful discussion.

References

1 Bajpai A & Raj V, *Polym Bull*, 78 (2021) 4109.
2 Sharma B, Bharti R & Sharma R, *Mater Today Proc*, 65 (2022) 3657.
3 Singh B, Sharma V, Kumar R & Mohan M, *Food Hydrocoll Heal*, 2 (2022) 100059.
4 Nejatian M, Abbasi S & Azarikia F, *Int J Biol Macromol*, 160 (2020) 846.
5 Nazarzadeh Zare E, Makvandi P & Tay F R, *Carbohydr Polym*, 212 (2019) 450.
6 Singh B & Sharma V, *Carbohydr Polym*, 157 (2017) 185.
7 Tischer C A, Iacomini M & Gorin P A J, *Carbohydr Res*, 337 (2002) 1647.
8 Polez R T, Morits M, Jonkergouw C, Phiri J, Valle-Delgado J J, Linder M B, Maloney T, Rojas O J & Österberg M, *Int J Biol Macromol*, 215 (2022) 691.
9 Verma C, Negi P, Pathania D, Sethi V & B Gupta, *Polym Int*, 68 (2019) 344.
10 Rimpy, Abhishek & Ahuja M, *Carbohydr Polym*, 174 (2017) 896.
11 Sullad A G, Manjeshwar L S & Aminabhavi T M, *J Appl Polym Sci*, 122 (2011) 452.
12 Veeramachineni A K, Sathasivam T, Paramasivam R, Muniyandy S & Pushpamalar J, *J Polym Environ*, 27 (2019) 1516.
13 Wang Q, Qu Y, Zhang Z, Huang H, Xu Y, Shen F, Wang L & Sun L, *Gels*, 8 (2022) 400.
14 Chang C & Zhang L, *Carbohydr Polym*, 84 (2011) 40.
15 Jabbari E & S Nozari, *Eur Polym J*, 36 (2000) 2685.
16 Ganguly S, Mondal S, Das P, Bhawal P, Maity P P, Ghosh S, Dhara S & Das N C, *Int J Biol Macromol*, 111 (2018) 983.
17 Behrouzi M & Moghadam P N, *Carbohydr Polym*, 202 (2018) 227.
18 Santos M B, dos Santos C H C, de Carvalho M G, de Carvalho C W P & Garcia-Rojas E E, *Int J Biol Macromol*, 134 (2019) 595.
19 Verma S & Ahuja M, *Int J Biol Macromol*, 98 (2017) 75.
20 Suhail M, Wu P C & Minhas M U, *J Saudi Chem Soc*, 25 (2021) 101212.
21 Fan Z, Cheng P, Zhang P, Gao Y, Zhao Y, Liu M, Gu J, Wang Z & Han J, *Int J Biol Macromol*, 208 (2022) 1.
22 Tanpichai S, Phoothong F & A Boonmahitthisud, *Sci Rep*, 12 (2022) 1.
23 Kannaujia R, Prasad V, Sapna, Rawat P, Rawat V, Thakur A, Majumdar S, Verma M, Rao G K, Gupta A P, Kumar H & Srivastava C M, *Mater Lett*, 252 (2019) 198.
24 Singh B, Sharma V & Kumar A, *Carbohydr Polym Technol Appl*, 2 (2021) 100062.
25 Malik S & Ahuja M, *Carbohydr Polym*, 86 (2011) 177.
26 Badwaik H R, Sakure K, Alexander A, Ajazuddin, Dhongade H & Tripathi D K, *Int J Biol Macromol*, 85 (2016) 361.

27 Kulkarni A R, Soppimath K S, Aminabhavi T M, Dave A M & Mehta M H, *J Control Release*, 63 **(**2000**)** 97.
28 Singh B & Singh B, *Int J Biol Macromol*, 99 **(**2017**)** 699.
29 Chung J T, Vlugt-Wensink K D F, Hennink W E & Zhang Z, *Int J Pharm*, 288 **(**2005**)** 51.
30 Singh B & Singh B, *Int J Biol Macromol*, 99 **(**2017**)** 699.
31 Goel H, Gupta N, Santhiya D, Dey N, Bohidar H B & Bhattacharya A, *Int J Biol Macromol*, 174 **(**2021**)** 240.
32 Singh B & Sharma V, *Polymer (Guildf)*, 91 **(**2016**)** 50.
33 Suryadevara V, Lankapalli S R, Thalamanchi B, Patcha A & Danda L H, *Asian J Pharm*, 10 **(**2016**)** 51.
34 Pal K & Pal S, *Mater Manuf Process*, 21 **(**2006**)** 325.
35 Fan Z, Cheng P, Gao Y, Wang D, Jia G, Zhang P, Prakash S, Wang Z & J Han, *Food Hydrocoll*, 123 **(**2022**)** 107162.
36 Yadav R & Purwar R, *Polym Test*, 93 **(**2021**)** 106916.
37 Bachra Y, Grouli A, Damiri F, Talbi M & Berrada M, *Int J Biomater*, 2021 **(**2021**)** 1.
38 Hasan A M A, Keshawy M & Abdel-Raouf M E S, *Mater Chem Phys*, 278 **(**2022**)** 125521.
39 Santos F B, Miranda N T, Schiavon M I R B, Fregolente L V & Wolf Maciel M R, *J Therm Anal Calorim*, 146 **(**2021**)** 2503.
40 Singh B, Varshney L, Francis S & Rajneesh, *Int J Biol Macromol*, 88 **(**2016**)** 586.
41 Sayadnia S, Arkan E, Jahanban-Esfahlan R, Sayadnia S & Jaymand M, *Polym Adv Technol*, 32 **(**2021**)** 262.
42 Wang W & Wang A, *J Appl Polym Sci*, 112 **(**2009**)** 2102.
43 Singh B & Singh B, *Int J Biol Macromol*, 159 **(**2020**)** 264.
44 Singh B & Rajneesh, *J Drug Deliv Sci Technol*, 47 **(**2018**)** 200.
45 Mukherjee K, Dutta P & T K Giri, *Int J Biol Macromol*, 232 **(**2023**)** 123448.
46 American Society for Testing and Materials, ASTM F 756-00, *Am Soc Test Mater*, **(**2000**)** 159.
47 Khan S & N Anwar, *Carbohydr Polym*, 257 **(**2021**)** 117617.
48 Lakouraj M M, Rezaei M & Hasantabar V, *Int J Biol Macromol*, 193 **(**2021**)** 609.

2023 10th International Conference on Signal Processing and Integrated Networks (SPIN) | 978-1-6654-9099-3/23/$31.00 ©2023 IEEE | DOI: 10.1109/SPIN57001.2023.10116812

CNTFET BASED M-DMTGDI (CMDMTGDI) DESIGN AND ITS LEAKAGE ANALYSIS

NEETIKA YADAV[a,b]
a. Department of Electronics and Communication Engineering, Delhi Technological University, Delhi, 110042, India

b.Amity Institute of Space Science and Technology, Sector 125, Noida 201303, India

yadav.neetika92@gmail.com

NEETA PANDEY[a]

a. Department of Electronics and Communication Engineering, Delhi Technological University, Delhi, 110042, India
n66pandey@rediffmail.com

DEVA NAND[a]
a. Department of Electronics and Communication Engineering, Delhi Technological University, Delhi, 110042, India
devkamboj07@gmail.com

***Abstract*— This work presents CNTFET based Modified DMTGDI design and CNTFET based DMTGDI design, referred to as CMDMTGDI design and CDMTGDI design respectively. The proposed CMDMTGDI overcomes the contention issue in CDMTGDI design. Further leakage reduction techniques- LECTOR, GALEOR and LCNT are proposed for CMDMTGDI design. 2-input type A NAND, NOR and XOR gates are used for simulative investigation using HSPICE tool with 32nm CNTFET Stanford model at 0.9V and 5fF load capacitance in static and dynamic mode. A maximum PDP reduction of 97.65% and 97.85% is achieved using CDMTGDI and CMDMTGDI as opposed to their CMOS counterparts. The proposed CMDMTGDI design achieves a maximum PDP reduction of 96.62% as compared to its C-DMTGDI counterparts. Further a maximum leakage power saving of 46.52%, 46.68% and 46.5% is achieved using LECTOR, GALEOR and LCNT respectively as compared to its C-MDMTGDI counterparts in static mode. Corresponding values are (40.65%, 40.94%, 40.75%) in dynamic mode.**

Keywords— CNTFET, DMTGDI, GALEOR, LCNT, LEAKAGE, LECTOR, MDMTGDI

I. INTRODUCTION

The paradigm shift towards energy-efficient designs has been made possible by the development of Internet of Things (IoT) applications and, consequently, portable devices [1]. For energy efficiency, designs based on MOSFETs have traditionally been investigated. For decades, the most widely used method for designing digital logics has been static CMOS [2]. Logic families that can replace static CMOS have been developed in an effort to have designs that are energy-optimized. The Dynamic Logic family [2], Gate Diffusion Input (GDI) [3], Transmission Gate Diffusion Input (TGDI) logic [4], Differential Cascode Voltage Switch Logic (DCVSL) [5], Dual Mode Logic (DML) [6-10] and DMTGDI [4] are representative of such logic styles. Among these, DMTGDI is a logic family that provides benefits of dual mode operation in a TGDI based design [4]. The logic function is implemented using TGDI logic, and two mode operation is made possible by an additional transistor (pre-charge/pre-discharge transistor) at output[4]. Here, mode signal is used, like DML [6-7], to allow static and dynamic mode of operation. All these previously described logic designs rely on traditional MOSFET technologies for their implementation. These MOSFET-based devices, however, suffer from increased leakage current, larger parametric fluctuations, a number of short channel effects, higher heat dissipation, and reduced gate control as a result of technological scaling [11-13].

To overcome these limitations of MOSFET based designs, CNTFET has been proposed as an alternative, mainly due to its similarities to MOSFET. In contrast to the conventional MOSFET structure, a CNTFET is a FET that uses carbon nanotubes as the channel [11]. The CNTFETs offer improved scaling and performance with less short-channel effects and increased carrier mobility. Due to its ballistic transport and low off-current characteristics, CNTFET based devices operate with high speed and less power [12]. These designs can be made more power efficient by incorporation of leakage reduction techniques. For MOSFET based designs, various leakage reduction techniques have been researched [14-16]. Some of the techniques have already been implemented for leakage reduction in CNTFET domain [13,17-19].

Till now, DMTGDI in CNTFET domain is not available in literature. This contribution introduces DMTGDI style implemented using CNTFETs. A CNTFET based TGDI (C-TGDI)[20] design is converted into DMTGDI by adding additional transistors at the output node, referred to as C-DMTGDI design. To overcome the contention issue in implemented C-DMTGDI design, a C-MDMTGDI design is proposed. Further leakage reduction techniques-LECTOR, GALEOR and LCNT- are investigated for the proposed C-MDMTGDI design.

The presented paper is arranged in four sections: the CNTFET overview is given in section 2. The proposed approaches are explained in section 3. The simulation results for NAND, NOR and XOR gates with 2-inputs based on proposed approaches in static and dynamic mode are stated in section 4. The work is concluded in section 5.

II. CNTFET OVERVIEW

A CNTFET is a form of FET that has one or more carbon nanotubes (CNTs) as the channel instead of silicon that is typically used in MOSFET designs [11]. To create a CNT, a graphite sheet is rolled up and wrapped around the chirality vector, which is controlled by the (m,n) chiral indices [12]. Chirality vector and diameter of the CNT are the parameters

Authorized licensed use limited to: DELHI TECHNICAL UNIV. Downloaded on May 15,2023 at 09:59:05 UTC from IEEE Xplore. Restrictions apply.

that determine the threshold voltage (Vth) of a CNTFET [12], given by Eq. (1)[12].

$$V_{th} = \frac{0.43}{DCNT(nm)} \quad (1)$$

where DCNT is CNT's diameter in nm

As a result, by adjusting the diameter of the CNT, CNFFETs offer a unique potential for threshold voltage control [12]. It has been shown that CNTFETs have MOSFET-like properties [14]. CNTFETs, like MOSFETs, can be of N-type (N-CNTFET) or P-type (P-CNTFET) Eq. (2) states ON current (I_{CNFET}) in CNTFET [21].

$$I_{CNFET} \approx \frac{Ng_{CNT}(V_{dd}-V_{th})}{1+g_{CNT}L_s\rho_s} \quad (2)$$

where N: No. of CNTs per device,
g_{CNT}: Transconductance per CNT,
VDD: Supply voltage,
Vth: Threshold voltage of the CNTFET,
Ls: Length of source,
ρ_s: Resistance of source per unit length

Eq.(3) states the delay value (τ_p) for a CNTFET [21].

$$\tau_p = \frac{C_{gg,CNFET}\,VDD}{I_{CNFET}} \quad (3)$$

where, $C_{gg,CNFET}$: Gate capacitance
V_{DD}: Supply voltage,
I_{CNFET} : ON current in CNTFET

The existing C-TGDI [20] cell with inputs (I0 and I1) with select lines (S, $\bar{S}$), is shown in Fig. 1(a).

III. PROPOSED APPROACHES

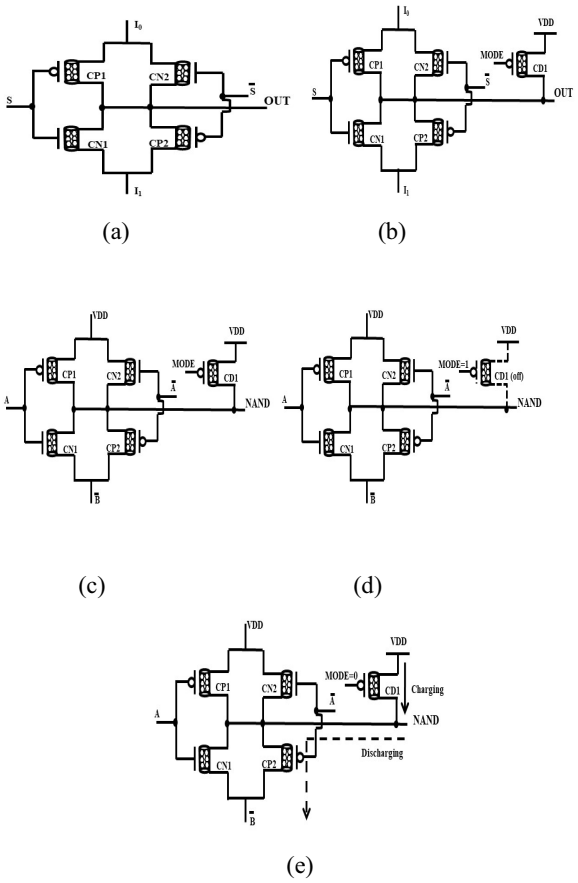
Three subsections constitute this section. The operation of the proposed CDMTGDI logic is briefly described in the first subsection. The second subsection proposes the C-MDMTGDI design and the third subsection describes the leakage reduction techniques-LECTOR, GALEOR and LCNT for proposed CNTFET based MDMTGDI logic.

A. C-DMTGDI logic

The standard CDMTGDI cell is obtained by adding pre-charge transistor (CD1) to the C-TGDI cell's output [20]. Inputs are (I0 and I1) with select lines (S, $\bar{S}$), depicted in Fig.1(b). MODE input of transistor, CD1 is used to switch the circuit in dynamic and static mode.

For static mode, transistor CD1 is made off by setting MODE=HIGH. The output of the cell is determined by the inputs provided to I0, I1, and select line S. A clock signal is used as the MODE input for dynamic mode, allowing for pre-charge and evaluation phases. During the pre-charge phase, transistor CD1 is on, the output node is charged to VDD. In evaluation phase, CD1 is turned off and the output is evaluated based on the logic function of the C-TGDI structure (CP1, CN2, CN1, and CP2 transistors) of the C-DMTGDI cell. Equation (4) describes the NAND function with inputs (A,B).

When operating a NAND gate with inputs (A,B)=(1,1) using the CDMTGDI circuit in static mode, transistor CD1 is turned off by setting MODE=HIGH. During dynamic mode, the circuit undergoes two phases of operation: precharge and evaluation. Transistor CD1 is on during the precharge phase, charging the output node to VDD. The output node is discharged during the evaluation phase as the lower half of the C-DMTGDI cell turns on (CN1 and CP2). However, the output voltage may be limited to a value less than VDD due to the path from the output node to ground, which can cause contention problems. Proper transistor sizing is necessary to obtain the correct output voltage. Transistor CD1 is turned off during the evaluation phase in dynamic mode when MODE=1, and the output is evaluated based on the applied inputs.



(a) (b) (c) (d) (e)

Fig.1. (a) CTGDI (b) CDMTGDI (c) CDMTGDI NAND gate (2-input) (d) static mode (e) precharge phase working for (A,B) = (1,1)

Authorized licensed use limited to: DELHI TECHNICAL UNIV. Downloaded on May 15,2023 at 09:59:05 UTC from IEEE Xplore. Restrictions apply.

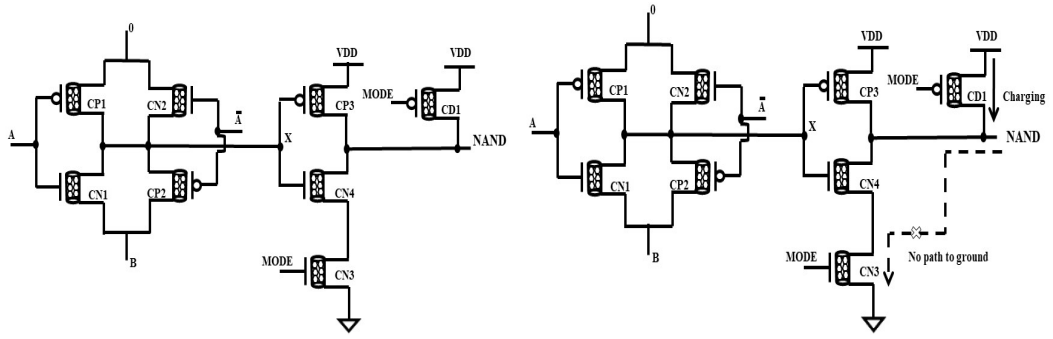
B. CMDMTGDI LOGIC

The proposed CMDMTGDI logic adds a type A inverter in footed DML configuration to the C-TGDI cell's output. In static mode, CD1 is turned off, footer transistor CN3 is turned on when the MODE input is set to a constant HIGH. The circuit generates an output in accordance with the logic implemented by the CTGDI block. In dynamic mode, a clock signal is applied to the MODE input, enabling precharge and evaluation phases. During the precharge phase, the output is precharged to VDD due to MODE=0, and in the evaluation phase, corresponding logic function is calculated as MODE=1.

A CMDMTGDI NAND gate (2-inputs) is shown in Fig. 2(a). In static mode, footer transistor CN3 is turned on while transistor CD1 is turned off, and output of NAND gate is determined by the applied inputs. During dynamic mode, the circuit works in two phases: precharge and evaluation. In the precharge phase, transistor CD1 turns on and charges the output node OUT to VDD as MODE=0, as illustrated in Fig. 2(b). The output node does not discharge since the footer transistor CN3 is off. Thus, the footer transistor's presence prevents contention at the output node, which produces proper output voltage. Evaluation of output is done in accordance with the applied inputs while the footer transistor is on and the mode transistor is off in evaluation phase.

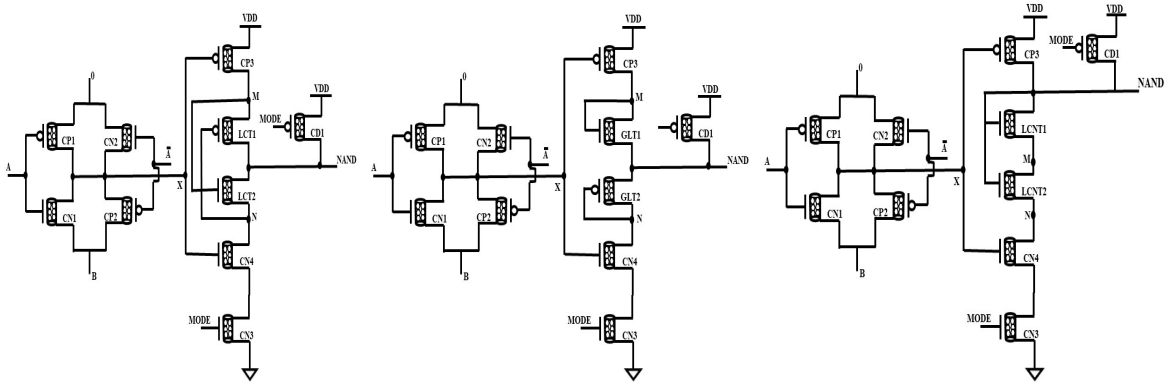
C. LEAKAGE REDUCTION TECHNIQUES FOR C-MDMTGDI LOGIC

The pre-charge transistor (CD1) in the proposed C-MDMTGDI NAND gate is turned off for static mode. There is some leakage current in off transistors as well as the off CD1 transistor, depending on the inputs applied. Current passes from the supply to the ground. Similar to this, transistor CD1 is utilised to charge the output to VDD during pre-charge phase of the dynamic mode, regardless of the applied inputs. Since transistor CN3 is off, the PDN should ideally have no current flowing through it. However, because of leakage in off transistors, there is leakage current from the supply to the ground. Off transistors produces leakage current during the evaluation phase and is controlled by the applied inputs. This sub-section proposes leakage reduction techniques-LECTOR, GALEOR and LCNT for reducing leakage power.



(a) (b)

Fig.2.(a) Proposed CMDMTGDI based type A NAND gate (2-input) (b) pre-charge phase with no contention



(a) (b) (c)

Fig.3. Type A NAND gate (2-input) (a) Proposed LECTOR based CMDMTGDI (b)Proposed GALEOR based CMDMTGDI (c) Proposed LCNT based CMDMTGDI

Authorized licensed use limited to: DELHI TECHNICAL UNIV. Downloaded on May 15,2023 at 09:59:05 UTC from IEEE Xplore. Restrictions apply.

Proposed CMDMTGDI logic incorporates LECTOR technique for leakage reduction, as shown in Fig. 3(a). To implement the NAND gate using this design, two transistors, LCT1 (PFET), LCT2 (NFET), are added between the PUN and PDN. LCT1 and LCT2 are connected through drain terminals to get output, which is also connected to the pre-charge transistor, CD1 (PFET). In static mode, the MODE=1, turning off CD1 and turning on transistor CN3. The output of the NAND gate is decided by inputs. If both inputs are HIGH, node X is charged to HIGH, and CP3 is off while CN4 is on. However, some amount of leakage is present in off transistors, which increases the effective resistance of path from power supply to ground due to presence of LCTs. LCT2 would be off. The analysis can be carried out similarly for all other input combinations in static mode.

In pre-charge phase, CD1 transistor charges the output node to VDD as MODE= 0 but leakage is dependent on inputs. Due to presence of LCTs, the amount of leakage decreases. In evaluation phase, MODE=1, CD1 is off, CN3 is on. According to the inputs applied, output is calculated. When (A, B) =(1,1), there is discharging of output node. Leakage current exists in off transistors, due to presence of off LCT transistor, LCT2, flow of leakage current is restricted. The analysis can be carried out similarly for all other input combinations in evaluation phase.

Another proposed approach for leakage reduction is incorporation of Gated Leakage Transistors (GLTs) in the CMDMTGDI design. Fig.3(b) illustrates a typical GLT based CMDMTGDI NAND gate. The GLTs are placed between PUN and PDN of output inverter. Gate and drain terminal of GLT1 and GLT2 are interconnected. The common source of GLT1 and GLT2 is used to get the output, NAND to which the mode transistor (CD1) is connected. In static mode, CD1 is off and CN3 is on. GLT1 and GLT2 switching is governed by voltages at node M and N. When (A, B)=(1,1), node X is charged to VDD, CP3 is off, CN4 is on. Transistor, GLT1 is off, due to which the resistance of path from supply to ground increases, which eventually reduces leakage. The analysis can be carried out similarly for all other input combinations. During precharge phase, transistor CD1 charges the output node to VDD as MODE=0, here the applied inputs determine leakage current. In evaluation phase (MODE=1), with (A,B)=(1,1), X is charged to VDD, GLT1 is off, which reduces the leakage current. The analysis can be carried out similarly for all other input combinations in evaluation phase.

The third proposed approach for leakage reduction in CMDMTGDI design is by introducing Leakage Control NMOS Transistors (LCNTs) between PUN and PDN of the output inverter of CMDMTGDI design. A LCNT based CMDMTGDI based NAND gate is depicted in Fig. 3(c). LCNTs are connected through gate terminals to get output, NAND to which the mode transistor, CD1 is connected. In static mode, CD1 is off and footer transistor, CN3 is on as MODE=1. When (A, B) =(1,1), the node X is at logic HIGH and the output node is at logic LOW. Both the LCNTs are turned off in this case, which leads to increase in resistance of supply to ground path. As a result, leakage current reduces. Similarly, for other inputs, analysis can be done in static mode.

In precharge phase, CD1 becomes on and it precharges the output node to VDD as MODE=0, here the leakage is reduced as stacking effect is introduced due to LCNT transistors. In evaluation phase, CD1 is off and CN3 is on as MODE=1. When (A, B) =(1,1), the output node is at logic LOW, due to which both the LCNTs are off and leakage current is reduced. All other input combinations can be analysed similarly in evaluation phase.

IV. SIMULATION RESULTS

The proposed CDMTGDI and CMDMTGDI designs are simulated for NOR, NAND and XOR circuits with 2-inputs using 32nm CNTFET Stanford model in HSPICE tool at 0.9V, with 5fF load capacitance. The proposed CDMTGDI and CMDMTGDI circuits are compared with their respective CMOS counterparts using 32nm PTM CMOS model in terms of delay, power, and PDP in static and dynamic mode.

Further leakage reduction techniques-LECTOR, GALEOR and LCNT- discussed above are implemented for CMDMTGDI design- LECTOR based CMDMTGDI, GALEOR based CMDMTGDI and LCNT based C-MDMTGDI. The proposed circuits are simulated with similar value of parameters as CMDMTGDI circuits. The functionality of the proposed circuits is verified in dynamic and static mode and a performance comparison is done.

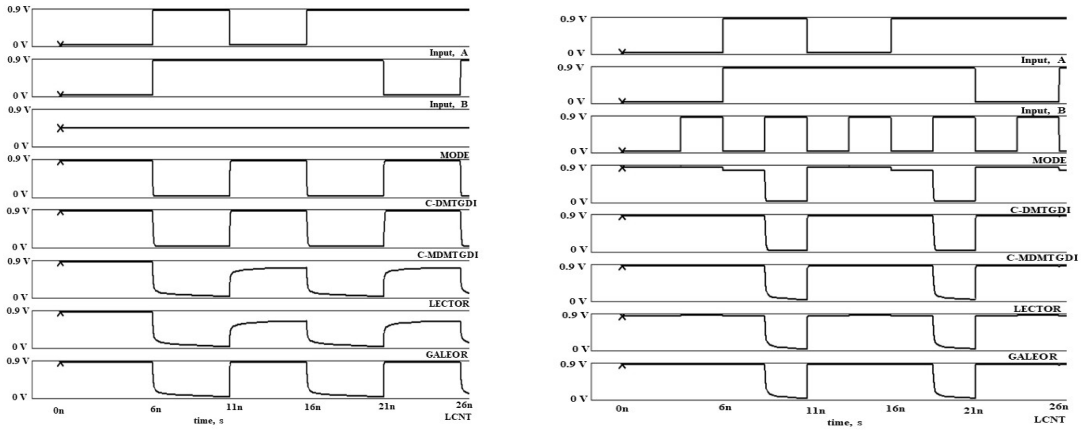
To illustrate the functionality of the proposed designs, the transient waveforms for NAND gate(2-input) in static and dynamic mode are depicted in Fig.4. Table 1 tabulates the performance metrics i.e., delay, power and PDP of existing CMOS based DMTGDI, CMOS based M-DMTGDI, CDMTGDI and CMDMTGDI based 2-input NAND, NOR and XOR gates in static and dynamic mode at 27°C. As observed, there is a PDP reduction of 71.52% to 97.85% for the proposed CDMTGDI and CMDMTGDI circuits as against CMOS designs. The percentage saving in PDP using proposed CDMTGDI and CMDMTGDI is illustrated in Fig. 5. A maximum PDP saving of 97.85% and 93.82% is achieved using the proposed circuits in static and dynamic mode respectively, as compared to CMOS designs. For proposed CNTFET based designs, the PDP of CMDMTGDI design in static mode deteriorates in contrast to CDMTGDI counterparts. However, the PDP improves significantly in dynamic mode i.e., energy efficiency of the CMDMTGDI design is high. As a result, the total PDP of CMDMTGDI designs is decreased in contrast to CDMTGDI designs. Further temperature and voltage variations impact on PDP of proposed CMDMTGDI based NAND is depicted in Fig.6.

The proposed CMDMTGDI based LECTOR, GALEOR and LCNT based NAND, NOR and XOR gates with 2-inputs are simulated using 32nm CNTFET Stanford model in HSPICE tool at 0.9V and load capacitance of 5fF. The total leakage power is evaluated over all input combinations of 2-input gates in both static and dynamic mode. For GALEOR based C-MDMTGDI design, high threshold voltage GLTs are used.

The total leakage power and delay values for NAND, NOR and XOR gates for CMDMTGDI, LECTOR based CMDMTGDI, GALEOR based C-MDMTGDI and LCNT based CMDMTGDI is tabulated in Table 2. It can be observed that a maximum leakage power saving of 36.18%, 46.68% and 41.19% is achieved using the proposed leakage

Authorized licensed use limited to: DELHI TECHNICAL UNIV. Downloaded on May 15,2023 at 09:59:05 UTC from IEEE Xplore. Restrictions apply.

reduction techniques in NAND, NOR and XOR gates respectively. GALEOR based CMDMTGDI is the most efficient at leakage power reduction followed by LECTOR based CMDMTGDI and LCNT based CMDMTGDI. However, there is a degradation of delay in each of the proposed leakage reduction technique. Further, the leakage energy saving achieved using the proposed leakage reduction techniques for CMDMTGDI based designs is illustrated in Fig.7. It can be observed that there is significant leakage energy saving for each of the proposed technique in static and dynamic mode.

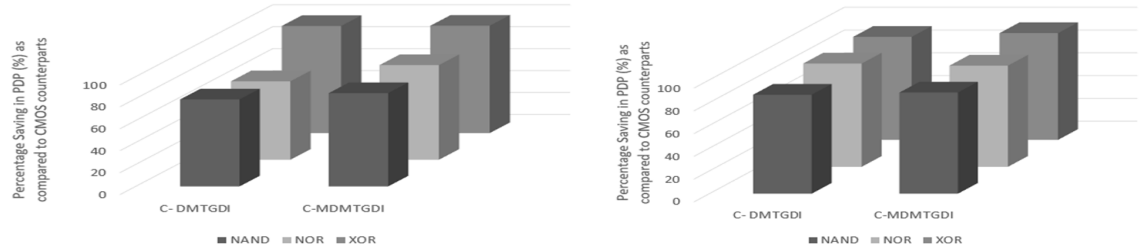


(a) (b)

Fig.4. Transient waveforms for proposed techniques based NAND (2-input) gate at 32nm at 27°C in different mode (a) Static (b) Dynamic

Mode	Circuit	Power(uW)				Delay(ps)				PDP(aJ)			
Static		CMOS DMTGDI	CMOS MDMTGDI	C-DMTGDI	C-MDMTGDI	CMOS DMTGDI	CMOS MDMTGDI	C-DMTGDI	C-MDMTGDI	CMOS DMTGDI	CMOS MDMTGDI	C-DMTGDI	C-MDMTGDI
	NAND	1.36	1.64	1.25	1.18	72	158.6	16.2	33	97.92	260.1	20.25	38.94
	NOR	0.95	1.12	0.81	0.69	47.9	146.4	16	32.6	45.51	163.97	12.96	22.49
	XOR	4.51	4.12	0.46	0.48	70.4	149.8	16.2	27.7	317.5	617.18	7.45	13.29
Dynamic													
	NAND	139.6	4.65	41.8	1.2	13.8	47.3	5.99	20.3	1926.48	219.95	250.38	24.36
	NOR	290.7	5.36	70.18	1.19	18	39.8	6.9	19.9	5232.6	213.33	484.24	23.68
	XOR	295.5	4.07	61.6	0.66	11.7	43.8	5.3	16.7	3457.35	178.27	326.48	11.02

Table 1 Power, delay and PDP of existing CMOS DMTGDI, CMOS MDMTGDI, proposed CDMTGDI and CMDMTGDI based NAND, NOR and XOR gates (2-input) in different modes at 32nm at 27°C



(a) (b)

Fig.5. Percentage Saving in PDP for proposed CDMTGDI and CMDMTGDI based NAND, NOR and XOR gates (2-input) at 32nm at 27°C in different mode (a) Static (b) Dynamic

Authorized licensed use limited to: DELHI TECHNICAL UNIV. Downloaded on May 15,2023 at 09:59:05 UTC from IEEE Xplore. Restrictions apply.

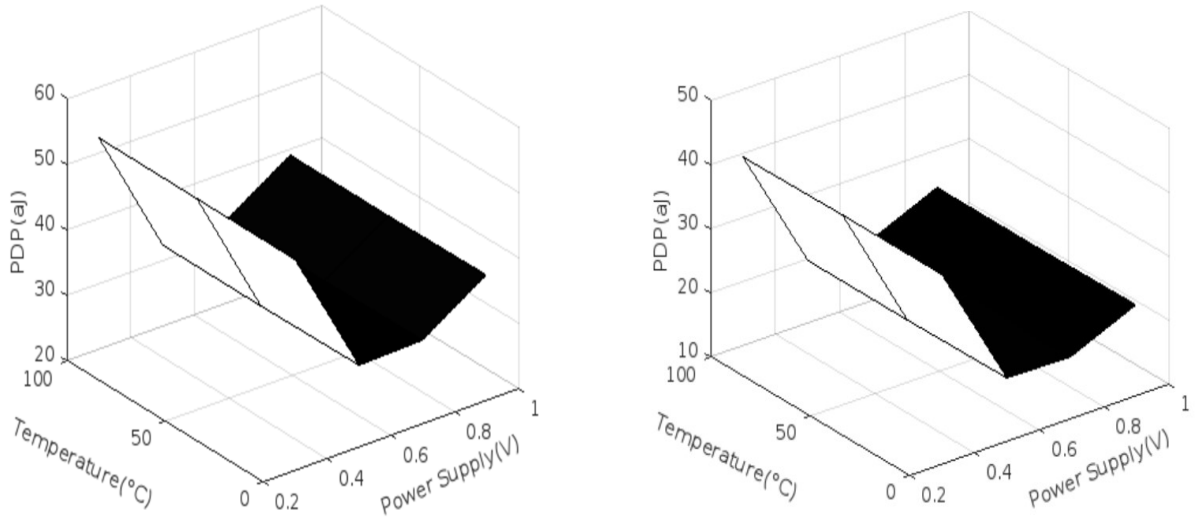


Fig.6. Temperature and voltage variations effect on the PDP of proposed CMDMTGDI based NAND gate (2-input) at 32nm at 27°C in different mode (a) Static (b) Dynamic

Mode	Circuit	Leakage Power(10^{-11} W)				Delay(10^{-11} s)			
Static		C-MDMTGDI	LECTOR based C-MDMTGDI	GALEOR based C-MDMTGDI	LCNT based C-MDMTGDI	C-MDMTGDI	LECTOR based C-MDMTGDI	GALEOR based C-MDMTGDI	LCNT based C-MDMTGDI
	NAND	72.48	46.77	46.26	46.75	3.3	3.89	4.19	3.66
	NOR	114.56	61.27	61.08	61.29	3.26	3.99	4.04	3.9
	XOR	83.74	49.59	49.25	50.56	2.87	3.53	3.57	3.48
Dynamic									
	NAND	115.21	81.99	81.18	81.81	2.09	2.39	2.61	2.23
	NOR	191.95	113.92	113.36	113.73	1.99	2.33	2.46	2.17
	XOR	134.06	89.08	88.43	99.99	1.87	2.21	2.3	2.15

Table 2 Leakage power and delay of CMDMTGDI, LECTOR based CMDMTGDI, GALEOR based CMDMTGDI and LCNT based CMDMTGDI for NAND, NOR and XOR gates (2-input) in static and dynamic mode at 32nm at 27°C

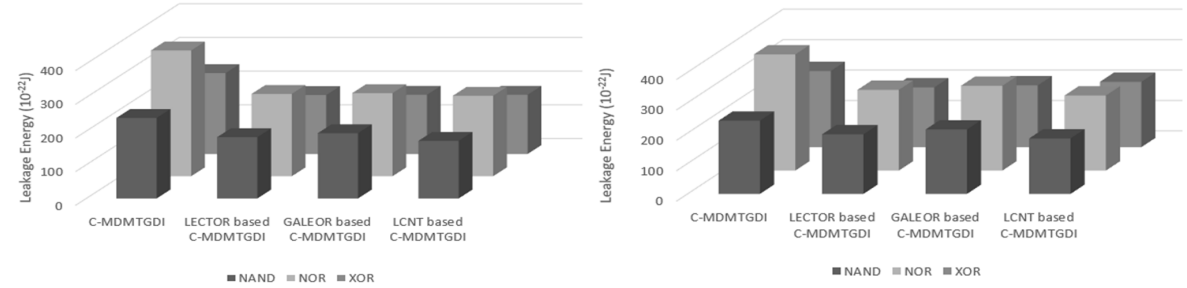


Fig.7. Leakage energy of CMDMTGDI, LECTOR based CMDMTGDI, GALEOR based CMDMTGDI and LCNT based CMDMTGDI for NAND, NOR and XOR gates at 32nm at 27°C (a) Static mode (b) Dynamic Mode

V. CONCLUSION

This work presents DMTGDI and M-DMTGDI design implemented using CNTFETs, referred to as CDMTGDI and CMDMTGDI circuits. The proposed designs are compared with their existing CMOS counterparts. The proposed CMDMTGDI design overcomes the contention issue present in CDMTGDI design. Simulative investigation reveals that the proposed designs are more efficient at reducing PDP than their CMOS counterparts. When compared to CMOS-based designs, the proposed designs yield a PDP reduction of 71.52% to 97.85%. Further, leakage reduction techniques i.e., LECTOR, GALEOR and LCNT- are implemented in the proposed CMDMTGDI design. These techniques prove to be efficient at reducing leakage power for the proposed CMDMTGDI circuits with a leakage power saving of 28.83% to 46.52%, 29.54% to 46.68% and 25.41% to 46.5% for

Authorized licensed use limited to: DELHI TECHNICAL UNIV. Downloaded on May 15,2023 at 09:59:05 UTC from IEEE Xplore. Restrictions apply.

LECTOR based CMDMTGDI, GALEOR based CMDMTGDI and LCNT based CMDMTGDI, respectively.

References

[1] M. Alioto, Enabling the internet of things: From integrated circuits to integrated systems, Springer International Publishing, 2018.

[2] S.-M. Kang, Y. Leblebici, and C. W. Kim, CMOS Digital Integrated Circuits Analysis & Design, 4th ed. New York, NY: McGraw-Hill Professional, 2014.

[3] A. Morgenshtein, A. Fish, and I. A. Wagner, "Gate-diffusion input (GDI): a power-efficient method for digital combinatorial circuits," IEEE Trans. Very Large Scale Integr. VLSI Syst., vol. 10, no. 5, pp. 566–581, 2002.

[4] E. Rastegar Pashaki and M. Shalchian, "Design and simulation of an ultra-low power high performance CMOS logic: DMTGDI," Integration, vol. 55, pp. 194–201, 2016.

[5] P. Bajpai, N. Pandey, K. Gupta, and J. Panda, "LECTOR incorporated differential cascode voltage swing logic (L-DCVSL)," Analog Integr. Circuits Signal Process., vol. 100, no. 1, pp. 221–234, 2019.

[6] V. Yuzhaninov, I. Levi, and A. Fish, "Design flow and characterization methodology for dual mode logic," IEEE Access, vol. 3, pp. 3089–3101, 2015.

[7] A. Kaizerman, S. Fisher, and A. Fish, "Subthreshold Dual Mode Logic," IEEE Trans. Very Large Scale Integr. VLSI Syst., vol. 21, no. 5, pp. 979–983, 2013.

[8] I. Levi, A. Kaizerman, and A. Fish, "Low voltage dual mode logic: Model analysis and parameter extraction," Microelectronics, vol. 44, no. 6, pp. 553–560, 2013.

[9] N. Yadav, N. Pandey, and D. Nand, "Leakage reduction in dual mode logic through gated leakage transistors," Microprocess. Microsyst., vol. 84, no. 104269, p. 104269, 2021.

[10] N. Yadav and P. Kumari, "Design of ALU using dual mode logic with optimized power and speed," in 2017 International Conference on Multimedia, Signal Processing and Communication Technologies (IMPACT), 2017.

[11] M. L. P. Tan, G. Lentaris, and G. Amaratunga Aj, "Device and circuit-level performance of carbon nanotube field-effect transistor with benchmarking against a nano-MOSFET," Nanoscale Res. Lett., vol. 7, no. 1, p. 467, 2012.

[12] A. Raychowdhury and K. Roy, "Carbon nanotube electronics: Design of high-performance and low-power digital circuits," IEEE Trans. Circuits Syst. I Regul. Pap., vol. 54, no. 11, pp. 2391–2401, 2007.

[13] H. Kumar, S. Srivastava, P. K. Khosla, and B. Singh, "High stable and energy efficient emerging nanoscale CNTFET SRAM cells using circuit level low power techniques," Silicon, vol. 14, no. 13, pp. 8031–8043, 2022.

[14] N. Hanchate and N. Ranganathan, "LECTOR: a technique for leakage reduction in CMOS circuits," IEEE Trans. Very Large Scale Integr. VLSI Syst., vol. 12, no. 2, pp. 196–205, 2004.

[15] R. Lorenzo and S. Chaudhury, "LCNT-an approach to minimize leakage power in CMOS integrated circuits," Microsyst. Technol., vol. 23, no. 9, pp. 4245–4253, 2017.

[16] S. Katrue and D. Kudithipudi, "GALEOR: Leakage reduction for CMOS circuits," in 2008 15th IEEE International Conference on Electronics, Circuits and Systems, 2008.

[17] V. K. Magraiya, T. K. Gupta, and B. Garg, "Design of CNTFET based domino wide OR gates using dual chirality for reducing subthreshold leakage current," Silicon, vol. 14, no. 14, pp. 8695–8706, 2022.

[18] R. P. Somineni, Y. P. Sai, and S. N. Leela, "Low leakage CNTFET full adders," in 2015 Global Conference on Communication Technologies (GCCT), 2015, pp. 174–179.

[19] A. Kumar, B. P. Shrivastava, and A. Kumar, "A new leakage-tolerant domino circuit for wide fan-in gates with CNTFET," in 2017 International Conference on Information, Communication, Instrumentation and Control (ICICIC), 2017.

[20] N. Yadav, N. Pandey, and D. Nand, "CNTFET based Transmission Gate Diffusion Input Logic (C-TGDI) design," in 2021 5th International Conference on Electrical, Electronics, Communication, Computer Technologies and Optimization Techniques (ICEECCOT), 2021.

[21] YB Kim Design methodology based on carbon nanotube field effect transistor (CNFET) PhD diss., Northeastern University, 2010.

Authorized licensed use limited to: DELHI TECHNICAL UNIV. Downloaded on May 15,2023 at 09:59:05 UTC from IEEE Xplore. Restrictions apply.

Comparative Analysis of Different Profiles of Riblets on an Airfoil using Large Eddy Simulations

Aryan Tyagi
Department of Mechanical Engineering
Delhi Technological University
New Delhi, India
tyagiaryan82@gmail.com

Aakash Ghosh
Department of Aerospace Engineering
Delft University of Technology
Delft, Netherlands
ag101099@gmail.com

Rajkumar Singh
Department of Mechanical Engineering
Delhi Technological University
New Delhi, India
rajkumarsingh@dce.ac.in

Abstract*—Nature has adapted throughout its existence, from humans to fishes, and amongst these adaptations, several nature-driven optimizations have made species better suited to the current environment. These optimizations can be found in Mako Sharks, which have developed geometric surface patterns that allow them to move faster. These patterns have been named riblets, and it is observed that they induce skew-induced secondary flows, which improve the overall flow behavior around the sharks. Secondary flows create a pocket of low-velocity air in the ridges, resulting in the high-speed flow being concentrated on the tips of the riblets, further resulting in reduced shear stress. Moreover, the vortical motion of the secondary flows allows a more significant transfer of energy in the boundary layer, which aids in delaying the boundary layer separation. Most of the numerical studies regarding various shapes of riblets have been carried out on flat plates using a Reynolds Averaged Navier-Stokes (RANS) approach. This study focuses on four profiles of riblets: sawtooth, scalloped, blade, and inverted U-shape, attached to the airfoil, and develops a Large Eddy Simulation (LES) framework to simulate the flow. LES resolves eddies of larger scales while modeling the smaller eddies. This allows the simulation to capture the secondary flow over the airfoil with much greater detail and accuracy when compared to RANS, which averages the fluid flow over time. The drag coefficient at various angles of attack was compared against the drag coefficient values of the bare airfoil. The scalloped riblets showed the maximum reduction in drag coefficient (8% lesser than the bare airfoil), followed by sawtooth, inverted U-shape, and blade-shape. The LES produced accurate contours of velocity, which conform to existing research. The wall shear stress was also post-processed to find similarities between existing research and the proposed LES framework. It was observed that the wall shear stress was concentrated on the riblet-tips instead of the whole upper surface of the airfoil. Another focus of this research was to reduce the simulation's computational load, which is done by using the Spalart-Allmaras DDES solver and reducing mesh time while maintaining the accuracy of the simulation framework.

TABLE OF CONTENTS

1. INTRODUCTION 1
2. METHODOLOGY 2
3. RESULTS AND DISCUSSION 4
4. SUMMARY 4
ACKNOWLEDGMENTS 6
REFERENCES 6
BIOGRAPHY 7

978-1-6654-9032-0/23/$31.00 ©2023 IEEE

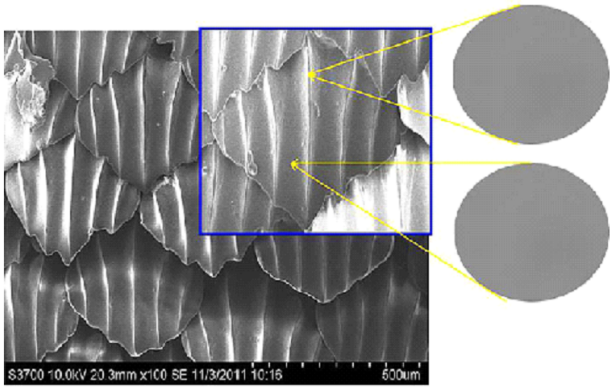


Figure 1: **Electron microscope picture of artificial shark-skin riblets [1]**

1. INTRODUCTION

Mako sharks have been known to have developed riblets, which allows these sharks to achieve higher speeds. These riblets are a product of evolution, and similar patterns have been seen on birds. Skimmer birds have developed riblets on the beaks which allow them to dive faster when trying to hunt for fish. Design based on the adaptations of nature has been known to help optimize current technology. One of the prime examples of biomimicry can be seen in commercial airplanes with their use of "winglets" or "sharklets" which are fitted to the end of the wings in order to decrease the formation of wing-tip vortices. Similarly, riblets also have the potential to be applied for further optimization. Pu et al. [1] present a SEM of a biomimetic shark skin membrane used for their study on hydrophobicity of biomimetic shark-skin membrane.

The patterns visible in figure 1 are known as riblets. These riblets have been known to induce secondary flows. Secondary flows are a micro-flow phenomenon which has been extensively studied. Secondary flows was first popularised by Edward S. Taylor in an Massachusetts Institute of Technology educational film called "Secondary Flows". The term "secondary flow" can be regarded as an umbrella term to localized flow in an existing flow region that travels perpendicular to the primary flow.

Secondary flows developed by riblets can be categorized into a third kind as it is seen to be a product of both geometry

Authorized licensed use limited to: DELHI TECHNICAL UNIV. Downloaded on May 18,2023 at 05:03:26 UTC from IEEE Xplore. Restrictions apply.

2023 IEEE Aerospace Conference | 978-1-6654-9032-0/23/$31.00 ©2023 IEEE | DOI: 10.1109/AERO55745.2023.10115937

and viscosity [2]. Experimental research of riblets has mainly been focused on their application on flat plates. Studies performed by Walsh [3] and Lee & Lee [4], both discussed the concentration of wall shear stress on the tips of the riblets. Walsh[3] further discusses how the geometrical parameters of V-shaped or sawtooth riblets can alter flow behavior. There has been a recent rise in interest on the optimization and modelling of riblet structures. This can be attributed to the potential of such biomimetic devices in improving current technology. Decreasing aerodynamic load on vehicles in crucial for reducing fuel usage, and riblets have proven to reduce that. A recent study by Lloyd et al. [5] presents an experimental study of the effect of riblet patterns on the boundary layer. The study tests the effect of riblets seen on denticles, which are seen on the skin of sharks. Llyod et al. [5] compares the denticles with riblets and ones without, concluding that the riblets reduce the overall wall shear stress on these surfaces which ultimately reduces the fluidic drag. There are two forms of drag induced on an object passing through a fluid namely, frictional drag and form drag. Frictional drag or skin friction drag is caused by friction between the fluid and the object's surface. Surface enhancements can be done to improve the frictional drag on an object. Airplanes and high performance automobiles are regularly polished and painted in order to ensure their smooth surface. Form drag is caused by a pressure difference between the front and the back of a body. Boundary layer separation is known to produce a wake field behind the body as the potential energy of the flow is transformed into the turbulent kinetic energy of the flow in the wake. Delaying the boundary layer separation on bodies have been studied for a long time; vortex generators are a device used to induce vortices in the flow to keep flows attached. These vortices increase the momentum of the boundary layer which keeps the flow attached to the surface for longer [6].

Delaying boundary layers separation on wings are important to reduce the fuel consumption and riblets can be used to achieve this. Only a limited number of studies have been conducted on the application of riblets on airfoils. A research on the effect of sweep angles and the riblets was conducted by Zhang et al. [7], and though there was a reduction in drag for most cases, the study reported an increase in pressure drag at sweep angle of 15°. Prior simulation-based research has also been conducted which have used metaheuristic optimization in order to find the optimal height-spacing ratio for sawtooth (V-shaped) riblets [8], [9].

Further research can be done by analyzing the effect of different shapes of riblets. As reported by a study done by Fu et al. [10] used RANS modelling to compare the turbulent kinetic energy between different shapes of riblets applied on a flat plate concluding that -shaped geometries increase drag and sawtooth, U and L-shaped riblets show reductions in drag. Guo et al. [11] researched the use of convergent-divergent patterns of riblets on a flat plate and noticed that increasing the height of the riblet makes the secondary flows stronger. However, such a strategy will not be suitable for applications in aerospace. A study by Raayai-Ardakani McKinley [12] discuss how unoptimized riblet geometry can increase drag.

The main objective of this study is to provide a comprehensive quantitative comparison between U-shaped, inverted U-shaped, sawtooth, and blade-shaped riblets over a NACA0012 airfoil. Figure 2 presents the schematic diagrams of the different types of riblet profiles used in this paper. The height to spacing ratio of each profile is kept as 0.8. Another focus of this study is to maintain a low-computation CFD framework to perform a Large-Eddy Simulation (LES). The paper discusses the CAD model and mesh development on OpenFOAM, the use of solvers based on OpenFOAM and how these are tuned to reduce the overall simulation time.

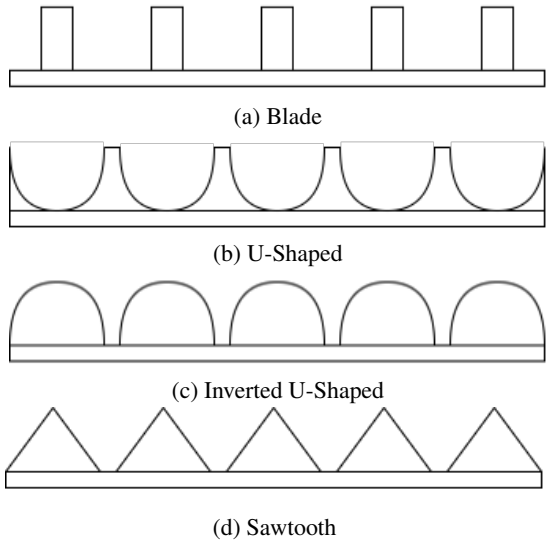


Figure 2: **Riblet Profiles used in present study**

2. METHODOLOGY

Geometry and Mesh Development

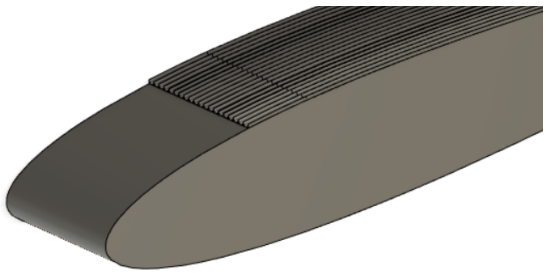
A NACA0012 airfoil with a chord length of 0.1m and span of 0.1m is considered for the analysis. The riblets on the surface of the airfoil were modeled using the CAD software Fusion 360 (Figure 3). The STL files of these models were then imported in the open-source CFD software called OpenFOAM. The mesh for the fluid domain is generated by the snappyHexMesh tool in OpenFOAM. A CAD of the bare airfoil was used to validate the accuracy of the solver by comparing the drag coefficient obtained from CFD with wind tunnel experiments.

The final mesh with 5 million elements consists of a fluid domain with a refinement region around the top of the airfoil to better capture the flow behavior between the riblets. The average time for the mesh to be generated was about 1000 seconds, with some variation depending on the geometrical complexity of the particular riblet profile.

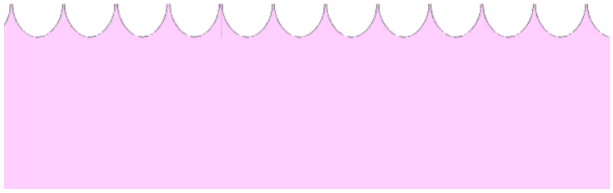
CFD Solver

Studies of the micro-structures on the surface of an airfoil have been carried out using the Reynolds-Averaged Navier Stokes (RANS) equations, but they do not provide the full picture of the flow behaviour at the riblet surfaces. Direct Numerical Simulation (DNS) and Large Eddy Simulation (LES) have the potential to capture the flow with high detail between the riblets, but the high computational cost makes them prohibitive for complex geometries. In this study, the Spalart Allmaras Delayed Detached Eddy Simulation (SA DDES) turbulence model has been used. The SA DDES model is a hybrid RANS-LES model based on the one equation Spalart Allmaras Model [13]. The DDES model is based on the Detached Eddy Simulation (DES) model originally proposed by Spalart et al. [14] in 1997. The DES model

Authorized licensed use limited to: DELHI TECHNICAL UNIV. Downloaded on May 18,2023 at 05:03:26 UTC from IEEE Xplore. Restrictions apply.

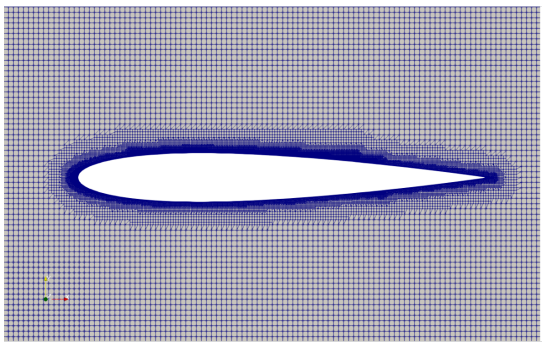


(a) Location of Riblets

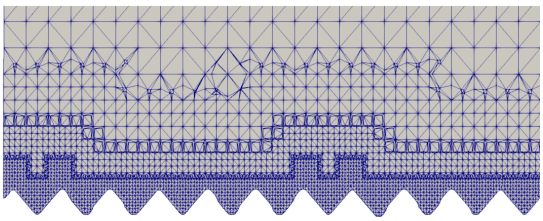


(b) Profile of the Riblets at 2-D section parallel to freestream velocity

Figure 3: **CAD Model of the airfoil with Riblets**



(a) Mesh of the Flow Domain



(b) Refined Mesh around the Riblets

Figure 4: **Slice of Mesh for Airfoil with Sawtooth Riblets at an Angle of Attack of 0**

is based on the one-equation Spalart Allmaras turbulence model. The length scale d in the Spalart Allmaras turbulence model is taken as the shortest distance at any point to the closest wall. For DES, this length scale is modified to be the minimum between the distance to the closest wall and a quantity that is proportional to the local mesh size.

$$d_{DES} = min\,(d, C_{DES}\Delta) \tag{1}$$

where C_{DES} is taken as a constant with a value of 0.65 in past studies. Δ denotes the local mesh size.
The hybrid turbulence model aims to have an accuracy comparable to that of LES, while also maintaining the computational power and time required at practical levels. It is a slightly modified version of the Detached Eddy Simulation. In the DES model, RANS equations are used for the attached boundary layers, and the LES model resolves the time-dependent, three-dimensional large eddies. For the Delayed DES, the length scale is modified by incorporating information about the molecular and turbulent viscosity to prevent a premature switch to LES within the boundary layers.

$$\tilde{d} = d - f_d max\,(0, d - C_{DES}\Delta) \tag{2}$$

$$f_d = tanh([8r_d]^3) \tag{3}$$

$$r_d = \frac{\nu_t + \nu}{\sqrt{U_{i,j}U_{i,j}}\kappa^2 d^2} \tag{4}$$

In this paper, the incompressible, transient state solver pisoFoam is used in OpenFOAM as the physics solver. The GAMG Solver in OpenFOAM is used to implicitly calculate the pressure at each iteration. We use a smoother to smoothen out the spikes in the residuals and reduce the error. For the pressure equations, the Gauss Seidel smoother is used. The tolerance is kept as 1e-6. The velocity and modified eddy viscosity are calculated using smoothSolver and the Gauss Seidel smoother, with a tolerance of 1e-7. The dimensions of the riblets were chosen according to the experimental data. The height and spacing values which showed the maximum reduction in drag in wind tunnel experiments were used for this study.

Boundary Conditions

At the inlet, a freestream boundary condition was given, with the inlet velocity of 48 m/s. At the walls of the fluid domain, the slip boundary condition along with zero pressure gradient setting were specified. The surface of the airfoil was given the no slip condition. The outlet was provided with a pressure condition and zero-gradient settings for velocity. The Reynolds Number is calculated as

$$Re = \frac{\rho u L}{\mu} \tag{5}$$

and comes out to be about 360,000 for the flow, falling in the laminar to turbulent transitional region. The CFD simulations were run on the airfoil with the different riblet profiles, namely, scalloped, u-shape, blade, and inverted u-shape. The simulations were run for 4 different angles of attack of the airfoil (-2°, 0°, 2°, 6°). The computations were done on a system with 36 cores and 64GB of RAM, and each simulation took roughly 2 hours to complete.

Grid Independence Test

The selection of mesh size and mesh settings is important in order to use the computational resources efficiently, without compromising on accuracy. Thus, a grid independence test was performed on an airfoil with riblets. Since the region near the riblets is where most of the flow alterations occur, the velocity field near the riblets is chosen as the parameter for the grid independence test. The velocity is plotted along a straight line starting from the trough of the riblets till the region where $U = U_\infty$. The different meshes are generated in the following steps:

1. Generate a mesh with sufficient detail, with global element size δ and run the CFD simulation.

2. Set $\delta' = 2 * \delta$ and run the CFD simulation with the same boundary conditions.

Authorized licensed use limited to: DELHI TECHNICAL UNIV. Downloaded on May 18,2023 at 05:03:26 UTC from IEEE Xplore. Restrictions apply.

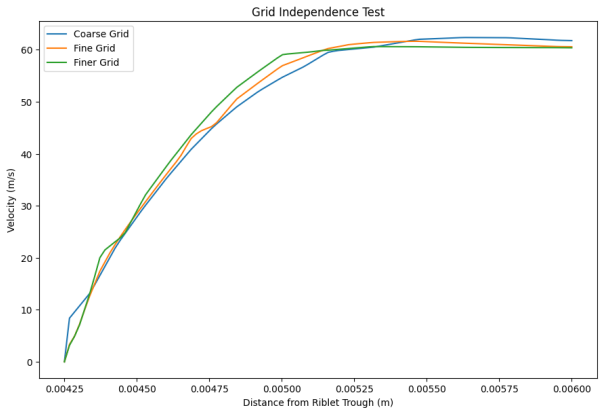


Figure 5: **Grid Dependency Test**

3. Set $\delta' = 0.5 * \delta$ and run the CFD simulation with the same boundary conditions.

4. Compare the behaviour of velocity along the straight line plotted from the trough till the point where $U = U_\infty$.

Figure 5 shows the results of the mesh independence test. It is clear from the graph that the results of our CFD simulations are independent of the mesh size.

3. Results and Discussion

Streamwise Velocity

Figure 6 shows the velocity contours around different shapes of riblets. All the riblets produce a similar pattern wherein, pockets of low velocity flow are created in the riblet valleys. The production of these low velocity valleys help reduce the wall shear stress over the wing. The shear stress of Newtonian fluids parallel to a plate can be mathematically represented as:

$$\tau = \mu \frac{\partial u}{\partial y} \tag{6}$$

Where, μ is the dynamic viscosity and the second term on the right is the velocity gradient perpendicular to the direction of fluid flow. It is evident that the wall shear stress is dependent on velocity. A slower velocity transition from the wall results in a lower shear stress. The sawtooth and U-riblets perform the best in creating pockets of low velocity. However, it is visible that the velocity gradient of the flow moving away from the wall is lower in case of the U-shaped riblets. The blade-shaped riblets perform poorly in terms of reducing the velocity gradient and a flow of greater velocity interacts with the walls. The inverted-U riblets perform well, however due to their shape a larger area is in contact with a higher velocity flow. As discussed before, drag experienced by the wing can be sub-categorized into two forms. The shear stress contributes to the skin friction drag. Table 1 can be used to further elaborate on the contours. Comparing the coefficients of drag, it is visible that the U-shaped riblets perform the best with an 8.11% reduction in drag, and the findings can be correlated to the reduced shear stress as well as shown in figure 7. The sawtooth riblets performed slightly worse than the U-shaped riblets with a drag reduction of 7.49%. The blade-riblets can be seen performing poorly relative to the other shapes which can also be linked to the poor velocity transition from the wall.

Table 1: **Summary of Drag Reduction at AOA = 0 °**

Profile	Cd	Drag Reduction
Sawtooth	0.00734	7.09%
U-Shaped	0.00726	8.11%
Blade	0.00764	3.31%
Inverted U-Shaped	0.00739	6.49%

Drag Reduction

Figure 8 plots the drag coefficient against four angles of attack for each riblet profile. The trend shows that riblets generally achieve a lower drag coefficient than the bare airfoil. The drag reducing effects of the riblets gets weaker as the angle of attack increases.

The best drag reduction by all riblet profiles is observed at an angle of attack of 0°. The results are summarised in Table 1. It is observed that the U-shaped riblets performs the best in reducing drag, it is chosen for detailed analysis and comparison with the bare airfoil.

Boundary Layer Separation

Figure 9 can be used to illustrate the effect on flow separation due to riblets. The bare airfoil shows flow separation occurring earlier than its ribletted-counterpart. As discussed before, riblets increase the momentum and energy of the boundary layer, this allows the boundary layer to stay attached for a longer distance.

Figure 9 (a) shows the velocity profile of the bare airfoil, and at point A, the flow can be seen to adversely interact with the surrounding flow. This results in a high velocity streak shown at point B with an overall turbulent flow. On the other hand, the airfoil with the riblets, keeps the flow attached for longer. Though a low velocity region can be seen in case of the ribletted airfoil, a large wake region is noticeable on the bare airfoil. This effect can be further elaborated using Q-criterion plots.

Q-Criterion

Q-criterion is helpful for visualizing vortices, as shown in figure 10, (a) shows the iso-surfaces of the bare airfoil and (b) gives the iso-surfaces of the airfoil fitted with riblets. It is clearly visible that the riblets induce higher vortical flow on the upper surface.

Another major observation can be made to further upholster the discussion on the wake field. An early flow separation can be clearly seen occurring in case of the bare airfoil and there is a much larger turbulent region behind the bare airfoil relative to the airfoil fitted with U-shaped riblets. Larger wake formation causes pressure drag to increase, this is effected by the early flow separation. Therefore, it is clear that by adding riblets onto the surface, the flow separation can be delayed and the wake generation can be reduced.

4. Summary

Different profiles of riblets were compared using Delayed Detached Eddy Simulations on OpenFOAM. The riblet pro-

Authorized licensed use limited to: DELHI TECHNICAL UNIV. Downloaded on May 18,2023 at 05:03:26 UTC from IEEE Xplore. Restrictions apply.

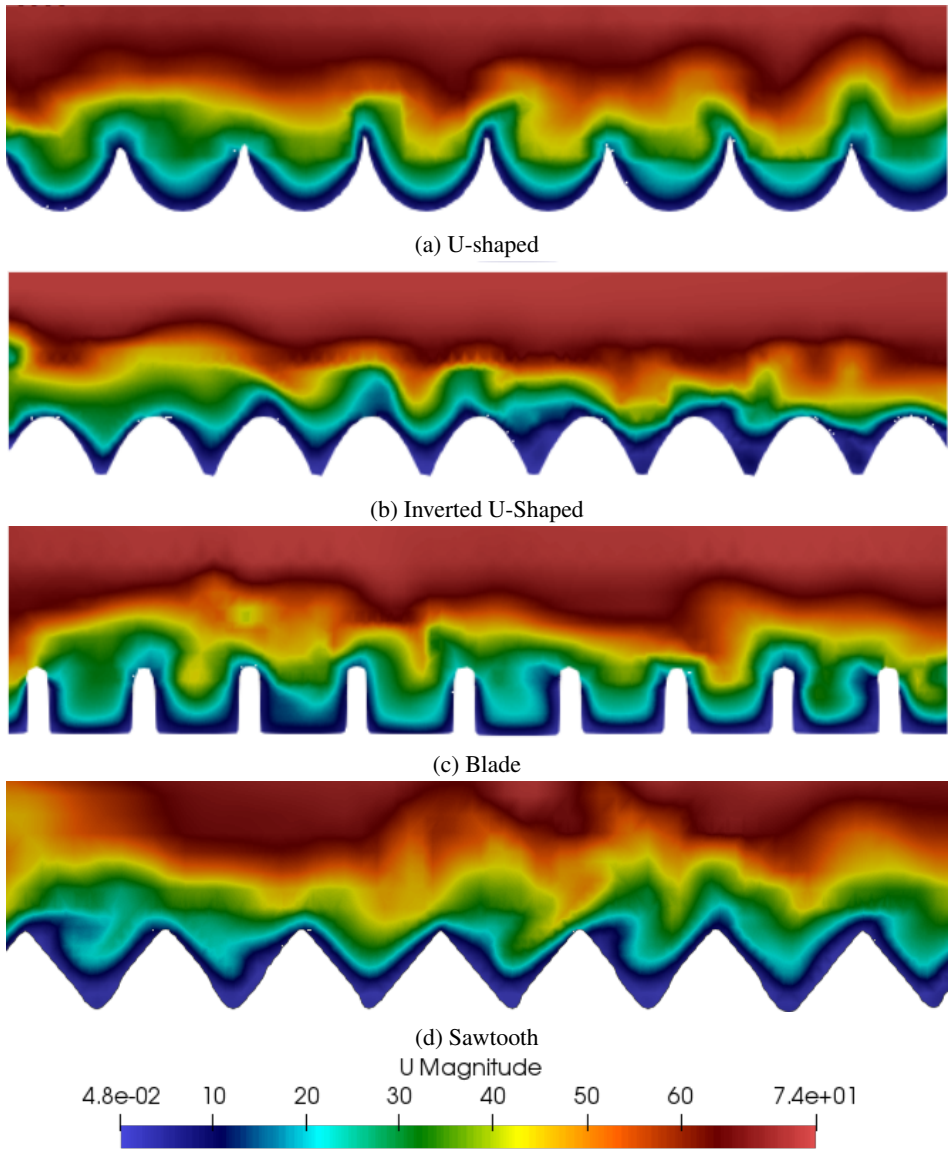


Figure 6: **Streamwise velocity contours at x/C = 0.3**

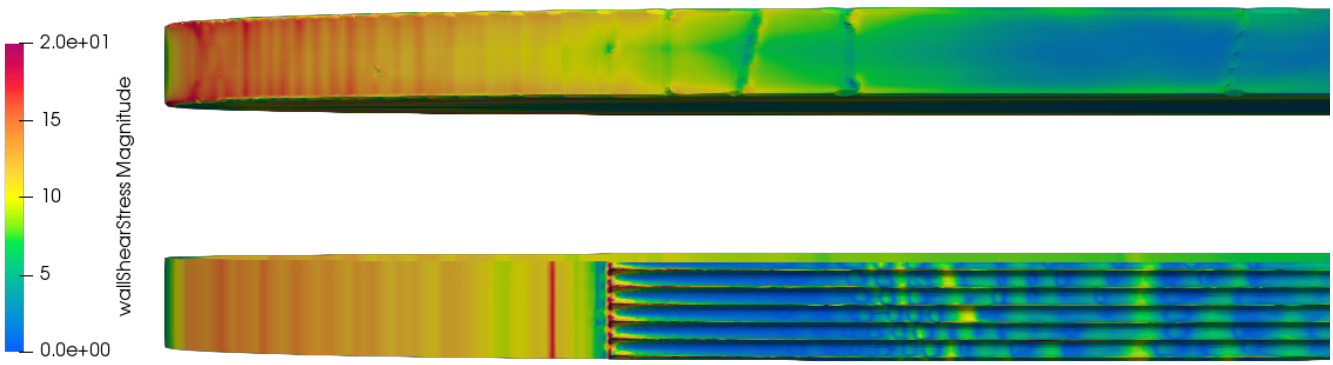


Figure 7: **Wall shear stress contours of bare airfoil (top) and airfoil with U-shaped riblets (bottom)**

Authorized licensed use limited to: DELHI TECHNICAL UNIV. Downloaded on May 18,2023 at 05:03:26 UTC from IEEE Xplore. Restrictions apply.

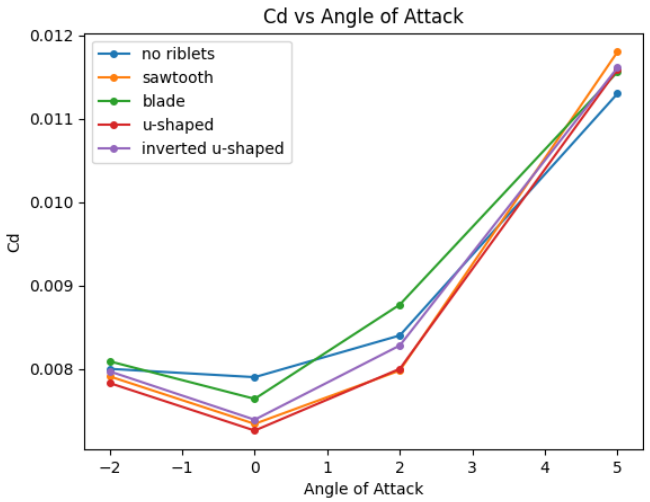
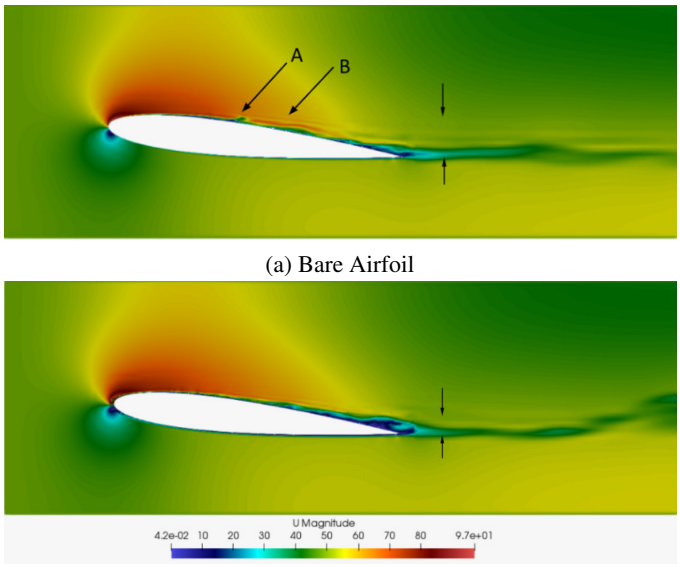


Figure 8: **Variation of Drag Coefficient with Angle of Attack for different riblet profiles**



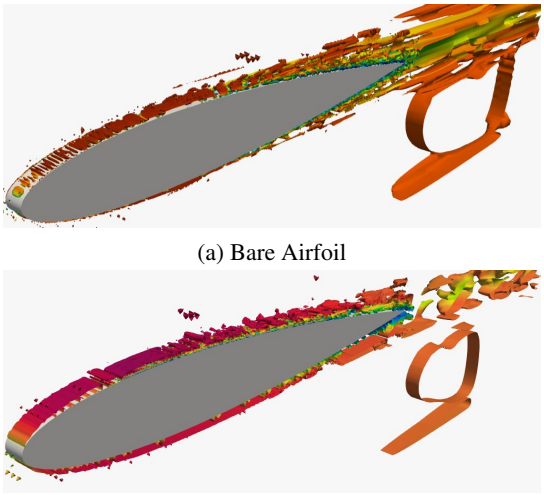
(a) Bare Airfoil

(b) Airfoil with U-shaped Riblets

Figure 9: **Visualizing flow separation using velocity contours**

files studied were sawtooth, blade, U-shaped, and inverted U-shaped. The drag reduction capabilities were compared, and the U-shaped riblet profile proved to be the best at drag reduction, reducing the coefficient of drag by 8.11%. The sawtooth is seen to provide similar drag reduction but the velocity gradient is seen to be much smaller in the U-shaped riblets. The blade riblets are seen to perform most poorly achieving a drag reduction of 3.31%.

The velocity contours and Q-criterion behaviors of a bare airfoil and an airfoil fitted with U-shaped riblets is further studied. It is found that the airfoil fitted with riblets is able to keep the flow attached for longer due to higher energy of the boundary layer, which leads to a smaller wake formation. The Q-criterion isosurfaces further aid in analyzing the wake formation and it is concluded that the airfoil fitted with riblets perform better at reducing wake.



(a) Bare Airfoil

(b) Airfoil with U-shaped Riblets

Figure 10: **Comparison of Q-Criterion between Bare Airfoil and Airfoil with U-shaped Riblets**

ACKNOWLEDGMENTS

The authors would like to thank the Fluid Mechanics Research Laboratory for providing the computational resources needed for the completion of this project.

REFERENCES

[1] X. Pu, G. Li, and H. Huang, "Preparation, anti-biofouling and drag-reduction properties of a biomimetic shark skin surface," *Biology open*, vol. 5, 03 2016.

[2] D. Goldstein and T.-C. TUAN, "Secondary flow induced by riblets," *Journal of Fluid Mechanics*, vol. 363, pp. 115 – 151, 05 1998.

[3] M. J. Walsh, "Riblets as a viscous drag reduction technique," *AIAA Journal*, vol. 21, no. 4, pp. 485–486, 1983. [Online]. Available: https://doi.org/10.2514/3.60126

[4] S. Lee and S. Lee, "Flow field analysis of a turbulent boundary layer over a riblet surface," *Experiments in Fluids*, vol. 30, pp. 153–166, 02 2001.

[5] C. Lloyd, J. Peakall, A. Burns, G. Keevil, R. Dorrell, P. Wignall, and T. Fletcher, "Hydrodynamic efficiency in sharks: the combined role of riblets and denticles," *Bioinspiration Biomimetics*, vol. 16, 03 2021.

[6] M. B. Bragg and G. M. Gregorek, "Experimental study of airfoil performance with vortex generators," *Journal of Aircraft*, vol. 24, no. 5, pp. 305–309, 1987. [Online]. Available: https://doi.org/10.2514/3.45445

[7] Y. Zhang, C. Yan, H. Chen, and Y. Yin, "Study of riblet drag reduction for an infinite span wing with different sweep angles," *Chinese Journal of Aeronautics*, vol. 33, 06 2020.

[8] S. Lulekar, P. Ghassemi, and S. Chowdhury, "Cfd-based analysis and surrogate-based optimization of bio-

Authorized licensed use limited to: DELHI TECHNICAL UNIV. Downloaded on May 18,2023 at 05:03:26 UTC from IEEE Xplore. Restrictions apply.

inspired surface riblets for aerodynamic efficiency," 06 2018.

[9] A. Ghosh, P. Gupta, Jayant, and R. K. Singh, "Metaheuristic optimization framework for drag reduction using bioinspired surface riblets," 2021. [Online]. Available: https://arxiv.org/abs/2109.09650

[10] Y. Fu, C. Yuan, and X. Bai, "Marine drag reduction of shark skin inspired riblet surfaces," *Biosurface and Biotribology*, vol. 3, no. 1, pp. 11–24, 2017.

[11] T. Guo, J. Fang, J. Zhang, and X. Li, "Investigation of the secondary flow by convergent-divergent riblets in a supersonic turbulent boundary layer over a compression ramp," *Physics of Fluids*, 09 2022.

[12] S. Raayai and G. McKinley, "Geometric optimization of riblet-textured surfaces for drag reduction in laminar boundary layer flows," *Physics of Fluids*, vol. 31, p. 053601, 05 2019.

[13] M. L. Shur, P. R. Spalart, M. K. Strelets, and A. K. Travin, "A hybrid rans-les approach with delayed-des and wall-modelled les capabilities," *International Journal of Heat and Fluid Flow*, vol. 29, no. 6, pp. 1638–1649, 2008.

[14] P. Spalart and S. Allmaras, "A one-equation turbulence model for aerodynamic flows," *AIAA*, vol. 439, 01 1992.

BIOGRAPHY



Aryan Tyagi *is an undergraduate student of Mechanical Engineering with specialization in Automotive Engineering at Delhi Technological University, New Delhi, India. His research interests include biofluid mechanics and aerodynamic shape optimization.*



Aakash Ghosh *received his Bachelors of Technology degree in Mechanical Engineering from Delhi Technological University in 2022. He is currently studying Aerospace Engineering at Delft University of Technology in Delft, Netherlands.*



Rajkumar Singh *received his Bachelors of Technology degree in Mechanical Engineering from Indian Institute of Technology, Kharagpur, India. He is currently a professor of Fluid Mechanics at Delhi Technological University, New Delhi, India. His research areas include aerospace engineering, fluid mechanics, and data-driven computational fluid dynamics.*

Authorized licensed use limited to: DELHI TECHNICAL UNIV. Downloaded on May 18,2023 at 05:03:26 UTC from IEEE Xplore. Restrictions apply.

Comparison of the Heat Transfer Capability of Various Nanofluids in a Flat Plate Solar Collector

Utkarsh Verma
Department of Mechanical Engineering
Delhi Technological University
New Delhi, India
vutkarsh2001@gmail.com

Shivraj Yadav
Department of Mechanical Engineering
Delhi Technological University
New Delhi, India
yadavshivraj096@gmail.com

Gaurav Kumar
Department of Mechanical Engineering
Delhi Technological University
New Delhi, India
gauravkmr716@gmail.com

Raj Kumar Singh
Department of Mechanical Engineering
Delhi Technological University
New Delhi, India
rajkumarsingh@dtu.ac.in

2023 9th International Conference on Electrical Energy Systems (ICEES) | 979-8-3503-4803-3/23/$31.00 ©2023 IEEE | DOI: 10.1109/ICEES57979.2023.10110182

***Abstract*—The aim of this study is to analyze and compare the performance of six nanofluids having 2 percent volumetric concentration when used in a flat plate solar collector using FVM analysis on ANSYS Fluent with a constant heat flux of 700 kW/m^2 and a flow velocity of 0.5 m/s to evaluate the heat transfer capability of each based on outlet temperatures, determining which is better as a working fluid for this solar energy collection device.**

Keywords— Nanofluids, Solar Energy, Solar Collector

I. Introduction

In response to the population growth, the energy demand has grown rapidly, which is needed for economic and technological advancement. Through 2040, the requirement for energy is anticipated to increase by 2.1% yearly. However, the world's precious energies are finite, primarily coming from unconventional sources. Despite recent reduction in numbers due to increased usage of renewable energy sources, fossil fuels continue to account for the 84 percent of majority of global energy use [1], [2]. Conventional energy sources contribute significantly to pollution in the form of greenhouse gases, which are the primary cause of global warming. Solar, wind, hydropower, geothermal, and biomass energy are a few types of renewable energy sources. Of all the viable renewable energy sources, solar energy is regarded as the most plentiful. The quantity of solar energy that reaches the surface of Earth is around 10,000 times more than what the entire planet needs in terms of energy. In terms of direct normal irradiance, the overall theoretical potential for solar electricity is relatively considerable. Current classifications of solar technology fall into two primary groups: (1) Photovoltaic: Using photovoltaic effects, sunlight is directly converted into electricity. (2) Thermal: Sunlight is heated and dried using thermal conversion. Using water or air as the working fluid, solar thermal energy systems transform the sun's energy directly into heat that is then stored. [3]. Several studies have been executed on flat plate solar collectors as an effective device for energy collection [4], [5]. The components of a conventional solar energy-based heating system are a collector device, a heat transfer loop with a fluid with circulation and a energy storage system with a heat exchanger. The energy a solar collector produces is significantly influenced by its size and shape, incidence angle, thermal properties of the working fluid and collector material [6], [7]. According to the latest data, wind and solar energy produced more than 10% of the world's electricity in 2021.

Tubes of circular cross section with U bent are most common in the application of heat exchangers, solar collectors, cooling of the electronic systems, chromatography etc. where heat is being transferred from one medium to another [8]. Spiral tubes have become quiet famous for application in above fields due to the compact geometry and manufacturing ease in addition to the increased rate of heat transfer due to increase in the heat transfer coefficient. It is quite complicated to understand the flow through the spiral tubes as it is much more complex than the flow in a straight circular cross sectioned tube due to the generation of secondary flows in the spiral tubes. These developed secondary flows are the reason for affecting the heat transfer capability of the spiral tubes. This is the first method to increase the heat transfer performance another method is to change the working fluid operating in the tubes by using a fluid with a high thermal conductivity. Solar applications mostly deal with rising the temperature of water for daily home uses and other purposes. So, changing the base working fluid is not a good option for a solar collector instead we can go for an innovative approach which is quite popular these days i.e. nanofluids [9], [10]. Nanofluids are colloidal solutions prepared from nanoparticles or particles with a nominal diameter smaller than one nanometer, in a base fluid. The whole point of using a nanofluid is to enhance the thermal conductivity of the base fluid by adding foreign material. If we compare the conductivity of ethylene glycol and other non-metal the conductivity of metal and their oxides are pretty much higher. Several researchers like Meibodi et al. [11], Rashidi et al. [12], Rashidi and Esfahani [13], Akbarzadeh et al. [10], Subramani et al. [14], Farshad et al. [15] performed various studies to analyse the effects on the heat transfer rates by nanofluids in heat transfer applications.

II. Problem Definition

A. CAD Model and Mesh

The size of flat solar collector plates is much larger than that of this paper. The size of the mesh should be minute enough to reveal the impact of the secondary developed flows because the goal of this research is to evaluate heat transfer variations utilising various turbulence-inducing devices. Also, due to this reason, the problem must be handled in three dimensions. The collector under investigation is 250 x 250 x 1.30 mm^3. The external diameter of the pipe is 6 mm with

Authorized licensed use limited to: DELHI TECHNICAL UNIV. Downloaded on May 04,2023 at 06:33:10 UTC from IEEE Xplore. Restrictions apply.

a thickness of 1 mm. The pipe and plate are both considered to be made of copper. Both the pipe and plate are press-welded together with 0.25 mm as the shared thickness. “Fig 1”, shows the geometry of the solar flat plate collector used in this research. For improving mesh accuracy, four inflation layers with a growth rate of 1.2 are incorporated throughout the length of the nanofluid. Grid Independence Test is performed using Parametric Analysis to refine the accuracy of the mesh and find the ideal mesh element size, which in this study comes out to be 1mm. For an element size of 1 mm, the number of nodes generated in the mesh is 4.244E +05 and the number of mesh elements is 1.4517E +06. “Fig. 2”, depicts a section of the mesh generated for 1mm mesh element size.

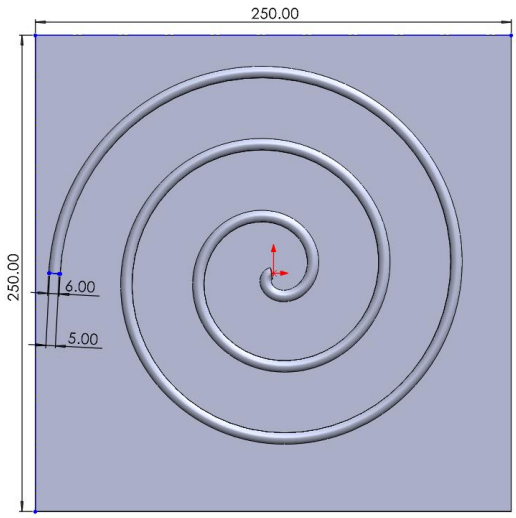


Fig. 1. CAD model of the solar collector with key geometric dimensions



Fig. 2. A portion of the mesh generated for simulation

B. Governing Equations

In this study a Newtonian, steady and three-dimensional flow of the working fluid is considered. To simulate a turbulent flow, the k-ε model is used. The concentration of the nanofluid is assumed to be homogeneous throughout the flow due to the existence of secondary flows in the flow of the nanofluid and changes in the path of the nanofluid flow. The physical system is modelled using the given equations[16]:

Equation of Conservation of Mass:

$$\frac{\partial \rho}{\partial t} + \nabla\nabla.(\rho\vec{v}) = S_m \tag{1}$$

where S_m is the mass generated.

Equation of Conservation of Momentum:

$$\frac{\partial \rho\vec{v}}{\partial t} + \nabla.(\rho\vec{v}\vec{v}) = -\nabla p + \nabla(\bar{\bar{\tau}}) + \rho\vec{g} + \vec{F} \tag{2}$$

Where $\rho, \vec{g}$ are the forces of gravity and external force respectively and $\bar{\bar{\tau}}$ is the stress tensor $\vec{J}$ is flux penetration of various types.

Equation of Conservation of Energy:

$$\frac{\partial \rho E}{\partial t} + \nabla.\left(\vec{v}(\rho E + P)\right) = \nabla\left(k_{e_{ff}}\nabla T - \sum_j h_j\overrightarrow{J_J} + \left(\tau_{e_{ff}}.\vec{v}\right)\right) + s$$

where s is a heat generated.

The stress tensor can be defined as follow:

$$\bar{\bar{\tau}} = \mu\left(\nabla\vec{v} + \nabla\vec{v}^T - \frac{2}{3}\nabla.\vec{v}I\right) \tag{4}$$

where I represents the second term tensor on the right side of effect of volume change and μ is molecular viscosity. The thermal performance of the model is defined by:

$$\eta = \left(\frac{Nu}{Nu_0}\right)\left(\frac{f_0}{f}\right)^{\frac{1}{3}} \tag{5}$$

$$Nu = \frac{h_m d_h}{k} \tag{6}$$

$$f = \frac{2\, d_h \Delta P}{\rho u^2 L} \tag{7}$$

where η is a dimensionless parameter which represents thermal performance. L represents the length of the tubes, and suffix 0 corresponds to the clear tube. The hydraulic diameter of the flow channel is denoted by d_h. The term h_m denotes the average heat transfer coefficient.

The working fluids used in this work are six nanofluids with the base fluid being water having homogeneous suspensions of the respective nanoparticles. These nanofluids are SiO_2-H_2O, Al_2O_3-H_2O, CuO-H_2O, TiO_2-H_2O, Ag-H_2O and diamond-H_2O having 2% volumetric concentration of the respective nanoparticles. The following equations are used to compute the thermophysical characteristics of the nanofluids, which are a crucial component of the governing equations:

Density:

$$\rho_{n_f} = \left(\frac{\phi}{100}\right)\rho_P + \left(1 - \frac{\phi}{100}\right)\rho_f \tag{8}$$

Heat Capacity:

$$C_{n_f} = \frac{(\phi/100)(\rho C)_P + \left(1-(\phi/100)\right)(\rho C)_f}{\rho_{n_f}} \tag{9}$$

Thermal Conductivity:

$$\frac{k_{n_f}}{k_f} = \frac{k_p + (n-1)k_f - (n-1)\phi\left(k_f - k_p\right)}{k_p + (n-1)k_f + \phi\left(k_f - k_p\right)} \tag{10}$$

Viscosity:

$$\mu_{n_f} = (1 + 2.5\phi)\mu_f \tag{11}$$

Here suffixes *f*, *p* and *nf* correspond to base fluid, nanoparticle and nanofluid respectively. Based on these equations and the thermal-physical properties of the base fluid and the nanoparticle materials, as shown in Table 1., the thermophysical properties of the respective nanofluids were calculated. These properties are listed in Table 2.

Authorized licensed use limited to: DELHI TECHNICAL UNIV. Downloaded on May 04,2023 at 06:33:10 UTC from IEEE Xplore. Restrictions apply.

TABLE I. THERMOPHYSICAL PROPERTIES OF BASE FLUID AND NANOPARTICLES

Material	ρ (kg/m³)	Cp (J/kg K)	k (W/m K)	μ (Ns/m²)
SiO_2	2200	703	1.2	-
Al_2O_3	3970	765	40	-
CuO	6500	535.6	20	-
TiO_2	4250	686.2	8.954	-
diamond	3150	497.26	1000	-
Ag	10500	235	429	-
H_2O	998.2	4182	0.613	0.001003

TABLE II. THERMOPHYSICAL PROPERTIES OF NANOFLUIDS

Nano -fluid	Nano -particle	ρ (kg/m³)	Cp (J/kg K)	k (W/m K)	μ (Ns/m²)
SiO_2-H_2O	SiO_2	1022.236	4032.25	0.6219	0.0010531
Al_2O_3-H_2O	Al_2O_3	1188.236	3925.47	0.6488	0.0010531
CuO-H_2O	CuO	1108.236	3754.26	0.6472	0.0010531
TiO_2-H_2O	TiO_2	1063.236	3902.53	0.6436	0.0010531
diamond-H_2O	diamond	1048.436	3935.28	0.6504	0.0010531
Ag-H_2O	Ag	1188.236	3484.44	0.6503	0.0010531

III. NUMERICAL SIMULATION

A. Details of Simulation

The numerical simulation was executed with the help of the ANSYS 2020 R1 Fluent programme by using the Finite Volume Method (FVM). In each case the working fluid is given the initial temperature as 300 K. The top face of the plate is constantly unveiled to a solar flux of 700 W/m^2. The flow velocity of the nanofluids is taken to be 0.5 m/s with the concentration of the nanoparticles to be 2% to form homogeneous fluids. As the concentration of the nanoparticles is very less the flow is modelled to be in single phase. The side faces and downward side of the collector plate are insulated. The discretization of kinetic energy, mass and momentum was obtained using the scheme of second-order upwind. The SIMPLE algorithm is used to investigate the relationship between pressure and velocity in this work. To find gradients the Green-Gauss cell-based technique is utilised and the convergence for the residuals of every equation is 10^{-9}.

B. Mesh Sensitivity Analysis

The grid independence test is used to find the ideal grid condition that has the minimal grids while providing the same simulation results. A unique synthesis methodology called parametric optimization uses a set of parameters and the accompanying bounds on their values to represent the design space. The input parameter, was selected mesh element size and adjusted to produce various mesh nodes and mesh elements. The output parameter was defined to be the outlet temperature. From the parametric optimization the outlet temperature is not varying for the element size lesser than 1mm. Therefore, 1mm is chosen as the element size.

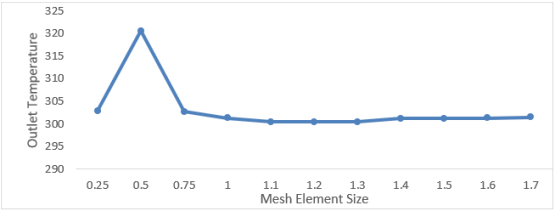


Fig. 3. Variation of outlet temperature with mesh element size

IV. VALIDATION

In order to verify the reliability and exactness of numerical model, the obtained Nusselt numbers calculated were compared with the Nusselt numbers predicted from the Gnielinski equation for the turbulent flow, which is defined by the following equation:

$$Nu_d = \frac{(f/8)(Re-1000)Pr}{1+12.7\sqrt{\frac{f}{8}}\left(Pr^{\frac{2}{3}}-1\right)} \quad (12)$$

which is applicable between $0.5 < Pr < 2000$ and $2300 < Re < 5106$. In the equation, the friction factor, f, is calculated as follows:

$$f = \frac{1}{(0.79\,ln\,Re-1.64)^2} \quad (13)$$

Nusselt numbers from Dittos-Boelter equation are calculated using the following relation between Nusselt number, Reynolds number and Prandtl number.

$$Nu_{DB} = \frac{h_f}{k_f} D_{eff} = Re^{0.8}\,Pr^{0.4} \quad (14)$$

The values of Nu, Nu_d and Nu_{DB} for all six nanofluids are represented in "Fig. 4", for application in the given solar flat plate collector.

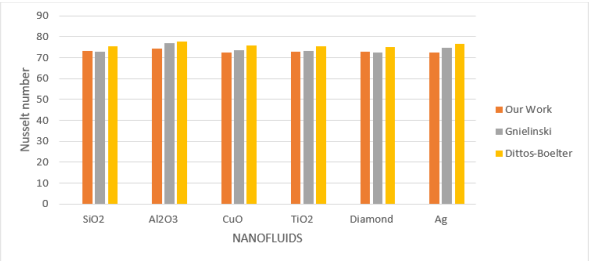


Fig. 4. Graph for validation of Nusselt number with Gnielinski correlation and Dittos-Boelter equation

V. RESULTS AND DISCUSSION

A. Temperature Distribution

There is currently a lot of research being performed to speed up transfer of heat in flat plate based solar collectors. An inexpensive and simple method of increasing the rate of heat transfer in heat exchange devices without using outer power. Nanofluids used in the collectors have comparatively higher heat transfer coefficient. "Fig. 5-10" show the various distributions of temperature on collector's top face.

Authorized licensed use limited to: DELHI TECHNICAL UNIV. Downloaded on May 04,2023 at 06:33:10 UTC from IEEE Xplore. Restrictions apply.

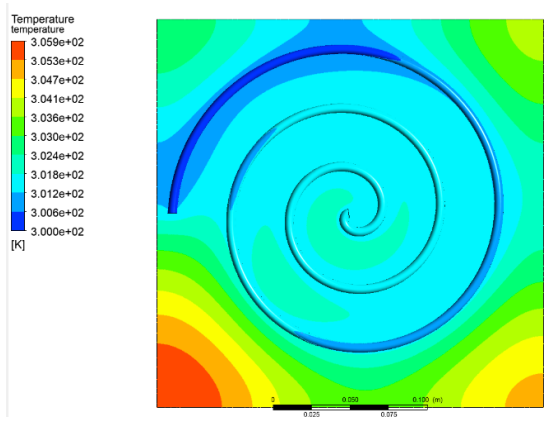


Fig. 5. Temperature variation of the top face of the solar collector for SiO_2-H_2O nanofluid

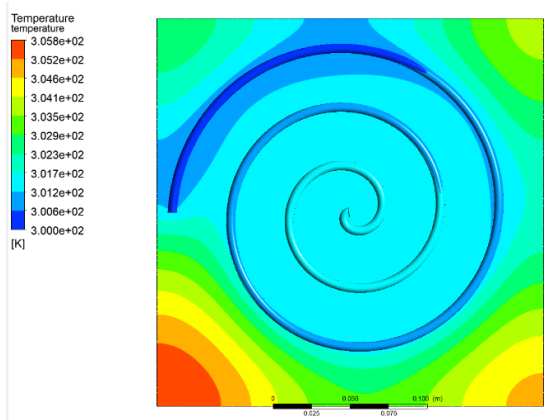


Fig. 6. Temperature variation of the top face of the solar collector for Al_2O_3-H_2O nanofluid

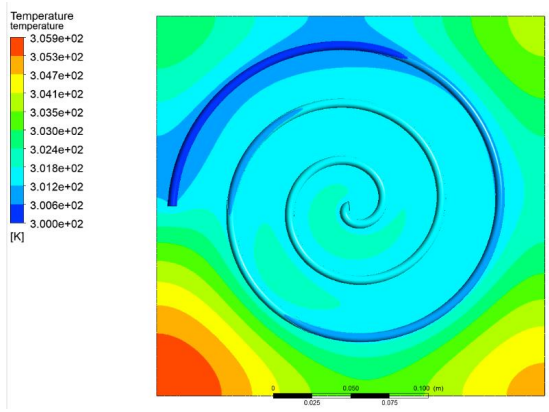


Fig. 7. Temperature variation of the top face of the solar collector for CuO-H_2O nanofluid

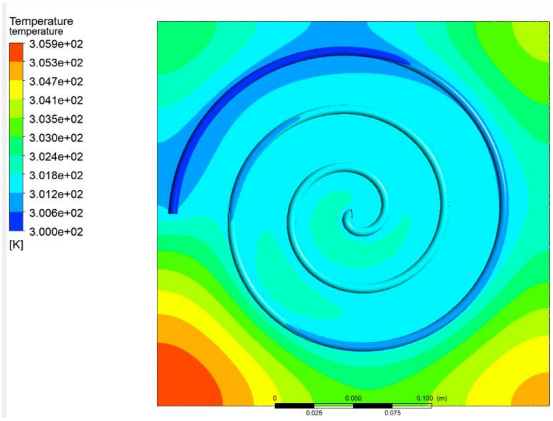


Fig. 8. Temperature variation of the top face of the solar collector for TiO_2-H_2O nanofluid

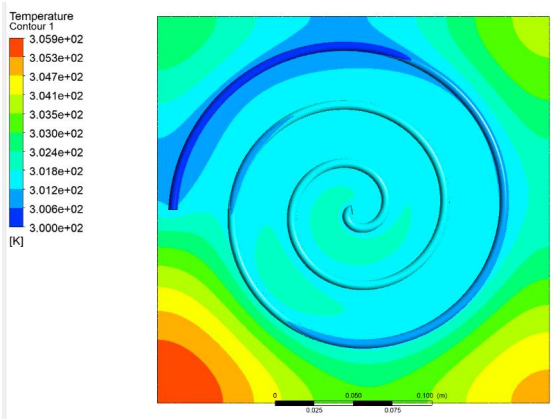


Fig. 9. Temperature variation of the top face of the solar collector for Diamond-H_2O nanofluid

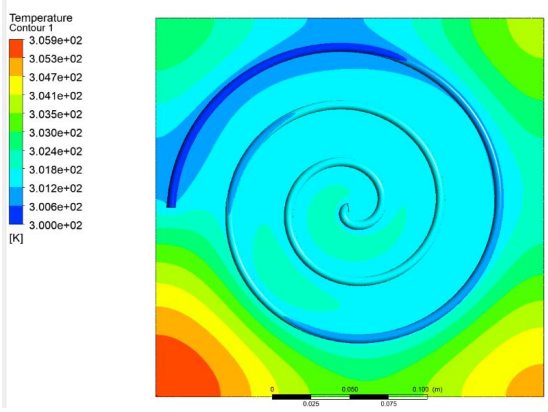


Fig. 10. Temperature variation of the top face of the solar collector for Ag-H_2O nanofluid

B. Outlet Temperature

By measuring the temperature at the outlet of the tubes the effectiveness can be compared with which the different nanofluids are able to transfer the heat from the collector plate and the tube to the fluid flowing in the it. Outlet temperatures for all the nanofluids were calculated and are represented in "Fig. 11". From the graph it is easily seen that the variation in the outlet temperatures are very negligible i.e. variations are present in only decimals of K which is due to the small scale of the model. The maximum outlet temperature observed is in

Authorized licensed use limited to: DELHI TECHNICAL UNIV. Downloaded on May 04,2023 at 06:33:10 UTC from IEEE Xplore. Restrictions apply.

SiO_2 and the minimum outlet temperature in Al_2O_3, which are 301.2869 K and 301.1366 respectively.

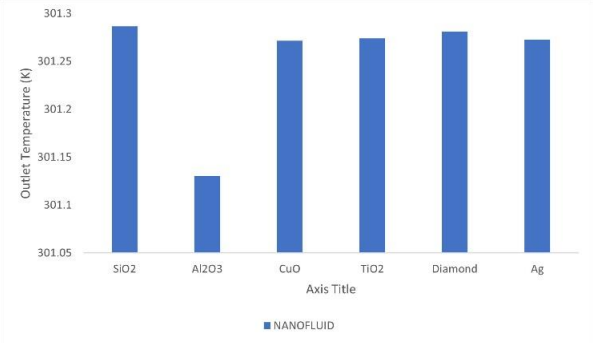


Fig. 11. Outlet temperatures of all six nanofluids when used in the given solar collector

VI. Conclusion

In this paper a comparative study of the performance of six water based nanofluids as a working fluid for a solar collector was made. Heat flux of 700w/m^2 was applied at the top surface of the flat plate collector. The inlet velocity of the fluid was 0.5m/s with inlet temperature of 300K the outlet temperatures are calculated using CFD. It was found that SiO_2-H_2O has the best performance as heat transfer fluid among the nanofluids considered. The heat transferred from the collector also depends on the area covered with the spiral which can be seen in the temperature distribution figures.

Acknowledgment

The authors of this paper express their gratitude towards all the researchers whose work functioned as the reference of the current work to help in the development of the numerical simulation model.

References

[1] M. Javidan, M. Asgari, M. Gholinia, M. Nozari, A. Asgari, and D. D. Ganji, "Thermal energy storage inside the chamber with a brick wall using the phase change process of paraffinic materials: A numerical simulation," *Theoretical and Applied Mechanics Letters*, vol. 12, no. 3, Mar. 2022, doi: 10.1016/j.taml.2022.100329.

[2] B. Shaker, M. Gholinia, M. Pourfallah, and D. D. Ganji, "CFD analysis of Al2O3-syltherm oil Nanofluid on parabolic trough solar collector with a new flange-shaped turbulator model," *Theoretical and Applied Mechanics Letters*, vol. 12, no. 2, Feb. 2022, doi: 10.1016/j.taml.2022.100323.

[3] R. Shaji, "A Review on India's Renewable Energy Potential," *Int J Sci Eng Res*, vol. 5, no. 4, 2014, [Online]. Available: http://www.ijser.org

[4] S. Lund and F. Struckmann, "Analysis of a Flat-plate Solar Collector," 2008.

[5] H. Bhowmik and R. Amin, "Efficiency improvement of flat plate solar collector using reflector," *Energy Reports*, vol. 3, pp. 119–123, Nov. 2017, doi: 10.1016/j.egyr.2017.08.002.

[6] B. Hellstrom, M. Adsten, P. Nostell, B. Karlsson, and E. Wackelgard, "The impact of optical and thermal properties on the performance of flat plate solar collectors," 2003. [Online]. Available: www.elsevier.com/locate/renene

[7] A. Ibrahim, M. Y. Othman, M. H. Ruslan, S. Mat, and K. Sopian, "Recent advances in flat plate photovoltaic/thermal (PV/T) solar collectors," *Renewable and Sustainable Energy Reviews*, vol. 15, no. 1. Elsevier Ltd, pp. 352–365, 2011. doi: 10.1016/j.rser.2010.09.024.

[8] T.-H. Shih, W. W. Liou, A. Shabbir, Z. Yang, and J. Zhu, "A NEW kt EDDY VISCOSITY MODEL FOR HIGH :REYNOLDS NUMBER TURBULENT FLOWS," 1995.

[9] M. Sheikholeslami, R. ul Haq, A. Shafee, Z. Li, Y. G. Elaraki, and I. Tlili, "Heat transfer simulation of heat storage unit with nanoparticles and fins through a heat exchanger," *Int J Heat Mass Transf*, vol. 135, pp. 470–478, Jun. 2019, doi: 10.1016/j.ijheatmasstransfer.2019.02.003.

[10] M. Akbarzadeh, S. Rashidi, N. Karimi, and N. Omar, "First and second laws of thermodynamics analysis of nanofluid flow inside a heat exchanger duct with wavy walls and a porous insert."

[11] S. Salavati Meibodi, A. Kianifar, H. Niazmand, O. Mahian, and S. Wongwises, "Experimental investigation on the thermal efficiency and performance characteristics of a flat plate solar collector using SiO2/EG-water nanofluids," *International Communications in Heat and Mass Transfer*, vol. 65, pp. 71–75, Jul. 2015, doi: 10.1016/j.icheatmasstransfer.2015.02.011.

[12] M. Akbarzadeh, S. Rashidi, N. Karimi, and R. Ellahi, "Convection of heat and thermodynamic irreversibilities in two-phase, turbulent nanofluid flows in solar heaters by corrugated absorber plates," *Advanced Powder Technology*, vol. 29, no. 9, pp. 2243–2254, Sep. 2018, doi: 10.1016/j.apt.2018.06.009.

[13] S. Rashidi, P. Javadi, and J. A. Esfahani, "Second law of thermodynamics analysis for nanofluid turbulent flow inside a solar heater with the ribbed absorber plate," *J Therm Anal Calorim*, vol. 135, no. 1, pp. 551–563, Jan. 2019, doi: 10.1007/s10973-018-7164-4.

[14] J. Subramani, P. K. Nagarajan, O. Mahian, and R. Sathyamurthy, "Efficiency and heat transfer improvements in a parabolic trough solar collector using TiO2 nanofluids under turbulent flow regime," *Renew Energy*, vol. 119, pp. 19–31, Apr. 2018, doi: 10.1016/j.renene.2017.11.079.

[15] S. A. Farshad, M. Sheikholeslami, S. H. Hosseini, A. Shafee, and Z. Li, "Nanofluid turbulent forced convection through a solar flat plate collector with Al2O3 nanoparticles," *Microsystem Technologies*, vol. 25, no. 11, pp. 4237–4247, Nov. 2019, doi: 10.1007/s00542-019-04430-2.

[16] M. N. Zadeh, M. Pourfallah, S. S. Sabet, M. Gholinia, S. Mouloodi, and A. T. Ahangar, "Performance assessment and optimization of a helical Savonius wind turbine by modifying the Bach's section," *SN Appl Sci*, vol. 3, no. 8, Aug. 2021, doi: 10.1007/s42452-021-04731-0.

Authorized licensed use limited to: DELHI TECHNICAL UNIV. Downloaded on May 04,2023 at 06:33:10 UTC from IEEE Xplore. Restrictions apply.

2023 9th International Conference on Advanced Computing and Communication Systems (ICACCS) | 979-8-3503-9737-6/23/$31.00 ©2023 IEEE | DOI: 10.1109/ICACCS57279.2023.10112776

Crocin: A Potent Secondary Metabolite As BACE1 Inhibitor In Alzheimer's Disease

Murali Mohan Mishra
Dept. of Biotechnology
Molecular Neuroscience and Functional Genomics Laboratory,
Delhi Technological University
Delhi – 110042, India
muralimohanmishra_2k21ibt13@dtu.ac.in

Pravir Kumar
Dept. of Biotechnology
Molecular Neuroscience and Functional Genomics Laboratory,
Delhi Technological University
Delhi – 110042, India
pravirkumar@dtu.ac.in

***Abstract*—The use of plants based secondary metabolites as BACE1 inhibitor in treating Alzheimer's disease (AD) has long been discussed due to their great potential to cross the blood brain barrier (a tissue and blood artery network with small cells that act together to prevent dangerous substances from entering the brain.), longer bioavailability, longer serum half-life and least or no side-effect on human brain. AD is caused due to aggregation of amyloid β peptides in the brain. β secretase also called β site amyloid precursor protein cleaving enzyme 1(BACE1) is accountable for initiating the synthesis of pernicious amyloid β peptide important in the pathogenesis of the disease. BACE1 is an important target for the development of therapeutic modalities to reduce the concentration of amyloid β aggregates in the brain. The present study is focused on the active role of plants based secondary metabolites in the clearance of amyloid β peptides and their role as a BACE1 inhibitor. We have performed Molecular docking to investigate the binding energy of BACE1 and the inhibitor complex. The binding energy of Crocin was observed to be the most negative suggesting it to be one of the most suitable secondary metabolites as BACE1 inhibitor and thus its usage can be considered as an important step in preventing or delaying the onset of Alzheimer's disease.**

Keywords—Alzheimer's disease, BACE1, bioavailabity, serum life, type-3-diabetes, amyloid β, molecular docking, binding energy, β-secretase, Crocin.

I. INTRODUCTION

Alzheimer's disease (AD) is a neurobiological disease which is caused due to the abnormal accumulation of amyloid β (a significant part of the amyloid deposits in the cerebrovascular disease, implications for the pathogenesis of Alzheimer disease.) in the brain forming senile plaques and hyperphosphorylation of the Tau protein resulting in the formation of neurofibrillary tangles and Aβ plaques[1]. It is characterized by the death of the neuronal cells, cognitive dysfunction of the nervous system, neuroinflammation and the loss of memory with the increasing age. Further, few more characteristics such as misfolding, aggregation and accumulation of Aβ peptides indicates that AD is one of the diseases caused by protein misfolding (protein folding disorder)[2].Approximately 44 million people are suffering from the disease worldwide and only one out every four patients is diagnosed with the disease [3]. AD is the sixth major reason for death in US population after cancers including breast and prostate cancers. Few of the other important cause of dementia are disturbance of equilibrium between the production and clearance of amyloid β, dystrophic neurites, impeded energy metabolism, prolonged oxidative stress, dysfunctioning of mitochondria, destruction of DNA and the hoisted expression of some pro- apoptotic genes and the respective signaling mechanism[4]. Recently scientists have found that the insulin resistance or the insulin like growth factors are also a promoting factor that leads to the progression of AD[5].

II. LITERATURE

A. Alzheimer's disease and diabetes

In a study it has been reported that disorders causing dementia especially the type 2 diabetes relate to Alzheimer's disease as well sharing few common characteristics such as elevated level of cholesterol, insulin resistance in CNS and PNS, deteriorated signaling cascades of IR, ageing associated problems and the most important i.e., degeneration of neuronal cells. The repeated fluctuation in the glucose level promotes the onset of AD and the associated symptoms and thus it was found that hyperinsulinemia may trigger the progression of AD to a greater extent as compared to the normal conditions [6]. Moreover, a relation between the abnormalities in the IR signaling cascade and the reduced expression of insulin encoding genes was established in the patients suffering from AD due to which sporadic AD was considered as a neuroendocrine disease. Since this condition has few common features as of type 1 and 2 diabetes, AD is now considered as the "Type 3 diabetes".

B. Secondary metabolites in AD

Amyloid β peptides have tendency of aggregation and forming fibrils and oligomers via bonding between amino-acids and the inter molecules [7]. The drug molecules that are found to have any role in the treatment of AD have potent side effects as well. Thus, plant-based products, mainly the secondary metabolites such as Curcumin, Fisetin, Luteolin, Oleuropein, Quercetin, Rutin, Dihydromyricetin, Rosmarinic acid, Epigallocatechin-3-gallate (ECGC), Salvianolic acid, Silibinin and crocin were studied for their antiaggregating role of beta amyloid peptides and the results showed the positive inhibitory effects. Plants based secondary metabolites do not cause any side effects, have better bioavailability, longer serum half-life and most importantly they have ability to cross

979-8-3503-9737-6/23/$31.00 ©2023 IEEE

Authorized licensed use limited to: DELHI TECHNICAL UNIV. Downloaded on May 11,2023 at 10:21:35 UTC from IEEE Xplore. Restrictions apply.

the blood brain barrier. These molecules were analyzed by the virtue of their noncovalent binding with amyloid beta peptide. In the amyloid beta fibrils, the amino end of the peptide is exposed to the other molecules for interaction whereas on the other side middle and the carboxyl terminal end of the peptide are associated with the inter and intra molecular binding within the amyloid beta peptide[8] . The most commonly used methods for the analysis of amyloid beta aggregation or its fibrillization are UV spectroscopy, thioflavin T assay, sandwich ELISA, atomic force microscopy, transmission electron microscopy and scanning electron microscopy.

C. *BACE1 protein and Alzheimer's disease*

BACE1 is a β secretase enzyme also known as β site amyloid precursor cleaving enzyme1 which initiates the synthesis of amyloid β peptides and thus are the prime therapeutic target for lowering the concentration of amyloid-β in the cerebellum. β- secretase cleave the APP into a membrane bound C- terminal fragment called C99. This C99 is further cleaved into amyloid β by the enzyme γ- secretase which is made up of four major transmembrane protein called- Nicastrin, Presenilin, Pen2 and Aph1. Then α-secretase cleaves APP at a region in amyloid β and thus triggers its formation. Since both the β and γ secretase are required for the synthesis of amyloid β peptides, modulation or the inhibition of these enzymes are considered to be an important goal in the therapeutic modalities for reducing the concentration of amyloid β peptide aggregates in patients with Alzheimer's diseases [9]..

D. *Secondary metabolites as a BACE1 inhibitory molecules*

X-Ray crystallography structure of BACE1 with the peptidomimetic inhibitors showed an important enzyme-inhibitor interactions[10]. Various plants based secondary metabolites have been identified which can substantially inhibits BACE1 and can be effectively utilized for the therapeutic effect in the treatment of Alzheimer's disease. They were found to have the ability to cross the blood brain barrier very easily, had good oral bioavailability and the longer serum half-life as compared to previously discovered BACE1 inhibitory molecules [11]. Target specific delivery of plant secondary metabolites can enhance the overall therapeutic efficacy of the natural BACE1 inhibitors. The BACE1 inhibiting characteristic of Quercetin, Fisetin and Dihydromyricetin was found to be significant enough to prevent the aggregation of amyloid β peptides and hence proved to be an important molecule for the treatment of Alzheimer's disease[12].

E. *Computational approach for establishing the inhibitory link between Plants secondary metabolites and BACE1 protein.*

The current study is majorly focused on establishing between plants based secondary metabolites and the BACE1 protein and to prove that these secondary metabolites are efficient inhibitor of the BACE1 protease using bioinformatics and computational tools. Molecular docking was performed using SWISS DOCK. Dedicated to the docking of tiny compounds on specific proteins is Swiss Dock. It is built on top of the EADock DSS engine and includes setup scripts for solving typical issues and getting the target protein and ligand input files ready[13].

Relationship between Type 2 Diabetes and Alzheimer's Disease is show in fig.1. Binding energy of all the plant secondary metabolites with BACE1 inhibitor is show in table.2

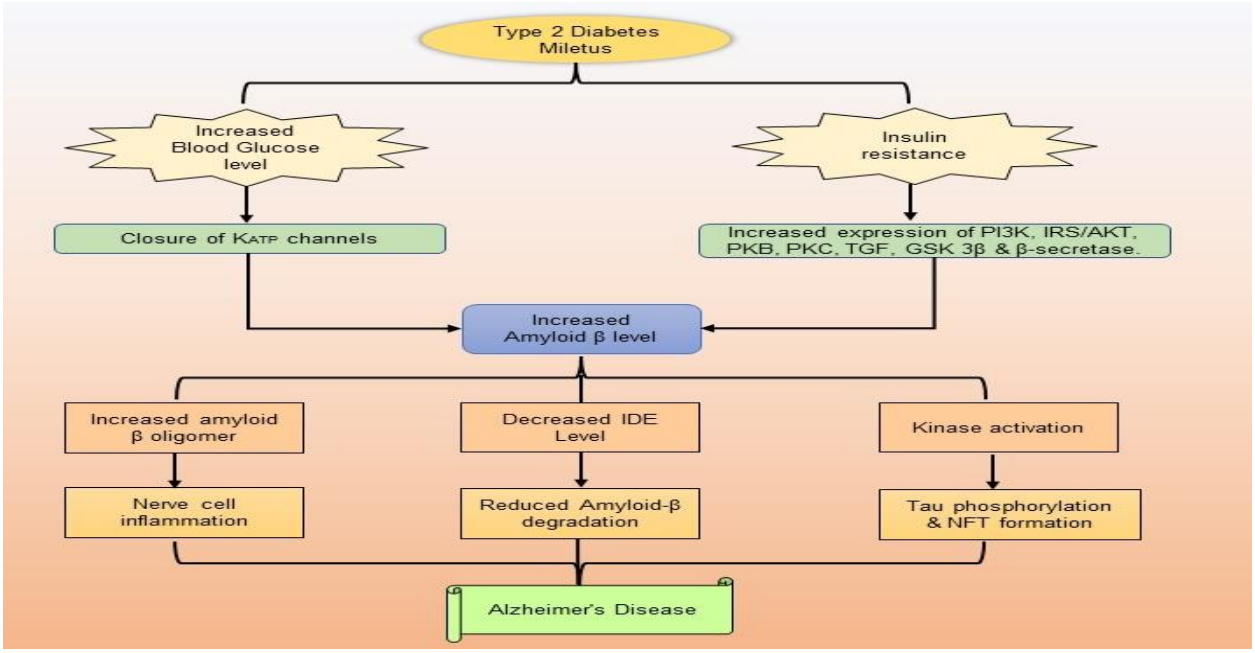


Fig. 1. Relationship between Type 2 Diabetes and Alzheimer's Disease. PI3K-phosphoinositide 3-kinase, IRS- insulin receptor substrate, AKT- a serine/threonine kinase family protein, PKB-protein kinase B, GSK- glycogen synthase kinase. IDE- Insulin degrading enzyme, NFT- neurofibrillary tangles.

Authorized licensed use limited to: DELHI TECHNICAL UNIV. Downloaded on May 11,2023 at 10:21:35 UTC from IEEE Xplore. Restrictions apply.

TABLE 2- BINDING ENERGY OF ALL THE PLANT SECONDARY METABOLITES WITH BACE1 INHIBITOR

S.No	Compound	Energy of full fitness (kcal/mol)	ΔG (kcal/mol)	Amino Acid bonded
1	Dihydromyricetin	-1752.95	-7.5	GLU200, ILE386, ASN385, TRP197, LYS224, TYR384, ARG195, ARG194
2	Epigallocatechin-3-gallate (ECGC)	-1761.80	-8.45	LYS321, GLY11, PHE108, THR231, THR72, ASN233, THR232, ARG307, GLN12, ILE110, PHE109, LYS107, TRP115, GLN73, ARG235,
3	Rosmarinic acid	-1778.62	-8.04	ASP32, GLN73, THR231, THR232, ASP228, GLY34, SER35, ILE118, GLY230, LEU30, ILE110, TYR71, PHE108, TRP115, GLY13, GLN12, GLY11, ARG235
4	Salvianolic acid	-1745.77	-9.01	ARG128, PRO70, GLN73, GLY11, ASP32, ILE126, SER36, TYR198, ILE226, THR72, ARG235, GLY34, SER35, ASN233, LYS321, THR232, GLN12, ILE110, THR231, VAL332, GLY230,
5	Silibinin	-1708.83	-8.59	PRO70, ARG128, ILE126, TYR198, SER36, ILE226, ARG235, THR72, GLY34, SER35, ASN233, LYS321, THR232, GLY11, GLH12, ILE110, THR231, VAL332, GLN73, GLY230, ASP228, ASP32, ILE118, TYR71,
6	Crocin	-1502.42	-12.37	GLN326, SER328, SER327, ARG235, THR72, TRP197, THR329, TYR198, LYS224, ASP223, TYR384, ILE386, ILE226, TYR71, GLY34, ASP228, THR231, VAL332, GLN73, SER35, ASN233, LYS321, GLU265, LEU263, GLY264, GLY264
7	Curcumin	1764.09	-8.43	GLN73, ARG235, GLY34, THR231, ILE118, GLN73, GLY74, LYS107, PHE108, TYR71, ILE110, TRP115, LEU30, GLY230, GLY13, GLN12, ASP32, SER35, AS228, THR329, THR72
8	Fisetin	-1744.35	-7.28	GLY34, ASP228, SER328
9	Luteolin	-1780.74	-8.05	LYS218, ASP381, ASP216, VAL204, CYS217, MET215, TYR220, VAL206, LYS214, ASP212, ARG205, THR376, LEU377, MET379, ASP378
10	Oleuropein	-1745.48-	-9.26	GLU310, GLN73, THR232, VAL309, LYS321, ARG307, SER10, ILE110, PHE108, GLY74, PHE109, PHE17, LYS107, TRP115, GLY13, LEU30, GLY230, GLN12, THR231, GLY11
11	Quercetin	-1760.53	-7.32	ASP216, CYS217, TYR220, ASP212, ARG205, LYS218, VAL204, MET215, VAL206, LYS214, THR376, LEU377, MET379, ASP378, CYS382, ASP381
12	Rutin	-1629.10	-9.63	GLU310, LEU267, LYS321, GLY11, GLN12, PHE109, LYS107, PHE47, PHE108, ILE110, GLN73, TRP115, ILE118, LEU30, GLY230, THR231, THR232, SER10, ARG307, PRO308, VAL309

III. PROPOSED METHODOLOGY

A. Protein preparation for docking

BACE1 protein was prepared using Discovery Studio 2021. 3D structure of BACE1 protease was download from the PubChem in SDF format. The redundant water molecules and ligand were removed, and the prepared protein was saved as .pdb file.

B. Ligand preparation for docking

Swiss Dock needs. mol2 format for the ligand. Using Discovery studio 2021, we saved all the secondary metabolites structure as. mol2 (sybyl MOL2 files) format.

C. Ligand-protein docking using Swiss Dock

Swiss Dock is a web-based service used for docking of proteins and ligands. The structure of protein in .pdb format and ligand structure in. mol2 format were uploaded individually on the docking portal (http://www.swissdock.ch/docking) and the docking was started.

D. Structure analysis of the protein-ligand interaction using UCSF chimera

Once the docking was terminated, chimera files were downloaded for all the protein-ligand complex. Using

Authorized licensed use limited to: DELHI TECHNICAL UNIV. Downloaded on May 11,2023 at 10:21:35 UTC from IEEE Xplore. Restrictions apply.

UCSF Chimera software (Version 1.16), the interaction of the complex was analyzed.

IV. Results And Discussion

A. *Interaction between BACE1 protease and secondary metabolites.*

The molecular docking method allows us to characterize how small molecules behave in the binding site of target proteins and to better understand basic biological processes by simulating the interaction between a small molecule and a protein at the atomic level. The docking results came out to be in the favor of positive interaction between BACE1 protease and the plants secondary metabolites. The energy of full fitness and ΔG of the docked molecules showed that the interaction between the BACE1 protease and secondary metabolites is of prime importance. The more negative the binding energy, more stable was the interaction among protein and ligand. The most negative ΔG was found to be for Crocin and the BACE1 complex with cluster 0 and element 6 that is-12.37kcal/mole and the respective full fit energy was recorded to be -1502.42kcal/mol. The structural analysis of the molecular interaction was done by using UCSF Chimera as shown in Fig 2. The full fitness energy and ΔG of all the secondary metabolites are listed in the table2.

TABLE 1- A. The average of the elements' most favorable energies to lessen the possibility of effects brought on by a select few complexes in the cluster B. ΔG (gives a rough senseof the intended pose of the docked structures)

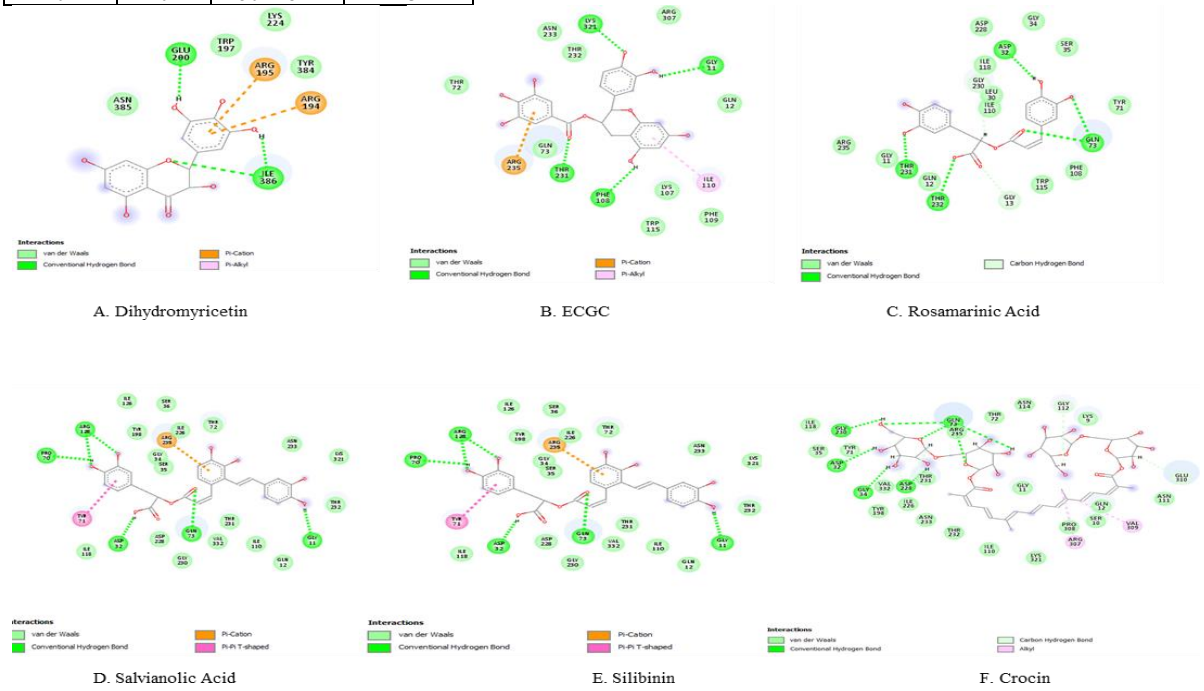
Cluster	Element	Full Fitness (kcal/mol)	Estimated ΔG (kcal/mol)
0	6	-1502.42	-12.37
0	7	-1502.42	-12.37
0	0	-1504.28	-12.23

B. *Amino Acid residues bonding*

A 2D picture of the complex was created from the structural analysis of every protein-ligand complex using UCSF Chimera which depicted all the interaction major and minor interactions of the protein and the secondary metabolites as shown in Fig 2. Out of all the major amino acid residues, ASP and ARG were found to be the most prominent amino acid residues found in all most all the complex. This suggests that ASP and ARG may contribute to inhibitory mechanism of BACE1 protease more as compared to other amino acid residues.

V. Conclusion

Abnormal accumulation of amyloid β peptides in the brain due to imbalance between the production and clearance of amyloid β results in the onset of Alzheimer's disease. Among various mechanisms of anti-amyloidβ fibrillization, the inhibition of BACE1 protein by β and γ secretase enzyme was found to be an important mechanism for preventing the amyloid β fibrillization process. Modulation or inhibition of β and γ secretase enzyme is an important step as the therapeutic approach for the Alzheimer's disease. Among all the listed plant secondary metabolites, Quercetin, Fisetin and Dihydromyricetin were found to be a proven BACE1 inhibitor. After completing the docking of rest metabolites, the results proposed that out of all the secondary metabolites, Crocin had most negative Estimated ΔG and thus showed most suitable interaction with target suggesting it to be an important BACE1 inhibitor. However, more research and studies need to be done on the same and to find out the possible mechanism for this result.



A. Dihydromyricetin B. ECGC C. Rosamarinic Acid

D. Salvianolic Acid E. Silibinin F. Crocin

Authorized licensed use limited to: DELHI TECHNICAL UNIV. Downloaded on May 11,2023 at 10:21:35 UTC from IEEE Xplore. Restrictions apply.

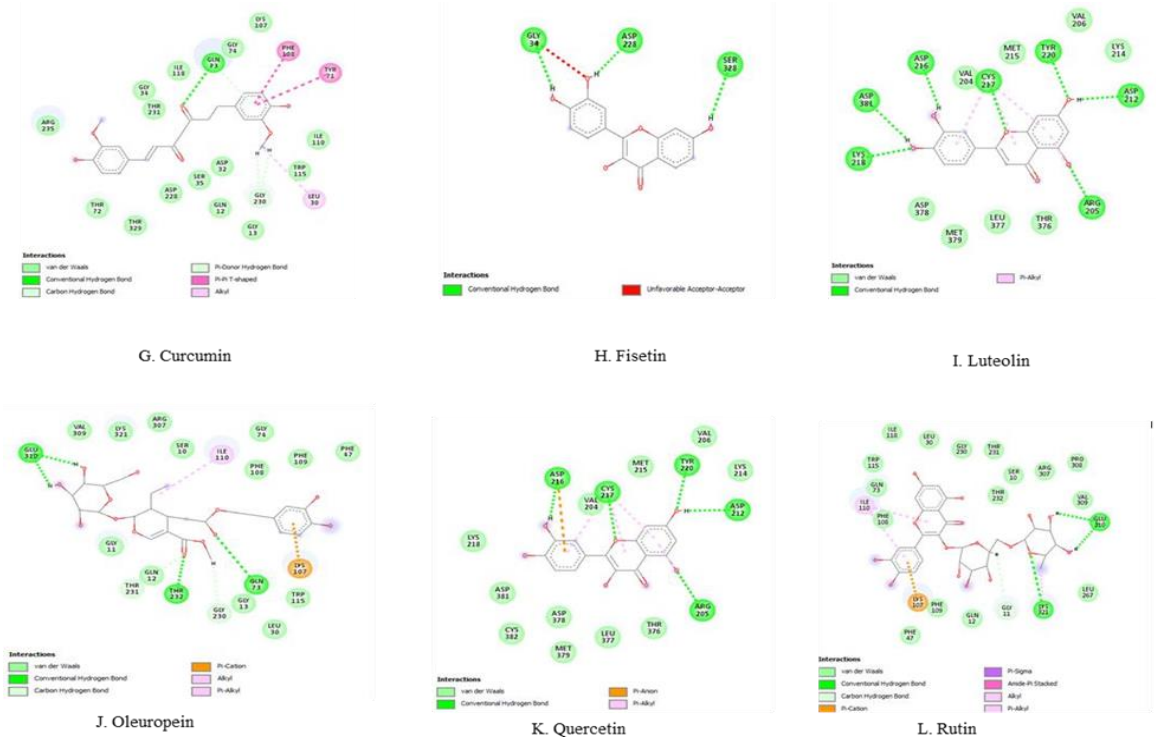


Fig 2. Docking results of various plant secondary metabolites with BACE1 protein.

REFERENCES

[1] N. K. Jha *et al.*, "Impact of insulin degrading enzyme and neprilysin in Alzheimer's disease biology: Characterization of putative cognates for therapeutic applications," *J. Alzheimer's Dis.*, vol. 48, no. 4, pp. 891–917, 2015, doi: 10.3233/JAD-150379.

[2] Z. Breijyeh and R. Karaman, "Comprehensive Review on Alzheimer ' s Disease :," 2020.

[3] "Alzheimer's Disease Statistics - Alzheimer's News Today." https://alzheimersnewstoday.com/alzheimers-disease-statistics/ (accessed Nov. 06, 2022).

[4] S. M. de la Monte, "Brain Insulin Resistance and Deficiency as Therapeutic Targets in Alzheimer's Disease," *Curr. Alzheimer Res.*, vol. 9, no. 1, p. 35, Jan. 2012, doi: 10.2174/156720512799015037.

[5] "IGF-1 and GLP-1 signaling: potential therapeutic target for... : Annals of Medicine and Surgery." https://journals.lww.com/annals-of-medicine-and-surgery/Fulltext/2023/01000/IGF_1_and_GLP_1_signaling__potential_therapeutic.14.aspx (accessed Feb.27, 2023).

[6] V. Hegde, N. V. Dhurandhar, and P. Hemachandra Reddy, "Hyperinsulinemia or Insulin Resistance: What Impacts the Progression of Alzheimer's Disease?," *J. Alzheimer's Dis.*, vol. 72, no. s1, pp. S71–S79, Jan. 2019, doi: 10.3233/JAD-190808.

[7] R. Stefanescu, G. D. Stanciu, A. Luca, L. Paduraru, and B. I. Tamba, "Secondary Metabolites from Plants Possessing Inhibitory Properties against Beta-Amyloid Aggregation as Revealed by Thioflavin-T Assay and Correlations with Investigations on Transgenic Mouse Models of Alzheimer's Disease," *Biomolecules*, vol. 10, no. 6, Jun. 2020, doi: 10.3390/BIOM10060870.

[8] T. Lührs *et al.*, "3D structure of Alzheimer's amyloid-β(1-42) fibrils," *Proc. Natl. Acad. Sci. U. S. A.*, vol. 102, no. 48, pp. 17342–17347, Nov. 2005, doi: 10.1073/PNAS.0506723102/SUPPL_FILE/06723FIG10.PDF.

[9] R. Yan and R. Vassar, "Targeting the β secretase BACE1 for Alzheimer's disease therapy," *Lancet Neurol.*, vol. 13, no. 3, pp. 319–329, 2014, doi: 10.1016/S1474-4422(13)70276-X.

[10] J. R. M. Coimbra *et al.*, "Highlights in BACE1 inhibitors for Alzheimer's disease treatment," *Front. Chem.*, vol. 6, no. MAY, p. 178, May 2018, doi: 10.3389/FCHEM.2018.00178/BIBTEX.

[11] V. Prakash Reddy, P. Aryal, S. Robinson, R. Rafiu, M. Obrenovich, and G. Perry, "Polyphenols in Alzheimer's Disease and in the Gut–Brain Axis," *Microorg. 2020, Vol. 8, Page 199*, vol. 8, no. 2, p. 199, Jan. 2020, doi: 10.3390/MICROORGANISMS8020199.

[12] R. Stefanescu, G. D. Stanciu, A. Luca, L. Paduraru, and B. I. Tamba, "Secondary Metabolites from Plants Possessing Inhibitory Properties against Beta-Amyloid Aggregation as Revealed by Thioflavin-T Assay and Correlations with Investigations on Transgenic Mouse Models of Alzheimer's Disease," *Biomolecules*, vol. 10, no. 6, Jun. 2020, doi: 10.3390/BIOM10060870.

[13] G. Bitencourt-Ferreira and W. F. de Azevedo, "Docking with SwissDock," *Methods Mol. Biol.*, vol. 2053, pp. 189–202, 2019, doi: 10.1007/978-1-4939-9752-7_12/COVER.

Authorized licensed use limited to: DELHI TECHNICAL UNIV. Downloaded on May 11,2023 at 10:21:35 UTC from IEEE Xplore. Restrictions apply.

ResearchGate

See discussions, stats, and author profiles for this publication at: https://www.researchgate.net/publication/370328686

Cross-domain learning for pulmonary nodule detection using Gestalt principle of similarity

Article *in* Soft Computing · April 2023

DOI: 10.1007/s00500-023-08252-3

CITATIONS
0

READS
4

3 authors:



Seba Susan
Delhi Technological University
129 PUBLICATIONS **1,278** CITATIONS
SEE PROFILE



Dhaarna Sethi
Delhi Technological University
6 PUBLICATIONS **79** CITATIONS
SEE PROFILE



Kriti Arora
Delhi Technological University
4 PUBLICATIONS **9** CITATIONS
SEE PROFILE

All content following this page was uploaded by Seba Susan on 28 April 2023.

The user has requested enhancement of the downloaded file.

THIS IS THE AUTHOR'S VERSION OF THE ARTICLE PUBLISHED IN SOFT COMPUTING JOURNAL. DOI: 10.1007/S00500-023-08252-3

Cross-Domain Learning for Pulmonary Nodule Detection using Gestalt Principle of Similarity

Seba Susan, Dhaarna Sethi, and Kriti Arora

Abstract—Transfer learning is a trending concept in computer vision that is based on the transfer of knowledge between the source and target domains. In the distant domain problem addressed in this paper, the source and target domains are totally unrelated but have similar visual structures, thereby infusing explainability in transfer learning. We specifically focus on the pulmonary nodule detection problem in which the task is to distinguish the image patches that contain lung nodules from those that do not. The Gestalt principle of similarity states that the human mind tends to club visually similar structures together based on some object attributes like shape and color. Though some structural differences may exist, these are imperceptible to the human eye since it focusses on "what it wants to see". This is the central idea behind our work that trains a deep convolutional neural network on commonly found natural scene images containing visual structures similar in appearance to cropped images of pulmonary nodules from Computed Tomography (CT) scans for the purpose of cancer diagnosis. Our transfer learning module comprises of a deep Convolutional Autoencoder (CAE) that is pre-trained on a source domain comprising of a small and selective subset of only two objects: flowers and rivers, that are selected by voting by human annotators to visually correlate with images of lung nodules and non-nodules, respectively. Our work thus presents a mechanism to make the learning process both human-interactive and explainable. Deep tuning our network on images from the benchmark Lung Image Database Consortium and Infectious Disease Research Institute (LIDC/IDRI) database yields higher classification scores as compared to the state of the art. Cost-sensitive learning or data augmentation can be additionally used to further improve the performance of the proposed model.

Index Terms—Gestalt principle of similarity, Lung nodule detection, Deep Learning, Transfer learning, Convolutional autoencoder, Medical image analysis.

1. INTRODUCTION

TRANSFER learning facilitates knowledge transfer between the source domain and target domain, with the objective of generating a prediction model for the target task that has got good generalization performance (Lu et al. 2015). By good generalization performance, we mean that the model is able to predict accurately when it sees test samples unlike those used for training (Bishop 1995). Such a scenario is not uncommon in the case of imbalanced datasets wherein the minority class indicating the diseased samples show a poor generalization performance due to insufficient representation. Biomedical image databases such as those associated with lung cancer and lung nodule Computed Tomography (CT) scans are cropped into smaller image patches that are scanned for the presence of cancer cells or nodules (Armato III 2011). However, these cells are found in rarity, reducing these samples to a minority class. On the other hand, cancer-free image patches are in a majority, rendering most problems in biomedical domain to a heavily imbalanced two-class problem. In data mining, undersampling, oversampling and hybrid sampling strategies have been proposed to balance the class distribution (Susan and Kumar 2021), and so are distance metric learning approaches that transform the input space (Kaushik and Susan 2021). Some researchers have directly adopted data sampling strategies to the biomedical domain, notably, Sui *et al.* (2015) and Krawczyk *et al.* (2016); here sampling is executed by directly replicating or eliminating image samples. To counter the class-imbalance problem in computer vision, specific remedies have been suggested. The chief among them is data augmentation that generates visually different synthetic samples through image transformations such as rescaling, rotation, shear etc.in order to increase the overall number of samples for training. Saini and Susan (2019) addressed the problem of class-imbalance in breast cancer histopathological biomedical dataset by augmenting the minority class such that the class-distribution is balanced prior to classification by pre-trained transfer networks. Cost-sensitive learning is another popular remedy for mitigating the effect of class imbalance, which modifies the loss function so that the model learns equally well from both the majority and minority classes (Fernández et al. 2018). In the previous work of the authors (Susan et al. 2021), the minority class loss was assigned a higher weight during the computation of the fitness function for lung nodule detection. Cost-sensitive learning and data augmentation are data-driven methods and their mode of application depend heavily on the characteristics of the imbalanced dataset (Cao et al. 2021).

In current times, there is an increasing interest in Explainable Artificial Intelligence (XAI) that focuses on understanding

Seba Susan is a Professor in the Department of Information Technology, Delhi Technological University, Shahbad Daulatpur, Delhi, India-42. Email: seba_406@yahoo.in, Ph: +91-9868850209. Dhaarna Sethi (dhaarna29@gmail.com) and Kriti Arora (kritiarora2110@gmail.com) are undergraduate students with the Department of Information Technology, Delhi Technological University, Shahbad Daulatpur, Delhi, India-42.

how deep models work and interpreting their learning methodology (Holzinger et al. 2022). A recent example of XAI is SCOUTER (Li et al. 2021) which is a slot-attention based classifier that provides explanations for positive and negative classes. Therefore, XAI provides explanations on how a model works and on the definition of what samples constitute a particular class. In the current work, we emphasize on the role of "explainable" transfer learning for the task of lung nodule detection in the presence of class imbalance. More specifically, we focus on cross-domain transfer learning of visually similar structures for improving the classification of lung nodule image patches segmented from CT scans.

Transfer learning was introduced by the likes of Thrun and Pratt (1998), Caruana (1997) and researchers in the NIPS workshop "Learning to learn" who advocated transfer of knowledge from another domain to handle the inadequacies of the original or target domain. The domains could be related (Blitzer et al. 2008), or totally unrelated leading to the term distant domain learning (Tan et al. 2017). Transfer learning is used for medical image analysis by fine tuning of pre-trained convolutional neural networks that are pre-trained on millions of images of objects that have no actual relevance to the medical problem at hand (Kim et al. 2022). In our work, we seek to bridge this gap, by compiling a source domain comprising of relevant objects that have high structural similarity to the medical images with and without pulmonary nodules. We use the Gestalt principles of psychology (Todorovic 2008) that suggests visual groupings of objects in the human perception of a scene. A human cognition experiment is first conducted to visually identify and compile objects from different domain datasets that visually identify with nodule and non-nodule images. A consensus on the objects: flowers and rivers, is reached. The encoder part of a deep CAE that is pre-trained on the manually compiled *Flower-River* dataset is combined with dense fully connected layers. The end-to-end deep network so formed is again pre-trained on the source *Flower-River* dataset and later fine-tuned on the target biomedical dataset, for classifying the image patches containing lung nodules that are indicative of potential cancer cells. Experiments are conducted to test the viability of the transfer approach. The contributions of our work are summarized as follows.

1. We propose a novel deep learning approach for pulmonary nodule detection in the presence of class imbalance.
2. We apply the Gestalt principle of similarity for selecting visually similar objects from real-world for pre-training the model. Our approach seeks to bring in "explainability" into the transfer learning process by pre-training on visually relevant objects only.
3. We have involved human subjects or annotators to select the most visually similar structures to lung nodules and non-nodules, paving way for human-interactive learning mechanisms.
4. We have compared our results extensively with the state of the art in lung nodule detection on a benchmark dataset which has an imbalanced class distribution.
5. We prove that our approach classifies effectively in the presence of class imbalance. The results can be further improvised through cost-sensitive learning or data augmentation which are the usual remedies for class imbalance correction.

The rest of this paper is organized as follows: A review of transfer learning strategies applied to biomedical datasets is given in Section 2, the proposed selective transfer methodology is described in Section 3, the experiments and the results are analyzed in Section 4 and the overall conclusion is summarized in Section 5.

2. DEEP LEARNING FOR LUNG NODULE DETECTION- A LITERATURE REVIEW

Convolutional Neural Network (CNN) is the backbone of most deep neural networks today. Proposed by LeCun et al. (2015), it outperforms all other neural networks in its power to process images in 2D through a flexible combination of filtering, max-pooling, dropout, regularization, followed by fully connected dense layers for learning the top-level activations. While the initial layers of CNN detect and learn low-level features such as the edges in an image, the intermediate and higher layers detect more semantically meaningful image parts. The features extracted from these layers hold crucial information that aid in highly efficient classification, which is the reason why deep CNNs win most of the visual challenge competitions.

Researchers in (Song et al. 2017) investigate simple CNN, Deep Neural Networks (DNN) and stacked autoencoders for a comparative performance analysis on lung nodule classification. CNN outperformed other networks in the task. Lai et al. (2021) proposed an attention sub-ConvNet architecture which introduced a squeeze-and-excitation block after every convolutional layer in order to learn feature maps more effectively for lung nodule detection. The authors proposed a combination of softmax loss during the training phase and the triplet loss during the testing phase for more effective learning. It is a well-known fact that CNN weights are learnt via the conventional stochastic gradient descent and hence are susceptible to local minima entrapping. Learning network weights from scratch for biomedical datasets is thus not always a reliable option due to class-imbalance problems that persist most medical image databases (Tajbakhsh et al. 2016). The randomly initialized weights converge to local minima with a strong bias towards the majority class. In this scenario, transferring knowledge from another domain containing visually similar structures and a balanced class-distribution is expected to mitigate the bias. This involves pre-training the CNN with the source dataset and fine-tuning the pre-trained model with the target biomedical dataset; this is the approach followed in our experiments as well. Gogineni et al. (2020) segmented the cancerous nodule region prior to transfer learning using DenseNet161 pre-trained network. The authors claimed that

identifying the regions of interest prior to transfer learning boosts the classification performance. An unsupervised clustering algorithm was used to segment the cancerous nodules.

Most applications of transfer learning for biomedical datasets in literature involve pre-trained deep CNN (Inception, AlexNet, ResNet, VGG16 etc.) that are trained on the massive ImageNet object database containing millions of natural images belonging to 1000 classes. An obvious disadvantage of these approaches from the perspective of biomedical datasets is the irrelevance of the images in the training database for the medical diagnosis task to be undertaken. However, researchers generally overlook this fact and achieve decent classification scores using these pre-trained networks. A common approach to transfer learning is the extraction of deep features from different layers of the pre-trained network that are trained on a suitable classifier. In a recent work on the classification of Breakhis breast cancer histopathological images, the Inception-v3 pre-trained network was used for deep feature extraction (from all layers) which were classified using weighted Support Vector Machines (SVM) (Saini and Susan 2019). A Decaf implementation of CNN pre-trained on 1000 categories of ImageNet was used in (Bar et al. 2015) for extracting features from the 5^{th}, 6^{th}, 7^{th} layers followed by fusion with a compact set of low-level features like SIFT, with the aim of diagnosing chest X-ray images as healthy or abnormal. Fusion of deep features with handcrafted features followed by classification by SVM is implemented for breast cancer diagnosis in (Antropova et al. 2017).

Other than deep feature extraction, the next important strategy in deep transfer networks is fine-tuning of pre-trained CNN models. Fine-tuning is of two types: shallow tuning that involves fine-tuning of the last stage of fully connected dense layers, or deep tuning that involves fine-tuning of all the layers in the network. As per investigation by Tajbakhsh et al. (2016), deep tuning of pre-trained networks in a layer-by-layer manner achieved higher accuracies of classification as compared to training a deep CNN from scratch. Layer-wise greedy supervised training was formally introduced in the case of autoencoders (Bengio et al. 2007), achieved by increasing (and learning the parameters of) hidden layers one at a time for improving the overall performance. Additional layers were added stage-by-stage until the desired performance was achieved. However, this technique is heavily dependent on the labeled training data for performance validation.

Convolutional autoencoders (CAE) were introduced by Masci *et al.* (2011) to preserve 2D spatial information in the autoencoder framework. Deep CAE models have been investigated in biomedical field, notably for Arrhythmia classification with LSTM (Yildrim et al. 2019) and Parkinson disease case study in (Martinez-Murcia 2018). The layers in a deep CAE are a flexible mix of filtering or convolutional layers, downsampling (in encoder part) and upsampling (in decoder part). The order of layers in the encoder and decoder modules are the reverse of each other as for any autoencoder. In our transfer approach involving CAE, following the cue from Tajbakhsh et al. (2016), we use a greedy approach to deep tuning the final network; the modules being consecutively trained are the (unsupervised) CAE (encoder part) and the (supervised) fully connected dense layers (FCN). More details are given in the next section.

3. PROPOSED TRANSFER LEARNING BASED ON THE GESTALT SIMILARITY PRINCIPLE

3.1 Motivation for our approach

We start with the definition of the basic principle of visual cognition that influences the way humans perceive objects in a scene. The Gestalt principle of similarity (Todorovic 2008) states that the human mind tends to club visually similar structures together. The object attributes that contribute to this phenomenon could be shape, color or texture (Peterson and Berryhill 2013). Though some structural differences may exist, these are imperceptible to the human eye since it focusses on "what it wants to see" (Wörgötter et al. 2004). This is the central idea behind our work that trains the neural network on visual structures from natural scenes that are similar in appearance to pulmonary nodules for lung cancer diagnosis. Our work seeks to make the transfer learning process "explainable" by training on visually similar structures only. Some recent works in AI have integrated the Gestalt principles for cognitive computing. The Gestalt principles of similarity and proximity were used to construct an attention-based model for online shopping in (Huang et al. 2021). This work stated that consumer attention was engaged by distracting products that were categorically similar and placed near to the focal object. The Gestalt principles were used recently by Fang et al. (2019) for video saliency detection by visual attention modeling.

In the distant domain problem, addressed in this paper, the source and target domains are totally unrelated. Relatively few works have addressed distant domain transfer learning for biomedical datasets and this forms the matter of investigation in our work. We specifically focus on the pulmonary nodule detection problem in which the task is to distinguish the image patches that contain lung nodules from those that do not. The two types of images are called "Nodule" and "Non-Nodule" respectively, examples are shown in Fig. 1. Lung cancer is detected from pulmonary nodules that are malignant. An undetected nodule may prove fatal to diagnosis while a wrongly detected nodule may be misleading. Direct learning from lung nodule datasets using randomly initialized neural networks is biased due to the small size of the datasets, the prevalent class-imbalance issue and local minima entrapping of network weights. This backdrop renders transfer learning as an attractive proposition for pre-training the network weights on a balanced source dataset. Contrary to the conventional transfer learning schemes that involve readily available pre-trained deep networks trained on millions of images from the ImageNet database, our method advocates pre-training on a select subset of relevant objects only, whose visual appearance resembles the structure and shape of the medical images we are classifying.

3.2 Pre-training with visually similar objects

Our source dataset for the pre-training phase is compiled from the benchmark datasets UK Flowers (Nilsback and Zisserman 2006) and UC Merced landscape dataset (Yang and Newsam 2010). The procedure behind the compilation process is explained in detail next. The compilation is the result of a rigorous human polling experiment on an initial collection of images comprising of flower images from UK Flowers dataset and *Soccer-ball* and *Bowling-ball* object categories from Caltech-256 (Griffin and Perona 2007) (resemblance to Nodule images); and *River, Overpass* and *Runway* landscape categories from the UC Merced landscape dataset (resemblance to Non-Nodule images). Samples of all datasets are shown in Fig. 2. For the *Flower* category, 100 images were selected out of the source images that is made available by us at the online link[1]. All the 100 images in each of the categories *River, Overpass* and *Runway* of the UC Merced landscape dataset are used for the polling. 100 out of 104 image files of the *Bowling-ball* category (017_0001.jpg to 017_0100.jpg) and 100 out of 174 images (193_0001.jpg to 193_0100.jpg) of the *Soccer-ball* category are selected. The Nodule and Non-Nodule images in Fig. 1 were given to three human annotators as a reference template to identify whether the real-world image in the compiled database resembles: a) Nodule and b) Non-nodule. The binary responses (Yes/No) were recorded for both a) Nodule and b) Non-nodule, on an individual basis for all three annotators, in a form-based response. The results of the human cognition experiment are compiled in Table 1 and we have made it available online as well[2] for the reference of readers.

The total votes obtained for each object category by the three annotators are summarized in Table 1. The object that resembles the nodules the most, were voted in a majority, to be *Flowers* from the UK flowers dataset with 300 votes. The non-nodule images were evaluated for their similarity with each image in the UC Merced landscape dataset, and the *River* category won the maximum votes (292) as compared to *Overpass* and *Runway*. Following the poll results, the *Flower* and *River* datasets, containing 100 images each, were given as input for our first phase of experiments involving pre-training of the CAE. Some samples of both categories are shown in Fig. 3. The online repository for our pre-training images of *Flower-River* is provided online[3].

3.3 "Explainable" transfer learning

In our proposed "explainable" transfer learning approach, in order to distinguish effectively between nodule and non-nodule images, we pre-train the deep network on visually similar objects – Flowers and Rivers. We incorporate a greedy-layer learning mechanism by pre-training the model on the *Flower-River* dataset in two phases. The flowchart for the entire process is shown in Fig. 4. In Phase 1 of the experiments, the Convolutional Autoencoder (CAE) is trained on the *Flower-River* images. The CAE architecture is shown in Fig. 5. In the second phase of our experiments, the encoder part of the trained CAE model is separated and stacked with randomly initialized dense fully connected layers to form an assembled Convolutional Neural Network (CNN) shown in the bottom-half of Fig. 5, and the combination is first pre-trained on the *Flower-River* dataset followed by deep tuning with the biomedical (lung-nodule) dataset. The FCN layers are shown connected to the encoder part of the CAE in Fig. 5; the combination is the new learning module for both the pre-training in the second phase and the ultimate deep tuning using the lung nodule dataset. The medical images used in the second phase of our experiments are cropped CT scan images and are categorized on the basis whether they contain pulmonary nodules or not. We also explore the effect of pre-training on an enlarged version of the *Flower-River* dataset. For the enlarged version of the dataset, we use Flower and River images from two benchmark datasets. The Kaggle flowers dataset[4] contains 4242 images of flowers that were collected from the internet. The real-time images of the Errenxi river in Taiwan[5] are available from Harvard Dataverse (Tsai 2020). We worked on the 4800 training images of this dataset. The enlarged Flower-River dataset is thus balanced (4242 vs 4800 images) and is suitable for pre-training our deep model. Table 2 summarizes the details of the datasets involved in our deep learning framework. Further details of the lung nodule dataset and the experimentation are explained in section 4. To summarize, in our model, there is two-phase pre-training with distant-domain images (first phase related to the training of CAE, and second phase involves training the final deep network in which CAE encoder layers are embedded). Once the pre-training stage is complete, the pre-initialized weights of both the CAE and FCN are fine-tuned using the training set of the lung nodule dataset. In deep tuning of the final network model, the parameters of the all the layers of the deep model are fine-tuned. The Validation set of the pulmonary nodule dataset is used for determining the optimal network hyperparameters for the testing phase. The Adam optimizer and mean square error loss function with a learning rate of 0.01 are used to converge the training cycle. 200 epochs with a batch size of 128 was used.

[1] https://drive.google.com/drive/folders/1Uk3VtwWBwjspiIhLOot0P7fAiCeodV_Y?usp=sharing

[2] https://drive.google.com/file/d/1Ew0qGaBTwfQJxyOn-W7F0JbcTeGzHjWf/view?usp=sharing

[3] https://drive.google.com/drive/folders/1Uk3VtwWBwjspiIhLOot0P7fAiCeodV_Y?usp=sharing

[4] https://www.kaggle.com/datasets/alxmamaev/flowers-recognition

[5] https://dataverse.harvard.edu/dataset.xhtml?persistentId=doi:10.7910/DVN/8FDC7P

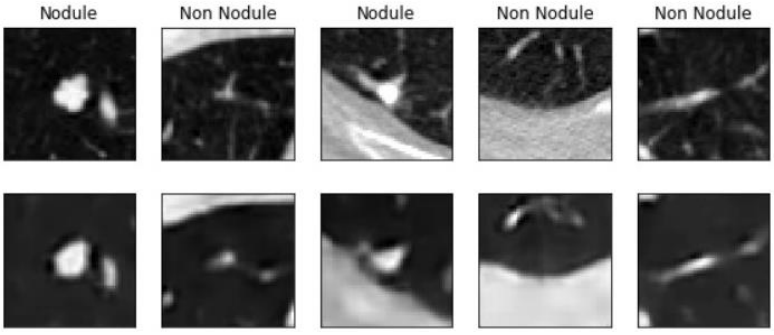


Fig. 1. Nodule and Non-nodule image patches (labeled) cropped from CT scans

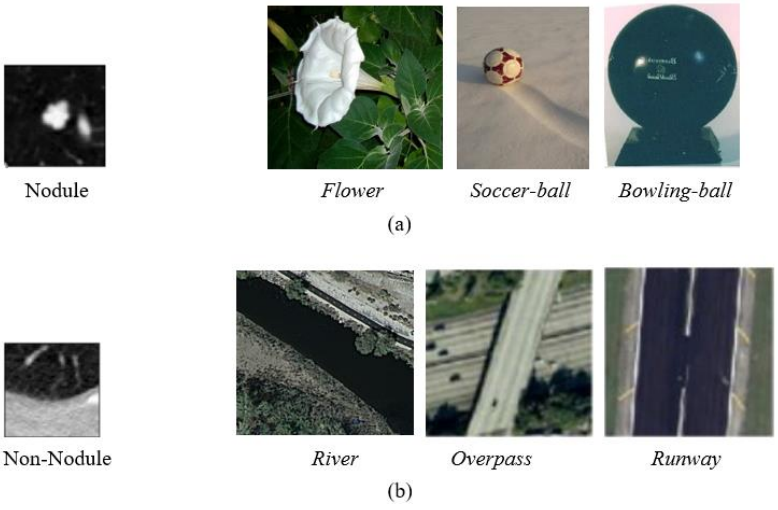


Fig. 2. Instances from the object and scene categories used for the human cognition experiment (a) categories resembling "Nodule" (b) categories resembling "Non-Nodule"

TABLE 1: DETAILS OF HUMAN COGNITION EXPERIMENT INVOLVING HUMAN ANNOTATORS FOR FINDING RESEMBLING OBJECTS

Type of experiment	*Dataset in experiment*	*Outcome of poll Online link*	*Relevant online links of benchmark/compiled dataset*
Cross-Domain Searching for visually similar objects as per Gestalt principle of similarity	Lung Nodule (closest resemblance to)	*Flower* (300 votes) *Soccer-ball* (73 votes) *Bowling-ball* (54 votes)	*Sources of benchmark datasets:* *Flower*: UK Flowers – 100 Nos. *Soccer-ball*- 100 Nos : Caltech-256 *Bowling-ball*- 100 Nos.: Caltech-256
	Non-Nodule (closest resemblance to)	*River* (292 votes) *Overpass* (230 votes) *Runway* (208 votes)	*Source of benchmark datasets:* Landscape: UC Merced Land database-100 Nos. in each of the three categories
Pre-training with compiled source dataset: *Flower-River*	*Flower*	All **100** Nos.	*Images of compiled Flower-River:* 200 images
	River	All **100** Nos.	



Fig. 3. Instances from the *Flower-River* dataset (a) *Flower* instances (b) *River* instances

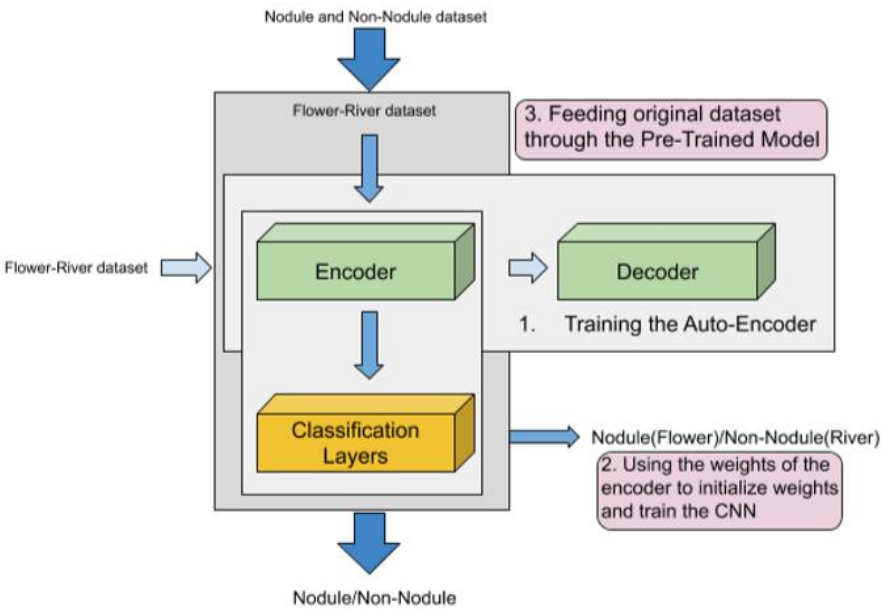


Fig. 4. Flowchart for the proposed cross-domain learning of visually similar structures

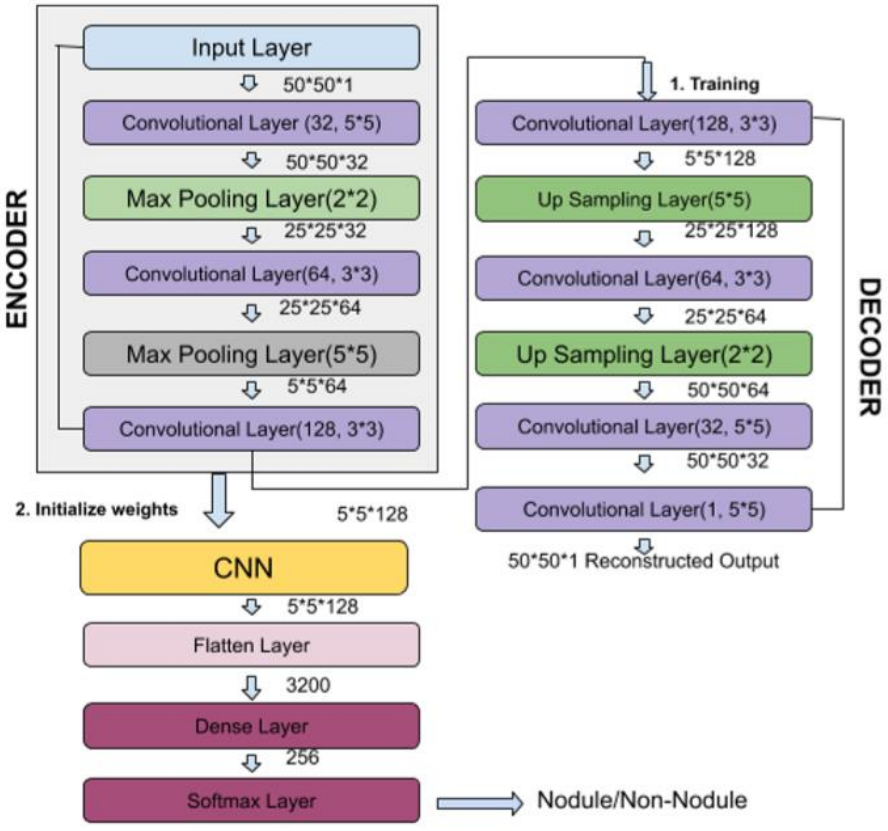


Fig. 5. Proposed CAE-FCN architecture for pulmonary nodule detection

TABLE 2: DETAILS OF DATASETS USED FOR TRAINING THE FINAL PROPOSED DEEP MODEL

Dataset	*Source*	*Train*	*Test*
Lung nodule dataset	LIDC lung nodule database (with pre-processing)	4342 (Non-nodule) 845 (Nodule)	1340 (Non-nodule) 282 (Nodule)
Flower-River (small version)	UK Flowers UC Merced Land database	100 (Flower) 100 (River)	--
Flower-River (enlarged version)	Kaggle Flowers Harvard Dataverse Taiwan River database- Training set	4242 (Flower) 4800 (River)	--

3.4 Cost-sensitive learning

Since the number of nodules is much less than the number of non-nodules in lung nodule datasets acquired from the real world, therefore we suggest addition of cost-sensitive learning to mitigate the effect of this class imbalance. Under this scheme, the loss function of the minority class is weighted by a factor w which is the imbalance ratio between the two classes, as shown in (1) and (2). The loss function would be then more sensitive to the underrepresented minority class which in our case is the set of nodule images. Modifying the loss function, induces fair decision making as proved in previous works on cost-sensitive learning for imbalanced datasets (Fernández et al. 2018, Cao et al. 2021, Susan et al. 2021).

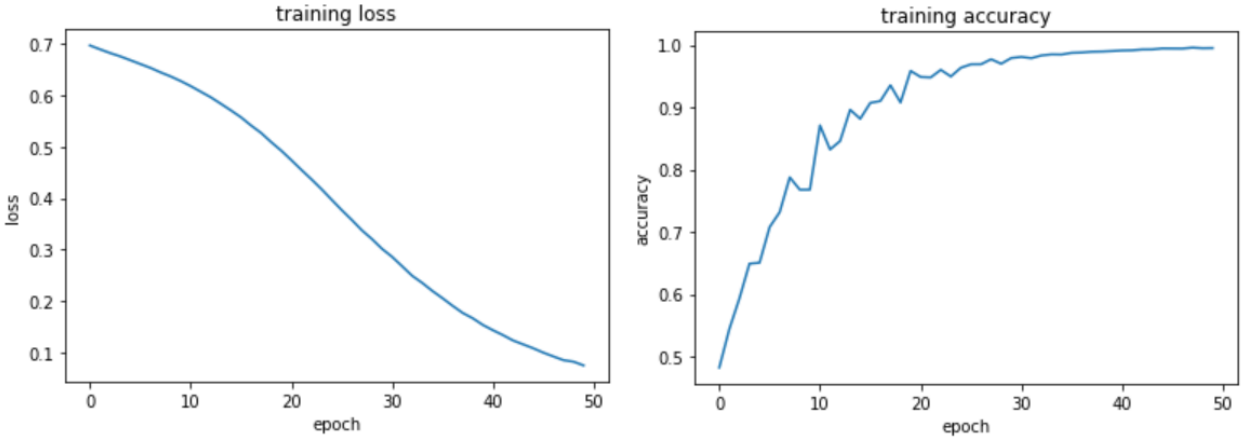
$$Loss = Majority_Loss + Minority_Loss \times w \tag{1}$$

where,

$$w = \frac{Total_population}{Minority_population} \tag{2}$$

4. RESULTS AND DISCUSSIONS

The images used for our experiments were obtained from the LUNA16 (Setio et al. 2017) challenge https://luna16.grand-challenge.org/ that is derived from the Lung Image Database Consortium and Infectious Disease Research Institute (LIDC/IDRI) database (Armato III 2011) available online at https://wiki.cancerimagingarchive.net/display/Public/LIDC-IDRI. This dataset consists of 888 CT scans with annotations describing coordinates and ground truth labels. The images were available in the .mhd format, which stores the header data and the .raw format, which stores the multidimensional image data. Each CT scan has dimensions of 512×512×*n,* where *n* is the number of axial scans. There are roughly 200 images in each CT scan. Since the amount of data was huge, we decided to use the annotations provided to crop each image around the coordinates. The final dataset comprised of 5187 training samples, 1297 validation samples and 1622 test samples where each sample is a 50×50 grayscale image applied as 2D input to our deep convolutional network. The hyperparameters of the deep network are tuned on the validation set. Some samples of Nodule/Non-Nodule images are shown in Fig. 1. The *Flower-River* dataset compiled by human annotators, and containing 100 images each, are used for pre-training, some samples of which are shown in Fig. 3 (a, b). A comparison between Figs. 1, 3 highlight the visual similarity between Nodule and *Flower*; and between Non-Nodule and *River*. Table 3 shows the results of the proposed model for different training combinations on this small *Flower-River* dataset. The best performance (94.45%) is obtained for the proposed schema of fine-tuning all layers of the CAE-FCN model with the *Flower-River* dataset followed by fine tuning on the lung nodule dataset. (The CAE in CAE-FCN refers to the encoder part of the trained CAE). We have made our code available online[6] for facilitating future research. The training loss and accuracy curves are shown in Fig. 6 for the enlarged *Flower-River* dataset containing 4242 *Flower* images and 4800 *River* images. The graphs in Fig. 6 show good convergence for the enlarged *Flower-River* dataset in terms of the training loss and accuracy graphs.



(a) (b)

Fig. 6. Training loss and accuracy curves for the enlarged *Flower-River* dataset shown for 50 epochs

We also apply cost-sensitive learning on the proposed model with enlarged *Flower-River* dataset. The weight *w*=6 is used for the cost-sensitive learning (Eq. (1) and Eq. (2)) since the total population/minority population for our benchmark dataset is 5187/845=6.13. Table 4 shows the comparison of the proposed method with the state of the art. We have compared our results with that of Deep Convolutional Neural Networks (CNN) (Song et al. 2017), Deep Convolutional Auto-encoder (CAE) (Yildrim et al. 2019), Stacked Convolutional Auto-encoder (CAE) (Masci et al. 2011), attention sub-ConvNet (Lai et al. 2021), regions of interest (cancerous nodules) learned by DenseNet161 (Gogineni et al. 2020), and RESNET-50 pre-trained deep neural network (He et al. 2018). The proposed method outperforms other methods in terms of accuracy, precision, recall, specificity, and F1-score and Mathew's Correlation Coefficient (MCC).

The hyperparameters of both the CAE and the final deep model are tuned on the validation set of the lung nodule dataset (Table 2). The Adam optimizer and mean square error loss function with a learning rate of 0.01 are used to converge the training cycle, for both CAE and the final deep model. 200 epochs with a batch size of 128 was used for training the models. While accuracy refers to the percentage of correct classification, F1-score refers to the harmonic mean of Precision and Recall. F1-score and MCC reflect the improvement in minority class scores even more than accuracy does. We also present results of data augmentation in our approach. Data augmentation is a popular tool for improving the performance of imbalanced datasets. The details of the data augmentation incorporated are as follows. The 200 *Flower-River* images were initially augmented to 2000 images for training the CAE by the transformations of rotation, horizontal flip, vertical shift and horizontal shift. In the second phase, involving training of the deep training module, the two datasets (augmented *Flower-River* and lung nodule dataset) were augmented on-the-fly by the affine transformations of rotation, horizontal flip, vertical shift and horizontal shift. Under this scheme, the training data is replaced by a fresh batch of augmented data in every epoch to introduce variety

[6] https://github.com/sebasusan/Cross-Domain-Learning-for-Pulmonary-Nodule-Detection

in the training cycle. The augmentations resulted in an improvement of the model accuracy from 94.45% to 95.25%, as observed from Table 4 indicating an improvement in the minority class performance.

Our experiments led to the following conclusions: 1) Cross-domain learning based on the Gestalt visual similarity principle is feasible for biomedical datasets by learning in small numbers on selective categories of visually similar objects Our approach advocates "explainable" AI development since transfer learning is performed using visually similar structures as per the psychology of human visual perception. 2) The choice of the visually similar structures used for pre-training affects the performance. This opens up a perspective on human-interactive learning mechanisms for deep models. 3) Fine-tuning the CAE and the fully connected dense layers in a greedy layer-wise manner is more effective than training the network from scratch and fine tuning of deep pre-trained networks 4) Data augmentation and cost-sensitive learning can be incorporated to further enhance the performance of the minority class. Introduction of a class bias of ratio 6:1 for the LUNA16 version of the LIDC dataset, for which the total population to minority population is 6:1, achieves the best classification scores outperforming the state of the art in terms of accuracy (95.56%), precision (0.92), recall (0.816), specificity (0.985), and F1-score (0.865) and MCC (0.840). Attention sub-ConvNet (Lai et al. 2021) is the second best method as observed from the scores in Table 4.

TABLE 3: PERFORMANCE EVALUATION FOR DIFFERENT TRAINING COMBINATIONS OF THE PROPOSED MODEL FINE-TUNED ON THE LUNG NODULE TEST DATASET WITH PRE-TRAINING ON THE SMALL FLOWER-RIVER DATASET HAVING 100 IMAGES EACH.

Model	*Pre-training*		*Fine-tuning*		*Test Accuracy*	*Remarks*
	CAE	*FCN*	*CAE*	*FCN*		
Proposed	Flower-River	Flower-River	Lung nodule	Lung nodule	94.45%	Pre-training and Deep tuning of all layers
	Flower-River	---	---	---	77.86%	No fine-tuning
	Flower-River	---	---	Lung nodule	91.12%	Shallow tuning
	Flower-River	---	Lung nodule	Lung nodule	93.89%	Deep tuning of all layers
Direct method	---	---	Lung nodule	Lung nodule	91.92%	No pre-training

TABLE 4: PERFORMANCE COMPARISON OF THE PROPOSED METHOD WITH STATE OF THE ART ON THE LUNG NODULE DATASET (VALUE IN BOLD INDICATES THE PROPOSED APPROACH)

Model	*Accuracy*	*Precision*	*Recall or Sensitivity*	*F1-score*	*Specificity*	*MCC*
Deep CNN (Song et al. 2017)	92.47%	0.803	0.752	0.7766	0.962	0.732
Deep CAE (Yildrim et al. 2019)	87.60%	0.697	0.507	0.587	0.954	0.526
Stacked CAE (Masci et al. 2011)	91.92%	0.781	0.745	0.763	0.956	0.714
RESNET -50 pre-trained network (He et al. 2016)	93.89%	0.853	0.784	0.817	0.972	0.781
CW-CAE (Susan et al. 2021)	93.34%	0.833	0.762	0.796	0.968	0.757
Attention sub-ConvNet (Lai et al. 2021)	95.25%	0.823	0.925	0.871	0.958	0.845
Regions of interest + DenseNet161 (Gogineni et al. 2020)	95.25%	0.873	0.851	0.862	0.974	0.833
Proposed model with limited pre-training using smaller *Flower-River* dataset	**94.45%**	**0.861**	**0.812**	**0.836**	**0.972**	**0.803**

Proposed model with limited pre-training using smaller *Flower-River* dataset and data augmentation	**95.25%**	**0.864**	**0.862**	**0.863**	**0.972**	**0.835**
Proposed model with improved pre-training using enlarged *Flower-River* dataset and cost-sensitive learning (final model)	**95.56%**	**0.92**	**0.816**	**0.865**	**0.985**	**0.840**

5. CONCLUSION

In this paper, we address the problem of pulmonary nodule detection from cropped images of lung CT scans through distant domain transfer learning. The system is based on learning visually similar structures using the Gestalt principle of similarity. We propose that training the deep network from scratch, on a select group of visually correlated cross-domain objects, is more fruitful than the existing complex pre-trained networks trained on a thousand image classes that may not be related to the medical image at all. A small though balanced source distribution of flowers and rivers is compiled from benchmark datasets by human annotators, and used to pre-train a Convolutional Auto-Encoder (CAE). Our deep network comprising of the trained CAE encoder and dense FCN layers are deep-tuned using both the source (*Flower-River*) and the target datasets (lung nodule images). Data augmentation and cost-sensitive learning was observed to further improve the performance of the proposed model. We achieved the highest accuracy of 95.56% by pre-training on an enlarged version of the Flower-River dataset, outperforming the state of the art on lung nodule detection. We additionally verified the efficacy of our approach using performance metrics such as Precision, Recall, F1-score, Specificity and MCC. Our results conclude that an efficient transfer of knowledge from natural images to the biomedical domain is made possible by pre-training with visually similar structures followed by layer-wise fine-tuning of the entire model. Our work opens up a new perspective on "explainable" transfer learning that promotes cross-domain transfer learning of objects that have visually similar characteristics to the objects that have to be classified. The visual similarity of the objects are qualitatively judged by human annotators. Our work thus presents a mechanism to make the learning process both human-interactive and explainable.

REFERENCES

Antropova, N., Huynh, B. Q., & Giger, M. L. (2017). A deep feature fusion methodology for breast cancer diagnosis demonstrated on three imaging modality datasets. Medical physics, 44(10), 5162-5171.

Armato III, S. G., McLennan, G., Bidaut, L., McNitt-Gray, M. F., Meyer, C. R., Reeves, A. P., ... & Clarke, L. P. (2011). The lung image database consortium (LIDC) and image database resource initiative (IDRI): a completed reference database of lung nodules on CT scans. *Medical physics*, *38*(2), 915-931.

Bar, Y., Diamant, I., Wolf, L., & Greenspan, H. (2015, March). Deep learning with non-medical training used for chest pathology identification. In Medical Imaging 2015: Computer-Aided Diagnosis (Vol. 9414, p. 94140V). International Society for Optics and Photonics.

Bengio, Y., Lamblin, P., Popovici, D., & Larochelle, H. (2007). Greedy layer-wise training of deep networks. In Advances in neural information processing systems (pp. 153-160).

Bishop, C. M. (1995). Neural networks for pattern recognition. Oxford university press.

Blitzer, J., Crammer, K., Kulesza, A., Pereira, F., & Wortman, J. (2008). Learning bounds for domain adaptation.

Cao, C., Cui, Z., Wang, L., Wang, J., Cao, Z., & Yang, J. (2021). Cost-sensitive awareness-based SAR automatic target recognition for imbalanced data. *IEEE Transactions on Geoscience and Remote Sensing*, *60*, 1-16.

Caruana, R. (1997). Multitask learning. Machine learning, 28(1), 41-75.

Fang, Yuming, Xiaoqiang Zhang, Feiniu Yuan, Nevrez Imamoglu, and Haiwen Liu. "Video saliency detection by gestalt theory." *Pattern Recognition* 96 (2019): 106987.

Fernández, A., García, S., Galar, M., Prati, R. C., Krawczyk, B., Herrera, F., ... & Herrera, F. (2018). Cost-sensitive learning. *Learning from Imbalanced Data Sets*, 63-78.

Gogineni, A. K., Kishore, R., Raj, P., Naik, S., & Sahu, K. K. (2020). Unsupervised Clustering Algorithm as Region of Interest Proposals for Cancer Detection Using CNN. In *Computational Vision and Bio-Inspired Computing: ICCVBIC 2019* (pp. 1386-1396). Springer International Publishing.

Griffin, G., Holub, A., & Perona, P. (2007). The caltech-256. Caltech Technical Report, 1.

He, K., Zhang, X., Ren, S., & Sun, J. (2016). Deep residual learning for image recognition. In Proceedings of the IEEE conference on computer vision and pattern recognition (pp. 770-778).

Holzinger, A., Goebel, R., Fong, R., Moon, T., Müller, K. R., & Samek, W. (2022, April). xxAI-beyond explainable artificial intelligence. In *xxAI-Beyond Explainable AI: International Workshop, Held in Conjunction with ICML 2020, July 18, 2020, Vienna, Austria, Revised and Extended Papers* (pp. 3-10). Cham: Springer International Publishing.

Huang, Bo, Carolane Juaneda, Sylvain Sénécal, and Pierre-Majorique Léger. "'Now You See Me': The Attention-Grabbing Effect of Product Similarity and Proximity in Online Shopping." *Journal of Interactive Marketing* 54 (2021): 1-10.

Kaushik, Ashu, and Seba Susan. "TWO-WAY METRIC LEARNING WITH MAJORITY AND MINORITY SUBSETS FOR CLASSIFICATION OF LARGE EXTREMELY IMBALANCED FACE DATASET." Jordanian Journal of Computers and Information Technology (JJCIT) 7, no. 04 (2021).

Kim, H. E., Cosa-Linan, A., Santhanam, N., Jannesari, M., Maros, M. E., & Ganslandt, T. (2022). Transfer learning for medical image classification: A literature review. *BMC medical imaging*, *22*(1), 69.

Krawczyk, B., Galar, M., Jeleń, Ł., & Herrera, F. (2016). Evolutionary undersampling boosting for imbalanced classification of breast cancer malignancy. Applied Soft Computing, 38, 714-726.

Lai, K. D., Nguyen, T. T., & Le, T. H. (2021). Detection of lung nodules on ct images based on the convolutional neural network with attention mechanism. *Annals of Emerging Technologies in Computing (AETiC)*, *5*(2), 78-89.

LeCun, Y., Bengio, Y., & Hinton, G. (2015). Deep learning. nature (2015). May; 521 (7553): 436 10.1038/nature14539.

Li, L., Wang, B., Verma, M., Nakashima, Y., Kawasaki, R., & Nagahara, H. (2021). SCOUTER: Slot attention-based classifier for explainable image recognition. In *Proceedings of the IEEE/CVF International Conference on Computer Vision* (pp. 1046-1055).

Lu, J., Behbood, V., Hao, P., Zuo, H., Xue, S., & Zhang, G. (2015). Transfer learning using computational intelligence: A survey. Knowledge-Based Systems, 80, 14-23.

Martinez-Murcia, F. J., Ortiz, A., Gorriz, J. M., Ramirez, J., Castillo-Barnes, D., Salas-Gonzalez, D., & Segovia, F. (2018, June). Deep convolutional autoencoders vs PCA in a highly-unbalanced Parkinson's disease dataset: a DaTSCAN study. In The 13th International Conference on Soft Computing Models in Industrial and Environmental Applications (pp. 47-56). Springer, Cham.

Masci, J., Meier, U., Cireşan, D., & Schmidhuber, J. (2011, June). Stacked convolutional auto-encoders for hierarchical feature extraction. In International conference on artificial neural networks (pp. 52-59). Springer, Berlin, Heidelberg.

Nilsback, M. E., & Zisserman, A. (2006, June). A visual vocabulary for flower classification. In 2006 IEEE Computer Society Conference on Computer Vision and Pattern Recognition (CVPR'06) (Vol. 2, pp. 1447-1454). IEEE.

Peterson, D. J., & Berryhill, M. E. (2013). The Gestalt principle of similarity benefits visual working memory. Psychonomic bulletin & review, 20(6), 1282-1289.

Saini, M., & Susan, S. (2019, July). Data augmentation of minority class with transfer learning for classification of imbalanced breast cancer dataset using inception-V3. In Iberian Conference on Pattern Recognition and Image Analysis (pp. 409-420). Springer, Cham.

Setio, Arnaud Arindra Adiyoso, Alberto Traverso, Thomas De Bel, Moira SN Berens, Cas Van Den Bogaard, Piergiorgio Cerello, Hao Chen et al. "Validation, comparison, and combination of algorithms for automatic detection of pulmonary nodules in computed tomography images: the LUNA16 challenge." *Medical image analysis* 42 (2017): 1-13.

Song, Q., Zhao, L., Luo, X., & Dou, X. (2017). Using deep learning for classification of lung nodules on computed tomography images. Journal of healthcare engineering, 2017.

Sui, Y., Wei, Y., & Zhao, D. (2015). Computer-aided lung nodule recognition by SVM classifier based on combination of random undersampling and SMOTE. Computational and mathematical methods in medicine, 2015.

Susan, S., Sethi, D., & Arora, K. (2021). CW-CAE: pulmonary nodule detection from imbalanced dataset using class-weighted convolutional autoencoder. In International Conference on innovative computing and communications (pp. 825-833). Springer, Singapore.

Susan, S., & Kumar, A. (2021). The balancing trick: Optimized sampling of imbalanced datasets—A brief survey of the recent State of the Art. Engineering Reports, 3(4), e12298.

Szegedy, C., Vanhoucke, V., Ioffe, S., Shlens, J., & Wojna, Z. (2016). Rethinking the inception architecture for computer vision. In *Proceedings of the IEEE conference on computer vision and pattern recognition* (pp. 2818-2826).

Tajbakhsh, N., Shin, J. Y., Gurudu, S. R., Hurst, R. T., Kendall, C. B., Gotway, M. B., & Liang, J. (2016). Convolutional neural networks for medical image analysis: Full training or fine tuning?. IEEE transactions on medical imaging, 35(5), 1299-1312.

Tan, B., Zhang, Y., Pan, S., & Yang, Q. (2017, February). Distant domain transfer learning. In Proceedings of the AAAI conference on artificial intelligence (Vol. 31, No. 1).

Thrun, S., & Pratt, L. (1998). Learning to learn: Introduction and overview. In Learning to learn (pp. 3-17). Springer, Boston, MA.

Todorovic, D. (2008). Gestalt principles. *Scholarpedia*, *3*(12), 5345.

Wörgötter, F., Krüger, N., Pugeault, N., Calow, D., Lappe, M., Pauwels, K., ... & Johnston, A. (2004). Early cognitive vision: Using gestalt-laws for task-dependent, active image-processing. Natural computing, 3(3), 293-321.

Yang, Y., & Newsam, S. (2010, November). Bag-of-visual-words and spatial extensions for land-use classification. In Proceedings of the 18th SIGSPATIAL international conference on advances in geographic information systems (pp. 270-279).

Yildirim, O., Baloglu, U. B., Tan, R. S., Ciaccio, E. J., & Acharya, U. R. (2019). A new approach for arrhythmia classification using deep coded features and LSTM networks. Computer methods and programs in biomedicine, 176, 121-133.

View publication stats

2023 6th International Conference on Information Systems and Computer Networks (ISCON)
GLA University, Mathura, India. Mar 3-4, 2023

2023 6th International Conference on Information Systems and Computer Networks (ISCON) | 979-8-3503-4696-1/23/$31.00 ©2023 IEEE | DOI: 10.1109/ISCON57294.2023.10111990

Cyber Attack Detection in IoT using Deep Learning Techniques

Kartik Tomar
Department of Computer Science and Engineering
Delhi Technological University
Delhi, India
kartiktomar97@gmail.com

Krishi Bisht
Department of Computer Science and Engineering
Delhi Technological University
Delhi, India
krishisinghbisht2000@gmail.com

Kshitiz Joshi
Department of Computer Science and Engineering
Delhi Technological University
Delhi, India
kshitizjoshi2k21@gmail.com

Rahul Katarya
Department of Computer Science and Engineering
Delhi Technological University
Delhi, India
rahuldtu@gmail.com

***Abstract*—The Internet of things (IoT) consists of millions of digital devices which interact with each other through minimum user interaction. IoT is one of the most rapidly expanding computing sectors; however, it is vulnerable to many attacks. An emerging concern in the Internet of Things (IoT) space is attack and strange placement on the IoT framework. Attacks and dangers on these systems are also growing proportionally because of the expanding IoT foundation usage across all industries. In this paper, a review of previous work is conducted, and several deep learning techniques are proposed for accurately predicting attacks on IoT systems. Injection attacks, Man-in-the-middle attacks, Information gathering, Malware attacks, and DDoS/Dos attacks are such attacks and irregularities that might occur in an IoT framework. Identifying such attacks and malicious traffic is important for the Internet of things (IoT) network to block unwanted traffic and unauthorized access. The Edge-IIoTset Cyber Security Dataset and the VGG16 and VGG19 algorithms are utilized to evaluate the effectiveness of the proposed solution; F1 score, precision, recall, and accuracy are the assessment metrics used.**

***Index Terms*—Cyber attack, IoT, VGG-16, VGG-19, Attack Detection.**

I. Introduction

A. Overview

The Internet of Things (IoT) consists of uniquely addressable physical devices with varying sizes and different degrees of sensing and processing capabilities [1]. These devices are interconnected to each other with the help of the Internet and Microchips which results in smooth communication among these devices. In simple terms, IoT is basically interconnected "things" that help make human life easier [2]. These things are the internet, sensors, and web-based communication and control technologies. Microchips track the environment, communicating information to people and the network. IoT is all around us, from connecting our smartwatch to our mobile phone to Smart AC which maintains the temperature according to the surroundings. According to [3], the overall number of IoT devices will be around 75.44 billion by 2025. From Smart healthcare systems to smart education, IoT is present everywhere to make our lives simpler, easier and better. The advent of IoT devices and their growth, as seen in the upcoming years, has led to the formation of a branch of systems, otherwise known as the ubiquitous systems, for example, smart home appliances interconnected in a system via an underlying network to bring ease in the life of the users. However, while having such beneficial purposes, IoT devices continue to face several security risks, such as cyberattacks. [4]. Combined with the fact that IoT devices are also used in health monitoring systems like PEDs and many other sensitive areas, it becomes necessary to secure them, which becomes the motivation behind our paper. Below is a summary of this paper's major contributions.

- Proposed modifications in VGG-16 and VGG-19 for IoT attack detection and classification.
- To enhance classification performance, pre-processing and training techniques have been used.
- In comparison with previous works proposed work has better accuracy in attack classification.
- Previous work on IoT attack detection with various other approaches has been studied and summarized.

B. Research Problem

To understand "normal" and "abnormal" behavior about how IoT devices and components interact with one another, DL are powerful method not only for the analysis of data. The data related to components of the IoT system is collected and examined to establish typical patterns of interaction, which in turn helps with early detection of intrusion on the system. Additionally, as DL techniques intelligently foresee forthcoming, unknown attacks by acquiring knowledge from previous examples, they may be essential for forecasting new attacks, typically mutations of previous ones. Based on these facts, our research problem becomes detecting such attacks on IoT devices and addressing them based on the type of attacks.

Authorized licensed use limited to: DELHI TECHNICAL UNIV. Downloaded on May 11,2023 at 10:18:12 UTC from IEEE Xplore. Restrictions apply.

TABLE I
A COMPARATIVE ANALYSIS OF THE LITERATURE ON IOT ATTACK DETECTION

S.No	Reference	Objectives	Techniques	Results	Advantages	Disadvantages
1.	Gaber et al. [5] 2022	Injection attacks detection on AWID	SVM, RF, DT	99% accuracy, 90% F1 Decision tree	Requires only eight features for attack detection	The proposed method only addresses injection attacks, not all security and privacy concerns in IoT.
2.	Nayak et al. [6] 2021	Decreased Rank, Version Number, Hello Flood attack on IoT Routing Attack Dataset (IRAD)	GAN-C, SVM	93% precision,92% recall and 92% f1-score for HF attack	The parallel GAN-C model significantly decreased the amount of training time.	The Dataset used is homogenous and only accounts for three kinds of attacks
3.	Almaraz-Rivera et al. [7] 2021	Transport and Application layer attack detection on Bot-IoT dataset	SVM, Random Forest, Decision Tree	100% Accuracy on RF and DT	The methodology suggested corrects the class imbalance issue of the original dataset.	In multiple IoT, the proposed intrusion detection system has not been reviewed.
4.	Bedi et al. [8] 2021	DOS, MC, SC, MO, WS, NL, DP, SP attacks detection on DS2OS dataset	LR, SVM, ANN,RF, DT	99.4% accuracy with RF	Data preprocessing is not required for the given dataset	The number of data points is very low for any particular attack other than a Normal attack.
5.	Zagrouba et al. [9] 2021	Botnet/DDoS Attacks detection on BoT-IoT dataset	Random Forest and Decision Tree	99.99% accuracy	With a false negative rate of 0.000 along with a true positive rate of 1.000, the accuracy is quite high.	Analyzing data, training the algorithms, and classifying different data sets are time-consuming.
6.	Bagui et al. [10] 2021	Botnet Attack detection on UCI's machine learning repository	LR, SVM, RF	99% accuracy with RF.	Very high attack detection rate.	Effective feature selection techniques have not been employed to select features.
7.	Aboelwafa et al. [11] 2020	Cyber Attacks detection on CICIDS-2017, UNSW-NB15, ICS Cyber Attack	LR, GNB, Simple RNN, GRU, CNN-LSTM, CNN, RF, AdaB, DT, KNN, LSTM, DNN	99.9% accuracy with RF for the CICIDS-2017 dataset	The method requires no labeled data and has an efficient data-cleaning algorithm.	If the attack preserves correlation among sensor readings, AutoEncoder might not detect it.
8.	Shafiq et al. [12] 2020	Bot-IOT attacks detection on Bot-IoT dataset	Decision Tree and Random forest	99.99% accuracy on RF	An efficient technique for selecting relevant features has been employed.	The system is inadequate in detecting Keylogging theft attacks.
9.	Kim et al. [13] 2020	Botnet attack detection on N-BaIoT dataset	CNN, RNN, LSTM, KNN, LR, RF, DT, and NB	99.7% accuracy	The F1 score of machine learning models is very high.	Multiclass classification models misclassify TCP as UDP rather than SYN and benign.
10.	Shafiq et al. [14] 2020	Bot-IoT attack detection on Bot-IoT dataset	Naive Bayes, BayesNet, DecisonTree, RF	99.79% Naive Bayes	The bijective soft set technique is used, which improves the accuracy of the machine learning model.	ML metrics used can be enhanced.

The paper is divided into four different sections, namely, 1) Introduction 2) Literature Review of prior Research word done on Attack detection in IoT using various other approaches. 3) Implemented modified version of VGG-16 & VGG-19 which increase attack detection efficiency. 4) Results. The dataset which we have used here is The Edge-IIoTset Cyber Security Dataset of IoT and IIoT [15]. This is different from other datasets because it is a real-world-based one. We have utilized VGG-16 and VGG-19 with some modifications to fit our dataset for training and testing. To our knowledge, these models have not been applied in any previous work related to complete attack classification and detection. The evaluation measures included in the presentation analysis include the F1 score, precision, recall, and accuracy.

C. Motivation

The increased demand for IoT in our lives inadvertently increases the danger of IoT security. IoT devices' widespread distribution generates a big, vulnerable surface, which introduces new security issues. Additionally, the IoT platform generates a significant amount of relevant data. A major privacy violation might ensue if this data is not transmitted and analyzed securely. If any data breach happens, this can affect millions of human lives. Each layer of the Internet of

Authorized licensed use limited to: DELHI TECHNICAL UNIV. Downloaded on May 11,2023 at 10:18:12 UTC from IEEE Xplore. Restrictions apply.

Things is susceptible to security flaws. These processes might start from internal networks or external systems and can be active or passive. While a passive attack gathers information about the IoT network without interfering with live services, an active attack disrupts the operation of running services. Denial of service (DoS) attacks can target IoT devices and services at any layer. Customer service suffers due to the device and network resources becoming unresponsive. Thus to curb such losses, we aim to provide a solution via this research paper.

II. Related Work

Table 1 is giving an overview of previous research work that employed deep learning and machine learning techniques for identifying attacks on IoT environments. The table covers multiple research papers from the years 2020-2022. The table includes a list of different algorithms used in these studies, such as SVM, RF, DT, LR, ANN, etc., and the pros and cons of the research paper being discussed. Most of the studies have a specific focus on detecting particular types of attacks, such as Bot-IoT, DDoS, Injection attacks, etc.

III. Methodology

The primary aim of the paper is cyber attack detection in the IoT environment. Hence, it helps in classifying if any cyber attack is being targeted on said IoT environment. Fig. 1 depicts a flowchart that describes the methodology used for training deep learning models capable of attack detection and classification, which has been further explained in the below-following subsections.

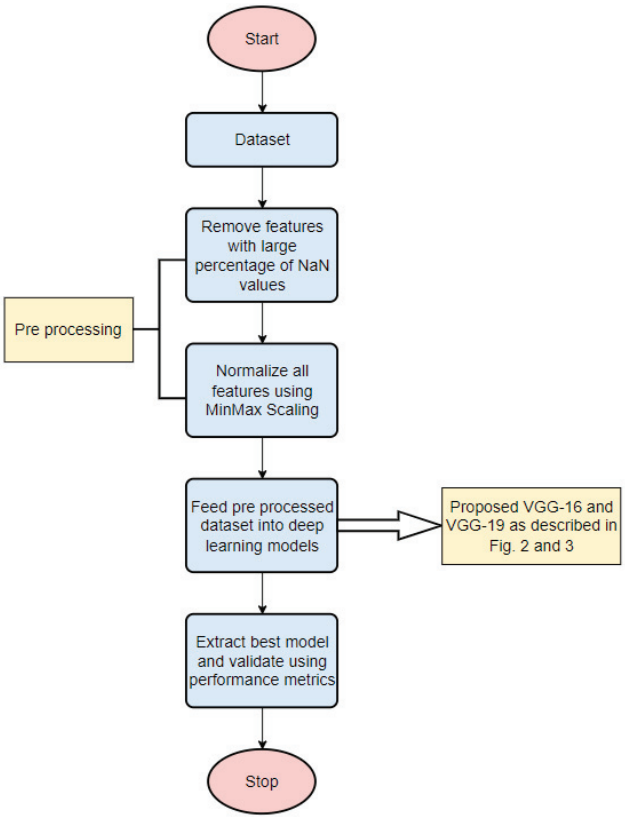


Fig. 1. Training deep learning model for attack detection and classification in IoT

A. Dataset

The Edge-IIoTset Cyber Security Dataset [16] has been utilized for this experiment which was designed by the authors of [15] recently in 2022.

This dataset can be utilized in various intrusion detection systems applying machine learning algorithms such as federated and centralized learning. The data was generated and gathered using multiple IoT devices of various different types(more than 10) forming an IoT testbed, for example, Ultrasonic sensors, pH Sensor Meters, Water level detecting sensors, Heart Rate sensors, Soil Moisture sensors etc.

In the dataset, the threats are classified into five major types such as Man in middle attacks, Information gathering, Injection attacks, Malware attacks, and DoS/DDoS attacks, which in turn have been subdivided into a total of 14 classes for attack types and 1 class depicting normal behavior. The authors in [15] have referred to multiple datasets, like the Bot-IoT dataset and the MQTTset dataset, to name a few.

In the paper, they argued the fact that these datasets do not depict real-world scenarios, and, thus, in turn, would hinder different machines and deep learning algorithms when used in the real-world landscape. To curb this, they have made significant use of real-world scenarios and have collected data from various IoT devices, as mentioned above. To implement the above-mentioned methodology, the authors created a realistic IoT testbed . They used various realistic cyber-attacks such as TCP-SYN and DNS Spoofing attacks, to name a few. They conducted their experiment for two months.

The next step taken up was to extrapolate features from the HTTP requests and adequately label the attacks to reach a final dataset.

B. Pre-Processing raw HTTP requests on IoT from dataset

We filtered features from the dataset that were irrelevant to our task or contained a large percentage of NAN(Not a Number) value. Following this, we arrived at a reasonably usable dataset containing 92 features and 19,04,671 data items.

To prevent one feature from having an enormous influence on the neural network weights, we also normalized the feature vectors using MinMax scaling normalization [17]. At this step, we have arrived at the dataset that will finally be fed to the neural networks.

The labels in the dataset, such as standard request, backdoor attack, SQL_injection attack, etc., were encoded to corresponding unique integer values representing the attack classification. We have used random shuffling on the datasets to ensure that there is a good mix of all the classes for training and testing purposes.

C. Cyber Attack analysis in IOT using Deep Learning techniques

As is the inherent nature of IoT devices and the environments involving them, data is sent and received via the

Authorized licensed use limited to: DELHI TECHNICAL UNIV. Downloaded on May 11,2023 at 10:18:12 UTC from IEEE Xplore. Restrictions apply.

internet using HTTP requests. Thus, the major brunt of cyber attacks on IoT devices occurs via these requests. The main idea behind the paper lies in the fact that if these requests can be used to detect and classify cyber attacks, we can prevent them from reaching the IoT gateway. For that purpose, we have utilized the above-mentioned dataset to simulate such HTTP requests and train models that can be capable of detecting and classifying these cyber attacks. For classifying and detecting attacks on the IoT environment, we have utilized two main Deep Learning Convolutional Models, that is, VGG-16 and VGG-19 [18]. Since our data items are not present as images, which is the traditional approach when using the above-mentioned models, certain modifications were made. The complete description of both models is given in the next two sections.

*1) **VGG-16**:* With the onset of Convolution networks [19] in the deep learning scenario, it was possible to extract low, medium, and high-level features from images, thus allowing us better accuracy in classification problems.

VGG-16 model, a Deep Convolutional Neural Network [18], was introduced in 2015 and achieved better accuracies than its predecessor Alexnet [20].

The focus on such networks has been prevalent for recognizing and classifying images. However, the same architecture can still be utilized for tasks other than that of computer vision to achieve better accuracies than other classification models and techniques. We have approached this research problem with the same method.

The VGG-16 ConvNet comprises of 13 Convolutional Layers and 5 MaxPooling layers. In addition to convolutional layers, flatten, dense, and softmax [19] layers are also utilized for classification purposes. The equation (1) denotes the mathematical representation of the softmax function, where σ represents the softmax value, x_i denotes the ith of value, and exp denotes the exponent e. The authors in [18] have utilized a (3x3) reception field, similar to which we have adopted for our use case.

In contrast to traditional VGG-16 models that use Conv2D and MaxPooling2D layers for image recognition purposes, we have utilized the appropriate Conv1D and MaxPooling1D layers to fit our needs owing to the nature of the data being processed. However, we have kept the activation function as ReLu [21], which is mathematically defined in equation (2). In addition to these changes, we have also utilized the ZeroPadding1D layer instead of directly passing the one-dimensional tensor as input data to the 1st convolutional layer.

When we built the model, we used the glorot uniform [22] for the kernel initialized with seed as 0. For the loss function, we have used categorical cross-entropy loss [23] and is defined in equation (3), where $\mathcal{L}_{CE}$ denotes the loss, M denotes the number of classes, the log is the natural log, y is the binary indicator (0 or 1) if class label i is the correct classification for observation o, and p denotes the predicted probability observation o is of class i. The optimizer used is Adam [24].

The model's general layout is shown in Fig. 2.

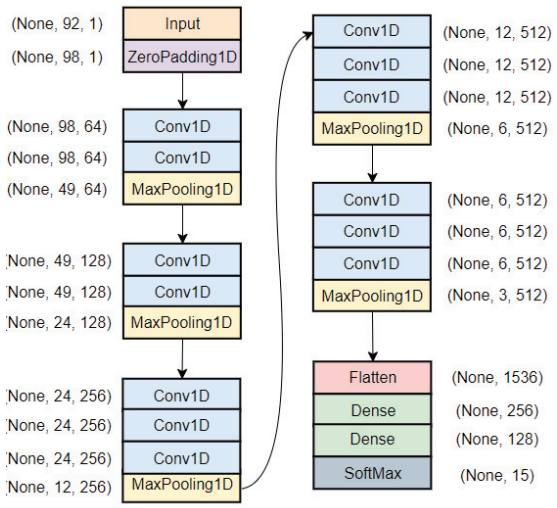


Fig. 2. VGG-16: Model Overview

$$\sigma(x_i) = \frac{\exp(x_i)}{\sum_j \exp(x_j)} \tag{1}$$

$$ReLu(x) = max(0, x) \tag{2}$$

$$\mathcal{L}_{CE} = -\sum_{i=1}^{M} y_{o,i} \log(p_{o,i}) \tag{3}$$

*2) **VGG-19**:* Similar to VGG-16, the VGG-19 ConvNet model follows similar architecture for weighted layers but instead of only 16 of them, it has 19 weighted layers.

The main ideology behind VGG-19 was to add more layers and increase the depth of the VGG-16 ConvNet model to increase accuracy by extracting more information from the data items.

Similarly, to make the model applicable to our dataset, we have used the same conforming changes as done in the VGG-16 model mentioned previously. The model's general layout is shown in Fig. 3.

The VGG-19 ConvNet comprises of 16 Convolutional Layers and 5 MaxPooling layers. In addition to convolutional layers, flatten, dense, and softmax [19] layers are also utilized for classification purposes. We have kept the activation function as ReLu [21]. We have also utilized the ZeroPadding 1D layer instead of directly passing the one-dimensional tensor as input data to the 1st convolutional layer.

Here, we also build the model using the glorot uniform [22] for kernel initializer with seed as 0. Similarly, for the loss function, we have used categorical cross entropy [23] and the optimizer used is Adam [24].

IV. Experimentation and Results

A. Result Metrics

To assess the effectiveness of our models, we have utilized majorly four performance evaluation parameters, namely accuracy, Precision, Recall, and F1 score, the mathematical

Authorized licensed use limited to: DELHI TECHNICAL UNIV. Downloaded on May 11,2023 at 10:18:12 UTC from IEEE Xplore. Restrictions apply.

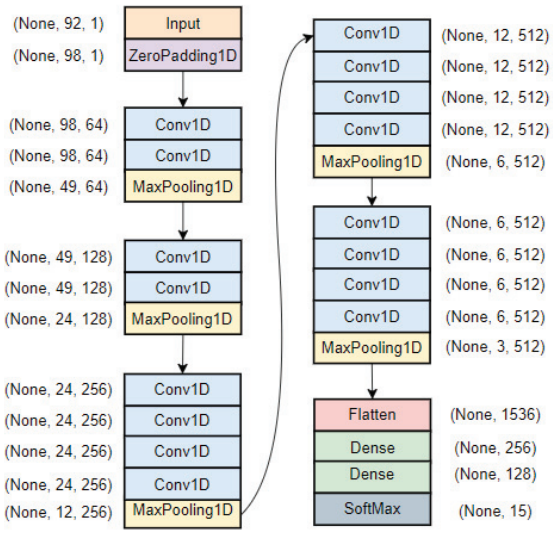


Fig. 3. VGG-19: Model Overview

denotation of which can be found in equations (4), (5), (6) and (7) respectively. We have measured the accuracy of 2 types: the first for attack classification based on the initially described 15 labels and the second for attack detection, namely two labels, that is, normal or an attack. Each metric has been defined below, along with the mathematical equation [25].

*1) **Accuracy**:* This depicts the ratio of data instances our model properly categorized as compared to all the data instances.

$$Accuracy = \frac{TP + TN}{TP + TN + FP + FN} \tag{4}$$

*2) **Recall**:* This depicts the number of instances the model correctly identified as relevant out of the total.

$$Recall = \frac{TP}{TP + FN} \tag{5}$$

*3) **Precision**:* This depicts the number of relevant instances out of the total instances the model retrieved.

$$Precision = \frac{TP}{TP + FP} \tag{6}$$

*4) **F1 score**:* It is determined as the harmonic mean of recall and precision.

$$F1 = \frac{2 * Precision * Recall}{Precision + Recall} = \frac{2 * TP}{2 * TP + FP + FN} \tag{7}$$

TP = True Positive TN = True Negative FP = False Positive FN = False Negative

B. Findings

Table 2 shows the findings of our experiment under the same conditions when both models were trained for 20 epochs, each with a batch size of 1024 data items. The findings are retrieved when the model is run on the validation dataset. The below-mentioned findings were observed without bias.

TABLE II
COMPARATIVE ANALYSIS WITH OTHER MODELS

S.No	Model	Attack Detection Accuracy	Attack Classification Accuracy	Recall	Precision	F1 score
1.	ResNet50 [26]	100%	92.78%	0.927	0.94	0.9299
2.	Proposed VGG-16	100%	94.865%	0.948	0.96	0.944
3.	Proposed VGG-19	99.999%	94.864%	0.948	0.951	0.947

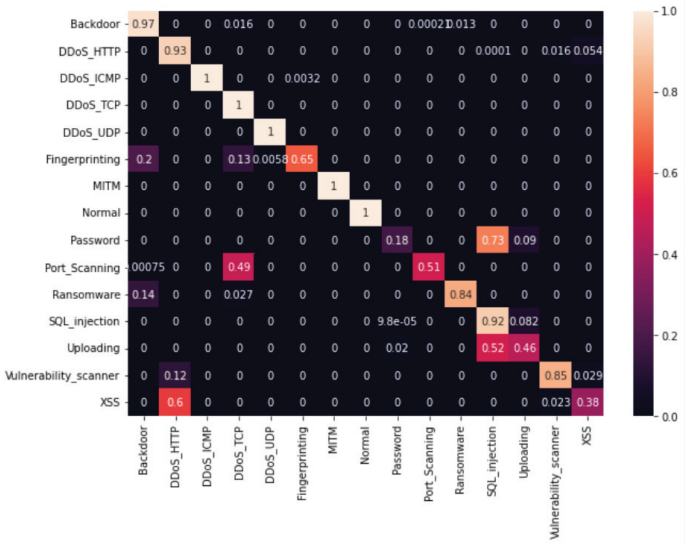


Fig. 4. VGG-16: Heatmap plot for validation dataset

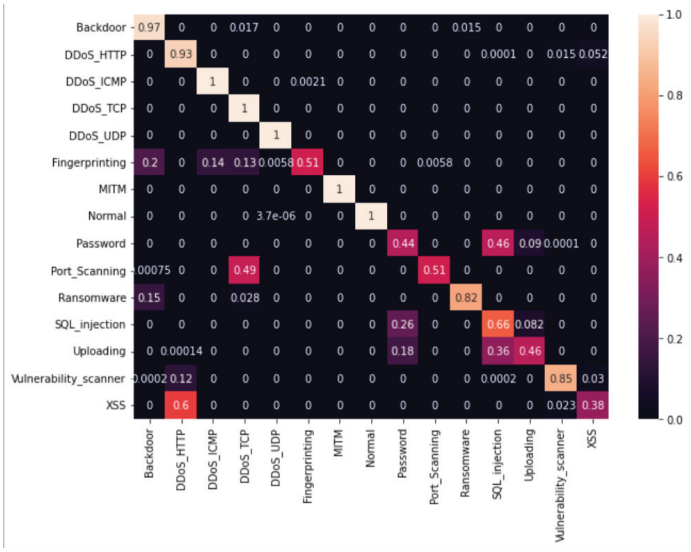


Fig. 5. VGG-19: Heatmap plot for validation dataset

Also, Fig. 4-5 describes the heatmap for both the models VGG-16 and VGG-19 when evaluated on the validation dataset. This helps us identify the misclassifications that the models make. For example, when we look at the intersection of the 'normal' class's row and column, we can infer that both

Authorized licensed use limited to: DELHI TECHNICAL UNIV. Downloaded on May 11,2023 at 10:18:12 UTC from IEEE Xplore. Restrictions apply.

models can identify a normal HTTP request from the harmful one.

When we compare the above-mentioned results, we can not declare which is better as both the models perform exceptionally well in detecting attacks and better in classifying attacks than previously trained models, as done here [26]. Thus both models work very well for intrusion detection from cyber-attacks and have better-classifying capabilities than previously trained models.

.

V. Conclusion and Future Work

Through this paper, we have carefully studied and researched the current field of thought on attack detection in the IoT landscape. We have compared and contrasted techniques currently used to detect attacks on IoT-based networks, such as different machine learning techniques like Naive Bayes using the bijective soft set approach, Random Forests, SVM(support vector machines), etc. We applied VGG-16 and VGG-19 deep convolutional neural networks with conforming changes made so that the dataset could fit into both models. Using different performance metrics we studied the results of both the models and thus concluded that both models perform equally well on the dataset, with a near-perfect attack detection accuracy and better attack classification accuracy than previous work.

Our work was mostly regarding attack detection. What further can be done on this is to provide security from these attacks using Blockchain Mechanism, a digitally formatted distributed database or ledger for storing information. The creation of cryptocurrencies such as Bitcoin is the most widely recognized use of blockchain technology. They are employed to keep a safe, decentralized record of each transaction carried out on a network. Once the transaction has been made, it is immutable. These qualities can all be utilized to make IoT devices/systems more secure.

The results of our experiments indicate that the proposed model utilizing the algorithm is efficient in detecting attacks in IoT applications with exceptional accuracy.

References

[1] A. B. Zebua, M. F. A. Husni, M. Naufal, Andri, and S. Irviantina, "Iot-based smart bin using smell, weight, and height sensors," in *2022 Seventh International Conference on Informatics and Computing (ICIC)*, 2022, pp. 1–5.

[2] M. Husamuddin and M. Qayyum, "Internet of things: A study on security and privacy threats," in *2017 2nd International Conference on Anti-Cyber Crimes (ICACC)*. IEEE, 2017, pp. 93–97.

[3] L. S. Vailshery, "Iot devices installed base worldwide 2015-2025," Nov 2016. [Online]. Available: https://www.statista.com/statistics/471264/iot-number-of-connected-devices-worldwide/

[4] D. Minoli and B. Occhiogrosso, "Blockchain mechanisms for iot security," *Internet of Things*, vol. 1, pp. 1–13, 2018.

[5] T. Gaber, A. El-Ghamry, and A. E. Hassanien, "Injection attack detection using machine learning for smart iot applications," *Physical Communication*, vol. 52, p. 101685, 2022.

[6] S. Nayak, N. Ahmed, and S. Misra, "Deep learning-based reliable routing attack detection mechanism for industrial internet of things," *Ad Hoc Networks*, vol. 123, p. 102661, 2021.

[7] J. G. Almaraz-Rivera, J. A. Perez-Diaz, and J. A. Cantoral-Ceballos, "Transport and application layer ddos attacks detection to iot devices by using machine learning and deep learning models," *Sensors*, vol. 22, no. 9, p. 3367, 2022.

[8] P. Bedi, S. Mewada, R. A. Vatti, C. Singh, K. S. Dhindsa, M. Ponnusamy, and R. Sikarwar, "Detection of attacks in iot sensors networks using machine learning algorithm," *Microprocessors and Microsystems*, vol. 82, p. 103814, 2021.

[9] R. Zagrouba and R. Alhajri, "Machine learning based attacks detection and countermeasures in iot," *International Journal of Communication Networks and Information Security*, vol. 13, no. 2, pp. 158–167, 2021.

[10] S. Bagui, X. Wang, and S. Bagui, "Machine learning based intrusion detection for iot botnet," *International Journal of Machine Learning and Computing*, vol. 11, no. 6, pp. 399–406, 2021.

[11] M. M. Aboelwafa, K. G. Seddik, M. H. Eldefrawy, Y. Gadallah, and M. Gidlund, "A machine-learning-based technique for false data injection attacks detection in industrial iot," *IEEE Internet of Things Journal*, vol. 7, no. 9, pp. 8462–8471, 2020.

[12] M. Shafiq, Z. Tian, A. K. Bashir, X. Du, and M. Guizani, "Corrauc: a malicious bot-iot traffic detection method in iot network using machine-learning techniques," *IEEE Internet of Things Journal*, vol. 8, no. 5, pp. 3242–3254, 2020.

[13] J. Kim, M. Shim, S. Hong, Y. Shin, and E. Choi, "Intelligent detection of iot botnets using machine learning and deep learning," *Applied Sciences*, vol. 10, no. 19, p. 7009, 2020.

[14] M. Shafiq, Z. Tian, Y. Sun, X. Du, and M. Guizani, "Selection of effective machine learning algorithm and bot-iot attacks traffic identification for internet of things in smart city," *Future Generation Computer Systems*, vol. 107, pp. 433–442, 2020.

[15] M. A. Ferrag, O. Friha, D. Hamouda, L. Maglaras, and H. Janicke, "Edge-iiotset: A new comprehensive realistic cyber security dataset of iot and iiot applications for centralized and federated learning," *IEEE Access*, vol. 10, pp. 40 281–40 306, 2022.

[16] "Edge-iiotset cyber security dataset of iot & iiot - kaggle.com," https://www.kaggle.com/datasets/mohamedamineferrag/edgeiiotset-cyber-security-dataset-of-iot-iiot, 2022, [Accessed 16-Jan-2023].

[17] L. Al Shalabi, Z. Shaaban, and B. Kasasbeh, "Data mining: A preprocessing engine," *Journal of Computer Science*, vol. 2, no. 9, pp. 735–739, 2006.

[18] K. Simonyan and A. Zisserman, "Very deep convolutional networks for large-scale image recognition," *arXiv preprint arXiv:1409.1556*, 2014.

[19] S. Albawi, T. A. Mohammed, and S. Al-Zawi, "Understanding of a convolutional neural network," in *2017 international conference on engineering and technology (ICET)*. Ieee, 2017, pp. 1–6.

[20] A. Krizhevsky, I. Sutskever, and G. E. Hinton, "2012 alexnet," *Adv. Neural Inf. Process. Syst*, pp. 1–9, 2012.

[21] S. R. Dubey, S. K. Singh, and B. B. Chaudhuri, "Activation functions in deep learning: A comprehensive survey and benchmark," *Neurocomputing*, 2022.

[22] X. Glorot and Y. Bengio, "Understanding the difficulty of training deep feedforward neural networks," in *Proceedings of the thirteenth international conference on artificial intelligence and statistics*. JMLR Workshop and Conference Proceedings, 2010, pp. 249–256.

[23] Y. Srivastava, V. Murali, and S. R. Dubey, "A performance evaluation of loss functions for deep face recognition," in *National Conference on Computer Vision, Pattern Recognition, Image Processing, and Graphics*. Springer, 2019, pp. 322–332.

[24] S. Ruder, "An overview of gradient descent optimization algorithms," *arXiv preprint arXiv:1609.04747*, 2016.

[25] K. P. Shung, "Accuracy, precision, recall and f1? — towardsdatascience.com," https://towardsdatascience.com/accuracy-precision-recall-or-f1-331fb37c5cb9, [Accessed 20-Jan-2023].

[26] "Resnet50-cnn1d -kaggle.com," https://www.kaggle.com/code/mohamedahmedae/resnet50-cnn1d, 2022, [Accessed 16-Jan-2023].

Authorized licensed use limited to: DELHI TECHNICAL UNIV. Downloaded on May 11,2023 at 10:18:12 UTC from IEEE Xplore. Restrictions apply.

Materials Research Express

ACCEPTED MANUSCRIPT • OPEN ACCESS

Damage identification in Concrete under impact loading at varying temperatures using voltage relations technique: An experimental and numerical study

To cite this article before publication: indrajeet singh *et al* 2023 *Mater. Res. Express* in press https://doi.org/10.1088/2053-1591/acd2a9

Manuscript version: Accepted Manuscript

Accepted Manuscript is "the version of the article accepted for publication including all changes made as a result of the peer review process, and which may also include the addition to the article by IOP Publishing of a header, an article ID, a cover sheet and/or an 'Accepted Manuscript' watermark, but excluding any other editing, typesetting or other changes made by IOP Publishing and/or its licensors"

This Accepted Manuscript is **© 2023 The Author(s). Published by IOP Publishing Ltd**.

As the Version of Record of this article is going to be / has been published on a gold open access basis under a CC BY 4.0 licence, this Accepted Manuscript is available for reuse under a CC BY 4.0 licence immediately.

Everyone is permitted to use all or part of the original content in this article, provided that they adhere to all the terms of the licence https://creativecommons.org/licences/by/4.0

Although reasonable endeavours have been taken to obtain all necessary permissions from third parties to include their copyrighted content within this article, their full citation and copyright line may not be present in this Accepted Manuscript version. Before using any content from this article, please refer to the Version of Record on IOPscience once published for full citation and copyright details, as permissions may be required. All third party content is fully copyright protected and is not published on a gold open access basis under a CC BY licence, unless that is specifically stated in the figure caption in the Version of Record.

View the article online for updates and enhancements.

This content was downloaded from IP address 14.139.251.98 on 11/05/2023 at 11:22

Damage identification in Concrete under impact loading at varying temperatures using voltage relations technique: An experimental and numerical study

Indrajeet Singh[1], Nirendra Dev[2], Shilpa Pal[3*]

[1] Research scholar, [2] Professor, [3] Associate Professor
Civil Engineering Department, Delhi Technological University, Delhi

* *Corresponding Author* shilpapal@dtu.ac.in

Abstract

Impact-loaded concrete structures cause severe and rapid damage, resulting in significant property and human life loss. As the temperature rises, the damage caused by impact loading becomes increasingly severe. Concrete structures need structural health monitoring (SHM) to avoid this damage and loss. In this study, the voltage strain relation technique was used to identify the damaged state of concrete under impact loads at various temperature conditions experimentally and numerically. For this purpose, an experimental study was performed on concrete cube specimens in which different piezo configurations (surface bonded, non-bonded, and jacketed) were installed to acquire the voltage data. Before applying an impact load to the top surface of the concrete specimen, it was preheated at 50 ^{o}C, 100 ^{o}C, and 150 ^{o}C to provide the temperature effect, and then a free-falling iron ball was dropped from 3 m heights on the top of the specimens. Furthermore, finite element analysis has been carried out to validate the experimental results with analytical results. The experimental results show that the voltage strain relation technique is well capable of detecting the damage in concrete under the temperature and impact loading conditions. The maximum absolute voltage value *(Vp)* of 17.11 V was recorded for the jacketed sensors under an impact height of 3 m at 100 ^{o}C. All the piezo sensor configurations are capable of finding the damage. Jacketed sensors are more efficient in the health assessment of concrete in terms of voltage relations. In terms of strain values, the analytical results are in good agreement with the experimental results.

Keywords:-Damage detection; Voltage relation; Piezo sensors; temperature loading; Impact Loading.

Accepted Manuscript

1 Introduction

In recent years, structures have become more vulnerable to terrorist attacks, blast waves, earthquakes, industrial accidents, etc. High loading rates often cause fire outbreaks and spread, exposing structures to harsh conditions. Limited studies have demonstrated the assessment of concrete damage caused by an impact load at various temperatures. The majority of studies only show the individual impact and temperature loading effects on concrete structures. Many areas of damage identification for pre and post-heated concrete under impact loading remain unexplored. The voltage relation technique has emerged as an advanced technique in structural health monitoring (SHM) in recent years due to its wide application in the field of piezoelectric materials.

Nomenclature

D_3	electric Displacement	E_s	Young's modulus
S_1	strain value in direction	μ	Poisson's ratio
d_{31}	piezoelectric strain coefficient	V	voltage generated across the PZT
E_3	external electric field	V_p	absolute peak voltage
T_1	axial stress in direction	S_p	strain values at the vicinity of PZT
$\overline{Y^E}$	complex young's modulus of elasticity of the PZT patch	h	thickness of PZT
		δ	dielectric loss tangent
$\overline{\varepsilon_{33}^T}$	complex electric permittivity	η	mechanical loss factor

When exposed to impact loads, concrete structures primarily fail in two ways: globally and locally. Local substantial failure is commonly caused by crushing, plug development, and scabbing, whereas global failure is caused by bending. The best method for examining the impact behaviour of concrete materials was the drop impact test [1]. Bischoff et al. [2] examined and explained concrete's behaviour under both static and impact loading conditions. The responses of different loading conditions were compared using strain value, strength and energy-absorption capacity. The behaviour of the slab, when subjected to impact loading has been investigated by several researchers [3]–[9][10]. Youmn Al Rawi et al. [11] investigated the behaviour of post-tensioned concrete slabs under the effect of impact load. For the purpose of analyzing the damage behaviour, two different grades of post-tensioned concrete slabs were

Accepted Manuscript

tested at a height of 20 m and a weight of 605 kg. Many researchers [12]–[16] investigated the impact load analysis of beams. Liu Jin et al. [17] tested 12 different types of simply supported beams with various stirrup ratios and steel fibre volume fractions to examine the impact resistance behaviour of steel fibre reinforced concrete beams. Additionally, a three-dimensional finite element simulation was performed, and it was found that the addition of steel fibres improved the steel fibre beam's capacity to withstand impacts.

Many researchers have already studied the effect of low and high temperatures on concrete [18]–[23][24][25]. One of the most significant advantages of concrete as a building material is its ability to withstand high temperatures. The disturbance caused by high temperatures in concrete manifests itself as surface cracking and spalling [26]. According to Wang et al. [27], because of anisotropy and porosity, thermal distribution and transmission in concrete are typically non-uniform and time-dependent, causing a negative correlation between temperatures and concrete Young's modulus/natural frequencies. Under conditions of higher temperatures, structural elements like beams and slabs show greater signs of deterioration [28], [29]. Researchers have recently become increasingly focused on detecting the many sorts of strength behaviour and damage situations in concrete, such as Sher. [30] , cracking pattern [31] [32], fracture performance [33], reduction due to explosion [34], corrosion monitoring using piezo sensors [35]–[39] and strength parameters [40] under the static and dynamic loading conditions.

Researchers have recently emphasized the behaviour of concrete structures element (beam and slab) under both loading condition impact and temperatures. The behaviour of concrete structures was studied by varying some key parameters of impact loading and temperature, such as the mass of the impactor, velocity of the impactor, geometry of the impactor, and at higher degrees of temperature. The complete literature review of the concrete structures subjected to both impact and temperatures is shown in Table 1.

Table 1 Literature review of the concrete subjected to both impact and temperatures

Configuration of Impact loading and temperature	**Conclusions**	**References**
Mass of drop weight = 105 kg, Impact Velocity = 6.86m/sec, Heating Time = 0,30,60,90 min,	With an increase in heating time duration, mid-span deflection rises.	[41]

Accepted Manuscript

Number of slab = 6		
Weight of hammer = 393 Kg Drop of impactor height = 1.5 m Velocity of Impact = 5.4 m/s Impact energy ($mv^2/2$) = 5730 J. Cylindrical Hammer = 200 mm Steel fibre volume fractions = 0 %, 1 % , 2 % and 3 % Different grades for the rebars = HRB400 and HPB300.	With more steel fibres, SFRC beams fail in flexure under impact loads, not shear. Steel fibre content has a minimal impact on the thermal and mechanical behaviour of damaged beams, limited to low-energy pre-impact.	[42]
Velocity of impact = 4 m/s , Three different temperature variations = 200 ºC, 500 ºC and 800 ºC	80 % degradation of concrete strength with an increase in temperature	[43]

1.1 Finite element analysis (FEM) of concrete structures under temperature and impact loading

FEM analysis has emerged as a superior technique for analyzing concrete structures in recent years because of its accurate interpretation and faster results. Due to these advantages, most researchers now employ the FEM technique to analyze concrete structures subjected to impact loading, thermal loading, and the combined effect of impact and thermal.

This section shows the literature review for the FEM analysis of a concrete structure subjected to thermal loading conditions. Many researchers have demonstrated that FEM analysis produces significant results when analyzing concrete under thermal loading conditions [44], [45]. The strengthening effect of glass fibre and polypropylene fibre-based engineered cementitious composites (GFPPECC) on fire-damaged reinforced concrete short exterior columns was explained by Bhuvaneshwari et al. [46], and the FEM analysis performed by ANSYS was compared with the experimental results and found that there was no deviation in both the experimental and numerical results. Song et al. [47] simulated the mass concrete freezing shaft lining and frozen soil wall under the influence of low temperatures. The ANSYS finite element software was used to perform the transient heat transfer analysis.

Ganesan P et al. [48] used ANSYS explicit dynamics software to perform FEM analysis of the RC and prestressed RC slab at low-velocity impact under two different boundary conditions, the opposite side simply supported and the adjacent side simply supported. Their analysis demonstrated that the boundary condition significantly impacted the slab's deflection. Singh I et al. [10] performed the FEM analysis of the conventional and geopolymer reinforced concrete beam and slab under the low and high-velocity impact using ANSYS explicit dynamics

Accepted Manuscript

software; the results shows that the geopolymer concrete performs better impact resistance behaviour in comparison to the conventional reinforced concrete.

FEM behaviour of a concrete structure subjected to thermal and impact loading was comprehensively studied [49]. The author also performed a three-dimensional finite element study of the RC slab when it was destroyed by fire and then loaded by impact. The fire effect was simulated using transient 3D FE thermo-mechanical analysis, whereas the impact loading was simulated using explicit multi-body dynamic analysis. According to the study's findings, the simulation can match the experimental results. Jin Liu et al. [50] investigated the effect of elevated temperature on dynamic compressive properties of heterogeneous concrete using a mesoscale numerical study. They divided the study into two steps, first simulating heat conduction behaviour and then simulating the dynamic mechanical behaviour of concrete using the first stage's output as the initial conditions. Previous researchers employed dynamic strain measurement utilizing the voltage strain relation approach to locate damage in concrete structures under impact load conditions and discovered that this voltage strain relation technique is quite capable of finding damage under impact load situations [51] [52].

The purpose of this research is to use various piezo configuration sensors to detect damage in concrete under different impact loading conditions at different temperatures conditions. For this purpose, experimental studies were carried out to extract the voltage data from these various sensors. For a better understanding of the damages, these extracted signatures data were further analyzed in various forms such as equivalent structural parameters like mass, damping, and stiffness and compared the experimental and equivalent plots. This study also illustrates the effect of damages under fixed boundary conditions (FBC). Further, to validate the experimental results, finite element analysis was performed on a concrete sample under free-free (FFBC) and fixed boundary conditions.

2 Background information for the research

This section discusses the research background, beginning with the dynamic strain measurement using PZT sensors and progressing to an introduction to the finite element method (FEM) analysis for the impact loading condition.

Accepted Manuscript

2.1 Dynamic strain measurement using PZT sensors

Materials with piezoelectric properties PZT has the ability to sense changes in its environment, such as changes in geometry, and mechanical or electrical properties, and respond quickly, which can be easily measured. The PZT operates under the effect of piezoelectricity, which has the ability to convert electrical responses into mechanical disturbances and mechanical disturbances into electric pulses. These effects are represented mathematically, with Equation 1 demonstrating the sensing behaviour of the PZT and Equation 2 demonstrating the actuation behaviour. One dimensional interaction between PZT Patch and the host structure is shown in Figure 1.

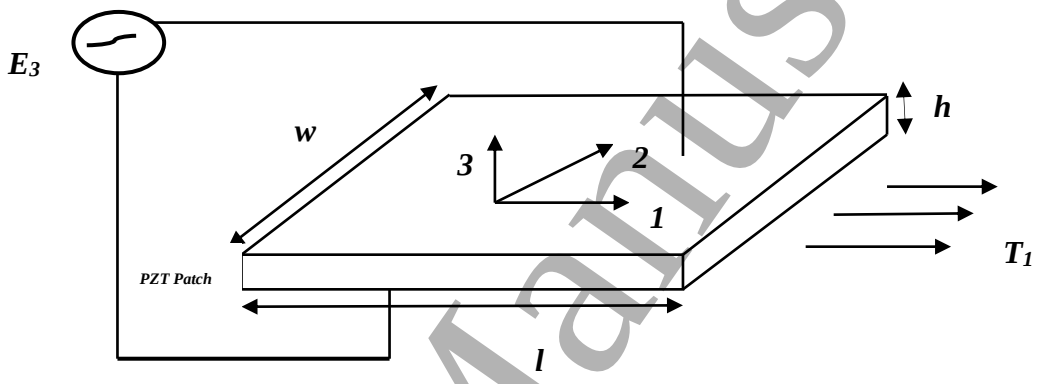


Figure 1 One-dimensional interaction of PZT patch under the action of electric field and stress

$$D_3 = \overline{\varepsilon_{33}^T} E_3 + d_{31} T_1 \quad \textbf{(1)}$$

$$S_1 = \frac{T_1}{\overline{Y^E}} + d_{31} E_3 \quad \textbf{(2)}$$

Where S_1 represents the strain value in direction '1'. D_3 is the electric displacement over the PZT patch, the piezoelectric strain coefficient is d_{31}, E_3 is the external electric field and T_1 is the axial stress in direction '1'. $\overline{Y^E}$ is the complex young's modulus of elasticity of the PZT patch at a constant electric field as shown in Equation 3

$$\overline{Y^E} = Y^E (1 + \eta i) \quad \textbf{(3)}$$

$\overline{\varepsilon_{33}^T}$ is the complex electric permittivity in direction '3' at constant stress as shown in Equation 4

$$\overline{\varepsilon_{33}^T} = \varepsilon_{33}^T (1 - \delta i) \text{ with } i = \sqrt{-1} \quad \textbf{(4)}$$

Accepted Manuscript

Where ɳ and δ represent the mechanical loss factor and the dielectric loss tangent respectively. As shown in Equation 5, Shanker et al. [67] developed a relationship between the voltage across the PZT patch and strain in the host structure at the point of attachment.

$$V = \left(\frac{d_{31}\,\overline{Y^E}h}{\overline{\varepsilon_{33}^T}}\right)S_1 \quad \textbf{(5)}$$

Where V represents the voltage generated across the PZT patch of the thickness h. The output voltage can be measured using the instrument oscilloscope and with the help of this measured voltage, strain-induced can be calculated using this equation.

The above Equation 5,

3 Experimental setup

This section covers the entire methodology starting with the fabrication and installation of different piezo configurations such as jacketed piezo sensors (JKTPS), surface-bonded piezo sensors (SBPS), and non-bonded piezo sensors (NBPS) in concrete specimens. Further, the experimental setup consisting of testing age, and collection of data procedures have been explained.

3.1 Fabrication and installation of different piezo configurations

As shown in Figure 2, all three different sensors are built in the laboratory and installed with the host structure. The JKTPS has a diameter of 25 mm and a height of 20 mm, as shown in Figure 3(c). It is constructed of rectangular PZT patches 10 mm x 10 mm x 0.2 mm in size, soldered with co-axial wire on positive and negative electrodes, placed in the centre, and epoxy resin provided at the top and bottom portions to protect the PZT from the effects of water and ambient conditions during the construction stages.

JKTPS sensors are installed at the centre of the concrete cube, i.e., 75 mm each from the top and bottom. During the casting process, great care was taken to ensure that all JKTPS sensors were installed in the centre of the concrete cube and were not displaced from their original location.

SBPS sensors, as shown in Figure. 3(b) were directly bonded on the concrete using epoxy at the centre on the side face of the concrete adjacent to the impactor face, and the upper face of the bonded PZT was again covered with epoxy to protect it from the environment. The NBPS,

Accepted Manuscript

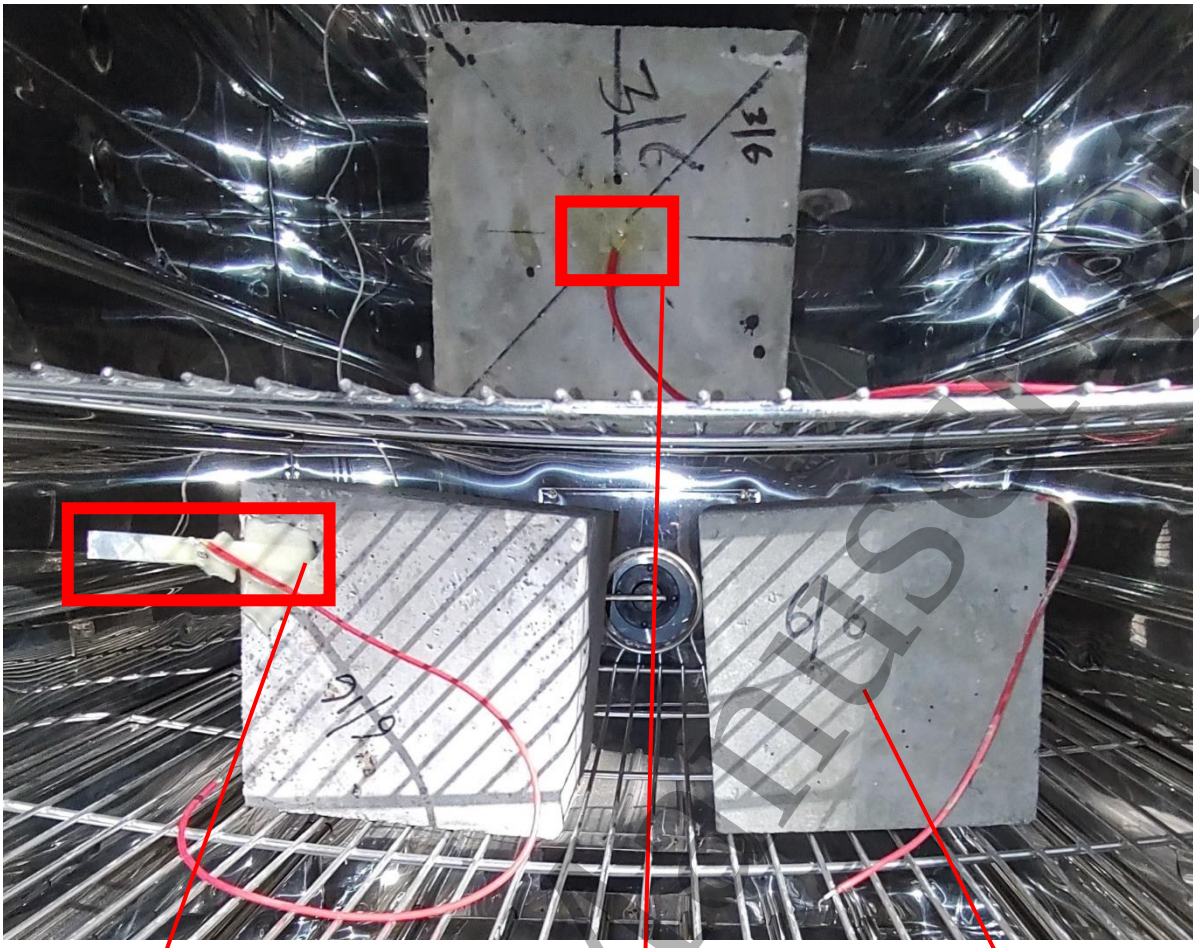


Figure 2 Arrangement of different piezo sensors configuration with the host structure



(a) **(b)** **(C)**

Figure 3 Closed view of the configuration of each different sensor a) NBPS b) SBPS c) JKTPS

as shown in Figure 3(a), was fabricated by using a surface-cleaned aluminium strip (100 mm x 10 mm x 3 mm) and a PZT patch (10 mm x 10 mm x 0.2 mm) fixed at the middle of the aluminium strip. Epoxy was used as a binding material to bond aluminium sheets and PZT, and special care was taken to ensure that they were adequately bonded. Furthermore, after

Accepted Manuscript

connecting with the aluminium strip, the PZT patch was soldered with the coaxial wire on the positive and negative electrodes, and an epoxy layer was applied above the soldered PZT after soldering to protect the PZT patch from environmental conditions. On the concrete side face adjacent to the impactor face, NBPS sensors were installed using adhesive epoxy.

3.2 Experimentation details and procedure

In this study, a standard 150 x 150 x 150 mm concrete cube with M30 grade was used, which has a 28-day strength of 30 N/mm^2. J.K Super ordinary Portland cement (OPC) grade 43 was employed as a binding material. Two varieties of coarse aggregate (10 mm and 20 mm) were used, as well as locally available well-graded fine aggregate that comes within Zone II of the Indian standard code (IS: 2386 (Part I)-1963) [53]. The casting of the concrete cube was done in the ratio of 1:1.84:3.48(Cement: Fine aggregate: Coarse aggregate) in a standard mould with proper mixing in the pan mixture as shown in Figure 4 (a) and compaction is done by vibrating table and left the mould for 24 hours as shown in Figure 4 (b). After 24 hours, all of the concrete moulds were de-moulded and placed in a curing tank as shown in Figure 4 (c) for 28 days for normal curing. Furthermore, until the samples were tested, they were all kept in a laboratory. The entire concrete cube sample is cast in the laboratory, which includes the embedded and non-bonded sensors type as well as the standard cube. Impact loads were applied from a 3 m height onto a concrete cube using a 5.45 kg free-falling spherical cast iron ball. The cast iron ball with a diameter of 11.5 cm falls through a PVC pipe with a thickness of 4 mm and an internal diameter of 15 cm. The PVC pipe is provided to guide the spherical ball for proper impact positioning on the concrete cube. All the concrete cubes were heated in the rectangular oven manufactured by Khera Instruments Pvt Ltd of size 605 x 605 x 910 mm. The experimental setup for testing the concrete cube under impact loading is depicted in Figure 5, which also includes a description of the experimental setup.

In this study, the damage was detected in the reference to voltage data recorded at the time of testing the cube. The first cube was subjected to three different temperatures, ranging from 50 °C, 100 °C and 150 °C, heated in the oven for 120 minutes then cooled for 60 minutes at room temperature. Furthermore, cooled cube samples were tested at the 3 m impact height and voltage data were recorded after each impact up to failure.

Accepted Manuscript



(a) **(b)** **(c)**

Figure 4 Preparation of concrete cube sample a) Pan concrete mixture b) Casting of concrete cube sample c) Curing tank

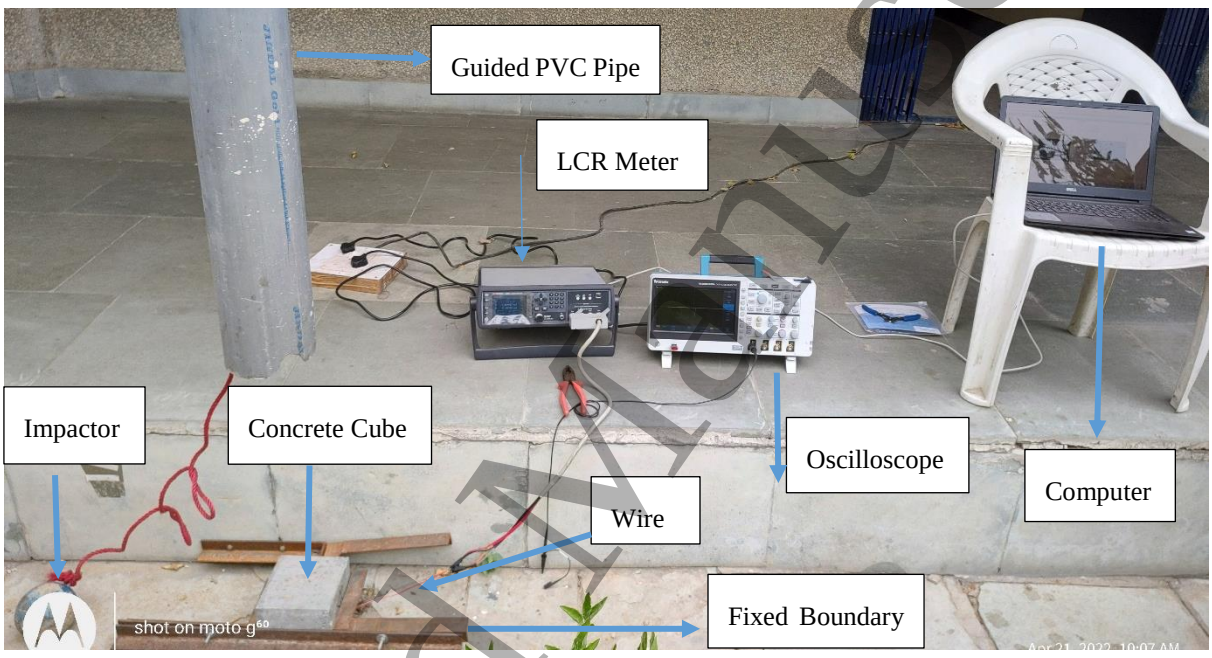


Figure 5 Experimental setup for impact test under FBC

3.3 Finite element modelling of the concrete sample

Two bodies are involved in finite element analysis, the concrete cube and the steel impactor. In the first stage, a concrete cube is subjected to thermal loading, which includes heating and cooling at room temperature. The transient thermal module in ANSYS was used to perform the thermal analysis, and the impact load analysis was performed using the explicit dynamics module in ANSYS.

3.3.1 Geometry and material properties

Table 2 shows the material and thermal properties at ambient temperature that were used in the finite element analysis in detail. Steel impactors with a specific gravity of 6839 kg/m^3 were

Accepted Manuscript

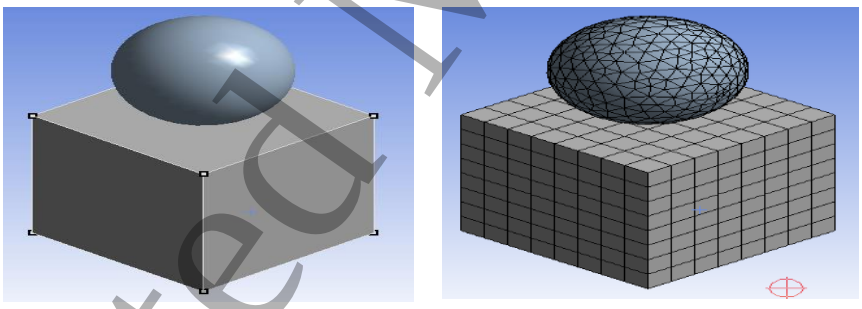
used, the same as in the experiment. Steel impactors were assumed to be linear elastic materials in the FEM analysis, with Young's modulus Es = 210 GPa and Poisson's ratio μ = 0.30.

Table 2 Properties of concrete cube and Impactor

Property	**Concrete Cube**	**Impactor**
Density*(kg/m^3)*	2340	6839
Young's mod., E (GPa)	30.91	210
Compressive strength(MPa)	29.7	-
Tensile strength (MPa)	2.88	-
Poisson's ratio	0.2	0.30
Bulk modulus (MPa)	17172	166,670
Shear modulus (MPa)	12879	76,923

3.3.2 Description of elements and meshing

For the modelling of the concrete cube in this FEM analysis, hexahedral solid elements were used. Frictional-type body interactions were used in the explicit dynamics module between the host structure (concrete cube) and the impactor (spherical ball).In this study, a 15 mm mesh size was used for both the concrete and the impactor, with the element mid-nodes dropped at the time of meshing. Figure 6 depicts the finite element model of a concrete sample with and without meshing.



(a) **(b)**

Figure 6 Finite element model of concrete sample a) without meshing b) with meshing

3.3.3 Boundary condition

In this study, concrete cubes were simulated with free boundary conditions (FBC), which were provided as same in the experiment.

Accepted Manuscript

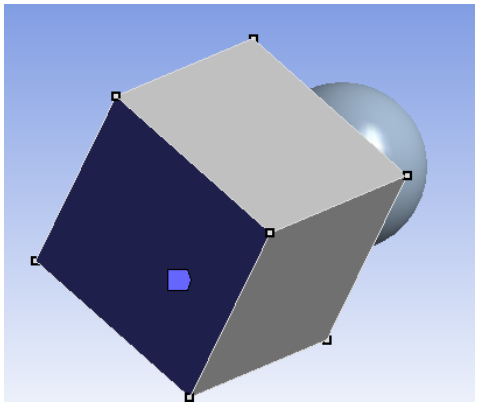


Figure 7 Free boundary condition for the concrete sample

Figure 7 depicts the free boundary condition (FBC) applied to a concrete cube with just the bottom portion of the cube fixed and the other remaining faces of the cube free.

3.4 Loading Condition

As mentioned in the previous section, concrete cubes that had previously been tested experimentally were simulated for a single drop of impact under thermomechanical and explicit dynamics loading conditions. In thermomechanical analysis, the initial thermal loading is given in terms of an initial temperature of 22 ^{o}C to be applied to the entire body of a concrete cube. There were two steps of analysis performed in thermomechanical analysis. In the first step, the concrete cube was heated for two hours using the convection method and then cooled down for one hour in which a linear decrement of ambient temperature occurs as in the experiment. The concrete cube was heated at three different temperature conditions of 50, 100 and 150 ^{o}C same as in the experiment.

After thermal exposure, concrete cubes were subjected to the spherical steel ball impact loading at the top surface of the concrete cube at the centre. Impact loading simulations were performed for the same height of 3 m as the experiment. The impact load is generated by free fall dropping of the steel ball of weight 5.45 kg mass from the velocity of 7.67 m/s.

4 Experimental Results and Discussion

This section is divided into two parts. First, discuss the experimental results of the voltage-time history and then go over the results of the finite element analysis (FEM) in detail.

Accepted Manuscript

4.1 Quantification of impact load using voltage-time history

In general, the impact load time histories are very minute, and hence, the loading's distinguishing features are highly evasive. A high acquisition rate digital oscilloscope was used to solve this problem (model Tektronix TBS 2104B series), which captured the impact value for intervals as short as 1 μs. The voltage generated by the PZT patch attached to the host structure was essentially captured by the oscilloscope. Voltage measurements were taken at a high acquisition rate, with acquisition times ranging from 500 ms to 2 s. The voltage-time histories were thoroughly examined to correlate the accumulating damage with strain. A total of typical 12 sensors were used to determine the effect of voltage with the impact loading under temperature variation for different sensors configuration. Absolute peak voltage (V_p) was identified for each impact loading. Furthermore, this obtained V_p were used to calculate the accumulated value of strain for each sensor. Figure 8 shows a typical variation of the voltage vs time graph for four different cube conditions. Figure 8 (a) depicts the voltage variation for cube C9, SBPS at ambient temperature conditions following the second impact, in which the voltage value first increases to 0.104 V and then decreases to 0.080 V. The graph in Figure 8 (b) shows the same pattern as the previous one, which depicts the voltage vs time graph for cube no. C5 after the second impact. Figure 8 (c) and (d) depicts the voltage variation for cube no. C12 and under C8 after the 3rd and 2nd impact respectively for SBPS and JKTPS sensors at the temperature variation of 150 ^{o}C, in both of them the voltage value first decreased and then increased.

Quantification of impact force is represented with the help of obtained peak voltage from each sensor at the time of impact and it was found that the peak voltage follows a continuously decreasing trend for the surface bonded and non-bonded sensors with the increase in the number of impact loads on each cube. This decreasing trend of peak voltage is due to the increase in damping of the cube. Peak voltage has followed the opposite trend for the JKTPS because they have been placed in the line of impact loading as a result strain development is more in this case. Table 3 displays all of the typical 12 cubes, which include the representation number, number of impacts up to failure and *Vp* value. Furthermore, strain values were calculated using Equation 6 with the help of PZT parameters and a *Vp* value.

$$S_p = \frac{\varepsilon_{33}^{T}}{d_{33} h Y^{E}} V_p \quad \textbf{(6)}$$

Accepted Manuscript

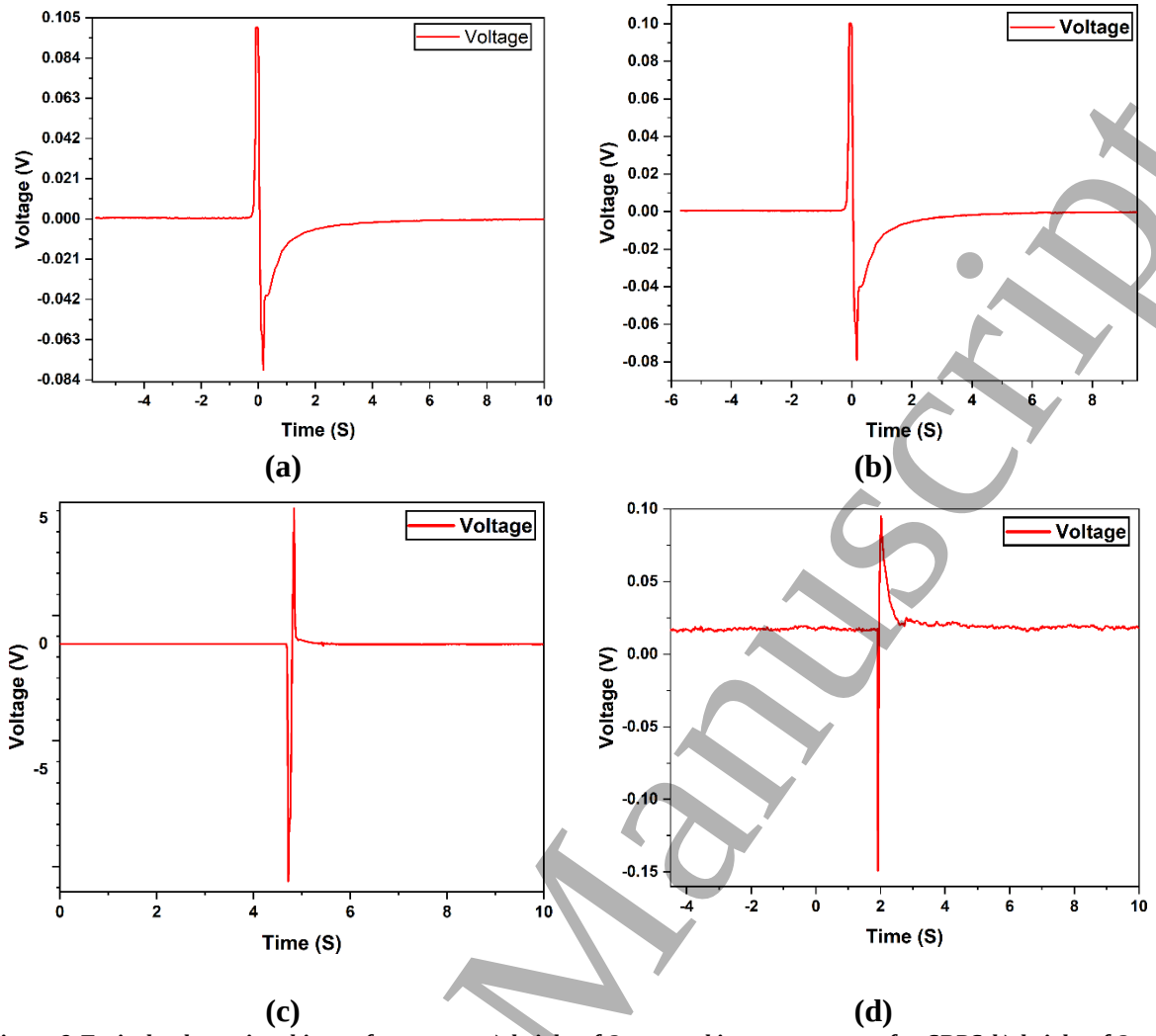


Figure 8 Typical voltage time history for sensors a) height of 3m at ambient temperature for SBPS b) height of 3m at ambient temperature for JKTPS c) height of 3 m at 150 ºC temperature for SBPS sensors d) height of 3 m at 150 ºC temperature for JKTPS

Table 3 depicts the *Vp* value for each cube, which is the maximum voltage recorded against the impact loading. The maximum absolute voltage value *(Vp)* of 17.11 V was recorded for the JKTPS sensors under an impact height of 3 m at 100 ºC, this is due to the Placing of JKTPS sensors in the line of impact. Furthermore, after the first impact, the peak voltage and strain value of each PZT installed in the cube were calculated as shown in Table 4.

Table 3 Representation of cube number, Absolute peak voltage (Vp) value and strain value for all different sensors with varying impact and temperature condition

S.No.	Type of Sensors	Impact Height	Temperature	Cube representation Number.	Total number of impact	Absolute Peak Voltage (V_p)
1	Non-Bonded PZT	3m	Ambient	C1	11	0.78
			50ºC	C2	11	0.33
			100ºC	C3	9	2.42

Accepted Manuscript

	(NBPS)		150°C	C4	7	10.58
2	Embedded (JKTPS)	3m	Ambient	C5	7	0.10
			50°C	C6	6	3.01
			100°C	C7	7	17.11
			150°C	C8	10	2.50
3	Surface Bonded (SBPS)	3m	Ambient	C9	8	0.100
			50°C	C10	8	10.58
			100°C	C11	7	11.71
			150°C	C12	12	6.41

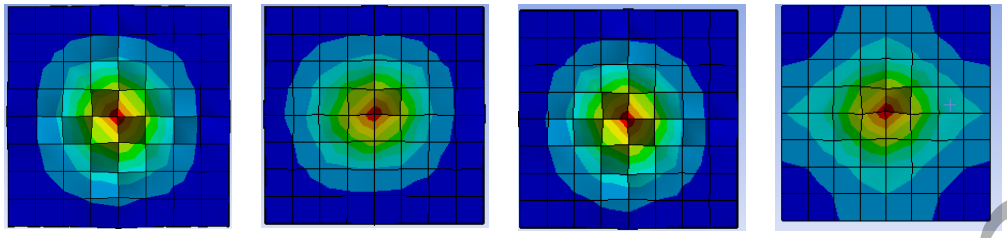
Table 4 Peak voltage and strain value after the first impact

S.No.	Cube representation no.	Peak voltage after 1st impact	Strain value against 1st impact x (10^{-6})
1	C1	0.24	1.14
2	C2	0.27	1.29
3	C3	1.46	6.86
4	C4	3.32	15.61
5	C5	0.10	0.473
6	C6	1.46	6.86
7	C7	4.02	18.90
8	C8	0.69	3.27
9	C9	0.100	0.47
10	C10	6.41	30.18
11	C11	3.13	14.75
12	C12	6.34	29.81

4.2 FEM Result and Discussion

The results of the thermomechanical and dynamic simulations are shown and discussed in this section. Figure 9 (a) - (d) illustrates the distribution of elastic strain at a 3 m height of impact with temperatures ranging from ambient to 150 °C. Maximum strain values of 0.0074913, 0.0077198, 0.0081335, and 0.0085585 were observed at different variable temperatures of ambient, 50,100, and 150 °C, respectively, and they clearly illustrate that the strain value was temperature-dependent and that it goes up with the increase in temperature.

Accepted Manuscript

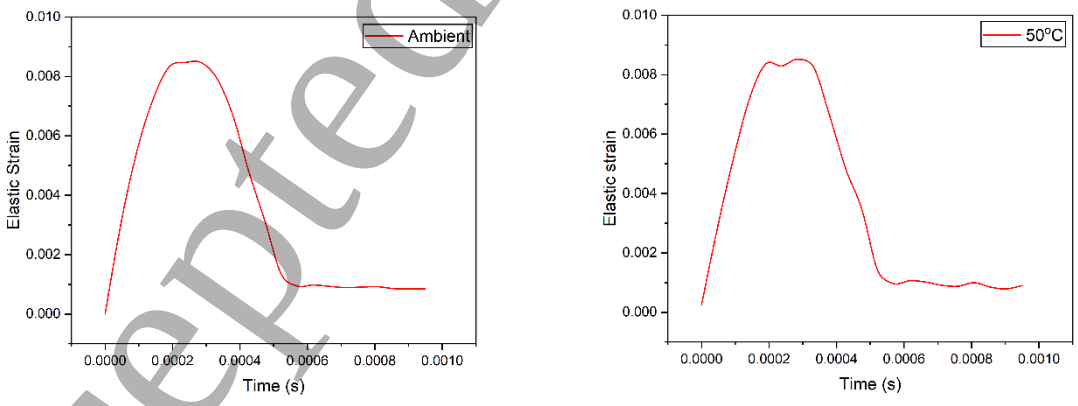


(a) **(b)** **(c)** **(d)**

Figure 9 Distribution of elastic strain for 3 m height of impact at varying temperature a) strain for 3 m height at ambient b) strain for 3 m height at 50 °C c) strain for 3m height at 100 °C d) strain for 3 m height at 150 °C

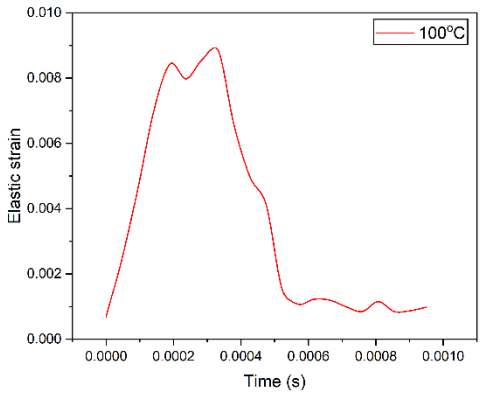
The distribution area of elastic strain became similar from ambient to 100 °C temperature. Figure 9 (d) shows the distribution of elastic strain at 150 °C temperature, it was observed that the distribution of elastic strain in the larger area for this temperature is as compared to the lower temperature. This was due to the loss of the stiffness of the concrete behaviour at the higher temperature.

The elastic strain time history curve of the concrete cube was also obtained for 3 m heights of impact at temperatures ranging from ambient temperature to 150 °C. Figure 10 (a)-(d) depicts the variation of the elastic strain time history curve under the height of 3 m impact loading from ambient to 150 °C. It shows that, as the temperature rises, the elastic strain values for the fixed height of impact loading at 3 m rise as well. For a better understanding of the elastic strain deviation with the increase in temperature, a combined graph of elastic strain value was shown in Figure 11, which clearly shows the higher peak value of elastic strain for the higher temperature.

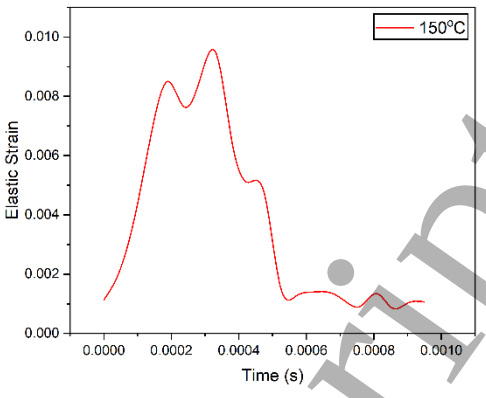


(a) **(b)**

Accepted Manuscript



(c)



(d)

Figure 10 The elastic strain time history curve for concrete cube under 3 m impacts at varying temperatures a) ambient b) 50 oC c) 100 oC d) 150 oC

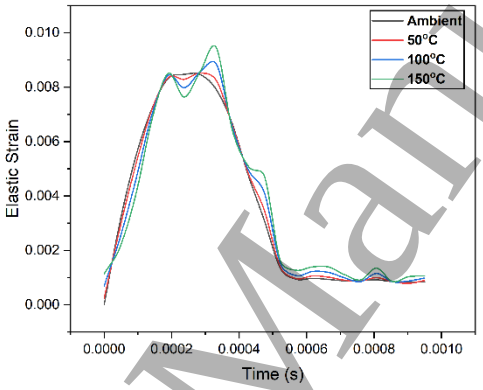


Figure 11 Elastic strain time history curve for concrete cube under different impact heights at varying temperatures for 3 m impact height

Table 5 shows all the maximum values of elastic strain for varying temperatures under 3 m height of impact. The maximum elastic strain values obtained for ambient, 50 ^{o}C , 100 ^{o}C and 150 ^{o}C temperatures were 0.0074913, 0.0077198, 0.0081335 and 0.0085585 respectively. As the temperature increases the elastic strain value gets increased i.e. higher for the 150 ^{o}C temperatures.

Table 5 Maximum elastic strain value at 3m height of impact for FFBC and FBC under varying temperature

Height of impact	Temperature variation	Maximum Elastic strain
3m	Ambient	0.0074913
	50 ^{o}C	0.0077198
	100 ^{o}C	0.0081335

Accepted Manuscript

	150 °C	0.0085585

To validate the experimental results and investigate the efficacy of numerical simulation analysis for concrete cubes under impact loading at various temperatures, the experimental results of the concrete cube were compared with the finite element analysis.

Table 6 Experimental and numerical strain values around the vicinity of sensors for FFBC

S.No.	Cube representation no.	Temperature	Height of impact	Experimental strain value around the vicinity of sensors x (10^{-6})	Numerical strain value around the vicinity of sensors x (10^{-6})
1	C5 (JKTPS)	Ambient	3m	0.473	0.49
2	C6 (JKTPS)	50	3m	6.87	7.05
3	C7 (JKTPS)	100	3m	18.9	21.20
4	C8 (JKTPS)	150	3m	3.27	35.50

The elastic strain value of each concrete cube obtained from the experiment and FEM analysis were compared. A typical example of the strain values for both experimental and numerical analysis were shown in Table 6. The strain value calculated experimentally using voltage data from an oscilloscope gives the strain around the vicinity of the sensors. Furthermore, this obtained experimental value of strain from the oscilloscope was compared with the FEM analysis. According to Table 6, the variation in the experimental and numerical values of elastic strain is less than 10 %. The difference in experimental and numerical values was due to the inability of providing the exact fixity at the base of the concrete cube in experimental conditions as compared to the numerical analysis. Based on the comparison of numerical and experimental results, the FEM analysis was found to be highly consistent with the experimental results, indicating that the proposed modelling methodology is useful for studying the impact-resistant behaviour of the concrete cube under varying temperatures.

5 Conclusion

This research described both the experimental and numerical simulations of a concrete cube subjected to the combined effects of temperature and impact loading. The voltage measurement technique was used to identify the damage caused by the combined effect of impact and temperature in concrete for all three piezo sensors of different configurations. Furthermore, the ANSYS explicit dynamics and transient thermal FEM software was used for the numerical simulation and the conclusions discussed below are based on the outcomes of the experimental and numerical simulation.

Accepted Manuscript

- All three sensors embedded, surface bonded, and non-bonded are capable of detecting damage in concrete caused by the combined effect of impact loading and temperatures.

- Peak voltage follows a continuously decreasing trend for the surface bonded and non-bonded sensors with an increase in the number of impact loads on each cube. This decreasing trend of peak voltage is due to the increase in damping of the cube.

- Peak voltage has followed the opposite trend for the JKTPS because they have been placed in the line of impact loading as a result strain development is more in this case.

- In terms of elastic strain value, the numerical simulation results based on explicit dynamics and a transient thermal programme agree well with the measured experimental results.

- This indicates that the experimental and numerical methodology proposed in this study was suitable and showed good agreement between them for detecting damages in concrete structures subjected to impact loading at varying temperatures.

Funding Statement

There was no specific grant for this research from public, private, or non-profit funding organisations.

Acknowledgements:

The authors would like to express their gratitude to Prof. Suresh Bhalla of the Department of Civil Engineering at the Indian Institute of Technology (IIT) Delhi for his unwavering assistance throughout the research experiment. The authors would also like to thank Prof. T. Visalakshi of the Department of Civil Engineering at Mahindra University in Hyderabad for his consistent guidance throughout this research. Furthermore, the authors thank Dr Tushar Bansal of Sharda University's Department of Civil Engineering in Greater Noida, Uttar Pradesh, for his invaluable advice throughout the research.

Conflict of Interest:

The authors declare that there is no potential for a conflict of interest in their research work.

Accepted Manuscript

References

[1] N. Banthia, S. Mindess, A. Bentur, and M. Pigeon, "Impact testing of concrete using a drop-weight impact machine," *Exp. Mech.*, vol. 29, no. 1, pp. 63–69, 1989, doi: 10.1007/BF02327783.

[2] P. H. Bischoff and S. H. Perry, "Impact Behavior of Plain Concrete Loaded in Uniaxial Compression," *J. Eng. Mech.*, vol. 121, no. 6, pp. 685–693, 1995, doi: 10.1061/(asce)0733-9399(1995)121:6(685).

[3] A. L. Mina, M. F. Petrou, and K. G. Trezos, "Resistance of an optimized ultra-high performance fiber reinforced concrete to projectile impact," *Buildings*, vol. 11, no. 2, pp. 1–18, 2021, doi: 10.3390/buildings11020063.

[4] P. Satya, T. Asai, M. Teshigawara, Y. Hibino, and I. Maruyama, "Impact of drying on structural performance of reinforced concrete beam with slab," *Materials (Basel).*, vol. 14, no. 8, 2021, doi: 10.3390/ma14081887.

[5] R. Smith-Gillis, R. Lopez-Anido, T. S. Rushing, and E. N. Landis, "Development of thermoplastic composite reinforced ultra-high-performance concrete panels for impact resistance," *Materials (Basel).*, vol. 14, no. 10, pp. 1–16, 2021, doi: 10.3390/ma14102490.

[6] S. J. Yoo, T. F. Yuan, S. H. Hong, and Y. S. Yoon, "Effect of strengthening methods on two-way slab under low-velocity impact loading," *Materials (Basel).*, vol. 13, no. 24, pp. 1–16, 2020, doi: 10.3390/ma13245603.

[7] S. Bright Singh and M. Murugan, "Performance of carbon fibre-reinforced pervious concrete (CFRPC) subjected to static, cyclic and impact loads," *Int. J. Pavement Eng.*, vol. 0, no. 0, pp. 1–16, 2021, doi: 10.1080/10298436.2021.1883017.

[8] M. Loganaganandan, G. Murali, and M. Parasuraman, "Experimental Study on GFRP Strips Strengthened New Two Stage Concrete Slabs under Falling Mass Collisions," 2020, doi: 10.1007/s12205-020-0331-8.

Accepted Manuscript

[9] J. H. Haido, A. A. Abdul-Razzak, M. M. Al-Tayeb, B. H. Abu Bakar, S. T. Yousif, and B. A. Tayeh, "Dynamic response of reinforced concrete members incorporating steel fibers with different aspect ratios," *Adv. Concr. Constr.*, vol. 11, no. 2, pp. 89–98, 2021, doi: 10.12989/acc.2021.11.2.089.

[10] I. Singh, N. Dev, S. Pal, and T. Visalakshi, *Finite Element Analysis of Impact Load on Reinforced Concrete*, vol. 203. Springer Singapore, 2022.

[11] Y. Al, Y. Temsah, O. Baalbaki, A. Jahami, and M. Darwiche, "Experimental investigation on the effect of impact loading on behavior of post- tensioned concrete slabs," *J. Build. Eng.*, vol. 31, no. September 2019, p. 101207, 2020, doi: 10.1016/j.jobe.2020.101207.

[12] T. Pham and H. Hao, "Effect of the Plastic Hinge and Boundary Conditions on the Impact Behavior of Effect of the Plastic Hinge and Boundary Conditions on the Impact Behavior of Reinforced Concrete Beams," no. December, 2016, doi: 10.1016/j.ijimpeng.2016.12.005.

[13] N. Kishi, M. Komuro, T. Kawarai, and H. Mikami, "Low-Velocity Impact Load Testing of RC Beams Strengthened in Flexure with Bonded FRP Sheets," *J. Compos. Constr.*, vol. 24, no. 5, p. 04020036, 2020, doi: 10.1061/(asce)cc.1943-5614.0001048.

[14] A. Bentur, S. Mindess, and N. Banthia, "The behaviour of concrete under impact loading: Experimental procedures and method of analysis," *Mater. Struct.*, vol. 19, no. 5, pp. 371–378, 1986, doi: 10.1007/BF02472127.

[15] S. M. Soleimani, N. Banthia, and S. Mindess, "Behavior of RC beams under impact loading: Some new findings," *Proc. 6th Int. Conf. Fract. Mech. Concr. Concr. Struct.*, vol. 2, no. Figure 1, pp. 867–874, 2007.

[16] Y. Fu *et al.*, "Investigating the failure behaviors of RC beams without stirrups under impact loading," *Int. J. Impact Eng.*, vol. 137, no. November 2019, p. 103432, 2020, doi: 10.1016/j.ijimpeng.2019.103432.

[17] L. Jin, R. Zhang, G. Dou, J. Xu, and X. Du, "Experimental and numerical study of reinforced concrete beams with steel fibers subjected to impact loading," *Int. J. Damage*

Accepted Manuscript

Mech., vol. 27, no. 7, pp. 1058–1083, 2018, doi: 10.1177/1056789517721616.

[18] M. S. Khan, J. Prasad, and H. Abbas, "Effect of High Temperature on High-Volume Fly Ash Concrete," *Arab. J. Sci. Eng.*, vol. 38, no. 6, pp. 1369–1378, 2013, doi: 10.1007/s13369-013-0606-1.

[19] A. Savva, P. Manita, and K. K. Sideris, "Influence of elevated temperatures on the mechanical properties of blended cement concretes prepared with limestone and siliceous aggregates," vol. 27, pp. 239–248, 2005, doi: 10.1016/j.cemconcomp.2004.02.013.

[20] H. Yang, H. Zhao, and F. Liu, "Residual cube strength of coarse RCA concrete after exposure to elevated temperatures," *Fire Mater.*, vol. 42, no. 4, pp. 424–435, 2018, doi: 10.1002/fam.2508.

[21] M. Potha Raju, K. Srinivasa Rao, and P. S. N. Raju, "Compressive strength of heated high-strength concrete," *Mag. Concr. Res.*, vol. 59, no. 2, pp. 79–85, 2007, doi: 10.1680/macr.2007.59.2.79.

[22] A. Powezka, J. Szulej, and P. Ogrodnik, "Effect of high temperatures on the impact strength of concrete based on recycled aggregate made of heat-resistant cullet," *Materials (Basel).*, vol. 13, no. 2, pp. 1–21, 2020, doi: 10.3390/ma13020465.

[23] A. Lau and M. Anson, "Effect of high temperatures on high performance steel fibre reinforced concrete," vol. 36, pp. 1698–1707, 2006, doi: 10.1016/j.cemconres.2006.03.024.

[24] D. Ai, Z. Yang, H. Li, and H. Zhu, "Heating-time effect on electromechanical admittance of surface-bonded PZT sensor for concrete structural monitoring," *Meas. J. Int. Meas. Confed.*, vol. 184, no. February, p. 109992, 2021, doi: 10.1016/j.measurement.2021.109992.

[25] I. Singh, N. Dev, and S. Pal, "Impedance based damage assessment of concrete under the combined effect of impact and temperature using different piezo configurations," *Sensors Actuators A Phys.*, vol. 345, no. July, p. 113763, 2022, doi: 10.1016/j.sna.2022.113763.

Accepted Manuscript

[26] Y. Xia, H. Hao, G. Zanardo, and A. Deeks, "Long term vibration monitoring of an RC slab: Temperature and humidity effect," *Eng. Struct.*, vol. 28, no. 3, pp. 441–452, 2006, doi: 10.1016/j.engstruct.2005.09.001.

[27] Y. Wang, G. Yuan, Z. Huang, J. Lyv, Z. Q. Li, and T. yan Wang, "Experimental study on the fire behaviour of reinforced concrete slabs under combined uni-axial in-plane and out-of-plane loads," *Eng. Struct.*, vol. 128, pp. 316–332, 2016, doi: 10.1016/j.engstruct.2016.09.054.

[28] Y. Jiao, H. Liu, X. Wang, Y. Zhang, G. Luo, and Y. Gong, "Temperature effect on mechanical properties and damage identification of concrete structure," *Adv. Mater. Sci. Eng.*, vol. 2014, 2014, doi: 10.1155/2014/191360.

[29] V. K. R. Kodur, "Innovative strategies for enhancing fire performance of high-strength concrete structures," *Adv. Struct. Eng.*, vol. 21, no. 11, pp. 1723–1732, 2018, doi: 10.1177/1369433218754335.

[30] J. Magnusson, M. Hallgren, and A. Ansell, "Shear in concrete structures subjected to dynamic loads," *Struct. Concr.*, vol. 15, no. 1, pp. 55–65, 2014, doi: 10.1002/suco.201300040.

[31] M. Szelag, "Development of cracking patterns in modified cement matrix with microsilica," *Materials (Basel).*, vol. 11, no. 10, 2018, doi: 10.3390/ma11101928.

[32] G. L. Golewski, "The Phenomenon of Cracking in Cement Concretes and Reinforced Concrete Structures: The Mechanism of Cracks Formation, Causes of Their Initiation, Types and Places of Occurrence, and Methods of Detection—A Review," *Buildings*, vol. 13, no. 3, p. 765, 2023, doi: 10.3390/buildings13030765.

[33] G. L. Golewski, "Fracture Performance of Cementitious Composites Based on Quaternary Blended Cements," *Materials (Basel).*, vol. 15, no. 17, 2022, doi: 10.3390/ma15176023.

[34] S. Park, J. Beak, K. Kim, and Y. J. Park, "Study on Reduction Effect of Vibration Propagation due to Internal Explosion Using Composite Materials," *Int. J. Concr. Struct. Mater.*, vol. 15, no. 1, 2021, doi: 10.1186/s40069-021-00467-8.

Accepted Manuscript

[35] T. Bansal, V. Talakokula, S. K. Rama Jyosyula, R. Vicente, and G. Ascensão, "Embedded Piezo-Sensor-Based Automatic Performance Monitoring of Chloride-Induced Corrosion in Alkali-Activated Concrete," *Sustain.*, vol. 14, no. 19, 2022, doi: 10.3390/su141912917.

[36] T. Bansal and V. Talakokula, "Deterioration of structural parameters due to corrosion in prestressed concrete identified by smart probe-based piezo sensor," *Eng. Res. Express*, vol. 3, no. 1, 2021, doi: 10.1088/2631-8695/abded9.

[37] T. Visalakshi, T. Bansal, and S. Bhalla, "RCC26 Corrosion Assessment in Rebars of Normal and Geopolymer Concrete," no. May, 2019.

[38] T. Bansal, V. Talakokula, and S. Bhalla, "Rebar corrosion assessment comparison of different piezo configurations in blended concrete," *Proc. 7th Asia-Pacific Work. Struct. Heal. Monit. APWSHM 2018*, no. January, pp. 914–925, 2018.

[39] T. Bansal, V. Talakokula, and S. Bhalla, "Model based corrosion assessment in rebars of different fly ash blended concrete using piezo sensors," *Proc. 7th Asia-Pacific Work. Struct. Heal. Monit. APWSHM 2018*, no. January, pp. 902–913, 2018.

[40] G. L. Golewski, "Combined Effect of Coal Fly Ash (CFA) and Nanosilica (nS) on the Strength Parameters and Microstructural Properties of Eco-Friendly Concrete," *Energies*, vol. 16, no. 1, 2023, doi: 10.3390/en16010452.

[41] Y. Liu, Z. Li, B. Jin, and J. Huo, "Experimental investigation on dynamic behavior of concrete after exposure to elevated temperatures," *Eur. J. Environ. Civ. Eng.*, vol. 0, no. 0, pp. 1–17, 2018, doi: 10.1080/19648189.2018.1500310.

[42] L. Jin, R. Zhang, G. Dou, and X. Du, "Fire resistance of steel fi ber reinforced concrete beams after low-velocity impact loading," *Fire Saf. J.*, vol. 98, no. November 2017, pp. 24–37, 2018, doi: 10.1016/j.firesaf.2018.04.003.

[43] J.-W. Nam and A. Hak-Chul Shin, "Damage Assessment of Concrete in Thermal and Dynamic Loadings," *J. Civ. Eng. Res.*, vol. 2, no. 6, pp. 49–56, 2012, doi: 10.5923/j.jce.20120206.01.

Accepted Manuscript

[44] M. Saeed Mirza and A. A. Mufti, "Nonlinear Finite Element Analysis of Reinforced Concrete Structures.," vol. 2, no. 6, pp. 403–417, 1974.

[45] M. M. Rafi, A. Nadjai, and F. Ali, "Finite element modeling of carbon fiber-reinforced polymer reinforced concrete beams under elevated temperatures," *ACI Struct. J.*, vol. 105, no. 6, pp. 701–710, 2008, doi: 10.14359/20098.

[46] P. Bhuvaneshwari and K. S. R. Mohan, "Strengthening of Fire-Damaged Reinforced Concrete Short Columns Using GFPPECC Composites," *Arab. J. Sci. Eng.*, vol. 45, no. 10, pp. 8619–8632, 2020, doi: 10.1007/s13369-020-04795-x.

[47] H. Song, H. Cai, H. Cheng, and Z. Yao, "Physical model testing and numerical simulation for temperature distribution of mass concrete freezing shaft lining in deep alluvium," *AIP Adv.*, vol. 8, no. 7, 2018, doi: 10.1063/1.5043454.

[48] P. Ganesan and S. Venkata Sai Kumar, "FE modelling of low velocity impact on RC and prestressed RC slabs," *Struct. Eng. Mech.*, vol. 71, no. 5, pp. 515–524, 2019, doi: 10.12989/sem.2019.71.5.515.

[49] J. Ožbolt, D. Ruta, and B. İrhan, "Impact analysis of thermally pre-damaged reinforced concrete slabs: Verification of the 3D FE model," *Int. J. Impact Eng.*, vol. 133, no. April, 2019, doi: 10.1016/j.ijimpeng.2019.103343.

[50] L. Jin, H. Hao, R. Zhang, and X. Du, "Determination of the effect of elevated temperatures on dynamic compressive properties of heterogeneous concrete: A meso-scale numerical study," *Constr. Build. Mater.*, vol. 188, pp. 685–694, 2018, doi: 10.1016/j.conbuildmat.2018.08.090.

[51] A. Dixit and S. Bhalla, "Prognosis of fatigue and impact induced damage in concrete using embedded piezo-transducers," *Sensors Actuators, A Phys.*, vol. 274, pp. 116–131, 2018, doi: 10.1016/j.sna.2018.03.005.

[52] P. Negi, R. Chhabra, N. Kaur, and S. Bhalla, "Health monitoring of reinforced concrete structures under impact using multiple piezo-based configurations," *Constr. Build. Mater.*, vol. 222, pp. 371–389, 2019, doi: 10.1016/j.conbuildmat.2019.06.100.

Accepted Manuscript

[53] IS:2386 (Part I), "Method of test for aggregate for concrete (Particle size and shape)," *Indian Stand.*, p. (Reaffirmed 2002), 1963.

Accepted Manuscript

Multimedia Tools and Applications
https://doi.org/10.1007/s11042-023-15444-4

Deep Siamese Network with Handcrafted Feature Extraction for Hyperspectral Image Classification

Pallavi Ranjan[1] · **Ashish Girdhar**[1]

Received: 15 January 2022 / Revised: 7 April 2022 / Accepted: 18 April 2023
© The Author(s), under exclusive licence to Springer Science+Business Media, LLC, part of Springer Nature 2023

Abstract
The prominence of deep learning models for classification of hyperspectral images is directly proportional to their ability to exploit spatial context and spectral bands jointly. The effectiveness of these deep learning models, however, is heavily reliant on a good amount of labelled training samples. In contrast, one of the biggest challenges with hyperspectral images is limited labelled samples availability as getting the samples annotated is a time consuming and labor-intensive process. Traditional machine learning algorithms are available for classification with a higher training time and very deep pre-trained networks like GoogleNet and VGGNet did not work well for hyperspectral image classification. The idea of one shot classification has been quite motivating in recent years to deal with the problems of limited labelled samples, imbalanced distribution of samples leading to poor classification results and overfitting. To implement one shot classification model and overcome these challenges, the proposed work is based on Siamese network that can work with limited samples or imbalanced samples. The proposed Siamese network has a handcrafted feature generation network that extracts discriminative features from the image. Experimental findings on two benchmark hyperspectral datasets demonstrate that the proposed network is capable of improving the classification performance with an overall accuracy of 95.17 and 93.25 for Pavia U and Indian Pines dataset respectively with a small scale trained data.

Keywords Hyperspectral Classification · Convolution Neural Network · Siamese CNN · Deep Learning · One shot classification · Feature Extraction

1 Introduction

Hyperspectral images contain abundant spatial and spectral information [39, 55]. Hyperspectral images are used in a wide variety of applications such as in defense, military, medical diagnosis, geological mapping and object recognition, environmental monitoring, anomaly detection, forensic analysis to name a few [25, 33–35].A fundamental and classic problem in the field of hyperspectral imaging is the ability to classify the ground objects accurately [56].

✉ Pallavi Ranjan
er.pallaviranjan@gmail.com

[1] Delhi Technological University, New Delhi, India

However, one major challenge while classifying supervised hyperspectral images is the availability of labelled samples [9, 38] and since annotating samples is a time consuming and labor-intensive process that needs a lot of ground campaign, the unavailability of which leads to poor classification performance [32, 52] since the success of deep learning models depend on the amount of training data. Unsupervised approaches, on the other hand, categorize incoming data without prior knowledge, but rather based on similarities and patterns in the data. Lately, supervised deep learning methods have outperformed unsupervised models in terms of performance [44]. However, because of the limited labeled data, they may not have learnt the huge spatial spectral features required for good HSI classification [41]. Second major challenge in the field of spectroscopy is the ability of deep learning models to train and categorize imbalanced datasets [13]. HSI data cannot ensure homogeneity in quantity distribution in each category owing to the random and unpredictable nature of ground truth distribution. For instance, Indian Pines dataset contains extremes to as low as 46 samples inside the category "Alfafa" and 2455 samples in "Soybean-mintill", Pavia University dataset contains 947 samples in "Shadows" and 18,649 samples in "Meadows" which is almost 20 times more than the former category [14]. This demonstrates the regular occurrence of uneven distribution of HSI samples. This makes it challenging for deep learning algorithms to recognize categories with small numbers.

A large number of supervised methods like linear discriminant analysis (LDA) maximize the separability between different classes but these linear transformation methods may not be suitable for classification of nonlinear data such as HSI [1]. A lot of feature extraction methods like Principal Component Analysis (PCA) [36], Independent Component Analysis [51], Locally Linear Embedding (LLE) [1], Nonlinear Kernel Mapping [28] have been used for extracting the spectral based properties, Other spatial-spectral information based feature extraction modules include Extended Morphological Profile (EMP) [11] or Morphological Attribute Profile (MAP) [7]. Traditional machine learning algorithms like support vector machines work well on classification problems with small training samples but need longer training time for large datasets. A new form of feature extraction approach known as deep learning automatically extracts features from training data, including models like Convolution Neural Networks [17, 20], Generative Adversarial Networks [47], Autoencoders [46, 48], Transfer Learning [4, 42], Recurrent Neural Networks [29] have gained popularity in recent years by performing classification tasks and achieving state of the art results. CNN seems to outperform all other models for hyperspectral image classification. However, sufficient training data is a constraint for deep models to give great classification results. Also the inadequacy of training data for deep learning models leads to a major problem of overfitting [20, 17, 47]. And pre-trained models like Google Net [48] and VGG Net [46] failed to perform well on classification of hyperspectral images [4, 31].

Significant attempts in the past, such as L2 regularization and dropout, have been investigated in recent years to address the issue of overfitting. Furthermore, while adding new classes or deleting existing ones, the network must be retrained. As a result, the notion of one shot training has been proposed [42], and Siamese network is utilized for this study to learn the similarity of sample pairs in order to train network with less data and avoid retraining. [26] worked on one shot image recognition using Siamese network to work on the overfitting issue induced by insufficient training data. This study makes use of many inputs despite the problem of insufficient training samples by creating SCNN (Siamese CNN). Miao et. al [43] introduced pairwise loss for the Siamese network by reducing the intra class distance in the feature space while increasing the inter class distance. Also, Siamese networks come in handy and provides good accuracy with an imbalanced class distribution [23, 24]. Therefore, to handle problems like imbalanced class distribution, limited

labelled samples and overfitting, the idea of one shot learning was considered. This idea is implemented using Siamese CNN with a handcrafted feature extraction module. The handcrafted feature extraction module is fine tuned in a way so that it generates the discriminative features by reducing the duplicate features since HSI data is high dimensional containing a lot of spectral bands. It enhances the discriminative information and modelling of spatial features making the proposed model an end to end model without a need of additional dimensionality reduction approaches. Also, the proposed model is less complex than current CNN models such as VGG Net or Inception Net and eliminates the overfitting problem [23]. With a larger number of layers and a smaller dataset, the lower layers are more likely to suffer from the vanishing gradient problem, which causes dense models to fail in such cases. If there is little data, a model with fewer layers paired with Siamese can successfully cope with issues like underfitting and overfitting.

The main contribution of this paper can be concisely summarized as follows:

1) The proposed work doesn't need too many instances of any class to train the network, rather uses adequate training data to build a strong network using Siamese as the base model to determine the similarity of input pairs;
2) Both the datasets are pre-processed after removal of the noisy bands to further escalate the classification accuracy. A novel feature generation module is handcrafted, fine-tuned and merged with the Siamese network that helps in increasing the classification performance by extracting finer discriminative features from the input image.
3) The proposed network alleviates the problem of overfitting and further reduces the problem of gradient vanishing by optimizing the network with Adam optimizer, binary cross entropy function and dropout layers.
4) To prove the worth of model, the proposed method is applied on two benchmark hyperspectral data sets, Indian Pines and Pavia University and results prove that the designed model is able to outperform other models even with small scale training data.

2 Related work

In 2008, a study by Gua et. al [15] extended the approach based on SVM using spectrally weighted kernels by highlighting the information that wasn't uniformly distributed among the spectral bands. They tried to associate between the spectral bands and ground truth by constructing spectral weights. This was concluded by great classification results, however the proposed work had severe risk of overfitting as new parameters were added into the layers. To tackle the problem of limited labelled samples and imbalanced class distribution, Zhu et. al [58] proposed spectral spatial dependent global learning (SSDGL) framework with a capability to focus on attention areas and achieve great classification performance even with imbalanced datasets like Indian Pines. In 2021, a study by Eeti and Buddhiraju [10] proposed an algorithm based on decision trees that can greatly increase the HSI classification performance with imbalanced datasets with a limitation of long computational time and validation required on other hyperspectral datasets. However, most of above mentioned approaches face significant obstacles, such as the curse of dimensionality and focus on spectral information only.

To address this challenge, [8] combined CNN and Capsule networks to make use of spectral-spatial variability, which addresses the issue of restricted sample supply while still providing reasonably acceptable classification accuracy. Because the nature of CapsNet is too complicated, efforts are required to enhance CapsNets, which take longer time than

CNN. [19] suggests the use of deep learning models over conventional machine learning models for image classification tasks. CNNs were first used by [12] and recently they seem to outperform all other models specifically in the area of image classification [6, 27]. The Indian Pines and Pavia University dataset was classified using CNN providing a greater accuracy with small training samples in comparison to traditional models like SVM. To make the performance even better, this study suggests the use of Siamese network as it has the capability to deal with data having small number of samples per category. This study also suggests the use of dropout layer to optimize the network. [21] worked on the problem of dimensionality of HSI by proposing spatial-spectral regularized sparse hypergraph embedding (SSRSHE) and possesses better classification performance by reducing the influence of noisy data. However the proposed model uses information in both spectral and spatial domain, therefore more time taking than the existing spectral models.

[43] proposed a framework based on Siamese network and autoencoders making full use of the limited labeled sample information to provide a classifier for HSI. This model was proven great in generating discriminative features even on the edges of cubes however accuracy of the model declines with training samples as low as one percent. In 2020, [20] came up with the idea of dual path Siamese network that provides better results in case of limited samples than models like CapsNet, SVM or CNN but still has a scope of improving accuracy. Recently, [50] proposed a method based on few show classification and attention mechanisms that solves the problem of annotating samples being a time-consuming and costly task. It explores the relationships between labelled and unlabeled samples using Siamese network to further analyze the intra class and inter class distances. However, the model did not produce great classification results. [13] and [54] use Siamese networks with the augmented data and calculating a similarity score. The former study works absolutely well with small and imbalanced samples with a limitation that when the samples in each category reach a satisfactory mark, the model may not work well. Later study [54] makes use of dynamic augmentation that changes the value of loss as per the augmentation with a risk of misclassification. [16] developed a model for limited samples, SaSiResNet based on superpixel segmentation using Siamese network that even works for unlabeled samples with a disadvantage to derive optimal number of superpixels and make the model computationally efficient. Table 1 summarizes the literature.

3 Proposed framework

3.1 Siamese network

Siamese Network presents a similarity measure that may be utilized for image classification challenges, particularly when the number of categories is large or the dataset has an imbalanced class distribution. [23, 24]. Distance based methods are quite common solution to such problems as they compute a similarity metric between the pattern to be classified and a database of stored patterns using the same neural network [5]. The motivation behind choosing Siamese network was the fact that this network weakens the importance of labels by setting labels as similar or dissimilar making it an appropriate network for the HSI due to the scarcity of labeled or supervised samples [43]. The overall working of proposed model is illustrated in Fig. 1. The proposed model encloses in it feature generation model that is applied to each image to generate the reduced feature vectors with discriminative features and eventually compute the similarity score. The core of Siamese

Table 1 Summary of related work

Ref	Year	Work Done	Limitations
[15]	2008	SVM + Spectrally weighted kernels produced great classification results	Risk of overfitting
[45]	2012	Addition of newer classes in existing dataset does not lead to retraining of network	Algorithm needs optimization and fine tuning
[19]	2015	Great accuracy with small training samples, Better than SVM	Can better perform with use of Siamese network optimized with dropout layer
[22]	2017	A pixel-pair way of classification combined with voting strategy, Able to learn more discriminative features	Greater classification with increased computational cost
[8]	2018	Combined CNN and Capsule networks	Need to enhance CapsNets, that takes longer time than CNN
[21]	2019	Worked on the problem of dimensionality by proposing SSRSHE and possesses better classification performance	Time taking than the existing spectral models
[43]	2019	Proposed a framework based on Siamese network + autoencoders making full use of the limited labeled sample information	Accuracy of the model declines with training samples as low as one percent
[16]	2020	Developed a model for limited samples, SaSiResNet based on superpixel segmentation using Siamese network that even works for unlabeled samples	Disadvantage to derive optimal number of superpixels and make the model computationally efficient
[50]	2020	Proposed a method based on few show classification and attention mechanisms, Solves the problem of annotating samples, Explores the relationships between labelled and unlabeled samples	The model did not produce great classification results
[58]	2021	Proposed SSDGL with attention mechanism	
[10]	2021	Increased classification performance	Limitation of long computational time and validation required on other hyperspectral datasets
[20]	2021	Proposed Dual Path Siamese network that provides better results in case of limited samples than models like CapsNet, SVM or CNN	Still has a scope of improving accuracy
[13]	2021	Use Siamese networks with the augmented data and calculating a similarity score. Works absolutely well with small and imbalanced samples	When the samples in each category reach a satisfactory mark, the model may not work well
[37]	2021	Proposed Attention Aware pseudo 3D CNN (AP3D) that pays attention to important features in the image at all level of convolutions	Complex model, Reduction in the model size required, Also classification accuracy needs to be improved
[40]	2021	Proposed a fine-tuned, SVM based algorithm that outperformed other machine learning based algorithms	Inclusion of a feature extraction module could have greatly improved the effectiveness of proposed method

Table 1 (continued)

Ref	Year	Work Done	Limitations
[54]	2022	Makes use of dynamic augmentation that changes the value of loss as per the augmentation	Risk of misclassification
[2]	2022	Performs HSI classification using attention mechanism and graph networks to generate relationship between features	Uses NVIDIA GTX1070 GPU for performing the experiments, therefore time consumption is lower
[18]	2022	Works on the problem of limited samples using a hybrid network combined point graph and distribution graph (DGCN), fully extracts features to study correlations	Still a scope of improving accuracy

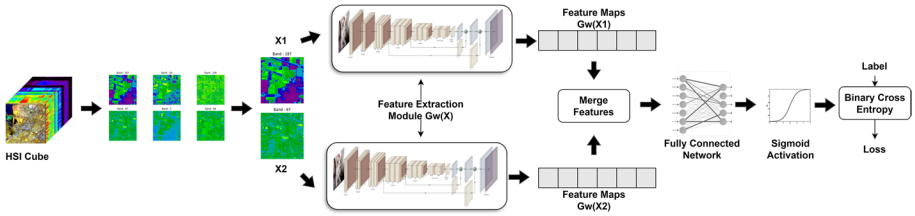


Fig. 1 Working of the proposed model

network is CNN and it is made up of convolution layers, pooling layers, dense layers, and dropout layers, each layer having its own importance. Convolutional layers store low, mid, and high level features. The image is delivered onto the network in the form of an HSI cube, which contains several bands. The feature extraction module takes input as bands and generates the feature maps, each feature map uses different convolutional kernel to analyze and extract different type of features. The objective behind pooling layer is to further reduce the dimensions of feature representations by scheming the mean or variance inside the subtle rotations. Our proposed model uses max pooling layer to calculate he maximum value among the neighboring pixels in a feature map. Lastly, the vectors pass through fully connected layers to better summarize the information followed by sigmoid activation.

This network creates usable batches to train the network. It takes image A and B as input and calculates similarity score between two images as output. This network lies on the basic assumption that if the input images belong to same group, the similarity score is 1 signifying complete resemblance and otherwise 0 signifying no resemblance. The random batches algorithm randomly picks the two sample input images, the first half from same category and second half from different category.

In 2016, a labelling scheme for pixel pairs was proposed by [30] that maps a pixel pair set to a multiclass label set. Let A is a input HSI including n labeled samples. The representation of training set for each category can be done by $\{(x_i, y_i)\}_{i=1}^{n}$ and labels $y_i \in \{1, 2, \ldots .C\}$ where C is the number of classes. $[x_i, x_j]$ is a random pixel pair vector selected from training set, the labelling strategy can be defined by the equation (i). This equation compares the two input pixels and returns the category "l" if two samples belong to the same label l, otherwise if the samples belong to different classes, the label doesn't change and remains as 0. [11] defines equation (ii) to test any pixel vector t, network computes the similarity score s_i of pixel pair (t, s_i) for the available pixels x_i and computes the label $\hat{l}$ by taking the maximum s_i as shown in equation (ii)

$$label([x_i, x_j]) = \begin{cases} l \; if \; x_i = x_j = l \\ 0 \; if \; x_i ! = x_j \end{cases} \tag{1}$$

$$\hat{l} = l_\text{argmax} s_i \tag{2}$$

Table 2 Number of classes with samples given for dataset Indian Pines (IP)

No	Class	Samples
1	Alfalfa	46
2	Corn-notill	1428
3	Corn-mintill	830
4	Corn	237
5	Grass-pasture	483
6	Grass-Trees	730
7	Grass-pasture-mowed	28
8	Hay-windrowed	478
9	Oats	20
10	Soybean-notill	972
11	Soybean-mintill	2455
12	Soybean-clean	593
13	Wheat	205
14	Woods	1265
15	Buildings-Grass-Trees-Drives	386
16	Stone-Steel-Towers	93

4 Dataset description

To validate our model, two benchmark opensource HSI datasets were chosen from [22]. First of them was Indian Pines (IP) that is captured over the Indian Pines region in Northwest Indiana, a mixed agricultural/forest area, each image consists of 145×145 pixels and 224 spectral channels having a total of 16 classes. Second dataset chosen was Pavia University acquired over the University of Pavia, 610×340 pixels in size and 103 spectral channels after the removal of the noisy bands with a total of nine ground-truth classes. Table 2 and 3 clearly show the categories in each dataset along with class wise sample distribution for both datasets. Figure 2 and 3 display the spectral bands and ground truth distribution for Indian Pines dataset, Similarly Fig. 4 and 5 display the spectral bands and ground truth distribution for Pavia U dataset.

Table 3 Number of classes with samples given for dataset Pavia University (PU)

	Class	Samples
1	Asphalt	6631
2	Meadows	18,649
3	Gravel	2099
4	Trees	3064
5	Painted Metal Sheets	1345
6	Bare Soil	5029
7	Bitumen	1330
8	Self-Blocking Bricks	3682
9	Shadows	947

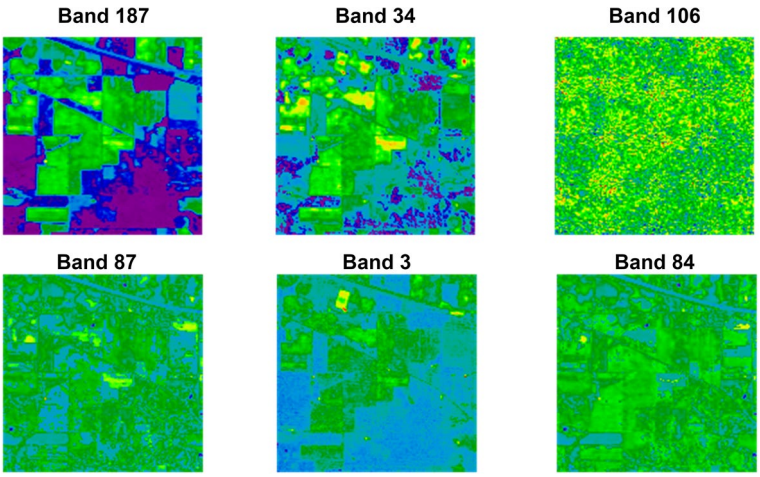
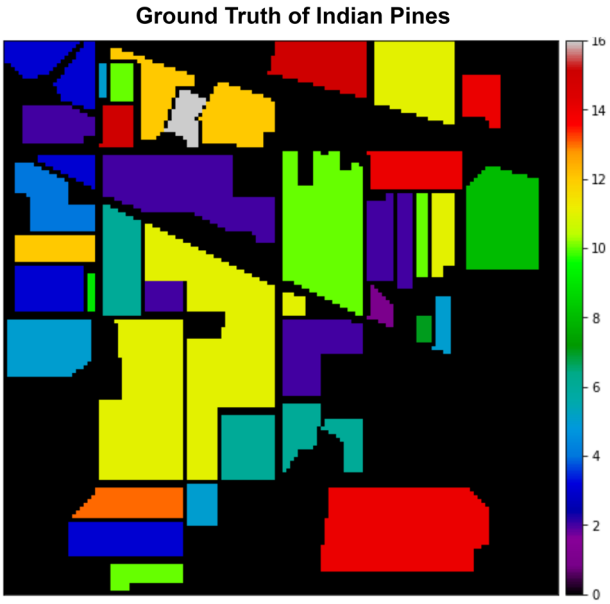


Fig. 2 Band images for dataset: Indian Pines

5 Preprocessing

Because hyperspectral pictures are high-dimensional data with improved spectral and temporal resolution, processing them often increases computational complexity [49]. Preprocessing of data is essential to choose for correct band selection and presentation in order to decrease the data dimensionality and complexity of images. As shown in Fig. 6, The original spectral-spatial dimension for the Indian Pines dataset was 145 * 145 * 224. After deleting the noisy bands, data left for preprocessing was 145 * 145 *

Fig. 3 Ground truth image dataset: Indian Pines



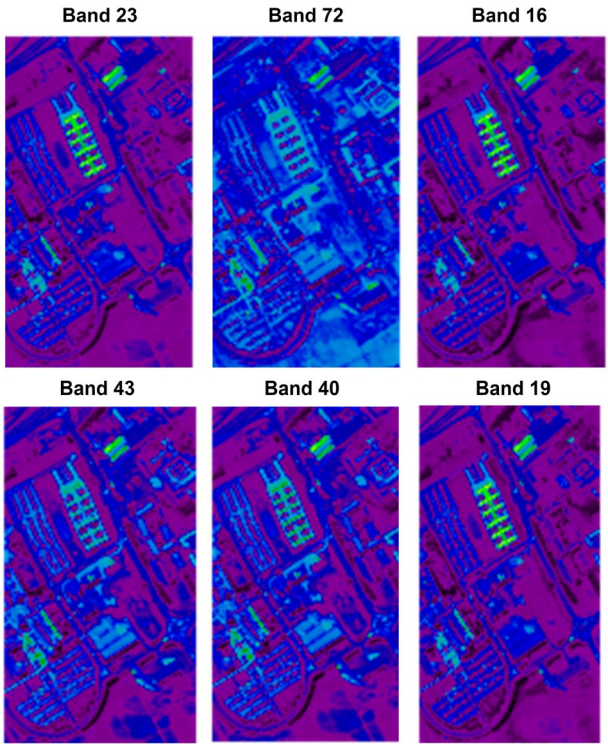


Fig. 4 Band images for dataset: Pavia U

220, where 145 *145 was the spatial dimension and 220 the number of spectral bands in the IP dataset, the number of pixels in each band 145 * 145 = 21,025 in number, for a total of 220 bands. This data was divided into 10% for training samples and 90% for testing samples. After dividing the data into 10–90, the total number of training samples was 2102, and testing was done on 18,923 samples. For the Pavia University Dataset, original hyperspectral cube had 610 * 340 *103 spectral-spatial dimensions, after extracting 103 bands the net image was scaled to 207,400 * 103 out of which data used for training was 20,740 and testing was 186,660 in number. Similar extraction was performed on the ground truth images having the spatial dimension as 145 X 145 pixels. Since ground truth forms the label or category for each data point. Thus, final data shape was 21,025 X 221 including bands and the target label for Indian Pines dataset and 610 X 340 X 103 (+ 1) = 207,400 X 104 pixels for Pavia U dataset.

6 Feature extraction module

The goal of having a similarity model was to make CNN extract discriminative features in order to enhance the classification. The similarity model is made up of two input layers that are given two separate data points at the same time. Using the feature extraction

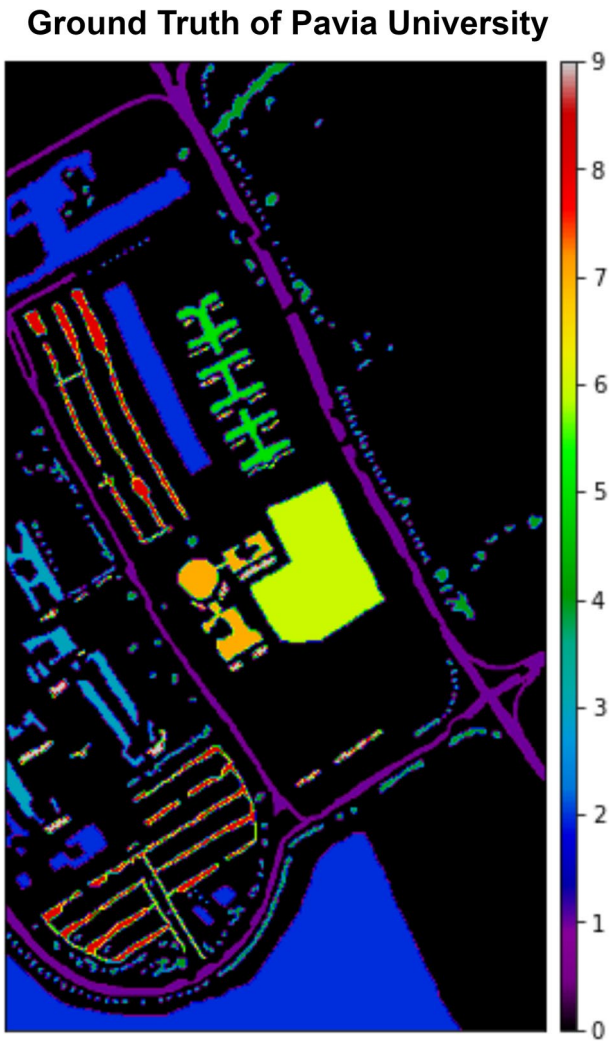


Fig. 5 Ground truth for dataset: Pavia U

approach, features are retrieved from both data points and concatenated using the concatenate layer, this is followed by fully connected network including dense and dropout layers and a sigmoid activation that aids in image classification with a probabilistic similarity score. As shown in Fig. 7, Two images A and B are fed into feature generation block and f(a), f(b) are the feature vectors produced by CNN inside the feature generation block. The similarity score is calculated using D(a,b), termed as Euclidean distance defined on f(a) and f(b), the feature vectors produced by the images A and B as shown in equation (iii). Equation (iv) defines the loss function where δ_+ is intraclass Euclidean distance, δ_- is the intra class Euclidean distance and μ is the mean. The proposed network learns features with loss function showing a high interclass and low intraclass distance.

$$D(a,b) = ||f(a) - f(b)||_2 \tag{3}$$

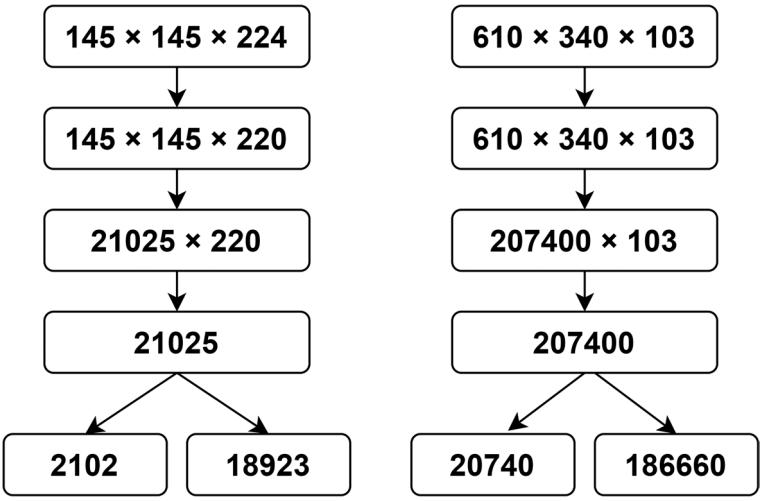


Fig. 6 Preprocessing for Indian Pines and Pavia U dataset

$$\delta = \max(0, \delta_+ +, \mu - \delta_-) \tag{4}$$

$$A = X(w * a + B) \tag{5}$$

The Feature Extraction Module is designed to extract discriminative features from the input image. The customized feature extraction module is built using four blocks of convolution layer followed by batch normalization layer. This module is depicted in Fig. 8 where input image is passed through the convolutional layer that applies convolutions resulting in reduced depth of the channels. Equation (v) defines the rectified linear unit (ReLu) activation function with function X(.) where a is the HSI cube, to which the convolution operation is applied with w and B as the filter and bias respectively. After every two such conv and batch normalization blocks follows a max-pooling layer. Max-pooling is a method for summarizing the features in a segment of a feature map developed by a convolution layer.

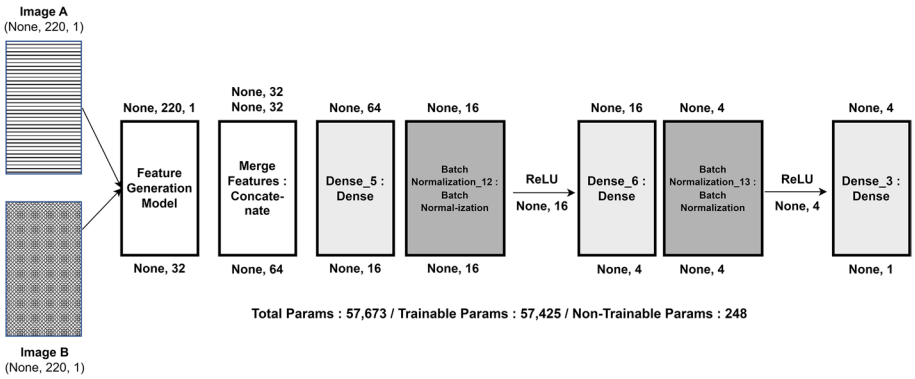


Fig. 7 Layers by layer description of the proposed model

As a result, the max-pooling layer produces a feature map containing the most discrimina-

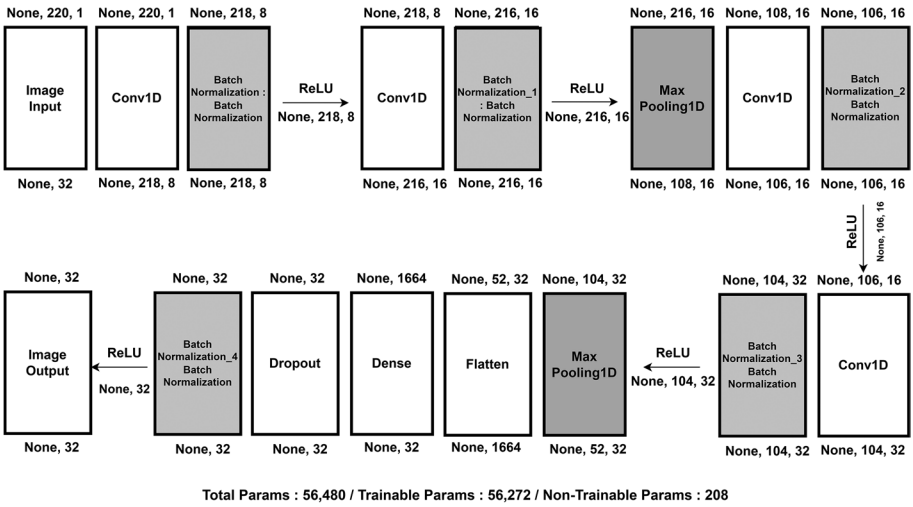


Fig. 8 Layer by layer description of feature extraction model

tive and variant features from the previous feature map. This is followed by a flatten layer, which results in a vector with only one dimension.

To avoid overfitting, the network is optimized using batch normalization and dropout layers. The rationale behind combining the dropout layer with batch normalization is that [57] advises combining the dropout layer with the batch normalization layer because it provides excellent performance even when learning rates are high and prevents overfitting. The batch normalization layer's objective is to determine the mean or variance of micro batches and deliver the batch normalized value as input to the following layer. Batch normalization, in particular, is employed in our approach to make the data linear. Following that is the max pooling layer, which reduces computational complexity by generalizing the convolutional layer's features. Feature maps become more durable and abstract after passing through the max pooling layer. After getting the maximum pooled data, the data is flattened with the flattening layer so that it may be single dimensional and sent to the dense layer, which decreases the dimensions further by employing each neuron. To reduce overfitting, a dropout layer with a rate of 0.5 is added.

As we can see in Fig. 8, the input to the model has dimensions 220 X 1, after passing through the model the dimension gets reduced to 32 X 1. The novelty in customizing the feature extraction module lies in placement of layers along with right parameters in such a way that it gives best classification accuracy with minimum run time. The placement of layers and their connections with each layer are clearly depicted in Fig. 8. Table 4 provides a detailed summary with output shape of each layer with respective parameters and connection.

The way band extraction process works is depicted in Fig. 9. The Indian Pines input data is a cube of 145 X 145 X 220 Width X height X spectral band as shown in 9(a). Randomly some of the bands were selected using randint() and are displayed in 9(b) and

Table 4 Similarity model with feature generation block, showing input layers and parameters

Layer (type)	Output Shape	Param #	Connected To
ImageA_Input (InputLayer)	[(None, 220, 1)]	0	
ImageB_Input (InputLayer)	[(None, 220, 1)]	0	
Feature Generation Model	**(Function (None, 32)**	**56,480**	**ImageA_Input[0][0], ImageB_Input [0][0]**
FeatureNet_ImageInput	(Input [(None, 220, 1)]	0	
conv1d_4 (Conv1D)	(None, 218, 8)	32	
batch_normalization_7	(Batch (None, 218, 8)	32	
activation_7 (Activation)	(None, 218, 8)	0	
conv1d_5 (Conv1D)	(None, 216, 16)	400	
batch_normalization_8	(Batch (None, 216, 16)	64	
activation_8 (Activation)	(None, 216, 16)	0	
max_pooling1d_2	(MaxPooling1 (None, 108, 16)	0	
conv1d_6 (Conv1D)	(None, 106, 16)	784	
batch_normalization_9 (Batch	(None, 106, 16)	64	
activation_9 (Activation)	(None, 106, 16)	0	
conv1d_7 (Conv1D)	(None, 104, 32)	1568	
batch_normalization_10	(Batch (None, 104, 32)	128	
activation_10 (Activation)	(None, 104, 32)	0	
max_pooling1d_3	(MaxPooling1 (None, 52, 32)	0	
flatten_1 (Flatten)	(None, 164)	0	
dense_4 (Dense)	(None, 32)	53,280	
dropout_1 (Dropout)	(None, 32)	0	
batch_normalization_11	(Batch (None, 32)	128	
activation_11 (Activation)	(None, 32)	0	
Total params: 56,480 Trainable params: 56,272 Non-trainable params: 208			
merge_features (Concatenate)	(None, 64)	0	FeatureGenerationModel[39][0]
dense_5 (Dense)	(None, 16)	1040	**Merge_feaures[0][0]**
batch_normalization_12	(BatchNo (None, 16)	64	dense_5[0][0]
activation_12 (Activation)	(None, 16)	0	batch_normalization_12[0][0]
dense_6 (Dense)	(None, 4)	68	activation_12[0][0]
batch_normalization_13	(BatchNo (None, 4)	16	dense_6[0][0]
activation_13 (Activation)	(None, 4)	0	batch_normalization_13[0][0]
dense_7 (Dense)	(None, 1)	5	activation_13[0][0]
Total params: 57,673 Trainable params: 57,425 Non-trainable params: 248			

corresponding ground truth image is shown in 9(c) where each category has a different label represented in different spectra. 9(d) clearly shows how each band is extracted and each pixel has been assigned a class that matches the ground truth indicating what category that specific pixel represents. Therefore the spectra is used to extracting data corresponding to different data points or pixels.

The feature extraction module consists of Conv layers, batch normalization, max pool, ReLU activation, flatten, dense and dropout layers. For the Indian Pines dataset, 220 bands after removing the noisy bands were passed into feature generation model. As shown in Fig. 8 and Table 4, there are four sets of Conv1D, Batch Normalization layers and activation functions, after every two such sets follows a max pooling layer.

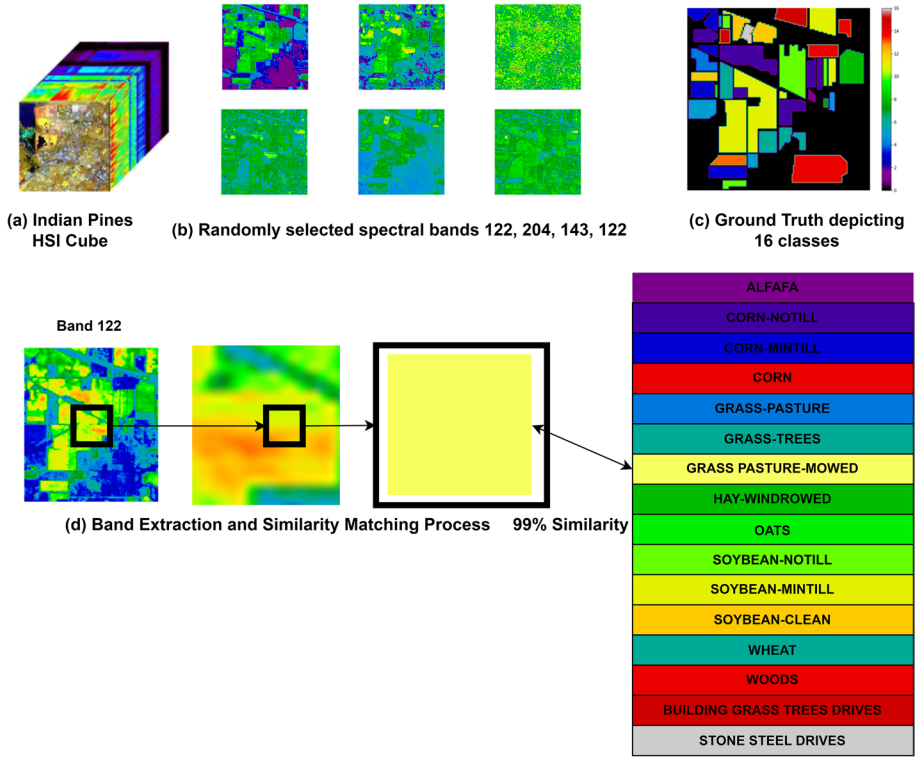


Fig. 9 Band extraction process for Indian Pines

The first block reduces the bands to 218 and second set further reduces it to 216. Max pooling further down samples it to 108 with 16 such feature maps. After passing it to second such block and second max pooling layer, spectral bands get reduced to 52 with 32 such feature maps. Flattening layer reduces it to 52 * 32 = 1664 one dimensional array. Finally this is passed to dense and dropout block with parameter 0.5, attaining a one dimensional feature vector of size 32. As shown in Fig. 7 and Table 4, these extracted features are passed to inputted Siamese network that takes two such inputs and computes the similarity. A fully connected layer with three dense and two batch normalization layers follows, whereby first two dense layers are linearly activated and third dense layer is activated with sigmoid activation function.

7 Binary cross entropy

The proposed network calculates the similarity score or distance using binary cross entropy as it is essentially a two class classification problem. It is a general approach for distance metric learning as it checks if the input images are similar or dissimilar. This log loss is shown mathematically with equation (vi) where n is the number of rows, m is the number of classes and p is the probability.

$$-\frac{1}{N}\sum_{i}^{n}\sum_{j}^{m} y_{ij}\log\left(p_{ij}\right) \tag{6}$$

8 Experimental settings

ADAM (Adaptive Moment Estimation) with a learning rate of 0.0001 is utilised as the optimizer when training the classification network. The maximum epoch is 120, and the maximum batch size is 64. Dropout is used to avoid overfitting. The dropout rate is set to 0.2 for the first layer, while the dropout rate in the remaining layers is set to 0.5. The framework used for metrics evaluation is Scikit Learn and for model implementation is TensorFlow. The system used for experimentation had 8 GB RAM and Intel i5 8th Gen processor with 480 GB system memory and RAM Type: DDR4, Windows operating system.

9 Results and discussions

This study was conducted on two benchmark hyperspectral datasets, the University of Pavia and Indian Pines. The performance is evaluated by proposed Siamese CNN for the classification of hyperspectral datasets. The features are extracted using the feature extraction module and passed through the proposed network to generate the classification score. The following sections delve deeper into settings and results.

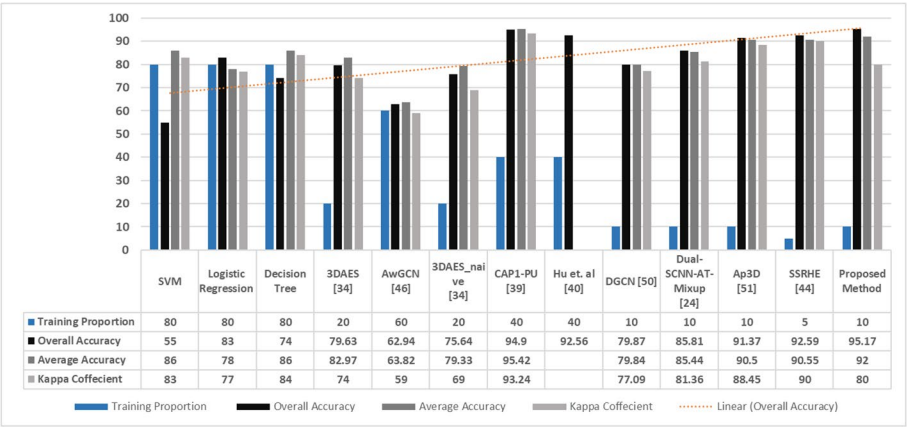
9.1 Data set descriptions

The ROSIS sensor captured the Pavia University images during an air campaign over Pavia, Northern Italy. This dataset has nine categories, 640*340 pixels, 103 spectral bands with a spatial resolution of 1.3 m. In June 1992, an aircraft visible/infrared imaging spectrometer sensor overflew the Indian Pines agricultural location in Northwestern Indiana. Indian Pines dataset has 16 categories with 145 * 145 pixels, 200 spectral bands after removal of 4 noisy bands, with a spatial resolution of 20 m per pixel. Table 2 and 3 show the name of classes and samples in each class. Indian Pines (IP) and Pavia University (PU) dataset after going through data preprocessing as described earlier in this paper.

9.2 Evaluation metrics

To make sure the comparison is fair and thorough; three types of categories were formed:

1. The first group comprised the most well-known and widely used machine learning techniques, such as support vector machine (SVM), decision trees (DT), and logistic regression (LR). These machine learning models produced reasonable results, but there was still room for improvement in categorization accuracy.
2. Deep learning methods came in second owing to their great performance in the field of hyperspectral image categorization. This category included the existing models



	SVM	Logistic Regression	Decision Tree	3DAES [34]	AwGCN [46]	3DAES_naive [34]	CAP1-PU [39]	Hu et. al [40]	DGCN [50]	Dual-SCNN-AT-Mixup [24]	Ap3D [51]	SSRHE [44]	Proposed Method
Training Proportion	80	80	80	20	60	20	40	40	10	10	10	5	10
Overall Accuracy	55	83	74	79.63	62.94	75.64	94.9	92.56	79.87	85.81	91.37	92.59	95.17
Average Accuracy	86	78	86	82.97	63.82	79.33	95.42		79.84	85.44	90.5	90.55	92
Kappa Coffecient	83	77	84	74	59	69	93.24		77.09	81.36	88.45	90	80

Fig. 10 Comparison chart for Pavia U dataset

including 3DAES [24], AwGCN [50], 3DAES_naive [24], CAP1-PU [8], Hu et. al [19], DGCN [18], Dual-SCNN-AT-Mix-up [20], Ap3D [37], SSRHE [21] for Pavia University dataset and CNN-PPF [30], SaSiResnet-2 [16], Hu et. al [19], CAG [2], w-S-SAN [43], DGCN [18], CNN [43], Ap3D [37], SSRHE [21]for Indian Pines dataset.

3. The third category includes the results by proposed network.

Following the related work, three evaluation measures were considered for evaluating the performance of models enclosed in all three categories.

1. Overall Accuracy (OA), The fraction of correctly recognised samples divided by the total number of samples.
2. Average Accuracy (AA) is the average of all classification accuracies obtained for all given classes.
3. Kappa Coefficient concludes the accuracy evaluation with the confusion matrix produced by the network. It assesses the compatibility of predicted labels with the ground truth.
4. The Confusion Matrix shows the percentage of samples from the row classes that were classified into the column classes. Each column/total row should have a value of one.

To avoid an accuracy imbalance for each class, the OA prioritizes the overall classification map, whereas the AA prioritizes each class. Using the kappa coefficient, it can efficiently quantify the correlations between classes.

9.3 Proposed model settings

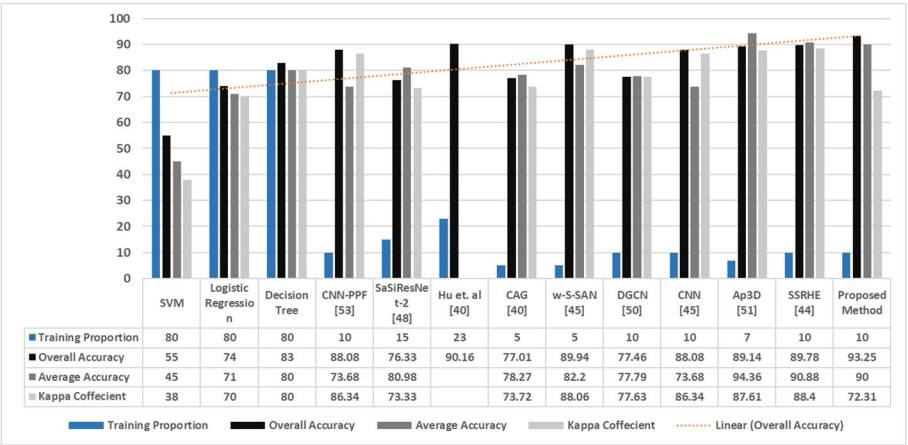
For the Indian Pines dataset, the input was 145 * 145 * 220 as spatial and spectral dimension. The 220 bands were extracted and ground truth was 145 * 145. The model was trained for 10% of samples and tested on 90% of the remaining data. For training the

Table 5 Class wise accuracy comparison for Pavia U (Best Values in Bold)

Class	Class Name	SVM [3]	CAPS1-PU [8]	Hu et. al [19]	Dual-SCNN-AT-Mix-up [20]	SSRHE [21]	DGCN-DC [18]	Ap3D [37]	Proposed
1	Asphalt	87.47	89.43	87.34	80.76	91.19	78.99	91.00	**92.27**
2	Meadows	93.86	96.86	94.63	89.96	98.12	80.91	97.13	**99.49**
3	Gravel	84.23	92.29	86.47	69.51	78.6	79.43	78.23	**98.62**
4	Trees	97.80	97.97	96.29	96.24	89.26	79.23	98.11	**99.49**
5	Painted Metal Sheets	99.86	100.0	99.65	99.49	**99.77**	80.97	98.96	97.08
6	Bare Soil	95.19	96.09	93.23	77.60	85.22	81.03	65.58	**99.33**
7	Bitumen	94.82	**98.31**	93.19	77.23	90.18	80.60	91.88	94.59
8	Self-Blocking Bricks	92.58	87.96	86.42	80.60	79.33	79.30	95.22	**98.94**
9	Shadows	99.93	99.85	**100.0**	97.59	100	78.33	98.42	95.48
OA	Overall Accuracy	92.97	94.90	92.56	85.81	92.59	79.87	91.37	**95.17**
AA	Average Accuracy	93.97	95.42		85.44	90.55	79.84	90.50	92.00
Kappa	Kappa Score		93.24		81.36	90.2	77.09	88.45	80.00

Table 6 Class wise accuracy comparison for Indian Pines (Best Values in Bold)

Class	Class Name	EMP_SVM [45]	CNN-PPF [40]	SaSiResNet [16]	SSRHE [21]	DGCN-DC [18]	Ap3D [37]	Proposed
1	Alfalfa	81.82	-	**95.88**	94.44	81.10	80.20	75.05
2	Corn-notill	78.85	92.99	66.61	88.17	76.20	90.94	**99.15**
3	Corn-mintill	90.75	96.66	81.92	80.46	73.82	**100**	99.46
4	Corn	73.96	-	80.51	84.04	75.50	93.29	79.15
5	Grass-pasture	95.10	98.58	89.18	96.55	73.83	97.27	88.01
6	Grass-Trees	96.99	100	89.71	97.02	78.46	99.77	**99.10**
7	Grass-pasture-mowed	87.50	-	100.00	100	80.80	88.45	81.48
8	Hay-windrowed	99.07	100	95.65	98.60	81.75	83.29	95.81
9	Oats	6.67	-	36.00	80.00	65.56	87.06	**1.0**
10	Soybean-notill	86.81	96.24	77.68	83.89	77.16	100	**98.16**
11	Soybean-mintill	96.80	87.80	59.23	89.50	78.44	95.10	**97.65**
12	Soybean-clean	85.75	98.98	75.96	83.71	81.07	96.97	**97.95**
13	Wheat	97.96	**-**	**98.59**	100	79.34	100	72.39
14	Woods	97.66	99.81	90.08	95.52	76.81	97.44	**1.0**
15	Buildings-Grass-Trees-Drives	92.03	-	81.14	83.57	79.00	**100**	95.37
16	Stone-Steel-Towers	68.85	-	77.47	97.59	85.80	100	89.71
OA	Overall Accuracy	91.09	**94.34**	76.33	89.78	77.46	89.14	***93.25***
AA	Average Accuracy	83.53	**96.78**	80.98	90.88	77.79	94.36	***90.00***
Kappa	Kappa Score	89.78	94.73	73.33	88.4	77.63	87.61	72.31



	SVM	Logistic Regression	Decision Tree	CNN-PPF [53]	SaSiResNet-2 [48]	Hu et. al [40]	CAG [40]	w-S-SAN [45]	DGCN [50]	CNN [45]	Ap3D [51]	SSRHE [44]	Proposed Method
Training Proportion	80	80	80	10	15	23	5	5	10	10	7	10	10
Overall Accuracy	55	74	83	88.08	76.33	90.16	77.01	89.94	77.46	88.08	89.14	89.78	93.25
Average Accuracy	45	71	80	73.68	80.98		78.27	82.2	77.79	73.68	94.36	90.88	90
Kappa Coffecient	38	70	80	86.34	73.33		73.72	88.06	77.63	86.34	87.61	88.4	72.31

Fig. 11 Comparison chart for Indian Pines dataset

network the images were first loaded into the memory, The labels were then converted using one hot encoding as 1 and 0, based upon whether two images belong to same or different class. Images along with converted labels were fed to the Similarity Model. The model was run for 110 epochs and batch size 64. Once the training was completed, model was tested for left 90% sample. Data was trained in random batches and passed through the Feature Generation model where image is passed through convolutions with a kernel size 3 and ReLU activation. The dropout parameter was tried and tested and finally set to 0.5 to reduce the overfitting. After passing two random images through the feature generation model, they were concatenated and further passed through three Dense layers with linear activation function and lastly with sigmoid activation to help achieve the similarity score probability. The model was trained for 110 epochs with 500 steps per epoch. The Siamese network was defined with batch size 32 where random batches were generated by converting the batches into half their equal size and network was fine tuning using adam optimizer with learning rate of 0.0001, binary cross entropy as the hyperparameters in an effort to calculate the mean absolute error, classification accuracy, recall and precision.

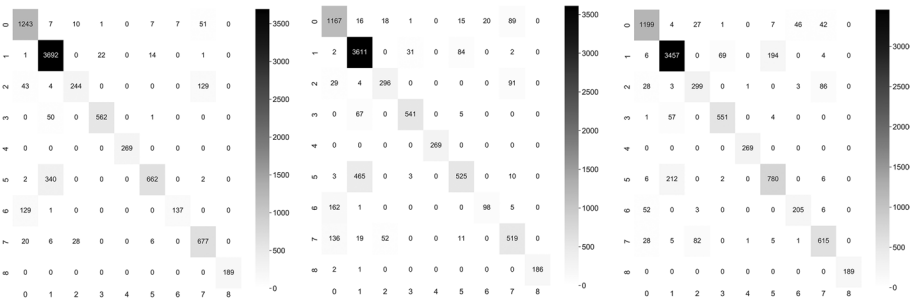


Fig. 12 (Left to Right) confusion matrix, dataset: **Pavia U** for (a) SVM (b) Logistic Regression (c) Decision Tree

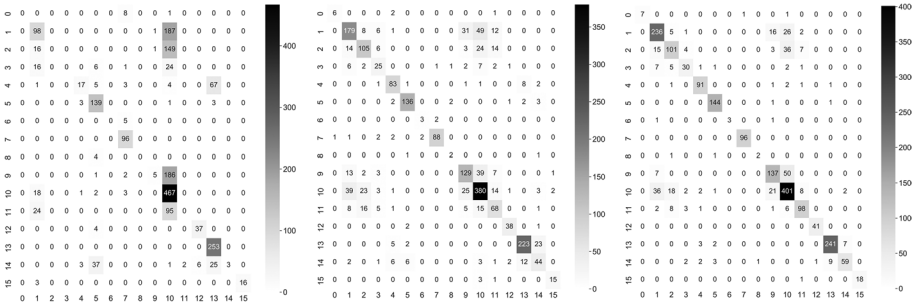


Fig. 13 (Left to Right) Confusion matrix, dataset: **Indian Pines** for (a) SVM (b) Decision Tree (c) Logistic Regression

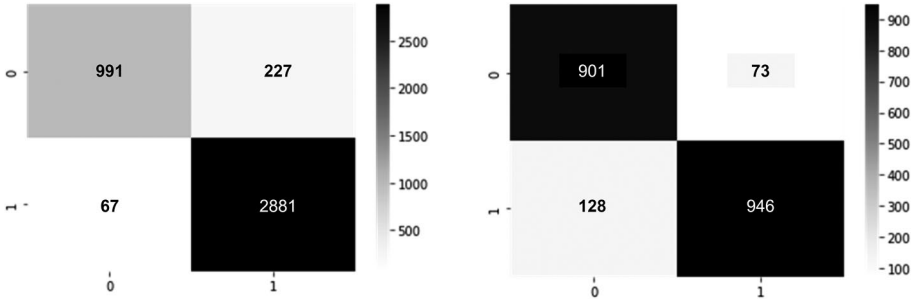


Fig. 14 Confusion matrix for Pavia U and Indian Pines

9.4 Experiment 1: Pavia University

Firstly the experiment was carried out on Pavia University dataset. The comparison of the proposed network with studies proposed literature is graphically represented in Fig. 10 by taking overall accuracy, average accuracy and Kappa coefficient as evaluation metrics. The classification accuracy of each class is shown in Table 5. It clearly shows that the proposed network produces great classification results, particularly the highest overall accuracy and highest accuracies for most of the categories. When the same dataset was classified using machine learning models like SVM, LR and DT the overall accuracy fell down to 55%, 83% and 74% respectively with as big as 80 percent training data. Our proposed model provides great accuracy with data as low as ten

Table 7 Training and testing time taken

Pavia University (610 * 340 * 103)			**Indian Pines** (145 * 145 * 220)		
Total Parameters	Training Time (s)	Testing Time (s)	Total Parameters	Training Time (s)	Testing Time (s)
$2.576 * 10^4$	300	11	$5.648 * 10^4$	280	7
Predicted consumption for 110 epoch(s): Energy: 0.946596 kWh CO2eq: 278.494358 g This is equivalent to: 2.313076 km travelled by car Carbon Tracker: Finished monitoring					

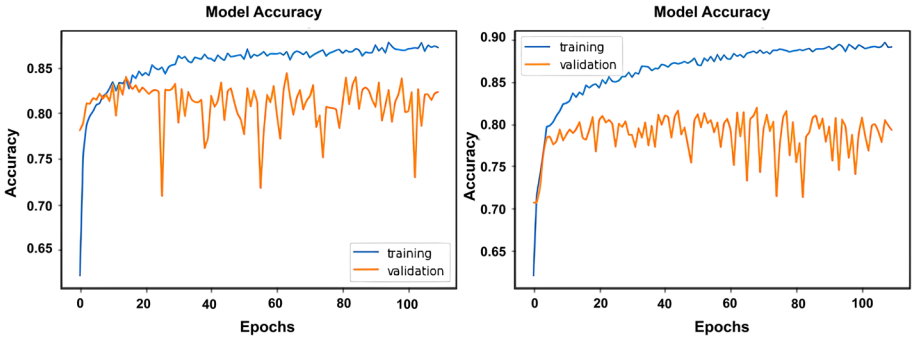


Fig. 15 (Left to Right) model accuracy for Pavia U and Indian Pines

percent. Specifically for the classes "Painted Metal Sheets", "Bitumen" and "Shadows", the accuracy of our model touches 95% or more.

9.5 Experiment 2: Indian Pines

The second experiment was performed on Indian Pines dataset. The class wise accuracy is displayed in Table 6 and overall comparison of evaluation metrics is displayed visually in Fig. 11. The proposed model provides 93.25% overall accuracy with only ten percent of training samples. Digging deep into the results, it can be noticed that the few classes have less data to train for instance, "Soybean-clean", "Oats", "Stone-Steel-Towers" and "Grass-pasture-mowed but still provide fairly good amount of classification accuracy. Our model achieved second best results among the compared models considering the fact that he model achieving highest accuracy has not considered the classes with less or a limited number of samples.

9.6 Confusion matrices

This is a simple way to portray the correctly predicted classes vs incorrectly predicted classes. Figure 12 shows the confusion matrix plotted for machine learning models for Pavia U dataset, Fig. 13 shows the same for Indian Pines dataset and Fig. 14 is the confusion matrix plotted for our proposed model. For the machine learning category, the number of misclassifications are quite high as seen in the matrix and also from the comparative accuracy chart. Figure 15 depicts the training and validation accuracy for the proposed model. The alleviation in overfitting validates the performance of the proposed model.

Figure 14 shows the confusion matrix plotted for the model proposed. This is done by plotting pairwise multilabel 2*2 confusion matrix for a multilabel problem. Since the proposed Siamese network uses binary cross entropy and if two samples do not output the similarity score as 1, it counts it as misclassification. Therefore, this type of pairwise matrix shows true behavior of model specifically in case of Siamese.

Our model was implemented on Windows operating system using 8 GB RAM and Intel i5 8th Gen processor with 480 GB system memory and RAM Type: DDR4 with Scikit

Learn and TensorFlow. As shown in Table 7, The training took 300 s for Pavia U and 280 s for Indian Pines and testing took 11 and 7 for Pavia U ad Indian Pines respectively. The proposed model provides great convergence and this could be improved by use of frameworks like Caffe to reduce the training and testing time.

10 Conclusion and future work

In comparison to current models in the literature, the proposed one shot classification model based on Siamese network with enhanced feature extraction achieves state-of-the-art classification accuracy. The feature extraction block is fine-tuned using hyperparameters to extract discriminative features that aids in boosting classification accuracy even when network is trained using limited data. Since this is fine tuned to extract the HSI features, it performs better than the predefined feature extraction models. This network is more robust to imbalanced data. In compared to current models in the literature, the feature extraction module is less dense providing superior results and faster convergence. As recommendations for future work, one interesting dimension would be to investigate the concept of transfer learning that involves training on data set and testing on other dataset with the same dimensions to solve the problem of labelling data.

Data Availability All the related data can be found at https://www.ehu.eus/ccwintco/index.php/Hyperspectral_Remote_Sensing_Scenes.

Conflict of interest The authors have no conflicts of interest to declare that are relevant to the content of this article.

References

1. Bandos TV, Bruzzone L, Camps-Valls G (2009) Classification of hyperspectral images with regularized linear discriminant analysis. IEEE Trans Geosci Remote Sens 47(3):862–873. https://doi.org/10.1109/TGRS.2008.2005729
2. Cai W, Wei Z (2022) Remote sensing image classification based on a cross-attention mechanism and graph convolution. IEEE Geosci Remote Sens Lett 19:1–5. https://doi.org/10.1109/LGRS.2020.3026587
3. Chapel L, Burger T, Courty N, Lefevre S (2012) Classwise hyperspectral image classification with PerTurbo method, in 2012 IEEE International Geoscience and Remote Sensing Symposium, Munich, Germany, 6883–6886. https://doi.org/10.1109/IGARSS.2012.6352581.
4. Chen Y, Jiang H, Li C, Jia X, Ghamisi P (2016) Deep feature extraction and classification of hyperspectral images based on convolutional neural networks. IEEE Trans Geosci Remote Sens 54(10):6232–6251. https://doi.org/10.1109/TGRS.2016.2584107
5. Chopra S, Hadsell R, LeCun R (2005) Learning a similarity metric discriminatively, with application to face verification in 2005 IEEE Computer Society Conference on Computer Vision and Pattern Recognition (CVPR'05), San Diego, CA, USA, 1:539–546. https://doi.org/10.1109/CVPR.2005.202
6. Ciresan D, Meier U, Schmidhuber J (2012) Multi-column deep neural networks for image classification in 2012 IEEE Conference on Computer Vision and Pattern Recognition, Providence, RI, 3642–3649. https://doi.org/10.1109/CVPR.2012.6248110
7. Dalla Mura M, Villa A, Benediktsson JA, Chanussot J, Bruzzone L (2011) Classification of hyperspectral images by using extended morphological attribute profiles and independent component analysis. IEEE Geosci Remote Sens Lett 8(3):542–546. https://doi.org/10.1109/LGRS.2010.2091253

8. Deng F, Pu S, Chen X, Shi Y, Yuan T, Pu S (2018) Hyperspectral image classification with capsule network using limited training samples. Sensors 18(9):3153. https://doi.org/10.3390/s18093153
9. Dopido I, Li J, Marpu PR, Plaza A, Bioucas Dias JM, Benediktsson JA (2013) Semisupervised self-learning for hyperspectral image classification. IEEE Trans Geosci Remote Sens 51(7):4032–4044. https://doi.org/10.1109/TGRS.2012.2228275
10. Eeti LN, Buddhiraju KM (2021) Two hidden layer neural network-based rotation forest ensemble for hyperspectral image classification. Geocarto Int 36(16):1820–1837. https://doi.org/10.1080/10106049.2019.1678680
11. Fauvel M, Chanussot J, Benediktsson JA, Sveinsson JR (2007) Spectral and spatial classification of hyperspectral data using SVMs and morphological profiles, in 2007 IEEE International Geoscience and Remote Sensing Symposium, Barcelona, Spain, pp. 4834–4837https://doi.org/10.1109/IGARSS.2007.4423943
12. Fukushima K (1988) Neocognitron: A hierarchical neural network capable of visual pattern recognition. Neural Netw 1(2):119–130. https://doi.org/10.1016/0893-6080(88)90014-7
13. Gao H, Zhang J, Cao X, Chen Z, Zhang Y, Li C (2021) Dynamic data augmentation method for hyperspectral image classification based on siamese structure. IEEE J Sel Top Appl Earth Obs Remote Sens 14:8063–8076. https://doi.org/10.1109/JSTARS.2021.3102610
14. Graña M, Veganzons M, Ayerdi B (2021) Computational Intelligence Group (GIC). Hyperspectral Remote Sensing Scenes. http://www.ehu.eus/ccwintco/index.php/Hyperspectral_Remote_Sensing_Scenes#Indian_Pines (Accessed Nov. 30, 2021)
15. Guo B, Gunn SR, Damper RI, Nelson JDB (2008) Customizing Kernel Functions for SVM-Based Hyperspectral Image Classification. IEEE Trans Image Process 17(4):622–629. https://doi.org/10.1109/TIP.2008.918955
16. He Z, He D (2020) Spatial-adaptive siamese residual network for multi-/hyperspectral classification. Remote Sens 12(10):1640. https://doi.org/10.3390/rs12101640
17. He K, Zhang X, Ren S, Sun J (2015) Deep residual learning for image recognition. ArXiv151203385 Cs. Accessed: Oct. 27, 2021. [Online]. Available: http://arxiv.org/abs/1512.03385
18. He X, Chen Y, Ghamisi P (2022) Dual graph convolutional network for hyperspectral image classification with limited training samples. IEEE Trans Geosci Remote Sens 60:1–18. https://doi.org/10.1109/TGRS.2021.3061088
19. Hu W, Huang Y, Wei L, Zhang F, Li H (2015) Deep convolutional neural networks for hyperspectral image classification. J Sens 2015:1–12. https://doi.org/10.1155/2015/258619
20. Huang L, Chen Y (2021) Dual-Path Siamese CNN for hyperspectral image classification with limited training samples. IEEE Geosci Remote Sens Lett 18(3):518–522. https://doi.org/10.1109/LGRS.2020.2979604
21. Huang H, Chen M, Duan Y (2019) Dimensionality reduction of hyperspectral image using spatial-spectral regularized sparse hypergraph embedding. Remote Sens 11(9):1039. https://doi.org/10.3390/rs11091039
22. Hyperspectral Remote Sensing Scenes - Grupo de Inteligencia Computacional (GIC). http://www.ehu.eus/ccwintco/index.php/Hyperspectral_Remote_Sensing_Scenes (accessed Jan. 31, 2022).
23. Javaid N, Jan N, Javed MU (2021) An adaptive synthesis to handle imbalanced big data with deep siamese network for electricity theft detection in smart grids. J Parallel Distrib Comput 153:44–52. https://doi.org/10.1016/j.jpdc.2021.03.002
24. Jia S et al. (2021) A semisupervised siamese network for hyperspectral image classification. IEEE Trans Geosci Remote Sens. 1–17. https://doi.org/10.1109/TGRS.2021.3116138
25. Khan MJ, Khan HS, Yousaf A, Khurshid K, Abbas A (2018) Modern trends in hyperspectral image analysis: A review. IEEE Access 6:14118–14129. https://doi.org/10.1109/ACCESS.2018.2812999
26. Koch G, Zemel R, Salakhutdinov R (2015) Siamese neural networks for one-shot Image Recognition 8
27. Krizhevsky A, Sutskever I, Hinton GE (2012) ImageNet classification with deep convolutional neural networks in advances in neural information processing systems 25. [Online]. Available: https://proceedings.neurips.cc/paper/2012/file/c399862d3b9d6b76c8436e924a68c45b-Paper.pdf
28. Kuo B-C, Li C-H, Yang J-M (2009) Kernel nonparametric weighted feature extraction for hyperspectral image classification. IEEE Trans Geosci Remote Sens 47(4):1139–1155. https://doi.org/10.1109/TGRS.2008.2008308
29. Li Y, Zhang H, Xue X, Jiang Y, Shen Q (2018) Deep learning for remote sensing image classification: A survey. WIREs Data Min Knowl Discov 8(6). https://doi.org/10.1002/widm.1264
30. Li W, Wu G, Zhang F, Du Q (2017) Hyperspectral image classification using deep pixel-pair features. IEEE Trans Geosci Remote Sens 55(2):844–853. https://doi.org/10.1109/TGRS.2016.2616355

31. Li Y, Xie W, Li H (2017) Hyperspectral image reconstruction by deep convolutional neural network for classification. Pattern Recognit 63:371–383. https://doi.org/10.1016/j.patcog.2016.10.019
32. Liang H, Bao W, Shen X (2021) Adaptive weighting feature fusion approach based on generative adversarial network for hyperspectral image classification. Remote Sens 13(2):198. https://doi.org/10.3390/rs13020198
33. Liao X, Yin J, Chen M, Qin Z (2021) Adaptive payload distribution in multiple images steganography based on image texture features. IEEE Trans. Dependable Secure Comput. 1–1. https://doi.org/10.1109/TDSC.2020.3004708
34. Liao X, Yu Y, Li B, Li Z, Qin Z (2020) A new payload partition strategy in color image steganography. IEEE Trans Circuits Syst Video Technol 30(3):685–696. https://doi.org/10.1109/TCSVT.2019.2896270
35. Liao X, Li K, Zhu X, Liu KJR (2020) Robust detection of image operator chain with two-stream convolutional neural network. IEEE J Sel Top Signal Process 14(5):955–968. https://doi.org/10.1109/JSTSP.2020.3002391
36. Licciardi G, Marpu PR, Chanussot J, Benediktsson JA (2012) Linear versus nonlinear PCA for the classification of hyperspectral data based on the extended morphological profiles. IEEE Geosci Remote Sens Lett 9(3):447–451. https://doi.org/10.1109/LGRS.2011.2172185
37. Lin J, Mou L, Zhu XX, Ji X, Wang ZJ (2021) Attention-Aware Pseudo-3-D convolutional neural network for hyperspectral image classification. IEEE Trans Geosci Remote Sens 59(9):7790–7802. https://doi.org/10.1109/TGRS.2020.3038212
38. Liu B, Yu X, Zhang P, Tan X, Yu A, Xue Z (2017) A semi-supervised convolutional neural network for hyperspectral image classification. Remote Sens Lett 8(9):839–848. https://doi.org/10.1080/2150704X.2017.1331053
39. Liu J, Yang Z, Liu Y, Mu C (2021) Hyperspectral remote sensing images deep feature extraction based on mixed feature and convolutional neural networks. Remote Sens 13(13):2599. https://doi.org/10.3390/rs13132599
40. Liu B, Yu X, Zhang P, Yu A, Fu Q, Wei X (2018) Supervised deep feature extraction for hyperspectral image classification. IEEE Trans Geosci Remote Sens 56(4):1909–1921. https://doi.org/10.1109/TGRS.2017.2769673
41. Makantasis K, Karantzalos K, Doulamis A, Doulamis N (2015) Deep supervised learning for hyperspectral data classification through convolutional neural networks in 2015 IEEE International Geoscience and Remote Sensing Symposium (IGARSS), Milan, pp. 4959–4962. https://doi.org/10.1109/IGARSS.2015.7326945
42. Meng S, Wang X, Hu X, Luo C, Zhong Y (2021) Deep learning-based crop mapping in the cloudy season using one-shot hyperspectral satellite imagery. Comput Electron Agric 186:106188 https://doi.org/10.1016/j.compag.2021.106188
43. Miao J, Wang B, Wu X, Zhang L, Hu B, Zhang JQ (2019) Deep feature extraction based on siamese network and auto-encoder for hyperspectral image classification in IGARSS 2019 - 2019 IEEE International Geoscience and Remote Sensing Symposium, Yokohama, Japan, 397–400. https://doi.org/10.1109/IGARSS.2019.8899230
44. Paoletti ME, Haut JM, Plaza J, Plaza A (2018) A new deep convolutional neural network for fast hyperspectral image classification. ISPRS J Photogramm Remote Sens 145:120–147. https://doi.org/10.1016/j.isprsjprs.2017.11.021
45. Pathak DK, Kalita SK, Bhattacharya DK (2021) Hyperspectral image classification using support vector machine: a spectral spatial feature based approach. Evol Intell. https://doi.org/10.1007/s12065-021-00591-0
46. Simonyan K, Zisserman A (2015) Very deep convolutional networks for large-scale Image Recognition. ArXiv14091556 Cs. Accessed: Nov. 26, 2021. [Online]. Available: http://arxiv.org/abs/1409.1556
47. Song H, Yang W, Yuan H, Bufford H (2020) Deep 3D-Multiscale densenet for hyperspectral image classification based on spatial-spectral information. Intell Autom Soft Comput 26(4):1441–1458. https://doi.org/10.32604/iasc.2020.011988
48. Szegedy C et al. (2014) Going deeper with convolutions. ArXiv14094842 Cs. Accessed: Nov. 26, 2021. [Online]. Available: http://arxiv.org/abs/1409.4842
49. Te-Ming Tu, Chen C-H, Jiunn-Lin Wu, Chang C-I (1998) A fast two-stage classification method for high-dimensional remote sensing data. IEEE Trans Geosci Remote Sens 36(1):182–191. https://doi.org/10.1109/36.655328
50. Tong X, Yin J, Han B, Qv H (2020) Few-shot learning with attention-weighted graph convolutional networks for hyperspectral image classification, in 2020 IEEE International Conference on Image Processing (ICIP), Abu Dhabi, United Arab Emirates. 1686–1690. https://doi.org/10.1109/ICIP40778.2020.9190752.

51. Villa A, Benediktsson JA, Chanussot J, Jutten C (2011) Hyperspectral image classification with independent component discriminant analysis. IEEE Trans Geosci Remote Sens 49(12):4865–4876. https://doi.org/10.1109/TGRS.2011.2153861
52. Wang G, Ren P (2020) Hyperspectral Image Classification with Feature-Oriented Adversarial Active Learning. Remote Sens 12(23):3879. https://doi.org/10.3390/rs12233879
53. Wang X, Ma L, Liu F (2013) Laplacian support vector machine for hyperspectral image classification by using manifold learning algorithms in 2013 IEEE International Geoscience and Remote Sensing Symposium - IGARSS, Melbourne, Australia, 1027–1030. https://doi.org/10.1109/IGARSS.2013.6721338
54. Wang W, Chen Y, He X, Li Z (2022) Soft augmentation-based siamese CNN for hyperspectral image classification with limited training samples. IEEE Geosci Remote Sens Lett 19:1–5. https://doi.org/10.1109/LGRS.2021.3103180
55. Xi J et al (2021) Dynamic wide and deep neural network for hyperspectral image classification. Remote Sens 13(13):2575. https://doi.org/10.3390/rs13132575
56. Yang X, Ye Y, Li X, Lau RYK, Zhang X, Huang X (2018) Hyperspectral image classification with deep learning models. IEEE Trans Geosci Remote Sens 56(9):5408–5423. https://doi.org/10.1109/TGRS.2018.2815613
57. Zhong Z, Li J, Luo Z, Chapman M (2018) Spectral–spatial residual network for hyperspectral image classification: A 3-D deep learning framework. IEEE Trans Geosci Remote Sens 56(2):847–858. https://doi.org/10.1109/TGRS.2017.2755542
58. Zhu Q et al. (2021) A spectral-spatial-dependent global learning framework for insufficient and imbalanced hyperspectral image classification. IEEE Trans Cybern 1–15. https://doi.org/10.1109/TCYB.2021.3070577.

Publisher's note Springer Nature remains neutral with regard to jurisdictional claims in published maps and institutional affiliations.

Springer Nature or its licensor (e.g. a society or other partner) holds exclusive rights to this article under a publishing agreement with the author(s) or other rightsholder(s); author self-archiving of the accepted manuscript version of this article is solely governed by the terms of such publishing agreement and applicable law.

AIP Conference Proceedings

RESEARCH ARTICLE | MAY 08 2023

Denoising of palm leaf manuscripts using Gaussian filter and conservative smoothing

Mayank Singh ✉; S. Indu

Check for updates

AIP Conference Proceedings 2521, 050005 (2023)
https://doi.org/10.1063/5.0142237

CrossMark

View Online Export Citation

Articles You May Be Interested In

Self-Consistent Ornstein-Zernike Approximation (SCOZA) and exact second virial coefficients and their relationship with critical temperature for colloidal or protein suspensions with short-ranged attractive interactions

J. Chem. Phys. (October 2013)

On the impossibility of defining adhesive hard spheres as sticky limit of a hard-sphere-Yukawa potential

J. Chem. Phys. (March 2011)

Investigation of electronic transport properties of some liquid transition metals

AIP Conference Proceedings (April 2018)

Downloaded from http://pubs.aip.org/aip/acp/article-pdf/doi/10.1063/5.0142237/17410495/050005_1_5.0142237.pdf



AIP Publishing

Denoising of Palm Leaf Manuscripts Using Gaussian Filter and Conservative Smoothing

Mayank Singh[1,a)], S. Indu[2,b)]
[1,2] *Delhi Technological University, Shahbad Daulatpur, Delhi-110042, India*
[a)] Corresponding author: mayanksingh9634@gmail.com
[b)] s.indu@dce.ac.in

Abstract. Text extraction is a very important step is language processing and pattern recognition. As the world is moving to digital era, the volume of digital images is increasing exponentially with most of thembeing distorted. Hence denoising of digital images is gaining importance. In this paper we are proposing a novel method of denoising by combining two methods, gaussian filtering and conservative smoothening.The proposed method is used for enhancing a manuscript image for extracting text from it. After converting colour space from BGR to HSV, Gaussian filtering followed by conservative smoothening is done for incorporating better entropy and PSNR features of both methods respectively. The method is validated using entropy and PSNR features

Keywords. Gaussian Filtering, Conservative Smoothening, Peak Signal to Noise Ratio, Entropy, mean, median.

INTRODUCTION

Palm leaves manuscripts were one of the most used writing materials in the olden days, especially the dried ones. Palm leaves are being used for writing purposes even before the history of writing started which was in 2500 B.C. The style of writing on palm leaves is a little bit different from the conventional style. To begin with, a sharp instrument is used to seam the palm leaf. This is done to imprint the character into the leaf. The next step would be to make the characters just embedded into the palm leaf visible, using natural dies to polish polishing the manuscript[1]. Palm leaf manuscripts carry lots of heritage information. Hence, we chose the enhancement of such manuscript image.

For any signal processing system, filtering is a very important step, which is described as predicting the degraded signal mostly by add-on arbitrary noise. For many years linear processing technique have been preferredfor many filtering algorithmsbecause of their simplicity. But for almost all of the filtering algorithms A gaussian model is taken for and then the parameters are optimized for the system model. Recently nonlinear methods are used more and more because of their ability to minimize Gaussian noise which retains the important signal elements like fine details and edges and also helps to remove deteriorations caused while transmission through non-linear channels or signal formation. Fuzzy-logic techniques are important in non-linear algorithms because of their ability to reason uncertain and vague information.[2]

The palm leaf chosen for this research paper is an ancient manuscript that has deteriorated over time. Figure 1 below shows a sample palm-leaf manuscript.



FIGURE 1. Palm leaf manuscript

In ancient times as there was no digital technology, these palm leaf manuscripts were all written by hand and there were many different techniques to do that. One of which is the technique used in Kerala, where an instrument

Advances in Manufacturing Technologies and Application of Artificial Intelligence
AIP Conf. Proc. 2521, 050005-1–050005-8; https://doi.org/10.1063/5.0142237
Published by AIP Publishing. 978-0-7354-4473-7/$30.00

Downloaded from http://pubs.aip.org/aip/acp/article-pdf/doi/10.1063/5.0142237/17410495/050005_1_5.0142237.pdf

in the shape of a pen-like Stylus called “Narayam” was utilized to embed the characters in the palm leaves. The juice of a plant called Chromalaena Odorata or “Communist Pacha” is used as a die for polishing which is widely available shown in Figure 2.



FIGURE 2. Chromalaena Odorata[3]

During ancient times the most popular exchangeable means of writing were the palm leaves, which is why these palm leaves are considered an incredible source of knowledge. As India is the originator of Ayurveda that’s why the medical details embedded in the palm leaf are immeasurable. However, the palm leaves turn fragile as time passes by and is also affected by environmental factors. Hence, as more and more palm leaves deteriorate more and more of them disappear which is the main reason to digitize the palm leaves. When digitizing an image, it needs to be made sure that the image is noise-free that’s why denoising algorithms are needed. However, the following complexities make this even harder.[3]

Palm leaf manuscripts are subjected to many kinds of noises over time like fungus, color fading, dust, stains. Manuscripts may also be affected by several other noises like varying and poor contrast, marks, ink sipping, noise from scanning, dots, ghosting noise, black borders, lines, textual specks, etc. All these different types of noises should be addressed by the denoising algorithm.Pre-processing is done before actual denoising begins because palm leaves were used as a writing material even before the 5th century BC therefore palm leaves with very high noise may also be present.

The main focus of this paper will be further enhancing the images after the initial noise removal of the image has been done through some methods. Various different filtering algorithms have been performed and compared in this paper for the same and finally the hybrid algorithm combining both Gaussian filtering and Conservative smoothing is found to give the best results.

The paper is organized as follows; Section 2 presents the Literature Review. Section 3 introduces the proposed methodology. Experimental results are displayed in section 4. The conclusions are drawn in section 5. The future scope is briefly discussed in section 6.

LITERATURE REVIEW

The existing noise removal algorithms are researched very thoroughly. An algorithm performing binarization over a wide range of parameter values and hence predicting the correct value by repeatedly narrowing the parameters’ range. was introduced by Badekas and Papamarkos[4]. A smoothing algorithm was established by Lu et al.[5] based on iterative polynomial where the identified stroke edges in characters decided the local threshold. A technique was invented by Lelore and Bouchara[6] where pixels were classified into different groups like background, foreground, etc. A parameter-independent algorithm was invented by Gatos et al[7]. Multiple threshold values were combined to obtain a single binarization value based on a cross-section sequence in Dawoud’s[8] method. A global energy function is optimized drawing on an in Howe’s approach[8]. Non-local means filtering algorithm is a method in which the filtering parameter depends on the standard deviation of the noise was developed by A. Buades, B. Coll, J. Morel[9]. Bayesian Optimization is used to binarize a document image in the algorithm introduced by Vats et al.[10]. Nikolaos Papamarkos, Nikolaos Mitianoudis, implemented Document Image Binarization was performed using Gaussian Mixture Modelling and Local Features[11].

The foreground and background contrast difference in the palm leaves makes it such that most of the algorithms are not suitable for denoising. Thus, algorithms especially suitable for this task are introduced by researchers. A technique where the color histogram is used to determine the background color is introduced by Z. Shi, S. Setlur, and V. Govindaraju[12]. A binarization method with a cognitive memory network basis was introduced by Kumar et al[13]. Gray-level Histograms were used to develop a method based on threshold selection by N. Otsu[14]. Niblack

Downloaded from http://pubs.aip.org/aip/acp/article-pdf/doi/10.1063/5.0142237/17410495/050005_1_5.0142237.pdf

executed a binarization method that does threshold calculation using a fixed-size sliding window that moves across the image[15]. The adaptive document image binarization technique[16] was developed by Sauvola and M. Pietikainen. This method enhances the Niblack one with the addition of dynamic standard deviation.
The existing algorithms do a fine job of removing noise from the image but the proposed algorithm works on enhancing the image by using a hybrid filtering technique which is a combination of Gaussian filtering and Conservative smoothing implemented successively. The Gaussian filter will enhance entropy and Conservative smoothening increase PSNRin the same order, because if even the order is reversed the function of the algorithm will change.

PROPOSED METHODOLOGY

The method proposed in this paper is briefly explained below. A flow chart is shown in Figure 3 briefly highlighting the steps in the whole process.

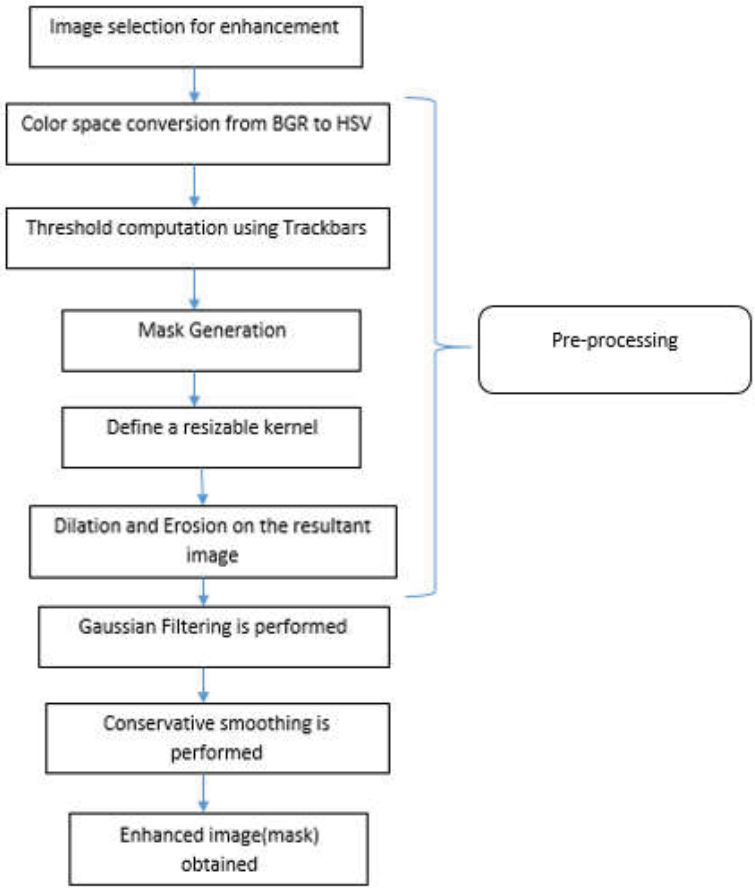


FIGURE 3. Flow chart of the proposed method

As indicated by the flow chart shown above, the major steps involved in the method proposed are image selection for enhancement, pre-processing, Gaussian filtering, and finally, conservative smoothing after which the final image is obtained.
The flow chart is explained below:

- First the image is selected among many images present in the dataset.
- Then the pre-processing is started:
  - First the color space[17] of the image is changed from BGR to HSV[18].
  - After which the different thresholds for hue, saturation, and value is calculated using trackbars.

Downloaded from http://pubs.aip.org/aip/acp/article-pdf/doi/10.1063/5.0142237/17410495/050005_1_5.0142237.pdf

    - When the above step is done, a mask will be obtained.
    - A resizable kernel window is defined[19].
    - Morphological operations like dilation and erosion is performed on the resultant mask[20].
- Gaussian filtering is performed on the image[21][22].
- Conservative smoothing is performed[2].
- Final image is obtained which will have more characters that are recognizable.

After the pre-processing is completed, the image obtained will have some noise which will result in not all of the characters being recognizable, that's why the filtering techniques are performed to reduce the noise in the image. Various filtering processes are explained in the following paragraphs.

Filtering

Multiple ways are present to conserve the image in image processing; image enhancement is one of them. Image enhancement is used to improve the image quality such that it looks inherently better. The resulting image after enhancement is observed to provide more details or having less noise or having a better contrast[23].

There are many ways to perform image enhancement like removing interference and additive noise, changing the contrast, abolishing the multiplicative interference, also minimizing the blurring. Then the image filtering process determines the best outcome among several filters.

Mean Filtering

Mean filter is one of the easiest linear filters to implement. A local mean operation is performed, and each pixel's value is substituted by the mean of the local neighbourhood pixel values:

$$h[i,j] = \frac{1}{M}\sum_{(k,l)\epsilon N} f[k,l] \quad (1)$$

where M gives the total number of pixels in the neighbourhood N[22][21]. For example, taking a 3 x 3 neighbourhood about [i, j] yields:

$$h[i,j] = \frac{1}{9}\sum_{k=i}^{i+1}\sum_{l=j-1}^{j+1} f[k,l] \quad (2)$$

Median Filter

The median filter is a digital filter of a non-linear kind and it operates by replacing the pixels in the image with the median value of the neighborhood pixels. Sharp signal changes can be preserved by the median filter. The median filter can be used to remove impulse noise (salt and pepper noise) because the gray level of the impulse noise is either higher or lower than the neighborhood pixels.

$$y[m,n] = median\{x[i,j], (i,j)\epsilon w\} \quad (3)$$

where "w" is a neighborhood site on the center around the location [m, n] in the image data[21][22][24].

Gaussian Filter

Gaussian filter or Gaussian smoothing is a filter that causes the image to blur. A gaussian filter can be used to reduce the image noise and detail simultaneously maintaining the color. The formula is given below.

Downloaded from http://pubs.aip.org/aip/acp/article-pdf/doi/10.1063/5.0142237/17410495/050005_1_5.0142237.pdf

$$G(x,y) = \frac{1}{2\pi\sigma^2} e - \frac{x^2 + y^2}{2\sigma^2} \quad (4)$$

where, 'x = horizontal axis' origin distance and 'y' vertical axis' origin distance, and 'σ' is the Gaussian distributions' standard deviation[22][23].

Conservative Smoothing

Its[2] a technique based on the reduction of noise. It is a straightforward fast filtering method used to preserve the high spatial frequency detail comprising the noise suppression power in an image.It can also remove the spikes made by noise in an imagei.e., the pixels with unusually low or high intensities (salt and pepper noise) and thus is somewhat less efficient for removing additive noise present in an image (Gaussian noise). The fact that noise has a high spatial frequency and can be attenuated with local operation is exploited by conservative smoothing. Thus, each pixel's intensity is approximately consistent with those of its nearest neighbors. Mean filtering accomplishes this by averaging local intensities and median filtering does the same by a non-linear rank selection technique. On the other hand, conservative smoothing makes sure that each pixel's intensity is within the range of intensities defined by its neighbors.

RESULTS

The dataset contains images of the manuscripts written on the palm leaves as shown in figure 4. Since these manuscripts are ancient, most of the leaves have deteriorated due to environmental effects. Contemporarily if researchers try to interpret the text written on these manuscripts, then it would be difficult due to degradation. Therefore, the filtering techniques are applied to the processed images to interpret them more easily.

TABLE 1. Filtering techniques comparison on image with threshold = 244

Type of filter	PSNR	Entropy
Mean Filter	27.80	6.89
Median Filter	27.86	6.85
Gaussian Filter	27.92	6.51
Conservative Smoothing	28.01	4.57
Gaussian Filter + Conservative Smoothing	27.97	6.61

PSNR and Entropy of the image is calculated before doing anything to it, after pre-processing and then after the image has gone through theproposed method, as represented in Table 2 and Table 3. Then, different filtering algorithms are proposed on the image and then it's PSNR and Entropy is calculated. Then the filtering algorithm having the best combination of PSNR and Entropy is chosen out of all the algorithms.

Table 1 performs various filtering algorithms when applied to the image obtained after pre-processing. It can be seen that while Mean filtering gives the best performance concerning Entropy[25] and Conservative Smoothing for PSNR[26] but collectively they don't do very good so a new method is tried out which is the combination of Gaussian Filtering and Conservative Smoothing which results in overall good results with a little increase in PSNR and a good improvement in Entropy which will result in a good final image.

The combination of Gaussian filtering and conservative smoothing has the most balanced results when compared to the PSNR and entropy of the original image.

TABLE 2: Comparison between the two methods based on PSNR

Image	Entropy
Original	6.603
After pre-processing	1.096
Proposed method	1.534

Downloaded from http://pubs.aip.org/aip/acp/article-pdf/doi/10.1063/5.0142237/17410495/050005_1_5.0142237.pdf

TABLE 3. Comparison between the two methods based on Entropy

Image	PSNR
Original Image, Image after pre-processing	28.153
Original Image, Proposed method Image	28.031



FIGURE 4. An image from the dataset

Figure 5 shown below depicts the text extracted from the manuscript image using BGR to HSV based text extraction incorporating slidebars at threshold = 244.

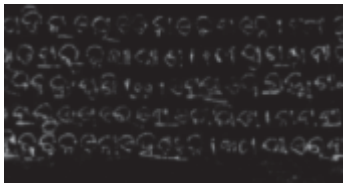


FIGURE 5. A small part of the output image after going through the method proposed (threshold = 244)

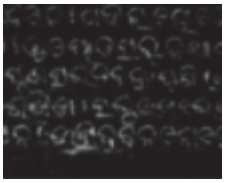


FIGURE 6. Gaussian filtering performed of the selected image

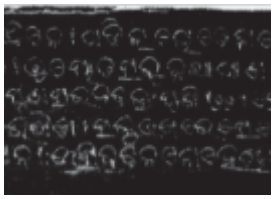


FIGURE 7. Conservative smoothing performed on the selected image

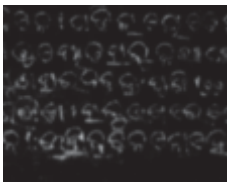


FIGURE 8. Gaussian Filtering + Conservative Smoothing performed on the selected image

Downloaded from http://pubs.aip.org/aip/acp/article-pdf/doi/10.1063/5.0142237/17410495/050005_1_5.0142237.pdf

CONCLUSIONAND FUTURE SCOPE

The method proposed here can be used for image noise removal and it also gives out good results when comparing to the algorithms performing individually. The method gives a balanced result focusing on both the measurement parameter, unlike some others which just gives a good result in one of the parameters and poor in another.

Further research can be done to improve the image quality, even more, using various hybrid techniques and thus gather relevant information from ancient scripts. Theoutput image can be further enhanced in quality using various methods.

This algorithm can be automated using deep learning or any other relevant method.

The algorithm can be further modified such that variation of hue in the image does not cause any changes to the image because it can be seen in the results that hue does not have a very significant impact on the results.

REFERENCES

[1] D. U. Kumar, G. V Sreekumar, and U. a Athvankar, "Traditional writing system in Southern India — Palm leaf manuscripts .," *Des. Thoughts*, no. July, pp. 2–7, 2009.

[2] M. Poulose, "Literature Survey on Image Deblurring Techniques," *Int. J. Comput. Appl. Technol. Res.*, vol. 2, no. 3, pp. 286–288, 2013, doi: 10.7753/ijcatr0203.1014.

[3] T. Ernakulam, "manuscripts using Image Gradient approximations," pp. 506–511, 2019.

[4] S. Lu, B. Su, and C. L. Tan, "Document image binarization using background estimation and stroke edges," *Int. J. Doc. Anal. Recognit.*, vol. 13, no. 4, pp. 303–314, 2010, doi: 10.1007/s10032-010-0130-8.

[5] T. Lelore and F. Bouchara, "Super-resolved binarization of text based on the FAIR algorithm," *Proc. Int. Conf. Doc. Anal. Recognition, ICDAR*, pp. 839–843, 2011, doi: 10.1109/ICDAR.2011.172.

[6] B. Gatos, I. Pratikakis, and S. J. Perantonis, "Adaptive degraded document image binarization," *Pattern Recognit.*, vol. 39, no. 3, pp. 317–327, 2006, doi: 10.1016/j.patcog.2005.09.010.

[7] I. Cross, S. Sequence, A. C. Section, and S. Graph, "О Проблеме Борсука Для (0, 1)- И (-1, 0, 1)-Многогранников В Пространствах Малой Размерности," *Труды Московского Физико-Технического Института*, vol. 4, no. 1–13, pp. 2150–2154, 2012.

[8] N. R. Howe, "Document binarization with automatic parameter tuning," *Int. J. Doc. Anal. Recognit.*, vol. 16, no. 3, pp. 247–258, 2013, doi: 10.1007/s10032-012-0192-x.

[9] J. Wang, Y. Guo, Y. Ying, Y. Liu, and Q. Peng, "Fast non-local algorithm for image denoising," *Proc. - Int. Conf. Image Process. ICIP*, no. 0, pp. 1429–1432, 2006, doi: 10.1109/ICIP.2006.312698.

[10] E. Vats, A. Hast, and P. Singh, "Automatic document image binarization using Bayesian optimization," *ACM Int. Conf. Proceeding Ser.*, pp. 89–94, 2017, doi: 10.1145/3151509.3151520.

[11] N. Mitianoudis and N. Papamarkos, "Document image binarization using local features and Gaussian mixture modeling," *Image and Vision Computing*, vol. 38. pp. 33–51, 2015, doi: 10.1016/j.imavis.2015.04.003.

[12] Z. Shi, S. Setlur, and V. Govindaraju, "Digital image enhancement using normalization techniques and their application to palmleaf manuscripts," *Cent. Excell. Doc. Anal. Recognit.*, no. February 2016, 2005, [Online]. Available: http://www.cedar.buffalo.edu/~zshi/Papers/kbcs04_261.pdf.

[13] N. S. Kumar, D. S. Kumar, S. Swathikiran, and A. P. James, "Ancient indian document analysis using cognitive memory network," *Proc. 2014 Int. Conf. Adv. Comput. Commun. Informatics, ICACCI 2014*, no. September, pp. 2665–2668, 2014, doi: 10.1109/ICACCI.2014.6968659.

[14] N. Otsu *et al.*, "Otsu_1979_otsu_method," *IEEE Trans. Syst. Man. Cybern.*, vol. C, no. 1, pp. 62–66, 1979.

[15] W. Niblack, "An introduction to digital image processing.," *An Introd. to Digit. image Process.*, 1986, doi: 10.1002/0470035528.ch15.

[16] "PRACHEENA KERALA LIPIKAL - RAVIVARMA L.A (www.malayalambooks.net).pdf." .

[17] R. G. Kuehni, "Color Space and Its Divisions," vol. 26, no. 3, 2001.

[18] G. Saravanan, G. Yamuna, and S. Nandhini, "Real Time Implementation of RGB to HSV / HSI / HSL and Its Reverse Color Space Models," pp. 462–466, 2016.

[19] V. Gupta, N. Sambyal, A. Sharma, and P. Kumar, "Restoration of artwork using deep neural networks," *Evol. Syst.*, no. 0123456789, 2019, doi: 10.1007/s12530-019-09303-7.

Downloaded from http://pubs.aip.org/aip/acp/article-pdf/doi/10.1063/5.0142237/17410495/050005_1_5.0142237.pdf

[20] R. M. Haralick and S. R. Sternberg, “Image Analysis Morphology,” no. 4, pp. 532–550, 1987.
[21] M. Mandar, D. Sontakke, M. Meghana, and S. Kulkarni, “Different Types of Noises in Images and Noise Removing Technique,” *Int. J. Adv. Technol. Eng. Sci.*, vol. 03, no. 01, pp. 102–115, 2015.
[22] A. C. Frery, “Image filtering,” *Digit. Doc. Anal. Process.*, pp. 55–70, 2013, doi: 10.1201/b10797-8.
[23] S. Z. Syed Zaini *et al.*, “Image Quality Assessment for Image Segmentation Algorithms: Qualitative and Quantitative Analyses,” *Proc. - 9th IEEE Int. Conf. Control Syst. Comput. Eng. ICCSCE 2019*, pp. 66–71, 2019, doi: 10.1109/ICCSCE47578.2019.9068561.
[24] M. R. Rakesh, B. Ajeya, and A. R. Mohan, “Hybrid Median Filter for Impulse Noise Removal of an Image in Image Restoration,” *Int. J. Adv. Res. Electr. Electron. Instrum. Eng.*, vol. 2, no. 10, pp. 5117–5124, 2013.
[25] C. H. Thum, “Measurement of the entropy of an image with application to image focusing,” *Opt. Acta (Lond).*, vol. 31, no. 2, pp. 203–211, 1984, doi: 10.1080/713821475.
[26] U. Sara, M. Akter, and M. S. Uddin, “Image Quality Assessment through FSIM, SSIM, MSE and PSNR—A Comparative Study,” *J. Comput. Commun.*, vol. 07, no. 03, pp. 8–18, 2019, doi: 10.4236/jcc.2019.73002.

Downloaded from http://pubs.aip.org/aip/acp/article-pdf/doi/10.1063/5.0142237/17410495/050005_1_5.0142237.pdf

This article has been accepted for publication in IEEE Transactions on Nanotechnology. This is the author's version which has not been fully edited and content may change prior to final publication. Citation information: DOI 10.1109/TNANO.2023.3280083

Density functional characterization of electronic and optical properties of strontium titanate under doping and strain for optoelectronic applications

Ashish Raturi, Poornima Mittal, and Sudhanshu Choudhary
Department of Electronics and Communication Engineering, Delhi Technological University Delhi, India
National Institute of Technology, Kurukshetra

***Abstract*—We perform first-principles calculations, to investigate the effect of doping of metal dopants (silver, gold, aluminum, and copper) on the electronic, structural, and optical properties of strontium titanate $SrTiO_3$. We further explore the impact of varying strains (compressive and tensile) on the optical and electronic properties of pristine and doped $SrTiO_3$. Our results suggest that the undoped $SrTiO_3$ exhibit a wide bandgap of 2.94 eV with high optical absorption only in the ultraviolet (UV) region. On doping the $SrTiO_3$ by metal dopants, the bandgap is significantly narrowed and most of the absorption peaks are found to shift towards the lower energies (red-shift). Subsequently, the absorption is enhanced in the visible region (~380 to 800 nm) of the optical spectrum. The decrease in the bandgap is highest for the dopant Cu. Further, on the application of the biaxial strain (tensile and compressive) on the doped-$SrTiO_3$, the optical absorption is enhanced in the visible region, particularly for the high compressive strain of 20%. The calculated refractive index and dielectric function for all the structures of $SrTiO_3$ are found to follow the trend of absorption. The enhanced absorption in the desired visible region through doping and strain may find prospective applications in the fabrication of photovoltaic, optoelectronic, and solar devices.**

***Index Terms*—Absorption, Strain, Optical, Doping, Perovskite.**

I. Introduction

Perovskite material is comprised of many compounds, which came into existence after the discovery of the mineral calcium titanate ($CaTiO_3$) in Russia in 1939 by Gustav Rose [1, 2]. Rose investigated its composition and named it after the renowned Russian mineralogist Lev Perovski [3]. Ideal perovskite exhibits the P-nma space group with cubical geometry. The fundamental formula of perovskite is ABO_3, where site A and site B are cations with site A larger than site B [4, 5]. The exceptional ability of perovskites to form complex structures by utilizing any element of the periodic table makes them favorable for the investigation of existing properties and promising for tuning them for the desired properties. The perovskites have tremendous structural and compositional diversity, which allows the structured synthesis of materials from perovskites by chemical and/or structural modification [6-8]. In the studies of optoelectronic devices, K Wu *et al.* [9] designed and fabricated a polycrystalline silicon light-emitting device and found visible light absorption in the range from 400 nm to 900 nm.

Among a wide volume of perovskites, Strontium titanate ($SrTiO_3$), widely known as STO is an interesting complex oxide having B site occupied by Ti [10, 11, 12]. STO has wide applicability in the fabrication of nano-electronic devices due to its exceptional and unique ferroelectric, and optical properties [10, 12, 13]. STO has usages in the fabrication of LED, optical switches, waveguides, memory cells, and gas sensors [14]. The experimentally reported bandgap of STO is 3.25 eV, which attributes the transitions of oxygen states (2p) to titanium states (3d) [15]. The stable stoichiometry with the simple cubic structure of STO attracts the attention of researchers, which has perspective applications in the various fields of optoelectronics and microelectronics [3, 10, 13, 15]. Fig. 1 illustrates the structural geometry of perovskite and STO. The STO is the most ascribed material for optoelectronic and solar applications and has extensively attracted the attention of researchers in recent years [10, 12, 14, 15]. It exhibits a significantly large dielectric constant value and behaves as paraelectric material in bulk form. In the low-temperature state, STO exhibits a growing ferroelectric state and prohibits long-range ferroelectric formation. Owing to the wide intrinsic bandgap, despite having so many tremendous properties, the applicability of STO is restricted and the optical and photovoltaic effectiveness of the STO is severely delimited [16, 17]. The wide bandgap of STO (>3 eV) results in the absorption in the UV region of the sunlight only, which is a small segment of the (~5%) available spectrum [18- 20]. STO can only exploit the UV wavelength of the available optical spectrum due to its wide bandgap of 3.25 eV [10, 12, 49]. Therefore, it is advantageous to modulate the electronic bandgap of the STO so that the optical absorption can be largely shifted towards the desired wavelengths i.e. towards the visible region [13, 16]. Thus, many attempts were made by researchers to reduce the bandgap of STO and to induce absorption in the visible wavelengths by mean of employing the techniques like doping, substitution, adsorption, and strain [10, 12, 13, 21, 22].

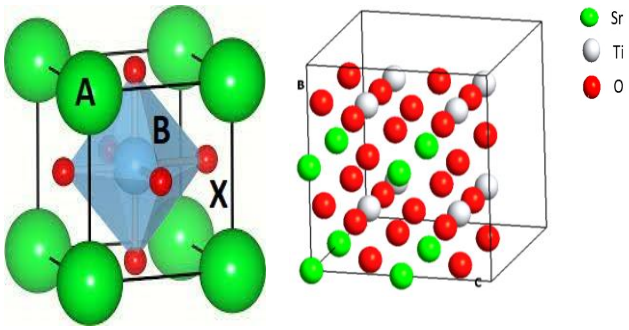


Fig. 1. (a) Perovskite Structure (b) $SrTiO_3$ Crystal.

In recent years, researchers have accepted doping and strain as effective techniques to reduce the bandgap of materials and subsequently improve visible absorption [13, 15, 17, 21-26]. As far as doping is considered, the dopant

Authorized licensed use limited to: DELHI TECHNICAL UNIV. Downloaded on May 31,2023 at 04:30:51 UTC from IEEE Xplore. Restrictions apply.
© 2023 IEEE. Personal use is permitted, but republication/redistribution requires IEEE permission. See https://www.ieee.org/publications/rights/index.html for more information.

This article has been accepted for publication in IEEE Transactions on Nanotechnology. This is the author's version which has not been fully edited and content may change prior to final publication. Citation information: DOI 10.1109/TNANO.2023.3280083

introduces the donor or acceptor levels in the empty forbidden band and shifts the absorption towards low energy ranges. The dopant introduces the discrete energy gaps in the pristine material and the electron can be exited from the valance to the conduction band using these gaps which ultimately enhance the absorption in the visible wavelengths [16, 25]. In STO, the doping creates impurity-isolated bands in the forbidden gap which significantly narrows down the bandgap and improves the visible region absorption. In the past few years, several types of research were carried out to enhance the optoelectronic behavior of STO [10, 12, 15]. Among them, the STO was subjected to the doping of various metals and further variation in various properties are investigated. Xin Zhou *et al.* [27] performed experimental and theoretical work to analyze the impact of doping with Fe and Mn on the optical behavior of STO, which is improved due to doping. N C Panoiu *et al.* [19] discussed the theoretical and experimental methods and computational tools for exploring the non-linear optical properties of nanostructures. Gillani *et al.* [10] and H. Irie *et al.* [28] studied the impact of doping on the STO with dopants Zn and Ag respectively. They found that doping with metals improves the absorption in the visible region and results in the widening of the acceptability of doped STO for optoelectronic applications. Among the wide variety of metals of the periodic table, we choose Silver (Ag), Aluminium (Al), Gold (Au), and Copper (Ag) as dopants, these dopants show plasmonic behavior and are very strong absorbers of light. Doping with these plasmonic metals can extend the absorption extraordinarily towards the visible wavelengths [13, 29-31]. Along with the doping, we further applied strain on pristine and doped STO to improve the optical response in the desired visible region. As far as strain engineering is concerned, it is reversible, and the application of strain on any material is a controllable process [23, 25, 32, 33]. Stain does not generate any additional defects and lattice damages in the crystal and advantageously alters the structure of the crystal which induces enormous prospects in various desirable applications. The strain engineering demonstrates the obvious or desired variation in the structure of the materials and shows unique properties for the applications of optoelectronics, photovoltaics, batteries, and photodetectors [33-35].

The doping, along with the application of strain, has proved itself an efficient approach to modulate the optoelectronic characteristics of the nanomaterials in the desired manner. Doping with metals like Ag, Al, Au, and Cu can improve the optoelectronic response of STO, which can be further enhanced by the application of strain [10, 13, 33-35]. Ghosh *et al.* [24] reported the impact of biaxial strain on the optoelectronic response of Iodide Perovskites. Ali *et al.* [25] reported that the high strain in the range of intensities 13% to 21% can effectively improve the optical behavior of the Sn2Bi. Yan Wang *et al.* [34] analyzed the impact of strain on the visible light absorption of SrTiO3/LaAlO3. These studies collectively advocate that the strain can participate significantly in modulating the optical properties of the materials. Ali *et al.* [35] performed the first principle computations on the Mn-SnS2 via stain and reported the blue and red shift due to the applied compressive and tensile strain. After undergoing a thorough literature review on STO, it is found that in the recent few years, there have been a significant number of efforts reported on the enhancement of the optoelectronic behavior of STO. However, there is a missing detailed investigation on the investigation of variation in the structural, and optoelectronic properties of M-STO (M- Ag, Al, Au, and Cu) due to the applied compressive and tensile strain of varying intensity using the first principle methods. Due to the wide acceptability of STO for optoelectronic applications, the study of applied biaxial strain on the doped STO can create new possibilities for optoelectronics and photovoltaic applications.

Herein, the pristine and M- STO (M= Ag, Al, Au, and Cu) are subjected to the compressive and tensile strain of varying intensities (5%, 10%, and 20%). The optical, structural, and electronic properties are computed and the impact of the strain on the properties is analyzed. For understating the electronic structure bandgap is computed for all the structures of STO. The optical behavior is understood by calculating the parameters like absorption, refractive index, and dielectric function. It is elucidated from the computed results that due to doping, the bandgap of STO is narrowed down and subsequently the absorption in the visible region is significantly improved. The lessening of the bandgap is due to the variation in the ideal stoichiometry because of metal doping. Further, on the application of the coexistence of doping and strain the lessening of the bandgap is increased and the optical properties are enhanced. The enhancements in the properties of doped-STO are the function of the type and intensity of the biaxial strain. All the results computed, altogether emphasize the fact that the coexistence of doping and strain is an effectual approach for modulating the optoelectronic behavior of the STO for photovoltaic and optoelectronic applications.

II. COMPUTATIONAL METHODOLOGY

In this paper, we execute the DFT computations to calculate the optical, structural, and electronic properties. All the DFT- simulations for the calculation of various properties of $SrTiO_3$ with doping and strain are executed on Quantum ATK atomic-scale modeling software [16, 18, 38]. Density Functional Theory (DFT) is a largely used computational technique that computes the properties of materials using electron density. DFT utilizes the electron density for the calculations, which is not a mathematical construct, but a physical characteristic of the materials [18]. The formularization of the electron density is independent of the number of electrons, which is advantageous and reduces the computational time for the DFT calculations. The important advantage of the DFT is its high computational accuracy without the additional computing time. Further, DFT can be utilized to perform calculations on the molecules like transition metals, which is not possible with traditional computational methods. In this work, the cubic cell of $SrTiO_3$ containing 40 atoms of Strontium (Sr), Oxygen, and Titanium (Ti) is created using the Quantum ATK. The geometry of $SrTiO_3$ is optimized to achieve the structure with the lowest possible ground state energy for further calculations. All the calculations related to geometry optimization are carried out using the LACO ATK-DFT calculator with k-point sampling (Monkhorst-Pack) of 7x7x7 [16, 36, 37] and exchange-correlation Generalized Gradient Approximation (GGA-PBE) [10, 12, 13, 16, 18, 50]. The optimization of the LBFGS (quasi-Newton) is utilized for geometry relaxation [16]. The geometry is relaxed till the interatomic forces between the atoms reach the limit of force tolerance of 0.05 eV/Å [16]. The maximum number of steps for geometry optimization is set to 200 and stress tolerance is

Authorized licensed use limited to: DELHI TECHNICAL UNIV. Downloaded on May 31,2023 at 04:30:51 UTC from IEEE Xplore. Restrictions apply.
© 2023 IEEE. Personal use is permitted, but republication/redistribution requires IEEE permission. See https://www.ieee.org/publications/rights/index.html for more information.

This article has been accepted for publication in IEEE Transactions on Nanotechnology. This is the author's version which has not been fully edited and content may change prior to final publication. Citation information: DOI 10.1109/TNANO.2023.3280083

set to 0.005 eV/Å^3. Afterward, the $SrTiO_3$ is doped through the metal dopants (M=Al, Ag, Au, and Cu) with the 5% doping concentration and biaxial strain (compressive and tensile) of varying intensities (5%, 10%, and 20%) is subjected on the pristine and M-$SrTiO_3$. The feasible intensity of the biaxial strain to be subjected to the $SrTiO_3$ is taken from the previous research conducted on perovskite structures. Specifically, Wu *et al.* [33] conducted a review on the research development of the influence of the strain on the perovskite structures and concluded that the perovskite can be applied with a strain of 20% without any structural breakdown. The electronic properties of all the $SrTiO_3$ structures are calculated by employing GGA approximation with the mesh cut-off of 150 Ry [10, 12, 13, 16, 18, 46, 48, 50]. However, meta-GGA Tran and Blaha (TB09) is used for calculating the optical properties as suggested in the literature available for DFT calculation of ATK VNL [16, 18, 39, 50]. The high accuracy basis set of tier 3 with HGH [Z=4] pseudopotentials is adopted in the calculations to achieve computational accuracy [16]. To validate the adopted DFT simulation parameters, properties of pristine $SrTiO_3$ are calculated first and are then compared with the past experimental and theoretical reported results [10, 12, 21, 28, 49]. The equivalence of our calculated results of undoped $SrTiO_3$ with the previously reported results advocates the validity of our DFT simulation model used for calculations (Table I).

TABLE I
Lattice parameters and bandgap of pure and doped $SrTiO_3$.

Model	a=b=c (Å)	Volume (Å^3)	Bandgap (eV)	Ref
Pristine	-	-	3.25	Experimental [49]
Pristine	3.90	59.31	-	Experimental [12]
Pristine	3.94	61.39	2.15	DFT [10]
Pristine	3.94	61.16	2.94	DFT [This work]
Ag- $SrTiO_3$	4.08	67.91	1.57	
Al- $SrTiO_3$	3.93	60.69	1.77	
Au- $SrTiO_3$	4.09	68.41	1.56	
Cu- $SrTiO_3$	4.07	67.41	1.54	

In the calculations, The Kubo–Greenwood is used to calculate the susceptibility tensor as below [38].

$$\chi_{i,j(\omega)} = -\frac{e^2\hbar^4}{\varepsilon_0 m^2\omega^2 V}\sum_{nm}\frac{f(E_m)-f(E_n)}{E_{nm}-\hbar\omega-i\Gamma}\pi^{t}_{nm}\,\pi^{j}_{mn} \quad (1)$$

The equation illustrated below is used to calculate the dielectric constant (χ), using response coefficients, polarizability (α), conductivity (σ), and susceptibility (χ) [42].

$$\varepsilon_r = 1 + \chi(\omega) \quad (2)$$

$$\alpha(\omega) = V\chi(\omega)\varepsilon_0 \quad (3)$$

$$\sigma(\omega) = -\mathrm{img}(\omega\chi(\omega)\varepsilon_0) \quad (4)$$

The dielectric constant in terms of extinction coefficient and refractive index is illustrated below.

$$\eta + i\kappa = \sqrt{\varepsilon_r} \quad (5)$$

The extinction coefficient (k), and refractive index (η) as a function of real (ε_1) and imaginary (ε_2) dielectric functions are illustrated as below.

$$\eta = \sqrt{\frac{\sqrt{{\varepsilon_1}^2+{\varepsilon_2}^2}+\varepsilon_1}{2}} \quad (6)$$

$$\kappa = \sqrt{\frac{\sqrt{{\varepsilon_1}^2+{\varepsilon_2}^2}-\varepsilon_1}{2}} \quad (7)$$

The value of the optical absorption coefficient α_α is illustrated in the terms of extinction coefficient (κ) below [42].

$$\alpha_a = 2\frac{\omega}{c}\kappa \quad (8)$$

III. Results and Analysis

In this segment of the paper, the optical, structural, and electronic properties of pristine and doped structures of $SrTiO_3$ are computed by employing the DFT computations. Further, the structures of pristine and doped-$SrTiO_3$ are subjected to strain (tensile and compressive) with intensities of 5%, 10%, and 20%. All the properties of strained-$SrTiO_3$ are calculated and variations in the properties due to strain are analyzed.

A. Structural properties and stability analysis

Under this segment, the structural properties of the $SrTiO_3$ (pristine and M- $SrTiO_3$, where M=Ag, Al, Au, and Cu) are computed. Along with structural properties, the total energies of all the structures of $SrTiO_3$ are calculated for stability analysis. The cubic cell (2×2×1) of $SrTiO_3$ (space group pm3m) is build for the calculations. As shown in fig. 1(b) the cubic cell of $SrTiO_3$ has 8 atoms of strontium and titanium each and 24 oxygen atoms [10, 12]. The computed lattice constants of pristine and doped $SrTiO_3$ after the geometry relaxation are illustrated in Table I. To validate our computational reliability, the calculated geometrical parameters of pure $SrTiO_3$ are equated with the previous research results. Our computation results show that the lattice constants of pristine $SrTiO_3$ are a=b=c=3.945 Å (Table I)and the computed lattice angles are $\alpha = \beta = \gamma = 90^{\circ}$. These values of structural parameters for pristine $SrTiO_3$ are in good agreement with the previous research results [10, 12, 17, 21]. Subsequently, the $SrTiO_3$ is doped through the metal dopants Ag, Al, Au, and Cu (doping concentration of 5%). The doping in $SrTiO_3$ is performed on the Ti site only as the existing research on $SrTiO_3$ advocates that the metal ions enter the Ti site preferably due to the comparable ionic radius [44, 48]. Furthermore, the pure and metal-doped $SrTiO_3$ are subjected to the strain of compressive and tensile with intensities of 5%, 10%, and 20%. We applied the compressive and tensile strain of intensities 5%, 10%, and 20% on the pristine and doped SrTiO3. The values of the intensities applied are taken from the available research on strain engineering of the materials. Wu *et al.* [34] mentioned that the feasible range of strain for

Authorized licensed use limited to: DELHI TECHNICAL UNIV. Downloaded on May 31,2023 at 04:30:51 UTC from IEEE Xplore. Restrictions apply.
© 2023 IEEE. Personal use is permitted, but republication/redistribution requires IEEE permission. See https://www.ieee.org/publications/rights/index.html for more information.

This article has been accepted for publication in IEEE Transactions on Nanotechnology. This is the author's version which has not been fully edited and content may change prior to final publication. Citation information: DOI 10.1109/TNANO.2023.3280083

tuning the band structure of the perovskites is 13% to 20%. Ali *et al.* [25] reported that the high strain in the range of intensities 13% to 21% can effectively improve the optical behavior of the Sn2Bi. Further, according to the previous research, the suitable range of the strain to be applied for tuning the band structure of the perovskites is from 10%–20% [24, 25, 33-35].

TABLE II
Energy (eV) of pure and doped-$SrTiO_3$.

Structure	Total Energy	Binding energy	Formation energy
Pure-$SrTiO_3$	-12239.6	-581.026	
Ag- Doped	-14248.96	-683.888	-145.213
Al- Doped	-12453.64	-627.449	-88.7743
Au- Doped	-14159.82	-678.331	-139.657

The strain is applied in the biaxial directions and is defined below [32].

$$\varepsilon = \frac{a-a_0}{a_0} \times 100\ \% \quad (9)$$

In the equation given above, a_o is the value of the lattice constant $SrTiO_3$ (relaxed and without strain) and a represents the lattice constant with strain. The positive value of ε represents the tensile strain and the negative value represents the compressive strain. Further, to investigate the structural stabilities of doped structures the total energy calculations are performed on pristine and doped $SrTiO_3$. The stability of any nanostructure can be effectively defined by utilizing the formation energy and binding energy. We computed the formation and binding energy of pure and doped $SrTiO_3$ by using the ground state total energy as illustrated in Table II with the relation given below [39, 45].

$$E_{Binding} = -\frac{(E_T - xE_{Sr} - yE_{Ti} - zE_O - kE_{M(Au,Al,Au,Cu)})}{x+y+z} \quad (10)$$

In the equation given above E_T is the computed energy ($SrTiO_3$ and M-$SrTiO_3$), E_{sr} is the computed energy of Sr, E is the computed energy of O, E_{Ti} is the computed energy of Ti, and E_m is the computed energy of the dopant. x, y, z, k, and N are the number of atoms. The formation energy is calculated by using the equation given below [38, 44].

$$E_{Formation} = -\frac{(E_{Doped} - E_{Pristine} - xE_{M(Au,Al,Au,Cu)})}{N} \quad (11)$$

In the equation given above $SrTiO_3$ is the computed energy of doped $SrTiO_3$, $E_{pristine}$ is the computed energy of pure $SrTiO_3$, and E_M is the computed energy of the dopant. x and N are the total numbers of dopant atoms and the total number of atoms in the nanocrystal respectively. The results of binding energy and formation energy illustrated in Table II show that the value of the binding energies is negative for all the structures of $SrTiO_3$, which indicates the stability in the doped and pristine $SrTiO_3$. The values of the binding energy of the doped $SrTiO_3$ are more negative in comparison to the pristine $SrTiO_3$, which shows that the doped structures reach more stability. In the doped structures of $SrTiO_3$, the value of binding and formation energy is the largest negative for the dopant Cu, which indicates that this structure is highly stable among all the doped structures and energetically more favorable for doping.

B. Electronic properties

In this segment of the paper, the band structure of pure and doped $SrTiO_3$ are computed and the effects of the applied strain (tensile and compressive) on the bandgap are analyzed. The calculated value of the bandgap for pristine $SrTiO_3$ is 2.94 eV the same is illustrated in fig. 2. This value of bandgap is in good equivalence with the existing research results [10, 12, 14, 17, 21, 28, 49].

TABLE III
Bandgap (eV) of pure and doped $SrTiO_3$ under strain.

Structure	Compressive			Tensile		
	5%	10%	20%	5%	10%	20%
Ag-doped	0.198	0.249	0.406	0.13	0.031	0.058
Al-doped	0.02	0.008	0.091	0.25	0.030	0.174
Au-doped	0.108	0.145	0.914	0.091	0.031	0.011
Cu-doped	0.104	0.148	0.012	0.074	0.026	0.049

The bandgap of the pristine and M-SrTiO3 (M=Ag, Al, Au, and Cu) are illustrated in Table I. For all the dopants the bandgap is remarkably lowered. The bandgap is decreased due to the introduction of impurity states due to doping. The lowering of the bandgap is further increased on the application strain of intensities 5%, 10%, and 20%. The bandgaps of strained M-SrTiO3 are illustrated in Table III. The lessening of the bandgap because of doping and strain is favorable for the possibilities of enhancement of the optical properties of the photovoltaic and optoelectronics applications.

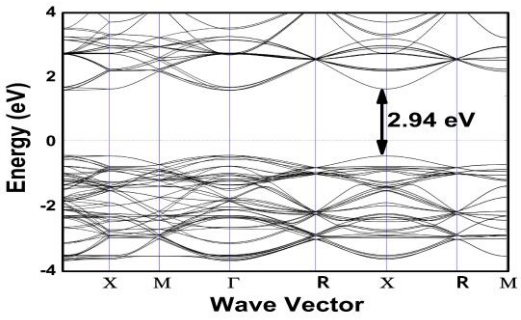


Fig. 1. Bandgap of pristine $SrTiO_3$ Crystal.

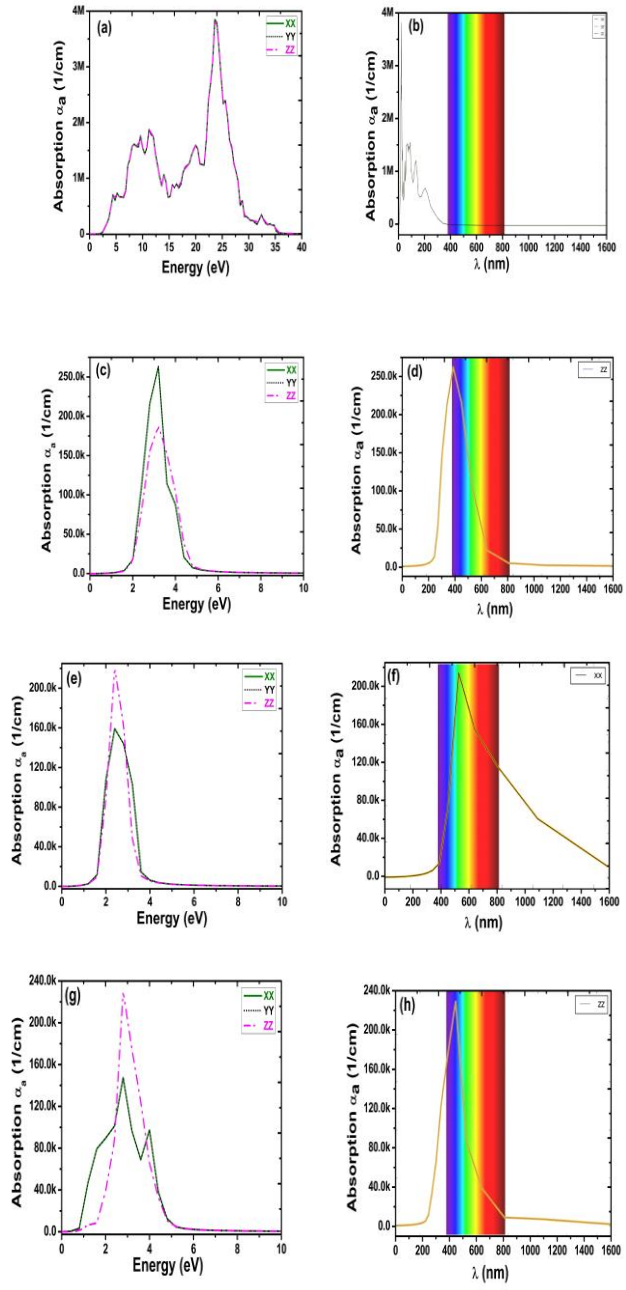
C. Optical Properties

In this section optical properties of pure and doped (M= Al, Ag, Au, and Cu) $SrTiO_3$ are calculated. Subsequently, the influence of the applied strain (tensile and compressive) of intensities of 5%, 10%, and 20% on the optical properties of $SrTiO_3$ (pure and doped) are evaluated. The calculations of the optical parameters are important to categorize the prospective utilization of the materials for various applications. The fundamental parameter for obtaining the optical properties of any material is the dielectric function, which is the elucidation of the interaction of the material with the applied electromagnetic field. We calculate the optical

Authorized licensed use limited to: DELHI TECHNICAL UNIV. Downloaded on May 31,2023 at 04:30:51 UTC from IEEE Xplore. Restrictions apply.
© 2023 IEEE. Personal use is permitted, but republication/redistribution requires IEEE permission. See https://www.ieee.org/publications/rights/index.html for more information.

This article has been accepted for publication in IEEE Transactions on Nanotechnology. This is the author's version which has not been fully edited and content may change prior to final publication. Citation information: DOI 10.1109/TNANO.2023.3280083

properties of all the structures of $SrTiO_3$ (pristine, doped, and strained) by utilizing the computed values of the dielectric function (real and imaginary). The dielectric function (real) of any material is related to the slowing down of the light and resembles the refractive index. Its large value is desired as it represents the lesser slowdown of the propagating light. The imaginary part is related to the optical absorption and represents the damping. In this work, the calculations of the optical properties are carried out along the xx, yy, and zz tensors [16, 39, 50]. However, the descriptions of the results are made limited to the zz tensor only and may be understood in the same way for all other tensors [16, 39, 50]. All the computations of the optical parameters are performed using the meta-GGA exchange-correlation of DFT. The acceptance of computation is validated by comparing our results calculated for pristine $SrTiO_3$ with the existing research work [10, 12, 14, 17, 21, 28, 49].



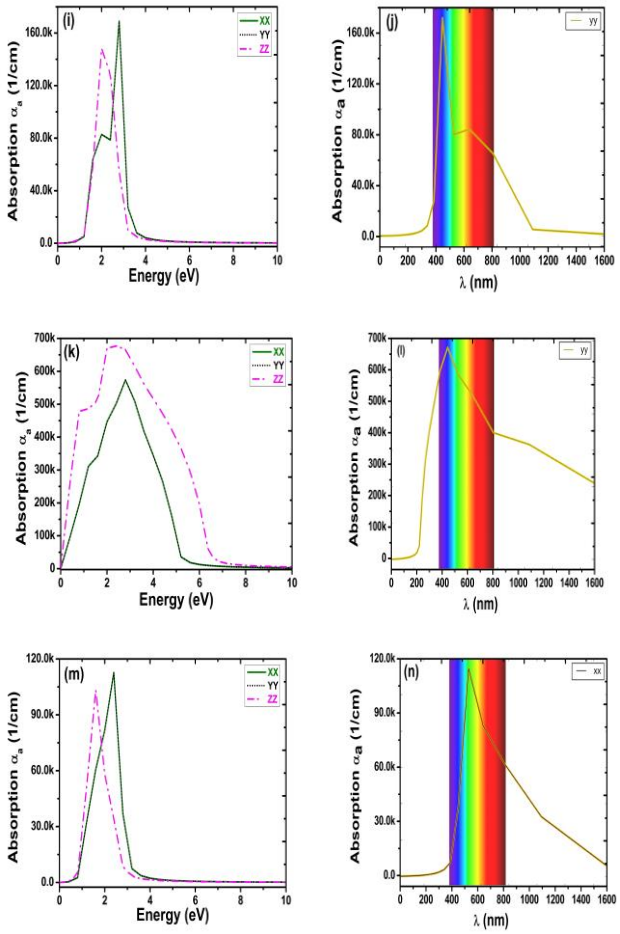


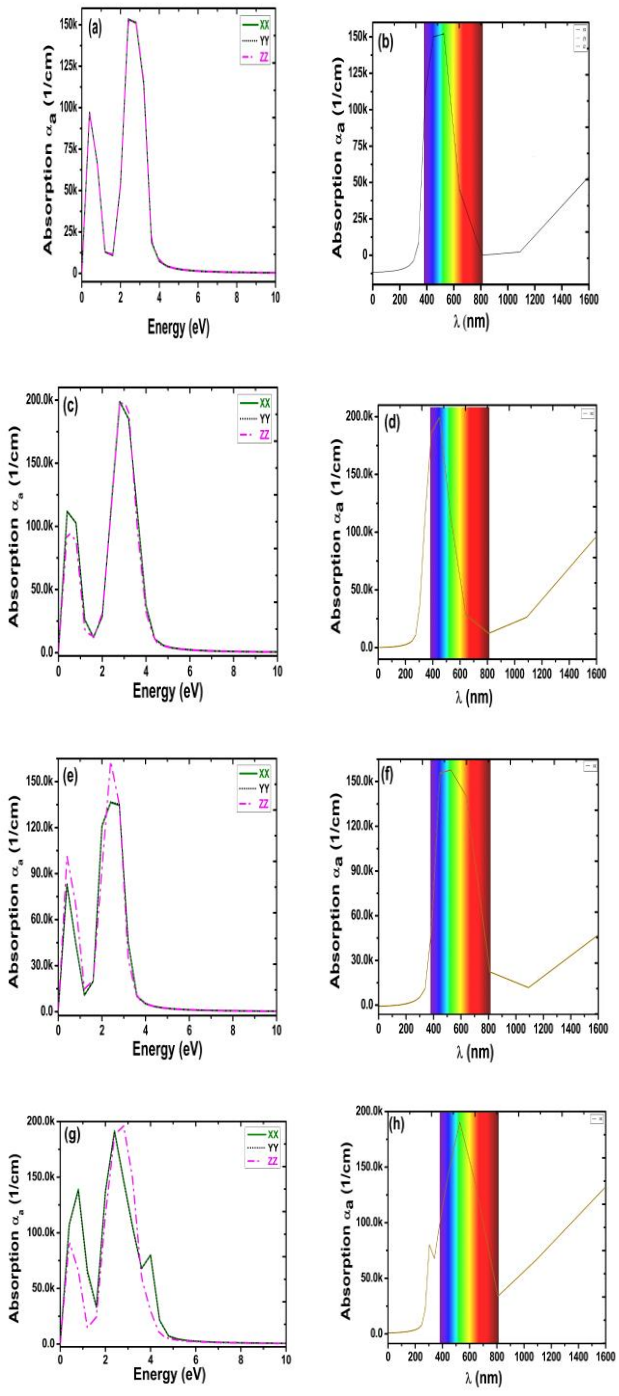
Fig. 3. Absorption coefficient of pristine $SrTiO_3$: Unstrained ((a) and (b)), and Strained (5% compressive (c) and (d), 5% tensile (e) and (f), 10% compressive (g) and (h), 10% tensile (i) and (j), 20% compressive (k) and (l), 20% tensile (m) and (n)).

To understand the impact of the applied biaxial strain on the optical response of $SrTiO_3$, the pristine structure of $SrTiO_3$ is subjected to the strain (tensile and compressive) of 5%, 10%, and 20% intensities. Furthermore, the absorption coefficients (function of energy and wavelength) of the strained crystals are calculated and compared with the unstrained crystal (fig. 3). For the pristine crystal of $SrTiO_3$, the absorption is limited only in the region of lower wavelengths and high energies, which limits its solar efficiency. The optical absorption for the pristine unstrained crystal of $SrTiO_3$ (fig. 3(a), and 3(b)) is predominantly found in the UV region (~0 to 200 nm) with heights peaks of the absorption in the high energy range (at ~ 25 eV). The absorption of the pristine $SrTiO_3$ begins around ~ 3 eV, which resembles the bandgap. On the applied strain, the optical absorption modulates depending on the type and intensity of the applied strain. For the compressive strain of 5%, 10% the absorption is found to shift significantly towards the visible and near visible region, starting from ~200 nm and is available till ~800 nm range (fig. 3(c), 3(d), 3(g), and 3(h)). For the compressive strain of 20%, the absorption is enhanced drastically in the visible region but there are non-zero absorption values for the high wavelengths region (IR) (fig. 3(k), and 3(l)). For the tensile strain of 5%, 10%, and 20% the absorption starts from ~400 nm and has a high value in the

Authorized licensed use limited to: DELHI TECHNICAL UNIV. Downloaded on May 31,2023 at 04:30:51 UTC from IEEE Xplore. Restrictions apply.
© 2023 IEEE. Personal use is permitted, but republication/redistribution requires IEEE permission. See https://www.ieee.org/publications/rights/index.html for more information.

This article has been accepted for publication in IEEE Transactions on Nanotechnology. This is the author's version which has not been fully edited and content may change prior to final publication. Citation information: DOI 10.1109/TNANO.2023.3280083

visible region. For the biaxial tensile strain of 5%, 10%, and 20%, the absorption is zero in the UV region and completely shifted towards the low energies(redshift), with improved value in the visible region absorption as compared to the unstrained crystal of $SrTiO_3$ (fig. 3(e), 3(f), 3(i), 3(j), 3(m), and 3(n)). Conclusively the tensile and compressive strain enhances the visible light absorption of $SrTiO_3$, which improves solar efficiency and is desired for optoelectronic applications. Further, the crystal of $SrTiO_3$ is doped through the metal dopants Ag, Al, Au, and Cu and subsequently, strain is applied to the doped crystals. The implementation of the coexistence of techniques (strain and doping) might be a more efficient method for modulating the optical properties of $SrTiO_3$ for desired applications.



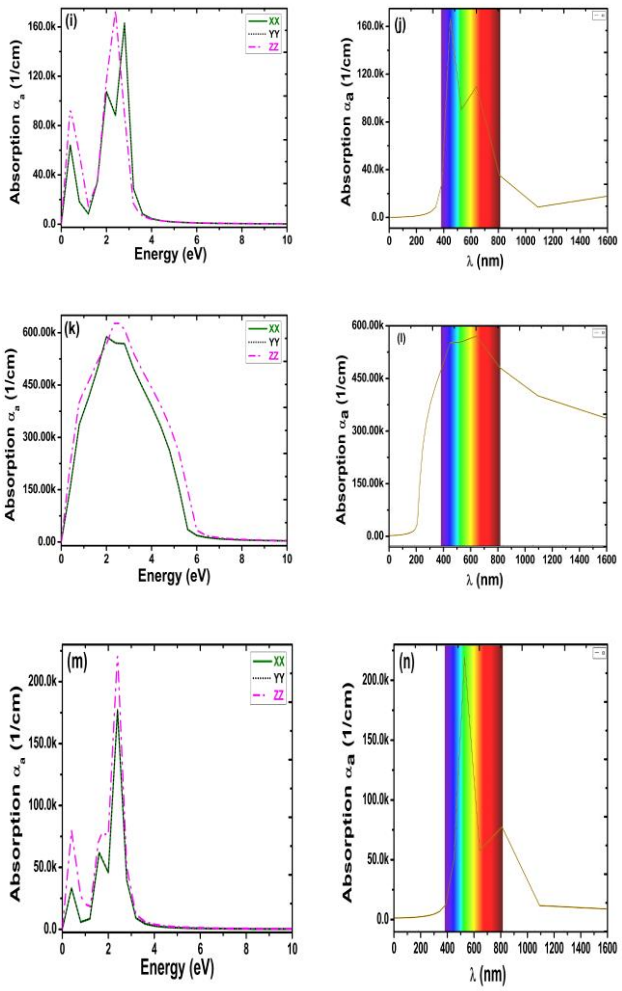
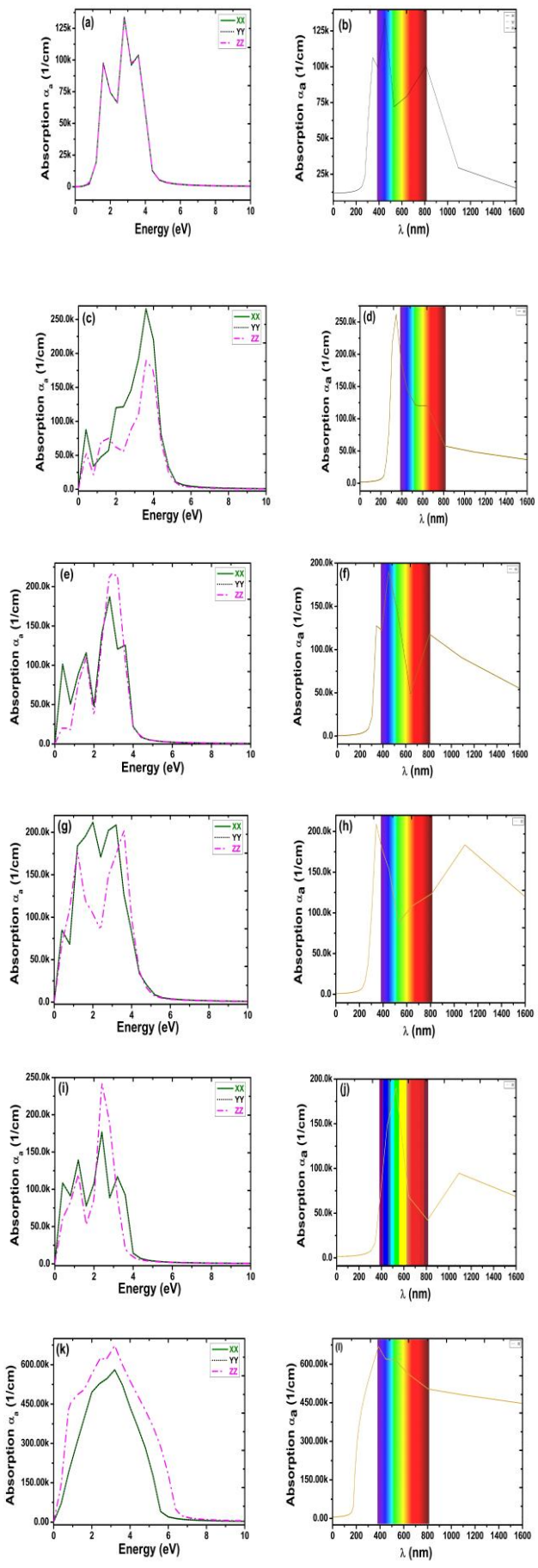


Fig. 4. Absorption coefficient of Silver-doped $SrTiO_3$: unstrained ((a) and (b)), and Strained (5% compressive (c) and (d), 5% tensile (e) and (f), 10% compressive (g) and (h), 10% tensile (i) and (j), 20% compressive (k) and (l), 20% tensile (m) and (n)).

The absorption coefficients for the Ag-doped $SrTiO_3$ and its strained structure (tensile and compressive) are plotted in fig. 4. Due to the doping of Ag, the absorption starts at the low energy (fig. 4(a), 4(b)), and the peak of the absorption is found at ~2.5 eV (redshift). The non-zero absorption in the UV region of the pristine crystal of $SrTiO_3$ is shifted towards the high wavelengths and is predominantly available in ~300 to 800 nm. Furthermore, on the applied compressive strain of intensities of 5%, and 10%, the absorption is available in the ~300 to 800 nm range with the enhanced value of visible region absorption (fig. 4(c), 4(d), 4(g), and 4(h)). Subsequently, the Ag-doped $SrTiO_3$, applied with the tensile biaxial strain of intensities of 5%, 10%, and 20% has almost zero absorption in the UV region but the absorption in the visible region is narrow and low as compared to the compressive strain (fig. 4). For the compressive strain of 20%, the absorption curve contains the peak at ~600 nm with an amplitude of ~650k, which is the highest among all the crustal of strained and unstrained Ag-doped $SrTiO_3$.

Authorized licensed use limited to: DELHI TECHNICAL UNIV. Downloaded on May 31,2023 at 04:30:51 UTC from IEEE Xplore. Restrictions apply.
© 2023 IEEE. Personal use is permitted, but republication/redistribution requires IEEE permission. See https://www.ieee.org/publications/rights/index.html for more information.

This article has been accepted for publication in IEEE Transactions on Nanotechnology. This is the author's version which has not been fully edited and content may change prior to final publication. Citation information: DOI 10.1109/TNANO.2023.3280083



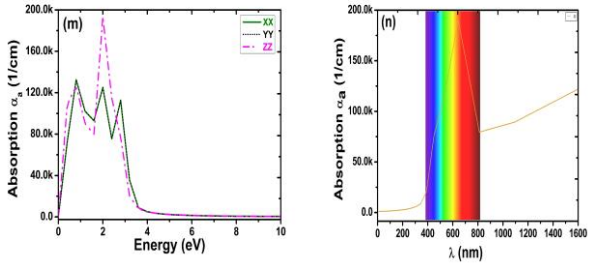
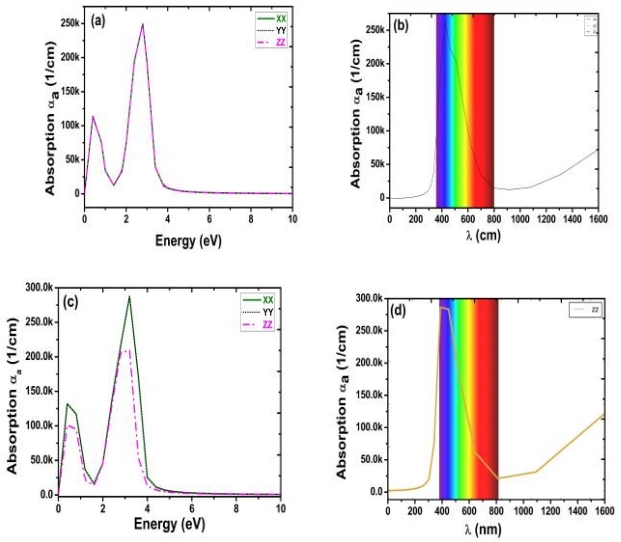


Fig. 5. Absorption coefficient of Aluminum-doped $SrTiO_3$: unstrained ((a) and (b)), and Strained (5% compressive (c) and (d), 5% tensile (e) and (f), 10% compressive (g) and (h), 10% tensile (i) and (j), 20% compressive (k) and (l), 20% tensile (m) and (n)).

For the Al-doped crystal of $SrTiO_3$, the absorption is shown in fig. 5. As shown in fig. 5(a), and 5(b), as a result of doping with Al, the absorption begins from ~0.5 eV and has non-zero peaks in the range of wavelengths ~300 to 1100 nm. The non-zero absorption is available in the high wavelength range and the values of absorption are amplified in the visible range as compared to the pure crystal of $SrTiO_3$. The Al-doped crystal of $SrTiO_3$, with the compressive applied strain of 5%, 10%, and 20%, has an enhanced visible absorption. Specifically, for the high compressive strain of 20%, the amplitude of the highest absorption peak is found at ~450 nm with an amplitude of ~600 k. The applied tensile strain on Al-doped $SrTiO_3$ shifts the absorption in the visible region with some extension towards the IR region. All the crystals of Al-doped $SrTiO_3$ under tensile strain have an absorption peak with a value of ~200k, which is larger than the absorption peak of unstrained crystals. Further, the doping of the Au on the crystal of $SrTiO_3$ tunes the absorption from ~400 to 800 nm, with an absorption peak of ~250k at ~500 nm (fig. 6). Also, the applied compressive strain shifts the absorption in the visible and near-visible-regions (~ 300 to 800 nm). The absorption peak is highest in the visible region for the compressive biaxial strain of large intensity of 20%. Nevertheless, the compressive strain also increases the absorption in the IR region slightly. The Cu doping on $SrTiO_3$ also tunes the absorption in the viable region, which further improves due to the strain having the highest value of visible region absorption for the compressive satin of 20% fig(7).



Authorized licensed use limited to: DELHI TECHNICAL UNIV. Downloaded on May 31,2023 at 04:30:51 UTC from IEEE Xplore. Restrictions apply.
© 2023 IEEE. Personal use is permitted, but republication/redistribution requires IEEE permission. See https://www.ieee.org/publications/rights/index.html for more information.

This article has been accepted for publication in IEEE Transactions on Nanotechnology. This is the author's version which has not been fully edited and content may change prior to final publication. Citation information: DOI 10.1109/TNANO.2023.3280083

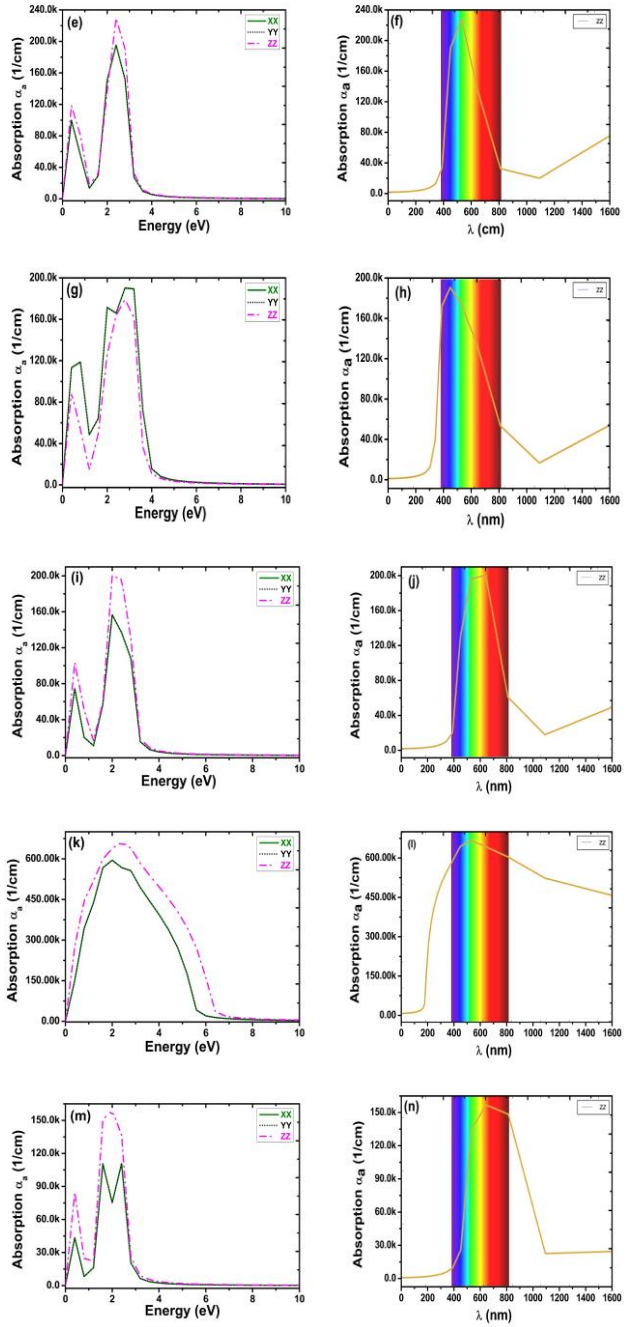
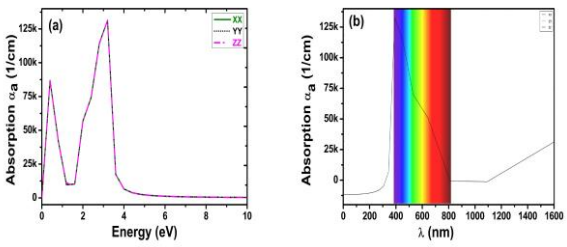


Fig. 6. Absorption coefficient of Gold-doped $SrTiO_3$: unstrained ((a) and (b)), and Strained (5% compressive (c) and (d), 5% tensile (e) and (f), 10% compressive (g) and (h), 10% tensile (i) and (j), 20% compressive (k) and (l), 20% tensile (m) and (n)).



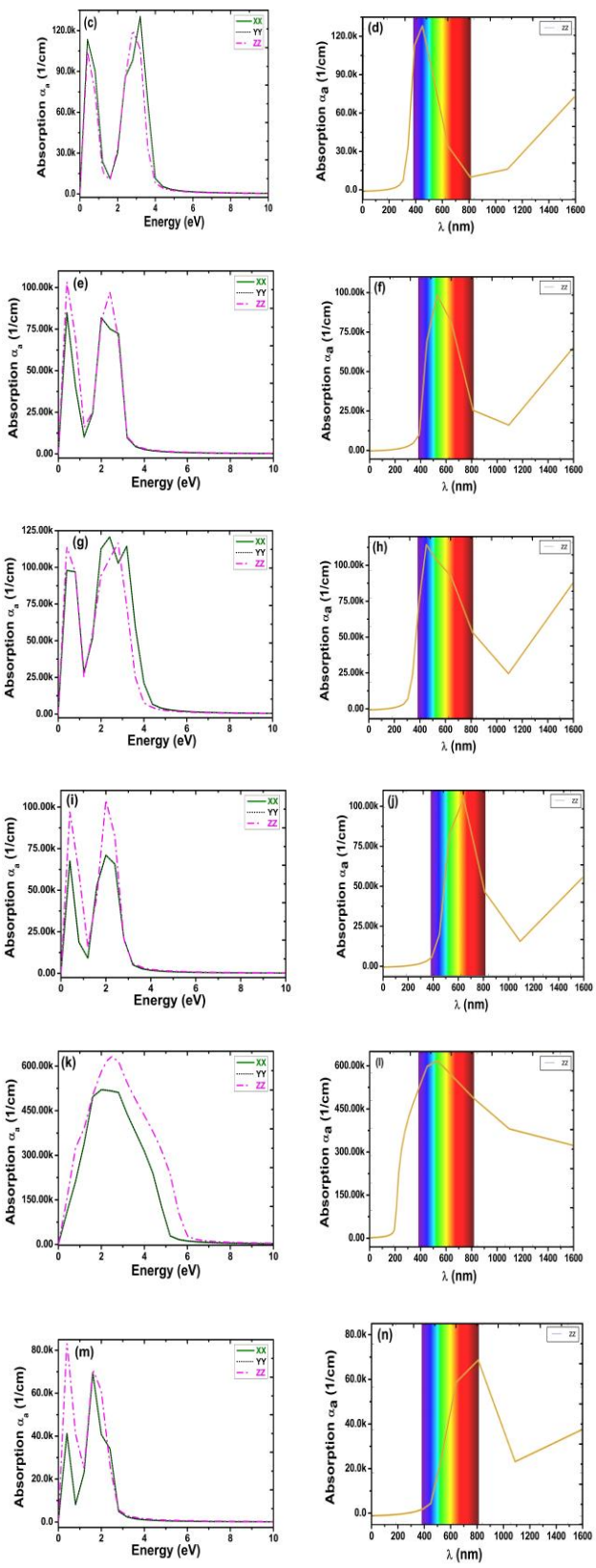


Fig. 7. Absorption coefficient of Copper-doped $SrTiO_3$: unstrained ((a) and (b)), and Strained (5% compressive (c) and (d), 5% tensile (e) and (f), 10% compressive (g) and (h), 10% tensile (i) and (j), 20% compressive (k) and (l), 20% tensile (m) and (n)).

It is evident from fig. 3(b), 4(b), 5(b), 6(b), and 7(b) that the UV region absorption of the pure $SrTiO_3$ is completely

Authorized licensed use limited to: DELHI TECHNICAL UNIV. Downloaded on May 31,2023 at 04:30:51 UTC from IEEE Xplore. Restrictions apply.
© 2023 IEEE. Personal use is permitted, but republication/redistribution requires IEEE permission. See https://www.ieee.org/publications/rights/index.html for more information.

This article has been accepted for publication in IEEE Transactions on Nanotechnology. This is the author's version which has not been fully edited and content may change prior to final publication. Citation information: DOI 10.1109/TNANO.2023.3280083

tuned towards the visible and near visible region due to the doping of plasmonic metals dopants. The increased absorption is due to the collective oscillation of the charge carriers (surface plasma effect). Among the plasmonic dopants, the Ag and Au show better plasmonic behavior in compressing to the Al and Au. Additionally, gold has excellent chemical stability and shows remarkable properties in the visible region. The reduction in the bandgap due to doping is lowest for the dopant Al, because of its lowest ionic radius among all the plasmonic dopants. Further, the large size of the dopant ion reduces the scattering of the light and increases the plasmonic effect. The same is evident from the lowest improvement in visible light absorption due to the doping of the Al (smallest ionic radius among all dopants)

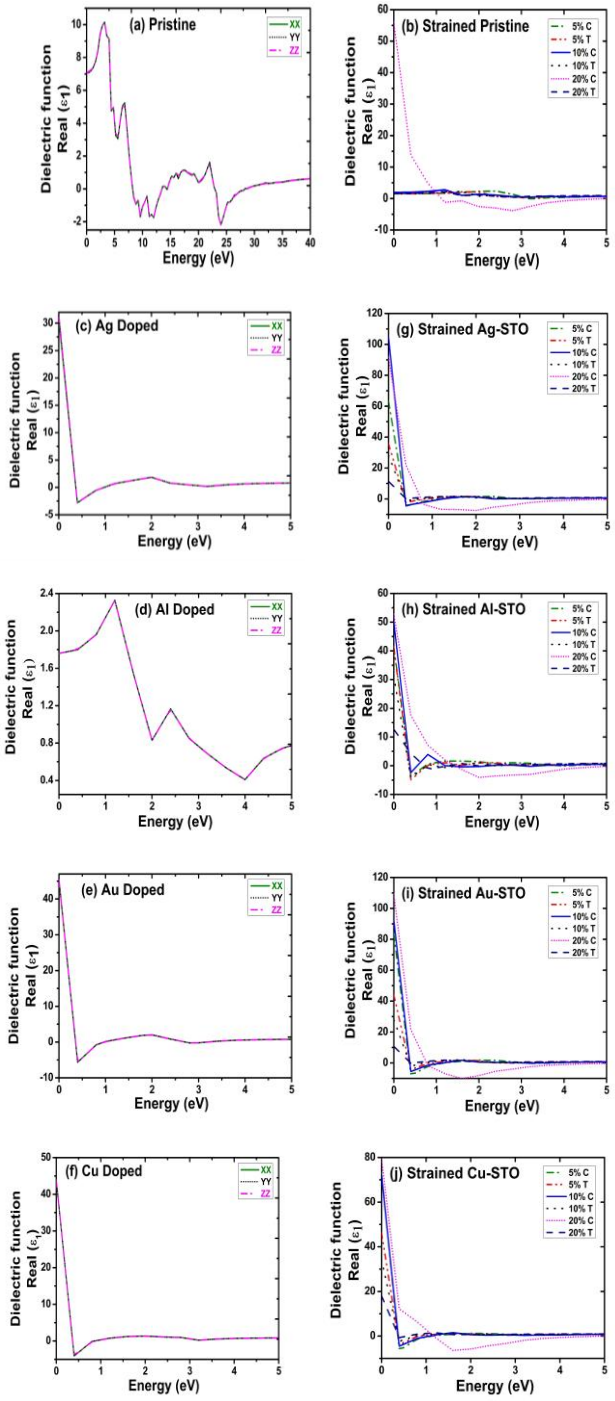


Fig. 8. Dielectric function (real) of $SrTiO_3$ (undoped, doped, and strained).

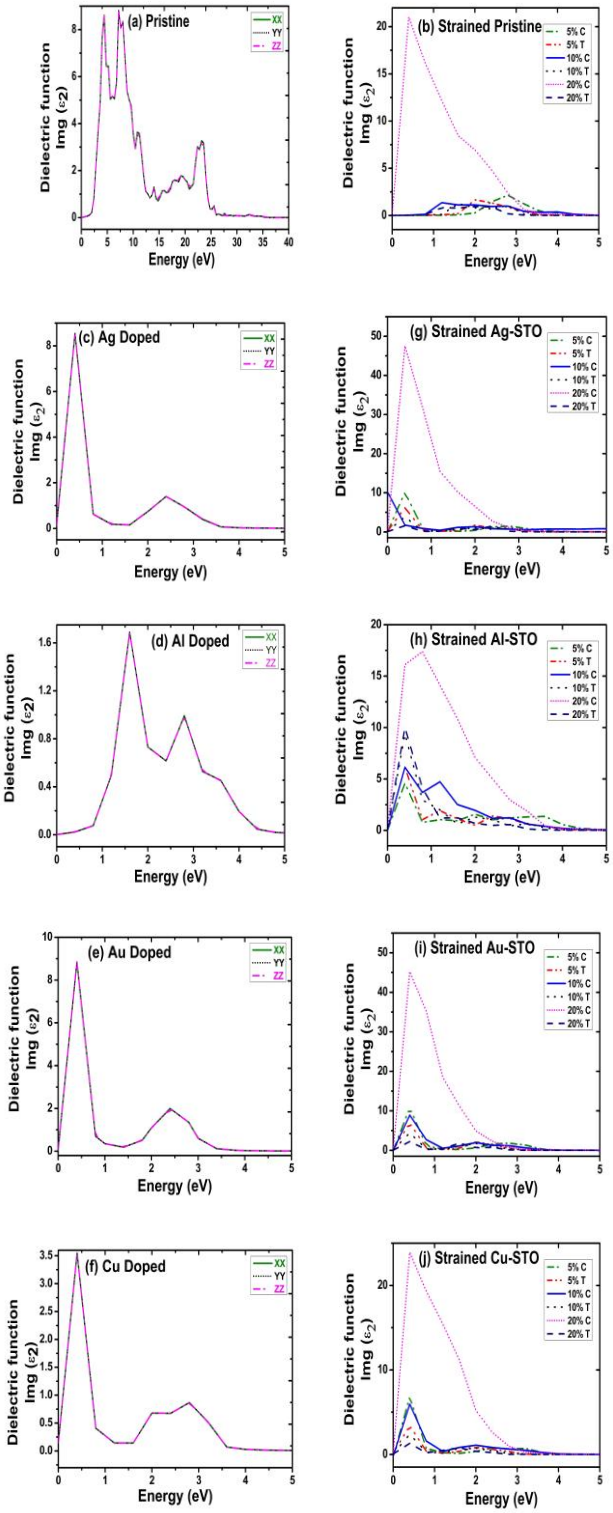


Fig. 9. Dielectric function (imaginary) of $SrTiO_3$ (undoped, doped, and strained).

The dielectric constants for the pristine, doped, and strained $SrTiO_3$, are shown in fig. 9 and fig. 10. As the dielectric constant is directly related to the absorption coefficient, the peaks of the dielectric constants are in accordance with the absorption coefficient. The value of the dielectric constants (imaginary) is increased due to the applied strain (fig. 9), which indicates the low value of the energy of excitation and improves the absorption. The value of the dielectric constant is highest for the compressive strain

Authorized licensed use limited to: DELHI TECHNICAL UNIV. Downloaded on May 31,2023 at 04:30:51 UTC from IEEE Xplore. Restrictions apply.
© 2023 IEEE. Personal use is permitted, but republication/redistribution requires IEEE permission. See https://www.ieee.org/publications/rights/index.html for more information.

This article has been accepted for publication in IEEE Transactions on Nanotechnology. This is the author's version which has not been fully edited and content may change prior to final publication. Citation information: DOI 10.1109/TNANO.2023.3280083

of 20%. The strained $SrTiO_3$ results in the border and stable absorption as compared to the pristine structure, which is useful for optoelectronics applications.

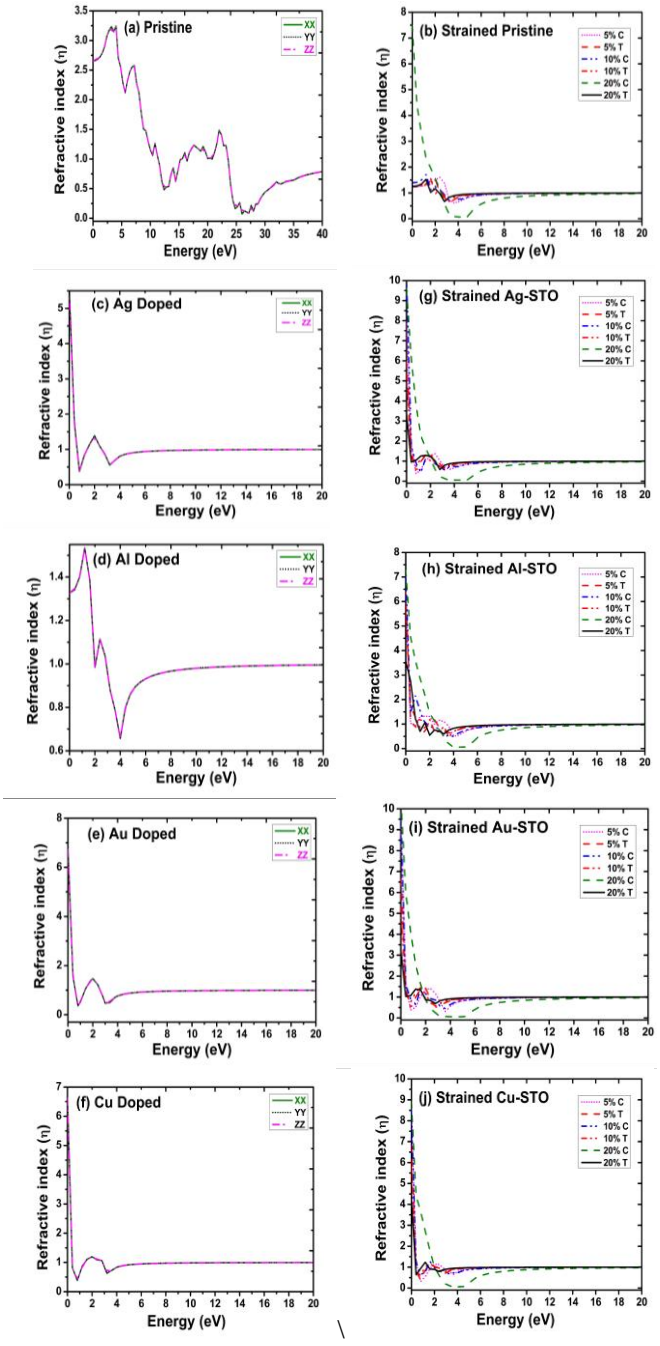


Fig. 10. Refractive index of $SrTiO_3$ (undoped, doped, and strained).

The refractive indexes for all the structures of $SrTiO_3$ are calculated from the value of the dielectric function and are represented in fig. 10. As shown in fig. 10, the refractive index of all the structures of $SrTiO_3$ is completely follows the trends of absorption coefficient and dielectric function. The peak of refractive index for the pristine $SrTiO_3$ is ~3 eV, which is in accordance with the peak of the dielectric constant. After doping, the values of the corresponding refractive index are high in the low energy region, and the value of the refractive index is further increased on the application of the strain. The large value of the refracting index corresponds to the large absorption and results in the long life of the light in the material. Similarly, the low values of the refractive index for high energy, after the doping and strain represent the lower absorption. The value of the intrinsic refractive index is ~2.7 for the pristine $SrTiO_3$ and the same becomes ~7 due to the applied compressive biaxial strain of intensity 20%. Similarly, the computed value of the intrinsic refractive index improved due to doping and increased further with strain having the largest value for the compressive strain of 20%. Improvements in the refractive index of $SrTiO_3$ due to the coexistence of doping and strain, increase photon absorption, which is favorable for solar and optoelectronics applications.

D. Photocatalytic properties

The photocatalysis water-splitting takes place with the oxidation of H+ to H_2 and reduction of H_2O to H+ and O_2. A material can act as a photocatalyst if its bandgap is smaller or equivalent to the energy of the illuminated photon. The low value of bandgap alone cannot guarantee the efficient photocatalytic behavior of any material. However, the appropriate positions of conduction band minima and valance band maxima can help in understanding the ability of the photocatalysis of any photocatalyst. For water splitting, the VBM of the photocatalyst must be lower than the water oxidation level, and CMB must be larger than the reduction level of water. The values of CBM and VBM of the undoped, doped, and STO are calculated by utilizing the equation below [14, 22, 28, 48].

$$E_{CBM} = -\frac{1}{2}E_g + \chi_{STO} + E_0 \quad (12)$$

$$E_{VBM} = \frac{1}{2}E_g + \chi_{STO} + E_0 \quad (13)$$

$$\chi_{STO} = (\chi_{sr}\chi_{ti}{\chi_o}^3)^{\frac{1}{5}} \quad (14)$$

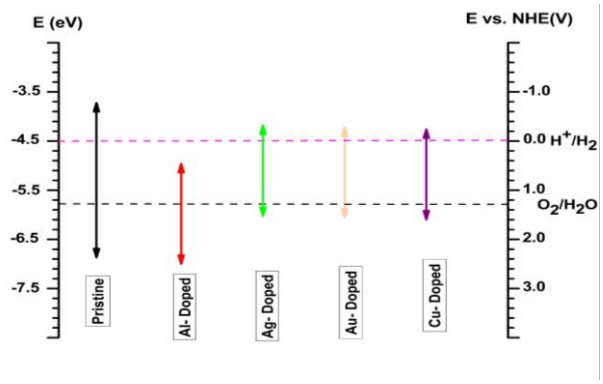


Fig. 11. Band edge alignment of pristine and doped $SrTiO_3$.

In the above equations,E_g is the bandgap of pristine $SrTiO_3$, E_0=-4.5 (scaling factor for NHE), χ=absolute electronegativity [46]. The values of the CBM and VBM for undoped $SrTiO_3$ are -0.879 eV and 2.271 eV, and are in good accordance with the existing results [14, 22, 28]. All the computed values of CBM and VBM of all the undoped and doped $SrTiO_3$ are shown in fig. 11. As shown in fig. 11, $SrTiO_3$ has a good reducing ability due to its CBM, which is negative in comparison to the reduction potential (water). Further for Ag, Au, and Cu, the downshifting in the CBM

Authorized licensed use limited to: DELHI TECHNICAL UNIV. Downloaded on May 31,2023 at 04:30:51 UTC from IEEE Xplore. Restrictions apply.
© 2023 IEEE. Personal use is permitted, but republication/redistribution requires IEEE permission. See https://www.ieee.org/publications/rights/index.html for more information.

This article has been accepted for publication in IEEE Transactions on Nanotechnology. This is the author's version which has not been fully edited and content may change prior to final publication. Citation information: DOI 10.1109/TNANO.2023.3280083

improves the photoreduction. Also, the upward shifting of VBM improves photo-oxidation. The improved photo reduction and oxidation of Ag, Au, and Cu-doped $SrTiO_3$ suggest that doping improves the photocatalytic behavior of $SrTiO_3$.

IV. Conclusion

In summary, density functional theory calculations are performed to investigate the application of the coexistence of doping and strain on the optoelectronic properties of the $SrTiO_3$. The calculated results advocate that the doping through the metal dopants (Ag, Al, Au, and Cu) on $SrTiO_3$ decreases the bandgap and tunes the absorption in the visible region. The optical response in the visible region is further improved on the application of strain (compressive and tensile) as compared to the pristine and doped $SrTiO_3$. The coefficient of absorption is seen enhanced for the doped structures and is further improved on the applied strain specifically for the high compressive strain of 20%. Likewise, the trend in the results of the absorption is following the calculated dielectric constant and refractive index. The results of optical properties of doped and strained $SrTiO_3$ indicate a significant enhancement in the adsorption in the desired visible region, so, increasing the acceptance of the $SrTiO_3$ in optoelectronics and solar-based applications.

References

[1] B. Yang, D. B. Geohegan, and K. Xiao, "Perovskite Materials: Solar Cell and Optoelectronic Applications," Encycl. Inorg. Bioinorg. Chem., pp. 1–14, 2011.

[2] C. S. Tan, "Lead-Free Ultra-Wide Direct Bandgap Perovskite EACaI 3," IEEE Trans. Nanotechnol., vol. 21, pp. 66–70, 2022.

[3] H. Huang, L. Polavarapu, J. A. Sichert, A. S. Susha, A. S. Urban, and A. L. Rogach, "Colloidal lead halide perovskite nanocrystals: synthesis, optical properties and applications," NPG Asia Mater., vol. 8, no. 11, pp. e328, 2016.

[4] R. Cai, X. Qu, H. Liu, H. Yang, K. Wang, and X. W. Sun, "Perovskite light-emitting diodes based on FAPb 1- x Sn x Br 3 nanocrystals synthesized at room temperature," IEEE Trans. Nanotechnol., vol. 18, pp. 1050–1056, 2019.

[5] S. Negi, P. Mittal, and B. Kumar, "Modeling and analysis of high-performance triple hole block layer organic LED based light sensor for detection of ovarian cancer," IEEE Trans. Circuits Syst. I Regul. Pap., vol. 68, no. 8, pp. 3254–3264, 2021.

[6] S. Casaluci, L. Cinà, F. Matteocci, P. Lugli, and A. Di Carlo, "Fabrication and Characterization of Mesoscopic Perovskite Photodiodes," IEEE Trans. Nanotechnol., vol. 15, no. 2, pp. 255–260, 2016, doi: 10.1109/TNANO.2016.2517239.

[7] H. M. Singh, B. Choudhuri, and P. Chinnamuthu, "Investigation of optoelectronic properties in germanium nanowire integrated silicon substrate using kelvin probe force microscopy," IEEE Trans. Nanotechnol., vol. 19, pp. 628–634, 2020.

[8] Z. Wang, M. Currie, P. Dianat, K. Montazeri, and B. Nabet, "Enhancement of optoelectronic properties of core--shell nanowires," IEEE Trans. Nanotechnol., vol. 17, no. 5, pp. 1058–1062, 2018.

[9] K. Wu, Y. Chen, J. Cheng, and K. Xu, "Use of carrier injection engineering to increase the light intensity of a polycrystalline silicon avalanche mode light-emitting device," Journal of Applied Physics, vol. 128, no. 17, p. 173104, 2020.

[10] S. S. A. Gillani, "First-principles investigation of structural, electronic, optical and thermal properties of Zinc doped SrTiO3," Optik (Stuttg)., vol. 201, p. 163481, 2020.

[11] P. Mittal, S. Yadav, and S. Negi, "Advancements for organic thin film transistors: Structures, materials, performance parameters, influencing factors, models, fabrication, reliability and applications," Mater. Sci. Semicond. Process., vol. 133, p. 105975, 2021.

[12] M. Rizwan, A. Ali, Z. Usman, N.R. Khalid, H.B. Jin, and C.B. Cao, "Structural, electronic and optical properties of copper-doped $SrTiO_3$ perovskite: A DFT study," Phys. B Condens. Matter., vol. 552, pp. 52-57, 2019.

[13] A. Raturi, P. Mittal, and S. Choudhary, "Effect of metal doping on visible light absorption and optical properties of lithium niobate (LiNbO3) crystal: a first-principles calculation," Bull. Mater. Sci., vol. 44, no. 3, pp. 1–10, 2021.

[14] B. L. Phoon, C. W. Lai, J. C. Juan, P.-L. Show, and W.-H. Chen, "A review of synthesis and morphology of SrTiO 3 for energy and other applications," Int. J. Energy Res., vol. 43, no. 10, pp. 5151–5174, 2019.

[15] C. E. Ekuma, M. Jarrell, J. Moreno, and D. Bagayoko, "First principle electronic, structural, elastic, and optical properties of strontium titanate," AIP Adv., vol. 2, no. 1, p. 12189, 2012.

[16] R. Kochar and S. Choudhary, "MoS2/Phosphorene Heterostructure for Optical Absorption in Visible Region," in *IEEE Journal of Quantum Electronics*, vol. 54, no. 4, pp. 1-6, Aug. 2018, Art no. 7000306, doi: 10.1109/JQE.2018.2850450.

[17] Y. Bi, M. F. Ehsan, Y. Huang, J. Jin, and T. He, "Synthesis of Cr-doped SrTiO3 photocatalyst and its application in visible-light-driven transformation of CO2 into CH4," J. CO2 Util., vol. 12, pp. 43–48, 2015.

[18] G. Yadav and S. Choudhary, "Tuning the Optical Properties of Zinc Sulfide Nanotube," IEEE Trans. Nanotechnol., vol. 17, no. 4, pp. 807–813, 2018.

[19] N. C. Panoiu, W. E. Sha, D. Y. Lei, and G.-C. Li, "Nonlinear optics in plasmonic nanostructures," Journal of Optics, vol. 20, no. 8, p. 083001, 2018.

[20] S. Negi, P. Mittal, and B. Kumar, "In-Depth Analysis of Structures, Materials, Models, Parameters, and Applications of Organic Light-Emitting Diodes," Spri. J. of Electr. Mater., vol. 49, pp. 4610–4636, 2020.

[21] H. Bentour, M. El Yadari, A. El Kenz, and A. Benyoussef, "DFT study of electronic and optical properties of (S--Mn) co-doped SrTiO3 for enhanced photocatalytic hydrogen production," Solid State Commun., vol. 312, p. 113893, 2020.

[22] S. Negi, P. Mittal, and B. Kumar, "Analytical modelling and parameters extraction of multilayered OLED," IET Circuits, Devices \& Syst., vol. 13, no. 8, pp. 1255–1261, 2019.

[23] Y. Chen et al., "Strain engineering and epitaxial stabilization of halide perovskites," Nature, vol. 577, no. 7789, pp. 209–215, 2020.

[24] D. Ghosh, A. Aziz, J. A. Dawson, A. B. Walker, and M. S. Islam, "Putting the squeeze on lead iodide perovskites: pressure-induced effects to tune their structural and optoelectronic behavior," Chem. Mater., vol. 31, no. 11, pp. 4063–4071, 2019.

[25] M. A. Mohebpour, S. I. Vishkayi, and M. B. Tagani, "Tuning electronic and optical properties of free-standing Sn2Bi monolayer stabilized by hydrogenation," J. Appl. Phys., vol. 127, no. 1, p. 14302, 2020.

[26] S. Negi, P. Mittal, and B. Kumar, "Impact of Different Layers on Performance of OLED," Spri. Micros. Techno., vol. 24, pp. 1-9, 2018.

[27] X. Zhou, J. Shi, and C. Li, "Effect of metal doping on electronic structure and visible light absorption of SrTiO3 and NaTaO3 (Metal= Mn, Fe, and Co)," J. Phys. Chem. C, vol. 115, no. 16, pp. 8305–8311, 2011.

[28] H. Irie, Y. Maruyama, and K. Hashimoto, "Ag+-and Pb2+-doped SrTiO3 photocatalysts. A correlation between band structure and photocatalytic activity," J. Phys. Chem. C, vol. 111, no. 4, pp. 1847–1852, 2007.

[29] F. Scotognella, G.D. Valle, A.R.S. Kandada, M.Z. Rossi, S. Longhi, S. Lanzani, and F. Tassone, "Plasmonics in heavily-doped semiconductor nanocrystals," The Euro. Phys. J. B., vol. 86, pp. 1-13, 2013.

[30] M. Jabeen and S. Haxha, "Increased Optical Absorption and Light--Matter Interaction in Silicon Thin-Film Solar Cell Nanostructure Using Graphene and 2-D Au/Ag Nanograting," IEEE J. Quantum Electron., vol. 54, no. 6, pp. 1–12, 2018.

[31] P. Chamola, and P. Mittal, "Impact of ZnTe, SbZnTe and SnZnTe Absorber Materials for Multi-layered Solar Cell: Parametric Extraction and Layer wise Internal Analysis," Optik, vol. 224, pp. 165626-165640, 2020

[32] R. Husin, F. W. Badrudin, M. F. M. Taib, and M. Z. A. Yahya, "Effects of strain on electronic and optical properties of LiNbO3: a first principles study," Mater. Res. Express, vol. 6, no. 11, p. 114002, 2019.

[33] J. Wu et al., "Strain in perovskite solar cells: origins, impacts and regulation," Natl. Sci. Rev., vol. 8, no. 8, p. nwab047, 2021.

[34] G.-Z. Wang, H. Chen, X.-K. Luo, H.-K. Yuan, and A.-L. Kuang, "Bandgap engineering of SrTiO3/NaTaO3 heterojunction for visible

Authorized licensed use limited to: DELHI TECHNICAL UNIV. Downloaded on May 31,2023 at 04:30:51 UTC from IEEE Xplore. Restrictions apply.
© 2023 IEEE. Personal use is permitted, but republication/redistribution requires IEEE permission. See https://www.ieee.org/publications/rights/index.html for more information.

This article has been accepted for publication in IEEE Transactions on Nanotechnology. This is the author's version which has not been fully edited and content may change prior to final publication. Citation information: DOI 10.1109/TNANO.2023.3280083

light photocatalysis," Int. J. Quantum Chem., vol. 117, no. 20, p. e25424, 2017.

[35] A. Ali et al., "First-principles investigation on electronic structure, magnetic states and optical properties of Mn-doped SnS2 monolayer via strain engineering," Phys. E Low-dimensional Syst. Nanostructures, vol. 134, p. 114842, 2021.

[36] J. P. Perdew, K. Burke, and M. Ernzerhof, "Generalized gradient approximation made simple," Phys. Rev. Lett., vol. 77, no. 18, p. 3865, 1996.

[37] K. Xu, "Silicon electro-optic micro-modulator fabricated in standard CMOS technology as components for all silicon monolithic integrated optoelectronic systems," Journal of Micromechanics and Microengineering, vol. 31, no. 5, p. 054001, 2021.

[38] A. Raturi, and S. Choudhary, "Simulation study on understanding the spin transport in MgO adsorbed graphene based magnetic tunnel junction," Spin, vol. 6, no. 3, pp. 1650011, 2016.

[39] A. Maniyar, and S. Choudhary, "Visible region absorption in TMDs/phosphorene heterostructures for use in solar energy conversion applications," RSC Advances, vol. 10, no. 53, pp. 31730-31739, 2020.

[40] R. H. Mitchell, A. R. Chakhmouradian, and P. M. Woodward, "Crystal chemistry of perovskite-type compounds in the tausonite-loparite series, (Sr 1- 2 x Na x La x) TiO3," Phys. Chem. Miner., vol. 27, no. 8, pp. 583–589, 2000.

[41] F. Tran and P. Blaha, "Accurate band gaps of semiconductors and insulators with a semilocal exchange-correlation potential," Phys. Rev. Lett., vol. 102, no. 22, p. 226401, 2009.

[42] G. R. Berdiyorov, "Optical properties of functionalized Ti3C2T2 (T= F, O, OH) MXene: First-principles calculations," Aip Adv., vol. 6, no. 5, p. 55105, 2016.

[43] R. M. Martin, Electronic structure: basic theory and practical methods. Cambridge university press, 2020.

[44] M. Barrimi et al., "An investigation of thermoelectric power factor of Mn and Nb doped SrTiO3 ceramics," Encephale, vol. 53, no. 1, pp. 59–65, 2013.

[45] A. Srivastava, M. I. Khan, N. Tyagi, and P. Swaroop Khare, "Doping induced structural stability and electronic properties of GaN nanotubes," Sci. World J., vol. 2014, 2014.

[46] J. P. Perdew, K. Burke, and M. Ernzerhof, "Generalized gradient approximation made simple," Phys. Rev. Lett., vol. 77, no. 18, p. 3865, 1996.

[47] R. W. Godby, M. Schlüter, and L. J. Sham, "Accurate exchange-correlation potential for silicon and its discontinuity on addition of an electron," Phys. Rev. Lett., vol. 56, no. 22, p. 2415, 1986.

[48] Y.-L. Liu, C.-L. Yang, M.-S. Wang, X.-G. Ma, and Y.-G. Yi, "Theoretical insight into the effect of Si-doped sites on the photocatalytic properties of SrTiO3," Appl. Phys. A, vol. 125, no. 6, pp. 1–9, 2019.

[49] K. van Benthem, C. Elsässer, and R. H. French, "Bulk electronic structure of srtio3: Experiment and theory," Journal of Applied Physics, vol. 90, no. 12, pp. 6156–6164, 2001.

[50] S. Choudhary and A. K. Garg, "Enhanced Absorption in MoS2/Hg0.33Cd0.66Te Heterostructure for Application in Solar Cell Absorbers," in IEEE Transactions on Nanotechnology, vol. 18, pp. 989-994, 2019.



Ashish Raturi was born in Uttarakhand, India in 1991. He received B. Tech Degree in Electronics and Communication Engineering, from GEU, Dehradun, India in 2013. He received M. Tech degree in VLSI Design from National Institute of Technology, Kurukshetra, India. He is presently pursuing Ph.D. at Delhi Technical University, New Delhi, India. His research interests include study of nanoelectronics, VLSI, microelectronics and DFT.



Dr. Poornima Mittal, Senior Member IEEE (Ph.D, M.Tech(H), B.Tech) has published 150+ international journal/conference papers/book chapters. Her research interests include design/modeling of flexible electronic devices, electronic and optical materials, thin film fabrication, OLED, Solar cell, memory cell, sense amplifier and low power VLSI circuits. She has published two patents on novel OTFT structure and SRAM cell. In addition, she has published a Text Book titled "Organic Thin-Film-Transistor Applications: Materials to Circuits" CRC Press, T&F, UK, 2016. One book on 'Labview' is in-press for publication. She is the reviewer of many IEEE transactions and other international journals of IEEE, Elsevier, Springer, IOP, AVS, Wiley and T&F. She has received the research awards in 2012 and 2015 for dedicated research at Graphic Era University, Dehradun, India. Also, she has received Premier and Commendable-Research-Awards in 2019, 2020, 2021 and 2022 at Delhi Technological University (DTU), Delhi, India. She is a life member of many professional societies. She has 17+ years of academic and research experience and presently, she is working as Professor in the department of ECE at DTU, Delhi, India.



Dr. Sudhanshu Choudhary was born in Lucknow, India, in 1980. He received the bachelor's degree from Birla Institute of Technology, Mesra, Ranchi, India, in 2002, the master's degree from the Indian Institute of Information Technology and Management Gwalior, India, in 2006, and the Ph.D. degree from the Department of Electrical Engineering, IIT Kanpur, India. Since 2013, he is an Assistant Professor with the National Institute of Technology, Kurukshetra, India. His research interests include microelectronics, very large-scale integration, and nanoelectronics. His current research focuses on molecular electronics simulations using density functional theory in combination with nonequilibrium green's function. He is on the panel of experts for several funding agencies and several international conferences.

Authorized licensed use limited to: DELHI TECHNICAL UNIV. Downloaded on May 31,2023 at 04:30:51 UTC from IEEE Xplore. Restrictions apply.
© 2023 IEEE. Personal use is permitted, but republication/redistribution requires IEEE permission. See https://www.ieee.org/publications/rights/index.html for more information.

2023 IEEE 8th International Conference for Convergence in Technology (I2CT)
Pune, India. Apr 7-9, 2023

2023 IEEE 8th International Conference for Convergence in Technology (I2CT) | 979-8-3503-3401-2/23/$31.00 ©2023 IEEE | DOI: 10.1109/I2CT57861.2023.10126494

Design & Validation of ANN based Reinforcement Learning Control Algorithm for Coupled Tank System

Digant Rastogi
Control of Dynamical Systems and Computation Lab
Dept. of Electrical Engineering
Delhi Technological University
Delhi, India
digant.dtu@gmail.com

Manika Jain
Control of Dynamical Systems and Computation Lab
Dept. of Electrical Engineering
Delhi Technological University
Delhi, India
manikajain11@gmail.com

Madan M. Rayguru
Control of Dynamical Systems and Computation Lab
Dept. of Electrical Engineering
Delhi Technological University
Delhi, India
mmrayguru87@gmail.com

Sudarshan K. Valluru
Control of Dynamical Systems and Computation Lab
Dept. of Electrical Engineering
Delhi Technological University
Delhi, India
sudarshan_valluru@dce.ac.in

***Abstract*—This paper presents a framework to apply Reinforcement Learning control algorithm on benchmark nonlinear dynamical systems. This work focuses on a novel Artificial Neural Network (ANN) based dynamic programming approach using Value Iteration to obtain optimal control for continuous-time nonlinear system. In particular, Coupled Tank System has been chosen to represent benchmark nonlinear dynamical system. The proposed Artificial Neural Network-Reinforcement Learning (ANN-RL) algorithm, Naive Reinforcement Learning (Naive-RL) algorithm and traditional PID control schemes are investigated on coupled tank system. The ANN-RL algorithm performs better than the Naive-RL and PID controllers in terms of steady state error, stability, oscillations and overshoot.**

***Keywords*—Reinforcement Learning, Artificial Neural Network, Value Iteration, PID Controller, Nonlinear dynamical system**

I. INTRODUCTION

Various traditional control techniques have been designed for solving linear-time-invariant systems, which are presumed to be fully understood. However, most practical systems are nonlinear and dynamical, i.e. whose state varies continuously with time and is governed by differential equations. Devising and validating the optimised algorithms for the control of nonlinear benchmark dynamical systems, has attracted researchers for many years now.

When the system is discrete and linear, control objectives are straightforward, and strategies developed to reach the objective are easy and intuitive. On the other hand, building control algorithms when the system possesses nonlinear and dynamical characteristics presents certain challenges. With recent advancements in both theory and computational technologies, Reinforcement Learning (RL) algorithms have become promising data-driven control of dynamical systems [1].

RL algorithms mimic the learning process of a child's brain, where the RL agent is equipped with basic capabilities and allowed to explore and exploit the surroundings. The RL agent interacts with environment to learn the optimal control policy [2]. RL algorithms present a simplified technique which progressively improves its knowledge [3]. Fig. 1 presents a schema followed by RL algorithms.

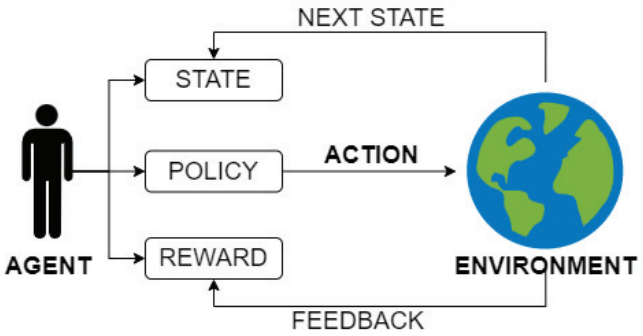


Fig. 1. RL agent-environment interaction

At present, RL has been applied to linear-time-invariant games [4] where there is a simple reward and the games have no dynamical nature. However, most real world control systems are nonlinear and dynamical. Thus it is imperative to find ways to apply RL to such practical systems. In this paper, a framework is proposed to use value iteration based algorithm which can be applied to control an interactive coupled tank

Authorized licensed use limited to: DELHI TECHNICAL UNIV. Downloaded on May 29,2023 at 05:46:00 UTC from IEEE Xplore. Restrictions apply.

system, which is a nonlinear dynamical system.

A novel ANN based RL control scheme to control liquid level in an interactive two-tank system is designed, to maintain a desired level of liquid in both tanks where there is an inflow and outflow of liquid in each tank. By discretizing a continuous system into different states, naive RL techniques like value iteration can be applied. Naive-RL in combination with a feed-forward ANN [5] is used to find optimal control of continuous nonlinear systems with the minimum error. The ANN is used as a regression analysis machine.

The PID, Fuzzy techniques or combinations have been long researched [6]- [8] but suffer from high overshoot and oscillations. The novel ANN-RL is compared to Naive-RL and PID algorithms and the performance of these techniques are examined for the level control of a coupled tank system.

This paper is organised as follows: Section II models the coupled tank system, Section III investigates the problem formulation, followed by Section IV which discusses the proposed algorithm. Section V presents the results and the comparative analysis of the three control mechanisms. The conclusions are presented in Section VI.

II. MATHEMATICAL MODELING OF COUPLED TANK SYSTEM

The coupled tank system is an experimental setup that mimics various industrial applications of the two-tank system found in the process control and petro-chemical industry. The task of this system is to maintain a required liquid height through controlling the input and output fluid rate. The system exhibits nonlinear and dynamical behaviour due to interaction of liquid between the two tanks through an orifice [6], [8].

The apparatus consists of two tanks, T1 and T2 as shown in Fig. 2. Let H_1 and H_2 represent the liquid heights in each tank at any instant. The input flow rate is defined as Q_{i1} and Q_{i2} respectively in the two tanks and the flow rate between tank 1 and tank 2 is defined as Q_{o3}. The output flow rate from tanks is Q_{o1} and Q_{o2} respectively. The input liquid is supplied by a variable speed pump to the two tanks.

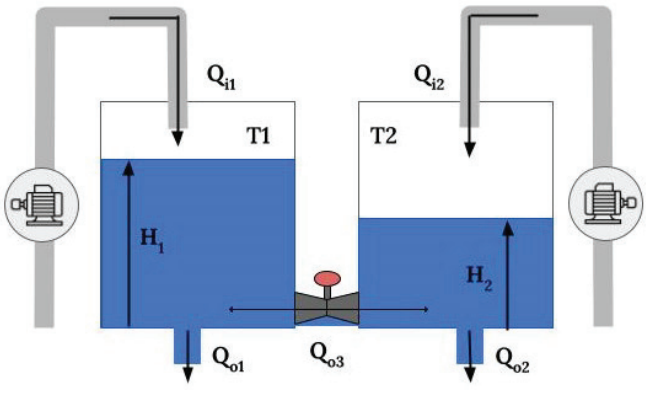


Fig. 2. Coupled Tank System Schematic

At any instant of time, the height of liquid in either tank is a function of the liquid input and output rate. This can be expressed as equations (1) and (2), where A_1 and A_2 are the cross-sectional areas of the two tanks respectively.

$$A_1 \frac{dH_1}{dt} = Q_{i1} - Q_{o1} - Q_{o3} \tag{1}$$

$$A_2 \frac{dH_2}{dt} = Q_{i2} - Q_{o2} + Q_{o3} \tag{2}$$

In equations (1) and (2) the flow rate Q_{03} depends on the gravitational constant and heights of liquid in the two tanks [6]. The state transition dynamics of the system are presented in equations (3) and (4). The proportionality constants α_1, α_2 are determined by the discharge coefficients, the cross-sectional area of each orifice, and the gravitational constant.

$$A_1 \frac{dH_1}{dt} = Q_{i1} - \alpha_1 \sqrt{H_1} - \alpha_3 \sqrt{H_1 - H_2} \tag{3}$$

$$A_2 \frac{dH_2}{dt} = Q_{i2} - \alpha_2 \sqrt{H_2} + \alpha_3 \sqrt{H_1 - H_2} \tag{4}$$

III. PROBLEM FORMULATION

It is evident from the state transition equations (3) and (4), that the system is dynamical and nonlinear. RL algorithms are used to find the global optimum control policy for a sequential decision-making process. Dynamic programming methods such as value iteration require a sequential process to be formulated as a Markov Decision Process (MDP). Hence it is imperative to model the coupled tank system as an MDP by discretizing the system variables [2].

The state S of the system is expressed as a linear array $S = [H_1, H_2]$. The action performed by the controller is to change the input flow rate of liquid Q_i, from the pump. The reward function, R is an essential part of the RL algorithm which communicates to the RL agent whether the control action it is performing is suitable or not. The actions for which the reward function is maximised are learnt as 'good' actions. The reward function is calculated for each state and action pair. For example, for state S = $[2, 3]$ an action Q_i = 10m^3/s is taken, then a reward value associated with this state-action pair $([2, 3], 10)$ will be estimated.

Hence, dynamic programming algorithm can simply learn to maximise reward and learn good actions for each state. The MDP can be formulated as the tuple (S, Q_i, T, γ, R) where:

- S - Current State [H_1, H_2]
- Q_i - Action taken by the controller, in terms of the input flow rate
- T - State transition equations
- γ - The discount factor has a value between $(0, 1]$, showing the importance of future rewards versus immediate rewards,
- R - Reward, which is defined for every ordered pair (S, Q_i)

Authorized licensed use limited to: DELHI TECHNICAL UNIV. Downloaded on May 29,2023 at 05:46:00 UTC from IEEE Xplore. Restrictions apply.

IV. DEVELOPMENT OF ANN BASED RL ALGORITHM

Value iteration algorithm is one of the most used RL algorithm for game-like decision processes. In the Section III, it was illustrated that the coupled tank system could be modelled like a game by discretizing the heights of liquid S ($[H_1, H_2]$) and the action space Q_i.

The flowchart in Fig. 3 describes the steps of the algorithm. There are 3 steps in the algorithm: Discretizing the continuous state-action space, applying Value iteration to discrete state-action space, and lastly using ANN to find the continuous control policy from the discrete policy returned by value iteration. The Algorithm 2 illustrates the pseudo-code for the ANN-RL algorithm. Each step is discussed in detail in the following subsections.

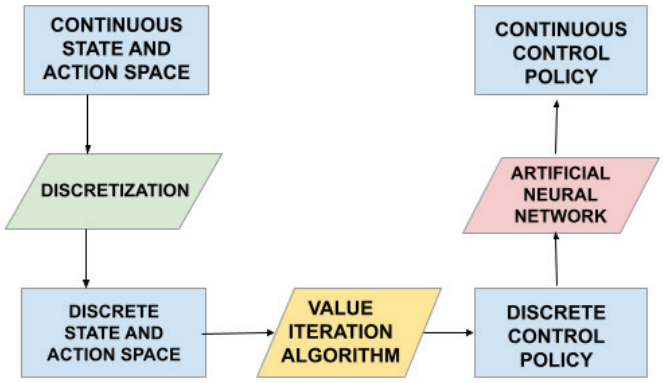


Fig. 3. Flowchart for ANN-RL algorithm

A. DISCRETIZATION OF THE SYSTEM

Naive-RL method deals with discrete states and actions where a finite number of actions exist for each of the states. The RL agent performs each action in every state, learns the best actions and forms a control policy. Hence, to successfully use Naive-RL algorithm, it is crucial to discretize a continuous system.

The system is described by two parameters: current state and the action taken. In dynamical systems like a coupled tank, these are continuous variables. After discretization, the coupled tank system can be represented as:

- $S = \{[H_1, H_2] \mid [H_1, H_2] \in$ finite numbers between (min, max)$\}$
- $Q_i = \{q_i \mid q_i \in$ finite numbers between (min, max)$\}$

Using the discrete state-action space, the system is easily modeled as an MDP, which allows us to use dynamic programming algorithms suitable for sequential decision process.

B. VALUE ITERATION

Value Iteration is a popular Naive-RL technique. Value iteration algorithm is based on the Bellman optimality equation that is used to calculate optimal value function for an MDP [2]. Value iteration estimates how good it is to perform an action in a state. The two forms of the optimal Bellman equation, are shown in equations (5) and (6) [2]. Here, $v_*(s)$ is the state-value function, where the best action is selected and the expected cumulative future rewards are calculated from the state. This state-value function can be simply converted into an iterative update, which converges to the optimal value function for each state [3]. The value function can be represented in another form as in (6) using $q_*(s, a)$, where for the given state, each action is selected one by one, and this state-action pair is assigned a value based on the expected future rewards if that action is performed in that state.

$$v_*(s) = \max_{a \in \mathcal{A}(s)} \sum_{s' \in \mathcal{S}, r \in \mathcal{R}} p(s', r|s, a)(r + \gamma v_*(s')) \quad (5)$$

$$q_*(s, a) = \sum_{s' \in \mathcal{S}, r \in \mathcal{R}} p(s', r|s, a)(r + \gamma \max_{a' \in \mathcal{A}(s')} q_*(s', a')) \quad (6)$$

In (5) and (6), r represents the reward, A and S represent action and state space. Here, $p(s', r|s, a)$ represents the transition dynamics from state s to s' when action a is performed, resulting in a reward value r. The pseudo-code for value iteration algorithm is presented in Algorithm 1. Each state is assigned a random state-value at the beginning. The state-value function is iteratively updated based on the cumulative reward that can be expected from the current state till the goal state is reached. Once the value function converges, the policy is extracted. The policy is extracted by choosing the action that yields a new state with the highest state-value of all possible next states. The reward function is designed to represent how far is the system is from the desired state. Equation (7) represents the reward function, where $H_{desired}$ represents the goal, i.e. the height to which liquid should be filled. The reward function has higher value as the system reaches closer to the desired state, which incentivises the agent to keep moving in that direction itself.

$$R(h_1) = -|h_{desired} - h| \quad (7)$$

Fig. 4 shows the discrete state transition based on control policy learnt by the RL Agent.

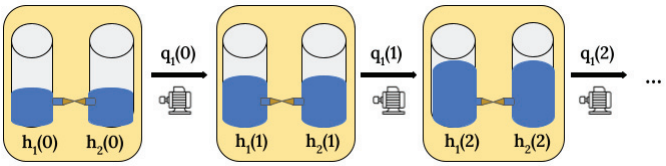


Fig. 4. Discrete State Transition based on Optimal Policy

C. ANN-RL CONTROL ALGORITHM

A discrete control policy is returned from value iteration. Discretization introduces error and loss similar to the effect of quantisation on analog signals. Quantization error yields poor performance by the controller. Hence, the true optimal control policy can only be found if the discrete control policy

Authorized licensed use limited to: DELHI TECHNICAL UNIV. Downloaded on May 29,2023 at 05:46:00 UTC from IEEE Xplore. Restrictions apply.

Algorithm 1 Value Iteration Algorithm

Require: π, the continuous policy to be evaluated
1: Initialize $V(s) = 0$, for all $s \in \mathcal{S}^+$
2: **repeat**
3: **for each** $s \in \mathcal{S}$ **do**
4: $v \leftarrow V(s)$
5: $V(s) \leftarrow \max_a \sum_{s',r} \mathcal{P}^a_{ss'}[\mathcal{R}^a_{ss'} + \gamma V(s')]$
6: $\Delta \leftarrow \max(\Delta, |v - V(s)|)$
7: **end for**
8: **until** $\Delta < \theta$ (a small positive number)
9: **return** $\pi_*(s) = \arg\max_a \sum_{s',r} \mathcal{P}^a_{ss'}[\mathcal{R}^a_{ss'} + \gamma V(s')]$

is translated to continuous space. This can be modelled as a simple regression task. The features, i.e. the input variable to the regression model is the state and the label, i.e. the output of the regression model can be the action taken. Hence, the regression model will learn a mapping between states and action, i.e. giving the true optimal policy. For regression, a feed-forward ANN is used to easily capture the nonlinearities in the control policy. The ANN uses the discrete state-action pairs, learns the best fit function, which gives us the continuous control policy. With the help of ANN, the discrete policy is translated to a continuous policy. The ANN-RL algorithm is designed and presented in Algorithm 2.

This continuous control policy learnt by the ANN can be used to predict favourable actions to take in any state.

Algorithm 2 ANN-RL Algorithm

Require: π, the continuous policy to be evaluated
Input: $H_{desired}, \gamma$, Reward(h)
1: **Initialize** $\mathcal{S}$ = {[H_1, H_2] | H_1, H_2 $\in$ whole numbers between [min, max]}
2: **Initialize** Q_i = {Q_i | Q_i $\in$ whole numbers between [min, max]}
3: **Initialize** $V(s) = 0$, for all $s \in \mathcal{S}$
4: **Call** Value Iteration Algorithm for $V(s)$
5: Train ANN on $\pi_*(s)$ calculated by Value Iteration
6: ANN works as continuous control policy
7: Use ANN to successively predict actions for current states until the goal state is reached

D. REALIZATION OF ALGORITHMS ON COUPLED TANK SYSTEM

The ANN-RL algorithm is applied to the coupled tank system. The height of the two tanks is taken to be 15m. The algorithm controls the inlet flow rate between 0 to a maximum of 20m^3/s in tank 1, and for simplicity, the inlet to tank 2 is closed. The value of γ (discount factor) is taken as 0.99.

The liquid levels in the tanks are discretized into finite states. Hence, the liquid levels of height 15m in each tank are discretized into 16 steps of 1m, giving 256 (16×16) possible states. The inlet flow of the value 20m^3/s is discretized into 21 steps each, giving us 21 possible actions for decision-making as depicted:

- S = {[H_1, H_2] | H_1, H_2 $\in$ whole numbers in [0, 15]}
- Q_i = {q_i | q_i $\in$ whole numbers in [0, 20]}

For experimental validation, the liquid is assumed to be incompressible and non-viscous. For these 256 states, a feed-forward ANN is trained on the discretized states and action to compute the optimal control policy. The ANN contains an 'Adam' optimiser for the neural network to minimize loss. The ANN contains two hidden layers, each containing 110 neurons and uses the 'Relu' activation function [9]. Hence, the ANN contains a feature set of 256 states and a label set of 21 possible actions.

To evaluate the ANN-RL algorithm, a comparison is drawn with the popular Proportional Integral Derivative (PID) control technique. A PID controller is based on a feedback technique that gives a continuous variation in a control loop feedback mechanism to accurately control the process. The PID controller works most efficiently when the gain values K_p, K_i and K_d are correctly tuned [10]. In most systems, K_p is responsible for process stability, K_i is responsible for minimizing the error and K_d for decreasing the overshoot and improving the transient response. The Zeigler-Nichols method was used to tune the PID gain values and they are depicted in the Table I.

TABLE I. ESTIMATED PID PARAMETERS

PID Gains	$\mathbf{K}_p$	$\mathbf{K}_i$	$\mathbf{K}_d$
Values	0.2	0.087	0.09

V. RESULTS

To evaluate the proposed ANN-RL algorithm, the results obtained from the ANN-RL control technique is contrasted with the results of Naive-RL and PID controllers. The three control algorithms are evaluated for different starting and desired states in the system to determine the stability of the system for the three control techniques.

Fig. 5 shows the control policy learnt by the Naive-RL Algorithm for the desired state of 7m height in tank 1 and starting state of 0m (empty tanks). It is observed from Fig. 5 that due to discretization, the Naive-RL control policy is not smooth and shows sudden changes and jumps. The ANN is then trained over this discrete optimal policy, for 50 epochs. Fig. 6 shows the loss magnitude after each epoch. The Mean Squared Error (MSE) is used as the loss function to train the ANN. After training, a loss of 5.4% and Mean Absolute Error (MAE) of 1.4% is observed.

The ANN learns the best fit function between discrete states and actions, giving us a function approximation of what the control policy would be in continuous state-action space. Fig. 7 shows the continuous control policy learnt by the ANN. It is evident from Fig. 5 and Fig. 7 that the ANN-RL policy is much smoother without sudden jumps. This is expected since the ANN-RL control policy represents the continuous state-action space.

The three algorithms are compared for the height of liquid in tank, i.e. the state of the system as a function of time.

Authorized licensed use limited to: DELHI TECHNICAL UNIV. Downloaded on May 29,2023 at 05:46:00 UTC from IEEE Xplore. Restrictions apply.

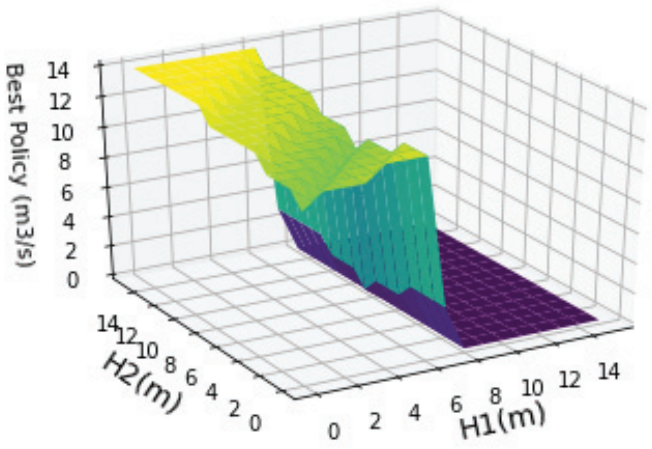


Fig. 5. Optimal Control Policy learnt by Naive-RL

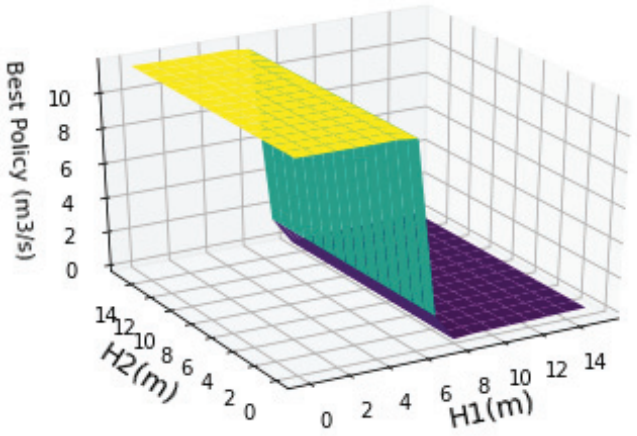


Fig. 7. Continuous Optimal Control Policy learnt by ANN-RL

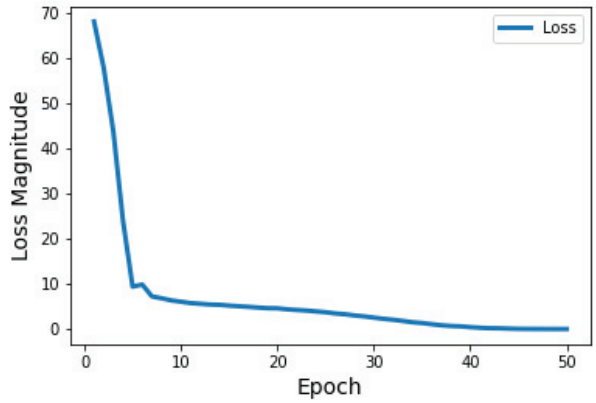


Fig. 6. Loss magnitude of the ANN after each epoch

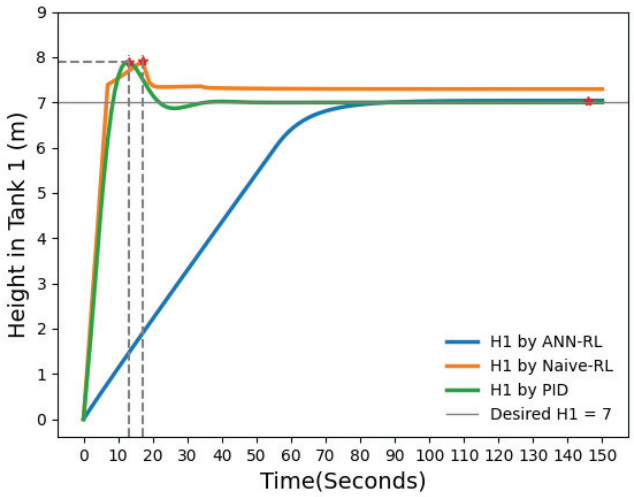


Fig. 8. Liquid height in tank 1 with time for goal state H_1=7m

Some of the crucial metrics to determine the performance of the control techniques are steady state error and percentage overshoot. The metrics obtained for the various test cases are presented in Table II. Fig. 8 shows the liquid height in tank 1 against time. The starting state for this test case was taken to be S = [0,0], i.e., tanks were initially empty. The goal state is taken as H_1 = 7.

It is visible in Fig. 8 that ANN-RL algorithm easily outperforms PID and Naive-RL as it presents no overshoot, no oscillation and no ripples. It is observed that PID and Naive-RL both exhibit a high overshoot. PID control mechanism exhibits oscillations but converges to the desired state. Naive-RL algorithm does not exhibit oscillations but it presents a high steady-state error and never converges to the goal. It also shows sharp changes and jitters.

Stability Analysis: The three control schemes are tested through simulation for different starting and goal states to check the system stability. One drawback of the ANN-RL control algorithm is that it exhibits a high rise time, hence as future work, better training algorithms can be deployed to reach the desired state faster as required in different industrial scenarios. Fig.9 shows the liquid height with time in tank 1 when the starting state was S=[1,1], i.e., liquid was present in each tank upto 1m level. Goal state of H_1 = 9m is taken. It is again observed that ANN-RL outperforms both PID and Naive-RL. Fig.10 shows the liquid height with time in tank 1 when the starting state was S=[2,1], i.e., liquid was present in tank 1 upto 2m level. A goal state of H_1 = 11m is taken. It is again observed that ANN-RL outperforms both PID and Naive-RL.

It should be observed from Fig. 8, Fig. 9 and Fig. 10, the PID algorithm requires re-tuning of gain values according to change in starting and goal states. However, the ANN-RL algorithm does not require any re-tuning while changing of starting and goal states.

Table II summarises the results obtained from the Experiments. All three control techniques are compared based on their steady state error, overshoot, and the ripples in the state. A significant advantage of the ANN-RL-based control approach is that it results in a smoother, oscillation free control than the simple Naive-RL and PID controller techniques and presents no steady state error.

Authorized licensed use limited to: DELHI TECHNICAL UNIV. Downloaded on May 29,2023 at 05:46:00 UTC from IEEE Xplore. Restrictions apply.

TABLE II. COMPARATIVE ANALYSIS OF THE 3 ALGORITHMS

START STATE	GOAL STATE	CONTROL ALGORITHM	OVERSHOOT (%age)	STEADY STATE ERROR(%age)	OSCILLATIONS
S = [0,0] H1 = 0m, H2 = 0m	H1 = 7m	PID	12.82	0.12	HIGH
		NAIVE-RL	13.09	4.14	HIGH
		ANN-RL	0.57	0.57	NIL
S = [1,1] H1 = 1m, H2 = 1m	H1 = 9m	PID	12.77	0.13	HIGH
		NAIVE-RL	5.11	3.82	HIGH
		ANN-RL	0.71	0.70	NIL
S = [2,1] H1 = 2m, H2 = 1m	H1 = 11m	PID	13.25	0.09	HIGH
		NAIVE-RL	5.18	1.19	HIGH
		ANN-RL	0.60	0.59	NIL

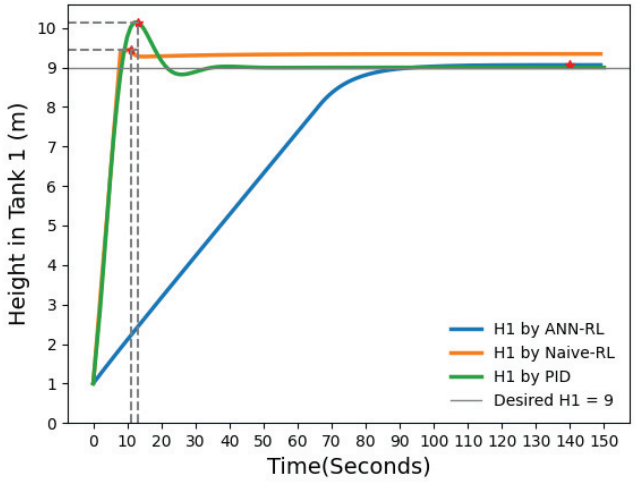


Fig. 9. Liquid height in tank 1 with time for goal state H_1=9m

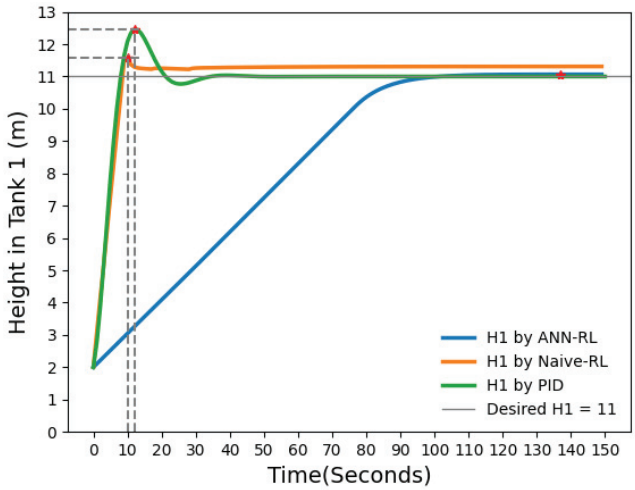


Fig. 10. Liquid height in tank 1 with time for goal state H_1=11m

VI. CONCLUSION

In this paper, a novel ANN-RL control algorithm is presented, to improve control of non-linear dynamical systems. The proposed algorithm uses value iteration to extract optimum policy for the discrete states and actions. Then, the optimal policy is approximated using a feed-forward ANN for the continuous state space. Further, a comparison is drawn along with a stability analysis between three different types of control techniques, namely, ANN-RL, Naive-RL and PID control methods, based on their steady-state error, oscillation and overshoot. The results indicate that the ANN-RL control approach results in enhanced performance with smoother control, no overshoot and minimal steady state error.

REFERENCES

[1] V. N. Vichugov, G. P. Tsapko and S. G. Tsapko, "Application of reinforcement learning in control system development," Proceedings. The 9th Russian-Korean International Symposium on Science and Technology, 2005. KORUS 2005., Novosibirsk, Russia, 2005, pp. 732-733, doi: 10.1109/KORUS.2005.1507888.

[2] R. S. Sutton and A. G. Barto, Reinforcement Learning: An Introduction. The MIT press, Cambridge MA, A Bradford Book, 1998.

[3] R. Siraskar, "Reinforcement learning for control of valves," Machine Learning with Applications, vol. 4, p. 100030, Jun. 2021, doi: 10.1016/j.mlwa.2021.100030.

[4] J. Martinez-Piazuelo, D. E. Ochoa, N. Quijano and L. F. Giraldo, "A Multi-Critic Reinforcement Learning Method: An Application to Multi-Tank Water Systems," in IEEE Access, vol. 8, pp. 173227-173238, 2020, doi: 10.1109/ACCESS.2020.3025194.

[5] Sudarshan K. Valluru, T.N. Rao, Introduction to Neural networks, Fuzzy Logic and Genetic algorithms (2nd ed.), Jaico Publishing House, Mumbai (2011).

[6] O. Geylani and B. Ata, "Adaptive Sliding Mode Control of a Coupled Tank System," 2022 International Congress on Human-Computer Interaction, Optimization and Robotic Applications (HORA), Ankara, Turkey, 2022, pp. 1-5, doi: 10.1109/HORA55278.2022.9799973.

[7] A. Muntaser and N. Buaossa, "Coupled Tank Non-linear System; Modeling and Level Control using PID and Fuzzy Logic Techniques," arXiv.org, 2021, doi: 10.48550/arXiv.2112.15506.

[8] S. Shamily, Praveena and N. S. Bhuvaneswari, "Intelligent control and adaptive control for interacting system," 2015 IEEE Technological Innovation in ICT for Agriculture and Rural Development (TIAR), Chennai, India, 2015, pp. 116-121, doi: 10.1109/TIAR.2015.7358542.

[9] R. Parhi and R. D. Nowak, "The Role of Neural Network Activation Functions," in IEEE Signal Processing Letters, vol. 27, pp. 1779-1783, 2020, doi: 10.1109/LSP.2020.3027517.

[10] S. K. Valluru et al., "Design of Multi-Loop L-PID and NL-PID Controllers: An Experimental Validation," 2018 2nd IEEE International Conference on Power Electronics, Intelligent Control and Energy Systems (ICPEICES), Delhi, India, 2018, pp. 1228-1231, doi: 10.1109/ICPEICES.2018.8897368.

Authorized licensed use limited to: DELHI TECHNICAL UNIV. Downloaded on May 29,2023 at 05:46:00 UTC from IEEE Xplore. Restrictions apply.

Journal of Religion and Health
https://doi.org/10.1007/s10943-023-01831-6

ORIGINAL PAPER

Development and Validation of Hindu Gratitude Scale (HGS-15): A *Rnas* Perspective

Naval Garg[1]

Accepted: 4 May 2023
© The Author(s), under exclusive licence to Springer Science+Business Media, LLC, part of Springer Nature 2023

Abstract

Researchers have proposed culture- and religion-based variations in experience and expression of gratitude. Accordingly, the present study developed and validated a Hindu Gratitude Scale (HGS) based on Hindu notion of *rnas.* The *rnas* are sacred obligations (duties) that every Hindu is supposed to fulfil during their lifetime. These pious obligations are practised to acknowledge, honour, and appreciate others' contribution in one's life. These five holy duties are *Pitṛ-yajna, Bhūta-yajna, Manuṣya-yajna, Deva-yajna,* and *Brahma-yajna.* The study started with *rnas*-based conceptualisation of gratitude followed by item generation using both inductive and deductive approaches. These statements were subjected to content validity and pretesting, which resulted in nineteen items. The psychometric properties of proposed HGS (with nineteen items) were analysed with the help of three studies. The first study evaluated factorial validity of the proposed HGS using exploratory factor analysis (EFA) and confirmatory factor analysis (CFA) using a sample of 1032 respondents. Poor factor loading in EFA suggested removal of three statements. The EFA recommended five dimensions of the HGS—appreciation for family, ancestors, and cultural values (AFF), appreciation for family, ancestors, and cultural values (AFF), appreciation for God, appreciation for knowledge, skills, and talents, and appreciation for ecosystem. Further, CFA also suggested removal of one statement. Lastly, the EFA and CFA result suggested adequate factorial validity of a fifteen-itemed five-factored HGS. The second study examined the reliability and validity of the HGS derived from CFA with the help of a sample of 644 participants. And, in the third study, the test–retest reliability was investigated by collecting the data twice. The results revealed significant positive correlations in two sets of data, thereby concluding test–retest reliability of the HGS. The study offered a novel fifteen-item Hindu Gratitude Scale, which could be used in future studies to explore gratitude level of Hindus.

✉ Naval Garg
naval.garg@dtu.ac.in

[1] University School of Management and Entrepreneurship, Delhi Technological University, New Delhi, India

Published online: 19 May 2023

Keywords Gratitude · Hindu · *Rnas* · Psychometric

Introduction

Gratitude has been revered as a special virtue in all major religions of the world (Mahipalan and Sheena, 2019). It is a highly valued and prized feature of Christian, Jewish, Muslim, Buddhist, and Hindu faith traditions (Peterson and Seligman, 2004). Modern literature has also revealed that religions are closely related to different conceptualisations, experiences, realisations, and expressions of gratitude. The linkage between religion and gratitude could be understood at two levels: general and specific. At the general level, associations have been suggested between gratitude and different tenants of religiosity. Emmons and Kneezel (2005) reported that various religious attributes such as frequency of engagement in religious practices, spiritual transcendence experience, and ascribing significance and due importance to religion are positively related with gratitude.

Watkins et al. (2003) suggested that people high on gratitude experience higher intrinsic religiosity, i.e., involvement with religion for one's own sake. Such people also exhibit lower extrinsic religiosity, i.e., engagement with religion for other gains, such as improved social status, and publicity. In addition, Kraus et al. (2014) recommended that otherworldly belief and religious salience are closely related to the experience of gratitude. Other studies have reported linkage between gratitude and religious commitment (Rosmarin et al., 2016), religious efficacy (Kraus et al., 2014), and religious involvement (Rothenberg et al., 2016). In a rare study, Morgan et al. (2017) asserted that Christians express higher gratitude than atheists. Apart from these empirical studies, researchers have also explored gratitude in the backdrop of major religions of the world.

Gratitude has always been central to Christianity, which is regarded as the world's largest religion (Emmons and Crumpler, 2000). The Hebrew Bible is full of motifs that support gratefulness for God for life, health, and sustenance (Emmons and McCullough, 2003). There are several thanksgiving psalms and prayers to express gratitude in Christianity. It is argued that Christianity gratitude is not limited to being thankful in normal or good times, it also includes a deep sense of gratitude even in adverse or difficult situations.

Similarly, Islam, the second largest religion of the world, also adores gratitude as Godly virtue. Different suras of the holy Koran repeatedly outline the necessity for gratitude and thankfulness to God. "If you are grateful, I will give you more" (Sura 14, verse 7). The prophet Mohammad also said "Gratitude for the abundance you have received is the best insurance that the abundance will continue" (Fadiman and Frager, 1976, p. 178). In addition, daily Islamic prayers are expressions of one's gratitude towards God. Another feature of Islam is fasting during the month of Ramadan. It is a unique and special Islamic tradition to express their thankfulness to almighty God, fellow-beings, and society.

In the same manner, Hinduism, the third largest religion, also gives special reverence to gratitude. Hinduism seems to represent the pinnacle of gratitude experience and expression (Garg, 2017a, 2017b). The intensity of gratitude is so high among

Indians that they worship almost everything including sun, moon, sky, air, mountains, rivers, planets, animals, birds, directions, and place (Saxena et al., 2020). It is a divine virtue (Shankar, 2014). Bhagavad Gita says, "YadrcchalabhaSantustoDvandvatitoVimatsarah" (verse 4.22). It adores the quality of being grateful for all material and spiritual possessions. Also, almost all Hindu *mantras* (holy hymns) have a word "*Namah*," which epitomises thankfulness for divinity. For inference "*Namo Bharanta Emasi*," (Rig Veda, verse 1.1.7) "*Om Namah Shivaya.*"

Hinduism offers a unique combination of intrapersonal, interpersonal, and transpersonal conceptualisation of gratitude. The intrapersonal connotation (gratefulness for self) is a distinctive feature of Hinduism. Several Hindu prayers, practices, and meditations are offered in reverence to one's own body, mind, spirit, virtues, knowledge, and skill sets. *Yog nidra*, *Chakra* meditation, *Basant panchami,* and *Vishwakarma jayanti* are practised/celebrated in honour of one's own self. In general, the literature refers to ten directions (East, West, North, South, North-East, North-West, South-East, South-West, up, and down). Hinduism refers to the eleventh direction (movement towards one's inner self) to acknowledge the importance of one's body and self. In addition, interpersonal outlook includes gratitude for both animate and inanimate (Garg et al., 2020). The experience and expression of gratitude for fellow-beings are common in all religions. But thankfulness for forms of life other than human beings and inanimate objects has got a special place in Hinduism.

Several festivals, rituals, traditions, and local customs appreciate contributions of animate and inanimate forms of life. Four out of ten *avatars* (incarnations) of Hindu God were in animal forms such as fish and tortoise. The four most essential elements (air, water, fire, and soil) are considered as deities. And, Hindu prayers and *yajnas* generally start with acknowledging and appreciating them (Navare and Pandey, 2022). As far as transpersonal nature of gratitude is concerned, Hindu philosophy also believes in transcendental gratitude that goes beyond benefit-triggered interpersonal gratitude restricted to specific person, event, and circumstance.

This novel and holistic perspective of gratitude could be understood through Hindu notion of *rnas* (Pandey and Navare, 2018). The *rnas* are sacred obligations (duties) that every Hindu is supposed to fulfil during their lifetime. These pious obligations are practised to acknowledge, honour, and appreciate others' contribution in one's life (Garg and Mehak, 2021). These five holy duties are *Pitṛ-yajna, Bhūta-yajna, Manuṣya-yajna, Deva-yajna,* and *Brahma-yajna.* The *Pitṛ-yajna* requires a Hindu to indulge in certain activities to repay the valuable benefaction of parents, ancestors, family, and relatives. Hinduism rates parents even higher than God. According to Hindu philosophy, it is better to serve and take care of parents than to pray to the almighty. It is a daily routine for Hindus to touch the feets of their parents first in the morning.

Also, Hindus express deep gratitude for their ancestors through worshipping them (Garg et al., 2021). There is a custom to worship ancestors on every new moon day among Hindus. In addition, Hindus celebrate a 15-day festival every year in honour and remembrance of their ancestors. The *Manuṣya-yajna* necessitates certain acts and deeds in appreciation of valuable contributions of fellow human beings in one's life. The Hindu philosophy has always believed in interconnectedness and interdependence of all humans. Every achievement is seen as a combined outcome of

the efforts of many individuals. Thus, a Hindu is supposed to gratefully reciprocate other's direct or indirect contributions in life. The *Bhūta-yajna* includes gratitude for the ecosystem (primarily for nonhumans). It advocates thankfulness for animals, birds, rivers, mountains, air, sun, moon, and other constituents of the ecosystem.

The *Deva-yajna* expects one to remain grateful towards God for its blessings. Hinduism offers multiple ways to express gratitude for the almighty. It includes prayers, fasting, meditation, *pranayam* (breathing techniques), *yajna*, celibacy, sacrifices, and a tendency to help others. Hindu philosophy believes that God resides in every living being. Thus, serving others is regarded as prayer to God. The *Brahma-yajna* requires a deep sense of appreciation for acquired knowledge and skills, both in the realm of matter and spirit (Pandey and Navare, 2018). Among Hindus, knowledge is ranked higher than money and power. And, thus, *gurus* and teachers have acquired status higher than even God.

Purposed of the Study

The present effort to develop and validate a gratitude scale on Hindu philosophy is motivated by two prominent reasons. First, the previous studies have highlighted religion- and culture-based differences in experience and expression of gratitude. "Gratitude may contain a common core with culturally ubiquitous features, in addition to socially constructed elements that change depending on the culture being studied" (Morgan et al., 2014). Sommers and Kosmitzki (1988) reported variations in gratitude among people of different cultures and nationalities. Tudge et al. (2015) reported culture-based variability of gratitude among American, Brazilian, Chinese, and Russian children.

Acknowledging the religious specificity of gratitude, Knabb et al. (2020) suggested emic approach to study gratitude in a particular religion or culture. Based on the emic perspective, they developed the Christianity Gratitude Scale (CGS) to capture thankfulness among Christains. They categorically outlined the importance of emic scales in future research and interventions contexts. Similarly, Amri et al. (2022) constructed and validated Islamic Gratitude Scale (IGS) for Muslim population. They argued that any gratitude scale for Muslim sample is incomplete without inclusion of Islamic notion of *Shukr,* which operationalises at three levels: heart (feelings), words, and actions. The present generation of indigenous psychology also advocates native view of psychological constructs such as gratitude, compassion, and trust (Sharma et al., 2022). It necessitates a gratitude scale based on the world's third largest religion (Hinduism).

Second, the Hindu notion of *rnas* offers a holistic conceptualisation of gratitude. The GQ-6 and GRAT-16 are two mostly used scales but they are often criticised for being based on a narrower perspective of gratitude that involves tangible benefits from others. On the other hand, the TGS is based on transcendental and transpersonal conceptualisation of gratitude. The Hindu's *rnas* perspective involves intrapersonal (gratitude for one's skill and talents), interpersonal (appreciation for fellow human beings), and transpersonal (gratefulness for ecosystem and God) connotations of gratitude. Thus, a scale based on *rnas* is poised to offer wider and

comprehensive conceptualisation of gratitude. Thus, a pursuit of wider conceptualisation and a dire need of a indigenous scale lead to the present study to develop a scale for Hindu population.

Scale Development

A new scale development follows four steps: (a) conceptualisation; (b) item generation; (c) content validity; and (d) analysis of psychometric properties of the scale (Arias et al., 2014; Boateng et al., 2018; Koenig and Al Zaben, 2021).

(1) *Conceptualisation:* The present study relies on above-discussed *rnas* conceptualisation of gratitude, which seems to offer theoretical explanations to a more holistic approach including intrapersonal, interpersonal, and transpersonal nature of gratitude.
(2) *Item generation:* Items are generated through deductive and inductive approaches. In the deductive method, existing literature and scales are analysed. And in the inductive approach, focus group or individual interviews are conducted to generate items. Here, as suggested by Boateng et al. (2018), both deductive and inductive approaches were used simultaneously. Firstly, existing gratitude scales such as McCullough et al.'s (2002) Gratitude Questionnaire (GQ-6), Watkins et al.'s (2003) Gratitude Resentment and Appreciation Scale-Short Form (GRAT-16), Hlava et al.'s (2014a; b) Transpersonal Gratitude Scale (TSG), Knabb et al.'s (2021) Christianity Gratitude Scale (CGS), and Rusdi et al.'s (2012) Islamic Gratitude Scale were explored. A few items such as "I couldn't have gotten where I am today without the help of many people" and "I think it's important to enjoy the simple things in life" were deduced from these scales.

Secondly, a focus group discussion of five university professors engaged in research work on spirituality, gratitude, indigenous psychology, and ethics was conducted to generate items of the scale. These two processes lead to the generation of thirty items.

(3) *Content validity and pretesting:* The content validity refers to the degree to which proposed items contain all the facets of the conceptual framework. It is often mistaken as synonymous with validity; rather, it should be considered only one way of validity examination (Koenig and Al Zaben, 2021). It mandates evaluation of proposed items by knowledgeable experts (Boateng et al., 2018). Accordingly, another focus group discussion of other five university teachers was conducted. They evaluated the content relevance, representative, technical quality, and comprehension of thirty generated items in the background of *rnas* conceptualisation of gratitude. The experts suggested elimination of eight statements for being repetitive, vague, or non-contextual.

The remaining twenty-two items were given to twenty Hindus (above 18 years and residing in India) for pretesting. The statements were discussed with each respondent for "what meaning they derive from the statements," and "where they are able to understand the question." Based on their inputs, three statements were deleted for being vague or too technical for understanding of common man, and a few other statements were rephrased for better clarity. Remaining nineteen statements were referred to as Hindu Gratitude scale (HGS) and subjected to psychometric analysis using three studies. The first study evaluated the construct and factorial validity of the scale using exploratory factor analysis (EFA) and confirmatory factor analysis (CFA). The second study investigated reliability and validity of the scale. And the third study explored the test–retest reliability of the HGS.

4) *Analysis of psychometric properties*

Study 1—Factorial Validity of the Hindu Gratitude Scale (HGS)

The purpose of the first study was to explore the factorial validity of the Hindu Gratitude Scale (HGS) using EFA and CFA conducted on two independent samples.

Participants and Instruments

This study is based on a sample of 1032 Hindu respondents. An online questionnaire using Google form was created. It was floated on major social media platforms such as Facebook, LinkedIn, Instagram, etc. The survey was open for adult Hindus residing in India. Table 1 illustrates demographic details of the sample. The questionnaire was divided into two parts. The first part is demographic information, and the second part measures the gratitude level of respondents using nineteen statements of proposed HGS on a five-point rating scale ranging from 1 (strongly disagree) to 5 (strongly agree).

Data Analysis

The sample of 1032 participants was divided into two equal parts using systematic sampling. The first subsample consisted of odd responses, and the second subsample included even responses. Koenig and Al Zaben (2021) suggested that EFA and CFA should be conducted on two different samples. Accordingly, EFA and CFA were conducted on subsample 1 and 2, respectively. Before EFA, the suitability of the data was ensured using the Kaiser–Meyer–Olkin (KMO) test and Bartlett's test of sphericity.

The KMO value of sampling adequacy is 0.870. A significant Bartlett's test of sphericity at a significance level of 0.05 was also reported. These results recommended suitability of the data for EFA. Then, EFA was applied using the promax method, which uses an oblique rotation. The oblique rotation is preferred when extracted factors are assumed to be correlated (Osborne, 2015). The EFA results showed inadequate factor loading (less than 0.40) for three items, and thus, these

Table 1 Descriptive statistics

Variables	Category	Sample 1	Sample 2
Gender	Male	550	358
	Female	482	286
Age	Less than 25 years	347	216
	26–35 years	310	233
	36–45 years	244	106
	Above 45 years	131	89
Income	Below 5 lakhs	265	156
	6–10 lakhs	378	190
	11–15 lakhs	330	177
	Above 15 lakhs	59	121
Marital status	Married	533	304
	Unmarried	476	316
	Separated	23	24
Occupation	Student	336	235
	Service	359	198
	Business	337	211
Total		1032	644

Source: primary data

items were discarded. These eliminated statements were "Life has been good to me," "I am thankful for my educational credentials as it helps me to earn bread and butter for my family," and "I deeply value trees and plants for their necessity for survival of life." Table 2 illustrates the following five-factor solution consisting of sixteen statements. The five dimensions of the HGS explain 66.43% of the variance.

- *Factor-1:* It has been referred to as "appreciation for fellow human beings" (AFH). It consists of statements such as "A lot of people have contributed positively in my life," and "It is important to acknowledge others' contributions in one's life." This factor expresses one's gratitude towards others for their invaluable contributions in one's life. The factor seems to capture the interpersonal nature of gratitude. It comprises four items and has an eigenvalue of 6.224.
- *Factor-2:* It has been named as "appreciation for family, ancestors, and cultural values" (AFF). This factor captures one's gratefulness for his/her parents, family members, ancestors, and cultural values. Indian joint family system, perennial parental assistance, and social support from family members and relatives make one's life relatively easier. Thus, they command a special revered place in Hindu culture. Hindu celebrates a 15-day long festival called "*Pitr paksha"* to express their gratitude towards parents and ancestors. This factor comprises items such as "I often feel good about my family and cultural values," and "I take great interest in rituals and festivals celebrated for reverence of ancestors (like Pitr paksha)." It has three items and an eigenvalue of 5.150.
- *Factor-3:* It is named as "appreciation for God" (AFG). The transpersonal connotation favours ethereal, spiritual, and transcendent conceptualisation of grati-

Table 2 Factor structure of the Hindu gratitude scale

S. No.	Statements	Loading	Eigenvalue
Factor-1 (Appreciation for fellow human beings)			
1	A lot of people have contributed positively in my life	0.889	6.224
2	It is important to acknowledge others' contributions in one's life	0.837	
3	I could not have gotten where I am today without the help of many people	0.770	
4	I could not imagine life without other's support	0.581	
Factor-2 (Appreciation for family, ancestors, and cultural values)			
5	I am thankful to my parents and grandparents for this beautiful life	0.855	5.150
6	I often feel good about my family and cultural values	0.812	
7	I take great interest in rituals and festivals celebrated for reverence of ancestors (like Pitr paksha)	0.784	
Factor-3 (Appreciation for God)			
8	I am thankful to the divine for this life	0.832	4.324
9	I often experience blessings of the divine	0.778	
10	I feel that practices such as prayer, fasting, and meditation are good ways to express our gratitude towards God	0.746	
Factor-4 (Appreciation for knowledge, skills, and talents)			
11	I am thankful to all teachers who have imparted knowledge and skills in me	0.864	2.524
12	I deeply appreciate my virtues, skills, and abilities for their valuable contribution in my life	0.835	
13	With age, I find development in my capabilities that help me in dealing with people, events, and situations	0.766	
Factor-5 (Appreciation for ecosystem)			
14	I often feel overwhelmed by the blessings of nature	0.814	1.860
15	I enjoy different prayers and rituals in respect of panch-mahabhuta (five basic constituents of the world), i.e., air, water, sky, fire, and earth	0.754	
16	I appreciate the contributions of animals and birds in human life	0.720	
	Total number of factors extracted	5	
	Total variance explained	66.43%	

Source: primary data, *satisfactory factor loadings (i.e., greater than |.40|.), results after deleting three items with loading < 0.40, based on a sample of 1032 respondents

tude. It promotes universal consciousness, interconnectedness, and oneness. Since Hindus believe in both form and formless incarnation of God, they follow varieties of expression of gratitude such as prayer, fasting, meditation, yoga, festivals, and introspection. This factor captures Hindu's profound gratefulness for almighty with statements such as "I often experience blessings of the divine," and "I feel that practices like prayer, fasting, meditation, are good ways to express our gratitude towards God." It has three items and an eigenvalue of 4.324.

- *Factor-4:* It has been referred to as "appreciation for knowledge, skills and talents" (AFK). It captures two paradigms of gratitude: (a) gratefulness for both knowledge givers (teachers, trainers, coaches, and guides) and (b) gratitude for one's own knowledge and talents. The first paradigm seems an expression of interpersonal gratitude, and the second one offers a new insight of intrapersonal gratitude, wherein one is grateful for his/her own skills and virtues. Hinduism has a special reference for intrapersonal gratitude. The factor has items such as "I deeply appreciate my virtues, skills, and abilities for their valuable contribution in my life," and "With age, I find development in my capabilities that help me in dealing with people, events and situations." It has three items and an eigenvalue of 2.546.
- *Factor-5:* It has been named as "appreciation for the ecosystem" (AFE). This factor includes gratefulness for elements of external elements such as air, rivers, mountains, birds, animals, and nature. Hindu philosophy has a deep sense of appreciation for them as they are honoured as deities. Even special festivals and prayers such as *Govardhan puja, Ganga aarti,* and *Nag panchami* are performed as a token of respect and appreciation. There are traditions of honouring mother earth, sun, fire, and water during all auspicious events and functions. Accordingly, the factor includes statements such as "I enjoy different prayers and rituals in respect of panch-mahabhuta (five basic constituents of the world) i.e., air, water, sky, fire, and earth," and "I appreciate the contributions of animals and birds in human life." It has three items and an eigenvalue of 18.60.

After EFA, the CFA was applied for the second subsample to check the factorial validity of the model proposed by EFA. Acceptable statistics used to recommend a model fit are the comparative ft index (CFI $\geq$ 0.95), root-mean-square error of approximation (RMSEA $\leq$ 0.06), Tucker–Lewis index (TLI $\geq$ 0.95), and standardised mean square residual (SRMR $\leq$ 0.08) (Koenig and Al Zaben, 2021). The default model with sixteen statements (five latent factors) showed underperforming models with CFI = 0.96, TLI = 0.92, RMSEA = 0.082, and SRMR = 0.068.

On observation, it was found that one of the statements (I could not imagine life without other's support) has a factor loading of 0.27. Since factor loading was less than the standard value of 0.30, it was deleted. The new fifteen items model reported good model fit with CFI = 0.93, TLI = 0.90, RMSEA = 0.077, and SRMR = 0.063. The EFA and CFA results suggest a fifteen-itemed five-factored HGS. The proposed fifteen-itemed Hindu Gratitude Scale needs further reliability and validity testing performed in the below-explained second study (Fig. 1).

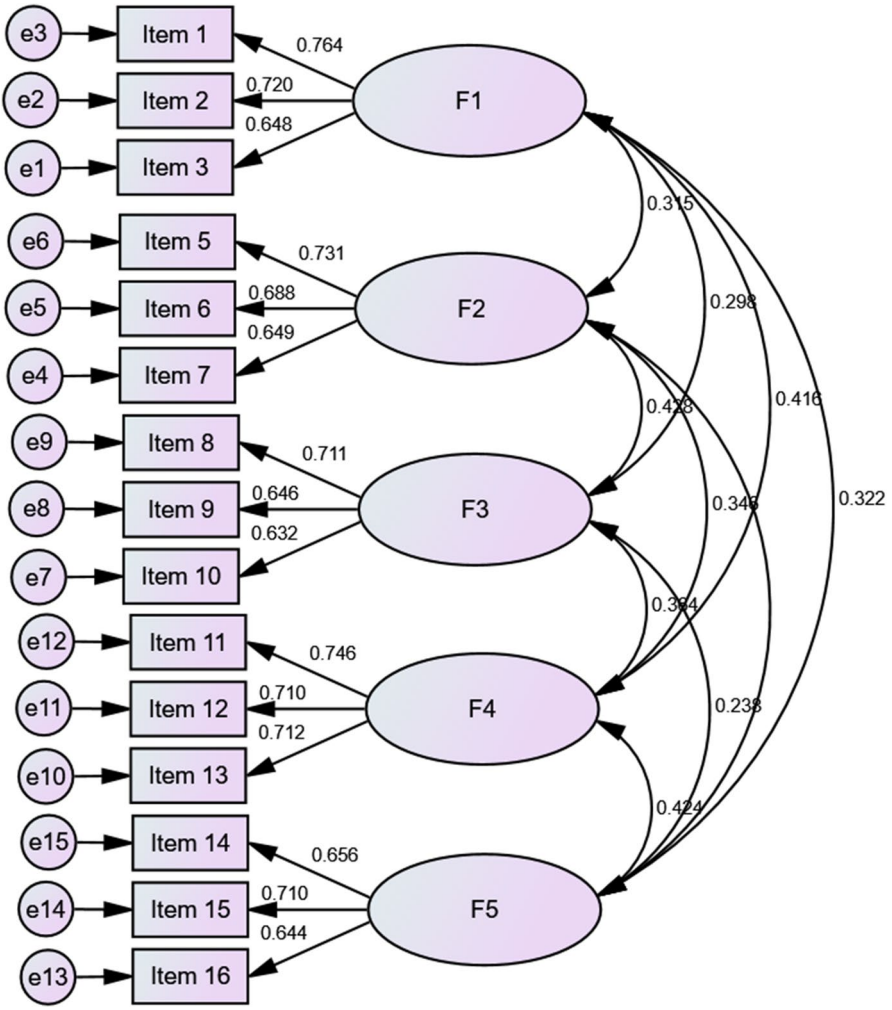


Fig. 1 Results of confirmatory factor analysis. *Source*: primary data, based on a sample of 1032 respondents

Study 2: Reliability and Validity of the HGS

The purpose of the second study was to evaluate the reliability and validity of the HGS.

Participants and Instruments

This study is based on another sample of 644 Hindu respondents. An online questionnaire using Google form was created and floated on major social media platforms

such as Facebook, LinkedIn, Instagram, etc. The survey was open for adult Hindus residing in India. Table 1 illustrates demographic details of the sample. The questionnaire was divided into five parts. The first part captures demographic information, and the second part measures the gratitude level of respondents using proposed HGS (fifteen items) on a five-point rating scale ranging from 1 (strongly disagree) to 5 (strongly agree). In the third part, McCullough et al.'s (2002) GQ-6 scale was used to measure an individual's dispositional gratitude. The scale comprised six statements rated on a seven-point scale ranging from 1 (strongly disagree) to 7 (strongly agree). A few items of the scale are "I have so much in life to be thankful for," and "If I had to list everything that I felt grateful for, it would be a very long list."

The fourth part assessed one's religious (10 items) and existential well-being (10 items) using Paloutzian et al.'s (2012) spiritual well-being scale (SWBS). Participants were requested to rate twenty items of SWBS on a six-point Likert scale, ranging from strongly disagree (1) to strongly agree (6). A few items of the scale are "I don't get much personal strength and support from my God," "I feel a sense of well-being about the direction my life is headed in," and "I believe that God is concerned about my problems." In the final part, Kessler Psychological Distress Scale (K10) was used to measure participants' distress levels (Kessler et al., 2003). The scale comprised ten items that measure the distress level of participants on a five-point scale ranging from 1 (none of the time) and 5 (all of the time). A few items of the scale are "In the past 4 weeks, about how often did you feel nervous?" and "In the past 4 weeks, about how often did you feel so nervous that nothing could calm you down?"

Data Analysis

The reliability of the HGS was evaluated with the help of Cronbach's alpha and composite reliability (CR) values, whose acceptable values are 0.70 or above (Cronbach and Shavelson, 2004; George and Mallery, 2008). Table 3 suggests that Cronbach's alpha values for appreciation for fellow human beings, appreciation for family, ancestors, and cultural values, appreciation for God, appreciation for knowledge, skills, and talents, and appreciation for ecosystem are 0.811, 0.780, 0.734, 0.827, and 0.717, respectively. Similarly, composite reliability estimates for appreciation

Table 3 Descriptive statistics, reliability, and validity estimates

Variable	Mean	S.D	CA	CR	AVE
Appreciation for fellow human beings	4.30	0.754	0.811	0.857	0.606
Appreciation for family, ancestors, and cultural values	4.18	0.860	0.780	0.858	0.668
Appreciation for God	4.43	1.114	0.734	0.829	0.618
Appreciation for knowledge, skills, and talents	3.85	0.664	0.827	0.862	0.677
Appreciation for ecosystem	3.40	0.583	0.717	0.807	0.583

Source: primary data

CA Cronbach's alpha, *CR* composite reliability, and *AVE* average variance explained, based on a sample of 644 respondents

for fellow human beings, appreciation for family, ancestors, and cultural values, appreciation for God, appreciation for knowledge, skills, and talents, and appreciation for ecosystems are 0.857, 0.858, 0.829, 0.862, and 0.807, respectively. These values establish the internal consistency reliability of fifteen-itemed HGS.

Furthermore, the convergent and divergent validity of the HGS was evaluated in two ways. Firstly, the average variance extracted (AVE) values and the Fornell and Larcker (1981) testing methods were used to check internal convergence and divergence of five dimensions of the HGS. Fornell and Larcker (1981) have recommended AVE values of 0.50 or greater to conclude the convergent validity of any scale.

Table 3 suggests that the AVE values for appreciation for fellow human beings, appreciation for family, ancestors, and cultural values, appreciation for God, appreciation for knowledge, skills, and talents, and appreciation for ecosystems are 0.606, 0.668, 0.618, 0.677, and 0.583. These values confirm internal convergence of five factors of the HGS. Further, the Fornell and Larcker (1981) testing method suggests that the AVE values of the factors should be greater than the squared correlation of the factors to recommend divergence between different dimensions of a scale. Table 4 reports higher AVE values than squared correlations coefficients, which concludes divergent internal validity of the scale.

Secondly, the external convergent and divergent validity of the HGS was examined using correlation coefficients between five dimensions of the HGS, GQ-6, and K-10 scores. Convergent validity is "the extent to which scores on a new scale are related to scores on an existing scale (or scales) that already has established validity in measuring the construct" (Koenig and Al Zaben, 2021, p. 3467).

Thus, to establish convergent validity of the HGS, it is hypothesised that five dimensions of the HGS correlate positively with the GQ-6 scores. Table 5 reports that GQ-6 scores are significantly positively correlated with appreciation for fellow human beings ($r=0.745$, $p<0.01$), appreciation for family, ancestors ($r=0.620$, $p<0.01$), and cultural values, appreciation for God ($r=0.460$, $p<0.01$), appreciation for knowledge, skills, and talents ($r=0.525$, $p<0.01$), and appreciation for ecosystems ($r=0.616$, $p<0.01$). Discriminant/divergent validity "is the extent to which a scale is not related to constructs that theoretically it should not be strongly related" (Koenig and Al Zaben, 2021, p. 3467). Accordingly, it is proposed that people high on gratitude would experience lower levels of distress. Table 5 reports

Table 4 Fornell and Larcker testing system

Factors	1	2	3	4	5
Appreciation for fellow human beings	1 (**0.606**)				
Appreciation for family, ancestors, and cultural values	0.205	1 (**0.668**)			
Appreciation for God	0.173	0.264	1 (**0.618**)		
Appreciation for knowledge, skills, and talents	0.305	0.238	0.174	1 (**0.677**)	
Appreciation for ecosystem	0.217	0.226	0.139	0.318	1 (**0.583**)

Source: primary data, AVE values are in bold (diagonally), based on a sample of 644 respondents

Table 5 Correlation matrix

Variables	1	2	3	4	5	6	7	8
AOF	1							
AOF	0.453*	1						
AOG	0.416*	0.514*	1					
AOK	0.553*	0.488*	0.418*	1				
AOE	0.466*	0.476*	0.374*	0.564*	1			
GQ-6	0.745*	0.620*	0.460*	0.525*	0.616*	1		
SWBS	0.664*	0.624*	0.529*	0.653*	0.510*	0.467*	1	
K10 score	−0.536*	−0.425*	−0.382*	−0.444*	−0.425*	−0.373*	−0.589*	1

Source: primary data

AOF appreciation for fellow human beings, *AOF* appreciation for family, ancestors, and cultural values, *AOG* appreciation for God, *AOK* appreciation for knowledge, skills, and talents, *AOE* appreciation for ecosystem, *GQ-6* gratitude questionnaire-6 score, *SWBS* spiritual well-being scale, and *K10* Kessler's distress scale, based on a sample of 644 respondents

*Sig. at 0.01

that K-10 scores are significantly negatively correlated with appreciation for fellow human beings ($r=-0.536$, $p<0.01$), appreciation for family, ancestors ($r=-0.425$, $p<0.01$), and cultural values, appreciation for God ($r=-0.382$, $p<0.01$), appreciation for knowledge, skills, and talents ($r=-0.444$, $p<0.01$), and appreciation for ecosystems ($r=-0.425$, $p<0.01$). These findings conclude the construct (convergent and divergent validity) of the HGS.

In addition, the criterion validity of the HGS was evaluated through examining the association between HGS and spiritual well-being scores. The previous researchers such as Garg et al. (2022), Loi and Ng (2021), and Feizi et al. (2020) have reported positive linkage between gratitude and spiritual well-being. Table 5 reports that SWBS scores are significantly positively correlated with appreciation for fellow human beings ($r=0.664$, $p<0.01$), appreciation for family, ancestors ($r=0.624$, $p<0.01$), and cultural values, appreciation for God ($r=0.529$, $p<0.01$), appreciation for knowledge, skills, and talents ($r=0.653$, $p<0.01$), and appreciation for ecosystems ($r=0.510$, $p<0.01$). These results conclude both construct and criterion validity of the HGS.

Study 3: Test–Retest Reliability

It refers to the degree of consistency of scores on repeated measures. Since data needto be collected twice, two hundred college students were approached with the HGS. Same students were requested to fill the questionnaire after 4 weeks. The sequence of items was changed to avoid any familiarity biasness. The findings revealed statistically significant positive correlations between two sets of data. The correlation coefficients for appreciation for fellow human beings, appreciation for family, ancestors, and cultural values, appreciation for God, appreciation for

knowledge, skills, and talents, and appreciation for the ecosystem are 0.765, 0.876, 0.919, 0.884, and 0.897. This study establishes test–retest reliability of the HGS.

Discussion

The present study aimed at developing and validating a scale to measure gratitude among Hindus. The previous researchers and indigenous psychologists have advocated an emic view to exploration and measurement of gratitude. Accordingly, the study attempted to derive a gratitude scale from Hindu notion of *rnas,* which obligates five duties for every Hindu. Based on Boateng et al. (2018) recommendations, the study started with *rnas*-based conceptualisation of gratitude followed by item generation using both inductive and deductive approaches.

Existing scales such as GQ-6, GRAT-16, CGS, IGS, and TGS were examined. Also, a focus group discussion was conducted between five university professors. It resulted in the culmination of thirty statements. The content validity of these thirty statements was ensured with the help of another focus group discussion, which resulted in elimination of eight statements. The remaining items were presented to twenty Hindus (from target population) for pretesting the scale, and their opinion led to elimination of other three statements. Now, the psychometric properties of proposed HGS (with nineteen items) were analysed with the help of three studies.

The first study evaluated factorial validity of the proposed HGS using EFA and CFA. Poor factor loading in EFA suggested removal of three statements. These statements were "life has been good to me," "I am thankful for my educational credentials as it helps me to earn bread and butter for my family," and "I deeply value trees and plants for their necessity for survival of life." The statement "life has been good to me" seems too general to fit into *rnas* conceptualisation of gratitude. The statement has been inducted from GRAT-16.

And interestingly, Garg and Mehak (2021) also suggested removal of the statement while analysing psychometric properties of GRAT-16 in the Indian context. The item related to educational credential also seems a slight mismatch as one might consider academic degrees and achievement as an outcome of one's own effort and hardwork. The EFA recommended five dimensions of the HGS—appreciation for family, ancestors, and cultural values (AFF), appreciation for family, ancestors, and cultural values (AFF), appreciation for God (AFG), appreciation for knowledge, skills, and talents (AFK), and appreciation for ecosystem (AFE). Further, CFA also suggested removal of one statement. Lastly, the EFA and CFA result suggested adequate factorial validity of a fifteen-itemed five-factored HGS.

The second study examined the reliability and validity of the HGS derived from CFA. The appropriate values of the Cronbach's alpha and composite reliability established the internal consistency reliability of the HGS. The AVE values recommended internal convergent validity of the scale. Also, HGS reported significant positive correlations with GQ-6 and K-10 scores, which confirmed external convergent and divergent validity of the scale. Lastly, as hypothesised, the HGS observed significant positive correlations with spiritual well-being scores, which recommended adequate scale's criterion validity. And, in the third study, the test–retest

reliability was investigated by collecting the data twice. The results revealed significant positive correlations in two sets of data, thereby concluding test–retest reliability of the HGS.

This study offers several theoretical and practical contributions to existing literature and researchers. Hindu philosophy has always cherished the virtue of gratitude as an essence of life. One of the most revered Hindu scriptures, *Ramayana,* states "Krte ca pratikartavyameshamdharmahsanatanah." It means "to repay a good deed of others" is the core of human life (Garg et al., 2021). Other Hindu epics such as *Veda, Upanishads, Gita, and Puran* also adored the importance of being grateful to others. But unfortunately, modern scientific exploration of gratitude is dominated by western researchers and academicians with very little studies on Hindus version of gratitude.

The proposed *rnas*-based conceptualisation and subsequent scale development are poised to attract the attention of modern researchers to examine Hindus view on gratitude. It might lead to scientific investigation on the significance and utility of various Hindu expressions of gratitude such as touching the feet of parents and elders, offering water to sun, and praying tools before usage. After thoughtful considerations, a few of these traditions might be developed and practised as gratitude interventions. The developed and validated Hindu Gratitude Scale could be used by future researchers for measuring gratefulness among Hindus. As discussed, the previous researchers have advocated culture- and religion-based examination of experience, expression, and interventions of gratitude. The HGS would provide an impetus to studies among Hindus who are in majority in several countries such as India and Nepal.

Limitations, Scope, and Conclusion

The study also offers an important insight into the positive association between gratitude and spiritual well-being of Hindus. Similar results were observed by other researchers such as Mills et al. (2015), Ajmal et al. (2018), and Elosua (2015). Accordingly, it is suggested to utilise a combination of western and Hinduism-based gratitude interventions to enhance the spiritual well-being of the people. The present study also concluded a negative relationship between gratitude and distress. It suggests that gratitude could be an effective tool to deal with respondents' distress. Further, although study offers interesting insights, it is marred with several limitations. First, the study is based on samples derived from Hindus residing in India only. Future research may explore psychometric properties of the HGS among Hindu living in other parts of the world too. Second, this study relied on self-report scales, which may lead to response bias. Also, various associations in the study are derived from cross-sectional data. Future researchers may use longitudinal or double-source data for better results.

In summary, although gratitude has special significance for Hindus, the empirical studies on gratitude among Hindus are scarce. One of the first and foremost steps for initiation of scientific explorations is the availability of a reliable and valid scale.

The Hindu Gratitude Scale might encourage researchers to give science-based evidence to different gratitude-based traditions of Hindus.

Funding The authors have not disclosed any funding.

Data availability Data could be procured from author upon reasonable request

Declarations

Conflict of interest We declare that they have no conflict of interest.

Ethical approval All procedures performed in the study are carried out in accordance with the ethical standards of the 1964 Helsinki Declaration and its later amendments or comparable ethical standards.

Informed consent Participants were duly informed of the study's purpose, and consent was procured from all the participants.

References

Ajmal, A., Abid, S., Bokhari, S. Z., & Rasool, A. (2018). Role of gratitude and forgiveness in spiritual well-being of teachers. *Pakistan Journal of Professional Psychology: Research and Practice*, *9*(2), 1–14.

Amri, M. A., Zaid, I., Md Nasser, N. A., & Abdul Khaiyom, J. H. (2022). Initial construction and validation of the islamic gratitude (I-Gratitude) scale. *Iium Journal of Human Sciences*, *4*(2), 52–64.

Arias, M. R. M., Lloreda, M. J. H., & Lloreda, M. V. H. (2014). *Psicometria*. Madrid: Alianza Editorial.

Boateng, G. O., Neilands, T. B., Frongillo, E. A., Melgar-Quiñonez, H. R., & Young, S. L. (2018). Best practices for developing and validating scales for health, social, and behavioral research: A primer. *Frontiers in Public Health*. https://doi.org/10.3389/fpubh.2018.00149

Cronbach, L. J., & Shavelson, R. J. (2004). My current thoughts on coefficient alpha and successor procedures. *Educational and Psychological Measurement, 64*(3), 391–418. https://doi.org/10.1177/0013164404266386

Elosúa, M. R. (2015). The influence of gratitude in physical, psychological, and spiritual well-being. *Journal of Spirituality in Mental Health*, *17*(2), 110–118. https://doi.org/10.1080/19349637.2015.957610

Emmons, R. A., & Crumpler, C. A. (2000). Gratitude as a human strength: Appraising the evidence. *Journal of Social and Clinical Psychology, 19*(1), 56–69. https://doi.org/10.1521/jscp.2000.19.1.56

Emmons, R. A., & Kneezel, T. T. (2005). Giving thanks: Spiritual and religious correlates of gratitude. *Journal of Psychology and Christianity*. http://transformationalchange.pbworks.com/f/Spiritual%20and%20Religious%20Correlates%20of%20Gratitude.pdf.

Emmons, R. A., & McCullough, M. E. (2003). Counting blessings versus burdens: An experimental investigation of gratitude and subjective well-being in daily life. *Journal of Personality and Social Psychology, 84*(2), 377–389. https://doi.org/10.1037/0022-3514.84.2.377

Fadiman, J., & Frager, R. A. (1976). Personality and Personal Growth. http://ci.nii.ac.jp/ncid/BA00975230

Feizi, S., Nasiri, M., Bahadori, H., Amiri, M. H., & Mirhosseini, H. (2020). The relationship between spiritual well-being and happiness among healthcare students: Application of the spiritual health questionnaire for the Iranian population. *Heliyon*. https://doi.org/10.1016/j.heliyon.2020.e05448

Fornell, C., & Larcker, D. F. (1981). Evaluating structural equation models with unobservable variables and measurement error. *Journal of Marketing Research, 18*(1), 39. https://doi.org/10.2307/3151312

Garg, N. (2017a). Workplace spirituality and employee well-being: An empirical exploration. *Journal of Human Values, 23*(2), 129–147. https://doi.org/10.1177/0971685816689741

Garg, N. (2017b). Workplace spirituality and organizational performance in Indian context: Mediating effect of organizational commitment, work motivation and employee engagement. *South Asian Journal of Human Resources Management, 4*(2), 191–211. https://doi.org/10.1177/2322093717736134

Garg, N. (2021). Gratitude resentment and appreciation scale (GRAT-16): Analyzing psychometrics properties in the Indian context. *Current Psychology*. https://doi.org/10.1007/s12144-021-02169-6

Garg, N., Jain, A., & Punia, B. (2020). Gratitude, social intelligence, and leadership among university teachers: Mediation and moderation analysis. *International Journal of Organizational Analysis, 29*(2), 368–388. https://doi.org/10.1108/ijoa-01-2020-2016

Garg, N., & Katiyar, N. (2021). Gratitude questionnaire (GQ-6)—Exploring psychometric properties in India. *Journal of Religion and Health, 60*(5), 3716–3731. https://doi.org/10.1007/s10943-021-01419-y

Garg, N., Kumari, S., & Punia, B. (2022). Resolving stress of university teacher: Exploring role of workplace spirituality and constructive workplace deviance. *South Asian Journal of Business Studies, 11*(3), 295–315. https://doi.org/10.1108/sajbs-04-2020-0118

George, D., & Mallery, P. (2008). *SPSS for windows step by step: A simple guide and reference, 16.0 update* (9th ed.). Allyn & Bacon.

Hlava, P., Elfers, J., & Offringa, R. (2014a). A transcendent view of gratitude: The transpersonal gratitude scale. *International Journal of Transpersonal Studies, 33*(1), 3. https://doi.org/10.24972/ijts.2014.33.1.1

Hlava, P., Elfers, J., & Offringa, R. (2014b). A transcendent view of gratitude: The transpersonal gratitude scale. *International Journal of Transpersonal Studies, 33*(1), 1–14. https://doi.org/10.24972/ijts.2014.33.1.1

Kessler, R. C., Barker, P. R., Colpe, L. J., Epstein, J. F., Gfroerer, J. C., Hiripi, E., Howes, M. J., Normand, S. L. T., Manderscheid, R. W., Walters, E. E., & Zaslavsky, A. M. (2003). Screening for serious mental illness in the general population. *Archives of General Psychiatry, 60*(2), 184. https://doi.org/10.1001/archpsyc.60.2.184

Knabb, J. J., Vazquez, V. E., & Wang, K. T. (2020). The Christian contentment scale: An *Emic* measure for assessing inner satisfaction within the Christian tradition. *Journal of Psychology and Theology, 49*(4), 324–341. https://doi.org/10.1177/0091647120968146

Knabb, J. J., Vazquez, V. E., Wang, K. T., & Pate, R. A. (2021). The Christian Gratitude Scale: An emic approach to measuring thankfulness in every season of life. *Spirituality in Clinical Practice*. https://doi.org/10.1037/scp0000278

Koenig, H. G., & Al Zaben, F. (2021). Psychometric validation and translation of religious and spiritual measures. *Journal of Religion and Health, 60*(5), 3467–3483. https://doi.org/10.1007/s10943-021-01373-9

Kraus, R., Desmond, S. A., & Palmer, Z. D. (2014). Being thankful: examining the relationship between young adult religiosity and gratitude. *Journal of Religion and Health, 54*(4), 1331–1344. https://doi.org/10.1007/s10943-014-9923-2

Loi, N. M., & Ng, D. L. (2021). The relationship between gratitude, wellbeing, spirituality, and experiencing meaningful work. *Psych*, *3*(2), 85–95. https://doi.org/10.3390/psych3020009

Mahipalan, M., & Sheena, S. (2019). Workplace spirituality and subjective happiness among high school teachers: Gratitude as a moderator. *Explore, 15*(2), 107–114. https://doi.org/10.1016/j.explore.2018.07.002

McCullough, M. E., Emmons, R. A., & Tsang, J. A. (2002). The grateful disposition: A conceptual and empirical topography. *Journal of Personality and Social Psychology, 82*(1), 112–127. https://doi.org/10.1037/0022-3514.82.1.112

Mills, P. J., Redwine, L., Wilson, K., Pung, M. A., Chinh, K., Greenberg, B. H., Lunde, O., Maisel, A., Raisinghani, A., Wood, A., & Chopra, D. (2015). The role of gratitude in spiritual well-being in asymptomatic heart failure patients. *Spirituality in Clinical Practice, 2*(1), 5–17. https://doi.org/10.1037/scp0000050

Morgan, B., Gulliford, L., & Kristjánsson, K. (2014). Gratitude in the UK: A new prototype analysis and a cross-cultural comparison. *The Journal of Positive Psychology, 9*(4), 281–294. https://doi.org/10.1080/17439760.2014.898321

Morgan, B., Gulliford, L., & Kristjánsson, K. (2017). A new approach to measuring moral virtues: The multi-component gratitude measure. *Personality and Individual Differences, 107*, 179–189. https://doi.org/10.1016/j.paid.2016.11.044

Navare, A., & Pandey, A. (2022). Karma yoga: Scale development and studies of the impact on positive psychological outcomes at the workplace. *International Journal of Cross Cultural Management, 22*(2), 271–299. https://doi.org/10.1177/14705958221111239

Osborne, J. W. (2015). What is rotating in exploratory factor analysis. *Practical Assessment, Research and Evaluation, 20*(2), 1–7. https://doi.org/10.7275/hb2g-m060

Paloutzian, R. F., Bufford, R. K., & Wildman, A. J. (2012). Spiritual well-being scale: Mental and physical health relationships. In M. Cobb, C. Puchalski, & B. Rumbold (Eds.), *Oxford textbook of spirituality in healthcare* (pp. 353–358). Oxford University Press.

Pandey, A., & Navare, A. V. (2018). Paths of yoga: Perspective for workplace spirituality. *The Palgrave Handbook of Workplace Spirituality and Fulfillment*. https://doi.org/10.1007/978-3-319-62163-0_4

Peterson, C., & Seligman, M. E. P. (2004). *Character strengths and virtues: A handbook and classification*. Oxford University Press.

Rosmarin, D., Alper, D., & Pargament, K. (2016). Religion, spirituality, and mental health. *Encyclopedia of Mental Health*. https://doi.org/10.1016/b978-0-12-397045-9.00190-7

Rothenberg, W. A., Hussong, A. M., Langley, H. A., Egerton, G. A., Halberstadt, A. G., Coffman, J. L., Mokrova, I., & Costanzo, P. R. (2016). Grateful parents raising grateful children: Niche selection and the socialization of child gratitude. *Applied Developmental Science, 21*(2), 106–120. https://doi.org/10.1080/10888691.2016.1175945

Rusdi, A., Sakinah, S., Bachry, P. N., Anindhita, N. P., & Hasibuan, M. a. I. (2021). The development and validation of the Islamic gratitude scale (IGS-10). *Psikis: Jurnal Psikologi Islami*, *7*(2), 120–142. https://doi.org/10.19109/psikis.v7i2.7872

Saxena, A., Garg, N., Punia, B., & Prasad, A. (2020). Exploring role of Indian workplace spirituality in stress management: A study of oil and gas industry. *Journal of Organizational Change Management, 33*(5), 779–803. https://doi.org/10.1108/jocm-11-2019-0327

Shankar, R. (2014). *Celebrating silence*. Van Duuren Media.

Sharma, N., Pathak, A., Lavanya, B. L., Garg, N., & Lata, K. (2022). Exploring the psychometric properties of personal optimism and self-efficacy optimism-extended (POSO-E) scale among Indian teachers. *Benchmarking: An International Journal*. https://doi.org/10.1108/bij-01-2022-0054

Sommers, S., & Kosmitzki, C. (1988). Emotion and social context: An American-German comparison. *British Journal of Social Psychology*, *27*(1), 35–49. https://doi.org/10.1111/j.2044-8309.1988.tb00803.x

Tudge, J. R., Freitas, L. B., & O'Brien, L. T. (2015). The virtue of gratitude: A developmental and cultural approach. *Human Development, 58*(4–5), 281–300. https://doi.org/10.1159/000444308

Watkins, P. C., Woodward, K., Stone, T., & Kolts, R. L. (2003). Gratitude and happiness: Development of a measure of gratitude, and relationship with subjective well-being. *Social Behavior and Personality: An International Journal, 31*(5), 431–451. https://doi.org/10.2224/sbp.2003.31.5.431

Publisher's Note Springer Nature remains neutral with regard to jurisdictional claims in published maps and institutional affiliations.

Springer Nature or its licensor (e.g. a society or other partner) holds exclusive rights to this article under a publishing agreement with the author(s) or other rightsholder(s); author self-archiving of the accepted manuscript version of this article is solely governed by the terms of such publishing agreement and applicable law.

JMEPEG
https://doi.org/10.1007/s11665-023-08302-9

©ASM International
1059-9495/$19.00

TECHNICAL ARTICLE

Effect of Intermetallic Compounds on Mechanical and Microstructural Properties of Dissimilar Alloys Al-7Si/AZ91D

Husain Mehdi, Sumit Jain, Velaphi Msomi, Sipokazi Mabuwa, and Chandrabhanu Malla

Submitted: 17 October 2022 / Revised: 7 February 2023 / Accepted: 9 April 2023

AZ91D (Mg alloy) and A356 (Al-7Si) were fabricated by friction stir welding (FSW) at different process parameters, affecting the welded joints' mechanical properties. The results demonstrated that preferred properties were observed when AZ91D was placed on the advancing side. Mechanical properties, microstructure, elemental mapping, and fractography were analyzed by optical microscopy (OM), scanning microscopy (SEM), and energy-dispersive x-ray spectrograph, etc. The primary Al and Mg diffraction peaks were present, and $Al_{12}Mg_{17}$ and Al_3Mg_2 were intermetallic in all of these joints. This occurred due to the inter-diffusion performance of Al and Mg atoms in the welding and formed intermetallic compounds. The $Al_{12}Mg_{17}$ phase mixed with the Mg phase has preferentially lowered to the weld surface where the AZ91D plate was placed, and legitimate liquation may occur and be observed in the eutectic microstructures. The maximum ultimate tensile strength (UTS) of 90.57 MPa was perceived at tool rotational speed (TRS) of 900 rev/min with a traverse speed (TS) of 100 mm min^{-1}, and the lower UTS (76.63 MPa) was found at TRS of 700 mm min^{-1}.

Keywords friction stir welding, microhardness, microstructure, tensile strength

1. Introduction

Important structural metals such as Mg and Al alloys are extensively employed in various automobile and aerospace applications. Mg and Al have combined to create greater design flexibility for their wide-ranging uses (Ref 1). In the past, several fusion welding procedures have been tried. However, their significant coarser grains, welding defects, intermetallic compounds (IMCs), and loss of strength have made them unsatisfactory (Ref 2, 3). It is not easy to join Al and Mg alloys using fusion welding due to the massive differences in their metallurgical and physical characteristics. Due to the formation of micro-defects and brittle IMCs in the welded zone, the fusion joining process cannot produce sound Mg-Al hybrid joints as a result of the dispersion of IMCs being disseminated under the combined action of high strain rate, low processing temperature, and severe plastic deformation during FSW. The worst strength of Mg-Al welded joints was observed due to brittle failure and IMCs. Although IMCs' elimination was quite challenging, reducing their thickness may be feasible (Ref 4). Much work has focused on the metallurgical characterization and materialization of the IMCs in the welded area. The FSW process has been primarily applied to join non-ferrous materials such as Mg and Al alloys. Both alloys have many attractive mechanical and physical properties. Al-7Si and AZ91D are widely used in automotive transmission pulleys, fuel tanks, aircraft joints, household equipment, aerospace, shipbuilding, and automotive sectors and have many applications for using joints between these metals (Ref 5-7). Various research articles have reported on different welding alloys by FSW (Ref 8-10).

While joining Al-Mg alloys, the main disadvantage is the materialization of brittle IMCs. The influence of TS and rotational speed on the FSWed joints of Al-Mg alloys was studied, where Mg alloys were kept on the advancing side (AS). The welding parameters (TRS, TS, tool offset, and material position) affected the joint efficiency of the FSWed joints of Mg-Al alloys. AZ31 should be kept on the retreating side (RS), while AA2024 should be placed on AS to improve joint efficiency (Ref 11). While aluminum alloy 6064 should be on the RS in the FSW of AZ31 and AA6064 (Ref 12), various cracks and defeats were observed when the FSW tool was placed at the center of both plates (Ref 4). The sharp edges of the parent metals are kept under high pressure during the FSW. Metallurgical bonds with each other can form due to the oxygen-free surface. However, a small oxide layer will remain in the welded region (Ref 13). The past work contains several reports on joining Al to Mg (Ref 14-19) by FSW and observing the materialization of the brittle IMC at the Mg-Al welded region, resulting in high residual stresses and microhardness at the welding interface. Numerous studies have been done on heterogeneous materials' interfaces to analyze their mechanical efficiency. Under certain conditions, the FSW may produce a complex nonlinear weld interface. The FSW with a tortuous weld was reported in the Mg-Al

Husain Mehdi, Mechanical Engineering Department, Meerut Institute of Engineering and Technology, Meerut, India; **Sumit Jain**, Mechanical Engineering Department, Delhi Technological University, New Delhi, Delhi, India; **Velaphi Msomi** and **Sipokazi Mabuwa**, Mechanical Engineering Department, Cape Peninsula University of Technology, Cape Town, South Africa; and **Chandrabhanu Malla**, Mechanical Engineering Department, Radhakrishna Institute of Technology and Engineering, Bhubaneswar, India. Contact e-mail: husainmehdi4u@gmail.com.

Published online: 19 May 2023

alloys (Ref 16, 18). The geometrically complex interface can enhance joint efficiency by 20-40% (Ref 20).

Many studies have revealed that brittle IMCs, including Al_3Mg_2 and $Al_{12}Mg_{17}$, were frequently responsible for the Al-Mg FSW joint's limited strength. $Al_{12}Mg_{17}$ may have been formed via constitutional liquation and increased joint hardness (Ref 21). Al_3Mg_2 and $Al_{12}Mg_{17}$ in the SZ might weaken the joint due to the generation of the liquid film (Ref 22). The joints' hardness and tensile strength distribution were affected by a thin IMC layer consisting of Al3Mg2 and $Al_{12}Mg_{17}$ along the interface (Ref 23). After curing and welding, the adhesive bonded zone is generated at the weld periphery. The residual adhesive was thermally decomposed during the welding, developing a path between the dissimilar alloys for SZ growth and formation. Lots of heat is employed for SZ growth during thermal decomposition resulting in heat accumulation and severe defects caused by the surrounding adhesive thickening IMC layers (Ref 24, 25). The segregated residual oxides at the dissimilar welded joint interface act as diffusion barriers preventing nucleation, intermetallic reaction, and growth of IMC layers (Ref 26). Due to high temperature, the IMCs $Al_{12}Mg_{17}$ and Al_3Mg_2 and non-equilibrium phase Al-Mg in the upper portion of the SZ formed during the solidification process. The Al_3Mg_2 precipitation in the lower and middle of the SZ resulted from the mobility of the Mg atom to the grain boundaries under severe plastic deformation (Ref 27). There are three stages of growth and formation of IMCs at the weld interface. The 1st stage involves the formation of a supersaturated solid solution due to atom diffusion in the interface. When the produced solid solution reaches saturation at the requisite pressure and temperature, it will change into IMCs in the 2nd stage. Finally, in the third stage, the solute atoms diffuse into the gradually growing IMCs layers. The high temperature, immense strain, strain rate, and high pressure promote the IMCs layer's growth in the FSW process (Ref 28).

In advanced industries, particularly in transportation, automobile, aerospace, and power energy, there is a considerable drive toward using multi-layer structures to achieve enhanced performance, cost, and weight reduction. Dissimilar materials such as Al/Mg alloys are functional materials whose welding quality is being explored to enhance the material performance. Combining Al and Mg alloys can help the modern push for lightweight structure hybridization. In contrast, the welding of Al and Mg alloys is complicated owing to the difference in their mechanical and physical properties (Ref 29). The literature mentioned above revealed that no systematic research had been done on the rotational tool speed on the metallurgical characterization of Al-7Si and AZ91D butt joints. The rotational tool speed modifies the flow and material mixing of dissimilar alloys. So, in this paper, FSW was used to join AZ91D and Al-7Si alloys; the mechanical and metallurgical characteristics of the FSWed joints were studied with different parameters. The process parameters could effectively enhance the weld strength. The reasons are reduced IMC concentration, improved material flow, and intense material mixing.

2. Materials and Methods

Samples with a dimension of 200 × 40 × 6.35 mm of extruded Al-7Si and AZ91D were welded in this experiment via FSW. The chemical composition and mechanical properties of the parent metals Al-7Si and AZ91D are revealed in Tables 1 and 2. Before FSW, the steel wire brush removed the oxide films on the base plates, and acetone was employed to remove the dust and oil from the base plates. The FSW tool was made of H13 tool steel with a 19.5-mm and 6-mm shoulder diameter and a pin diameter of 5.5-mm tool pin length. During the FSW, Al-7Si was placed at the AS., and AZ91D was placed at the RS. These two plates were welded according to the processing parameters (range of TRS 700-1000 rev/min, and constant TS of 100 mm min^{-1}) with a constant TS of 100 mm/min by FSW.

Figure 1 presents the schematic diagram of FSW. The motion actuator creates the necessary hydraulic pressure during the welding process. Welding trials were accomplished with an AZ91D plate on both AS. and RS. and a tool offset of 0-2 mm toward Al-7Si. The EDM machine cut the welded plates per the ASTM E8 standard for tensile test specimens, and the tensile test was conducted on the universal testing machine (UTM). After the tensile test, the fractured surface was examined by the microscopic scanning (SEM) machine (ZEISS EVO 50). The Vicker hardness machine examined the hardness per the ASTM 381–41 standard. A total of 20 indentations were measured with 300 g from the AZ91D to the Al-7Si with 1-mm spacing between the points. A loading time of 10 s was used. The OM specimens were sliced using an electrical discharge machine perpendicular to the FSW direction and polished with silicon carbide emery sheets of grit sizes from 300 to 2200, followed by Al_2O_3 powder, and etched with a solution of 5% HF., 10% H_2SO_4, and 85% H_2O for 20-30 s from the Al-7Si side. The AZ91D side of the welded joint was etched with 2 mL of glacial acetic acid, 2 mL of water, and 14 mL of picric acid for 6 s. Additionally, following a brief period of swabbing, the samples were cleaned with ethanol. After that, the polished surface was analyzed by an Olympus OM machine to measure the IMC layer thickness. The BRUKER D8 ADVANCE XRD machine carried out the phase detection based on CuKα radiation at 1.52 Å. The conversion of the diffraction peaks to d-spacing enables metal identification since each material has a distinct d-spacing.

3. Results and Discussion

3.1 Aluminum and Magnesium Phase Diagram

The equilibrium phase diagram includes two solid terminal solutions, i.e., Mg(Al) and Al(Mg), and two IMCs, $Al_{12}Mg_{17}$ and Al_3Mg_2. At room temperature, the $Al_{12}Mg_{17}$ and Al_3Mg_2 phases will occur when Al and Mg are in the stir zone (SZ) with the same weight percentage. But the material flow is quite difficult for dissimilar alloys during the FSW. Thus, the presence of IMCs leads to poor weld strength. The elongated and coarse eutectic phases were broken during the welding process into fine particles. Dynamic recrystallization (DRX) depends on the dispersion and size of the particles. The non-dissolved and coarse particles accelerate DRX, while the tiny dispersions can impede recrystallization by preventing the early development of DRX grains (Ref 22, 30); numerous investigations have noted the Zener pinning effect's ability to inhibit grain development. The phase diagram of aluminum and magnesium (Ref 33) was used to elucidate the welded zone's microstructure. Al-7Si and AZ91D were not pure, while the

Table 1 Chemical composition of AZ91D and Al-7Si

Materials	Al	Si	Mn	Zn	Cu	Fe	Ti	Mg
AZ91D	8.95	0.09	0.28	0.65	0.02	0.01	0.02	Balance
Al-7Si	Balance	7.01	0.04	0.06	0.12	0.14	0.11	0.28

Table 2 Mechanical properties of AZ91D and Al-7Si

Alloys	UTS, MPa	YTS, MPa	% Elongation	Hardness, HV
AZ91D	195	122	19.5	66
Al-7Si	242	136	12.4	102

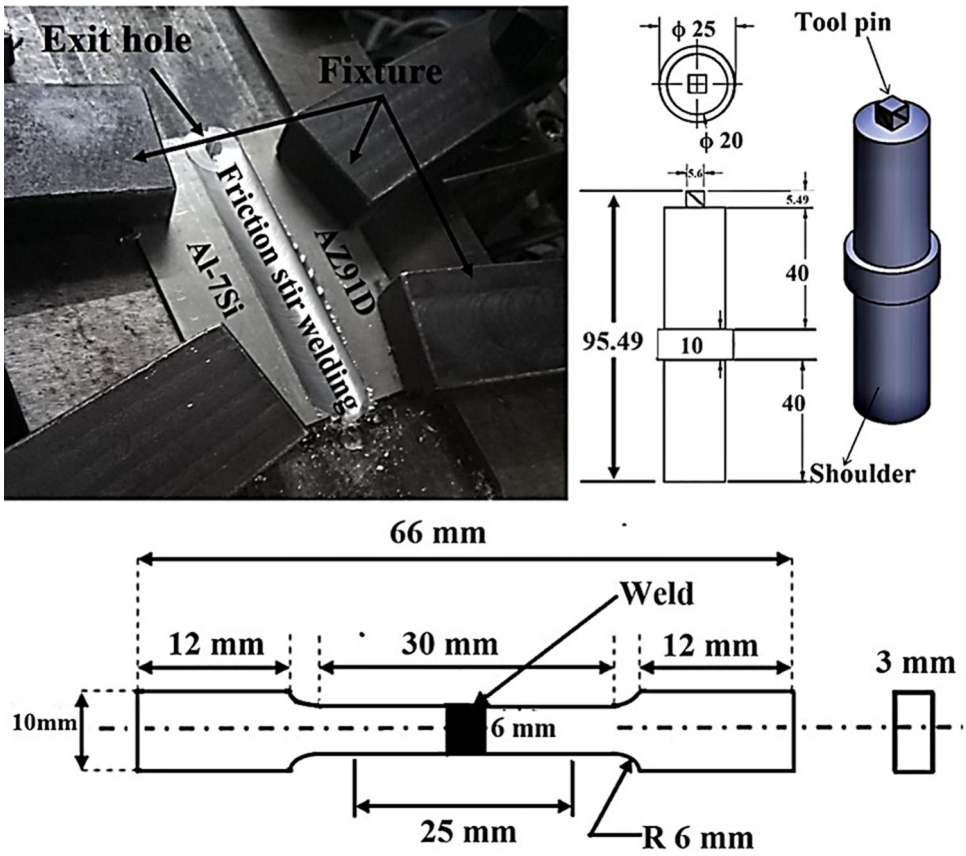


Fig. 1 Schematic diagram of FSW

Mg-Al phase diagram can easily understand the materialization of IMCs ($Al_{12}Mg_{17}$ and Al_3Mg_2) and the welding process of different alloys. The appearance of intermetallic and metallic compounds depends on the base metals' cooling speed, welding process, and chemical composition (Ref 31, 32). During FSW, the Al12 Mg17 lamellar precipitation phase discontinuously precipitates near the eutectic β-Al12 Mg17, located at the boundary of the new form of refined grains, hindering the mobility of the grains boundary (Ref 15, 33).

3.2 Microstructure Analysis

The optical microstructure reveals the metal dispersion and IMC layer of the FSWed joint of Al-7Si and AZ91D at high TRS, as revealed in Fig. 2. When the Al-7Si was positioned on the AS with 0 tools offset, then the surface produced a heavy flash, zigzag line, uneven, insufficient intermixing, and expelled out of the welded region. The weld appearance became interlocked with less irregularity at 0.4-mm tool offset from the Al-7Si side. When the AZ91D was placed on the AS

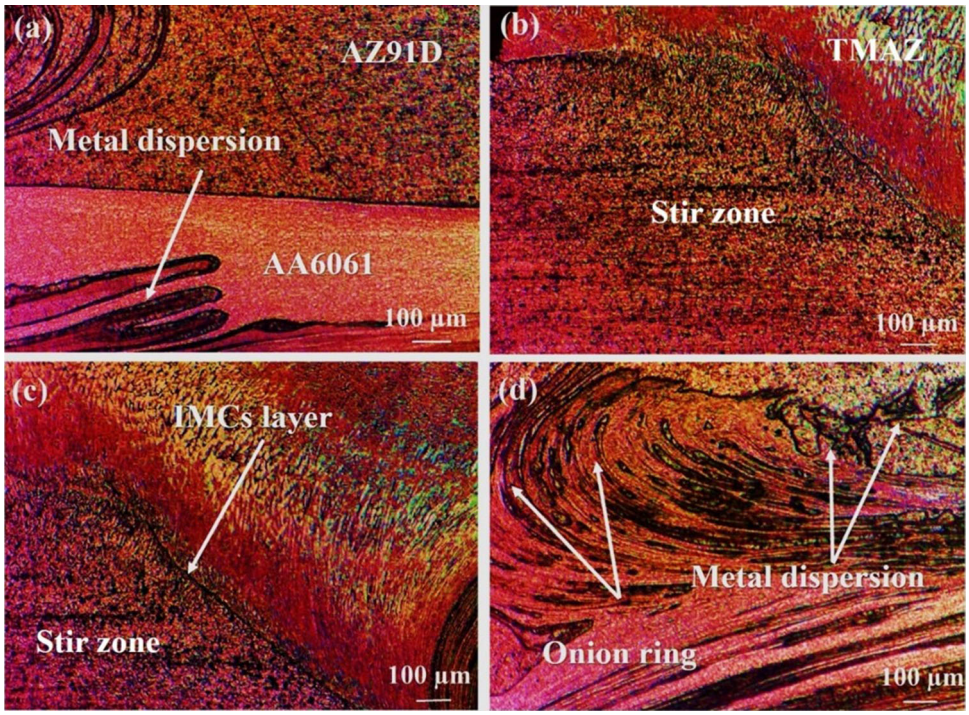


Fig. 2 Metal dispersion and IMC layer of the FSWed joint of Al-7Si and AZ91D at high TRS

with zero tool offset, the surface defect was not found, and the surface of the welded region looked smooth with semicircular traces. The maximum weld offset UTS was accomplished at the tool pin of 0.2 mm toward the harder metal. Hard material particles were fragmented in the soft material matrix at a high offset. This fragmentation was large enough to form voids, decreasing the weld UTS in the bimetallic welded joint via FSW (Ref 34). The optical microstructure of the FSWed joint with different welding zones and base metals (AZ91D and Al-7Si) is shown in Fig. 2. The tensile properties of AZ91D and Al-7Si depend on the distribution of Mg-Al IMCs. For enhancement of joint efficiency, the precipitates must be suppressed. The effect of tool offset on Al-7Si and AZ91D welded joints was considered, and it was found that with zero offsets, the weld appearance was smooth, with a minimum amount of flash formation during the fabrication process (Ref 35). The material flow underneath the rotating tool pin promoted a swirl zone, a vortex flow pattern (Ref 36). The AS material near the rotating tool pin adjacent to the tool shoulder surface is located in the rotational flow around the rotating pin. It becomes trapped by the metal's radial influx at the rotating pin's top surface.

The FSWed joints were not symmetrical at the weld center due to tool rotation. The materials were displaced downward in the S. Z's inner area and upward at its outer perimeter by the onion wing flow that surrounds the rotating tool (Fig. 3) (Ref 30). The SZ on the AS was characterized by substantial mixing of Mg and Al alloys (Ref 15, 37-39), with more severe mixing perceived on the AS. In Fig. 3a-d, the material flow from the RS to the AS was noticeable in the aluminum-rich elongated bands material, which was expatriated from the upper to the bottom side of the magnesium alloy plate (Ref 40). The FSWed joints with higher TRS reveal further pronounced vertical transport through this area (Ref 41, 42). The microstructure at the SZ observed recrystallized grains with delicate IMC phases. Various intermixing phases at the SZ are revealed in Fig. 4a-d. On the cross-section of the FSWed joints, there are two main zones of material flow: one at the bottom of the tool pin, which displaces material to the AS when it penetrates the lowest sheet, and another on the surface below the tool shoulder. When a rotating tool is used in a pin-driven region, the material flows with each rotation, layer by layer. The welding parameters such as T.S and TRS significantly influenced the microstructure and developed the SZ. When FSW combined aluminum and magnesium alloys, the chaotic mixing of Al-7Si and AZ91D was seen, where lamellae were created comprising different phases, leading to a similar intercalated structure (Ref 43-46). Due to the material being absorbed into a rotating tool on a tiny scale, lamellae development was noticed. The microstructure in the SZ in which DRX occurred consisted of grains which were equiaxed and smaller compared to the severely elongated base metal microstructure. The grain misorientation angle for the DRX zone revealed a flatter distribution. Some grains in the SZ were left with dislocation tangles at the grain boundaries resulting in recrystallization that may still need to be completed. However, these grains resemble cells rather than fully recovered grains. The majority of grains have no dislocation tangles with clear boundaries. The grain size in the DRX region was perceived to be stable at the SZ of FSWed joints of AZ91D and A-7Si.

Figure 4 demonstrates the SEM image of the FSWed joint of AZ91D and Al-7Si at TRS of 700-1000 rev/min with a TS of 100 mm/min at the SZ, and it was observed that there was fiercely intermixing at the interface of AZ91D and Al-7Si alloys. The layer of metal oxide generated at the lower surface of the base plate was fragmented (Ref 47) under the effect of acoustic action. A tight gripping of both base metals across the interfaces was observed due to metal-to-metal higher-order interaction (Ref 48). The recrystallization was perceived in the SZ and resulted in refined grains, so the weld fabrication via

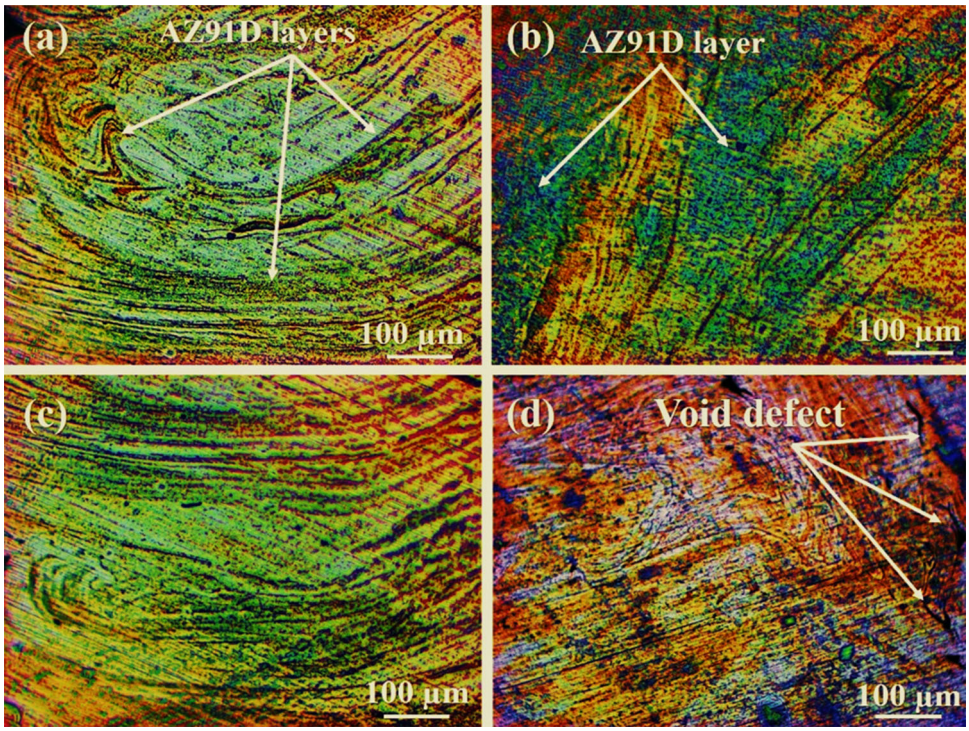


Fig. 3 Optical images of welded joint at the SZ zone, (a) TRS of 700 rev/min, (b) TRS of 800 rev/min, (c) TRS of 900 rev/min, and (d) TRS of 1000 rev/min

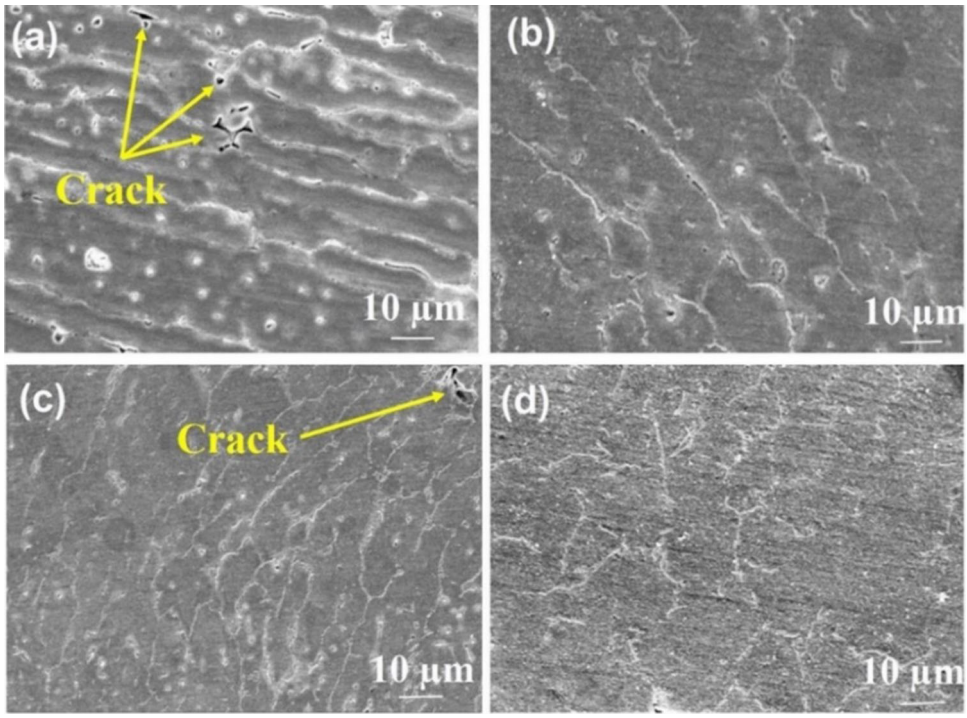


Fig. 4 SEM images of FSWed joint of AZ91D and Al-7Si at SZ, (a) TRS of 700, (b) TRS of 800, (c) TRS of 900 rev/min, and (d) TRS of 1000 rev/min

acoustic assistance may reveal higher strength at high TRS. Many refined and equiaxed grains were found in the SZ at high TRS. High-angle grain boundaries with finer and recrystallized grains in the SZ were produced by DRX, which was made possible by the high peak temperature associated with plastic deformation. Due to the increased strain and immense heat gradient from the tool shoulder to the upper surface of the welded joint of Al-7Si and AZ91D, many fragmented grains continued to exist in the SZ (Ref 49, 50). Due to the temperature plastic strain's heterogeneity, a heterogeneous

microstructure generates. The SZ perceived equiaxed and refined grain structure due to the DRX, which was brought on by plastic deformation mixed with immense temperature (Ref 9). Extreme heat in the SZ causes the grains to recrystallize while other grains nucleate. They were divided into little, equally spaced grains by the spinning tool. Because the heat from the bottom SZ could quickly move to the base plate and backing plate, the temperature of the higher SZ was relatively high. The grains in the bottom SZ have less time to grow because of the reduced temperature. Due to the high energy, the joints may experience continuous DRX and intermittent during the hot deformation process (Ref 51). Figure 5 and 6 shows the EDX and elemental mapping of the major alloying elements of Al, Mg, Zn, Si, Mn, and Cu acquired from the marked regions and evenly distributed in the SZ. The aluminum and magnesium percentages on the grains boundary were lower than within the grains and confirmed that these flow patterns were composed of Mg (green color) and Al (red color) shear bands; moreover, Al-7Si and AZ91D were swirled together and generated an intermittent lamellar structure. The refine grain size in the SZ in FSWed joints is due to grain stirring and DRX.

In contrast with the HAZ, which was related to a thermal cycle and modest strain rate, the TMAZ region also observed refined grains. The temperature experiences different levels of plastic strain as it passes from the weld center to the base materials. A substantial amount of plastic strain was experienced by the material at the SZ, which increases the temperature relative to the other zones (TMAZ and HAZ).

Figure 7 demonstrates the TEM images of the SZ. The TEM samples were sliced from the weld center, and the thinnest portion of the specimen was near the IMC layer. The recrystallized grains are compared to the elongated grains, and a pertinent lack of dislocation and pinning of the precipitates within the grain boundaries in the recrystallized region seemed. The deep penetration welding was too delicate to agree with proper penetration, as apparent from the various cracks. The elongated and coarse grains comprising uniform dislocation dissemination pinned by the preferred direction and hardening precipitates are visible. The dislocation orientation was parallel to the grains' boundary in this zone. The presence of Al-7Si and AZ91D at the SZ was reliable with the portion of the Mg-Al phase resulting in eutectic reaction Al + Al_3Mg_2 (450°) and Mg + $Al_{12}Mg_{17}$ (435°). The IMCs (Al_3Mg_2 and $Al_{12}Mg_{17}$) were predominant on both sides. The primary Al and Mg diffraction peaks, $Al_{12}Mg_{17}$ and Al_3Mg_2, were present in these joints. This occurred due to Al and Mg atoms' inner-diffusion behavior in welding and forming IMCs. During welding, the original grains and sub-grains of the parent metals were replaced with equiaxed and refined grains formed by a DRX.

3.3 XRD Analysis

The phase composition of the FSWed joint of AZ91D and Al-7Si with different parameters is demonstrated in Fig. 8. The obtained results reveal the existence of brittle IMCs, which led to cracks after welding. The primary Mg and Al diffraction peaks were present, and $Al_{12}Mg_{17}$ and Al_3Mg_2 were intermetallic in all of these joints. This occurred due to the inner-diffusion behavior of Mg and Al atoms in the welding and the materialization of IMCs. The temperature of both the eutectic

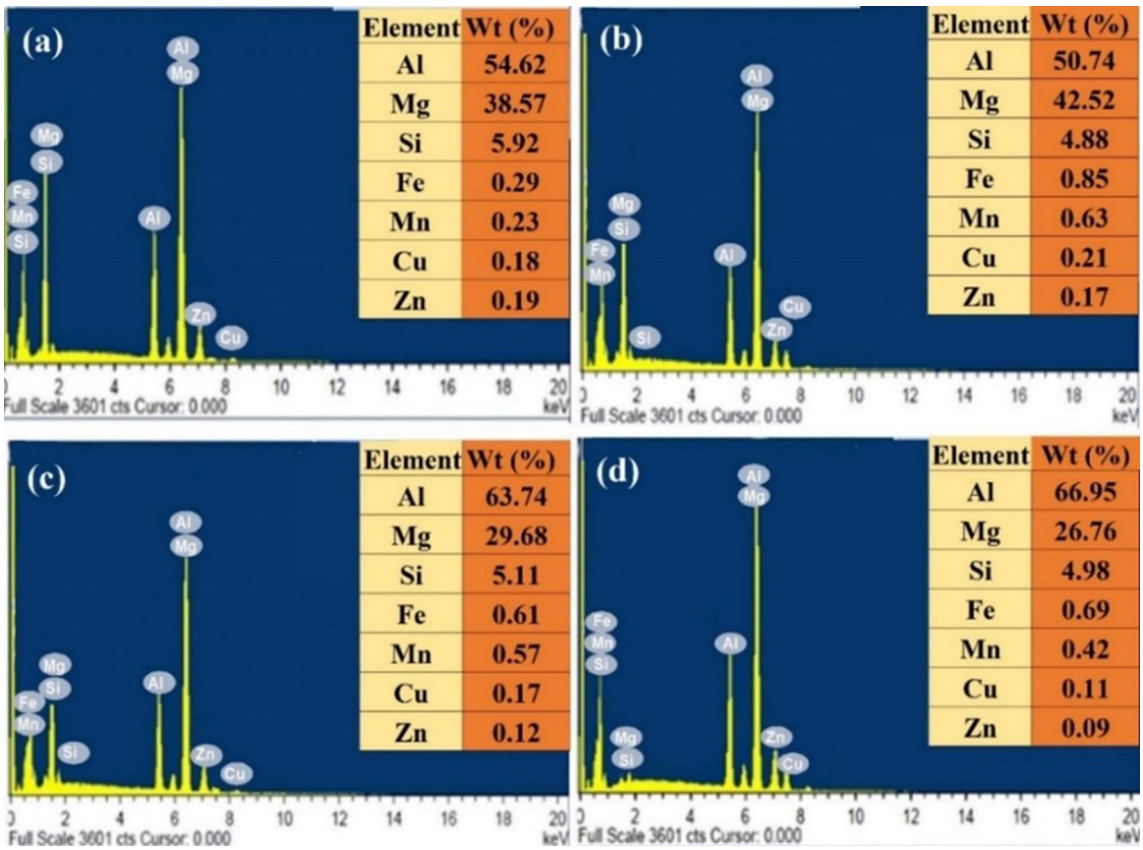


Fig. 5 EDX analysis of FSWed joint of AZ91D and Al-7Si, (a) TRS of 700, (b) 800, (c) 900, and (d) 1000 rpm

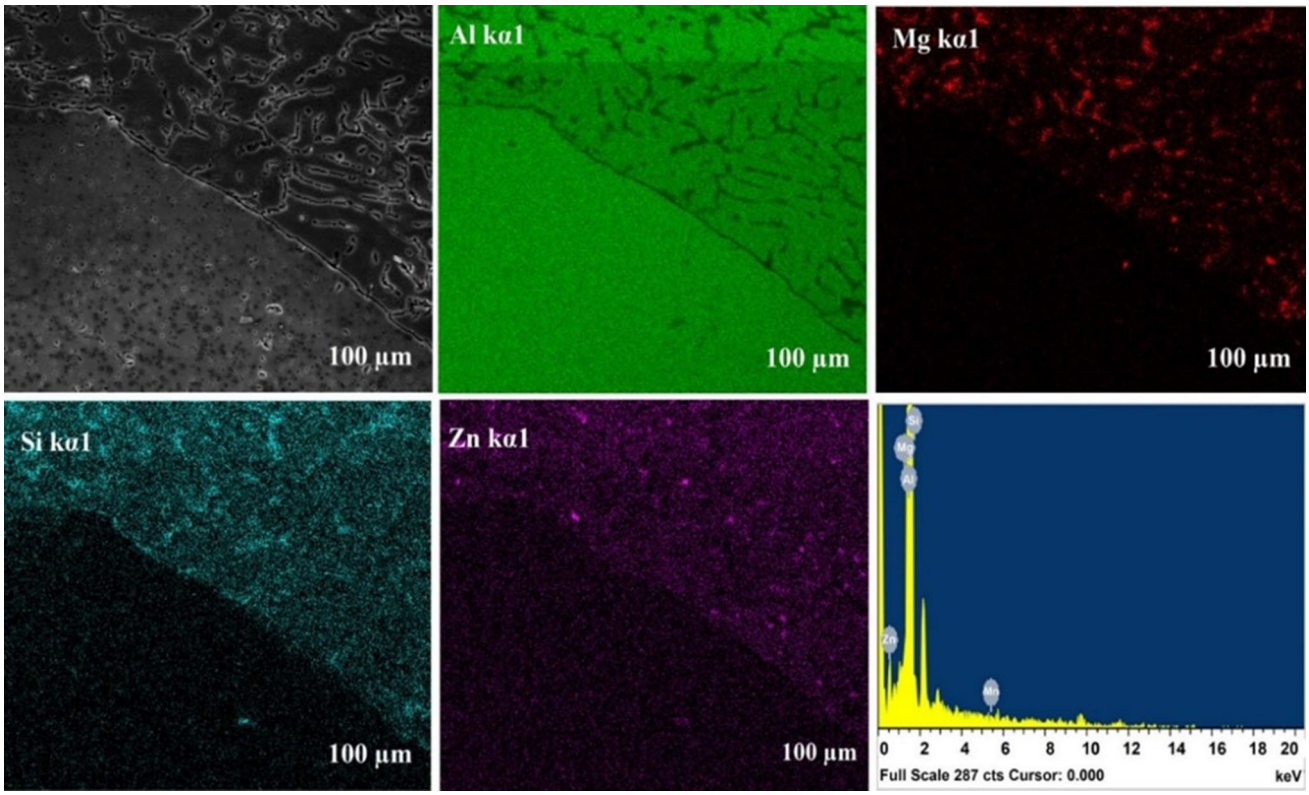


Fig. 6 Elemental mapping of FSWed joint of Al-7Si and AZ91D

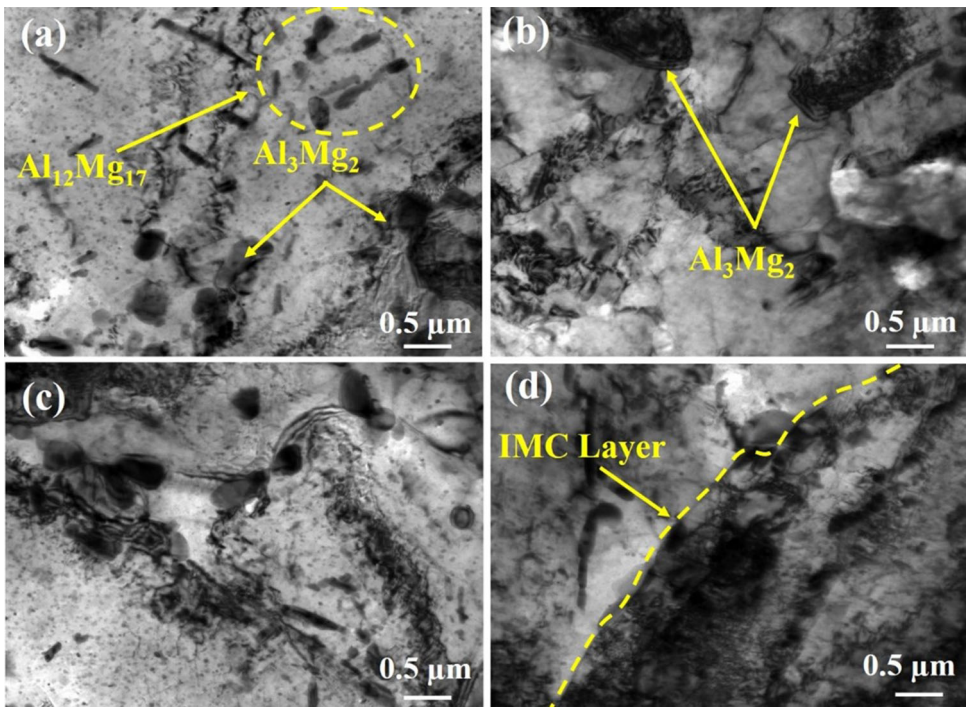


Fig. 7 TEM images of the FSWed joint of AZ91D and Al-7Si at SZ, (a) TRS of 700, (b) 800, (c) 900, and (d) 1000 rpm

Al + Al_3Mg_2 (450°) and Mg + $Al_{12}Mg_{17}$ (435°) has potentially been exceeded as per the binary phase diagram (Ref 33, 52). The IMCs (Al_3Mg_2 and $Al_{12}Mg_{17}$) were predominant on both sides. The IMC (Al_3Mg_2) remained in the lower portion of the SZ, near the Al-7Si plate.

In contrast, the $Al_{12}Mg_{17}$ phase mixed with the Mg phase has specially lowed to the joining surface where the AZ91D material was placed, and liquation may have occurred and been observed in the eutectic microstructures. This may occur due to the high concentration of aluminum, the high viscosity, and the

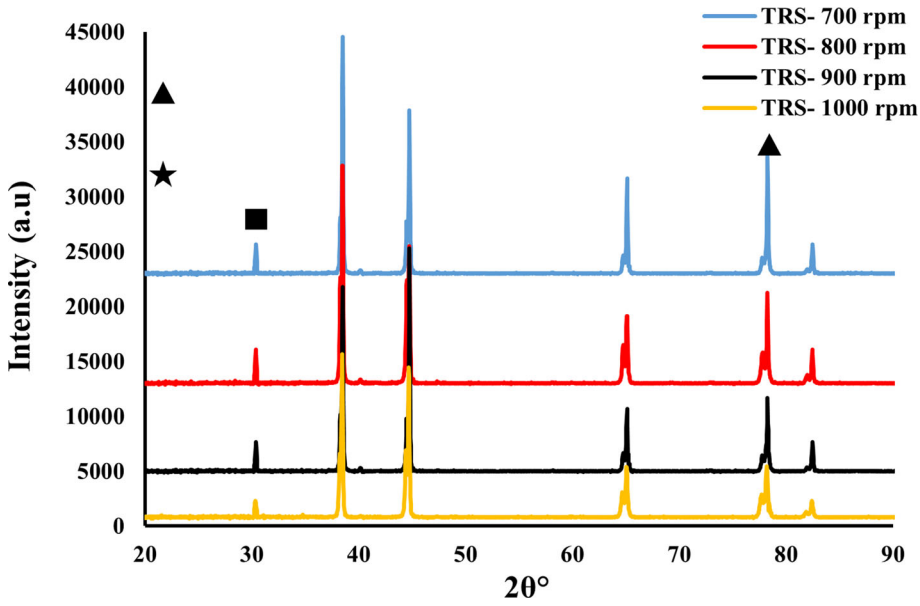


Fig. 8 XRD analysis of FSWed joints of Al-7Si and AZ91D at different tools rotational speed

high temperature in the Al + Al_3Mg_2 and $Al_{12}Mg_{17}$ intermetallic, which may constrain intermixing and material flow in the FSWed joint of Al-7Si and AZ91D. A thick layer of $Al_{12}Mg_{17}$ and Mg + $Al_{12}Mg_{17}$ was observed in the SZ with lower rotational and TS. This may be attributed to inappropriate processing parameters, leading to the IMCs materialization in the SZ, resulting in reduced mechanical properties. Low TS increases the heat input, which leads to the various IMC combinations in the SZ. At the same time, higher TRS and TS occur in the suspension of voids, sufficient intermixing of alloys, and dispersion of IMC were achieved. The SZ demonstrated the adequate mixing of AZ91D and Al-7Si and observed the high peaks of Al_3Mg_2 and $Al_{12}Mg_{17}$ at low TRS and the low peak at high TRS. The XRD peaks also predict the non-uniform dissemination of the IMCs in the SZ. The IMC Al_3Mg_2 has a higher hardness than the $Al_{12}Mg_{17}$ (Ref 53), so the hardness value of the SZ is greater than the parent material (AZ91D) shown in Fig. 8.

3.4 Effect of Heat Input

The heat input affects the material flow and formation of intermetallic compounds of FSWed joints of AZ91D and Al-7Si alloys. Let Ω, T, and t are the rotational tool speed (rpm), torque, and time (sec), respectively. The influence of tool rotational speed to the input heat Q_Ω (Jules) may be expressed as follows (Ref 54):

$$Q_\Omega = \int_0^t T\left(\frac{2\pi\Omega}{60}\right)\mathrm{d}t \qquad \text{(Eq 1)}$$

Similarly, let F_x be the force (N), and v_x be the traverse speed along the direction of the welding. The influence of the heat input to tool travel is as follows:

$$Q_F = \int_0^t F_x v_x \mathrm{d}t \qquad \text{(Eq 2)}$$

The total heat input may be expressed as follows:

$$Q = Q_\Omega + Q_F \qquad \text{(Eq 3)}$$

Table 3 Heat input at different process parameters of FSWed joint of AZ91D and Al-7Si

Tool rotation speed, rpm	Traverse speed, mm/min	Heat input(KJ)
700	100	7.23
800		8.95
900		14.25
1000		28.37

$$Q = \left(\frac{2\pi\Omega}{60}\right)\int_0^t M_Z \mathrm{d}t + \int_0^t F_x \mathrm{d}t \qquad \text{(Eq 4)}$$

Heat input increases as the rotational tool speed increase with constant traverse speed, as shown in Table 3. The heat input in dissimilar metal welding is lower than that of similar metal welding (Ref 22) because viscous dissipation influences to the heat input for Al-7Si but fewer for AZ91D. The high heat input (28.37 kJ) was achieved at a TRS of 1000 rev/min, while the minimum heat input (7.23 kJ) was observed at a TRS of 700 rpm. The input heat can be minimized by a reduction of rotational tool speed or higher traverse speed because of the direct correlation between rotational speed/traverse speed and heat input (Ref 55).

3.5 Tensile Strength

Tables 4 and 5 show the UTS and percent strain value of FSWed joints of AZ91D and Al-7Si at a 95% confidence interval. Only defect-free FSWed joints were analyzed for UTS. The ductility and strength of the FSWed joints are remarkably inferior to the parent material. The traverse and TRS affected the yield and ultimate UTS of the FSWed joints. The AZ91D alloy exhibited a UTS of 195 MPa, while the UTS of Al-7Si was perceived to be 508 MPa. The maximum UTS of 90.57 MPa was perceived at a TRS of 900 rev/min with a TS of 100 mm/min, and the lower UTS (76.63 MPa) was found at a TRS of 700 rev/min. The low UTS of the welded joint at low

Table 4 UTS of the FSWed joints of AZ91D and Al-7Si

Tool rotation speed, rpm	TS, mm/min	UTS, MPa			Mean UTS, MPa	Standard deviation (SD)	Standard error, SE	95% CI	
		Specimen 1	Specimen 2	Specimen 3				Minimum	Maximum
700	100	76.8	77.9	75.2	76.63	1.36	0.78	75.10	78.17
800		82.4	83.9	81.5	82.60	1.21	0.70	81.23	83.97
900		90.1	89.8	91.8	90.57	1.08	0.62	89.35	91.79
1000		86.5	85.7	87.8	86.67	1.06	0.61	85.47	87.87

Table 5 % strain of the FSWed joints of AZ91D and Al-7Si

Tool rotation speed (rpm)	TS, mm/min	Strain, %			Mean strain,%	SD	SE	95% CI	
		Specimen 1	Specimen 2	Specimen 3				Minimum	Maximum
700	100	13.5	12.8	13.2	13.17	0.35	0.20	12.77	13.56
800		13.9	14.2	14.3	14.13	0.21	0.12	13.90	14.37
900		14.5	14.4	14.7	14.53	0.15	0.09	14.36	14.71
1000		13.8	13.9	13.6	13.77	0.15	0.09	13.59	13.94

Table 6 Microhardness value at SZ of the FSWed joints of AZ91D and Al-7Si

Tool rotation speed, rpm	TS, mm/min	Hardness at SZ, HV			Mean hardness, HV	SD	SE	95% CI	
		Specimen 1	Specimen 2	Specimen 3				Minimum	Maximum
700	100	88	89	88	88.33	0.58	0.33	87.68	88.99
800		82	84	85	83.67	1.53	0.88	81.94	85.40
900		73	72	71	72.00	1.00	0.58	70.87	73.13
1000		81	78	77	78.67	2.08	1.20	76.31	81.02

TRS could be attributed to forming of a brittle layer of the β-phase (Ref 53). The failure of the welded joints was characterized by brittle material behavior at small stresses occurring in the elastic zone. The enhancement of mechanical properties was found at high TRS. At the same time, low TS reveals more liquidation and unfavorable material flow produced by the high heat, which might have been the reason for the lower joint strength (Ref 41, 42).

Additionally, at low rotational speed, low peak temperature, and low heat generation, the resulting insufficient interlocking and inadequate material flow were observed between the AZ91D and Al-7Si, leading to weak welded joints. Moreover, the IMC could not crack up at low TRS, and poor intermetallic particle dissemination caused lower strength (Ref 56, 57). The highest point efficiency of 46.44% was observed at the TRS of 900 rpm compared to the AZ91D. During the tensile test, the fracture occurred along the TMAZ and HAZ regions at high TRS, while the fracture occurred at the SZ at low TRS.

Due to inadequate heat generation, the fabrication of FSWed joint of Al-7Si and AZ91D at TRS of 700 and 800 rpm observed the tunnel defects and coarse grain structure. At 1000 rpm, excessive heat generation was noticed, leading to plasticized metal's improper and surplus flow. The FSWed joint at TRS of 900 rpm was found defect-free joint due to the adequate flow of the plasticized material around the rotating tool surface in a uniform and desirable manner leading to excellent mechanical properties of the welded joint. Beyond the TRS of 900 rpm, a surplus amount of flash and excessive input heat was observed, resulting in defective joints, which reveals that the proper combination of process parameters plays a significant role in enhancing the microstructure and mechanical properties of the welded joints.

3.6 Hardness Distribution

Table 6 and Fig. 9 demonstrate the microhardness value at a 95% confidence interval and the hardness distribution of the welded joints of AZ91D and Al-7Si along the transverse axis from the weld centre. The uneven microhardness distribution was observed in the SZ and measured at a maximum hardness of 88.33 HV in the SZ. The microhardness value in the SZ was inferior to the Al-7Si but higher than that of AZ91D. The lamellae and complex vortexes were responsible for the spikes and a wide variation in the hardness values in the welded region. The hardness value depends on the lamellae band. The hardness in the SZ was more significant than in the adjacent areas (HAZ and TMAZ). The HAZ reveals a minimum hardness inferior than the parent materials due to the softening of HAZ (Ref 58). The DRX in the SZ resulted in the

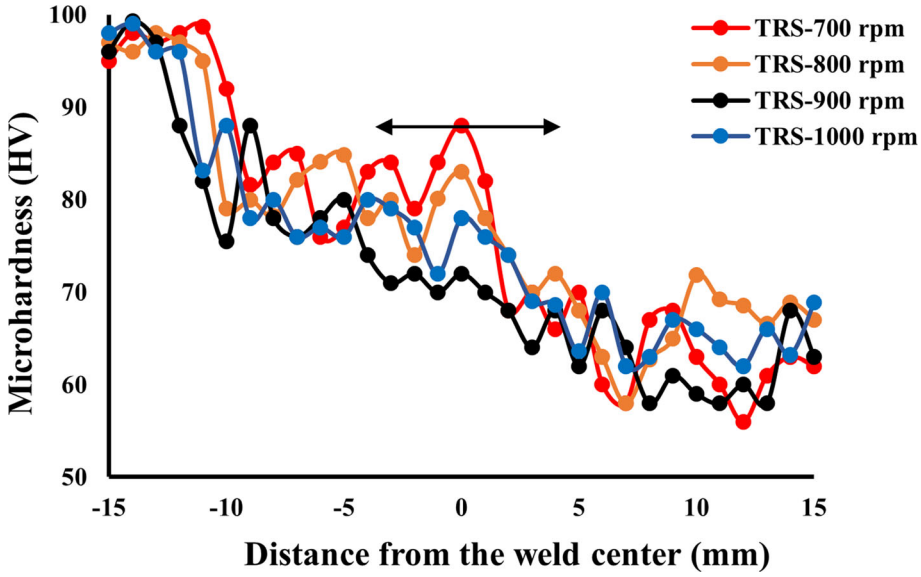


Fig. 9 Hardness variation of the FSWed joints of AZ91D and Al-7Si from the weld center

materialization of equiaxed and fine-grained structures, which may be a cause for the high microhardness.

Moreover, grain boundaries and dislocation density increase the intensity of plastic deformation in the SZ. Due to IMC materialization in the SZ, higher hardness values in the middle and lower regions of the SZ were observed as compared to the upper region (Ref 59). Due to excessive heat observed at high TRS and low TS, the welded joints experienced lower hardness. The AZ91D alloy is a precipitate-strengthening alloy and susceptible to high temperatures (more than 200 °C), so the welded joints were affected. The SZ hardness depends on the grain size as per the Hall–Patch correlation (Ref 60), so the UTS of the SZ may be associated with other factors, i.e., dislocation density and precipitations (Ref 61, 62), such as Al_3Mg_2 and $Al_{12}Mg_{17}$. It means that the welding temperature and heat input by FSW may minimize the brittle IMCs formation. As per the Hall–Petch equation, the microhardness in the SZ depends on the grain size of the FSWed region. The hardness enhances by the reciprocal root of the grain size of the metal. The correlation between the grain size and the hardness may be written as $H = \mathrm{H}_0 + k_H\, d^{-1/2}$, where d is the mean grain size diameter, H_0 and k_H are the constant (Ref 57).

3.7 Fractography

The SEM machine examined the fractography of the welded joints AZ91D and Al-7Si. Figure 10 reveals the fractured surface of the Al-7Si side of a tensile specimen and observes that the fracture appearance was not the same throughout the samples. The tensile test specimen fractured at the joint center where the microhardness value was sharp, according to Fig. 10. The large area of the fractured surface demonstrates brittle failure with cleavage facets, demonstrating that the dissimilar weld fractured through brittle failure. Low plasticity was attributed to the low toughness and high hardness generated at the weld interface. Along the perimeter of the tensile test specimen, the shear plane at 45° to the tensile axis was observable and found that various sized dimples in the welded region.

Conversely, the joining surface subjected to the low TRS revealed some pores and cracks at the root of some dimples, and these kinds of flaws are hazardous because they weaken the welded region. Ductile dimples, pores, deep dimples, and cleavage facets are present in the high TRS welded joints. The brittle failure occurs due to the continuous IMC layers in the AZ91D and Al-7Si interface, and its crack propagation may occur due to the brittle zone. While in the high TRS and TS, necking was perceived, and the rupture area showed a swirl-like pattern, indicating extensive plastic deformation. Since the IMCs layer will not be eliminated, some FSW techniques may have been employed to eliminate the destructive effect of the IMCs. The failure occurs in the SZ and TMAZ zone, which supports those processing parameters that significantly affect the FSWed joints and control microstructure, IMCs, and suppression of voids or cracks, which control the tensile characteristics. The tensile failure may occur through the Al-7Si into the inter-penetrating feature. The fracture surface demonstrates brittle failure at high TRS on the large area of the welded region, with confirmation of some ductility in the mid-section of the fracture surface. The microvoid coalescence on the fracture surfaces occurs in the areas where Al features were prolonged into configurations that generate mechanical locking.

4. Conclusions

The fabrication of dissimilar welded joints of AZ91D and Al-7Si was successfully done and observed the following conclusions.

- The SZ's uneven hardness distribution was caused by the intercalated microstructure produced in some areas of the SZ by a complex flow pattern. Extreme heat in the SZ causes the grains to recrystallize while other grains nucleate. They were divided into tiny, equally spaced grains by the rotating tool. The SZ displayed grain refinement as a

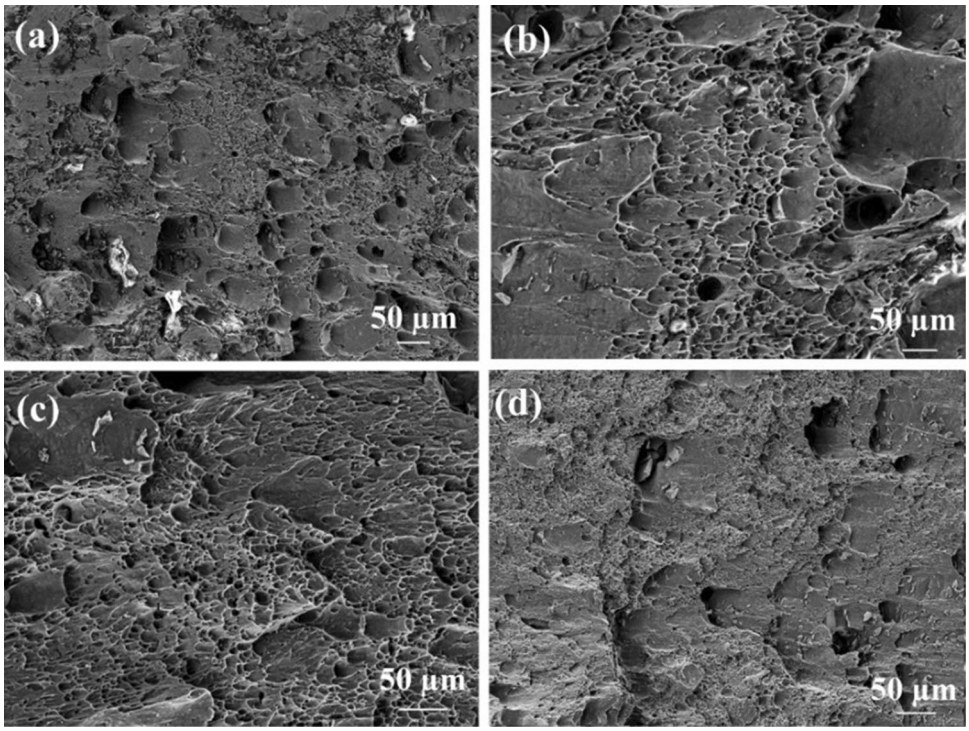


Fig. 10 Fractography of the FSWed joints of AZ91D and Al-7Si of different specimens

result of DRX.

- The maximum UTS of 90.57 MPa was perceived at a TRS of 900 rev/min with a TS of 100 mm/min, and the lower UTS (76.63 MPa) was found at a TRS of 700 mm/min. The excessive heat the joints endured while being subjected to high TRS and low TS led to the welded joints' reduced hardness. Since the AZ91D alloy is precipitate-strengthened, it is sensitive to temperatures exceeding 200 °C, which harms the joint.
- The SZ with lower rotational and TS observed a thick layer of IMCs ($Al_{12}Mg_{17}$ and Mg + $Al_{12}Mg_{17}$). This may be attributed to inappropriate processing parameters, leading to the intermetallic compound's materialization in the SZ, resulting in reduced mechanical properties. The $Al_{12}Mg_{17}$ phase mixed with the Mg phase has preferentially lowed to the weld surface where the AZ91D plate was placed, and constitutional liquation may occur and be perceived in the eutectic microstructures.
- The failure occurs in the SZ and TMAZ zone, which supports those processing parameters that significantly affect the FSWed joints and control microstructure, IMCs, and suppression of voids or cracks, which affect the tensile properties of the welded joints.

Conflict of interest

The authors declare no conflict of interest.

References

1. T.T. Zhang, W.X. Wang, W. Zhang, Y. Wei, X.Q. Cao, Z.F. Yan, and J. Zhou, Microstructure Evolution and Mechanical Properties of an AA6061/AZ31B Alloy Plate Fabricated by Explosive Welding, *J. Alloy. Compd.*, 2018, **735**, p 1759-1768. https://doi.org/10.1016/j.jallcom.2017.11.285
2. A.W. Hashmi, H. Mehdi, R.S. Mishra, P. Mohapatra, N. Kant, and R. Kumar, Mechanical Properties and Microstructure Evolution of AA6082/Sic Nanocomposite Processed by Multi-Pass FSP, *Trans. Indian Inst. Metals*, 2022 https://doi.org/10.1007/s12666-022-02582-w
3. B.L. Fu, G.L. Qin, F. Li, X.M. Meng, J.Z. Zhang, and C.S. Wu, Friction Stir Welding Process of Dissimilar Metals of 6061–T6 Aluminum Alloy to AZ31B Magnesium Alloy, *J. Mater. Process. Tech.*, 2015, **218**, p 38–47. https://doi.org/10.1016/j.jmatprotec.2014.11.039
4. A. Kostka, R.S. Coelho, J. dos Santos, and A.R. Pyzalla, Microstructure of Friction Stir Welding of Aluminium Alloy to Magnesium Alloy, *Scripta Mater.*, 2009, **60**, p 953–956.
5. S. Hirano, K. Okamoto, M. Doi, O. Kamura, M. Inagaki, and Y. Aono, Microstructure of the Interface in Magnesium Alloy to Aluminium Alloy Dissimilar Joints Produced by Friction Stir Welding, *Weld. Int.*, 2004, **18**, p 702–708.
6. C.L. Yang, C.S. Wu, and X.Q. Lv, Numerical Analysis of Mass Transfer and Material Mixing in Friction Stir Welding of Aluminum/Magnesium Alloys, *J. Manuf. Process.*, 2018, **32**, p 380–394. https://doi.org/10.1016/j.jmapro.2018.03.009
7. X.Q. Lv, C.S. Wu, C.L. Yang, and G.K. Padhy, Weld Microstructure and Mechanical Properties in Ultrasonic Enhanced Friction Stir Welding of Al Alloy to Mg Alloy, *J. Mater. Process. Tech.*, 2018, **254**, p 145–157. https://doi.org/10.1016/j.jmatprotec.2017.11.031
8. A.W. Hashmi, H. Mehdi, S. Mabuwa, V. Msomi, and P. Mohapatra, Influence of FSP Parameters on Wear and Microstructural Characterization of Dissimilar TIG Welded Joints with Si-rich Filler Metal, *SILICON*, 2022 https://doi.org/10.1007/s12633-022-01848-8
9. A.N. Salah, S. Mabuwa, H. Mehdi, V. Msomi, M. Kaddami, and P. Mohapatra, Effect of Multipass FSP on Si-rich TIG Welded Joint of Dissimilar Aluminum Alloys AA8011-H14 and AA5083-H321: EBSD and Microstructural Evolutions, *SILICON*, 2022 https://doi.org/10.1007/s12633-022-01717-4
10. H. Mehdi and R.S. Mishra, Mechanical Properties and Microstructure Studies in Friction Stir Welding (FSW) Joints of Dissimilar Alloy- A Review, *J. of Achiev. Mater. Manuf. Eng.*, 2016, **77**(1), p 31–40.
11. X.Q. Lv, C.S. Wu, and G.K. Padhy, diminishing Intermetallic Compound Layer in Ultrasonic Vibration Enhanced Friction Stir

Welding of Aluminum Alloy to Magnesium Alloy, *Mater. Lett.*, 2017, **230**, p 81–84. https://doi.org/10.1016/j.matlet.2017.05.090
12. S.A. Khodir and T. Shibayanagi, Dissimilar Friction Stir Welded Joints between 2024–T3 Aluminum Alloy and AZ31 Magnesium Alloy, *Mater. Trans.*, 2007, **48**, p 2501–2505.
13. J.C. Yan, Z.W. Xu, Z.Y. Li, L. Li, and S.Q. Yang, Microstructure Characteristics and Performance of Dissimilar Welds Between Magnesium Alloy and Aluminum Formed By Friction Stirring, *Scripta. Mater.*, 2005, **53**, p 585–589.
14. A.A. McLean, G.L.F. Powell, I.H. Brown, and V.M. Linton, Friction stir welding of magnesium alloy AZ31B to aluminium alloy 5083, *Sci Tech. Weld. Join.*, 2003, **8**(6), p 462–464.
15. Y.C. Chen and K. Nakata, Friction Stir Lap Joining Aluminum and Magnesium Alloys, *Scripta Mater.*, 2008, **58**, p 433–436.
16. M.A. Mofid, A. Abdollah-zadeh, and C.H. Gür, Investigating the Formation of Intermetallic Compounds During Friction Stir Welding of Magnesium Alloy to Aluminum Alloy in Air and under Liquid Nitrogen, *Int. J. Adv. Manuf., Technol.*, 2014, **71**, p 1493–1499. https://doi.org/10.1007/s00170-013-5565-x
17. P. Venkateswaran, Z.H. Xu, X. Li et al., Determination of Mechanical Properties of Al–Mg Alloys Dissimilar Friction Stir Welded Interface by Indentation Methods, *J. Mater. Sci.*, 2009, **44**, p 4140–4147. https://doi.org/10.1007/s10853-009-3607-4
18. M. Haghshenas and A.P. Gerlich, Joining of Automotive Sheet Materials by Friction-Based Welding Methods: A Review, *Eng. Sci. Technol., Int. J.*, 2018, **21**(1), p 130–148.
19. C. Liu, D.L. Chen, S. Bhole, X. Cao, and M. Jahazi, Polishing-assisted galvanic corrosion in the dissimilar friction stir welded joint of AZ31 magnesium alloy to 2024 aluminum alloy, *Materials Characterization*, 2009, **60**, p 370–376.
20. C.B. Jagadeesha, FSW between Al Alloy and Mg Alloy: the Comparative Study, *J. Mech. Behav. Mater.*, 2017, **26**(1–2), p 25–42.
21. Y.S. Sato, S.H.C. Park, M. Michiuchi, and H. Kokawa, Constitutional Liquation During Dissimilar Friction stir Welding of Al and Mg Alloys, *Scr. Mater.*, 2004, **50**, p 1233–1236. https://doi.org/10.1016/j.scriptamat.2004.02.002
22. V. Firouzdor and S. Kou, Al-to-Mg Friction Stir Welding: Effect of Material Position, Travel Speed, and Rotation speed, *Metall. Mater. Trans. A*, 2010, **41**, p 2914–2935. https://doi.org/10.1007/s11661-010-0340-1
23. A.H. Baghdadi, Z. Sajuri, S.N.F.M. Selamat, M.Z. Omar, Y. Miyashita et al., Effect of Intermetallic Compounds on the Fracture Behavior of Dissimilar Friction Stir Welding Joints of Mg and Al Alloys, *Int. J. Min. Met. Mater.*, 2019, **26**, p 1285–1298. https://doi.org/10.1007/s12613-019-1834-5
24. H. Zhao, G. Zhang, Q. Zhang, C. Zhang, and Y. Li, Joining Mechanism and Mechanical Properties of Metallic Bump Assisted Weld-Bonded (MBaWB) Joints of AA6061-T6 and Bare DP590, *J. Manuf. Process.*, 2020, **50**, p 204–215.
25. R. Chen, C. Zhang, M. Lou et al., Effect of Al-Si Coating on Weldability of Press-Hardened Steels, *J. Mater. Eng. Perform.*, 2020, **29**, p 626–636. https://doi.org/10.1007/s11665-020-04555-w
26. C. Zhang, J.D. Robson, S.J. Haigh et al., Interfacial Segregation of Alloying Elements During Dissimilar Ultrasonic Welding of AA6111 Aluminum and Ti6Al4V Titanium, *Metall. Mater. Trans. A*, 2019, **50**, p 5143–5152. https://doi.org/10.1007/s11661-019-05395-7
27. Xu. Yang, L. Ke, S. Ouyang, Y. Mao, and P. Niu, Precipitation Behavior of Intermetallic Compounds and their Effect on Mechanical Properties of Thick Plate Friction Stir Welded Al/Mg Joint, *J. Manuf. Process.*, 2021, **64**, p 1059–1069.
28. M.D. Sameer, Mechanical and Metallurgical Properties of Friction Stir Welded Dissimilar Joints of AZ91 Magnesium Alloy and AA 6082–T6 Aluminium Alloy, *J. Mag. Alloys*, 2019, **7**, p 264–271.
29. M. Paidar, S. Mehrez, B. Babaei, S. Memon, and H.M. Lankarani, Dissimilar Welding of AA5083 to AZ31 Mg Alloys Using Modifed Friction Stir Clinching Brazing, *Mater Lett*, 2021 https://doi.org/10.1016/j.matlet.2021.129764
30. J. Luo, S. Liu, R. Moslem Paidar, V. Vignesh, and S. Mehrez, Enhanced Mechanical and Tribological Properties of AA6061/CeO2 Composite Fabricated by Friction Stir Processing, *Mater. Lett.*, 2022, **318**, p 132210.
31. V. Firouzdor and S. Kou, Al-to-Mg Friction Stir Welding: Effect of Positions of Al and Mg With Respect to the Welding Tool, *Welding Journal (Miami, Fla).*, 2009, **88**, p 213S-S224.
32. H. Eftekharinia, A.A. Amadeh, A. Khodabandeh et al., Microstructure and Wear Behavior of AA6061/SiC Surface Composite Fabricated Via Friction Stir Processing with Different Pins and Passes, *Rare Met.*, 2020, **39**, p 429–435.
33. J. Mohammadi, Y. Behnamian, A. Mostafaei, H. Izadi, T. Saeid, A.H. Kokabi, and A.P. Gerlich, Friction Stir Welding Joint of Dissimilar Materials between AZ31B Magnesium and 6061 Aluminum Alloys: Microstructure Studies and Mechanical Characterizations, *Mater. Charact.*, 2015, **101**, p 189–207.
34. Baghdadi AH, Selamat NFM, Sajuri Z. Effect of tool offsetting on microstructure and mechanical properties dissimilar friction stir welded Mg-Al alloys, IOP Conference series: materials science and engineering, 238. IOP Publishing Ltd.; 2017:012018
35. T. Watanabe, H. Takayama, and A. Yanagisawa, Joining of Aluminium Alloy to Steel by Friction Stir Welding, *J. Mater. Process. Technol.*, 2006, **178**(1), p 342–349.
36. A. Gerlich, P. Su, M. Yamamoto, and T.H. North, Material Flow and Intermixing During Dissimilar Friction Stir Welding, *Sci. Technol. Weld. Joining*, 2008, **13**, p 254–264.
37. S. Liu, M. Paidar, and S. Mehrez, Development of AA6061/316 Stainless Steel Surface Composites via Friction Stir Processing: Effect of tool rotational speed, *Mater. Charact.*, 2022, **192**, 112215
38. R. Zettler, A.A.M. Da Silva, S. Rodrigues, A. Blanco, and J.F. Dos Santos, Dissimilar Al to Mg Alloy Friction Stir Welds, *Adv. Eng. Mater.*, 2006, **8**, p 415–421.
39. M. AbbasiGharacheh, A.H. Kokabi, G.H. Daneshi, B. Shalchi, and R. Sarrafi, The Influence of the ratio of "Rotational Speed/Traverse Speed" (ω/v) on Mechanical Properties of AZ31 Friction Stir Welds, *Int. J. Mach. Tools Manuf*, 2006, **46**, p 1983–1987.
40. R.S. Mishra and Z.Y. Ma, Friction Stir Welding and Processing, *Mater. Sci. Eng. R. Rep.*, 2005, **50**, p 1-78P.
41 H. Mehdi and R.S. Mishra, Microstructure and mechanical characterization of tungsten inert gas-welded joint of AA6061 and AA7075 by friction stir processing, *Proceed. Instit. Mech. Eng., Part L: J. Mater.: Des. Appl.*, 2021, **235**(11), p 2531–2546. https://doi.org/10.1177/14644207211007882
42. H. Mehdi and R.S. Mishra, Effect of Multi-Pass Friction Stir Processing and SiC Nanoparticles on Microstructure and Mechanical Properties of AA6082-T6, *Adv. Ind. Manuf. Eng.*, 2021, **3**, p 100062. https://doi.org/10.1016/j.aime.2021.100062
43. Y. Morisada, H. Fujii, T. Nagaoka, K. Nogi, and M. Fukusumi, Fullerene/A5083 Composites Fabricated By Material Flow During Friction Stir Processing, *Compos. A Appl. Sci. Manuf.*, 2007, **38**, p 2097–2101.
44. A.C. Somasekharan and L.E. Murr, Characterization of Complex, Solid-State Flow and Mixing in the Friction-Stir Welding (FSW) of Aluminum Alloy 6061–T6 to Magnesium Alloy AZ91D Using Color Metallography, *J. Mater. Sci.*, 2006, **41**, p 5365–5370.
45. L.E. Murr, Y. Li, R.D. Flores, E.A. Trillo, and J.C. McClure, Intercalation Vortices and Related Microstructural Features in the Friction-Stir Welding of Dissimilar Metals, *Mater. Res. Innovations*, 1998, **2**, p 150–163.
46. L.E. Murr, A Review of FSW Research on Dissimilar Metal and Alloy Systems, *J. Mater. Eng. Perform.*, 2010, **19**, p 1071–1089.
47. B. Strass, G. Wagner, C. Conrad, B. Wolter, S. Benfer, and W. Fürbeth, Realization of Al/Mghybrid-Joints by Ultrasound Supported Friction Stir Welding - Mechanical Properties, Microstructure and Corrosion Behavior, *Adv. Mater. Res.*, 2014, **966–967**, p 521–535.
48. S. Kumar, C.S. Wu, Z. Sun, and W. Ding, Effect of Ultrasonic Vibration on Welding Load, Macrostructure, and Mechanical Properties of Al/Mg Alloy Joints Fabricated By Friction Stir Lap Welding, *Int. J. Adv. Manuf. Technol.*, 2019, **100**, p 1787–1799.
49. J. Fayomi, A.P.I. Popoola, O.M. Popoola, O.P. Oladijo, and O.S.I. Fayomi, Tribological and Microstructural Investigation of Hybrid AA8011/ZrB2-Si3N4 Nanomaterials for Service Life Improvement, *Results in Phys.*, 2019, **14**, 102469
50. X. Chen, Y. Peng, S. Peng, S. Yao, C. Chen, and P. Xu, Flow and Fracture Behavior of Aluminum alloy 6082–T6 at different Tensile Strain Rates and Triaxialities, *PLoS ONE*, 2017, **12**(7), p e0181983.
51. T. Dursun and C. Soutis, Recent Developments in Advanced Aircraft Aluminium Alloys, *Mater. Des.*, 2014, **1980–2015**(56), p 862–871.
52. P. Venkateswaran and A.P. Reynolds, Factors Affecting the Properties of Friction Stir Welds Between Aluminum and Magnesium Alloys, *Mater. Sci. Eng., A*, 2012, **545**, p 26–37.

53. Morishige T, Kawaguchi A, Tsujikawa1 M, Hino M, Hirata T, Higashi K (2008) Dissimilar welding of Al and Mg alloys by FSW [J]. Materials Transactions, , 49(5): 1129−1131
54. Y.K. Yang, H. Dong, H. Cao, Y.A. Chang, and S. Kou, Liquation of Mg Alloys in Friction Stir Spot Welding, *Weld. J.*, 2008, **87**, p 167s–177s.
55. R. Kumar, K. Singh, and S. Pandey, Process Forces and Heat Input as Function of Process Parameters in AA5083 Friction Stir Welds [J], *Trans. of Nonferrous Metals Soc. China*, 2012, **22**(2), 288298
56. V. Firouzdor and S. Kou, Al-to-Mg Friction Stir Welding: Effect of Positions of Al and Mg with Respect to the Welding Tool, *Weld. J.*, 2009, **88**, p 213–224.
57. S.H.C. Park, Y.S. Sato, and H. Kokawa, Microstructural Evolution and its Effect on Hall-Petch Relationship in Friction Stir Welding of Thixomolded Mg Alloy AZ91, *Mater. Sci.*, 2003, **38**, p 4379–4383.
58. R.K.R. Singh, C. Sharma, D.K. Dwivedi, N.K. Mehta, and P. Kumar, The Microstructure and Mechanical Properties of Friction Stir Welded Al−Zn−Mg Alloy in as Welded and Heat Treated Conditions [J], *Mater. Des.*, 2011, **32**(2), p 682–687.
59. X.W. Li, D.T. Zhang, C. Qiu, and W. Zhang, Microstructure and Mechanical Properties of Dissimilar Pure Copper/1350 Aluminum Alloy Butt Joints by Friction Stir Welding [J], *Trans. Nonferrous Metals Soc. of China*, 2012, **22**(6), p 1298–1306.
60. Y. Morisada, H. Fujii, T. Nagaoka, and M. Fukusumi, MWCNTs/AZ31 Surface Composites Fabricated by Friction Stir Processing [J], *Mater. Sci. Eng., A*, 2006, **419**(1), p 344–348.
61. H. Mehdi and R.S. Mishra, Modification of Microstructure and Mechanical Properties of AA6082/ZrB2 Processed by Multipass Friction Stir Processing, *J. Mater. Eng. Perform.*, 2022 https://doi.org/10.1007/s11665-022-07080-0
62. A. Heidarzadeh, H. Khodaverdizadeh, A. Mahmoudi and A.E. Nazari, Tensile behavior of friction stir welded AA 6061–T4 aluminum alloy joints [J], *Mater. Des.*, 2012, **37**, p 166–173.

Publisher's Note Springer Nature remains neutral with regard to jurisdictional claims in published maps and institutional affiliations.

Springer Nature or its licensor (e.g. a society or other partner) holds exclusive rights to this article under a publishing agreement with the author(s) or other rightsholder(s); author self-archiving of the accepted manuscript version of this article is solely governed by the terms of such publishing agreement and applicable law.

Effective Brain Tumor Segmentation for MRI Image Analysis using Dual Attention Network based YOLACT++

Neil Roy
Department of Computer Engineering
Delhi Technological University
Delhi, India
neilroy_co20b1_15@dtu.ac.in

Sandip Kumar Roy
S P Jain School of Global Management
Dubai, UAE
sandipr@hotmail.com

Preeta Sharan
Department of E&C
The Oxford College of Engineering
Bangalore, India
sharanpreeta@gmail.com

***Abstract*—A Brain Tumor is an abnormally growing clump of cells inside or around the brain, which can lead to a fatal situation if not detected at an earlier stage. Therefore, we present an Artificial Intelligence (AI) approach based on the YOLACT++ image segmentation model. In this technique, we introduced a two Dual attention network on the YOLACT++ architecture for the identification and segmentation of scanned MRI (Magnetic Resonance Imaging) for a brain tumor. We have applied the concepts of transfer learning by using RESNET-50 with Feature Pyramid Networks (FPN) as the backbone of our work. The experiment setup includes 400 images as a training set, and the results show that the proposed method achieved 94.71% segmentation accuracy for each segmentation. The proposed method is significantly higher than the previously published dice score of 88% for the Convolutional Neural Network (CNN) based approach.**

Keywords— Segmentation, Brain Tumor, Computer Vision, Magnetic Resonance Imaging, YOLACT, CNN.

I. INTRODUCTION

The intracranial tumor, also known as a brain tumor, occurs when a cell regulatory system in an aberrant mass of tissue appears and has no effect on the uncontrollable multiplication of the cells. If not detected at an early stage of formation, a tumor could result in a life-threatening situation. In contrast to invasive treatments like tissue biopsies, medical personnel often uses MRI, Computer Tomography (CT) scans to get a comprehensive picture of the brain for initial analysis [1] as it generates various contrast of tissues in each imaging modality and is often utilized by the medical specialist. However, the task of manually segmenting and analyzing is a time-consuming and quite tedious role. Therefore, a need for an automatic and robust segmentation technique is needed. The goal of segmentation of brain tumors is to isolate the region of abnormal growth of tissue. Segmenting tumors can assist clinicians in a better and faster diagnosis. Following the above multiple studies have been made to achieve optimal segmentation[4-6]. Most methods utilize Convolutional Neural networks (CNN) as they are known to be the state of the art methods in the field of segmentation because they can learn the essential features without the need for any feature selection or any form of manual design. But it remains a challenge for the existing methods to accurately segment a tumor from an MRI scan since the tumor's location and size are variable and the presence of ambiguous lines between the tumor and normal tissue. In this work we aim to develop a model that can accurately segment the tumor regardless of its size and location.

The main Contribution we made in this paper is:

- Introduction of the position attention module to the FPN architecture of YOLACT++ for spatial inter dependencies and Channel Attention Module for modeling the channel dependencies.
- To Demonstrate that the proposed addition to the architecture increases the accuracy of the segmentation when compared with related work done.

The structure of the paper is as follows. Section II describes the previous work done in brain tumor segmentation and more. In section III, the dataset and the architecture are discussed, and section IV demonstrates the achieved result and ends with a conclusion and future work in areas V and VI, respectively.

II. LITERATURE REVIEW

The main intention of Computer-aided image analysis is to reduce diagnostic errors, thus reducing false negative rates of specialists analyzing medical pictures. Various studies have been conducted for segmentation and classification tasks using deep learning methods. Using a ten-fold cross-validation procedure, the author fed an improved hybrid-feature dataset to four ML classifiers: multilayer perceptron (MLP), SVM, random forest (RF), and J48.MLP had an overall accuracy of 95.78% [13]. Kalpathy, C. J. presented the performance of biomedical image retrieval systems [14].

In brain tumor analysis, we found several methods involving both conventional approaches and deep learning methods. Techniques such as K-nearest neighbor are used by [2] to segment the FLAIR-MRI brain pictures into bright and dark anomalies in low and medium background grey level values. In [3], more emphasis is on superpixel segmentation than voxel processing. The relationship between neighboring superpixels is handled as multi-level Gabor wavelet filter features for training the SVM Deep Learning algorithms. This method allows data to be used to understand the hierarchy of complicated characteristics. CNN models are widely recognized as the state of the art method. In the field of image processing because CNN models have the benefit's

Authorized licensed use limited to: DELHI TECHNICAL UNIV. Downloaded on May 11,2023 at 10:23:37 UTC from IEEE Xplore. Restrictions apply.

of considering context and being utilized with raw data as it runs.

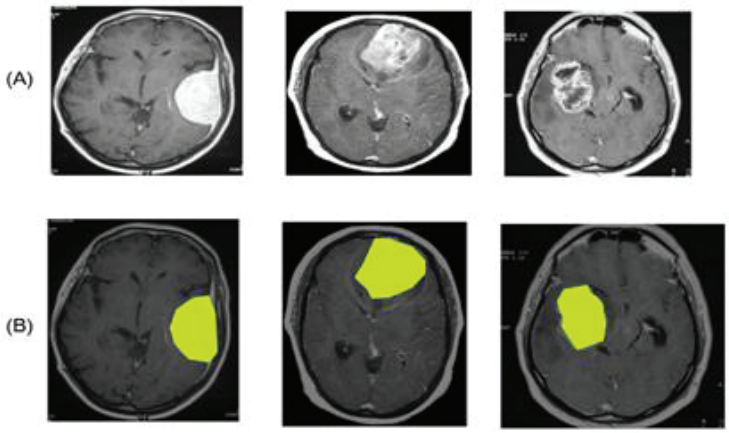


Fig. 1. Referenced Brain scans with corresponding labels. (a) Image, (B) Ground Truth

Ref [4] employed a shallow CNN with one Fully-connected layer, One SoftMax layer, and two convolutional layers. Ref [5] Used Ax pooling with stride 3 to separate the convolutional layers. In a 3D CNN with 11 layers and two parallel paths, local and contextual information to produce better segmentation results. The 3D filter may make use of the image's 3D character. However, its main drawback is increased network size and computational expense. As a result, 2D-CNNs often are in use in brain tumor segmentation techniques. In ref [6,] a deep convolutional network based on U-Net was employed for segmentation.

The attention model has received a lot of interest in recent years for several Deep learning problems such as audio recognition, image recognition, and natural language processing. The goal of attention modules is to capture an image's essential features. Attention modules have previously been used for biomedical segmentation .In ref [7] An attention module was proposed on the U-NET architecture along with custom edge filters. In ref [8], the authors applied the channel attention module to the U-NET architecture and achieved an highly accurate gland segmentation with a dice score of 91%.

AI-based segmentation technique is for treatment planning and follow-up evaluation. Since most of the segmentation work is manual, which is not just time-consuming but also subject to errors, such reasons, medical experts use a rough estimate for evaluation. Segmentation of brain tumors is challenging due to factors such as intensity inhomogeneity in MRI images, shape, structure, and tumor location. Much of previous work using attention has been done on the U-NET architecture. Our work is novel in terms of introducing position and channel attention module networks to the FPN architecture. The combination of the dual attention network will increase the segmentation performance of YOLACT++[9] as it will enable better feature selection.

III. Methodology

This section presents the data description, data annotation and model architecture.

A. Dataset Description

The MRI images used for this work are from Kaggle's Brain tumor classification dataset [17]. The dataset consists of images of 3 different types of brain tumors meningioma, glioma, and pituitary tumor. The dataset was used for training the proposed algorithm. Figure 1 shows the sample of MRI scanned images.

B. Dataset annotation

In this study, a total of 400 Images were randomly divided into training (250), validation (150), and test (100). The data augmentation technique like increasing the image noise and adding photo metric distortion are used extensively. To avoid over fitting, this method increases the variety of the dataset in both the training and validation sets. The following data augmentation resulted in the training set is expanded to 400 images, and the validation set is developed to 300. As it was meant for model evaluation, no augmentation was performed on the test image set. Figure 2 shows the referenced MRI brain scans with corresponding labels (high contrast area) and ground truth (green color).

C. Model Architecture

1) Feature Extraction

Our study employed a residual network with 50 layers (Resnet-50) [23] to extract features. Reset 50 is noted for being less computationally demanding and learning more quickly. Moreover, on C_3 –C_5, fig.2 a Deformable Convolutional Neural Network (DCN) [24] was deployed. The reason for adding DCN is that YOLACT is a one-shot sampling. Thus, it does not have a resampling process. Still, adding DCN can enhance the network's performance by improving its ability to handle different aspect ratios, rotation, and scale

Authorized licensed use limited to: DELHI TECHNICAL UNIV. Downloaded on May 11,2023 at 10:23:37 UTC from IEEE Xplore. Restrictions apply.

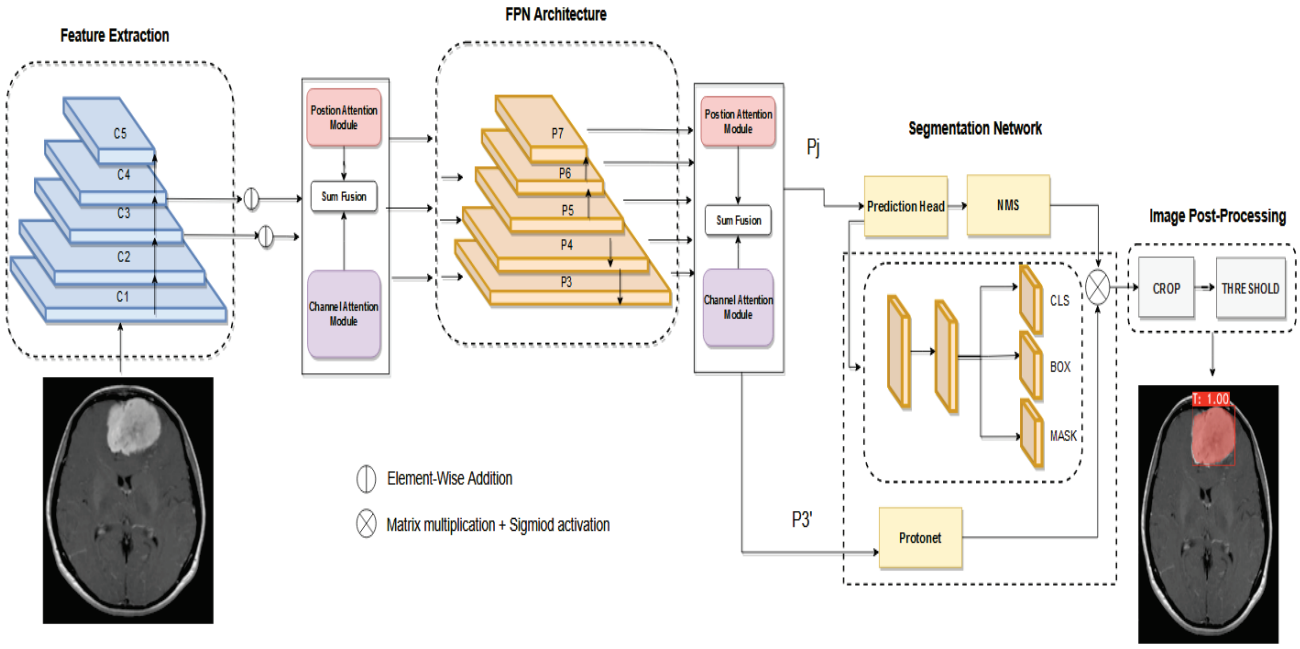


Fig. 2. Dual Attention Network YOLACT++

2) Channel Attention Module

Fig 3 Shows the Channel Attention Module (CAM) module used in this study. Unlike a Position Attention Module the channel attention maps are directly calculated X $\in R^{C\times C}$ from A $\in R^{C\times H\times W}$ i.e. the original features. A is reshaped to R^{CxN} after which matrix multiplication is performed between **A** and transpose of **A.**

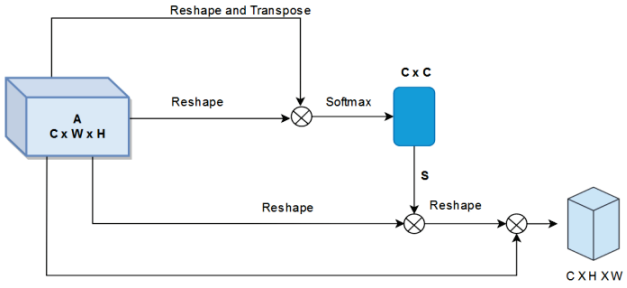


Fig. 3. Channel Attention Module

In the end, soft max layer is applied for obtaining the channel attention map **X ∈ $R^{C\times C}$.** The result of matrix multiplication of **X** and **A** which is then reshaped to $R^{C\times H\times W}$ is the multiplied with scaling parameter β and also applying element wise sum operation on **A** to achieve the result E ∈ $R^{C\times H\times W}$.

2) Position Attention Module

Position Attention Module [25], Fig.4 models contextual relationships over local features by encoding a broader variety of contextual information into local feature thus boosting its representation capability. Firstly, a local feature **A** $\in R^{C\times H\times W}$ which is then passed through a convolution layer to generate two feature maps B and C {B, C} $\in R^{C\times H\times W}$.

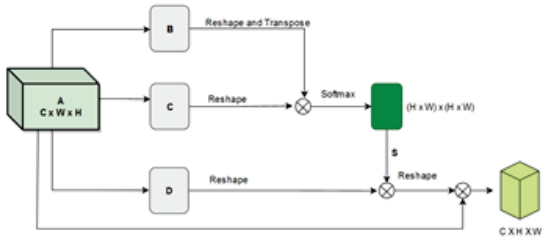


Fig. 4. Position Attention Module

After which reshaping of $R^{C\times H\times W}$ to $R^{C\times N}$ takes place, N is the number of pixels. Then perform matrix multiplication on transpose of B and C. A is also passed through convolution layers to generate a new feature map **D** $\in R^{C\times H\times W}$ and reshape it to the result to $R^{C\times N}$ which then is multiplied with a scale parameter α.

3) Feature Pyramid Architecture

P_3 through P_7 in the FPN structure were created by passing the convolutional layer C_5 via one convolutional layer. Then, using a bilinear interpolation technique, the size of feature map P_5 was doubled. Next, the convolution of C_4 was added, and feature maps P_4 and P_3 were created using the same process. Convolution and down sampling of feature maps P_5 and P_6 eventually led to the creation of the feature maps P_6 and P_7.

Authorized licensed use limited to: DELHI TECHNICAL UNIV. Downloaded on May 11,2023 at 10:23:37 UTC from IEEE Xplore. Restrictions apply.

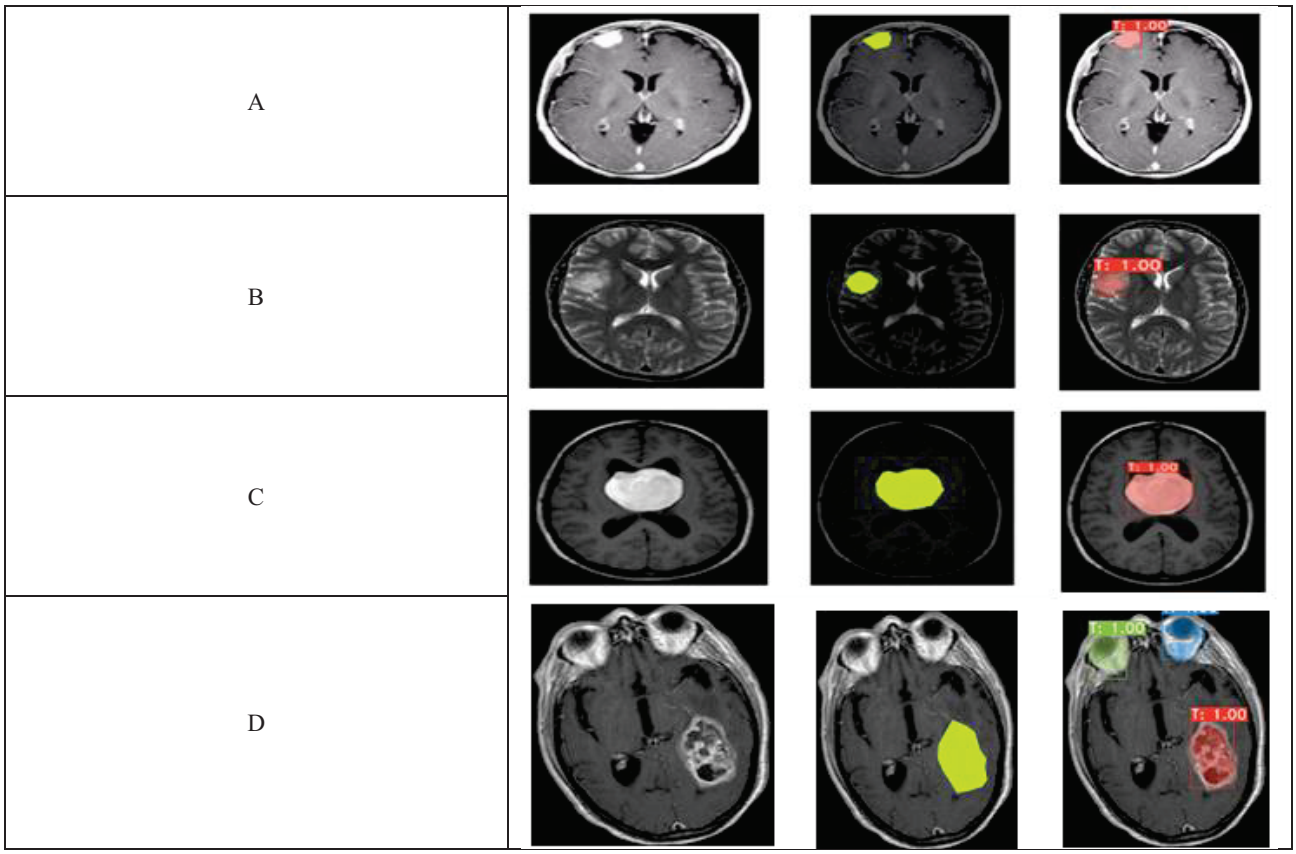


Fig. 5. Example images of segmentation results. (A) Small sized tumor, (B) tumor with low visibility, (C) Larger Tumor. (D) Detection of Eyes as tumor.

4) Segmentation Networks

The input of the segmentation network is from the features maps obtained from the FPN network Segmentation. Using a Fully Convolutional Neural Network (FCN), the protonet (Fig. 2) was utilized to create a K-many prototype mask with dimensions equivalent to the original image. The prototype masks were constructed using the feature map P3 as the input, and the output mask dimensions are 138 X 138. A shared convolutional network is used by the Prediction Head structure (Fig. 2) to increase segmentation speed. The prediction head takes the five feature maps P_3 - P_7 as input from the feature extraction network to execute the three tasks: Target Classification Losses prediction, Bounding Box Prediction, and Mask Coefficient prediction. The highest confidence mask coefficients are obtained using the quick Non-Maximum Suppression (NMS) technique. Using the sigmoid function and simple matrix multiplication, Protonet branches and Prediction head outputs are acquired from the mask.

$$M = \sigma\,(PC_T) \qquad (1)$$

P: Prototype Mask, C: Mask Coefficient of matrix n

5) Loss Functions

In this work, 3 loss are used to train the mode Classification Loss (L_{cls}), Box Regression Loss (L_{box}) and mask loss (L_{mask}) Equation (2) show the total loss function

$$L = \alpha\, L_{cls} + \beta\, L_{box} + \gamma\, L_{mask} \qquad (2)$$

The definition of L_{cls} and L_{box} is the same as [6] and L_{mask} is defined as Equation (3)

$$L_{mask} = \sigma\left(\left(-p_i^* log\left[p_i^* p_i + \left(1 - p_i^*\right)(1 - p_i)\right]\right)\right) \qquad (3)$$

$$\sigma(x) = \frac{1}{1+e^{-x}} \qquad (4)$$

In this study, many criteria were employed to objectively determine the performance of the suggested technique. They are the Mean Intersection Over Union(mIoU) and F1/Dice score. The segmentation accuracy of the tumor as a whole is represented by the F1 score given by Equation (5).

$$F_1 = 2 * \left(\frac{P*R}{P+R}\right) \qquad (5)$$

P = Precision, R = Recall.

The mIoU is formed by joining two sets of predicted tumor and ground truth data. Better segmentation is related to a

Authorized licensed use limited to: DELHI TECHNICAL UNIV. Downloaded on May 11,2023 at 10:23:37 UTC from IEEE Xplore. Restrictions apply.

higher mIoU value. MIoU is determined by the given Equation (6).

$$\frac{TP}{(TP+FN+FP)} \quad (6)$$

IV. Results

We trained our model on AMD Ryzen 7 4800H with 2.90GHZ processor, 32 GB RAM, NVIDIA Ge Force RTX 2060 GPU with 6GB of graphics memory. We used transfer learning to fine-tune the Image-net classification model's pre-trained parameters with a batch size of 8 using Stochastic gradient descent for 600,000 iterations starting with an initial learning rate of 10-3, weight decay of 5×10−4, and momentum of 0.9.in the α, β, γ are set to 1,1.5 and 6.125. Figure 7 demonstrates the total loss values at different iterations. We could see that the loss values gradually converge and stabilizes. Out of 100 test images, our proposed method was able to segment 91 images successfully with an mIOU of 94.71%. The accuracy, recall, F1/Dice scores, mIOU, and total time required to segment the 100 test pictures are shown in Table 1. We chose 0.5 as our mIOU threshold for brain tumor

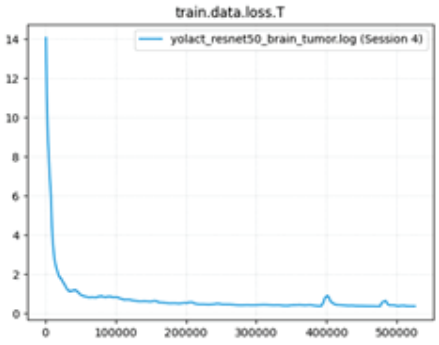


Fig. 6. The total loss values corresponding

Segmentation. Fig 8 shows the segmentation results of the tumor found in various positions. From the above experiment, we determined that the proposed method showed promising segmentation with accurate and precise edges. Experiments also showed that the model sometimes detects the eye's as tumors, Fig 5-(D), and improvement could be made by providing the model images with higher resolution or improving the dataset accordingly.

TABLE I. METRICS FOR MODEL PERFORMANCE

Model	Precision	Recall	Dice Score	mIOU	Total Time
YOLACT++ with Dual Attention Network	96.71	96.45	96.5	94.71	8.31

We compared the proposed method's performance to that of various state-of-the-art instance segmentation methods for additional validation. Table 2 In comparison to other models. The comparison demonstrates that the suggested strategy outperformed others regarding segmentation performance. This could be credited to YOLACT++'s high-level mask quality since the mask created is from the original feature without the ability to change and perhaps slight misalignment of the features. The attention module improved the performance by extracting the features of the tumor.

TABLE II. COMPARISON OF RELATED WORK

Author	Model	Dice Score
Urban G. et al. [18]	3D CNN architecture using 3D convolutional filters	0.87
Dvorak and Menze [19]	Local structured prediction with CNN and k-means	0.83
Pereira et al. [20]	CNN with small (3x3) filters for deeper architecture	0.88
Proposed Method in present work	Yolact++ with Dual Attention Network	0.965

The comparison demonstrates that the suggested strategy outperformed others regarding segmentation performance. This could be credited to YOLACT++'s high-level mask quality since the mask created is from the original feature without the ability to change and perhaps slight misalignment of the features. The attention module improved the performance by extracting the features of the tumor.

V. Conclusion

AI provides an opportunity where one gets a chance to work with established and rapidly evolving platforms that handle massive amounts of events and images. The implementation requires new initiatives to automate, enhance, maintain, and scale services in a rapidly-scaling environment. Clinical data provides the best understanding of disease behavior. Based on the available clinical data [17], an innovative YOLACT++-based image segmentation technique is presented in this work for segmenting brain tumors from MRI scans. The comparison of the outcome of the proposed method with some of the recent publications is shown in Table 2. The presented technique has an accuracy of 96.5%. The accuracy is significantly higher than the previously published 88% for the Convolutional Neural Network (CNN) based approach [18] due to YOLACT++'s high quality of mask produced and the increase in the effectiveness of feature extraction due to the presence of the dual attention network. It should be noted that the technique given here is meant to augment rather than replace existing options for tumor diagnosis. Because in the present approach, AI interprets the images with high accuracy, which may minimize the need for a third-party expert in the long run. Since this technique involves continuous learning, with time, the system gets enriched with each case it detects.

VI. Future Work

The future use cases will be based on the AI capability to provide cost-effective analysis of MRI scans. How disease attacks can be prevented or how a particular brain tumor can further be spread with time can be some of the future applications using AI. Future lies in proposing and implementing creative, efficient solutions for MRI scan analysis and contribute to expanding implementation area beyond current diseases.A key area of research could be live video segmentation of diseases which could directly be used by the clinician during the scan,this would allow for a faster diagnosis. Another key area for future growths is to conduct technical performance benchmarking and studies to help engineers make choices. Using more sophisticated real time

Authorized licensed use limited to: DELHI TECHNICAL UNIV. Downloaded on May 11,2023 at 10:23:37 UTC from IEEE Xplore. Restrictions apply.

video, algorithms can be evolved for improved image segmentation, 3D reconstruction and classification.

REFERENCES

[1] J. Ker, L. Wang, J. Rao, and T. Lim, "Deep Learning Applications in Medical Image Analysis," IEEE Access, vol. 6, pp. 9375–9389, 2018.

[2] Khalid, Noor Elaiza Abdul, Shafaf Ibrahim, and P. N. M. M. Haniff., "MRI Brain Abnormalities Segmentation using K- Nearest Neighbors (k-NN)", International Journal on Computer Science and Engineering 3.2 ,2011, 980-990.

[3] Wu, W., Chen, A. Y., Zhao, L., & Corso, J. J. "Brain tumor detection and segmentation in a CRF (conditional random fields) framework with pixel-pairwise affinity and super pixel-level features", International journal of computer assisted radiology and surgery, 9(2), 241- 253, 2014

[4] Georgiadis, P., Cavouras, D., Kalatzis, I., Daskalakis, A., Kagadis, G. C., Sifaki, K., ... & Solomou, E. (2008). Improving brain tumor characterization on MRI by probabilistic neural networks and non-linear transformation of textural features. *Computer methods and programs in biomedicine*, *89*(1), 24-32.

[5] Kamnitsas, K., Ledig, C., Newcombe, V. F., Simpson, J. P., Kane, A. D., Menon, D. K., ... & Glocker, B. (2017). Efficient multi-scale 3D CNN with fully connected CRF for accurate brain lesion segmentation. *Medical image analysis*, *36*, 61-78.

[6] Dong, H., Yang, G., Liu, F., Mo, Y., & Guo, Y. , "Automatic brain tumor detection and segmentation using U-Net based fully convolutional networks", In annual conference on medical image understanding and analysis, pp. 506-517, 2017, Springer, Cham.

[7] Song, H., Wang, Y., Zeng, S., Guo, X., & Li, Z. (2023). OAU-net: Outlined Attention U-net for biomedical image segmentation *Biomedical Signal Processing and Control*, *79*, 104038.

[8] Ulutan, O., Iftekhar, A. S. M., & Manjunath, B. S., "VSGNET: Spatial attention network for detecting human object interactions using graph convolutions", In Proceedings of the IEEE/CVF conference on computer vision and pattern recognition, 2020, pp. 13617-13626.

[9] Bolya, D., Zhou, C., Xiao, F., & Lee, Y. J., "Yolact++: Better real-time instance segmentation", IEEE transactions on pattern analysis and machine intelligence, 2020.

[10] Jamshidi, M., Lalbakhsh, A., Talla, J., Peroutka, Z., Hadjilooei, F., Lalbakhsh, P., ... & Mohyuddin, W. (2020). Artificial intelligence and COVID-19: deep learning approaches for diagnosis and treatment. *Ieee Access*, *8*, 109581-109595.

[11] Roy, S., Menapace, W., Oei, S., Luijten, B., Fini, E., Saltori, C., ... & Demi, L. (2020). Deep learning for classification and localization of COVID-19 markers in point-of-care lung ultrasound. *IEEE transactions on medical imaging*, *39*(8), 2676-2687.

[12] Castellino, RA., "Computer aided detection (CAD): an overview", Cancer Image,2005, 5, pp. 17–19.

[13] Naeem, S., Ali, A., Qadri, S., Khan Mashwani, W., Tairan, N., Shah, H.; Fayaz, M., Jamal, F., Chesneau, C., Anam, S. Machine-Learning Based Hybrid-Feature Analysis for Liver Cancer Classification Using Fused (MR and CT) Images. Appl. Sci. 2020, 10, 3134. https://doi.org/10.3390/app10093134

[14] Kalpathy-Cramer J, de Herrera AGS, Demner-Fushman D, Antani S, Bedrick S, Müller H. Evaluating performance of biomedical image retrieval systems – an overview of the medical image retrieval task at ImageCLEF 2004–2013. Comput Med Imaging Graph. 2015,39, 55–61.

[15] You D, Simpson M, Antani S, Demner-Fushman D, Thoma GR., "Annotating image ROIs with text descriptions for multimodal biomedical document retrieval", Paper presented at: IS&T/SPIE Electronic Imaging; 2013.

[16] Charles E, Kahn J, Thao C., "GoldMiner: a radiology image search engine", Am J Roentgenol. 2007,pp. 188,1475–8

[17] Online Resource: https://www.kaggle.com/datasets/sartajbhuvaji/brain-tumor-classification-mri

[18] Urban G. et al., Multi-modal brain tumor segmentation using deep convolutional neural networks. MICCAI Multimodal Brain Tumor Segmentation Challenge (BraTS) 2014, pp. 31–35

[19] Dvorak P, Menze B. Structured prediction with convolutional neural networks for multimodal brain tumor segmentation. MICCAI Multimodal Brain Tumor Segmentation Challenge (BraTS), 2015, 13–2

[20] Pereira, S., Pinto, A., Alves, V., & Silva, C. A. (2016). Brain tumor segmentation using convolutional neural networks in MRI images. IEEE transactions on medical imaging, 35(5), 1240-1251.

[21] R. K. Pathak, S. Mishra, P. Sharan and S. K. Roy, "Nodule Detection in Infrared Thermography Using Deep Learning," 2022 IEEE 7th International conference for Convergence in Technology (I2CT), 2022, pp. 1-6, doi: 10.1109/I2CT54291.2022.9824313.

[22] S. Mishra, A. Prakash, S. K. Roy, P. Sharan and N. Mathur, "Breast Cancer Detection using Thermal Images and Deep Learning", 2020 7th International Conference on Computing for Sustainable Global Development (INDIACom), pp. 211-216, 2020.

[23] He, K., Zhang, X., Ren, S., & Sun, J. (2016). Deep residual learning for image recognition. In *Proceedings of the IEEE conference on computer vision and pattern recognition* (pp. 770-778).

[24] Dai, J., Qi, H., Xiong, Y., Li, Y., Zhang, G., Hu, H., & Wei, Y. (2017). Deformable convolutional networks. In *Proceedings of the IEEE international conference on computer vision* (pp. 764-773).

Authorized licensed use limited to: DELHI TECHNICAL UNIV. Downloaded on May 11,2023 at 10:23:37 UTC from IEEE Xplore. Restrictions apply.

Journal of Power Sources 572 (2023) 233112

Contents lists available at ScienceDirect

Journal of Power Sources

journal homepage: www.elsevier.com/locate/jpowsour

Efficient photosensitive light harvesting dye sensitized solar cell using hibiscus and rhodamine dyes

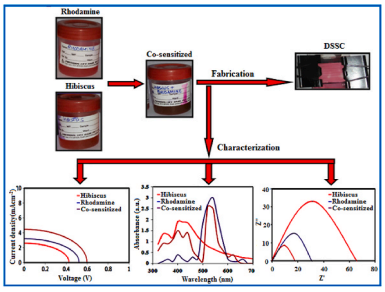
Geetam Richhariya [a], Anil Kumar [b,c,*], Akash Kumar Shukla [d], Kailash Nath Shukla [e], Issara Chanakaewsomboon [f]

[a] Department of Electrical & Electronics Engineering, OIST College, Bhopal, 462 022, India
[b] Department of Mechanical Engineering, Delhi Technological University, Delhi, 110 042, India
[c] Centre for Energy and Environment, Delhi Technological University, Delhi, 110 042, India
[d] Department of Electrical Engineering, Ujjain Engineering College, Ujjain, 456010, India
[e] Department of Electrical Engineering, LNCT College, Bhopal, 462021, India
[f] Faculty of Environmental Management, Prince of Songkla University, Hat Yai, 90110, Thailand

HIGHLIGHTS

- Co-sensitization is a powerful technique for achieving photosensitive light harvesting.
- Natural dye from Hibiscus sabdariffa and synthetic organic dye from Rhodamineare used to fabricate DSSC.
- Impedance spectra of dyes showed minimum impedance of 17.5 Ω for mixed dye.
- Co-sensitized dye solar cell has highest current density of 4.02 mA and efficiency of 1.23%.

GRAPHICAL ABSTRACT



ARTICLE INFO

Keywords:
Dye sensitized solar cell
Hibiscus sabdariffa
Rhodamine dye
Fill factor
Power conversion efficiency
Co-sensitized dye

ABSTRACT

Co-sensitization is a powerful technique for achieving photosensitive light harvesting and enhancing dye sensitized solar cell (DSSC) performance. In this article, potential of extracted natural dye from Hibiscus sabdariffa and synthetic organic dye from Rhodamine as single dye source and mixed dyes are used to examine the performance of cells. The UV–Vis absorption spectra showed that examined dye mixture has cumulative absorption properties, such that its absorption spectra overlapped the spectral area. Moreover, DSSCs are characterized using UV–Vis Spectroscopy and Scanning electron microscopy (SEM). FTIR study was used to observe the functional groups of dye molecules to ensure the anchoring ability of dye to adsorb onto TiO_2 layer. X-Ray diffraction spectrum analysis (XRD), Photovoltaic performance of cells, Energy dispersive spectroscopy (EDS), and Electrochemical impedance spectroscopy (EIS) were also conducted on the cells. The impedance spectra of dyes show minimum impedance of 17.5 Ω in case of mixed dye. XRD analysis recognizes small crystalline size that reveals anatase crystal phase of TiO_2. Co-sensitized dye solar cell shows highest current density (Jsc) of 4.02mA and power conversion efficiency of 1.23%. The outcomes can be attributed to the light harvesting, the

* Corresponding author. Department of Mechanical Engineering, Delhi Technological University, Delhi, 110 042, India.
E-mail address: anilkumar76@dtu.ac.in (A. Kumar).

https://doi.org/10.1016/j.jpowsour.2023.233112
Received 28 February 2023; Received in revised form 2 April 2023; Accepted 22 April 2023
Available online 28 April 2023
0378-7753/© 2023 Elsevier B.V. All rights reserved.

good optical condition, and the appropriate energy levels of the co-sensitized dye. Moreover, the homogenous dispersion causes effective dye loading on the surface of semiconductor.

1. Introduction

The forever-rising challenge for sustainable energy has prompted academic and corporate researchers to focus on developing low-priced photovoltaic technology. Dye-sensitized solar cells (DSSCs) are being researched as a proficient choice to traditional solar cells because of attractive ecological and economic aspects, ease of manufacture, and atomic design options to modify optical properties [1–4]. For such cells, best reported efficiency using perovskite dyes is currently 13% [5]. The operation of DSSCs is based on photosynthesis process, and the dye plays an imperative character in expanding the phantom reaction of the cells. After photo exciting the sensitizer dye, the excited electrons are transmitted through a cascade mechanism, resulting in charge separation and rapid regeneration of oxidized dyes [6,7]. DSSCs sensitized with organic and porphyrin dyes produced the preeminent results [8]. The toxicity, harmful and radical compounds cause impure water for synthetic dyes, resulting in dangerous environmental issues. Therefore, protective actions were required to bind the amount of such dye for approaching the worldwide stream calamity and related risks. To encounter the challenges in progressing water handling applications, numerous approaches have been suggested by various research organizations and government firms. Alternatively, natural dyes have been measured as a useful approach to allocate water waste problems and reduce the influence of similar commercial actions. Natural dyes are obtained from viable natural resources. The dyes are ecological and economical and can be a useful replacement for hazardous synthetic dyes. Such dyes are extracted from different parts of plants and used as an adequate photosensitizer for DSSCs [9]. A natural dye should possess a few characteristics to be capable as a good sensitizer: (i) light absorption capability in the visible and near-infrared regions should be broad and strong, (ii)it should be stable and causes efficient charge injection, (iii) it should have suitable LUMO (lowest unoccupied molecular orbital) and HOMO (highest occupied molecular orbital) energy levels to attain a strong electronic incorporate to capable for charge injection into the conduction band (CB) of the semiconductor and also regeneration of the oxidized dye from the electrolyte [10]. To reduce the toxicity of synthetic dyes, causing severe environmental issues, mixed dye concept is promoted. The synthetic dye with natural dye reduces the toxicity level and thus improves the environmentally friendly atmosphere. The co-sensitization technology also enhances DSSC photovoltaic performances. Co-sensitization is a factual advancement to improve the light-harvesting capabilities of DSSCs by co-adsorbing two or more distinct dyes with corresponding spectral reactions on the semiconductor surface [11]. A maximum power conversion efficiency of 28.90% was accounted for by combining two sensibly preferred sensitizers under ambient illumination, capable of indoor utilization in a low-light situation [12]. It has appeared that the performance of DSSCs can be increased by using co-sensitization via chlorophyll and anthocyanin pigments may be due to greater absorption. It revealed that chlorophylls are conscientious in capturing and transmitting light energy to photosynthesis [13]. Many natural dyes have been extracted from hibiscus sabdariffa, bougainvillea, dragon fruit, marigold etc. [14]. Hibiscus shows the presence of anthocyanin pigment accounts for red to pink color. A power conversion efficiency of 0.046% was observed via Hibiscus sabdariffa as natural dye [15]. On the other side, organic dyes also showed better performance of DSSCs. An accountable efficiency has been revealed using eosin Y, rhodamine, methyl violet blue, bromophenol blue, pyronin, carbol fuchsin [16]. Rhodamine dye is a more widespread dye that showed high absorbance and less costly high power conversion Efficiency. A power conversion Efficiency and current density of 5% and 12.12mAcm^{-2}was observed using Rhodamine dye adsorb on TiO_2 [17]. An improvement in power conversion efficiency of 5.37% was observed by the mixed dye prepared by Beetroot and Cranberries as natural dyes due to enhancement in the light absorption capability of dyes [18].

The main objectives of the article are discussed as follows.

- The potential of the dyes extracted from Hibiscus Sabdariffa as natural dye and Rhodamine dye as metal free synthetic organic dye for application in dye sensitized solar cells like individual sensitizer and mixed sensitizers are used.
- The absorbance of various dyes was assessed with a UV–visible spectrophotometer.
- In the subsequent phase, characterization procedures were achieved to examine particle size, phase detection of semiconductor material using scanning electron microscopy, and XRD analyzer respectively.
- The photovoltaic performance of the single and cocktail dye based dye sensitized solar cells was observed to measure voltage-current curves in standard AM 1.5 G (global) solar radiations. The internal impedance of various prepared DSSCs is observed by using Electro impedance spectroscopy (EIS).

2. Materials and methods

The chemicals used in the current phase were of analytic grade and employed with no more purification process. Rhodamine dye was purchased by Jwalaa Traders (India). Polyethylene gycol 400 {HO (C_2H_4O)}, Titanium dioxide (TiO_2) and polyethylene gycol 400 {HO (C_2H_4O)} were bought from Solaronix, Switzerland and were used to prepare semiconductor paste. Transparent conductive oxide glass; Fluorine doped tin oxide was purchased by company Solaronix Switzerland and used as substrates for dye solar cell. Electrolyte was bought from Solaronix Switzerland and was used to give conductivity between the substrates. In the present work, DSSC was fabricated using dye extracted from Rhodamine and Hibiscus using ethanol as a solvent. The cocktail dye was prepared by adding two single dye extracts in a 1:1 ratio. TiO_2 was used as semiconductor coated onto conducting face of FTO using doctor blade technique. Counter electrode is prepared to employ carbon as a catalyst. The working and counter electrode were joined by filling liquid electrolyte through the drilled hole. X-Ray diffractometer (Co.Bruker) was employed to obtain X-Ray diffraction (XRD) patterns of TiO_2. Scanning microscope (model-JEOL/JSM-6390A) was used to obtain surface morphological structure of TiO_2. UV–Vis spectrometer was used to inspect the absorption spectrum analysis for the sensitizers. Electrochemical impedance of all the developed DSSCs was obtained using impedance analyzer instrument. Ethanol was used to extract different dyes and overall cleansing work. The Hibiscus Sabdariffa was collected from locally available plants surrounding the campus and natural dye was extracted using ethanol solution.

2.1. Preparation of dye

The petals of Hibiscus Sabdariffa flowers were used to extract natural dye using ethanol solution for extraction. The petals were washed properly to eliminate dirt; after that, it is left to dry in an open-air system in a dark place. After that, a fine powder was made by crushing the dried petals of Hibiscus Sabdariffa. Then, 1g of finely powdered petals was dissolved with 10 ml of solution of ethanol and left for one day in dark. Prepared solution was filtered using filter paper and then concentrated into 3 ml dye solution. The prepared dye was ready to mix with other synthetic organic dye to make cocktail dye solution. Next procedure is to

prepare synthetic organic dye i.e Rhodamine dye. This dye was prepared by adding 1g of Rhodamine dye powder in 10 ml ethanol solution and concentrating it into 3 ml dye solution. The cocktail dye was prepared by adding an equal amount of natural and synthetic organic concentrated solution.

2.2. Fabrication of photo anode

Fluorine doped tin oxide glass was dipped isopropanol solution to remove the impurity on the surface of the FTO; after that kept to dry for further application. TiO_2 paste was prepared by mixing titanium dioxide semiconductor white colored powder in polythelene glycol in equal ratio using mortar pestle in clockwise direction for half an hour to make a fine paste without any lumps. The prepared paste was then coated using glass rod on FTO conducting side. The conductive side of the FTO glass was previously checked using multi-meter by observing resistance of both glass sides. TiO_2 coated FTO was left for half an hour at room temperature. The TiO_2 coated sintered FTO was left for cooling purposes. Finally, sintered FTO with a coating of TiO_2 was dipped into the prepared dye solution.

2.3. Fabrication of counter electrode and assembling the DSSCs

The cleansing procedure of FTO for counter electrode was the same as that for photo anode. After drying the FTO a fine layer of carbon particles dropped onto the conductive face of TCO. To assemble the cell, an iodide tri-iodide electrolyte solution was filled between photo anode and counter electrode, and the two electrodes were sandwiched using binder clips to make the cell, as mentioned in Fig. 1.

3. Results and discussion

3.1. UV–Vis spectrum analysis

The UV–Vis spectroscopy analysis is carried out to find the capability of extracted dyes to imprison illumination in its visible range, i.e., 400–800nm. Dye solar cell performances depend upon capability of dye material to absorb electrons. Fig. 2 illustrates the UV–Vis absorption spectrum of dyes. The dye extracted from Hibiscus sabadriffa revealed two absorption peaks at 400 nm and 440nm wavelength; this shows a mark indicating the presence of anthocyanin [19,20]. Similarly, the existence of anthocyanin in Rhodamine dye was demonstrated by a strong absorption crest finding around 520–560nm of the dye solution. It is observed that each single and mixed dye has different potential for absorbing energy depending upon a definite wavelength range.

The maximum absorbance of mixed dye is shown in the 520–540nm range. It is revealed that the absorbance spectrum shows the presence of anthocyanin group. The maximum absorbance of the mixed dye is adjusted with HOMO-LUMO energy levels of anthocyanin group of dye material [21]. The anthocyanin molecules contain carbonyl and hydroxyl groups that attach to the semiconductor layer, increasing the reaction rate from the dye molecule to the semiconductor conduction band. Table 1 shows maximum absorbance of various natural and synthetic organic dyes.

3.2. Photovoltaic performance of DSSCs

The photovoltaic performance of various DSSCs fabricated using Hibiscus sabadariffa (A), Rhodamine dye (B) and mixed dye (C) on the

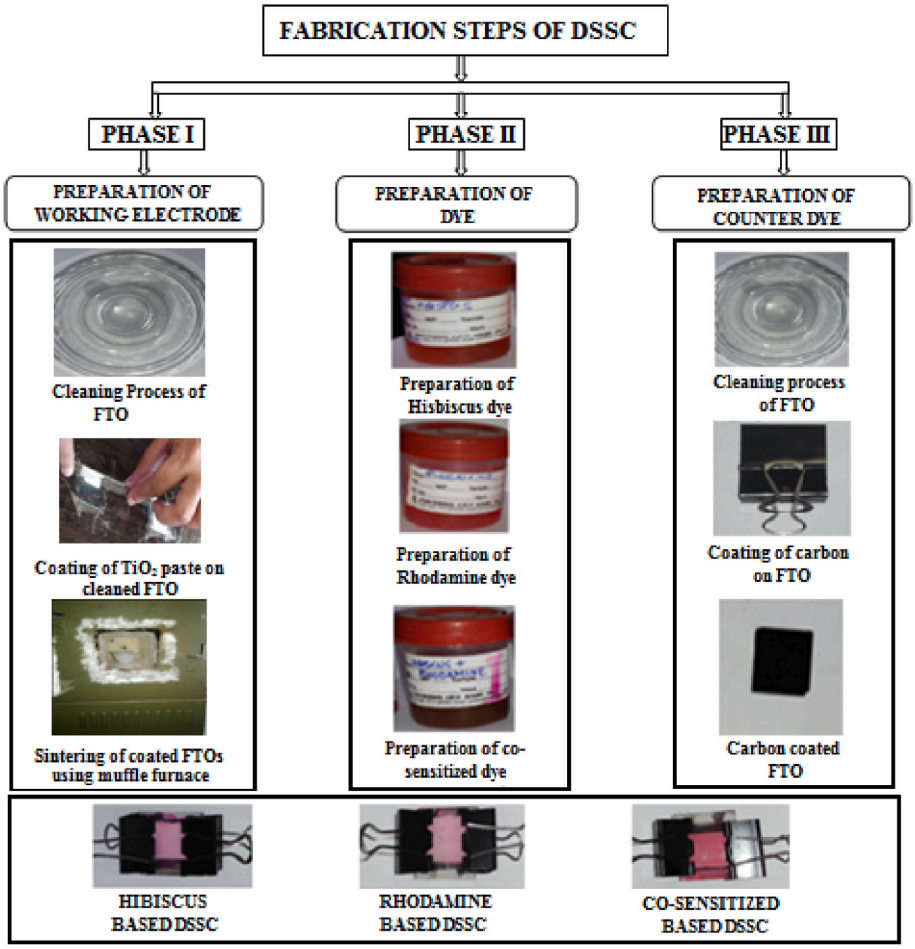


Fig. 1. Experimental diagram of DSSC.

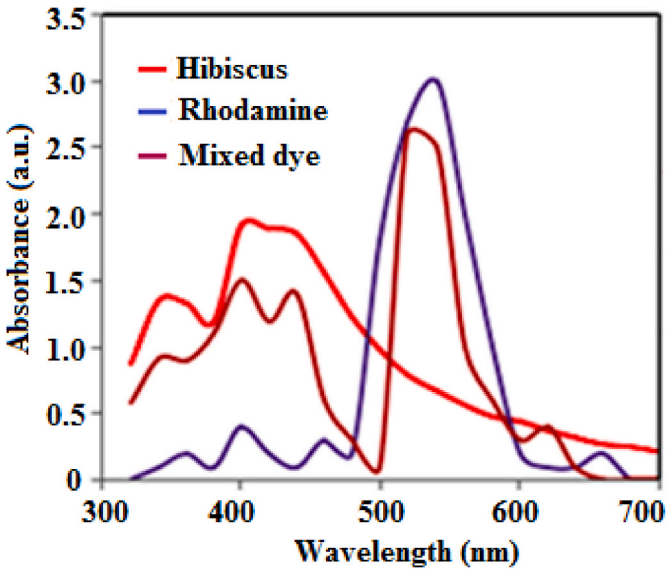


Fig. 2. UV–Vis spectrum of dyes.

Table 1
Absorbance of dyes.

Dye	Maximum Absorbance (nm)	Reference
Rosella	519	[22]
Remazole Red RB-133	520	[22]
7 Methyl Coumanin	417	[22]
Talinum Fruticosum	460	[23]
Telfairia Occidentalis	438	[24]
Caesalpinia Pulcherrima	538	[24]
M. Pudica	434	[23]
Yellow Nasturtium flowers dye	315	[25]
Orange Nasturtium flowers dey	345	[25]
Beetroot and Strawberry	332	[26]
Hibiscus Sabadariffa	400	[27]
Eosin Y	540	[27]
Hibiscus Sabadariffa with eosin Y	440	[27]
Hibiscus Sabadariffa	440	**[Present work]**
Rhodamine	560	**[Present work]**
Hibiscus Sabadariffa with Rhodamine	520	**[Present work]**

TiO_2 photo anode have been observed under the illumination of 100 mW/cm^2. The structure performance relationship for mixed dye was observed using various photovoltaic performances. The addition of mixed dye in DSSCs has shown an improvement in the photovoltaic parameters such as open circuit voltage (V_{oc}), short circuit current density(Jsc), fill factor (FF) and overall efficiency (η) of the devices. Fig. 3 shows photovoltaic performance of all the devices sensitized from single dyes and mixed dye.

The analogous photovoltaic observations are shown in Table 2. It is observed that the DSSC sensitized by mixed dye showed better photo conversion efficiency compared to the devices using single dyes.

3.3. Electrochemical impedance spectroscopy and X-ray diffraction spectrum analysis

Electrochemical impedance spectroscopy (EIS) measurement techniques were used to obtain carrier transportation behavior and observe interfacial charge recombination in individual and co-sensitized DSSCs [36–39]. In present study, impedance analyzer was used to observe EIS Spectra over a frequency range of 1Hz to 100 kHz. In this investigation,

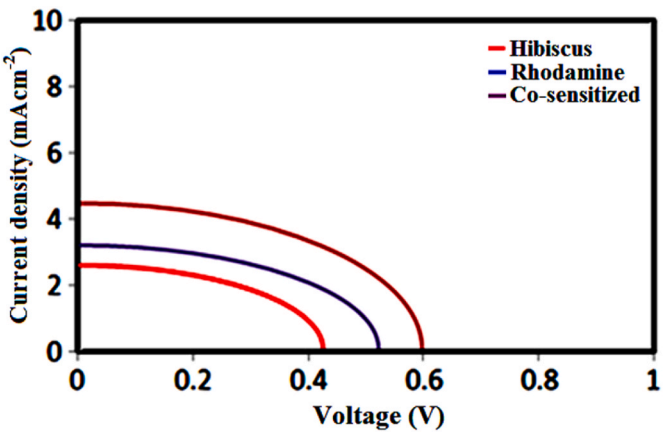


Fig. 3. I–V characteristic of DSSCs.

Table 2
Photovoltaic parameters of DSSCs.

Natural/Synthetic organic dye	V_{oc} (V)	J_{sc} (mAcm^{-2})	FF	η (%)	Ref
Rosella with Blue Pea	0.382	0.82	0.47	0.15	[28]
Phloxine B with Bromophenol	0.606	5.6	0.53	1.13	[29]
Cu with Fe	0.74	8.78	0.50	3.25	[30]
Malva verticillata with Syzygium cumini	0.37	0.53	0.39	0.31	[31]
ZnP-triazine-$(gly)_2$/D	0.70	14.78	0.71	7.34	[32]
XW22+XW24+CDCA (Porphyrin dye)	0.73	16.42	0.71	0.86	[33]
Metal free organic dye + Squaraine dye	0.75	12.32	0.68	6.31	[34]
Metal free carbazole dye + Ru II complex	0.672	22.85	0.62	9.55	[35]
Hibiscus sabdariffa	0.42	2.69	0.37	0.41	[Present work]
Rhodamine	0.53	3.2	0.43	1.03	[Present work]
Hibiscus + Rhodamine	0.60	4.02	0.52	1.23	[Present work]

co-sensitized dye solar cell shows charge transfer resistance of 17.52 Ω. In contrast, Rhodamine and Hisbiscus sabdariffa based dye solar cells show 31.2Ω and 67.5 Ω charge transfer resistance, respectively (Fig. 4). Thus, EIS analysis of various DSSCs revealed that co-sensitized dye plays crucial role in dropping the dark current in co-sensitized dye solar cell. X-ray diffraction (XRD) spectrum analysis determines crystalline size as well as crystal structure of titanium dioxide. The phase detection of

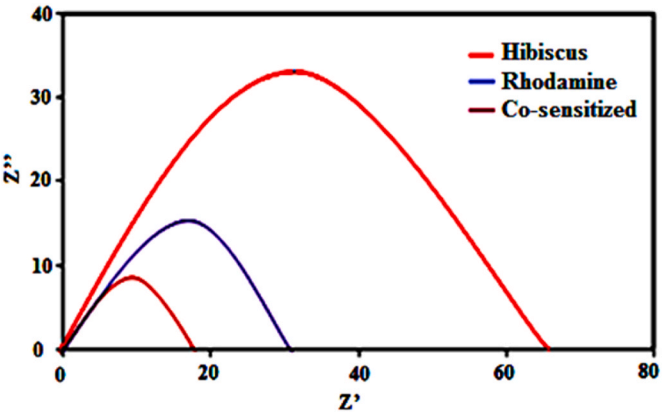


Fig. 4. EIS of various DSSCs.

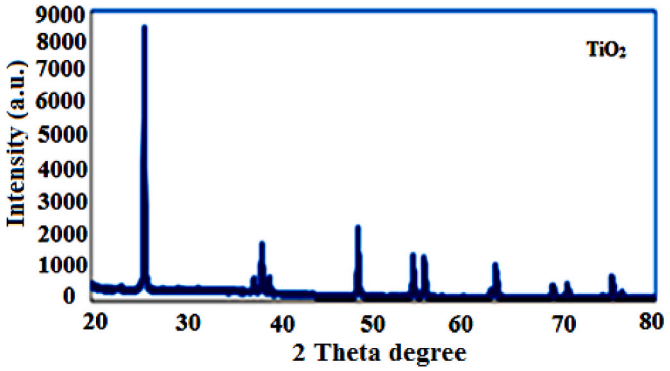


Fig. 5. XRD of TiO_2.

Table 3
X-ray diffraction parameters and crystalline size of TiO_2 nanoparticles.

Nanocomposite	2θ degree	β (radian)	D (nm)
TiO_2	26.7	0.0056831	24.8

titanium dioxide semiconductor was determined by calcinations temperature. In this investigation, XRD pattern of titanium dioxide powder was observed by calcined TiO_2 powder at nearly 500 °C for 2h. The XRD spectrum of TiO_2 is revealed in Fig. 5. The XRD analysis shows small crystalline size in the nanoscale range due to the appearance of broad XRD peaks that are attributed anatase crystal phase of the TiO_2(Table 3). At 2 theta scale, the diffraction peaks were recorded as 25.02, 38.10, 47.21, 51.03, 56.01, 62.17 and 69.02 in diffraction faces of (101), (004), (201), (105), (210), (204) and (114) respectively. The XRD pattern showed strong diffraction peaks at 25 and 48, revealing anatase phase of TiO_2 [40]. The peaks were obtained at 25.5° (101), 38.3° (004) and 48.4° (200) for TiO_2 nano-material under XRD patterns revealing anatase form of TiO_2 [41].

3.4. Scanning electron microscopy and energy dispersive spectroscopy of TiO_2

The key factors of semiconductor materials (i.e., shape, size and composition of materials) affect the performance of dye solar cell. The arrangement of corner states below the conduction band, dye loading behavior, the electron diffusion length in the semiconductor layer, effective area of surface of semiconducting materials are the

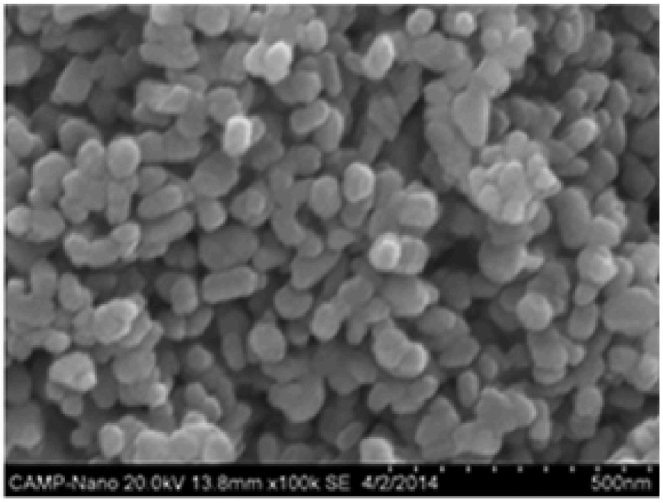


Fig. 6. SEM images of TiO_2.

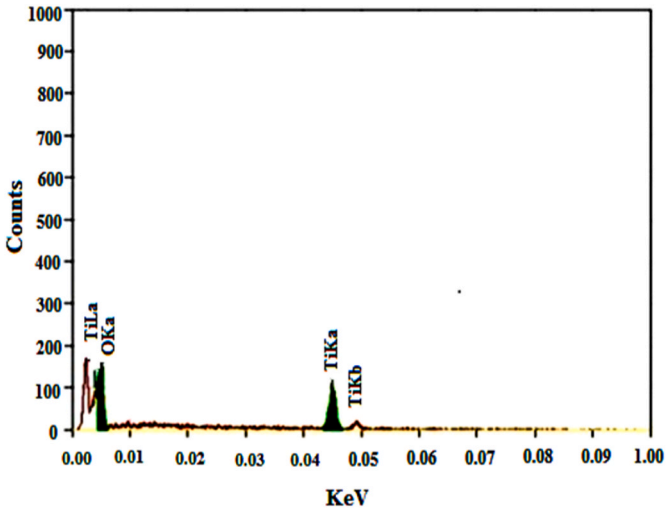


Fig. 7. EDS of TiO_2.

Table 4
Typical quantitative analysis.

Elements	KeV	Mass%	Counts	Atom%	K
O K*	0.519	22.64	1023.17	48.22	0.3881
Ti K	4.507	76.25	1285.55	51.78	1.0000

morphological characteristics of the surface of TiO_2 based photo-anode [42]. The small particle size due to increased surface area in photo anode causes higher dye adsorption on the photo anode surface, ensuring the production of many charge carriers and thus enhancing the photovoltaic performance of solar cell. Although, the larger particles increase light scattering and thus decrease effective light power in the dye solar cell. Thickness of dye coating is also a key factor that needs to be considered during the formation of the thickness over surface area of photo anode [43]. The larger thickness results in more absorbance of the dye. However, it increases effective charge transfer resistance. Therefore optimum thickness should be considered, including the size, nature and electron transportation of the coated material for photo anode [44]. The TiO_2 photo-anode film surfaces on FTO conductive glass substrates are homogenous, porous, and contain well distributed nanoparticles of the size range of 10–30 nm, according to the SEM pictures. The increased dye loading on the TiO_2 surface was made possible by high surface porosity and the resulting increase in surface area as shown in Fig. 6. SEM analysis shows that surface of TiO_2 is quite porous. The occurrence of Ti and O with 75.54 and 22.66 mass percent, respectively, has been observed during the energy dispersive spectroscopy (EDS) analysis as revealed in Fig. 7.

In the analysis, no impurity is observed in the spectra; therefore, it shows pure form of prepared sample. The counts have represented in X axis as well as energy levels of counts on Y axis. The spectrum shows emitted X-rays with K and L series, which recognize the elements onto the surface of TiO_2. This is noticed; oxygen showed Ka line, whereas titanium exhibited La, Ka and Kb line. The quantitative analysis is explained in Table 4.

3.5. FTIR analysis

The Fourier transform infrared spectroscopy works on the premise that some IR radiation is absorbed when it passes through a material. It is noted which radiation enters the sample. The spectra can be employed to recognize and differentiate between molecules since different molecules, due to their various structures, emit various spectra. To access chemical interactions, the FTIR spectra of the powder made from dried pigments were carefully examined. While the peak vibrations, which

came at approximately 1042 cm^{-1}, were attributable to C–O stretching, the stretching vibrations, which appeared at approximately 3500 cm^{-1}, were indicative of the OH group. The dyes show C═O stretching vibrations at about 1740 cm^{-1}. The FTIR spectra for each dye are displayed in Fig. 8, which demonstrates the existence of carbonyl and hydroxyl groups in the dyes' molecular structure. The characteristic band at 3087 cm^{-1} indicated aromatic C–H vibrations for the Rhodamine dye [17].

4. Conclusion

In this work, mixed dye prepared by synthetic organic and natural dye has been demonstrated as a positive way to enhance overall performance of the DSSCs. The Rhodamine dye (synthetic organic) with Hibiscus sabdariffa as natural dye was used as sensitizer for fabrication of DSSC. The UV Vis absorption analysis showed high molar extinction coefficient and the absorption spectra overlapped maximum region. More significantly, the co-sensitized dye showed wider absorption in the 440–560 nm range. Photovoltaic results showed highest short circuit current of 4.02 $mAcm^{-2}$ with the highest incident power conversion efficiency of 1.23%. This improvement is attributed to panchromatic light harvesting as well as good optical activity. The adsorption of co-sensitized dye on the TiO_2 surface was improved, attributable to the smaller size of semiconductor surface aggregated pigment molecules. Based on electrochemical analysis, the charge transfer resistance of co-sensitized dye is less as compared to the single dye sensitized solar cells, which also contributes to high performances of the DSSC. It has been observed from the various experimental results that co-sensitized dye is a more prominent dye for the performance of dye solar cells. Co-sensitized cell performance improvements could be very encouraging and effective for further DSSC development. As an alternative to pure synthetic dyes based on Ruthenium complexes, the application of various combinations of synthetic organic dyes and natural dyes has the potential to improve the general performance of cells. Moreover, carbon fuschin, methyl violet, bromophenol, pyronin synthetic organic dyes with various natural sources are proposed to enhance the light scattering. It has been observed that better sensitization and enhanced photovoltaic properties can be obtained by combining effect of the different dyes for the recognition of more efficient DSSCS.

Ethics approval and consent to participate

Not Applicable.

Consent for publication

Not Applicable.

Availability of data and materials

Here critical analysis has been done with reference to earlier research work. This is a kind of comprehensive review. Hence, there is no data used.

Funding

There is no funding

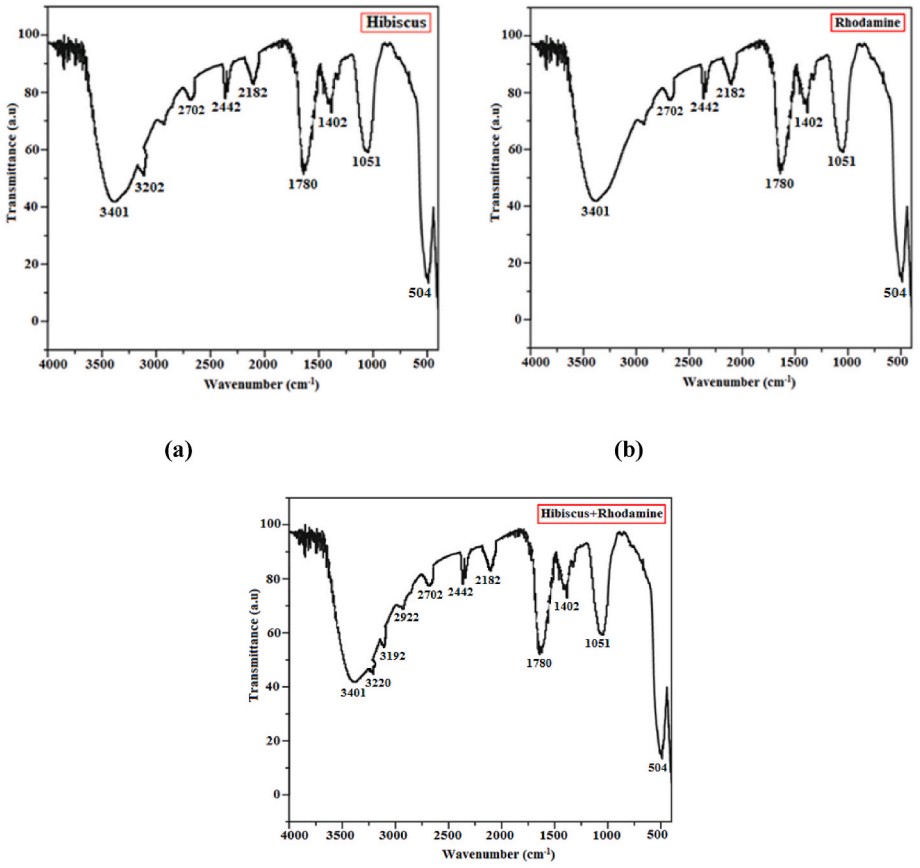


Fig. 8. FTIR analysis of the prepared dyes.

CRediT authorship contribution statement

Geetam Richhariya: Methodology, Writing – original draft, Investigation. **Anil Kumar:** Conceptualization, Writing – review & editing, Visualization, Supervision. **Akash Kumar Shukla:** Investigation, Writing – review & editing. **Kailash Nath Shukla:** Investigation, Writing – review & editing. **Issara Chanakaewsomboon:** Conceptualization.

Declaration of competing interest

The authors declare that they have no known competing financial interests or personal relationships that could have appeared to influence the work reported in this paper.

Data availability

Data will be made available on request.

Acknowledgment

Authors are highly thankful to Centre for Energy and Environment, Delhi Technological University, for providing the basic facility for this compiling.

Nomenclature

DSSCs	Dye sensitized solar cells
FF	Fill factor
FTO	Fluorine doped tin oxide
IPCE	Incident photon-to-electron conversion efficiency
NDSSCs	Natural dye sensitized solar cell
Ru	Ruthenium
V_{oc}	Open circuit voltage
J_{sc}	Short circuit current density
HOMO	Highest occupied molecular orbital
LUMO	Lowest unoccupied molecular orbital

Greek letter

H	The energy conversion efficiency

Subscript

Oc	Open circuit
Sc	Short circuit

References

[1] M.A. Green, Review of technologies and commercial status, Thin. Film Solar Cells (2005) 1–10.
[2] J. Gong, J. Liang, K. Sumathy, Review on dye sensitized solar cells (DSSCs): fundamental concepts and novel materials, Renew. Sustain. Energy Rev. 16 (2012) 5848–5860.
[3] N.A. Ludin, AM-Al Alwani Mahmoud, B. Mohamad, A.A.H. Kadhum, K. Sopian, N. S.A. Karim, Review on the development of natural dye photo sensitizer for dye sensitized solar cells, Renew. Sustain. Energy Rev. 31 (2014) 386–396.
[4] G. Richhariya, A. Kumar, P. Tekasakul, B. Gupta, Natural dyes for dye sensitized solar cell:A review, Renew. Sustain. Energy Rev. 69 (2017) 705–718.
[5] A. Suzuki, H. Okumura, Y. Yamasaki, T. Oku, Fabrication and characterization of perovskite type solar cells using phthalocyanine complexes, Appl. Surf. Sci. 488 (2019) 586–592.
[6] U. Mehmood, S. Rahman, K. Harrabi, I.A. Hussein, B.V.S. Reddy, Review Article: recent advances in dye sensitized solar cells, Adv. Mater. Sci. Eng. 1–13 (2014).
[7] Geetam Richhariya, Anil Kumar, Akash Kumar Shukla, K.N. Shukla, Bhim Charan Meikap, Effect of different counter electrodes on power conversion efficiency of DSSCs, J. Electron. Mater. 52 (2023) 60–71.
[8] S. Atsushi, K. Kobayashi, T. Oku, K. Kikuchi, Fabrication and characterization of porphyrin dye-sensitized solar cells, Mater. Chem. Phys. 129 (2011) 236–241.
[9] H. Hug, M. Bader, P. Mair, T. Glatzal, Biophotovoltaics: natural pigments in dye sensitized solar cells, Appl. Energy 115 (2014) 216–225.
[10] R.N. Monishka, Review: dye sensitized solar cells based on natural photo-sensitizers, Renew. Sustain. Energy Rev. 16 (2012) 208–215, 2012.
[11] H.P. Wu, Z.W. Ou, T.Y. Pan, C.M. Lan, W.K. Huang, E.W.G. Diau, et al., Molecular engineering of cocktail co-sensitization for efficient panchromatic porphyrin-sensitized solar cells, Energy Environ. Sci. 5 (2012) 9843–9848.
[12] M. Freitag, J. Teuscher, Y. Saygili, X. Zhang, F. Giordano, P. Liska, J. Hua, S. M. Zakeeruddin, J.E. Moser, et al., Dye sensitized solar cells for efficient power generation under ambient lighting, Nat. Photonics 11 (2017) 372.
[13] R. Chandra, H.M. Iqbal, G. Vishal, H.-S. Lee, S. Nagra, Algal biorefinery: a sustainable approach to valorize algal-based biomass towards multiple product recovery, Bioresour. Technol. 278 (2019) 346–359.
[14] A. Lim, P. Ekanayake, L.B.L. Lim, J.S. Bandara, Co-dominant effect of selected natural dye sensitizers in DSSC performance, Spectrochim. Acta Mol. Biomol. Spectrosc. 167 (2016) 26–31.
[15] M.Ahmad EliD, I. Maxwell, D. Ezra, A. Francis, S. Sarki, Dye sensitized solar cells using natural dyes extracted from roselle (Hibiscus Sabdariffa) flowers and Pawpaw (Carica Papaya) leaves as sensitizers, J. Energy Nat. Resour. 5 (1) (2016) 11–15.
[16] G. Richhariya, A. Kumar, Performance evaluation of mixed synthetic organic dye as sensitizer based dye sensitized solar cell, Opt. Mater. 111 (2021), 110658.
[17] S. Kazemifard, L. Naji, F.A. Taromi, Enhancing the photovoltaic performance of bulk heterojunction polymer solar cells by adding Rhodamine B laser dye as co-sensitizer, J. Colloid Interface Sci. 515 (2018) 139–151.
[18] W. Shah, S.M. Faraz, Z.H. Awan, Photovoltaic properties and impedance spectroscopy of dye sensitized solar cells co sensitized by natural dyes, Phys. B Condens. Matter 654 (1) (2023), 414716.
[19] B.C. Mphande, A. Pogrebnoi, Impact of extraction methods upon light absorbance of natural organic dyes for dye sensitized solar cells application, J. Energy Nat. Resour. 3 (2014) 38–45.
[20] W. Wu, F. Meng, J. Li, X. Teng, J. Hua, Co-sensitization with near-IR absorbing cyanine dye to improve photoelectric conversion of dye sensitized solar cells, Synt. Met. 159 (2009) 1028–1033.
[21] B.P. Kafle, B.R. Pokhre, R. Gyawali, A. Kafle, T.M. Shrestha, R. Shrestha, Absorbance of natural and synthetic dyes: prospect of application as sensitizers in dye sensitized solar cell, Adv. Appl. Sci. Res. 5 (2014) 8–12.
[22] E.M. Abdou, H.S. Hafez, E. Bakir, M.S.A. Abdel-Mottaleb, Photostability of low cost dye-sensitized solar cells based on natural and synthetic dyes, Spectrochim. Acta Mol. Biomol. Spectrosc. 115 (2013) 202–207.
[23] S.C. Ezike, C.N. Hyelnasinyi, M.A. Salawu, J.F. Wansah, A.N. Ossai, N.N. Agu, Synergestic effect of chlorophyll and anthocyanin co-sensitizers in TiO_2 based dye sensitized solar cells, Surface. Interfac. (2021), 100882.
[24] K.M. Darkwa, F.O. Agyemang, D. Ye, S. Akromah, Dye-sensitized solar cells based on graphene oxide and natural plant dye extract, Mater. Today Proc. 38 (2021) 514–521.
[25] S. Singh, I. C Maurya, S. Sharma, S.P.S. Kushwaha, P. SrivastavaL. Bahadur, Application of new natural dyes extracted from Nasturtium flowers (Tropaeolum majus) as photosensitizer in dye-sensitized solar cells, Optik 243 (2021), 167331.
[26] K. Sahu, M. Dhonde, V.V.S. Murty, Efficiency of solar cells employing natural dyes with plasmonicnano particle based photo anode, Int. J. Nanosci. 18 (2019), 1850049.
[27] G. Richhariya, A. Kumar, Fabrication and characterization of mixed dye: natural and synthetic organic dye, Opt. Mater. 79 (2018) 296–301.
[28] K. Wongcharee, V. Meeyoo, S. Chavadej, Dye-sensitized solar cell using natural dyes extracted from rosella and blue pea flowers, Sol. Energy Mater. Sol. Cells 91 (2007) 566–571.
[29] S. Kushwaha, L. Bahadur, Enhancement of power conversion efficiency of dye sensitized solar cells by co-sensitization of Phloxine B and Bromophenol blue dyes on ZnO photoanode, J. Luminescene 161 (2015) 426–430.
[30] S. Cakara, 1,10 phenanthroline 5,6 diol metal complex (Cu, Fe) sensitized solar cells: a cocktail dye effect, J. Power Sour. 435 (2019), 226825.
[31] M. Golshan, S. Osfouri, R. Azin, T. Jalali, N.R. Moheimani, Co-sensitization of natural and low-cost dyes for efficient panchromatic light-harvesting using dye-sensitized solar cells, J. Photochem. Photobiol. Chem. 417 (2021), 113345.
[32] Ganesh D. Sharma, Panagiotis A. Angaridis, Sophia Pipou, Galateia E. Zervaki, Vasilis Nikolaou, Rajneesh Misra, G. Athanassios, Coutsolelos, Efficient co-sensitization of dye-sensitized solar cells by novel porphyrin/triazine dye and tertiary aryl-amine organic dye, Org. Electron. 25 (2015) 295–307.
[33] J. Pan, H. Song, C. Lian, H. Liu, Y. Xie, Cocktail co-sensitization of porphyrin dyes with additional donors and acceptors for developing efficient dye-sensitized solar cells, Dyes Pigments 140 (2017) 36–46.
[34] H. Lee, J. Kim, D.Y. Kim, Y. Seo, Co-sensitization of metal free organic dyes in flexible dye sensitized solar cells, Org. Electron. 52 (2017) 103–109.
[35] P. Naik, R. Su, M.R. Elmorsy, A. El-Shafei, A.V. Adhikari, New carbazole based dyes as effective co-sensitizers for DSSCs sensitized with ruthenium (II) complex (NCSU-10), J. Energy Chem. 27 (2018) 351–360.
[36] J. Bisquert, Chemical capacitance of nanostructured semiconductors: its origin and significance for nanocomposite solar cells, Phys. Chem. Chem. Phys. 5 (2003) 5360–5364.
[37] F.F. Santiago, J. Bisquert, G. Garcia-Belmonte, G. Boschloo, A. Hagfeldt, Influence of electrolyte in transport and recombination in dye-sensitized solar cells studied by impedance spectroscopy, Sol. Energy Mater. Sol. Cell. 87 (2005) 117–131.
[38] Q. Wang, J.-E. Moser, M. Grätzel, Electrochemical impedance spectroscopic analysis of dye-sensitized solar cells, J. Phys. Chem. B 109 (2005) 14945–14953.
[39] G. Li, M. Liang, H. Wang, Z. Sun, L. Wang, Z. Wang, S. Xue, Significant enhancement of open-circuit voltage in indoline-based dye-sensitized solar cells via retarding charge recombination, Chem. Mater. 25 (2013) 1713–1722.

[40] A.K. Swarnkar, Sanjay Sahare, Nikhil Chander, Rajesh K. Gangwar, S.V. Bhoraskar, Tejashree M. Bhave, Nanocrystalline titanium dioxide sensitised with natural dyes for eco-friendly solar cell application, J. Exp. Nanosci. 10 (13) (2014).
[41] S. Sathyajothi, R. Jayavel, A. Clara Dhanemozhi, The fabrication of natural dye sensitized solar cell (dssc) based on TiO2 using henna and Beetroot dye extracts, Mater. Today Proc. 4 (2017) 668–676.
[42] F. Gracia, J.P. Holgado, A.R.G. Elipe, PhotoEfficiency and optical, microstructural, and structural properties of TiO2 thin films used as photoanodes, Langmuir 20 (2004) 1688–1697.
[43] H.J. Ahn, J.S. Lee, H.S. Kim, I.T. Hwang, J.H. Hong, J. Shin, C.H. Jung, Fabrication of large Pt nanoparticles-decorated rGO counter electrode for highly efficient DSSC, J. Ind. Eng. Chem. (Seoul, Repub. Korea) 65 (2018) 318–324.
[44] H. Wang, J. Gao, J. Zhu, J.Y. Ma, H. Zhou, J. Xiao, M. Wu, Design bifunctional nitrogen doped flexible carbon sphere electrode for dye-sensitized solar cell and supercapacitor, Electrochim. Acta 334 (2020) 135–582.

International Journal of Environmental Science and Technology
https://doi.org/10.1007/s13762-023-04953-2

ORIGINAL PAPER

End-of-life solar photovoltaic panel waste management in India: forecasting and environmental impact assessment

A. Sharma[1] · P. Mahajan[1] · R. Garg[1]

Received: 12 January 2022 / Revised: 30 January 2023 / Accepted: 18 April 2023
© The Author(s) under exclusive licence to Iranian Society of Environmentalists (IRSEN) and Science and Research Branch, Islamic Azad University 2023

Abstract
Presently, India is in the stage of installation of solar photovoltaic panels and no focus is being given towards the impending problem of handling solar waste. The absence of adequate regulations, guidelines and operational infrastructure for photovoltaic waste in the country may lead to waste being inappropriately landfilled or incinerated in a manner that may be detrimental to human health and the environment. Business as usual projection estimates 6.64 million tonnes and 5.48 million tonnes of waste generation due to the early and regular losses using the Weibull distribution function, respectively by 2040 in India. The current study also systematically investigates various policies and legislation developments on the end-of-life of photovoltaic modules in various regions of the world, to identify gaps for further assessment. Using life cycle assessment methodology, this paper compares the environmental impacts of landfilling end-of-life crystalline silicon panels with avoided burden approach due to the recycling of materials. It has been demonstrated that solar photovoltaic recycling and reusing the recovered materials will result in impact reduction in the forthcoming production phase by as high as 70%. Further, the outcomes of carbon footprint, single score indicator with the application of Intergovernmental Panel on Climate Change also predicts lower values for avoided burden approach due to recycling (15,393.96 kgCO_2 eq) in comparison to landfill approach (19,844.054 kg CO_2 eq). The outcomes of this study aim to illuminate the importance of the sustainable management of photovoltaic panels at end-of-life.

Keywords Circular economy · Landfill · Life cycle assessment · Recovery · Recycling · Solar waste generation

Introduction

With the advent of new technologies and products in markets, older products are rapidly becoming obsolete. The volume of waste, particularly, e-waste is growing rapidly. A developing country like India has become a dumping ground, because of waste accumulation not only from waste generated within the country but also from waste being dumped illegally from developed countries (Arya and Kumar 2020; Kumar and Dixit 2018, pp. 36–52). On one hand, India is still grappling with challenges to find solutions for the e-waste problem and on another hand, with growth and rapid advancement in the deployment of solar energy resources in the country, the chances of solar waste turning into a bigger environmental problem are looming large (Chaudhary and Vrat 2018, pp. 5–14; Prabhu et al 2022, pp. 507–534; BTI, 2019). World over, the major thrust is on the improvement of production efficiency, and very little or no attention is paid to the slowly but surely increasing the photovoltaic (PV) waste problem. The PV effect involves the conversion of light (photons) into electricity. The complete system of energy generation from the PV system can be divided into two parts viz. the balance of system (BOS) and PV modules. BOS is a collection of devices that includes an inverter, transformer, wiring, mounting and tracking systems, charge regulators, sun trackers, and batteries. Several studies on PV waste assessment conducted the world over have excluded the BOS wastes and focussed only on the wastes generated from the PV module or panel (Dias et al 2016, pp. 220–225; Xu et al 2018, pp. 450–458; Yi et al 2014, pp. 797–807). Solar PV panels can be broadly classified into three generations: (1) crystalline silicon (c–Si)

Editorial responsibility: Senthil Kumar Ponnusamy.

✉ A. Sharma
abhiabhi30@gmail.com

[1] Department of Electrical Engineering, Delhi Technological University, Shahbad Daulatpur, Main Bawana Road, 110042 Delhi, India

Published online: 07 May 2023

wafer based (monocrystalline or polycrystalline); (2) thin-film (amorphous silicon, cadmium telluride, copper indium gallium selenide—CIGS); and (3) concentrator photovoltaic and emerging technologies (CPV solar panels, dye-sensitized solar panels, organic solar panels, and hybrid panels). Out of these different types of PV panel modules, the most prevalent module types are wafer-based (monocrystalline and polycrystalline) and thin-film. Wafer based silicon panels in comparison to thin film solar panels have higher conversion efficiency and are the most widely used solar panels commercially. Wafer-based PV technology accounted for nearly 95% of the total production in the year 2019 (FISES, 2020). The modelling in the current study is done based on the rate of installation of crystalline technology since it is anticipated that crystalline Si-wafer-based technology will dominate the solar PV panels market share in the next decades. From the perspective of PV waste determination, the complete life cycle of a solar PV module can be divided into the following stages

a. Processing and production stage

In comparison to polycrystalline panels, the making of monocrystalline panels results in production of more waste since they are made from silicon ingot slices—leaving off-cuts, etc. However, this waste can be further utilized to make polycrystalline or multi-crystalline PV modules. In thin-film silicon panels there is a reduction in the volume of material needed as they are made by spraying a thin layer of silicon onto the surface, so has the potential to reduce impacts and waste. Production waste is the most easily managed waste as manufacturers are well equipped to handle such waste and production waste is not a societal waste management problem (IEA, 2016).

b. Transportation stage

Panels may get damaged due to their transportation from the manufacturing to the installation site. The major reason is the ill-handling of PV modules during the loading and unloading of PV panels.

c. Operation stage

Faulty installation practices along with extreme weather conditions like hailstorms, floods, cyclones, etc. may also result in the generation of solar waste during the initial and active life cycle of solar panels.

d. End-of-life stage

PV modules reach their end-of-life (EoL) stage when the overall power output of modules drops below 80% of the initial quoted value at the time of manufacture (CERC 2011). This stage will contribute to maximum waste generation typically after the actual life cycle of 25–30 years of the solar PV module (CERC 2017; Domínguez and Geyer 2017, pp. 29–41; IEA, 2016; Lugo-Laguna et al. 2021, pp. 3238; Mahmoudi et al. 2019, pp. 192–205; Paiano 2015, pp. 99–112). The exponential growth in the installation of PV capacity in recent years means there will also be a rapid increase in the number of panels reaching their EoL stage (Shin et al 2017, pp. 1–6).

Figure 1 shows various stages of solar PV waste generation during the complete life cycle of the solar PV module. The cycle shown in the continuous line is an open cycle, however, if dotted lines are incorporated, the use of raw materials is not only minimized but also burdens on the environment are also minimal. Currently, in absence of any significant waste recycling techniques, there is a high dependency on the supply of raw materials from natural resources during the production stage.

European countries played a key pioneering role during the early developments of PV. Asia's share started to grow rapidly in 2012 and it has not abated since then. Asia represented around 57% of the total cumulative installed solar PV capacity in 2019 primarily driven by China, India, Japan, Korea, and others. During 2019, around 115 GW of PV systems have been installed and commissioned in the world leading to a total cumulative installed capacity of 627 GW. Despite the shrinkage of the Chinese PV market for the second year in a row from 53.0 GW in 2017 to 43.4 GW in 2018 and 30.1 GW in 2019, China remained the leader in terms of total capacity with almost one-third of the global PV installed capacity. During 2019, India's annual market reached 9.9 GW which also includes around 1.1 GW of distributed and off-grid installations. In the top 10 countries, there are China, India, Japan, Vietnam, Australia, and Korea representing Asia–Pacific countries, three European countries namely Spain, Germany, and Ukraine, and one country in the Americas i.e., the USA (IEA, 2020).

In this paper, an attempt for estimation of solar PV waste in India by 2040 has been made using the Weibull distribution function. The study also explores the prospects of the circular economy by comparison of the environmental impacts of landfilling with avoided burden approach due to the recycling of materials that will result in substituting virgin raw materials with recycled materials in the forthcoming production stage. The paper is organised as follows: first, an analysis of the literature survey reviewed and motivation for the study, followed by a discussion on the overall methodology adopted for performing solar PV waste estimation is carried out. Next, the national and international scenarios for solar PV waste management and proposed solar PV waste reduction strategies for India are discussed. Lastly, the life cycle assessment using SimaPro software is carried out. This

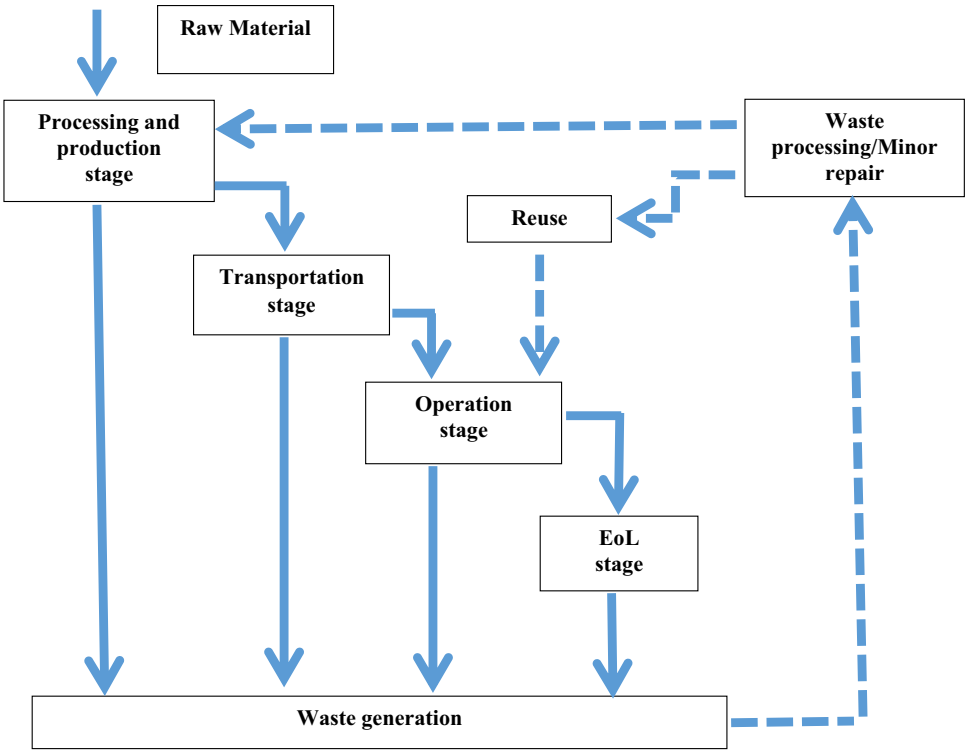


Fig. 1 Various stages of solar PV waste generation

is followed by a discussion on the overall life cycle impact comparison amongst different PV waste disposal methods and the conclusion of the study along with recommendations for future work. Finally, Appendix (Tables 4, 5, 6 and 7) is included at the end of the text, the first one showing tonnes per megawatt (t/MW) variation of Waaree solar panels, the second one showing the list of various uncertainties encountered throughout the conduct of the present study, the third one giving list of background input datasets used in life cycle inventory analysis and the last one giving the amount of recovered materials.

Different studies conducted in different regions across the world have estimated different values of accumulation of solar waste. Domínguez and Geyer (2017, pp. 29–41) estimated that in Mexico for each GW of installed PV capacity, around 4 million PV modules waste will be generated by 2045, and PV modules will constitute 691 thousand metric tonnes of PV waste. In another study done for the USA by the same authors (Domínguez and Geyer 2018, pp. 1188–1200), it is estimated between 2030 and 2060, a total of 9.8 million metric tons of PV waste will be generated that includes 6.6 million metric tons of PV modules waste, 2.7 million metric tons BOS waste, 0.3 million metric tons inverters waste, and 0.215 million metric tons transformers waste. Paiano (2015, pp. 99–112) projected the PV crystalline silicon waste amount in Italy for two periods i.e., between 2012–2038 and 2039–2050 based on the 25 years lifetime of PV panels. The estimated amount during 2012–2038 is 1,957,099 tonnes, corresponding to the photovoltaic installations from 1987 to 2013, and the amount during the period 2039–2050 as 6,281,868 tonnes, corresponding to the installations during 2014–2025. Peeters et al (2017, pp. 14–26) highlighted the uncertainty in estimating the PV waste volumes owing to the rapid development of PV technology. The authors estimated the amount and material composition of waste from silicon-based PV modules based on the theory of the bathtub curve in Flanders, Belgium. Faircloth et al (2019, pp. 260–272) estimated that in Thailand, 5000 t of PV waste will have accumulated by 2025 and by 2030, the country will be producing at least 8000 t of PV waste per year. Similarly, actual PV installation in Australia from 2001 to 2018 formed the basis for the fact that 0.8 million tonnes of cumulative PV waste will be generated by the year 2047 based on the study by Mahmoudi et al. (2019, pp. 192–205). Corcelli et al (2018, pp. 37–51) used SimaPro 8.0.4.30 and ReCiPe midpoint impact assessment method to compare two treatment scenarios that include high and low recovery rates in a laboratory scale and highlighted that the recycling of the PV panels generates large environmental benefits at the material recovery level as well as the scale of the biosphere (pollution prevention). A pilot-scale project named full recovery end-of-life photovoltaic (FRELP) for the treatment of the EoL crystalline PV modules was studied by Latunussa et al (2016b) for conducting the environmental impact assessment of the EoL PV panels based on the industry data. This study excludes the analysis of the production of secondary raw materials. For India, Pankadan et al (2021, pp. 1361–1371) predicted 0.4 million tonnes and 0.038 million tonnes of waste due to early and regular losses

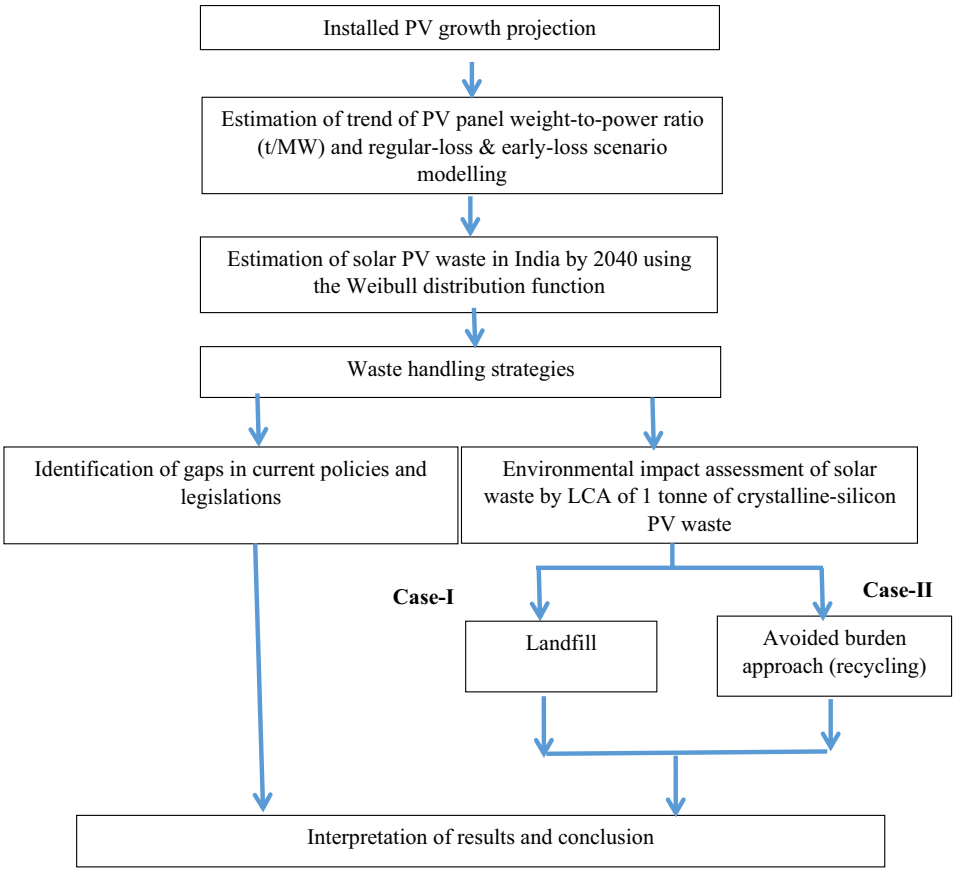


Fig. 2 Description of paper methodology

respectively by 2030, and 7.99 million tonnes and 3.61 million tonnes, due to early and regular losses respectively by 2050.

It is revealed from the literature review that most of the studies are concentrated particularly towards solar PV waste estimation, life cycle, and economic assessment of PV panels, but still, there are considerable gaps in these studies, as the success of the EoL solution of solar PV panels depends on the robustness of local regulatory and policy framework and overall participation of various stakeholders viz. original equipment manufacturers, solar PV system installers, consumers, recyclers, and various government organizations. None of these studies conducted so far has highlighted the enormity of the impending solar PV waste problem in India. In comparison to the available scattered literature on solar PV waste estimation in India, the present study also highlights the effect of the COVID-19 pandemic on waste volumes. Presently, solar PV module and battery waste are considered general electronic waste and its effective and safe disposal come under the Ministry of Environment, Forest and Climate Change (MoEFCC), and even despite the presence of the e-waste regulation in place since 2011, only 5% of the estimated e-waste is recycled in the organized or formal sector (Turaga et al 2019, pp. 127–162). India is undergoing a clean energy transition. The government is implementing various programmes and regulatory measures into place to raise the percentage of renewable energy sources in the overall mix of electricity. Among different renewable energy sources, significant capacity addition in solar energy in the form of rooftop and utility-scale solar installation has been made. Solar power from an energy requirement point of view promises a bright future for India, but behind the gleam is a growing mountain of e-waste. With the current growth rate of solar PV, the solar waste problem will turn into a serious environmental problem in the next decades unless addressed at this stage. The country lacks even conventional recycling facilities to separate glass and aluminium frames from the modules.

To this end, the present study is undertaken to estimate the volume of solar PV waste in India, particularly at the time when the country is undergoing a massive solar capacity expansion programme and also presents an environmentally benign strategy to policymakers for the handling of solar waste using life cycle assessment (LCA) methodology. The role of avoided burden approach due to recycling of materials from the point of view of circular economy prospects has been discussed. Additionally, the breakups of the amount of materials that can be recovered along with environmental gains associated with their replacement from virgin material are also discussed.

Materials and methods

PV panel waste volume will increase along with the PV deployment rate. One of the easiest ways to predict waste streams is by considering a fixed loss scenario. This scenario assumes that after the lifetime of the PV panel (25–30 years) it will be discarded. On the other hand, the cumulative PV waste generation can be obtained more accurately for regular-loss and early-loss scenarios by the multiplication of the probability distribution function with the weight of panels installed in a particular year. In this paper, the methodology as shown in Fig. 2 has been adopted. Despite every effort that has been made in the present study to predict the solar waste data and its effect on the environment with accuracy, various assumptions have been taken throughout the study that may affect the outcomes. The probable sources of some of the uncertainties are given in the Appendix (Table 5).

Solar PV waste estimation

Without waiting for the end of life of solar cells which typically varies from 25 to 30 years the slowly and surely increasing problem of solar waste can be best addressed by estimating solar waste using a mathematical probability distribution function based on its projected growth. In India, significant solar PV installation started near the year 2010, the corresponding PV waste due to regular loss scenario should be generated by 2035–2040 (RS 2021b) and it can be said that the critical point from a waste generation point of view, will reach by 2040. To estimate the solar PV waste in India firstly, futuristic PV installed capacity is projected under two scenarios i.e., the business as usual (BAU) scenario and the ambitious scenario. Secondly, tonnes/MW projection to estimate the weight of waste generated is carried out. Finally, mathematical modelling using Weibull distribution is carried out to predict waste volumes.

Installed PV growth projection

In India, the cumulative capacity of solar PV installation as on 31.03.2022 is 53997 MW and that constitutes a share of 13.5% in overall installed capacity compared to 10 MW in 2010 (MoP 2022; NITI 2021).

The government of India is committed to achieving an already set target of 100 GW of solar energy by 2022 (RS 2021a). With the BAU scenario, cumulative solar installed capacity will reach around 339 GW by 2040. The genesis of the ambitious scenario is the numbers provided by NITI Aayog given under the draft national energy policy (NITI 2017). The anticipated cumulative capacity at the end of 2040 will be 395 GW. The anticipated maximum solar capacity of India is 750 GW (PIB 2020), therefore even if the ambitious scenario is considered; only approximately 50% of the maximum solar capacity of India will be achieved by 2040. These anticipated projections will form the basis for the estimation of solar PV waste.

Tonnes/MW estimation

Waste estimation depends on the weight of the panel being used for installation. The advancement of technology has resulted in thinner frames, glass layers, and wafers along with improved efficiencies thereby resulting in lighter solar panels in other words given the same weight of the panel, more wattage can be accommodated now. The factor t/MW or kg per watt depends on the type of solar technology, size & weight of the panel, solar cell efficiency, and other characteristics of the panels. Earlier studies across the world have taken this factor in the range of 90–100 t/MW (HBR 2021; Sander et al 2007). However, in the present study, no constant factor for t/MW has been taken rather its value has been extrapolated, and thus values are more reflective of the expected future weights of installed solar PV panels. The major challenge encountered in obtaining this information from ecoinvent or from the datasheet of solar modules is the lack of availability of data pertaining to the weight of the PV model vis-a-vis its manufacturing year. Therefore, in the present study, the information pertaining to the yearly variation of t/MW of one of the major solar PV manufacturer companies in India i.e., Waaree renewable technologies ltd. has been obtained via correspondence through email Appendix (Table 4).

The obtained data have been fitted appropriately to an exponentially decreasing function given by Eq. 1.

$$\text{Mass to power ratio } \left(\frac{t}{MW}\right) \textit{for } i^{th} \text{ year} = A \cdot e^{-i/B} \quad (1)$$

where, $A = 89.416$ t/MW, B (exponential time constant) $= 37.037$ and the value R^2 corresponding to the

Table 1 Values of the average lifetime of solar panels reported in various studies

Region	Global (IEA, 2016)	Europe (Lugo-Laguna et al. 2021, p. 3238)	Italy (Paiano 2015, pp. 99–112)	Mexico (Domínguez and Geyer 2017, pp. 29–41)	Australia (Mahmoudi et al. 2019, pp. 192–205)	India (Present study)
Average lifetime (year)	30	25	25	30	30	25

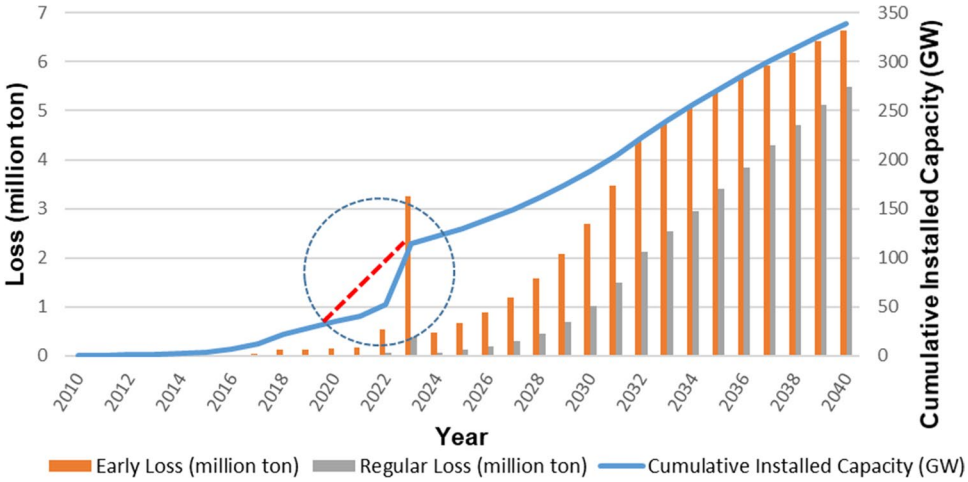


Fig. 3 Estimation of PV panel waste using early and regular loss scenarios for India

coefficient of determination of fitting has been taken as 0.9691.

Mathematical modelling using Weibull distribution

Solar module failures like a failure in other equipment, subsystem, or components follow the "bathtub" curve i.e., most common failures occur near the beginning and near the end of the component's lifetime. The three main PV panel failure phases are 1. Infant mortality failure, 2. Midlife failure, and 3. Wear-out failure (IEA, 2014).

Infant mortality occurs at the commencement of the working life cycle, and midlife failures of PV occur from five to eleven years after installation. Further, wear-out failures like delamination, occur from after 12 years of installation to 25–30 years i.e., at the end of the lifetime of PV modules (IEA, 2016).

The anticipated lifetime of PV modules spans several decades in the range of 25–30 years. Device lifespan is the amount of time a device operates as intended, in accordance with design standards, and under predetermined circumstances, before failing. Device life expectancy typically follows a probability distribution. The materials used for manufacturing solar PV cells and design are continually changing to reduce the levelised cost of energy (LCOE) (Sharma et al 2021, pp. 126–147) and the researchers cannot wait for the end of the anticipated life of 25–30 years to identify the failure modes and mechanisms. In the present study for carrying out failure and reliability analysis of solar modules, Weibull statistics have been utilized. Weibull statistics is one of the most widely used lifetime distributions in reliability engineering and is used to assess product reliability, analyse life data, and model failure time. Weibull models can include up to three parameters: shape (α), lifespan or scale (δ), and failure-free life or location (θ). In a two-parametric Weibull model, the location parameter (θ) is set to 0.

The probability density function can be written as: (Kumar and Sarkar 2013, pp. 129–134)

$$f(x) = \frac{\alpha}{\delta}\left(\frac{x-\theta}{\delta}\right)^{\alpha-1} e^{-\frac{(x-\theta)\alpha}{\delta}} \tag{2}$$

The Weibull function for reliability can be deduced from Eq. 2 and is given by Eq. 3 as:

$$R(x) = e^{-\frac{(x-\theta)\alpha}{\delta}} \tag{3}$$

The Weibull failure rate function i.e. $\lambda(x)$ is the ratio $f(x)$ to $R(x)$ and is given as

$$\lambda(x) = \frac{f(x)}{R(x)} = \frac{\alpha}{\delta}\left(\frac{x-\theta}{\delta}\right)^{\alpha-1} \tag{4}$$

Thus, to estimate the failure rate over time, the parameters α and δ need to be determined.

The above Weibull cumulative distribution function can be transformed into a straight-line equation form i.e., $Y = \mathrm{mX} + b$: (Kumar and Sarkar 2013) as given in Eq. 5

$$F(t) = 1 - e^{-\left(\frac{t}{T}\right)^{\alpha}} \tag{5}$$

where, t = time in years and T = average lifetime. The shape parameter α controls the typical S shape of the Weibull curve and describes how the failure rate changes over time. If, $\alpha < 1$, the failure rate decreases with time and is commonly associated with infantile failures or early life failures. If $\alpha = 1$ means the failure rate is constant. If $\alpha > 1$ means the failure rate increases with time and is associated with failures related to mechanical wear-out failures. Different studies the world over have taken different values of the average lifetime of solar panels varying between 25 and 30 years. An overview of the value of the average lifetime reported in various studies is given in Table 1. The average lifetime of 25 years is taken in the present study based on the Ministry of New and Renewable Energy (MNRE) regulation (CERC 2017).

The shape factor α determines the probability of regular-loss and early-loss scenarios during the panel life cycle. The present study uses 2.4928 and 5.3759 as the values of shape factors (α) for early-loss and regular-loss scenarios respectively (IEA-PVPS 2014a; IEA-PVPS 2014b; SunPower Corp, 2011).

PV panel waste projections: analysis and comparison with other studies

The COVID-19 outbreak affected the solar industry sector at a time when the country's solar project execution was at its peak. India has ambitious targets of achieving 100GW solar energy target by 2022 (RS 2021a).

Due to COVID-19, India's installed solar capacity suffered a 56% decline in the calendar year 2020 as compared to 2019 (MERCOM India 2019) mainly due to the disruption of supply chains, workforce availability, and a brake on solar equipment imports from China. The fact is evident from the dip in installed capacity during the year 2020–2021 as shown in Fig. 3. The purpose of the dotted circle in Fig. 3 is to highlight the effect of the COVID-19 pandemic on solar PV installation in India. The COVID-19 pandemic has posed tough challenges by impacting the pace of development and commissioning of renewable energy projects. Accordingly, several steps were initiated like an auction of new tenders, extensions of deadlines, advising states to maintain the sanctity of agreements, and ensuring certainty in supporting regulations for renewables to bring the sector back to the path of recovery (BTI 2020). Figure 3 also depicts an increase in installed capacity after a decline in 2020–21 due to the increased pace of implementation of projects that could not be implemented due to various COVID restrictions and lockdowns. Similar trends have also been obtained under the analysis of an ambitious scenario wherein a cumulative capacity of 395 GW will be achieved by 2040. Based on cumulative installed capacity by 2040 under BAU, the cumulative PV waste generation due to early and regular loss scenarios are 6.64 million tonnes and 5.48 million tonnes respectively and under the ambitious scenario by 2040, the cumulative PV waste generation due to early and regular loss scenario is 10.30 million tonnes and 8.51 million tonnes respectively.

India's solar waste prediction was also carried out by IEA (2016) and Pankadan et al (2021, pp. 1361–1371). IEA study predicted solar PV waste could average 50,000–320,000 tonnes by 2030, possibly ending in 4.4 to 7.5 million tonnes by 2050. Similarly, another study by Pankadan et al (2021, pp. 1361–1371) predicted 0.4 million tonnes and 0.038 million tonnes of PV waste generation due to early and regular losses, respectively for India by 2030, and 7.99 million tonnes and 3.61 million tonnes of waste generation due to early and regular losses, respectively by 2050. The main reason for the variation of waste volumes in the present study and studies conducted earlier for India is the variation in the projection of installed capacities since the present study includes the disruptions of the solar market due to the COVID-19 pandemic otherwise the figure would have followed the dotted path (Fig. 3) and accordingly early loss figures would be quite less secondly present study assumes a 25-year lifetime for solar panels, in contrast to 30 year lifetime in IEA (2016) study and 25–30 year in the study conducted by Pankadan et al (2021, pp. 1361–1371). Thirdly present study uses power-to-weight ratio trends of an Indian solar manufacturer i.e., Waaree for the period 2015–2021 while the IEA study uses panel datasheet of leading producers of the world for the period 1980–2013 and the other study is silent on values of power-to-weight ratios.

Waste management: national and international scenario

India will likely face serious challenges regarding mechanisms to address the management of solar PV waste and its disposal in the near future as solar power waste management is a neglected sector and follows an unregularised, unscientific, and informal approach (Sheoran, Sharma and Kumar, 2020). An online PV waste monitoring system either at the early stage or EoL stage will help in assessing the flow of all discarded modules. This assessment will provide input for authorities and other stakeholders to develop regulations and policies. In a developing country like India, the model commonly found is based on a linear economy, in which different extracted raw materials are processed to make the end product, then transported to the user site, and finally discarded as waste at the EoL cycle of the product. However, in a circular economy, waste streams by different processes are converted into basic raw materials thus a continuous closed cycle will be initiated by bringing back waste to the material flow cycle. India notified the E-waste management rules, 2016 (CPCB 2018) and as compared to the E-waste (management & handling) rules, 2011, the key difference is the provision of extended producer responsibility (EPR) to ensure that electronic products are recovered for safe recycling. However, the rules are silent about solar PV waste and there is always a risk that waste PV modules end up in uncontrolled or not environmentally sound disposal operations such as uncontrolled or illegal landfills or open land (EU 2021). Lack of incentives, regulatory policies, and knowledge about the value of extractable materials and their corresponding environmental impacts are major hindrances in the safe disposal of PV waste material. Globally, it has been estimated that only 10% of the total solar PV waste is currently recycled which indicates a massive gap in the availability of the operational infrastructure (Lunardi et al 2018, pp. 9–27). With prodigious growth, the problem of solar PV waste management is inching slowly to an alarming stage in absence of a legislative and regulatory framework. Except for waste regulation for solar PV in European Union, all other

major countries lack regulation on solar PV waste disposal and relies on non-regulatory approaches to managing solar PV waste. A list of development in some major regions of the world is summarised below (IEA, 2018; Pankadan et al 2021, pp. 1361–1371; SunShot 2016).

1. *United States of America*: There is no specific federal law or regulations so presently only laws pertaining to general waste apply however, some states like California, and Washington are developing their regulation or law for PV module utilization and recycling.
2. *European Union*: First Waste electric and electronic equipment (WEEE) directive of 2003 was silent on tackling PV waste. However, modified WEEE include EoL management of PV module and as per the latest WEEE directive, PV manufacturers will have the main liability for the costs of collection, handling, and treatment of PV waste irrespective of the location of the manufacturing facility. The modified directive is applicable to all European Union members.
3. *China*: At present, there is no federal law or disposal mechanism however, PV Recycling and Safety Disposal Research programme by National High-tech R&D has provided recommendations for developing policy guidelines for addressing PV waste challenges.
4. *Japan*: The country is still in stage of developing guidelines for PV recycling. However, substantial progress is made in developing and testing technology for the recycling of PV panels.
5. *India*: In India, there is no central regulation and PV waste is treated under general waste regulations that have limited scope and apply to household electronics products only.

Strategies for India

Both the Indian government and the Indian solar industry use the E-Waste Management Rules 2016 as reference law in the absence of any rules. For example, the guidelines of Solar Energy Corporation of India Limited (SECI) for setting up grid-connected solar PV plants state that "the solar power developer will ensure that all solar PV modules from their plant after their 'end-of-life' (when they become defective/ non-operational/ non-repairable) are disposed of in accordance with the "e-waste (management and handling) rules, 2011" notified by the government and as revised and amended from time to time." (SECI 2017). Thus, there is significant scope for a regulated approach to solar waste management that will lead to environmental benefits and enhance the prospects of the circular economy by substituting virgin material manufacturing with recycled material. The following section discusses the probable waste mitigation strategies for India along with their limitations.

Reduce

The thumb rule for handling waste is first to reduce, reuse, and then recycle. Solar waste volumes can be considerably reduced by improvement in the design of products and manufacturing processes. The use of various hazardous materials like lead, cadmium, and selenium can be limited by extensive research and development. Similarly, the use of silver can be avoided due to advancements in inkjet and screen-printing technologies. New and innovative techniques in printing and pastes have been projected to reduce silver consumption from 0.16 g/Wp in 2005 to less than 0.1 g/Wp in 2020 (Perez-Santalla 2013). Efforts should be made to design a product with fewer amounts of hazardous materials. Careful handling of modules during transportation and operation stages will also result in a decrease in waste volumes.

Reuse

Both reusing and recycling strive to achieve a common goal but are different terms that are not interchangeable. Reuse is a means to prevent waste streams from entering landfills. It is the action or practice of using an item, whether for its original purpose or to fulfil a different function thus increasing the occupational well-being of citizens by taking useful products discarded by those who no longer want them and providing them to those who do. Further, recycling results in keeping waste materials out of the landfill by "collecting, segregating, processing, and manufacturing collected goods into new products" (Kralj and Markic 2008, pp. 409–418). The flaws and imperfections discovered during the early phase of a PV panel's lifecycle can be easily handled by imparting specific training and skill on PV panel repairs. In addition to extending the lifespan of PV panels, this will create a market where repaired PV panels can be sold at a lower market price than new or as used panels. A second-hand market can be developed for repaired panels and for panels that have lived up to their nominal lifetime, after necessary repairs.

Recycle

Not only solar-panel production is a highly energy-intensive process but also the presence of hazardous materials like lead, cadmium in the end-of-life panels can cause significant pollution and health issues if discharged into the environment. Therefore, the recycling of waste solar panels can reduce energy waste and environmental pollution (Cucchiella et al 2015, pp. 263–272). In the comparison of P–V and I–V characteristics of old, recycled, and new PV modules, it is observed that the characteristics of the recycled module are at par with the new module (Ashfaq et al 2017, pp. 22–28). Recycling constituent materials of solar PV

back to manufacturing will cut down imports from natural resources. There is a scope for reduction in the EoL solar PV waste in the range of 60%-90% due to the high potential of recyclability rates of the constituent solar PV materials (Domínguez and Geyer 2017, pp. 29–41; Domínguez and Geyer 2018, pp. 1188–1200; Santos and Alonso-García, 2018, pp. 1613–1628).

Based on the above discussions, dedicated PV panel recycling plants are needed to be created, even though waste recovery models are not economically viable at the present stage owing to low to moderate values of PV waste generation. The government may consider incentivizing the waste recovery units for a few initial years. The treatment of solar PV waste requires significant importance not only from environmental benefits arising from the treatment of waste but also has economic significance since the recovery of materials can be used as raw material during different stages of solar PV panels production. The solar PV waste recycling industry can be considered a secondary mining industry.

Landfill

Improper waste disposal at landfill sites as the case with e-waste disposal will result in the leaching of lead and cadmium into groundwater and will result in further worsening groundwater quality. Leaching of lead may result in reduced growth of flora and fauna, destruction of habitat, and adverse health hazards on the nervous, kidney, immune, and reproductive function systems in the human body. It may also result in impaired brain development in children. Cadmium is a highly toxic carcinogen and is linked to lung, human prostate and renal cancer (BTI, 2019). Landfill as an option for solar waste disposal is the easiest to implement but not only it results in the loss of valuable materials but also results in economic loss and should be assigned the lowest priority while designing solar waste disposal strategies. The improper treatment of PV waste may result in the loss of potentially conventionally reusable materials like aluminium and glass which have a share of 88% in terms of weight (Latunussa et al 2016a, pp. 101–111). Not only this, but the landfill will also result in the loss of rare and/or critical metals (e.g., silicon metal) and precious metals like silver, a well-known conductor, though found in a small quantity. WEEE directive based on EPR encourages resource efficiency through reuse, recycling, and minimising the dumping of waste in landfills (Farrell et al 2020).

In April 2019, the MNRE issued a blueprint under the directions of the National Green Tribunal in Delhi, MNRE has released the concept note for the disposal, utilization, manufacturing, and import of solar PV but no progress has been made since then (MERCOM India 2019). Apart from the '3Rs' concept of sustainable waste management, i.e. reduce, reuse, and recycle, a multi-sector and multi-stakeholder coordinated approach among various ministries like MNRE, MoEFCC, Ministry of Power (MoP), SECI, solar PV manufacturers, and other stakeholders along with extended producer responsibility legislation that will cover collection, recovery, and recycling of solar PV modules is the need of the hour to tackle solar PV waste challenges.

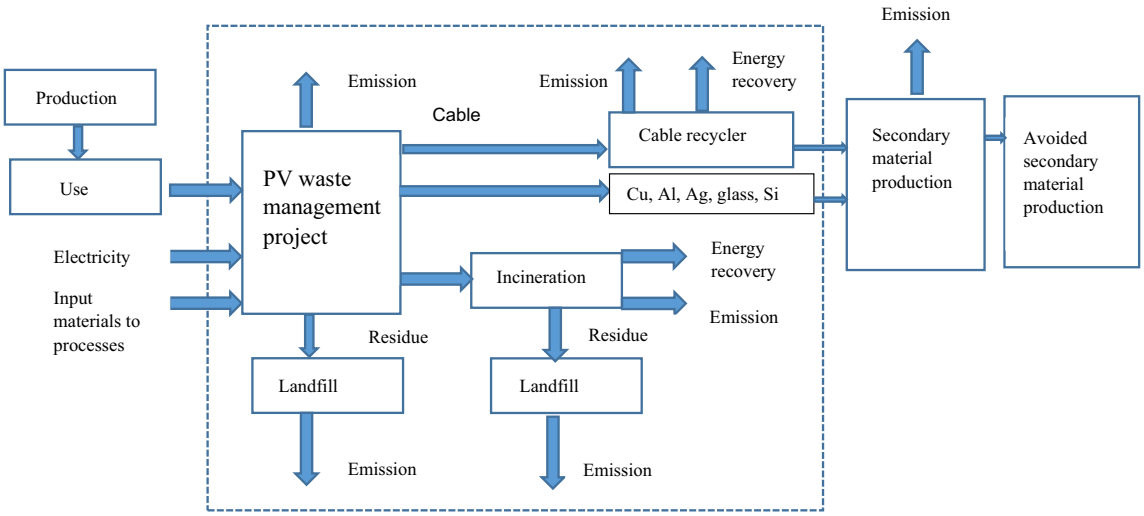


Fig. 4 System boundaries for FRELP (Latunussa et al 2016b)

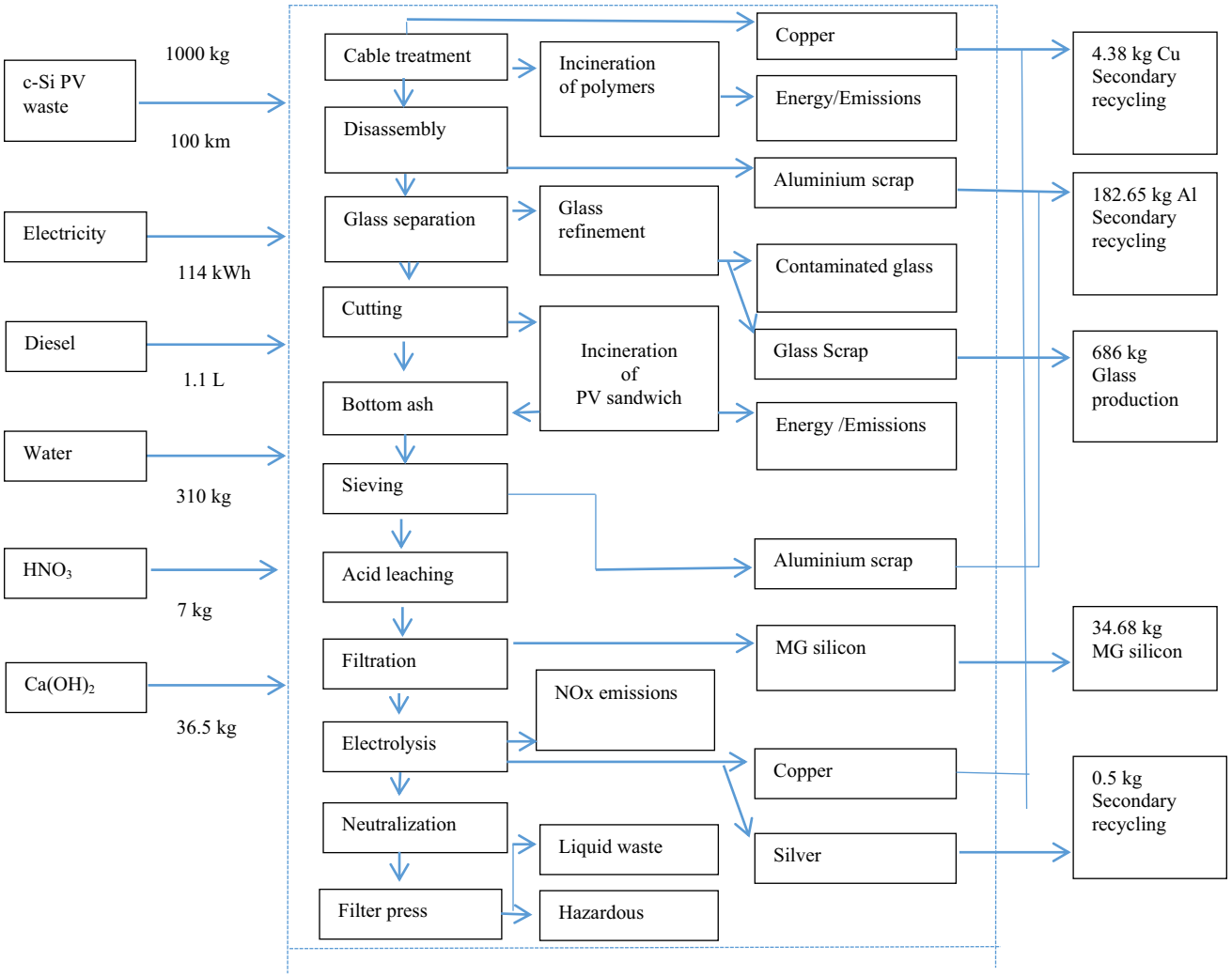


Fig. 5 System diagram showing input and output stream for the FRELP recycling process (FRELP, 2015)

Life cycle assessment methodologies

The LCA is an objective procedure for assessing the energy and environmental loads related to a process or activity, carried out by identifying the energy and materials used, and the waste released into the environment (SETAC 2019). According to ISO 14040 series (ISO 2016), the analysis of LCA consists of four consecutive steps. A LCA study is initiated by defining the goals & scope, the functional unit, and the system boundary of the study in the first step. Identifying the inputs and outputs related to each stage of a product's life cycle is the next step, referred to as a life cycle inventory (LCI). In the life cycle impact assessment (LCIA) step, the evaluation of potential impacts based on the inventory is carried out. The results of the impact assessment are analysed in final step known as the interpretation phase. The analysis of the data completeness, sensitivity, and consistency is also part of interpretation step. To carry out an LCA study, the goals and scope of the study must be explicitly stated. On basis of the inventory of energy and material, the evaluation of potential environmental impacts is assessed. The functional unit (FU) that provides a reference to which the inputs and outputs can be related must be clearly defined. The FU in the present analysis is the treatment of 1000 kg of c–Si PV waste in a recycling facility. The system boundary of an LCA should be in accordance with the stated goal of the study and it defines the unit processes to be included in the system for analysis. Presently there is no EoL recycling legislative framework in India for the

Table 2 Overall impacts of solar manufacturing process

Impact category	Unit	Solar PV manufacturing (c–Si)
Global warming	kg CO_2 eq	22,749.859
Stratospheric ozone depletion	kg CFC11 eq	0.007307048
Ionizing radiation	kBq Co-60 eq	108.91387
Ozone formation, Human health	kg NOx eq	48.103837
Fine particulate matter formation	kg PM2.5 eq	21.617138
Ozone formation, Terrestrial ecosystems	kg NOx eq	50.23211
Terrestrial acidification	kg SO_2 eq	75.725588
Freshwater eutrophication	kg P eq	2.036668
Marine eutrophication	kg N eq	0.66197535
Terrestrial ecotoxicity	kg 1,4-DCB	174,726.93
Freshwater ecotoxicity	kg 1,4-DCB	10.334238
Marine ecotoxicity	kg 1,4-DCB	58.395577
Human carcinogenic toxicity	kg 1,4-DCB	2.6683154
Human non-carcinogenic toxicity	kg 1,4-DCB	330.18233
Land use	m^2a crop eq	400.1602
Mineral resource scarcity	kg Cu eq	88.426529
Fossil resource scarcity	kg oil eq	5198.4594
Water consumption	m^3	564.27006

processing of PV waste. Laminated glass recycling facility processing does not require a dedicated recycling plant but recovers only aluminium, glass, and copper while various recoverable from solar cells are not recovered and this facility requires small batches of PV waste rather than a constant stream (Faircloth et al 2019, pp. 260–272) while FRELP method developed an Italian PV waste company SASIL S.p.a for recycling of PV is considered to be most advanced method and reduces the lifetime environmental impact by 10–15% as compared to other recycling methods is used in the present study (Latunussa et al 2016b). The system boundaries of the FRELP process (see Fig. 4) that have been taken in the present analysis exclude processing of the aluminium, glass, copper, silver, and silicon in additional plants for the production of secondary materials (Latunussa et al 2016b). The objective of this study is not only to measure the absolute values in each impact category of various disposal cases but rather to compare commonly used disposal methods to come to more definitive conclusions about how PV waste should be disposed of rationally to minimize environmental burdens.

The LCA analysis is done using SimaPro software version 8.0 (SimaPro 2021a). The ReCiPe 2016 midpoint V1.03/World (2010) method is used to analyse environmental impacts under 18 impact categories (SimaPro

Table 3 An overall impact comparison of LCIA results (SimaPro 2021a)

Impact category	Unit	Landfill (Case I)	Avoided burden approach (recycling) (Case II)	% Impact change
Global warming	kg CO_2 eq	73.7527	− 5124.95	− 22.5274
Stratospheric ozone depletion	kg CFC-11 eq	1.29E-05	− 0.00069	− 9.44294
Ionizing radiation	kBq Co-60 eq	0.169903	− 9.68052	− 8.88823
Ozone formation, Human health	kg NOx eq	0.151898	− 11.0117	− 22.8915
Fine particulate matter formation	kg PM2.5 eq	0.016694	− 3.42764	− 15.8561
Ozone formation, Terrestrial ecosystems	kg NOx eq	0.155352	− 11.1429	− 22.1828
Terrestrial acidification	kg SO_2 eq	0.091477	− 21.9033	− 28.9246
Freshwater eutrophication	kg P eq	0.000387	− 0.60427	− 29.6695
Marine eutrophication	kg N eq	0.000167	− 0.01886	− 2.84905
Terrestrial ecotoxicity	kg 1,4-DCB	184.0005	− 6151.99	− 3.52092
Freshwater ecotoxicity	kg 1,4-DCB	0.139588	− 3.33188	− 32.2412
Marine ecotoxicity	kg 1,4-DCB	0.128903	− 20.8427	− 35.6923
Human carcinogenic toxicity	kg 1,4-DCB	0.182906	− 0.85843	− 32.1712
Human non-carcinogenic toxicity	kg 1,4-DCB	0.965908	− 37.1778	− 11.2598
Land use	m^2a crop eq	2.635054	− 137.462	− 34.3517
Mineral resource scarcity	kg Cu eq	0.035884	− 62.3286	− 70.4863
Fossil resource scarcity	kg oil eq	8.492743	− 978.131	− 18.8158
Water consumption	m^3	0.156098	− 27.0175	− 4.78804

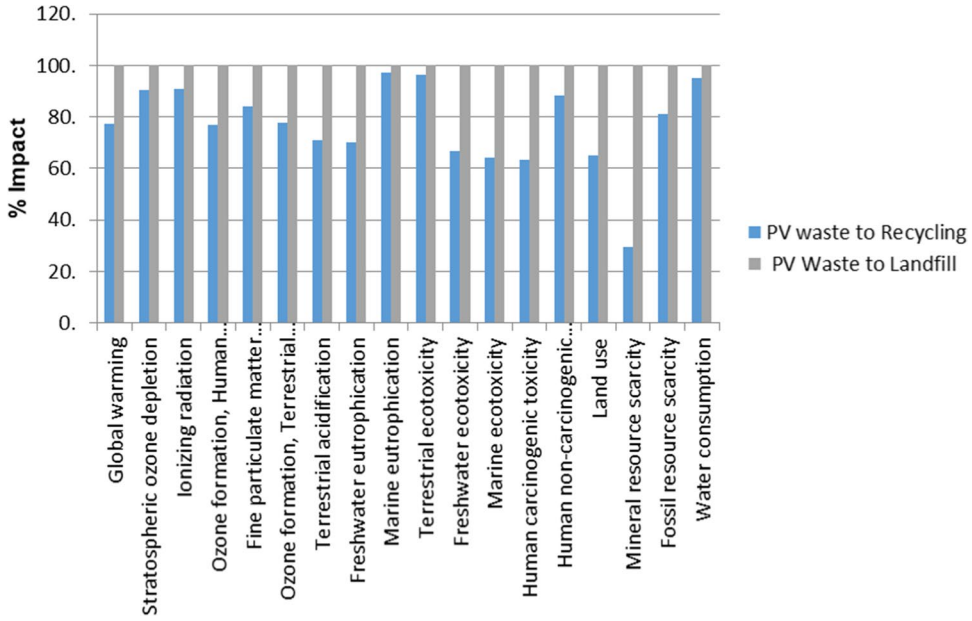


Fig. 6 Comparative illustration of LCA results

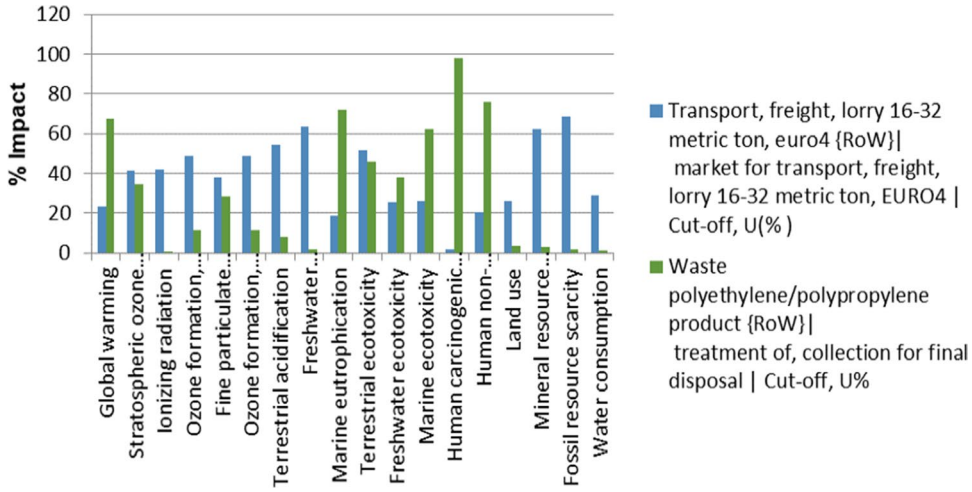


Fig. 7 Effect of transport and waste product treatment on various impact categories

2021b). SimaPro allows users to model and analyse complicated life cycles in a systematic, transparent manner in accordance to recommendations of ISO 14040 series. The input to the software is life cycle inventory (LCI) data for different cases. The present study has relied on European data set in case of the absence of a relevant Indian dataset. The LCI for the EoL phase is collated using the FRELP method. The results and their subsequent interpretation are discussed in the following section. The list of selected background input datasets used in the LCI modelling of 1000 kg solar PV waste in the present study is given in the Appendix (Table 6).

The laboratory tests provided by the FRELP are used to determine the composition of the PV module and the amount of materials that can be recovered are presented in the Appendix (Table 7). The system diagram for the FRELP process used by the SASIL group in Italy for recovering materials from 1000 kg of PV waste is given in Fig. 5 (FRELP, 2015).

The embodied energy requirement for the entire EoL treatment of c-Si PV modules is around114 kWh/tonne of PV waste as per the FRELP process. The electrical and thermal energy quantities recovered from the incineration process of cable polymer and PV encapsulation layer are

248.84 MJ and 502.84 MJ respectively (Latunussa et al 2016a, pp. 101–111). These quantities have been credited to the FU in terms of avoided impacts on the production of electricity and heat from conventional sources.

Firstly, the LCA analysis has been undertaken to assess the impact of 1 tonne of solar panel production (72.72 m^2). The overall results from solar manufacturing impact assessments are presented in Table 2. Large amounts of energy are used to convert silica sand into the high-purity silicon required for photovoltaic wafers. The purification of metallurgical-grade (MG) silicon into electronic-grade silicon during the process of producing PV cells requires 1190 MJ/panel (Stoppato 2008, pp. 224–232). Due to the addition of high-energy content aluminium framing and glass roofing, the PV module assembly process also consumes a lot of resources. The 18 impact categories that Recipe midpoint method models to assess the potential environmental impacts are global warming, stratospheric ozone depletion, ionizing radiation, ozone formation, human health, fine particulate matter formation, ozone formation, terrestrial ecosystems, terrestrial acidification, freshwater eutrophication, marine eutrophication, terrestrial ecotoxicity, freshwater ecotoxicity, marine ecotoxicity, human carcinogenic toxicity, human non-carcinogenic toxicity, land use, mineral resource scarcity, fossil resource scarcity, and water consumption.

For the solar PV manufacturing process, fossil fuel and energy use impact climate change and air quality (acidification, particulate matter, etc.) as a large amount of greenhouse gas (GHG) and hazardous pollutants are released into the atmosphere. There is a large amount of consumption of energy and material such as aluminium, copper, glass, etc. The process entails the extraction of raw material, manufacture, i.e., cell–matrix production, cutting of foils and washing of glass, laminate production, isolation, and the aluminium frame of the panel.

India has no specific regulations for solar module waste disposal, thus, the main portion of solar waste is regarded as general e-waste and dumped in an unscientific manner in landfills (EU, 2021) therefore in case I, the LCA analysis has been undertaken considering that all the material at EoL goes in a landfill and impacts associated with same are studied.

In case II, avoided burden approach has been considered wherein it has been considered that solar waste materials are sent for recycling and the impact includes avoided burden due to material recycling. The recovered materials at the EoL phase are recycled back to the manufacturing phase to gauge circular economy prospects in terms of the reduction of various environmental parameters. The potential environmental impacts associated with the production of secondary material result in avoided burden as the solar PV recycling process yields recyclable materials such as aluminium, glass, copper, and other materials, the input of virgin material into the solar PV manufacturing process can be replaced with recycled material.

Results and discussion

Table 3 provides results of LCIA comparison for the case I and Case II and it can be observed from the results that impact produced under a landfill of 1000 kg c-Si PV panels produces greater environmental impacts in all 18 impact categories as compared to avoided burden approach due to recycling of materials using FRELP. The LCA analysis is done on SimaPro software version 8.0 (SimaPro 2021a) using the ReCiPe 2016 midpoint V1.03/World (2010) method to analyse environmental impacts under 18 impact categories. A list of background data sets given in the Appendix (Table 6) is used to undertake the analysis.

Figure 6 gives a comparative illustration of LCA results for the case I and case II. The major impacts associated with the case I are due to the transport and collection and treatment of waste polyethylene/polypropylene products.

Figure 7 gives a comparative percentage share due to these two parameters across all 18 impact categories and it is observed that the effect of collection, and treatment of waste polyethylene/polypropylene products under human carcinogenic toxicity is around 98%, human non-carcinogenic toxicity (76%), marine eutrophication (72%) and global warming (67%).

While the effect of transport is highest under fossil resource scarcity is around 68% freshwater eutrophication (64%), mineral resource scarcity (62%) and terrestrial acidification (54%). The overall environmental impacts are lower in all categories under case II on account of the obvious reason of recycling benefit of the material as it will result in the reduction of virgin material usage. Resource extraction and material production are some of the highest impact contributors to solar PV production, thus recycling solar PV module components can result in avoidance of the use of virgin material for production, and lesser energy and resources for extraction and further processes will be required. A ton of aluminium (virgin metal) produced in India can have GHG emissions in the range of 16–20 T CO_2 (Hindalco 2020), however as aluminium is recyclable, at EoL if aluminium products are recycled back into the manufacturing stream, the GHG emissions are reduced by 92% as the recycling aluminium requires 95% lesser energy than the virgin metal production (NITI

2019). Similarly, other materials such as glass, copper, silicon, silver etc. also require extensive energy, and recycling the material at the EoL back into the manufacturing and process stream can significantly reduce environmental impacts across all impact categories. Recycling of aluminium resulted in an 82% reduction in the stratospheric ozone depletion category, a 76% reduction across global warming, and an ozone formation category. Recycling glass resulted in a 44% reduction in the stratospheric ozone depletion category. Recycling silver resulted in an 88% reduction in the marine ecotoxicity category.

From the analysis and comparison of solar PV production and avoided burden approach due to recycling, it can be observed that recycling in the overall life cycle assessment of solar PV can result in much higher benefits for impact reduction throughout solar PV recycling. The last column of Table 3 provides a summary of % impact reduction in the solar PV manufacturing process by incorporating material recycling.

Incorporating solar PV recycling will result in an impact reduction for the solar PV manufacturing process by as high as 70%. The major reduction impacts can be seen in mineral resource scarcity, marine ecotoxicity land use, freshwater ecotoxicity and human carcinogenic toxicity categories. The impact reduction results from the aspects of avoidance of primary material production due to the recycling of solar PV components at EoL.

Nowadays, a carbon footprint, single score indicator with the application of the IPCC (Intergovernmental Panel on Climate Change) 2013, GWP model is commonly used in LCA, especially for PV panels. On basis of IPCC 2013 GWP 100a V1.03. The comparative score for solar PV manufacturing (c–Si) is 19784.976 kg Co_2 eq and the corresponding values for landfill and avoided burden approach (recycling) are 19,844.054 and 15,393.96 kgCo_2 eq respectively.

Conclusion

With ambitious solar installation targets, solar waste is bound to increase in India. The waste projection results as per the BAU scenario estimated that the PV waste could reach up to 6.64 million tonnes due to the early loss scenario and 5.48 million tonnes due to the regular loss scenario while in the ambitious scenario, the waste estimation is 10.30 million tonnes due to the early loss scenario and 8.51 million tonnes due to the regular loss scenario by the end of 2040 in India. These results of the present study vary from the results of earlier studies, mainly on account of COVID-19 pandemic disruptions, variation of t/MW factor, and the lifetime of solar panels. The PV waste if not tackled appropriately can result in a significant impact on the environment due to mishandling as well as disposal of waste in landfills. While the EU has pioneered PV electronic waste regulations including PV-specific collection, recovery and recycling other leading solar-installed capacity countries including India lack a systematic regulatory approach to handle PV waste. The present study proposes the following strategies to handle the ever-growing solar waste problem in India:

- Establishing an online monitoring system to track the flow of all discarded modules at all stages of the PV life cycle that will provide input for authorities and other stakeholders to develop regulations and policies.
- Imparting skills in PV panel repairs will enable the development of the second-hand market of solar PV modules wherein modules can be sold and purchased after doing necessary minor repairs.
- In the long term, extensive R&D will limit waste production & the establishment of pilot recycling plants to recover the secondary materials. Though, the viability of waste recovery models cannot be guaranteed owing to low to moderate values of PV waste generation. The government may therefore consider incentivizing the waste recovery units for a few initial years.
- A multi-sector and multi-stakeholder coordinated approach among various stakeholders including ministries and manufacturers along with EPR legislation that will cover the provision of collection, recovery, and recycling of solar PV.

The LCA analysis for different aspects relating to solar PV recycling and disposal was undertaken as part of the study to identify and highlight the most environmentally friendly solution for solar PV recycling. The LCA analysis has been undertaken considering that all the material at EoL goes in a landfill and impacts associated with same are studied in case I and in case II, avoided burden approach has been considered wherein it has been considered that solar waste materials are sent for recycling and the impact includes avoided burden due to material recycling. Avoided burden approach due to the recycling of materials will result in substituting virgin raw materials

with recycled materials in the forthcoming production stage will result in an impact reduction for solar PV by as high as 70%. Moreover, the reuse of recovered aluminium, glass, and silver in the manufacturing phase of the PV module will not only be beneficial from an environmental impact point of view but also from an economic standpoint. The probable sources of some of the uncertainties in the present study that may affect outcomes of solar waste estimation and its effect on the environment are discussed in the Appendix (Table 5). This study aims to apprise researchers, policymakers, and other stakeholders of impending problems that may arise due to EoL solar PV e-waste in India. Lack of infrastructure, waste handling, and recycling guidelines put India in a precarious position for achieving the twin objectives of energy security and sustainability.

The absence of availability of accurate data like life span, shape and scale parameters etc. relating to BOS is the main hindrance behind their inclusion in the present analysis. As a potential avenue of future research, the analysis carried out in the present study can be further enhanced by the inclusion of BOS along with PV modules. Another opportunity for future research lies in carrying out sensitivity and cost–benefit analysis of the recycling process.

Appendix

See Tables 4, 5, 6 and 7.

Table 4 Variation (t/MW) of Waaree solar panels (Source: Correspondence through author email)

Year	Weight to power ratio (t/MW)
2016	74.02
2017	72.05
2018	70.13
2019	68.26
2020	66.44
2021	64.67

Table 5 List of Probable source of Uncertainties in the present study

S. No	Probable uncertainties
1	Uncertainty due to projected solar PV capacity The present solar PV growth rate forms the basis of 339 GW solar PV cumulative installed capacity by 2040 in BAU scenario and the basis for 395 GW solar PV cumulative installed capacity by 2040 in an ambitious scenario is estimations provided under draft national energy policy (NITI 2017) report. Both these estimations introduce uncertainties in final PV waste figures as in the BAU scenario the installed capacity figures up to 2021 are extrapolated to obtain estimated values by 2040. In an ambitious scenario, it is difficult to judge the reliability of estimations provided in said study. The estimations provide indicative figures of waste volumes that will be generated. Further, series of Covid-19 pandemic waves are also creating uncertainty in capacity additions
2	Uncertainty due to tonnes per MW ratio With the improvement of technology PV modules are becoming lighter and lighter. The mass to power ratio till the year 2040 has been predicted from past data fitting to an exponentially decreasing curve. In the absence of availability of year-wise panel weight data in the public domain, the past data in present estimation has been obtained from a leading solar PV manufacturer in India through e mail correspondence
3	Uncertainty due to cut off point for EoL It is not necessary panels will become obsolete after 25 years and in many cases it has been observed that the PV module would still deliver enough power after their end-of-life period of 25 years. This will be more predominant in the case of solar PV panels installed at the rooftop of residential buildings. This will introduce uncertainties in the figure of waste streams
4	Uncertainty due to solar technology This study takes into consideration that c-Si technology will remain and continue to dominate the PV market in the coming years. Any significant change in the market share of c-Si technology will affect the solar waste estimation projection and LCA results. A further change in proportions of various raw materials in the PV module will affect the mass percentage of the recoverable from recycling process

Table 6 List of background input datasets used in the life cycle inventory modelling

Item	Used for the process phase	Datasets
Electricity	Solar panel disassembly, electrical cable treatment, separation of glass and refinement, PV sandwich layer cutting, sieving, acid leaching, filtration, electrolysis, neutralisation and filter press	Electricity, high voltage {IN-Western grid}| market for electricity, high voltage
Thermal energy	Heat	Heat, central or small-scale, other than natural gas {RoW}| heat production, light fuel oil, at boiler 10 kW, non-modulating
Transport	PV waste transportation to the recycling plant	Transport, freight, lorry 16–32 metric ton, euro4 {RoW}| market for transport, freight, lorry 16–32 metric ton, EURO4
	PV waste transportation to local collection point; cables transportation to cable treatment plant and cable polymer transportation to the incineration plant; transport of glass residue to landfill; PV sandwich transportation to incinerator; transport of ash to the treatment plant; transportation of fly ash to special landfill	Transport, freight, lorry 16–32 metric ton, euro4 {RoW}| market for transport, freight, lorry 16–32 metric ton, EURO4
	Sludge transportation from the recycling plant to landfills	Transport, freight, lorry 16–32 metric ton, euro4 {RoW}| market for transport, freight, lorry 16–32 metric ton, EURO4
Landfilling of the contaminated glass	Glass refinement	Waste glass {GLO}| waste glass treatment, unsanitary landfill, moist infiltration class
Disposal of fly ash in a landfill	Incineration	Fly ash and scrubber sludge {RoW}| treatment of, hazardous waste incineration
Water	Acid leaching, electrolysis, neutralisation	Water, unspecified natural origin, IN
Nitric acid	Acid leaching	Nitric acid, without water, in 50% solution state {RoW}| market for nitric acid, without water, in 50% solution state
$Ca(OH)_2$	Neutralisation	Lime, hydrated, loose weight {RoW}| market for lime, hydrated, loose weight
Limestone residue	Landfill	Limestone residue {RoW}| treatment of, inert material landfill
Landfilling of sludge with metal residuals	Filter press	Sludge, pig iron production {CH}| treatment of, residual material landfill

Table 7 Amount of recovered materials based on mass composition in BAU and ambitious scenario (C. E. L. Latunussa et al. 2016a, pp. 101–111)

Component	Mass composition of 1 ton of crystalline-silicon PV waste as input to the recycling process		Mass composition of PV waste as input to the recycling process				Mass composition of PV waste as input to the recycling process			
			BAU Scenario				Ambitious Scenario			
			2030 (t/MW = 50.72)		2040 (t/MW = 38.72)		2030 (t/MW = 50.72)		2040 (t/MW = 38.72)	
	Quantity	Percentage	Regular-loss scenario Quantity	Early-loss scenario Quantity	Regular-loss scenario Quantity	Early-loss scenario Quantity	Regular-loss scenario Quantity	Early-loss scenario Quantity	Regular-loss scenario Quantity	Early-loss scenario Quantity
	(kg)	(%)	(*t*)	(*t*)	(t)	(*t*)	(*t*)	(*t*)	(*t*)	(*t*)
Glass, containing antimony (0.01–1%/kg of glass)	700	70%	717,317	1,883,976	3,838,327	4,645,641	791,636	2,079,169	5,955,818	7,208,502
PV frame, made of aluminium	180	18%	184,453	484,451	986,998	1,194,593	203,564	534,643	1,531,496	1,853,615
Polymer-based adhesive (EVA) encapsulation layer	51	5.1%	52,262	137,261	279,650	338,468	57,676	151,482	433,924	525,191
Solar cell, containing silicon metal	36.5	3.65%	37,403	98,236	200,141	242,237	41,278	108,414	310,553	375,872
Back-sheet layer (based on Polyvinyl Fluoride)	15	1.5%	15,371	40,371	82,250	99,549	16,964	44,554	127,625	154,468
Cables (containing copper and polymers)	10	1%	10,247	26,914	54,833	66,366	11,309	29,702	85,083	102,979
Internal conductor, aluminium	5.3	0.53%	5431	14,264	29,062	35,174	5994	15,742	45,094	54,579
Internal conductor, copper	1.14	0.114%	1168	3068	6251	7566	1289	3386	9699	11,740
Silver	0.53	0.053%	543	1426	2906	3517	599	1574	4509	5458
Other metals (tin, lead)	0.53	0.053%	543	1426	2906	3517	599	1574	4509	5458
Total	1000	100%	1,024,739	2,691,395	5,483,325	6,636,630	1,130,909	2,970,241	8,508,311	10,297,859

Acknowledgements The authors wish to thank all who assisted in conducting this study especially M/s Waaree renewable technologies ltd for sharing power to weight ratio data with authors.

Funding The authors did not receive support from any organization for the submitted work.

Declarations

Conflict of interest The authors declare no competing interests.

References

Arya S, Kumar S (2020) E-waste in India at a glance: Current trends, regulations, challenges and management strategies. J Cleaner Prod 271:122707. https://doi.org/10.1016/j.jclepro.2020.122707

Ashfaq H, Hussain I, Giri A (2017) A comparative analysis of old recycled and new PV modules. J King Saud Univ Eng Sci 29(1):22–28. https://doi.org/10.1016/j.jksues.2014.08.004

Bridge to India (BTI) (2019) 'Managing India's PV module waste'. Available at: https://bridgetoindia.com/backend/wp-content/uploads/2019/04/BRIDGE-TO-INDIA-Managing-Indias-Solar-PV-Waste-1.pdf (Accessed: 30 June 2022)

Bridge to India (BTI) (2020) 'Covid-19: Impact on global solar market'. Available at: https://bridgetoindia.com/backend/wp-content/uploads/2020/06/ISA-BRIDGE-TO-INDIA-report-on-COVID-19-impact-May-2020.pdf (Accessed: 30 June 2022)

Central Electricity Regulatory Commission (CERC) (2011) 'Performance of solar power plants in India'. Available at: https://cercind.gov.in/2011/Whats-New/PERFORMANCE%20OF%20SOLAR%20POWER%20PLANTS.pdf (Accessed: 30 June 2022)

Central Electricity Regulatory Commission (CERC) (2017) 'Terms and Conditions for Tariff determination from Renewable Energy Sources Regulations, 2017'. Available at: https://cercind.gov.in/2017/regulation/Noti131.pdf (Accessed: 30 June 2022)

Central Pollution Control Board (CPCB) (2018) 'E-waste'. Available at: https://cpcb.nic.in/e-waste/ (Accessed: 30 June 2022)

Chaudhary K, Vrat P (2018) Analysis of long term impact of the end of life solar panels as e-waste in India. Ind Eng J 10(10):5–14. https://doi.org/10.26488/IEJ.10.10.70

Corcelli F, Ripa M, Leccisi E, Cigolotti V, Fiandra V, Graditi G, Sannino L, Tammaro M, Ulgiati S (2018) Sustainable urban electricity supply chain – Indicators of material recovery and energy savings from crystalline silicon photovoltaic panels end-of-life. Ecol Indic 94(3):37–51. https://doi.org/10.1016/j.ecolind.2016.03.028

SunPower Corporation (2011) 'Degradation mechanisms in Si module technologies observed in the field, technologies observed in the field, their analysis and statistics'. Available at: https://www.irishellas.com/files/Degradation-Mechanisms-in-Si-Module.pdf (Accessed: 30 June 2022)

Cucchiella F, D'Adamo I, Lenny Kok SC, Rosa P (2015) Recycling of WEEEs: An economic assessment of present and future e-waste streams. Renew Sustain Energy Rev 51:263–272. https://doi.org/10.1016/j.rser.2015.06.010

Dias P, Javimczik S, Benevit M, Veit H, Bernardes AM (2016) Recycling waste electrical and electronic equipment (WEEE): extraction and concentration of silver from waste crystalline silicon photovoltaic modules. Waste Manage 57:220–225. https://doi.org/10.1016/j.wasman.2016.03.016

Domínguez A, Geyer R (2017) Photovoltaic waste assessment in Mexico. Resour Conserv Recycl 127:29–41. https://doi.org/10.1016/j.resconrec.2017.08.013

Domínguez A, Geyer R (2018) Photovoltaic waste assessment of major photovoltaic installations in the United States of America. Renew Energy 133:1188–1200. https://doi.org/10.1016/j.renene.2018.08.063

European Union (EU)-India Technical Cooperation Project: Energy (2021) 'PV waste management in India: Comparative analysis of state of play and recommendations'. Available at: https://www.cecp-eu.in/uploads/documents/events/pv-waste-management-report-25-01-2021.pdf (Accessed: 30 June 2022)

Faircloth CC, Wagner KH, Woodward KE, Rakkwamsuk P, Gheewala SH (2019) The environmental and economic impacts of photovoltaic waste management in Thailand. Resour Conserv Recycl 143:260–272. https://doi.org/10.1016/j.resconrec.2019.01.008

Farrell CC, Osman AI, Doherty R, Saad M, Zhang X, Murphy A, Harrison J, Vennard ASM, Kumaravel V, Al-Muhtaseb AH, Rooney DW (2020) Technical challenges and opportunities in realising a circular economy for waste photovoltaic modules. Renew Sustain Energy Rev 128:109911. https://doi.org/10.1016/j.rser.2020.109911

Fraunhofer Institute for Solar Energy Systems (FISES) (2020) 'Photovoltaics Report'. Available at: https://www.ise.fraunhofer.de/content/dam/ise/de/documents/publications/studies/Photovoltaics-Report.pdf (Accessed: 30 June 2022)

Full Recovery End-of-Life Photovoltaic (FRELP) (2015) *Objectives* [Online]. Available at: https://frelp.info/participants/pvcycle/ (Accessed 30 June 2022)

Harvard Business Review (HBR) (2021) *The Dark Side of Solar Power* [Online]. Available at: https://hbr.org/2021/06/the-dark-side-of-solar-power (Accessed: 30 June 2022)

Hindalco (2020) 'Sustainability report FY 2019–20'. Available at: http://www.hindalco.com/upload/pdf/sustainability-report-2019-20.pdf (Accessed: 30 June 2022)

MERCOM India (2019) *MNRE suggests mandatory recycling of solar panel glass containing antimony* [Online]. Available at: https://mercomindia.com/mnre-recycling-solar-panel-glass/ (Accessed: 30 June 2022)

International Energy Agency (IEA) (2014) 'Review of failures of photovoltaic modules: Photovoltaic power systems programme'. Available at: https://iea-pvps.org/wp-content/uploads/2020/01/IEA-PVPS_T13-01_2014_Review_of_Failures_of_Photovoltaic_Modules_Final.pdf (Accessed: 30 June 2022)

International Energy Agency (IEA) (2016) 'End-of-life management solar photovoltaic panels'. Available at: https://www.irena.org/-/media/Files/IRENA/Agency/Publication/2016/IRENA_IEAPVPS_End-of-Life_Solar_PV_Panels_2016.pdf (Accessed: 30 June 2022)

International Energy Agency (IEA) (2018) 'End of life management of photovoltaic panels: Trends in PV module recycling technologies'. Available at: https://iea-pvps.org/wp-content/uploads/2020/01/End_of_Life_Management_of_Photovoltaic_Panels_Trends_in_PV_Module_Recycling_Technologies_by_task_12.pdf (Accessed: 30 June 2022)

International Energy Agency (IEA) (2020) 'Snapshot of global photovoltaic markets'. Available at: https://iea-pvps.org/wp-content/uploads/2020/04/IEA_PVPS_Snapshot_2020.pdf (Accessed: 30 June 2022)

International Energy Agency-Photovoltaic Power Systems (IEA-PVPS) (2014a) 'Review of failures of photovoltaic modules'. Available at: https://engineering.case.edu/centers/sdle/sites/engineering.

case.edu.centers.sdle/files/iea-pvps_t13-01_2014a_review_of_failures_of_photovoltaic_modules_final.pdf (Accessed 30 June 2022)

International Energy Agency-Photovoltaic Power Systems (IEA-PVPS) (2014b) 'Trends 2014b in Photovoltaic Applications: Survey report of selected IEA countries between 1992 and 2013'. (Accessed: 30 June 2022)

International Organization for Standardization (ISO) (2016) *ISO 14040:2006 standard* [Online]. Available at: https://www.iso.org/standard/37456.html (Accessed: 30 June 2022)

Kralj D, Markic M (2008) Building materials reuse and recycle. WSEAS Trans on Environ Dev 4(5):409–418

Kumar A, Dixit G (2018) An analysis of barriers affecting the implementation of e-waste management practices in India: A novel ISM-DEMATEL approach. Sustainable Prod Consum 14:36–52. https://doi.org/10.1016/j.spc.2018.01.002

Kumar S, Sarkar B (2013) Design for reliability with Weibull analysis for photovoltaic modules. Int J Current Eng Technol 3(1):129–134

Latunussa CEL, Ardente F, Blengini GA, Mancini L (2016a) Life cycle assessment of an innovative recycling process for crystalline silicon photovoltaic panels. Sol Energy Mater Sol Cells 156:101–111. https://doi.org/10.1016/j.solmat.2016.03.020

Latunussa, C.E.L., Mancini, L., Blengini, G.A., Ardente, F., and Pennington D. (2016b) 'Analysis of material recovery from silicon photovoltaic panels', *Publications Office of the European Union EUR 27797*, https://doi.org/10.2788/786252

Lugo-Laguna D, Arcos-Vargas A, Nuñez-Hernandez F (2021) A european assessment of the solar energy cost: key factors and optimal technology. Sustainability 13:3238. https://doi.org/10.3390/su13063238

Lunardi MM, Alvarez-Gaitan JP, Bilbao JI, Corkish R (2018) A review of recycling processes for photovoltaic modules. In: Zaidi B (ed) Solar panels and photovoltaic materials. Intechopen, London, pp 9–27. https://doi.org/10.5772/intechopen.74390

Mahmoudi S, Huda N, Behnia M (2019) Photovoltaic waste assessment: Forecasting and screening of emerging waste in Australia. Resour Conserv Recycl 146:192–205. https://doi.org/10.1016/j.resconrec.2019.03.039

Ministry of Power (MoP) (2022) *Power Sector at a Glance All India* [Online]. Available at: https://powermin.gov.in/en/content/power-sector-glance-all-india (Accessed: 30 June 2022)

National Institution for Transforming India (NITI) (2017) 'Draft National Energy Policy'. Available at: https://niti.gov.in/writereaddata/files/new_initiatives/NEP-ID_27.06.2017.pdf (Accessed: 30 June 2022)

National Institution for Transforming India (NITI) (2019) 'Strategy on resource efficiency in aluminium sector'. Available at: https://www.eu-rei.com/pdf/publication/NA_MoM_Strategy%20on%20RE%20in%20Aluminium%20Sector_Jan%202019.pdf (Accessed: 30 June 2022)

National Institution for Transforming India (NITI) (2021) *India Energy Dashboards (IED)* [Online]. Available at: http://www.niti.gov.in/edm/#reCapacity (Accessed: 30 June 2022)

Paiano A (2015) Photovoltaic waste assessment in Italy. Renew Sustain Energy Rev 41:99–112. https://doi.org/10.1016/j.rser.2014.07.208

Pankadan, S., Nikam, S., and Anwer, N. (2021) 'An analysis for management of end-of-life solar PV in India' in Bose, M. and Modi, A. (eds.) In: *Proceedings of the 7th international conference on advances in energy research*. Springer Proceedings in Energy. Singapore: Springer, pp. 1361–1371. https://doi.org/10.1007/978-981-15-5955-6

Peeters JR, Altamirano D, Dewulf W, Duflou JR (2017) Forecasting the composition of emerging waste streams with sensitivity analysis: A case study for photovoltaic panels in Flanders. Resour Conserv Recycl 120:14–26. https://doi.org/10.1016/j.resconrec.2017.01.001

Perez-Santalla, M. (2013) *Silver use: Changes & outlook* [Online]. Available at: https://www.bullionvault.com/gold-news/silver-use-103020132 (Accessed: 30 June 2022)

Prabhu VS, Shrivastava S, Mukhopadhyay K (2022) Life cycle assessment of solar photovoltaic in India: A circular economy approach. Circular Economy Sustainability 2:507–534. https://doi.org/10.1007/s43615-021-00101-5

Press Information Bureau (PIB) (2020) *MNRE: Year end review-2020* [Online]. Available at: https://pib.gov.in/Pressreleaseshare.aspx?PRID=1685046 (Accessed: 30 June 2022)

Rajya Sabha (RS) (2021a) *Rajya Sabha unstarred question - 927 solar energy target* [Online]. Available at: https://pqars.nic.in/annex/254/Au927.pdf (Accessed: 30 June 2022)

Rajya Sabha (RS) (2021b) *Rajya Sabha unstarred question - 1733 solar energy target* [Online]. Available at: https://pqars.nic.in/annex/254/AU1733.pdf (Accessed: 30 June 2022)

Sander, K., Schilling, S., Reinschmidt, J., Wambach, K., Schlenker, S., Müller, A., Springer, J., Fouquet, D., Jelitte, A., Stryi-Hipp, G., and Chrometzka, T. (2007) *Study on the development of a take back and recovery system for photovoltaic products*. Hamburg: Ökopol GmbH.

Santos JD, Alonso-García MC (2018) Projection of the photovoltaic waste in Spain until 2050. J Clean Prod 196:1613–1628. https://doi.org/10.1016/j.jclepro.2018.05.252

Sharma A, Mahajan P, Garg R (2021) Analysing the impact of various incentives on solar tariff in India. Int J Sustain Energ 41(2):126–147. https://doi.org/10.1080/14786451.2021.1900184

Sheoran M, Sharma S, Kumar P (2020) Compatible standard policy measure to tackle solar photovoltaic waste in Indian scenario. J Phys Conf 1504:012012. https://doi.org/10.1088/1742-6596/1504/1/012012

Shin J, Park J, Park N (2017) A method to recycle silicon wafer from end-of-life photovoltaic module and solar panels by using recycled silicon wafers. Sol Energy Mater Sol Cells 162:1–6. https://doi.org/10.1016/j.solmat.2016.12.038

SimaPro (2021a) *LCA software for fact-based sustainability* [Online]. Available at: https://simapro.com/ (Accessed: 30 June 2022)

SimaPro (2021b) *SimaPro database manual* [Online]. Available at: https://simapro.com/wp-content/uploads/2020/10/DatabaseManualMethods.pdf (Accessed: 30 June 2022)

Society of Environmental Toxicology and Chemistry (SETAC) (2019) *Life Cycle Assessment* [Online]. Available at: https://www.setac.org/page/sciencelca (Accessed: 30 June 2022)

Solar Energy Corporation of India Limited (SECI) (2017) *Request for selection (RfS) document for setting up of 5MW grid connected solar PV project at ordnance factory, Kanpur under VGF scheme* [Online]. Available at: https://www.seci.co.in/web-data/docs/RfS_5MW_OFCK.pdf (Accessed: 30 June 2022)

Stoppato A (2008) Life cycle assessment of photovoltaic electricity generation. Energy 33(2):224–232. https://doi.org/10.1016/j.energy.2007.11.012

SunShot (2016) 'PV module recycling RFI summary'. Available at: https://www.energy.gov/sites/prod/files/2016/12/f34/2014_PV_Recycling_RFI_Summary.pdf (Accessed: 30 June 2022)

Turaga RMR, Bhaskar K, Sinha S, Hinchliffe D, Hemkhaus M, Arora R, Chatterjee S, Khetriwal DS, Radulovic V, Singhal P, Sharma H (2019) E-Waste management in India: Issues and strategies. J

Decision Makers 44(3):127–162. https://doi.org/10.1177/0256090919880655

Xu Y, Li J, Tan Q, Peters AL, Yang C (2018) Global status of recycling waste solar panels: a review. Waste Manage 75:450–458. https://doi.org/10.1016/j.wasman.2018.01.036

Yi YK, Kim HS, Tran T, Hong SK, Kim MJ (2014) Recovering valuable metals from recycled photovoltaic modules. J Air Waste Manag Assoc 64(7):797–807. https://doi.org/10.1080/10962247.2014.891540

Springer Nature or its licensor (e.g. a society or other partner) holds exclusive rights to this article under a publishing agreement with the author(s) or other rightsholder(s); author self-archiving of the accepted manuscript version of this article is solely governed by the terms of such publishing agreement and applicable law.

2023 10th International Conference on Signal Processing and Integrated Networks (SPIN) | 978-1-6654-9099-3/23/$31.00 ©2023 IEEE | DOI: 10.1109/SPIN57001.2023.10117416

Estimation of Respiratory Rate from a Corrupted PPG Signal using Time-Frequency Spectrogram

Pankaj
Department of Electronics and Communication Engineering
Bennett University
Uttar Pradesh, India
er.pankaj08@gmail.com

Ashish Kumar
School of Electronics Engineering
Vellore Institute of Technology
Chennai, India
akumar.1june@gmail.com

Rama Komaragiri
Department of Electronics and Communication Engineering
Bennett University
Uttar Pradesh, India
rama.komaragiri@bennett.edu.in

Manjeet Kumar
Department of Electronics and Communication Engineering,
Delhi Technological University (DTU)
Rohini, Delhi.
manjeetchhillar@gmail.com

Abstract - Illnesses like pneumonia, influenza, lung cancer, chronic obstructive pulmonary disease, asthma, and many heart problems, including congestive heart failure, are life-threatening. Respiration rate (RR) is a vital indicator for checking the health status of a subject and can be a marker of early clinical diagnosis. Continuous monitoring of RR can provide an early indication of abnormalities, thereby saving lives. The real-time RR monitoring device is only available in hospitals due to the size and cost of the device.

Analyzing the PPG signal change due to respiratory modulations helps estimate RR. This paper describes an algorithm for RR estimation using a PPG sensor signal. During daily activities, inaccuracy in estimating RR using the PPG signal occurs due to motion artifacts. Thus, to improve the accuracy of the RR estimation in real-time, this work investigated the potential of superlet transform-based separation of true RR signal components and the motion artifacts components, thus improving the accuracy of the RR estimation in real-time. The algorithm comprises signal segmentation, pre-processing, and signal transformation using superlet transform to achieve the least mean absolute error (MAE) and robustness to noise. The algorithm is based on the superlet transform technique that includes separating RR peak and motion artifacts peak and detecting high-intensity peak frequency to estimate RR. The proposed algorithm obtained an MAE, and the root mean square error (RMSE) of 0.67 breaths per minute (BPM) and 1.56 BPM, respectively, indicates that embedding the proposed algorithm in a wearable device can be used reliably at home and in hospitals.

Keywords - Morlet wavelet, Photoplethysmography (PPG), Pulse oximeter, Respiratory-induced intensity variation, Respiratory rate (RR), Wearable device.

I. Introduction

Monitoring of vital signs such as respiratory rate (RR) in real-time is essential to assess the patient's health. The blood flow volume changes during the inhalation and exhalation process [1]. RR is a vital sign to assess the change in blood flow. Generally, RR in an adult does not change significantly. Thus, a slight change in RR can be a sign of any illness. RR is the number of breaths a person takes in one minute. During rest position, the average RR of a person is 12 to 20 breaths per minute (BPM). Impedance pneumography, abdominal plethysmography belts, nasal pressure transducers, and capnography are used to measure RR. However, the complexity of these devices limits their hospitals only. Routinely, in hospitals, RR is measured by manually counting the breaths. Thus, healthcare industries need a user-friendly device in the portable and wearable form to monitor RR in real time. In recent times, with the emergence of wearable devices, photoplethysmography (PPG) has gained the interest of the healthcare industry. PPG is an optical technique used to measure the variation in blood volume in tissues. The widespread wearable health monitoring devices estimate blood oxygen saturation, HR, and BP [2]. These devices do not have the feature to estimate RR. Out of the various vital signs, RR is a valuable bio-marker, estimated using PPG for real-time prognosis and diagnosis. Thus, accurate and reliable estimation of RR using user-friendly, low-cost wearable sensors not only manifests PPG as a monitoring device but also helps quantify the risk of patient deterioration. The algorithm proposed in the literature to estimate RR from the PPG signal have certain limitations. Initially, the digital filters-based technique to filter out noise signals and estimate RR is proposed. The performance of the digital filter depends on the selection of their cut-off frequency. Moreover, the presence of motion artifacts within the desired estimation range makes these approaches unreliable.

In [3] autoregressive model time-frequency (TF) domain-based approach is proposed to estimate RR. In [4], an empirical mode decomposition (EMD) based RR estimation approach is proposed. However, this approach becomes less practical due to the requirement of manual selection of intrinsic mode function and mode-mixing. Ensemble EMD and principal component analysis approach are proposed to estimate RR in [5] by overcoming the manual selection issue. This approach faces the mode-mixing problem and high computational complexity. Thus in [6], Fourier–Bessel series expansion-based empirical wavelet transform-based approach is proposed to estimate RR. The algorithm proposed in [7] is susceptible to noise and is thus not preferred for real-time analysis. In [8], an algorithm is proposed to estimate child RR. The proposed algorithm automatically discards the PPG signal segment contaminated by motion artifacts. In [9], a joint sparse signal reconstruction and spectra fusion-based RR estimation approach is proposed. Further in [10], an intelligent fusion method based on EEMD is proposed to estimate RR. In [11], an approach was proposed based on particle filter-based TF PPG signal analysis to measure the amplitude fluctuations in the PPG signal to estimate the RR. In [12], an accelerometer sensor-based RR estimation approach is proposed. In [13], PPG-based RR estimation precision is conducted at various body sites with normal and deep respiration. An algorithm is proposed in [14] to account

Authorized licensed use limited to: DELHI TECHNICAL UNIV. Downloaded on May 15,2023 at 09:51:08 UTC from IEEE Xplore. Restrictions apply.

for the respiration-induced variabilities by a fusion-based wavelet synchro-squeezed spectrum to analyze the variability in PPG signal due to respiration. Recently, a machine learning (ML) approach has been proposed to estimate RR from motion artifact affected PPG signal [15]. The raw PPG signal is decomposed for motion artifact suppression using the variational mode decomposition technique. Then feature is extracted to train the ML model for RR estimation. In [16], the EEMD-based motion artifacts suppression and fusion technique-based RR estimation is proposed. The above approach is computationally inefficient and requires additional motion artifacts suppression stage.

The recorded PPG signal is non-stationary, meaning the properties vary over time. Thus, TF analysis is widely used to estimate the RR from the PPG signal. Short-time Fourier Transform (STFT) [17] and continuous wavelet transforms (CWT) [18] are the two widely used TF approach for RR estimation. In addition to this TF analysis, in [19], the variable-frequency complex demodulation (VFCDM) approach is proposed to estimate RR. However, VFCDM provides a better TF resolution than STFT and CWT. Still, the need for minimum sixty-second data and high computational complexity makes this approach infeasible in real-time RR monitoring wearable devices.

Both TF analysis approaches, STFT and CWT, have inherent limitations. The STFT provides good frequency resolution but poor relative temporal resolution at high frequencies. With increasing frequency, the CWT provides a good temporal resolution throughout the spectrum but degrades in frequency resolution. Thus, a computationally efficient approach for real-time RR estimation based on time-frequency analysis of PPG signal is still in great demand. This paper proposes a computationally efficient RR algorithm based on superlet transform to estimate the RR in real-time.

The rest of the paper is organized as follows: Section II describes the proposed framework for RR estimation. The experimental results and comparison with the state of the art work are mentioned in Section III, Section IV consists of the related discussion, and Section V summarizes the paper.

II. Method and Materials

The processing sequence of the proposed framework in RR estimation from a PPG signal is shown in Fig. 1. The framework consists of four steps: pre-processing of the acquired PPG signal, Transform of time domain PPG signal into TF super-resolution spectrogram, detection of the high-intensity peak, estimation of RR.

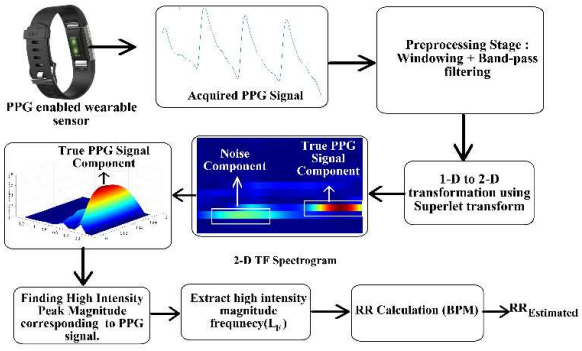


Fig. 1. Block-wise representation of proposed framework for RR estimation from PPG sensor signal

A. Data Acquisition Stage

This work considers the publicly-available CapnoBase benchmark dataset to test the efficacy of the proposed framework for RR estimation. The CapnoBase dataset represents a younger subject population and contains simultaneously recorded PPG, ECG, and reference RR signals. The CapnoBase dataset is recorded with 59 pediatrics aged between 1 to 17 years with an average age of 9 years and 35 adult subjects undergoing routine anesthesia aged between 26 to 76 years with an average age of 52 years. The CapnoBase dataset was recorded with a sampling frequency of 300 Hz for both the PPG signal and the reference capnography respiratory signal. Of the dataset, 42 subjects are randomly selected, of which 29 are pediatric, and 13 are adult subjects. Each signal in the Capnobase dataset is recorded for a duration of eight-minute. A research expert manually labeled the simultaneously recorded gold standard reference capnogram signal waveforms for each respiratory cycle to calculate the reference RR value.

B. Pre-processing Stage

In this work, the acquired PPG signal from the Capnobase dataset $P_S[n]$ is represented in Eq. (1). In Eq. (1), $P_S[n]$ consists of $C_P[n]$, the clean PPG signal component and the noise component $N_P[n]$.

$$P_S[n] = C_P[n] + N_P[n] \quad (1)$$

As per the dataset protocol, to compare the estimate RR with the reference RR, the acquired corrupted PPG signals are segregated into consecutive windows of Q samples. Eq. (2) shows the relation between the segregated consecutive window.

$$P_S^k = \left(P_S\left((k-1)\times w\right)+1 \;\cdots\; P_S\left((k-1)\times w\right)+Q\right) \quad (2)$$

The acquired PPG signal is divided using an overlapping windowing scheme for a thirty-two-second window. Each window (k) consists of Q number of samples. For k = 1 (first window), to estimate RR, the foremost Q samples of the corrupted PPG signal are used. After the first window, each succeeding window is shifted by a step size (w). Thus, from the second window onwards, to assign Q samples of the kth window, (Q-w) samples from the $(k-1)^{th}$ window are concatenated with w new samples to obtain Q samples of the kth window. Table 1 represents the sample number assigned to each window of length Q. As per Capnobase dataset Q is 9600, and the step size is 900. As shown in Table 1, for the first window (k = 1), the sample number was assigned from 1 to 9600. After the first window, to obtain 9600 samples in the next window, 900 new samples are concatenated with 8700 samples from the first window.

Table 1: Allotment of range of sample number to assign Q samples of each window.

Window's number (k)	Range of sample number	Total samples allotted for each window (Q)
1	1: 9600	9600
2	901: 10500	9600
3	1801: 11400	9600
4	2701: 12300	9600
.	.	.
.	.	.
151	13500: 144600	9600

This work considers Q = 9600 and w = 900 to match the reference RR available in the CapnoBase dataset. After window segmentation, the Q samples window is passed through a 5th-order Butterworth band-pass filter [0.1-1 Hz] corresponding to 6 to 60 breaths per minute (BPM). The signal filtering is done to filter out unwanted frequency components lie outside the desired RR spectrum.

Authorized licensed use limited to: DELHI TECHNICAL UNIV. Downloaded on May 15,2023 at 09:51:08 UTC from IEEE Xplore. Restrictions apply.

C. *Separation of Clean PPG signal Component from the Corrupted PPG Signal.*

Separation of the clean PPG signal components from the corrupted PPG signal is challenging as PPG and the noise signal components have coinciding frequency components between 0.1 Hz to 1 Hz. Due to spectral overlap between PPG and noise components such as motion artifacts, the estimation of RR provides inaccurate estimation. Thus, accurate and reliable estimation of RR using a PPG-enabled wearable device requires separating the clean PPG signal component and the motion artifact components. The superlet transform has the potential to accurately separate the corrupted PPG signal into clean PPG signal and motion artifacts component. The superlet transforms the PPG signal into a TF spectrogram to analyze the PPG signal for RR estimation [20].

The superlet transform uses a Morlet wavelet to provide the multi-resolution TF representation of the pre-processed PPG signal. Superlet transform consists of multiple wavelets with a fixed center frequency instead of a single wavelet used in CWT [20]. Hence provides better TF information on the PPG signal. Morlet wavelet with multiple order called superlet is represented in Eq. (3).

$$SL_{f,g} = \left\{ \psi_{s,d} \,\middle|\, d = d_1, d_2, \cdots, d_g \right\} \tag{3}$$

Here, g represents the order of superlet (number of wavelets utilized to obtain the super-resolution). Superlet also overcomes the limitation of CWT at a higher frequency by increasing the order of the superlet. In Eq. (3) the number of base cycles allotted to each wavelet is indicated by d.

The final response of the superlet transform to pre-processed PPG signal is given by the geometric mean of the individual wavelet response shown in Eq. (4).

$$R\left[SL_{f,g} \right] = \sqrt[g]{\prod_{i=1}^{g} R\left[\psi_{s,d_i} \right]} \tag{4}$$

Fig. 2 represents the 2-D representation of the TF spectrogram. The spectrogram represents time and frequency on the x and y-axis, and the color represents the normalized amplitude. The geometric mean of the g order superlet transform represents a high-intensity systolic peak information of the PPG signal representing the clean PPG signal, as the systolic peak of the PPG signal exists at the same frequency and time for multiple wavelets.

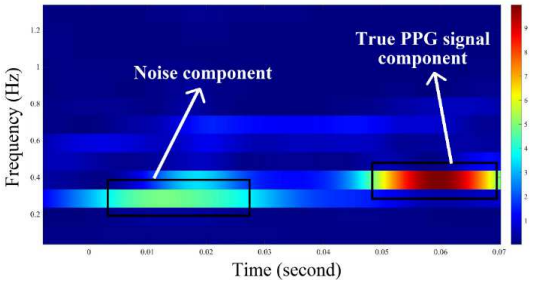


Fig. 2. 2-D TF spectrogram of the PPG signal.

However, the existence of motion artifacts and noise signal is random, thus in the TF spectrogram, the geometric mean of the noisy component occurs with a low-intensity magnitude, as shown in Fig. 2. Therefore, the frequency of the high-intensity peak represents the frequency of a systolic peak of clean PPG signal to estimate the RR.

Fig.3 shows the 3-D TF spectrogram, representing the separation of motion artifacts components and the clean PPG signal components. The color bar in the TF spectrogram indicates a large amplitude with bright red color, and the lowest amplitude indicates with blue color.

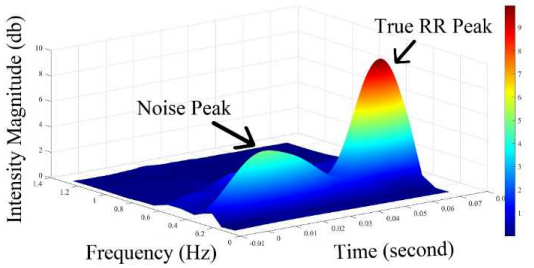


Fig. 3. 3-D TF spectrogram of the PPG signal.

Fig.2 and Fig.3 clearly shows that the transformation of a PPG signal into a TF superlet spectrogram has the potential to separate RR spectral lobe and motion artifacts lobe, thus improving the robustness of the proposed framework for real-time RR estimation from a corrupted PPG signal.

D. *Detection of the high-intensity peak for RR estimation*

The frequency components of the PPG signal changes with different rates with different physical motions, as the nature of the PPG signal is non-stationary. Thus, with a superlet transform with an order greater than one, the TF spectrogram improves the separability between a clean PPG signal and the motion artifacts component.

The clean PPG signal component is indicated by a high-intensity lobe centered on a frequency corresponding to the RR. In this work, firstly, the highest intensity magnitude is detected from the 2-D superlet transform spectrogram. Then the frequency of the detected magnitude (L_F) is used to estimate the RR using the relation given in Eq. (5).

$$RR_{estimated}(k) = L_F \times 60 \tag{5}$$

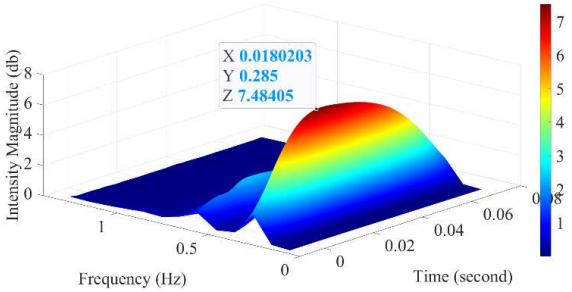


Fig. 4. Detection of high-intensity magnitude from TF PPG spectrogram

Table 2: The frequency value extracted from the detected high intensity lobe and calculated RR value for randomly selected windows for subject 009 of the Capnobase dataset.

Window Number (k)	Lobe Frequency (L_F) in Hz *At* (d_1=3)	Calculated RR (BPM) $L_F \times 60$	Reference RR (BPM)
1	0.29	17.4	17.98
5	0.31	18.6	18.40
17	0.30	18	17.79
25	0.29	17.4	17.22
41	0.32	19.2	19.23
43	0.30	18	18.10
46	0.29	17.4	16.09
60	0.34	20.4	20.64
71	0.36	21.6	21.45
125	0.33	19.8	19.95
137	0.31	18.6	18.61
142	0.32	19.2	19.62

Fig. 4 represents the 3-D view of the TF spectrogram, showing the high-intensity peak, the magnitude of the high-intensity peak (Z), the time value (X), and the corresponding

Authorized licensed use limited to: DELHI TECHNICAL UNIV. Downloaded on May 15,2023 at 09:51:08 UTC from IEEE Xplore. Restrictions apply.

frequency of the high-intensity peak (Y). Table 2 shows the frequency value extracted from the detected high-intensity lobe for randomly selected twelve windows out of one-fifty-one of subject-009 of the Capnobase
dataset. For a window, by multiplying the extracted frequency value of a high-intensity peak by 60, the RR value of that window is calculated, as shown in Table 2. Thus, the proposed framework automatically estimates RR by extracting the detected high-intensity magnitude frequency (L_F). The last column of Table 2 indicates the reference RR value of each window, used to correlate the reference RR value with estimated value. The difference between the reference RR and the estimated RR value indicates that the proposed framework automatically estimates RR by extracting the frequency of high-intensity magnitude peaks.

III. Results and Comparison

Monitoring continuous RR in real-time with high accuracy and minimum computation complexity is challenging. The proposed computationally efficient framework consistently achieves high accuracy for RR estimation even when the signal consists of motion artifacts components added to subjects' movement. The performance of the proposed framework is evaluated with the benchmark Capnobase dataset. Mean absolute error (MAE) and root mean square error (RMSE) of the $RR_{estimated}$ and RR_{ref} are computed to analyze the performance of the proposed framework. Eq. (6) and Eq. (7) describe the relations used to compute MAE and RMSE.

$$MAE = \frac{1}{W}\sum_{b=1}^{W}\left|RR_{ref}(k) - RR_{estimated}(k)\right| \quad (6)$$

$$RMSE = \sqrt{\frac{1}{W}\sum_{b=1}^{W}\left(RR_{ref}(k) - RR_{estimated}(k)\right)^2} \quad (7)$$

Table 3 A comparison between the proposed work and works from the literature

Author	Database	Methodology	Metrics	Results
Motin et al. [21] 2019	MIMIC Database	Empirical mode decomposition	MAE RMSE	5.03 --
Motin et al. [22] 2020	Own Database	Empirical mode decomposition	MAE RMSE	3.05 -
Jarch et al. [23] 2018	BIDMC Database	Accelerometer Sensor	MAE RMSE	2.56 -
Pirhonen et al. [24] 2018	Vortal Database	Wavelet Transform	MAE RMSE	2.33 3.68
Zhang et al. [25] 2017	Capnobase Dataset	Joint Sparse Signal Reconstruction	MAE RMSE	-- 2.89
Birrenkott et al. [26] 2017	MIMIC Database Capnobase Dataset	Respiratory Quality Index + Fusion Technique	MAE RMSE	0.71 --
Shuzan et al. [27] 2021	Vortal Database	Machine learning	MAE RMSE	1.91 2.57
Khreis et al. [28] 2021	Capnobase dataset	Respiratory Quality Index	MAE RMSE	1. 10 --
Baker et al. [29] 2021	MIMIC-III Database	Respiratory signal quality quantification + Neural network	MAE RMSE	0.711 1.73
Bian et al. [30] 2020	Capnobase Dataset	Deep Neural Network	MAE RMSE	2.5 -
Stankoskhi et al. [31] 2022	Two Own Dataset	Manual Feature Extraction + Machine Learning Model	MAE RMSE	1.38
Iqbal et al., 2022	BIDMC Database	selective windowing + Welch filtering	MAE RMSE	2.05 2.47
Proposed work	Capnobase Dataset	Superlet Transform	MAE RMSE	0.67 1.53

Here, RR_{ref}(k) and $RR_{estimated}$(k) are the reference RR and the estimated RR with the proposed framework, respectively, for the kth observation, and W is the total number of windows.

Table 3 compares MAE (BPM) and RMSE (BPM) with various techniques proposed in the literature. The MAE and RMSE values of the proposed framework are 0.67 and 1.53, respectively. The MAE and the RMSE value of the proposed framework outperform all similar work reported in the literature. Further, to analyze the performance of the proposed RR detection framework in detail, Fig. 5 and Fig. 6 compare $RR_{estimated}$ with RR_{ref} of two randomly selected subjects Subject-009 and Subject-0028 from the Capnobase dataset. All three figures show the estimated RR track the reference RR with high accuracy almost for all time windows. Besides the MAE and RMSE, the Pearson correlation coefficient Bland-Altman plot is introduced to analyze the efficacy of the proposed framework. In Fig. 7 the pearson correlation coefficient of 0.997 represents a linear relationship between RR_{ref} and $RR_{estimated}$.



Fig. 5. Comparison of $\boldsymbol{RR_{ref}}$ and $\boldsymbol{RR_{estimated}}$ on Subject-009



Fig. 6. Comparison between $\boldsymbol{RR_{ref}}$ and $\boldsymbol{RR_{estimated}}$ for the Subject-0028

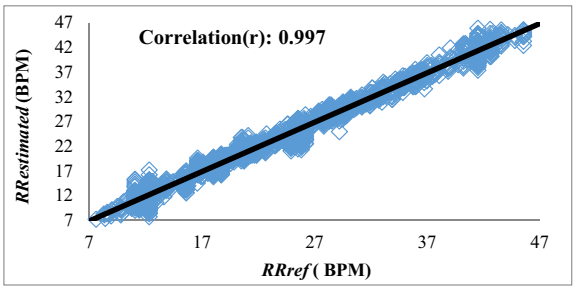


Fig. 7. Correlation plot between $\boldsymbol{RR_{ref}}$ and $\boldsymbol{RR_{estimated}}$ for all subjects from the Capnobase dataset

In the correlation plot, RR_{ref} is taken on the x-axis, and $RR_{estimated}$ on the y-axis. The graph indicates a linear relation between RR_{ref} and $RR_{estimated}$ with correlation of 0.997. Further Bland-Altman plot shown in Fig. 8 compares RR_{ref} and $RR_{estimated}$ graphically. Fig. 8 shows the Bland-Altman plot, plotted the difference between RR_{ref} and $RR_{estimated}$ versus the average of RR_{ref} and $RR_{estimated}$. The correlation between RR_{ref}

Authorized licensed use limited to: DELHI TECHNICAL UNIV. Downloaded on May 15,2023 at 09:51:08 UTC from IEEE Xplore. Restrictions apply.

and $RR_{estimated}$ for all the forty-two subjects in the Capnobase dataset is plotted as the Bland-Altman plot and is shown in Fig. 8. The LOA value for the signals from the Capnobase dataset is between – 2.87 to 3.49 BPM with a bias of 0.31 BPM and standard deviation (SD) 1.62 BPM. Fig. 8 shows that maximum points lie within the 95% agreement limit.

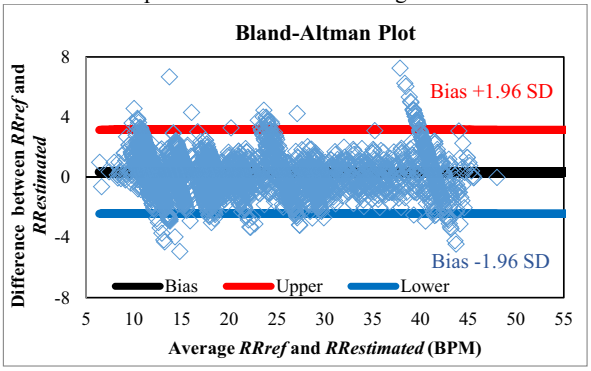


Fig. 8. The Bland–Altman plot for all Capnobase dataset

This indicates error difference between *RRref* and $RR_{estimated}$ is low, showing that the proposed framework performs well with high accuracy.

IV. Discussion

The constraints in a real-time monitoring wearable device are computational complexity and energy consumption, as the wearable device has limited system resources. As a wearable device has limited energy sources, it is essential to reduce hardware and computational complexity to increase battery life. The proposed work is intended for the accurate and reliable estimation of RR using a motion artifact corrupted PPG signal.

The methodology used in the similar work, proposed in the literature to estimate RR have some inherent limitation. In Table 3, the work proposed in [21], [22] used EMD technique to estimate RR from a PPG signal. The EMD is an efficient frequency domain technique used to extract feature, however EMD and its variant algorithms are based on an empirical and heuristic procedures. Thus, the mathematical modelling of the of the algorithm become more complex. Moreover, EMD also faces limitation of aliasing, mode mixing and detrend uncertainty. The work proposed in [23], require additional accelerometer sensor signal to extract the RR information. The work proposed in [24] based on wavelet transform. The wavelet transform provides better time resolution but degrades in frequency resolution at high frequency. Moreover, efficacy of the wavelet-based approach depends on the accurate selection of number of decomposition level and mother wavelet.

This work proposes a motion artifacts suppression method to estimate RR based on superlet transform. The proposed framework reduces the need for separate motion artifacts filtering steps and additional reference accelerometer signals. RR estimation performances with the proposed framework outperformed those obtained from the state-of-the-art technology with less computational cost. Superlet transform with multiple wavelets improves the separability between the desired signal and the noise.

Detection of high-intensity magnitude from the spectrogram will provide a robust way to estimate RR with a wearable device. Moreover, for accurate estimation of RR in real-time when the subject indulged in physical activities, finding an optimum value of input base cycle (d) provides an enhanced TF representation.

Table 4 shows the effect of input base cycle value on RR estimation performance for a randomly selected subject 0032.

Table 4 Variation in MAE with change in d.

Input base cycle (d)	MAE (BPM)	Input base cycle (d)	MAE (BPM)
1	4.53	7	0.84
2	3.54	8	0.84
3	0.85	9	0.83
4	0.85	10	0.83
5	0.84	11	0.83
6	0.84	12	0.82

As seen from Table 4, the changes in MAE after d = 3 are insignificant. Still, finding an optimum value of d can play a vital role in estimating RR accurately in real-time. For implementation in a wearable device, there is a trade-off between computational complexity and the value of d. Increasing the input base cycle will increase the computational time of the device.

The Capnobase dataset was recorded when the subject was not indulged in any physical movement. Thus, the signals are not affected by the motion artifacts. Thus, to analyze the proposed framework on the Capnobase dataset, this work considers d = 3 as an optimum value with minimum computational complexity. In the future, to test the effectiveness of the proposed framework for real-time monitoring and to select an optimum value of d, the proposed framework needs to test on real-time acquired PPG recording, where the subject undergoes substantial physical activity. Further, the framework can be implemented on hardware with low computational complexity to estimate and monitor the real-time RR. The CPU time require to obtain the RR of a thirty-two-second window with proposed framework is 1.015 second.

V. Conclusion

This work proposes a superlet transform based RR estimation algorithm using a PPG signal only. The proposed algorithm consists of three steps: pre-processing, signal transformation using superlet transform, and respiratory rate estimation stage. The pre-processing stage consists of signal segmentation and band-pass filtering to remove the signal outside the undesired frequency range. The acquired PPG signal is a super-resolution TF spectrogram in the signal transformation stage. In the last stage, the algorithm estimates RR from the frequency obtained from the detected high-intensity peak. To analyze the performance of the proposed framework, the publicly available Capnobase dataset is used, and calculate the MAE, RMSE, and Pearson correlation coefficient. One of the aims of this study is to determine the impact of different values of d on the estimation of the RR. Table 4 shows a trade-off between MAE and computational complexity while selecting parameter d for real-time RR estimation. Table 4 shows that a d = 3 is best for RR estimation using the Capnobase dataset. For d = 3, the algorithm gives acceptable MAE values with the least computational complexity. The optimum value of d to estimate accurate RR with minimum computational complexity can differ with different datasets recorded under different physiological conditions. In the future, the proposed algorithm will be improved to obtain the generalized value of d to estimate the RR in real-time, which will eventually reduce the MAE and computational complexity of the system. a required parameter while designing a wearable and portable real-time RR estimation device. The performance of the proposed algorithm will make it possible to embed the proposed RR estimation algorithm for remote and intensive care units.

Authorized licensed use limited to: DELHI TECHNICAL UNIV. Downloaded on May 15,2023 at 09:51:08 UTC from IEEE Xplore. Restrictions apply.

REFERENCES

[1] Pankaj, A. Kumar, R. Komaragiri, and M. Kumar, "A Review on Computation Methods Used in Photoplethysmography Signal Analysis for Heart Rate Estimation," Archives of Computational Methods in Engineering, vol. 29, no. 2. Springer Science and Business Media BV, pp. 921–940, Mar. 01, 2022. doi: 10.1007/s11831-021-09597-4.

[2] Pankaj, A. Kumar, R. Komaragiri, and M. Kumar, "Reference signal less Fourier analysis-based motion artifact removal algorithm for wearable photoplethysmography devices to estimate heart rate during physical exercises," Comput Biol Med, vol. 141, Feb. 2022, doi: 10.1016/j.compbiomed.2021.105081.

[3] J. Lee and K. H. Chon, "An autoregressive model-based particle filtering algorithms for extraction of respiratory rates as high as 90 breaths per minute from pulse oximeter," IEEE Trans Biomed Eng, vol. 57, no. 9, pp. 2158–2167, Sep. 2010, doi: 10.1109/TBME.2010.2051330.

[4] A. Garde, W. Karlen, P. Dehkordi, J. M. Ansermino, and G. A. Dumont, "Empirical Mode Decomposition for Respiratory and Heart Rate Estimation from the Photoplethysmogram."

[5] M. A. Motin, C. K. Karmakar, and M. Palaniswami, "Ensemble empirical mode decomposition with principal component analysis: a novel approach for extracting respiratory rate and heart rate from photoplethysmographic signal," IEEE J Biomed Health Inform, vol. 22, no. 3, pp. 766–774, May 2018, doi: 10.1109/JBHI.2017.2679108.

[6] R. Katiyar, V. Gupta, and R. B. Pachori, "Fbse-ewt-based approach for the determination of respiratory rate from ppg signals," IEEE Sens Lett, vol. 3, no. 7, Jul. 2019, doi: 10.1109/LSENS.2019.2926834.

[7] W. Karlen, S. Raman, J. M. Ansermino, and G. A. Dumont, "Multiparameter respiratory rate estimation from the photoplethysmogram," IEEE Trans Biomed Eng, vol. 60, no. 7, pp. 1946–1953, 2013, doi: 10.1109/TBME.2013.2246160.

[8] S. A. Shah, S. Fleming, M. Thompson, and L. Tarassenko, "Respiratory rate estimation during triage of children in hospitals," J Med Eng Technol, vol. 39, no. 8, pp. 514–524, Nov. 2015, doi: 10.3109/03091902.2015.1105316.

[9] X. Zhang and Q. Ding, "Respiratory rate estimation from the photoplethysmogram via joint sparse signal reconstruction and spectra fusion," Biomed Signal Process Control, vol. 35, pp. 1–7, May 2017, doi: 10.1016/j.bspc.2017.02.003.

[10] M. Abdul Motin, K. Karmakar, D. Kant Kumar, and M. Palaniswami, PPG Derived Respiratory Rate Estimation in Daily living Conditions. 2020. doi: 10.0/Linux-x86_64.

[11] M. Pirhonen, M. Peltokangas, and A. Vehkaoja, "Acquiring respiration rate from photoplethysmographic signal by recursive bayesian tracking of intrinsic modes in time-frequency spectra," Sensors (Switzerland), vol. 18, no. 6, Jun. 2018, doi: 10.3390/s18061693.

[12] D. Jarchi, S. J. Rodgers, L. Tarassenko, and D. A. Clifton, "Accelerometry-Based Estimation of Respiratory Rate for Post-Intensive Care Patient Monitoring," IEEE Sens J, vol. 18, no. 12, pp. 4981–4989, Jun. 2018, doi: 10.1109/JSEN.2018.2828599.

[13] V. Hartmann, H. Liu, F. Chen, W. Hong, S. Hughes, and D. Zheng, "Toward accurate extraction of respiratory frequency from the photoplethysmogram: Effect of measurement site," Front Physiol, vol. 10, no. JUN, 2019, doi: 10.3389/fphys.2019.00732.

[14] M. Pirhonen and A. Vehkaoja, "Fusion enhancement for tracking of respiratory rate through intrinsic mode functions in photoplethysmography," Biomed Signal Process Control, vol. 59, May 2020, doi: 10.1016/j.bspc.2020.101887.

[15] M. N. I. Shuzan et al., "A Novel Non-Invasive Estimation of Respiration Rate from Motion Corrupted Photoplethysmograph Signal Using Machine Learning Model," IEEE Access, vol. 9, pp. 96775–96790, 2021, doi: 10.1109/ACCESS.2021.3095380.

[16] IEEE Engineering in Medicine and Biology Society. Annual International Conference (42nd : 2020 : Online), IEEE Engineering in Medicine and Biology Society,

[17] D. Jarchi, P. Charlton, M. Pimentel, A. Casson, L. Tarassenko, and D. A. Clifton, "Estimation of respiratory rate from motion contaminated photoplethysmography signals incorporating accelerometry," Healthc Technol Lett, vol. 6, no. 1, pp. 19–26, 2019, doi: 10.1049/htl.2018.5019.

[18] Y. der Lin, Y. H. Chien, and Y. S. Chen, "Wavelet-based embedded algorithm for respiratory rate estimation from PPG signal," Biomed Signal Process Control, vol. 36, pp. 138–145, Jul. 2017, doi: 10.1016/j.bspc.2017.03.009.

[19] K. H. Chon, S. Dash, and K. Ju, "Estimation of Respiratory Rate From Photoplethysmogram Data Using Time-Frequency Spectral Estimation," IEEE Trans Biomed Eng, vol. 56, no. 8, pp. 2054–2063, 2009, doi: 10.1109/TBME.2009.2019766.

[20] Pankaj, A. Kumar, M. Kumar, and R. Komaragiri, "STSR: Spectro-Temporal Super-Resolution Analysis of a Reference Signal Less Photoplethysmogram for Heart Rate Estimation During Physical Activity," IEEE Trans Instrum Meas, vol. 71, pp. 1–10, 2022, doi: 10.1109/TIM.2022.3192831.

[21] M. A. Motin, C. K. Karmakar, and M. Palaniswami, "Selection of empirical mode decomposition techniques for extracting breathing rate from PPG," IEEE Signal Process Lett, vol. 26, no. 4, pp. 592–596, Apr. 2019, doi: 10.1109/LSP.2019.2900923.

[22] IEEE Engineering in Medicine and Biology Society. Annual International Conference (42nd : 2020 : Online), IEEE Engineering in Medicine and Biology Society,

[23] D. Jarchi, S. J. Rodgers, L. Tarassenko, and D. A. Clifton, "Accelerometry-Based Estimation of Respiratory Rate for Post-Intensive Care Patient Monitoring," IEEE Sens J, vol. 18, no. 12, pp. 4981–4989, Jun. 2018, doi: 10.1109/JSEN.2018.2828599.

[24] M. Pirhonen, M. Peltokangas, and A. Vehkaoja, "Acquiring respiration rate from photoplethysmographic signal by recursive bayesian tracking of intrinsic modes in time-frequency spectra," Sensors (Switzerland), vol. 18, no. 6, Jun. 2018, doi: 10.3390/s18061693.

[25] X. Zhang and Q. Ding, "Respiratory rate estimation from the photoplethysmogram via joint sparse signal reconstruction and spectra fusion," Biomed Signal Process Control, vol. 35, pp. 1–7, May 2017, doi: 10.1016/j.bspc.2017.02.003.

[26] D. A. Birrenkott, M. A. F. Pimentel, P. J. Watkinson, and D. A. Clifton, "A robust fusion model for estimating respiratory rate from photoplethysmography and electrocardiography," IEEE Trans Biomed Eng, vol. 65, no. 9, pp. 2033–2041, Sep. 2018, doi: 10.1109/TBME.2017.2778265.

[27] M. N. I. Shuzan et al., "A Novel Non-Invasive Estimation of Respiration Rate from Photoplethysmograph Signal Using Machine Learning Model," Feb. 2021, [Online]. Available: http://arxiv.org/abs/2102.09483

[28] S. Khreis, D. Ge, H. A. Rahman, and G. Carrault, "Breathing Rate Estimation Using Kalman Smoother with Electrocardiogram and Photoplethysmogram," IEEE Trans Biomed Eng, vol. 67, no. 3, pp. 893–904, Mar. 2020, doi: 10.1109/TBME.2019.2923448.

[29] S. Baker, W. Xiang, and I. Atkinson, "Determining respiratory rate from photoplethysmogram and electrocardiogram signals using respiratory quality indices and neural networks," PLoS One, vol. 16, no. 4 April, Apr. 2021, doi: 10.1371/journal.pone.0249843.

[30] IEEE Engineering in Medicine and Biology Society. Annual International Conference (42nd : 2020 : Online), IEEE Engineering in Medicine and Biology Society.

[31] "Breathing Rate Estimation from Head-Worn Photoplethysmography Sensor Data Using Machine Learning _ Enhanced Reader".

Authorized licensed use limited to: DELHI TECHNICAL UNIV. Downloaded on May 15,2023 at 09:51:08 UTC from IEEE Xplore. Restrictions apply.

J. Inst. Eng. India Ser. A
https://doi.org/10.1007/s40030-023-00740-x

ORIGINAL CONTRIBUTION

Estimations of Wind-Generated Effects on a Regular Tower of Varying Cross-Sectional Shape

Abhishek Prakash Paswan[1] · Bhagya Jayant[1] · Ark Rukhaiyar[1] · Kunal Dahiya[1] · Ritu Raj[1] · Rahul Kumar Meena[1,2]

Received: 4 December 2022 / Accepted: 6 May 2023
© The Institution of Engineers (India) 2023

Abstract Tall Buildings are coming up all around the world since the land availability in the plan shape is limited hence irregular plan cross-sectional shape are designed. Wind load standards of different countries are also silent about the modification of tall building. The present study analysed the wind effects on the tall building where modification is provided in the vertical plane of the structure and the tall building is consisting of two types of cross-sectional shape such as square and plus shape. Wind effects are investigated from 0° to 90° wind incidence angles at the interval of the 30°. The result is presented in various graphical forms such as pressure contours stream lines in plan and average pressure coefficient on each surface of the tall building. Cross-sectional shape has a significant impact on reducing the wind effects, also it is observed that the recirculation zone of wind is most effective on one-third height of the leeward face for such type of modifications. Positive pressure was noted on the wind ward face, while suction that is negative pressure is observed on the leeward and side faces of the tall building for most of the wind incidence angle.

Keywords Tall building · Varying cross section · Pressure contours · Streamlines · Wind load

Introduction

Modern urban infrastructure is dominated by tall buildings, which are increasingly common because of the number of reasons such population expansion, a lack of available land and economic concerns. However, as buildings get taller or rise in vertical height then high-rise buildings are exposed to more environmental factors, such as wind effects, which can significantly affect a building structural parameters and occupant comfort. Understanding the necessity of construction of the tall buildings and examining how wind is affecting them are therefore essential for assuring the safety and comfort. Wind effects can be investigated by wind tunnel test and CFD test. Wind tunnel testing has high acceptance when designing tall buildings but this is costly and time taking. However, a shift to computational fluid dynamics analysis has been observed for an in-depth study at the early design stage in areas with lower to moderate turbulence. While both methods are moderate to highly accurate, wind tunnel testing takes months to analyse, whereas CFD analysis is faster and cost-effective. It provides direct reporting in comparison to abstract reporting in wind tunnel testing. The wind tunnel is, however, preferred in studies dealing with higher turbulent winds by resolving unsteady gusts and eddies directly. Another advantage of CFD analysis is its capability to eliminate scaling and probes that may influence the measurements. It provides mapping of results and precise resolution in an informative and with better visual way. The structural designer can design the regular shape structure with the help of various international standards [1–12] all these standards are for regular shapes. Wind load changes as the shape of the structure changes.

Various studies such as Tian et al. [13] performed RANS simulation on rectangular cylinder and observed that the vortex shedding is almost independent on the aspect ratio while

✉ Rahul Kumar Meena
rahulmeena@pec.edu.in

[1] Department of Civil Engineering, Delhi Technological University, New Delhi, India

[2] Department of Civil Engineering, Punjab Engineering College, Chandigarh, India

Published online: 20 May 2023

the drag force is highly dependent on the aspect ratio. Diez et al. [14] investigated performance of the rear cavities in different shape of the high-rise building, it is observed that the slanted cavity may perform better in comparison to the straight cavity to increase the structural performance. Different research such as Baraigi and Dalui [15] on "Set back building", Sanyal and Dalui [16–18] on "Y", Meena et al. [19] on "L" and different researcher [20–28] have investigated the wind effect using either CFD or wind tunnel test and observed that the improving cross-sectional shapes leads to reduced wind-induced vibrations, and implementing dynamic facades using different methods could mitigate wind-induced effects, thus improving the safety of civil infrastructures and their performance. While wind tunnel testing has been widely accepted when designing tall buildings, a shift to CFD analysis has been observed for an in-depth study at the early design stage in areas with lower to moderate turbulence. CFD analysis is faster and cost-effective, providing direct reporting in comparison to abstract reporting in wind tunnel testing, and it is capable of eliminating scaling and probes that may influence the measurements. Wind flow is mainly influenced by the characteristics of the building model [29, 30].

This manuscript aims to investigate the wind effects for determining wind flow characteristics of tall buildings with varying cross sections (G + 64) using Computational Fluid Dynamics (CFD) approach. The manuscript also highlights the advantages of using CFD analysis over wind tunnel testing in estimating the wind effects on tall building at a faster rate and using cost-effective tools. Most of the available studies are either discussing the wind effects on regular shape or irregular shape tall building, while the present study is investigating the wind effects on the tall building where modification in the plan cross-sectional shape is presented in the form of the square and plus shape. Hence this study is different from past available studies also the various results such as pressure contours and stream lines in both vertical and horizontal plan are presented.

Numerical Model Development

Numerical Model

Numerical analysis is performed using a computational fluid dynamics tool ANSYS CFX. Numerical studies done in the field of wind engineering are done using the $k-\varepsilon$ turbulence model. This model performs more efficient, and the result obtained is more or less identical to the wind tunnel results. In order to anticipate the wind response for the wind engineering issue, the $k-\varepsilon$ model requires fewer computer resources. The $k-\varepsilon$ turbulence model solves two transport equations, one for turbulent kinetic energy (k) and one for turbulent dissipation rate (ε), making it a two-equation model.

The $k-\varepsilon$ turbulence model is advantageous since it does not require geometry-specific parameters for result prediction. It is necessary to include two new variables in the model system of equations: the turbulent kinetic energy and the turbulence dissipation rate.

The inlet value of turbulence kinetic energy (k) is given by Eq. (1)

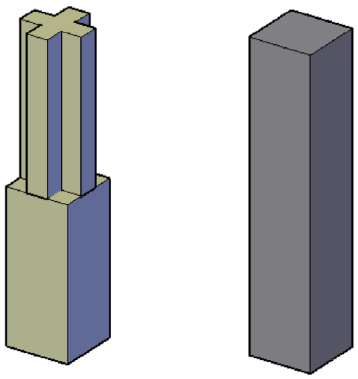
$$k = \frac{3}{2}\left(U_{\text{avg}} I\right)^2 \tag{1}$$

$$\in = \frac{c_{\mu k^2}}{\nu\left(\mu_\tau/\mu\right)} \tag{2}$$

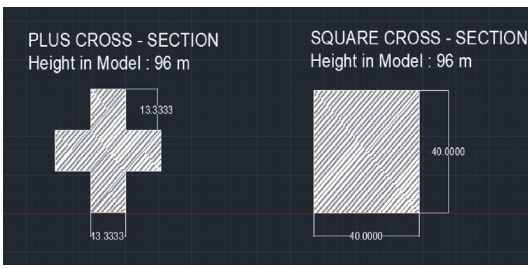
where c_μ is a non-dimensional constant, K is the turbulent kinetic energy, ν is the kinematic viscosity, μ_τ/μ is the eddy viscosity ratio.

Geometry and Meshing

In this study, Model A was designed using AutoCAD 3D modelling software, as illustrated in Fig. 1. Model A is a G + 64 building, standing 192 m tall, with two types of cross



Model A and Model X



Different Types of cross – sections

Fig. 1 Plan and elevation of the high-rise building

sections—square and plus, each with a height of 96 m, as depicted in Fig. 1. The model was compared with a reference isolated model X, which is shown in Fig. 1.

The ANSYS analysis can be conducted in five steps such as Geometry, Mesh, Setup, Solution, and Result. To prevent flow re-circulation, the domain was established based on wind tunnel manual [31, 32] and various guidelines available to investigate the wind effects, where the boundaries are set at a distance of 5 h from the windward face (A), lateral faces (C and D), and roof of the model, and 15 h from the leeward face (B) (where h represents the height of the model). A meshing for the different part is adopted and a tetrahedral meshing is used for the large domain with a size of 0.2 m, and meshing with inflation of 15 layers was provided at the boundaries of building model to the ground of the domain for smooth flow. Meshing is presented in Fig. 2.

Grid Convergence and Validation

Grid convergence analysis is a necessary prerequisite for CFD programming since it suggests the meshing pattern for the entire numerical simulation. For the purposes of this investigation on model A is performed at wind incidence angle 0° and it is found that the meshing pattern 4 as shown in Fig. 4 is with least error hence for the entire numerical simulation mp-4 is adopted. Domain used for the numerical simulation with the dimensions is presented in Fig. 3 and different meshing are graphically plotted in Fig. 4. Meshing on domain and meshing on building with inflation is presented in Fig. 2.

The grid convergence approach described by Celik et al. [33] and Derakhshandeh and Alam [29] is used in this investigation. Initially geometry of the tall building is created and then the geometry of the building is divided into the small elements and these elements are of different shapes for the present study the tetrahedron meshing is adopted for the domain. The flow is computed into these grids and stiffness matrix is solved for each grid and these how the solution is obtained for the wind engineering problem solved through the computational fluid dynamics tool.

To validate the present study and its adherence to Indian Standard IS: 875 (part-3): 2015, an independent reference model, referred to as Model X, was constructed and evaluated. Model X has a height of 192 m and a square cross section with dimensions of 40 m by 40 m (Fig. 1). The analysis was performed in ANSYS CFX mode, and the resulting coefficient of pressure (C_p) values for each face (A, B, C, and D) were tabulated in Table 1 below. These values were

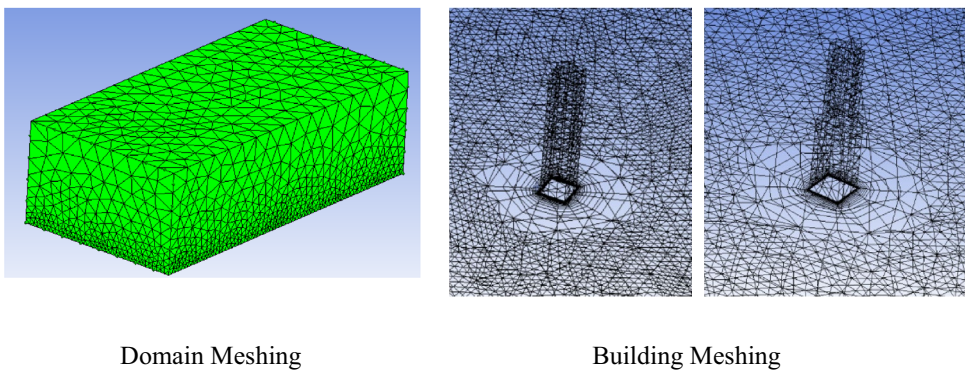


Fig. 2 Different type of meshing

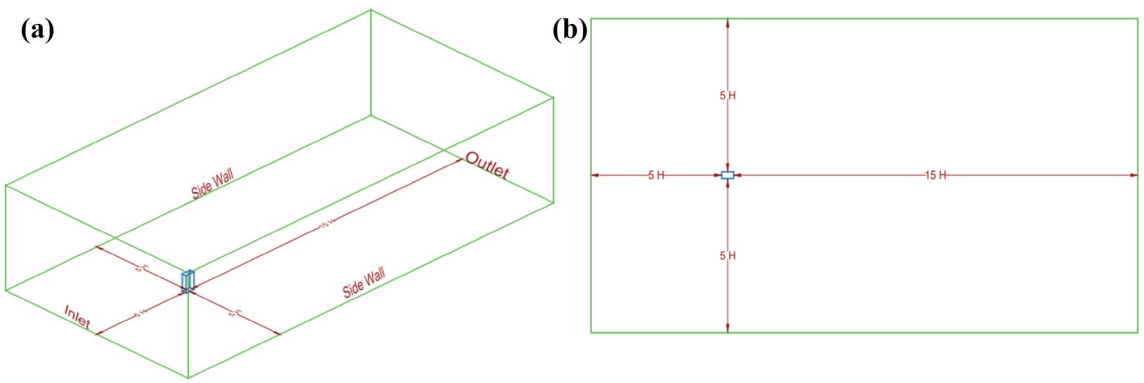
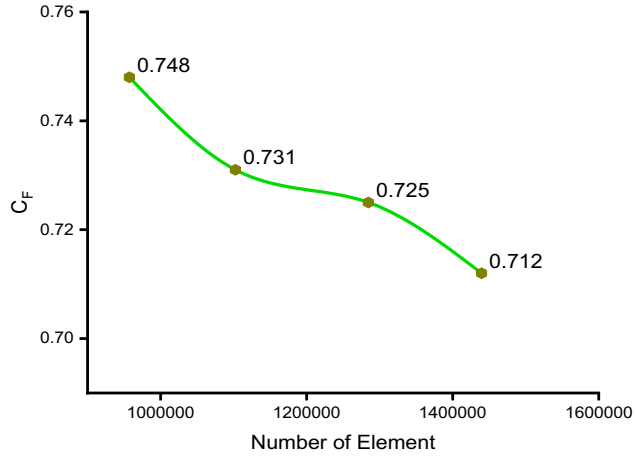
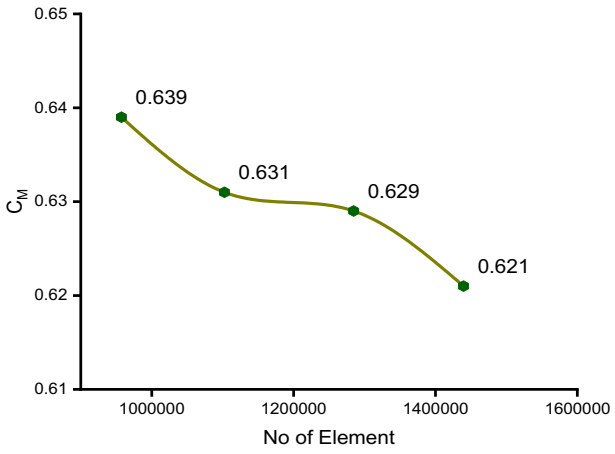


Fig. 3 Domain **a** elevation and **b** plan



C_F for model-X at 0^0 wind incidence angle



C_M for model-X at 0^0 wind incidence angle

Fig. 4 Grid test result for model-A

Table 1 Comparing C_p values of Model X with acceptable C_p values in accordance with IS: 875 pt-3

Coefficient of pressure (C_p)	Faces of model X			
	A	B	C	D
IS: 875 (Part III)—2015	+0.8	−0.25	−0.8	−0.8
Model X	+0.66	−0.28	−0.65	−0.65

then compared against the allowable ranges specified in IS: 875 (part-3): 2015.

The validation process is an essential step in the investigation of the wind effects on tall buildings using ANSYS CFX. The purpose of the validation is to ensure the accuracy and reliability of the results obtained from the numerical simulations. In this process, an independent reference model is developed and assessed for the purpose of verifying the present study outcome with Indian Standard IS: 875 (part-3): 2015. By validating the results obtained from the numerical simulations with the reference model, it can ensure that the simulation methodology used in the present study is accurate and reliable. This, in turn, provides the results obtained for the tall building under consideration. The validation process also serves as a benchmark for future studies and helps to establish the credibility of the simulation methodology used. The present study investigates the wind effect in the varying cross-sectional shape tall building.

CFD Pre-simulations

To make sense of the data generated by ANSYS setup and solution processes, the power law is applied for interpretation of wind generated result on complex shape building. Figure 5 depicts the power law profile and virtual domain used in this study to investigate the results produced by this simulation with the following input parameters:

$\alpha = 0.147$
$Z_{\text{ref}} = 1$ m
$U_{\text{ref}} = 10$ m/s

For the purpose of determining pressure, a power law is applied (Eq. 3).

$$P = U_{\text{ref}} \left(\frac{z}{Z_{\text{ref}}} \right)^{\alpha} \tag{3}$$

After the programme has been executed for almost an hour, the outcomes are analysed. The pressure coefficient variation is then calculated (Eq. 4).

$$C_{\text{P}} = \frac{\left(P - P_{\text{ref}}\right)}{\left(\frac{1}{2}\rho_{\text{a}} V_{\text{ref}}\right)} \tag{4}$$

V_{ref} is reference wind speed which is calculated as per the guidelines available in Indian Standard and wind tunnel manual and kept as 10 m/s.

As a result, the density of air is calculated to be $\rho_a = 1.225$ kg/m^3

The wind load effect on Model A is analysed for 17 faces. The faces are named as shown in Fig. 6. Windward side is that side which is facing the on—coming wind. The side resisting this on—coming wind is called as the Leeward side. Classification of faces is done majorly based on four directions into faces A, B, C and D as the "front faces" as shown in Fig. 6. The remaining faces are classified into subscripts

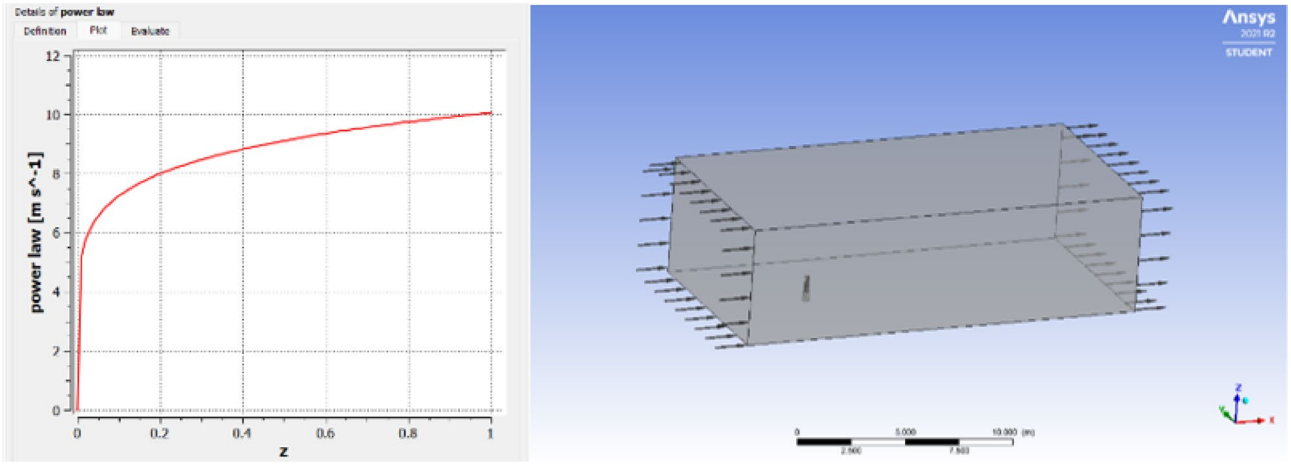


Fig. 5 Representation of setup in ANSYS CFX

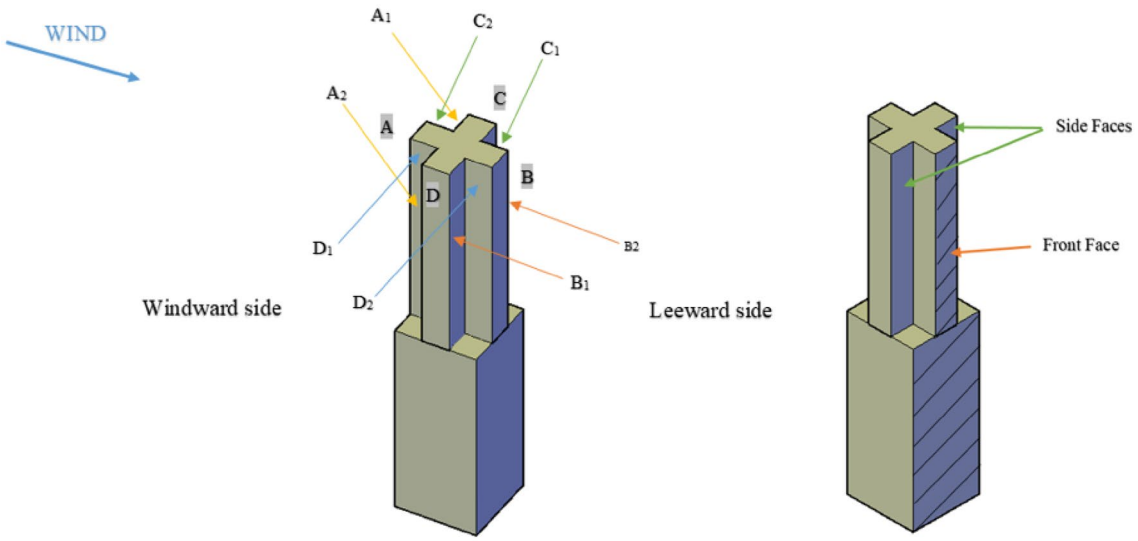


Fig. 6 Representation of front and side faces of Model A

of 1 and 2 of front face as "side faces". As explained in Fig. 7, each direction or front face will have 2 side faces. The side face to the left of front face is subscripted to 1 (A_1/B_1/C_1/D_1) while the one to the right is subscripted to 2 (A_2/B_2/C_2/D_2).

Also, for wind analysis in ANSYS further cases for each face will be considered for wind angle incident at 0°, 30°, 60°, and 90° on the $x-y$ plane.

Results and Discussion

The outcomes of regular and irregular shape models with equal plan area are explored, and the results are presented in various visualizations.

Pressure Contours

The distribution of wind pressure across each face of a tall building is depicted in a pressure contours diagrams for tall building model in Fig. 7. Usually, a range of pressure levels are shown on the figure, with the greatest values denoted by the different colour shades. Constant pressure values fluctuate across a surface, the contours are utilized to show the variation. When displaying a variable pressure contours different colour is presented in the figures by default settings of ANSYS, but in a contour plot with more or less equal pressure colour bands are some difficult to measure the exact pressure, the areas of colour are more continuous. The following observations of pressure contours for all faces are listed and classified into different cases as below. The cases

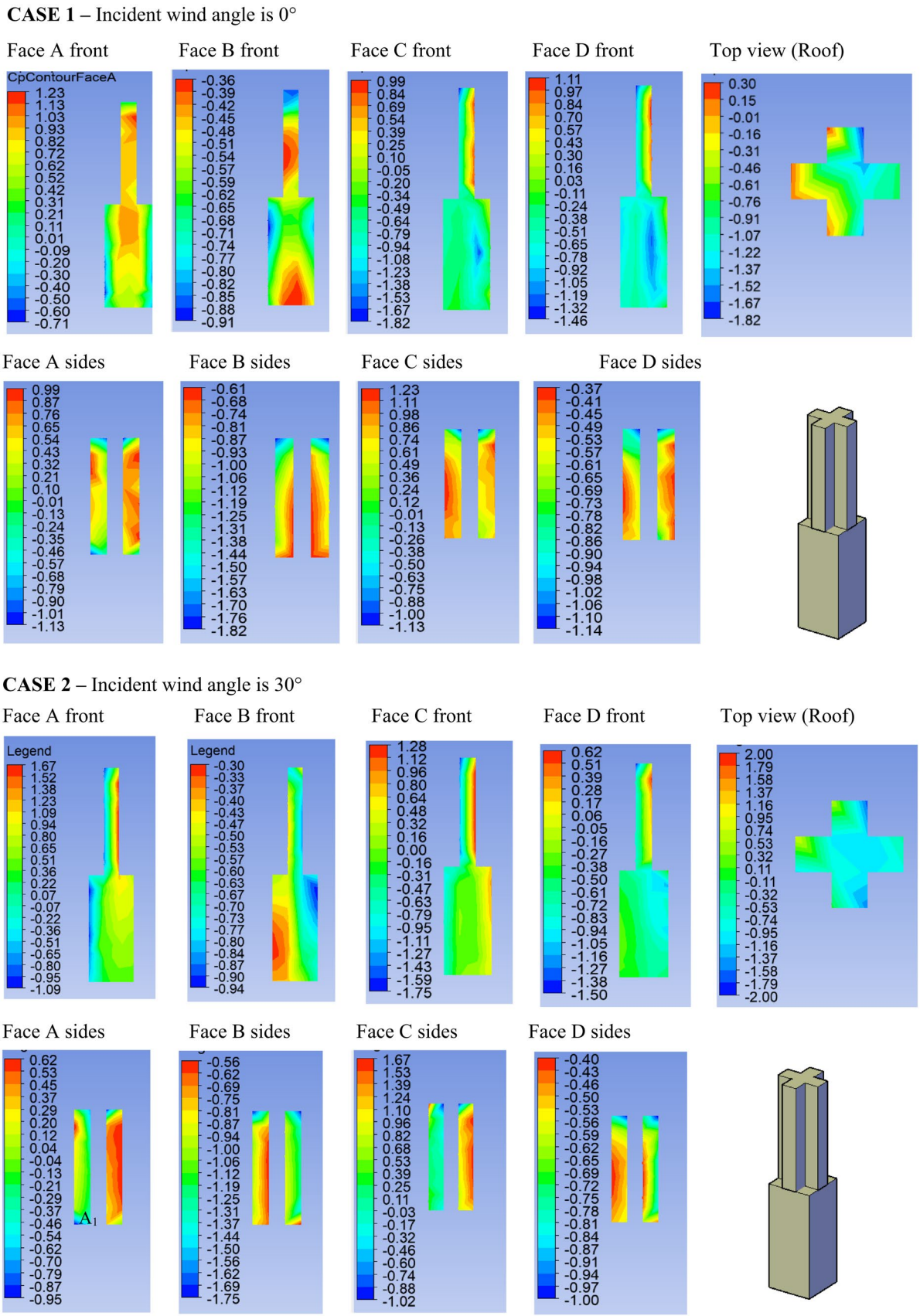
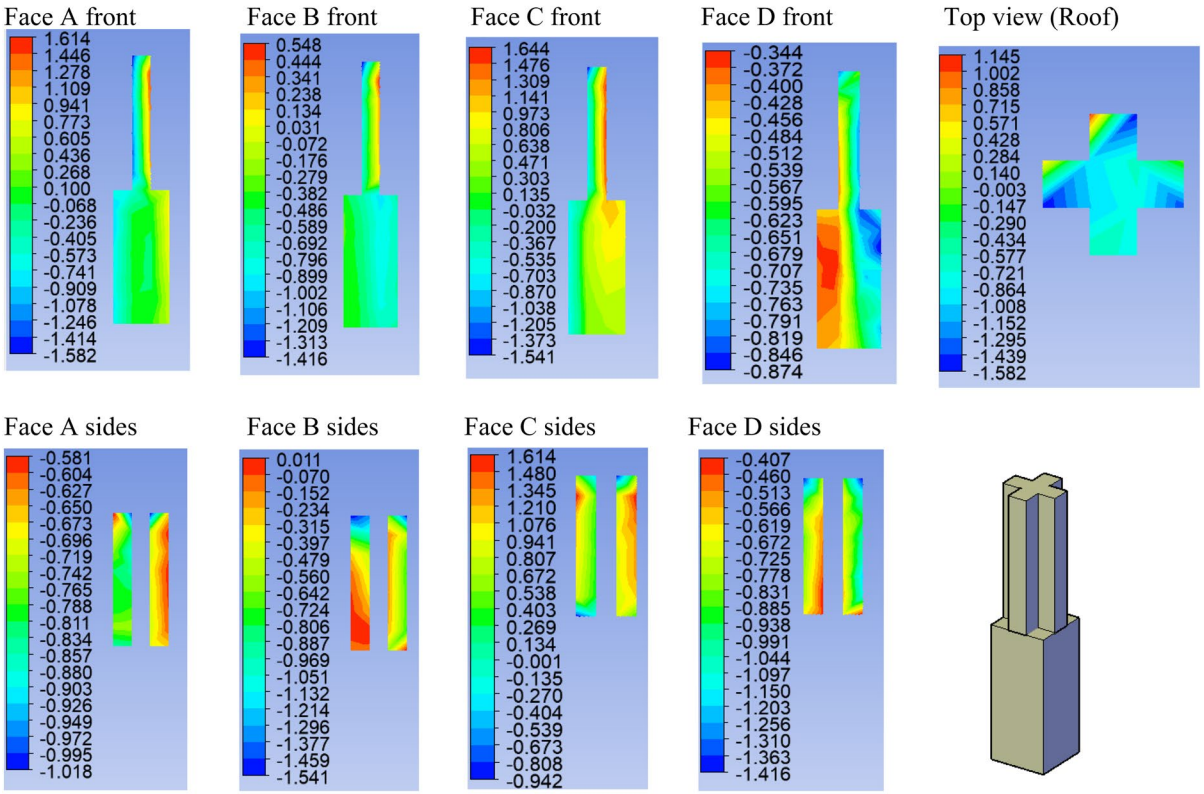


Fig. 7 Pressure contours for different face of the building model A and X

CASE 3 – Incident wind angle is 60°



CASE 4 – Incident wind angle is 90°

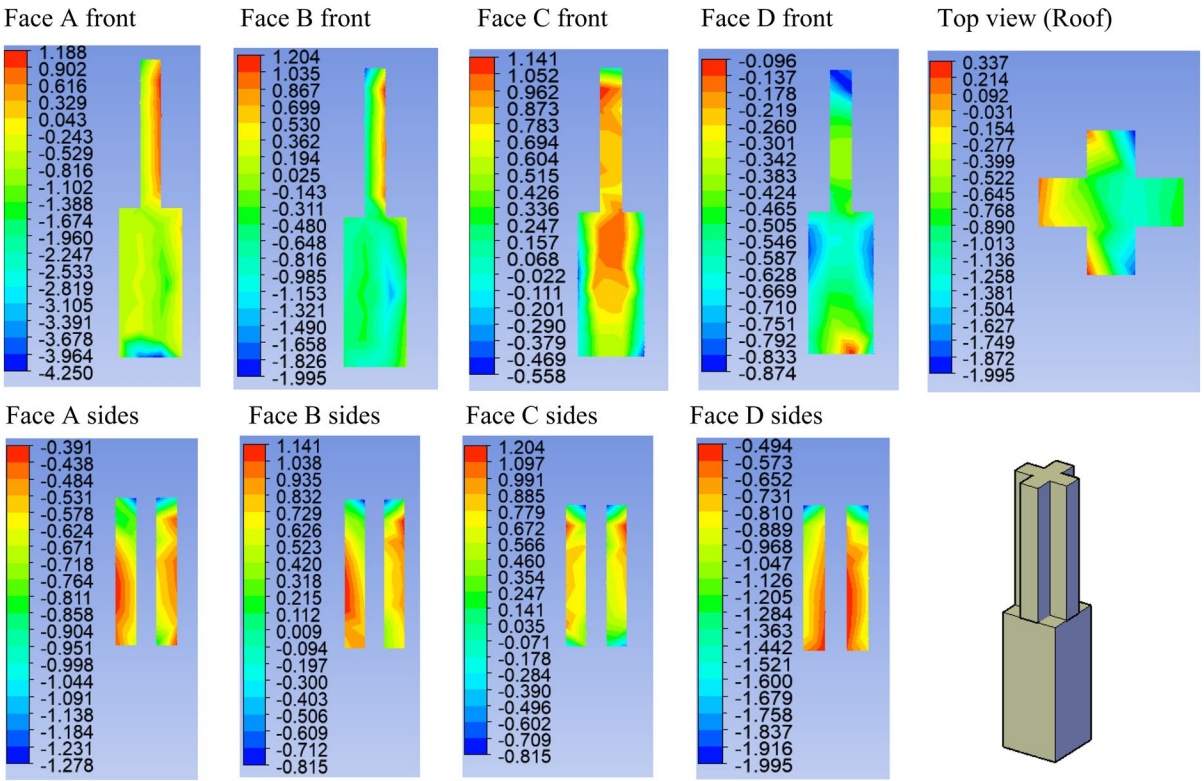


Fig. 7 (continued)

Model X – From Model X, pressure contours were obtained for wind incident angle 0°.

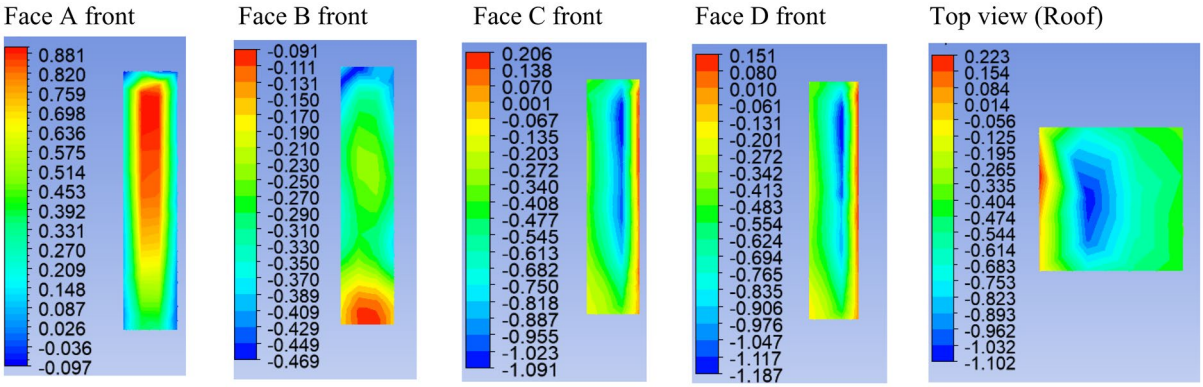


Fig. 7 (continued)

are classified into 1, 2, 3, and 4 on the basis of incident wind angle—0°, 30°,60°, and 90°. Figure 7 reiterates the classification of faces of Model A. The face which is left to the front face is subscripted to A and the other on the right is subscripted to D. The following pressure contours are evaluated using ANSYS for Model A and Model X (Fig. 8).

- Variation in C_p range is highest in case 3 for incident wind angle 60°. Therefore, most wind effect on Model A is observed in this case, whereas least variation in C_p range is observed for incident wind angle 90°. Therefore, least wind effect on Model A is observed in this case.
- For wind direction $<=30°$ on the horizontal plane, C_p values of faces C and D were almost similar and C_p variation across these faces were similar too. Therefore, the sides of the Model A experience similar pressure impact.
- For wind direction $>=30°$ on the horizontal plane, contours of plus cross section were symmetrical (except for Face A and its side faces where slight disturbances were observed).

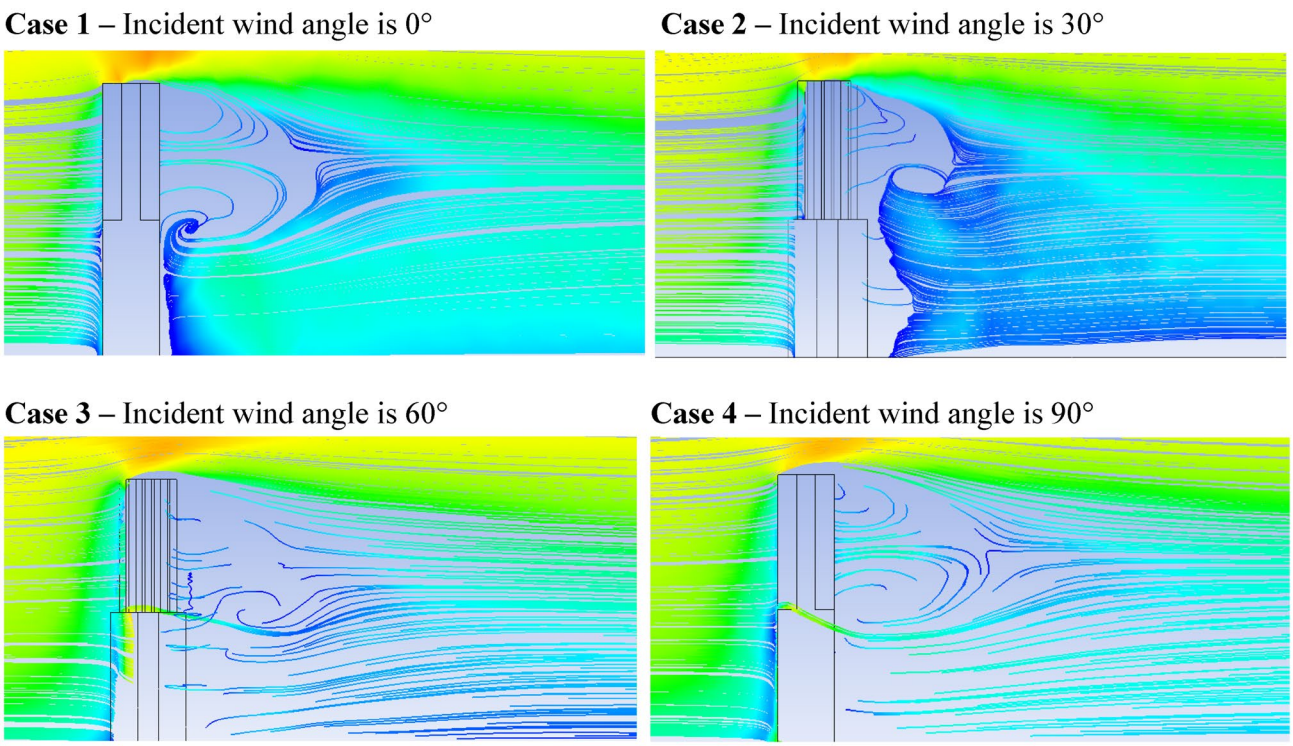


Fig. 8 Velocity streamline in vertical planes

- Also Cp range for Model X is comparable to Model A. Value of C_p for roof faces is constant over its entire area, although slight variation was observed with change in wind direction.
- For Model A with an incidence wind angle of 0 degrees, the value of C_p is between (−0.86084) and (0.666623). The maximum negative pressure coefficient was −0.86084, acting on face B2, while the maximum positive pressure coefficient was 0.666623, acting on face D1. Therefore, the most important sides here are B2 and D1.
- C_p for Model A with an incidence wind angle of 30° may be found in the interval [−1.10667, 1.14674]. The maximum negative pressure coefficient was 1.10667, which acted on face B2, while the maximum positive pressure coefficient was 1.14674, which acted on face C2. It follows that B2 and C2 are the most important faces here. In this particular circumstance, C_p has a wider range than it did in the 0° scenario.
- A value of C_p between − 1.03526 and 1.1391% for an incidence wind angle of 60° on Model A may be found between these two ranges. Both a maximum of −1.03526 (on face D1) and a maximum of 1.1391 (on face A1) were the maximum negative and positive pressure coefficients, respectively. The most important sides in this scenario are D1 and A1. C_p now has a larger range than it had at 0°.
- C_p on Model A, with an incidence wind angle of 90°, has a range of [−0.85415, 0.642927]. Face D1 was subjected to a maximum negative pressure coefficient of −0.85415, whereas face B2 was subjected to a maximum positive pressure coefficient of 0.642927. As a result, D1 and B2 are the most important faces here. In this instance, the C_p range is analogous to the 0° instance.
- The interval [−0.734214, 0.623015] contains the values that may be expected for C_p in Model X. The maximum negative and positive pressure coefficients were -0.734214 on face D and 0.623015 on face A. For Model X, the C_p range is comparable to the 0° of Model A.

Streamlines

When fluid particles move vertically around a tall building, they follow imaginary paths called "streamlines" in the vertical plane. These streamlines are essential in the design of tall buildings since they aid engineers and architects in understanding how the wind moves around the building and locating potential weak points. In the construction of tall structures, computational fluid dynamics (CFD) simulations are often used to assess streamlines in the vertical plane. These simulations are able to simulate the wind flow around a building and produce images of the ensuing streamlines. The structural performance of the structure can be improved by making design changes in parts of the building that may be subject to increased wind pressures, such as corners or edges, by studying the streamlines in the vertical plane. Overall, comprehending the streamlines in the vertical plane is a vital step in the design of tall buildings since it enables structural engineers to maximize the structural performance to resist the wind loads.

Vertical Streamlines

The discovered vertical streamlines lead to the following conclusions:

- The wake region of Model A exhibits a reversal in wind direction at an incidence wind angle of 0 degrees, producing a separation zone. At the peak of the structure, or Model A, where the streamlines switch directions, higher velocities are seen. Since the streamlines are symmetrical, the structure will be less affected by the wind.
- At a distance from the building or model A, a leeward recirculation zone or vortex forms when the incident wind angle is 30°. The windward side of the structure, also known as Model A, experiences flow reattachment. At the highest point of the structure, or Model A, where the streamlines change direction, the velocity is highest.
- Flow separation is seen at the wake region when the incident wind angle is 60° on Model A. Fewer lines of circulation are seen. At the highest point of the structure, or Model A, the streamlines speed up and reverse the direction with reference to wind ward face.
- A re-circulation zone forms on the leeward side of Model A when the wind is blowing at an incidence angle of 90°. The wake zone exhibits flow separation, most notably on the leeward side of the plus cross section of the structure. Fewer lines of circulation are seen. At the highest point of the structure, or Model A, the streamlines speed up and reverse path. A re-circulation zone forms on the leeward side of Model A when the wind is blowing at an incidence angle of 90 degrees. The wake zone exhibits flow separation, most notably on the leeward side of the plus cross section of the structure. Fewer lines of circulation are seen. At the highest point of the structure, or Model A, the streamlines speed up and reverse path with respect to positive pressure on building face.

Horizontal Streamlines

For Model X, horizontal streamlines were obtained for wind flow at four different heights (incident wind angle 0°). In the present study, the following observations were made regarding the wind behaviour on Model A and Model X and the streamlines are presented in Figs. 9 And 10:

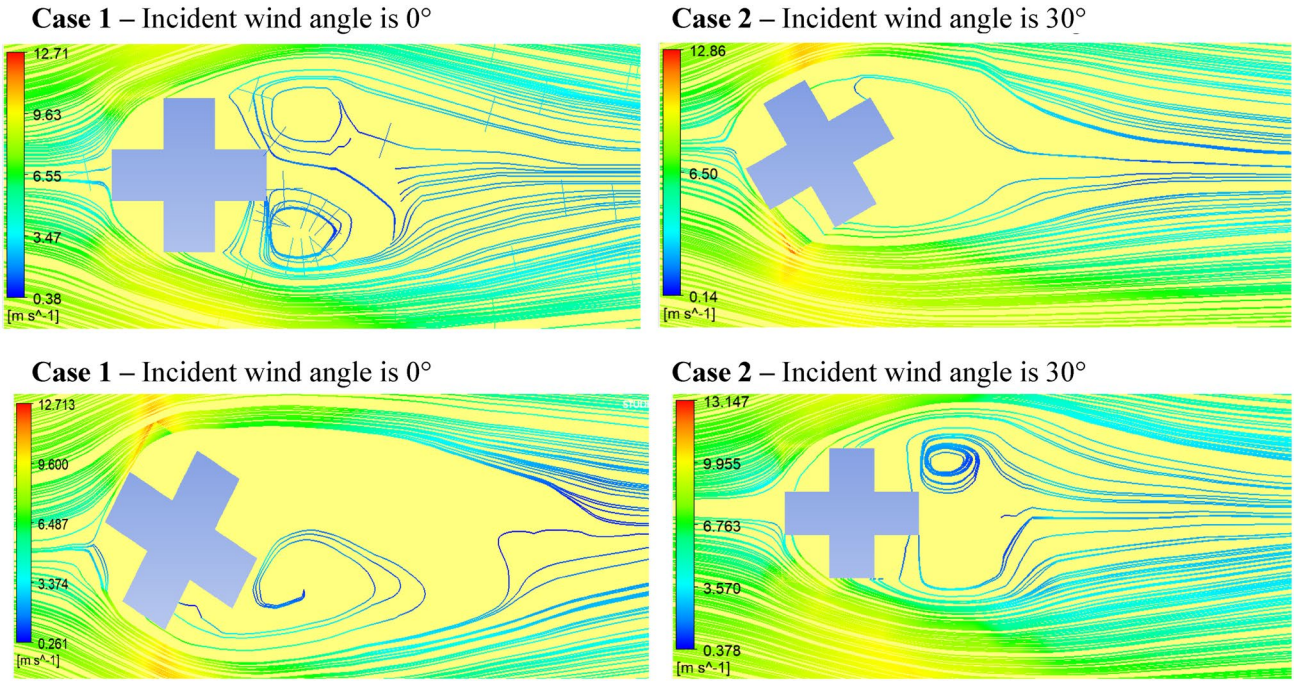


Fig. 9 Velocity streamline in horizontal planes for model A

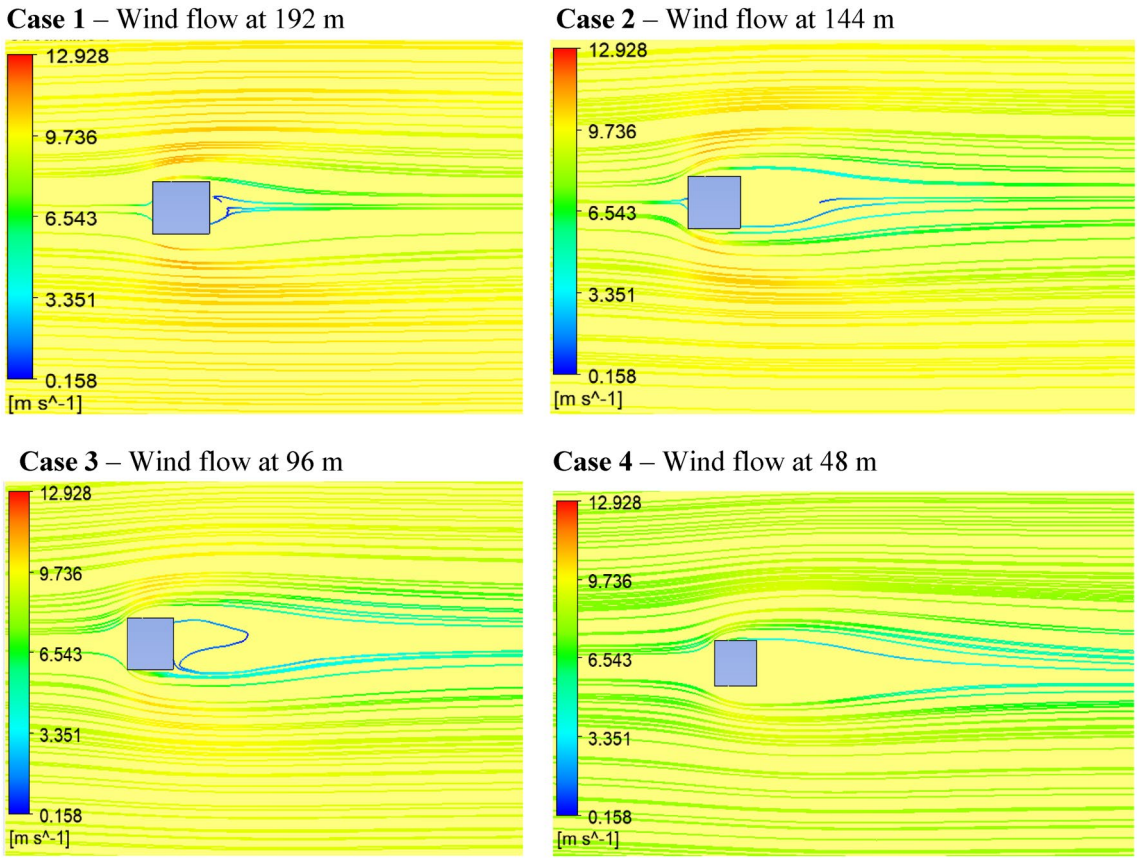


Fig. 10 Velocity streamline in horizontal planes for model X

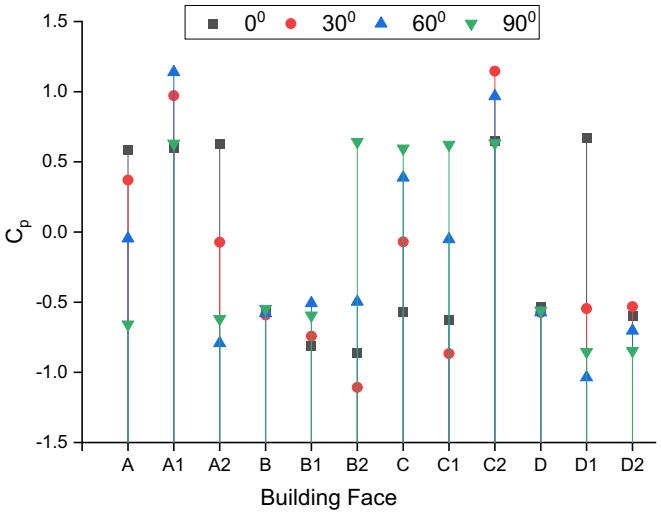
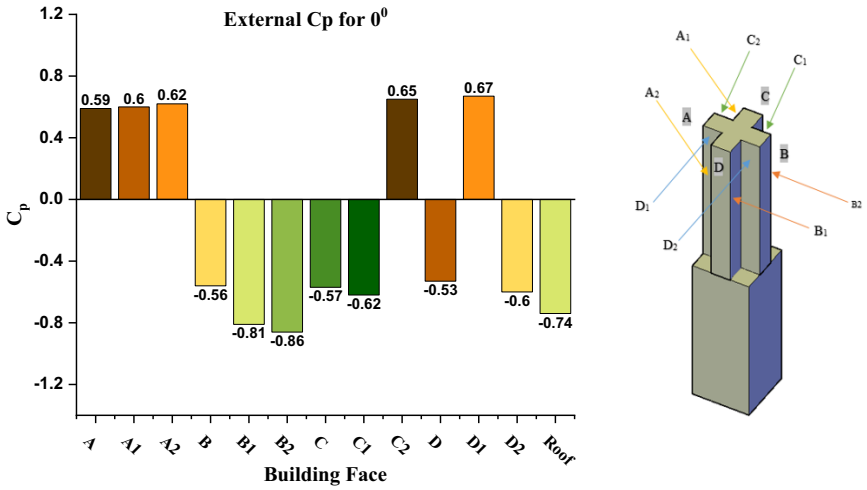


Fig. 11 External pressure coefficient for model A

Case-1 External Cp for 0⁰



Case-2 External Cp for 30⁰

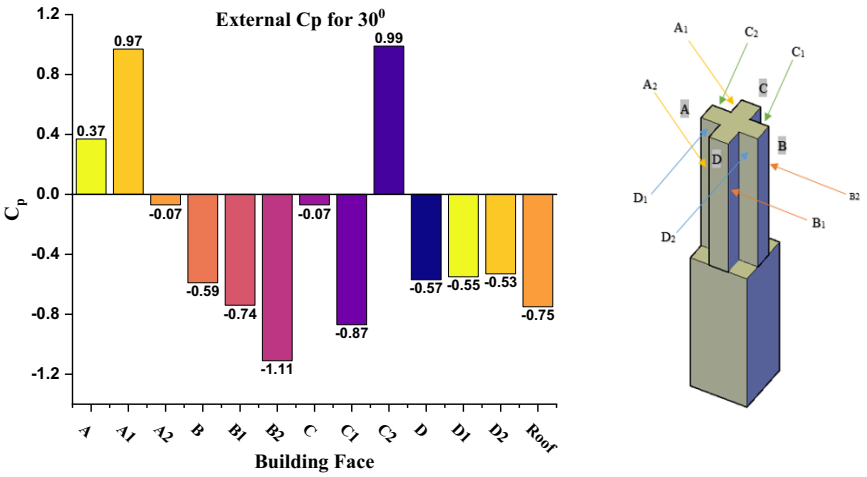
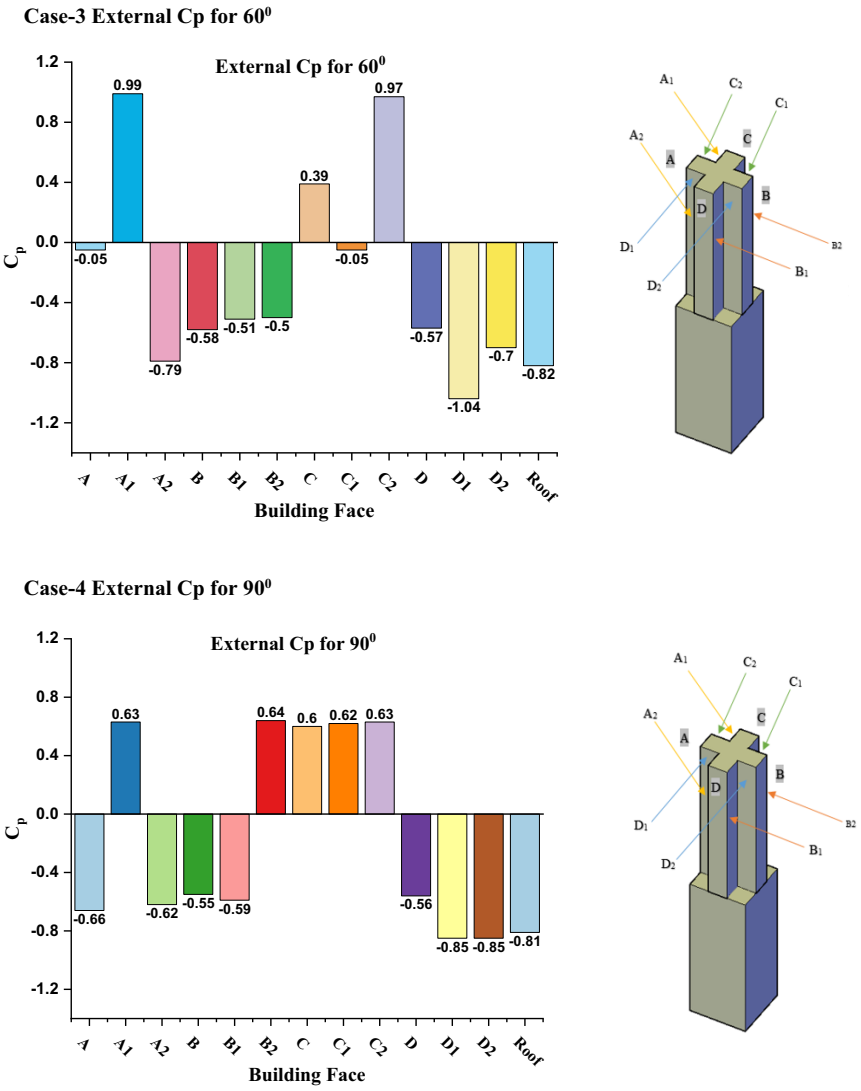


Fig. 11 (continued)



- At an incident wind angle of 0 degrees on Model A, two symmetric vortices or recirculation zones are formed near faces C1 and B2, and B1 and D2, resulting in a separation zone. However, at the highest point of the structure, symmetrical streamlines are observed, indicating minimal wind effect on the structure.
- At a wind angle of 30°, symmetrical streamlines are observed on Model A, suggesting that the wind has a minimal impact on the structure.
- At a wind angle of 60°, a vortex or recirculation zone is formed near face D (leeward face) on Model A, indicating that this region is unsuitable for providing openings for windows, etc.
- At a wind angle of 90° on Model A, a vortex or recirculation zone is observed near faces C1 and D2, making this region unsuitable for providing openings for windows, etc.
- On the other hand, Model X shows symmetrical horizontal streamlines with minimal turbulence and no recirculation zone nearby, indicating an ideal cross section shape for tall buildings. Therefore, it is safely designed.

External Pressure Coefficient

The pressure coefficients (C_p) obtained from the ANSYS analysis for Model A were used to classify each face as windward or leeward. A positive C_p value indicates that the face is in the windward region, while a negative value indicates that it is in the leeward region. The results were plotted in the form of bar charts for each incident wind angle, as shown below.

From Fig. 11, the following conclusions are drawn.

- For Case 1—Incident wind angle is 0°, the highest negative value of C_p is -0.9 (rounded—off) on face B_2 and the highest positive value of C_p is 0.67 (rounded—off) on face D_1. Independent groups of side faces (A_1 & A_2, B_1 & B_2, C_1 & C_2, D_1 &D_2) have similar pressure impact. Faces A, B, C, D have almost equal value of coefficient of pressure, $C_p \approx 0.6$.
- For Case 2—Incident wind angle is 30°, the highest negative value of C_p is -1.1 (rounded—off) at face B_2 and the highest positive value of C_p is 1.15 (rounded—off) at face C_2. C_p values for side faces A_1 & A_2 and C_1 & C_2 have high variation in comparison to side faces B_1 & B_2 and D_1 & D_2 which show low variation in values. C_p (faces B & D) ≈ -0.6. With respect to 0° case, values of C_p for faces A & C decreased and for faces B & D increased very slightly (negligible).
- For Case 3—Incident wind angle is 60°, the highest negative value of C_p is -1.03526 at face D_1 and the highest positive value of C_p is 1.139 at face A_1. C_p values for side faces B_1 & B_2 have equal pressure impact with $C_p \approx 0.5$. Whereas, C_1 & C_2 show high variation in comparison to side faces A_1 & A_2 and D_1 & D_2 which show medium variation in C_p values. C_p (faces B & D) ≈ -0.57. C_p values of faces A & C obtained in this case is equal to C_p values of C & A respectively obtained in Case 2 (for incident wind angle 30°). With respect to 0° case, values of C_p for faces A & C decreased and for faces B & D increased very slightly (negligible).
- For Case 4—Incident wind angle is 90°, the highest negative value of C_p is -0.854 at face D_1 and the highest positive value of C_p is 0.6304 at face A_1. Independent side faces (A_1 & A_2, B_1 & B_2, C_1 & C_2, D_1 & D_2) have similar pressure impact. Faces A, B, C, D have almost equal value of coefficient of pressure, $C_p \approx 0.6$.

Conclusions

The turbulent and unpredictable nature of wind poses a challenge for understanding its behaviour when interacting with tall buildings where modifications are applied in the tall building along the height of the building. Therefore, investigating the wind flow characteristics of such type of structures is essential. This paper presents the following conclusions:

- International standards are typically used for analysing wind effects on tall buildings with simple cross sections. To analyse a tall building with a more complex cross section (Model A), this study adopted CFD analysis and the k-ε turbulence model in ANSYS: CFX mode.
- Model A is validated by comparing its C_p values with those obtained from IS: 875 (Part III)—2015, which were found to be in closer range for external C_p provided in the Indian standards.
- Wind flow characteristics were analysed for all faces of Model A in terms of pressure contours and vertical and horizontal streamlines for four incident wind angles (0°, 30°, 60°, and 90°). Pressure behaviour changes at different faces of Model A due to changes in incident wind angle. Faces A, B, C, and D have similar pressure impact ($C_p \approx 0.6$) for incident wind angles of 0° and 90°. However, C_p values for faces A and C decrease for incident wind angles of 30° and 60°.
- The study found that changing cross sections have a significant influence on the stability of the structure. For incident wind angle 30°, a recirculation zone was formed at the leeward side of Model A at one-third of its height. Windward faces exhibited positive values of the coefficient of pressure. Additionally, C_p values for faces A and C were interchanged for incident wind angles of $-30°$ and 60°.
- CFD analysis is a better alternative to traditional wind tunnel testing methods, as it is more time-efficient and cost-effective.
- In summary, this study provides valuable insights into the complex behaviour of wind flow on tall buildings with non-standard cross sections and highlights the importance of considering changing wind angles and cross sections for designing stable structures.

Future Scope of the Paper

Next steps for this work include testing the dynamic response of the wind on the suggested model of this research (Model A) by changing the heights of the cross sections. To further evaluate how well the code performed, the resulting results would be entered into ETABs.

Funding No specific funding is received for this study.

Declarations

Conflict of interest The authors declares that they have no known competing financial interest or personal relationship that could have appear to influence the work reported in this paper.

References

1. ASCE: 7-16(2017), in *Minimum Design Loads and Associated Criteria for Buildings and Other Structures* (Structural Engineering Institute of the American Society of Civil Engineering, Reston, 2017). https://doi.org/10.1061/9780872629042
2. AS/NZS:1170.2(2011), in *Structural Design Actions—Part 2: Wind Actions* (Standards Australia/Standards New Zealand, Sydney, 2011)
3. National Research Council of Canada, Canadian commission on building and fire codes. Natl. Build. Code Canada **2015**(1), 708 (2015)
4. T. Standard, I. Ministry, Engineering Standard for Flow Instruments Original Edition, 1998 (1997)
5. GB 5000902001, National Standard of the People's Republic of China (2002)
6. IS: 875 (2015), in *Indian Standard Design Loads (Other Than Earthquake) for Buildings and Structures-Code of Practice, Part 3(Wind Loads)* (2015)
7. B. European Committe for Standardization, EN 1991-1-4 (2005) (English): Eurocode 1: Actions on structures—Part 1–4: General actions—Wind actions (2011)
8. Ethiopian Standard, ES ISO 4354 (2012) (English): Wind actions on structures (2012). http://scholar.google.com/scholar?start=10&q=asi+interface&hl=es&as_sdt=0,5#6
9. Hong Kong Building Department, Code of Practice on Wind Effects in Hong Kong 2019 (2019)
10. MNBC, Myanmar National Building Code 2020, International relation and legal Section Department of Building Minis (2020)
11. NSCP C101-15, National Structural Code of the Philippines 2015 (2015)
12. P. Planning, U. Development, Nepal national building code (1994)
13. X. Tian, M.C. Ong, J. Yang, D. Myrhaug, Unsteady RANS simulations of flow around rectangular cylinders with different aspect ratios. Ocean Eng. **58**, 208–216 (2013). https://doi.org/10.1016/j.oceaneng.2012.10.013
14. M. Lorite-Díez, J.I. Jiménez-González, L. Pastur, O. Cadot, C. Martínez-Bazán, Drag reduction on a three-dimensional blunt body with different rear cavities under cross-wind conditions. J. Wind Eng. Ind. Aerodyn. (2020). https://doi.org/10.1016/j.jweia.2020.104145
15. A.K. Bairagi, S.K. Dalui, Wind environment around the setback building models. Build. Simul. **14**, 1525–1541 (2021). https://doi.org/10.1007/s12273-020-0758-3
16. P. Sanyal, S.K. Dalui, Forecasting of aerodynamic coefficients of tri-axially symmetrical Y plan shaped tall building based on CFD data trained ANN. J. Build. Eng. **47**, 103889 (2022). https://doi.org/10.1016/j.jobe.2021.103889
17. P. Sanyal, S.K. Dalui, Effects of side ratio for 'Y' plan shaped tall building under wind load. Build. Simul. (2020). https://doi.org/10.1007/s12273-020-0731-1
18. P. Sanyal, S.K. Dalui, Effects of internal angle between limbs of "Y" plan shaped tall building under wind load. J. Build. Eng. **33**, 101843 (2021). https://doi.org/10.1016/j.jobe.2020.101843
19. R.K. Meena, R. Raj, S. Anbukumar, *Numerical Investigation of Wind Load on Side Ratio of High-Rise Buildings* (Springer, Singapore, 2021)
20. N. Gaur, R. Raj, P.K. Goyal, Interference effect on corner—configured structures with variable geometry and blockage configurations under wind loads using CFD. Asian J. Civ. Eng. (2021). https://doi.org/10.1007/s42107-021-00400-0
21. R. Raj, S. Jha, S. Singh, S. Choudhary, Response analysis of plus shaped tall building with different bracing systems under wind load. Int. J. Adv. Res. Eng. Technol. **11**, 371–380 (2020). https://doi.org/10.34218/IJARET.11.3.2020.032
22. A. Kumar, R. Raj, CFD study of flow characteristics and pressure distribution on re-entrant wing faces of L-shape buildings. Civ. Eng. Arch. **10**, 289–304 (2022). https://doi.org/10.13189/cea.2022.100125
23. R. Raj, T. Rana, T. Anchalia, U. Khola, Numerical study of wind excited action on H Plan-shaped tall building. Int. J. Emerg. Technol. **11**, 591–605 (2020)
24. F.Q. Meng, B.J. He, J. Zhu, D.X. Zhao, A. Darko, Z.Q. Zhao, Sensitivity analysis of wind pressure coefficients on CAARC standard tall buildings in CFD simulations. J. Build. Eng. **16**, 146–158 (2018). https://doi.org/10.1016/j.jobe.2018.01.004
25. A.K. Bairagi, S.K. Dalui, Estimation of wind load on stepped tall building using CFD simulation, Iran. J. Sci. Technol. Trans. Civ. Eng. **45**, 707–727 (2021). https://doi.org/10.1007/s40996-020-00535-1
26. T. Stathopoulos, B.A. Baskaran, Computer simulation of wind environmental conditions around buildings. Eng. Struct. **18**, 876–885 (1996). https://doi.org/10.1016/0141-0296(95)00155-7
27. J. Revuz, D.M. Hargreaves, J.S. Owen, On the domain size for the steady-state CFD modelling of a tall building. Wind Struct. Int. J. **15**, 313–329 (2012). https://doi.org/10.12989/was.2012.15.4.313
28. C.R. Zheng, Y.C. Zhang, Numerical investigation on the drag reduction properties of a suction controlled high-rise building. J. Zhejiang Univ. Sci. A **11**, 477–487 (2010). https://doi.org/10.1631/jzus.A0900593
29. J.F. Derakhshandeh, M.M. Alam, Flow structures around rectangular cylinder in the vicinity of a wall. Wind Struct. Int. J. **26**, 293–304 (2018). https://doi.org/10.12989/was.2018.26.5.293
30. R. Raj, A. Rukhaiyar, B. Jayant, K. Dahiya. *CFD Analysis for wind flow characteristics of varying cross section tall building using ANSYS* (2022). https://doi.org/10.21203/rs.3.rs-1471297/v1
31. ASCE Manuals and Reports on Engineering practice No. 67, Wind Tunnel Studies of Buildings and Structures (1999). https://doi.org/10.1061/9780784403198
32. G.A. Kopp, Full-Scale Methods for Examining Wind Effects on Buildings, n.d. https://doi.org/10.3389/978-2-88945-510-2.
33. I. Celik, M. Klein, J. Janicka, Assessment measures for engineering LES applications. J. Fluids Eng. Trans. ASME. **131**, 0311021–03110210 (2009). https://doi.org/10.1115/1.3059703

Publisher's Note Springer Nature remains neutral with regard to jurisdictional claims in published maps and institutional affiliations.

Springer Nature or its licensor (e.g. a society or other partner) holds exclusive rights to this article under a publishing agreement with the author(s) or other rightsholder(s); author self-archiving of the accepted manuscript version of this article is solely governed by the terms of such publishing agreement and applicable law.

J. Inst. Eng. India Ser. B
https://doi.org/10.1007/s40031-023-00887-y

ORIGINAL CONTRIBUTION

Experimental Investigation of Modern Control Algorithms for Power Quality Improvement for Single-Phase Grid-Connected Photo-Voltaic System

Prakash Chittora[1] · **Alka Singh**[1] · **Madhusudan Singh**[1] · **Hemant Saxena**[1]

Received: 23 November 2021 / Accepted: 13 April 2023
© The Institution of Engineers (India) 2023

Abstract This paper deals with the design and development of single-phase grid-connected Photo-Voltaic (PV) system. Three control algorithms, namely Synchronous Reference Frame Theory, Notch Filter and Second-Order Generalized Integrator are tested on the developed system. Various loading conditions as well as solar irradiance consideration are modeled in MATLAB. After successful validation by simulation, hardware prototype is developed in the laboratory in which dSPACE1104 is used as Digital Signal Processor (DSP). A single-phase nonlinear load is considered and different conditions of availability of load and PV are considered. Experimental results with a PV simulator have been recorded to have flexibility and control on various PV conditions. The novelty of the paper is that single-stage grid-connected PV system is used which removes the requirement of boost converter. Further, a low cost DSP can be used for the proper operation of the system hence cost effective solution is proposed in this paper. Three control algorithms are compared on various aspects, viz. performance, complexity and nature. After rigorous simulation and hardware study, conclusions are discussed in this paper.

Keywords Photo-voltaic (PV) system · Static synchronous compensator · Power quality (PQ) · Renewable energy sources (RES)

✉ Prakash Chittora
prakashchittora@dtu.ac.in

[1] Electrical Engineering Department, Delhi Technological University, Delhi 110042, India

Introduction

Solar PV integration to electric grid has seen a phenomenal rise in the recent years [1, 2]. This increasing trend is also observed due to fall of prices of solar modules, government policies and initiatives for increasing use of renewable energy sources such as PV, wind. Moreover, the availability of traditional sources of energy for electricity generation such as coal, petroleum and natural gases is limited. The solar energy is abundant in nature and also free, hence there is renewed focus on developing advanced technology to harness solar energy. Therefore, the operation, control and integration of renewable energy sources such as PV, wind are important issues of concern.

Choosing an appropriate equivalent model of a PV cell [3] is essential to simulate the actual solar cell behavior. There are basically two models, viz. single diode and two diode equivalent model of a PV cell [4, 5] discussed widely in literature and single-diode model is used in this paper.

Power Quality (PQ) is an important expect for the power distribution system [6]. Passive capacitive compensation is normally used to improve the power factor of distribution system and it also supports reactive power locally hence system losses are reduced and efficiency increases. Dynamic compensation using Static Var Compensation (SVC) automatically controls the power factor under heavy load. The Static Compensator (STATCOM) [6] is the latest shunt compensation device which has advantage over SVC is that it can provide ±Q (reactive power) compensation regardless of the value of terminal voltage and compensation is also constant over a wide range of voltages. In this paper, a H-bridge inverter along with a DC link capacitor is modeled as distribution STATCOM (DSTATCOM). The DSTATCOM is made functional by providing proper pulses for its operation using suitable control algorithms.

Published online: 28 April 2023

Designing a proper control algorithm is also very important to effectively improve PQ of the connected system economically. Several conventional control algorithms such as Synchronous Reference Frame Theory (SRFT) [7], Power Balance Theory (PBT), Instantaneous Reactive Power theory (IRPT) [8] have been developed for the control of DSTATCOM. These conventional control algorithms are successful in mitigating PQ issues but their convergence and speed of response are not adequate under wide range of operating conditions. Hence, their dynamic response needs to be studied thoroughly. Several new control algorithms such as conductance-based technique [9], adaptive generalized maximum Versoria criterion [10], Adaptive spline-based PLL [11], Proportional Resonant Filter [12] are reported in the literature. These algorithms are reported to be faster than traditional control algorithms. However, their limitation may be in their optimal parameter selection.

Another control group consists of adaptive controllers such as Least Mean Square (LMS) algorithms [13]. Several latest LMS techniques such as Kalman LMS [14], Variable Forgetting Factor Recursive Least Square [15], Modified recursive Gauss Newton (MRGN) [16], Hopfield LMS [17] etc. are also reported in the literature. Besides these controllers, Second-Order generalized Integrator (SOGI) [18], Improved adaptive linear element (ADALINE) [19], Adaptive Enhanced Phase Locked Loop (A-EPLL) [20], etc. control algorithms are available in the literature for proper control of DSTATOM. With such a wide choice of control algorithms available in the literature, it becomes imperative to compare the performance of a few commonly used algorithms. This paper attempts to bridge such a gap, especially for PV-integrated single-phase distribution system.

In this paper, a thorough and detailed analysis of traditional as well and advanced control algorithms for DSTATCOM is performed for improving the PQ parameters of the single-phase grid-connected PV system. Three control algorithms, viz. SRFT, Notch Filter (NF) and SOGI are implemented on the proposed grid connected PV system. This is a unique work and has not been reported in the latest literature. Exhaustive study in MATLAB simulation environment suggests important utility of the three developed control algorithms for taking care of PQ issues such as harmonics in load, demand- supply unbalance. Simulation study is verified by hardware results. When the demand is lower than PV generation then excess energy is fed back to the grid or when PV is absent, load demand is supplied by grid. A single stage PV array is integrated at the DC link, a dedicated MPPT technique is avoided which reduces burden on the DSP, moreover boost converter is not needed. The developed system is a single stage system and very conveniently can be used in our power distribution system.

System Description

Figure 1 presents the layout of the proposed single stage PV incorporated grid connected system. A PV simulator having its voltage equal to DC link, is connected in parallel to the DC side capacitor of DSTATCOM. DSTATCOM configuration comprises four IGBT switches with anti-parallel diodes connected in H- Bridge configuration. The PV source is integrated at the DC link of the DSTATCOM and suitable gating pulses to improve the PQ of the connected system. Single-phase nonlinear load is also connected at Point of Common Coupling (PCC). The PV simulator feeds real power into the system which is also integrated with DSTATCOM control.

Design of the Proposed System

The calculations for the designed DSTATCOM voltage, DC link capacitor, PV simulator and sensors are discussed here. Table 1 shows the various parameters of the proposed system and actual hardware values used.

In the current setup, the PV output from the PV simulator is selected as 250 V, which is V_{oc} for the PV system. Thus from the PV curve obtained from the PV simulator, V_{mp} is obtained around 200 V. The PV output is directly connected

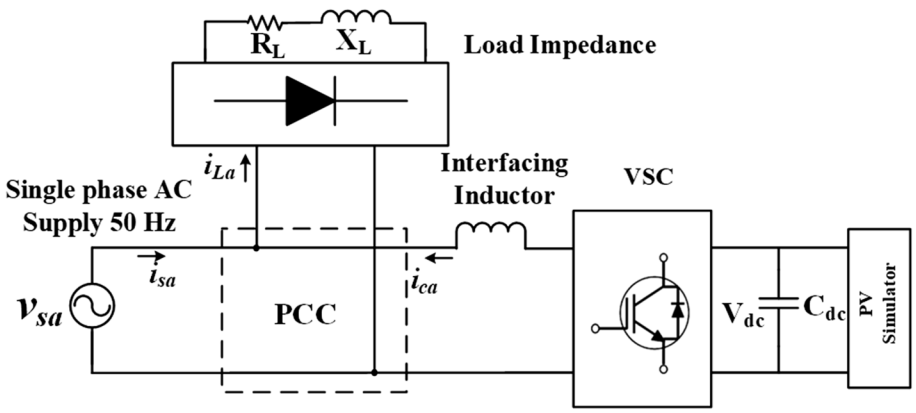


Fig. 1 System under consideration

Table 1 Design parameters of proposed single stage PV connected to Grid system

S. No	Design parameter	Design criterion/equations involved	Practical value selected	Remarks
1	PV Simulator	Electrical, mechanical, customer and environmental	300 W capacity	
2.1	DSTATCOM-DC link voltage	$V_{\text{peak}} = \sqrt{2}V_{\text{s}}$ (1)	200 V	Selected as reference
2.2	DSTATCOM-DC link capacitor	$C_{\text{b}} = \frac{P_{\text{pv}}}{2\pi \times f_{\text{sw}} \times V_{\text{boost}} \times \Delta V_{\text{boost}}}$ (2)	1600 µF	Semikron Make
2.3	DSTATCOM-AC Interfacing Inductor	$L_i = \frac{\sqrt{3} * m * V_{dc}}{12 * o * f_s * i_{rcpp}}$ (3)	1 mH, 10 A	
3	Voltage and current sensors	As per hardware requirement	400 V and 25 A	LEM make

to the single-phase system at the DC link of VSC. The value selected for DC link of H bridge inverter is also 200 V. A PI controller is designed to maintain the DC link to 200 V. Controllers are designed to generate proper compensating currents for PQ improvement. In the single stage configuration selected, MPPT is also automatically ensured. This ensures high efficiency and low component requirement.

Development of Control Algorithms for Improving Power Quality of Single Stage PV Incorporated Grid Connected System

This section deals with the development of control algorithms, namely SRFT, NF and SOGI for improving PQ in single stage PV incorporated grid connected system. MPPT technique is not required as discussed in section 3.1. The above three control algorithms have performed well for load compensation. The in depth details of control flow of three control algorithms developed are discussed below.

Unit Templates Generation

Unit templates are the synchronizing signals, which are used to calculate reference current for DSTATCOM. In single phase a unique signal having phase as per grid voltage and a unity magnitude is termed as unit template. The unit template calculation is shown in Fig. 2. Figure 2a shows calculation of peak grid voltage (V_t). Figure 2b shows two components, In-phase and quadrature-phase templates. The quadrature component is obtained by incorporating a $T/4$ delay where T is the time period of standard 50 Hz signal. They are termed as sinθ and cosθ as shown in fig. Various Eqs. (4)–(5) used for unit templates are shown as follows:

$$V_t = \sqrt{v_s^2 + v_{s\beta}^2} \tag{4}$$

$$\sin\theta = \frac{v_s}{V_t}; \cos\theta = \frac{v_{s\beta}}{V_t} \tag{5}$$

Calculation of Feed Forward Factor (*IFF*) for PV

Integration of PV to the grid requires a feed forward factor (I_{ff}) to be calculated. This term shall be subtracted from the fundamental active load component (I_{Ld}) to compute effective component of current to be feed from the grid. The I_{ff} is computed as

$$I_{\text{ff}} = \frac{2 \times V_{\text{mp}} \times I_{\text{mp}}}{V_{\text{t}}} \tag{6}$$

where V_{mp} and I_{mp} are voltage and current corresponding to maximum power point of PV.

Since PV simulator is directly connected to DC link so Eq. 6 is modified as

$$I_{\text{ff}} = \frac{2 \times V_{\text{dc}} \times I_{\text{pv}}}{V_{\text{t}}} \tag{7}$$

where I_{pv} is the output current of PV at voltage V_{dc}.

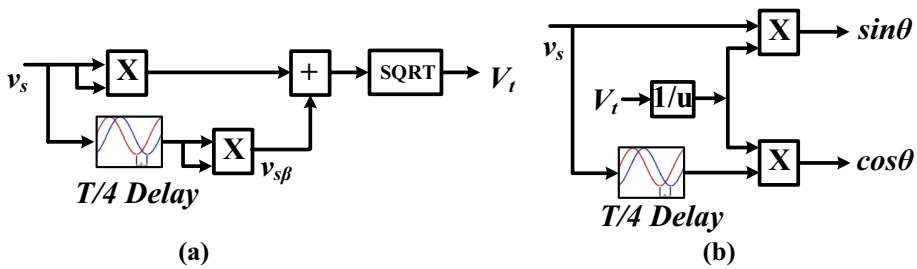


Fig. 2 Generation of unit templates for single-phase system **a** calculation of V_t, **b** generation of sinθ and cosθ

This I_{ff} is used further to obtain the magnitude of the reference current for DSTATCOM and also discussed in section "Extraction of Effective Fundamental Active Power Component and Reference Current Generation."

Extraction of Effective Fundamental Active Power Component and Reference Current Generation

This section discusses mathematical analysis of the three control algorithms namely SRFT, NF and SOGI. The aim of all three control algorithms are to extract fundamental component from the load current in the presence of PV. The details are shown as follows:

Synchronous Reference Frame Theory (SRFT) Based Control Algorithm

Figure 3a shows the SRFT control algorithm developed for single stage PV incorporated grid connected system. The sensed load current (i_L) and T/4 phase shifted load current ($i_{L\beta}$) are operated by Park's transformation to obtain direct and quadrature axis components i_{Ld} and i_{Lq} as follows

$$\begin{bmatrix} i_{Ld} \\ i_{Lq} \end{bmatrix} = \begin{bmatrix} cos\theta & sin\theta \\ -sin\theta & cos\theta \end{bmatrix} \begin{bmatrix} i_L \\ i_{L\beta} \end{bmatrix} \tag{8}$$

The direct axis component i_{Ld} of load current is filtered using low pass filter to obtain I_{Ld}. The switching loss occurring in IGBT switches can be determined by calculating I_{loss}. For calculating I_{loss} DC link voltage is compared with a reference voltage and passed through a PI controller as shown in Eq. 9

$$I_{loss}(k) = I_{loss}(k-1) + K_p\{(e_{dc}(k) - e_{dc}(k-1)\} + K_I\left[e_{dc}(k)\right] \tag{9}$$

The PI regulator gain are K_p and K_I which need to be tuned properly. The PV feed forward term I_{ff} is now considered to obtain effective fundamental active power component (I_{eff}) as

$$I_{eff} = I_{Ld} + I_{loss} - I_{ff} \tag{10}$$

To obtain reference current i_s^* for DSTATCOM, I_{eff} is multiplied by unit template $\sin\theta$

$$i_s^* = I_{eff} * \sin\theta \tag{11}$$

Now with the help of Hysteresis Current controller (HCC), the reference current (i_s^*) and actual current (i_s) are compared. The HCC has a hysteresis band of 0.2. The HCC generates proper gating pulses for H-bridge DSTATCOM, through which compensation is performed.

Notch Filter (NF) Based Control Algorithm

Figure 3b shows the NF control algorithm developed for single stage PV incorporated grid connected system. The

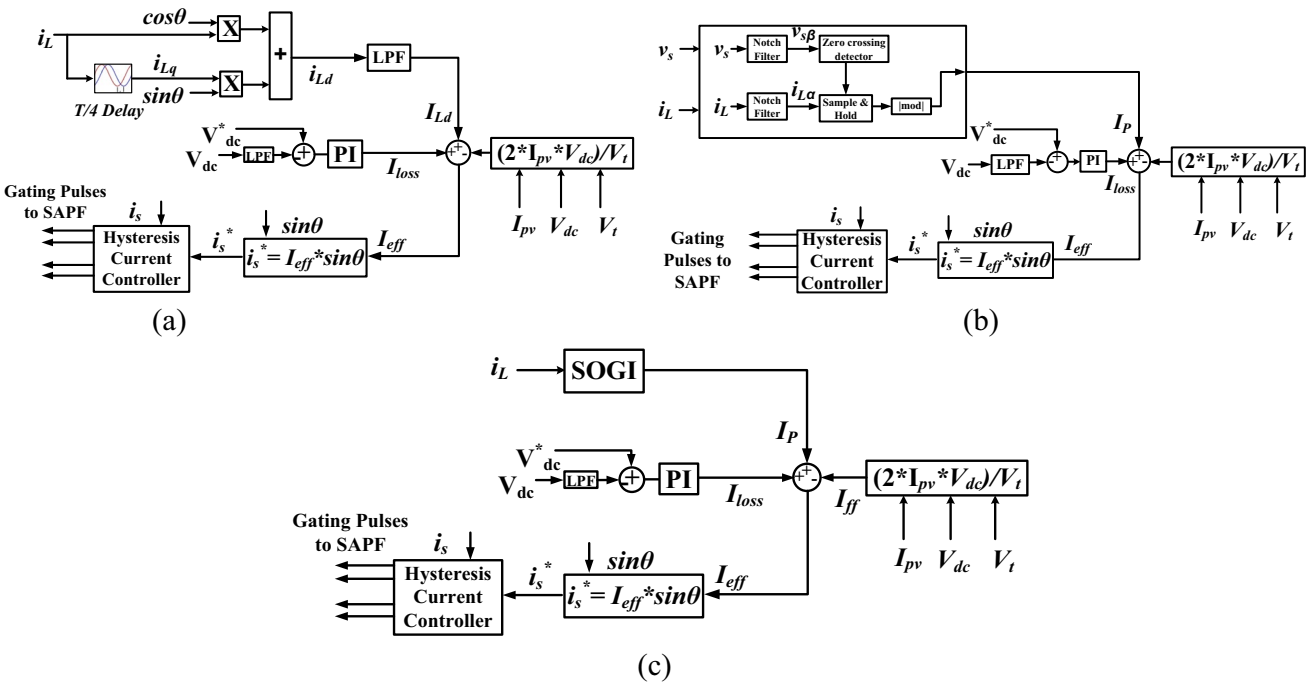


Fig. 3 Block diagram of **a** SRFT based, **b** NF based and **c** SOGI based control algorithm implementation for single-phase grid connected PV system

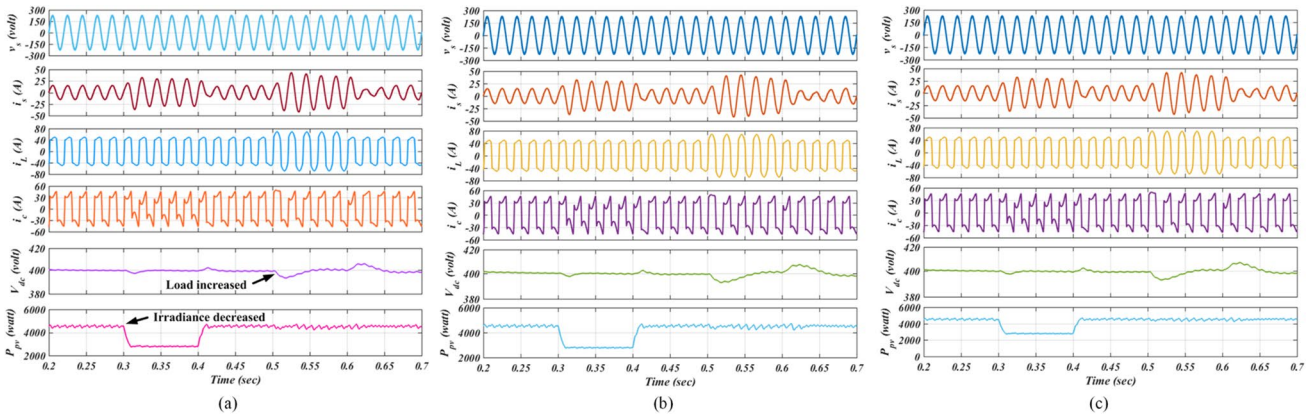


Fig. 4 Simulation results for **a** SRFT, **b** NF and **c** SOGI based control algorithm

load current alpha ($i_{L\alpha}$) and supply voltage beta ($v_{s\beta}$) components are calculated using following equations.

$$i_{L\alpha} = \frac{s\varepsilon\phi}{s^2 + s\varepsilon\phi + \phi^2} i_L \tag{12}$$

$$v_{s\beta} = \frac{s\phi^3}{s^2 + s\varepsilon\phi + \phi^2} v_s \tag{13}$$

where ϕ is the phase angle of input signals (i_L and v_s), 's' denotes the Laplace operator, ε is damping constant of system.

The $i_{L\alpha}$ and $v_{s\beta}$ components are used along with sample and hold circuit. The sample and hold circuit calculates the fundamental active power component of load current I_P. To incorporate PV, a feed forward factor I_{ff}, needs to be calculated. It is already discussed in Section "Calculation of Feed Forward Factor (IFF) for PV." The I_{eff} is now computed as follows

$$I_{eff} = I_P + I_{loss} - I_{ff} \tag{14}$$

To obtain reference current i_s^* for DSTATCOM, I_{eff} is multiplied by unit template sinθ.

$$i_s^* = I_{eff} * \sin\theta \tag{15}$$

Now with the help of Hysteresis Current controller (HCC), the reference current (i_s^*) and actual current (i_s) are compared. The HCC has a hysteresis band of 0.2. The HCC generates proper gating pulses for H-bridge DSTATCOM, through which compensation is performed.

Second-Order Generalized Integrator (SOGI) Based Control Algorithm

Figure 3c shows the SOGI control algorithm developed for single stage PV incorporated grid connected system. With the help of SOGI, in-phase (i_{Lj}) and quadrature phase (i_{Lk}) fundamental load current components are computed as follows:

$$\frac{i_{Lj}}{i_L} = \frac{W\omega_0 s}{s^2 + W\omega_0 s + \omega_0^2} \tag{16}$$

$$\frac{i_{Lk}}{i_L} = \frac{W\omega_0^2}{s^2 + W\omega_0 s + \omega_0^2} \tag{17}$$

where i_{Lj}, i_{Lk} are SOGI obtained in-phase and quadrature phase outputs of load current, ω_0 is fundamental frequency and W is constant gain.

Now the I_P is calculated as

$$I_p = \sqrt{i_{Lj}^2 + i_{Lk}^2} \tag{18}$$

The I_{eff} is now calculated as

$$I_{eff} = I_P + I_{loss} - I_{ff} \tag{19}$$

To obtain reference current i_s^* for DSTATCOM, I_{eff} is multiplied by unit template sinθ.

$$i_s^* = I_{eff} * \sin\theta \tag{20}$$

Now with the help of Hysteresis Current controller (HCC), the reference current (i_s^*) and actual current (i_s) are compared. The HCC has a hysteresis band of 0.2. The HCC generates proper gating pulses for H-bridge DSTATCOM, through which compensation is performed. The sections below show the simulation and hardware performance of all three control algorithms.

Simulation Results

All three control algorithms, viz. SRFT, NF and SOGI are modeled in MATLAB/SIMULINK environment. In

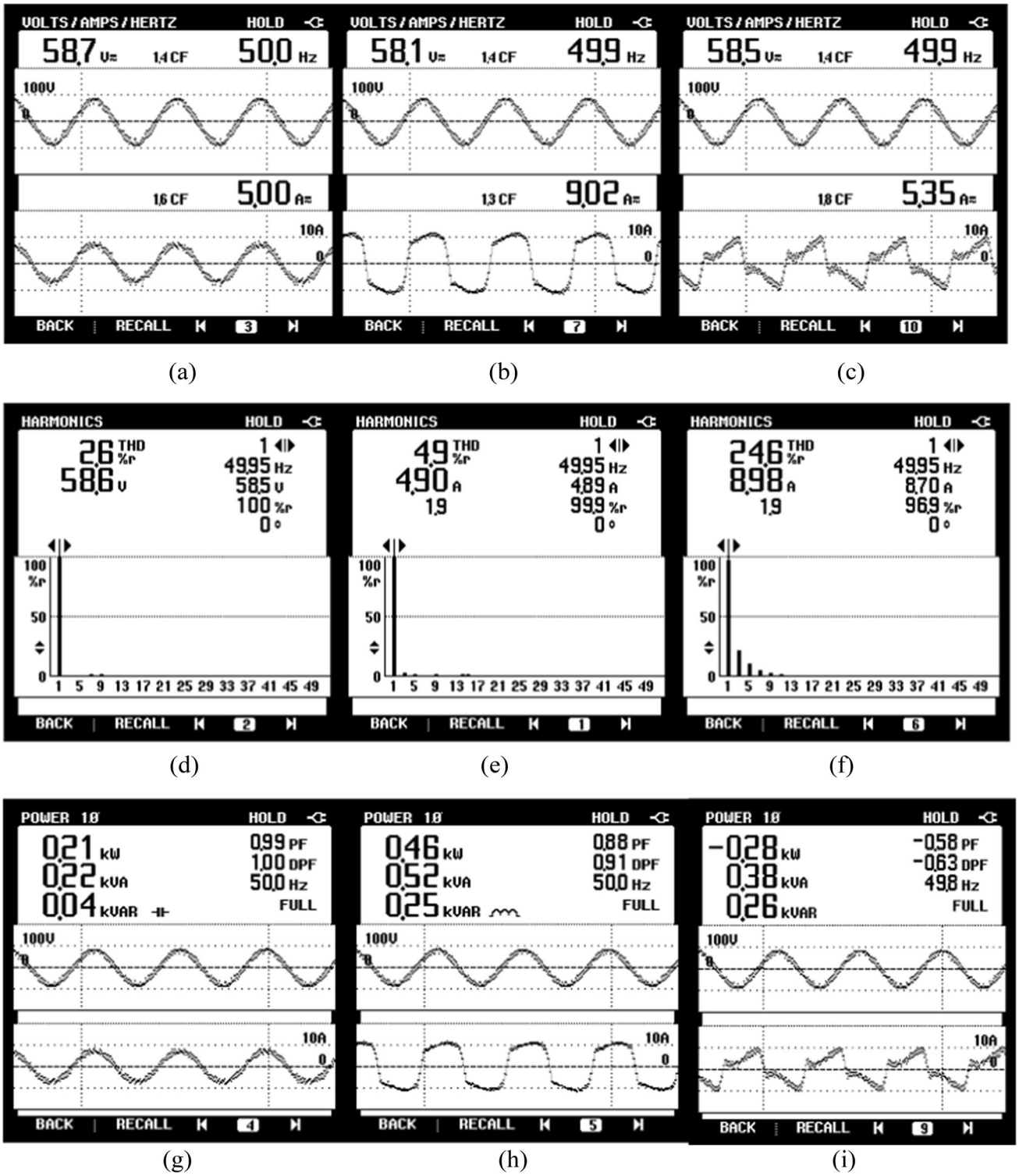


Fig. 5 Steady state results for single stage PV incorporated grid connected system using SRFT **a–c** Waveforms of **a** i_s, **b** i_L, **c** i_c, **d–f** THD analysis **d** v_s, **e** i_s, **f** i_L, **g–i** active and reactive power for **g** supply, **h** load, **i** compensator

simulation PV system with a capacity of 5 kW is considered. The single-phase grid voltage is kept at 230 V. Simulation results analysis for load variation and irradiance change is shown in Fig. 4a–c.

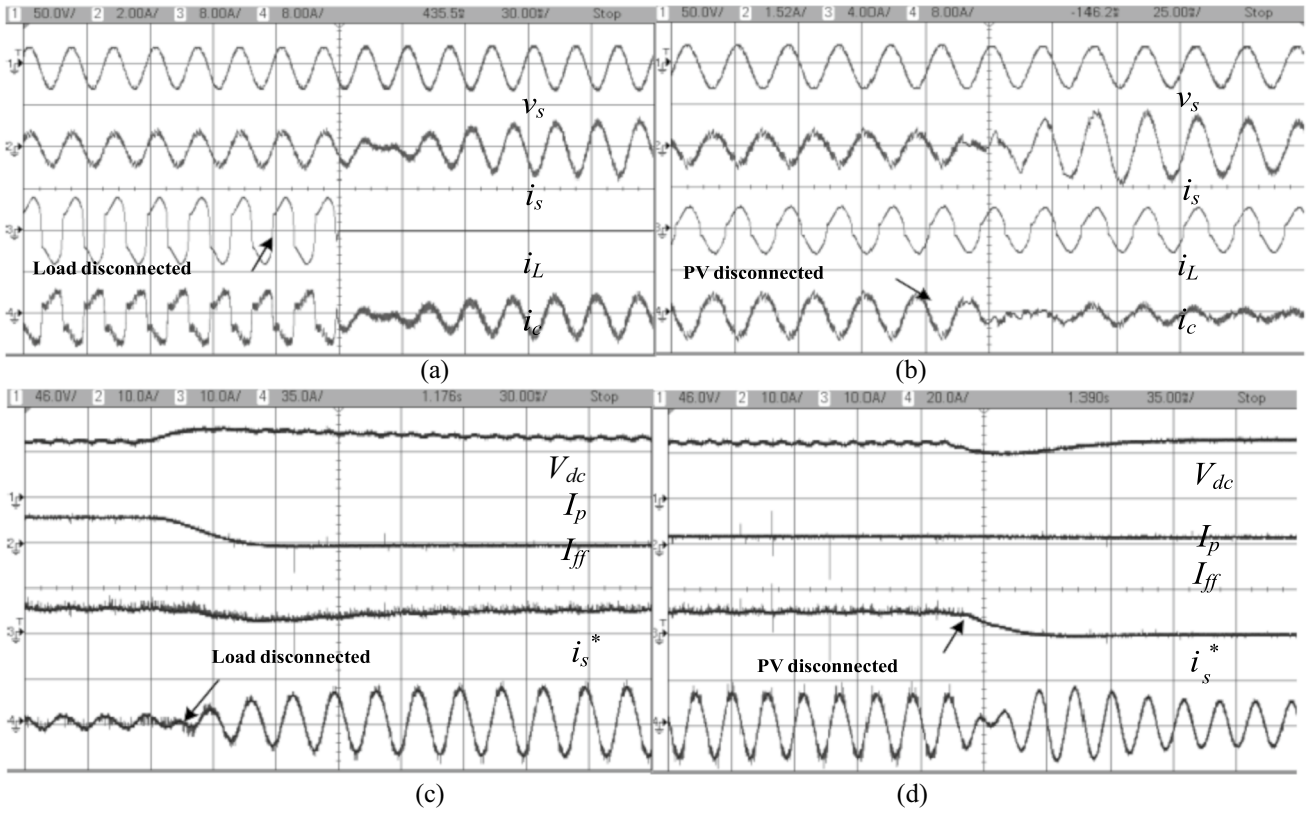


Fig. 6 Dynamics results using SRFT control algorithm **a** v_s, i_s, i_L, i_c, **b** v_s, i_s, i_L, i_c, **c** V_{dc}, I_P, I_{ff}, i_s^*, **d** V_{dc}, I_P, I_{ff}, i_s^*

Figure 4a–c shows the source voltage (v_s), source current (i_s), load current (i_L), compensator current (i_c), DC link voltage (V_{dc}) of DSTATCOM and PV power (P_{pv}). When the irradiance is varied from 1000 to 600 W/m^2 at $t = 0.3$ s, there is a corresponding reduction in PV power (P_{pv}). In this case, the load is kept constant so the load will now be supplied by grid. So in Fig. 4a–c, there is a rise in source current when irradiance is decreased. Later at time $t = 0.5$ s, there is an addition of load, which can be seen by increased load current. In this case also, since the PV output is fixed at its rated power of 4500 W, the source current increases to meet the increased demand. The DC link shows some transients for both irradiance change and load change, which get settled by PI controller action. In Fig. 4a–c DSTATCOM output current also changes as per the system condition. The source current remains balanced and sinusoidal during load change as well as irradiance change. All the three algorithms have achieved PQ compensation for single stage PV incorporated grid connected system.

Experimental Results

All three control algorithms discussed above are tested for effectiveness on a developed prototype in laboratory. A Chroma-make PV simulator is used along with dSPACE 1104. The steady state and dynamic hardware results are obtained using Fluke power analyzer and DSO. The results are discussed below.

Synchronous Reference Frame Theory-Based Control Algorithm

With the help of PV simulator available in the laboratory, 500 W output power is connected to DC link of DSTATCOM. Nonlinear load is connected at PCC. Using SRFT control algorithm, the load current compensation as well as PV incorporation using single stage method has been achieved successfully. Figure 5a–e shows the steady state results of proposed system using SRFT control algorithm. Figure 5a–c shows source current (i_s), load current (i_L) and compensator current (i_c) along with source voltage (v_s). It is observed that source current magnitude is lower than load current since PV is also supplying to load via DSTATCOM. There is a real power flow between PV system and nonlinear load. Figure 5d–f shows Total harmonic Distortion (THD) analysis of source voltage (v_s), source current (i_s) and load current (i_L). The source current THD obtained in this case is 4.9% which is less than 5% as prescribed in IEEE 519 [21] and IEEE 1547 [22]. Figure 5g–i shows active and reactive

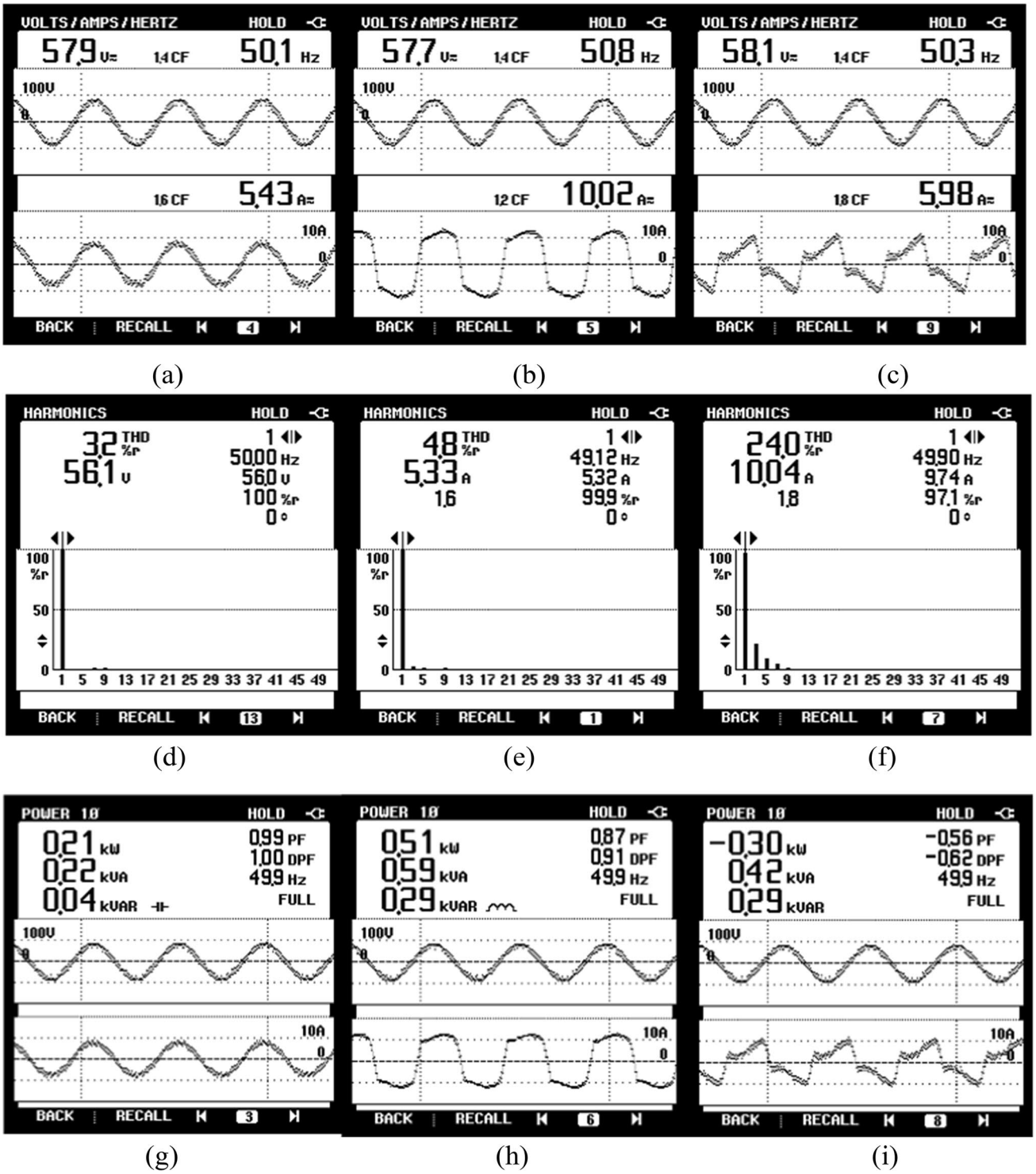


Fig. 7 Steady state results for single stage PV incorporated grid connected system using NF **a–c** Waveforms of **a** i_s, **b** i_L, **c** i_c, **d–f** THD analysis **d** v_s, **e** i_s, **f** i_L, **g–i** active and reactive power for **g** supply, **h** load, **i** compensator

power flow between source, load and compensator. The grid is supplying 210 W of real power at PCC. The reactive power burden of source is only 40 VARs and a PF of 0.99 is achieved. The load active and reactive power requirement are 460 W and 250 VARs. The DSTATCOM active and reactive power flow is 280 W and 260 VARs. The PV system is able to inject active power successfully at PCC.

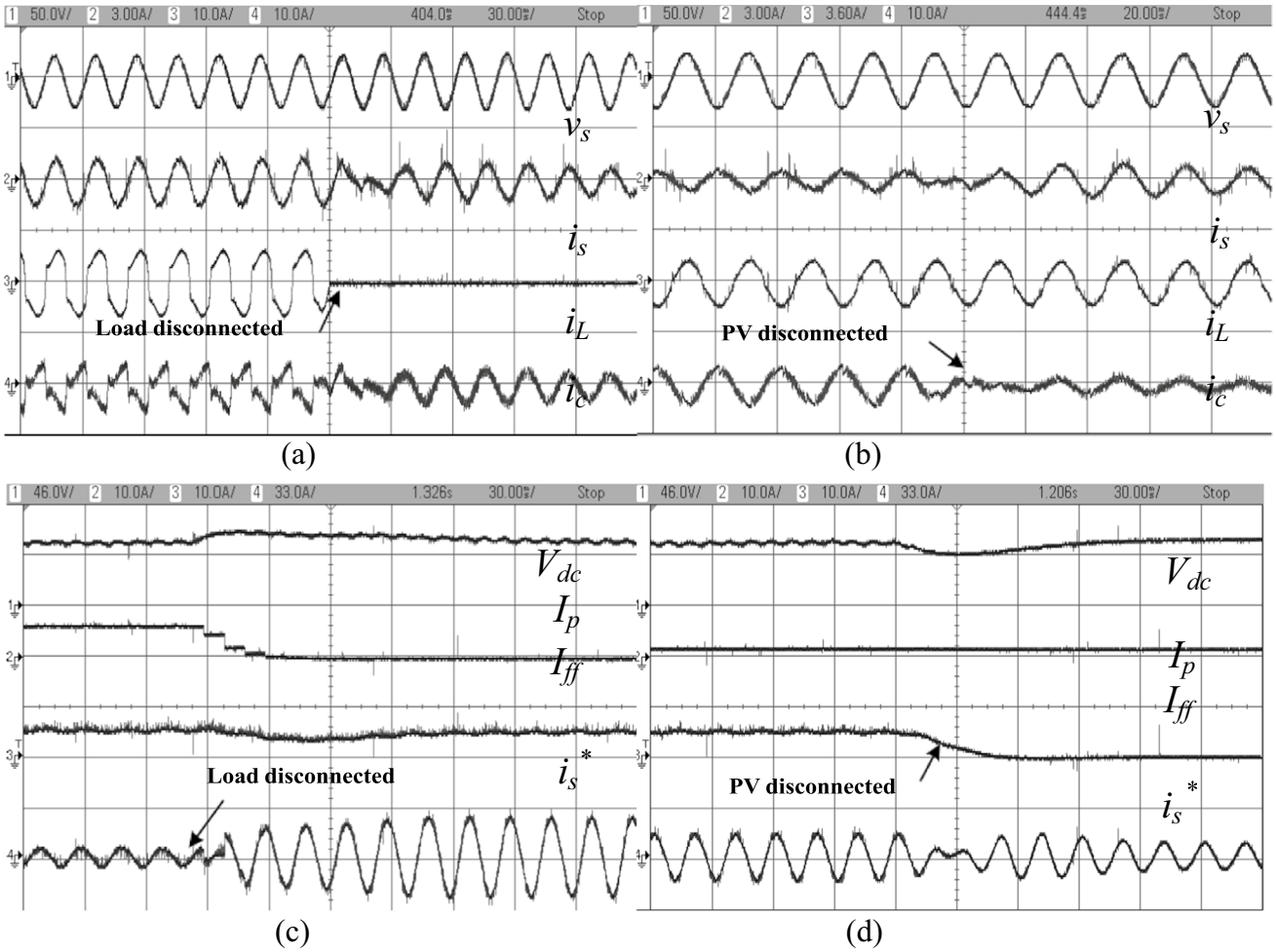


Fig. 8 Dynamics results using Notch Filter based control algorithm **a** v_s, i_s, i_L, i_c, **b** v_s, i_s, i_L, i_c, **c** V_{dc}, I_P, I_{ff}, i_s^*, **d** V_{dc}, I_P, I_{ff}, i_s^*

Figure 6 shows the dynamics result of SRFT control algorithm on the proposed system. Figure 6a shows source voltage (v_s), source current (i_s), load current (i_L) and compensator current (i_c). In this figure load is removed and dynamics are captured. The source current is now in phase opposition of source voltage. Since the load is absent, all power from PV is now getting absorbed by grid. This condition will also arise when the PV generation will be greater than real power load demand. Figure 6b shows source voltage (v_s), source current (i_s), load current (i_L) and compensator current (i_c). In this case PV is disconnected and transients are captured. The compensator current magnitude as well as phase changes. As PV output is zero, the compensator is consuming power which is equal to switching losses of IGBT switches. The source current phase is in accordance with source voltage. Figure 6c shows DC link voltage (V_{dc}), fundamental active power component (I_d), PV feed forward factor (I_{ff}) and reference current (i_s^*). For constant PV output I_{ff} is nearly the same. When the load is disconnected, the DC link has some transients but settles down soon to its reference value. Since the load is absent, reference current has only I_{ff} component thus phase of reference current is in opposition of the source voltage. This is an example of PV to grid power transfer. Figure 6d shows DC link voltage (V_{dc}), fundamental active power component (I_d), PV feed forward factor (I_{ff}) and reference current (i^*). When PV is disconnected, the PV output reduces to zero, which is indicated by I_{ff} but the fundamental active component extracted by SRFT remains same because load is constant. The reference current is now in phase with the source current and load is getting its supply from grid.

Notch Filter-Based Control Technique

Figure 7a–i shows the steady state hardware results for single stage PV incorporated grid connected system using Notch Filter control algorithm. The source current THD achieved using NF is 4.8% which is allowable as per IEEE 519 and 1547. The THD of source voltage is 3.2%. The source active and reactive power flow are 210 W and 40 VARs. The load demand is 510 W of real power and 290 VARs of reactive

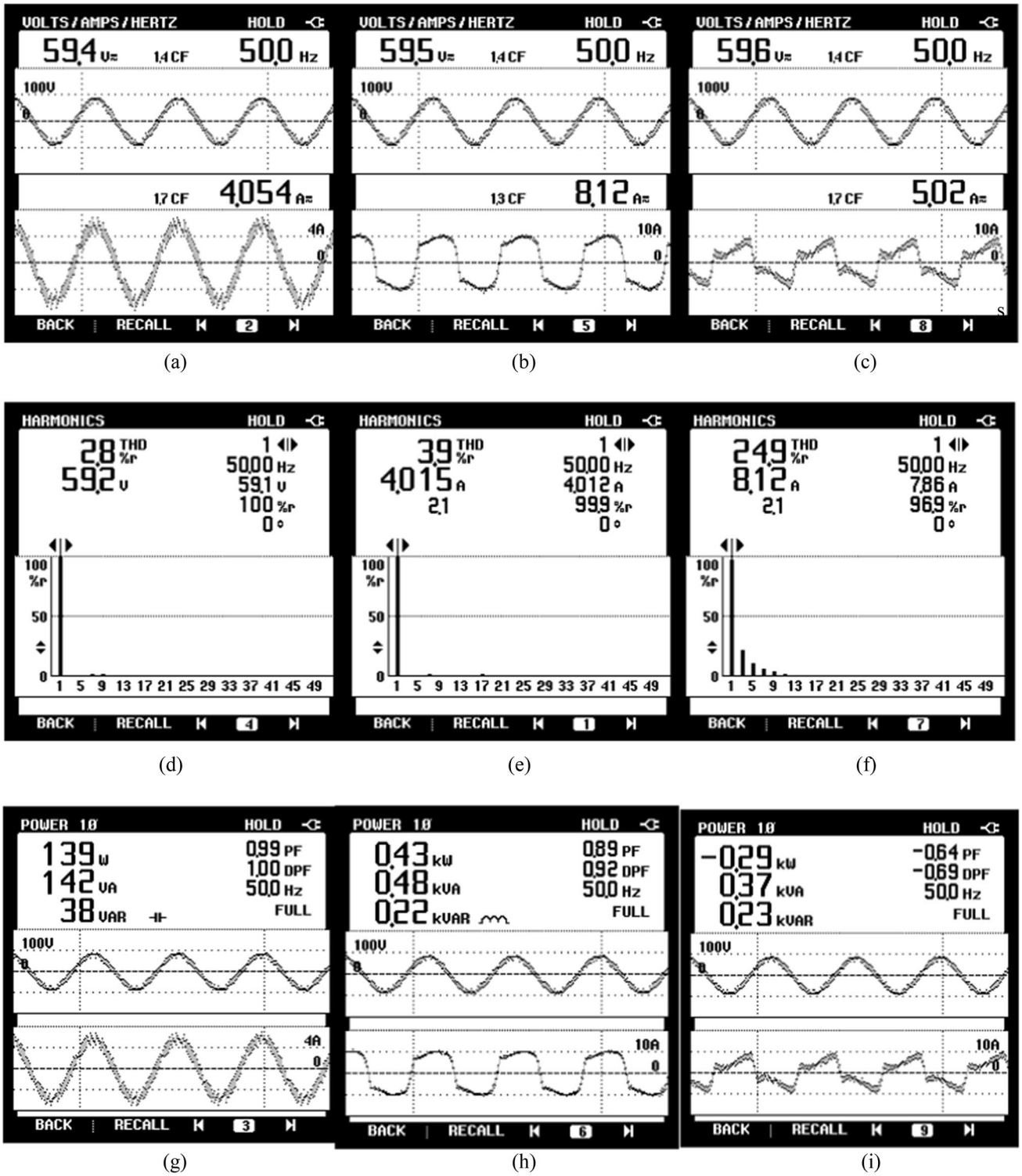


Fig. 9 Steady state results for single stage PV incorporated grid connected system using SOGI **a–c** Waveforms of **a** i_s, **b** i_L, **c** i_c, **d–f** THD analysis **d** v_s, **e** i_s, **f** i_L, **g–i** active and reactive power for **g** supply, **h** load, **i** compensator

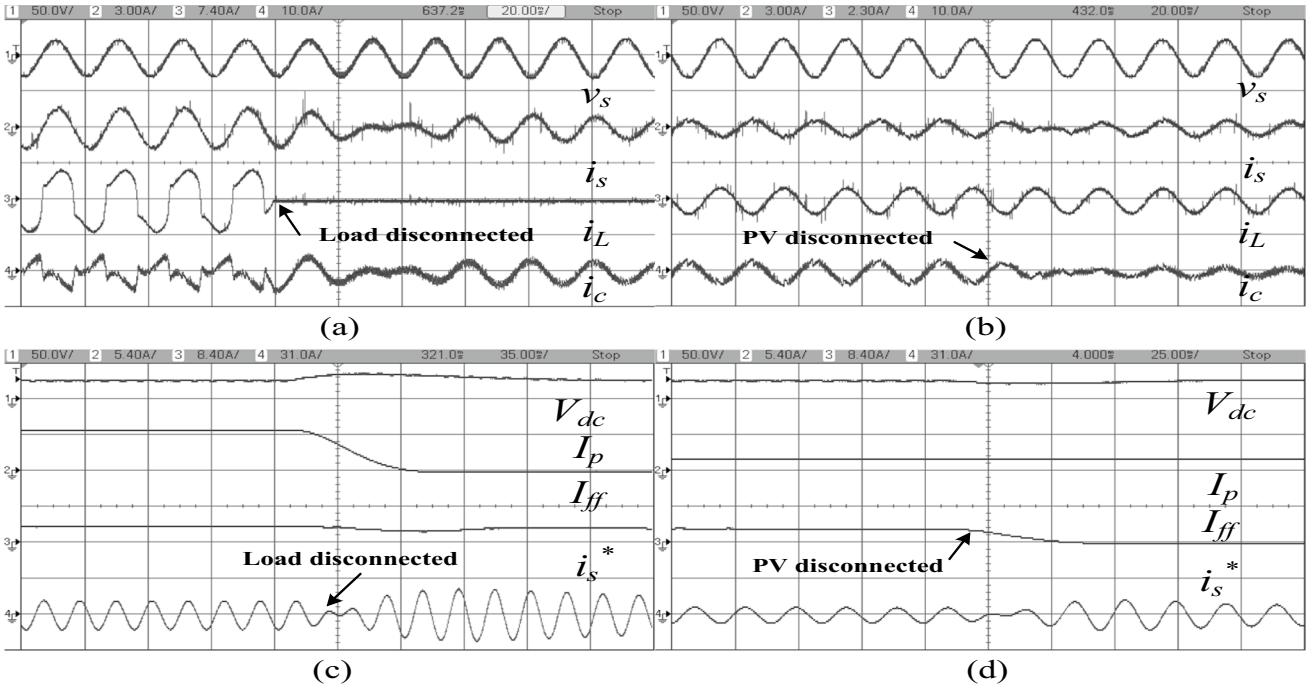


Fig. 10 Dynamic results using SOGI based control algorithm **a** v_s, i_s, i_L, i_c, **b** v_s, i_s, i_L, i_c, **c** V_{dc}, I_P, I_{ff}, i_s^*, **d** V_{dc}, I_P, I_{ff}, i_s^*

power. The compensator active and reactive power flow are 300 W of and 290 VARs, respectively. The load reactive power demand matches with DSTATCOM reactive power delivered. Dynamic state results for PV/Load disconnection are shown in Fig. 8. Figure 8a shows source voltage (v_s), source current (i_s), load current (i_L) and compensator current (i_c). In Fig. 8b source voltage (v_s), source current (i_s), load current (i_L) and compensator current (i_c) are shown. The results are similar in nature to that of obtained using SRFT control algorithms. In Fig. 8c DC link voltage (V_{dc}), fundamental active power component ($I_p^{'}$), PV feed forward factor (I_{ff}) and reference current (i_s^*) are shown. In this case also load is disconnected and results are captured. In Fig. 8d, DC link voltage (V_{dc}), fundamental active power component ($I_p^{'}$), PV feed forward factor (I_{ff}) and reference current (i_s^*) are shown. The NF control algorithm performs satisfactorily under load /PV disconnection conditions.

Second-Order Generalized Integrator-Based Control Algorithm

Steady state experimental results using SOGI control algorithm for single stage PV incorporated grid connected system are shown in Fig. 9a–i. The THD of source current and load current is 3.9%, 24.9%, respectively. The THD of PCC voltage is 2.8%. The supply active and reactive power flow are 139 W of real power and 38 VARs of reactive power and the source power factor is 0.99 PF. The load active and reactive power flow is 430 W and 220 VARs, respectively. The compensator active and reactive power flow is 290 W and 230 VARs, respectively. The load real power demand is met by source as swell as PV. The PV system has certain losses and is not delivering its rated capacity. The reactive power of load is counterbalance by DSTATCOM.

Dynamic state result for PV/Load disconnection are shown in Fig. 10. Figure 10a shows source voltage (v_s), source current (i_s), load current (i_L) and compensator current (i_c). The load is disconnected and all power from PV is going directly to grid. In Fig. 10b source voltage (v_s), source current (i_s), load current (i_L) and compensator current (i_c) are shown. The results are similar in nature to that of obtained using SRFT and NF control algorithms. In Fig. 10c, DC link voltage (V_{dc}), fundamental active power component (I_{p}), PV feed forward factor (I_{ff}) and reference current (i_s^*) are shown. In Fig. 10d, DC link voltage (V_{dc}), fundamental active power component (I_{p}), PV feed forward factor (I_{ff}) and reference current (i_s^*) are shown. The SOGI controller also performs satisfactorily under load /PV disconnection conditions.

PV Output for MPPT and Without MPPT Conditions

In this paper, a PV simulator (Chroma make) is used for testing instead of actual PV panel so that the study can be more flexible and controllable. PV output capacity of 300 W is considered and corresponding results at 1000 W/m^{2}and 600 W/m^2 are given in Figs. 11 and 12, respectively. PV

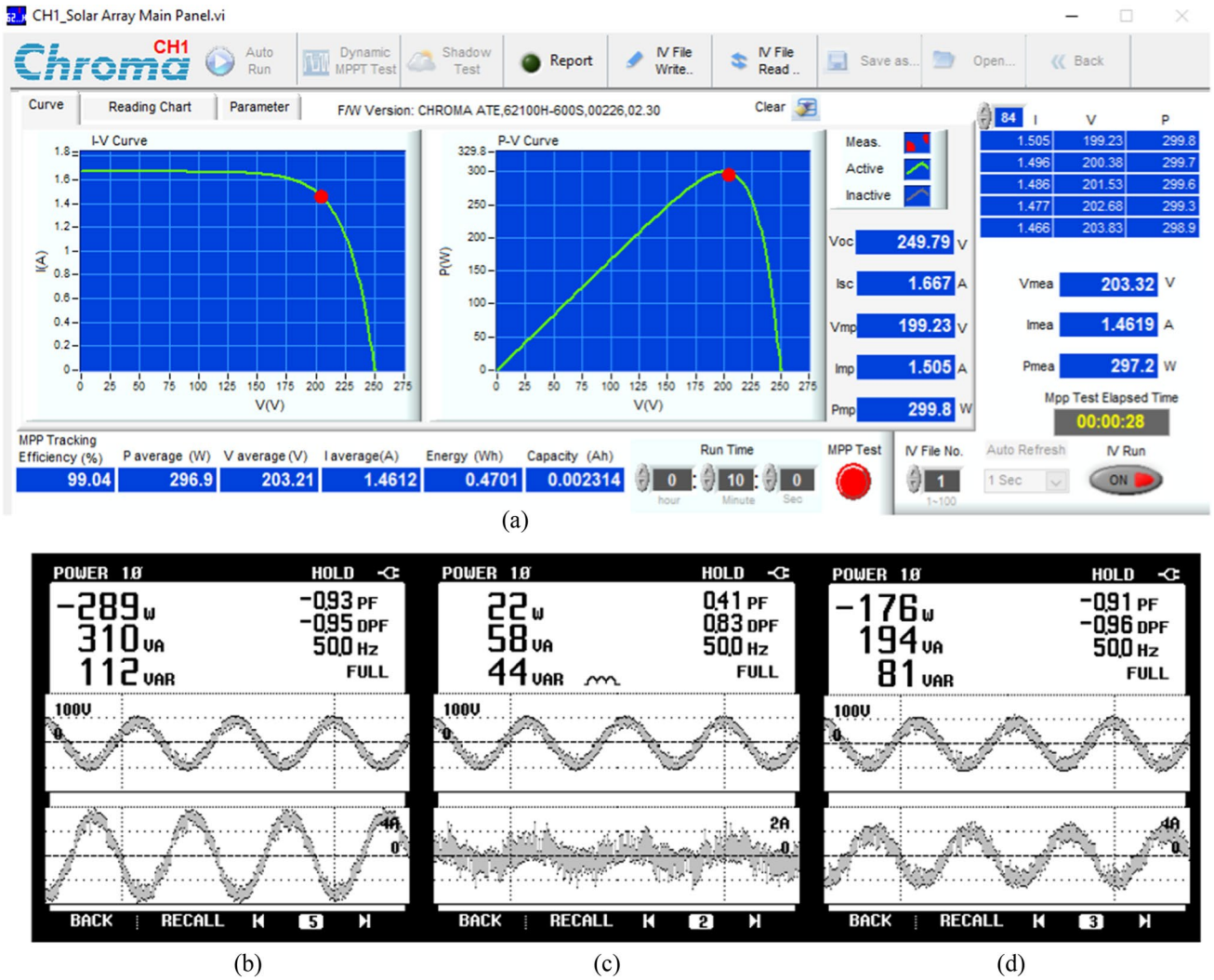


Fig. 11 PV output at 1000 W/m^2 **a** PV and IV curve with V_{mp} and I_{mp}. **b** PV output at VSC with MPPT, **c** switching losses in VSC

curve generated by simulator shows its power, voltage and efficiency level is also presented.

From these figures it is seen that PV output (for 1000 W/m^{2}irradiance) is 299.8 W at 99.04% efficiency level. In this case V_{mp} is 199.23 V and I_{mp} is 1.505 A. The switching loss in VSC is 22 W, and final output of PV to the system via VSC is 289 W. The same PV power get reduced to 176 W (Fig. 11d), when MPPT condition is not reached, Here PV power results are taken directly from PV simulator software whereas the VSC switching losses and its output power are captured using single-phase power quality analyzer FLUKE 43B.

Similarly PV output at irradiance level of 600 W/m^2 is 179.9 W at 98.32% efficiency level. In this case, V_{mp} is 199.23 V and I_{mp} is 0.903 A. The switching loss in VSC is 22 W, and final output of PV to the single-phase system via VSC at MPPT is 167 W.

The above results are presented in Table 2. The DSTATCOM DC link voltage is maintained by grid and MPPT voltage is selected by PV simulator. When the DC link voltage is set as 200 V, which also is MPPT voltage for PV system, the output is maximum. And when DC link voltage is selected as 224 V which is not MPPT voltage, the PV output reduces significantly.

Comparative Performance Analysis

Table 3 enlists a thorough comparison of the three control algorithm, viz. SRFT, NF and SOGI. Both simulation as well as hardware results are considered for finding out the best controller for shunt compensation in PV incorporated system.

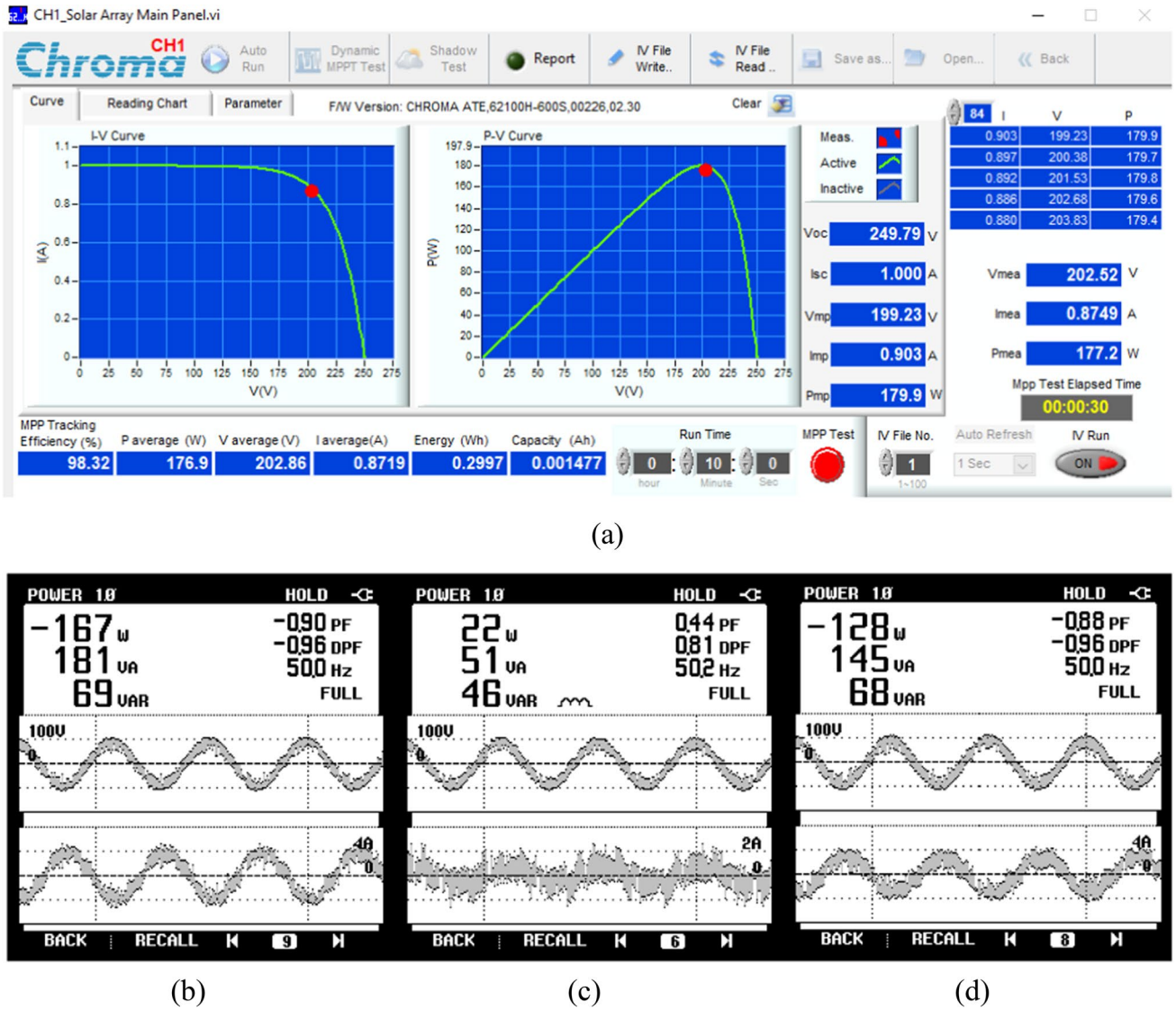


Fig. 12 PV output at 600 W/m^2, **a** PV and IV curve with V_{mp} and I_{mp}. **b** PV output at VSC with MPPT, **c** switching losses in VSC, **d** PV output at VSC without MPPT, **d** PV output at VSC without PT

Table 2 Comparison of VSC output at MPPT and Without MPPT conditions

S. No	Irradiance (W/m^2)	*V*dc (V)	VSC output (W)	Difference (W)
1	1000	200	289	113
2	1000	224	176	
3	600	200	167	39
4	600	224	128	

The current THD obtained using SOGI, SRFT, NF control algorithms are 3.9%, 4.9% and 4.8%, respectively. The load current THD is almost same in all three cases. So it is inferred that for similar operating conditions, SOGI controller is providing lowest THD. A lower value of THD means the source current is more closer to a sinusoidal waveform, which is the desired condition from the point of view of a healthy power system. In Table 3, various other parameters are also considered. The sampling time is the minimum time required for DSP unit to run the hardware without any internal delay. The sampling time is also least by SOGI controller.

On several other parameter also, SOGI is found to be superior to the rest two. The SOGI controller is used in this paper to enable DSTATCOM for shunt compensation but SOGI can also be used as PLL which SRFT and NF cannot. So from the above discussion, it is evident that for the proposed system SOGI controller is giving superior performance.

Table 3 Comparative performance of SOGI, SRFT and NF control algorithms

S. No	Features		SOGI	SRFT	Notch
1	PLL required		No	Yes	No
2	Park's transformation required		No	Yes	No
3	Convergence (average weight) steady state		0.021 s (~1 cycle)	0.043 s (~2 cycles)	0.031 s (~2 cycles)
4	THD of current	Supply current	4.015 A, THD = 3.9%	4.90 A, THD = 4.9%	5.33 A, THD = 4.8%
5	THD of current	Load Current	i_{La} = 8.12 A, THD = 24.9%	8.98 A, THD = 24.6%	10.0, THD = 24.0%
6	Weight convergence		Fastest	Slow	Moderate
7	Sampling time		55 µs	70 µs	55 µs
8	Overall performance		Best	Moderate	Moderate
9	Performance as filter (input and output)		No lag associated	NA	Lag associated

Conclusions

The novel contribution of this paper is to compare three algorithms on a single stage PV incorporated grid connected system. The boost converter is eliminated in the single stage and PV is directly connected at the DC link of DSTATCOM system. This has an added advantage as a low-cost DSP can be used for the compensation of distribution system. Three control algorithms, viz. SRFT, NF and SOGI are modeled and extensive simulation and hardware analysis have been performed. The paper also shows the performance of all the three algorithms under PV disconnection and load disconnection modes. Simulation results are supported by hardware results. In experimental results, phase reversal of source current is shown which happens when the PV generation is greater than load demand. The DSTATCOM is easily able to switch into different modes when load is present or absent and also for PV connected/disconnected operation. A comparative analysis of all three algorithms is discussed in Section "Comparative Performance Analysis." The analysis of Table 3 shows that the SOGI controller outperforms the SRFT and NF control algorithms.

References

1. E. Acha, V.G. Agelidis, O. Anaya-Lara, T.J.E. Miller, *Power Electronics Control in Electrical System* (Newnes Power Engineering Series, New York, 2002)
2. H.A. Khan, M. Zuhaib, M. Rihan, A review on voltage and frequency contingencies mitigation technologies in a grid with renewable energy integration. J. Inst. Eng. India Ser. B **103**, 2195–2205 (2022)
3. X.H. Nguyen, M.P. Nguyen, Mathematical modeling of photovoltaic cell/module/arrays with tags in Matlab/Simulink. Environ. Syst. Res. **4**(1), 24–36 (2015)
4. N.M.A.A. Shannan, N.Z. Yahaya, B. Singh, Single-diode model and two-diode model of PV modules: A comparison, in *2013 IEEE International Conference on Control System, Computing and Engineering* (Mindeb, 2013), pp. 210–214
5. H. Bellia, R. Youcef, M. Fatima, A detailed modeling of photovoltaic module using MATLAB. NRIAG J. Astron. Geophys. **3**, 53–61 (2014)
6. D.B. Kanase, H.T. Jadhav, Three-phase distribution static compensator for power quality improvement. J. Inst. Eng. India Ser. B **103**, 1809–1826 (2022)
7. B. Singh, P. Jayaprakash, D.P. Kothari, Three-leg voltage source converter integrated with T-connected transformer as three-phase four-wire distribution static compensator for power quality improvement. Electric. Power Compon. Syst. **37**(8), 817–831 (2019)
8. M.B. Latran, A. Teke, Y. Yoldaş, Mitigation of power quality problems using distribution static synchronous compensator: a comprehensive review. IET Power Electron. **8**(7), 1312–1328 (2015)
9. A. Pandey, A. Singh, Development of conductance based algorithm for compensation in highly unbalanced and distorted grid, in *2019 International Conference on Power Electronics, Control and Automation (ICPECA)* (2019), pp. 1–6
10. M. Badoni, A. Singh, A.K. Singh, H. Saxena, R. Kumar, Grid tied solar PV system with power quality enhancement using adaptive generalized maximum Versoria criterion. CSEE J. Power Energy Syst. (2021)
11. H. Saxena, A. Singh, J. N. Rai, Adaptive spline-based PLL for synchronisation and power quality improvement in distribution system. IET GTD (Feb 2020)
12. P. Chittora, A. Singh, K. Singh, Design, analysis, and implementation of proportional-resonant filters for shunt compensation. Int. Trans. Electric. Energy Syst. **27**(10), 1–13 (2017)
13. S.K. Patel, S.R. Arya, R. Maurya, Optimal step LMS-based control algorithm for DSTATCOM in distribution system. Electric. Power Compon. Syst. **47**(8), 675–691 (2019)
14. P. Chittora, A. Singh, M. Singh, Performance evaluation of a new Kalman filter based least mean square algorithm for power quality improvement, in *2016 IEEE 1st International Conference on Power Electronics, Intelligent Control and Energy Systems (ICPEICES)* (Delhi, 2016), pp. 1–5
15. M. Badoni, A. Singh, B. Singh, Variable forgetting factor recursive least square control algorithm for DSTATCOM. IEEE Trans. Power Deliv. **30**(5), 2353–2361 (2015)
16. P. Chittora, A. Singh, M. Singh, Gauss–Newton-based fast and simple recursive algorithm for compensation using shunt active power filter. IET Gener. Transm. Distrib. **11**(6), 1521–1530 (2017)
17. P. Chittora, A. Singh, M. Singh, Application of hopfield neural network for harmonic current estimation and shunt compensation. Electric. Power Compon. Syst. **46**(3), 290–301 (2018)
18. P. Chittora, A. Singh, M. Singh, Simple and efficient control of DSTATCOM in three-phase four-wire polluted grid system using

MCCF-SOGI based controller. IET Gener. Transm. Distrib. **12**(5), 1213–1222 (2018)
19. H. Saxena, A. Singh, J.N. Rai, Design and performance analysis of improved Adaline technique for synchronization and load compensation of grid-tied photovoltaic system. Int. Trans. Electric. Energy Syst. (March 2020)
20. P. Chittora, A. Singh, M. Singh, Adaptive EPLL for improving power quality in three-phase three-wire grid-connected photovoltaic system. IET Ren. Power Gener. **13**(9), 1595–1602 (2019)
21. IEEE Recommended Practice and Requirements for Harmonic Control in Electric Power Systems, in *IEEE Std 519-2014* (Revision of IEEE Std 519-1992, June 11, 2014), pp.1–29
22. IEEE Standard for Interconnection and Interoperability of Distributed Energy Resources with Associated Electric Power Systems Interfaces. in *IEEE Std 1547-2018* (April 6, 2018, Revision of IEEE Std. 1547-2003), pp 1–138

Publisher's Note Springer Nature remains neutral with regard to jurisdictional claims in published maps and institutional affiliations.

Springer Nature or its licensor (e.g. a society or other partner) holds exclusive rights to this article under a publishing agreement with the author(s) or other rightsholder(s); author self-archiving of the accepted manuscript version of this article is solely governed by the terms of such publishing agreement and applicable law.

Extractive Text Summarization

Abhishek Kumar
Department of Computer Science and Engineering
Delhi Technological University
New Delhi, India

Garima Chhikara
Department of Computer Science and Engineering
Delhi Technological University
New Delhi, India

***Abstract* - In the last decade, there has been a significant growth in the fields of Artificial Intelligence (AI), Machine Learning (ML), and Data Science. These fields have shown immense potential in various industries, including healthcare, finance, transportation, and more. One of the areas where AI and ML have made remarkable progress is in Natural Language Processing (NLP), which involves processing and understanding human language by machines. Text summarization is one such application of NLP, where machines are used to summarize large amounts of text into shorter, more concise summaries. This project shows small and effective use of extractive text summarization technique. Here we are going to use BERT,GPT-2, KL-summarizer, Luhn, LEX and Word Rank summarization to show the extractive text summarization technique. Once the extractive summarization is obtained it is matched with the human text summarized text. The summary score is obtained between both the texts. Here we are going to use three summary score: Rouge Score, BERT Score and MoverScore.**

Keywords- Artificial Intelligence, Natural Language Processing, BERT (Bi-directional Encoder Representation from Transformers), GPT-2(Generative Pretrained Transformer), KL-summarizer, Luhn, LEX and Word Rank, BERT Score and Mover Score.

I. INTRODUCTION

Text Summarization technique is a summarization of given text. It is very important in Natural Language processing used for data mining. Through Text summarization we can able to extract important information from large text file [1]. There are various models used for text summarization like transformers, KL-summarizer, Luhn, LEX and Word Rank, GPT-1, GPT-2 and Bert Model.

There are basically two types of text summarization techniques:

1. Extractive Text Summarization
2. Abstractive Text Summarization

Extractive Text Summarization-It is carried out when important word, lines or sentences are taken out from paragraph and they are combined to summary of the paragraph [2].

Example: Harry and Jimmy rode on a car to attend the party in Washington. In the city, Jimmy adopted dog named Tommy.

Output: Harry and Jimmy attend party Washington. Jimmy adopted Tommy.

Abstractive Text Summarization – Abstractive text summarization is a process that involves creating new phrases and sentences that effectively convey the essential information, even if they are not found in the original text. Compared to extractive text summarization, which involves choosing and combining existing sentences or phrases from the source text to produce a summary, abstractive text summarization is more difficult. It necessitates a more thorough comprehension of the text and the ability to generate grammatically correct and coherent sentences [3].

Output: Harry and Jimmy came to Washington where Tommy was born.

A. Problem Statement

When comparing a model summary to a humansummary, the issue is obtaining the text appropriately summarized.

B. Objective

- Propose few algorithms for Extractive Text Summarization which can select highly relevant sentences from a given textual unit.
- We intend to use BERT, GPT-2, KL-summarizer, Luhn, LEX and Word Rank summarization for the process of generating summaries.
- Further, we show the quantitative goodness of our proposed algorithm by using ROUGE metric, BERT metric and MoverScore metric.

II. LITERATURE REVIEW

Here we are using two different datasets, i.e., the CNN Daily Mail dataset [4] and the BBC News dataset [5]. Both the datasets consist of text that is to be summarized by models and a human text summary of that text.

Once the model-generated summary is out, we compare the resulting summary with a human-generated summary. The extractive text summarization model here that we have used is BERT, GPT-2, KL-summarizer, Luhn, LEX, and Word Rank summarization for the process of generating summaries.

Furthermore, we use the ROUGE score, the BERT score, and the Movers score to demonstrate the quantitative quality of our suggested approach.

III. PROPOSED METHODOLOGY

A. *BERT*

BERT, an acronym for Bidirectional Encoder Representations from Transformers, is a potent natural language processing approach that has been widely utilized in various fields, including text summarization [6]. Extractive summarization based on BERT involves utilizing a pre-trained BERT model to determine the crucial sentences or phrases in a document and then extracting them to create a summary.

The steps involved in BERT-based extractive summarization are as follows:

1. Text pre-processing: Stop words, unnecessary punctuation, and other non-essential components are removed from the original text.

2. Tokenization: The pre-processed text is tokenized into individual words and sentences.

3. BERT encoding: Each sentence in the pre-processed text is encoded using a pre-trained BERT model, which generates a high-dimensional representation of the sentence.

4. Sentence scoring: The significance of the encoded phrases to the text's overall meaning determines how well they perform. Various methods can be used to score sentences, such as cosine similarity or a learned scoring function.

5. Sentence selection: A summary is created by choosing and concatenating the top-ranked sentences [7].

BERT-based extractive summarization has shown promising results in several benchmarks and evaluations, outperforming traditional methods such as TF-IDF and TextRank. Despite its effectiveness, BERT-based summarization requires significant computational resources and an extensive amount of training data to attain optimum outcomes. Furthermore, the quality of the generated summary is closely tied to the quality of the pre-trained BERT model used and the scoring function applied.

B. *GPT-2*

GPT-2 (Generative Pre-trained Transformer 2) is a type of language model that utilizes unsupervised learning techniques to produce text that closely resembles that written by humans. While GPT-2 is primarily used for generative tasks such as language modeling, it can also be used for extractive summarization.

The process of GPT-2-based extractive summarization is similar to BERT Model. It involves the similar process as BERT i.e., Text pre-processing, Tokenization, GPT-2 encoding, Sentence scoring, Sentence selection.

GPT-2-based extractive summarization has shown promising results in some benchmarks and evaluations. However, GPT-2 is primarily a generative language model and may not be as effective at extractive summarization as models specifically designed for that task. The effectiveness of the summary is heavily reliant on both the caliber of the pre-trained GPT-2 model utilized and the scoring function that is applied.

C. *KL-Summarizer*

KL Summarizer is a text summarization algorithm that uses the Kullback-Leibler (KL) Divergence to rank sentences and select the most informative ones to form a summary.

The difference between two probability distributions is measured by the KL Divergence. The probability distribution of words in a phrase and the probability distribution of words throughout the full text are compared in text summarization to determine the difference. Sentences with a high KL Divergence score, meaning they have a significantly different distribution than the rest of the document, are considered to be more informative and are selected for the summary.

The KL Summarizer algorithm works in the following steps:

1. Sentence Pre-processing: The input text is first pre-processed by tokenizing it into individual sentences and removing stop words and punctuation.

2. Document Word Frequency Calculation: Each word's frequency inside the text is determined.

3. Sentence Word Frequency Calculation: Each word's frequency inside each phrase is determined.

4. Probability Distribution Calculation: The probability distribution of words in each sentence and the entire document is calculated.

5. KL Divergence Calculation: The KL Divergence is calculated between the probability distribution of each sentence and the entire document.

6. Sentence Ranking: The top N sentences are chosen to make up the summary after sentences are sorted according to their KL Divergence scores.

The KL Summarizer algorithm is simple yet effective in identifying the most informative sentences in a document. However, it may not always produce the most coherent and readable summary, as it solely relies on statistical measures of word distribution and does not take into account semantic relationships between words and sentences [1].

D. LUHN

Hans Peter Luhn devised the Luhn algorithm, an extractive text summarizing method, in 1958. The most significant phrases in a text have the highest frequency of key terms, according to the algorithm. Here are the main steps of the Luhn algorithm:

1. Tokenize the text into individual words and remove stop words (such as "the", "and", "is", etc.) and punctuation.

2. Determine the frequency of each word in the text, then give each one a weight based on that frequency.

3. Divide the text into a set of candidate sentences, such as by splitting the text at each period or other punctuation mark.

4. Each candidate sentence's "score" is determined by adding the weights of the words it includes.

5. Choose the top N sentences—where N is the required length of the summary—with the greatest scores as the summary.

Although it has significant drawbacks, the Luhn algorithm provides a quick and efficient technique to create extractive summaries. For instance, it does not consider how words relate to one another or how sentences fit together. Therefore, it may not be as accurate or informative as more advanced summarization techniques [8].

E. LEX

The LEX (Logistic Regression with Regularization based summarizing) method of extractive text summarizing chooses the most crucial passages from a given document using logistic regression with regularization. The fundamental principle of LEX is to score each sentence according to its significance within the text, then choose the top-ranked sentences to serve as the summary.

To calculate the score of each sentence, LEX uses a set of features that capture various aspects of the sentence such as its position in the document, length, and similarity to other sentences in the document. These features are used to train a logistic regression model that assigns a score to each sentence.

The regularization term in LEX encourages sparsity in the selected sentences, meaning that the model tends to select a small number of highly informative sentences rather than many less informative ones. This helps to produce more concise and informative summaries.

Overall, LEX is a simple but effective extractive summarization technique that has been shown to perform well on a variety of datasets and languages [1].

F. Word Rank

Word Rank is another extractive text summarization technique that ranks the importance of words based on their frequency and position in the text. The basic idea is that important words tend to occur frequently in the text and are located in important positions such as the beginning or end of sentences.

The Word Rank algorithm first tokenizes the input text into words and removes stop words and punctuation. Then, it calculates the frequency of each word and assigns a score based on its position in the text. The score of each word is calculated as the product of its frequency and a position weight factor. The position weight factor is determined by the position of the word in the sentence and the number of sentences in the text.

Finally, the algorithm selects the top-ranked words and generates a summary by including the sentences that contain these words. Setting a limit on the number of chosen words or the percentage of the original text can regulate how long the summary is.

Overall, Word Rank is a simple and effective approach for extractive text summarization that does not require any training data or complex models. However, it may not capture the semantic meaning of the text and may overlook important phrases or concepts that are not represented by high-frequency words [1].

G. ROUGE SCORE

To evaluate the efficiency of machine translation and automatic summarization systems, a set of metrics known as ROUGE (Recall-Oriented Understudy for Gisting Evaluation) is employed. The measurements were established to gauge how well a generated summary or translation matched up with a collection of examples of summaries or translations produced by human experts.

ROUGE scores are determined by comparing the overlap between the generated summary or translation and the reference summary or translation. Usually, the scores are determined at the level of individual words, n-grams (contiguous groups of n words), or phrases.

ROUGE metrics comprise several variations such as ROUGE-1, ROUGE-2, ROUGE-L, and ROUGE-S. ROUGE-1 evaluates the agreement between the produced and reference summaries or translations based on unigram (single word) overlap, while ROUGE-2 considers the agreement between bigrams (pairs of nearby words). On the other hand, ROUGE-S evaluates the agreement based on skip-bigram overlap between the two sets of text, while ROUGE-L measures the longest common subsequence (LCS) between the generated and reference summaries or translations. A higher ROUGE score denotes better similarity between the produced and reference texts; values range from 0 to 1 [9].

H. BERTScore

BERTScore is a form of automatic evaluation metric used to evaluate the efficacy of text generation systems. Unlike conventional approaches that compute syntactical similarity at the token level, BERTScore concentrates on determining the semantic similarity between tokens in the reference and hypothesis sets. The creators of the metric applied it to image captioning and machine translation tasks and discovered that it correlates more closely with human assessments compared to other popular methods.

The process of determining the contextualized word embeddings for both the reference and candidate texts involves passing them through a pre-trained BERT model. Subsequently, the n x m similarity matrix, where n is the number of words in the reference text and m is the number of words in the candidate text, is generated by calculating the cosine similarity between every pair of embeddings. Following this, the maximum similarity score for each word in the candidate text is identified from among all the words in the reference text. This essentially involves finding the most comparable word in the reference text for every word in the candidate text.

Upon identifying the most similar words between the reference and candidate texts, precision, recall, and F1-score (harmonic mean of precision and recall) are calculated based on the number of words that are matched correctly.

Overall, BERT Score provides a more accurate and robust measure of text similarity compared to traditional methods such as BLEU and ROUGE, particularly for tasks involving complex language generation [10].

I. MoverScore

MoverScore is an evaluation metric used to assess the quality of text generation, with a focus on measuring the semantic similarity between the reference and candidate text at the sentence level. The metric is based on the "earth mover's distance" concept, which determines the minimum amount of effort needed to convert one distribution to another.

In the case of MoverScore, the distribution is represented by the sentence embeddings of the reference and candidate sentences, which are generated using pre-trained language models such as BERT. The earth mover's distance between these two distributions is then calculated to determine the similarity between the two sentences.

In a variety of text production tasks, including machine translation, summarization, and picture captioning, MoverScore has shown to be more efficient than other commonly used assessment metrics, such BLEU and ROUGE [11].

IV. EXPERIMENTAL RESULTS

Here we have used Bert Model designed by [12] *Hugging Face*. The vocabulary size for the transformers baseline is 30522 words, the hidden size is 768, there are 12 hidden levels for the transformers, 12 layers for attention, and there are 3072 feed forward layers in the transformer encoder.

Secondly, the GPT-2 model, which was made available by *OpenAI*[13] in 2019, has a variation called GPT-2 Medium. It is bigger and more potent than the lesser GPT-2 models thanks to its 355 million parameters, but smaller than the biggest GPT-2 model (which has 1.5 billion parameters). The model is pre-trained using a causal language modelling objective on a sizable corpus of English text, which means it is taught to predict the following word in a sequence given the preceding ones.

We have worked on 2 different dataset i.e CNN/Dailymail and BCC New Datasets.

A. CNN/Dailymail Dataset

The CNN/Daily Mail news publication served as the source for the dataset. The dataset consists of 500 different articles for different news. Every news story has been traversed, and extractive text summarization has been taken out. When a human-generated summary is compared to an extractive synthesis, the summary evaluation metric is calculated.

TABLE I

Rouge Score	**Rouge 1 Recall**	**Rouge 1 Precision**	**Rouge 1 F-Measure**
BERT	0.47	0.23	0.29
GPT 2	0.47	0.23	0.3
KL SUMMARIZER	0.32	0.24	0.27
LUHN	0.44	0.24	0.3
LEX	0.42	0.25	0.31
WORD RANK	0.49	0.21	0.29

TABLE II

Rouge Score	Rouge 2 Recall	Rouge 2 Precision	Rouge 2 F-Measure
BERT	0.18	0.08	0.1
GPT 2	0.18	0.08	0.11
KL SUMMARIZER	0.12	0.08	0.09
LUHN	0.17	0.08	0.11
LEX	0.15	0.08	0.1
WORD RANK	0.2	0.07	0.1

TABLE III

Rouge Score	Rouge L Recall	Rouge L Precision	Rouge L F-Measure
BERT	0.44	0.21	0.27
GPT 2	0.44	0.21	0.27
KL SUMMARIZER	0.3	0.22	0.25
LUHN	0.4	0.22	0.28
LEX	0.38	0.23	0.28
WORD RANK	0.46	0.2	0.27

According to Recall, Precision, and F-Measure scores, different models are categorized into Rouge 1, Rouge 2, and Rouge L in the Table I, II, and III.

TABLE IV

BERT Score	Precision	Recall	F -Measure
BERT	0.76	0.83	0.79
GPT 2	0.76	0.83	0.8
KL SUMMARIZER	0.77	0.79	0.78
LUHN	0.76	0.82	0.79
LEX	0.77	0.81	0.79
WORD RANK	0.75	0.82	0.79

The Table IV shows BERT Score based on Recall, Precision and F-Measure score for different models.

TABLE V

MoverScore	Score
BERT	0.56
GPT 2	0.56
KL SUMMARIZER	0.55
LUHN	0.55
LEX	0.56
WORD RANK	0.55

The Table V shows BERT Score for different extractive text summarization models.

B. BBC News Datasets

There are news archives from business, entertainment, politics, sports, and technology in the BBC News Databases. 510 articles are dedicated to business, 386 to entertainment, 417 to politics, 511 to sports, and 401 to technology, in contrast. The combined dataset consists of 2225 articles. According to 2225 distinct BBC news article, the average rouge score (roughly) for recall, precision, and F-measure is shown in the table below.

TABLE VI

Rouge Score	Rouge 1 Recall	Rouge 1 Precision	Rouge 1 F-Measure
BERT	0.43	0.57	0.47
GPT 2	0.43	0.58	0.48
KL SUMMARIZER	0.48	0.46	0.46
LUHN	0.75	0.56	0.63
LEX	0.66	0.53	0.58
WORD RANK	0.56	0.51	0.51

TABLE VII

Rouge Score	Rouge 2 Recall	Rouge 2 Precision	Rouge 2 F-Measure
BERT	0.3	0.43	0.34
GPT 2	0.3	0.45	0.34
KL SUMMARIZER	0.34	0.33	0.33
LUHN	0.65	0.46	0.53

LEX	0.53	0.43	0.47
WORD RANK	0.41	0.39	0.38

TABLE VIII

Rouge Score	Rouge L Recall	Rouge L Precision	Rouge L F-Measure
BERT	0.42	0.55	0.46
GPT 2	0.42	0.57	0.47
KL SUMMARIZER	0.47	0.45	0.45
LUHN	0.74	0.55	0.63
LEX	0.64	0.52	0.57
WORD RANK	0.55	0.5	0.5

The Table VI, VII, VIII shows Rouge based on Recall, Precision and F-Measure score for different models classified into Rouge 1, Rouge 2 and Rouge L.

TABLE IX

BERT Score	Precision	Recall	F Measure
BERT	0.85	0.83	0.84
GPT 2	0.86	0.83	0.84
KL SUMMARIZER	0.81	0.81	0.81
LUHN	0.83	0.88	0.85
LEX	0.83	0.86	0.84
WORD RANK	0.84	0.85	0.85

The Table IX shows BERT Score based on Recall, Precision and F-Measure score for different models.

TABLE X

MoverScore	Score
BERT	0.6
GPT 2	0.6
KL SUMMARIZER	0.6
LUHN	0.64
LEX	0.63
WORD RANK	0.61

The Table X shows MoverScore for different extractive text summarization models.

V. CONCLUSIONS

When working with vast amounts of text, extractive summarization can help you save time and work more effectively. It cannot create new material, for instance, or accurately capture the entire context and meaning of the original document. Despite these drawbacks, extractive summarization is nonetheless a helpful tool for a variety of tasks, including writing news stories, academic papers, and legal documents.

We took two different datasets CNN/Dailymail Dataset, BBC News Datasets. From the working mechanism we could implement Rouge metric, BERT metric and MoverScore metric between human text summarized and different model summarized text. On the CNN/Dailymail Dataset, we get GPT-2 as the best model and for the BBC New Dataset we get Luhn as the best Model.

REFERENCES

[1] Nenkova, Ani, and Kathleen McKeown. "A survey of text summarization techniques." Mining text data (2012): 43-76.

[2] Moratanch, N., and S. Chitrakala. "A survey on extractive text summarization." In 2017 international conference on computer, communication and signal processing (ICCCSP), pp. 1-6. IEEE, 2017.

[3] Moratanch, N., and S. Chitrakala. "A survey on abstractive text summarization." In 2016 International Conference on Circuit, power and computing technologies (ICCPCT), pp. 1-7. IEEE, 2016.

[4] https://www.kaggle.com/datasets/gowrishankarp/newspaper-text-summarization-cnn-dailymail

[5] https://www.kaggle.com/datasets/pariza/bbc-news-summary

[6] Devlin, Jacob, Ming-Wei Chang, Kenton Lee, and Kristina Toutanova. "Bert: Pre-training of deep bidirectional transformers for language understanding." arXiv preprint arXiv:1810.04805 (2018).

[7] Liu, Yang. "Fine-tune BERT for extractive summarization." arXiv preprint arXiv:1903.10318 (2019). arXiv:1810.04805 (2018).

[8] H. P. Luhn, "The Automatic Creation of Literature Abstracts," in *IBM Journal of Research and Development*, vol. 2, no. 2, pp. 159-165, Apr. 1958, doi: 10.1147/rd.22.0159.

[9] Lin, Chin-Yew. "Rouge: A package for automatic evaluation of summaries." In Text summarization branches out, pp. 74-81. 2004.

[10] Zhang, Tianyi, Varsha Kishore, Felix Wu, Kilian Q. Weinberger, and Yoav Artzi. "Bertscore: Evaluating text generation with bert." arXiv preprint arXiv:1904.09675 (2019).

[11] Zhao, Wei, Maxime Peyrard, Fei Liu, Yang Gao, Christian M. Meyer, and Steffen Eger. "MoverScore: Text generation evaluating with contextualized embeddings and earth mover distance." arXiv preprint arXiv:1909.02622 (2019).

[12] https://github.com/huggingface/transformers

[13] https://en.wikipedia.org/wiki/OpenAI

Fake News Detection using Attention Based Model

Khushi Jain
Department of Electronics and Communication Engineering
Delhi Technological University
Delhi,India
khushijain_2k19ec094@dtu.ac.in

Harsh Bansal
Department of Electronics and Communication Engineering
Delhi Technological University
Delhi,India
harshbansal_2k19ec070@dtu.ac.in

Gaurav Saxena
Department of Electronics and Communication Engineering
Delhi Technological University
Delhi,India
gauravsaxena_2k19ec059@dtu.ac.in

Rohit Kumar
Department of Electronics and Communication Engineering
Delhi Technological University
Delhi,India
rohit.kumar@dtu.ac.in

2023 10th International Conference on Signal Processing and Integrated Networks (SPIN) | 978-1-6654-9099-3/23/$31.00 ©2023 IEEE | DOI: 10.1109/SPIN57001.2023.10117332

***Abstract*—With the inception of big data, there is a lot of information that goes unfiltered, contributing to fake news. This false information can lead to catastrophic results in the long run. Hence, to curb this spread, we aim to provide constructive techniques that can help detect this kind of misleading news. In this paper, we have introduced a novelty model, the LSTM-Attention Network, and shown the comparison of the novelty model with existing machine learning algorithms like Naive Bayes, SVM, BERT, and DeBERTa. The analysis is based on the dataset, which was extracted from diverse sources and contains over 20,000 news samples. The proposed work results in an accuracy ranging from 85.7% to 99.9%, which is very good for classifying most of the information.**

Keywords—— Naïve Bayes, SVM, BERT, DeBERTa,LSTM-Attention Network.

I. INTRODUCTION

The phenomenon of fakin thee news has become a widespread issue in this world, affecting people from all walks of life. Not only is it spread deliberately by those with nefarious intentions, such as gaining political power or spreading propaganda against certain groups, but it is also often unknowingly shared by individuals who are not aware of its false nature. The proliferation of social media has made it easier than ever for false information to reach a large audience. With advancements of internet and the widespread use of social media, an overwhelming amount of information is readily available to the public, but determining its credibility can be a challenging task. "Fake news" is a term used to describe information that is false and intended to harm the reputation of an organisation, individual, or group, or to gain financially or politically. The spread of fake news not only undermines trust in media and institutions but also has the potential to create societal divisions, sow confusion, and lead to dangerous consequences. It is crucial that individuals take the time to fact-check information and question its source before sharing it with others. Additionally, media and social media platforms have a responsibility to take steps to combat the spread of fake news by verifying information and providing resources for fact-checking. It is a collective effort by everyone to counter the spread of false information and ensure that accurate information is being disseminated. Therefore, it is important for people to stay vigilant and educate themselves about the potential dangers of fake news and how to identify and avoid it.

Identify applicable funding agency here. If none, delete this text box.

The spread of false information, commonly referred to as "fake news," has become a major concern in today's age of instant global communication. The misinformation can lead to confusion and undue stress among the public and has the potential to harm democracy and individual freedoms. It is often used for personal or political gain and can result in violence and mistrust in government and media institutions. This practise is referred to as 'infodemic," which, just like the pandemic that we all went through in the recent years, spreads false information quickly. It is crucial for individuals to be discerning when consuming information and for authorities to take action to combat the spread of fake news.[1].

In this research, a new and innovative approach is proposed: the LSTM-Attention Network for detecting fake news using state-of-the-art deep neural network models that incorporate attention mechanisms such as BERT and DeBERTa. The effectiveness of these attention-based models is assessed by evaluating their performance in terms of accuracy when applied to both training and validation datasets. This paper is structured in a logical and coherent manner, with the first section providing a comprehensive introduction to the subject matter. The second section delves into the existing algorithms that have been used for the detection of fake news, while the third section describes the methodology employed in this research. The fourth section presents a detailed comparison of the results obtained from the proposed algorithm with other existing algorithms. Finally, the fifth section concludes the paper by summarising the key findings and discussing potential future work in this field.

II. LITERATURE REVIEW

A. Fake News on social media

Social media encompasses wikis, microblogging, social bookmarking, forums, social websites, and other similar platforms[2][3].The ease of sharing and the large reach of social media make it a prime channel for the dissemination of fake news. Fake news's effects on social media can be significant, as it can affect common people's opinions and lead to the spread of misinformation. Furthermore, it can also lead to political interference, manipulation of public opinion, and even manipulation of stock markets[4].

B. Natural Language Processing

NLP is an area of AI that focuses on the interaction between computers and human language. It uses various techniques to analyze, understand, and generate human language. It has a variety of applications, including speech-to-text and text-to-speech systems, analysis of emotions, machine translation, and information retrieval. Recently, the

Authorized licensed use limited to: DELHI TECHNICAL UNIV. Downloaded on May 15,2023 at 09:52:28 UTC from IEEE Xplore. Restrictions apply.

advancement of deep learning techniques has greatly improved the performance of NLP, resulting in more accurate and natural language understanding.

The creation of tools for separating actions from speech is a crucial topic of NLP research. This requires the usage of numerous pipelines that speak various languages, including Chunking, Named Entity Recognition (NER), Parts of Speech (POS) Taggers, Emotion Analysis and Detection, and Semantic Role Labelling. Together, these methods enable us to recognise and properly extract the intended meaning from spoken language.

Recent advancements in NLP have also led to the development of chatbots and virtual assistants that are able to understand and respond to natural language input. This has led to the widespread use of NLP in industries such as customer service and e-commerce, where it is used to improve customer engagement and automate repetitive tasks..

Overall, NLP is a highly dynamic and rapidly evolving field that has the potential to revolutionize the way we interact with technology. With the continued advancements in machine learning techniques, it is likely that NLP will continue to play a significant role in shaping the future of human-computer interaction.

C. Naive Bayes

The Naive Bayes Classifier algorithm is a statistical method that is based on Bayes' theorem and is commonly used in machine learning problems such as text classification and spam filtering. The algorithm makes the assumption that the predictors in the dataset are independent of each other, which is often referred to as the "naive" assumption [5]. Despite this assumption, the Naive Bayes Classifier algorithm has been shown to be highly effective in many real-world applications.

One such application is in the detection of fake news on social media sites. The Naive Bayes Classifier algorithm can be used to classify news articles as either real or fake based on a variety of features such as the text of the article, the source of the article, and the number of shares and likes the article receives. By training the algorithm on a large dataset of known real and fake news articles, it can be used to accurately identify and flag potentially fake news articles on social media platforms.

Another application of Naive Bayes Classifier is in the field of natural language processing where it can be used to identify text as spam or ham. The algorithm can be trained on a dataset of known spam and ham messages, and then used to classify new incoming messages as either spam or ham. It can also be used in sentiment analysis to classify text as positive, negative, or neutral.

Overall, the Naive Bayes Classifier algorithm is a powerful tool that can be used in a wide range of machine learning problems. Its simplicity and effectiveness make it a popular choice for many practitioners and researchers.

D. Support Vector Machine

A well-liked machine learning method for classification and regression applications is the Support Vector Machine (SVM). It is a technique for determining the best border (hyperplane) that categorizes the data points while maximizing the margin—the distance between the nearest data points in each class and the boundary[6]. The SVM algorithm works by plotting the data points in an n-dimensional space, where n is the number of features. Each data point is represented by a coordinate that corresponds to the values of each feature. The algorithm then tries to find the most suitable hyperplane that separates the data points into different classes. The data points closest to the boundary are known as support vectors, and they have a crucial role in determining the location of the hyperplane.

The SVM algorithm is especially useful in scenarios where the data cannot be separated by a simple straight line, this is known as non-linearly separable data. To address this issue, the algorithm can use a technique called the kernel trick. This method transforms the data into a higher-dimensional space, where a linear boundary can be used to separate the data. This technique allows the SVM algorithm to find a boundary even when the data is not linearly separable.

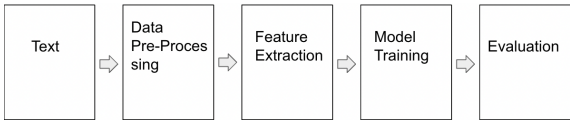
In addition to classification, SVM can also be used for regression problems, in which case the goal is to find a function that best maps the input data to the output variable[7].

Overall, the Support Vector Machine algorithm is a powerful tool that can be used for a wide range of machine learning tasks, and its ability to work well with non-linearly separable data make it a popular choice among practitioners and researchers.

III. METHODOLOGY

This paper presents the use of NLP techniques for identifying misleading news stories, commonly known as fake news. This section provides an overview of the architecture of the model. It includes information about the dataset used for training and evaluation.

The dataset is collected from Kaggle, followed by preprocessing, feature extraction, training of the model, and finally evaluation. Figure 1 describes the system



methodology.Figure 1: Methodology Process

A. Dataset

The project's dataset came from https://www.kaggle.com/c/fake-news/train.csv, from where it was downloaded. a complete training set having the following characteristics:

- Id: unique id.
- Title: the title of a news article.
- Text: Content in the article
- Label: a label that marks the article as fake.

B. Data Pre-Processing

The data on social media is extremely amorphous; the bulk of it is casual announcements with typos, slang, and poor grammar. For better inference, it is essential to clean the data before it can be used for extrapolative modelling. So, fundamental pre-processing was completed on the training data. Data Pre-processing comprises the following steps:

- **Conversion to Lower case**: To avoid using the same words more than once, the text was first converted to lower case. For instance, "Quick" and "quick" are both full of dissimilar terms when determining the word count.

Authorized licensed use limited to: DELHI TECHNICAL UNIV. Downloaded on May 15,2023 at 09:52:28 UTC from IEEE Xplore. Restrictions apply.

- **Removal of Punctuations**:Removal of Punctuation mark will help the model to treat all the text equally.For eg. the word Hi and Hi! will be treated equally after the process of punctuation removal. Punctuation typically don't convey much meaning on its own.
- **Stop-words removal**: The majority of frequently occurring words that are insignificant are known as stop-words. These include a, the, of, on, at, etc. as examples. They frequently categorise a text based on its structure rather than its context. It would lead to a deficient presentation if viewed as a feature. Stop-words are therefore not included in the training data as it helps the model focus more on important information and not on low-level information like stop-words.
- **Tokenization**: It means breaking the text up into groups of words or sequences of words, such as bigrams, trigrams, etc. To acquire frequency-based vector values for these tokens, tokenization was done.
- **Lemmatization**: It breaks down words into their underlying word forms. It does morphological analysis to identify the root word with the aid of a lexicon. Lemmatization was used in this study to raise the quality of the frequency-based vector values.
- **Handling missing or duplicate values**: When missing or duplicate values are found, the next step is to choose whether to drop them or impute them. While imputing values may inject bias into the dataset, dropping missing values could result in the loss of crucial data. Duplicate values should be eliminated to prevent the model from being trained on the same data more than once. You can achieve this by eliminating duplicates or by preserving only the first instance of a duplicate value.

C. *Feature Extraction*

Feature Extraction is the process of selecting and extracting relevant information from text data that can be used as input to a machine learning model. The goal of feature extraction is to extract the most informative and relevant features from the text that can help the model make accurate predictions. Feature Extraction steps are:

- **Count Vector**: It is a feature extraction technique to represent the frequency of words in a text. It is a simple method of converting text data into numerical feature vectors. This is done by counting the number of occurrences of each word in the text and then representing each word as a dimension in the feature vector. The count of the word in the text is the value of that dimension. The resulting vector is a sparse vector.
- **Term Frequency-Iverse Document Frequency(TF-IDF)**: It is a feature extraction approach used to depict a word's significance within a document. To calculate the term frequency of a word in a corpus of documents, the term frequency of a word in a document is multiplied by the word's inverse document frequency. As a result, terms that are used frequently in one text but not frequently across the corpus are given more weight.
- **Word Embeddings**: The representation of words as high-dimensional vectors that accurately convey their meaning is a feature extraction technique. Word embeddings are designed to map vocabulary words to a dense vector space, where each dimension of the vector corresponds to a distinct semantic or syntactic aspect of the word. Words with comparable meanings are clustered together in the resulting vector space, capturing the similarity between words.

D. *Algorithms*

- **Bidirectional Encoder Representations from Transformers (BERT)**: It is designed to understand the context of a sentence by analyzing the relationship between words in a sentence, rather than just their individual meanings. BERT has been trained on a large corpus of text and has the ability to understand the meaning of words in context. This allows it to perform well on a wide range of natural language processing tasks such as text classification, question answering, and language translation [8]. In addition to its pre-training and fine-tuning capabilities, BERT's architecture is designed to handle long sequences of text, making it well-suited for handling news articles. It also has the ability to handle out-of-vocabulary words, which is important for handling new and emerging words or phrases in the context of fake news detection. Overall, BERT's pre-training, fine-tuning capabilities, and ability to handle long sequences of text and out-of-vocabulary words make it a powerful tool for fake news detection and a wide range of other NLP tasks.
- **Deeply Bidirectional Encoder Representations from Transformer-based Pre-training (DeBERTa)**:DeBERTa's architecture is similar to BERT, but with some modifications such as a longer sequence length, more layers, and more attention heads. One of the features of DeBERTa is the use of dynamic masking. This technique adaptively masks different tokens for each input, which results in a more robust language model. This allows DeBERTa to better handle text data with a high degree of variability, such as social media posts or informal text. DeBERTa also uses a technique called "span-based masked language model" which helps to better understand the relationship between words in a sentence, which in turn helps it to perform better on tasks such as coreference resolution, where understanding the relationships between different words is crucial.
- **LSTM-Attention Network:**Long short-term memory (LSTM) is a type of recurrent neural network (RNN) architecture that was designed to address the vanishing gradient problem of traditional RNNs. LSTM networks are particularly effective at modelling sequential data due to their ability to selectively remember or forget information over time. In an LSTM, the network contains memory cells that are responsible for storing and transmitting information over time steps. These memory cells are governed by gating mechanisms that control the flow of information into, out of, and between the cells. An attention layer is stacked on the LSTM layer. The attention mechanism assigns a weight to each input element based on its relevance to the current state of the model. The weights are used to compute a weighted sum of the input elements, which becomes the input for the next layer of the model. This mechanism can improve the accuracy of the model by allowing it to more effectively capture long-term dependencies and handle variable-length input sequences.

Authorized licensed use limited to: DELHI TECHNICAL UNIV. Downloaded on May 15,2023 at 09:52:28 UTC from IEEE Xplore. Restrictions apply.

E. Evaluation

The dataset after preprocessing is split into a training and validation dataset in the ratio of 80:20, respectively.

Measuring the performance of machine learning algorithms is an important task to ensure that they are working correctly and achieving the desired results. One of the most commonly used metrics for evaluating the performance of classification algorithms is classification accuracy.

Classification accuracy is the capacity of a model or system to correctly identify the true class of an observation. It is described as the percentage of examples in a dataset that were correctly categorized. This indicates that it is determined by dividing the total number of occurrences in the dataset by the number of cases that were correctly categorized.

A model or system that can accurately identify the true class of an observation with a high frequency is said to be functioning well. This is indicated by a higher classification accuracy. Generally speaking, the model is thought to function better the higher the classification accuracy. Although accuracy is often the greatest indicator for assessing a model's performance, additional metrics like precision, recall, and F1-score should also be taken into account.

IV. RESULT

Five classifiers have been implemented, and their performance on how well they were able to classify the given news article is compared. For the comparison, we have used the accuracy metric.

The following are the four algorithms that are used to detect fake news:

- Naive Bayes
- Support Vector Machine
- LSTM-Attention Network
- BERT
- DeBERTa

Algorithms	Accuracy Score
Naive Bayes	91.34%
Support Vector Machine	89.57%
LSTM-Attention Network	94.46%
BERT	99.5%
DeBERTa	99.9%

Table 1: Comparison of accuracy score

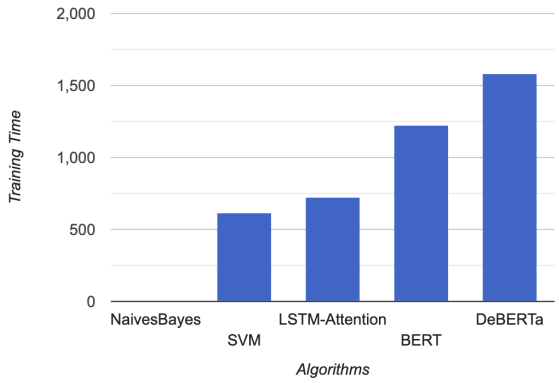


Figure 2: Training time for all Algorithms

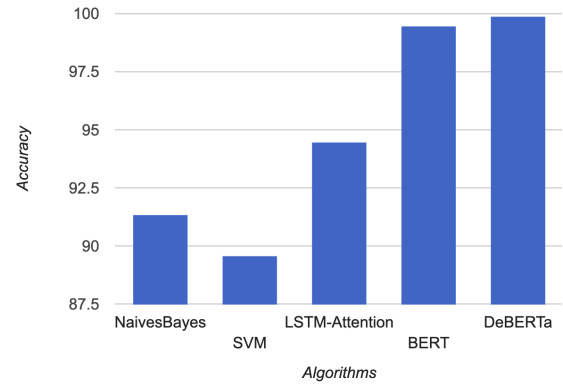


Figure 3: Accuracy results of all Algorithms

Figure 2 expresses the training time for all the algorithms. We can see that Naive Bayes requires the least amount of training time (about 3.7s), followed by SVM (276s). Naive Bayes takes 1/100th of the processing time taken by SVM because Naive Bayes assumes that features are independent of each other, thus it does not have to learn all the possible correlations between the features, whereas SVM looks for correlation between the features. The DeBERTa model takes the most training time of 1581s.

Figure 3 expresses the accuracy score for all the algorithms .We can see that DeBERTa model has the highest accuracy of 99.9%, followed by BERT model with 99.5%. SVM has the least accuracy of 89.57%.

V. CONCLUSION

The objective of this research is to address the challenging task of classifying news articles, as the input data is in text format and news can have a wide range of features that must be taken into account. This paper presents a novelty model, the LSTM-Attention Network, for identifying fake news on social media. The first stage focuses on defining the key concepts and characteristics of fake news, while the second stage reviews the comparison of the novelty model with existing methods for detecting fake news using various supervised learning algorithms. We propose a model with an accuracy of 94.46%. There are several potential hypotheses that can be made as to why a

Authorized licensed use limited to: DELHI TECHNICAL UNIV. Downloaded on May 15,2023 at 09:52:28 UTC from IEEE Xplore. Restrictions apply.

model may perform well on one dataset but not as well on another. The model may be overfitting to the training dataset and not generalising effectively to new data, which is one scenario that could apply. This indicates that the model has discovered patterns in the training data that only apply to that dataset and not to others. Another potential reason is that the features used in the model may not be relevant or informative for the new dataset. The model may be using features that are specific to the training dataset and are not present in the new dataset, causing the model to perform poorly.

A combination of factors such as overfitting, irrelevant features, covariate shift, and different styles of writing may contribute to a model performing well on one dataset but not as well on another. These variables should be taken into account when assessing a model's performance and when developing new models.

With huge computational power required for the attention-based models to be fine tuned, which will be costly and does not provide much improvement over traditional machine learning algorithms like Naive Bayes and SVM, which require much less computational power compared to attention-based models, and execution times for these models are also much less than attention-based models,

In the future, we plan to continue this research by experimenting with multi-model-based approaches and We plan to develop a hybrid approach for detecting fake news by incorporating information from the content, context, and structure of the news articles. This approach will make use of graph-based techniques to analyse the relationships between different entities in the news. We'll also look into how varying kernel sizes for parallel channel-based deep neural networks might help with performance. This approach will be able to better detect patterns and features that are indicative of fake news, as well as use visual information-based analysis for real-time detection in videos and images. Furthermore, we aim to incorporate domain experts' knowledge and fact-checking techniques for more accurate classification.

REFERENCES

[1] Ramya, S. P., and R. Eswari. "Attention-based deep learning models for detection of fake news in social networks," *IJCINI* vol.15, no.4, pp.1-25,2021

[2] Mu-Yen Chen, Yi-Wei Lai, and Jiunn-Woei Lian., "Using deep learning models to detect fake news about covid-19". *ACM Transactions on Internet Technology*, vol. 0,May 2022.

[3] F. Yu, Q. Liu, S. Wu, L. Wang, and T. Tan, "A convolutional approach for misinformation identification," in *Proc. 26th Int. Joint Conf. Artif. Intell*., Aug. 2017, pp. 3901–3907.

[4] Galli, A., Masciari, E., Moscato, V. *et al.* "A comprehensive Benchmark for fake news detection," *J Intell Inf Syst,* vol. 59, pp.237–261,2022.

[5] Zolnierek, A., Rubacha, B. "The empirical study of the naive bayes classifier in the case of markov chain recognition task,"*Advances in Soft Computing*, Springer, vol 30, pp. 329-335,2005

[6] M. A. Hearst, S. T. Dumais, E. Osuna, J. Platt and B. Scholkopf, "Support vector machines," in *IEEE Intelligent Systems and their Applications*, vol. 13, no. 4, pp. 18-28, July-Aug. 1998.

[7] Zhang, Y,"Support vector machine classification algorithm and its application,"*Information Computing and Applications,*Springer, vol 308,pp.179-188, 2012

[8] Devlin, J., Chang, M., Lee, K., & Toutanova, K., "Bert: pre-training of deep bidirectional transformers for language understanding," *North American Chapter of the Association for Computational Linguistics: Human Language Technologies,*vol. 1,pp. 4171–4186,2019

Authorized licensed use limited to: DELHI TECHNICAL UNIV. Downloaded on May 15,2023 at 09:52:28 UTC from IEEE Xplore. Restrictions apply.

Finding the Network of Unsocial Elements

Rajesh Kumar Yadav*, Archit Gupta*, Areeshaa Parveen*

* Department of Computer Science and Engineering, Delhi Technological University, New Delhi, 110042, India

Abstract- Smartphones have become an essential commodity for humans. It is used by a daily person and is used in retrospective units, and that is why today it is not uncommon that in all cases, the first step in resolving a crime is to break down the CDR of the defendant. Today in almost every case of criminal misconduct, the suspect's cell phone testing plays an essential role in detecting wrongdoing. To track down suspects/criminals, intelligence officials need to process a suspect's Call Detail Record (CDR) that has changed designs from professional co-operatives. It is noteworthy that the anti-friendship groups have their own organisation and relationships with different offenders and are opposed to sections of society. They are often linked together by doing evil, or they may be familiar with the abuse. Many of their partners could not be convicted or their names kept in old cases. Writing a CDR to cover the benefit of the knowledge base is a sensible organisation to provide tangible evidence of potential suspects in a variety of contexts. This test paper examines a case-killing case model using CDR.

Index Terms- Graph theory, Call Detail Record

I. Introduction

The purpose of the misinformation is to identify the design and examples that exist between offenders and those that are anti-social. Such an investigation will help deal with many rare cases and provide sensitive information to an organisation that understands the relationship between offenders. Police divisions often come with their own data when fraud, photography, malpractice and many other essential details related to crime are removed[2]. Despite the fact that these structures are very different from office by the organisation, the key objectives and powers are the same. These structures are essential sources of information in police investigations and law enforcement. Especially today, it is an excellent battle for wise and prudent investigators to regain the lead in their office structures. Most of the time, advanced systems develop the skills to create paper reports and get one case at a time. All in all, these modified plans do not give you the option to download much of the information needed for test purposes. There are various sources of information on trial offices that are widely used to investigate a case. One of them is the Call Detail Record (CDR)[8]. A caller ID record (CDR) is a record of information created by trading on the phone or other broadcast communication gear that archives call deception or exchange of broadcast communications (e.g., instant messaging) travelling through that particular office or gadget In this work, we look at a model that shows how the Call Detail Record (CDR) Database, which contains CDR from past cases and hoodlums who have been sued, may be used to research a topic.

II. Problem Statement and Research Objective

Today it is not unexpected that in all cases the primary purpose of dealing with crime is to disband the Call Records of the Suspects. This often requires some investment and effort. Time and complexity of the investigation increase compared to the CDR volume collected. CDR testing has become an integral part of all sin tests. However, it is evident that in most cases, the analytical offices usually collect CDR when preparing the case with the suspects explicitly. They often break it down by looking at specific issues and filing individual suspects. These CDRs are deleted once the case is closed. CDR testing is also recognised as a difficult and time-consuming job, necessitating the use of a product tool. There are other such instruments on the market; nevertheless, as previously said, they can assist in distinguishing CDR from litigation and prosecution. We suggest that CDR linked to older cases and hoodlums can be stored in an integrated database, which may be called a CDR Website, for testing and the reason for testing in different contexts. A CDR-based assessment can be helpful in distinguishing the relationships of habitual offenders or the like, who are involved in a large number of other cases.

III. Proposed Model

This paper proposes a diagram based on a comprehension model using a CDR data set. The CDR data set contains CDR for old cases and hoodlums related to those malicious actions. The goal of this research paper is to help the analytical office to investigate cases with the help of CDR. It is noteworthy that the anti-friendly parts have their own organisation and relationships with the various hoodlums and the private parts[1][19]. Often they are related to doing wrong or they may be acquainted with each other's trials and wrong actions. Many of their partners could not be convicted or their names kept in old cases. Assuming that CDR of older cases and suspects are placed in a centralised information base, it is often helpful for testing. Investigating this relationship between the opposing parties can help the analytical office by breaking down many values[12]. However, recognising visitor numbers and their communication on equal information is very difficult. We therefore use graphical expressions, based on the drawing concept. This diagram can show with a picture what the telephone numbers / IMEI are like related to other IMEI calls /numbers. Figure 1 depicts the diagrammatic representation of the proposed model.



Figure 1: The flow diagram of the model.

IV. IMPLEMENTATION

This section shows our CDR test model. For representation reasons we used a complete cycle and presented the CDR table in a more precise format, although it actually contains many fields and features that are important for testing. The most essential fields in the CDR are Dialler's Number, Dialler's IMEI number, Caller Number, in addition, Dialler's location and more. For representation reasons we show a few fields in the model. IMEI number is quint essential field of the CDR, which is not mentioned in the framework to reduce the complexity of the diagrammatical representation. IMEI number is essential for identification of items and is vital if the suspect changes the sim cards on the device being used. The subsequent sections discusses the proposed model handling the hidden objects within the model.

call details record contains metadata - information about information - that contains information handles that indicate a specific example of media transfer. It does not include text content. The record has various telephone attributes, for example, duration, length, duration, source number, and purpose number.

As a rule, a call log information showing a specific call may include the following:

- Dialler's contact number
- Receiver's contact number
- Call start time
- Duration of the call
- Billing device contact number
- IMEI number of the devices
- Unique identification number of call
- Call type (connected, missed etc.)
- Mode of communication (Voice, SMS, etc.)
- Any matter of experience and so on.

Modern CDRs (Call Detail Records) are much more informative and details containing numerous attributes including the approximate smartphone GPS location (Latitude and Longitude), cell phone tower connected for the call. These details may vary from one subscription provider to another and is proprietary in nature to protect the privacy of its subscriber base[15]. Management needs and a wide variety of strategies vary from professional engagement to a particular organisation[13]. Call Recording Data provided by professional media transfer organisations to the police is usually subject to an ordinary empty organisation (for example,*.xlsx or *.csv document formatting (See Figure 3). These records are obtained on special requests

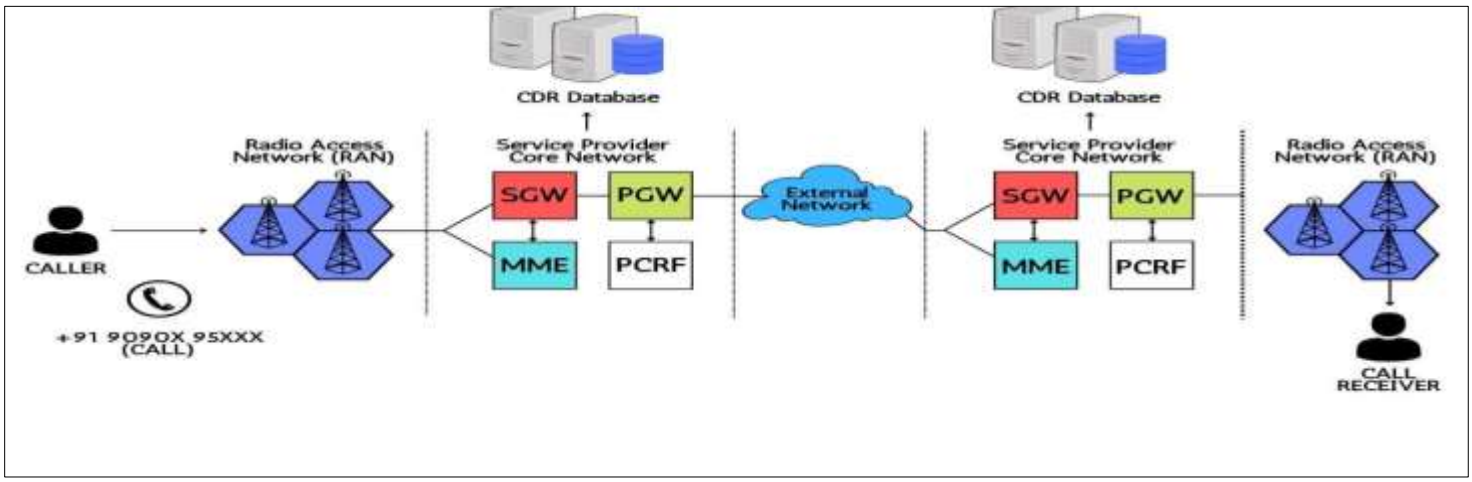


Figure 2: Source of generation of various CDRs for different Telecom providers.

A. CDR Analysis

Today in many negative tests, the Call Record Data test plays an important role. The analytical office collects a record of the details of the calls of the suspects from the portable professional body. A call record (CDR) record is information that is transmitted by telecommunications or a different communication gear that contains call or other communication transactions (e.g., instant messaging) passing through that office or gadget[3]. The made by the analytics team, which is followed up with privacy related legal issues removal. This record in the organisation, even for a while, contains horrible records. It is a diagnostic function for the specialist to investigate and make any disturbances [5].

The analytical office takes the help of in-house devices to perform CDR investigations. They often break it down by looking at specific cases and prosecuting individual suspects. If the case is handled, these CDRs are discarded.

We suggest that this CDR for individual cases be included in the data set for long-term testing. The opposition parties have their own organisation and relationships with different and hostile crooks in the public sphere. They are often associated with wrongdoing or, on the other hand, are more likely to be acquainted with abuse. Exploring these relationships between opposing parties can help a professional organisation break down too many values[9]. In any case, distinguishing visitor numbers and their connection to open information is very difficult. Appropriately we use image presentation based on a chart view. The diagram shown may show how phone numbers are associated with other phones. To clarify the whole cycle, in the following area, we accept one situation. The name and number displayed in the model are created.

B. Utilising CDRs for Crime Investigation

To demonstrate the usage of Graph Theory (Social Graph and Identifying Churn Nodes)[14][20], we will take an example scenario. Let's assume a planned robbery occurred at Palika Bazaar, Connaught Place, New Delhi, on February 13, between 1800 hrs to 1900 hrs. To narrow down the search, we get our hands on a potential suspect from location where incident was reported during a specified date, time and location of the crime[10].

C. Identifying a Potential Suspect

In the case mentioned above, the crime investigation department would gather the CDR from Telecom providers for a particular telephone tower situated near the crime scene, here Palika Bazaar[11]. To narrow down the possible suspects, they would investigate the call records within the given time span of one hour, i.e. 1800-1900hrs. We can request this as a simple SQL query such as:

SELECTDialer_Number, Reciever_ Number, Start_Time, Duration WHERE
Tower_Number ='4132'
OR Tower_Number ='4133'
OR Tower_Number = '4134'A
ND Start_Time BETWEEN 18:00 AND 19:00;

The SQL query returns all the entries in the CDRs for all the calls initiated within the given hour span with the three nearest cell phone towers located nearby Paalika Bazaar, Connaught Place, and New Delhi.

Let's assume that the above SQL query returns 10 records, as shown in Table. This narrows down the number of potential perpetrators or suspects to these ten users. In this 4G-5G era and with high connectivity, this number would run into hundreds and thousands and it would be practically impossible to narrow down the search for suspects. This task is no longer humanly possible. This is where our proposed model comes into the picture, where automation can reduce the number of man-hours and help us identify the network of anti-social elements.

TABLE I. SAMPLE CALL DETAIL RECORDS

S. No	Dialer's Number	Reciever's Number	Time (in hrs)	Duration (in mins)
1	99XX6216X1	99XX6315X1	18:15:05	5
2	99XX6216X2	99XX6315X2	18:20:19	6
3	99XX6216X3	99XX6315X3	18:27:37	1
4	99XX6216X4	99XX6315X4	18:29:28	7
5	99XX6216X5	99XX6315X5	18:31:48	2
6	99XX6215X1	99XX6316X1	18:33:26	8
7	99XX6215X2	99XX6316X2	18:40:59	8
8	99XX6215X3	99XX6316X3	18:46:08	4
9	99XX6215X4	99XX6316X4	18:47:16	1
10	99XX6215X5	99XX6316X5	18:55:03	3

D. Graph plotting to identify perpetrators.

We desperately need more tests to find our culprit. The above CDR (Table 1) can be combined with the CDR data set. CDRs for previous cases and linked hoodlums can be found in the CDR database. We can only assume there's a link between these visitors and another scheme involving veteran situations.That would be a nice place to start if we believe we observe such a visitor. The number of suspects can be decreased from thousands to hundreds if a sufficient amount of testing is done[6].Table 2 depicts one such scenario. Table 2 contains lines that allude to visitor numbers that have something to do with the convicted offender. We're currently putting together a CDR of ideas (last 30-50 days). These CDRs can be linked to the CDR database for additional inquiry to see whether they have any ties to the relevant criminals or are part of previous cases[4]. This is our suspects' second point of contact.The visual effects of their association may look as shown in Figure 4:

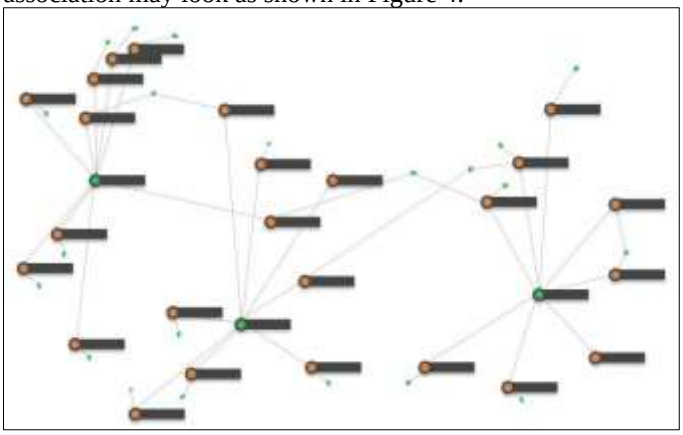


Figure 3: Graph for calls made up to second degree connection of all the probable suspects.

TABLE 2. POSSIBLE SUSPECTS (HIGHLIGHTED ROWS)

S. No	Dialer's Number	Reciever's Number	Time (in hrs)	Duration (in mins)
1	99XX6216X1	99XX6316X1	18:15:05	5
2	99XX6216X2	99XX6316X2	18:20:19	6
3	99XX6216X3	99XX6316X3	18:27:37	1
4	99XX6216X4	99XX6316X4	18:29:28	7
5	99XX6216X5	99XX6316X5	18:31:48	2
6	99XX6215X1	99XX6315X1	18:33:26	8
7	99XX6215X2	99XX6315X2	18:40:59	8
8	99XX6215X3	99XX6315X3	18:46:08	4
9	99XX6215X4	99XX6315X4	18:47:16	1
10	99XX6215X5	99XX6315X5	18:55:03	3

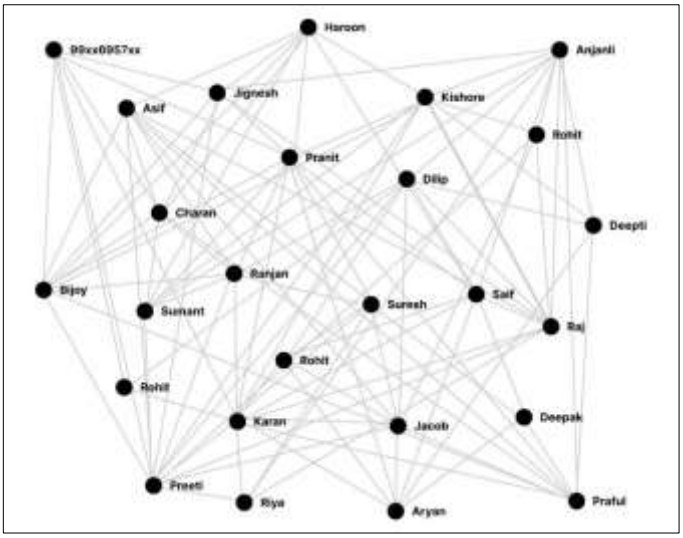


Figure 4: Network of users with anti-social elements.

The calls made by each of our suspicions are shown above. We need to track down the persons our suspicions are calling in order to figure out who they are. Figure 4 depicts the defendants' apparent exposure as well as their interactions with authorities related to the section of the wrongdoing recorded in the police report. As you can see from Figure 4, investigators recognise individual names. It can be implied from the CDR police database acknowledges the offender's name, so compiling a number against a number is a word you can think of. This provides easy access for the observer to separate the connection. The representation of the drawing makes it easy to look for and find related people. The diagram above depicts how our suspects are organised. Remote testing with Excel or normal scientific tools would be required for that data.

V. USING GRAPH THEORY AND CHURN PREDICTION

After separating the suspects, the next step is to visually inspect their organisation to zero down the suspect. Currently, in our model, we would find observation of 3 suspects with police history, 99XX6216X2, 99XX6215X4 and 99XX6216X3. Figure 4 shows the organisation of our 3 suspects and a convicted criminal on a police record. The diagram is really thick, and in this way, it is difficult to read and analyse. From the chart above, we can select any suspects to see the accused and convicted organisations, as shown in Figure 5.

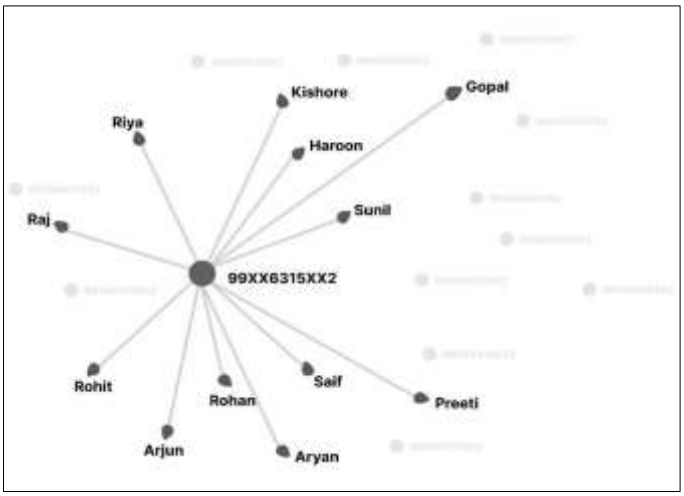


Figure 5: Connections of users with convicted criminals.

After investigating the suspected perpetrator associated with the alleged offenders, the police inspector is unable to identify many of the suspects' suspects without hesitation. The strength and weight of the interactive feature can be determined by the variable dynamics such as the number of calls, traded messages and more. In our model case, suspect 99XX6315X2 is closely related (Figure 6) to two convicted conspirators: Rohan and Arjun The agent also found the criminal history or background of Rohan and Arjun who had been involved in similar crimes. Rohan and Arjun are not involved in the criminal investigation we are investigating. Still, they are in contact with a suspect (for example, 99XX6315X2 about our situation) and possibly a criminal who has done so. We should focus on our testing of him.

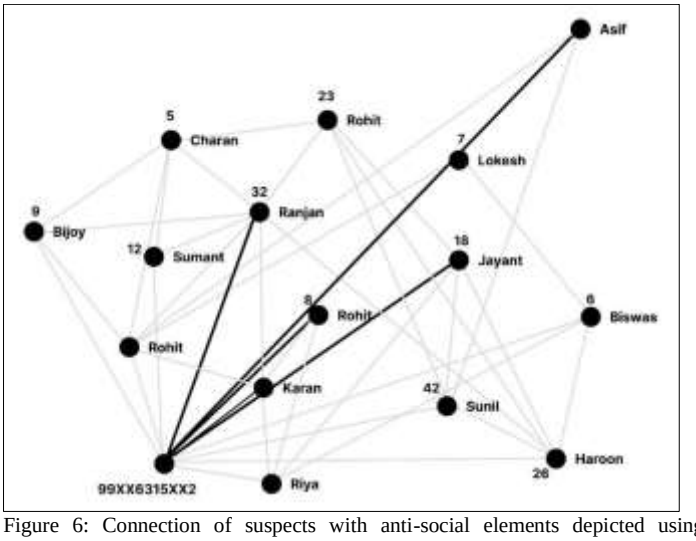


Figure 6: Connection of suspects with anti-social elements depicted using weighted graphs.

VI. CONCLUSION

With the help of our proposed model, not only can we utilise it for crime detection. We can single out suspects to narrow down on the list of perpetrators. To achieve this result, we used the our

own to power the charts, which gave us an amazing insight into case-cutting. Negative testing is one of the areas where diagram testing can be used, as well as additional human strategies, to gain experience in complex knowledge. Examining the case using the CDR document may provide additional information if comments are made from the profiles of the organisation of convicted and convicted offenders[17]. As the informal community enjoys more information about the individual, it is often very helpful in testing[16]. We are currently trying to accommodate investigative procedures using CDR next to the Social Network profile appropriately[7].

As a large dataset of CDR is being used hence storing CDR records and their retrieval might be a problem which can be done using hive based retrieval optimization technique[18].

ACKNOWLEDGMENT

Thanks to the contributions of many people, we were able to complete our task and achieve academic success. We would like to express our gratitude to everyone who has helped us. We owe a special debt of gratitude to Dr. Rajesh Kumar Yadav for his indispensable supervision and guidance throughout the project. His motivation and direction have been essential to our development. We also want to thank the department's lecturers for their unwavering encouragement and motivation. Not least of all, we appreciate our parents' support during these tough times.

REFERENCES

[1] F. Ozgul, C. Atzenbeck, A. Celik and Z. Erdem, "Incorporating data sources and methodologies for crime data mining," Intelligence and Security Informatics (ISI), 2011 IEEE International Conference on, Beijing, 2011, pp. 176-180.

[2] Lawrence McClendon and Natarajan Meghanathan, "Using Machine Learning To Analyze Crime Data", Machine Learning and Applications: An International Journal (MLAIJ) Vol.2, No.1, March 2015.

[3] Weiss, G.M. Data Mining in Telecommunications. In Data Mining and Knowledge Discovery Handbook; Springer: Boston, MA, USA, 2005; pp. 1189–1201.

[4] H. Chen, W. Chung, J. J. Xu, G. Wang, Y. Qin and M. Chau, "Crime data mining: a general framework and some examples," in Computer, vol. 37, no. 4, pp. 50-56, April 2004.

[5] Ilona Murynets and Roger PiquerasJover. 2012. Crime scene investigation: SMS spam data analysis. In Proceedings of the 2012 ACM conference on Internet measurement conference (IMC '12). ACM, New York, NY, USA, 441-452.

[6] Scott, J. Social Network Analysis: Developments, Advances, and Prospects. Soc. Netw. Anal. Min. 2011, 1, 21–26.

[7] Scott, J. Social Network Analysis; Sage Publications: Thousand Oaks, CA, USA, 2012.

[8] R. Becker et al., "Clustering anonymized mobile call detail records to find usage groups", Proc. PURBA, pp. 1-8, Jun. 2011.

[9] Richter, Y.; Yom-Tov, E.; Slonim, N. Predicting Customer Churn in Mobile Networks through Analysis of Social Groups. In Proceedings of the SIAM International Conference on Data Mining (SDM 2010), Columbus, OH, USA, 29 Apri–1 May 2010; pp. 732–741.

[10] Wei, C.P.; Chiu, I.T. Turning Telecommunications Call Details to Churn Prediction: A Data Mining Approach.

[11] Nadaf, M.; Kadam, V. Data Mining in Telecommunications. Int. J. Adv. Comput. Theory Eng. 2013, 2, 92–96.

[12] Wasserman, S.; Faust, K. Social Network Analysis: Methods and Applications; Cambridge University Press: Cambridge, UK, 1994.

[13] Hung, S.Y.; Yen, D.C.; Wang, H.Y. Applying Data Mining to Telecom Churn Management. Expert Syst. Appl. 2006, 31, 515–524. [CrossRef]

[14] Amin, A.; Rahim, F.; Ramzan, M.; Anwar, S. A prudent based approach for customer churn prediction. In Proceedings of the International Conf. Beyond Databases, Architectures and Structures (BDAS 2015), Ustron´, Poland, 26–29 May 2015; pp. 320–332.

[15] Amin, A.; Al-Obeidat, F.; Shah, B.; Adnan, A.; Loo, J.; Anwar, S. Customer churn prediction in telecommunication industry using data certainty. J. Bus. Res. 2019, 94, 290–301. [CrossRef]

[16] Yang, C.; Shi, X.; Jie, L.; Han, J. I Know You'll Be Back: Interpretable New User Clustering and Churn Prediction on a Mobile Social Application. In Proceedings of the 24th ACM SIGKDD International Conference on Knowledge Discovery & Data Mining, London, UK, 19–23 August 2018; pp. 914–922.

[17] Xevelonakis, E.; Som, P. The impact of social network-based segmentation on customer loyalty in the telecommunication industry. J. Database Mark. Cust. Strategy Manag. 2012, 19, 98–106. [CrossRef]

[18] Droftina, U.; Štular, M.; Košir, A. A diffusion model for churn prediction based on sociometric theory. Adv. Data Anal. Classi. 2015, 9, 341–365. [CrossRef]

[19] Peng, X., Liu, L., & Zhang, L. (2020). A Hive-Based Retrieval Optimization Scheme for Long-Term Storage of Massive Call Detail Records. IEEE Access, 8, 431–444. https://doi.org/10.1109/access.2019.2961692

[20] Dileep, G. K., & Sajeev, G. P. (2021, July 1). A Graph Mining Approach to Detect Sandwich Calls. https://doi.org/10.1109/CONECCT52877.2021.9622627

AUTHORS

First Author – Rajesh Kumar Yadav, Assistant Professor, Delhi Technological University, Delhi, India, 110042,
Second Author – Areeshaa Parveen, Student, Delhi Technological University, Delhi, India, 110042,
Third Author – Archit Gupta, Student, Delhi Technological University, Delhi, India, 110042,

Correspondence Author – Areeshaa Parveen, Student, Delhi Technological University, Delhi, India, 110042.

2023 IEEE 8th International Conference for Convergence in Technology (I2CT)
Pune, India. Apr 7-9, 2023

Forest Fire Detection using Convolutional Neural Network Model

Shubham Sah
Department of Software Engineering
Delhi Technological University
Delhi, India
shubhamsah_2k19se121@dtu.ac.in

Suneet Prakash
Department of Software Engineering
Delhi Technological University
Delhi, India
suneetprakash_2k19se130@dtu.ac.in

Shweta Meena
Department of Software Engineering
Delhi Technological University
Delhi, India
shwetameena@dtu.ac.in

2023 IEEE 8th International Conference for Convergence in Technology (I2CT) | 979-8-3503-3401-2/23/$31.00 ©2023 IEEE | DOI: 10.1109/I2CT57861.2023.10126370

***Abstract*— Everyone recalls the destruction brought on by the Australian forest fires in 2019. Even though there isn't much we can do to battle forest fires on our own, we can always rely on technology. By this we are trying to predict the accuracy of these models on forest fire data set. We are trying to detect forest fire in dense forest; our data set is very diverse and consist of images having forest fires, smokes, non-smoke and fire images. We have found out that Sensor detection and real-time geological data analysis are two methods for detecting forest fires. However, using image classification, for which Deep learning is the most efficient solution, is one of the best methods for detecting fire. In addition, these algorithms can be integrated with drones using deep learning techniques so that images can be taken frequently from the sky with ease, smoke can be detected in dense forests, and the authorities can be notified to take immediate action. The convolutional neural network algorithm for fire detection was the sole focus of our paper. The value of various epochs is used to evaluate these results.**

Keywords*— *Machine learning, convolutional neural net- works, algorithms, forest fire.

I. INTRODUCTION

A forest fire detection is a software program that can predict the occurrence of a forest fire by analysing the still images of a forest. To ensure the safety of everyone it is very important to put out the fire before it gets out of control. Experts use a variety of frameworks for observation and discovery. Eyewitnesses for the type of watches or observation peaks are remembered, along with ethereal and satellite checking, more complex discovery and checking frameworks based on optical camera sensors, various types of location sensors, or their combination. The accompanying part provides a brief overview of the world's programmed and self-loading frameworks for fire assurance, as well as practical experience with these frameworks and an appraisal of their effectiveness in terms of proficiency, precision, adaptability, and other important attributes. Forest fire detection refers to the process of identifying the presence of a forest fire and determining its location. This is typically done using a combination of satellite imagery, ground-based Once a forest fire is detected, authorities can be alerted and appropriate action can be taken to contain and extinguish the fire. Before the advance machine learning models to detect forest, fire there were many traditional and manual methods to look out for the forest fire, its range of coverage and alert to the general public. In the past, forest fire detection relied heavily on ground-based systems such as lookout towers and patrols. These methods were effective in some cases, but they were limited in their ability to detect fires quickly, particularly in remote or inaccessible areas. As a result, many fires were not detected until they had already grown to a significant size. With the development of satellite technology, it became possible to detect forest fires from space using specialized sensors. These systems are able to detect the heat and smoke associated with fires, allowing for earlier detection and faster response times. In recent years, other technologies such as aerial surveillance and ground-based sensors have also been used to improve the accuracy and effectiveness of forest fire detection. This project aims to build a machine-learning model that processes image files and classifies them into correct identification of fire or no fire. Different types of machine learning solutions and algorithms are able to solve this problem, like Recurrent Neural Networks (RCONVOLUTIONAL NEURAL NETWORK), Artificial Neural Networks (ANN) and Convolutional Neural Networks (CONVOLUTIONAL NEURAL NETWORK). For this project, we focus on building a CONVOLUTIONAL NEURAL NETWORK that can accurately identify the forest fire using different image files.

A. Uses for forest fire detection

- Protecting human life and property: By detecting forest fires early on, authorities can take action to prevent the fires from spreading and potentially threatening human lives and property.
- Containing and extinguishing the fire: Once a forest fire is detected, firefighters and other emergency responders can be alerted and dispatched to the area to contain and extinguish the fire.
- Reducing the environmental impact of the fire: Forest fires can have devastating effects on the environment, including the destruction of wildlife habitat, air pollution, and soil erosion. By detecting and responding to forest fires quickly, it is possible to minimize these impacts.
- Protecting natural resources: Forest fires can destroy valuable natural resources such as timber, water, and other resources. By detecting and responding to forest fires, authorities can protect these resources and preventsignificant economic losses.

B. Application of Machine Learning

- Sensor-based approach : This method uses many sensors spread out over the forest to help detecting

Authorized licensed use limited to: DELHI TECHNICAL UNIV. Downloaded on May 29,2023 at 05:53:29 UTC from IEEE Xplore. Restrictions apply.

forest fires. These sensors monitor the levels of gases like carbon monoxide and oxygen. The information is then evaluated in conjunction with other elements like temperature and humidity levels. The data collected is then used as a data set to train machine learning models. The machine learning algorithm alerts forest officials of impending forest fires whenever an abnormality is found.

- Image-based approach : A machine learning model has been trained to recognize forest fires in this strategy. The model receives a picture data set of forests and other large areas of vegetation. The models learn to differentiate between photos with and without forest fires after that. The machine learning model can be used by drones with sensors that fly over areas of deep, dense vegetation. Based on what it has learned, the drone sends fire warnings with precise location coordinates automatically. This can help put out a fire before it spreads to a large area.

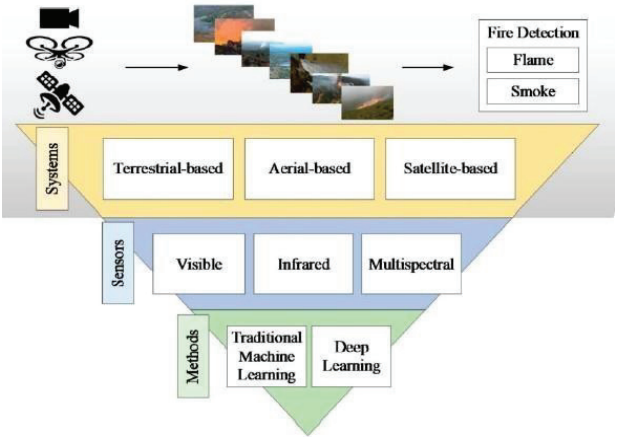


Fig. 1. Application of Machine learning

II. RELATED WORK

A. Literature

Forest fires have the potential to seriously harm the ecosystem, wildlife, and people. Controlling the spread of forest fires and lessening their effect requires prompt detection and action. Deep learning and artificial intelligence (AI) algorithms for detecting forest fires have gained popularity in recent years.

Historically, ground-based and aerial surveillance methods have been used to find forest fires. For instance, to find and watch fires, ground-based monitoring employs routine patrols, lookout towers, and weather sensors. On the other hand, aerial monitoring uses planes and satellites to take pictures and find differences in the vegetation that might be signs of a fire. However, these techniques may not be quick enough to stop fires from spreading and may not be able to spot fires in remote or inaccessible areas.

Convolutional Neural Networks, a type of deep learning model, have been created to identify forest fires using remote sensing data in order to get around these restrictions. Convolutional neural networks are a particular kind of deep learning model that work well for image-based fire detection because they can automatically learn to identify features in images. Numerous studies have shown how well convolutional neural networks work at spotting woodland fires. For instance, the authors of a research that was published in the Journal of Applied Remote Sensing employed a convolutional neural network-based strategy to identify forest fires from satellite images. The suggested method had a 95% detection success rate.

Another research that was published in the Journal of Computational Science suggested a hybrid strategy for detecting forest fires that combined a convolutional neural network-based model with conventional machine learning algorithms. The accuracy of the suggested method in identifying forest fires from aerial pictures was 98%. Recurrent Neural Networks (RNNs) and Long Short-Term Memory (LSTM) networks, in addition to convolutional neural networks, have also been used to identify forest fires from remote sensing data. With accuracy levels between 90% and 99%, these models have produced encouraging outcomes.

As a result, deep learning models like convolutional neural networks have demonstrated significant promise in the detection of woodland fires from remote sensing data. These models can get around the limitations of conventional monitoring methods and offer reliable and on-time forest fire discovery. To improve these models and create more durable and dependable fire detection systems, additional study is necessary.

B. Additional techniques for spotting forest fire

- Visual Detection: This is the oldest and most basic method of spotting forest fires. A person or lookout tower is used to physically scan the forest for any indications of a fire, such as smoke or flames.
- Infrared Detection: Infrared devices or cameras can identify the heat produced by a fire even if no smoke is visible. This technique is especially helpful for finding fires at night or in heavily forested regions.
- Smoke Detection: Smoke sensors can identify the existence of smoke, which is frequently a sign of a fire before it has fully developed. For greater coverage, these sensors can be integrated into wireless sensor networks (WSNs) or put in crucial areas throughout the forest.
- Satellite Imagery: Forest fires can be discovered using remote sensing methods that use satellite footage. This technique involves looking through satellite images for any anomalies, like a rise in temperature or the existenceof smoke.
- Unmanned aerial vehicles (UAVs): UAVs fitted with infrared cameras or other instruments are capable of spotting forest fires. These drones can rapidly cover vast areas and give fire managers real-time data.

III. RESEARCH METHODOLOGY

We have used deep learning techniques for our project “Object Detection using deep learning techniques”. Deep learning can be thought of as a subset of machine learning. The study of computer algorithms is the foundation for independent learning and development in this field. While deep learning makes use of artificial neural networks created to imitate how people think and learn, machine learning is

Authorized licensed use limited to: DELHI TECHNICAL UNIV. Downloaded on May 29,2023 at 05:53:29 UTC from IEEE Xplore. Restrictions apply.

based on more fundamental principles. Networks of convolutional neural networks. The following actions were taken during the construction of our model.

A. Python libraries

Tensor flow is a free software library for artificial intelligence and machine learning. Deep neural network (DNN) work can be utilized for a wide range of tasks . Although deep neural net- work training and inference are given special attention, it can be used for a variety of tasks.

B. Data Augmentation

The accuracy of deep learning models is largely due to the developer's data quality and quantity. We can improve our accuracy by simply adding more data to the data. This extra data is been created keeping two things in mind which are:

- Resizing
- Re scaling

We generated our enriched augmented dataset by scaling and resizing our model and creating more than 7,000 images within it. Parameters which were used to create new data were re-scale units, horizontal flips, vertical flips, zoom and shear range, width shifts and height shift range and at last the validation splits.

C. Training and Validation

To achieve good results, we divided our data into training and validation sets. We are unable to train a machine learning model on a single dataset each time, and even if we do, we will not be able to evaluate its performance. As a result, we divided our source data into datasets for training, testing, and validation.

D. CONVOLUTIONAL NEURAL NETWORK Architecture

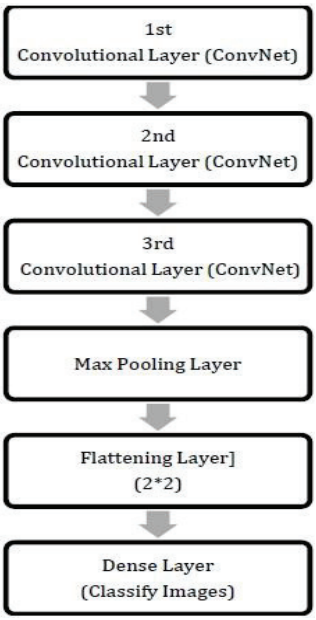


Fig. 2. Convolutional neural network architecture

IV. RESULTS

This section gives out the results which we got through all the experimentations and Final implementation. It includes graphical and visual representations of audio files and of their various features. Also, it consists of the final testing accuracy.

Results:

TABLE I. THE TABLE SHOWS ACCURACY ON DIFFERENT EPOCHS

EPOCHS	Results of CONVOLUTIONAL NEURAL NETWORK	
	LOSS	*ACCURACY*
1/50	0.0254	0.992
2/50	0.0094	0.998
3/50	0.0093	0.9982
4/50	0.0029	0.9992
5/50	0.0026	0.993
6/50	0.0023	0.9994
7/50	0.0017	0.9996
8/50	0.0416	0.9965
9/50	0.0048	0.9991
10/50	0.0048	0.9965

The graph shows accuracy of convolutional neural network model on varied Epochs.

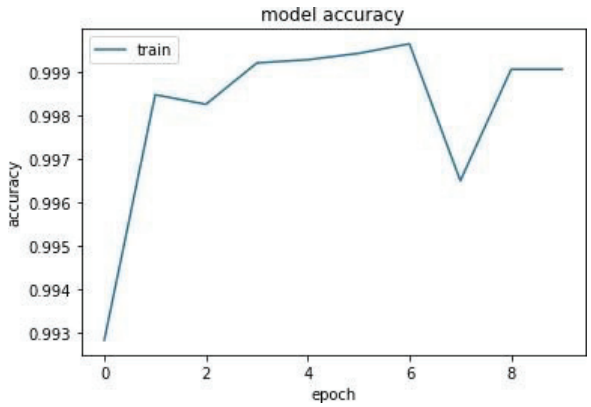


Fig. 3. Graphical representation of Accuracy vs epoch

The graph shows change in loss of convolutional neural networkmodel on varied Epochs.

Authorized licensed use limited to: DELHI TECHNICAL UNIV. Downloaded on May 29,2023 at 05:53:29 UTC from IEEE Xplore. Restrictions apply.

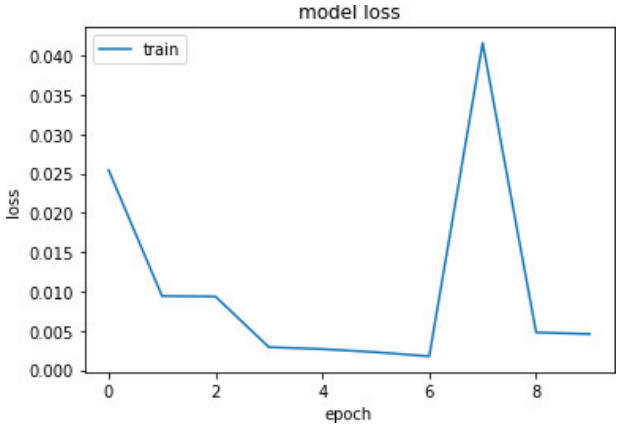


Fig. 4. Graphical representation of Loss vs epoch

Our convolutional neural network model correctly predicted whether an image is a fire or smoke

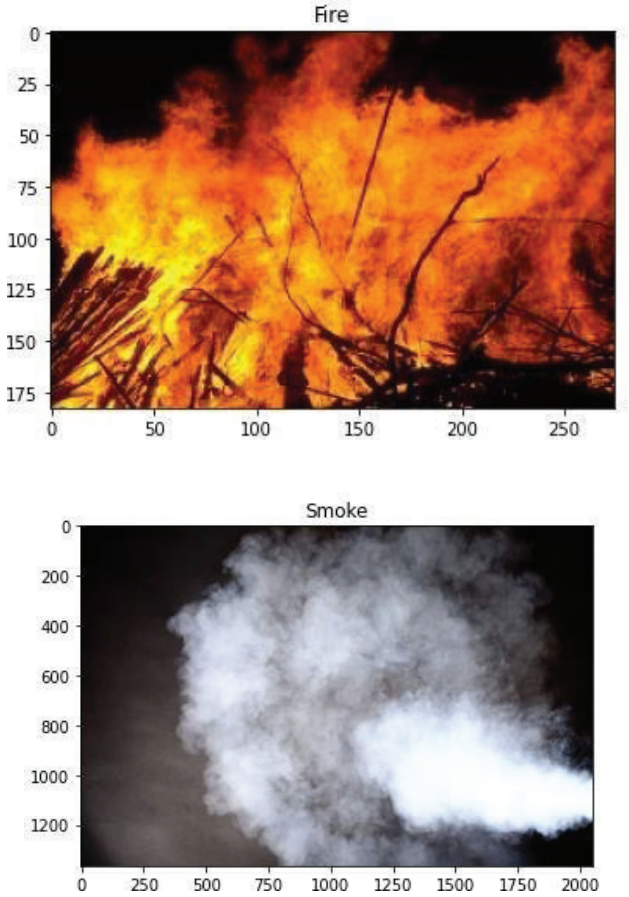


Fig. 5. Fire and Smoke Detected

V. LIMITATIONS

This section looks as to what are the different threats or limitations that are there in the method that have been used for the project and approaches used.

A. Threats to validity

Our model was created using a pre-defined dataset with fewer photos than the large Deep learning models. This model is only capable of developing results of photos which is a drawback of our model and we will be working on detecting fire from real- time video surveillance method. The use of video would be a practical and effective technique to deal with forest fires since it can provide precise information on the effects that are actually beneficial or falsely negative. Our model explains the most effective method for identifying a fire in an image based on our successful results with convolutional neural network. By combining geological data, such as a change in temperature in a specific forest region or any change in the environmental factor that helps identify the forest fire, regression can be used to evaluate the data. The validity of our model will be enhanced by these elements. By comparing our model to geological data, we could determine which area is most susceptible to forest fires, and we could then use a drone to take pictures there. By doing so we may raise the percentage of accuracy to detect fire in the forest with our deep learning models.

VI. CONCLUSION

Artificial intelligence in sustainability can be used to fight forest fires and prevent them from starting in the first place. Fire is the most dangerous abnormal event because, if not controlled at an early stage, it can cause enormous disasters that result in losses in terms of human, ecological, and financial resources. AI, machine learning, and other related technologies have enormous potential in the fire and safety domain. The cameras can be used to identify fire accidents. As a result, we have here suggested a convolutional neural network approach for using cameras to detect fires. Our method can locate the fire that is being monitored by cameras.

Additionally, our suggested solution uses dataset tweaking to strike a compromise between the size of the model and the accuracy of fire detection. For convolutional neural network, we found accuracy of 99 percent. These numbers demonstrate how much better the model's forecast is. We have done experiments using datasets gathered from fire recording, and we have compared the results to our suggested system. The convolutional neural network model's adequate accuracy for fire detection, the size of the fire, and the frequency of false alarms can all help emergency response teams quickly contain fires.

A. Future Work

Goal of the project is to identify fire occurrences that are being monitored. Future work might concentrate on building demanding and accurate data set. Natural catastrophes cause hundreds of billions of dollars' worth of property damage and thousands of deaths each year. For decades, experts have struggled with ways to mitigate the consequences of catastrophic disasters to save lives and protect infrastructure. However, a potential next step is to use AI to identify natural calamities. During calamities, AI may support communities, individuals, and livelihoods.

REFERENCES

[1] Kinaneva, D., Hristov, G., Raychev, J., Zahariev, P. Early forest fire detection using drones and artificial intelligence. In 201942nd International Convention on Information and Communication Technology, Electronics and Microelectronics (MIPRO) (pp. 1060 - 1065). IEEE 2019.

[2] Festag, S. Analysis of the effectiveness of the smoke alarm obligation–Experiences from practice. Fire safety journal, 119, 103263, 2021.

Authorized licensed use limited to: DELHI TECHNICAL UNIV. Downloaded on May 29,2023 at 05:53:29 UTC from IEEE Xplore. Restrictions apply.

[3] Sun, F., Yang, Y., Lin, C., Liu, Z., Chi, L. ForestFire Compound Feature Monitoring Technology Based on Infrared and Visible Binocular Vision. In Journal of Physics: Conference Series (Vol. 1792, No. 1, p. 012022). IOP Publishing, 2021.

[4] Alkhatib, A. A, "A review on forest fire detection techniques", International Journal of Distributed Sensor Networks, 10(3), 597368, 2014.

[5] Guede-Ferna´ndez, F., Martins, L., de Almeida, R. V., Gamboa, H., Vieira, P.. A deep learning based object identification systemfor forest fire detection. Fire, 4(4), 75, 2021.

[6] Dubey, V., Kumar, P., Chauhan, N. Forest fire detection system using IoT and artificial neural network. In International Conference on Innovative Computing and Communications (pp. 323-337). Springer, Singapore, 2019.

[7] Mahmoud, M. A. I., Ren, H. Forest fire detection and identification using image processing and SVM. Journal of Information Processing Systems, 15(1), 159-168, 2019.

[8] Parashar, A., Biswas, S. The impact of forest fire on forest biodiversity in the Indian Himalayas (Uttaranchal). In XII World Forestry Congress (Vol. 358), 2003.

[9] P. Barmpoutis, P. Papaioannou, K. Dimitropoulos, & Grammalidis, N. A review on early forest fire detection systems using opticalremote sensing. Sensors, 20(22), 6442, 2020.

[10] Jiao, Z., Zhang, Y., Xin, J., Mu, L., Yi, Y., Liu, H., & Liu, D. A deep learning-based forest fire detection approach using UAV and YOLOv3. In 2019 1st International conference on industrial artificial intelligence (IAI) (pp. 1-5), 2019.

[11] Yuanbin W, Xianmin M. Fire Detection Based on Image Processing in CoalMine.Internet Computing & Information Services (ICICIS), 2011 InternationalConference on. IEEE, Proc.431-434, 2011.

[12] Yang, X., Tang, L., Wang, H., He, X. Early detection of forest fire based on unmaned aerial vehicle platform. In 2019 IEEE International Conference on Signal, Information and Data Processing (ICSIDP) (pp. 1-4). IEEE, 2019.

[13] Pan, H., Badawi, D., Zhang, X., Cetin, A. E. Additive neural network for forest fire detection. Signal, Image and Video Processing, 14(4), 675-682, 2020.

[14] Zhang, J., Zhu, H., Wang, P., Ling, X. ATT squeeze U- Net: a lightweight network for forest fire detection and recognition. IEEE Access, 9, 10858-10870, 2021.

[15] Xue, Z., Lin, H., Wang, F. A Small Target Forest Fire Detection Model Based on YOLOv5 Improvement. Forests, 13(8), 1332, 2022.

[16] Dampage, U., Bandaranayake, L., Wanasinghe, R., Kottahachchi, K., Jayasanka, B. Forest fire detection system using wireless sensor networks and machine learning. Scientific reports, 12(1), 1-11, 2022.

[17] Khan Muhammad, Jamil Ahmad, Sung Wook Baik. Early fire detection using convolutional neural networks during surveillance for effective disaster management, 2017.

[18] Ahmed M. Elshewey, Amira. A. Elsonbaty. Forest Fires Detection Using Machine Learning Techniques, 2020.

[19] Xu, R., Lin, H., Lu, K., Cao, L., Liu, Y. A forest fire detection system based on ensemble learning. Forests, 12(2), 217, 2021.

Authorized licensed use limited to: DELHI TECHNICAL UNIV. Downloaded on May 29,2023 at 05:53:29 UTC from IEEE Xplore. Restrictions apply.

2023 10th International Conference on Signal Processing and Integrated Networks (SPIN) | 978-1-6654-9099-3/23/$31.00 ©2023 IEEE | DOI: 10.1109/SPIN57001.2023.10116674

FPGA IMPLEMENTATION OF A HIGH THROUGHPUT LOW POWER ADVANCED ENCRYPTION STANDARD (AES-128) CIPHER

Jaideep kala
Department of Electronics and Communication
Delhi Technological University
New Delhi, India
jaideepkala_2k21spd04@dtu.ac.in

Jeebananda Panda
Department of Electronics and Communication
Delhi Technological University
New Delhi, India
jpanda@dce.ac.in

Lavi Tanwar
Department of Electronics and Communication
Delhi Technological University
New Delhi, India
lavi.tanwar@dtu.ac.in

***Abstract*— Ensuring secure transmission and storage of digital information is critical for any organization to function properly. To address this issue, encryption algorithms are commonly used. Advanced Encryption Standard (AES) has been globally adopted as the mainstay cipher algorithm for securing transmission networks and storage devices due to its easy implementation and compatibility with both hardware and software applications. Another reason for its widespread popularity is its uncompromisable nature against existing brute force attacks, making it practically unbreakable on existing computing power. AES implementation for battery operated devices requires an algorithm with low power consumption and high-speed encryption/decryption of digital data. This paper proposes an FPGA implementation of a high throughput parallel pipelined 128-bit AES algorithm with a low power key expansion mechanism for iterative stages. A 128-bit symmetric key has been used for undertaking 10 rounds of transformations. All the encryption and decryption transformations are simulated using iterative design methodology in order to minimize hardware consumption. Xilinx Artix-7 FPGA device is used for hardware evaluation and Verilog HDL for programming. Simulation and synthesis task has been performed on Xilinx Vivado v2021.1 IDE. The results exhibit high-rate encryption of 68 Gb/s and low energy consumption of 7 pJ/bit.**

Keywords*— *AES, Encryption, FPGA, Low Power, Secure, Simulation, Throughput.

I. INTRODUCTION

Information security is a critical part of any communication system. At the heart of this security system is a cryptographic algorithm that manipulates the input message or plain text into cipher text with the help of a key [1]. An Encryption algorithm ensures that data is safely transmitted from sender to the receiver without any unauthorized manipulations or attacks. Advanced encryption standard (AES) is widely used encryption algorithm that has been adopted globally by governments and organizations for secure communication and data storage. Developed by National Institute of Standards and Technology in the year 2001, AES is a symmetric key cipher with a fixed block size of 128 bits. Meaning it uses the same key for encryption and decryption process and all operations are performed on 128 bits of data [2]. AES is the successor of Data encryption standard (DES) algorithm which was prone to hacking hence needed to be replaced by a much stronger algorithm. AES utilizes cipher key of sizes 128,192 and 256 bits for encryption hence making it one of the most secure and robust algorithms. It has proven to be safe from brute force attacks with not a single registered case of its failure against known attacks. Encryption techniques like AES are based on Shannon's theory of confusion and diffusion (1945) [3]. Here confusion aims at complicating the relationship between cipher message and symmetric key whereas diffusion aims at dispersing the features of input message throughout the encrypted message. It can be efficiently used for both hardware and software applications One of the major limitations of AES algorithm is its high computational complexity which leads to high power consumption, making it less suitable for battery operated devices. Another area for improvement in AES is the speed of the algorithm [4]. Faster encryption and decryption processes are highly desirable for real time communication and data storage. For hardware implementation, AES algorithms that takes less area for implementation, has high throughput and low power consumption are preferable and is a topic of constant research [5].

II. LITERATURE SURVEY

There have been significant efforts in the past aimed at reducing the power consumption and increasing throughput of the AES algorithm. Bui et al. [6] proposed a hardware optimization strategy for AES implementation in ultra-low power IoT applications to provide multilevel security using different key sizes. Power and energy optimization has been performed for both data path and key expansion. This led to significant reduction in energy per bit to a value of 1 pJ/b at 10 MHz at 0.6 V and throughput of 28 Mb/s. Duran et al. [7] proposed an AES-128/256 S-box acceleration scheme which uses a custom S-box unit connected as a logic unit. All S-box calculations were performed using pipelined and pure combinational approach resulting in lower memory access and lower energy consumption of 9.7 pJ/bit. A large portion of the energy consumed in an AES circuit is during the substitution process, hence S-box architecture plays a crucial role. Morioka et al. [8] proposed a low power S-box architecture in which signal arrival time at gates are very close if their depth from main input is identical. This led to a minimalistic power consumption of 29 μW at 10 MHz using 0.13 μm CMOS technology. In recent studies, pipelining of AES architecture has proven to significantly increase the throughput of the encryption system and accompanied power reduction. Chellappa et al. [9] proposed a fully pipelined 256-bit AES design with pulse clocked latches connecting the pipeline stages that can be made transparent when in use resulting a 7.6% decrease in energy. This design could deliver 64 Gb/s encryption when fabricated on 90 nm technology. Oukili et al. [10] presented a 5-stage pipeline S-box design to increase the maximum speed and frequency of the AES system. S-box transformations plays a crucial role in the complexity of AES algorithm therefore parallel processing using pipelined stages helped the proposed method to achieve a throughput of 79 Gbps. Kshirsagar et al. [11] proposed interchanging of byte substitution and shift rows operations in the AES implementation which helped to streamline the processing of 16 data blocks into 4 parallel blocks of data. This led to significant reduction in hardware area consumption by 56%

Authorized licensed use limited to: DELHI TECHNICAL UNIV. Downloaded on May 15,2023 at 07:04:33 UTC from IEEE Xplore. Restrictions apply.

and increasing the throughput by 4.25%. Contributions of the proposed algorithm are:

- This paper intends to incorporate power saving strategies and obtaining high throughput using parallel pipelined 128-bit AES.
- Maintaining design simplicity.
- Ease of implementation.
- Low hardware area consumption.

III. Methodology

AES algorithm makes use of iterative process to obscure the relationship between the key and the cipher text. Each iteration step performs fixed number of substitutions and permutations to encrypt the input message. The number of iterations depends on the size of the cipher key used. Key can be of size 128,192 and 256 bits and subsequently the number of iterations are 10,12 or 14 respectively. Similarly, during the decryption process the encrypted message is passed through these iterative steps in reverse order to obtain the original input message. Each of these steps consists of four processes named (1) Substitute bytes (2) Shift rows (3) Mix Column (4) Add round keys the details of which has been discussed in brief in this section [12]. Before the first iteration is performed, a pre round transformation takes place along with key expansion in which the size of cipher key is extended from 4 words (in case of 128 bits key) to 44 words, where each word is of size 4 bytes. Four words of this expanded key is then supplied to each of the 10 iterative rounds as well as to the pre-round transformation. All operations on the data are performed on a block size of 128 bits in the AES irrespective of the key size, hence the input message is divided into 4x4 matrices where each element in the matrix is of size 1 byte. After each operation the results are stored in a 4x4 intermediate state matrix on which further operations are performed [13]. Figure 1 shows the flow of input data through N rounds of transformation where each round is provided with extended key. The cipher key is first XORed with the input data matrix in the pre-round transformation to produce the state matrix which then acts as the input for subsequent rounds.

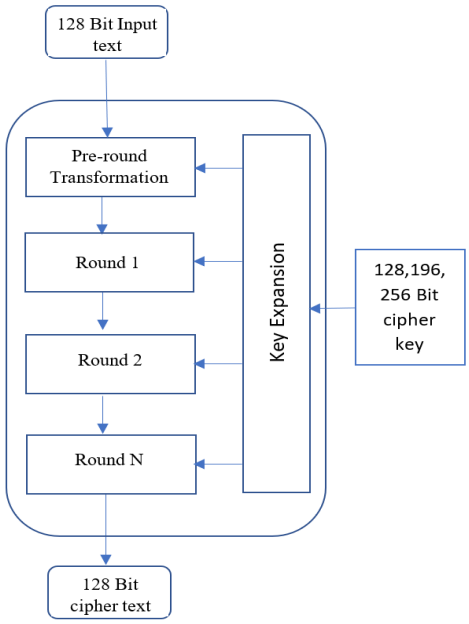


Fig.1. Block diagram of N rounds 128-bit AES algorithm.

A. Key Expansion

The cipher key is supplied by the user as a plain text which is first converted to hexadecimal form. Consider a 128 bit key arranged in the form of a 4x4 matrix with each column representing a 4 byte word as shown in Figure 2. This 4-word representation of the original key is expanded to 44 words and supplied to the pre-round transformation stage along with 10 transformation rounds [14]. The first 4 words of the expanded key representation is the original key itself which is XORed with the input message (in hex) and the intermediate state matrix is passed on to round 1 as input.

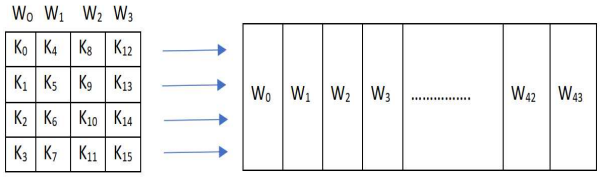


Fig.2. Key Expansion process for 128-bit symmetric key.

Figure 3 depicts the process of obtaining the next four words (W_4-W_7) from the first 4 words (W_0-W_3) of the original cipher key using the "g" function.

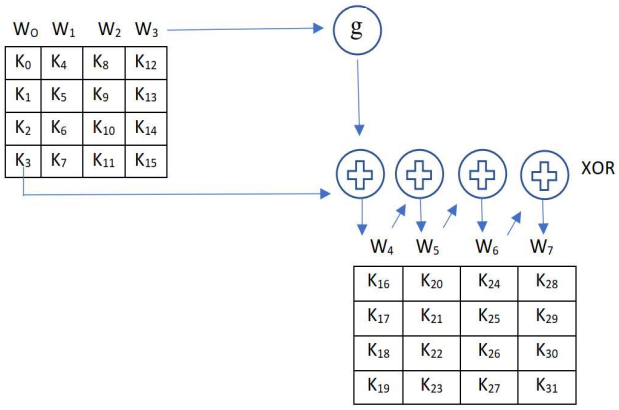


Fig.3. Key expansion operation for obtaining next 4 key words.

Mathematically this can be defined as:

$$W_4 = W_0 \oplus g(W_3) \quad (1)$$

$$W_5 = W_4 \oplus W_1 \quad (2)$$

$$W_6 = W_5 \oplus W_2 \quad (3)$$

$$W_7 = W_6 \oplus W_3 \quad (4)$$

Here $g(W_3)$ is obtained by performing a 3-step process, one-byte circular left shift of the word W_3 to get X_1 and then performing a byte substitution on each byte of X_1 using S-box to get Y_1.

Finally,

$$g(W_3) = Y_1 \oplus R_{CON}[j] \quad (5)$$

Here $R_{CON}[j]$ is the round constant described for each iteration round as shown in Table 1.

Authorized licensed use limited to: DELHI TECHNICAL UNIV. Downloaded on May 15,2023 at 07:04:33 UTC from IEEE Xplore. Restrictions apply.

Table 1. Round constant table for 10 rounds of transformation in AES.

R1	R2	R3	R4	R5	R6	R7	R8	R9	R10
01	02	04	08	10	20	40	80	1B	36
00	00	00	00	00	00	00	00	00	00
00	00	00	00	00	00	00	00	00	00
00	00	00	00	00	00	00	00	00	00

Figure 4 depicts the four processes in round 1 to 9 of the 128-bit AES algorithm with a cipher key size of 128 bit. The final round R10 has only 3 internal processes as the Mix column operation is excluded from it.

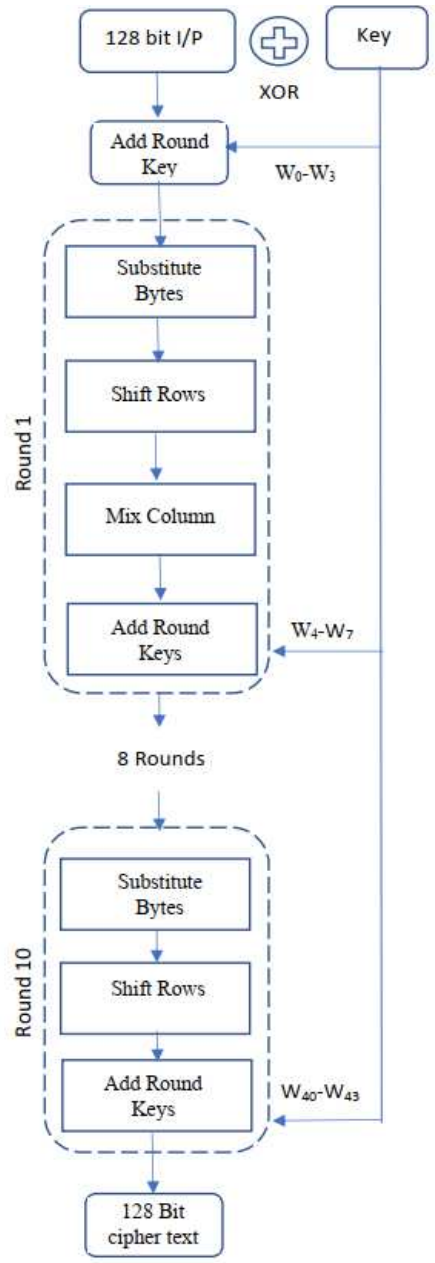


Fig.4. XOR of expanded key with each round of AES.

B. Substitute Bytes

Substitute byte forms the first step in each round. Here the output of pre-round transformation is used as an input to this step in which the elements of intermediate state matrix are replaced using an S-box table as shown in Figure 5. S-box is a major component of any cryptography algorithm, which performs substitution. It is a 16x16 Look Up Table (LUT) with its elements ranging from 00 to FF. Substitution has the largest share in power consumption and is one of the most complex process in the entire algorithm [15].

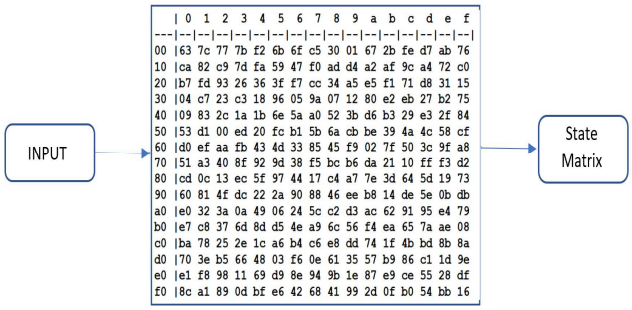


Fig. 5. Substitution byte transformation using 16x16 S-box

C. Shift Rows

The result obtained from substitution then undergoes shift rows operation in which circular left shift is performed on the state array as shown in figure 6. There is no shift in the first row of the matrix, a 1-byte circular left shift in second row, followed by 2 and 3 bytes circular left shift in row 3 and 4 respectively [16].

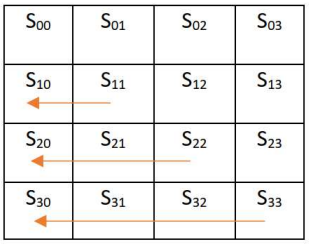


Fig 6. Shift rows operation on 128-bit block size data

D. Mix Columns

In this step, the state matrix obtained from shift row operation undergoes word by word multiplication with a constant matrix as shown in figure 7 [17].

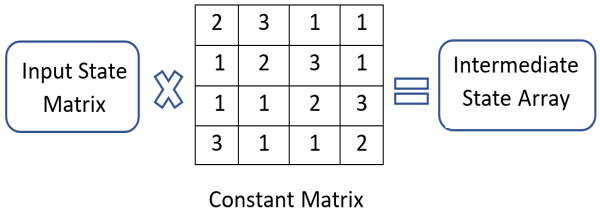


Fig. 7. Multiplication of state matrix with constant matrix

Authorized licensed use limited to: DELHI TECHNICAL UNIV. Downloaded on May 15,2023 at 07:04:33 UTC from IEEE Xplore. Restrictions apply.

E. Add Round Keys

In this final step round keys are XORed with the output obtained from mix column operation and the results are passed on to the next round [18]. After all the 4 steps are performed iteratively for all the 10 rounds final cipher text is obtained. This encrypted message is in hexadecimal form. For performing decryption, a similar approach is undertaken where the encrypted message is passed through the 10 rounds of transformation with inverted Mix Columns and inverted shift rows. An inverted S-box is used in the substitute bytes step and the output obtained is the original message in hexadecimal form which can be further converted to plain text.

F. Pipelined Architecture

All operation inside the AES is performed on 128-bit block size of data, that means the input message (in hex) needs to be broken to and presented in 128-bit 4x4 matrices before being processed inside the AES [19]. Since the data blocks passes through the 10 iterative rounds in a sequential manner therefore only one block is processed at a given time in a particular round leaving the subsequent stages unused or idle. Parallel pipelining enables multiple data blocks to be processed parallelly in different stages hence making the encryption process of large messages or images faster [20].

IV. Results

To perform encryption of "*sample message 1*" with 128 bit key "*secure password1*" the resulting 128-bit encrypted output will be "786e4e6532761c57e253cc34814c233c".

The decryption module will take this 128-bit hexadecimal encrypted data as input and same 128 bit key as input to generate the decipher text message "sample message 1". The energy consumed per bit in transformation during the entire process was 7 pJ/bit and throughput of encrypted results was 68 Gbps. Figure 8 and 9 shows the produced encryption and decryption outputs.

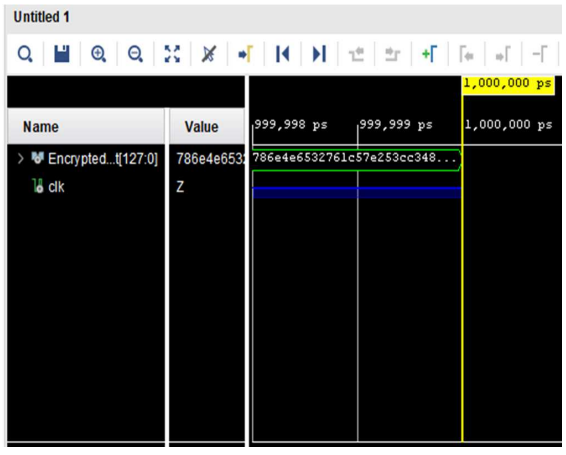


Fig. 8. Encrypted 128-bit hexadecimal output.

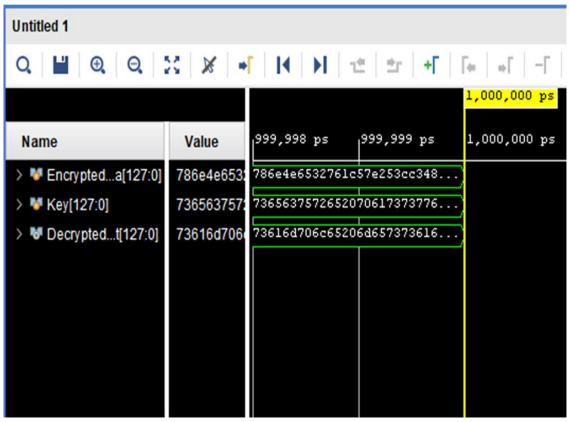


Fig. 9. Shows the Encrypted 128-bit hexadecimal results and decrypted message.

Xilinx Artix-7 FPGA device based on 28nm technology was used for hardware evaluation and Verilog HDL for programming. This FPGA provides highest performance/watt and has 215,360 logic cells for design implementation. For the AES-128 implementation, a total of 23,689 logic cells were used which comes to about 11% resource utilization on the FPGA. Simulation and synthesis task has been performed on Xilinx Vivado v2021.1 IDE. Figure 10 shows simulation of the given algorithm run for 1000ns and the encryption status in Vivado tcl console, peak memory used, gain, and time elapsed in producing simulation results.

```
# run 1000ns
Encrypted_Message = 786e4e6532761c57e253cc34814c233c
Decrypted_output = sample message 1
Encryption success!
xsim: Time (s): cpu = 00:00:13 ; elapsed = 00:00:10 . Memory (MB): peak = 2137.082 ; gain = 32.738
INFO: [USF-XSim-96] XSim completed. Design snapshot 'TB_behav' loaded.
INFO: [USF-XSim-97] XSim simulation ran for 1000ns
launch_simulation: Time (s): cpu = 00:00:17 ; elapsed = 00:00:50 . Memory (MB): peak = 2137.082 ; gain = 38.902
```

Fig. 10. simulation runtime and status of encryption.

Figure 11. shows the AES top module in Xilinx Vivado simulator with 128 bits of input data and cipher key and the clock pulse. Dataout[127:0] is the encrypted output message in hex form. Figure 12. Shows the Rounds operation module with datain[127:0], keyin[127:0], clk, rc[3;0] input vectors and keyout[127:0], rndout[127:0] output vectors.

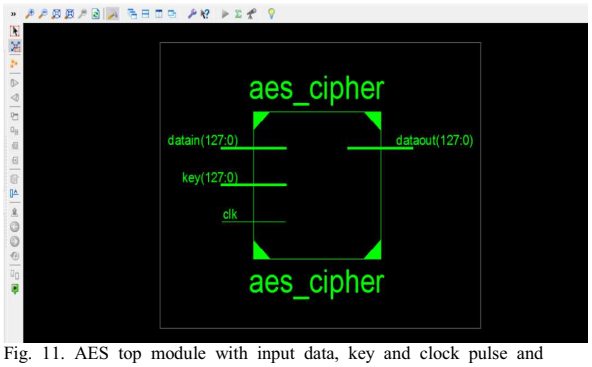


Fig. 11. AES top module with input data, key and clock pulse and encrypted output.

Authorized licensed use limited to: DELHI TECHNICAL UNIV. Downloaded on May 15,2023 at 07:04:33 UTC from IEEE Xplore. Restrictions apply.

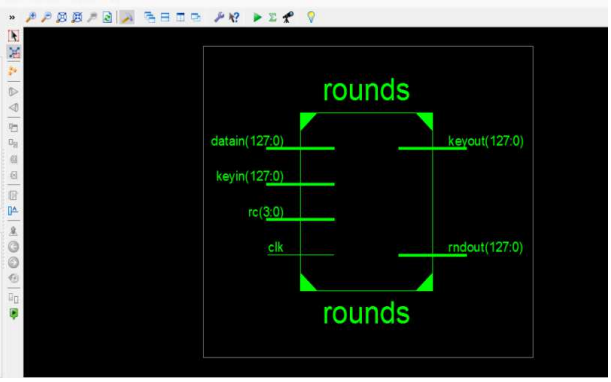


Fig. 12. Round transformation module with its input and output vectors

Table 2. shown below provides a variation in the energy/bit (pJ/b) of the design with varying temperature in kelvin at various input supply voltages (V).

Table 2. Energy/bit variation with temperature and input voltage

S. No	Temperature (K)	Input Voltage (V)	Energy/bit (pJ/b)
1	290	0.9	7
2	300	1	7.09
3	310	1.05	7.23
4	320	1.1	8.10

Table 3. shown below provides a variation in the dynamic power (W) and the leakage power (W) at various input supply voltages (V).

Table 3. Input voltage vs dynamic and leakage power

S. No	Input Voltage (V)	Dynamic Power (W)	Leakage Power (W)
1	0.9	0.69	0.09
2	1	0.83	0.11
3	1.05	0.9	0.12
4	1.1	1.01	0.14

Table 4 shown below provides a comparison of the throughput and energy consumed in per bit transformation of the presented parallel pipelined architecture with existing work.

Table 4. Result comparison of presented method with existing research.

S.No	Author	Algorithm	Through-put	Energy	Frequency
1	D.H Bui (2017) [6]	Data Path optimization	28 Mb/s	1 pJ/bit	10 MHz
2	C. Duran (2022) [7]	S-box acceleration	-	9.7 pJ/bit	100 MHZ
3	S. Chellapa	Fully Pipelined	64 Gbps	-	500 MHz
	(2015) [9]				
4	This Paper	Parallel Pipelining	68 Gbps	7 pJ/bit	531.2 MHz

V. Conclusions

This paper proposes an efficient high throughput pipelined architecture of 128-bit AES cipher algorithm. A detailed study of the transformation processes in encryption/decryption of data has been presented to analyze the results obtained from each stage of the AES. The results exhibit high-rate encryption of 68 Gbps and a low energy consumption of 7 pJ/bit. Both encryption and decryption processes have been demonstrated for an alphanumeric text message using a 128-bit symmetric cipher key. This architecture proved to be more efficient and easier to implement as compared to other techniques adopted for low energy AES. Making it useful for applications in battery operated devices which have speed and power consumption constraints.

References

[1] W. H. Baker and L. Wallace, "Is Information Security Under Control?: Investigating Quality in Information Security Management," in IEEE Security & Privacy, vol. 5, no. 1, pp. 36-44, Jan.-Feb. 2007, doi: 10.1109/MSP.2007.11.

[2] H. S. Deshpande, K. J. Karande and A. O. Mulani, "Efficient implementation of AES algorithm on FPGA," 2014 International Conference on Communication and Signal Processing, pp. 1895-1899, 2014 doi: 10.1109/ICCSP.2014.6950174.

[3] C. E. Shannon, "Communication theory of secrecy systems," in The Bell System Technical Journal, vol. 28, no. 4, pp. 656-715, Oct. 1949, doi: 10.1002/j.1538-7305.1949.tb00928.x.

[4] O. Hajihassani, S. K. Monfared, S. H. Khasteh and S. Gorgin, "Fast AES Implementation: A High-Throughput Bitsliced Approach," in IEEE Transactions on Parallel and Distributed Systems, vol. 30, no. 10, pp. 2211-2222, 1 Oct. 2019, doi: 10.1109/TPDS.2019.2911278.

[5] P. Hamalainen, T. Alho, M. Hannikainen and T. D. Hamalainen, "Design and Implementation of Low-Area and Low-Power AES Encryption Hardware Core," 9th EUROMICRO Conference on Digital System Design (DSD'06), pp. 577-583, 2006 doi: 10.1109/DSD.2006.40.

[6] D. -H. Bui, D. Puschini, S. Bacles-Min, E. Beigné and X. -T. Tran, "AES Datapath Optimization Strategies for Low-Power Low-Energy Multisecurity-Level Internet-of-Things Applications," in IEEE Transactions on Very Large Scale Integration (VLSI) Systems, vol. 25, no. 12, pp. 3281-3290, Dec. 2017, doi: 10.1109/TVLSI.2017.2716386.

[7] C. Duran and E. Roa, "A 10pJ/bit 256b AES-SoC Exploiting Memory Access Acceleration," in IEEE Transactions on Circuits and Systems II: Express Briefs, vol. 69, no. 3, pp. 1612-1616, March 2022, doi: 10.1109/TCSII.2021.3126984.

[8] M. Sumio, and A. Satoh. "An optimized S-Box circuit architecture for low power AES design." In *International Workshop on Cryptographic Hardware and Embedded Systems*, pp. 172-186. Springer, Berlin, Heidelberg, 2002.

Authorized licensed use limited to: DELHI TECHNICAL UNIV. Downloaded on May 15,2023 at 07:04:33 UTC from IEEE Xplore. Restrictions apply.

[9] S. Chellappa, C. Ramamurthy, V. Vashishtha and L. T. Clark, "Advanced encryption system with dynamic pipeline reconfiguration for minimum energy operation," Sixteenth International Symposium on Quality Electronic Design, pp. 201-206, 2015 doi: 10.1109/ISQED.2015.7085425.

[10] S. Oukili and S. Bri, "High speed efficient advanced encryption standard implementation," 2017 International Symposium on Networks, Computers and Communications (ISNCC), 2017, pp. 1-4, doi: 10.1109/ISNCC.2017.8071975.

[11] R. V. Kshirsagar and M. V. Vyawahare, "FPGA Implementation of High Speed VLSI Architectures for AES Algorithm," 2012 Fifth International Conference on Emerging Trends in Engineering and Technology, pp. 239-242, 2012 doi: 10.1109/ICETET.2012.53.

[12] K. -L. Tsai, Y. -L. Huang, F. -Y. Leu, I. You, Y. -L. Huang and C. -H. Tsai, "AES-128 Based Secure Low Power Communication for LoRaWAN IoT Environments," in IEEE Access, vol. 6, pp. 45325-45334, 2018, doi: 10.1109/ACCESS.2018.2852563.

[13] C. Lu and S. Tseng, "Integrated design of AES (Advanced Encryption Standard) encrypter and decrypter," Proceedings IEEE International Conference on Application- Specific Systems, Architectures, and Processors, pp. 277-285, 2002 doi: 10.1109/ASAP.2002.1030726.

[14] B. Subramanyan, V. M. Chhabria and T. G. S. Babu, "Image Encryption Based on AES Key Expansion," 2011 Second International Conference on Emerging Applications of Information Technology, pp. 217-220, 2011 doi: 10.1109/EAIT.2011.60.

[15] S. Kumar, V. K. Sharma and K. K. Mahapatra, "Low latency VLSI architecture of S-box for AES encryption," 2013 International Conference on Circuits, Power and Computing Technologies (ICCPCT), pp. 694-698, 2013,doi: 10.1109/ICCPCT.2013.6528906.

[16] B. Bhat, A. W. Ali and A. Gupta, "DES and AES performance evaluation," International Conference on Computing, Communication & Automation, pp. 887-890, 2015 doi: 10.1109/CCAA.2015.7148500.

[17] K. Wu, Ramesh Karri, G. Kuznetsov and M. Goessel, "Low cost concurrent error detection for the advanced encryption standard," 2004 International Conference on Test, pp. 1242-1248, 2004, doi: 10.1109/TEST.2004.1387397.

[18] F. J. D'souza and D. Panchal, "Advanced encryption standard (AES) security enhancement using hybrid approach," 2017 International Conference on Computing, Communication and Automation (ICCCA), pp. 647-652, 2017, doi: 10.1109/CCAA.2017.8229881.

[19] D. Punia and B. Singh, "Speed Optimization of the AES Algorithm Using Pipeline Hardware Architecture," 2019 International Conference on Communication and Electronics Systems (ICCES), pp. 2070-2074, 2019, doi: 10.1109/ICCES45898.2019.9002086.

[20] Q. Liu, Z. Xu and Y. Yuan, "A 66.1 Gbps single-pipeline AES on FPGA," 2013 International Conference on Field-Programmable Technology (FPT), pp. 378-381, 2013, doi: 10.1109/FPT.2013.6718392.

Authorized licensed use limited to: DELHI TECHNICAL UNIV. Downloaded on May 15,2023 at 07:04:33 UTC from IEEE Xplore. Restrictions apply.

Research Square

Preprints are preliminary reports that have not undergone peer review.
They should not be considered conclusive, used to inform clinical practice,
or referenced by the media as validated information.

Gate Engineered Ferroelectric Junctionless BioFET for Label-Free Detection of Biomolecules

Snehlata yadav
Delhi Technological University
Sonam Rewari (rewarisonam@gmail.com)
Delhi Technological University
Rajeshwari Pandey
Delhi Technological University

Research Article

Keywords:

Posted Date: May 5th, 2023

DOI: https://doi.org/10.21203/rs.3.rs-2880988/v1

License: This work is licensed under a Creative Commons Attribution 4.0 International License. Read Full License

Abstract

A Gate Engineered Ferroelectric Junctionless BioFET is proposed and investigated for label-free detection of various biomolecules. A nanocavity is created by etching a part of the gate oxide material on the top and bottom of the device, which allows biomolecules to get immobilized. The immobilization of biomolecules in the cavity causes changes in electrostatic characteristics such as surface potential, input and output characteristics, transconductance, output conductance, gate capacitance, and cut-off frequency used as sensing metrics. The biosensor is also examined at different biomolecule concentrations, such as -1e12, 0, and 1e12. The transistor's sensitivity is then understood by looking at the fluctuation in threshold voltage, subthreshold swing, and switching ratio. Ferroelectric Junctionless BioFET and Gate Engineered Ferroelectric Junctionless BioFET performances have been compared. It has been found that the Gate Engineered Ferroelectric Junctionless BioFET shows the maximum improvement for protein (1202.4%, 111%, and 565%) and DNA (787.5%, 117.3%, and 600%). For ultrasensitive bio-sensing applications, the Gate Engineered Ferroelectric Junctionless BioFET is shown to be suitable.

1. Introduction

The current research focus has been addressing challenges that conventional CMOS technology faces, including voltage scaling and short-channel effects (SCEs) [1]. The junctionless dual gate MOSFET, immune to short-channel effects and possesses several unique features, is an outstanding alternative device architecture for CMOS technology [2]. The most prominent challenge in fabricating short-channel devices is forming source/channel and channel/drain junctions in typical MOSFETs [3]. Several advantageous qualities of junctionless MOSFETs include the absence of sharp junctions, which are challenging to create, a streamlined fabrication technique, and others [4]. Field effect transistor-based electrochemical biosensors have garnered the most attention in the research community because they have numerous benefits over other biosensors, including compatibility with CMOS, label-free detection, increased scaling, and inexpensive production costs. They could be suitable for use in upcoming biosensor applications because of these qualities. FET-based biosensors have many applications, including label-free detection of charged bio-analytes [5]. The biomolecules change the sensors' electrical responses by modifying the gate terminals' functioning. Dielectrically regulated Field Effect Transistors, which exploit the dielectric constant of biomolecules, have recently sparked much attention [6]. This technology can detect charged and uncharged biomolecules at various concentrations. Larger sensitivity in terms of current is required to detect biomolecule species at very low concentrations. When the device is operated in the subthreshold range, the maximum current sensitivity for FET-based biosensors can be achieved [7], [8]. On the other hand, the Boltzmann tyranny limits the subthreshold swing (SS) in typical FET-based biosensors to a minimum of 60 mV/decade at ambient temperature, lowering the maximum current sensitivity [9]. As technology has improved, efficiency has become much more in demand. Therefore, shifting to a new technology that can handle these difficulties is mandatory. Negative Capacitance FETs (NCFETs), a form of the steep-switching device based on ferroelectrics, offer a potential solution to overcome the Boltzmann limit of SS and achieve a swing of less than 60 mV/decade [9]. Recent research shows that HfO2 exhibits ferroelectric behavior when doped with elements such as Y, Zr, Al, Si, and others at different mole concentrations and annealing temperatures [10]. It has been found in previous research that the mechanical encapsulation of thin sheets of zirconium-doped hafnium oxide (HZO) forms an orthorhombic phase. It possesses a piezoelectric response, and polarization tests have proved that it is ferroelectric. According to studies, HZO has a low dielectric constant (about 30), indicating that it can be scaled down to meet existing technological nodes [11]. As a result, these materials are excellent candidates for application as ferroelectric materials. The benefits of the ferroelectric layer and junctionless structures, as well as the creation of cavities in the oxide regions for inserting the biomolecules, is what distinguishes our work. A dielectric-modulated FET can be used to implement this form of a biosensor [12]. Even though simulation and modeling of dielectric modulated FETs have been documented in many publications, they are typically used for sensing biomolecules in dry environments [12]–[14]. Therefore, a Gate Engineered Ferroelectric Junctionless BioFET (GE-FJ-BioFET) capable of detecting diverse biomolecules such as enzymes, proteins, and DNAs [15] is described in this study. This device could be a significant contender for CMOS technology in the future since it can overcome the critical limitations of complex fabrication methods and operate at lower voltage limits, thereby eliminating the problem of excessive chip heating [16]. Furthermore, various studies have outlined fabrication methods for JL transistors and FeFETs [17], [18], [19]; as a result, the suggested device may be produced using current technologies. Section 2 describes the device structure, simulation of Gate Engineered Ferroelectric Junctionless BioFET and calibration with the experimental work. The results and discussion are covered in Section 3. Section 4 concludes the work.

2. Device Structure, Simulation, and Calibration

Figure 1 depicts a 2D schematic cross-sectional view of the GE-FJ-BioFET. The device employs an n-type doped, symmetric double gate junctionless transistor with a ferroelectric layer and two biomolecule nano-cavities. The doping concentrations are assumed to be 10^{19} cm^{-3} across the source, drain, and channel. The thicknesses of the ferroelectric (t_{fe}), oxide (t_{ox}), and channel (t_{ch}) are 5nm, 2nm, and 20nm, respectively. GE-FJ-BioFET analyses each dielectric constant to identify biomolecules, including biotin, APTES, protein, and DNA [20]. The biomolecules are inserted into the gate stack's nano-cavities. The dielectric constant of each of the biomolecules is shown in Table 1. The biomolecules are placed in the nano-cavities created in the gate stack. The cavity region is filled with air in the absence of biomolecule, i.e., ($\varepsilon = 1$) and when dielectric constant,i.e., ($\varepsilon > 1$), the cavity region is infused with biomolecules. The calibration of the simulated work with the experimental work [21] is shown in Fig. 2(a). The simulations are performed using the Silvaco ATLAS TCAD simulator, with the Lombardi CVT model, Shockley-Read-Hall (SRH) recombination, fermi, and Landau-Khalatnikov (LK) models [22] explained in Table 2.

Table 1
Biomolecule with dielectric constant variations.

Biomolecule	Dielectric constant
Biotin [23]	2.63
APTES [24]	3.57
Protein [25]	6
DNA [26]	8

Table 2
Physical Model used for the simulations.

Models	Description
Lombardi CVT model	This model overrides any other mobility models which may be specified in the MODELS statement.
Shockley-Read-Hall (SRH) recombination model	Shockley-Read-Hall (SRH) recombination model with concentration-dependent lifetimes accounts for the recombination of minority carriers.
Fermi model	This model introduces fermi statistics recombination into intrinsic concentration calculation.
Landau-Khalatnikov Ferro model	The model is enabled by specifying the flag LKFERRO on the INTERFACE statement, along with the LKCORECIVE and LKREMNANT parameters.

Figure 3 depicts the contour plots for electron concentration in the channel region at different dielectric constants. When biomolecules are added to the cavity region, charges are induced in the channel below the cavity. As shown from Fig. 3, the amount of charge produced depends on the biomolecule's dielectric constant.

3. Results and Discussion

Biomolecules have dielectric properties as well as charge concentration. Variations of biomolecule species and their concentrations have been investigated for biomolecule detection. The dielectric variation of biomolecules is taken into account when examining the electrical characteristics of GE-FJ-BioFET for biomolecules with dielectric properties and concentrations. The biomolecule concentration used to analyze the electrical properties of GE-FJ-BioFET with charge density variation and constant dielectric are -1×10^{12} cm^{-2},0 cm^{-2}, and 1×10^{12} cm^{-2}.

A. GE-FJ-BioFET as a Biomolecule species sensor

Table 2 illustrates the device sensitivity with dielectric constant variations. As seen in Fig. 4 (a), changes in the dielectric constant have an impact on the GE-FJ-BioFET surface potential. As illustrated, a drop in the potential is observed as the biomolecule with increasing dielectric constant is introduced. A drop in the potential reduces the drain current in the device and raises the threshold

voltage. The influence of GE-FJ-BioFET as a biomolecule species sensor can be reflected on device electrical parameters is investigated using device transfer characteristics, transconductance (gm), threshold voltage (V_{th}), I_{on}/I_{off} ratio, and subthreshold swing (SS). Figures 5 (a) and (b) demonstrate the drain current and transconductance fluctuation for different biomolecule species. The drain current reduces as the biomolecule dielectric increases because of a fall in the surface potential of the device in the channel region. Also, as shown in Fig. 5 (b), the transconductance decreases as the dielectric constant increases. Figure 6 depicts the changes in output characteristics and output conductance with biomolecules' dielectric constant. As observed, the output characteristics decreases with an increase in the dielectric constant. It can also be evident from the figures that the performance of GE-FJ-BioFET is high when compared to FJ-BioFET. Figures 7 (a) and (b) shows the total gate capacitance (C_{GG}) and cut-off frequency (f_T), which depicts that both parameters increases when the dielectric constants are increased. The threshold voltage sensitivity is investigated with increasing dielectric constant concerning air in the cavity depicted in Fig. 8 (a). The figure shows that the threshold voltage sensitivity increases as the dielectric constant increases, allowing biomolecules to be detected. Furthermore, the GE-FJ-BioFET biosensor's sensitivity concerning SS, and Ion/Ioff is illustrated in Figs. 8 (b) and (c). The sensitivity can be formulated as [27]:

$$S_{V_{th}} = \frac{V_{th,bio} - V_{th,air}}{V_{th,air}} \quad (1)$$

$$S_{SS} = \frac{SS_{bio} - SS_{air}}{SS_{air}} \quad (2)$$

$$S_{I_{on}/I_{off}} = \frac{I_{on}/I_{off_{bio}} - I_{on}/I_{off_{air}}}{I_{on}/I_{off_{air}}} \quad (3)$$

As evident from the figure, GE-FJ-BioFET is highly sensitive for protein and DNA when compared with the other device. The sensitivity in terms of V_{th}, SS and $I_{on/loff}$ with variations in dielectric constants are listed in Table 3. The biomolecules such as protein and DNA show a more significant sensitivity improvement. The % improvement for protein is 1202.4%, 111%, and 565%, whereas for DNA, it's 787.5%, 117.3%, and 600%. The devices are compared, and it is found that GE-FJ-BioFET is highly sensitive and can be a good choice for biosensing applications.

Table 3
Device sensitivity with dielectric constant variations.

Dielectric constant (ε)	S_{Vth}			$S_{Ion/Ioff}$			S_{SS}		
	FJ-BioFET	GE-FJ-BioFET	% improvement	FJ-BioFET	GE-FJ-BioFET	% improvement	FJ-BioFET	GE-FJ-BioFET	% improvement
Biotin	0.00633	0.00949	50%	0.1066	0.18488	73.4%	0.01587	0.03333	110%
APTES	0.00949	0.0427	350%	0.18441	0.33564	82%	0.03175	0.1	215%
Protein	0.00949	0.1236	1202.4%	0.35151	0.74205	111%	0.04762	0.31667	565%
DNA	0.01899	0.16854	787.5%	0.4720	1.02601	117.3%	0.04762	0.33333	600%

B. GE-FJ-BioFET as a biomolecule concentration sensor

The biomolecule concentration changes the device surface potential, as shown in Fig. 4 (b). It illustrates that negatively charged biomolecules decrease the device's potential in the channel region while positively charged biomolecules increase it. When the potential increases, the current flow increases, and the threshold voltage decreases, but when the potential decreases, the current flow decreases and the threshold voltage increases. The influence of biomolecule charge concentration fluctuation on device electrical parameters such as device transfer characteristics, transconductance (gm), threshold voltage (V_{th}), I_{on}/I_{off} ratio and subthreshold swing have been investigated (SS).

The fluctuation in device transfer characteristics and transconductance with biomolecule charge concentration is depicted in Figs. 9 (a) and (b). The drain current is higher for positively charged biomolecule because surface potential is higher in the channel region and lower for negatively charged biomolecule because surface potential is lower in the channel region. Additionally, the transconductance is also higher for positively charged biomolecule. The output characteristics have been depicted in Figs. 10 (a) and (b), which shows that the performance of GE-FJ-BioFET is quite well than the FJ-BioFET. The investigation of sensitivity in terms of V_{th}, SS, and $I_{on/Ioff}$ with positively as well as negatively charged biomolecule about neutral biomolecules in the cavities, is illustrated in Figs. 11 (a), (b), and (c). It depicts higher sensitivity for GE-FJ-BioFET in terms of V_{th}, SS, and $I_{on/Ioff}$, for negatively charged Biomolecule.

Table 4

Device sensitivity with biomolecule charge concentration

Charge Density	S_{Vth}			$S_{Ion/Ioff}$			S_{SS}		
	FJ-BioFET	GE-FJ-BioFET	% improvement	FJ-BioFET	GE-FJ-BioFET	% improvement	FJ-BioFET	GE-FJ-BioFET	% improvement
-1e12	0.0085	0.17879	2003.4%	0.61403	1.22997	100.3%	0.03226	0.26667	726.6%
0	0.00946	0.16816	1677.5%	0.47436	1.03164	117.5%	0.04762	0.11667	145%
1e12	0.00719	0.14528	1920.5%	0.39914	0.84623	112%	0.04762	0.18333	285%

Table 4 shows the comparison of GE-FJ-BioFET and FJ-BioFET at different biomolecule concentration with respect to V_{th}, SS, and $I_{on/Ioff}$.

Improvement in the sensitivity is 2003.3% for V_{th}, 100.3% for I_{on}/I_{off} and 726.6% for SS in DNA biomolecule. Therefore, it can concluded that the GE-FJ-BioFET is more sensitive than FJ-BioFET.

4. Conclusion

Gate Engineered Ferroelectric Junctionless BioFET (GE-FJ-BioFET) sensor has been investigated owing to its strong sensing capability. Various sensing parameters such as input and output characteristics, g_m, V_{th}, SS, I_{on}/I_{off}, C_{gg} and f_T have been considered for detecting the immobilized biomolecules in the cavity area. Sensitivity has been obtained by varying the dielectric of biomolecule species and their concentration. The comparison between GE-FJ-BioFET and FJ-BioFET is done and it is found that the GE-FJ-BioFET transistor shows an excellent improvement in sensitivity. The % improvement for protein is 1202.4%, 111% and 565% whereas for DNA it's 787.5%, 117.3% and 600%. As a result, the research presented in this study demonstrates that GE-FJ-BioFET transistor-based biosensor is better suited for applications requiring ultrasensitive biosensing.

Declarations

Declaration of interests

The authors declare that they have no known competing financial interests or personal relationships that could have appeared to influence the work reported in this paper.

References

1. IRDS Systems and Architectures Team, "International Roadmap for Devices and Systems: Executive Summary," *IEEE Adv. Technol. Humanit.*, p. 63, 2020, [Online]. Available: https://irds.ieee.org/images/files/pdf/2020/2020IRDS_ES.pdf.
2. P. Kumar, M. Vashishath, and N. Gupta, "Analytical Modeling and Performance Analysis of Surface Potential for Junctionless MOSFET," in *Journal of Physics: Conference Series*, 2021, vol. 1916, no. 1, doi: 10.1088/1742-6596/1916/1/012026.

3. N. Gupta, J. B. Patel, and A. K. Raghav, “A study of conventional and junctionless MOSFET using TCAD simulations,” in *International Conference on Advanced Computing and Communication Technologies, ACCT*, 2015, vol. 2015-April, pp. 53–56, doi: 10.1109/ACCT.2015.51.
4. S. Sahay and M. J. Kumar, “Fundamentals of Junctionless Field-Effect Transistors,” *Junctionless Field-Effect Transistors*, pp. 67–123, 2019, doi: 10.1002/9781119523543.ch3.
5. D. Sadighbayan, M. Hasanzadeh, and E. Ghafar-Zadeh, “Biosensing based on field-effect transistors (FET): Recent progress and challenges,” *TrAC Trends Anal. Chem.*, vol. 133, p. 116067, Dec. 2020, doi: 10.1016/J.TRAC.2020.116067.
6. P. Dwivedi, “Influence of Transistor Architecture on the Performance of Dielectric Modulated Biosensor,” no. June, 2021, doi: 10.13140/RG.2.2.21183.43680.
7. S. K. Parija, S. K. Swain, S. M. Biswal, S. Adak, and P. Dutta, “Performance Analysis of Gate Stack DG-MOSFET for Biosensor Applications,” *Silicon*, vol. 14, no. 14, pp. 8371–8379, 2022, doi: 10.1007/s12633-021-01622-2.
8. D. Singh and G. C. Patil, “Dielectric-Modulated Bulk-Planar Junctionless Field-Effect Transistor for Biosensing Applications,” *IEEE Trans. Electron Devices*, vol. 68, no. 7, pp. 3545–3551, Jul. 2021, doi: 10.1109/TED.2021.3083212.
9. T. Manimekala, R. Sivasubramanian, and G. Dharmalingam, “Nanomaterial-Based Biosensors using Field-Effect Transistors: A Review,” *J. Electron. Mater. 2022 515*, vol. 51, no. 5, pp. 1950–1973, Feb. 2022, doi: 10.1007/S11664-022-09492-Z.
10. H. Mulaosmanovic, E. T. Breyer, S. Dünkel, S. Beyer, T. Mikolajick, and S. Slesazeck, “Ferroelectric field-effect transistors based on HfO2: a review,” *Nanotechnology*, vol. 32, no. 50, p. 502002, Sep. 2021, doi: 10.1088/1361-6528/AC189F.
11. T. Ali *et al.*, “Silicon doped hafnium oxide (HSO) and hafnium zirconium oxide (HZO) based FeFET: A material relation to device physics,” *Appl. Phys. Lett.*, vol. 112, no. 22, p. 222903, 2018, doi: 10.1063/1.5029324.
12. K. N. Priyadarshani, S. Singh, and M. K. A. Mohammed, “Dielectric/charge density modulated junctionless FET based label-free biosensor,” *Inorg. Chem. Commun.*, vol. 148, no. October 2022, p. 110350, 2023, doi: 10.1016/j.inoche.2022.110350.
13. P. Kaur, A. S. Buttar, and B. Raj, “Design and Performance Analysis of Proposed Biosensor based on Double Gate Junctionless Transistor,” *Silicon*, vol. 14, no. 10, pp. 5577–5584, 2022, doi: 10.1007/s12633-021-01335-6.
14. D. Sen, A. De, B. Goswami, S. Shee, and S. K. Sarkar, “Noise immune dielectric modulated dual trench transparent gate engineered MOSFET as a label free biosensor: proposal and investigation,” *J. Comput. Electron.*, vol. 20, no. 6, pp. 2594–2603, 2021, doi: 10.1007/s10825-021-01780-x.
15. A. Goel, S. Rewari, S. Verma, S. S. Deswal, and R. S. Gupta, “Dielectric Modulated Junctionless Biotube FET (DM-JL-BT-FET) Bio-Sensor,” *IEEE Sens. J.*, vol. 21, no. 15, pp. 16731–16743, 2021, doi: 10.1109/JSEN.2021.3077540.
16. M. Singh, G. Kumar, S. Bordoloi, and G. Trivedi, “A study on modeling and simulation of Multiple- Gate MOSFETs,” *J. Phys. Conf. Ser.*, vol. 759, no. 1, 2016, doi: 10.1088/1742-6596/759/1/012093.
17. M. Hoffmann, B. Max, T. Mittmann, U. Schroeder, S. Slesazeck, and T. Mikolajick, “Demonstration of High-speed Hysteresis-free Negative Capacitance in Ferroelectric Hf0.5Zr0.5O2,” *Tech. Dig. - Int. Electron Devices Meet. IEDM*, pp. 31.6.1-31.6.4, Jan. 2019, doi: 10.1109/IEDM.2018.8614677.
18. Q. Xu *et al.*, “Physical Thickness 1.5-nm HfZrO Negative Capacitance NMOSFETs,” *IEEE Trans. Electron Devices*, vol. 68, no. 7, pp. 3696–3701, Jul. 2021, doi: 10.1109/TED.2021.3082109.
19. L. Stucchi-Zucchi, A. R. Silva, and J. A. Diniz, “Junctionless-FET device fabrication using silicon etching in NH4OH solution: Device behaviour according to etching time,” *SBMicro 2019 - 34th Symp. Microelectron. Technol. Devices*, pp. 2–5, 2019, doi: 10.1109/SBMicro.2019.8919301.
20. A. Dixit, D. P. Samajdar, and V. Chauhan, “Sensitivity Analysis of a Novel Negative Capacitance FinFET for Label-Free Biosensing,” *IEEE Trans. Electron Devices*, vol. 68, no. 10, pp. 5204–5210, 2021, doi: 10.1109/TED.2021.3107368.
21. Q. H. Luc *et al.*, “First experimental demonstration of negative capacitance InGaAs MOSFETs with Hf0.5Zr0.5O2 ferroelectric gate stack,” *Dig. Tech. Pap. - Symp. VLSI Technol.*, vol. 2018-June, pp. 47–48, Oct. 2018, doi: 10.1109/VLSIT.2018.8510644.
22. D. S. Software, “Atlas User Manual,” no. 408, pp. 567–1000, 2019.
23. R. Gautam, M. Saxena, R. S. Gupta, and M. Gupta, “Numerical model of gate-all-around MOSFET with vacuum gate dielectric for biomolecule detection,” *IEEE Electron Device Lett.*, vol. 33, no. 12, pp. 1756–1758, 2012, doi: 10.1109/LED.2012.2216247.
24. S. I. Amin, L. Gajal, and S. Anand, “Analysis of dielectrically modulated doping-less transistor for biomolecule detection using the charge plasma technique,” *Appl. Phys. A Mater. Sci. Process.*, vol. 124, no. 9, pp. 1–8, Sep. 2018, doi: 10.1007/S00339-018-2003-

9/FIGURES/8.

25. A. Chattopadhyay, S. Tewari, and P. S. Gupta, “Dual-Metal Double-Gate with Low-k/High-k Oxide Stack Junctionless MOSFET for a Wide Range of Protein Detection: a Fully Electrostatic Based Numerical Approach,” *Silicon*, vol. 13, no. 2, pp. 441–450, 2021, doi: 10.1007/s12633-020-00430-4.
26. S. A. Hafiz, Iltesha, M. Ehteshamuddin, and S. A. Loan, “Dielectrically Modulated Source-Engineered Charge-Plasma-Based Schottky-FET as a Label-Free Biosensor,” *IEEE Trans. Electron Devices*, vol. 66, no. 4, pp. 1905–1910, 2019, doi: 10.1109/TED.2019.2896695.
27. A. Chakraborty and A. Sarkar, “Analytical modeling and sensitivity analysis of dielectric-modulated junctionless gate stack surrounding gate MOSFET (JLGSSRG) for application as biosensor,” *J. Comput. Electron.*, vol. 16, no. 3, pp. 556–567, 2017, doi: 10.1007/s10825-017-0999-2.

Figures

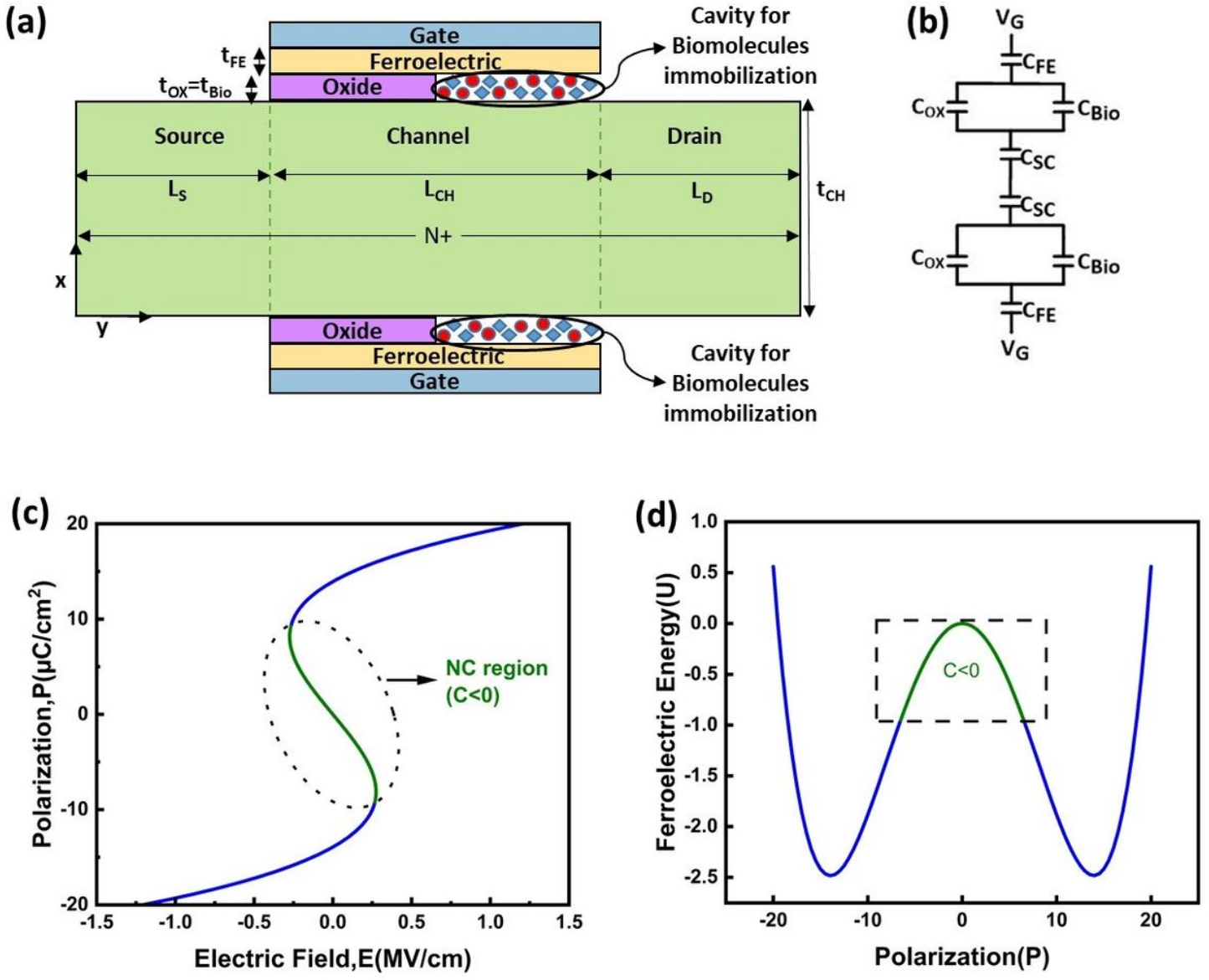


Figure 1

(a) Schematic of Gate Engineered Ferroelectric Junctionless BioFET (GE-FJ-BioFET), **(b)** equilavent capacitance model, **(c)** the double well ferroelectric energy versus polarization using LK theory, and **(d)** ferroelectric polarization as a function of electric field.

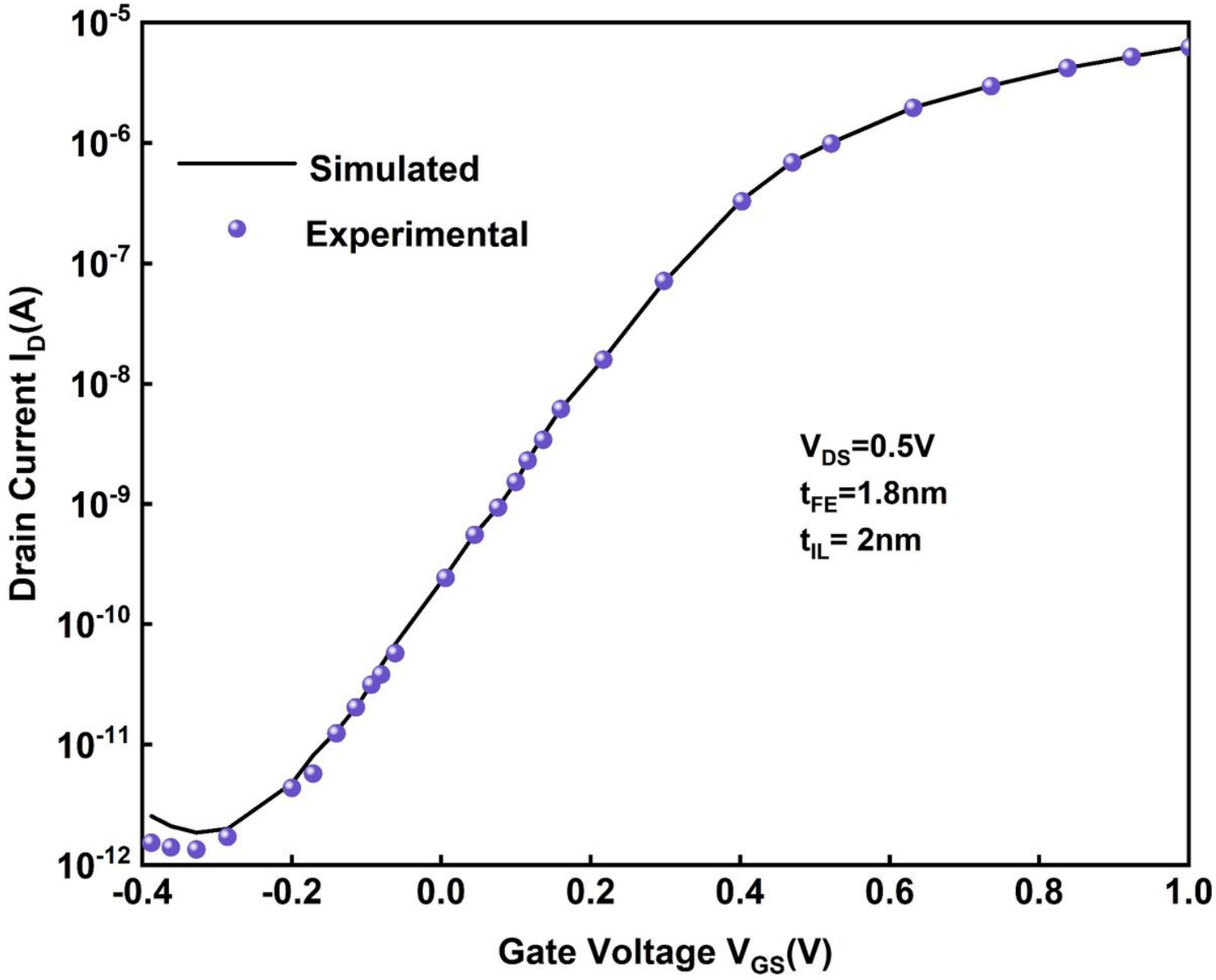


Figure 2

Calibration with the experimental work.

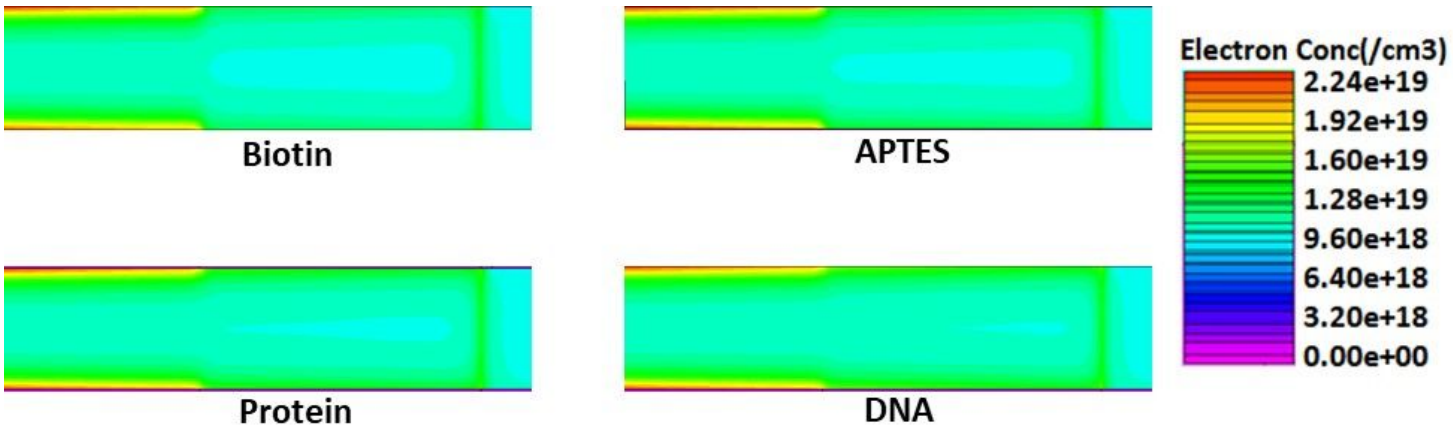


Figure 3

Electron concentration in the channel region of GE-FJ-BioFET at different dielectric constants

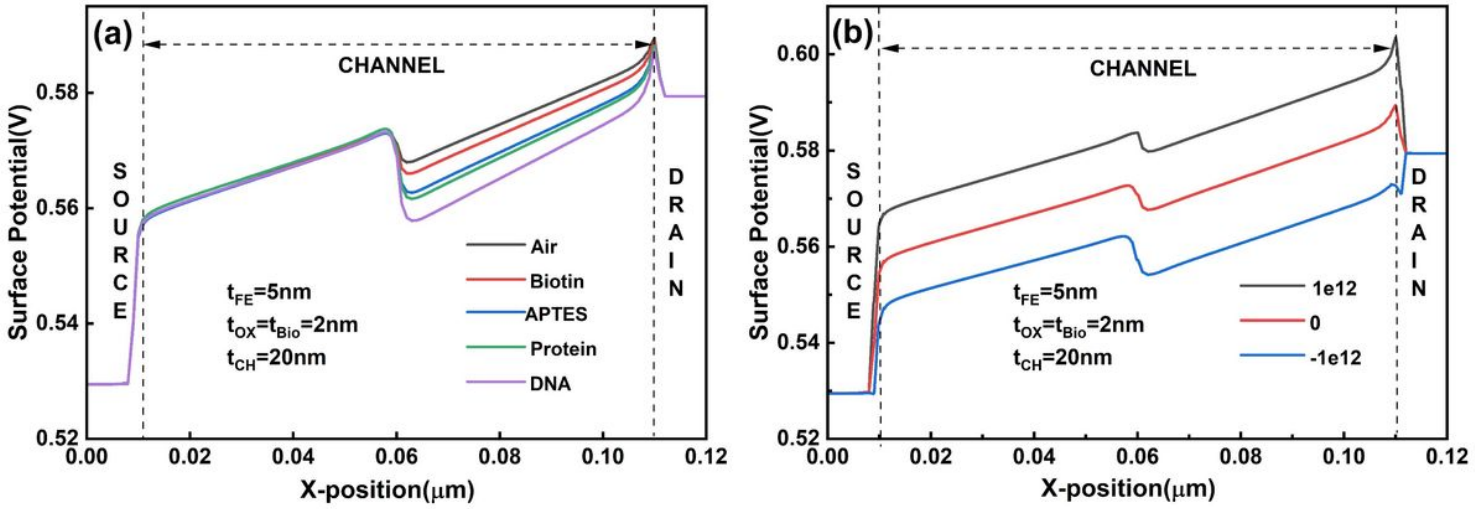


Figure 4

Surface potential of GE-FJ-BioFET at varying **(a)** dielectric constants, and **(b)** biomolecule concentration.

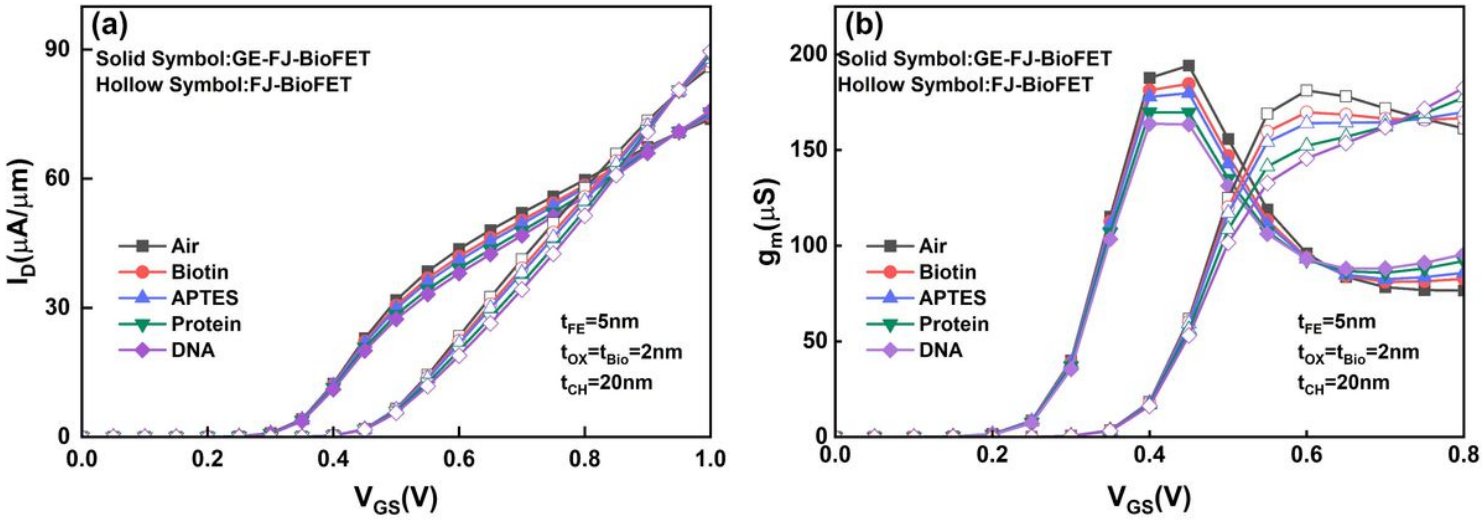


Figure 5

(a) Transfer characteristics, and **(b)** transconductance of devices with variations in dielectric constants.

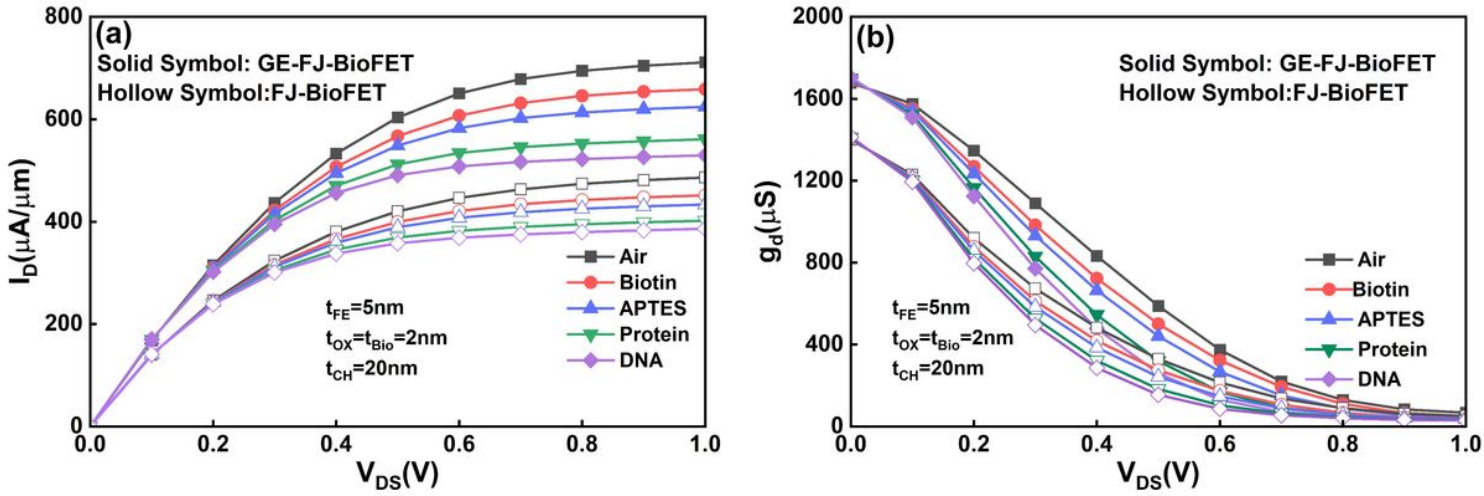


Figure 6

(a) Output characteristics, and **(b)** output conductance for different biomolecules dielectric constants

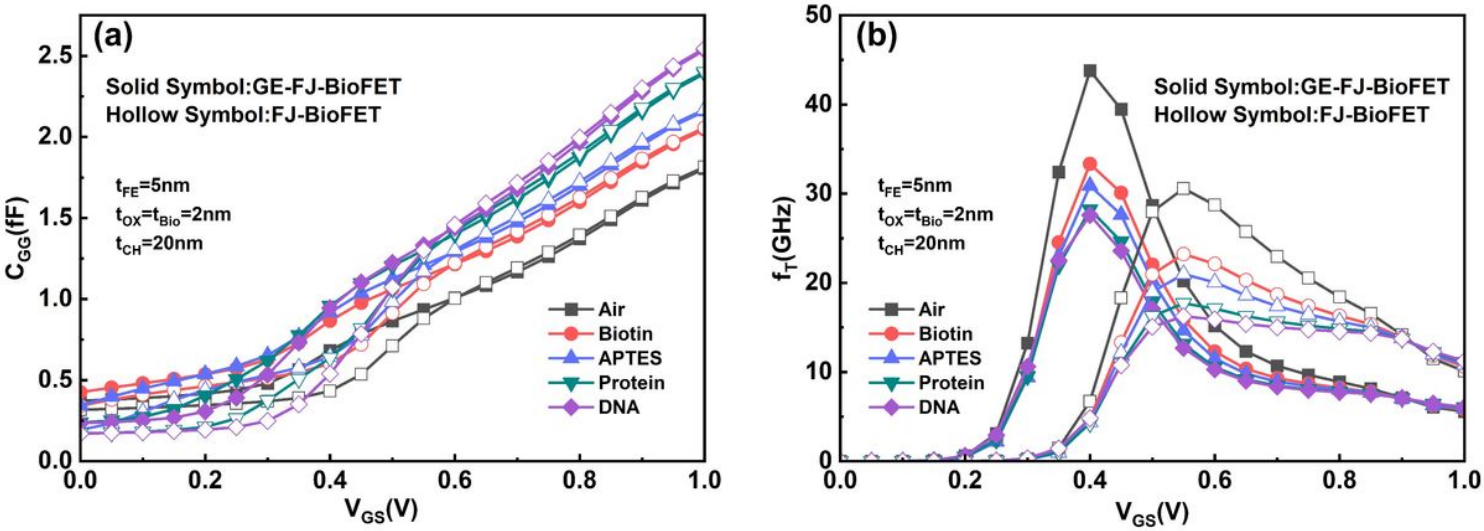


Figure 7

(a) Total gate capacitance, and **(b)** cut off frequency of the devices for different biomolecule species.

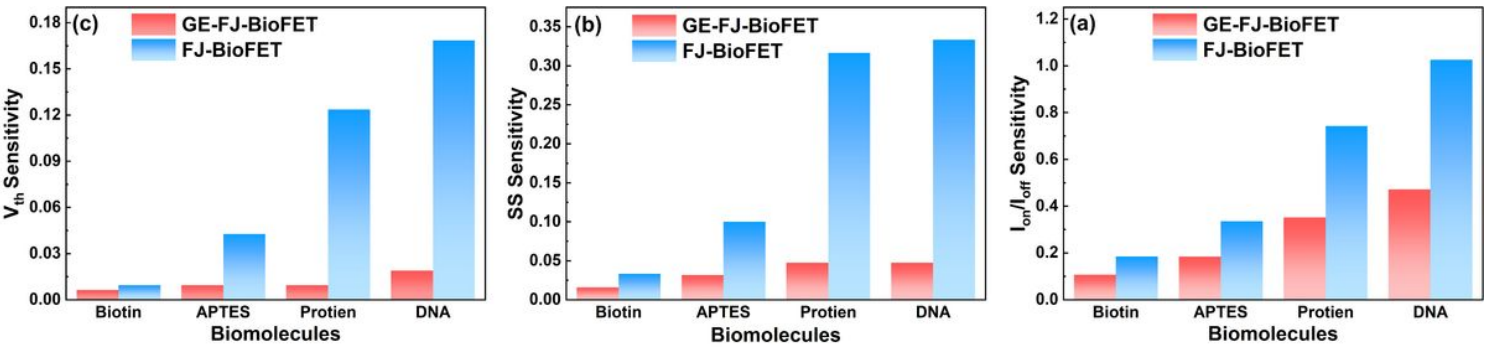


Figure 8

Sensitivity comparison of in terms of **(a)** V_{th}, **(b)** SS, and **(c)** I_{on}/I_{off} ratio for different biomolecule species.

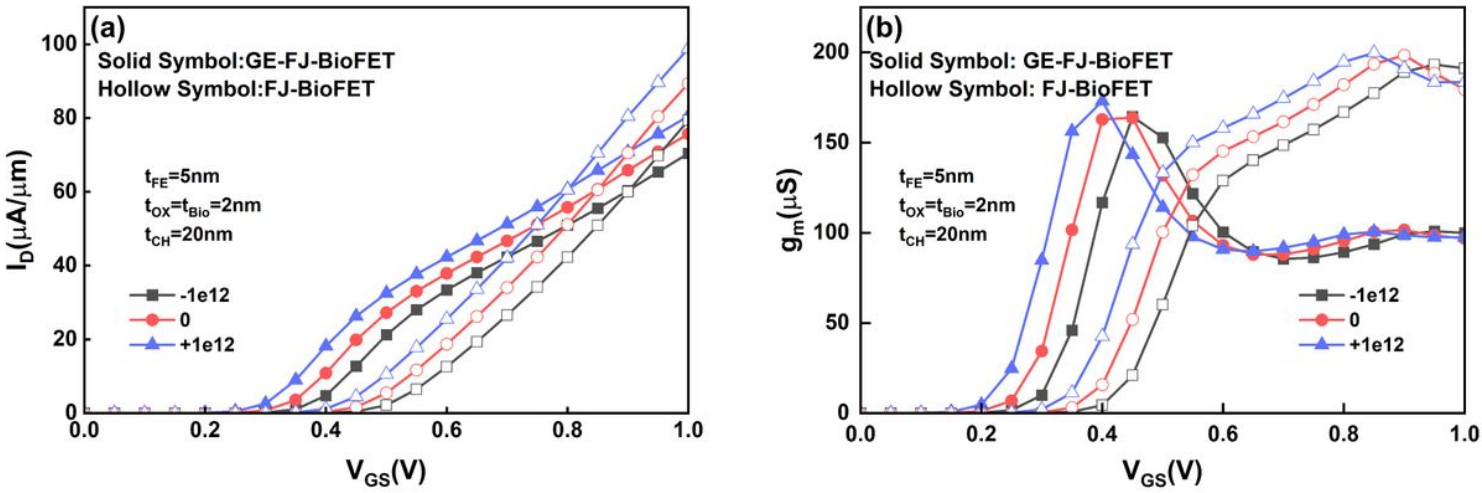


Figure 9

(a) Transfer characteristics, and **(b)** transconductance at different biomolecule concentration.

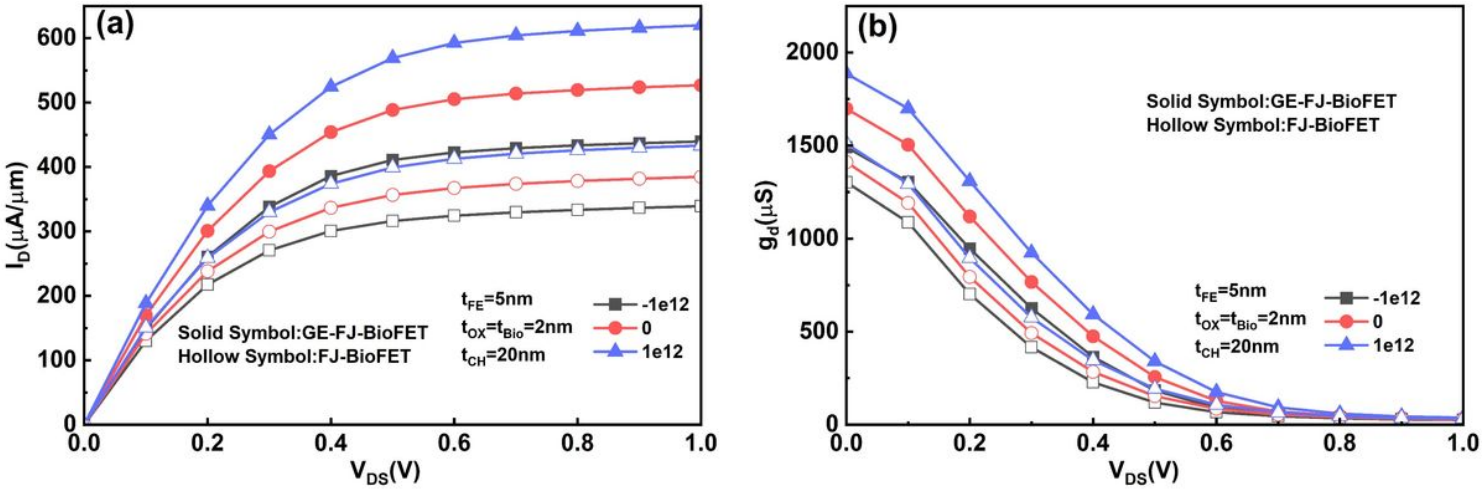


Figure 10

(a) Output characteristics, and **(b)** output conductance at different biomolecule concentration.

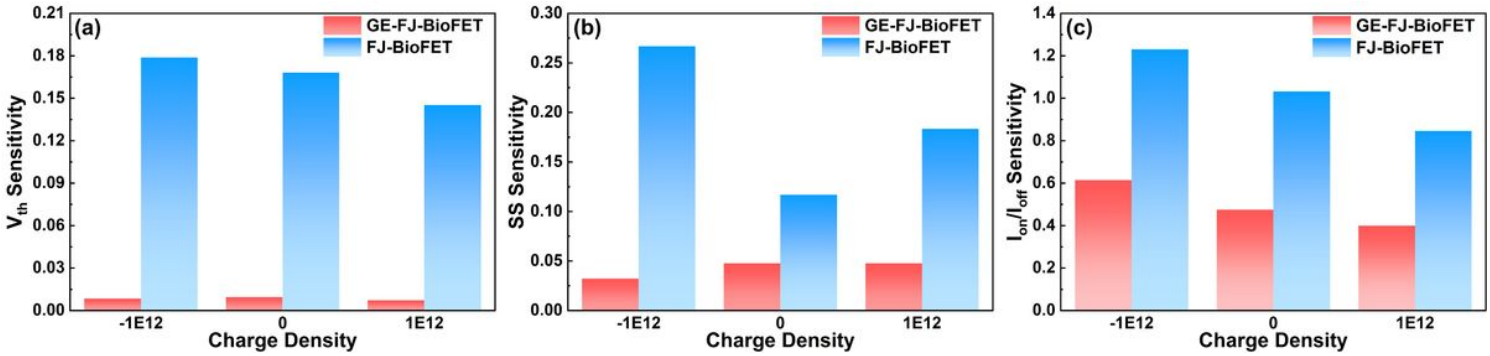


Figure 11

Sensitivity comparison in terms of **(a)** V_{th}, **(b)** SS, and **(c)** I_{on}/I_{off} ratio at different biomolecule concentration.

Helping Local Businesses by using IoT Embedded Systems

Dr. Ajai Kumar Gautam*, Ritvick A. Lohani*, Sudeep Saurabh*, Swapnil Gour*

*Department of Electronics and Communication Engineering

**Delhi Technological University, NewDelhi, India

***Abstract*— In today's world, businesses require a large amount of data to be gathered about their customers, which is then analysed to help optimize business decisions to increase sales and profits. Multinational companies spend large amounts of money annually on gathering demographic information about their customers and developing methods to analyse it. In this paper, we have designed prototype embedded systems that can help businesses to improve without having to take a major risk and is cost-effective.**

***Index Terms*— IoT, AI, Embedded system, Customer, business, Android, Database**

I. INTRODUCTION

Businesses are essential to any economy, and every major chain of stores was once a local business in their own country. In India, it's said that all the Indian family-owned companies have been contributing to almost 70% of India's GDP. A local business is significant to a developing country like India, providing jobs and stimulating the economy. If American companies come to India, even though they are creating jobs, the profit is sent back to the US stock market. It helps to stimulate the economy as more money comes in from another nation.

In the case of local businesses, all money is kept within the country, allowing local company owners to spend that money elsewhere and help stimulate the economy. As technology progresses, the problem with local businesses is that they need to catch up with big international companies with technology that allows them to maximize their profit in multiple ways. Companies like Burger King, McDonald's, Pizza Hut, and Domino's, which are trendy fast-food restaurants, have been using technology to improve and make their company maximum profit. Dominos uses GPS to track its employees to maximize labour efficiency and profit. Google and Netflix have been using ML algorithms to recommend the best customer experience, maximizing profit. Technology is even used in colleges nowadays; the best example is the attendance system used by the college to keep track of their faculty and staff.

Most people in India are scared to take significant risks; that's why we can say India is among the countries with the highest fixed deposit amount. So even when an Indian family wants to take the risk of starting a business, they try to limit their risks by being cost-efficient and not trying new techniques to improve their business. Most Indian companies are still working orthodoxly; the only significant difference is the UPI system. We want to change that by building a very cheap system that does not seem risky and is easy to use for anyone. We will make it simple but efficient so that even though it has little change, it will change for more profit in the longer term.

II. LITERATURE REVIEW

A. AI and IOT use in Business

Artificial intelligence is helping businesses grow exponentially with the aid of IoT or the Internet of things, making business work swiftly in modern times. These devices are quicker than humans and are crucial for profitability. They are easy to assemble and maintain.

Technologies make life easy for us, and this work aims to help small businesses make great profits. Internet of things majorly means connecting small devices to the internet so they can be operated from all around the globe.[8] It is basically connecting sensors with the help of micro-controllers so as to work smartly with these physical objects. Communication is easy to establish with the internet, the connection is permanent and data is rendered regularly. IoT is perfect for automation purposes.[10] The user can control the switching of lights, intensity of light in a room, build a driverless automated car and what not. The system is cheap and easy to operate, with reduced response time IoT increases productivity and efficiency, reminding users when maintenance is required, thus avoiding any failure in the system. It has great opportunities for revenue generation. With widespread penetration of the Internet of things, there is an excellent scope for future development and home automation and connected industries. Less human labour is involved, thus letting employees to focus on the designated work. The system's efficiency increases drastically when IoT is enabled with Artificial Intelligence and Machine Learning. [5]

B. Smart Security

Without security, individuals often become complacent and miss the unusual behaviour of civilians, employees, and others around them. Awareness is an ongoing activity, and people want to do the right thing, so security guides a positive and proactive culture. That's why we require their introduction of smart solutions to them, where a smart security system has been introduced. In this system, where there a microcontroller or microprocessor in the middle that act as the brain of the system then you act various senor and locks to help secure the place entry of an unauthorized person into places like a house, shop, even bank, and other institutes[9]. The whole purpose of the system is to not be operated on a daily basis by humans but rather be automated, as it is more cost-effective and even safer than a human being. This machine will be also working 24 hours a day, only required initial cost, power supply, and maintenance once a week or wherever broke rather than having to hire multiple security guards and having to pay for them to watch the system. Various research papers have used Arduino as the central brain of operations, as it is very cheap a microcontroller and easy to use and maintain. [4]

One of the ways to make smart security was built by using Arduino as the central brain and securing the house using a keypad lock, solenoid lock, and temperature sensor. In this system, they made so the door open only if you had put in the right password and you are given the right signal in the solenoid lock.[13] A solenoid lock is a lock that is operated by an electrical signal and relates on electromagnetic force to open the door. They have used electromagnetic force, like keycards or similar, which send electrical signals to the solenoid lock to open up the system. In the system, there are is two cases when a person wants to open the door, one is when they had put the right password in the keypad lock, and the electrical signal sent to the solenoid lock then the lock opens up.[6] Otherwise even if one of them is wrong or both are wrong then the system sends a notification to the owner asking whether the person is the owner or not, if the owner replies no, then there option of calling the police.

The temperature sensor is used similarly to the flame sensor we planning to use as it focuses more than just security but also gives an alert when the place gets a bit hot or cold, which can be used for a comfortable style of living. It will alert when too high temperature considers a fire, and it will alert the owner of the risk of their place being on fire, and give them the option to call the fire station or see the place for them and react accordingly. Another benefit of the temperature senor was you could find the temperature sensor of the place according to according either your air conditioning or heater depending on temperature and make the place comfortable for yourself while being at home or while coming back home.

Systems for fire alarms are crucial for warning people before a fire consumes lives and property.[12] It's crucial to have a responsive and effective system so that the fire station may be notified first in order to have a quicker alerting system. If there is a fire and it spreads to the entire building. By suggesting a fire alarm system that can contact the owner remotely to alert them if there is a fire at their property.

Some classical fire alarm systems like the "NestProtect" [3] connect the user and sensing module through Wi-Fi, whereas this system creates a sensing module that will be connected through IoT and Cloud Messaging. The system was designed to alert, monitor, and handle real-time accidents. Notification to the user and fire station will be sent immediately. Helping small businesses to grow to keep them safe from any sort of unforeseen situation is essential to install this system.

III. HARDWARE DESCRIPTION

A. Raspberry Pi

We use a Raspberry Pi 4 computer as a server. The Raspberry Pi 4 is a cheap credit card-sized computer that can also act as a microcontroller. One can even use it as a complete replacement for a laptop. This device component detects the flame detection sensor signal and Passive Infrared Red Sensors on receiving further necessary action. I am using a Raspberry Pi 4 computer to detect the signal and automatically send the signal over the internet. I wrote the script that handles this operation in Java. The Raspberry Pi 4 doesn't need to be connected to any other computer for the project's operation and only needs to be connected to a power source, as it has its wireless communication equipment [11].

B. Flame sensor

This is a flame sensor PCB that is based on a YG1006 NPN Phototransistor. It consists of 3 pins, which are for 5V input, ground, and digital output. It has many surface-mounted devices on it, such as a 10-kilo ohm potentiometer for controlling the sensitivity of flame detection and an LM393 Voltage comparator IC. The working of the flame sensor is based upon the LM393 and the phototransistor. When there is no flame in the range of the phototransistor, the LM393 produces a HIGH digital output. When light in the range of the flame is produced in front of the phototransistor, a voltage is produced in the base terminal of the transistor. This causes current to flow from the collector of the circuit to the emitter of the circuit, reducing the potential at the LM393 which changes the digital output of the flame sensor. This digital output signal is sent to pin 18 of the Raspberry Pi 4

C. Passive Infrared Sensor

Passive Infrared which is used in this project, is also called motion sensor. It consists of 3 pins, which are for 5V input, ground, and for digital output. The word Passive in Infrared Sensor tells us the about the sensor being inactive. It rather focuses on Infrared that is emit by human body, and detect it. The required of senor was to count people coming in, and the decoration of Passive Infrared Senor match. PIR has two slots. These holes are constructed from a unique, IR-sensitive substance. The Fresnel lens is utilised to ensure that

the two PIR slots can view beyond a certain range. A human body will block the first slot of the PIR sensor when it passes by. Positive differential change results between the two slots as a result of this. The sensor generates a negative differential change between the two slots once a human body leaves the detecting region, changing the digital output signal. This digital output signal is sent to pin 15 of the Raspberry Pi 4.

D. Google Firebase Cloud Messaging

This is the service that app developers use to send notifications to the users of their apps. Essentially, all Android and iOS devices have a direct connection to Firebase servers, allowing them to receive notifications from apps instantly with low power and performance consumption.

When an App Developer needs to send a message, data or a notification to a user while their app isn't open, rather than sending the message directly to the user's device; instead, the app developer sends a letter from their own server to Firebase. Firebase then relays the message to the user or users to which the message was to be delivered through the persistent connection that the android device has to the firebase servers. This allows all app developers to be able to send notifications regarding their apps to the user without any usage of power or performance.

E. Android App Client

This is an Android app that I have written which receives notifications from the Raspberry Pi. The app needs to be opened one after it is installed. This registers the device to be able to receive notifications from Firebase [7].

F. Database

The database is used to store information about the registered business locations, such as the username and the encrypted password hash used to login by the application client by that location. It also stores the information gathered by the sensors located at the business location. We are using the Cloud Firestore NoSQL cloud database service provided by Google. This can allow multiple business locations to simultaneously access as well as upload new data to the database simultaneously. We can also develop a client for the restaurant chain to read the data presently stored on the database of all locations, as well as register new locations to the system.

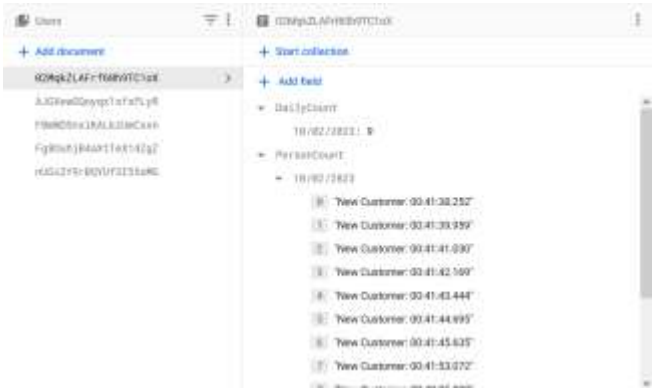


Fig 3.1: Firestore GUI showing the stored customer data of a restaurant.

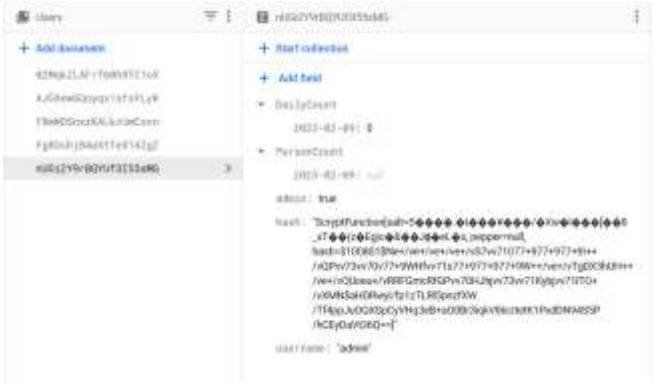


Fig 3.2: Firestore GUI showing the stored authentication information of Admin User, with encrypted password hash.

IV. IMPLEMENTATION

Currently in the project we have 5 Java classes which define various objects and methods that the project needs to work on the IoT embedded system running on the Raspberry Pi.

A. The Main Class

The **Main** class contains the main() method of the project which is the first thing that runs on the JVM when we run the program. It invokes the different functions that are defined in the other classes. This helps keep the program modular which allows us to add or remove various functions as the project progresses. For example, if we were to implement a Graphical User Interface then we would use the main class to invoke the functions responsible for drawing the interface windows. If we were to create a web client then the main class can be used to simultaneously launch the web server used to host the website along with the project.

B. The init Class

The **init** class stores the initialiseFirebase() function which is used at the startup of the program to sign in to Google Firebase from which we use the Google Firestore database

service as well as the Google Firebase Cloud Messaging service. There is a private file 'serviceaccountkey.json' which contains the required private API keys for logging in to the Firebase service that we have created for our project. Anyone who wishes to use our project must first register and obtain their own Firebase Service Account API keys for using our code. The function reads the API keys and logs in accordingly.

C. The User Class

The **User** class which defines the User object. Each User object has its own username and encrypted password hash for logging in to the system. It also has an admin property which is used to separate between normal users and administrators, or in our case to separate location management and chain management. This is important as both have different uses of the project available to them. The location management should be able to view data for their own location while the chain management should be able to view data for all of the locations. The chain management also has the ability to create or delete accounts as necessary. The User class also has the DailyCount property which is a map of a date String and Integers used to store the date and number of persons that visited that location. It also has the PersonCount map which stores the timestamp of every new customer which was detected by the sensor. It has two methods addcount() and viewCount() which are used for adding and viewing the customer data of that user.

D. The User Database

The **UserDatabase** class which is used as a login system and to store and manipulate User objects. The main() function loads this class which then starts by displaying a screen asking for the username and password of a user through the loginscreen() method. If a user with authentication level 1 logs in then the databaseRestaurant() method loads with that User class as its argument. This method lets the user choose between Viewing or adding customer data for their own restaurant as shown in the use case diagram. At the start of this method it invokes a PersonCounter object which is then run as a separate thread in the background.

If a user with the admin Boolean value as true logs in then the databaseAdmin() method is invoked with that User class. This method contains administrator level options such as registering, deleting and viewing a list of users, and to view or add customer data for any of the registered locations.

There is also the userdatabase() method which is the method that the projects main() function invokes and this method acts as the main method of the class. It invokes the loginscreen() function which asks the user to input their username. After receiving the input credentials, the program queries the Firestore database to check if a user with the username exists. If that user exists, it asks for the password of the user and then uses attempts to find if it matches with the password hash stored in the database which was generated using the Scrypt cryptographic key derivation algorithm. On successful authentication, the information of the user is retrieved from the database and a User class is generated using the retrieved data. The function then according to whether the user is an admin launches the corresponding function.

E. IoT EmbeddedSystem

The **IoTEmbeddedSystem** class is used to communicate with the hardware component of the project. We are using a Raspberry Pi 4, Flame Sensor and a Passive Infrared Sensor. Flame Sensor is to detect the fire happening inside the store. Passive Infrared Sensor to detect motion and to count the number of people that are entering the business location. This project uses the Pi4J java library to communicate with the Raspberry Pi's General Purpose Input Output (GPIO) pins. It also uses the Firebase library, which we will use in the future as a possible security system. It implements the Thread for multithreading, as it runs in the background counting persons while the restaurant is logged in to the database. This class also uses the java.time library for using the time to determine when the business is opened and closed and when to add to the person count or to act as an alarm system . It also alerts in case of fire.

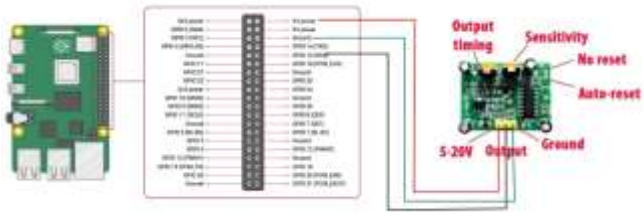


Fig 4.1 Circuit Diagram for Detecting System

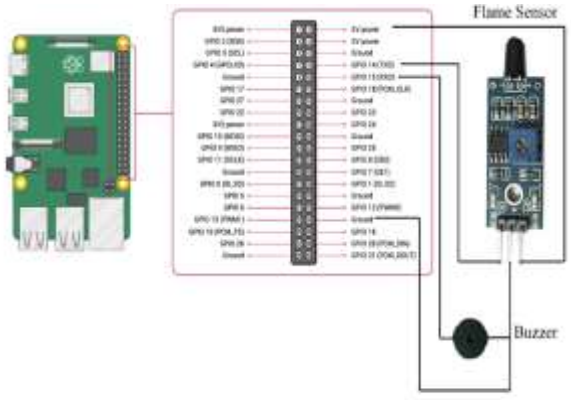


Fig 4.2 Circuit Diagram for Fire Alarm

F. Android App

The final major component of the project is the Android app, when run for the first time, registers the Android to Firebase. After this one-time registration, the phone will start receiving any security and fire from the system anywhere in the world through the internet. It also mentions how many people enter the store today, and a log of recent alarm events. It can be used to login to the Firestore database and view information logged on the system.

V. WORKING

As stated before, our embedded system has three functions and the results are below with function

1. The first function would be trying to collect data and use it wisely to improve company profit by helping utilize the data effectively. In these functions, we are ready with the collection of data parts. Every time a customer is detected the timestamp is uploaded onto the Firestore database.

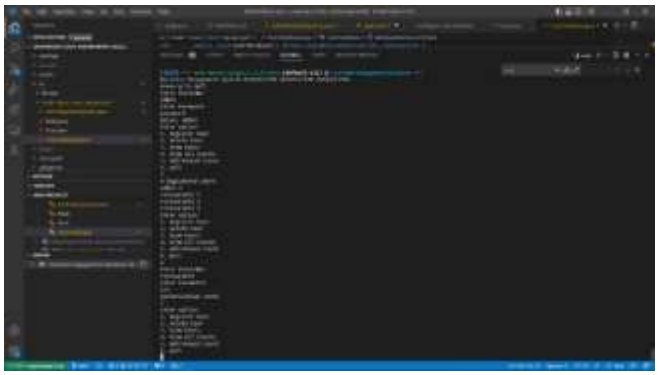


Figure 5.1 Chain Manager

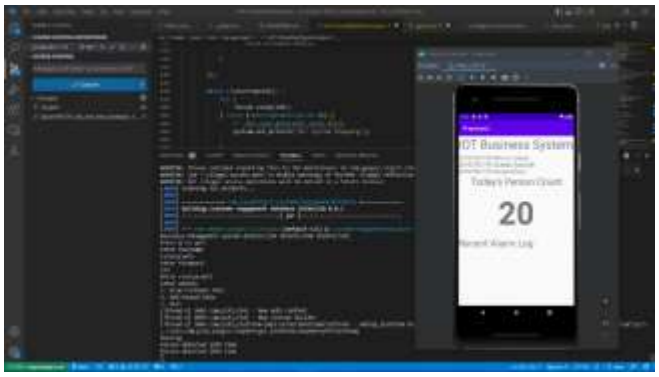


Figure 5.2 Store Manager

2. The Second function would be to create a security system. In these functions, we have made it, so that owner or store manager has put the time store will close. If the Passive Infrared sensor detects anyone coming inside the stores then it considers the person an invader. Then it notifies the Raspberry Pi and then an alert will show on the notification on the phone. The alert is shown as notification which is shown below, and it include the time when the person was detected by the senor.



Figure 5.3 Security Alert

3. The last function we required our system to do was to detect the fire. In the function, we use the flame sensor to detect the fire. If their fire detects the sensor send information to Raspberry PI, which then sends a notification to the phone of the owner or stores a similar security function. It also same a similar notification to the last function where it tells you Fire detection, and tell u the time it detects the time.

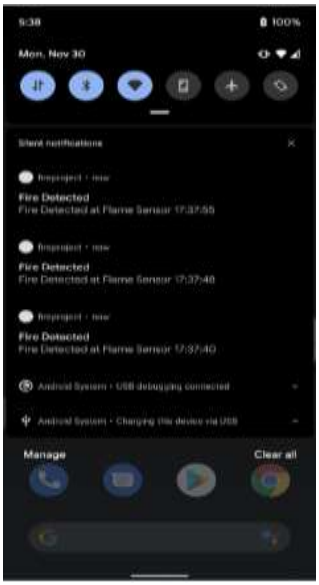


Fig 5.4 Fire Alarm alert

4. We have made our own application for the Android OS which receives alerts from the Embedded System through the internet. It is also able show the current customer count of that day.

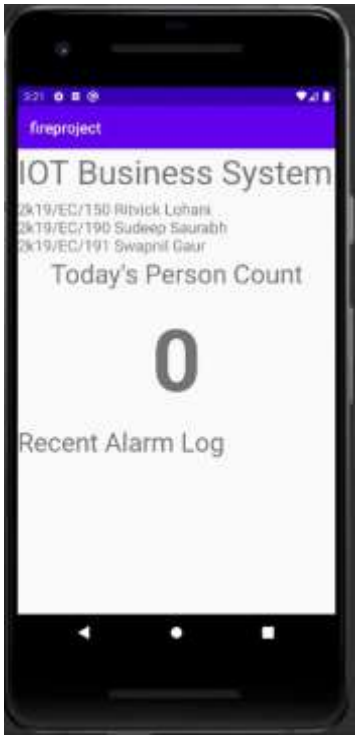


Fig 5.5 APP

VI. Conclusion and Future Scope

In today's world of technology, companies are investing billions of dollars annually on data and using that data to efficiently increase the growth of their company using methods which include optimizing the flow of customers, the supply and demand of the products that they provide. We have proposed a design for a low-cost Internet-of-Things enabled embedded system prototype which would help the small retail business to get data, and able to use that data further to increase its growth. The prototype is cost-efficient as it costs just under ₹2,500. The prototype currently works as data collection device which updates a remote database, as well as an emergency fire and security alarm.

The device is able to gather the number of people that visit a retail location and update a database in real-time, which can be viewed by the authorized user. Any data or necessary alerts are instantly sent to the mobile devices of the user who have installed and authenticated with the app we have made for the system. Many wonder what the applications are of the information gathered, and here are some examples:

1. We can determine and optimize the number of employees working at the location using this information. The device can accurately determine the customer footfall of the shop on an hourly and seasonal basis which helps decide the required number of retail employees, cash POS systems, security and safety measured required to be present in the retail shop at that moment of time. The retail shops should collect data over period of time, and see what hour of time during the day the shop is most active and they can have more employees present and that moment.

2.With the customer footfall information, the store can help identity various pointers on business as to why the growth of the business is doing well or not.

a) If the number of people visiting grows, and the growth of company profits happens at the same time, that mean that company is doing well.

b) If the number of people visiting grows, but the company profits and the item sales are not at a growth then that indicates that the company has been doing well with their advertising, but not with their product lineup or their pricing.

c) If the profits of the company grow, but the people visiting the store has been declining, this indicates that the company has been doing well with their pricing and has been selling desirable products, but not doing well enough with their advertising which can potentially be improved to increase sales.

Acknowledgment

We would like to express our gratitude to everyone who has helped us through our academic journey. They have made major contributions towards our success in both our academics and the major project. We are indebted to Dr. Ajai Kumar Gautam for his invaluable supervision and guidance throughout the project. His leadership and inspiration have been instrumental in our progress. We like to also thanks our department for the support they provided throughout our journey. We would finally like to thank our parents for the assistance they provided.

VII. References

[1] Lohani, Gour, Saurabh, "Source code for Major Project: Helping Businesses with IoT Embedded Systems", 26 Apr. 2022, https://doi.org/10.5281/zenodo.7413899

[2] Lohani, Gour, Saurabh, "Source code for Major Project: Helping Businesses with IoT Embedded Systems - Android Client", 8 Dec. 2022, https://doi.org/10.5281/zenodo.7413822

[3] Mahgoub, Asma, et al. "IOT-Based Fire Alarm System." 2019 Third World Conference on Smart Trends in Systems Security and Sustainablity (WorldS4), 2019, https://doi.org/10.1109/worlds4.2019.8904001.

[4] Sharma, Aman, and Anjana Goen. "Smart Home Security System." 2018 International Conference on Advanced Computation and Telecommunication (ICACAT), 19 Dec. 2018, https://doi.org/10.1109/icacat.2018.8933780.

[5] Regmi, Swesh Raj, et al. "Customer Market Segmentation Using Machine Learning Algorithm." 2022 6th International Conference on Trends in Electronics and Informatics (ICOEI), 2022, https://doi.org/10.1109/icoei53556.2022.9777146

[6] Schiopu, Paul, and Aurelian Costea. "Design of Anti Burglar Alarm Systems Detection and Signaling." 2011 IEEE 17th International Symposium for Design and Technology in Electronic Packaging (SIITME), 15 Dec. 2011, https://doi.org/10.1109/siitme.2011.6102698

[7] Meegahapola, Lakmal, and Indika Perera. "Enhanced in-Store Shopping Experience through Smart Phone Based Mixed Reality Application." 2017 Seventeenth International Conference on Advances in ICT for Emerging Regions (ICTer), 15 Jan. 2018, https://doi.org/10.1109/icter.2017.8257810

[8] Archana Sharma. "Internet of Things: Impact of IoT in Business Environment and Challenges in Secure Implementation." 2020 International Journal of Recent Technology and Engineering (IJRTE) Volume-9 Issue-2,, July,2020; ISSN: 2277-387

[9] Kumar, S., Tiwari, P. & Zymbler, M. Internet of Things is a revolutionary approach for future technology enhancement: a review. J Big Data 6, 111 (2019). https://doi.org/10.1186/s40537-019-0268-2

[10] Angelova, N., et al. "The Great Impact of Internet of Things on Business." Trakia Journal of Science, vol. 15, no. Suppl.1, 2017, pp. 406–412., https://doi.org/10.15547/tjs.2017.s.01.068

[11] Muheden, Karwan, et al. "Design and Implementation of the Mobile Fire Alarm System Using Wireless Sensor Networks." 2016 IEEE 17th International Symposium on Computational Intelligence and Informatics (CINTI), 19 Feb. 2017, https://doi.org/10.1109/cinti.2016.7846411

[12] Mori, Hideki, et al. "Configuration-Free Propagation System for Early Fire Alerts." 2016 IEEE International Conference on Pervasive Computing and Communication Workshops (PerCom Workshops), 21 Apr. 2016, https://doi.org/10.1109/percomw.2016.7457100

[13] Nayyar, Chetana, et al. "Home Security and Energy Efficient Home Automation System Using Arduino." 2017 International Conference on Communication and Signal Processing (ICCSP), 8 Feb. 2018, https://doi.org/10.1109/iccsp.2017.8286573

First Author – Dr.Ajai Kumar Gautam, Professor, Delhi Technological University, Delhi, India, 110042,
Second Author Ritvick A. Lohani, Student, Delhi Technological University, Delhi, India, 110042,
Third Author – Sudeep Saurabh, Student, Delhi Technological University, Delhi, India, 110042,
Fourth Author – Swapnil Gour, Student, Delhi Technological University, Delhi, India, 110042, .

Correspondence Author – Sudeep Saurabh, Student, Delhi Technological University, Delhi, India, 110042,

Hexagonal lattice twin core photonic crystal fiber based chemical sensor

2023 10th International Conference on Signal Processing and Integrated Networks (SPIN) | 978-1-6654-9099-3/23/$31.00 ©2023 IEEE | DOI: 10.1109/SPIN57001.2023.10117365

Vishal Chaudhary
Dept. of Electronics and Communication Engineering,
Delhi Technological University, Shahbad Daulatpur, Delhi, India
vishalchaudhary_2k21phdec14@dtu.ac.in

*Sonal Singh
Dept. of Electronics and Communication Engineering,
Delhi Technological University, Shahbad Daulatpur, Delhi, India
sonalsingh@dtu.ac.in

* Corresponding Author

***Abstract*— In this work, a chemical sensor based on twin-core photonic crystal fiber (TC-PCF) is presented. In the TC-PCF structure's cross-sectional arrangement, two solid cores are positioned with a vertically aligned elliptical hole in between them. These cores are then filled with different chemicals, such as ethanol, benzene, and water. The proposed sensor incorporates a unique configuration of elliptical air holes, which provides it with a competitive advantage in achieving high sensitivity compared to other currently available structures. High birefringence is a distinctive feature of this sensor, which operates based on the principle of mode coupling between its two fiber cores. Through the employment of the finite element method (FEM), we have conducted a quantitative analysis and simulation of the TC-PCF chemical sensor proposed. With a fiber length of 0.03 cm, the maximum sensitivity of 6667 nm/RIU is obtained. With such small fiber length, our proposed TC-PCF design will help overcome the geometry restrictions towards its practical designing and fabrication, as compared to conventional PCFs. The primary goal is to deploy TC-PCF as a chemical sensor application in the industrial sector to identify dangerous chemicals.**

Keywords*— Twin core PCF, Chemical sensor, Mode coupling, Birefringence, Transmission signal

I. INTRODUCTION

The development of photonic crystal fibers (PCFs), which have salient optical characteristics, has demonstrated the potential advantages of optical fibers in sensing applications [1]–[4]. These micro structured fibers stand out especially for chemical and biological sensing due to their exceptional qualities, including their tiny size and relative compatibility [5]–[7]. While in conventional fibers, designing is so difficult, the size of the core is constrained, selection of material is tough etc. Additionally, these geometry restrictions make the system less flexible to identify the characteristics of fibers, such as birefringence [6], confinement loss [8], dispersion [6], relative sensitivity [9] etc. PCF enables long-distance light propagation that was previously impossible. It is possible to control the characteristics of light propagation by modifying the air holes in the core and cladding region. In the areas of nonlinear optics [10], sensing [11] and optical communications [9], numerous research investigations have previously been conducted. It has been suggested to use a PCF refractive index (RI) sensor that is based on the surface plasmon resonance (SPR) phenomena. Because the inside side of the air holes in these fibers contains metal, they are particularly challenging to make. As a result, the use of fibers based on SPR has extremely few applications. Simple twin core PCF sensors are extremely effective because they have high sensitivity, easy fabrication, simple design and require less metal wires for their construction.

In this research work, we proposed a novel type of chemical sensing fiber with two solid cores separated by a vertical elliptical hole. The sensitivity of the TC-PCF can be determined by examining the variation in the transmission curve of the TC-PCF caused by changes in the refractive index of different chemicals, such as ethanol, benzene, and water. The proposed TC-PCF configuration is designed by the FEM-based COMSOL Multiphysics version 5.2a.

II. PCF DESIGN AND RESULT ANALYSIS

Figure (1) shows the configuration of a proposed hexagonal lattice twin core PCF chemical sensor. Two air holes are eliminated from this design, creating two PCF solid cores. The twin-fiber cores of the proposed TC-PCF are separated by a vertical elliptical hole and filled with different chemicals such as ethanol, benzene and water. The proposed Photonic Crystal Fiber will have elliptical air holes with a pitch length (Λ) of 2 µm. The minor axis of the elliptical hole is 0.9 µm, while the major axis is 1.4 µm. The background material selected is pure silica and its refractive index (R.I.) is determined by the Sellmeier equation [12] and R.I. of air (n_{air} = 1) is considered. The refractive index of various analytes like ethanol (n = 1.354), benzyne (n = 1.366) and water (n = 1.33) is considered [13]. When compared to other complex structures that have been previously published, this form of PCF structure is quite simple to fabricate. Here, a normal mode of Mesh analysis is chosen to investigate the proposed PCF using COMSOL Multiphysics software.

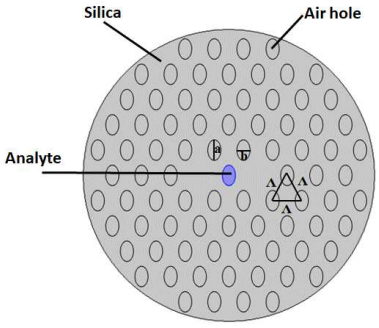


Figure (1) Cross-section of proposed twin-core PCF.

Authorized licensed use limited to: DELHI TECHNICAL UNIV. Downloaded on May 15,2023 at 09:56:51 UTC from IEEE Xplore. Restrictions apply.

Four super modes in the x and y-polarization are possible according to the theory of PCF mode coupling [14]. Due to the distinct cores, these four super-modes are possible. The electric field profile distribution of the four super modes at 1.55 µm are shown in Figure (2).

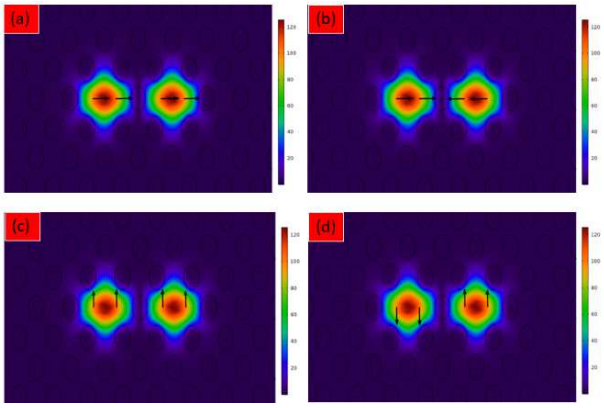


Figure (2) The distribution of the amplitude and vector of the electric field for four super-modes: (a) and (b) are x-polarization with even and odd symmetry, respectively, while (c) and (d) are y-polarization with even and odd symmetry, respectively

The PCF sensing setup, as illustrated in Figure (3), requires crucial equipment such as a temperature controller, broadband light source, and optical spectrum analyzer. Light can be introduced into the fiber-core A using a single-mode fiber (SMF) from the broadband light source, while the output signal can be observed from the fiber core B using another SMF and an optical spectrum analyzer.

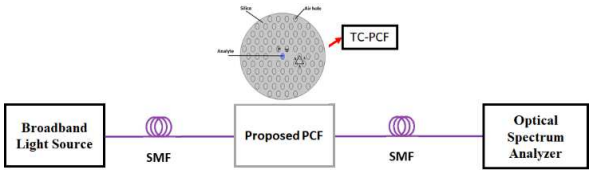


Figure (3) TC-PCF sensing arrangement for chemical sensor

The n_{eff}^{x} even and odd modes at 1.55 µm are 1.410891625 and 1.407693967, respectively, while the n_{eff}^{y} even and odd modes at 1.55 µm are 1.411224356 and 1.408240529, respectively. Figure (4) shows how the n_{eff} of the even and odd modes for x-polarized and y-polarized vary with wavelength. As the wavelength increases, the n_{eff} decreases.

Figure (5) shows the Δn_{eo} fluctuation, where $\Delta n_{eo} = |n_e - n_o|$, for the x and y polarized modes. When there is an increase in the wavelength of light, the Δn_{eo} between the core and cladding of a fiber also increases. The increase in the Δn_{eo} of the proposed PCF indicates that the confinement of light in the core has become stronger.

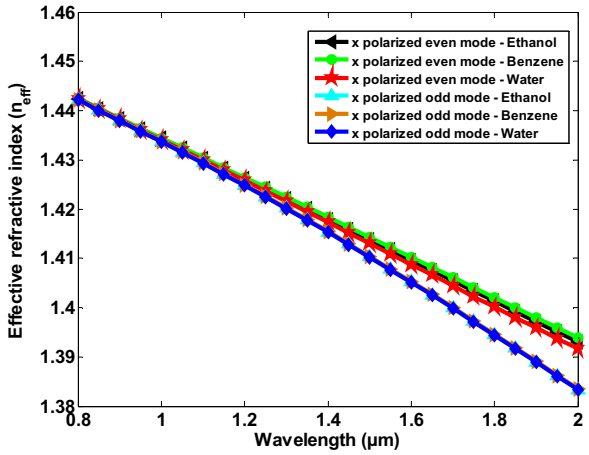


Figure (4) Variation in n_{eff} with wavelength

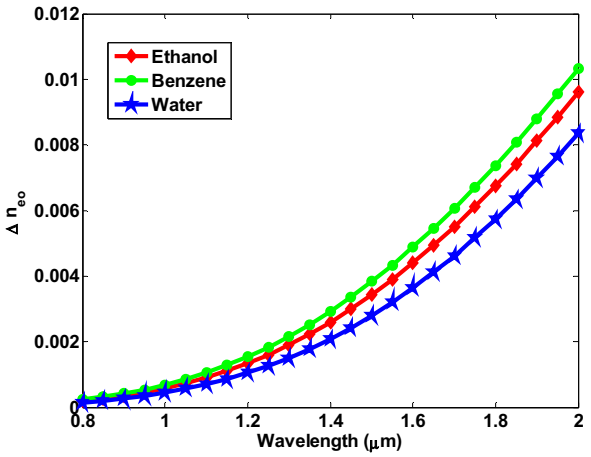


Figure (5) Variation in Δn_{eo} with wavelength

The coupling length of the proposed PCF is computed using Eq. (1).

$$L_c = \frac{\pi}{|\beta_e^i - \beta_o^i|} = \frac{\lambda}{2|n_e^i - n_o^i|} \quad (1)$$

The TC-PCF has even and odd mode propagation constants represented by β_e^i and β_o^i, respectively, where i is either x or y. Additionally, even and odd effective R.I. are denoted by n_e^i and n_o^i, respectively [15], [16]. We have determined the coupling length value for various wavelengths using Eq. (1). The coupling length variation as a function of wavelength when the central hole of the TC-PCF is filled with different chemicals such as ethanol, benzene and water shown in Figure (6). It should be noticed that the coupling length decreases with increasing wavelength. The TC-PCF coupling length varies depending on the chemical used and when water is poured into the central hole of the TC-PCF, it can provide a maximum coupling length of 0.24 mm at a 1.55 µm wavelength. Also, a small coupling length results in a greater mode coupling between the two fiber cores.

Authorized licensed use limited to: DELHI TECHNICAL UNIV. Downloaded on May 15,2023 at 09:56:51 UTC from IEEE Xplore. Restrictions apply.

The birefringence of the proposed PCF, which is the cause of the double-refraction phenomenon, is computed using Eq. (2). In the presence of a birefringent material, the polarization of a light ray leads to its division into two rays, which propagate in separate directions.

$$B = \left|Re\left(n_{eff}^{x}\right) - Re\left(n_{eff}^{y}\right)\right| \qquad (2)$$

Where the effective refractive indices of the x and y polarized modes is denoted as n_{eff}^{x} and n_{eff}^{y}, respectively [17]. At 1.55 µm wavelength, the high birefringence of 3.327x10^{-4} and 5.466x10^{-4}, respectively is attained for the even and odd modes when water is poured into the central hole of the TC-PCF. Figure (7) illustrates how birefringence changes with operational wavelength.

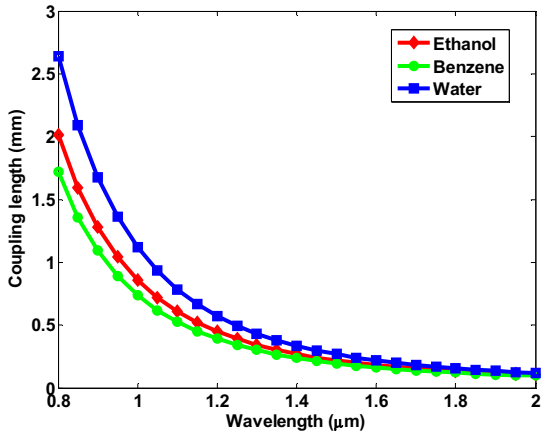


Figure (6) The variation of coupling length with wavelength

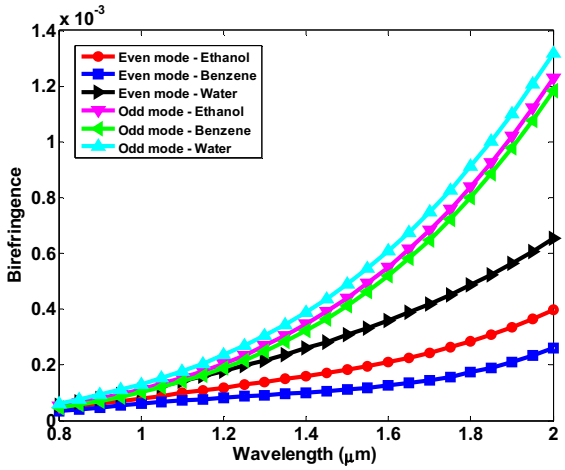


Figure (7) The variation of birefringence with wavelength

Equation (3) is used to calculate the power transfer of the TC-PCF after a length L.

$$\mathrm{I}(\lambda) = \sin^2\left(\frac{\pi}{\lambda}\Delta n_{eo} L\right) \qquad (3)$$

In the given context, the effective refractive indices difference is denoted as (Δn_{eo}) and the effective refractive indices of the even and odd modes are denoted as n_e^i and n_o^i respectively [15]. Figure (8) depicts the power transmission graph of TC-PCF for different chemicals when the PCF length is just 0.03 cm. The proposed power transmission graph for TC-PCF displays a sinusoidal pattern, which should be duly noted.

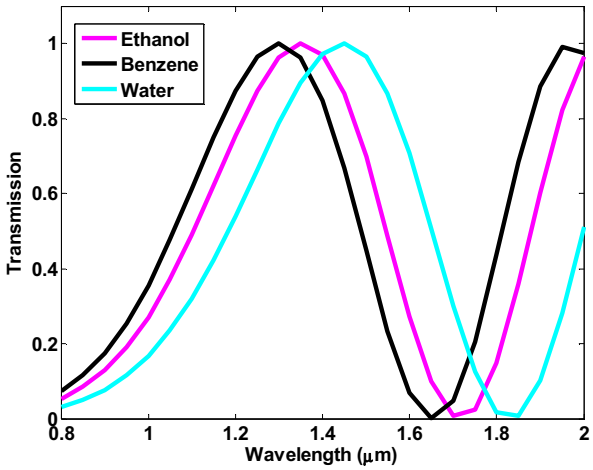


Figure (8) The transmission characteristics of TC-PCF, with a specific length of 0.03 cm

To evaluate the proposed TC-PCF sensitivity for chemical sensing, the shifting of transmission peaks is observed by changing the refractive index (RI) of different chemicals. The TC-PCF temperature sensitivity can be described as

$$S_\lambda(nmRIU^{-1}) = \Delta\lambda_{peak}/\Delta n_a \qquad (4)$$

where $\Delta\lambda_{peak}$ represent the overall shift in transmission curve and Δn_a is the shift in RI of different chemicals [18]. The sensitivity of the twin-core PCF, which is 6667 nm/RIU, is achieved for a fiber length of only 0.03 cm. With other published papers, we have compared the proposed design sensitivity response. Using a gold nanofilm coated photonic crystal fiber, Zhen-Kai Fan et al. demonstrated a SPR sensor in 2019 achieving a RI sensitivity of around 3978 nm/RIU [19]. In their study of a SPR sensor based on a PCF with large-sized microfluidic channels, P. Bing and group found that the sensor had a maximum wavelength sensitivity of 2000 nm/RIU for a RI detection range of 1.33 to 1.39 [20]. G. An et al. presented a PCF-SPR sensor with a maximum wavelength sensitivity of around 3233 nm/RIU and an extra-wide RI detection range of 1.30 to 1.79 [21]. C. Liu et al. presented a SPR sensor in 2018 achieving a RI sensitivity of around 6300 nm/RIU [22]. The main benefits of a proposed chemical sensor based on TC-PCF are its inexpensive price, compact size and improved stability.

Table 1 summarizes the suggested sensor performance. Table 1 shows that the sensor presented in this study exhibited superior performance compared to the PCF sensors that were reported recently.

Authorized licensed use limited to: DELHI TECHNICAL UNIV. Downloaded on May 15,2023 at 09:56:51 UTC from IEEE Xplore. Restrictions apply.

Table 1 Comparison of the performance of various PCF sensors, including the PCF sensor proposed in this study

Reference	Sensitivity
[19]	3978 nm/RIU
[20]	2000 nm/RIU
[21]	3233 nm/RIU
[22]	6300 nm/RIU
Proposed PCF	6667 nm/RIU

III. CONCLUSION

This research presents a chemical sensor based on twin-core photonic crystal fiber (PCF) with a hexagonal lattice structure. The sensitivity of the sensor is evaluated using the Finite Element Method and COMSOL software by analyzing the coupling length and transmission spectrum. The results demonstrate the potential of the proposed PCF sensor for chemical sensing applications. The highest sensitivity achieved for the proposed fiber sensor is 6667 nm/RIU when the fiber length is 0.03 cm. The result reveals that the size of the proposed TC-PCF chemical sensor is very compact, of simple design, and easy to fabricate when compared to other reported works. The small fiber length can help to overcome associated practical physical constraints during designing and achieve a less complex PCF architecture.

REFERENCES

[1] S. Geerthana, A. S. Raja, and D. S. Sundar, "Design and optimization of photonic crystal fiber with improved optical characteristics," *J. Nonlinear Opt. Phys. Mater.*, vol. 24, no. 4, 2015, doi: 10.1142/S0218863515500514.

[2] M. Hossain, E. Podder, A. Adhikary, and A. Al-Mamun, "Optimized Hexagonal Photonic Crystal Fibre Sensor for Glucose Sensing," *Adv. Res.*, vol. 13, no. 3, pp. 1–7, 2018, doi: 10.9734/air/2018/38972.

[3] S. Kim, Y. S. Lee, C. G. Lee, Y. Jung, and K. Oh, "Hybrid square-lattice photonic crystal fiber with broadband single-mode operation, high birefringence, and normal dispersion," *J. Opt. Soc. Korea*, vol. 19, no. 5, pp. 449–455, 2015, doi: 10.3807/JOSK.2015.19.5.449.

[4] V. Chaudhary and D. Kumar, "Design and analysis of refractive index sensor based on dual-core photonic crystal fiber (DC-PCF) with rectangular air hole lattice structure," *Lect. Notes Electr. Eng.*, vol. 546, pp. 207–213, 2020, doi: 10.1007/978-981-13-6159-3_22.

[5] A. M. R. Pinto and M. Lopez-Amo, "Photonic crystal fibers for sensing applications," *J. Sensors*, vol. 2012, 2012, doi: 10.1155/2012/598178.

[6] D. Chen, M. L. V. Tse, and H. Y. Tam, "Optical properties of photonic crystal fibers with a fiber core of arrays of sub-wavelength circular air holes: Birefringence and dispersion," *Prog. Electromagn. Res.*, vol. 105, pp. 193–212, 2010, doi: 10.2528/PIER10042706.

[7] O. S., N. Seifouri, M., A., Abadi, and M. S. E., "Low Nonlinear Effects Index-Guiding Nanostructured Photonic Crystal fiber," *Int. J. Chem. Mol. Nucl. Mater. Metall. Eng.*, vol. 9, no. 2, pp. 253–257, 2015.

[8] K. R. Priya, A. S. Raja, and D. S. Sundar, "Design of a dual-core liquid-filled photonic crystal fiber coupler and analysis of its optical characteristics," *J. Opt. Technol.*, vol. 83, no. 9, p. 569, 2016, doi: 10.1364/jot.83.000569.

[9] M. B. Hossain, A. A.-M. Bulbul, M. A. Mukit, and E. Podder, "Analysis of Optical Properties for Square, Circular and Hexagonal Photonic Crystal Fiber," *Opt. Photonics J.*, vol. 07, no. 11, pp. 235–243, 2017, doi: 10.4236/opj.2017.711021.

[10] H. Ademgil, "Highly sensitive octagonal photonic crystal fiber based sensor," *Optik (Stuttg).*, vol. 125, no. 20, pp. 6274–6278, 2014, doi: 10.1016/j.ijleo.2014.08.018.

[11] E. K. Akowuah, T. Gorman, H. Ademgil, S. Haxha, G. K. Robinson, and J. V. Oliver, "Numerical analysis of a photonic crystal fiber for biosensing applications," *IEEE J. Quantum Electron.*, vol. 48, no. 11, pp. 1403–1410, 2012, doi: 10.1109/JQE.2012.2213803.

[12] A. A. Rifat, G. A. Mahdiraji, Y. M. Sua, R. Ahmed, Y. G. Shee, and F. R. M. Adikan, "Highly sensitive multi-core flat fiber surface plasmon resonance refractive index sensor," *Opt. Express*, vol. 24, no. 3, p. 2485, 2016, doi: 10.1364/oe.24.002485.

[13] V. S. Chaudhary and D. Kumar, "TOPAS based porous core photonic crystal fiber for terahertz chemical sensor," *Optik (Stuttg).*, vol. 223, no. August, p. 165562, 2020, doi: 10.1016/j.ijleo.2020.165562.

[14] W.-P. Huang, "Coupled-mode theory for optical waveguides: an overview," *J. Opt. Soc. Am. A*, vol. 11, no. 3, p. 963, 1994, doi: 10.1364/josaa.11.000963.

[15] K. Saitoh, Y. Sato, and M. Koshiba, "Coupling characteristics of dual-core photonic crystal fiber couplers," *Opt. Express*, vol. 11, no. 24, p. 3188, 2003, doi: 10.1364/oe.11.003188.

[16] Z. Wang, T. Taru, T. A. Birks, J. C. Knight, Y. Liu, and J. Du, "Coupling in dual-core photonic bandgap fibers: theory and experiment," *Opt. Express*, vol. 15, no. 8, p. 4795, 2007, doi: 10.1364/oe.15.004795.

[17] A. Ortigosa-Blanch *et al.*, "Highly Birefringent Photonic Crystal Fibers," *Opt. Photonics News*, vol. 12, no. 12, p. 17, 2001, doi: 10.1364/opn.12.12.000017.

[18] B. Gauvreau, A. Hassani, M. Fassi Fehri, A. Kabashin, and M. A. Skorobogatiy, "Photonic bandgap fiber-based Surface Plasmon Resonance sensors," *Opt. Express*, vol. 15, no. 18, p. 11413, 2007, doi: 10.1364/oe.15.011413.

[19] Z. K. Fan, S. B. Fang, S. G. Li, and Z. Y. Wei, "Refractive index sensor based on high-order surface plasmon resonance in gold nanofilm coated photonic crystal fiber," *Chinese Phys. B*, vol. 28, no. 9, 2019, doi: 10.1088/1674-1056/ab327a.

[20] P. Bing, J. Yao, Y. Lu, and Z. Li, "A surface-plasmon-resonance sensor based on photonic-crystal-fiber with large size microfluidic channels," *Opt. Appl.*, vol. 42, no. 3, pp. 493–501, 2012, doi: 10.5277/oa120306.

[21] G. An *et al.*, "Extra-broad Photonic Crystal Fiber Refractive Index Sensor Based on Surface Plasmon Resonance," *Plasmonics*, vol. 12, no. 2, pp. 465–471, 2017, doi: 10.1007/s11468-016-0286-2.

[22] C. Liu *et al.*, "Birefringent PCF-Based SPR Sensor for a Broad Range of Low Refractive Index Detection," *IEEE Photonics Technol. Lett.*, vol. 30, no. 16, pp. 1471–1474, 2018, doi: 10.1109/LPT.2018.2856859.

Authorized licensed use limited to: DELHI TECHNICAL UNIV. Downloaded on May 15,2023 at 09:56:51 UTC from IEEE Xplore. Restrictions apply.

Computers and Electrical Engineering 108 (2023) 108733

Contents lists available at ScienceDirect

Computers and Electrical Engineering

journal homepage: www.elsevier.com/locate/compeleceng

Hybrid deep learning with improved Salp swarm optimization based multi-class grape disease classification model

Shtwai Alsubai [a], Ashit Kumar Dutta [b], Ahmed Hussein Alkhayyat [c,*], Mustafa Musa Jaber [d,e], Ali Hashim Abbas [f], Anil Kumar [g]

[a] Department of Computer Science, College of Computer Engineering and Sciences in Al-Kharj, Prince Sattam bin Abdulaziz University, Al-Kharj 151, Saudi Arabia
[b] Department of Computer Science and Information Systems, College of Applied Sciences, AlMaarefa University, Riyadh, Ad Diriyah 13713, Saudi Arabia
[c] Scientific Research Centre of the Islamic University, The Islamic University, Najaf, Iraq
[d] Department of Medical Instruments Engineering Techniques, Al-Turath University College, Baghdad 10021, Iraq
[e] Department of Medical instruments engineering techniques, Al-Farahidi University, Baghdad 10021, Iraq
[f] College of Information Technology, Imam Ja'afar Al-Sadiq University, Al-Muthanna 66002, Iraq
[g] Tula's Institute, Dehradun, India

ARTICLE INFO

This paper is for CAEE special section VSI-siot. Reviews processed and recommended for publication to the Editor-in-Chief by Guest Editor Dr. Deepak Gupta.
Editor Name: Deepak Gupta

Keywords:
Precision agriculture
Grape leaf disease
Computer vision
Artificial intelligence
Deep learning

ABSTRACT

The recent revolutions in Computer Vision (CV) and Artificial Intelligence (AI) techniques have found many applications in grapevine and smart agriculture processes. Recently, Deep Learning (DL) techniques like Convolutional Neural Networks (CNN) have been broadly applied in smart agriculture, leaf disease recognition, and scene perception. In this background, the current study develops a Hybrid Deep Learning with Improved Salp Swarm Optimization-based Multi-class Grape Disease Classification (HDLISSA-MGDC) model. The proposed HDLISSA-MGDC model focuses on the classification of grape leaf images into four distinct classes such as black measles, black rot, Isariopsis leaf spot and healthy. Initially, the Median Filtering (MF) technique is applied for image pre-processing, which eliminates the noise present in the images. In addition, the HDLISSA-MGDC model designs a feature extractor with the help of Dilated Residual Network (DRN) and Adam optimizer. For grape disease classification, the Convolutional Neural Network-Gated Recurrent Unit (CNN-GRU) model is employed in this study. Finally, the ISSA is exploited to adjust the hyperparameter values of the CNN-GRU method. The proposed HDLISSA-MGDC method was simulated using the plant leaf disease dataset. The simulation results show the significant performance of the proposed HDLISSA-MGDC model.

1. Introduction

Agricultural crop protection is highly significant to preserve the food sources. It is important to ensure that the agricultural crops

This paper was recommended for publication by Associate Editor Dr. Gupta DeepakThis paper is for special section VSI-siot. Reviews were processed by Guest Editor Dr. Gupta Deepak

* Corresponding author.
E-mail addresses: sa.alsubai@psau.edu.sa (S. Alsubai), adotta@mcst.edu.sa (A.K. Dutta), dr.ahmedalkhayyat85@gmail.com (A.H. Alkhayyat), mustafa.jaber@turath.edu.iq (M.M. Jaber).

https://doi.org/10.1016/j.compeleceng.2023.108733
Received 16 December 2022; Received in revised form 10 April 2023; Accepted 13 April 2023
Available online 28 April 2023
0045-7906/© 2023 Published by Elsevier Ltd.

are maintained healthy as it affects the yield and accordingly the agricultural outcome too. If it is not maintained properly, then it may lead to economic loss as well. Plant diseases are caused by fungi, viruses, and microbes [1]. Unexpected temperatures and risky meteorological conditions may spur the growth and development of plants by spreading harmful creatures. This in turn destroys the crops or severely decreases the yields. Additionally, globalization and global travel increase the risks of infection with transboundary diseases [2]. Grapes are considered to be a widespread and significant fruit that is used either as a beverage or food. Based on the spread and seriousness, the grape diseases cause 5%−80% of the crop loss [3]. Grape plants are highly susceptible to diseases such as isariopsis leaf spots, black measles, and black rot. Grape leaf diseases are now controlled by repetitive fungicide treatments, all over the season [4,5]. It is challenging to mitigate the costs of treatment from economic and environmental views. So, prompt recognition and early treatment of downy mildew infection remain a good solution to reduce and control the spread of downy mildew in large areas [6].

In recent years, vision-related disease detection techniques have been formulated for the detection of plant diseases [7]. It can be carried out by deriving the visual features (for example, the color of leaf lesion, texture, and shape) of leaf imageries and utilizing machine learning techniques (for example, linear regression, support vector machine and so on) for detection and recognition of the diseases. But, due to complicate feature extraction and image pre-processing requirements, such techniques have less recognition efficiency [8.9]. Recently, Convolutional Neural Networks (CNNs) have been formulated as an end-wise DL method. These techniques leverage image-based big datasets, find the discriminatory features from the original images, evade complex image preprocessing requirements and minimize the memory footprints [10]. CNNs can be employed in the diagnosis of crop diseases [11,12]. But, several problems persist in realizing the real-time recognition of grape leaf disease, because of the subsequent features of grape leaf-diseased spots. Many dense and small diseased spots tend to appear on similar leaves with different shapes [13]. Furthermore, the environmental components and the protection of other leaves even affect the recognition of grape leaf diseases.

The current study presents a Hybrid Deep Learning with Improved Salp Swarm Optimization-based Multi-class Grape Disease Classification (HDLISSA-MGDC) model. In the proposed HDLISSA-MGDC model, the Median Filtering (MF) technique is applied for image pre-processing. Besides, the HDLISSA-MGDC model designs a feature extractor using the Dilated Residual Network (DRN) with an Adam optimizer. For grape disease classification, the ISSA with Convolutional Neural Network-Gated Recurrent Unit (CNN-GRUs) model is employed. The proposed HDLISSA-MGDC model was experimentally validated using the plant leaf disease dataset.

Rest of the paper is organized as follows: Section 2 presents related work. Section 3 analyzes and studies the proposed model, taking into account feature extraction and grape disease classification utilizing a simple mathematical model. Results and discussion are presented in Section 4. Finally, we conclude in Section 5.

2. Related works

In literature [14], novel multi-class SVM and image processing methods were employed to classify and diagnose the grape leaf diseases as leaf blight, black measles, and black rot. The region that showed the disease symptoms was separated from the healthy parts of the leaves using K-means clustering mechanically. Then, the features were derived in three color methods such as l*a*b, RGB, and HSV. In this work, SVM was employed as an effective classifier technique and PCA was executed to reduce the feature dimensions. In the study conducted earlier [15], the authors intended to identify the grape leaf diseases. So, an accurate and a fast detection technique related to fused deep features that are derived from CNNs and an SVM were devised. Initially, the images were resized in the study to address the input needs of the CNN network; then, the deep features of the input images were derived through a particular deep feature layer that belonged to CNN networks. Two types of features from various networks were merged through different fusion techniques so as to enhance the effectual classification of feature information.

In literature [16], ML technique was implemented to detect the grape leaf disease at the initial stage itself and distinguish different classes of disease with high precision. Additionally, an improvised K- Nearest Neighbor (IKNN) method and CNN-related Classification (CNNC) technique were presented for the classification of leaf diseases. High-quality histogram and the extended histogram features were acquired to offer boundary, structural, discriminative information, and pattern. In the study conducted earlier [17], an accurate and a fast identification approach, related to Canonical Correlation Analysis (CCA), was modelled. This model compiled various deep features derived from the CNN and SVM techniques. In this work, three types of existing CNN, seven species of deep features, and multiclass SVM techniques were learnt based on open data. Initially, the images were resized to address the input needs of CNN. Math and Dharwadkar [18] developed a Deep CNN (DCNN) method to classify and identify the grape diseases, related to the RGB leaf images. The novelty of this method was that the CNN classifier method can be framed from scratch which renders accurate or more importance than the accuracy gained for certain pre-trained techniques utilizing TL.

In literature [19], a united Convolutional Neural Network (CNN) architecture, relevant to the integrated technique, was devised. The architecture of the modelled CNNs i.e., UnitedModel was devised to differentiate the leaves with common grape diseases like caryopsis, black rot, and esca leaf spot from the normal leaves. The integration of many CNNs allowed the devised UnitedModel to extract the complementary discriminatory features. In the study conducted earlier [20], the authors devised an artificial intellectual method for grape foliage disease classification and detection. The stretch-oriented enhanced method was implemented for image enhancement. At the end, two techniques i.e., Bayesian Classifier and Multi–Support Vector Machine were devised to determine the category of grape foliage disease.

Diana Andrushia et al. [21] aimed at detecting the diseases in grape leaves using convolutional capsule networks. Capsule network is a promising neural network in DL algorithms. This network exploits a collection of neurons as capsules and efficiently represents the spatial information of the features. The novelty of the proposed work lies in the addition of convolutional layers before the primary caps layer. This characteristic indirectly reduces the number of capsules and accelerates the dynamic routing method. Lin et al. [22]

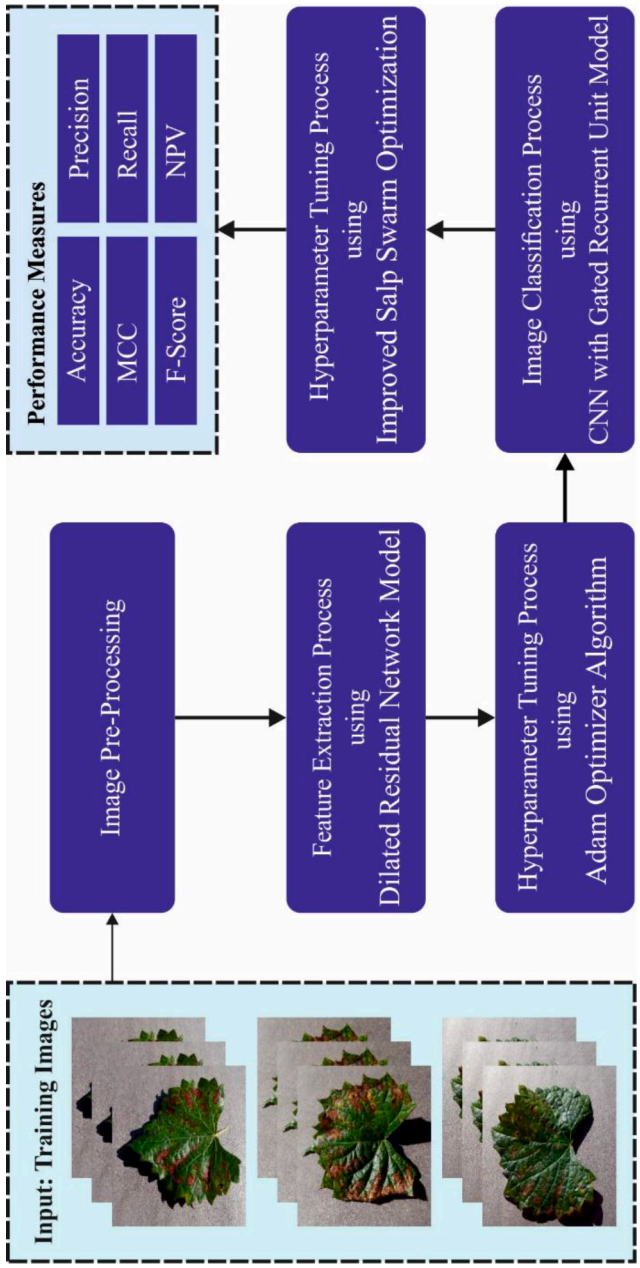


Fig. 1. Block diagram of the proposed HDLISSA-MGDC system.

developed a lightweight CNN model named 'GrapeNet' to detect different levels of symptoms exhibited by specific grape diseases. The building blocks of GrapeNet model are convolution block attention modules, residual blocks, and the Residual Feature Fusion Blocks (RFFBs). To mitigate the degraded performance of the CNN due to a considerable amount of hidden layers, this study developed the RFFB module based on the residual block. Lu et al. [23] introduced an accurate and effective method based on ghost-convolution and transformer networks to identify the grape leaves in the field. Ghost network was adopted in this study as the convolutional backbone to generate the intermediate feature maps with cheap linear operation. Further, the model also incorporated the transformer encoders with multi-head self-attention to extract deep semantic features. From this study, the Ghost Enlightened Transformer model i.e., GeT was attained.

3. The proposed model

In the current study, an automated grape disease classification model named HDLISSA-MGDC model has been developed. The presented HDLISSA-MGDC model classifies the grape leaf images under four distinct classes namely, Isariopsis leaf spot, Black measles, healthy, and black rot. In the presented HDLISSA-MGDC model, a series of processes is involved namely, the MF-based noise removal, Adam with DRN feature extraction, CNN-GRU classification, and ISSA hyperparameter tuning. Fig. 1 represents the block diagram of the proposed HDLISSA-MGDC system.

3.1. Image pre-processing

At first, the MF is applied to remove the noise from grape leaf images. MF refers to a filtering method that is employed to remove the noise from signals and images [24]. MF is the most significant technique used in the domain of image processing as it preserves the edges at the time of noise removal. The main task of this filter is to scan all the input datasets, interceding overall entries, with a median function called 'window' technique. The window is somewhat more complicated than the high-dimensional signals. The median count can be set as per the count of windows and falls under even and odd categories.

3.2. Feature extraction

To produce a set of feature vectors from the pre-processed images, the DRN is exploited with Adam optimizer. The ResNet 3×3 Visual Geometry Group (VGG) framework is the best framework available on the market for transfer learning. Afterwards, the modified data is provided to the ReLU layer. ReLU is activated after two convolution layers. The ResNet model depends on the GoogLeNet architecture at an initial point. After the convolution layers up to 64 and 7×7 layers become two strides, the 3×3 input channels are used. It is possible to interconnect the output of the convolution layer with the single input. One of the possibilities is to increase the channel count. Further 1×1 convolutional layer is required. ReLU is considered to be a non-linear input. This layer exerts no effects on its channel previous. Due to the presence of a small volume of the diseased spots in leaf images, the DRN architecture assists in the recognition of images only with a small amount of disease. A wide range of dilated architecture-based features would be available, thanks to the presence of high-quality leaf images in the ResNet model. By utilizing the preceding layers and the samples, it is possible to retain fine-grained features. Thus, a light-weighted ResNet-18 architecture has been proposed by conducting tests with different dilation rates and convolutional scales. Hence, the concatenation process reduces the computation cost, when increasing the number of fine-grained features. Consequently, the sample should be gathered for combining the lowest-level components into the highest-level map. The top and the bottom layers must be combined together to increase the detection of a smaller volume of illness in leaves. Each of the 64 filters contains 7×7 dimensions with an overall value being 64. Generally, Conv1 features considerably have large 7×7 dimensions, 64 filters, and 2 strides. The MaxPool 2×2 stride length is 2. The feature extraction process is followed by deep structure; the study additionally selects the features with low computation difficulty. The weight of the features in the neighbourhood can be evaluated based on the distance measures. So, it is possible to minimize the size of the feature vector through Neighbourhood Component Analysis (NCA) that represents the "nonparametric and supervised" type of analysis. This technique enables the modification and enhancement of the KNN architecture. Then, this technique is used for reducing the number of feature vectors, attained from the leaf image. This is because the positive weights are assigned to all the features whereas the feature rank is calculated through NCA. The Adam optimizer is used for fine-tuning the hyperparameters of the DRN model.

Adam is a first-order stochastic gradient-oriented optimization technique that is highly adaptable to the fitness function which changes for the features. The important advantage of this algorithm is its computation efficacy and fewer memory requirements. The text classification exploits the DRN for text [25]. The following steps detail about the Adam optimizer.

Step 1: Initialization

The initial step signifies the initialization of bias correction process in which $\widehat{q}$ indicates the corrected bias of the initial moment estimation and $\widehat{ml}$ signifies the corrected bias of the second-moment estimation.

Step 2: Discovery of error

Bias error can be evaluated for selecting the optimal weight in order to train the DRN. Now, the error is called as an error function

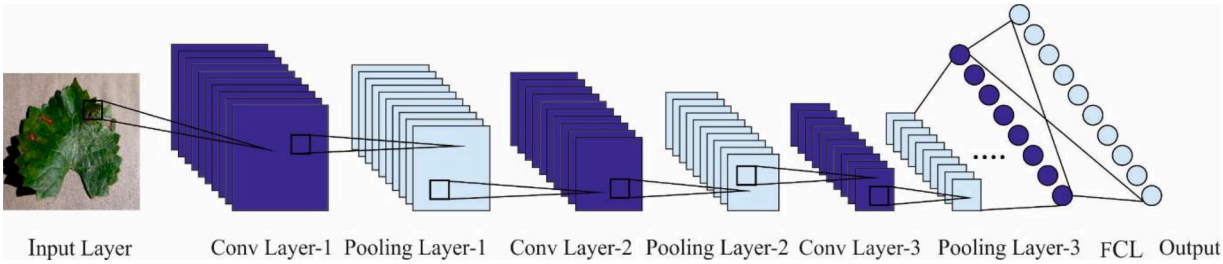


Fig. 2. Architecture of CNN.

that results in the optimum global solution.

$$Err = \frac{1}{f}\sum_{l=1}^{f}(O_l - \kappa)^2 \tag{1}$$

Here, f denotes the overall dataset, κ represents the output produced by DRN, and O_l specifies the expected value.

Step 3: Discovery of upgrading bias

Adam can be utilized to enhance the optimization outcomes and the convergence behavior. This approach generates smooth variations with low memory requirement and effective computation efficacy.

$$\theta_l = \theta_{l-1} - \frac{\alpha\widehat{q}_l}{\sqrt{\widehat{m}l + \varepsilon}} \tag{2}$$

Here, α indicates the step size, $\widehat{q}_l$ represents the corrected bias, $\widehat{m}_l$ shows the bias-corrected second-moment estimation, ε signifies a constant and θ_{l-1} indicates the variable at a prior time instant $(l-1)$:

$$\widehat{q}_1 = \frac{q_l}{(1-\eta_1^l)} \tag{3}$$

$$\widehat{q}_1 = \eta_1 q_{l-1} + (1-\eta_1)G_l^1. \tag{4}$$

The corrected bias of the second-order moment is given as follows.

$$\widehat{m} = \frac{ml}{(1-\eta_2^l)} \tag{5}$$

$$\widehat{m}_l = \eta_2 m_{l-1} + (1-\eta_2)H_l^2 \tag{6}$$

$$H_l = \nabla_\theta 1oss(\theta_{l-1}). \tag{7}$$

Step 4: Determination of a better solution: A better solution can be defined by errors whereas the best solution can be applied to classify the text.
Step 5: Termination: The optimal weight is repeatedly generated, until the iteration is accomplished.

3.3. Grape disease classification

For the identification of grape diseases, the CNN-GRU method is applied in this study. In RNN, the GRU network is frequently performed to manage the gradient vanishing problems [26]. GRU is better than LSTM since it involves three crucial gates and neither one of them contains internal cell state. Within the GRU, the dataset is kept in a hidden format for protection. Both backward and forward data can be jointly offered to update the gate (z). Moreover, the preceding data can be stored in the reset gate (r). The present memory gate uses the reset gate to maintain and save the basic data which already exists in the system, in its previous state. It is promising to integrate the non-linearity with the input of the modulation gate while at the same time, concurrently providing it with the property of zero means. This can be attained in a two-fold method and is mathematically expressed herewith.

$$L_\tau = \sigma(Z_\tau \cdot K_{xr} + R_{\tau-1} \cdot W_{hr} + C_r) \tag{8}$$

$$M_\tau = \sigma(Z_\tau \cdot K_{xz} + R_{\tau-1} \cdot W_{hz} + C_z) \tag{9}$$

Here, K and K denote the weight parameters, C_r and C refer to the bias vectors. The CNN-GRU method encompasses three Fully Connected layers (FC), three max-pooling layers and four Convolution Layers (CL). The activation function (ReLU) is executed since it

may not be able to activate all the neurons at the same time, which enables the algorithm to learn faster and implement the process better. At first, the input image dataset is provided with a dimension size of (50, 50, and3) in CL. This implies that the height and width of the image is 50 pixels, whereas the channel is 3. The CNN-GRU architecture needs a feature for extraction by-passing through the CL. In these cases, the output of the feature map is 128. Furthermore, the parameter is set so that the stride is 1 and the kernel size (3×3) of CL, correspondingly. Then, the ReLU is utilized by CL to reduce the nonlinearity dimension. After the initial CL, the output feature maps become 128 with a size of (50, 50). Moreover, the pooling layer reduces the variable of training to (48, 4s8). To prevent the model from over-fitting problems, the training variable (48, 48, 128) is passed over from the dropout layers and afterwards, the pooling layers too. Fig. 2 illustrates the structure of CNN.

To enhance the classification outcomes of the CNN-GRU method, the ISSA is used. The Salps population is classified into followers and leaders [27]. The leader of the Salps lies at the front of the food chain whereas the rest of the Salps are regarded as followers. The leaders lead the population whereas the follower follows one another (direct or indirect leaders).

Population initialization:

$$X_j^i = rand(N,\ D) \times (ub(\mathrm{j}) - lb(j)) + lb(j) \tag{10}$$

Initializing the position of slaps; $X_j^i(i = 1, 2,\ N, j = 1, 2,\ D)$.

The leader's location updating equation is given herewith.

$$x_j^i = \begin{cases} F_j + c_1\left(\left(ub_j - lb_j\right)\right)c_2 + lb_j c_3 \geq 0.5 \\ F_j - c_1\left(\left(ub_j - lb_j\right)\right)c_2 + lb_j c_3 < 0.5 \end{cases} \tag{11}$$

In Eq. (11), χ_j^i denotes the leader's location at *j-th* parameter. The initial Salp is selected as the leader. Further, F_j shows the location of the food source at *j-th* variable, ub_j denotes the upper boundary at *j-th* parameter, lb_j indicates the lower boundary at *j*-th variable, and c_1, c_2, *and*c_3 indicate random numbers. c_1 represents a significant variable in SSA since it balances the exploration and exploitation phases and it can be determined as follows.

$$c_1 = ze^{-\left(\frac{4l}{L}\right)^2} \tag{12}$$

Here, l denotes the existing iteration and L indicates the maximal iteration count.

The equation to update the location of the followers is as follows.

$$\chi_j^i = \frac{1}{2}\left(X_j^i + X_j^{i-1}\right) \tag{13}$$

Here, $i \geq 2$, χ signifies the location of the *i-th*follower at *j*-th parameter.

A chaotic map generates chaotic numbers within [0, 1] instead of generation the random integers through the original method. The chaotic sequence could frequently accomplish the best outcomes in comparison with the arbitrarily-generated numbers during operations like mutation, population initialization, selection, and crossover. In the presented method, the PWLCM chaotic map is utilized for initializing the location of the Salps' population.

$$X_j^i = lb_i + (ub_i - lb_i)y_j^i \tag{14}$$

$$X\left((+1) = F_p(X(T)) = \begin{cases} X((\mathrm{t})/p,\ 0 < X(t) < p \\ \dfrac{X-p}{0.5-p},\ p < X(T) < 0.5 \\ \dfrac{1-X(T)-p}{O.5-p},\ 0.5 < X(T) < 1-p \\ \dfrac{1-X(T)}{p}, 1-p < X(T) < 1-p \end{cases}\right. \tag{15}$$

Whereas $\in (O, 0.5)$.

The leader's location updating equation is given herewith.

$$\chi_j^i = \begin{cases} F_j + c_1\left(\left(ub_j - lb_j\right)\right)c_2 + lb_j & c_3 \geq 0.5 \\ F_j - c_1\left(\left(ub_j - lb_j\right)\right)c_2 + lb_j & c_3 < 0.5 \end{cases} \tag{16}$$

In the original algorithm, the initial Salps are chosen as the leader whereas only the primary one is easier to get trapped in the local optima. So, the current study prefers the first third of the Salps as the leader. The location of the follower's updating equation depends on the Newton's law of motion as given below.

$$V_t = V_0 + at \tag{17}$$

$$x = V_0 T + \frac{1}{2}at^2 \tag{18}$$

Table 1
Dataset details.

Label	Class	No. of Samples
Class 0	black measles	400
Class 1	black rot	400
Class 2	isariopsis leaf spot	400
Class 3	Healthy	400
Total number of samples		**1600**



Fig. 3. Sample images.

$$a = \frac{V_{final} - V_0}{t} \tag{19}$$

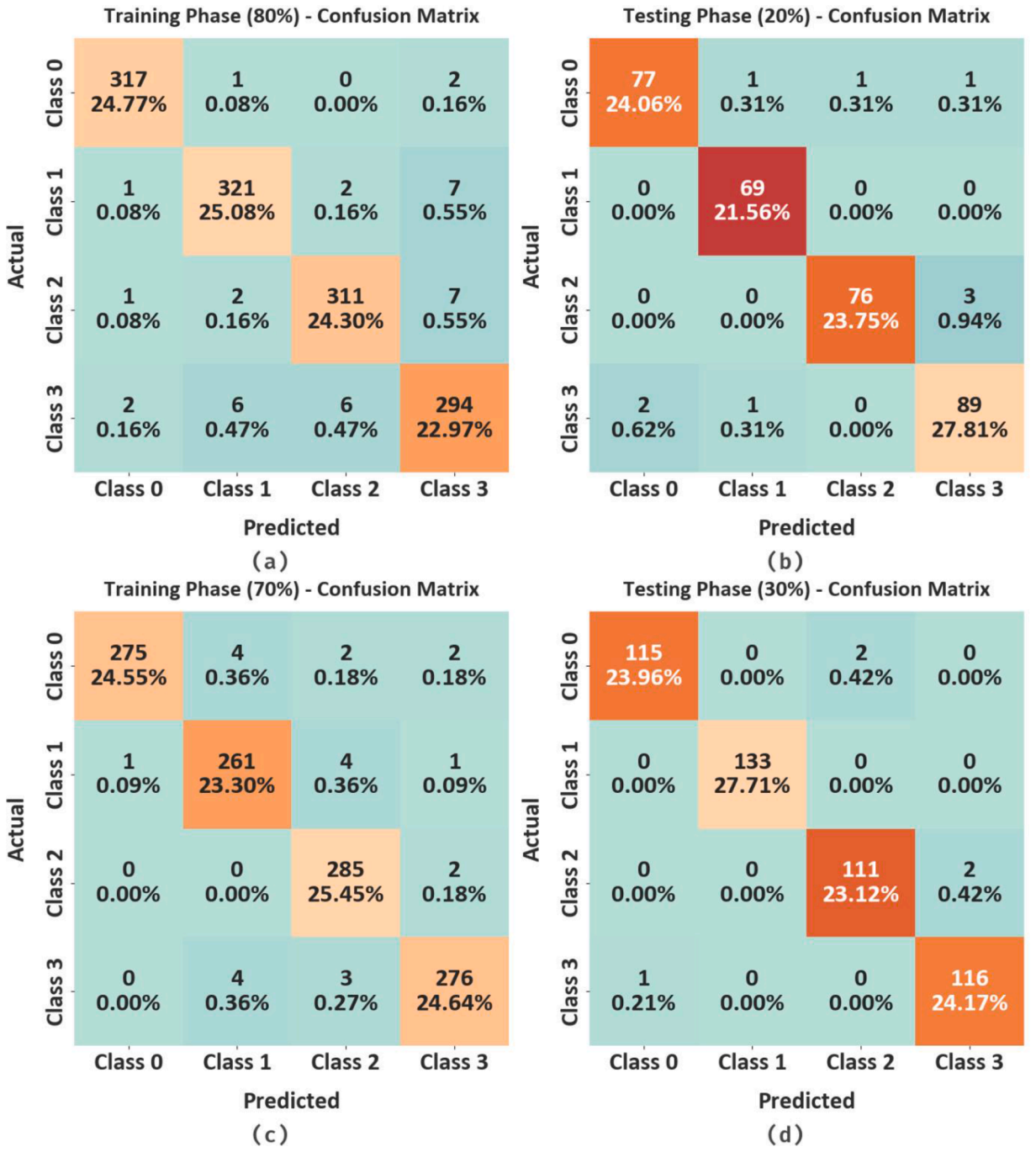


Fig. 4. Confusion matrices of the HDLISSA-MGDC system (a-b) TR and TS databases of 80:20 and (c-d) TR and TS databases of 70:30.

$$V_{final} = \frac{x_j^{i-1} - x_j^i}{\tau} \tag{20}$$

which also gets

$$\chi_j^i = \frac{1}{2}\left(\chi_j^i - \chi_j^{i-1}\right) \tag{21}$$

The current study upgrades Eq. (21) as followers. Certain steps are demonstrated in Algorithm 1. The ISSA method derives the Fitness Function (FF) to have enhanced classification outcomes. It defines a positive value to signify the superior outcomes of the

Table 2
Analytical results of the proposed HDLISSA-MGDC system under 80:20 of TR and TS databases.

Labels	$Accu_y$	$Prec_n$	$Reca_l$	F_{score}	MCC	NPV
Training Phase (80%)						
Class 0	99.45	98.75	99.06	98.91	98.54	99.69
Class 1	98.52	97.27	96.98	97.13	96.13	98.95
Class 2	98.59	97.49	96.88	97.19	96.25	98.96
Class 3	97.66	94.84	95.45	95.15	93.60	98.56
Average	**98.55**	**97.09**	**97.10**	**97.09**	**96.13**	**99.04**
Testing Phase (20%)						
Class 0	98.44	97.47	96.25	96.86	95.82	98.76
Class 1	99.38	97.18	100.00	98.57	98.19	100.00
Class 2	98.75	98.70	96.20	97.44	96.62	98.77
Class 3	97.81	95.70	96.74	96.22	94.68	98.68
Average	**98.59**	**97.26**	**97.30**	**97.27**	**96.33**	**99.05**

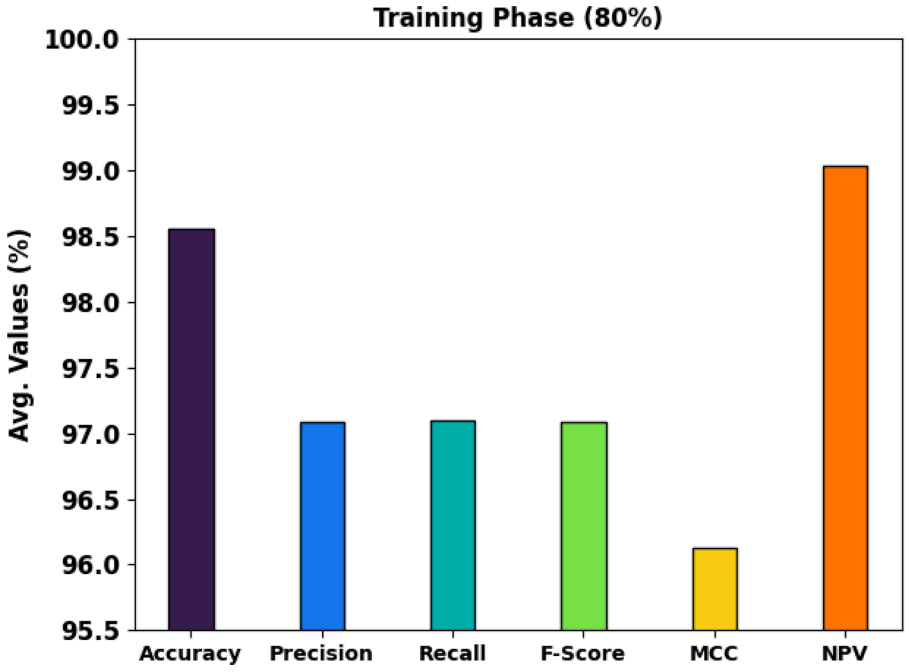


Fig. 5. Average analysis outcomes of the HDLISSA-MGDC system under 80% of TR database.

candidate solutions. In this work, the reduction of the classifier error rate corresponds to FF, as given in Eq. (22).

$$fitness(x_i) = \frac{number\ of\ misclassified\ samples}{Total\ number\ of\ samples} * 100 \tag{22}$$

4. Results and discussion

The proposed model was simulated using Python 3.6.5 tool on a PC with configurations such as i5–8600k, GeForce 1050Ti 4GB, 16GB RAM, 250GB SSD, and 1 TB HDD. The parameter settings followed for the study are as follows; learning rate: 0.01, dropout: 0.5, batch size: 5, epoch count: 50, and activation: ReLU. In this section, the grape leaf disease detection performance of the proposed HDLISSA-MGDC model was validated using a dataset [28], comprising 1600 images. The details of the dataset are given in Table 1. The dataset holds both healthy as well as diseased images (with 3 classes). Fig. 3 shows some of the sample images.

In Fig. 4, the confusion matrices generated by the proposed HDLISSA-MGDC model on grape leaf disease detection process are depicted. The results clearly show that the HDLISSA-MGDC model recognized both healthy and diseased grape leaf images in an effective manner.

Table 2 reports the overall results achieved by the proposed HDLISSA-MGDC model on 80% of TR and 20% of TS datasets. Fig. 5 reveals the average classification outcomes accomplished by the proposed HDLISSA-MGDC model on 80% of the TR database. The results imply that the HDLISSA-MGDC model properly recognized all the four class labels. In addition, the results demonstrate that the HDLISSA-MGDC model gained an average $accu_y$ of 98.55%, $prec_n$ of 97.09%, $reca_l$ of 97.10%, F_{score} of 97.09%, MCC of 96.13%, and an

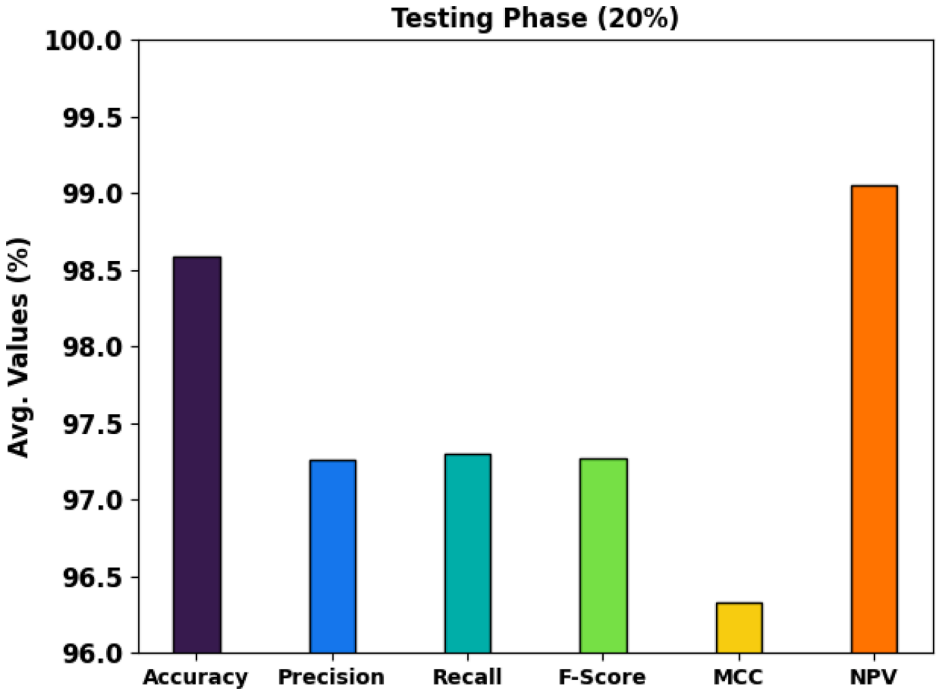


Fig. 6. Average analysis outcomes of the HDLISSA-MGDC system under 20% of TS database.

Table 3
Analytical results of the proposed HDLISSA-MGDC system under 70:30 of TR and TS databases.

Labels	$Accu_y$	$Prec_n$	$Reca_l$	F_{score}	MCC	NPV
Training Phase (70%)						
Class 0	99.20	99.64	97.17	98.39	97.87	99.05
Class 1	98.75	97.03	97.75	97.39	96.57	99.29
Class 2	99.02	96.94	99.30	98.11	97.46	99.76
Class 3	98.93	98.22	97.53	97.87	97.16	99.17
Average	**98.97**	**97.96**	**97.94**	**97.94**	**97.26**	**99.32**
Testing Phase (30%)						
Class 0	99.38	99.14	98.29	98.71	98.30	99.45
Class 1	100.00	100.00	100.00	100.00	100.00	100.00
Class 2	99.17	98.23	98.23	98.23	97.69	99.46
Class 3	99.38	98.31	99.15	98.72	98.31	99.72
Average	**99.48**	**98.92**	**98.92**	**98.92**	**98.57**	**99.66**

NPV of 99.04%.

Fig. 6 portrays the average classification outcomes attained by the proposed HDLISSA-MGDC method on 20% of TS database. The outcomes exhibit that the HDLISSA-MGDC method properly recognized all the four class labels. The study results confirm that the proposed HDLISSA-MGDC technique obtained an average $accu_y$ of 98.59%, $prec_n$ of 97.26%, $reca_l$ of 97.30%, F_{score} of 97.27%, MCC of 96.33%, and an NPV of 99.05%.

Table 3 displays the overall results accomplished by the HDLISSA-MGDC technique on 70% of TR and 30% of TS databases. Fig. 7 illustrates the average classification outcomes of the HDLISSA-MGDC technique on 70% of the TR database. The outcomes display that the HDLISSA-MGDC technique properly recognized all the four class labels. The results infer that the HDLISSA-MGDC technique achieved an average $accu_y$ of 98.97%, $prec_n$ of 97.96%, $reca_l$ of 97.94%, F_{score} of 97.94%, MCC of 97.26%, and an NPV of 99.32%.

Fig. 8 illustrates the average classification outcomes attained by the proposed HDLISSA-MGDC technique on 30% of the TS database. The outcomes exhibit that the HDLISSA-MGDC approach properly recognized all the four class labels. Moreover, the HDLISSA-MGDC algorithm achieved an average $accu_y$ of 99.48%, $prec_n$ of 98.92%, $reca_l$ of 98.92%, F_{score} of 98.92%, MCC of 98.57%, and an NPV of 99.66%.

The TACC and VACC values of the HDLISSA-MGDC technique were examined in terms of grape disease classification performance and the results are portrayed in Fig. 9. The figure exhibits that the HDLISSA-MGDC approach achieved an improved performance with high TACC and VACC values. It is to be noted that the HDLISSA-MGDC algorithm obtained the maximum TACC outcomes.

The TLS and VLS values, attained by the HDLISSA-MGDC technique in terms of grape disease classification performance, are

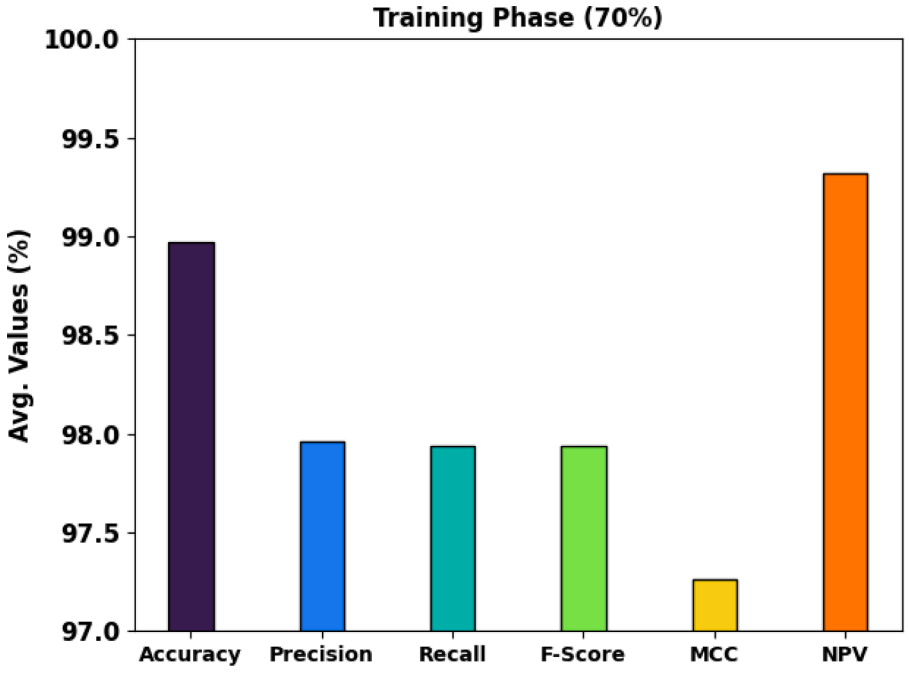


Fig. 7. Average analysis outcomes of HDLISSA-MGDC system under 70% of TR database.

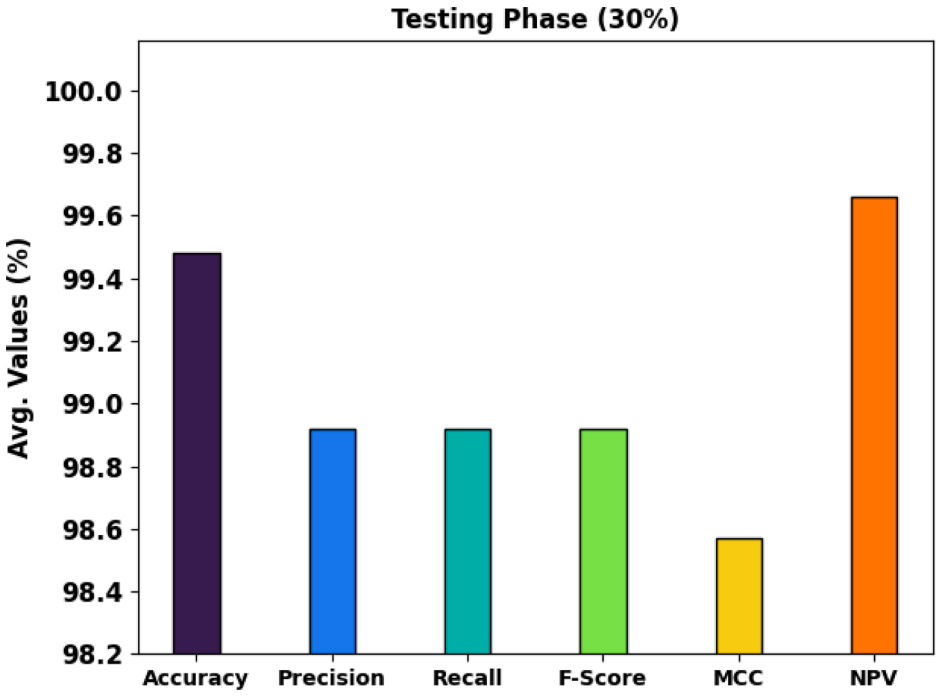


Fig. 8. Average analysis outcomes of the proposed HDLISSA-MGDC system under 30% of TR database.

presented in Fig. 10. The figure displays that the HDLISSA-MGDC approach achieved a better performance with minimal TLS and VLS values. It is to be noted that the HDLISSA-MGDC technique achieved low VLS outcomes.

In Table 4, the detailed grape disease classification results achieved by the proposed HDLISSA-MGDC model and other DL models are portrayed [29]. Fig. 11 reports the comparative $accu_y$ and F_{score} analysis between the HDLISSA-MGDC model and other recent models. The results indicate the improved performance of the HDLISSA-MGDC method over other ones. For example, in terms of $accu_y$, the HDLISSA-MGDC method gained a high $accu_y$ of 99.48% whereas the SqueezeNet, Inceptionv3, MobileNetv2, ResNet50, Xception,

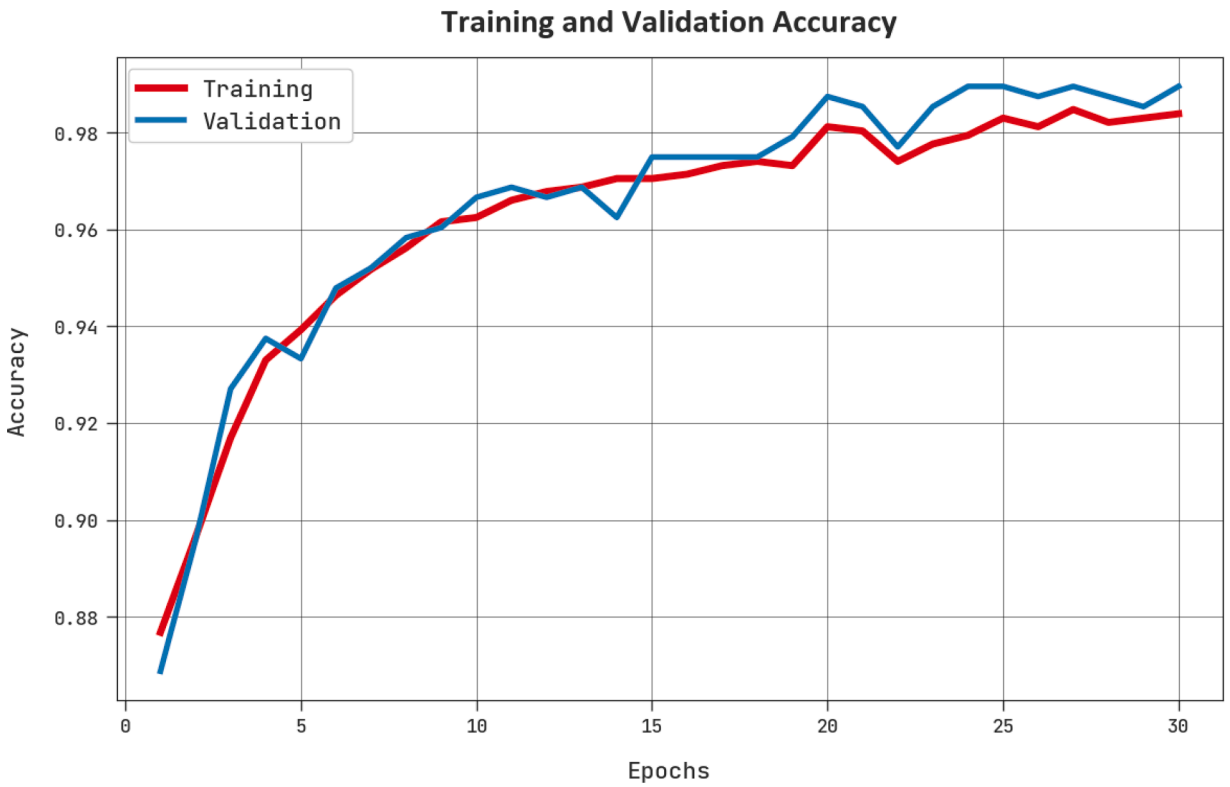


Fig. 9. TACC and VACC analysis results of the HDLISSA-MGDC system.

and the ShuffleNet models obtained the least $accu_y$ values such as 98.25%, 97.23%, 97.33%, 98.04%, 98.05%, and 98.17% respectively. Meanwhile, in terms of F_{score}, the proposed HDLISSA-MGDC approach produced the maximum F_{score} of 98.92%, while the SqueezeNet, Inceptionv3, MobileNetv2, ResNet50, Xception, and the ShuffleNet methods accomplished the least F_{score} values such as 98.74%, 98.24%, 97.83%, 97.67%, 98.81%, and 98.43% correspondingly.

Fig. 12 reports the comparative $prec_n$ and $reca_l$ analyses outcomes accomplished by the proposed HDLISSA-MGDC method and other recent methods. The outcomes exhibit the superior performance of the HDLISSA-MGDC model over other ones. For example, in terms of $prec_n$, the HDLISSA-MGDC technique obtained a maximum $prec_n$ of 98.92%, while the SqueezeNet, Inceptionv3, MobileNetv2, ResNet50, Xception, and the ShuffleNet methods gained the least $prec_n$ values such as 97.85%, 98.56%, 98.01%, 97.31%, 98.17%, and 98.51% correspondingly. In the meantime, in terms of $reca_l$, the presented HDLISSA-MGDC methodology achieved a maximum $reca_l$ of 98.92%, while the SqueezeNet, Inceptionv3, MobileNetv2, ResNet50, Xception, and the ShuffleNet methods accomplished the least $reca_l$ values such as 97.69%, 98.74%, 98.20%, 98.33%, 98.45%, and 98.33% correspondingly.

The results obtained and discussed earlier assure the enhanced performance of the HDLISSA-MGDC model on grape disease recognition process.

5. Conclusion

In this study, an automated grape disease classification model is proposed, named Hybrid Deep Learning with Improved Salp Swarm Optimization-based Multi-class Grape Disease Classification (HDLISSA-MGDC). The proposed HDLISSA-MGDC model classifies the grape leaf images into four distinct classes: Isariopsis leaf spot, Black measles, healthy, and black rot. Where, a series of processes is involved namely, MF noise removal, Adam with DRN feature extraction, CNN-GRU classification, and ISSA hyperparameter tuning. To further improve the overall performance, the ISSA is exploited to adjust the hyperparameter values of the CNN-GRU method. The proposed HDLISSA-MGDC method was simulated using the plant leaf disease dataset. The simulation results show the significant performance of the HDLISSA-MGDC model with an increased accuracy of 99.48%. In the future, the ensemble voting-based DL methods can be integrated to foster the efficiency of the HDLISSA-MGDC model.

Ethics approval

This article does not contain any studies with human participants performed by any of the authors.

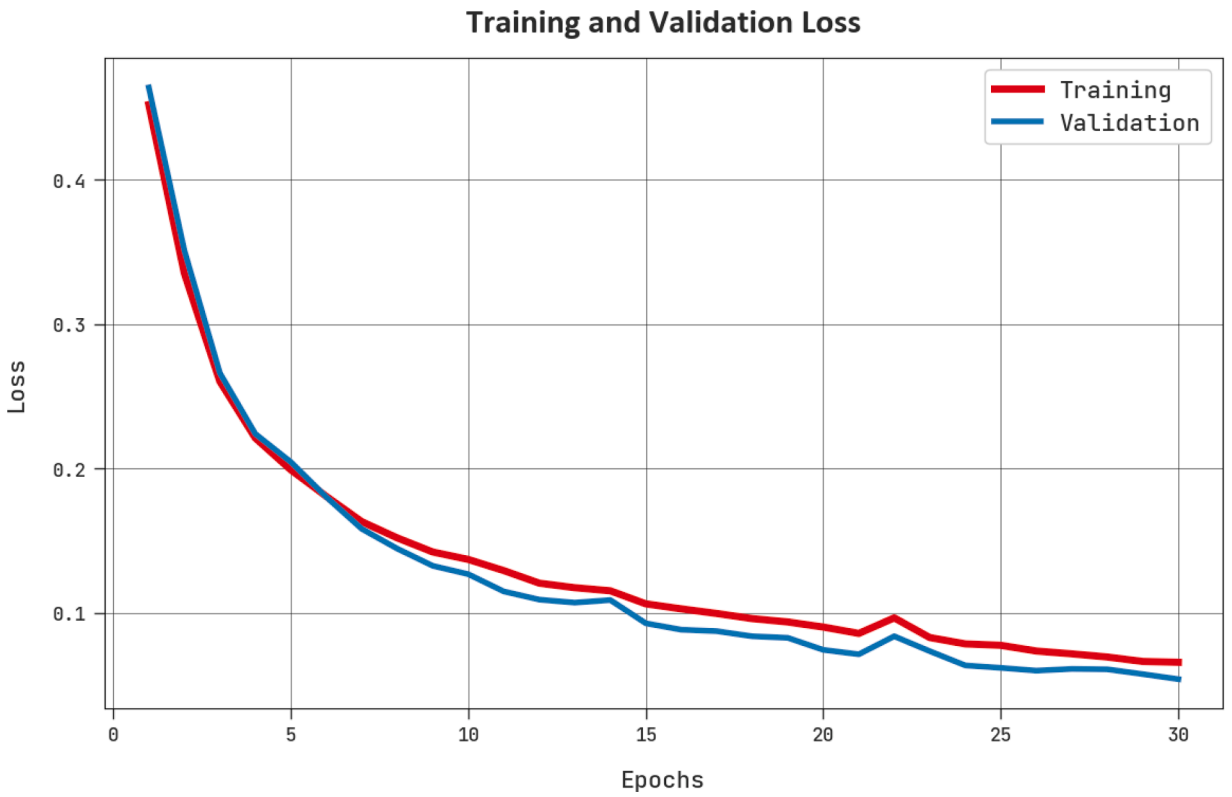


Fig. 10. TLS and VLS analyses results of the proposed HDLISSA-MGDC system.

Table 4
Comparative analysis results of the HDLISSA-MGDC system and other existing approaches.

Methods	$Accu_y$	$Prec_n$	$Reca_l$	F_{score}
HDLISSA-MGDC	99.48	98.92	98.92	98.92
SqueezeNet	98.25	97.85	97.69	98.74
Inceptionv3	97.23	98.56	98.74	98.24
MobileNetv2	97.33	98.01	98.20	97.83
ResNet50	98.04	97.31	98.33	97.67
Xception	98.05	98.17	98.45	98.81
ShuffleNet	98.17	98.51	98.33	98.43

Algorithm 1
Pseudocode of ISSA.

Inputs: testing set, training set, population size, the maximal iteration count
Initialization:
The PWLCM chaotic map based on Eqs. (14) & (15) initializing the position matrix A of the Salps Optimization technique:
When $iter < Tmax_iter$
The fitness value of Salps can be evaluated
Rank the fitness function value
If the optimum fitness value < the food position
Allocate the location of optimum fitness function values to the food location
Produce c_1 based on Eq. (12), randomly produce c_2, c_3
The first one-third of the Salps upgrade the location of the leader based on Eq. (16)
The back of Salps upgrades the location of followers based on Eq. (21)
$Iter = iter + 1$
Output: Optimum Salps location

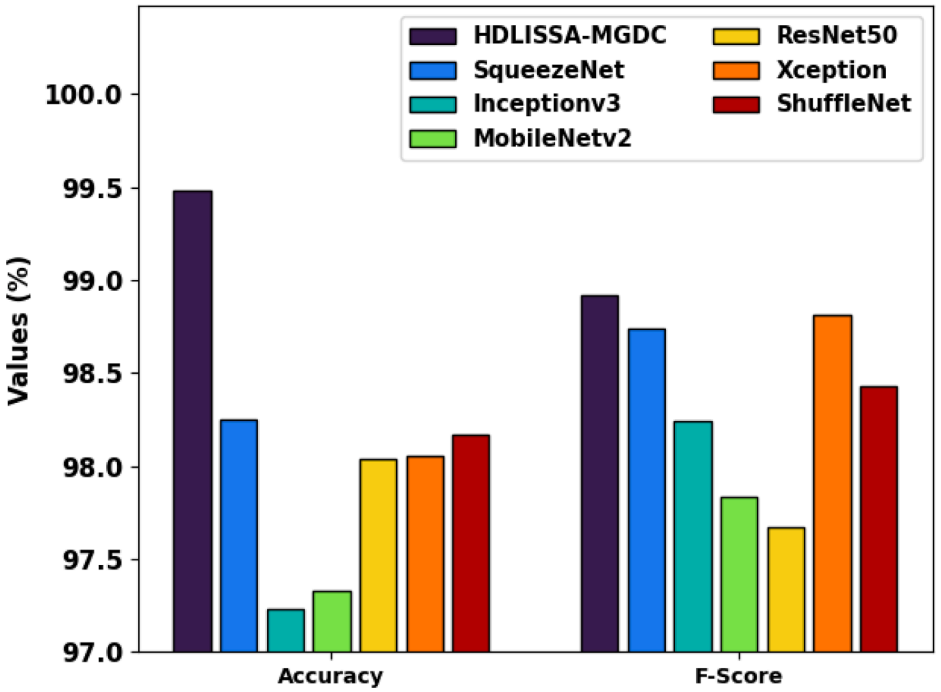


Fig. 11. $Accu_y$ and F_{score} analysis results of the HDLISSA-MGDC system and other existing approaches.

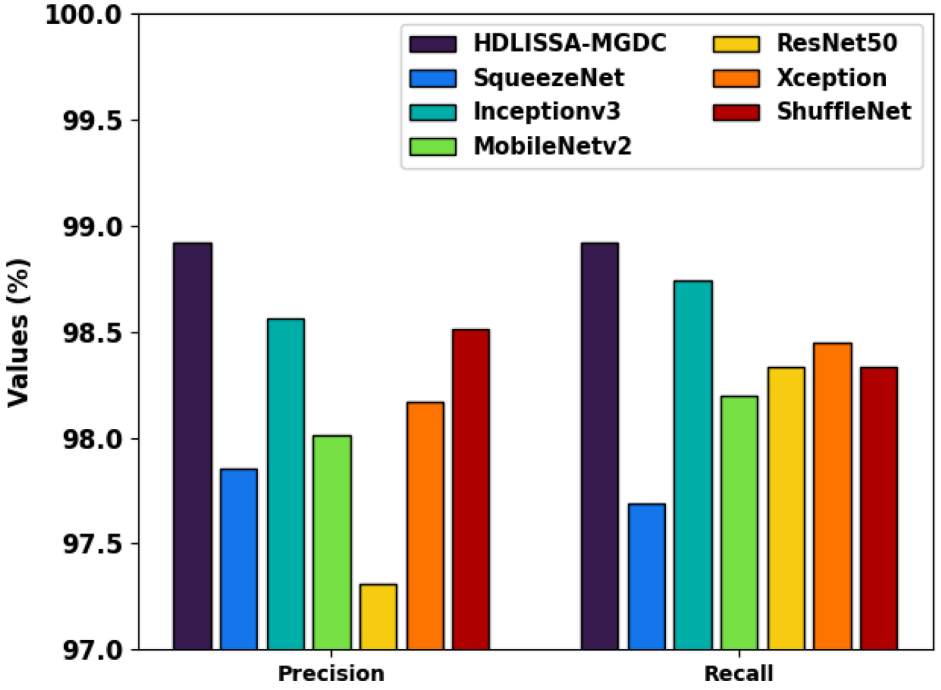


Fig. 12. $Prec_n$ and $Reca_l$ analyses results of the HDLISSA-MGDC system and other existing approaches.

Consent to participate

Not applicable.

Informed consent

Not applicable.

Declaration of Competing Interest

The authors declare that they have no conflict of interest. The manuscript was written through contributions of all authors. All authors have given approval to the final version of the manuscript.

Data availability

Data sharing not applicable to this article as no datasets were generated during the current study.
No data was used for the research described in the article.

Acknowledgment

.The authors would like to acknowledge the support provided by AlMaarefa University while conducting this research work. This study is supported via funding from Prince Sattam bin Abdulaziz University project number (PSAU/2023/R/1444).

References

[1] Landa V, Shapira Y, David M, Karasik A, Weiss E, Reuveni Y, Drori E. Accurate classification of fresh and charred grape seeds to the varietal level, using machine learning based classification method. Sci Rep 2021;11(1):1–15.
[2] Franczyk B, Hernes M, Kozierkiewicz A, Kozina A, Pietranik M, Roemer I, Schieck M. Deep learning for grape variety recognition. Procedia Comput Sci 2020;176:1211–20.
[3] Shantkumari M, Uma SV. Machine learning techniques implementation for detection of grape leaf disease. Multimedia tools and applications. 2023. p. 1–23.
[4] Landa, V., Shapira, Y., David, M., Karasik, A., Weiss, E., Reuveni, Y. and Drori, E., 2020. Utilizing machine-learning-based 3D image analysis for classifying charred grape seeds to the varietal level.
[5] Zhang Z, Qiao Y, Guo Y, He D. Deep learning based automatic grape downy mildew detection. Front Plant Sci 2022:13.
[6] Santos TT, de Souza LL, dos Santos AA, Avila S. Grape detection, segmentation, and tracking using deep neural networks and three-dimensional association. Comput Electron Agric 2020;170:105247.
[7] Qiao Y, Zhang Z, Guo Y, He D. Deep learning based grape mildew disease severity classification. In: 2022 ASABE annual international meeting. American Society of Agricultural and Biological Engineers; 2022. p. 1.
[8] Chen Y, Wu Q. Grape leaf disease identification with sparse data via generative adversarial networks and convolutional neural networks. Precis Agric 2023;24(1):235–53.
[9] Farahani G, Mousavi S, Farahani A, Farahani H. Identification of grape leaf diseases using proposed enhanced VGG16. In: 2022 27th International Conference on Automation and Computing (ICAC). IEEE; 2022. p. 1–6.
[10] Mohona SA, Aktar S, Ahamad MM. Efficient computation of leaf disease classification techniques using deep learning. In: 2021 3rd International Conference on Electrical & Electronic Engineering (ICEEE). IEEE; 2021. p. 149–52.
[11] Ji M, Wu Z. Automatic detection and severity analysis of grape black measles disease based on deep learning and fuzzy logic. Comput Electron Agric 2022;193:106718.
[12] Chauhan A, Singh M. Computer vision and machine learning based grape fruit cluster detection and yield estimation robot. J Sci Ind Res 2022;81(08):866–72.
[13] Kirti K, Rajpal N, Yadav J. Black measles disease identification in grape plant (Vitis vinifera) using deep learning. In: 2021 International Conference on Computing, Communication, and Intelligent Systems (ICCCIS). IEEE; 2021. p. 97–101.
[14] Javidan SM, Banakar A, Vakilian KA, Ampatzidis Y. Diagnosis of grape leaf diseases using automatic K-means clustering and machine learning. Smart Agric Technol 2023;3:100081.
[15] Peng Y, Zhao S, Liu J. Fused-deep-features based grape leaf disease diagnosis. Agronomy 2021;11(11):2234.
[16] Shantkumari M, Uma SV. Grape leaf image classification based on machine learning technique for accurate leaf disease detection. Multimedia tools and applications. 2022. p. 1–11.
[17] Peng Y, Zhao S, Liu J. Fused deep features-based grape varieties identification using support vector machine. Agriculture 2021;11(9):869.
[18] Math RM, Dharwadkar NV. Early detection and identification of grape diseases using convolutional neural networks. J Plant Dis Protect 2022;129(3):521–32.
[19] Ji M, Zhang L, Wu Q. Automatic grape leaf diseases identification via UnitedModel based on multiple convolutional neural networks. Inf Process Agric 2020;7(3):418–26.
[20] Mohammed KK, Darwish A, Hassenian AE. Artificial intelligent system for grape leaf diseases classification. Artificial intelligence for sustainable development: theory, practice and future applications. Cham: Springer; 2021. p. 19–29.
[21] Diana Andrushia A, Mary Neebha T, Trephena Patricia A, Umadevi S, Anand N, Varshney A. Image-based disease classification in grape leaves using convolutional capsule network. Soft Comput 2023;27(3):1457–70.
[22] Lin J, Chen X, Pan R, Cao T, Cai J, Chen Y, Peng X, Cernava T, Zhang X. GrapeNet: a Lightweight Convolutional Neural Network Model for Identification of Grape Leaf Diseases. Agriculture 2022;12(6):887.
[23] Lu X, Yang R, Zhou J, Jiao J, Liu F, Liu Y, Su B, Gu P. A hybrid model of ghost-convolution enlightened transformer for effective diagnosis of grape leaf disease and pest. J King Saud Univ-Comput Inf Sci 2022;34(5):1755–67.
[24] Noor A, Zhao Y, Khan R, Wu L, Abdalla FY. Median filters combined with denoising convolutional neural network for Gaussian and impulse noises. Multimed Tools Appl 2020;79(25):18553–68.
[25] Abdalla HB, Ahmed AM, Zeebaree SR, Alkhayyat A, Ihnaini B. Rider weed DRN-based incremental model for text classification using multidimensional features and MapReduce. PeerJ Comput Sci 2022;8:e937.

[26] Wang X, Ahmad I, Javeed D, Zaidi SA, Alotaibi FM, Ghoneim ME, Daradkeh YI, Asghar J, Eldin ET. Intelligent hybrid deep learning model for breast cancer detection. Electronics (Basel) 2022;11(17):2767.
[27] Qin X, Zhang S, Yin D, Chen D, Dong X. Two-stage feature selection for classification of gene expression data based on an improved Salp swarm algorithm. Math Biosci Eng 2022;19(12):13747–81.
[28] Pandian JA, Geetharamani G. Data for: identification of plant leaf diseases using a 9-layer deep convolutional neural network. Comput Electr Eng 2019;76:323–38.
[29] Fraiwan M, Faouri E, Khasawneh N. Multiclass classification of grape diseases using deep artificial intelligence. Agriculture 2022;12(10):1542.

Ashit Kumar Dutta is working as a Full Professor in the Department of Computer Science and Information Systems at Allmaarefa University. His-specialization is in the fields of artificial intelligence and cyber security.

Shtwai Alsubai is an assistant professor in Computer Science at the Prince Sattam Bin AbdulAziz University. His-research interests include XML, XML query processing, XML query optimization, machine learning and natural language processing

Ahmed Hussein Alkhayyat received the B.*Sc*. degree from KUFA University, Iraq, in 2007, the M.*Sc*. degree from the DIT, India, in 2010, and PhD from Cankaya University, Turkey, in 2015. He organized a several IEEE conferences. He is currently a dean of international relationship in the Islamic university. In addition, he is head of Islamic University centre for Scientific Research.

Mustafa Musa Jaber is a Ph.D. holder from the technical university of Malaysia and Currently working as a postdoctoral fellow at Universiti Tenaga Nasional, his interest in telemedicine,

machine learning, and the human factor.

Ali Hashim Abbas received the B.S. degree in communication engineering from Al-Furat Al-Awsat Technical University, in 2010 and the M.S. degree in digital system and computer electronics(DSCE) from Jawaharlal Nehru Technological University Hyderabad, India, in 2014, and Ph.D. degrees in Communication engineering, Clustering of Vehicular Ad-Hoc Networks (VANETs) from UTHM University Tun Hussein Onn Malaysia, Johor, Malaysia, in 2019.

Anil Kumar is currently working as a Professor Computer Science & Engineering, Accreditation Coordinator, and Head of Data Science Research Group, DIT University, India. Prof. Anil Kumar received his M.Tech from Delhi College of Engineering and Ph.D. from Manipal University. He has more than 26 years teaching. He is an IEEE Senior Member and ACM.

2023 10th International Conference on Signal Processing and Integrated Networks (SPIN) | 978-1-6654-9099-3/23/$31.00 ©2023 IEEE | DOI: 10.1109/SPIN57001.2023.10116874

Image flare removal using Deep Convolutional Generative Adversarial Networks

Ishan Prakash*
Department of Electrical Engineering
Delhi Technological University
Delhi, India
ishan.0114@gmail.com

Aryan*
Department of Electrnoics and Communication Engineering
Delhi Technological University
Delhi, India
aryanmangal2022@gmail.com

S. Indu
Department of Electrnoics and Communication Engineering
Delhi Technological University
Delhi, India
s.indu@dce.ac.in

Mini Sreejeth
Department of Electrical Engineering
Delhi Technological University
Delhi, India
minisreejeth@dce.ac.in

***Abstract*—In this paper, a novel approach is proposed for removing flare artefacts from images using a two-stage method. Flare is a phenomenon that occurs when a strong source of light hits the lens of the camera. The converging light rays are scattered due to imperfections in the lens, creating a glare or halo effect in the image. This degrades the image quality and can make it challenging to extract useful information from the image, making it problematic for industries such as autonomous driving and medical robotics that rely heavily on image processing algorithms. To solve this problem, we utilize a flare removal model based on a conditional generative network. This model is trained on a dataset created using computer vision techniques. The dataset creation process involves scraping internet images of different scenes under various lighting conditions without the presence of flare. These images are then pre-processed to extract the flare-corrupted images, which serve as input for the flare removal model, which produces flare-free output. However, in order to make the model more generalizable and able to handle real-world data, we incorporate the flare removal module in a self-supervised setting along with a flare addition module. This allows us to fine-tune the flare removal model using real images and improve its performance. The flare removal module achieves an SSIM score of 0.916, which was previously 0.887. Our approach can be used in a variety of applications, such as autonomous driving and camera photo optimization, and has the potential to be further improved by incorporating a flare mask detector module.**

Keywords—Generative Adversarial Networks, Flare Removal, Convolution Neural networks

I. Introduction

Flare artefacts in images are a common problem caused by unwanted reflections and light dispersion inside the camera. These artefacts can appear in various shapes, locations, and colours, making it challenging to spot and fully remove them from an image. These artefacts can cause false information in the image, which can negatively impact the performance of computer vision-based solutions that rely on accurate visual information.

Previous research [13], [14] has mainly relied on deep convolutional neural networks for removing flares, but these approaches may be unable to differentiate between light sources and flare artefacts as they rely on predetermined flare intensity and geometry priors. Our approach solves this problem by using a self-supervised generative modelling approach, a machine learning technique that includes automatically recognizing and learning the patterns or regularities from incoming data.

We use Generative Adversarial Networks (GANs) to accurately determine the flare in an image and remove it successfully. Our self-supervised framework utilizes GANs to understand the underlying patterns in the information and generate new, flare-free images. The performance of our model is evaluated using similarity metrics, and we show that it outperforms previous methods [18]. Our approach can be used in a variety of applications, such as autonomous driving and camera photo optimization, and has the potential to be further improved by incorporating a flare mask detector module.

To summarize, the major contributions of this paper are:

- We created an algorithm that leverages self-supervision as opposed to previous state-of-the-art techniques which utilize supervised learning techniques.
- We worked on synthetic data generation to train the initial model before self-supervised training, which ensures better training
- We optimize the algorithm to have high accuracy and low latency and, at the same time, low memory and energy consumption.

II. Related Work

The three categories of current flare suppression technologies are (a) Computational methods, (b) Hardware-Software co-design based methods, and (c) Learning based Image decomposition.

A. Computational methods

Numerous post-processing methods have been suggested in recent years to address the issue of lens flare in imaging. Deconvolution is a common technique that has been used to reduce flare in HDR photography [3] and X-ray imaging [1], [2]. However, these techniques primarily rely on the notion that the flare's point spread function is constant across the image, which is often not the case. Another class of solutions [4]–[6] involves a two-stage process, in which flare is first detected based on characteristics such as shape, location, or

Authorized licensed use limited to: DELHI TECHNICAL UNIV. Downloaded on May 15,2023 at 09:56:12 UTC from IEEE Xplore. Restrictions apply.

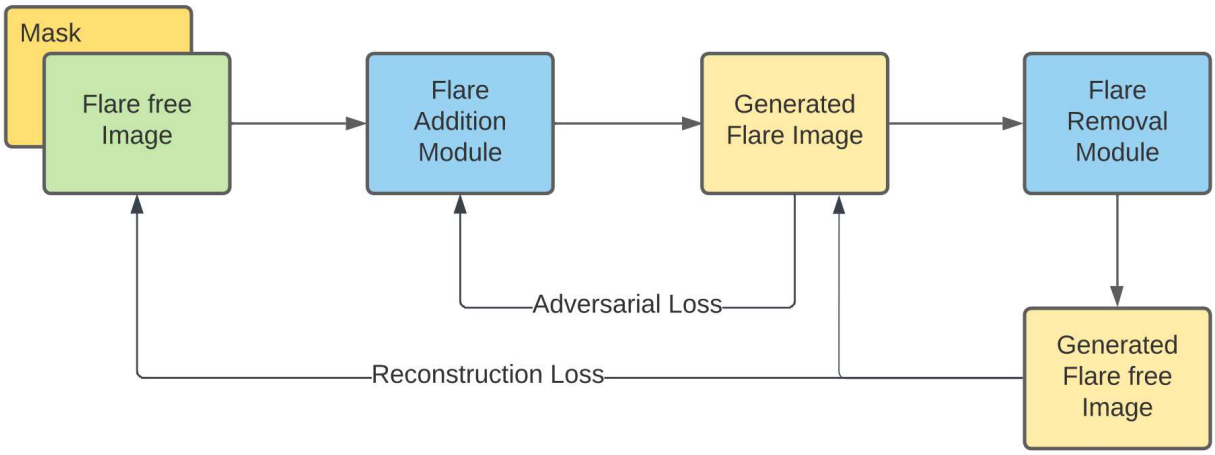


Fig. 1. The Architecture of self-supervised training module

intensity, and then the underlying scene is recovered using inpainting [7] techniques. However, these methods are limited to specific types of flare and can lead to the bright region's misclassification in the flared image. Furthermore, they treat lens flare as a binary phenomenon, ignoring the fact that it is often better modelled on top of the underlying scene as a semi-transparent layer.

B. *Co-design of Hardware–software*

Recently, scientists have investigated the use of computational imaging methods for lens flare removal. The camera hardware and image processing algorithms work together in this method. To reconstruct the flare-free scene using either direct-indirect separation or a light field-based technique, Talvala et al. and Raskar et al. proposed utilizing structured occlusion masks to block flare light in their publications [8], [9] While these methods demonstrate promising results, they have a significant drawback in that they require specialized hardware, which limits their practicality. Therefore, more research is needed to develop computational imaging-based methods that can be implemented using standard camera equipment.

C. *Learning-based image decomposition*

Despite lens flare being a common problem in photography, there are currently very few learning-based methods for getting rid of flare. To related tasks like reflection removal [10]–[12], rain removal [13], [14], and denoising [15], numerous recent publications have, however, used learning-based techniques [16]. These techniques use neural network training to separate a picture into "clean" and "corrupted" parts. The accessibility of excellent, domain-specific training datasets is crucial to the success of these techniques. In this study, we suggest a novel method for producing these datasets that will allow the development of learning-based flare removal methods. We believe that this is the first time in the history of the field that such an attempt has been undertaken.

III. DATASET GENERATION

Obtaining a dataset having pairs of flare-free and flare corrupted images is a challenging task, particularly in a supervised learning setting. This is in contrast to many other vision-related problems, where such datasets are more readily available. To solve this issue, we proposed a novel, physically realistic, semi-synthetic pipeline for creating pairs of flare-free and flare-corrupted images.

Given that light is additive, we model flare as an artefact that is added to an "ideal" image without affecting the illumination strength of the "ideal" rays. To achieve this, we will first discuss methods for modelling and producing scattering and reflecting flares. Our pipeline utilizes these models to generate flare-corrupted images and corresponding flare-free images, providing a valuable dataset for the development of flare removal techniques which are mainly learning-based.

A. *Types of Flare*

In an ideal scenario, a camera lens should direct all light rays from a point light source to a single spot on the sensor when the camera is in focus. However, in reality, lenses reflect and scatter light in unexpected ways, leading to flare effects in images. Although flare is constantly present, it is typically not visible in pictures because the dispersed and reflected light is usually a small fraction of the incident light. However, if a powerful source of light, for example, the sun, is much brighter than the surrounding area, a small percentage of its scattered and reflected rays will cause noticeable artefacts at other pixels in the image. These artefacts are characterized by visual patterns that are produced by the dispersion geometry from scratches dust as well as the geometry of the many reflections. Flare can be broadly categorized into two groups: reflection and scattering.

Scattering flare: Actual lenses, unlike an ideal lens, have various imperfections that cause light to scatter, making them not entirely refractive. These imperfections can be a result of regular wear or manufacturing flaws such as dust and scratches. Therefore, in addition to the main rays, which are refracted, another set of rays deviate from their intended paths by being scattered or diffracted. This results in the phenomenon of lens flare, an unwanted artefact that is present in images captured by cameras.

Reflective flare: In actual lens systems, every interaction between glass and air presents the potential for a small amount of reflection, generally around 4%. These reflected rays can then be directed towards the sensor after an even number of reflections, resulting in a reflection pattern; this type of flare is called a reflection flare.

Authorized licensed use limited to: DELHI TECHNICAL UNIV. Downloaded on May 15,2023 at 09:56:12 UTC from IEEE Xplore. Restrictions apply.

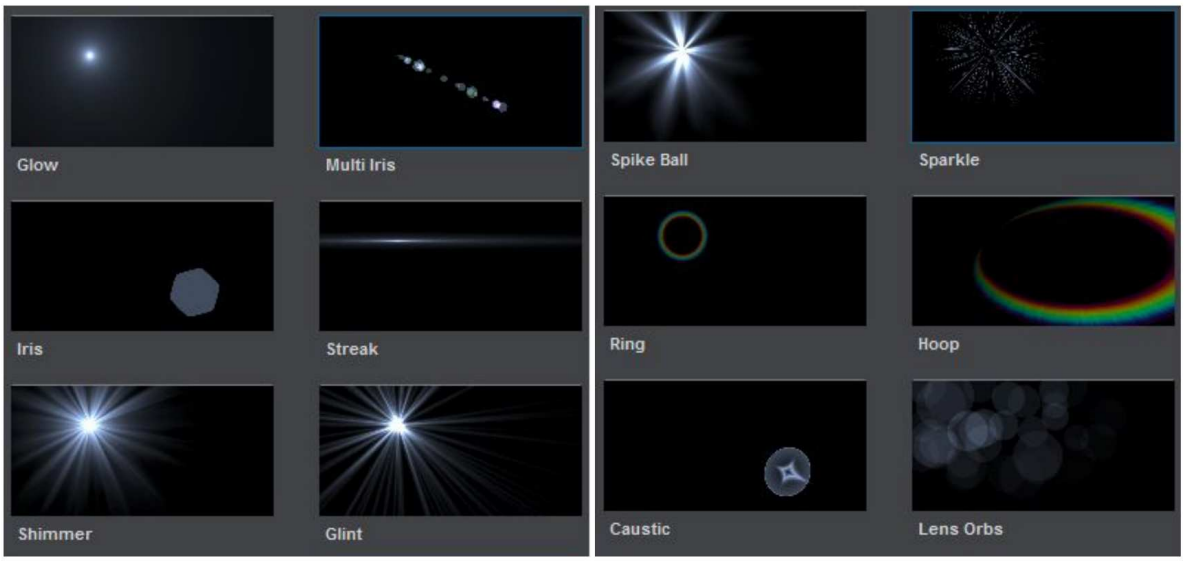


Fig. 2. Different types of flares

B. Pairs of Flare Free and Flare Corrupted Images

To create a synthetic image IF with flare corruption, we add a flare-only image F to a clear image I0. To simulate varying noise levels commonly found in real situations, we add random Gaussian noise with a standard deviation derived from a scaled chi-square distribution, $\sigma^2 \sim 0.01 \cdot \chi^2$.

$$I_F = I_O + F + N(0, \sigma^2) \quad (1)$$

The clear image I_O is selected from a 24k image dataset on Flickr and undergoes random flipping and brightness adjustments. The Flickr images have already been gamma-encoded, so to approximately linearize them. We apply an inverse gamma curve with a gamma value randomly selected from the range [1.8, 2.2]. This compensates for the fact that the exact gamma value is often unknown.

The flare-only image F is obtained from a combination of real-world captures and simulated data to provide a diverse set of flares. To enhance the robustness of the dataset, random affine transformations, such as translation, scaling, shearing, and rotation, are applied to the flare-only images. The diversity of the dataset is also increased by applying white balance adjustments to these images.

IV. METHODOLOGY

The proposed method for flare removal in images has two main modules: The Flare Removal Module and the Flare Addition Module. These modules are designed to work together in a self-supervised finetuning process. The Flare Removal Module is responsible for removing flare from an image, while the Flare Addition Module is responsible for adding flare to a flare-free image. The self-supervised finetuning process combines these two modules to improve the overall performance of the method. Additionally, specific loss functions are employed for both the individual modules and the finetuning process to ensure optimal results.

A. Flare Removal Network

The Flare Removal Module is a crucial component of the proposed method for removing the flare from an input image. This module utilizes the technique of Image-to-Image translation in Deep Learning to shift image representations from the source domain (Flare Images) to the target domain (Flare-Free Images) while maintaining the representations of the content.

To achieve this, we make use of the concept of Conditional Generative Adversarial Networks (cGANs) [17]. These networks are capable of generating images based on a conditional input, in this case, a flare-free image. The cGANs consist of two main components: a discriminator and a generator. The generator is responsible for creating new images, while the discriminator is responsible for evaluating the authenticity of the generated images.

Given $I_F \in [512\times512\times3]$, a flare-corrupted image, the goal of the Flare Removal Module is to train a network $f(I_F, \theta)$ such that it can predict a flare-free image $\hat{I_0}$, where θ is the trainable network weights. The architecture of the Generative Adversarial Network used for Image-to-Image translation is shown in Fig. 4.

B. Flare Addition Network

The Flare Addition module works by taking a flare-free input image and outputting a flare-corrupted image. The module utilizes a Generative Adversarial Network (GAN) architecture similar to the one used in the Flare Removal module. The input for this module is a flare-free image or the original image. The generator network is trained to generate realistic flare patterns, while the discriminator network is trained to differentiate between synthetic and real flare patterns.

Additionally, the module can also take in other modalities for a finer generation, such as the type of flare, by encoding that information in the form of masks. The mask contains information about the type and location of the flare, which

Authorized licensed use limited to: DELHI TECHNICAL UNIV. Downloaded on May 15,2023 at 09:56:12 UTC from IEEE Xplore. Restrictions apply.

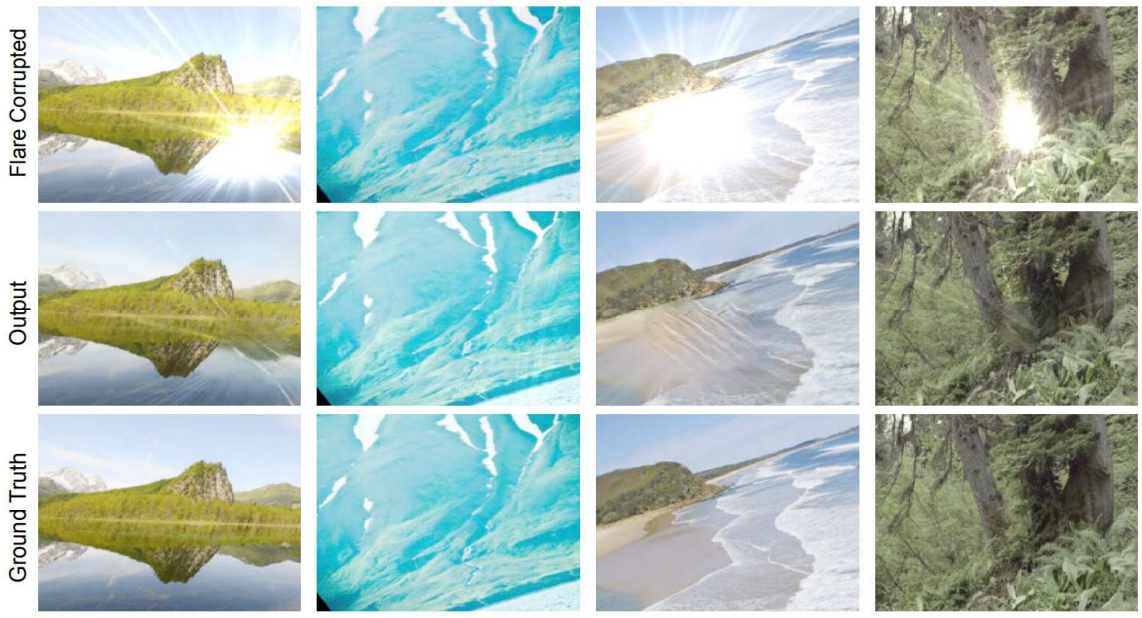


Fig. 3. Qualitative Results for Flare Removal

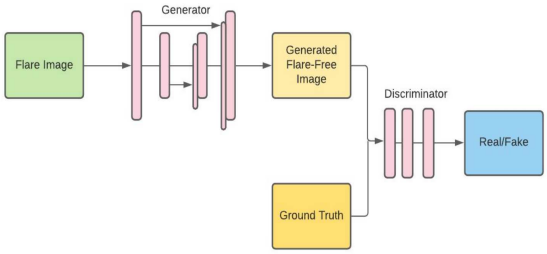


Fig. 4. The Architecture of generative Adversarial Network

helps the generator network to create more accurate flare-free images. The discriminator and generator are trained using an adversarial loss, which is a measure of how well the generator can fool the discriminator into thinking that the synthetic flare patterns are real. The adversarial loss is discussed in more detail in the next section.

C. *Self-Supervised Domain Adaptation*

This section presents our self-supervised training approach using both the Flare Removal and Flare Addition modules. The process begins by passing an input image from the internet through the Flare Addition Module, which adds a flare mask to the image. The resulting flared image is then passed through the Flare Removal Module, with the goal of producing the original, flare-free image. To train the framework, an Image Reconstruction Loss is used. The image reconstruction loss compares the Flare Removal Module output with the original flare-free image and measures the difference between the two. By minimizing this loss, the network learns to accurately remove flare from an image.

D. *Losses*

1) Image-to-Image translation: Loss The objective that we minimize can be presented as follows

$$L_{cGAN} = E_{x,y}[logD(x,y) + E_{x,z}[log\big(1 - D\big(x, G(x,z)\big)\big)] \quad (2)$$

here G, the generator, is used to minimize the objective against the discriminator D, which maximizes it, x is the input flared image, which is mapped to y, and the label, which is flare free. The noise, z, is not added separately since the model learns to ignore the noise. The final objective is

$$G* = (arg(min_G(max_D(L_{cGAN}(G, D)))) \quad (3)$$

2) Image Reconstruction Loss: The image reconstruction loss, LR, aims to enforce similarity between the ground truth I0 and the =predicted flare-free image ˆI0 both perceptually and photometrically. It consists of two terms:

- Photometric term: L1 loss between the intensity values of $\hat{I_O}$ and I_O.
- Perceptual term: Difference between the outputs of a pre-trained VGG-19 network applied to $\hat{I_O}$ and I_O at specific feature layers (conv1_2, conv2_2, conv4_2, and conv5_2). The absolute difference is penalized.

In short, the image reconstruction loss can be expressed as:

$$L_R = ||\hat{I_O} - I_O|| + \sum_l \lambda_l ||\phi(\hat{I_O}) - \phi(I_O)|| \quad (4)$$

The activation outputs of the encoder convolutions are represented by $\phi(I_0)$ and $\phi(\hat{I_0})$. In self-supervised finetuning, the image reconstruction loss is used to train both the flare removal and flare addition modules by backpropagating the loss through both of them.

Authorized licensed use limited to: DELHI TECHNICAL UNIV. Downloaded on May 15,2023 at 09:56:12 UTC from IEEE Xplore. Restrictions apply.

V. EXPERIMENTAL RESULTS

A. Implementation Details

Our model is trained with a learning rate of 0.0002. We optimise the generator and the discriminator model using the Adaptive Moment Estimation or ADAM algorithm. We adopted a minibatch size of 16 during our training. The individual modules are pretrained for 300 epochs each, and self-supervised finetuning is performed for another 300 epochs. The module consisted of a pre-trained VGG-19 backbone for the generator.

B. Comparison to State-of-the-art-methods

The performance of the proposed module is evaluated with three baselines. For the first baseline, we compare it with classical non-learning-based computer vision algorithms, which perform a set of morphological operations along with other transformations to identify and remove flare-corrupted regions. We also fine-tune an Autoencoder to perform flare removal. The Decoder and Encoder are based on the ResNet18 model [18].

Table I presents a comparison of the proposed methods and baselines based on the Structural Similarity Index (SSIM). It can be observed that our proposed model outperforms baselines with a significant difference. The self-supervised training paradigm has the highest score of 0.916. Upon further training of the module, this score can increase.

Figure 3 present the qualitative results for the model. The outputs demonstrate that the proposed model can correctly identify and remove Flare from the images and regenerate the area containing flare.

Figure 6 present the generator and discriminator losses for the Flare Removal module. We can see that the generator loss decreases as the number of epochs increases; therefore, we can conclude that upon further training, the generator cost function will converge. This is also shown in the discriminator loss as it is increasing, which means that the generator is able to generate relatively accurate flare-free images.

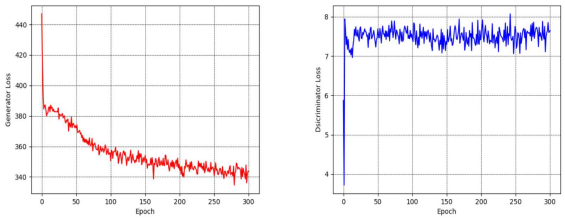


Fig. 5. The Generator and Discriminator Losses for Flare Addition Module

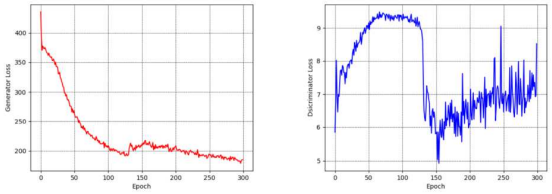


Fig. 6. The Generator and Discriminator Losses for Flare Removal Module

Figure 5 presents the generator and discriminator losses for the Flare addition module. It can be seen that the losses are following a similar trend as Flare Addition losses validating the training of the Flare Addition module.

TABLE I. COMPARISON OF FLARE REMOVAL TECHNIQUES BASED ON SSIM

	Dilation	***Resnet-18***	***Flare Removal Module***	***SSL***
SSIM	0.752	0.861	0.887	0.916

VI. ABLATION STUDIES

To prove the effectiveness of self-supervised finetuning, we compare the SSIM scores of the Flare Removal module before and after self-supervised finetuning. The scores after finetuning are 0.916, and the scores before finetuning are 0.887. This indicates that the self-supervised training with the Flare addition module helps in augmenting the capabilities of the Flare Removal module and also reduces dependency on labelled data.

VII. CONCLUSION

In this work, we presented a novel approach to remove flare artefacts from images using a combination of two methods. The first method is a Flare Removal module, which is trained to remove flare from images using a flare-free image as a reference. The second method is trained to add flare to images using a flare mask as an input. The Flare Addition and Removal modules work together to fine-tune the Flare Removal module. We evaluated the performance of our approach using various accuracy and similarity metrics. Our results show that our approach can effectively remove flare artefacts from images. Furthermore, we incorporated the flare removal module in a self-supervised setting along with the flare addition module, which allows the network to learn from images without the need for labels. This method can be used to train on a larger dataset of flare free images, which is useful in applications a large amount of data is required for training. This self-supervised training paradigm increases the accuracy by decreasing the dependency on labelled data, which can be inaccurate and limited. After fine-tuning the flare removal module in this environment, we were able to achieve an SSIM score of 0.916, which was previously 0.887. We expect this method to play an important role in various applications like autonomous driving, camera photo optimization and in any application where images are captured in challenging lighting conditions. In future, we envision using a flare mask detector module to add an auto-generated flare mask for better training. This will further improve the performance of our model.

REFERENCES

[1] Faulkner, K., C. J. Kotre, and M. Louka. "Veiling glare deconvolution of images produced by x-ray image intensifiers." In Third International Conference on Image Processing and its Applications, 1989., pp. 669-673. IET, 1989

[2] Seibert, J. Anthony, O. Nalcioglu, and W. Roeck. "Removal of image intensifier veiling glare by mathematical deconvolution techniques." Medical physics 12, no. 3 (1985): 281-288.

[3] Reinhard, Erik, Wolfgang Heidrich, Paul Debevec, Sumanta Pattanaik, Greg Ward, and Karol Myszkowski. High dynamic range imaging: acquisition, display, and image-based lighting. Morgan Kaufmann, 2010.

[4] Asha, C. S., Sooraj Kumar Bhat, Deepa Nayak, and Chaithra Bhat. "Auto removal of bright spot from images captured against flashing light source." In 2019 IEEE International Conference on Distributed

Authorized licensed use limited to: DELHI TECHNICAL UNIV. Downloaded on May 15,2023 at 09:56:12 UTC from IEEE Xplore. Restrictions apply.

Computing, VLSI, Electrical Circuits and Robotics (DISCOVER), pp. 1-6. IEEE, 2019.

[5] Chabert, Floris. "Automated lens flare removal." In Technical report. Department of Electrical Engineering, Stanford University, 2015.

[6] Vitoria, Patricia, and Coloma Ballester. "Automatic flare spot artifact detection and removal in photographs." Journal of Mathematical Imaging and Vision 61, no. 4 (2019): 515-533.

[7] Criminisi, Antonio, Patrick Pérez, and Kentaro Toyama. "Region filling and object removal by exemplar-based image inpainting." IEEE Transactions on image processing 13, no. 9 (2004): 1200-1212.

[8] Jacobs, Axel. "High dynamic range imaging and its application in building research." Advances in building energy research 1, no. 1 (2007): 177-202.

[9] Raskar, Ramesh, Amit Agrawal, Cyrus A. Wilson, and Ashok Veeraraghavan. "Glare aware photography: 4D ray sampling for reducing glare effects of camera lenses." In ACM SIGGRAPH 2008 papers, pp. 1-10. 2008.

[10] Fan, Qingnan, Jiaolong Yang, Gang Hua, Baoquan Chen, and David Wipf. "A generic deep architecture for single image reflection removal and image smoothing." In Proceedings of the IEEE International Conference on Computer Vision, pp. 3238-3247. 2017.

[11] Li, Chao, Yixiao Yang, Kun He, Stephen Lin, and John E. Hopcroft. "Single image reflection removal through cascaded refinement." In Proceedings of the IEEE/CVF Conference on Computer Vision and Pattern Recognition, pp. 3565-3574. 2020.

[12] Zhang, Xuaner, Ren Ng, and Qifeng Chen. "Single image reflection separation with perceptual losses." In Proceedings of the IEEE conference on computer vision and pattern recognition, pp. 4786-4794. 2018.

[13] Qian, Rui, Robby T. Tan, Wenhan Yang, Jiajun Su, and Jiaying Liu. "Attentive generative adversarial network for raindrop removal from a single image." In Proceedings of the IEEE conference on computer vision and pattern recognition, pp. 2482-2491. 2018.

[14] Wei, Wei, Deyu Meng, Qian Zhao, Zongben Xu, and Ying Wu. "Semi-supervised transfer learning for image rain removal." In Proceedings of the IEEE/CVF conference on computer vision and pattern recognition, pp. 3877-3886. 2019.

[15] Brooks, Tim, Ben Mildenhall, Tianfan Xue, Jiawen Chen, Dillon Sharlet, and Jonathan T. Barron. "Unprocessing images for learned raw denoising." In Proceedings of the IEEE/CVF Conference on Computer Vision and Pattern Recognition, pp. 11036-11045. 2019.

[16] Xuaner Zhang, Ren Ng, and Qifeng Chen. Single image reflection separation with perceptual losses. CVPR, 2018

[17] Gauthier, Jon. "Conditional generative adversarial nets for convolutional face generation." Class project for Stanford CS231N: convolutional neural networks for visual recognition, Winter semester 2014, no. 5 (2014): 2.

[18] He, Kaiming, Xiangyu Zhang, Shaoqing Ren, and Jian Sun. "Deep residual learning for image recognition." In Proceedings of the IEEE conference on computer vision and pattern recognition, pp. 770-778. 2016.

Authorized licensed use limited to: DELHI TECHNICAL UNIV. Downloaded on May 15,2023 at 09:56:12 UTC from IEEE Xplore. Restrictions apply.

e-ISSN: 2582-5208
International Research Journal of Modernization in Engineering Technology and Science
(Peer-Reviewed, Open Access, Fully Refereed International Journal)
Volume:05/Issue:04/April-2023 Impact Factor- 7.868 www.irjmets.com

INDUSTRY 4.0 AND THE SMART FACTORY: A REVIEW OF EMERGING TECHNOLOGIES AND APPLICATIONS

Ravi Prakash[*1], Somnath Pal[*2], Ashok Kumar Madan[*3]

[*1,2,3]Mechanical Engineering, Delhi Technological University, Shahbad, Bawana Road, Rohini, Delhi, India.

ABSTRACT

The emergence of Industry 4.0 has revolutionized the manufacturing industry with the implementation of smart factories. Smart factories have integrated advanced technologies such as the Internet of Things (IoT), artificial intelligence (AI), and robotics to optimize production processes and achieve higher efficiency, productivity, and profitability. This research article provides a comprehensive review of the emerging technologies and applications of Industry 4.0 in smart factories. A systematic literature review was conducted to identify relevant studies and sources, and the results were analyzed and interpreted to discuss the implications for future research. The findings suggest that Industry 4.0 technologies such as predictive maintenance, digital twin, and blockchain can enhance the performance of smart factories. Successful implementations of Industry 4.0 technologies were also identified, providing examples of how manufacturers can realize the benefits of smart factories. The article concludes with a discussion of the implications of the research for the industry and recommendations for future research.

Keywords: Industry 4.0, Smart Factory, Emerging Technologies, Internet Of Things, Artificial Intelligence.

I. INTRODUCTION

Industry 4.0 and the concept of the smart factory have emerged as key drivers of the fourth industrial revolution, aiming to transform traditional manufacturing processes through the integration of digital technologies. The emergence of these technologies presents new opportunities for manufacturers to enhance productivity, reduce costs, and improve quality. However, the implementation of Industry 4.0 and smart factory technologies also poses challenges related to data management, cybersecurity, and workforce upskilling.

The objective of this research article is to provide a comprehensive review of the emerging technologies and applications of Industry 4.0 in the smart factory context. The paper will explore the latest research and practical examples of how these technologies are being used to improve manufacturing processes and productivity, and also examine the implications of these developments for the industry.

The paper will begin with an overview of Industry 4.0 and smart factories, followed by a review of emerging technologies in Industry 4.0 and their applications in smart factories. The article will also compare traditional factories with smart factories and explore the potential benefits and challenges associated with these new developments.

The methodology section will explain the research method used, selection of relevant studies and sources, and criteria for inclusion/exclusion of studies. The results section will present the findings from the literature review, discussing the emerging technologies and their applications in smart factories, as well as examples of successful implementations of Industry 4.0 technologies in smart factories.

The discussion section will analyze and interpret the findings, comparing the results to previous research and exploring the implications for future research. Finally, the conclusion section will summarize the key findings, discuss the implications of the research for the industry, and provide limitations and suggestions for future research.

Overall, this research article aims to contribute to the understanding of Industry 4.0 and smart factories, their emerging technologies, and applications, and to highlight the potential benefits and challenges associated with these developments.

II. METHODOLOGY

In this research paper, a literature review methodology is used to explore and analyze the current state of the art of Industry 4.0 and the smart factory. The literature review approach involves an extensive search of

e-ISSN: 2582-5208
International Research Journal of Modernization in Engineering Technology and Science
(Peer-Reviewed, Open Access, Fully Refereed International Journal)
Volume:05/Issue:04/April-2023 Impact Factor- 7.868 www.irjmets.com

relevant published and unpublished sources, including academic articles, conference proceedings, reports, and industry publications.

Selection of Relevant Studies and Sources

To identify relevant sources, a systematic search was conducted using several electronic databases, including Scopus, Web of Science, and IEEE Xplore. The search was limited to articles published in English between 2015 and 2023. The following keywords and combinations of keywords were used to search for relevant literature: Industry 4.0, smart factory, emerging technologies, Internet of Things (IoT), big data, artificial intelligence (AI), machine learning (ML), cyber-physical systems (CPS), and digital twins.

Criteria for Inclusion/Exclusion of Studies

The initial search resulted in a large number of articles. To narrow down the search results and ensure the relevance and quality of the studies included, the following inclusion and exclusion criteria were applied:

Inclusion criteria:

Articles that focused on Industry 4.0 and/or smart factories

Articles that discussed emerging technologies and their applications in smart factories

Articles published in peer-reviewed academic journals, conference proceedings, or industry publications

Exclusion criteria:

Articles that focused on Industry 4.0 and smart factories in non-manufacturing industries (e.g., healthcare, logistics)

Articles that did not discuss emerging technologies and their applications in smart factories

Articles published in non-peer-reviewed sources, such as blogs or news articles

After applying the inclusion and exclusion criteria, a final set of relevant studies was identified and included in the literature review. The selected studies were analyzed and synthesized to answer the research questions and achieve the research objectives.

III. DISCUSSION

The findings of the literature review suggest that Industry 4.0 and smart factories have the potential to revolutionize the manufacturing industry, enabling manufacturers to be more efficient, flexible, and adaptable than ever before. Emerging technologies such as IoT, big data analytics, AI, ML, CPS, cloud computing and digital twins etc. are key enablers of this transformation.

The comparison of traditional factories vs. smart factories suggests that smart factories have several advantages over traditional factories, including increased efficiency, flexibility, and adaptability. Smart factories are also better equipped to deal with the challenges of an increasingly complex and dynamic manufacturing environment.

The implications of the research for the industry are significant. Manufacturers need to embrace Industry 4.0 and invest in emerging technologies to remain competitive in an increasingly global and dynamic marketplace. However, there are also several challenges that need to be addressed, such as the need for skilled workers and the integration of different systems and technologies.

IV. RESULTS

The literature review identified a range of emerging technologies in Industry 4.0 that are being applied in smart factories, including IoT, big data analytics, AI, ML, CPS, cloud computing, and digital twins. These technologies are enabling the development of smart factories that are more efficient, flexible, and adaptable than traditional factories.

IoT technologies, such as sensors and actuators, are being used to collect and transmit data in real-time, allowing for real-time monitoring and control of factory processes. Big data analytics is being used to analyze large volumes of data generated by IoT devices, enabling manufacturers to identify patterns and insights that can be used to optimize production processes.

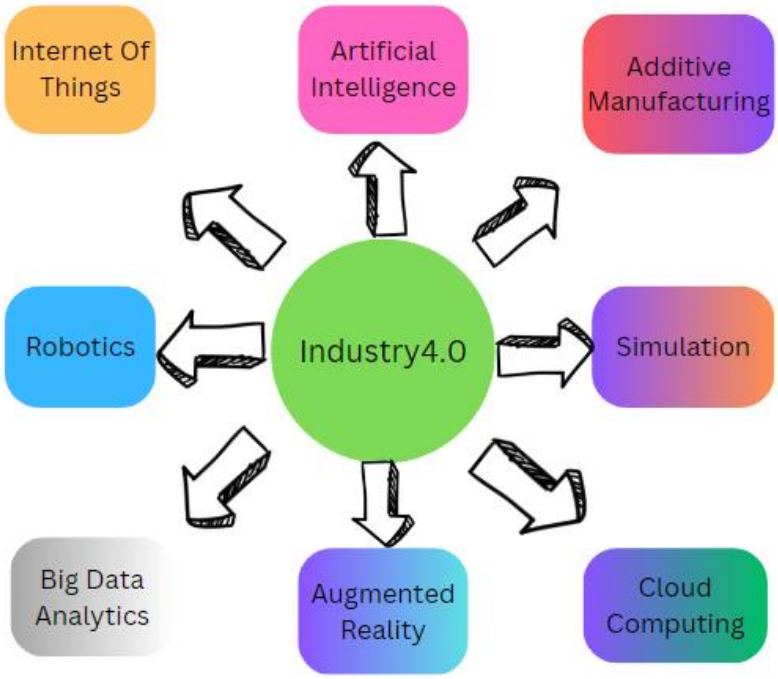
AI and ML technologies are being used to automate and optimize various processes in smart factories, such as predictive maintenance, quality control, and supply chain management. CPS technologies are being used to

e-ISSN: 2582-5208
International Research Journal of Modernization in Engineering Technology and Science
(Peer-Reviewed, Open Access, Fully Refereed International Journal)
Volume:05/Issue:04/April-2023 Impact Factor- 7.868 www.irjmets.com

integrate physical and digital systems, enabling more efficient and effective communication and coordination between different parts of the production process.

Digital twin technology is also being used to create virtual replicas of physical systems and processes, enabling manufacturers to simulate and test different scenarios before implementing changes in the real world.

Examples of successful implementations of Industry 4.0 technologies in smart factories include the Siemens Amberg Electronics Plant, which uses digital twin technology to optimize production processes, and the Bosch Rexroth smart factory in Homburg, Germany, which uses AI and IoT technologies to automate and optimize production processes.



V. CONCLUSION

In conclusion, the literature review suggests that Industry 4.0 and smart factories are key drivers of the future of manufacturing. Emerging technologies such as IoT, big data analytics, AI, ML, CPS, and digital twins etc. are enabling manufacturers to be more efficient, flexible, and adaptable than ever before. However, there are also several challenges that need to be addressed to fully realize the potential of Industry 4.0.

Limitations of the research include the limited scope of the literature review and the focus on published sources in English. Future research could explore the challenges and opportunities of Industry 4.0 in more detail, as well as the implications for different industries and regions.

This literature review has provided a comprehensive analysis of emerging technologies in Industry 4.0 and their applications in smart factories. The review highlights that smart factories are transforming the manufacturing industry, providing several advantages over traditional factories, including increased efficiency, flexibility, and adaptability. The integration of IoT, big data analytics, AI, ML, CPS, and digital twin technologies is key to realizing the full potential of Industry 4.0.

The successful implementation of these technologies in real-world examples, such as the Siemens Amberg Electronics Plant and the Bosch Rexroth smart factory, demonstrates the significant impact Industry 4.0 can have on manufacturing.

The findings of this review have significant implications for the industry, emphasizing the need for manufacturers to invest in emerging technologies and adapt to the rapidly changing manufacturing environment. However, there are also several challenges that must be addressed, including the need for skilled workers and the integration of different systems and technologies. Future research should focus on addressing

these challenges and developing practical solutions for the successful implementation of Industry 4.0 in smart factories.

VI. REFERENCES

[1] Sharma, S., & Jain, S. (2020). A Review of Industry 4.0 Applications in Manufacturing. Materials Today: Proceedings, 33(4), 2348-2356.

[2] Priyadharshini, A., & Aravindan, S. (2021). Smart Factory: A Literature Review. Materials Today: Proceedings, 47(1), 182-187.

[3] Singh, S., Kumar, A., & Kumar, R. (2021). Industry 4.0 Technologies in Manufacturing: A Comprehensive Review. Journal of Manufacturing Technology Management, 32(4), 732-764.

[4] Li, C., Li, J., & Wang, J. (2019). Smart Factory for Industry 4.0: A Review. IEEE Access, 7, 83616-83628.

[5] Khan, H., Khan, R. M., & Hassan, M. M. (2021). Smart Manufacturing: A Review of Technologies and Applications. Computers & Industrial Engineering, 159, 107258.

[6] Rathi, M. G., & Singh, A. K. (2021). Industry 4.0 and Smart Manufacturing: A Review of Research Issues and Challenges. Journal of Manufacturing Systems, 60, 472-491.

[7] Akella, S. S. R., & Padhy, S. K. (2021). A Review of Emerging Technologies for Industry 4.0. Journal of Manufacturing Systems, 60, 100-117.

[8] Zhang, T., Li, Z., & Liu, Y. (2018). Industry 4.0 and Smart Factory: A Review of the Literature. IEEE International Conference on Industrial Engineering and Engineering Management (IEEM), 1424-1428.

[9] Farooq, U., Ashraf, U., & Aijaz, A. (2020). Industry 4.0 and Smart Factory: A Review of the Literature. In Proceedings of the 2020 International Conference on Computer Science and Artificial Intelligence (CSAI), 210-214.

[10] Jawale, M. D., & Bapat, S. S. (2020). Industry 4.0 and Smart Manufacturing: A Literature Review. Procedia Manufacturing, 51, 1138-1145.

[11] Kagermann, H., Wahlster, W., & Helbig, J. (2013). Securing the future of German manufacturing industry: Recommendations for implementing the strategic initiative INDUSTRIE 4.0. Final report of the Industrie 4.0 working group.

[12] Wang, L., Törngren, M., & Onori, M. (2015). Current status and advancement of cyber-physical systems in manufacturing. Journal of Manufacturing Systems, 37, 517-527.

[13] Lee, J., Bagheri, B., & Kao, H. A. (2015). A cyber-physical systems architecture for Industry 4.0-based manufacturing systems. Manufacturing Letters, 3, 18-23.

[14] Tao, F., Zhang, M., & Nee, A. Y. C. (2019). A digital twin-driven approach to lifeline maintenance of machinery and equipment in smart factories. Journal of Manufacturing Systems, 50, 42-50.

[15] Schuh, G., Potente, T., & Westkämper, E. (2017). Industrie 4.0 and smart manufacturing-a review of research issues and application examples. International Journal of Precision Engineering and Manufacturing-Green Technology, 4(4), 401-420.

[16] Hermann, M., Pentek, T., & Otto, B. (2016). Design principles for Industrie 4.0 scenarios. In Proceedings of the 49th Hawaii International Conference on System Sciences, 3928-3937.

[17] Li, X., Liu, Z., Yan, Y., & Li, J. (2020). A cloud-based architecture for digital twin-driven smart manufacturing. Journal of Intelligent Manufacturing, 31(1), 143-154.

[18] Zhang, L., Hu, Y., Wu, D., & Xu, X. (2019). A survey on industrial applications of digital twin. IEEE Access, 7, 176784-176802.

[19] Jazdi, N. (2014). Cyber physical systems in the context of Industry 4.0. In Proceedings of the 2014 IEEE International Conference on Automation, Quality and Testing, Robotics, 1-4.

[20] Wang, X., Chen, X., Yin, H., & Shi, Y. (2019). Digital twin-driven product design, manufacturing and service with big data. Journal of Intelligent Manufacturing, 30(2), 665-678.

[21] Wang, X., Xu, X., & Li, X. (2020). A survey on applications of digital twin in manufacturing. Journal of Intelligent Manufacturing, 31(6), 1493-1507.

[22] Wang, X., Zeng, Z., Chen, X., & Yin, H. (2019). A review of digital twin: Concepts, applications, and challenges. IEEE Access, 7, 94524-94540.

International Journal of Advances in Engineering and Management (IJAEM)
Volume 5, Issue 4 April 2023, pp: 1838-1842 www.ijaem.net ISSN: 2395-5252

INDUSTRY 4.0 –The Industry Internet of Things (Computer aided manufacturing)

A.k Madan[1], Mohit Raj[2], Saksham Agrawal[3]

[1]*Faculty of department mechanical engineering,* [2,3]*Production and Industrial Engineering (Dept. of mechanical engineering)Delhi Technological University Formely Delhi College of EngineeringBawana Road, ShahbadDaulatpur, Rohini, Delhi 110042, India,*

Date of Submission: 20-04-2023 Date of Acceptance: 30-04-2023

ABSTRACT

We are currently living in the era of Industry 4.0, and particularly over the past few years, major developments have been made in the quickly expanding field of Manufacturing Technology due to the extraordinary efforts of both scientists and leaders in business.The regeneration of production and its material and technical base is fundamentally connected with the modernization of the Indian economy and its transition to an innovative development path.In recent years, there has been a trend towards increasing the economic potential of highly developed nations through scientific, technological, and advancements in technology, with the government playing an active role. There is a shift towards a digital industry focusing on Industry 4.0. This results in enormous setup of cyber physical systems in production, the advancement of modern digital technologies such as Computer-Aided Design (CAD) and Computer-Aided Manufacturing (CAM) has been vital, automation of most production processes, the endowment of devices with artificial intelligence, and the introduction of a variety of other advanced technologies in the field by optimizing and streamlining procedures, lowering manufacturing costs, and improving the quality of manufactured parts.

Keywords: CAD/CAM/CAx systems, design and manufacturing features, geometric modelling, tool-paths generation, Industry 4.0, digital-twins, CIM – computer integrated manufacturing (ERM/MRP – CAD/CAM), CAD/CAM for additive manufacturing

I. INTRODUCTION

Industry 4.0 is a concept that encompasses a promise of the flexible technological advancements of the industrial revolution, which linked improved production techniques with the IoT (Internet of Things), CAM (Computer aided manufacturing), CAD (Computer Aided Design). The goal is to develop new and integrated manufacturing systems capable of communicating, utilizing information, and analyzing data to drive intelligent activities in the physical environment. As a result, it is also known as the Fourth Industrial Revolution.

The concepts behind Industry 4.0 followed by the fourth industrial age are getting more popular, and they have turned into more than just words; behind them are trustworthy projects that are making their way into our lives. The fourth industrial revolution is a combination of industry and digital technologies, resulting in the development of digital industries or smart factories and factories in which all devices, machines, merchandise, and people interface with one another via digital technologies and the Internet. In fact, Industry 4.0 is an industrial Internet connection and connecting people or industry with the computer based technology like CAM , CAD, Industry 4.0 allows you to create mass production of individual orders, while the price of products will be lower.

Industry 4.0, which is interchangeably used with the fourth worldwide industrial revolution, signifies another step in the organisation and manages the on-the-ground value chain.

It has the following **characteristics:**

- More automation than the third revolution
- IIoT-enabled cyber-physical systems bridge the gap between the digital and physical worlds.
- A considerable movement from central industrial control to a location where the most

International Journal of Advances in Engineering and Management (IJAEM)
Volume 5, Issue 4 April 2023, pp: 1838-1842 www.ijaem.net ISSN: 2395-5252

advanced intelligent products define the manufacturing phases.
- Data models and closed-loop control systems
- Product personalization/customization

The concept of Industry 4.0 is closely related to the incorporation of advancements in Information Technology into manufacturing technology and systems. As its name implies, it is a revolution in industry, aiming at a higher level of automation and digitization that will lead to the overall improvement of processes, services, and products. Several tools and technologies, such as Internet of Things, cloud computing and CAM ,CAD,CIM, and big data analytics are already used for this purpose. However, the shift from the automated manufacturing concept to intelligent manufacturing is of particular importance. In advanced manufacturing, intelligence is a key element for future development and progress. The aforementioned shift can be accomplished by including algorithms and methods relevant to soft computing or computational methods, for optimization in industrial practice. These methods are capable of providing fast simulation models or resolve industry-related problems efficiently. Especially, in the case of hard engineering problems, it is possible to adopt a rapidly converging optimization method as a part of the decision-making system, which will receive information in real time from the physical processes in the industrial environment and provide reliable results. Computational optimization techniques have proven to be critical for this purpose and a lot of research has already been performed in this field. As a result, many methods and various techniques have been proposed and applied in manufacturing technology problems.

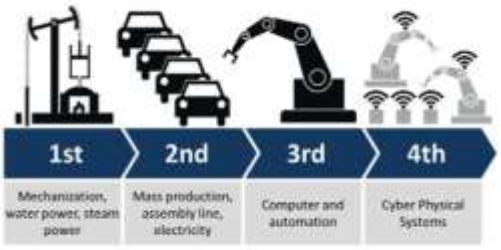
1. The three pillars that allowed the development of this engineering field are:

- **Mathematical models:** From the point of view of design (CAD), innovative mathematical solutions have enabled the more precise representation of complex shapes, as well as the development of new tools and technologies, such as virtual reality, geometric design for Additive Manufacturing (3D printing), and new structural design (lattice structure), which ultimately facilitate the designer's work. To optimise production from the standpoint of manufacturing (CAM), new algorithms that improve tool-path computation, as well as new alternatives for tool trajectories, have been developed.

- **New functions**: modern CAD/CAM functionalities have been developed to meet new technical needs and advance the state of the industry. CAD/CAM for Additive Manufacturing (3D printing), CAD/CAM and Virtual Reality, Digital-Twin technology, and reverse engineering are a few examples.

- Industry 4.0 era: real-time data collected during design and manufacturing processes can be used to optimise production and feed into new generations of CAD/CAM.

2. Transition to the fourth industrial revolution: Industry 4.0



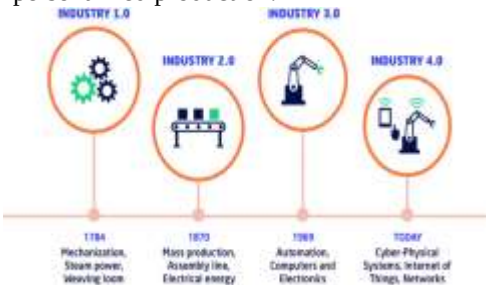
- The discovery of a steam engine in the second half of the 17th century in Great Britain triggered the first industrial revolution. However, the revolution occurred between the XVIII and XIX centuries, and it did not occur simultaneously in all countries. Steam engines were first employed in pumps, then in locomotives, steamboats, and in manufacturing. Steam power has had an impact on the advancement of metallurgy, mechanical engineering, transportation, and other industries. There was a shift from manual to machine labour, and productivity increased dramatically.
- Henry Ford's creation of the conveyor belt and in-line production are associated with the second industrial revolution. The time spans the second half of the nineteenth to the beginning of the twentieth centuries. Many other inventions were also created during this time period, including the Bessemer process of steel smelting, which was the first low-cost method of creating high-quality steel, electric energy, widespread use of chemicals, telephone, telegraph, and so on. Electricity allows for the division of labour in the manufacture of bats.

- The third industrial revolution, often known as the "Digital revolution," occurred around the end of the twentieth century (since 1970) and is related with the development of electronics,

International Journal of Advances in Engineering and Management (IJAEM)
Volume 5, Issue 4 April 2023, pp: 1838-1842 www.ijaem.net ISSN: 2395-5252

digitalization, computerization, information systems, and the advent of a robot. Industrial production has become more automated as a result of advances in electronics and information technology.

- The fourth industrial revolution originates in 2011 , as the German public-private Industries 4.0 program within which the German companies with assistance of the federal government in the form of grants create digital, clever productions which devices and products interact with each other and provide the personalized production.



3. **Industry 4.0 principles :**

- Compatibility is a feature of all devices and machines to communicate with one another in the same language via the Internet of Things, i.e. they must be compatible.
- Transparency is the construction of a digital duplicate of the product, as well as the collecting of data from microarrays and sensors that allows devices to connect with one another. As a result, the most complete information about all processes that occur with equipment, smart products, production in general, and so on is accumulated.
- Technical support is software that collects, analyses, systematises, visualises sensor data and assists a person in making a decision or makes it automatically, thereby freeing up human resources. This assistance may even include the entire replacement of humans with machines during hazardous or routine procedures.
- Decentralization of management decisions, automation of various solutions by systems, maximum human replacement. Employees are assigned the role of supervisors who can connect in emergency and non-standard situations.

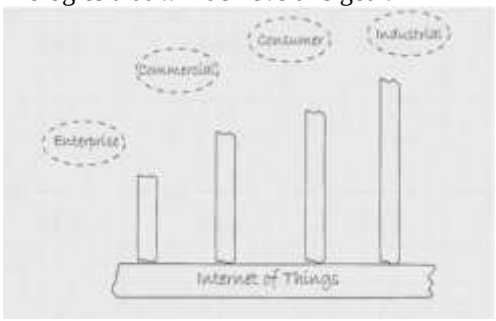
4. Computer-aided manufacturing and Industry 4.0

- The kind of intelligent system design will enhance computer-aided manufacturing by providing higher quality assurance more efficiently. However, CAM plays a larger role as part of a larger, integrated product and service delivery process. New design principles will be required, and new technology will have a significant impact on computer-aided manufacturing and its future role.
- In existing Industry 3.0, networks and processes are limited to a single factory. Individual industrial borders will most likely no longer exist in Industry 4.0. Computer-aided manufacturing will grow increasingly networked until everything is interconnected. As a result, the complexity of production and supplier networks will increase.

5. CAM's Success Factors Are Changing :

Currently, success in manufacturing is defined as producing a high-quality service or product at the lowest possible cost. Factories strive to do this through optimising performance and volume. More complex variables will be incorporated in the future of CAM. Monitoring and fault diagnosis, components and systems will self-diagnose and self-predict, providing additional insight into the status of the process and delivering self-healing and adaptive solutions.

Computer-aided manufacturing and IoT will necessitate orchestration throughout the entire value chain, from product creation, product management, manufacture and assembly, through digital service provision and service management. The necessity for orchestration will reflect the convergence and interdependence of the emerging technologies that will achieve this goal.



6. The Negative Effects of Industry 4.0

- The Industry4.0 medal has a disadvantage. Mass robotization and automation will result in job independence; a huge number of people may be out of work; retraining of specialists to other professions will be required; but many new professions will emerge.

International Journal of Advances in Engineering and Management (IJAEM)
Volume 5, Issue 4 April 2023, pp: 1838-1842 www.ijaem.net ISSN: 2395-5252

- The value of low- and middle-skilled labour will be dramatically diminished, perhaps reducing middle-class income and material goods. The move to highly trained labour will be arduous and not available to all. The middle class is a large segment of the country's population, and a drop in middle-class wages can lead to the country's democratic system collapsing.
- There is also a presumption that the population's low purchasing power as a result of Industry 4.0 will lead to poor demand for items, putting the profitability of many firms producing non-vital products in jeopardy.
- It is also a danger that automation will replace the mental and physical activities of people, production workers will only observe robots, and thus people can atrophy memory and other brain functions. It is necessary to involve people in various tasks for universal development.

7. Industry4.0implementation examples

- The leaders in this area are Microsoft, GE, PTC and Siemens. Microsoft is developing solutions for IoT platforms that are closely related to the infrastructure (IaaS + PaaS) that is, operating on the basis of the IaaS server of the cloud provider. The technology is already being used by BJC HealthCare, a health care provider that manages 15 hospitals in Missouri and Illinois. The company uses an IoT platform to save in the supply chain.
- Combining IoT and big data is a that Bosch uses to transform digital technologies at its Bosch Automotive Diesel System plant in Wuxi, China. The company connects its equipment to control the entire production process to a single distribution center of the plant. To do this, sensors are installed on all machines of the factory, which are used to collect data on the state of the machines and their time of operation. The company BoschRexroth equipped equipment for the production of valves (and the valves themselves) with special radio frequency identification (RFID), so that the working equipment "understands" what steps need to be performed and how to adapt each individual operation.
- Along with robotics and intelligent systems, additive manufacturing, or 3D printing, is a key technology that stimulates the development of the 4.0 Industry. One of the World economic forum's best intelligent factories in the world, Fast Radius, uses its own technology platform for 3D printing.
- Siemens has developed and used virtual and augmented reality capabilities to develop a virtual training module for its Comos software. Using a 3D model and augmented reality glasses, the module helps staff cope with emergencies in virtual simulation mode. In this virtual world, operators learn to interact with equipment using a digital presentation, change equipment parameters and display operating indicators and repair instructions.

- An example is Siemens PLM Software's Tecnomatix, a family of software products designed to automate production preparation and optimization tasks.

II. CONCLUSIONS

- The fourth industrial revolution will cause major changes in practically every aspect of human life. The following are the most likely effects of Industry 4.0 development: The fundamental transformation of the economy, the predominant development of sectors of the economy that have access to large amounts of data; the growth of social classification as a result of the disappearance of the importance of a large number of professions, intellectual and creative opportunities will become the main value in the labour market; The removal of routine and standard tasks as a result of the automation of the great majority of such activities; world transparency as a result of the interpenetration of the real and virtual worldsdigital environment, new opportunities for digital control of undesirable social phenomena and events.
- Industry 4.0 is slowly but surely entering our world. Industry 4.0 will make it possible to reach a new level of human development and quality of life. It will change the attitude of people and people themselves.



REFERENCES

[1]. Martinov G M 2019 Digital manufacturing technologies according to Industry 4.0 concept Automation in industry
[2]. Sergeeva O Y «Industry 4.0» as «Smart manufacturing» 2018 Nanotechnology in construction: scientific online journal 2 100-13
[3]. Shustova I S 2019 «The internet of things» as the most perspective technology of the Industry 4.0 changing business models of the companies In the collection: World economy in the 21st century: Value and Values. collection of materials of the International academic and research conference
[4]. Kantonen, T., Woodward, C., & Katz, N.
[5]. (2010). Mixed reality in virtual world teleconferencing. In Proc. IEEE Virtual Reality, Waltham, Massachusetts, USA, March 20 – 24 (pp. 179–182).
[6]. Rosen, D. (2007). Computer-aided design for additive manufacturing of cellular structures. Computer-Aided Design and Applications, 4(5), 585–594.
[7]. Palmarini, R., Erkoyuncua, J. A., Roy, R., &Torabmostaedi, H. (2018). A systematic review of augmented reality applications in maintenance. Robotics and ComputerIntegrated Manufacturing, 49, 215–228. Peruzzini, M., Grandi, F., &Pellicciari, M. (2017). Benchmarking of tools for user experience analysis in Industry 4.0. Procedia Manufacturing, 11, 806–813.
[8]. vercator.com/blog/the-future-of-computer-aided-manufacturing
[9]. E. D. Rekow, A. G. Erdman, D. R. Riley, and B. Klamecki, "CAD/CAM for dental restorations—some of the curious challenges," IEEE Transactions on Biomedical Engineering, vol. 38, no. 4, pp. 314–318, 1991.
[10]. "Internet of Things (IoT) 2013 to 2020 market analysis: Billions of things trillions of dollars", Rep. 243661, Oct. 2013.
[11]. L. D. Xu, W. He and S. Li, "Internet of Things in industries: A survey", IEEE Trans. Ind. Inform., vol. 10, no. 4, pp. 2233-2243, Nov. 2014.
[12]. American Machinist. The CAD/CAM hall of fame, 1998; Available at: http://www.Americanmachinist.Com/304/Issue/Article/False/9168/Issue. Accessed August 13, 2010.
[13]. Kanazawa M, Inokoshi M, Minakuchi S, Ohbayashi N. Trial of a CAD/CAM system for fabricating complete dentures. Dent Mater J 2011; 30: 93-B. Khoshnevis et al.

2023 IEEE 8th International Conference for Convergence in Technology (I2CT)
Pune, India. Apr 7-9, 2023

In-silico approach to DNA codon optimization of Zaire Ebola Virus Genes for Vaccine Development

Ruchi Tirkey
Department of Biotechnology
Delhi Technological University
Delhi, India
ruchitirkey458@gmail.com

Soniya
Department of Biotechnology
Delhi Technological University
Delhi, India
soniyaj861@gmail.com

Yasha Hasija*
Department of Biotechnology
Delhi Technological University
Delhi, India
yashahasija06@gmail.com
*Corresponding Author

2023 IEEE 8th International Conference for Convergence in Technology (I2CT) | 979-8-3503-3401-2/23/$31.00 ©2023 IEEE | DOI: 10.1109/I2CT57861.2023.10126407

***Abstract*—Ebola Virus is the causative agent of one of the longest known pandemics Ebola Virus Disease (EVD) in history of deadly outbreaks with a zoonotic origin. EVD outbreaks originate through zoonotic transmission, spread within humans via direct or indirect contact with contaminated bodily fluids. With a high mortality rate, EBOV has created havoc in Middle African countries. To curb such pandemics, a strong immunogenic vaccine is always a problem which can be solved by Codon Optimization. In the present study, tools available online were used to optimize all the seven protein coding genes of EBOV. A significant increase in the Codon adaptation Index (CAI) and GC content was observed along with a considerable decrease in ENC values as compared to the wild type strain. Our results demonstrate that the optimized genes other than GP can be beneficial for elevated translation of target proteins in the host and also helpful in increasing the immunogenic response.**

Keywords— Zaire Ebola virus, codon optimization, vaccine, codon usage bias, GC content.

I. INTRODUCTION

Initially known as *Zaire ebolavirus, Ebola virus* (EBOV) belonging to the Filoviridae family, was responsible for the 2013-2016 Ebola virus disease epidemic. The outbreak had majorly affected the West African countries with 28000 confirmed cases and 11000 deaths being reported, indicating the highly infectious nature of the virus.[1] EBOV has shown high transmission rates amongst humans, by the means of contaminated body fluids like blood, semen. Clinical manifestations of the infection include fever, fatigue, joint pain and acute hemorrhagic conditions leading to organ failure and death. Young age pregnancy and no use of contraceptives have also been found to increase the mortality risks. Although the morbidity rate of the virus is high, certain patients do survive and, in some cases may develop different autoimmune conditions [1]. Currently knowledge about the EBOV in survivors is limited to transmission and persistence of the virus even after the disappearance of clinical symptoms and disease [1].

EBOV has a pleomorphic shape with a diameter and length ranging from 50-80 nm and 10,000-14,000 nm respectively [2]. It has a negative sense, single stranded RNA genome which is approximately 19 kb in size and comprises seven genes that encode - nucleoprotein (NP), virion protein (VP35), VP30, glycoprotein (GP), RNA-dependent RNA polymerase (L), matrix proteins (VP40 and VP24). The helical nucleocapsid of the virion is surrounded by an envelope that is embedded with GP spikes. These 10 nm long spikes are responsible for the pathogenicity of the virus and hence have been a major target for vaccine development. VP24 and VP35 help in nucleocapsid assembly, virus release and immune response suppression. L is responsible for the activation of viral RNA synthesis and NP for the encapsidation of the newly synthesized viral RNA. VP40 helps in maintaining the structural integrity of the developing virus-like particles [1], [2].

II. CODON OPTIMIZATION

As we recently witnessed one of the biggest pandemics of all time, COVID-19, it becomes all the more important to prevent any such future possibilities that may arise. There are currently two vaccines approved for Ebola Virus, one is Ervebo which is a recombinant vaccine made up of vesicular stomatitis virus containing Ebola GP gene. The other one is a two-dose vaccine, called Zabdeno and Mvabea which is futile in case of an outbreak that demands an immediate response. Now that we are left with only one approved vaccine for EVD, new strategies should be considered for developing treatments from these deadly viruses.

The antigens of pathogens like viruses, bacteria, fungi, and parasites are encoded in DNA vaccines, commonly referred to as "naked DNA" or nucleic acid vaccines [3]. But when expressed in larger organisms, they have shown less immunogenic properties. Maximizing its expression in the immunized host is a viable strategy for improving its immunogenicity.

DNA codon optimization helps in increasing the yields of translated heterologous proteins. As we know that the genetic code is degenerate, except Methionine and Tryptophan, multiple codons code for one amino acid which leads to synonymous codon usage. This degeneracy differs in frequency in different genomes but is not random. In one organism, one codon might be used to synthesize an amino acid but in different organisms another set of synonymous codon might be used. This is called codon usage bias and it is species specific. Similarly, isoacceptor tRNAs modification can also alter the tRNA-mRNA base pairing as the interaction is not one-on-one and the third position of a codon is wobble.

Authorized licensed use limited to: DELHI TECHNICAL UNIV. Downloaded on May 29,2023 at 05:54:43 UTC from IEEE Xplore. Restrictions apply.

Protein translation can become more efficient if codon usage aligns with presence of specific tRNA isoacceptors [4]. Generally viruses do not show a lot of Codon Usage bias and thus are able to survive in a wide variety of hosts [5]. Codon optimization allows increased expression of rarely used sets of codons in a heterologous host native to an individual organism. This can increase the immunogenicity of a particular antigen which can also come handy in development of vaccines. Codon optimization presents an inexpensive and convenient strategy for different laborious experiments [5], [6].

Therefore, the aim of this study was to prepare optimized codon sequences of all seven genes of Zaire Ebola Virus for their over expression in *Escherichia coli K-12* as a host. The optimization was such that there was no effect on the amino acid sequence of any of the seven genes ensuring there was no change in the immunogenicity and functional properties of the genes. DNA codon optimization has a huge array of applications specifically in immunotherapy and immunodiagnostics due to its ability to increase the expression of target protein and reduce the codon usage bias without posing any major side effects.

III. METHODOLOGY

A. Collection of sequences

Through NCBI-Genbank (https://www.ncbi.nlm.nih.gov), nucleotide sequences (CDS) of genes - NP, VP35, GP, VP40 and VP24 of Zaire Ebola virus were retrieved (Accession number: L11365.1).

B. Codon optimization

OPTIMIZER is a freely accessible, web based application that helps in predicting and increasing gene expression levels by optimizing its codon usage in a heterologous host system (http://genomes.urv.es/OPTIMIZER). Along with optimization, Codon Adaptation Index (CAI), G+C% and A+T% were also calculated for the retrieved DNA sequences. The respective scores obtained were used for analyzing the expression of the optimized sequences.

C. In-silico Translation

Using Expasy's online translation tool (https://web.expasy.org/translate/), all the optimized sequences were translated into peptide sequences. These peptide sequences were then taken to analyze the immunogenicity profile of specific viral genes.

D. Immunogenicity analysis

Immunogenicity profiling was done via IEDB (Immune Epitope Database) Analysis Resource which is an online tool available for predicting properties of immune epitopes. The protein sequences were processed via MHC-I processing tool (http://tools.iedb.org/processing/) following some parameters and each of the 9-mer peptides were then subjected to the T-cell immunogenicity prediction test (http://tools.iedb.org/immunogenicity/). The results were analyzed. All the parameters were compared for wild type and optimized sequences by plotting graphs and calculating the percentage increase or decrease from the native type.

IV. RESULTS

Table 1 outlines the codon usage for the different Zaire Ebola virus genes, including the nucleoprotein, VP35 virion protein, glycoprotein, RNA dependent RNA polymerase, VP40/VP24 matrix protein, and VP30 minor nucleoprotein. Their codons were modified with reference to *Escherichia coli K12.* The current study demonstrated a significant increase in CAI (Codon Adaptation Index) values & G+C% content, and a decrease in ENC (Effective Codon Number) values of all genes. The immunogenicity values acquired from IEDB for both wild and optimized sequences remained exactly the same. After optimization, differences in CAI, A+T%, G+C% and ENC values were noted. An increment of 31% for NP, 33% for VP24, 35% for VP30, 51% for VP35, 40% for VP40 34% for GP and 23% for polymerase (L) for CAI was observed (Fig. 1). ENC showed a dip of 12% for NP, 13% for VP24, 9% for VP30, 7% for VP35, 18% for VP40, 9% for GP and 13% for polymerase (Fig. 2). G+C% was increased in all the 7 genes by 6% in NP, 11% in VP24, 22% in VP30, 16% in VP35, 11% in VP40, 7% in GP and 20% in polymerase. (Fig 3.) A+T% in all genes were decreased (Fig 4.) and immunogenicity of the proteins obtained after optimization showed no changes. GP showed highest immunogenicity among the 7 viral genes (Fig. 5). Hence, it can be inferred that with increase in codon adaptation index and G+C%, the expression of required genes increased with enhanced stability in the immunized host, without hampering the functional profile of the antigen.

V. DISCUSSION

In a time where any and every pathogen has the capacity to cause disasters like the COVID-19 pandemic, it is very important to curb any such possibilities. Zaire Ebola Virus is the deadliest of all the Ebola virus strains and developing better strategies for therapeutics should be our key motive of research. One such innovative technique of preparing high

TABLE I. CODON OPTIMIZATION PARAMETERS FOR NP, VP24, VP30, VP35, VP40, GP AND POLYMERASE GENES OF EBOLA VIRUS FOR BOTH WILD TYPE AND OPTIMIZED VARIANT

Gene Name	CAI		ENC		GC		AT	
	Wild type	Optimized	Wild Type	Optimized	Wild type	Optimized	Wild type	Optimized
NP	0.519	0.682	57	50	47	49.9	53	50.1
VP24	0.507	0.674	55	48	42.7	47.4	57.3	52.6
VP30	0.456	0.69	54	49	44.4	54.3	55.6	45.7
VP35	0.495	0.659	56	52	45.5	52.7	54.5	47.3
VP40	0.483	0.674	55	45	48.5	53.6	51.5	46.4
GP	0.507	0.678	56	51	47.8	51.2	52.2	48.8
Polymerase L	0.461	0.569	31	27	42.6	51.2	57.4	48.8

.

Authorized licensed use limited to: DELHI TECHNICAL UNIV. Downloaded on May 29,2023 at 05:54:43 UTC from IEEE Xplore. Restrictions apply.

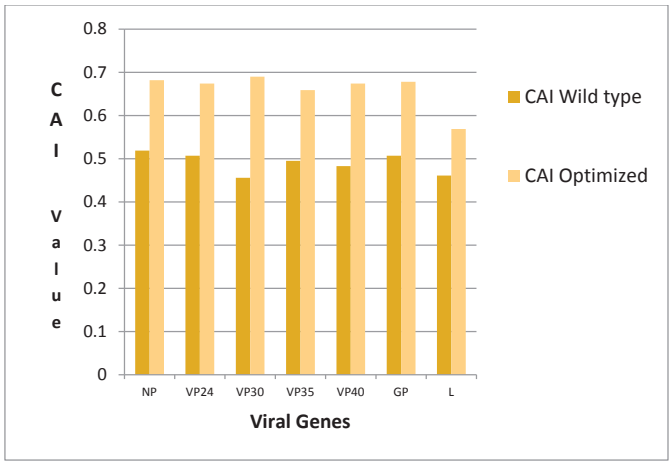


Fig. 1. Comparing Codon Adaptation Index of wild type and optimized gene sequences.

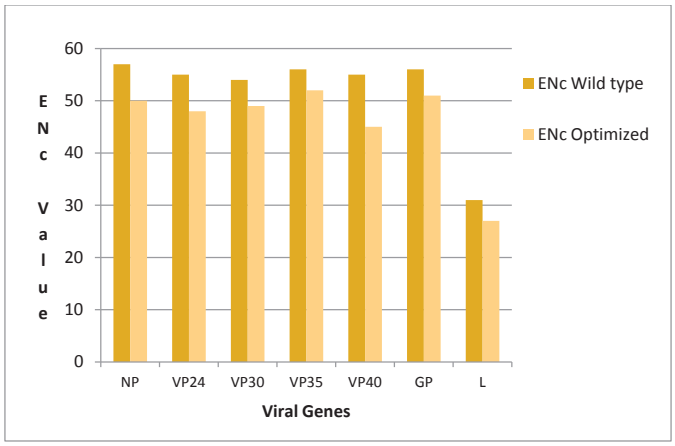


Fig. 2. Comparing ENC Values of wild type and optimized gene sequences.

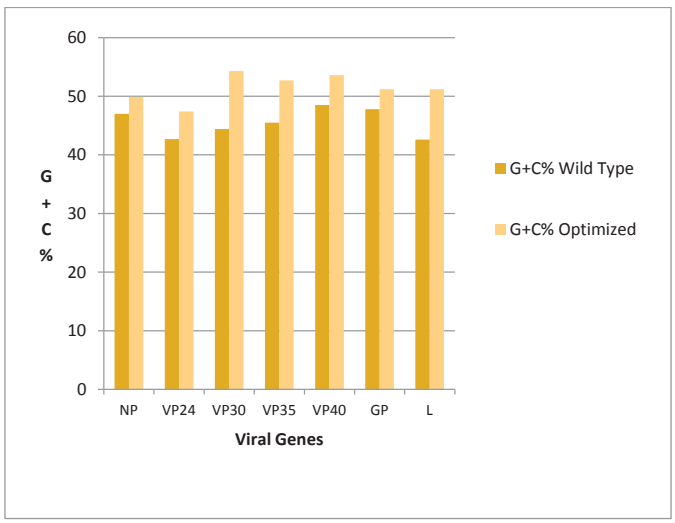


Fig. 3. Comparing GC Content of wild type and optimized gene sequences.

response yielding vaccines is Codon Optimization. It is an in-silico approach to increase the amount of expression of target proteins in hosts using synonymous codon bias. With higher levels of expressed proteins, their functional properties are also accelerated.

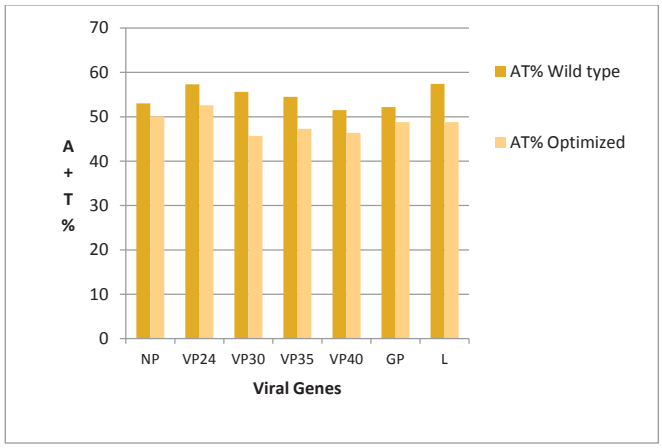


Fig. 4. Comparing AT Content of wild type and optimized gene sequences.

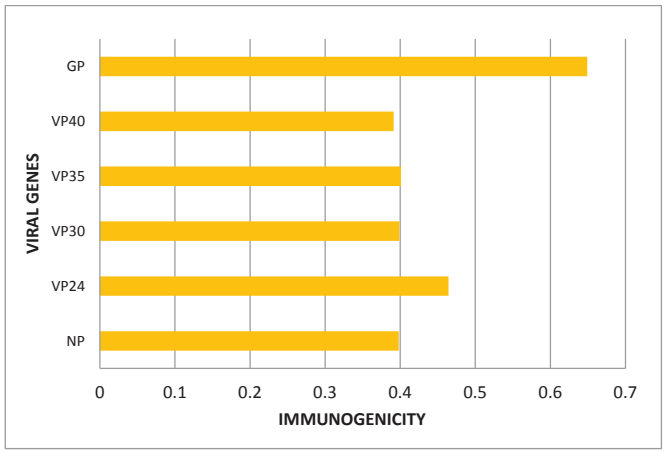


Fig. 5. Comparison of Immunogenicity scores of each gene of Zaire Ebola Virus.

To analyze the results obtained, it is important to understand some parameters. 1. CAI - Codon optimization Index is a quantitative measure to check the expression level of specific sequence in an organism [7]. Its value can range from 0 to 1.0, 0 being minimum and 1 being maximum level of expression. By comparing the codon utilization rate of a gene with a set of highly expressed genes from a species, one can calculate the CAI for that gene. Using Optimization tools, CAI can be easily increased [8].

Effective Codon number (ENC) value measures codon bias as a divergence from a distribution of synonymous codon usage that is expected to be neutral. Within a range of 20-61, highly expressed genes give lower values due to high codon preference [9]. Unlike ENC, CAI evaluates the degree of bias towards a specific set of adaptive codons. Lower ENC and higher CAI are indicators of stronger codon bias [8]. Increase in GC content at third position and smaller length of sequence is also a characteristic feature of most of the highly expressed genes. A high GC content also ensures stability leading to enhanced expression. However as it can be seen there is no change in the immunogenicity profiles of any of the genes, optimization of sequences has not proven to be degrading the quality of our possible antigens.

Authorized licensed use limited to: DELHI TECHNICAL UNIV. Downloaded on May 29,2023 at 05:54:43 UTC from IEEE Xplore. Restrictions apply.

VI. CONCLUSION

Zaire Ebola Virus has been a topic of concern since 2013 when it caused the largest viral Pandemic. The disease starts with fever and ends up hampering the immune system of the body. From 2013-2016, Ebola virus is responsible for 28,652 human infections and 11,325 deaths in the areas of Middle Africa. With better diagnostic techniques like Real time RT-PCR, the understanding of EVD has significantly increased [10].This knowledge led to development of efficacious vaccines. To add onto the list of efficacious vaccines, this study used codon optimization strategy using Optimizer for every gene sequence of Zaire Ebola virus and checked their expression level using CAI and ENC values. It was evident that using *E.coli* as a reference, CAI values significantly increased for all the genes. While inspecting for immunogenicity of each viral protein in IEDB Analysis Resource, Envelope protein GP could elicit maximum immune response. This value coincides with recent studies. In a trial conducted in 2015, *C. macaques* were vaccinated with DNA plasmids expressing codon optimized GP genes of EBOV and the neutralizing antibodies and IgG titer levels obtained after vaccination were significantly higher [11]

Another research demonstrated optimizing GP1 sequence removed pseudoknots from the native gene and increased its translational efficacy. As presence of GC increases the possibility of formation of pseudoknots, the study used optimization to reduce GC content. Many such parameters can be taken into account and modified according to the requirements of the recombinant vaccine [12].

However, Codon optimization poses some disadvantages as well. Not all optimized genes have shown higher expression in lab conditions. It is a good strategy to increase the production or activity of industrial enzymes, however in case of recombinant applications, better algorithms should be developed to ensure native conformation of the protein. It is not well supported by research in mammals. Anyhow we are inducing DNA changes which can add to the safety issues of the product. The ultimate goal of Codon optimization, besides increased expression, should be increased safety. [13]

We propose that other than GP, optimized VP24 and VP35 genes can also be used as a probable antigen for EVD vaccines as they showed significant immunogenic response. Future work should be done in-vitro to authenticate the results of the present study. With better algorithms keeping added parameters in mind can help increase the safety of using optimized sequences in therapeutics.

REFERENCES

[1] M. Rojas *et al.*, "Ebola virus disease: An emerging and re-emerging viral threat," *J. Autoimmun.*, vol. 106, no. December 2019, p. 102375, 2020, doi: 10.1016/j.jaut.2019.102375.

[2] B. Zawilińska and M. Kosz-Vnenchak, "General introduction into the Ebola virus biology and disease," *Folia Med. Cracov.*, vol. 54, no. 3, pp. 57–65, 2014.

[3] L. Deml *et al.*, "Multiple Effects of Codon Usage Optimization on Expression and Immunogenicity of DNA Candidate Vaccines Encoding the Human Immunodeficiency Virus Type 1 Gag Protein," *J. Virol.*, vol. 75, no. 22, pp. 10991–11001, 2001, doi: 10.1128/jvi.75.22.10991-11001.2001.

[4] K. Jitobaom *et al.*, "Codon usage similarity between viral and some host genes suggests a codon-specific translational regulation," *Heliyon*, vol. 6, no. 5, p. e03915, 2020, doi: 10.1016/j.heliyon.2020.e03915.

[5] A. M. Butt, I. Nasrullah, R. Qamar, and Y. Tong, "Evolution of codon usage in Zika virus genomes is host and vector specific," *Emerg. Microbes Infect.*, vol. 5, no. 10, pp. 1–14, 2016, doi: 10.1038/emi.2016.106.

[6] C. Elena, P. Ravasi, M. E. Castelli, S. Peirú, and H. G. Menzella, "Expression of codon optimized genes in microbial systems: Current industrial applications and perspectives," *Front. Microbiol.*, vol. 5, no. FEB, 2014, doi: 10.3389/fmicb.2014.00021.

[7] R. Jansen, H. J. Bussemaker, and M. Gerstein, "Revisiting the codon adaptation index from a whole-genome perspective: Analyzing the relationship between gene expression and codon occurrence in yeast using a variety of models," *Nucleic Acids Res.*, vol. 31, no. 8, pp. 2242–2251, 2003, doi: 10.1093/nar/gkg306.

[8] H. M. W. Salim and A. R. O. Cavalcanti, "Factors influencing codon usage bias in genomes," *J. Braz. Chem. Soc.*, vol. 19, no. 2, pp. 257–262, 2008, doi: 10.1590/S0103-50532008000200008.

[9] P. Puigbò, E. Guzmán, A. Romeu, and S. Garcia-Vallvé, "OPTIMIZER: A web server for optimizing the codon usage of DNA sequences," *Nucleic Acids Res.*, vol. 35, no. SUPPL.2, pp. 126–131, 2007, doi: 10.1093/nar/gkm219.

[10] S. T. Jacob *et al.*, *Ebola virus disease*, vol. 6, no. 1. Springer US, 2020. doi: 10.1038/s41572-020-0147-3.

[11] R. J. Grant-Klein *et al.*, "Codon-optimized filovirus DNA vaccines delivered by intramuscular electroporation protect cynomolgus macaques from lethal Ebola and Marburg virus challenges," *Hum. Vaccines Immunother.*, vol. 11, no. 8, pp. 1991–2004, 2015, doi: 10.1080/21645515.2015.1039757.

[12] Z. Zou, J. Misasi, N. Sullivan, and P. D. Sun, "Overexpression of Ebola virus envelope GP1 protein," *Protein Expr. Purif.*, vol. 135, pp. 45–53, 2017, doi: 10.1016/j.pep.2017.04.010.

[13] V. P. Mauro, "Codon Optimization in the Production of Recombinant Biotherapeutics: Potential Risks and Considerations," *BioDrugs*, vol. 32, no. 1, pp. 69–81, 2018, doi: 10.1007/s40259-018-0261-x.

Authorized licensed use limited to: DELHI TECHNICAL UNIV. Downloaded on May 29,2023 at 05:54:43 UTC from IEEE Xplore. Restrictions apply.

e-ISSN: 2582-5208
International Research Journal of Modernization in Engineering Technology and Science
(Peer-Reviewed, Open Access, Fully Refereed International Journal)
Volume:05/Issue:05/May-2023 Impact Factor- 7.868 www.irjmets.com

INTEGRATION OF DIMENSIONING AND TOLERANCING INTO CAD SYSTEMS: A SYSTEMATIC APPROACH USING TTRS

AK Madan[*1], Arko Sardar[*2], Ankush Kapoor[*3], Badal Singh[*4]

[*1]Professor, Mechanical Engineering, Delhi Technological University, Delhi-42, India

[*2,3,4]B.Tech. Student, Mechanical Engineering, Delhi Technological University, Delhi-42, India

DOI : https://www.doi.org/10.56726/IRJMETS38249

ABSTRACT

This paper presents the developments done in the field of Dimensioning and tolerances and Integration of CAM and CAD, using The Technologically and Topologically Related Surfaces (TTRS) concepts. TTRS involved description of object geometry in terms of surfaces which incorporates dimensions and tolerances into an information tree built in 3D. The process of analysis a geometry for CAM in to CAD utilises many techniques like Minimum Geometric Datum Elements (MGDE), Tolerance Transfer Methods (TTM), etc this allows us to develop and propose new techniques that can improve efficiency, accuracy, and performance.

Keywords: CAD/CAM, Machining, TTRS, Tolerance analysis.

I. INTRODUCTION

CAD/CAM has now days much importance in manufacturing industries as the need is now to produce much better job with low cost and time involvement. And as computers and software helps us a lot in achieving these goals so industry tends to use these wherever and whenever possible. And as the need of today is precision and accuracy too, so it is important that part features should be of controlled size, form, orientation, surface and texture. So research topics like tolerance modelling, tolerance specification, tolerance analysis, tolerance allocation, tolerance transfer and evaluation comes in picture. Tolerance modelling mainly concerns how to reasonably and effectively present, interpret and represent tolerance semantics. It requires construction of three different kinds of models: presentation model, interpretation model and representation model. Various types of tolerances in a unified way which can be understandable to civilization are presented in the presentation model. We need industry domain experts of the respective fields to understand these types of models because mostly presentation model exists in drawing indication form. In interpretation model the meaning of presentation model is interpreted. This is also the intermediate between presentation model and representation model. These models are available in form of mathematical expressions, and cannot be read by computers. The only models which can be understood and read by computers are representation models. Many of researchers started to update the existing or developing new knowledge representation languages that can construct their tolerance representation models since computer readability has been always a problem with these models. These constructed models are categorized on the base of what knowledge representation language is used. These are:

- Unified modeling language (UML),
- Extensive markup language (XML),
- Geo spelling formal language model (GPS),
- Categorical language model,
- Web ontology language model (OWL)

The idea is to develop a system for path planning, and technical constraint addition, as well as improvements in handling multiple disconnected objects. The aim is to extend the idea of the smart grid and optimize results in network planning for LOM. The proposed methods are expected to lead to better PR planning systems and represent a significant advancement in the state of the art. This study develops a web-based system, vision process, feature recognition and classification method, database and matching algorithm for shop-floor applications in the manufacturing industry of mussels. The system uses two-dimensional image information, has fast processing speed, and is suitable for a network-based system. The matching technique is designed and validated experimentally and can be generalized for general shapes when distortion and shape height differences recorded by the camera are not severe. An effective OMM planning method is proposed, including a

e-ISSN: 2582-5208
International Research Journal of Modernization in Engineering Technology and Science
(Peer-Reviewed, Open Access, Fully Refereed International Journal)
Volume:05/Issue:05/May-2023 Impact Factor- 7.868 www.irjmets.com

series of tasks, such as an appropriate number of measurement points, their locations, and optimal survey paths to minimize measurement errors and time.

The results and conclusions obtained through the experiment are as follows:

(1) The features and their features are classified into the CAD database for shape recognition, and the results are stored in the database.

(2) The system uses two-dimensional image information, with fast processing speed, suitable for web-based systems;

(3) The matching technology is designed and verified in experiments, and can generally be used for general shapes to achieve the degree of distortion of images captured by cameras.

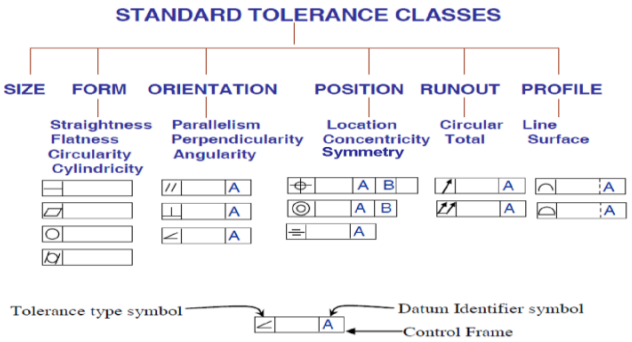


Figure1: Different classes of tolerances in the standards

II. TTRS MODEL

It stands for technologically and topologically related surfaces. It can be seen as objects representing sets of related surfaces on the same part. So a part can be seen as list of this model in which each of them regrouping a subset of all functional surfaces. TTRS model can be defined as Set composed of two surfaces belonging to the same space and located on same kinematic loop in a mechanism.

Before moving further let's understand some basic things.

- Surface is the exterior or upper boundary of any body, or a plane or curved 2D locus of points.
- Association process is binary.
- Association process is recursive.
- Associations are guided by kinematic loops in a mechanism.

Surfaces	Degrees of invariance	MGDE
spherical	3 rotations	point
plane	1 rotation 2 translations	plane
cylindrical	1 rotation 1 translation	line
helical	1 rotation + translation coupled	point + line
revolution	1 rotation	point + line
prismatic	1 translation	line + plane
complex	no degree of invariance	point + line + plane

Figure2

e-ISSN: 2582-5208
International Research Journal of Modernization in Engineering Technology and Science
(Peer-Reviewed, Open Access, Fully Refereed International Journal)
Volume:05/Issue:05/May-2023 Impact Factor- 7.868 www.irjmets.com

Dimensioning and Tolerancing TTRS

It consists of two steps:

1. Dimensioning and tolerancing elementary surfaces.
   For elementary surfaces dimensions are in diameters and distances and tolerances are for form or profile.
   For Surface associations dimensions are in distances and angles while tolerances are for location, orientation and runout.
2. Dimensioning and tolerancing MGDE associations.
   These are some MGDE Combination rules:

a. Basic MGDE issued from the same original MGDE are not dimensioned or tolerance with respect to one another.
b. Number of cases to be considered is equal to summation of MGDE involved minus one.
c. Each basic MGDE involved must be implicated in at least one of the association cases considered.
d. We shall give priority to association cases involving at least one line.

REPRESENTATION OF THE STRUCTURED KNOWLEDGE

DL definitions of terminologies are most common way in which structured knowledge in a domain exist. We should in first place identify terminologies and their definitions for representing the structured knowledge of CPT for POHs in tolerancing standards. Composite positional tolerances, pattern of holes, segments, upper segments, PLTZF, rectangular patterns of holes, circular pattern, resultant tolerances zones, feature control frame, FRTZF and lower segment are the major terminologies used to define the CPT for POHs. And these are needed to be defined by DL terminologies axioms.

REPRESENTATION OF THE CONSTRAINT KNOWLEDGE

It consists of some rules which computer can understand and which tells constraints relation to the objects and relation in this field. So determining the constraint relation which needs to be explained is the initiating step to representing constraint knowledge of CPT for POHs in tolerancing standards.

The three aspects of constraint relationships of CPT are:

1. Relationship of constraint between upper segment and PLTZF
2. Relationship of constraints between lower segment and its FRTFZF.
3. Relationship of constraints between the variational geometry and the intersection of PLTZF and FRTZF.

The semantics of constraint knowledge of CPT for POHs can be represented through determining the constraints relationships that require to be described, using HORN rules to describe these constraints relationships, and assigning a model theoretic semantics to each horn rule.

REPRESNTATION OF THE INDIVIDUAL KNOWLEDGE-

Individual knowledge in any field is to be seen as few computer readable statements of concrete individuals in this domain. So firstly extracting the concrete individuals in CPT is required to represent individual knowledge of CPT. For extracting these concrete individuals from the system the application program interface can be useful of a CAD/CAM system. Next we have to describe these extracted concrete individuals using computer readable statements. Resultant tolerances zone and variational geometry must be firstly established in order to represent the detailed semantics of a CPT. After this step, detailed semantics can also be described by DL assertional axioms.

In brief the representation process of individual knowledge of CPT for POHs can be explained:

- Extract the CPT information from systems using APIs of CAD/CAM.
- Establish the resultant tolerances zone and variational geometry of this tolerances by applying establishment methods.
- Describe the extracted tolerance information and established resultant tolerances zones and variational geometry using DL assertional axioms.

ADVANTAGES OF THE APPROACH

1. Consistency checking of the CPT ontology. It ensures whether there are inconsistencies in the DL definitions of concepts and roles and whether instantiations of concepts and role could create inconsistencies.

e-ISSN: 2582-5208
International Research Journal of Modernization in Engineering Technology and Science
(Peer-Reviewed, Open Access, Fully Refereed International Journal)
Volume:05/Issue:05/May-2023 Impact Factor- 7.868 www.irjmets.com

2. Knowledge reasoning on CPT ontology. Knowledge reasoning on the ontology takes as input the explicit knowledge in CPT representation and returns as output the implicit knowledge in representation.
3. Semantic interoperability of the information of CPT. This aims to exchange the semantics of tolerance information between heterogeneous CAD/CAM systems to overcome the limitations of old STEP based method.

III. LITERATURE REVIEW

The paper discusses the development of various systems and algorithms for different applications in the manufacturing industry. The first study proposes an effective inspection planning strategy for measuring etched surfaces, while the second study develops a web-based system for shape recognition and classification using image information. The third study presents an open-architecture process planning system for vector-based rapid prototyping, and the final study focuses on the development of new algorithms for garbage disposal and path planning. All studies contribute to the advancement of their respective fields, and propose new techniques that can improve efficiency, accuracy, and performance. Further research is needed to address the remaining challenges and improve the proposed methods. The study presents an effective inspection planning strategy for measuring etched surfaces using the OMM system. The effectiveness of the proposed method is studied using an experimental verification procedure. The method is to move the measurement points to the CC points, locate more measurement points in areas where the maximum error probability is higher, and use the TSP algorithm to minimize the inspection time. To validate the proposed efficient inspection planning strategy, experimental inspections are performed on sculpted surfaces. The model provides designers with systematic dimensioning and tolerancing aids, and TFRS and its corresponding MGDE are also a sensible approach to integrating dimensioning and tolerancing into CAD systems. In addition, the model shows promise in several related areas, such as mathematical formulation of tolerance zones, modelling of gaps and spaces, and solving tolerance analysis and synthesis problems. Finally, it provides a solid basis for representing tolerance zones via dies or screws, and can be adapted to represent gaps and gaps within mechanisms. The most important details of this article are the generation of measurement sequences, the generation of process-oriented TTRS and the implementation of these ideas. Generating a measurement series involves measuring a surface using a coordinate measuring machine (CMM), while generating a process-oriented TTRS involves generating an "I'TRS" representing a machining operation and its associated dimensions and tolerances. Implementing these ideas took a lot of development, but some of them have been approved and look promising. Work in this area is far from complete and the authors hope that the method will be useful in the future. The main details of this article are the proposed open-architecture process planning system for vector-based rapid prototyping. The system allows for easy modification/replacement of individual modules, as well as connection to feedback sensors which may require specific procedures to implement adaptive techniques. The main contribution of this work is to show that while RP techniques save time in prototyping, they themselves are currently rather inefficient, and better geometry methods could be used to improve their temporal performance. The scope of this work is quite broad and we hope to be able to handle all the parts that commercial STL-based systems can handle. The research also raises several interesting new technical and geometric questions, which we plan to investigate in the near future. The most important details of this article are the development of new algorithms for garbage disposal, the ability to handle multiple (disconnected) objects, the addition of technical constraints to the optimization results, and improvements in the methods of path planning. For LOM, the researchers hope to extend the idea of the smart grid by developing new garbage disposal algorithms, the ability to handle multiple (disconnected) objects, the ability to analyse more objective measures of quality, adding from technical constraints to the network to optimize results, improving road planning methods. This research represents a significant advance in the state of the art and paves the way for better PR planning systems.

IV. RESULTS AND DISCUSSION

The TTRS model provides for the discriminating of the solutions using the orientation of the constraints and allows for the explicit dimensioning and positioning of any surface with respect to any other surface using constraints from the list of the 13 constraints. The TTRS model explicitly identifies and locates the tolerance zone of any element in the tolerancing field using signed constraints and its own datum. The TTRS model eventually allows for the automatic execution of dimensional inspection constructs in order to inspect such

tolerances. One has access to an integrated model that enables precision, consistency, and explicit specification in the disciplines of metrology, tolerancing, and dimensioning.

V. CONCLUSION

It has been shown that a sequential order can be incorporated into the TTRS building process, expanding the TTRS representation's intended use beyond simple geometry. Additionally, tolerancing data has been integrated using the idea of TTRS attributes, further advancing the technological aspects of TTRS. Last but not least, the creation of precise criteria to recognise and extract tolerancing chains enables the automation of a time-consuming and laborious operation. Overall, the suggested method enables the modeling of design and production data using a common model and includes a numerical evaluation of the consequences of the associated tolerance transfer.

VI. REFERENCES

[1] Clément, André & Rivière, Alain &Serré, Philippe &Valade, Catherine. (1998). The TTRS: 13 Constraints for Dimensioning and Tolerancing. 122-129. 10.1007/978-1-4615-5797-5_9.
[2] ASME Y14.5–2009 Dimensioning and Tolerancing, 2009, ASME, New York, NY
[3] Liu, Jiandong& Wilhelm, Robert. (2001). Genetic Algorithms for TTRS tolerance analysis. 73-82. 10.1007/978-94-017-1691-8_8.
[4] Desrochers, Alain. (2003). A CAD/CAM representation model applied to tolerance transfer methods. Journal of mechanical design. 125. 10.1115/1.153974.
[5] Ameta, Gaurav & Samper, Serge & Giordano, Max. (2011). Comparison of Spatial Math Models for Tolerance Analysis: Tolerance-Maps, Deviation Domain, and TTRS. Journal of Computing and Information Science in Engineering. 11. 10.1115/1.3593413.
[6] Wang, Liming & Chen, Zezhong. (2014). A new CAD/CAM/CAE integration approach to predicting tool deflection of end mills. The International Journal of Advanced Manufacturing Technology. 72. 10.1007/s00170-014-5760-4.
[7] Qin, Yuchu & Lu, Wenlong & Qi, Qunfen & Li, Tukun & Huang, Meifa & Scott, Paul & Jiang, Xiang. (2017). Explicitly representing the semantics of composite positional tolerance for patterns of holes. International Journal of Advanced Manufacturing Technology. 90. 2121–2137. 10.1007/s00170-016-9457-8.
[8] Gao, Jian & Zheng, D.T. & Gindy, N.. (2004). Extraction of machining features for CAD/CAM integration. International Journal of Advanced Manufacturing Technology. 24. 573-581. 10.1007/s00170-003-1882-9.
[9] Alvares, Alberto & Ferreira, Joao & Lorenzo, Roman. (2008). An integrated web-based CAD/CAPP/CAM system for the remote design and manufacture of feature-based cylindrical parts. Journal of Intelligent Manufacturing. 19. 643-659. 10.1007/s10845-008-0117-1.
[10] Cho, Myeong-Woo & Seo, Taekyu. (2002). Inspection Planning Strategy for the On-Machine Measurement Process Based on CAD/CAM/CAI Integration. International Journal of Advanced Manufacturing Technology. 19. 607-617. 10.1007/s001700200066.
[11] Advances in Manufacturing Technology by P. F. McGoldrick

Interpolative AMBTC based Reversible Data Hiding In Encrypted Images using Rhombus Mean

2023 International Conference on Device Intelligence, Computing and Communication Technologies, (DICCT) | 978-1-6654-7491-7/23/$31.00 ©2023 IEEE | DOI: 10.1109/DICCT56244.2023.10110223

Sezal Mittal
Department of Computer Science and Engineering
Delhi Technological University
Delhi, India
sezalmittal@gmail.com

Sanya Goyal
Department of Computer Science and Engineering
Delhi Technological University
Delhi, India
sanyagoyal2001@gmail.com

Shruti Aggarwal
Department of Computer Science and Engineering
Delhi Technological University
Delhi, India
shrutiagg001@gmail.com

Rajeev Kumar
Department of Computer Science and Engineering
Delhi Technological University
Delhi, India
rajeevkumar@dtu.ac.in

***Abstract*—This paper proposes an interpolative absolute moment block truncation coding (IAMBTC) based reversible data hiding method in encrypted images (RDHEI) using rhombus mean. The proposed method aims to increase the embedding efficacy by reserving more room before encryption, for embedding the confidential data. For this, the cover image is divided into a checkerboard pattern - grey cells and white cells. Grey cells are calculated using rhombus mean to group the same intensity pixels. Next, the IAMBTC is employed first on the grey cells and difference errors are stored. Afterward, the white cells are compressed using IAMBTC and their difference is also stored. The complete difference information is then compressed using Huffman coding to condense its size and make bigger rooms for embedding. Experimental results demonstrate that the suggested method outperforms existing related methods in terms of hiding efficiency.**

Keywords— AMBTC; Image Compression; Interpolation; Huffman-encoding; PSNR.

I. INTRODUCTION

The burgeoning digitization of the World has made everything accessible on the fingertips of people in a matter of milliseconds. The transmission and exchange of files over the web has become very convenient and prompt. However, this has also led to a rise in network security issues and nefarious activities such as hacking and phishing. Data hiding was introduced as a technique to mask additional data to ensure the authenticity of the files [1, 2]. The recovery of cover media can be made lossless, i.e., the data integrity is maintained when the hidden data is retrieved from the encrypted image [3]. This is referred to as Reversible Data Hiding in Encrypted Images (RDHEI). RDHEI is used to incorporate confidential information, such as timestamps, watermarks, and/or copyright data, into images that are encrypted. [4]. The sender, the data-concealer, and the recipient are the three individuals involved in the process. After encrypting the cover image, the sender uploads it to the cloud. Secret information is concealed in the encrypted image by a data-concealer who is not aware of the cover image or encryption key. At the recipient's side, the hidden information is extracted, and the cover image is reconstructed.

The main aim of RDH methods is to achieve the maximum data embedding capacity with the least distortion. However, in RDHEI methods, the prime issue has been the conflict between reversibility and embedding capacity. So, in this paper, our main objective is to increase room size for embedding and bring a significant improvement in hiding capacity of images. At the same time, the proposed method will also ensure the complete reversibility with error free data extraction.

The rest of the paper is organized as follows: In section II, related works have been analyzed. Section III and IV discuss the proposed work and experimental results, respectively. Finally, Section V summarizes the papers and presents the conclusion.

II. RELATED WORKS

The related works section is divided into two sections. In the first section, an overview of Interpolative AMBTC is provided. The second section briefly discusses a series of existing and related works.

2.1 Overview of Interpolative AMBTC

Lema and Mitchell [5] come up with the idea of Absolute Moment Block Truncation Coding (AMBTC), a variation of Block Truncation Coding (BTC) which uses a bi-clustering approach. It provides better image quality and preserves the upper and the lower mean of each block to quantize the output with a lower computation complexity.

Absolute Moment Block Truncation Coding (AMBTC) is a proficient and prompt lossy compression technique for images. Its implementation is simpler as compared to other methods of transform coding. Interpolative AMBTC is an enhanced version of AMBTC compression. In this method, the image is divided into blocks and two statistical means, L_{AMBTC} and $H_{AMBTC,}$ are computed for each block using the following equations:

$$L_{AMBTC} = \frac{1}{p}\sum_{x_i \le \bar{x}}^{n} x_i \quad (1)$$

$$H_{AMBTC} = \frac{1}{q}\sum_{x_i > \bar{x}}^{n} x_i \quad (2)$$

where x_i is the i[th] pixel of the block, $\bar{x}$ is the mean of the block, p and q are the number of values below and above the mean, respectively. A bitmap is created for the block using

Authorized licensed use limited to: DELHI TECHNICAL UNIV. Downloaded on May 04,2023 at 06:31:25 UTC from IEEE Xplore. Restrictions apply.

1 for H_{AMBTC} and 0 for L_{AMBTC}. The compressed code for each block consists of (L_{AMBTC}, H_{AMBTC}, bitmap).

X_1	X_5	X_9	X_{13}
X_2	X_6	X_{10}	X_{14}
X_3	X_7	X_{11}	X_{15}
X_4	X_8	X_{12}	X_{16}

Fig 1. Reduced bitmap for Interpolative AMBTC

To recreate the image at the decoder side of AMBTC, the pixel values for each block are generated as follows:

$$x_i' = \begin{cases} H_{AMBTC}, & if\ y_i = 1 \\ L_{AMBTC}, & if\ y_i = 0 \end{cases} \quad (3)$$

where x'_i is the decoded i[th] pixel of the block and y_i is the corresponding bit in the bitmap for the i[th] pixel. Interpolative AMBTC was introduced to enhance the performance of AMBTC. In Interpolative AMBTC, only the pixel values of alternate cells (shown in white color of Fig. 1) are stored. This reduces the bitmap size greatly as the size is reduced to 8 bits from 16 bits that were stored in AMBTC [6]. To reconstruct the image at the recipient's end, the pixel values are obtained as:

$$x_i' = \begin{cases} \frac{x_{i-1}+x_{i+1}+x_{i+4}}{3} & if\ i = 2 \\ \frac{x_{i-1}+x_{i+4}}{2} & if\ i = 4 \\ \frac{x_{i-4}+x_{i+1}+x_{i+4}}{3} & if\ i = 5 \\ \frac{x_{i-4}+x_{i-1}+x_{i+1}+x_{i+4}}{4} & if\ i = 7{,}10 \\ \frac{x_{i-4}+x_{i-1}+x_{i+4}}{3} & if\ i = 12 \\ \frac{x_{i-4}+x_{i+1}}{2} & if\ i = 13 \\ \frac{x_{i-1}+x_{i+1}+x_{i-4}}{3} & if\ i = 15 \end{cases} \quad (4)$$

2.2. Literature Review

In this sub-section, we will briefly review several related and popular data hiding schemes introduced in the last decade and so. Zhang [7] was the first to present a RDHEI scheme. He proposed a method that leverages the spatial relationship between pixels to embed and extract data. The technique entails dividing the encrypted image into blocks, flipping the LSBs of half of the pixels within the block, and identifying the flipped portion for image recovery and data extraction using a fluctuation function. As the block size was reduced, the method allowed for more data to be embedded, but it has limitations in its use of pixels and consideration of pixel correlations at the border of adjacent blocks, resulting in a reduction in data extraction accuracy. Hong et al. [8] enhanced Zhang's method [7] by introducing a novel technique for estimating the smoothness of blocks by using the summation of the two neighbouring pixels to lower the error rate of data extraction using side-matching technique. Bhardwaj and Aggarwal's [9] method considers only boundary pixels like Zhang's [7] and segments pixel blocks into sub-blocks where each sub-block carries one additional bit. Wang et.al [10] discuss a new block selection mechanism in which auxiliary data is embedded only in ECBs (Error-correction blocks). Liao et al. [11] present a new fluctuation function and estimate the complexity of image blocks by calculating the absolute mean difference of pixels and their neighboring pixels. Data embedding ratio was fully considered as was the dependence of reversibility on block size. However, computational complexity was very high.

Previously, all methods were trying to vacate space after encrypting the image. Many techniques were also proposed to make room for data embedding before encryption, Ma et al. [12] suggests a Reversible Data Hiding approach for encrypted images that improves full reversibility, PSNR, and data extraction/decryption separability by shifting the encrypted histogram of anticipated errors. The complexity of this method increased with embedding rates. Ma et al. [13] proposes a method that uses traditional Reversible Data Hiding to embed LSBs into other pixels, then encrypted the image. This allowed for data to be inserted in the encrypted image and separated data extraction from image decryption. It also improved real reversibility and PSNR for given embedding rates and enlarged the range of embedding rates for acceptable PSNR. Cao et al. [14] also separate data extraction from image decryption. By dividing the images into patches and then using sparse coding, they were able to conceal secret data using patch-level sparse representation and pixel replacement. Their method allowed for separate and error-free data extraction and original image restoration processes.

Yin et al. [15] were the pioneers of a reversible data hiding (RDH) method for AMBTC-compressed and encrypted images. They achieved this by encrypting the quantization levels through an XOR operation to preserve correlation, followed by a bitmap replacement and prediction error-based RDH to make room for secret messages. Nguyen et al. [16] put forward a technique where an image is divided into pixel blocks, compressed using an AMBTC algorithm, and blocks with lower compression errors are chosen to maintain space for data embedding. The resulting image is then encrypted, resulting in a decrypted image of better quality. In 2018, Shiu et al. [17] suggested a high payload RDHEI scheme for images that was based on interpolative AMBTC and Huffman coding. Their scheme ensures the restoration of the original image and has the highest hiding capacity of any similar method at the time however the method is susceptible to outliers. To address this concern up to a great extent, we propose a new IAMBTC based RDHEI method which makes use of rhombus mean to club similar intensity pixels for efficient compression by IAMBTC. This in turn helps in increasing embedding capacity.

III. PROPOSED SCHEME

In this section, a method is proposed based on Interpolative AMBTC [17-18]. It is based on the RRBE (Reserve Room Before Encryption) framework which exploits the similarity of the adjacent pixels. The method includes four stages : A) Image Pre-processing B) Image Encryption and Data Embedding C) Image Encoding and D) Data Extraction.

A. Image Pre-processing

In this phase, the pixels are classified into grey and white pixels. The grey and white pixels are compressed separately and the difference information from the original image is compressed using Huffman coding and stored.

a. Classification

Step 1. Enter an image of size S x S.

Authorized licensed use limited to: DELHI TECHNICAL UNIV. Downloaded on May 04,2023 at 06:31:25 UTC from IEEE Xplore. Restrictions apply.

Step 2. Split the image into a checkerboard format into white and grey cells.

Step 3. Compute expected pixel value for grey cells using rhombus mean.

Step 4. Store the pairs of expected pixel value and original value in grey_list and sort this on the basis of expected pixel values. Compression will be applied on the sorted grey_list.

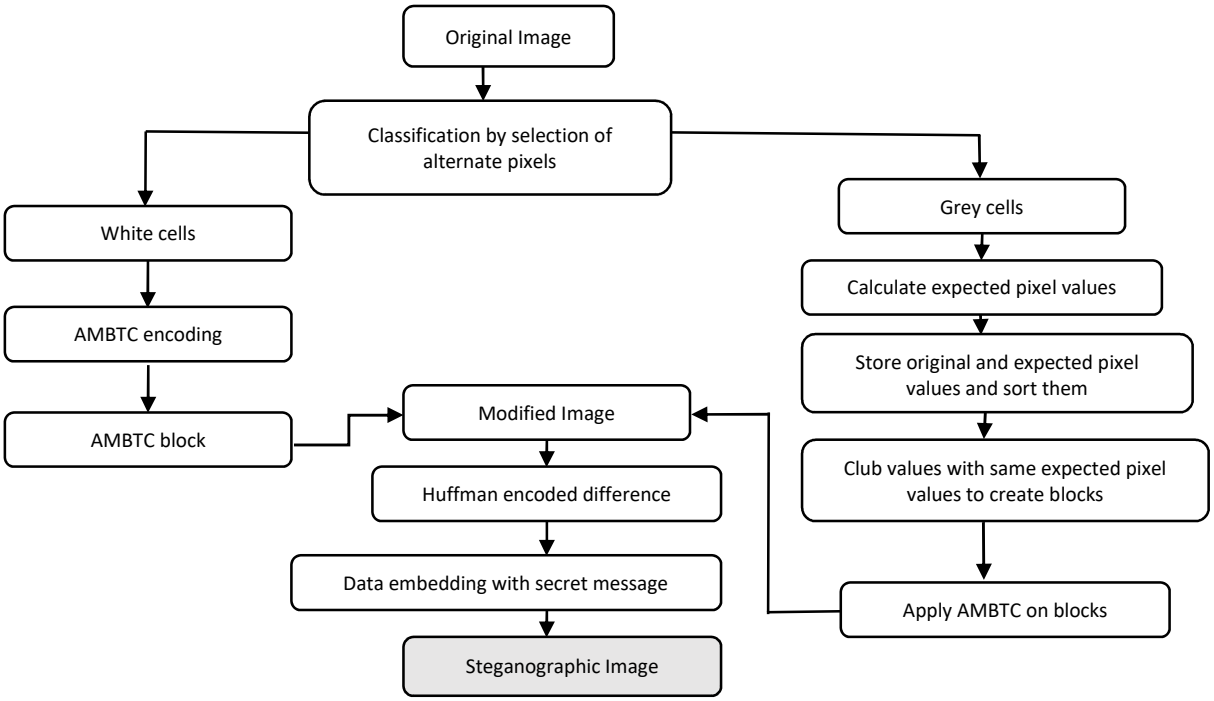


Fig 3. Flowchart of proposed data embedding

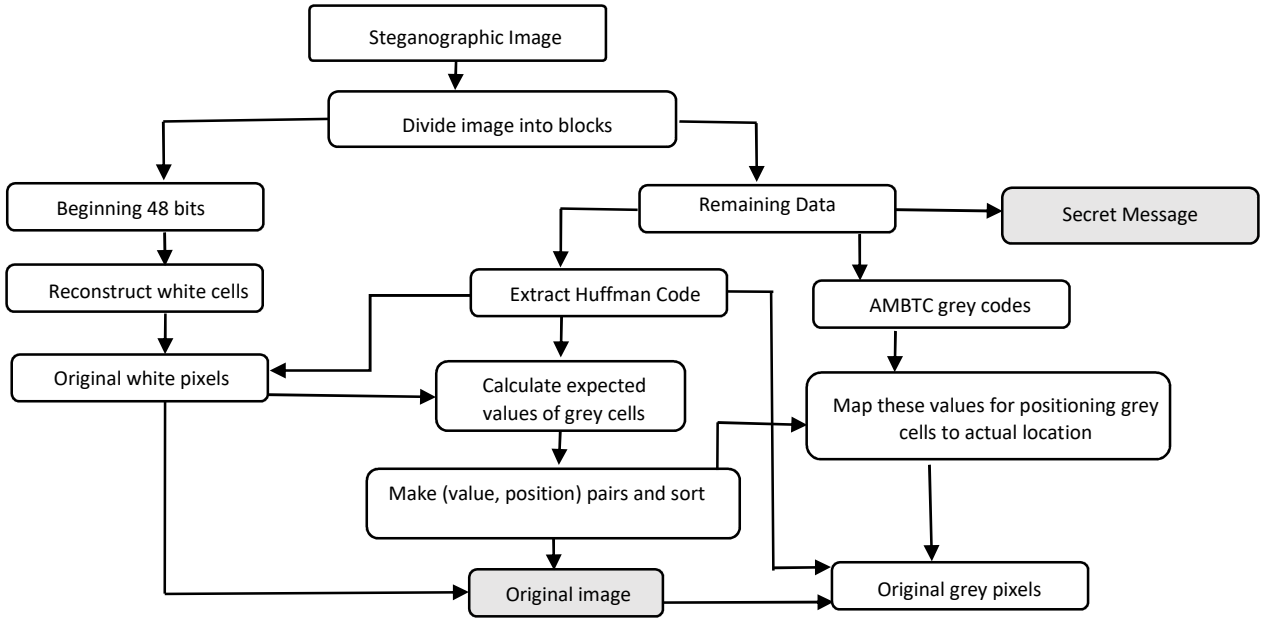


Fig 4. Flowchart of proposed data extraction and image recovery decryption

b. Compression of grey cells

Step 1. Club the values in the grey_list with the same expected pixel values to form the blocks.

Step 2. Perform IAMBTC technique on these obtained blocks and generate the bitmaps using Eq.3 and 4.

Step 3. Group bitmaps of all the blocks in a consecutive manner to form a binary string as shown in Fig. 5.

Step 4. Store L_{AMBTC}, H_{AMBTC} values for all the blocks followed by the compressed bitmap.

c. Compression of white cells

Authorized licensed use limited to: DELHI TECHNICAL UNIV. Downloaded on May 04,2023 at 06:31:25 UTC from IEEE Xplore. Restrictions apply.

Step 1. Split the picture into non-intersecting squares of size f×f.

Step 2. Apply IAMBTC on each block.Then, store the compressed code (L_{AMBTC}, H_{AMBTC}, bitmap)

for the block using equations (1), (2) and (3).

d. Compression of Difference block

Compression of both white and grey cells are done using AMBTC method. It is a lossy compression technique. To reconstruct the whole image from the

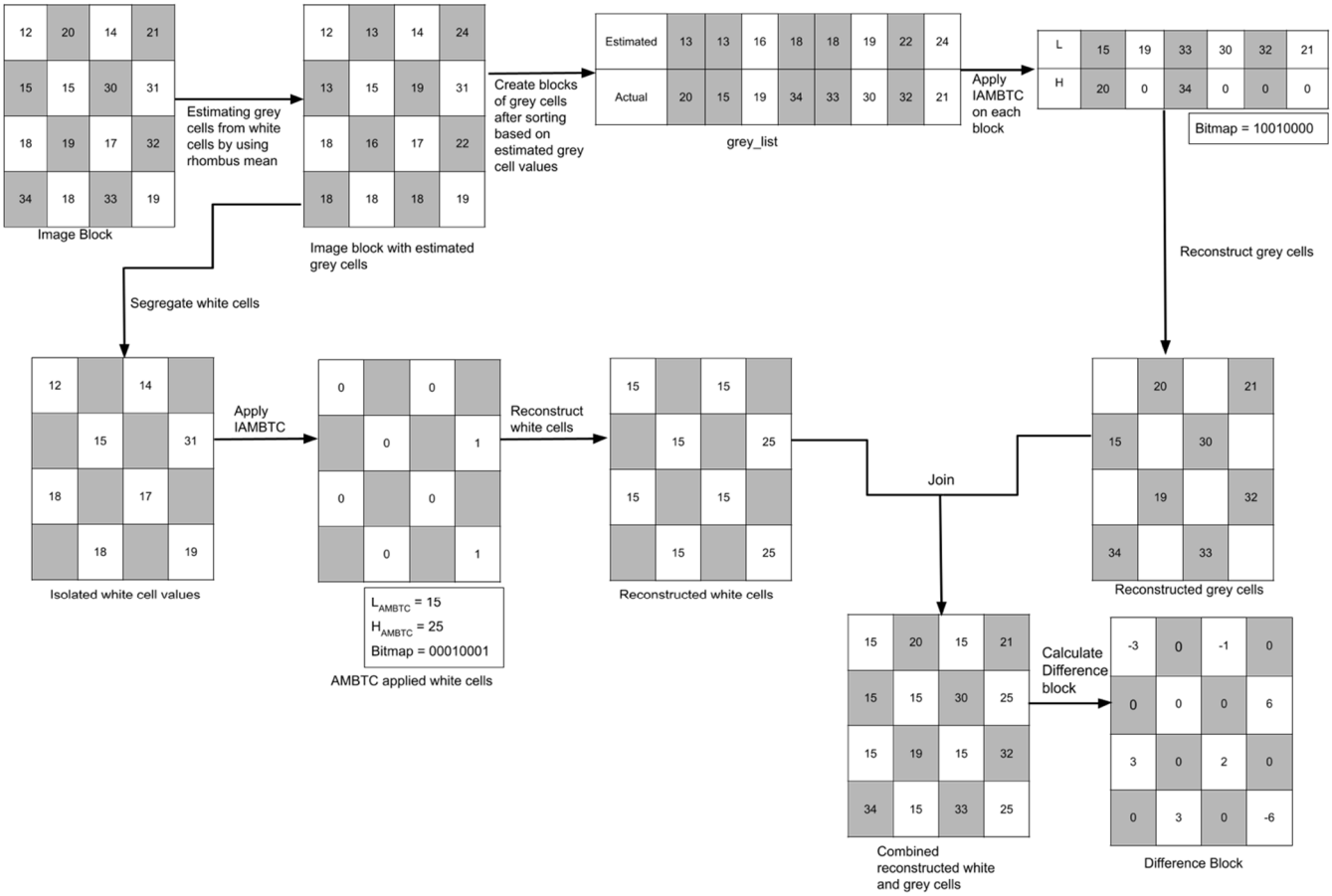


Fig 5. Example depicting the proposed procedure for vacating space for embedding using our method.

compressed blocks, the difference between the actual image and the reconstructed image blocks is stored. The difference between the reconstructed AMBTC block and the original block is found to be normally distributed, meaning that the data follows a bell-shaped curve. Huffman coding is used to compress this difference, also known as the difference block, as it is well-suited for compressing normally distributed data, resulting in more efficient encoding of the data.

B. Image Encryption and Data Embedding

During this phase, two keys are generated to encrypt and hide the data. An encryption key is used to encrypt the AMBTC codes for the grey and white cells and the Huffman codes associated with them. To integrate secret information, hiding key is used.

C. Image Encoding

Step 1. Divide the picture into white and grey cells.

Step 2. Compress the white and grey cells as described in III-B and III-C.

Step 3. Decode the AMBTC code for the white and grey cells to get the reconstructed image block. Calculate the difference block and compress it using Huffman coding as mentioned in section III-D.

Step 4. Divide the picture into 8×8 squares. In every square, store the compressed AMBTC code (48 bits) in the first 6 cells, then use remaining cells to hide the Huffman code for the difference block, AMBTC code for grey cells, and secret data using raster scan.

Step 5. 13 bits are allocated at the beginning of an image to store the length of the Huffman tree, and 24 bits for the length of the compressed message. Once these lengths have been recorded, the Huffman tree can be placed in the image, followed by the compressed message.

Step 6. For grey cells, there will be 256 using 4096 bits (256 × (8 + 8)) to store the L and H components of the AMBTC code. The blocks also include a 10-bit field

Authorized licensed use limited to: DELHI TECHNICAL UNIV. Downloaded on May 04,2023 at 06:31:25 UTC from IEEE Xplore. Restrictions apply.

specifying the length of the compressed AMBTC bitmap and the AMBTC bitmap itself.

D. *Data Extraction*

I. Extraction of white cells

Step 1. Split the picture into non-intersecting squares of size f×f, where f = 8.

Step 2. Extract first 48 bits of each block as (L_{AMBTC}, H_{AMBTC}, bitmap) and using this information, reconstruct the white cells of the whole image.

Step 3. Extract the remaining data in raster scan manner, skipping the first six cells of each block.

Step 4. Generate the reconstructed AMBTC blocks by applying decoding of white cells.

Step 5. Retrieve the original order of the Huffman tree, Huffman code, AMBTC compressed data of grey cells and the secret data by performing conjugate permutation with the hiding key.

Step 6. Generate the difference array D by decoding the codes and dictionary generated by the Huffman's algorithm.

Step 7. Recover the original white cells by adding D to the steganographic image.

II. Extraction of grey cells

Step 1. Expand the extracted AMBTC code (L_{AMBTC}, H_{AMBTC}) and grey_bitmap by traversing the compressed version multiple times equal to its length, adding a specific number of bits to the grey_bitmap in each pass until the entire grey_bitmap is expanded.

Step 2. From the recovered white cells, obtain the expected values of the grey cells using equation (4).

Step 3. Make a list of pairs of expected values calculated in Step 1 and positions of the grey cells, say grey_position_list. Sort this list based on the expected values.

Step 4. Match grey_position_list with grey_bitmap, create blocks of same expected value, apply AMBTC decoding on each block, replace 1s in bitmap with block's H_{AMBTC} value and 0s with block's L_{AMBTC} value.

Step 5. Place the values in their position deduced from the second values of the pairs in the grey_position_list.

Step 6. Finally for all grey cells, add the difference between the primary pixel and the reconstructed pixel to the reconstructed block.

Fig. 5 gives an example for embedding data using our proposed scheme in an image. We use rhombus mean to generate the expected grey cell values and filter out the white cell values and isolate them as they are operated on separately. AMBTC is then performed on the expected values of grey cells after sorting them on the basis of expected values while Interpolative AMBTC is applied on the white cells. We then combine the reconstructed white and grey cells and find the difference block by finding difference with the original image.

IV . EXPERIMENTAL RESULTS

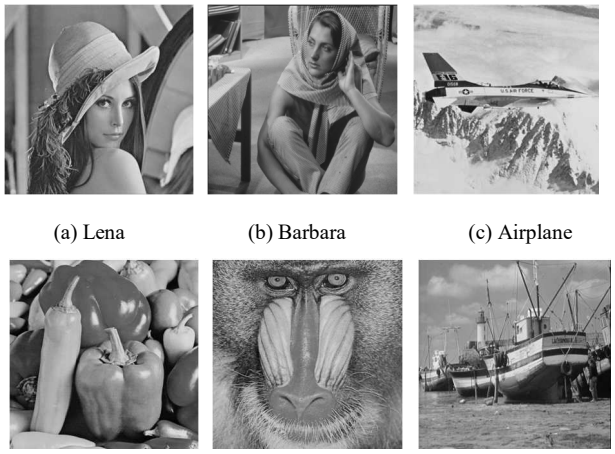
This section demonstrates the experimental results of the proposed results and their comparative analysis with existing RDHEI methods. All experiments are performed with six frequently used grayscale images of size 512 × 512: "Lena", "Barbara" , "Airplane", "Peppers", "Baboon" and "Boat" as used in [17].

The PSNR between two pictures is measured in decibels(dB). It is used to compare the quality of the input image to that of a compressed image. A higher PSNR value indicates a higher quality reconstruction of the image, while a lower value indicates a lower quality reconstruction. It is expressed as a logarithmic quantity in decibel scale.

$$PSNR = 10\log_{10}\frac{255^2}{\frac{1}{M \times N}\sum_{i=1}^{M}\sum_{i=1}^{N}(x_{i,j} - x'_{i,j})^2} \quad (5)$$

where $x_{i,j}$ and $x'_{i,j}$ are pixel values of original and transformed images respectively and M × N is the size of the image.

Embedding/Hiding capacity is calculated by finding the difference between bits required to build the original image and the white cells encoding, grey cells encoding and Huffman encoding.



(a) Lena (b) Barbara (c) Airplane

(d) Peppers (e) Baboon (f) Boat

Fig. 6 Test images

Figure 7 shows the maximum embedding capacity (EC) achieved by the proposed method on different test images. The results of maximum embedding capacity are displayed in terms of bits stored per pixel (bpp). Additionally, the PSNR attained at the maximum EC is also marked. It can be observed from the Figure 7 that the highest PSNR is in the case of Lena" i.e., 32.17 dB ,while the most bits could be stored in "Airplane". Although, the quality of "Baboon" is observed to be the lowest at 26.02 dB, we observe an average quality of images at 29.82 db. An average bpp of 2.065 is observed over all the images. Even in the worst case, the bpp is 1.07 for "Baboon".

Table 1 compares the maximum hiding capacity for all the test images for our proposed technique and other seven techniques [7-8,12-14,16-17]. Our method achieves better hiding capacity than all the other schemes for all images.

Authorized licensed use limited to: DELHI TECHNICAL UNIV. Downloaded on May 04,2023 at 06:31:25 UTC from IEEE Xplore. Restrictions apply.

Therefore, the analysis shows that the proposed scheme is better than the previous techniques in terms of embedding capacity with an acceptable distortion to the cover image.

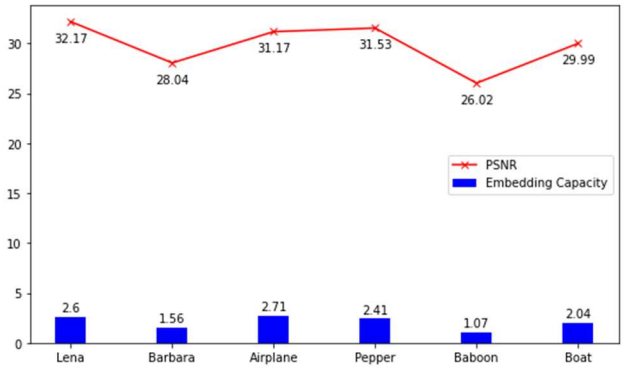


Fig 7. Maximum embedding capacity and PSNR (on the same) for different test images

TABLE 1: Maximum EC comaprision of the proposed method with other related RDHEI methods on different test images

Scheme	Maximum Embedding Capacity (EC)					
	Lena	Barbara	Airplane	Peppers	Baboon	Boat
Proposed	**2.60**	**1.56**	**2.71**	**2.41**	**1.07**	**2.04**
Shiu et al. [17]	2.34	1.22	2.49	2.41	0.73	2.01
Hong et al. [8]	0.001	0.00122	0.0162	0.0147	0.0086	0.016
Zhang et al. [7]	0.033	0.02	0.04	0.022	0.01	0.041
Ma et al. [12]	0.04	0.036	0.071	0.0367	0.012	0.069
Ma et al. [13]	0.5	0.2454	0.4738	0.3202	0.1462	0.2334
Cao et al. [14]	0.74	0.4778	1.0207	0.5044	0.2666	0.5135
Nyugen et al. [16]	0.12	0.131	0.279	0.158	0.034	0.104

V . CONCLUSION

In this paper, an Interpolative AMBTC based reversible data hiding scheme for encrypted images was proposed using rhombus mean to ameliorate hiding capacity. The proposed method divided the image into a checkboard pattern. Interpolative AMBTC was applied in different ways on the two types of cells generated. Huffman coding was used to condense the difference information. By combining IAMBTC with Huffman coding, it was therefore possible to achieve a balance between compression efficiency and visual quality. The original image could also be recovered completely. Thus, we were able to make more room for secret data to be encrypted and obtained an increased hiding capacity for images. However, there was a slight reduction in the quality of the images.

REFERENCES

[1] R. Kumar, S. Chand and S. Singh, "A reversible data hiding scheme using pixel location," *Int Arab J Inf Technol,* vol. 15, no. 4, pp. 763–768, 2018.

[2] R. Kumar, S. Chand and S. Singh, "An Improved Histogram-Shifting-Imitated reversible data hiding based on HVS characteristics," *Multimedia Tools and Appl.,* vol. 77, no. 11, pp. 13445- 13457, 2018.

[3] A.Malik, S. Singh and R. Kumar, "Recovery based high capacity reversible data hiding scheme using even-odd embedding," *Multimedia Tools and Appl.*, vol. 77, no. 12, pp. 15803–15827, 2018.

[4] A.K. Rai, N. Kumar, R. Kumar , H. Om, S. Chand and K.H. Jung, "Intra-block correlation based reversible data hiding in encrypted images using parametric binary tree labeling," *Symmetry*, vol. 13, no. 6, pp. 1072, Jun. 2021.

[5] M.D. Lema and O.R. Mitchell, "Absolute moment block truncation coding and its application to color images," *IEEE Transactions on Communications*, vol. 32, no. 10, pp. 1148-1157, Oct. 1984.

[6] R. Kumar, N. Kumar and KH. Jung, "Enhanced interpolation-based AMBTC image compression using Weber's law," *Multimedia Tools and Appl.*, vol. 81, no. 15, pp. 20817-20828, 2022.

[7] X. Zhang, "Separable reversible data hiding in encrypted image," *IEEE Transactions on Information Forensics and Security*, vol. 7, no. 2, pp. 826-832, April 2012.

[8] W. Hong, T.S. Chen and H.Y. Wu, "An improved reversible data hiding in encrypted image using side match," *IEEE Signal Processing Letters*, vol. 19, no. 4, pp. 199-202, April 2012.

[9] R. Bhardwaj and A. Aggarwal, ''An improved block based joint reversible data hiding in encrypted images by symmetric cryptosystem,'' *Pattern Recognit. Lett.*, vol. 139, pp. 60–68, Nov. 2020.

[10] Y. Wang, G. Xiong and W. He, "An Improved Reversible Data Hiding in Encrypted Image Method Based on Block Selection," *IEEE Access*, vol. 8, pp. 227036-227047, 2020.

[11] X. Liao and C. Shu, "Reversible Data Hiding in Encrypted Images Based on Absolute Mean Difference of Multiple Neighboring Pixels," *Journal of Visual Communication and Image Representation*, vol. 28, pp. 21-27, Jan. 2015.

[12] W. Zhang, K. Ma and N. Yu, "Reversibility improved data hiding in encrypted images," *Signal Process*., vol. 94, pp. 118–127, 2014.

[13] K. Ma, W. Zhang, X. Zhao, N. Yu and F. Li, "Reversible data hiding in encrypted images by reserving room before encryption," *IEEE Trans. Inform. Forensics Secur.,* vol. 8, no. 3, pp. 553–562, 2013.

[14] X. Cao, L. Du, X. Wei, D. Meng and X. Guo, "High capacity reversible data hiding in encrypted images by patch-level sparse representation," *IEEE Transactions on Cybernetics*, vol. 46, no. 5, pp. 1132-1143, May 2016.

[15] Z. Yin, X. Niu, X. Zhang, J. Tang and B. Luo," Reversible Data Hiding in Encrypted AMBTC images," *Multimedia Tools and Applications*, vol. 77, no. 14, pp. 18067- 18083, July. 2018.

[16] T.S. Nguyen, C.C. Chang and W.C. Chang, "High capacity reversible data hiding scheme for encrypted images," *Signal Process.: Image Commun.,* vol. 44, pp. 84–91, 2016.

[17] P.F. Shiu, W.L. Tai, J.K. Jan, C.C. Chang and C.C. Lin, "An Interpolative AMBTC-based high-payload RDH scheme for encrypted images," *Signal Processing: Image Communication,* vol. 74, pp. 64–77, 2019.

[18] R. Kumar and K.H. Jung, "A systematic survey on block truncation coding based data hiding techniques," *Multimedia Tools Appl,* vol. 78, pp. 32239–32259, 2019.

Authorized licensed use limited to: DELHI TECHNICAL UNIV. Downloaded on May 04,2023 at 06:31:25 UTC from IEEE Xplore. Restrictions apply.

2023 6th International Conference on Information Systems and Computer Networks (ISCON)
GLA University, Mathura, India. Mar 3-4, 2023

Light-Weight Deep Learning Model for Human Action Recognition in Videos

Rahul Kumar
Department of Computer Science & Engineering
Delhi Technological University
Delhi, India
rahuldtucs@gmail.com

Shailender Kumar
Department of Computer Science & Engineering
Delhi Technological University
Delhi, India
shailenderkumar@dce.ac.in

2023 6th International Conference on Information Systems and Computer Networks (ISCON) | 979-8-3503-4696-1/23/$31.00 ©2023 IEEE | DOI: 10.1109/ISCON57294.2023.10111975

***Abstract*— Human Action Recognition (HAR) from a visual stream has recently attained much researcher consideration in the domain of computer vision. Due to its large applications like monitoring of health, home automation, and tele-immersion, among others. However, it still faces human variances, occlusion, lighting changes, and complicated backgrounds. The evaluation criteria rely on the features collection approach as well as learning data being performed correctly. The success of Deep Learning (DL) has resulted in a variety of impressive outcomes, including neural networks. Nonetheless, a robust features vector is required for an efficient classifier to give the class label. Features serve as the essential component of any data set. Indeed, feature extraction may affect the algorithm's performance and computational cost. For this research framework, we used pre-trained deep learning models VGG19, Dense Net and Efficient Net for feature extraction from the sequence of images and classified each action with the help of the SoftMax layer. UCF50 action dataset used, which contains 50 sections and evaluates performance with the help of precision, recall, f1-score and AUC score. Testing accuracy from models achieved VGG19-90.11, DenseNet-92,57 and EfiicientNet-94.25.**

Keywords—Transfer Learning, CNN, VGG19, UCF50

I. INTRODUCTION

In HAR, an action is an observable thing that may be seen by the human eye or by some sensor device. In fact, engaging in an activity like walking requires constant attention to a person located inside the field of view. Actions may be separated into four categories depending on the body components needed to do them. [1].

- Gesture: It's based on facial expression. Don't need any action or verbal way of communication.
- Action: Walking, playing, punching human action comprised.
- Interaction: It Consist human object interaction as well human interaction like handshake, hugging is example of interaction.
- Group activity: when more than two action is happening is known as group activity like combination of gesture and interaction. Two or more than two actor is involved for performing action.

Over the course of the last two decades, HAR has emerged as an essential component of research into computer vision. Based on a collection of observations, HAR is designed to detect and identify activities carried out by one or more persons. This may be done for any number of people. This had developed into a need for the further development of human–computer interaction. Many researchers from different parts of the globe are drawn to this field of study due to the wide range of domains in which it may be used. Surveillance video, the labeling and retrieving of visuals, monitoring of health, automation, and environmental modelling are but a few of its most prominent applications[1]. Human activities have an intrinsic hierarchical structure that denotes their many levels, which may be categorized at three levels. First, there is an atomic element at the lowest level, and these action primitives represent increasingly complicated human actions. The actions/activities level follows the action primitive level as the second level. The greatest level of categorization for human activities is represented by complex interactions. Each of these categories is sufficiently extensive to need its own area of study. This is mostly due to the unpredictability and ambiguity of human acts in a real-world situation. HAR faces several barriers and obstacles. Gender discrimination, multi-subject interactions, and disparities in inter-class activity are some examples. Human action recognition form videos have four stage process. In first step we extract feature from given sequences of images. In the feature extraction process, handcrafted methods just like SIFT (scale invariant feature transform), SURF (Speed up Robust Feature), Shape-based, Pose-based, and optical flow, to mention a few, may be used [1]. Feature extraction can be done with deep learning method automatically in this approach model learn itself all feature from sequences of images. It involves the extraction of poses and gesture patterns from frames and sequences of visuals depicting human activities. Therefore, it is a challenging task due to obstacles such as size fluctuations, poor illumination, incorrect viewpoints, and backdrop clutter.

In a subsequent stage, actions are learned and recognized based on extracted features. Learning new models that are taught by extracted features is an important part of action learning and recognition, as is determining which features are relevant to which action classes and assessing those features with the aid of classifiers. The Machine Learning (ML) technique and the DL method are two of the most notable approaches to solve the HAR issue. The former, the most conventional kind of Artificial Intelligence, takes a more deterministic approach, requiring the user to layout, dictate, and fine-tune the extracted features and characterize action. Using the latter strategy, however, we anticipate that the deep neural network (DNN). When we use the latter approach, on the other hand, we predict that the DNN will solve all of the attributes on its own by act as the function of the human brain [1][2].

Figure 1 depict ML and DL base classification for HAR.

Authorized licensed use limited to: DELHI TECHNICAL UNIV. Downloaded on May 11,2023 at 10:20:11 UTC from IEEE Xplore. Restrictions apply.

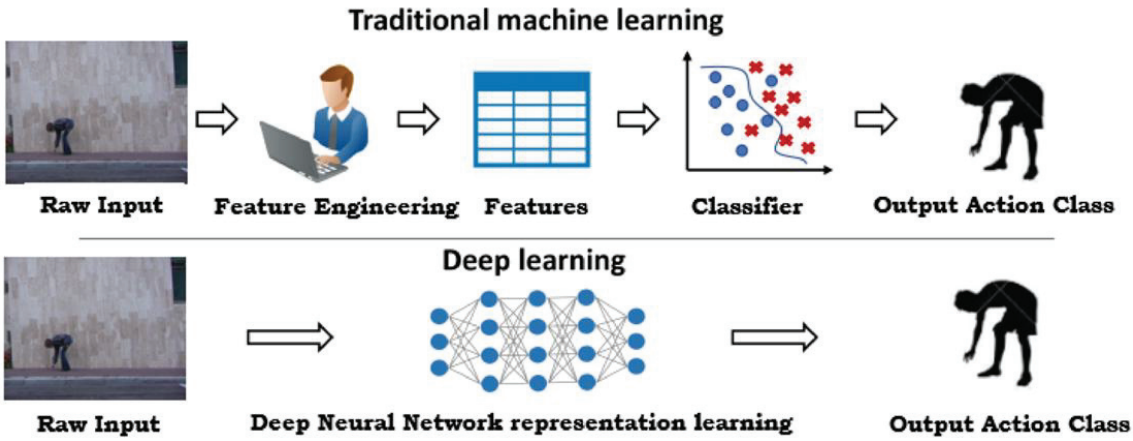


Fig. 1. A graphical representation of the conventional ML methods and the cutting-edge DL methods employed for HAR [2].

ML base methods such as random forest (RF), Bayesian networks (BN), Markov models (MM), and support vector machine (SVM) have been employed for decades to try to solve the HAR issue associated with it like clutter background, noise issue, class similarity issue. Accustomed ML algorithms have been able to attain excellent performance in settings with limited data inputs and stringent restrictions. Machine learning algorithm time consuming and need special attention due to preprocessing step with the handcrafted feature; they need to perform better When the data size is huge. DL has attained lot of gained in last years. This is due to the fact that research that is focused on deep learning has achieved excellent performance in a variety of study fields, such as detection of object in frames and recognition of action, classification of frames, and natural language processing.

By unmanned features pull out through numerous hidden layers, DL significantly reduces the effort required to select the appropriate features compared to traditional ML algorithms, and its structure has been shown to be effective for unsupervised learning and reinforcement learning. Because of this, there has been a rise in the number of proposed deep learning-based HAR frameworks.

The following is a summarization of the research paper:

In the first section, we provide a high-level overview of human action identification and then examine machine and deep learning techniques for this task. Following that, in Section 2, we will talk about the modalities and accuracy levels of previously proposed techniques to human action recognition. Methods and results on the dataset are discussed in Section 3. Section 4 summarizes the work done and the planned future development in the area of computer vision.

II. Related Work

In domain of human action recognition lots of work has been done. Due to its wide variety of application, there is lot of scope to improve the prediction of human action. Many manually produced and automated learned feature-based techniques for human activity detection in visuals have been developed during the last decade. Earlier techniques to human activity identification relied on handmade characteristics that were primarily focused on small atomic activities that seem to be less relevant for actual applications [3].Despite obtaining a model with a high degree of accuracy, the primary downside of these methods is that they need extensive data preprocessing and are difficult to generalize in practice. Following the success of convolutional neural networks (CNNs) in text and visual classification, many spatiotemporal approaches for video activity analysis have been created; these algorithms can automatically train and classify from raw RGB video [4].

Shuiwang Ji et al.[5] introduced a 3D convolution method for extracting spatial and temporal video data for action identification. As a result, the envisioned architecture creates many channels of data from the video sequence and applies convolution and subsampling to each channel individually. Gu et al. offered a DL based method to identify locomotive motions relevant to indoor localization and navigation. Their solution made use of stacked denoising auto-encoders that learnt data characteristics automatically, decreasing the requirement to manually build the relevant features [6]. Higher precision attained claimed in proposed research framework as compare to another classifier. Aubry et al.[7] came up with a new way to figure out what an action is by looking at RGB (Color model) footage. To do this, first the video's motion has to be taken out and provide the human skeleton extraction. Open Pose [8] , a Deep Neural Network (DNN)-employ identification method that pulls out a 2-D skeleton with 18 known joints from each body, was used to do this extraction. In the second instance, motion patterns are turned into RGB pictures with the help of an image classifier. R, G, B Channels used to store motion information. This makes an RGB picture for an action sequence. In the future, neural networks that are used to classify images could be used to recognize actions.

Dual stream model suggested by researcher Dai et al.[9] which use attention-based LSTM structure for localizing action in frames of visuals. They said they had solved the problem of ignoring visual attention. With the UCF11 dataset, the architecture was 96.9% accurate, with the UCF Sports dataset it was 98.6% accurate, and with the j-HMDB dataset it was 76.3% accurate. Du et al. [10] came up with a skeleton-based method for recognizing actions employing a hierarchical RNN model. Also, their suggested techniques was evaluated(compared) to five different deep RNN designs that were based on it. During their whole evaluation, they used the MSR Action-3D dataset, the Berkeley MHAD dataset, and the HDM05 dataset. Majd and Safabakhsh[11] devised the Correlational Convolutional LSTM by incorporating spatial and motion information into a

Authorized licensed use limited to: DELHI TECHNICAL UNIV. Downloaded on May 11,2023 at 10:20:11 UTC from IEEE Xplore. Restrictions apply.

preexisting LSTM module in addition to establishing temporal linkages. Their work was assessed on the UCF101 and HMDB51 benchmark datasets, both of which are widely used, and they achieved correctness(accuracy) of 92.3% and 61.0%, respectively. For the purpose of recognizing both group and individual activities, Qi et al.[12] offered a different approach to building a semantic RNN known as stag-Net. They added a fourth dimension to their semantic network model—time—with the help of a structural RNN. Using this method, 90.5% of the Volleyball dataset was completed as a team and 8.5% as an individual effort.

Posture-based characteristics are extracted from a 3D convolutional neural network (ConvNet) in Huang et. al.[13] by fusing 3-D pose, 2-D appearance, and information of motion. The 3-D CNNs attained of features of color joint in frames is expected to be computationally intensive, thus we perform convolution in each of the heatmap's 15 channels to reduce the noise. The (BN-inception) network architecture was used by Wang et al. in Inception and Batch Normalization [14]. The aforementioned approach, like two-stream networks, employs RGB variation frames (to simulate appearing alteration) and optical flow fields in conjunction to RGB and optical flow frames (to inhibit background motion).

The author in [15] utilized the GCN with channel attention strategy for joints and graph pooling network. Finally, the SGP design incorporated the human skeletal network and improved the convolution. Kernel receptive regions are used to collect particular human body data. The suggested SGP technique has the potential to considerably improve GCNs' capacity to gather based on motion characteristics while also lowering computation costs.

Context stream and fovea stream designs employed in research article [16]. The context channel receives frames at half their original resolution, but the fovea channel receives the center region at full resolution. The study trains a model to detect three separate pattern classes: Early Fusion, Late Fusion, and Slow Fusion using each video as a collection of small, fixed-length clips. CNN may create single-frame animations by combining time and space in various ways. Singh et. al.[17] proposed a highly linked ConvNet with RGB frames as the top layer for identifying human activities-term, bidirectional-LSTM. The lowest layer of the ConvNet model is learned(trained) with the help of individual DMI. The ConvNet-Bi-LSTM model is trained from scratch for RGB frames to improve the features of the pre-trained CNN, while the uppermost layers of the pre-trained ConvNet are adjusted(fine-tune) to extract temporal information from video streams. Features are combined at the decision layer to get a higher precision value using a late fusion technique following the SoftMax layer. Four RGB-D (depth) datasets including both single-person and multiple-person activities are employed to examine the effectiveness of the suggested model.

III. METHODOLOGY

The DL model for HAR shows the impactful result on the classification of each activity. We discussed some deep-learning models, how they work and classify each action accurately. Deep learning model training is required from scratch and requires lots of computing power. Compared to transfer learning models are trained, learning models. They are learned on the huge amount of data ImageNet [18]. ImageNet has more than 1 M of images suitable for training transfer learning models. This research paper used various transfer learning models to classify each action & compared them with state-of-the-art methods. This research paper compared various transfer learning models to recognizing human action. Figure 2 represents the Human Action Recognition model with the pre-trained deep learning model.

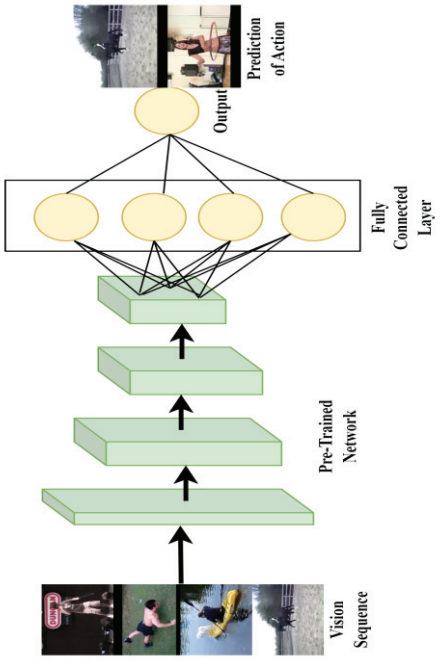


Fig. 2. HAR using pre-trained DL method.

Dense Net[19] are used to evaluate transfer learning (TL)-based methodologies. Dense Net neural networks were chosen for their new techniques to coping with vanishing or growing gradients, as well as their particular design, which allows one layer to learn from the feature maps of preceding layers, allowing feature reuse. VGG[20] is also trained via transfer learning-based HAR approach because to its very deep architecture, which is accomplished by using tiny (3 3) filters. As a result of their complexity, VGG models often experience gradient explosions. To address this problem, we employed VGG models with batch normalization layers to keep gradients under control. Efficient Net[21] method is also used to evaluate performance of framework.

A. *Dense Net*

A dense Convolution neural network (Dense Net)[19] uses a feed-forward fashion to interconnect each subsequent network layer; this extensive interconnectedness has earned it the moniker Dense Net. The data is first routed via a Conv2D layer with a high filter size, then through a dense block that establishes dense connections with all following layers. Each Dense Net layer receives new inputs from all previous layers and broadcasts its feature-maps to all subsequent layers.

B. *VGG*

VGG [20] is a CNN architecture that we also included into the TL-based approach to identify human actions. The pictures provided to VGG for training are images of a strict ratio, i.e., 512 by 512 pixels (224, 224, 3). These images have been processed using a stack of convolutional layers with 3-by-3-pixel filters. Following specific conv2D layers,

Authorized licensed use limited to: DELHI TECHNICAL UNIV. Downloaded on May 11,2023 at 10:20:11 UTC from IEEE Xplore. Restrictions apply.

five max-pooling layers do spatial pooling. A stack of convolutional layers is followed by dense layers with full connection and a SoftMax prognostication layer.

Figure 3 represent the VGG19 architecture where conv belongs to convolution layer, pool represent pooling layer and FC belong to fully connected layer

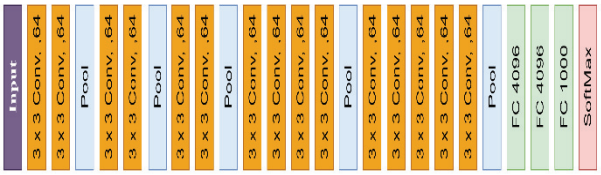


Fig. 3. VGG19 Architecture

C. *EfficientNet*

Efficient Net[21] is an architectural and scaling strategy for convolutional neural networks that scales all parameters of depth/width/resolution evenly utilizing a compound coefficient. Unlike current practice, which randomly scales these elements, the Efficient Net scaling technique uniformly adjusts network breadth, depth, and resolution using a set of predefined scaling factors. Efficient Net [21] It is a one-of-a-kind CNN network with high parameter estimation efficiency and speed. Efficient Net [21] used a simple and complicated scaling approach to more systematically scale up CNN models by scaling network characteristics like as depth, breadth, and resolution uniformly. In classification tasks, Efficient Net [21] was utilized also as spatial feature extraction network. There were seven CNN models dubbed EfcientNet-B0 through EfcientNet-B7 in the Efficient Net family. With the same input size, EfcientNet-B0 outperformed Resnet-50[22] with less parameters and FLOPs (floating-point operations per second) precision, indicating that EfcientNet-B0 is capable of efficient feature extraction.

D. *Dataset*

UCF50[23] dataset used for evaluation of model performance. This dataset was proposed by Reddy et al. in 2012. Online platforms like YouTube are used for the collection of videos. All videos have a realistic environment and are not taken from a controlled environment. This dataset is an updated version of the UCF11 dataset. It contains 50 action classes like basketball, shooting, tabla playing, biking, violin playing etc. There are a total of 6618 films featuring a variety of activities ranging from general sports to everyday life activities. Each activity class is separated into 25 homogeneous groups, including at least four movies for each activity. Films in the same category may have some characteristics, such as the same person, backdrop, or perspective. Figure 4 represents the action snippets of the UCF 50 dataset.

IV. DISCUSSION AND RESULTS

To classify each activity, we used three pre-trained deep-learning models Dense Net, VGG19 and Efficient Net. We applied pre-trained deep learning to capitalize on the information gathered from massive datasets such as ImageNet. The transfer learning approach transfers information from a previously-trained model to a neural network to train a new domain. Evaluation of the UCF50

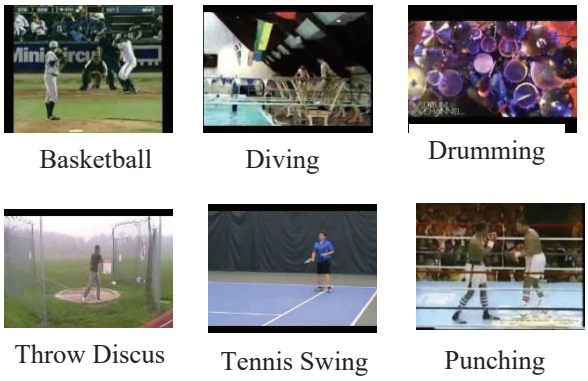


Fig. 4. UCF50 Action Dataset Frames.

action dataset, which contains various groups of images. We compared various deep learning model performances onthe above dataset in this approach and compared accuracy with state-of-the-art methods. Firstly, frames were extracted from each group of action videos and fed into a pre-trained deep-learning model. Figure 5-7 depicts the confusion matrix for recognizing 50 activities from UCF 50 dataset using the VGG19 model, Dense Net 161,EfficientNet b7.

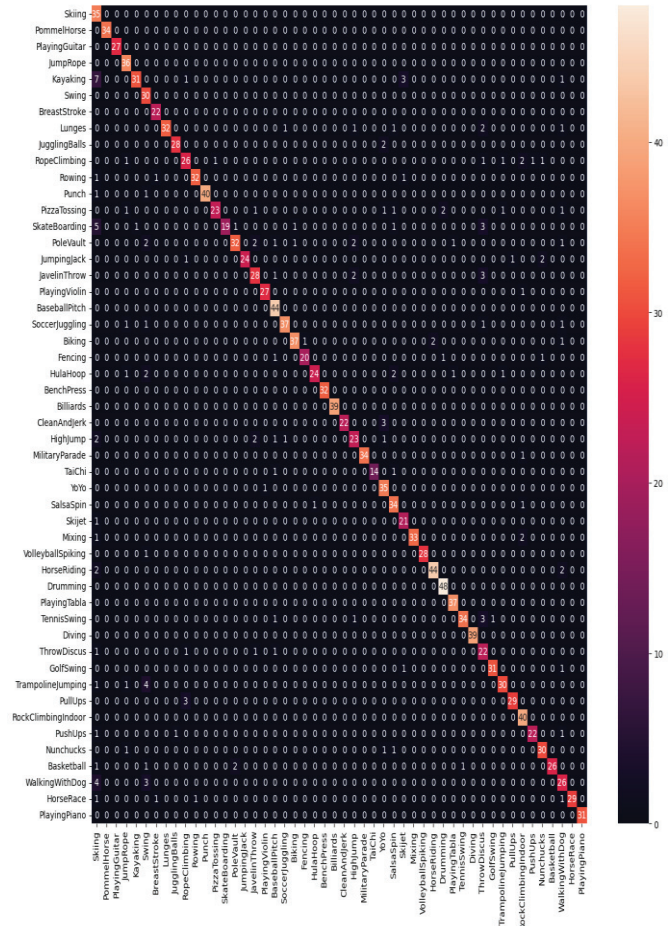


Fig. 5. VGG19 model confusion matrix for action recognition.

Authorized licensed use limited to: DELHI TECHNICAL UNIV. Downloaded on May 11,2023 at 10:20:11 UTC from IEEE Xplore. Restrictions apply.

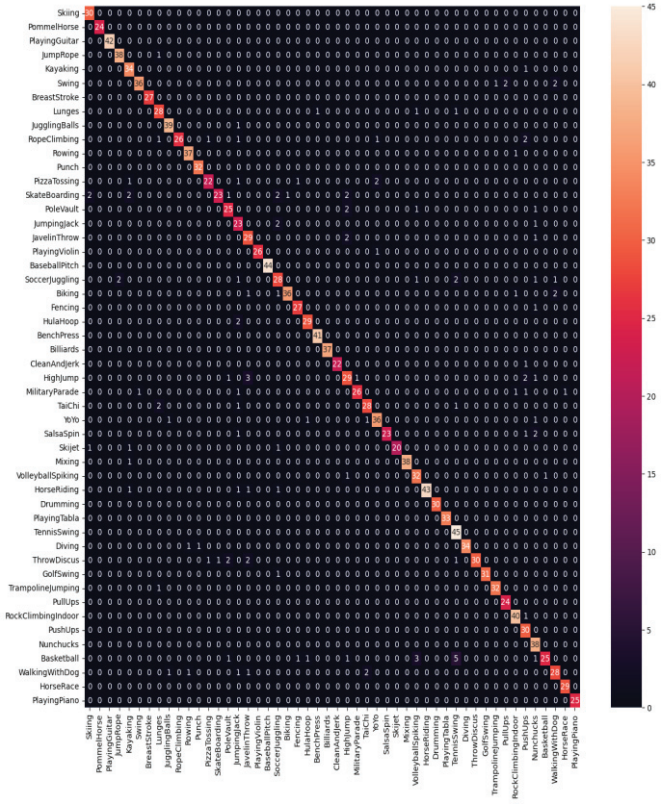


Fig. 6. Utilizing Dense Net 161 model, a confusion matrix for action recognition.

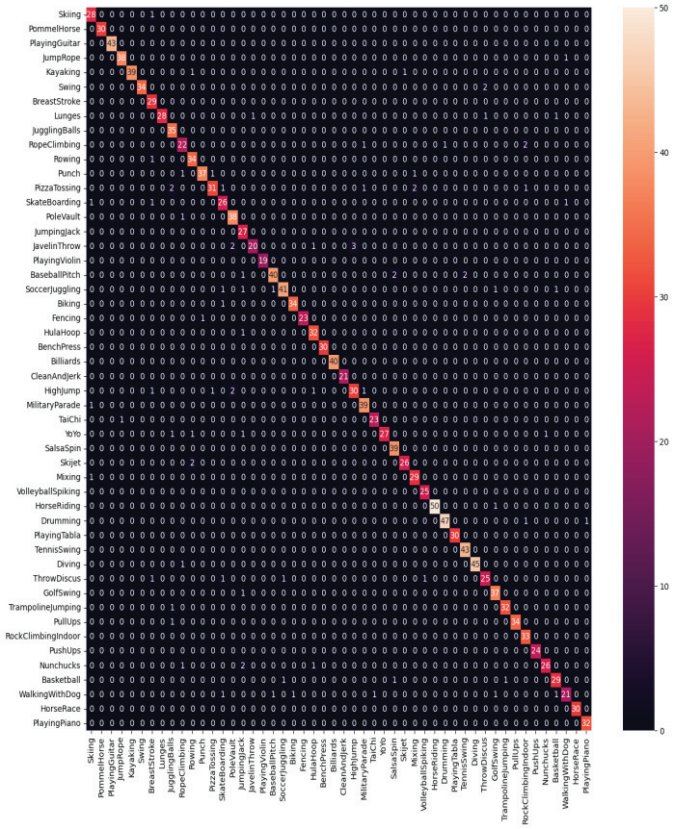


Fig. 7. Confusion matrix for action prediction from Efficient Net b7 model.

Classification result on activity dataset UCF 50 is shown as a Confusion matrix. Most of the activities classify accurately and with high confidence. On the UCF50 action dataset, Table 1 compares models evaluation metrices utilising TL techniques. Training, validation, and testing phases were used to partition the recovered frames during the implementation phase. Figure 8 shows a graphic illustration of this. Comparison with different state of the art methods shown in Table2:

TABLE I. COMPARISON OF VARIOUS LIGHT WEIGHT DL METHOD.

Model	Accuracy (%)	Precision (%)	Recall (%)	F1-Score (%)
VGG19	90.11	91.92	90.34	90.53
Dense Net 161	92.57	93.06	92.45	92.43
Efficient Net b7	94.25	94.92	94.79	94.71

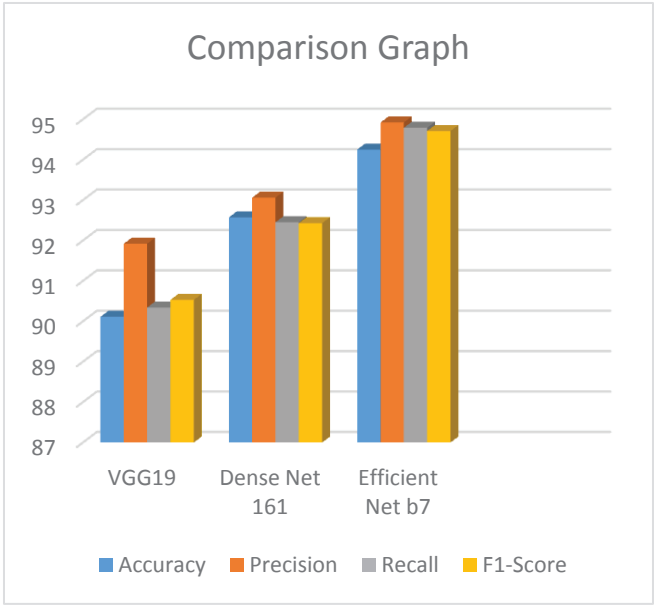


Fig. 8. Comparison graph for evaluation metrices.

TABLE II. COMPARISON OF LIGHT WEIGHT DL METHOD WITH EXISTING APPROACH.

Researcher	Dataset	Accuracy (%)
L. Zhang et al[24]	UCF50	88.0
H. Wang et al[25]	UCF50	89.1
Q. Meng et. al[26]	UCF50	89.3
Ahmad Jalal et. al[27]	UCF50	90.48
VGG19_bn	UCF50	**90.11**
Dense Net 161	UCF50	**92.57**
Efficient Net_b7	UCF50	**94.25**

On the UCF 50 dataset, we evaluated our approach's performance with that of a number of other methods that did not involve transfer learning. The findings of the experiment demonstrated whether employing transfer learning to a similar dataset improved recognition score. Their classification performance is enhanced by 1-4 % when pre-trained deep learning is used.

Authorized licensed use limited to: DELHI TECHNICAL UNIV. Downloaded on May 11,2023 at 10:20:11 UTC from IEEE Xplore. Restrictions apply.

V. CONCLUSION

Pre-trained deep learning models are used to classify human action from UCF 50 action dataset. UCF50 action dataset contains 50 different action categories into 25 groups, each containing at least 4 videos. Various evaluation matrices were used for testing model accuracy and effectiveness like precision, recall,f1 score and AUC score.VGG19, Dense Net 161, and Efficient Net models classify each dataset action. This work also compared state-of-the-art methods applied to the UCF50 dataset. These pre-trained deep learning models perform better as compared to state-of-the-art methods. Efficient Net performs better than other pre-trained deep learning models with 94 % accuracy.

In the future, we can extend this work to classify another dataset action, real action monitoring, abnormal action detection, and crowd behavior. This research goes on to adjust the framework of the pre-trained deep learning model, such as adding an attention layer, such that the pre-trained deep learning model may be employed with Bi-LSTM.

REFERENCES

[1] P. Pareek and A. Thakkar, "A survey on video-based Human Action Recognition: recent updates, datasets, challenges, and applications," Artif Intell Rev, vol. 54, no. 3, pp. 2259–2322, Mar. 2021, doi: 10.1007/s10462-020-09904-8.

[2] P. K. Singh, S. Kundu, T. Adhikary, R. Sarkar, and D. Bhattacharjee, "Progress of Human Action Recognition Research in the Last Ten Years: A Comprehensive Survey," Archives of Computational Methods in Engineering, vol. 29, no. 4, pp. 2309–2349, Jun. 2022, doi: 10.1007/s11831-021-09681-9.

[3] A. Ladjailia, I. Bouchrika, H. F. Merouani, N. Harrati, and Z. Mahfouf, "Human activity recognition via optical flow: decomposing activities into basic actions," Neural Comput Appl, vol. 32, no. 21, pp. 16387–16400, Nov. 2020, doi: 10.1007/s00521-018-3951-x.

[4] K. Simonyan and A. Zisserman, "Two-Stream Convolutional Networks for Action Recognition in Videos."

[5] S. Ji, W. Xu, M. Yang, and K. Yu, "3D Convolutional neural networks for human action recognition," IEEE Trans Pattern Anal Mach Intell, vol. 35, no. 1, pp. 221–231, 2013, doi: 10.1109/TPAMI.2012.59.

[6] F. Gu, K. Khoshelham, and S. Valaee, "Locomotion activity recognition: A deep learning approach," in IEEE International Symposium on Personal, Indoor and Mobile Radio Communications, PIMRC, Feb. 2018, vol. 2017-October, pp. 1–5. doi: 10.1109/PIMRC.2017.8292444.

[7] S. Aubry, S. Laraba, J. Tilmanne, and T. Dutoit, "Action recognition based on 2D skeletons extracted from RGB videos," MATEC Web of Conferences, vol. 277, p. 02034, 2019, doi: 10.1051/matecconf/201927702034.

[8] Z. Cao, G. Hidalgo, T. Simon, S. E. Wei, and Y. Sheikh, "OpenPose: Realtime Multi-Person 2D Pose Estimation Using Part Affinity Fields," IEEE Trans Pattern Anal Mach Intell, vol. 43, no. 1, pp. 172–186, Jan. 2021, doi: 10.1109/TPAMI.2019.2929257.

[9] C. Dai, X. Liu, and J. Lai, "Human action recognition using two-stream attention-based LSTM networks," Applied Soft Computing Journal, vol. 86, Jan. 2020, doi: 10.1016/j.asoc.2019.105820.

[10] Y. Du, W. Wang, and L. Wang, "Hierarchical Recurrent Neural Network for Skeleton Based Action Recognition."

[11] M. Majd and R. Safabakhsh, "Correlational Convolutional LSTM for human action recognition," Neurocomputing, vol. 396, pp. 224–229, Jul. 2020, doi: 10.1016/j.neucom.2018.10.095.

[12] M. Qi, Y. Wang, J. Qin, A. Li, J. Luo, and L. van Gool, "StagNet: An Attentive Semantic RNN for Group Activity and Individual Action Recognition," IEEE Transactions on Circuits and Systems for Video Technology, vol. 30, no. 2, pp. 549–565, Feb. 2020, doi: 10.1109/TCSVT.2019.2894161.

[13] Y. Huang, S.-H. Lai, and S.-H. Tai, "Human Action Recognition Based on Temporal Pose CNN and Multi-Dimensional Fusion."

[14] Wang Limin et al., Computer Vision – ECCV 2016, vol. 9912. Cham: Springer International Publishing, 2016. doi: 10.1007/978-3-319-46484-8.

[15] Y. Chen et al., "Graph convolutional network with structure pooling and joint-wise channel attention for action recognition," Pattern Recognit, vol. 103, Jul. 2020, doi: 10.1016/j.patcog.2020.107321.

[16] A. Karpathy, J. Johnson, and L. Fei-Fei, "Visualizing and Understanding Recurrent Networks," Jun. 2015, [Online]. Available: http://arxiv.org/abs/1506.02078

[17] T. Singh and D. K. Vishwakarma, "A deeply coupled ConvNet for human activity recognition using dynamic and RGB images," Neural Comput Appl, vol. 33, no. 1, pp. 469–485, Jan. 2021, doi: 10.1007/s00521-020-05018-y.

[18] O. Russakovsky et al., "ImageNet Large Scale Visual Recognition Challenge," Int J Comput Vis, vol. 115, no. 3, pp. 211–252, Dec. 2015, doi: 10.1007/s11263-015-0816-y.

[19] G. Huang, Z. Liu, L. van der Maaten, and K. Q. Weinberger, "Densely connected convolutional networks," in Proceedings - 30th IEEE Conference on Computer Vision and Pattern Recognition, CVPR 2017, Nov. 2017, vol. 2017-January, pp. 2261–2269. doi: 10.1109/CVPR.2017.243.

[20] K. Simonyan and A. Zisserman, "Very Deep Convolutional Networks for Large-Scale Image Recognition," Sep. 2014, [Online]. Available: http://arxiv.org/abs/1409.1556

[21] M. Tan and Q. v. Le, "EfficientNet: Rethinking Model Scaling for Convolutional Neural Networks," May 2019, [Online]. Available: http://arxiv.org/abs/1905.11946

[22] K. He, X. Zhang, S. Ren, and J. Sun, "Deep residual learning for image recognition," in Proceedings of the IEEE Computer Society Conference on Computer Vision and Pattern Recognition, Dec. 2016, vol. 2016-December, pp. 770–778. doi: 10.1109/CVPR.2016.90.

[23] K. K. Reddy and M. Shah, "Recognizing 50 Human Action Categories of Web Videos."

[24] L. Zhang and X. Xiang, "Video event classification based on two-stage neural network," Multimed Tools Appl, vol. 79, no. 29–30, pp. 21471–21486, Aug. 2020, doi: 10.1007/s11042-019-08457-5.

[25] H. Wang, D. Oneata, J. Verbeek, and C. Schmid, "A Robust and Efficient Video Representation for Action Recognition," Int J Comput Vis, vol. 119, no. 3, pp. 219–238, Sep. 2016, doi: 10.1007/s11263-015-0846-5.

[26] Q. Meng, H. Zhu, W. Zhang, X. Piao, and A. Zhang, "Action recognition using form and motion modalities," ACM Transactions on Multimedia Computing, Communications and Applications, vol. 16, no. 1s, Apr. 2020, doi: 10.1145/3350840.

[27] A. Jalal, I. Akhtar, and K. Kim, "Human posture estimation and sustainable events classification via Pseudo-2D stick model and K-ary tree hashing," Sustainability (Switzerland), vol. 12, no. 23, pp. 1–24, Dec. 2020, doi: 10.3390/su12239814.

Authorized licensed use limited to: DELHI TECHNICAL UNIV. Downloaded on May 11,2023 at 10:20:11 UTC from IEEE Xplore. Restrictions apply.

2023 10th International Conference on Signal Processing and Integrated Networks (SPIN) | 978-1-6654-9099-3/23/$31.00 ©2023 IEEE | DOI: 10.1109/SPIN57001.2023.10116165

Machine Learning Aided Techniques for Constraints Elimination in Optimal Power Flow Problem

Chaitanya Agarwal
Dept. of Electrical Engineering
Delhi Technological University
Delhi, India
chaitanyaagarwal_2k19ee081@dtu.ac.in

Kabir
Dept. of Electrical Engineering
Delhi Technological University
Delhi, India
kabir_2k19ee130@dtu.ac.in

Vinod Kumar Yadav
Dept. of Electrical Engineering
Delhi Technological University
Delhi, India
vinodkumar@dtu.ac.in

***Abstract*— With the rapid integration of Renewable Energy Sources (RESs) for power generation introduces greater uncertainties. The real time optimal power flow (OPF) solution is required faster and with greater accuracy. This paper develops and compare a machine learning and a deep learning approach for optimizing the real-time operation of electric power grids. In particular, feasible solutions to the OPF problem are realized with no violations in constraints and negligible optimality gaps. The aim of the OPF problem is identifying optimal operational conditions that minimize the power losses and/or generation costs or any other objective function that we aim for. Due to the computational challenges which occur while solving this nonconvex problem, many efforts have been made on linearizing or approximating the problem in order to solve the OPF on faster timescales. However, even after many approximations of the actual system state, there is still a need to solve an optimization problem, which can be time consuming for large networks. In this work, an approach to remove one of the OPF constraint entirely prior to building models using machine learning and deep learning, enabling us to find nearly optimal and realizable OPF solutions. This allows us to skip the nonconvexity of OPF problem, resulting in a significant decrease in computational burden.**

Keywords—optimal power flow, backward and forward sweep, random forest regressor, recurrent neural networks

I. INTRODUCTION

The rise of RESs contribution to the power grid also facilitates an increase in the uncertainties in the load dispatch predictions. The resulting imbalance makes it difficult to maintain both economic efficiency and system reliability and security. Optimal Power Flow (OPF) is the most important tools employed for power system analysis and network optimization. Grid operator run the OPF algorithms based on the demand to make the dispatch decisions. The uncertain and variable nature of RES require these decision parameters to be solved in real time to avoid curtailment. However, the nonlinearity and nonconvexity of the OPF model led to a high computational burden.

Many advancements have been made to the approaches to solve an OPF. For example, linearization of the constraints and objective function [1], [2], but the iterative process used to solve the extensive sample size render the computations too slow to be used in real time. The computational time can be reduced by sacrificing the accuracy of the results [3]– [5]. This deterministic approach, assuming point forecasts of exogenous power injections results in high forecast errors. The underlying distributed feedback controllers, which must manage the transients brought on by these inaccuracies, are pushed closer to stability limits by growing forecast errors [6].

Recently, the focus has been shifting towards the stochastic optimal power flow methods that explicitly incorporate forecast errors, in order to lessen the strain on feedback controllers and more effectively balance between economic efficiency and risk. They have been shown to tackle complex OPF problem with nonconvex cost functions and discrete control variables with desired robustness and convergence parameters. Many formulations assume that uncertain forecast errors follow a prescribed probability and utilize analytically tractable reformulations of probabilistic constraints. However, the complexity and nonlinear phenomena in emerging power networks are increasing, thus these assumptions in the model cannot be supported, and can significantly underestimate risk. Thus, the computational efficiency is still a bottleneck.

A modern way to decrease the computational complexity and time is to model the power system using Machine Learning (ML) techniques. Accurate models can be devised and trained for a particular grid section to help the operator predict the future load dispatch. Machine learning (ML) is among the most advanced mathematical tools that can be employed for analyzing this data and providing meaningful insights for system operators to make fast and efficient decisions [7]. Machine learning tools are used in many disciplines, such as finance, marketing, healthcare, social media, surveillance, voice and face recognition, recommendation system, robotics, and energy [8]. The development in the hardware sector has facilitated the models to run in real time, reducing the prediction errors. The implementation of end-to-end modelling results in high test accuracy, but constraint violation in this method makes the results unusable [9]. A hybrid approach to the problem has proven to reduce computational cost while minimizing the constraint violations. In hybrid method some parameters are calculated with the machine learning model within the feasible space and proceed with physics-based solvers to get the total dispatch.

This paper discusses the various models for machine learning side to study and compare the results, providing us with the advantages and short coming of each method in different scenarios. The following methods are employed to predict the bus voltage for each bus based on the variation in the demanded load, further the output voltages are used in the physics-based solver to obtain the injected active and reactive powers of the bus:

1. Machine learning algorithm Random Forest classifier performs several tasks which increases the accuracy of training and testing. Random forest classifier is used because of its good performance in case of multi feature solution space. Each unique decision tree in the random forest classifier divides into a class prediction and the class with the most votes become our model's prediction. The basic concept behind

Authorized licensed use limited to: DELHI TECHNICAL UNIV. Downloaded on May 15,2023 at 09:49:58 UTC from IEEE Xplore. Restrictions apply.

random forest classifier is an easy algorithm but powerful one – the intelligence of crowds [10]. Using Machine learning approach to solve OPF problems have been proven to improve the computational efficiency.

2. The multi-input multi-output and sequential nature of OPF makes it a perfect candidate for Recurrent Neural Network where the penalty functions further optimize for the inequality constraints. The neural network model takes the active and reactive load on each bus as the input and processes it through a feature map implemented through nodes in hidden layer and outputs the decision variables values. It takes in account the forecasting data available to train the model.

II. Problem Formulation

First Major issue with machine learning models is that while training the models OPF constraints get violated which results in less accuracy of the model, and hence, less prediction capability. However, with the ability to eliminate the constraints of the OPF problem, the accuracy of the machine learning should increase. In this paper voltage constraint is eliminated using MATLAB and power of the buses is calculated, the Random Forest model and Recurrent neural network model is then trained on the power to get the output voltage. This approach proved to be highly successful with good accuracy and less error rate for both the models.

A security constrained OPF problem is formulated as optimization problem, which aims to minimize the power loss in the system, as follows.

$$\min \sum_{n=1}^{N} r_n l_n \tag{1}$$

Subject to

$$\sum_{k:\, n\to k} P_k = p_n + P_n - r_n l_n \tag{2}$$

$$\sum_{k:\, n\to k} Q_k = q_n + Q_n - x_n l_n \tag{3}$$

$$v_n = v_{\pi_n} - 2r_n P_n - 2x_n Q_n + (r_n^2 + x_n^2) l_n \tag{4}$$

$$l_n . v_{\pi_n} = P_n^2 + Q_n^2 \tag{5}$$

And the objective function is,

(6)

where N, is the set of bus.

After solving with the machine learning models, the bus voltages are acquired, thus, eliminating the v_n constraint.

III. Methodology

In this paper, Random Forest and Convolutional Neural Network have been used for predicting the uncertain data and making insightful predictions.

Before discussing about these, random forest has been discussed below in sub-section A, multivariate regression trees have been discussed in sub-section B and RNN have been discussed in sub-section C.

A. Random Forest

Regression trees are used for predicting the continuous data. Constructing a regression tree follows two steps mainly:

1. The feature space is divided—that is, the set of possible values for $X_1, X_2, X_3, X_4, \dots X_p$ —into K distinct and non-overlapping regions, $R_1, R_2, R_3, R_4, \dots R_K$.
2. For every observation, a prediction is made which is the mean of the response values for the training observations in R_K.

For ease of interpretation of the model let us consider the feature space to be divided into rectangular boxes.

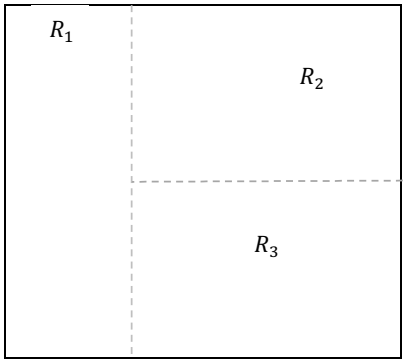


Fig 1. feature space divided into subspaces

From the figure above, the goal is to find the boxes $R_1, R_2, \dots R_K$ that minimize the MEAN SQAURED ERROR, given by

$$\sum_{k=1}^{K} \sum_{i \in R_k} \left(y_i - \hat{y}_{R_k}\right)^2 \tag{7}$$

where $\hat{y}_{R_k}$ is the response of the observation present in the k^{th} box. But this approach is computationally expensive, so top-down greedy approach known as Recursive binary splitting is followed. In this predictor X_k and cut point c is selected such that splitting the predictor space into $\{X|X_k < c\}$ *and* $\{X|X_k \geq c\}$ leads to the maximum possible reduction in mean squared error.

$\{X|X_k < c\}$ means that the space in which X_k takes value is less than c.

The Random Forest predictor comes under an ensemble predictor which encompasses random feature sub spacing and bagging to construct accurate and best possible regression or classification ensembles of decision trees. Both bagging and random sub spacing are proven to be effective ensemble methods. These ensemble methods force the tree to learn rather than form a specialized prediction rule, increasing the diversity amongst the classifiers by limiting the scope of the methods. During prediction, each of the tree 'vote' for the prediction that are then mapped to its limited scope. The final prediction is made by combining the votes using aggregation method.

1) Bagging

This ensemble method helps in reducing the variance in a dataset. It introduces diversity in the ensemble by taking only subset of the samples (with replacement). Bagging is an effective method for both classification and regression models. However, it has limitations. Bagged ensembles work best well only with unstable classifiers such as Classification and regression trees (CART) as the inferred rules are

Authorized licensed use limited to: DELHI TECHNICAL UNIV. Downloaded on May 15,2023 at 09:49:58 UTC from IEEE Xplore. Restrictions apply.

significantly affected by changes in the training data for these classifiers.

2) Random Feature Subspacing

Considering a two-dimensional N x M matrix of the training data — where features are represented by columns and example instances are represented by rows, and a single cell represents a value of that instance — bootstrap sampling repeatedly selects (with replacement) a random row from the matrix and adds it to the current bootstrap sample, until the original matrix size becomes equal to the bootstrap sample size.

B. Multivariate Regression Trees

In this paper, there are multiple outputs as each bus will have a predicted voltages thus, it becomes a multi-output prediction problem. This problem can be easily addressed by multivariate regression trees (MRT) which have the capability to make predictions for multiple regression related tasks. The objective is to minimize the sum of squared errors amongst the child nodes.

$$\phi(s,t) = SS(t) + SS(t_L) + SS(t_R) \tag{8}$$

where SS(t) is the sum of squared error in node t which is defined as

$$SS(t) = \sum_{i \in t} \left(y_i - \bar{y}(t)\right)^2 \tag{9}$$

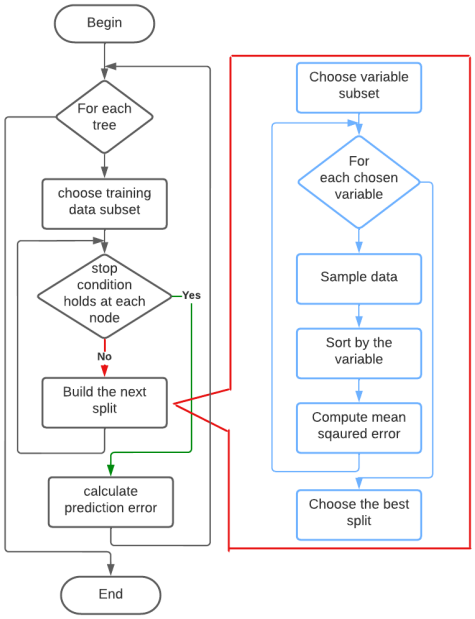


Fig 2. Flowchart of the random forest regression

C. Recurrent Neural Networks

Recurrent neural networks, also known as RNNs, are a class of neural networks (ML models) which allow previous outputs to be used as input. It is the most suitable model to analyze sequential data and predict future trends. Fig. 1 shows the architecture of a sample RNN. For each time step T, the previous step's output is added to its hidden layer.

The recurrent networks models sequential data such as the available data is used to predict the future response to the input. This is the differentiating feature that differentiates them from regular multilayer neural networks, like feed-forward neural networks, that does not have memory and can only learn a mapping between input and output patterns.

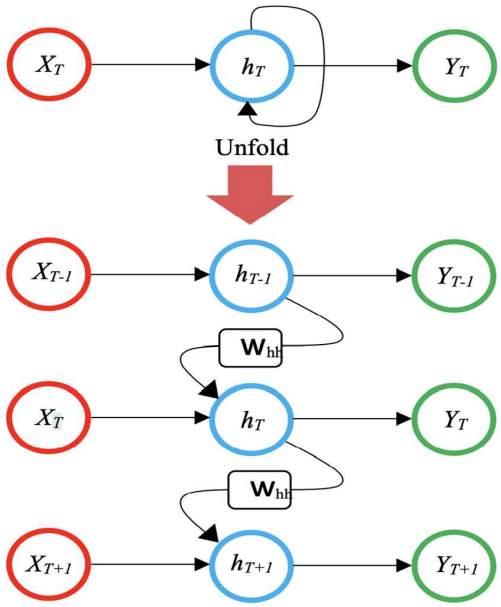
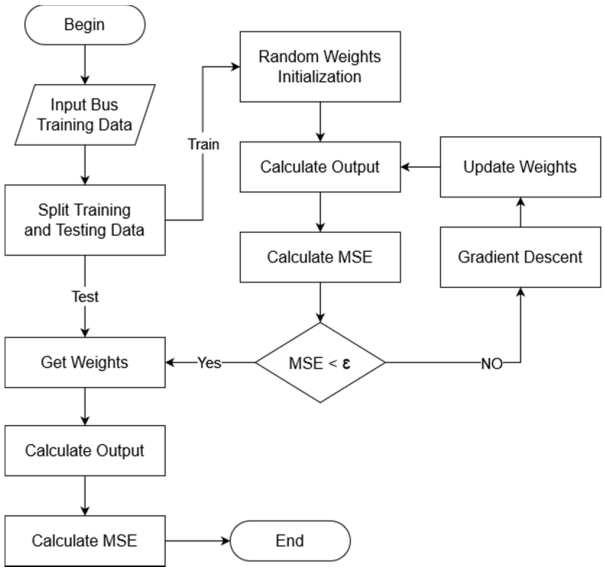


Fig 3. A common structure of recurrent neural network

RNN is trained using backpropagation, but the error is summed at each step, in contrast of backpropagation of feed forward neural network where the error is calculated individually for each output. In the case of a recurrent neural network, the loss function L of all time steps is defined based on the loss at every time step as follows:

$$L(\hat{y}, y) = \sum_{t=1}^{T} L\left(\hat{y}^{\langle t \rangle}, y^{\langle t \rangle}\right) \tag{10}$$

Backpropagation is done at each point in time. At timestep T, the derivative of the loss L with respect to weight matrix W is expressed as follows:



Authorized licensed use limited to: DELHI TECHNICAL UNIV. Downloaded on May 15,2023 at 09:49:58 UTC from IEEE Xplore. Restrictions apply.

$$\frac{\partial L^{(T)}}{\partial w} = \sum_{t=1}^{T} \frac{\partial L^{(t)}}{\partial w}\Big|_t \quad (11)$$

Fig 4. Flowchart of recurrent neural networks training

RNNs frequently experience the two issues of exploding gradients and vanishing gradients throughout this process. This issue arises due to magnitude of the gradient, gradient is defined as the slope of the loss function. When the gradient's value gets too small, it continues to exponentially decrease with respect to the number of layers, as the weight parameters updating depends upon the gradient, they become negligible—i.e., 0 for the case of vanishing gradient. The model stops learning when this happens. In the case of the exploding gradient, it becomes too large, resulting in an unstable system. The weight parameters continue to grow larger, exceeding the data type size limit and be represented as NaN.

Gradient clipping: To encounter the problem of exploding gradients gradient clipping is employed, by capping the maximum value for the gradient, the scenario of exponentially increasing gradient is avoided.

IV. Results and Discussion

In this section, the performance of the proposed hybrid models is evaluated in solving an OPF problem. The training of the proposed ML and RNN algorithm is performed on a GPU (Nvidia GeForce RTX 3050). A desktop with Intel i5-1135G7 4-core CPU and Gurobi solver are used.

To test and train the models datasets were generated using a 12-bus system was considered for which a standard snapshot for demanded load for each bus was taken and split in to 100 variations were generated using normal distribution around the standard value, which were capped at 10% variance from the standard value. Distribution of active power demand for the second bus is shown in the graph.

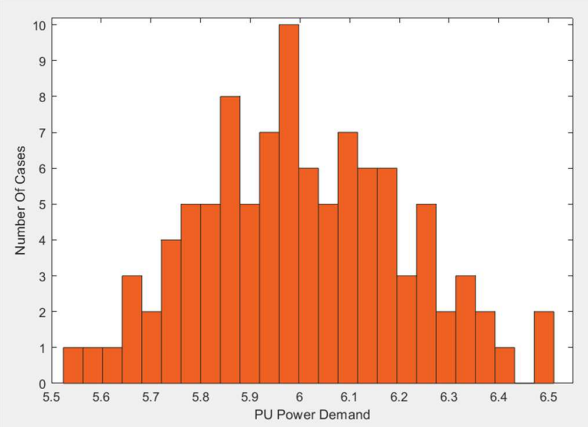


Fig 5. Active power demand distribution for the 2nd bus

A. Random forest model

In While training the model, special focus was given on the "max_depth" (depth of the tree) and "n_estimators" (number of trees) to prevent overfitting of the data. Depth and number of trees were set to 4 and 100 respectively after using a grid search and rest of the parameters such as "criterion", "max_samples" did not need tuning.

After training the model on the Active and reactive power and keeping the constraints in check, the model achieved an accuracy of 98.048%. The model achieved an error rate of 6.90754E-07. Time taken to train the model on Bus 12 dataset was only 0.07750 seconds

Graph of mean voltage of every bus in the test data and mean voltage of the ones predicted using the model were plotted for comparing the deviation in the voltages. Graphs for predicted value and actual voltages overlap significantly as shown in the figure owing to the high accuracy of the model. The graphs illustrate that the model performed excellently with exceptionally low error rate.

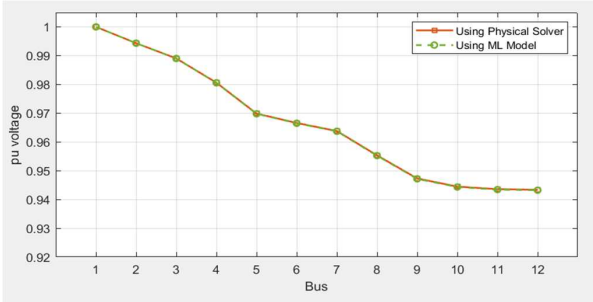


Fig 6. Combined plot of Actual Voltage and Predicted Voltage obtained using RF Model

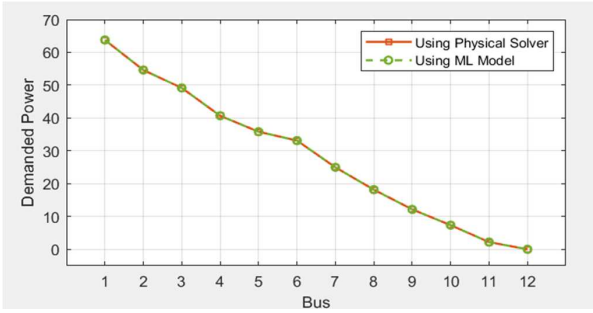


Fig 7. Combined plot of Actual Power over Predicted Voltage obtained using RF Model

B. Recurrent Neural Network

Root-mean-square error (RMSE) was used to evaluate the performance of the forecasting models. The models based on the RNN were implemented and trained on MATLAB R2018a with the default learning rate $\alpha = 10^{-3}$ and a maximum of 250 epochs.

In the training of was completed in 28 epochs for and accepted error of 1e-5. The training was completed in 0.02 sec. For the training, vanishing gradient was not considered as the data is not sequential in time.

After training the model on the Active and reactive power and keeping the constraints in check, the model achieved an accuracy of 92% over the iterations with an average error of 0.2695% per bus.

Graph of mean voltage of every bus in the test data and mean voltage of the ones predicted using the model were plotted for comparing the deviation in the voltages. The predicted voltage closely follows the

Authorized licensed use limited to: DELHI TECHNICAL UNIV. Downloaded on May 15,2023 at 09:49:58 UTC from IEEE Xplore. Restrictions apply.

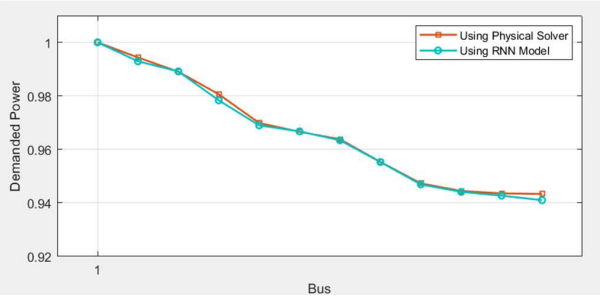


Fig 8. Combined plot of Actual Voltage and Predicted Voltage obtained using RNN Model

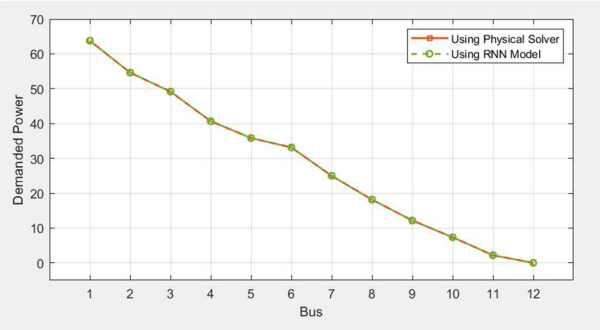


Fig 9. Combined plot of Actual Power over Predicted Voltage obtained using RNN Model

Using the physical solver, the program run for 2.8645 seconds and using the hybrid model the computational time was reduced to 1.5814 using RF model and 1.6592 seconds using the RNN model.

V. Conclusion

In this paper, a framework was prepared and compared for solving OPF problems using machine learning and deep learning model to predict the voltage of every bus. Moreover, the approach to eliminate one of the constraints before building the model proved to be extremely helpful. Both the approaches showed acceptable results, provided a method to pursue feasibility and realize the solution in the original OPF problem by training the model on strictly feasible solutions keeping the constraints in check and then solving the OPF equations to recover the reactive power generation values. From start to finish, both the approaches could recover a feasible solution to the OPF problem extremely quickly with negligible sacrifices in optimality. Thus, both the frameworks developed are faster and provide a more accurate solution than other methods that are used to solve OPF quickly, such as approximating power flow equations.

References

[1] S. M. Fatemi, S. Abedi, G. B. Gharehpetian, S. H. Hosseinian, and M. Abedi, “Introducing a novel DC power flow method with reactive power considerations,” IEEE Trans. Power Syst., vol. 30, no. 6, pp. 3012–3023, Nov. 2015.

[2] Z. Yang, H. Zhong, A. Bose, T. Zheng, Q. Xia, and C. Kang, “A linearized OPF model with reactive power and voltage magnitude: A pathway to improve the MW-only DC OPF,” IEEE Trans. Power Syst., vol. 33, no. 2, pp. 1734–1745, Mar. 2018.

[3] A. Schellenberg, W. Rosehart, and J. Aguado, “Cumulant-based probabilistic optimal power flow (P-OPF) with Gaussian and gamma distributions,” IEEE Trans. Power Syst., vol. 20, no. 2, pp. 773–781, May 2005.

[4] A. Vaccaro and D. Villacci, “Radial power flow tolerance analysis by interval constraint propagation,” IEEE Trans. Power Syst., vol. 24, no. 1, pp. 28–39, Feb. 2009.

[5] A. Kazemdehdashti, M. Mohammadi, and A. R. Seifi. “The generalized cross-entropy method in probabilistic optimal power flow,” IEEE Trans. Power Syst., vol. 33, no. 5, pp. 5738–5748, Sep. 2018.

[6] P. Kundur, N. J. Balu, and M. G. Lauby, Power System Stability and Control, vol. 7. New York, NY, USA: McGraw-Hill, 1994.

[7] I. H. Witten, E. Frank, M. A. Hall, and C. J. Pal, Data Mining: Practical machine learning tools and techniques. Morgan Kaufmann, 2016.

[8] M. I. Jordan and T. M. Mitchell, "Machine learning: Trends, perspectives, and prospects," Science, vol. 349, no. 6245, pp. 255-260, 2015.

[9] J. Rahman, C. Feng and J. Zhang, "Machine Learning-Aided Security Constrained Optimal Power Flow," 2020 IEEE Power & Energy Society General Meeting (PESGM), 2020, pp. 1-5, doi: 10.1109/PESGM41954.2020.9281941.

[10] V. Geetha, A. Punitha, M. Abarna, M. Akshaya, S. Illakiya and A. P. Janani, "An Effective Crop Prediction Using Random Forest Algorithm," 2020 International Conference on System, Computation, Automation and Networking (ICSCAN), 2020, pp. 1-5.

Authorized licensed use limited to: DELHI TECHNICAL UNIV. Downloaded on May 15,2023 at 09:49:58 UTC from IEEE Xplore. Restrictions apply.

e-ISSN: 2582-5208
International Research Journal of Modernization in Engineering Technology and Science
(Peer-Reviewed, Open Access, Fully Refereed International Journal)
Volume:05/Issue:04/April-2023 Impact Factor- 7.868 www.irjmets.com

MACHINE LEARNING APPROACHES TO MANUFACTURING

AK Madan[*1], Rohin Verma[*2], Rudansh Singh[*3], Ritik Kamboj[*4]

[*1]Prof., Mechanical Engineering department, Delhi Technological University, New Delhi, India.

[*2,3,4]Student, Mechanical Engineering, Delhi Technological University, New Delhi, India.

ABSTRACT

Manufacturing companies need constant development to remain competitive, which calls for adaptable workplaces and staff members that value lifelong learning. They also profit from systems for processing information and materials that are flexible and progressive. Machine learning has grown in popularity across a variety of industries, including entertainment, business, and industrial applications. It is a type of artificial intelligence that focuses on autonomous knowledge acquisition. Due to its adaptability and accessibility, new avenues for innovation have emerged, notably in the manufacturing sector. Machine learning techniques are becoming increasingly popular as the manufacturing sector moves towards Smart Manufacturing and Industrie 4.0. This study examines a decade's worth of manufacturing papers to assess how much machine learning is being used in that sector.

I. INTRODUCTION

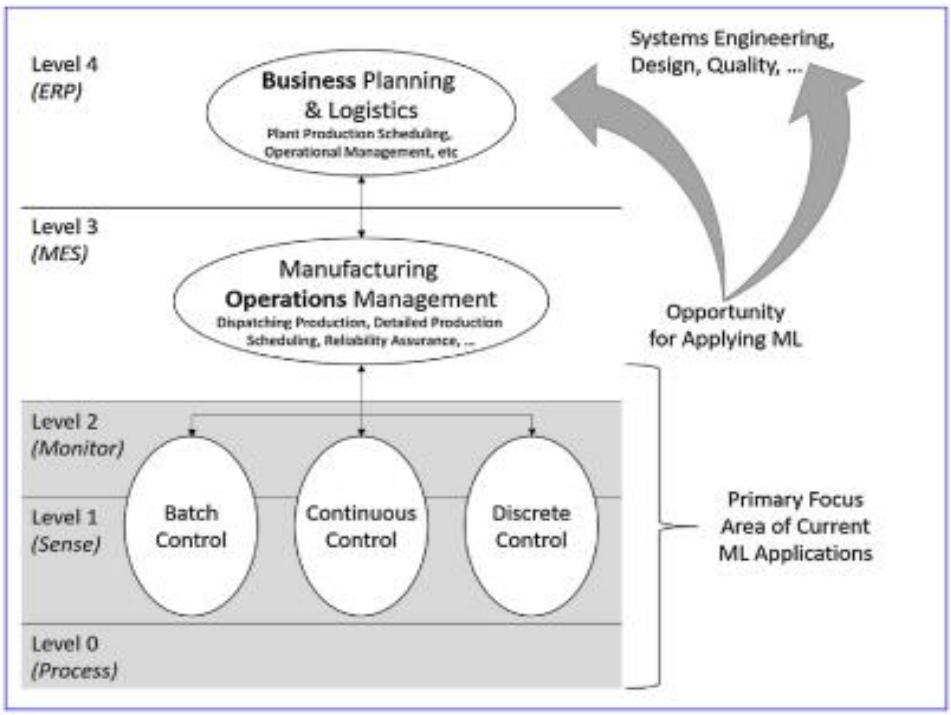
The rapid advancement of CAD/CAM technology, notably in prosthetic and restorative dentistry, has had a significant impact on the discipline of dentistry. Dental education has improved in terms of cost, time, and predictability with the integration of these systems with biomaterials like high-strength zirconium oxide ceramics. To incorporate the advantages of CAD/CAM technology into dental care, three primary procedures have been developed: digital impressions, digital models, and virtual articulators and face bows. The ability to generate a broad range of restorations for The enormous differences in acquisition techniques, CAD design mechanisms, and CAM production processes can make it difficult to develop specialized prosthetic solutions.a broad variety of restorations for unique prosthetic solutions might be difficult to build because of the wide variation in acquisition methods, CAD design tools, and CAM production techniques.

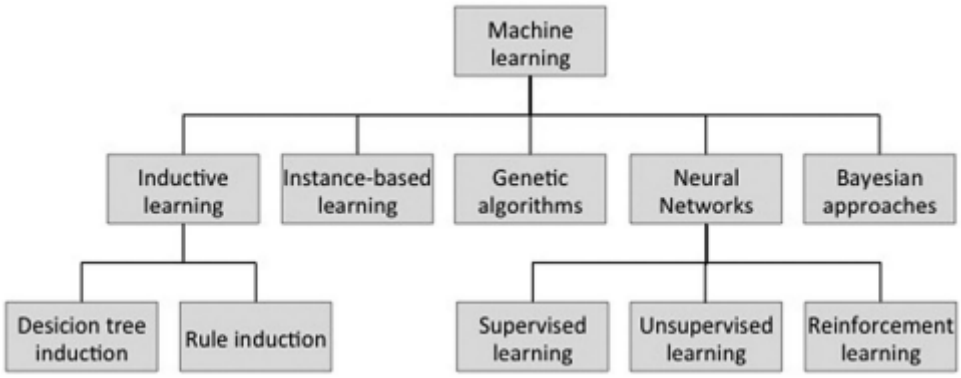
Machine learning (ML) has witnessed an increase in use in manufacturing over the past 20 years, with two surges in the 1980s and present utilization. Even though machine learning (ML) received a lot of attention in the 1980s, there was little industry adoption as a result of the challenges associated with using the methodologies with the available technology. In recent studies, cross-domain models for tying together information throughout the product life cycle have received less attention than domain-specific models.

However, as technologies like the Industrial Internet of Things, Industrie 4.0, and smart manufacturing are more widely used, more data is being produced, necessitating the use of automated ways to gather, transmit, evaluate, and take appropriate action on the data. Dynamically generating knowledge bases and figuring out minimum information requirements require ML tools that can analyse data, apply context, and build knowledge, especially earlier in a product's life cycle. This can lower the negative consequences of choices and raise the cost-effectiveness and standard of production programmes.

The paper seeks to make the case for why machine learning is a valuable tool for addressing current and future challenges in manufacturing, from a production perspective. It introduces relevant terminology and provides an overview of the different areas of machine learning, proposing a comprehensive structure. The paper also discusses the advantages and drawbacks of various methods for manufacturing applications, aiming to give readers a broad understanding of the topic.

e-ISSN: 2582-5208
International Research Journal of Modernization in Engineering Technology and Science
(Peer-Reviewed, Open Access, Fully Refereed International Journal)
Volume:05/Issue:04/April-2023 Impact Factor- 7.868 www.irjmets.com





II. CHALLENGES OF THE MANUFACTURING DOMAIN

The importance of the industrial sector cannot be emphasized, despite its long history. Despite the fact that the manufacturing sector's GDP contribution has decreased in several industrialised economies over the past few decades, initiatives to revive it have been taken recently. For instance, the European Union started the "Factories of the Future" program, and the US announced "Executive Actions to Strengthen Advanced Manufacturing in America." The manufacturing challenges of today are different from those of the past, and various international studies have outlined the main issues.. These include the adoption of advanced manufacturing technologies, the increasing significance of high-value product manufacturing, the use of advanced knowledge, information management, and AI systems, the use of sustainable manufacturing processes and products, agile and flexible enterprise capabilities and supply chains, and innovation in goods, services, and procedures.

Advantages of machine learning application in manufacturing

In industrial systems, machine learning (ML) approaches have a number of benefits. Their capacity to handle high-dimensional, multivariate data and extract implicit relationships from huge, complicated datasets, especially in chaotic circumstances, is one of their main advantages. In engineering and industry, where challenges are frequently data-rich yet knowledge-scarce, this is especially helpful. In some NP-hard manufacturing challenges, ML can reduce cycle time and scrap while increasing domain expertise and resource utilization, while reducing cycle time and scrap in certain NP-hard manufacturing problems.

e-ISSN: 2582-5208
International Research Journal of Modernization in Engineering Technology and Science
(Peer-Reviewed, Open Access, Fully Refereed International Journal)
Volume:05/Issue:04/April-2023 Impact Factor- 7.868 www.irjmets.com

Different ML techniques have varying advantages, but the ability to cope with high dimensionality is generally considered a positive feature. Additionally, user-friendly programs like Rapidminer make it easy to apply ML algorithms and adjust parameters for improved classification performance. Another significant advantage is ML's capacity to uncover implicit knowledge and relationships in data that was previously unknown.

ML algorithms can learn and adapt to dynamic, uncertain, and complex manufacturing systems, making them a powerful tool for continuous quality improvement. Their ability to quickly adapt to changing environments is often faster than traditional methods. While specific ML algorithms may have unique requirements for data availability and other factors, the overall effectiveness of ML in manufacturing has been successfully demonstrated

Applications in manufacturing

In the following sections, grouped by topics, a roster of applications of ML in manufacturing is presented. For each topic, a general introduction is followed by a description of major research projects as offered by our contributors and reported in major periodicals and selected conference materials.

III. DESIGN

Several researchers have applied machine learning techniques to diverse design issues. Beginning with a specific problem situation where a fixed design model is assumed, the talk moves on to a method that combines model development with optimisation. Later, particular production system design issues are addressed. By filling in the design and manufacturing details of new, identical parts using data from current components, a design retrieval system, for instance, can reduce the amount of design work required. In order to accomplish this, a set of completely defined, representative parts is used to anticipate the missing information on a new, partially defined part. Parts have been grouped using the COBWEB method based on an assessment of the likelihood that attribute values would be correctly predicted. A different suggested system retrieves design solutions through functional associations and can mutate the retrieved cases to further configurations. However, recognizing geometric invariance remains an unsolved issue. Finally, a four-layer ANN is suggested for the function specification step.

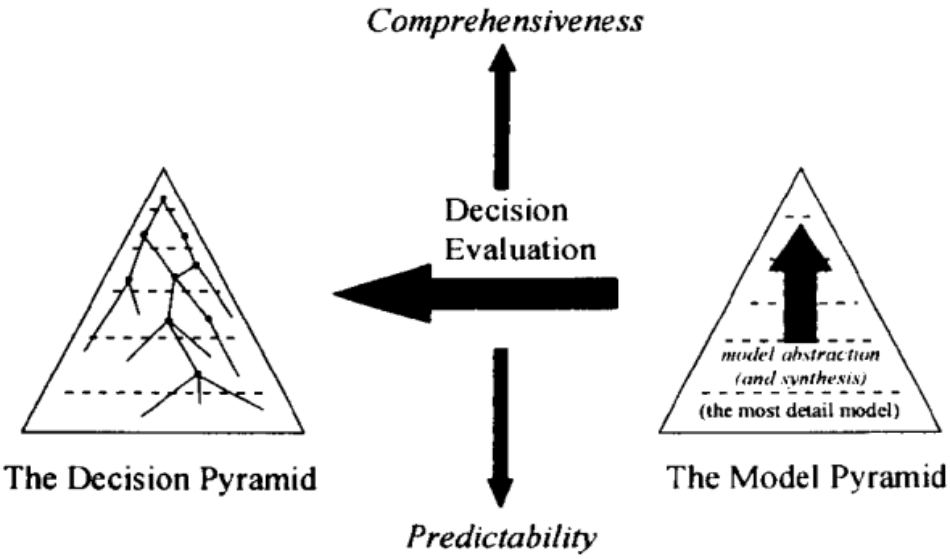


Figure 8.
A hierarchy of the model pyramid [128]

Process planning

Process planning has been highly successful in applying various learning methods, mainly due to the complexity of process planning expertise and the interrelated knowledge from multiple sources. Numerous applications have made use of easily accessible tools and methods, and research in this area has yielded useful outcomes

e-ISSN: 2582-5208
International Research Journal of Modernization in Engineering Technology and Science
(Peer-Reviewed, Open Access, Fully Refereed International Journal)
Volume:05/Issue:04/April-2023 Impact Factor- 7.868 www.irjmets.com

outside of the technical community. The research in this discipline is categorised by application area in the following parts.

Process modeling, monitoring, and control

Several indications, including force, torque, temperature, mechanical vibration, and acoustic emission, which are the focus of various monitoring and control algorithms, can be used to evaluate manufacturing processes. It hasn't been possible to find a signal that works reliably under all circumstances and from all viewpoints, though. As a result, the incorporation of sensors has been acknowledged as a crucial step in this area, providing advantages including information redundancy. In the event of sensor failures or mistakes, this redundancy can reduce total uncertainty and improve system reliability.

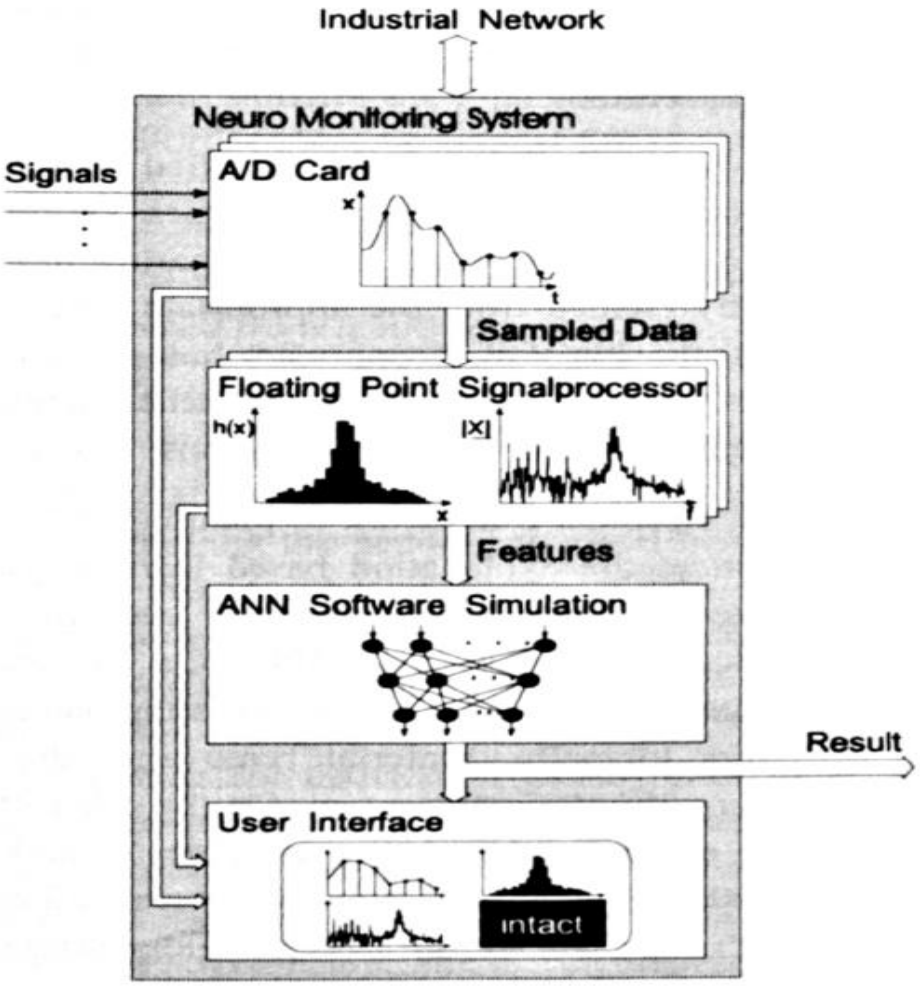


Figure 11.
Schematic of neuro monitoring and diagnostic systems

Automated inspection, diagnostics and quality control

Competition and the need to minimise costs on the one hand, and the rising demand for quality and dependability on the other, create conflicting demands for modern manufacturing. In order to achieve maximum efficiency, process parameters are frequently pushed to the limits of machine tools, yet high-quality standards can only be met under reasonable machining settings. Complex quality control procedures are needed in highly automated, just-in-time manufacturing to guarantee error-free assembly of parts. Manufacturing requires the use of inspection, diagnosis, and quality control. High accuracy measurements of deviations in dimensions, form, and position are made using coordinate measuring machines (CMMs). For sporadic process measurements, interchangeable measuring heads are utilised. These heads can be connected to controllers so that any necessary adjustments can be made.

e-ISSN: 2582-5208
International Research Journal of Modernization in Engineering Technology and Science
(Peer-Reviewed, Open Access, Fully Refereed International Journal)
Volume:05/Issue:04/April-2023 Impact Factor- 7.868 www.irjmets.com

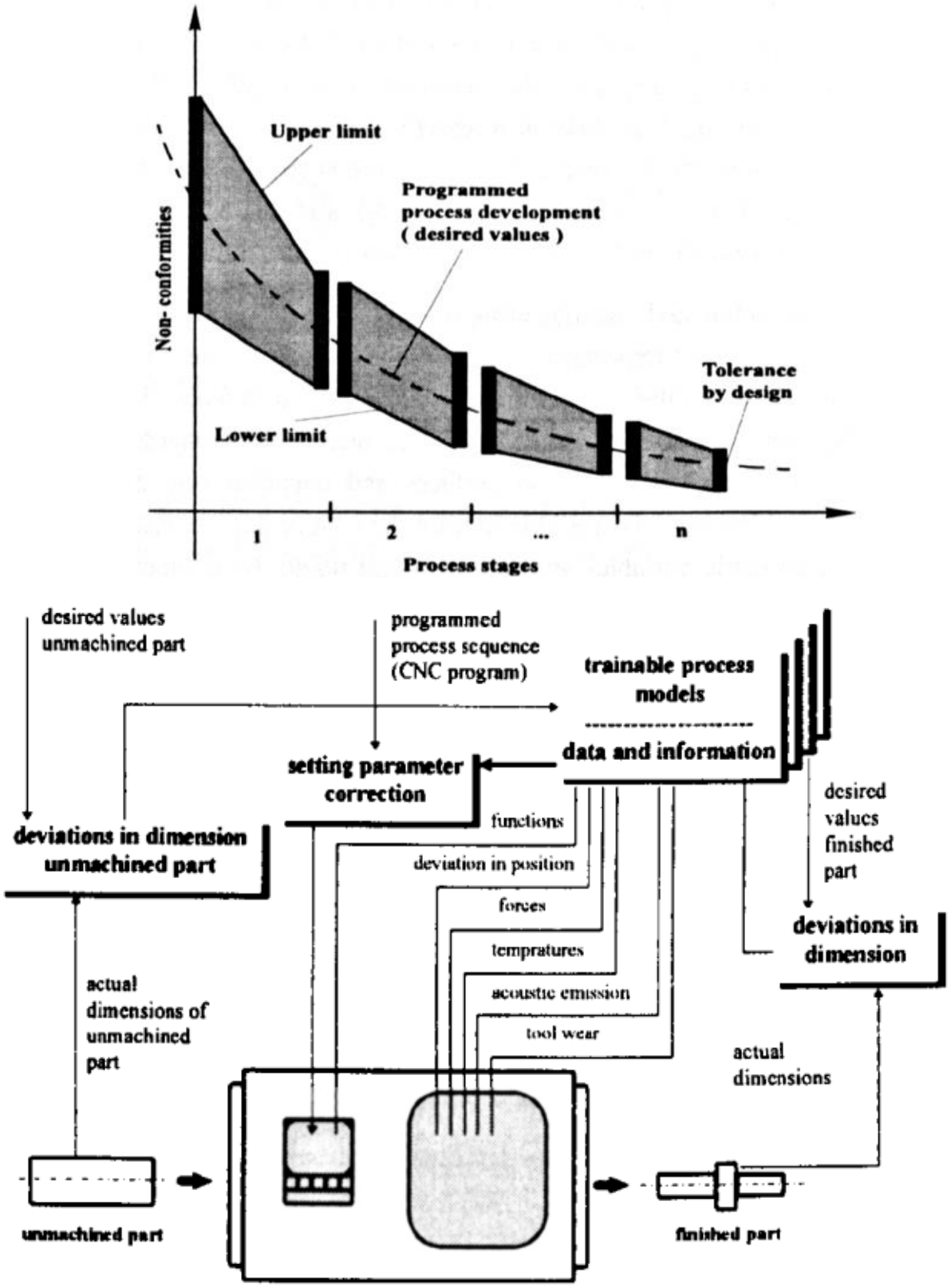


Figure 19.
Quality control loop for zero-defect manufacturing [242]

e-ISSN: 2582-5208
International Research Journal of Modernization in Engineering Technology and Science
(Peer-Reviewed, Open Access, Fully Refereed International Journal)
Volume:05/Issue:04/April-2023 Impact Factor- 7.868 www.irjmets.com

Production planning and control

It was acknowledged in 1990 that scheduling lacked expert and heuristic knowledge since there weren't enough human experts who could be validated. This issue has been addressed by a system that uses the production system's history database to make suitable scheduling decisions in a dynamic context. The system combines goal-directed conceptual clustering, case- and rule-based methods, and simulation to provide synergistic effects. Another study modified system performance by combining weighted heuristic priority rules with an induction module. The name of this simulation system is KBSim. In another study, the performance of a "artificial memory" system and a traditional heuristic algorithm were evaluated in order to handle the scheduling problem of knowledge organisation. The outcomes demonstrated that the former performed only a little bit better.

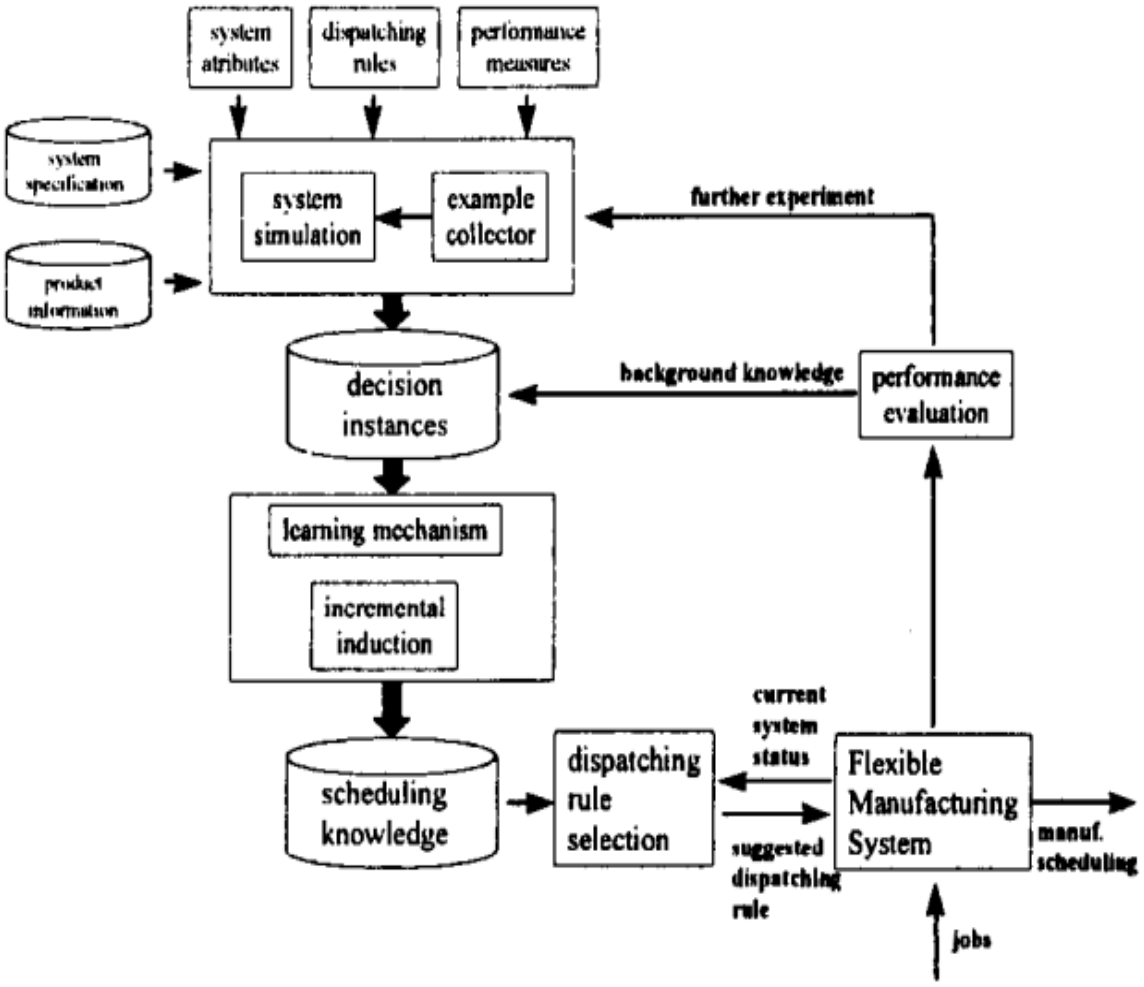


Figure 20.

Architecture of the learning-based dynamic scheduling system

Robotics and assembly

Machine learning can be used to improve a variety of learning tasks found in robotics and assembly. During the development and deployment of robots, machine learning can support a variety of tasks, including initial knowledge acquisition, programme generation (i.e., robot programming and world-model acquisition), and action and world knowledge refinement. (i.e., acquiring new knowledge to solve new tasks, refining existing knowledge, and correcting it to help the robot adapt to uncertain and changing environments).

e-ISSN: 2582-5208
International Research Journal of Modernization in Engineering Technology and Science
(Peer-Reviewed, Open Access, Fully Refereed International Journal)
Volume:05/Issue:04/April-2023 Impact Factor- 7.868 www.irjmets.com

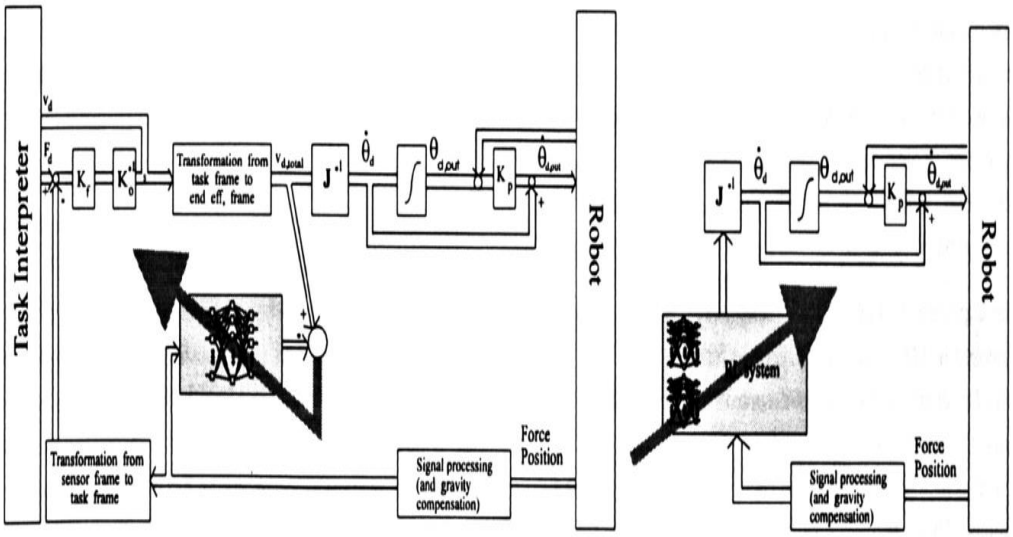


Figure 23.
Learning control architectures: supervised training in the KA phase (left) and RL phase (right) [172]

IV. CONCLUSION

1. In today's industry, efficient management and manufacturing are crucial for progress and improvement. An effective system is needed to help industries overcome challenges.

2. Computers have been an essential tool in many fields, including manufacturing, aerospace, and healthcare. Integrations that synchronize data and provide better results have become increasingly important. CAD/CAM (Computer-Aided Design and Computer-Aided Manufacturing) is a popular integration that has brought significant efficiencies to the industry.

3. CAD is used to create designs on modern computers, which are then simulated and manufactured.

4. CAD applications can be combined with artificial intelligence and machine learning to optimize designs and make the system more advanced and creative.

5. CAM is similar to CAD, but it manages manufacturing tasks and resources, including materials and personnel, to find the best solution.

6. Adding AI and machine learning to CAM can improve system performance and efficiency. CAD/CAM integration streamlines the design and manufacturing process by providing a single system application for all operations and data flow.

7. CAD/CAM integration has also improved computer graphics systems, making it easier to perform automated drawings and engineering analyses such as stress-strain.

V. REFERENCE

[1] Groover M. P.(2000), "Automation, Production Systems, and Computer Aided Manufacturing", Prentice Hall of India, New Delhi.

[2] Bohlen, I. S., Fieret, J., Holmes, A. S., Lee K. W., 2003, CAD/CAM Software for an Industrial Laser Manufacturing Tool, Photon Processing in Microelectronics and Photonics Ii, 4977 198- 206.

[3] Kalpakjian, Serope and Schmid, Steven, R, "Manufacturing Engineering & Technology", Prentice Hall, Fifth edition, 2002

[4] David Twigg, Christopher A. Voss, Graham M. Winch "Implementing Integrating Technologies (1992): Developing Managerial Integration for CAD/CAM", International Journal of Operations & Production Management, 12 (7/8), 76-91.

[5] Rishi Kumar Shukla, Dinesh, B. Deshmukh,(2015) "A Review on Role of CAD/CAM in Designing for SkillDevelopment", ITMVU, at Vadodara, with 1,827 Reads.

[6] Rohit Pandey, Arvind Singh Tomar & Nishant Sharma,(2016): "A Recent Role of CAD/CAM in Designing, Developing and Manufacturing in Modern Manufacturing Technologies" Imperial Journal of Interdisciplinary Research (IJIR), 2(3),399

[7] A survey of the advancing use and development of machine learning in smart manufacturing Michael Sharp, Ronay Ak, Thomas Hedberg Jr. ∗ Engineering Laboratory, National Institute of Standards and Technology, 100 Bureau Drive, Stop 8260, Gaithersburg, MD 20899, US

[8] Barschdorff, D.; Bothe, A.; WOstenkUhler, G., 1990, Vergleich lernender Mustererkennungs-verfahren und neuronaler Netze zur Prufung und Beurteilung von Maschinengerauschen, Proc. Schalltechnik'90, VOl Berichte, Nr. 813, pp. 23-42.

[9] Barschdorff, D.; Monostori, L., 1991, Symbolicism and connectionism: Rivals or allies in intelligent manufacturing?, Proc. of The 23rd CIRP Int. Seminar on Manufacturing Systems, 6-7 June, Nancy, France, Section 4, pp. 14-28.

[10] Barschdorff, D.; Monostori, L.; Kottenstede, T.; Warnecke, G.; MUller, M., 1993, Cutting tool monitoring in turning under varying cutting conditions via artificial neural networks, Proc. of The Sixth Int. Conf. on Industrial & Engineering Applications of Artificial Intelligence & Expert Systems, June 1-4, Edinburgh, Scotland, Gordon and Breach Science Publishers, pp. 353-359.

[11] Barschdorff, D.; Monostori, L.; Ndenge, A.F.; Wostenkuhler, G.W., 1991, Multiprocessor systems for connectionist diagnosis of technical processes, Computers in Industry, Elsevier, Spec. Issue on Learning in IMSs, pp. 131-145.

[12] Barschdorff, D.; Monostori, L.; WOstenkUhler, G.W.; Egresits, Cs.; Kadar, B., 1995, Approaches to coupling connectionist and expert systems in intelligent manufacturing, Proc. ofthe Second Int. Workshop on Learning in IMSs, Budapest, Hungary, April 20-21, pp. 591-608.

[13] Smart Manufacturing through Machine Learning: A Review, Perspective, and Future Directions to the Machining Industry A. S. Rajesh , 1 M. S. Prabhuswamy,2 and Srinivasan Krishnasamy 3 1 Department of Mechanical Engineering, JSS Science and Technology University, Mysuru, Karnataka 570006, India 2 Department of Mechanical Engineering, JSS Science and Technology University, Mysuru, Karnataka 570006, India 3 Arba Minch University, Arba Minch, Ethiopia

[14] Bohner, P., 1995, A multi-agent approach with distributed fuzzy logic control, Computers in Industry, Vol. 26, pp.219-227.

[15] Bose, P., 1992, An abstraction-based search and learning approach for effective scheduling., Artificial Intelligence Applications in Manufacturing, (ed: A. Famili, D. S. Nau, S. H. Kim) AAAI Press / The MIT Press, pp. 187-197.

[16] A smooth and undistorted toolpath interpolation method for 5-DoF parallel kinematic machines Robot. Comput. Integr. Manuf. (2019)

[17] Agarwal, R., J. Singh, and V. Gupta. 2022. "Predicting the Compressive Strength of Additively Manufactured PLA-Based Orthopedic Bone Screws: A Machine Learning Framework." Polymer Composites 438: 5663–5674. John Wiley and Sons Inc. 10.1002/PC.26881

[18] Zangaro, Francesco, Stefan Minner, and Daria Battini. 2020. "A supervised machine learning approach for the optimization of the assembly line feeding mode selection." International Journal of Production Research.

[19] A survey of machine learning in additive manufacturing technologies Jingchao Jiang Received 04 Mar 2022, Accepted 29 Jan 2023, Published online: 14 Feb 2023

[20] Machine learning and artificial intelligence in CNC machine tools, A review Mohsen Soori a, Behrooz Arezoo b, Roza Dastres c Received 11 October 2022, Revised 17 December 2022, Accepted 13 January 2023, Available online 14 January 2023.

Mitigating YouTube Recommendation Polarity using BERT and K-Means Clustering

Zoheb Ahmad
Dept. of Software Engineering
Delhi Technological University
New Delhi, India
zoheb.ahmad100@gmail.com

Danish Quasim
Dept. of Computer Engineering
Delhi Technological University
New Delhi, India
danishquasim31@gmail.com

Shreeya Garg
Dept. of Computer Engineering and Bioscience
IIIT Delhi
New Delhi, India
shreeya18415@iiitd.ac.in

Vinod Kumar
Dept. of Computer Engineering
Delhi Technological University
New Delhi, India
vinod_k@dtu.ac.in

***Abstract*— YouTube's recommendation system is famous for its success in maintaining high retention rates. The cause of its success is its ability to learn and predict an individual user's preferences appropriately. An unintended consequence, however, is that users get stuck in what is known as their own "echo chambers" when dealing with and feeding users back their preferences. These echo chambers can cause increasing perspective bias within users, making it difficult for users to understand differing opinions. This work aims to prepare a model that counteracts YouTube's recommendation system by forcefully exposing users to content from varying viewpoints. The SSKA pipeline (Suno Sabki, Karo Apni) is a complementary deep learning model that involves Natural Language Processing (NLP) and K-Means clustering. It utilizes modern software libraries such as the YouTube API (Application Programming Interface) for data collection and was trained and tested on a varied set of users. The results prove that the model is successful in decreasing the bias recommendation by exposing users to the content of varying opinions and helping them break away from their echo chambers. The proposed methodology of explicitly exposing users to the content of varying opinions can positively impact local societies and the global community.**

Keywords*— *Bidirectional Encoder Representations from Transformers (BERT), K-Means Clustering, Encoder, Google Universal Encoder (GUE), Polarity Co-efficient, Natural Language Processing (NLP)

I. INTRODUCTION

Ever since the origin of the user-centric internet, every big player has been trying to take a crack at learning user patterns and recommending them relevant content. This is done to increase user retention on their platforms. In the black-and-white days of the early 2000s, corporations such as Google, Instagram, and many more procured their learning and recommendation architectures [1]. These rudimentary architectures employed different types of language processing and pattern coupling to suggest content to users. However, even being purely text-based, these systems were often limited and were engulfed with various types of problems (such as biases or noise) [1]. The system would often suffer by giving weight to irrelevant patterns, and users would often be recommended content not particularly of interest. These problems would only be apparent for a platform as complex and intricate as YouTube.

In 2015, YouTube updated its learning and prediction architecture by incorporating deep learning [2]. In their early white paper, YouTube's team recognized three significant problems scale, freshness, and noise [2]. Scale refers to the sheer massiveness of the YouTube data set. The obstacle is that YouTube not only houses over a billion videos but has been growing at an increasing rate since its formation. Freshness refers to the need to stay true to modern trends. Users should always be provided with content that is not only relevant to their request but is closest to what is true at the time of searching. Finally, noise refers to the irrelevant pieces of data that can potentially guide the model toward drawing out contradictory or even untrue trends, patterns, and predictions. The overall YouTube recommendation and ranking of videos constituted two neural networks, candidate generation, and ranking [2]. Candidate generation takes past activity from individuals' history as input and produces a small subset from the relatively large collection. Candidate generation uses only collaborative filtering of data. The ranking algorithm finalizes the subset of videos by assigning a score to each video according to the desired objective function using a very large set of features. According to the YouTube white paper [2], millions of classes have been used to train the model. After ranking, the video with the highest score is presented first and accordingly. The amalgamation of the two methods results in a recommendation list from a very large collection of videos for everyone.

As understood, social media outlets utilize (amongst other methods) the recommendation system to increase user retention time. While modern recommendation systems are tasked with providing users with content relevant to the user, an unintended consequence of these systems is the reinforcement of "echo chambers" and widespread bias-based misinformation. The psychological presupposition [3], [4], [5] is that the above-mentioned phenomenon increases populace-based opinion polarity. Furthermore, people do not

Authorized licensed use limited to: DELHI TECHNICAL UNIV. Downloaded on May 11,2023 at 10:11:17 UTC from IEEE Xplore. Restrictions apply.

shy away from voicing their opinion on social media [6] if they truly believe in something. Effectively, content created by people is presented specifically to like-minded users, creating "echo chambers." The qualitative surveys that were conducted as a part of this research articulated said polarity. This entire phenomenon is no less a threat given the detrimental impact internet-based services have shown to have on youngsters, for example, with respect to their cognitive growth [7]. The aim is to utilize modern machine learning techniques to mitigate such biases and expose the public to diverse opinions. The speculation is that supplemented as a feature on social media platforms (YouTube for the sake of this paper), an explicit enumeration of content from differing views on a given topic can help reintroduce the said exposure. Furthermore, the hypothesis is that such exposure can bring down polarity levels amongst different users.

The first obstacle was to successfully extract meaning out of text (wherever it is being extracted from). Universally, this objective has been named "natural language processing" (NLP) and branches out to various use cases (including "sentiment analysis"). Around the 1960s, notable progress started [8] happening when researchers opened the gates to artificial intelligence-based methodologies by studying the more rule-based paradigm of natural languages [8]. Such methodologies include a rudimentary frequency count of words (coined the "Bag-of-words"' technique) and the Term Frequency-Inverse Document Frequency (TF-IDF) technique that works to reduce redundancy by ignoring common placeholder words such as "a," "the," "was," etc. However, it took the reintroduction of probabilistic and statistical methods (seen as the backbone of modern machine learning today) around the late 1980s to early 1990s [9] that really propelled the industry-level applicability of natural language processing research. It allowed researchers to incorporate the concept of error mitigation for the sake of simulating real "learning." This transition allowed researchers to dive into complex, statistically driven machine learning [9]. Roughly around early 2010 [10], researchers capitalized on the then-modern machines and started utilizing neural networks on NLP-based problems. True groundbreaking work in NLP occurred with the proposition of a technique that vectorizes words based on definition-based similarity (now commonly implemented using the Word2Vec library) [10]. The model essentially cracked the problem of understanding the context of words by introducing the continuous bag-of-words model and the continuous skip-gram model. At first, researchers jumped on the Recurrent Neural Network (RNN) bandwagon and tried to make progress. However, a major obstacle with RNNs was that they suffered long-term memory degradation. This was especially undesirable in the case of NLP.

A lasting obstacle has been opinion extraction. Online content is an immense pool of unending opinions. Much work has been done in trying to explicitly extract context-contingent words and deriving the closest approximation of intended opinion [11]. However, a revolution in general NLP occurred when researchers introduced the concept of "transformers." These architectural components work by using positional encoding, attention, and, more particularly, self-attention. While early neural networks using transformers made great progress, the most famous in the industry today are the Generative Pre-trained Transformer (GPT) [12], BERT [13], and the Text-to-Text Transfer Transformer (T5) [14] models, as shown in Fig 1.

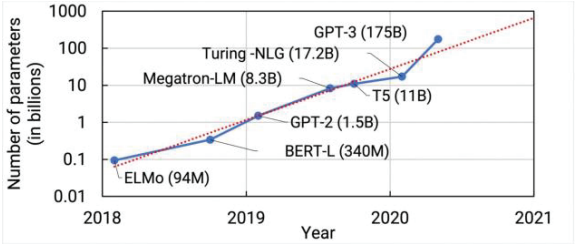


Fig. 1. Comparison of NLP-Models

Finally, the other relevant machine learning problem type is the unsupervised clustering objective. This problem type requires relative clustering of input data based purely on said data. The dimensionality of the clustering plane depends on the number of features. Researchers were quick in procuring a strong clustering model when they developed the K-Means clustering architecture [15]. This architecture, like most other architectures, takes in as many input features as needed and formulates a Cartesian coordinate for each entity. The so-called" clusters" form when entities (that share certain similar drivers) end up having coordinates closer to each other than entities that have genuinely different drivers. However, it also takes a constant "k" value that determines exactly how many clusters the given input data is to be divided into. Proposing the SSKA model; an amalgamation of the NLP BERT and the K- Means clustering architectures, the model utilizes state-of-the-art machine learning algorithms to classify videos relatively based on the user's choice, the topic at hand, and the public opinion. The model was then implemented as the brains of an entire Google Chrome extension that would detect when a user is currently watching a controversial video. It then prescribes an evenly divided set of random videos for different labels where the general idea behind the labelling is an indexing of different opinions and a potentially singular "neutral" opinion. As mentioned, the hypothesis is such that such an explicit exposure of videos with differing opinions will bring down opinion polarity levels amongst the public.

II. Architecture

Two subject matters were selected to procure the architecture, as shown in Fig 2, and ensure the model gets trained on recent development. Since the SSKA recommendation system works entirely on YouTube, the first order of business was to gather relevant videos for each topic. This was made possible by utilizing the official YouTube API.

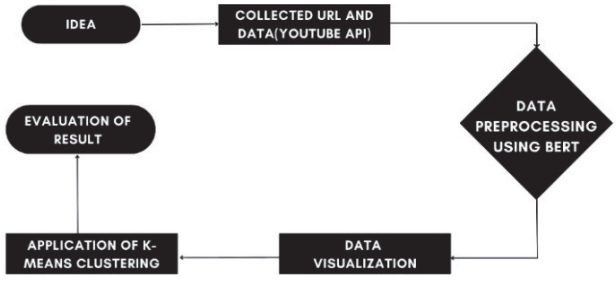


Fig. 2. Architecture of the SSKA Architecture

Authorized licensed use limited to: DELHI TECHNICAL UNIV. Downloaded on May 11,2023 at 10:11:17 UTC from IEEE Xplore. Restrictions apply.

Utilizing the YouTube API returned 575 video uniform resource locators (URL) for Topic 1 and 519 video URLs for Topic B. To output, the model mapped each video to one of three labels (this applies separately to each topic). Three videos were manually added, each discernibly representing an opinion (for each topic). The number of videos for Topic 1 was 578 and for Topic 2 was 522. The need for segregating exactly one video for each label will be explained later. These URLs were then saved in a list based on the topic they were on. Using the lists and going back to the YouTube API, all relevant text items were extracted from each video and stored (with respect to their videos) in their respective lists. At this point, the Topic 1 list constituted a size of 578 x 4, and the Topic 2 list constituted a size of 522 x 4, where the columns represent the title of the video, an identification value, the tags, the description, and the top five comments (based on likes).

The columns (other than the identification value) for each topic were then separately (based on topic) passed through the Google Universal Encoder. Primarily based on the BERT NLP algorithm, the GUE makes use of various modern techniques to vectorize textual input. As explained above, BERT makes use of positional encoding and self-attention to maximize context-based definition derivation of each word passed into it. In return, the GUE returns a complete enumeration of the words for each video. The dimensions of this enumerated list were 578 x 512 for Topic 1 and 522 x 462 for Topic B, where each row represented a video, and the corresponding columns made up the textual sentiment embedding. The number of columns (the size of the second dimension) is completely procured by the GUE's BERT model. The textual sentiment embedding is, in fact, the final features list and can be used in the next step of the machine learning architecture. However, as it can clearly be seen, the size of the features needs some space-based optimization. This is because, while modern hardware can easily handle the features list currently available, not only can the model work faster with a smaller feature size, but optimizing the size of the features list can help make it easier for the model to focus on only the most relevant parts of each feature. Reducing the feature size should help the model home in on the true drivers behind opinion-relevant sentiment rather than be distracted by the irrelevant "noise" (as it is called) surrounding said drivers. To mitigate all potential noise, the model utilizes Principal Component Analysis (PCA) on the enumerated data. The final dimensions of the features list of Topic 1 and Topic 2 were 578 x 288 and 522 x 260, respectively. Now, the encoder was ready to hand over the input data to the K-Means clustering model. While most of the difficult work with NLP was taken care of by the GUE, one of the best ways to show relative clusters was by simply utilizing K-Means. Fig 3 shows the K-Means clustering visualization of videos from the Topic 1 data frame for all the labels (each being color coded). It is important to note that the axis doesn't hold any contextual meaning relevant to the videos, their textual encoding, or the knowledge extraction from the textual encodings. Since the clustering was relatively successful in having little to no outliers, it wasn't necessary to procure and utilize a modified algorithm inspired by [16]. As mentioned, the architectural implementation was done on each topic separately. K-Means clustering simply recognizes trends between videos and allots similar videos closer to each other.

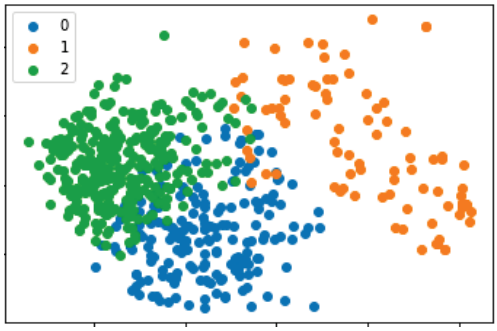


Fig. 3. Clusters formed on videos after applying SSKA from Topic 1

However, the K-Means clustering algorithm has no understanding of what the clusters mean. Thus, even a clear visual output without context meant there was no way to objectively discern which color represents which opinion. In the beginning of the architecture, when three videos were manually appended to the data frame of the topic (a video representing the extreme of an opinion), it came in handy to solve this lack of translation. Since the opinion name of the three videos was known, the derivation process can be reversed and the color output from the clustering algorithm can be renamed to reflect the opinion. This means, to return the actual opinion label for an output, the color labels returned by the K-Means algorithm must be renamed to the opinion they represent based on what the opinion of their respective "extreme" video holds. These extreme videos can be thought of as analogous to the "support vectors" found in the Support Vector Machine algorithm. This marks the completion of the machine-learning model. At this point, videos remotely relevant to the subject may be appended and the algorithm is expected to be able to map the video voicing a similar opinion or sentiment. This is because the clustering model works entirely based on the possibility of opinion derivation from the encoded textual data provided.

III. Implementation

Python data management and analysis libraries were imported and utilized. A script was then run to extract videos with respect to each of the two topics chosen. The videos were then stored in their respective data frames. An "extreme" video that could be arguably used to "represent" one of the views for each opinion is also appended to its respective data frame. Furthermore, a separate set of lists (one for each topic) was created that stores the label to the video believed to be representing it. With the complete list of YouTube video URLs, the YouTube API was used to extract textual data points for each video. The data points were stored related to their respective videos by appending columns to the two data frames. At this point, the data frames simply allocate each video with the text that makes up their title, their tags, their description, and their comments (top five based on likes). After cleaning up the data frames (removing null values and ensuring appropriate dimensionality), the model separately fed said data frames into the Google Universal Encoder. The GUE can take as input any form of textual data. While early BERT implementations used sentence-based embeddings, the model has advanced to the ability to take even a list of varying lengths of text (words, sentences, and even paragraphs). The BERT model ran multiple epochs that then

Authorized licensed use limited to: DELHI TECHNICAL UNIV. Downloaded on May 11,2023 at 10:11:17 UTC from IEEE Xplore. Restrictions apply.

started embedding the words of each textual data as one matrix (per video). The matrices are then passed back, and the original data frame is readjusted to accommodate the change in dimension. Now, for each topic, the videos in their respective data frames are paired with the sentiment-based textual embedding that has, within it, patterns matching videos with similar sentiments. This embedding is crucial (and is literally the very backbone of) the entire process of clustering the videos. However, as explained in the architecture, it was necessary to optimize the embeddings by extracting only the driving components and removing irrelevant components. To accomplish this, the Principal Components Analysis method from the "sklearn" module was imported, each data frame was passed through the PCA, and an optimization was observed (effectively decreasing the size of the second dimension for each data frame). Finally, from the "sklearn.cluster" module, the K-Means clustering model was imported. Since three opinions for each topic was decided upon (two completely opposite views/labels and one as the "neutral" view/label), the "n clusters" argument was set to three and the data frame fitting process was executed. One last time, the data frames were readjusted to have, instead of textual embeddings paired with each video, a final label representing where the video falls. However, the integer values being displayed in the labels' column don't hold any contextual meaning. To provide context, the list made in the beginning of the process, which stored an "extreme" video, labelled according to the opinion it represented, is required. Utilizing this list, it is possible to name the data frame each video is in with the label each video has been allotted (in the earlier list).

IV. Results and Discussion

To finally test the effectiveness of the model, it needed to be exposed to the public. After procuring the final clustering, the model was integrated with the front end and brought test subjects to use YouTube with and without the model. The front end would simply recommend a set of random videos that each belong to one of the labels. As explained, while YouTube brings recommendations strictly based on the patterns of personal preference for the user, the recommendation system lists videos belonging to each of the different labels prescribed. The test subjects were allotted to either one of the topics. Before using the extension, the users were tasked with watching videos YouTube was recommending them on the topic they were allotted for a constant period. Tabs were kept on how many videos of each opinion YouTube recommended for the test subjects. Based on the number of videos suggested, the polarity coefficient was calculated between the different videos.

Videos of one opinion were labelled "A," the opposing opinion labelled "B," and the neutral opinion labelled "N." Also, the number of videos under label A were denoted as vA, videos under label B denoted as vB, and videos under label N denoted as vN. The coefficient of polarization is calculated for each user by the given equation in (1).

$$|vA - vB| / (vA + vB + vN)| \quad (1)$$

Graphing the count of recommended videos (based on opinion) and the derived coefficient of polarity for each test subject results in the relations seen in Table I.

TABLE I. Results without Extension

ID	Age	Gender	Topic	Videos of Opinion A (vA)	Videos of Opinion B (vB)	Videos of a Neutral Opinion (vN)	Polarity Coefficient
1	49	Male	Article 370	11	0	1	91.67
2	49	Female	Article 370	3	13	0	62.5
3	16	Female	US Elections	2	13	1	68.75
4	54	Male	Article 370	6	1	0	71.43
5	25	Female	US Elections	2	9	1	58.33
6	18	Male	Article 370	4	9	3	31.25
7	51	Male	Article 370	2	8	6	37.5
8	42	Male	Article 370	6	3	1	30
9	36	Female	Article 370	10	4	3	35.29
10	55	Male	US Elections	13	2	10	44
11	20	Male	Article 370	5	0	4	55.56
12	25	Male	Article 370	10	4	7	28.57
13	21	Female	Article 370	1	8	10	36.84
14	38	Male	US Elections	1	9	3	61.54
15	19	Female	US Elections	6	4	9	10.53
16	30	Male	Article 370	3	0	3	50
17	27	Male	Article 370	9	2	5	43.75
18	46	Female	US Elections	7	3	5	26.67
19	47	Female	US Elections	11	3	1	53.33
20	35	Male	Article 370	8	2	3	46.15
21	30	Female	Article 370	2	9	6	41.18
22	28	Male	Article 370	8	5	3	18.75
23	52	Male	Article 370	1	7	1	66.67
24	36	Female	Article 370	3	9	2	42.86
25	24	Male	Article 370	9	5	8	18.18
26	49	Female	Article 370	10	2	4	50
27	38	Female	US Elections	4	12	6	36.36

Authorized licensed use limited to: DELHI TECHNICAL UNIV. Downloaded on May 11,2023 at 10:11:17 UTC from IEEE Xplore. Restrictions apply.

TABLE II. RESULTS WITHOUT EXTENSION

ID	Age	Gender	Topic	Videos of Opinion A (vA)	Videos of Opinion B (vB)	Videos of a Neutral Opinion (vN)	Polarity Coefficient
1	49	Male	Article 370	7	4	3	21.43
2	49	Female	Article 370	5	1	6	33.33
3	16	Female	US Elections	2	8	2	50
4	54	Male	Article 370	7	3	0	40
5	25	Female	US Elections	5	4	7	6.25
6	18	Male	Article 370	4	6	2	16.67
7	51	Male	Article 370	6	3	5	21.43
8	42	Male	Article 370	4	4	6	0
9	36	Female	Article 370	4	9	7	25
10	55	Male	US Elections	5	7	7	10.53
11	20	Male	Article 370	6	5	3	7.14
12	25	Male	Article 370	8	3	10	23.81
13	21	Female	Article 370	5	4	9	5.56
14	38	Male	US Elections	6	4	7	11.76
15	19	Female	US Elections	6	5	7	5.56
16	30	Male	Article 370	4	7	3	21.43
17	27	Male	Article 370	5	6	8	5.26
18	46	Female	US Elections	3	4	5	8.33
19	47	Female	US Elections	8	5	7	15
20	35	Male	Article 370	4	6	6	12.5
21	30	Female	Article 370	5	7	8	10
22	28	Male	Article 370	4	4	4	0
23	52	Male	Article 370	6	3	7	18.75
24	36	Female	Article 370	4	5	4	7.69
25	24	Male	Article 370	3	5	4	16.67
26	49	Female	Article 370	7	6	4	5.88
27	38	Female	US Elections	6	8	14	7.14

TABLE III. ABSOLUTE AND PERCENTAGE REDUCTION IN POLARITY AFTER USING THE EXTENSION

ID	Age	Gender	Topic	Reduction in Polarity after Using Extension	Percentage Reduction in Polarity After Using the Extension
1	49	Male	Article 370	70.24	76.62
2	49	Female	Article 370	29.17	46.67
3	16	Female	US Elections	18.75	27.27
4	54	Male	Article 370	31.43	44
5	25	Female	US Elections	52.08	89.29
6	18	Male	Article 370	14.58	46.66
7	51	Male	Article 370	16.07	42.85
8	42	Male	Article 370	30	100
9	36	Female	Article 370	10.29	29.16
10	55	Male	US Elections	33.47	76.07
11	20	Male	Article 370	48.42	87.15
12	25	Male	Article 370	4.76	16.66
13	21	Female	Article 370	31.28	84.91
14	38	Male	US Elections	49.78	80.89
15	19	Female	US Elections	4.97	47.2
16	30	Male	Article 370	28.57	57.14
17	27	Male	Article 370	38.49	87.98
18	46	Female	US Elections	18.34	68.77
19	47	Female	US Elections	38.33	71.87
20	35	Male	Article 370	33.65	72.91
21	30	Female	Article 370	31.18	75.72
22	28	Male	Article 370	18.75	100
23	52	Male	Article 370	47.92	71.88
24	36	Female	Article 370	35.17	82.06
25	24	Male	Article 370	1.51	8.31
26	49	Female	Article 370	44.12	88.24
27	38	Female	US Elections	29.22	80.36

Authorized licensed use limited to: DELHI TECHNICAL UNIV. Downloaded on May 11,2023 at 10:11:17 UTC from IEEE Xplore. Restrictions apply.

After some time, a qualitative survey of all the test subjects was taken and their opinions were mapped to their allotted topic. Then, the users were tasked with watching videos on the same subject, but now with the SSKA extension activated. The test subjects were only allowed to watch videos recommended to them from the front end of the extension. Again, the count of recommended videos and derived coefficient values were graphed to get Table II.

The model searched randomly and gave the test subjects a set of relevant videos from each label, as expected. The video links were recorded and, after conducting the experiment for a period, a qualitative survey of the overall experience of each test subject was taken. Several test subjects that had once insisted on watching videos closer to their opinion, expressed genuine interest in content from the "other side". Table III shows the absolute and percentage-based polarity change between the recommended videos with and without the SSKA extension.

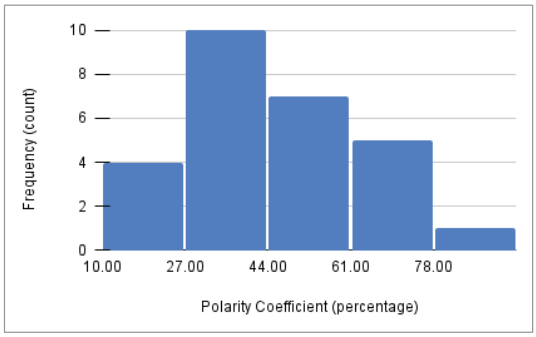


Fig. 4. Frequency of videos for different polarity ranges (without extension)

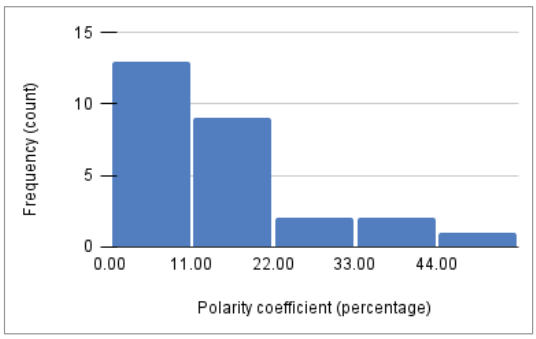


Fig. 5. Frequency of videos for different polarity ranges (with extension)

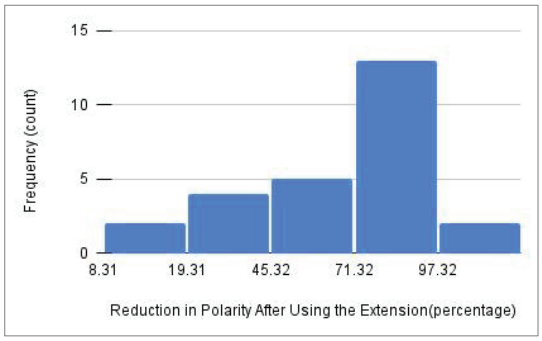


Fig. 6. No. of users experiencing percentage reduction in polarity

To drive the point, a clear visual difference between Figs 4 and 5 can be observed. Fig 4 represents the frequency of videos shown in different polarity ranges without the extension; Fig 5 shows the frequency in polarity ranges with the extension. Both histograms map the polarity range to the frequency of exposure based on the recommendation system used.

As can be seen, the frequency of exposure for more extensive polarity ranges decreased drastically, whereas the frequency of lower polarity ranges increased just as drastically. This difference has been mapped in Fig 6, where the different percentage reductions of polarity and how many users experienced it are shown.

V. Conclusion

The SSKA architecture was proposed; with the intent of extensively bias-based content exposure as seen on YouTube. The model learns and presents YouTube content based on varying opinions, effectively decreasing the observable polarity in the view of users. It searches for relevant videos to a topic and divides videos based on their different views. It then exposes users to this new set of recommendations. The results have clearly shown a reduction in the polarity of views of the subjects, thus showing great potential in helping people appropriately acknowledge views they may be biased against. For example, one test subject exclaimed how "invested," they had become "in the humanness behind the opinion opposing my own."

In contrast, another test subject admitted that "great industrial potential exists in the application." The qualitative evidence of the frequency shift, as seen in the interviews taken of the test subjects, gives hope of greater harmony amongst people, caused simply by the ability to understand where the many perspectives on a subject matter are coming from. Walking in another's shoes is an old and proven way of increasing understanding and wisdom among the average human. However, there is no doubt that much more can be accomplished with the SSKA model. The model needs to be adaptable to other social media outlets and other types of content, and it needs extensive work in its feature set.

The technologically meaningful and psychologically healthy growth as a potential of this model and its implementation in the proposed problem set gives great hope. This model should be a source for much development in the field of polarity mitigation, effectively decreasing individual bias and misinformation across the world. The technology used can find a place and grow in all types of systems (even outside of social media recommendation systems). Whether that be increasing the label columns and textual embeddings (to support the ability of representing more views and opinions) or implementing the model on different technology systems (such as native apps, cloud-based systems, or even fully fledged artificial intelligence networks).

References

[1] J. Liu, E. Pedersen, and P. Dolan, 'Personalized News Recommendation Based on Click Behavior', in 2010 International Conference on Intelligent User Interfaces, 2010.

[2] P. Covington, E. Sargin, and J. Adams, "Deep Neural Networks for YouTube recommendations," Deep Neural Networks for YouTube Recommendations. Available: https://static.googleusercontent.com/media/research.google.com/en//pubs/archive/45530.pdf.

Authorized licensed use limited to: DELHI TECHNICAL UNIV. Downloaded on May 11,2023 at 10:11:17 UTC from IEEE Xplore. Restrictions apply.

[3] F. P. Santos, Y. Lelkes, and S. A. Levin, "Link recommendation algorithms and dynamics of polarization in online social networks," Proceedings of the National Academy of Sciences, vol. 118, no. 50. Dec. 06, 2021. doi: 10.1073/pnas.2102141118.

[4] A. Matakos, E. Terzi, and P. Tsaparas, "Measuring and moderating opinion polarization in social networks," Data Mining and Knowledge Discovery, vol. 31, no. 5. Springer Science and Business Media LLC, pp. 1480–1505, Jul. 15, 2017. doi: 10.1007/s10618-017-0527-9.

[5] J. Cho, S. Ahmed, M. Hilbert, B. Liu, and J. Luu, "Do Search Algorithms Endanger Democracy? An Experimental Investigation of Algorithm Effects on Political Polarization," Journal of Broadcasting & Electronic Media, vol. 64, no. 2. Informa UK Limited, pp. 150–172, Apr. 27, 2020. doi: 10.1080/08838151.2020.1757365.

[6] G. Vashisht and Y. N. Sinha, "Sentimental Study of CAA by location-based tweets," International Journal of Information Technology, vol. 13, no. 4, pp. 1555–1567, March. 22, 2021 doi: 10.1007/s41870-020-00604-8.

[7] G. Tripathi and M. A. Ahad, "Impact of excessive use of internet on cognitive development of youngsters," International Journal of Information Technology, vol. 9, no. 3, pp. 281–286, July. 22, 2017. doi: 10.1007/s41870-017-0028-5.

[8] NLP - Overview. Available: https://cs.stanford.edu/people/eroberts/courses/soco/projects/2004-05/nlp/overview_history.html.

[9] G. W. Blackwood, "Lattice rescoring methods for statistical machine translation: Semantic scholar," Semantic Scholar, 01-Jan-1970. Available:https://ethos.bl.uk/OrderDetails.do?uin=uk.bl.ethos.596707

[10] T. Mikolov, K. Chen, G. Corrado, and J. Dean, "Efficient estimation of word representations in vector space," arXiv.org, 07-Sep-2013. Available: https://arxiv.org/abs/1301.3781.

[11] T. K. Tran and T. T. Phan, "Mining opinion targets and opinion words from online reviews," International Journal of Information Technology, vol. 9, no. 3, pp. 239–249, Jul. 31, 2017. doi: 10.1007/s41870-017-0032-9.

[12] A. Radford and K. Narasimhan, "Improving language understanding by generative pre-training: Semantic scholar," undefined, 01-Jan-1970. Available: https://gwern.net/doc/www/s3-us-west-2.amazonaws.com/d73fdc5ffa8627bce44dcda2fc012da638ffb158.pdf .

[13] J. Devlin, M.W. Chang, K. Lee, and K. Toutanova, BERT: Pre-training of Deep Bidirectional Transformers for Language Understanding Proceedings of the 2019 Conference of the North, 2019. doi: 10.18653/v1/n19-1423.

[14] C. Raffel et al., "Exploring the Limits of Transfer Learning with a Unified Text-to-Text Transformer." arXiv, 2019. doi: 10.48550/ARXIV.1910.10683.

[15] C. Ding and X. He, "K-Means Clustering with Distributed Dimensions," Twenty-first international conference on Machine learning - ICML '04, 2004. doi: 10.1145/1015330.1015408.

[16] S. K. Sahu, P. Kumar, and A. P. Singh, "Modified K-NN algorithm for classification problems with improved accuracy," International Journal of Information Technology, vol. 10, no. 1, pp. 65–70, 2017, Nov. 11, 2017. doi: 10.1007/s41870-017-0058-z.

Authorized licensed use limited to: DELHI TECHNICAL UNIV. Downloaded on May 11,2023 at 10:11:17 UTC from IEEE Xplore. Restrictions apply.

2023 6th International Conference on Information Systems and Computer Networks (ISCON)
GLA University, Mathura, India. Mar 3-4, 2023

2023 6th International Conference on Information Systems and Computer Networks (ISCON) | 979-8-3503-4696-1/23/$31.00 ©2023 IEEE | DOI: 10.1109/ISCON57294.2023.10112085

MonkeyPox, Measles and ChickenPox Detection through Image-Processing using Residual Neural Network (ResNet)

Kapil Sharma
Dept of Computer Science and Engineering
Delhi Technological University
New Delhi, India
kapilsharma7575@gmail.com

Kishlay
Dept of Computer Science and Engineering
Delhi Technological University
New Delhi, India
kishlay1105@gmail.com

Mayank Mittal
Dept of Computer Science and Engineering
Delhi Technological University
New Delhi, India
mayankmittal1410@gmail.com

Vinod Kumar
Dept of Computer Science and Engineering
Delhi Technological University
New Delhi, India
vinod_k@dtu.ac.in

***Abstract*—Timely detection of Measles, Mpox (Monkeypox), and Chickenpox can help in effective treatment and computer-aided decision-making for faster diagnosis. In today's scenario, measles is spreading throughout India and Mpox is spreading worldwide. This issue requires a solution because it has the potential to grow into a major problem in the future and even cause a pandemic. The contribution of Deep Learning to large-scale medical data research has been invaluable, offering new approaches and opportunities for diagnostic techniques. In this research-based project, we tried to explore how deep learning models such as CNNs and Residual Neural Networks (ResNets) using datasets containing images of skin lesions can be used to classify various Measles, ChickenPox and MonkeyPox. We tried to highlight the challenges (including dataset size and quality) in using the publicly available "Monkeypox Skin Lesion Dataset (MSLD)" to develop our Proposed ResNet model and then compare the results of VGG 16, Inception V3 and CapsuleNet. Images used in the dataset are collected through various sources by web scraping. To increase the sample size, we have used data augmentation. We have developed a custom RESNET-18-based model and compared it with various other models such as VGG-16, RESNET-50, InceptionV3, Ensemble etc. Our model achieved an accuracy of 84.59% in the classification of monkeypox, measles and chickenpox.**

Keywords—pox classification, monkeypox, measles, chickenpox, Deep Learning

I. INTRODUCTION

In 2019 Novel Corona Virus started spreading and affected the whole world. WHO has confirmed more than 660 million cases and more than 6 million deaths till now [1]. The COVID-19-affected aftereffects, whether social or economic, are still evident as of 2022. Being an infectious disease, COVID has a significant impact on our daily lives. Lockdowns were announced all across the world to stop this, which hindered economic activity and caused many people to lose their employment.

Several people were forced into poverty due to employment losses, and now that COVID is nearly completely contained, the monkeypox disease now known by the WHO as Mpox is spreading throughout many western nations. As a result, it has been deemed a public health emergency. Though Mpox till now has not affected India in the way it did in countries like the USA, Canada, etc, however measles which is another type of pox-causing disease has started to pop up in some parts of India like Mumbai, UP, and Bihar. Monkeypox virus causes a disease that is of less severity than smallpox. Monkeypox before spreading in the world could be found in two African regions known as West African Clade and Central African Clade [2]. CDC states [3], there are some key characteristics that differentiate Mpox from chickenpox and measles. Mpox lesions are firm, circumscribed, and develop a umbilication. They generally occur in areas near the genital or in the mouth. The lesions are painful and go through different stages before scabbing over. The various stages of lesions are Enanthem, Macules, Papules, and Vesicles which have a duration of 1-2 days each, and then Pustules which last for 5-7 days. Mpox illness period is 2-4 weeks and severity depends on the initial health of the individual.

According to WHO [3], Measles is a disease that spreads through contact. A vaccine for measles was invented in 1963 which prevented epidemics that used to occur at the interval of every 2-3 years. These epidemics used to kill at least 2 million people each time. Most of the people who died in these epidemics were children. Even now, since the vaccine has been invented a few years ago, children are the prime target of this disease, as seen in Maharashtra, India in 2022, measles took the lives of at least 700 children.

The CDC has warned [4] people of all age groups about measles, although according to it children in the age group below 5 years and adults above 20 years old along with pregnant women and people with comparatively weakened immune systems owing to diseases like HIV/AIDS are more prone to risks. According to WHO [3], during the initial time of Measles, one might have a high fever initially, following which white spots inside the cheeks, cough, or a runny nose might be there as well. Once several days have passed rashes begin to erupt. They generally start with the face and the

Authorized licensed use limited to: DELHI TECHNICAL UNIV. Downloaded on May 11,2023 at 10:13:23 UTC from IEEE Xplore. Restrictions apply.

neck but over the next 3 days spread to the hand and feet too. These rashes last for about 6 days and then fade away.

According to WHO [5], chickenpox is a highly contagious disease that transmits through droplets, aerosols, or direct contact with respiratory secretion. It is mid in childhood but can be severe in adults. According to CDC [6], chickenpox lasts about 4 to 7 days and symptoms are rash that turns into crust-like things. The pimples first occur on the chest, followed by the back before spreading over the entire body. Chicken pox symptoms that occur after a rash are fever, tiredness, loss of appetite, and headache.

Deep learning algorithms like CNN are proven to be quite effective in the medical profession. The CNN-based model correctly categorized Covid and Non-Covid Lung Xrays. Similarly, we may utilize deep learning models to assist us to determine if the skin lesion is caused by Chickenpox, Monkeypox, or Measles. In this study, we used the Monkeypox Skin Lesion Dataset (MSLD) [7] and created a ResNet-based architecture, which gives an accuracy of 84% ± 1.5% and f1 score of 84% ± 1.5% on the enhanced train data.

II. Related Work

Many researchers have recently used various deep-learning approaches for monkeypox detection. In [7], the authors have used Monkey Pox Skin Lesion Dataset and have employed pre-trained VGG16, Resnet50, and InceptionV3 deep learning techniques which gave an accuracy of 81.48%, 82.59%, and 74.07% respectively. They also developed their own ensemble model giving an accuracy of 79.26%.

In [8], the author has tried to integrate CBAM which is a convolutional block attention module to do the classification of monkeypox disease in humans. They have implemented various models such as EfficientNetB3, Xception, VGG19, MobileNetV2, and DenseNet121 and have integrated CBAM layers which gave a validation accuracy of 83.89%.

In [9], the authors first developed their own dataset which they have used to train their ML models for the classification of monkeypox. Further, they modified VGG 16 which achieved an accuracy of 83%. Apart from this, they tested their model on an imbalanced dataset which gave an accuracy of 78%.

In [14], the study focused on the use of transfer learning techniques in medical image processing. It showed how the Resnet-50 model could be used in chest X-rays, and how this could lead to the development of an accurate and fast COVID-19 detection system. It is believed that this technology could help in addressing the current screening and diagnosing issues related to COVID-19. The proposed model was able to achieve a 96 percent accuracy rate and was very sensitive to the data.

III. Proposed Work

A. Convolutional Neural Network

CNNs are part of deep learning algorithms that are particularly well-suited for image and video recognition tasks [10]. The organization of the visual cortex in humans is allegedly said by many to be the inspiration for them. They can learn filters that can identify specific aspects of an image. This enables them to differentiate between objects in an image and perform tasks such as object recognition and image classification [14].

CNN architecture is composed of several layers, each of which performs a specific function. The convolutional layer, which is the first layer of CNNs, aims at extracting the features of the input image(s) provided. The next layer, the pooling layer, reduces the dimensions by trying to summarize the information it got from the previous layer. The final layer i.e. the fully-connected (FC) layer makes use of the results from previous layers to classify the image [15].

Compared to other neural network architectures, CNNs have several advantages. First, they can capture spatial and temporal dependencies in an image, which enables them better to understand the relationships between different parts of the image. Second, they require less preprocessing than other methods, which makes them more efficient. Finally, they can learn filters that are more effective than hand-engineered filters, which leads to better performance on image recognition tasks. Overall, CNNs have proven to be a powerful tool for image and video recognition [16].

B. Residual Neural Network

Researchers have found [11], that convolutional neural networks are more effective when they have a deeper structure. This is because deeper networks have a larger parameter space and can adapt to a wider range of data. However, after a certain depth, the performance of these networks begins to degrade. This problem was one of the limitations of the VGG network, which was unable to achieve the desired depth without losing its generalization ability.

With the advent of residual networks [12], often known as ResNets, the issue of training incredibly deep networks has been overcome. These networks are made up of residual blocks, each of which has a special "skip connection" that omits a layer or layers. The output of the layer can be different than it would have been without this skip link thanks to it. If skip connections are not included, we get H(x) by adding bias after multiplying x with the weight of layers, and then we passed it through the activation function f(x) in equations 1,2.

$$H(x) = f(wx+b) \tag{1}$$

$$H(x) = f(x) \tag{2}$$

Output changes to the following after including skip connections in equation 3:

$$H(x) = f(x) + x \tag{3}$$

Padding to extend the dimensions of the skip connection is one technique to solve the problem of mismatched dimensions between the input and output of a convolutional or pooling layer. Projection is the method in which we give 1x1 convolutional layers to the input which get matched to the output's dimension.

$$H(x) = f(x) + w1.x \tag{4}$$

As one could observe, an extra parameter has been added in equation 4. Resnet uses skip connections to overcome the problem of vanishing gradient due to which we were able to

Authorized licensed use limited to: DELHI TECHNICAL UNIV. Downloaded on May 11,2023 at 10:13:23 UTC from IEEE Xplore. Restrictions apply.

train models with large depths without performance issues. The extra layers that we added learn the identity function such that it doesn't degrade the performance in comparison to the ordinary CNN. This guarantees that the output of these layers is equivalent to their input, preventing performance deterioration despite the complexity-added complexity of additional levels. This method allows us to retain the shallow network's performance while also taking advantage of the deep network's increased capacity. Layers have been seen to rapidly acquire identity functions when residual blocks are present. It is evident from the formulas provided in the above equations. The outcome in simple networks is:

$$H(x) = f(x) \tag{5}$$

Therefore, f(x) must equal x to learn an identity function in equation 5, which is more difficult to do than ResNet, which gives the following output in equations 6,7 and 8:

$$H(x) = f(x) + x \tag{6}$$

$$f(x) = 0 \tag{7}$$

$$H(x) = x \tag{8}$$

Setting f(x) = 0 is all that is necessary when input is equal to get x as the output in equation 7.

In the best situation, adding layers to the neural network can greatly minimize the error and offer a more accurate approximation of the mapping to output 'y' from input 'x'. As a result, we believe ResNet will perform on par with or better than the fundamental deep neural networks. plain-34 has a much higher error% than ResNet-34 in networks with 34 layers, which is a considerable difference.ResNet18 is a convolutional neural network (CNN) architecture that was developed by Microsoft researchers and introduced in a paper published in 2016. The name "ResNet" is short for "Residual Network," and the "18" states the number of layers in the network. Additionally, ResNet-18 and plain-18 have nearly identical error percentages [17].

C. The Dataset

In order to classify monkeypox from chickenpox and measles, we used the Monkeypox Skin Lesion Dataset (MSLD) [13].

This dataset is comprised of 228 images of measles and chickenpox, some of which could be seen in Fig 1 provided below. The chosen dataset contains both original as well as augmented images, split into Train and Test sets with proportions of 70:30. Fig 2 and Fig 3 show the distribution of data belonging to different classes used for training and testing purposes.



Fig. 1. Chicken Pox Skin Lesion Sample, Measles Skin Lesion Sample, and MonkeyPox Skin Lesion Sample from MonkeyPox Skin Lesion Dataset

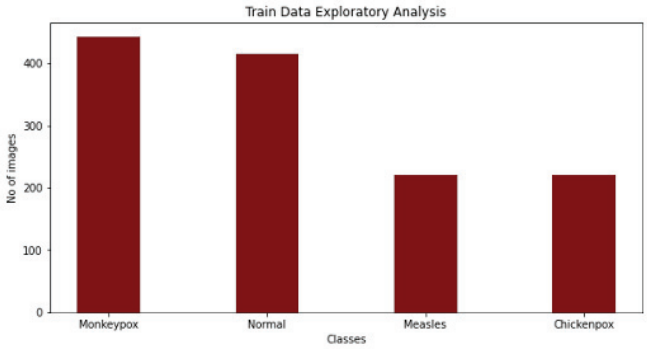


Fig. 2. Bar graph representation of the distribution of images from Monkeypox, Measles, Chickenpox, and Normal class used in training the model

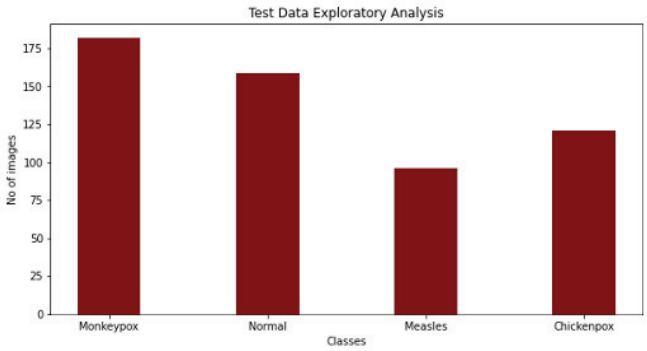


Fig. 3. Bar graph representation of the distribution of images from Monkeypox, Measles, Chickenpox, and Normal class used in testing the model

D. Image Pre-Processing

To preprocess the images, the following steps were performed:

1) Data Augmentation
2) Resizing images to 128 by 128 pixels
3) Converting the images to grayscale

E. Implementation

We have already seen that the results given to us by CNNs increase as we go deeper or in other terms increase the number of layers but this happens only up to a certain point after which this technique does not prove fruitful. This is due to a phenomenon called Vanishing gradient, which causes the gradients to be either too small or too large resulting in an increase in the magnitude of the error.

The ResNets solved this issue by introducing something known as the Residual Blocks. The networks containing these used the technique of skip connections [18]. The skip connections as the name suggest used to skip some of the

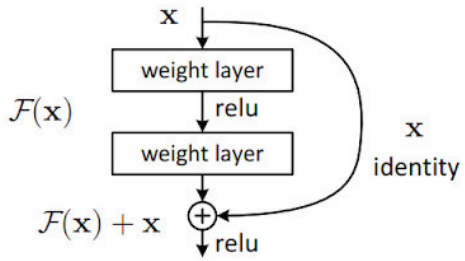


Fig. 4. Skip Connections

Authorized licensed use limited to: DELHI TECHNICAL UNIV. Downloaded on May 11,2023 at 10:13:23 UTC from IEEE Xplore. Restrictions apply.

layers and connect the activation of the current layers to a layer further ahead. This has been discussed in detail in the previous sections as well. Fig. 4 also encapsulates the concept visually.

The base model used in our project is Resnet-18, where the latter numerical signifies that the Resnet has 18 deep layers (and 72 architectural layers). During our project, we tried experimenting with additional layers as well. Observing the effects of various types of layers of varying sizes and activation functions, we concluded that the addition of three linear layers after the fully connected layer of our Resnet yielded the best possible results. There was a downgrade in the result on both increasing as well as decreasing the number of additional linear layers. Among the activation functions tried and tested, the ReLu function gave the best results and hence was used as an activation function in all three linear layers.

The model comprises around 11.7 million trainable parameters. A different number of optimizers were tested as well including the Adam optimizer, SGD optimizer, and the others available with the torch library. The use of SGD optimizer yielded the best results and was hence used in the study. It is a variant of gradient descent, which is an iterative method that finds the minimum of a function by taking small steps in the direction of the negative gradient. In SGD, the gradient is calculated using a single training example, rather than using the entire training dataset as in standard gradient descent. This makes SGD much faster and more efficient, particularly for large datasets [19].

IV. Experiments and Results

A. Dataset and Setup

The MonkeyPox Skin Lesion Dataset(MSLD) [7] has been used to classify monkeypox among chickenpox, measles, and monkeypox. The Monkey Pox Skin Lesion Dataset was assembled by gathering and adjusting images from numerous websites, news portals, and openly available case reports. Table I provides details on the dataset. The trials were carried out on Google Colab, and a Python program called PyTorch was used to create the ResNet-based model. Table II shows the hyperparameters of the proposed model.

TABLE I. Dataset Description

Classes	Chickenpox	Measles	Monkeypox	Normal
No. of images	329	313	630	585
Size of images	256 by 256	256 by 256	256 by 256	256 by 256

TABLE II. Hyperparameter Tuning

Epochs	50
Training Batch Size	10
Test Batch Size	12
Learning Rate	0.001
Optimizer	SGD
Loss	Cross Entropy Loss

B. Evaluation Metrics

The most prominent statistical methods, including accuracy, precision, recall, and F1-score, are employed to measure and present the overall experimental outcome [20].

- Accuracy: Metric used to evaluate how often a model predicts correctly.
- Precision: Metric that counts the proportion of accurate positive predictions a model makes out of all positive ones.
- Recall: Metric that determines the number of accurate positive predictions a model made out of all real positive cases.
- F1 Score: Metric that combines Precision and Recall into one measurement by taking their harmonic mean. A higher F1 score denotes a better balance between recall and precision. It is usually used for binary categorization tasks.

C. Results

We divided the dataset used into 70% training and validation samples and 30% testing samples. We simultaneously validated the weights and trained the model. Fig. 5 displays the training and validation accuracy. The evaluation criteria are displayed in Table III and include recall, precision, class-wise, and averaged F-measures.

D. Comparative Analysis

We compared our model with modern models used for monkeypox classification. In [7], transfer learning was applied to pre-trained VGG16, ResNet50, and InceptionV3 models, achieving accuracies of 81.48%, 82.96%, and 74.07%, respectively. The authors also developed their own ensemble model, which achieved an accuracy of 79.26%. In [8], the Xception BAM-Dense model was proposed, achieving an accuracy of 83.39%. Table IV provides the summarized comparative results. The ResNet-based model proposed in this study yields.

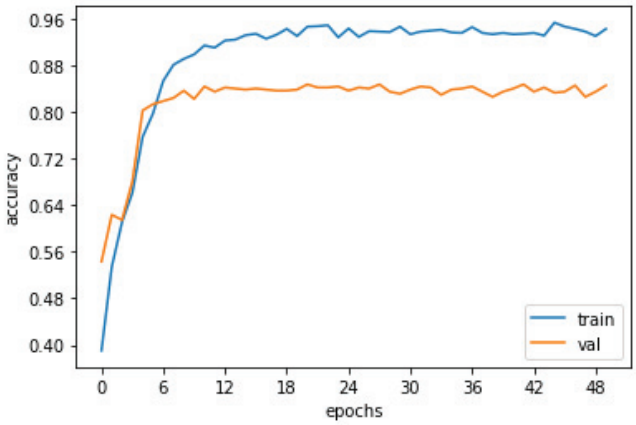


Fig. 5. accuracy curve of proposed model on Monkeypox Skin Lesion Dataset

TABLE III. Accuracy, Precision, Recall, and F1 Score of the Proposed Model on MLSD.

Accuracy	Precision	Recall	F1 Score
84.59	84.67	84.59	84.63

Authorized licensed use limited to: DELHI TECHNICAL UNIV. Downloaded on May 11,2023 at 10:13:23 UTC from IEEE Xplore. Restrictions apply.

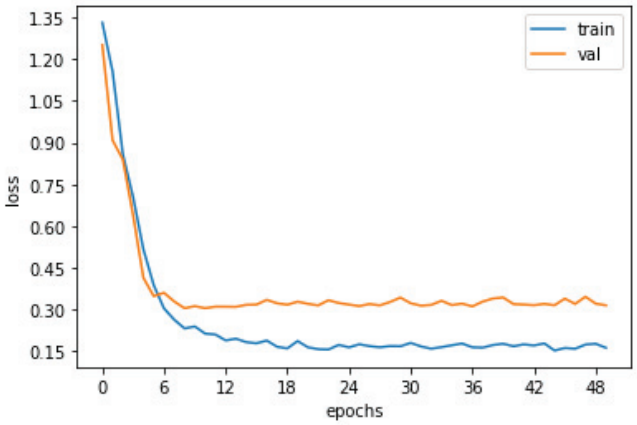


Fig. 6. . loss curve of proposed model on Monkeypox Skin Lesion Dataset

V. CONCLUSION

In the study that was performed, our proposed model was used to detect Monkeypox, measles, and chickenpox through images of skin lesions of patients of different classes by using the Monkeypox Skin Lesion Dataset (MSLD). We have augmented the images and aimed that no infected person is classified in any other way. Preliminary analysis can be done by medical experts with the help of this study. In this study we have concluded that for less complex and smaller datasets, ResNets is more effective than other CNN equivalents. Less training data is required to train ResNets because they are capable of recognizing the spatial arrangement. The proposed study produced superior findings compared to other studies using the same dataset. One of the major drawbacks to the proper training of the proposed model is the extremely small number of original images of Monkeypox and other diseases in the dataset. In future, we hope to design a more optimized model and train it on larger datasets of human lesion disease images. There is a limited database for Monkeypox as it is new in medical research and therefore calls for effective methodologies that could yield promising results to avoid overfitting and enhance the classifier's generalizability. We are also hoping for the development of new methods for feature extraction [21] and representation that are better suited to the specific characteristics of the images being classified, such as using wavelets or other transforms to capture spatial and spectral information more accurately.

TABLE IV. SUMMARIZED COMPARATIVE RESULTS

Paper	Model	Dataset	Accuracy
Monkeypox Skin Lesion Detection Using Deep Learning Models: A Feasibility Study [7]	VGG16 ResNet50 InceptionV3 Ensemble	Monkey Pox Skin Lesion Dataset	81.48% 82.96% 74.07% 79.26%
Classification of Human Monkeypox Disease Using Deep Learning Models and Attention Mechanisms [8]	Xception BAM-DenseModel	Monkey Pox Skin Lesion Dataset	83.39 %
Image Data collection and implementation of deep learning-based model in detecting Monkeypox disease using modified VGG16 [9]	VGG 16 based Model	Monkeypox 2022 dataset	83%
Our Study	**ResNet18 Based Model**	**Monkey Pox Skin Lesion Dataset**	**84.59%**

REFERENCES

[1] Who coronavirus (COVID-19) dashboard (2022) World Health Organization. World Health Organization. Available at: https://covid19.who.int/ (Accessed: January 12, 2023).

[2] Who director-general declares the ongoing monkeypox outbreak a public health emergency of international concern (2022) World Health Organization. World Health Organization. Available at:https://www.who.int/europe/news/item/23-07-2022-who-director-general-declares-the-ongoing-monkeypox-outbreak-a-public-health-event-of-international-concern (Accessed: January 12, 2023).

[3] Measles (2019) World Health Organization. World Health Organization. Available at: https://www.who.int/news-room/fact-sheets/detail/measles (Accessed: January 12, 2023).

[4] Measles signs and symptoms (2020) Centers for Disease Control and Prevention. Centers for Disease Control and Prevention. Available at: https://www.cdc.gov/measles/symptoms/signs-symptoms.html (Accessed: January 12, 2023)..

[5] Varicella (2016) World Health Organization. World Health Organization. Available at: https://www.who.int/teams/health-product-policy-and-standards/standards-and-specifications/vaccine-standardization/varicella (Accessed: January 12, 2023).

[6] About chickenpox (2022) Centers for Disease Control and Prevention. Centers for Disease Control and Prevention. Available at: https://www.cdc.gov/chickenpox/about/index.html (Accessed: January 12, 2023).

[7] Ali, S. N., Ahmed, M. T., Paul, J., Jahan, T., Sani, S. M. Sakeef, Noor, N., & Hasan, T. (2022). Monkeypox Skin Lesion Detection Using Deep Learning Models: A Preliminary Feasibility Study. arXiv preprint arXiv:2207.03342.

[8] Haque, Md. E., Ahmed, Md. R., Nila, Razia S., and Salekul Islam. (2022) "Classification of Human Monkeypox Disease Using Deep Learning Models and Attention Mechanisms." arXiv preprint arXiv:2211.15459..

[9] Ahsan, Md M., Uddin, Muhammad R., Farjana, Mithila, Sakib, Ahmed N., Momin, Khondhaker A., and Shahana A. Luna. (2022) "Image Data collection and implementation of the deep learning-based model in detecting Monkeypox disease using modified VGG16." arXiv preprint arXiv:2206.01862.

[10] S. M. Bujar Baruah, U. Hazarika, and S. Roy, “Edge detection and segmentation type responses in primary visual cortex,” Lecture Notes in Networks and Systems, pp. 141–148, 2022..

[11] K. He, X. Zhang, S. Ren, and J. Sun, “Deep residual learning for image recognition,” 2016 IEEE Conference on Computer Vision and Pattern Recognition (CVPR), 2016.

[12] F. He, T. Liu, and D. Tao, “Why resnet works? residuals generalize,” IEEE Transactions on Neural Networks and Learning Systems, vol. 31, no. 12, pp. 5349–5362, 2020.

[13] V. Sreejith and T. George, “Detection of COVID-19 from chest X-rays using resnet-50,” Journal of Physics: Conference Series, vol. 1937, no. 1, p. 012002, 2021.S. Cerutti, and A. M. Bianchi, “Detection of sleep

[14] apnea from surface ECG based on features extracted by an autoregressive model,” in 2007 29th Annual International Conference of the IEEE Engineering in Medicine and Biology Society, IEEE, Aug. 2007.

[15] R. Yamashita, M. Nishio, R. K. Do, and K. Togashi, “Convolutional Neural Networks: An overview and application in Radiology,” Insights into Imaging, vol. 9, no. 4, pp. 611–629, 2018.

[16] S. Albawi, T. A. Mohammed, and S. Al-Zawi, “Understanding of a convolutional neural network,” 2017 International Conference on Engineering and Technology (ICET), 2017.

Authorized licensed use limited to: DELHI TECHNICAL UNIV. Downloaded on May 11,2023 at 10:13:23 UTC from IEEE Xplore. Restrictions apply.

[17] R. Chauhan, K. K. Ghanshala, and R. C. Joshi, “Convolutional Neural Network (CNN) for Image Detection And Recognition,” 2018 First International Conference on Secure Cyber Computing and Communication (ICSCCC), 2018.

[18] Y. Hu, H. Tang, and G. Pan, “Spiking deep residual networks,” IEEE Transactions on Neural Networks and Learning Systems, pp. 1–6, 2021.

[19] O. K. Oyedotun, K. A. Ismaeil, and D. Aouada, “Why is everyone training very deep neural network with skip connections?,” IEEE Transactions on Neural Networks and Learning Systems, pp. 1–15, 2022.

[20] E. YAZAN and M. F. Talu, “Comparison of the stochastic gradient descent based optimization techniques,” 2017 International Artificial Intelligence and Data Processing Symposium (IDAP), 2017.

[21] M. Fatourechi, R. K. Ward, S. G. Mason, J. Huggins, A. Schlögl, and G. E. Birch, “Comparison of evaluation metrics in classification applications with imbalanced datasets,” 2008 Seventh International Conference on Machine Learning and Applications, 2008.

[22] A. O. Salau and S. Jain, “Feature extraction: A survey of the types, techniques, applications,” 2019 International Conference on Signal Processing and Communication (ICSC), 2019.

Authorized licensed use limited to: DELHI TECHNICAL UNIV. Downloaded on May 11,2023 at 10:13:23 UTC from IEEE Xplore. Restrictions apply.

Research Square

Preprints are preliminary reports that have not undergone peer review.
They should not be considered conclusive, used to inform clinical practice,
or referenced by the media as validated information.

Next-LSTM: A novel LSTM-based Image Captioning technique

Priya Singh (priya23294@gmail.com)
Delhi Technological University https://orcid.org/0000-0001-7656-7108
Chandan Kumar
Delhi Technological University
Ayush Kumar
Delhi Technological University

Research Article

Keywords: Computer Vision, Image Captioning, Long Short-Term Memory, Convolutional Neural Network

Posted Date: May 8th, 2023

DOI: https://doi.org/10.21203/rs.3.rs-2770378/v1

License: This work is licensed under a Creative Commons Attribution 4.0 International License.
Read Full License

Abstract

Recently, Image Captioning has evolved into an immensely popular area in the field of Computer Vision. It strives to generate natural language sentences in order to describe the salient parts of a given image. Research in this area is active and various Machine learning-based Image Captioning models have been proposed in the literature. The main challenge with the existing approaches is effectively extracting image features to generate adequate image captions. Further, there is a need to improve the generalizability of the results on large and diverse datasets. In the current paper, a novel method framework, namely Next-LSTM is proposed for Image Captioning. It first extracts the image features using ResNeXt. It is a powerful convolution neural network-based model that is adopted for the first time in the Image Captioning domain. Later, it applies a Long-short term memory network on the extracted features to generate accurate captions for the images. The proposed framework is then evaluated on the benchmark Flickr-8k dataset on Accuracy. The performance of the proposed framework is also compared to the state-of-the-art approaches and it outperforms the existing approaches.

1 Introduction

The main objective of Image Captioning is to enhance the user experience by producing automatic descriptions. That may be used for image identification, living with disabled people, social media sites, and other NLP (Natural Language Processing) requests. Image captioning provides a narrative explanation for a collection of images. Which creates NLP captions based on the information detected in a image, it is a crucial aspect of scenario comprehension, which integrates Computer Vision with NLP skills, when it comes to Image Captioning, it can be considered a sequence of steps that can be considered as an end-of-series challenge. This occurs when the program changes images from a set of pixels to a set of phrases. A language model is essential to present NLP. For this reason, it is necessary to process both the words or remarks and the visuals. The program uses a combination of Long Short-term Memory (LSTM) and CNN (Convolutional Neural Network) to provide the language content.

The quantity of data available on the internet is growing at an exponential rate, and with it, the quantity of image data. News, internet articles, blogs, advertising, informatic diagrams, NFTs, and other resources can be used to collect image data. People can detect the background in photos for a small number of images but not for a large number of images. As a result, the necessity for technology enters the scene. Computers can automate Image Captioning, but they cannot recognize the context in images like humans. As a result, Image Captioning powered by Deep Learning (DL) entered the image.

DL approaches have grown in popularity in the area of Image Captioning due to their capacity to properly manage the complexity and variety of images and provide human-like captions. Some popular DL architectures for Image Captioning include CNN, Recurrent Neural Networks (RNN), and encoder-decoder models. These models use various combinations of convolutional layers, recurrent layers, and attention mechanisms to capture the features and context of an image and generate a corresponding textual

description. These architectures make DL techniques unique in solving the Image Captioning problem, as they are capable of modeling both the visual and textual information in an end-to-end way.

Extraction and language models are two characteristics of DL. The process of lowering the dimensionality of information by translating raw data into a reduced set of features that capture the underlying patterns is known as feature extraction. It aids in the analysis and prediction jobs by minimizing data complexity. DL frequently employs feature extraction in Computer Vision and NLP to extract significant characteristics from images and texts, respectively. In the instance of Image Captioning, the goal is to predict caption sequences using feature vectors acquired from the trained network using a model based on LSTM.

There are various techniques available in literature for unique caption generation. Although, the existing techniques work well only on large sized datasets but fail miserably on small to medium sized datasets. In the present work proposed a novel Image Captioning model named Next-LSTM, in an attempt to make the model work equally well on datasets and different sized datasets and further improve the performance in terms of Accuracy. To achieve the same, firstly CNN is exploited to generate the features that are later fed to Next-LSTM for creation of effective image captions. Next-LSTM utilizes a novel improved technique in which ResNeXt is used to Extract features from the images and LSTM is used to generate the image captions.

To summarize, ResNeXt is a simple and modular DL framework for picture classification. Repeating building blocks that aggregate a number of alterations with similar topologies are used to construct the network, which yields a homogeneous, multi-branch architecture with a limited number of high energies. The size of the set of transformations, sometimes referred to as "cardinality," is a crucial element in network design along with length and breadth. ResNeXt is a powerful and flexible deep learning architecture that has achieved ground-breaking results on a variety of benchmarks for image classification. Due to its modular architecture and multi-branch structure, it is a popular option among researchers and professionals engaged in image-related tasks.

The rest of the paper is arranged as follows. The review of the literature is presented in Section 2. Section 3 elaborates on the proposed work. Later, the experimental results are reported in Section 4. Finally, in Section 5 conclusion are drawn and future works are explored.

2 Literature Review

Automatic picture captioning is becoming a potential topic of research thanks to recent developments in deep neural network models. Encoder-decoder architecture, merge-model architecture, sequential models, and attention-based models are just a few of the methodologies, models, and architectures that have been investigated in the past and present for picture captioning. These techniques have been utilized by researchers to create word sequences, extract characteristics from images, and create captions by combining text and image data. Researchers have also looked into models based on reinforcement learning to create captions for photos that are better described. Researchers are looking at new methods

to enhance the effectiveness of these systems as picture captioning develops further. Now let's go through a few techniques to better understand how the researchers approached this assignment.

Narula et al. [1] applied DL to explore image description. The purpose of the study is to investigate the different deep-learning approaches used in Image Captioning. The authors provide a clear description of the dataset and explain the CNN-based image caption generation approach and its key components. The study focuses on investigating the different deep-learning techniques used in Image Captioning.

Rasheed et al. [2] created models to provide precise image descriptions. They also utilise some DL methods to create descriptions for videos and images. In the paper, researchers are expanding the area to include DL-based robotic description creation for photos and videos to assist persons with various disabilities.

Jiang et al. [3] developed a model for generating captions on images that used a Dense-Net network system and adaptable focus. The researchers propose an adaptable focus approach with an optical sensor in this paper. The model applies Dense-Net to collect any images universal characteristics. A LSTM network is employed as language creation architecture for image description tasks to enhance the Accuracy of image description results. The dataset which is used in this paper is for Image Captioning is Flickr30k.

Singh et al. [4] explored three different DL models for Image Captioning. These models were CNN with LSTM, CNN with KNN and Attention Based LSTM for IC. These models were trained on the Flicker8k dataset. Further, these models were evaluated on three performance metrics BLEU, METEOR and ROGUE to compare the results. In their study Attention based LSTM model displayed better results than CNN with KNN and CNN with LSTM models on all the three performance measures.

Leekha et al. [5] performed CNN Text Recognition Research. In this paper, researchers built the model where they employed a CNN for image encoding and an RNN for language models for prediction. They suggested a method for language caption production.

P. Mathur. [6] explored various deep-learning methods for image description. Images are comprehended employing Computer Vision, semantics & syntax are comprehended employing NLP, and descriptions are produced using ML. CNN is employed to understand images, whereas RNN is employed to produce language.

Phukan et al. [7] employed deep neural network algorithms to create an efficient method for image description. Fully automated captioning is essential in the case of image data because objects on the web must be properly recognized and managed. In this paper, researchers create a successful and distinct technique for performing autonomous image descriptions on individual photos, and they describe how to improve its performance and usefulness.

Sharma et al. [8] employed CNN and LSTM to image description to include explicit resources. In this paper, researchers presented a method for improved image description that includes all internal and

outside information using explicit resources like Concept-Net. They demonstrated how to produce image descriptors using two sets of datasets, Flickr30k & Flickr8k.

Wang et al. [9] employed improved perceptual g-LSTM to construct a photo translation algorithm. Here researchers developed a method for directing LSTM(g-LSTM), during which visual input from RoI is retrieved and employed as directing details in g-LSTM to produce more precise image descriptions.

Sudhakar et al. [10] developed a method for caption generation and audio conversion for the created caption. The authors of the paper presented a model for generating English sentence captions for images using a combination of CNNs, RNNs, and sentence generation. The model is fed a image, and the resultant captions are then transformed to audio utilizing Google's Text to Sound service (GTTS). The model is based on the 8k Flickr dataset.

Kanimozhiselvi et al. [11] proposed an Image Captioning model that combines CNN architecture with LSTM to improve results. The model employs three distinct CNN and LSTM architectures and is training utilizing three CNN architectures (InceptionV3, Xception, and ResNet50) for extraction of visual characteristics and the LSTM for caption creation.

Aljawarneh et al. [12] investigated several Image Captioning algorithms that included DL techniques such as CNNs and LSTMs. The researchers began their survey study by discussing the methodologies utilized in earlier Image Captioning efforts, such as learning and framework systems. The emphasis subsequently turned to neural network-based approaches, which produce more current findings. Based on specific frameworks, these approaches have been divided into subcategories, and each topic is extensively described. Finally, cutting-edge approaches are tested on benchmark datasets.

Shinde et al. [13] performed a centrally controlled analysis to determine which Image Captioning techniques are most effective. They used algorithms like InceptionV3, ResNet, RNN, CNN, and VGG16 in their system and took into account all the important factors that impact Image Captioning to maximize the results. The dataset used in the analysis is the Flickr 8k. The paper discusses the fundamentals of these approaches, evaluates their performance, strengths, and limitations.

Rao et al. [14] The authors of the paper proposed a method to generate visual captions using a combination of CNN and LSTM for the In-depth Reading method. The CNN is used to encode images into compact representations, and then the LSTM is used to create captions for the input images. The Flickr8k dataset was used to train the model

K. Rage [15] provided an in-depth review of various DL approaches for Image Captioning, such as CNN, Deep Neural Networks (DNN), Auto-Encoders(AE), RNN with Gated Recurrent Units(GRU), LSTM and ConvLSTM, Reinforcement Learning Learning(DRL), Adversarial Networks (GAN), and (DBN). They thoroughly examined these strategies and weighed their advantages and disadvantages.

In the current work, we have proposed novel Next-LSTM model for Image Captioning. To the best of our knowledge none yet has explored ResNeXt for Image Captioning. We first employ CNN for feature

extraction and later exploits ResNeXt for effective Image Captioning generation

3 Proposed Work

In this paper we have proposed a novel method for image caption generation. In order to get superior outcomes, we have designed a model that makes use of the deep learning algorithm. In order to have a successful model for Image Captioning, the first thing that has to be done is feature extraction from the picture, and then the captions for the photos need to be generated. We made use of ResNeXt for feature extraction, and LSTM was the algorithm of choice for producing captions. In the next part (3.1), we will provide a quick introduction to the framework of the model, and the following section (3.2) will discuss the specifics of the ResNeXt Model.

3.1 Architecture of the proposed system

This is a description of a merge-model architecture-based Image Captioning model. The ResNeXt50 (32x4d) CNN is used to retrieve visual features. To generate the next phrase in the caption, the encoded characteristics and encrypted text data produced by an LSTM are combined in a multi-modal layer. Before being input into the model, the text data is pre-processed. The model is divided into five stages: extraction of features, text processing, output predictions, model and results fitting, and caption production. The overall architecture is presented in Fig. 1. This architecture has the advantage of using pre-processed text data in the model rather than raw data.

3.2 Dataset Descriptions

The proposed system in the paper prepares a model for text detection using the Flickr8k image dataset. The dataset contains 8091 JPEG format images, each with 5 distinct captions. The captions explain the events, items, or people depicted in the photograph. The photographs were picked from six separate Flickr communities and do not depict any famous individuals or places. Figure 2 provides a sample image from Flickr8k dataset. A dictionary of all unique terms from the 40455 captions is developed during processing. For training, 6000 captioned images are used, 1000 for validation, and 1000 for testing. The dataset comes with a text file called "Flickr8k.token.txt" that contains the brand logo, caption number (0–4), and real description for each image and its five captions.

3.3 CNN based feature extraction

Before feeding the input into the model, it needs to be pre-processed. The feature extractor requires an image with size 224x224x3, so the images need to be resized to meet this requirement. The ResNeXt50 (32x4d) model is used for feature extraction in the Image Captioning model. The model is pre-trained on the ImageNet dataset and the features are extracted from the output shortly before the final classification layer. The model is further improved using a dense layer, and the output is transformed into a vector of length 2048 for each image. This vector represents the feature representation of the image, which is used in the caption generation process. This process is performed for all images in the dataset, and the extracted features are then mapped to the image names, creating a dictionary.

3.4 ResNeXt

ResNeXt is a form of neural network that necessitates less hyperparameters than normal ResNet. It uses cardinality, which is an additional dimension that defines the number of evolutions in the set, to achieve this reduction.

Figure 3. represents the ResNeXt frame, which has a number of clusters of 32 and applies the same transitions 32 times before being aggregated. The combination of ResNets repetition strategy and InceptionV3 Network's split-transform-merge strategy yields a network frame that divides the input, converts it, and combines it to make the products, for each block following the very same configuration. This method aids in overcoming the limitations that VGG-nets, ResNets, and InceptionV3 Networks face when adapting to new datasets.

Additionally, ResNeXt introduces a new dimension, called cardinality, which indicates to the number of parallel branches in the network. This allows ResNeXt to learn a more diverse set of transformations, reducing the number of hyperparameters required compared to conventional ResNet. The use of cardinality, combined with the sharing of hyperparameters and the width adjustment, makes ResNeXt a more flexible and efficient architecture for image classification tasks.

Table 1
ResNet-50 on left and ResNeXt-50 with a 32×4d template on right

stage	output	ResNet-50	ResNeXt-50 (32x4d)
conv l	112 x 112	7×7, 64, stride 2	7×7, 64, stride 2
conv2	56 x 56	3×3 max pool, stride 2	3×3 max pool, stride 2
		$\begin{bmatrix} 1\times1, 64 \\ 3\times3, 64 \\ 1\times1, 256 \end{bmatrix} \times 3$	$\begin{bmatrix} 1\times1, 128 \\ 3\times3, 128, C=32 \\ 1\times1, 512 \end{bmatrix} \times 3$
conv3	28 x 28	$\begin{bmatrix} 1\times1, 128 \\ 3\times3, 128 \\ 1\times1, 512 \end{bmatrix} \times 4$	$\begin{bmatrix} 1\times1, 256 \\ 3\times3, 256, C=32 \\ 1\times1, 1024 \end{bmatrix} \times 4$
conv4	14 x 14	$\begin{bmatrix} 1\times1, 256 \\ 3\times3, 256 \\ 1\times1, 1024 \end{bmatrix} \times 6$	$\begin{bmatrix} 1\times1, 512 \\ 3\times3, 512, C=32 \\ 1\times1, 2048 \end{bmatrix} \times 6$
conv5	7 x 7	$\begin{bmatrix} 1\times1, 512 \\ 3\times3, 512 \\ 1\times1, 2048 \end{bmatrix} \times 3$	$\begin{bmatrix} 1\times1, 1024 \\ 3\times3, 1024, C=32 \\ 1\times1, 2048 \end{bmatrix} \times 3$
	1 x 1	global average pool 1000-d fc, softmax	global average pool 1000-d fc, softmax
# params.	**25.5**×10^6	**25.0**×10^6	
FLOPs	**4.1**×10^9	**4.2**×10^9	

As seen in Table 1, The ResNeXt-50 has a number of clusters of 32, which implies that the clustered layer contains 32 groups, and this grouping is repeated four times in the network's depth. The dimensions in the table represent residue left frame constructions, and the figures beside them indicate the number of stacked blocks.

The network architectures described in Fig. 4. illustrate what a clustered convolution is and how it outperforms the other two-layer structures. (a) represents a common ResNeXt frame that has already been observed. It employs the divided approach and has a number of clusters of 32. (b) appears to be a variation on Inception-ResNet. However, networking blocks in Inception or Inception-ResNet do not maintain the very same architecture. (c) is connected to the clustered convolution descfribed in the Proposed approach. The value 32*4 in (a)-and-(b) has been replaced with 128 in short, indicating that the division is done by a clustered convolution operation. Similarly, the transformation is carried out by another grouped convolutional layer, which does 32 convolution groupings. Clustering occurs afterwards. Among the three options shown above, (c) proved to be the most practical due to its ease of implementation.

3.5 Selected state of the art models for comparison

ResNet50

The ImageNet dataset, which comprises millions of annotated pictures, was used to train the pre-trained DL model ResNet50 (Fig. 5) on a significant image classification job. When there is not enough labelled data available to train a model from scratch, employing pre-trained models can help. These models take advantage of the information obtained during training on a big dataset to address comparable issues. The ResNet (Residual Network) architecture, which was created to solve the issue of disappearing gradients in very deep neural networks, has a variation called ResNet50. 48 convolutional layers, 1 max pooling layer, 1 average pooling layer, and skip connections that let data skip one or more levels make up this system. ResNet50 is a computationally demanding model with around 3.8 billion floating-point operations.

InceptionV3

An enhanced version of Inception V2, Inception V3 is a pre-trained convolutional neural network (CNN) model. While still utilising the fundamental components of the Inception module, Inception V3 was created to alleviate some of the shortcomings of Inception V2. The architecture of the Inception V3 model is complex and consists of many Inception modules as well as different layers including softmax, max pooling, and average pooling. Figure 5 of the original study article, which illustrates the model's intricate structure, depicts the architecture of Inception V3.

Xception

The researchers came up with the deep CNN architecture known as Xception (Fig. 7). Since it is built on the Proposed approach but employs an extreme variation of depth-wise separable convolutions, the term "Xception" stands for "Extreme Inception".

With fewer parameters and calculations needed for each layer thanks to the Xception architecture, deep neural networks are more effective and accurate. To do this, insight separated convolution layer, essentially split the temporal and channel dimensions of the information and perform a complexity

combination succeeded by a point-wise combination, are used in place of the conventional convolutional layers.

3.6 Long Short-Term Memory

LSTMs are a type of RNN that can handle the issue of vanishing gradients and learn order dependencies in sequence prediction problems. LSTMs are widely used in various applications such as speech recognition, machine translation, etc. LSTMs have the ability to remember previous inputs for a longer period of time compared to traditional RNNs. This is achieved through the use of gates in the LSTM architecture (Fig. 8), which control the flow of information through the network. LSTMs can also be made bidirectional to consider both past and future context while making predictions. This enhances the performance of the LSTM model in sequence-to-sequence problems.

3.7 Text Pre-processor

All of the captioning list's phrases are recovered within the same list, and then each of their individual words are deleted and placed into a separate list. To summarize, the captions in the dataset are first extracted, tokenized, and translated to numerical values by assigning each word a unique number. Then the tokenized captions are padded to the same length, using the "0" value for padding and marked with the "start" and "end" delimiters. This processed text data is then ready to be used as input to the DL model for caption generation.

3.8 Output Predictor

This is a description of a DL architecture for an image-captioning model. The image is processed using a Dense layer with ReLU activation and the extracted features are repeated 40 times. The text captions are processed through tokenization, encoding, sequencing and padding, followed by an Embedding layer. The image and text representations are merged and then passed through two Dense layers, with the final layer predicting the next word in the caption using the SoftMax activation.

3.9 Fitting the Model

After it has been constructed, the model is fitted that use the training data. The algorithm is expected to run over 100 epochs, with the prediction fit chosen by calculating the prediction error on the Flickr8k experimental dataset. For caption construction, the model with the least error function is chosen.

3.10 Image Caption Generation

To test our trained model, to create descriptions for a specific input image, a trained model is employed. The image is first processed by the feature extractor and then the generated features are used to predict the words in the caption sequentially, word-by-word. The words with maximum weights are selected for each iteration and appended to the final caption. The caption is generated until a delimiter is found or the caption size meets the set maximum length. Following that, the final caption is shown beside the input image.

3.11 Evaluation Metric

Accuracy and loss are two frequently used metrics when assessing the performance of a machine learning model, but they don't always give a clear picture of how well the model is working. Although it does not account for the distribution of classes in the data, accuracy represents the proportion of accurate predictions generated by the model. A model that consistently predicts class A, for instance, would achieve a 90% accuracy rate on a dataset where 90% of samples belong to class A and just 10% to class B, but it would not be a useful model. Loss, on the other hand, is a gauge of how successfully a model can reduce the discrepancy between its forecasts and the actual values. A better-performing model generally has a lower loss; however, this might vary depending on the amount of the data and the loss function used.

3.12 Comparison

The suggested novel technique is then trained using various state-of-the-art CNN models i.e., Resnet50, Xception, InceptionV3. The results of the experiment are being compared using the accuracy metric to determine the performance of the novel technique relative to the established models. This comparative study aims to evaluate the effectiveness of the proposed technique and provide insights into its potential usefulness in classification tasks.

4 Results and Discussions

In this proposal, we provide a unique ResNeXt and LSTM-based method for automated picture captioning. The suggested model was constructed via merge model architecture. We used ResNeXt, a convolutional neural network, to compress an image's graphical elements into a compact representation. Following this, an LSTM language model was used to construct the descriptive phrase. We used a smaller dataset (Flickr8k) due to limited processing power in order to successfully complete what was outlined in the project proposal. Our model is capable of seeing an image and producing semantically accurate output in user-selected languages, based on the available terms in its dictionary, which is constructed based on the different words in existing captions contained in the training dataset. The purpose of the built model is to increase the chance of a phrase being produced based on a given image. We evaluated the model using Flickr8K's training photos and the results were positive. We evaluate the model's precision based on its accuracy and loss. If a comparable model is applied to a bigger dataset, consisting of more photos, the accuracy may be increased.

Table 2
Performance comparison of Models

Model	Accuracy	Loss
InceptionV3	0.6212	1.5505
Xception	0.6223	1.4970
ResNet50	0.7586	0.8839
ResNext50 (32x4d)	**0.7719**	**0.8778**

Table 2 presents the accuracy and loss metrics for four different models: InceptionV3, Xception, ResNet50, and ResNext50 (32x4d). The accuracy metric measures the proportion of correctly classified instances out of the total number of instances, while the loss metric indicates the error in the model's predictions.

According to the Table 2, ResNext50 (32x4d) has the highest accuracy score of 0.7719, followed by ResNet50 with an accuracy score of 0.7586. InceptionV3 and Xception have lower accuracy scores of 0.6212 and 0.6223, respectively.

In terms of loss, ResNext50 (32x4d) and ResNet50 have the lowest values of 0.8778 and 0.8839, respectively, indicating that these models have the least amount of error in their predictions. InceptionV3 and Xception have higher loss values of 1.5505 and 1.4970, respectively, suggesting that these models have a higher degree of error in their predictions. Overall, it provides a comparison of the accuracy and loss metrics for four different models, which can be used to evaluate their performance and guide decision-making in selecting the best model for a given task. Here, various examples of images from both within and outside the dataset are examined. Further, Fig. 9 portrays the generated captions for sample images.

5 Conclusion and Future Scope

We have proposed a novel Next-LSTM that utilizes CNN for feature extraction and later exploits ResNeXt for effective Image Captioning generation. The results are evaluated on Accuracy and compared with InceptionV3, Xception, ResNet50. The performance of the models indicate that the novel Next-LSTM outperforms the state-of-the-art models.

While memory size and training time can undoubtedly have an impact on the functionality and restrictions of neural networks, it isn’t the only ones. The quantity and calibre of training data, the model's complexity, and the selection of hyperparameters are a few other variables that can affect how well neural networks learn and generalise. Our model takes 4 hours to train on computer with Intel Xeon Processor and 256 GB of ram.

Our proposed model can be improved by increasing the number of epochs used to train the model. Also, there are large datasets like MS COCO, Flickr 30k, etc. Which could further increase the accuracy of the model. The DL approaches produced relevant descriptions for photos comparable to those found in the datasets we used. We utilized the CNN approach for feature extraction and the LSTM model for caption synthesis. Three CNN designs have been given training into the algorithm: InceptionV3, Xception, and ResNet50. ResNeXt provided the greatest Accuracy of 77.9% for 100 epochs among the three CNN models tested.

Declarations

Compliance with Ethical Standards

Disclosure of potential conflicts of interest

There are no conflicts of interest (financial or non-financial) applicable in conducting the research.

Research involving Human Participants and/or Animals

No human participants and/or animals were involved in conducting the research.

Informed consent

No informed consent was required as the research did not involve any human participants during conducting the research.

References

1. M. S. Alam, V. Narula, R. Haldia and G. Nikam Ganpatrao, "An Empirical Study of Image Captioning using Deep Learning," *2021 5th International Conference on Trends in Electronics and Informatics (ICOEI)*, Tirunelveli, India, 2021, pp. 1039-1044, doi: 10.1109/ICOEI51242.2021.9452919.
2. S. Amirian, K. Rasheed, T. R. Taha and H. R. Arabnia, "Automatic Image and Video Caption Generation With Deep Learning: A Concise Review and Algorithmic Overlap," *in IEEE Access,* vol. 8, pp. 218386-218400, 2020, doi: 10.1109/ACCESS.2020.3042484.
3. Z. Deng, Z. Jiang, R. Lan, W. Huang, Xiaonan Luo, Image captioning using DenseNet network and adaptive attention, Signal Processing: Image Communication, Vol. 85, 2020, 115836, ISSN 0923-5965, doi:10.1016/j.image.2020.115836. (https://www.sciencedirect.com/science/article/pii/S092359652030059X)
4. P. Singh, P. Gupta and H. Jain, "A Comparative Study of Machine Learning Based Image Captioning Models," *2022 6th International Conference on Trends in Electronics and Informatics (ICOEI)*, Tirunelveli, India, 2022, pp. 1555-1560, doi: 10.1109/ICOEI53556.2022.9777153.

5. S. Kalra & A. Leekha (2020) Survey of convolutional neural networks for Image Captioning, *Journal of Information and Optimization Sciences*, doi:10.1080/02522667.2020.1715602
6. P.Mathur, 2021, August. A Survey on Various Deep Learning Models for Automatic Image Captioning. *In Journal of Physics: Conference Series (Vol. 1950, No. 1, p. 012045)*. IOP Publishing.
7. B.B.Phukan, A.R.Panda, (2021). An Efficient Technique for Image Captioning Using Deep Neural Network. *In: Mallick, P.K., Bhoi, A.K., Marques, G., Hugo C. de Albuquerque*, V. (eds) Cognitive Informatics and Soft Computing. Advances in Intelligent Systems and Computing, vol 1317. Springer, Singapore. doi:10.1007/978-981-16-1056-1_38
8. H.Sharma and A.H.Jalal, 2020. Incorporating external knowledge for Image Captioning using CNN and LSTM. Modern Physics Letters B, 34(28), p.2050315.
9. P.Cao, Z.Yang, L.Sun, et al. Image Captioning with Bidirectional Semantic Attention-Based Guiding of Long Short-Term Memory. Neural Process Lett 50, 103–119 (2019). doi:10.1007/s11063-018-09973-5
10. J. Sudhakar, V. V. Iyer and S. T. Sharmila, "Image Caption Generation using Deep Neural Networks," 2022 International *Conference for Advancement in Technology (ICONAT)*, Goa, India, 2022, pp. 1-3, doi: 10.1109/ICONAT53423.2022.9726074.
11. C. S. Kanimozhiselvi, K. V, K. S. P and K. S, "Image Captioning Using Deep Learning," *2022 International Conference on Computer Communication and Informatics (ICCCI)*, Coimbatore, India, 2022, pp. 1-7, doi: 10.1109/ICCCI54379.2022.9740788.
12. Z. Al-Jamal, M. J. Bani-Amer and S. Aljawarneh, "Image Captioning Techniques: A Review," *2022 International Conference on Engineering & MIS (ICEMIS*), Istanbul, Turkey, 2022, pp. 1-5, doi: 10.1109/ICEMIS56295.2022.9914173.
13. S. Shinde, D. Hatzade, S. Unhale and G. Marwal, "Analysis of Different Feature Extractors for Image Captioning Using Deep Learning," *2022 3rd International Conference for Emerging Technology (INCET)*, Belgaum, India, 2022, pp. 1-5, doi: 10.1109/INCET54531.2022.9824294.
14. S. Rao, S. Santhosh, K. Preethi Salian, T. Chidananda, Prathyakshini and S. Sandeep Kumar, "A Novel Approach to Generate the Captions for Images with Deep Learning using CNN and LSTM Model," *2022 International Conference on Distributed Computing, VLSI, Electrical Circuits and Robotics (DISCOVER)*, Shivamogga, India, 2022, pp. 176-179, doi: 10.1109/DISCOVER55800.2022.9974750.
15. K. Rage, "A Study on Different Deep Learning Architectures on Image Captioning," *2022 8th International Conference on Smart Structures and Systems (ICSSS)*, Chennai, India, 2022, pp. 1-9, doi: 10.1109/ICSSS54381.2022.9782260.
16. Xie, Saining, Ross B. Girshick, Piotr Dollár, Zhuowen Tu and Kaiming He. “Aggregated Residual Transformations for Deep Neural Networks.” *2017 IEEE Conference on Computer Vision and Pattern Recognition (CVPR)* (2016): 5987-5995.
17. K. He, X. Zhang, S. Ren and J. Sun, "Deep Residual Learning for Image Recognition," *2016 IEEE Conference on Computer Vision and Pattern Recognition (CVPR)*, Las Vegas, NV, USA, 2016, pp. 770-778, doi: 10.1109/CVPR.2016.90.

Figures

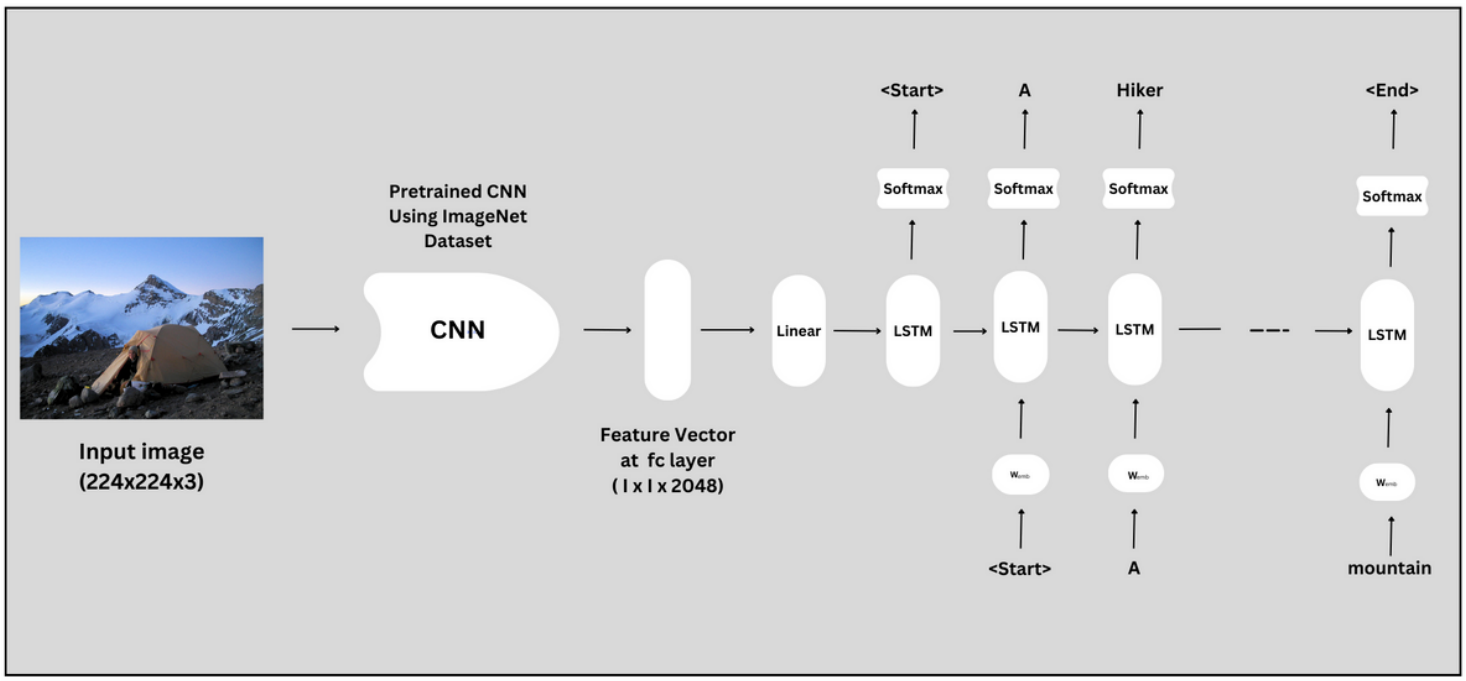


Figure 1

Process of image caption generation using the proposed system



Toddler sits on a pile of rocks.
A toddler sitting on a pile of rocks holding a rock at a beach.
A small boy is playing with rocks.
A baby is stacking rocks on the beach.
A baby is sitting on and playing with smooth rocks.

Figure 2

Sample image from Flickr8k dataset

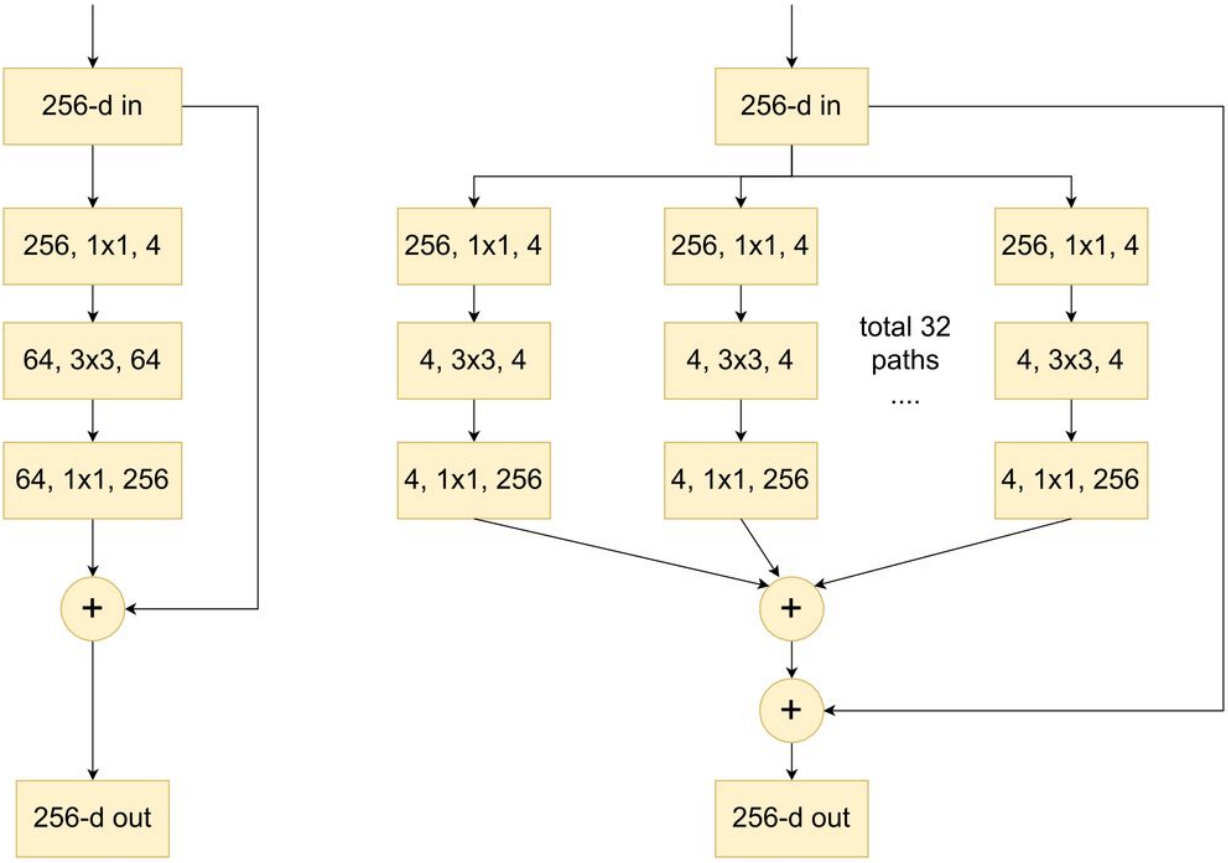


Figure 3

A frame of ResNet on left and a frame of ResNeXt on right.

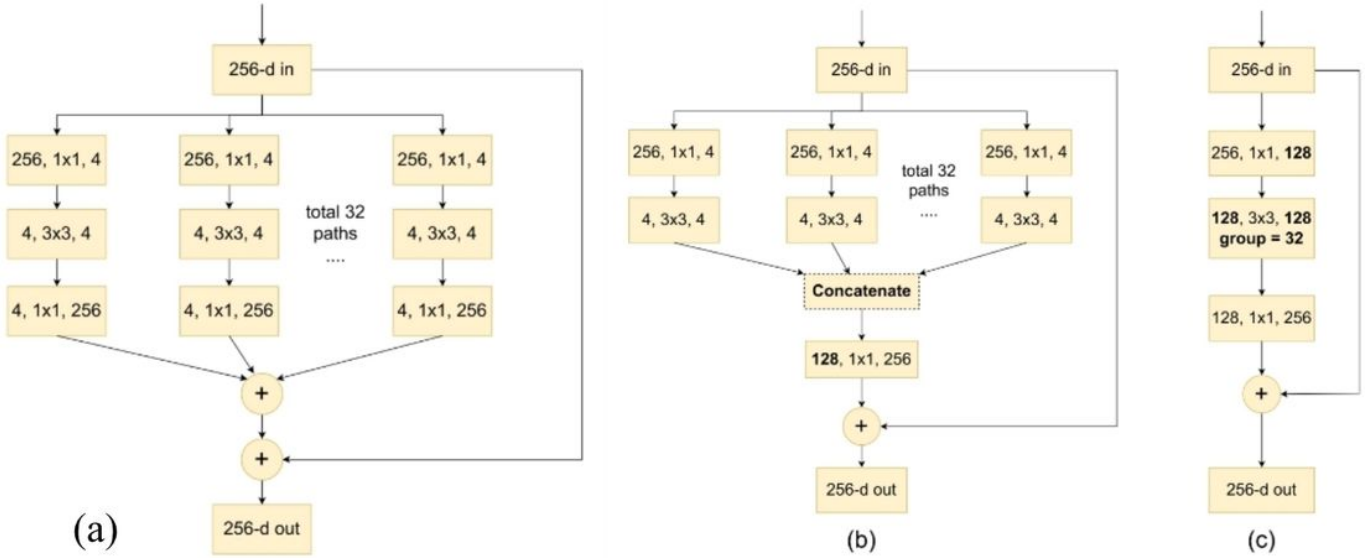


Figure 4

Equivalent construction blocks of ResNeXt **(a):** Aggregated residual transformations, identical to those in Figure. 3 right (a). **(b):** An early concatenation block that is equal to (a). **(c):** Grouped convolutions are used to create a block that is identical to (a, b). Bold text annotations draw attention to the reformulation adjustments. The (number of input channels, filter size, and number of output channels) denotes a layer.

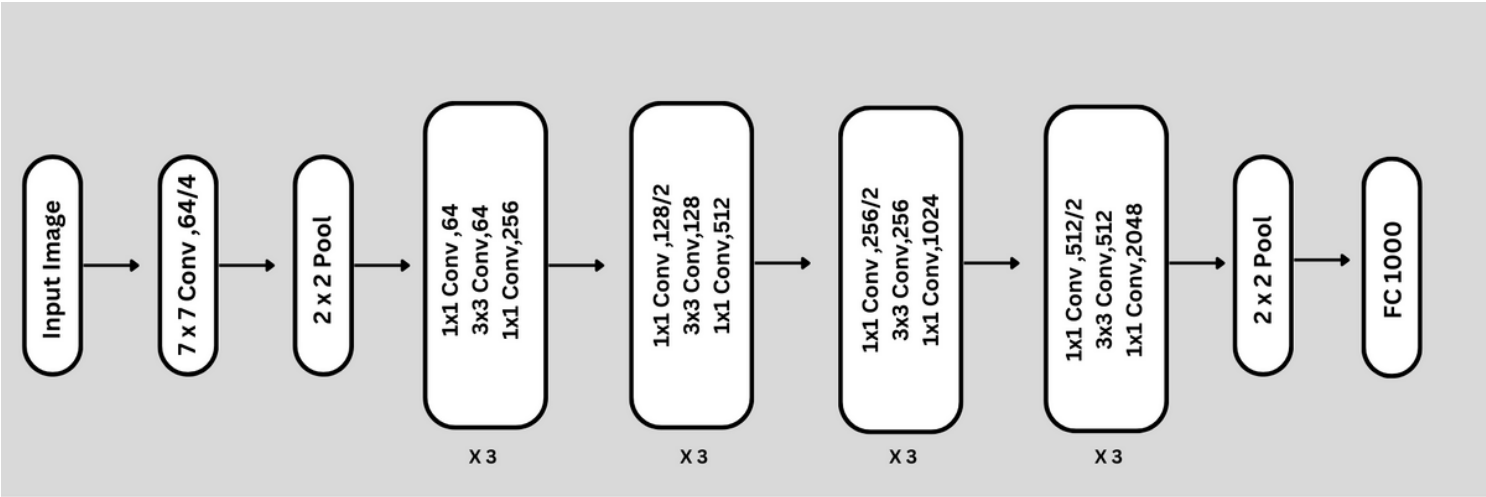


Figure 5

Architecture of ResNet50

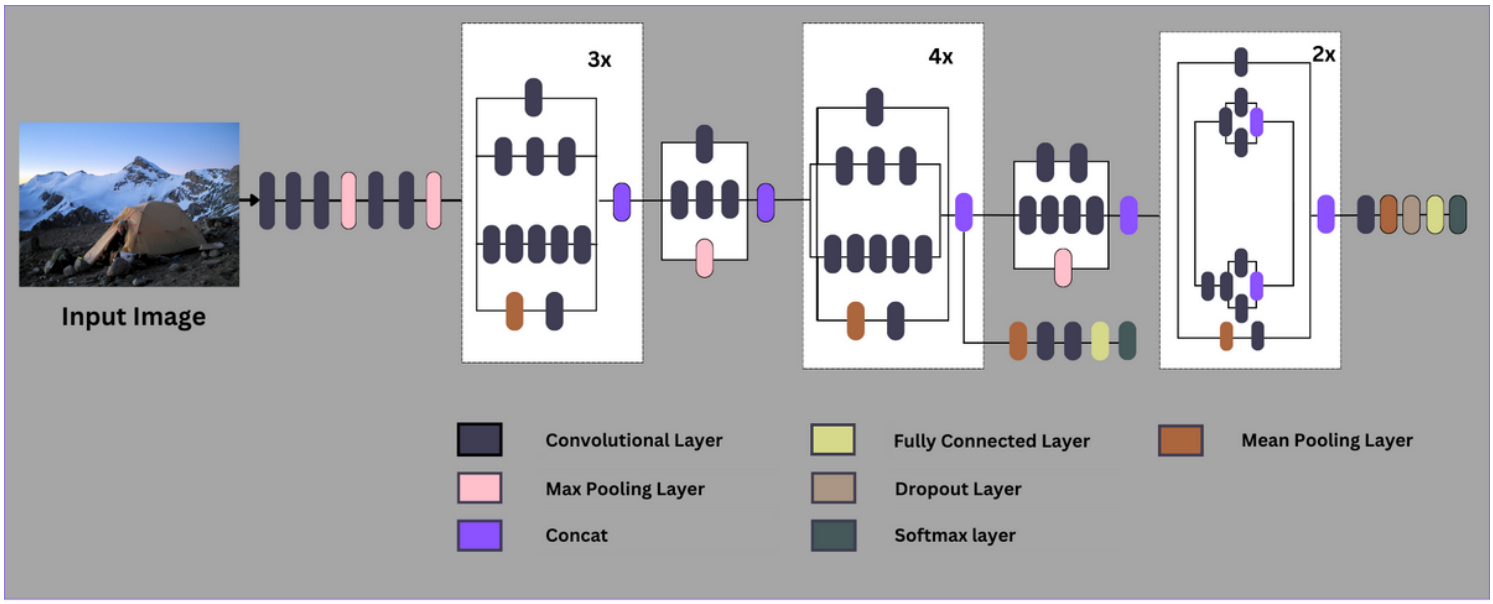


Figure 6

Architecture of InceptionV3

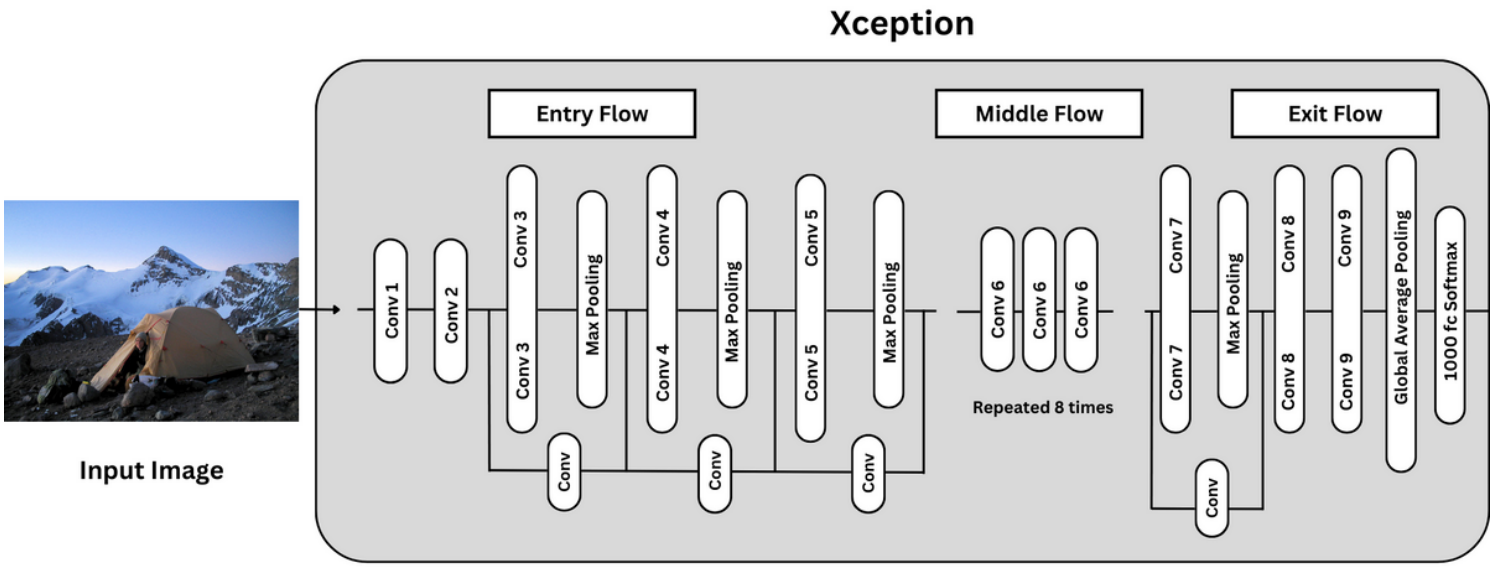


Figure 7

Architecture of Xception

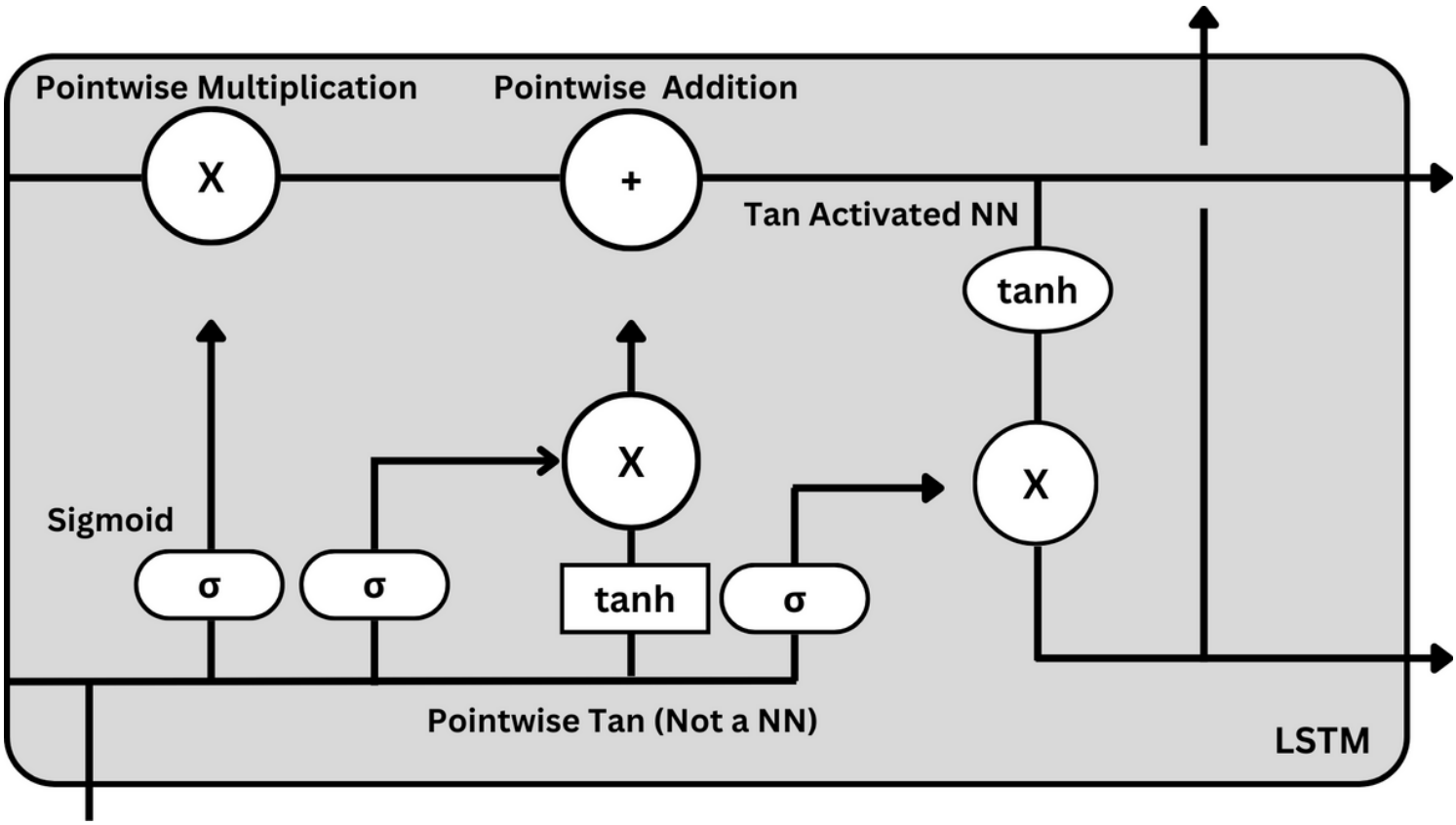


Figure 8

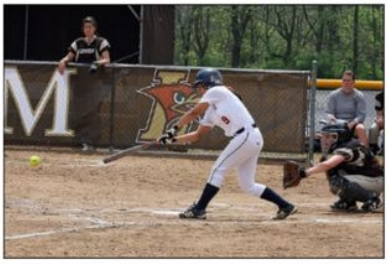
LSTM Architecture



Actual
A large brown dog runs after a tennis ball in a field .
A German shepherd dog is running toward a tennis ball .
A dog with a red leash still attached chases over the grass toward a tennis ball .
"A dog trailing a leash chases a tennis ball across a grassy area ."
A brown dog is chasing a ball on the grass
Predicted
a dog jumps to catch a ball .



Actual
A panting brown dog walking on the grass .
A brown dog with white paws is trotting through a field of green grass .
A brown dog is walking on the grass .
A brown dog is running through the grass panting .
A brown dog in running on grass .
Predicted
a brown dog runs across the grass .



Actual
A girl at bat in a softball game
A batter swings at a ball .
A baseball player swings at the ball as onlookers watch .
A baseball player punting .
A baseball player in white swings for the ball as the player in brown is waiting to intercept .
Predicted
a young boy playing baseball .



Actual
The motocross rider jumps high in the air on his bike .
A person on a dirt bike is in midair making a jump on a dirt track .
a motocross bike is jumping through the air between two lines of red tape .
A man performs a dirt bike stunt over the sand .
A dirt bike rider jumps in the air .
Predicted
a motorcycle rider jumps over a wall as his cyclists watch .

Figure 9

Generated captions for some sample images

Iranian Journal of Science
https://doi.org/10.1007/s40995-023-01469-9

RESEARCH PAPER

Optimal Control Strategies to Cope with Unemployment During the Covid-19 Pandemic

Charu Arora[1] · **Sudhakar Yadav**[2]

Received: 14 September 2022 / Accepted: 3 March 2023
© The Author(s), under exclusive licence to Shiraz University 2023

Abstract
In the present paper, a mathematical model using the non-linear differential equations depicting the impact of Covid-19 on unemployment is discussed. The stability of the system is studied and model is reformulated as an optimal control problem. To assess the impact of unemployment on human population, two time-dependent controls are used. Providing education and training of job-oriented persons act as first control and campaigning about the awareness of coronavirus disease and self-employment business is the second control. Necessary conditions for optimal control are derived by Pontryagins maximum principle. Further, the results are illustrated by numerical simulation.

Keywords Modified unemployment model · Covid-19 · Stability analysis · Control strategies · Numerical simulation

1 Introduction

Unemployment is the state of a person who is willing to work but is not able to get the job. Unemployment is a big problem across the globe and it effects the socio-economic condition of a region. It is vividly a matter of concern for government authorities as it holds a major role in taxation and budgets. Hence, providing adequate number of jobs to meet the challenge of unemployment is a major agenda for every government body in elections. Apparently, supporting education from the primary classes itself is an essential and elementary step towards the solution of a bigger problem. Unfortunately, covid crisis has impacted the condition of unemployment in a more worse manner. Many people have lost their jobs due to the Covid-19 pandemic and their economic, mental and social health have suffered a lot. Advances in technology adds to the development economically but the advancement should be made in a planned and controlled way like proper training, developing skills etc. These factors often increases the employment. Also, entrepreneurship increases the employment in an efficient way (Yousefpour et al. 2020; Mallick and Biswas 2017). The rate of unemployment has increased dejectedly today than from the previous years due to the worldwide lockdown and curfews. According to research, India's unemployment rate has increased to 7.1% in 2020 from 5.2% in 2019. In 2021–2022, unemployment rate is almost the same as 2019–2020 (https://www.businesstoday.in/jobs/story/india-unemployment-in-2020-at-worst-level-in-29-years-shows-study-297195-2021-05-28). One of the significant study depicts the cost effective measures for the control of unemployment which is to embed the control strategies on temporary employees and regular employees while creating some temporary and regular vacancies (Munoli et al. 2017). In Munoli et al. (2017) and Munoli and Gani (2016), models include the schemes of retirement, unavoidable circumstances like death, termination from job etc. and control analysis is executed by adopting the Pontryagin's maximum principle. In Abu Arqub and Shawagfeh (2021), optimal control problem is solved by the method of reproducing kernel Hilbert space. Inverse problems are analyzed for diffusion equations with fractional Sturm–Liouville operator for space (Djennadi et al. 2021a) and fractional derivatives in time (Djennadi et al. 2021b). The class of fractional delay differential equations with Atangana-Baleanu fractional derivatives is discussed in Sweis et al. (2022). Effective measures like various policies to provide temporary or regular employ-

✉ Charu Arora
charuarora099@gmail.com

Sudhakar Yadav
sudhakarbhu10@svc.ac.in

[1] Department of Applied Sciences, Bharati Vidyapeeth's College of Engineering, Delhi 110063, India

[2] Department of Applied Mathematics, Delhi Technological University, Delhi 110042, India

Published online: 26 May 2023

ment are discussed and numerical simulations are employed to validate the theoretical results. A mathematical model in Mallick and Biswas (2020) analyzes the stability conditions of a system which comprises of vacancies, employment and unemployment compartments. Optimal control techniques are adopted and model is simulated. The optimal control conditions for unemployment problem with effective use of policies in providing temporary and regular employment by creating new vacancies are derived. The study calculates the Unemployment Averted Ratio (UAR) and Incremental Cost-Effectiveness Ratio (ICER) to investigate the cost effectiveness of all possible combinations of four control measures.

In this paper, we make an attempt to study and deal with this major problem of unemployment that has even increased more due to Covid-19 pandemic. Section 2 of the paper explains the formulation of the model and discusses the basic preliminaries of the proposed model. Global stability is examined in Sect. 3. Section 4 studies the model with control followed by the numerical simulation in Sect. 5. Section 6 concludes the paper with discussion and future scope.

2 Formulation and Basic Preliminaries of the Model

Misra and Singh (2011) studied an employment model by assuming three classes such as U, T and R representing the unemployed class, temporarily employed and regularly employed persons at any time t which leads to the following model;

$$\begin{aligned}
\frac{dU}{dt} &= \Lambda - k_1 U(R_a - R) - k_2 U(T_a - T) \\
&\quad -\alpha_1 U + \gamma_1 T + \gamma_2 R, \\
\frac{dT}{dt} &= k_2 U(T_a - T) - k_3 T(R_a - R) - \alpha_2 T - \gamma_1 T, \\
\frac{dR}{dt} &= (k_1 U + k_3 T)(R_a - R) - \alpha_3 R + \gamma_2 R V. \qquad (1)
\end{aligned}$$

We assume U_1, U_2, E and V as the unemployed class, unemployment occurred due to the pandemic, employed class and number of vacancies created at the time t. So, the proposed model comprises of the following variables;

(1) Unemployed persons due to the factors other than Covid-19 (U_1).
(2) Unemployed persons due to Covid-19 (U_2).
(3) Employed persons (E).
(4) Unfilled vacancies (V).

It is depicted in the proposed system about the unemployed class U_1 getting employment to fill the vacancies which follows a linear functional pattern. On the other hand, unemployed persons due to the crisis of Covid-19, U_2 gets employed following a different functional response (Fig. 1).

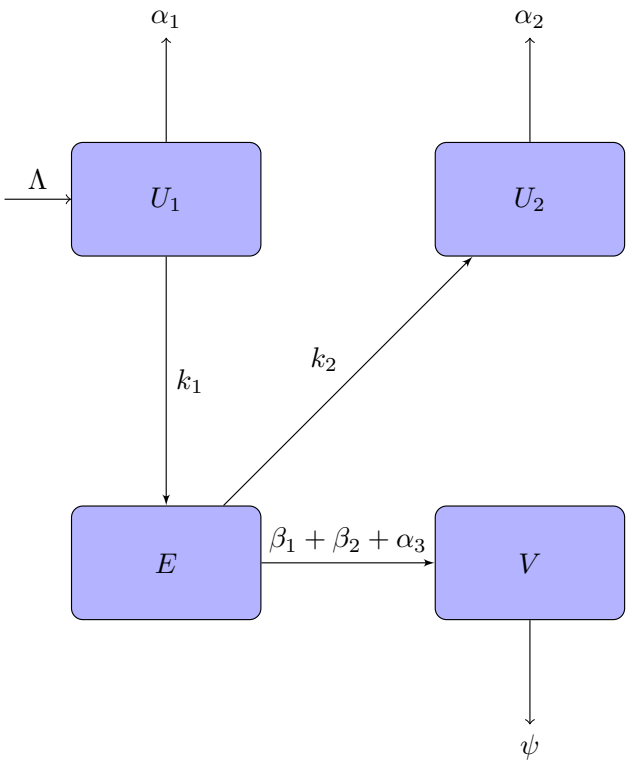


Fig. 1 Diagram of the compartment model

We differentiate the unemployed class into two subclasses i.e. unemployed persons due to Covid (U_1) and unemployed persons due to factors other than Covid (U_2). Based on the above concepts, we reformulate the model given by Misra and Singh (2011) which is given as;

$$\begin{aligned}
\frac{dU_1}{dt} &= \Lambda - k_1 U_1 V - \alpha_1 U_1 + \beta_1 E, \\
\frac{dU_2}{dt} &= \frac{k_2 U_2 V}{1 + \delta V} - \alpha_2 U_2 + \beta_2 E, \\
\frac{dE}{dt} &= k_1 U_1 V - \frac{k_2 U_2 V}{1 + \delta V} - \alpha_3 E - \beta_1 E - \beta_2 E, \\
\frac{dV}{dt} &= \alpha_3 E + \beta_1 E + \beta_2 E - \psi V. \qquad (2)
\end{aligned}$$

The parameters used in the system are interpreted in Table 1.

Lemma 1 *Every solution of the system (2) with respect of initial conditions existing in* $[0, \infty)$ *remain positive for all* $t > 0$.

Table 1 Details of the parameters in the system 1

Parameter	Meaning
Λ	Constant number by which employment rises
k_1	Rate of conversion of unemployed class to employed class
k_2	Rate of conversion of employed class to unemployed class due to Covid 19 situation
α_1	Loss of persons due to natural death in usual unemployed persons
δ	Mortality rate of human population
α_2	Loss of persons due to death in the unemployed class due to the infection
β_1	Rate of employed persons who become unemployed
β_2	Rate of employed persons who become unemployed due to the effect of disease
α_3	Loss of unemployed class due to death
δ	Time in which employed gets unemployed
ψ	Loss in vacancies

Proof The proposed model with initial conditions $(U_1(0), U_2(0), E(0), V(0))^T \in R_+^4$ is written in the matrix equation form as,

$$\frac{dH}{dt} = G(H(t)),$$

where $H(t) = (U_1, U_2, E, V)^T$ such that $H(0) = (U_1(0), U_2(0), E(0), V(0))^T \in R_+^4$ (Khajanchi 2014; Gakkhar and Singh 2012).

$$G(H(t)) = \begin{pmatrix} G_1(H(t)) \\ G_2(H(t)) \\ G_3(H(t)) \\ G_4(H(t)) \end{pmatrix} = \begin{pmatrix} \Lambda - k_1 U_1 V - \alpha_1 U_1 + \beta_1 E, \\ \frac{k_2 U_2 V}{1+\delta V} - \alpha_2 U_2 + \beta_2 E, \\ k_1 U_1 V - \frac{k_2 U_2 V}{1+\delta V} - \alpha_3 E - \beta_1 E - \beta_2 E, \\ \alpha_3 E + \beta_1 E + \beta_2 E - \psi V. \end{pmatrix},$$

where $G : R^4 \to R_+^4$ and $G \in C^\infty(R^4)$ such that $G_i(H_i) \mid_{H_i=0} \geq 0$, for $i = 1, 2, 3, 4$. By the classical theory proposed by Nagumo (1942), the solution is positive for all finite and positive time t.

Lemma 2 *Every solution of system* (2) *with respect to initial conditions are bounded for all* $t \geq 0$.

Proof Let $N(t) = U_1(t) + U_2(t) + E(t)$.

Assuming $0 < \eta_1 \leq min(\alpha_1, \alpha_2, \alpha_3)$ and $0 < \eta_2 \leq \psi$. Then,

$$\frac{dN}{dt} + \eta_1 N = \Lambda - \alpha_1 U_1 - \alpha_2 U_2 - \alpha_3 E + \eta_1 U_1 + \eta_1 U_2 + \eta_1 E,$$
$$\frac{dV}{dt} + \eta_2 V = \alpha_3 E + \beta_1 E + \beta_2 E + V(\eta_2 - \psi),$$

which implies,

$$\frac{dN}{dt} + \eta_1 N \leq \Lambda,$$
$$\frac{dV}{dt} + \eta_2 V \leq \Lambda'(say).$$

If, $\frac{\Lambda}{\eta_1} + \frac{\Lambda'}{\eta_2} \leq \frac{\lambda}{\eta}$.
Hence, we obtain,
$\lim_{t\to\infty} Sup\ (N(t) + V(t)) \leq \frac{\lambda}{\eta}$.
This proves the boundedness property as discussed in Birkhoff and Rota (1982).

2.1 Existence and Stability of Nonzero Equilibrium Point

The formulated system 2 possesses the nonzero equilibrium point (U_1^*, U_2^*, E^*, V^*), where,

$$U_1^* = \mathcal{A} + \frac{\mathcal{B} k_2 V^*}{k_1(\alpha_2 + \alpha_2 \delta V^* - k_2 V^*)},$$
$$U_2^* = \frac{\mathcal{B}(1+\delta V^*) V^*}{\alpha_2 + \alpha_2 \delta V^* - k_2 V^*}, \quad (3)$$
$$E^* = \frac{\psi V^*}{\beta_1 + \beta_2 + \alpha_3},$$

and V^* is the root of quadratic equation defined by,

$$(k_1\beta_1 \mathcal{C}\alpha_2\delta - k_1 k_2 \beta_1 \mathcal{C} - k_1\alpha_2\delta + k_1 k_2 - \mathcal{B} k_1 k_2) V^{*2} + (\alpha_2 \delta k_1 \Lambda - k_1 k_2 \Lambda + k_1 \alpha_2 \beta_1 A - k_1 \alpha_1 \alpha_2 \mathcal{C}^2 \delta - \mathcal{C}^2 k_1 k_2 \alpha + \beta k_2 \alpha_1 - \mathcal{C}^2 k_1^2 \alpha_2) V^* + k_1 \Lambda \alpha_2 - \mathcal{C}^2 \alpha_1 \alpha_2 k_1 = 0, \quad (4)$$

where $\mathcal{A} = \frac{\psi}{k_1}$, $\mathcal{B} = \frac{\beta_2 \psi}{\beta_1 + \beta_2 + \alpha_3}$, $\mathcal{C} = \frac{\psi}{\beta_1 + \beta_2 + \alpha_3}$.

By using Descartes rule of signs which depends upon the number of changes in sign of coefficients (Wang 2004), the quadratic equation 4 has a unique positive real root V^* if any one of the following condition holds true,

1. • $\beta_1 \mathcal{C}\alpha_2\delta - k_2\beta_1\mathcal{C} - \alpha_2\delta + k_2 - \mathcal{B}k_2 > 0$.
   • $\alpha_2\delta k_1\Lambda - k_1 k_2 \Lambda + k_1\alpha_2\beta_1 A - k_1\alpha_1\alpha_2\mathcal{C}^2\delta - \mathcal{C}^2 k_1 k_2 \alpha + \beta k_2 \alpha_1 - \mathcal{C}^2 k_1^2 \alpha_2 > 0$.
   • $\Lambda - \mathcal{C}^2\alpha_1 < 0$.
2. • $\beta_1 \mathcal{C}\alpha_2\delta - k_2\beta_1\mathcal{C} - \alpha_2\delta + k_2 - \mathcal{B}k_2 > 0$.

- $\alpha_2\delta k_1\Lambda - k_1k_2\Lambda + k_1\alpha_2\beta_1 A - k_1\alpha_1\alpha_2\mathcal{C}^2\delta - \mathcal{C}^2k_1k_2\alpha + \beta k_2\alpha_1 - \mathcal{C}^2k_1^2\alpha_2 < 0.$
- $\Lambda - \mathcal{C}^2\alpha_1 < 0.$

3. - $\beta_1\mathcal{C}\alpha_2\delta - k_2\beta_1\mathcal{C} - \alpha_2\delta + k_2 - \mathcal{B}k_2 < 0.$
   - $\alpha_2\delta k_1\Lambda - k_1k_2\Lambda + k_1\alpha_2\beta_1 A - k_1\alpha_1\alpha_2\mathcal{C}^2\delta - \mathcal{C}^2k_1k_2\alpha + \beta k_2\alpha_1 - \mathcal{C}^2k_1^2\alpha_2 > 0.$
   - $\Lambda - \mathcal{C}^2\alpha_1 > 0.$
4. - $\beta_1\mathcal{C}\alpha_2\delta - k_2\beta_1\mathcal{C} - \alpha_2\delta + k_2 - \mathcal{B}k_2 < 0.$
   - $\alpha_2\delta k_1\Lambda - k_1k_2\Lambda + k_1\alpha_2\beta_1 A - k_1\alpha_1\alpha_2\mathcal{C}^2\delta - \mathcal{C}^2k_1k_2\alpha + \beta k_2\alpha_1 - \mathcal{C}^2k_1^2\alpha_2 < 0.$
   - $\Lambda - \mathcal{C}^2\alpha_1 > 0.$

Thus, U_1^*, U_2^* and E^* can easily be obtained using V^*.

Now, the jacobian matrix corresponding to the system 2 is given by,

$$J = \begin{bmatrix} \mathcal{A} & 0 & \beta_1 & \mathcal{B} \\ 0 & \mathcal{C}' - \alpha_2 & \beta_2 & \mathcal{D} \\ \mathcal{G} & -\mathcal{C}' & \mathcal{E} & -\mathcal{B} - \mathcal{D} \\ 0 & 0 & -\mathcal{E} & -\psi \end{bmatrix},$$

where $\mathcal{A} = -k_1V - \alpha_1$, $\mathcal{B} = -k_1U_1$, $\mathcal{C}' = \frac{k_2V}{1+\delta V} - \alpha_2$, $\mathcal{D} = \frac{k_2U_2}{1+\delta V} - \frac{k_2U_2V\delta}{(1+\delta V)^2}$, $\mathcal{E} = -\alpha_3 - \beta_1 - \beta_2$, $\mathcal{G} = k_1V$.

In addition, the characteristic equation at nonzero equilibrium point is given by,

$$\lambda^4 + A_1\lambda^3 + A_2\lambda^2 + A_3\lambda + A_4 = 0, \tag{5}$$

where

$A_1 = -\mathcal{A} + \psi - \mathcal{D} - \mathcal{E}$,

$A_2 = -\psi\mathcal{A} + \mathcal{A}\mathcal{D} + \mathcal{A}\mathcal{E} + \psi\mathcal{D} - \psi\mathcal{E} + \mathcal{D}\mathcal{E} - \mathcal{E}(\mathcal{B}+\mathcal{D}) + \mathcal{E}\mathcal{C}' + \mathcal{D}\mathcal{G}$,

$A_3 = \psi\mathcal{A}\mathcal{E} + \psi\mathcal{A}\mathcal{E} - \mathcal{A}\mathcal{D}\mathcal{E} + \mathcal{A}\mathcal{E}(\mathcal{B}+\mathcal{D}) - \mathcal{A}\mathcal{E}\mathcal{C}' - \psi\mathcal{D}\mathcal{E} + \mathcal{D}\mathcal{E}(\mathcal{B}+\mathcal{D}) + \psi\mathcal{E}\mathcal{C}' - \mathcal{F}\mathcal{C}'\mathcal{E} - \psi\mathcal{D}\mathcal{G} - \mathcal{D}^2\mathcal{G}$,

$A_4 = -\psi\mathcal{A}\mathcal{D}\mathcal{E} - \mathcal{A}\mathcal{E}\mathcal{D}(\mathcal{B}+\mathcal{D}) - \psi\mathcal{A}\mathcal{E}\mathcal{C}' + \mathcal{A}\mathcal{F}\mathcal{C}'\mathcal{E} + \mathcal{D}^2\mathcal{G}$.

Using Routh Hurwitz criteria, the stability conditions become,

(i) $A_1 > 0$,
(ii) $A_4 > 0$,
(iii) $A_1A_2A_3 > {A_3}^2 + {A_1}^2A_4$.

3 Global Stability

Global stability signifies the high resistance property pertaining to the changes in the system. Section 3 analyzes the global stability conditions of nonzero equilibrium point using the positive definite function based on the work in Santoprete and Xu (2018). Considering a positive definite function as follows,

$$\begin{aligned} V = {} & a_1\left(U_1 - U_1^* - U_1^*\frac{\ln U_1}{U_1^*}\right) \\ & + a_2\left(U_2 - U_2^* - U_2^*\frac{\ln U_2}{U_2^*}\right) \\ & + a_3\left(E - E^* - E^*\frac{\ln E}{E^*}\right) \\ & + a_4\left(V - V^* - V^*\frac{\ln V}{V^*}\right). \end{aligned} \tag{6}$$

Differentiating with respect to 't', we get,

$$\begin{aligned} \frac{dV}{dt} = {} & a_1\left(1 - \frac{U_1^*}{U_1}\frac{dU_1}{dt}\right) \\ & + a_2\left(1 - \frac{U_2^*}{U_2}\frac{dU_2}{dt}\right) + a_3\left(1 - \frac{E_2^*}{E}\frac{dE}{dt}\right) \\ & + a_4\left(1 - \frac{V^*}{V}\frac{dV}{dt}\right). \end{aligned} \tag{7}$$

$$\begin{aligned} V = {} & a_1\frac{(U_1 - U_1^*)}{U_1}\big(k_1(U_1^*V^* - U_1V) \\ & + \alpha(U_1^* - U_1) - \beta_1(E^* - E)\big) \\ & + a_2\frac{(U_2 - U_2^*)}{U_2}\left(k_2\left(\frac{U_2V}{1+\delta V} - \frac{U_2^*V^*}{1+\delta V^*}\right)\right. \\ & \left. + \alpha_2(U_2^* - U_2) + \beta_2(E - E^*)\right) \\ & a_3\frac{(E - E^*)}{E}\left(k_1(U_1V - U_1^* - V^*)\right. \\ & + k_2\left(\frac{U_2^*V^*}{1+\delta V^*} - \frac{U_2V}{1+\delta V}\right) \\ & \left. + \alpha_3(E^* - E) + \beta_1(E^* - E) + \beta_2(E^* - E)\right) \\ & + a_4\left(\frac{V - V^*}{V}\right) \\ & \Big(\beta_1(E - E^*) + \beta_2(E - E^*) \\ & + \alpha_3(E - E^*) + \psi(V^* - V)\Big). \end{aligned}$$

After the simplification process, we get the following as,

$$\begin{aligned} \frac{dv}{dt} = {} & a_1\left(\frac{-\alpha_1}{U_1} - \frac{-k_1V}{U_1}\right)(U_1 - U_1^*)^2 \\ & + a_2\left(\frac{-\alpha_2k_1}{U_2} + \frac{Vk_2}{U_2(1+\delta V)(1+\delta V^*)}\right. \\ & \left. + \frac{\delta VV^*}{U_2(1+\delta V)(1+\delta V^*)}\right)(U_2 - U_2)^2 \end{aligned}$$

$$+a_3\left(\frac{-\alpha_3 k_2}{E}-\frac{\beta_1 k_2}{E}-\frac{\beta_2 k_2}{E}\right)(E-E^*)^2$$
$$-\frac{a_4 k_3 \psi}{V}(V-V^*)^2$$
$$+\left(\frac{a_1\beta_1}{U_1}+\frac{a_3 k_1 V}{E}+\frac{a_1 k_1 V}{E}\right)(E-E^*)(U_1-U_1^*)$$
$$+\left(\frac{a_2\beta_2 k_1}{U_2}+\frac{a_3 V}{E(1+\delta V)(1+\delta V^*)}\right.$$
$$\left.+\frac{a_3\delta V V^*}{E(1+\delta V)(1+\delta V^*)}\right)$$
$$(E-E^*)(U_2-U_2^*)$$
$$+\left(\frac{a_4\beta_1 k_3}{V}+\frac{a_4\beta_2 k_3}{V}+\frac{a_4\alpha_3 k_3}{V}+\frac{a_3 k_1 U_1^*}{E}+\right.$$
$$\left.\frac{a_3 U_2^*}{E(1+\delta V)(1+\delta V^*)}\right)(E-E^*)(V-V^*)$$
$$+\frac{k_1 U_1^* a_1}{U_1}(V-V^*)(U_1-U_1^*)$$
$$+\frac{U_2^* a_2}{U_2(1+\delta V)(1+\delta V^*)}(V-V^*)(U_2-U_2^*).$$

Since, $m_i \le U_i \le M_i$, $i=1,2$, $m_3 \le E \le M_3$, $m_4 \le V \le M_4$.

$$\frac{dv}{dt} \le -a_1\left(\frac{\alpha_1}{M_1}+\frac{k_1 m_4}{M_1}\right)(U_1-U_1^*)^2$$
$$-a_2\left(\frac{-\alpha_2 k_1}{M_2}-\frac{M_4 k_2}{m_2(1+\delta m_4)(1+\delta V^*)}\right.$$
$$\left.-\frac{\delta M_4 V^*}{m_2(1+\delta m_4)(1+\delta V^*)}\right)(U_2-U_2)^2$$
$$-a_3\left(\frac{\alpha_3 k_2}{M_3}+\frac{\beta_1 k_2}{M_3}+\frac{\beta_2 k_2}{M_3}\right)(E-E^*)^2$$
$$-\frac{a_4 k_3 \psi}{M_4}(V-V^*)^2$$
$$+\left(\frac{a_1\beta_1}{m_1}+\frac{a_3 k_1 M_4}{m_3}+\frac{a_1 k_1 M_4}{m_3}\right)$$
$$(E-E^*)(U_1-U_1^*)$$
$$+\left(\frac{a_2\beta_2 k_1}{m_2}+\frac{a_3 M_4}{m_3(1+\delta m_4)(1+\delta V^*)}\right.$$
$$\left.+\frac{a_3\delta M_4 V^*}{m_3(1+\delta m_4)(1+\delta V^*)}\right)(E-E^*)$$
$$(U_2-U_2^*)$$
$$+\left(\frac{a_4\beta_1 k_3}{m_4}+\frac{a_4\beta_2 k_3}{m_4}+\frac{a_4\alpha_3 k_3}{m_4}+\frac{a_3 k_1 U_1^*}{m_3}\right.$$
$$\left.+\frac{a_3 U_2^*}{m_3(1+\delta m_4)(1+\delta V^*)}\right)$$
$$(E-E^*)(V-V^*)+\frac{k_1 U_1^* a_1}{m_1}(V-V^*)(U_1-U_1^*)$$
$$+\frac{U_2^* a_2}{m_2(1+\delta m_4)(1+\delta V^*)}(V-V^*)(U_2-U_2^*).$$

If $Z=\left((U_1-U_1^*),(U_2-U_2^*),(E-E^*),(V-V^*)\right)$ and $D=Diag(a_1,a_2,a_3,a_4), a_i>0, i=1,2,3,4.$

So, $\frac{dV}{dt}=\frac{1}{2}Z(DH+H^TD)Z^T$, with,

$$H=\begin{bmatrix} a & 0 & b & c \\ 0 & d & e & f \\ g & h & k & l \\ 0 & 0 & m & n \end{bmatrix},$$

where

$$a=-a_1\left(\frac{\alpha_1}{M_1}+\frac{k_1 m_4}{M_1}\right),\quad b=\frac{\beta_1}{m_1}+\frac{k_1 m_4}{m_3},$$
$$c=\frac{k_1 U_1^*}{m_1},$$
$$d=-a_2\left(\frac{-\alpha_2 k_1}{M_2}-\frac{M_4 k_2}{m_2(1+\delta m_4)(1+\delta V^*)}\right.$$
$$\left.-\frac{\delta M_4 V^*}{m_2(1+\delta m_4)(1+\delta V^*)}\right),$$
$$e=\frac{\beta_2 k_1}{m_2},\quad f=\frac{U_2^*}{m_2(1+\delta m_4)(1+\delta V^*)},\quad g=\frac{k_1 m_4}{m_3},$$
$$h=\frac{m_4}{m_3(1+\delta m_4)(1+\delta V^*)}+\frac{\delta V^* m_4}{m_3(1+\delta m_4)(1+\delta V^*)},$$
$$k=-a_3\left(\frac{\alpha_3 k_2}{M_3}+\frac{\beta_1 k_2}{M_3}+\frac{\beta_2 k_2}{M_3}\right),$$
$$l=\frac{k_1 U_1^*}{m_3}+\frac{U_2^*}{m_3(1+\delta V^*)(1+\delta m_4)},$$
$$m=\frac{\beta k_3}{m_4}+\frac{\beta_2 k_3}{m_4}+\frac{\alpha_3 k_3}{m_4},$$
$$n=-\frac{a_4 k_3 \psi}{M_4}.$$

All the principal minors of the matrix $-H$ are positive when the following holds,

(i) $adk-aeh-bdg>0$,
(ii) $adkn-adlm-aehn+afhm-bdgn+cdgm>0$.

The matrix H is invertible provided the determinant is nonzero i.e., $cdgm-bdgn-aehn+afhm+adkn-adlm \neq 0$.

4 Model with Optimal Control

The various ways in optimal control develop optimal strategies to control the factors that affect the system. In this section, we develop a model using control variables and verify how effective controls in the model work. Pontryagin's maximum technique provides the necessary conditions for the principle of optimal control system (Schättler and

Ledzewicz 2012; Lenhart and Workman 2007). An optimal control problem is an optimization technique and defined as the process of designing control and state trajectories over time in order to maximize (or minimize) a performance index. The collection of variables used to represent the mathematical state of the system is referred as the state variables. The Cost functional is formulated using state and control variables in an optimal control problem. Let $u(t)$ be the control variable that is used on the state variable $P(t)$, and the state variable constitutes the differential equation that is dependent on the control variable i.e. $P'(t) = g(t, P(t), u(t))$. The goal is to find a control $u(t)$ and its corresponding state variable $P(t)$. The objective functional (maximize/minimize) is given as,

$$\begin{aligned} &\max_u / \min \int_{t_o}^{t_1} f(t, P(t), u(t))dt, \\ &\text{subject to } P'(t) = g(t, P(t), u(t)), \\ &P(t_o) = P_o \text{ and } P(t_1)\ free. \end{aligned} \tag{8}$$

Necessary Conditions Let $u(t)$ be a control affecting the differential equation (DE) and state function $P(t)$ that satisfies the differential equations(DE). Defining Hamiltonin H as

$$H(t, P, u, \lambda) = f(t, P, u) + \lambda g(t, P, u)$$

Let u^* is an optimal control and P^* be the corresponding state. Then the following conditions hold true,
$\frac{\partial H}{\partial u} = 0$ at $u^* \implies f_u + \lambda g_u = 0$ (optimality condition),
$\lambda^{'} = -\frac{\partial H}{\partial p} \implies \lambda^{'} = -(f_p + \lambda g_p)$ (adjoint equation),
$\lambda(t_1) = 0$(transversality condition).

Sufficient Conditions

Theorem 1 *Consider*

$$\begin{aligned} &J(u) = \int_{t_o}^{t_1} f(t, p(t), u(t))dt, \\ &\text{subject to } p'(t) = g(t, p(t), u(t)),\ p(t_0) = p_0. \end{aligned}$$

Assuming $f(t, P, u)$ and $g(t, P, u)$ as both continuously differentiable functions in their arguments and concave in P and u. If u^* is a control with associated states p^*, and λ are the piecewise differentiable functions. Moreover, u^*, P^* and λ fulfil on $t_0 \le t \le t_1$ and,

$$\begin{aligned} &f_u + \lambda g_u = 0, \\ &\lambda' = -(f_P + \lambda g_p), \\ &\lambda(t_1) = 0, \\ &\lambda(t) \ge 0. \end{aligned}$$

Then, for all controls u, we have $J(u^*) \ge J(u)$.

When the problem is minimization rather than maximizing, a similar approach gives the same required conditions. We minimise the Hamiltonian pointwise in a minimization problem, and the inequality in Pontryagin's Maximum Principle is reversed. However, f and g are convex in u in minimization problem.

Optimal control assessment is performed to study the effectiveness of all possible combinations of control measures in the system. The Covid-19 problem has a significant impact on employment across the globe. The set of measures to improve employment, includes the monetary and fiscal policies, education and training to decrease structural unemployment, geographic incentives to encourage businesses to invest in struggling regions, a lower national salary to minimize the real pay unemployment, more flexible labor markets and easy measures to hire employees. For economic growth and sustainable development, a transformational strategy is adopted. The strategy is supported by seven engines, including logistical infrastructure, mass transit, rivers, airports, and trains. This strategy provides numerous career and business options. The comprehensive effect of all these measures are anticipated to increase output and create jobs jointly. The creation of job possibilities is another goal of infrastructure development and industrial corridors. The aforementioned strategies can all be used as a control to enhance employment. Firstly, providing education and training of job-oriented and secondly, campaigning about awareness of the corona and self-employment business are the two taken control measures. The self-employment business means drop shipping, blogging, chocolate making, toy making, brew making, interior designer/home decorator, event planning, fashion designing, dog walking, makeup artist, personal trainer/gym instructor, landscaper architecture, tutoring, food cart franchise, logo designing, E-Bay merchant, computer repairing, picture framing, local tour guide, recycling services, soap/detergent making, repair services, food business, home-based restaurant, laundry services, social media expert, resume writing, agriculture works etc. Hence, a model is considered on unemployment by taking two time-dependent controls. Initially, the formulated problem is studied with its existence of control and time dependent control parameters are considered. The total impact of all measures in controlling unemployment due to corona is examined. The optimal level needed to control unemployment is minimizing the number of unemployment population. The model is discussed by inculcating the following two controls: (i) u_1-providing education and training of job-oriented and (ii) u_2-campaigning about the awareness of corona and self-employment business especially during the pandemic times. The control functions, $u_1(t)$ and $u_2(t)$ are bounded and Lebesgue integrable functions. So, the model with two control strategies is given below,

$$\begin{cases} \frac{dU_1}{dt} = \Lambda - k_1 U_1 V - \alpha_1 U_1 + \beta_1 E - b_1 u_1 U_1, \\ \frac{dU_2}{dt} = \frac{k_2 U_2 V}{1+\delta V} - \alpha_2 U_2 + \beta_2 E - b_2 u_2 U_2, \\ \frac{dE}{dt} = k_1 U_1 V - \frac{k_2 U_2 V}{1+\delta V} - \alpha_3 E - \beta_1 E - \beta_2 E, \\ \frac{dV_1}{dt} = \beta_1 E + \beta_2 E + \alpha_3 E - \psi V. \end{cases} \tag{9}$$

$$J(u_1, u_2) = \min_{u_1,u_2} \int_0^{T_f} (A_1 U_1(t) + A_2 U_2(t) + A_3 u_1^2(t) + A_4 u_2^2(t))dt, \tag{10}$$

where $A_1 > 0$, $A_2 > 0$, $A_3 > 0$ and $A_4 > 0$ are weights. A_1 corresponds to the unemployed class and A_2 associates with the unemployed class due to Covid-19. A_3 and A_4 are the parameters attached with ${u_1}^2$ and ${u_2}^2$ respectively.

$$J(u_1^*, u_2^*) = min\{J(u_1, u_2) | u_1.u_2 \in U\}, \tag{11}$$

where U is control set defined as,

$$U = \{u(t) | u(t) \text{ lebesgue measurable with } 0 \le t \le 1,\ t \in [0, T]\}. \tag{12}$$

Based on the relative significance, the weights of state variables are allocated. Using Pontryagin's maximum principle (Pontryagin et al. 1962), the evaluation criteria is obtained for the control value such that J is optimized. Occurrence of this feasible control is recognized as optimal control (Clark 1990; Lenhart and Workman 2007).

Theorem 2 *Given the objective functional* $J(u_1, u_2) = \min_{u_1,u_2} \int_0^{T_f} (A_1 U_1(t) + A_2 U_2(t) + A_3 u_1(t)^2 + A_4 u_2(t)^2)dt$, *with initial data* $U_1(0) = U_{10} > 0$, $U_2(0) = U_{20} > 0$, $E(0) > 0$, $V(0) > 0$, $t \in [0, T_f]$. $u(t)$ *is measurable with* $0 \le u(t) \le 1$, *then there are optimal controls* $u_1^*(t)$ *and* $u_2^*(t)$ *to minimize the objective functional* $J(u_1, u_2)$ *such that* $J(u_1^*, u_2^*) = min\{J(u_1, u_2) | 0 \le u_1(t), u_2(t) \le 1\}$.

Proof To prove the existence of optimal control, the following conditions are to be fulfilled,

(i) The non empty state variables and controls.
(ii) The control set U is closed and convex.
(iii) Objective functional is convex in U.
(iv) The system of the state must be bounded by a linear function having state and control variables with coefficients as dependent on state and time.
(v) The integrand bounded below by $c_1(|u|^2)^{\frac{\beta}{2}} - c_2$ for $c_1 > 0$, $c_2 > 0$ and $\beta > 1$.

Using (Fleming and Rishel 2012; Lenhart and Workman 2007), the above stated conditions are true. Clearly, the state and control variables attain non-negative values and convexity of the objective functional in $u(t)$ exist in the minimization problem. The control along with the admissible Lebesgue measurable control variables set $u(t)$ are convex and closed. Further, $f(t, , u_1, u_2) = (A_1 U_1(t) + A_2 U_2(t) + A_3 u_1^2(t) + A_4 u_2^2(t))$ is convex in u_1 and u_2. For verifying (iv), RHS of equation (9) is written as,

$$\overrightarrow{g}(t, \overrightarrow{P}, u) = \overrightarrow{\alpha}(t, \overrightarrow{P}) + \overrightarrow{\beta}(t, \overrightarrow{P})u, \tag{13}$$

where $\overrightarrow{P} = (U_1, U_2, E, V)$, $\overrightarrow{\alpha}$, $\overrightarrow{\beta}$ as vector valued function of $\overrightarrow{P}$ and $u = (u_1, u_2)$,

$$\begin{aligned} |\overrightarrow{g}(t, \overrightarrow{P}, u)| &\le \left| \begin{pmatrix} \frac{N}{m} & 0 & \beta_1 & 0 \\ 0 & \frac{K}{\delta} & \beta_2 & 0 \\ 0 & 0 & 0 & k_1 M \\ 0 & 0 & \beta_1 + \beta_2 + \alpha_3 & 0 \end{pmatrix} \begin{pmatrix} U_1 \\ U_2 \\ E \\ V \end{pmatrix} \right| \\ &\quad + \begin{pmatrix} -b_1 u_1 U_1 \\ -b_2 u_2 U_2 \\ 0 \\ 0 \end{pmatrix} \\ &\le C_1 |P| + C_2 |u|. \end{aligned}$$

where $m \le U_1 \le M$. C_1 depends on the coefficients of the system and C_2 is maximum norm value. For the last conditions,

$$\begin{aligned} &A_1 U_1(t) + A_2 U_2(t) + A_3 u_1^2(t) + A_4 u_2^2(t) \\ &\quad \ge A_3 u_1^2(t) + A_4 u_2^2(t) \ge c_1(|u_1|^2 + |u_2|^2)^{\frac{\beta}{2}} - c_2. \end{aligned}$$

Thus, the integrand bounded below by $c_1(|u_1|^2 + |u_2|^2)^{\frac{\beta}{2}} - c_2$ for $c_1 > 0$, $c_2 > 0$ and $\beta > 1$.

Theorem 3 *If* $u_1^*(t)$ *and* $u_2^*(t)$ *be an optimal control which minimize* $J(u_1, u_2)$. *Let* $U_1^*(t)$, $U_2^*(t)$ $E^*(t)$ *and* $V^*(t)$ *be the optimal state solutions of control system* (9), *such that there exist adjoint variables* $\lambda_1(t)$, $\lambda_2(t)$, $\lambda_3(t)$ *and* $\lambda_4(t)$ *which leads to the following:*

$$\begin{cases} \frac{d\lambda_1}{dt} = -A_1 + \lambda_1(\alpha_1 + b_1 u_1) + (\lambda_1 - \lambda_3) k_1 V, \\ \frac{d\lambda_2}{dt} = -A_2 - \lambda_2 \left(-\alpha_2 - b_2 u_2 + \frac{k_2 V}{\delta V + 1}\right) + \frac{\lambda_3 k_2 V}{\delta V + 1}, \\ \frac{d\lambda_3}{dt} = -\lambda_3(-\alpha_3 - \beta_1 - \beta_2) - \lambda_4(\alpha_3 + \beta_1 + \beta_2) \\ -\beta_1 \lambda_1 - \beta_2 \lambda_2, \\ \frac{d\lambda_4}{dt} = \lambda_4 \psi + \lambda_1 k_1 U_1 \\ -\lambda_2 \left(\frac{k_2 U_2}{\delta V + 1} - \frac{\delta k_2 U_2 V}{(\delta V + 1)^2}\right) - \lambda_3 \left(\frac{\delta k_2 U_2 V}{(\delta V + 1)^2} - \frac{k_2 U_2}{\delta V + 1} + k_1 U_1\right), \end{cases}$$

with the transversality conditions as,

$$\lambda_i(T_f) = 0 \text{ for } i = 1, 2, 3, 4.$$

Further, the optimal control variable u_1^* and u_2^* that minimize $J(u_1, u_2)$ are given by,

$$u_1^*(t) = min\left\{max\left\{0, \frac{b_1\lambda_1 U_1}{2A_3}\right\}, 1\right\}.$$
$$u_2^*(t) = min\left\{max\left\{0, \frac{b_2\lambda_2 U_2}{2A_4}\right\}, 1\right\}.$$

Proof The transversality and adjoint conditions as given in Lenhart and Workman (2007), Kamien and Schwartz (2012) and Schättler and Ledzewicz (2012) and using the Hamiltonian function H, we get,

$$H(t, \overrightarrow{P}, \overrightarrow{u}) = f(t, \overrightarrow{P}, \overrightarrow{u}) + \lambda_i \sum_{i=1}^{4} g_i(t, \overrightarrow{P}, \overrightarrow{u}),$$

where $f(t, \overrightarrow{P}, \overrightarrow{u})$ is integrand of the functional and $g_i(t, \overrightarrow{P}, \overrightarrow{u})$ are state equations.

$$\begin{aligned}
&H(t, \lambda(t), P(t))\\
&= A_3u_1^2 + A_4u_2^2 + A_1U_1 + A_2U_2 + \lambda_1\\
&\quad(-b_1u_1U_1 + \beta_1 e - k_1U_1V + N - \alpha_1U_1)\\
&\quad+ \lambda_2\left(-b_2u_2U_2 + \beta_2 e + \frac{k_2U_2V}{\delta V + 1} - \alpha_2U_2\right)\\
&\quad+ \lambda_3\left(-\alpha_3 e - \beta_1 e - \beta_2 e - \frac{k_2U_2V}{\delta V + 1} + k_1U_1V\right)\\
&\quad+ \lambda_4(\alpha_3 e + \beta_1 e + \beta_2 e - V\psi),
\end{aligned}$$

where $\lambda_1(t), \lambda_2(t), \lambda_3(t)$ and $\lambda_4(t)$ are the adjoint functions. Using the Pontryagin's maximum principle (Schättler and Ledzewicz 2012) provides adjoint system, which can be followed as,

$$\begin{aligned}
\frac{d\lambda_1}{dt} &= -\frac{\partial H}{\partial U_1} = -A_1 + \lambda_1(\alpha_1 + b_1u_1) + (\lambda_1 - \lambda_3)k_1V,\\
\frac{d\lambda_2}{dt} &= -\frac{\partial H}{\partial U_2} = -A_2 - \lambda_2\left(-\alpha_2 - b_2u_2 + \frac{k_2V}{\delta V + 1}\right)\\
&\quad+ \frac{\lambda_3k_2V}{\delta V + 1},\\
\frac{d\lambda_3}{dt} &= -\frac{\partial H}{\partial E} = -\lambda_3(-\alpha_3 - \beta_1 - \beta_2)\\
&\quad- \lambda_4(\alpha_3 + \beta_1 + \beta_2) - \beta_1\lambda_1 - \beta_2\lambda_2,\\
\frac{d\lambda_4}{dt} &= -\frac{\partial H}{\partial V} = \lambda_4\psi + \lambda_1k_1U_1\\
&\quad- \lambda_2\left(\frac{k_2U_2}{\delta V + 1} - \frac{\delta k_2U_2V}{(\delta V + 1)^2}\right)\\
&\quad- \lambda_3\left(\frac{\delta k_2U_2V}{(\delta V + 1)^2} - \frac{k_2U_2}{\delta V + 1} + k_1U_1\right).
\end{aligned}$$

The transversality conditions are,

$$\lambda_i(T_f) = 0 \text{ for } i = 1, 2, 3, 4.$$

The optimality condition provides,

$$\begin{aligned}
\frac{\partial H}{\partial u_1} &= 2A_3u_1 - b_1\lambda_1U_1 = 0 \, at \, u_1 = u_1^*(t),\\
&\Rightarrow u_1^*(t) = \frac{b_1\lambda_1U_1}{2A_3}.
\end{aligned}$$

Using bound on control (Lenhart and Workman 2007), we obtain optimal control,

$$u_1^*(t) = \begin{cases} \frac{b_1\lambda_1U_1}{2A_3}, & \text{if } 0 \le \frac{b_1\lambda_1U_1}{2A_3} \le 1,\\ 0, & \text{if } \frac{b_1\lambda_1U_1}{2A_3} < 0,\\ 1, & \text{if } \frac{b_1\lambda_1U_1}{2A_3} > 1. \end{cases}$$

Further, $u_1^*(t)$ can be represented in a compact form (by combining all the above three cases) as,

$$u_1^*(t) = min\left\{max\left\{0, \frac{b_1\lambda_1U_1}{2A_3}\right\}, 1\right\},$$

and

$$\begin{aligned}
\frac{\partial H}{\partial u_2} &= 2A_4u_2 - b_2\lambda_2U_2 = 0 \, \text{at} \, u_2 = u_2^*(t),\\
&\Rightarrow u_2^*(t) = \frac{b_2\lambda_2U_2}{2A_4}.
\end{aligned}$$

Using bound on control (Lenhart and Workman 2007), we obtain,

$$u_2^*(t) = \begin{cases} \frac{b_2\lambda_2U_2}{2A_4}, & \text{if } 0 \le \frac{b_2\lambda_2U_2}{2A_4}\} \le 1,\\ 0, & \text{if } \frac{b_2\lambda_2U_2}{2A_4} < 0,\\ 1, & \text{if } \frac{b_2\lambda_2U_2}{2A_4} > 1. \end{cases}$$

Further, $u_2^*(t)$ is represented in compact form by combining all the cases (above).

$$u_2^*(t) = min\left\{max\left\{0, \frac{b_2\lambda_2U_2}{2A_4}\right\}, 1\right\}.$$

4.1 Optimal System

The optimal system (includes the adjoint system and state system) along with the initial and transversality conditions is,

$$\begin{aligned}
\frac{dU_1}{dt} &= N - k_1U_1V\\
&\quad- \alpha_1U_1 + \beta_1E - b_1U_1\, min\left\{max\left\{0, \frac{b_1\lambda_1U_1}{2A_3}\right\}, 1\right\},
\end{aligned}$$

$$\frac{dU_2}{dt} = \frac{k_2 U_2 V}{1+\delta V} - \alpha_2 U_2 + \beta_2 E - b_2 U_2 \, min\left\{max\left\{0, \frac{b_2\lambda_2 U_2}{2A_4}\right\}, 1\right\},$$

$$\frac{dE}{dt} = k_1 U_1 V - \frac{k_2 U_2 V}{1+\delta V} - \alpha_3 E - \beta_1 E - \beta_2 E,$$

$$\frac{dV_1}{dt} = \beta_1 E + \beta_2 E + \alpha_3 E - \psi V,$$

$$\frac{d\lambda_1}{dt} = -A_1 + \lambda_1\left(\alpha_1 + b_1 \, min\left\{max\left\{0, \frac{b_1\lambda_1 U_1}{2A_3}\right\}, 1\right\}\right) + (\lambda_1 - \lambda_3) k_1 V,$$

$$\frac{d\lambda_2}{dt} = -A_2 - \lambda_2\left(-\alpha_2 - b_2 \, min\left\{max\left\{0, \frac{b_2\lambda_2 U_2}{2A_4}\right\}, 1\right\} + \frac{k_2 V}{\delta V + 1}\right) + \frac{\lambda_3 k_2 V}{\delta V + 1},$$

$$\frac{d\lambda_3}{dt} = -\lambda_3(-\alpha_3 - \beta_1 - \beta_2) - \lambda_4(\alpha_3 + \beta_1 + \beta_2) - \beta_1\lambda_1 - \beta_2\lambda_2,$$

$$\frac{d\lambda_4}{dt} = \lambda_4\psi + \lambda_1 k_1 U_1 - \lambda_2\left(\frac{k_2 U_2}{\delta V + 1} - \frac{\delta k_2 U_2 V}{(\delta V + 1)^2}\right) - \lambda_3\left(\frac{\delta k_2 U_2 V}{(\delta V + 1)^2} - \frac{k_2 U_2}{\delta V + 1} + k_1 U_1\right),$$

and subject to the following conditions,

$$U_1(0) = U_{10},\ U_2(0) = U_{20},\ E(0) = E_0,$$
$$V(0) = V_0,\ \lambda_i(T_f) = 0 \text{ for } = 1, 2, 3, 4.$$

5 Numerical Simulation of the Model

As the optimal control problem is arduous to solve, so forward-backward sweep method with the help of fourth order Runge–Kutta method is used and the successive steps are given in Lenhart and Workman (2007) and Kar and Ghosh (2012).

To solve the optimality system, we use the Runge–Kutta forward-backward sweep procedure, which is a more accurate and effective technique. Firstly, we start with the initial guess of the control variable and then the system of state equations are approximately solved with the given initial condition forward in time. After that, all adjoint is simultaneously solved backward in time. Thus, the state equation is solved in forward time using the Runge–Kutta method with initial conditions as P_{10} and P_{20}. Using initial guessed control value and state values, the adjoint equations are solved backward in time along with transversality conditions.

Subsequently, the value of control is updated using the state values, adjoint values together with the average value of previous control and new control. Thus, the process is repeated for updating control until convergence occurs. The choices of the bound for the control are selected between 0 and 1 because the control would not be 100% effective. In this problem, we have considered hypothetical data for the purpose of verifying the results.

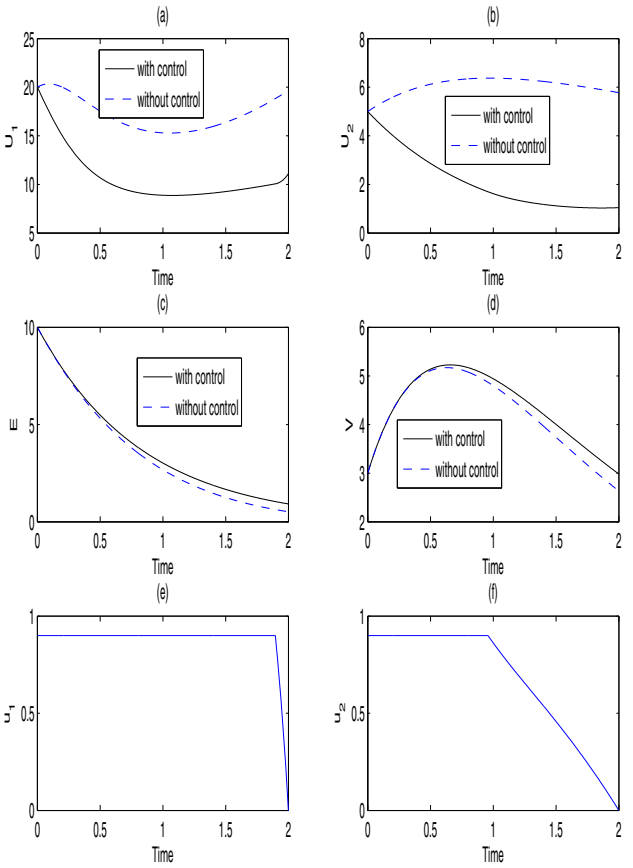


Fig. 2 Representation of U_1, U_2, E, V and control variables with respect to time, where the values of the parameters are $A_1 = 1$, $A_2 = 1$, $A_3 = 1$, $A_4 = 1$, $b_1 = 2$, $b_2 = 2$, $n = 38$, $k_1 = 0.5$, $\beta_1 = 0.4$, $\delta = 0.7$, $\alpha_1 = 0.2$, $k_2 = 0.003$, $\alpha_2 = 0.2$, $\beta_2 = 0.45$, $\alpha_3 = 0.3$, $\psi = 1$, $U_{10} = 20$, $U_{20} = 5$, $E_0 = 10$, $V_0 = 3$, and $t = 2$

In Fig. 2, the computational analysis on the control of unemployment populations is addressed. The results represent the unemployment and employment populations due to Covid-19 in the presence and absence of control. In Fig. 2a, U_1 population is 10.1 unit in the presence of control, while 20 units in the absence of control. In Fig. 2b, U_2 is approximately 0.5 unit populations with control and 5.9 without control. Consequently, the unemployment declines in the presence of control as compared to the absence of control. Further, Fig. 2c, d show that the population of E and V increase in the presence of control.

Figure 2e, f show the variation and convergence of the control. Figure 3 represents the variation of the adjoint variables $\lambda_1, \lambda_2, \lambda_3$ and λ_4 with respect to time. In Fig. 4, the numerical output of control problem shows the variation in unemployed and employed population with the optimal strategy compared to prey populations not having a control technique. Here,

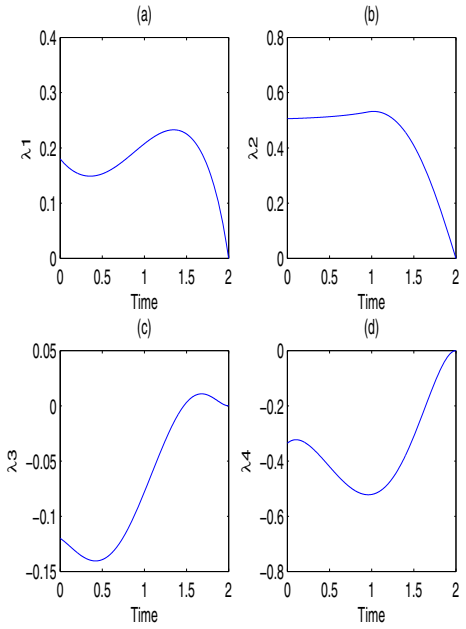


Fig. 3 Variation of adjoint variables with respect to time for $A_1 = 50$, $A_2 = 10$, $A_3 = 1$, $r_1 = 0.8$, $i_1 = 0.3$, $d_1 = 1$, $c_1 = 0.4$, $m_1 = 0.9$, $r_2 = 0.6$, $i_2 = 0.4$, $c_2 = 0.5$, $d_2 = 1$, $U_{10} = 20$, $U_{20} = 5$, $E_0 = 10$, $V_0 = 3$, and $t = 2$

we take some other value of the parameters compared to Fig. 2, i.e., $A_3 = 0.1$, $A_4 = 0.1$, $k_1 = 0.3$, $\beta_1 = 0.35$, $\delta = 0.7$, $\alpha = 0.3$, $k_2 = 0.003$, which are shown in Fig. 4. In Fig. 4, U_1 population has an approximate value of 12 individuals and 28 individuals with control and without control respectively at 2 units time. Similarly, U_2 population has a value of approximately 1 individual with control and 5.8 value without control at 2 units time. Further, the population E and V have more value with control compared to without control. In Fig. 4, the cost-effectiveness is less compared to Fig. 2. Figure 4e, f show the variation and convergence of the control variables. The Figs. 3 and 5 represent the four adjoint variables λ_1, λ_2, λ_3, and λ_4 in the population, and we solve these adjoint by a backward fourth-order Runge–Kutta procedure. It is seen in Fig. 3 that declination in the value of λ_1 leads to decline in control u_1. Similarly, when the value of λ_2 declines, the control u_2 plunges too. Initially, the values of λ_3 and λ_4 are extremely low, but after sometime, the values of adjoint variables grow with respect to time t. Figure 5 depicts the variation of λ_1, λ_2, λ_3, and λ_4 when different parameter values are varied in comparison to Fig. 3.

6 Discussion and Future Scope

In this study, we have presented mathematical model with control and without control using a system of ordinary differential equations. Various parameters used in the model

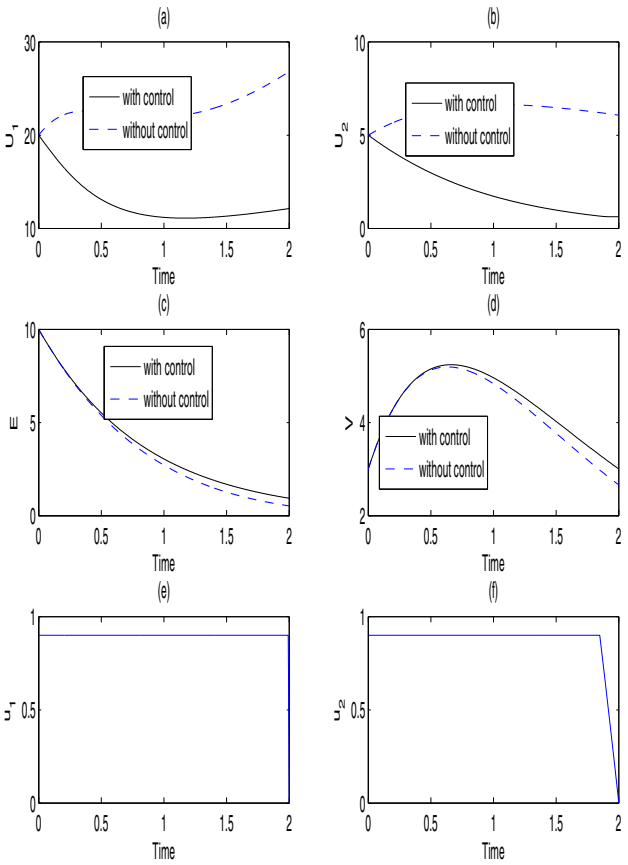


Fig. 4 Representation of U_1, U_2, E, V and control variables with respect to time, where the values of the parameters are $A_1 = 1$, $A_2 = 1$, $A_3 = 0.1$, $A_4 = 0.1$, $b_1 = 2$, $b_2 = 2$, $n = 38$, $k_1 = 0.3$, $\beta_1 = 0.35$, $\delta = 0.6$, $\alpha_1 = 0.3$, $k_2 = 0.003$, $\alpha_2 = 0.2$, $\beta_2 = 0.5$, $\alpha_3 = 0.2$, $\psi = 1$, $U_{10} = 20$, $U_{20} = 5$, $E_0 = 10$, $V_0 = 3$, and $t = 2$

influences the system and the proposed approach. Like k_1 and k_2 illustrates the conversion rate of unemployed class to employed and employed class to unemployed respectively. High or low value of these parameters will lead to increase or decrease the class of population (Unemployed and employed). Similarly, other parameters are highly impactful for optimizing the process of employment. Local and global stability results are derived. Two controls have been introduced in the model where providing education and training of job-oriented is one control parameter, and the other one is campaigning about awareness of the corona and self–employment business. Further, b1 and b2 are the coefficients of control variables which are used to reduce the number of jobless people and raise the number of employed people. In examining the effect of optimal control strategies, we have analysed the existence conditions for optimal control. Further, the control model is solved by numerical techniques by taking assumed suitable parameters and various numerical results which are obtained with different values of parameters. Figures 2 and 4 shows that the unemployment is reduced

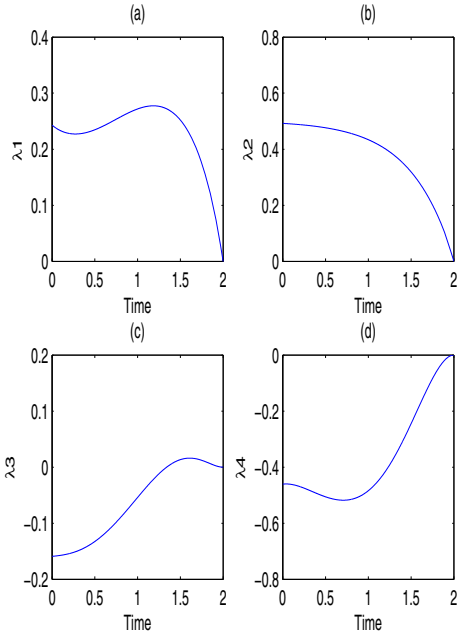


Fig. 5 Variation of adjoint variables with respect to time for $A_1 = 1$, $A_2 = 1$, $A_3 = 0.1$, $A_4 = 0.1$, $b_1 = 2$, $b_2 = 2$, $n = 38$, $k_1 = 0.3$, $\beta_1 = 0.35$, $\delta = 0.6$, $\alpha_1 = 0.3$, $k_2 = 0.003$, $\alpha_2 = 0.2$, $\beta_2 = 0.5$, $\alpha_3 = 0.2$, $\psi = 1$, $U_{10} = 20$, $U_{20} = 5$, $E_0 = 10$, $V_0 = 3$, and $t = 2$

in the presence of control variables. More focus can be drawn on taking some other control in place of the present examined control in the future or remodel the system by introducing more parameters to provide an alternative way of controlling the predator, which also restores the balance of the ecosystem.

Funding No funding is received for this research paper.

Declarations

Conflict of interest The authors declare no conflict of interest.

References

Abu Arqub O, Shawagfeh N (2021) Solving optimal control problems of Fredholm constraint optimality via the reproducing kernel Hilbert space method with error estimates and convergence analysis. Math Methods Appl Sci 44(10):7915–7932

Birkhoff G, Rota GC (1982) Ordinary differential equations. Ginn, Boston

Clark CW (1990) Mathematical bioeconomics: the optimal management of renewable resources, vol 1. Willy, New York, pp 9–62

Djennadi S, Shawagfeh N, Arqub OA (2021a) A fractional Tikhonov regularization method for an inverse backward and source problems in the time-space fractional diffusion equations. Chaos Solitons Fractals 150:111127

Djennadi S, Shawagfeh N, Osman MS, Gómez-Aguilar JF, Arqub OA (2021b) The Tikhonov regularization method for the inverse source problem of time fractional heat equation in the view of ABC-fractional technique. Phys Scr 96(9):094006

Fleming WH, Rishel RW (2012) Deterministic and stochastic optimal control, vol 1. Springer, Berlin

Gakkhar S, Singh A (2012) Control of chaos due to additional predator in the Hastings–Powell food chain model. J Math Anal Appl 385(1):423–438

Kamien MI, Schwartz NL (2012) Dynamic optimization: the calculus of variations and optimal control in economics and management. Courier Corporation, North Chelmsford

Kar TK, Ghosh B (2012) Sustainability and optimal control of an exploited prey predator system through provision of alternative food to predator. Biosystems 109(2):220–232

Khajanchi S (2014) Dynamic behavior of a Beddington–DeAngelis type stage structured predator–prey model. Appl Math Comput 244:344–360

Lenhart S, Workman JT (2007) Optimal control applied to biological models. CRC Press, Boca Raton

Mallick UK, Biswas MHA (2017) Optimal control strategies applied to reduce the unemployed population. In: 2017 IEEE Region 10 humanitarian technology conference (R10-HTC). IEEE, pp 408–411

Mallick UK, Biswas MHA (2020) Mathematical approach with optimal control: reduction of unemployment problem in Bangladesh. J Appl Nonlinear Dyn 9(2):231–246

Misra AK, Singh AK (2011) A mathematical model for unemployment. Nonlinear Anal Real World Appl 12(1):128–136

Munoli SB, Gani S (2016) Optimal control analysis of a mathematical model for unemployment. Optim Control Appl Methods 37(4):798–806

Munoli SB, Gani S, Gani SR (2017) A mathematical approach to employment policies: an optimal control analysis. Int J Stat Syst 12(3):549–565

Nagumo M (1942) Über die lage der integralkurven gewöhnlicher differentialgleichungen. In: Proceedings of the physico-mathematical society of Japan. 3rd Series, vol 24, pp 551–559

Pontryagin LS, Boltyanskii VG, Gamkrelidze RV, Mishchenko EF (1962) The maximum principle. The mathematical theory of optimal processes. Wiley, New York

Santoprete M, Xu F (2018) Global stability in a mathematical model of de-radicalization. Phys A 509:151–161

Schättler H, Ledzewicz U (2012) The pontryagin maximum principle: from necessary conditions to the construction of an optimal solution. In: Geometric optimal control. Springer, New York, pp 83–194

Sweis H, Shawagfeh N, Arqub OA (2022) Fractional crossover delay differential equations of Mittag–Leffler kernel: existence, uniqueness, and numerical solutions using the Galerkin algorithm based on shifted Legendre polynomials. Results Phys 41:105891

Wang X (2004) A simple proof of Descartes's rule of signs. Am Math Mon 111(6):525

Yousefpour A, Jahanshahi H, Bekiros S (2020) Optimal policies for control of the novel coronavirus disease (COVID-19) outbreak. Chaos Solitons Fractals 136:109883

Springer Nature or its licensor (e.g. a society or other partner) holds exclusive rights to this article under a publishing agreement with the author(s) or other rightsholder(s); author self-archiving of the accepted manuscript version of this article is solely governed by the terms of such publishing agreement and applicable law.

Optimization of PV array with PID controller and MPPT(P&O)

Shilpa Saxena
Electrical Engineering dept.
Amity University Uttar Pradesh Noida
Noida, India
shilpasxna@gmail.com

V.K Tayal
Electrical Engineering dept.
Amity University Uttar Pradesh Noida
Noida, India

H.P Singh
Electrical Engineering dept.
Amity University Uttar Pradesh Noida

Vinod Kumar Yadav
Electrical Engineering dept.
Delhi Technological University Delhi
Delhi, India

2023 International Conference on Device Intelligence, Computing and Communication Technologies, (DICCT) | 978-1-6654-7491-7/23/$31.00 ©2023 IEEE | DOI: 10.1109/DICCT56244.2023.10110277

***Abstract*— Due to depletion in fossil fuel resources, alternate energies are gaining importance. Further, adverse effects of global warming, increased installation and fuel costs of conventional energy sources in remote areas motivates to switch to suitable renewable resources including fuel cells, wind energy, photovoltaic cells etc. Such renewable energy resources are clean, pollution free and cost effective as compared to conventional fuels. Due to readily availability of the photovoltaic energy, it finds most usage. There is continuous rise in applications of photovoltaic (PV) solar panels, however the output voltage obtained from it is very low. Thus, there is need for suitable control technique to enhance the output voltage level. This paper presents the comparison of two techniques namely PID control and maximum power point tracking (MPPT) techniques for voltage enhancement of a PV panel. The MPPT technique utilizes perturb and observe (P&O) algorithm. The output results of Simulink models indicates that there is a substantial increase in output voltage with good stability by MPPT (P&O) technique.**

Keywords— Solar energy, Photovoltaic, Boost converter, PID controller, MPPT and P&O.

I. INTRODUCTION

Renewable energy resources are the need of hour due to increased global warming. Also, everyone across the world is running towards energy crisis with increase in population. So, for survival one should switch towards the use of renewable energy resources as early as possible.

In real time, various renewable resources options available such as tidal energy, wave energy, ocean currents, biomass, geothermal, wind, photovoltaic etc. This paper discusses PV array panels as a renewable resource. There are certain limitations of PV array panel modules such as (a) cost of installation is too high (b) Efficiency of conversion is low (c) non-linear power- voltage curves (d) weather dependents.

Hence maximum power point should be searched so that whole photovoltaic system (converters, photovoltaic panel, etc.) works at optimized efficiency and generates optimized power at output.

Various methods have been implemented to track maximum power point which can broadly classified as direct and indirect methods and can be used for intelligent (using artificial intelligence) and optimization purpose as and when required as per the application[1]. Different techniques are already discussed with their pros and cons[2–4]. The main aim is to harvest efficiently the energy from renewable energy resources (here PV array) and which can optimally be used with desired loads. As efficiency of solar panels are very low [5, 6] hence there is a great need of increasing it and also efficiency decreases further if no load matching is there hence it is the necessity to operate the panels at its maximum output [7]. Also due to use of non linear loads which lead to increasing no of power quality problems which in turn lead to decreased performance of microelectronic circuits. Thus can be minimized using active filters [8]. Also controlled output should be available at load terminal thus different control techniques using controller can be used such as PID [9], robust, infinity loop, fuzzy logic [10, 11], MPPT[12], PO [13] etc. Many different techniques were introduced to optimize the performance of different renewable energy resources such as PV array system [14, 15], fuel cell [16–20], wind etc in a hybrid mode [21–24] and implemented in MATLAB and Simulink environment and compared implementing different control techniques such as fuzzy logic control technique, sliding mode and many more robust control techniques along with the application of artificial intelligence.

This paper proposed the two techniques to enhance the voltage at the output side of photovoltaic array (here six solar cells of equal rating 3 volts, connected in series) thereby improving the efficiency and thus optimizing the performance. Firstly a boost converter-closed loop PID controller is incorporated with the photovoltaic panel and secondly same setup but with MPPT(P&O)-boost converter is implemented. The analysis of simulation results shows: (a) Output voltage using boost converter- PID controller is varying from 40 volts to 80 volts with a average value of 60 volts. However with boost converter –MPPT (P&O) , it is constant at a value of 160 volt (b) The percentage increase in voltage at the output side with MPPT(P&O) - boost converter is much higher.

This paper is organized as follows: PV array conversion process is explained in section II whereas as design of controller (PID) and MPPT using Perturb and Observe alogorithm are introduced in sections III and IV respectively. Detailed simulink and MATLAB modelling has been discussed in section V. Results and conclusions are presented in section VI and VII respectively, after comparing the scope results obtained after implementing different techniques.

II. PV ARRAY

The proposed system comprises of series connected six solar cells of equal rating of 3V to form photovoltaic array

Authorized licensed use limited to: DELHI TECHNICAL UNIV. Downloaded on May 04,2023 at 06:36:30 UTC from IEEE Xplore. Restrictions apply.

panel which is implemented for photon energy to electrical energy conversion.

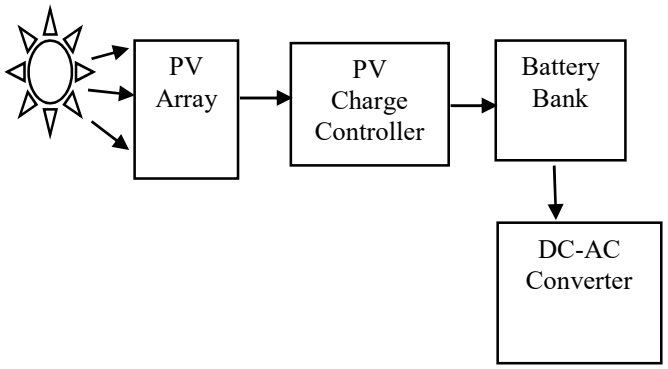


Fig. 1. PV Array Conversion process

Fig.1 depicts the PV Array conversion process. This process is divided into following steps:-

(a) Absorption of solar irradiations by PV array (b) Conversion of solar energy into electrical energy (c) Storage of electrical energy (DC) in battery bank using charge controller (charge controller regulates the charging of battery bank) (d) Conversion of DC into AC using DC-AC converters (e) Supply to the utility grid and which can further be used for any desired application.

III. PID Controller Design

The PID controllers has wide industrial applications used to regulate pressure, speed, temperature, etc. It produces an output signal with a feedback loop control which is proportional to (a) error signal (b) integral of error signal and (c) derivative of the error signal.

This controller with feedback loop provides very good accuracy and stability. The proportional controller provides the advantages of stablized gain and shows a steady state error of constant magnitude, further the integral controller eliminitates or reduces this error whereas rate of change of error is reduced using derivative controller.

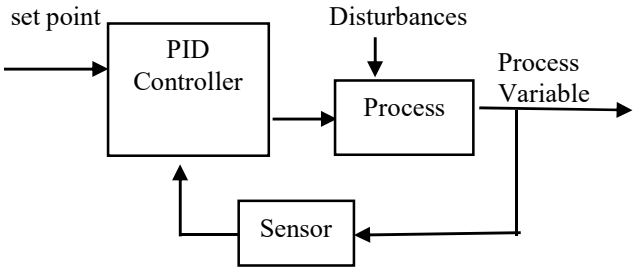


Fig. 2. Schematic of PID control Process

Fig. 2. depicts schematic of PID control process.The process can be explained as follows:

The set point input is the desired value. It is fed to the PID controller after comparing with feedback signal i.e the output. Controller gives the output in a manner so as to maintain the setpoint value. Some disturbances may eventually added to the process, which actually produces the deviations of process variables from set point hence must be controlled as far as possible for stable operation.

IV. Maximum Power Point Tracking (MPPT) Design

The primary limitation of photovoltaic array is low conversion efficiency because of dependency on weather conditions i.e irradiance available. Thus maximum power point is searched using different approaches such as direct or indirect approaches. Also these techniques can further divided according to applications like: (a) For classical approach (Constant Voltage, Adaptive Reference voltage, Perturb and Observe etc) (b) For Intelligent Approach (Artificial neural networks, fuzzy logic controller, sliding mode controller etc) (c) For Optimization (Particle swarm Optimization, Grey wolf optimization,cuckoo search, ant colony optimization, artificial Bee Colony MPPT, etc).

This paper presents the MPPT technique using Perturb and Observe (P&O) algorithm.

V. Simulink and MATLAB Modelling

The proposed system is modelled with two control techniques in MATLAB and Simulink R2017b environment namely- PV array firstly with PID controller- boost converter and secondly with MPPT (P&O) -boost converter

A. PV array with boost converter and PID controller

In this, six solar cells of 3 volts each are joined in series to make a photovoltaic array. Now the output of PV array is increased to a suitable value by using boost converter by suitably selecting the values of L and C and closed loop PID controller (Fig. 3.) and (Fig. 4.) . As shown in TABLE I, PID controller is set with mentioned gain values. Then the voltage is measured at two points before and after the combined setup of boost converer and PID controller. Scope results shows a significant increase in voltage level between the two outputs.

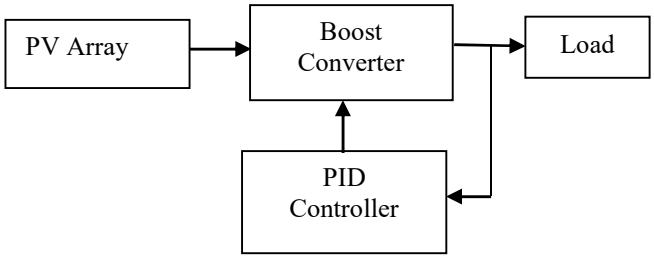


Fig. 3. Block Diagram of PV array with boost converter and PID controller

Fig. 3. and Fig. 4. depicts the block diagram and Simulink model of proposed technique respectively. It comprises of PV array to absorbs sunlight and convert it to electrical energy. The output of PV array system is connected to boost converter. Boost converter is used to enhance the voltage level. The output of boost converter is given to load. PID controller is set with a suitable value then output voltage is adjusted w.r.t set value.

TABLE I. PID Controller Gain Values

PID Controller gain values		
Proportional (K_p)	**Integral (K_i)**	**Derivative (K_d)**
0.00001	7	0.00001

Authorized licensed use limited to: DELHI TECHNICAL UNIV. Downloaded on May 04,2023 at 06:36:30 UTC from IEEE Xplore. Restrictions apply.

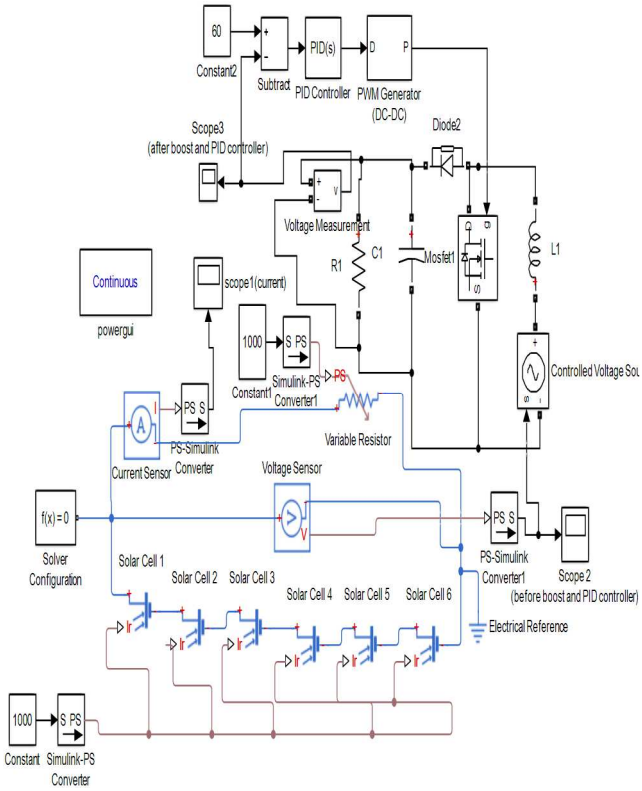


Fig. 4. Simulink model of PV array with boost converter and PID controller

B. *PV array with boost converter and MPPT (P&O)*

In this, six solar cells of three volts each are joined in series to make photovoltaic array. Now the output is increased to suitable value w.r.t boost converter by appropriate selection of L and C values. This output is also based on duty ratio which is controlled by P&O algorithm by utilizing MPPT technique by programming in MATLAB. MPPT is basically a technique to achieve a maximum efficiency for solar PV array (Fig. 5.) and (Fig. 6.). Then again voltage is measured at two points before and after the boost converter and MPPT (P&O). Scope results shows again a considerable rise in the voltage level between the outputs.

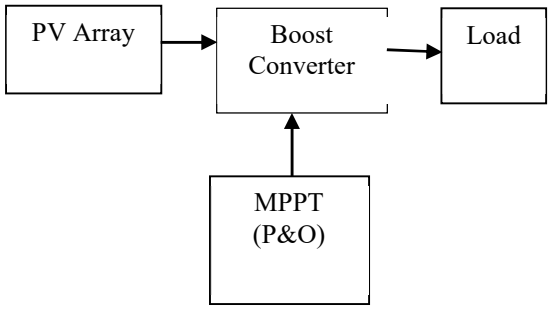


Fig. 5. Block Diagram of PV array with boost converter and MPPT (P&O)

Fig. 5. and Fig. 6. depicts the block diagram and Simulink model of proposed technique respectively. It comprises of PV array which absorbs sunlight and convert it to electrical energy. Output of PV array system is connected to boost converter. Boost converter is used to increase the voltage level. Output of boost converter is given to desired load (here a resistance is taken for simplicity). Boost converter's duty ratio is controlled here using P&O algorithm using MPPT algorithm by programming in MATLAB. Thus, system is searching and set to a maximum output point always.

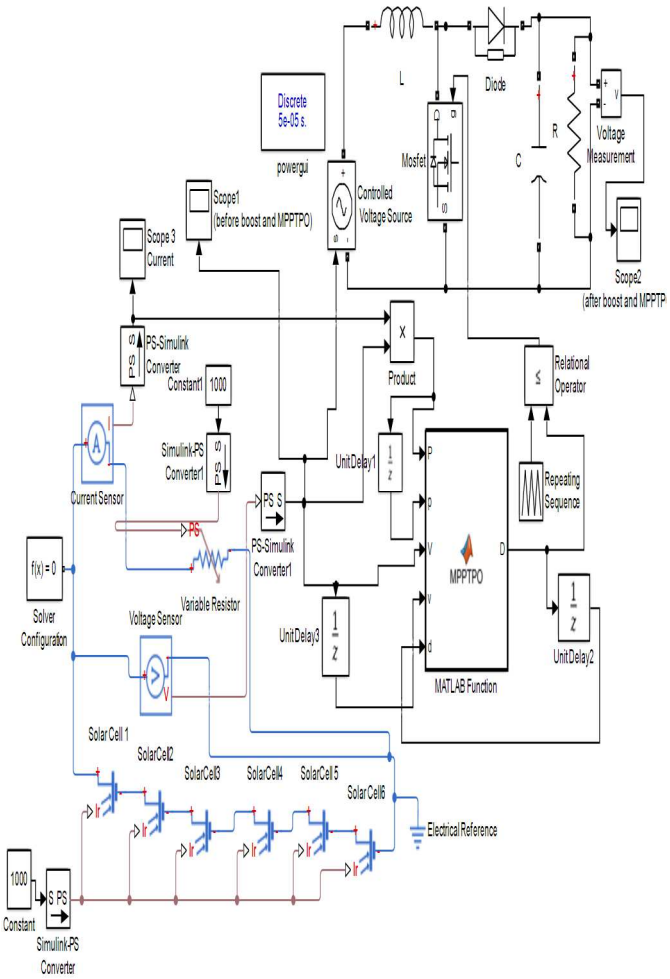


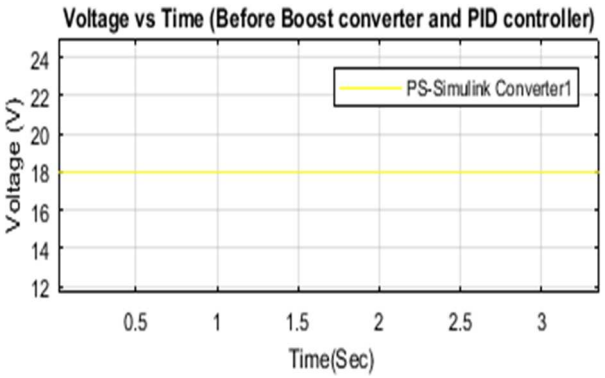
Fig. 6. Simulink model of PV array with boost converter and MPPT (P&O)

VI. Simulation Results

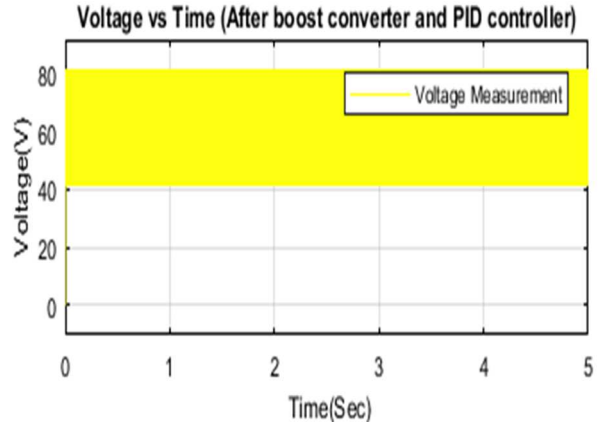
In order to obtain improved output voltage and higher efficiency, six series connected solar cells (3 Volts each) constituting a PV array panel and boost converter combination are connected with PID and MPPT (P&O) controllers as depicted in Fig. 4 and Fig. 6 respectively. The measured output voltage before and after boost converter-PID controller are shown in Fig. 7. (a)-(b). Before PID-boost converter the output of photovoltaic array is 18 Volts. Further after PID-boost converter application the output voltage is increased to 60 Volts. Thus, proposed PID controller yields in increased output voltage.

In second control scheme, the duty cycle is controlled using P&O algorithm using MPPT technique. Here, the output voltage is increased to 160 volts as shown in Fig. 8 (b).

Authorized licensed use limited to: DELHI TECHNICAL UNIV. Downloaded on May 04,2023 at 06:36:30 UTC from IEEE Xplore. Restrictions apply.

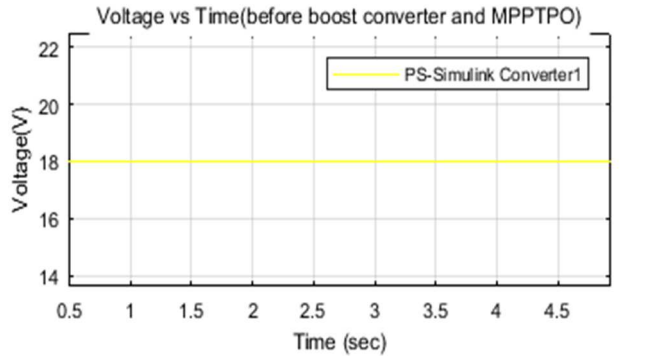


(a)

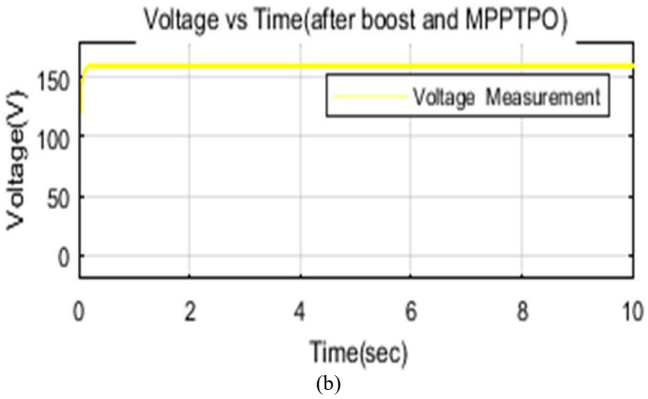


(b)

Fig. 7. Simulation outputs of PV array (a) Before boost converter and PID controller (b) With boost converter and PID controller



(a)



(b)

Fig. 8. Simulation outputs of PV array (a) Before boost converter and MPPT (P&O) (b) With boost converter and MPPT (P&O)

The comparative data analysis is presented in Table II. This has been observed that by using proposed PID controller or MPPT (P&O) algorithm, the output voltage is enhanced significantly. The output voltage obtained using PID controller is varying from 40 to 80 volts, however, by application of MPPT(P&O) algorithm stable output voltage of 160 volt is obtained.

TABLE II. COMPARISON OF PERFORMANCE ANALYSIS OF PV ARRAY WITH PROPOSED TECHNIQUES

System Parameter ↓	**Before Boost converter and controller (V_i)**	**After boost converter with PID Controller (Vo)**	**After boost converter with MPPT(P&O) (Vo)**
Voltage (V)	18	60	160
Increase in Voltage (%) $= [(V_i \sim V_o)/V_i] X 100$	NA	233	788.8

VII. CONCLUSION

In practice, the output voltage obtained from a series PV solar cells is very low. This paper presents implementation of PID and MPPT(P&O) techniques to increase the output voltage from series solar PV cells. This has been observed that output voltage of PV array has been considerably improved by using boost converter-PID controller or by using boost converter-MPPT(P&O) controller. The increment in output voltage obtained by boost converter MPPT(P&O) is stable and much higher in magnitude. Thus, the MPPT(P&O) technique is superior in performance enhancement of PV array as compared to PID control technique .

REFERENCES

[1] R. B. Bollipo, S. Mikkili, and P. K. Bonthagorla, "Critical Review on PV MPPT Techniques: Classical, Intelligent and Optimisation," *IET Renewable Power Generation*, vol. 14, no. 9. Institution of Engineering and Technology, pp. 1433–1452, Jul. 06, 2020. doi: 10.1049/iet-rpg.2019.1163.

[2] H. Bounechba, A. Bouzid, K. Nabti, and H. Benalla, "Comparison of perturb & observe and fuzzy logic in maximum power point tracker for PV systems," in *Energy Procedia*, 2014, vol. 50, pp. 677–684. doi: 10.1016/j.egypro.2014.06.083.

[3] M. Kamran, M. Mudassar, M. R. Fazal, M. U. Asghar, M. Bilal, and R. Asghar, "Implementation of improved Perturb & Observe MPPT technique with confined search space for standalone photovoltaic system," *Journal of King Saud University - Engineering Sciences*, vol. 32, no. 7, pp. 432–441, Nov. 2020, doi: 10.1016/j.jksues.2018.04.006.

[4] S. Kannaiyan, N. D. Bokde, and Z. W. Geem, "Solar collectors modeling and controller design for solar thermal power plant," *IEEE Access*, vol. 8, pp. 81425–81446, 2020, doi: 10.1109/ACCESS.2020.2989003.

[5] T. Paul and N. B. Sc, "Thermal performance of a solar hot water system : model versus measurement," 1984, doi: 10.14288/1.0096148.

[6] J. Ma, "I-V characteristic data of photovoltaic systems operating under partial shading conditions," vol. 1, 2021, doi: 10.17632/YY288MJCN2.1.

[7] J. J. Nedumgatt, K. B. Jayakrishnan, S. Umashankar, D. Vijayakumar, and D. P. Kothari, "Perturb and observe MPPT algorithm for solar PV systems-modeling and simulation," *Proceedings - 2011 Annual IEEE India Conference: Engineering Sustainable Solutions, INDICON-2011*, 2011, doi: 10.1109/INDCON.2011.6139513.

[8] T. Esram and P. L. Chapman, "Comparison of photovoltaic array maximum power point tracking techniques," *IEEE Transactions on Energy Conversion*, vol. 22, no. 2, pp. 439–449, Jun. 2007, doi: 10.1109/TEC.2006.874230.

Authorized licensed use limited to: DELHI TECHNICAL UNIV. Downloaded on May 04,2023 at 06:36:30 UTC from IEEE Xplore. Restrictions apply.

[9] R. Arora, V. K. Tayal, H. P. Singh and, and S. Singh, "PSO Optimized PID Controller Design for Performance Enhancement of Hybrid Renewable Energy System," in *IEEE 9th Power India International Conference (PIICON)*, 2020, pp. 1–5.

[10] D. J. Petrovic, M. M. Lazic, B. v. Jovanovic Lazic, B. D. Blanusa, and S. O. Aleksic, "Hybrid Power Supply System with Fuzzy Logic Controller: Power Control Algorithm, Main Properties, and Applications," *Journal of Modern Power Systems and Clean Energy*, vol. 10, no. 4, pp. 923–931, Jul. 2022, doi: 10.35833/MPCE.2020.000069.

[11] S. Liu, T. Zhang, Z. Lin, Y. Liu, Y. Ding, and L. Yang, "Controlled Islanding Strategy Considering Uncertainty of Renewable Energy Sources Based on Chance-constrained Model," *Journal of Modern Power Systems and Clean Energy*, vol. 10, no. 2, pp. 471–481, Mar. 2022, doi: 10.35833/MPCE.2020.000411.

[12] B. Bendib, F. Krim, H. Belmili, M. F. Almi, and S. Boulouma, "Advanced fuzzy MPPT controller for a stand-alone PV system," in *Energy Procedia*, 2014, vol. 50, pp. 383–392. doi: 10.1016/j.egypro.2014.06.046.

[13] M. Kesraoui, A. Lazizi, and A. Chaib, "Grid Connected Solar PV System: Modeling, Simulation and Experimental Tests," in *Energy Procedia*, 2016, vol. 95, pp. 181–188. doi: 10.1016/j.egypro.2016.09.043.

[14] N. Kannan and D. Vakeesan, "Solar energy for future world: - A review," *Renewable and Sustainable Energy Reviews*, vol. 62. Elsevier Ltd, pp. 1092–1105, Sep. 01, 2016. doi: 10.1016/j.rser.2016.05.022.

[15] B. Parida, S. Iniyan, and R. Goic, "A review of solar photovoltaic technologies," *Renewable and Sustainable Energy Reviews*, vol. 15, no. 3. pp. 1625–1636, Apr. 2011. doi: 10.1016/j.rser.2010.11.032.

[16] C. Kunusch, C. Ocampo-Martinez, and M. Ines Valla, "Modeling, Diagnosis, and Control of Fuel-Cell-Based Technologies and Their Integration in Smart Grids and Automotive Systems," *IEEE Transactions on Industrial Electronics*, vol. 62, no. 8, pp. 5143–5145, Aug. 2015, doi: 10.1109/TIE.2015.2440212.

[17] J. S. Lai and M. W. Ellis, "Fuel Cell Power Systems and Applications," *Proceedings of the IEEE*, vol. 105, no. 11, pp. 2166–2189, Nov. 2017, doi: 10.1109/JPROC.2017.2723561.

[18] K. W. E. Cheng, "Energy storage, fuel cell and electric vehicle technology," in 2020 8th International Conference on Power Electronics Systems and Applications: Future Mobility and Future Power Transfer, PESA 2020, Dec. 2020. doi: 10.1109/PESA50370.2020.9343950.

[19] K. K. T. Thanapalan, G. C. Premier, and A. J. Guwy, "Model based controller design for hydrogen fuel cell systems," *Renewable Energy and Power Quality Journal*, vol. 1, no. 9, pp. 671–676, May 2011, doi: 10.24084/repqj09.419.

[20] V. Khubchandani, K. Pandey, V. K. Tayal and, and S. K. Sinha, "'PEM Fuel Cell integration with using Fuzzy PID technique' IEEE 1st International Conference on Power Electronics, Intelligent Control and Energy Systems (ICPEICES)," in *IEEE 1st International Conference on Power Electronics, Intelligent Control and Energy Systems (ICPEICES)*, 2016, pp. 1–4.

[21] A. Vahidi, A. Stefanopoulou, and H. Peng, "Current management in a hybrid fuel cell power system: A model-predictive control approach," *IEEE Transactions on Control Systems Technology*, vol. 14, no. 6, pp. 1047–1057, Nov. 2006, doi: 10.1109/TCST.2006.880199.

[22] A. Bharatee, P. K. Ray, and A. Ghosh, "A Power Management Scheme for Grid-connected PV Integrated with Hybrid Energy Storage System," *Journal of Modern Power Systems and Clean Energy*, vol. 10, no. 4, pp. 954–963, Jul. 2022, doi: 10.35833/MPCE.2021.000023.

[23] M. Uzunoglu, O. C. Onar, and M. S. Alam, "Modeling, control and simulation of a PV/FC/UC based hybrid power generation system for stand-alone applications," *Renew Energy*, vol. 34, no. 3, pp. 509–520, Mar. 2009, doi: 10.1016/J.RENENE.2008.06.009.

[24] M. Khemariya and A. Mittal, "Modeling & Simulation of different components of a stand-alone Photovoltaic and PEM Fuel Cell Hybrid System," *International Journal on Emerging Technologies*, vol. 1, no. 0975–8364, pp. 60–67, 2010.

Authorized licensed use limited to: DELHI TECHNICAL UNIV. Downloaded on May 04,2023 at 06:36:30 UTC from IEEE Xplore. Restrictions apply.

2023 IEEE 8th International Conference for Convergence in Technology (I2CT)
Pune, India. Apr 7-9, 2023

Optimized Pair Trading Strategy using Unsupervised Machine Learning

Vanshika Gupta
Computer Science Department
Delhi Technological University
Delhi, India
vanshikagupta_2k19co421@dtu.ac.in

Vineet Kumar
Computer Science Department
Delhi Technological University
Delhi, India
vineet_2k19co428@dtu.ac.in

Yuvraj
Computer Science Department
Delhi Technological University
Delhi, India
yuvraj_2k19co447@dtu.ac.in

Manoj Kumar
Computer Science Department
Delhi Technological University
Delhi, India
mkumarg@dce.ac.in

2023 IEEE 8th International Conference for Convergence in Technology (I2CT) | 979-8-3503-3401-2/23/$31.00 ©2023 IEEE | DOI: 10.1109/I2CT57861.2023.10126289

***Abstract*— Pair trading is a popular trading strategy that involves taking advantage of the correlation between two stocks to generate profits. However, traditional pair trading strategies have limitations, such as the difficulty in identifying the most suitable pairs of stocks, determining the optimal trading parameters and large computational cost. To address these challenges, this paper proposes an approach that leverages unsupervised machine learning techniques to improve computation time and identify the best pairs of stocks. The presented model uses PCA and DBSCAN algorithm for dimensionality reduction and clustering. Furthermore, the paper attempts to optimize the pair selection criteria using Engle-Granger test and the trading algorithm using moving averages. The proposed strategy is then tested on historical National Stock Exchange data and the results demonstrate great performance of the proposed approach with respect to the NIFTY-50 Global benchmark.**

Keywords—Pairs trading; Hedge funds; Spreads; Optimization;

I. INTRODUCTION

Pairs trading strategy is one of the most successful trading techniques developed in 1980s by the team of scientists, mathematicians and computer scientists and has since become one of the most well-liked and effective quantitative methodologies. This approach uses computer algorithms for trading without human decision.

Pair trading is a two stage method. The initial stage is to identify stock combinations that belong to the same market sector or have a similar market cap. The second step in the trading cycle is to monitor their separation from one another. It is believed that if the pairs are mean reverting and at the same time, the overachieved stock is short and the under-achieved stock is long, the spread between them will converge when the distance between them suddenly increases. The investor closes out every trade at a profit when spreads converge.

One of the big reasons that pair trading has become so popular is because of the advantages that it holds over trading manually. The biggest benefit is speed because algorithms are created beforehand and run automatically. These exchanges take place at a rate that is fractions of a second slower than human perception. Trading with algorithms has the advantage of swiftly examining and responding to a large number of indicators.

Since trades are limited by a pre-determined set of parameters, another significant benefit of this type of trading is its capacity to eliminate human emotion from the markets. Back testing is also a benefit of algorithm trading. It is possible to test the algorithms against historical data to see if they have previously been successful. This skill offers a significant benefit because it enables the user to fix any trading system defects before implementing it in real time. Other advantages include better accuracy and reduced cost.

In this study, we have applied our strategy to NSE (National Stock Exchange) data for the past five years and tested results against the NIFTY-50 stocks as a benchmark. The PCA algorithm is used to reduce dimensionality and clustering is used to reduce the computational cost. DBSCAN clustering algorithm is selected in the presented model for clustering stocks. Furthermore, the pair selection criteria uses Engle-Granger test and trading algorithm is optimized using moving averages.

II. CONCEPTS USED

We can think of pair trading as trading of two stocks showing similar behavior due to similarity in industry, etc. We can use this property to invest in market through pair trading which makes the trade market neutral. This is because if the market goes up for one stock of the pair it is likely that it will go up for the other stock also and vice versa. This makes the trade less risky.

In pairs trading, investment decisions are based on forecasts of the spread between two stocks rather than the level of future stock prices. If the gap between the two stocks grows, we can sell the overvalued stock short and buy the undervalued stock. Later, when the spread between the stocks mean-reverts to its equilibrium level, the advantage will become apparent.

Trading pairs, a market-neutral strategy, may be beneficial during an upswing, a downtrend, or a sideways market movement.

Cointegrated stocks exhibit a tendency to drift towards and apart from each other. During some periods, the spread

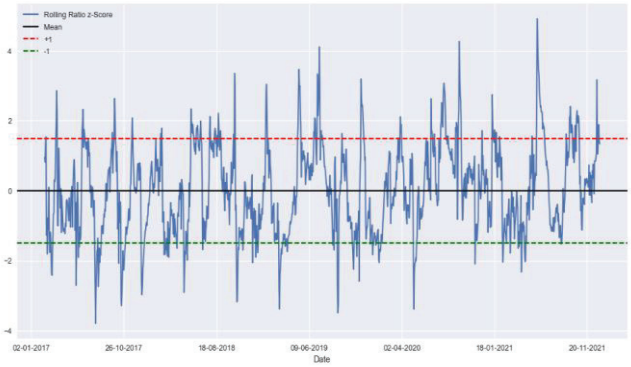


Fig. 1. Spread of ratio of 2 equities

Authorized licensed use limited to: DELHI TECHNICAL UNIV. Downloaded on May 29,2023 at 05:46:47 UTC from IEEE Xplore. Restrictions apply.

between the two securities may be high, while during others, it may be low. A pairs trade is used to take advantage of this phenomenon by purchasing one security and selling another.

This approach allows the trader to remain market neutral when both securities move up or down together, neither gaining nor losing money. In the case of two cointegrated time series, such as X and Y, which follow $Y = \alpha X + e$, profits can be made when the ratio (Y/X) reverts to its mean value α. To identify trading opportunities, we observe instances when X and Y diverge considerably, meaning α is either too high or too low. There are two types of trades that can be made:

- Going Long – Placing a bet by buying Y and selling X when the ratio is anticipated to rise and is lower than usual.
- Going Short - Placing a bet on the ratio by selling Y and buying X occurs when the ratio is higher than normal and predicted to fall.

In order to ensure that a short position profits if the security sold loses value and a long position profits if a security gains value, it is crucial to notice that all positions are hedged. As a result, the trader's profit or loss is unaffected by the general market movement. The gain or loss will only be determined by the proportional movement of the securities X and Y.

III. Trading Strategy

In terms of statistics, the absolute ratio is not particularly useful. The normalisation of our signal by considering it as a z-score is more beneficial. Z score helps us to get a better idea of the deviation from the equilibrium.

To find z score we can use the formula,

$$Z\ Score = (V — M) / SD$$

Where,

- *V* is data point ,
- *M* is the mean value,
- *sd* is the standard deviation of stock

Thus, according to the strategy-

- We compute the rolling mean, rolling standard deviation and the z-score
- Go long the ratio whenever the z-score is below -1.5.
- Go “Short” the ratio when the z-score is above 1.5.
- And exit the positions in case the z-score approaches zero.

However, this is just an example, in actual implementation we would want to compute a more optimal weighting for how many shares to hold for S1 and S2 You would also want to trade using constantly updating statistics. Instead of taking a statistic over the entire sample size, which can have unfavourable effects, it is essential to use statistics that depend on more recent data. For instance, your average price over the past few years might not be indicative of the present if the market is rising and both assets are rising along with it. It is crucial to employ statistics that depend on rolling windows of the most recent data because of this.

As a result, we computed the z score using the 1d Moving Average rather than the ratio values, and the mean and standard deviation were determined using the 30d Moving Average and 30d Standard Deviation.

IV. Dataset

The data set is sourced from finance.yahoo.com. Our data collection covers the period of 5 years from January 1, 2017, to December 31, 2021. Because pairs trading necessitates the consistency of the data of two stocks, we must first perform some data preprocessing. Consistent means that every feed for both securities should have data and a time that exactly match. The original data set contains 1027 NSE (National Stock Exchange) equities.

Each security has data from January 1, 2017, through December 31, 2021, as well as the closing price as an attribute. The type of industry they work in is another consideration in the calculations. We used the data for further research after daily percent change processing of the data.

V. Proposed framework and Implementation

At this point, our goal is to investigate how an investor might find relevant pairs without having to subject himself to the disadvantages of traditional methods of pair searching. On one hand, if he limits his search to stocks within the same sector, the investor is less likely to select pairs not yet being traded in big quantities, leaving a little margin for profit.

On the other hand, if the investor leaves the search unrestricted, he may need to look into excessive combinations and maybe find bogus associations. We aim to reach equilibrium by applying an unsupervised learning to find valuable asset clusters to find relevant pairs.

A. Dimensionality reduction

We first tried to find the concise representation of each value to minimise modelling data columns or input variables. There shouldn't be many features because an unsupervised learning approach would be used to these data. The presence of high data complexity poses two problems. The first is that it is more likely that irrelevant characteristics will be discovered as the number of attributes rises.

The problem of the curse of dimensionality, which is caused by the exponential increase in volume caused by the introduction of extra dimensions to the space, is another one. Our method is severely hampered if the dimensionality is too high.

We used the PCA (Principal Component Analysis) for dimensionality reduction. Using the scikit-learn toolkit, which offers the PCA class that can be fitted on a dataset and used to modify a training dataset and any additional dataset in the future, we utilised PCA to create a projection of a dataset.

We reduced our data with the first 3 principal component loadings for efficient results.

B. Unsupervised learning

A clustering approach may be used once each asset has been given a compact representation. It is first necessary to identify certain problem-specific requirements in order to determine which method is better suitable:

Authorized licensed use limited to: DELHI TECHNICAL UNIV. Downloaded on May 29,2023 at 05:46:47 UTC from IEEE Xplore. Restrictions apply.

- There's no need to predetermine the number of clusters.
- There's no need to combine all securities. rigid assignment that takes into consideration outliers.
- Make no assumptions about the geometry or shape of the clusters.

Given these constraints, a density-based clustering algorithm appears like the best option. Since it creates clusters of any shapes, no gaussian presumptions are required. Since it does not group every data point in the data set, it is inherently resilient against outliers. Furthermore, the number of clusters need not be specified.

K-means clustering is one of the easiest and most used unsupervised machine learning techniques. Unsupervised algorithms frequently draw inferences from a dataset using simply input vectors, without relying on planned or labelled results. But, we decided to use DB-SCAN algorithm in place of K-means because it has some advantages over the latter algorithm. All stocks are not clustered in DBSCAN. That which does not cleanly fit into a cluster of stocks is excluded. In a similar manner, the number of clusters is not required in this algorithm. The DB-SCAN algorithm in a nutshell, looks for point clusters based on density. As a result, the DBSCAN method was employed to generate clusters.

Two criteria must be established in order to achieve that:

- The first parameter is eps value - This tells the closeness of neighbours to form a cluster. We used eps value as 0.13.
- The second parameter is minimum points that are needed to form our cluster. We fixed it as 2 (as we can have pairs as clusters)

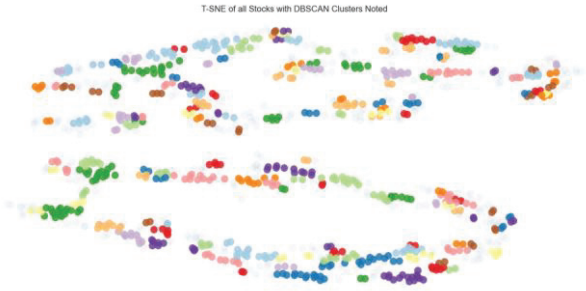


Fig. 2. Visualization of all stock clusters

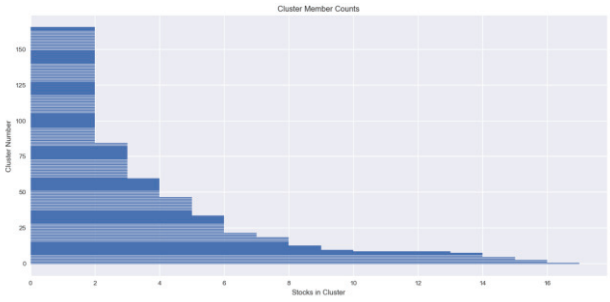


Fig. 3. Clusters with number of stocks in each cluster

C. Pairs selection criteria

After forming the cluster, we developed a set of rules to select co-integrated pairs that are suitable for trading. It is essential that the pairings' balance persist. We propose merging approaches from many research programmes to realise this reality. If a couple satisfies the four conditions stated below, it is selected using the specified criteria. First, only stocks that are cointegrated are selected as a pair. We propose applying the Engle-Granger test, created by Granger and Engle in 1987, because it is straightforward. We test both potential permutations of the dependent variable and choosing the one that yields the lowest t-statistic in order to address the test reliance on the dependent variable. There will be periods when the spread is high and periods when it is low because two cointegrated time series drift toward and away from one another. A pair transaction is one in which we acquire one security and sell another. Thus, regardless of whether the value of both assets increases or decreases, we will retain our market neutrality.

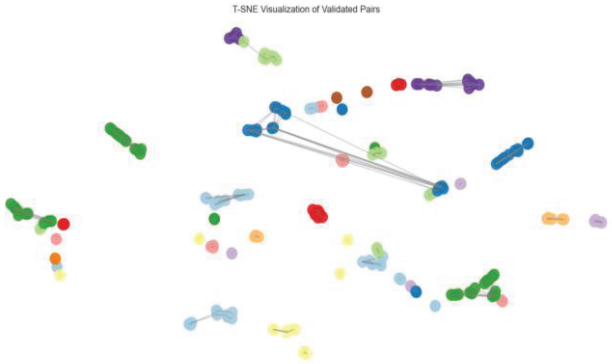


Fig. 4. Visualization of valid stock pairs

D. Pairs selection criteria

These are some examples of clusters formed by DB-SCAN algorithm. These clustered how highly co-integrated. They are generally but not limited to the same industry sector. This is due to the openness of the DBSCAN algorithms that has no restrictions on attributes or size of cluster. Thus, the clustering is not just based on the same industry, but is true for a lot of cases due to similar trends in the stocks.

HertageFood and JublFood are in a cluster as they are both under the Food Processing industry.

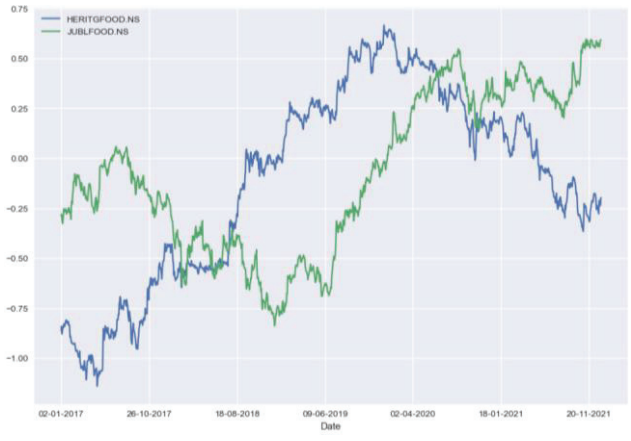


Fig. 5. Stock time series for cluster with 2 stocks

HCL tech, Infyosys, Omaxe and Wipro are part of the IT sector and are cointegrated with each other. With this 6 pairs are formed to be traded according to our strategy.

Authorized licensed use limited to: DELHI TECHNICAL UNIV. Downloaded on May 29,2023 at 05:46:47 UTC from IEEE Xplore. Restrictions apply.



Fig. 6. Stock time series for cluster with 4 stocks

E. Trading Algorithm

```
def trade(S1, S2,money, window1=1, window2=30):
    # If window length is 0, algorithm doesn't make sense, so exit
    if (window1 == 0) or (window2 == 0):
        return 0
    # Compute rolling mean and rolling standard deviation
    ratios = S1/S2
    ma1 = ratios.rolling(window=window1,
                                center=False).mean()
    ma2 = ratios.rolling(window=window2,
                                center=False).mean()
    std = ratios.rolling(window=window2,
                            center=False).std()
    zscore = (ma1 - ma2)/std
    # Simulate trading
    # Start with no money and no positions
    countS1 = 0
    countS2 = 0
    first_time = [0,0]
    profit=0
    c1=0
    c2=0
    mon_list = pd.Series(index=returns.index)
    mon_list[mon_list.index==returns.index[0]] = money
    for i in range(len(ratios)):

        # Sell short if the z-score is > 1,5
        if zscore[i] > 1.5 and money>max(S1[i],S2[i]) and c1==0:
            countS1 -= int((money/2)/S1[i])
            countS2 += int((money/2)/S2[i])
            first_time = [S1[i],S2[i]]
            money -= -countS1*S1[i] +  countS2*S2[i]
            c1=1
        # Buy long if the z-score is < -1.5
        elif zscore[i] < -1.5 and money>max(S1[i],S2[i]) and c2==0:
            countS1 += int((money/2)/S1[i])
            countS2 -= int((money/2)/S2[i])
            first_time =  [S1[i],S2[i]]
            money -= countS1*S1[i] - countS2*S2[i]
            c2=1

        # Clear positions if the z-score between -.1and .1
        elif abs(zscore[i]) < 0.1:
            profit= countS1*(S1[i]-first_time[0]) + countS2*(S2[i]-first_time[1])
            if(c1==1):
                money += -countS1*first_time[0] + countS2*first_time[1] + profit
                c1=0
            if(c2==1):
                money += countS1*first_time[0] - countS2*first_time[1] + profit
                c2=0
            countS1 = 0
            countS2 = 0
            mon_list[mon_list.index==data.index[i]] = money


        #if(i == len(ratios)-1):

            #money += abs(countS1)*first_time[0] + abs(countS2)*first_time[1]
            #mon_list[mon_list.index==data.index[i]] = money


            #mon_list.append((data.index[i],money))
    return mon_list
```

Fig. 7.

VI. Results

The strategy was tested against Nifty-50 performance using 5 years data between 2017 and 2021 giving very promising results. From this technique we have found 47 pairs that out-performs NIFTY-50 (buy and hold for 5 years) with maximum profit of 469% on single-pair. (between SETUINFRA AND SNOWMAN). These results show the efficiency of our strategy when compared to other strategies of pair trading and also against the global standard NIFTY 50. But there is still a need to focus on portfolio creation to distribute capital appropriately between these stock pairs based on risks.

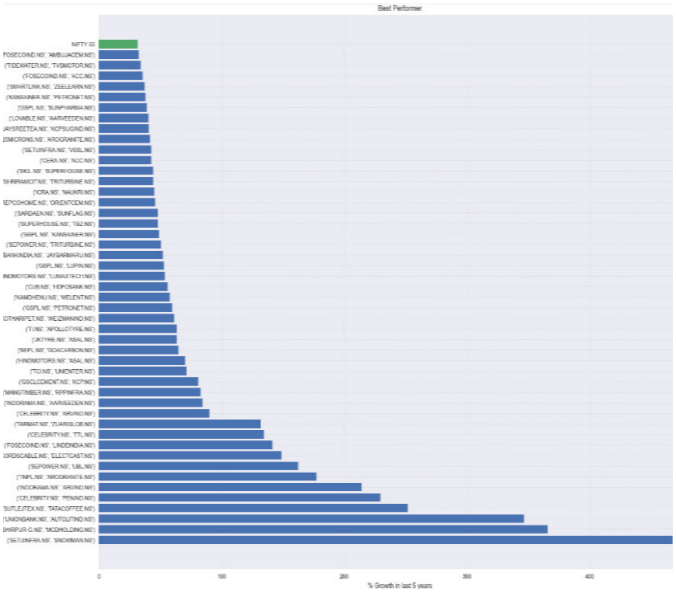


Fig. 8. Top pair performance against Nifty-50 standard

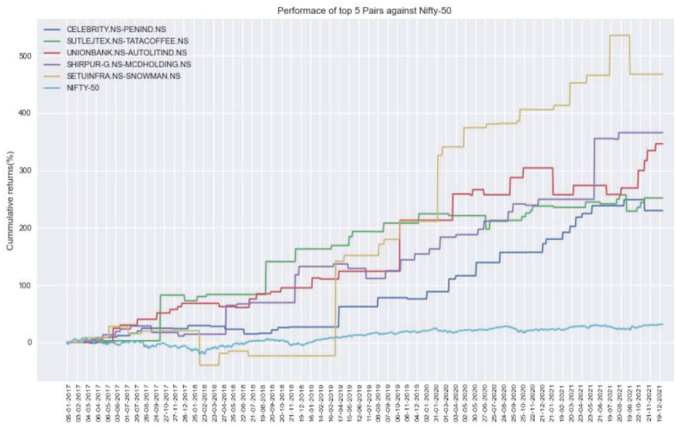


Fig. 9. Top 5 pairs performance against Nifty-50

TABLE I. Observations

NIFTY-50 benchmark calculated	31%
Pairs passing co-integrated test	181 pairs
Pairs outperforming NIFTY-50	47 pairs
Maximum profit on a single pair	469% (Setuinfra and Snowman)

VII. Conclusion

We applied the unsupervised learning technique DB-SCAN algorithm for efficient pair selection which gives more number of pairs and better results than other algorithms like KNN algorithm.

We also used moving averages over 30 days rather than overall averages for more efficient prediction due to more relevant and recent results. We optimized our strategy at

Authorized licensed use limited to: DELHI TECHNICAL UNIV. Downloaded on May 29,2023 at 05:46:47 UTC from IEEE Xplore. Restrictions apply.

each step of pair trading computation to obtain overall optimized results which can be seen in our results.

The results show that our strategy is very effective against the standard Nifty-50 leading to good profits and pair selections. But, the model has slightly better performance in prediction spread and pairs than profitability. This is because profitability depends on various other market factors.

REFERENCES

[1] Vidyamurthy, G. (2004) Pairs Trading - Quantitative Methods and Analysis, John Wiley & Sons, Inc., New JerseyJ.

[2] Gatev, E., W.N. Goetzmann, and K.G. Rouwenhorst "Pairs trading: Performance of a relative-value arbitrage rule." Review of Financial Studies, Vol. 19 (2006), pp. 797–827

[3] Ghosh, Indranil and Chaudhuri, Tamal and Singh, Priyam, Application of Machine Learning Tools in Predictive Modeling of Pairs Trade in Indian Stock Market (April 10, 2018). The IUP Journal of App

[4] Riedinger, Stephanie, Demystifying Pairs Trading: The Role of Volatility and Correlation (June 7, 2017)

[5] Caldeira, Joao and Moura, Guilherme Valle, Selection of ˜ a Portfolio of Pairs Based on Cointeg

[6] Rudy, J., Dunis, C., Giorgioni, G. and Laws, J. (2010) Statistical Arbitrage and High-Frequency Data with an Application to Eurostoxx 50 Equities. Social Science Electronic Publishing, Rochester.

[7] Huang, C. F., Hsu, C. J., Chen, C. C., Chang, B. R., & Li, C.- A. (2015). An intelligent model for pairs trading using genetic algorithms. Comp

[8] Dunis, Christian and Laws, Jason and Rudy, Jozef, Mean Reversion Based on Autocorrelation: A Comparison Using the S&P 100

[9] Constituent Stocks and the 100 Most Liquid ETFs (January 31, 2011). ETF Risk, 2013, October, 36-41.

[10] Dingli, Alexiei & Fournier, Karl. (2017). Financial Time Series Forecasting – A Deep Learning Approach. International Journal of Machine Learning and Computing. 7. 118-122. 10.18178/ijmlc.2017.7.5.632.

[11] Perry J. Kaufmann, Alpha Trading: Profitable Strategies That Remove Directional Risk, Wiley; 1 edition (March 8, 2011)

[12] Sinclair, E. 2013. Volatility Trading, Hoboken, New Jersey, John Wiley and Sons.

[13] Board of Governors of the Federal Reserve System (US) (2019). 3-Month Treasury Bill: Secondary Market Rate. https://fred.stlouisfed.org/series/TB3MS. Accessed: 2019-07-11.

[14] Sutskever, I., Vinyals, O., & Le, Q.V. (2014). Sequence to sequence learning with neural networks. CoRR, abs/1409.3215

Authorized licensed use limited to: DELHI TECHNICAL UNIV. Downloaded on May 29,2023 at 05:46:47 UTC from IEEE Xplore. Restrictions apply.

Semiconductor Optoelectronics
ISSN: 1001-5868

PERFORMANCE EVALUATION OF BISMUTH TELLURIDE SEMICONDUCTOR BASED PARABOLIC DISH CONCENTRATED SOLAR THERMOELECTRIC GENERATOR IN REALISTIC METEOROLOGICAL CONDITIONS OF CENTRAL INDIA

Sanjeev Kumar Bhukesh[1,*], Anil Kumar[2] and Suresh Kumar Gawre[3]
[1]Energy Centre, Maulana Azad National Institute of Technology, Bhopal -462003 (India)
[2]Dept. of Mechanical Engineering, Delhi Technological University, Delhi-110 042 (India)
[3]Dept. of Electrical Engineering, Maulana Azad National Institute of Technology Bhopal-462003 (India)

Abstract
Maintaining desired temperature difference between hot and cold sides (ΔT) in thermoelectric generator without harming environment, with feasible cost is a greater challenge. In this research an attempt has been made to maintain ΔT within a certain limit by means of DC fan air cooling which is powered by TEG itself. A 10W Bi_2Te_3 semiconductor based thermoelectric generator is fabricated where heat input is received from solar parabolic dish concentrator. Various operating parameters such as Global radiation, concentrated radiation, diffuse radiation, ambient temperature, hot and cold side temperature, ambient air velocity, ambient relative humidity, voltage and current are observed after regular interval of time. Max. hot side temperature 210°C, cold side temperature 45°C, TEG output voltage of 10V instead of 12V (rated), TEG output current of 0.694 A instead of rated current 1 A at a beam radiation of 726 W/m^2 are observed. Maximum electrical TEG power output was calculated ≈7 W instead of rated power 10 W. Experimental observationsare used for performance evaluation of developed TEG in terms overall system efficiency. The overall Parabolic dish concentrated solar thermoelectric generator PDCSTEG system efficiency are determined as 0.6207%. Concentrated solar power integrated TEG is a feasible renewable power solution.

Keywords: Thermoelectric Generator; Solar Power; temperature difference; Overall efficiency

1. Introduction

Population explosion and industrial growth has raised a need to examine various renewable energy resources. Globally 6 major **Global Horizontal Irradiation (GHI)**hotspots are identified (Australia, the Arabian Peninsula, Southern, Northern, Eastern and South Western Africa, Western South America) having rich value of >2200 kWh/m^2 annually and 6 major **Direct Normal Irradiation (**DNI) hotspots as (Australia, Tibetan Plateau, North Western Arabian Peninsula, South Western Africa, Western South America, South Western North America) having potential of >2500 kWh/m^2**[1].**India is blessed with 300 sun shine days per year, irradiation of 4-7 kWh/m^2 /day and across the country between 2300 and 3200 sunshine hours. National Institute of Solar Energy, India (NISE) admits India's solar power potential

around 750 GW **[2].**The largest SPV plant (750 MW) has been approved by the state government of Madhya Pradesh, India. By the year 2022, India is committed to achieve its renewable energy target of 220 GW out of which 100 GW would be contributed by the solar power which was earlier 20 GW**[3].** Nowadays most of the solar energy is harnessed through photovoltaic systems which deal with the direct conversion of incoming solar radiation into electrical energy using solar cells. The efficiency of solar cells is not very high (usually ≤ 20%) and demand large area of land**[4].Thermo-Electric Generator**(TEG)is a solid state robust device that converts heat from various sources into useful electric power and has gained popularity among researcher and renewable energy stakeholders in the energy market. Solid state device nature, absence of moving part, operable at high temperature and stability in harsh environment due to its robustness are the features of this technology that suits for standalone power conversion or in hybrid solar thermal-electrical power systems. TEG integrated with parabolic dish forms PDCSTEG that harnesses solar energy from sun through concentrating solar power (CSP) technology. Concentrated radiations gets convert into heat to drive TEG **[4],[5].**

TE power generation mechanism converts directly heat into electric power via Seebeck effect. A electrical potential difference is generated between two junctions of two dissimilar material conductors and semiconductors due to temperature difference between the two junctions**[6].**

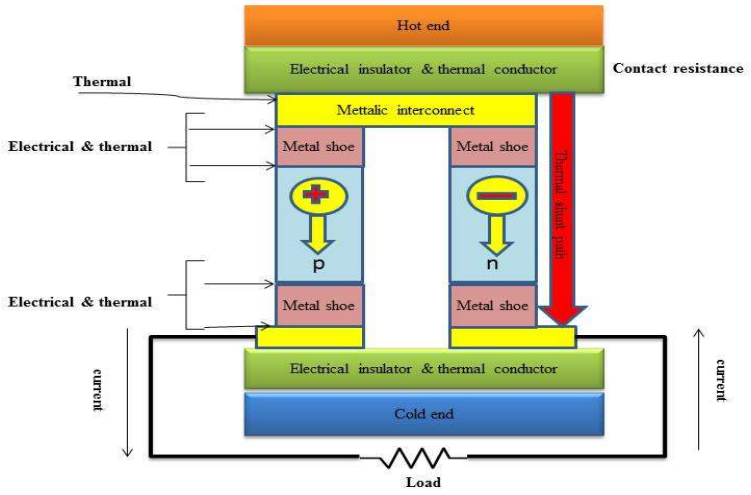


Figure 1. Electrical and thermal interfaces in the architecture of a single p-n leg of a TEG[7]

A large number of p-type and n-type TE elements connected alternately electrically in series and thermally in parallel in a TEG module **[7]. Energy** efficient TEGs need to be fabricated with a high performance TE material, high figure of merit, higher temperature difference ΔT and with the ability of efficiently recovery of waste heat from various heat sources**[7], [8].**Metal based, semiconductor based, ceramic based and polymer based TE materials are recommended for wide range of figure of merit (ZT)**[9].** TEG operate at various operating temperature in the range 250-650 ºC with high figure of merit TE material ZT of >2by enhancing the power factor and reducing thermal conductivity**[7].**In a PDCSTEG system, concentrated solar radiation

absorption increases at receiver, which ultimately results increased temperature gradient across TEG device **[4].** There are two main approaches of increasing the temperature difference in **PDCSTEG**: (i) optical concentration enhancement of sunlight to increase the heat flux at the absorber surface, and (ii) increase thermal concentration, which means larger area of highly thermally conducting absorber than the area of the TE legs, allowing increased heat flux through the legs. Latter approach demonstrates STEG efficiencies of 4.6% and 5.2% with light intensities corresponding to 1 kW/m^2 and 1.5 kW/m^{2}respectively**[8].**The maximum output power and TE conversion efficiency also depends on an optimal length ratio of the segmented TE leg. This ratio does not only depend on the TE properties of the material but also on geometry and heat transfer conditions**[10].**By improving TE leg with the help of segmented TE material and using high-temperature (600ºC) spectrally selective solar absorber, thereby combining optical and thermal concentration, at an optically concentrated normal solar irradiance of 211kW/m^2. **Chen et al.** investigated CSTEGs with a peak efficiency of 9.6% and 7.4% after considering optical concentration losses **[5].**Length of the TE leg affects the optimized shape parameter, if contact resistance is taken into account**[11].**By keeping element length constant, reducing the cross-sectional area of TE element and increasing the substrate area, thermal concentration increases that lead to efficiency improvement**[5],[12].** Through desired geometry optimization of TE leg, TEG performance in terms of output power and efficiency can be improved and having constant cross section area of TE leg maximum output power per unit mass can be achieved for an ideal ATEG.Protic and Aprotic Ionic liquid TE cell based TEG sandwiched between a heated and a cooled electrode, which works in the range of room temperature and 300°C, exhibit temperature-dependent current, voltage and power output characterization **[13].**The maximum efficiency also depends upon number of TEG modules integrated in an assembly. **Kurt** used the performance data of a full one year cycle solar irradiation to optimize the number of commercial TEGs for heat to electricity conversion in CSTEG**[14].**It was observed that with an assembly of less TEGs, high concentration ratio and high temperature difference is achieved with more electric power as compared to an assembly of more number of TEGs **[15]**.Light spectrum is also responsible for improved efficiency of TEG. UV and visible solar spectrum energy is converted by photovoltaic, and IR spectrum energy can be utilized by thermo-electrics. The utilized spectrum range can be extended by combining and optimizing PV and TE hybrid system, hence improved efficiency can be achieved[15]**.**The structure, area and receiver material are also determinants of efficiency of a TEG. Fem to second laser irradiation creates anano-structure surface on Al receiver that enhances absorption of UV and visible spectrum with small emissivity in infrared. Power generating capacity and efficiency of STEG integrated with Al foil receiver increased significantly[16]**.**Semiconductor based multilayer selective absorber could be an appropriate option for non-concentrated sunlight which shows low emissivity in the thermal wavelength range and high absorptivity for the visible solar spectrum. Therefore, solar concentrators can be avoided for medium temperature solar applications[17]**.** The highest efficiency ever reported by TEG is 15% across$T_h - T_c$ =1000–200°C by combining several next generation TE material**.**High flux solar furnace and selective solar absorber are used to achieve TEG efficiency greater than 15% **[8].** Hollaran determines the power and efficiency of a commercial TEG with the help of LabVIEW data acquisition system[18]**. Chen et al.** investigated the performance of a TEG under the influence of sinusoidal temperature distribution at the hot side

or cold side surface[19]**.** TEG performance is not affected by the time period of temperature oscillations. Increase in concentration ratio increases the efficiency of PDCSTEG [20]**.** Various concentrating technologies have been used to harness the solar energy like, A solar tracker based on mosaic set of mirrors integrated with Bi_2Te_3 based CSTEG with running water cooling achieve hot side temperature of 200◦C and the cold side temperature 50◦C, produces 20W of electrical energy and 200W of thermal energy stored in water with a temperature of 50◦C[21]**.Date et al.** developed a Fresnel lens (heat flux 50000 W/m^2) based CSTEG with solar water heating. Heat pipe condenser immersed in water tank passively cool the cold side with a higher heat transfer coefficient[22].Heat source like phase change material, geothermal heat or solar pond (low-grade heat source) show continuity for thermal-electrical energy conversion therefore suitable for TE power generation investigated [21]**.** PCM based R- STEG provides 60% and 86% higher peak energy conversion efficiency for solar irradiance of 1 kW m^{-2} and 1.5 kW/m^2 as compared to typical STEG, therefore PCM can help to generate steady electrical energy **[23].**

For the evaluation of prototype CSTEG **PENG LI et al.**[20]developed a discrete numerical model by dividing TE leg into finite elements and considered temperature dependence of the TE material properties, achieved improved conversion efficiency for higher temperature gradient with increase in concentration ratio**. Tobereret al.[24]**developed a novel detailed balance model for CSTEG and applied this model for an incident flux 100 kW/m^2 and T_h - 1000^0C and ensure 15.9% efficiency and with ZT =2, 30.6%**.Manikandan et al** developed and analysed an irreversible and exoreversible thermodynamic model of the combined TEG-TEC compatible system in MATLAB environment with consideration of temperature dependent TE properties and with maximum power point tracker**[25].**Seebeck effect, modelling of TE phenomenon and TEG system geometry is investigated through an ANSYS computer program that involves modelling of complicated geometry of real objects, application of differentiable or discontinuous functions, which enable description of physical parameters and boundary conditions through finite element method (FEM). It reveals that increasing ΔT between hot and cold reservoir leads to produce higher voltage and electric power**[26].** By means of ANSYS, the finite element analysis (FEA) was conducted on a model of the solar waste heat recovery based TEG attached with Al plate on the hot side. If area and thickness of the Al plate increased, the temperature gradient between hot and cold sides of TEG increases because of the increase in thermal resistance of Al plate. Thereby voltage produced gets increased **[27].** By developing a Simulink model and thermal concentration optimization in realistic terrestrial environment for CSTEG, It was observed that thermal concentration in realistic environment gets doubled as compared to standard test condition[19]**.** A thermodynamic model for a CSTEG was developed and optimized in MATLAB environment. For maximum energy efficiency of 5.85% and maximum exergy efficiency of 6.29% optimized concentration ratio is achieved as 180 and load resistance ratio as 1.3 respectively, with corresponding power output of 4.213W **[28]**. An equivalent model based on 3-dimensional finite element scheme advocates that the thermal concentration ratio gets increased by keeping element length constant, reducing the cross-sectional area of TE element and increasing the substrate area that leads to improvement in efficiency and performance of CSTEG**[12].Q. Cao et al.** developed a genera lised model for investigating various effects of geometry configuration and contact resistance of an annular TEG**[11]**. Desired optimization of TE leg led to improve the performance of TEG in terms of

output power**.**In a Solar heat pipe based cylindrical annular TEG (SATEG) the thermal energy output and thermal exergy efficiency with overall exergy efficiency of SATEG are found little bit lower than that of the SFTEG, however with the higher FOM TE materials, SATEG will gain its importance in near future **[29]**.

The solar heat pipe/thermoelectric hybrid system in which the TE modules combined with solar heat pipe provide an ultimate device for simultaneous electricity generation **[30].**A concentrating photovoltaic/thermoelectric hybrid generator was developed by **T.H Kil et al**. consisting of single-junction GaAs-based solar cell and a conventional TE module and achieved a 3% higher efficiency as compared to the single CPV cell at the solar concentration of 50 suns**[31].**Typical applications of the solar-driven thermoelectric refrigeration and the solar-driven TE power generation are presented **[32].**It is an estimation of scientists and researchers that almost 70% of world energy is wasted in the form of heat to the atmosphere and led to a major factor in global warming **[4].**TEGs have potential to harvest the heat of human body and waste heat from various sources**[33], [34].**
Therefore, heat generated from CSP technology and waste heat from various sources can be utilized by TEG in more efficient way**.** Small scale power generation confines the area of receiver plate, due to which complexity in design of small scale power generating PDCSTEG system gets increased, if CSP technology is employed. In this research to examine a TEG sandwiched between aluminium receiver plate (without any selective absorber coating) and aluminium heat sink integrated with solar parabolic dish concentrator at Energy centre (Bhopal City 23^0 16'N, 77^0 36'E), a trade of between the concentrator aperture area and the absorber plate has been set which keeps ΔT within specified range. For central India it is a very first kind of study of performance of concentrated solar thermoelectric generator which could help to provide renewable power solution for Indian villages.

2. Materials and Methods

2.1. Experimental Setup of PDCSTEG System

The arrangement of solar parabolic dish thermoelectric generator is shown in **Figure 2**.A parabolic dish concentrator is integrated with a set of two thermoelectric modules (each 5 watt) connected in series, sandwiched between uncovered flat plate aluminium solar thermal absorber/receiver (hot side) and aluminium air cooled heat sink (cold side) and hence a PDCSTEG is so constructed. The TEG set is placed on a focal plane of solar PDC.

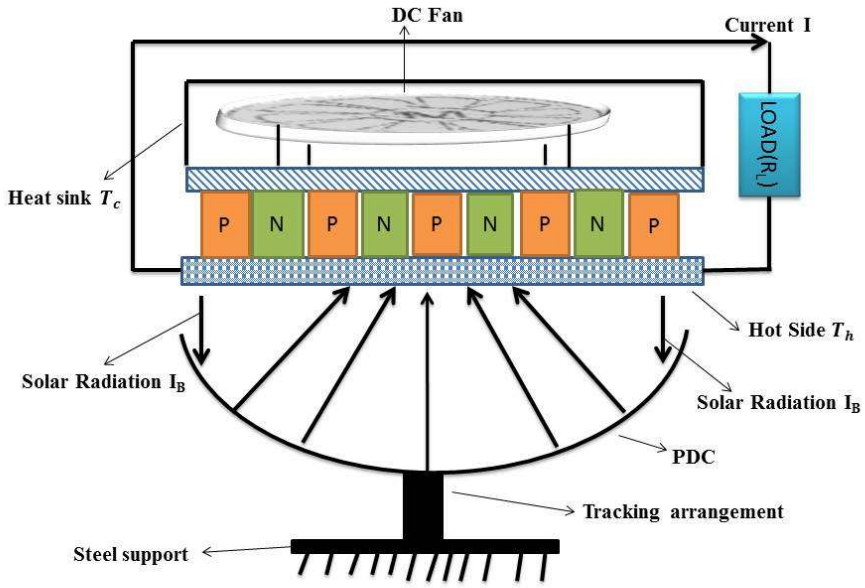


Figure 2. Arrangement of PDCSTEG

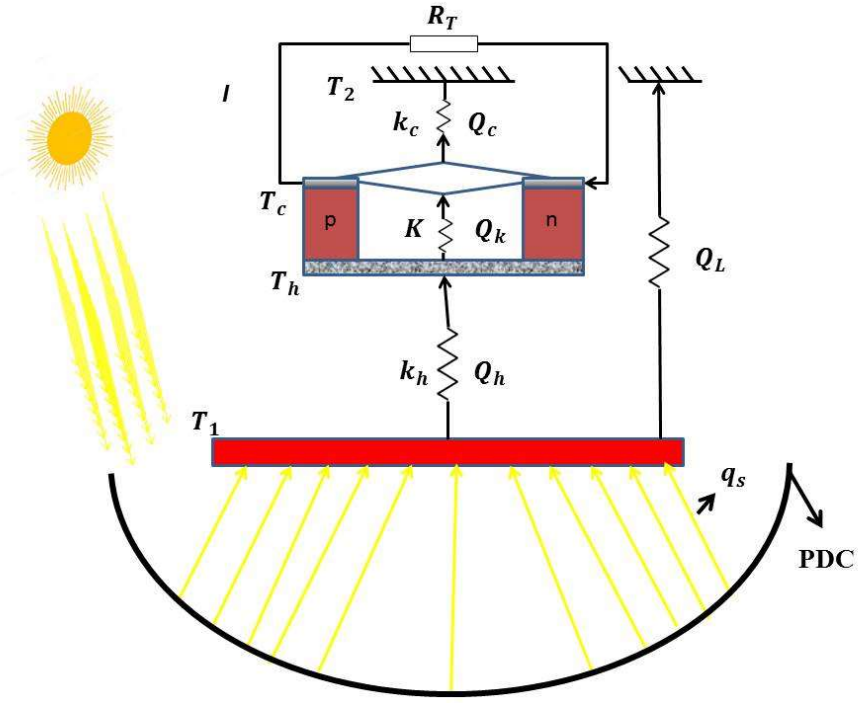


Figure 3. Heat transfer in a PDCSTEG

2.2. Various tests on PDCSTEG

The complete experimental setup was installed in the yard area of the Energy Centre, Maulana Azad National Institute of Technology Bhopal (Latitude: **23^0 16'N,** Longitude: **77^0 36'E**), India. Photographs of the experimental set up are shown in **Figure 4**. The focal point of the solar PDC is the position where the absorber/receiver plate is positioned. Sun is tracked

manually with one axis rotation of the dish. Dish parameters are measured as open mouth diameter of 1.4 m, focus of 0.285 m, height of 0.43 m and aperture angle of 101.7^0. For absorption of solar concentrated radiation from PDC, two TE modules (each 5watt) connected in series are sandwiched between the hot side of receiver and heat sink. For testing purpose the TE modules are loaded with an electrical Resistance of 16.94 Ω in accordance with the maximum power transfer theorem. Mass flow rate of fan's air tries to maintain the cold side temperature at 35-43ºC.

Table 1.Air velocity and Relative humidity Variation with time

Parameter	**Min Value at 1430 hrs**	**Max Value at 1300 hrs**	**Value at 1100 hrs**	**Value at 1400 hrs**
Ambient air velocity V_a	0.13 m/s	1.20 m/s	0.85 m/s	0.18 m/s
Relative humidity Rh_a	12.1% at 1615 hrs	30.1% at 800 hrs	21.2%	14.2%.

The best performance analysis time duration is between 1100 hrs to 1400 hrs as shown in table 1. The maximum value and minimum value of both the parameter are very effective parameter to affect the temperature gradient and ultimately the power generated.



Figure 4.(a)- Top view of PDCSTEG(b) Side view of PDCSTEG(c) Focussed concentrated radiation(d) TEG, Load Box, Ammeter, Voltmeter

2.2.1. No Load Test/Open Circuit Test

The first test conducted on the PDCSTEG was an open circuit test in the yard of Energy Centre, by connecting the module output wires to a DC voltmeter as shown in **Figure5.**open circuit voltage can be measured. The sun was tracked manually throughout the day from 800 hrs to

1645 hrs. Observations were recorded at each 15 minutes interval. The open circuit voltage was also recorded for given time intervals until it reaches at steady-state. The constant input solar power was recorded using a solar power meter, made by Ambient Weather**.** The open circuit voltage varies between 6.1volts(min) to 9.5volts(max) during 1100 hrs and 1400 hrs.

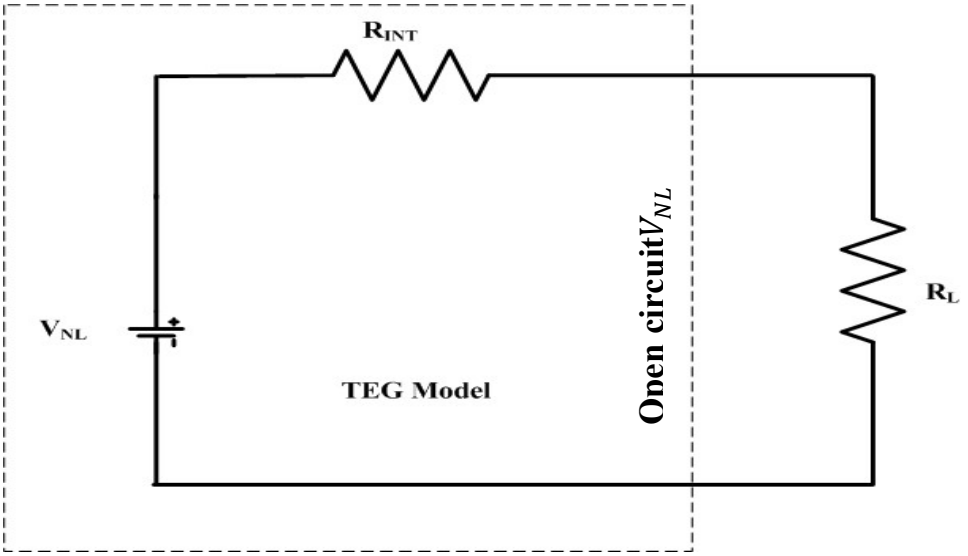


Figure 5. Circuit diagram of a TEG model

2.2.2. Loaded Tests

For the load test of the PDCSTEG, the TEG assembly was first placed at the focus of solar PDC where maximum concentrated radiations were received. The device is kept for about an hour to allow the entire device to reach ambient temperature. When the PDCSTEG was moved into the sun, the solar power input (Beam radiation) and output voltage were measured at every 15 minute from 800 hrs to 1645 hrs on 4th May 2021. A decade box was connected to the output wires of the module as the resistive load and a DC voltmeter is connected across the load and ammeter is connected in series with R_T. The test isconducted for: 1-Fan load (96 Ω) 2- Half load (R_T = 28.28 Ω) 3-Full load R_T = 14.4 Ω. **(R_T=R_{FAN}‖ R_L)**as shown in **Figure 6**.

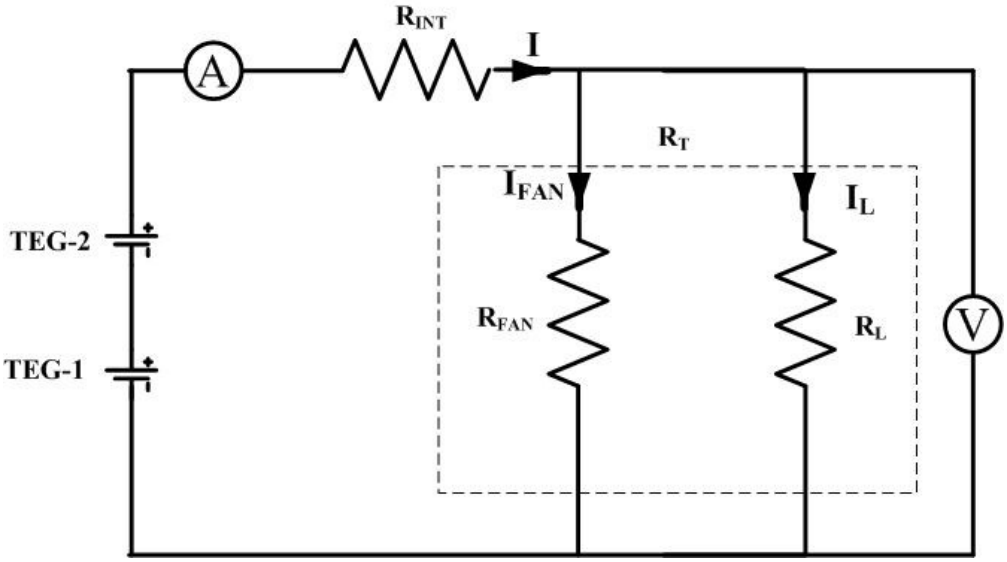


Figure 6. Circuit diagram of a TEG with DC fan resistance and load resistance

$$V_L = V_{NL}\frac{R_L}{R_{INT}+R_L} \quad (1)$$

$$I_L = \frac{V_L}{R_L} \quad (2)$$

$$P_L = V_L . I_L \quad (3)$$

Steady state energy balance equation can be written by considering following assumptions

I. Intercept factor can be taken as unity as PDC tracks the sun.
II. The solar intensity doesn't affect the optical properties of solar PDC.
III. Solar flux received on the surface of the receiver is distributed uniformly.
IV. All the equations are incorporated for one dimensional heat transfer analysis.

The contact resistance between the faces of modules, aluminium absorber plateand the surface of aluminium heat sink are neglected.

3. Energy balance for complete PDCSTEG system (Thermal Analysis)

3.1. Solar Parabolic Dish Concentrator

It had been provided by Gargthe standard mathematical formulas for computation of the parabolic dish collector parameters, such as mouth opening diameter D, depth of dish h, focal distance f, and aperture angle. The concentrated solar radiation heat received by the absorber/receiver surface, the optical efficiency of PDC and the useful energy delivered by the absorber unit of the solar PDC, which works as input to the TEG are determined from the equations given below **[12]-[14]** and **[35], [36]:**

$$q_s = I_B \rho (\tau\alpha)_e \gamma C_R \quad (4)$$

$$\eta_o = \rho_c (\tau\alpha)_e \gamma \quad (5)$$

$$Q_u = q_s A_r - U_L A_r (T_1 - T_a) \quad (6)$$

The useful energy gain in the absorber plate in interval of time is:

$$Q_u = (mC)_{plate}(T_f - T_i) \quad (7)$$

The instantaneous thermal efficiency of the PDC is:

$$\eta_{ith} = \frac{Q_u}{A_{PDC} I_B} \quad (8)$$

3.2. Aluminium absorber Plate

Uncoated aluminium absorber/receiver plate's surface area is exposed to the aperture area of PDC, thus absorbs the concentrated heat and this concentrated heat is then supplied to operation of TEG. Concentration ratio is the determining factor for the amount of heat absorbed and it can be defined as[22]**:**

$$C_R = \frac{A_{PDC}}{A_r} \quad (9)$$

3.3. Working Principle of Thermoelectric Generator

TEG works on the principle of Seebeck effect. When a temp gradient is applied to the junctions of two dissimilar conductor or semiconductor, an electric potential is developed, this is known as TE effect or Seebeck effect[15]**,** [16]**.**

As per the discussed Seebeck effect the hot junction absorbed the heat flux $\alpha I T_h$and $\alpha I T_c$ is rejected by the cold junction. There are three additional effects known as Joule heating effect

caused by electric current, heat leakage caused by heat conduction between two junctions and the Thomson heat caused by the temperature gradient and electric current[16], [17]. If the effect of the Thomson heat is considered negligible, then to overcome the Peltier effects, the heat conduction and the joule heating, the equations governing the heat input rate and heat rejection can be obtained by considering the energy supply or removal [20] and **[35]-[37].**

Heat input to TEG:

$$Q_h = \alpha I T_h + K(T_h - T_c) - 0.5 I^2 R_{INT} \quad (10)$$

Heat removal from TEG:

$$Q_c = \alpha I T_c + K(T_h - T_c) + 0.5 I^2 R_{INT} \quad (11)$$

The heat removal rate from the module to the cooling medium is found as:

$$Q_c = k_c(T_{mf} - T_c) \quad (12)$$

By the Newtonion law Q_h and Q_c may be expressed as-

$$Q_h = k_h(T_1 - T_h) \quad (13)$$

$$Q_c = k_c(T_2 - T_c) \quad (14)$$

The electrical power produced by the TE module can be obtained from:

$$P_{TE} = Q_h - Q_c = \alpha I(T_h - T_c) - I^2 R_n = R_L I^2 \quad (15)$$

Electrical efficiency of TEG is quantified as:

$$\eta_{TEG} = \frac{P_{TE}}{Q_h} \quad (16)$$

The overall electrical efficiency of the PDCSTEG system is**[24]-[28]**:

$$\eta = \frac{P_{TE}}{I_B A_{PDC}} = \frac{Q_h}{I_B A_{PDC}} \frac{P_{TE}}{Q_h} = \eta_{PDC}\eta_{TEG} \quad (17)$$

Where η_{PDC} is the thermal efficiency of the solar PDC.$\eta_{TEG}$is the electrical efficiency of the TEG. Computation of the properties of bismuth telluride alloys TE modules can be done as **[25]:**

Seebeck coefficient:

$$\alpha = (22224 + 930.6\,T - 0.9905T^2)10^{-9} V/K \quad (18)$$

Electrical Resistivity:

$$\rho = (5112 + 163.4T - 0.6279T^2 + 0.4131T^2)10^{-4}\Omega - m \quad (19)$$

Thermal conductivity:

$$k = (62605 - 277.7T + 0.4131T^2)10^{-4} \text{ W/mK} \quad (20)$$

For a parabolic dish concentrator and flat plate receiver the following values are approximately valid**[8],[38]-**

For concentration ratio 100 and beam radiation 1000 W/m^2 the standard values of TE device parameters are as follows**[28], [38].**

Table 2.Thermoelectric material (Bi_2Te_3) characteristics and TE device factors on Standard test condition

S.N	Parameters	Value
1.	C_R=A_{PDC}/A_a	*100*
2.	I_B	1000W/m^2
3.	η_{TEG}	0.75
4.	T_h	300 K
5.	α_n	-1.95×10^{-4} V/K
6.	α_p	2.3×10^{-4}V/K

7.	ρ_n	1.35×10^{-5} Ω-m
8.	ρ_p	$1.75 \times 10^{-5}\Omega$-m
9.	k_n	1.4W/mK
10.	k_p	1.2 W/mK
11.	A_n/L_n	0.01 m
12.	A_p/L_p	0.01 m
13.	k_h	0.2W/K
14.	k_c	0.1W/K

Z and k may be expressed as **[28]-**

$$Z = [\frac{(\alpha_P - \alpha_n)}{\sqrt{k_n \rho_n}+\sqrt{k_p \rho_p}}]^2 \quad (21)$$

$$k = \frac{k_n A_n}{L_n} + \frac{k_p A_p}{L_p} = \frac{A_n}{L_n}\left(k_n + \sqrt{\frac{k_n k_p \rho_p}{\rho_n}}\right) \quad (22)$$

For the geometric configuration of the TEG the optimal conditions may expressed as **[9],[10]-**

$$\frac{L_n/A_n}{L_p/A_p} = \sqrt{\frac{k_n \rho_p}{k_p \rho_n}} \quad (23)$$

where$A_p$and $L_p$are the cross-sectional area and the length of the *p*-type semiconductor element. The ratio of area to length of the TE element can be defined as aspect ratio.

Thermoelectric maximum efficiency and Figure of merit [25],[27]:

$$\boldsymbol{\eta_{TEG}} = \frac{\boldsymbol{T_h - T_c}}{\boldsymbol{T_h}} \frac{\sqrt{(1+ZT)}-1}{\sqrt{(1+ZT)}+\frac{T_c}{T_h}} \quad (24)$$

$$\boldsymbol{ZT} = \frac{\boldsymbol{\alpha^2 \sigma T}}{\boldsymbol{k}} \quad (25)$$

Where$\boldsymbol{\alpha} = \frac{\Delta V}{\Delta T}$is the Seebeck coefficient, $\boldsymbol{\sigma}$ is the electrical conductivity, k is the thermal conductivity which can be divided into two parts (k_e and k_l the electrical and lattice respectively)**[7]**and T is the average temperature$T = \frac{T_h+T_c}{2}$, Z is the effective figure of merit across the temperature gradient, $\frac{\boldsymbol{T_h - T_c}}{\boldsymbol{T_h}}$isCarnot efficiency**[8].**

4. Results and Discussion

The performance characteristics of a class of thermoelectric generator using solar energy as a heat source are discussed through a thermodynamic model. There are always four irreversibility exist in a solar thermoelectric generator like-finite-rate heat transfer between the thermoelectric device and the external heat reservoirs, heat leakage through the thermoelectric device, ohmic heat generated inside the thermoelectric device and heat loss in the solar absorber[19]**, [28]**. On the performance parameters these are investigated with the help of non-equilibrium thermodynamics and finite-time thermodynamics. The variation of Solar Radiation (Global, Concentrated, Diffuse, Beam) with respect to time from 800 hrs to 1645 hrsthroughout the day at each time interval of 15 minute with total 36 observations were recorded. All the radiation between minimum and maximum value during 1100 hrs to 1400 hrs varies as Global Radiation $\boldsymbol{I_G}$ (810-1020 W/m^2), concentrated radiation$\boldsymbol{I_C}$(1200-1621 W/m^2), diffuse radiation $\boldsymbol{I_D}$(99-151

W/m^2), beam radiation$\boldsymbol{I_B}$ (659-892 W/m^2) as shown in **Figure 7**. Parameters$\boldsymbol{T_a}$, $\boldsymbol{T_h}$, $\boldsymbol{T_c}$,$\boldsymbol{V_a}$,$\boldsymbol{Rh_a}$, **V, I** are also observed at every 15 minutes interval from 800 hrs to 1645 hrs and $\boldsymbol{I_B}$, **T, ΔT, P** are calculatedand the overall efficiency of PDCSTEG, the optimal operating temperature of solar receiver/absorber, the optimal matched load resistance and some other novel results are found.

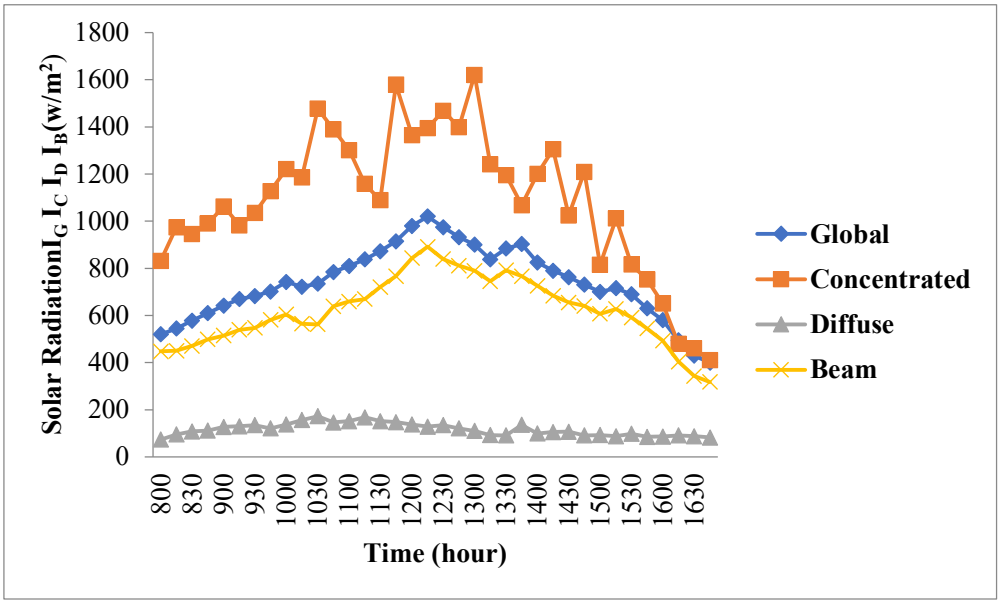


Figure7. Variation of solar radiations during sun shine hourat **23^0 16'N, 77^0 36'E**

PDCSTEG is simply constructed consist of a TEG and solar collector/concentrator as shown in **Fig. 3**.The *p*-type and *n*-type legs are the primary elements of TEG **[26].**
The amount of energy $I_B A_{PDC}$ is received by the aperture area A_{PDC} (1.54 m^2) by the concentrator and it supplied heat to the receiver/absorber with aperture area A_r at the rate q_s , thus the total insolation $q_s = I_B \rho_c (\tau\alpha)_e \gamma C_R$ is received by the absorber is expressed by **Equation (4)**[19]**,** whereI_B is the solar insolation.

The reflectivity of parabolic dish material (Anodized aluminium) is 0.84, effective transmissivity and absorptivity product of the receiver surface is 0.80. The PDC concentrate only the beam radiations that start to raise the temperature of hot side. The heat input rate to the thermoelectric generator from the solar receiver/absorber is Q_h at temperature $T_h$and heat rejection from TE device to heat sink takes place at rate Q_c at temperature T_c according to **Equation (10 and 11)[29]**.The heat leakage through the TE device is $Q_k$and heat loss of the solar receiver/absorber is considered as Q_L=$U_L A_r (T_1 - T_a)$according to **Equation-(6)[30].**

The electrical power P, at current I is produced by the TEG and it is transferred to the load resistance R_L and fan resistance R_{FAN} as per the Equations (1, 2, 3). T_h and $T_c$are the temperatures of the two junctions in the thermoelectric device, whose variation during 1100 to 1400 hrs was observed as hot side temperature (150-210 ºC), cold side temperature (37-45ºC) and hence the average temperature T (93.5-127.5ºC), ΔT(113-165ºC) at ambient temperature (38.9-40.2ºC) are shown in **Figure 8**. The useful energy delivered to thermoelectric generator

by the receiver unit is computed by $Q_u = q_s A_r - U_L A_r (T_r - T_a)$ as per **Equation (6)**, where $A_r$is the absorber area of the solar collector and $\eta_{lth} = \frac{Q_u}{A_{PDC} I_B}$is the instantaneous thermal efficiency as per equation (8)[16].

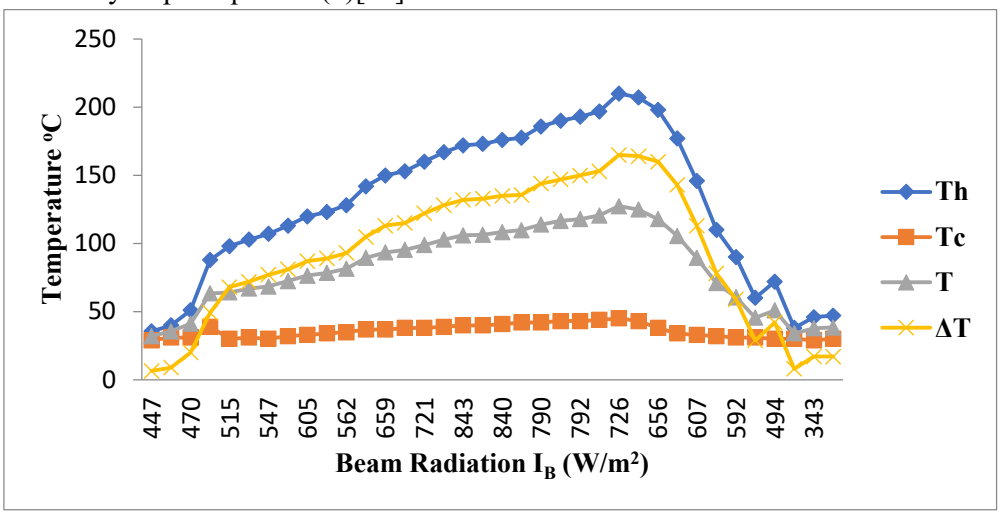


Figure8. Variation of temperatures with beam radiations

Here, Seebeck effect is the most important factor due to which TE device works as a generator, heat flux $\alpha I T_h$ is absorbed at hot junction and $\alpha I T_c$ is the heat flux rejected at cold junction, where $\alpha$is the Seebeck coefficient. αdoes not only depend upon the properties of semiconductor material but also is a function of temperature according to the **Equation (18)[32]**i.e., $\alpha = \alpha(T)$. Three additional effects also exist in TE device: Joule heating due to the electrical current, heat leak between the two junctions, Thomson heat due to both the temperaturegradient in the TE device and the electrical current**[33].**The TE device which has negligible Thomson coefficient, their performance is not influenced by the Thomson coefficient and α may be approximately considered as a constant**[39].** Thomson heat is taken as negligible in this research. The TE device is insulated both electrically and thermally from the surrounding except at the junction-reservoir contacts, it is assumed for the purpose of analysis, such that the net rates of heat input q_h is $\alpha I T_h + K(T_h - T_c) - 0.5 I^2 R_{INT}$and heat rejection$q_c$*is* $\alpha I T_2 + K(T_h - T_c) + 0.5 I^2 R_{INT}$ as per **Equations (10, 11).**Where *K* and $R_{INT}$are the thermal conductance and the total internal electrical resistance of the TE device. Joule heat produced inside the thermoelectric device flows equally to the hot and the cold junctions that is why a factor of 1/2 in $R_{INT} I^2$ term appears**[40]**. According to the above assumptions α may be considered as a constant, the electrical power P produced by TE modules is $q_h - q_c$ which is equal to $\alpha(T_h - T_c)I - R_{INT} I^2 = R_T I^2$ as per **Equation (15)[41]**. If α is considered as function of temperature and the effect of the Thomson heat has to be considered[42], the performance of PDCSTEG remains to be investigated further. The more analytical model for a PDCSTEG can be established by considering the effect of the irreversibility of finite-rate heat transfer between the TE device and its external heat reservoirs. Newtonian law is also obeyed by the heat transfer so $q_h$and $q_c$may be expressed as from **Equations (13, 14)-**

$Q_h = k_h(T_1 - T_h)$and $Q_c = k_c(T_2 - T_c)$

Where $k_h$is the thermal conductance between the solar absorber and hot junction and $k_c$is the thermal conductance between the cold junction and the heat sink.Using the above equations, we derived the efficiency of a PDCSTEG and discuss its optimal performance.

4.1. Optimization of Load for a PDCSTEG system in view of no load and loaded tests-
In this project we used TEG module (32 ×32 mm) for our experiment. Bismuth telluride alloy is the material of which module is made of and the length of the TE element is 1.72 mm. Specifications of TEG according to the supplier are-figure of Merit of TE material (Z=1), rated power 5 W, rated voltage 12 V, rated current 1 A at T_h= 220 ^{0}C andT_c= 30^{0}C. The internal resistance of TEG module is 1.84 Ω at maximum working temperature of 220 ^{0}C. The maximum processing temperature of TEG is 220 ^{0}C. Open circuit test and load tests(R_{fan}=96 Ω, R_L=16.94 Ω, R_T=R_{fan}‖R_L=14.4 Ω) are performed to analyse the performance of TE module, but the TEG produces output voltage in the range (6.3-10 V), current in the range (0.437-0.7 A) and Power in the range (2.94-6.94≈7 W). The PDC concentrate only the beam radiations that start to raise the temperature of hot side. The Voltage build up process starts atT_h 35.5 ^{0}C with a value of 0.75 V and reaches to the value of 10 V at 210 ^{0}C instead of rated voltage of 12 V, current 0.7 A instead of 1 A and power 6.94≈7 W instead of 10 W for the solar beam radiation ranging from 726 w/m^2, because of the decrement in ΔT due to increased air velocity and relative humidity, these all parameters doesn't match with the supplier's specification. The maximum overall efficiency of PDCSTEG system for hot Side Temperature (T_h) 210 ºC, Cold Side Temperature (T_c) 45 ºC, Average receiver temperature (T) 127.5 ºC, maximum output Voltage 10 V, Current 0.7 A, Power 7 W is obtained 0.6207%.

Maximum power to the load is transferred in the case only when load resistance equals the internal resistance of the TEG. Ironically, at this operating point, equal amount of power will be dissipated within both the load and the internal resistance of the generator (i.e., electrical efficiency will be 50%) **[34].**To obtain maximum electrical power output the load resistance is kept equal to internal resistance of TEG. The overall efficiency of the PDCSTEG system can be better for the higher value of beam radiations (more sunshine) with less wind velocity and relative humidity**[35]**. Further discussion about the results and optimization of load is as follows.

The device was kept under sunshine for an hour so that it could achieve steady state. As the incoming solar radiation increases during the day, the hot side temperature increases, the DC fan maintains cold side temperature between 35-42 **ºC**during 1100 hrs to 1400 hrs. At the starting of the day around 800 hrs when T_h =35 **ºC**and T_c = 27**ºC,** No load voltage or open circuit voltage build up process starts up at ΔT 8**ºC**and observed as 0.78 V as shown in **Figure9**. As the time passes after 800 hrs solar radiation increases, which leads to increase hot side temperature that raises open circuit voltage. The maximum no load voltage is achieved as 11.27 V at 1400 hrs when beam radiations are observed as 726 W/m^2.

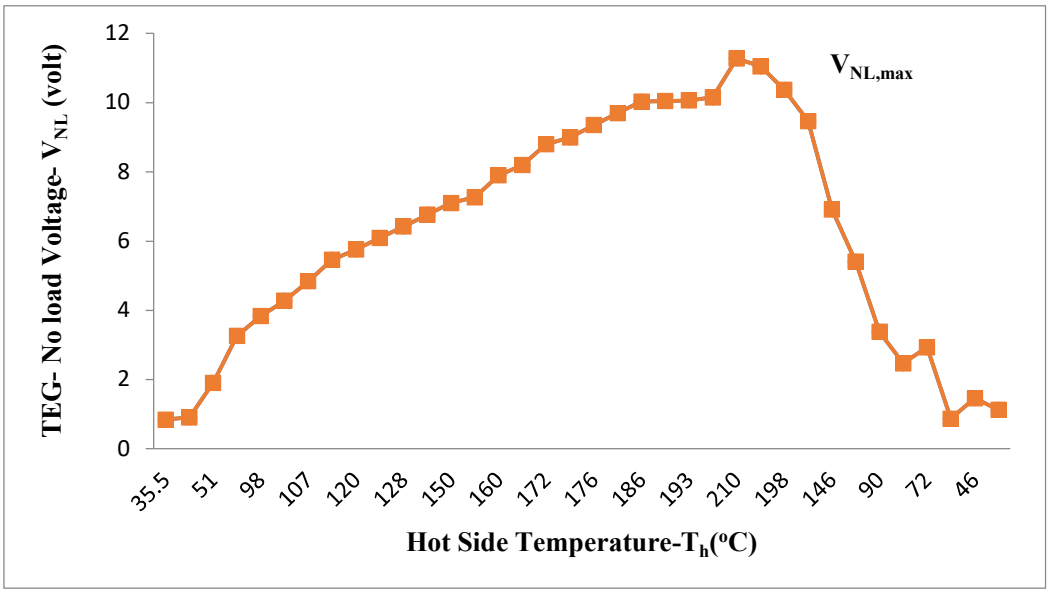


Figure9. Open Circuit Voltage v/s Hot side Temperature

The no load test and load test were conducted simultaneously on the TEG after each 15 minute interval. For every beam radiation value open circuit voltage was observed, at the same moment TEG was loaded with connected half load and full load ($\mathbf{R_T}$) consecutively and hence all other parameters like voltage, current and power of TEG were observed and calculated as shown in **Fig. 10**. The maximum load voltage 10V, load current of 0.694 A were observed and power 7 W calculated for no load voltage (TEG output voltage) 11.27 V at solar beam radiation of 726 W/m^2.

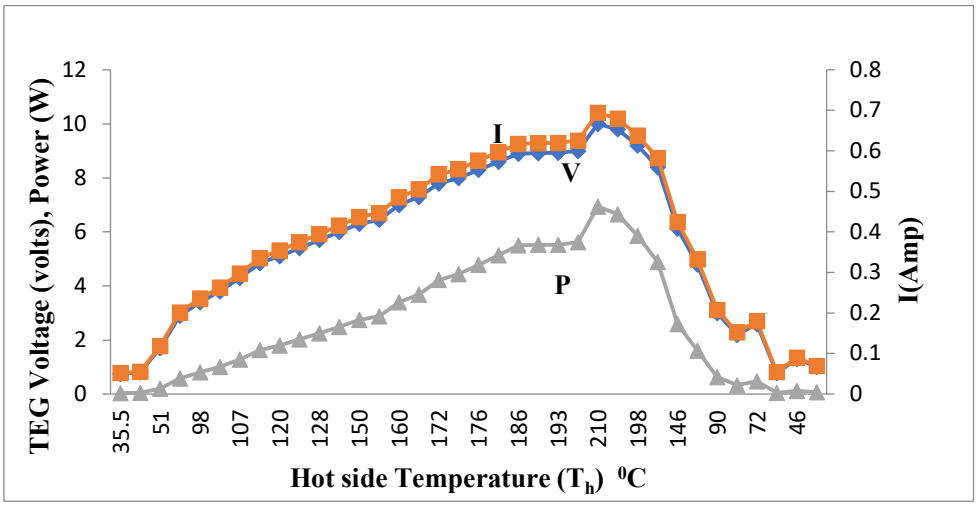


Figure10. Variation of output TEG voltage, Current and power for various operating hot side temperature(T_h v/s V_L, I, P curve, Tc: 35-43 ^{0}C, R_{fan}=96 Ω R_L=16.94 Ω R_T=14.4 Ω)

The electrical power output of a thermoelectric generator is $P_{TE} = I_B A_{PDC}\,\eta$ as per **Equation (15)**. It can be easily proved that when the efficiency of a PDCSTEG with a given quantity$I_B A_{PDC}$attains its maximum, the power output also attains maximum. It is here clearly manifested that both the maximum power output and the maximum efficiency of a PDCSTEG

are identical states. But maximum power transfer to the load R_L is so important in designing TEG systems. TEGs inherently don't work as regulated power supplies**[43].** At any given ΔT, if the load resistance decreases, the output voltage also decreases and as the load resistance increases, the output voltage will also increase**[44].** There is no inherent output regulation (We can provide additional circuit to regulate the voltage). Because every TEG has considerable amount of internal resistance, it refers that as more current will be drawn by the electrical load (e.g., as load resistance decreases), more of the available power will be dissipated within the TEG**.** Moreover there will be a considerable voltage drop across this internal resistance. Analysis of the voltage drop with the help of electrical model of TEG system is accomplished in this article. If there is a no-load voltage (i.e., the open-circuit voltage output of a TEG) applied to a series circuit consisting of the module's internal resistance R_{INT} and the total electrical load $R_T$as shown in **Figure6**,there will be a voltage drop in proportion to the resistance according to voltage divider rule. Thus, if we consider no-load voltage 7V, the internal resistance is 1.86 Ω and the Full load R_T = 14.4 Ω **(R_T=R_{fan}‖ R_L),** then from equation-(1) there would be a 6.2 V drop across the load. This decrement in load voltage can be seen in **Figure11.**

$$V_L = V_{NL}\frac{R_T}{R_{INT}+R_T} V_L = 7V\frac{14.4\Omega}{1.86\Omega+14.4\Omega} = 6.2V$$

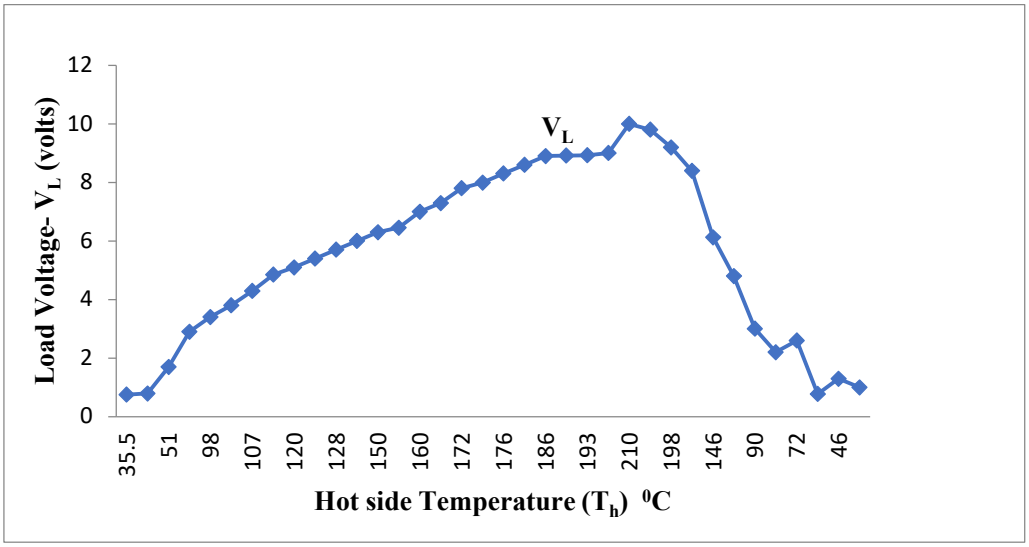


Figure11.Variation of Load Voltage with Hot side Temperature (T_h v/s $V_L$curve,Tc: 35-43 ^{0}C, R_{fan}=96 Ω R_L=16.94 Ω R_T=R_{fan}‖R_L=14.4 Ω)

Therefore, the maximum power transfer to the load is a major concern here. Therefore for any electrical circuit maximum power can be transferred to the load if the load resistance equals the internal resistance of the voltage source (TEG)**[43], [44].** Here it is to be noted that this point of operation will not provide us the maximum amount of voltage or current, but the greatest power can be derived at that point. For any no load voltage the following formulas are

used to determine load voltage, current and power for various load resistances from **Equations (1, 2, 3)**:

$$V_L = V_{NL}\frac{R_L}{R_{INT}+R_L}, I_L = \frac{V_L}{R_L}, P_L = V_L.I_L$$

The variation of TEG output current and power delivered to load with load voltage can be seen in **Figure12**.with rise in TEG generated voltage, the load voltage also increases, the demand of load power at required load current is fulfilled. The maximum power is delivered to the load at maximum voltage.

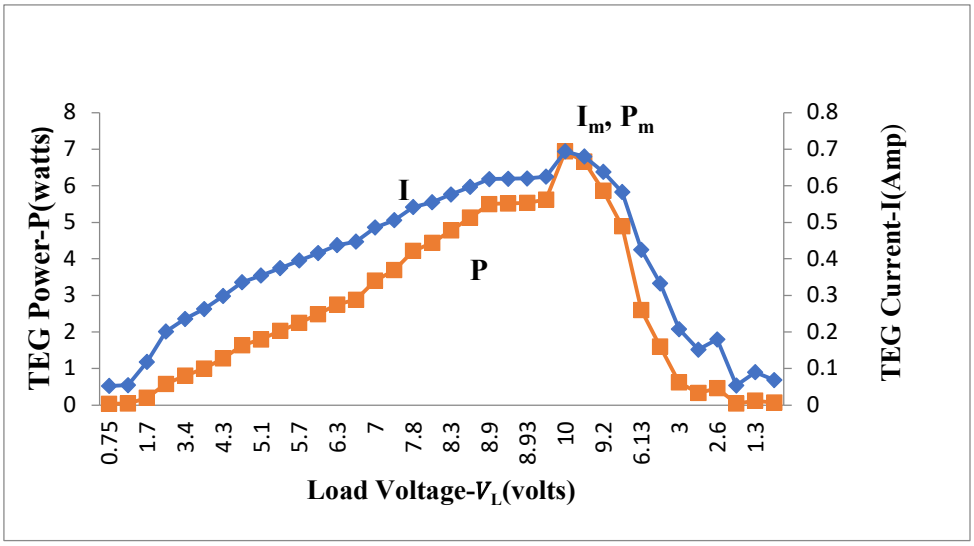


Figure 12. Electrical performance of thermoelectric module (I-V and P-V curve, Tc: 35-43 ^{0}C, R $_{fan}$=96 Ω R_L=16.94 Ω R_T=14.4 Ω)

It is fairly tricky to match the loads. It can be easily done when a TEG is customised for a particular project, then the optimization of the pallet configuration can be done for the specific application **[20], [30]**. On the other hand, the best job of load-matching is the series/parallel module combination, for which the designer is left to arrive at. Moreover complicating matters in many cases will be the fact that operating conditions may change over time and our design may be matched for one set of circumstances but not for another**[25],[26].** For the dynamic ambient environment and/or variable load resistance, the TEG must be designed to the worst case and then manage surplus capacity with a regulatory circuit**[26], [27].**

Sometimes maximum power transfer couldn't be the priority, especially in those systems whose heat source is not waste heat. Here power conversion efficiency(which occurs at a somewhat different operating point) may be the greater issue. Even then TEG is made to compromise a bit toward enhancing power transfer**[27], [19]**. A significant power boost can be achieved by sacrificing a little bit of efficiency. Practically most TEG system designs will be at least somewhat mismatched**[29], [30].** For a discrete building block (i.e., individual TEG modules) only a given resistance with series/parallel combination can be approximated. Generally, it is better to err on the side of having load resistance exceed internal resistance (efficiency is a much more slippery slope when it is the other way around). In the general cases, we obtain the required load resistance at the maximum power output, i.e. the optimal load

matching. In the special case the optimal value of the load resistance must be **[37]-**

$$R_{L,opt} > R_{INT}$$

The calculative results of the optimal load resistance provide an important theoretical basis for the optimal operation of PDCSTEG.

4.2. Variation of internal resistance with operating temperature and dynamic ambient conditions-

Design solutions of TEGs are significantly depend on temperature-dependent properties of TE material according to **equation (18, 19 and 20)**, Which create more challenges in arriving at design solutions. The module has internal resistance of 1.84Ω at an average temperature ($T = \frac{T_h+T_c}{2}$) of 115 °C, it may reach 2.84Ω at 150°C. This affect output voltage, current and power as operating temperature changes. For this module for instance, if 115°C is the average operating temperature, the no-load voltage is 10 V and the load resistance is 14.4 Ω, it gives a resulting load voltage of 8.86V with a load current of 0.52 amps (P_L = 4.6 W). Due to some dynamic ambient conditions throughout the day and continuous operation if the average operating temperature then drifted to 150° C while keeping constant no-load voltage, there will be the decrement in load voltage to 8.3 V with a load current draw of 0.50 A (P_L = 4.17 watts-nearly a 9.3% decrease). Therefore, if there is any variation in operating conditions, there will be a need to look at the range of module resistance that may provide result according to variable ambient condition. So it is quite clear that TEG system designing should be done, keeping in mind worst case condition and ensure that the system should provide sufficient power even when ΔT is low and high current demand and it should have the capacity of excess generation at all other operating points.

4.3. Maximum efficiency of PDCSTEG system-

As per equation (17, 24 and 25)

$$\eta = \frac{P_{TE}}{I_b A_{PDC}} = \frac{Q_h}{I_b A_{PDC}} \frac{P_{TE}}{Q_h} = \eta_{PDC}\eta_{TEG}$$

shows clearly that the efficiency η of a PDCSTEG is equal to the product of the thermal efficiency $\eta_{PDC}$of the solar collector and the TEG efficiency$\eta_{TEG}$of the thermoelectric generator. For a PDC as a heat engine **[38]**η_{PDC} decreases with an increase in the operating temperature $T_h$of the solar collector after an optimum temperature $T_{h,opt}$ and η_{TEG}increases with an increase in the operating temperature $T_h$upto210^0C. It clearly specifies that there should be an optimum operating temperature $T_{h,opt}$at which the efficiency of the PDCSTEG will be maximum**[5], [38]**. By incorporating above information, we plotted the curve of PDCSTEG efficiency varying with the operating temperature of the solar absorber/receiver, as shown in **Figure13**. It is seen from **Figure13** that for a given area A_r, the efficiency increases when hot side temperature increases upto 210^0C. There will be an optimal maximum current $I_m$at which the efficiency of PDCSTEG will be maximum, as shown in **Figure 12 and Figure 13**.

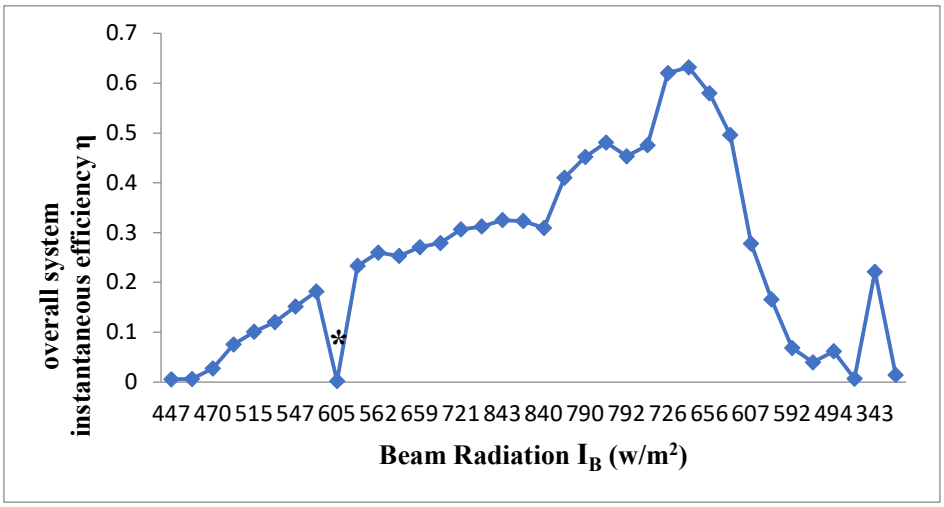


Figure13. Variation of Instantaneous overall PDCSTEG system efficiency with beam radiation η_{max}isan important parameter of PDCSTEG, because it determines an upper bound for the efficiency of a class of TEG, whose source is solar energy. It is worthwhile to note that the electrical current at the maximum efficiency $\eta_{max}$is another important parameter of PDCSTEG.

Instantaneous maximum overall system efficiency of PDCSTEG from Equation-17:-

$$\eta_{max} = \frac{Maximum\ Power\ Output}{Power\ input}$$

Maximum Power Output $= 6.94 \approx 7$ w

Aperture Area of the PDC $= 1.54\text{m}^2$

Beam radiation $= 726\ \text{w/m}^2$

Power i/p $=$ Aperture Area of the PDC $(\text{m}^2) \times$ Beam radiation(W/m^2)

$\eta_{\max} = 0.6207\ \%$

It can be observed clearly from **Figure 12 and Figure13** that for a given receiver area A_r, both η_{max} and $I_m$increases when ΔT increases and both decrease when ΔT decreases. At * point the efficiency is very low 0.0019%, because ΔT is very low due to dynamic ambient conditions. There is always a finite-rate heat-transfer between the TE device and the external heat reservoirs and heat leakage between two junctions of TE device so the maximum efficiency is achieved at the maximum electrical current I_m. **Figure 13** shows the instantaneous overall system efficiency of the PDCSTEG ranges as (0.2709-0.6207%), which is to be as low as 0.2709% at lower beam radiation of 659 W/m^2 at operating temperature of 150 °C. Increment in operating temperature gradually increases the overall system efficiency. The PDCSTEG achieve a maximum efficiency of 0.6207% when the solar beam radiation reaches the value of 726 W/m^2 at temperature 210°C. Increase in velocity of ambient air and relative humidity decrease the operating temperature of hot side and cold side that results decrease in ΔT, which ultimately reduces the overall system efficiency and vice-versa. Air velocity during the whole day varies in the range of (0.18-1.20 m/s) and relative humidity is in the range of (14.2-21.2%).

5. Artificial Intelligence in PDCSTEG

ANN commonly referred to as neural networks, had been extensively used in a large variety of programs. Those applications consist of pattern popularity, function Approximation, optimization, simulation, and estimation can be automated amongst many different software

regions and furthermore studies have produced a large number of community Paradigms. Nowadays, ANN have been skilled to remedy Complex troubles which are hard to resolve by way of conventional Techniques. ANN conquers the restrictions of the Traditional methods by means of extracting the desired statistics viause of the input statistics. An ANN does now not need such a selected Equation shape, however it requires enough input-output records. Additionally, it may continuously be re-educated, so that it may readily adapt to new facts. An ANN has been investigated to cope with the troubles related to incomplete or obscure input facts. An essential degree of a neural network is the training Step, in which an input is added to the network collectively with the favoured output; the weighs and bias values are initially Chosen randomly and the weighs are adjusted so that the Network tries to produce the desired output. The weighs after training, contain significant statistics, while before training, they're random and don't have any means. When a Great level of overall performance is reached, the training stops, and the network makes use of the weighs to make choice. Many Alternate education techniques are being incorporated including back propagation that has different editions. The purpose of any training set of rules to limit the mistakes including mean % Error, root-mean-square (rms) etc. An ANN model records processing paradigm that is inspired by way of the way the biological apprehensive structures such as the brain manner information. The key element of this paradigm is the radical structure of the statistics processing machine. It Composed of a big range of distinctly inter related Processing factors (neurons) running in unison to clear up Particular trouble. The network usually consists of an input Layer, one hidden layer and an output layer. Ann is like a human being that Examine through instance as biological structures involves Adjustment to the synaptic connections that exist among the Neurons. ANNs operate a complete lot like a “black field” version, requiring no specific statistics about the function. An artificial neuron is a tool with many inputs and one output. The neuron has modes of operation; the Education mode and the checking out mode. In the training mode, Neuron can be trained to fireplace (or not now state) for precise input Styles. In the checking out mode, whilst a taught input sample is detected on the entry level, its associated output will become the modern-day Output.

5.1. Heat maps of PDCSTEG

Each square shows the correlation between the variables on each axis. Correlation ranges from -1 to +1. Values closer to zero means there is no linear trend between the two variables. While values closer to 1 the correlation more positively correlated; that is as one variable increases, so does the other and as it reaches to closer to 1 the stronger the relationship is. A correlation closer to -1 is similar, however instead of both increasing, one variable will decrease as the other increases. The diagonals are all 1/dark green because those squares are correlating each variable to itself (so it's a perfect correlation). For the rest of the values, the larger the number and darker the colormanifest the higher correlation between the two variables. The plot as shown in **Figure14**is also symmetrical about the diagonal since the same two variables are being paired together in those squares.

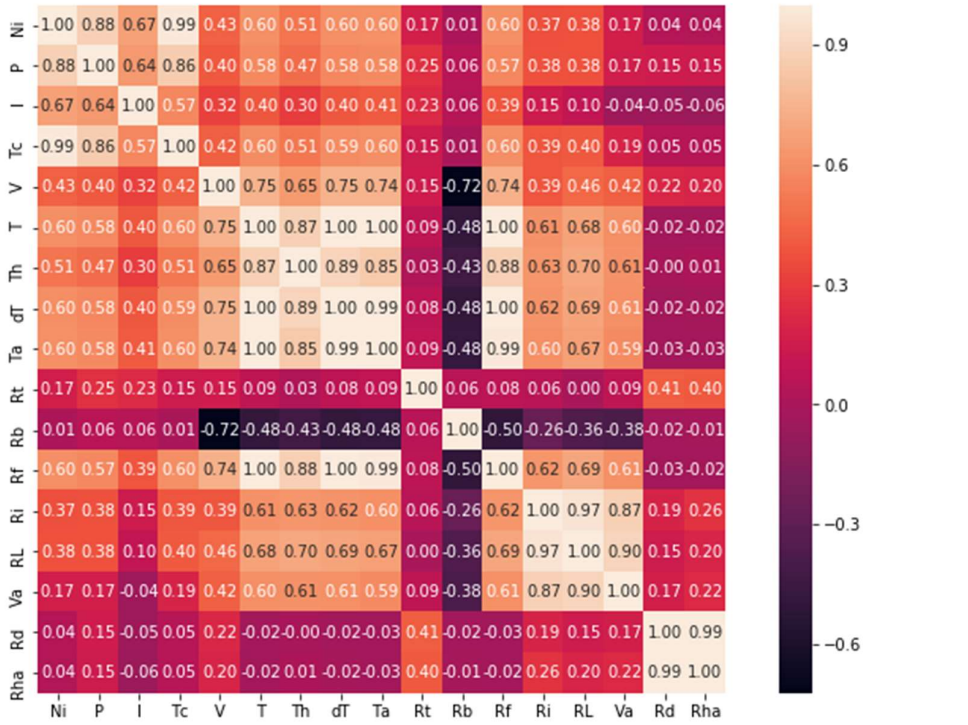


Figure 14. Visual representation of Heat map

The PDCSTEG system modeled by ANN has eight inputs and one output. The input variables of Solar collector systems are the (Rb) beam radiation, hot side temperature (Th), (Tc) cold side temperature, (dt) temperature difference between hot and cold side, (Rha) relative humidity,(V) voltage, (I) current, (R_L) load resistance, and (Rt) total resistance all these parameters were taken into consideration to calculate and predict (Ni) total efficiency of the system. All network calculations were performed using python Jupyter lab Platform. The original data set was having 19 features which was reduced to 9 data features on the basis of heatmap used for correlation between different factors. The data set for the efficiency of the system available included 108 data pattern for each. From these 81 data patterns were used for training the ANN. The remaining 27 patterns were used as the test data set. The Architecture for ANN is shown in **Figure15**, the optimizer used was Adam optimizer or adaptive moment estimation which is an algorithm for optimization technique for gradient descent.

5.2. The ANN Model of PDCSTEG (with 8 inputs)

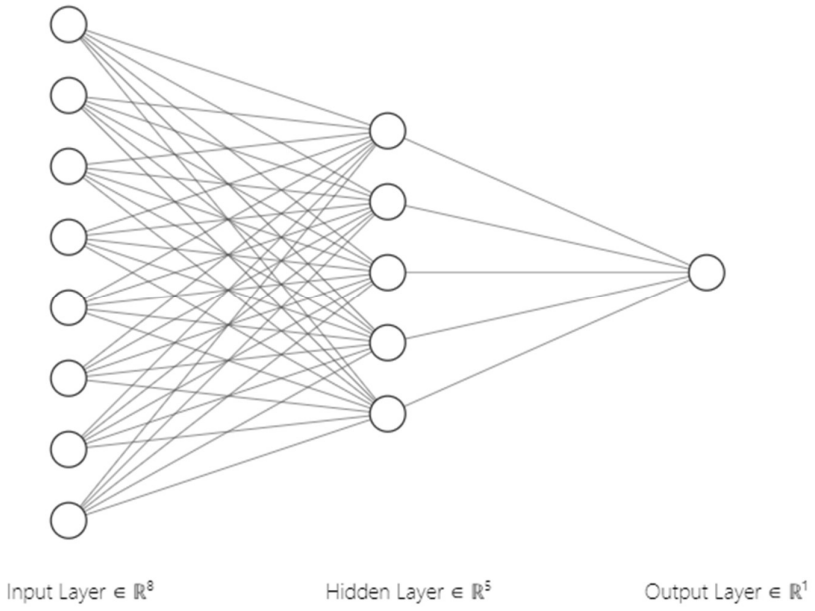


Figure15. Diagrammatic representation of Multilayer Neural network model

The predicted values obtained from the ANN model for PDCSTEG is shown in **Figure**16 reveal the best trained data with minimum error. Efficiency with a mean square error (MSE), root mean square error (RMSE), mean absolute error value is 0.00223354, 0.04726043 and 0.02570740 respectively. In this case, these results confirm that the experimental values are closer to ANN predicted results.

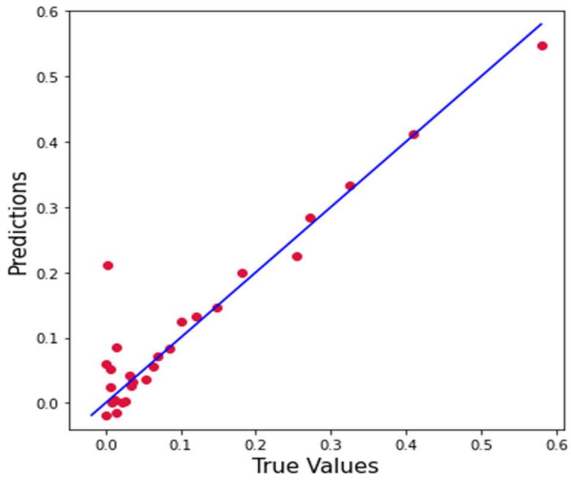


Figure16. Prediction Curve for efficiency (Best Linear Fit For predicted And True values)

6. Conclusions and future phase of work

An experimental prototype of Solar concentrating thermoelectric generator using parabolic dish concentrator, absorber/receiver, heat sink cooling system and TEG modules is fabricated

and the potential of thermo electric cells combined with concentrating solar energy as a power generation system has been tested and illustrated. The following conclusions were drawn:

I. By incorporating parabolic dish concentrator technology without maximum power point tracking overall PDCSTEG system maximum efficiency is achieved as 0.6207% at the solar beam radiation of 726 W/m^2 and a minimum of 0.2709% at a minimum solar beam radiation of 659 W/m^2 during 1100 hrs and 1400 hrs for the 10 W capacity TEGs with passive air cooling and without any maximum power point tracker.

II. The parameters are achieved as hot side temperature 210^{o}C and Cold side temperature 45 ^{o}C that's why ΔT=165^{o}C instead of 170^{0}C is achieved i.eΔTdecreased by 5^{0}C and hence maximum Power output approximately 6.94 W ≈7 W at 10 V voltage and 0.694 A current with an overall system efficiency of 0.6207% with passive air cooling and without any maximum power point tracker.

III. The power transfer to the load can be maximum, only when the load resistance would be equal to internal resistance of the TEG module.

IV. The maximum power output 7W is found just near to rated power of 10W as specified by supplier, however not matched with the supplier's specifications. This Power gap is mainly caused by the reduction in ΔT due to dynamic ambient conditions, like increased air velocity and humidity.

V. The experimental and theoretical values of generated power of the PDCSTEG were within 30% accuracy.

VI. The experimental results showed a considerable agreement with the mathematical model as well as its potential applications without considering losses.

VII. Further investigation of the PDCSTEG can be studied by incorporating all the losses. It is observed that the perspective applications for such power system is strongly depend on the development of the thermoelectric material, types of concentrator, various absorber, absorber coating, various substrates, various heat sinks, therefore research about exploring the latest improved TE material with other design parameters under the current PDCSTEG system is recommended**.** Performance can be improved by implementing maximum power point solar tracker however it increases the cost of TEG power generation.

VIII. PDCSTEG could be a perspective and feasible device of the renewable energy based power source from small scale to large scale application without harming environment.

Authors Contribution:

Sanjeev Kumar Bhukesh: Conceptualization, Methodology, Writing- Original draft preparation, Investigation, Data curation**, Anil Kumar**: Supervision, Reviewing and Editing,**Suresh Kumar Gawre**:Supervision, Reviewing and Editing

Acknowledgement: Authors are highly thankful to Maulana Azad National institute of Technology, Bhopal, India for providing all basic research facility.

Data Availability Statement:

The data that support the findings of this study are available from the corresponding author upon reasonable request.

Declaration of competing interest:

The authors declare that they have no known competing financial interests or personal relationships that could have appeared to influence the work reported in this paper.

Nomenclature

A_{PDC}: Aperture area of the solar parabolic dish collector, **m^2**
A_r: Aperture area of the receiver plate, **m^2**
A_n: Cross-sectional area of n-type TE element leg
A_p: Cross-sectional area of p-type TE element leg
C: Coefficient of performance
C_R: Concentration ratio
I_G: Global radiation **W/m^2**
I_C: Concentrated Radiation **W/m^2**
I_D: Diffuse Radiation **W/m^2**
I_B: Beam Radiation incident on the concentrator surface, **W/m^2**
I: Output Electric Current **A (Ampere)**
I_L: Load current **A (Ampere)**
I_m: Maximum output Electric Current **A (Ampere)**
K: Thermal conductance of the thermoelectric device, **W/K**
k**:** Thermal conductivity of thermoelectric material, **W/m-K**
K_c: Heat transfer coefficient between the module cold side and the cooling medium, **W/m^2K**
k_h: Thermal conductance between the solar receiver/absorber and hot junction, **W/K**
k_c: Thermal conductance between the cold junction and the heat sink, **W/K**
L_n: Length of n-type TE element leg
L_p: Length of p-type TE element leg
m: mass of the receiver plate, **Kg**
P_{TE}: Electrical power produced by TE module, **W**
P_L: Power delivered to load
q_s: Heat supplied to the absorber/receiver, **W/m^2**
Q_h: Absorbed heat flux at hot junction, **W**
Q_C: Heat rejection from the TEG/Heat flux rejected at cold junction, **W**
Q_u: Useful energy delivered to TEG by the absorber, **W**
Rh_a: Relative Humidity **%**
R_{INT}: Internal resistance of TEG, **Ohm**
R_{fan}: DC fan resistance **Ohm**
R_L: Load resistance **Ohm**
$R_{L,opt}$: Optimum load resistance, **Ohm**
R_T: Total electrical load resistance **Ohm**
T_a: Ambient Temperature **^{0}C**
T_1: Receiver/absorber plate temperature **^{0}C**
T_2: Heat sink temperature **^{0}C**

T_h: Hot junction side Temperature of the TEG **^{0}C**
$T_{h,opt}$: Optimum hot side temperature of the TEG **^{0}C**
T_c: Cold junction side Temperature of the TEG **^{0}C**
T: Average Temperature of receiver/absorber **^{0}C**
ΔT: Temperature difference between hot side and cold side **^{0}C**
T_{mf}: Mean fluid (air) temperature at aluminium sink box device ^{0}C
T_f: Final temperature of the receiver/absorber plate ^{0}C
T_i: Initial temperature of the receiver/absorber plate ^{0}C
Time: Hours
V_a: Air Velocity **m/s**
V_L: Load voltage **V**
V_{NL}: No load voltage **V**
U_L: Overall heat Loss Coefficient (radiative, conductive, convective)
V: Output voltage **V (Volt)**
ΔV: Change in voltage with change in temperature
Z: Figure of merit of thermoelectric material

Abbreviation

Min: minimum
Max: maximum
PDCSTEG: Parabolic Dish concentrated Solar Thermoelectric Generator
PDC: Parabolic dish concentrator
STC: Solar Thermal collectors
TEG: Thermoelectric Generator
TE: Thermoelectric
hrs: hours

Greek Symbols

η_o**:** Instantaneous optical efficiency of PDC **%**
η_{ith}**:** Instantaneous thermal efficiency of PDC **%**
η_{TEG}**:** Instantaneous electrical efficiency of TEG **%**
$\eta_{TEG\ max}$**:** Instantaneous maximum electrical efficiency of TEG **%**
η**:** Instantaneous overall system efficiency **%**
η_{max}**:** Instantaneous maximum overall PDCSTEG system efficiency **%**
γ: Intercept factor
τ: transmissivity of the receiver
∝: absorptivity of the receiver
$(\tau \propto)_e$: Effective transmissivity and absorpitivity product of receiver surface
ρ_c : Reflectivity of the concentrating surface
ρ: Electrical resistivity of the thermoelectric material
α: Seebeck coefficient of thermoelectric material

References

[1] R. Prăvălie, C. Patriche, and G. Bandoc, "Spatial assessment of solar energy potential at global scale. A geographical approach," *J. Clean. Prod.*, vol. 209, pp. 692–721, 2019,

doi: 10.1016/j.jclepro.2018.10.239.

[2] M. K. Hairat and S. Ghosh, "100 GW solar power in India by 2022 – A critical review," *Renew. Sustain. Energy Rev.*, vol. 73, no. November 2016, pp. 1041–1050, 2017, doi: 10.1016/j.rser.2017.02.012.

[3] R. Singh, "Energy sufficiency aspirations of India and the role of renewable resources: Scenarios for future," *Renew. Sustain. Energy Rev.*, vol. 81, no. June, pp. 2783–2795, 2018, doi: 10.1016/j.rser.2017.06.083.

[4] E. Ogbonnaya and L. Weiss, "Micro Solar Thermal Power Harvesting using Thermoelectric Generator," *Natl. Soc. Black Eng. Proc. 38thAnnual Conv. Pittsburgh, PA*, pp. 88–95, 2012, [Online]. Available: http://www2.latech.edu/~lweiss/Site/Vitae_files/NSBE_2012.pdf.

[5] D. Kraemer *et al.*, "Concentrating solar thermoelectric generators with a peak efficiency of 7.4%," *Nat. Energy*, vol. 1, no. 11, 2016, doi: 10.1038/nenergy.2016.153.

[6] W. He, G. Zhang, X. Zhang, J. Ji, G. Li, and X. Zhao, "Recent development and application of thermoelectric generator and cooler," *Appl. Energy*, vol. 143, pp. 1–25, 2015, doi: 10.1016/j.apenergy.2014.12.075.

[7] D. K. Aswal, R. Basu, and A. Singh, "Key issues in development of thermoelectric power generators: High figure-of-merit materials and their highly conducting interfaces with metallic interconnects," *Energy Convers. Manag.*, vol. 114, pp. 50–67, 2016, doi: 10.1016/j.enconman.2016.01.065.

[8] M. L. Olsen *et al.*, "A high-temperature, high-efficiency solar thermoelectric generator prototype," *Energy Procedia*, vol. 49, pp. 1460–1469, 2013, doi: 10.1016/j.egypro.2014.03.155.

[9] M. Hamid Elsheikh *et al.*, "A review on thermoelectric renewable energy: Principle parameters that affect their performance," *Renew. Sustain. Energy Rev.*, vol. 30, pp. 337–355, 2014, doi: 10.1016/j.rser.2013.10.027.

[10] G. Zhang *et al.*, "A comprehensive design method for segmented thermoelectric generator," *Energy Convers. Manag.*, vol. 106, pp. 510–519, 2015, doi: 10.1016/j.enconman.2015.09.068.

[11] Q. Cao, W. Luan, and T. Wang, "Performance enhancement of heat pipes assisted thermoelectric generator for automobile exhaust heat recovery," *Appl. Therm. Eng.*, vol. 130, pp. 1472–1479, 2018, doi: 10.1016/j.applthermaleng.2017.09.134.

[12] W. H. Chen, C. C. Wang, C. I. Hung, C. C. Yang, and R. C. Juang, "Modeling and simulation for the design of thermal-concentrated solar thermoelectric generator," *Energy*, vol. 64, pp. 287–297, 2014, doi: 10.1016/j.energy.2013.10.073.

[13] E. Laux *et al.*, "Development of thermoelectric generator based on ionic liquids for high temperature applications," *Mater. Today Proc.*, vol. 5, no. 4, pp. 10195–10202, 2018, doi: 10.1016/j.matpr.2017.12.265.

[14] L. Kütt, J. Millar, M. Lehtonen, and M. Märss, "Optimization of concentrated solar thermoelectric generator system for highest yearly electric output," *2015 56th Int. Sci. Conf. Power Electr. Eng. Riga Tech. Univ. RTUCON 2015*, pp. 3–8, 2015, doi: 10.1109/RTUCON.2015.7343170.

[15] P. Huen and W. A. Daoud, "Advances in hybrid solar photovoltaic and thermoelectric generators," *Renew. Sustain. Energy Rev.*, vol. 72, no. October 2016, pp. 1295–1302,

2017, doi: 10.1016/j.rser.2016.10.042.

[16] T. Y. Hwang, A. Y. Vorobyev, and C. Guo, "Enhanced efficiency of solar-driven thermoelectric generator with femtosecond laser-textured metals," *Opt. Express*, vol. 19, no. S4, p. A824, 2011, doi: 10.1364/oe.19.00a824.

[17] N. H. Thomas, Z. Chen, S. Fan, and A. J. Minnich, "Semiconductor-based Multilayer Selective Solar Absorber for Unconcentrated Solar Thermal Energy Conversion," *Sci. Rep.*, vol. 7, no. 1, pp. 3–8, 2017, doi: 10.1038/s41598-017-05235-x.

[18] S. O'halloran and M. M. Rodrigues, "AC 2012-3976: POWER AND EFFICIENCY MEASUREMENT IN A THER-MOELECTRIC GENERATOR degrees in mechanical engineering from Kansas State University. Power and Efficiency Measurement in a Thermoelectric Generator," no. 2000, 2000.

[19] M. K. Rad, M. Omid, A. Rajabipour, F. Tajabadi, L. A. Rosendahl, and A. Rezaniakolaei, "Optimum thermal concentration of solar thermoelectric generators (STEG) in Realistic Meteorological Condition," *Energies*, vol. 11, no. 9, 2018, doi: 10.3390/en11092425.

[20] P. Li, L. Cai, P. Zhai, X. Tang, Q. Zhang, and M. Niino, "Design of a concentration solar thermoelectric generator," *J. Electron. Mater.*, vol. 39, no. 9, pp. 1522–1530, 2010, doi: 10.1007/s11664-010-1279-0.

[21] L. C. Ding, A. Akbarzadeh, and L. Tan, "A review of power generation with thermoelectric system and its alternative with solar ponds," *Renew. Sustain. Energy Rev.*, vol. 81, no. August 2017, pp. 799–812, 2018, doi: 10.1016/j.rser.2017.08.010.

[22] A. Date, A. Date, C. Dixon, and A. Akbarzadeh, "Theoretical and experimental study on heat pipe cooled thermoelectric generators with water heating using concentrated solar thermal energy," *Sol. Energy*, vol. 105, pp. 656–668, 2014, doi: 10.1016/j.solener.2014.04.016.

[23] M. S. Kim, M. K. Kim, S. E. Jo, C. Joo, and Y. J. Kim, "Refraction-Assisted Solar Thermoelectric Generator based on Phase-Change Lens," *Sci. Rep.*, vol. 6, pp. 1–9, 2016, doi: 10.1038/srep27913.

[24] L. L. Baranowski, G. J. Snyder, and E. S. Toberer, "Concentrated solar thermoelectric generators," *Energy Environ. Sci.*, vol. 5, no. 10, pp. 9055–9067, 2012, doi: 10.1039/c2ee22248e.

[25] S. Manikandan and S. C. Kaushik, "Thermodynamic studies and maximum power point tracking in thermoelectric generator-thermoelectric cooler combined system," *Cryogenics (Guildf).*, vol. 67, pp. 52–62, 2015, doi: 10.1016/j.cryogenics.2015.01.008.

[26] S. Radkowski, K. Lubikowski, M. Wikary, and K. Szczurowski, "Seebeck phenomenon, calculation method comparison," *J. Power Technol.*, vol. 95, pp. 63–67, 2015.

[27] M. N. Zulkifli, I. Ilias, A. Abas, and W. M. W. Muhamad, "Finite element analysis on the thermoelectric generator for the waste heat recovery of solar application," *AIP Conf. Proc.*, vol. 1877, 2017, doi: 10.1063/1.4999894.

[28] R. Lamba, S. Manikandan, and S. C. Kaushik, "Performance Analysis and Optimization of Concentrating Solar Thermoelectric Generator," *J. Electron. Mater.*, vol. 47, no. 9, pp. 5310–5320, 2018, doi: 10.1007/s11664-018-6410-7.

[29] S. Manikandan and S. C. Kaushik, "Energy and exergy analysis of solar heat pipe based annular thermoelectric generator system," *Sol. Energy*, vol. 135, pp. 569–577, 2016, doi:

10.1016/j.solener.2016.06.031.

[30] K. S. Ong, "Review of solar, heat pipe and thermoelectric hybrid systems for power generation and heating," *Int. J. Low-Carbon Technol.*, vol. 11, no. 4, pp. 460–465, 2016, doi: 10.1093/ijlct/ctv022.

[31] T. H. Kil *et al.*, "A highly-efficient, concentrating-photovoltaic/thermoelectric hybrid generator," *Nano Energy*, vol. 37, no. April, pp. 242–247, 2017, doi: 10.1016/j.nanoen.2017.05.023.

[32] H. Xi, L. Luo, and G. Fraisse, "Development and applications of solar-based thermoelectric technologies," *Renew. Sustain. Energy Rev.*, vol. 11, no. 5, pp. 923–936, 2007, doi: 10.1016/j.rser.2005.06.008.

[33] O. H. Ando Junior, A. L. O. Maran, and N. C. Henao, "A review of the development and applications of thermoelectric microgenerators for energy harvesting," *Renew. Sustain. Energy Rev.*, vol. 91, no. March, pp. 376–393, 2018, doi: 10.1016/j.rser.2018.03.052.

[34] Y. Kishita, Y. Ohishi, M. Uwasu, M. Kuroda, H. Takeda, and K. Hara, "Evaluating the life cycle CO2 emissions and costs of thermoelectric generators for passenger automobiles: A scenario analysis," *J. Clean. Prod.*, vol. 126, pp. 607–619, 2016, doi: 10.1016/j.jclepro.2016.02.121.

[35] S. Shanmugam, M. Eswaramoorthy, and A. R. Veerappan, "Modeling and analysis of a solar parabolic dish thermoelectric generator," *Energy Sources, Part A Recover. Util. Environ. Eff.*, vol. 36, no. 14, pp. 1531–1539, 2014, doi: 10.1080/15567036.2011.555352.

[36] C. Thornsberry, *Methicillin-resistant staphylococci*, vol. 9, no. 2. 1989.

[37] G. A. Moore, "Modern Thermoelectrics," *Electronics and Power*, vol. 30, no. 9. p. 733, 1984, doi: 10.1049/ep.1984.0389.

[38] J. Chen, "Thermodynamic analysis of a solar-driven thermoelectric generator," *J. Appl. Phys.*, vol. 79, no. 5, pp. 2717–2721, 1996, doi: 10.1063/1.361143.

[39] H. B. Gao, G. H. Huang, H. J. Li, Z. G. Qu, and Y. J. Zhang, "Development of stove-powered thermoelectric generators: A review," *Appl. Therm. Eng.*, vol. 96, pp. 297–310, 2016, doi: 10.1016/j.applthermaleng.2015.11.032.

[40] R. Mal, R. Prasad, V. K. Vijay, and A. R. Verma, "The design, development and performance evaluation of thermoelectric generator (TEG) integrated forced draft biomass cookstove," *Procedia Comput. Sci.*, vol. 52, no. 1, pp. 723–729, 2015, doi: 10.1016/j.procs.2015.05.085.

[41] B. D. In, H. I. Kim, J. W. Son, and K. H. Lee, "The study of a thermoelectric generator with various thermal conditions of exhaust gas from a diesel engine," *Int. J. Heat Mass Transf.*, vol. 86, pp. 667–680, 2015, doi: 10.1016/j.ijheatmasstransfer.2015.03.052.

[42] B. Orr, A. Akbarzadeh, M. Mochizuki, and R. Singh, "A review of car waste heat recovery systems utilising thermoelectric generators and heat pipes," *Appl. Therm. Eng.*, vol. 101, pp. 490–495, 2016, doi: 10.1016/j.applthermaleng.2015.10.081.

[43] H. P. Garg, *Advances in Solar Energy Technology. Volume 1: Collection and Storage Systems*, vol. 1. 1987.

[44] J. A. Duffie and W. A. Beckman, "Solar Engenierring of Thermal Process." p. 893, 2006.

[45] Verde, Giuseppe. "Thermal operating machine." *Int. J. Mech. Prod. Eng. Res. Dev* 7.5 (2017): 311-322.

[46] Kumar, A. N. I. L., M. Chopkar, and A. Swarnakar. "Effect of Milling Time and Milling Media on the Formation of CrSi2 from their Constituent Elements for Thermoelectric Materials." *Int. J. Metall. Mater. Sci. Eng* 5 (2015): 1-8.

[47] Saleh, B., and M. S. Youssef. "Parametric analysis of an ejector refrigeration cycle activated by renewable energy." *International Journal of Mechanical and Production Engineering Research and Development (IJMPERD)* 9.3 (2019): 1143-1156.

[48] Senthil, R. "Effect of secondary reflector on thermal performance of linear fresnel concentrated solar collector." *International Journal of Mechanical and Production Engineering Research and Development* 8.4 (2018).

[49] Deshpande, Shripad V., and P. R. Devale. "Recent trends in using wireless sensor networks in industrial environment." *International Journal of Computer Networking Wireless and Mobile Communication (IJCNWMC)* 3 (2013): 11-20.

[50] Kumar, Raja Ram, et al. "Design, control and experimental investigation of fault-tolerant five phase PMSG for wind power application." (2018).

Thermal Science and Engineering Progress 42 (2023) 101882

Contents lists available at ScienceDirect

Thermal Science and Engineering Progress

journal homepage: www.sciencedirect.com/journal/thermal-science-and-engineering-progress

Performance evaluation of indirect type domestic hybrid solar dryer for tomato drying: Thermal, embodied, economical and quality analysis

Mukul Sharma [a], Deepali Atheaya [a], Anil Kumar [b,c,*]

[a] Department of Mechanical Engineering, Bennett University, Greater Noida 201310, India
[b] Department of Mechanical Engineering, Delhi Technological University, Delhi 110042, India
[c] Centre for Energy and Environment, Delhi Technological University, Delhi 110042, India

ARTICLE INFO

Keywords:
Solar dryer
Tomato
Embodied energy
Carbon mitigation
Payback period
Domestic

ABSTRACT

This study evaluated the performance of an indirect type domestic hybrid solar dryer (ITDHSD) for drying tomato flakes in terms of thermal, environmental, economical, and quality parameters. The dryer achieved a final moisture content of 9% (wb) in 10 h during November 2021. Average heat utlisation factor and coefficient of performance during experimentation for drying system were 0.67 and 0.33 respectively. Embodied energy during dryer fabrication was estimated as 1434.176 kWh. Energy payback time, total CO_2 mitigation, and earned carbon credit for tomato drying in dryer were projected as 4.21 years, 12.28 Tonnes, and US$364. Initial capital cost for drying system fabrication was US$245. The drying system can pay back all initial costs in 6 months of operation as estimated for tomato flakes drying. Moreover, quality of dried tomato flakes in dryer and open sun drying was estimated and compared. Indirect type domestic hybrid solar dryer provided better quality dried tomato flakes than open sun drying method as estimated from sensory analysis, rehydration ratio, shrinkage and hardness test. Further, present system was duly compared and found superior among several existing solar drying systems in terms of drying efficiency and total CO_2 mitigation. The significance of the system performance lies in its potential to provide an economical, efficient, and environmentally friendly alternative to traditional drying methods. The results demonstrate that the ITDHSD system can help reduce energy consumption, greenhouse gas emissions, and improve the quality of dried products, making it an attractive option for domestic users as well as small-scale agricultural producers. The findings of this study can provide useful insights for designing and implementing sustainable and cost-effective drying systems for other food products.

1. Introduction

Crop drying is essential for food processing and preservation [1]. Drying removes moisture from crop and enhances its lifespan [2]. Food drying is commonly performed using conventional dryers that run over high-grade electrical energy [3]. This energy is generally produced by combustion of fossils and this combustion cause emission of greenhouse gases such as CO_2 into the environment [4]. Furthermore, this usage of electrical energy is costly. Therefore, solar food drying is encouraged among users. A general method of solar food drying is open sun drying. It is free of cost and has no greenhouse gas emissions from this method, but it has some disadvantages [5]. Food is kept open in the environment, which increases the chances of deterioration of food quality and the efficiency of this process is very low [6]. To address these issues originating from conventional drying and open sun drying, the usage of dedicated devices named solar food dryers is encouraged.

Solar food dryers are highly efficient than open sun drying due to controlled environment drying. During operation, these have zero greenhouse gas (GHG) emissions [7]. Moreover, it is more economical than conventional dryers in terms of initial and operating costs [8]. Solar food dryers can be used for food drying applications in domestic, medium, and small-scale as well as large-scale industries [9]. Solar dryers are preferable for crop drying due to their better efficiency than open sun drying. Although the dryers didn't use any conventionally produced energy during operation, preparation of material used in dryer fabrication can be manufactured using conventional energy. This conventional energy used for dryer fabrication is termed embodied energy and generation of this conventional energy releases a significant amount of GHGs (primarily CO_2). Embodied energy and CO_2 released should be accounted and to become environmentally friendly devices, solar dryers should save at least energy equal to their embodied energy and mitigate

* Corresponding author at: Centre for Energy and Environment, Delhi Technological University, Delhi 110042, India.
E-mail addresses: E20SOE803@bennett.edu.in (M. Sharma), deepali.atheaya@bennett.edu.in (D. Atheaya), anilkumar76@dtu.ac.in (A. Kumar).

https://doi.org/10.1016/j.tsep.2023.101882
Received 20 March 2023; Received in revised form 16 April 2023; Accepted 30 April 2023
Available online 4 May 2023
2451-9049/© 2023 Elsevier Ltd. All rights reserved.

Nomenclature

A	Aperture area of the solar dryer, in m^2
A_c	Area of solar collector in m^2
$C_{initial}$	Initial capital
D_C	Price of carbon credit
D_s	Total sunshine hours
E_{di}	Daily input energy in kWh
E_{do}	Daily thermal output in kWh
E_y	Annual energy output, in kWh
I_c	Global solar radiation falls over solar collector in W/m^2
$I_m(t)$	Mean incident solar radiation on the solar dryer, in W/m^2
M	Mass moisture evaporated in a day, in g
M_e	Equivalent moisture content
$M_{f(wb)}$	Final moisture content
$M_{i(wb)}$	Initial moisture content on wet basis
N_d	No. of sunshine days in a year for a crop
N_h	Daily sunshine hours
P_{net}	Net profit
T_t	Mass of dried tomato per hour
V_{actual}	Actual volume
V_{final}	Final Volume
W_B	Mass of bone dried crop in kg
W_M	Mass of moisture in crop in kg
W_T	Total mass of crop in kg
λ	Latent heat of vaporization of water i.e. 2.26×10^6 J/kg
η_{daily}	Daily efficiency of the system
η_O	Overall efficiency

CO_2 which was used during their fabrication. Several studies have been carried out on different solar dryers for performance and environmental analysis such as energy payback time (EPBT) and CO_2 mitigation which have been tabulated in Table 1. Concluding remarks of each study have been discussed as follows:

Simple and modified greenhouse dryer performance, EPBT, CO_2 mitigation, and total carbon credit were evaluated and compared for groundnut drying, and modified dryer was found superior [10]. Performance parameters and drying kinetics of heat exchanger-evacuated tube assisted drying system for drying garlic was evaluated and overall drying efficiency of drying system was observed as 25.1% [11]. Tomato crop was dried in a hybrid active greenhouse solar dyer integrated with evacuated solar collector. Payback period and CO_2 mitigation were reported as 1.73 years and 169.10 Tonnes, respectively [12]. Overall drying efficiency of indirect type solar dryer (ITSD) was reported as 31.42% [13]. Large-scale solar dyer integrated with phase change material had EPBT 6.82 years and lifetime CO_2 mitigation of 99.60 Tonnes [14]. EPBT for an indirect solar dryer used for drying bitter gourd was reported as 2.21 years and CO_2 mitigation assessed for lifetime of the system was 33.52 years [15]. Sajith and Muraleedharan (2020) reported payback period, benefit-cost ratio, and EPBT as 9.3 years, 1.61, and 2.25 years for indirect solar dryer embedded with hybrid photovoltaic thermal air heater for drying amla [16]. The embodied energy, EPBT, and carbon credit of a domestic direct type multi-shelf solar dryer were stated as 339.015 kWh, 7.57 years, and INR 2055, respectively [5].

A convective dryer used for drying wood chips had drying chamber's exergy efficiency from 41.84% to 98.07%, and drying system's average overall exergy efficiency varied from 1.32% to 4.01% [17]. Thermo-environomical assessment of a north wall insulated greenhouse dryer under natural and forced mode drying gave EPBT as 1.68 years and 2.35 years, net Carbon dioxide mitigation as 33.04 and 36.34 Tonnes, respectively [18]. Embodied energy, EPBT, and CO_2 mitigation of an indirect solar drying system were 1081.83kWh, 4.36 years, and 391.52 kg per year, respectively for drying fenugreek [19]. For potato drying in modified solar greenhouse dryer during active and passive mode drying, the corresponding values of payback period and earned carbon credits were 1.9 years, 1.25 years, and INR 37,826 and INR 37,882 [20]. Payback period, embodied energy, and EPBT was reported as 1.9 years, 628.7287 years, and 1.14 years, respectively for tomato drying in modified greenhouse dryer [21]. Payback period of indirect type solar dryer for bitter gourd drying was estimated as 3.26 years [22].

Agricultural products can be preserved via solar drying, which also lowers post-harvest losses and boosts food security. The environmental and financial viability of various solar drying systems, however, is still a subject of interest and research. While earlier studies have evaluated the environmental and economic factors of various solar dryers. However, most research has focused on greenhouse-type, direct-type, and flat-plate collector-based indirect-type solar dryers. Surprisingly, no studies have investigated the environmental and economic feasibility of domestic hybrid solar dryers for tomato crop drying. Additionally, previous evaluations of embodied energy in solar dryers did not consider the PV module's embedded energy. This study aims to fill this research gap by focusing on a unique PV-integrated compact hybrid solar dryer with a rectangular corrugated collector suitable for domestic and small-to-medium-scale industrial applications. The study investigates the thermal performance, environomical factors, and economic viability of an indirect-type domestic hybrid solar dryer (ITDHSD) for tomato drying. Furthermore, the study includes quality analysis viz. sensory analysis, rehydration ratio, shrinkage, and hardness, to evaluate the dried product outcomes from ITDHSD.

This study's novelty and significance come from its contribution to the development of environmentally friendly and economically viable drying systems for agricultural products. This work provides insights into the performance and feasibility of novel drying technology for tomato crops by concentrating on a unique PV-integrated compact hybrid dryer. A comprehensive analysis of the ITDHSD's performance is also provided by the inclusion of quality analysis, which may be used to design and execute high-quality, sustainable drying systems for different food products. Finally, this investigation gives more precise assessment of the environmental impact of solar drying systems by taking into account the embedded energy in PV modules. The results of this study have major repercussions for post-harvest loss reduction, lowering the carbon footprint of the food industry, and sustainable food production.

2. Materials and method

2.1. Experimental system information

An indirect type domestic hybrid solar dryer (ITDHSD) was constructed and installed on the rooftop of Department of Mechanical Engineering, Delhi Technological University (DTU), Delhi, India [23]. The schematic and actual picture of experimental set-up was demonstrated in Figs. 1 to 3, respectively.

Drying system consists of a drying cabinet, solar collector, rectangular corrugated galvanized iron (GI) absorber plate, 03 stainless steel wire mesh trays, and a DC fan installed at the dryer outlet. A toughened glass (8 mm) was used to cover the newly developed drying system. This drying system can be operated in both indirect and mixed modes. While working as an indirect solar dryer, toughened glass placed over the drying cabinet was covered using polystyrene of thickness of 5 mm, which obstructs the penetration of solar insolation inside the drying cabinet. Various components of developed drying system and their dimensions have been displayed in Table 2.

Table 1
List of several solar drying systems, crop dried and parameters investigated in the literature.

Literature	System	Crop	Parameters investigated
Shimpy et al. (2022)	Simple and modified greenhouse dryer	Groundnut	Performance, EPBT, CO_2 mitigation, and total carbon credit
Kushwah et al. (2021)	Heat exchanger-evacuated tube assisted drying system	Garlic	Drying kinetics, performance parameters and color index
Singh and Gaur (2021)	Hybrid active greenhouse solar dyer integrated with evacuated solar collector	Tomato	Moisture ratio, sustainability assessment, payback period and CO_2 mitigation
Lingayat et al. (2021)	Indirect type solar dryer (ITSD)	Tomato and Brinjal	Drying kinetics and performance parameters
Atalay and Cankurtaran (2020)	Large-scale solar dyer integrated with phase change material	Strawberry	Energy, exergy, exergoeconomic, and exergo-environmental analysis
Vijayan et al. (2020)	Indirect solar dryer	Bitter gourd	Exergo-environmental analysis
Sajith and Muraleedharan (2020)	Indirect solar dryer embedded with hybrid photovoltaic thermal air heater	Amla	Payback period, benefit-cost ratio, and EPBT
Jain et al. (2019)	Domestic direct type multi-shelf solar dryer	Fenugreek	Embodied energy, EPBT, and carbon credit
Zohrabi et al. (2019)	Pilot-scale convective dryer	Wood Chips	Exergetic efficiencies of drying system and drying chamber at different air velocities
Chauhan et al. (2018)	North wall insulated greenhouse dryer	Bitter gourd	Embodied energy, EPBT, and carbon credit under natural and forced mode drying
Shrivastava and Kumar (2017)	Indirect solar dryer	Fenugreek	Embodied energy, EPBT, CO_2 mitigation, total carbon credit, and payback period
Prakash et al. (2017)	Modified solar greenhouse dryer	Potato	Embodied energy, EPBT, CO_2 mitigation, total carbon credit, and payback period under active and passive mode drying
Prakash and Kumar (2014)	Modified greenhouse dryer	Tomato	Embodied energy, EPBT, CO_2 mitigation, and payback period
Sreekumar et al. (2008)	Indirect solar dryer	Bitter gourd	Performance and economic analysis

2.2. Experiment details

Experiments for tomato crop drying were carried out five times from 21st to 30th November 2021. 03 kg of tomatoes were purchased from local market and washed thoroughly before slicing. 3–5 mm thick flakes were prepared and kept on wire mesh trays inside the ITDHSD system [23]. Tomatoes slice drying experimentation was performed from 09:30 to 16:30 h in ITDHSD as well as in open sun. Experimental observations were noted down at an interval of one hour. For calculation, hourly average of the readings was taken into consideration.

2.3. Instrumentation

Temperature across the ITDHSD system was estimated using twelve K-type thermocouples attached at twelve different places inside the system. These were further connected to 12 channel temperature indicator device. Solar intensity was measured using solar power meter. Temperature and relative humidity were measured using a digital thermo-hygrometer. Air velocity was measured using a thermal anemometer. The details of equipment used during experimentation have been given in Table 3.

2.4. Uncertainty analysis

Various factors contributed to the uncertainty in the experimental readings, such as inappropriate instrument selection, environmental conditions, imprecise measurements, and human errors. To account for this uncertainty, it was necessary to evaluate potential sources of error in the drying experiment's independent parameters, including velocity, solar insolation, weight, and temperature, as well as key design parameters such as air flow rate, efficiency, drying rate, and heat gain [15]. Table 4 provides a summary of the uncertainties associated with these parameters.

To anticipate potential outcomes, function E was used, which represents the relationship between independent variables (v_1, v_2, … v_n) and unrelated variables. The uncertainties in the estimated outcomes, represented by x_{EP}, were determined based on the uncertainties in the independent variables (x_1, x_2, … x_n) that make up the function EP.

$$x_{EP} = \sqrt{\left(\frac{\partial E}{\partial v_1}x_1\right)^2 + \left(\frac{\partial E}{\partial v_2}x_2\right)^2 + \cdots + \left(\frac{\partial E}{\partial v_n}x_n\right)^2} \quad (1)$$

2.5. Moisture content and thermal performance parameters

The moisture content is the amount of moisture present in a crop. It plays an essential role in defining the efficacy of any drying system. It is given as [24]:

$$W_T = W_M + W_B \quad (1)$$

2.5.1. Moisture content wet basis (M_{wt})

It is the percentage equivalent ratio of water weight present in the crop to total bone-dried weight of crop. It can be expressed as [25]:

$$M_{wt} = \frac{W_M - W_B}{W_M} \quad (2)$$

2.2.5.2. Moisture ratio (MR). It is the ratio of moisture content present in the crop at any time to that of initial moisture content of the crop. It can be expressed as [25]:

$$MR = \frac{M_{f(wb)} - Me}{M_{i(wb)-Me}} \quad (3)$$

2.2.5.3. Overall daily thermal efficiency (η_O). It is a measure of how effectively a dryer uses input energy while drying the crop and can be determined [23]:

$$\eta_O = \frac{l_w \sum_{i=1}^{t} M_{wt}(t)}{3600 \times A_c \sum_{i=1}^{t} I_c(t)} \quad (4)$$

2.2.5.4. Heat utilisation factor (H.U.F.). It is the ratio of temperature reduction due to air cooling during drying and temperature raised due to air heating. It can be expressed as [24,26]:

$$H.U.F. = \frac{T_{wf} - T_{cr}}{T_{wf} - T_a} \quad (5)$$

Where, T_{wf} is working fluid (air) temperature, T_{cr} is crop temperature and T_a is ambinet temperature.

2.2.5.5. Coefficient of performance (C.O.P.). C.O.P. of drying system can be given as [24,27]:

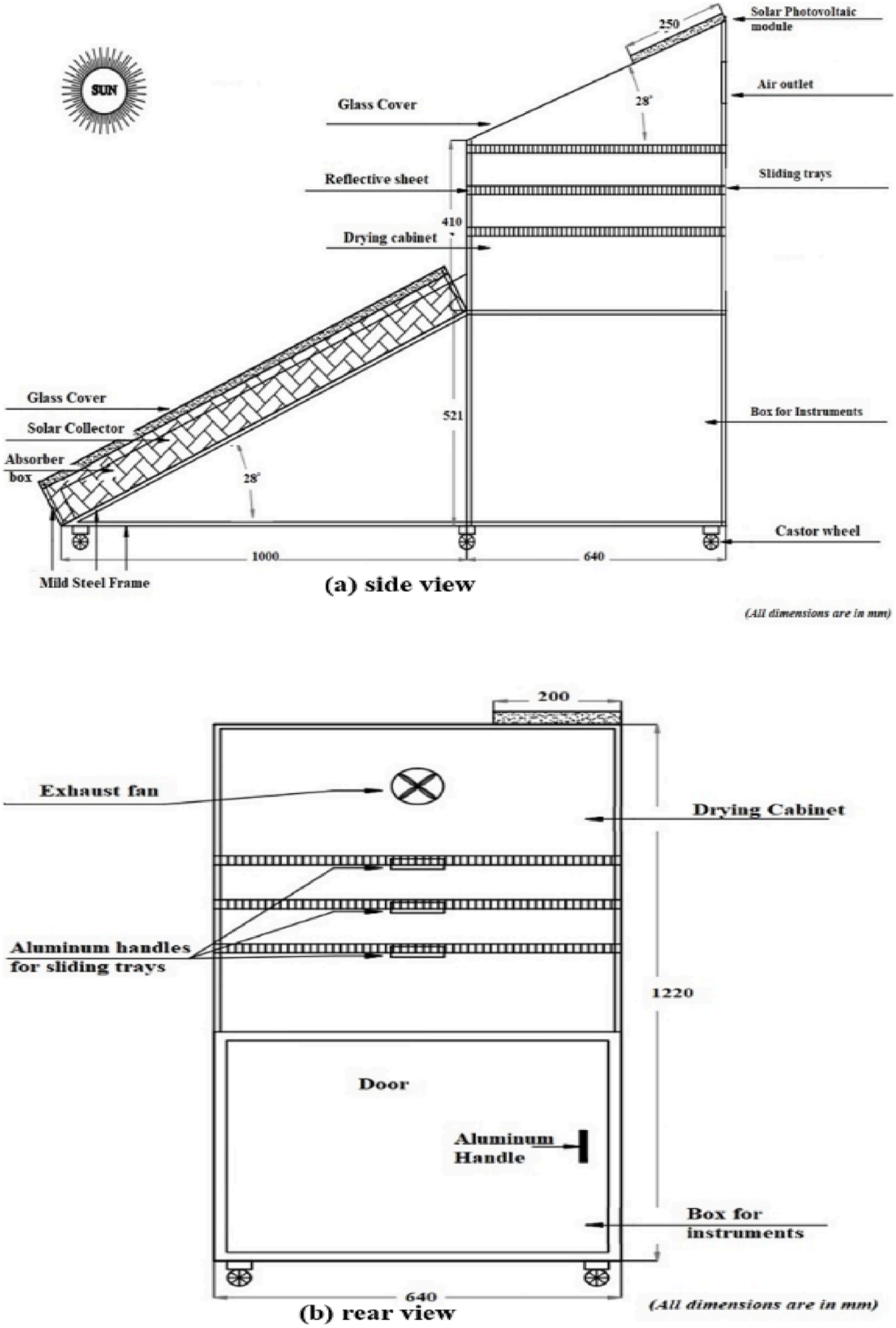


Fig. 1. Schematic layout of novel drying system.

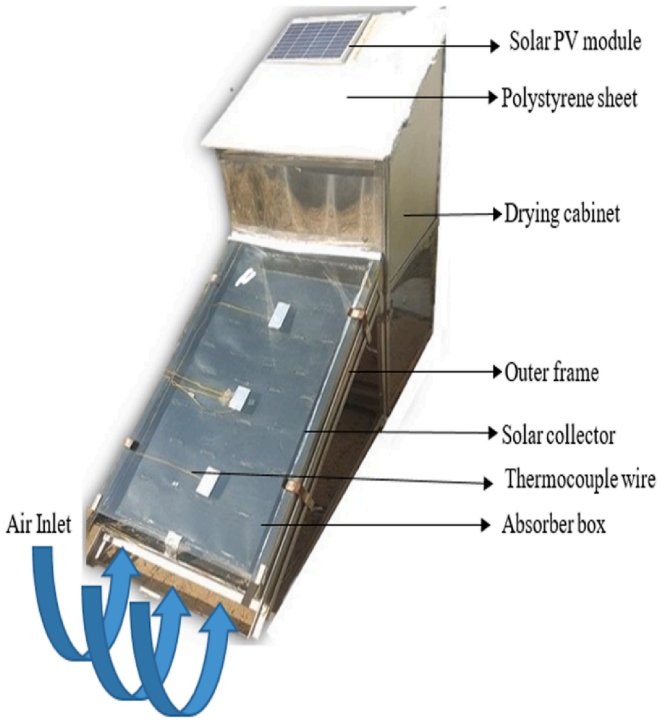


Fig. 2. Pictorial view of indirect type domestic hybrid solar dryer.

$$\text{C.O.P.} = \frac{T_{cr} - T_a}{T_{wf} - T_a} \tag{6}$$

2.6. Energy assessment of indirect type domestic hybrid solar dryer (ITDHSD)

Energy assessment is a study that contemplates on surge in fuel prices, raw materials, and environmental impact. Thus, it is essential to conduct energy assessment for the drying system. Energy assessment for indirect type domestic hybrid solar dryer (ITDHSD) includes the assessment of embodied energy, energy payback time (EPBT), yearly CO_2 emissions, carbon mitigation, and carbon credit.

2.6.1. Embodied energy

The energy desired for manufacturing objects, services, or things is depicted as embodied energy [5]. It can be called an indication of the global environmental impact of systems and materials. The consumption of energy generates CO_2, which adds emissions of greenhouse gases. It is an essential factor to study in the assessment of life cycle of a product and it relates straight to sustainability of built environment.

2.6.2. Energy payback time (EPBT)

Energy payback time is the time it takes for a product, service, or thing to recover its embodied energy [5,28]. It is an important factor to evaluate viability of any product by considering payback of energy consumed during its production. It can be assessed as [29]:

$$EPBT = \frac{Embodied\ Energy}{Annual\ Energy\ Output} \tag{7}$$

2.6.3. CO_2 emissions

Throughout the process of coal-based electricity generation, average emission of CO_2 is equivalent to 0.98 kg CO_2/kWh [30]. Hence, yearly CO_2 emissions can be assessed as [29]:

$$CO_2\ emissions\ per\ year = \frac{Emboided\ Energy \times 0.98}{Lifetime} \tag{8}$$

Table 2
Design specifications of ITDHSD.

Component	Materials used for fabrication	Dimensions
Solar collector	FRP (fiber-reinforced plastic) sheet, Toughened glass, Iron angles	1100 × 620 × 85 mm^3
Absorber box	Galvanized Iron (GI) sheet	1000 × 500 × 60 mm^3
Drying cabinet	FRP (fiber-reinforced plastic) sheet, Toughened glass, Iron angles	410 × 640 × 640 mm^3
Wire mesh trays	Stainless steel wire mesh, Aluminum angles, Plywood, Aluminum handle	500 × 500 mm^2
Collector's inclination angle	–	28°
Outlet diameter	–	100 mm

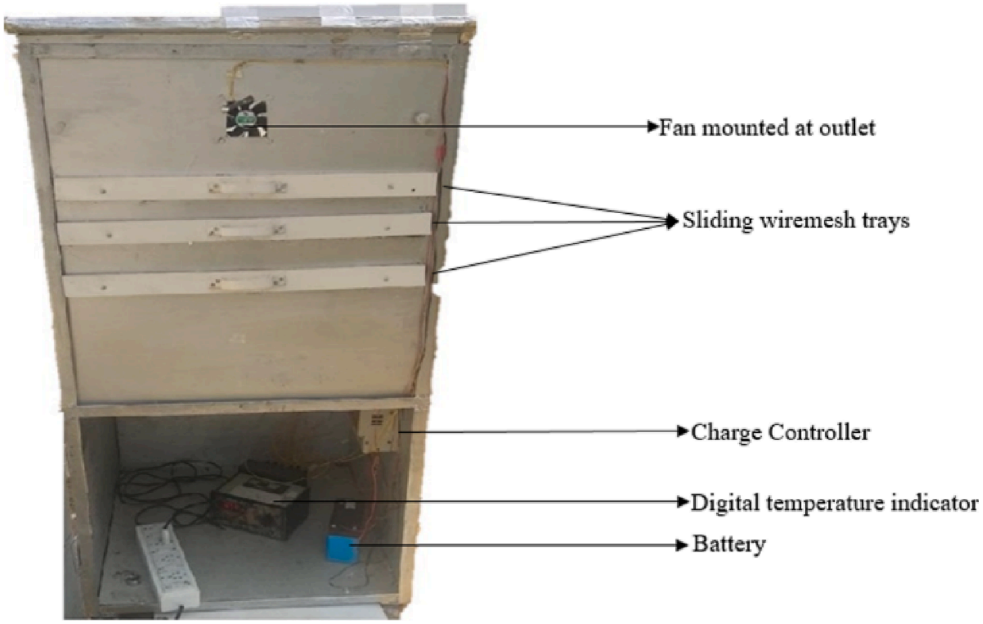


Fig. 3. Rear pictorial view of indirect type domestic hybrid solar dryer.

Table 3
Details of instruments used during the tomato drying experiments.

Instruments used	Specification	Use	Accuracy
K-Type thermocouple sensors (Tempsens T-101)	0 to 400 °C	Temperature sensing	±1°C
Solar power meter (General tools DBTU-1300)	0 to 2000 W/m^2	Solar irradiation	± 10 W/m^2
Thermo-hygrometer (Testo-625)	0 to 100%	Relative humidity	±2.5%
Thermal anemometer (Testo-405)	0 to 10 m/s	Wind velocity	± 0.1 m/s
12-channel data logger (Sun Pro Instruments (India))	−50 °C to + 1210 °C	Temperature indicator	±0.5%
Weighing balance (Swisser SWIID06)	Up to 6 kg	Weight	±0.2g

Table 4
Uncertainty values of various measured variables during the tomatoes drying experiment.

Independent variables	Uncertainty
Air velocity measurement (x_A)	±0.1 m/s
Temperature measurement (x_T)	±0.1 °C
Weight measurement (x_W)	±0.001 kg
Solar insolation measurement (x_I)	± 10 W/m^2
Relative humidity measurement (x_R)	±3%

2.6.4. Carbon mitigation and earned carbon credit

Climate change potential is measured as Carbon mitigation. The net CO_2 mitigations are examined per kilowatt-hour; hence, its comparison with other power production systems is extremely possible. In ITDHSD, CO_2 mitigation is evaluated. Carbon credit is termed an essential factor of national and international emissions trading programs that have been applied to mitigate- global warming [21]. Purchasing and trading carbon credits on a global market or in a corporation are currently possible. It applies to monetary carbon reduction initiatives.

System's daily efficiency can be considered as [18]:

$$\eta_{daily} = \frac{daily\ output\ energy}{daily\ input\ energy} = \frac{E_{do}}{E_{di}} \times 100 \tag{9}$$

Dryer's daily thermal output (E_{do}) in kWh can be evaluated [5]:

$$E_{do} = \frac{M \times \lambda_w}{3.6 \times 10^6} \tag{10}$$

Daily input energy (E_{di}) can be computed as [19]:

$$E_{di} = I_m(t) \times N_h \times A \times 10^{-3} \tag{11}$$

Dryer's yearly energy output (E_y) can be given as [24]:

$$E_y = E_{do} \times N_d \tag{12}$$

The transmitted power is equal to $\frac{1}{1-L_t}$ Units when all energy losses by the end-user in domestic equipment ($L_t = 10\%$) are taken into account. In distribution and transmission, there is an L_{dt} (45%) loss of energy per unit. As a result, the amount of energy produced by a power plant can be expressed as $\frac{1}{1-L_t} \times \frac{1}{1-L_{dt}}$ Units [5].

Given that coal-based energy has an average carbon dioxide equivalent intensity of 0.98 kg of CO_2/kWh, the system's overall CO_2 mitigation (X_m) is as follows [5]:

$$X_m = \frac{1}{1-L_t} \times \frac{1}{1-L_{dt}} \times 0.98 = 2.01\ \text{kg/unit}$$

The CO_2 mitigation can be calculated as [15]:

$$CO_2\ mitigation\ during\ life\ of\ solar\ dryer = E_y \times X_m \tag{13}$$

Hence, net mitigation of CO_2 during lifetime (kg) = Total CO_2 mitigation – Total CO_2 emissions.

$$Net\ mitigation\ of\ CO_2\ during\ life\ time(kg) = E_y \times n \times X_m - E_m \tag{14}$$

$$Earned\ Carbon\ Credit = \text{net mitigation of } CO_2 \text{ during life time(kg)} \times D_C \tag{15}$$

2.7. Economic analysis

The economic analysis of the indirect type domestic hybrid solar dryer is important as it directly comprises the financial traits for commercial application. The cost of an indirect solar dryer is assessed by taking the totality of the cost of materials utilized in the construction of the dryer and working capital cost [31]. The payback period of the dryer is defined as the time required to recover the original cash investment and it is evaluated as [31]:

$$\text{Payback period} = \frac{C_{initial}}{P_{net}} \tag{16}$$

where,

Net profit (P_{net}) is the total income obtained excluding the working capital cost and can be depicted as [31]:

P_{net} = Gross income – working capital cost.

The quantity of annually dried tomato flakes (DT_{annual}) is considered as the product of the mass of dried tomato per hour with total sunshine hours for it [24,34].

$$DT_{annual} = T_t \times D_s \tag{17}$$

According to climatic conditions in Delhi (India), the average yearly sunny days are 250 and the average annual sunshine hours are 1500. The sale price of dried products is considered as per present market rates.

2.8. Quality assessment of tomato flakes

The quality characteristics of the dehydrated tomato flakes are assessed in terms of sensory analysis, rehydration ratio, shrinkage, and hardness. Further, it is compared with the open sun-dried tomato flakes.

2.8.1. Sensory analysis

Sensory analysis criteria such as color, taste, flavor, mouth feel, and general acceptance were used to assess the quality of dried tomato flakes produced by drying in the open sun and ITDHSD [32,33]. Forty untrained panelists were chosen among the university's academic personnel, students, and technicians. The panelists rated the dried samples for color, taste, mouth feel, flavor, and general acceptance of dried tomato flakes using a five-point hedonic scale, with 1 being severely disliked and 5 being extremely liked. The dried samples were coded and placed at random. After evaluating each sample, panelists were told to rinse their mouths out with water before moving on to the next.

2.8.2. Rehydration ratio

To evaluate the rehydration ratio of tomato flakes, a 10 g dried tomato slice sample was used and boiled in water with 1% salt content for 10 min, and then the final weight was observed [32]. The rehydration ratio is estimated using the following equation:

$$\text{Rehydration ratio} = \frac{m_{final}}{m_{initial}} \tag{18}$$

Where m_{final} and $m_{initial}$ is the final and initial weight of tomato slices in kg.

2.8.3. Shrinkage

Shrinkage is the difference in volume between dried tomato flakes and fresh tomato flakes expressed as a percentage [38]. It is given as follows:

$$\text{Percentage of shrinkage} = \frac{(V_{actual} - V_{final})}{V_{final}} \times 100 \quad (19)$$

2.8.4. Hardness

Hardness is one of the most significant characteristics in the quality evaluation of dried tomato flakes. It is the most significant force applied during the first bites observed in grams [38]. The hardness of the dried tomato flakes was studied next to rehydration, using the CT3 Texture Analyser. The result of hardness was concluded by taking an average of 10 observations.

3. Results and discussion

3.1. Ambient parameters

Experimentation of tomato slice drying was performed during winter month of November 2021. The conditions during the experimentation were clear sky. Solar insolation and ambient temperature during experimentation varied between 424–670 W/m^2 and 21–26 °C, respectively, as depicted in Fig. 4. From Fig. 5, it can be noted that relative humidity and air velocity were in the range of 40.5%−57.7% and 0.15–1 m/s, respectively.

3.2. Moisture content and thermal performance parameters

Fig. 6 shows raw tomato flakes evenly kept over the wire mesh tray of ITDHSD. From equation (1)-(3), initial moisture content of tomato flakes was evaluated as 95% which was dried in 10 h to final moisture content of 9% [23]. Using equation (4), overall daily thermal efficiency of the system was 41.05%. The drying curve can be seen in Fig. 8. During initial hours of drying, flakes were dried rapidly due to removal of free moisture content and internal heat generation. Afterward, drying rate decreased progressively due to shortage of free water molecules. Furthermore, a solid layer had formed on the tomato slice surface due to high water evaporation, responsible for the reduced drying rate [34,35]. Tomato flakes in ITDHSD were dried to 9% moisture content in 10 h, while in open sun, final moisture content of 14% was achieved in 14 h. Dried tomato flakes obtained from ITDHSD can be seen in Fig. 7.

Fig. 9 shows the Heat Utilization Factor (H.U.F.) and Coefficient of Performance (C.O.P.) of the drying system during the experimentation evaluated using equations (4) and (5). Heat utilization factor and C.O.P. for drying system were in the range of 0.59–0.84 and 0.16–0.44, respectively. Average heat utilization factor and coefficient of performance during experimentation for drying system were 0.67 and 0.33 respectively. It is evident from Fig. 9 that the H.U.F. increases gradually over time, as the temperature difference between the drying air and the wet crop decreases due to the reduction in moisture content. However, the heat supplied to the dryer decreases with time due to the reduction in solar insolation. On the other hand, the C.O.P. decreases with time during the day, indicating that the energy efficiency of the system reduces as the day progresses. A similar trend can be observed on day 2. Prakash et al. [36] discussed variations of HUF and C.O.P. during crop drying.

3.3. Embodied energy analysis

The embodied energy of the indirect type domestic hybrid solar dryer (ITDHSD) and coefficient of embodied energy for various items utilized in the fabrication of dryer is displayed in Table 5. The overall embodied energy for the fabrication of the ITDHSD was estimated 1434.2 kWh. Daily output and input energy calculated using equations (10) and (11) for ITDHSD for tomato drying were 1.3623 kWh and 1.9145 kWh, respectively. The daily efficiency of ITDHSD was estimated using equation (9) and found to be 71.16%. Annual energy output was

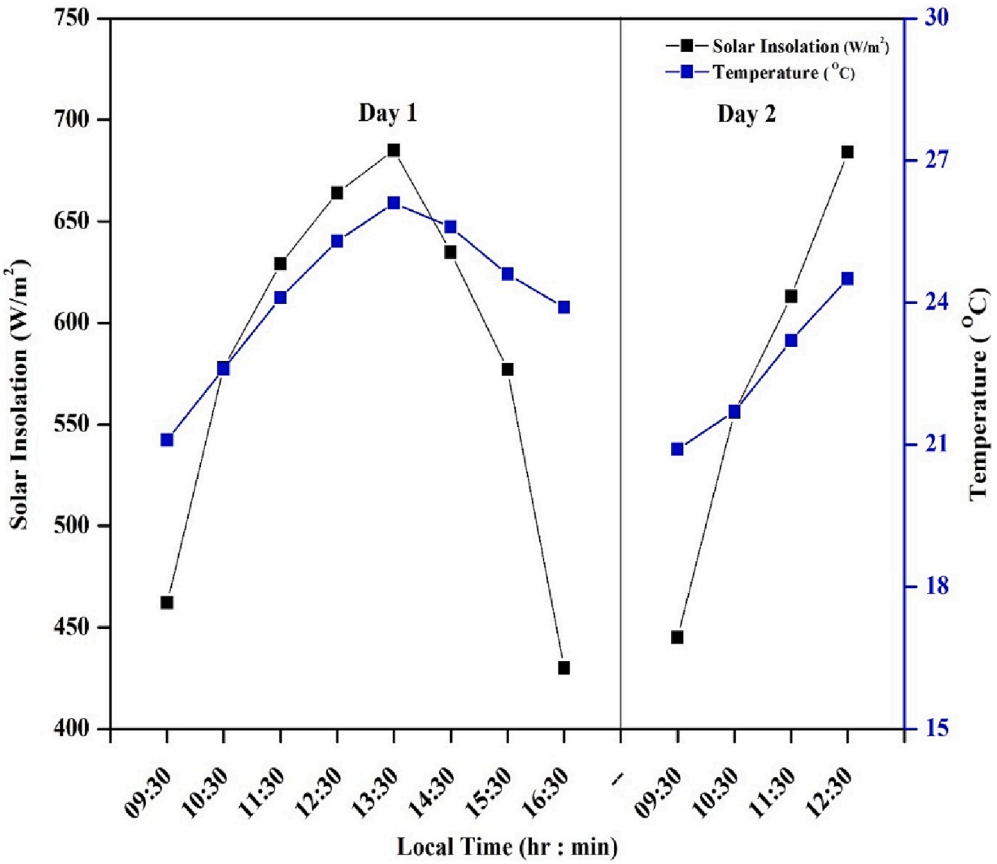


Fig. 4. Mean ambient solar insolation and temperature Vs local time during drying experimentation.

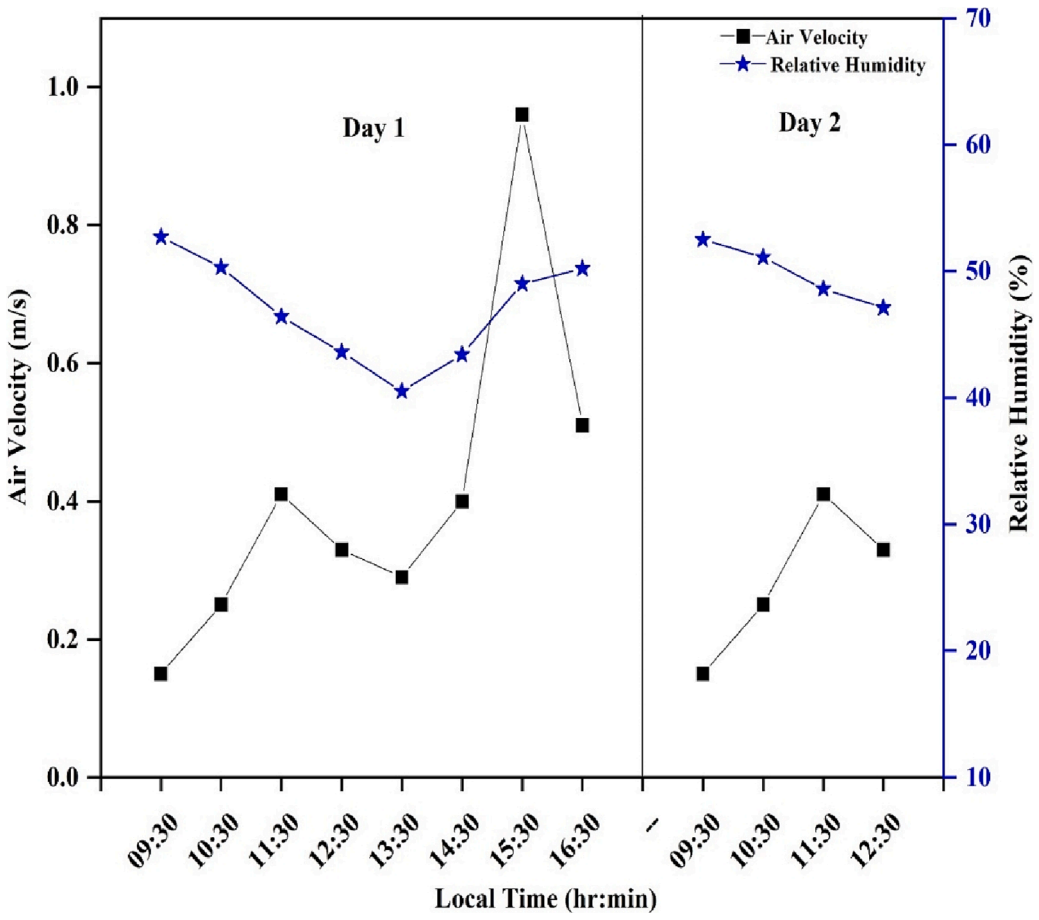


Fig. 5. Mean ambient air velocity and relative humidity Vs local time.



Fig. 6. Raw tomato flakes evenly kept over the wire mesh tray.



Fig. 7. Dried tomato flakes obtained from dryer.

assessed 340.6 kWh/year from equation (12), considering 250 sunshine days in a year.

EPBT calculated using equation (7) for ITDHSD was 4.21 years. The evaluated quantity of carbon dioxide emissions during the fabrication of the ITDHSD system was 1405.5 kg. The net CO_2 mitigation for tomato flakes drying by ITDHSD during its estimated lifetime of 20 years was computed using equation (14) as 12.28 Tonnes. Earned carbon credit for ITDHSD system for tomato drying was calculated. Present rate of carbon credit is US $30.83/Tonne (carboncredits.com). The computed value for earned carbon credit by ITDHSD for tomato drying has been noted as US $364 (US $1 = ₹81.84 as of 09/04/2023).

The contribution of materials used for fabrication of ITDHSD in total embodied energy can be seen in Fig. 10. The value of EPBT was observed to be less as compared with lifetime of ITDHSD, which signifies that the fabricated dryer is economical. It saves more energy during operation than the energy consumed by different materials used during its fabrication. Carbon mitigation shows a way to restrict the impact of greenhouse effect emissions on a commercial scale by capping aggregate yearly emissions and giving a chance to compensate for any shortage of allotted mitigation of greenhouse gas emissions. ITDHSD can save 12.28 Tonnes of CO_2 emissions, which helps sustain the environment.

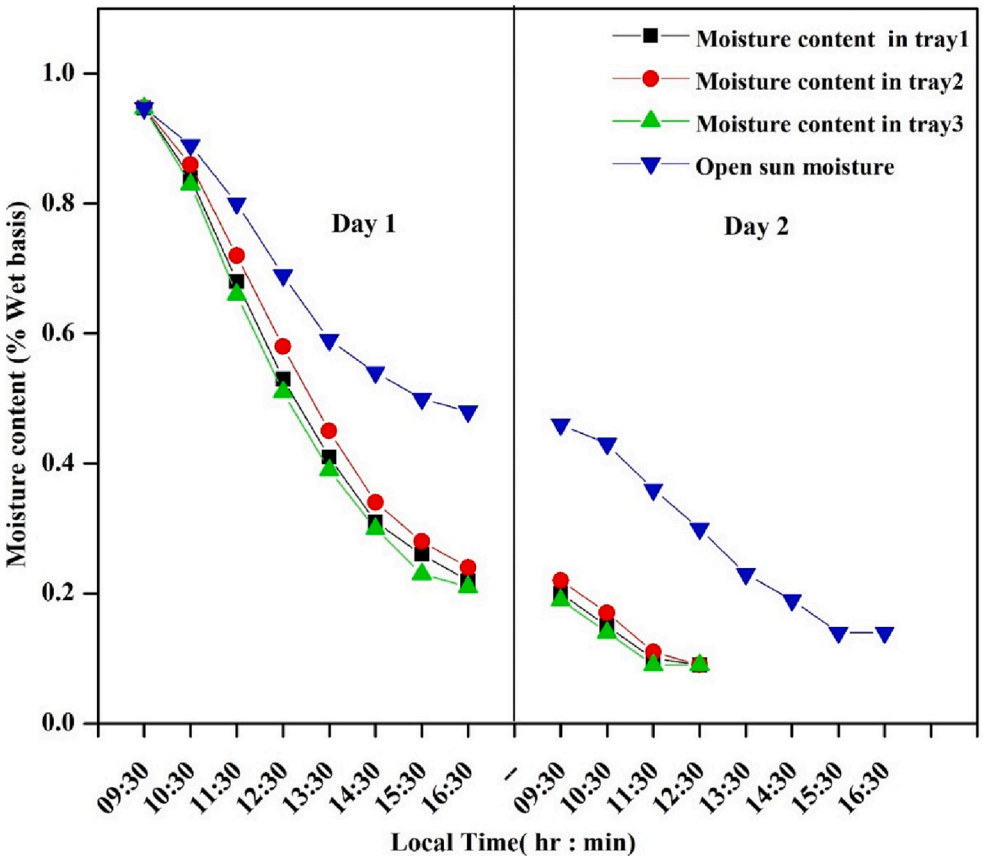


Fig. 8. Mean moisture content (wet basis) of tomatoes flakes during drying experimentation.

3.4. Economical analysis

Table 6 presents the economic evaluation of the ITDHSD system for drying tomato flakes. Total initial capital for fabrication of ITDHSD system was US$245. Operating cost of ITDHSD for tomato drying throughout the year (considering 250 sunshine days) was estimated as US$563. The operator purchased 3 kg raw material (tomato) from a nearby vegetable market for dried crops and further washed and sliced. It took 10 h to dry a single batch of 3 kg crop. Therefore, in a year, 530 kg of tomatoes can be dried, providing dried tomato flakes of 71 kg per year. This dried tomato can easily be sold at US$14-38 per kg at local markets and online market platforms. Net profit from selling the dried product at minimal selling price of US$14.66/kg was estimated US$478.

Furthermore, ITDHSD system's payback period was computed using equation (16) as 6 months because the initial capital was minimal. Since ITDHSD's payback period is far shorter than its projected lifespan of 20 years, tomato slice drying can be done for free for 95% of its useful life. ITDHSD was constructed with the support of locally skilled laborers and materials were procured from the local market. This makes ITDHSD economical in terms of initial capital cost. Furthermore, operating cost of ITDHSD, which comprised all expenses, including raw material and operator cost was less. ITDHSD provides high-quality dried products that can be sold at high cost at local and online marketplaces. Therefore, ITDHSD covers its initial capital quickly and can generate employment and livelihood in small and medium scale industries.

3.5. Quality assessment

Results obtained from sensory analysis of dried tomato flakes from ITDHSD and open sun drying are displayed in Fig. 11. Dried tomato flakes obtained from ITDHSD had higher acceptance rate among the panelists than open sun dried samples. The colour of dried flakes obtained from ITDHSD was closer to original colour of raw tomato. Other attributes such as taste, mouthfeel and flavour of ITDHSD dried tomato flakes were also ranked superior to that of open sun dried tomato flakes. The acceptance of ITDHSD dried tomato flakes was 4.2 while that of the open sun dried sample was 3.01. A similar analysis has been performed by Notfia et al. [33].

Rehydrated tomato slice observations are provided in Table 7. Rehydration is an essential parameter of effective drying. Tomato has a good rehydration capacity. The flakes dried through ITDHSD during active mode had a higher rehydration capacity than flakes dried under open sun. Tomato flakes with 14% final moisture content, which dried under the open sun shrunk radially and uniformly, while the flakes have lower moisture content i.e., those dried in the ITDHSD revealed a shriveled appearance with uneven curling. Moreover, the hardness of dried tomato flakes was found greater due to controlled airflow in ITDHSD. Open sun-dried tomato flakes were softer than dried flakes obtained from ITDHSD as the removal of moisture in open sun was less. Obtained values for the shrinkage and hardness have been summarized in Table 7.

Variations in the moisture content, pressure, and temperature gradient during drying resulted in generation of contractile stresses in tomato flakes. Majumdar et al. [38] discussed the reason for shrinking and hardening of crop during drying. Flakes dried inside the drying system had lost high moisture content than open sun drying. Therefore, Tomato flakes dried inside ITDHSD dryer had a higher shrinkage value (74%) than those dried in open sun. Furthermore, hardness of dried tomato flakes obtained from ITDHSD was comparatively higher (171 g) than open sun drying. The color of the dried product in the ITDHSD system was nearer to the original color than the product dried under open sun. The color of dried tomato flakes under open sun faded because of the loss of volatile contents due to the direct fall of solar radiation over tomato flakes. ITDHSD gave superior quality dried products due to

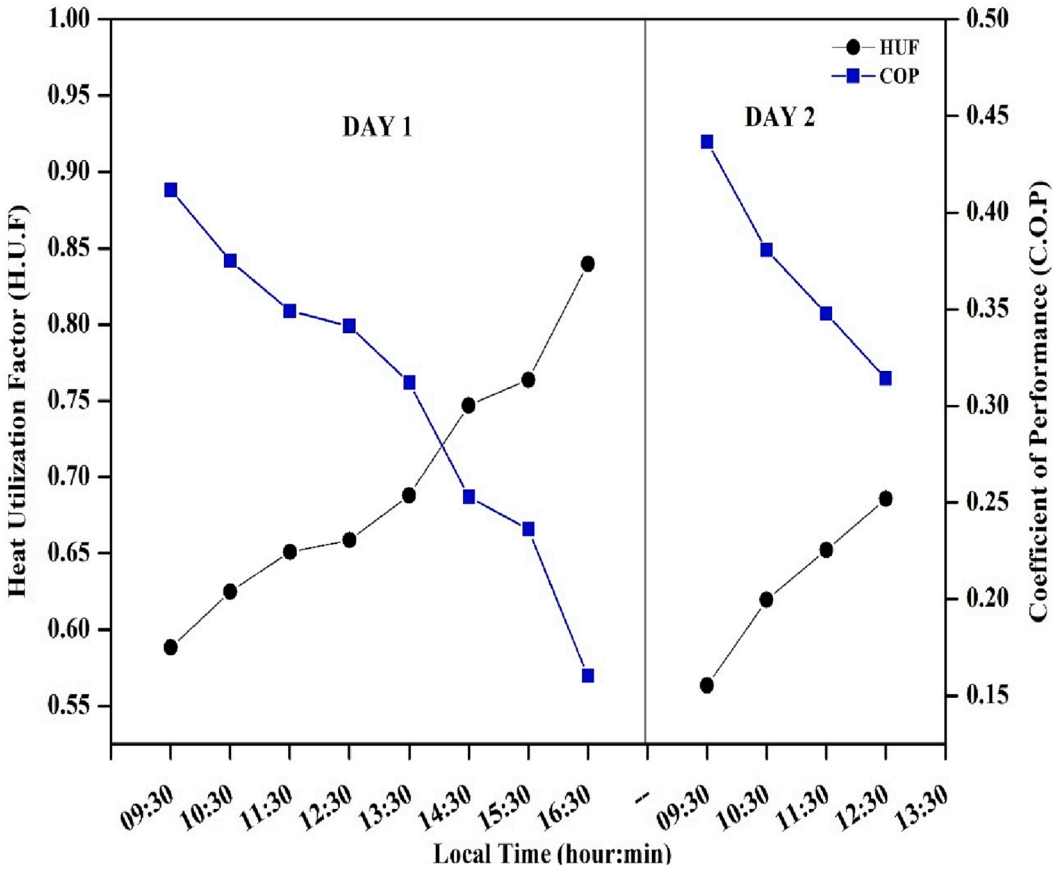


Fig. 9. Variation of heat utilisation factor and coefficient of performance with time during experimentation.

Table 5
Embodied energy of different materials used in fabrication of ITDHSD system.

S. No.	Items	Embodied energy coefficient (kWh/kg)	Amount (kg)	Total embodied energy (kWh)	Reference
1	Glass sheet	7.28	20	145.6	[19,37]
2	Iron angles	9.72	26	252.7	
3	FRP Sheet	41.67	1.5	62.51	
4	GI Sheet	9.67	2	19.34	[37]
5	Stainless steel wire mesh	8.89	0.5	4.45	
6	Plywood	2.89	15.5	44.8	
7	Fan	19.44	0.15	2.92	[20]
8	Aluminium frame	55.28	0.4	22.1	[37]
9	Glass wool	4.06	0.8	3.3	[18]
10	Rubber seal	30.56	0.8	24.5	[37]
11	Aluminium Sheet	55.28	1.5	82.92	
12	Paint (solvent based)	27.25	1	27.25	
13	Polystyrene	32.5	0.122	3.97	
14	Copper wire	19.61	0.2	3.92	[20,29]
15	Fittings	–	1.2	47.99	
16	Solar PV module 20 W,12 V	–	–	607	
17	Battery	148.45	–	46	
18	Solar charge controller	–	–	33	
Total				**1434.2 kWh**	

favorable drying conditions inside the dryer.

3.6. Comparison with existing drying systems

A comparison of ITDHSD with existing solar drying systems has been reported in Table 8. Modified and Simple convection greenhouse dryers had overall drying efficiency of 26.23% and 23.34%, with total CO_2 mitigation of 1.45 and 1.26 Tonnes, respectively [10]. Heat exchanger-evacuated tube assisted drying system had dryer efficiency of 25.1% [11]. Indirect solar drying unit had an efficiency of 31.42% and EPBT of 4.36 years. It mitigated 7.83 Tonnes of CO_2 in 20 years [19]. An ITSD system had a drying efficiency of 31.4% for tomato slices drying [13]. The present ITDHSD system is superior in overall drying efficiency, which was 41.05% [23]. Total CO_2 mitigated by ITDHSD was 12.28 Tonnes.

4. Conclusions and future directions

Tomato drying experimentation in ITDHSD system was performed at Delhi Technological University (DTU), Delhi, India, in November 2021 (winter). The following conclusions have been drawn from the present work:

- Final moisture content of 9% (wb) in tomato flakes was achieved after 10 h of drying in ITDHSD while in open sun drying 14% (wb) moisture content was achieved after 14 h.
- Heat utilization factor and C.O.P. for ITDHSD were in the range of 0.59–0.84 and 0.16–0.44, respectively.
- Embodied energy in fabrication of ITDHSD system was evaluated as 1434.176 kWh and corresponding EPBT was calculated as 4.21 years.

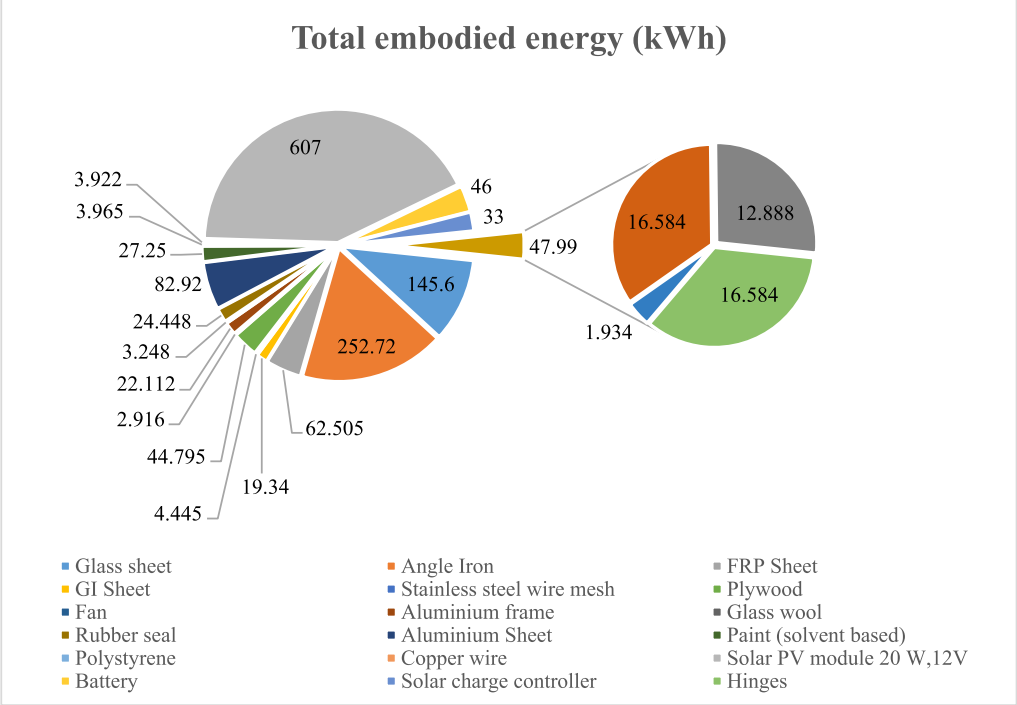


Fig. 10. Contribution graph embodied energy of material utilized for constructing ITDHSD system.

Table 6
Economic investigation of tomato drying in drying system.

Parameter	Value
Initial capital (Cost of ITDHSD system)	US$245
Operating cost	
I. Raw Material @ $0.37/kg for 530 kg	US$196
II. Maintenance and repair cost @ 10% of initial capital	US$25
III. Labour cost @ $1.22/day for 250 days	US$305
IV. Packaging charge	US$37
Total Operating cost (I + II + III + IV)	***US$563***
Selling price of dried product @ US$14.66/kg for 71 kg	US$1041
Net annual income	US$478
Simple payback period	6 months 3 days
Life of solar dryer	20 years
Loading capacity	3 kg
No. of working days	250 days
Total dried tomato flakes per year	520 kg

- Total CO_2 mitigation using ITDHSD for tomato drying in lifetime of 20 years was estimated 12.28 tonnes.
- Earned carbon credit by ITDHSD for tomato drying was evaluated as US$364.
- Total initial capital and operating cost for ITDHSD system were computed as US$245 and US$563, respectively and the corresponding payback period for selling dried tomato flakes was estimated as 6 months.
- Dried tomato flakes obtained from ITDHSD were of good quality in terms of sensory analysis, rehydration ratio, shrinkage and hardness compared to open sun dried tomato flakes.
- ITDHSD system has been found economical in terms of monetary value as well as in terms of carbon mitigation.

Present ITDHSD system can be useful for domestic users and small and medium scale industries and could provide livelihood to the farmers. The outcomes of present work could be very useful to students, researchers and engineers in assessment of energy and environmental parameters for any system. However, this analysis has been limited to tomato crop drying during winter season. To provide a comprehensive

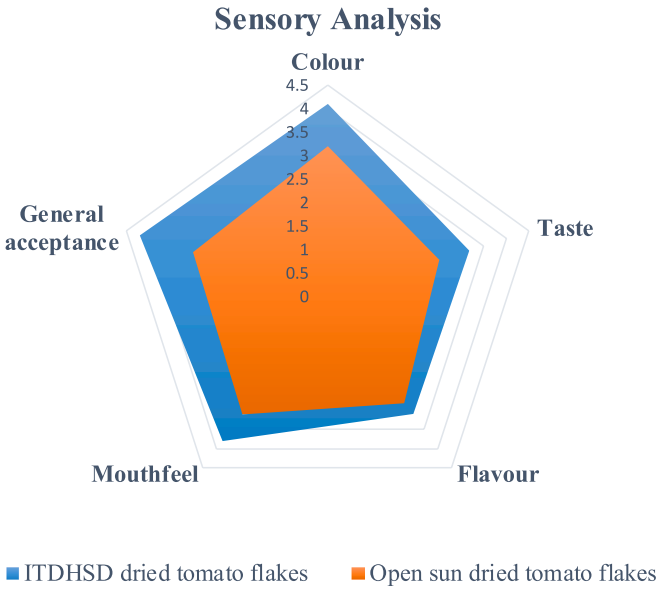


Fig. 11. Sensory analysis of dried tomato flakes obtained from ITDHSD and open sun drying.

Table 7
Results of quality estimation of dried tomatoes flakes.

Parameters	Open sun drying	ITDHSD
Shrinkage (%)	68	74
Rehydration ratio (g of water in 10 g of dried sample)	12.5	15.8
Hardness (g)	140	171

Table 8
Comparison of ITDHSD with existing solar drying systems.

Drying system	Overall drying efficiency (%)	EPBT (Years)	Total CO_2 mitigation (Tonnes)	References
Modified convection greenhouse dryer	26.23	2.28	1.45	[10]
Simple convection greenhouse dryer	23.34	1.27	1.26	[10]
Heat exchanger-evacuated tube assisted drying system	25.1	–	–	[11]
Indirect solar drying unit	31.42	4.36	7.83	[19]
Indirect type solar dryer (ITSD) system	31.4	–	–	[13]
ITDHSD system	41.05	4.21	12.28	**Present system**

understanding of the drying process for various crops, future studies should integrate economic, environmental, and quality analysis across all four seasons.

CRediT authorship contribution statement

Mukul Sharma: Writing – original draft, Methodology, Formal analysis. **Deepali Atheaya:** Writing – review & editing, Resources, Visualization, Supervision. **Anil Kumar:** Conceptualization, Writing – review & editing, Investigation, Supervision.

Declaration of Competing Interest

The authors declare that they have no known competing financial interests or personal relationships that could have appeared to influence the work reported in this paper.

Data availability

Data will be made available on request.

Acknowledgment

There is no direct funding for this research work. Authors are highly thankful to Bennett University, Greater Noida, India, and Centre for Energy and Environment, Delhi Technological University, for providing basic infrastructure for compiling this work.

References

[1] M. Sharma, D. Atheaya, A. Kumar, Recent advancements of PCM based indirect type solar drying systems: a state of art, Mater. Today Proc. 47 (2021) 5852–5855.
[2] F.A.N. Fernandes, S. Rodrigues, C.L. Law, A.S. Mujumdar, Drying of exotic tropical fruits: a comprehensive review, Food Bioprocess Technol. 4 (2011) 163–185, https://doi.org/10.1007/s11947-010-0323-7.
[3] O. Prakash, A. Kumar, Y.I. Sharaf-Eldeen, Review on Indian solar drying status, Curr. Sustain. Energy Rep. 3 (2016) 113–120, https://doi.org/10.1007/s40518-016-0058-9.
[4] D. Tiwari, D. Atheaya, A. Kumar, N. Kumar, Analysis of organic rankine cycle powered by N-number of solar collectors in series, Energy Sources, Part A Recover. Util. Environ. Eff. 44 (2022) 6678–6697, https://doi.org/10.1080/15567036.2022.2096726.
[5] A. Jain, M. Sharma, A. Kumar, A. Sharma, A. Palamanit, Computational fluid dynamics simulation and energy analysis of domestic direct-type multi-shelf solar dryer, J. Therm. Anal. Calorim. 136 (1) (2019) 173–184, https://doi.org/10.1007/s10973-018-7973-5.
[6] P. Singh, V. Shrivastava, A. Kumar, Recent developments in greenhouse solar drying: a review, Renew. Sustain. Energy Rev. 82 (2018) 3250–3262, https://doi.org/10.1016/j.rser.2017.10.020.
[7] V. Shrivastava, A. Kumar, P. Baredar, Developments in Indirect Solar Dryer : A Review, Dev. Indirect Sol. Dry. a Rev. 3 (2014) 67–74.
[8] M. Aghbashlo, H. Mobli, S. Rafiee, A. Madadlou, A review on exergy analysis of drying processes and systems, Renew. Sustain. Energy Rev. 22 (2013) 1–22, https://doi.org/10.1016/j.rser.2013.01.015.
[9] Shimpy, M. Kumar, A. Kumar, Designs, performance and economic feasibility of domestic solar dryers, Food Eng. Rev. 15 (1) (2023) 156–186, https://doi.org/10.1007/s12393-022-09323-1.
[10] Shimpy, M. Kumar, A. Kumar, R.K. Sahdev, H. Manchanda, Comparison of groundnut drying in simple and modified natural convection greenhouse dryers: thermal, environmental and kinetic analyses, J. Stored Prod. Res. 98 (2022), 101990, https://doi.org/10.1016/j.jspr.2022.101990.
[11] A. Kushwah, A. Kumar, M. Kumar, A. Pal, Garlic dehydration inside heat exchanger-evacuated tube assisted drying system: thermal performance, drying kinetic and color index, J. Stored Prod. Res. 93 (2021), 101852, https://doi.org/10.1016/j.jspr.2021.101852.
[12] P. Singh, M.K. Gaur, Sustainability assessment of hybrid active greenhouse solar dryer integrated with evacuated solar collector, Curr. Res. Food Sci. 4 (2021) 684–691, https://doi.org/10.1016/j.crfs.2021.09.011.
[13] A. Lingayat, V.P. Chandramohan, V.R.K. Raju, S. Suresh, Drying kinetics of tomato (Solanum lycopersicum) and Brinjal (Solanum melongena) using an indirect type solar dryer and performance parameters of dryer, Heat Mass Transf. Und Stoffuebertragung 57 (2021) 853–872, https://doi.org/10.1007/S00231-020-02999-3.
[14] H. Atalay, E. Cankurtaran, Energy, exergy, exergoeconomic and exergo-environmental analyses of a large scale solar dryer with PCM energy storage medium, Energy 216 (2021), 119221, https://doi.org/10.1016/j.energy.2020.119221.
[15] S. Vijayan, T.V. Arjunan, A. Kumar, Exergo-environmental analysis of an indirect forced convection solar dryer for drying bitter gourd slices, Renew. Energy. 146 (2020) 2210–2223, https://doi.org/10.1016/j.renene.2019.08.066.
[16] K.G. Sajith, C. Muraleedharan, Analysis of Economic and Environmental Factors of Solar Dryer Integrated With a Hybrid Photovoltaic-, 39 (2020) 335–345.
[17] S. Zohrabi, S.S. Seiiedlou, M. Aghbashlo, H. Scaar, J. Mellmann, Enhancing the exergetic performance of a pilot-scale convective dryer by exhaust air recirculation, Dry. Technol. 38 (2020) 518–533, https://doi.org/10.1080/07373937.2019.1587617.
[18] P.S. Chauhan, A. Kumar, C. Nuntadusit, Thermo-environomical and drying kinetics of bitter gourd flakes drying under north wall insulated greenhouse dryer, Sol. Energy 162 (2018) 205–216, https://doi.org/10.1016/j.solener.2018.01.023.
[19] V. Shrivastava, A. Kumar, Embodied energy analysis of the indirect solar drying unit, Int. J. Ambient Energy 38 (2017) 280–285, https://doi.org/10.1080/01430750.2015.1092471.
[20] O. Prakash, A. Kumar, P. Tekasakul, A.M. Abdel-Ghany, I.M. Al-Helal, Environomical analysis and mathematical modeling of potato chips drying in a modified solar greenhouse dryer, Heat Transf. Res. 48 (2017) 1497–1514, https://doi.org/10.1615/HeatTransRes.2017012421.
[21] O. Prakash, A. Kumar, Environomical analysis and mathematical modelling for tomato flakes drying in a modified greenhouse dryer under active mode, Int. J. Food Eng. 10 (2014) 669–681, https://doi.org/10.1515/ijfe-2013-0063.
[22] A. Sreekumar, P.E. Manikantan, K.P. Vijayakumar, Performance of indirect solar cabinet dryer, Energy Convers. Manag. 49 (2008) 1388–1395, https://doi.org/10.1016/j.enconman.2008.01.005.
[23] M. Sharma, D. Atheaya, A. Kumar, Exergy, drying kinetics and performance assessment of Solanum lycopersicum (tomatoes) drying in an indirect type domestic hybrid solar dryer (ITDHSD) system, J. Food Process. Preserv. n/a (2022) e16988.
[24] O. Prakash, A. Kumar, in: Solar Drying Systems, 1st ed., CRC Press, Boca Raton, 2020 https://doi.org/10.1201/9780429299353.
[25] M. Aghbashlo, M.H. Kianmehr, A. Arabhosseini, Modeling of thin-layer drying of potato slices in length of continuous band dryer, Energy Convers. Manag. 50 (2009) 1348–1355, https://doi.org/10.1016/j.enconman.2009.01.004.
[26] P.S. Chauhan, A. Kumar, Heat transfer analysis of north wall insulated greenhouse dryer under natural convection mode, Energy 118 (2017) 1264–1274, https://doi.org/10.1016/j.energy.2016.11.006.
[27] P.S. Chauhan, A. Kumar, C. Nuntadusit, Heat transfer analysis of PV integrated modified greenhouse dryer, Renew. Energy 121 (2018) 53–65, https://doi.org/10.1016/j.renene.2018.01.017.
[28] M.A. Eltawil, M.M. Azam, A.O. Alghannam, Energy analysis of hybrid solar tunnel dryer with PV system and solar collector for drying mint (MenthaViridis), J. Clean. Prod. 181 (2018) 352–364, https://doi.org/10.1016/J.JCLEPRO.2018.01.229.
[29] I. Nawaz, G.N. Tiwari, Embodied energy analysis of photovoltaic (PV) system based on macro- and micro-level, Energy Policy 34 (2006) 3144–3152, https://doi.org/10.1016/j.enpol.2005.06.018.
[30] O.H.R. Watt M. E., Johnson A. J., Ellis M., Life-cycle Air Emissions from PV Power Systems, Prog. Photovoltaics Res. Appl. (1998). doi:10.1002/(SICI)1099-159X(199803/04)6:2<127::AID-PIP214>3.0.CO;2-Z.
[31] D. Atheaya, Economics of Solar Drying, in: O. Prakash, A. Kumar (Eds.), Sol. Dry. Technol. Concept, Des. Testing, Model. Econ. Environ., Springer Singapore, Singapore, 2017: pp. 441–462. doi:10.1007/978-981-10-3833-4_1.
[32] K. Jayathunge, R. Kapilarathne, B. Thilakarathne, K. Palipane, P. Prasanna, Development of a methodology for production of dehydrated tomato powder and study the acceptability of the product, J. Agric. Technol. 8 (2012) 765–773. www.philippineherbalmedicine.org.
[33] Y. Noutfia, A. Benali, I. Guirrou, K. El Fazazi, H. Tantaoui, Effect of two drying methods on key physicochemical properties and sensory profile of dried figs (Ficus Carica L.), J. Agri. Sci. 2 (2021) 61–65. www.techagro.org.

[34] O. Prakash, A. Kumar, Solar drying technology: concept, design, testing, modeling, economics, and environment, Springer Publication (2017). ISBN 978-981-10-3833-4. https://doi.org/10.1007/978-981-10-3833-4..

[35] E.E. Abano, H. Ma, W. Qu, Influence of air temperature on the drying kinetics and quality of tomato slices, J. Food Process. Technol. 02 (05) (2011), https://doi.org/10.4172/2157-7110.1000123.

[36] O. Prakash, A. Kumar, V. Laguri, Performance of modified greenhouse dryer with thermal energy storage, Energy Rep. 2 (2016) 155–162, https://doi.org/10.1016/j.egyr.2016.06.003.

[37] G. Baird, A. Alcorn, P. Haslam, The energy embodied in building materials - updated New Zealand coefficients and their significance, IPENZ Trans. 24 (1997) 46–54.

[38] P. Majumder, A. Sinha, R. Gupta, S.S. Sablani, Drying of selected major spices: characteristics and influencing parameters, drying technologies, quality retention and energy saving, and mathematical models, Food Bioprocess Technol. 14 (2021) 1028–1054, https://doi.org/10.1007/s11947-021-02646-7.

BioNanoScience
https://doi.org/10.1007/s12668-023-01125-x

Phytochemical-Based Synthesis of Silver Nanoparticle: Mechanism and Potential Applications

Ritu[1] · Krishan Kumar Verma[1] · Asmita Das[1] · Prakash Chandra[1]

Accepted: 6 May 2023
© The Author(s), under exclusive licence to Springer Science+Business Media, LLC, part of Springer Nature 2023

Abstract
Nanoparticles, nowadays, are being used in multiple applications such as therapeutics, industries, healthcare, cosmetics, and wound healing. Nanoparticles are entirely distinct from bulk particles as they have a giant surface area to volume ratio, therefore, showing various mechanical, electrical, physical, chemical, and optical properties, and thus, being used in different properties. As there are so many applications of metallic nanoparticles, there is a requirement for an efficient method for nanoparticle synthesis because the conventional chemical methods used to synthesize nanoparticles have limitations such as high cost and negative environmental impact. To overcome these drawbacks, green methods for nanoparticle synthesis have emerged as an eco-friendly and cost-efficient alternative. The green method for nanoparticle amalgam is cost-efficient and eco-friendly, unlike the chemical technique for nanoparticle synthesis. A variety of dimensions of nanoparticles can be synthesized by a substitute of the plant's extract. Moreover, there is no requirement for external stabilizing agents and the involvement of harmful chemicals. This review aims to investigate how plant compounds can be used to synthesize silver nanoparticles and to evaluate the potential of plant extracts as reducing and stabilizing agents in the green synthesis of metallic nanoparticles. This review seeks to investigate the green production of metallic nanoparticles using plant-derived chemicals and to assess the potential of plant extracts as reducing and stabilizing agents. The study investigates the function of numerous plant substances in the synthesis process, such as flavonoids, alkaloids, terpenoids, saponins, and phenols. The paper also examines various methods for figuring out the morphology of nanoparticles created from various plant parts and their prospective uses as antibacterial agents, wastewater treatment, and reactive oxygen species modulators. This review offers insightful information about the possible uses of metallic nanoparticles by highlighting the advantages of environmentally friendly processes for the manufacture of silver nanoparticles.

Keywords Metal nanoparticles · Flavonoids · Alkaloids · Terpenoids · Saponins · Amino acids · Polyphenol groups · Green synthesis · Antimicrobial activity · Applications · Top-down and bottom-up · Silver nanoparticles

1 Introduction

Nanobiotechnology has emerged as a promising field that combines the power of biotechnology and nanotechnology to unlock the potential of nanomaterials in various life sciences applications such as healthcare, medicine, and cosmetics [1].

Nanotechnology offers a means of understanding the correlation between nanoparticle size, shape, and surface conditions concerning their electrical, magnetic, and other properties. Metallic nanoparticles are being used in textiles, wound dressing, and medical devices with antibacterial coating due to their novel properties, including their giant surface area to volume ratio, better mechanical properties, the high charge on the surface, antimicrobial activity, and better permeability through biological barriers [2]. Silver nanoparticles have attracted the most attention among the metallic nanoparticles because of their numerous uses in the healthcare, pharmaceutical, food, and medical industries. Additionally, silver nanoparticles can help with drug delivery [3]. The biological methods of nanoparticle synthesis also provide cost-effective, easy, energy-saving platforms for lofty output. By using

✉ Prakash Chandra
prakash0111@gmail.com

Ritu
ritu_2k19phdbt13@dtu.ac.in

Asmita Das
asmitadas1710@dce.ac.in

[1] Department of Biotechnology, Delhi Technological University, Main Bawana Road, 110042 Delhi, India

Published online: 23 May 2023

living cells to synthesize nanoparticles, bio nanotechnology can produce environmentally friendly nanoparticles. The use of natural or environmentally friendly sources to synthesize nanoparticles is referred to as the "green synthesis" of silver nanoparticles. By doing so, dangerous chemicals are avoided and the environmental damage caused by chemical pollutants is reduced [4]. This method offers several advantages such as cost-effectiveness, simplicity, and sustainability compared to previous studies that use chemical methods to synthesize nanoparticles [5]. The combination of biotechnology and nanotechnology has opened up new avenues for the development of nanomaterials with enhanced properties and reduced environmental impact, providing a promising future for the field of nanobiotechnology.

Nanoparticles have become an increasingly popular area of research due to their potential applications in various fields such as medicine, agriculture, and water treatment. The characterization of biosynthesized nanoparticles can be done through a variety of approaches, including TEM, SEM, DLS, AFM, zeta potential, and XRD [6]. Recent advancement in nanotechnology is to study the interaction of nanoparticles with the living world for instance plants, animals, cells, and tissues for the toxicity of nanoparticle analysis. This would allow the identification of a specific biological response by the metal nanoparticles [7]. The researchers attributed improvements to the catalytic properties of the silver nanoparticles, which enhanced the combustion efficiency of the engine. A study evaluates the impact of green synthesized silver nanoparticles blended with biodiesel on the performance and emissions of a 4-stroke diesel engine. The addition of silver nanoparticles has been shown to improve engine performance and reduce emissions. Although further research is needed to optimize the synthesis and application of silver nanoparticle-based fuel additives for sustainable diesel engines [8]. The findings suggest that the use of green synthesized silver nanoparticles as a fuel additive could lead to more efficient and environmentally friendly diesel engines [9]. The shape, size capping, agglomeration, and dissolution rate of the metallic nanoparticles depend upon the variety of reducing agents used [10]. The combination of chemical and physical methods is the most efficient way to synthesize nanoparticles. Numerous studies have explored the potential applications of green synthesized silver nanoparticles [11]. It has been demonstrated that these nanoparticles exhibit strong antibacterial activity against a variety of pathogenic microbes and improve the combustion efficiency of diesel engines. Silver nanoparticles made with green synthesis have also been applied to the creation of new catalysts, biosensors, and antibacterial drugs. Silver nanoparticles produced by plants have demonstrated promise as samples with heavy metal contamination are examined. Additionally, numerous studies have been done on the use of various plant extracts, including aloe vera, neem, and turmeric, for the green synthesis of silver nanoparticles [12]. In 2022, Nayak et al. investigated the potential application of plant-mediated gold and silver nanoparticles for the detection of heavy metal contamination in food and environmental samples. The researchers created gold and silver nanoparticles from plant extracts and assessed how well they worked as lead, cadmium, and copper ion detectors. As a result of the heavy metal ions, the synthesized nanoparticles displayed a color shift, which indicated heavy metal contamination. The study also discovered that the nanoparticles have good lead ion selectivity. The method's eco-friendliness was emphasized by using plant extracts as green reducing and stabilizing agents. Overall, the study suggests that plant-mediated gold and silver nanoparticles can provide a simple and cost-effective approach for detecting heavy metal contamination in various samples [13]. Another study found that the *Jatropha curcas* seed cake extract for synthesizing silver nanoparticles through a biogenic method could be a promising approach for producing nanoparticles with antibacterial activity [14]. Pradeep et al. (2021) biosynthesized silver and gold nanoparticles using areca nut husk extract and evaluated their anticandidal and antioxidant activities. The study emphasizes the potential of using areca nut husk extract for producing nanoparticles with significant biomedical applications [15].

The unique features and possible uses of greenly synthesized silver nanoparticles, which have attracted a lot of interest lately, are insightfully summarized in this paper. In place of current processes that rely on hazardous chemicals, plant extracts can be used as reducing and capping agents for the manufacture of silver nanoparticles. These nanoparticles are potential prospects for a variety of applications, including medicine, agriculture, and water treatment due to their distinctive qualities, such as their antibacterial and catalytic capabilities. When synthesizing silver nanoparticles, phytochemicals with known antimicrobial properties may increase their effectiveness and decrease their toxicity. AgNPs' control of ROS and RNS also sheds light on the potential therapeutic uses that they may have for treating a variety of illnesses. As they can be made using readily available plant extracts, green synthesized silver nanoparticles have the potential to be used in water treatment. This lowers their cost significantly. Additionally, it has been demonstrated that these nanoparticles are efficient at removing impurities from water, making them a potential remedy for the world's water crisis. In conclusion, there are many advantages, such as eco-friendliness, sustainability, and cost-effectiveness, to using plant-based extracts in the production of silver nanoparticles. These nanoparticles have the potential to revolutionize the way we approach medicine, agriculture, water treatment, and other related industries because of their potential uses in a variety of fields. However, further research is necessary to

fully understand their underlying mechanisms and evaluate their safety and efficacy in clinical settings.

2 Methods for Nanoparticle Synthesis

A bottom-up method and a top-down method can be used to synthesize nanoparticles. In the top-down method of nanoparticle synthesis, particles of atomic levels are combined to form a nanoparticle [16]. There are several approaches for the development of the nanoparticle, this includes layer-by-layers self-assembly, molecular self-assembly, direct assembly, coating, growth, etc. In contrast, in the bottom-up approach, bulk particles are reduced to the nano level by a variety of methods which includes e-beam lithography, scanning probe lithography, atomic force microscopy lithography, laser ablation, sputtering, etc. (Fig. 1) [17, 18].

The implementations of metal nanoparticles are growing rapidly daily, thereby the requirement for an efficient method for nanoparticle synthesis was felt. The conventional chemical method of nanoparticle synthesis deals with the involvement of hazardous chemicals which not only affect the health of human beings but also pose a danger to the territory and marine health. Therefore, the green method is allied as a highly recommended method for metal nanoparticle synthesis [21].

3 The Green Method

In the green method or biological method, the benefit of using plant extract is that it works as a reducing agent, does not require any external stabilizing agent, rapid synthesis, and synthesis at lenient pressure, temperature, and pH which aims to avoid harmful features of nanoparticle synthesis. Hence, only the extract of plants can be utilized to serve both the purpose of reducing and capping as well [22]. Metal nanoparticle synthesis by the green synthesis approach requires the involvement of extraction of plants and metal salt solution [3]. On the blending of the metal salt solution with the extraction of plants, there will be a color change. As the color changes, metal nanoparticles are being synthesized. Several phytochemicals contribute to the formation of metal nanoparticles, including cellulose, flavonoids, protein, polysaccharides, alkaloids, and secondary metabolites (Fig. 2) [23]. The dimension of the nanoparticle depends upon the quantity of the reducing agents present in the extraction. The hydroxyl group of polysaccharides oxidized to the carboxylic group, which means there is a bit part of the hydroxyl group in the depletion of metal ions into the metal nanoparticle [24]. It has also been reported that bacteria, fungi, and algae produce metal nanoparticles, such as silver, gold, copper, alginate, and magnesium nanoparticles, although a complete understanding has yet to be reached (Fig. 1).

These plant-based compounds are very efficient for the synthesis of nanoparticles. This approach to nanoparticle synthesis has so many benefits in contrast to the ordinary method of nanoparticle synthesis, some of which are the low operational cost, the potential for high yields, and no involvement of hazardous chemicals [26]. Out of all these sources, plants are considered to be the most effective source, since, in microorganism-based metal nanoparticle synthesis, the variety of sizes and shapes of metal nanoparticles is very limited as compared to the plant-based method [26]. Moreover, plants present a much faster rate

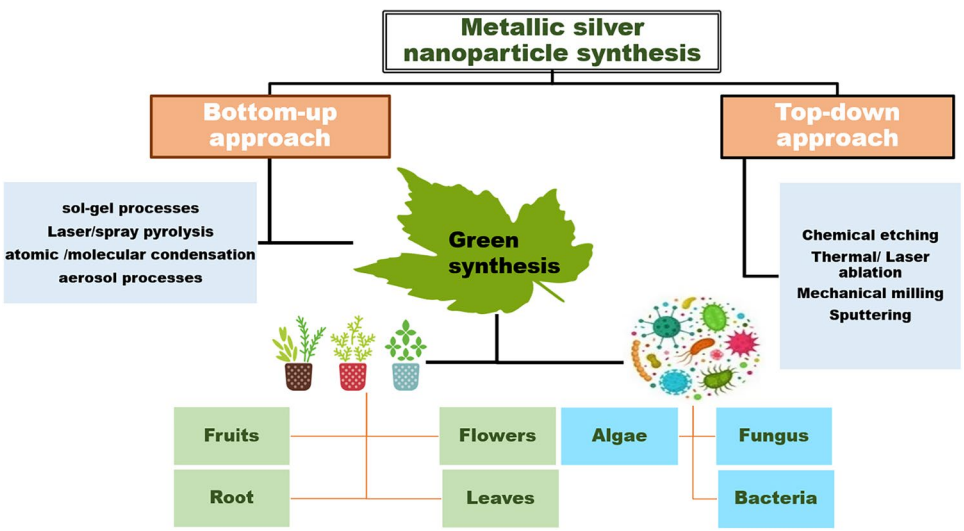


Fig. 1 The flowchart depicts multiple approaches for synthesizing metallic silver nanoparticles. These methods vary in terms of their techniques and ingredients. Overall, the chart provides an overview of the diverse ways in which silver nanoparticles can be produced [19, 20]

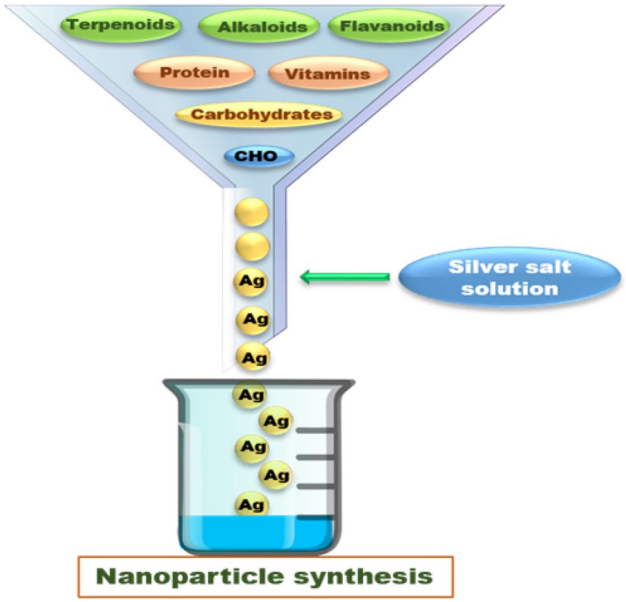


Fig. 2 This schismatic representation highlights the key steps involved in nanoparticle synthesis, from the selection and preparation of precursor materials to the final purification and characterization of the nanoparticles [25]

of synthesis and stable metallic nanoparticle synthesis. By substituting the temperature, concentration, and pH of the solution one can alter the shape and size of nanoparticles [27].

Plant extracts like leaves, fruits, stems, flowers, petals, whole plants, and seeds are used for the development of the Ag-NP from silver nitroxide. The carbohydrate, fats, proteins, pigments, and other phytohormones existing in the extraction of plants help in the stabilization of the nanoparticles and thus behave as a well-organized deoxidizer for the synthesis of the silver nanoparticles [28]. There are numerous advantages to the green method, such as the fact that it is environmentally friendly, cost-effective, and does not produce harmful chemicals as a by-product [29]. Different parts of a plant can synthesize metal nanoparticles, including bark, leaves, calluses, fruit, stems, seeds, petals, flowers, and rhizomes Table 1. By depleting metal salts into metal nanoparticles, phytochemicals present in the extract of different plant organs contribute to metal nanoparticle formation (Fig. 3). When the type of solvent and the reaction time are changed, nanoparticles can be manufactured in a variety of shapes and sizes. Nanoparticle synthesis using the green method involves the interaction of phytocomponents with metal ions [30].

The metal ion M + was reduced to the M0 due to the action of the plant extract's components, now this reduced form of metal aggregates and capped to form the silver nanoparticles. As a reduction agent for the transformation of metal ions into metal nanoparticles, the plant's extract must be used in the right concentration, as well as the pH, when synthesizing nanoparticles. The nanoparticle dimension depends upon the phytochemicals or components in the extraction of plants which are being used for the depletion of the metal ions into the metal nanoparticles [87]. These are terpenoids, aldehydes, alkaloids, amino acids, ketones, flavonoids, and carboxylic acid. These compounds were identified and confirmed by spectroscopic studies [18, 88].

4 Plant-Based Metal Nanoparticle Synthesis

Metal nanoparticles can be synthesized using plant extracts as reductants and stabilizers. Mixing plant extracts with metal salt solutions causes the formation of nanoparticles. The reaction will cause a color change and thus, mark the formation of nanoparticles. It has been shown that a variety of phytochemicals can result in metal nanoparticles, including alkaloids, flavonoids, proteins, polysaccharides, cellulose, and phenolic compounds (Fig. 2). Different amounts of reducing agents result in different sizes of nanoparticles. The hydroxyl group of the polysaccharide is oxidized to a carboxylate group, meaning that there is a role for the hydroxyl group in the reduction of metal ions into metal nanoparticles [24]. The synthesis of the silver nanoparticle will be confirmed by the UV-spectrometer and peak at 420 nm.

5 Compounds Present in Plants

Alkaloids can act as reducing agents, flavonoids and terpenoids can act as stabilizing and capping agents, while carbohydrates and proteins can act as reducing and stabilizing agents during the conversion of metallic salts to metallic nanoparticles. Each component plays a complementary role in the formation of stable and well-dispersed nanoparticles Table 2.

5.1 Flavonoids

are well-known secondary metabolites found in plants. Biotic and abiotic stress causes the production of secondary metabolites in plants, one such secondary metabolite is a flavonoid. The flavonoid can vary in its structure and can have different routes of synthesis. Thus, they can be found in leaves, flowers, fruit skin, etc. Anthocyanidins, flavanols, flavanones, flavan3-ols, flavones, and isoflavones are some examples of flavonoids [106]. Flavonoids have carbohydrate and hydroxy groups which make them water-soluble and groups like methyl and isopentyl make

Table 1 This table summarizes the different plant parts used for silver nanoparticle synthesis and the corresponding synthesis methods and characterization techniques used for each. Leaves and stem bark are commonly used for green synthesis methods, while seeds and fruits are more frequently used for biological synthesis methods. Flowers are more often used for chemical synthesis methods. Common characterization techniques include UV–Vis spectroscopy, TEM, XRD (X-ray diffraction), and DLS (dynamic light scattering), with applications in medicine, electronics, agriculture, FTIR (Fourier transform infrared spectrophotometer), TEM (transmission electron microscopy), SEM (scanning electron microscopy), GA-XRD (grazing angle X-ray diffraction), SAED (selected area electron diffraction), AFM (atomic force microscopy), EDS (energy-dispersive X-ray spectroscopy), ZPM (zero-point energy measurement), NMR (nuclear magnetic resonance), FE-SEM (field-emission scanning electron microscopy), EDAX (energy dispersive analysis of X-rays), XPS (X-ray photoelectron spectroscopy) and PSA (particle size analysis) and more

S no	Plant's name	Plant part used	Shape and size	Applications	Characterization techniques	Ref
1	*Abutilon indicum*	leaf	25 nm	It works by hampering drug-resistant gram-positive and gram-negative bacteria	XRD, TEM, SEM, UV	[31]
2	*Azadirachta indica*	leaf	30–34 nm	It is most effective at inhibiting the growth of gram-positive and gram-negative bacteria and is used in water purification	TEM, DLS, UV–visible	[32]
3	*Allium sativum*	fruit	3–10 nm	It is antibacterial against both gram-negative and gram-positive bacteria and has a high antimicrobial potency	TEM, GA-XRD, FTIR, SEM	[33]
4	*Eucalyptus camaldulensis*	Leaf extract	9–14 nm	Shows Efficient bactericidal and antifungal activity	UV–visible,	[34]
5	*Acacia Seyal*	Gum	80 nm	Shows radical scavenging activity, antioxidant properties, and anti-microbial properties. It also helps in the reduction of cellular infiltration and granulomatous inflammation in ankle joint tissues	FTIR, XRD, TEM, UV	[35]
6	*Acalypha hispida*	leaf	30–50 nm, spherical	Detection of Mn(II) ions in real wastewater or industrial effluents	UV, XRD, FTIR	[36]
7	*Aloe vera*	leafs	70–200 nm, spherical shaped	Shows antibacterial activity against pathogenic bacteria	XRD, SEM	[37]
8	*Acacia Senegal*	Gum and leaf	80 nm, rods and spherical	It has antiseptic properties against both gram-negative and gram-positive bacteria	UV, TEM, XRD, AFM, FTIR	[38]
9	*Allium cepa*	Bulb and fruit	10–14 nm and up to 100 nm, spherical	It is an ecofriendly approach for synthesis and works as an excellent catalyst for the reduction of toxic and hazardous dyes	UV, ZPM, FTIR, TEM	[39]
10	*Acacia nilotica*	Leaf	30–140 nm, spherical	Nanoparticle induces cytotoxicity and shows antiproliferative and anticancer activity in cancer also antibacterial and antifungal activity against pathogenic microorganism	SEM, UV, EDX, FTIR	[40]
11	*Adansonia digitata*	Leaf, pulp, and fruit	5–60 nm, spherical	Shows antimicrobial activity against various microorganisms	FTIR, XRD, UV, AFM	[41]
12	*Datura stramonium*	Leaf	15–20 nm, crystalline	Antimicrobial property	UV, FTIR, XRD, TEM	[42]
13	*Solanum trilobatum*	fruit	12–42 nm Spherical	Antigenic properties show against pathogen	UV, TEM, XRD, EDAX, FTIR	[43]
14	*Coriandrum sativum*	Seed and leaf	13 and 26 nm, spherical structure	Antimicrobial property	FITR, SEM, TEM, XRD	[44]
15	*Jatropha curcas*	Seed extract	15–50 nm, crystalline, spherical	Anti-microbial property	HRTEM, UV–visible, XRD	[45]

Table 1 (continued)

S no	Plant's name	Plant part used	Shape and size	Applications	Characterization techniques	Ref
16	*Cyperus rotundus*	Complete plant	20–30 nm	The anticancer and antibacterial property	FTIR, UV, SEM, EDX	[46]
17	*Elettaria Cardamomom*	Seeds	40–70 nm	Antimicrobial properties against pathogenic microbial strains like *Bacillus subtilis* and *Klebsiella plantticolla*	EDAX, SEM, XRD, UV-spectrophotometer, FTIR	[47]
18	*Cassia occidentails*	Leaf	31 nm	Antioxidant and Antibacterial against Escherichia coli	EDAX, TEM, SEM, XRD	[48]
19	*Fagonia cretica*	Leaf, Complete plant	16–50 nm, crystalline, spherical	Shows antibacterial efficacy	HPLC, TEM, UV, FTIR	[49]
20	*Coffee arabica*	Seed	10–50 nm, crystalline, cubic, spherical, and ellipsoidal	Diminished growth of several bacteria like *E.coli, S.aureus*	SEM-EDXA, TEM, FTIR, DLS	[50]
21	*Cucurbita maxima*	Petal extract	76.1 nm roughly spherical	Catalyze degradation of methylene blue and also shows antibacterial property	UV–Vis spectroscopy, DLS, Zeta-sizer, FTIR, Fe-SEM	[51]
22	*Citrus sinensis(navel orange)*	Peel	34 nm, spherical	Antibacterial activity against several bacteria	AFM, XRD, FTIR,UV, TEM, SEM, DLS	[52]
23	*Carum carvi*	Leaf	10 nm, spherical	Shows antifungal activity against *Candida albicans*	XRD, TEM, SEM, EDS	[53]
24	*Catharanthus roseus*	Leaf	67–48 nm, crystalline with FCC geometry	Shows anti-microbial properties against pathogen strains	UV, XRD, SEM, EDX	[54]
25	*Benzoin gum*	Plant Extract	12–38 nm, Spherical	High free radical scavenging activity and promising anti-microbial activity against few pathogens	UV–vis spectroscopy, IR, XRD	[55]
26	*Mangifera indica*	Leaf	32 and 100 nm, crystalline, flake-like structure	Nanoparticles are reinforced with Glass Ionomer Cement because it has anti-microbial activity and it can prevent microbial growth in mediated part	SEM, EDS, XRD, PSA	[56]
27	*Olea europaea L*	Leaf and seed	20–34 nm	Shows anti-microbial activity	FTIR, TEM, ZPM, UV–visible, EDAX	[57, 58]
28	*Moringa oleifera*	Leaf, seed	4–10 nm, spherical	Antibacterial activity and photocatalytic oxidation for water treatment	EDS, TEM, SEM, UV, XRD	[51, 59]
29	*Phoenix dactylifera*	Leaf and seed	14–30 nm, spherical	Effective against Methicillin-resistant Staphylococcus aureus (MRSA)	XRD, SEM, UV–visible, HR-TEM, DLS	[60]
30	*Coriandrum sativum*	Leaf Extract	13.9 nm, Spherical, and non-uniform	Antimicrobial activity	UV–Vis Spectroscopy, IR, XRD, FTIR	[61]
31	*Foeniculum vulgare*	Seed	11–25 nm, spherical	Antibacterial activity	FTIR, SEM, UV–visible, XRD, EDS	[62]
32	*Lantana Camara*	Leaf	14–27 nm, crystalline nanoparticles	Efficient bactericidal activity	XRD, SAED, XPS, FTIR, UV, XPS	[63]
33	*Nigella sativa*	Seed	10–20 nm	Inhibit the growth of microorganisms causing urinary tract infection	ZPM, TEM, UV, FTIR	[64]
34	*Phyllanthus amarus*	Complete plant	30–36 nm, flower-like structure	Shows excellent Antimicrobial and catalytic effect	FTIR, DLS, UV, TEM, XRD	[65]
35	*Glycyrrhiza uralensis*	Root Extract	Cubic shape	Antibacterial and antioxidant properties	UV–Visible spectroscopy, FE-TEM, XRD	[66]
36	*Mentha piperta*	Leaf	35 nm, spherical shape	Antibacterial and anti-odor properties	UV–visible, SEM, TEM	[67]
37	*Kigelia Africana*	fruit	10 nm	It has antibacterial and antifungal properties against both gram-negative and gram-positive bacteria	TEM, XRD, SEM, FTIR, UV–visible	[68]

Table 1 (continued)

S no	Plant's name	Plant part used	Shape and size	Applications	Characterization techniques	Ref
38	*Hibiscus sabdariffa*	Leaf extract	5–60 nm	Shows catalytic activity for reduction of 4-nitrophenol	XRD, FTIR, UV–visible, SEM, TEM	[69]
39	*Rosa Indica*	Petal Extract	20–60 nm, Spherical	A human colon adenocarcinoma cancer cell line was shown to have antibacterial, anticancer, and antiinflammatory properties	UV-Spectroscopy, DLS, XRD, FTIR, HRTEM, FE-SEM, EDAX	[70]
40	*Piper nigrum*	fruit	20 nm, Spherical shape	Shows cytotoxic effect against MCF-7 and hep-2 with good anticancer property	HR-TEM, FTIR, UV	[71]
41	*Pimpinella anisum*	Seed	3.2–16 nm	Shows toxicological/cytotoxic effect against hSSCs cells and colon cancer cells	EDS, TEM, XRD, UV	[72]
42	*Lawsonia inermis*	Leaf	30 nm	Anti-bacterial activity against pathogenic bacteria	FTIR, XRD, TEM, UV	[73]
43	*Syzygium Jambos*	Leaf and bark extract	Spherical	5–8 nm	UV–vis. Spectroscopy, TEM, XRD, FTIR, NMR	[74]
44	*Tinospora cordifolia*	Complete plant	34.5 nm	Showed pharmacological activity against cancer, arthritis, diabetes mellitus	UV, DLS, FTIR	[75]
45	*Zingiber officinale*	Rhizome, leaf	3–22 nm	Antioxidant, antibacterial, and anti-pancreatic cancer properties	TEM, SEM, XRD, FTIR, UV	[44, 76]
46	*Tribulus Terrestris*	Fruit	16–28 nm, spherical shaped	Showed antibacterial properties against multidrug-resistant bacteria	UV, TEM, FTIR, AFM	[77]
47	*Artemisia marschalliana*	Aerial part extract	5–50 nm, Spherical	Shows anti-oxidant, anti-microbial activity, anti-cancer against human gastric carcinoma, and induces apoptosis in cancer cell	UV- Visible spectroscopy, SEM, TEM, XRD, FTIR	[78]
48	*Withania somnifera*	Leaf	12–110 nm, spherical shape	Anti-microbial activity against human pathogens	AFM, XRD, LDA, UV, TEM	[79, 80]
49	*Tamarindus indica*	Fruit	10 nm, spherical	Shows dose-dependent cytotoxicity in breast cancer cell line (MCF-7)	TEM, AFM, UV, FTIR	[81]
50	*Ricinus communis*	Leaf	30–40 nm, spherical	This compound has antibacterial and photocatalytic properties, as well as anti-oxidant properties	FTIR, UV, SAED, XRD, TGA, UV	[82]
51	*Hydrastis Canadensis*	Whole plant Extract	90.87 nm, Spherical	Antioxidant and anti-microbial activity	UV- Visible spectroscopy, DLS, TEM, FTIR, AFM, XRD, CD	[83]
52	*Calotropis Procera*	Leaf	26–38 nm, Spherical	Act as an antioxidant and possess significant antimicrobial property	XRD, UV–visible, SEM	[84]
53	*Dodonaea viscosa*Land*Capparis decidua*	Leaf	60–90 nm, spherical	Shows antimicrobial, anti-inflammatory, and antiproliferative activity	UV–visible, FTIR, SEM, XRD	[85]
54	*Capsicum annum L*	Leaf	42.3–45.9 nm	Antimicrobial activity	SAED, XRD, TEM, FTIR, XPS, UV-visible	[86]

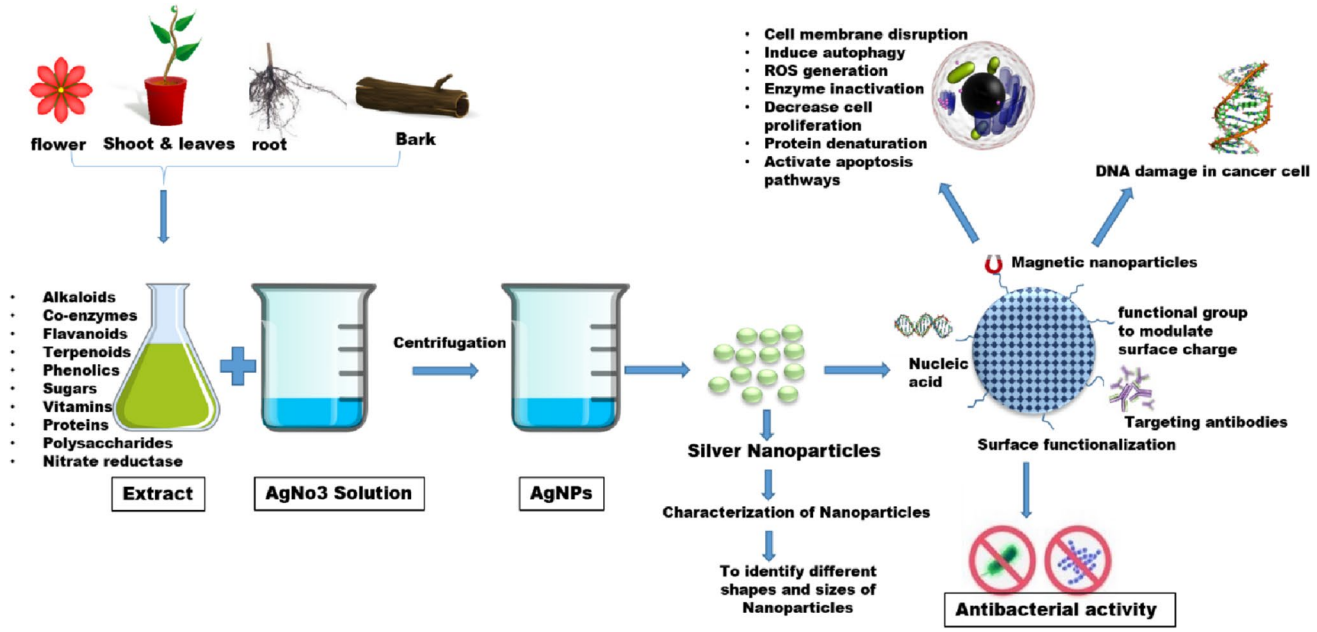


Fig. 3 A diagram depicting the formation of nanoparticles from various phytochemicals. The extract is mixed with a metal salt solution and heated under reflux conditions, forming a coating on the surface of the nanoparticles. The resulting nanoparticle suspension can be characterized using various techniques and has many potential applications in fields such as medicine and electronics. This method is eco-friendly and provides a sustainable alternative to traditional synthesis methods [22]

them water-insoluble compounds. Studies show that flavonoids have electron and hydrogen-donating capability which makes them suitable for nanoparticle synthesis [107]. Also, the flavonoids contain a variety of functional groups which allows them to work as a reducing agent. The reactive hydrogen of flavonoids is removed due to the tautomeric transformation and the enol group is converted to the keto group allowing the depletion of the metal ion into the metal nanoparticle [108].

5.1.1 The Mechanism of Metal Nanoparticle Synthesis

The production of nanoparticles included several steps to follow. This includes depletion of ions, aggregation, and progression. The different classes of flavonoids are found in large amounts in a variety of plants. One such polyphenolic flavonoid is quercetin with the molecular formula of C15H10O7, which is found in a variety of fruits, vegetables, leaves, and other types of plants [52]. It was also

Table 2 The table highlights the diverse applications and potential uses of silver nanoparticles in various fields, which can be attributed to the use of different secondary metabolites as precursors, reducing and stabilizing agents for their formation

Secondary metabolite	Example(s)	Activity	References
Flavonoids	Quercetin, Kaempferol, Epicatechin	Antibacterial, antifungal, antioxidant	[89, 90]
Phenolics	Catechins, Cinnamic acid, Gallic acid	Antibacterial, antifungal, antioxidant	[91–93]
Terpenoids	Limonene, Menthol, Thymol, carvacrol	Antibacterial, antifungal, Antioxidant, anticancer	[94, 95]
Alkaloids	Vincristine, Nicotine, Berberine	Antibacterial, antifungal, anticancer	[96]
Tannins	Ellagitannins, Punicalagins, Arjunic acid	Antibacterial, antifungal, antiviral	[97, 98]
Saponins	Quillaja saponin, Sapindus saponin, Ginsenosides	Antibacterial, antifungal, anti-inflammatory	[99]
Carotenoids	Lycopene, β-carotene, Astaxanthin	Antioxidant, antitumor, anti-inflammatory	[100]
Coumarins	Scopoletin, Umbelliferone, Aesculetin	Anticoagulant, anti-inflammatory, antioxidant	[101]
Quinones	Juglone, Anthraquinone, Alizarin	Antibacterial, antifungal, antiviral	[102]
Glycosides	Stevioside, Oleandrin, Gentiopicrin	Cardiotonic, anti-inflammatory, antioxidant	[103]
Lignans	Secoisolariciresinol, Sesamin, Lignan-Lariciresinol	Antioxidant, anticancer, anti-inflammatory	[104]
Polyacetylenes	Falcarinol, Falcarindiol, Panaxydiol	Antimicrobial, anticancer, anti-inflammatory	[105]

proposed that the flavonoid in the leaf extract of the guava, i.e., quercetin releases the hydrogen which then reduces the silver ion into the silver nanoparticle and gets oxidized to form quinone. The most accepted reason for nanoparticle synthesis is the release of reactive hydrogen from the flavonoids due to the tautomeric transformation of the flavonoid in which the enol group is transformed into the keto group and releases the hydrogen. That hydrogen reduces the metal ion to the metal nanoparticles [109].

5.2 Terpenoids

Terpenoids are natural substances that plants produce in response to both abiotic and biotic stresses. The stimulus causes the activation of the terpene synthase gene and thus the formation of terpenes takes place. Terpenes are naturally organic chemicals that are formed from the five-carbon isoprene units and assemble variably. Sesquiterpenoid and monoterpenoid are produced by the combination of those units [110]. Terpenoid is the oxygenated form of terpenes. Terpenoids are a group of a composite combination of eruptive organic compounds and also the part of essential oils presents in the plant. There are approximately 3000 known essential oils out of which 300 have commercial importance. In the terpenoid and all other secondary metabolites, the commonly found compound isoprenoid, which is a basic hydrocarbon molecule [111]. The very fundamental unit of terpenoid is isoprenoid which unites from monoterpenoids and sesquiterpenoids, and they have a salient role in the plant hormone genesis and other important plant components [110]. They are also accountable for the color and taste of the fruits of plants. The presence of hydroxyl in the terpenoids diminishes the silver ions and thus forms the silver nanoparticles. The major terpenoids intricate in the formation of metal nanoparticles are monoterpenoids and sesquiterpenoids. Terpenoids such as linalool, eugenol, and methyl chavicol (estragole) have been demonstrated to have great promise to deplete silver ions into metal oxide nanoparticles [107].

5.2.1 The Mechanism Behind Metal Nanoparticle Synthesis by Terpenoid Compounds of Plants

The terpenoid in plants, for example, Eugenol, has the phenol group on its benzene ring. There are also two highly electron-withdrawing groups which are allyl and methoxy groups. Eugenol now releases a proton due to the presence of the phenol group, changing itself into the activated state. Eugenol has two electron-removing groups at the para and ortho positions of the phenol group, increasing its degradation efficiency. After releasing a proton, eugenol stabilizes due to the resonance and because of the inductive effect, eugenol releases two electrons at the same time. Ultimately, these two electrons are utilized by a metal ion and get converted into a metal nanoparticle [112].

5.3 Alkaloids

Alkaloids are also secondary metabolites, having more than 12,000 different structures, the alkaloids also have some medicinal properties. Alkaloids have compounds having a low molecular weight and also have heterocyclic nitrogen which might have come from the amino acids. Alkaloids are being used in various pharmacotherapy applications. Alkaloids have also been used in life-threatening diseases as a drug. For example, atropine is an alkaloid that is being used as an insecticide. Paclitaxel and its derivative are used to treat ovarian carcinoma [113]. Quinine is another example of an alkaloid that is present in the bark of cinchona trees [114]. Morphine is another alkaloid that is used to alleviate pain. Alkaloids are found in active tissues of plants, which include meristematic tissue at the stem and root apices. In the epidermal and hypodermal tissues, vascular sheaths of plants, and the latex vessels of the present. Studies show that 10% of the total alkaloids are present in the bark of the Cinchona tree. Also, in living cells, alkaloids are present in the vacuole as an acid or as a salt of acids. The synthesis of alkaloids starts with the formation of amino acids like ornithine, proline, etc. these amino acids get transformed into alkaloids [115].

5.4 Proteins, Carbohydrate Ketones, and Acids of Plants

The metabolites of plants consist of amino acids, carbohydrates, fatty acids, and other compounds that help the plant to grow. The proteins of plant extract provide the electron which can turn down the metal ions into metal nanoparticles after their stabilization. Also, there is a study, in which the part of the protein in the consolidation of silver nanoparticles, using *Capsicum annum*, was described. The UV absorption spectra manifest high absorption at 210 nm, specifying the presence of amino acids. Moreover, absorption at 280 nm indicates the existence of amino acids like tyrosine and phenylalanine. Thus, described the role of amides in the depletion of silver ions into the silver nanoparticles [107]. Moreover, the hydroxyl, amine, and thiols groups present in the extraction of plants provide a way to donate the electrons to the metal ions and reduce them into metal nanoparticles [116]. It has also been studied that protein-rich content in the extract of soybean leaf efficiently reduces the metal ion viz. palladium ions into the palladium nanoparticles [117].

5.5 Saponin

Saponin is the secondary metabolite that is produced by many species of plants that have the capability of defending plants from pathogens and other stress-inducing agents. Saponins also have been known to reduce blood cholesterol levels and inhibit cancer growth. Furthermore, it has also shown the potential of stabilizing oil-in-water emulsions and also nano emulsions. The saponin-mediated nanoparticles can also be formed by using the pH-driven method. The encapsulation and stabilization capabilities of saponin-mediated nanoparticles were found to be better than the synthetic surfactant. This can be used in food, supplement, and pharmaceutical preparations. The nanoparticles synthesized by the curcumin have shown potential applications in health-related issues [118].

Saponins are the glycosides that can alter the permeability of the membrane and hence destabilize it. The saponin-mediated nanoparticles were synthesized by a study with a size of 2–15 nm. It was also described that the FTIR analysis of saponin-mediated nanoparticle formation manifested the presence of C-O, C = O, and O–H groups of saponin, and their electron vibrations were intricated in the depletion and equilibration of the nanoparticles. These nanoparticles have shown potential application in the prevention of bacterial infection, wound healing, and also in the healing of burned patients [119].

5.6 Tannin/Tannic Acid

Tannins belong to compounds that are natural, non-toxic, and biodegradable, and can be extracted from plants. They are found in a good quantity in the leaf, bark, fruit, and wood of a plant. The secondary metabolites are fabricated by plants to combat the biotic and abiotic agents like herbivores, pathogens, and other agents [120]. The existence of hydroxyl groups in the construction of tannin allows it to interconnect with the various metal ions and form complexes with them. The most commonly present tannin is tannic acid whose ortho-dihydroxy or trihydroxy benzene group interacts with metal ions [121]. Tannic acid is a polyphenolic compound consisting of glucose molecules at the center to which end groups of gallic and benzoic acid are attached to the glucose molecule via ester linkages [122]. Now, at low pH, tannic acid acts as a frail reducing agent, which can begin the extension of nanoparticles at room temperature. At high pH, gallic acid can form nanoparticles from the silver nitrate but cannot stabilize them, hence conducting the accumulation of particles. Moreover, glucose can stabilize the reduced particle at room temperature but lacks reducing capability. Hence, tannic acid appears to be the potential candidate for reducing and stabilizing the metal nanoparticle at room temperature. The presence of phenolic groups in the tannic acid allows the metal ions to reduce to the metal nanoparticle and at the same time stabilize them to prevent further aggregation. The reducing properties of tannic acid are due to the presence of phenol groups, these phenol groups donate electrons which lower the oxidation of the metal ions in the metal salt solution and thus synthesize the metal nanoparticles [123]. It was found that tannic acid can also be used for wound healing, by eliminating ROS and increasing the emergence of capillary vessels and proliferation of the fibroblasts. Moreover, the nanoparticles synthesized by the tannic acid are more stabilized. Thus, it was found that tannic acid is the most desirable candidate for metal nanoparticle synthesis [124].

6 Metallic Nanoparticle Analysis

Characterization of the nanoparticles allows for evaluation of the size, safety, behavior, and structure of metal nanoparticles. There are numerous methods for analyzing how nanoparticles are portrayed. These include scanning electron microscopy (SEM), atomic force microscopy (AFM), dynamic light scattering (DLS), transmission electron microscopy (TEM), X-ray photoelectron spectroscopy (XPS), and UV–Vis spectroscopy [2].

6.1 UV–Vis Spectroscopy

It provides a simple and effective method for determining the basic or primary characterization of synthesized nanoparticles. Silver nanoparticles interconnect with a particular wavelength of light due to their optical properties [125]. UV–Vis spectrophotometer can characterize several forms of nanoparticles. It is an expeditious, convenient, and delicate technique for the characterization of nanoparticles [38]. The convection and valence bands lie near each other so the movement of electrons is allowed. Surface plasmon resonance (SPR) formation due to these free electrons happens because of the oscillation of electrons in the presence of light waves. The particle size and chemicals in the surroundings affect the absorption of light by the nanoparticles [126, 127].

6.2 X-ray Diffraction

It is a common technique for the analysis of nanoparticles; it aims to investigate crystalline formations, statistical magnification of synthetic complexes, analyses of different chemical types, crystallinity extent, and physical properties [128–130]. Applying Bragg's law to the property of the polycrystalline material will reveal interference when the scattered X-rays interact with one another [131].

Consequently, X-ray diffraction analysis can explore a wide range of materials including biomolecules, polymers, superconductors, glasses, and so on [2]. Diffraction peaks are the sole method for analyzing the aforementioned components. This technique can be used to examine the chemical and physical properties of crystal molecules [132]. It is suitable for examining both inorganic and organic crystalline materials [133, 134].

6.3 Fourier Transform Infrared Spectrophotometer (FTIR)

Through this method, it is possible to determine how biomolecules contribute to the production of metallic nanoparticles by analyzing the physiochemical properties of the particles [135]. FTIR can also reveal the information interaction uniting substrate and enzyme during the catalytic reaction, as the functional molecules will be grafted onto the metal [111, 136]. An infrared beam of radiation passes through the sample in this process, and the rest is absorbed or infiltrated. The evolving spectrum comes up with information on the radiation absorbed and transmitted by the sample. FTIR allows the rapid collection of data and less heating of the sample. Therefore, it is observed as a valuable, non-invasive, and convenient approach for nanoparticle characterization [134, 137].

6.4 X-ray Photoelectron Spectroscopy (XPS)

An empirical formula of a molecule can be estimated quantitatively using spectroscopic surface chemical analysis [138–140]. It is executed under a high vacuum state. In this technique, a ray beam of X-rays is estimated onto the specimens. The irradiation causes the emission of electrons from the sample. Analyzing XPS spectra, determining the number of electrons emitted by the sample, and estimating their kinetic energy. Due to this technique, P = S, aromatic ring, C-O, and C = O groups can be recognized by this technique [141].

6.5 Dynamic Light Scattering (DLS)

Nanoparticle average diameter and crystallinity can be ascertained using dynamic light scattering (DLS). Measurements of hydrodynamic radius in Brownian motion are the basis of this approach. The particle scatters the laser light at different intensities when it is allowed to fall on it. The Stokes–Einstein relationship is used to analyze the fluctuations. Therefore, the size of the nanoparticle can be measured by this technique. It measures the particle's size which is in the Brownian motion [18].

6.6 Scanning Electron Microscopy (SEM)

It is the electron microscopy approach, which captured the surface topology of the molecules. It helps in analyzing the dimensions and distribution of nanoparticles [142]. It uses high-energy electron beams to project onto samples, which are then scanned over by a detector, scattering back electron beams and providing information about the samples [143]. Energy dispersive X-ray spectroscopy (EDX) is a chemical analysis approach that is combined with the SEM to get insight constitution of the sample [144]. Using an SEM, only the surface of a sample can be analyzed, not what is inside; instead, purity and aggregates can be determined [145].

6.7 Transmission Electron Microscopy (TEM)

It is an efficient process for the analyses of the volume fraction, and the morphology of the nanoparticles. It provides finer structural resolution and also has the potential for supplementary analytical measurements [2, 146].TEM utilizes the beam of electrons that interconnects with the sample and thus forms a depiction on the photographic plate. This method can determine the chemical and electronic structure of individual nanoparticles [147]. Therefore, TEM offers better resolution and presents better information about the sample [134].

6.8 AFM

Atomic force microscopy (AFM) is a powerful characterization technique used to analyze the morphology and topography of nanoparticles. AFM can provide valuable insights into the structural features and size distribution of these nanoparticles. AFM operates on the principle of scanning a sharp tip over the surface of a sample. The tip interacts with the surface and generates a three-dimensional topographical image [148]. The resolution of AFM can be in the range of sub-nanometers to tens of nanometers, making it a highly precise technique. The size of silver nanoparticles can be determined from the height and diameter measurements obtained from the AFM images. The size distribution of the nanoparticles can also be analyzed using statistical methods. The shape of the nanoparticles can be characterized using the AFM images, which can provide information on whether the nanoparticles are spherical, cubic, or other shapes [149]. AFM can also be used to study the interaction between nanoparticles and other materials, such as biological samples. This technique can provide insights into the surface properties of the nanoparticles and how they interact with the surrounding environment [150]. AFM can be a valuable tool in the field of nanotechnology, providing crucial information on the properties of these unique materials.

7 Potential Applications of the Silver Nanoparticles

Nanoparticles are easily applied to many surfaces because they self-assemble quickly under appropriate conditions without promoting bacterial growth or damaging substrates during application. Additionally, synthetic nanoparticles have a high potential to replace toxic chemicals in daily products since they do not emit harmful compounds when applied to various materials**.** Metal nanoparticles have boundless applications in multiple disciplines (Fig. 4). The novel properties (like-size and shape which depends upon the optical properties, magnetic properties, and electrical properties) shown by the nanoparticles allowed them to be the potential candidate for multiple fields like textile, biomedical, environment, catalysis, health care, and much more. A variety of applications have been developed with AgNPs, including utensils, food storage, biomedical devices, and the health care industry. So many book chapters and reviews have been written concerning the use of AgNPs in various fields. Metallic nanoparticles are renowned for their antibacterial properties, lending them to antimicrobial drug development. Furthermore, silver nanoparticles have demonstrated immense opportunities for use as catheter coatings, orthopedics, dental implants, and wound dressings. Cancerous cells can also be targeted using nanoparticles for drug delivery, and angiogenesis pathways can be inhibited to suppress tumor growth [151]. Aside from being effective in drug delivery, AgNP-based nanosystems and nanomaterials may also be used for wound dressings, tissue scaffolding, and protective coatings. Our research focused on using Ag nanoparticles to treat biological and biomedical conditions such as infectious diseases, antifungals, antivirals, inflammation, and cancer. We specifically address highly influential papers that have previously been published and provide a brief update on current revelations throughout this text.



Fig. 4 Applications of metal nanoparticles in different fields. Metal nanoparticles have diverse applications across various fields, including medicine, electronics, energy, environment, and catalysis. Their use ranges from drug delivery and imaging in medicine to sensing and pollution control in the environment. The versatility of metal nanoparticles demonstrates their potential impact and significance in various domains

7.1 Medical Application

(a) Catheters—catheters are being used for urinary complications, for people who cannot empty their bladder naturally. Catheters are more prone to bacterial or microbial contamination which can further aggravate the situation of the patient. Hence, the biofilm of AgNP can be used as a coat on a catheter which can prevent microbial contamination. The coating of the silver nanoparticle, for example, is a gradual reversible process. The silver nanoparticles were released from the coated surface for approximately 10 days. Therefore, the gradual release of nanoparticles would provide long-term protection from microbial contamination. The coating at the luminal and external sides would provide double protection from microbial contamination [152]. In a test using central venous catheters coated with AgNPs, both Gram-positive and Gram-negative bacteria developed biofilms in a markedly inhibited manner. It is the most common complication associated with urinary catheterization that causes catheter-associated urinary tract infection (CAUTI) [153]. Using AgNPs as the surface of a polymer matrix, it has been shown that bacterial biofilms were prevented from forming as well as proteins and electrolytes were deposited, which prevented microorganisms from adhering to the surface and incruding [154].

(b) Orthopedic implants—even though osseous-tissue replacement strategies are becoming increasingly aware, severe morbidity and mortality can occur via opportunistic contamination of orthopedic implants. Regenerative and restorative processes take place in the bone due to its intrinsic and complex mechanisms. Due to some orthopedic complications, implants are used to ease the life of the patients. But in orthopedic surgeries, bacterial contamination worsens the cases [155]. Whenever bacterial activity is present in bone defects, self-repairing capabilities can be limited. The antibacterial properties of AgNPs are broader than those found in normal antibiotics. Hence, the coating of silver nanoparticles can be used to prevent such contaminations [156]. Comparatively, to other nanoparticles, AgNPs have been found to naturally enhance the delineation of MC3T3-1 pre-osteoblast cells and the resulting mineralization of bone-like tissue [157]. Previous studies have shown that titanium implants implanted with AgNPs exhibit enhanced antibacterial properties as well as excellent osteoblast compatibility because of the micro-galvanic effects [154].

(c) Wound dressing—because hydrogels have a high-water content and can absorb wound exudates better, they are used to promote wound healing. When the hydrogel is coated with silver nanoparticles (AgNP), it enhances the antibacterial activity and prevents further aggravation of the wound. Both gram-negative and gram-positive bacteria will be susceptible to it. Therefore, nanoparticles have an important application in wound dressing [158].

7.2 Consumer Goods and Personal Care Products

The use of silver nanoparticles in deodorants, soaps, hand washing, shampoo, room spray, and many more, is very frequent nowadays. The silver nanoparticles are known to reduce the dye and also remove it. Additionally, metal nanoparticles can be applied as a nano fertilizer, nano pesticide, nano herbicide, and other important drugs for plants [156].

7.3 Optical Application

The metal nanoparticles have an optical property by which the interaction of antigen and antibody can be measured on a real-time basis. Surface plasmon resonance effects of the silver nanoparticles enable real-time measurement with greater sensitivity. The local surface plasmon resonance (LSPR) property can be used for in-vivo testing [159]. With better optical properties than gold nanoparticles (AuNPs), AgNPs can assist in biosensing and bioimaging, as they have higher plasmon excitation efficiency.

7.4 Anticancer Properties of AgNPs

The side effects of many chemotherapeutic agents are enormous, and administering them intravenously is a tedious process due to their many side effects. To avoid systemic side effects, it is therefore imperative to develop technologies. Inhibitors of poly (ADP-ribose) polymerase (PARP) have recently gained approval for clinical use in cancer patients with mutated BRCA genes [160]. Nanomaterials are currently being investigated as a potential tool for developing formulations that can target tumor cells more effectively than current techniques [161]. As a result of studying the molecular mechanism of AgNPs, Gopinath, and colleagues noted that the degree of programmed cell death depended on the concentration of AgNPs [162]. AgNPs alter cell morphology, viability, and metabolic activity by damaging mitochondria and producing reactive oxygen species (ROS) [11, 163]. Biologically synthesized AgNPs may significantly induce cell death in cancer cells, based on morphology analysis. Several human cancerous cell lines have been examined closely concerning AgNPs' anticancer effects, including endothelial cells, lung fibroblasts, glioblastoma cells, and breast cancer cells, such as MDA-MB-231 and MR-90 [164]. Silver nanoparticles can be delivered directly to cancer cells using chitosan as a carrier molecule [165]. They then used a battery of biochemical assays to determine cytotoxic efficiency. They discovered an increase in intracellular ROS in HT 29 cells [166]. Several studies have found that different AgNP shapes, sizes, doses, and concentrations have different anticancer activities in cancer cells. The pH of tumors, the uv treatment, the primary cells, and the extracellular matrix of tumors also greatly affect AgNP's antitumor activity. A study found that the cytotoxicity and genotoxicity of AgNPs vary with their size, owing to differences in the reaction mechanism of absorption, intracellular acquisition, and excretion. It is generally assumed that smaller AgNPs will produce greater cytotoxicity than larger AgNPs, due to their higher endocytosis and exocytosis efficiency [167]. An effective therapeutic effect for humans or animals depends on how pharmaceutical compounds are administered. A hybrid molecular unit composed of AgNPs was successfully chosen to target inflammation, infectious diseases, and malignancies by modulating their performance with thermal, optical, or pH modulation. The hybrid molecular units are exceptionally biocompatible and viable for nanoscale-derived therapeutic settings, making them particularly attractive to clinical trials.

7.5 AgNPs in Gene Therapy and Diagnosis

As a novel nanostructured platform, AgNPs could be successfully utilized for the diagnosis and treatment of different types of cancer. As a result of their broad-spectrum bioactivity, AgNPs can be applied to the fight against infections, as well as to the fight against cancer and multidrug resistance [168]. The specific and selective delivery of therapeutic agents has become a major focus of current human healthcare practice, and nanoparticles have been given much attention in the design of novel and enhanced drug-delivery systems. AgNPs could enhance the biomedical efficacy of cancer therapies and wound healing by delivering known therapeutic genes as well as their biomedical properties. The benefits of AgNPs coupled with their capacity to deliver genes could be leveraged synergistically with a strategy such as this to provide better therapies.

In addition to detecting blood sugar levels, enzyme levels, malignant cell marker levels, pathogens, and other parameters, nanoparticles containing AgNPs can be utilized as biosensors. Also, in combination with drug candidates, metallic nanoparticles (MNPs) can provide a targeted approach to prevent undesirable side effects associated with traditional anticancer agents [169]

7.6 Antimicrobial Mechanism of Metallic Nanoparticles

The metallic nanoparticles are known to have antimicrobial properties. They act against fungi, bacteria, and viruses. The pathway of the killing of a microbe by a nanoparticle is ambiguous. There has still been a suggestion that nanoparticles become associated with bacterial cell walls, which in turn causes nanoparticles to penetrate into the cytoplasm [111]. By contacting the nanoparticles with the cell wall, the nanoparticle destroys the cell wall, releasing the cellular material outside the cell and ultimately causing the cell's death.

Silver nanoparticles can penetrate the microbial cell wall and gain access to its interior. Nanoparticles are categorized by their size according to their toxic properties. The smaller the nanoparticle, the high will be the toxicity. Most of the studies of nanoparticles suggested the formation of free radicals, which can be detected by electron spin resonance (ESR) at their peak. In the living system, these nanoparticles attack the membrane lipids, which damages and dissociates the cell and prevents the growth of the cell, hence ultimately killing the cell. The study conducted on E. coli demonstrated that Ag + ions can penetrate the cell wall, leading to severe damage at the point of entry, ultimately resulting in cell death. This damage is caused by the permeation of Ag + ions through the cell wall, which disrupts the integrity of the wall and leads to its degradation [170]. A negatively charged membrane of a microbial cell interacts with positively charged silver ions, leading to inhibition of the growth of the cell. Due to this interaction, there is the development of a trench in the microbial cell membrane which permeates to the main components of the cell and thus forms reactive oxygen species, as a result causing the death of the bacterial cell [26]. It was also suggested that the positively charged silver ions show great affinity towards the electron donation groups like sulfhydryl, amino, imidazole, and phosphate which are present on the cellular membrane or protein [171]. The thiol group of protein is negatively charged which can bind strongly with the silver ions. This alters the protein structure and blocks the binding sites of the proteins. Moreover, the silver ions can block the potassium ion channel which can block the ATP formations and thus lead to the death of microbial cells [172]. A phosphate atom in DNA makes it negatively charged, thus attracting the silver ions, which upon binding with silver ions, impairs the DNA replication and growth of cells. The reactive oxygen species produced by the silver ions include hydrogen peroxide, hydroxyl radical, superoxide anions, singlet oxygen, etc. [173]. They are the by-product of aerobic respiration, but they are eliminated and held at on very low level due to the functions of scavengers. The free radicals directly damage the mitochondrial membrane and damage the DNA strand, and affect the microbial cell negatively (Fig. 5) [174].

Furthermore, nanoparticles that are smaller than 10 nm are considered to be the most lethal because they are capable of piercing the cell membrane and interacting with biomolecules like proteins, lipids, DNA, and other cellular components, producing reactive oxygen species(ROS) [170] such as hydroxyl, superoxide, and hydrogen peroxide, which can damage the cellular components by oxidative stress. The metallic nanoparticles (silver nanoparticles) when interacting with microbial cells disturb the normal functions of the cells such as respiration and protein synthesis. Therefore, it causes the cell to get deprived of normal functions and the cell dies (Fig. 5) [171].

In addition to their green and cost-effective nature, the ROS and RSN mechanisms in the green synthesis of AgNPs using plant extracts also have advantages over other synthetic methods. For example, the ROS mechanism can lead to the formation of highly uniform and monodisperse AgNPs, while the RSN mechanism can facilitate the use of a wide range of plant extracts for AgNP synthesis. AgNPs have emerged as potential candidates for the treatment of various diseases due to their remarkable antimicrobial, anticancer, antidiabetic, and anti-neurodegenerative properties.

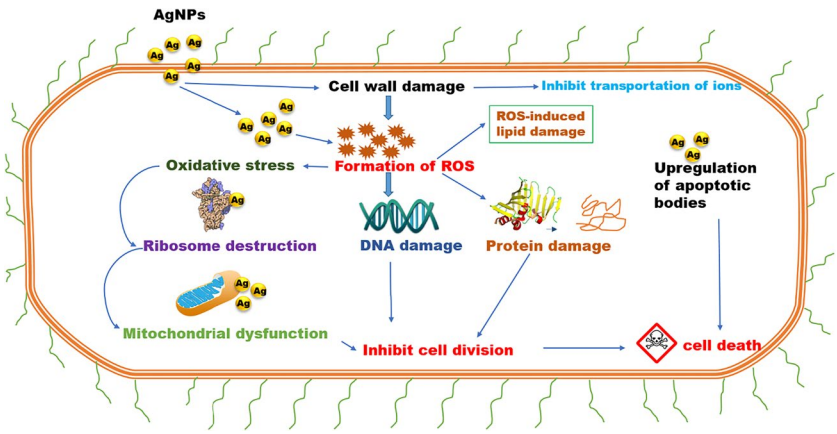


Fig. 5 Mechanisms of cell death induced by ROS and RSS generation by silver nanoparticles. Silver nanoparticles can generate ROS, through electron transfer and catalytic reactions, leading to oxidative stress and cell death by apoptosis or necrosis. These mechanisms illustrate the potential toxicity of silver nanoparticles and the importance of understanding their underlying mechanisms to ensure their safe use [18]

The underlying mechanisms of these effects involve the modulation of reactive oxygen species (ROS) and reactive nitrogen species (RNS) in cells [172]. AgNPs can modulate ROS and RNS levels in cells through several mechanisms, including the generation of ROS/RNS, scavenging of ROS/RNS, and inhibition of ROS/RNS-generating enzymes [173]. AgNPs have been reported to induce ROS generation in bacteria, fungi, and cancer cells, leading to cell death. Moreover, AgNPs can scavenge ROS and RNS in diabetic models, reducing oxidative stress and improving glucose homeostasis [174]. AgNPs have also been found to inhibit ROS-generating enzymes such as NADPH oxidase, reducing the proliferation and invasion of cancer cells. In the case of anti-neurodegenerative effects, AgNPs have been shown to protect neurons from oxidative stress and inflammation, which are common features of neurodegenerative diseases such as Alzheimer's and Parkinson's disease [175]. AgNPs can scavenge ROS/RNS in neuronal cells, reducing inflammation and protecting against oxidative stress-induced damage.

8 Future Prospective of AgNPs in Cancer Therapeutics

Because of the frequently occurring side effects of radiation and chemotherapy therapy, academic and industrial researchers are exploring AgNPs as anticancer therapeutics of the future. A novel approach to cancer treatment and other angiogenesis-related diseases could be achieved by using AgNPs according to the development of these molecules as anti-angiogenic molecules. An entirely new field of chemotherapeutics called cancer nanomedicine has emerged as a result of nanoparticles' unique physical and chemical properties. Such molecules can overcome issues related to drug resistance as well as poor delivery. While using AgNPs in biomedical studies, several factors must be considered, including raw material source, production process, consistency, targeted delivery, controlled drug release, acquisition, cell-specific targeting, and eventually toxicological concerns. It remains unclear whether AgNPs and antibiotics have synergistic effects on antibacterial activity/tumor reduction, despite various methods available. To understand the synergistic effect at a single time point of the two different cytotoxic agents, further studies are required.

9 Conclusions

Nanoparticles have numerous applications, and there is a growing demand for an efficient and environmentally friendly method of their synthesis. The conventional chemical method is hazardous to both human health and the environment, while the physical method requires large amounts of energy and is not cost-effective. Therefore, a green synthesis method that utilizes plant extracts is gaining popularity. This method involves using the various phytochemicals and phytocomponents in plant extracts, such as terpenoids, alkaloids, and carbohydrates, to neutralize metal ions and transform them into metal nanoparticles. As a result, there is no need for external stabilizing agents as required in the chemical method, and the green method is more cost-effective. Silver nanoparticles (AgNPs) have attracted significant attention due to their attractive physicochemical properties, low cytotoxicity, and strong antibacterial performance. The green method is used for the production, characterization, and bioapplication of AgNPs. The green synthesis of AgNPs has several advantages over other methods, such as cost-effectiveness, reduced toxicity, and environmental friendliness. The phytochemicals and phytocomponents present in plant extracts play a crucial role in stabilizing the AgNPs, ensuring their biocompatibility and bioactivity. The green method involves simple steps and can be easily scaled up for large-scale synthesis, making it an attractive alternative to conventional chemical and physical methods. AgNPs have shown promise as potential chemotherapeutic agents due to their ability to induce cell death in cancer cells while sparing healthy cells. They can also enhance the efficacy of traditional chemotherapy drugs by improving drug delivery and reducing drug resistance. AgNPs have been shown to target various signaling pathways involved in cancer development and progression, making them a promising candidate for cancer therapy. The modulation of ROS and RNS mechanisms by AgNPs during their green synthesis using plant extracts offers several advantages including controlled nanoparticle size and shape, enhanced physical, chemical, and biological properties, biocompatibility, sustainability, and enhanced antimicrobial properties. This makes them suitable for use in a variety of applications, such as wound healing, disinfectants, and food packaging and presents a promising approach for various biomedical and industrial applications. In conclusion, the green synthesis of AgNPs using plant extracts is an efficient and environmentally friendly method for the production, characterization, and bioapplication of AgNPs. AgNPs have promising potential for non-conventional biological applications, specifically in cancer therapy. Further research is needed to explore their safety and efficacy in vivo, but the green synthesis method offers a promising approach for the large-scale production of AgNPs for future biomedical applications.

Acknowledgements The authors would like to acknowledge the Department of Biotechnology at Delhi Technological University in India for their ongoing assistance. A special thank you is extended to the University Grants Commission, India for funding the research of Ms. Ritu.

Author Contribution All authors have reviewed and approved this manuscript.

Funding The University Grants Commission provided Ms. Ritu with financial support for this research.

Data Availability Not applicable.

Declarations

Competing interests The authors declare no competing interests.

Ethical Approval Based on the ethical guidelines of Delhi Technological University, this study does not require ethical approval because neither humans nor animals are involved.

Informed Consent A written informed consent statement is not required as it was an observation study.

Conflict of Interest The authors declare no competinginterests.

References

1. Beg, M., et al. (2017). Green synthesis of silver nanoparticles using Pongamia pinnata seed: Characterization, antibacterial property, and spectroscopic investigation of interaction with human serum albumin. *Journal of Molecular Recognition, 30*(1), 1–8. https://doi.org/10.1002/jmr.2565
2. Zhang, X. F., Liu, Z. G., Shen, W., & Gurunathan, S. (2016). Silver nanoparticles: Synthesis, characterization, properties, applications, and therapeutic approaches. *Int J Mol Sci, 17*, 9. https://doi.org/10.3390/ijms17091534
3. Salem, S. S., & Fouda, A. (2021). Green synthesis of metallic nanoparticles and their prospective biotechnological applications: An overview. *Biological Trace Element Research, 199*(1), 344–370. https://doi.org/10.1007/s12011-020-02138-3
4. Singh, J., Dutta, T., Kim, K. H., Rawat, M., Samddar, P., & Kumar, P. (2018). 'Green' synthesis of metals and their oxide nanoparticles: Applications for environmental remediation. *Journal of Nanobiotechnology, 16*(1), 1–24. https://doi.org/10.1186/S12951-018-0408-4
5. Ghotekar, S., Pagar, T., Pansambal, S., & Oza, R. (2020). A review on green synthesis of sulfur nanoparticles via plant extract, characterization and its applications. *Advanced Journal of Chemistry-Section B: Natural Products and Medical Chemistry, 2*(3), 128–143. https://doi.org/10.22034/AJCB.2020.109501
6. Biswal, A. K., & Misra, P. K. (2020). Biosynthesis and characterization of silver nanoparticles for prospective application in food packaging and biomedical fields. *Mater Chem Phys, 250*, 123014. https://doi.org/10.1016/j.matchemphys.2020.123014
7. Albanese, A., Tang, P. S., & Chan, W. C. W. (2012). The effect of nanoparticle size, shape, and surface chemistry on biological systems. *Annual Review of Biomedical Engineering, 14*(1), 1–16. https://doi.org/10.1146/annurev-bioeng-071811-150124
8. Nayak, S., Shet, V. B., Rao, C. V., & Joshi, K. (2018). Performance evaluation and emission characteristics of a 4 stroke diesel engine using green synthesized silver nanoparticles blended biodiesel. *Mater Today Proc, 5*(2), 7889–7897. https://doi.org/10.1016/J.MATPR.2017.11.470
9. Yusof, S. N. A., Sidik, N. A. C., Asako, Y., Japar, W. M. A. A., Mohamed, S. B., & Muhammad, N. M. A. (2021). A comprehensive review of the influences of nanoparticles as a fuel additive in an internal combustion engine (ICE). *Nanotechnol Rev, 9*(1), 1326–1349. https://doi.org/10.1515/NTREV-2020-0104/ASSET/GRAPHIC/J_NTREV-2020-0104_FIG_003.JPG
10. Carlson, C., et al. (2008). Unique cellular interaction of silver nanoparticles: Size-dependent generation of reactive oxygen species. *Journal of Physical Chemistry B, 112*(43), 13608–13619. https://doi.org/10.1021/jp712087m
11. Zhang, X. F., Liu, Z. G., Shen, W., & Gurunathan, S. (2016). Silver nanoparticles: Synthesis, characterization, properties, applications, and therapeutic approaches. *Int J Mol Sci, 17*, 9. https://doi.org/10.3390/IJMS17091534
12. Nayak, S., Goveas, L. C., & Vaman Rao, C. (2017). Biosynthesis of silver nanoparticles using turmeric extract and evaluation of its anti-bacterial activity and catalytic reduction of methylene blue. *Materials, Energy and Environment Engineering*, 257–265. https://doi.org/10.1007/978-981-10-2675-1_31
13. Nayak, S., Goveas, L. C., Kumar, P. S., Selvaraj, R., & Vinayagam, R. (2022). Plant-mediated gold and silver nanoparticles as detectors of heavy metal contamination. *Food and Chemical Toxicology: An International Journal Published for the British Industrial Biological Research Association*, 167. https://doi.org/10.1016/J.FCT.2022.113271
14. Nayak, S., Sajankila, S. P., Rao, C. V., Hegde, A. R., & Mutalik, S. (2019). Biogenic synthesis of silver nanoparticles using Jatropha curcas seed cake extract and characterization: evaluation of its antibacterial activity. *Energy Sources, Part A: Recovery, Utilization, and Environmental Effects, 43*(24), 3415–3423. https://doi.org/10.1080/15567036.2019.1632394
15. Pradeep, B., Hemba, P., Kunnathuli Jagadeesh, A., Ganappa Ramakkanavar, C., Nayak, S., & Vaman Rao, C. (2021). Anticandidal and antioxidant activity of silver and gold nanoparticles biosynthesised using matured areca nut husk extract. *International Journal Nanoparticles, 13*(1), 21–32.
16. Qi, Y., et al. (2020). In-situ synthesis of metal nanoparticles@metal−organic frameworks: Highly effective catalytic performance and synergistic antimicrobial activity. *Journal Hazardous Materials, 387*, 121687. https://doi.org/10.1016/j.jhazmat.2019.121687
17. Ahmadi Tehrani, A., Omranpoor, M. M., Vatanara, A., Seyedabadi, M., & Ramezani, V. (2019). Formation of nanosuspensions in bottom-up approach: Theories and optimization. *DARU, Journal of Pharmaceutical Sciences, 27*(1), 451–473. https://doi.org/10.1007/s40199-018-00235-2
18. Hembram, K. C., Kumar, R., Kandha, L., Parhi, P. K., Kundu, C. N., & Bindhani, B. K. (2018). Therapeutic prospective of plant-induced silver nanoparticles: Application as antimicrobial and anticancer agent. *Artif Cells Nanomed Biotechnol, 46*(sup3), S38–S51. https://doi.org/10.1080/21691401.2018.1489262
19. Yadi, M., et al. (2018). Current developments in green synthesis of metallic nanoparticles using plant extracts: A review. *Artif Cells Nanomed Biotechnol, 46*(sup3), S336–S343. https://doi.org/10.1080/21691401.2018.1492931
20. Ahmed, S., Ahmad, M., Swami, B. L., & Ikram, S. (2016). A review on plants extract mediated synthesis of silver nanoparticles for antimicrobial applications: A green expertise. *Journal of Advanced Research, 7*(1), 17–28. https://doi.org/10.1016/j.jare.2015.02.007
21. Singh, R., Sahu, S. K., & Thangaraj, M. (2014). Biosynthesis of silver nanoparticles by marine invertebrate (polychaete) and assessment of its efficacy against human pathogens. *Journal of Nanoparticles, 2014*, 1–7. https://doi.org/10.1155/2014/718240
22. Mittal, A. K., Chisti, Y., & Banerjee, U. C. (2013). Synthesis of metallic nanoparticles using plant extracts. *Biotechnology Advances, 31*(2), 346–356. https://doi.org/10.1016/j.biotechadv.2013.01.003

23. Bawazeer, S., et al. (2021). Green synthesis of silver nanoparticles using Tropaeolum majus: Phytochemical screening and antibacterial studies. *Green Processing and Synthesis, 10*(1), 85–94. https://doi.org/10.1515/gps-2021-0003
24. Patil, M. P., & Do Kim, G. (2017). Eco-friendly approach for nanoparticles synthesis and mechanism behind antibacterial activity of silver and anticancer activity of gold nanoparticles. *Applied Microbiology Biotechnology, 101*(1), 79–92. https://doi.org/10.1007/s00253-016-8012-8
25. Borase, H. P., et al. (2014). Plant extract: A promising biomatrix for ecofriendly, controlled synthesis of silver nanoparticles. *Applied Biochemistry and Biotechnology, 173*(1), 1–29. https://doi.org/10.1007/s12010-014-0831-4
26. Siddiqi, K. S., Husen, A., & Rao, R. A. K. (2018). A review on biosynthesis of silver nanoparticles and their biocidal properties. *Journal of Nanobiotechnology, 16*(1), 1–28. https://doi.org/10.1186/S12951-018-0334-5
27. Hasnain, M. S., et al. (2019). Purple heart plant leaves extract-mediated silver nanoparticle synthesis: Optimization by Box-Behnken design. *Materials Science and Engineering C, 99*(January), 1105–1114. https://doi.org/10.1016/j.msec.2019.02.061
28. Okaiyeto, K., Hoppe, H., & Okoh, A. I. (2021). Plant-based synthesis of silver nanoparticles using aqueous leaf extract of salvia officinalis: Characterization and its antiplasmodial activity. *Journal of Cluster Science, 32*(1), 101–109. https://doi.org/10.1007/s10876-020-01766-y
29. Fahmy, T. Y. A., & Mobarak, F. (2011). Green nanotechnology: A short cut to beneficiation of natural fibers. *International Journal of Biological Macromolecules, 48*(1), 134–136. https://doi.org/10.1016/j.ijbiomac.2010.10.010
30. "(PDF) Green synthesis of silver nanoparticles by using plant extract and its antibacterial activity." https://www.researchgate.net/publication/307990615_Green_Synthesis_of_Silver_Nanoparticles_by_using_Plant_Extract_and_its_Antibacterial_Activity (accessed Jun. 22, 2021).
31. Jayaram, U. C., & Gurusamy, A. (2018). Biosynthesis and Characterization of Silver Nanoparticles Using Leaf Extract Abutilon indicum Active lithiatic compound encapsulation potential of natural polymeric nanoparticles in medicinal plant View project "Characterization and toxicology evaluation of various nanoparticles on embryonic and neural development of zebrafish" View project.
32. Roy, P., Das, B., Mohanty, A., & Mohapatra, S. (2017). Green synthesis of silver nanoparticles using azadirachta indica leaf extract and its antimicrobial study. *Applied Nanoscience (Switzerland), 7*(8), 843–850. https://doi.org/10.1007/s13204-017-0621-8
33. Rastogi, L., & Arunachalam, J. (2011). Sunlight based irradiation strategy for rapid green synthesis of highly stable silver nanoparticles using aqueous garlic (Allium sativum) extract and their antibacterial potential. *Materials Chemistry and Physics, 129*(1–2), 558–563. https://doi.org/10.1016/j.matchemphys.2011.04.068
34. Mohammed, A. E. (2015). Green synthesis, antimicrobial and cytotoxic effects of silver nanoparticles mediated by Eucalyptus camaldulensis leaf extract. *Asian Pacific Journal of Tropical Biomedicine, 5*(5), 382–386. https://doi.org/10.1016/S2221-1691(15)30373-7
35. Ahmed, R. H., & Mustafa, D. E. (2019). Green synthesis of silver nanoparticles mediated by traditionally used medicinal plants in Sudan. *International Nano Letters, 10*(1), 1–14. https://doi.org/10.1007/S40089-019-00291-9
36. Sithara, R., Selvakumar, P., Arun, C., Anandan, S., & Sivashanmugam, P. (2017). Economical synthesis of silver nanoparticles using leaf extract of Acalypha hispida and its application in the detection of Mn(II) ions. *Journal of Advanced Research, 8*(6), 561–568. https://doi.org/10.1016/j.jare.2017.07.001
37. Tippayawat, P., Phromviyo, N., Boueroy, P., & Chompoosor, A. (2016). Green synthesis of silver nanoparticles in aloe vera plant extract prepared by a hydrothermal method and their synergistic antibacterial activity. *Peer J, 2016*(10). https://doi.org/10.7717/PEERJ.2589/SUPP-2
38. Kudle, K., Kudle, M., … Y. P.-I. J., & 2014, undefined. (n.d.). Silver nanoparticles synthesis, stabilization and characterization by different concentrations of Acacia senegal (l.) Willd. Extract and evaluation of their. Impactfactor.Org. Retrieved May 16, 2023, from http://impactfactor.org/PDF/IJPPR/6/IJPPR,Vol6,Issue2,Article12.pdf
39. Sharma, P., Pant, S., Rai, S., Yadav, R. B., & Dave, V. (2018). Green synthesis of silver nanoparticle capped with allium cepa and their catalytic reduction of textile dyes: An ecofriendly approach. *Journal of Polymers and the Environment, 26*(5), 1795–1803. https://doi.org/10.1007/s10924-017-1081-7
40. Rao, T. N., Riyazuddin, Babji, P., Ahmad, N., Khan, R. A., Hassan, I., Shahzad, S. A., & Husain, F. M. (2019). Green synthesis and structural classification of Acacia nilotica mediated-silver doped titanium oxide (Ag/TiO2) spherical nanoparticles: Assessment of its antimicrobial and anticancer activity. *Saudi Journal of Biological Sciences, 26*(7), 1385. https://doi.org/10.1016/J.SJBS.2019.09.005
41. Kumar, C. M. K., Yugandhar, P., & Savithramma, N. (2016). Biological synthesis of silver nanoparticles from Adansonia digitata L. fruit pulp extract, characterization, and its antimicrobial properties. *Journal of Intercultural Ethnopharmacology, 5*(1), 79. https://doi.org/10.5455/JICE.20160124113632
42. Gomathi, M., Rajkumar, P. V., Prakasam, A., & Ravichandran, K. (2017). Green synthesis of silver nanoparticles using Datura stramonium leaf extract and assessment of their antibacterial activity. *Resource-Efficient Technologies, 3*(3), 280–284. https://doi.org/10.1016/j.reffit.2016.12.005
43. Ramanathan, S., Gopinath, S. C. B., Anbu, P., Lakshmipriya, T., Kasim, F. H., & Lee, C. G. (2018). Eco-friendly synthesis of Solanum trilobatum extract-capped silver nanoparticles is compatible with good antimicrobial activities. *Journal of Molecular Structure, 1160*, 80–91. https://doi.org/10.1016/J.MOLSTRUC.2018.01.056
44. Nazeruddin, G. M., Prasad, N. R., Prasad, S. R., Shaikh, Y. I., Waghmare, S. R., & Adhyapak, P. (2014). Coriandrum sativum seed extract assisted in situ green synthesis of silver nanoparticle and its anti-microbial activity. *Industrial Crops and Products, 60*, 212–216. https://doi.org/10.1016/j.indcrop.2014.05.040
45. Bar, H., Bhui, D. K., Sahoo, G. P., Sarkar, P., Pyne, S., & Misra, A. (2009). Green synthesis of silver nanoparticles using seed extract of Jatropha curcas. *Colloids and Surfaces A: Physicochemical and Engineering Aspects, 348*(1–3), 212–216. https://doi.org/10.1016/j.colsurfa.2009.07.021
46. Nichita, C., Mikhailef, A.-B. F., Vasile, E., & Stamatin, I. (n.d.). Silver nanoparticles synthesis. bioreduction with gallic acid and extracts from cyperus rotundus L. *Digest Journal of Nanomaterials and Biostructures, 15*(2), 419–433.
47. GnanaJobitha, G., Annadurai, G., & Kannan, C. (2012). Green synthesis of silver nanoparticle using Elettaria cardamomom and assesment of its antimicrobial activity. *International Journal of Pharmaceutical Sciences and Research, 3*(3), 323–330.
48. Saravanakumar, A., Ganesh, M., Jayaprakash, J., & Jang, H. T. (2015). Biosynthesis of silver nanoparticles using Cassia tora leaf extract and its antioxidant and antibacterial activities. *Journal of Industrial and Engineering Chemistry, 28*, 277–281. https://doi.org/10.1016/J.JIEC.2015.03.003
49. Bibi, N., Ali, Q., Tanveer, Z. I., Rahman, H., & Anees, M. (2019). Antibacterial efficacy of silver nanoparticles prepared using Fagonia cretica L. leaf extract. *Inorganic and Nano-Metal Chemistry, 49*(8), 260–266. https://doi.org/10.1080/24701556.2019.1661440

50. Dhand, V., Soumya, L., Bharadwaj, S., Chakra, S., Bhatt, D., & Sreedhar, B. (2016). Green synthesis of silver nanoparticles using Coffea arabica seed extract and its antibacterial activity. *Materials Science and Engineering C, 58*, 36–43. https://doi.org/10.1016/j.msec.2015.08.018
51. Nayak, D., Pradhan, S., Ashe, S., Rauta, P. R., & Nayak, B. (2015). Biologically synthesised silver nanoparticles from three diverse family of plant extracts and their anticancer activity against epidermoid A431 carcinoma. *Journal of Colloid and Interface Science, 457*, 329–338. https://doi.org/10.1016/j.jcis.2015.07.012
52. Anwar, A., et al. (2019). Antimicrobial activities of green synthesized gums-stabilized nanoparticles loaded with flavonoids. *Science and Reports, 9*(1), 1–12. https://doi.org/10.1038/s41598-019-39528-0
53. Nasiri, S., & Nasiri, S. (2016). Biosynthesis of silver nanoparticles using carum carvi extract and its inhibitory effect on growth of candida albicans. *Avicenna Journal of Medical Biochemistry, 4*(2), 37504. https://doi.org/10.17795/ajmb-37504
54. Mukunthan, K. S., Elumalai, E. K., Patel, T. N., & Murty, V. R. (2011). Catharanthus roseus: A natural source for the synthesis of silver nanoparticles. *Asian Pacific Journal of Tropical Biomedicine, 1*(4), 270–274. https://doi.org/10.1016/S2221-1691(11)60041-5
55. Du, J., Singh, H., & Yi, T. H. (2016). Antibacterial, anti-biofilm and anticancer potentials of green synthesized silver nanoparticles using benzoin gum (Styrax benzoin) extract. *Bioprocess and Biosystems Engineering, 39*(12), 1923–1931. https://doi.org/10.1007/s00449-016-1666-x
56. Sundeep, D., Vijaya Kumar, T., Rao, P. S. S., Ravikumar, R. V. S. S. N., & Gopala Krishna, A. (2017). Green synthesis and characterization of Ag nanoparticles from Mangifera indica leaves for dental restoration and antibacterial applications. *Prog Biomater, 6*(1–2), 57–66. https://doi.org/10.1007/s40204-017-0067-9
57. Sadeghi, B. (2014). Green synthesis of silver nanoparticles using seed aqueous extract of Olea europaea. *International Journal of Nano Dimension, 5*(6), 575–581. https://doi.org/10.7508/IJND.2014.06.010
58. Sadeghi, B. (2014). Green synthesis of silver nanoparticles using seed aqueous extract of Olea europaea. *International Journal of Nano Dimension*, vol. 5, no. Issue 6, pp. 575–581, Accessed: Jul. 04, 2021.. Available: www.IJND.ir
59. Mehwish, H. M., et al. (2021). Green synthesis of a silver nanoparticle using Moringa oleifera seed and its applications for antimicrobial and sun-light mediated photocatalytic water detoxification. *J Environ Chem Eng, 9*(4), 105290. https://doi.org/10.1016/j.jece.2021.105290
60. Rashid, M. I., et al. (2016). One-step synthesis of silver nanoparticles using Phoenix dactylifera leaves extract and their enhanced bactericidal activity. *Journal of Molecular Liquids, 223*, 1114–1122. https://doi.org/10.1016/J.MOLLIQ.2016.09.030
61. Sathishkumar, P., et al. (2016). Anti-acne, anti-dandruff and anti-breast cancer efficacy of green synthesised silver nanoparticles using Coriandrum sativum leaf extract. *Journal of Photochemistry and Photobiology B: Biology, 163*, 69–76. https://doi.org/10.1016/j.jphotobiol.2016.08.005
62. Thiyagarajan, M. et al., (2014). Rapid green synthesis of silver nanoparticles using seed extract of foeniculum vulgare and screening of its antibacterial activity.
63. Ajitha, B., Ashok Kumar Reddy, Y., & Sreedhara Reddy, P. (2015). Green synthesis and characterization of silver nanoparticles using Lantana camara leaf extract. *Materials Science and Engineering: C, 49*, 373–381. https://doi.org/10.1016/J.MSEC.2015.01.035
64. Ranjan, P., et al. (2013). Green synthesis and characterization of silver nanoparticles from Nigella sativa and its application against UTI causing Bacteria. *Journal of Academia and Industrial Research, 2*(1), 45.
65. Ajitha, B., Reddy, Y. A. K., Jeon, H. J., & Ahn, C. W. (2018). Synthesis of silver nanoparticles in an eco-friendly way using Phyllanthus amarus leaf extract: Antimicrobial and catalytic activity. *Advanced Powder Technology, 29*(1), 86–93. https://doi.org/10.1016/j.apt.2017.10.015
66. Huo, Y., et al. (2018). Biological synthesis of gold and silver chloride nanoparticles by Glycyrrhiza uralensis and in vitro applications. *Artif Cells Nanomed Biotechnol, 46*(2), 303–312. https://doi.org/10.1080/21691401.2017.1307213
67. Khatoon, A., et al. (2018). Silver nanoparticles from leaf extract of Mentha piperita: Eco-friendly synthesis and effect on acetylcholinesterase activity. *Life Sciences, 209*, 430–434. https://doi.org/10.1016/j.lfs.2018.08.046
68. Kalainila, P., Ravindran, R., … R. R.-J. N., & 2015, undefined. (n.d.). Anti-bacterial effect of biosynthesized silver nanoparticles using Kigelia africana. Academia.Edu. Retrieved May 16, 2023, from https://www.academia.edu/download/53292614/Anti-Bacterial_Effect_of_Biosynthesized_Silver_Nanoparticles_Using_Kigelia_Africana.pdf
69. Kalita, N. K., & Ganguli, J. N. (2017). Hibiscus sabdariffa L. Leaf extract mediated green synthesis of silver nanoparticles and its use in catalytic reduction of 4-nitrophenol. *Inorganic and Nano-Metal Chemistry, 47*(5), 788–793. https://doi.org/10.1080/15533174.2016.1218506
70. Manikandan, R., et al. (2015). Biosynthesis of silver nanoparticles using ethanolic petals extract of Rosa indica and characterization of its antibacterial, anticancer and anti-inflammatory activities. *Spectrochim Acta A Mol Biomol Spectrosc, 138*, 120–129. https://doi.org/10.1016/J.SAA.2014.10.043
71. Arul, T. K. (2016). Green synthesis of silver nanoparticles using piper nigrum concoction and its anticancer activity against MCF-7 and Hep-2 cell lines. https://doi.org/10.4172/2472-1212.1000123
72. Alsalhi, M. S., et al. (2016). Green synthesis of silver nanoparticles using Pimpinella anisum seeds: Antimicrobial activity and cytotoxicity on human neonatal skin stromal cells and colon cancer cells. *International Journal of Nanomedicine, 11*, 4439–4449. https://doi.org/10.2147/IJN.S113193
73. Said, A., Abu-Elghait, M., Atta, H. M., & Salem, S. S. (2023). Antibacterial activity of green synthesized silver nanoparticles using lawsonia inermis against common pathogens from urinary tract infection. *Applied Biochemistry and Biotechnology*, 1–14. https://doi.org/10.1007/S12010-023-04482-1/TABLES/3
74. Dutta, P. P., et al. (2017). Antimalarial silver and gold nanoparticles: Green synthesis, characterization and in vitro study. *Biomedicine and Pharmacotherapy, 91*, 567–580. https://doi.org/10.1016/j.biopha.2017.04.032
75. Begum, J., Ramamurthy, V., & Senthil Kumar, S. (2019). Study of synthesis and characterization of silver nanoparticles from Tinospora cordifolia. *The Pharma Innovation Journal, 8*(1), 612–615.
76. Wang, Y., Chinnathambi, A., Nasif, O., & Alharbi, S. A. (2021). Green synthesis and chemical characterization of a novel anti-human pancreatic cancer supplement by silver nanoparticles containing Zingiber officinale leaf aqueous extract. *Arabian Journal of Chemistry, 14*(4), 103081. https://doi.org/10.1016/j.arabjc.2021.103081
77. Gopinath, V., MubarakAli, D., Priyadarshini, S., Priyadharsshini, N. M., Thajuddin, N., & Velusamy, P. (2012). Biosynthesis of silver nanoparticles from Tribulus terrestris and its antimicrobial activity: A novel biological approach. *Colloids and Surfaces. B, Biointerfaces, 96*, 69–74. https://doi.org/10.1016/j.colsurfb.2012.03.023

78. Salehi, S., et al. (2016). Phytosynthesis of silver nanoparticles using artemisia marschalliana sprengel aerial part extract and assessment of their antioxidant, anticancer, and antibacterial properties. *International Journal of Nanomedicine, 11*, 1835–1846. https://doi.org/10.2147/IJN.S99882
79. Marslin, G., Selvakesavan, R. K., Franklin, G., Sarmento, B., & Dias, A. C. (2015). Antimicrobial activity of cream incorporated with silver nanoparticles biosynthesized from Withania somnifera. *International Journal of Nanomedicine, 10*, 5955. https://doi.org/10.2147/IJN.S81271
80. Alagesan, V., & Venugopal, S. (2019). Green synthesis of selenium nanoparticle using leaves extract of withania somnifera and its biological applications and photocatalytic activities. *Bionanoscience, 9*(1), 105–116. https://doi.org/10.1007/s12668-018-0566-8
81. Gomathi, A. C., Xavier Rajarathinam, S. R., Mohammed Sadiq, A., & Rajeshkumar, S. (2020). Anticancer activity of silver nanoparticles synthesized using aqueous fruit shell extract of Tamarindus indica on MCF-7 human breast cancer cell line. *J Drug Deliv Sci Technol, 55*, 101376. https://doi.org/10.1016/j.jddst.2019.101376
82. Ojha, S., Sett, A., & Bora, U. (2017). Green synthesis of silver nanoparticles by Ricinus communis var. carmencita leaf extract and its antibacterial study. *Advances in Natural Sciences: Nanoscience and Nanotechnology, 8*(3), 35009. https://doi.org/10.1088/2043-6254/aa724b
83. Das, S., Das, J., Samadder, A., Bhattacharyya, S. S., Das, D., & Khuda-Bukhsh, A. R. (2013). Biosynthesized silver nanoparticles by ethanolic extracts of Phytolacca decandra, Gelsemium sempervirens, Hydrastis canadensis and Thuja occidentalis induce differential cytotoxicity through G2/M arrest in A375 cells. *Colloids and Surfaces. B, Biointerfaces, 101*, 325–336. https://doi.org/10.1016/j.colsurfb.2012.07.008
84. Biological evaluation and green synthesis of silver nanoparticles using aqueous extract of Calotropis procera. https://www.cabdirect.org/globalhealth/abstract/20143080352 (accessed Jul. 04, 2021).
85. Giridharan, T., Masi, C., Sindhu, S., & Arumugam, P. (2014). Studies on green synthesis, characterization and anti-proliferative potential of silver nano particle using dodonaea viscosa and Capparis decidua. *Biosciences, Biotechnology Research Asia, 11*(2), 665–673. https://doi.org/10.13005/bbra/1320
86. Li, S., et al. (2007). Green synthesis of silver nanoparticles using Capsicum annuum L. Extract. *Green Chemistry, 9*(8), 852–885. https://doi.org/10.1039/b615357g
87. Eaton, P., et al. (2017). A direct comparison of experimental methods to measure dimensions of synthetic nanoparticles. *Ultramicroscopy, 182*, 179–190. https://doi.org/10.1016/j.ultramic.2017.07.001
88. Rai, M., Kon, K., Ingle, A., Duran, N., Galdiero, S., & Galdiero, M. (2014). Broad-spectrum bioactivities of silver nanoparticles: The emerging trends and future prospects. *Applied Microbiology and Biotechnology, 98*(5), 1951–1961. https://doi.org/10.1007/s00253-013-5473-x
89. Jia, J. L., Xu, H. H., Li, D. Q., Ye, W. H., & Liu, W. J. (2015). Biosynthesis of silver and gold nanoparticles using Huangdan (Camellia sinensis) leaf extract. *Synthesis and Reactivity in Inorganic, Metal-Organic and Nano-Metal Chemistry, 45*(7), 941–946. https://doi.org/10.1080/15533174.2013.862817
90. Mohapatra, B., Kaintura, R., Singh, J., Kuriakose, S., & Mohapatra, S. (2015). Biosynthesis of high concentration, stable aqueous dispersions of silver nanoparticles using citrus limon extract. *Advanced Materials Letters, 6*(3), 228–234. https://doi.org/10.5185/AMLETT.2015.5731
91. Masooleh, A. K., Ahmadikhah, A., & Saidi, A. (2019). Green synthesis of stable silver nanoparticles by the main reduction component of green tea (Camellia sinensis L.). *IET Nanobiotechnology, 13*(2), 183–188. https://doi.org/10.1049/IET-NBT.2018.5141
92. Fatima, M., Zaidi, N. U. S. S., Amraiz, D., & Afzal, F. (2016). in vitro antiviral activity of cinnamomum cassia and its nanoparticles against H7N3 influenza A virus. *Journal Microbiology Biotechnology, 26*(1), 151–159. https://doi.org/10.4014/JMB.1508.08024
93. Alavi, M., Yarani, R., Sreedharan, M., & Thomas, S. (2023). Micro and nanoformulations of catechins for therapeutic applications: Recent advances and challenges. *Micro Nano Bio Aspects, 2*(1), 8–19. https://doi.org/10.22034/MNBA.2023.382922.1021
94. Echeverry-Chica, J., Naranjo-Díaz, A., & Araque-Marín, P. (2020). Silver nanoparticles functionalized in situ with D-Limonene: Effect on antibacterial activity. *Revista ION, 33*(1), 79–92. https://doi.org/10.18273/REVION.V33N1-2020008
95. MubarakAli, D., Thajuddin, N., Jeganathan, K., & Gunasekaran, M. (2011). Plant extract mediated synthesis of silver and gold nanoparticles and its antibacterial activity against clinically isolated pathogens. *Colloids and Surfaces. B, Biointerfaces, 85*(2), 360–365. https://doi.org/10.1016/J.COLSURFB.2011.03.009
96. Bhushan, S., Sharma, D., Rakshant, Kaul, S., Dhar, M. K., & Sharma, M. (2023). Recent strategies to engineer alkaloid biosynthesis in medicinal plants. *Medicinal Plants*, 391–416. https://doi.org/10.1007/978-981-19-5611-9_15
97. Deshmukh, A. R., Dikshit, P. K., & Kim, B. S. (2022). Green in situ immobilization of gold and silver nanoparticles on bacterial nanocellulose film using Punica granatum peels extract and their application as reusable catalysts. *International Journal of Biological Macromolecules, 205*, 169–177. https://doi.org/10.1016/J.IJBIOMAC.2022.02.064
98. Yadav, S., Kaushik, S., Chhikara, S. K., Singh, S., Yadav, J. P., & Kaushik, S. (2022). Terminalia arjuna (Arjun Tree): A Sacred plant with high medicinal and therapeutic potential. *Res J Pharm Technol, 15*(12), 5859–5867. https://doi.org/10.52711/0974-360X.2022.00989
99. Muniyan, A., Ravi, K., Mohan, U., & Panchamoorthy, R. (2017). Characterization and in vitro antibacterial activity of saponin-conjugated silver nanoparticles against bacteria that cause burn wound infection. *World Journal of Microbiology & Biotechnology, 33*(7), 1–12. https://doi.org/10.1007/S11274-017-2309-3/TABLES/1
100. Sridhar, K., Inbaraj, B. S., & Chen, B. H. (2021). Recent advances on nanoparticle based strategies for improving carotenoid stability and biological activity. *Antioxidants, 10*(5), 713. https://doi.org/10.3390/ANTIOX10050713
101. Bilal, M., Rasheed, T., Iqbal, H. M. N., Hu, H., Wang, W., & Zhang, X. (2017). Macromolecular agents with antimicrobial potentialities: A drive to combat antimicrobial resistance. *International Journal of Biological Macromolecules, 103*, 554–574. https://doi.org/10.1016/J.IJBIOMAC.2017.05.071
102. Faridul Hasan, K., Hridam, D., Mostafizur Rahman, M., Neaz Morshed, M., Al Azad, S., & Genyang, C. (2016). A review on antibacterial coloration agent's activity, implementation & efficiency to ensure the ecofriendly & green textiles. *American Journal of Polymer Science & Engineering, 4*, 39–59. Available: http://www.ivyunion.orghttp://www.ivyunion.org/index.php/ajpse/http://www.ivyunion.org. Accessed 24 Apr 2023
103. View of Investigation on some main glycosides content of Stevia rebaudian B. under different concentrations of commercial and synthesized silver nanoparticles. https://publish.kne-publishing.com/index.php/PBR/article/view/140/5581 (accessed Apr. 24, 2023).
104. Anjum, S. (2018). Green synthesis of antimicrobial nanoparticles (silver and zinc oxide) and production of commercially important secondary metabolites from in vitro-derived.

accessed: Apr. 24, 2023.. Available: http://173.208.131.244:9060/jspui/handle/123456789/4956
105. Ahmed, S. S. T., Fahim, J. R., Youssif, K. A., Amin, M. N., Abdel-Aziz, H. M. H., Khadra, I. A., Rateb, M. E., Abdelmohsen, U. R., & Hamed, A. N. E. (2022). Comparative study of the chemical composition and anti-proliferative activities of the aerial parts and roots of Apium graveolens L. (celery) and their biogenic nanoparticles. *South African Journal of Botany, 151*, 34–45. https://doi.org/10.1016/J.SAJB.2021.11.002
106. Jain, S., & Mehata, M. S. (2017). Medicinal plant leaf extract and pure flavonoid mediated green synthesis of silver nanoparticles and their enhanced antibacterial property. *Science and Reports, 7*(1), 1–13. https://doi.org/10.1038/s41598-017-15724-8
107. Ovais, M., et al. (2018). Role of plant phytochemicals and microbial enzymes in biosynthesis of metallic nanoparticles. *Applied Microbiology and Biotechnology, 102*(16), 6799–6814. https://doi.org/10.1007/s00253-018-9146-7
108. Singh, J., Dutta, T., Kim, K. H., Rawat, M., Samddar, P., & Kumar, P. (2018). 'Green' synthesis of metals and their oxide nanoparticles: Applications for environmental remediation. *J Nanobiotechnology, 16*(1), 1–24. https://doi.org/10.1186/s12951-018-0408-4
109. Huang, J., et al. (2011). Biogenic silver nanoparticles by cacumen platycladi extract: Synthesis, formation mechanism, and antibacterial activity. *Industrial and Engineering Chemistry Research, 50*(15), 9095–9106. https://doi.org/10.1021/ie200858y
110. Mashwani, Z.-U.-R., Khan, M. A., Khan, T., & Nadhman, A. (2016). Applications of plant terpenoids in the synthesis of colloidal silver nanoparticles. *Advanced Colloid Interface Sci, 234*, 132–141. https://doi.org/10.1016/j.cis.2016.04.008
111. Gurunathan, S., Han, J. W., Kwon, D. N., & Kim, J. H. (2014). Enhanced antibacterial and anti-biofilm activities of silver nanoparticles against Gram-negative and Gram-positive bacteria. *Nanoscale Research Letters, 9*(1), 1–17. https://doi.org/10.1186/1556-276X-9-373
112. Singh, A. K., Talat, M., Singh, D. P., & Srivastava, O. N. (2010). Biosynthesis of gold and silver nanoparticles by natural precursor clove and their functionalization with amine group. *Journal of Nanoparticle Research, 12*(5), 1667–1675. https://doi.org/10.1007/s11051-009-9835-3
113. Kampan, N. C., Madondo, M. T., Mcnally, O. M., Quinn, M., & Plebanski, M. (2015). *Paclitaxel and its evolving role in the management of ovarian cancer*. https://doi.org/10.1155/2015/413076
114. Schläger, S., & Dräger, B. (2016). Exploiting plant alkaloids. *Current Opinion in Biotechnology, 37*, 155–164. https://doi.org/10.1016/j.copbio.2015.12.003
115. Formation, A., Plants, I. N., Accumulation, T. H. E. (1953). Alkaloid formation in plants* by w. 0. james, m.a., f.r.s. 809–822.
116. Neu, T. R., & Lawrence, J. R. (2014). Investigation of microbial biofilm structure by laser scanning microscopy. *Advance Biochemical Engineering Biotechnology, 123*, 127–141. https://doi.org/10.1007/10_2014_272
117. Kharissova, O. V., Dias, H. V. R., Kharisov, B. I., Pérez, B. O., & Pérez, V. M. J. (2013). The greener synthesis of nanoparticles. *Trends in Biotechnology, 31*(4), 240–248. https://doi.org/10.1016/j.tibtech.2013.01.003
118. Gupta, A., Briffa, S. M., Swingler, S., Gibson, H., Kannappan, V., Adamus, G., Kowalczuk, M., Martin, C., & Radecka, I. (2020). Synthesis of silver nanoparticles using curcumin-cyclodextrins loaded into bacterial cellulose-based hydrogels for wound dressing applications. *Biomacromolecules, 21*(5), 1802. https://doi.org/10.1021/ACS.BIOMAC.9B01724
119. Muniyan, A., Ravi, K., & Mohan, U. (2017). Characterization and in vitro antibacterial activity of saponin- conjugated silver nanoparticles against bacteria that cause burn wound infection. *World Journal of Microbiology & Biotechnology*. https://doi.org/10.1007/s11274-017-2309-3
120. Lawal, A., & Odums, C. (2015). Tanning of different animal skins/hides and study of their properties for textile application. *Br J Appl Sci Technol, 5*(6), 588–594. https://doi.org/10.9734/bjast/2015/12938
121. Raji, P., Samrot, A. V., Bhavya, K. S., Sharan, M., Priya, S., & Paulraj, P. (2019). Greener approach for leather tanning using less chrome with plant tannins and tannins mediated nanoparticles. *Journal of Cluster Science, 30*(6), 1533–1543. https://doi.org/10.1007/s10876-019-01597-6
122. Herrera-Becerra, R., Rius, J. L., & Zorrilla, C. (2010). Tannin biosynthesis of iron oxide nanoparticles. *Applied Physics A: Materials Science & Processing, 100*(2), 453–459. https://doi.org/10.1007/s00339-010-5903-x
123. Ahmad, T. (2014). Reviewing the tannic acid mediated synthesis of metal nanoparticles. *Journal of Nanotechnology*, 2014. https://doi.org/10.1155/2014/954206
124. Orlowski, P., et al. (2018). Tannic acid-modified silver nanoparticles for wound healing: The importance of size. *International Journal of Nanomedicine, 13*, 991–1007. https://doi.org/10.2147/IJN.S154797
125. Leung, A. B., Suh, K. I., & Ansari, R. R. (2006). Particle-size and velocity measurements in flowing conditions using dynamic light scattering. *Applied Optics, 45*(10), 2186–2190. https://doi.org/10.1364/AO.45.002186
126. Link, S., & El-Sayed, M. A. (2003). O Ptical P roperties and U Ltrafast D Ynamics of M etallic N anocrystals. *Annual Review of Physical Chemistry, 54*(1), 331–366. https://doi.org/10.1146/annurev.physchem.54.011002.103759
127. Noginov, M. A., et al. (2007). The effect of gain and absorption on surface plasmons in metal nanoparticles. *Applied Physics B, 86*(3), 455–460. https://doi.org/10.1007/s00340-006-2401-0
128. Cabral, M., Pedrosa, F., Margarido, F., & Nogueira, C. A. (2013). End-of-life Zn-MnO2 batteries: Electrode materials characterization. *Environmental Technology (United Kingdom), 34*(10), 1283–1295. https://doi.org/10.1080/09593330.2012.745621
129. Dey, A., Mukhopadhyay, A. K., Gangadharan, S., Sinha, M. K., & Basu, D. (2009). Characterization of microplasma sprayed hydroxyapatite coating. *Journal of Thermal Spray Technology, 18*(4), 578–592. https://doi.org/10.1007/s11666-009-9386-2
130. Singh, D. K., Pandey, D. K., Yadav, R. R., & Singh, D. (2013). A study of ZnO nanoparticles and ZnO-EG nanofluid. *Journal of Experimental Nanoscience, 8*(5), 731–741. https://doi.org/10.1080/17458080.2011.602369
131. Scherzer, O. (1936). Uber einige Fehler von Elektronenlinsen (some defects of electron lenses). *Optik (Stuttg), 101*(9–10), 593–603. https://doi.org/10.1007/BF01349606
132. Varberg, T. D., & Skakuj, K. (2015). X-ray diffraction of intermetallic compounds: A physical chemistry laboratory experiment. *Journal of Chemical Education, 92*(6), 1095–1097. https://doi.org/10.1021/ed500804b
133. Patil, V., & Sastry, M. (1997). Electrostatically controlled diffusion of carboxylic acid derivatized Q-state CdS nanoparticles in thermally evaporated fatty amine films. *Journal of the Chemical Society - Faraday Transactions, 93*(24), 4347–4353. https://doi.org/10.1039/a704355d
134. Rajeshkumar, S., & Bharath, L. V. (2017). Mechanism of plant-mediated synthesis of silver nanoparticles – A review on biomolecules involved, characterisation and antibacterial activity. *Chemico-Biological Interactions, 273*, 219–227. https://doi.org/10.1016/j.cbi.2017.06.019
135. Wadhwa, P., Sharma, S., Sahu, S., Sharma, A., & Kumar, D. (2022). A review of nanoparticles characterization techniques.

Current Nanomaterials, 7(3), 202–214. https://doi.org/10.2174/2405461507666220405113715
136. Kumar, S., & Barth, A. (2010). Following enzyme activity with infrared spectroscopy. *Sensors, 10*(4), 2626–2637. https://doi.org/10.3390/s100402626
137. Rohman, A., & Man, Y. B. C. (2010). Fourier transform infrared (FTIR) spectroscopy for analysis of extra virgin olive oil adulterated with palm oil. *Food Research International, 43*(3), 886–892. https://doi.org/10.1016/j.foodres.2009.12.006
138. Acosta, E. J., Gonzalez, S. O., & Simanek, E. E. (2005). Synthesis, characterization, and application of melamine-based dendrimers supported on silica gel. *Journal of Polymer Science Part A: Polymer Chemistry, 43*(1), 168–177. https://doi.org/10.1002/pola.20493
139. Desimoni, E., & Brunetti, B. (2015). X-ray photoelectron spectroscopic characterization of chemically modified electrodes used as chemical sensors and biosensors: A review. *Chemosensors, 3*(2), 70–117. https://doi.org/10.3390/chemosensors3020070
140. Manna, A., Imae, T., Aoi, K., Okada, M., & Yogo, T. (2001). Synthesis of dendrimer-passivated noble metal nanoparticles in a polar medium: Comparison of size between silver and gold particles. *Chemistry of Materials, 13*(5), 1674–1681. https://doi.org/10.1021/cm000416b
141. Gautam, S. P., Sharma, A. K. G. A., & Gautam, T. (2013). Synthesis and analytical characterization of ester and amine terminated PAMAM dendrimers. *Global Journal of Medical research Pharma, 13*(3), 7–15.
142. Ajitha, B., Ashok Kumar Reddy, Y., & Reddy, P. S. (2014). Biogenic nano-scale silver particles by Tephrosia purpurea leaf extract and their inborn antimicrobial activity. *Spectrochim Acta A Molecular Biomolecules Spectroscopy, 121*, 164–172. https://doi.org/10.1016/j.saa.2013.10.077
143. Buhr, E., Senftleben, N., Klein, T., Bergmann, D., Gnieser, D., Frase, C. G., & Bosse, H. (2009). Characterization of nanoparticles by scanning electron microscopy in transmission mode. *Measurement Science and Technology, 20*(8), 084025. https://doi.org/10.1088/0957-0233/20/8/084025
144. Anandalakshmi, K., Venugobal, J., & Ramasamy, V. (2016). Characterization of silver nanoparticles by green synthesis method using Pedalium murex leaf extract and their antibacterial activity. *Applied Nanoscience (Switzerland), 6*(3), 399–408. https://doi.org/10.1007/s13204-015-0449-z
145. Lavoie, D. M., et al. (1995). Environmental scanning electron microscopy of marine aggregates. *Journal of Microscopy, 178*(2), 101–106. https://doi.org/10.1111/j.1365-2818.1995.tb03585.x
146. Joshi, M., Bhattacharyya, A., & Ali, S. W. (2008). Characterization techniques for nanotechnology applications in textiles. *Indian Journal of Fibre & Textile Research, 33*(3), 304–317.
147. Asoro, M. A., Kovar, D., & Ferreira, P. J. (2013). In situ transmission electron microscopy observations of sublimation in silver nanoparticles. *ACS Nano, 7*(9), 7844–7852. https://doi.org/10.1021/nn402771j
148. Bellotti, R., Picotto, G. B., & Ribotta, L. (2022). AFM Measurements and tip characterization of nanoparticles with different shapes. *Nanomanufacturing and Metrology, 5*(2), 127–138. https://doi.org/10.1007/S41871-022-00125-X/FIGURES/11
149. Mourdikoudis, S., Pallares, R. M., & Thanh, N. T. K. (2018). Characterization techniques for nanoparticles: Comparison and complementarity upon studying nanoparticle properties. *Nanoscale, 10*(27), 12871–12934. https://doi.org/10.1039/C8NR02278J
150. Kiio, T. M., & Park, S. (2020). Nano-scientific application of atomic force microscopy in pathology: From molecules to tissues. *International Journal of Medical Sciences, 17*(7), 844. https://doi.org/10.7150/IJMS.41805
151. Hoshyar, N., Gray, S., Han, H., & Bao, G. (2016). The effect of nanoparticle size on in vivo pharmacokinetics and cellular interaction. *Nanomedicine, 11*(6), 673–692. https://doi.org/10.2217/nnm.16.5
152. Roe, D., Karandikar, B., Bonn-Savage, N., Gibbins, B., & Baptiste Roullet, J. (2008). Antimicrobial surface functionalization of plastic catheters by silver nanoparticles. *Journal of Antimicrobial Chemotherapy, 61*(4), 869–876. https://doi.org/10.1093/jac/dkn034
153. Yassin, M. A., Elkhooly, T. A., Elsherbiny, S. M., Reicha, F. M., & Shokeir, A. A. (2019). Facile coating of urinary catheter with bio–inspired antibacterial coating. *Heliyon, 5*(12). https://doi.org/10.1016/J.HELIYON.2019.E02986
154. Qing, Y., et al. (2018). Potential antibacterial mechanism of silver nanoparticles and the optimization of orthopedic implants by advanced modification technologies. *International Journal of Nanomedicine, 13*, 3311. https://doi.org/10.2147/IJN.S165125
155. Ribeiro, M., Monteiro, F. J., & Ferraz, M. P. (2012). Infection of orthopedic implants with emphasis on bacterial adhesion process and techniques used in studying bacterial-material interactions. *Biomatter, 2*(4), 176. https://doi.org/10.4161/BIOM.22905
156. Rafique, M., Sadaf, I., Rafique, M. S., & Tahir, M. B. (2017). A review on green synthesis of silver nanoparticles and their applications. *Artif Cells Nanomed Biotechnol, 45*(7), 1272–1291. https://doi.org/10.1080/21691401.2016.1241792
157. Mahmood, M., et al. (2011). Nanostructural materials increase mineralization in bone cells and affect gene expression through miRNA regulation. *Journal of Cellular and Molecular Medicine, 15*(11), 2297–2306. https://doi.org/10.1111/J.1582-4934.2010.01234.X
158. Liao, C., Li, Y., & Tjong, S. C. (2019). Bactericidal and cytotoxic properties of silver Nanoparticles. *International Journal of Molecular Sciences, 20*(2). https://doi.org/10.3390/IJMS20020449
159. Abbasi, E., et al. (2016). Silver nanoparticles: Synthesis methods, bio-applications and properties. *Critical Reviews in Microbiology, 42*(2), 173–180. https://doi.org/10.3109/1040841X.2014.912200
160. Xu, L., Wang, Y. Y., Huang, J., Chen, C. Y., Wang, Z. X., & Xie, H. (2020). Silver nanoparticles: Synthesis, medical applications and biosafety. *Theranostics, 10*(20), 8996. https://doi.org/10.7150/THNO.45413
161. Bae, K. H., Chung, H. J., & Park, T. G. (2011). Nanomaterials for cancer therapy and imaging. *Molecules and Cells, 31*(4), 295. https://doi.org/10.1007/S10059-011-0051-5
162. Gopinath, P., Gogoi, S. K., Chattopadhyay, A., & Ghosh, S. S. (2008). Implications of silver nanoparticle induced cell apoptosis for in vitro gene therapy. *Nanotechnology, 19*(7). https://doi.org/10.1088/0957-4484/19/7/075104
163. Dayem, A. A., Hossain, M. K., Lee, S. Bin, Kim, K., Saha, K., Yang, G.-M., Choi, H. Y., & Cho, S.-G. (2017). *Molecular sciences the role of reactive oxygen species (ROS) in the biological activities of metallic nanoparticles*. https://doi.org/10.3390/ijms18010120
164. Ratan, Z. A. et al., (2020). Green chemistry synthesis of silver nanoparticles and their potential anticancer effects. Cancers *(Basel)*, *12*(4). https://doi.org/10.3390/CANCERS12040855.
165. Sharma, S., Chockalingam, S., Sanpui, P., Chattopadhyay, A., & Ghosh, S. S. (2014). Silver nanoparticles impregnated alginate-chitosan-blended nanocarrier induces apoptosis in human glioblastoma cells. *Advanced Health Materials, 3*(1), 106–114. https://doi.org/10.1002/ADHM.201300090
166. Sanpui, P., Chattopadhyay, A., & Ghosh, S. S. (2011). Induction of apoptosis in cancer cells at low silver nanoparticle concentrations using chitosan nanocarrier. *ACS Applied Materials & Interfaces, 3*(2), 218–228. https://doi.org/10.1021/AM100840C
167. Ferdous, Z., & Nemmar, A. (n.d.). *Health impact of silver nanoparticles: A review of the biodistribution and toxicity following various routes of exposure*. https://doi.org/10.3390/ijms21072375

168. Rai, M., Kon, K., Ingle, A., Duran, N., Galdiero, S., & Galdiero, M. (2014). Broad-spectrum bioactivities of silver nanoparticles: The emerging trends and future prospects. *Applied Microbiology and Biotechnology, 98*(5), 1951. https://doi.org/10.1007/S00253-013-5473-X
169. Khursheed, R., et al. (2022). Biomedical applications of metallic nanoparticles in cancer: Current status and future perspectives. *Biomedicine & Pharmacotherapy, 150*, 112951. https://doi.org/10.1016/J.BIOPHA.2022.112951
170. Dakal, T. C., Kumar, A., Majumdar, R. S., & Yadav, V. (2016). Mechanistic Basis of Antimicrobial Actions of Silver Nanoparticles. *Frontiers Microbiological, 7*, 1831. https://doi.org/10.3389/FMICB.2016.01831
171. Crisan, C. M., Mocan, T., Manolea, M., Lasca, L. I., Tăbăran, F. A., & Mocan, L. (2021). Review on silver nanoparticles as a novel class of antibacterial sol2021utions. *Applied Sciences (Switzerland), 11*(3), 1–18. https://doi.org/10.3390/app11031120
172. Ciociola, T., et al. (2014). Antibodies as an unlimited source of anti-infective, anti-tumour and immunomodulatory peptides. *Science Progress, 97*(3), 215–233. https://doi.org/10.3184/003685014X14049273183515
173. Durán, N., Durán, M., de Jesus, M. B., Seabra, A. B., Fávaro, W. J., Nakazato, G. (2016). Silver nanoparticles: A new view on mechanistic aspects on antimicrobial activity. *Nanomedicine: Nanotechnology Biology and Medicine,* 12(3), 789–799. https://doi.org/10.1016/j.nano.2015.11.016.
174. Tang, S., & Zheng, J. (2018). Antibacterial activity of silver nanoparticles: Structural effects. *Adv Healthc Mater, 7*(13), 1–10. https://doi.org/10.1002/adhm.201701503
175. Jagaran, K., & Singh, M. (2021). Nanomedicine for neurodegenerative disorders: Focus on alzheimer's and parkinson's diseases. *International Journal of Molecular Sciences, 22*(16). https://doi.org/10.3390/IJMS22169082

Publisher's Note Springer Nature remains neutral with regard to jurisdictional claims in published maps and institutional affiliations.

Springer Nature or its licensor (e.g. a society or other partner) holds exclusive rights to this article under a publishing agreement with the author(s) or other rightsholder(s); author self-archiving of the accepted manuscript version of this article is solely governed by the terms of such publishing agreement and applicable law.

2023 9th International Conference on Advanced Computing and Communication Systems (ICACCS) | 979-8-3503-9737-6/23/$31.00 ©2023 IEEE | DOI: 10.1109/ICACCS57279.2023.10112733

Plant Disease Detection And Prevention Using Deep Learning

Prashant Giridhar Shambharkar
Department of Computer Science and Engineering
Delhi Technological University
New Delhi, India
prashant.shambharkar@dtu.ac.in

Saurabh Sharma
Department of Computer Science and Engineering
Delhi Technological University
New Delhi, India
ss12saurav@gmail.com

***Abstract*—Identifying disease in plants is a major research topic in agriculture and it is also important so that no crops are going to waste. As India has a large population, it becomes more important to fulfill the increasing demand and for enhancing the yield of crops we need to save the crops which are affected by the diseases. We can find the disease of the plants by classifying the type of disease the crop has and then we can apply prevention methods. It is done by some experts by using some chemicals to find the disease and it is also time consuming and costly. If we can make an automatic system which can detect the disease by analyzing plant leaves then we can make this process cheaper as well as faster with respect to time taken for finding the disease in crops. For that we can use deep learning models which are used to classify the leaves based on disease they have. In this paper, we are finding the disease on the cassava plant. Because people also eat the leaves of this plant. The aim of this paper is to increase the accuracy and efficiency in comparison to the previously proposed models. Deep learning models are more effective than the machine learning models which we got to know while reading about the work which was done previously on plant disease detection. So that is why we used a deep learning model. In this, we used EfficientNet-B0 with k-fold cross validation. EfficientNet is known as best classification models because they are faster and scale on width, depth, and resolution. Our model gives accuracy of 96.68 on the dataset which we collect from kaggle.**

Keywords—Plant Disease, CNN, Classification, EfficientNet, K-fold cross validation

I. INTRODUCTION

Cassava is a very important African crops , of which Africa is the single largest producer cassava is a crop which is successfully cultivated in any climate , nonproductive soil and drought included . though the crops faces several difficulties during the time of production , i.e. not of good quality , leaf diseases , of which The primary cause of reduced production is leaf diseases , which affects income of the farmers . the identification and treatment of such leaf diseases must be done on priority to regain capacity of production, detect automatically is a step which is very important to detect such diseases in crops on crop leaves [1]. In India, approx 70% of the population depends on agriculture. So, it becomes more necessary to detect the disease in plants and cure the disease before it causes trouble for other plants. In India peoples are leaving farming because they are not getting good profit because their crops are damaged because of some disease. So, if disease can be detected before it causes loss then we can help farmers because some crops' leaves show the effect before and we can treat them before they come in the situation where we cannot do anything [21]. Agriculture contributes to the economy in India and also a primary source of revenue. During COVID-19 restrictions on food cause a food crisis in the whole world so for that we also need to save crops from the diseases [2]. The food supply chain also gets disturbed during the pandemic. Nowadays farmers are using pesticides to increase the quantity of food but it decreases the quality of food and these pesticides are dangerous for health because they are responsible for around 300,000 deaths in the whole world. Several artificial intelligence algorithms like SVM(support vector machine), KNN(k nearest neighbor), logistic regression, and decision tree are used for detecting disease through which plants are suffering. Recently DNN(deep neural network) and CNN(convolution neural network) prove that they can give better results [3].So The model which we proposed is using a deep learning model which is good to arrange the type of disease by using a classification algorithm. There is many CNN based models which give very promising results in plants like tomato plants. But for cassava plants we have no model which can give better results. So, for that this model is proposed.

The rest of the paper is ordered as follows. Section II discussed about related work; Section III discussed about Overview of CNN; section IV explains about proposed work; section V illustrated about the Implementation and Result discussion; section VI concludes the work along with future scope.

II. RELATED WORK

In order to achieve sustainable development in addition to prevent irrelevant waste, including fiscal and other resources, the identification of diseases of plant within time are crucial. There have been many conventional machine learning models which are proposed in the last ten years for detecting and classifying diseases in plant. Al-Hiary et al. [22] identified five different types of leaf diseases in plants based on the features derive in the preprocessing step, we clustered them using K-Means, split the lesion area, and extracted features based on color and texture to classify these areas using artificial neural networks (ANN). The method proposed by Revathi and Hemalatha [23] identifies disease on cotton leaves of six types. In their procedure, they use particle swarm optimization (such as colors, edges, and textures) for selecting features from feature vectors, and diseases are classified using deep forward

979-8-3503-9737-6/23/$31.00 ©2023 IEEE

Authorized licensed use limited to: DELHI TECHNICAL UNIV. Downloaded on May 11,2023 at 10:16:37 UTC from IEEE Xplore. Restrictions apply.

neural networks with cross-information gain. An algorithm called GMDH logic algorithm was recently proposed by J. Chen et al. [14] to detect plant diseases automatically. Deep learning progresses alot over the last few years, with convolutional neural networks (CNN) making great strides in recognizing targets and classes of images. This success of CNN is attributed to CNN's capability to distinguish learning, which extracts deep features automatically and completes the learning of deep feature. A significant deal of research has been done on the use of CNN for identifying crops diseases, which has shown excellent results. Several deep learning methods are used to diagnose and classify medical imaging diseases. Further, a comprehensive article published in 2019 concentrated on the use of deep learning in monitoring and sorting the disease in plant leaf. Using CNN models (such as AlexNet and GoogleNet) Mohanty et al. [11] classified plant diseases. They achieved 99.35% classification accuracy in their research. According to et al., CNN models like VGG 16, ResNet 50, ResNet 152, DenseNets 121 and Inception V4 were used. According to reports, the DenseNet architecture had less computation time, less parameters, and attain the highest experiment accuracy i.e., 99.75 in research% when compared to other models. Adedoja et al. [24] took Plant village data set nad did migration learning on the it using the NASNet trained network model. The test's accuracy was 93.82%. This strategy failed to create a network topology that was appropriate for data on plant diseases. Chen et al. [16] proposed a new model named MobileNet-Beta for detection of plant disease by including the classification activation map into the pre-trained model of MobileNet V2. To test the suggested model, they used their own dataset as well as the Plant Village dataset. It is found in the tests that the MobileNet-Beta model on the Plant Village data set gives accuracy up to 99.85% accurate and give accuracy of 99.11% on its own data set. The earlier studies show that deep learning frameworks are being utilised more frequently in the published works to identify disease in plant leaf. Still, more research needs to be done on the use of deep learning frameworks which is era-adapted for detection of disease in plant leaf. In particular, it is unavoidable that an effective model with fewer parameters, a quicker training time, and no performance impact will exist [4].

A. *Efficientnet*

Alina Maryum, Anum Abdul Salam and Muhammad Usman Akram uses model EfficientNet model B4 [5] which gives accuracy of 89.09% on cassava plant dataset [6]. EfficientNet was created by Google in 2019. It uses compound coefficients to scale models in simple and effective ways. It uses depth wise, width wise and resolution scaling. So, if the image is of more resolution then more features can be extracted from the images. So, the question is how we find the depth and width for scaling. It gives better results than any other model. It is fast so that it can be used in real life.

$$f = \alpha^{\phi}.\beta^{\phi}.\gamma^{\phi} \quad (1)$$

Here α is depth of the network, β is width and γ is resolution. In this value of, and are constants. Values of β, α and γ are 1.1, 1.2 and 1.15 respectively. And the value of ϕ is found out by performing grid search which is also called coefficient. It works on 380x380 images.

B. *Resnet50 And SVM Classifier*

Sedat METLEK uses the cassava dataset [6] and applies the Resnet50 and SVM Classifier Model which gives 85.4% and 84.4% accuracy respectively [7].

1) Resnet50: ResNet50 is a 50 layer deep neural network. ResNet stands for Residual Network. It is inspired by the VGG-19 architecture in which shortcut connections are added to overcome the problem of vanishing gradient. It has 48 convolution layers and one layer of max pooling and one layer of average pooling[8]. Disadvantage of ResNet is that is it has vanishing gradient problem. Skip connections are used to resuce this problem in neural networks. In skip connections many connections are skipped directly. The result is not the same after the connections are skipped.

2) SVM Classifier : SVM is a popular supervised learning algorithm used for both regression and classification. Typically, though, this is basically used for problems related to classification in machine learning. Using SVM, we are able to divide n dimensional space into classes and can put any new data point into the right category easily in the coming time by drawing the best line or decision boundary. A hyperplane represents this best decision boundary. In SVM, extremum points and vectors are used to create hyperplanes. Support vectors are these extremum cases, so the Support Vector Machine algorithm derives its name from that. A hyperplane is used to classify two distinct categories [9].

C. *MobileNet-SSD*

Amanda Ramcharan uses the MobileNet-SSD model [10] on the cassava Dataset [6] which gives accuracy of 80.6%. It is a light weighted deep neural network.As we can see that its name suggests it is used to create applications which can be used in mobile. It uses depthwise separable convolution. Single shot detector was developed by google which can work in real time and can run on embedded devices.It is the same as the Efficient convolutional neural network which can run on mobile.

D. *Alexnet*

Sharada P. Mohanty, Marcel Salathe and David P. Hughes ´ use the plant village dataset [11] and apply the AlexNet Model [12] which gives 99.27% accuracy. In this there are 8 weighted layers in this model [13]. There are 5 convolution layers with activation function as ReLU and max pooling operation and there are 3 fully connected layers [17]. First 7 layers of alexnet use the ReLU activation function. After conv5 there is a pooling layer and at last there are two fully connected layers have a dropout layer at last which has a dropout ratio as 0.5.

E. *Deep-CNN*

G Geetharamani uses the plant village dataset [11] and applies the Deep CNN Model [14] which gives 96.46%

Authorized licensed use limited to: DELHI TECHNICAL UNIV. Downloaded on May 11,2023 at 10:16:37 UTC from IEEE Xplore. Restrictions apply.

accuracy. In this they use a total 5 weighted layers where 3 layers are convolution layers and each layer is followed by ReLU function as activation function,uses max pooling operation for pooling and two fully connected layers. They trained model for thirty epochs with a learning rate of 0.5 and batch size of 64.

F. DenseNet and VGG-19

Junde Chen uses the Maize plant village dataset [11] and applies the Dense Net [15] and VGG-19 [16] Model which gives 98.5% and 92% accuracy respectively.

1) *DenseNet:*In DenseNet all the results from the preceding layer is the input for the next layer. In this all the layers are densely connected. After each dense block there is one convolution layer and one pooling layer. In this to increase the accuracy then the number of layers need to increase. But after a limit of layers the problem of vanishing gradient takes place.

2) *VGG-19:* The VGG-19 model is a nineteen layer deep model. In this there are sixteen convolution layers and three fully connected layers. There are five Pooling layers. First pooling layer is after two layers, second pooling layer is after four layers, third is after eight layers, fourth id after twelve layers and fifth is after sixteen layers. At last there is a softmax layer and the last three layers before softmax are fully connected layers. Performance Comparision is show in table .1

TABLE I. PERFORMANCE COMPARISION

Author	Dataset	Method	Accuracy
Alina Maryum	Cassava dataset	fficientNet model B4	89.09%
Sedat METLEK	Cassava Dataset	ResNet50	85.4%
Sedat METLEK	Cassava Dataset	SVM Classifier	84.4%
A Ramacharan	Cassava dataset	bilenet- SSD	80.60%
Mohanty et al	Plant Village	AlexNet	99.27%
a Ramani et al	Plant Village	CNN	96.46%
chen et al	aize Plant Village	DenseNet	98.5%
chen et al	aize Plant Village	VGG-19	92%

III. OVERVIEW OF CONVOLUTION NEURAL NETWORK

CNNs are frequently utilised in a variety of applications, including target recognition, target detection, image recognition, speech recognition, recommendation systems, and image classification. Following their investigation of the cat's visual nerve, Hubel and Wiesel put out the idea of a receptive field and later identified a connection between the processing and categorization of input from external and the visual cortex of the brain. The visual input cells and space that make up the visual cortex can be duplicated to actualize precise computer vision techniques, they added, which is a key idea in the concept of the sensory field [20]. These notions are then used to generate CNNs, which can be further separated into three categories. Here, first layer is input image, then, for feature extraction, there is convolutional and pooling layer. Then, the third component called joining layer separates and combines the features of the image into a column vector.

A. Convolutional Layer

Convolutional layer has an optimal solution for backpropagation, and together they create a convolution unit. A convolution layer is made up by multiple convolution units. Low-level aspects like edges, lines, and faces of an image, are determined via a convolution operation. A network can bring out more complicated characteristics from low-level information with each additional convolution layer. For example, the first layer uses pixels to extract the information about points and edges, which is then used as the input for the 2nd layer. Squares, circles, and other shapes are identified from the edges and points in the second layer, which serves as the input for the subsequent layers, and so on. This procedure continues until a level of abstraction appropriate for the matching task is attained. The total count of convolutions and features to extract can be changed depending on the desired outcome because there are so many characteristics that can be extracted.

B. Pooling Layer

Through the pre-set convolution layer, which is disposed to overfitting, we acquire abstract features. As a result, it is important to downscale the features dimension in the pooling layer. The average or maximum pooling method reduces the dimension of features by obtaining the average or maximum value in a specific area. This approach can both maintain image details and avoid overfitting.

C. Fully Connected Layer

This layer joins every feature in the form of column vector to make two-dimensional feature map output by using the first layer. Then, the classifier takes the output values and classifies them into different classes. Mapping from original data into feature space is done by convolution and pooling layers. It helps in increasing the precision of feature matrix and abstraction of original data. Then, we convert feature space into column vector to input it to the classifier. then the next layer help in mapping of pooling layer and convolution output to a linear separable space. This layer can simplify the parameter model, extract high order features from pooling and convolution operations, and decrease the number of training parameters and neurons.

IV. PROPOSED SYSTEM

In our proposed model we used pretrained EfficientNet-b0 with k fold cross validation where k is 5. Why do we choose Efficient Net? The answer for this question is that it is faster and it scale on depth of the model and width and

Authorized licensed use limited to: DELHI TECHNICAL UNIV. Downloaded on May 11,2023 at 10:16:37 UTC from IEEE Xplore. Restrictions apply.

resolution of the images. So, if the image resolution is high then we can extract more features from the images and we can classify better. In this we use 5-fold cross validation. So, the Error in this is find by the equation.

$$E = \frac{1}{k}\sum_{i=0}^{k} E_i \qquad (2)$$

In this equation error(E) is equal to the average of the error in each fold. Where Ei is the error in ith fold. Efficient Net was created by Google in 2019. It uses compound coefficients to scale models in simple and effective ways. It uses depth wise, width wise and resolution scaling. So, if the image is of more resolution then more features can be extracted from the images. So, the question is how we find the depth and width for scaling. It gives better results than any other model. It is fast so that it can be used in real life. As you can see in equation 1 Here α is depth of the network, β is width and γ is resolution. In this value of, and are constants. Values of β, α and γ are 1.1, 1.2 and 1.15 respectively. And the value of ϕ is found out by performing grid search which is also called coefficient. It works on 380x380 images. Efficient Net are of 8 types from b0-b7. As the number increases then the resolution of the images increases. The Efficient Net B0, Efficient Net B1, Efficient Net B2, Efficient Net B3, Efficient Net B4, Efficient Net B5, Efficient Net B6 and Efficient Net B7 in all these the resolution of the images increases so that it can extract more features and use it to find more feature from the images. [18] As you can see the values of β, γ and α are in the table II. These values are the standard values but the values are made constant so that it becomes easy to use for everybody. The constant values of β, α and γ are 1.1, 1.2 and 1.15 respectively. In our Model we used the EfficientNet-b0 which works on the images of resolution 224 and uses fivefold cross validation in which the data set is split into five equal slices which is 4279 images in each part and which gives us the accuracy of 96.68.

TABLE II. PERFORMANCE COMPARISION OF EFFICIENTNETS

Model	Width(β)	Depth(α)	Resolution(γ)
Efficient net B0	1.0	1.0	224
Efficient net B1	1.0	1.1	240
Efficient net B2	1.1	1.2	260
Efficient net B3	1.2	1.4	300
Efficient net B4	1.4	1.8	380
Efficient net B5	1.6	2.2	456
Efficient net B6	1.8	2.6	528
Efficient net B7	2.0	3.1	600

A. *K-Fold Cross-Validation:*

In machine learning, cross-validation is a method of evaluating models by resampling limited samples of data. Data samples are divided into groups according to a parameter called k indicating the number of groups to be formed. Hence, the procedure is known as k fold cross-validation. Let us say if k=5 is selected, then the reference to the model would be 5-fold cross validation. In our machine learning model, cross-validation is used primarily to evaluate a machine learning model's skill on given data. It uses small data sample to estimate how good the model will perform when we predict result which was not used during training [19]. Due to its simplicity and the fact that it usually yields a less biased or more optimistic estimate of the model skill than other methods, such as training and testing, it is widely used. Work Flow Is show in fig.1

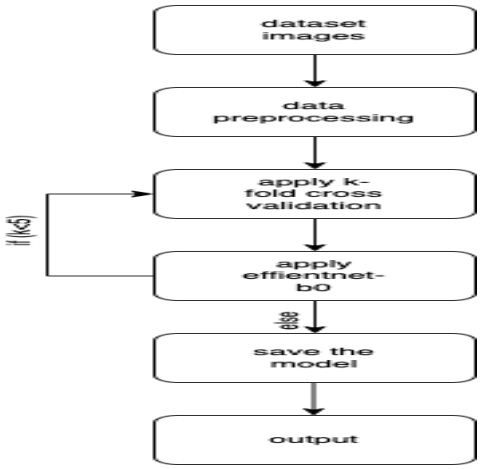


Fig. 1. Work Flow

Steps of K-fold cross validation:

Step 1: Jumble up the dataset arbitrarily.
Step 2: Divide the dataset into k segments.
Step 3: For every segment:

- Consider it as a test dataset or hold out segment.
- Consider all remaining segments as training dataset.
- Train the model using training dataset and examine it on test dataset.
- Note the score of performance evaluation and drop the model.

Step 4: Using the sample of model evaluation scores, conclude about the skill of the model.

B. *Configuration Of K*:

Data samples require careful selection of k values. When k is chosen poorly, the model may have a misrepresentative idea of its skill, like high variance (which can be influenced by the data which is used to fit the model), or highly bias (like overestimation). The following are three common ways to choose k:

- Representative: It is important to choose k such that each train and test group represents the broader dataset statistically.
-
- k=10: It has been proved experimentally that if we set k as 10 then model will have low bias and modest variance.
- k=n: For every test *sample* should be considered in the hold-out dataset, k is permanent at n, where n is define as the number of records in the dataset. It is called cross validation with one out (leave-one-out).

If k is not chosen at a value that evenly splits the sample, then a remainder of the examples will be included in one group. For model skill scores to be comparable across the

Authorized licensed use limited to: DELHI TECHNICAL UNIV. Downloaded on May 11,2023 at 10:16:37 UTC from IEEE Xplore. Restrictions apply.

k groups, it is preferable to divide the data sample into k equal samples.

V. Implementation And Result Discussion

A. Dataset

The dataset which is used in this is cassava dataset which was taken from the kaggle [6]. It contains images of cassava plant leaves of five types: one is of healthy leaves and other four are of different diseases. Other four are Cassava mosaic disease, Cassava bacterial blight, Cassava brown streak disease and Cassava green mite. As shown in fig 9 there 0 represents the total count of images of cassava bacterial blight,1 represents the total count of images of Cassava brown streak disease,2 represents the total count of images of Cassava green mite,3 represents the total count of images of cassava Mosaic disease and 4 represents the total count of images of healthy leaf. As shown in fig 13. Number of images in each disease is show in fig.2

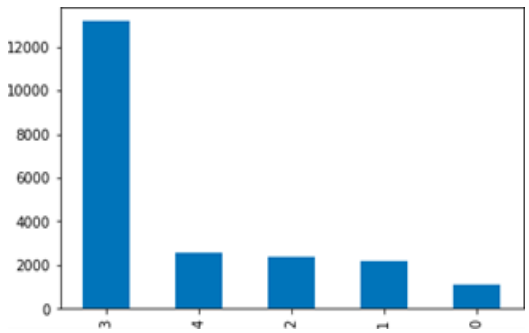


Fig. 2. Number of images in each disease

1) Healthy Leaves: Cassava leaves are rich in protein,vitamins and minerals so that's why people of south africa also eat these leaves. But it is grown for its roots and leaves are considered as a byproduct. So the healthy cassava plant leaves are green which shows that the plant is not caused by any disease and good for eating.

2) Cassava Bacterial Blight: This cassava disease was first found in brazil. Then found in different countries where cassava crops are produced. It is the most dangerous disease for cassava plants after the cassava mosaic disease. This causes more damage to crops. Starch in roots are in low quantity because of cassava bacterial blight. The leaves become brownish and yellow as you can see in the fig. It can cause loss of new roots and planting material. Because leaves become dry then leaves start falling due to which they lose leafy vegetables.

3) Cassava Mosaic Disease: It is the too much dangerous and it is most widely spread disease which limits the production of crops in africa. It shows a wide variety of symptoms which are mosaic, mottling, misshapen and twisted leaflets. It also shows that the size of leaves and plants reduces because of cassava mosaic disease.

Cassava Brown Streak Disease : This disease is very dangerous disease for cassava plants and it is widely spread in the east region of africa. Two viruses called ugandan brown streak virus i.e UCBSD and cassava brown streak virus i.e CBSD causes this disease. Both Ugandan brown streak virus i.e UCBSD and cassava brown streak virus i.e CBSD are different genetically but both show the same symptoms on the cassava plants including leaf chlorosis, brown streaks on stems of the plants, and on storage roots brown corky necrosis. Architecture of EfficientNet B0 is show in fig.3

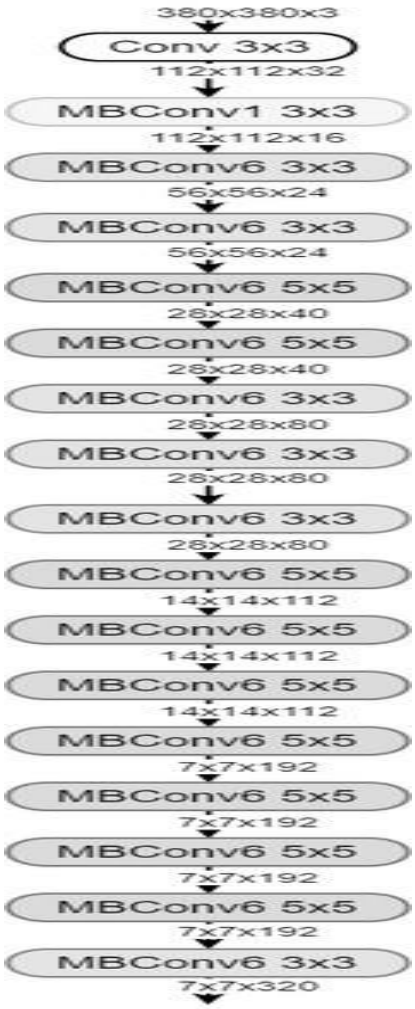


Fig. 3. Architecture of EfficientNet B0

4) Cassava Green Mite: This is the disease which is caused by the mites. These mites sucks juice from the leaves and resulting which leaves become yellow and dead. Because of which leaves start falling from the plants. This can be detected by checking the color of the plant leaves and if the leaves start falling. This disease spreads from plant to plant. These mites take 12 days from egg to adult and spreads on the nearby plants also.

Authorized licensed use limited to: DELHI TECHNICAL UNIV. Downloaded on May 11,2023 at 10:16:37 UTC from IEEE Xplore. Restrictions apply.

B. Algorithm Used

In this we used EfficientNet-B0 which is known as best in terms of classification after the AlexNet and ResNet. As shown in fig 19. So, the advantage of using this model is that it is faster than any other model and it can work on high resolution images which is helpful to extract more features from images. It scales on width, depth and resolution which make it different from other models which work on depth only to give good results [20]. Then we apply k-fold cross validation on our dataset. Which divides our data into five equal parts and trains model one by one on each. It divides it into 5 parts because we used 5-fold cross validation. Proposed model gives better results than the existing models which are used for cassava dataset. It gives 96.68% accuracy which is better than the other model as you can see in the comparison table III.

TABLE III. PERFORMANCE COMPARISION

Author	Method	Accuracy
roposed Model	cientNet with k-fold cross validation	96.68%
Alina Maryum	EfficientNet	89.09%
Sedat METLEK	ResNet50	85.4%
Sedat METLEK	SVM Classifier	84.4%
A Ramacharan	MobileNet-SSD	80.60%

VI. CONCLUSION AND FUTURE SCOPE

Plant disease detection is very crucial to prevent the crops from various type of diseases. Chemical testing is not feasible for every plant because it is very expensive and time consuming. So, we detect plant disease by doing plant image classification using deep learning and machine learning approaches. In past years, researchers have made many models such as ResNet, EfficientNet, CNN etc., to detect plant disease. In this paper, proposed model detects Cassava plant disease using EfficientNet with k-fold cross validation with value of k as 5 which outperforms the existing models. In future, we will extend our model to the other crops also and increase the accuracy and we will then integrate our model with the drones. Then with the help of drones we will take the images of plants and find the plants which are affected by disease and apply prevention methods on them by finding which disease causes that plant so that it can become disease free. We will make our model more accurate. So that we can use this model in real life. We will try to increase the accuracy by optimizing the model. This will decrease the time of farmers in finding the plants which are affected by disease and increase the growth of the crop.

REFERENCES

[1] Vishakha, B. S., Sharma, N., Bhushan, B., & Kaushik, I. (2021). Blockchain-based cultivating ideas for growth: A New AGRONOMICS PERSPECTIVE. Advances in Computing Communications and Informatics, 195–219. https://doi.org/10.2174/9781681088624121010012

[2] Sethi, R., Bhushan, B., Sharma, N., Kumar, R., & Kaushik, I. (2020). Applicability of Industrial IoT in Diversified Sectors: Evolution, Applications and Challenges. Studies in Big Data Multimedia Technologies in the Internet of Things Environment, 45-67. doi:10.1007/978-981-15-7965-3_4..

[3] Gao, Fei, Jiming Sa, Zhuoer Wang, and Zhongyu Zhao. ”Cassava disease detection method based on EfficientNet.” In 2021 7th International Conference on Systems and Informatics (ICSAI), pp. 1-6. IEEE, 2021.

[4] Maryum, Alina, Muhammad Usman Akram, and Anum Abdul Salam. ”Cassava leaf disease classification using deep neural networks.” In 2021 IEEE 18th international conference on smart communities: improving quality of life using ICT, IoT and AI (HONET), pp. 32-37. IEEE, 2021.

[5] https://www.kaggle.com/competitions/cassava-disease/data

[6] METLEK, Sedat. ”Disease detection from cassava leaf images with deep learning methods in web environment.” International Journal of 3D Printing Technologies and Digital Industry 5, no. 3 (2021): 625-644.

[7] Ali, Luqman, Fady Alnajjar, Hamad Al Jassmi, Munkhjargal Gocho, Wasif Khan, and M. Adel Serhani. ”Performance evaluation of deep CNN-based crack detection and localization techniques for concrete structures.” Sensors 21, no. 5 (2021): 1688.

[8] Hearst, Marti A., Susan T. Dumais, Edgar Osuna, John Platt, and Bernhard Scholkopf. ”Support vector machines.” IEEE Intelligent Systems and their applications 13, no. 4 (1998): 18-28.

[9] Ramcharan, Amanda, Peter McCloskey, Kelsee Baranowski, Neema Mbilinyi, Latifa Mrisho, Mathias Ndalahwa, James Legg, and David P. Hughes. ”A mobile-based deep learning model for cassava disease diagnosis.” Frontiers in plant science (2019): 272.

[10] Hughes, David, and Marcel Salathe. ”An open access repository of ´ images on plant health to enable the development of mobile disease diagnostics.” arXiv preprint arXiv:1511.08060 (2015).

[11] Mohanty, Sharada P., David P. Hughes, and Marcel Salathe. ”Using ´ deep learning for image-based plant disease detection.” Frontiers in plant science 7 (2016): 1419.

[12] Alom, Md Zahangir, Tarek M. Taha, Christopher Yakopcic, Stefan Westberg, Paheding Sidike, Mst Shamima Nasrin, Brian C. Van Esesn, Abdul A. S. Awwal, and Vijayan K. Asari. ”The history began from alexnet: A comprehensive survey on deep learning approaches.” arXiv preprint arXiv:1803.01164 (2018).

[13] Geetharamani, G., and Arun Pandian. ”Identification of plant leaf diseases using a nine-layer deep convolutional neural network.” Computers & Electrical Engineering 76 (2019): 323-338.

[14] Chen, Junde, Wenhua Wang, Defu Zhang, Adnan Zeb, and Yaser Ahangari Nanehkaran. ”Attention embedded lightweight network for maize disease recognition.” Plant Pathology 70, no. 3 (2021): 630-642.

[15] Chollet, Franc¸ois. ”Xception: Deep learning with depthwise separable convolutions.” In Proceedings of the IEEE conference on computer vision and pattern recognition, pp. 1251-1258. 2017.

[16] Chen, Chih-Cheng, Ju Yan Ba, Tie Jun Li, Christopher Chun Ki Chan, Kun Ching Wang, and Zhen Liu. ”EfficientNet: A low-bandwidth IoT image sensor framework for cassava leaf disease classification.” Sens. Mater 33 (2021): 4031.

[17] Tan, Mingxing, and Quoc Le. ”Efficientnet: Rethinking model scaling for convolutional neural networks.” In International conference on machine learning, pp. 6.

[18] Rao, Patike Kiran. ”Cassava leaf disease classification using separable convolutions UNet.” Turkish Journal of Computer and Mathematics Education (TURCOMAT) 12, no. 7 (2021): 140-145.

[19] Tan, Mingxing, and Quoc Le. ”Efficientnet: Rethinking model scaling for convolutional neural networks.” In International conference on machine learning, pp. 6105-6114. PMLR, 2019

[20] Himanshu, Rana, R., Sharma, N., Kaushik, I., & Bhushan, B. (2021). Blockchain technology for Industry 4.0 Applications. Big Data Analysis for Green Computing, 147–171. https://doi.org/10.1201/9781003032328-10

[21] Aggarwal, V. K., Sharma, N., Kaushik, I., Bhushan, B., & Himanshu. (2021). Integration of Blockchain and IoT (B-IoT): Architecture, Solutions, & Future Research Direction. IOP Conference Series: Materials Science and Engineering, 1022, 012103. https://doi.org/10.1088/1757-899x/1022/1/012103

Authorized licensed use limited to: DELHI TECHNICAL UNIV. Downloaded on May 11,2023 at 10:16:37 UTC from IEEE Xplore. Restrictions apply.

[22] Al-Hiary, Heba, et al. "Fast and accurate detection and classification of plant diseases." *International Journal of Computer Applications* 17.1 (2011): 31-38.

[23] Revathi, P., and M. Hemalatha. "Classification of cotton leaf spot diseases using image processing edge detection techniques." *2012 International Conference on Emerging Trends in Science, Engineering and Technology (INCOSET)*. IEEE, 2012.

[24] Adedoja, Adedamola, Pius Adewale Owolawi, and Temitope Mapayi. "Deep learning based on nasnet for plant disease recognition using leave images." *2019 international conference on advances in big data, computing and data communication systems (icABCD)*. IEEE, 2019.

Authorized licensed use limited to: DELHI TECHNICAL UNIV. Downloaded on May 11,2023 at 10:16:37 UTC from IEEE Xplore. Restrictions apply.

Computational Materials Science 226 (2023) 112252

Contents lists available at ScienceDirect

Computational Materials Science

journal homepage: www.elsevier.com/locate/commatsci

Full Length Article

Potential application of novel graphene/diamane interface in silicon-based heterojunction with intrinsic thin layer solar cell

Naima, Pawan K. Tyagi *, Vinod Singh

Department of Applied Physics, Delhi Technological University, New Delhi 110042, India

ARTICLE INFO

Keywords:
HIT solar cell
Transparent Conducting Electrode (TCE)
Emitter layer
2D material
Diamane
Graphene
AFORS-HET version 2.5 software

ABSTRACT

In this article, the patentability of novel graphene/diamane interface in HIT solar cell has been explored by simulated a structure modelled as: graphene (TCO) / n-diamane / a-Si: H (i) / p-cSi / Ag (back contact) with the help of software AFORS-HET version 2.5. Here, n-type diamane is used as an emitter layer and graphene as TCO. An efficiency of 31.2 % is achieved with this structure by varying various parameters of n-type diamane, p-crystalline silicon and hydrogenated intrinsic amorphous silicon layer which is pressed in between the two oppositely doped wafer (diamane and c-Si). Furthermore, when ITO is used as TCO then a comparatively low efficiency 27.15 % is achieved and when the commercially available values of silicon's parameters is used for the validation of results then an efficiency of 24.15 % is obtained. Some parameters of a-Si: H (i) has been further optimized and the optimum efficiency 31.2 % has been found at minimum thickness of 3 nm at bandgap 1.6 eV. Finally, we have demonstrated that only carbon material has an ability that its two-dimensional allotropes can be used as an emitter layer as well as efficient transparent conducting electrode.

1. Introduction

The holy grail hurdle in the profitable expansion of photovoltaic solar cell is to make them cost effective as well as exhibits high efficiency. For this motive, a number of solar cells have been explored and fabricated with different materials in order to increase its efficiency [1,2]. Recently, a new 2D material called diamane (Dn) has been used as an emitter layer by Naima *et. al.* [3] and elaborated the significance of using diamane in silicon heterojunction solar cell for enhancing its efficiency to good extent. In order to further proceed the possibility of achieving higher efficiency, we have explored a HIT (heterojunction solar cell with intrinsic thin layer) module where 2D carbon material (diamane) is used as an emitter layer. It is reported that 26.6 % and more than 30 % efficiency can be achieved for different HIT modules [4,5].

Furthermore, to ease the movement of photons from the emitter layer to the external circuit a transparent conducting oxide (TCO) is needed which must be highly transparent as well as low sheet resistance and high carrier mobility. In this search graphene is found to be potential candidate which possess 97.4 % optical transparency with sheet resistance approximately, 125 Ωsq^{-1} [6] for monolayer graphene and its work function can be manipulate in the range 3.10 eV to 5.57 eV [7,8]. It is reported that HIT module with graphene/MoS_2 interface is commendable for achieving higher efficiency 25.61 % [9]. Similarly, another HIT cell has also been simulated previously, in which up to 20.23 % efficiency has reached for the area of 156 mm × 156 mm active layer of silicon [2]. Therefore, it is plausible to use graphene/diamane interface in HIT solar cells with intention of improving efficiency.

Previously, numerous studies have been done on the excellent optoelectronic properties of various 2D materials and their heterojunctions [10-12]. In 2009, 2-D ultra-thin layer of diamond called diamane was predicted and studied [13,14]. The effective mass of conduction electron in diamane is very small (0.55 m_0) and it has wide bandgap which is diverse ranging from 3.1 eV to 4.5 eV [14,15]. In addition, the carrier' mobility in diamane is also very high as 2732 cm^2/Vs for electrons and 1565 cm^2/Vs for holes for its different forms [15]. Its work function can also be tuned in range 6.78 eV to 7.24 eV by vacuum annealing at 350 ^{0}C [16]. Doping of diamane with nitrogen makes it n-type as well as highly stable material which can be used in different electronic applications. Also, diamane is a sp^3 hybridized C_2H based layered structure on the bilayer graphene which is also sp^3 hybridized and the neighbouring carbon atoms of both materials are covalently bonded with the hydrogen atoms located out there. In this way, we can state that the graphene/diamane interface would be stable [13] and this heterostructure can find applications in electronic devices.

* Corresponding author.
E-mail addresses: pawankumartyagi@gmail.com, pawantyagi@dtu.ac.in (P.K. Tyagi).

https://doi.org/10.1016/j.commatsci.2023.112252
Received 9 January 2023; Received in revised form 17 April 2023; Accepted 7 May 2023
Available online 21 May 2023
0927-0256/© 2023 Elsevier B.V. All rights reserved.

Since, to the best of our knowledge this material is not tested in solar cell's structure yet therefore, we have selected this material as emitter layer in HIT solar cell and studied the patentability of novel graphene/diamane interface.

The nature of diamane layer is considered isotropic during the entire simulation [15]. The motive of this simulation is to attain the maximum possible efficiency of HIT solar cell by optimizing various parameters of both doped and one intrinsic layer as well as front and back contacts at minimum possible thin substrate. The main objective of this report is to examine the effect of graphene layer using as TCE and diamane layer as an emitter layer in HIT solar cell for higher efficiency and to achieve the highest conversion efficiency of HIT solar cell by using thinnest possible silicon substrate or wafer.

2. Simulation and structural details and junction formation

2.1. Simulation and structural details

For all simulation work, a software called AFORS-HET version 2.5 is used in this report which automatize the simulation for heterostructures. This software is a one-dimensional numerical computer program which modelled multi-layer hetero as well as homojunction solar cells and also do modelling for some common solar cell characterization methods [17]. This software usually solves one-dimensional semiconductor equations for both carriers' electrons and holes by using finite difference at different conditions [17]. Within each semiconductor layer the Poisson equation and the transport and continuity equations for electrons and holes have been solved in one-dimension given by:

Poissońs equation,

$$\frac{\varepsilon_o \varepsilon_r}{q}\frac{\partial^2 \varphi(x,t)}{\partial x^2} = p(x,t) - n(x,t) + N_D(x) - N_A(x) + \sum_{trap} \rho_{trap}(x,t) \quad (2)$$

Where, p (x, t) and n (x, t) are the local particle densities in the system q is the electronic charge and ε_o *and* ε_r are the absolute and relative permittivity, respectively.

Continuity and transport equation for electrons and holes to be solved in one - dimension:

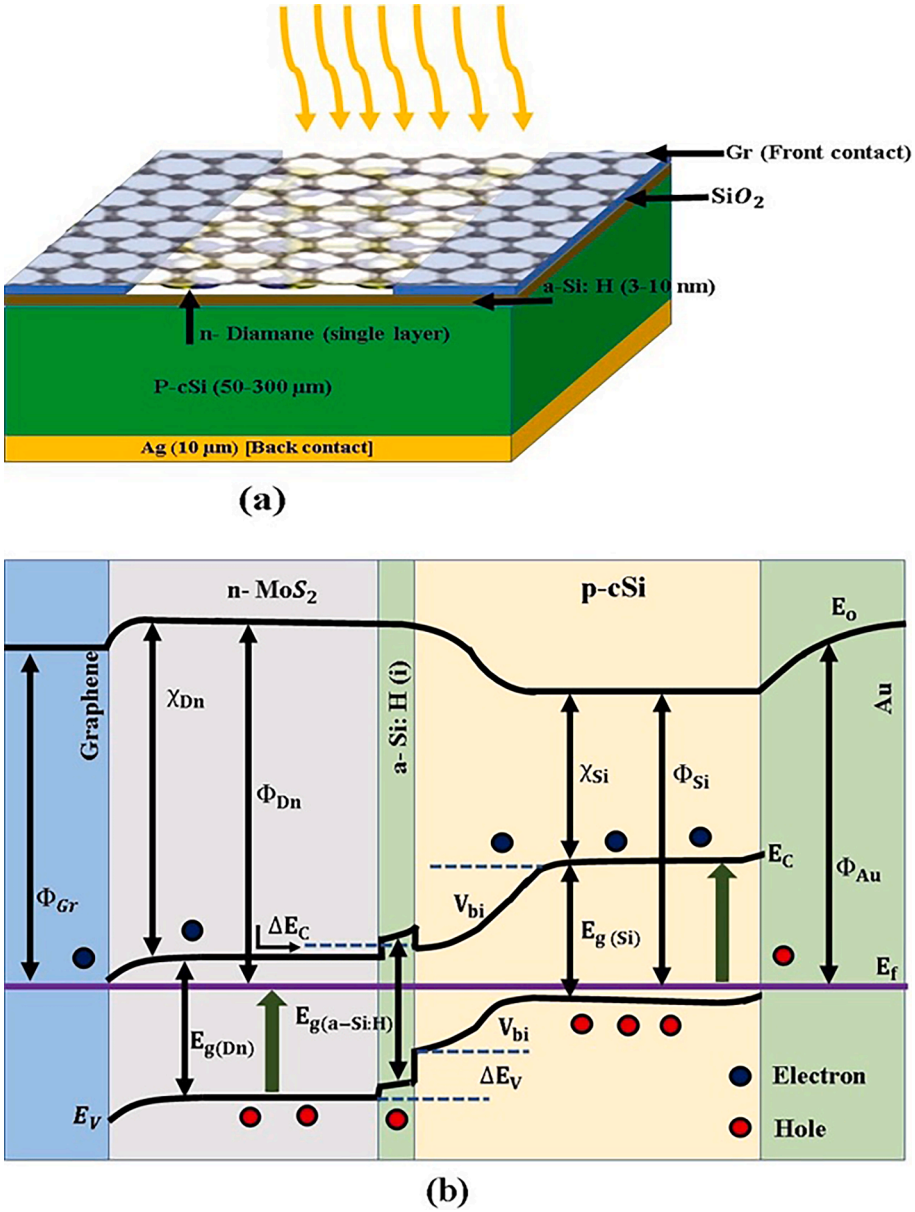


Fig. 1. **(a)** Schematic of designed HIT module. **(b)** energy band diagram for the designed HIT structure showing separation of charges at the interfaces.

$$-\frac{1}{q}\frac{\partial j_n(x,t)}{\partial x} = G_n(x,t) - R_n(x,t) - \frac{\partial}{\partial t}n(x,t) + \frac{1}{q}\frac{\partial j_p(x,t)}{\partial x}$$
$$= G_p(x,t) - R_p(x,t) - \frac{\partial}{\partial t}p(x,t) \quad (3)$$

Where, $G_n(x,t)$ and $G_p(x,t)$ are the electron and hole super-bandgap generation rates and R_n (x, t) and R_p (x, t) are their corresponding recombination rates [17].

In the presented report, electronic nature of both diamane as well as graphene has been considered as 3D instead of 2D. To make sure that Schottky junction will form at the interface, intentionally we have made the electric contacts along the c-axis so that maximum number of charge carriers could collect. The intrinsic amorphous silicon can be deposited on a SiO_2 patterned silicon substrate by using plasma-enhanced chemical vapor deposition method (PECVD) or hot wire CVD method [2] at low temperature in order to prevent thermal damage to the silicon layer. After deposition of the amorphous silicon on the patterned substrate, few layer graphene can be directly transferred by chemical methods used by Sukang Bae *et.al* [6] and these transferred few graphene can be converted to a diamane layers by using chemical fluorination route [14,16]. Furthermore, another layer of graphene can also be directly transferred on diamane 6]. Finally, the back electrode (Ag) at the back surface may be screen printed or deposited in order to extract the light-generated current [2]. In this way, we have a structure Gr / n-Dn / a-Si: H (i) / p-cSi / Ag shown in Fig. 1 (a).

Furthermore, we have explored the HIT solar cell by optimizing the values of some parameters in their possible ranges and by setting some parameters to their default values as well. We have used here both electrical and optical simulation. The HIT structure of solar cell modelled here is; graphene (TCE) / n-Dn / a-Si: H (i) / p-cSi / Ag can be seen in Fig. 1 (a). The front and back contacts are selected on taking the account of their optical transparency as well as conductivity. The ranges of parameters for these two contacts have been taken from the literature available [18-22]. The details of front and back contacts are given in Table 1 and details about the interfaces are given in Table 2. The parameters of different layers used in the simulation are given in Table 3. MS- Schottky interface is consider for graphene / n-Dn and p-cSi / Ag interfaces similarly drift–diffusion interface is chosen for n-Dn / a-Si: H (i) and a-Si: H(i) / p-cSi the interfaces, respectively. The drift–diffusion model drives the interface current. No defects are considered for the interface regions except drift–diffusion interface to avoid additional recombination centres. The electron and hole recombination velocities are taken as 4×10^7 cm/sec at the MS- Schottky interface and tunnelling

Table 1
List of parameters used as front and back contacts [18-22].

Parameters	Front contact			Back contact
	Before simulation	After simulation		
Material	Graphene	ITO	Al	Ag
Thickness	1L–5L (1L = 0.334 nm)	80 nm	80 nm	10 μm
Optical properties	n = 2.7, k = 1.45	ITO nk (default)	n = 1.19 k = 7.05	Ag nk (default)
Work function (eV)	4.3–4.9	4.4–4.5	4.06–4.26	4.64–4.74
Absorption loss	0.023	ITO abs (default)	0.056	0
External reflection	1L = 0 2L = 0.023 3L = 0.046 4L = 0.070 5L = 0.092	ITO Ref (default)	0.868	0
Surface condition	Plane	Plane	Plane	Plane
Internal reflection	0	0	0	0

Table 2
List of range of values of parameters used [32-35].

Parameter	n-Dn	a-Si: H (i)	p-cSi
Thickness	1L – 5L (1L = 0.34 nm)	3–10 nm	50–500 μm
Dielectric constant (ε_r)	8–11	11.9	11.9
Electron affinity χ (eV)	3.6–4.1	3.9	4.05–4.5
Band gap E_g (eV)	0.3 – 1.4	1.6–1.7	1.12
N_C (cm^{-3})	9×10^{17} to 1×10^{21}	0	3×10^{19} to 3×10^{21}
N_V (cm^{-3})	9×10^{17} to 1×10^{21}	0	3×10^{19} to 3×10^{21}
μ_n ($cm^2V^{-1}s^{-1}$)	2732	20	1104
μ_p ($cm^2V^{-1}s^{-1}$)	1565	5	420
N_A (cm^{-3})	0	0	1×10^{16} to 1×10^{19}
N_D (cm^{-3})	2×10^{12} to 8×10^{17}	0	0
V_e (cms^{-1})	1×10^7	1×10^7	1×10^7
V_h (cms^{-1})	1×10^7	1×10^7	1×10^7
Layer density (gcm^{-1})	2.328	2.328	2.328
Auger electron recombination coefficient (cm^6s^{-1})	0	0	2.20×10^{-31}
Auger hole recombination coefficient (cm^6s^{-1})	0	0	9.90×10^{-31}
Band- to- band recombination coefficient (cm^3s^{-1})	0	0	9.50×10^{-15}
Defect type	Conduction tail	Single	Valance tail
Defect charge	Donor	Acceptor	Acceptor
Total defect density (cm^{-3})	1×10^{14}	2.75×10^{16}	1×10^{10}
Specific defect density ($cm^{-3}eV^{-1}$)	6.67×10^{14}	2.75×10^{16}	1.43×10^{11}
Defect level energy (eV)	0.15 (Urbach)	0.6	0.07 (Urbach)
Electron and hole capture cross section (cm^{-2})	1×10^{-14}	7×10^{-19}	1×10^{-14}
Optical properties	n = 1.4, k = 0.75	a-Si nk (default)	c-Si nk (default)

Table 3
List of parameters used at interfaces.

Interface	Model applied
Graphene/n-Dn	MS-Schottky contact
n-Dn/a-Si:H (i)	Drift diffusion model
a-Si:H (i)/p-cSi	Drift diffusion model
p-cSi/Ag	MS-Schottky contact

is kept activated (new feature added in AFORS-HET software version 2.5) during the simulation. The simulation is carried by taking 20 steps to get the better accuracy. Front contact of the cell is taken at positive pole whereas the negative pole is assigned for the back contact of the solar cell. The simulation is carried for the boundary voltage of 0.7 V at temperature 300 K. The front contact of the cell is illuminated with monochromatic light of photon flux 1×10^{16} $cm^{-2}s^{-1}$, spectral width of 10 nm with power density 100 mW/cm^2 under the AM 1.5. When the cell is operated under these conditions an amount of light or photon flux is get absorbed by the super-bandgap of the semiconductor layer which creates electron-hole pairs and to calculate this super-bandgap generation rate $G_n = G_p$ $\left(\frac{hc}{\lambda} \geq E_g\right)$ Lambert-Beer absorption optical model has been chosen [17] which specifies the reflectivity of the semiconductor and calculates the resulting absorption within the semiconductor layer by using only the specified values of extinction coefficient k(λ). In this model, generation rate G_n is calculated from the resulting absorption by doing integration over all incident wavelength range. There are some models to describe the recombination in semiconductors, in diamane layer the recombination is described by Shockley-Read-Hall recombination model [Sze & Kwok, 2007]. In p-cSi semiconductor dangling

bond recombination is used to described the recombination [Sah & Shockley, 1958].

The structure designed as graphene (TCE) / n-Dn / a-Si: H(i) / p-cSi / Ag is displayed in Fig. 1 (a). Amorphous and crystalline silicon solar cell technologies are used to design it [23]. Single layer graphene is chosen as the front contact or the transparent conducting electrode which allows maximum photons flux to pass through it and no internal and external reflection is chosen for this layer to avoid efficiency loss at the front contact of the cell. The front surface is textured by anisotropic etching to reduce reflection [5]. Additionally, no mismatching between the layers of the cell is considered. An ideal 2D semiconductor follows a condition $< t > \leq \lambda_F$, where λ_F is the Fermi wavelength given by $\sqrt{\frac{2\pi}{n_{2D}}}$ nm here n_{2D} is the carrier density in cm^{-2} [24]. It is reported that graphene and therefore diamane do not satisfy this condition [25] and the interlayer space increases due to doping [26]. Therefore, both diamane and graphene are considered as quasi 3D in nature in spite of considering them 2D. For to improve J_{SC}, the quantum confinement is accomplished by controlling the number of layers of diamane and the carrier transport is taken along the c-axis. In order to avoid the efficiency losses due to defects present on the surface of p-cSi layer an intrinsic hydrogenated amorphous silicon layer is inserted on the p-cSi layer which develops a p-n heterojunction. This intrinsic silicon passivates the defects of crystalline silicon which reduces the chances of tunnelling through the localised states present on the doped crystalline silicon due to defects which makes V_{OC} decreased. In this manner the passivation of intrinsic amorphous silicon just improved V_{OC} and consequently efficiency of HIT solar cell and gives the excellent temperature coefficient. The intrinsic amorphous silicon also reduced dangling bond and recombination rate which also became the reason of improved V_{OC} [27]. No thermal losses are considered as the deposition is done by CVD under low temperature [28]. An insulating SiO_2 layer is used to avoid surface recombination between the front contact and silicon layer as shown in Fig. 1(a). For diamane layer donor concentration, effective conduction and valance band density, band gap, electron affinity, dielectric constant and layer numbers are being optimized by keeping the parameters of remaining layers to some specified values. For intrinsic hydrogenated amorphous silicon layer, the parameters which have been optimized are; N_C/N_V, E_g and thickness of the thin intrinsic layer. Further, the optimized parameters in case of p-cSi are; N_A, N_C/N_V, χ, thickness of p-cSi wafer. Layer number as well as work function of graphene layer is also being optimized as well as material and work function of front and back contact have also been optimized. The details of front and back contacts as well as the details of all three optimized layers are tabulated in Tables 1 and 2.

2.2. Junction formation

In n-Dn /p-cSi heterojunction, the diamane and crystalline silicon interface performs main role in the conversion of energy. When n-diamane and p-cSi comes in contact which has work-function difference then the electrons in the silicon layer get depleted and the energy band gets bended close to the Fermi level to form a built-in electric field. The energy band-diagram is shown in Fig. 1(b). The built-in potential further separates the excess electrons and holes generated by the light incident and then convert light energy into electrical energy in form of current flows in external circuit. The built-in potential (eV_{bi}) is given by;

$$(eV_{bi}) = E_{g(Dn)} + \Delta E_V + kT\ln\left(\frac{N_A N_D}{N_{V(Si)}N_{C(Dn)}}\right) = E_{g(Si)} - \Delta E_C + kT\ln\left(\frac{N_A N_D}{N_{V(Si)}N_{C(Dn)}}\right) \quad (1)$$

Where, e is the electric charge, E_g, ΔE_V and ΔE_C are the bandgap, valence band offset and conduction band offset, respectively and k, T are Boltzmann constant, temperature [K]. N_A and N_D are the acceptor and donor concentration and N_C and N_V are the conduction and valence band density, respectively [9].

At the graphene / diamane interface there is Schottky junction formed and a barrier for the transportation of hole is built corresponding to the potential energy of eV_{bi} given by;

$$eV_{bi} = e(\phi_{Dn} - \phi_{Gr}) \quad (2)$$

where, ϕ_{Dn} and ϕ_{Gr} is the work-function of diamane and graphene, respectively [29]. Since the work-function of the graphene layer can be modulated between 4.5 eV and 4.9 eV [7,30] then with large work-function, the built-in potential gets amplified at the junction which consequently, increases the capacity of collecting the photo-generated charge carriers of the heterojunction. The shift in the Fermi level of graphene at heterojunction graphene/diamane performs better in conduction [31]. Since, the dangling bonds over the p-cSi layer degrades the V_{OC} and also the efficiency of solar cell therefore, a perfect passivation is required to improve the overall efficiency. For this type of passivation, intrinsic hydrogenated amorphous silicon wafer is pressed between the heterojunction n-Dn/p-cSi which successfully prevent the tunnelling through localized states present in p-cSi layer because of the presence of many defects and decrease the recombination rate and hence improve the efficiency of HIT solar cell.

3. Result and discussion

3.1. Optimization of diamane layer

In this section, influence of various parameters of n-type diamane on the performance of HIT solar cell has been examined. To do so, the very first parameter we have optimized here is the donor concentration (N_D) of the n-type diamane layer while keeping the remaining parameters at some viable values and the results are shown in Fig. 2 (a and b). The values of parameters used for diamane are taken from the previous literature [32-35]. The a-Si: H (i) layer (3 nm thick) and c-Si layer (500 μm thick) is kept constant at values given in Table 4. The range in which N_D is being varied is 2×10^{12} cm^{-3}–8×10^{17} cm^{-3}, and it is noticed from Fig. 2 (a and b) that V_{OC}, J_{SC}, FF and η remained almost constant during the optimization. There is a very slight change observed in case of FF only. The FF is infinitesimally increased from 83.95 % to 83.96 % as the value of N_D is increased from 6×10^{17} cm^{-3}–8×10^{17} cm^{-3}. Therefore, the optimum donor concentration for n-Dn is 8×10^{17} cm^{-3}. The reason behind the constant value of V_{OC} (698 mV) is that it does not depend on N_D until and unless it does not follow the condition $\Delta n_o \gg N_D$, where Δn_o denotes the excess electron-hole pairs [36]. J_{SC} remained constant during the optimization at 53.04 mA/cm^2, this is because as we increase the donor concentration the mobility of photo-generated charge carriers does not change and therefore there is not a slight change observed in the value of J_{SC} as shown in Fig. 2 (b). Since there is not observed any variation in the values of V_{OC}, J_{SC} and FF on increasing N_D within the range 2×10^{12} cm^{-3}–8×10^{17} cm^{-3} therefore, the value of efficiency will also remain same at 31.08 % as shown in Fig. 2(a). The best optimized value of N_D we have noticed here is 8×10^{17} cm^{-3} which we will keep constant throughout the further optimization of HIT cell.

After getting best optimized value of N_D for the designed HIT solar cell, we will now further optimize the parameter conduction and valance band density (N_C/N_V) in the range from 9×10^{17} cm^{-3} to 1×10^{21} cm^{-3} and the result obtained is shown in Fig. 2 (c and d). From Fig. it is observed that, as the value of N_C/N_V is increased in the chosen limit there is a continuous decrement in the value of V_{OC} from 699.7 mV to 580.6 mV, this is because of the reduction in barrier height which offers less charge carriers near the junction. As a result, small built-in potential is formed near the junction resulted in lower V_{OC}. The value of J_{SC} is found to be constant at 53.04 mA/cm^2 as N_C/N_V goes from 9×10^{17} cm^{-3} to 3×10^{19} cm^{-3} and then start decreasing and reached 52.97 mA/cm^2 at 1×10^{21} cm^{-3}. The reason behind the J_{SC} being constant may be the decrement in the minority carrier density which probably get

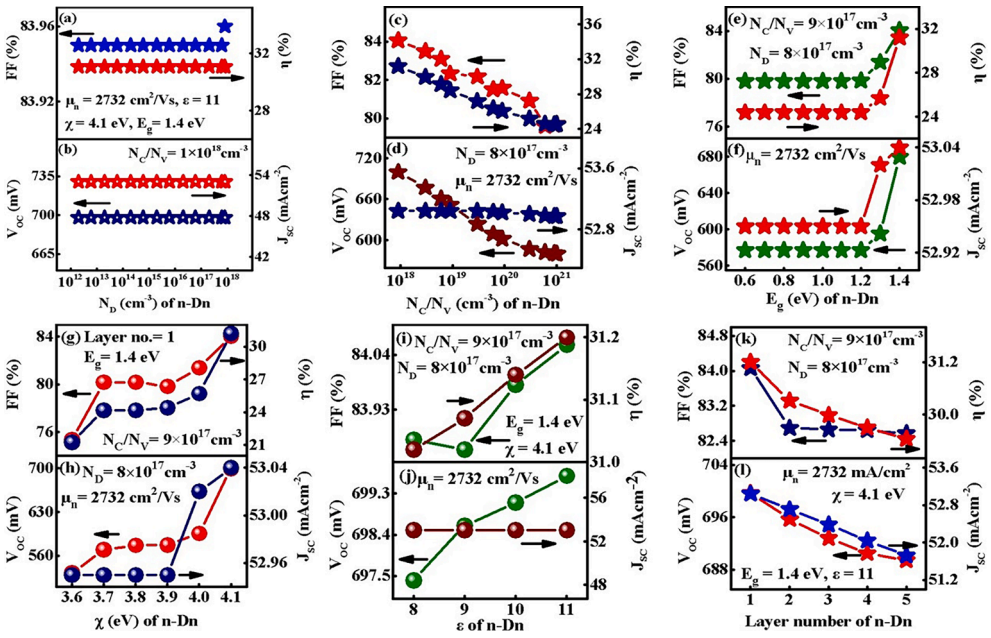


Fig. 2. Simulation of diamane layer by keeping the parameters of remaining layers at values given in Table 4. (a and b) optimization of N_D (cm^{-3}), (c and d) optimization of N_C (cm^{-3}), (e and f) optimization of E_g (eV), (g and h) optimization of χ (eV), (i and j) optimization of ε_r, (k and l) optimization of layer numbers of diamane by keeping its other parameters at optimum set of values.

Table 4
List of initially taken values of parameters.

Parameter	a-Si: H (i)	p-cSi
Thickness	3 nm	500 μm
Dielectric constant (ε_r)	11.9	11.9
Electron affinity χ (eV)	3.9	4.05
Band gap E_g (eV)	1.6	1.12
N_C (cm^{-3})	2×10^{21}	3×10^{19}
N_V(cm^{-3})	2×10^{21}	3×10^{19}
N_A (cm^{-3})	0	1×10^{19}
N_D (cm^{-3})	0	0

declined due to the short life-time of photogenerated charge carriers and trapping of free charge carriers across the interface. Another reason behind the constant value of J_{SC} can be the recombination of photogenerated charge carriers across the interface and due to which these new photogenerated charge carriers do not play an active role in the process. On further increasing the value of N_C/N_V the barrier height gets decreased according to Equation (1) and therefore J_{SC} decreased after N_C/N_V reached 3×10^{19} cm^{-3}. These reduction in the values of V_{OC} and J_{SC} could be the reason for reduction in the values of FF and η from 84.06 % to 79.71 % and 31.2 % to 24.51 %, respectively. In this way 9×10^{17} cm^{-3} is the optimum value of N_C/N_V where we got maximum efficiency 31.2 %.

After optimizing the parameters N_D and N_C/N_V, the next parameter we have optimized here is the bandgap of the n-type diamane layer within the range 0.3 eV to 1.4 eV and the results obtained are displayed in Fig. 2 (e and f). It is observed from figure that, as the bandgap increased from 0.3 eV to 1.1 eV, no variation is found in the values of V_{OC}, J_{SC}, FF and η and they remained constant at 577.1 mV, 52.95 mA/cm², 79.8 % and 24.38 %, respectively. On further increasing the range of bandgap from 1.2 eV to 1.4 eV, the values of all these parameters get increased because of the increment in the barrier height according to Equation (1) as increased V_{bi} separates the photogenerated charge carriers very effectively across the interface and hence increase the value of J_{SC}. In this way, the best efficiency 31.2 % was found at the bandgap 1.4 eV.

The next parameter after N_D, N_C/N_V and bandgap, we have simulated the electron affinity of the diamane layer within 3.6 eV- 4.1 eV and the results are shown in Fig. 2 (g and h). On increasing electron affinity, barrier height increases resulting in increment in the value of V_{OC} from 532.8 mV to 699.7 mV, higher barrier height increases the minority charge carriers which consequently increase the current density from 52.95 mA/cm² to 53.04 mA/cm², and therefore the FF and the efficiency also get increased from 75.35 % to 84.06 % and 21.25 % to 31.2 %, respectively as shown in Fig. 2 (g and h).

The optimization of the parameter, dielectric constant (ε_r) of the diamane layer is shown in Fig. 2 (i and j). We have optimized the value of dielectric constant within the values 8 to 11. It is observed from figure that, as the dielectric constant increases from 8 to 11, V_{OC} and efficiency get increase from 697.4 mV to 699.7 mV and from 31.02 % to 31.2 %, respectively as efficiency was found largely dependent on V_{OC}. The reason behind the increment of V_{OC} is the more electron-hole pair generation in diamane layer on increasing dielectric constant according to the Coulomb's law; $F\propto\frac{1}{\varepsilon_r}$, where F is the electrostatic force between the electrons and holes [29]. From Fig. it is found that J_{SC} is constant at 53.04 mA/cm² throughout the variation of relative permittivity and FF is slightly increased from 83.87 % to 84.06 %. Therefore, the maximum efficiency 31.2 % we obtained at dielectric constant (ε_r) value of 11.

After optimizing various parameters as mentioned above, number of diamane layers was optimized to see its effect on the working of HIT solar cell. The layers were varied up to 5 and the result obtained is shown in Fig. 2 (k and l). As the layers number increased the transmittance decreased [9] which raise difficulty for photons in reaching to the junction and therefore the electron-hole pair generation rate decreased which results in poor efficiency. Therefore, V_{OC} decreased from 699.7 mV to 689.4 mV, J_{SC} decreased from 53.04 mA/cm² to 51.72 mA/cm² and efficiency decreased from 31.2 % to 29.44 % as number of layers increased from 1 to 5. Since the sheet resistance decreases on increasing the number of layers. Therefore, the value of FF also gets reduced from 84.06 % to 82.57 % as shown in Fig. 2 (k). In this way maximum efficiency 31.2 % was achieved at single layer diamane.

3.2. Optimization of a-Si: H(i) layer

Since, an extremely high-quality thin a-Si: H(i) layer plays main role

in proving HIT solar module better than general heterojunction solar cell module, because it passivates the defects present in the silicon layer which causes the poor conversion efficiency of heterojunction solar cells. The placing of thin a-Si: H(i) layer enhances V_{OC} because it decreases the interface recombination velocity [23,27]. This thin layer also contributes in the depletion region, drift current and electric field strength as well [37]. Therefore, it became essential to inspect the effect of optimizing the parameters of this thin layer on the working of HIT solar cell. To do this simulation the optimized parameters of diamane layer are used and the parameters of p-cSi and remained parameters of a-Si: H (i) are kept at their initial taken values. In order to do so we first have optimized the effective conduction and valance band density (N_C/N_V) of a-Si: H(i). We have optimized N_C/N_V in the range 1.5×10^{21} cm^{-3}–3×10^{21} cm^{-3} by keeping the thickness of a-Si: H(i) at 3 nm and bandgap at 1.6 eV. The obtained results are depicted in Fig. 3 (a and b). It is noticed from the figure that on increasing the value of N_C/N_V, V_{OC} and J_{SC} remains constant at 699.7 mV and 53.04 mA/cm^2. The value of FF gets slightly increased from 84.04 % to 84.06 % and therefore there was certainly tiny increment observed in the value of efficiency also, it increased from 31.19 % to 31.20 % which is really tiny increment. Therefore, the optimization of the parameter N_C/N_V of a-Si: H(i) does not seem to have any major effect on the efficiency of HIT solar module and the maximum efficiency 31.2 % was obtained in the range 1.5×10^{21} cm^{-3}–3×10^{21} cm^{-3}.

By assigning a value 2×10^{21} cm^{-3} to the N_C/N_V we further have optimized the bandgap of a-Si: H(i) at two values 1.6 eV and 1.7 eV and the results are shown in Fig. 3 (c and d). From Fig. it is noticed that on increasing the bandgap from 1.6 eV to 1.7 eV, V_{OC} get decreased from 699.7 mV to 696.3 mV. The values of J_{SC}, FF and efficiency were also decreased from 53.04 mA/cm^2 to 53.02 mA/cm^2, 84.06 % to 82.43 % and 31.2 % to 30.43 %, respectively. The deterioration in the value of J_{SC} is because the number of photons which get absorbed only when their energy is less than the bandgap of intrinsic hydrogenated amorphous layer, decreased. This decrement in the absorbed photon numbers leads to decrease the number of electron-hole pairs which consequently decreases J_{SC}. For the better performance of the HIT solar cell, 1.6 eV is the best optimized bandgap for a-Si: H (i) at which efficiency is maximum 31.2 % as shown in Fig. 3 (c). This is maybe probably because of the absorbed photons by the diamane layer corresponding to the bandgap value of a-Si: H (i) layer [9].

After getting our best optimized values of N_C/N_V and bandgap for a-Si: H (i), next we have optimized the thickness of a-Si: H (i) which majorly effects the performance of HIT solar cell module. The thickness of a-Si: H (i) is optimized between 3 nm and 10 nm and the obtained results are shown in Fig. 3 (e and f). As the thickness increase from 3 nm to 7 nm V_{OC} remains constant at 699.7 mV but as the thickness increase further it gets decrease from 699.7 mV to 698.6 mV as shown in Fig. 3 (f). This happens because as the thickness of amorphous layer increases more dangling bonds will affect the efficiency of the solar cell, as more photogenerated charge carriers get trapped by these dangling bonds which causes the deterioration of V_{OC} [27]. The J_{SC} was also found to decreases from 53.04 mA/cm^2 to 44.67 mA/cm^2 as shown in Fig. 3 (f). This decrement in the value of J_{SC} is because of the increased sheet resistance in thicker intrinsic layer [9]. The FF decrease from 84.06 % to 83.68 % which consequently leads to the decrement in the conversion efficiency from 31.2 % to 26.11 % on increasing the thickness from 3 nm to 10 nm, results are shown in Fig. 3 (e). Therefore, on increasing thickness of the a-Si: H (i) layer the power conversion efficiency of the HIT solar cell decreases. In this way, the best optimized efficiency is achieved at the thickness 3 nm shown in Fig. 3 (e). The passivation is done by using the high quality thinnest possible intrinsic hydrogenated amorphous silicon layer in HIT structured solar cells.

3.3. Optimization of p-cSi layer

Since, an intrinsic amorphous silicon layer is introduced in between two doped layers of diamane and crystalline silicon like; graphene (TCE) / n-Dn / a-Si: H(i) / p-cSi / Ag displayed in Fig. 1 (a) therefore, the processing of c-Si layer of achieving good efficiency get improved as the effective lifetime of the cell becomes lower which improves efficiency with higher V_{OC}. The inserted intrinsic layer basically passivates crystalline silicon layer which drastically change the working principle of c-Si wafer or active layer which affects the power conversion efficiency of HIT structured solar cell in a positive way. This passivation improves the efficiency of cell in a such a way that the active layer effectively separates the generated charge carriers which reduce the recombination velocity at the interface and improve V_{OC}. This improved V_{OC} then improve the efficiency and temperature coefficient of the HIT solar cell [38]. If the recombination velocity is low as in the case of HIT solar cells, then it became easy for thinner silicon wafer to maintain excess carrier density and that is how V_{OC} improves [28] and more cost-effective solar cell is achieved. In this section we have discussed about the effect of optimization of the parameters of the p-cSi wafer on the power conversion efficiency of HIT structured solar cell. While doing the simulation up on the p-cSi wafer the parameters of n-Dn layer and a-Si: H(i) layer was fixed to their best optimal values. For doing so, initially we have simulated the acceptor concentration N_A of p-cSi wafer in the rage 1×10^{16} cm^{-3} to 1×10^{19} cm^{-3} and the results are depicted in Fig. 4 (a and b). V_{OC}, J_{SC}, FF and η was found to increase from 622.6 mV to 699.7 mV, 39.88 mA/cm^2 to 53.04 mA/cm^2, 83.06 % to 84.06 % and 20.62 % to 31.2 %, respectively. The improvement in the value of V_{OC} is because of the increment of barrier height on increasing the acceptor concentration according to Eq. (1). Since the higher eV_{bi} deteriorates the recombination rate due to which photo-generated charge carriers move rapidly from the depletion region to the contact region and no trapped effect is experienced by the carriers in the neutral region [9,39]. Therefore, J_{SC} get increased which reduced the sheet resistance consequently, FF increases. The increment in these parameters leads in an

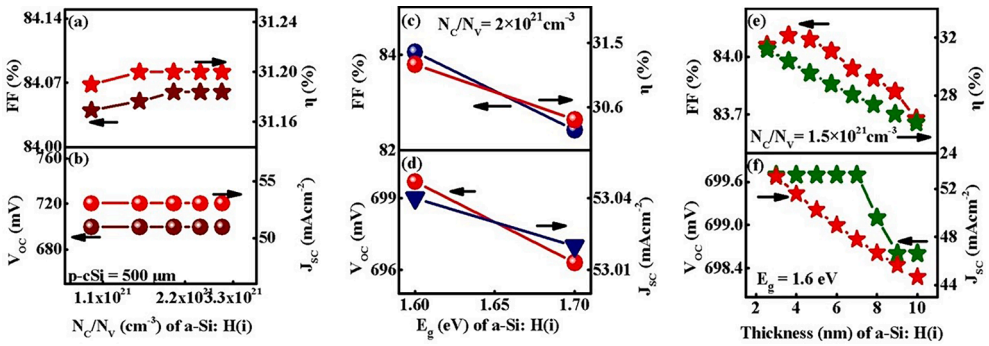


Fig. 3. Simulation of a-si: h (i) at optimized diamane and other layers at the previous set of values (Table 4). (a and b) optimization of N_C/N_V (cm^{-3}), (c and d) optimization of E_g (eV), (e and f) optimization of thickness (nm).

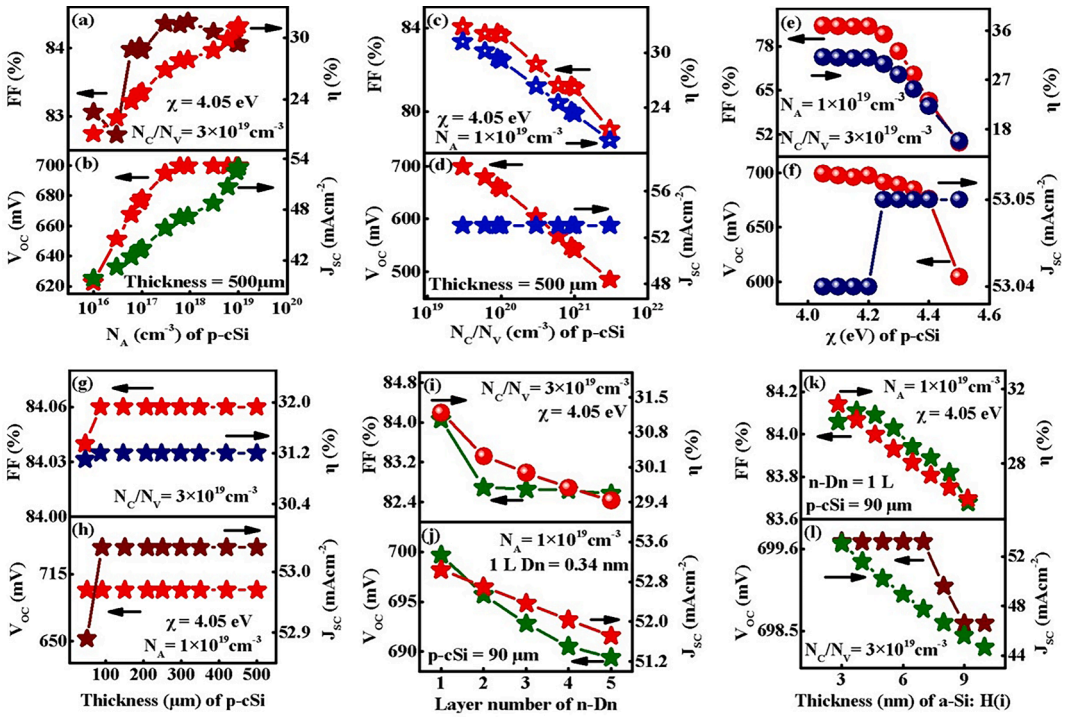


Fig. 4. Simulation of p-csi layer at optimized diamane as well as a-si: h(i) layer. (a and b) optimization of N_A (cm^{-3}), (c and d) optimization of N_V (cm^{-3}), (e and f) optimization of χ (eV), (g and h) optimization of thickness (μm), (i and j) optimization of layer numbers of diamane at fully optimized cell, (k and l) optimization of thickness (nm)of a-Si: H (i) again at fully optimized cell.

increased efficiency. In this way, the maximum efficiency 31.2 % was obtained at N_A 1 × 10^{19} cm^{-3}.

After obtaining the best optimized value of N_A, we have optimized the value of N_C/N_V of p-cSi layer from 3 × 10^{19} cm^{-3} to 3 × 10^{21} cm^{-3} and the results are shown in Fig. 4 (c and d). From Fig. it is shown that, as N_C/N_V increases V_{OC} decreases linearly from 699.7 mV to 485.6 mV. It is because according to Eq. (1), barrier height decreases as N_V of p-cSi increases which makes V_{OC} to decrease. The value of J_{SC} was found to remained constant at 53.04 mA/cm^2 as we go from 3 × 10^{19} cm^{-3} to 3 × 10^{21} cm^{-3} this might be happened because of the recombination and trapping of carriers across the interface. The FF on increasing the N_C/N_V gets decrease from 84.06 mA/cm^2 to 79.15 mA/cm^2 which leads to decrease the efficiency from 31.2 % to 20.39 %. Therefore, the optimum value of N_C/N_V for p-cSi wafer is 3 × 10^{19} cm^{-3}.

The next parameter to get optimized in this report after optimizing N_A and N_C/N_V of p-cSi layer is the electron affinity of p-cSi layer. The electron affinity we have optimized in the range from 4.05 eV to 4.5 eV and the desired results are depicted in Fig. 4 (e and f). Figure shows that on increasing the χ, V_{OC} decreased from 699.7 mV to 604.7 mV and FF decreased from 84.06 % to 49.52 % and therefore the efficiency also dropped from 31.2 % to 15.89 %. The reason behind this deterioration is may be the variation in the work-function of p-cSi layer which consequently reduce the transportation of the charge carriers across the p-cSi layer. This reduction in the transportation rate of charge carriers through the p-cSi layer increase the series resistance in the p-cSi layer due to which FF and η decreased. A tiny increment was observed in the value of J_{SC} from 53.04 mA/cm^2 to 53.05 mA/cm^2 as shown in Fig. 4 (f).

Since, in this report we have simulated the result keeping in mind to reduce the production cost of solar cell therefore the next parameter we have optimized here is the thickness of p-cSi wafer because the thickness of p-cSi wafer enhanced the manufacturing cost of solar cell. So, we have simulated the keeping the thickness of p-cSi wafer within the range of 50 μm to 300 μm and the result is shown in Fig. 4 (g and h). As we increase the thickness, the V_{OC} does not change at all and it remains uniform throughout maintaining the value 699.7 mV as shown in Fig. 4 (h). As the thickness increases photogenerated charge carriers increases but at the same time the recombination and trapping of these charge carriers also increases due to the defects present in the p-cSi layer, which restricts the V_{OC} either to get increased or decreased therefore it remains constant as the thickness increases. Further, J_{SC} was found to slightly increased from 52.89 mA/cm^2 to 53.04 mA/cm^2 as the thickness increased. This is because of the increased photogenerated charge carriers on increasing the thickness of layer. The FF and η also get slightly increased from 84.04 % to 84.06 % and 31.1 % to 31.2 %, respectively as shown in Fig. 4 (g). The reduction in series resistance of the p-cSi layer maybe the reason behind this small improvement in the value of FF [9]. Since HIT structure solar cell has tendency of getting good efficiency even for thin silicon wafer therefore, the best efficiency of the solar cell is achieved at the thickness 90 μm which makes it comparatively less costly.

After achieving the best optimized parameters of n-Dn, a-Si: H (i) and p-cSi layers, the cell then again simulated by optimizing the layer numbers of diamane and thickness of intrinsic amorphous silicon to see the effect of changing the layer number of n-Dn and the thickness of a-Si: H (i) wafer on the best simulated solar cell and the results are shown in Fig. 4 (i and j) and (k and l) respectively. From Fig. 4 (i and j) it is shown that, all the parameters such as V_{OC}, J_{SC}, FF and η decreased as the number of diamane layers increased from 1 to 5. V_{OC} decreased from 699.7 mV to 689.4 mV, J_{SC} decreased from 53.04 mA/cm^2 to 51.71 mA/cm^2, FF varies from 84.06 % to 82.57 % and efficiency decreased from 31.2 % to 29.44 %. This deterioration in the values of these parameters is because of the reduction of absorbed photons as the transmittance increases on increasing the layers. From figure it is shown that as the thickness of a-Si: H (i) wafer increases from 3 nm to 10 nm the values of V_{OC}, J_{SC}, FF and η decreases from 699.7 mV to 698.6 mV, 53.04 mA/cm^2 to 44.67 mA/cm^2, 84.06 % to 83.68 % and 31.2 % to 26.11 % respectively. This happened probably because of addition of more dangling bonds and less excitations of charge carriers on increasing the thickness of intrinsic layer [40]. Minimum efficiency 26.11 % was seen at the thickness 10 nm and therefore the maximum efficiency 31.2 % was

achieved for 3 nm thick a-Si: H (i) layer.

3.4. Optimization of the TCE (graphene) parameters

In this section, we have optimized the work-function as well as layer numbers of graphene which is used as transparent conducting electrode in the present article. It is now well established that graphene can be transferred on the other substrate by using chemical route [41]. To study the influence of the work function and layer numbers of graphene layer (TCO) on the efficiency of solar cell we have varied the layer from 1 to 5 and the work function in the range from 4.3 eV to 4.9 eV and the results are shown in Fig. 5 (a and b) and (c and d) respectively. From Fig. 5 (a and b) it is shown that, as the layer numbers increases from 1 to 5 where the thickness of single layer graphene is 0.334 nm and the external reflection, we have considered zero for single layer graphene, the value of V_{OC} decreased from 699.7 mV to 111.4 mV and J_{SC} decreased from 53.04 mA/cm^2 to 48.02 mA/cm^2. The FF and the efficiency also decreased from 84.06 % to 49.97 % and from 31.2 % to 2.672 % as shown in Fig. 5 (a and b). The reason behind the decrement in the value of efficiency is that as the layer number increases the reflection coefficient of the graphene layer increases which opposes the photons to enter into the cell and therefore the efficiency gets decline. Fig. 5 (c and d) shows that, on increasing the work function of graphene layer at single layer diamane and graphene at 90 μm thickness of c-Si layer, the V_{OC} decreases from 699.7 mV to 114.3 mV on increasing the work function of graphene from 4.30 eV to 4.90 eV. J_{SC} decreases very slightly from 53.04 mA/cm^2 to 53.01 mA/cm^2. Furthermore, noticeable decrement in the value of fill factor is also noticed from 84.06 % to 50 % while increasing the value of work function from 4.30 eV to 4.90 eV. As a result, the overall efficiency of the HIT cell decreased from 31.2 % to 3.028 % as work function decreases in the considered range of values. The deterioration in the value of V_{OC} on increasing the work function of graphene layer is maybe due to the reduction of the potential barrier energy eV_{bi} of graphene/n-Dn following equation (2). It is also reported that if the work function of TCO in case of Si HIT cells, is low then the direction of eV_{bi} of TCO/n-type emitter and n-type emitter/p-type Si will be in the same direction [9]. Conversely, if the work function of TCO is high then eV_{bi} of TCO/n-type emitter will be in the opposite direction that of n-type emitter/p-type Si [9]. Furthermore, the increment in the work function of the TCO in case of Si HIT cells causes the depletion in the emitter regions to gets widen which in result the overlapping of TCO/n- diamane emitter region and n-type emitter/p-cSi region coincide if the emitter layer is also not sufficiently thick [42]. Therefore, an increment in the work function of graphene layer may increase the chances of overlapping between the graphene/n-type emitter depleted region and n-type emitter/p-cSi depleted region and subsequently an overall deterioration in the value of V_{OC} can be seen [9] from Fig. 5 (d). The reason for J_{SC} being decreased can be understood by the fact that on

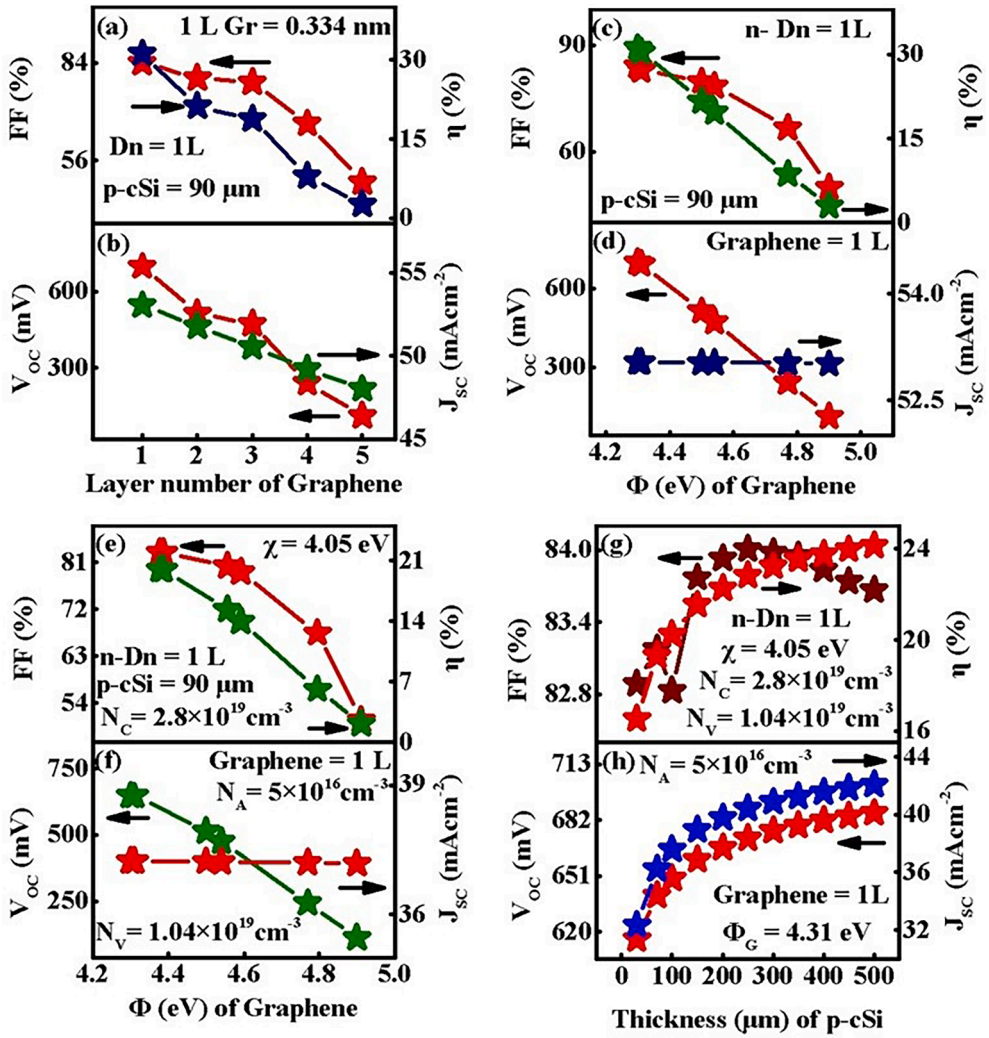


Fig. 5. Simulation of graphene (TCE) at optimized cell. (a and b) optimization of layer numbers, (c and d) optimization of ϕ (ev) at single layer graphene, (e and f) optimization of ϕ (ev) of graphene layer by taking commercially available values of p-csi layer. (g and h) thickness of p-csi layer at single layer graphene with ϕ = 4.31 eV (other parameters of p-cSi layer are at practically available set of values).

increasing the work function of graphene layer, since the depletion region of graphene/n-type emitter and n-type emitter/p-cSi gets overlap which causes the eV_{bi} of n-Dn/p-cSi layer to get influenced or decreased which in turn reduces the built-in electric field and this poor electric field gets unable to push the photogenerated charge carrier to its respective electrode under short circuit condition. Therefore, the J_{SC} gets declined as shown in Fig. 5 (d). Since, there is a decrement in the values of V_{OC} and J_{SC} is found therefore the overall efficiency and FF will also suffer and gets declines on increasing work function from 4.30 eV to 4.90 eV as shown in Fig. 5 (c). In this manner the highest efficiency 31.2 % was achieved at the lowest value 4.30 eV of work function for pristine graphene.

The optimization is further carried out to optimized value of work function and thickness of graphene layer for commercially available parameters of crystalline silicon layer and the results are shown in Fig. 5 (e and f) and (g and h), respectively. This optimization is carried at the single layer graphene and single layer diamane. During this optimization of graphene's work function the thickness of p-cSi is taken as 90 μm and for optimizing the thickness of silicon layer the best optimized work function 4.31 eV is considered as revealed from Fig. 5 (e and f) and (g and h), respectively. We have extended this work to validate the best simulated results and to make a comparison at all best optimized parameters of diamane and a-Si: H (i) and the commercially available data of p-cSi layer is picked from the available literature [43]. From Fig. 5 (e and f) it is shown that, the maximum efficiency 19.98 % is achieved at the smaller value of work-function 4.30 eV as we increase it from 4.30 eV to 4.9 eV. This indicates that as the work function of graphene layer increased the efficiency decreased in the same manner as happened for our best optimized results, shown in Fig. 5 (c and d) and the best optimized value of work function 4.30 eV in Fig. 5 (e and f) is also so close to the best optimized results, Fig. 5 (c and d). In the same manner, it is found from Fig. 5 (g and h) that the maximum efficiency 24.15 % is obtained for 500 μm thickness of p-cSi layer which is also valid for the best optimized cell as shown in Fig. 4 (g and h).

3.5. Optimization and simulation of front and back contact material

To investigate the effect of material selected as the front contact and the back contact on the performance or efficiency of the photovoltaic cell, we have further done the simulation by varying the material used as the front and back contact and its parameters. The simulation is done at the fully optimized cell with single layer diamane and 90 μm thick p-cSi layer and the results are shown in Fig. 6. A comparison has been made between the front contact materials: graphene, ITO and aluminium by varying their work function in order to find the optimum material with its optimum work function. The work function of graphene is already optimized in the above section of the report and we have found that the maximum efficiency 31.2 % is gained at work function 4.3 eV whereas, the maximum efficiency attained by ITO is 27.15 % at the work function 4.4 eV and in case of Al the maximum attainable efficiency is found to be 2.27 % at 4.06 eV of work function as shown in Fig. 6 (a and b) and (c and d), respectively. The thickness of ITO was taken 80 nm and its work function is varied in the range 4.40 eV-4.50 eV [44] whereas, the work function of aluminium is varied within the range 4.06 eV-4.26 eV. These results clearly show that the optimum material for to use as the front contact is graphene with its work function 4.3 eV. After deciding the optimum front contact material, the next optimization is carried around the work function of the back contact Ag. The work function of Ag is varied from 4.64 eV and 4.74 eV and the thickness is considered as 10 μm the results are shown in Fig. 6 (e and f). It is seen from the Figure that, the V_{OC} and J_{SC} is constant at values 699.7 mV and 53.04 $mAcm^{-2}$ as the work function is increased from the value 4.64 eV to 4.74 eV whereas, the value of FF and efficiency are increased from 83.99 % to 84.06 % and 31.17 % to 31.2 %, respectively. Therefore, the maximum efficiency 31.2 % is achieved at the work function 4.74 eV. In this way, Ag is chosen as the back contact with optimum work function 4.74 eV.

Finally, to validate the method applied in our work, we have also simulated previously reported model as gr/MoS_2/c-Si in [45] and we have attained an efficiency of 15.68 % with V_{OC} = 468 mV, J_{SC} = 42.93 mA/cm^2 and FF = 78.08 %. These results are found to be much convincing with the reported values of the conversion efficiency 15.8 %, V_{OC} = 590 mV, J_{SC} = 36.80 mA/cm^2 and FF = 73 %. Similarly, another evidence regarding this method has already been provided by our research group in their report [25] in which they have attained an efficiency of 9.81 % which was in close approximation of experimentally obtained results (η = 9.27 %) [46] . Furthermore, to show the novelty of the presented work a comparison between our work and previously reported similar work on Si-based solar cells along with their sizes and parameters has been tabulated in Table 5.

Additionally, in our knowledge till date no one has used graphene/diamane interface in silicon based solar cells except for our work.

4. Conclusion

In this work, we have examined potentiality of graphene/diamane interface in Si-HIT solar cell. we have also made a comparison between ITO and graphene to be used as TCO and diamane as emitter layer which is not ever done so far. Also, various parameters of hydrogenated intrinsic thin amorphous silicon layer have also been optimized except its bandgap. Due to which the efficiency of considered HIT cell get influenced and found to increase from 25.61 % to 31.2 % from the previous report. Furthermore, a comparison has been made between the theoretical and commercially possible cell to validate the obtained results which are found in accordance. The maximum efficiency for the commercially possible cell is reported to be 24.15 % at graphene (TCO) work function 4.3 eV, single layer diamane and 500 μm thick silicon wafer which is matched with the theoretical results. The independent

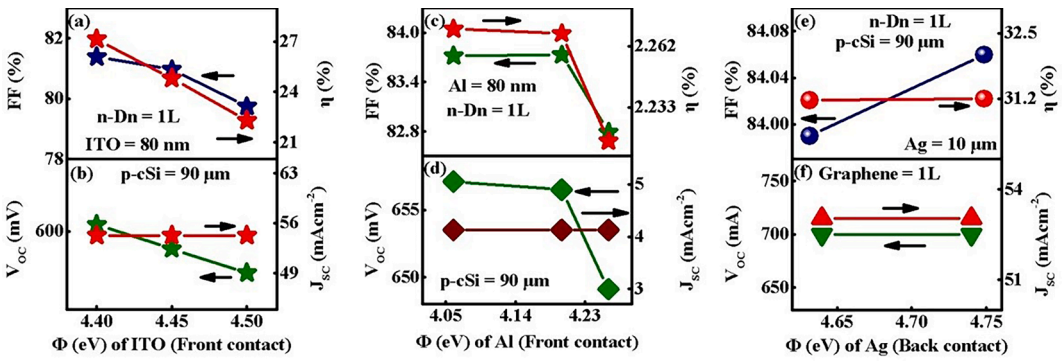


Fig. 6. Simulation of front as well as back contact surfaces for final optimized cell. (a and b) optimization of the work function (eV) of ITO at thickness 80 nm, (c and d) optimization of work function (eV) of Al (front contact) at thickness 80 nm, (e and f) optimization of work function (eV) of Ag (back contact) at thickness 10 μm.

Table 5
Crystalline silicon based solar cells.

Nature of study	Structure	Area/thickness	V_{OC}	J_{SC}	FF	η	Ref.
Experimental	ITO/Gr/MoS_2/n-cSi/Ag	3 mm × 3 mm	590 mV	36.8 mA/cm^2	73 %	15.8 %	[45]
Experimental	TCO/p-aSi/(i) aSi:H/n-cSi/(i) aSi;H/n-aSi/TCO	100.5 cm^2	725 mV	39.09 mA/cm^2	79.10 %	22.30 %	[47]
Experimental	ITO/p-MoO_x/(i) aSi:H/n-cSi/(i) aSi:H/n-aSi/ITO/Ag	3.93 cm^2	725.4 mV	38.60 mA/cm^2	80.36 %	22.50 %	[48]
Theoretical	Ag/TCO/p-aSi/(i) aSi:H/n-cSi/(i) aSi:H/n-aSi/TCO/Ag	161 μm	747.1 mV	39.56 mA/cm^2	84.98 %	25.11 %	[49]
Theoretical	Gr/n-MoS_2/a-Si:H/p-cSi/Au	500 μm	697 mV	44.25 mA/cm^2	82.95 %	25.61 %	[11]
Experimental	TCO/(i)aSi:H/n-cSi/(i) aSi;H/(n/p)aSi/Electrode	165 μm	744 mV	42.30 mA/cm^2	83.80 %	26.30 %	[50]
Experimental	TCO/(i)aSi:H/n-cSi/(i) aSi;H/(n/p)aSi/Electrode	180 cm^2	740 mV	42.50 mA/cm^2	84.60 %	26.60 %	[5]
Theoretical	Gr/n-Dn/a-Si:H(i)/p-cSi/Ag	90 μm	699.7 mV	53.04 mA/cm^2	84.06 %	31.20 %	Our Work

effect of different parameters of n-diamane and p-cSi layer have also been studied. The variation in layer numbers of graphene has also been carried out and it is found that the maximum efficiency 31.2 % can be only achieved for single layer graphene. The obtained results suggest that graphene and diamane can be used as the good transparent conducting electrode and emitter layer.

Declaration of Competing Interest

The authors declare that they have no known competing financial interests or personal relationships that could have appeared to influence the work reported in this paper.

Data availability

Data will be made available on request.

Acknowledgement

The author is thankful to the financial support provided by the Delhi Technological University, New Delhi for providing DTU fellowship and authors appreciatively accredited Helmholtz-Zentrum Berlin who provided AFORS-HET simulation software.

References

[1] S.R. Bera, S. Saha, Fabrication of CdTe/Si heterojunction solar cell, Appl. Nanosci. 6 (2016) 1037–1042, https://doi.org/10.1007/s13204-015-0516-5.
[2] X. Yang, J. Bian, Z. Liu, S. Li, C. Chen, S. He, HIT Solar cells with N-type low-cost metallurgical Si, Adv. Optoelectronic (2018) 7368175, https://doi.org/10.1155/2018/7368175.
[3] Naima, P.K. Tyagi, V. Singh, N-type diamane: An effective emitter layer in crystalline silicon heterojunction solar cell, Carbon Trends. 9 (2022), 100209, https://doi.org/10.1016/j.cartre.2022.100209.
[4] M. Alla, V. Manjunath, N. Chawki, D. Singh, S.C. Yadav, M. Rouchdi, F. Boubker, Optimized CH3NH3PbI3-XClX based perovskite solar cell with theoretical efficiency exceeding 30%, Opt. Mater. (Amst). 124 (2022), 112044 https://doi.org/10.1016/j.optmat.2022.112044.
[5] K. Yoshikawa, W. Yoshida, T. Irie, H. Kawasaki, K. Konishi, H. Ishibashi, T. Asatani, D. Adachi, M. Kanematsu, H. Uzu, K. Yamamoto, Exceeding conversion efficiency of 26% by heterojunction interdigitated back contact solar cell with thin film Si technology, Sol. Energy Mater. Sol. Cells. 173 (2017) 37–42, https://doi.org/10.1016/j.solmat.2017.06.024.
[6] S. Bae, H. Kim, Y. Lee, X. Xu, J.-S. Park, Y. Zheng, J. Balakrishnan, T. Lei, H. Ri Kim, Y. Il Song, Y.-J. Kim, K.S. Kim, B. Özyilmaz, J.-H. Ahn, B.H. Hong, S. Iijima, Roll-to-roll production of 30-inch graphene films for transparent electrodes, Nat. Nanotechnol. 5 (2010) 574–578, https://doi.org/10.1038/nnano.2010.132.
[7] J.-H. Kim, J.H. Hwang, J. Suh, S. Tongay, S. Kwon, C.C. Hwang, J. Wu, J. Young Park, Work function engineering of single layer graphene by irradiation-induced defects, Appl. Phys. Lett. 103 (2013), 171604, https://doi.org/10.1063/1.4826642.
[8] P. Lazar, R. Zbořil, M. Pumera, M. Otyepka, Chemical nature of boron and nitrogen dopant atoms in graphene strongly influences its electronic properties, Phys. Chem. Chem. Phys. 16 (2014) 14231–14235, https://doi.org/10.1039/C4CP01638F.
[9] C.K. Borah, P.K. Tyagi, S. Kumar, The prospective application of a graphene/MoS_2 heterostructure in Si-HIT solar cells for higher efficiency, Nanoscale Adv. 2 (2020) 3231–3243, https://doi.org/10.1039/D0NA00309C.
[10] M.J. Abdulameer, S.S. Abed Al-Abbas, H.R. Jappor, Tuning optical and electronic properties of 2D Zn I_2/CdS heterostructure by biaxial strains for optical nanodevices: a first principles study, J. Appl. Phys. 129 (2021), 225104, https://doi.org/10.1063/5.0054365.
[11] A. Bafekry, M. Faraji, M.M. Fadlallah, Two-dimensional porous graphitic carbon nitride C_6N_7 monolayer: first-principles calculations, Appl. Phys. Lett. 119 (2021), 142102, https://doi.org/10.1063/5.0060496.
[12] A. Bafekry, M.M. Fadlallah, H.R. Jappor, S. Karbasizadeh, M. Ghergherehchi, D. Gogova, Biphenylene monolayer as a two-dimensional nonbenzenoid carbon allotrope: a first-principles study, J. Phys.: Condens. Matt. 34 (2022), 015001, https://doi.org/10.1088/1361-648X/ac2a7b.
[13] L.A. Chernozatonskii, P.B. Sorokin, A.G. Kvashnin, D.G. Kvashnin, Diamond-like C_2H nanolayer, diamane: simulation of the structure and properties, JETP Lett. 90 (2009) 134–138, https://doi.org/10.1134/S0021364009140112.
[14] L.A. Chernozatonskii, V.A. Demin, D.G. Kvashnin, Fully hydrogenated and fluorinated bigraphenes–diamanes: theoretical and experimental studies, C. 7 (2021), https://doi.org/10.3390/c7010017.
[15] T. Cheng, Z. Liu, Z. Liu, High elastic moduli, controllable bandgap and extraordinary carrier mobility in single-layer diamond, J. Mater. Chem. C. 8 (2020) 13819–13826, https://doi.org/10.1039/D0TC03253K.
[16] K.J. Rietwyk, S.L. Wong, L. Cao, K.M. O'Donnell, L. Ley, A.T.S. Wee, C.I. Pakes, Work function and electron affinity of the fluorine-terminated (100) diamond surface, Appl. Phys. Lett. 102 (2013) 91604, https://doi.org/10.1063/1.4793999.
[17] R. Stangl, Numerical Simulation of Solar Cells and Solar Cell Characterization Methods: the Open-Source on Demand Program AFORS-HET, in: C. Leendertz (Ed.), IntechOpen, Rijeka, 2010: p. Ch. 14. https://doi.org/10.5772/8073.
[18] R. Schlaf, H. Murata, Z.H. Kafafi, Work function measurements on indium tin oxide films, J. Electron Spectrosc. Relat. Phenom. 120 (2001) 149–154, https://doi.org/10.1016/S0368-2048%2801%2900310-3.
[19] M. Uda, A. Nakamura, T. Yamamoto, Y. Fujirnoto, Work function of polycrystalline Ag, Au and A1, J. Electron Spectrosc. Relat. Phenom. 88–91 (1998) 643–648, https://doi.org/10.1016/S0368-2048(97)00236-3.
[20] C. Nunes de Carvalho, A. Luis, G. Lavareda, E. Fortunato, A. Amaral, Effect of thickness on the properties of ITO thin films deposited by RFPERTE on unheated, flexible, transparent substrates, Surf. Coat. Technol. 151–152 (2002) 252–256, https://doi.org/10.1016/S0257-8972(01)01641-3.
[21] P. Hess, Thickness of elemental and binary single atomic monolayers, Nanoscale Horiz. (2020) 385, https://doi.org/10.1039/c9nh00658c.
[22] Y. Shin, J. Kim, Influences of the Ag and the ITO thicknesses on the optical and the electrical properties of ITO/Ag/ITO multilayer films, J. Korean Phys. Soc. 74 (2019) 871–875, https://doi.org/10.3938/jkps.74.871.
[23] Y. Tsunomura, Y. Yoshimine, M. Taguchi, T. Baba, T. Kinoshita, H. Kanno, H. Sakata, E. Maruyama, M. Tanaka, Twenty-two percent efficiency HIT solar cell, Sol. Energy Mater. Sol. Cells. 93 (2009) 670–673, https://doi.org/10.1016/j.solmat.2008.02.037.
[24] S. Das Sarma, S. Adam, E.H. Hwang, E. Rossi, Electronic transport in two-dimensional graphene, Rev. Mod. Phys. 83 (2011) 407–470, https://doi.org/10.1103/RevModPhys.83.407.
[25] K. Patel, P.K. Tyagi, P-type multilayer graphene as a highly efficient transparent conducting electrode in silicon heterojunction solar cells, Carbon N. Y. 116 (2017) 744–752, https://doi.org/10.1016/j.carbon.2017.02.042.
[26] Z. Lin, B.R. Carvalho, E. Kahn, R. Lv, R. Rao, H. Terrones, M.A. Pimenta, M. Terrones, Defect engineering of two-dimensional transition metal dichalcogenides, 2D Mater. 3 (2016) 22002, https://doi.org/10.1088/2053-1583/3/2/022002.
[27] K. Patel, O.S. Panwar, A. Bisht, S. C., S. Kumar, C.M.S. Rauthan, Simulation studies on heterojunction and HIT solar cells, in: Proc.SPIE, 2012: p. 85490E. 10.1117/12.927395.
[28] S. Tohoda, D. Fujishima, A. Yano, A. Ogane, K. Matsuyama, Y. Nakamura, N. Tokuoka, H. Kanno, T. Kinoshita, H. Sakata, M. Taguchi, E. Maruyama, Future directions for higher-efficiency HIT solar cells using a Thin Silicon Wafer, J. Non. Cryst. Solids. 358 (2012) 2219–2222, https://doi.org/10.1016/j.jnoncrysol.2012.03.025.
[29] J. Singh, Semiconductor Devices : Basic Principles, Wiley India Pvt, Limited, 2007 https://books.google.co.in/books?id=BYoin_6TNZEC.

[30] Y. Shi, K.K. Kim, A. Reina, M. Hofmann, L.-J. Li, J. Kong, Work function engineering of graphene electrode via chemical doping, ACS Nano 4 (2010) 2689–2694, https://doi.org/10.1021/nn1005478.
[31] V.A. Dao, S. Kim, Y. Lee, S. Kim, J. Park, S. Ahn, J. Yi, High-Efficiency Heterojunction with Intrinsic Thin-Layer Solar Cells: A Review, Current Photovoltaic Research 2 (2013) 73-81. pISSN 2288-3274.
[32] M. Raeisi, B. Mortazavi, E. V. Podryabinkinc, F. Shojaeid, X. Zhuang, A. V. Shapeevc, High thermal conductivity in semiconducting Janus and non-Janus diamanes, cond-mat.mtrl-sci. (2006) 04091. 10.48550/arXiv.2006.04091.
[33] S. Bouzidi, M. Barhoumi, M. Said, Optical properties of Janus and non-Janus diamanes monolayers using ab-initio calculations, Optik – Int. J. Light and Electron Optics 235 (2021), 166642, https://doi.org/10.1016/j.ijleo.2021.166642.
[34] P. V. Bakharev, M. Huang , M. Saxena , S. W. Lee, S. H. Joo , S. O Park, J. Dong, D. C. Camacho-Mojica, S. Jin, Y. Kwon , M. Biswal, F. Ding , S. K. Kwak, Z. Lee , R. S. Ruoff , Chemically induced transformation of chemical vapour deposition grown bilayer graphene into fluorinated single-layer diamond, Nature Nanotechnology. https://doi.org/10.1038/s41565-019-0582-z.
[35] W. Shen, Y. Pan, S. Shen, H. Li, Y. Zhang, G. Zhang, Electron affinity of boron-terminated diamond (001) surface: a density functional theory study, J. Mater. Chem. C 7 (2019) 9756–9765, https://doi.org/10.1039/C9TC02517K.
[36] A. Sachenko, V. Kostylyov, M. Gerasymenko, R. Korkishko, N. Kulish, M. Slipchenko, I. Sokolovskyi, V. Chernenko, Silicon solar cells efficiency analysis. Doping type and level optimization, cond-mat.mtrl-sci (2015) . https://doi.org/10.48550/arXiv.1506.03132.
[37] W. Lisheng, C. Fengxiang, A. Yu, Simulation of high efficiency heterojunction solar cells with AFORS-HET, J. Phys. Conf. Ser. 276 (2011) 12177, https://doi.org/10.1088/1742-6596/276/1/012177.
[38] L. Korte, E. Conrad, H. Angermann, R. Stangl, M. Schmidt, Advances in a-Si:H/c-Si heterojunction solar cell fabrication and characterization, Sol. Energy Mater. Sol. Cells. 93 (2009) 905–910, https://doi.org/10.1016/j.solmat.2008.10.020.
[39] Y. Zhao, C. Liang, H. Zhang, D. Li, D. Tian, G. Li, X. Jing, W. Zhang, W. Xiao, Q. Liu, F. Zhang, Z. He, Anomalously large interface charge in polarity-switchable photovoltaic devices: an indication of mobile ions in organic–inorganic halide perovskites, Energy Environ. Sci. 8 (2015) 1256–1260, https://doi.org/10.1039/C4EE04064C.
[40] H. Sakata, T. Nakai, T. Baba, M. Taguchi, S. Tsuge, K. Uchihashi, S. Kiyama, 20.7% highest efficiency large area (100.5 cm^2) HIT/sup TM/ cell, in: Conf. Rec. Twenty-Eighth IEEE Photovolt. Spec. Conf. - 2000 (Cat. No.00CH37036), 2000: pp. 7–12. https://doi.org/10.1109/PVSC.2000.915742.
[41] S. Gorantla, A. Bachmatiuk, J. Hwang, H. Alsalman, J.Y. Kwak, T. Seyller, J. Eckert, M. Spencer, M. Rümmeli, A universal transfer route for graphene, Nanoscale (2013), https://doi.org/10.1039/C3NR04739C.
[42] L. Zhao, C.L. Zhou, H.L. Li, H.W. Diao, W.J. Wang, Design optimization of bifacial HIT solar cells on p-type silicon substrates by simulation, Sol. Energy Mater. Sol. Cells. 92 (2008) 673–681, https://doi.org/10.1016/j.solmat.2008.01.018.
[43] L. Zhao, H.L. Li, C.L. Zhou, H.W. Diao, W.J. Wang, Optimized resistivity of p-type Si substrate for HIT solar cell with Al back surface field by computer simulation, Sol. Energy. 83 (2009) 812–816, https://doi.org/10.1016/j.solener.2008.11.007.
[44] Y. Park, V. Choong, Y. Gao, B.R. Hsieh, C.W. Tang, Work function of indium tin oxide transparent conductor measured by photoelectron spectroscopy, Appl. Phys. Lett. 68 (1996) 2699–2701, https://doi.org/10.1063/1.116313.
[45] J. Ma, H. Bai, W. Zhao, Y. Yuan, K. Zhang, High efficiency graphene/MoS_2 /Si Schottky barrier solar cells using layer controlled MoS_2 films, Solar Energy 160 (2018) 76–84,, https://doi.org/10.1016/j.solener.2017.11.066.
[46] X. Li, D. Xie, H. Park, M. Zhu, T.H. Zeng, K. Wang, J. Wei, D. Wu, J. Kong, H. Zhu, Ion doping of graphene for high-efficiency heterojunction solar cells, Nanoscale 5 (2013) 1945–1948, https://doi.org/10.1039/c2nr33795a.
[47] Y. Tsunomura, Y. Yoshimine, M. Taguchi, T. Kinoshita, H. Kanno, H. Sakata, E. Maruyama, M. Tanaka, Twenty-two percent efficiency hit solar cell, Sol. Energy Mater. Sol. Cells 93 (2009) 670–673, https://doi.org/10.1016/j.solmat.2008.02.037.
[48] J. Geissbühler, J. Werner, S.M. de Nicolas, L. Barraud, A. Hessler-Wyser, M. Despeisse, S. Nicolay, A. Tomasi, B. Niesen, S. De Wolf, C. Ballif, 22.5% efficient silicon heterojunction solar cell with molybdenum oxide hole collector, Appl. Phys. Lett. 107 (2015), 081601, https://doi.org/10.1063/1.4928747.
[49] W. Long, S. Yin, F. Peng, M. Yang, L. Fang, X. Ru, M. Qu, H. Lin, X. Xu, On the limiting efficiency for silicon heterojunction solar cells, Sol. Energy Mater. Sol. Cells 231 (2021), 111291, https://doi.org/10.1016/j.solmat.2021.111291.
[50] K. Yoshikawa, H. Kawasaki, W. Yoshida, T. Irie, K. Konishi, K. Nakano, T. Uto, D. Adachi, M. Kanematsu, H. Uzu, K. Yamamoto, Silicon heterojunction solar cell with interdigitated back contacts for a photoconversion efficiency over 26%, Nature Energy 2 (2017) 17032, 10.1038/nenergy.2017.32.

This article has been accepted for publication in IEEE Access. This is the author's version which has not been fully edited and
content may change prior to final publication. Citation information: DOI 10.1109/ACCESS.2023.3274732

IEEE Access
Multidisciplinary | Rapid Review | Open Access Journal

Date of publication xxxx 00, 0000, date of current version xxxx 00, 0000.

Digital Object Identifier 10.1109/ACCESS.2022.DOI

Power Quality Disturbances Detection and Classification Based on Deep Convolution Auto-encoder Networks

PORAS KHETARPAL[1], NEELU NAGPAL[2], (Senior Member, IEEE), MOHAMMED AL-NUMAY[3], (Senior Member, IEEE), PIERLUIGI SIANO [3,4] (Senior Member, IEEE), YOGENDRA ARYA [5], (Senior Member, IEEE), and NEELAM KASSARWANI [2]

[1]Information Technology Department, Bharati Vidyapeeth's College of Engineering, New Delhi 110063, India
[2]Electrical and Electronics Engineering Department, Maharaja Agrasen Institute of Technology, Delhi 110086, India
[3]Electrical Engineering Department, College of Engineering, King Saud University, 800, Riyadh 11421, Saudi Arabia.
[4]Department of Management and Innovation Systems, University of Salerno, 84084 Fisciano, Italy
[5]Department of Electrical Engineering, J.C. Bose University of Science and Technology, YMCA, Faridabad 121006, India

Corresponding authors: Pierluigi Siano, Neelu Nagpal (psiano@unisa.it, nagpalneelu1971@ieee.org)

ABSTRACT Power quality issues are required to be addressed properly in forthcoming era of smart meters, smart grids and increase in renewable energy integration. In this paper, deep auto-encoder (DAE) networks is proposed for power quality disturbance (PQD) classification and its location detection without using complex signal processing techniques and complex classifiers. In this technique, Gabor filter is used to extract a set of general Gabor features from the convolution of PQD image. Subsequently, through sparse based DAE network, essential and optimal features are extracted and learnt which are used by a simple classifier (SoftMax) to classify the PQD type. Furthermore, the temporal information of the PQD is obtained using the PQD image to correctly locate the disturbance's initiating and terminating instants. The proposed DAE network has the benefits of deep learning-based networks in terms of automatic feature selection, but it requires smaller data sets. The issue of obtaining optimised, robust, and strong features from the PQD signal is thus resolved. Excellent classification accuracy of PQD is obtained with appropriate network parameter setting of the proposed DAE network. The proposed technique is compared with three other methods support vector machine (SVM), stacked auto-encoder (SAE) and principal component analysis (PCA) for PQD classification by implementing all the four techniques on python platform using the same data set. It has an overall classification accuracy of more than 97% at a signal to noise ratio (SNR) of 20dB, which is on the higher side when compared to other methods of PQD detection under noisy environment. Additionally, this method requires less computation time with the same data set than alternative approaches like SVM. Thus, the proposed method outperforms existing methods for PQD classification and detection of single disturbance and multi-disturbance in terms of greater accuracy and reduced computation complexity and computation time.

INDEX TERMS Power Quality Monitoring, Power Quality Disturbance, Deep Auto-encoders, Optimal Feature Extraction, Power Quality Event Detection

I. INTRODUCTION

A. BACKGROUND AND LITERATURE SURVEY

With the advances in electrical and electronic devices and increase in the use of non-linear power electronics-based devices (converters, flexible AC transmission system (FACTS) devices, etc.) and non-linear loads (Variable frequency drives), different power quality (PQ) issues or disturbances are often encountered in the power system. This causes various issues resulting in reduced efficiency of the devices to damage the instrument in case the disturbance is severe. Hence, accurate and efficient monitoring of these PQDs become essential. The emerging smart grid trends with smart meters requires continuous monitoring and detection of PQDs from economic and technical point of view [1]. General PQ issues include voltage variations which are momentary (voltage sag, voltage swell, voltage interruptions,

This work is licensed under a Creative Commons Attribution-NonCommercial-NoDerivatives 4.0 License. For more information, see https://creativecommons.org/licenses/by-nc-nd/4

This article has been accepted for publication in IEEE Access. This is the author's version which has not been fully edited and
content may change prior to final publication. Citation information: DOI 10.1109/ACCESS.2023.3274732

etc.), harmonics, oscillatory transients and their combinations. In addition to IEC 61000-2-5:1995, IEC 61000-2-1: 1990 standards, an IEEE work group 1159-2019 [2] has compiled a list of power quality related definitions and mentions the relevant standards for PQDs. These standards are summarized along with main PQ events as mentioned in [3]. Further, a comprehensive state-of-the-art for different detection and classification techniques of PQDs along with main international standards such as IEC 61000 and EN 50160 have been presented [4].

The general procedure of classifying PQDs involves three major steps: segmentation, feature extraction, and classification [5]. The presence of a PQD signal is identified in the segmentation section, and the disturbance component is extracted from the normal power signal. The transient component is detected, and the disturbance is separated. Following that, in the feature extraction section, various signal processing techniques such as Wavelet transform (WT), S transform (ST), Hilbert Huang transform (HHT), and others are used to extract optimal, strong, and non-redundant features from the power disturbance signal. The disturbance signal is decomposed in WT, yielding multiple signals with varying resolution levels. Detailed version of disturbance signal is obtained in this process to get the features [6]. ST has advantage of multi-resolution analysis (like WT) and uses frequency variables like that of Fourier Transform (FT) [7]. Empirical mode decomposition (EMD) method is used to disintegrate the power disturbance signal in HHT followed by the analysis using Hilbert transform (HT) [8]. Finally, in the classification process, the optimal features of the disturbance is classified using a suitable classifier [9]. SVM, Artificial Neural Network (ANN) etc. are among popular classifiers for PQD classification. ST has been used in [10]–[13], WT in [14]–[16], HHT in [17], [18] as the feature extraction technique for PQD signal. In [16], [19]–[21] SVM and in [10], [22]–[24] ANN based technique is used for classification purpose of PQD. It is inferred from [25] that better results of classification can be obtained with suitable pairing of signal processing technique and artificial intelligence (AI) based classifiers. Accurate classification of PQD can be possible with the selection of optimal features from the set of features obtained from the power disturbance signal [26]. From the set of features, Some of these are ignored to get accurate and fast classification. After feature extraction, a optimal feature selection (OFS) model has been used for extracting optimal features from the feature set to remove redundant features and improve classification accuracy and computation time. The developing field of deep learning (DL) addresses the issue of optimal feature extraction and classification jointly to make the process optimized and rich features are learnt automatically from the feature set [27], [28].

The application of DL in the field of image processing has discovered low level structures as well as mid-level structures of images such as edges and shapes [29]. In this way, features extracted by DL networks perform exceptionally well for feature extraction in the presence of noise, outperforming hand-engineered features for classification [30]. Nevertheless, DL-based approaches necessitate large data sets, expensive training, and long training time. In this proposed work, a DL-based auto-encoder technique is used to learn optimized, robust, and strong features from a PQD image, requiring a smaller data set than other DL learning-based methods. It also does not necessitate complex signal processing or machine learning based classification techniques, as previously discussed. As a result, the proposed PQD classification technique requires lesser time and computation effort. A neural network model known as autoencoder (AE) that encodes the high dimensional data and then decodes the compressed version and reconstructs the input could be used to compress data [31]. Multiple layers of AE forms SAE or DAE, a deep neural network. DAE can extract essential and rich features from the images easily which could be classified through a classifier with good accuracy. Rich features are learned during the reconstruction process, and after the training process, the decoding part is discarded, and the features can be used for classification of PQD data or images.

B. PROPOSED WORK

In this paper, Gabor filters are used to extract features from PQD images, and an improved deep convolution autoencoder for PQD image classification is designed using convolution to select strong features. The convolution layer aids in the acquisition of features, after which DAE easily discriminates and learns the rich and essential features, resulting in improved classification accuracy. These strong features are then used with a Softmax classifier to classify PQD types. Following the model's training with noisy PQD images, this method also classifies noisy PQD.

The major contribution of the research is highlighted as below:

- Gabor features are extracted from simple and complex PQD images without noise and with noise at different levels, and optimal and strong features are learned using a deep neural network with a sparse auto-encoder. Gabor features are being used for the first time for PQD classification.
- The proposed DAE network can correctly classify the type of PQD in the images and also accurately determine the location of the disturbance in the PQD image. Hence, temporal information of the PQD can also be determined accurately.
- Excellent classification accuracy of PQD is achieved by appropriate network parameter setting. The features obtained through the DAE network are powerful and outperforms the handcrafted features used without DAE network. Also, less computation time is required using this method with the same data set as compared with other popular methods like SVM.
- DAE network requires less data set as compared to deep learning-based architectures and also does not require complex signal processing techniques like wavelet, FFT etc. hence, it has benefits of deep learning-based net-

This work is licensed under a Creative Commons Attribution-NonCommercial-NoDerivatives 4.0 License. For more information, see https://creativecommons.org/licenses/by-nc-nd/4

This article has been accepted for publication in IEEE Access. This is the author's version which has not been fully edited and
content may change prior to final publication. Citation information: DOI 10.1109/ACCESS.2023.3274732

works which are obtained with comparatively smaller data sets.

The rest of this paper is structured as follows. In Section II, the proposed convolution based deep neural network is presented in detail. In section III, PQD data analysis along with data set generation and parameter selection for the proposed deep neural network is given. Section IV, presents the experiments, results and discussions in detail. Finally, the conclusion is summarized in Section V.

II. PROPOSED METHOD

This paper proposes a new PQD classification and detection method using image processing and neural networks-based auto-encoders. This auto-encoder is based on deep learning for robust and strong feature learning. Firstly, through simulation fifteen types of PQD signals are generated. These PQD signals are converted into images. Fig. 1 represents the block diagram to depict the whole process of detection and classification of PQD. Convolution is done for the PQD image with Gabor filter to obtain a set of original Gabor features. These features are then passed through into a DAE neural network, which is trained to learn optimal, strong, and non-redundant features. The DAE network is trained with supervised learning. SoftMax classifier is then used for classification of PQD. For correct detection of temporal information (starting time and ending time) of the disturbance in the image, the image is first converted to grey image (refer Fig. 1). According to [32], grey images reflect the presence and type of PQD in the image. If grey intensity of the PQD image is considered, the grey intensity of the region around sag or voltage interruption is found be darker than the normal part of the signal image. Similarly, the intensity of grey are is found to be lighter than the corresponding part of the signal image for voltage swell. As a result, the beginning and end of this intense section are used to pinpoint the exact location of PQD in the image.

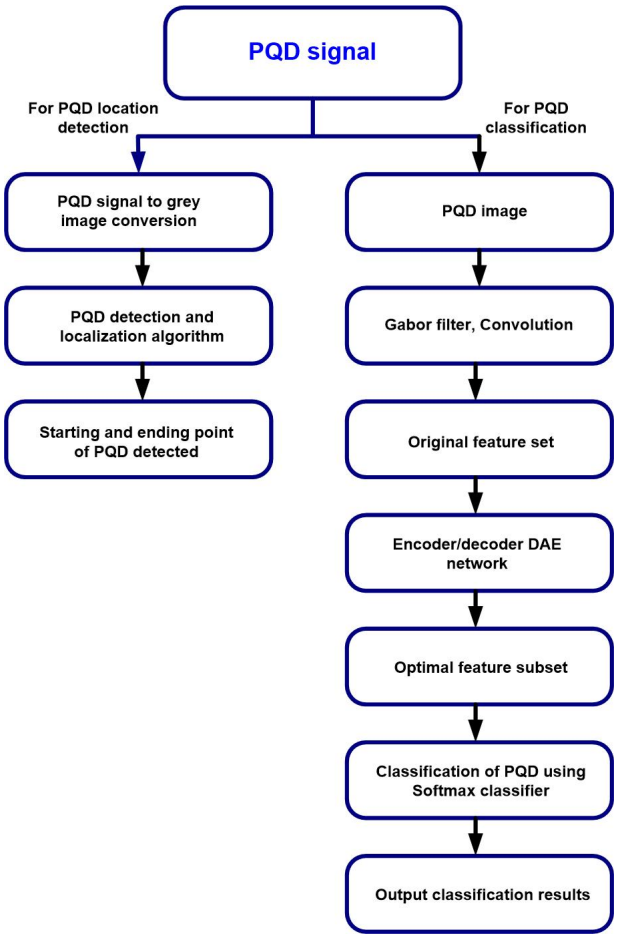


FIGURE 1: PQD detection and classification block diagram.

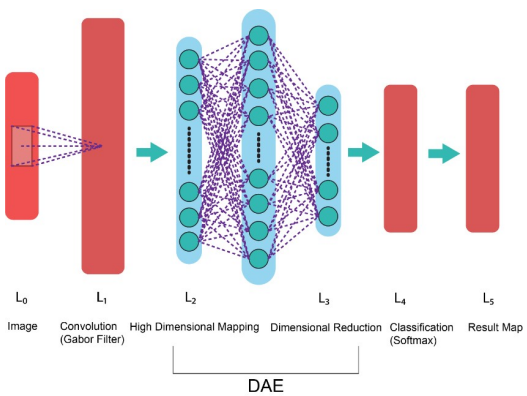


FIGURE 2: Proposed DAE network for PQD classification.

A. DAE NETWORK

In this section, the deep neural network having DAE for PQD image classification is proposed. The deep network is composed of five layers, as shown in Fig. 2. The process is divided into three steps: texture analysis, feature optimization and classification.

1) Texture analysis

The PQD classification requires extraction of the texture features from PQD images using Gabor filter as convolutional unit. Gabor filter is a type of Gaussian kernel function that function similarly to band-pass filter and can be tuned in terms of central frequency, bandwidth, and orientation. [34]. In case of unsupervised texture, segmentation Gabor filter has the ability to perform well [33]. In Fig. 2, L_0 and L_1 layer could be considered for texture analysis. Given the PQD image P, the mean and variance is computed below.

$$O_1(x,y) = \frac{1}{(2m+1)^2} \sum_{i=-m}^{w} \sum_{j=-m}^{m} P(x+i, y+j)$$

$$O_2(x,y) = \frac{1}{(2m+1)^2} \sum_{i=-m}^{w} \sum_{j=-m}^{m} [P(x+i, y+j)^2 - O_1(x+1, y+j)]^2 \quad (1)$$

This work is licensed under a Creative Commons Attribution-NonCommercial-NoDerivatives 4.0 License. For more information, see https://creativecommons.org/licenses/by-nc-nd/4

This article has been accepted for publication in IEEE Access. This is the author's version which has not been fully edited and
content may change prior to final publication. Citation information: DOI 10.1109/ACCESS.2023.3274732

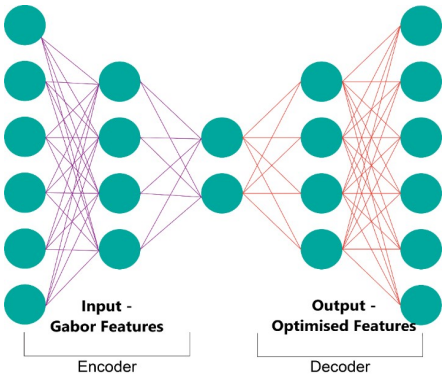


FIGURE 3: Layers of deep neural network as encoder and decoder.

where x and y represent the positions of the pixels in the PQD image, $2m+1$ represents the window size of the filters, $O1(x,y)$ represents the mean, and $O2(x,y)$ represents the variance.

Multi-scale and multi-directional features of the PQD in the frequency domain are obtained with Gabor transform which is similar to Fourier transform combined with Gauss function. The two-dimensional Gabor filter is presented as:

$$G(x_0,y_0,\omega_0,\theta)=\frac{1}{2\pi\sigma^2}exp(-\frac{x_0^2+y_0^2}{2\sigma^2})[e^{j\omega_0 x_0}-e^{-\frac{\omega_0^2\sigma^2}{2}}] \tag{2}$$

Also, with $x_0 = xcos + ysin\theta$ and $y_0 = -xsin\theta + ycos\theta$, centre frequency of the filter is represented by ω_0. Standard deviation of the Gauss function is represented by σ. Orientation of the Gabor filter is represented by θ. $e^{-\frac{\omega_0^2\omega^2}{2}}$ represents the direct current compensation and $e^{jw_0x_0}$ represents the alternating current component. Convolution of the PQD image, $P(x,y)$ with Gabor filter gives multi-scale features of the PQD image. The image is convolved with the Gabor filters present in the first layer which are its convolutional units. The original image is decomposed into multiple filtered images. Each image has some spectral information and hence, texture features are obtained as a multidimensional matrix of features. To overcome speckle noise effects and reduce computation complexity average pooling is used after obtaining the features. The most important advantage of Gabor filters is their invariance to rotation, scale, and translation [35], [36]. Ten Gabor filters in five scales and eight orientations are applied in the layer L_1 and PQD images used in this present experiments are of size $640 * 480$ pixels. Hence, the dimension of the feature vector is $640 * 480 * 10 = 3,072,000$. Due to the high correlation of adjacent pixels in the image, the feature images are down sampled. The proposed work has used a down sampling or feature reduction factor of four hence, size of the feature vector would have a size of $3,072,000/4 = 768000$. Many of these features are not required for good classification accuracy as a large number of features reduces accuracy and consumes an excessive amount of computation time. After application of DAE network, a vector of 8 essential features are obtained. In the following step, feature optimization is used to learn the best, compact, strong, and non-redundant feature set to be used for PQD classification.

2) Feature learning

After obtaining the texture features, important distinct and rich features are learnt using two sparse autoencoders in the network. In Fig. 2, layer L_2 and L_3 correspond for the feature extraction part as high dimensional mapping part (encoder) and low dimensional mapping part (decoder) respectively. In sparse encoders, the hidden layers are penalized for activation hence, smaller number of hidden units are activated [37], [38]. The reconstruction error is minimized between the input data and output data of encoder and decoder unit of sparse encoder respectively. Fig.3 shows encoder and decoder based neural network layer. In encoding step, a linear mapping is used with nonlinear activation function to represent an input, where n represent the n^{th} layer of the encoder and is represented as $z_i^n = f_n(W_n x_i^n + b_n)$. The decoding in the decoder step is given by running the stack in reverse order and reconstructed output is obtained as $\hat{x}_i^n = g_k(W_n z_i^n + \hat{b}_n)$ Weight matrices of encoder and decoder part are represented by W_n and $\hat{W}_n$ for the layer respectively. Similarly, the weight biases for encoder and decoder units are represented by b_n and $\hat{b}_n$ respectively. Also, encoder and decoder functions are represented by $f_n(.)$ and $g_n(.)$, and these functions are normally $\tanh$ or sigmoid function. The loss function which is optimized for the n^{th} layer autoencoder is given below.

$$J_{SAE}(W_n,b_n,\hat{W}_n,\hat{b}_n) = J(W_n,b_n,\hat{W}_n,\hat{b}^n)+ \sigma\sum_{j=1}^{i_n} KL(\beta||\hat{\beta}_j) \tag{3}$$

where, $J_{SAE}(W_n,b_n,\hat{W}_n,\hat{b}^n)$ is the loss function which does not include sparse constraint and represented as:

$$J_{SAE}(W_n,b_n,\hat{W}_n,\hat{b}^n) = arg^{min}_{W_n,b_n,\hat{W}_n,\hat{b}^n}\sum_{i=1}^{k}||x_i^n-\hat{x}_i^n||^2 + \frac{\mu}{2}||W_n||_F^2 \tag{4}$$

where, μ denotes the parameter for weight decay, total number of samples are denoted by k. Also, hidden values of $(n-1)^{th}$ layers acts as the inputs for the nth layer, i.e., $x_i^n = z_i^{n-1}$, Sparsity penalty is represented by α. Count of hidden neurons of nth layer is represented by i_n. Further, $KL(\beta||\hat{\beta}_j$ represents Kullback–Leibler divergence ranging between β and $\hat{\beta}_j$ defined as:

$$KL(\beta||\hat{\beta}_j) = \beta\, log\frac{\beta}{\hat{\beta}_j} + (1-\beta)log\frac{1-\beta}{1-\beta_j} \tag{5}$$

where, β represents the sparsity parameter. k^{th} hidden unit average activation over the sample set is represented by $\hat{\beta}_j$

This work is licensed under a Creative Commons Attribution-NonCommercial-NoDerivatives 4.0 License. For more information, see https://creativecommons.org/licenses/by-nc-nd/4

This article has been accepted for publication in IEEE Access. This is the author's version which has not been fully edited and
content may change prior to final publication. Citation information: DOI 10.1109/ACCESS.2023.3274732

TABLE 1: Numerical modeling of the simulated PQ disturbances [21]

PQ Event	Numerical Model	Parameters
Pure sine (C1)	$V(t) = Asin(\omega t)$	A=1 (pu), $\omega = 2\pi$ 50 rad/s
Sag (C2)	$V(t) = (1 - \alpha(u(t-t_1) - u(t-t_2)))sin\omega t$	$0.1 \leq \alpha \leq 0.9, T \leq (t_2 - t_1) \leq 9T$
Swell (C3)	$V(t) = (1 + \alpha(u(t-t_1) - u(t=t_2)))sin\omega t$	$0.1 \leq \alpha \leq 0.8, T \leq (t_2 - t_1) \leq 9T$
Interruption (C4)	$V(t) = \alpha(u(t-t_1) - u(t=t_2)))sin\omega t$	$0.9 \leq \alpha \leq 1.0, T \leq (t_2 - t_1) \leq 9T$
Harmonics (C5)	$V(t) = \alpha_1 sin(wt) + \alpha_3 sin(3wt) + \alpha_5 sin(5wt) + \alpha_7 sin(7wt)$	$0.05 \leq \alpha_3, \alpha_5, \alpha_7 \leq 0.15, \sum \alpha_i^2 = 1$
Oscillatory transient (C6)	$V(t) = sin\omega t + \alpha e^{\frac{(t-t_1)}{\tau}} sin\omega_n(t-t_1)(u(t_2 - u(t_1))$	$(0.1 \leq \alpha \leq 0.8, 0.5T \leq (t_2 - t_1) \leq 3T$ 8 ms $\leq t \leq$ 40 ms, $300 \leq f_n \leq 900$ Hz $\leq \tau$
Flicker (C7)	$V(t) = (1 + \alpha_f sin(\beta\omega t))sin\omega t$	$0.1 \leq \alpha_f \leq 0.2, 5 \leq \beta \leq 20Hz$
Impulse transient (C8)	$V(t) = sin\omega t + \text{sign}(sin\omega t) \times$ $[\sum_{n=0}^{9} K\{u(t-(t_1+0.02n)) - u(t-(t_2+0.02n))\}]$ $0.1 \leq \alpha_f \leq 0.2, 5 \leq \beta \leq 20Hz$	$0.1 \leq K \leq 0.4, 0 \leq t_1, t_2 \leq o, 5T$ $0.01 \leq (t_2 - t_1) \leq 0.05T$
Notch (C9)	$V(t) = sin\omega t - \text{sign}(sin\omega t) \times$ $[\sum_{n=0}^{9} K\{u(t-(t_1+0.02n)) - u(t-(t_2+0.02n))\}]$	$0.1 \leq K \leq 0.4, 0 \leq t_1, t_2 \leq o, 5T$ $0.01 \leq (t_2 - t_1) \leq 0.05T$
Sag with Harmonics (C10)	$V(t) = (1 - \alpha(u(t-t_1) - u(t-t_2)))$ $\alpha_1 sin(wt) + \alpha_3 sin(3wt) + \alpha_5 sin(5wt) + \alpha_7 sin(7wt)$	$0.1 \leq \alpha \leq 0.9, T \leq (t_2 - t_1) \leq 9T$ $0.05 \leq \alpha_3, \alpha_5, \alpha_7 \leq 0.15, \sum \alpha_i^2 = 1$
Swell with Harmonics (C11)	$V(t) = (1 + \alpha(u(t-t_1) - u(t-t_2)))$ $\alpha_1 sin(wt) + \alpha_3 sin(3wt) + \alpha_5 sin(5wt) + \alpha_7 sin(7wt)$	‘$1.1 \leq \alpha \leq 1.8, T \leq (t_2 - t_1) \leq 9T$ $0.05 \leq \alpha_3, \alpha_5, \alpha_7 \leq 0.15, \sum \alpha_i^2 = 1$
Sag with oscillation (C12)	$v(t) = A[sin(-\phi)(1 - \alpha(u(t-t_1) - u(t-t_2)))$ $+\beta e^{(-(t-t_3)/\tau)} sin(\omega_n(t-t_3) - \nu)((u(t-t_4) - u(t-t_3)))]$	‘$1.1 \leq \alpha \leq 1.8, T \leq (t_2 - t_1) \leq 9T$ $0.05 \leq \alpha_3, \alpha_5, \alpha_7 \leq 0.15, \sum \alpha_i^2 = 1$
Swell with oscillation (C13)	$v(t) = A[sin(\omega t - \phi)(1 + \beta(u(t-t_1) - u(t-t_2)))$ $+ \beta e^{(-(t-t_3)/\tau)} sin(\omega_n(t-t_3) - \nu)((u(t-t_4) - u(t-t_3)))]$	‘$1.1 \leq \alpha \leq 1.8, T \leq (t_2 - t_1) \leq 9T$ $0.05 \leq \alpha_3, \alpha_5, \alpha_7 \leq 0.15, \sum \alpha_i^2 = 1$
Swell with Harmonics and Oscillations (C13)	$V(t) = (1 - \alpha(u(t-t_1) - u(t-t_2)))$ $\alpha_1 sin(wt) + \alpha_3 sin(3wt) + \alpha_5 sin(5wt) + \alpha_7 sin(7wt)$	$0.9 \leq \alpha \leq 1.0, T \leq (t_2 - t_1) \leq 9T$ $0.05 \leq \alpha_3, \alpha_5, \alpha_7 \leq 0.15, \sum \alpha_i^2 = 1$
Sag with Harmonics and Oscillations (C14)	$V(t) = A[sin(-\nu_1) + (-\alpha(u(t-t_1) - u(t-t_2))) +$ $\sum_{(n=1)}^{5}[\alpha_n(sin(n)]t - \nu_n)\alpha_1 sin(\omega t)$ $+ \alpha_3 sin(3\omega t) + \alpha_5 sin(5\omega t) + \alpha_7 sin(7\omega t)$	$0.9 \leq \alpha \leq 1.0, T \leq (t_2 - t_1) \leq 9T$ $0.05 \leq \alpha_3, \alpha_5, \alpha_7 \leq 0.15, \sum \alpha_i^2 = 1$
Swell with Harmonics and Oscillations (C15)	$V(t) = A[sin(\omega t - \nu_1) + (\beta(u(t-t_1) - u(t-t_2))) +$ $\sum_{(n=1)}^{5}[\alpha_n(sin(n)]t - \nu_n)\alpha_1 sin(\omega t)$ $+ \alpha_3 sin(3\omega t) + \alpha_5 sin(5\omega t) + \alpha_7 sin(7\omega t)$	$0.9 \leq \alpha \leq 1.0, T \leq (t_2 - t_1) \leq 9T$ $0.05 \leq \alpha_3, \alpha_5, \alpha_7 \leq 0.15, \sum \alpha_i^2 = 1$

i.e., $\hat{\beta}_j = \frac{1}{K} \sum_{i=1}^{K} f_{n,j}(x_i^n)$.

Two sparse autoencoders are used one after the other. The sparse encoder (first one) is designed with number of hidden units greater than that of the input layer so that linear features are obtained. After the first encoder, the second encoder is designed in such a way such that the number of hidden units are lesser than the input so that the feature set dimension is reduced. After the layers of encoders, SoftMax classifier is applied [39]. The neural network's raw output is finally converted into probabilities by the SoftMax classifier, and classification is completed. The SoftMax classifier normalizes the probability values of output received from the autoencoder. The learning rate of 0.6 is chosen after repeated simulation tests. The deep neural network develop needs to be initialized first, so, ReLU (rectified linear activation function) function is used to initialize the deep neural network. After assigning weights, biases are optimised jointly. Method of gradient descent is applied to update the autoencoder and classification layer parameters.

3) Classification

The final layer $L4$, or the SoftMax classifier, classifies the image or images after the biases and weights have been optimised. Softmax classifier is a ML based algorithm. It is a supervised learning algorithm that is used for multiple classes of classification. It assigns probability distribution (PD) to each class. The class with highest probability is given a normalized value of ‘1’ as PD and PD of other classes are scaled accordingly. This classifier works with PD and is preferred here due to its faster execution time for multiple class based classifiers. The classifier results in high accuracy of classification. It computes the probability of the image sample x_i belonging to the o^{th} class.

$$p(y_i = o|x_i; W_4, b_4) = \frac{e^{{W_4}^{(o)}{}^T x_i + b_4^{(o)}}}{(\sum_{j=1}^{z} e^{{W_4}^{(j)}{}^T x_i + b_4^{(j)}}} \tag{6}$$

The weights portion and biases portion in the o^{th} class is denoted by $W_4^{(o)}$ and $b_4^{(o)}$ respectively. Total number of classification categories is represented by z. We get maximal probability of the sample x_i and hence, the classification label is determined through equation:

$$\text{class}(x_i) = \arg max(t = 1, ., ., ., ., c) p(y_i = o|x_i; W_4, b_4) \tag{7}$$

III. PQD ANALYSIS

In this section, PQDs are generated using MATLAB environment to develop required data set and then, the data is converted to images. Further, the analysis of the disturbances is carried out following the process proposed in section II.

A. PQD DATASET GENERATION

A dataset of PQDs is required for proper PQ disturbance classification. The availability of PQD data in large numbers is difficult to obtain since the occurrence of all types of PQ disturbances is not guaranteed, and the location and

This work is licensed under a Creative Commons Attribution-NonCommercial-NoDerivatives 4.0 License. For more information, see https://creativecommons.org/licenses/by-nc-nd/4

This article has been accepted for publication in IEEE Access. This is the author's version which has not been fully edited and
content may change prior to final publication. Citation information: DOI 10.1109/ACCESS.2023.3274732

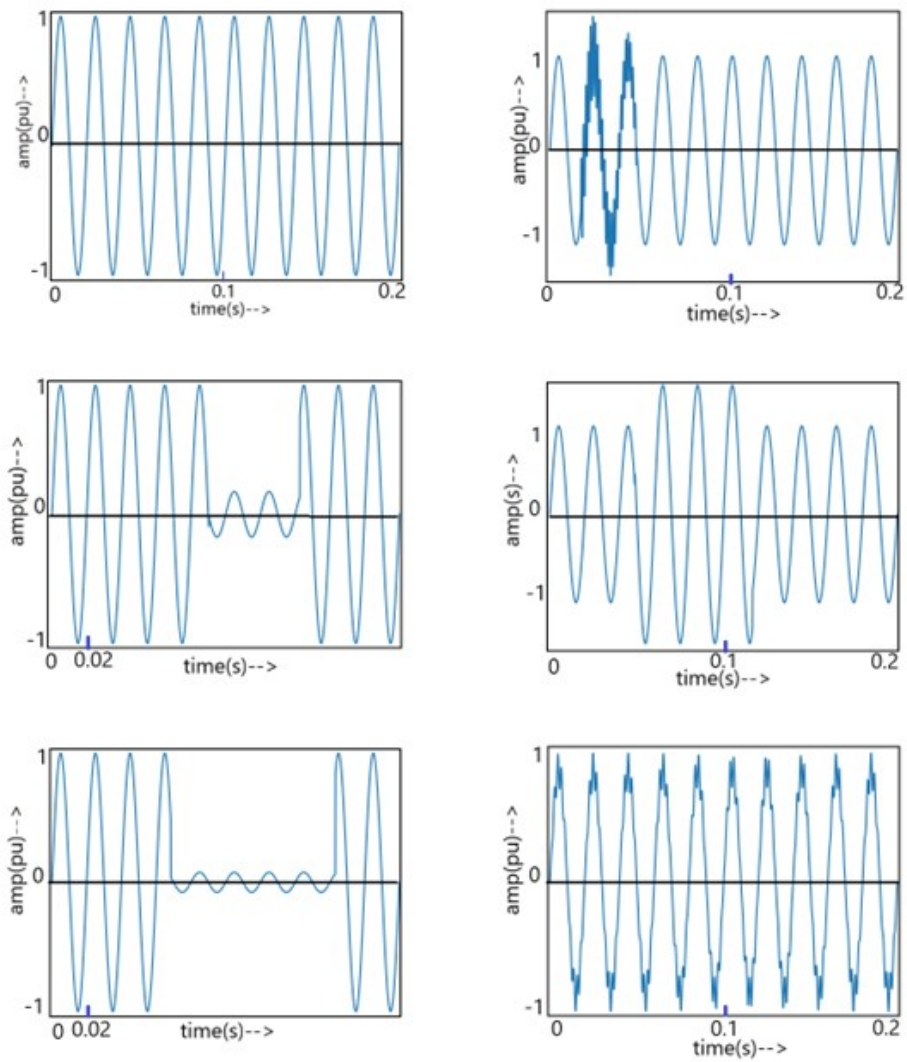


FIGURE 4: PQD images (a) Normal voltage waveform (b) Oscillatory transient (c) Voltage sag (d) Voltage swell (e) Voltage interruption (f) Voltage flicker.

time are also not fixed. As a result, synthetic PQDs data is widely used for training neural network layers [40]. PQDs are simulated in MATLAB using numerical models imitating the PQ disturbances and these simulated PQDs are very close to the real PQ disturbances that could be used for training and testing of deep neural networks. Further to accommodate the modelling uncertainty from real signal, white Gaussian noise (WGN) is added to these signals that is a general practice in power system modelling [41], [42], [43]. Single PQD as well as multiple PQDs are developed using the numerical models [44] which are presented in Table 1.

Fifteen types of PQD named as standard voltage signal (C1), voltage sag (C2), voltage swell (C3), voltage interruption (C4), voltage harmonics (C5), transient oscillation (C6), voltage flicker (C7), impulse transient (C8), voltage notch (C9), voltage sag with harmonics (C10), voltage swell with harmonics (C11), voltage sag with oscillation (C12), voltage swell with oscillation (C13), voltage sag with harmonics and oscillation (C14), voltage swell with harmonics and oscillation (C15) are developed through the numerical modelling. The signal is is chosen that is generated with fundamental frequency of 50 Hz and sampling rate of 3200 Hz. Length of 10 cycles is chosen for each signal. The single dimension PQD signal data is obtained in CSV format which is then converted to two-dimensional image with the use of Matplotlib library of python. Fig. 4 shows some of the PQD waveform images generated through process. Fig. 4(a) presents normal 50Hz sinusoidal voltage. Fig. 4(b) presents an oscillatory transient (OT). OT is a frequency change in voltage with both positive and negative polarity values. Fig. 4(c) presents sag in voltage waveform. Sag is a fall in RMS value of normal sinusoidal voltage signal ranging between 0.1 pu and 0.9 pu with a time period ranging between 0.5 cycles to 1 minute. Fig. 4(d) is swell in voltage signal. Swell

This work is licensed under a Creative Commons Attribution-NonCommercial-NoDerivatives 4.0 License. For more information, see https://creativecommons.org/licenses/by-nc-nd/4

This article has been accepted for publication in IEEE Access. This is the author's version which has not been fully edited and
content may change prior to final publication. Citation information: DOI 10.1109/ACCESS.2023.3274732

is a rise in RMS voltage which is above 1.1 pu and exists for a duration ranging from 0.5 cycles to 1 minute. Fig. 4(e) is interruption in voltage signal. In this the voltage supply falls below 0.1 pu for time duration which is less than 1 minute. Fig. 4(f) is flicker in voltage and is continuous and fast variations in voltage waveform.

The developed data set contains 1000 images of 15 different types of PQDs. Each image has a resolution of $480 * 640$ pixels. For training, 750 images of each PQD type are used, out of which 250 images of each PQD type are used for testing. In addition, images with the same number are generated by adding white Gaussian noise to the PQD data with SNRs of 20dB, 30dB, and 40dB. The proposed model is also trained with noisy PQD images for classification of PQD.

TABLE 2: Classification accuracy computed with different features (in %age)

Class	Pixel(%)	Gabor(%)	GLCM(%)
OA	87.53	95.33	89.53
AA	90.23	99.4	93.66

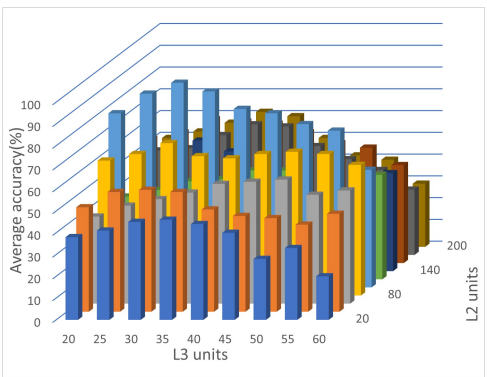


FIGURE 5: Comparison of classification performance when window size(s) of Gabor filter is changed.

B. PARAMETER SELECTION

The classification accuracy of the proposed deep neural network greatly depends upon its structure and selection of parameter values. As discussed in section II, ten Gabor

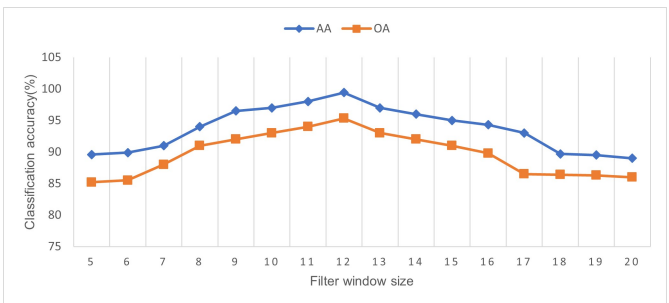


FIGURE 6: Comparison of classification performance when L_2 and L_3 units are varied.

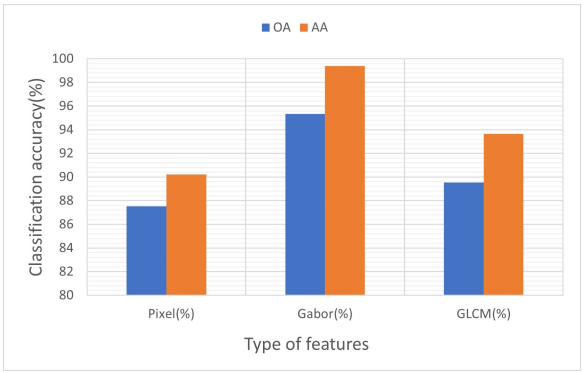


FIGURE 7: Classification accuracy comparison of different features.

filters are used for texture analysis with five scales and eight orientations including $[0, (\pi/8), (\pi/4), (3\pi/8), (\pi/2), (5\pi/8), (3\pi/4), (7\pi/8)]$ in the layer L_1 to obtain the initial feature set of the PQD image. The original PQD image is convolved with the Gabor filters and decomposed into multiple filtered images. Each obtained image has some spectral information. As a result, a multidimensional matrix of features is obtained. In general, the classification accuracy of a machine learning (ML) model/deep learning model is the ratio of correct classifications made by the model for each class and total number of classifications made for each class. The classification performance of the proposed model is evaluated by the indexes termed as average accuracy (AA) and overall accuracy (OA). AA is defined as the ratio of the total sum of accuracy of classification for each class and the total number of classes available for classification where as OA of a machine learning based model is defined as the ratio of total number of correct classification predictions made by the machine learning/deep learning model and the total number of classification predictions made by the model.

As discussed in section II A, average pooling is done after obtaining the set of Gabor features to reduce the complexity of computation and reduce speckle noise effect. Variance filter and mean filter size are used to determine window size of average pooling. Classification accuracy with different values of s is shown in Fig. 5 where, s is ranged from 4 to 20 and this indicates the effect on classification accuracy when window size of the convolution filter is changed. Further, it is worthy to note from the results that if pooling is done appropriately, the effect of noise is limited and also the size of window should not be too large. It is found that when $s = 12$, the performance of the network is found to be satisfactory. Layer L_2 and layer L_3 represent the two layers of DAEs and number of units present in each layer are represented by L_2 and L_3 respectively. The classification accuracy of the deep neural network depends upon the parameters s, L_2 and L_3. The hyper parameters μ, α, and β are set to 0.005, 0.01, and 0.5 respectively. L_2 and L_3 are set to 90 and 30 respectively. Fig. 6 shows the classification accuracy of the deep neural network with different values of L_2 and L_3, setting L_2 from

This work is licensed under a Creative Commons Attribution-NonCommercial-NoDerivatives 4.0 License. For more information, see https://creativecommons.org/licenses/by-nc-nd/4

This article has been accepted for publication in IEEE Access. This is the author's version which has not been fully edited and
content may change prior to final publication. Citation information: DOI 10.1109/ACCESS.2023.3274732

20 to 200 and L_3 from 20 to 60. The experiment was executed four times with a set of parameters and mean value was calculated for each case.

The deep neural network performs best when $L_2 = 90$ and $L_3 = 30$ with good OA. Keeping L_4 fixed, the DAE network achieved a good performance when L_2 ranged between 90 and 140. The result indicated that with high-dimensional mapping the classification accuracy could be improved by increasing the value of L_2, but after increasing L_2 beyond a certain value, it was observed that the performance was not affected much. Hence, it could be concluded that since L_2 is used for high dimensional mapping and L_3 is used for dimension reduction, this abrupt reduction may be responsible for weakening of important information. It is also observed that the value of L_3 should neither be too high and nor too low. Hence, high value of L_3 may lead to overfitting problem in classifier training and low value of L_3 may lead to loss of important features. Hence L_3 was chosen to be between 25 to 40 and corresponding values of L_2 was found out to be between 90 and 140.

IV. RESULTS AND ANALYSIS

A DAE network is created as described in section II, and parameters are configured as described in section III B. After selecting and setting the perfect parameters for DAE network (s=12, L_2=90 and L_3=30), the experiments are performed. 25% percent of the units of L_2 layer and 25% of the units of L_3 layer are dropout to control the overfitting problem. Gabor filter is used for feature extraction in L_1 layer. For proper analysis, many different features are learnt which are then compared in Table 2 for their classification accuracy after learning process. The features considered for analysis are pixel features which are learnt from the PQD original image, Gabor features from L_1 layer and grey level co-occurrence matrices (GLCM) features from L_1 layer. It could be seen from Table 2 that Gabor and GLCM features perform better than the pixel features and Gabor features lead to better classification accuracy than GLCM features. Fig. 7 depicts a graphical comparison of OA and AA for the classification of PQD using pixel, Gabor, and GLCM features. Hence, the use of Gabor features are preferred in this proposed work.

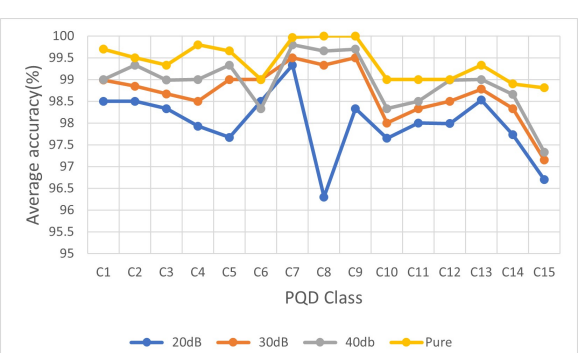


FIGURE 8: Classification accuracy of PQ events (%) with different values of SNR.

TABLE 3: Average accuracy of PQD classification of proposed work with different SNR ratios

Class	Accuracy (%) 20dB	Accuracy(%) 30dB	Accuracy(%) 40dB	Pure (%)
C1	98.5	98.99	99	99.7
C2	98.5	98.85	99.33	99.5
C3	98.33	98.67	98.99	99.33
C4	97.93	98.5	99	99.8
C5	97.67	99	99.33	99.66
C6	98.5	99	98.33	99
C7	99.33	99.5	99.8	99.97
C8	96.3	99.33	99.66	100
C9	98.33	99.5	99.7	100
C10	97.65	98	98.33	99
C11	98	98.33	98.5	99
C12	97.99	98.5	98.99	99
C13	98.53	98.78	99	99.33
C14	97.73	98.33	98.66	98.9
C15	96.7	97.15	97.33	98.81
Avg. Acc	97.99	98.69	98.93	99.4

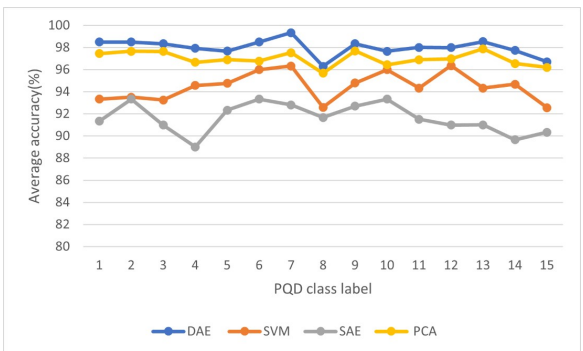


FIGURE 9: Classification accuracy comparison different methods for each class of PQ event.

A. PERFORMANCE ANALYSIS UNDER NOISY PQDS

The efficacy of the proposed method to classify single and multiple PQDs under different noise conditions such as without noise and with noise at different levels. PQD signals with 20dB, 30dB and 40dB of noise were generated and the training and testing of the proposed model was done considering these conditions. With the incursion of noise in the signal, the quality of PQD images degrades. However, the proposed technique has the ability to extract the strong features of images. The classification accuracy of fifteen different PQDs (refer Table 1) with varying signal to noise (SNR) ratios, such as 20 dB, 30 dB, and noiseless PQD signal, is shown in Table 3. As it could be seen from this Table that although the average classification accuracy (AA) declines as the noise level increases but in the proposed method, PQD images with no noise achieves 99.4% AA, 98.93% AA of PQD with SNR of 20dB, 98.69% AA is obtained for PQD with SNR of 30dB, and 97.99% AA is obtained for PQD with SNR of 40dB using Gabor features. Fig. 8 compares the classification accuracy of PQ events with different values of SNR as mentioned in Table 3. The experimental results mentioned in this table indicates the efficacy of the proposed model in classifying PQD with better accuracy, even under noisy conditions.

This work is licensed under a Creative Commons Attribution-NonCommercial-NoDerivatives 4.0 License. For more information, see https://creativecommons.org/licenses/by-nc-nd/4

This article has been accepted for publication in IEEE Access. This is the author's version which has not been fully edited and
content may change prior to final publication. Citation information: DOI 10.1109/ACCESS.2023.3274732

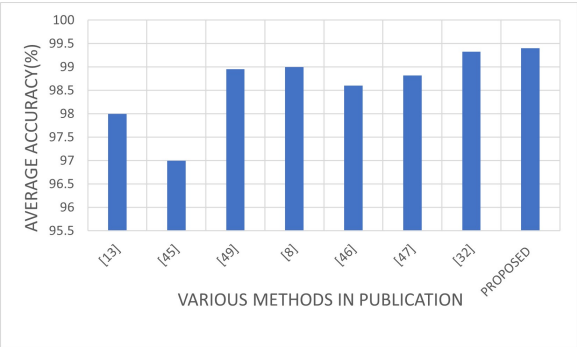


FIGURE 10: Comparison of recent PQD classification techniques with the proposed method.

TABLE 4: Classification accuracy (OA) and time of computation (s) comparison of different methods with different SNR ratio.

Class	DAE	SVM	SAE	PCA
Pure (%)	99.4	95.45	93.33	98.66
20DB (%)	97.99	94.48	91.61	96.65
30DB (%)	98.69	94.75	92.33	97.64
40DB (%)	98.93	95.33	93.12	97.99
Time(s)	0.013	0.024	0.023	0.021

B. PERFORMANCE COMPARISON

A comparison of the proposed work is carried out with three other common approaches, SVM [34] and SAE [37] and Principal component analysis (PCA). We have implemented all the four PQD classification techniques on python platform and used the same data set to conduct extensively comparative experiments to verify the superiority of the proposed framework. SVM is a well-established method that can work using limited data sets. We have applied kernel SVM using sigmoid function to convert non-linear data into simple linear data. Support vector classifier (SVC) is used for the classification purpose. Regularization constant (C) is obtained by using grid search technique. In the above comparison method, independent component analysis (ICA) is applied to the feature set obtained after convolution with Gabor filter to reduce the number of features and select good features. 75% of the samples are taken as training samples and rest 25% as testing samples. In SAE method, Gabor features are not considered and features are learnt directly through a single layer of autoencoder and classification is done by SoftMax classifier. In PCA based method, the PQD image is convolved with the Gabor filter and PCA is used for feature selection rather than sparse autoencoder with same data set. The results are shown in Table 4 and Table 5. Table 4 gives the comparison of overall classification accuracy (OA) for 15 different classes and execution time of the proposed method with SVM, SAE, and PCA based methods. It could be observed from this table that the proposed method outperforms the other three methods in terms of overall classification accuracy and execution time. The proposed method's PQD classification accuracy (AA) for each class is compared in

TABLE 5: AA of different methods for each class of PQ event

Class	AA DAE 20dB(%)	AA SVM 20dB(%)	AA SAE 20dB(%)	AA PCA 20dB(%)
C1	98.5	93.33	91.33	97.45
C2	98.5	93.5	93.33	97.66
C3	98.33	93.25	90.99	97.64
C4	97.93	94.56	89	96.66
C5	97.67	94.76	92.33	96.89
C6	98.5	95.99	93.33	96.77
C7	99.33	96.33	92.8	97.53
C8	96.3	92.58	91.66	95.67
C9	98.33	94.78	92.7	97.68
C10	97.65	95.99	93.33	96.43
C11	98	94.33	91.5	96.89
C12	97.99	96.35	90.99	96.98
C13	98.53	94.33	91	97.87
C14	97.73	94.67	89.66	96.54
C15	96.7	92.55	90.33	96.2
AA	97.99	94.48	91.61	96.65

Table 5 with methods based on SVM, SAE, and PCA for 20 dB SNR. This table and corresponding Fig. 9 show that, in comparison to the other three alternatives, the proposed method provides good PQD classification accuracy for each class in the presence of noise with a 20 dB SNR. It could be seen that our proposed method for PQD classification (DAE) performs far better than the three methods. According to the results, with and without different levels of noise, features extracted automatically through DAE perform better than features extracted automatically through ICA in SVM method and automatic feature learning in simple SAE method. In addition, the classification process takes less computational time than all the three methods. It is observed that proposed DAE network selects and learns more discriminating features from the feature sets as compared to other three methods.

Table 6 and Fig. 10 compares various latest methods for PQD classification available. In [13], multi-resolution ST is used for optimal feature extraction from PQD signal and then simple fuzzy logic-based classifier is used for classification. A good classification accuracy is obtained which is around 98%. Multi-resolution ST technique used here is complex since it is using convolution along with Fast Fourier Transform to obtain a complex feature matrix whereas in the proposed method, simple Gabor features are extracted without any complex mathematical algorithm and then efficient features are learnt using DAE giving an average accuracy of 99.4%. In [45] a modified ST technique is used for efficient feature extraction and SVM variant is used for classification of nine types of PQD. A run time of 13.4 ms is reported for the proposed method (excluding training and testing times) whereas proposed method takes 13 ms of run time with greater accuracy. In [15], discrete wavelet transform (DWT) is clubbed with SVM as a classifier for 11 types of PQD classification. As compared to the proposed method, DWT as a feature extraction technique along with SVM as a classifier is complex. Classification accuracy of 98.95% is achieved which is less than that of proposed method. In [8], HHT along with ELM is applied for the purpose of PQD classification,

This work is licensed under a Creative Commons Attribution-NonCommercial-NoDerivatives 4.0 License. For more information, see https://creativecommons.org/licenses/by-nc-nd/4

This article has been accepted for publication in IEEE Access. This is the author's version which has not been fully edited and
content may change prior to final publication. Citation information: DOI 10.1109/ACCESS.2023.3274732

Ref. paper	Feature Extraction Method	Classifier Type	Data Type	With Noise	No.of PQ Events	Total Efficiency
[8]	HHT	Extreme learning machine (WBELM)	Real and Artificial	Yes	16	95.5 % and 99 %
[13]	ST	Fuzzy Logic	Artificial	yes	14	98 %
[15]	DWT	SVM	Artificial	yes	11	98.95%
[32]	-	Random Forest (RF)	Artificial	Yes	9	99.33 %
[45]	S-transform Variant	Support Vector Machines (DAG-SVMs)	Artificial	Yes	9	97%
[46]	Sparse Auto Encoder (SAE)	Independent Component Analysis (ICA)	Artificial	No	> 7	98.6%
[47]	Variational Mode Decomposition (VMD)	Kernel Extreme Learning Machine (KELM)	Artificial	No	15	98.82%
[48]	WT	NN	Artificial	Yes	7	94.93%
[49]	WT	SVM	Artificial	Yes	8	98.95%
[50]	Ensemble Empirical Mode Decomposition (EEMD)	Rank Wavelet Support Vector Machine (RWSVM)	Artificial	Yes	8	92.8%
Proposed Method	Deep Auto Encoder	Softmax classifier	Artificial	Yes	15	99.4%

TABLE 6: Comparison of recent PQD classification techniques with the proposed method.

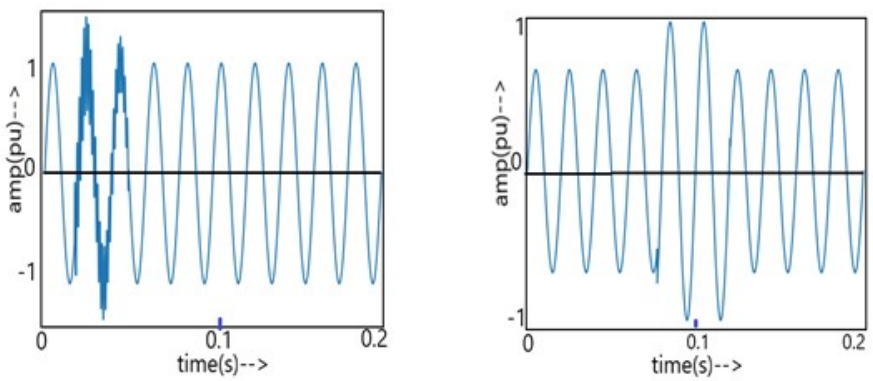


FIGURE 11: PQD images (a) Oscillatory transient (C6). (b) Voltage swell (C3).

HHT is fast and advanced signal processing technique, but average run time mentioned is 19 ms which is greater than the proposed technique's run time, accuracy for both the techniques nearly matches with proposed technique having accuracy on higher side. In [46], ICA is used with SAE along with SoftMax classifier to classify PQDs. ICA is used for feature set extraction and SAE for choosing the right features. As compared, features obtained in the proposed methods are easier to obtain and also higher accuracy is obtained for PQD classification. In [47] VMD is applied with a variant of extreme learning machine, the technique gives very good results and selects optimum features, but its run time is approximately 27.4 ms which is greater than the proposed method which has a run time of 13 ms. In [32], image processing is used for the purpose of PQD classification, PQD image is first processed with three types of image enhancement techniques, features are extracted and then important features are selected based on Gini importance and finally disturbance classification is done with RF classifier with an accuracy of 99.33% for nine types of artificially generated PQDs. Whereas an accuracy of 99.40% is obtained with the proposed method with simple feature extraction and selection process. Important point is that in both the methods, image processing techniques are being used for PQD classification, but the proposed method is less complex and straightforward. It is inferred that the proposed DAE method outperforms all other methods in terms of classification accuracy.

TABLE 7: PQD time detection.

Class label	PQ event	Starting time (s)	Ending time (s)
C6	Oscillatory transients	0.0162	0.0531
C3	Voltage swell	0.0842, 0.143	0.0881, 0.182

C. PQD TIME DETECTION

Images of the PQ signals are taken in batches and there is one class which denotes normal voltage signal and the rest others have disturbance in between the image batch. The

This work is licensed under a Creative Commons Attribution-NonCommercial-NoDerivatives 4.0 License. For more information, see https://creativecommons.org/licenses/by-nc-nd/4

This article has been accepted for publication in IEEE Access. This is the author's version which has not been fully edited and
content may change prior to final publication. Citation information: DOI 10.1109/ACCESS.2023.3274732

proposed DAE network can classify the type of PQD present in the image along with the starting and ending times of the disturbance. This may be the sudden change or transient that happens in the normal sinusoidal voltage that gives the information regarding the presence with onset and ending times of disturbance in voltage signal. Time detection of PQD is restricted to appearance since when disturbance appears in a normal sinusoidal voltage, the transient that occurs gives the starting point of the PQD. If this PQD is converted to a grey image then the intensity of the grey part after the start and in duration of PQD is different from normal sinusoidal voltage grey image. Hence, this difference in grey image intensity gives the starting and ending point of PQD.

For correct detection of temporal information (starting time and ending time) of the disturbance in the image, the image is first converted to a grey image as shown in Fig. 1. According to [32], grey images reflect the presence and type of PQD in the image. If the grey intensity of the PQD image is considered, the grey intensity of the region around sag or voltage interruption is found be darker than the normal part of the signal image. Similarly, for voltage swell the intensity of grey area is found to be lighter than the corresponding part of the signal image hence, starting and ending of this intense part is used to give the exact location of PQD in the image. The proposed DAE network can classify the type of PQD present in the image along with the starting and ending times of the disturbance. Table 7 gives the starting and ending times of some of the PQD events as shown in Fig. 11..

V. CONCLUSION

This paper has successfully performed PQD classification and occurrence time detection using a new image recognition technique based on an improved deep autoencoder to obtain the best features with minimum data set, less complexity and computation time. In this technique, the redundant and unnecessary features are neglected from the original feature set obtained through convolution using Gabor filter. Subsequently, the optimised features learned through the improved DAE network are used for classification of 15 different types of PQ events, including the normal voltage waveform. The main advantages of the proposed method include: high accuracy classification of real and noisy PQDs, requirement of lesser computation time using this method with the same data set contrarily to other popular methods like SVM, use of Gabor filter to extract features from PQD images hence, complex signal processing techniques are not required, and accurate determination of temporal information (starting and ending time) of the PQD. The proposed model achieves an overall classification accuracy of more than 97% with an SNR of 20dB, which is on the higher side when compared to other popular methods for PQD classification. As a result, it is concluded that the proposed technique has the potential to identify any problems with power quality quickly and accurately.

ACKNOWLEDGMENT

The authors, Pierluigi Siano and Mohammed AL-Numay acknowledge financial support from the Distinguished Scientist Fellowship Program, King Saud University, Riyadh, Saudi Arabia.

REFERENCES

[1] A. Bose, “Smart transmission grid applications and their supporting infrastructure,” *IEEE Trans. Smart Grid*, vol. 1, no. 1, pp. 11–19, Jun. 2010.

[2] "IEEE Recommended Practice for Monitoring Electric Power Quality," *IEEE Std 1159-2019 (Revision of IEEE Std 1159-2009)* , vol., no., pp.1-98, 13 Aug. 2019, doi: 10.1109/IEEESTD.2019.8796486.

[3] N. Kassarwani, "Performance study of dynamic voltage restorer for mitigation of voltage sags", 2019.

[4] G. S. Chawda et al., "Comprehensive Review on Detection and Classification of Power Quality Disturbances in Utility Grid With Renewable Energy Penetration," *IEEE*, vol. 8, pp. 146807-146830, 2020, doi: 10.1109/ACCESS.2020.3014732.

[5] Poras Khetarpal, Madan Mohan Tripathi, A critical and comprehensive review on power quality disturbance detection and classification, *Sustainable Computing: Informatics and Systems*, Volume 28, 2020, 100417, ISSN 2210-5379. https://doi.org/10.1016/j.suscom.2020.100417.

[6] S. Santoso, E. J. Powers, and W. M. Grady, “Power quality disturbance data compression using wavelet transform methods,” *IEEE Trans. On Power Delivery*, vol. 12, no. 3, pp. 1250–1256, July 1997.

[7] The s-transform from a wavelet point of view sergi ventosa, carine simon, martin schimmel, juan jose dañobeitia, and antoni mànuel *IEEE transactions on signal processing*, vol. 56, no. 7, July 2008.

[8] M. Sahani and P. K. Dash, "Automatic Power Quality Events Recognition Based on Hilbert Huang Transform and Weighted Bidirectional Extreme Learning Machine," *IEEE Transactions on Industrial Informatics*, vol. 14, no. 9, pp. 3849-3858, Sept. 2018.

[9] U. Singh and S. N. Singh, "Optimal Feature Selection via NSGA-II for Power Quality Disturbances Classification," *IEEE Transactions on Industrial Informatics*, vol. 14, no. 7, pp. 2994-3002, July 2018.

[10] S. Mishra, C. N. Bhende and B. K. Panigrahi, "Detection and Classification of Power Quality Disturbances Using S-Transform and Probabilistic Neural Network," *IEEE Transactions on Power Delivery*, vol. 23, no. 1, pp.280-287, Jan.2008.

[11] I. W. C. Lee and P. K. Dash, "S-transform-based intelligent system for classification of power quality disturbance signals," *IEEE Transactions on Industrial Electronics*, vol. 50, no. 4, pp. 800-805, Aug. 2003.

[12] R. Kumar, B. Singh, D. T. Shahani, A. Chandra and K. Al-Haddad, "Recognition of Power-Quality Disturbances Using S-Transform-Based ANN Classifier and Rule-Based Decision Tree," *IEEE Transactions on Industry Applications*, vol. 51, no. 2, pp. 1249-1258, March-April 2015.

[13] M. V. Chilukuri and P. K. Dash, Closure on "Multiresolution S-transform-based fuzzy recognition system for power quality events"," *IEEE Transactions on Power Delivery*, vol. 20, no. 1, pp. 540-, Jan. 2005.

[14] H. He and J. A. Starzyk, "A self-organizing learning array system for power quality classification based on wavelet transform," *IEEE Transactions on Power Delivery*, vol. 21, no. 1, pp. 286-295, Jan. 2006.

[15] J. Huang, Z. Jiang, L. Rylands and M. Negnevitsky, "SVM-based PQ disturbance recognition system," *IET Generation, Transmission & Distribution*, vol. 12, no. 2, pp. 328-334, 30 1 2018.

[16] W. Lin, C. Wu, C. Lin and F. Cheng, "Detection and Classification of Multiple Power-Quality Disturbances With Wavelet Multiclass SVM," *IEEE Transactions on Power Delivery*, vol. 23, no. 4, pp. 2575-2582, Oct. 2008.

[17] N. Senroy, S. Suryanarayanan and P. F. Ribeiro, "An Improved Hilbert–Huang Method for Analysis of Time-Varying Waveforms in Power Quality," *IEEE Transactions on Power Systems*, vol. 22, no. 4, pp. 1843-1850, Nov. 2007.

[18] S. Alshahrani, M. Abbod and G. Taylor, "Detection and classification of power quality disturbances based on Hilbert-Huang transform and feed forward neural networks," 2016 51st International Universities Power Engineering Conference (UPEC), Coimbra, 2016, pp. 1-6.

[19] P. Janik and T. Lobos, "Automated classification of power-quality disturbances using SVM and RBF networks," *IEEE Transactions on Power Delivery*, vol. 21, no. 3, pp. 1663-1669, July 2006.doi: 10.1109/TPWRD.2006.874114.

This work is licensed under a Creative Commons Attribution-NonCommercial-NoDerivatives 4.0 License. For more information, see https://creativecommons.org/licenses/by-nc-nd/4

This article has been accepted for publication in IEEE Access. This is the author's version which has not been fully edited and
content may change prior to final publication. Citation information: DOI 10.1109/ACCESS.2023.3274732

[20] Z. Liu, Y. Cui and W. Li, "A Classification Method for Complex Power Quality Disturbances Using EEMD and Rank Wavelet SVM," *IEEE Transactions on Smart Grid*, vol. 6, no. 4, pp. 1678-1685, July 2015

[21] S. Naderian and A. Salemnia, "Method for classification of PQ events based on discrete Gabor transform with FIR window and T2FK-based SVM and its experimental verification," *IET Generation, Transmission & Distribution*, vol. 11, no. 1, pp. 133-141, 5 1 2017.

[22] B. Biswal, M. Biswal, S. Mishra and R. Jalaja, "Automatic Classification of Power Quality Events Using Balanced Neural Tree," *IEEE Transactions on Industrial Electronics*, vol. 61, no. 1, pp. 521-530, Jan. 2014.

[23] Zwe-Lee Gaing, "Wavelet-based neural network for power disturbance recognition and classification," *IEEE Transactions on Power Delivery*, vol. 19, no. 4, pp. 1560-1568, Oct. 2004.

[24] M. Valtierra-Rodriguez, R. de Jesus Romero-Troncoso, R. A. Osornio-Rios and A. Garcia-Perez, "Detection and Classification of Single and Combined Power Quality Disturbances Using Neural Networks," *IEEE Transactions on Industrial Electronics*, vol. 61, no. 5, pp. 2473-2482, May 2014.

[25] Serkan Gunal, Omer Nezih Gerek, Dogan Gokhan Ece, Rifat Edizkan,The search for optimal feature set in power quality event classification, *Expert Systems with Applications*, Volume 36, Issue 7, 2009, Pages 10266-10273, ISSN 0957-4174.

[26] U. Singh, S. N. Singh, A New Optimal Feature Selection Scheme for Classification of Power Quality Disturbances based on Ant Colony Framework, *Appl. Soft Comput.* 74 (2019) 216-225.

[27] Yaping Deng, Lu Wang, Hao Jia, Xiangqian Tong, Feng Li, A Sequence-to-Sequence Deep Learning Architecture Based on Bidirectional GRU for Type Recognition and Time Location of Combined Power Quality Disturbance, *IEEE Trans. Industrial Informatics*, 15(8) (2019) 4481-4493.

[28] Y. Deng, H. Jia, P. Li, X. Tong and F. Li, "A Deep Learning Method based on Long Short Term Memory and Sliding Time Window for Type Recognition and Time Location of Power Quality Disturbance," 2018 Chinese Automation Congress (CAC), Xi'an, China, 2018, pp. 1764-1768.

[29] F. Zhang, B. Du, and L. Zhang, "Saliency-guided unsupervised feature learning for scene classification," *IEEE Trans. Geosci. Remote Sens.*, vol. 53, no. 4, pp. 2175–2184, Apr. 2015.

[30] M. Liu, Y. Chen, Z. Zhang and S. Deng, "Classification of Power Quality Disturbance Using Segmented and Modified S-Transform and DCNN-MSVM Hybrid Model," in IEEE Access, vol. 11, pp. 890-899, 2023, doi: 10.1109/ACCESS.2022.3233767.

[31] N. Rahal, M. Tounsi, A. Hussain and A. M. Alimi, "Deep Sparse Auto-Encoder Features Learning for Arabic Text Recognition," *IEEE Access*, vol. 9, pp. 18569-18584, 2021, doi: 10.1109/ACCESS.2021.3053618.

[32] L. Lin, D. Wang, S. Zhao, L. Chen and N. Huang, "Power Quality Disturbance Feature Selection and Pattern Recognition Based on Image Enhancement Techniques," *IEEE Access*, vol. 7, pp. 67889-67904, 2019, doi: 10.1109/ACCESS.2019.2917886.

[33] Hofmann, T., Puzicha, J., Buhmann, J. M. (1998). Unsupervised texture segmentation in a deterministic annealing framework, *IEEE Transactions on Pattern Analysis and Machine Intelligence*, 20(8), 803-818.

[34] P. Rai and P. Khanna, "A gender classification system robust to occlusion using Gabor features based 2D2PCA," J. Vis. Commun. *Image Represent.*, vol. 25, no. 5, pp. 1118–1129, Jul. 2014.

[35] Kamarainen, Kyrki, & Kalviainen, 2006; Liu & Wechsler, 2002; Meshgini, Aghagolzadeh, & Seyedarabi, 2013; Shen, Bai, & Fairhurst, 2007.

[36] Gabor, D. (1946). Theory of communication. Part 1: The analysis of information, *Journal of the Institution of Electrical Engineers-Part III:Radio and Communication Engineering*, 93(26), 429-441.

[37] J. Feng, L. Liu, X. Cao, L. Jiao, T. Sun and X. Zhang, "Marginal Stacked Autoencoder With Adaptively-Spatial Regularization for Hyperspectral Image Classification," *IEEE Journal of Selected Topics in Applied Earth Observations and Remote Sensing*, vol. 11, no. 9, pp. 3297-3311, Sept. 2018.

[38] A. J. Larrazabal, C. Martínez, B. Glocker and E. Ferrante, "Post-DAE: Anatomically Plausible Segmentation via Post-Processing With Denoising Autoencoders," *IEEE Transactions on Medical Imaging*, vol. 39, no. 12, pp. 3813-3820, Dec. 2020.

[39] X. Ye and Q. Zhu, "Class-Incremental Learning Based on Feature Extraction of CNN With Optimized Softmax and One-Class Classifiers," *IEEE Access*, vol. 7, pp. 42024-42031, 2019, doi: 10.1109/ACCESS.2019.2904614.

[40] M. Gouda, M. M. A. Salama, M. R. Sultan, and A. Y. Chikhani, "Power quality detection and classification using wavelet multiresolution signal decomposition," *IEEE Trans. Power Del.*, vol. 14, no. 4, pp. 1469–1476, Oct. 1999.

[41] H. H. Alhelou, H. Parthasarathy, N. Nagpal, V. Agarwal, H. Nagpal and P. Siano, "Decentralized Stochastic Disturbance Observer-Based Optimal Frequency Control Method for Interconnected Power Systems With High Renewable Shares," *IEEE Transactions on Industrial Informatics*, vol. 18, no. 5, pp. 3180-3192, 2022, doi: 10.1109/TII.2021.3107396.

[42] J. Liu, H. Song, H. Sun and H. Zhao, "High-Precision Identification of Power Quality Disturbances Under Strong Noise Environment Based on FastICA and Random Forest," in IEEE Transactions on Industrial Informatics, vol. 17, no. 1, pp. 377-387, Jan. 2021, doi: 10.1109/TII.2020.2966223.

[43] L. Fu, T. Zhu, G. Pan, S. Chen, Q. Zhong, Y. Wei Q, "Power Quality Disturbance Recognition Using VMD-Based Feature Extraction and Heuristic Feature Selection", *Applied Sciences*, vol. 9, no. 3, pp. 4901, 2019, https://doi.org/10.3390/app9224901

[44] A. M. Gargoom, N. Ertugrul and W. L. Soong, "Automatic Classification and Characterization of Power Quality Events," *IEEE Transactions on Power Delivery*, vol. 23, no. 4, pp. 2417-2425, Oct. 2008, doi: 10.1109/TPWRD.2008.923998.

[45] J. Li, Z. Teng, Q. Tang and J. Song, "Detection and Classification of Power Quality Disturbances Using Double Resolution S-Transform and DAG-SVMs," *IEEE Transactions on Instrumentation and Measurement*, vol.65, no. 10, pp. 2302-2312, Oct.2016.

[46] X. Shi, H. Yang, Z. Xu, X. Zhang and M. R. Farahani, "An Independent Component Analysis Classification for Complex Power Quality Disturbances With Sparse Auto Encoder Features," *IEEE Access*, vol. 7, pp. 20961-20966, 2019.

[47] T. Chakravorti and P. K. Dash, "Multiclass power quality events classification using variational mode decomposition with fast reduced kernel extreme learning machine-based feature selection," *IET Science, Measurement & Technology*, vol. 12, no. 1, pp. 106-117, 1 2018.

[48] H. He and J. A. Starzyk, "A self-organizing learning array system for power quality classification based on wavelet transform," in IEEE Transactions on Power Delivery, vol. 21, no. 1, pp. 286-295, Jan. 2006.

[49] J. Huang, Z. Jiang, L. Rylands and M. Negnevitsky, "SVM-based PQ disturbance recognition system," *IET Generation, Transmission and Distribution*, vol. 12, no. 2, pp. 328-334, 30 1 2018.

[50] Z. Liu, Y. Cui and W. Li, "A Classification Method for Complex Power Quality Disturbances Using EEMD and Rank Wavelet SVM," *IEEE Transactions on Smart Grid*, vol. 6, no. 4, pp. 1678-1685, July 2015.

This work is licensed under a Creative Commons Attribution-NonCommercial-NoDerivatives 4.0 License. For more information, see https://creativecommons.org/licenses/by-nc-nd/4

This article has been accepted for publication in IEEE Access. This is the author's version which has not been fully edited and
content may change prior to final publication. Citation information: DOI 10.1109/ACCESS.2023.3274732



PORAS KHETARPAL is currently working as an Assistant Professor in Information Technology Department at Bharati Vidyapeeth's College of Engineering (Affiliated to Guru Gobind Singh Indraprastha University), New Delhi, India. He completed his M.Tech degree from IIT Delhi in power electronics, electrical machines and drives. His area of interest includes artificial intelligence and machine learning. He has published more than 20 research papers in reputed journals and conferences. He has received research excellence award from Delhi technological university, New Delhi in the year 2021.



NEELU NAGPAL (Senior Member, IEEE) is currently an Associate Professor in GGSIP University, has been working since last 17 years in EEE Department of Maharaja Agrasen Institute of Technology, Delhi. Her Ph.D in Electrical Engineering was accomplished in Delhi Technological University, Delhi, India. She was the recipient of commendable research award from Delhi Technological University during her PhD course. She completed her Masters with distinction from Delhi University in Control and Instrumentation specialization. Prior to that, she graduated in Electrical Engineering in first division from Delhi College of Engineering. Besides having 21 years of experience in teaching, she has 5 years of industrial experience and a lot more educational contributions to her name. She has 20 research publications in top-tier journals, Transactions, and conferences. Her area of research is Investigations on the Dynamics, Control, and Estimation in the field of Power systems and Robotics. Her research interest includes Stochastic and nonlinear control, state estimation, smart grid technologies, renewable energy integration and artificial intelligence. She has grant of one Australian patent. She is Vice-chair, IEEE Smart Cities Ambassador Program 2023.



MOHAMMED S. AL-NUMAY (Senior Member, IEEE) was born in Riyadh, Saudi Arabia. He received the B.S. degree (Hons.) in electrical engineering from King Saud University, Riyadh, Saudi Arabia in 1986, the M.S. degree in electrical engineering from Michigan State University, East Lansing, MI, USA, in 1990, and the Ph.D. degree in electrical engineering from the Georgia Institute of Technology, Atlanta, GA, USA, in 1997. Since 1998, he has been with the Electrical Engineering Department, College of Engineering, King Saud University, where he is currently a Full Professor. From 2002 to 2006, he was the Dean of Admissions and Registration, King Saud University. He is a board member in 2 universities and 4 private colleges. In January 2018, he became the Vice President for Educational and Academic Affairs, King Saud University. His research interests include modeling and control of switched mode power supplies, computer science, renewable energy, and applications of AI.



PIERLUIGI SIANO (Senior Member, IEEE) (M'09–SM'14) received the M.Sc. degree in electronic engineering and the Ph.D. degree in information and electrical engineering from the University of Salerno, Salerno, Italy, in 2001 and 2006, respectively. He is a Professor and Scientific Director of the Smart Grids and Smart Cities Laboratory with the Department of Management & Innovation Systems, University of Salerno Since 2021 he has been a Distinguished Visiting Professor in the Department of Electrical & Electronic Engineering Science, University of Johannesburg and since 2023 he has been Fellow of the Distinguished Scientist Fellowship Program with the Department of Electrical Engineering, College of Engineering, King Saud University. His research activities are centered on demand response, energy management, the integration of distributed energy resources in smart grids, electricity markets, and planning and management of power systems. In these research fields, he has co-authored more than 700 articles including more than 410 international journals that received in Scopus more than 17000 citations with an H-index equal to 63. In the period 2019-2022 he has been awarded as a Highly Cited Researcher in Engineering by Web of Science Group. He has been the Chair of the IES TC on Smart Grids. He is Editor for the Power & Energy Society Section of IEEE Access, IEEE TRANSACTIONS ON POWER SYSTEMS, IEEE TRANSACTIONS ON INDUSTRIAL INFORMATICS, IEEE TRANSACTIONS ON INDUSTRIAL ELECTRONICS, IEEE SYSTEMS.



YOGENDRA ARYA (Senior Member, IEEE) is currently working as an Associate Professor with the Department of Electrical Engineering, J.C. Bose University of Science and Technology, YMCA, Faridabad, India. He has published 50+ research papers in reputed International journals. He has placed among "Top 2% of Researchers" by Stanford University, USA for 2019, 2020, and 2021. He is Fellow of IETE and Senior Member of IEEE. He is Academic/Associate Editor of few SCIE journals. His area of research is power system operation and control.



NEELAM KASSARWANI is currently an Associate Professor in GGSIP University, has been working since last 15 years in EEE Department of Maharaja Agrasen Institute of Technology, Delhi. She received her doctorate in electrical engineering from the National Institute of Technology, Kurukshetra, India. She completed her Masters in Power System from Delhi University in Power System and Apparatus specialization. Prior to that, she graduated in Electrical Engineering in first division from Madan Mohan Malviya Engineering College, Gorakhpur, India. She was a National Scholarship Holder from year 1980-87 for her education. Besides having 20 years of experience in teaching, she has 10 years of industrial experience. She has 8 research publications in International journals, and conferences. Her area of research is investigations on the Power System modelling and control, power quality, dynamic voltage restore, artificial intelligence, and renewable energy systems.

This work is licensed under a Creative Commons Attribution-NonCommercial-NoDerivatives 4.0 License. For more information, see https://creativecommons.org/licenses/by-nc-nd/4

ResearchGate

See discussions, stats, and author profiles for this publication at: https://www.researchgate.net/publication/371032596

Pre-training Meets Clustering: A Hybrid Extractive Multi-document Summarization Model

Conference Paper · May 2023

DOI: 10.1007/978-3-031-27409-1_48

CITATIONS
0

READS
15

2 authors:



Akanksha Karotia
Delhi Technological University
2 PUBLICATIONS **0** CITATIONS
SEE PROFILE



Seba Susan
Delhi Technological University
133 PUBLICATIONS **1,334** CITATIONS
SEE PROFILE

All content following this page was uploaded by Akanksha Karotia on 29 May 2023.

The user has requested enhancement of the downloaded file.

This is the author's version of the paper published in the conference Hybrid Intelligent Systems (HIS 2022). DOI: 10.1007/978-3-031-27409-1_48

Pre-training meets Clustering: A Hybrid Extractive Multi-Document Summarization Model

Akanksha Karotia*[0000-0003-4070-8137], Seba Susan[0000-0002-6709-6591]

Department of Information Technology
Delhi Technological University, Delhi, India.
akankshakarotia@gmail.com*

Abstract. In this era where a large amount of information has flooded the Internet, manual extraction and consumption of relevant information is very difficult and time-consuming**.** Therefore, an automated document summarization tool is necessary to excerpt important information from a set of documents that have similar or related subjects. Multi-document summarization allows retrieval of important and relevant content from multiple documents while minimizing redundancy. A multi-document text summarization system is developed in this study using an unsupervised extractive-based approach. The proposed model is a fusion of two learning paradigms: - the T5 pre-trained transformer model and the K-Means clustering algorithm. We perform the experiments on the benchmark news article corpus Document Understanding Conference (DUC2004). The ROUGE evaluation metrics were used to estimate the performance of the proposed approach on the DUC2004. Outcomes validate that our proposed model shows greatly enhanced performance as compared to the existent unsupervised state-of-the-art approaches.

Keywords: Multi-document, Extractive Summarization, Clustering Algorithm, Unsupervised Technique, Text Summarization.

1 INTRODUCTION

In light of the exponential growth in information resources, the readers are overburdened with tons of data. Getting a piece of relevant information and summarizing it manually in a short period is a very challenging and time-consuming task for humans [1]. By eliminating information redundancy, we can save time and save resources, so it is imperative to remove information redundancy. To address this problem, text summarization has become an increasingly important tool. Text summarization is a task that is considered a sequence-to-sequence operation. Machine translation is one other application of sequence-to-sequence learning that has gained success and popularity over time [2]. The automatic text summarizer selects the most relevant and meaningful information and compresses it into a shorter version while preserving the original meaning [3]. The aim is to create short, to-the-point summaries that deliver the most important information and keep readers engaged, without taking more time to get the

https://github.com/Akankshakarotia/Pre-training-meets-Clustering-A-Hybrid-Extractive-Multi-Document-Summarization-Model

knowledge they require. Current researches on automatic text summarization focus on summarizing multiple documents rather than single documents [4]. When a summary is derived from one document, it is referred to as a single-document summary, while when it is retrieved from a set of documents on a specific topic, it is referred to as a multi-document summary [5]. As of yet, almost all current extractive text summarization models lack the ability to efficiently summarize multi-document data. Consequently, this paper aims to manage this gap.

This work makes the subsequent main additions:

1. We propose an extractive-based unsupervised algorithm for extracting summaries from multiple documents based on the integration of the T5 pre-trained transformer model and the K-Means clustering algorithm.

2. We extracted the salient texts in two-stages: - generation of abstractive summaries using the T5 pre-trained model followed by clustering of the abstractive summaries using the K-means clustering algorithm; the extracted salient text's benefits to generate the final meaningful summary.

3. We use the ROUGE-1, ROUGE-2, ROUGE-3, ROUGE-4, ROUGE-S, and ROUGE-SU metrics to evaluate the performance of our proposed work with respect to nine existing unsupervised extractive-based summarization methods for multiple documents on the standard DUC2004 corpus.

The remaining sections of the paper are arranged as follows. Related work is described in Section 2. Detailed information about the proposed method is given in section 3. Our experiments and results are presented in Section 4. Section 5 of this paper summarizes the work and outlines future directions.

2 BACKGROUND

Natural language processing (NLP) chores have been refined by advancements in transformer-based frameworks [18, 19]. Encoder-decoder models have been deployed for generative language tasks such as abstractive-based summarization and question-answering systems [14, 15]. The competence of transformers to achieve semantic learning has also been enhanced significantly.

With the ability to automatically group similar items, one can discover hidden similarities and key concepts and organize immense quantities of information into smaller sets. Data can be condensed to a considerable extent using clustering techniques [16]. Since the documents in multi-document summarization are taken from different origins, they are verbose and redundant in articulating beliefs, and the summary contains only a few key points. Based on the distance between sentences, we can form semantic clusters that can be compressed into a particular sentence representing the important content of each cluster [17]. Applications of clustering are finding documents in similar categories, organizing enormous documents, redundant content, and recommendation models.

Using statistics derived from word frequencies and distributions, Luhn [6] used machine learning techniques to calculate the importance of sentences and created summaries based on the best sentence scores obtained. Edmundson and Wyllys proposed a

https://github.com/Akankshakarotia/Pre-training-meets-Clustering-A-Hybrid-Extractive-Multi-Document-Summarization-Model

method [7] that is an improvement on the Luhn method described above. What sets this summarizer apart from other summarizers is that it requires three additional heuristics to measure sentence importance which includes bonus words, stigma words, and stopwords. Mihalcea and Tarau proposed a TextRank algorithm in [8]. Graph-based representations are utilized for summarizing content by calculating intersections between texts. LexRank uses eigenvector centrality, another node centrality method that was introduced in [9]. Based on common content between words and sentences, PageRank is a system for summarizing documents and identifying the central sentence in a document. Latent Semantic Analysis (LSA) [10] is a powerful summarization tool that identifies the patterns of relationships between terms and concepts using the singular value decomposition technique. Kullback-Leibler Divergence (KLD) [11] calculates the difference between two probability distributions. This approach takes a matrix of KLD values of sentences from an input document and then selects sentences with a lower KLD value to form a summary. SumBasic [12] uses the average sentence score to break links and iteratively selects the sentence containing the highest content word score. GenCompareSum [13] is a recently introduced method for single document summarization that first divides the document into sentences, and then combines these sentences into segments. Each segment is fed to a transformer model to generate multiple text fragments per segment. A similarity matrix is then computed between the text fragments and the original document using the BERT score. As a result, a score is generated per sentence by adding the values of the text fragments. A summary is formed by compiling the *N* sentences with the highest scores.

3 METHODOLOGY

This work is motivated in parts by the research work of Bishop et al. in [13], who introduced the model named GenCompareSum, described briefly in Section 2. The proposed model is an unsupervised hybrid extractive-based strategy for a multi-document news article. It is a fusion of the T5 pre-trained transformer model and the K-Means clustering technique. Fig. 1 shows the proposed model architecture.

3.1 Extracting the key texts from each document using the T5 pre-trained transformer model

The dataset contains a total of *T* documents. It is organized into *C* folders, with an average of *n* documents per folder, i.e. $D = \{D_1, D_2, D_3, \dots, D_n\}$. A T5 pre-trained transformer model was used to generate summaries for all documents separately $Sum = \{Sum_1, Sum_2, Sum_3, \dots, Sum_n\}$. Each document has k sentences on average $D_{\mathrm{i}} = \{q_1, q_2, q_3, \dots, q_k\}$. The output produced for each document from the T5 pre-trained transformer model is $D_i' = \{q_1', q_2', q_3', \dots, q_l'\}$, where l refers to how many sentences there are. Combine the summaries obtained from *n* documents into one. This consolidated summary document shows key information from each document that guides subsequent modules in creating the final summary.

https://github.com/Akankshakarotia/Pre-training-meets-Clustering-A-Hybrid-Extractive-Multi-Document-Summarization-Model

3.2 Extracting the salient texts using the K-Means Clustering strategy with the help of key texts extracted in the above section

The summary document generated in the above section is first tokenized into sentences and then pre-processed, such as removing stop words and converting uppercase letters to lowercase letters. Furthermore, to create the sentence vector, we used word embedding Word2Vec, a vector representation of all the words that make up the sentence, and used their average to arrive at a composite vector. After creating the sentence vector, we employed the K-Means clustering technique to group the sentence embeddings into a pre-defined number of clusters. In this case, we chose the number of clusters to be 7. Any cluster of sentence embeddings can be depicted as a group of sentences with the same meaning. These sentences have more or less the same information and meaning that can be expressed with only one sentence from each cluster. The vector representation of sentences with the lowest Euclidean distance from the cluster center represents the whole cluster. More the number of additional sentences in a group, the more vital that sentence is. Therefore, the text fragments obtained from i clusters $F = \{f_1, f_2, f_3, \dots, f_i\}$ are associated with the count of sentences in that group, which is the weight w_t of the particular fragment f_t.

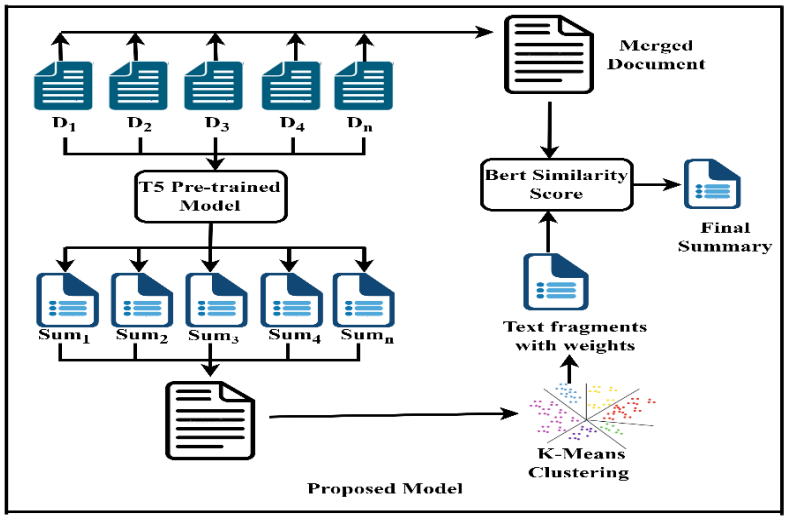


Fig. 1. Proposed model architecture

3.3 Final Summary generation

Here, based on the BERT score we extract the sentences for the final summary. First, we create a merged document of the initial input documents. Next, we calculate the similarity between the text fragments obtained using the K-Means clustering technique and the merged input document using the BERT score. This similarity matrix is multiplied by the paired text fragment weights and summed to get the sentence scores. The

https://github.com/Akankshakarotia/Pre-training-meets-Clustering-A-Hybrid-Extractive-Multi-Document-Summarization-Model

top-scored sentences are fetched for the final summary and these extracted sentences are organized in the ordered fashion as they were in the original document to get the final meaningful summary.

Eq (1) shows the formula used to calculate the similarity scores between the original document and text fragments to get the final sentence scores for each sentence *r*, where *i* is the number of clusters of text fragments that we get from the K-Means clustering algorithm and *s* is a sentence from the original merged document.

$$Sentence\ Score_r = \sum_{t=1}^{t=i} w_t * BERTSCORE(s_r, f_t) \quad (1)$$

4 RESULTS AND EVALUATION

Google Colab online platform with 12 GB of RAM is used to perform the experiments. Our code is made available online[1] for facilitating future research. Results are evaluated on the DUC2004 dataset containing four human-generated summaries. We calculate the ROUGE scores between the four gold summaries and the system-generated summaries and average those scores to obtain the final ROUGE score as shown in Table 1, Fig. 2, Fig. 3, Fig. 4, Fig. 5, Fig. 6, and Fig. 7. The results are presented in detail below.

4.1 Dataset used

We have evaluated the performance of all the models on the dataset DUC2004 [20] for multi-document summarization. It contains a total of 500 news articles (documents) that are segregated into 50 folders, and each folder has ten documents on average. Each folder is associated with four different human-written summaries.

4.2 Performance Evaluation Metrics

ROUGE [21] is a performance metric used to evaluate the accuracy of generated summaries by comparing them to reference/gold summaries. It is a universally recognized benchmark used to evaluate machine-generated summaries and has also become the standard evaluation criterion for DUC collaborative work, making it popular for summary evaluation. Simply put, it works by comparing word occurrences in generated and referenced summaries.

4.3 Discussion on Results

Table 1, Fig. 2, Fig. 3, Fig. 4, Fig. 5, Fig. 6, and Fig. 7 show the comparative analysis of various unsupervised state-of-the-art techniques, including the proposed system. Our model performs best with the highest ROUGE-1, ROUGE-2, ROUGE-3, ROUGE-4, ROUGE-S, and ROUGE-SU F1 average scores of 34.013, 8.266, 2.951, 1.253, 10.366, 10.71. The least performing technique is Luhn method in ROUGE-1 F1 average score with 26.132**,** Latent Semantic Analysis (LSA) method in ROUGE-2 F1 average score with 3.837, LSA method in ROUGE-3 F1 average score with 0.804, LSA method in

[1] https://github.com/Akankshakarotia/Pre-training-meets-Clustering-A-Hybrid-Extractive-Multi-Document-Summarization-Model

https://github.com/Akankshakarotia/Pre-training-meets-Clustering-A-Hybrid-Extractive-Multi-Document-Summarization-Model

ROUGE-4 F1 average score with 0.241, Luhn method in ROUGE-S F1 average score with 5.319, Luhn method in ROUGE-SU F1 average score with 5.458. The deviation of ROUGE scores strongly depends on parameters such as the number of clusters selected to obtain salient texts. As shown in Table 2, we note that our model performed best when the number of clusters is 7. Fig. 3 is the sample of the output summary from our model and the gold summary from the DUC2004 dataset.

Table 1. Performance evaluation of various multi-document summarization models on the DUC2004 dataset using the ROUGE metric

Methods	Rouge-1	Rouge-2	Rouge-3	Rouge-4	Rouge-S	Rouge-SU
LSA	28.756±0.311	3.837±0.1857	0.804±0.1047	0.241±0.0469	6.244±1.3214	6.758±0.9288
Edmundson	30.272±0.3581	5.587±0.5128	1.506±0.3232	0.567±0.2134	7.961± 0.2085	8.24 ± 0.2176
Luhn	26.132±0.4364	5.535±0.1789	1.518±0.0293	0.595±0.0498	5.319± 0.2311	5.458± 0.2543
SumBasic	31.095±0.7055	4.613±0.1362	1.085±0.1564	0.295±0.1187	7.877± 0.4189	8.34 ± 0.4148
TextRank	26.146±0.5377	5.71 ± 0.2947	1.481 ± 0.184	0.544 ± 0.11	5.394± 0.2701	5.563± 0.2827
Lead	32.634±0.4501	6.704±0.4952	1.991±0.1885	0.783±0.1283	9.248± 0.2846	9.571± 0.2819
Random	30.681±0.3746	5.007±0.2447	1.189±0.1584	0.442 ± 0.084	8.088± 0.1344	8.426± 0.1316
GencopareSum	31.272±1.5372	6.965±0.6824	2.288±0.3661	0.977±0.2448	9.042± 0.9351	9.481± 0.9372
KLDivergence	30.079±0.6514	6.441±0.4692	1.584±0.3825	0.557±0.2391	8.167± 0.3169	8.49 ± 0.3251
Our Model	**34.013±0.8079**	**8.266±0.7509**	**2.951±0.4178**	**1.253±0.2422**	**10.366±0.4009**	**10.713±0.3988**

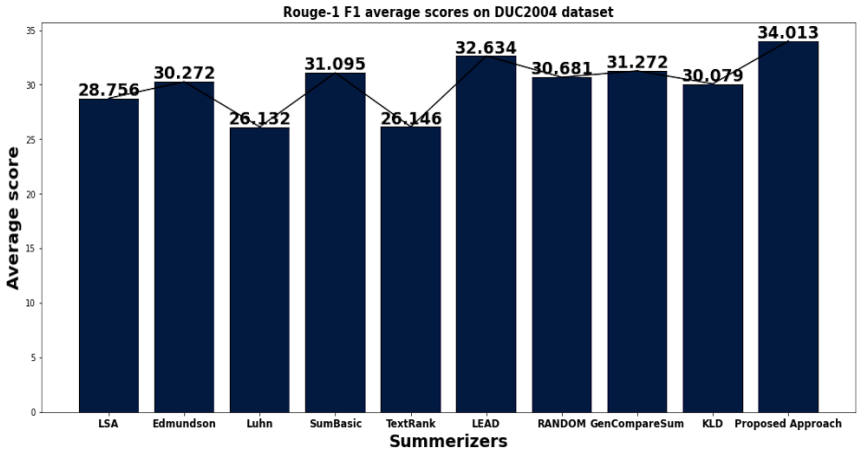


Fig. 2. Comparison between summarization models with ROUGE-1 F1 average score on the DUC2004 dataset

https://github.com/Akankshakarotia/Pre-training-meets-Clustering-A-Hybrid-Extractive-Multi-Document-Summarization-Model

Table 2. ROUGE F1 average scores with different numbers of clusters on the DUC2004

Number of Clusters	Rouge-1	Rouge-2	Rouge-3	Rouge-4	Rouge-S	Rouge-SU
3	33.185±0.9684	7.553±0.9602	2.585±0.5183	1.1 ± 0.3483	10.003±0.4343	10.349±0.4357
5	33.387±0.5468	7.776±0.3528	2.651±0.1398	1.167 ± 0.132	10.066±0.2851	10.49 ± 0.2276
7	**34.013±0.8079**	**8.266±0.7509**	**2.951±0.4178**	**1.253±0.2422**	**10.366±0.4009**	**10.713±0.3988**
9	33.944±0.6066	8.225±0.4657	2.935±0.2674	1.22 ± 0.161	10.284±0.3443	10.625±0.3433
11	33.878±0.5115	8.071±0.2487	2.787±0.3742	1.216±0.1949	10.288±0.3194	10.63±0.3164

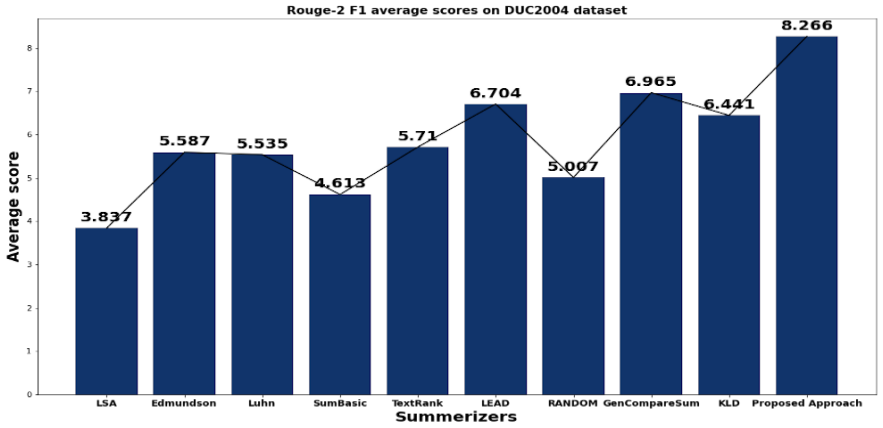


Fig. 3. Comparison between summarization models with ROUGE-2 F1 average score on the DUC2004 dataset

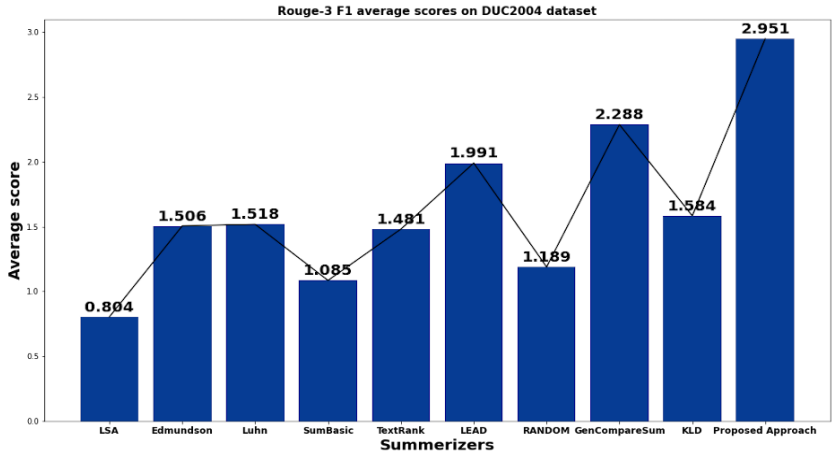


Fig. 4. Comparison between summarization models with ROUGE-3 F1 average score on the DUC2004 dataset

https://github.com/Akankshakarotia/Pre-training-meets-Clustering-A-Hybrid-Extractive-Multi-Document-Summarization-Model

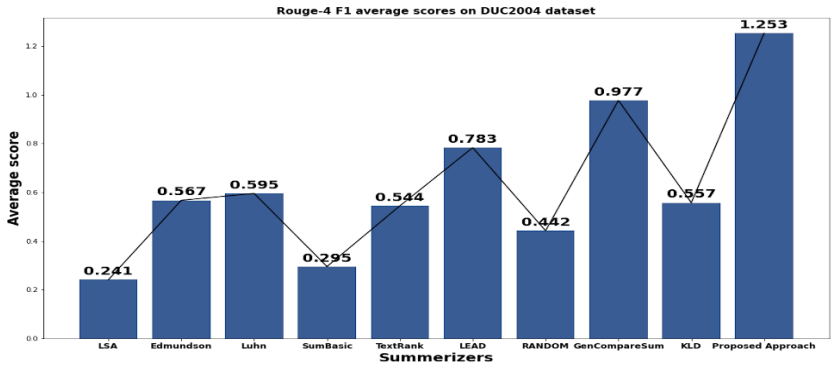


Fig. 5. Comparison between summarization models with ROUGE-4 F1 average score on the DUC2004 dataset

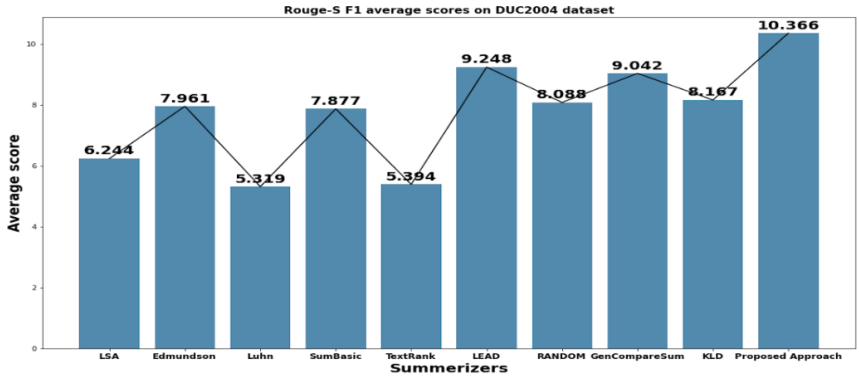


Fig. 6. Comparison between summarization models with ROUGE-S F1 average score on the DUC2004 dataset

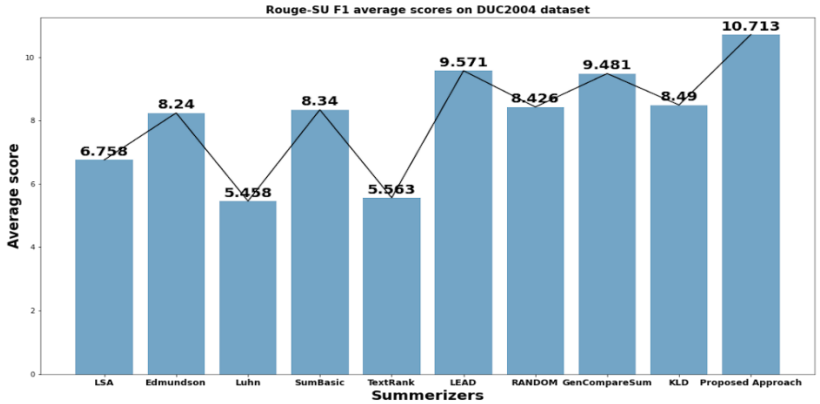


Fig. 7. Comparison between summarization models with ROUGE-SU F1 average score on the DUC2004 dataset

https://github.com/Akankshakarotia/Pre-training-meets-Clustering-A-Hybrid-Extractive-Multi-Document-Summarization-Model

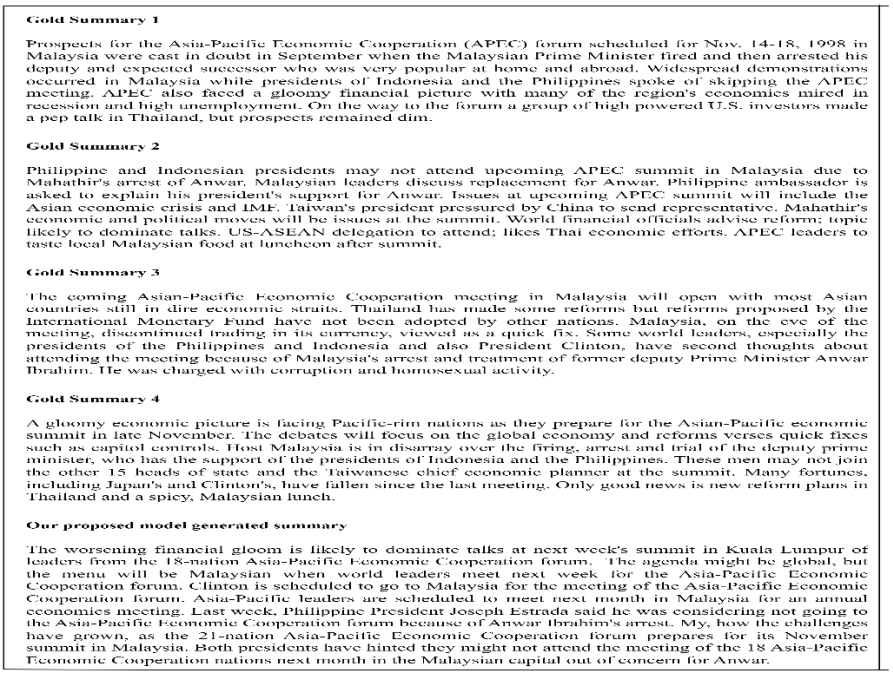


Fig. 8. This figure shows the four given human-written summaries/ground-truth/gold summaries from the DUC2004 dataset and the summary generated from our proposed system

5 CONCLUSION

This work aims to develop an unsupervised extractive-based text summarization system for multi-documents. The developed system is two-stage, it uses both the T5 pre-trained transformer model and the K-Means clustering technique to get a salient text that helps to retrieve the most relevant sentences that can be represented as summaries for the collection of documents. System performance was evaluated using the ROUGE metric on the DUC2004 benchmark dataset, which indicates that our proposed model outperformed all other unsupervised state-of-the-art summarization models. For further improvement, we will be exploring more combinations of pre-trained models and clustering algorithms from the vast literature available.

References

1. Rezaei, Afsaneh, Sina Dami, and Parisa Daneshjoo. "Multi-document extractive text summarization via deep learning approach." In *2019 5th Conference on Knowledge Based Engineering and Innovation (KBEI)*, pp. 680-685. IEEE, 2019.
2. Mallick, Ritam, Seba Susan, Vaibhaw Agrawal, Rizul Garg, and Prateek Rawal. "Context-and sequence-aware convolutional recurrent encoder for neural machine translation." In Proceedings of the 36th Annual ACM Symposium on Applied Computing, pp. 853-856. 2021.

https://github.com/Akankshakarotia/Pre-training-meets-Clustering-A-Hybrid-Extractive-Multi-Document-Summarization-Model

3. Tsoumou, Evrard Stency Larys, Linjing Lai, Shichong Yang, and Mbembo Loundou Varus. "An extractive multi-document summarization technique based on fuzzy logic approach." In 2016 international conference on network and information systems for computers (ICNISC), pp. 346-351. IEEE, 2016.
4. Yapinus, Glorian, Alva Erwin, Maulhikmah Galinium, and Wahyu Muliady. "Automatic multi-document summarization for Indonesian documents using hybrid abstractive-extractive summarization technique." In 2014 6th International Conference on Information Technology and Electrical Engineering (ICITEE), pp. 1-5. IEEE, 2014.
5. T. Hirao, T. Fukusima, M. Okumura, C. Nobata and H. Nanba. Corpus and Evaluation Measures for Multiple Document Summarization with Multiple Sources. In Proceedings of the Twentieth International Conference on Computational Linguistics (COLING), pp. 535–541, 2004.
6. Luhn, Hans Peter. "The automatic creation of literature abstracts." *IBM Journal of research and development* 2, no. 2 (1958): 159-165.
7. Edmundson, H. P., & Wyllys, R. E. (1961). Automatic abstracting and indexing—survey and recommendations. Communications of the ACM, 4(5), 226–234.
8. Mihalcea, Rada, and Paul Tarau. "A language independent algorithm for single and multiple document summarization." In *Companion Volume to the Proceedings of Conference including Posters/Demos and tutorial abstracts*. 2005.
9. Erkan, Günes, and Dragomir R. Radev. "Lexrank: Graph-based lexical centrality as salience in text summarization." Journal of artificial intelligence research 22 (2004): 457-479.
10. Ozsoy MG, Alpaslan FN, Cicekli I (2011) Text summarization using latent semantic analysis. J Inf Sci 37(4):405–417.
11. Allahyari, Mehdi, Seyedamin Pouriyeh, Mehdi Assefi, Saeid Safaei, Elizabeth D. Trippe, Juan B. Gutierrez, and Krys Kochut. "Text summarization techniques: a brief survey." arXiv preprint arXiv:1707.02268 (2017).
12. Nenkova, A., & Vanderwende, L. (2005). The impact of frequency on summarization. MSRTR-2005-101.
13. Bishop, Jennifer, Qianqian Xie, and Sophia Ananiadou. "GenCompareSum: a hybrid unsupervised summarization method using salience." In Proceedings of the 21st Workshop on Biomedical Language Processing, pp. 220-240. 2022.
14. Raffel, Colin, Noam Shazeer, Adam Roberts, Katherine Lee, Sharan Narang, Michael Matena, Yanqi Zhou, Wei Li, and Peter J. Liu. "Exploring the limits of transfer learning with a unified text-to-text transformer." J. Mach. Learn. Res. 21, no. 140 (2020): 1-67.
15. Cachola, Isabel, Kyle Lo, Arman Cohan, and Daniel S. Weld. 2020. “TLDR: Extreme Summarization of Scientific Documents.” Findings of the Association for Computational Linguistics: EMNLP 2020. 4766-4777.
16. Yu, Hui. "Summarization for internet news based on clustering algorithm." In 2009 International Conference on Computational Intelligence and Natural Computing, vol. 1, pp. 34-37. IEEE, 2009.
17. Zhao, Jinming, Ming Liu, Longxiang Gao, Yuan Jin, Lan Du, He Zhao, He Zhang, and Gholamreza Haffari. "Summpip: Unsupervised multi-document summarization with sentence graph compression." In *Proceedings of the 43rd international acm sigir conference on research and development in information retrieval*, pp. 1949-1952. 2020.
18. Goel, Raman, Sachin Vashisht, Armaan Dhanda, and Seba Susan. "An empathetic conversational agent with attentional mechanism." In 2021 International Conference on Computer Communication and Informatics (ICCCI), pp. 1-4. IEEE, 2021.
19. Goel, Raman, Seba Susan, Sachin Vashisht, and Armaan Dhanda. "Emotion-aware transformer encoder for empathetic dialogue generation." In 2021 9th International Conference on Affective Computing and Intelligent Interaction Workshops and Demos (ACIIW), pp. 1- 6. IEEE, 2021
20. https://www.kaggle.com/datasets/usmanniazi/duc-2004-dataset
21. Lin, C., & Rey, M. (2001). ROUGE: A Package for Automatic Evaluation of Summaries.

https://github.com/Akankshakarotia/Pre-training-meets-Clustering-A-Hybrid-Extractive-Multi-Document-Summarization-Model

View publication stats

MĀPAN-Journal of Metrology Society of India
https://doi.org/10.1007/s12647-023-00664-8

REVIEW PAPER

Prospects and Challenges with Legal Informatics and Legal Metrology Framework in the Context of Industry 6.0

S. Chourasia[1], S. M. Pandey[2]* and A. K. Keshri[3]

[1]Department of Mechanical Engineering, Delhi Technological University, Delhi, India

[2]Department of Mechanical Engineering, National Institute of Technology, Patna, India

[3]Department of Metallurgical and Materials Engineering, Indian Institute of Technology, Patna, India

Received: 13 November 2022 / Accepted: 10 May 2023

© Metrology Society of India 2023

Abstract: Industry 6.0 is viewed as a futuristic industrial evolution. It aims to set the synergy between man and robot by providing the wealth affluence away from the trade, and customers solutions that would provide progress to the world in every field across all planetary boundaries. Industry 6.0 comprises numerous promising technology such as quantum computing, artificial intelligence, machine learning, cloud computing, and quantum artificial computing. These technologies have the massive capabilities to help the legal industry, metrology industry and many other organizations attain their goals by delivering excellent and best-suited insights. In the future, these technologies will assist the lawmaker and jurisprudence in improving the old law justice system into the advanced one. In this article, we first introduce a glimpse of industry 6.0 from the outlook of legal information, digital transformation in metrology, and strength, limitation, opportunities, and threat analysis in brief. Then we discuss key technologies of industry 6.0, framework of legal informative, a futuristic model for a legal informatics system based on quantum-based AI, machine learning, and digital legal metrology and its challenges in adoption in regard's Industry 6.0. In subsequent sections, we discussed requirements, challenges, and progress in developed countries, preparedness of academia and industry in India. Then, we brief challenges for legal metrology in the future, opportunities for legal metrology in future legal challenges faced by lawyers and legal metrology, limitations of the study, research implication, and conclusion. Finally, the finding shows that industry 6.0 technologies have enormous capabilities to bring a revolutionary change in the legal industry but are present in the new born growth stage.

Keywords: Legal informative; Metrology; Legal metrology; Frame work; Legal system; Quantum computing; AI; Robot judges; Robot lawyer; Industrial revolution (IR); Machine learning (ML); I.6.0 (Industry 6)

1. Introduction

During the last many years, manufacturing industries and business organizations have willingly moved toward the adoption of new technologies for improving their production system efficiency, data transparency, sustainable production, and real-time monitoring. In the present scenario, the digital transformation, the unification of new technologies and information technology, such as electronic communication, electronic sensors, IoT, cloud computing, artificial intelligence, quantum computing, and anti-fragile concepts in metrology are at their peak stage and it resulted to the birth of industry 6.0 and gave birth of Atma Nirbhar (Self-reliant Bharat) Bharat of GOI (Government of India) missions [1, 2]. For instance, the sensors, distinguish methodologies and other digital technologies would play a significant role in the evolution of industry 6.0 for setting the connection between the real world to the virtual world. As an entire summary, the efficacious implementation of industry 6.0 needs the use of present-day digital technologies such as quantum computing, AI, cloud computing, data storage, and security. For example, the EM (European metrology) department is using metrology clouds for checking the accuracy of the process, its valuation as well as the market observation that would help them in developing the base of a digital solitary arcade from the European viewpoint [3]. That is why, the need for industry 6.0

*Corresponding author, E-mail: smp.me@nitp.ac.in

Published online: 25 May 2023

and digital technologies in metrological amenities are required for achieving the digital quality structure for speeding the industrial development, growth, conventionality assessment, innovation, market checking, and standardization of the product [4]. Industry 6.0 is defined as the futuristic idea where every individual's thought would be commanded through engaging the human brain and work performed with the help of automatic robots by enwrapping all the cosmopolitan boundaries [5]. As a result, business organizations, and manufacturing industries are rapidly exploring industry 6.0 to meet the worldwide challenges of inconsistency, optimization of processes, and environment-friendly technology with low economic cost [6]. Industry 6.0 is the assortment of human intelligence [7], quantum computing [8], the co-working culture of humans and robots, artificial intelligence, and anti-fragile sustainable goals [5]. It is capable of connecting the physical system to the digital world [6] outside the planetary boundaries. According to Chourasia [5], industry 6.0 gathers various ideas from industrialists, business people, leaders, scientists, and researchers. It works on the exclusive concept of customer-driven, customer-oriented, effervescent supply chain management, robotic flexibility, magnificent interconnected industries, and business-to-appropriate interactions among the intensive and extensive across the world and managerial areas. On the next side, a radical change occurs in digital transformation in production, business model, and value creation which creates new challenging environments for enterprises in day-to-day business life [9]. With the intention of this, organizations have to develop new strategies in an adequate frame of time under the government law, statutory provisions, and judicial bodies to reduce the risk of accountabilities under criminal and civil law for the organization and their bodies [9]. In the present scenario, the inducement of technologies is spreading its wings with the speed of light, because of which government policies, laws, and judiciary systems are changing abruptly and creating lots of complexities for the adoption of legal castigations and use of technology in LM (legal metrology). Metrology is the study of measurements that introduces the units and distinguishes techniques for weighing and measuring, based on laws and regulations globally. But due to progression in science and technology as well continuous enhancement in digital technologies push the metrology toward the legality. Therefore, to measure the weight for profitable drive and trading business purpose there is used of legal metrology, where it retracted the standards of weight and measurement Act 1985. In simple words, legal metrology is the claim of legal requirements to measuring and measurements the instruments [10]. Technological change triggered the development of distinguish variety of nobel measuring instruments and processes that expands the opportunity of metrology [11]. The technology's predictable challenges includes introduction of digital weighing equipment's, fast flow of equipment in market, cost of maintenance of metrology devices, calibrations for various weighing equipment's cost in metrology and criminal law, civil law, legal liability, data security, trade boundaries, data rights [12], and data mismanagement [13]. Additionally, it is vigorous to explain the right interaction of digital technology of industry 6.0 with legal constitution. But alliances of digital technologies with legal trials must have enhanced the probabilities of data threat, legal liability, data security and hacking of data information system. To address all these current issues, the concept of a legal information system has been addressed in industry 6.0 and would also play a crucial role in developing a legal information system. Legal information system came into the existence in 1995 and illustrates the relationship between jurisprudence and computer [14]. Legal informatics is the synergy between man and machines in statutory processes to solve their problems, about all the laws, data protection, right to seclusion, and data security [15]. Legal information system has a tremendous ability of legal conscripting to accomplish several law activities and a tendency to create new legal cognitive models. Moreover, legal information is an area that is growing in the field of technologies too such as artificial intelligence, cloud computing, cyber security, big data, additive manufacturing, smart factories, and virtual reality [7, 8, 16]. The application of industry 6.0 would also show an imperative part of the legal informative system as a reinforcement of jurisprudence activities. In industry 6.0, all the technologies such as data science, quantum computing, cloud computing, artificial intelligence, cyber physical system, automated robots would have work together to create a legal paradigm that make the work easier and substantiate. The computational and data science-driven legal innovative populations models would be made for improvement of existing legal models. The new models will be developed with the use of industry 6.0 tools such as artificial intelligence, quantum computing, cloud computing, cyber physical system, and automated robots. Implementation of legal informatics in industry 6.0 would guide the industrialist, businessmen and clients on the several matters related to data privacy, management information system, litigations, compliance, and security-related issues and efficiently manage all the legal tranquil in internal and external processes of the organization in cutting throat competitive environment [17]. Further, quantum computing [8], AI, cloud computing, Internet of Things, cyber security and system integration [18] have all

the possible abilities to bring the changes in the era of legal informative and metrology sector. For instance, in metrology quantum lies measurement technologies would simplify the accuracy and precision of the measurements that is keep concern with SI (International Sytem of Units) for several applications [19]. Industry 6.0 is the futuristic concept where technologies would provide system integration, simulation support, real-time data information and big data that support to recognize the system fault, miscalculation, optimizing the production flow and also mending the legal informative services in perspective of industry 6.0 [20]. AI is the powerful tool of industry 6.0 where lawyers, can easily fetch the all past and existing information regarding to judicial cases and make work smoother. Industry 6.0 has tendency to develop unique insight into the legal circle in seconds using the technology of AI [21]. The industry 6.0 works on the various pillars of digital technologies such as IoT, quantum computing, antifragility, digital twins, transparency in data, and dynamic supply chain 22]. While a usage of quantum computing technology, lawyer to streamline their study and paper work. Quantum computing would provide enough advancements in field of law through which system would be able to generate automated legal advice to lawyer. This is one of the powerful tool of industry 6.0, it would provide predictive analytics that could help law practices to understand outcomes of cases and refined results. It would also assist the lawyer to understand client behavior and selection of right prosecutor for national and international cases [23]. The incorporation of industry 6.0 digital technologies with legal system would definitely come out with the outstanding results in operational efficiencies, cost-effective solutions, precise law decisions practices, real-time status of cases and revamp the eminence of legal services in entire the globe without debilitating the human rights [23, 24]. The central objective of this research paper is to study the role of industry 6.0 technologies in legal informative field, to find out legal potential challenges and legal risks factors to implementation of legal informative system with industry 6.0 and also to prosper the connection between them. On account of all, the legal informative system should able to embrace the digital transformations of industry 6.0 so that rapid transfer of right information, data security, AI-based solutions, legal analytics using quantum computing, document automation [25], electronic contract generation, legal mechanism [26], smart legal contracts in license data and right to personal information [27], robot attorney's [28] can affirms. It has been seen that few extent research has done over industry 6.0 which keep concern with the sustainable legal informative domain. Thus, the following research questions are to be addressed in present research work:

Question 1: To study the need for industry 6.0 in the legal informative system and digital transformation in the metrology system.
Question 2: To find out the techniques which could support a legal informative system in the context of industry 6.0
Question 3: To develop a hypothesis framework and futuristic model for a legal informatics system based on quantum-based AI, machine learning concepts, and a framework of digital metrology based on cloud computing and its adoption challenges.
Question 4: To study the requirement, challenges, and progress in developed countries and the preparedness of academia and industries in India in the context of digital metrology.
Question 5: To study legal challenges and opportunities in legal informative and legal metrology in industry 6.0.

2. Need for Industry 6.0 in Legal Informative

The need for digital technologies in law/jurisprudence has been a growing trend in the last few years. In developing countries like India, the legal system is negligibly touched with IT support and industry 6.0 technologies such as quantum computing, the Internet of Things, cloud computing, artificial intelligence, machine learning, and other IT-enabled advancements. The law system is still working with its traditional style, demanding lots of resources and hard work. These hard-core law conditions can be improvised with the futuristic concept of Industry 6.0 technologies. These technologies can provide outstanding support to the present judicial system instead of enormous, complex work. Indian legal system has infinite possibilities for improvement that can be accomplished with collaboration with industry 6.0 technologies. In of present scenario, the Indian law jurisprudence system of developing countries is very sluggish and disorganized where maximum cases are still pending due to the fewer numbers of the ratio of judges per case and time-consuming court proceedings. Regardless, the above-said condition is still not improved over the last many years because of many constraints such as political, financial, technological, and many more. Thus, now it is time to take a wake-up call for legal communities to reconnoiter themselves and explore a new perspective of innovative processes and computational methods that can enhance their existing worse condition of the justice system. The art of the state of industry 6.0 can give a new look to the jurisprudence system with the assistance of enabling artificial intelligence, quantum computing, IoT, and machine learning in a more effective, efficient, and optimized way. That is why there is a need for industry 6.0 in

legal information so that tremendous change could be brought in the area of the legal province with the assistance of digital transformation.

2.1. Need for Digital Transformation in a Metrology System

Each country possesses its own individual vigorous measurement system that consists of a chain of laboratories, standardized facilities, and accreditation governing bodies as per the need for national quality infrastructure. The legal metrology department of any country makes the rules and regulations and imposes on the metrology trade and BIS (Bureau of Indian standard) that deals with written standards of products and services [29]. Now digital metrology is a need of the metrological department. Digital metrology would bring a good understanding that would be beyond the measure. It would help to develop, interpret, and apply the measurement outcomes to detailed situations. By using enabling technologies of industry 6.0, the VL (virtual links) of distinguish calibration laboratories or testing laboratory can perform their jobs remotely or online through the transfer of data despite the physical transport of instruments. By using enabling technologies of industry 6.0 in the future data can be transferred from the testing laboratories to client scenes electronically. The digital transformations in legal metrology can only be established by implementing, cloud metrology, IoT-based digital framework, big data, AI and digital twins would be adopted in the future that is why there is a need for industry 6.0 in legal metrology so that tremendous change could be brought in the area of the metrology province with the assistance of digital transformation. Table 1 shows strengths, limitations, opportunities, and threats during the adoption of digital transformation in metrology [29].

Contrasting the Internet, cloud computing is in its initial state in the field of legal metrology. From the literature, it has been studied that in 2012, the European Commission estimated that 250 euro billion in GDP can be generated in an upcoming year, i.e., 2020 by the implementation of cloud approachable policies in contradiction of 88 billion euros in the environment of "NO INTERVENTION" environment and bringing to more collective controls from 2015 to 2020 of 600 euro billion with the generation of 2.5 million more jobs [30]. Cloud will work effectively when countries have good IT infrastructure for their consumers and stakeholders. Now cloud technology is not un-touch with the legal metrology field. No doubt, cloud computing would bring new prospects in the field of measuring systems that are bare to legal control. Cloud computing offers servals aspects to manufacturers of measuring the world and they are utilizing it by use of virtualized infrastructure in developed countries. For instance, legally relevant measuring data are stored remotely or complete data is transferred to clouds, i.e., on external servers. In the cloud, all data of individual measurement is stored easily for all the instruments and make experts surveillance work easier, when they wish to test the instrument from a remote area. Hence, the native instruments can reduce physical sensor that is combined with minimum communication unit that are providing admittances to open network. For instance, sensors, that assist technologies as proposed by Europe in the digital agenda in 2020 [31].

3. Literature Review

The present paperwork has been categorized into 10 phases. In the very beginning phase, the basic introduction of legal informatics, legal metrology, and industry 6.0 is explained. In the second phase, the need for industry 6.0 in legal Informative and legal metrology is illustrated. Iin the third phase, the literature review and the transformation journey from industry 4.0 to industry 6.0 are addressed. In contrast, in the fourth phase, key technologies of industry 6.0 have been illustrated. The fifth phase of the paper covers the framework of industry 6.0 in the legal Informatics system with its challenges in the adoption of the framework. In the seventh phase, a futuristic model for a legal informatics system based on quantum-based AI and machine learning in Industry 6.0, is explained in brief. Further, in the eighth phase, the framework of digital legal metrology in context with cloud metrology is explained as its challenges in the adoption of the framework. In the ninth phase of the paper, we discussed requirements, challenges, and progress in developed countries. In the tenth phase, we discussed the preparedness of academia and industry in India in the context of digital metrology. And at the end of the paper, the limitations of the study research implications, and conclusions in the future were addressed.

3.1. Revolution Voyage from I.4.0 to Industry I.6.0

We, humans, have been encroaching toward the up-gradation of industrial revolutions to chase effective and efficient production throughout history. The IR-1 started in late 1784–1800 and was lied on the concept of the mechanical production system, the introduction of the steam engine, and water power usage [28]. IR-2 (1870-1914) has one step ahead of the previous one; mass production use of electricity for production and assembly lines was the core theory of IR-1. The IR-2 is extended further and turned into the IR-3, and computer-based knowledge and automation come into the picture or the transformation of hard analog systems into the digital system [12]. As time

Table 1 Shows strengths, limitations, opportunities, and threats during the adoption of digital transformation in metrology

S. no	Strength	Limitations	Opportunities	Threat
1	Capability to develop the economy of the country and society	Required highly skilled and qualified workforce to understand digital technologies	Coordination of conformity valuation and market observation	Required strict security system and protocols for sharing and coordinating measurement information
2	Make strong legal metrology standardization process, accreditation, market lookup, and confirm the assessment	Quantum-based digital technology is expensive and required a huge infrastructure setup	Online checking of faults, condition monitoring, and self-decision-making	Requires excellent metrological traceability and self-identify intelligent system
3	Fix the link between the non-virtual and virtual worlds	Remote maintenance is the biggest challenge in digital communications	Synchronization in legal metrology standards, documentation, and market observation. and service standards	Chances of arguments may be created between legal people and technological people
4	Employing the development of a smart metrology system, a single digital market for metrologists	Remote diagnostics and calibration are the challenges in front of the metrology department while using digital technologies	Chance for developing 5G communication channel	Required cloud services for storing the real-time data of measurement
5	Generate new job chances and innovations in the field of legal metrology	High-budget infrastructure with 5G enabling Internet connectivity	Finding new ways to lessen	Semantic methods or technologies are required for fixing the link between virtual and physical systems

passed, IR-3 entered into the new paradigm of revolution, i.e., IR-4. Currently, industries are working on the impression of industry 4.0, which is based on mass customization rather than mass production, the conceptualization of modularity, cyber physical system, 3D printing, real-time data capability, and robotization. IR-4 concept came to light in 2011 and pushed the entire world to digital automation [5]. As we move further, IR-5 comes into the frame with supporting high-tech technologies such as artificial intelligence, machine learning, deep learning, and the Internet of Things., strengthening the IR-5 [32]. According to Demir et al. [33] co-working culture of humans and robots, the growth of smart societies, artificial intelligence-enabled robots, data unification, mobilization, sustainability, and bio-economy led to starting of IR-5. The core idea of IR 5 is moving from mass customization to personal customization. IR-6 is the futuristic vision of researchers that believes in anti-fragile manufacturing, mind control machines, cloud renewable energy, human co-robot-centric, homogeneous assets, hyper-connected industries, quantum computing, etc. Figure 1 shows the transformation journey from industry 1.0 to industry 6.0. Moreover, industry 6.0 is based on quantum computing and real-time information transfer to several systems and their sub-components to bring transparency to work and enhance digitalization in the whole service chain. Quantum computing is a new technology that works 158 million times faster than any supercomputer globally. It comprises a high-performance capacity that easily gauges the millions of data through qubits, can run millions of algorithms, and performs predictive analysis and data analytics in seconds [34]. In today's time, QC works as a powerful weapon where clients' data privacy is a topmost priority, especially in the time of excellent cloud and distributed computing. Quantum computing has the inherent supremacy to expand AI-based systems in forthcoming years. Such quantum computing can develop digital subordinates which would be AI-enabled with actual circumstantial responsiveness and can easily coordinate, interact and make the people understand [23]. Here researchers hope that QC has high computational supremacy that would meet the exponential singularities of AI. It has been found that AI can work excellently flourishes when a huge amount of data is given to the AI system to analyze, store, recognize, classify, and more accurately, precisely organize and categorize huge data as per specific requirements [35]. Quantum computing systems have excellent memory to save enormous data that can be processed at a very high speed and are easier to cater to as artificial intelligence. AI analyzes the set to remove several irregularities from data and produce authenticated ones [36]. However, these irregularities in the data create lots of trouble and yield huge challenges in front of professionals to get accurate data on an internal working system. Quantum computing is the backbone of AI because it is observed that without quantum computing and no artificial intelligence and machine learning can work [34]. Because AI and ML require millions of data for generating algorithms and to achieve precise results. And

these data can only be provided through quantum computing. In quantum computing, computers work with countless numbers at an implausible rate and super speed of data searches [36]. It is observed that AI can work excellently flourishes when a huge amount of data is provided to the AI system and AI analyses, store, recognize, classify and accurately, organize and categorize huge data as per specific requirements, and provide excellent results. The collaborative work of quantum computing with AI would enhance the operational efficiency of the legal system. It can also help them make the right decisions in the law industry and maintain authentic records of important information. Quantum computing is the high-tech technology that would make computers faster, about 50-quilt in the future, and smarter through factors prime, statics, algorithms, complex coding, maths, and simulation [37]. These technologies are used to solve unbelievably complex processes and calculations with a huge amount of data. Most researchers believe that quantum computers will take artificial intelligence at a great pace forward. And it would prove highly safe and reliable for data evaluation and forecasting over tasks in the future [38]. Industry 6.0 focuses on quantum AI computing, where quantum computing and AI will work together to compute ML (machine learning) algorithms. Because of the advantages of QC, AI would be able to achieve these results that were not thinkable to attain from classical computers [39]. Although AI is a problem-solving technique that enhances the efficiency of collected data in several ways over the past periods, it has still not yet come out from many technological constraints, such as artificial general intelligence (AGI). AGI is the depiction of broad human intellectual/cerebral abilities in software so that the developed software can face all the unfamiliar tasks. It can perform every task that human is competent in [39]. These constraints can be eliminated in the future with the assistance of quantum computing, where QC can be used for creating optimized algorithms by providing rapid training to machine learning models. A secure and optimized artificial intelligence offered by QC could utter years of data analysis in a minimal period [40]. Further, cloud computing uses remote servers for storing data, managing, and processing the data to achieve better and improved services that would be most cost-effective, reliable, and possess good quality [41]. Currently, quantum-based cloud computing is in its initial phases of development. It would open the door for all the possibilities to enter the era of automation of composite legal reasoning which is called computational law. The progress in the infrastructure of cloud quantum computing would have the ability to create the CLA (computational law applications), would be highly proficient in computing and analyzing several compound patterns at less power consumption to provide as per the demand of the client or on-demand legal assistance. If a legal firm can use quantum cloud computing models, the firm can make maximum profit in terms of money, services, client satisfaction, etc. Big data is the technology that helps an organization make critical and complex decisions by using millions of data, whereas quantum computing can boost the value of big data. In the instance of big data, quantum computing has numerous promising capabilities to deal with various decisions and predicting factors and form more accessible predictable prototypes that can deal with loads of big data and add more feasible variables in the equations without slow downing the process with effective use of data [42].

3.2. Legal Informatics

The term coined legal informatics consist of two separate words. The first one is legal, which refers to the law. And second denotes informatics, defined as an area of information science that belongs to information processing and computer technology [43]. In my own simple words, legal informatics is the science that involves the several applications of legal rules and principles to the dispensation of information and confirming its submission with the law that pertains to obligations, right, data protection, and individual privacy rights. Many individuals and

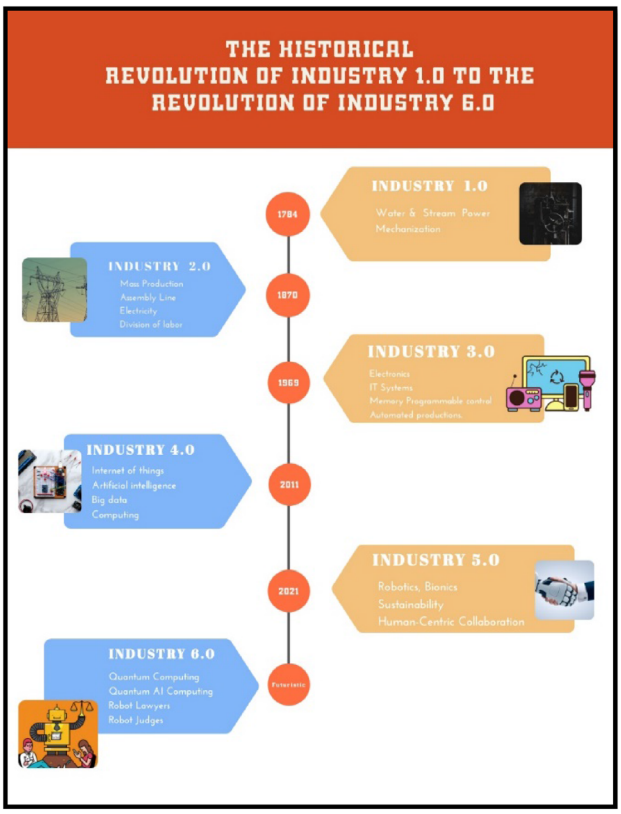


Fig. 1 Transformation journey from industry 1.0 to industry 6.0

associations have different points of view toward the legal informatics system. According to the American library association, legal informatics combines information structure and technology that provides access to the organization for storing, retrieving, and distributing information in the legal environment [14]. As per the view of Professor Peter Seipel, legal informatics is Jurimetrics. The jurimetrics keep province with the quantitative analysis rather than qualitative, where all the information, computational, and communication theory in the legal system uses mathematical formulas, logic, and calculus for predicting the solutions to legal problems [9]. In the current scenario, legal informatics is widely contributing to society in various fields such as case management, law office automation, legal administration [44, 45], and E-governance [46]. Due to increasing trends of ease of digital technology and computerization, all the administrative governance, E-governance, and legal system is heading toward digitalization. According to Don Tap Scott, an E-government is a government that connects new technologies to the central legal system; it turns everyone, such as taxpayers, business people, lawyers, judiciary system, and connects everything digitally [46]. According to Hinson [47], the main aim of the legal system is to keep the focus on the information technology field and its advanced technologies that can be used in the legal system. Daksh [48] has developed a regulatory framework for justice authorities. At the same time, the E-legal platform was developed by Sharma et al. [49] to stir the current Indian justice system. Sharma et al. [24] described the involvement of AI (artificial intelligence), ML (machine learning), NPL (natural language processing), DP (deep learning), and IT (information technology) in the legal system. These technologies would help people file their complaints and queries from any place to the police station with a secure line and eliminate individual visits to the police station. According to Saarenpaa et al. [50], LI deals with legal information, information law, legal information processing, and ICT law. Legal informatics does not only keep concerned with the information and computer law which provides information but also closely emphasizes the application of information technology in law.

Scherer [51] discussed AI and legal informatics, where the author concluded that AI could help law practitioners resolve legal clashes with their patrons by using AI algorithms to provide many solutions to single problems. Currently, digitization in legal communities is not so easy because of global corruption, lack of understating, financial barriers, swift changes in technologies, cyber risk, IT advancements, and polyglot information management. Usually, these challenges are faced by the law system due to rapid transformation in information technologies that require enough skill [9]. As per the author's knowledge, the legal system should have learned the depth of technologies to employ and get better and more effective results. They have to come out from the fear that the growing association with digital technology and law will tend to unemployability in the law industry [52].

Further, it has been observed from many law-based studies that if the legal system keeps focusing on its managerial actions, formal documentation of legal requirements [53], good governance, and correct decision-making processes, then it would become easy for the legal system to reduce the gap between the client and legal law with a peak of client satisfaction. Moreover, the application of industry 6.0 would have the ability to bring the dynamic explosion in the legal firm to providing quantum decision-making solutions to the judiciary system within seconds, easy retrieval and solve of colossal algorithms [5], ease the law practice between the advocates and legal profession [52], ease the client's legal justice system automatic generation of receipts, text mining [53], and robot assistance lawyers (AI Bot) to legal advisory institutions. The robot assistance lawyers (AI Bot) will elucidate the advice and dependability and correlate several factors in real judiciary case issues [54].

3.3. Role of Industry 6.0 in Legal Informatics

Industry 6.0 is defined as the futuristic idea where every individual's thought would be commanded by engaging the human brain, and work would be performed with the help of automatic robots by enwrapping all the cosmopolitan boundaries [5]. Industry 6.0 would develop the link between the lawyers, the judiciary system, clients, and robots. The researcher, academician, and lawyers have started to work together to develop a high-technology robot lawyer; if it succeeds in the future so it will open a new horizon for the legal system and will make legal advice ease for all the immigrant people from multilingual backgrounds and also transforms the face of legal informatics area. With the arrival of robots in the legal judiciary system, the law would sense an immense change in its system, and that would make lawyers' and judges' work more accessible by reducing the cost as well as constraints which are ingress to legal services for a person due to high cost that can be only afforded by rich people [55]. Industry 6.0 will focus on robot judges and robot lawyers. It seems to be a real-life science-fiction concept, but this would come true in industry 6.0.

4. Industry 6.0 Key Technologies and its Challenges

With the tremendous growth of digital technologies, the world insanity is moving toward digital transformation

where tonnes of data are continuously obtained from IoT, nearly transforming the whole world toward the concept of industry 6.0. Quantum computing, AI computing, AI, IoT, machine learning, and other industry 6.0 technologies can assist law developers in supporting the legal judicial system. The implementation of industry 6.0 technologies in legal informatics can help the clients, lawyers, government, and judiciary system keep proper documentation of records, monitoring and analyzing the judiciary cases and their impacts on the legislation system [56]. Implementation of industry 6.0 will motivate the law people and citizens to participate and understand the new methods of the legislative process. Table 2 presents the key digital technologies of Industry 6.0

5. Framework of Industry 6.0 in LI System

Developing a legal informatics framework for the legal system will provide the stage and authority to the legal system that can provide legal assistance to the legal industry in the future. The primary profit of developing the LI framework for the legal industry is to assist the legal judiciary system, justice-ability to legal process, and accountability to stage authority. After an inclusive literature review, the present study proposes a framework for legal informatics that could help the legal system in a future perspective. Figure 2 illustrates the framework of the legal informatics system. The theoretical framework of a legal informatics system consists of seven components such as first industry 6.0 technologies, legal education and documentation, cyber legal law, operating parameters, regulatory bodies, legal challenges, and LI system implementation. In the first component of the LI framework, digital technologies of industries 6.0 will be introduced into the legal system. A brief description of the following is addressed below:

5.1. Introduction of Industry 6.0 Technologies in Legal System

The primary purpose of introducing these technologies in the legal system is to provide the ease of accessibility of legal services to every client. At present, the law system of India is very complex and steady; the proceedings in court take a much longer time to reach the final judgment or a few years. This is due to less awareness of digital technologies and their implantation in the legal industry they are still working with an inefficient, traditional approach that demands enormous numbers of human resources, energy, more time, and enough financial support. The ultimate focus of these technologies is to use the supremacy of digital technologies of industry 6.0 such as quantum computing, artificial intelligence, machine learning, and artificial cloud computing to transform traditional legal informatics systems into digital legal informatics systems. Industry 6.0 technologies tend to revise, renovate, reshape, and modernize the present legal system to make it more efficient and easy to use for all people. Industry 6.0 would be proved a boon to manufacturing industries by connecting them through a dynamic supply chain, transparency in information flow, and increased industries' profit in every aspect [5]. From the literature review, it has been found that the UK government has started to use AI-based services to deal with civil legal cases that arise from road casualties by virtual modes. This kind of AI assisting virtual hearing can help clients with casualties and improve customer services with minimal costs [69].

By using AI, customers need not go outside the city where they are working or live; they can avail of the AI services. Industry 6.0 is also moving forward with the future vision for establishing a legal and ethical framework for quantum computing. This would ease the work of legal informatics systems such as solving the case pendency, judicial decision on numerous cases, time-consuming tasks, and the poor ratio of cases over judge's calculations. It can easily be solved by using a legal and ethical framework for quantum computing where several components of QC are armed with artificial intelligence, so the binary codes, neural network technology, and quantum software will provide outstanding results to all the above-said problems [35]. Further application of quantum computing to quantum analysis, sense, quantum simulation the millions of legal documents in seconds with the help of a quantum algorithm and would provide outstanding results [42]. In the upcoming days, a collaboration between AI and auantum will bring a new skyline to the whole legal system of the world.

Moreover, suppose quantum computing AI technology implementation has started in a legal firm. In that case, it will accelerate the entire legal profession's practice and bring a revolutionary change in the legal paradigm, and will teach lawyers new technologies that make their work easy. The sole target of introducing quantum computing and quantum computing AI is to fill the gap between the legal system and technology so that the legal activities of lawyers, judges, and judiciary system can be sped up and clients and society can be benefitted. Nowadays, cloud

Table 2 Key digital technologies of Industry 6.0

S. no	Industry 6.0 technologies	Explanations	Advantages	Barriers	Applications
A	Quantum computing	• It is a sort of computation that binds the several properties of quantum phases like interference, entanglement, and the concept of superposition for solving quantum computations [57] • It works on qubits which is the basic unit of computing and useful for the security of data stored in a quantum field [58]	• This technology makes the calculation much faster than the traditional system [38] • It helps law firms with data analytics by providing sufficient advancement in technology • This technology will provide automated legal advice to lawyers and judges by interpreting laws freely [23] • It tends to solve any calculation in 200 s • It tends to transform cybersecurity before 2030 or may be beyond [59] • This technology can solve complex problems with extraordinary speed [59]	• It is costly technology and is still on under development • It performs calculations errors up to 10 to 100 times more than classical computers • It provides noise and interference of qubits because of which errors are produced	• Cryptography • Banking Sector • Automobiles • Health sector • Travel and Transport
B	Quantum artificial intelligence computing	• It is the combination of quantum computing and artificial intelligence, where they work together and would provide insignificant results to the law system • Quantum AI employs a machine learning algorithm for computation purposes [60] • Quantum artificial intelligence is the sort of computing in which AI algorithms are specially designed for quantum computing to perform a task. Both work simultaneously and contribute to fast calculation in minimum time with numerous benefits [60]	• This technology provides a less mistake-prone and more powerful system • It can be used as an open-source model and for training purposes • Persuasive applications of artificial intelligence help quantum computing to perform unbeatable results [39]	• One of the highly vigorous challenges in implementing QAI computing is the scarcity of resources for design • Lack of organization/system interest in embracing new technologies • The design of the algorithm structure and its verifications is one more challenge [61] • The organization required a huge-scale quantum computing circuit system for efficient execution which required architecture support [62]	• Climate Change predictions [61] • Quantum Property Testing [62] • Automobile • Health care system [61] • Space exploration [41]
C	Artificial intelligence	• It is the technology that refers to the imitation of man's intelligence to machines through proper programming by using AI algorithms [63] • It is a part of information technology where it comprises probability, data mining, statistics, problem-solving models, decision models, and maths [63] • AI reconnoiter several data by using various open data sources by coalescing ANN (artificial neural networks), the Internet of Things, Mathematical models, genetic algorithms, etc. [41]	• It reduces the time to perform the job • It helps to take fast and accurate decision-making during the judgment time • It helps to reduce human error. Because AI uses all previously gathered data and a group of algorithms before giving any decisions • It provides digital assistance to customers. eg chat-bot • It helps the medical system to solve intricate problems. Eg Recently AI-based technologies were used to predict the starting phase of breast cancer in women	• Its implementation in legal informatics systems requires high costs • It will have increased unemployment because AI-based lawyers would replace human lawyers [64] • AI does not contain ethics and moral values like humans and that can be very difficult to integrate into an AI. So there would be more chances that AI will wipe out all of humanity [64] • Neuromorphic cognitive models, adaptive machine learning, or reasoning under vagueness are approximately fundamental challenges of AI	• Banking Sector • Automobiles • Health sector • Legal system • E-commerce • Gaming • Finance • Education • Surveillance • Agriculture [13]

Table 2 continued

S. no	Industry 6.0 technologies	Explanations	Advantages	Barriers	Applications
D	Cloud computing	• Cloud computing is a technology that relies on the Internet • It uses an outskirts server to store the data, manage the data, and effectively processed the data economically [65]	• Cloud-based technologies enhance the reliability of the system by lowering the fear of losing the data of clients • It helps the legal system to store a large amount of data in clouds and save human and IT and machine resources • It reduces the attorney's time that is consumed during arranging appointments, managing legal documents, billings, voicing, etc. [66]	• One of the biggest challenges in cloud computing is the safety of personal/confidential customers' or clients' data • Data privacy • The anxiety of handing over control of data [71] • Data Hacking • Third-party admittance issues [66]	• Education Sector • Entertainment Industry • Health care Sector
E	Robot judges and robot lawyers	• Robot judges and lawyers reduce the workload of human judges and lawyers by using their programming abilities that are enabled by AI, ML, QC, and deep learning • This technology will be designed in such a way that it will understand all the multilingual languages, able to articulate hypotheses and monitor the changes that occur in the legal system [67]	• Robot judges will edify the legal reasoning of human judges [68] • Better decision-making by using algorithms [68]	• Increase rate of unemployment • Lack of emotions • Robots could develop their communication language as occurred in the Facebook project. That could be proof very dangerous to humans [67]	• Judiciary system • Legal Informatics • Courts
F	Big Data	• This is the technology that extracts data from large and complex database and analyzes it, process it, and extract the information as per the requirement of users which is an impossible task for old data processing software system [68] • This technology helps the legal firm as well as other organizations also to take complex decisions [67]	• Big data would bring transparency to legal operations and tell the Clients about the fees means should have to know how much money they are paying for which services • This technology would develop building a client strong base	• Access of control • Data privacy • Data integrity • Rules and regulations • Data breach [14]	• Faster courtroom process • Believe in maintaining a client base • Health sector

computing keeps transforming the face of the legal industry by offering cost-effective services and profit to time-strapped attorneys. Cloud-based technology provides data protection and backup services to lawyers [70] and allows clients to take follow-ups of their cases from any place through real-time data monitoring [71]. Machine learning technology uses algorithms capable of developing empirical models by gathering information by pattern followed by received data. If these empirical models are correct, ML develops automated several decisions related to the case for a future perspective that helps the judiciary system a lot. From the perspective of big data, it would help the government administrations and judiciary system understand the ML and deep learning process to identify the several possibilities of illegal, criminal activities and cybercrime for mitigating actions [72].

5.2. Role of Legal Education and Documentation in Legal Informative System

The ultimate aim of legal education in legal informatics is to develop multi-purpose and inter-discipline purpose learnings that strengthen the entire legal structure. According to S.P. Sathe, a successful product of the education system is a lawyer that should be capable in the future of contributing toward the growth of the nation and

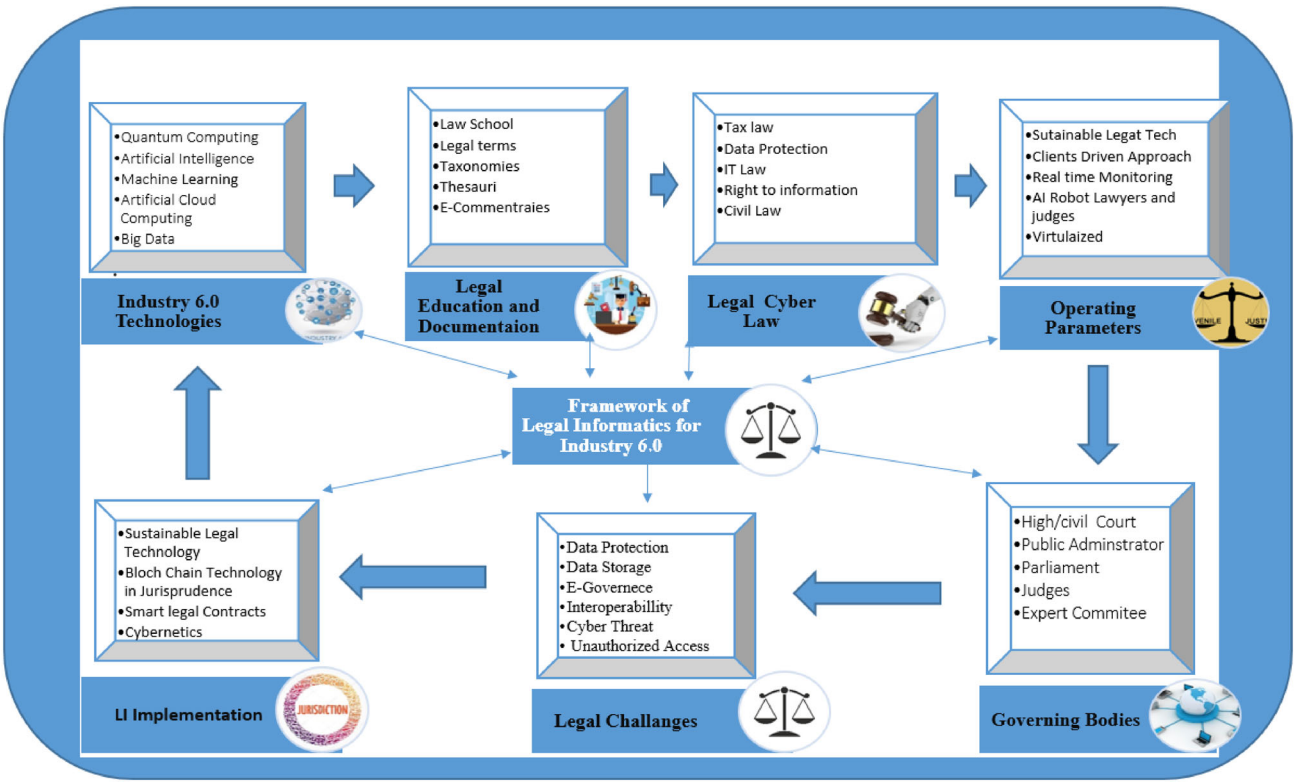


Fig. 2 Framework of legal informatics system

society and bringing substantial social change in a positive manner [73]. Industry 6.0 can transform the era of legal education and will produce exciting opportunities through which the future of law graduates and postgraduate law students can be transformed constructively. Industry 6.0 gives the massive propagation of digital technologies of auantum computing, simulation, AI, ML, deep learning, and cloud computing, high technology enables mobiles and 5G and 6G Internet connectivity which would offer a new paradigm and set a new path for educating students. This innovative education approach in law will reform the old trend of legal education. Law students are no longer required to study on university/college campuses to study the law; they would be able to take their bar lectures/classes from any part of the country [74].

The futuristic student of industry 6.0 will be the students who will emerge with the amalgamation of digital technologies and novelties. These students are the ones who would be incarnate in an atmosphere where everything would be automated and more organized. The legal system is highly affected by lots of paperwork used during the time of herrings of the cases and judicial judging. So, to solve this problem, the concept of E-review could be introduced in case management. So that judges and lawyers can manage the case comfortably from their homes or where are they. On the other hand, lawyers are not required not to worry about supervising the files, documents, and affidavits of pending case judgments in several cases. Because the industry 6.0 cloud-based monitoring system will ring the automatic alert alarm to remind the date for them. Further, all the files and documents would be virtual in the CMS (case management system); lawyers are only supposed to bring their laptops/tablets to court.

5.3. Legal Cyber Law

Legal cyber law or IT law is the paperless law in the paperless ecosphere, which relates to the law of the Internet, where the legal system is sketched in such a way that it should be proficient in dealing with computers, the Internet, cyberspace, and more legal issues [87]. It is also in accord with the legal informatics that handles data flow, software commerce, and data security. According to the Ministry of Electronics and Information Technology of the Government of India, the identification of cyber law is to work with electronic documents and provide support to electronic-filling and electronic commerce and also decrease cybercrimes [88]. The critical areas of cybercrimes covered by the Indian IT act are illustrated in Fig. 3 [57]:

The birth of the cyber law or IT act came into existence after establishing the constitution, i.e., in the year 2000 on 17th October, to furnish with E-commerce and crimes attacks/cybercrimes in India. There are some IT Act guidelines published by Indian legislation in Table 3.

The main governing body of cyber law is the central government of India. Under this IT act, people can register their complaint or FIR to any police station by online mode without physically visiting that place. In addition, industry 6.0 technologies provide a wide range of access by using digital tools to effectively deal with complex crime cases. Additionally, lawyers should have adequate knowledge of these budding technologies of industry 6.0 to understand their consequences on law and its risks and have a tendency to develop a safeguard against them. In India, ITA (Information Technology Act) is the prime regulator of the legal justice system and was applied in the year 2000 [24, 77]. The main goal of ITA is to provide significant legal shielding and make E-commerce flexible services by providing actual information to the government at every period. Quantum computing and law would be proved cognate to each other, but presently, there are no particular regulations and laws in India that keep concerned with quantum computing. Hoever, MEITY (Ministry of Electronics and Information Technology) is answerable for all the policies regarding matters to IT and ADIT (Administration of the Information Technology), Act 2000 [78]. One more study in the USA reveals that Australia, China, and other European countries are moving faster to lead in quantum technologies. Now, India has also commenced nearly legal reforms in quantum computing, and these reforms are broadly associated with the laws adopted by developed countries [79]. Similarly, India has implemented the export of some information security systems by using quantum cryptography under the Foreign Trade Act, of 1992 but still working on quantum computing.

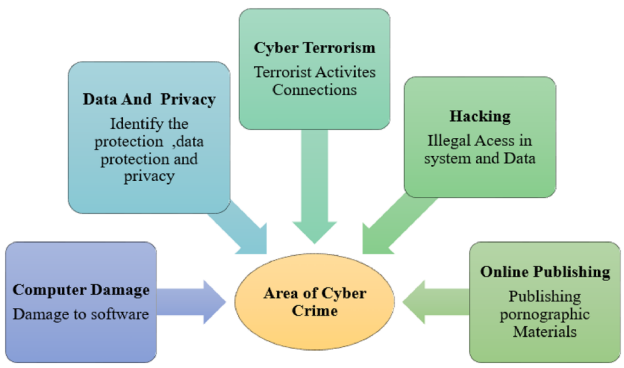


Fig. 3 Critical areas of cybercrimes are covered beneath the Indian IT act

5.4. Operating Parameters in Legal Informatics

Currently, sustainable legal tech is the new primacy of an informative legal system where law firms are continuously expanding their feet toward adopting new technologies for improving efficiency and law values. Sustainable legal tech intends to develop a judicial system that can make solid operational functions for the judiciary system so that members of the law industry could easily access it [80]. In sustainable legal tech, lawyers not only to adapt the changing economy and part of society but also work as a leader who would bring positive change to a law firm on a magnificent scale [81]. Innovation in the legal system is often driven by customer/client demands. So it is the responsibility of lawyers to employ their knowledge, experience, and expertise for goodwill to their clients and identify their needs and preferences to defend them [82].

To make healthy relationships with clients, lawyers must embrace the innovative skillset in the legal profession to be able to meet the requirements of their clients. This indicates that for achieving a sustainable legal tech firm or informative legal system, legal administration, lawyers, and judiciary system are required to set a sustainable legal mind in the law profession and to understand clients, their human rights, social challenges, and the digitalized world in the more economical way [81]. On the other hand, Industry 6.0 would focus on lawyer robots, which would be proved a boon for tomorrow's attorneys, and also be capable of providing prodigious legal assistance to every client. Robot lawyers and judges will assist human lawyers and judges in researching the cases, and the history of clients, drafting briefs and complicated paperwork, and also providing counseling to clients in the legal profession [83]. The dream of a robot lawyer can be accomplished by using industry 6.0-enabled digital technologies such as quantum computing, artificial intelligence, and machine learning and also make lawyer work more accessible and safe than ever thought.

5.5. Regulatory Bodies in Legal Informatics

The constitution of India provides guarantees lifetime protection, defense of fundamental rights, and personal liberty to everyone. The regulatory bodies in legal informatics have bonds with government administration, the supreme court, the high court, subordinate courts, legal aid, public prosecuting attorneys, experts, etc. [84]. The governing regulatory bodies are the backbone of the legal system. It becomes highly subtle when forming sustainable laws and policies for the legal system. Law-making governing bodies need to consider the emerging technologies of industry 6.0. This industry 6.0 revolution would bring a new revolution in the era of the legal system by providing

Table 3 Guidelines of Indian Legislation under the IT Act

S. no	Sections	Explanations	Penalty	References
1	43	This section refers to aggravation or attack on a computer system deprived of owner permission will be liable to this punishment	In such cases, lifetime imprisonment	[71]
2	65	This section refers to Snooping with the source code documents The source codes document is the collection of codes written so that humans can read	In such cases, imprisonment of up to 3 years and an Rs. 2 Lakh fine will be applied	[75]
3	66	This section refers to computer systems and cybercrime hacking, which involves computers and networks	In such cases, imprisonment of up to 3 years and an Rs. 5 Lakh fine will be applied	[75, 76]
4	66B	This section refers to imposing a fine for getting a stolen computer, communication device, and digital device	In such cases, imprisonment of up to 3 years and an Rs. 1 Lakh fine will be applied	[75, 76]
5	66C	This section refers to cheating, breaching the password	In such cases, imprisonment of up to 3 years and an Rs.1 Lakh fine will be applied	[75, 76]
6	66D	This section refers to Internet fraud or cheating using computer resources. or These sections miens into the matter related to Internet fraud or providing wrong information to the victim for taking money, property, and inheritance	In such cases, imprisonment of up to 3 years and an Rs. 1 Lakh fine will be applied	[75, 76]
7	66F	This section refers to the act of cyberterrorism	In such cases, lifetime imprisonment	[75, 76]
8	70	This section refers to attempting to open secure access to a password-protected system	In such cases, as much as possible fine and 3 years of imprisonment	[75, 76]
9	72	Fissure/Breach of confidentiality and privacy	In such cases, imprisonment of up to 2 years and an Rs. 1 Lakh fine will be applied	[75, 76]

accurate monitoring data information, transparency in the legal system and public administration, and promoting responsibility.

5.6. Legal Technology Challenges

Legal technology is changing the face of the legal firm with the velocity of light incredibly. This technology has an enormous capacity to change the map of the whole practice of the law system. But cyber threats, data protection, unauthorized access, extensive investment in technology, and global fraud are significant challenges to legal informatics systems. Data protection is the arranged application of official, technical and physical protection that saves personal data and privacy [85]. Legal firms are continuously working to maintain their clients' privacy and sensitive information. With emerging technology, interoperability is another challenge, where lawyers get various solutions to their case-related problems with the help of AI, IoT, etc. Still, it is difficult to decide which solution will connect and fit with the existing problem in the future [86].

5.7. Legal Informatics Implementation

It has been seen that lawyers are complaining about their workload and that they are overloaded. So to reduce their workload, the legal system is heading toward the implementation of sustainable legal technologies such as blockchain, digital business, and smart legal contracts. In the legal system framework, blockchain technology is assumed to be an essential part of it, which keeps all the recording details of transactions between two or more two parties by considering secure design [87]. This technology would help jurisprudence to perform proper verifications of legal documents and provide damage immune proof examinations that will enhance the judicial system's effectiveness and efficiency. The implementation of blockchain technology in the legal system will ensure the stoppage of unethical use of technology and financial fraud [23]. On the other hand, smart legal contracts are the legal contracts that bind all the contractual obligations, which are clearly explained in the form of or/and codes and performed spontaneously by a computer system. Its primary purpose is to increase efficiency and effectiveness with certainty in the legal system and reduce errors for client satisfaction [86]. Sometimes, smart legal contracts also create challenges in front of clients due to the complex languages or terms of the law mentioned in documents, due

to which clients have to face problems in understanding the documents [81]. Studies have observed that if blockchain were a part of the legal industry, it would provide accessibility, cost savings, transparency, data integrity, and automation in work. The use of blockchain in a legal firm leverages lawyers' work to be more simplified and streamlined by using smart contracts and digitally signed and automated contracts. The automated contract management system decreases the unnecessary time spent on the preparation of law documentation and maintaining personal records. Using this technology in a legal firm, the cost can be saved significantly. Moreover, if blockchain is implemented in legal law, it provides complete freedom to the legal justice system by reducing customer difficulties and lawyers' hefty fees [88]. Cybernetics is the science that investigates the rules, regulations, constraints, and opportunities inside the system. The main aim of cybernetics in the legal system is to understand the functioning of numerous processes such as hardware, computer device, and IT technologies that are part of the system. It works either in a circular form, chain form, or many others forms. And lastly, it senses the forms and equates them parallel with the ultimate goal so that the final goal can be attained. Cybernetics is also called "Kubernetes," which means steersman. The word cybernetics explains the information which flows from one system to another and its impact on the control system. This novel approach works on cognitive, normality, and interpretative theory, which were introduced by cybernetics. It can change the direction of the legal field, socially and economically, so that industry 6.0 can regulate all the processes effectively by using various technologies. Moreover, lawyers spend 48% of their time on administrative paperwork like the transfer of legal documents and related information midst the software to the client, making a list of clients, etc. Using this technology, excessive manual work can be reduced and reduces the legal herrings cost [89]. Figure 4 shows the summarize flow diagram of legal informatics.

6. Challenges in Adoption of Legal Informatics Framework

6.1. Legal Challenges for Lawyers in Future

The Indian judiciary system is continuously facing many challenges that are produced during the time of the COVID-19 pandemic and still trying to overcome this by using online services for urgent matters through video conferencing. The legal system has to understand the importance and potential of digital technologies in the legal industry. So, it's time for the judicial system to open its eyes and move from traditional to digitalized law practice using industry 6.0 key technologies. But currently, the Indian judiciary system has many intrinsic flaws that prevent the law system from using technology in a 100 percent efficient way. So, firstly legal system has to overcome these challenges, and then only it would be capable of embracing the digital technologies of industry 6.0. Some glitches in the present legal system are discussed here.

6.2. Architecture Structure

Because during the online herrings of court, lawyers and clients have to use either their own devices such as laptops/mobile phones to continue the hearings or the devices provided by the court. Now the biggest challenge is the insufficiency of the physical system (Laptop/Desktop/Mobile) utilized during the time of court proceedings. Thus, the E-committee of the supreme court has also faced lots of trouble during the online proceedings, E-filling, and operating virtual courts through video conferencing due to less availability of essential infrastructure in the legal system. Because India is a developing country, where about 65.07% of people belong to rural areas [90], in such a scenario, vast numbers of clients cannot afford the expense of digital devices.

6.3. Difficulty in Embracing Digital Technologies in the Legal System

The legal jurisprudence system has been working on traditional law systems for many years, but now it's time to renovate the law system by adopting legal Tech and new computational technologies to improve the efficiency and effectiveness of the legal system. But it has been seen that for the last some years, the majority of the lawyers and judges are not ready to embrace the new technologies because they know that it would require a set of new skills, and they have to learn these skills to deal with them, and they deny to adopt the technologies due to dearth of understanding and it will put an adverse effect on the jurisprudence system.

6.4. Uniformly Admittance of New Technology

The next challenge for the judiciary system is the availability of technologies in every corner of the country without affecting their economic conditions. Another challenge is uniform access to technology in all places so that lawyers, judges, and clients can use it conveniently. Before going into the law system in the digitalized world, all litigators should have proper knowledge of technologies and know-how to use them to maintain court dignity. Because the tradition of the Indian litigation system is supposed to be archetypal and combative. While abstaining

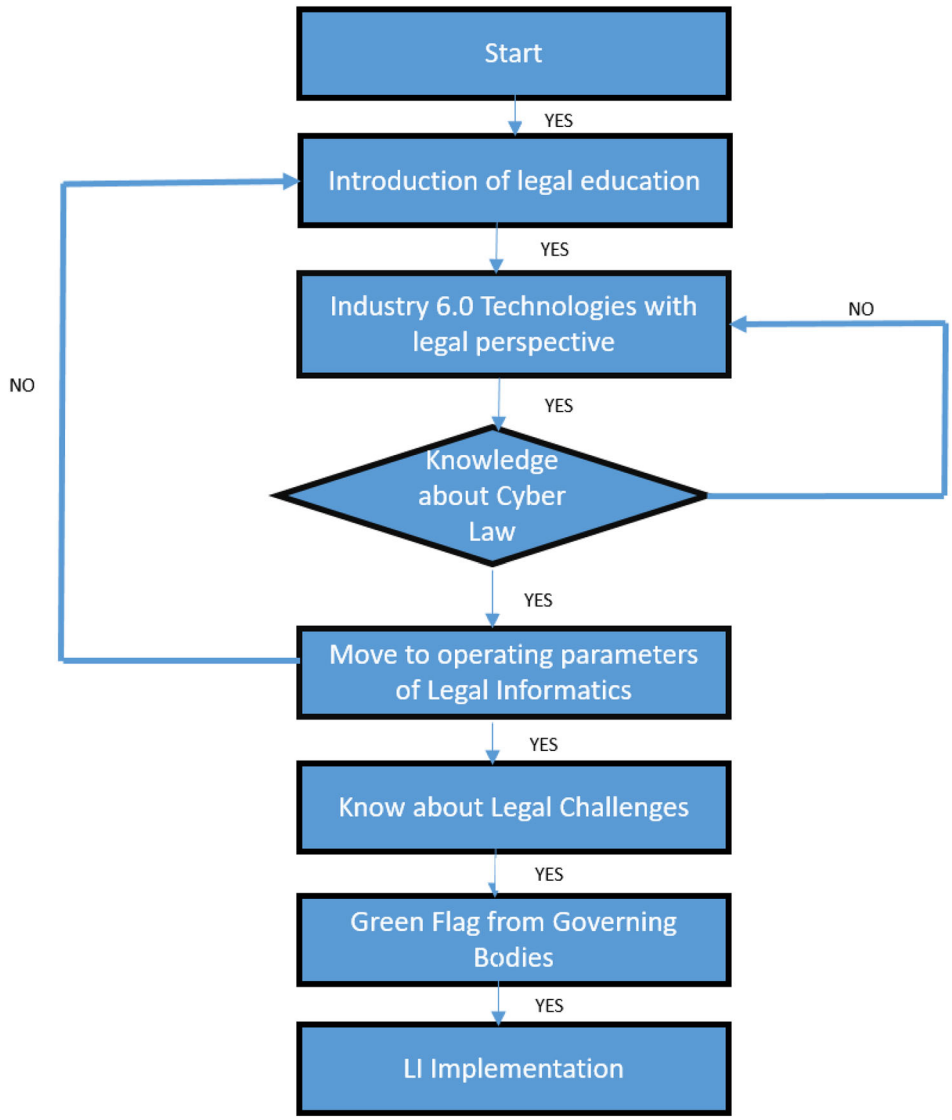


Fig. 4 Summary of the flow diagram of legal informatics

from discussing the profit and loss of this stereotypical culture, if the condition of culture is archetypal and combative, it will raise the burden on a virtual platform and result in interruptions of proceedings [58].

6.5. Internet Connectivity

India is moving toward the digital India concept, where every service is made available to customers electronically, and online services are provided to customers by enhancing Internet connectivity or making people empowered in technology. To achieve the aim of digital India, the government has to provide 6G and 7G Internet connections. High-speed Internet is the first step toward digitalization. In the absence of high-speed Internet connectivity, embracing digital technologies will remain a dream. It will never come true and just remain a dream. It has been noticed from many legal blogs that approximately 60 court cases come to different courtrooms of the supreme court on Friday or Monday. In a simple calculation, 1140 court cases have to be heard daily. The question is whether our present Internet connectivity can support the supreme court in all 60 cases simultaneously. We cannot make proper judgments and confident statements in India toward adopting industry 6 technologies [58].

6.6. Standard Operating Procedure, Protocols, and Unvarying Platform

Presently, it has been noticed that different courts, lawyers, and judges are using various online platforms (Skype, Zoom, hats app, and Microsoft teams) for proceedings that are creating trouble for clients and courts to understand the app's functioning. That is why it is necessary to adopt a

uniform platform and uniform protocol with the standard operating process for proceedings in-country and hearings to remove the complexity of understanding among the clients, lawyers, and judges. The legal system would have to ensure that all the records regarding hearings, proceedings, etc. It should be maintained in a pleasant way to quickly be understood. The platform should comprehend such an option that one can show the objection in between the hearing or in arguments without speaking a single word. These objections should be kept in such a way that it automatically recorded in the software itself and to help the judge to mention them to the alike later. These challenges recently brought fundamental changes in standard operating procedures on April 15, 2021 [33]. In this comprehensive standard procedure, only the team/party can address the court; if there is any objection to the opposition team, they can raise their hands in teams/Zoom; otherwise, all have to remain mute till directed by the court to unmute.

6.7. Internet and Bandwidth Connectivity

To achieve the aim of digital India, the government has to provide 6G and 7G Internet broadband speed. Because high-speed Internet is the first step toward digitalization. But due to the absence of high-speed Internet connectivity, the dream of embracing digital technologies will remain to be a dream and will never come true and just remain a dream. It has been noticed from many legal blogs that approximately 60 court cases come to different courtrooms of the supreme court every Friday or Monday. In a simple calculation, 1140 court cases have to be heard daily. Whether our present Internet connectivity can simultaneously support the supreme court in all 60 cases? At present, we are not able to make the right judgment and confident statement in India toward adopting industry 6 technologies.

6.8. Infrastructure and Technology Training

The conduction of virtual courts is not as easy as we think. Virtual processing requires seamless robust architecture infrastructure and secure audio–video and Internet connectivity with trustworthy technologies that should have the capability to hold all the conference meeting data securely. After seeing all these requirements, the E-committee of the supreme court has placed some solutions to deal with the present problem. They suggested that the fund comes for phase 2 E courts could be used to improve the speed of Internet connectivity. If these solutions are thoughtfully implemented, maximum problems related to infrastructure and technology can be reduced.

6.9. Issue of Cybersecurity

Cyber security is one more challenging issue legal system while implementing the concept of virtual courts. All the technologies work on Internet-based technologies, where all the data are stored in the cloud. As such, data security is the biggest challenge. The present study also provides the theoretical framework of LI and a futuristic model for the legal informatics system. This futuristic model is based on quantum-based AI and machine learning techniques of Industry 6.0 to improve and advance legal informatics systems. Industry 6.0 technologies have enormous capability to bring man and machine (robot judges and lawyers) together to make the decision-making process easy without taking time years and provide a collaborative solution to judges relevant to cases lawyers and judges [9].

7. Futuristic Model for Legal Informatics System based on Quantum-Based AI and Machine Learning in Industry 6.0

The quantum-enabled ML and AI models can be proved helpful in solving complex problems in legal industries. Studies have found that if quantum computing works collectively with machine learning and AI, AI and ML will rise as a more powerful weapons in the field of law in the future [91]. Quantum computing has enormous potential to bring enormous improvement in artificial intelligence and machine learning. Machine learning is the branch of AI and CS (computer science) that use data and AI algorithms and try to copy human behavior as he learns, reacts, behaves, etc., so that significant improvement can be achieved in ML with precision and accuracy. It also tends to prove itself as the most powerful technology in the field of law in the future. ML can predict system behavior after learning the system model. In the last many years, ML models have been employed several areas to tackle many challenging problems such as weather predictions and earthquake forecasting. In the present study, the hypothesis-based quantum machine learning and AI models [57] represent the legal system. Quantum, ML, and AI-based models have more extraordinary abilities to gather data using mechanical origin.

This model will work on two concepts; the very first one is the quantum database, i.e., if we are applying in the field of law, the database will be the total number of cases, pending cases, solved cases, complaints recorded, Lawsuits, herrings, judicial decisions, etc. And the second one is hybrid quantum–classical models. Figure 5 shows the Futuristic model for a legal informatics system based on quantum-based AI and machine learning in Industry 6.0. In this model, a large circuit is divided into small sub-circuits,

and they are evaluated distinctly either by using a quantum processor or using a classical supercomputer running a quantum simulator [69].

In the very initial stage, for solving the cases, herrings, and counts of pending cases., a quantum database will be prepared which will cover all the information regarding cases, herrings, and counts of pending cases. with all the data that keep concerned with these issues. And these data are denoted as multi-dimensional arrays of numbers called quantum tensors. Multi-dimensional array implies an array that contains more than two dimensions. If we co-relate this with the legal system, a multi-dimensional array will be court hearing cases containing several solutions. In the second stage, as per all the quantum data gathered for specific court cases, the basis of that one quantum neural network will be selected. Quantum neural networks are network models based on computational neural networks and work on quantum mechanics concepts. The primary purpose of this is to take out concealed information in an entangled form. In the third stage, quantum stats or averages are measured by extracting classical information of value from the random variables. In the previous stage, classical information related to the court case of the client is converted into classical data; now, in the subsequent step, evaluation of the classical neural network model will be performed by using deep learning, machine learning, and AI techniques that would be used to study the relationships among the various variables. After receiving the proper correlation between the problem and its solution variables. After that, the cost function will be evaluated. The cost function is the function that helps ML to understand the fundamental difference between the assumed value and the value which exists [92]. The accuracy of the result of the cost function could be based on how intelligently the model had selected to perform functions when quantum data was categorized, or any other measures were taken. And at the last stage, after evaluating the cost function, gradients are evaluated as well as if there is any change, new parameters will be updated [93]. Using this quantum-based AI and ML can improve the decision-making system of the Law industry.

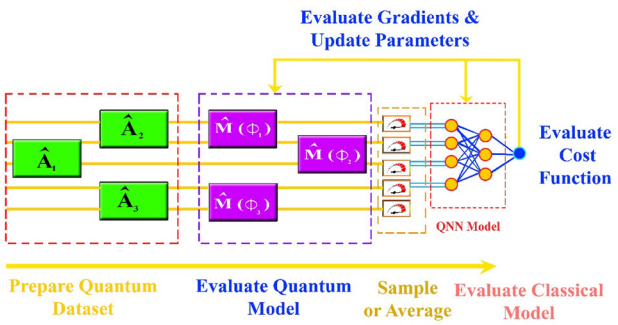


Fig. 5 Futuristic model for a legal Informatics system based on quantum-based AI and machine learning in Industry 6.0

8. Framework of Digital Legal Metrology

Legal digital metrology would bring an excellent output that would be beyond the measure. It will help to develop, interpret and apply the measurement results to the specific situation. It has been observed that approximately 4 to 6 percent of shares of EU countries which is equal to 660–990 million euros annually are saved due to the adoption of a legal measurement system. That is why in India lots of efforts are required from the legal metrology department, Bureau of Indian Standards (BIS), National Metallurgical Laboratory (NML), and Quality Council of India (QCI) to establish the digital metrological quality structure in India so that it can subsidize the GDP and economy of India. Developing a legal informatics framework for the legal digital metrology system will provide the stage and authority to the legal system that can provide legal assistance to the legal metrology industry in the future. The primary profit of developing the LI framework for the legal metrology industry is to assist the National Metallurgical Laboratory (NML) and Quality Council of India (QCI) legally and accountable to stage authority. After an inclusive literature review, the present study proposes a framework for legal metrology informatics that could help the legal digital metrology system in a future perspective. Figure 6 shows the framework for legal metrology informatics that could help the legal digital metrology system in a future perspective.

8.1. System of a Unit Digital Framework for Digital Metrology

It has been noted that the International Committee for Weight and measures (CIPM) has formed a workgroup on a digital system of the unit to perform some tasks. Here, SI digital metrology would use for developing a uniform measuring system throughout the world. The digital system that would be designed should be explicit and in data secured format by using enabling technologies of industry 6.0 such as IoT-based networks that would be SI entirely described in the present SI booklet [94]. This target can only be achieved by proper coordination with pertinent stakeholders by fixing appropriate connections. Legal metrology industries have to propose such a broacher that can be machine-readable.

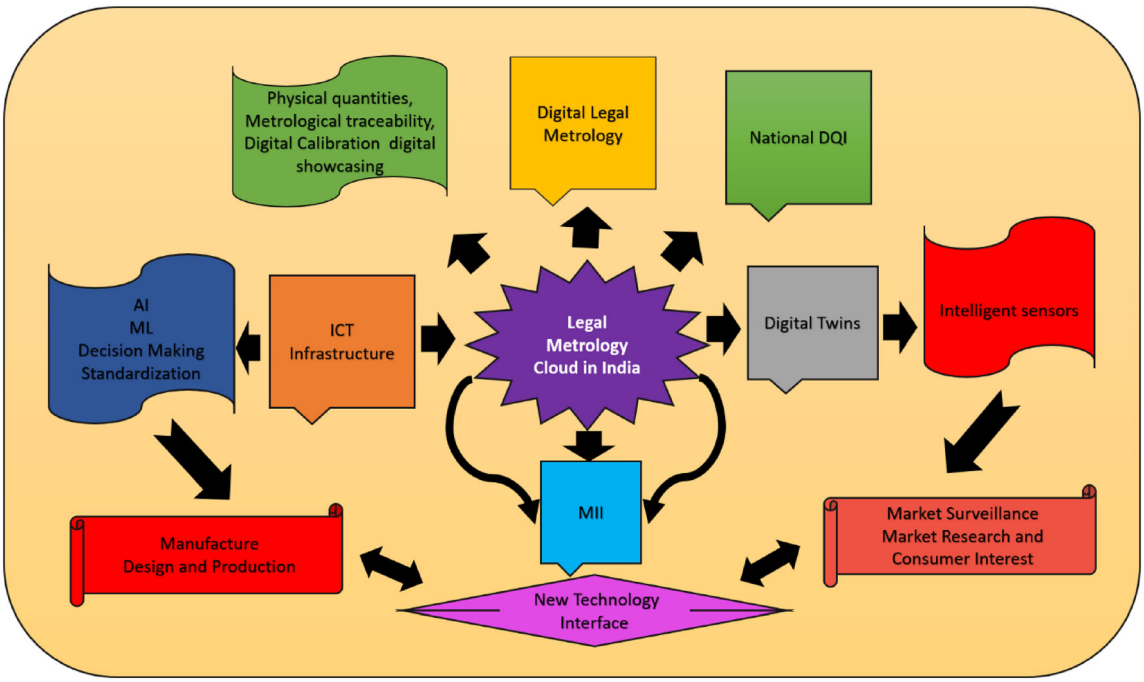


Fig. 6 Framework for legal metrology informatics that could help the legal digital metrology system in a future perspective

8.2. Measurement of Information Structure

MII is defined as the group of normative standards that could explicatively define the data, its structures, service ethics, certification, conformity assessment, and market survey which is digitally connected with a digital network and behaves like an interoperable [9]. In simple words, in MII all the measurements should be linked to a digital system and each system communicates with the other without doing any manual data processing, or transcription work [95]. The demand for digital transformation in every field such as manufacturing and production has swiftly increased. To establish the quality structure with the adoption of all challenges, digital transformations are needed in the field of legal metrology by adapting proper quality assurance, conformity assessment, certification, market survey, etc. by using a digitally enabled platform that would act as an interoperable.

8.3. Legal Metrology Clouds and Digital Structure

The developed countries such as Germany, National Metrology Institute has recently started a program that is related to the development of EDQI (European digital quality infrastructure). In this program, the metrological institute predicted to use the of metrology as a main platform in every state, country, and city for designing, supporting, and streamlining the regulatory courses by connecting all the infrastructures, and databases to the single point of communication for all the stake holders [96]. The EU aims to apply digital metrology to strengthen the rank of Europe in the field of innovation, and data-driven and to develop a single digital metrology market in Europe [97]. The same approach and efforts can also be applied in India with more innovation in legal metrology perspectives for establishing a national digital quality infrastructure for helping the manufacturers and share-holders. If we see at the perspective of India, CSIR and NPL play an important role in establishing and developing the basic to standard concepts and pillars of cloud-based legal metrology. In India, such kind of transformation needs the embracement of digital technologies in legal metrology.

8.4. Digital Data and Digital Twins in Legal Metrology

To decrease the managerial load over the businesses and manufactures and accelerate the harmony between the administrative process of conventionality assessment, market survey and digital-enabled infrastructure is needed in India by adopting the industry 6.0 technologies such as digital twins and AI. A digital twin is the copy model of physical assets, natural environment, and processes. This uses real-time data from distinguished assets. Digital twins would play a significant role in establishing digital legal metrology. Digital twins would involve a replica model, a set of data related to that model, and able to update and change the model according to the availability of data [98].

This model will contain all the information related to measuring instruments, their substructure, and particular information about the instruments. Digital twins will contain all the information about the instruments, sensors, and authorization of profiles. In a generalized way, the establishment of digital twins would bring new development in the history of measurement standards with a high degree of accuracy and precision. The main challenge in the implementation of digital twins is the repairing of software, its streamlining, and validation support [29]. The flowchart for digital metrology is shown in Fig. 7.

8.5. Challenges in the Adoption of Legal Metrology Framework in the Future

The COVID-19 has brought a massive pace of digital transformation all over the globe. In legal metrology, one of the primary challenges is the transition from current working practices to digitized solutions. For instance, digital twins. Digital twins based on virtual models of the non-virtual system. The digital object model will be made first which would evolve all the possible sets of data or the model can be adjusted as per the requirement of data. In a generalized manner, the digital model will give precise decision-making when the set of data received from the measure would be accurate. Reliable data is one of the biggest challenges in legal metrology [99, 100]. Another challenge in adopting digital transformation in legal metrology is the cost of digital instruments, standardization of measuring instruments, training required as well as government policies toward the adoption of digital technologies in the field of legal metrology [11]. The security of data is another risk which is associated with cloud computing. There is a chance of loss of control of data if there is inadequate security contrivance. These risks are data breaches, insecure interfaces, hijacking of accounts, data loss, etc. After seeing these risks, there is no doubt that cloud computing can come under the risk of cyber attack and data theft.

8.6. Opportunities in the Adoption of Legal Metrology in the Future

Digital transformation has the tremendous capability to bring significant change in the field of legal metrology by instituting digital quality measurement instruments,

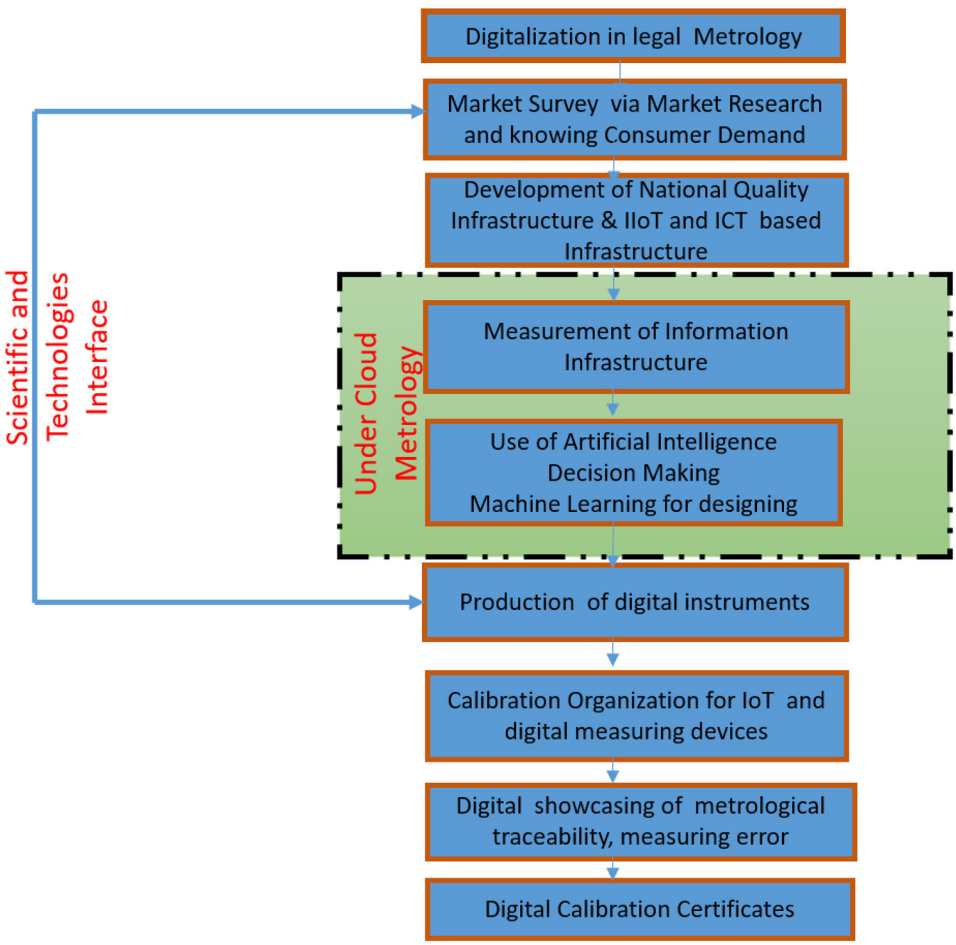


Fig. 7 Flowchart for digital legal metrology

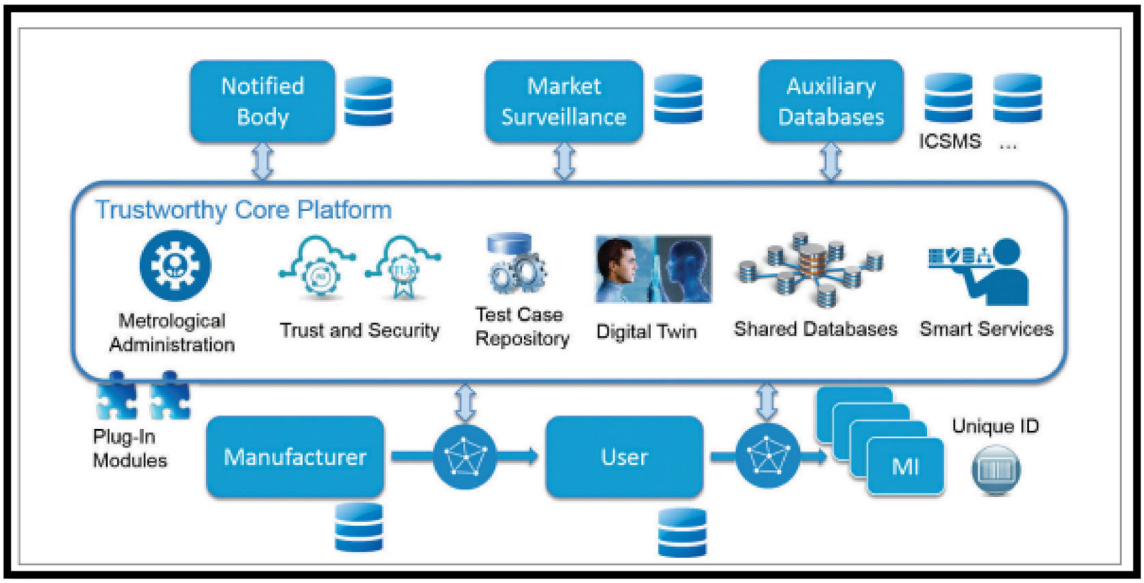


Fig. 8 Proposed concept of a faithful core platform for state members [96] [103]

digitally enabled infrastructure, nurturing economic and trade growth, standardization of market scrutiny, conventionality assessment, and legal metrology. The inducement of digital technology in legal metrology would be crucial in keeping the founding of legal metrology clouds enabled by machine learning for developing the excellent quality structure for metrology, enhancement of industrial growth, innovations, and many more. Machine learning is quality data-dependent and can efficiently handle and process the data. For instance, machine learning. Machine learning is data-dependent. The right quality of data in ML provides precise results. Machine learning has tremendous capability to process the data effectively by using filtering techniques to filter incorrect, non-accurate data and systematic error data that are caused by mature aged measurement devices. The next digital technology. IoT can also increase the effectiveness of measurement in metrology by the usability of data for marked requests and outside parties. The trusted data produced by IoT helps the stakeholders to taking accurate decisions. Consequently, a significant social impact can be produced by using this industry 6.0 technology by introducing quality data metrics with IoT in metrology. The IoT-based sensors make metrologies work easier by securing the non-virtual system to digital traceability series potentially by using digital twins.

9. Requirements, Challenges, and Progress in Developed Countries

In the present time, fast change in developing technologies like BD (big data) and CC (cloud computing) can be seen in the market of instruments and measurement. These changes bring huge changes in the globalized market and increase the efficiency of work and the demands of the customers. In India, products are loaded onto the ships, and adjacently legal deals take place in the Netherlands, and the UK monitored and controlled the automatic weight measuring in Indonesia The importance of this is that new developments and changes are read to endure solely any framework of legal metrology. The external forces are controlling the driving forces [101]. ICT (information and communication technologies) are not only contributing to developing innovation in products but in innovation in processes and structural arrangement of legal metrology. As per the view of the industry, it is time for moving toward the DSM (Digital Single Market) where the single point of communication for all the stakeholders. The digital single market is the market that provides great access to consumers, industries, and businesses and provides online services across Europe [102]. To this end, in this study, the framework proposed by Europe on European Metrology Cloud for setting the digital quality infrastructure in legal metrology. The concept proposed by Europe for the single digital market for European legal metrology focuses on the founding of a data infrastructure by using the trust full platform of the European Metrology Cloud core platform. The proposed concept of a faithful core platform for state members is shown in Fig. 8. This platform helps the legal metrology market to support the processes of conventionality assessment and market survey. So that if the digital transformation has been embraced by legal metrology the distinguished benefits in measurements can be achieved by stakeholders and industrialists in lesser time. The crucial

prerequisite of the manufacturers of technologies and its possibilities have provided the guiding aim for achieving conformity assessment, market survey, and digital quality infrastructure for legal metrology services based on the future of measuring instruments and data-driven metrological services to the European country. To attain the said objective the following actions are proposed as Link Infrastructures an databases, references architectures, streamlined with the inducement of new metrological services and European COE (center of Excellence). In joint infrastructure and databases, a single quality digital infrastructure and database will be provided to stakeholders, and industrialists by providing a core platform to every state member of legal metrology. This platform will serve as a communiqué and service-providing platform rather than a data-discarding environment.

In reference architectures, industries needed new technologies such as digital twins, IoT, cloud computing, and Big data. These are the important pillars of future European digital quality infrastructure to complete the need for a legal metrology system. These technologies would make work easier, and provide sufficient security and easy verification of measurement data [103]. In streamlined with the inducement of new metrological services, the concept of digital twins will be introduced, where the administration will contain all the descriptive data of individual measurement instruments and may present DQI (digital quality infrastructure) and can be easily accessed by official parties. The 100 million data of measurements are used in the European single market which generates huge data in volumes over the complete life cycle in the distinct database. This merging of data definitely will produce a brook of metrological data through which new data-based smart services can be consequent for industrialists, and stakeholders to make their work easy in present controlled processes [102]. This concept of Europe also emphasizes developing novel technology and data-dependent metrological services for quality infrastructure to endorse manufacturer innovations and could sustenance harmony in Europe. In this regard, a project proposal for the development and implementation of future digital quality infrastructure was succumbed by Europe in industries in Call 2017 to the EMPIR (European Metrology Programme for Innovation And Research) to the EMPIR (European Metrology Programme for innovation and Research) and that would be funded by EMPIR participating countries. The main challenge in the proposed framework is the security costs that would be paid to IT, and the technology gap between the manufacturers and notified authorized bodies of market investigation agencies. Authorities may refuse new technologies and innovative solutions in the legal metrology field.

9.1. Preparedness of Academia and Industry in India in the Context of Digital Technologies

In the revolution of industry 6.0, universities will have to play an important role. Universities have to take a dynamic step in developing and describing the prospects of industry 6.0 and its enabling technologies. Now it's time for universities to redefine their roles, responsibilities, and way of delivering knowledge to students. Now the universities have to adopt new adaptive learning models, collective educating models of teaching and learning for professors and learners that should be enabled with digital technologies such as AI, ML, and DM. Universities are required to motivate for developing a curriculum that offers opportunities to students and professors to examine their knowledge, caliber, and competency in their study and teaching methodology respectively to acquire the latest skills, critical and creative thinking, digital literacy physical skill, and cognitive learning. The power of digital or IT tools such as ML, and AI, can play a prime role that could be more in the form of democratic approaches in dealing with, transferring, and circulating knowledge from universities to industries to society. But in India, the present scenario, the scope of AI and ML is in the initial stage but its pace is slow. To see this lap, DRDO (Defence Research and Development Organisation) has started an autonomous college (Defence Institute of Advanced Technology) and announced short-term courses on AI, and ML with cybersecurity. This is an online course for 10 h where learners can learn about basic and advanced concepts of AL and ML such as (BDA) big data analytics, probability theory, AR (augmented reality), deep learning, and related advancements in technologies. After the completion of courses, DRDO conducts for giving the course successful completion of courses [104]. In the same way, ISRO has also launched the course for DL and ML. These courses are developed for students who are pursuing their degree in sensing data in distinguished applications. In these course classes, fundamental to advance of ML, fuzzy-dependent ML, ANN, and CNN [105]. IIT Madras is offering a master's program in AI to motivate students who belong to distinguish backgrounds to learn about new technologies. The main goal of introducing these technologies in the curriculum is to develop the concept of new technologies such as AI and ML so that the students can become the future leader of India as well as all over the world and also fill the gap between the source and demand of the AI and ML in India. IIT Hyderabad provides excellent laboratory amenities with state of art in research areas, good Internet connectivity, and hardware and software support. In the same way. IISC Bangalore, VIT Vellore, and many more are offering specialization in AI and ML for upgrading the skills of students for achieving the future vision of India

[106]. At the end, by developing technology-based literacy among the students, every citizen of India can help the development of society and attain the goal of industry 6.0. Presently, India is facing many challenges in adopting these digital technologies in their industries due to less strategic planning, less training in these technologies, and increasing difficulties among the technology and industries. As per the report of IBEF (Indian Brand Equity Foundation), the GOI (Government of India) has fixed a determined target for attaining the impact of manufacturing output from 25% of GDP by 2025 which is 16% at present. The government also has taken steps for the green corridor and Make in India initiatives. According to the IBEF report, IoT is the biggest weapon for India and it is expected that it will cover 20% of the share in the next 5 years. Metro states of India are taking wits to embrace digital technologies. Andhra Pradesh took a chance to capitalize on the IoT caliber in the country. The Andhra Pradesh government has an IoT policy with the agenda of turning itself into an IoT hub by 2020 and also achieved the 10% of the market share economy. In recent, the first smart factory in India is turning automation into autonomy. In this concept of automation to autonomy, the machines talk with another machine, this arrangement is being set up in Bengaluru. IISc Bengaluru, (CPDM) center for product design and manufacturing is working on this project with the monetary investment of Boeing Company. According to the reports, the concept of digitalization in the industry will touch 215bn US dollars by 2025 in India [107]. On an ending note, the capability to cuddle industry 6.0 enabling digital technology would provide enormous opportunities to industries, and businesses that would be the key to success.

10. Limitations of the Study and Research Implications

The present work is based on the theoretical perspective of the legal informative system and legal metrology for developing the framework of LI and a futuristic model for a legal informatics system based on quantum-based AI and machine learning for Industry 6.0. In upcoming work in the future, the quantitative perspective of LI will be considered by employing quantitative techniques to validate the results of the findings.

In current findings of work, it observed that industry 6.0 is a futuristic revolutionary idea that would have an affinity to change the entire scenario of the law system and legal metrology system. But due to this futuristic idea, the author has found minimal studies that show a detailed explanation of the problems faced by metrologists, lawyers, judges, and clients in legal industries in all respect either, socially, economically, and technologically. In legal Tech, Industry 6.0 technologies will bring opportunities and a challenging environment to lawyers, clients, and judges that will help them improve their skills and decision-making system with the help of digital technologies and robot lawyers and judges. At present time in India, industries are using 40-year-old measurement systems for weighing. This is the one implication that can be filled by proper training in the legal metrology field. The practice of digital measurement with digital enabling technologies requires high-skill in-house training for understanding digital practice. The next implications are the use of software in measuring apparatus. For instance, measuring software will work on some operating systems and sometimes it seems to become very difficult for metrologists to use OS (operating system). OS is programmed with high-level codes which need deep knowledge to understand. Lastly, the client's trust and confidence can be increased in legal metrology, jurisprudence, legal services, and sustainability when the industry 6.0 technological vision is embraced by the law and metrology communities.

11. Conclusion and Future

This study is based on an analysis of the legal industry in the context of industry 6.0. And how the critical technologies of industry 6.0 can benefit the Indian legal system and legal metrology in the future. In this study, the following conclusions can be manifested:

- This study found that necessary cyber security and data privacy are compassionate issues, yet no rigid rules and regulations are built up.
- The government has to look up these issues and must establish a powerful jurisprudence system in India that would have the capability to help the law industries protect their data from cyber threats.
- The implementation of industry 6.0 technologies pillars in the law system should focus not only on the effective working of the law system but also on client, lawyer, and judge satisfaction toward the insouciance of decisions that come out through digital technology data security.
- This study investigates how industry 6.0 technologies, such as quantum computing, AI, and ML, can provide excellent decision-making prop up to the legal system and its people.
- The implementation of the legal metrology framework in India could require inhibitors among the manufacturers and the government governing bodies because the inducement of new technologies in legal metrology could create fear among the manufacturers due to the technology gap.

- The cost of digital technologies and the security of data will be the main concern among the stakeholders, manufacturers, and notified bodies.
- The main challenge in the implementation of digital twins is the repairing of software, its streamlining, and validation support.
- The practice of digital measurement with digital enabling technologies requires high-skill in-house training for understanding digital practice.

References

[1] S. Desiraju, ATMANIRBHAR BHARAT_ Innovation through technology−Commercialization (2022). [Online]. Available: https://www.isbr.in/blogs/atmanirbhar-bharat-innovation-through-technology-commercialization/.

[2] D. Gürdür Broo, O. Kaynak, and S. M. Sait, Rethinking engineering education at the age of industry 5.0, J. Ind. Inf. Integr., **25** (2022). https://doi.org/10.1016/j.jii.2021.100311.

[3] A. Schütze, N. Helwig and T. Schneider, Sensors 4.0−Smart sensors and measurement technology enable Industry 4.0, J. Sens. Sens. Syst., **7**(1) (2018) 359–371. https://doi.org/10.5194/jsss-7-359-2018.

[4] T. Hackel, N. Savinov, L. Ladicky, J. D. Wegner, K. Schindler, and M. Pollefeys, Semantic3D.Net: a new large-scale point cloud classification benchmark, ISPRS Ann. Photogr. Remote Sens. Spat. Inf. Sci., **4**(1W1) (2017) 91–98. https://doi.org/10.5194/isprs-annals-IV-1-W1-91-2017.

[5] S. Chourasia, A. Tyagi, S.M. Pandey, R.S. Walia and Q. Murtaza, Sustainability of Industry 6.0 in global perspective: benefits and challenges. Mapan-J. Metrol. Soc. India, **37**(2) (2022) 443–452. https://doi.org/10.1007/s12647-022-00541-w.

[6] Y. D. Ravinda Kumar, R. K. Singh, Application of industry 4.0 technologies in SME for ethical and sustainable operations: analysis of challenges, https://doi.org/10.1016/j.jclepro.2020.124063.

[7] C. Atwell, Yes, industry 5.0 is already on the horizon|machine design, *Machinedesign.Com* (2017) pp. 4–6. [Online]. Available: https://www.machinedesign.com/automation-iiot/article/21835933/yes-industry-50-is-already-on-the-horizon, Accessed on 22 December 2021.

[8] C.F. Bowman, What is quantum computing? How Things Work (2022) pp. 215–234. https://doi.org/10.1201/9781003143437-10.

[9] D. Habrat, Legal challenges of digitalization and automation in the context of Industry 4.0, Procedia Manuf., **51** (2020) 938–942. https://doi.org/10.1016/j.promfg.2020.10.132.

[10] S. Dash, What is legal metrology_complete concept and laws−Corpbiz. [Online]. Available: https://corpbiz.io/learning/what-is-legal-metrology-complete-concept-and-laws, Acesssed on 21/12/2022

[11] N.F. Wanjiru, A research report presented in partial fulfillment for award of the degree of masters of arts in project planning and management (2012).

[12] M.K. Marcelo Negri Soares and R.O.J. Fortaleza, Industry 4.0: horizontal integration and intellectual property law strategies In England (2018). [Online]. Available: https://doi.org/10.12662/2447-6641OJ.V16I23.P268-289.2018.

[13] S. Agrawal, A. Sahu and G. Kumar, A conceptual framework for the implementation of Industry 4.0 in legal informatics, Sustain. Comput. Informatics Syst., **33**(July 2021) (2022) 100650. https://doi.org/10.1016/j.suscom.2021.100650.

[14] F.V. less, A. Biasotti, E. Francesconi, M. Palmirani and G. Sartor, Legal informatics and management of legislative documents (2008). Corpus ID: 15034062.

[15] A. Saarenpää and A. Wiatrowski, Society trapped in the network: Does it have a future? (2016) [Online]. Available: https://research.ulapland.fi/en/publications/society-trapped-in-the-network-does-it-have-a-future, Accessed 29/3/2022.

[16] X. Xu, Y. Lu, B. Vogel-Heuser and L. Wang, Industry 4.0 and industry 5.0—inception, conception and perception, J. Manuf. Syst., **61**(October) (2021) 530–535. https://doi.org/10.1016/j.jmsy.2021.10.006.

[17] A. Teichholz, Industry guide to legal: How the legal industry is changing in the age of digital transformation (2019) [Online]. Available: https://blogs.opentext.com/industry-guide-to-legal-how-the-legal-industry-is-changing-in-the-age-of-digital-transformation/, Accessed 29/3/2022.

[18] J.P. Pauli Kuosmanen, T. Villman, E. Annanperä, M. Jurmu, J. Kaivo-oja, P. Kettunen, M. Knudsen, T. Lauraéus and J. Majava, From industry X to industry 6.0: antifragile manufacturing for people, planet, and profit with passion.

[19] Q. Sensors and B. Goldstein, NIST on a chip: revolutionizing metrology through deployable quantum based sensors (2020) 30–31. https://doi.org/10.5162/SMSI2020/2.

[20] C. Stergiou, K.E. Psannis, B.B. Gupta and Y. Ishibashi, Security, privacy & efficiency of sustainable Cloud Computing for Big Data & IoT. Sustain. Comput. Informat. Syst., **19** (2018) 174–184. https://doi.org/10.1016/j.suscom.2018.06.003.

[21] S. Sanjana, Role of artificial intelligence in law, *iPleaders* (2021) [Online]. Available: https://blog.ipleaders.in/role-of-artificial-intelligence-in-law/. Accesed on 29 March 20222.

[22] L. Chung, B.A. Nixon, E. Yu and J. Mylopoulos, Non-functional requirements in software engineering, (2000). https://doi.org/10.1007/978-1-4615-5269-7.

[23] S. Flynn, What is quantum computing and how is it disrupting law firms, *LawTechnologyToday* (2020). [Online]. Available: h https://www.lawtechnologytoday.org/2020/12/what-is-quantum-computing-and-how-is-it-disrupting-law-firms/, Accessed on 30 March 2022

[24] S. Sharma and R.S. Al, eLegalls: enriching a legal justice system in the emerging legal informatics and legal tech Era.

[25] M. Javaid and A. Haleem, Impact of industry 4.0 to create advancements in orthopaedics, J. Clin. Orthop. Trauma, **11**(xxxx) (2020) S491–S499. https://doi.org/10.1016/j.jcot.2020.03.006.

[26] 6 Benefits of using technology in the legal industry−Legodesk [Online]. Available: https://legodesk.com/blog/legal-practice/6-benefits-of-using-technology-in-the-legal-industry/, Accessed on 30 March.

[27] H. Arya, Could your next lawyer be a robot (2022). [Online]. Available: https://www.digit.in/features/machine-learning-and-ai/could-your-next-lawyer-be-a-robot-62785.html,Accessed on 30 March 2022.

[28] K.A. Demir and H. Cicibaş, The next industrial revolution: industry 5.0 and discussions on industry 4.0, Ind. 4.0 MIS Perspect., (January 2019) (2019), 247–260.

[29] N. Garg, S. Rab, A. Varshney, S.K. Jaiswal and S. Yadav, Significance and implications of digital transformation in metrology in India, Meas. Sens., **18** (2021). https://doi.org/10.1016/j.measen.2021.100248.

[30] Communication from the commision to european parliment, the council, the European Economics And Social Committee and the committee of the regions unleashing the Potential of Cloud Computing in Europe [Online]. Available: https://eur-

lex.europa.eu/legal-content/EN/TXT/HTML/?uri=CELEX:52012DC0529, Accessed on 13/1/2023.
[31] J. Bergendahl, A transformational agenda for the digital age, Digital Europe's 2020 vision, Digit. Eur. (2009), [Online]. Available: https://www.tubisad.org.tr/tr/images, Acessed on 13/1/2023.
[32] A. Haleem and M. Javaid, Industry 5.0 and its applications in orthopaedics, J. Clin. Orthop. Trauma, **10**(4) (2019) 807–808. https://doi.org/10.1016/j.jcot.2018.12.010.
[33] K.A. Demir, G. Döven and B. Sezen, Industry 5.0 and human-robot co-working. Procedia Comput. Sci., **158** (2019) 688–695. https://doi.org/10.1016/j.procs.2019.09.104.
[34] M. Smith, Quantum computing: definition, facts & uses (2022). [Online]. Available: https://www.livescience.com/quantum-computing, Accessed on 28/4/2022.
[35] Himanshi, Quantum computing_the future of computing.pdf. [Online]. Available: https://www.legalserviceindia.com/legal/article-5900-quantum-computing-the-future-of-computing.html , Accesed on 28/4/2022.
[36] N. Parvez, Quantum computing in data science: the weird yet profitable duo. [Online]. Available: https://www.analyticsinsight.net/quantum-computing-in-data-science-the-weird-yet-profitable- https://www.analyticsinsight.net/quantum-computing-in-data-science-the-weird-yet-profitable-duo/, Accessed on 28/4/2022.
[37] N.P. Firoz Khan, G. Dalawai, Impact of quantum computing in India and it's applications, p. Volume & Issue: NCAIT−2020.
[38] Asisoso, Advantages and disadvantages of quantum computing relation to digital marketing. [Online]. Available: https://www.asioso.com/en/blog/advantages-and-disadvantages-of-quantum-computing-in-relation-to-digital-marketing-b536, Accesed on 7 May 2022.
[39] C. Dilmegani, In-depth guide to quantum artificial intelligence, *AI Multipe*. 2022. [Online]. Available: https://research.aimultiple.com/quantum-ai, Accessed on 26/11/2022.
[40] S. Ranjitha, What is artificial general intelligence (AGI)? (2021) [Online]. Available: https://www.techtarget.com/searchenterpriseai/definition/artificial-general-intelligence-AGI. Accessed on 7 May 2020.
[41] A. Sahu, S. Agrawal and G. Kumar, Integrating Industry 4.0 and circular economy: a review, J. Enterpr. Inf. Manag., **35**(3) (2022) 885–917. https://doi.org/10.1108/JEIM-11-2020-0465.
[42] C.L. Stergiou, K.E. Psannis and B.B. Gupta, Iot-based big data secure management in the fog over a 6G wireless network. IEEE Internet Things J., **8**(7) (2021) 5164–5171. https://doi.org/10.1109/JIOT.2020.3033131.
[43] J.A. Reed, Chris, Computer law: the law and regulation of information technology. 6th Ed., Oxford University Press, Oxford, 200. [Online]. Available: 0.
[44] M. Kuehn, M.K. Leong and K. Tanaka-Ishii, Lecture notes in artificial intelligence (subseries of lecture notes in computer science): introduction, vol. 3248 (2005). https://doi.org/10.1007/978-3-540-30211-7_78.
[45] S. He, Informatics: a brief survey, Electron. Libr., **21**(2) (2003) 117–122. https://doi.org/10.1108/02640470310470480.
[46] R. Smith, Consolidated version of the treaty on European union, *Core EU Legis.* (2015) pp. 1–14. https://doi.org/10.1007/978-1-137-54482-7_1.
[47] C.L. Hinson, Legal informatics: opportunities for information science, J. Edu. Libr. Inf. Sci., **46**(2) (2005) 134. https://doi.org/10.2307/40323866.
[48] W. Series, O. N. Generation, and J. Platform, "LEGAL," no. September, 2019.
[49] A. Correia Simões, A. Lucas Soares and A.C. Barros, Factors influencing the intention of managers to adopt collaborative robots (cobots) in manufacturing organizations, J. Eng. Technol. Manag.—JET-M, **57**(May) (2020) 101574. https://doi.org/10.1016/j.jengtecman.2020.101574.
[50] A. Saarenpanpää, Information and law in the constitutional state, Lect. Notes Comput. Sci. (Incl. Subser. Lect. Notes Artif. Intell. Lect. Notes Bioinformat.), **3183** (2004) 443–452. https://doi.org/10.1007/978-3-540-30078-6_76.
[51] M. Scherer, Artificial intelligence and legal decision-making: The wide open? A study examining international arbitration, J. Int. Arbitr., **36**(5) (2019) 539–573.
[52] Y. Liao, F. Deschamps, E. De Freitas and R. Loures, Past , present and future of Industry 4.0—a systematic literature review and research agenda proposal, Int. J. Prod. Res., **7543**(March) (2017) 0. https://doi.org/10.1080/00207543.2017.1308576.
[53] J.H. Ho, G.G. Lee and M.T. Lu, Exploring the implementation of a legal AI bot for sustainable development in legal advisory institutions, Sustain., **12**(15) (2020) 1–17. https://doi.org/10.3390/su12155991.
[54] K. Flinders, Affordable legal advice for all—from a robot, *ComputerWeekly.com* (2021). [Online]. Available: https://www.computerweekly.com/news/252497338/Affordable-legal-advice-for-all-from-a-robot, Accesed on 10 May 2022.
[55] R.V.B. Waltl, Explainable artificial intelligence—the new frontier in legal informatics.
[56] Technological trends in legal sectorlLegaltech.
[57] National Mission on Quantum Technologies: government needs to address legalstrategy to unlock dual -use tech. [Online]. Available: https://government.economictimes.indiatimes.com/news/technology/national-mission-on-quantum-technologies-government-needs-to-address-legal-strategy-to-unlock-dual-use-tech/76026658, Acessed on 14/5/2022.
[58] hWhat is the Information Technology Amendment Act 2008 (IT Act 2008). [Online]. Available: https://www.techtarget.com/whatis/definition/Information-Technology-Amendment-Act-2008-IT-Act-2008#:~:text=The Information Technology Amendment Act 2008 %28IT Act,2008 and came into force a year later, Acessed on18/5/2022.
[59] M. Singh, C. Dhara, A. Kumar, S.S. Gill and S. Uhlig, Quantum artificial intelligence for the science of climate change, Artif. Intell. Mach. Learn. Blockchain Quantum Satell. Drone Netw., (2017) 199–207. https://doi.org/10.1201/9781003250357-13.
[60] AI applications of quantum computing. [Online]. Available: https://www.uts.edu.au/research-and-teaching/our-research/centre-quantum-software-and-information/qsi-research/qsi-research-programs/ai-applications-quantum-computing, Accessed on 18/5/ 2022.
[61] K.B.C.G. Almudever, L. Lao, X. Fu, N. Khammassi, I. Ashraf, D. Iorga, S. Varsamopoulos, C. Eichler, A. Wallraff, L. Geck, A. Kruth, J. Knoch and H. Bluhm, The engineering challenges in quantum computing, Test Eur. DATE 2017 (2017), pp. 836–845. [Online]. Available: https://doi.org/10.23919/DATE.2017.7927104.
[62] Artificial intelligence_ What it is and how it is used. [Online]. Available: https://www.investopedia.com/terms/a/artificial-intelligence, Accessed on 18/5/ 2022.
[63] F. Tao, Q. Qi, L. Wang and A.Y.C. Nee, Digital twins and cyber-physical systems toward smart manufacturing and industry 4.0: correlation and comparison. Engineering, **5**(4) (2019) 653–661. https://doi.org/10.1016/j.eng.2019.01.014.
[64] S. Nadella, Real world artificial intelligence applications in various sectors, *Tech Vidvan* (2022). [Online]. Available: https://techvidvan.com/tutorials/artificial-intelligence-applications/, Accessed on 18/5/ 2022.
[65] W. Wu, T. Zhang and P.X. Chen, Quantum computing and simulation with trapped ions: on the path to the future. Fundam.

Res., **1**(2) (2021) 213–216. https://doi.org/10.1016/j.fmre.2020.12.004.
[66] L.I. Min, Cloud computing applications, (2015), pp. 45–49. [Online]. Available: https://www.javatpoint.com/cloud-computing-applications, Accessed on 18/5/2022.
[67] 5 Applications of big data in law industry. [Online]. Available: https://www.analyticssteps.com/blogs/5-applications-big-data-law-industry, Accessed on 18/5/ 2022.
[68] S. Sharma, U.S. Tim, J. Wong, S. Gadia and S. Sharma, A brief review on leading big data models, Data Sci. J., **13** (2014) 138–157. https://doi.org/10.2481/dsj.14-041.
[69] R. Computing, Quantum computing in DNA, [Online]. Available: https://vimeo.com/222107093, Acessed on 12/5/2022.
[70] S. Sharma, V. Chang, U.S. Tim, J. Wong and S. Gadia, Cloud and IoT-based emerging services systems, Cluster Comput., **22**(1) (2019) 71–91. https://doi.org/10.1007/s10586-018-2821-8.
[71] S.G.G. Contissa, G. Francesco, The future of cybersecurity: major role of artificial intelligence, machine learning, and deep learning in cyberspace B, vol. 15. Springer, Singapore (2019). https://doi.org/10.1007/978-981-10-8681-6.
[72] S. Mishra and | Views, Legal education system in India. [Online]. Available: https://www.legalserviceindia.com/legal/article-199-legal-education-system-in-india.html, Accesed on 13/5/2022.
[73] B. Xing and T. Marwala, Implications of the fourth industrial age on higher education, Tap chí Nghiên cuu dân toc, **23** (2018). https://doi.org/10.25073/0866-773x/87.
[74] P.S. Amirnuddin, Transforming legal education in the era of fourth industrial revolution (IR4.0), no. February, 2020.
[75] Offences and penalties under information technology Act (2000) [Online]. Available: https://taxguru.in/corporate-law/offences-penalties-information-technology-act-2000.html, Acessed on 16/8/2022.
[76] A. Ho, Announcing tensorflow quantum: an open source library for quantum machine learning. [Online]. Available: https://blog.tensorflow.org/2020/03/announcing-tensorflow-quantum-open.html, Accessed on 15/9/2022.
[77] C. Kitchener, Sustainable technology solutions: a new priority in legal. [Online]. Available: https://www.lawtechnologytoday.org/2021/02/sustainable-technology-solutions-a-new-priority-in-legal, Accessed on 15/5/2022.
[78] L. and T. counselling world Wide, Nishith Desai Associates.pdf. [Online]. Available: https://www.nishithdesai.com/SectionArticleList/32/Areas-of-Service/4509/QuantumComputing.html, Accessed on 15 May 2022.
[79] B. Raina, Government of India transaction of business rules (1961). [Online]. Available: https://www.isrgrajan.com/government-of-india-transaction-of-business-rules-1961.html, Accessed on 18/9/2022.
[80] Sustainability is the future of law. [Online]. Available: https://www.aija.org/sustainability-is-the-future-of-law, Accessed 15/8/2022.
[81] State of the legal profession: client driven innovation. [Online]. Available: https://practice.findlaw.com/practice-guide/state-of-the-legal-profession-client-driven-innovation.html, Accessed on 16/10/2022.
[82] Robots are coming for the lawyers which may be bad for tomorrow's attorneys but great for anyone in need of cheap legal assistance. [Online]. Available: https://theconversation.com/robots-are-coming-for-the-lawyers-which-may-be-bad-for-tomorrows-attorneys-but-great-for-anyone-in-need-of-cheap-legal-assistance-157574, Accessed on 16/9/2022.
[83] Website of ministry of social justice and empowerment|National Portal of India. [Online]. Available: https://www.india.gov.in/official-website-ministry-social-justice-and-empowerment, Accessed on 14/10/2022.
[84] Data privacy_ Emerging area for legal professionals _ Deccan Herald.pdf.
[85] M. Jeyaraman, A. Nallakumarasamy, and N. Jeyaraman, Industry 5.0 in orthopaedics, Indian J. Orthop., (September) (2022). https://doi.org/10.1007/s43465-022-00712-6.
[86] Technology adoption challenges for law firms and legal departments. [Online]. Available: https://www.spectrumwise.com/2019/12/technology-adoption-challenges-for-law-firms-and-legal-departments, Accessed on 14/6/2022
[87] P. Casanovas, L. de Koker and M. Hashmi, Law, socio-legal governance, the internet of things, and industry 4.0: a middle-out/inside-out approach, J, **5**(1) (2022) 64–91. https://doi.org/10.3390/j5010005.
[88] The 2018 legal trends report. [Online]. Available: https://www.clio.com/resources/legal-trends/2018-report/, Accessed on 23/12/2022.
[89] Blockchain in the legal industry. [Online]. Available: https://consensys.net/blockchain-use-cases/law/, Accessed on 27/5/2022.
[90] India—rural population (2021). [Online]. Available: https://tradingeconomics.com/india/rural-population-percent-of-total-population-wb-data.htmla/rural-population-percent-of-total-population-wb-data.html0n, Accessed 12/12/202.2
[91] A-Z Guide on cyber law & becoming a cyber lawyer—iDreamCareer. [Online]. Available: https://idreamcareer.com/blog/career-in-cyber-law/, Accessed on 20/5/2022.
[92] A.J. da Silva, T.B. Ludermir and W.R. de Oliveira, Quantum perceptron over a field and neural network architecture selection in a quantum computer, Neural Netw., **76** (2016) 55–64. https://doi.org/10.1016/j.neunet.2016.01.002.
[93] M. Suchara, Y. Alexeev, F. Chong, H. Finkel, H. Hoffmann, J. Larson, J. Osborn and G. Smith, Hybrid quantum-classical computing architectures, (November 2020) (2018), 1–4.
[94] CIPM task group on the digital SI (CIPM-TG-DSI). [Online]. Available: https://www.bipm.org/en/committees/ci/cipm/wg/cipm-tg-dsi, Accessed on 12/1/2023.
[95] M. Kuster, A measurement information infrastructure's benefits for industrial metrology and IoT, in 2020 IEEE int. work. metrol. ind. 4.0 IoT, MetroInd 4.0 IoT 2020—proc. (2020) pp. 479–484. https://doi.org/10.1109/MetroInd4.0IoT48571.2020.9138200.
[96] F. Thiel, M. Esche, F. Grasso Toro, A. Oppermann, J. Wetzlich, and D. Peters, The European metrology cloud, **09001** (2017) 09001. https://doi.org/10.1051/metrology/201709001.
[97] Digital single market: bringing down barriers to unlock online opportunities. [Online]. Available: https://www.fiware.org/2015/05/08/digital-single-market-bringing-down-barriers-to-unlock-online-opportunities, Accessed on 11/1/2023.
[98] Digital twin and its legal implications. [Online]. Available: https://abounaja.com/blogs/digital-twin-legal-implications, Accessed on 11/1/2023.
[99] F. Tao, M. Zhang and A.Y.C. Nee, Digital twin and virtual reality and augmented reality/mixed reality, Digit. Twin Driven Smart Manuf., (2019) 219–241. https://doi.org/10.1016/b978-0-12-817630-6.00011-4.
[100] L. Wright and S. Davidson, How to tell the difference between a model and a digital twin, Adv. Model. Simul. Eng. Sci., **7**(1) (2020). https://doi.org/10.1186/s40323-020-00147-4.
[101] F. Thiel and J. Wetzlich, The European metrology cloud: impact of European regulations on data protection and the free flow of non-personal data, **01001** (2019) 01001. https://doi.org/10.1051/metrology/201901001.
[102] Eurostat, What is the digital single market about? *Profile of the digital society & businesses* (2018). [Online]. Available:

https://ec.europa.eu/eurostat/cache/infographs/ict/, Accessed on 12/01/2023.
[103] F. Thiel, Digital transformation of legal metrology—the European metrology cloud, OIML Bull., **59**(1) (2018) 10–21 [Online]. Available: https://www.bipm.org/en/committees/ci/cipm/wg/cipm-tg-dsi, Accessed on 12/1/2023.
[104] DRDO offers online courses on AI and ML. [Online]. Available: https://indiaai.gov.in/news/drdo-offers-online-courses-on-ai-and-ml, Accessed on 16/1/2023.
[105] Free AI_ML & deep learning courses launched by ISRO in 2021. [Online]. Available: https://content.techgig.com/upskilling-at-techgig/these-are-the-top-free-courses-launched-by-isro-in-2021/articleshow/88120060.cms, Accessed on 16/1/2023.
[106] Top masters programmes in artificial intelligence in India for students in 2021. [Online]. Available: https://www.analyticsinsight.net/top-masters-programmes-in-artificial-intelligence-in-india-for-students-in-2021, Accessed on 16/1/2023.
[107] F. M. Fadul, Industry 4.0: basic understanding and readiness of India (2019).

Publisher's Note Springer Nature remains neutral with regard to jurisdictional claims in published maps and institutional affiliations.

Springer Nature or its licensor (e.g. a society or other partner) holds exclusive rights to this article under a publishing agreement with the author(s) or other rightsholder(s); author self-archiving of the accepted manuscript version of this article is solely governed by the terms of such publishing agreement and applicable law.

Psyche.ly: Personality Detection for Hindi Text-based Dataset

Rijul Chauhan*, Prakhar Mehta*, Nikhil Chauhan*, Garima Chhikara*

*Department of Computer Science and Engineering, Delhi Technological University, New Delhi, 110042, India

***Abstract*— Personality traits significantly influence our daily life decisions, emotions, motivation, and mental patterns. Automatic personality trait recognition has numerous real-world applications, including sentiment analysis, mental health diagnosis, and forensics. However, the majority of studies in this field have focused on English language datasets, limiting their generalizability to Hindi language. With this paper we have proposed a classifier which would classify whether a dialogue porrtrays the character as 'introvert', 'extrovert' or 'N/A'. The Hindi Language dataset was curated from a well-known Bollywood web series called "AARYA" in order to automatically identify personality traits. To accomplish this, Support Vector Machine (SVM) and Artificial Neural Network (ANN) models were used. It also proposes future research directions to overcome these limitations.**

***Index Terms*— Hindi Personality Detection, Support Vector Machine, Artificial Neural Network, Hindi Dataset**

I. Introduction

An individual's conduct, emotion, motivation, and mental patterns make up their personality. Our personalities greatly influence our lives; they have an impact on our lifestyle decisions, happiness, health, and a variety of other preferences. Numerous crucial real-world uses can be made of automatic personality trait recognition. For instance, when using sentiment analysis, a user should only be given goods and services that have received favorable reviews from other users who share their personality type. Since the same notion might have distinct meanings to different sorts of people, personality detection can also be used to clarify word polarity in sentiment lexicons. Certain diagnoses in mental health diagnosis are correlated with particular personality qualities. Knowing personality traits in forensics aids in narrowing the suspect list.

In the existing literature, multiple formal definitions of personality can be found. However, in a broad sense, personality encompasses an individual's social and emotional behavior, cognitive abilities, and decision-making skills. By examining these traits, we can gain a deeper understanding of individuals and develop effective strategies for managing them.

Personality assessment has been used since the 1920s, primarily for detecting indications of post-traumatic stress disorder (PTSD) and improving recruitment procedures, particularly within the military. Even today, organizations including the National Aeronautics and Space Administration (NASA) employ various group exercises to assess characteristics essential for survival in high-risk situations.

As a result, automatic personality assessment holds significant potential for advancements in various sectors mentioned earlier. New research has investigated ways to assess personality by utilizing various datasets such as social media information[9], anonymously written pieces, videos of self-introductions, simulations of contact center interactions, and observations of performance during group discussions. These studies have employed different techniques to measure personality traits.

The research utilizing these datasets has the following limitations, albeit offering fascinating insights into the personalities of their subjects.

- To begin with, a significant portion of existing personality assessment methods often overlook a crucial element: the social environment.
- Furthermore, it is noteworthy that a significant amount of research in the field of personality assessment has primarily focused on the English language, with limited literature available on the application of these advances to the Hindi language dataset.

II. Literature Survey

A. Personality Measures

There are various contemporary psychological theories that attempt to understand human personality through different approaches. In this brief discussion, we will touch on some of them, while noting that more information can be found in psychological surveys and books. The Trait Theory, which views human behavior as traits such as Extraversion and Emotional Stability, has been around for a long time and uses a lexical approach. Cattell's 16PF model, on the other hand, employs 16 factors such as Dominance, Perfectionism, and Privateness to analyze human behavior, while Eysenck's PEN model employs the factors of Psychoticism, Extraversion, and Neuroticism to describe personality dimensions. Fig. 1 depicts the big 5 personality traits. Personality traits are often analyzed using questionnaires that require subjects to respond to specific inquiries. The Myers-Briggs Type Indicator (MBTI)[3] is a commonly used self-report test that categorizes individuals based on four dimensions: Introversion or Extraversion, Sensing or Intuition, Thinking or Feeling, and Judging or Perception, which examine their decision-making process. Lastly, the Five-Factor model, also known as the Big Five model, is a widely accepted and popular approach used for personality assessment in the literature.

Dimension	High Scores	Low Scores
Openness	imaginative, creative, original, prefers variety, curious, liberal	down-to-earth, uncreative, conventional, uncurious, conservative
Conscientiousness	hard-working, well-organized, punctual, ambitious, persevering	negligent, lazy, disorganized, late, aimless, quitting
Extraversion	affectionate, joiner, talkative, fun loving, active, passionate	reserved, loner, quiet, sober, passive, unfeeling
Agreeableness	soft-hearted, trusting, generous, acquiescent, lenient, good-natured	ruthless, suspicious, stingy, antagonistic, critical, irritable
Neuroticism	anxious, temperamental, self-pitying, self-conscious, emotional	calm, even-tempered, self-satisfied, comfortable, unemotional

Fig. 1. Big 5 Personality Traits

B. *Personality Assessment: Dataset*

Numerous studies have examined human personality traits; nevertheless, the ways in which they model the personalities of particular people vary greatly. The experimental designs of this research range widely, from examining participants' telephone calls to judging these attributes based on their resumes. This section explains the most common experimental methodologies and datasets used by researchers to evaluate personality.

- **Text-based analysis** Wang's study utilized social media data to predict personality traits by analyzing the language used by individuals on these platforms. The dataset for this study consisted of approximately 90,000 individuals and their most recent tweets, which were used to forecast MBTI[4] personality traits.In a similar vein, some scholars have investigated personality characteristics by analyzing written essays by participants, using approaches such as a benchmark dataset developed by Pennebaker and King that forecasts five qualities[14] based on these essays. Moreover, researchers have shown significant interest in automating the estimation of impressions on personality based on the spoken content of video blogs.
- **Audio and Vision based analysis** compiled the PersIA dataset, which featured a number of phone calls between individuals that simulated call center activity. Additionally, they discovered that the individuals' verbal backchanneling responses served as accurate personality predictions[5]. It has also been extensively pursued through audio and video-based automatic personality assessment in the form of vlogs.. The ChaLearn dataset has been extensively tested in this area.

III. Psyche.ly's Dataset

To train and test our Artificial Intelligence (AI) model, we created our own dataset using the web series AARYA (Season 1). The series consisted of nine episodes, with a duration of approximately 45 minutes each. We analyzed each dialogue spoken by the characters and classified them into three personality types: 'introvert', 'extrovert', or 'not applicable'.

To ensure the accuracy and reliability of our dataset, each dialogue was manually classified by three independent raters, and any discrepancies were resolved through discussion. The dataset includes a total of [6737] dialogues and their corresponding personality classifications, which were used to train and test our AI model. Fig. 2 depicts the graphical statistics of the dataset curated.



Fig. 2. Psyche.ly's Dataset Statistics

IV. Models Used

A. ***Support Vector Machine (SVM)***

1) Introduction: Support Vector Machine (SVM) is a widely adopted supervised learning technique for classification and regression tasks. Although SVM is primarily used in Machine Learning Classification[6] problems, its main objective is to determine an optimal decision boundary or hyperplane, that can effectively divide n-dimensional space into classes for efficient categorization of new data points in the future. SVM selects extreme vectors and points that contribute to the hyperplane, known as support vectors, to represent these critical situations.

Fig. 3 illustrates how a decision boundary or hyperplane is utilized to separate two distinct categories.

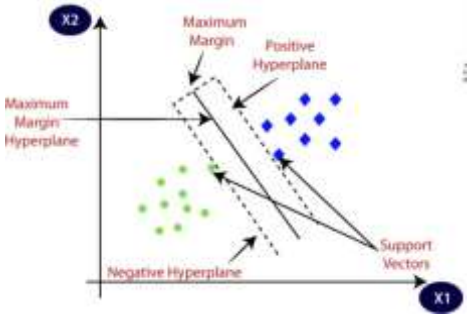


Fig. 3. SVM Algorithm

In this project the scikit-learn library was utilized to train SVM model. The Scikit-SVM learn library can receive as input either a dense or sparse sample vector, in the form of a numpy.ndarray that can be transformed to numpy.asarray, or a scipy.sparse sample vector. To obtain predictions for sparse data, an SVM model must have been previously fitted on such data. To achieve the best performance, it is recommended to use a C-ordered numpy.ndarray with dtype=float64 for dense data, or a scipy.sparse.csr matrix with the same dtype for sparse data.

2) How we used SVM: Our SVM model uses a couple of libraries.

- The first library, **"numpy"** is being imported using the alias "np". Numpy is a library for scientific computing in Python which in turn provides support for arrays, matrices, and other numerical operations.
- The second library, **"matplotlib.pyplot"** is being imported using the alias "plt". Matplotlib is a data visualization library in Python that provides tools for creating charts, graphs, and other visual representations of data.
- The third library, **"pandas"** is being imported using the alias "pd". Pandas is a library for data manipulation and analysis in Python that provides data structures like Series and DataFrame.
- The fourth library, **"nltk"** is being imported. NLTK (Natural Language Toolkit) is a library for working with human language data, providing tools for processing text and working with various types of language data like corpora and lexicons.

By importing these libraries, the subsequent code will have access to their functions and capabilities.

A CSV file containing data on the personality types of Hindi-speaking individuals was utilized. The data was imported into the study using the "readcsv" function from the pandas library, which reads the file contents and returns a pandas DataFrame object that stores the data in a tabular format. The imported data was then analyzed and processed using various Python libraries and functions to gain insights into the personality types of the individuals surveyed.

To prepare the data for analysis, certain columns of the "data" DataFrame were identified as unnecessary and thus removed. The "drop" function of the pandas library was used to remove the second and third columns of the DataFrame, which were specified by their respective indices within a list. The removal was performed along the columns axis, leaving the remaining columns necessary for further analysis. This step of removing unnecessary columns ensured that only relevant data was retained for analysis, reducing computational overhead and facilitating efficient analysis. NULL values were also analyzed and rows containing NULL values were removed.

To investigate the personality types of the Hindi-speaking[15] individuals surveyed, new columns were added to the existing "data" DataFrame. Using the pandas Series, three new columns were created, namely "introvert", "extrovert", and "NA". These columns were based on the values in the "TYPE: 1. INTROVERT 2. EXTROVERT 3. N/A" column of the DataFrame.

A for loop was implemented to assign values of 1 or 0 to the "introvert", "extrovert", and "NA" columns based on the corresponding personality types. If the value was "1", the "introvert" column was assigned a value of 1, and the "extrovert" and "NA" columns were assigned values of 0. If the value was "2", the "extrovert" column was assigned a value of 1 and the "introvert" and "NA" columns were assigned values of 0. If the value was "3", the "NA" column was assigned a value of 1, and the "introvert" and "extrovert" columns were assigned values of 0.

the "data" DataFrame was split into training and testing sets using the scikit-learn library's "traintestsplit" function. The first column of the "data" DataFrame was used as the input feature, while all columns except the first two columns were used as the output target variables.

The "traintestsplit" function was called with the "train-size" parameter set to 0.80 and the "testsize" parameter set to 0.20, indicating that 80 percent of the data is for training the model, and 20 percent of the data is for testing the model.

A random state of 48 was set using the "random state" parameter to ensure that the same random data split was obtained each time the code was executed. This step ensured consistency and reproducibility of the results obtained from the machine learning model.

In order to prepare the text data for the machine learning model, the "TfidfVectorizer"[12] from the sci-kit-learn library was used for the conversion of text into a numerical representation. The "mindf" parameter was set to 2, which specified that the words occurring in the text corpus less than twice would be ignored.

The "ngramrange" parameter was set to (1,3) which specified that unigrams, bigrams, and trigrams[2] were to be considered while vectorizing the text. This allowed the model to capture the contextual meaning of the words.

The "mytokenizer" function was defined to split the text into individual words. A list of stop words in Hindi was defined in the "stopwords" variable, which was to be

ignored during the vectorization process.

The "encoding" parameter was set to 'utf-8', which specified that the text was to be encoded in UTF-8 format. The "TfidfVectorizer" function was called with the above parameters to create a vectorizer object named "vectorizer". This object was used to transform the text data into a numerical representation that could be fed into the machine learning model.

Next, we trained a Support Vector Machine (SVM) classifier[13] using the sci-kit-learn library to predict personality types based on Hindi text data. We first used the TfidfVectorizer function to transform the text data into a vectorized form, which represents the significance of each term in the document corpus. Stop words were removed during the vectorization process to eliminate insignificant terms. The SVM model was trained using the vectorized data and the personality types provided in the dataset.

Next, SVM Multiclass classification[11] was used:

- **Data transformation:** The training data was transformed into a vectorized form using the TfidfVectorizer object. This process represents the significance of each term in the document corpus, and the transformed data was stored for further processing.
- **Test data transformation:** Similarly, the test data was transformed into the same vectorized form using the TfidfVectorizer object. The transformed data were stored for subsequent use.
- **SVM model creation:** An SVM model was instantiated with a linear kernel, a regularization parameter C of 1, and a "one-vs-rest" (ovr) strategy for multi-class classification.
- **Model training:** The SVM model was trained on the training data, where the target labels for the training data were used for model training.
- **Prediction:** The SVM model was used to make predictions on the test data, and the predicted labels were stored for evaluation.
- **Accuracy calculation:** The precision of the SVM (Support Vector Machine) model was assessed by utilizing the accuracy score function to compare the anticipated labels with the actual labels of the test data. The calculated accuracy was converted into a percentage and reported as the final output.

Fig. 4 represents the graphical respresentation of SVM Multiclass classification.

We used the SVC function to create a linear kernel SVM model, which was then trained on the training data using the fit method. The predict method was utilized to generate predictions on the test data, and the accuracy score function was employed to compute the accuracy of the model on the test data. The resulting accuracy of the model was determined to be 71.84%.

B. *Artificial Neural Network*

1) Introduction:: Neural Networks refer to an AI method that is used to teach computers how to ideally process our data in a way that is nearly identical to how a human brain

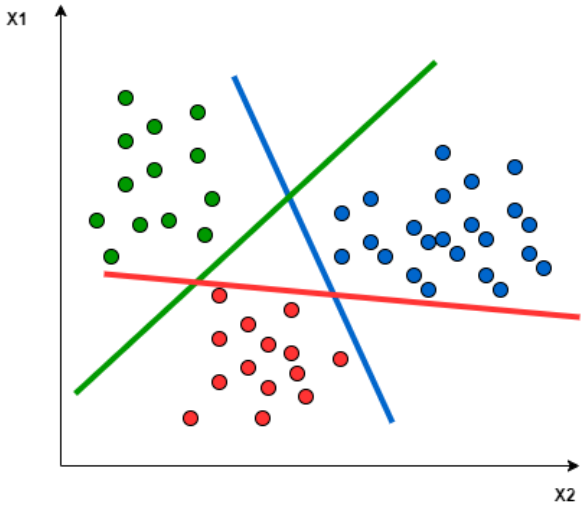


Fig. 4. SVM Multiclass classification

works. A type of ML process is deep learning which consists of multiple nodes or neurons that are interconnected in multiple layers- namely Input, hidden and output layers that would resemble the structure of a human brain. It is basically a system that adapts, learns from its own mistakes and uses the learnings to continuously adapt and improve. This the model helps solve problems with much greater accuracy, some examples of problems it solves could be recognizing human faces and summarizing docs.

A typical neural network consists of multiple layers each having a network of artificial neurons or nodes connected internally, there are 3 layers mentioned below:

- **Input Layer:** The input layer is also known as first contact layer and this is the layer where any data or information from the outside world can enter the artificial neural network. The nodes or neurons in the input layer analyze the information and categorizes it before it passes to the next layer which is the hidden layer.
- **Hidden Layer:** This layer gets its input passed in from the Input layer, there might be multiple hidden layers that co-exist in an artificial neural network. Each of those hidden layers does analyze the output it gets from the previous layer, processes it further and then hand it to the next hidden layer until the last hidden layer which passes it on to the output layer.
- **Output Layer:** The last layer that is the output layer displays the eventual or final result that we get after all the processing is done by the layers of the neural network. The output layer can also consist of a single node or multiple nodes. If the type of problem is based on binary classification, the output from the output layer will return the value 1 or 0 whereas for a multi-class problem, the output layer will have multiple artificial neurons or nodes.

Fig. 5 depicts the Artificial Neural Network Architecture i.e. Input, Output and Hidden layers.

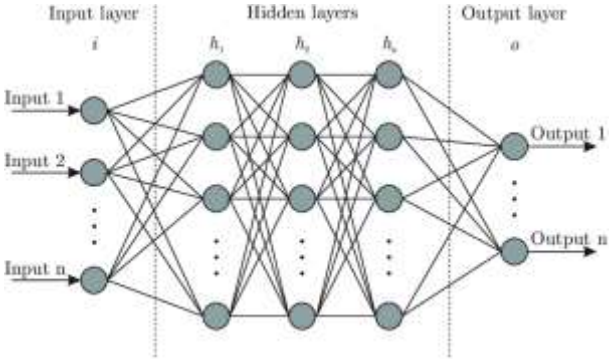


Fig. 5. Artifical neural network architecture



Fig. 6. ANN Accuracy attained for different classes

2) How we used ANN : We used the TensorFlow Hub library to load and utilize a pre-trained model called "XLM-RoBERTa" for text encoding. The pre-trained model consists of a preprocessor module and an encoder module, both of which are loaded from specific URLs in TensorFlow Hub. The encoder module, implemented as a Keras layer, is set to be trainable.

To encode text inputs conveniently, we implemented the encode data function, which takes a list of text inputs, preprocesses them using the preprocessor module, encodes them using the encoder module, and returns the encoded output's 'pooled output'. This allows for easy encoding of text inputs using the pre-trained deep learning model for further downstream processing or analysis.

Furthermore, we developed a function that takes a DataFrame of text data and encodes it using the previously defined XLM-RoBERTa model, enabling the handling of large amounts of data by saving the encoded representations in separate files.

Next, we defined a neural network model using the Keras API of TensorFlow. The model architecture was specified using the Sequential class of Keras, which consists of a sequence of layers. The input data is first flattened into a 1-dimensional vector using the Flatten layer, followed by seven hidden layers, each containing 500 neurons with the ReLU activation function. The final layer comprises a single neuron with the sigmoid activation function, producing a binary output (0 or 1).

The model was compiled using the compile method, with the binary cross-entropy loss function and the Adam optimizer with a learning rate of 1e-5. The model was also configured to compute accuracy as a training metric. The fit method was employed to train the model on a set of input data and corresponding target labels. The training was conducted for 200 epochs with a batch size of 50, and the validation data was provided using the validation data argument. The training progress was displayed with a verbosity level of 1.

The Validation accuracy attained for the 'Introvert class' was 91.6%, the 'Extrovert' class was 75.56% and for the 'N/A' class was 67.9% and Fig. 6 depicts the line graph of the same.

V. Use cases of the project

- **Recruitment:** Personality detection software can be used to assess the personality traits of job candidates during the recruitment process. This can help identify candidates who are more likely to succeed in the role and fit in with the company culture. It can also help eliminate unconscious biases in the hiring process[8].
- **Marketing:** Personality detection software can be used to personalize marketing messages based on a person's personality traits. This can help increase engagement and conversion rates. For example, a company could use personality data to determine which type of advertising message would resonate best with different personality types.
- **NASA** used an observation-based personality model for their astronaut selection for nearly 20 years as a preliminary test to see if the candidate is the right fit for the mission ahead of them.
- **Healthcare:** By analyzing a person's conversational data, the software can detect patterns in speech and identify potential mental health issues. This can help healthcare professionals provide targeted treatment plans for individuals.
- **Law Enforcement:** By analyzing conversational data, the software can detect patterns in language that may indicate violent or threatening behavior. This can help law enforcement agencies intervene before a potentially dangerous situation occurs.

VI. Recommendations for future work

In light of the wide-ranging diversity observed in the Psyche.ly dataset, this section presents several potential avenues for future research exploration:

- **Adding more information to the preparation set:** There is currently only a small amount of training data for personality detection in Hindi text. To work on the precision of models, future research might concentrate on gathering additional diverse and extensive datasets.
- **Enhancing feature representation quality:** Highlights that function admirably in English text probably won't be as successful in Hindi text. The development of new highlights or the modification of existing ones in

order to better capture the subtleties of Hindi could be the subject of future research.

- **Including differences between regions:** Hindi is spoken in a variety of dialects and accents in various parts of India. Future models may be developed to recognize and adapt to these regional variations in order to improve accuracy.
- **Paying attention to orientation and social preferences:** Orientation and social inclinations can be an issue for character location models[10]. These predispositions could be identified and addressed in Hindi text-based models in future research.
- **Making models for specific applications:** Recruitment, mental health diagnosis, and customer service are just a few of the applications that can be made of personality detection models. Custom models for these applications could be the focus of future research in the context of Hindi text.
- **Enhancing interpretability further:** Like with any model for machine learning, interpretability is a major concern. Future research may focus on developing models that are simpler and more obvious, which may aid in establishing trust in the innovation.

VII. Conclusions

In our research paper, we introduced a cutting-edge personality detection system named 'Psyche.ly', which utilizes advanced Machine Learning techniques, specifically Support Vector Machine (SVM) and Neural Network models. Our system is specifically designed to analyze dialogues or utterances from a popular Bollywood web series called 'AARYA', with the aim of accurately predicting the personality traits of characters based on their dialogues.

To create our system, we first compiled a comprehensive database of dialogues from the web series, which served as the training data for our SVM model. We then implemented the SVM model, utilizing its ability to find optimal decision boundaries in n-dimensional space to classify dialogues into different personality traits. The resulting accuracy of our SVM model was determined to be 71.84%, showcasing its effectiveness in predicting personality traits from the dialogues in the 'AARYA' web series.

Furthermore, we also utilized Artificial Neural Network (ANN) models in our system to further enhance the accuracy of personality detection. Our ANN model achieved impressive validation accuracy of 91.6% for the 'Introvert' class, 75.56% for the 'Extrovert' class, and 67.9% for the 'N/A' class. This highlights the effectiveness of our system in accurately predicting personality traits using the dialogues from the 'AARYA' web series, as demonstrated by the high accuracy achieved by both SVM and ANN models.

Overall, our research paper presents a novel personality detection system, 'Psyche.ly', that utilizes Machine Learning techniques to analyze dialogues from a popular Bollywood web series. The high accuracy achieved by our system using SVM and ANN models showcases its potential in various applications, such as character analysis, content recommendation, and audience engagement in the field of entertainment and beyond.

References

[1] ES. Khan, M. Leekha, J. Shukla and R. Shah, "Vyaktitv: A Multimodal Peer-to-Peer Hindi Conversations based Dataset for Personality Assessment," in 2020 IEEE Sixth International Conference on Multimedia Big Data (BigMM), New Delhi, India, 2020 pp. 103-111.

[2] N. Majumder, S. Poria, A. Gelbukh and E. Cambria, "Deep Learning-Based Document Modeling for Personality Detection from Text" in IEEE Intelligent Systems, vol. 32, no. 02, pp. 74-79, 2017.

[3] S. Möller, T. Polzehl and F. Metze, "Automatically Assessing Personality from Speech," in 2012 IEEE Sixth International Conference on Semantic Computing, Pittsburgh, Pennsylvania USA, 2010 pp. 134-140.

[4] A. Ariyanto, E. C. Djamal and R. Ilyas, "Personality Identification of Palmprint Using Convolutional Neural Networks," 2018 International Symposium on Advanced Intelligent Informatics (SAIN), 2018, pp. 90-95, doi: 10.1109/SAIN.2018.8673353.

[5] A. V. Kunte and S. Panicker, "Using textual data for Personality Prediction:A Machine Learning Approach," 2019 4th International Conference on Information Systems and Computer Networks (ISCON), 2019, pp. 529-533, doi: 10.1109/ISCON47742.2019.9036220.

[6] B. Y. Pratama and R. Sarno, "Personality classification based on Twitter text using Naive Bayes, KNN and SVM," 2015 International Conference on Data and Software Engineering (ICoDSE), 2015, pp. 170-174, doi: 10.1109/ICODSE.2015.7436992.

[7] Pennebaker, James W., Ryan L. Boyd, Kayla Jordan, and Kate Blackburn. The development and psychometric properties of LIWC2015. 2015.

[8] Katarya, R. and Maan, S., 2020, December. Predicting Mental health disorders using Machine Learning for employees in technical and non-technical companies. In 2020 IEEE International Conference on Advances and Developments in Electrical and Electronics Engineering (ICADEE) (pp. 1-5). IEEE.

[9] Ross, C., Orr, E.S., Sisic, M., Arseneault, J.M., Simmering, M.G. and Orr, R.R., 2009. Personality and motivations associated with Facebook use. Computers in human behavior, 25(2), pp.578-586.

[10] Gosling, S.D., Augustine, A.A., Vazire, S., Holtzman, N. and Gaddis, S., 2011. Manifestations of personality in online social networks: Self-reported Facebook-related behaviors and observable profile information. Cyberpsychology, Behavior, and Social Networking, 14(9), pp.483-488.

[11] Khan, A.S., Ahmad, H., Asghar, M.Z., Saddozai, F.K., Arif, A. and Khalid, H.A., 2020. Personality classification from online text using machine learning approach. International Journal of Advanced Computer Science and Applications, 11(3), pp.460-476.

[12] Choong, En Jun, and Kasturi Dewi Varathan. "Predicting judging-perceiving of Myers-Briggs Type Indicator (MBTI) in online social forum." PeerJ 9 (2021): e11382.

[13] Utami, Ninda Anggoro, Warih Maharani, and Imelda Atastina. "Personality classification of facebook users according to big five personality using SVM (support vector machine) method." Procedia Computer Science 179 (2021): 177-184.

[14] Bharadwaj, Srilakshmi, Srinidhi Sridhar, Rahul Choudhary, and Ramamoorthy Srinath. "Persona traits identification based on Myers-Briggs Type Indicator (MBTI)-a text classification approach." In 2018 international conference on advances in computing, communications and informatics (ICACCI), pp. 1076-1082. IEEE, 2018.

[15] Sumit Singh, Pawankumar Jawale, and Uma Tiwary. 2022. silpa_nlp at SemEval-2022 Tasks 11: Transformer based NER models for Hindi and Bangla languages. In Proceedings of the 16th International Workshop on Semantic Evaluation (SemEval-2022), pages 1536–1542, Seattle, United States. Association for Computational Linguistics.

Authors

First Author – Rijul Chauhan, Student, Delhi Technological University, Delhi, India, 110042,

Second Author – Prakhar Mehta, Student, Delhi Technological University, Delhi, India, 110042,prakharme-

Third Author – Nikhil Chauhan, Delhi Technological University, Delhi, India, 110042,

Fourth Author - Ms. Garima Chhikara, Assistant Professor, Delhi Technological University, Delhi, India, 110042,

Correspondence Author – Rijul Chauhan, Student, Delhi Technological University, Delhi, India, 110042, ri-

axioms

MDPI

Article

Radius of Uniformly Convex γ-Spirallikeness of Combination of Derivatives of Bessel Functions

Stanislawa Kanas [1,*] and Kamaljeet Gangania [2,3]

[1] Department of Mathematical Analysis, Rzeszow University, Al. Rejtana 16c, 35-959 Rzeszów, Poland
[2] Department of Applied Mathematics, Delhi Technological University, Delhi 110042, India
[3] Department of Mathematics, Bhagwan Parshuram Institue of Technology, Delhi 110089, India
* Correspondence: skanas@ur.edu.pl

Abstract: We find the sharp radius of uniformly convex γ-spirallikeness for $N_\nu(z) = az^2 J_\nu''(z) + bzJ_\nu'(z) + cJ_\nu(z)$ (here $J_\nu(z)$ is the Bessel function of the first kind of order ν) with three different kinds of normalizations of the function $N_\nu(z)$. As an application, we derive sufficient conditions on the parameters for the functions to be uniformly convex γ-spirallikeness and, consequently, generate examples of uniform convex γ-spirallike via $N_\nu(z)$. Results are well-supported by the relevant graphs and tables.

Keywords: γ-spirallike functions; uniformly convex functions; bessel function and derivatives; radius problem

MSC: 30C45; 30C15

1. Introduction

Let $\mathcal{A}$ be the class of analytic functions normalized by the condition $f(0) = 0 = f'(0) - 1$ in the unit disk $\mathbb{D} := \mathbb{D}_1$, where $\mathbb{D}_r := \{z \in \mathbb{C} : |z| < r\}$. Now let Γ_w be the image of an arc $\Gamma_z : z = z(t)$, $(a \le t \le b)$ under the function $w = f(z)$, and let w_0 be a point not on Γ_w. Let $\gamma \in \left(-\frac{\pi}{2}, \frac{\pi}{2}\right)$. The arc Γ_w is γ-spirallike with respect to w_0 if

$$\arg \frac{z'(t)f'(t)}{f(z) - w_0}$$

lies between γ and $\gamma + \pi$. Further, an arc Γ_w is convex γ-spirallike if

$$\arg\left(\frac{z''(t)}{z'(t)} + \frac{z'(t)f''(z)}{f'(z)}\right)$$

lies between γ and $\gamma + \pi$. In the form of one variable, equivalently, we say that a function $f \in \mathcal{A}$ is γ-spirallike of order α if and only if

$$\mathrm{Re}\left(e^{-i\gamma}\frac{zf'(z)}{f(z)}\right) > \alpha \cos\gamma,$$

where $\gamma \in \left(-\frac{\pi}{2}, \frac{\pi}{2}\right)$ and $0 \le \alpha < 1$. We denote the class of such functions by $\mathcal{S}_p^\gamma(\alpha)$. In view of the well-known Alexander's relation, let $\mathcal{CS}_p^\gamma(\alpha)$ be the class of convex γ-spirallike functions of order α, which is defined below:

$$\mathrm{Re}\left(e^{-i\gamma}\left(1 + \frac{zf''(z)}{f'(z)}\right)\right) > \alpha \cos\gamma.$$

Spacek [1] introduced and studied the class $\mathcal{S}_p^\gamma(0)$. Each function in $\mathcal{S}_p^\gamma(\alpha)$ is univalent in $\mathbb{D}$, but they are not necessarily starlike. Further, it is worth mentioning that, for general

check for updates

Citation: Kanas, S.; Gangania, K. Radius of Uniformly Convex γ-Spirallikeness of Combination of Derivatives of Bessel Functions. *Axioms* **2023**, *12*, 468. https://doi.org/10.3390/axioms12050468

Academic Editors: Andriy Bandura and Oleh Skaskiv

Received: 5 April 2023
Revised: 2 May 2023
Accepted: 4 May 2023
Published: 12 May 2023

Copyright: © 2023 by the authors. Licensee MDPI, Basel, Switzerland. This article is an open access article distributed under the terms and conditions of the Creative Commons Attribution (CC BY) license (https://creativecommons.org/licenses/by/4.0/).

values of $\gamma(|\gamma| < \pi/2)$, a function in $\mathcal{CS}_p^{\gamma}(0)$ need not be univalent in $\mathbb{D}$. For example, $f(z) = i(1-z)^i - i \in \mathcal{CS}_p^{\pi/4}(0)$, but this is not univalent. In this context, see Figure 1. Indeed, $f \in \mathcal{CS}_p^{\gamma}(0)$ is univalent if $0 < \cos\gamma < 1/2$; see Robertson [2] and Pfaltzgraff [3]. Note that, for $\gamma = 0$, the classes $\mathcal{S}_p^{\gamma}(\alpha)$ and $\mathcal{CS}_p^{\gamma}(\alpha)$ reduce to the classes of starlike and convex functions of order α, given by

$$\mathrm{Re}\left(\frac{zf'(z)}{f(z)}\right) > \alpha \quad \text{and} \quad \mathrm{Re}\left(1 + \frac{zf''(z)}{f'(z)}\right) > \alpha,$$

which we denote by $\mathcal{S}^*(\alpha)$ and $\mathcal{C}(\alpha)$, respectively.

In the above context and using the idea of uniformly starlike and uniformly convex functions introduced and studied in [4–8], Ravichandran et al. [9] introduced the concept of uniformly γ-spiral functions as described below:

Definition 1 ([9]). *The function f is a uniformly convex γ-spiral function if the image of every circular arc Γ_z with center at ζ lying in $\mathbb{D}$ is a convex γ-spiral.*

We denote the class of such functions by $\mathcal{UCSP}(\gamma)$. These functions have an analytic characterization (see [9]) as follows:

$$f \in \mathcal{UCSP}(\gamma) \Leftrightarrow \mathrm{Re}\left\{e^{-i\gamma}\left(1 + \frac{(z-\zeta)f''(z)}{f'(z)}\right)\right\} \geq 0, z \neq \zeta, z, \zeta \in \mathbb{D}.$$

Indeed, authors in [9] obtained the one-variable characterization as:

$$f \in \mathcal{UCSP}(\gamma) \Leftrightarrow \mathrm{Re}\left(e^{-i\gamma}\left(1 + \frac{zf''(z)}{f'(z)}\right)\right) > \left|\frac{zf''(z)}{f'(z)}\right|.$$

Special functions and their geometric properties frequently appear in univalent function theory. In the recent past, normalized function properties have been explored in terms of radius problems [10–13]. In particular, for a normalized special function f, we define

$$\mathcal{S}^*(\alpha) - radius := \sup\left\{r \in \mathbb{R}^+ : \mathrm{Re}\left(\frac{zf'(z)}{f(z)}\right) > \alpha, z \in \mathbb{D}_r\right\}$$

and, similarly, one may define the $\mathcal{C}(\alpha)$-radius. In this direction, the $\mathcal{S}^*(\alpha)$-radius of Bessel functions was obtained in [10], and Ramanujan-type entire functions were dealt with in [11]. A unified treatment of the radius of Ma–Minda classes [14] and more for some special functions was studied in [13,15,16].

However, to the best of our knowledge, the $\mathcal{UCSP}(\gamma)$-radius has not been studied to date for the above-mentioned special functions. Therefore, we define the $\mathcal{UCSP}(\gamma)$-radius here:

Definition 2. *Let f in $\mathcal{A}$ be a special function. Then, the radius of a uniformly convex γ-spirallike is found as:*

$$R_{ucs}(\gamma; f) = \sup\left\{r \in \mathbb{R}^+ : \mathrm{Re}\left(e^{-i\gamma}\left(1 + \frac{zf''(z)}{f'(z)}\right)\right) > \left|\frac{zf''(z)}{f'(z)}\right|, z \in \mathbb{D}_r\right\}.$$

In the present investigation, we consider our special normalized functions to be the derivatives of Bessel functions. Recall that the Bessel function of the first kind of order ν is defined by ([17], p. 217):

$$J_\nu(z) = \sum_{n=0}^{\infty} \frac{(-1)^n}{n!\Gamma(n+\nu+1)}\left(\frac{z}{2}\right)^{2n+\nu} (z \in \mathbb{C}). \tag{1}$$

We know that all its zeros are real for $\nu > -1$. Here we consider the general function

$$N_\nu(z) = az^2 J_\nu''(z) + bzJ_\nu'(z) + cJ_\nu(z),$$

which was studied by Mercer [18]. Here, as mentioned in [18], we take $q = b - a$ and $(c = 0$ and $q \neq 0)$ or $(c > 0$ and $q > 0)$. From (1), we now have the power series representation

$$N_\nu(z) = \sum_{n=0}^{\infty} \frac{Q(2n+\nu)(-1)^n}{n!\Gamma(n+\nu+1)} \left(\frac{z}{2}\right)^{2n+\nu} \quad (z \in \mathbb{C}), \tag{2}$$

where $Q(\nu) = a\nu(\nu-1) + b\nu + c$ $(a, b, c \in \mathbb{R})$. There are three important reference works dealing with the function N_ν. Firstly, in Mercer's paper [18], it is proved that the k^{th} positive zero of N_ν increases with ν in $\nu > 0$. Secondly, Ismail and Muldoon [19], under the conditions $a, b, c \in \mathbb{R}$ such that $c = 0$ and $b \neq a$ or $c > 0$ and $b > a$, showed the following behavior of roots:

(i) For $\nu > 0$, the zeros of $N_\nu(z)$ are either real or purely imaginary.
(ii) For $\nu \geq \max\{0, \nu_0\}$, where ν_0 is the largest real root of the quadratic $Q(\nu) = a\nu(\nu - 1) + b\nu + c$, the the zeros of $N_\nu(z)$ are real.
(iii) If $\nu > 0$, $\left(a\nu^2 + (b-a)\nu + c\right)/(b-a) > 0$ and $a/(b-a) < 0$, the zeros of $N_\nu(z)$ are all real, except for a single pair that is conjugate and purely imaginary.

In 2016, Baricz et al. [20] obtained the sufficient and necessary conditions for the starlikeness of a normalized form of N_ν by using the results of Mercer [18], Ismail and Muldoon [19], and Shah and Trimble [21].

Since the function N_ν does not belong to $\mathcal{A}$, to prove our results, we consider the following normalizations of the function N_ν as given by:

$$f_\nu(z) = \left[\frac{2^\nu \Gamma(\nu+1)}{Q(\nu)} N_\nu(z)\right]^{\frac{1}{\nu}}, \tag{3}$$

$$g_\nu(z) = \frac{2^\nu \Gamma(\nu+1) z^{1-\nu}}{Q(\nu)} N_\nu(z), \tag{4}$$

$$h_\nu(z) = \frac{2^\nu \Gamma(\nu+1) z^{1-\frac{\nu}{2}}}{Q(\nu)} N_\nu(\sqrt{z}). \tag{5}$$

In the rest of this paper, for the quadratic $Q(\nu) = a\nu(\nu-1) + b\nu + c$, we will always assume that $a, b, c \in \mathbb{R}$ $(c = 0$ and $a \neq b)$ or $(c > 0$ and $a < b)$. Moreover, ν_0 is the largest real root of the quadratic $Q(\nu)$ defined according to the above conditions.

Since the functions $N_\nu(z)$ and $N_\nu'(z)$ are entire functions of order zero, then they have infinitely many zeros. According to the Hadamard factorization theorem [22], we may write

$$N_\nu(z) = \frac{Q(\nu) z^\nu}{2^\nu \Gamma(\nu+1)} \prod_{n \geq 1} \left(1 - \frac{z^2}{\lambda_{\nu,n}^2}\right) \tag{6}$$

and

$$N_\nu'(z) = \frac{Q(\nu) z^{\nu-1} \nu}{2^\nu \Gamma(\nu+1)} \prod_{n \geq 1} \left(1 - \frac{z^2}{\lambda_{\nu,n}'^2}\right), \tag{7}$$

where $\lambda_{\nu,n}$ and $\lambda_{\nu,n}'$ denote the n^{th} positive zero of $N_\nu(z)$ and $N_\nu'(z)$, respectively. For recent updates on the geometric properties of Bessel functions, readers are urged to see [20,23–28] and references therein.

In this paper, we find the radius of uniformly convex γ-spirallike for the functions $f_\nu(z)$, $g_\nu(z)$, and $h_\nu(z)$ to be defined by (3)–(5) when $\nu \geq \max\{0, \nu_0\}$. The key tools in their proofs are special properties of the zeros of the function N_ν and their derivatives.

2. Zeros of Hyperbolic Polynomials and the Laguerre–Pólya Class of Entire Functions

In this section, we recall some necessary information about polynomials and entire functions with real zeros. An algebraic polynomial is called hyperbolic if all its zeros are real. We formulate the following specific statement that we shall need; see [25] for more details. By definition, a real entire function ψ belongs to the Laguerre–Pólya class $\mathcal{LP}$ if it can be represented in the form

$$\psi(x) = cx^m e^{-ax^2+\beta x} \prod_{k\geq 1}\left(1+\frac{x}{x_k}\right)e^{-\frac{x}{x_k}},$$

with $c, \beta, x_k \in \mathbb{R}$, $a \geq 0$, $m \in \mathbb{N}\cup\{0\}$, and $\sum x_k^{-2} < \infty$. Similarly, ϕ is said to be of type $\mathcal{I}$ in the Laguerre–Pólya class, written $\varphi \in \mathcal{LPI}$, if $\phi(x)$ or $\phi(-x)$ can be represented as

$$\phi(x) = cx^m e^{\sigma x} \prod_{k\geq 1}\left(1+\frac{x}{x_k}\right),$$

with $c \in \mathbb{R}$, $\sigma \geq 0$, $m \in \mathbb{N}\cup\{0\}$, $x_k > 0$, and $\sum x_k^{-1} < \infty$. The class $\mathcal{LP}$ is the complement of the space of hyperbolic polynomials in the topology induced by the uniform convergence on the compact sets of the complex plane, while $\mathcal{LPI}$ is the complement of the hyperbolic polynomials whose zeros possess a preassigned constant sign. Given an entire function φ with the Maclaurin expansion

$$\varphi(x) = \sum_{k\geq 0} \mu_k \frac{x^k}{k!},$$

its Jensen polynomials are defined by

$$P_m(\varphi; x) = P_m(x) = \sum_{k=0}^{m} \begin{pmatrix} m \\ k \end{pmatrix} \mu_k x^k.$$

The next result of Jensen [29] is a well-known characterization of functions belonging to $\mathcal{LP}$.

Lemma 1. *The function φ belongs to $\mathcal{LP}$ ($\mathcal{LPI}$, respectively) if and only if all the polynomials $P_m(\varphi; x)$, $m = 1, 2, \ldots$, are hyperbolic (hyperbolic with zeros of equal sign). Moreover, the sequence $P_m(\varphi; z/n)$ converges locally uniformly to $\varphi(z)$.*

The following result is a key tool in the proof of the main results.

Lemma 2 ([30])**.** *The function $z \longmapsto \Psi_\nu(z) = \frac{2^\nu \Gamma(\nu+1)}{Q(\nu) z^\nu} N_\nu(z)$ has infinitely many zeros, and all of them are positive, if $\nu \geq \max\{0, \nu_0\}$. Denoting by $\lambda_{\nu,n}$ the n^{th} positive zero of $\Psi_\nu(z)$, under the same conditions, the Weierstrassian decomposition*

$$\Psi_\nu(z) = \prod_{n\geq 1}\left(1-\frac{z^2}{\lambda_{\nu,n}^2}\right)$$

is valid, and this product is uniformly convergent on compact subsets of the complex plane. Moreover, if we denote by $\lambda'_{\nu,n}$ the nth positive zero of $\Phi'_\nu(z)$, where $\Phi_\nu(z) = z^\nu \Psi_\nu(z)$, then the positive zeros of $\Psi_\nu(z)$ are interlaced with those of $\Phi'_\nu(z)$. In other words, the zeros satisfy the chain of inequalities

$$\lambda'_{\nu,1} < \lambda_{\nu,1} < \lambda'_{\nu,2} < \lambda_{\nu,2} < \lambda'_{\nu,3} < \lambda_{\nu,3} < \cdots.$$

3. Main Results

Our principal result establishes the radius of $\mathcal{UCSP}(\gamma)$, see Table 1, and reads as follows:

Theorem 1. *Let* $\gamma \in \left(-\frac{\pi}{2}, \frac{\pi}{2}\right)$. *The following statements hold:*

(a) *If* $\nu \geq \max\{0, \nu_0\}$, $\nu \neq 0$, *then the radius of uniformly convex* γ*-spirallikeness of the function* f_ν *is the smallest positive root of the equation*

$$\frac{rN_\nu''(r)}{N_\nu'(r)} + \left(\frac{1}{\nu} - 1\right)\frac{rN_\nu'(r)}{N_\nu(r)} = \frac{\cos\gamma}{2}.$$

(b) *If* $\nu \geq \max\{0, \nu_0\}$, *then the radius of uniformly convex* γ*-spirallikeness of the function* g_ν *is the smallest positive root of the equation*

$$\frac{r^2N_\nu''(r) + (2-\nu)rN_\nu'(r)}{rN_\nu'(r) + (1-\nu)N_\nu(r)} = \nu - \frac{\cos\gamma}{2}.$$

(c) *If* $\nu \geq \max\{0, \nu_0\}$, *then the radius of uniformly convex* γ*-spirallikeness of the function* h_ν *is the smallest positive root of the equation*

$$\frac{\sqrt{r}N_\nu''(\sqrt{r})}{N_\nu'(\sqrt{r})} + \frac{\sqrt{r}N_\nu'(\sqrt{r})}{N_\nu(\sqrt{r})} = 1 - \cos\gamma.$$

Proof. We first prove part (a). From (3), we have

$$1 + \frac{zf_\nu''(z)}{f_\nu'(z)} = 1 + \frac{zN_\nu''(z)}{N_\nu'(z)} + \left(\frac{1}{\nu} - 1\right)\frac{zN_\nu'(z)}{N_\nu(z)},$$

and by means of (6) and (7), we obtain

$$1 + \frac{zf_\nu''(z)}{f_\nu'(z)} = 1 - \left(\frac{1}{\nu} - 1\right)\sum_{n\geq 1}\frac{2z^2}{\lambda_{\nu,n}^2 - z^2} - \sum_{n\geq 1}\frac{2z^2}{\lambda_{\nu,n}'^2 - z^2}.$$

For $1 \geq \nu > \max\{0, \nu_0\}$, we get

$$\begin{aligned}
&\operatorname{Re}\left(e^{-i\gamma}\left(1 + \frac{zf_\nu''(z)}{f_\nu'(z)}\right)\right)\\
&= \operatorname{Re}(e^{-i\gamma}) - \operatorname{Re}\left(e^{-i\gamma}\left(\sum_{n\geq 1}\frac{2z^2}{\lambda_{\nu,n}'^2 - z^2} + \left(\frac{1}{\nu} - 1\right)\sum_{n\geq 1}\frac{2z^2}{\lambda_{\nu,n}^2 - z^2}\right)\right)\\
&\geq \cos\gamma - \left(\frac{1}{\nu} - 1\right)\sum_{n\geq 1}\frac{2r^2}{\lambda_{\nu,n}^2 - r^2} - \sum_{n\geq 1}\frac{2r^2}{\lambda_{\nu,n}'^2 - r^2}\\
&\geq \cos\gamma + \frac{rf_\nu''(r)}{f_\nu'(r)} \qquad (8)
\end{aligned}$$

where $|z| = r$. Moreover, observe that if we use the inequality ([31], Lemma 2.1)

$$\mu\operatorname{Re}\left(\frac{z}{a-z}\right) - \operatorname{Re}\left(\frac{z}{b-z}\right) \geq \mu\frac{|z|}{a-|z|} - \frac{|z|}{b-|z|},$$

where $a > b > 0$, $\mu \in [0,1]$ and $z \in \mathbb{C}$ such that $|z| < b$, then we see that the inequality (8) is also valid when $\nu \geq 1$. Here we have seen that the zeros of N_ν and N_ν' are interlacing according to Lemma 1. In view of the Definition 2 and the above inequalities (8), let us define $T_{f_\nu} : (0, \lambda_{\nu,1}') \to \mathbb{R}$, which is given by

$$T_{f_\nu}(r) = \cos\gamma - 2\left(\left(\frac{1}{\nu} - 1\right)\sum_{n\geq 1}\frac{2r^2}{\lambda_{\nu,n}^2 - r^2} + \sum_{n\geq 1}\frac{2r^2}{\lambda_{\nu,n}'^2 - r^2}\right).$$

Clearly, it can be seen that

$$T_{f_\nu}(0) = \cos\gamma > 0 \quad \text{and} \quad \lim_{r \nearrow \lambda'_{\nu,1}} T_{f_\nu}(r) = -\infty$$

for all $r \in (0, \lambda'_{\nu,1})$. Moreover, for $r \in (0, \lambda'_{\nu,1})$ using Lemma 2,

$$T'_{f_\nu}(r) = 2\left\{ -\left(\frac{1}{\nu} - 1\right) \sum_{n\geq 1} \frac{4r\lambda^2_{\nu,n}}{(\lambda^2_{\nu,n} - r^2)^2} - \sum_{n\geq 1} \frac{4r\lambda'^2_{\nu,n}}{(\lambda'^2_{\nu,n} - r^2)^2} \right\} < 0.$$

Now let $R_{ucs}(\gamma; f_\nu)$ be the smallest positive root of the equation $T'_{f_\nu}(r) = 0$. Hence, the inequality

$$\mathrm{Re}\left(e^{-i\gamma} \left(1 + \frac{zf''(z)}{f'(z)} \right) \right) > \left| \frac{zf''(z)}{f'(z)} \right|$$

holds whenever the following inequality is valid:

$$\cos\gamma + \frac{rf''_\nu(r)}{f'_\nu(r)} > -\frac{rf''_\nu(r)}{f'_\nu(r)}.$$

The above inequality may be equivalently read as $T_{f_\nu}(r) > 0$, which is valid for all $|z| = r < R_{ucs}(\gamma; f_\nu)$. The sharpness of the radius constant $R_{ucs}(\gamma; f_\nu)$ can be observed, in view of the maximum and minimum modulus principles by taking $z = r > R_{ucs}(\gamma; f_\nu)$ such that the following reverse inequality holds:

$$\begin{aligned} \min_{|z|=r} \mathrm{Re}\left(e^{-i\gamma} \left(1 + \frac{zf''(z)}{f'(z)} \right) \right) &= \cos\gamma + \frac{rf''_\nu(r)}{f'_\nu(r)} \\ &< \max_{|z|=r} \left| \frac{zf''(z)}{f'(z)} \right| \\ &= -\frac{rf''_\nu(r)}{f'_\nu(r)}. \end{aligned}$$

This completes the proof of part (a).

For the other parts, in view of Lemma 2, note that the functions g_ν and h_ν belong to the Laguerre–Pólya class $\mathcal{LP}$, which is closed under differentiation, that their derivatives g'_ν and h'_ν also belong to $\mathcal{LP}$, and that the zeros are real. Thus assuming $\delta_{\nu,n}$ and $\gamma_{\nu,n}$ to be the positive zeros of g'_ν and h'_ν, respectively, we have the following representations:

$$g'_\nu(z) = \prod_{n\geq 1} \left(1 - \frac{z^2}{\delta^2_{\nu,n}} \right) \quad \text{and} \quad h'_\nu(z) = \prod_{n\geq 1} \left(1 - \frac{z}{\gamma_{\nu,n}} \right),$$

which yield

$$1 + \frac{zg''_\nu(z)}{g'_\nu(z)} = 1 - \sum_{n\geq 1} \frac{2z^2}{\delta^2_{\nu,n} - z^2} \quad \text{and} \quad 1 + \frac{zh''_\nu(z)}{h'_\nu(z)} = 1 - \sum_{n\geq 1} \frac{z}{\gamma_{\nu,n} - z}.$$

Further, reasoning along the same lines as in part (a), the result follows at once. □

Table 1. Radii of uniformly convex $\frac{\pi}{3}-$spirallike for $f_{1/2}$, $g_{1/2}$, and $h_{1/2}$ in Theorem 1.

	$b=3$ and $c=0$			$a=1$ and $c=0$			$a=1$ and $b=2$		
	$a=2$	$a=3$	$a=4$	$b=2$	$b=3$	$b=4$	$c=2$	$c=3$	$c=4$
f_ν	0.087	0.067	0.050	0.099	0.113	0.121	0.172	0.192	0.208
g_ν	0.122	0.094	0.0703	0.138	0.157	0.169	0.241	0.269	0.292
h_ν	0.040	0.024	0.013	0.052	0.068	0.078	0.162	0.204	0.240

Example 1. *For the value $\nu = 1/2$, we may express the function $N_\nu(z)$ in terms of the elementary trigonometric functions as follows:*

$$N_{1/2}(z) = \frac{4(b-a)z\cos z + \left[a\left(3-4z^2\right) - 2b + 4c\right]\sin z}{2\sqrt{2\pi}\sqrt{z}}.$$

Consequently, we get

$$f_{1/2}(z) = \frac{\left[4(a-b)z\cos z + \left(4az^2 - 3a + 2b - 4c\right)\sin z\right]^2}{(a-2b-4c)^2 z},$$

$$g_{1/2}(z) = \frac{4(a-b)z\cos z + \left(4az^2 - 3a + 2b - 4c\right)\sin z}{a-2b-4c},$$

and

$$h_{1/2}(z) = \frac{4(a-b)z\cos\sqrt{z} + (4az - 3a + 2b - 4c)\sqrt{z}\sin\sqrt{z}}{a-2b-4c}.$$

An immediate consequence of the proof of Theorem 1 is the following sufficient conditions for functions to be uniformly convex γ-spirallike. In fact, Tables 2–4 explain the sufficient conditions for uniformly convex γ-spirallikeness by giving the minimum value of the ν with respect to the given equations in Corollary 1. Also, Figures 1–3 represent image domains of the unit disk in view of Corollary 1.

Corollary 1. *(Sufficient condition.) Let $\gamma \in \left(-\frac{\pi}{2}, \frac{\pi}{2}\right)$ and $\nu \geq \max\{0, \nu_0\}$. Then, the following statements hold:*

(a) Let $\nu \neq 0$. The function f_ν is uniformly convex γ-spirallike if

$$\frac{\cos\gamma}{2} + \frac{N_\nu''(1)}{N_\nu'(1)} + \left(\frac{1}{\nu} - 1\right)\frac{N_\nu'(1)}{N_\nu(1)} > 0.$$

(b) The function g_ν is uniformly convex γ-spirallike if

$$\frac{\cos\gamma}{2} - \nu + \frac{N_\nu''(1) + (2-\nu)N_\nu'(1)}{N_\nu'(1) + (1-\nu)N_\nu(1)} > 0.$$

(c) The function h_ν is uniformly convex γ-spirallike if

$$\frac{N_\nu''(1)}{N_\nu'(1)} + \frac{N_\nu'(1)}{N_\nu(1)} > 1 - \cos\gamma.$$

In particular, $\gamma = 0$ provides sufficient conditions for functions to be uniformly convex.

Table 2. Minimum value of ν for uniformly convex γ-spirallike of f_ν in Corollary 1.

	$b=3$ and $c=0$			$a=1$ and $c=0$			$a=1$ and $b=2$		
	$a=2$	$a=3$	$a=4$	$b=2$	$b=3$	$b=4$	$c=2$	$c=3$	$c=4$
$\gamma=\pi/3$	0.8921	3.6136	1.0762	0.8229	0.7432	0.6999	0.4802	0.3938	0.3395
$\gamma=\pi/4$	0.8910	3.2130	1.0770	0.8211	0.7408	0.6973	0.4748	0.3883	0.3342
$\gamma=0$	0.8895	2.8790	1.0779	0.8188	0.7376	0.6937	0.4674	0.3806	0.3268

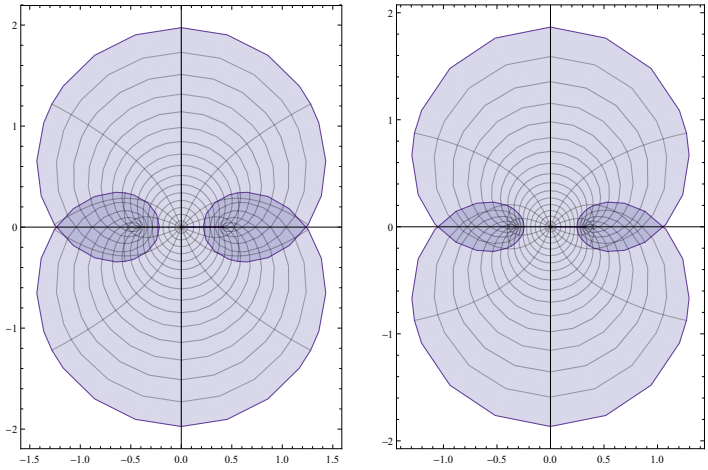


Figure 1. Image domains of the unit disk under f_1 with $a=2, b=3$, and $c=0$ for $\gamma=\pi/3$, and $f_{0.5}$ with $a=1, b=2$, and $c=2$ for $\gamma=\pi/4$ using Table 2.

Remark 1. *In light of Spacek [1], here we see that* $f_1 \in \mathcal{CS}_p^{\pi/3}(0)$ *for* $a=2, b=3$, *and* $c=0$, *and* $f_{0.5} \in \mathcal{CS}_p^{\pi/4}(0)$ *for* $a=1, b=2$, *and* $c=2$, *but that these are not univalent in* $\mathbb{D}$, *as shown in Figure 1.*

Table 3. Minimum value of ν for uniformly convex γ-spirallike of g_ν in Corollary 1.

	$b=3$ and $c=0$			$a=1$ and $c=0$			$a=1$ and $b=2$		
	$a=2$	$a=3$	$a=4$	$b=2$	$b=3$	$b=4$	$c=2$	$c=3$	$c=4$
$\gamma=\pi/3$	8.6224	8.6936	8.7315	8.5568	8.4404	8.3404	8.5008	8.4730	8.4455
$\gamma=\pi/4$	6.7337	6.8160	6.8604	6.6591	6.5297	6.4220	6.5785	6.5387	6.4993
$\gamma=0$	5.3610	5.4540	5.5048	5.2783	5.1385	5.0258	5.1675	5.1128	5.0586

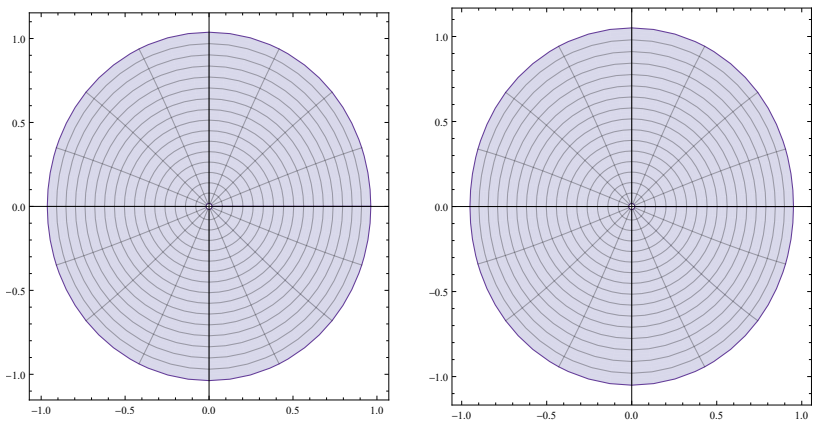


Figure 2. Image domains of the unit disk under the function g_9 with $a=2, b=3$, and $c=0$ for $\gamma=\pi/3$, and the function g_7 with $a=1, b=2$, and $c=2$ for $\gamma=\pi/4$ using Table 3.

Table 4. Minimum value of ν for uniformly convex γ-spirallike of h_ν in Corollary 1.

	$b=3$ and $c=0$			$a=1$ and $c=0$			$a=1$ and $b=2$		
	$a=2$	$a=3$	$a=4$	$b=2$	$b=3$	$b=4$	$c=2$	$c=3$	$c=4$
$\gamma=\pi/3$	1.0778	1.2061	1.2908	0.9895	0.8818	0.8210	0.5378	0.3990	0.3134
$\gamma=\pi/4$	1.0709	1.2003	1.2856	0.9818	0.8732	0.8119	0.5177	0.3741	0.2863
$\gamma=0$	1.0614	1.1923	1.2786	0.9713	0.8614	0.7996	0.4890	0.3377	0.2463

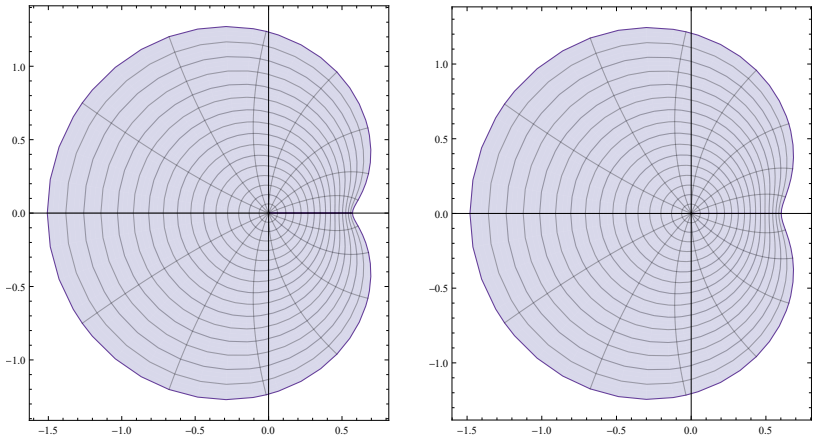


Figure 3. Image domains of the unit disk under function $h_{3.5}$ with $a=2, b=3$, and $c=0$ for $\gamma=\pi/3$, and function h_1 with $a=1, b=2$, and $c=2$ for $\gamma=\pi/4$ using Table 4.

Remark 2. *In Tables 2–4, the entries with the choice $\gamma=0$ generate ample examples of uniformly convex functions via the special function $N_\nu(z)=az^2J_\nu''(z)+bzJ_\nu'(z)+cJ_\nu(z)$, studied by Mercer [18].*

In Theorem 1, letting $\gamma=0$, we obtain the radius of uniform convexity for the functions $f_\nu(z)$, $g_\nu(z)$, and $h_\nu(z)$ as defined by (3), (4), and (5), respectively.

Corollary 2. *(Radius of uniform convexity). Let $\nu\geq\max\{0,\nu_0\}$. The following statements hold:*

(a) If $\nu\neq 0$, then the radius of uniform convexity of the function f_ν is the smallest positive root of the equation

$$\frac{rN_\nu''(r)}{N_\nu'(r)}+\left(\frac{1}{\nu}-1\right)\frac{rN_\nu'(r)}{N_\nu(r)}=\frac{1}{2}.$$

(b) The radius of uniform convexity of the function g_ν is the smallest positive root of the equation

$$\frac{r^2N_\nu''(r)+(2-\nu)rN_\nu'(r)}{rN_\nu'(r)+(1-\nu)N_\nu(r)}=\nu-\frac{1}{2}.$$

(c) Then the radius of uniform convexity of the function h_ν is the smallest positive root of the equation

$$\frac{\sqrt{r}N_\nu''(\sqrt{r})}{N_\nu'(\sqrt{r})}+\frac{\sqrt{r}N_\nu'(\sqrt{r})}{N_\nu(\sqrt{r})}=0.$$

Now, from Theorem 1, we deduce that:

Example 2. *Let $\nu=1/2$, $a=1$, $b=2$, $c=0$, and $\gamma=\pi/3$, see Figure 4. The following statements are true.*

(a) *The radius of uniformly convex* $\frac{\pi}{3}-$*spirallikeness of the function* $f_{1/2}$ *is the smallest positive root of the equation*

$$\frac{1+48t^4+(-1+2t^2-192t^4+32t^6)\cos 2t+2t(-1-16t^2+80t^4)\sin 2t}{(-4t\cos t+\sin t+4t^2\sin t)(2t(-1+4t^2)\cos t+(-1+20t^2)\sin t)}+\frac{1}{4}=0.$$

(b) *The radius of uniformly convex* $\frac{\pi}{3}-$*spirallikeness of the function* $g_{1/2}$ *is the smallest positive root of the equation*

$$\frac{t(20t\cos t+(15-4t^2)\sin t)}{(-3+4t^2)\cos t+12t\sin t}+\frac{1}{4}=0.$$

(c) *The radius of uniformly convex* $\frac{\pi}{3}-$*spirallikeness of the function* $h_{1/2}$ *is the smallest positive root of the equation*

$$\frac{(1+24t)\sqrt{t}\cos\sqrt{t}+(-1+(23-4t)t)\sin\sqrt{t}}{2(-7+4t)\sqrt{t}\cos\sqrt{t}+2(1+16t)\sin\sqrt{t}}+\frac{1}{4}=0.$$

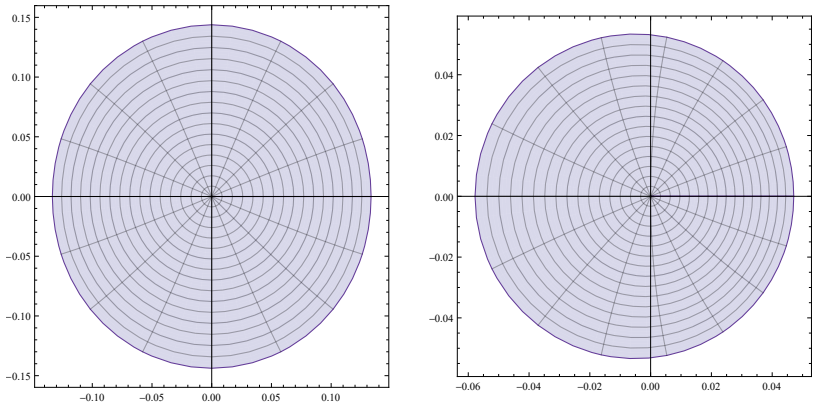


Figure 4. Image domains of $g_{1/2}$ for $|z| < 0.1386$ and $h_{1/2}$ for $|z| < 0.0524$, respectively, with $a = 1, b = 2$, and $c = 0$ for $\gamma = \pi/3$.

4. Conclusions

For the three different kinds of normalizations, namely (3), (4), and (5) of the function $N_\nu(z) = az^2J_\nu''(z) + bzJ_\nu'(z) + cJ_\nu(z)$, where $J_\nu(z)$ is the Bessel function of the first kind of order ν, we obtained the sharp radius of uniformly γ-spirallikeness. As a byproduct, we obtained the conditions on parameters for the normalized forms to be uniform γ-spirallike functions. Thus, we created a category of examples of uniform γ-spirallike functions from special functions.

Author Contributions: All authors contributed equally. All authors have read and agreed to the published version of the manuscript.

Funding: This research received no external funding.

Data Availability Statement: Not applicable.

Acknowledgments: The authors would like to thank the anonymous reviewers for their insightful comments.

Conflicts of Interest: The authors declare no conflict of interest.

References

1. Spacek, L. Contribution á la thèorie des fonctions univalentes. *Casop Pest. Mat.-Fys.* **1933**, *62*, 12–19.
2. Robertson, M.S. Univalent functions $f(z)$ for which $zf'(z)$ is spirallike. *Mich. Math. J.* **1969**, *16*, 97–101. [CrossRef]
3. Pfaltzgraff, J.A. Univalence of the integral of $f'(z)^\lambda$. *Bull. Lond. Math. Soc.* **1975**, *7*, 254–256. [CrossRef]
4. Kanas, S.; Wiśniowska, A. Conic domains and starlike functions. *Rev. Roumaine Math. Pures Appl.* **2000**, *45*, 647–657.
5. Kanas, S.; Wiśniowska, A. Conic regions and k-uniform convexity. *J. Comput. Appl. Math.* **1999**, *105*, 327–336. [CrossRef]

6. Goodman, A.W. On uniformly convex functions. *Ann. Pol. Math.* **1991**, *56*, 87–92. [CrossRef]
7. Goodman, A.W. On uniformly starlike functions. *J. Math. Anal. Appl.* **1991**, *155*, 364–370. [CrossRef]
8. Ronning, F. Uniformly convex functions and a corresponding class of starlike functions. *Proc. Am. Math. Soc.* **1993**, *118*, 189–196. [CrossRef]
9. Ravichandran, V.; Selvaraj, C.; Rajagopal, R. On uniformly convex spiral functions and uniformly spirallike functions. *Soochow J. Math.* **2003**, *29*, 393–405.
10. Baricz, Á.; Kupán, P.A.; Szxaxsz, R. The radius of starlikeness of normalized Bessel functions of the first kind. *Proc. Am. Math. Soc.* **2014**, *142*, 2019–2025. [CrossRef]
11. Deniz, E. Geometric and monotonic properties of Ramanujan type entire functions. *Ramanujan J.* **2020** *55*, 103–130. [CrossRef]
12. Kazımoğlu, S.; Deniz, E. The radii of starlikeness and convexity of the functions including derivatives of Bessel functions. *Turk. J. Math.* **2022**, *46*, 894–911. [CrossRef]
13. Saliu, A.; Jabeen, K.; Al-shbeil, I.; Oladejo, S.O.; Cătaş, A. Radius and Differential Subordination Results for Starlikeness Associated with Limaçon Class. *J. Funct. Spaces* **2022**. [CrossRef]
14. Ma, W.C.; Minda, D. A unified treatment of some special classes of univalent functions. In Proceedings of the Conference on Complex Analysis, Tianjin, China, 19–23 June 1992; Conf Proc Lecture Notes Anal I; Int Press: Cambridge, MA, USA, 1992; pp. 157–169.
15. Gangania, K.; Kumar, S.S. $\mathcal{S}^*(\psi)$ and $\mathcal{C}(\psi)$-radii for some special functions. *Iran. J. Sci. Technol. Trans. A Sci.* **2022**, *46*, 95966.
16. Gangania, K.; K; Kumar, S.S. Certain Radii problems for $\mathcal{S}^*(\psi)$ and Special functions. *arXiv* **2023**, arXiv:2007.07816v2.
17. Oliver, F.W.J.; Lozier, D.W.; Boisvert, R.F.; Clark, C.W. (Eds.) *NIST Handbook of Mathematical Functions*; Cambridge Univ. Press: Cambridge, UK, 2010.
18. Mercer, A.C. The zeros of $az^2 J_\nu''(z) + bz J_\nu'(z) + c J_\nu(z)$ as functions of order. *Internat. J. Math. Math. Sci.* **1992**, *15*, 319–322. [CrossRef]
19. Ismail, M.E.H.; Muldoon, M.E. Bounds for the small real and purely imaginary zeros of Bessel and related functions. *Meth. Appl. Anal.* **1995**, *2*, 1–21. [CrossRef]
20. Baricz, Á.; Çağlar, M.; Deniz, E. Starlikeness of bessel functions and their derivatives. *Math. Inequal. Appl.* **2016**, *19*, 439–449. [CrossRef]
21. Shah, S.M.; Trimble, S.Y. Entire functions with univalent derivatives. *J. Math. Anal. Appl.* **1971**, *33*, 220–229. [CrossRef]
22. Levin, B.Y. Lectures on Entire Functions. *Am. Math. Soc. Transl. Math. Monogr.* **1996**, *150, 248.*
23. Baricz, Á.; Orhan, H.; Szász, R. The radius of $\alpha-$ convexity of normalized Bessel functions of the first kind. *Comput. Method. Func. Theo.* **2016**, *16*, 93–103. [CrossRef]
24. Deniz, E.; Szász, R. The radius of uniform convexity of Bessel functions. *J. Math. Anal. Appl.* **2017**, *453*, 572–588. [CrossRef]
25. Deniz, E.; Kazımoğlu, S.; Çağlar, M. Radii of Starlikeness and Convexity of Bessel Function Derivatives. *Ukr. Math. J.* **2022**, *73*, 1686–1711. [CrossRef]
26. Szász, R. About the radius of starlikeness of Bessel functions of the first kind. *Monatshefte Für Math.* **2015**, *176*, 323–330. [CrossRef]
27. Frasin, B.A.; Aldawish, I. On Subclasses of Uniformly Spirallike Functions Associated with Generalized Bessel Functions. *J. Funct. Spaces* **2019**, *2019*, 1329462.
28. Kazımoğlu, S.; Gangania, K. Radius of γ-Spirallikeness of order α for some Special functions. *arXiv* **2022**, arXiv:2211.13232.
29. Jensen, J.L.W.V. Recherches sur la théorie des équations. *Acta Math.* **1913**, *36*, 181–195. [CrossRef]
30. Kazımoğlu, S.; Deniz, E. Radius Problems for Functions Containing Derivatives of Bessel Functions. *Comput. Method. Func. Theo.* **2022**, 1–26. [CrossRef]
31. Baricz, Á.; Szász, R. The radius of convexity of normalized Bessel functions of the first kind. *Anal. Appl.* **2014**, *12*, 485–509. [CrossRef]

Disclaimer/Publisher's Note: The statements, opinions and data contained in all publications are solely those of the individual author(s) and contributor(s) and not of MDPI and/or the editor(s). MDPI and/or the editor(s) disclaim responsibility for any injury to people or property resulting from any ideas, methods, instructions or products referred to in the content.

ISSN 2063-5346

RECENT FINDINGS ON PLASTIC WASTE POLLUTION AND BIOTRANSFORMATION

Tushar Agarwal and Jai Gopal Sharma*

Article History: **Received:** 01.02.2023 **Revised:** 07.03.2023 **Accepted:** 10.04.2023

Abstract

Plastic waste is generated in large quantities globally, and its disposal poses significant environmental challenges as it is non-biodegradable and can persist in the environment for hundreds of years. It is estimated that over 8 million tons of plastic waste end up in our oceans every year. Biodegradation is an eco-friendly approach to managing plastic waste as it does not result in the formation of toxic by-products. Types of plastic waste, degradation methods, and different microorganisms impacting biodegradation are discussed in this review. Overall, microbial bioremediation has the potential to provide an eco-friendly solution to the problem of plastic waste, and recent advances in this field have shown promising results. However, further research is needed to optimize bioremediation processes and to develop new microorganisms that can efficiently degrade and transform plastic waste.

Keywords: Bioremediation; Environment awareness; Biotransformation; Biodegradation; Plastic waste

Delhi Technological University, Shahbad Daulatpur Village, Rohini, New Delhi, Delhi 110042

DOI: 10.31838/ecb/2023.12.s1.079

Introduction

Plastic waste is generated in large quantities globally, and its disposal poses significant environmental challenges as it is non-biodegradable and can persist in the environment for hundreds of years [1,2]. It is estimated that over 8 million tons of plastic waste end up in our oceans every year [3]. Plastic waste can also release toxic chemicals and greenhouse gases when burned, contributing to air pollution and climate change [4,5]. As plastic waste continues to be a major environmental problem, innovative solutions are required to address the challenges posed by plastic waste. This includes the development of new technologies and methods for the efficient and sustainable management of plastic waste, as well as awareness-raising and education efforts to encourage individuals and businesses to reduce their plastic consumption and waste. Efforts to manage plastic waste include recycling, reuse, reduction, and disposal [6]. Recycling involves the conversion of plastic waste into new plastic products [7]. Reuse involves finding new uses for plastic products, such as using plastic bags for shopping multiple times. Reduction involves reducing the amount of plastic used in products, such as by using reusable water bottles instead of disposable plastic ones. Finally, disposal involves the safe and environmentally friendly disposal of plastic waste, such as through landfilling or incineration.

Plastics can also be degraded into simpler compounds that can be absorbed or assimilated by the environment [8,9]. This process can occur naturally through physical, chemical, or biological means. Physical degradation occurs due to the action of external factors such as sunlight, heat, and mechanical stress [10]. Exposure to UV light and heat can cause the degradation of plastic, leading to the breaking of chemical bonds, which results in the formation of smaller molecules. Mechanical stress, such as grinding or shredding, can also break down plastic waste into smaller fragments. Chemical degradation involves the use of chemicals to break down the polymer chains of plastic into simpler compounds [9]. Chemicals such as acids, bases, and oxidizing agents can be used to degrade plastic waste. For example, hydrolysis is a common chemical method used to break down the ester linkages in PET plastics. However, not all plastics are easily biodegradable, and some may require special conditions or pre-treatments to enhance biodegradation. For example, polyethylene (PE) and polypropylene (PP) are difficult to biodegrade, and it can take hundreds of years for them to degrade in the environment [8]. This has led to the development of new technologies, such as the use of engineered microorganisms or enzymes to degrade specific types of plastics.

Bioremediation is an eco-friendly approach to tackle this problem, and it involves using microorganisms such as bacteria, fungi, and algae to break down plastic waste into simpler, non-toxic compounds (Figure 1) [11]. These microorganisms secrete enzymes that can break down the polymer chains of plastic into smaller molecules. Microbial bioremediation of plastic waste can be classified into two categories: biodegradation and biotransformation [12]. Biodegradation involves the complete breakdown of plastic waste into carbon dioxide and water [13]. This process is carried out by microorganisms such as bacteria and fungi, which secrete enzymes that break down the polymer chains of plastic into smaller molecules that can be used as an energy source for the microorganisms. The biodegradation of plastic waste has been extensively studied, and several microorganisms have been identified that can efficiently degrade plastic waste [14,15]. Biotransformation, on the other hand, involves the conversion of plastic waste into non-toxic compounds by microorganisms. This process is particularly useful for plastics that are difficult to biodegrade, such as polyvinyl chloride (PVC) and polystyrene (PS). Biotransformation can be carried out by microorganisms such as white rot fungi, which secrete enzymes that can break down the chemical bonds of plastic waste, resulting in the formation of non-toxic compounds.

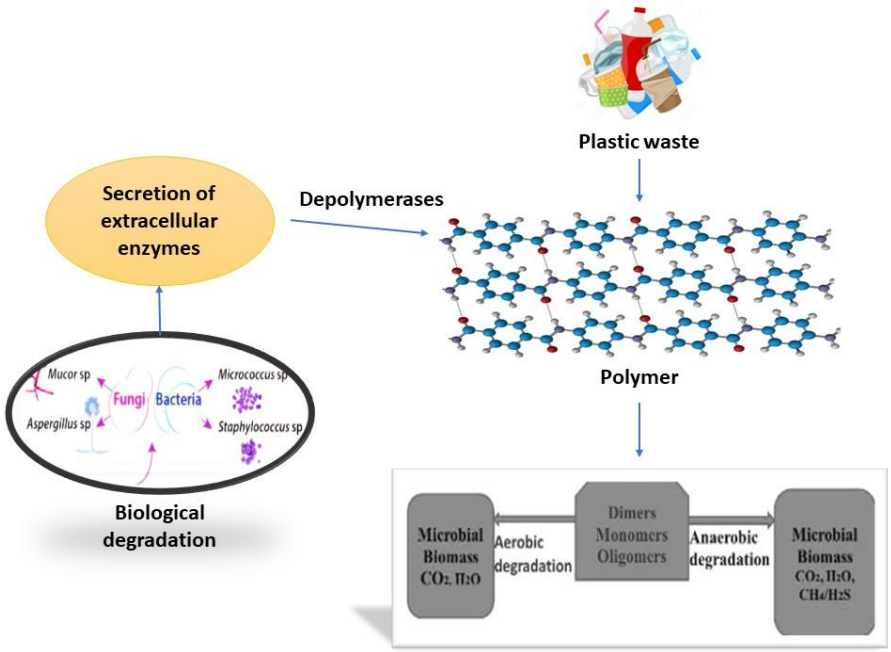


Figure 1: Process of biodegradation of plastic waste

Recent advances in microbial bioremediation for the disposal of plastic waste include the development of new microorganisms that can efficiently degrade and transform plastic waste, as well as the optimization of bioremediation processes to increase their efficiency. For example, genetic engineering has been used to develop microorganisms that can degrade specific types of plastics, such as polyethylene terephthalate (PET), which is commonly used in plastic bottles. In addition, bioremediation processes have been optimized by using pre-treatments such as mechanical shredding or chemical treatments to increase the surface area of plastic waste and make it more accessible to microorganisms. Overall, microbial bioremediation has the potential to provide an eco-friendly solution to the problem of plastic waste, and recent advances in this field have shown promising results. However, further research is needed to optimize bioremediation processes and to develop new microorganisms that can efficiently degrade and transform plastic waste.

Types of plastic waste

Plastic waste refers to any discarded or abandoned plastic material that has served its intended purpose and is no longer useful. It can accumulate in landfills, oceans, rivers, and other water bodies, causing harm to wildlife and ecosystems [16]. Plastics vary in their properties and degradation rates, and some are more environmentally friendly than others. Some plastics are easily recyclable, while others are difficult to recycle or not recyclable at all. It is essential to properly sort and dispose of plastic waste according to its type and to make efforts to reduce plastic waste in general. Plastics can be classified into various types based on their chemical structure and properties. The following are the most common types of plastic:

1. **Polyethylene (PE):** PE is a type of polymer made from the monomer ethylene. It is one of the most widely used plastics in the world and can be found in a variety of applications, including packaging, toys, pipes, and medical devices. PE is popular due to its low cost, versatility, and ease of manufacturing. It is also lightweight, moisture-resistant, and can be recycled, making it a popular choice for sustainable products. It can be produced in various forms, including high-density polyethylene (HDPE), low-density polyethylene (LDPE), and linear low-density polyethylene (LLDPE). HDPE is known for its strength, stiffness, and resistance to impact, while LDPE is known for its flexibility and transparency. LLDPE is a blend of the two and is used for

applications that require a combination of the properties of HDPE and LDPE [17,18].

2. **Polypropylene (PP):** PP is a thermoplastic polymer made from the monomer propylene. It is a versatile material with a wide range of applications due to its excellent chemical and heat resistance, high stiffness, and low density. PP is commonly used in packaging, textiles, automotive parts, yogurt cups, bottle caps, straws and consumer goods. It is also used in the medical industry for applications such as surgical instruments and medical devices. Its resistance to chemicals and sterilization makes it a popular choice for these applications. PP is often produced in a variety of forms, including homopolymer, copolymer, and random copolymer. Homopolymer is the most common form and is used in applications that require high strength and stiffness. Copolymer and random copolymer have improved impact resistance and are often used in applications that require more flexibility. PP is a highly recyclable material and is often used in products that promote sustainability. It is also lightweight, which makes it an attractive option for manufacturers looking to reduce the weight of their products [19].
3. **Polyvinyl Chloride (PVC):** PVC is a synthetic thermoplastic polymer made from the monomer vinyl chloride. It is one of the most widely used plastics in the world due to its versatility, durability, and low cost. PVC is commonly used in a variety of applications, including construction, electronics, automotive, pipes, vinyl flooring, window frames, and healthcare. In the construction industry, PVC is used for pipes, flooring, roofing, and siding due to its durability, weather resistance, and ease of installation. In the healthcare industry, PVC is used for medical tubing, blood bags, and other medical devices due to its biocompatibility and sterilization resistance [20]. PVC can be produced in different forms, including rigid and flexible PVC. Rigid PVC is used in applications that require strength, durability, and rigidity, while flexible PVC is used in applications that require flexibility, such as electrical cables and hoses. However, PVC has also been associated with environmental concerns due to the release of dioxins during its manufacturing process and when it is burned. Efforts are being made to improve the sustainability of PVC production and reduce its impact on the environment. Additionally, PVC can be recycled, although it requires specialized processing to remove additives and impurities.
4. **Polystyrene (PS):** PS is a synthetic thermoplastic polymer made from monomer styrene. It is a widely used plastic due to its versatility, low cost, and good insulation properties. PS is commonly used in a variety of applications, including packaging, disposable insulation, foam cups, disposable cutlery, and consumer electronics. Its excellent insulation properties make it a popular choice for insulation boards and packaging materials. In the food industry, PS is used for disposable food containers and packaging due to its low cost and durability. PS can be produced in different forms, including crystal and expandable. Crystal PS is a clear and rigid plastic used for products such as disposable cutlery and CD cases. Expandable PS is a foam plastic used for packaging materials and insulation. However, PS is also associated with environmental concerns due to its slow rate of decomposition and the difficulty of recycling. When disposed of improperly, PS can contribute to litter and pollution. Efforts are being made to reduce the environmental impact of PS through recycling programs and the development of biodegradable alternatives [21].

5. **Polyethylene Terephthalate (PET):** PET is a type of thermoplastic polymer that is commonly used in the manufacture of plastic bottles, food containers, and other products. It is a clear, strong, and lightweight material that is resistant to moisture and many chemicals. PET is made by polymerizing ethylene glycol and terephthalic acid or by using dimethyl terephthalate and ethylene glycol as starting materials. PET has several advantages as a packaging material, including its low cost, versatility, and recyclability. It is widely used in the food and beverage industry because it is safe for food contact and does not react with the contents of the container. PET can also be easily recycled, which makes it an environmentally friendly choice. However, PET also has some disadvantages. It is not heat-resistant and can deform at high temperatures, and it is also susceptible to UV degradation. PET can also take a long time to decompose in the environment, which can lead to pollution if not properly disposed of or recycled [22,23].
6. **Polycarbonate (PC):** PC is a type of thermoplastic polymer that is known for its strength, durability, and clarity. It is commonly used in the manufacture of a wide range of products, including electronic components, automotive parts, medical equipment, and sports equipment. PC is made by reacting bisphenol A (BPA) and phosgene, which produces a polymer that is tough, lightweight, and resistant to impact. It has a high melting point and is able to withstand high temperatures, making it suitable for use in applications where high heat resistance is required [24].

   One of the most notable properties of PC is its clarity. It is often used in place of glass in applications where impact resistance is needed, such as in safety glasses, windows, and skylights. PC is also used in the manufacture of electronic components because of its excellent electrical insulation properties. However, there are concerns about the potential health risks associated with PC, particularly regarding the use of BPA in its production. BPA is a chemical that has been linked to a range of health problems, including reproductive disorders, diabetes, and cancer. As a result, some manufacturers have begun to shift away from using PC in their products and are instead exploring alternatives such as PET or PP.
7. **Acrylonitrile Butadiene Styrene (ABS):** ABS is a thermoplastic polymer that is commonly used in the manufacture of a wide range of products, including automotive parts, toys, appliances, and piping systems. It is a copolymer made by polymerizing styrene and acrylonitrile in the presence of polybutadiene. ABS has several desirable properties, including its strength, impact resistance, and toughness. It is also resistant to heat and chemicals, making it suitable for use in harsh environments. ABS has a relatively low melting point, which means that it can be easily molded into complex shapes using injection molding or extrusion techniques. ABS is also known for its aesthetic qualities. It can be easily colored and has a shiny, glossy appearance that makes it a popular choice for consumer products such as toys and electronic devices.

   One of the disadvantages of ABS is that it can release toxic fumes when burned, which can be harmful to health. This makes it important to use proper ventilation and safety precautions when working with or disposing of ABS products. Additionally, ABS is not biodegradable, which can lead to environmental concerns if it is not properly disposed of or recycled [25].

Degradation methods of plastic waste

There are several methods available for the degradation of plastic waste, including

physical, chemical, and biological methods [26,27].

1. **Physical methods**

Physical methods of plastic degradation involve breaking down plastic waste into smaller pieces through mechanical or physical means. These methods do not involve any chemical reactions and are typically less energy-intensive than chemical methods. Physical methods of plastic degradation have some advantages over chemical methods, such as being less energy-intensive and producing fewer emissions. However, they may not be suitable for all types of plastic waste, and some methods may produce by-products that are difficult to dispose of. Additionally, physical methods may not completely break down plastic waste and may only produce smaller particles that can still pose environmental risks. Here are a few examples of physical methods of plastic degradation:

Shredding or Grinding: This involves shredding or grinding plastic waste into smaller pieces, which can then be used as feedstock for other processes, such as recycling or fuel production.

Pyrolysis: This involves heating plastic waste in the absence of oxygen to break down the long chains of polymers into smaller hydrocarbons, which can be used as feedstock for fuel production.

Hydrogenation: This involves adding hydrogen to plastic waste under high pressure and temperature, which breaks down the long chains of polymers into smaller molecules that can be used as feedstock for fuel production.

Mechanical recycling: This involves sorting and cleaning plastic waste and then mechanically processing it into pellets or flakes, which can be used as feedstock for the production of new plastic products.

2. **Chemical methods**

Chemical methods of plastic degradation involve breaking down plastic waste through chemical reactions. These methods typically require more energy and resources than physical methods but can be more effective in breaking down plastic waste into its constituent molecules. Chemical methods of plastic degradation can be effective in breaking down plastic waste into its constituent molecules, which can then be used as feedstock for the production of new plastic products. However, these methods typically require more energy and resources than physical methods and can produce hazardous by-products if not properly managed. Additionally, some chemical methods may not be suitable for all types of plastic waste. Here are a few examples of chemical methods of plastic degradation:

Depolymerization: This involves breaking down the long chains of polymers that make up plastic waste into their constituent monomers using chemical reactions. The monomers can then be purified and used as feedstock for the production of new plastic products.

Solvolysis: This involves breaking down plastic waste using a solvent, such as an acid or a base, to dissolve the polymers into their constituent molecules. The resulting solution can then be purified and used as feedstock for the production of new plastic products.

Gasification: This involves heating plastic waste in the presence of oxygen or steam to break down the polymers into their constituent gases, such as methane and carbon dioxide. These gases can then be used as fuel or feedstock for the production of new plastic products.

Hydrolysis: This involves breaking down plastic waste using water and an acid or a base to break the long chains of polymers into their constituent monomers. The resulting monomers

can then be purified and used as feedstock for the production of new plastic products.

3. **Biological methods**

Biological methods of plastic degradation involve using microorganisms, such as bacteria or fungi, to break down plastic waste. Biological methods of plastic degradation are considered more environmentally friendly than physical and chemical methods, as they use natural processes to break down plastic waste. However, these methods may require specific environmental conditions to be effective and may not be suitable for all types of plastic waste. Additionally, some methods may produce hazardous by-products if not properly managed. Here are a few examples of biological methods of plastic degradation:

Biodegradation: This involves using microorganisms to break down plastic waste into simpler compounds, such as carbon dioxide and water. Some microorganisms, such as certain bacteria and fungi, are capable of breaking down certain types of plastic, such as polyhydroxyalkanoates (PHAs) or polylactic acid (PLA).

Composting: This involves using microorganisms, such as bacteria and fungi, to break down organic waste, including certain types of plastic, into nutrient-rich compost. Composting requires specific environmental conditions, such as moisture, temperature, and oxygen levels, to be effective.

Anaerobic digestion: This involves breaking down organic waste, including certain types of plastic, using microorganisms in the absence of oxygen. This process produces biogas, which can be used as fuel, and a nutrient-rich digestate that can be used as fertilizer.

Enzymatic degradation: This involves using enzymes, such as lipases and proteases, to break down certain types of plastic, such as PET and polyurethane (PU), into smaller molecules.

Plastic-degrading microorganisms

Biodegradation of plastic waste by microorganisms involves the breakdown of the plastic polymer into smaller compounds by the action of enzymes produced by microorganisms. There are various microorganisms capable of degrading plastic waste, including bacteria, fungi, and algae. The following are some examples of microorganisms that can degrade plastic:

***Pseudomonas putida*:** This bacterium has been found to have the ability to degrade certain types of plastic. Specifically, it has been shown to be capable of degrading PET, which is commonly used in the production of plastic bottles and packaging. The degradation process involves the production of certain enzymes, such as PET hydrolase, by *Pseudomonas putida*. PET hydrolase is able to break down the long chains of polymers that make up PET into smaller, more manageable molecules. These smaller molecules can then be used as feedstock for the production of new plastic products or for other purposes, such as fuel production. Overall, *Pseudomonas putida*'s application in plastic breakdown has the potential to be a successful and sustainable way to cut down on plastic waste [28,29].

***Bacillus subtilis*:** *Bacillus subtilis* is a type of bacteria that has been found to have the ability to degrade certain types of plastic. Specifically, it has been shown to be capable of degrading polyethylene, which is commonly used in the production of plastic bags and packaging. The degradation process involves the production of certain enzymes, such as lipases and esterases. These enzymes are able to break down the long chains of polymers that make up polyethylene into smaller, more manageable molecules. These smaller molecules can then be used as feedstock for the production of new plastic products or for other purposes, such as fuel production. Overall, the use of Bacillus subtilis in plastic degradation has the potential to be an effective and environmentally-friendly method for reducing plastic waste [30].

***Aspergillus niger*:** *Aspergillus niger* is a type of fungus that has been found to have the ability to degrade LDPE types of plastic. Specifically, it has been shown to be capable

of degrading polyurethane, which is commonly used in the production of foams, coatings, and adhesives. The degradation process involves the production of certain enzymes, such as polyurethanease and esterase. These enzymes are able to break down the long chains of polymers that make up polyurethane into smaller, more manageable molecules. These smaller molecules can then be used as feedstock for the production of new plastic products or for other purposes, such as fuel production [31,32].

***Rhizopus arrhizus*:** *Rhizopus arrhizus* has been found to be effective in degrading PU plastics. Specifically, it has been shown to be capable of degrading PS, which is commonly used in the production of disposable cups, containers, and packaging materials. The degradation process involves the production of certain enzymes, such as styrene monooxygenase and laccase, by *Rhizopus arrhizus*. These enzymes are able to break down the long chains of polymers that make up PS into smaller, more manageable molecules. These smaller molecules can then be used as feedstock for the production of new plastic products or for other purposes, such as fuel production [33].

***Penicillium simplicissimum*:** *Penicillium simplicissimum* has been found to be effective in degrading PVC plastics. Specifically, it has been shown to be capable of degrading PET, which is commonly used in the production of plastic bottles and packaging materials. The degradation process involves the production of certain enzymes, such as PETase and MHETase. These enzymes are able to break down the long chains of polymers that make up PET into smaller, more manageable molecules. These smaller molecules can then be used as feedstock for the production of new plastic products or for other purposes, such as fuel production. Overall, the use of *Penicillium simplicissimum* in plastic degradation has the potential to be an effective and environmentally-friendly method for reducing plastic waste, particularly in the case of PET plastics [34,35].

***Saccharomyces cerevisiae*:** This yeast has been shown to degrade polycaprolactone (PCL) plastics. While *S. cerevisiae* is not known to have any direct involvement in plastic degradation, it is possible that it could be used indirectly in the production of bio-based plastics. Bio-based plastics are made from renewable sources such as plant materials or microorganisms like algae, and *S. cerevisiae* has been used in the fermentation of various types of plant materials for bio-based plastic production. Although there is no proof that *Saccharomyces cerevisiae* can break down plastics directly, a recent study indicates that it might be viable to use this yeast as a component of a biohybrid system for breaking down plastic [36].

***Chlorella vulgaris*:** *Chlorella vulgaris* is a type of freshwater microalgae that has been studied for its potential in bioremediation, including the degradation of two common types of plastic, i.e., PE and PVC. The degradation process involves the production of certain enzymes by the algae, which are able to break down the long chains of polymers that make up the plastic into smaller, more manageable molecules. In addition to degrading plastic, *Chlorella vulgaris* has also been shown to have potential in other areas of bioremediation, such as wastewater treatment and carbon capture. However, more research is needed to fully understand the potential of this microalga in plastic degradation and other applications [37].

Conclusion

Due to biodegradation, thermo-oxidative degradation, photodegradation, thermal, and hydrolysis processes in the ecosystem, the concentration of in the aquatic environment has grown dramatically, which is very detrimental for both marine and freshwater organisms as well as humans owing to their impact on the food chain. To completely remove these polymers from the environment, effective biodegradable strategies are required. Polymers are generally difficult to eliminate or break down due to their hydrophobic and inert properties. Microbes have also shown promise as a means of degrading these polymers, complementing physical and chemical approaches. The use of microorganisms in plastic degradation has shown promising results in laboratory settings. However, there are still challenges that need to be addressed before this method can be scaled up for large-scale industrial applications. These challenges

include optimizing the conditions for the growth and activity of microorganisms, developing cost-effective methods for producing and using the necessary enzymes, and ensuring that the by-products of the degradation process are safe and environmentally friendly. However, it is important to note that the efficiency of plastic degradation by microorganisms can be affected by various factors such as temperature, pH, nutrients, and the structure and properties of plastic waste. Therefore, further research is required to optimize the conditions for the efficient and sustainable biodegradation of plastic waste by microorganisms (Figure 2).



Figure 2: Future of biodegradable plastics

More evaluation utilizing original polymers polluted wastewater is required to assess the possible usage of microorganisms for polymer removal. Further work is needed on issues related to plastic cleanup, plastic toxicity, and microbe use. It is important to effectively advocate for the transfer of plastic polymers from wastewater to a suitable area for deposition/incineration to prevent them from entering the aquatic environment, which includes rivers and seas. Evaluating the cumulative impact on ecosystems requires coordinated long-term cleaning efforts.

References

[1] H. Sahni, N. Chopra, P. Gadhavi, The Social Rendition of Plastic Waste Management Initiatives in India, in: 2023: pp. 31–58. https://doi.org/10.1108/S2043-052320230000019003.

[2] T.D. Moshood, G. Nawanir, F. Mahmud, F. Mohamad, M.H. Ahmad, A. AbdulGhani, Sustainability of biodegradable plastics: New problem or solution to solve the global plastic pollution?, Curr. Res. Green Sustain. Chem. 5 (2022) 100273. https://doi.org/10.1016/j.crgsc.2022.100273.

[3] A.T. Williams, N. Rangel-Buitrago, The past, present, and future of plastic pollution, Mar. Pollut. Bull. 176 (2022) 113429. https://doi.org/10.1016/j.marpolbul.2022.113429.

[4] M. Bardales Cruz, E. Saikawa, M. Hengstermann, A. Ramirez, J.P. McCracken, L.M. Thompson, Plastic waste generation and emissions from the domestic open burning of plastic waste in Guatemala, Environ. Sci. Atmos. 3 (2023) 156–167. https://doi.org/10.1039/D2EA00082B.

[5] A. Gómez-Sanabria, G. Kiesewetter, Z. Klimont, W. Schoepp, H. Haberl, Potential for future reductions of global GHG and air pollutants from circular waste management systems, Nat. Commun. 13 (2022) 106. https://doi.org/10.1038/s41467-021-27624-7.

[6] T.-D. Bui, J.-W. Tseng, M.-L. Tseng, M.K. Lim, Opportunities and challenges for solid waste reuse and recycling in emerging economies: A hybrid analysis, Resour. Conserv. Recycl. 177 (2022) 105968.

https://doi.org/10.1016/j.resconrec.2021.105968.

[7] O. Dogu, M. Pelucchi, R. Van de Vijver, P.H.M. Van Steenberge, D.R. D'hooge, A. Cuoci, M. Mehl, A. Frassoldati, T. Faravelli, K.M. Van Geem, The chemistry of chemical recycling of solid plastic waste via pyrolysis and gasification: State-of-the-art, challenges, and future directions, Prog. Energy Combust. Sci. 84 (2021) 100901. https://doi.org/10.1016/j.pecs.2020.100901.

[8] A.P. Asiandu, A. Wahyudi, S.W. Sari, A Review: Plastics Waste Biodegradation Using Plastics-Degrading Bacteria, J. Environ. Treat. Tech. 9 (2020) 148–157. https://doi.org/10.47277/JETT/9(1)157.

[9] H. Sharma, D.K. Neelam, Understanding challenges associated with plastic and bacterial approach toward plastic degradation, J. Basic Microbiol. 63 (2023) 292–307. https://doi.org/10.1002/jobm.202200428.

[10] M. Brebu, Environmental Degradation of Plastic Composites with Natural Fillers—A Review, Polymers (Basel). 12 (2020) 166. https://doi.org/10.3390/polym12010166.

[11] R. Husain, N. Vikram, S. Pandey, G. Yadav, S.K. Bose, A. Ahamad, M. Shamim, K.G. Kumar, N.A. Khan, M. Zuhaib, T. Hussain, Microorganisms: An Eco-Friendly Tools for the Waste Management and Environmental Safety, in: Biotechnol. Innov. Environ. Bioremediation, Springer Nature Singapore, Singapore, 2022: pp. 949–981. https://doi.org/10.1007/978-981-16-9001-3_36.

[12] N. Tiwari, B. Garua, J.G. Sharma, Microbial diversity, interactions, and biodegradation/biotransformation of organic and inorganic contaminants, in: Wastewater Treat. React., Elsevier, 2021: pp. 341–372. https://doi.org/10.1016/B978-0-12-823991-9.00001-0.

[13] A. Priya, K. Dutta, A. Daverey, A comprehensive biotechnological and molecular insight into plastic degradation by microbial community, J. Chem. Technol. Biotechnol. 97 (2022) 381–390. https://doi.org/10.1002/jctb.6675.

[14] T. Matjašič, T. Simčič, N. Medveščck, O. Bajt, T. Dreo, N. Mori, Critical evaluation of biodegradation studies on synthetic plastics through a systematic literature review, Sci. Total Environ. 752 (2021) 141959. https://doi.org/10.1016/j.scitotenv.2020.141959.

[15] Z. Qin, J. Mou, C.Y.H. Chao, S.S. Chopra, W. Daoud, S. Leu, Z. Ning, C.Y. Tso, C.K. Chan, S. Tang, Z.J. Hathi, M.A. Haque, X. Wang, C.S.K. Lin, Biotechnology of Plastic Waste Degradation, Recycling, and Valorization: Current Advances and Future Perspectives, ChemSusChem. 14 (2021) 4103–4114. https://doi.org/10.1002/cssc.202100752.

[16] L.K. Ncube, A.U. Ude, E.N. Ogunmuyiwa, R. Zulkifli, I.N. Beas, An Overview of Plastic Waste Generation and Management in Food Packaging Industries, Recycling. 6 (2021) 12. https://doi.org/10.3390/recycling6010012.

[17] R.M. Patel, Polyethylene, in: Multilayer Flex. Packag., Elsevier, 2016: pp. 17–34. https://doi.org/10.1016/B978-0-323-37100-1.00002-8.

[18] S. Dai, C. Chen, Direct Synthesis of Functionalized High-Molecular-Weight Polyethylene by Copolymerization of Ethylene with Polar Monomers, Angew. Chemie. 128 (2016) 13475–13479. https://doi.org/10.1002/ange.201607152.

[19] Hisham A. Maddah, Polypropylene as a Promising Plastic: A Review, Am. J. Polym. Sci. 6 (2016) 1–11. https://doi.org/10.5923/j.ajps.20160601.01.

[20] S. Oberoi, M. Malik, Polyvinyl Chloride (PVC), Chlorinated Polyethylene (CPE), Chlorinated Polyvinyl Chloride (CPVC), Chlorosulfonated Polyethylene (CSPE), Polychloroprene Rubber (CR)—Chemistry, Applications and Ecological Impacts—I, in: Ecol. Heal. Eff. Build. Mater., Springer International Publishing, Cham, 2022: pp. 33–52. https://doi.org/10.1007/978-3-030-76073-1_3.

[21] K. Kik, B. Bukowska, P. Sicińska, Polystyrene nanoparticles: Sources, occurrence in the environment, distribution in tissues, accumulation and toxicity to various organisms, Environ. Pollut. 262 (2020) 114297. https://doi.org/10.1016/j.envpol.2020.114297.

[22] R. Nisticò, Polyethylene terephthalate (PET) in the packaging industry, Polym. Test. 90 (2020) 106707. https://doi.org/10.1016/j.polymertesting.2020.106707.

[23] T.N. Tsironi, S.M. Chatzidakis, N.G. Stoforos, The future of polyethylene terephthalate bottles: Challenges and sustainability, Packag. Technol. Sci. 35 (2022) 317–325. https://doi.org/10.1002/pts.2632.

[24] T. Artham, M. Doble, Biodegradation of Aliphatic and Aromatic Polycarbonates, Macromol. Biosci. 8 (2008) 14–24. https://doi.org/10.1002/mabi.200700106.

[25] P. Singh, P. Katiyar, H. Singh, Impact of compatibilization on polypropylene (PP) and acrylonitrile butadiene styrene (ABS) blend: A review, Mater. Today Proc. 78 (2023) 189–197. https://doi.org/10.1016/j.matpr.2023.01.350.

[26] A. Lee, M.S. Liew, Tertiary recycling of plastics waste: an analysis of feedstock, chemical and biological degradation methods, J. Mater. Cycles Waste Manag. 23 (2021) 32–43. https://doi.org/10.1007/s10163-020-01106-2.

[27] F. Zhang, Y. Zhao, D. Wang, M. Yan, J. Zhang, P. Zhang, T. Ding, L. Chen, C. Chen, Current technologies for plastic waste treatment: A review, J. Clean. Prod. 282 (2021) 124523. https://doi.org/10.1016/j.jclepro.2020.124523.

[28] O.F. Brandenberg, O.T. Schubert, L. Kruglyak, Towards synthetic PETtrophy: Engineering Pseudomonas putida for concurrent polyethylene terephthalate (PET) monomer metabolism and PET hydrolase expression, Microb. Cell Fact. 21 (2022) 119. https://doi.org/10.1186/s12934-022-01849-7.

[29] S. Fontanazza, A. Restuccia, G. Mauromicale, A. Scavo, C. Abbate, Pseudomonas putida Isolation and Quantification by Real-Time PCR in Agricultural Soil Biodegradable Mulching, Agriculture. 11 (2021) 782. https://doi.org/10.3390/agriculture11080782.

[30] Y. Xu, X. Liu, J. Zhao, H. Huang, M. Wu, X. Li, W. Li, X. Sun, B. Sun, An efficient phthalate ester-degrading Bacillus subtilis: Degradation kinetics, metabolic pathway, and catalytic mechanism of the key enzyme, Environ. Pollut. 273 (2021) 116461. https://doi.org/10.1016/j.envpol.2021.116461.

[31] R. Sangeetha Devi, V. Rajesh Kannan, D. Nivas, K. Kannan, S. Chandru, A. Robert Antony, Biodegradation of HDPE by Aspergillus spp. from marine ecosystem of Gulf of Mannar, India, Mar. Pollut. Bull. 96 (2015) 32–40. https://doi.org/10.1016/j.marpolbul.2015.05.050.

[32] B. Mousavi, M.T. Hedayati, N. Hedayati, M. Ilkit, S. Syedmousavi, Aspergillus species in indoor environments and their possible occupational and public health hazards, Curr. Med. Mycol. 2 (2016) 36. https://doi.org/10.18869/ACADPUB.CMM.2.1.36.

[33] B. Nowak, J. PająK, S. Labuzek, G. Rymarz, E. Talik, Biodegradation of poly(ethylene terephthalate) modified

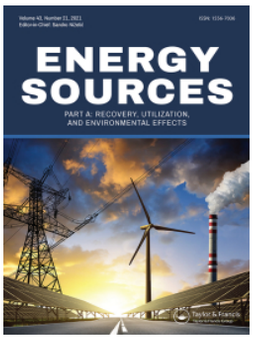
with polyester "Bionolle®" by Penicillium funiculosum, Polimery/Polymers. 56 (2011) 35–44. https://doi.org/10.14314/POLIMERY.2011.035.

[34] H. V. Sowmya, Ramalingappa, M. Krishnappa, B. Thippeswamy, Degradation of polyethylene by Penicillium simplicissimum isolated from local dumpsite of Shivamogga district, Environ. Dev. Sustain. 17 (2015) 731–745. https://doi.org/10.1007/S10668-014-9571-4.

[35] H. Sowmya, M. Krishnappa, B.T.-Environment, undefined development, undefined 2015, Degradation of polyethylene by Penicillium simplicissimum isolated from local dumpsite of Shivamogga district, Springer. (n.d.). https://link.springer.com/article/10.1007/s10668-014-9571-4 (accessed November 25, 2022).

[36] S. Jaiswal, B. Sharma, P. Shukla, Integrated approaches in microbial degradation of plastics, Environ. Technol. Innov. 17 (2020) 100567. https://doi.org/10.1016/j.eti.2019.100567.

[37] P.K. Akao, H. Mamane, A. Kaplan, I. Gozlan, Y. Yehoshua, Y. Kinel-Tahan, D. Avisar, Iohexol removal and degradation-product formation via biodegradation by the microalga Chlorella vulgaris, Algal Res. 51 (2020) 102050. https://doi.org/10.1016/j.algal.2020.102050.



Taylor & Francis
Taylor & Francis Group

Energy Sources, Part A: Recovery, Utilization, and Environmental Effects

ISSN: (Print) (Online) Journal homepage: https://www.tandfonline.com/loi/ueso20

Review on advancement in solar and waste heat based thermoelectric generator

Sanjeev Kumar Bhukesh, Suresh Kumar Gawre & Anil Kumar

To cite this article: Sanjeev Kumar Bhukesh, Suresh Kumar Gawre & Anil Kumar (2023) Review on advancement in solar and waste heat based thermoelectric generator, Energy Sources, Part A: Recovery, Utilization, and Environmental Effects, 45:2, 4982-5002, DOI: 10.1080/15567036.2023.2206370

To link to this article: https://doi.org/10.1080/15567036.2023.2206370

Published online: 02 May 2023.

Submit your article to this journal

View related articles

View Crossmark data

Full Terms & Conditions of access and use can be found at
https://www.tandfonline.com/action/journalInformation?journalCode=ueso20

ENERGY SOURCES, PART A: RECOVERY, UTILIZATION, AND ENVIRONMENTAL EFFECTS
2023, VOL. 45, NO. 2, 4982–5002
https://doi.org/10.1080/15567036.2023.2206370

Taylor & Francis
Taylor & Francis Group

Check for updates

Review on advancement in solar and waste heat based thermoelectric generator

Sanjeev Kumar Bhukesh[a], Suresh Kumar Gawre[b], and Anil Kumar[c,d]

[a]Energy Centre, Maulana Azad National Institute of Technology, Bhopal, India; [b]Deptartment of Electrical Engineering, Maulana Azad National Institute of Technology, Bhopal, India; [c]Deptartment of Mechanical Engineering, Delhi Technological University, Delhi, India; [d]Centre for Energy and Environment, Delhi Technological University, Delhi, India

ABSTRACT

Clean energy production has become flagship program of all countries as per the agenda of UNFCCC COP-27. Thermoelectric generator (TEG) has become popular candidate for Green energy. This paper reviews the principle of thermoelectricity, developmental history of solar and waste heat-based thermoelectric power generation, thermoelectric hybrid systems, thermoelectric materials (silicon, ceramics and polymers) with conventional, segmented and cascaded arrangement, operating temperature range, figure of merit, popular modeling and simulation tools, environmental impact, future improvements, exploitation of TEGs in various fields starting from low-power applications (wearable devices) to high-power applications (automotive engines and aerospace). This paper also handles performance of various solar concentrators (parabolic dish, Fresnel lens, solar furnace, etc.) with their optical concentration, heat recovery TEG systems and potential of TEG to generate electricity from human body. This review helps the academia, researchers, and industrialist with deep insights into customization of TEG projects in qualitative and quantitative ways before actual realization.

ARTICLE HISTORY
Received 19 October 2021
Revised 13 March 2023
Accepted 13 April 2023

KEYWORDS
Thermoelectric generator; TE-material; solar; operating-temperature; modeling-simulation; environment

Introduction

Pollution and emission of heat and greenhouse gases result in global warming caused by using conventional technologies. Aim of availing green and clean energy alternatives could be better served by converting the thermal energy into valuable electrical energy, that is, via thermoelectric power generation. The key elements of a TEG are n-type as well as p-type legs. Legs are made up of TE material, alternately connected, that is, thermally in parallel and electrically in series. Segmented TE legs provide more conversion efficiency and output power than simplex (Tian et al. 2015). The figure of merit of TE element is very important factor (Xi, Luo, and Fraisse 2007).

First of all, heating source is the primary concern in concentrating TEG. The manufacturer tries to optimize the concentrator for high optical concentration (0.1×-1000×) to achieve maximum efficiency because the concentrator's produced heat at receiver drives TEG and losses at the receiver can be calculated by developing a numerical model. By using available selective surfaces and advanced thermoelectric materials, 13% thermoelectric conversion efficiency is exhibited for this high concentration. In case of lens type concentrator, that is, the refracted solar thermoelectric generator (RSTEG) the refraction of the phase change material gets changed, leading to change in transmittance and hence refraction for sunlight gets changed and results 60–86% peak conversion efficiency. Another important heat source is solar pond. In solar pond, TEG converts the available heat present at the low

CONTACT Anil Kumar anilkumar76@dtu.ac.in Department of Mechanical Engineering, Delhi Technological University, Delhi 110 042, India

© 2023 Taylor & Francis Group, LLC

convective zone (LCZ) and produces electricity. A TEG system with 2 cold sinks and four TEMs provides 11W from solar pond (Chang, Guan, and Yang 2013).

Waste heat from automobiles, furnaces, and so on, can also be heat source for TEG. TEGs have been employed in automobiles for many reasons, like reducing carbon emissions and enhancing the engine's overall efficiency. Challenges and opportunities for Electric Turbocharged (ETC) engine and TEG systems used in compact cars powered through a turbocharged SI engine and an analysis for investigating the extraordinary characteristics attained by the ETC and TEG were analyzed (Arsie et al. 2015). Experimental analysis for heavy-duty diesel engine (DE) and TEM test rig was done over the exhaust gas recirculation (EGR) path, and a good agreement was observed with a simulated one. Both the models were equipped with the prototype TEG and improved efficiency was achieved (Lan et al. 2018).

Along with transmittance and reflectance of concentrator, properties of the absorber play significant role in determining overall efficiency of the system. Spectrally selective ($\varepsilon = 0.13$ and $\alpha = 0.954$) solar absorber integrated with Fresnel lens produces good amount of heat. TE module's efficiency of conversion significantly affects the overall system efficiency as well as the cost. To attain high efficiency, it is practically approached to generate electrical power by utilizing thermal energy with cogeneration system (Sathawane et al. 2014). Regarding simulation and modeling, the FEA method through ANSYS, COMSOL Multi-physics 5.4 and MATLAB can be used for numerical simulation and modeling of TEG under steady state. Non-uniform transient heat flux, waste heat flux, solar energy flux can be simulated through ray tracing Soltrace software (Shittu et al. 2020). Various advantages of TEG are silent operation, the operating life span of TEG is very long (20–25 years), and does not produce any hazardous by-products (Tellurex 2010). It can be extensively used in isolated places and remote areas. Numerous developments have been made.

The researchers cover only one or some aspects of thermoelectric technology in various studies; however, this article aims to highlight updated research oriented information covering all aspects of thermoelectric system advancement in holistic approach. This review will help the researchers and industries to customize their TEG project in qualitative and quantitative ways as per the climatic conditions of their region, solar radiation in their region, compatibility, availability of waste heat from automobiles and industries, hybridization of thermoelectric technologies, hot side temperature, materials, modeling and simulation techniques, and TEG applications.

in Section 1 introduction is discussed, Section 2 describes thermoelectricity concept, Section 3 covers knowledge about solar energy-based TEGs, Section 4 emphasizes waste heat recovery through TEGs, Section 5 covers waste heat recovery from human body, Section 6 throw light on hybrid TEG, Section 7 describes the operating temperature range, Section 8 elaborates various modeling and simulation techniques for TEG systems, Section 9 explains environmental impact of TEG and its applications and Section 10 concludes with remarks discussion.

Thermoelectricity concept

Electrical energy can be produced directly from heat received by renewable and nonrenewable sources through TEG with the Seebeck effect, which is termed thermoelectricity. A commercial TEG module is shown in Figure 1(a) and conduction of charge carrier in single stage TEG is shown in Figure 1(b). The conduction of the majority of charge carriers in n-leg, that is, electrons is shown in Figure 2(a) and majority of charge carriers in p-leg, that is, holes are shown in Figure 2(b).

Seebeck effect is the voltage induction between two junctions of different conductors kept at different temperatures (Hamid Elsheikh et al. 2014). When temperature gradient is applied to a conductor or semiconductor, voltage is developed, which depends on the conducting material's various qualities. Seebeck tried various materials, including the natural semiconductors ZnSb and PbS.

The constituents of TEG are thermopiles. N-number of thermocouples (TCs) are integrated electrically in series and thermally in parallel to form each thermopile, as shown in Figures 3 and 4(a).

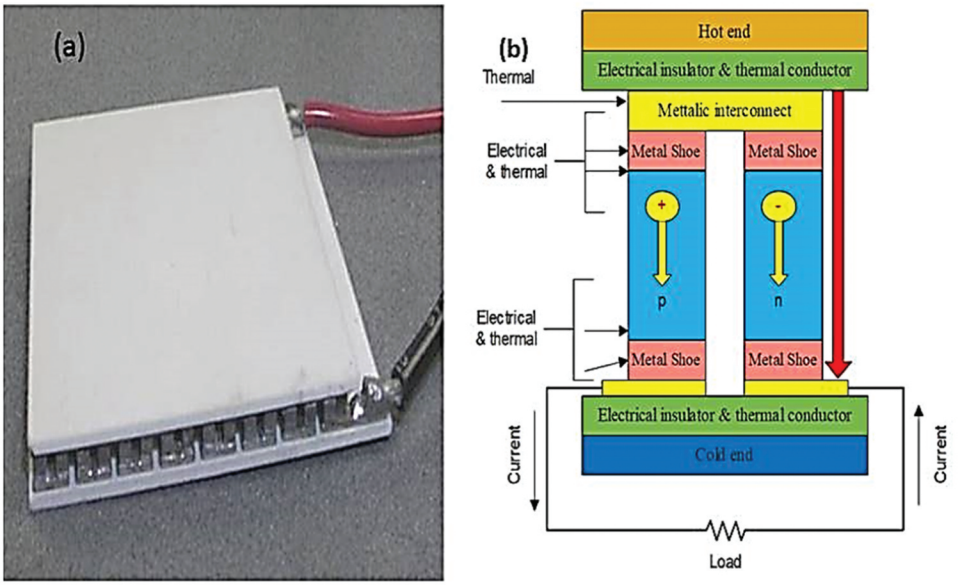


Figure 1. (a) Thermoelectric generator module (b) Conduction in single-stage (n-leg and p-leg) TEG.

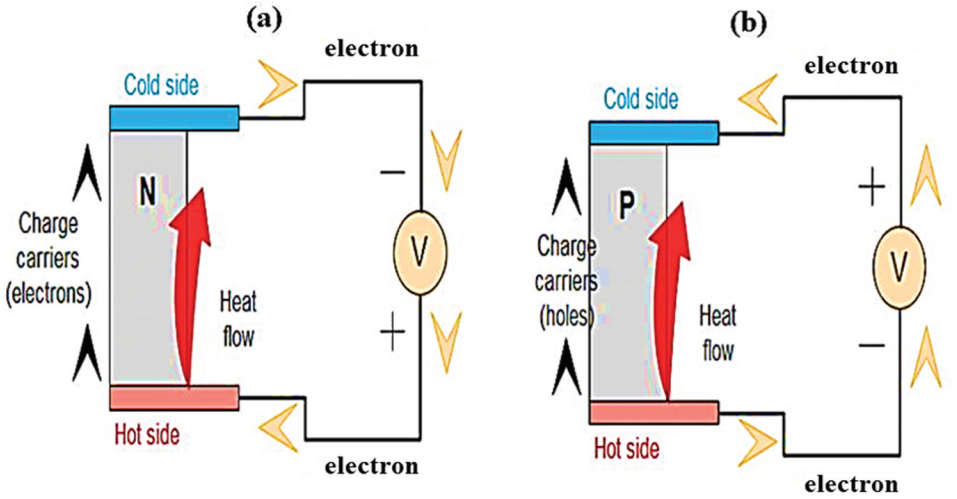


Figure 2. (a) Charge career flow in n-type leg (b) Charge career flow in p-type leg (Tellurex 2010).

Instead of one thermopile, several thermopiles are connected to enhance the output power. Two different materials, whose Seebeck coefficient is opposite, are joined end-to-end to form one thermocouple. When thermocouple joints are exposed to a temperature difference $\Delta T = T_{hot} - T_{cold}$, the Seebeck effect causes electric voltage production. The expression of voltage and power can be given as (Aswal, Basu, and Singh 2016):

$$V_{out} = N\alpha_{AB}\Delta T \tag{1}$$

where N is the integrated thermocouples, the Seebeck coefficient for a thermocouple constituted by two materials A and B can be termed as $\alpha_{AB,}$ and can be calculated as ($\alpha_{AB} = \alpha_A - \alpha_B$), the internal resistance of each thermocouple is added. Thus total internal resistance becomes proportional to

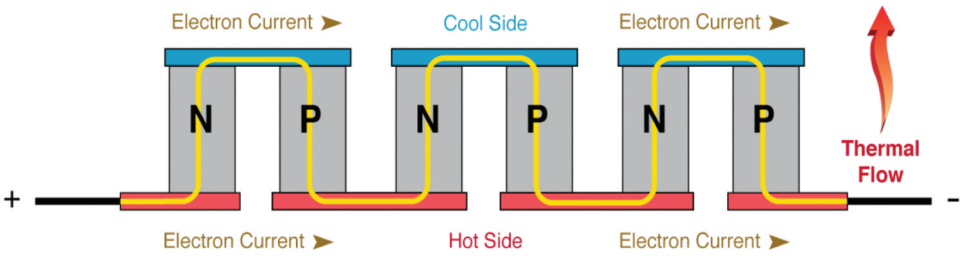


Figure 3. Charge career flow in multi-stage TEG (Tellurex 2010).

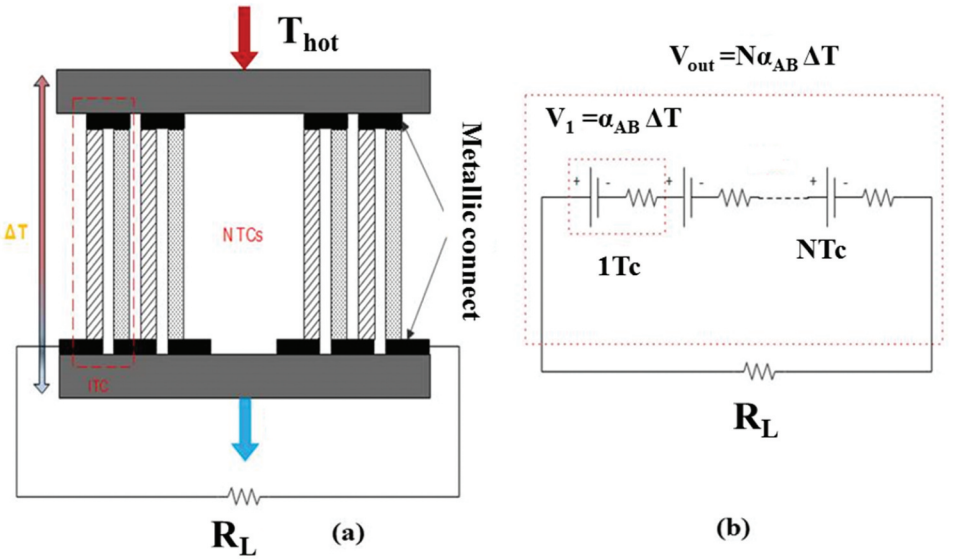


Figure 4. (a) Principle of working (b) Electrical circuit of TEG.

N. Although an increasing number of thermocouples (TCs) lead to increase in voltage yet it will increase the total internal resistance as shown in Figure 4(b). TEG's total internal resistance R_{TEG} can be computed as:

$$R_{TEG} = N\left(\frac{\rho_A L_A}{S_A} + \frac{\rho_B L_B}{S_B} + 2\frac{\rho_C L_C}{S_C}\right) \tag{2}$$

$\rho_A, \rho_B and \rho_C$ stand for electrical resistivity of A, B and metal contact. Heat flows through the lengths of arms (L_A and L_B) of thermocouples and the length of metal contact L_C. Cross-sectional areas of A, B and metal contacts are shown as S_A, S_B and S_C. Total output power (P) delivered by TEG can be expressed as:

$$P = V_{out}^2 R_L / (R_{TEG} + R_L)^2 \tag{3}$$

where R_L and R_{TEG} stand for resistance of external load and internal resistances of TEG as shown in Figure 4(b). V_{out} is the output voltage. The TEG can transfer maximum power output if load resistance R_L matches the total internal resistance R_{TEG} of the TEG. Expression of the maximum output power can be given as:

$$P_{max} = \frac{V_{out}^2}{4R_{TEG}} \tag{4}$$

Instantaneous efficiency of TEG and Figure of merit:

$$\eta_{TEG} = \frac{T_h - T_c}{T_h} \times \frac{\sqrt{(1+ZT)} - 1}{\sqrt{(1+ZT)} + \frac{T_c}{T_h}} \tag{5}$$

$$ZT = \left(\alpha^2 \sigma T\right)/k \tag{6}$$

where $\alpha = \frac{\Delta V}{\Delta T}$ is the Seebeck coefficient, Δv and ΔT are change in voltage and change in temperature between hot and cold side, σ is the electrical conductivity, k is the thermal conductivity combination of k_e and k_l the electrical and lattice thermal conducivity, respectively, and T is the average temperature $T = \frac{T_h + T_c}{2}$, Z is the effective figure of merit across the temperature gradient, $\frac{T_h - T_c}{T_h}$ is Carnot efficiency.

State-of-the-art solar energy-based TEG

To meet the energy demand in India, concentrated solar power can play a unique role. Solar flux at TEG's hot end can be changed through various collector options available like parabolic dishes, fresnel lens, parabolic troughs (Sundarraj et al. 2016), solar furnaces (Olsen et al. 2013) and flat plates (Kraemer et al. 2012). Solar TEG efficiency is the product of the efficiency of TEG, optical efficiency and thermal efficiency. For the materials of ZT = 1, about 100°C temperature difference, a 5% efficiency is attained by the state-of-the-art solar TEG systems. Conversion efficiency is the major commercial barrier for solar TEG technologies that is much lower than other solar electricity technologies, such as 18% efficiency exhibited by solar cells. In the future, efficiency with higher conversion rate is expected by enhancing the solar collector design and enhancing the figure of merit (ZT) of TE materials (Hamid Elsheikh et al. 2014).

Parabolic dish collectors

Solar dish collector is defined as a "concentrating solar collector that reflects optically and directs the sun's solar energy over a small receiving area through strips of metals (anodized aluminum), as shown in Figure 5. Depending on the dish's location and size, it may lead to 100–1000°C temperature generation (Kraemer et al. 2012). Targeting upon the systems with high optical concentrations of 0.1–1000 using multiple material systems of dish strip, a 35°C temperature difference and 5.5W output power, 13% conversion efficiency is possible in solar TEGs (Maslamani Abdu Idris Omer and A 2014).

The CSP is undoubtedly a unique renewable technology. Moreover, the focus should be on a solid-state device that converts electrical power from a heat flux, that is, a TEG works on Seebeck effect. Table 1 presents the research of various authors who dedicatedly worked on optimizing and designing the CSP system, which is assembled as the TEG-Concentrator that uses various material systems to hike the efficiency to its maximum over a difference in the temperature range.

In a parabolic dish collector, if radiations (DNI) are reduced from 950 to 430 W/m^2, temperature reduces from 602K to 375K means radiation reduction of 520 W/m^2 leads to temperature reduction of 227K. A higher concentration of 0.1–1000 can generate a good amount of power (5.5 W) at 35°C temperature difference at 13% of conversion efficiency. Solar pond-based thermoelectric plant shows maximum potential of generating 4.384 kWh/year m^2, while Cogeneration system with Fresnel lens exhibits better overall system performance, providing 1.4 W electrical power and 76.1 W thermal power. Annular TEG is capable of generating 50% more power as compared to normal flat plate TEG. Solar annular TEG (SATEG) produces power output at 5.02% combined system efficiency.

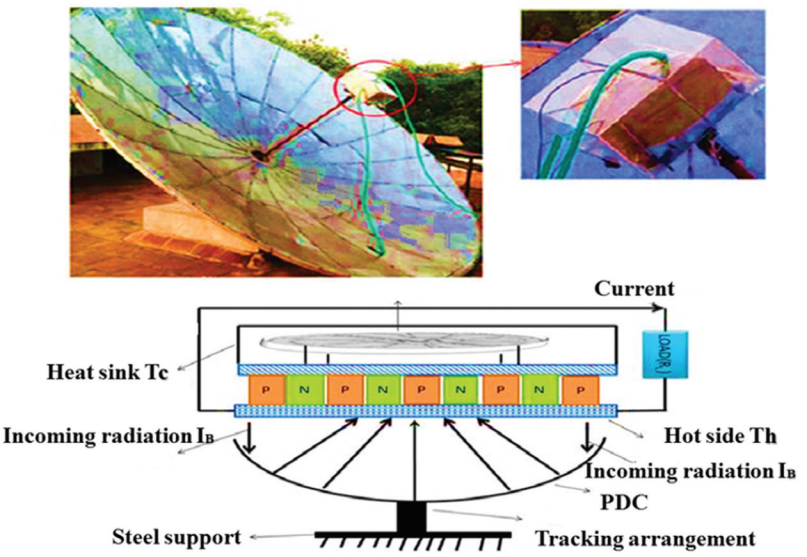


Figure 5. Parabolic dish concentrated solar thermoelectric power generation (Muthu, Shanmugam, and Veerappan 2014) .

Table 1. Various CSP (concentrated solar power) technologies for TEGs.

TEG using concentrating solar power (CSP)	Methodology	Research Findings	Ref.
Exergy and energy analysis of annular TEG systems based upon heat pipe	Thermal modeling of annular thermoelectric generator	Solar TEG's combined system exergy, electrical exergy, and power output are 5.02%, 2.63%, and 1.92W at 1000W/m^2 of solar radiation and 308K of $T_{water.}$	(Manikandan and Kaushik 2016; Remeli et al. 2015)
Solar parabolic dish TEG	Solar parabolic dish	Maximum solar beam radiation = 950 W/m^2 maximum efficiency= 0.78%, solar beam radiation= 431 W/m^2, minimum overall efficiency= 0.22%	(Shanmugam, Veerappan, and Eswaramoorthy 2014)
Solar TE cogenerator with evacuated tube solar collector	Cogenerating electrical power as well as thermal energy together in single system.	Hybrid system enhances overall efficiency of the TEPG system.	(Sathawane et al. 2014)
Experimental study on solar parabolic dish TEG	A satellite dish antenna is used with a concentrator surface made of polished Al sheet.	Solar beam radiation 950W/m^2, maximum temperature= 602K and at 430W/m^2 minimum temperature = 375K. The maximum output power =11W.	(Eswaramoorthy, Shanmugam, and Veerappan 2013)
Development of STEG	Systems with high optical concentrations of 0.1–1000X, which utilize multiple material systems	The system produced a 5.5W of electric power at 35°C temperature difference.	(Maslamani Abdu Idris Omer and A 2014)
Effect of non-uniform and transient heat flux over STEG	PCM (phase change material)	When the height of the PCM is hiked by 5–20 mm then the STEG's efficiency, temperature difference and peak power output fall by 32.87%, 30.71% and 52.11%	(Nguyen and Pochiraju 2013)
Refraction-assisted STEG	Based on PCM	Compared with the typical STEG, the RTEG's maximum energy conversion efficiencies are 86% and 60% higher at the 1.5kW/m^2 and 1kW/m^2 solar intensities, respectively.	(Kim et al. 2016)
Performance of thermoelectric generators	Transient model couples with solar pond	4.384 kWh/year m^2 at 15% heat extraction of the average horizontal solar radiation produced during the year while having 80°C temperature of average LCZ. Overall 'η_t' is within the range of 1% to 1.5% from extracted heat.	(Ding, Akbarzadeh, and Date 2016)

Fresnel lens

Initially, solar concentrator Fresnel lens was developed with concentrating photovoltaic applications. To face the sun, the "solar concentrator Fresnel lens" design is made as Plano-convex to face the integrated photovoltaic cells. These lenses are also utilized in solar furnace as a concentrator for solar energy. This configuration design is made to collect parallel lights over a single spot. Fresnel lenses of shorter focal length are brought in an application in detectors or/and sensors. Regarding Fresnel lens-TEG integration, TEGs are coupled with Fresnel lenses to concentrate the sunlight on hot side to produce electricity (Olsen et al. 2013). The electricity generation from TEG through energy received from sunlight is implemented based on solar radiation concentration for attaining higher hot side surface for efficiency of higher conversion order. Fresnel lens promises this up to a greater extent. To achieve high-efficiency STEGs, higher optical concentration will be effective. Hence this approach can be utilized in solar thermal and concentrated photovoltaic applications. These comprise parabolic troughs, parabolic dish, heliostat conjunction within the system used at central receiving and Fresnel lenses. In a cogeneration system fresnel lens-based TEG produces power at 18.39% (Banakar et al. 2017). The optical efficiency, the needed tracking system and the level of concentration attained are the pertinent characteristics that are used in STEGs. Optimizing concentrating lenses, thus improving optical concentration, 7.4% of peak efficiency is attained for concentrated TEG (Figure 6) (Kraemer et al. 2016). A design that uses a phase change lens was developed that provides solar energy with twice focus strength (Atouei et al. 2018). This mechanism provided efficiency of 60% for peak energy conversion of RSTEG, which is higher in comparison with the typical STEG by 86% at 1 kW/m^2 and 1.5 kW/m^2 solar intensities, respectively (Kim et al. 2016).

Solar furnace

Solar furnace is designed to produce high temperature by capturing sunlight and applying industries through a curved mirror that works as a parabolic reflector. The curved mirror concentrates the light over a focal length. Focal length can reach up to 6330F (i.e. 3500°C) and generated heat can produce nanomaterial, hydrogen fuel, melting steel and electricity generation. To attain high temperatures, solar energy is concentrated inside the solar furnace. It constitutes heliostats or parabolic mirrors for concentrating light over a focal length. It has a mechanical structure and complex optical structure

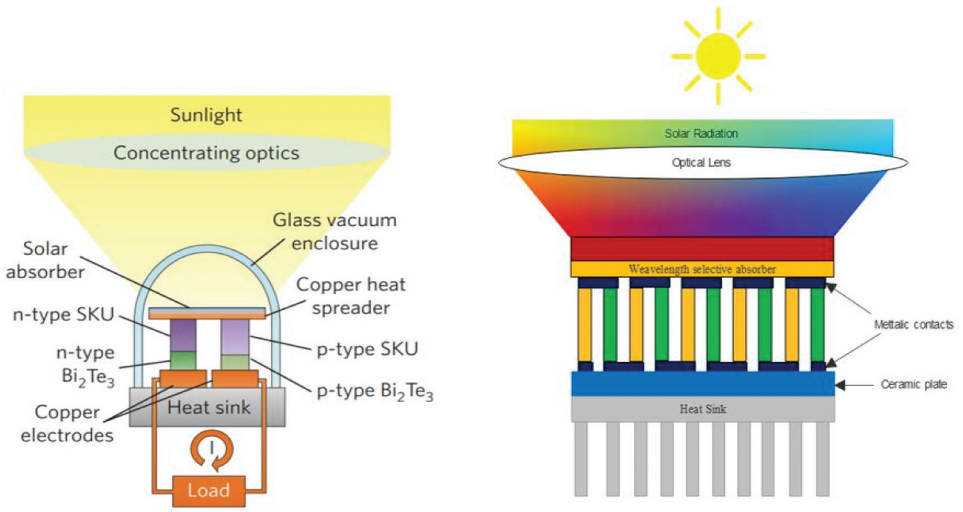


Figure 6. Thermoelectric power generation through optical concentration (Kraemer et al. 2016).

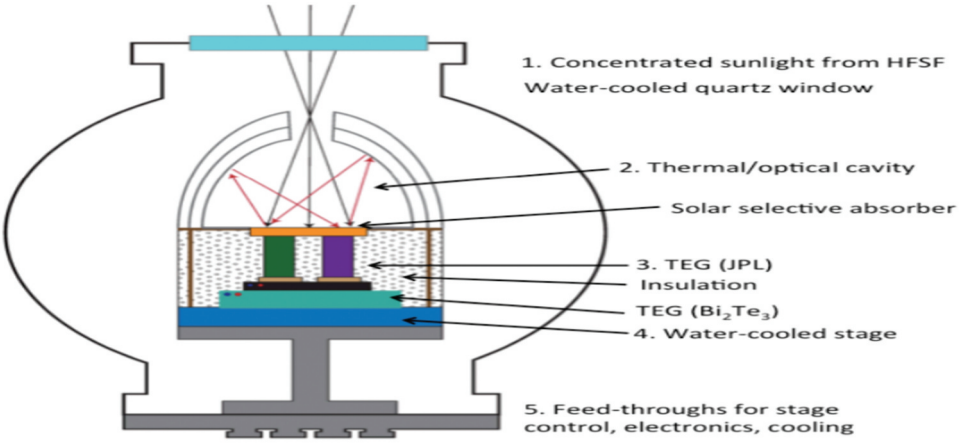


Figure 7. Highly efficient TE power generation through high flux solar furnace (HFSF) (Olsen et al. 2013).

with a system that is controlled automatically. Solar furnace principle is applied to solar water pasteurization, solar powered barbecues, and low-cost solar cookers.

The potential of STEGs can be observed by higher converting rate of solar energy, that is, higher efficiency of 15% (Goupil et al. 2016). Lifetime analysis and performance analysis of STEGs were made for optimizing prototype model and were also tested at NREL's HFSF (Figure 7) (Olsen et al. 2013).

From Table 1, it is quite clear that parabolic dish type concentrators (efficiency-13%) are less efficient than Fresnel lens and solar furnace because fresnel lens-based TEG produces power at 18.39% while higher efficiency of 15% is achieved via solar furnace-based TEG.

Waste heat recovery through TEGs

Many waste heat recovery methods can recover the waste heat and thus decrease overall energy consumption of any power-consuming device/system (Jouhara et al. 2018). Durability, scalability, small size, silence, no wear-tear, corrosion, and low maintenance are the desirable attributes for the waste heat recovery system compared to any other recovery methods where these desirable attributes are unavailable. TEG system possess these key attributes due to the absence of chemical reaction and having no moving parts (Orr et al. 2016). Recuperative burner integrated with TEG possesses all these attributes. Waste Heat recovery through Recuperative burner is shown in Figure 8. Heat exchanger is an important part of burner, It's surface absorb heat from the gases that pass through the burner's body. TEG is fixed on the surface of heat exchanger to absorb the heat to produce electricity.

Waste heat recovery through TEG also protects environment indirectly. Environmental protection issues and the global energy crisis have been reasons for the increased demand for energy recovery technologies for a long time. Heat recovery ventilation, heat recovery steam generators, and water heat recycling are the techniques for energy recovery. Various researchers use waste products (smoke) of an automotive exhaust pipe in power and energy harvesting systems through TEGs to convert heat into electricity in their experiments shown in Table 2.

Waste heat recovery through TEGs from human body

Wearable electronics can be powered by utilizing the low temperature continuous heat of human body. Such type of development has been in continuation for the last decade (Musleh et al. 2020). Therefore testing and research on 3D printed, nanostructure-based, thin film flexible TEG modules are in trend in the research World to fulfill the demand of the garment industry and other industries (Jaziri et al. 2019). The human body-TEG and TEG-air thermal contacts are the main hurdles in

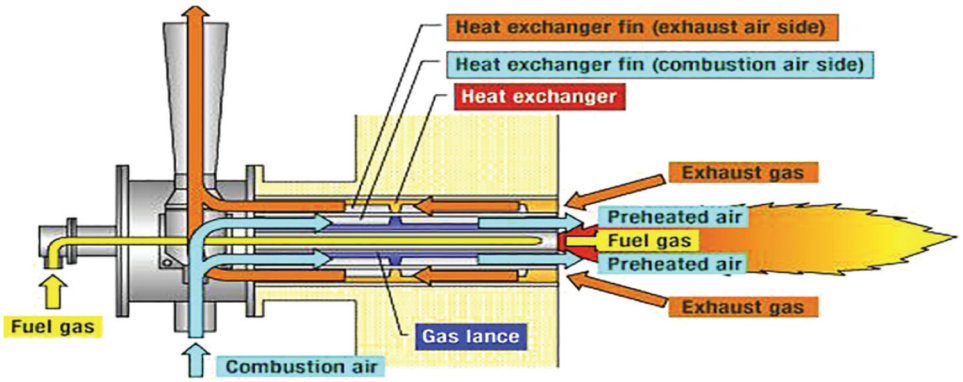


Figure 8. Waste heat recovery through recuperative burner (Jouhara et al. 2018).

Table 2. Waste heat recovery from different systems through TEG.

TE waste heat recovery technology studies	Methodology	Research findings	Ref.
Thermoelectric power generation used by Energy harvesting system for the applications of automobiles	Use of heat pipe and TEG for waste heat	There is a significant rise in the rate of maximum power output and the heat transfer of TEG when the ratio of lower duct's mass flow rate is lower than the upper duct's mass flow rate (increase in the effectiveness of the heat pipe from 67.9% to 72.4%)	(Date et al. 2014)
Exergy and Energy analysis of an advanced ATEG on the basis of the cook-stove	Thermodynamic modeling of ATEG when atmospheric temperature is considered as 30°C.	With time, the combustion air temperature passes over the TEG's annular fins because a variation in the temperature of cold junction is also seen within the range of 30 to 150°C.	(Duraisamy et al. 2019)
Harvesting body heat for generating power, wearable TEG is used	Miniaturized accelerometer	At ΔT=50 K, the developed wearable TEG generates an open-circuit voltage of 37.2 mV and has low internal resistance (1.8 Ω). 16.7μW/cm^2 and 192.6μW are the calculated corresponding power density and output power, respectively.	(Wang et al. 2018)
With humidified flue gas, exergy and energy analysis of TEG system	Using humidified flue gas as heat source	Efficiency in respect of exergy, at beginning goes down and then hikes up as the module area increases.	(Atouei et al. 2018)
Development of stove-powered TEG	Cooking/water heating stove design.	Batteries are available with the electrical power of 5 W. for thoroughly analyzing the temperature of the stove, effectiveness of the heat sink and the TE's location; theoretical analysis is required, especially in respect of the cooling and combustion system via numerical simulation.	(Goupil et al. 2016)

developing a flexible TEG module that makes the temperature difference between hot and cold sides very low (Champier 2017).

TEGs provide sufficient energy from living beings. From human body, temperature difference of 50 K is obtained to operate wearable TEG. Also, the solar cells of human beings are outperformed by them. At 22°C temperature and ZT = 1, available power in unobtrusive devices mounted over the human body is limited to **10 mW**, as shown in Figure 9. In contrast, large animals such as cattle can provide several mili watts by placing TEG on their body.

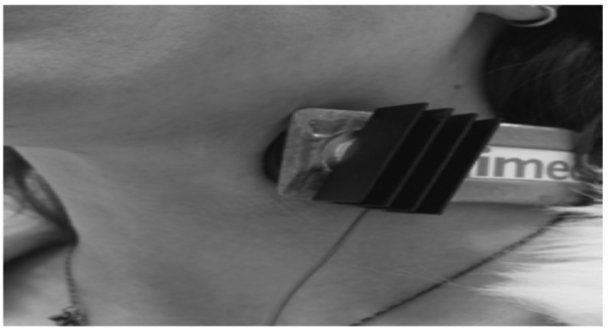


Figure 9. Extracted heat from body utilized in TEG (Leonov and Vullers 2007).

However, the thermoelectric scavengers will compete with the scavengers equipped with batteries only in terms of the fabrication cost, which decreases dramatically in TEG (Leonov and Vullers 2007).

Table 2 shows that low-grade heat (waste heat) can also be utilized to produce electricity, as from table lamp 10W heat produces 1 mW electrical power via TEG. From the human body at $\Delta T = 50K$, 192.6 μW power is generated, which means humans and other animals can provide significant power. Cookstove-based TEG possesses good qualities to be the best candidate for electrical power generation, especially for rural areas. However, to figure out the size and location where TEG is to be mounted, module rating, load value and numerical simulation are required. Nowadays, cookstove TEGs are working on an average TEG efficiency of 5%. Even though the power generation is low in a marine engine, the complete assembly of no. of TEGs will produce significant power.

Hybrid TEG

Many researchers have thoroughly studied hybrid solar TEG (HSTEG) systems to improve both electrical and thermal efficiency (Li et al. 2014). The performance, stability, and higher efficiency explain hybrid solar systems' current interest in contrast with individual solar devices. Hybrid solar photovoltaic-TEG system exhibits electrical efficiency of 15.6% and 12.2%, respectively.

Photovoltaic system is the most widely studied and used, and the simplest system is the photovoltaic panel attached to a heat extractor with running air or water. Crystalline silver solar photovoltaic module with 14% conversion efficiency is brought into use. It cools down the temperature by extracting heat (Goupil et al. 2016). TEG-PV system is observed as the most promising hybrid system. To utilize a broad spectrum of solar energy, photovoltaic and thermoelectric systems are integrated to develop the power system Figure 10. "Spectrum beam splitting" technique is applied, using higher frequency (short wavelength) radiations to produce electrical energy from PV cells, While thermal energy of moderate to high grade is produced by utilizing long-wave radiations, this heat can be used by thermoelectric system to produce electricity, as shown in Figure 10. In another solar hybrid system 6 serially connected Bi_2Te_3 TEG modules generate 20W of electrical energy and byproduct 200W of thermal energy stored in water with a temperature of around 50 °C. This system utilizes running water for cooling purpose, which maintains 50°C temperature at cold side. In the countries where abundant solar radiations are available throughout the year like India, Mexico, china and West Asian countries, the photovoltaic/thermal systems can be replaced by these hybrid systems. Performance of different combinations of hybrid TEG is concluded in Table 3.

Hybrid systems are also good combination. Hybrid PV-TEG system increases overall efficiency of the system by increasing the temperature and decreasing the losses. In a parabolic trough-based hybrid solar TEG, we found significant improvements in the electrical as well as in thermal efficiency, like

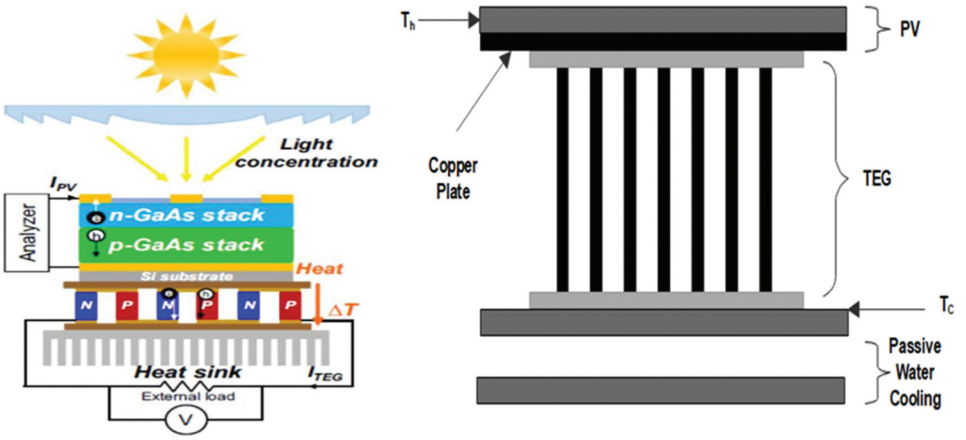


Figure 10. Hybrid concentrated photovoltaic and thermoelectric system and schematic of different layers (Kil et al. 2017).

Table 3. Performance of different combinations of hybrid TEG.

Hybrid TEG study	Methodology	Research findings	Ref.
TEGs with solar hybrid systems	Hybrid system with non-concentrated sunlight	PV operating at higher temperature with TEG's inclusion within the hybrid concentrating system will improve the system's electrical and thermal stability by hiking the temperature and decreasing the loss.	(Li et al. 2014)
Theoretical analysis and comparison of Solar PV-TGS were done in different conditions	For the analysis of PV-TGS (Photovoltaic- Thermoelectric Generation System) performance of the 1D steady state model, MATLAB software was used.	With the increase in light intensity, Power P increases but η decreases. But even having lower T_{cell} in photovoltaic- Thermoelectric Cooling system (PV-TCS) compared to PV-TGS, it has both lower η as well as P.	(Weinstein et al. 2014)
Hybrid solar TEG's performance analysis	A parabolic trough collector is used in the vacuum-enclosed HSTEG for concentrating sunlight on a solar-selective coated TEG.	Estimated highest electrical efficiency of the V-HSTEG and B-HSTEG is 15.6% and 12.2%, respectively and 60.3% and 61.9% are the corresponding thermal efficiency.	(Sundarraj et al. 2016)
Thermoelectric generator system and photovoltaic cell are applied with the algorithm of lock-on mechanism MPPT.	MPPT algorithm/fixed step hill climbing algorithm	SEPIC converter with input source algorithm is better and fast as compared to algorithm of conventional fixed step hill climbing	(Goupil et al. 2016)

electrical efficiency in V-Hybrid Solar TEG (HSTEG with evacuated glass tube) and B-HSTEG (without evacuated glass tube) is 15.6% and 12.2% as shown in Table 3.

Selection of TEG according to operating temperature

TEG can further be classified based on operating temperature range: cold side Temperature; 67–300°C, hot side temperature; 147–1000°C, making it versatile for exploitation from multiple heat sources.

Low temperature (<250 °C) TEGs

Ovens, air compressors, furnace doors, electronic circuits, refrigeration/air-conditioning condensers are the major sources in this temperature range. For the materials and metallic-buffer interconnection, the low temperature range was reported for TEG (<250°C) (Aswal, Basu, and Singh 2016). At low

Table 4. Various low temperature range TE material.

Thermo elements type	T_h/T_c	Interconnect material	Buffer layers at the ends	Efficiency (%)	Remarks	Ref.
p-type Bi_2Te_3	150°C/ 24°C	N/A	Nickel	5.8	Thermo electric and efficiency measurements under large temp. difference	(Olsen et al. 2013)
$MgAg_{0.965}Ni_{0.005}Sb_{0.99}$	245°C/ 20°C	Silver	N/A	8.5	High thermoelectric conversion efficiency of Mg-Ag-based materials	(Goupil et al. 2016)
p-type poly[Cu_x(Cu-ett)] and n-type poly[Na_x(Ni-ett)]	147°C/ 67°C	At hot end aluminum is mounted and at cold end silver is mounted	Gold	N/A	Organic thermoelectric materials	(Goupil et al. 2016)

temperature range (100–250°C), bismuth telluride/selenite exhibit high ZT. Thus for the fabrication of TEGs, these materials have been widely used. Instead of bismuth telluride/selenite, various efforts were made to develop organic material-based TEGs (Manikandan and Kaushik 2016) to obtain low temperature for TEG's input. Performance of Various low-temperature range TE materials is summarized in Table 4.

Mid temperature range (250–650 °C) TEG

Mid temperature range (250–650°C) is reported among various TEGs. This temperature source comprises automotive exhaust, steam boiler exhaust, drying and baking ovens, gas turbine exhaust, etc (Kraemer et al. 2012). Because of the lower cost and ease of synthesis, BiCuSeO, $Ca_3Co_4O_9$, In_2O_3, $NaCo_2O_4$, $CaMnO_3$, $LaNiO_3$ and $SrTiO_3$ are the thermodynamic materials that have gained much attention. The thermoelectric performance of these materials is attained best at high temperature>650°C. Performance of Various mid temperature range TE material is shown in Table 5.

High temperature range (>650 °C) TEG

Hydrogen plants, steel heating furnaces, metal refining furnaces, and so on, are included in this temperature source. High-temperature heat (800–1000°C) is also produced by the radio-isotopes natural decaying (e.g. Pu_{238}). "Radio-isotope thermoelectric power generators" (RTG) is used for such high temperature TEG. In 1964, at temperature>600°C, for thermoelectric power generation, iron di Silicide (b-$FeSi_2$) was proposed because of its stability in respect of evaporation and oxidation sublimation and toxic elements, which are present in it (Shanmugam, Veerappan, and Eswaramoorthy 2014). Performance of high temperature range TE material is concluded in Table 6.

Based on the different materials' performance, an overview of TE performance is summarized in Table 4 , Tables 5 and 6. These research groups across the globe have used several different potential TE materials. Performance of different temperature range materials is shown. Regarding collector and receiver, some materials can enhance the reflectivity of collector and receiver absorptance of receiver, like yttria-stabilized zirconia cermet, can increase the solar absorptance of receiver up to ~0.95.

Various modeling and simulation techniques for TEG systems

The performance is numerically (through simulations and modeling) analyzed for various geometric types to improve the practical devices' design with different methodologies discussed by various authors. Most of the time, these methodologies are adopted through CFD and FEA schemes. For example, maximum efficiency of 4.15% of the system is provided by the smallest element having $90 \times 90\ mm^2$ of the substrate area. It is feasible to enhance the performance in order to decrease the thermoelectric elements cross-sectional area at a given length of TE leg. Simulation and modeling tools

Table 5. Various mid temperature range TE material.

Types of thermoelements	T_h/T_c	Interconnect material	Buffer layers at the ends	Efficiency (%)	Remark	Ref.
n-type PbTe p-type TAGS 85	500°C/ 100°C	Stripe of Ag	Ag/Fe/Ag + Fe	6	By diffusion bonding, contacts are formed	(Aswal, Basu, and Singh 2016)
p-type ZnSb n-type Constantan	420°C/ 20°C	N/A	N/A	5.8	P and n-type wires are directly joined in the form of Thermocouple, Thermo electric Generators	(Maslamani Abdu Idris Omer and A 2014)
skutterudite of p-type and n-type	500°C/ 40°C	Aluminum	Molybdenum	7	Through brazing, the contacts are formed	(Muthu, Shanmugam, and Veerappan 2014)
skutterudite of p-type and n-type	550°C/ 70°C	N/A	Co_2Si in p-type and $CoSi_2$ in n-type	9	Energy harvesting materials	(Tian et al. 2015)
Sb_2Te_3/PbTe as p-type and Bi_2Te_3/PbTe as n-type	600°C/ 10°C	Copper (Cu)	$Co_{0.8}Fe_{0.2}$ for PbTe side and Ni at Bi_2Te_3/Sb_2Te_3 sides	11	Contact formation by liquid In-Ga eutectic alloys, Segmented TEG, thermoelectric materials for energy environment science	(Manikandan and Kaushik 2016)

Table 6. High temperature range TE material.

Thermoelements	T_h/T_c	Materials interconnected	Buffer layers at the ends	Efficiency (%)	Remark	Ref.
n- & p-type SiGe alloys	870°C/ 31°C	Molybdenum	Pressure contact	7	Thermo electric power generators	(Aswal, Basu, and Singh 2016)
n- & p-type SiGe alloys	1000°C/ 300°C	With Ti layer, hot shoes connected. p- and n-type SiMo (i.e. $MoSi_2$ in the Si matrix)	N/A	N/A	Si-Ge Unicouple materials	(Weinstein et al. 2014)
n-type $Ca_{0.92}La_{0.08}MnO_3$ & p-type $Ca_{2.75}Gd_{0.25}Co_{4O9}$ p-type	773°C/ 383°C	Connection among the p and n-type are made through Pt wire.	N/A	1.1	Fabrication of all oxide thermoelectric generators	(Ding, Akbarzadeh, and Date 2016; Mondol, Vogel, and Bastian 2015)
Segmented leg of p-type ($Yb_{14}MnSb_{11}$/ $Ce_{0.9}Fe_{3.5}Co_{0.5}Sb_{12}$) and n-type ($La_3$-$xTe_4$/(Ba, $YbCo_4Sb_{12}$)	1000°C/ 152°C	N/A	N/A	15	Production of Nuclear Emerge technology space	(Banakar et al. 2017), (Manikandan and Kaushik 2015)
Segmented leg of n-type [$CoSb_3$+ $Bi_2(Te/Se)_3$] and p-type [$Zn_{4-x}CdxSb_3$ +Zn_4Sb_3 + $(Bi/Sb)_2Te_3$]	700°C/ 27°C	N/A	N/A	15	High efficiency Segmental thermoelectric Uni-couples	(Aswal, Basu, and Singh 2016; Kraemer et al. 2012)
n-type $MnSi_{1.75}Ge_{0.01}$ and p-type $Mg_2Si_{0.53}Sn_{0.4}Ge_{0.05}Bi_{0.02}$	735°C/ 50°C	Copper on cold side and Mo on hot side	Cu on n-type and Ni/ Pb/Ni on p-type	5.3	Characterization, assembly and design of the materials, which are based on silica	(Fateh et al. 2014)

used in various TEG projects by researchers are incorporated in Table 7. MATLAB, ANSYS, COMSOL-MULTIPHYSICS, and so on, are popular tools available for TEG modeling and simulation before the realization of the TEG project. MATLAB Simulink tool was used in a project to determine the cold side temperature (35.7°C) via active-cooling mechanism in TEG/LED system. CFD analysis is accomplished for many automobile exhaust-based TEG through ANSYS and COMSOL multi-physics. These tools are best suited for 3D Finite element analysis (Lee et al. 2014).

COMSOL, ANSYS, ABAQUS, and IMHO have widely used modeling and simulation tools for thermoelectric systems. They can serve different objectives. COMSOL is equation-based software. As far as finite element analysis (nm size) is concerned, COMSOL-Multiphysics provides user-friendly interface and various complex physics phenomenon and multiple equations at a time can easily be handled regardless of time. Work on objectives with nm size can be done easily in COMSOL, while with ABAQUS, it is impossible. In case of COMSOL, difficulty occurs in geometrical modeling. However, the geometry can be imported from other tools. It also provides inbuilt model facility. Modeling & mesh generation can be accomplished smoothly. Scientists, who are familiar with MATLAB or any equation-based software, prefer COMSOL (Yu and Chau 2009).

ANSYS is element-based software and considered more relevant for structural analysis, general physics phenomena, CFD simulations, and saving time. Solution control is much better in ANSYS for complex flow problem for getting converged solution. ANSYS has two types of modelers: workbench and classic. Workbench is used for CAD-programme in industries, while classic ANSYS is used with APDL programing. ANSYS workbench can be availed through ANSYS student version, including ANSYS-Design Xplorer, ANSYS-Space Claim, ANSYS-Autodyn, ANSYS-CFD, ANSYS-FLUENT and ANSYS- Mechanical. For beginners, ANSYS WB is easier, however meshing quality is not up to the mark. High quality mesh can be obtained through ANSA or Hyper-mesh. Depending on the requirement, both can be applied simultaneously i.e. for stress/strain analysis-ANSYS and complicated multi-physics analysis-COMSOL, in a single project. If fluid dynamics is added to COMSOL, numerical simulation technology can be dominated by it.

ABAQUS dominates the automobile industry, while ANSYS dominates the energy industry. ABAQUS CAE has replaced ANSYS APDL because it has become outdated for almost 20 years. Though the parametric design language of ANSYS is very useful, the same results can be obtained through python with ABAQUS. ANSYS can't offer application programing interface (API) to interface with RST. Therefore, it would be trouble if anybody wanted to develop a model based on ANSYS results (file.rst). An excellent API can be accessed through ABAQUS with a structurally managed database. Developing UMATs in ABAQUS is mostly preferred as compared to ANSYS.

ANSYS versions are available as ANSYS-CFX, ANSYS-FLUENT, etc.; one has to pay each separately. ABAQUS versions are available as ABAQUS-TOSCA, ABAQUS-fe-safe, ABAQUS-Simpack, ABAQUS-XFlow, ABAQUS-XFEM. However, there is no need to purchase all of them, but can be purchased in tokens as per the need of product development. For aerospace applications NASTRAN is more relevant and in academia COMSOL is accepted with great recognition. For product development, one should look at the software family as a whole and the product demand, which requires electromagnetics, acoustics, explicit, CFD, multi-body, fatigue, optimization, etc.

Environmental impact and applications of various TEG systems

The performance of TEGs based on environmental impact, using different methodologies, that is, theoretically and experimentally, is investigated by a group of researchers and authors and has been reviewed here. In wet flue-gas TEG's analysis, it is found that as compared to the dry flue gas, the maximum output of wet flue gas is 5.8 times more, with the humidity of 30%, at the same gas temperature of 150°C and mass flow rate of flue gas. Thus required fuel gas reduces (Banakar et al. 2017). For CO_2 life cycle scenario, TEG is integrated with an exhaust pipe. It was found that for the average driving pattern, it is essential to decrease the $LCCO_2$ (Life cycle CO_2 emissions) to zero, for this the thermoelectric figure of merit is enhanced by the factor of 1.9. The current price of TEGs must

Table 7. Various models of TEG.

S.No.	Modeling in Various Researches	Simulation Technique	Software	Assumptions	Ref.
	Mathematical modeling for self-sufficient energy recycling of TEG module with high-power light-emitting diode and active-cooling. In comparison with the passive-cooling LED device, the active cooling mechanism of the proposed LED/TEG module exhibits a far better ability to cool at 87.5% of working temperature. Compared with one of the TEG/LED modules, the temperature at which the passive cooling heat sink arrives is 35.7°C, i.e., higher.	Numerical Simulation-	MATLAB /Simulink	(i)-Uniform air circulation through DC fan (ii)-Assume that interconnected metals and ceramic plates possess high thermal conductivity	(Tsai and Le 2016)
	In automobile TEGs, experimental as well as numerical analysis for exhaust heat exchangers. 7 baffles enhance heat transfer and maximum heat of 1737W is transferred by the serial plate structure. In a suburban driving cycle, a maximum pressure drop of 9.7 kPa is also produced by it	Numerical Simulation: CFD Analysis	ANSYS	At the inlet and outlet the amount of heat is equal	(Liu et al. 2015)
	ANSYS is used for simulation and modeling for the design of thermal-concentrated solar TEG. The smallest element of TEG system gives the maximum efficiency of 4.15% as the best performance.	Numerical Simulation:3-D Finite element scheme	ANSYS	N/A	(Weinstein et al. 2014)
	Optimization of the design and investigation of IC engine exhaust-based TEG (ETEG) system. The development of ETEG's 3-D numerical model is made. ETEG system is used to recover the waste heat, which brought down the engine's fuel consumption rate by 0.6%. Efficiency of TEG modules is equal to 4% with the waste heat recovery.	Numerical Simulation:3-D Numerical model	FLUENT (ANSYS)	Effect of increased temperature of the jacket water is assumed to be negligible on the engine	(Niu et al. 2014)
	For enhancing the operational life, analysis and design of the TE Module using ANSYS. The possibility of enhancing the structural integrity of the TEMs is investigated. Compared to the typical rectangular geometry, the Von Mises stresses and efficiency of the circular geometry of TE modules are 13% and 42%, respectively lower and even shear stresses are lower.	Numerical Simulation: Finite element method	ANSYS Workbench	(i) Set of P-type or N-type TE elements is considered isolated. (ii) Due to the same location Stresses existed on a P-N pair in both rectangular and circular layout designs	(Goupil et al. 2016)

(*Continued*)

Table 7. (Continued).

S.No.	Modeling in Various Researches	Simulation Technique	Software	Assumptions	Ref.
	Simulation and modeling (geometrical equivalent model) is carried out to design the concentrated solar TEG and numerical method is adopted for its investigation considering TE properties.	Numerical Simulation-three-dimensional finite element scheme	ANSYS	(i)- Steady-state-TEG (ii)- Identical-p-type and n-type elements (ii)-Temperature dependent-TE material properties (iv)-Material properties of the electrode, substrate, solar absorber- constants. (v)-Vacuum environment- convective losses neglected (vi)-Radiation heat transfer only takes place between the environment and hot-side surface (vii)-Heat sink and the solar absorber are not incorporated in the computational process; however, with the help of boundary conditions, their effect is described	(Chen et al. 2014)
	Simulation and modeling (mathematical modeling) of TEG under Mediterranean climatic conditions	Numerical Simulation-MATLAB/SIMULINK environment	MATLAB	(i)-The Seebeck factor (α), electrical conductivity (s) and thermal conductivity (k) are constants and temperature independent. (ii)-These are calculated at the average temperature (T) (iii)-Model is valid for n number of legs (iv)-Hot side temperature > ambient temperature, Cold side temperature< ambient temperature Weather-Autumn and spring	(Al-Nimr, Tashtoush, and Jaradat 2015)
	Theoretical modeling of TEG incorporating effect of average Seebeck coefficient, temperature dependence of TE materials, Thomson effect and considering heat transfer effect from side surface	Numerical simulation- finite element method	MATLAB	One-dimensional linear temperature distributions	(Shen et al. 2016)
	To investigate TEG-solar pond system through transient heat transfer mathematical model	Numerical simulation-MATLAB/SIMULINK environment	MATLAB	(i)-One-dimensional Conductive heat transfer takes place though the infinite size solar pond (ii)-across the layers of the pond, physical properties are constant (iii)-throughout the year, the temperature of the aquifer is constant (iv)-average ambient temperature =UCZ temperature (v)-Heat exchanger provides $T_h\tilde{T}_L$ and $T_c\tilde{T}_{am}$ (vi)-Heat exchanger-No heat loss	(Ding, Akbarzadeh, and Date 2016)
	Electric and thermal performance via TEG multiphysics simulations	Numerical transient simulation	ANSYS CFX	Glass fibres is used to insulate the sides of the hot block –no leakage of heat flux	(Li et al. 2015)
	Development of thermal model of wearable TEG without heat sink, fabrication and its experimental testing	Numerical FEA simulations	Comsol-Multiphysics	Human body distributes uniform heat	(Francioso et al. 2017)

(*Continued*)

Table 7. (Continued).

S.No.	Modeling in Various Researches	Simulation Technique	Software	Assumptions	Ref.
	TEG Modeling and simulation for heat extraction from ocean	Numerical simulation	N/A	Heat flow between energy storage material (thermal resistance) and seawater	(Falcão Carneiro and Gomes de Almeida 2018)
	Modeling and fabrication of a prototype TEG utilizing heat from hot exhaust gases	Mathematical simulation	N/A	At any cross-section of exhaust- uniform temperature distribution	(Mostafavi and Mahmoudi 2018)
	Dynamic electrical and thermal performance of TEG are investigated via Geometrical model and Multiphysics simulations	Numerical Simulation	ANSYS 15.0	Uniform temperature over the surface of heater	(Li et al. 2017)
	Two 3-D models are developed of a TEG with different boundary conditions Numerical model	Numeric Simulation	ANSYS FLUENT	Two different thermal boundary conditions: (i)-Fixed temperature at boundaries (ii)- Fixed convective heat transfer	(Niu et al. 2015)

be reduced by 10–40% to make TEGs profitable with respect to their life cycle (Kraemer et al. 2012). In Passenger automobile's exhaust, bismuth telluride-based TEG is integrated. 0.07~0.30% CO_2 emission of the city was reduced (Kim et al. 2016). In Hybrid Commercial Vehicles, the hike in the efficiency of the fuel was observed by upto 20%. It is the outcome of converting waste heat to electricity by 10% (Date et al. 2014). In Heavy duty vehicles, waste heat recovery leads to 20% increase in fuel efficiency (Orr et al. 2016). Remote power, aerospace, communication, military, biomedical, healthcare, etc., are the various application areas of TEGs operating at different temperature ranges. Negative temperature gradient makes possible microprocessor's thermoelectric cooling (Hamid Elsheikh et al. 2014).

Conclusion and future directions in field

TEG can support global commitment to energy demand and reduction in pollution. In this comprehensive review, the key aspects of TE system are focused such as utilization and applications in power production and heating-cooling processes, energy resources for TEG, thermodynamics, material principles. Summing up the advantages from this critical review, the review findings can be quantified as: parabolic dish type concentrators are less efficient than solar furnaces (efficiency-15%). Cogeneration system with Fresnel lenses exhibits better overall system performance, providing 1.4 W electrical power and 76.1 W thermal power. TEG based on heat released by human body generates 192.6 μW power at $\Delta T = 50K$ and an open-circuit voltage of 37.2 mV. Solar absorbers' material plays a significant role in TEG's efficiency, and a high figure of merit is the key factor for higher efficiency. Having various properties different TE materials are available in the market, which include polymers (flexibility), ceramics (high temperature) and semiconductors. Mostly alloys of Bi-Te materials are utilized because of their high figure of merit (ZT). Materials having ZT = 1 at temperature difference of 100°C provides 5% efficiency. With rise in FOM (ZT > 1) high temperature material p-type ($Yb_{14}MnSb_{11}/Ce_{0.9}Fe_{3.5}Co_{0.5}Sb_{12}$) and n-type ($La_3$-$xTe_4/(Ba,YbCo_4Sb_{12})$ achieved the best ZT of~1.8 at 790°C and produced 848°C temp difference to provide 15% efficiency. Mid-temperature material p-type Sb_2Te_3/PbTe and n-type Bi_2Te_3/PbTe achieved the best ZT of~2.2 at 600°C and produced 590°C temp difference to provide 11% efficiency. Low temperature material $MgAg_{0.965}Ni_{0.005}Sb_{0.99}$ achieved the best ZT of~1.86 at 225°C temp difference, providing 8.5% efficiency.

Solar hybrid TEG system can be a reasonable alternative to the traditional electric/thermal solar hybrid system. Thermoelectric materials have made good progress in recent years; therefore, in the upcoming years, performance of the TEG-based systems can be advantageous over the traditional solar PV hybrid systems. This comprehensive review of compiled information will help researchers, academicians, industrialists, scientists, and environmentalists to advance research and customize their projects accordingly. Future research can be conducted in areas: higher ZT materials, numerical simulation of human body, heat sink, unconverted heat, the power electronic circuit to get smooth DC voltage, and an active temperature control mechanism to control temperature difference ΔT and cost reduction.

Nomenclature

T_h	Hot junction side Temperature of the TEG °C
T_c	Cold junction side Temperature of the TEG °C
T	Average Temperature of receiver/absorber °C
$T_{water.}$	Hot water Temperature
Greek Symbols	
ε	Emissivity of the receiver
$\propto$	Absorptivity of the receiver

Acknowledgments

The authors would like to acknowledge Energy Centre, Maulana Azad National Institute of Technology, Bhopal, India and Department of Mechanical Engineering, Delhi Technological University, Delhi (India) for using all the resources.

Disclosure statement

No potential conflict of interest was reported by the authors.

Notes on contributors

Sanjeev Kumar Bhukesh is a research scholar at Energy Centre, Maulana Azad National institute of Technology, Bhopal, India. He completed his B.Tech. in Electrical and Electronics Engineering, M.Tech. in Renewable Energy in 2015. His area of research is design and development of Solar thermoelectric generator, Solar energy applications etc. He has published 4 research papers in international journal and 2 in international conference.

Dr Suresh Kumar Gawre is Assistant Professor in Department of Electrical Engineering, Maulana Azad National institute of Technology, Bhopal (India). He did his Ph.D. in electrical engineering. He has more than 19 years of experience in the teaching, research and development in power quality monitoring, solar PV systems, analog and digital electronics, IoT applications, machine learning. Dr. Gawre has authored around 51 research papers and 7 book chapters.

Dr Anil Kumar is Associate Professor, Mechanical Engineering Department, Delhi Technological University, Delhi (India). His research area is clean energy technologies. He has guided 10 Ph.D. scholars. Dr. Kumar has authored around 350 manuscripts (200 in Int. Journal of repute), 4 patents. He has received 4350+ citations with 36 h-index (SCOPUS). He is authors 12 books. He appears as most cited number Information Systems (IS) researchers featured in the World Ranking of "Top 2% scientists created by Stanford University since 2019".

References

Al-Nimr, M. A., B. M. Tashtoush, and A. A. Jaradat. 2015. Modeling and simulation of thermoelectric device working as a heat pump and an electric generator under Mediterranean climate. *Energy* 90:1239–50. doi:10.1016/j.energy.2015.06.090.

Arsie, I., A. Cricchio, C. Pianese, V. Ricciardi, and M. De Cesare. 2015. Modeling analysis of waste heat recovery via thermo-electric generator and electric turbo-compound for CO2 reduction in automotive SI engines. *Energy Procedia* 82:81–88. doi:10.1016/j.egypro.2015.11.886.

Aswal, D. K., R. Basu, and A. Singh. 2016. Key issues in development of thermoelectric power generators: High figure-of-merit materials and their highly conducting interfaces with metallic interconnects. *Energy Conversion and Management* 114:50–67. doi:10.1016/j.enconman.2016.01.065.

Atouei, S. A., A. Rezania, A. A. Ranjbar, and L. A. Rosendahl. 2018. Protection and thermal management of thermo-electric generator system using phase change materials: An experimental investigation. *Energy* 156:311–18. doi:10.1016/j.energy.2018.05.109.

Banakar, A., A. Motevali, M. Emad, and B. Ghobadian. 2017. Co-generation of heat and power in a thermoelectric system equipped with Fresnel lens collectors using active and passive cooling techniques. *Renew Energy* 112:268–79. doi:10.1016/j.renene.2017.05.052.

Champier, D. 2017. Thermoelectric generators: A review of applications. *Energy Conversion and Management* 140:167–81. doi:10.1016/j.enconman.2017.02.070.

Chang, H., J. Guan, and M. Yang. 2013. A new design of mobile thermoelectric power generation system. *International Journal of Electrical, Computer, Energetic, Electronic and Communication Engineering* 7 (8):101–106. doi:10.5281/zenodo.1335542.

Chen, W. H., C. C. Wang, C. I. Hung, C. C. Yang, and R. C. Juang. 2014. Modeling and simulation for the design of thermal-concentrated solar thermoelectric generator. *Energy* 64:287–97. doi:10.1016/j.energy.2013.10.073.

Date, A., A. Date, C. Dixon, and A. Akbarzadeh, 2014. "Theoretical and experimental study on heat pipe cooled thermoelectric generators with water heating using concentrated solar thermal energy," *Solar Energy*105: 656–68. doi: 10.1016/j.solener.2014.04.016.

Ding, L. C., A. Akbarzadeh, and A. Date. 2016. Transient model to predict the performance of thermoelectric generators coupled with solar pond. *Energy* 103:271–89. doi:10.1016/j.energy.2016.02.124.

Duraisamy, S., M. Sundararaj, K. Raja, G. K. Poongavanam, and I. Selvarasan. 2019. Energy and Exergy Analysis of an Advanced Cookstove-Based Annular Thermoelectric Cogeneration System. In *Biomass for Bioenergy-Recent Trends and Future Challenges*. IntechOpen. doi:10.5772/intechopen.84237.

Eswaramoorthy, M., S. Shanmugam, and A. Veerappan. 2013. Experimental study on solar parabolic dish thermoelectric generator. *International Journal of Energy* 3 (3):62–66. doi:10.5963/ijee0303001.

Falcão Carneiro, J., and F. Gomes de Almeida. 2018. Model and simulation of the energy retrieved by thermoelectric generators in an underwater glider. *Energy Conversion and Management* 163 (February):38–49. doi:10.1016/j.enconman.2018.02.031.

Fateh, H., C. A. Baker, M. J. Hall, and L. Shi. 2014. High fidelity finite difference model for exploring multi-parameter thermoelectric generator design space. *Applied Energy* 129:373–83. doi:10.1016/j.apenergy.2014.04.088.

Francioso, L., C. De Pascali, V. Sglavo, A. Grazioli, M. Masieri, and P. Siciliano. 2017. Modelling, fabrication and experimental testing of an heat sink free wearable thermoelectric generator. *Energy Conversion and Management* 145:204–13. doi:10.1016/j.enconman.2017.04.096.

Goupil, C., H. Ouerdane, K. Zabrocki, W. Seifert, N. F. Hinsche, and E. Müller. 2016. Thermodynamics and Thermoelectricity. *Continuum Theory and Modeling of Thermoelectric Elements* 1–74. doi:10.1002/9783527338405.ch1.

Hamid Elsheikh, M., D. A. Shnawah, M. F. M. Sabri, S. B. M. Said, M. Haji Hassan, M. B. Ali Bashir, and M. Mohamad. 2014. A review on thermoelectric renewable energy: Principle parameters that affect their performance. *Renewable and Sustainable Energy Reviews* 30:337–55. doi:10.1016/j.rser.2013.10.027.

Jaziri, N., A. Boughamoura, J. Müller, B. Mezghani, F. Tounsi, and M. Ismail. 2019. A comprehensive review of thermoelectric generators: Technologies and common applications. *Energy Reports* 6:264–87. doi:10.1016/j.egyr.2019.12.011.

Jouhara, H., N. Khordehgah, S. Almahmoud, B. Delpech, A. Chauhan, and S. A. Tassou. 2018. Waste heat recovery technologies and applications. *Thermal Science and Engineering Progress* 6 (January):268–89. doi:10.1016/j.tsep.2018.04.017.

Kil, T. H., S. Kim, D. -H. Jeong, D. -M. Geum, S. Lee, S. -J. Jung, S. Kim, C. Park, J. -S. Kim, J. M. Baik, et al. 2017. A highly-efficient, concentrating-photovoltaic/thermoelectric hybrid generator. *Nano Energy*. 37(April):242–47. doi:10.1016/j.nanoen.2017.05.023.

Kim, M. S., M. K. Kim, S. E. Jo, C. Joo, and Y. J. Kim. 2016. Refraction-assisted solar thermoelectric generator based on phase-change lens. *Scientific Reports* 6:1–9. doi:10.1038/srep27913.

Kraemer, D., Q. Jie, K. McEnaney, F. Cao, W. Liu, L. A. Weinstein, J. Loomis, Z. Ren, and G. Chen. 2016. Concentrating solar thermoelectric generators with a peak efficiency of 7.4%. *Nature Energy* 1 (11). doi:10.1038/nenergy.2016.153.

Kraemer, D., K. McEnaney, Z. Ren, and G. Chen. 2012. Solar thermoelectric power conversion. (April 2015):1–16. doi:10.1201/b11892-28.

Lan, S., Z. Yang, R. Chen, and R. Stobart. 2018. A dynamic model for thermoelectric generator applied to vehicle waste heat recovery. *Applied Energy* 210 (June 2017):327–38. doi:10.1016/j.apenergy.2017.11.004.

Lee, S. W., Y. Yang, H. -W. Lee, H. Ghasemi, D. Kraemer, G. Chen, and Y. Cui. 2014. An electrochemical system for efficiently harvesting low-grade heat energy. *Nature Communications* 5 (1):1–6. doi:10.1038/ncomms4942.

Leonov, V. and R. J. M. Vullers. 2007. Thermoelectric generators on living beings. *Engineering*.

Li, W., M. C. Paul, A. Montecucco, A. R. Knox, J. Siviter, N. Sellami, X. L. Meng, E. F. Fernandez, T. K. Mallick, P. Mullen, et al. 2015. Multiphysics simulations of a thermoelectric generator. *Energy Procedia* 75:633–38. doi:10.1016/j.egypro.2015.07.473.

Li, W., M. C. Paul, A. Montecucco, J. Siviter, A. R. Knox, T. Sweet, M. Gao, H. Baig, T. K. Mallick, G. Han, et al. 2017. Multiphysics simulations of thermoelectric generator modules with cold and hot blocks and effects of some factors. *Case Studies in Thermal Engineering*. 10(October 2016):63–72. doi:10.1016/j.csite.2017.03.005.

Liu, X., C. Li, Y. D. Deng, and C. Q. Su. 2015. An energy-harvesting system using thermoelectric power generation for automotive application. *International Journal of Electrical Power & Energy Systems* 67:510–16. doi:10.1016/j.ijepes.2014.12.045.

Li, Y., S. Witharana, H. Cao, M. Lasfargues, Y. Huang, and Y. Ding. 2014. Wide spectrum solar energy harvesting through an integrated photovoltaic and thermoelectric system. *Particuology* 15:39–44. doi:10.1016/j.partic.2013.08.003.

Manikandan, S., and S. C. Kaushik. 2015. Thermodynamic studies and maximum power point tracking in thermoelectric generator-thermoelectric cooler combined system. *Cryogenics (Guildf)* 67:52–62. doi:10.1016/j.cryogenics.2015.01.008.

Manikandan, S., and S. C. Kaushik. 2016. Energy and exergy analysis of solar heat pipe based annular thermoelectric generator system. *Solar Energy* 135:569–77. doi:10.1016/j.solener.2016.06.031.

Maslamani Abdu Idris Omer, T. M., and M. M. A. 2014. Development of solar thermoelectric generator. *European Scientific Journal* 10 (9):1857–7881.

Mondol, A. S., B. Vogel, and G. Bastian. 2015. Large scale water lens for solar concentration. *Optics Express* 23 (11):A692. doi:10.1364/oe.23.00a692.

Mostafavi, S. A., and M. Mahmoudi. 2018. Modeling and fabricating a prototype of a thermoelectric generator system of heat energy recovery from hot exhaust gases and evaluating the effects of important system parameters. *Applied Thermal Engineering* 132:624–36. doi:10.1016/j.applthermaleng.2018.01.018.

Musleh, A. M., E. V. Topriska, D. Jenkins, and E. Owens. 2020. Thermoelectric generator characterization at extra-low-temperature difference for building applications in extreme hot climates: Experimental and numerical study. *Energy and Buildings* 225:110285. doi:10.1016/j.enbuild.2020.110285.

Muthu, G., S. Shanmugam, and A. R. Veerappan. 2014. Solar parabolic dish thermoelectric generator with acrylic cover. *Energy Procedia* 54:2–10. doi:10.1016/j.egypro.2014.07.244.

Nguyen, N. Q., and K. V. Pochiraju. 2013. Behavior of thermoelectric generators exposed to transient heat sources. *Applied Thermal Engineering* 51 (1–2):1–9. doi:10.1016/j.applthermaleng.2012.08.050.

Niu, Z., H. Diao, S. Yu, K. Jiao, Q. Du, and G. Shu. 2014. Investigation and design optimization of exhaust-based thermoelectric generator system for internal combustion engine. *Energy Conversion and Management* 85:85–101. doi:10.1016/j.enconman.2014.05.061.

Niu, Z., S. Yu, H. Diao, Q. Li, K. Jiao, Q. Du, H. Tian, and G. Shu. 2015. Elucidating modeling aspects of thermoelectric generator. *International Journal of Heat and Mass Transfer* 85:12–32. doi:10.1016/j.ijheatmasstransfer.2015.01.107.

Olsen, M. L., E. L. Warren, P. A. Parilla, E. S. Toberer, C. E. Kennedy, G. J. Snyder, S. A. Firdosy, B. Nesmith, A. Zakutayev, A. Goodrich, et al. 2013. A high-temperature, high-efficiency solar thermoelectric generator prototype. *Energy Procedia* 49:1460–69. doi:10.1016/j.egypro.2014.03.155.

Orr, B., A. Akbarzadeh, M. Mochizuki, and R. Singh. 2016. A review of car waste heat recovery systems utilising thermoelectric generators and heat pipes. *Applied Thermal Engineering* 101:490–95. doi:10.1016/j.applthermaleng.2015.10.081.

Remeli, M. F., L. Kiatbodin, B. Singh, K. Verojporn, A. Date, and A. Akbarzadeh. 2015. Power generation from waste heat using heat pipe and thermoelectric generator. *Energy Procedia* 75:645–50. doi:10.1016/j.egypro.2015.07.477.

Sathawane, N. S., P. V. Walke, N. S. Sathawane, and P. V. Walke. 2014. A review on solar thermoelectric cogenerator with evacuated tube solar collector. *International Journal of Advanced Research in Science, Engineering* 8354 (3):36–41. [Online]. Available. http://www.ijarse.comwww.ijarse.com.

Shanmugam, S., A. R. Veerappan, and M. Eswaramoorthy. 2014. An experimental evaluation of energy and exergy efficiency of a solar parabolic dish thermoelectric power generator. *Energy Sources Part A: Recovery, Utilization, and Environmental Effects* 36 (17):1865–70. doi:10.1080/15567036.2011.578110.

Shen, Z. G., S. Y. Wu, L. Xiao, and G. Yin. 2016. Theoretical modeling of thermoelectric generator with particular emphasis on the effect of side surface heat transfer. *Energy* 95:367–79. doi:10.1016/j.energy.2015.12.005.

Shittu, S., G. Li, Q. Xuan, X. Xiao, X. Zhao, X. Ma, and Y. G. Akhlaghi. 2020. Transient and non-uniform heat flux effect on solar thermoelectric generator with phase change material. *Applied Thermal Engineering* 173 (October 2019):115206. doi:10.1016/j.applthermaleng.2020.115206.

Sundarraj, P., S. S. Roy, R. A. Taylor, and D. Maity. 2016. Performance analysis of a hybrid solar thermoelectric generator. *Energy Sources Part A: Recovery, Utilization, and Environmental Effects* 38 (20):2977–84. doi:10.1080/15567036.2016.1180331.

Tellurex. 2010. Frequently asked questions about our power generation technology. *Technology*. Accessed October 15, 2021. https://pdfcoffee.com/seebeck-faq-pdf-free.html.

Tian, H., N. Jiang, Q. Jia, X. Sun, G. Shu, and X. Liang. 2015. Comparison of segmented and traditional thermoelectric generator for waste heat recovery of diesel engine. *Energy Procedia* 75:590–96. doi:10.1016/j.egypro.2015.07.461.

Tsai, H. L., and P. T. Le. 2016. Self-sufficient energy recycling of light emitter diode/thermoelectric generator module for its active-cooling application. *Energy Conversion and Management* 118:170–78. doi:10.1016/j.enconman.2016.03.077.

Wang, Y., Y. Shi, D. Mei, and Z. Chen. 2018. Wearable thermoelectric generator to harvest body heat for powering a miniaturized accelerometer. *Applied Energy* 215 (October 2017):690–98. doi:10.1016/j.apenergy.2018.02.062.

Weinstein, L., D. Kraemer, K. McEnaney, and G. Chen. 2014. Optical cavity for improved performance of solar receivers in solar-thermal systems. *Solar Energy* 108:69–79. doi:10.1016/j.solener.2014.06.023.

Xi, H., L. Luo, and G. Fraisse. 2007. Development and applications of solar-based thermoelectric technologies. *Renewable and Sustainable Energy Reviews* 11 (5):923–36. doi:10.1016/j.rser.2005.06.008.

Yu, C., and K. T. Chau. 2009. Thermoelectric automotive waste heat energy recovery using maximum power point tracking. *Energy Conversion and Management* 50 (6):1506–12. doi:10.1016/j.enconman.2009.02.015.

2023 IEEE 8th International Conference for Convergence in Technology (I2CT)
Pune, India. Apr 7-9, 2023

Review on Ultrasound-Image Analysis of Fetus Using Deep Learning

1st Lavendra Gautam
Department of Computer Science and Engg.
Delhi Technological University
Delhi, India
lavendragautam$_2k21afi18@dtu.ac.in$

2nd Gull Kaur
Department of Computer Science
Delhi Technological University
Delhi, India
gullkaur@dtu.ac.in

2023 IEEE 8th International Conference for Convergence in Technology (I2CT) | 979-8-3503-3401-2/23/$31.00 ©2023 IEEE | DOI: 10.1109/I2CT57861.2023.10126500

***Abstract*—Deep learning Techniques are rapidly becoming the industry level for analyzing fetal ultrasound pictures. Despite the significant number of survey studies that have previously been published on this subject, the majority focus on image analysis-related Medical Science or do not include all fetal Ultrasound deep learning applications. We have collected 30 research papers released after 2016; this study examines the most recent work on the subject. Each study is evaluated and commented on from both a technique and an application standpoint. The studies were considered for the analysis of anatomical fetus structure. The primary limits and open concerns for each category are mentioned. Summary tables are supplied to make it easier to compare the various techniques. Also presented are publicly accessible data sets and key performance metrics indicators widely used to evaluate algorithmic Behaviour regarding deep learning techniques used. Here studies wrap up with a condemning overview of the present date in Deep learning algorithms for fetal Ultrasound image processing and a conclusion of nowadays problems that researchers working in the field must address to transform research techniques into practical clinical practice.**

***Index Terms*—anatomical structure analysis, biometry estimation, deep learning, Fetal ultrasound processing ,plan detection,survey.**

I. Introduction

Because of its mobility, cheap cost, and non-invasive nature, ULTRASOUND (US) imaging is a popular method for diagnosing, clocking, and prescribing a wide range of disorders. Over the years, US imaging has emerged as the primary tool of prenatal screening. It is frequently used to check fetal improvement, as well as to observe pregnancy and determine medication impression. Clinicians may find it challenging to assess US images because of artefact such sonic reflections, impulse noise, movement blurring, and lacking boundaries caused by the complex interactions between Ultrasound waves and both mother and infant. Over the last several decades, deep learning (DL), and in particular convolutional neural systems (CNNs), have increasingly been used in the analysis of fetal ultrasound images to aid clinicians in coming to conclusions.

In the last various years, survey articles in the field have been published, Regardless of how many of them there are focused on the larger domain of medical image analysis or study DL methods for Ultrasound picture analysis outside the fetal field where segmentation and classification algorithms are discussed, which examine approaches for fetal cardiology imaging; which quickly outline DL methods for fetal anomaly diagnosis; and, which analyses research publications from a medication viewpoint. A re-evaluation of the most modern research on the topic of processing images of the fetus using deep convolutional neural network (DL) may be a useful and condensed source of information for emerging scholars in addition to a reference overview article for those already engaged in the field. The steps taken to evaluate the well-being of infants in clinical practice are recreated in these sections. A unique section called "Assorted" gathers studies on new tasks, ranging from less common newborn assessment applications to explored movement control.

The following research inquiries served as the basis for our survey method: What are the most studied tasks in the area of Deep learning-based analysis of fetal US images? What are the main concerns in infant examination that DL is presently used to address? Can robust DL algorithms be developed and tested using frequently used datasets? What problems in the field does Deep learning still need to address? With all these issues in mind, we created a list of keywords for their survey, which included language for prenatal examination and organs along with categorization, recognition, fragmentation, fetal, ultrasound, and deep learning. The research databases used were IEEE Xplore, Google, SpringerLink, Researchgate, and Pubmed. Each article that was generated seems to have its bibliography carefully examined. To better focus on the latest and noteworthy developments while minimizing duplication with past review efforts, we looked at index journal and conference publications published in 2017.

II. DataSets and Performance Metrics

This section will discuss publicly accessible datasets for algorithm development and testing as well as the quantitative metrics used to assess the performance of Deep learning algorithms.

A. Available datasets

Collecting and disseminating high-quality annotated fetal Ultrasound datasets is difficult. Depending on the task, labeling large datasets may take a while (for example, pixel-level labeling for segmentation takes much longer

Authorized licensed use limited to: DELHI TECHNICAL UNIV. Downloaded on May 29,2023 at 05:56:27 UTC from IEEE Xplore. Restrictions apply.

than image-level labeling for classification). Data sharing is further hampered by worries about data security and privacy. To address these problems, international medical institutions are compiling and disseminating publicly accessible information to promote algorithm research and impartial algorithm comparison.

The Challenge Ultrasound: Biometric Measurements from Fetal Ultrasound Images, organized in 2012 in cooperation with and with aid from ISBI, was the first challenge of its kind. The task was to assess common biometric characteristics by autonomously segmenting the fetal head, belly, and femur. Despite the dataset's acknowledged importance, its size (270 photos) makes it impossible for academics to create Deep learning algorithms that are generalizable.

With the publication of the HC18 challenge sample in 2018, the ability of Deep learning for biometric parameter estimation was made available. It was necessary to develop algorithms for autonomously estimating the fetal head circumference (HC) using training and testing sets of 990 and 325 2D ultrasound pictures, respectively. The photos were annotated by a qualified technologist and a medical researcher.

Big sample photos from the U.s.a. taken as part of standard prenatal fetal screening have just been made public. It contains 7136 2D training photos from 888 patients, broken down into six categories: the thorax, the femur, the brain, the cervix of the mother, and others. The photographs were manually labeled by a qualified fetal doctor.

B. Performance Metrics

The F1-score (F1) measure is also commonly used, particularly for unbalanced datasets. These metrics may be computed for each patch, each image, or each patient.

When it comes to segmentation tasks, the Correlation coefficient (DSC) and Intersection over Union (IOU) are widely used to gauge model performance (IoU). DSC is defined as follows and is equivalent to F1. :

$$DSC = \frac{2|XZ|}{|X| + |Z|} = \frac{2TP}{FP + FN + 2TP} = F1$$

where X and Z represent the expected and labelled masks. The IoU is defined as follows:

$$IoU = \frac{X \cup Y}{X \cap Y}$$

Despite the fact that the two measures are significantly related, IoU penalizes single occurrences of subpar fragmentation more significantly than DSC, which assesses performance more in line with the average.

You may also utilize the Hausdorff length (HL), which measures the separation between the labeled segmentation mask and the anticipated segmentation : max(h(X, Z), h(X, Z)) = HD(X, Z)

Performance is measured for localization tasks using the average accuracy (AP), which is the P rec averaged across all Rec values between 0 and 1. The area under the precision-recall curve may be thought of as AP. P rec and Rec are routinely calculated at different IoU thresholds between the predicted and labeled bounding boxes. For detection tasks requiring the detection of multiple structures in an image,

The mean AP (MAP) is employed.

$$mAP = \frac{\sum_{n=1}^{k} APi}{K}$$

K represents how many courses there are Popular metrics for regression jobs where a total score must be anticipated (such as for biometric recognition estimate) include: The average of the squares error between both the expected and actual values is calculated using the Average Squared Error (MSE) formula:

$$MSE = \frac{1}{N}\sum_{i=1}^{N}(y - y)^2$$

It is frequently used as a loss function during training due to its differentiable nature.

$$MAE = \frac{1}{N}\sum_{i=1}^{N}|Y - Yi|$$

Difference error (DF):

$$DF = \frac{1}{N}\sum_{i=1}^{N}(Y - Yi)$$

Euclidean distance (ED):

$$ED = \frac{1}{N}\sum_{i=1}^{N}\sqrt{(Y - Yi)^2}$$

Evaluation of the mask contours produced by segmentation algorithms may also be done using regression metrics. Additionally used are AUC variations from Judd et al.. The AUC is determined using the TP and FP rates that are displayed below. The proportion of correct positives to total compulsions, where actual positives are defined as sift attribute values over the threshold at focused pixels, is known as the T P rate given a threshold limit.

Authorized licensed use limited to: DELHI TECHNICAL UNIV. Downloaded on May 29,2023 at 05:56:27 UTC from IEEE Xplore. Restrictions apply.

TABLE I
PERFORMANCE METRICS.

Index	Description
Accuracy (Acc)	(TP+TN)/(N)
Recall (Rec)	T P/(T P +F N)
Specificity (Spec)	T N/(T N+F P)
Precision (P rec)	T P/(T P +F P)
F1-score (F1)	(2PrecSpec)/(Prec+Spec)
AUC	Area Under the Receiver Operating Characteristic curve
Intersection Over Union (IoU)	eq ii
Hausdorff distance (HD)	eq. iii
mean Average precision (mAP)	Eq. v
Mean absolute error (MAE)	Eq. vii
Difference (DF)	Eq. viii
Mean squared error (MSE)	Eq. vi
Euclidean distance (ED)	Eq. ix

III. ANATOMICAL-STRUCTURE ANALYSIS

The procedures for analyzing the foetal heart (Section 3-A), brain (Section 3-B), and placental and synovial fluid (Section 3-C) are covered in this section. While Sec. 3-E offers methods for multi-structure analysis, Sec.3-D contains DL approaches for analyzing diverse foetal anatomical structures. The primary tasks covered in the literature on anatomical structure analysis are summarised in Table II.

A. Heart

Fetal cardiac evaluation is critical for detecting heart diseases like congenital heart disease (CHD) and intrauterine growth restriction. Cardiac examination often includes cardiac function analysis as well as heart anatomical evaluation, which includes heart size and form. Heart and heart-structure identification is the focus of several deep learning algorithms in the area. The left atrial capillary vein angle, apex superior vena cava, moderator band, and many ribs in 4CH are among the anatomical heart components that are detected using an SSD system with aggregation residual visual blocks.

The presence, viewing plane, location, and direction of the foetal heart are all predicted using a recurrent CNN. 91 films of 12 participants' prenatal cardiac screenings have annotations at the frame level. Leaving out one purposeful sampling across each individual is used, yielding 12 fold validations, to evaluate the accuracy of categorization and localization.

B. Brain

It is critical to assess foetal brain development in order to calculate foetal growth and diagnose brain pathologies. Several structures are evaluated in clinical practice to determine prenatal brain development and well-being. Clinicians find this challenging owing to issues including significant intra- and inter-structure fluctuation. Automated fetal-brain analysis frequently includes the location, segmentation, categorization, and measuring of anatomical structures. Many works on DL methods for foetal brain analysis concentrate on segmenting the brain utilizing encoder-decoder architectures. The study suggests an architecture based on deep learning for segregating the posterior cerebral artery and giving the sonographer the gate position on Doppler Ultrasound pictures. A from before the dilated residual network is employed as the encoder, while massive upsampling convolution blocks are employed as the decoder.

To divide the CSP and determine its width in order to look for anomalies, we offer a deep attention network that was motivated by the U-Net encoder-decoder architecture.

In between the encoder and the decoder, a channel awareness module is introduced, with VGG11 acting as the foundation of the encoding path.

ResU-Net reduces the number of training parameters while encoding convolutions and elongated convolutions to restore the encoder's degraded spatial resolution.

C. Placenta amniotic fluid

The placenta is an organ that supplies oxygen and nutrition to the foetus, regulates temperature, and eliminates waste from the foetus' blood. This structure is strongly tied to foetus health: improper placental function can damage foetus growth and, in severe situations, even risk the fetus's life. Given its importance, numerous clinical evaluations are conducted to check the state of the placenta as well as the health of the foetus. Placenta segmentation may offer automated measurement of placenta volume and shape in these circumstances. A variety of methods are used to segment the placenta from 2D Ultrasound pictures. The method presented in employs a U-Net-inspired CNN.

D. Others

1) Lungs: The primary cause of neonatal respiratory morbidity is immature foetal lung development. Quantitative US imaging at the 4CH level is frequently utilized as a noninvasive method for foetal lung ability evaluation. Although there are a few minor textural differences, normal foetal lung echogenicity is quite comparable to that of the adjacent liver. However, in the presence of an aberration, echogenicity can either increase or decrease. The problems of foetal US image lung analysis are now being addressed by deep learning algorithms, notably for calculating GA.

Authorized licensed use limited to: DELHI TECHNICAL UNIV. Downloaded on May 29,2023 at 05:56:27 UTC from IEEE Xplore. Restrictions apply.

TABLE I
SUMMARY OF PERFORMANCE METRICS OF FETUS ORGAN ON DEEP LEARNING ALGORITHM.

Organ	Paper(Year)	Technique Used	Dataset	Performance Metrics
heart	Dong et al.,(2019) [1]	Residual block network (ARvB-Net)	3986 2D	mAP=0.93
heart	Huang et al.,(2017) [2]	CNN's i;e ResNet18, ResNet34, ResNet50,	91videos	acc=.70
heart	Gao et al.,(2017) [3]	Two Stream ConVNet	412 videos	ACC=0.90, Prec=0.85, Rec=0.89
heart	Rachmatullah et al., (2021) [4]	CNN using U-Net Arch	517 2D	IoU=0.94, Acc=0.96
heart	Xu et al.,(2020) [5]	Cascaded U-net with SSIM	1709 2d	Dsc=0.86, Hd=3.34,ACC=0.92
heart	Tan et al., (2020) [6]	Automated Data curation and Classification using DL	110 subject*	P rec=0.85, Rec=0.86,F1=0.86, AUC=0.93
heart	Komatsu et al.,(2021) [7]	CNN to detect barcode like timeline	247 videos (363 subjects*)	mAP=0.70, AUC=0.83
heart	Qiao et al., (2022) [8]	Neural Network to image manipulation	2102 2D (101 subjects)	P rec=0.92, Rec=0.92
heart	Pu et al.,(2021)[9]	CNN arch i;e Xception, ResNet, MobilNet	737 videos (350 subjects*)	Acc=0.95, Rec=0.93, Spec=0.94, F1=0.95
Brain	Wyburd et al.,(2021) [10]	DL based model i;e Sylvion fissure, calcarine sulsus	811 3D	MAE=4.1, Mae=5.2, Mae=4.8,
Brain	Lee et al.,(2020) [11]	Baysian Neural Network to estimate GA	9237 2d	Rmse=13.86, Mae=16.06
Brain	Moser et al.,(2020) [12]	Manual segmentation and registration algorithm	1186 3d	Ed=1.37 mm,Hd=9.06 mm, Dsc=0.95
Brain	Venturini et al.,(2020) [13]	CNN based upon atlas label ALgo	527 3d	DSC=0.84, Ed=2.25 mm, Hd=4.52 mm
Brain	Huang et al.,(2018) [14]	VP-Nets using CNN	246 3d	IoU=0.65
Brain	Singh et al.,(2021) [15]	DL algo ResU-Net-c	735 2d	Dsc=0.88, HD=28.16,Rec=0.87, Prec=0.91
Brain	Wyburd et al., (2020) [16]	CNN alongwith V-Net	310 3d	Dsc=0.83, BCE=0.10
Placenta	Yang et al., (2017)	3D fully RNN	104 3d (104 sub*)	DSC=0.64, HD=24.54mm
Placenta	Looney et al.,(2017) [17]	Fully CNN network (OxNNet)	300 3d (3064 subj*)	Dsc=0.73, Hd=27 mm
Placenta	Oguz et al., (2018) [18]	CNN (PVcnn) with SGA10	(47 subj*)	DSC=0.86
Placenta	Hu et al., (2021) [19]	CNN architecture	13384 2d (321subj*)	Acc=0.81, Rec=0.88,Spec=0.65
Placenta	Hu et al.,(2019) [20]	U-Net with CRF-RNN	1567 2d (248sub*)	Dsc=0.91, Acc=0.92
Placenta	Zimmer et al.,(2019)	3D-CNN Architecture	43 3d (31 sub*)	Dsc=0.81
Placenta	Looney et al., (2018) [21]	OxNNet to estimate SGA	2393 3d (3105 sub*)	DSC=0.85, Hd=14.7mm
Plecenta	Zimmer et al., (2020) [22]	CNN with U-Net	32228 2d (66 sub*)	DSC=0.82, Hd=31.85 mm
head	Cerrolaza et al., (2018) [23]	Two level CNN	70 3D	DSC=0.84, IoU=0.71
head	Perez-Gonzalez et al.,(2020) [24]	11 3D (19 sub*)	8 3D (19 sub*)	DSC=0.80, AUC=0.81
head	Wang et al.,(2020) [25]	Cyclic Consistent GANs with DGCC	999 2D	DSC=0.93
Amniotic Fluid	Li et al., (2017) [26]	CNN with Pooling	1302 2D	Acc=0.77, IoU=0.55
Amniotic Fluid	Cho et al.,(2021) [27]	DL network (AF-Net)	435 2D (156 subjects*)	DSC=0.88, Prec=0.87,Rec=0.86, Spec=0.98

Authorized licensed use limited to: DELHI TECHNICAL UNIV. Downloaded on May 29,2023 at 05:56:27 UTC from IEEE Xplore. Restrictions apply.

2) Kidney: For completing a pre-diagnosis of renal disorders, in-utero kidney testing is essential. A greater danger of kidney failure in adulthood has been associated with low kidney improvement. Decreased kidney functioning after delivery is also associated with poor foetal growth, providing a 3D U-Net for kidney fragmentation in this area that utilizes 3D B-mode and Power Sonic volumes. Instead of the small number of testing volumes, the algorithm obtains mean Dsc, IOU, and Hd of 0.82, 0.68, and 8.95 mm when tested on 20 3D pictures.

3) Spine: Scoliosis, masses, diastematomyelia, vertebra segmentation abnormalities, sacral agenesis, spinal dysgenesis, and spondylothoracic or spondylocostal dysplasia, among other abnormalities, have an influence on the length of the foetal spine, which provides information on foetal development. The study mainly focuses on the detection of the spine center line from 3D Ultrasound images to offer an evaluation of foetal spine. Spine segmentation is carried out using a CNN, which analyses pictures of various sizes and fields of view. The forecast is sent into a model-based tracing method that draws the spine centerline.

4) HEAD: An important aspect of sonographic testing is the appraisal of the foetal head. This assessment is based on the supervisor's practiced and intrinsic Ultrasound image features. To mitigate this argument, Deep learning algorithms in the article primarily focus on foetal head segmentation and present a 2 stage method for skull segmentation in neonatal 3D Ultrasound. The skull is loosely segmented using a 3D U-Net. This segmentation was sent into a second 3D UNet along with two extra channels. Upon testing on 15 volumes, the model achieves DSC and Intersection over union values of 0.84 and 0.71, respectively.

DISCUSSION AND CONCLUSION

This study looked at a wide range of contemporary Deep learning methods for analyzing foetus ultrasound images. Fetal Ultrasound image analysis has been around since the middle of the 20th century, and there is a sizable and varied collection of research available today. Among the most explored jobs, according to our data, are conventional plane identification.

What are the most studied tasks inside the field of deep learning for foetal picture analysis?The foetal brain, abdomen, and heart standard planes have received the greatest attention in standard plane detection since biometric measures and abnormality diagnosis are mostly done on these planes. For evaluating the quality of each examined plane, it is essential to identify certain feature points; hence classifiers or awareness processes are heavily used in this field. The HC is the measurement that has received the most investigation regarding biometric recognition parameter estimation. The most often used methodologies are segmentation (with potential pre-processing for head localization) followed by fitting algorithms.

The foetal cardiac examination described in the literature is intended to discover heart defects and genetic disorders as early as possible. The detection rate is frequently increased by first detecting the major foetal cardiac planes.

What are the primary issues in foetal examination that are now being addressed by employing Deep learning?According to our study, In order to help clinicians in a wide range of therapeutic applications, DL is now able to handle USimage-related challenges such homogeneities, blemishes (such as shades), poor contrast, and trans and cross collection and measurement variability.

Existing Deep learning methods are reliable for handling sole center datasets gathered and annotated by 1 or 2 specialists, frequently from a single Ultrasound computer, for classical plane detection.

Deep learning has proven to be a crucial approach for assisting in the segmentation method of various anatomical structures, which might also differ in form and size throughout GA, in the anatomical-organ competition.

Are the regularly used datasets sufficient for the creation and testing of robust Deep Learning algorithms?In the field of medical image analysis, gathering and disseminating significant explain for the creation of algorithms using deep learning is a well-known problem.

Only a few datasets are currently available in the American foetal field. Aside from practical difficulties (annotating data is a time-consuming procedure), social and ethical concerns must be addressed. All of these elements should be carefully examined in collaboration with non-technical people in order to allay their worries (e.g., lawyers, ethicists, ...).The creation of reliable and generalized results algorithms depends on this phase. Almost all of the articles that were assessed had fewer than 1000 pictures, and some of them included as little as 300.

Additionally, several of the publications don't mention how many photographs were used.

The patient number, which is necessary to prevent utilizing the same female's scan in both the training/validation and test sets, must always be supplied in order to ensure a high level of resilience.

Cross-validation is strongly advised when there is a tiny data sample available, particularly when dealing with a number of co-scenarios.

IV. FUTURE WORK

Following that, we describe the key outstanding challenges and future research initiatives in the field of foetal Ultrasound image analysis that we have discovered.

A. Multi-expert image annotation:

A significant disadvantage nowadays is that many practitioners do not annotate photos. This multi-expert markup is crucial for the development of efficient Deep learning techniques and the accurate analogy of algorithm performance, despite the fact that it is undoubtedly expensive in terms of both money

Authorized licensed use limited to: DELHI TECHNICAL UNIV. Downloaded on May 29,2023 at 05:56:27 UTC from IEEE Xplore. Restrictions apply.

and time to have several expert annotators. Additionally, inter-clinician variability, a metric for picture complexity, might be investigated.

When using hand annotation as the level of standardization for the study, it is important to carefully consider result interpretation in light of these restrictions.

B. Semi, weak and self-supervised learning:

Researchers in related fields are putting forth semi, weakly, or self-supervised techniques to address the problem of having small datasets of labeled data. Only 8 of 30 papers in the foetal US area address the possibility of such techniques. These include the classification and detection of planes, as well as the investigation of cross-device adaption difficulties. For scan plane recognition, foetal position estimate, probe movement estimation, and foetal 3D reconstruction, self-supervised approaches are applied. Other intriguing approaches suggest unsupervised learning strategies for multi-organ categorization and biometry estimation in low-cost US devices.

REFERENCES

[1] J. Dong, S. Liu, and T. Wang, "ARVBNet: Real-time detection of anatomical structures in fetal ultrasound cardiac four-chamber planes," in Machine Learning and Medical Engineering for Cardiovascular Health and Intravascular Imaging and Computer Assisted Stenting.Springer, 2019, pp. 130–137.

[2] W. Huang, C. P. Bridge, J. A. Noble, and A. Zisserman, "Temporal HeartNet: towards human-level automatic analysis of fetal cardiac screening video," in International Conference on Medical Image Computing and Computer-Assisted Intervention. Springer, 2017, pp. 341–349.

[3] Y. Gao and J. A. Noble, "Detection and characterization of the fetal heartbeat in free-hand ultrasound sweeps with weakly-supervised twostreams convolutional networks," in International Conference on Medical Image Computing and Computer-Assisted Intervention. Springer,2017, pp. 305–313.

[4] M. Rachmatullah, S. Nurmaini, A. Sapitri, A. Darmawahyuni, B. Tutuko, and F. Firdaus, "Convolutional neural network for semantic segmentation of fetal echocardiography based on four-chamber view," Bulletin of Electrical Engineering and Informatics, vol. 10, no. 4, pp. 1987–1996, 2021.

[5] S. An, H. Zhu, Y. Wang, F. Zhou, X. Zhou, X. Yang, Y. Zhang, X. Liu, Z. Jiao, and Y. He, "A category attention instance segmentation network for four cardiac chambers segmentation in fetal echocardiography," Computerized Medical Imaging and Graphics, vol. 93, p. 101983,2021.

[6] J. Tan, A. Au, Q. Meng, S. FinesilverSmith, J. Simpson, D. Rueckert,R. Razavi, T. Day, D. Lloyd, and B. Kainz, "Automated detection of congenital heart disease in fetal ultrasound screening," in Medical Ultrasound, and Preterm, Perinatal and Paediatric Image Analysis. Springer, 2020, pp. 243–252.

[7] M. Komatsu, A. Sakai, R. Komatsu, R. Matsuoka, S. Yasutomi, K. Shozu, A. Dozen, H. Machino, H. Hidaka, T. Arakaki et al., "Detection of cardiac structural abnormalities in fetal ultrasound videos using deep learning," Applied Sciences, vol. 11, no. 1, p. 371, 2021.

[8] S. Qiao, S. Pang, G. Luo, S. Pan, Z. Yu, T. Chen, and Z. Lv, "Rlds: An explainable residual learning diagnosis system for fetal congenital heart disease," Future Generation Computer Systems, vol. 128, pp. 205–218,2022.

[9] B. Pu, N. Zhu, K. Li, and S. Li, "Fetal cardiac cycle detection in multiresource echocardiograms using hybrid classification framework," Future Generation Computer Systems, vol. 115, pp. 825–836, 2021.

[10] M. K. Wyburd, L. S. Hesse, M. Aliasi, M. Jenkinson, A. T. Papageorghiou, M. C. Haak, and A. I. Namburete, "Assessment of regional cortical development through fissure based gestational age estimation in 3D fetal ultrasound," in Uncertainty for Safe Utilization of Machine Learning in Medical Imaging, and Perinatal Imaging, Placental and Preterm Image Analysis. Springer, 2021, pp. 242–252.

[11] L. H. Lee, E. Bradburn, A. T. Papageorghiou, and J. A. Noble, "Calibrated bayesian neural networks to estimate gestational age and its uncertainty on fetal brain ultrasound images," in Medical Ultrasound, and Preterm, Perinatal and Paediatric Image Analysis. Springer, 2020, pp. 13–22.

[12] F. Moser, R. Huang, A. T. Papageorghiou, B. W. Papiez, and A. I.Namburete, "Automated fetal brain extraction from clinical ultrasound volumes using 3D convolutional neural networks," Communications in Computer and Information Science, p. 151–163, 2020.

[13] L. Venturini, A. T. Papageorghiou, J. A. Noble, and A. I. Namburete,"Multi-task CNN for structural semantic segmentation in 3D fetal brain ultrasound," Communications in Computer and Information Science, p. 164–173, 2020.

[14] R. Huang, W. Xie, and J. A. Noble, "Vp-nets: Efficient automatic localization of key brain structures in 3D fetal neurosonography," Medical Image Analysis, vol. 47, pp. 127–139, 2018.

[15] V. Singh, P. Sridar, J. Kim, R. Nanan, N. Poornima, S. Priya, G. S. Reddy, S. Chandrasekaran, and R. Krishnakumar, "Semantic segmentation of cerebellum in 2D fetal ultrasound brain images using convolutional neural networks," IEEE Access, vol. 9, pp. 85 864– 85 873, 2021.

[16] M. K. Wyburd, M. Jenkinson, and A. I. L. Namburete, "Cortical plate segmentation using CNNs in 3D fetal ultrasound," in Medical Image Understanding and Analysis, B. W. Papiez, A. I. L. Namburete, ˙ M. Yaqub, and J. A. Noble, Eds. Springer International Publishing, 2020, pp. 56–68.

[17] "Automatic 3D ultrasound segmentation of the first trimester placenta using deep learning," in 2017 IEEE 14th International Symposium on Biomedical Imaging. IEEE, 2017, pp. 279–282.

[18] B. U. Oguz, J. Wang, N. Yushkevich, A. Pouch, J. Gee, P. A. Yushkevich, N. Schwartz, and I. Oguz, "Combining deep learning and multi-atlas label fusion for automated placenta segmentation from 3DUS," in Data Driven Treatment Response Assessment and Preterm, Perinatal, and Paediatric Image Analysis. Springer, 2018, pp. 138–148.

[19] Z. Hu, R. Hu, R. Yan, C. Mayer, R. N. Rohling, and R. Singla, "Automatic placenta abnormality detection using convolutional neural networks on ultrasound texture," in Uncertainty for Safe Utilization 29 of Machine Learning in Medical Imaging, and Perinatal Imaging, Placental and Preterm Image Analysis. Springer, 2021, pp. 147–156.

[20] R. Hu, R. Singla, R. Yan, C. Mayer, and R. N. Rohling, "Automated placenta segmentation with a convolutional neural network weighted by acoustic shadow detection," in 2019 41st Annual International Conference of the IEEE Engineering in Medicine and Biology Society, 2019, pp. 6718–6723.

[21] P. Looney, G. N. Stevenson, K. H. Nicolaides, W. Plasencia, M. Molloholli, S. Natsis, and S. L. Collins, "Fully automated, real-time 3D ultrasound segmentation to estimate first trimester placental volume using deep learning," JCI insight, vol. 3, no. 11, 2018.

[22] V. A. Zimmer, A. Gomez, E. Skelton, N. Ghavami, R. Wright, L. Li,J. Matthew, J. V. Hajnal, and J. A. Schnabel, "A multi-task approach using positional information for ultrasound placenta segmentation," in Medical Ultrasound, and Preterm, Perinatal and Paediatric Image Analysis. Springer, 2020, pp. 264–273.

[23] J. J. Cerrolaza, M. Sinclair, Y. Li, A. Gomez, E. Ferrante, J. Matthew,C. Gupta, C. L. Knight, and D. Rueckert, "Deep learning with ultrasound physics for fetal skull segmentation," in 2018 IEEE 15th International Symposium on Biomedical Imaging, 2018, pp. 564–567.

[24] J. Perez-Gonzalez, N. H. Montiel, and V. M. Banuelos, "Deep learning ˜spatial compounding from multiple fetal head ultrasound acquisitions,"in Medical Ultrasound, and Preterm, Perinatal and Paediatric Image Analysis. Springer, 2020, pp. 305–314.

[25] L. Wang, D. Guo, G. Wang, and S. Zhang, "Annotation-efficient learning for medical image segmentation based on noisy pseudo labels and adversarial learning," IEEE Transactions on Medical Imaging,2020.

[26] Y. Li, R. Xu, J. Ohya, and H. Iwata, "Automatic fetal body and amniotic fluid segmentation from fetal ultrasound images by encoderdecoder network with inner layers," in 2017 39th Annual International Conference of the IEEE Engineering in Medicine and Biology Society. IEEE, 2017, pp. 1485–1488.

[27] H. C. Cho, S. Sun, C. M. Hyun, J.-Y. Kwon, B. Kim, Y. Park, and J. K.Seo, "Automated ultrasound assessment of amniotic fluid index using deep learning," Medical Image Analysis, vol. 69, p. 101951, 2021

Authorized licensed use limited to: DELHI TECHNICAL UNIV. Downloaded on May 29,2023 at 05:56:27 UTC from IEEE Xplore. Restrictions apply.

e-ISSN: 2582-5208
International Research Journal of Modernization in Engineering Technology and Science
(Peer-Reviewed, Open Access, Fully Refereed International Journal)
Volume:05/Issue:05/May-2023 Impact Factor- 7.868 www.irjmets.com

REVIEW PAPER ON AIR GAUGING FOR INDUSTRY 4.0

Aditya Mudgal[*1], Anmol Sharma[*2], AK Madan[*3]

[*1,2]Student, Department Of Mechanical Engineering, Delhi Technological University, New Delhi, India.

[*3]Professor, Department Of Mechanical Engineering, Delhi Technological University, New Delhi, India.

ABSTRACT

The aim of this paper is to study the uses and applications of Air Gauging in Industry 4.0. This paper reviews how air gauging has improved in both static and dynamic states in context with the fourth industrial revolution. This papers talks about the control, monitoring and integration of computer systems to air gauges according to industry 4.0.

I. INTRODUCTION

Pneumatic devices were perhaps originally used for dimensional measurements as early as 1917. Tanner examined the past and future of air gauging in 1958 and predicted: "As electronics are increasingly employed as the "brains" of automatic machining, air-operated gauges will be selected as the "eyes," to assess and signal or transmit impulses in accordance with the process's progress." After fifty years, in 2008, Schuetz enumerated the benefits of air gauging and said, "It is difficult to understand how a small hole could be so important."

The phrase "Industry 4.0" was first used in 2011 to define the digital transformation of production as a fourth industrial revolution. It grew in prominence despite some scholars claiming there was no systematic strategy exhibiting the specific features of an Industry 4.0 revolution. Instead, Industry 4.0 is typically defined as the fusion of various ideas and technologies that integrate biological, digital, and physical processes and that result in a fund.

Big Data & Analytics, which covers the processing of all sorts and quantities of data through data collection, ordering, record and storage, retrieval, real-time analysis, and dissemination that may go beyond simple automation and process optimisation.

Simulation is the process of creating a model of a system, either real or hypothetical, to describe and analyse the system's performance, which includes creating a model, which is typically a condensed set of assumptions expressed by a mathematical or logical relationship, and allowing the model to run over time while simulating the process of interrelated elements.

The Industrial Internet of Things (IIoT) facilitates the integration of operational technologies (OT) and information technology (IT) domains via the automation of industrial processes important to machine-to-machine communication, especially where a considerable quantity of data is involved Robots have a high degree of autonomy and can complete tasks in real time without the need for human intervention.

Protection of manufacturing systems from cyberattacks that could have a negative impact, such as (1) infrastructure sabotage or machine and component sabotage, (2) denial of basic network and computer functions, (3) crimes such as intellectual property theft, (4) safety violations and environmental pollution.(5) Workplace risks and potentially fatal situations.

Vertical system integration focuses on the alignment of people, equipment, organisations, and products, whereas horizontal system integration connects procurement, planning, management, and customer services with business counterparties.

The cloud provides almost endless on-demand processing, storage, and communication capabilities.

Layers of a raw material may be added to make items and components utilising a number of additive manufacturing procedures. The purpose of augmented reality, a sort of "immersive technology," was to enhance workplace interactions by increasing visual awareness of adjacent things without really replacing virtual objects for the real thing.

e-ISSN: 2582-5208
International Research Journal of Modernization in Engineering Technology and Science
(Peer-Reviewed, Open Access, Fully Refereed International Journal)
Volume:05/Issue:05/May-2023 Impact Factor- 7.868 www.irjmets.com

Four of them, in particular—Additive Manufacturing, AI, the Internet of Things, and Big Data—could be named as essential technologies that support circular product lives through improved product design, maintenance, redistribution, and recovery. Implementing Industry 4.0 ideas thus contributes significantly to industrial innovation and sustainability.

II. AIR GAUGING FOR INDUSTRY 4.0

Monitoring and control are the instruments most commonly used in industrial operations in the context of the Industry 4.0 plan , and air gauges have historically been used in this type of control systems, and in-process control may be seen as one of the forerunners of real-time process monitoring and decision-making. Indeed, "some of the development of in-process gauging systems for turning machines has been developed along the principle of air gauging."

Raghavendra cited non-contact examination, minimal gauging force, the potential for varied inspection (size variability), and the potential for attribute inspection (GO) as key benefits of air gauges in his guidebook.

It is widely acknowledged that air gauges are ideal measuring tools for a final examination of machine parts such as shafts and inspection of nuclear graphite's machined pieces. More specifically, air gauges can be used to measure cutting force, 2D roughness, surface topography, moving surfaces, wheel-tooling gap measurement in extrusion machinery, continuous tool wear monitoring, or gap control between machined pieces.

Numerous summaries and reviews on the subject were published during the century-long development of air gauging . However, as reports on other, recently developed measurement methods increased, scientific interest in air gauging significantly decreased in recent decades. Limiting the time frame to the years 2012–2022, it was determined that it was crucial to analyse the most recent research publications in the current study. It is consistent, at least in part, with the finding that Intelligent Manufacturing in the year 2000 was primarily related to computer-aided design (CAD), flexible manufacturing systems, expert systems, fuzzy logic, and neural networks, whereas the development of contemporary Smart Manufacturing in the year 2010 was centred on Industry 4.0 and automation. In order to address the constantly expanding need for mass-customized items, smart manufacturing must be implemented in today's society, claim Baroroh et al. The era of Industry 4.0 necessitates that traditional manufacturing technologies empowered by artificial intelligence and by the Industrial Internet of Things (IIoT) have become "smart" at handling the extremely complex tasks as a result of recent advancements in both information and operation technologies (IT and OT) .What does it signify for air gauging is the purpose of the current investigation. Will it be abandoned or will there be a new opportunity for development?

Industry 4.0 is widely regarded as the primary strategy for increasing the competitiveness of the manufacturing sector. It is motivated by advances in information, communication, and automation technologies, particularly the internet of things, artificial intelligence, big data, collaborative and cooperative robots, modelling and simulation, and is triggered by the need for shorter innovation and development cycles.

Lack of regulation and expertise may be a barrier for industry when it comes to implementing new technologies, but other challenges include a lack of knowledge of the design of the processes or deciding which of the existing solutions may be modified to meet the demands . It appears necessary to collect more data in order to provide high reliability of the models because the technologies that fall under the umbrella of Industry 4.0 are relatively new and the models are still in development.

Manufacturing's primary concern is dimensional metrology, which is also one of the pillars of mechanical engineering .Instead of using individual measuring instruments, Industry 4.0 employs dispersed measuring devices and sensor networks, making traceable co-calibration difficult, and a comprehensive method for a metrological assessment of all sensor networks is required by giving a clear assessment of measurement uncertainties, namely requirements, repeatability, and reproducibility.

Since air gauges still provide adequate magnification and high reliability in tolerance measurements that far exceed the capabilities of mechanical gauges, they appear to be able to meet those requirements. Air gauges are comparators that may be used in metrology and inspection procedures unique to the additive manufacturing process. They evaluate the difference between the actual dimension and the standard rather than performing an absolute measurement. Frequently, conventional probes and gauges are too big to be used for micropart

e-ISSN: 2582-5208
International Research Journal of Modernization in Engineering Technology and Science
(Peer-Reviewed, Open Access, Fully Refereed International Journal)
Volume:05/Issue:05/May-2023 Impact Factor- 7.868 www.irjmets.com

inspection. Systems for measuring must assess the characteristics or dimensions of a part using air, light, or other noncontact scanning techniques. Micromanufacturing is increasingly dependent on 3D metrology for micro/nanodevices and features . Air gauging might offer an effective way to measure the size of the hole in the turbine blade between the tight-fitting plug and the loose one, but this approach only performs effectively over a very small range of hole sizes . Additionally, it is unable to recognise crucial aspects of the holes' flaws. Air injection devices can be utilised in aerosol-assisted procedures for the creation of submicron particles ,but they are ineffective in this situation as a tool for measuring dimensions. Nevertheless, there are numerous reports on the use of air gauging in AGILE systems (Air Gauge Improved Levelling) to level a die correctly and lessen the reliance of lithography scanner control on the process . Since the AGILE application is a for-profit system offered by ASML, little is known about how it functions except that it offers measurement correction for the level sensor . By correcting for the optical effects, Dong et al. modified the AGILE approach to enhance the optical level sensor. In their method, the scanner was permitted to produce "optical-to-air-gage" focus corrections for each lot or each exposed wafer. Despite some drawbacks, the authors discovered that using AGILE in the 40 nm Via-PH process can be beneficial for the lithographic technology node, where calibration of the optical level sensor was carried out using an air gauge sensor with AGILE system.

Investigations into the Static Properties of Air Gauges

The primary characteristics of compressed air, thermodynamic processes, and some fluid mechanics rules with regard to the geometry of the flow-through components must all be taken into account while projecting and utilising air gauges . Jermak discussed the intricate phenomena, highlighting the supersonic regions and the emergence of a vacuum ring in the flapper-nozzle region, which led to discontinuity and hysteresis in the metrological characteristics. The author also looked at the compressed air stream's expansion in the measurement chamber immediately following the entrance nozzle. Based on the findings, he made some recommendations for the nozzles' geometrical characteristics and for the best placement of the pressure transducer within the measurement chamber. Burazer et al. looked at how the angle of a measuring nozzle affected the pressure distribution on the surface being measured, as well as how that affected the air gauge's sensitivity and measurement range. Despite not finding a clear trend regarding the changes in sensitivity caused by the measuring nozzle inclination, the authors showed that the inclination had a positive effect on the performance of the air gauge. The vacuum zone in the flapper-nozzle region was determined to have moved away from the nozzle's longitudinal axis after analysis. This implies that there will be a decrease in impurities accumulating. Measurement of nozzle tilt is advantageous from the standpoint of pneumatic metrology applications since it reduces the size of the vacuum area. The translation of the vacuum zone away from the axis of the measurement nozzle is another advantageous result of nozzle tilt.

Jakubowicz and Derezynski proposed an automated, computerised laboratory setup for the experimental assessment of air gauge static properties, with three distinct systems: pneumatic, electrical, and mechanical. The mechanical and pneumatic systems interact in the region around the flapper-nozzle, and the electronic system gathers signals from both while performing critical control activities.

According to the authors, in addition to measuring back pressure and air temperature and mass flow, correctly prepared compressed air flows to an air gauge after passing via an air flow metre. The test rig was designed for analysis of an open-jet straight cascade gauge, in which compressed air passed from a feeding chamber through a restriction to the measuring chamber, through the measuring nozzle and flapper-nozzle slot to the atmosphere. The air gauge may represent any type of constructional structures. To test the air gauges of the necessary metrological properties, such as multiplication and measurement, both the inlet and measuring nozzles are interchangeable. The authors used specialised software developed by their team, with an easy-to-use user interface that enables real-time management of the measuring procedure and online tracking of the data. This makes it possible to effectively link the created test rig with the experimentally discovered air gauge properties to the IoT and big data analysis, essential for the Industry 4.0 concept.

Various models for estimating air gauge performance were proposed globally throughout the twentieth century. One option is to calculate the air flow using the air-electric equivalency approach, which takes both the air flow and the electric current into account. The potential energy of an electric current is represented by voltage, while the potential energy of an air flow is represented by air flow pressure.

e-ISSN: 2582-5208
International Research Journal of Modernization in Engineering Technology and Science
(Peer-Reviewed, Open Access, Fully Refereed International Journal)
Volume:05/Issue:05/May-2023 Impact Factor- 7.868 www.irjmets.com

Because the thermodynamic phenomena in the air gauge cascade were so complex, numerous researchers combined theoretical formulas with experimental findings . In a steady-state empirical-mechanistic modelling, first- and second-order empirical polynomial approximation functions were integrated with mathematical calculations based on the existing theoretical background

III. DYNAMICS CHARACTERISTICS INVESTIGATION

For a long time, the dynamic characteristics of air gauges were thought to be their weak point. However, it was demonstrated that under certain conditions, the air gauging system's time constant could be improved to several milliseconds , which was made possible by modifications in construction that allowed the direct use of piezoresistive pressure transducers in the measurement chamber's smaller capacities.

Jermak et al. investigated several mathematical models for the dynamic properties of air gauges, where the back-pressure is time-dependent pk(t) due to the unstable condition of the input value z(t), and discovered that the second key air flow characteristics, which mostly depend on the geometry of the nozzles used in the actual arrangement of the air gauges, could be used to approximate air flow in the most accurate way.

Jakubowicz et al. investigated the effect of input nozzle diameter on the dynamic performance of an air gauge. The air gauges' dynamics deteriorated as expected.

IV. UNCERTAINTY ESTIMATES FOR AIR GAUGING SYSTEMS

Because the reduction of uncertainty should be correlated with an increase in information, the Industry 4.0 concept calls for special attention to be paid to the uncertainty budget . Jermak and his study group have looked at the uncertainty of an air gauging and, in particular, of a corresponding test rig . It was possible to identify between the mechanical, electrical, and air supply systems during the analysis. Since the laboratory was isolated from vibrations and constantly monitored for ambient pressure, humidity, and temperature, it was found that the controlled laboratory conditions were able to minimise the environmental effect. While the entire measurement process was fully automated, the operator's influence on the measurement results was reduced to the fixation of the examined air gauge, zero setting, and initial data input. The mechanical test rig system, reference inductive gauge, back-pressure indicators, and data processing each have their own estimates of uncertainties. They found that for a single measurement U0.95 = 0.260 kPa, which matched the dimensions measurement of 0.52 m, they had the findings with the biggest enlarged uncertainty (degree of confidence, 95%). Finally, equipment variation (EV) was calculated, accounting for both test rig and air gauge testing uncertainties. It contained variations for various air gauge designs and for various static characteristic points.

Similar to that, evaluated and reported on the uncertainty estimation for the dynamical properties. Different input frequencies could be set using the dynamic calibration apparatus, which produced mechanical sine input with an eccentric shaft. The studies were run for various air gauge measuring chamber volumes, ranging from Vmin = 0.5 cm3 to Vmax = 4.0 cm3. The authors identified three main sources of uncertainty: one relating to the pneumatic system (air supply, geometry of the air gauge components, pressure transducer, etc.), another relating to the mechanical system generating the periodically changing slot, and a third relating to data processing (averaging, smoothing algorithms, interpolation, linearization, etc.). The maximum frequency f 0.95—which represented the working frequency when the dynamic error of the amplitude did not exceed 5%—was calculated from the acquired amplitude-frequency graph. According to the JCGM recommendations , Type A standard uncertainty u(x) was considered to be equal to the standard deviation because the findings showed a distribution that was near to the Gaussian one. For a time constant of 0.001 seconds, the authors calculated expanded uncertainties for coverage factor k = 2, which corresponded to a 95% confidence level.

V. COMPUTER SYSTEMS INTEGRATED WITH AIR GAUGES

Air gauges may be combined with computers to construct sophisticated computer systems since the back-pressure signal can be easily converted to digital form . A computer, an electrical module, and a pneumatic system are the three components that make up Jermak's unique Pneustar measuring equipment . In order to adapt multiplication to the actual measuring task, the entrance nozzle was built in the shape of a programmable needle restrictor. The computer was given a set of theoretical static characteristics so that calibration could be done with just one setting ring. Through the calibration table, the exchangeable measuring head's respective

e-ISSN: 2582-5208
International Research Journal of Modernization in Engineering Technology and Science
(Peer-Reviewed, Open Access, Fully Refereed International Journal)
Volume:05/Issue:05/May-2023 Impact Factor- 7.868 www.irjmets.com

linearized characteristics are recorded and are readily accessible. On the other hand, linearity improvement in larger range was possible through application of three or more setting masters, thus, in fact, stitching together digi- tally several sections of the same air gauge characteristic . The authors showed that this method increased the measurement range by 50% while maintaining a linearity error of 1%. These capabilities, together with additional data processing options, might be regarded as requirements required for Industry 4.0 applications. With them, air gauge can be integrated to IoT device system possessing data storage, processing ability, system software, operating systems, preloaded applications, and communication resources.

VI. RECENT APPLICATIONS OF SPECIFIC AIR GAUGE

Tanaka and Koshy demonstrated the viability of a pneumatic sensor application for in-process monitoring of grinding wheel performance. The nominal distance in millimetres (m) between the measuring nozzle surface and the edge of the wheel. Due to the porous nature of the monitoring wheels, the scientists were able to use smaller nozzle sizes, but their use appeared to be limited.

The use of flood grinding fluid had no effect on the air gauging technique, and wheels for grinding with metal bonding were shown.

The experimental setup for a burnishing procedure, according to Stalin John et al. , involved measuring the penetration allowed using an air gauge, recording it, and then processing the data using the FANUC programme. The penetration allowed was fine-tuned for each attempt and measured once more using air gauges, while the bore diameters following burnishing were measured by additional digital air gauges.

Yen et al. designed an online quality inspection method based on air gauging for the production of automobile components, using a real-time monitoring module to collect signals from the manufacturing process and then analysing the feature values. The authors identified three stages of development: (1) signal processing and feature extraction; (2) implementation of quality inspection rules and thresholds; and (3) product development.

Third, tests were performed to collect data on vibrations and control signals and compare them with relevant quality inspection data from the air gauge in order to determine the relationship between vibration and cutting accuracy. Authors developed thresholds and guidelines for online precision diagnosis using big data from a historical data collection, and then deployed the system by connecting each subsystem to the actual manufacturing line for validation.

When the results of their unique system were compared to those of the reference Taylor-Hobson Talyrond 365 equipment, the relative error of the results was less than 10%.

Damir et al. investigated surfaces with complicated geometry such as truncated grooves and milled surfaces at various speeds and derived a relationship between back-pressure and displacements from the registered air gauge response, demonstrating good agreement between theoretical estimates and actual findings.

VII. CONCLUSION

This analysis of recent research reports on air gauging yielded several significant findings. For starters, despite a dramatic decline in the number of articles published, research is still being done to improve air gauges and, more importantly, to make them compatible with the Industry 4.0 concept and technologies. Notably, back-pressure air gauges were the focus of the studies.

Both static and dynamic features are investigated in order to produce better parameters and mathematical models; the use of more exact models that integrate theoretical formulae with practical data is shown and justified, as is the use of simpler models with acceptable accuracy.

The researchers demonstrated that open jet back-pressure type air gauges provide excellent accuracy while retaining all of the well-known benefits of pneumatic measurement, such as the lack of mechanical contact and friction, the ability of the measured surface to self-clean, or indifference to ambient work circumstances. It was demonstrated that steady-state measurement uncertainty for air gauging systems combined with electronic transducers and computer systems could be less than 0.52. Most of the Industry 4.0 constituent technologies are mentioned in the papers under review and are linked to air gauging in some way. Authors increasingly link air gauges with big data analytics, modelling and simulations, and integration with IT into IIoT systems, while keeping the. Digitization of measurement findings with further data processing in sensor network frames is

critical for Industry 4.0 installations. The publications that were reviewed suggested this line of inquiry and relevant equipment. The suggested techniques, in particular, allowed for digital linearization, streamlined calibration procedures, and automatic recall of the recorded features.

The maturity and readiness of Industry 4.0 deployment will be discussed in reports on attempts to integrate air gauges to existing or developed industrial. Additionally, it appears inevitable that some research will focus on using artificial intelligence in the filtration and interpretation of the signal from the air gauge. Algorithm verification, machine-readable calibration, the use of metrology cloud technology are all expected to surface in the near future.

VIII. REFERENCES

[1] Kebisek, M.; Tanuska, P.; Spendla, L.; Kotianova, J.; Strelec, P. Artificial Intelligence Platform Proposal for Paint Structure Quality Prediction within the Industry 4.0 Concept. IFAC Pap. **2020**, 53, 11168–11174

[2] Koehn, C. In-Process Air Gaging. Qual. Mag. **2014**, 53, 22–23.

[3] Stout, K. Quality Control in Automation; Kogan Page: London, UK, 1985.

[4] Eichstädt, S.; Keidel, A.; Tesch, J. Metrology for the digital age. Meas. Sens. **2021**, 18, 100232.

[5] Jain, V.K. Manufacturing Processes; CRC Press: Boca Raton, FL, USA, 2013.

[6] Jermak, C.J.; Rucki, M. Static Characteristics of Air Gauges Applied in the Roundness Assessment. Metrol. Meas. Syst. **2016**, 23,85–96.

[7] Jakubowicz, M. Accuracy of roundness assessment using air gauge with the slot-shaped measuring nozzle. Measurement **2020**,155, 107558.

[8] Schuetz, G. It is Never Too Late to Teach an Old Custom Gage New Tricks. Qual. Mag. **2022**, 61, 14.

[9] Jermak, C. Concept of the pneumatic devices PneuStar for dimensional measurement. Apar. Badaw. Dydakt. **2013**, 18, 25–30.(In Polish).

[10] Gluchow, W.J.; Tupolew, A.A. Non-contact pneumatic measuring control devices for the production of workpieces with discontin-uous surfaces. Feingeratetechnik **1974**, 23, 69–73. (In German).

[11] Balakšin, O.B. Automation of the Industrial Pneumatic Dimensional Measurement; Mashinostroenie: Moscow, Russia, 1964.(In Russian).

Journal of The Electrochemical Society

The Electrochemical Society
Advancing solid state & electrochemical science & technology

ACCEPTED MANUSCRIPT • OPEN ACCESS

Review—Magneto-Electrochemical-based Biosensors Devices for Recognition of Tumour Vesicles from Blood Plasma

To cite this article before publication: Anusuiya Bora *et al* 2023 *J. Electrochem. Soc.* in press https://doi.org/10.1149/1945-7111/acd350

Manuscript version: Accepted Manuscript

Accepted Manuscript is "the version of the article accepted for publication including all changes made as a result of the peer review process, and which may also include the addition to the article by IOP Publishing of a header, an article ID, a cover sheet and/or an 'Accepted Manuscript' watermark, but excluding any other editing, typesetting or other changes made by IOP Publishing and/or its licensors"

This Accepted Manuscript is **© 2023 The Author(s). Published on behalf of The Electrochemical Society by IOP Publishing Limited**.

As the Version of Record of this article is going to be/has been published on a gold open access basis under a CC 4.0 licence, this Accepted Manuscript is available for reuse under the applicable CC licence immediately.

Everyone is permitted to use all or part of the original content in this article, provided that they adhere to all the terms of the applicable licence referred to in the article – either https://creativecommons.org/licenses/by/4.0/ or https://creativecommons.org/licenses/by-nc-nd/4.0/

Although reasonable endeavours have been taken to obtain all necessary permissions from third parties to include their copyrighted content within this article, their full citation and copyright line may not be present in this Accepted Manuscript version. Before using any content from this article, please refer to the Version of Record on IOPscience once published for full citation and copyright details, as permissions may be required. All third party content is fully copyright protected and is not published on a gold open access basis under a CC licence, unless that is specifically stated in the figure caption in the Version of Record.

View the article online for updates and enhancements.

This content was downloaded from IP address 14.139.251.98 on 11/05/2023 at 11:09

Review—Magneto-Electrochemical-based Biosensors Devices for Recognition of Tumour Vesicles from Blood Plasma

Journal:	*Journal of The Electrochemical Society*
Manuscript ID	JES-109521.R1
Manuscript Type:	Review Paper
Date Submitted by the Author:	27-Mar-2023
Complete List of Authors:	Bora, Anusuiya; Vellore Institute of Technology Sharma, Rashi; Delhi Technological University Gupta, Ishi; Vellore Institute of Technology Singh, Mahika; Vellore Institute of Technology Mukherjea, Nilabha; VIT Bhopal University Bartaria, Yuvraj Ranjan; Vellore Institute of Technology Chadha, Utkarsh; University of Toronto - St George Campus, Bhardwaj, Preetam; Vellore Institute of Technology, School of Electronics Engineering; Vellore Institute of Technology, VIT University Vellore Latha, Srinivasan; Vellore Institute of Technology Chakravorty, Arghya; Vellore Institute of Technology
Keywords:	Biosensor, Electrochemical Biosensor, Cancer Detection, Biomarkers

SCHOLARONE™
Manuscripts

Accepted Manuscript

Review—Magneto-Electrochemical based Biosensors Devices for Recognition of Tumour Vesicles from Blood Plasma

Anusuiya Bora,[1] Rashi Sharma,[2] Ishi Gupta,[3] Mahika Singh,[4] Nilabha Mukherjea,[5] Yuvraj Ranjan Bartaria,[4] Utkarsh Chadha,[6,z] Preetam Bhardwaj,[7,8] Srinivasan Latha,[9,z] and Arghya Chakravorty[1,8]

[1]School of Bio Science and Technology, Vellore Institute of Technology, Vellore, Tamilnadu, India – 632014;
[2]Department of Biotechnology, Delhi Technological University, Bawana, New Delhi - 110042, India
[3]School of Electronics Science and Engineering (SENSE), Vellore Institute of Technology, Vellore, Tamilnadu, India – 632014
[4]School of Chemical Engineering, Vellore Institute of Technology, Vellore, Tamilnadu, India – 632014
[5]School of Bio Engineering, Vellore Institute of Technology, Bhopal, Madhya Pradesh 466114, India
[6]Department of Materials Science and Engineering, Faculty of Applied Sciences and Engineering, School of Graduate Studies, University of Toronto, Toronto, Ontario ON M5S 2Z9
[7]Research and Development Cell, Battrixx, Kabra Extrusion Technik Limited, Chakan Industrial Area, Phase II, Village Bhamboli, Chakan, Tal-Khed, Pune-410501 India
[8]Center for Nanotechnology Research (CNR), School of Electronics Engineering (SENSE), Vellore Institute of Technology, Vellore, Tamilnadu, India – 632014
[9]Department of Chemistry, School of Advanced Sciences (SAS), Vellore Institute of Technology, Vellore, Tamilnadu, India – 632014

[z]E-mail: utkarsh.chadha@mail.utoronto.ca; latha.chinnu@gmail.com

Abstract

Today, cancer is analyzed after it has metastasized throughout the body. This understanding demands earlier identification of cancer to enable better opportunities for a cure. Viable and well-defined strategies to discover cancer and clinical determination are the need of the hour. Biosensors are devices intended to recognize a particular natural analyte by recognizing an organic element (i.e., protein, DNA, RNA) to produce the signals as an electrical signature that can be distinguished and investigated. The utilization of biosensors in disease recognition and observation holds immense potential in diagnosis and treatment. Biosensors can detect cancer biomarkers and decide drug adequacy at different objective destinations. Innovations attributed to biosensors can give a quick and exact location, dependable imaging of cancer cells, observe angiogenesis and disease metastasis, and have the capacity to decide the adequacy of anticancer chemotherapy for specialists. This review briefly summarizes the growing utilization of magneto-electrochemical biosensors as indicative devices and some of its future uses of biosensor innovation.

1. Introduction

Cancer is the most incessant and hazardous infection, with the most elevated death rate globally [1, 2]. In those instances, new cases of cancer have been reported worldwide [3, 4]. Determination of disease at the beginning phase can assume a basic part of its viable and effective treatment. Organic markers, in some cases called disease biomarkers (CB), shows superb hereditary attributes of the carcinogenic cells or any substance, design, or deal with that can be estimated in the body or its items and impact or, on the other hand, foresee the frequency of result or sickness. Biosensors are broadly utilized in detecting biomarkers worldwide as the most solid, quick, and exact logical technique [5-7]. To recognize disease biomarkers, biosensors use different bio-recognition components like antibodies, compounds, deoxyribonucleic corrosive (DNA), ribonucleic corrosive (RNA), cancer cells, corrosive nucleic tests, or other explicit biomolecules which are immobilized on a transducer surface [8]. The transducer changes natural signs acquired from the collaboration between target biomarkers and bio-recognition atoms into quantifiable signals, either electrical or optical [5].

Extracellular vesicles (EV) serve as a transmitter inside the cells which regulate cancer cell growth and survival chances. They are secreted by the cells, to regulate and help in signaling in cellular processes. EV act as the container for nucleic

Accepted Manuscript
For Review Only

acids, proteins, and lipids that can alter the neighbouring cells. Every transmission between the cells helps create metastatic activities inside the cells for cancer to spread [9]. Such vesicles hold their component in the lipid bilayer, which helps them to prevent degradation [9]. These cell-mediated vesicles are the ultimate carriers of maintaining cell balance, hence they are used for treatments to stop cancer growth [9]. EVs also contribute to drug delivery systems, as they have commendable biosafety and stability systems.

Biopsies have been used by clinicians to diagnose and manage the disease for 1,000 years. There are many difficulties in obtaining a tissue biopsy—including the discomfort suffered by the patient, inherent clinical risks to the patient, potential surgical complications, and economic considerations—meaning that multiple or serial biopsies are often impractical. The considerable interpatient heterogeneity of the primary tumor and metastases located at different sites does not reveal enough information to help with treatment decisions. When we discuss liquid biopsies, we refer to the application of circulating tumor cells (CTC) and cell-free circulating tumor DNA (ctDNA) released into the immediate environment of the tumor. [10] This method has its fair share of challenges which embodies the chances of contamination of the specimen and ctDNA post-blood collection from the patient. On the same tangent future studies must be conducted to understand the possibility of ctDNA-inducing apoptosis. [11] Though ctDNA sequencing methods provide greater sensitivity to detect extremely low levels of mutation, effective implementation remains a challenge. In light of these limitations on the use of single biopsies, new ways like biosensing have evolved.

With the onset of new technologies, new inventions stand to enter the market with ease and newfound efficiency. Whether based on intelligence, technologies, or diagnosis, biosensors have thrown a ray of light on such advances in past years. The working mechanism of biosensors is highly reliable, cost-effective, and accurate. Biosensors have grounded the foundation for diagnosis based on the extraordinarily reliable sensing scheme for researchers. Its diversified applications have led to a user-friendly detection system with high accuracy, cost-effectiveness, and sensitivity [12]. Various biosensors are attributed to different departments of detection, including biomedical, agricultural, environmental, security, healthcare, and food analysis (Figure 3) [13-18]. Biosensors have contributed to the development of humankind in ways for easy and promising detection. Such sensors are currently being devoted as a diagnostic measure patient's condition using handy instruments.

Biosensor detection is based on a recognition system in which three components, the analyte, bio receptor, and the transducer, come into the role (Figure 2) [19, 20]. Bio-receptors recognize the analyte, and the transducer converts the signal according to the output [19-22]. Brolo, A. G has mentioned that the futuristic goals of medical instruments are the miniaturized version, so biosensors play the utmost role here [23]. Whenever biosensors are discussed, it is worth noting the applications and domains of sensors attributed to diagnosing various pathogens, diseases, viruses, enzymes, bacteria, or any other biological biomarker. Much research has been conducted on these biosensors, like electrochemical, optical, or mass-based sensors. Electrochemical biosensors have been well known for their biological and clinical studies on various analytes interacting with the transducer surface and the recognition element [24, 25]. Since pathogens can be detected using various biotechnology strategies, like ELISA and other culturing methods. However, these processes seem to be lengthy and time-consuming, chances of contamination are high. Electrochemical sensors have shown major applications for these limitations. While on the other hand, they are highly specific, sensitive, and can be reused [24]. Povedeno, E et al. have mentioned the advantage of using an electrochemical-based sensing scheme for DNA methylation detection in the sequence [25].

Moreover, these sensors have carbon and metal nanomaterials incorporated in their configurations that can detect toxins [26]. An optical biosensor with point-of-care detection was developed by Doulou, S et al., which is used to detect severe infections like sepsis that are life-threatening to patients [27]. Optical biosensors are a promising technique as they are non-invasive and allow real-time monitoring since they are highly sensitive and robust, based on the evanescent wave principle [27, 28]. Biomarkers recognition processes are mostly centered around the following proteins on the layer surface of growth cells and disease-related microRNA [29]. Although a few elective strategies were accounted for such biomarker conclusion, an electrochemical technique is favored due to its moderate expense, quick reaction, simplicity of activity, promptly quantifiable probability of scaling down, and high responsiveness and selectivity with a lower detection limit. Electrochemical biosensors include the biorecognition component, signal transducer, and three anode-based electrochemical frameworks (Figure 3). In biosensors, change in electrical sign causes electrochemical responses with target parts at the anode surface that are then observed and recorded [5, 30-32]. Among all the sensor components, the interface has most of the attention, having different architectures and functions. Many biorecognition components distinguish cancer biomarkers like antibodies, proteins, and engineered particles (for

Accepted Manuscript
For Review Only

example, aptamers, DNA pieces, peptides, and so forth). Contingent upon the particular bio-recognition components being utilized, biosensors are arranged into Immunosensors, Aptasensors, enzymatic biosensors, and Geno biosensors (corrosive nucleic biosensors).

The survival rate of a cancer patient greatly relies on early diagnosis. Thus, an early and secure way of detection is of utmost requirement. Biosensors have played a vital role in safe and accurate detection for a very long time. Wide research has been conducted for cancer diagnosis using biomarkers present in the fluid. Different markers account for different types of cancer (Figure 4).

Magneto-electrochemical biosensors in various destructive biomarker recognition techniques for cancer tumors have been discussed in the present scenario. Different approaches and alterations conducted heretofore are highlighted in this review, enlightening the future perspective of diagnosis in cancer diagnosis. Magneto-electrochemical sensors can be a promising area that will bolster point-of-care detection for several patients to avoid ending up at the last stage of treatments.

2. Biosensors

Ever since the massive revolution in the field of biotechnology, various types of biosensors have been developed. Depending on the field, detection, and applications, they are classified into the following types, enzyme-based, tissue-based, immuno-sensors, DNA biosensors, and thermal and piezoelectric biosensors. Table 1. mentions the different transduction techniques used to detect cancer using biomarkers.

Table 1. Different transduction principles for the diagnosis of cancer using various cancer biomarkers

Cancer Biomarker	Type of Cancer	Transduction Principle	Detection Limit	Result	Ref.
miRNA	Oral cancer	Magnetic controllable electrochemical biosensor	0.22 aM (2.2 x 10^{-19} M)	Oral squamous cell carcinoma is successfully detected via miRNA through saliva samples through the present sensor setup.	[33]
Glutathione S-transferase P1 (GSTP1) gene	Prostate cancer	Electrochemical Geno sensor	2.92 pM	A label-free electrochemical Geno sensor can detect the GSTP1 using DNA oligonucleotide and PCR process.	[34]
Cytokeratin 19 fragments 21-1 (CYFRA21-1)	Lung cancer	Electrochemical immunoassay	43 pg mL^{-1}	CYFRA21-1 was marked successfully using the serum samples via immunoassay for lung cancer diagnosis.	[35]
- 8-hydroxydeoxyguanosine (8-OHdG)	Prostate cancer	Silicon nanowire-based biosensor	3.5 nM	The author presented silicon nanowire-based biosensor to detect prostate cancer and effectively marked the biomarker 8-OHdG	[36]
Human epidermal growth factor receptor-3(HER-3)	Cancer-specific biomarker	Electrochemical biosensor	0.2–1.4 pg mL^{-1}.	Herein, an immunological biosensor characterized by electrochemical modifications has been proposed to detect HER-3 cancer biomarker	[37]
Human Epidermal growth factor Receptor 2 (HER2-ECD)	Breast cancer	Electrochemical Immunosensors	10–150 ng/ml	A human serum sample was preferred to show the presence of HER2-ECD for detecting breast cancer using quantum dots as a label.	[38]
α-Enolase (ENO1)	Lung cancer	Electrochemical Immunosensors	11.9 fg/mL	Electrochemical Immunosensors have been used as a base biosensor for diagnosing lung cancer by marking the ENO1 biomarker.	[39]

2.1 Electrochemical Biosensors

The most widely investigated and used biosensors rely on the electrochemical properties of the analyte and the transducer. Electrochemical biosensors exhibit high sensitivity, selectivity, and the capability of detection. These sensors detect the electrochemical reaction that occurs on the transducer surface better than the bioreceptor and analyte producing detectable electrochemical signals in terms of voltage, current, impedance, and capacitance.

The benefits of an electrochemical biosensor are well known. For their biological and clinical studies on various analytes interacting with the transducer surface and the recognition element. The electrochemical biosensors are highly

Accepted Manuscript For Review Only

advantageous for extracellular vesicles (EVs) detection and possess the potential to be applied in cancer screening, patient prognosis, and therapy. However, the challenge of surface functionalization, sample matrix effects, and reproducibility are some sources of concern in the application of biosensors that require further research. [40]

On another account, electrochemical immuno-sensors are biosensors that rely on the electrochemical detection of the interactions between the target antigen and specific antibodies that are immobilized on a transducer surface. To make any biosensor an effective source of cancer diagnosis, the apparatus must be highly selective, sensitive, cost-effective, and efficient in providing an analysis. Electrochemical immuno-sensors exhibit all of the above.

Amperometric-based sensors are the most common electrochemical sensor. [41]

Electrochemical sensors are highly sensitive, selective, and portable. But the problem arises when the biological antigens are bounded onto the sensing surface, which causes steric hindrance of an electron, which can reduce the signalling pathway. Moreover, this technique is time-consuming, also these sensors cannot be reused due to the immobilized antigens on the surface. Therefore, magnetic particles are considered to avoid such limitations for electrochemical sensors [42], hence the importance of magneto-electrochemical biosensors arises.

3. Magneto-electrochemistry

Magneto-electrochemistry, is the study of magnetic effects in the realm of electrochemistry. It offers numerous advantages, primarily seen through the ability to control and understand electrochemical reactions which are quite tricky to regulate in conventional electrochemical fields. When considering the future development of magneto-electrochemistry devices chemical transformation processes must be studied in-depth to understand the relations between chemical and thermal stability under a magnetic field. [43]

3.1 Magento-electrochemical Biosensor

Surface modification and functionalization are vital for this avenue of biosensor applications. Based on the fact that sensor surfaces are very sensitive due to the immobilization of the biomolecule, hence magnetic or electric properties could be useful for signal amplification throughout the process. To overcome this limitation, X. Zhu et al. has introduced a magneto-controlled moveable architecture (MCMA) to fabricate reusable biosensor [24]. They have placed the sensing interface over the colloidal magnetic nanoparticles (MNPs), which are further controlled by a magnetic field that is easy to move, enabling the model to move architecturally.

The MCMA will then be attached to the working electrode surface instead of being placed in one position. They have tried to incorporate the magnetic effect on the movable sensor surface. Magneto's essays have shown their exemplary performance when it comes to detection [24, 41, 44]. So, innovations are heading towards magneto-electrochemical sensors for diagnosing diseases like cancer [45, 46]. An electrochemical biosensor can be very efficient for cancer theragnostic, contributing to its advantage of sensitivity, high selectivity, low cost, and simplicity. Furthermore, electrochemical biosensors can be synthesized in a miniaturized version as per the application it is being used for and also allows mass fabrication, which grants them a better fit for point-of-care (POC) applications [47].

Introducing magnetic fields with electrochemical sensors will help overcome such biosensors' sensitivity. Moreover, these magnetic particles can be immobilized onto the sensor surface via physical adsorption or chemical processes. Research has made the electrochemical sensors reusable, but the problem arises when the recognition element has to be renewed. Therefore, using magnetic nanoparticles, we can easily avoid the renewable issues for a better sensing scheme.

Compact biosensor technology allows a technician to screen out tumour vesicles from blood plasma and is being used to detect cancer cells early in blood plasma. This design of a biosensor is based on an integrated magnetic-electrochemical screening mechanism in which tumour cells are filtered through the given sample provided by the patient in an immuno-magnetic manner [46]. This sample is later profiled through electrochemical reactions. This enables the lab technician to function the biosensor at high sensitivity, making it easier to detect cell-specific exosomes by combining magnetic enrichment and enzymatic therapy. [48] Miniature circuits have come to use, considering their great portability and accurate measurements.

Accepted Manuscript
For Review Only

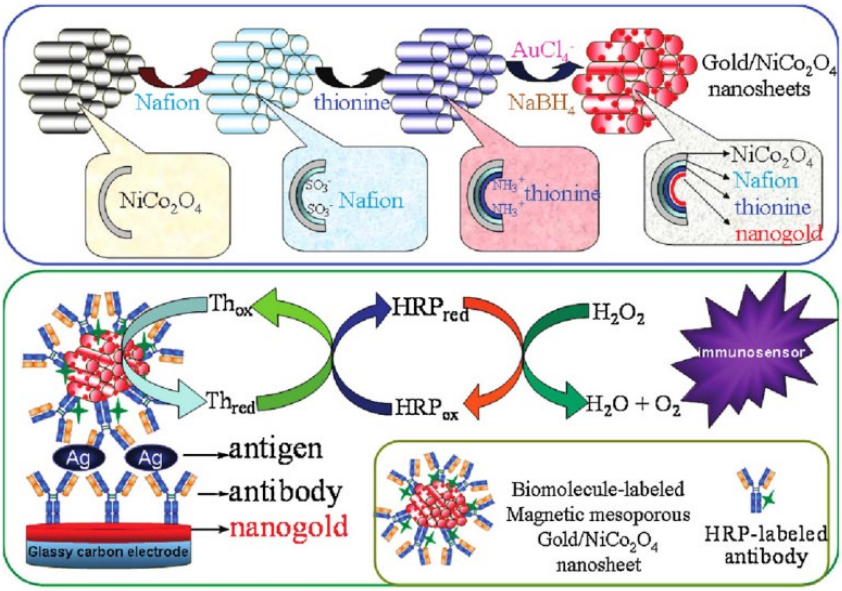


Figure 1. Discussing Nanomaterial composition and Fabrication details for Magneto electrochemical sensors

Researchers have been working on magnetic field-based sensors for reusable sensors, which are highly effective in terms of signalling as well. The approach that is being followed is to introduce a solid-phase layer of magnetic particles, that will separate the biorecognition and antigen binding sites, for the sensors to be utilized again. These magnetic particles are coated with the desired linkage element to bind with the antigens. This process provides the binding space for the antibodies, with limited size for the process to follow smoothly. This step too comes with a limitation in itself, if the unsynthesized magnetic particles are used often they can form a cluster when exposed to the biorecognition elements. Hence, the synthesized magnetic particles are being used for the desired purpose without any hindrance onto the sensor surface.

3.1 Magneto-Immunoassays

Magnetic particles are considerably useful as solid phases to help separation. Magneto-immunoassays are widely applicable as point-of-care test systems for their high stability. Immunoassay-based magnetic nanoparticles (MNPs) are able to take into account numerous labels and have lower interference from the background. Superparamagnetic; occurring in Ferromagnetic and Ferrimagnetic particles are used as labels for molecular detection. This allows for less noise in the detection background, grants the ability of the magnetic sensors to be integrated on-chip (enabling miniaturization), and finally, more efficient immunoassays which are possible by concentrating targets within a sensing zone. [49]

Molecular imaging along with biomarker detection and monitoring is the key to preventing and increasing survival rates of patients with cancer. The combination of biomarker sensing and novel anti-cancer therapeutics is essential for more effective, less harmful, and more economical cancer treatments. [41]

3.2 Material of choice

Nanomaterials are the most promising material that stands to solve the lack of reusability and stability of any biorecognition element that is commonly used in biosensors. [41] The main challenges as reported in the progress of biosensors its ability to i) efficiently capture the biorecognition signals and convert them into electrochemical, electrical, optical, gravimetric, or acoustic signals (transduction process), ii) improve their sensitivity, sharper response time and low detection limits, and iii) miniaturization.

Integration of sensing technology with nanomaterials, which range from zero to three-dimensional structures, large surface-to-volume ratio, good conductivities, shock-bearing abilities, and color tunability. Nanomaterials (NMs) automatically invite the application of nanoparticles (NPs) in the development of biosensors. [50]

Magnetoplasmonic nanoparticles (MagPlas NPs) are unique composites combining magnetic and plasmonic (deals with generation, detection, and manipulation of signals) materials within a defined nanoscale area that simultaneously show magnetic and plasmonic characteristics. The usual use of Fe, Co, or Ni-based magnetic materials and noble-metal

Accepted Manuscript
For Review Only

(e.g., Au, Ag, Cu, or Pt) plasmonic components. MagPlas NPs are emerging multifunctional materials in numerous fields, with their application in electronics being the most interesting of others. As a biosensor, MagPlas NPs possess commendable biocompatibility. [51]

3.3 Application of a Magneto-electrochemical biosensor

As reported by Tran et al. magnetic beads attached to the surface of a working electrode allows for electrochemical measurements by using an external magnetic field. The group also reports great advantages in the identification of the target analyst. Magnetic beads were used to capture exosomes, where the sensor had been fabricated using the combined two orthogonal modalities of magnetic selection and electrochemical detection. Captured exosomes were detected by electrochemical methods. Reliable recovery of the bead-bound vesicles was also seen. [51]

4. Biomarkers in Cancer

Cancer is among those critical diseases in which early detection could improve the patient's safety. Abnormal prothrombin (APT), Alpha-fetoprotein (AFP), and Lectin-reactive alpha-fetoprotein (AFP-L3) are common liver-cancer biomarkers. The presence of APT above the average concentration of 0.1 AU mL-1 (in healthy individuals) indicates the onset of hepato-carcinoma. The diagnosis can be further confirmed by detecting the other two biomarkers at a high concentration level. An immuno-sensor has been developed by Zhang H et al. (2013) to mark all three biomarkers at once. The design analyses human serum samples through an electrochemical sandwich with high specificity toward the APT biomarker [52, 53].

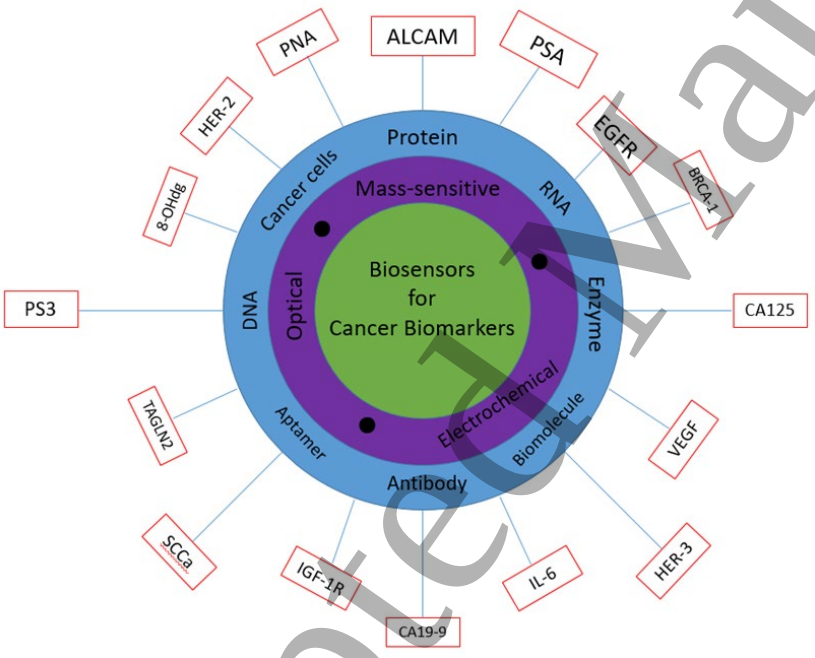


Figure 2. Cancer biomarkers: an overview.

Mucin 1 (Muc1), also known as cancer antigen 15-3 (CA15-3), is a common cancer biomarker related to breast and ovarian cancer. The biomarker concentration increases as the disease progress into advanced stages. The average concentration levels are 30 U mL-1 in healthy individuals. The magnetic beads are coated with Streptavidin and are conjugated with biotinylated horseradish peroxidase (HRP). Anti-CA 15-3 biotinylated monoclonal Antibody affinity-based biosensor is used to detect the CA-15-3 marker in a patient's blood serum or plasma [54]. The limit of detection (LOD) is about 1.5 x 10-5 U mL-1, which provides detection of the onco-biomarker in samples of less quantity [53, 54].

C-reactive protein (CRP) is a common biomarker utilized as a prognostic marker for inflammation in the body and a diagnostic marker indicating cardiovascular diseases and various types of cancer like lymphoma, renal cell carcinoma, thymic carcinoma, colorectal cancer, pancreatic, ovarian cancer, head and neck carcinoma [53]. Given its universal application, several detection methodologies are now present. Affinity-based nano-biosensors like indium tin oxide

Accepted Manuscript
For Review Only

(ITO) and anti-CRP antibody biosensors are utilized for increased sensitivity [55]. The LOD for this biosensor is 4.55 x 10-7 ng mL-1 providing the highest sensitivity toward CRP [53, 55].

Cancer antigen 125 (CA-125) is another biomarker for ovarian cancer diagnosis. The high level of the present biomarker ensures the growth of cancer. This biomarker is directly secreted into the blood, which can be detected easily [32]. Hence, Chang L et al. (2022) have developed the idea of microfluidic chips that enable direct isolation with the help of CD 9 and epithelial cell adhesion molecule (EpCAM) biomarkers from the serum.

Exosomes, nano-sized derived vesicles, have derived attention as biomarkers during the liquid biopsy. [48, 56] Exosomes are studied as they are released by cells during the fusion of endosomes and the plasma membrane [57]. Their function inside the cells is to transfer RNA and proteins to recipient cells for cell-to-cell communication. However, their expressions alter in some cases, which allows us to differentiate and understand different diseases such as cancer, cardiovascular, infectious, diabetes, and neurodegenerative disorders. The exosomes secreted by cancerous cells can be the reason for tumour growth, migration of cancerous cells, and invasion. Hence, it is why exosomes can be preferred as biomarkers for cancer detection [46, 57].

5. Detection of cancer from blood plasma

5.1 Extracellular vesicles & Exosomes

Extracellular vesicles (EV), including exosomes, are nanoscale vesicles that carry molecular information of parental cells. They are seen as competent biomarkers of cancers that are difficult to detect or serially follow. EV detection by nucleic acid, proteins, antibodies, and aptamers. The resulting sensor is based on an integrated magnetic-electrochemical assay which allows for the exosomes to be immunomagnetically captured from patient samples and profile through an electrochemical reaction. Magnetic enrichment and enzymatic amplification allow for highly sensitive, cell-specific exosome detection, sensor miniaturization, and scale-up for high throughput measurements. Extracellular vesicles, like the tumor-derived exosomes, carry several types of substances from the parent cells, like membrane transport proteins, fusion proteins [58], and materials from tumor cells that are oncogenic [59]. The transfer of oncogenic substances from a tumor microenvironment can lead to metastasis of the cancer type in the body. These exosomal secretions in the plasma can be biomarkers in several cancer types. We also see a high correlation in protein expression between CD63-positive exosomes and their parent cells (Figure 3). [48]

5.2 Circulating tumor DNA (ctDNA)

The research group of Jeong et al. (2016) devised an electrochemical magnet-Immunosensors containing magnetic beads to identify and analyze ovarian cancer surface proteins present on exosomal secretions in plasma. It could identify and perform expression profiling of CA125, CD24, CD63, and epithelial cell adhesion molecule (EpCAM) surface biomarkers, with the detection sensitivity being 3 ×103 exosomes per μL [46, 60]. Circulating tumor DNA (ctDNA) are DNA materials secreted by tumor cells into the bloodstream of cancer patients. It consists of the characteristics of the secreting tumor cells, linking ctDNA to the origin of the disease. Due to their presence in a free-form manner, they are considered biomarkers that can be detected in blood plasma. These methods are also known as liquid biopsy. [10] Electrochemical biosensors have the potential to identify ctDNA. In prostate cancer, circulating tumor cells (CTC) are also observed in the bloodstream. These can be detected by a highly sensitive biosensor designed by Moscovici et al. (2013). It is a micro-fabricated glass chip device based on lab-on-a-chip technology. The device contains a gold electrode array with a sensor surface having anti-EpCAM antibodies attached to the surface. The binding of Prostate CTCs leads to an electron transfer reaction of a redox reporter, leading to signal detection in fifteen (15) minutes [60, 61].

To utilize circulating tumor DNA (ctDNA) as a potential biomarker for the early diagnosis of cancer, methods that are accurate and robust must be investigated to quantify the levels of ctDNA. This quantification poses a unique challenge because of its short half-life and minimal presence in the patient in the early stages of cancer. The resulting biosensor is an ultrasensitive electrochemical biosensor for the rapid detection of ctDNA in whole blood. The sensing of ctDNA is based on hybridization on a network of probe DNA-modified gold-coated magnetic nanoparticles (DNA-Au@MNPs). This DNA-Au@MNPs biosensor can selectively detect short- and long-strand DNA targets. For the 101 nucleotide ctDNA target, a dynamic range from 200 aM to 20 nM was achieved with a detection limit of 5 fM. This biosensor provides a promising method to achieve 20-minute response time and a minimally invasive cancer early diagnosis approach.

Accepted Manuscript
For Review Only

5.3 Double-stranded DNA (dsDNA)

One such setup was reported by Ruiyi et al. (2015), where a nitrogen-doped multiple graphene aerogels/gold Nano star (N-doped MGA/GNS) is used. It can detect double-stranded DNA (dsDNA) in a three-dimensional structure, leading to bioconjugation. As bioconjugate formation occurs, a differential pulse voltammetric (DPV) signal is observed towards dsDNA. The signal is linearly proportional to the presence of dsDNA. The detection limit of the sensor is 3.9×10-22 g/ml [60, 62]. Authors reported the facile synthesis of nitrogen-doped multiple graphene aerogel/gold nanostar (termed as N-doped MGA/GNS) and its use as the electrochemical sensing platform for the detection of double-stranded (dsDNA). The unique structure of the biosensor, involving N-doped MGA and hybridized GNS makes it easy to combine with dsDNA to form the electroactive bioconjugate. This integration triggers an ultrafast DNA electron and charge transfer but also realizes a significant synergy between N-doped MGA, GNS, and dsDNA.

5.4 Micro-RNA (miRNA)

In the context of cancer disease development and progression epigenetic alterations are considered one of the key drivers. The levels of circulating microRNAs provide valuable information about cancer disease at its early stages, which makes them promising candidates for early cancer diagnosis and prognosis. The authors utilize magnetic beads for the capture of the target microRNA from the solution and bring the concentrated sample to the sensor surface. The modified magnetic beads with locked nucleic acids (LNA), have high affinity and specificity to their complementary microRNA sequence. [63]

5.5 Proteins: Glycoproteins & Antibodies

Epidermal growth factor receptor (EGFR) is a transmembrane glycoprotein on the cell surface of tumor cells. EGFR is a cancer biomarker indicating the prognosis of different cancers like ovarian and cervical cancers, head and neck, and esophageal cancers. Elshafey et al. (2013) devised an immuno-biosensor that can detect the presence of EGFR in human plasma with a detection limit of 0.88 pg/mL. The electrodes contained immobilized protein G. Anti-EGFR antibodies are then bound on the protein G-modified electrode. EGFR is detected when it binds with the non-antigenic fragment crystallizable (Fc) regions of anti-EGFR antibodies. The immuno-biosensor is characterized by using cyclic voltammetry (CV), square wave voltammetry (SWV), and Electrochemical impedance spectroscopy (EIS) in the presence of $[Fe(CN)6]^{3-}$ / $[Fe\ (CN)6]^{4-}$ redox probe. EIS helps measure impedance and detection of EGFR [5, 64].

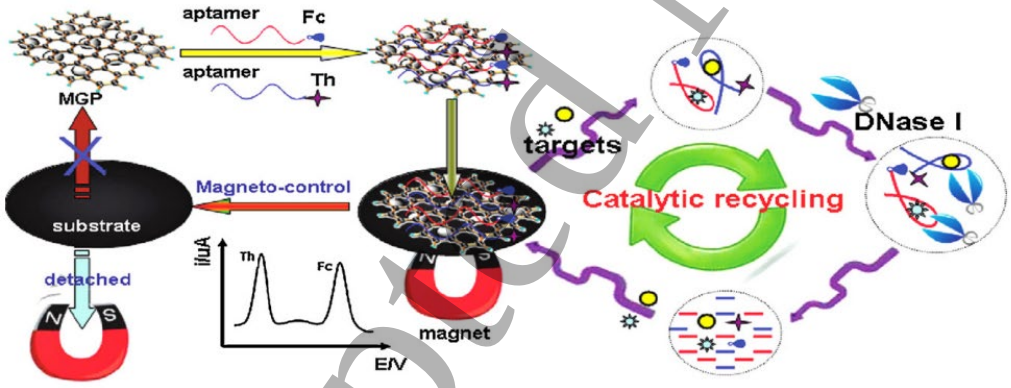


Figure 3. Target action using a magnetic platform and DNase I-based catalytic recycling of the analyte.

6. Conclusion

The present study focuses on magneto-electrochemical biosensors and their development area for cancer treatment. Cancer is the most common life-threatening disease, with the highest overall mortality rate. A cancer diagnosis at an early stage can play a critical role in effective and successful treatment. Long-established cancer screening technologies are expensive, time-consuming, and counterproductive for repeated screenings. On the other hand, a biomarker-based cancer diagnosis is taking shape as one of the most significant measures for early diagnosis, disease progression monitoring, and succeeding cancer treatment. [5]. There is a high demand for efficient biosensors to rapidly analyze cellular alterations to detect related biomarkers and improve cancer prognosis and therapeutic interventions. This review examined various recently reported electrochemical biosensors and their control mechanisms and designs for detecting cancer biomarkers. However, new approaches such as nanofabrication and

Accepted Manuscript For Review Only

clinical applications are required to develop low-cost lab-on-chips and next-generation novel biosensors. With the reliance on the analysis of large samples of a target biomarker, extremely high sensitivity could be counterintuitive. Therefore, considering the use of iron oxide magnetic NP (large surface area, fast diffusion, perfect magnetic and dispersion) allows for the development of an effective immuno-sensor. [41] Because circulating cancer biomarkers are typically found in trace amounts amongst the enormous amount of nontarget cells, EVs, and biomolecules, the combination of magnetic nanomaterials and electrochemical biosensors is being tailored to overcome the detection challenge [60].

Electrochemical biosensors are the most commonly reported sensing method for cancer biomarker detection. Nanostructured materials and nanocomposites are crucial in the fabrication and design of various electrochemical biosensors, and they are expected to be used more in scientific investigations [65]. This technique shows the levels of biomarkers and promises a patient-friendly detection technique, simple and less invasive, along with high sensitivity [66]. Among these biomarkers, the major focus is exosomes secreted by the cells and actively involved in cell-to-cell communication, cancer development, metastasis, and immune regulation [67, 68]. Table 2, employs the application of electrochemical biosensors, in cancer detection.

Table 2. Applications of Electrochemical biosensor

Area of application	Review	Ref.
Cancer Diagnosis	The authors have introduced a metal-organic framework as the platform for electrochemical sensor detection for cancer biomarkers.	[69]
SARS COV-2 (Severe acute respiratory syndrome coronavirus 2)	Hereunder, the electrochemical biosensors have been attributed to detect the existence of SARS COV 2 virus for diagnosing COVID-19 disease by various means.	[70]
Detection of DNA Damage	This study highlights various electrochemical sensor setups to detect DNA damage during the interactions between pharmaceutical compounds.	[71]
Detection of protein biomarkers	Electrochemical biosensors can be fused with various biological elements for diagnostic purposes or detection. Hence, peptide as a biological element has been used with electrochemical sensors to mark protein biomarkers.	[72]
Studying the interactions of biometal with biomarkers	The given review highlights the electrochemical sensors for analyzing the interactions between the transition metal with the protein or biomarker.	[73]
Detection of Amyloid beta (Aβ) into Amyloid plaques and hyperphosphorylated Tau	When it comes to Alzheimer's disease, amyloid beta, and Tau are the potential inhibitors to diagnose the disease. Electrochemical biosensors holding a convincing role in diagnostic approaches have put forward the medical field's research. Based on the same approach, electrochemical sensors detect the present Aβ and Tau for Alzheimer's.	[74]

As discussed earlier, magnetic beads have several advantages when diagnosing cancer. It can be used as a potential biomarker. However, due to the limitations on the usage of beads, few studies have come up with electrochemical detection on-chip, allowing less user involvement [68]. As already mentioned, EVs carry the potential to detect cancer in patients. J. Park et al. has highlighted the high–throughput EV analysis integrated with magneto-electrochemical extracellular vesicle named high-throughput integrated magneto-electrochemical extracellular vesicle (HiMEX). In this technique, the EVs are directly profiled from the sample. HiMEX is then applied to the sample. The sample is taken as blood from patients with colorectal cancer who underwent chemotherapies and heat surgeries and some patients without colorectal cancer. Through this process, the EVs enabled the detection of colorectal cancer with high accuracy. Also, according to the EV levels, the screening highlighted high-risk and low-risk patients [44].

Materials science must improve. Iron oxide composites with graphene, carbon dots, or core-shell structures with noble metal as well as using iron oxide nanomaterials as labels on biomolecules have shown to perform better than usual labels. Iron oxide NPs stand to be a paragon candidate for immuno-sensor due to their high conductivity and biocompatibility. Nanomaterials integrated with biochips or lab-on-chip allows for superior handling and analysis for clinical diagnosis. [50] Ensuring commercially available prototypes is an exciting avenue to explore shortly.

Accepted Manuscript
For Review Only

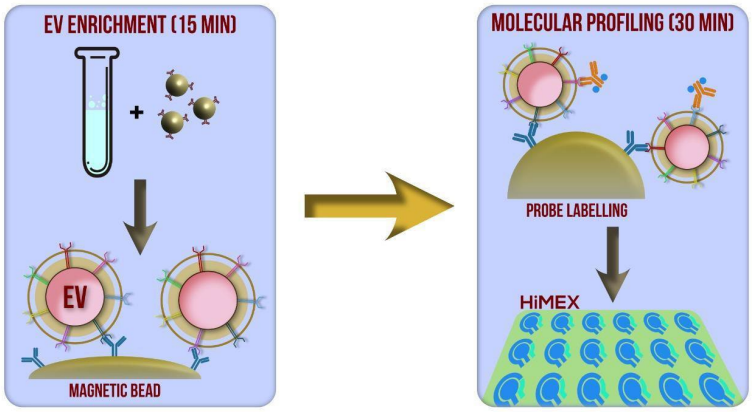


Figure 4. Working of HiMEX approach.

Utilizing the magnetic and intrinsic enzyme-like activity of Fe-based NPs is an exciting opportunity to incorporate it into simple biosensing strategies with the requirements of expensive devices.

One of the definitive objectives of biosensor technology is the point of care (POC) disease finding. Point-of-care testing (POCT), or analytic testing is done nearby, is a field wherein biosensors could have a significant effect, permitting the patient and clinical staff to come across results quickly and without any problem. POCT takes into account quicker conclusions and can altogether lessen costs. However, multi-target recognition of different biomarkers is essential to move biosensors toward POC devices.

Moreover, POCT and multi biosensors, while bringing biosensor innovation to the patient's bedside, should keep up with the precision and dependability of the laboratory. LOC biosensors are somewhat of a promising innovation. The significant impacts of nanotechnology on biosensor advancement include nanomaterials, especially quantum dabs, as they cannot work with finding and following disease cells, yet additionally can convey medications to target locales with accuracy and take into consideration more delicate imaging frameworks that can recognize malignant growth early.

In the following 5-10 years, it is sure that nanotechnology will alter malignant growth diagnostics and treatment. Coordinating nanomaterials and biosensors will permit us to identify illness prior, further develop cancer imaging, and help in the analysis and/or visualization and advance medication conveyance while limiting antagonistic responses. Cancer happens on the nanoscale level; it justifies that fighting this illness additionally happens at the nanoscale. Although the intricacy and variety of cancer have presented many difficulties in the clinical field, biosensor innovation can give quick, precise outcomes while keeping up with cost adequacy. Indeed, electrochemical biosensors with magneto sensing applications manifest as the most acceptable and reliable technology for meeting regulatory requirements and overcoming industrial implementation barriers because a lab-on-chip device with the desired analytical properties and adapted to specific industrial needs can be achieved at a foreseeably low cost [75-77].

Data Availability Statement: All the data is included in the manuscript.

Conflicts of Interest: The authors declare no conflict of interest.

References

1. S. I. Kaya, G. Ozcelikay, F. Mollarasouli, N. K. Bakirhan, and S. A. Ozkan, "Recent achievements and challenges on nanomaterial based electrochemical biosensors for the detection of colon and lung cancer biomarkers," Sensors Actuators B Chem., 2022, doi: 10.1016/j.snb.2021.130856.
2. P. Nenclares and K. J. Harrington, "The biology of cancer," Medicine (United Kingdom). 2020, doi: 10.1016/j.mpmed.2019.11.001.
3. R. L. Siegel, K. D. Miller, and A. Jemal, "Cancer statistics, 2020," CA. Cancer J. Clin., 2020, doi: 10.3322/caac.21590.
4. R. L. Siegel, K. D. Miller, H. E. Fuchs, and A. Jemal, "Cancer Statistics, 2021," CA. Cancer J. Clin., 2021, doi: 10.3322/caac.21654.
5. M. R. Hasan et al., "Recent development in electrochemical biosensors for cancer biomarkers detection," Biosensors and Bioelectronics: X. 2021, doi: 10.1016/j.biosx.2021.100075.

Accepted Manuscript
For Review Only

6. A. Roointan et al., "Early detection of lung cancer biomarkers through biosensor technology: A review," Journal of Pharmaceutical and Biomedical Analysis. 2019, doi: 10.1016/j.jpba.2018.10.017.
7. B. Bohunicky and S. A. Mousa, "Biosensors: The new wave in cancer diagnosis," Nanotechnology, Science and Applications. 2011, doi: 10.2147/NSA.S13465.
8. S. D. Alharthi, D. Bijukumar, S. Prasad, A. M. Khan, and M. T. Mathew, "Evolution in Biosensors for Cancers Biomarkers Detection: A Review," J. Bio- Tribo-Corrosion, 2021, doi: 10.1007/s40735-020-00463-7.
9. Tao, S. C., & Guo, S. C. (2020). Role of extracellular vesicles in tumour microenvironment. Cell Communication and Signaling, 18(1), 1-24.
10. J. Wu et al., "Tumor circulome in the liquid biopsies for cancer diagnosis and prognosis," Theranostics. 2020, doi: 10.7150/thno.40532.
11. K. Pantel and C. Alix-Panabières, "Real-time Liquid Biopsy in Cancer Patients: Fact or Fiction?," Cancer Res., vol. 73, no. 21, pp. 6384–6388, Oct. 2013, doi: 10.1158/0008-5472.CAN-13-2030.
12. K. M. Polizzi, "Biosensors," in Comprehensive Biotechnology, 2019.
13. R. Karunakaran and M. Keskin, "Biosensors: components, mechanisms, and applications," in Analytical Techniques in Biosciences, 2022.
14. Q. Wang et al., "Development of the DNA-based biosensors for high performance in detection of molecular biomarkers: More rapid, sensitive, and universal," Biosensors and Bioelectronics. 2022, doi: 10.1016/j.bios.2021.113739.
15. M. Zain et al., "Applications of nanotechnology in biological systems and medicine," in Nanotechnology for Hematology, Blood Transfusion, and Artificial Blood, 2022.
16. Z. Kotsiri, J. Vidic, and A. Vantarakis, "Applications of biosensors for bacteria and virus detection in food and water–A systematic review," Journal of Environmental Sciences (China). 2022, doi: 10.1016/j.jes.2021.04.009.
17. Y. Song, D. Mukasa, H. Zhang, and W. Gao, "Self-Powered Wearable Biosensors," Accounts Mater. Res., 2021, doi: 10.1021/accountsmr.1c00002.
18. J. Zhang, Q. Wu, X. Zhang, H. Wan, and P. Wang, "Acoustic Transducer and Its Applications in Biosensors," in Handbook of Cell Biosensors, 2021.
19. T. Vo-Dinh and B. Cullum, "Biosensors and biochips: Advances in biological and medical diagnostics," Fresenius' Journal of Analytical Chemistry. 2000, doi: 10.1007/s002160051549.
20. B. D. Malhotra and A. Chaubey, "Biosensors for clinical diagnostics industry," Sensors Actuators, B Chem., 2003, doi: 10.1016/S0925-4005(03)00075-3.
21. V. Perumal and U. Hashim, "Advances in biosensors: Principle, architecture, and applications," Journal of Applied Biomedicine. 2014, doi: 10.1016/j.jab.2013.02.001.
22. F. W. Scheller, U. Wollenberger, A. Warsinke, and F. Lisdat, "Research and development in biosensors," Current Opinion in Biotechnology. 2001, doi: 10.1016/S0958-1669(00)00169-5.
23. A. G. Brolo, "Plasmonics for future biosensors," Nature Photonics. 2012, doi: 10.1038/nphoton.2012.266.
24. X. Zhu, C. Feng, Z. Ye, Y. Chen, and G. Li, "Fabrication of magneto-controlled moveable architecture to develop reusable electrochemical biosensors," Sci. Rep., 2014, doi: 10.1038/srep04169.
25. E. Povedano et al., "Electrochemical affinity biosensors for fast detection of gene-specific methylations with no need for bisulfite and amplification treatments," Sci. Rep., 2018, doi: 10.1038/s41598-018-24902-1.
26. L. Reverté, B. Prieto-Simón, and M. Campàs, "New advances in electrochemical biosensors sfor the detection of toxins: Nanomaterials, magnetic beads and microfluidics systems. A review," Analytica Chimica Acta. 2016, doi: 10.1016/j.aca.2015.11.050.
27. S. Doulou et al., "A novel optical biosensor for the early diagnosis of sepsis and severe Covid-19: the PROUD study," BMC Infect. Dis., 2020, doi: 10.1186/s12879-020-05607-1.
28. D. Petrovszki et al., "An integrated electro-optical biosensor system for rapid, low-cost detection of bacteria," Microelectron. Eng., 2021, doi: 10.1016/j.mee.2021.111523.
29. M. Mascini and S. Tombelli, "Biosensors for biomarkers in medical diagnostics," Biomarkers. 2008, doi: 10.1080/13547500802645905.
30. N. Zare-Shehneh, F. Mollarasouli, and M. Ghaedi, "Recent Advances in Carbon Nanostructure-Based Electrochemical Biosensors for Environmental Monitoring," Critical Reviews in Analytical Chemistry. 2021, doi: 10.1080/10408347.2021.1967719.
31. P. Singh, S. K. Pandey, J. Singh, S. Srivastava, S. Sachan, and S. K. Singh, "Biomedical Perspective of Electrochemical Nanobiosensor," Nano-Micro Letters. 2016, doi: 10.1007/s40820-015-0077-x.
32. J. Min, J. R. Sempionatto, H. Teymourian, J. Wang, and W. Gao, "Wearable electrochemical biosensors in North America," Biosens. Bioelectron., 2021, doi: 10.1016/j.bios.2020.112750.
33. Z. W. Wang et al., "A novel electrically magnetic-controllable electrochemical biosensor for the ultra sensitive and specific detection of attomolar level oral cancer-related microRNA," Biosens. Bioelectron., 2013, doi: 10.1016/j.bios.2013.02.007.
34. S. N. Topkaya, D. Ozkan-Ariksoysal, B. Kosova, R. Ozel, and M. Ozsoz, "Electrochemical DNA biosensor for detecting cancer biomarker related to glutathione S-transferase P1 (GSTP1) hypermethylation in real samples," Biosens. Bioelectron., 2012, doi: 10.1016/j.bios.2011.11.029.
35. Y. Zeng et al., "A sandwich-type electrochemical immunoassay for ultrasensitive detection of non-small cell lung cancer biomarker CYFRA21-1," Bioelectrochemistry, 2018, doi: 10.1016/j.bioelechem.2017.11.003.
36. M. A. Mohd Azmi et al., "Highly sensitive covalently functionalised integrated silicon nanowire biosensor devices for detection of cancer risk biomarker," Biosens. Bioelectron., 2014, doi: 10.1016/j.bios.2013.08.030.

Accepted Manuscript
For Review Only

37. M. Ç. Canbaz, Ç. S. Şimşek, and M. K. Sezgintürk, "Electrochemical biosensor based on self-assembled monolayers modified with gold nanoparticles for detection of HER-3," Anal. Chim. Acta, 2014, doi: 10.1016/j.aca.2014.01.041.
38. M. Freitas, M. M. P. S. Neves, H. P. A. Nouws, and C. Delerue-Matos, "Quantum dots as nanolabels for breast cancer biomarker HER2-ECD analysis in human serum," Talanta, 2020, doi: 10.1016/j.talanta.2019.120430.
39. J. A. A. Ho et al., "Diagnostic detection of human lung cancer-associated antigen using a gold nanoparticle-based electrochemical immunosensor," Anal. Chem., 2010, doi: 10.1021/ac1001959.
40. H. Xie et al., "Extracellular vesicles based electrochemical biosensors for detection of cancer cells: A review," Chinese Chem. Lett., 2020, doi: 10.1016/j.cclet.2020.02.049.
41. T. Kavetskyy et al., "Magneto-immunoassay of cancer biomarkers: Recent progress and challenges in biomedical analysis," Microchemical Journal. 2021, doi: 10.1016/j.microc.2021.106320.
42. Xu, Y., & Wang, E. (2012). Electrochemical biosensors based on magnetic micro/nano particles. Electrochimica Acta, 84, 62-73.
43. S. Luo, K. Elouarzaki, and Z. J. Xu, "Electrochemistry in Magnetic Fields," Angew. Chem. Int. Ed Engl., vol. 61, no. 27, p. e202203564, Jul. 2022, doi: 10.1002/anie.202203564.
44. J. Park et al., "An integrated magneto-electrochemical device for the rapid profiling of tumour extracellular vesicles from blood plasma," Nat. Biomed. Eng., 2021, doi: 10.1038/s41551-021-00752-7.
45. Y. An, R. Li, F. Zhang, and P. He, "Magneto-Mediated Electrochemical Sensor for Simultaneous Analysis of Breast Cancer Exosomal Proteins," Anal. Chem., 2020, doi: 10.1021/acs.analchem.0c00106.
46. S. Jeong, J. Park, D. Pathania, C. M. Castro, R. Weissleder, and H. Lee, "Integrated Magneto-Electrochemical Sensor for Exosome Analysis," ACS Nano, 2016, doi: 10.1021/acsnano.5b07584.
47. F. Cui, Z. Zhou, and H. S. Zhou, "Review—Measurement and Analysis of Cancer Biomarkers Based on Electrochemical Biosensors," J. Electrochem. Soc., 2020, doi: 10.1149/2.0252003jes.
48. S. Li, M. Yi, B. Dong, X. Tan, S. Luo, and K. Wu, "The role of exosomes in liquid biopsy for cancer diagnosis and prognosis prediction," International Journal of Cancer. 2021, doi: 10.1002/ijc.33386.
49. B. M. de Boer, J. A. H. M. Kahlman, T. P. G. H. Jansen, H. Duric, and J. Veen, "An integrated and sensitive detection platform for magneto-resistive biosensors," Biosens. Bioelectron., vol. 22, no. 9, pp. 2366–2370, Apr. 2007, doi: 10.1016/j.bios.2006.09.020.
50. V. Naresh and N. Lee, "A Review on Biosensors and Recent Development of Nanostructured Materials-Enabled Biosensors," Sensors, vol. 21, no. 4, Art. no. 4, Jan. 2021, doi: 10.3390/s21041109.
51. V. T. Tran, J. Kim, L. T. Tufa, S. Oh, J. Kwon, and J. Lee, "Magnetoplasmonic Nanomaterials for Biosensing/Imaging and in Vitro / in Vivo Biousability," Anal. Chem., vol. 90, no. 1, pp. 225–239, Jan. 2018, doi: 10.1021/acs.analchem.7b04255.
52. H. Zhang, L. Liu, X. Fu, and Z. Zhu, "Microfluidic beads-based immunosensor for sensitive detection of cancer biomarker proteins using multienzyme-nanoparticle amplification and quantum dots labels," Biosens. Bioelectron., 2013, doi: 10.1016/j.bios.2012.10.076.
53. D. Sadighbayan, K. Sadighbayan, M. R. Tohid-kia, A. Y. Khosroushahi, and M. Hasanzadeh, "Development of electrochemical biosensors for tumor marker determination towards cancer diagnosis: Recent progress," TrAC - Trends in Analytical Chemistry. 2019, doi: 10.1016/j.trac.2019.05.014.
54. S. Akbari Nakhjavani, B. Khalilzadeh, P. Samadi Pakchin, R. Saber, M. H. Ghahremani, and Y. Omidi, "A highly sensitive and reliable detection of CA15-3 in patient plasma with electrochemical biosensor labeled with magnetic beads," Biosens. Bioelectron., 2018, doi: 10.1016/j.bios.2018.08.047.
55. M. N. Sonuç Karaboğa and M. K. Sezgintürk, "A novel silanization agent based single used biosensing system: Detection of C-reactive protein as a potential Alzheimer's disease blood biomarker," J. Pharm. Biomed. Anal., 2018, doi: 10.1016/j.jpba.2018.03.016.
56. I. Martins et al., "Liquid biopsies: Applications for cancer diagnosis and monitoring," Genes. 2021, doi: 10.3390/genes12030349.
57. C. Liu, Y. Yang, and Y. Wu, "Recent Advances in Exosomal Protein Detection Via Liquid Biopsy Biosensors for Cancer Screening, Diagnosis, and Prognosis," AAPS Journal. 2018, doi: 10.1208/s12248-018-0201-1.
58. A. Poliakov, M. Spilman, T. Dokland, C. L. Amling, and J. A. Mobley, "Structural heterogeneity and protein composition of exosome-like vesicles (prostasomes) in human semen," Prostate, 2009, doi: 10.1002/pros.20860.
59. T. L. Whiteside, "Tumor-Derived Exosomes and Their Role in Cancer Progression," in Advances in Clinical Chemistry, 2016.
60. K. M. Koo, N. Soda, and M. J. A. Shiddiky, "Magnetic nanomaterial–based electrochemical biosensors for the detection of diverse circulating cancer biomarkers," Current Opinion in Electrochemistry. 2021, doi: 10.1016/j.coelec.2020.100645.
61. M. Moscovici, A. Bhimji, and S. O. Kelley, "Rapid and specific electrochemical detection of prostate cancer cells using an aperture sensor array," Lab Chip, 2013, doi: 10.1039/c2lc41049d.
62. L. Ruiyi, L. Ling, B. Hongxia, and L. Zaijun, "Nitrogen-doped multiple graphene aerogel/gold nanostar as the electrochemical sensing platform for ultrasensitive detection of circulating free DNA in human serum," Biosens. Bioelectron., 2016, doi: 10.1016/j.bios.2015.12.092.
63. M. Keshavarz, M. Behpour, and H. A. Rafiee-Pour, "Recent trends in electrochemical microRNA biosensors for early detection of cancer," RSC Advances. 2015, doi: 10.1039/c5ra01726b.
64. R. Elshafey, A. C. Tavares, M. Siaj, and M. Zourob, "Electrochemical impedance immunosensor based on gold nanoparticles-protein G for the detection of cancer marker epidermal growth factor receptor in human plasma and brain tissue," Biosens. Bioelectron., 2013, doi: 10.1016/j.bios.2013.05.063.
65. K. K. Reddy et al., "Recent Trends in Electrochemical Sensors for Vital Biomedical Markers Using Hybrid Nanostructured Materials," Advanced Science. 2020, doi: 10.1002/advs.201902980.

Accepted Manuscript
For Review Only

66. I. Heidrich, L. Ačkar, P. Mossahebi Mohammadi, and K. Pantel, "Liquid biopsies: Potential and challenges," International Journal of Cancer. 2021, doi: 10.1002/ijc.33217.
67. W. Yu et al., "Exosome-based liquid biopsies in cancer: opportunities and challenges," Annals of Oncology. 2021, doi: 10.1016/j.annonc.2021.01.074.
68. Y. Choi et al., "Exosome-mediated diagnosis of pancreatic cancer using lectin-conjugated nanoparticles bound to selective glycans," Biosens. Bioelectron., 2021, doi: 10.1016/j.bios.2021.112980.
69. S. Zhang et al., "Metal–organic frameworks (MOFs) based electrochemical biosensors for early cancer diagnosis in vitro," Coordination Chemistry Reviews. 2021, doi: 10.1016/j.ccr.2021.213948.
70. S. S. Mahshid, S. E. Flynn, and S. Mahshid, "The potential application of electrochemical biosensors in the COVID-19 pandemic: A perspective on the rapid diagnostics of SARS-CoV-2," Biosens. Bioelectron., 2021, doi: 10.1016/j.bios.2020.112905.
71. A. M. Chiorcea-Paquim and A. M. Oliveira-Brett, "Dna electrochemical biosensors for in situ probing of pharmaceutical drug oxidative dna damage," Sensors (Switzerland). 2021, doi: 10.3390/s21041125.
72. V. Vanova, K. Mitrevska, V. Milosavljevic, D. Hynek, L. Richtera, and V. Adam, "Peptide-based electrochemical biosensors utilized for protein detection," Biosensors and Bioelectronics. 2021, doi: 10.1016/j.bios.2021.113087.
73. S. Li and K. Kerman, "Electrochemical biosensors for biometal-protein interactions in neurodegenerative diseases," Biosens. Bioelectron., 2021, doi: 10.1016/j.bios.2021.113035.
74. L. M. T. Phan et al., "Nanomaterial-based Optical and Electrochemical Biosensors for Amyloid beta and Tau: Potential for early diagnosis of Alzheimer's Disease," Expert Review of Molecular Diagnostics. 2021, doi: 10.1080/14737159.2021.1887732.
75. G. Ruiz-Vega, T. Garcia-Berrocoso, J. Montaner, and E. Baldrich, "Paper microfluidics on screen-printed electrodes for simple electrochemical magneto-immunosensor performance," Sensors Actuators, B Chem., 2019, doi: 10.1016/j.snb.2019.126897.
76. Chadha, Utkarsh, Preetam Bhardwaj, Rushali Agarwal, Priyanshi Rawat, Rishika Agarwal, Ishi Gupta, Mahek Panjwani et al. "Recent progress and growth in biosensors technology: A critical review." Journal of Industrial and Engineering Chemistry, 2022, doi: 10.1016/j.jiec.2022.02.010
77. Mamdiwar, S. D., Shakruwala, Z., Chadha, U., Srinivasan, K., & Chang, C. Y. (2021). Recent advances on IoT-assisted wearable sensor systems for healthcare monitoring. Biosensors, 11(10), 372, doi: 10.3390/bios11100372

Accepted Manuscript
For Review Only

RGB-D Dataset: The Impact of Yoga and Gym Exercise for Human Activity Recognition

Vishal Sharma
Electronics & communication engineering
Delhi technological university
Delhi, India
vishalsharma_2k19ec212@dtu.ac.in

Bhavana Sharma
Electronics & communication engineering
Delhi technological university
Delhi, India
bhavana_2k19phdec@dtu.ac.in

Jeebananda Panda
Electronics& communication engineering
Delhi technological university
Delhi, India
jpanda@dce.ac.in

2023 International Conference on Device Intelligence, Computing and Communication Technologies, (DICCT) | 978-1-6654-7491-7/23/$31.00 ©2023 IEEE | DOI: 10.1109/DICCT56244.2023.10110291

***Abstract*— Gesture technology is the future technology because it is widely used in different fields like computer game and sports, e-commerce, assistant system and Human robot interaction. Body gesture one of the most important recognition gesture for navigation automation cars, surveillance, 3D-animations, health sector and so many. Therefore, in this paper two types of datasets Gym dataset and yoga dataset are created for body gesture recognition. Gym dataset contains total body exercises RGB images 1992 of 1080 x 608 pixels with two subjects and two classes and same in yoga dataset total RGB images are 3012 of 2336 x 1080 pixels with one subject and four classes. All datasets are captured by camera at different views which has special configuration. This dataset is free to use for only experiment purpose.**

Keywords*— *Dataset creation, human activity recognition, pose estimation, machine learning

I. INTRODUCTION

Value of the data

- In Table 1, it is described that dataset comprehends two classes in gym dataset and four classes in yoga dataset. Separate files contain the representation of static bodily movements through both RGB images and depth images.
- These datasets can be applied for human activity classification, pose recognition and human machine interaction especially for body gesture recognition [1], [2].
- These datasets used as an instructor in gyms and yoga centers and also train to models of deep leaning and machine learning To identify the body gestures present in the datasets through the use of a single mode of information (RGB or Depth), or utilizing both modes simultaneously.
- This decomposition serves as a benchmark dataset for evaluating models.

Specifications of parameters of both datasets is described in Table 1. These datasets are designed in form of RGB images from recorded videos. for static body gestures as well dynamic body gesture. The full data of gym dataset and yoga dataset is available at [3][4]

TABLE 1 SPECIFICATIONS OF GYM DATASET AND YOGA DATASET

Subject	Computer vision , Human computer interaction
Specific subject area	Body gesture recognition and image processing
Type of data	Images (RGB)
How data were acquired	These datasets contain images, which are taken by one camera
Data format	Raw
Parameters for data collection	The acquisitions have been conducted, considering different body positions and orientation
Description of data collection	These datasets consist of 1992 images of 2 exercise of body gesture of gym & 3012 images of 4 yoga possess acquired by one camera
Data source location	Delhi technological university, Delhi ,India
Data aaccessibility	gym dataset [3] yoga dataset [4]

II. DATA DESCRIPTION

Gesture recognition is a vital area for human-device interplay research due to the fact that it is one of the maximum natural techniques for people to talk. We know that data is modern fuel because its use to identify the modern problem predictions and better user experience. Here, we use exercise dataset of yoga and gym because in modern era technology is gradually changes that's why the reason teaching phase also changes. Thanks to machine learning that we can learn anything without any human and trained machine learning models can be used as an instructor for learn the correct possess of exercise [5].



Original Image 1	Original Image 2	Original Image 1

Authorized licensed use limited to: DELHI TECHNICAL UNIV. Downloaded on May 04,2023 at 06:32:40 UTC from IEEE Xplore. Restrictions apply.



Fig 1 sample images of Gym dataset with three classes



Fig 2 sample images of Yoga dataset with four classes

Multi model datasets are available, such as the one presented in Fig 1 and Fig 2, where static gestures have been collected in the form of RGB and Depth frames specially and temporally aligned. The demerits of these datasets is that only one gesture per image is shown and the body is far to camera make these datasets suitable for object detector models that goal is to identify gestures in cluttered surroundings. However, the gestures are proposed mostly in dynamic and intricate, better suited for gaming and computer interactions rather than industrial settings where straightforward and uncomplicated gestures are required [6].

We create these datasets in form of videos with the help of smart phone camera. The gym videos are converted into 1992 RGB frames and Yoga videos are converted into 3012 frames by using Open CV (a python library) [7]. Gestures in Fig 1 have three variants by performing Bench-press, no exercise, and shoulder-press in the raw data. In this dataset two subjects are performing different activities. Similarly, in Fig 2 Yoga dataset, where we get 3012 frames. We extract four images of four different possess of yoga sequentially Pawanmuktasana, Balasana, Uttanpadasana and Halasana.

In Fig 1 and Fig 2, also the results of R-CNN (Region-based Convolutional Neural Network) technique is shown, which is used to identify a subset of regions in an image that might contain an object. Therefore, the result of object detection shows different objects which are doing different activities in both datasets.

III. Device Description and Camera View

Both Gym dataset and Yoga dataset are created by camera in the form of raw video data. The description of camera is described in Table 2.

TABLE 2 DESCRIPTION OF RECORDING DEVICE

Subject	Gym dataset	Yoga dataset
Video length	1:06 sec	1:40 sec
Video Memory	17.9 MB	242 MB
Camera used	Rear camera	Front camera
Autofocus	Yes	No
Camera resolutions	8MP	25MP
Video Resolution	1080 x 608	2336 x 1080

A. Gym dataset

For gym dataset the captured video length is one minute six second and converted into 1992 RGB frames and yoga dataset has video length one minute forty second and converted into 3012 RGB frames. During capturing videos camera is set at some different angles so the frames has multi view angles [8].

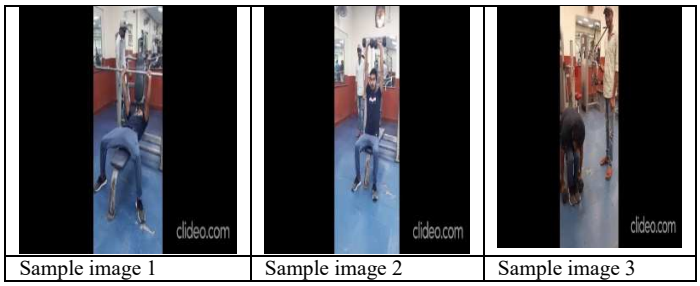


Fig 3 Description of multi view images of Gym dataset

The datasets with multiple modalities and view variant can be found at different angles of camera [9]. the captured static gestures through RGB and Depth frames that are spatially and temporally synchronized. However, the downside of these datasets is that they only display one gesture per image and the body is distant from the camera, making them suitable for object detection models. Some sample images with their angle and distance from camera are described in Fig 3. The camera captures two subjects in one frame is 20 degrees right from objects and 3 meters back from first subject who perform exercise hold rod in 30 degrees from chest and 7 meter far from second subject, which is shown in sample image 1.

Similarly, camera captures two subjects of 20 degrees right from other subject and 3 meters' distance from second subject. One performs exercise by holding dumbbells at 90 degrees from his shoulders and 5 meters' distance from second subject who standing behind of first subject in sample image 2 in Fig 3. And camera adjusting in sample image 3 of Fig 3 is 30 degrees and left from subject and 3 meters' distance of from first subject holds the dumbbells at 90

Authorized licensed use limited to: DELHI TECHNICAL UNIV. Downloaded on May 04,2023 at 06:32:40 UTC from IEEE Xplore. Restrictions apply.

degrees from ground and distance between both dumbbells from legs is 1 cm and 4.5 meters' distance from second subject and distance between first and second subject is around 0.5 meter.

B. *Yoga dataset*

The pose estimation of yoga is very useful for so many applications related to health concern [10], [11]. In Fig 4, there are four sample images of yoga dataset.For yoga dataset camera postion is almost same and clearly focus to object with high resolution. In sample image 1 , the subject is performing Pawanmuktasana. The camera adjust 10 meter far from the subject and view taken 15 degrees tillted back holding by camera with stand length of 3 meter from ground. In sample image 2 of Fig 4, The object performs Balasana with distance of head of subject is 30 cm from ground and toes are 150 cm from ground as well as distance between knees and chin is 5 cm.



Fig 4 description of multi view images of Yoga dataset

Camera position slightly changes of 1 to 2 degres left side but this time distance between camera and subject is 8 meters. In sample image 3, subject performs Uttanpadasana with distance between index fingers and head is almost 2 meters. In sample image 4 of Fig 4, the camera position is almost same but distance from object is again 8 meter, where subject is perfoming Halasana, where the distance of object head and ground is almost 30 to 35 cm and distance between subject toes and gound is 1 meter and angle between subject upper body and leges is 45 degress.

IV. VIDEO TO FRAMES CONVERSION

Python programming language is used to complex statistical calculations, data analysis, data optimization as well data formation or we can say data creation. It is suitable for all machine language and artificial intelligence works. For creating this data set used python programing language conversion of raw data which is in the form of video to frames [12]. The algorithm for video to frame conversion is describing below.

Import CV2 to solve computer vision problem
Cv2.video capture
Take input as video format
isOpened()
Conversion of video to frames
Imwrite()
save to image in storage device
release()
released acquired lock
Cv2.destroyAllWindows
Allows to close all windows any time after exiting the script

V. RESULTS

RGB-D datasets have a variety of applications, including fitness tracking, physical therapy, sports training, and injury prevention. These dataset can be used to track progress, identify areas for improvement, and provide personalized feedback to individuals. The gym and yoga datasets can also be used to promote a healthy lifestyle and aid medical research, as well as serve as a reference for human robotics. The datasets are adaptable for various applications, including web and android applications, and different algorithms can be implemented using them.

A. *Applications.*

- **Fitness tracking:** By monitoring and recognizing different yoga and gym exercise activities, RGB-D datasets can be used to track fitness progress over time, identify areas for improvement, and provide personalized feedback to individuals.
- **Physical therapy:** RGB-D datasets can be used to track the progress of individuals undergoing physical therapy, monitoring their movements and postures during exercise routines and providing feedback to therapists to help tailor treatment plans.
- **Sports training**: RGB-D datasets can be used to analyze the movements and postures of athletes during training and provide feedback on areas for improvement, helping athletes to optimize their performance and reduce the risk of injury.
- **Injury prevention:** By analyzing the movements and postures of individuals during yoga and gym exercise activities, RGB-D datasets can be used to identify potential areas of risk for injury and provide guidance on proper form and technique.

B. *Merits*

- Gym dataset and yoga dataset help to promoting healthy life style as well as medical research areas.
- Refer both dataset for human robotics as instructor.
- The most important machine learning module is so adaptable for web application, android application, IOT gadgets.
- Different algorithms can be implemented by using these datasets.

Authorized licensed use limited to: DELHI TECHNICAL UNIV. Downloaded on May 04,2023 at 06:32:40 UTC from IEEE Xplore. Restrictions apply.

C. Demerits

- Security and privacy are very important concerns.
- In gym dataset, there is overlapping of two objects, means occlusion is introduced here.

The summary of Gym dataset is described in Table 3 with some important parameters like gesture classes, number of subjects and video length.
Similarly, in Table 4, there is brief information of Yoga dataset

TABLE 3 SUMMARY OF GYM DATASET

Feature	value
Gestures classes	2
Subjects	2
Frames	1992
frames per class	400-570 (of two exercise)
Video length	1:06 sec
Frame rate	30 fps
Video Resolution	1080 x 608
Frame resolution	1080 x 608
Horizontal resolution	96 dpi
Horizontal resolution	96 dpi
Camera motion	Yes ,slightly

TABLE 4 SUMMARY OF YOGA DATASET

Feature	value
Gestures classes	4
Subject	1
frames	3012
frames per class	550-650 (of yoga possess)
Video length	1:40 sec
Frame rate	30 fps
Video Resolution	2336 x 1080
Frame resolution	2336 x 1080
Horizontal resolution	96 dpi
Vertical resolution	96 dpi
Camera motion	Yes ,slightly

D. Difference of existing and gym and yoga datasets

TABLE 5 EXISTING AND GYM AND YOGA DATASETS

Dataset	2D/ 3D	Video/ Image	Static/ Dynamic	Frames
Gym99	2D	Video	Dynamic	14,850
UCF101-Yoga	2D	Video	Both	3000
Yoga-82	Both	Video	Both	58,920
UCF11	2D	Video	Dynamic	280,000
Yoga And Gym (ours)	2D	Video	Static	Yoga-3012 Gym-1992

In above Table 5, here we show similarities and difference between our dataset and other existing datasets like frames, dimension etc.

VI. CONCLUSION

The creation of the Gym dataset and Yoga datasets for body gesture recognition is a significant contribution to the field of human-device interaction. These datasets consist of images captured by one camera and are available for free for experimental purposes. The Gym dataset consist of 1992 images of exercise for body gestures and 3012 images of four classes of yoga poses in the Yoga dataset. These datasets are valuable for human activity classification, pose recognition, and human-machine interaction, especially for body gesture recognition.

These datasets can serve as a benchmark for evaluating models, as a guide in fitness and yoga studios as well as training data and testing data for machine learning algorithms. The presence of both RGB and depth images offers the flexibility to use either a single mode of information or both modes concurrently. The results of the datasets show that they can be used in computer games, sports, e-commerce, assistant systems, and human-robot interactions.

REFERENCES

[1] Nuzzi C, Pasinetti S, Pagani R, Coffetti G, Sansoni G. HANDS: an RGB-D dataset of static hand-gestures for human-robot interaction. Data in Brief. 2021 Apr 1; 35:106791.

[2] Perera AG, Wei Law Y, Chahl J. UAV-GESTURE: A dataset for UAV control and gesture recognition. InProceedings of the European Conference on Computer Vision (ECCV) Workshops 2018 (pp. 0-0).

[3] Gym dataset: https://drive.google.com/drive/u/0/folders/1GckJjjT4srbr1mYRDDwkSUq4k-r2JpY6

[4] Yoga dataset: https://drive.google.com/drive/u/0/folders/1wAa8f26sg7_pK5rrffPcm2hCaFB86YhO

[5] Shukla D, Erkent Ö, Piater J. A multi-view hand gesture RGB-D dataset for human-robot interaction scenarios. In2016 25th IEEE international symposium on robot and human interactive communication (RO-MAN) 2016 Aug 26 (pp. 1084-1091). IEEE.

[6] Lopes A, Souza R, Pedrini H. A survey on RGB-D datasets. Computer Vision and Image Understanding. 2022 Sep 1; 222:103489.

[7] Raschka S, Patterson J, Nolet C. Machine learning in python: Main developments and technology trends in data science, machine learning, and artificial intelligence. Information. 2020 Apr;11(4):193.

[8] Beery S, Wu G, Rathod V, Votel R, Huang J. Context r-cnn: Long term temporal context for per-camera object detection. In Proceedings of the IEEE/CVF Conference on Computer Vision and Pattern Recognition 2020 (pp. 13075-13085).

[9] Hoang VT. HGM-4: A new multi-cameras dataset for hand gesture recognition. Data in brief. 2020 Jun 1; 30:105676.

[10] Anilkumar A, KT A, Sajan S, KA S. Pose estimated yoga monitoring system. In Proceedings of the International Conference on IoT Based Control Networks & Intelligent Systems-ICICNIS 2021 Jul 8.

[11] Kumar D, Sinha A. Yoga pose detection and classification using deep learning. LAP LAMBERT Academic Publishing; 2020 Nov.

[12] Conway AM, Durbach IN, McInnes A, Harris RN. Frame-by-frame annotation of video recordings using deep neural networks. Ecosphere. 2021 Mar;12(3): e03384.

Authorized licensed use limited to: DELHI TECHNICAL UNIV. Downloaded on May 04,2023 at 06:32:40 UTC from IEEE Xplore. Restrictions apply.

Journal of Mechanical and Construction Engineering, 2023,
Vol. 03, Iss. 01, S. No. 002, pp. 1-8
ISSN (Online): 2583-0619

Scenario of Offshore Wind Power Generation in India

Anubhav Singh[1], Dharmraj Meena[2], Shanti Lal Meena[3], Shiv Lal[4]

[1,2,3,4]Department of Mechanical Engineering, Rajasthan Technical University, Kota, India
[1]anubhav.20me422@rtu.ac.in, [2]dharmraj942@gmail.com, [3]slmeena@rtu.ac.in, [4]sl@rtu.ac.in

How to cite this paper: A. Singh, D. Meena, S. L. Meena and S. Lal, "Scenario of Offshore Wind Power Generation in India," *Journal of Mechanical and Construction Engineering (JMCE),* Vol. 03, Iss. 01, S. No. 002, pp. 1–8, 2023.

https://doi.org/10.54060/jmce.v3i1.28

Received: 02/01/2023
Accepted: 12/03/2023
Published: 25/04/2023

Copyright © 2023 The Author(s).
This work is licensed under the Creative Commons Attribution International License (CC BY 4.0).
http://creativecommons.org/licenses/by/4.0/

Open Access

Abstract

An exponential increase has been seen in the human population in the last few years. To meet the electricity requirement production has to be increased. The dependence on fossil fuels for generation has to be minimized. The practices of fossil fuel have contributed to the environmental degradation and its resources depleted continuously, that's why the whole world is switching to an alternate or renewable energy options. The electricity sector has to develop more generation capacity to maintain this development. According to 2012 data, only a small fraction (26GW) of India's total installed electricity capacity (210GW) produced from renewable sources. Hence Indian Government wants to shift to renewable forms of energy source share 40-42% of the total energy production i.e., 166GW. The share of wind energy is 60% of the total renewable energy basket, but the contribution from the offshore wind farms is lacking, as the wind energy generated in India is mostly through onshore wind farms. Promotion of offshore wind energy will farm will lead to reduction in dependency on fossil fuels, deplete in greenhouse emission, increase in environmental conservation and increase employment in India. India is coping up with the industry. Offshore wind energy is an emergent renewable energy industry, and it will become as main source of the future energy for India. This paper deals with the present situation and drift of offshore wind industries in India.

Keywords

Wind power, offshore wind farms, Present scenario of wind industry

1. Introduction

India's power producing capacity must be increased to meet the country's rising electrical consumption. India needs to move to sustainable energy fuels because it has historically powered its generators with fossil fuels. Wind power generation can be increased by increasing the power generation of already running farms are increasing the efficiency of the windmills. These two criteria can't meet our energy demand because stable wind is available only in the offshore areas, so it is to be emphasized to develop new projects in the offshore areas [1, 2].

In order to help India's growth of offshore wind power, the government of India joined forces with an association led by the Global Wind Energy Council (GWEC) and funded by the European Union (EU) in 2013 to work on the Facilitating Offshore Wind Energy in India (FOWIND) project in India. The FOWIND project resulted in a number of comprehensive research articles, including the pre-feasibility studies, evaluations of the supply chains, port facilities and logistics and a grid infrastructure study. Off the coasts of Gujarat and Tamil Nadu, offshore wind energy development was the focus of the study. For the Government of India to take into account as it develops the framework for offshore wind projects to be bid and ultimately implemented between 2018 and 2032, the FOWIND project outlined five essential route items in 2017 [3].

India is world's 2nd most populated country with population of 140.76 crores as of 2021, i.e., 17.7% of the total world population. The energy sector has seen many changes over time due to the introduction of new technologies [4]. To meet the energy demands of such a large population, energy generation has to be extraordinarily increased. In 1897, Darjeeling was the 1st place where power development was started, and then a hydropower station was built at Sivasamudram in Karnataka around 1902. Wind energy is domestic and can be of great help in reducing the need to generate energy from fossil fuels, owing to the variable heating of the earth's surface by the sun, wind occurrence takes place.

The wind power installed capacity is presented in figure 1, the installed wind power capacity and generation in India since 2007 is presented in figure 2. The installed wind capacity by state up to 31 March 2021 is presented in figure 3. India has installed capacity in the year 2022 of 40358W of wind energy and the renewable energy sources currently accounted by 27.78% (109885MW) of overall installed power capacity of India (which is 395608MW in 2022). 60% of the overall renewable energy basket is made up of wind energy. Yet, as onshore wind farms produce the majority of India's wind energy, the contribution of offshore wind farms is minimal. No systematic study was done till 2012 to estimate the available offshore wind energy (OWE) potential off the coasts of India [5].

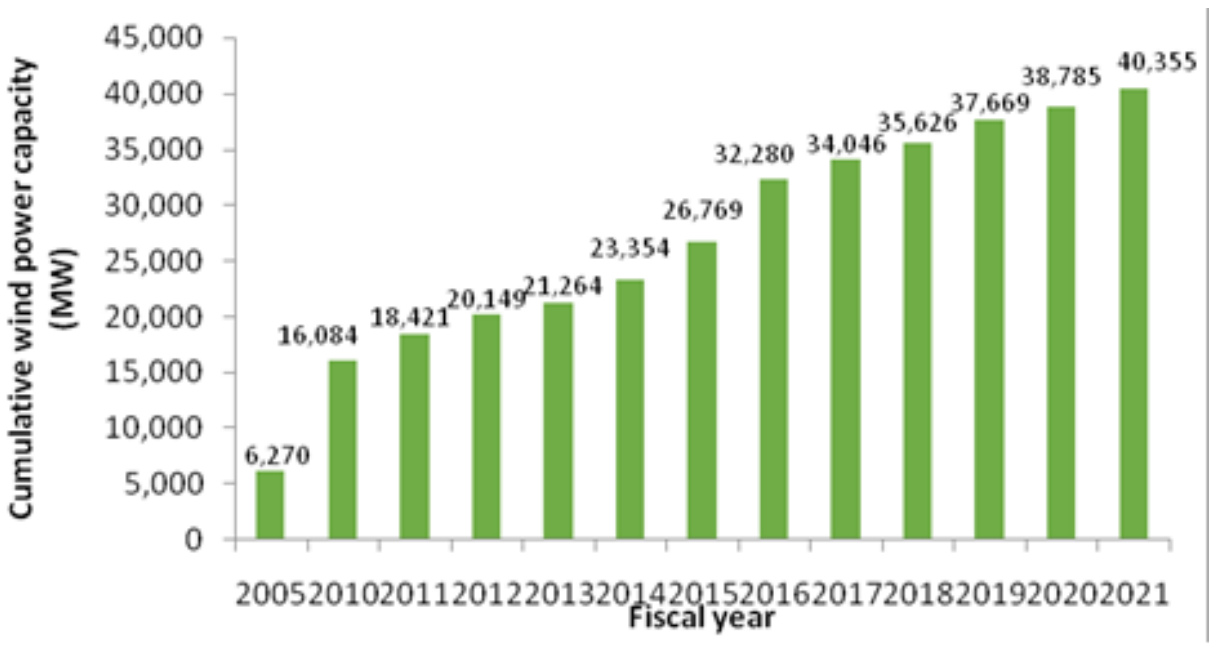


Figure 1. Installed Wind Power Capacity of India

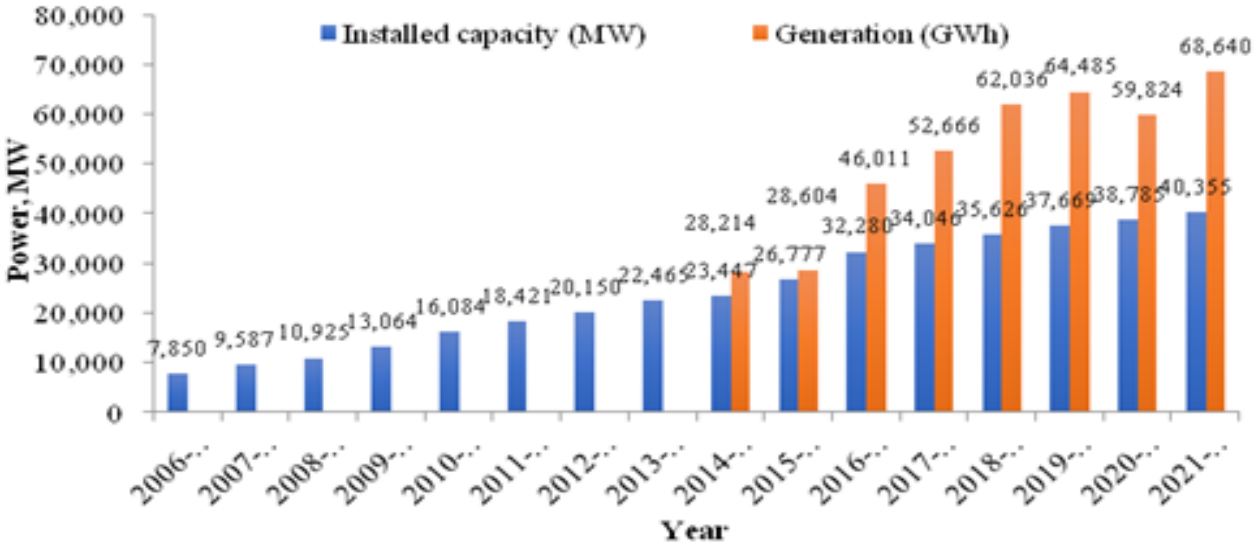


Figure 2. Installed wind power capacity and generation in India since 2007 [6]

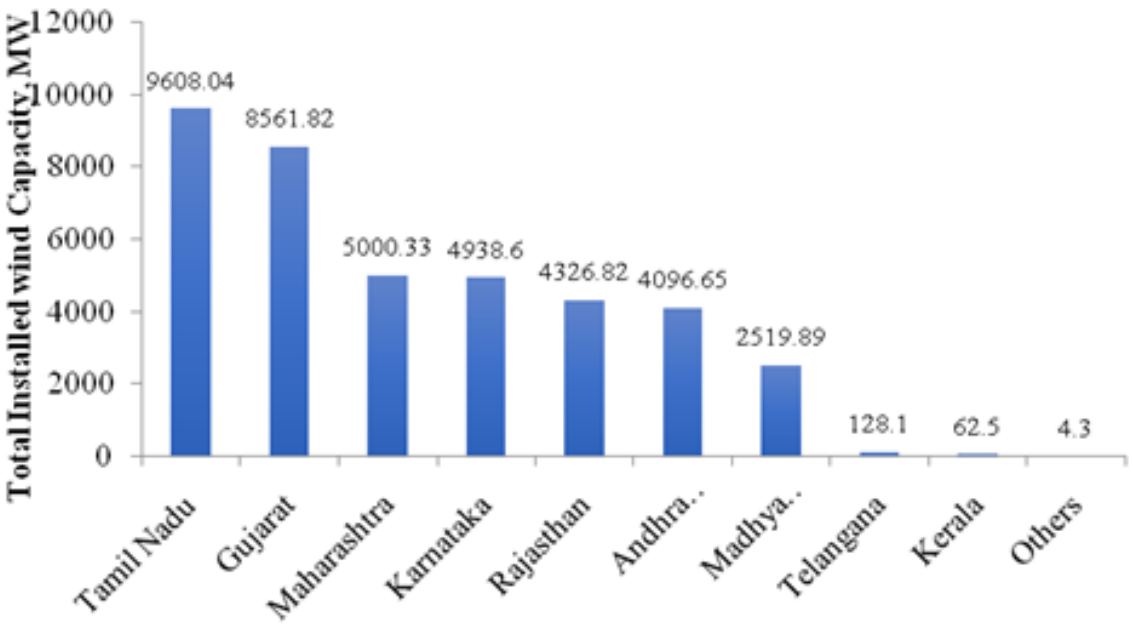


Figure 3. Installed wind capacity by state as of 31 March 2021 [7]

India has a large coastline of 75000km which have a great potential for the installation of offshore wind farms. As of 30 September 2022, the total installation wind capacity was 41.666GW, the fourth largest installed wind capacity in India power. The future Indian power economy in which renewable, wind and solar, could meet 80% of anticipated 2040[8]. The wind speed availability is more on the coastal areas of India as shown in figure 4. At any offshore wind development site, water depth is crucial for identifying an appropriate foundation technology [9].

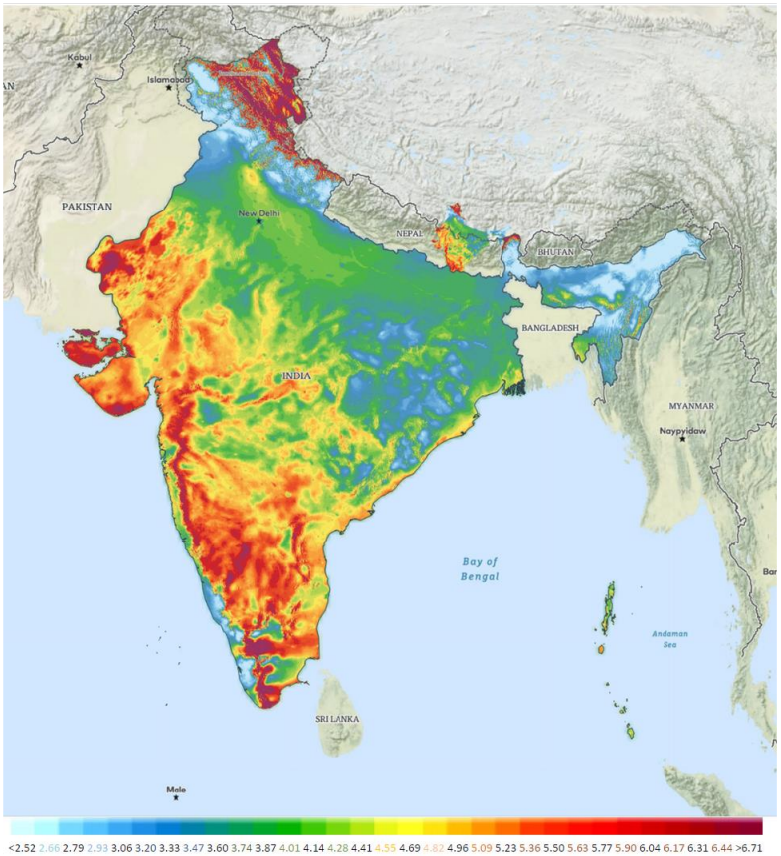


Figure 4. Wind speed (m/s) potential in India

The Indian Exclusive Economic Zone's offshore wind farm development is boosted by the Wind Energy Policy 2015 (EEZ) [9]. By 2030, India pledged to lower its intensity of greenhouse gas emissions by 35% from 2005 levels [11]. Exploration of offshore wind is becoming more practical, and several programs have been successful. The greatest installed wind power producing capacity is in Tamil Nadu, which contributes 23 percent of all installed wind capacity in India, or 37,505 MW [12], Gujrat has 142,560MW wind power potential at 120m above ground level [13], Gujrat is followed by Rajasthan with 127,155MW, Karnataka with 124,155MW, It was noted that from 2006 to 2012, Karnataka's energy consumption increased by 8% while the supply increased by just 6%, resulting in steadily growing energy deficits [14].

The ground level wind potential for Maharashtra is 98,213 MW, and for Andhra Pradesh it is 74,906 MW. Onshore wind farms have a more noticeable aesthetic influence on the landscape than some other power facilities, although they are more expensive than brand-new coal and gas plants. Offshore wind farms have a lower visual effect and produce more energy per installed capacity with fewer swings. Offshore wind power is growing even though there is now less of it and the expenses of production and maintenance are greater. The region between the southern and south-western coasts had the lowest annual average wind speed and WPD, whereas the area near the southernmost tip of India had the highest annual average wind speed and WPD [15].

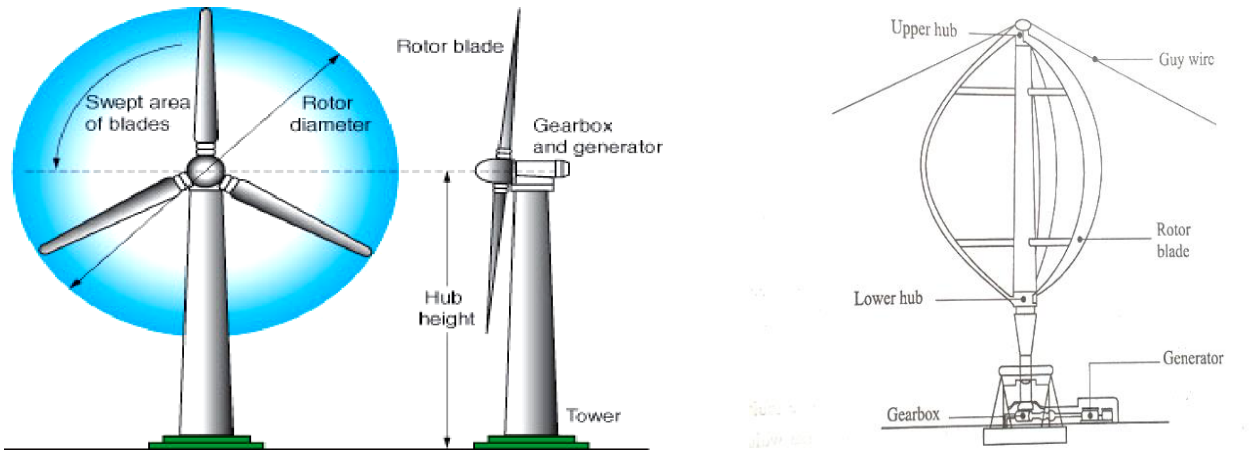
The first SAR operation in India Among other SAR missions, RISAT-1 fills the data void in coastal regions [16]. China and India are now relevant locations to investigate patterns of technology transfer that have supported the creation of multiple top wind power technology enterprises because they are the two largest emerging country wind power marketplaces in the world [17].

2. Material and Methods

2.1 Types of wind Turbines used in India

Wind turbines can be divided into two distinct types, based on the direction of the rotating axis.

- Horizontal axis wind turbines (HAWT) – It is a turbine with a rotor axis that is parallel to both the ground and the wind stream.
- Vertical axis wind turbines (VAWT) – It is a turbine in which the rotor is rotated along vertical axis.



(a) Horizontal axis wind turbines (HAWT) (b) Vertical axis wind turbines (VAWT)

Figure 5. Types of wind turbines used in India for offshore wind power generation

2.2 Benefits of offshore

The offshore wind measures higher speed as compared to onshore [18]. This is a very efficient way to produce wind energy. Near aquatic bodies, offshore wind farms are built. In comparison to on-land wind, offshore wind generates greater energy. A total of 55 offshore areas in 10 different European countries are home to over 1,662 wind turbines that produce enough electricity to power nearly 500 000 homes. Because of its economy, India does not deploy offshore wind turbines to generate much wind energy, offshore wind farms can be installed near to the major urban centers, which required shorter transmission lines to bring the wind power generated electrical energy to the high electrical energy price market [19]. Although the Indian economy is not strong enough to support the establishment of an offshore wind sector, some businesses have stepped forward to install offshore wind turbines because of the potential of this form of energy generation.

Offshore wind energy is a perpetually renewable and clean energy source that emits no damaging greenhouse gases during the process of converting wind to power. Offshore wind farms are distant from the coastline therefore cancelling the effect of noise produced due to the rotation of wind turbine blades. Due to its large coastline, there is large space for multiple installations. The government predicts that an increase in offshore wind capacity to 40 GW during the same time period will support up to 60,000 new employments. Because offshore wind generation is cost-effective, electricity costs will go down. It has no impact on the real estate value of land. Several factors, including stronger winds for effective electricity generation, make offshore wind farms appealing. In order to facilitate workflow, barriers to the effectiveness of India's wind energy policies and programs have been carefully examined [20].

2.3 Challenges in offshore installation

The installation is not easy as we reach practical installation. The primary obstacles to the effective use of offshore wind energy are its high present costs. [21]. Large wind turbines are challenging to erect on the open ocean. In comparison to onshore turbines, offshore wind turbines have significantly bigger dimensions and capacity. The plant load factor will be higher for offshore wind turbine as compared to the onshore turbines. The offshore wind farms may create disturbance in marine life [22] that's why the increase in electricity generation from offshore wind must be assess the effects on maritime birds and possible negative effects on bird populations in regions with wind farms [23]. Depending on the sea depth, an offshore wind generating project will cost 50–100% more per MW than an onshore installation. The presence of cyclones and sea breezes affects the wind resource of India's northwest. [24]. It creates No-go areas for commercial shipping. The Interaction Agency Model implies that when considering offshore wind growth generally, the sorts of policy tools, the direction of public values and norms, and the caliber of institutions are significant in both an independent and interacting manner. [25].

2.4 Present global and Indian offshore wind power scenario

Globally, the UK tops the list of offshore wind markets. The UK has the largest portfolio of offshore wind projects, with 1200 MW of offshore wind power generating electricity there, followed by Germany, Taiwan, China, which has a coastline of more than 4000 kilometers and USA [26-28]. The China has the largest existing offshore wind power capacity, but the UK has the biggest pipeline. In 2021, 7.4 MW was the average offshore wind turbine installed capacity, which was slightly less than 7.6MW in 2020 and it was also significantly higher 3.3 in 2011. In 2021, the global offshore wind energy market was valued at USD31.2 billion [30-31]. Capacity potential was firstly restricted geospatially using a GIS methodology to exclude EEZ areas, globally, that are infeasible for development [29]. In India by survey done by NIWE within the identified zones suggests 36GW of offshore wind energy potential exists off the coast of Gujrat and nearly 35GW of offshore wind energy potential exists off the Tamil Nadu coast. India's coastline of 76000km, the country has vast potential for OWE. The government of India has announced its intention of installation 5GW of offshore wind installation by 2022 and 30GW by 2030.

3. Conclusions

Offshore wing energy has started advancing in India. Policies have been set up to speed up the pace and due to the large coastline, the potential for its immense expansion. Targets are set so that the existence and potential of offshore wind energy can be tapped to the fullest. Ministry of new and renewable energy (MNRE), government of India have started the establishment procedure and installations of offshore wind farms in various states. It is also benefitted because the stable wind is available at the offshore sites. Indian coastland having large area that's why the possibility of offshore wind farms is more. Due to the installation of offshore windmills the wind power generation contribution will be 24% till 2030 in India.

References

[1]. T. Dhingra & S. Mani, "Policies to accelerate the growth of offshore wind energy sector in India," Renewable and Sustainable Energy Reviews, vol.24, pp.473-482, 2013.

[2]. V.Fuskele, P..Baredar, R.M. Sarviya, et al., "Wind Turbine Nacelle Cooling Systems: A review," WIRE-Energy and Environment Journal (Wiley), vol.11, no.6, pp.1-13, 2022.

[3]. P. B. Dash, "Developing Offshore wind energy in India," Assessed on pp.1-25, 2022. https://mnre.gov.in/img/documents/uploads/2e423892727a456e93a684f38d8622f7.

[4]. R. M. Murali, P. J. Vidya, P. Modi, et al., "Site selection for offshore wind farms along the Indian coast," Indian Journal of Geo-Marine Sciences, vol.43, no.7, pp.1401-1406, 2014.

[5]. R. Kumar, T. Stallard and P. K. Stansby, “Large-scale offshore wind energy installation in northwest India: Assessment of wind resource using Weather Research and Forecasting and levelized cost of energy,” Wind Energy, vol.24, no.2, pp.174-192, 2021.
[6]. S. H. Jain, “Overview of renewable power generation, CEA,” Archived from the original on Retrieved January 2023.https://cea.nic.in/renewable-project-monitoring/?lang=en
[7]. Offshore wind| Ministry of New and Renewable Energy, Government of India" Retrieved January 2023. https://mnre.gov.in/wind/offshore-wind/
[8]. T. Lu, P. Sherman, S. Chen, et al., “India’s potential for integrating solar and on-and offshore wind power into its energy system,” Nature communications, vol.11, no.1, pp.1-10, 2020.
[9]. N. Garlapati, V. Savasani, N. K. Naidu, et al., “Application of reanalysis data to estimate offshore wind potential in EEZ of India based on marine ecosystem considerations,” Energy, vol.118, pp.622-631, 2017.
[10]. C. R. Kumar, V. Kumar, M. Mazid, et al., “Offshore wind energy status, challenges, opportunities, environmental impacts, occupational health, and safety management in India,” Energy & Environment, vol.32, no.4, pp.565-603, 2021.
[11]. K. Boopathi, K. Balraman, J. Bastin, et al, “Assessment of wind power potential in the coastal region of Tamil Nadu India,” Ocean Engineering, vol.219, 2021.
[12]. R. Krishnamoorthy, K. Raju, L. M. Popa, et al., “An Assessment of Onshore and Offshore Wind Energy Potential in India Using Moth Flame Optimization,” Energies, vol.13, no.12, pp.1-41, 2021.
[13]. Gadad, S, Sanjeev and P. C. Deka, “Offshore wind power resource assessment using Oceansat-2 scatterometer data at a regional scale,” Applied Energy, vol.176, pp.57-170, 2016.
[14]. N. Garlapati, N. Naidu, V. Savsani, et al., “Feasibility study for offshore wind power development in India based on bathymetry and reanalysis data,” Energy Sources, Part A: Recovery, Utilization, and Environmental Effects, vol.39, no.5, pp.497-504, 2017.
[15]. S. V. V. A. Kumar, J. Prajapati, and R. Kumar, “Evaluation of offshore wind energy resources for power generation based on scatter meter and SAR data along the Indian coast,” Remote Sensing of the Oceans and Inland Waters: Techniques, Applications, and Challenges SPIE Asia Pacific, vol. 9878, 2016.
[16]. J. I. Lewis, “Building a national wind turbine industry: experiences from China India and South Korea,” International Journal of Technology and Globalisation, vol.5, no.3-4, pp.281-305, 2011.
[17]. S. B. Kore, A. Lole, S. S. Shinde, et al., “Feasibility of offshore wind farm in India,” Int. Res. J. Eng. Technol, vol.3, no.11, pp.2395-3225, 2016.
[18]. Bilgili, Mehmet, A. Yasar, et al., “Offshore wind power development in Europe and its comparison with onshore counterpart,” Renewable and Sustainable Energy Reviews, vol.15, no.2, pp.905-915, 2011.
[19]. S. Sharma and S. Sinha, “Indian wind energy & its development-policies-barriers: An overview,” Environmental and Sustainability Indicators, vol.1, 2019.
[20]. T. Smit, M. Junginger and R. Smits, “Technological learning in offshore wind energy: Different roles of the government,” Energy policy, vol.35, no.12, pp.6431-6444, 2007.
[21]. S. Jay, “Planners to the rescue: Spatial planning facilitating the development of offshore wind energy,” Marine pollution bulletin, vol.60, no.4, pp.493-499, 2010.
[22]. R. W. Furness, H. M. Wade, E. A. Madson, et al., “Assessing vulnerability of marine bird populations to offshore wind farms,” Journal of environmental management, vol.119, pp.56-66, 2013.
[23]. N. Garlapati, S. S. Kachhwaha, V. Savsani, “Estimation of technical and economic potential of offshore wind along the coast of India,” Energy, vol.138, no.1, pp.79-91, 2017.
[24]. C. Makridis, “Offshore wind power resource availability and prospects: A global approach,” Environmental science & policy, vol 33, pp.28-40, 2013.
[25]. C. Mattar and D. Borvaran, “Offshore wind power simulation by using WRF in the central coast of Chile,” Elsevier, vol.94, pp.22-31, 2016.
[26]. D. Toke, “The UK offshore wind power programmed: A sea-change in UK energy policy,” Energy Policy, vol.39, no.2, pp.526-534, 2011.

[27]. E. A. Madson, “Renewable energy developments in an uncertain world: the case of offshore wind and birds in the UK,” Marine Policy vol.51, pp.169-172, 2015.
[28]. J. Bosch, J. Staffell and A. D. Hawkes, “Temporally explicit and spatially resolved global offshore wind energy potentials,” Energy, vol.163, no.15, pp.766-781, 2016.
[29]. C. Makridis, “Offshore wind power resource availability and prospects: A global approach,” Environmental science & policy, vol.33, pp.28-40, 2018.
[30]. F. Pimenta, K. Willett and R. Garvine, “Combining meteorological stations and satellite data to evaluate the offshore wind power resource of Southeastern Brazil,” Renewable Energy, vol.33, no.11, pp.2375-2387, 2018.

Authors Profile



Mr. Anubhav Singh is a Graduate Engineering Student of Rajasthan Technical University Kota. He is working with offshore wind from last few years and chosen the same work in his seminar and other related academic works.



Mr. Dharmraj Meena is working as a guest faculty in Department of Mechanical Engineering, Rajasthan Technical University Kota (India). He is very much interested in the work of new horizons. He is working in the field of design and development of new and innovative systems, Renewable energy, Mechanical and Thermal Stress and Strain analysis.



Dr. Shanti Lal Meena currently working as an Assistant Professor in department of mechanical engineering, Rajasthan technical university Kota, India. He did his masters and PhD degree from Delhi Technological University Delhi, India. His main research directions include Manufacturing Technology, friction stir welding, modern machining methods, measurement and testing of various equipments with quality assurance. He has published many research papers in national/international journals and conferences. He can be contacted at email: slmeena@rtu.ac.in.



Dr. Shiv Lal is an Associate Professor in Department of Mechanical Engineering, Rajasthan Technical University Kota (India). He did his PhD from Indian Institute of Technology (IIT) Delhi. He is working in the field of Renewable energy options, Energy analysis, Energy economics, Biodiesel, Thermal Engineering and Heat Transfer Analysis, Energy and Exergy analysis of the thermal systems, Passive heating and cool-ing of buildings, green buildings. He has one year Industrial and 24-year teaching experience.

e-ISSN: 2582-5208
International Research Journal of Modernization in Engineering Technology and Science
(Peer-Reviewed, Open Access, Fully Refereed International Journal)
Volume:05/Issue:04/April-2023 Impact Factor- 7.868 www.irjmets.com

SIMULATION AND PERFORMANCE ANALYSIS OF A MULTIFUNCTIONAL OFF-BOARD EV CHARGER WITH SOLAR PV INTEGRATION AND IMPROVED POWER QUALITY USING MATLAB/SIMULINK

Sohail Ahmad[*1], Tarun[*2], Tushar[*3], Vishal Kumar[*4],
Aniruddha B Bhattacharya[*5]

[*1,2,3,4]Student, Electrical Engineering, Delhi Technological University,
New Delhi, India.

[*5]Assitant Professor, Electrical Engineering, Delhi Technological University,
New Delhi, India.

ABSTRACT

In this research paper, MATLAB Simulation & Analysis of a PV Integrated Multifunctional Off-Board EV Charger with Improved Grid Power Quality is described. The proposed solution utilizes an adaptive notch filter (ANF) and a multilevel topology for the grid-facing converter to accurately estimate the fundamental EV current and grid voltage, generating pure sinusoidal reference current and synchronizing voltage template. The charger can operate in grid connected (GCO) and standalone (SO) modes, offering grid current harmonic compensation, reactive power support, and backup power during emergencies. The simulation uses a DC Link system to directly charge the Electrical Vehicle, Energy Storage System and in case of cloudy conditions the 7-level cascaded H-bridge bidirectional dual-converter (CHBDC) converts Alternate Current from the Grid to charge the Electric Vehicle. A grid synchronization technique is employed for a smooth transition between modes. The simulation results show that the proposed system effectively achieves improved power quality with reduced harmonic distortion while maintaining stable DC link voltage regulation. This system has the potential to contribute to the sustainable development of EV charging infrastructure, reduce carbon footprint, and promote the use of renewable energy sources. Overall, this research is significant as it presents a promising solution for the integration of renewable energy sources in the EV charging system, leading towards a cleaner and sustainable future.

Keywords: EV Charger, Renewable Energy Sources, Grid Power Quality, Adaptive Notch Filter, Harmonic Mitigation, Bidirectional Dual Converter.

I. INTRODUCTION

With the growing popularity of electric vehicles (EVs) as an eco-friendly alternative to traditional fossil-fuel powered vehicles, the demand for efficient and effective charging infrastructure has been on the rise. According to the International Energy Agency's Renewables 2022 report, renewable energy accounted for almost 30% of electricity generation globally in 2021. The report also notes that the share of renewable energy in the global electricity mix is expected to grow over the next decade. As a result, Off-board EV chargers with solar PV integration have emerged as a potential solution to address the challenges of high electricity demand, limited grid capacity, and the need for renewable energy sources.

The current scenario of EV charging stations has some limitations in terms of charging time, grid capacity, and the availability of renewable energy sources. Traditional charging stations typically rely on grid power, which can lead to overloading and voltage fluctuations, causing power quality issues. This can result in power outages, damage to the equipment, and increased energy costs. Moreover, the lack of renewable energy sources limits the sustainability and long-term viability of traditional EV charging stations.

Therefore, there is a need for a multifunctional off-board EV charger with solar PV integration that can address these issues. Such a system can provide a sustainable and cost-effective solution for EV charging, while also improving power quality by minimizing voltage fluctuations and reducing the load on the grid.

The project will use MATLAB to simulate and analyze system's performance, considering the various components such as the solar PV system, battery storage, and charging infrastructure. The simulation will also

e-ISSN: 2582-5208
International Research Journal of Modernization in Engineering Technology and Science
(Peer-Reviewed, Open Access, Fully Refereed International Journal)
Volume:05/Issue:04/April-2023 Impact Factor- 7.868 www.irjmets.com

consider different scenarios such as changing weather conditions, varying load demand, and grid instability to evaluate the system's reliability and efficiency.

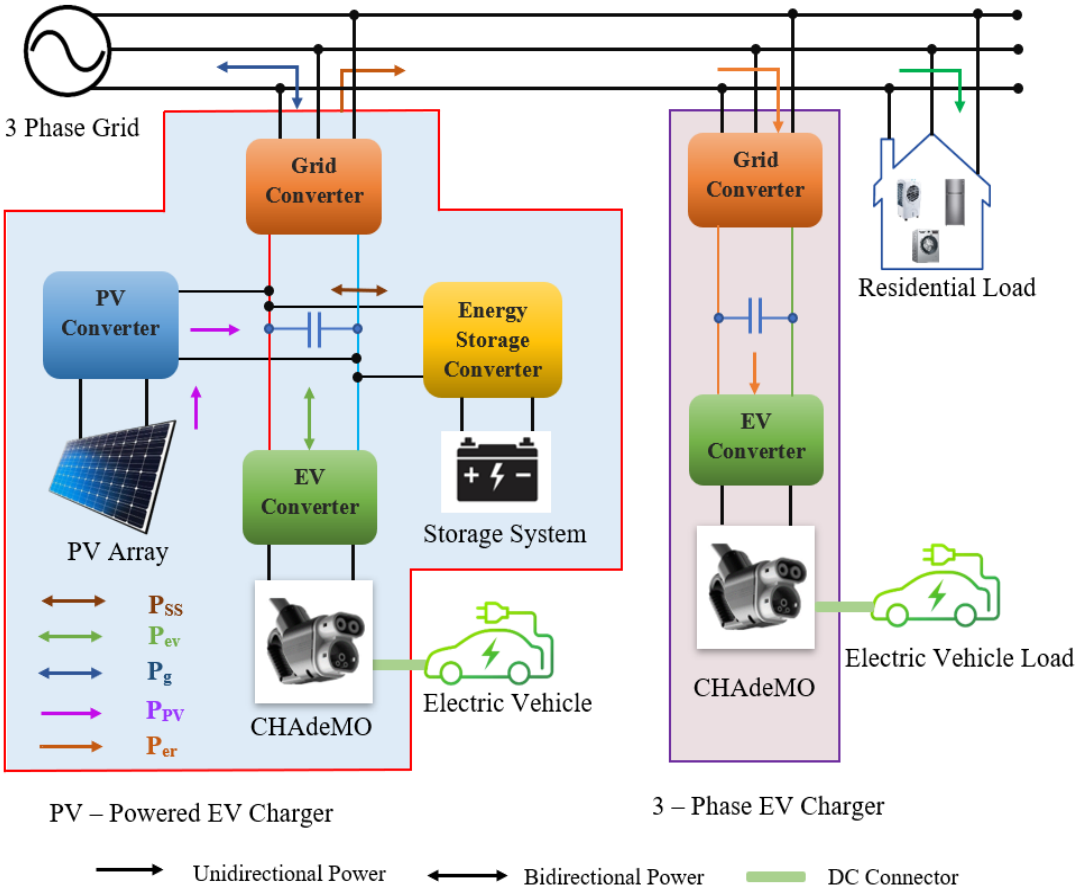


Figure 1: A Typical Photovoltaic (PV) powered EV charging System.

The global environmental crisis, caused by increased greenhouse gas emissions, has led to a growing concern about the impact of transportation on the environment. In response to this challenge, many countries have started to promote the adoption of Electric Vehicles (EVs) to reduce carbon emissions and mitigate the effects of climate change. EV charging systems, including the integration of renewable energy sources, of significant importance. It can help to address the challenges related to the adoption of EVs and contribute to the development of sustainable and reliable charging solutions for EVs.

In many instances, the Electric Vehicle (EV) batteries are utilized to alleviate issues arising from Photovoltaic (PV) intermittency and utility grid faults. However, this often leads to undesirable charging and discharging cycles of the EV batteries, ultimately reducing their lifespan. Therefore, this research paper proposes the integration of a Battery Energy Storage System (ESS) into the charger topology to improve the longevity of the EV batteries and ensure system reliability. An EV charging system consisting of ESS (Energy storage system) is shown in fig 1. The integration of Renewable Energy Source (RES) based Electric Vehicle (EV) chargers into the power grid poses various challenges to the system. The literature reports multiple studies focusing on the issues such as voltage deviation and drops, increased peak loads, distribution system losses, transformer lifespan reduction and significant investment costs. It also presents a range of opportunities for the system such as utilizing the power electronics circuitry of the EV charger to provide other services such as vehicle to grid (V2G) operation, vehicle to home (V2H) operation, four-quadrant charger operation, and grid current harmonics reduction.

The current time need is to create a renewable energy system (RES) based infrastructure for electric vehicle (EV) charging. In this paper, we propose a photovoltaic (PV) integrated system that provides various operations such as (1) grid connected/ standalone operation (GCO/SO), (2) four quadrant operation of the

e-ISSN: 2582-5208
International Research Journal of Modernization in Engineering Technology and Science
(Peer-Reviewed, Open Access, Fully Refereed International Journal)
Volume:05/Issue:04/April-2023 Impact Factor- 7.868 www.irjmets.com

charger (G2V/ V2G), (3) smooth transition between operation modes during grid synchronization, (4) grid current harmonic reduction, (5) reactive power support to the grid, and (6) simultaneous operation of the charger for improving grid power quality and EV charging using an active noise filter (ANF) based control algorithm. By implementing these features, the proposed model aims to enhance the reliability and efficiency of EV charging while improving the overall power quality of the grid. This research paper focuses on the following function implementation.

- This system employs solar PV generation to charge electric vehicles while also providing power to residential loads, in both grid-connected and standalone mode.
- To prevent undesirable charging or discharging of electric vehicles during regulation of DC link voltage when photovoltaic energy is intermittent, an energy storage system (ESS) is incorporated into the EV charger setup for the same purpose. This integration also enhances the dependability of charging and the supply of residential loads.
- A unified control algorithm based on ANF is utilized to ensure the grid current remains free of harmonics, with a total harmonic distortion (THD) of less than 5%, and to deliver reactive power support to the grid as required.
- During non-ideal grid voltage conditions, which include unbalanced and distorted voltage, the effectiveness of the ANF-based synchronizing voltage template estimator is evaluated and compared to the SOGI (Second Order Generalized Integrator) and PLL (Phase Locked Loop) methods that are currently in use.
- An ANF-based technique for minimizing phase errors is employed to synchronize the grid, enabling smooth transitions between grid-connected operation (GCO) and standalone operation (SO) and vice versa, and enhancing system reliability during grid outages.
- The charger control function has the capability to enable on-demand vehicle-to-grid (V2G) operation during grid-connected operation (GCO) and vehicle-to-home (V2H) operation during standalone operation (SO), thereby maximizing the utilization of the electric vehicle battery.

II. LITERATURE SURVEY

Literature Survey For Problem Identification And Specification

1. An off-board three-port integrated topology (TPIT) has been proposed by V. Monteiro, J. G. Pinto, and J. L. Afonso to connect solar photovoltaic (PV) panels and electric vehicles (EVs) to the electrical power grid. The TPIT consists of three power converters that are connected by a single common dc link and can function in four different ways to interact with future smart grids. These modes include the grid-to-vehicle, vehicle-to-grid, renewable-to-grid, and renewable-to-vehicle configurations. These modes can be rearranged to create new combination operation modes. The paper explains the power theory that is used to regulate the TPIT, the current management techniques used to manage the currents in the ac and dc sides of the TPIT, and the hardware and digital control system of the TPIT prototype. The acquired experimental results support the TPIT functioning modes.

2. A new control strategy for integrating solar photovoltaic (PV) with battery storage to a single-phase grid for residential and electric car applications has been proposed by N. Saxena, I. Hussain, B. Singh, and A. L. Vyas. The goal is to maintain a steady flow of electricity to the grid and increase the system's battery energy storage's viability. Power and load levelling are achieved because of the battery charging and discharging process, which also improves system reliability. The voltage-source converter reduces harmonics, compensates for reactive power, and functions as an active power filter. The suggested system has a special control mechanism that makes it possible to resynchronize the grid when a failure has been mitigated. The system control can be adjusted to a variety of real-world circumstances, such as cutting off the grid, the battery, and the PV array from the system. Additionally, the paper offers a thorough design and control strategy for the suggested system.

3. S. J. Gunter, K. K. Afridi, and D. J. Perreault have proposed a framework and optimization approach for the design of grid-connected systems that incorporate plug-in electric vehicle chargers, distributed generation, and storage. The process was used to create the best structures for a domestic charging case to show how useful it was. The study discovered that while maximizing grid power use might reduce system lifespan costs, systems with solar photovoltaic generation may be more cost-effective than those without depending on the location's

e-ISSN: 2582-5208
International Research Journal of Modernization in Engineering Technology and Science
(Peer-Reviewed, Open Access, Fully Refereed International Journal)
Volume:05/Issue:04/April-2023 Impact Factor- 7.868 www.irjmets.com

sun irradiance patterns. Micro wind turbines and Li-ion storage, however, are currently more expensive than alternative options.

4. The Multilevel inverter technology, which has emerged as an attractive option in high-power medium-voltage energy regulation, is the primary focus of the paper by J. Rodrguez, J.S. Lai, and F.Z. Peng. The paper discusses a number of topologies, such as cascaded multicell with separate DC sources, diode-clamped inverters, and capacitor-clamped topologies. Also covered are cutting-edge topologies like soft-switched multilevel inverters and asymmetric hybrid cells. The most important modulation and control techniques created for these converters are also covered in the study, including space-vector modulation, multilevel sinusoidal pulse width modulation, and multilevel selective harmonic elimination. The latest uses of these converters, including laminators, conveyor belts, and unified power-flow controllers, are highlighted by the authors. The article also covers several circuit topologies and examines the necessity of an active front end at the input side for inverters feeding regenerative loads. The paper concludes by discussing optical sensors, high-voltage high-power devices, and other potential future development areas.

III. ELECTRIC VEHICLE CHARGING MODEL

The proposed electric vehicle charging model is a multi-purpose off-board EV charger that integrates solar photovoltaic (PV) panels, an energy storage system (ESS), and a bidirectional charger to provide grid-connected operation (GCO) and standalone operation (SO). The model uses an adaptive notch filter (ANF) and includes several instruments such as a Bidirectional static switch, 7-level cascaded H-bridge dual converter (CHBDC) and bidirectional DC-DC converter for charging and discharging purposes.

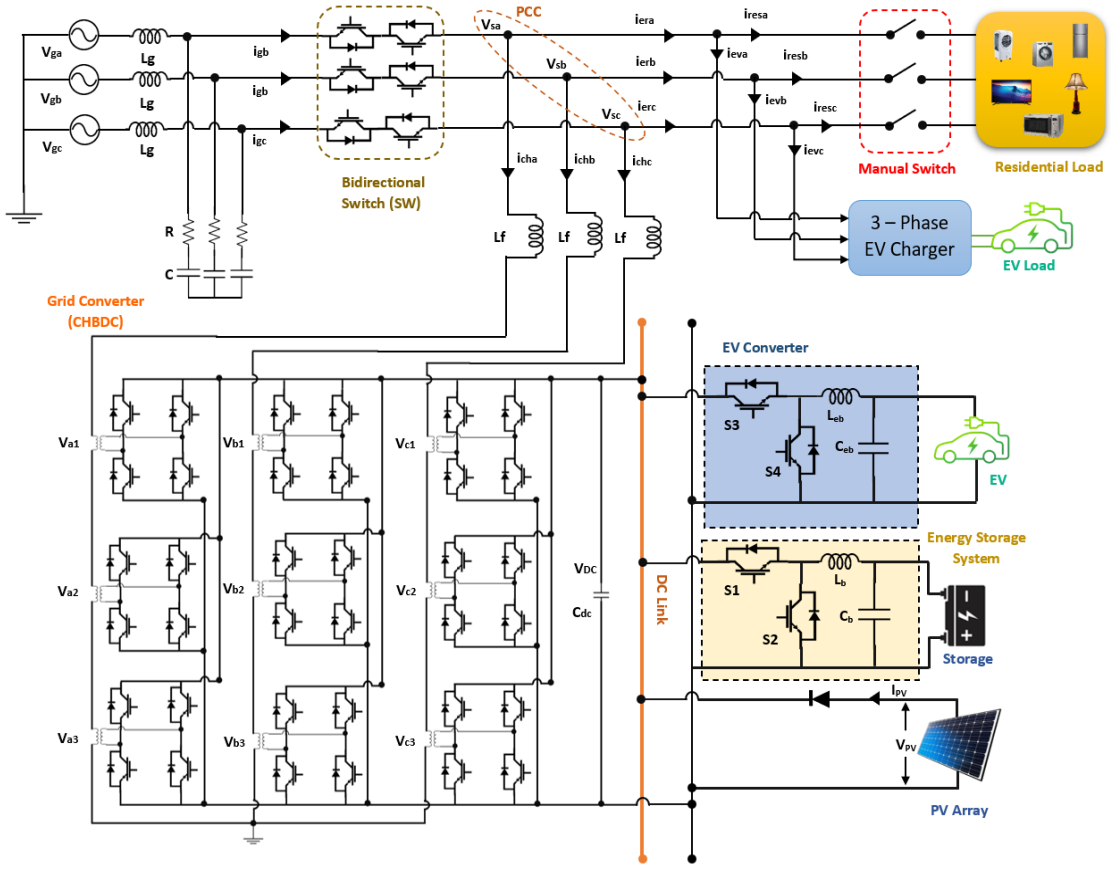


Figure 2: Proposed EV charger circuit

In the proposed model, a photovoltaic (PV) module is utilized to generate power. Instead of a PV boost converter, a diode is used to connect the PV array with the DC link, reducing the size of the system. The DC link is then connected to a 7-level cascaded H-bridge dual converter (CHBDC), which is linked to the grid at the point of common coupling (PCC) through an L-filter to enhance the output voltage of CHBDC. The energy storage converter and EV converter are connected to the DC link, allowing the energy storage battery and EV

e-ISSN: 2582-5208
International Research Journal of Modernization in Engineering Technology and Science
(Peer-Reviewed, Open Access, Fully Refereed International Journal)
Volume:05/Issue:04/April-2023 Impact Factor- 7.868 www.irjmets.com

battery to be charged and discharged in both directions. As shown in Figure 2, these converters are bidirectional DC-DC converters responsible for both charging and discharging of the EV and storage battery.

To couple the PCC with the grid, an inductor and a bidirectional switch are used, and an RC filter is used to mitigate switching harmonics. A manual switch is used to connect the PCC to the residential load, as demonstrated in Figure 2. EVs connected at the grid (PCC) are charged through the grid, while EVs connected at the DC link are charged with the assistance of a bidirectional DC-DC converter.

Overall, the proposed model provides a multifunctional solution that not only charges EVs but also enhances grid power quality and provides backup power supply to residential loads during emergencies. The use of a diode instead of a boost converter to connect the PV array with the DC link reduces the size of the system, making it more cost-effective. The bidirectional DC-DC converters allow for the efficient charging and discharging of both the EV and energy storage batteries, improving overall system performance. Finally, the use of an RC filter helps to mitigate switching harmonics and ensures a smooth transition from one charging mode to another.

IV. DIFFERENT OPERATIONS OF THE MODEL

The focus of this model is to propose an effective solution for an Electric Vehicle (EV) charging system that charges the EV in both Grid-Connected Operation (GCO) and Standalone Operation (SO), while also enhancing the power quality of the grid and providing backup power supply to residential loads in case of emergencies. One of the key challenges in designing this system is to ensure that the transition from GCO to SO or vice versa is smooth and seamless.

To address these challenges, the proposed model incorporates a battery energy storage system (ESS) and a multi-level topology for the grid-facing converter. The adaptive notch filter (ANF) is utilized for accurate estimation of fundamental EV current and grid voltage, generating pure sinusoidal reference current, and synchronizing voltage template. The model employs a DC Link system to directly charge the EV and ESS, and in case of cloudy conditions a 7-level cascaded H-bridge bidirectional dual-converter (CHBDC) converts Alternating Current from the grid to charge the EV.

Moreover, the proposed system offers grid current harmonic compensation, reactive power support, and backup power supply during emergencies. The integration of renewable energy sources and the use of a bidirectional converter enables the vehicle-to-grid (V2G) operation and vehicle-to-home (V2H) operation, allowing for the EV charger to provide additional services. The simulation results indicate that the proposed model effectively achieves improved power quality, reduced harmonic distortion, and stable DC link voltage regulation.

V. MATLAB SIMULATION OF THE MODEL

The proposed model has been simulated in MATLAB, the simulation presents an EV charging infrastructure that integrates solar PV and an energy storage system (ESS) for maximizing PV utilization and grid integration. The simulation model includes a 7-level cascaded H-bridge bidirectional dual-converter, bidirectional DC-DC converters, a PV array and an ANF-based control algorithm for grid synchronization and harmonic mitigation. The model is designed to operate in grid-connected mode and standalone mode, with a seamless transition between modes using a switch. The MATLAB Simulink is utilized to model the complete system and test its performance under different operating conditions. The simulation results demonstrate the effectiveness of the proposed ANF-based control algorithm. Overall, the simulation results validate the effectiveness of the proposed EV charging infrastructure in enhancing the reliability, efficiency, and flexibility of EV charging systems.

e-ISSN: 2582-5208
International Research Journal of Modernization in Engineering Technology and Science
(Peer-Reviewed, Open Access, Fully Refereed International Journal)
Volume:05/Issue:04/April-2023 Impact Factor- 7.868 www.irjmets.com

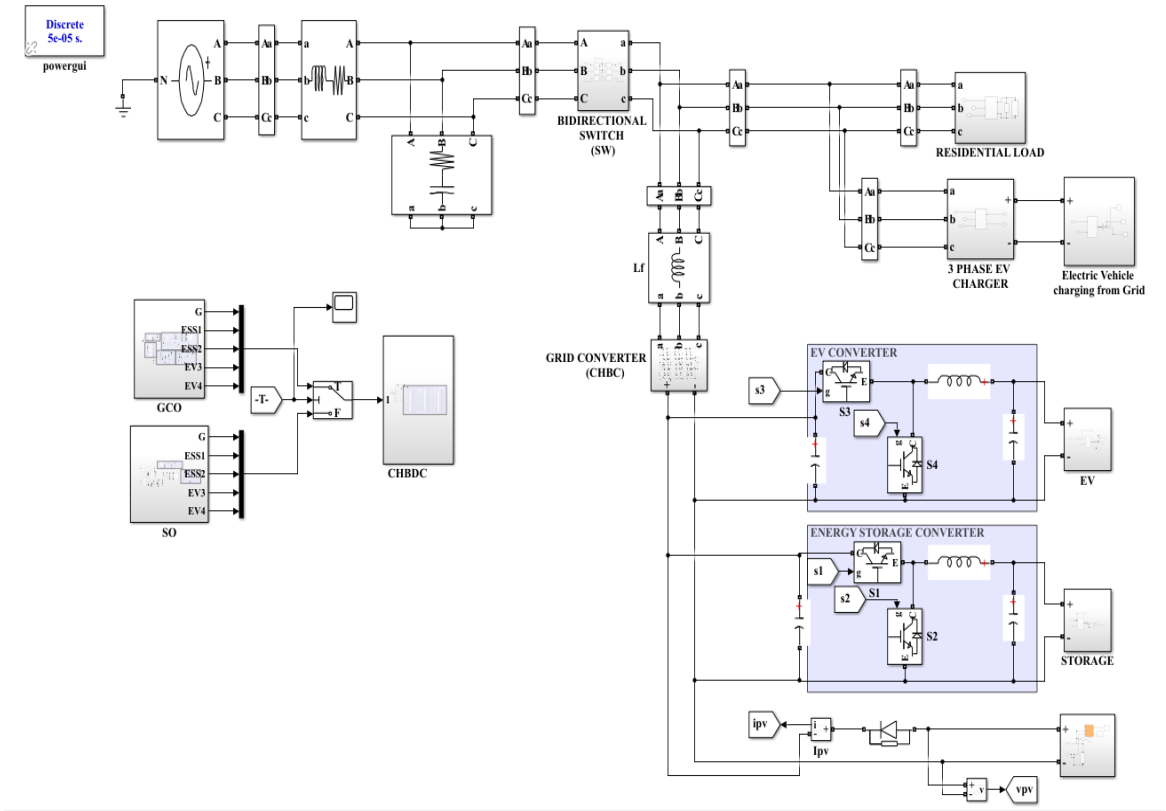


Figure 3: MATLAB Simulation of EV charging in GCO and SO mode

1. Grid-connected operation (SW=1)

In GCO, the control algorithm is mainly designed to compensate for the harmonic and reactive power demands of the residential and EV load during ideal and non-ideal grid voltage circumstances in order to maintain pure sinusoidal grid current at UPF. Fig. 3 shows the MATLAB model of GCO controller structure.

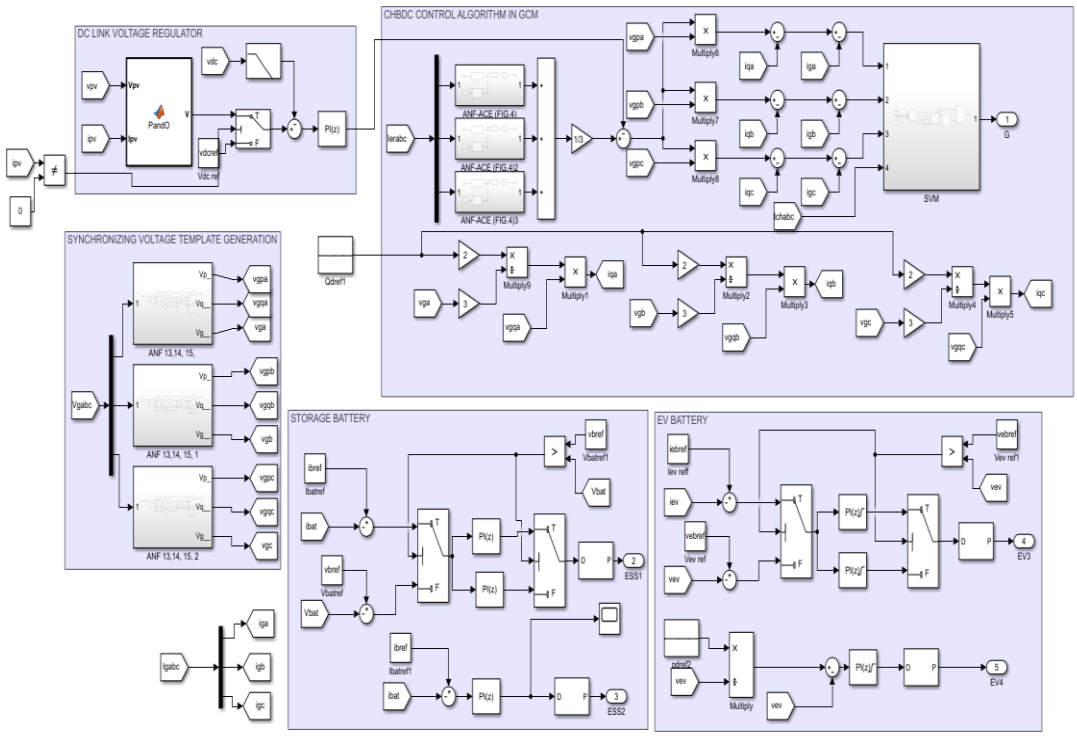


Figure 4: Grid Connected Operation (GCO)

e-ISSN: 2582-5208
International Research Journal of Modernization in Engineering Technology and Science
(Peer-Reviewed, Open Access, Fully Refereed International Journal)
Volume:05/Issue:04/April-2023 Impact Factor- 7.868 www.irjmets.com

The Simulink model depicts a control algorithm for electric vehicle (EV) charging stations in grid-connected operation (GCO), which maintains a pure sinusoidal grid current at unity power factor (UPF) while compensating for harmonic and reactive power demand of the residential and EV load in both ideal and non-ideal grid voltage conditions.

The CHBDC control algorithm block serves as the primary control algorithm for the system in GCO mode, utilizing ANF-based active power control, SH-based reactive power control, and MPPT algorithm for the PV array. The ANF-ACE block, which is an Adaptive Notch Filter (ANF) based active component extractor, estimates the active component of the nonlinear load current in two steps, ensuring estimation efficiency regardless of EV load current distortion and non-ideal grid voltage conditions. The structure of ANF-ACE is shown in Fig 5.

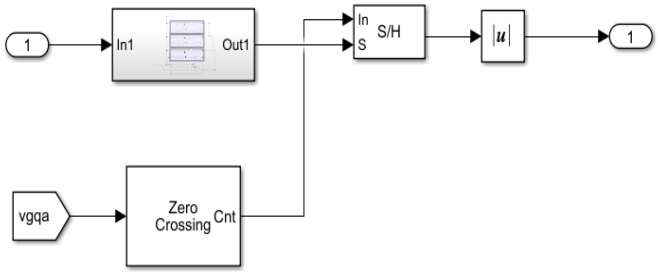


Figure 5: Structure of ANF-ACE

The GCO mode utilizes space vector modulation (SVM) technique for high-quality output waveforms and reduced harmonic distortion.

The Bidirectional DC-DC Converter (BDDC) controls the charging and discharging of the energy storage battery in GCO mode, with charging modes of constant current (CC) or constant voltage (CV) and discharging modes of constant current or constant power. The same charging technique is applied for EV charging at the DC link, with the discharging mode being constant power, determined by the charger operator based on the EV owner's convenience.

2. Standalone mode operation (SW=0)

To implement the standalone mode operation (SW=0) of the charger controller with solar PV and energy storage battery for uninterruptable charging of EV, a detailed control algorithm has been developed and simulated in MATLAB Simulink. The Simulink model consists of three major subsystems: CHBDC control, energy storage BDDC control, and EV BDDC control. Figure 6 shows the MATLAB model of SO controller structure.

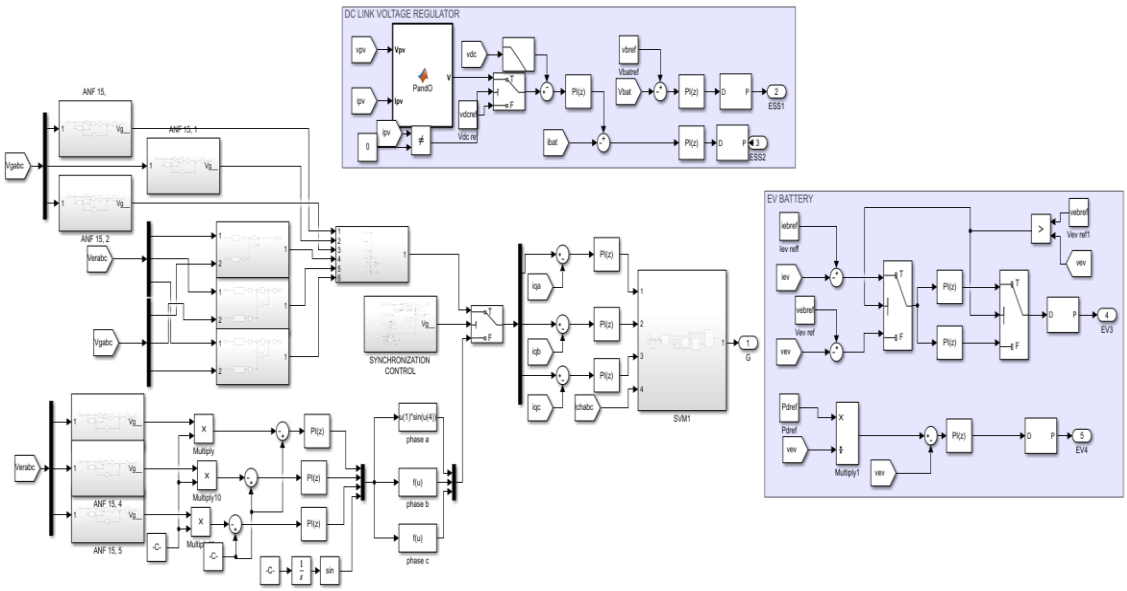


Figure 6: Standalone Operation (SO)

e-ISSN: 2582-5208
International Research Journal of Modernization in Engineering Technology and Science
(Peer-Reviewed, Open Access, Fully Refereed International Journal)
Volume:05/Issue:04/April-2023 Impact Factor- 7.868 www.irjmets.com

In the CHBDC control subsystem, an ANF-based controller estimates the reference voltage magnitude and phase, which are then compared with the measured PCC voltage to generate the error signal. The error signal is processed through a PI controller to minimize the error and generate the reference charger current. The reference current is compared with the actual measured current, and the error signal is fed to the space vector modulation (SVM) technique to generate gating pulses for switches.

The energy storage BDDC control subsystem regulates the DC link voltage to achieve MPP operation of the PV array, and the reference DC link voltage selection depends entirely on the availability of PV. The detailed controller structure is presented in Figure 7.

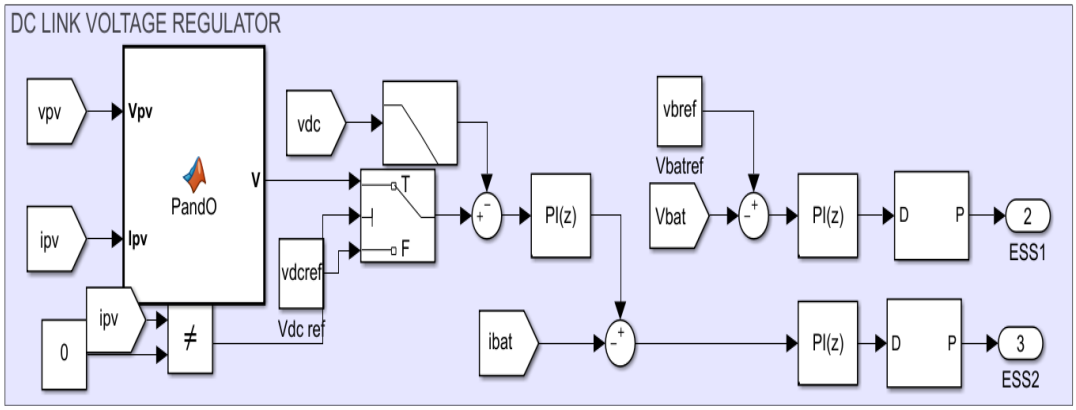


Figure 7: Storage battery BDDC control in SO of the charger

The EV BDDC control subsystem uses the same control algorithm as in the case of GCO, given in Fig. 2. The CC/CV mode of battery charging and constant power control is implemented to charge the EV battery.

To ensure a seamless transition from standalone mode to grid-connected operation (GCO), an ANF-based grid synchronization technique is employed. The ANF continuously estimates the phase of PCC voltage and compares it with the grid voltage phase. The phase error is then fed to a PI controller for minimization, which converts the phase error to frequency error. With the frequency error, the updated new frequency of the charger controller for reference generation is calculated, and the CHBDC generates the PCC voltage until the phase error is zero. The control logic continuously compares phase, frequency, and magnitude error with their maximum permissible limits to generate the control signal SW. When all the error lies below the maximum permitted limit, the control signal enables the bidirectional power electronic switch by setting SW=1 and connecting the PCC to the grid.

VI. RESULTS AND DISCUSSION

Steady state performance of the charger in GCO

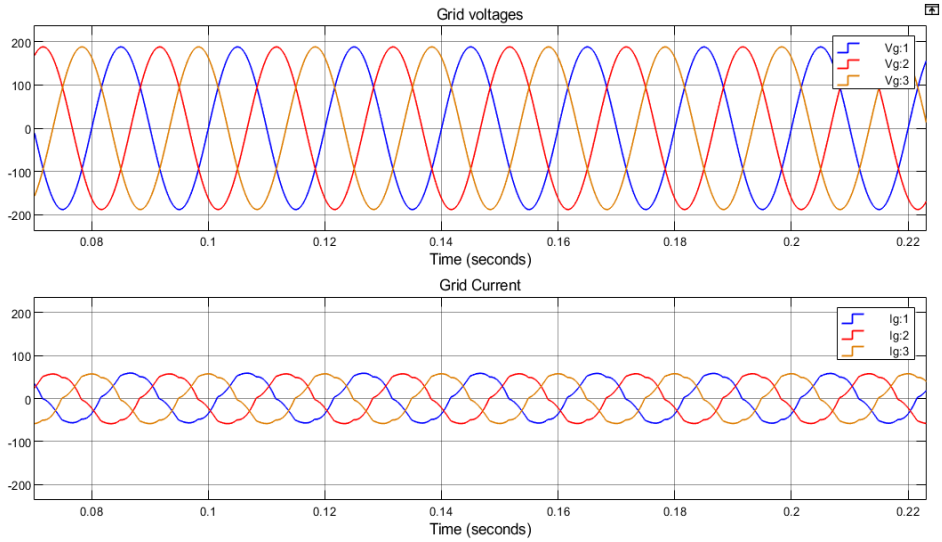


Figure 8: A, b and c-phase grid voltage (vga, vgb, vgc) and gird current (iga, igb, igc)

e-ISSN: 2582-5208
International Research Journal of Modernization in Engineering Technology and Science
(Peer-Reviewed, Open Access, Fully Refereed International Journal)
Volume:05/Issue:04/April-2023 Impact Factor- 7.868 www.irjmets.com

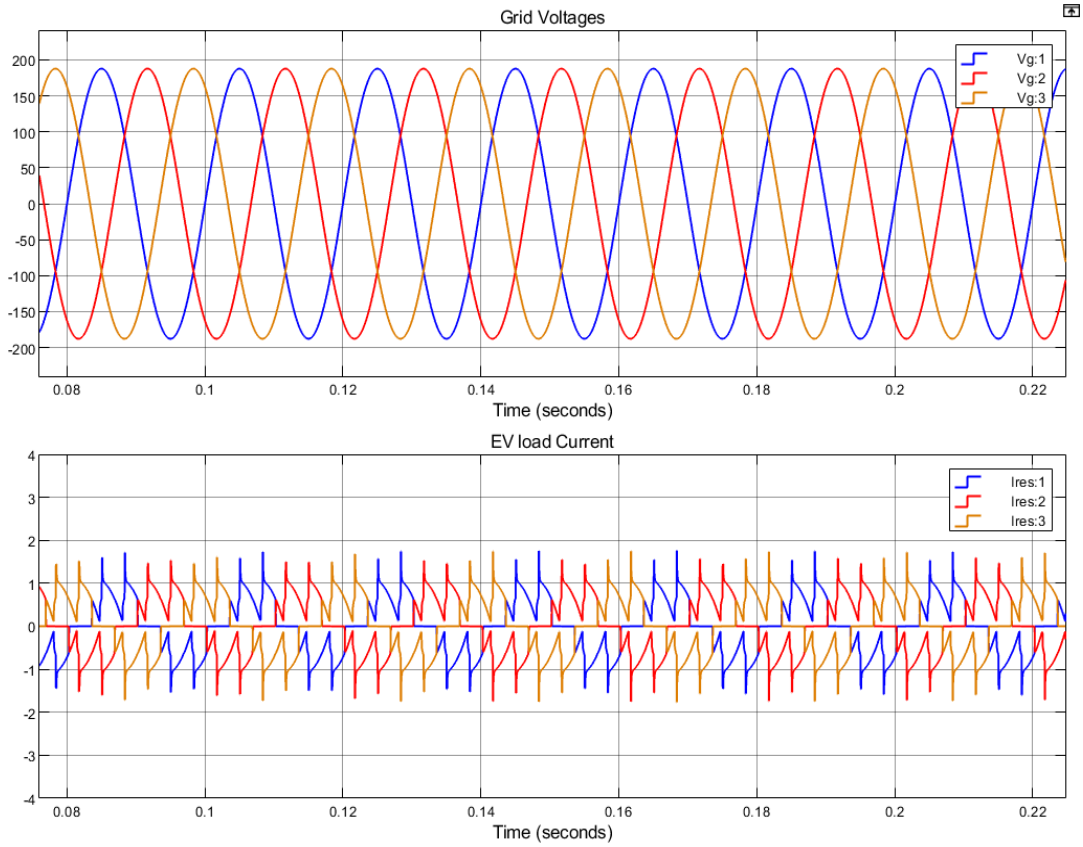


Figure 9: A, b and c-phase grid voltages (vga, vgb, vgc) and EV load current

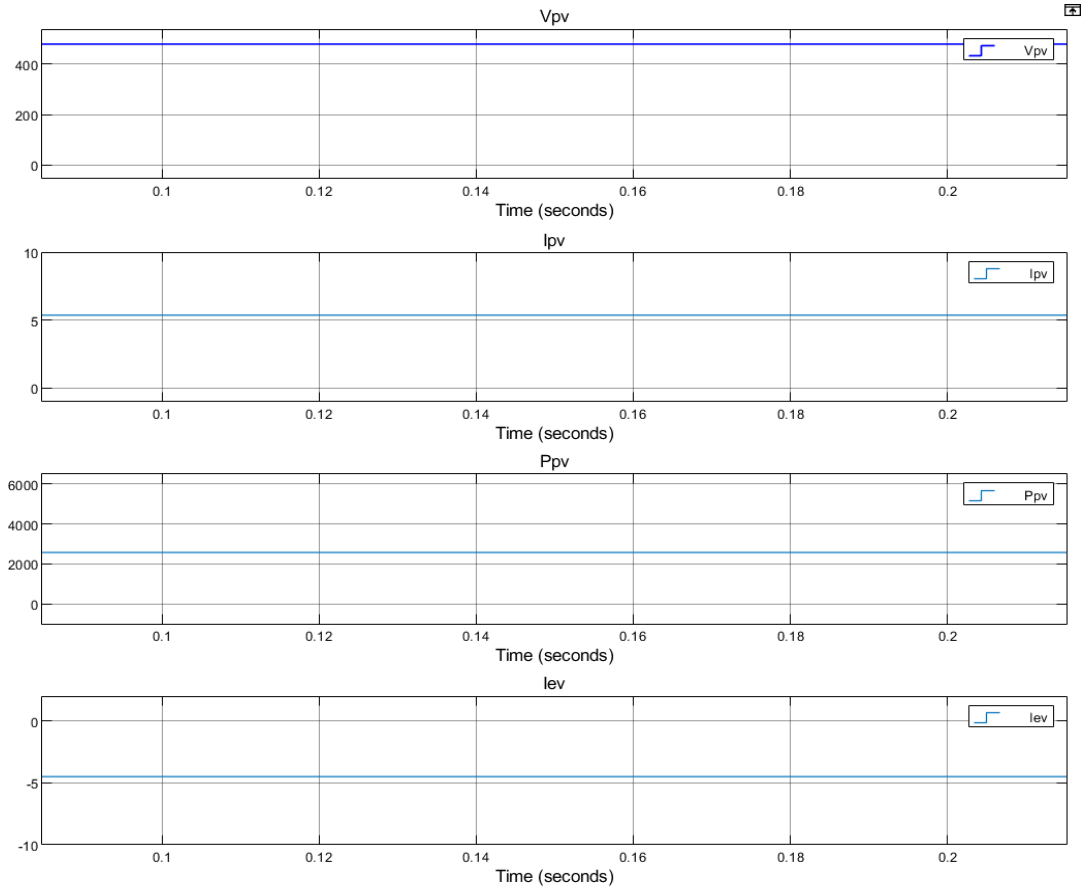


Figure 10: V_{PV}, I_{PV}, P_{PV} and I_{ev}

e-ISSN: 2582-5208
International Research Journal of Modernization in Engineering Technology and Science
(Peer-Reviewed, Open Access, Fully Refereed International Journal)
Volume:05/Issue:04/April-2023 Impact Factor- 7.868 www.irjmets.com

Dynamic performance of the charger

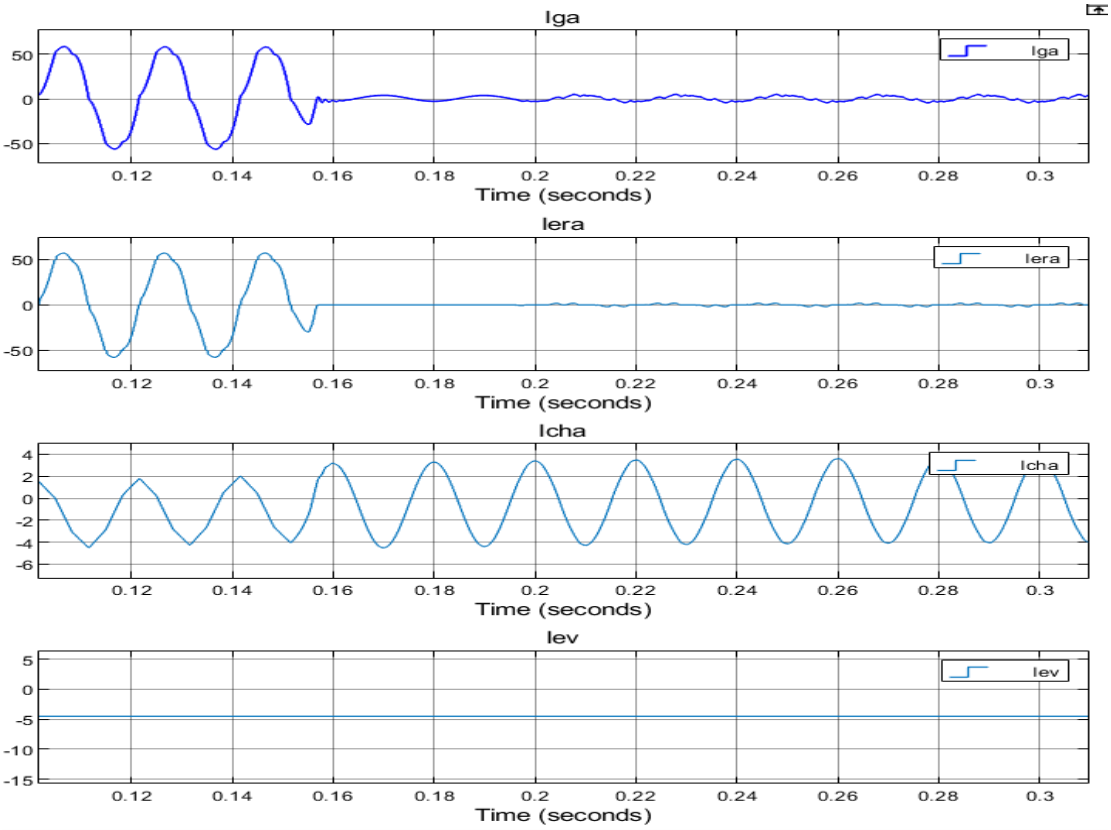


Figure 11A: E*V* load disconnected.

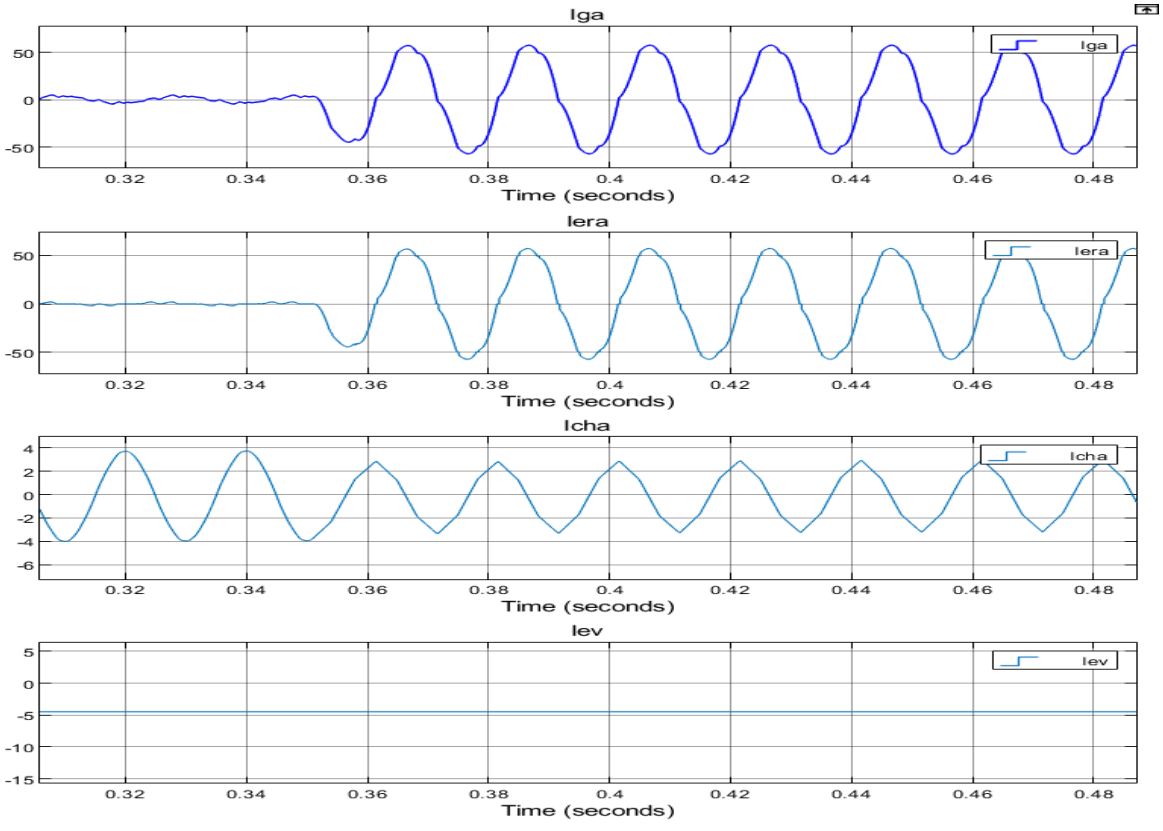


Figure 11b: E*V* load connected.

e-ISSN: 2582-5208
International Research Journal of Modernization in Engineering Technology and Science
(Peer-Reviewed, Open Access, Fully Refereed International Journal)
Volume:05/Issue:04/April-2023 Impact Factor- 7.868 www.irjmets.com

Grid current harmonic compensation during nonideal gird voltage conditions

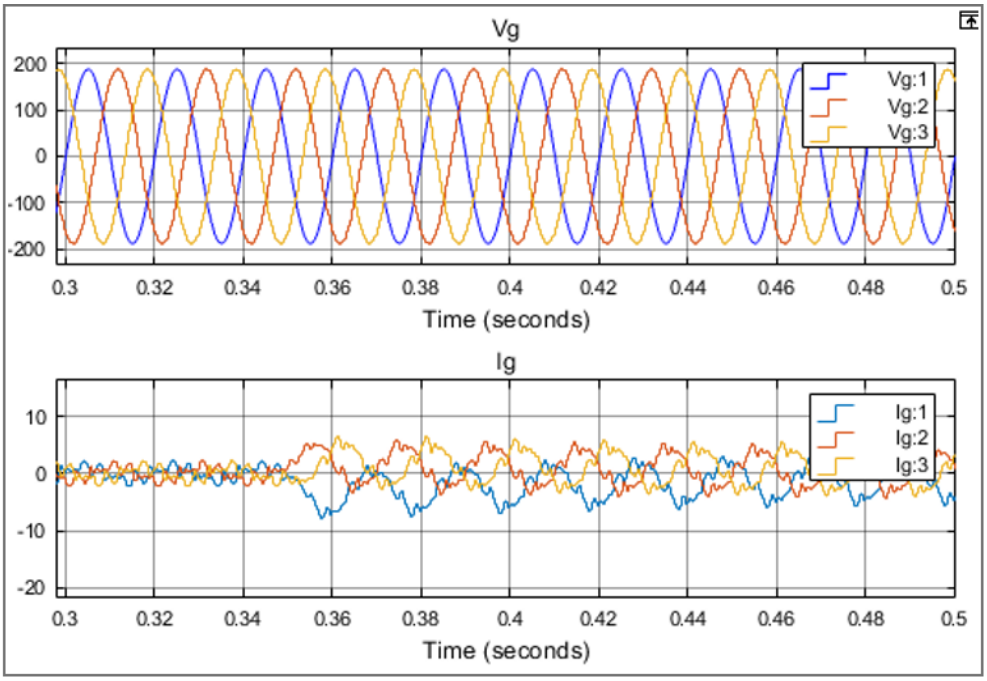


Figure 12: grid voltage (vga, vgb, vgc) and a-phase grid current (iga), before and after harmonic compensation using ANF

Charger in Standalone Operation

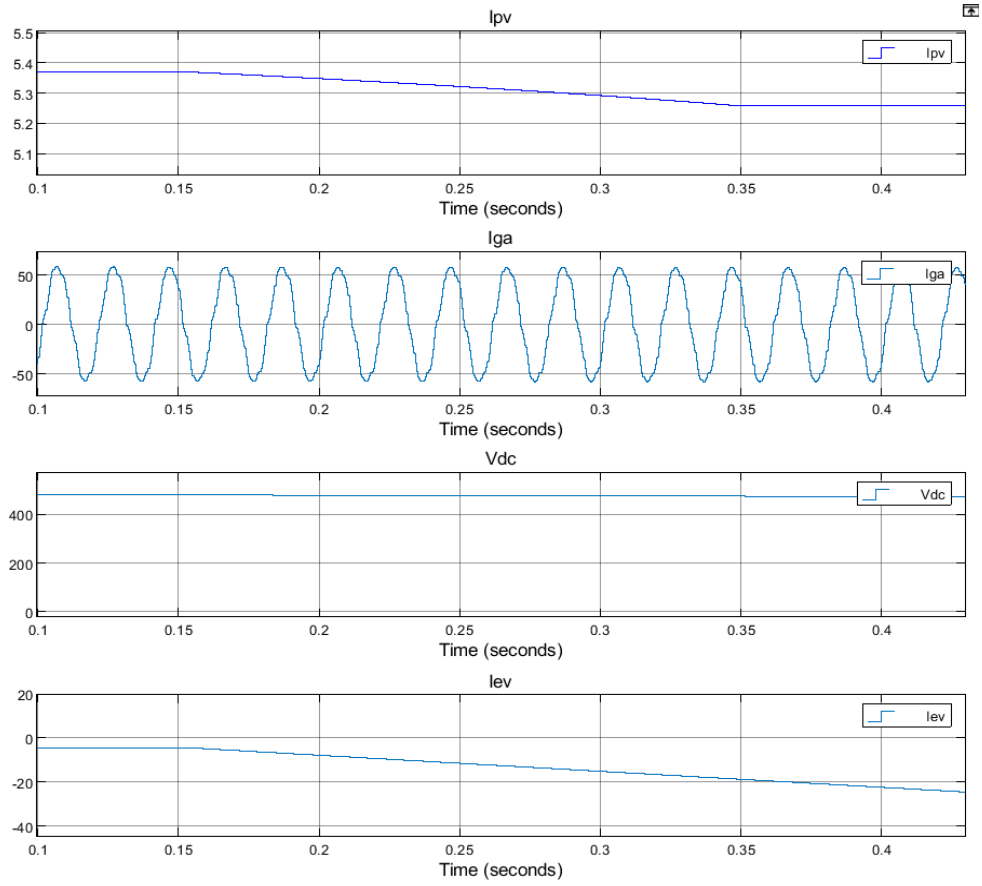


Figure 13: Performance of the charger with a decrease in solar irradiance.

e-ISSN: 2582-5208
International Research Journal of Modernization in Engineering Technology and Science
(Peer-Reviewed, Open Access, Fully Refereed International Journal)
Volume:05/Issue:04/April-2023 Impact Factor- 7.868 www.irjmets.com

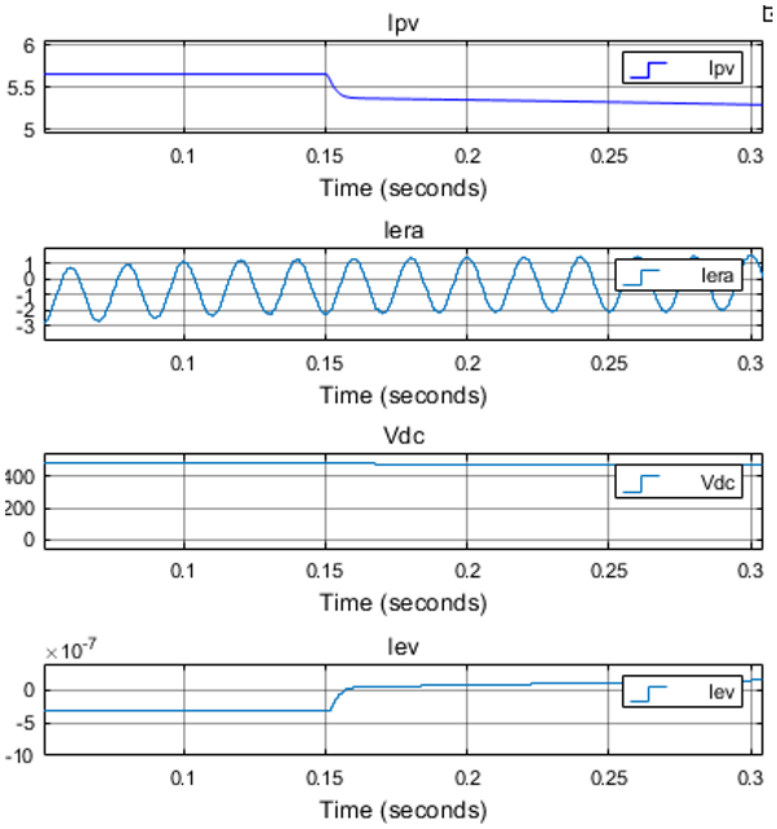


Figure 14: Performance of the charger with a decrease in solar irradiance in SO.

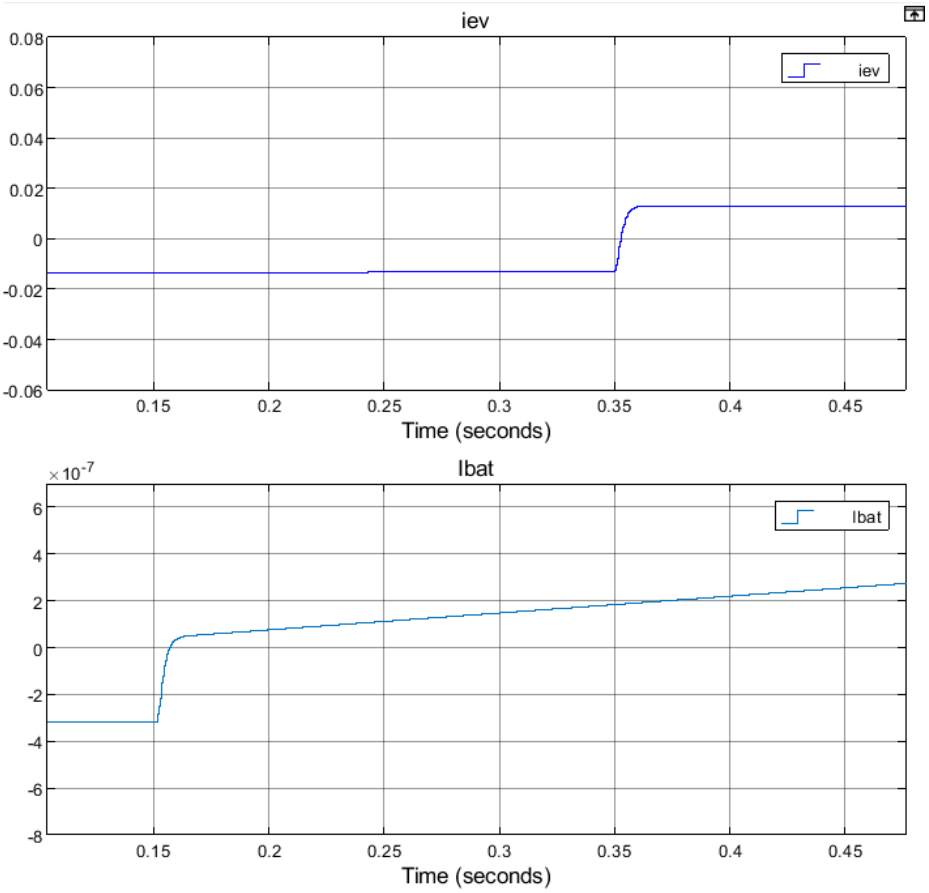


Figure 15: Performance of the charger with discharging of EV connected at DC link.

e-ISSN: 2582-5208
International Research Journal of Modernization in Engineering Technology and Science
(Peer-Reviewed, Open Access, Fully Refereed International Journal)
Volume:05/Issue:04/April-2023 Impact Factor- 7.868 www.irjmets.com

VII. CONCLUSION

The aim of this study is to Simulate a control strategy for a multifunctional EV charger powered by a grid-connected PV system using MATLAB Simulink, which can charge EVs and improve the power quality of the grid. The results obtained from the proposed control algorithm demonstrate its effectiveness in improving the grid power quality, even under non-ideal grid voltage conditions. The charger always maintains the grid voltage and current within the limits set by the IEEE-519 standard, and it operates satisfactorily in both GCO and SO modes. The proposed ANF based grid synchronization technique ensures a smooth transition from GCO to SO and vice versa. Additionally, the charger provides uninterrupted EV charging, reactive power support, grid current harmonic compensation, and backup power supply to the residential load. The charger optimally draws power from the PV system, regardless of its intermittent nature during all operating conditions. In GCO mode, the CHBDC control efficiently operates the PV system at MPP, while in SO mode, a storage battery converter achieves this. Furthermore, the V2G operation of the EV battery connected to the DC link maximizes the system utilization. Experimental results show that the EV battery charger operates stably in both steady-state and dynamic conditions.

VIII. REFERENCES

[1] International Energy Agency- Global EV Outlook 2020 Available https//webstore.iea.org/ download/ direct/ 3007.

[2] N. Saxena,I. Hussain, B.Singh and A.L. Vyas, “perpetration of a grid-integrated PV-battery system for domestic and electrical vehicle operations” IEEE Trans. Ind.Electron.,vol. 65,no. 8,pp. 6592 – 6601,Aug. 2018.

[3] International Energy Agency- World Energy Outlook 2020.(Online). Available: https//www.iea.org/reports/global-energy-review2020/renewables.

[4] P.M. de Quevedo,G. Muñoz- Delgado andJ. Contreras," Impact of Electric Vehicles on the Expansion Planning of Distribution Systems Considering Renewable Energy, Storage, and Charging Stations," IEEE Deals on Smart Grid,vol. 10,no. 1,pp. 794- 804,Jan. 2019.

[5] V. Monteiro, J.G. Pinto and J.L. Afonso, “ Experimental confirmation of a Three- Port Integrated Topology to Interface Electric Vehicles and Renewables With the Electrical Grid, ” IEEE Trans. Ind.Informat.,vol. 14,no. 6,pp. 2364- 2374, June 2018.

[6] S.J. Gunter, K.K. Afridi, andD.J. Perreault, “ Optimal design of grid connected PEV charging systems with integrated distributed coffers, ” IEEE Trans. Smart Grid, vol. 4,no. 2,pp. 956 – 967,Jun. 2013.

[7] A.S. Satpathy, N.K. Kishore, D. Kastha, and N.C. Sahoo, “ Control scheme for a standalone wind energy conversion system, ” IEEE Trans. Energy Convers.,vol. 29,no. 2,pp. 418 – 425,Jun. 2014.

[8] F. Marra,G.Y. Yang,C. Træholt, and E. Larsen, “ EV charging installations and their operation in LVfeeders with photo voltaics, ” IEEE Trans. Smart Grid, vol. 4,no. 3,pp. 1533 – 1540,Sep. 2013.

[9] N. Erdogan, F. Erden, and M. Kisacikoglu, “ A fast and effective coordinated vehicle- to- grid discharging control scheme for peak paring in power distribution system, ” Journal of Modern Power Systems and Clean Energy,vol. 6,no. 3,pp. 555- 566, May 2018.

[10] P.M. de Quevedo,G. Muñoz- Delgado andJ. Contreras," Impact of Electric Vehicles on the Expansion Planning of Distribution Systems considering Renewable Energy, Storage and Charging Stations," 2018 IEEE Power & Energy Society General Meeting(PESGM), 2018,pp. 1- 1,

[11] Monteiro, J.G. Pinto and J.L. Afonso," Operation Modes for the Electric Vehicle in Smart Grids and Smart Homes Present and Proposed Modes," in IEEE Deals on Vehicular Technology, vol. 65,no. 3,pp. 1007-1020, March 2016,

Proceedings of the 7th International Conference on Trends in Electronics and Informatics (ICOEI 2023)
IEEE Xplore Part Number: CFP23J32-ART; ISBN: 979-8-3503-9728-4

Simulation of an Elevator Controller with Weight Sensing Mechanism using VHDL

Rahul Sharma
Department of Electronics and Communication
Delhi Technological University
Delhi, India
rahul.sharma200010@gmail.com

Saarthak Shakargaye
Department of Electronics and Communication
Delhi Technological University
Delhi, India
shakargayesaarthak@gmail.com

Rohit Kumar
Department of Electronics and Communication
Delhi Technological University
Delhi, India
rohit.kumar@dtu.ac.in

Sachin Taran
Department of Electronics and Communication
Delhi Technological University
Delhi, India
taransachin2@gmail.com

2023 7th International Conference on Trends in Electronics and Informatics (ICOEI) | 979-8-3503-9728-4/23/$31.00 ©2023 IEEE | DOI: 10.1109/ICOEI56765.2023.10125939

***Abstract*— Modern infrastructure involves good connectivity. In high rise apartments, malls and several other buildings this connectivity is supplied with the help of stairs, escalators or moving stairs and elevators or lifts. While have their own advantages and disadvantages, elevators have proved to be most efficient and are being used extensively. A lot of designs have been proposed for an elevator controller implemented on hardware description language, this paper proposes a redesign and study of a five-storey elevator with a weight sensor mechanism, which though conventionally available in elevators hasn't been integrated in an FPGA controller. The field programmable gate array is used for the advantages it has such as reusability and quicker and cost-effective prototyping. The basic design involves a finite state machine, which has the various states described as various floors, again each floor branching into two different states, for closed and open door. The input to the elevator controller is given with the help of button that would be provided inside as well as outside the cabin. Several sensors are used to take inputs from the user for the weight. The controller has been successfully implemented on Xilinx and simulated in a FPGA environment.**

Keywords*— *Elevator, Weight sensor, Hardware language, Finite state machine

I. INTRODUCTION

A typical elevator in high rise buildings can be defined as a cabin which transports the user vertically parallel to the height of the building and this transport is carried out with the help of electric motors [1]. In the study, digital model of a machine with weight sensor mechanism has been discussed. A similar elevator controller has been designed on VHDL but with some limitations and without a weight sensor [3].

Hardware Description Languages (HDLs) are a tool commonly used to describe the behavior and structure of circuit and system designs. VHDL and Verilog are two common HDLs. The present project utilizes VHDL, a rich, deterministic, strongly typed, and verbose language, to design an elevator controller [2]. VHDL prioritizes unambiguous semantics and facilitates tool portability [8]. Traditional elevator controllers are based on microcontrollers or Programmable Logic Controllers (PLCs), but these systems have limitations in the number of inputs and outputs they can handle [9][12]. To overcome these constraints, the current project uses a Field Programmable Gate Array (FPGA), which allows for complex system designs requiring parallel processing [6]. FPGAs have a less sophisticated and more manageable flow routine than traditional systems and require less manual intervention. Routing, placement, and timing are largely handled by software to conform with the specification defined by the programmer. Additionally, FPGAs offer various advantages over its counter parts like the ability of reuse [10].

Although various elevator models have been implemented in various other controllers including the FPGA, the important feature of an overload alert has been missing. Due to the limited tensile strengths of the materials responsible for the suspension of the elevator cabin [12], the weight cannot be exceeded more than a specific safe limit. In general, this limit is usually set to 1000kgs or more, although the implementation discussed in this study allows the designer to select an appropriate limit depending on the actual specifications. The weight sensor included will halt the operation until the safe limit is reached. The implementation and results of this sensing mechanism have been discussed in design as well as simulation and results section.

To implement an elevator controller, one of the better techniques is the finite state machine, which is widely used in the theory of computation as well in digital electronics to model the functioning mathematically [7]. The use of a finite state machine has been justified in the algorithm section of Design Model.

II. DESIGN MODEL

A. Design Flow

A procedure for designing a digital system on an FPGA Board involves the following steps:

1. Choose a model in VHDL or Verilog to create the finite state machine. This can be a behavioral or a structural model.
2. Run simulation and design should be debugged.
3. Synthesize the design with the target device in mind.
4. Use a mapping/partitioning program to divide the state diagram into segments or portions that have their own singular properties.

Authorized licensed use limited to: DELHI TECHNICAL UNIV. Downloaded on May 31,2023 at 04:30:07 UTC from IEEE Xplore. Restrictions apply.

5. A program which is usually the part of the compilation can be used to place the partitioned logic blocks into their desired locations.
6. Use a program that will help in translating the code into a bit pattern that would allow programming the FPGA.
7. Load the translated bit pattern and burn it on the FPGA card and with the help of appropriate instruments test the functioning of the hardware.

B. Structure

The elevator system is operated by the elevator controller, which typically responds to the buttons that provide the input from inside the cabin, usually the floor number and the buttons that provide the input from outside the cabin usually the up and down calls [4]. Proximity sensors located on the floors detect the elevator's alignment and check for obstructions between the elevator doors when closing to ensure greater safety and reliability [5]. A weight sensor is fixed on the floor of the elevator and the elevator doesn't respond to calls until the weight is optimal.

C. Code

Although Verilog is commonly used to implement the elevator controller because the code is more compact [1], VHDL was chosen because of its wide use in the research domain as well as popularity. The FSM defined to model the functioning of the elevator controller has been segmented into blocks according to the logic [11]. The most significant block which is a switch statement is again segmented into multiple cases, where each case is the floor state and the code under a particular case defines the transitions that would be triggered once a particular set of inputs have been recorded by the FPGA [14]. These transitions are the vertical movement of the elevator cabin in which special emphasis has been given to the priority in which the inputs would be responded to in order to extract the efficiency of an FPGA to the fullest. The inputs are the control signals for the VHDL code [3] Also the machine is a mealy machine because it takes in input which effect the nature of the output.

III. METHODOLOGY

A. Algorithm

The code written for this paper in VHDL defined five floors or storeys, but this can be extended easily for any number of floors. The algorithm uses a finite state machine, with transition between the various states depending on a set of conditions, that includes the input from the users, both outside and inside the elevators and safety call such as the safe weight limit. The input output signals and their corresponding functions are defined in the table 1.

Table 1: IO signals and their significance

IO Signals	**Definition**
floor	Input from inside the cabin, floor 1 to 5 in our case.
up	Input from outside the cabin calling the elevator to go to a higher floor.
down	Input from outside the elevator for a call to a lower floor.
curr_flr	This displays the floor number in binary representation in the waveform.
wt	This represents the weight of the passengers in binary form.
w	This is a flag which is high or low based on if the weight of the passenger is optimum and safe.
clk	This is the clock input that drives the whole controller
Reset	If reset is high, the elevator returns to the ground floor and doesn't operate until it is set to low.

The choice of algorithm was made keeping in mind the advantages. The FSM states for the various floors help to realise the functioning in a logical sequence which also enables quicker understanding [13]. Because of the logical design, the algorithm enables predicatbility and quicker developemnt. It reduces the chances of errors by a huge amount increasing the reliability because only one state is active at a point of time. Increased reliability due to the use of FSM increase safety and allows better monitoring.

B. FSM Diagram

A diagram depicting the flow of the states according to the inputs is provided below in figure 1. In this, the 5 states are representing the five storeys. If we take for instance the third state or the 2nd floor, we can move to the 1st floor if f2, f1, u1, u2, d2 are high and similarly we can move to the 3rd floor if the corresponding inputs to the transition are high. Also, along with the states, a necessary condition i.e., w needs to be low all time in order for the elevator to function according to the safe weight limit.

Also, if two inputs are high at once, the one which is parallel to the direction of the movement of the lift will be followed and the other input will be stored and the operation will be carried out later. In the state diagram below, figure 1, the f represents floor buttons signaling the inputs from inside the cabin. U represents up calls and d represent down calls. W represents the flag bit for the safe weight limit.

Authorized licensed use limited to: DELHI TECHNICAL UNIV. Downloaded on May 31,2023 at 04:30:07 UTC from IEEE Xplore. Restrictions apply.

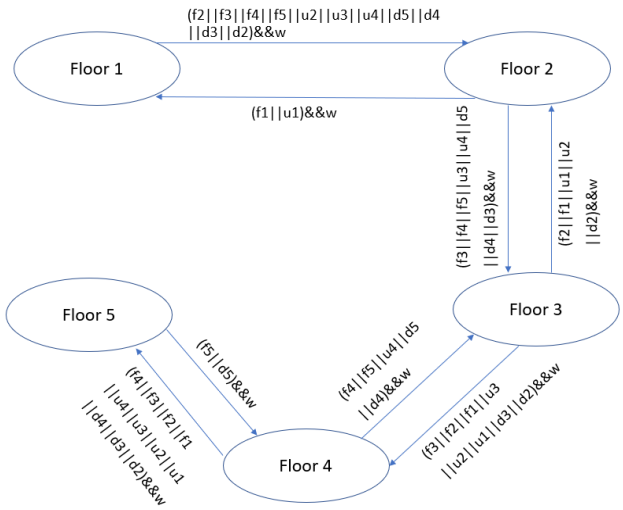


Figure 1: FSM state diagram

When an alteration is detected in any of the inputs, the elevator will start moving towards the designated floor. Since it's not possible for an elevator to immediately jump from, say, floor 1 to floor 4, it must gradually move through the intermediate floors. The state diagram depicts this process, indicating transitions through intermediate floors without stopping to open the doors, until the elevator reaches its final destination. The weight sensors sense the weight of the passengers and this is compared against the safe weight limit. This is done by converting the numerical weight into its binary equivalent. This is done by defining the precision with which the weight should be divided and the safe limit is set to 1000 kgs for reference. The flag bit for safe weight is turned off and further transition takes place accordingly. An illustration of this concept is detailed in 4th section - Simulation and Results.

IV. Simulation and Results

Simulation is the process by which the functioning of a hardware is tested out in a non-hardware typically a software environment that would eliminate the risks. Various simulators are used for this purpose, by running the RTL code and ensuring if the functioning is in conformation with the desired outcome of the logic. A testbench is written in VHDL, which triggers the 'clk' pulse, 'reset' switch, and other inputs such as the weight flag and emergency flags while also verifying system behaviour. This model observes the lift behavior upon receiving specific inputs in a specific order, as indicated by the 'curr_flr' signals. The elevator controller's timing diagram is depicted in Figure 2. This model was simulated utilizing the Xilinx Vivado ISE 14.7. All the figures were produces in the above simulation environment by generating a waveform. The waveform has inputs given by the testbench, and the time of simulation is selected before running the waveform [15].

The initial testing involved verifying the reset condition, which demonstrated that when the 'reset' signal is high, the elevator defaults to 'open1' state, indicating that it is on the first floor with open doors. Once the 'reset' pulse is set to low, the elevator detects clock cycles and transitions between floors based on the input it receives. The elevator's doors will only open when alignment sensors a proper alignment with the floor level. The inputs from the buttons placed outside as well as inside the elevator cabin can be used to feed the desired floor to the elevator controller. All potential transitions were tested in accordance to the testbench, and the lift behaved as per the expectations. An input of '0' says no input signal from the particular source, while numbers 1 through 5 are the floors that the elevator is desired to travel by the user. This is shown in figure 2 and 3.

For instance, if the elevator is in the ground floor, which is the default 0 states, and there is a call of down 4 which means that there's a person standing in the 4th floor who wants to go down, the elevator will respond by making a smooth transition from the ground floor to the 4th floor, each transition taking the required amount of time depending on the speed of the movement of the elevator. The elevator won't stop at any of the transitioning states or floor because that is not required, and as soon as it reaches the fourth floor, the alignment sensors will send a high signal to the controller, triggering the opening of the doors which will remain opened for a clock cycle and then be closed on getting a low input from the obstacle signals. And once inside the cabin, the user will make the floor selection and the elevator will start moving to the particular floor.

The other part of the simulation was aimed at testing the ability of the controller to handle two calls simultaneously We consider an event where a person standing in the 4th floor gives a down call and another person standing in the 1st floor wants to go down as well. The controller stores both the calls and prioritizes the down call from the 1st floor because at that particular moment the elevator was moving down from the 3rd to the 2nd floor. The call is prioritized based on the direction of the movement and if it is parallel to the call. The controller stores the other call until both are successfully executed and then only resets all the inputs. This means that the elevator will follow the calls that will help it to save time and power and increase its overall efficiency, which is already a great feature in modern day elevators. Figure 5 depicts the RTL schematic of the elevator controller. The RTL schematic is generated automatically in the Xilinx ISE simulation environment and can be accessed using the navigation bar.

Also, it is visible in figure 3 and 4 that when the weight is greater than the safe limit, the w bit is turned high. The w bit when high, stops the transition or the mobility of the elevator compartment and the instructions are stored for future use, as soon as the elevator might reach its safe weight. Figure 5 shows the RTL structure of the elevator controller where all the gates and components used are visible.

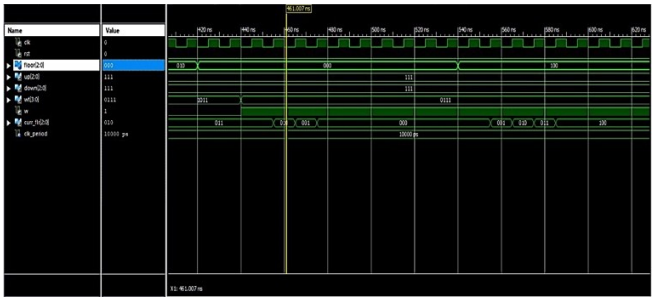


Figure 2: Floor call is 5 and the elevator ascends from 1 to 5 without stopping at floors 2,3 and 4

Authorized licensed use limited to: DELHI TECHNICAL UNIV. Downloaded on May 31,2023 at 04:30:07 UTC from IEEE Xplore. Restrictions apply.



Figure 3: No floor change takes place after w flag is low

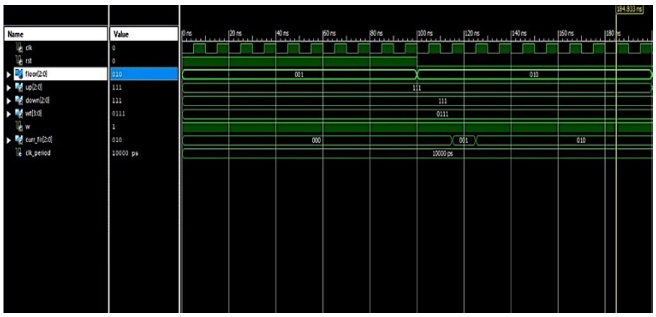


Figure 4: No floor transition takes place while reset pin in high

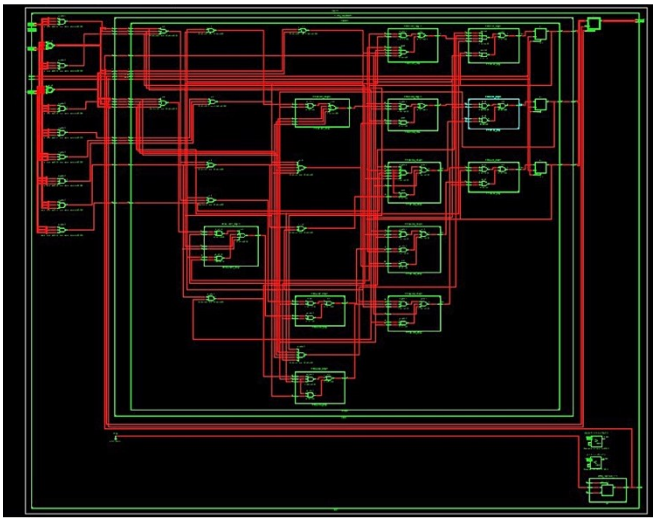


Figure 5: RTL schematic

V. CONCLUSION

Our team designed and simulated a VHDL-based elevator controller model with five floors and a weight sensing mechanism. Controller state-based model is then implemented on the Xilinx Zedboard Zynq 7000 FPGA board, and achieved excellent results. The proposed model is highly efficient, using minimal resources and consuming very little power. Additionally,the model has many advantages over traditional microcontroller-based elevator systems, including increased efficiency and reduced cost. To make it more functional a timer can be included which would help controlling the time of opening and closing of the doors.

REFERENCES

[1] S. Ekanayake, R. Ekanayake, S. Sanjayan, S. Abeyratne and S. Dewasurendra, "FPGA Based Elevator Controller with Improved Reliability", in UKSim 15th International Conference on Computer Modelling and Simulation IEEE, 2013.

[2] M. Kumar, P. Singh and S. Singh, "A VLSI Implementation of Four-Phase Lift Controller Using Verilog HDL", in International Conference on Materials, Alloys and Experimental Mechanics, India, 2017.

[3] J. Varghese, L. Philip, S. Mammen, Y. Thomas and R. Cheriyan, "FPGA Implementation of Elevator Controller", in International Conference on Emerging Trends in Technology and Applied Sciences, 2015.

[4] M. Siddiqui and K. Hasan, "Synthesis & Simulation Model of Parallel Lift Controller Using Verilog", International Journal of Engineering Development and Research, vol. 3, no. 3, pp.1-5, 2015.

[5] P. Kiran Babu and H. Rao, "A VLSI Implementation of Three-Lift Controller Based on Verilog", International Journal of Engineering Trends and Technology, vol. 6, no. 1, pp.43-47, 2013.

[6] N. Sulaiman, Z. Assi Obaid, M. Marhaban and M. Hamidon, "Design and Implementation of FPGA-Based Systems - A Review", Australian Journal of Basic and Applied Sciences, vol. 3, no. 4, pp. 3575-3596, 2009.

[7] B. Vaidya and D. Anupam, "A Study of different Finite state machine design and efficient coding techniques", Journal of Information, Knowledge and Research in Electronics and Communication Engineering, vol. 2, no. 2, pp. 493-496, 2008.

[8] I. Chiuchisan, A. Potorac and A. Graur, "Finite State Machine Design and VHDL Coding Techniques", in 10th International Conference on Development and Application Systems, Suceava, Romania, 2018.

[9] M. Bhuyan, M. Haque, M. Rauf and M. Khan, "Design and Implementation of a Microcontroller Based Elevator Control Systems", Proceedings of the Conference on Engineering Research, Innovation and Education 2011, pp. 504-507, 2011.

[10] M. Ullah and M. Saeed, "Design and Implementation of Efficient Elevator Control System using FPGA", International Journal of Innovation and Applied Studies, Vol. 9 No. 4, pp. 1541-1546, Dec. 2014.

[11] S. Huseinbegovic, S. Kreso and O. Tanovic, "Design and Implementation of the CAN Based Elevator Control System", 2009 XXII International Symposium on Information, Communication and Automation Technologies, Bosnia, pp. 1-6, 2009.

[12] O. Shete, D. Shete and S. Pise, "A Survey Paper on Design & Control of an Elevator for Smart City Application", International Journal of Advanced Research in Electrical, Electronics and Instrumentation Engineering, Vol. 6 No. 2, pp. 3021-3027, Apr. 2017.

[13] Michael D.Ciletti, "Advanced digital design with the VERILOG HDL", Prentice-hall of India ltd, India

[14] H.P.A.P. Jayawardana, H.W.K.M. Amarasekara, P.T.S. Peelikumbura, W.A.K.C. Jayathilaka, S.G. Abeyaratne, S.D. Dewasurendra, " Design and implementation of a statechart based reconfigurable elevator controller", International Conference on Industrial and Information Systems - ICIIS, 2011 IEEE

[15] "XILINX Triple Module Redundancy Design Techniques for Virtex FPGAs", Application Note (Virtex Series)

Authorized licensed use limited to: DELHI TECHNICAL UNIV. Downloaded on May 31,2023 at 04:30:07 UTC from IEEE Xplore. Restrictions apply.

AI in Civil Engineering

ORIGINAL ARTICLE

Open Access

Simulation of reservoir outflows using regression tree and support vector machine

Vijay Kaushik[1*] and Noopur Awasthi[1]

Abstract

Water stored in reservoirs has a lot of crucial function, including generating hydropower, supporting water supply, and relieving lasting droughts. During floods, water deliveries from reservoirs must be acceptable, so as to guarantee that the gross volume of water is at a safe level and any release from reservoirs will not trigger flooding downstream. This study aims to develop a well-versed assessment method for managing reservoirs and pre-releasing water outflows by using the machine learning technology. As a new and exciting AI area, this technology is regarded as the most valuable, time-saving, supervised and cost-effective approach. In this study, two data-driven forecasting models, i.e., Regression Tree (RT) and Support Vector Machine (SVM), were employed for approximately 30 years' hydrological records, so as to simulate reservoir outflows. The SVM and RT models were applied to the data, accurately predicting the fluctuations in the water outflows of a Bhakra reservoir. Different input combinations were used to determine the most effective release. For cross-validation, the number of folds varied. It is found that quadratic SVM for 10 folds with seven different parameters would give the minimum RMSE, maximum R^2, and minimum MAE; therefore, it can be considered as the best model for the dataset used in this study.

Keywords Reservoir outflow, Regression tree, Support vector machine, Error analysis

1 Introduction

As tangible constructs (either artificial or natural), reservoirs are used as water storage for supervision, monitoring and maintenance of water supply (Hussain et al., 2011), forming the most valuable element in water resources systems. Due to environmental issues, however, construction of new dams is not an easy task; therefore, it is important that active reservoirs be boosted for the maximum effectiveness, so as to handle any present and future water-related challenges. Reservoirs are built with a dam across a flow. The major feature of a reservoir is the rule of herbal streamflow with the aid of storing surplus water within moist seasons and liberating the saved water in destiny dry seasons, thus complementing the discount in river flows. The intention is to balance streamflows and change the sequential and three-dimensional water availability. The water stored in a reservoir can be distributed later for advantageous uses, giving rise to sequential changes or reroutes through waterways or pipelines to outlying locations, and thus resulting in three-dimensional changes. Reservoir outflow projection is guided by various potential constraints, such as water storage, inflow of water, water level, evaporation, infiltration, geomorphology, and other factors, all of which need to be considered, so as to understand the ambiguity. Plentiful methods have been used in forecasting hydrological practices over the past years. Traditional tactics used are of linear mathematical relationships based on the capability of machinists, a simple set of curve fitment, and standards employed to quote reservoir water outflows (Tokar & Markus, 2000). However, poor performances are found in numerical models, due to their unavailability and complexity of statistics, missing datapoints and overemphasized constraints. Various

*Correspondence:
Vijay Kaushik
vijaykaushik_2k20phdce01@dtu.ac.in
[1] Research Scholar, Department of Civil Engineering, Delhi Technological University, Delhi 110042, India

© The Author(s) 2023. **Open Access** This article is licensed under a Creative Commons Attribution 4.0 International License, which permits use, sharing, adaptation, distribution and reproduction in any medium or format, as long as you give appropriate credit to the original author(s) and the source, provide a link to the Creative Commons licence, and indicate if changes were made. The images or other third party material in this article are included in the article's Creative Commons licence, unless indicated otherwise in a credit line to the material. If material is not included in the article's Creative Commons licence and your intended use is not permitted by statutory regulation or exceeds the permitted use, you will need to obtain permission directly from the copyright holder. To view a copy of this licence, visit http://creativecommons.org/licenses/by/4.0/.

machine learning algorithms have been used in previous research, with an intention to overcome these concerns and estimate reservoir water outflows (Mokhtar et al., 2014; Seckin et al., 2013). Subsequently, many Machine Learning (ML) models, including Artificial Neural Networks (ANNs), Radial Basis Neural Networks (RBNN), Support Vector Machines (SVMs), Adaptive Neuro-Fuzzy Inference Systems (ANFIS), Logistic Regression (LR), etc., have been deployed in water management systems progressively, so as to improve the consistency and precision of the estimation models (Ahmadlou et al., 2019; Bowden et al., 2002; Naghibi & Pourghasemi, 2015). Modelling a machine to work and improvise on its own without explicit programming each time is called ML. In intellectual studies, ML shows the capability to solve complex problems at a high level of accuracy and can make predictions as demanded for certain future periods (Mullainathan & Spiess, 2017). Nowadays, AI models have been extended successfully to the field of reservoir operation. Compared to conventional physical prediction models, ML models can, with the help of historical dataset, learn numerous hydrological operations independently at acceptable correct operating rates. Advantages of such modelling lie in the capability of their software system to map input–output models (Hejazi & Cai, 2009; Hipni et al., 2013; Najah et al., 2011). To forecast daily water levels, five different ANN models were tested each with an increasing number of inputs, finding that the accuracy began to decrease with the addition of many inputs. The reason for this is that the network started to be obsolete and irrelevant, as explained in the research (Nwobi-Okoye & Igboanugo, 2013). By comparing the performance of SVM and multilayer perceptron (MLP), it is found that due to the optimization algorithms, SVM has a great deal of capacity to resolve a linearly constrained quadratic programming function, and the optimum kernel function in this case is a radial basis kernel function (Khan & Coulibaly, 2006). During the process of creating fuzzy membership functions, a study on the ANFIS technique observed that triangular and trapezoid membership functions were deemed to be more suitable than bell-shaped membership functions (Shafaei & Kisi, 2016). In addition, a genetic algorithm (GA) was successfully utilized in optimizing reservoir operations; and by using data collected in a longer period of time, the GA model could be further improved for reservoir water levels (Onur Hınçal et al., 2011). Many more AI methods, such as the adaptive network-based fuzzy inference system (ANFIS), genetic algorithm (GA) and decision tree, have been effectively applied in the reservoir operation field, in addition to these AI algorithms . In fact, many reservoirs in California have used the improved decision tree (DT) algorithms, classification methods and regression trees to estimate water storage or release (Yang et al., 2016).

In this study, five models of the SVM algorithm and Regression tree (RT) algorithm were compared with an increasing number of inputs by using 5-, 10- and 20-fold cross-validation for original data, so as to accurately forecast fluctuations of the water level of Rupnagar's Bhakra reservoir (Ropar). A lot of quantitative metrics, including root mean square error (RMSE), correlation coefficient (R^2), and mean absolute error (MAE), were used to validate and compare these models; and MATLAB R2021b was used to design and code the modelling and data procedures.

2 Materials and methods

2.1 The study area

Bhakra Dam on the Sutlej River (Bilaspur, Himachal Pradesh) is a concrete gravity dam in the northern part of India, with geographic coordinates of 31°24′39″N latitude and 76°26′0″ E longitude. The dam is considered to be the highest gravity dam in the world. The Sutlej River, a major tributary of the Indus River, originates in Tibet and flows into the Indo-Gangetic plains near Bhakra. The overall upriver catchment area of the Bhakra River is 56,980 km^2. The precipitation in the catchment changes around an annual average of about 875 mm. Situated in a canyon near the (now submerged) upstream Bhakra community in the Himachal Pradesh district of Bilaspur, the dam is 226 m high, 518.25 m long and 9.1 m wide. Its "Gobind Sagar" reservoir can hold up to 9.34 billion cubic metres of water. The Bhakra dam generates a 90-km-long reservoir, covering 168.35 square kilometres and forming India's third-largest reservoir in terms of water storage capacity. The Bhakra Beas Management Board (BBMB) is in charge of the dam's operation and maintenance.

As a straight gravity cum concrete dam, Bhakra Dam has four radial spillway gates and an 8212 cumec designed overflow capacity. The location of the study area is shown on the map in Fig. 1. The Nangal reservoir is built with a 28–95 m high dam, situated at about 11 km downstream of the Bhakra dam. It controls irrigation releases by acting as a head regulator. During the monsoon, the dam would retain extra water; and then, it would release the water gradually throughout a year. It also prevents flood damage caused by monsoon rains. This dam feeds the Bhakra canal, which irrigates 10 million acres (40,000 km^2) of land in Haryana Punjab and Rajasthan. Table 1 shows the characteristics of the Bhakra Nagal dam and reservoir.

2.2 Data collection

A total of 2976 historical data points (for 30 years) were used, including: the reservoir level (M), the monthly

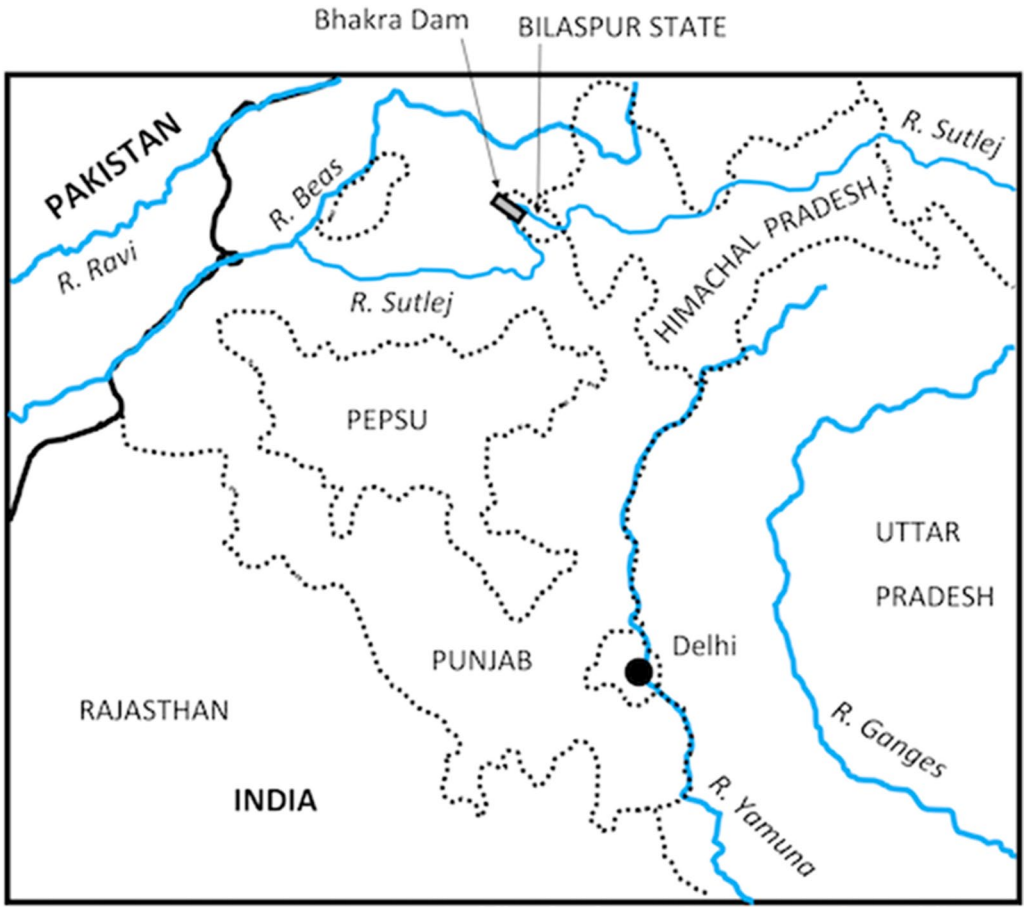


Fig. 1 Bhakra Dam's location

Table 1 Characteristics of Bhakra Nagal Dam and Reservoir

Item	Description
Catchment area	56,980 square kilometers
Dead storage level	EL. 512.06 m (EL.1680 feet)
Dead storage level	EL.445.62 m
New area irrigated	60 lakh acres
Area of the reservoir	162.48 square kilometers (62.78 sq. miles)
Length of the reservoir	96.56 km
Live storage capacity at EL.1680 ft	6911 million cum (5.60 MAF)
Gross storage capacity at EL.1680 ft	9340 million cum (7.57 MAF)
Dead storage capacity	2430 million cum (1.97 MAF)

Table 2 Data acquired with descriptive statistics

Input	Unit	Minimum	Maximum	Average	Count
Inflow	MCM	352.04	10,267.8	1764.88	372
Reservoir level	Meter	450.45	512.06	489.01	372
Monthly reservoir storage	BCM	0.2	6.23	3.13	372
Evaporation	MCM	− 28.1	41.2	− 6.8	372
Previous inflow	MCM	352.04	10,267.8	1764.62	372
Previous outflow	MCM	402.3	8942.3	1819.95	372

reservoir storage (BCM), the previous inflow of reservoir (MCM), the current inflow of reservoir (MCM), the evaporation of reservoir (MCM), the previous outflow of the reservoir (MCM), and time (months) and release of the reservoir. All the data were acquired from the following websites: "UK Centre for Ecology and Hydrology", "Bhakra Beas Management Board" and "India Meteorological Department". The range of the reservoir's water level is determined by the hydraulic features of the Bhakra dam, with the maximum water level at 512.06 m and the minimum operating level at 450.45 m. Table 2 shows the essential statistical properties of the inputs, such as the minimum, maximum and total count values.

One of the tasks during modelling nonlinear hydrological processes was to select the most significant variables from the whole set of input variables (Bahrami & Wigand, 2018; Hu & Wan, 2009). The major goal of data

collection in this study is to choose appropriate input variables, depending on the data available. Also known as feature selection, the choice of the best subset of the inputs in the model was made based on certain defined governing rules (Sharafati et al., 2019), so as to increase the model's accuracy and efficiency. Therefore, during the modelling phase of this study, various combinations of input variables were used. For this study, five scenarios are initially defined at different folds, as shown in Table 3, so as to find out the most effective output. Then, the prediction accuracy was evaluated for each scenario.

2.3 Support vector machine (SVM)

Support Vector Machine has gained popularity as a novel statistical learning method over recent two decades. Used for both classification and regression, it proves an efficient and reliable approach (Collobert & Bengio, 2001; Drucker et al., 1996; Vapnik, 1995). Unlike the traditional chaotic methods, the SVM method is based on the idea of mapping input data into a high-dimensional feature space, so as to help with classification and simulate unknown relationships between the set of input variables and the set of output variables. Based on the mechanism's simplicity, two advantages of this method are that it is sufficiently known by scientists and that it dominates prediction. It has a level of precision that sets it apart from several other approaches. SVM is a strategy that uses a kernel trick to understand an issue, while simultaneously lowering the complexity and prediction errors of models. SVM classification is the first step in making a decision limitation for the feature space, which is delivered by generating an ideal separation hyperplane between two classes, so as to maximize the margin by minimizing the generalization error. In theory, SVM classification has the potential to predict outcomes, which can be comprehended with three essential concepts: (1) Function of the kernel; (2) The soft-margin; and (3) The separation hyperplane (Cristianini & Shawe-Taylor, 2000; Schwefel, 1981). Polynomial, radial basis and sigmoid, functions are exemplary kernel functions. Algorithms like SVM are mostly used to forecast classification problems and support vector regression (SVR) is an expansion of SVM by adding an insensitive loss function, so that it can be used in regression analysis (Drucker et al., 1996; Kim et al., 2012). In other words, in a classification problem, SVM is utilised to partition data into "+1" and "− 1" classes. On the other hand, SVR is a generalized SVM approach to predict random real values (Basak et al., 2007; Gunn, 1988). To improve forecasting of reservoir inflows, a modified SVM-based prediction system was created (Li et al., 2010). Climatic data from previous time periods were used, in addition to highly connected climate precursors. To understand non-linear patterns underlying climatic systems more flexibly, SVM parameters were determined in a genetic algorithm-based parameter determination approach. The median of forecasts from the created models was then used to reduce the variation in the prediction by using bagging to construct several SVM models. In terms of the predictive ability, the suggested modified SVM-based model outperformed a bagged multiple linear regression (MLR), a simple SVM, and a simple MLR model.

Regression with an alternate loss function is an example of SVM. Loss functions are frequently used in estimation, model selection, and prediction; and they are critical in determining any disparities between the null and nonparametric models' fitted values (Hong & Lee, 2009). In terms of hydrology, researchers must consider loss functions when making predictions. In this study, a hydrologic loss function is used to link two primary variables: rainfall and runoff. A distance measure must be supplied, which necessitates a change in the loss function (Smola & Scholkopf, 2004). SVR's main notion is to nonlinearly translate the initial data into a higher-dimensional feature space, so as to solve the linear regression issue (Fig. 2). As a result, SVR is usually required to construct a suitable function $f(x)$ to reflect the non-linear relationship between feature x_i and target value y_i, as demonstrated in Eq. (4).

$$f(x_i) = w\varphi(x_i) + b\|w\|^2 \tag{1}$$

where w denotes the coefficient vector, $\varphi(x_i)$ denotes the transformation function, and w and b denote the weight

Table 3 The selected scenarios for input combinations

Number	Different input combinations	Output
1	Inflow, Evaporation	Output
2	Inflow, Reservoir level, Evaporation	Output
3	Inflow, Reservoir level, Evaporation, Monthly reservoir storage	Output
4	Inflow, Reservoir level, Evaporation, Monthly reservoir storage, Previous inflow	Output
5	Inflow, Reservoir level, Evaporation, Monthly reservoir storage, Previous inflow, Previous outflow	Output

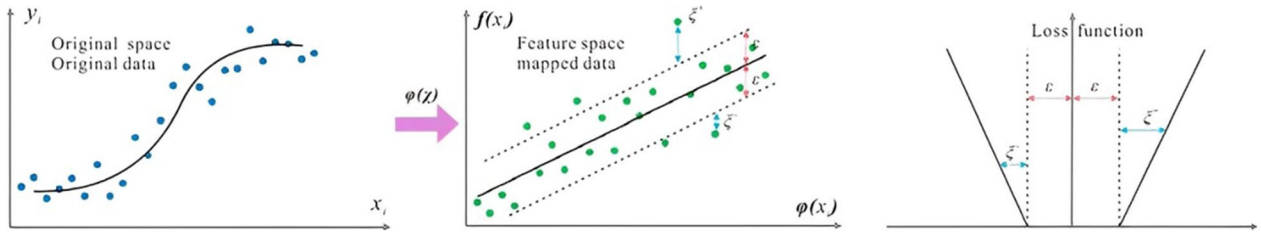


Fig. 2 Schematic diagram of SVR (Zhang et al., 2018)

and bias, respectively, which are calculated by minimising the so-called regularised risk function, as shown in Eq. (5).

$$\mathrm{R(w)} = \frac{1}{2}\|w\|^2 + c\sum_{i=1}^{n} L_\varepsilon(y_i, \mathrm{f}(x_i)) \tag{2}$$

where $\frac{1}{2}\|w\|^2$ is the regularization term; c is the penalty coefficient; and $L\varepsilon(y_i, \mathrm{f}(x_i))$ is the ε-insensitive loss function, which is calculated according to Eq. (6).

$$L\varepsilon\left(y_i, \mathrm{f}(x_i)\right) = \max\{0, \left|y_i - \mathrm{f}(x_i)\right| - \varepsilon\} \tag{3}$$

where ε signifies the allowed error threshold, which will be ignored if the projected value is within the scope of the threshold; otherwise, the loss will equal to a number greater than ε.

To find out the optimization boundary, two slack factors, ξ^+ and ξ^-, are introduced:

$$\min f\left(\mathrm{w}, \xi^+, \xi^-\right) = \frac{1}{2}\|w\|^2 + c\sum_{i=1}^{n}(\xi^+, \xi^-) \tag{4}$$

Subject to

$$y_i - [\mathrm{w}.\varphi(x_i)] - \mathrm{b} \le \varepsilon + \xi^-, \xi^- \ge 0$$

$$[\mathrm{w}.\varphi(x_i)] + \mathrm{b} - y_i \le \varepsilon + \xi^+, \xi^+ \ge 0 \tag{5}$$

The minimization of a Lagrange function, which is formed from the objective function and the problem constraints, yields the dual version of this optimization problem:

$$\begin{aligned}\max\alpha, \alpha^* = &\frac{1}{2}\sum_{i,j=1}^{N}(\alpha_i - \alpha^*{}_i), (\alpha_j - \alpha^*{}_j)\mathrm{K}(x_i, x_j) \\ &- \varepsilon\sum_{i=1}^{N}\left(\alpha_i + \alpha^*{}_i\right) + \varepsilon\sum_{i=1}^{N} y_i\left(\alpha_i - \alpha^*{}_i\right),\end{aligned} \tag{6}$$

$$\begin{aligned}\text{s.t} \quad &\sum_{i=1}^{l}(\alpha_i - \alpha^*{}_i) = 0, \quad \mathrm{i} = 1 \text{ to } N, \\ &\alpha_i, \alpha^*{}_i \ge 0 \quad i = 1 \text{ to } N, \\ &-\alpha_i, -\alpha^*{}_i - \ge -C \quad i = 1\text{to } N.\end{aligned} \tag{7}$$

The inner product$\{\varphi(x_i), \varphi\left(x_j\right)\}$ in the feature space is denoted by the function $K(x\ i,\ x\ j)$ in the dual formulation of the issue.

Any function $K(x_i, x_j)$ can become a kernel function, if it satisfies the inner product criteria. Hence, the regression function can be expressed as follows:

$$f(\mathrm{x}) = \sum_{i=1}^{N}(\alpha_i - \alpha^*{}_i)\mathrm{K}(x_i, x_j) + \mathrm{b} \tag{8}$$

2.4 Regression tree (RT)

As a machine-learning algorithm for building prediction models from datasets, Regression Tree employs a clustering tree with post-pruning processing. The clustering tree algorithm is often referred to as the forecasting clustering tree and the monothetic clustering tree (Chavent, 1988; Vens et al., 2010). Regression Tree is used for model-dependent variables having a finite number of values which are not arranged in order, with prediction errors commonly assessed as the squared difference between the predicted and observed values (Loh, 2011). Clustering tree algorithms are based on the top-down induction technique of decision trees (Quinlan, 1986). Regression Tree algorithms take a collection of data for training and create a new internal node as good as possible. Based on the decreased variance, such algorithms choose the top test scores. The lower the variance, the more homogeneous the cluster and the more accurate the forecast. If none of the tests significantly reduce variance, a leaf will be generated and marked as data representative (Chavent, 1988; Vens et al., 2010). By recursively splitting the data space and fitting a prediction model within each partition, a hierarchical tree-like division of the input space can be created (Breiman, 2017). A

sequence of recursive splits divides the input space into local regions, which are designated by a series of recursive splits. Internal decision nodes and terminal leaves make up the tree finally. Starting at the root node, a sequence of tests and decision nodes will determine the path through the tree, till it approaches a terminal node, providing a test data point. A prediction is made at the terminal node based on the model linked to that node locally.

2.5 K-fold cross-validation

The holdout approach can be employed when the amount of data available for training and testing are limited. In this approach, a subset of data is saved for validation, while the rest is for training. It is a common practice in engineering to keep one-third data for validation and utilize the other two-thirds for training and testing (Witten & Frank, 2000). By dividing the obtained data into a specified number of equally sized observations or folds (k), the holdout approach can be further improved. The dataset used for testing is chosen from these (k) folds, whereas the rest (k-1) is employed in the training process. This procedure will be repeated for k times, with a different fold being tested in each time and the remaining folds (k-1) serving as the training dataset. As a result, the approach would generate k different degrees of accuracy. The variance of the resulting estimate diminishes as (k) will be increased. Consider a fivefold cross-validation scenario ($k=5$). Figure 3 shows how the dataset is divided into five folds. The first fold is used to test the model, while the others are used to train the model in the first iteration. Then, the second iteration uses the second fold as the testing set and the rest as the training set. This procedure will be repeated until each of the five folds has served as a testing set.

3 Results and discussions

The best value of each grouping would result in the most precise estimating model; and later, the unsurpassed grouping combination would be chosen. The data were divided into two categories: Regression tree and SVM analysis. Following this process, two models were employed to make data projections based on five diverse scenarios. The most appropriate and exact prediction scenario was determined by each model's best estimation. To decide whether a model was best, the estimating power of both models was examined. To evaluate the suggested model's execution in varied in preparing, checking and testing information, three types of measurable assessments were used, i.e., RMSE, MAE and R^2. Figures 4 and 5 show the comparison of the observed values with the predicted values of outflows by using SVM and RT models for 5-, 10- and 20-fold cross-validation. It can be clearly seen from the figures that the predicted values are much closer to the observed ones for Scenario 5 with tenfold cross-validation using SVM model. Figures 6 and 7 depict the residuals obtained by using SVM and RT models for different cross-validation conditions. Residuals obtained are the minimum for SVM models as compared to RT models and are best for tenfold cross-validation condition. Table 4 contrasts the calculations statistically for the model SVM computed by using fivefold cross-validation. Data observed from the table clearly show that Scenario 5 relates to the lowest RMSE, MAE values and a maximum R^2 value amid all the situations. Moreover, data forecasting in Scenario 5 offers the most accurate results, while Scenario 4 provides the second lowest result. Besides, Scenario 3 has erratic forecasts, compared to all other scenarios. The lowest value for authentication oversights RMSE is also held by Scenario 5. Continuous development can be seen in the results from Scenarios 1–2 in SVM Regression. A big inaccuracy from Scenarios 2 to 3 of the SVM was recorded in the values of RMSE; MAE would increase, while the coefficient of correlation decreased from 0.87 to 0.85.

Table 5 compares and contrasts the statistical evaluations for the SVM model using tenfold cross-validation. It can be observed that Scenario 5 for SVM using tenfold cross-validation does necessarily produce better results than fivefold cross-validation. The RMSE and

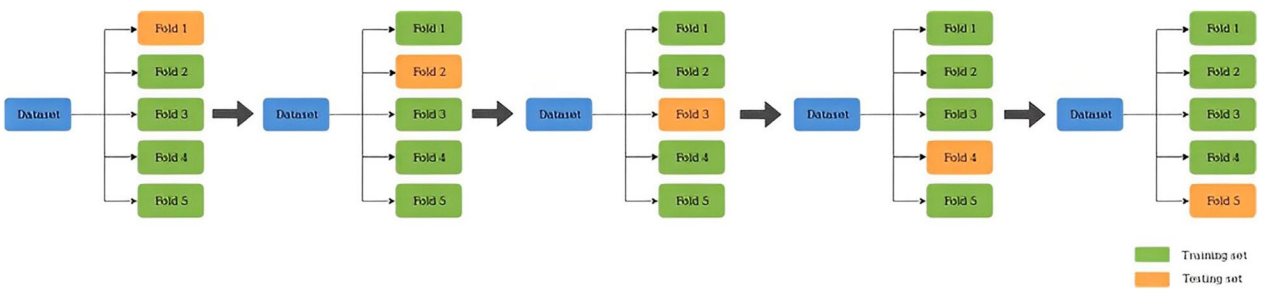


Fig. 3 Cross-validation in different folds

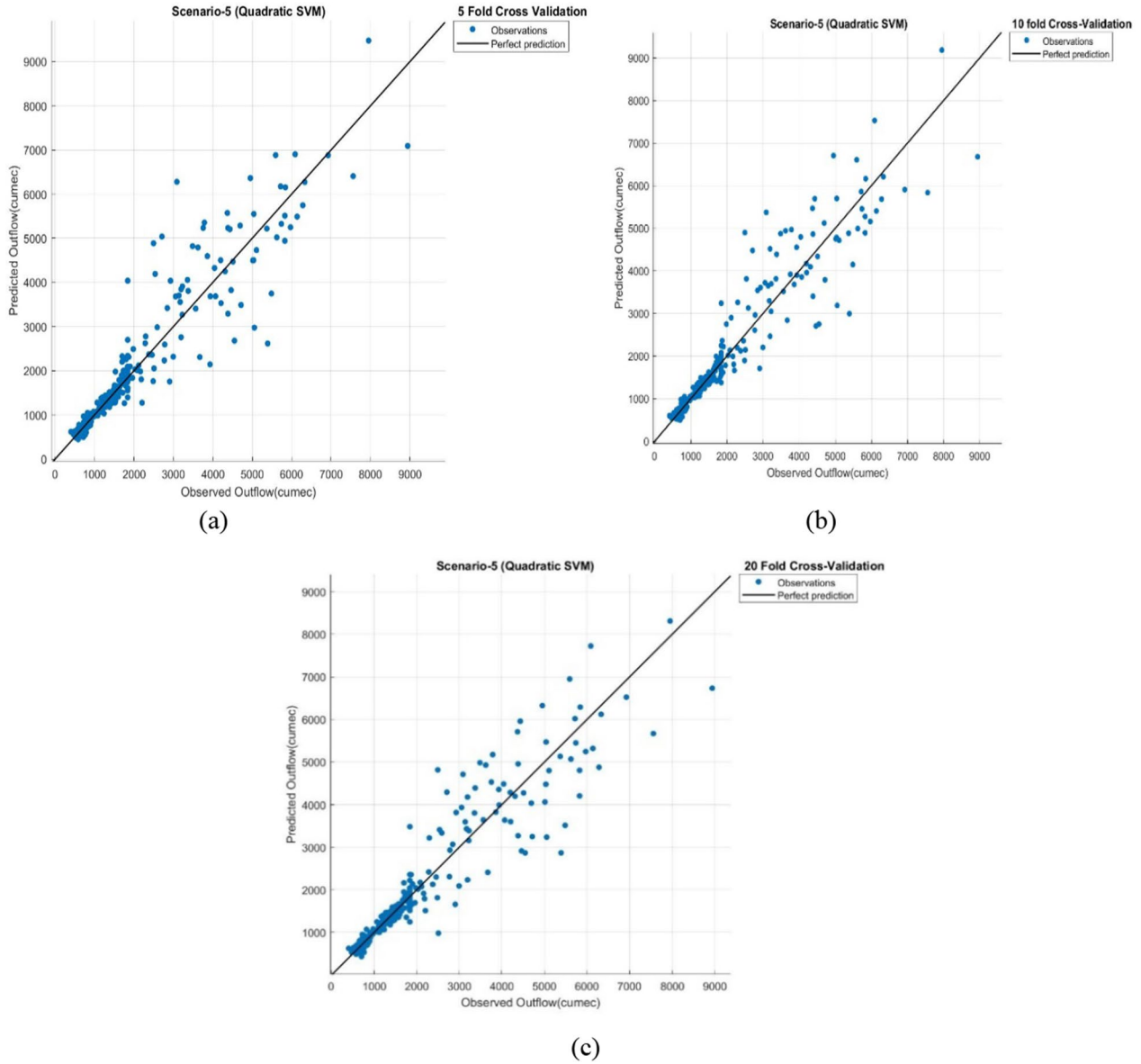


Fig. 4 Relationship between the observed outflow and the predicted outflow by using SVM, fivefold (**a**), tenfold (**b**) and 20-fold (**c**)

MAE values obtained with tenfold cross-validation seem to be more accurate than those obtained with fivefold cross-validation, as shown in Table 4. On the other hand, R^2 has the same value as fivefold cross-validation. Except for the R square value, i.e., 0.9, tenfold cross-validation yields better results than fivefold cross-validation for all parameters, which is the same as fivefold cross-validation. In the same way, Table 6 shows a comparison of the statistical assessments for the SVM model using 20-fold cross-validation, purposed to determine whether a greater cross-validation number may minimise the predicting errors. It shows that SVM model Scenario 5, which uses 20-fold cross-validation, may not always deliver better results than fivefold and tenfold cross-validation. Scenario fivefold and tenfold cross-validation yields lower RMSE values than 20-fold cross-validation. Fivefold and tenfold cross-validation has R square values closer to 1 as compared to 20-fold cross-validation. Table 7 displays the results of fivefold cross-validation using regression tree models under various assessment criteria. It can be observed that all of the scenarios have extremely strong prediction ability ($R^2 > 0.77$), according to the statistical assessment standards of this study. Scenario

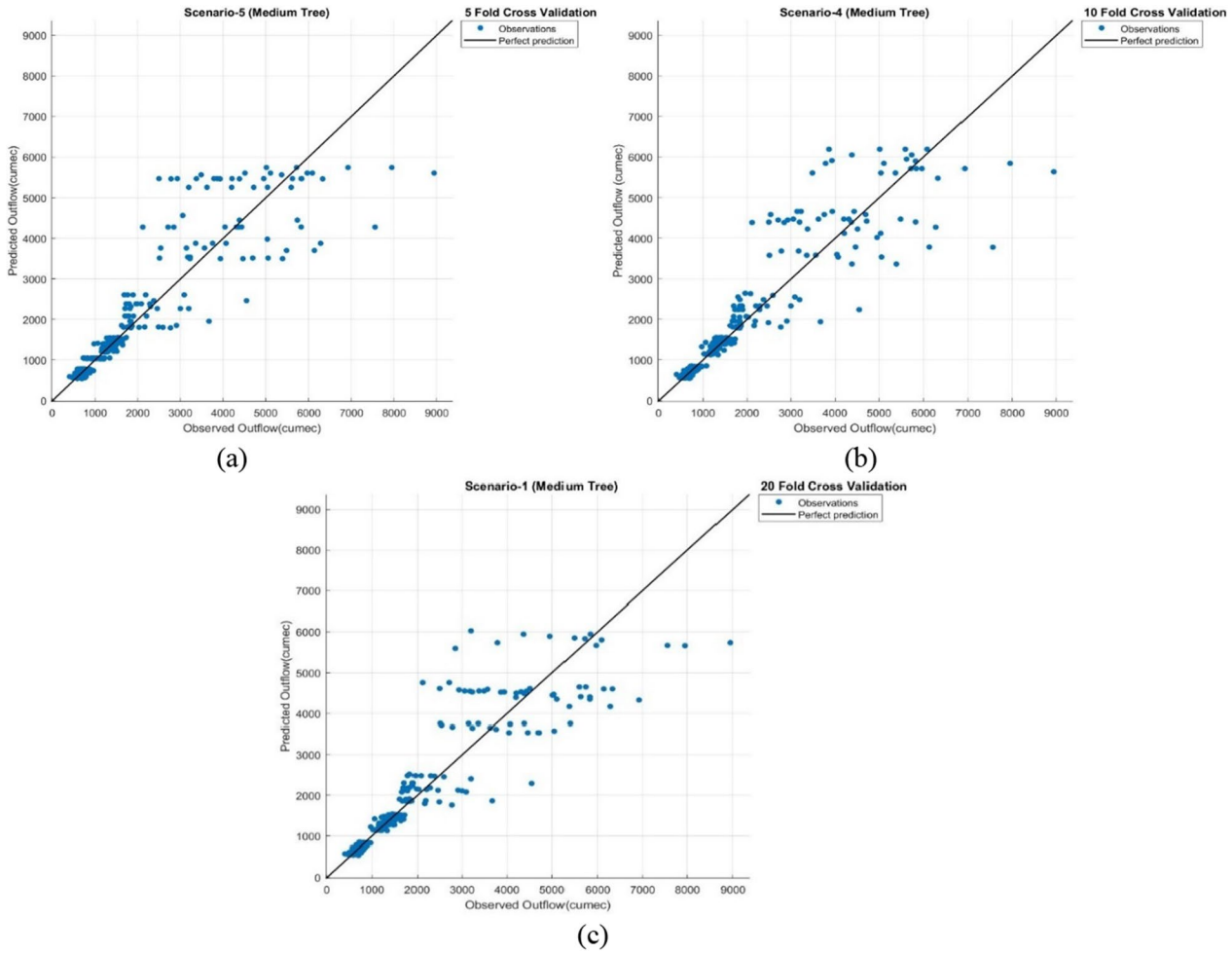
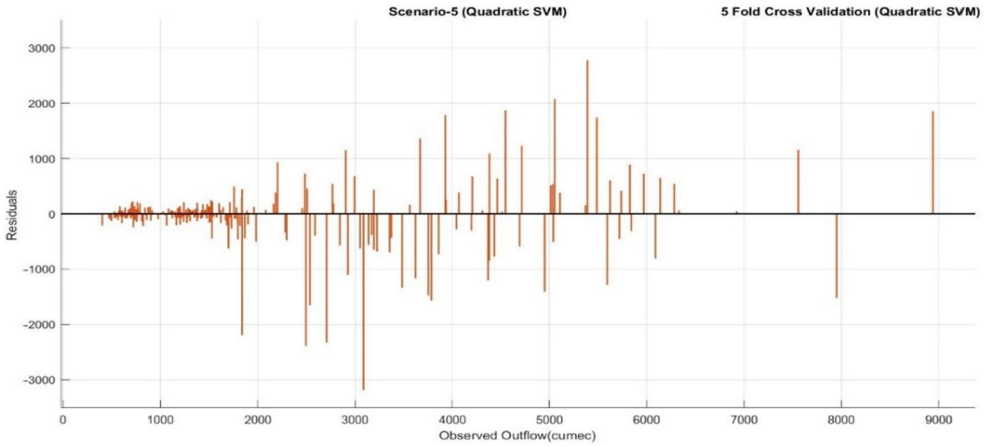


Fig. 5 Relationship between the observed outflow and the predicted outflow by using RT, fivefold (**a**), tenfold (**b**) and 20-fold (**c**)

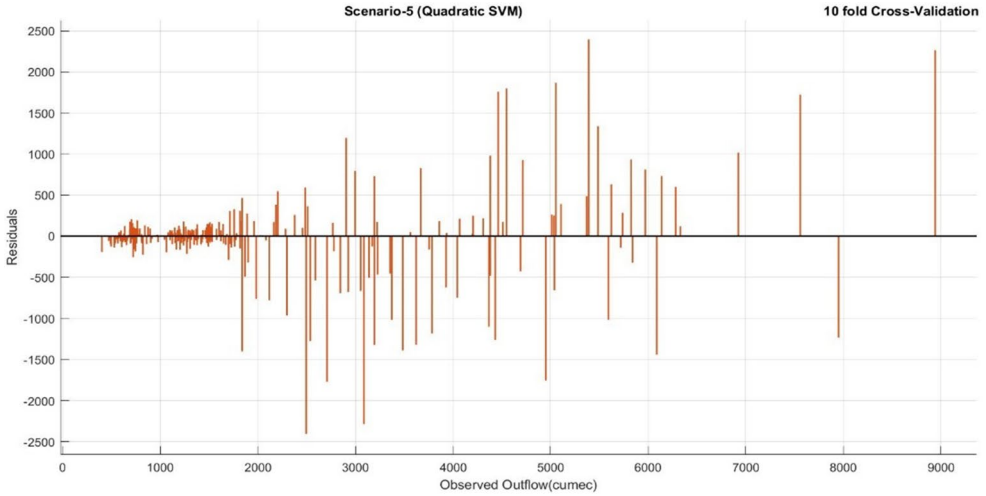
3 achieves the best result, since it has the highest R^2 value (0.82), followed by Scenarios 2, 4, 1 and 5. In terms of RMSE, Scenario 5 gives the best predictive power (602.8), followed by Scenarios 3, 4, 2 and 1. Table 8 shows that Scenario 4 of Regression tree model using tenfold cross-validation has very good predictive ability, since it gives the best R^2 value (0.85), the lowest RMSE (557.48) and the lowest MAE (270.23), followed by Scenario 2. As clearly seen in Table 9, the results of the Regression tree of Scenario 1 using 20-fold cross-validation are overall better than those for both fivefold and tenfold cross-validation. The computed RMSE values are higher than tenfold cross-validation. Table 10 compares the predicted outcomes based on two distinct AI models, i.e., Regression Tree and Support Vector Machine, united with various parameters of the model. The findings reveal that the SVM model with tenfold cross-validation [RMSE (452.17), R^2 (0.9)] performs the best when compared to other SVM and RT models.

4 Conclusion

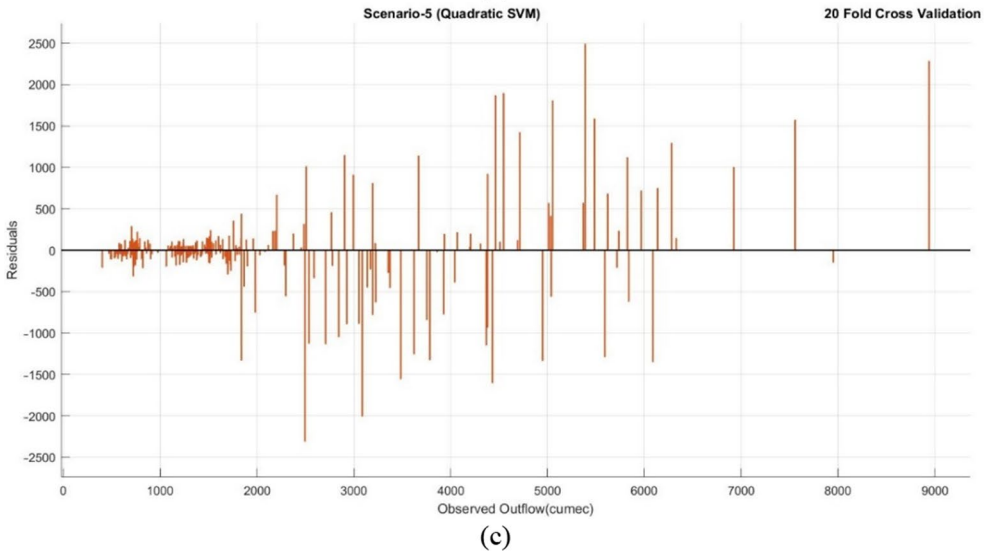
Over the past decades, traditional hydrological forecasting models have greatly changed, with SVM taking the prominence, because it can offer accurate data forecasts for a variety of hydrological processes. The ability to accurately estimate changes in reservoir water levels is beneficial for the planning and management of reservoir water usage in the long run. By examining two distinct Machine Learning approaches, i.e., Regression Tree and Support Vector Machine, this study tries to find which one is the most accurate in predicting water levels based on monthly hydrological records collected in the past 30 years, so as to simulate reservoir outflows. To get the best parameters, this study evaluated a variety of scenarios based on a variety of data



(a)

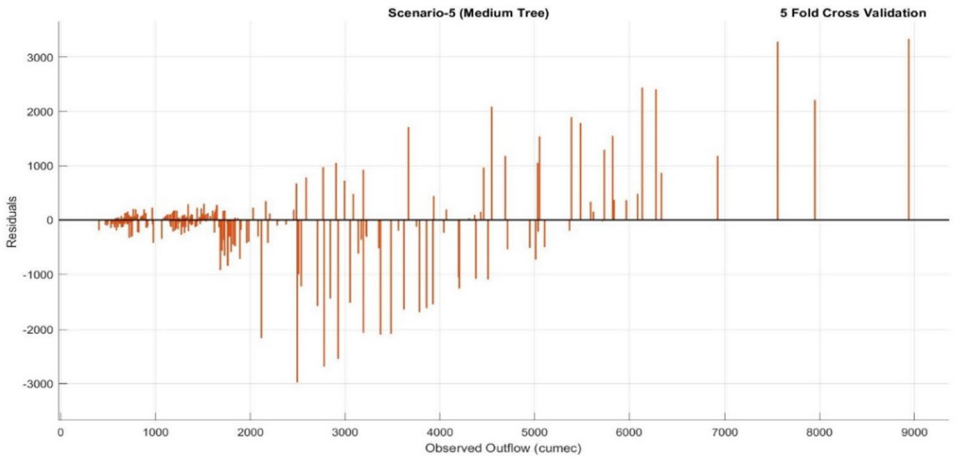


(b)

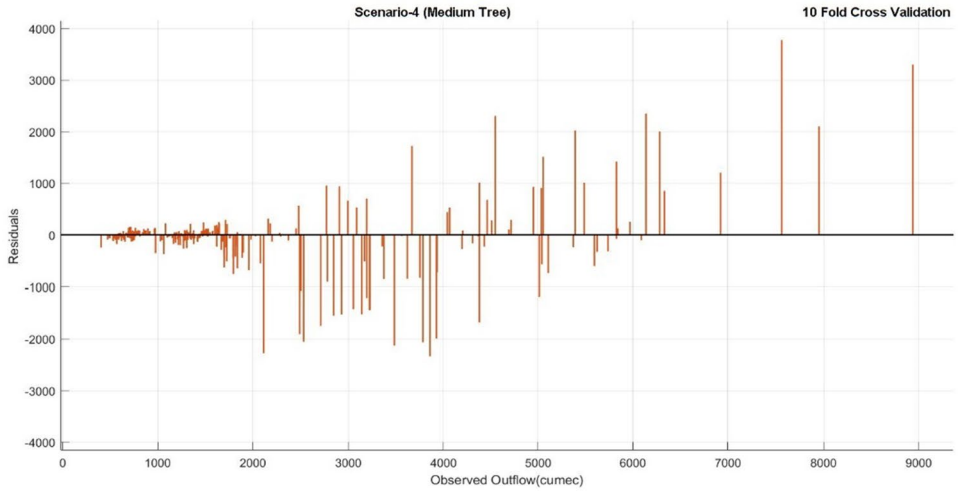


(c)

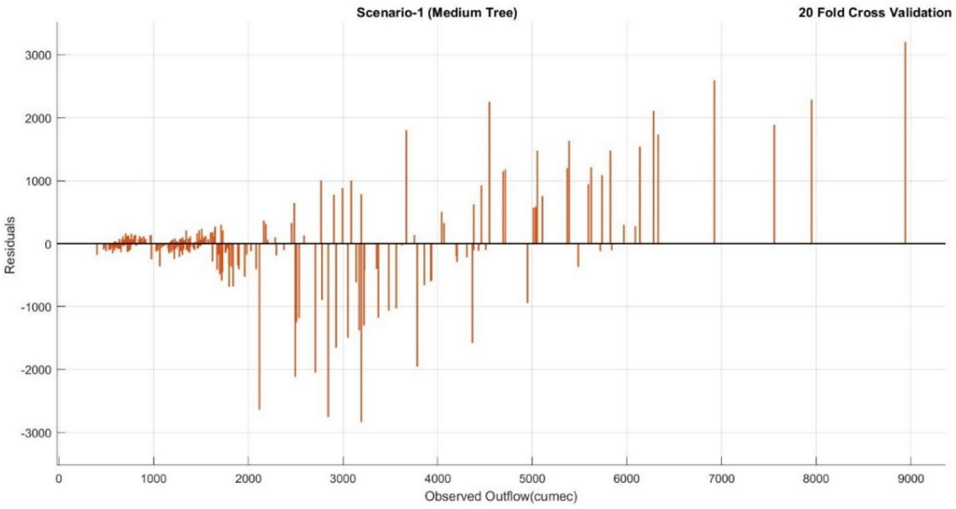
Fig. 6 Residue plots for the SVM model at the monthly scale, fivefold (**a**), tenfold (**b**) and 20-fold (**c**)



(a)



(b)



(c)

Fig. 7 Residue plots for the RT model at monthly scale, fivefold (**a**), tenfold (**b**) and 20-fold (**c**)

Table 4 Statistical evaluation of support vector machine for fivefold cross-validation

Cross-validation		Kernel function	RMSE	R^2	MAE
5-FOLD	Scenario 1	QUADRATIC	524.26	0.87	245.53
	Scenario 2	QUADRATIC	518.02	0.87	241.24
	Scenario 3	QUADRATIC	570.40	0.85	268.98
	Scenario 4	QUADRATIC	483.79	0.89	231.79
	Scenario 5	QUADRATIC	465.81	0.90	232.66

Table 5 Statistical evaluation of support vector machine for tenfold cross-validation

Cross-validation		Kernel function	RMSE	R^2	MAE
10-FOLD	Scenario 1	QUADRATIC	544.16	0.86	255.37
	Scenario 2	QUADRATIC	523.53	0.87	246.41
	Scenario 3	QUADRATIC	496.54	0.88	238.37
	Scenario 4	QUADRATIC	483.46	0.89	234.78
	Scenario 5	QUADRATIC	452.17	0.90	219.68

Table 6 Statistical calculation of Support Vector Machine for 20-fold cross-validation

Cross-validation		Kernel function	RMSE	R^2	MAE
20-FOLD	Scenario 1	QUADRATIC	545.27	0.86	254.21
	Scenario 2	QUADRATIC	527.27	0.87	246.36
	Scenario 3	QUADRATIC	513.03	0.87	247.30
	Scenario 4	QUADRATIC	487.11	0.89	235.82
	Scenario 5	QUADRATIC	471.98	0.89	226.78

Table 7 Statistical calculation of Regression tree for fivefold cross-validation

Cross-validation		Kernel function	RMSE	R^2	MAE
5-FOLD	Scenario 1	FINE	631.57	0.81	294.51
	Scenario 2	MEDIUM	633.14	0.81	289.25
	Scenario 3	FINE	610.93	0.82	282.70
	Scenario 4	FINE	623.00	0.81	292.39
	Scenario 5	MEDIUM	602.80	0.78	322.53

inputs. For this purpose, RMSE, MAE and R^2 indices are used to quantify the performance of the forecasting models. In summary, Scenario 5 shows the optimum combination of input data, which comprise inflow, evaporation, water level, reservoir storage, previous inflow and previous outflow. The best SVM regression is with quadratic kernel function, and the best V-fold

Table 8 Statistical calculation of regression tree for tenfold cross-validation

Cross-validation		Kernel function	RMSE	R^2	MAE
10-FOLD	Scenario 1	MEDIUM	602.59	0.83	288.27
	Scenario 2	FINE	625.43	0.81	297.57
	Scenario 3	COARSE	645.52	0.80	325.17
	Scenario 4	MEDIUM	596.34	0.84	274.07
	Scenario 5	FINE	613.99	0.82	284.99

Table 9 Statistical calculation of regression tree for 20-fold cross-validation

Cross-validation		Kernel function	RMSE	R^2	MAE
20-FOLD	Scenario 1	MEDIUM	596.2	0.83	279.73
	Scenario 2	MEDIUM	622.46	0.82	294.46
	Scenario 3	FINE	622.17	0.82	294.26
	Scenario 4	FINE	615.97	0.82	291.07
	Scenario 5	COARSE	629.35	0.81	309.94

Table 10 Statistical calculation of regression tree model and support vector machine model

Cross-validation	Model	RMSE	R^2	MAE
5-FOLD	SVM	465.81	0.9	232.66
	Regression tree	610.93	0.82	282.7
10-FOLD	SVM	452.17	0.9	219.68
	Regression tree	596.34	0.84	274.07
20-FOLD	SVM	471.98	0.89	226.78
	Regression tree	596.2	0.83	279.73

cross-validation is tenfold, which is employed for the optimal scenario selection. In the comparative analysis of water level prediction by the two algorithms, SVM is proven to be the best algorithms for water level prediction. However, when performing water level prediction individually, Regression tree with tenfold cross-validation shows that the SVM model can make accurate predictions. This highlights its unique capabilities and benefits in detecting hydrological time series with nonlinear properties. Therefore, SVM has certain generality and can be used as a model for reservoir water level prediction. More kind of hydrological data, such as infiltration rates, transpiration rates, low inflow conditions and other relevant parameters, should be added in future studies, so as to deliver more precise forecasts.

Acknowledgements
The authors would like to express their deepest appreciation to the anonymous reviewers for their time spent on this paper.

Author contributions
Both authors read and approved the final manuscript.

Funding
Not applicable.

Availability of data and materials
The data used in this study is available in digital platform.

Declarations

Competing interests
The authors reported no potential conflicts of interest related to the work submitted for publication.

Received: 19 October 2022 Revised: 12 November 2022 Accepted: 21 March 2023
Published online: 28 April 2023

References

Ahmadlou, M., Karimi, M., Alizadeh, S., Shirzadi, A., Parvinnejhad, D., Shahabi, H., & Panahi, M. (2019). Flood susceptibility assessment using integration of adaptive network-based fuzzy inference system (anfis) and biogeography-based optimization (bbo) and bat algorithms (ba). *Geocarto International, 34*, 1252–1272.

Bahrami, S., & Wigand, E. (2018). Daily streamflow forecasting using nonlinear echo state network. *International Journal Advance Research Science Engineering Technology, 5*, 3619–3625.

Basak, D., Pal, S., & Patranabis, D. C. (2007). Support vector regression. *Neural Information Processing-Letters and Reviews, 11*, 203–224.

Bowden, G. J., Maier, H. R., & Dandy, G. C. (2002). Optimal division of data for neural network models in water resources applications. *Water resources research, 38*(2), 2–1.

Breiman, L. (2017). *Classification and regression trees*. Routledge.

Chavent, M. A. (1988). Monothetic clustering method. *Pattern Recognition Letters, 19*, 989–996.

Collobert, R., & Bengio, S. (2001). SVM Torch: Support vector machines for large-scale regression problems. *Journal of Machine Learning Research, 1*, 143–160.

Cristianini, N., & Shawe-Taylor, J. (2000). *An introduction to support vector machines and other Kernel-based learning methods*. Cambridge University Press.

Drucker, H., Burges, C. J. C., Kaufman, L., Smola, A., Vapnik, V. (1996). Support vector regression machines. *Advance in Neural Information Processing System* 155–161.

Gunn, S. R. (1988). Support vector machines for classification and regression. *ISIS Technical Report, 14*, 5–16.

Hejazi, M. I., & Cai, X. M. (2009). Input variable selection for water resources systems using a modified minimum redundancy maximum relevance algorithm. *Advances in Water Resources, 32*(4), 582–593.

Hipni, A., El-shafie, A., Najah, A., Karim, O. A., Hussain, A., & Mukhlisin, M. (2013). Daily forecasting of dam water levels: Comparing a Support Vector Machine (SVM) Model with Adaptive Neuro Fuzzy Inference System (ANFIS). *Water Resour. Manag., 27*, 3803–3823.

Hong, Y., Lee, Y. J. (2009). Citing Websites. A loss function approach to model specification testing and its relative efficiency to the GLR test. Retrieved 3rd February 2013.

Hu, C., Wan, F. (2009). Input Selection in Learning Systems: A Brief Review of Some Important Issues and Recent Developments. *In Proceedings of the IEEE International Conference on Fuzzy Systems*, Jeju Island, Korea, 20–24 August, pp. 530–535.

Hussain, H. W., Ishak, W., Ku-mahamud, K. R., & Norwawi, N. (2011). Neural network application in reservoir water level forecasting and release decision. *International Journal of New Computer Architectures and Their Applications, 1*, 265–274.

Khan, M. S., & Coulibaly, P. (2006). Application of support vector machine in lake water level prediction. *Journal of Hydrologic Engineering, 11*(3), 199–205.

Kim, S. J., Ryoo, E. C., Jung, M. K., Kim, J. K., & Ahn, H. C. (2012). Application of support vector regression for improving the performance of the emotion prediction model. *Journal of Intelligent Information System, 18*, 185–202.

Li, P. H., Kwon, H. H., Sun, L., Lall, U., & Kao, J. J. (2010). A modified support vector machine based prediction model on streamflow at the Shihmen Reservoir, Taiwan. *International Journal of Climatology, 30*, 1256–1268.

Loh, W. Y. (2011). Classification and regression trees. *Wiley Interdisciplinary Reviews Data Mining and Knowledge Discovery., 1*(1), 14–23.

Mokhtar, A. S., Wan Ishak, W. H., Md Norwawi, N. (2014). Modelling of reservoir water release decision using neural network and temporal pattern of reservoir water level. *In: Proceedings of the fifth international conference on intelligent systems, modelling and simulation*, pp 127–130.

Mullainathan, S., & Spiess, J. (2017). Machine learning: An applied econometric approach. *Journal of Economic Perspective, 31*, 87–106.

Naghibi, S. A., & Pourghasemi, H. R. (2015). A comparative assessment between three machine learning models and their performance comparison by bivariate and multivariate statistical methods in groundwater potential mapping. *Water Resources Management., 29*, 5217–5236.

Najah, A. A., El-Shafie, A., Karim, O. A., & Jaafar, O. (2011). Integrated versus isolated scenario for prediction dissolved oxygen at progression of water quality monitoring stations. *Hydrology and Earth System Sciences Discuss, 8*, 6069–6112.

Nwobi-Okoye, C. C., & Igboanugo, A. C. (2013). Predicting water levels at Kainji dam using artifcial neural networks. *Nigerian Journal of Technology, 32*(1), 129–136.

Onur Hınçal, A., Burcu Altan-Sakarya, A., & Ger, M. (2011). Optimization of multireservoir systems by genetic algorithm. *Journal Water Resource Management, 25*, 1465–1487.

Quinlan, J. (1986). Induction of decision trees. *Machine Learning, 1*, 1–81.

Schwefel, H. P. (1981). *Numerical optimization of computer models*. John Wiley & Sons Inc.

Seckin, N., Cobaner, M., Yurtal, R., & Haktanir, T. (2013). Comparison of artifcial neural network methods with l-moments for estimating food fow at ungauged sites. *Water Resour Manage J, 27*(7), 2103–2124.

Shafaei, M., & Kisi, O. (2016). Lake level forecasting using Wavelet-SVR, Wavelet-ANFIS and Wavelet-ARMA conjunction models. *Water Resources Management, 30*(1), 79–97.

Sharafati, A., Khosravi, K., Khosravinia, P., Ahmed, K., Salman, S. A., Yaseen, Z. M., & Shahid, S. (2019). The potential of novel data mining models for global solar radiation prediction. *International Journal of Environmental Science and Technology, 16*, 7147–7164.

Smola, A. J., & Scholkopf, B. (2004). A tutorial on support vector regression. *Statistics and Computing, 14*(3), 1–24.

Tokar, A. S., & Markus, M. (2000). Precipitation-runoff modeling using artificial neural networks and conceptual models. *Journal of Hydrologic Engineering, 5*(2), 156–161.

Vapnik, V. (1995). *The nature of statistical learning theory*. Springer-Verlag.

Vens, C., Schietgat, L., Struyf, J., Blockeel, H., Kocev, D., & Džeroski, S. (2010). *Inductive databases and constraint-based data mining* (pp. 365–387). Springer.

Witten, I. H., & Frank, E. (2000). *Data mining: Practical machine learning tools and techniques with java implementations*. Morgan Kaufmann Publishers.

Yang, T., Gao, X., Sorooshian, S., & Li, X. (2016). Simulating California reservoir operation using the classification and regression-tree algorithm combined with a shuffled crossvalidation scheme. *Water Resources Research, 52*, 1626–1651.

Zhang, D., et al. (2018). Modeling and simulating of reservoir operation using the artificial neural network, support vector regression, deep learning algorithm. *Journal of Hydrology, 565*, 720–736.

Publisher's Note

Springer Nature remains neutral with regard to jurisdictional claims in published maps and institutional affiliations.

Journal of Current Research in Engineering and Science
Bi-Annual Online Journal (ISSN : 2581 - 611X)

Volume 6- Issue 1, Paper 9 ,January 2023

Software Testing using Genetic Algorithms- A review

IshaanRajora, Lakshay Sandhu,
Mohammad Yamin Bhat, Rohit Beniwal
Dept .of computer science & Engineering
Delhi Technological University

Abstract

Software testing is the process of assessing and verifying that a software or application is working in the manner it is programmed. This paper is a literature review that reflects the evolution of genetic algorithms (GA) and how they have been efficiently used in different types of test case generation during functional software testing. We have focussed on set-based GA, cluster-based GA and hyper volume genetic algorithms which have been used for automated test data generation and for optimisation of that test data for solving variouscomplexproblemsrelatingtosoftwaretesting.Thispaperhighlightstheideasoftwaretestingusingvariouskindsofgeneticalgorithmsforoptimumresults.

Keywords - software testing, test-data generation, genetic algorithm, test-case prioritisation

Introduction

1.1 Overview

The role and significance of software status has expanded in recent years, as software has become increasingly vital in the global economy and societal evolution. Imperfect software can result in not just costly maintenance, but also major asset loss and, in certain cases ,serious national security or environmental risks. Software testing is of utmost importance in software programming since it is utilised to ensure the quality of softwares. Software testing has been shown to account for more than half of project expenditures in the overall life cycle of softwares. Furthermore, referring to Boehm's studies, if an issue is found later, it takes much more money and is costlier to rectify. So, it becomes crucial to improve the softwaretesting'sefficiency.Softwaretestingapproachesareprimarilyfordeterministicsoftware.In fact many actual programmes contain various forms of uncertainty, like randomness or

fuzziness, implying that their behaviour is unpredictable.When executing the programmewithuncertaintymultipletimeswiththesametestdata,itmaytakevariouspathways,wrapp ingdifferentstatements,orevenproducedistinctresults.Previoustestadequacyrequirementsarenolo ngerapplicableinthissituation.

Software testing has been one of the most important processes to develop a reliablesoftwaresystembutitcanbesignificantlytimeconsuming.Thegoalistousetheleast amount of test data to find as many faults as possible. Testing particularly manual andad-hoccouldbesufficientforsmallbuildsbutforlargerset-ups automation testing comes into play. As software complexes further and further, testing becomes more and more challenging. In recent years, genetic algorithms (GA) have proven to be highly cost effectiveand efficient for test data generation. Moreover, GA is now being preferred for solving various software optimization problems.

Regression testing, a software testing practice that makes sure the unchanged partsof software sit well with the updated ones.The overall stability and functionality of theexisting features is dependent on it. For cost reduction, TCP is utilised for scheduling theofthetestcasestoenhancetheircapabilityforrevealingfaults.Orderingthetestcasestoexecute eventually is called Test case prioritization. Prioritising test cases aids in meetingtwo significant limitations, namely cost-time cost and budget cost-in software testing, toenhancethefaultdetectionrateasearlyaspossible.

1.2 Motivation

Therehavebeenvariousstudyresultsaimedattestingaprogrammewithnondeterminismin the past, but hardly any of these studies have focused on programmes containing ran-domness.Randomness-aware programmes, on the other hand, are common in actuality.Softwares for gaming, the Windows operating system as well as network software are fewexamples where randomness-aware programmes are used for instance when a user chal-lengesasoftwareprogramtoagameofChinesechess.Ingeneral,theprogram'sexecutionis determined by a set of strategies.However, certain random decisions may be included intheplan.Asnon-deterministicoptions,thecomputerdecisionswillbekeptundetermined.As a result, research into testing a programme using randomisation is both required andimportant.The program'sstabilitywill be ensured ifthe random behaviour'simpact couldbe determined on the programme. This could be achieved if some test cases could be

madeusingsomerandomvariables.

Asuiteshouldbediscoveredintheprogramme'sinputdomainundertrialforan

Awarded set of programme goals ,it should be such that in the whole test suite there should be at least one test datum which could cover each target. Various experimental objectives have distinct requirements for testing.

2.1 Literature Review

NSGA-II was performed on difficult test problems by Kalyanmoy Deb et al.[1] and concluded that it will provide better solutions and converge better when compared with Pareto-archived evolution strategy (PAES) and strength- Pareto EA (SPEA). PAES were able to converge closer to the true Pareto-optimal front only in one single case. They proposedthatNSGAIIisstatedtobethebetteramongothermethodsobservedbecauseofutilisingdiversity preserving mechanism. Although this has been a matter of ongoing research insingle-objective evolutionary algorithm studies, this study displays that epistatic difficulties may also cause problems for MOEAs.They also introduced an extension to definedominance for mannered multi-objective optimisation, which when used with the real-coded NSGA- II and with this stated definition has been presented to solve these different difficulties much better than another recent stated approach.

Christopher C. et al. [2] talks about automatic software test data generation by usinggenetic algorithm.They described the execution of a genetic based system and observed theefficiency of this method. With their previous observation of this study they also examinethe complexity problem by executing their system on a number of synthetic programswithvaryingdifficulties.Theyconcludedtheirresultsbyperformingfourexperiments with the help of dynamic test data generation. In their experiment, the analysis of randomtestgenerationforcomparativelylargerprogramsdeclinedinperformance.Accordingto them, the increase in complexity of the program causes an increasing complexity fornonrandomtestgenerationmethods.However,standardgeneticalgorithmgavethebestresults forprogramswithvaryingdifficulties.Moreovertheyfoundthemostefficientwaystogeneratetestdatabysatisfyingmanyrequirementswhichwerehighlyunlikelyandtheirdiscovery will help in solving most of the similar test generation problems and might

leadtosignificantdifferencesbetweenoptimisationanddynamictestdatagenerationissues.

AnautomatedtestcasegenerationbasedonGAwasdiscussedbyYuehuaDongetal.[3]thatpropose danimprovedGAforsoftwaretestinganddatageneration.TheimprovedGAhasmoreenhancedresults thanthebasicGAbyproficiencyandvirtueonthetestcasegeneration.Theyusedabinaryencodingmeth oddduetoitseasyencodinganddecoding,simpletoattaincrossoverandmutationpotency.Toimproveth eaccuracyof selection operation of GA they decided to refrain in variation and crossover operation tomaintain best solutions and also decided to use preservation and roulette wheel selectionmethod for conjunction to fasten the overall convergence rate.For the mutation operation,theyusedthebasicbitmutationi.e.toselectavariationindividualarbitrarily,thenchoose a random place for a variation point.According to them fitness function affectsstraightlytotheconvergencespeedofGAandthepotentialtofindoptimalsolutionsotheypropos edafitnessfunctionaccordingtotheirrequirementofexperimentalproblem.Intheirexperimentanalys is,theimprovedGAbasedtestdatageneration wascomparedwith the basic GA based test data generation approach and observed dominance on timeefficiencyandsearchcapability.

PraveenR.Srivastavaetal.proposedthecuckooandtabusearchalgorithms(CSTS)forautoma tion of test data generation. Tabu Search reduced the general complication of thealgorithmbycuttingthenumberofiterationsandexecutiontime.TheyusedLévyflightin solving the issues of getting stuck in local optima, thereby inspecting the search space moreeffectively. They combined the strength of the cuckoo algorithm to converge in minimumtimeusingthebacktrackingtabumechanismbyLévyflight[4].Theirexperimentswere basedonrelativelysimpleexampleswherethealgorithmprovedefficientingeneratingoptimal test cases and it performed significantly improved than previous approaches andvariousothermetaheuristictechniques.

2.2 ConceptsandTerminologies

To answer some research questions, Dario D. Nucci et al.[5] considered testing criteriawhich were distinct and widely used in previous TCP work: execution cost criterion, pastfaults coverage criterion, and statement coverage criterion [6].This study is a clear exampleofhypervolumebasedindicatorsandtheiradvantagesoversimpleAUCbasedmetrics.Th ecriteria shows how the Hypervolume-based metric can satisfy any type of testing criteria.Utilising the testing models depicted over, the creators inspected two distinct

definitions ofthe TCP issue: Two criteria (Single- objective). The objective is to calculate an ideal orderof experiments or test cases which limits the execution cost and maximises the statementcoverage, three criteria (Two- objective).For this detailing, the authors considered thepreviousflawsinclusionasathirdmeasuretobeamplified.

2.2.1 Testadequacycriteria

Inordertotestasoftwareproductatestsuiteneedstobegeneratedaccordingtoacriteria.Thenthefaultsa nderrorsareobtainedbyrunningtheprogram[7].Toguaranteetheappropriatenessofthetest,theauthor ssetforwarddefinitetststandardstorunthetestingresults.Particulartestgoalsrelatetodefinitetestmo dels.Forinstance,executablestatementsareneedforstatementcoverageruleorcriteria.Asobserved generally when comparing, the coverage measure method is more complex than the branchconvergemethod.Similarlywhencomparedbranchcoveragecriteriatothestatementcoverage model,branchcoverageisobservedtobemorecomplex.

2.2.2 Multi-objectiveTestOptimisationProblems

We discuss a total of three multi-objective test optimisation problems: test suite minimi-sation(TSM),testcaseprioritisation(TCP),testcaseselection(TCS)[8].

With the evolution of a software project or application, the associated test suite contin-ues to grow alongside.Without careful maintenance of the test suite, it can easily lead toexcessively long test execution times, lowering the benefits of regression testing as bugs getdiscoveredlateindevelopmentorevenafterrelease.TSMisdesignedtosolvetheproblemoflong-runningtestsuitesbyremovingunnecessarytestcases[9].

TCP and TCS have helped software developers to get timely feedback on their productorapplicationastheyhaveimprovedregressiontestingthroughselectionandprioritisationoft estcases[10].ThegoalofTCPinsimpletermsisfindingtheorderinwhichagivensetoftestcaseswil lbeexecuted,thusoptimisingagivenobjectivefunctionandsatisfyingtimeconstraintswhichhelp sinachievingtestinggoals[11].

TCS includes selection of a subset from a test suite which is used to check the changesmade in the software i.e. to check whether the changes made to the software affects theperformance of the unmodified parts [12]. The identity of the modified parts of softwareprogrammaybecompletedbytheusageofuniquetechniques.Thedetailsofthedifferents electing approaches differ on how a selected approach defines, seeks and identifies adjust-

ments within the application under test [13]. After the identification of test cases for theunmodified parts through a particular technique, we can use an optimisation algorithm,forinstancetheadditionalgreedy,forselectingaminimalsetofthosetestcasesinrelatio ntoacertaintestingcriteria[14].

2.2.3 Hypervolume

Thereisadevelopingpatternofsolvingmany-objectiveissuesutilisingqualityscalarmark-ers or indicators to consolidate various objectives into a solitary one [15].In this manner,rather than optimising the objective functions first, indicator-based algorithms discover asolutionsetthataugmentstheunderlyingqualityindicatortothemaximum[15].Perhaps

the most famous indicator is the hypervolume. It observes the nature and standard of thesolutionsuiteasthecompleteobjectivespace,whichinturniscontrolledby(atleastone)of such arrangements (combinatorial union [15]).For two objective and three objectiveproblems,thehypervolumereferstotheareaunderthecurveandthevolumerespectively.

3. ComparisonsofGeneticAlgorithms

3.1 Setbased genetic algorithm

Xiangjuan Yao et al.[7] introduced a special software testing generation approach forsoftwares with randomness and uncertainty, while previous practices of test data generationfrequently drop in efficiency.An algebraic model followed by a novel test adequacy criterionisputforwardtoprovidevitalitytothetestingsoftwares,accordingtothisanewapproachf ordecipheringtheoptimizationmodelbysetbasedGAisset.

Atestdatagenerationapproachformulti-pathcoverage,basedonageneticalgorithmwasintroducedwithlocalevolutiontoensuretheadequ acybyfindingerrorsbyrunningaprogramofthetestdata.Theydescribedthetraditionaltestingade quacycriterionfor a given software with set of test target and stated them valid for (softwares withoutuncertainties) test details awning a target with probability 0, 1 and for softwares withuncertainties and randomness coverage of test details for a target is not determined i.e.softwaremaybedistinctwhileexecutingthesametestdatum.

Followedbythestatedcriterionforsoftwareswithrandomness,tosolvetheoptimiza-tion model formulated by them, branch coverage criterion is seen as an instance to buildoptimised

structure for softwares with uncertainties and a set based genetic algorithm isproposedandformulatedaccordingly.

Firsttheygovernthevaluesofcontrolledparameters,likethenumberoftestdata,thresholdetc,followedbycreatingandgeneratingarandominitialpopulationcontaininga number of individuals. Although the chances to be selected to the next generation isgreaterifthefitnessvalueofanindividualissubstantialandifthisconditionissatisfiedthan performing the genetic operation with selection, crossover and mutation operation isdone.

Their experiment analysis is based on ten C programs with random numbers.Theexperimental outcomes portray that the stated approach can resolve the difficulty of testdataforsoftwarewithuncertainnumbers.

3.2 Clusterbasedgeneticalgorithm

Dipesh Pradhan et al.proposed a CBGA-ES+ in addition to the previous CBGA-ESalgorithm for Multi-Objective Test Optimization [8].The design of CBGA-ES+ is to selectnon-dominated elite solutions from a group of clusters of the population that is where itdiffers from CBGA-ES as it includes only dominant elite solutions. These solutions will beused to generate the offspring solutions which will form the next generation. The clustersare sorted with the cluster dominance strategy and then the non-dominant solutions areselected among these clusters. The cluster dominance strategy has been used to draw adominance relation between two clusters.Each of the two clusters has a centre i.e.themean fitness of solutions of the cluster such that the cluster with a lower value of centredominatestheonewithahighervalue.

CBGA-ES+ is intended to compute a variety of multi objective test optimization challenges. As a result, the inputs for CBGA-ES+ contains the initial test suite to be optimisedas well as a collection of parameters to be adjusted, such as population size, cluster size,and elite population minimum size.The minimal size of the elite population was set in order to avoid the algorithm from converging prematurely as a function of the added elitist selection. The algorithm initialises a random population of a given size. Solutions that are having similar fitness value are clustered using Lloyd's algorithm. Lloyd's algorithm selects one solution from Pt at random for each cluster and labels the

objectives as the cluster centres, respectively .It is important to note that the solutions chosen for each cluster have to be distinct, such that there aren't two clusters having the same centres.

Onceverysolutiongetspartitionedintoclusters,theclustercentresareupdatedusingthemeanofsolutions.Whenthereisachangeinthevaluesofclustercentres,everysolutionisclusteredbycalculatingtheEuclideandistancebetweenthesolutionsandthecentresofthenewclusters.Followingthat,allofthecclustercentresareupdatedagain,andtheprocedureiscontinueduntilthevaluesofthecluster centredonot change for two consecutive iterations.Eventually,the clusters that we regenerated ae delivered,with each cluster consisting of a group of related solutions with regard to the pre-defined objectives.Following that,theLloyd's algorithm clusters are organized using the cluster dominance strategy,and the elite population is initialized with non-dominated solutions, which the nuses the algorithm dominance comparator.In particular,the non-dominated solutions from the best clusters are added to the elite population by comparing every solution with the solutions in the cluster.

The algorithm of dominance comparator takes the values of two solutions and checks whether one is dominated by the other, and then returns the outcome. The addition of solution is done to the elite population only when it's not dominant for any solution in the given cluster. This process is continued until either all of the solutions in the cluster are compared to one another or the size of the elite population equals the required population size. When the structure of the returned elite population is less than the given mini elitepopulationsize,computationsfromthenextdominatingclusterarepickedfortheelitepopulationusingthesameupdatedelitepopulationalgorithmuntilthesizeoftheelitepopulationequalsrequiredpopulationsize.

3.3 Hyper-volumebasedgeneticalgorithm

Test case prioritization is just generation of test cases to reveal specific faults in software. So it is a special case of test case generation.Ordering the test cases to execute eventually is called Test case prioritization.Prioritising test cases aids in meeting two significant limitations, namely cost-time cost and budget cost-in software testing, to enhance the fault detection rate as early as possible. In this paper, the case prioritised by Dario DiNucci et al.[5] is regression faults in software. Regression testing—a software

testingpractice;thatmakessuretheunchangedpartsofsoftwaresitwellwiththeupdatedones.Since the capability of fault detection is not known before executing tests, the majority of the methodologies that are put forth for TCP use substitutes like coverage criteria with the possibility that experiments with better code coverage will reveal faults at a higherprobability.Once the coverage criterion is decided, search algorithms execute in a way that they find the order of maximizing that criterion.

Legitimate fitness functions are chosen and developed. Now, each of these fitness functions measures AUC addressed by the combined coverage and cost scores acquired aftersteadilyperformingtheexperiments(executingtestcases)asindicatedbyadistinctorder(prioritization). Numerous points in the cost-coverage space are consolidated into a soli-tary scalar value and utilised as a fitness fn for meta-heuristics, like single-objective GAs.Later work on search-based TCP likewise utilised multi- objective GAs, taking differentAUC-basedmetricsasvariousobjectivesforoptimization.

Hypervolume,usedinmany-objectiveoptimizationproblems,isjustanadvancedformof the AUC metric. Thus, A. Panichella et al. proposed HGA, which is a genetic algorithmbased on Hypervolume, to address the issue of TCP when multiple test coverage criteriaare used.They consider that it can deal with both— single cumulative code coveragecriteriaandmultipletestingcriteriainasinglescalarvalue.

Threeseparatecasestudieswerecarriedouttoaddresstheresearchquestion—IsHGAa lot quicker than GA and NSGA-II regarding efficiency.Furthermore, concerning Addi-tional Greedy, when the size of the program and the test suite increase, the effectivenessstaysunaffected.

While contrasting HGA and many-objective search based algorithms (e.g., MOEA/D-DEandGDE3),it was noted that it is more or just as effective,and the efficiency was 3times ber.

4. Results

CBGA-ES+algorithm has conclusivel yout performedallthealgorithmsfromTable4.1, 4.2 and 4.3 for TSM, TCP and TCS respectively [8]. HGA, on an average, is 1.89 times faster than GA. We already know number of test cases adversely affects the performance of GA. Indeed, with increasing number of test cases the ratio between the time required by GA and HGA increases.

HGA performs better than Additional Greedy in most cases—cost-effectiveness wise but

Journal of Current Research in Engineering and Science
Bi-Annual Online Journal (ISSN : 2581 - 611X)
Volume 6- Issue 1, Paper 9 ,January 2023

efficiency is lesst.On the two-criteria formulation,HGA and GA perform the same interms of fault detectionability. However,the former has better efficiency than the latter thanks to our algorithm for the fast computation of the hyper volume. On the three-cri-teria, HGA is often has higher effectiveness and always has a higher efficiency than NSGA-II.

Table 4.1:CBGA-ES+ comparative performance for TSM

ComparedWith	$\hat{A}12$
CBGA-ES	0.71
MOCell	0.77
NSGA-II	0.79
PAES	1.00
SPEA	0.66

Table4.2:CBGA-ES+comparativeperformanceforTCP

ComparedWith	$\hat{A}12$
CBGA-ES	0.80
MOCell	1.00
NSGA-II	1.00
PAES	1.00
SPEA	0.62

Table4.3:CBGA-ES+comparativeperformanceforTCS

ComparedWith	Aˆ12

CBGA-ES	0.67
MOCell	1.00
NSGA-II	1.00
PAES	1.00
SPEA	0.99

5 .Conclusion

CBGA-ES+ performed better compared to its predecessor algorithms (CBGA, MOCell, NSGA-II, PAES and SPEA) for multi-objective test optimization problems. More of these optimization problems can be applied to test the CBGA-ES+ algorithm. In terms of cost effectiveness, HGA is better than Additional Greedy.HGA generated solution is not dominated by NSGA-II generated solution. Statistically, Additional Greedy is more efficient than NSGA-II and HGA, while HGA is faster than GA and NSGA-II.

Reference

[1] K.Deb,A.Pratap,S.Agarwal,andT.Meyarivan,"Afastandelit-istmultiobjectivegenetic algorithm: NSGA-II," IEEE Trans. Evol. Comput., vol. 6, no. 2, pp. 182–197,Apr.2002.

[2] C. C. Michael, G. McGraw and M. A. Schatz, "Generating software test data byevolution," in IEEE Transactions on Software Engineering, vol. 27, no. 12, pp. 1085-1110,Dec.2001

[3] Dong, YuehuaPeng, Jidong. (2011). Automatic generation of software test casesbasedonimprovedgeneticalgorithm.10.1109/ICMT.2011.6002999.

[4] Srivastava, Dr. PraveenKhandelwal, RahulKhandelwal, ShobhitKumar, SanjayRanganatha, Suhas. (2012). Automated Test Data Generation Using Cuckoo

SearchandTabuSearch(CSTS)Algorithm.JournalofIntelligentSystems

[5] D. Di Nucci, A. Panichella, A. Zaidman and A. De Lucia, ”A Test Case PrioritizationGeneticAlgorithmGuidedbytheHypervolumeIndicator,”inIEEETrans actionsonSoftwareEngineering,vol.46,no.6,pp.674-696,1June2020

[6] Z. Li, M. Harman and R. M. Hierons, ”Search Algorithms for Regression Test CasePrioritization,” in IEEE Transactions on Software Engineering, vol. 33, no. 4, pp.225-237,April2007

[7] X. Yao, D. Gong, B. Li, X. Dang and G. Zhang, ”Testing Method for Software WithRandomness Using GeneticAlgorithm,” inIEEE Access,vol. 8,pp. 61999-62010,2020

[8] D.Pradhan,S.Wang,S.Ali, T. Yue and M. Liaaen, ”CBGA-ES+: A Cluster-Based Genetic Algorithm with Non-Dominated Elitist Selection for Supporting Multi-Objective Test Optimization,” in IEEE Transactions on Software Engineering, vol. 47,no.1,pp.86-107,1Jan.2021

[9] Noemmer, R., Haas, R. (2020). An Evaluation of Test Suite Minimization Techniques.In:Winkler,D.,Biffl,S.,Mendez,D.,Bergsmann,J.(eds)SoftwareQuality:Qu al-ity Intelligence in Software and Systems Engineering. SWQD 2020. Lecture Notes inBusinessInformationProcessing,vol371.Springer,Cham.

[10] Pan, RongqiBagherzadeh, MojtabaGhaleb, TaherBriand, Lionel. (2022). TestCase Selection and Prioritization Using Machine Learning:A Systematic LiteratureReview.EmpiricalSoftwareEngineering

[11] D. Marijan, A. Gotlieb and S. Sen, ”Test Case Prioritization for Continuous RegressionTesting: An Industrial Case Study,” 2013 IEEE International Conference on SoftwareMaintenance,2013,pp.540-543

[12] G.RothermelandM.J.Harrold,“Analyzingregressiontestselectiontechniques,” IEEETransactionsSoftwareEngineering,vol.22,no.8,pp.529-551,Aug.1996

[13] S. Yoo and M. Harman, “Regression testing minimization selection and prioritization:A survey,” Software Testing Verification Reliability, vol. 22, no. 2, pp.

67-120, Mar.2012.

[14] A. Panichella, R. Oliveto, M. D. Penta and A. De Lucia, ”Improving Multi-ObjectiveTest Case Selection by Injecting Diversity in Genetic Algorithms,” in IEEE Transac-tions onSoftwareEngineering,vol.41,no.4,pp.358-383,1April2015

[15] A. Auger, J. Bader, D. Brockhoff, and E. Zitzler, “Theory of the hypervolume indica-tor: Optimal m-distributions and the choice of the reference point,” in Proc. SIGEVOWorkshopFound.GeneticAlgorithms,2009,pp.87–102.

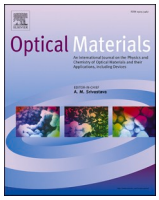
Optical Materials 140 (2023) 113910



Contents lists available at ScienceDirect

Optical Materials

journal homepage: www.elsevier.com/locate/optmat



Research Article



Spectroscopic studies of Pr^{3+} doped red-emitting BaO–ZnO– Li_2O–P_2O_5 glasses for luminescent devices applications

Kartika Maheshwari [a,b], Ravita [c], Aman Prasad [d], Yasha Tayal [a,b], A.S. Rao [a,*]

[a] Department of Applied Physics, Delhi Technological University, Bawana Road, Delhi, 110042, India
[b] ABES Engineering College, Ghaziabad, 201 009, India
[c] Department of Physics, Chaudhary Bansi Lal University, Bhiwani, 127021, India
[d] Department of Physics and Computer Science, Dayalbagh Educational Institute (DEI), Agra, 282005, India

ARTICLE INFO

Keywords:
Glasses
Luminescence
Decay kinetics
J-O Theory
Activation energy

ABSTRACT

Pr^{3+} doped BaO–ZnO– Li_2O–P_2O_5 (BZLP) glass samples synthesised through melt quenching route were studied. The x-ray diffraction (XRD) confirms the amorphous non-crystalline nature of undoped and doped BZLP glass. Absorption spectra show several bands in ultraviolet, visible and infrared regions. The absorption data was used in Judd-Ofelt (J-O) theory to evaluate various radiative parameters. Three peaks are visible in the photoluminescence (PL) emission spectra with the strongest peak positioned at 604 nm for which stimulated emission cross section and quantum efficiency has been assessed. The CIE color coordinates of the samples lie in the red region. The decay time values for 604 nm emission decreased with increased Pr^{3+} concentration. The luminescence intensity decreased to 88.12% and 82.61% of maximum value at 423 K and 473 K respectively showing high thermal stability. These BZLP glasses can work as an effective deep red-emitting component for w-LEDs and other photonic applications.

1. Introduction

Lighting is one of the most fundamental and essential parts of our everyday lives. A variety of electricity-based artificial lighting technologies are available and are being used for indoor/outdoor illumination and lighting industries, complexes, and other areas [1,2]. Solid-state lighting (SSL) technology is one of the advanced artificial lighting technologies. It is eco-friendly in nature and more efficient thereby saving enormous energy in various sectors [3,4]. The white light emitting diodes (w-LEDs) are most widely researched amongst all SSL devices. w-LEDs are developed by mixing a yellow color emitting phosphor with an inorganic compound (epoxy resin) and coated over a blue InGaN chip [5]. This technique has some shortcomings likee less color rendering index, inappropriate correlated color temperature and a halo-effect owing to absence of a red color component. To overcome the drawbacks as mentioned above, numerous other approaches were explored and published [3,6]. These approaches involved usage of inorganic phosphors having less thermal stability, which reduced efficiency and performance of illuminating devices [7]. Therefore, a suitable glass doped with an appropriate lanthanide/transition metal ions is the best replacement for a phosphor. So, in this work, thermally stable red-emitting inorganic glasses were synthesised and explored for lighting applications.

Inorganic oxide formers like phosphates are used to prepare excellent glasses for usage in numerous applications due to eco-friendliness, high transparency, ease of synthesis, low preparation cost, better mechanical and thermal stability etc. [8,9]. Also, high transparency in ultraviolet (UV) to infrared (IR) regions and high rare-earth solubility make phosphates a superior glass host material for photonic applications as compared to borate and silicate glasses [10,11]. But phosphate glass are hygroscopic in nature, which restricts their utility in many applications. The hygroscopic nature of phosphate glasses can be tackled by adding ZnO, which constitutes P–O–Zn bonds and makes the glass moisture resistant [12,13]. Also, the addition of ZnO offers superior characteristics like direct bandgap, non-toxicity, less cost, non-hygroscopic and large exciton binding energy [14]. Alkaline earth metal oxide can work as an active network modifier, which can disrupt the glass network thereby leading to creation of nonbridging oxygen groups and bringing down the melting temperature of glass compositions [15,16]. The addition of alkali oxide in glass compositions may reduce the non-radiative losses, heighten the stability of host matrix. Addtion of lithium oxide to the host leads to the intensification of

* Corresponding author.
E-mail address: drsrallam@gmail.com (A.S. Rao).

https://doi.org/10.1016/j.optmat.2023.113910
Received 5 April 2023; Received in revised form 9 May 2023; Accepted 15 May 2023
Available online 23 May 2023
0925-3467/© 2023 Elsevier B.V. All rights reserved.

transition temperature and lowering of thermal expansion coefficient [17]. With aforementioned characteristics in mind, we were able to synthesize BaO–ZnO–Li_2O–P_2O_5 (BZLP) glass that is highly transparent, moisture-resistant, has less phonon energy, is thermally and mechanically stable with excellent optical characteristics.

Lanthanide ions exhibit a ladder like energy level structure in the ultraviolet (UV) to infra-red (IR) range which is extremely useful for lasing and other photonic device applications [18,19]. The radiative emissions in the lanthanide ions are due to the f-f transitions of 4f shells that are screened by the $5s^2/5p^6$ orbitals [17,20]. Europium, praseodymium and samarium ions in trivalent states produce radiative emission in orange/red regions via pumped by UV/near-UV/blue radiations [21]. Among these lanthanides, Pr^{3+} ions can effectively absorb blue emission emanating from blue LED chips and has significant fluorescence emission in the conspicuous deep-red range of the electromagnetic spectrum [22,23].

In this work, various optical and morphological characteristics of highly transparent Pr^{3+} doped BZLP glass samples have been examined in detail. Absorption data was used to determine the bandgap of the as prepared glass. Photoluminescence (PL) excitation and emission studies were conducted on the glass samples. Under 445 nm excitation, the glasses show a sharp band centered at 604 nm. Decay curves for 604 nm emission were plotted as well. Temeperature dependent PL studies were performed to check whether or not the samples are thermally stable. The aim of performing all the aforementioned studies was to check the applicability of Pr^{3+} glass in w-LEDs and SSL applications.

2. Experimental work and characterizations

2.1. Preparation of glass

Trivalent praseodymium (Pr^{3+}) doped glass samples were synthesised by employing melt quenching route. The doped and undoped glass samples have the molar configuration as follows:

$$(15 - x)\ BaO - 15ZnO - 10Li_2O - 60P_2O_5 : xPr_6O_{11}$$

In the above-mentioned molar composition, *x* represents the amount of Pr^{3+} ions in BZLP glasses. In this study, x varies as 0.0, 0.01, 0.05 0.1, 0.5, 1.0, 1.5, 2.0 & 2.5 mol% and the glasses have been assigned names as BZLP, BZLP:0.01Pr, BZLP:0.05Pr, BZLP:0.1Pr, BZLP:0.5Pr, BZLP:1.0Pr, BZLP:1.5Pr, BZLP:2.0Pr and BZLP:2.5Pr respectively.

Annular grade precursors and 99.9% pure rare earth materials were employed to prepare undoped and Pr^{3+} doped glass samples. The raw chemical powders were weighed as per the composition calculation. The chemicals were ground using the agate mortar and pestle with ethanol as dispersing medium for 1 h. Then, this homogenous and smooth chemical mixture was transferred to an alumina crucible and heated in a muffle furnace from room temperature till 1150 °C at a rate of 5 °C per minute and a hold at 1150 °C for 1 h. This homogeneous melt mix was then taken out and swiftly pressed between preheated (320 °C) brass plates to form glass of desired shape and thickness. To eradicate bubbles and thermal strain, the prepared glass was annealed at 320 °C for 1 h. Finally, the undoped and Pr^{3+} doped BZLP glass samples were ready for the structural, optical and other characteristations.

2.2. Characterization techniques

The physical characteristics for Pr^{3+} doped BZLP glass samples such as density and refractive index and other related parameters were assessed using Archimedes principle (H_2O used as a measuring medium) and He–Ne laser (650 nm). Diffraction patterns of undoped and Pr^{3+} doped BZLP glass samples were recorded at room temperature (300 K) via Bruker D8 Advance X-Ray diffractometer attached with a Ni filter and Cu (K_α) radiation source in $20^\circ \leq 2\theta \leq 70^\circ$ range. Using a spectrophotometer JASCO V 670, optical absorption spectral investigations were measured in the UV to near-infrared (NIR) range.The photoluminescence studies for Pr^{3+} doped BZLP glass samples were carried out via spectrofluorophotometer JASCO 8300FL at 300 K. Decay profile for Pr^{3+} doped BZLP glass samples were recorded via EdinburgFLS980 coupled with a microsecond Xenon flash lamp. Temperature-dependent photoluminescence (TD-PL) features were observed with FLAME- S-XR1-ES Ocean optics spectrophotometer and sample holder attached with heating assembly.

3. Results and discussion

3.1. Physical properties of Pr^{3+} doped BZLP glass samples

The density and refractive index of the samples were calculated using Archemedes' principle and Brewster's angle method respectively [24]. Other related physical parameters were also calculated using formulae from relevant articles in literature and have been presented in Table 1 [25].

The physical parameters for Pr^{3+} doped BZLP glass samples showed variation with an increase in Pr^{3+} ions concentration due to altered environment around the Pr^{3+} ions. The values of parameters like molar refraction, average molecular weight, optical dielectric constant, molar refraction and reflection losses were seen to be increasing with increase in the Pr^{3+} ions concentration in BZLP glass samples whereas polaron radius and interatomic distance decreased with increasing Pr^{3+} ions.

3.2. Glass structural analysis

Diffraction patterns for BZLP and BZLP:0.1Pr glass samples have been recorded at room temperature and shown in Fig. 1. The spectra shows a broad ranging hump and absence of any sharp peaks thereby confirming the amorphous nature of the glass. Also, the doping of Pr^{3+} ions in BZLP glass does not affect the amorphous properties of the doped glasses.

3.3. Absorption properties of glass

Fig. 2 shows the absorption spectra from UV to IR region for BZLP glasses doped with Pr^{3+} ions that were measured at room temperature. The absorption profile exhibits numerous peaks in 300–2000 nm wavelength range. In the spectra, three peaks related to $^3H_4 \rightarrow {}^3P_{2,\ 1,\ 0}$ transitions and one peak related to $^3H_4 \rightarrow {}^1D_2$ transition is present in the visible range and the residual three peaks were related to $^3H_4 \rightarrow {}^1G_4$, $^3F_{4,3,2}$ transitions present in NIR region [26]. These transitions are in agreement with Carnall's work [27]. The absorption intensity increased with increase in the concentration of Pr^{3+} ions. The $^3H_4 \rightarrow {}^3P_2$ transition is hypersensitive in nature $[|\Delta S| = 0, |\Delta L| \leq 2\ and\ |\Delta J| \leq 2]$ which predominantly depends upon on the neighbourhood of Pr^{3+} ions and correspondingly affects the J-O intensity parameters [28]. The hypersensitive transition's peak position is shifted towards shorter wavelengths as depicted in Fig. 2 when the concentration of Pr^{3+} ions rises. This change in shift arises due to nephelauxetic effect [29]. For the mentioned band positions in absorption spectra, nephelauxetic ratio (β and bonding parameters (δ) were assessed for Pr^{3+} doepd BZLP glasses by employing expression in literature [29,30]. Bonding parameters can represent the covalent or ionic character of as-prepared glasses by having + ve or -ve values respectively. Table 2 shows that the bonding parameter values are positive, indicating the covalent character of as prepared glasses. This covalent nature increases in the as prepared glasses as the concentration of Pr^{3+} ions rises.

An essential parameter, the experimental oscillator strength (fexp), has been evaluated using the area under the absorption peaks and applying the specified formula:

$$f_{exp} = \frac{2.303mc^2}{N\pi e^2} \int \varepsilon(\vartheta) d\vartheta \quad (1)$$

Table 1
Physical Properties of Pr^{3+} doped BZLP glasses.

Physical Property	BZLP: 0.01Pr	BZLP: 0.05Pr	BZLP: 0.10Pr	BZLP:0.50Pr	BZLP:1.00Pr	BZLP:1.50Pr	BZLP:2.00Pr	BZLP:2.5Pr
Refractive index (n_d)	1.78	1.81	1.84	1.86	1.89	1.93	1.94	1.96
Density (gm/cm^3)	2.99	3.09	3.14	3.18	3.20	3.22	3.26	3.28
Average molecular weight	208.61	208.96	209.39	212.86	217.20	221.54	225.89	230.23
Pr^{3+} ion concentration N (10^{22} ions/cm^3)	0.008	0.04	0.09	0.45	0.88	1.32	1.73	2.14
Polaron radius (r_p) (Å)	9.10	5.27	4.16	2.43	1.94	1.70	1.55	1.44
Inter-atomic distance (r_i) (Å)	22.60	13.09	10.33	6.05	4.82	4.23	3.85	3.59
Optical band gap (eV)	3.57	3.51	3.48	3.64	3.92	3.94	4.02	4.07
Dielectric constant (Ɛ)	3.16	3.27	3.38	3.45	3.57	3.72	3.76	3.84
Optical dielectric constant (Ɛ-1)	2.16	2.27	2.38	2.45	2.57	2.72	2.76	2.84
Molar refraction (R_m) (cm^{-3})	29.18	29.14	29.45	30.10	31.30	32.67	33.19	34.09
Reflection losses (R %)	4.25	4.51	4.78	4.96	5.23	5.59	5.69	5.87

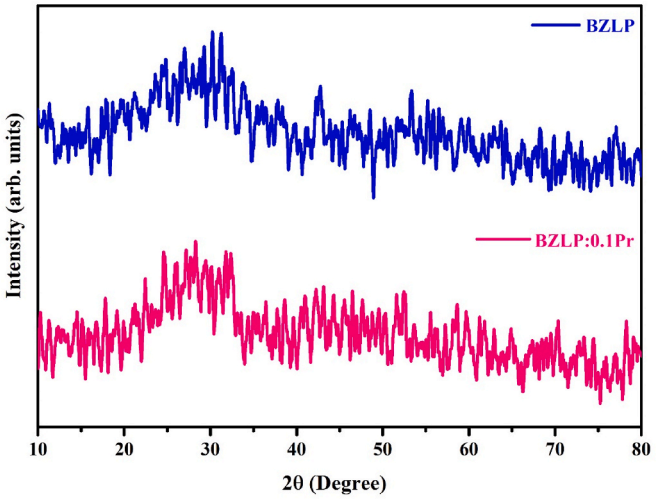


Fig. 1. XRD patterns recorded for BZLP and BZLP:0.1Pr glasses.

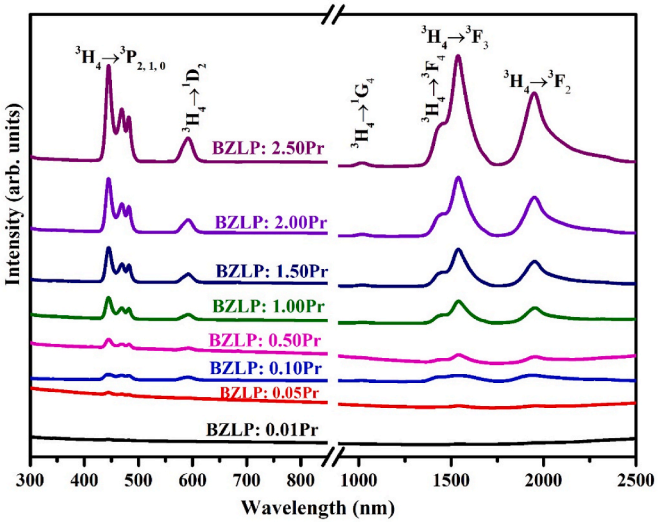


Fig. 2. Absorption spectra of doped BZLP glasses with varying concentrations of Pr^{3+} from 0.01 to 2.5 mol%.

where m, e, and c denotes for mass, charge of an electron and speed of light respectively. Also, N here stands for the Avagadro's Number, while $\varepsilon(\vartheta)$ is the molar extinction coefficient for the wave number ϑ (cm^{-1}.) The evaluated values are have been presented in Table 2. The calculated oscillator strength (f_{cal}) and J-O parameters (Ω_2, Ω_4, Ω_6) were estimated through experimental oscillator strength (f_{exp}). Least square fit method is used to evaluate the calculated oscillator strength for measured electric dipole transitions within $4f^2$ configuration using following relevant equation:

$$f_{cal} = \left[\frac{8\pi^2 mcv}{3h(2J+1)}\right]\left[\frac{(n^2+1)^2}{9n}\right]\sum_{\lambda=2,4,6}\Omega_\lambda\left(\Psi J \parallel U^\lambda \parallel \Psi' J'\right)^2 \quad (2)$$

Where, ϑ is the wave number for ground state (φ_J) to excited state $(\varphi_{J'}^{i})$ transition, m is electron's mass, c is the speed of light in free space and $\|U^\lambda\|^2$ is doubly reduced matrix element. The best fit between f_{exp} and f_{cal} is assessed through the root mean square deviation (δ_{rms}) that can be calculated by employing the subsequent formula:

$$\delta_{rms} = \left[\frac{\sum\left(f_{exp} - f_{cal}\right)^2}{N}\right]^{\frac{1}{2}} \quad (3)$$

Here N represents the overall number of peaks used in the fitting. The values of f_{cal}, f_{exp}, and δ_{rms} for BZLP glasses are shown in Table 2. Table 3 lists the evaluated J-O intensity parameters together with the values of other reported glasses from the literature [31–34]. J-O parameters emulate the uniform trend ($\Omega_4 > \Omega_2 > \Omega_6$) for all reported glass samples. The intensity parameter Ω_2 is a depiction of covalent character of metal ligand bond whereas other two parameters Ω_4 and Ω_6 indicate the rigidity and viscosity of host glass matrix. The Ω_2 parameter of the BZLP 0.1Pr glass is greater than those of the earlier reported glasses [31,32,35–37] and is comparable to those of Pr^{3+}doped ZnAlBiB glasses reported by Mahamuda et al. [26]. The higher value of Ω_2 parameter observed for BZLP 0.1Pr glass implies a greater degree of covalency of the Pr^{3+} ions bonding with the oxygen ligand, which is verified by the bonding parameters listed in Table 2 and may also be an indication of a greater degree of asymmetry in the ion sites around the Pr^{3+} ions. In contrast, higher value of Ω_4 implies more rigidty of host medium around the Pr^{3+} ions [38,39]. For the present glass system, J-O intensity parameter Ω_4 increases as the concentration of Pr^{3+} ions rises from BZLP:0.01Pr to BZLP:0.1Pr and then decreases up to BZLP:2.5Pr. Greater the value of Ω_4 intensity parameter for prepared glasses indicates the rigidty of host material in which Pr^{3+} ions are located [26].

The optical band gap is a vital parameter and was calculated for Pr^{3+} ions doped BZLP glass samples based on recorded absorption spectra. According to Davis and Mott's relation, the optical band gap for glass samples was estimated through the following relation [14]:

$$\alpha(\nu) = \left(\frac{B}{h\nu}\right)\left(h\nu - E_{opt}\right)^n \quad (4)$$

here, $h\nu$ denotes the incident photon energy, E_{opt} signifies the optical energy band gap, B stands for the band tailing parameter, n is an index number.The type of transition depends on the value of parameter n. For direct and indirect permissible transitions, the prescribed values are $n =$ ½ and $n = 2$ respectively. The value of $\alpha(\nu)$ was estimated using the following expression [40]:

Table 2
Experimental (f_{exp}) (x10^{-6}), calculated (f_{cal}) (x10^{-6}) oscillator strengths, r.m.s deviation (δ_{rms}), nephelauxetic ratio ($\bar{\beta}$), and bonding parameters (δ) for Pr^{3+} ions in BZLP glasses.

Transitions from $^3H_4$→	BZLP:0.01Pr		BZLP:0.05Pr		BZLP:0.1Pr		BZLP:0.5Pr		BZLP:1.0Pr		BZLP:1.5Pr		BZLP:2.0Pr		BZLP:2.5Pr	
	f_{cal}	f_{exp}	f_{exp}	f_{cal}	f_{exp}	f_{cal}	f_{exp}	f_{cal}	f_{exp}	f_{cal}	f_{exp}	f_{cal}	f_{exp}	f_{cal}	f_{exp}	f_{cal}
$^3F_2$	4.76	4.73	5.79	5.76	9.73	9.72	5.74	5.75	4.21	4.22	4.09	4.11	3.95	3.98	3.73	3.76
$^3F_3$	6.05	6.31	6.83	7.18	10.4	10.3	6.89	6.50	5.55	5.22	5.12	4.70	4.67	3.99	4.56	3.83
$^3F_4$	–	–	3.5	3.64	3.65	5.05	1.87	3.18	1.63	2.55	1.43	2.30	0.37	1.65	0.21	1.56
$^1D_2$	–	–	8.77	1.17	12.8	1.65	5.86	1.04	4	0.84	2.78	0.75	2.67	0.60	2.63	0.581
$^3P_0$	5.72	5.18	6.03	3.94	6.54	5.94	2.36	3.79	1.93	3.15	1.32	2.75	1	3.13	0.78	3.10
$^3P_1$	–	–	2.29	4.01	2.66	6.04	2.3	3.86	2.22	3.21	1.93	2.80	1.81	3.19	1.77	3.16
$^3P_2$	7.61	3.05	7.75	3.71	12.9	5.14	9.28	3.27	5.9	2.65	4.04	2.36	3.88	1.84	3.7	1.76
δ_{rms} (x 10^{-6})	2.29		3.41		5.34		3.06		1.85		1.23		1.55		1.58	
$\bar{\beta}$	0.997		0.995		0.994		0.993		0.998		0.998		0.997		0.997	
δ	0.03		0.05		0.06		0.07		0.12		0.15		0.20		0.21	
																0.2115

Table 3
Judd-Ofelt Parameters ($\Omega_\lambda \times 10^{-20} cm^2$) of Pr^{3+} ions in BZLP glasses along with various reported hosts.

Glass System	Ω_2	Ω_4	Ω_6	Trend	References
BZLP: 0.01Pr	2.57	5.20	3.05	$\Omega_4 > \Omega_2 > \Omega_6$	Present work
BZLP: 0.05Pr	5.34	5.40	4.47	$\Omega_4 > \Omega_2 > \Omega_6$	Present work
BZLP: 0.1Pr	7.86	9.98	5.88	$\Omega_4 > \Omega_2 > \Omega_6$	Present work
BZLP: 0.5Pr	4.94	5.45	3.67	$\Omega_4 > \Omega_2 > \Omega_6$	Present work
BZLP: 1.0Pr	3.48	4.00	2.87	$\Omega_4 > \Omega_2 > \Omega_6$	Present work
BZLP: 1.5Pr	3.23	3.38	2.50	$\Omega_4 > \Omega_2 > \Omega_6$	Present work
BZLP: 2.0Pr	3.03	3.22	1.61	$\Omega_4 > \Omega_2 > \Omega_6$	Present work
BZLP: 2.5Pr	2.87	3.72	1.48	$\Omega_4 > \Omega_2 > \Omega_6$	Present work
$(Ge_{30}Ga_5Se_{65})_{100-x}$ $(Pr_2 Se_3)x$	6.00	16.8	5.00	$\Omega_4 > \Omega_2 > \Omega_6$	[31]
$59.99TeO_2$ –$25WO_3$ – $15PbF_2$ – $0.01Pr_6O_{11}$	4.782	6.148	2.208	$\Omega_4 > \Omega_2 > \Omega_6$	[32]
TeWLiK	8.56	9.64	2.80	$\Omega_4 > \Omega_2 > \Omega_6$	[33]
TeWNaK	9.39	9.55	2.81	$\Omega_4 > \Omega_2 > \Omega_6$	[33]
Phosphate	4.19	4.29	6.40	$\Omega_6 > \Omega 2 > \Omega_4$	[35]
Mixed halide	2.70	4.40	5.40	$\Omega_6 > \Omega 2 > \Omega_4$	[36]
ZnAlBiB 1.0Pr	7.36	4.46	4.17	$\Omega_2 > \Omega 4 > \Omega_6$	[26]
ZBP5	3.94	1.34	1.23	$\Omega_2 > \Omega_4 > \Omega_6$	[37]
$40GaS_{3/2}$.$40GeS_2$.20Cs	9.05	7.26	7.28	$\Omega_2 > \Omega_6 > \Omega_4$	[34]

$$\alpha(\nu) = \left(\frac{1}{d}\right) ln\left(\frac{I_0}{I_T}\right) \quad (5)$$

Here, the thickness of glass denotes by d. The absorbance varies by a factor of $ln\ (I_0\ /I_T)$. The E_{opt} values were acquired for indirect allowed transitions by extrapolating the linear section of the Tauc's plot [$(ah\nu)^{1/n}$ versus $(h\nu)$] as presented in Fig. 3 with $n = 2$. The estimated bandgap E_{opt} values for Pr^{3+} ions doped BZLP glass samples have been listed in Table 1 and lie in the range 3.48–4.07 eV.

3.4. PL characteristics of glass

PL excitation spectrum of BZLP1.0Pr glass sample was recorded in 400–500 nm range with monitoring emission wavelength $\lambda_{em} = 604$ nm and has been presented in Fig. 4. Three excitation peaks ascribed to $^3H_4 \rightarrow {}^3P_2$, $^3P_1$,$^3P_0$ transitions of Pr^{3+} ions, respectively can be seen. The most intense excitation was seen at 445 nm corresponding to $^3H_4 \rightarrow {}^3P_2$ transition and this was selected for recording the photoluminescence emission spectra of all prepared glass samples at room temperature [27].

The PL emission spectra of Pr^{3+}doped BZLP glasses at $\lambda_{ex} = 445$ nm have been presented in Fig. 5. Emission peaks were noticed at 604, 616 and 647 nm corresponding to $^1D_2 \rightarrow {}^3H_4$, $^3P_0 \rightarrow {}^3H_6$ and $^3P_0 \rightarrow {}^3F_2$ transitions of Pr^{3+} ions respectively. Among the emission peaks, the dominant one is due to $^1D_2 \rightarrow {}^3H_4$ transition at 604 nm. In the emission spectra ranging between 600 and 620 nm, emission bands ($^1D_2 \rightarrow {}^3H_4$ and $^3P_0 \rightarrow {}^3H_6$) are observed, which are overlapped in proximity. The peak observed in the red region: $^3P_0 \rightarrow {}^3H_6$ has better sharpness as the concentration of Pr^{3+} ions is increased beyond 0.5 mol% while $^1D_2 \rightarrow {}^3H_4$ transition loses its sharpness at this concentration. The band maxima shifts from 604 nm to 616 nm as the concetration of dopant ion is increased [41–43]. The intensity of the peaks increased with increase in Pr^{3+} ions content up 0.1 mol% and decreased afterwards. This is due to concentration quenching. This occurs as soon as the interionic distance among the Pr^{3+} ions becomes lesser than the critical distancei.e the minimum distance between two doping ions. In this condition, the energy migration amongst dopant Pr^{3+} ions happens via radiationless transfer either by multiphonon or cross-relaxation process [44].The inset plot of Fig. 5 demonstrates the change in PL intensity with concetration of Pr^{3+} ions in BZLP glasses.

The excitations, non-radiative and radiative emissions of Pr^{3+} ions in BZLP glass and cross-relaxation channels (CRC) were well clarified by the energy level diagram as demonstrated in Fig. 6. The energy level diagram shows the absorption of specific energy and subsequently movement of ions from the ground state to a specific excited state. After a certain time, the excited ions return to the ground level via radiationless and radiative emissions. As per the energy of presented levels of Pr^{3+}, the possible CRC responsible for the concentration quenching are as below [26]:

CRC 1: $^3P_0 + {}^3H_4 \rightarrow {}^1D_2 + {}^3H_6$

CRC 2: $^3P_0 + {}^3H_4 \rightarrow {}^3H_6 + {}^1D_2$

CRC 3: $^3P_0 + {}^3H_4 \rightarrow {}^1G_4 + {}^1G_4$

The non-radiative energy transfer takes place in rare-earth-doped luminescent materials due to the multipolar interaction among dopant ions. Dexter theory predicts three kinds of mechanisms for interionic multipolar interactions between the dopant ions. As per the theory the PL intensity is related to the amount of doping ion content in the host system as [45]:

$$log\left(\frac{I}{c}\right) = logf - \frac{s\ log(c)}{d} \quad (6)$$

here I denotes the PL intensity, c is the Pr^{3+} ion concentration in BZLP glass samples, d denotes the dimension of the compound having the value of $d = 3$. f signifies a constant, which is unaffected by doping ion concentration. The parameter s describes the type of multipolar

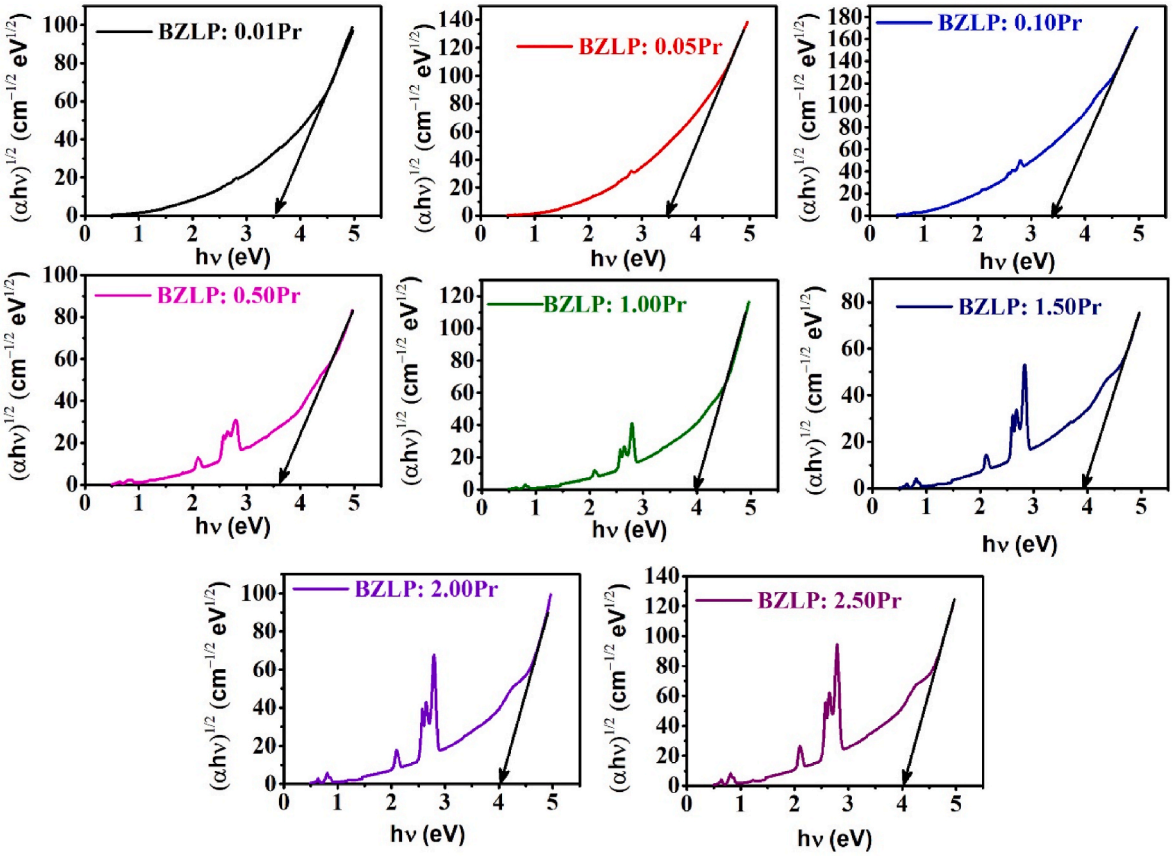


Fig. 3. Indirect bandgap plot of Pr^{3+} doped BZLP glasses with varying concentration from 0.01 to 2.50 mol%.

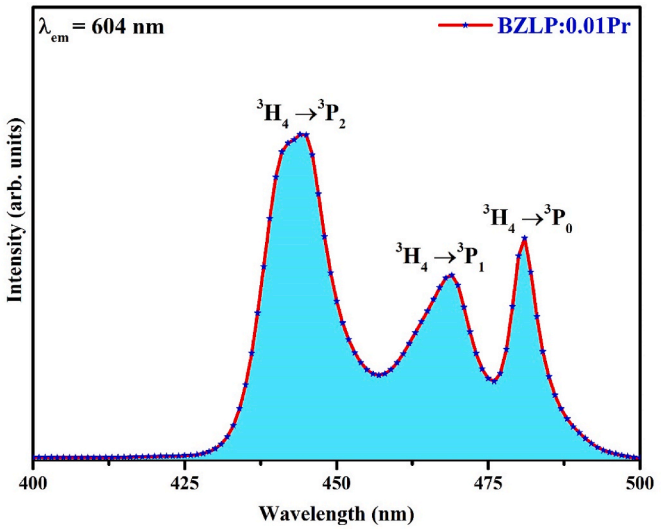


Fig. 4. The excitation spectrum recorded for BZLP:0.01Pr glass under 604 emission wavelength.

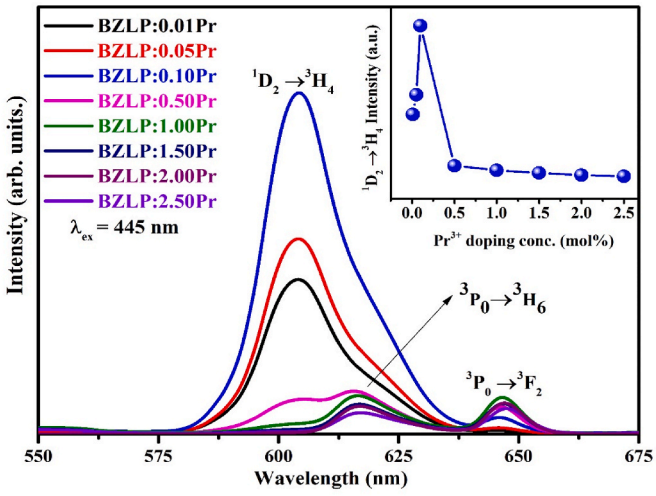


Fig. 5. Emission spectra of Pr^{3+} doped BZLP glasses with varying the doping concentration from 0.01 to 2.50 mol%. Inset plot shows the variation of the emission intensity related to $^1D_2 \rightarrow {}^3H_4$ transition with Pr^{3+} ions concentration.

interaction within the adjacent Pr^{3+} ions in BZLP glass samples. The value of parameter *s* is 6 for dipole-dipole interaction, 8 for dipole-quadrupole inetraction and 10 for quadrupole-quadrupole multipolar interaction [16]. For this research work, the value of parameter *s* was estimated using the slope of the linear fitted plot of $log\ (I/c)$ versus $log(c)$ as shown in Fig. 7 and was found to be 1.485. Therefore the estimated value of parameter *s* was 4.455 which is close to 6. This proves that the non-radiative multipolar interaction between the Pr^{3+} ions is dipole-dipole in nature. In accordance with Dexter Theory, the emission and absorption spectrum of doped glasses will overlap. The visible range emission and absorption spectrum of the $^1D_2$ transition, as well as the cross relaxation channel overlap as shown in Fig. 8 [44]. This spectral overlap enables us to comprehend the resonant energy transfer between excited and unexcited Pr^{3+} ions.

The photoluminescence performance for Pr^{3+} doped BZLP glasses is estimated by calculating the parameters like radiative transition probability (A_R), total transition probability (A_T),radiative lifetime (τ_R) and

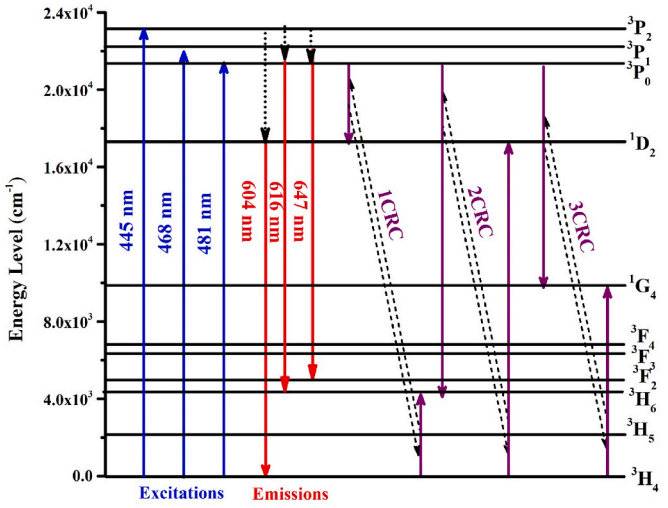


Fig. 6. Energy level diagram of Pr^{3+} doped BZLP glasses.

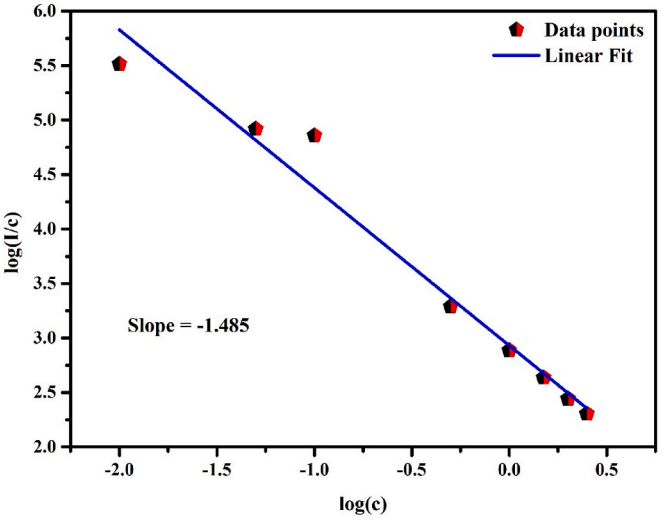


Fig. 7. Relation between log (I/c) and log (c) for different concentrations of Pr^{3+}.

luminescence branching ratio (β_R) with the aid of J-O intensity parameters measured from the absorption spectra. These parameters have been listed in Table 3. To explore the luminescent process, the radiative transition probability (A_R) for flouroscent levels can be computed by using the following equation [46]:

$$A_R(a_J, b_{J'}) = \frac{64\pi^4 \vartheta}{3h(2J+1)}\left[\frac{n(n^2+2}{9} s_{ed}(a_J, b_{J'}) + n^3 S_{md}(a_J, b_{J'})\right] \quad (7)$$

The total transition probability (A_T) for flouroscent levels can be computed by using the following equation [46]:

$$A_T = \sum_{b_{J'}} A_R(a_j, b_{j'}) \quad (8)$$

The radiative lifetime $\tau_R\ (a_j, b_{j'})$ and the luminescence branching ratio $\beta_R\ (a_j, b_{j'})$ from a ground state a_j to an excite state $b_{j'}$ are given by [46]:

$$\tau_R(a_j, b_{j'}) = \frac{1}{\sum_{b_{j'}} A_R(a_j, b_{j'})} \quad (9)$$

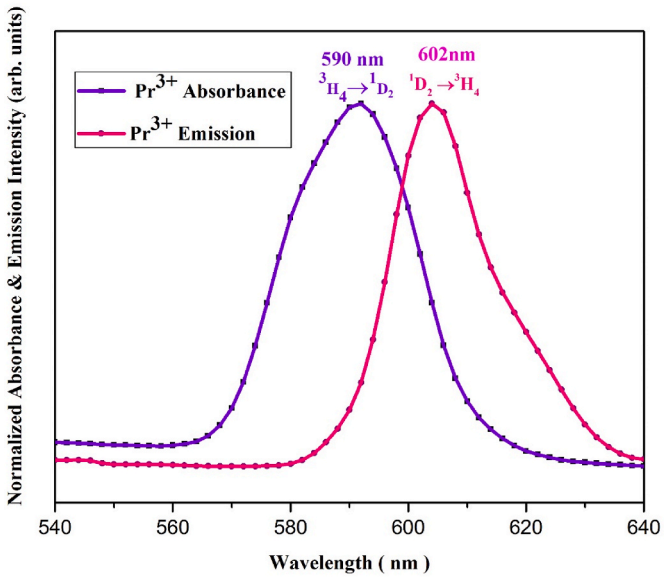


Fig. 8. Spectral overlap of absorbance & emission spectrum of BZLP:0.1 glass for transition $^1D_2 \rightarrow {}^3H_4$.

$$\beta_R\ (a_j, b_{j'}) = A_R(a_j, b_{j'}).\tau_R(a_j, b_{j'})$$

An essential parameter is stimulated emission cross-section (σ_{se}) and its value dictates high gain and low threshold for lasing applications. It is given by the following expression [46,47]:

$$\sigma_{se} = \frac{\lambda_p^4}{8\pi c n^2 \Delta\lambda_p} A_R \quad (10)$$

Where λ_p represents the peak wavelength, $\Delta\lambda_p$ is the effective width of the emission transition and c, n and A_R symbolize speed of light in free space, refractive index and radiative transition probability of flouroscent levels respectively.

A_R, A_T, β_R and τ_R radiatitve parameters computed for Pr^{3+} doped BZLP glasses for all fluoroscent transitions are listed in Table 4. Other radiative parameters like λ_p (peak wavelength), $\Delta\lambda_p$ (effective band width), β_R, β_{exp} (radiative and experimental brnching ratio) , σ_{se}(stimulated emission cross section), σ_{se} x $\Delta\lambda p$ (gain bandwidth) and σ_{se} x τ_R (optical gain parameters) are represented in Table 5 for all reported glasses. Fluoroscent Branching ratio (β_R) is another significant parameter for lasing action and its value should be around 0.5. From Tables 5

Table 4
Transition probability (A_R) (s^{-1}), luminescence branching ratio (β_R), total transition probability (A_T) (s^{-1}) and radiative lifetime (τ_R) (μs) for the observed emission transitions of Pr^{3+} ions in BZLP glass.

Sample name	Transition	A_R	A_T	β_R	τ_R
BZLP: 0.01Pr	$^3P_1 \rightarrow {}^3F_3$	10071.61	48833.47	0.2062	20
	$^1D_2 \rightarrow {}^3H_4$	978.62	3947.08	0.2479	253
BZLP: 0.05Pr	$^3P_1 \rightarrow {}^3F_3$	17721.88	66333.76	0.2672	15
	$^1D_2 \rightarrow {}^3H_4$	1372.52	6371.21	0.2154	156
BZLP: 0.1Pr	$^3P_1 \rightarrow {}^3F_3$	32900.21	110698.7	0.2972	9
	$^1D_2 \rightarrow {}^3H_4$	2001.65	11082.17	0.1806	90
BZLP: 0.5Pr	$^3P_1 \rightarrow {}^3F_3$	19264.42	68643.08	0.2806	14
	$^1D_2 \rightarrow {}^3H_4$	1293.03	6665.77	0.194	150
BZLP: 1.0Pr	$^3P_1 \rightarrow {}^3F_3$	13848.99	54324.4	0.2549	18
	$^1D_2 \rightarrow {}^3H_4$	1073.6	5003.91	0.2146	199
BZLP: 1.5Pr	$^3P_1 \rightarrow {}^3F_3$	13504.31	51079.94	0.2644	19
	$^1D_2 \rightarrow {}^3H_4$	1000.98	4811.39	0.208	207
BZLP: 2.0Pr	$^3P_1 \rightarrow {}^3F_3$	13605.71	53053.52	0.2565	18
	$^1D_2 \rightarrow {}^3H_4$	816.25	4636.94	0.176	215
BZLP: 2.5Pr	$^3P_1 \ {}^3F_3$	13488.58	52998.95	0.2075	18
$^1D_2 \rightarrow {}^3H_4$		799.31	4589.27	0.1742	217

Table 5
Emission peak wavelength (λ_P)(nm), effective band widths ($\Delta\lambda_P$)(nm), measured and experimental branching ratios (β_R& β_{exp}), stimulated emission cross-sections (σ_{se}) (cm^2), gain band width ($\sigma_{se} \times \Delta\lambda_P$) ($cm^3$) and optical gain parameter ($\sigma_{se} \times \tau_R$) ($cm^2$ s) parameters for the emission transitions for Pr^{3+} ions in BZLP glasses.

Spectral parameters	BZLP:0.01Pr	BZLP:0.05Pr	BZLP:0.1Pr	BZLP:0.5Pr	BZLP:1.0Pr	BZLP:1.5Pr	BZLP:2.0 Pr	BZLP:2.5Pr
$^1D_2 \rightarrow {}^3H_4$								
λ_P	604	604	604	604	604	604	604	604
$\Delta\lambda$p	18.67	18.90	19.54	16.01	14.97	14.50	14.19	15.63
β_R	0.2479	0.2154	0.1806	0.1940	0.2146	0.2080	0.1760	0.1742
β_{exp}	0.88	0.94	0.95	0.37	0.48	0.45	0.56	0.39
σ_{se}	29.20	39.13	53.42	41.21	35.45	32.71	26.97	23.50
$\sigma_{se} \times \Delta\lambda_P$	54.54	73.98	104.41	66.00	53.07	47.45	38.30	36.74
$\sigma_{se} \times \tau_R$	7.39	6.10	4.80	6.18	7.05	6.77	5.79	5.10

and it is noticed that β_R values for high intense transition $^1D_2 \rightarrow {}^3H_4$ decreases as the concentration of Pr^{3+} ions increases up to 0.1 mol% and after that increases as the concentration increases up to 2.5 mol%. This might be due to fluorescent quenching of $^1D_2 \rightarrow {}^3H_4$ transition [26,32,46,48]. Moreover, higher value of stimulated emission cross-section (σ_{se} is essential for luminescent transition thereby showing that the glass can be used as an active medium for laser. From Tables 5 it is noticed that σ_{se} has maximum value for BZPL:0.1Pr glass for transition $^1D_2 \rightarrow {}^3H_4$ transition.

Furthermore, a glassy materials doped with rare earth ions having high values of gain bandwidth (σ_{se} x $\Delta\lambda$p) and optical gain parameters (σ_{se} x τ_R) can be used in construction of optical fibres. As is evident from Table 5, BZLP:0.1Pr glass has high values for all radiatitve parameters as compared to other reported glasses. Therefore, BZLP:0.1Pr i.e 0.1 mol% of Pr^{3+} doped BZLP glass is best fitted for reddish –orange laser transition at 604 nm.

3.5. Colorimetric study

Chromaticity color coordinates of Pr^{3+} doped BZLP glass samples were evaluated based on PL results at $\lambda_{ex} = 445$ nm and have been shown in Table 6. The estimated color coordinates lie in the red region of the CIE chromaticity diagram as shown in Fig. 9. Further, the color purity is one of the vital parameters stating how pure or monochromatic a light for utilization in photonic applications. The color purity (CP) for all the glass samples were calculated via using formula as mention in equation (11) [49,50]:

$$CP\ (\%) = \sqrt{\frac{(x - x_{ee})^2 + (y - y_{ee})^2}{(x_d - x_{ee})^2 + (y_d - y_{ee})^2}}\ x\ 100 \qquad (11)$$

here (x, y) indicates the estimated chromaticity color coordinates, (x_{ee}, y_{ee}) signify the standard white point coordinates (0.33, 0.33) and (x_d, y_d) is coordinates for the maximum wavelength. The calculated color purity for the optimized glass was found to be 98.61%. The highly pure color of the Pr^{3+} doped BZLP glass samples makes them an ideal candidate as a red light-emitting constituent in W-LEDs.

Table 6
CIE co-ordinates of Pr^{3+} ions in BZLP glasses.

Name of the sample	CIE co-ordinates	
	X co-ordinate	*Y* co-ordinate
BZLP: 0.01Pr	0.606	0.386
BZLP: 0.05Pr	0.628	0.363
BZLP: 0.1Pr	0.629	0.367
BZLP: 0.5Pr	0.571	0.416
BZLP: 1.0Pr	0.554	0.4231
BZLP: 1.5Pr	0.544	0.440
BZLP: 2.0 Pr	0.532	0.307
BZLP: 2.5 Pr	0.506	0.469

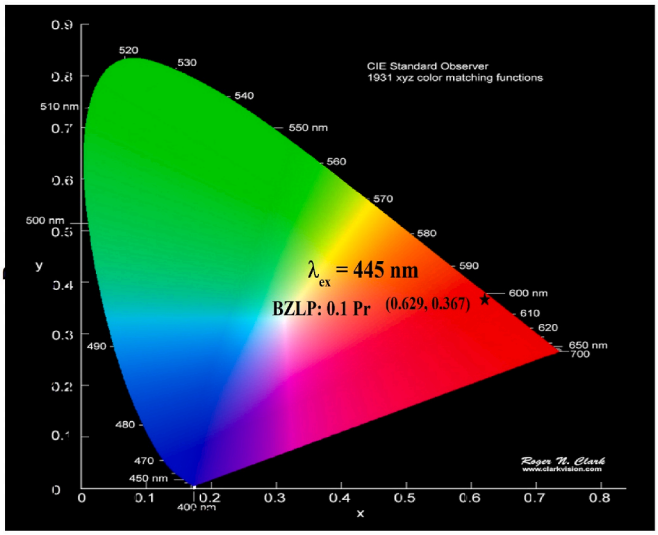


Fig. 9. CIE chromaticity coordinates of BZLP:0.10Pr glass.

3.6. PL decay analysis

PL decay profiles for Pr^{3+} doped BZLP glass samples have been documented at $\lambda_{ex} = 445$ nm and $\lambda_{em} = 604$ nm and shown in Fig. 10. The curves follow an exponential behaviour. The most proper fitting was attained for the bi-exponential function given by Ref. [51]:

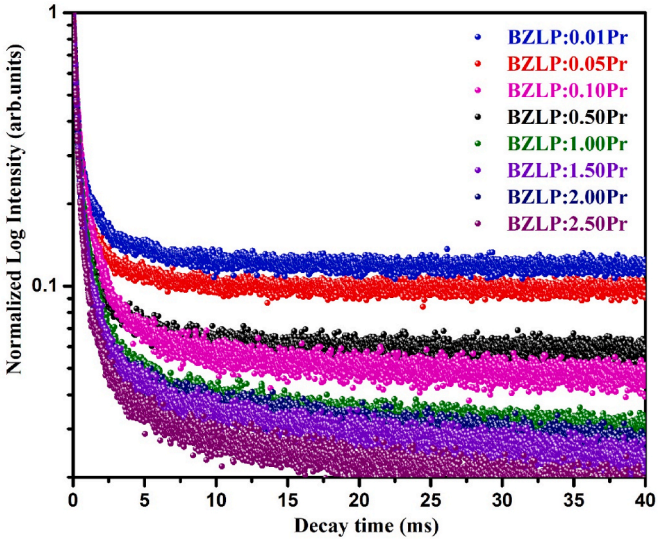


Fig. 10. PL decay curves of Pr^{3+} doped BZLP glasses with varying the doping concentration from 0.01 to 2.50 mol% under 445 nm excitation and emission at 604 nm.

$$I(t) = I_0 + A_1\ exp\left(-\frac{t}{\tau_1}\right) + A_2\ exp\left(-\frac{t}{\tau_2}\right) \quad (12)$$

here τ_1 and τ_2 symbolize slow and fast decay times in the exponential equation, respectively. Two fitting constants in equations designated by A_1 and A_2. $I(t)$ and I_0 are the emission intensities at time $= t$ sec and time $= 0$ s, respectively. The average (τ_{avg}) decay time for Pr^{3+} doped BZLP glass samples was assessed with the help of formula [16,52]:

$$\tau_{avg} = \frac{A_1\tau_1^{\ 2} + A_2\tau_2^{\ 2}}{A_1\tau_1 + A_2\tau_2} \quad (13)$$

The τ_{avg} recorded decay profile of all glass samples was depicted in Table 7. The average decay time decreased with an increase of Pr^{3+} ions in the glass lattice. This is due to reduced distance between the Pr^{3+} ions thereby enhancing the non-radiative energy transfer. The estimated average decay time for BZLP:0.1Pr was $\tau_{avg} = 2.57$ ms which reduced to $\tau_{avg} = 1.23$ ms for BZLP:2.50 Pr glass. From Table 7 it is seen that τ_{exp} values are less than τ_R. This small variation between τ_{exp} and τ_R values arises due to multi phonon relaxation process. In this case τ_{exp} , τ_R and non-radiative decay rate (W_{NR}) are related as:

$$W_{NR} = \frac{1}{\tau_{exp}} - \frac{1}{\tau_R} \quad (14)$$

Table 7 contains the W_{NR} values determined using the aforementioned equation. Another crucial factor utilised to assess the luminescence intensity of reported glasses is the quantum efficiency (η %). By calculating the ratio between τ_{exp} and τ_R, quantum efficieny for prepared glasses has been estimated and presented in Table 7. It is evident from Table 7 that up to 0.1 mol% (BZLP:0.1Pr) glass, the value of η % rises and after that declines with increasing Pr^{3+} ions concentration. Furthermore, Table 8 represents the comparision between several radiative parameters with the other reported glasses in literature [44,53,54]. It has been observed that stimulated emission cross section of the Pr^{3+} BZLP doped glasses have larger value than other reported glasses [53,54] and are comparable with that of Pr^{3+} doped LiPbAlB glass reported by Nisha et al. [44]. From the data in Table 8, BZLP:0.1Pr glass had the best quantum efficiency and stimulated emission cross section as compared to other reported glasses. Therefore, under 445 nm excitation, BZLP:0.1Pr glass is most suited for lasing emission in the reddish orange region.

3.7. Temperature-dependent PL (TD-PL) characteristics

Thermal stability is one of the vital requirements of the luminescent materials for utility in W-LEDs. So, using the temperature dependent-photoluminescence (TD-PL) spectra, the thermal stability of the prepared glass samples was examined.The TD-PL spectra were reported at excitation wavelength of $\lambda_{ex} = 445$ nm as presented in Fig. 11. It is evident that with an increase in temperature from 300 K to 473 K, PL intensity diminishes gradually but the spectral shape/peak position is unaffected. Further, the activation energy (ΔE) was evaluated using the Arrhenius equation [55–57]:

Table 7
Experimental lifetime (τ_{exp}) (μs), radiative lifetime (τ_R) (μs), quantum efficiency (η), and non-radiative decay rates (W_{NR}) (s^{-1}) for Pr^{3+} ions in BZLP glasses.

Sample	τ_{exp} (μs)	τ_R (μs)	η (%)	W_{NR}
BZLP: 0.01Pr	91	253	35.96	7036
BZLP: 0.05Pr	89	156	57.05	4825
BZLP: 0.1Pr	87	90	96.66	383
BZLP: 0.5Pr	86	150	57.33	4961
BZLP: 1.0Pr	85	199	42.71	6739
BZLP: 1.5Pr	83	207	40.09	7217
BZLP: 2.0 Pr	80	215	37.20	7848
BZLP: 2.5 Pr	75	217	34.56	8725

Table 8
Comparison of emission characteristics parameters like effective band widths ($\Delta\lambda_P$)(nm), measured branching ratio (β_R) and stimulated emission cross-sections (σ_{se} x 10^{-22}) (cm^2) of transition $^1D_2 \rightarrow {}^3H_4$ in different Pr^{3+} doped glasses.

Name of the sample	$\Delta\lambda_P$	β_R	σ_{se}	η (%)	References
BZLP: 0.01Pr	18.67	0.2479	29.20	35.96	Present work
BZLP: 0.05Pr	18.90	0.2154	39.13	57.05	Present work
BZLP: 0.1Pr	19.54	0.1806	53.42	96.66	Present work
BZLP: 0.5Pr	16.01	0.1940	41.21	57.33	Present work
BZLP: 1.0Pr	14.97	0.2146	35.45	42.71	Present work
BZLP: 1.5Pr	14.50	0.2080	32.71	40.09	Present work
BZLP: 2.0 Pr	14.19	0.1760	26.97	37.20	Present work
BZLP: 2.5 Pr	15.63	0.1742	23.50	34.56	Present work
0.1 Pr:NaAlGdP	16.50	0.82	27.64	78	[53]
ZNBBP-1	26.48	0.34	16.49	–	[54]
LiPbAlBPr 1.0	18.09	0.41	46.1	86	[44]

$$I_T = \frac{I_0}{1 + C\ exp\left(-\frac{\Delta E}{K_B T}\right)} \quad (15)$$

In above expression I_0 and I_T indicate PL intensity at room temperature 300 K and at any temperature T (in Kelvin), respectively. K_B Symbolizes the Boltzmann constant and C is an arbitrary constant. The value of ΔE was assessed via the slope of the linear fitted plot between $ln((I_0/I_T)-1)$ and $1/K_BT$ as shown in Fig. 12 [49]. The activation energy was found to $\Delta E = 0.175$ eV for BZLP:0.1Pr glass. Inset plot of Fig. 12 reveals the PL intensity reduced from 88.12% at 423 K to 82.61% at 473 K, which shows that glass samples have brilliant thermal stability.

4. Conclusions

Trivalent praseodymium doped BZLP glass samples were synthesised through melt quenching route and their structural,physical and optical properties were studied for utility in luminescent device applications. The diffraction pattern confirmed the unstructured and nonexistent crystalline character of host glass. Absorption spectra showed several bands in ultraviolet, visible and infrared regions. The indirect optical bandgap was estimated using Tauc's plot for each glass and was found to be in the range 3.48–4.07 eV. Using J-O parameters derived from the absorption spectrum, several radiative parameters were assessed for the reported fluorescence peaks of Pr^{3+} ions in BZLP glass samples. The PL spectra at 445 nm excitation shows prominent emission peak at 604 nm due to $^1D_2 \rightarrow {}^3H_4$ transition of Pr^{3+} ions. Beyond 0.10 mol% of Pr^{3+} ion concentration, quenching effect is observed due to dipole-dipole type of interaction between the dopant ions as confirmed by the Dexter plot. For the stransition $^1D_2 \rightarrow {}^3H_4$, stimulated emission cross-section,branching ratios and quantum efficiency were assessed. The CIE coordinates for the as prepared glasses fall in deep-red region. The average lifetime values at $\lambda_{ex} = 445$ nm for 604 nm emission were observed to decrease with an increase in Pr^{3+} ion content in BZLP glasses. The TD-PL study shows that the glass has an excellent thermal stability with activation energy $\Delta E = 0.175$ eV. After analysing the several evaluated radiative parameters, it was revealed that amongst all the Pr^{3+} doped BZLP glass samples, BZLP:0.1Pr glass can be used as a deep red-emitting component in blue pumped white LED and other luminescent device applications.

CRediT authorship contribution statement

Kartika Maheshwari: Writing, experimentation, Conceptualization, synthesis of samples. **Ravita:** Formal analysis. **Aman Prasad:** Formal analysis, editing, writing. **Yasha Tayal:** Formal analysis. **A.S. Rao:** Supervision, Writing – review and editing.

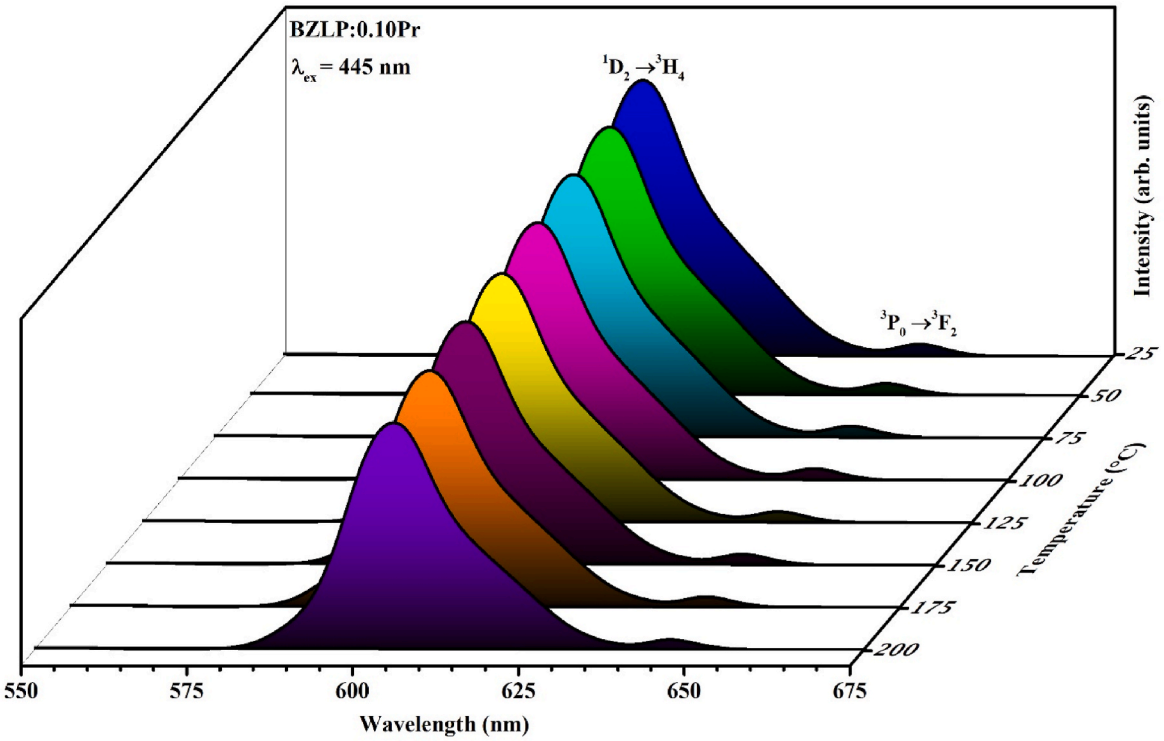


Fig. 11. TD-PL spectra of optimized BZLP:0.10Pr glass with temperature varying from 27 °C to 200 °C under 445 nm excitation wavelength.

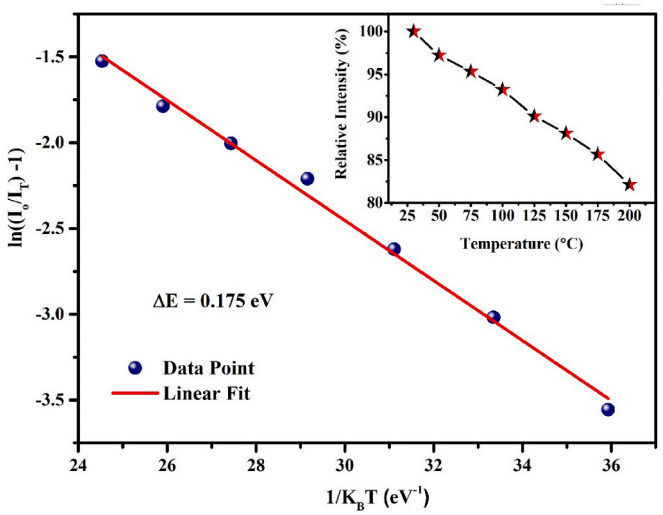


Fig. 12. Graph between $\ln[(I_o/I_T)-1]$ and $(1/K_BT)$ for BZLP:0.10Pr glass. The inset plot shows the decrease in relative emission intensity with rise in temperature from 27 °C to 200 °C.

Declaration of competing interest

The authors declare that they have no known competing financial interests or personal relationships that could have appeared to influence the work reported in this paper.

Data availability

The authors do not have permission to share data.

Acknowledgments

The authors are thankful to Delhi Technological University, Delhi for providing the necessary infrastructure and a conducive work environment to perform this research.

References

[1] A.S. Rao Ravita, Effective energy transfer from Dy^{3+} to Tb^{3+} ions in thermally stable KZABS glasses for intense green emitting device applications, J. Lumin. 239 (2021), 118325, https://doi.org/10.1016/j.jlumin.2021.118325.

[2] T.H. Kim, W. Wang, Q. Li, Advancement in materials for energy-saving lighting devices, Front. Chem. Sci. Eng. 6 (2012) 13–26, https://doi.org/10.1007/s11705-011-1168-y.

[3] X. Chen, P. Dai, X. Zhang, C. Li, S. Lu, X. Wang, Y. Jia, Y. Liu, Phosphor via dual energy transfers for white light-emitting diodes, Inorg. Chem. 53 (2014) 3441–3448.

[4] R.J. Xie, N. Hirosaki, N. Kimura, K. Sakuma, M. Mitomo, 2-Phosphor-Converted white light-emitting diodes using oxynitride/nitride phosphors, Appl. Phys. Lett. 90 (2007), 191101, https://doi.org/10.1063/1.2737375.

[5] J. Chen, Y. Liu, L. Mei, H. Liu, M. Fang, Z. Huang, Crystal structure and temperature-dependent luminescence characteristics of $KMg_4(PO_4)_3:Eu^{(2+)}$ phosphor for white light-emitting diodes, Sci. Rep. 5 (2015) 9673, https://doi.org/10.1038/srep09673.

[6] S.M. Rafiaei, A. Bahrami, The effects of boric acid on crystal structure, nano-/microstructure and photoluminescence characteristics of rare earth-doped Y_2O_3/YBO_3 composite compounds, J. Nanostructure Chem. 7 (2017) 367–373, https://doi.org/10.1007/s40097-017-0246-1.

[7] N. Deopa, A.S. Rao, Photoluminescence and energy transfer studies of Dy^{3+} ions doped lithium lead alumino borate glasses for w-LED and laser applications, J. Lumin. 192 (2017) 832–841, https://doi.org/10.1016/j.jlumin.2017.07.052.

[8] N. Deopa, A.S. Rao, Spectroscopic studies of Sm^{3+} ions activated lithium lead alumino borate glasses for visible luminescent device applications, Opt. Mater. 72 (2017) 31–39, https://doi.org/10.1016/j.optmat.2017.04.067.

[9] R.A. Talewar, S. Mahamuda, K. Swapna, A.S. Rao, Sensitization of Yb^{3+} by Nd^{3+} emission in alkaline-earth chloro borate glasses for laser and fiber amplifier applications, J. Alloys Compd. 771 (2019) 980–986, https://doi.org/10.1016/j.jallcom.2018.08.270.

[10] K. Jha, M. Jayasimhadri, D. Haranath, K. Jang, Influence of modifier oxides on spectroscopic properties of Eu^{3+} doped oxy-fluoro tellurophosphate glasses for visible photonic applications, J. Alloys Compd. 789 (2019) 622–629, https://doi.org/10.1016/j.jallcom.2019.02.277.

[11] J. Gou, J. Fan, S. Zuo, M. Luo, Y. Chen, X. Zhou, Y. Yang, B. Yu, S.F. Liu, Highly thermally stable and emission color tunable borate glass for white-light-emitting

diodes with zero organic resin, J. Am. Ceram. Soc. 100 (2017) 4011–4020, https://doi.org/10.1111/jace.14951.
[12] M. Jayasimhadri, K. Jang, H.S. Lee, B. Chen, S.S. Yi, J.H. Jeong, White light generation from Dy^{3+} -doped ZnO- B_2O_3 - P_2O_5 glasses, J. Appl. Phys. 106 (2009), https://doi.org/10.1063/1.3159899.
[13] K. Maheshwari, A.S. Rao, Photoluminescence downshifting studies of thermally stable Dy^{3+} ions doped phosphate glasses for photonic device applications, Opt. Mater. 129 (2022), 112518, https://doi.org/10.1016/J.OPTMAT.2022.112518.
[14] K. Jha, M. Jayasimhadri, Structural and emission properties of Eu^{3+} -doped alkaline earth zinc - phosphate glasses for white LED applications, J. Am. Ceram. Soc. (2017) 1402–1411, https://doi.org/10.1111/jace.14668.
[15] C. Zuo, Z. Zhou, L. Zhu, A. Xiao, Y. Chen, X. Zhang, X. Ding, Q. Ge, Spectroscopic properties of Ce^{3+}-doped borosilicate glasses under UV excitation, Mater. Res. Bull. 83 (2016) 155–159, https://doi.org/10.1016/j.materresbull.2016.06.001.
[16] N. Deopa, B. Kumar, M.K. Sahu, P.R. Rani, A.S. Rao, Effect of Sm^{3+} ions concentration on borosilicate glasses for reddish orange luminescent device applications, J. Non-Cryst. Solids 513 (2019) 152–158, https://doi.org/10.1016/j.jnoncrysol.2019.03.025.
[17] M. Kumar, A.S. Rao, Concentration-dependent reddish-orange photoluminescence studies of Sm^{3+} ions in borosilicate glasses, Opt. Mater. 109 (2020), 110356, https://doi.org/10.1016/j.optmat.2020.110356.
[18] C.B. Annapurna Devi, S. Mahamuda, M. Venkateswarlu, K. Swapna, A. Srinivasa Rao, G. Vijaya Prakash, Dy^{3+} ions doped single and mixed alkali fluoro tungsten tellurite glasses for Laser and white LED applications, Opt. Mater. 62 (2016) 569–577, https://doi.org/10.1016/j.optmat.2016.11.016.
[19] Ravita, A. Prasad, P. Rohilla, A. Shandilya, A.S. Rao, Photoluminescence and energy transfer studies on Tm^{3+}/Dy^{3+}/Eu^{3+}doped borosilicate glasses for color tunability and warm white light generation, J. Non-Cryst. Solids 606 (2023) 122192, doi:10.1016/j.jnoncrysol.2023.122192.
[20] W. Hordijk, G. Blasse, Energy transfer by sensitizer-activator pairing in calcium sulphate, J. Lumin. 6 (1973) 137–139, https://doi.org/10.1016/0022-2313(73)90050-1.
[21] K.R. Vighnesh, B. Ramya, S. Nimitha, A. Wagh, M.I. Sayyed, E. Sakar, H.A. Yakout, A. Dahshan, S.D. Kamath, Structural, optical, thermal, mechanical, morphological & radiation shielding parameters of Pr^{3+} doped ZAlFB glass systems, Opt. Mater. 99 (2020), 109512, https://doi.org/10.1016/j.optmat.2019.109512.
[22] C.Y. Morassuti, L.H.C. Andrade, J.R. Silva, M.L. Baesso, F.B. Guimarães, J. H. Rohling, L.A.O. Nunes, G. Boulon, Y. Guyot, S.M. Lima, Spectroscopic investigation and interest of Pr^{3+} -doped calcium aluminosilicate glass, J. Lumin. 210 (2019) 376–382, https://doi.org/10.1016/j.jlumin.2019.02.051.
[23] D. Manzani, D. Pabœuf, S.J.L. Ribeiro, P. Goldner, F. Bretenaker, Orange emission in Pr^{3+}-doped fluoroindate glasses, Opt. Mater. 35 (2013) 383–386, https://doi.org/10.1016/j.optmat.2012.09.030.
[24] Ravita, A. S.Rao, Effective sensitization of Eu^{3+} visible red emission by Sm^{3+} in thermally stable potassium zinc alumino borosilicate glasses for photonic device applications, J. Lumin. (2021) 118689, doi:10.1016/j.jlumin.2021.118689.
[25] P.P. Pawar, S.R. Munishwar, R.S. Gedam, Physical and optical properties of Dy^{3+}/Pr^{3+} Co-doped lithium borate glasses for W-LED, J. Alloys Compd. 660 (2016) 347–355, https://doi.org/10.1016/J.JALLCOM.2015.11.087.
[26] S. Mahamuda, K. Swapna, A. Srinivasa Rao, T. Sasikala, L. Rama Moorthy, Reddish-orange emission from Pr^{3+} doped zinc alumino bismuth borate glasses, Phys. B Condens. Matter 428 (2013) 36–42, https://doi.org/10.1016/j.physb.2013.07.010.
[27] W.T. Carnall, P.R. Fields, K. Rajnak, Electronic energy levels of the trivalent lanthanide aquo ions. I. Pr^{3+}, Nd^{3+}, Pm^{3+}, Sm^{3+}, Dy^{3+}, Ho^{3+}, Er^{3+} and Tm^{3+}, J. Chem. Phys. 49 (1968) 4424–4442, https://doi.org/10.1063/1.1669893.
[28] T.H.S. Tanabe, T. Ohyagi, N. Soga, Compositional dependence of judd-ofelt parameters of Er^{3+} ions in alkali- metal borate glasses, Phys. Rev. B 46 (2018) 3305, https://doi.org/10.1103/PhysRevB.46.3305.
[29] M.B. Saisudha, J. Ramakrishna, Optical absorption of Nd $^{3+}$, Sm $^{3+}$ and Dy $^{3+}$ in bismuth borate glasses with large radiative transition probabilities, Opt. Mater. 18 (2002) 403–441, https://doi.org/10.1016/S0925-3467(01)00181-1.
[30] S. Mahamuda, K. Swapna, M. Venkateswarlu, A.S. Rao, S.L. Shakya, G.V. Prakash, Spectral characterization of Sm^{3+} ions doped oxy-fluoroborate glasses for visible orange luminescent applications, J. Lumin. (2014), https://doi.org/10.1016/j.jlumin.2014.05.017.
[31] P Nemec, M. Frumar, Synthesis and properties of Pr $^{3+}$ -doped Ge – Ga – Se glasses, J. Non-Cryst. Solids 302 (2002) 1018–1022, https://doi.org/10.1016/S0022-3093(01)01127-9.
[32] M. Venkateswarlu, M.V.V.K.S. Prasad, K. Swapna, S. Mahamuda, Pr $^{3+}$ doped lead tungsten tellurite glasses for visible red lasers, Ceram. Int. 40 (2014) 6261–6269, https://doi.org/10.1016/j.ceramint.2013.11.084.
[33] C.B. Annapurna, S. Mahamuda, K. Swapna, M. Venkateswarlu, A.S. Rao, G. V. Prakash, Pr^{3+} ions doped single alkali and mixed alkali fluoro tungsten tellurite glasses for visible red luminescent devices, J. Non-Cryst. Solids 498 (2018) 345–351, https://doi.org/10.1016/j.jnoncrysol.2018.03.034.
[34] L. Sojka, Z. Tang, D. Furniss, H. Sakr, A. Oladeji, E.B. Pawlik, H. Dantanarayana, E. Faber, A.B. Seddon, T.M. Benson, S. Sujecki, Broadband, mid-infrared emission from Pr^{3+} doped GeAsGaSe chalcogenide fiber, optically clad, Opt. Mater. 36 (2014) 1076–1082, https://doi.org/10.1016/j.optmat.2014.01.038.
[35] M. Czaja, Optical properties of Pr^{3+} , Sm^{3+} and Er^{3+} doped P $_2$O $_5$ – CaO – SrO – BaO phosphate glass, Opt. Mater. 32 (2010) 547–553, https://doi.org/10.1016/j.optmat.2009.11.011.
[36] M.A. Newhouse, R.F. Bartholomew, B.G. Aitken, L.J. Button, N.F. Borrelli,Pr-doped mixed-halide glasses for 1300 nm amplification, IEEE Photon. Technol. Lett. 6 (1994) 189–191.
[37] I. Pal, A. Agarwal, S. Sanghi, M.P. Aggarwal, Structural , absorption and fluorescence spectral analysis of Pr3+ ions doped zinc bismuth borate glasses 509 (2011) 7625–7631, https://doi.org/10.1016/j.jallcom.2011.04.114.
[38] M. Vijayakumar, K. Marimuthu, Structural and luminescence properties of Dy^{3+} doped oxyfluoro-borophosphate glasses for lasing materials and white LEDs, J. Alloys Compd. 629 (2015) 230–241, https://doi.org/10.1016/j.jallcom.2014.12.214.
[39] V.H. Rao, P.S. Prasad, K.S. Babu, Visible luminescence characteristics of Pr $^{3+}$ ions in TeO $_2$ – Sb $_2$O $_3$ – WO_3 glasses, Opt. Mater. 101 (2020), 109740, https://doi.org/10.1016/j.optmat.2020.109740.
[40] K. Jha, M. Jayasimhadri, Spectroscopic investigation on thermally stable Dy^{3+} doped zinc phosphate glass for white light emitting diodes, J. Alloys Compd. 688 (2016) 833–840, https://doi.org/10.1016/j.jallcom.2016.07.024.
[41] M. So, A. Górny, L. Zur, M. Ferrari, G.C. Righini, W.A. Pisarski, J. Pisarska, White light emission through energy transfer processes in barium gallo- germanate glasses co-doped with Dy $^{3+}$ -Ln $^{3+}$ (Ln = Ce , Tm), Opt. Mater. 87 (2019) 63–69, https://doi.org/10.1016/j.optmat.2018.05.071.
[42] H.H. Caspers, H.E. Rast, R.A. Buchanan, Energy levels of Pr^{3+} in LaF_3, J. Chem. Phys. 43 (1965) 2124, https://doi.org/10.1063/1.1697083.
[43] P. Ramakrishna, R.K. Padhi, S. Kumar, D.K. Mohapatra, H. Jena, B.S. Panigrahi, Effect of U on the photoluminescence of Pr and structural properties of U/Pr doped and co-doped Li $_2$ O – ZnO – SrO borophosphate glass, Opt. Mater. 134 (2022), 113121, https://doi.org/10.1016/j.optmat.2022.113121.
[44] N. Deopa, A.S. Rao, S. Mahamuda, M. Gupta, M. Jayasimhadri, D. Haranath, G. V. Prakash, Spectroscopic studies of Pr^{3+} doped lithium lead alumino borate glasses for visible reddish orange luminescent device applications, J. Alloys Compd. 708 (2017) 911–921, https://doi.org/10.1016/j.jallcom.2017.03.020.
[45] Y. Tayal, A.S. Rao, Spectroscopic analysis of Dy^{3+} ions activated borosilicate glasses for photonic device applications, Opt. Mater. 117 (2021), 111112, https://doi.org/10.1016/j.optmat.2021.111112.
[46] D.V.R. Murthy, B.C. Jamalaiah, T. Sasikala, L. Rama Moorthy, M. Jayasimhadri, K. Jang, H.S. Lee, S.S. Yi, J.H. Jeong, Optical absorption and emission characteristics of Pr^{3+}-doped RTP glasses, Phys. B Condens. Matter 405 (2010) 1095–1100, https://doi.org/10.1016/J.PHYSB.2009.11.012.
[47] P. Karthikeyan, R. Vijayakumar, K. Marimuthu, Luminescence studies on Dy^{3+} doped calcium boro-tellurite glasses for White light applications, Phys. B Condens. Matter 521 (2017) 347–354, https://doi.org/10.1016/j.physb.2017.07.018.
[48] G. Lakshminarayana, K.M. Kaky, S.O. Baki, S. Ye, A. Lira, I.V. Kityk, M.A. Mahdi, Concentration dependent structural, thermal, and optical features of Pr^{3+}-doped multicomponent tellurite glasses, J. Alloys Compd. 686 (2016) 769–784, https://doi.org/10.1016/j.jallcom.2016.06.069.
[49] G. Zhu, Z. Li, C. Wang, X. Wang, F. Zhou, M. Gao, S. Xin, Y. Wang, Highly Eu $^{3+}$ ions doped novel red emission solid solution phosphors Ca $_{18}$ Li $_3$ (Bi,Eu)(PO $_4$) $_{14}$: structure design, characteristic luminescence and abnormal thermal quenching behavior investigation, Dalton Trans. 48 (2019) 1624–1632, https://doi.org/10.1039/c8dt04047h.
[50] G. Swati, S. Bishnoi, P. Singh, N. Lohia, V.V. Jaiswal, M.K. Dalai, D. Haranath, Chemistry of extracting high-contrast invisible fingerprints from transparent and colored substrates using a novel phosphorescent label, Anal. Methods 10 (2018) 308–313, https://doi.org/10.1039/c7ay02713c.
[51] V. Naresh, B.S. Ham, Influence of multiphonon and cross relaxations on $^3P_0$ and $^1D_2$ emission levels of Pr^{3+} doped borosilicate glasses for broad band signal amplification, J. Alloys Compd. 664 (2016) 321–330, https://doi.org/10.1016/j.jallcom.2015.12.246.
[52] Y. Wang, W. Zheng, Y. Lu, P. Li, S. Xu, J. Zhang, Effect of alkaline earth metals on luminescence characteristic in Eu-Doped oxynitride phosphate glasses, J. Lumin. 237 (2021), 118152, https://doi.org/10.1016/j.jlumin.2021.118152.
[53] N. Wantana, E. Kaewnuam, N. Chanthima, H.J. Kim, J. Kaewkhao, Optik Tuneable Luminescence of Pr $^{3+}$ -doped Sodium Aluminium Gadolinium Phosphate Glasses for Photonics Applications, 2022, p. 267, https://doi.org/10.1016/j.ijleo.2022.169668.
[54] V. Hegde, C.S.D. Viswanath, N. Chauhan, K.K. Mahato, S.D. Kamath, Photoluminescence and thermally stimulated luminescence properties of Pr^{3+} -doped zinc sodium bismuth borate glasses, Opt. Mater. 84 (2018) 268–277, https://doi.org/10.1016/j.optmat.2018.06.064.
[55] U. Farooq, Z. Zhao, Z. Sui, C. Gao, R. Dai, Z. Wang, Z. Zhang, Tm^{3+}/Dy^{3+}/Eu^{3+} (Sm^{3+}) tri-activated Y_2WO_6 as one potential single-phase phosphor for WLEDs, J. Alloys Compd. 778 (2019) 942–950, https://doi.org/10.1016/j.jallcom.2018.11.091.
[56] K. Maheshwari, A.S. Rao, Down-shifting photoluminescent properties of Tb^{3+} doped phosphate glasses for intense green-emitting devices applications, Opt. Mater. 137 (2023), 113533, https://doi.org/10.1016/j.optmat.2023.113533%0A.
[57] Ravita, A. S. Rao, Tunable photoluminescence studies of KZABS: RE $^{3+}$ (RE $^{3+}$ = Tm $^{3+}$, Tb $^{3+}$ and Sm $^{3+}$) glasses for w-LEDs based on energy transfer, J. Lumin. 251 (2022) 119194, doi:10.1016/j.jlumin.2022.119194.

Speed Control of Three-Phase Induction Motor Using PI, Fuzzy and ANFIS Controllers

Naman Gogia
Dept. of Electrical Engineering
Delhi Technological University
Delhi, India
namangogia2001@gmail.com

Rishabh Prasad
Dept. of Electrical Engineering
Delhi Technological University
Delhi, India
rishabhprasad11@gmail.com

Ritik Arora
Dept. of Electrical Engineering
Delhi Technological University
Delhi, India
ritikarora656@gmail.com

Bharat Bhushan
Dept. of Electrical Engineering
Delhi Technological University
Delhi, India
bharat@dce.ac.in

Prem Prakash
Dept. of Electrical Engineering
Delhi Technological University
Delhi, India
premprakash@dtu.ac.in

2023 10th International Conference on Signal Processing and Integrated Networks (SPIN) | 978-1-6654-9099-3/23/$31.00 ©2023 IEEE | DOI: 10.1109/SPIN57001.2023.10116308

***Abstract*— Induction motors are one of the most common motors in use today because of their high robustness and low maintenance. To achieve high efficiency and maximum toque, controlling the speed of the induction motor becomes essential. This paper compares the performance of Proportional-Integral (PI) Controller, Fuzzy Logic Controller (FLC) and Adaptive Neuro-Fuzzy Inference System (ANFIS) for controlling the speed and torque of a three-phase induction motor model. The effectiveness of each method is analyzed and presented with the help of simulation results. By comparing the effect in transient and state parameters, ANFIS shows higher efficiency and robustness than FLC and PI Controller for speed control.**

Keywords*— *Induction motor, PI Controller, Fuzzy Logic Controller, ANFIS, Speed Control, Simulink

I. INTRODUCTION

By far, the most common motor in use today is the AC induction motor. They are mostly utilized in drive applications having constant and variable speed requirements but do not consider dynamic processes. This situation is changing rapidly due to the development of several newer control technologies recently, namely vector control. The fundamental cause of this is that, in such situations, the squirrel cage induction motor is far more affordable and durable than its competitor, the DC motor [1][2].

Using the vector control technique, an induction motor can be controlled using a normal PI controller. Due to the significant advantages of vector control, AC drives will not use scalar control as the approved industry standard [3][4].

PI controllers are sensitive to any undesired disturbances, parameter fluctuations, and system non-linearities. AI-based intelligent controllers can be used to solve these limitations. Fuzzy Logic, Adaptive Neuro-Fuzzy Inference System (ANFIS) and other Artificial Neural Networks (ANN) are the most widely used techniques for intelligent controllers, which have demonstrated better performance in comparison to controllers used conventionally [5][6].

The following sections are part of this paper: Section II describes the system architecture and components of the three-phase induction motor drive used. Section III deals with the methodology used to implement Field Oriented Control (FOC). Section IV deals with the different optimization techniques used for speed control. Section V discusses the results of the simulation performed. Section VI concludes the simulation results followed by references.

II. SYSTEM ARCHITECTURE

The system consists of three major parts which are the FOC Block, the motor and the inverter.

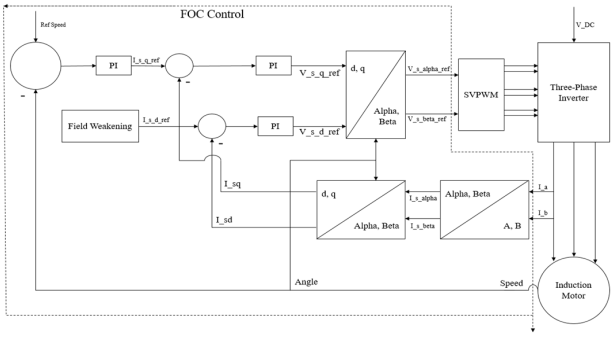


Fig 1. Block Diagram for Field Oriented Control (FOC)

FOC controls the output magnetic field and the current stator torque. This in turn allows the component producing torque to be at a right angle to the rotor flux which helps in producing maximum torque.

The final step of the FOC utilizes SVPWM which helps in determining the pulse-width modulation signals for the inverter switch to produce the voltages required.

A. FOC of Induction Motor

FOC is first of the many technologies which controls the flux of the motor and the torque by converting of the three-phase induction motor's stator currents into a two-component system – d and q which are orthogonal and can be symbolized as a vector. The component d signifies the motor's magnetic flux, while q signifies motor torque. These components are independently controlled, hence providing better control of the motor parameters [7]. FOC has various advantages such as it gives better torque response and can also be controlled at low ranges of speed and frequency which results into less consumption of power [8].

To keep the motor current component which is measured relative to the current component values which are desired, Proportional-integral (PI) controllers are utilized. Switching signals to the transistor in accordance with the stator voltage references, which are the output of the PI controllers, are provided by SVPWM.

Authorized licensed use limited to: DELHI TECHNICAL UNIV. Downloaded on May 15,2023 at 07:03:33 UTC from IEEE Xplore. Restrictions apply.

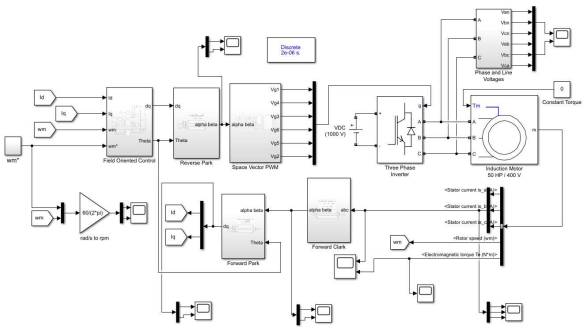


Fig 2. Simulink Model of the FOC block

TABLE I. EQUIVALENT CIRCUIT PARAMETERS AND VALUES

Parameter	Nomenclature	Values
Stator Voltage	V_s	400 V
Supply frequency	F	50 Hz
Stator Resistance	R_s	0.09 Ω
Stator Inductance	L_s	0.0001 H
Rotor Resistance	R_r	0.23 Ω
Rotor Inductance	L_r	0.0008 H
Magnetizing Inductance	L_m	0.035 H
Inertia	J	0.662 Kg–m^2
Poles	P	4

B. Clark's Transformation

The conversion of the stator currents (abc reference frame) to a two-component stationary orthogonal frame of reference (αβ reference frame) is done using the Clark transformation. The equations which implement Clark Transformation are as follows: [9][10]

$$\alpha(t) = \frac{2}{3}a(t) - \frac{1}{3}b(t) - \frac{1}{3}c(t) \quad (1)$$

$$\beta(t) = \frac{1}{\sqrt{3}}b(t) - \frac{1}{\sqrt{3}}c(t) \quad (2)$$

The matrix shown below converts the abc components to αβ components,

$$\begin{bmatrix}\alpha\\ \beta\\ 0\end{bmatrix} = \frac{2}{3}\begin{bmatrix}1 & -\frac{1}{2} & -\frac{1}{2}\\ 0 & \frac{\sqrt{3}}{2} & -\frac{\sqrt{3}}{2}\\ \frac{1}{2} & \frac{1}{2} & \frac{1}{2}\end{bmatrix}\begin{bmatrix}a\\ b\\ c\end{bmatrix}, \quad (3)$$

C. Park's Transformation

The conversion of two-component stationary orthogonal frame of reference (αβ) into a rotating orthogonal frame of reference (dq) is done using Park transformation. The frame having I_α and I_β (along the α and β axes) perpendicular to each other is the stationary orthogonal reference frame. The frame having I_d at θ angle to the α-axis and perpendicular components I_q and I_d along the q-axis is the rotating orthogonal frame of reference. [11]

$$i_d = i_\alpha \cos\theta + i_\beta \sin\theta \quad (4)$$

$$i_q = -i_\alpha \sin\theta + i_\beta \cos\theta \quad (5)$$

The crux of the matter is to convert the three-phase system into a time-invariant two-coordinate system which means any time delays on the input should correspond to the time delays of the output function. This linear time-invariant system when produced, simplifies and eases the procedure of implementing PI controllers while also simplifying the control of the flux and the current components producing torque (d and q).

D. Space Vector Pulse Width Modulation (SVPWM)

SVPWM is a modulation technique used to produce gate signals using the α and β components of the voltage. It helps in reducing the Total Harmonic Distortion (THD) [12][13]. FOC provides the corrected α-β voltage components which are fed to the SVPWM controller which produces gate signals fed to the three-phase inverter.

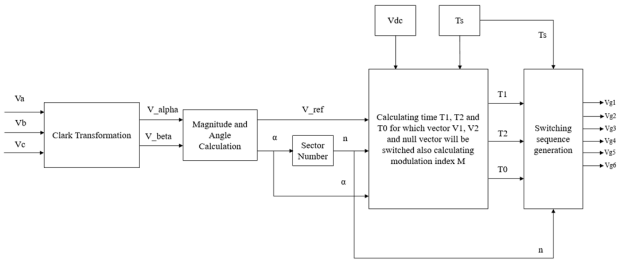


Fig 3. Block Diagram of SVPWM

III. METHODOLOGY

Field Oriented Vector Control has been implemented in the induction motor drive. This technique controls the d-axis (magnetizing component) and q-axis (motor torque component) of the stator current which helps in achieving higher starting torque and higher low-speed torque along with more effective speed control. SVPWM is used for generating gate signals for the three-phase inverter due to flexible control of output voltage, output frequency and lower Total Harmonic Distortion (THD) [14]. The process is as follows:

- Measuring the three-phase induction motor's stator phase currents.
- Converting the three-phase stator current to a stationary two-axis αβ coordinate system with Clark Transformation.
- Converting the current vector to the rotatory two-axis DQ coordinate system with Park Transformation.
- Controlling the DQ components, obtained after Park Transformation, independently by a control mechanism of choice. The output is a corrected voltage.
- Converting the voltage components back from DQ coordinate system to αβ coordinate system using Reverse Park Transformation.
- Generating gate signals from the corrected voltage using SVPWM for the three-phase inverter.

IV. OPTIMIZATION TECHNIQUES

The discrepancy between the induction motor's reference and actual speed must be minimized to adjust the speed and

Authorized licensed use limited to: DELHI TECHNICAL UNIV. Downloaded on May 15,2023 at 07:03:33 UTC from IEEE Xplore. Restrictions apply.

torque of the induction motor. There are some optimization techniques, like PI controller, Fuzzy Controller and ANFIS that can be used to achieve this.

A. Proportional Integral (PI) Controller

Comparing the direct component of current (I_d) and quadrature component of current (I_q) with their respective reference values gives us an error. Then, two PI controllers handle this error for I_d and I_q separately. PI controllers adjust the current values and produce the corresponding direct component (V_d) and quadrature component (V_q) of voltage to generate the required torque and speed [7].

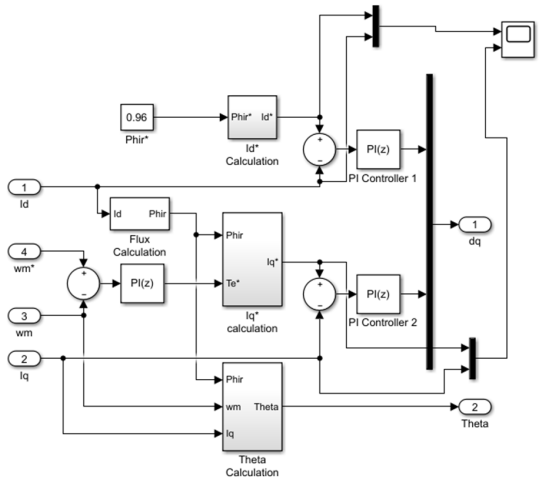


Fig 4. Field Oriented Control Block with PI Controller

In Fig. 4, the value of Proportional Gain (k_p) and Integral Gain (k_i) has been set to 100 and 26 of the given PI controllers.

B. Fuzzy Logic Controller

In Boolean logic system, either the particular situation has absolute true value i.e 1 or absolute false value i.e 0. But when a real-world situation is encountered, they can't just simply be categorized into absolute true or absolute false value. So, in order to handle these kind of situations, fuzzy logic provides the flexibility of reasoning in which the truth value can be an intermediate between 0 and 1 which defines how much the situation is partially true or partially false [15].

In this optimization technique, the reasoning capability of the control system is similar to a human which facilitates handling the uncertainties of the situation. Due to the fact that it resembles human logic, it provides very efficient and optimal solution to very complex problems by consuming very little memory.

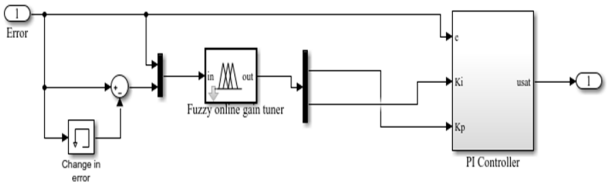


Fig 5. Fuzzy Tuned PI Controller

In Fig. 5, Fuzzy Online Gain Tuner takes two inputs which are change in error (ce) and error (e) and sets the value of k_i and k_p of the PI controller by using the set of rules which have been defined in TABLE I and TABLE II.

The Mamdani method has been employed by Fuzzy online gain tuner to compute the values of the output variables k_i and k_p based on the values of the input variables which are change in error (ce) and error (e). Furthermore, Generalized bell membership function (gbellmf) has been set for the input variables and Gaussian membership function (gaussmf) has been set for the output variables [16][17].

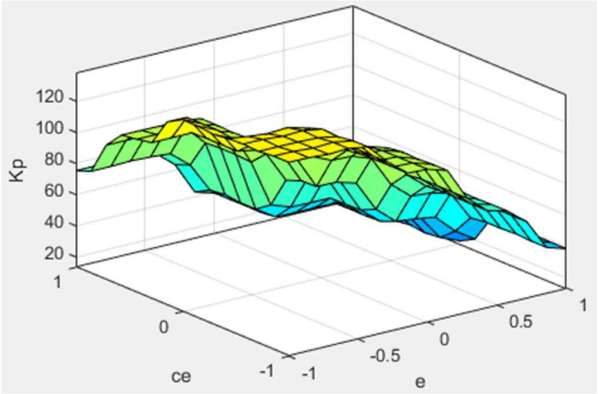


Fig 6. Fuzzy Controller Output's Surface view for the output variable k_p

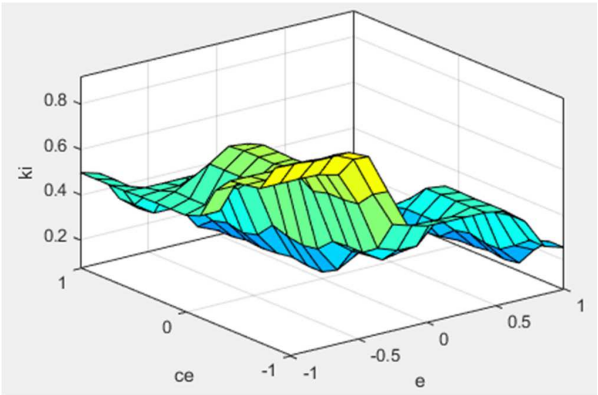


Fig 7. Fuzzy Controller Output's Surface view for the output variable k_i

e / ce	NB	NS	ZZ	PS	PB
NB	VVB	VVB	B	B	M
NS	VB	VB	M	B	S
ZZ	B	VB	S	M	S
PS	B	B	S	S	S
PB	B	M	S	S	S

TABLE II. RULE BASE FOR OUTPUT VARIABLE K_p

e / ce	NB	NS	ZZ	PS	PB
NB	VVB	VVB	VB	B	M
NS	VVB	VVB	VB	B	M
ZZ	VVB	VB	B	M	S
PS	VB	VB	M	M	S
PB	B	B	M	M	S

TABLE III. RULE BASE FOR OUTPUT VARIABLE K_i

Authorized licensed use limited to: DELHI TECHNICAL UNIV. Downloaded on May 15,2023 at 07:03:33 UTC from IEEE Xplore. Restrictions apply.

C. *Adaptive Neuro-Fuzzy Inference System (ANFIS)*

It is a method of optimization that is a hybrid of two computational techniques which are Fuzzy Logic and Neural Networks which provides the advantage of both computing methods within one framework. Initially ANFIS requires the values for input variables and corresponding output variables which are collected in the form of a dataset. Then ANFIS gets trained for that dataset so that it can pre-compute the values of output variables for the given values of input variables [18].

ANFIS's fundamental architecture combines five layers of ANN along with sugeno fuzzy model [19]. The input values are represented by the first layer of an ANN's structure, then the input values get fuzzified by the second layer, the fuzzy rule evaluation is represented by the third and fourth layers, and defuzzification is represented by the last layer [20].

For the sampling process, the data of error in stator current (which corresponds to the error in the motor speed output) and output of the fuzzy controller has been collected. Further, the data for I_d and I_q components of stator current has been collected separately. This data is in the form of 2D array which forms the training data for ANFIS controller.

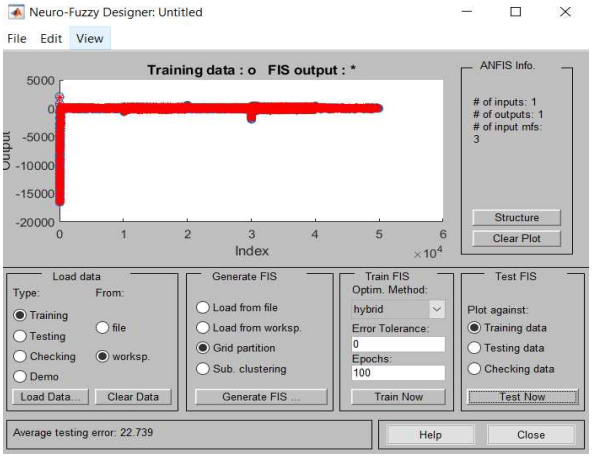


Fig 8. Training ANFIS

V. Simulation Results And Discussion

A. *PI Controller*

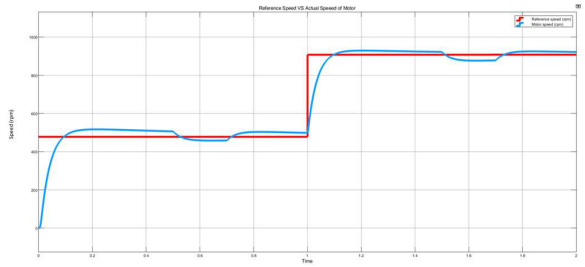


Fig 9. Reference Speed (variable) vs Motor Speed (Loaded condition) with PI Controller

In Fig. 9, the red and blue lines are the reference and actual speed of the motor respectively under loaded condition with PI controller.

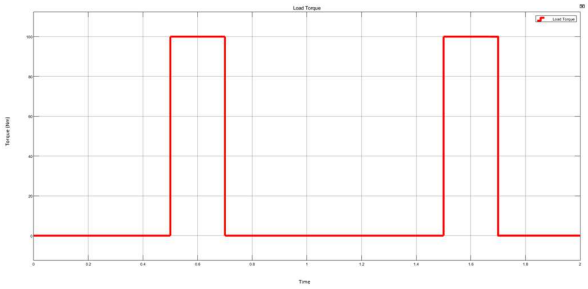


Fig 10. Mechanical load torque applied on the shaft of the induction motor

In Fig. 10, a mechanical load torque of 100 N–m has been applied on the shaft of the induction motor twice for a time duration of 0.2 seconds.

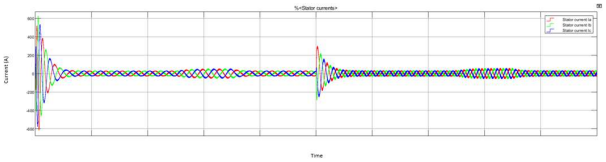


Fig 11. Stator current with PI Controller

In Fig. 11, a spike in stator current is observed when the reference speed or load torque is varied.

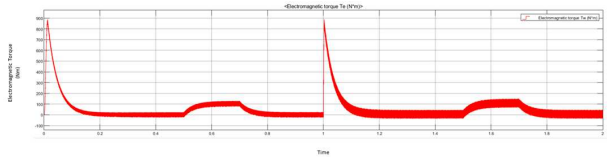


Fig 12. Electromagnetic Torque with PI Controller

In Fig. 12, a spike in electromagnetic torque is observed when the reference speed or load torque is varied.

B. *Fuzzy Logic Controller*

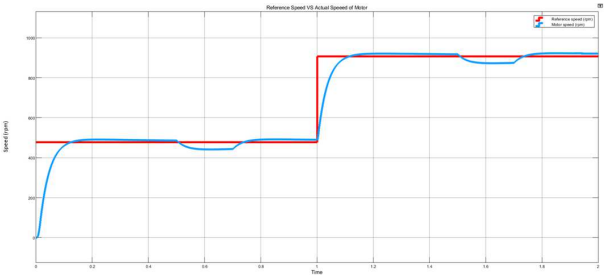


Fig 13. Reference Speed vs Motor Speed (Loaded condition) with FLC

In Fig. 13, the reference vs actual speed has been shown under loaded condition with FLC. It can be observed that in comparison to the PI Controller, the overshoot and steady state error has been significantly reduced.

Authorized licensed use limited to: DELHI TECHNICAL UNIV. Downloaded on May 15,2023 at 07:03:33 UTC from IEEE Xplore. Restrictions apply.

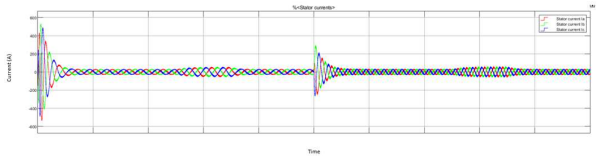


Fig 14. Stator current with FLC

In Fig. 14, a spike in stator current is observed when the reference speed or load torque is varied.

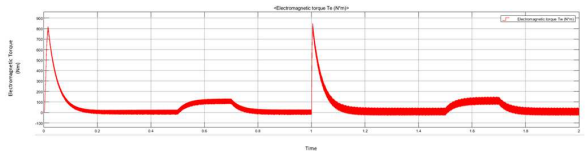


Fig 15. Electromagnetic Torque with FLC

In Fig. 15, a spike in electromagnetic torque is observed when the reference speed or load torque is varied.

C. ANFIS

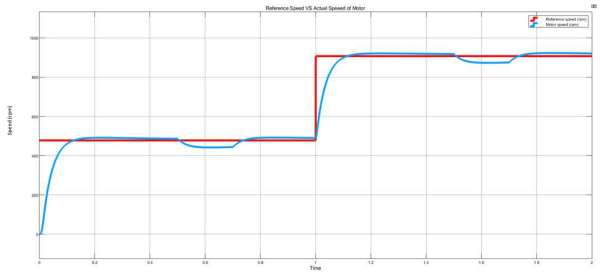


Fig 16. Reference Speed vs Motor Speed (Loaded condition) with ANFIS

In Fig. 16, the reference speed vs motor speed has been shown under loaded condition with ANFIS Controller. The overshoot and steady state error has been significantly reduced in the case of PI controller and there is a slight improvement over FLC.

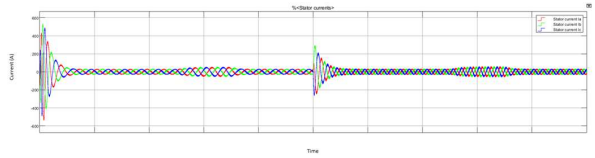


Fig 17. Stator current with ANFIS

In Fig. 17, a spike in stator current is observed when the reference speed or load torque is varied.

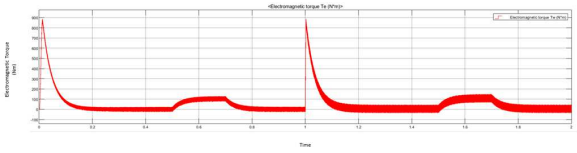


Fig 18. Electromagnetic Torque with ANFIS

In Fig. 18, a spike in electromagnetic torque is observed when the reference speed or load torque is varied.

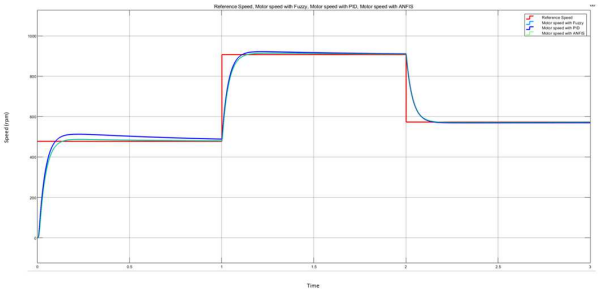


Fig 19. Reference Speed vs Motor speed (PI, Fuzzy, ANFIS) – No Load Condition

In Fig. 19, the results of the reference speed vs motor speed has been shown under no-load condition for all the optimization techniques covered (PI Controller, FLC, ANFIS Controller).

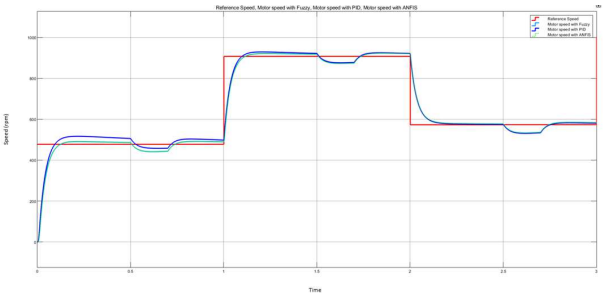


Fig 20. Reference Speed vs Motor speed (PI, Fuzzy, ANFIS) – Loaded Condition

In Fig. 20, the results of the reference speed vs motor speed has been shown under loaded condition for all the optimization techniques covered (PI Controller, FLC, ANFIS Controller). It can be observed that the overshoot and steady state error is maximum in the case of PI controller and reduces significantly in the case of FLC. There is a slight improvement in the results of FLC when ANFIS is applied

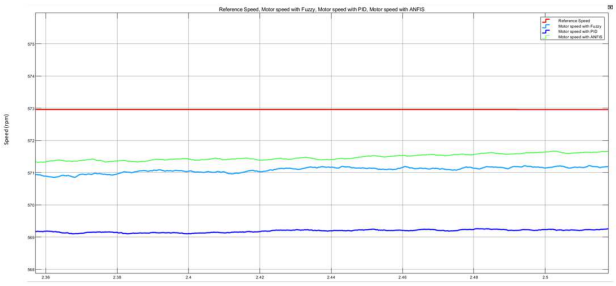


Fig 21. Reference Speed vs Motor speed (PI, Fuzzy, ANFIS) Zoomed-In

In Fig. 21, it can be clearly seen how the steady state value of the motor speed is closest to the reference speed in the case of ANFIS controller followed by FLC and PI Controller.

Authorized licensed use limited to: DELHI TECHNICAL UNIV. Downloaded on May 15,2023 at 07:03:33 UTC from IEEE Xplore. Restrictions apply.

Control Type	Rise Time (sec)	Settling Time (sec)	Overshoot (%)	Peak Time (sec)	Steady State Value (RPM)
PI	0.0591	1.0797	7.4262	0.2159	479.0108
Fuzzy	0.0668	0.5110	3.0951	0.2243	478.2389
ANFIS	0.0692	0.1159	1.8460	0.2333	477.4197

TABLE IV. TIME DOMAIN SPECIFICATIONS

Table IV shows the comparison of the different optimization techniques with respect to several time domain specification parameters. It can be determined that the PI Controller shows the minimum Rise Time and Peak Time. The overshoot and settling time are maximum for PI Controller while they are minimum for the ANFIS Controller. The steady state value is closest to the reference speed (477.4648 rpm) in the case of ANFIS.

VI. CONCLUSION

Several optimization techniques namely PI Controller, Fuzzy Logic Controller and ANFIS have been used to perform speed and torque control of a three-phase induction motor and performed simulations of the same in MATLAB/Simulink. Fuzzy Logic Controller was used to dynamically update the values of K_p and K_i using the formulated fuzzy rule base applied for different values of error and change in error. Training data for ANFIS was collected from the input and output values of Fuzzy Logic Controller and the training of collected data was performed for 100 epochs.

The response of the controller was analyzed for both changes in reference speed and load torque applied. When the system is subjected to load, Fuzzy-tuned PI Controller quickly regains stability. All the control mechanisms are compared on several time domain specifications including Settling Time, Overshoot, Rise Time, Steady State Value and Peak Time. The settling time observed in case of ANFIS was the minimum. It was also observed that overshoot was maximum in case of the PI controller whereas in case of Fuzzy-tuned PI Controller and ANFIS the steady state error, overshoot and settling time are reduced.

REFERENCES

[1] Mhaisgawali, Madhavi L.. “Speed Control of Induction Motor using PI”

[2] Stephen J. Chapman. Induction Motor, in Electric Machinery Fundamentals . 5th Edition, McGraw Hill cop. , New York, USA, 2012.

[3] M. H. Rashid, Power Electronics Handbook. Academic Press, 2010. doi: 10.1604/9780080467658 and PID Controller.” IOSR Journal of Engineering 03 (2013): 25-30”.

[4] S. S, V. K. K, S. R. V, S. Kulkarni and P. M. M, "An implementation of soft computing approach of smart control for induction motor using ANFIS," 2022 4th International Conference on Smart Systems and Inventive Technology (ICSSIT), Tirunelveli, India, 2022, pp. 1410-1413, doi: 10.1109/ICSSIT53264.2022.9716455.

[5] G. A. Olarinoye, C. Akinropo, G. J. Atuman and Z. M. Abdullahi, "Speed Control of a Three Phase Induction Motor using a PI Controller," 2019 2nd International Conference of the IEEE Nigeria Computer Chapter (NigeriaComputConf), Zaria, Nigeria, 2019, pp. 1-7, doi: 10.1109/NigeriaComputConf45974.2019.8949624.

[6] M. Y. Zidani, N. Brakta and O. Bendjeghaba, "Dynamic Performance Improvement of DFIM based on Hybrid Computational Technique," 2021 IEEE 11th Annual Computing and Communication Workshop and Conference (CCWC), NV, USA, 2021, pp. 0213-0217, doi: 10.1109/CCWC51732.2021.9376017.

[7] Mikhael, Hanan & Jalil, Hussein & Ibrahim, Inaam. (2016). Speed Control of Induction Motor using PI and V/F Scalar Vector Controllers. International Journal of Computer Applications. 151. 36-43. 10.5120/ijca2016911831.

[8] Wu, Bin, and Mehdi Narimani. High-Power Converters and AC Drives. Wiley-IEEE Press, 2016.

[9] Brandao Faria, Jose. (2007). Application of Clarke's transformation to the modal analysis of asymmetrical single-circuit three-phase line configurations. European Transactions on Electrical Power. 10. 225 - 231. 10.1002/etep.4450100405.

[10] K.K.Pandey and Dr.P.H.Zope, “Analysis and Simulation of Three-phase Induction motor using Clarke’s transformation,” International Journal of Engineering Research & Technology, vol. 2, no. 4, Jul. 2018, doi: https://doi.org/10.17577/IJERTCONV2IS04087.

[11] A. Sguarezi, Model Predictive Control for Doubly-Fed Induction Generators and Three-Phase Power Converters. 2022.

[12] M. A. K. A. Biabani and S. M. Ali, "Control of induction motor drive using space vector PWM," 2016 International Conference on Electrical, Electronics, and Optimization Techniques (ICEEOT), Chennai, India, 2016, pp. 3344-3351, doi: 10.1109/ICEEOT.2016.7755324.

[13] Waheed Ahmed and Syed M Usman Ali. Comparative study of SVPWM SPWM based three-phase voltage source inverters for variable speed drive. IOP Conf. Series: Materials Science and Engineering, 2013.

[14] P. Farhadi, F. A. Baroogh and M. Gheydi, "Comparative study of conventional SVPWM algorithms in terms of producing harmonics and the effect of the harmonics on induction motor," 2017 IEEE International Conference on Environment and Electrical Engineering and 2017 IEEE Industrial and Commercial Power Systems Europe (EEEIC / I&CPS Europe), Milan, Italy, 2017, pp. 1-5, doi: 10.1109/EEEIC.2017.7977716.

[15] A. N. Mohammed and G. A. -R. Ghoneim, "Fuzzy-PID Speed Controller Model-Based Indirect Field Oriented Control for Induction Motor," 2020 International Conference on Computer, Control, Electrical, and Electronics Engineering (ICCCEEE), Khartoum, Sudan, 2021, pp. 1-6, doi: 10.1109/ICCCEEE49695.2021.9429623.

[16] H. Humaira, R. Rasyidah and I. Rahmayuni, "Designing Mamdani Fuzzy Inference Systems for Decision Support Systems," 2019 2nd International Conference on Applied Information Technology and Innovation (ICAITI), Denpasar, Indonesia, 2019, pp. 111-115, doi: 10.1109/ICAITI48442.2019.8982153.

[17] S. Ali, S. A. R. Kashif, H. Q. Ali and K. Toqueer, "Direct Torque Control of Inverter Fed Three Phase Induction Motor by Implementing Fuzzy Logic Controller," 2019 IEEE 6th International Conference on Engineering Technologies and Applied Sciences (ICETAS), Kuala Lumpur, Malaysia, 2019, pp. 1-8, doi: 10.1109/ICETAS48360.2019.9117481.

[18] R. Simon and A. Geetha, "Comparison on the performance of Induction motor control using fuzzy and ANFIS controllers," 2013 IEEE International Conference ON Emerging Trends in Computing, Communication and Nanotechnology (ICECCN), Tirunelveli, India, 2013, pp. 491-495, doi: 10.1109/ICE-CCN.2013.6528549.

[19] C. -W. Chang and C. -W. Tao, "A Novel Approach to Implement Takagi-Sugeno Fuzzy Models," in IEEE Transactions on Cybernetics, vol. 47, no. 9, pp. 2353-2361, Sept. 2017, doi: 10.1109/TCYB.2017.2701900.

[20] R. A. Gupta, R. Kumar and R. S. Surjuse, "ANFIS Based Intelligent Control of Vector Controlled Induction Motor Drive," 2009 Second International Conference on Emerging Trends in Engineering & Technology, Nagpur, India, 2009, pp. 674-680, doi: 10.1109/ICETET.2009.35

Authorized licensed use limited to: DELHI TECHNICAL UNIV. Downloaded on May 15,2023 at 07:03:33 UTC from IEEE Xplore. Restrictions apply.

arXiv:2305.11190v1 [gr-qc] 18 May 2023

Statistical and cosmological analysis of Weyl-type $f(Q,T)$ models using Pantheon+ dataset

Gaurav N. Gadbail,[1,*] Harshita,[2,†] Amine Bouali,[3,‡] and P.K. Sahoo[1,§]

[1] *Department of Mathematics, Birla Institute of Technology and Science-Pilani, Hyderabad Campus, Hyderabad-500078, India.*
[2] *Department of Applied Mathematics, Delhi Technological University, Delhi-110042, India,*
[3] *Laboratory of Physics of Matter and Radiation, Mohammed I University, BP 717, Oujda, Morocco,*

We study the $f(Q,T)$ gravity in the framework of Weyl geometry (known as Weyl-type $f(Q,T)$ gravity), where Q denotes the non-metricity scalar, and T denotes the energy-momentum tensor trace. In this work, we consider the $f(Q,T)$ model, which is defined as $f(Q,T) = \alpha Q^{m+1} + \frac{\beta}{6\kappa^2}T$ and investigating two scenarios: (I) $m = 0$ (linear model) and (II) $m \neq 0$ (nonlinear model). For both scenarios, we find the explicit solution for the field equations by using the barotropic equation of state as $p = \omega\rho$, where ω is the equation-of-state (EoS) parameter. Further, we study the obtained solutions statistically using the $Pantheon^{+}$ dataset with 1701 data points. For both models, the best-fit values of model parameters for $1-\sigma$ and $2-\sigma$ confidence level are mentioned in table I and II. We statistically compare our models to the ΛCDM model using χ^2_{min}, χ^2_{red}, AIC and ΔAIC. We also examined the current values of cosmological parameters such as deceleration and EoS parameters to determine the current acceleration expansion of the universe. Furthermore, we test our model using Om diagnostic and compare it to the ΛCDM model to determine its dark energy profile. Finally, we draw the conclusion that, statistically speaking, Weyl $f(Q,T)$ model I (linear model) is more compatible with the ΛCDM model than Weyl $f(Q,T)$ model II (nonlinear model).

Keywords: Hubble constant; equation-of-state parameter; $f(Q,T)$ gravity; Pantheon+ data; Dark energy

I. INTRODUCTION

Modern astronomical discoveries, such as high redshift Type Ia supernovae (SNe Ia), observational Hubble parameter data (OHD), matter power spectra, cosmic microwave background radiation (CMBR), and others [1–6] have demonstrated that our universe is currently entered an accelerated expansion era. To explain this universe's acceleration mechanism, the cosmologist suggested the presence of a new negative pressure fluid called Dark energy (DE). The most well-known candidate for DE is the so-called Λ-cold-dark-matter (ΛCDM), which has been confirmed to be very prosperous in explaining many aspects of the observed universe. Despite its enormous success, the ΛCDM model has some issues, such as cosmic coincidence and fine-tuning problems [7, 8]. As a result, this prompts the investigation of potential alternatives. In this view, there are two types of alternative possibilities: modifying matter content in the Einstein-Hilbert action and modifying the gravitational part of the Einstein-Hilbert action called modified gravity. The modified theory has recently emerged as one of the most favored alternatives for explaining the DE problem. In order to explain the acceleration of the universe in early and late times, several authors have discussed various modified theories such as $f(R)$ theory (where R is Ricci scalar) [9, 10], $f(\mathcal{T})$ theory (where $\mathcal{T}$ is Torsion scalar) [11], $f(R,T)$ theory (where T denotes the energy-momentum tensor trace) [12], $f(G)$ theory (where G is Gauss-Bonnet invariant) [13], and $f(G,T)$ theory [14], etc.

Recently, a new theory of gravity (known as symmetric teleparallel theory) has been developed based on a geometrical variable called non-metricity Q, which describes the properties of gravitational interaction [15]. Geometrically, the non-metricity Q characterizes a vector's length interpretation under parallel transport. Further, the symmetric teleparallel theory was developed into the $f(Q)$ theory [16]. Various physical and geometrical aspects of $f(Q)$ gravity theory have been studied in the literature [17–24]. Later, Yixin et al. [25] investigated the most general extension of $f(Q)$ gravity named $f(Q,T)$ gravity theory, which is based on nonminimal coupling between the scalar non-metricity Q and the trace of the matter energy-momentum tensor T. Despite its novelty, the $f(Q,T)$ gravity theory has some interesting applications in the literature. Arora et al. [26–28] have investigated the viability of the $f(Q,T)$ gravity as a method to explain the present and late-time cosmic acceleration and provide a feasible solution to the dark energy problem. In the presence of $f(Q,T)$ theory, gravitational baryogenesis has been studied in [29]. Also, the cosmological perturbation theory in the framework of $f(Q,T)$ theory has been studied in [30]. Gadbail et al. [31] have reconstructed the $f(Q,T)$ models for various cosmological

* gauravgadbail6@gmail.com
† harshitagupta1224@gmail.com
‡ a1.bouali@ump.ac.ma
§ pksahoo@hyderabad.bits-pilani.ac.in

scenarios and show the model's validity. Additionally, in $f(Q,T)$ gravity, some work is done on the astrophysical object [32, 33].

In this paper, we look at a specific type of $f(Q,T)$ theory, in which the non-metricity $Q_{\sigma\mu\nu}$ of the space-time is depicted in its standard Weyl form, and it is completely determined by a vector field w_μ. More precisely, we make use of Weyl geometry and explicitly express non-metricity as $Q_{\sigma\mu\nu} = 2\,w_\sigma\,g_{\mu\nu}$. We will also look at the flat geometry restraint, which requires that the Weyl curvature scalar vanish. This condition is added to the action through a Lagrange multiplier λ. Furthermore, the field equation of Weyl-type $f(Q,T)$ gravity is obtained by varying the action with respect to metric tensor together with a vector field. Yixin et al. [34] studied the cosmological implication of Weyl-type $f(Q,T)$ gravity for three types of $f(Q,T)$ model and obtained solutions showing both the decelerating and accelerating phase of the universe. They demonstrated that the Weyl-type $f(Q,T)$ theory is an alternate and useful strategy for describing the early and late stages of cosmological evolution. Yang et al. [35] studied the Raychaudhuri equation, Geodesic deviation, tidal force, and Newtonian limit in Weyl-type $f(Q,T)$ theory. Furthermore, the power law and viscous cosmology were studied in Weyl-type $f(Q,T)$ theory [36, 37].

The main goal of the present study is to examine the Weyl-type $f(Q,T)$ theory by using the barotropic equation of state $p=\omega\rho$. For this study, we took two type of $f(Q,T)$ models: (I) $f(Q,T) = \alpha Q + \frac{\beta}{6\kappa^2}T$ (linear) and (II) $f(Q,T) = \alpha Q^{m+1} + \frac{\beta}{6\kappa^2}T$ (nonlinear). After that, we find two solutions to the field equation for both linear and nonlinear models. We further analyze the obtained solutions statistically using observational datasets. We observe that some cosmological parameters, like equation-of-state and deceleration parameters, are crucial in defining the cosmic evolution of the universe. And it is well comprehended that the equation-of-state parameter implies a variety of fluid universe descriptions. As a result, using observational data to restrict this parameter is intriguing. For this purpose, we use the *Pantheon*$^+$ dataset, which contains 1701 data points. Later on, we statistically compare our models to the ΛCDM model using χ^2_{min}, χ^2_{red}, AIC and ΔAIC. In order to identify the dark energy profile of our model, we also test it using the Om diagnostic and compare it to the ΛCDM model.

The layout of the article is as follows. In section II, we present the basic formulation of Weyl-type $f(Q,T)$ gravity. In section III, we find the solution of the generalized Friedmann equation by using the barotropic EoS parameter $p=\omega\rho$ for both linear and nonlinear models. In section IV, we study the statistical analysis of Weyl $f(Q,T)$ models by using the *Pantheon*$^+$ dataset and present our results. In section V, we test our model using Om diagnostic and compare it to the ΛCDM model to determine its dark energy profile. In section VII, we conclude our final results.

II. BASIC FORMULATION OF WEYL-TYPE $f(Q,T)$ THEORY

In 1918, Weyl proposed an essential generalization of Riemannian geometry, which served as the mathematical foundation for general relativity, by assuming that during the parallel transport of vectors, both the orientation and magnitude of a vector change [38]. Weyl introduced the intrinsic vector field w_μ and a semi-metric connection to express the simultaneous change of direction and length,

$$\widetilde{\Gamma}^{\lambda}_{\ \mu\nu} \equiv \Gamma^{\lambda}_{\ \mu\nu} + g_{\mu\nu}w^{\lambda} - \delta^{\lambda}_{\mu}w_{\nu} - \delta^{\lambda}_{\nu}w_{\mu} \tag{1}$$

where tilde shows the quantities defined in Weyl geometry, and the Christoffel symbol $\Gamma^{\lambda}_{\ \mu\nu} = \frac{1}{2}g^{\lambda\sigma}\left(\partial_\mu g_{\sigma\nu} + \partial_\nu g_{\sigma\mu} - \partial_\sigma g_{\mu\nu}\right)$.

With the help of a semi-metric connection, one can obtain the result in Weyl geometry,

$$\widetilde{\nabla}_\sigma g_{\mu\nu} = 2w_\sigma g_{\mu\nu} \tag{2}$$

The scalar non-metricity is defined as

$$Q \equiv -g^{\mu\nu}\left(L^{\alpha}_{\ \beta\nu}L^{\beta}_{\ \nu\alpha} - L^{\alpha}_{\ \beta\alpha}L^{\beta}_{\ \mu\nu}\right), \tag{3}$$

where $L^{\lambda}_{\ \mu\nu}$ is the disformation tensor read as

$$L^{\lambda}_{\mu\nu} = -\frac{1}{2}g^{\lambda\gamma}\left(Q_{\mu\gamma\nu} + Q_{\nu\gamma\mu} - Q_{\gamma\mu\nu}\right). \tag{4}$$

The nonmetricity tensor $Q_{\lambda\mu\nu}$ is defined as the covariant derivative of the metric tensor with respect to the semi-metric connection $\widetilde{\Gamma}^{\lambda}_{\ \mu\nu}$,

$$Q_{\lambda\mu\nu} \equiv \widetilde{\nabla}_\lambda g_{\mu\nu} = \partial_\lambda g_{\mu\nu} - \widetilde{\Gamma}^{\rho}_{\ \lambda\mu}\,g_{\rho\nu} - \widetilde{\Gamma}^{\rho}_{\ \lambda\nu}\,g_{\rho\mu} = 2w_\lambda g_{\mu\nu}. \tag{5}$$

Inserting Eq. (5) in Eqs. (3) and (4), we obtained the important relation

$$Q = -6w^2. \tag{6}$$

The action of Weyl-type $f(Q,T)$ theory of gravity coupled with matter Lagrangian $\mathcal{L}_m$ is provided by [34]

$$S = \int d^4x\sqrt{-g}\left[\kappa^2 f(Q,T) - \frac{1}{2}\tilde{m}^2 w_\mu w^\mu - \frac{1}{4}W_{\mu\nu}W^{\mu\nu} + \lambda\left(R + 6\nabla_\alpha w^\alpha - 6w_\alpha w^\alpha\right) + \mathcal{L}_m\right], \tag{7}$$

with $\kappa^2 = \frac{1}{16\pi G}$. Here, $f(Q,T)$ is an arbitrary function of Q (non-metricity scalar) and T (energy-momentum tensor trace). The particle's mass to the vector field w_μ is denoted by $\tilde{m}$. The second and third terms in action are the mass term and ordinary kinetic term of w_μ, respectively. Furthermore, under the assumption of total scale curvature vanishing, a condition is introduced to the action through a Lagrange multiplier λ.

Further, the generalized Proca equation by varying the action (7) with respect to a vector field is

$$\nabla^{\nu}W_{\mu\nu}-\left(\tilde{m}^2+12\kappa^2 f_Q+12\lambda\right)w_{\mu}=6\nabla_{\mu}\lambda. \quad (8)$$

We obtained the generalized field equation by varying the action (7) with regard to the metric tensor together with a vector field,

$$\begin{aligned}\frac{1}{2}\left(T_{\mu\nu}+S_{\mu\nu}\right)-\kappa^2 f_T\left(T_{\mu\nu}+\Theta_{\mu\nu}\right)&=-\frac{\kappa^2}{2}g_{\mu\nu}f\\ -6k^2 f_Q w_{\mu}w_{\nu}+\lambda\left(R_{\mu\nu}-6w_{\mu}w_{\nu}+3g_{\mu\nu}\nabla_{\rho}w^{\rho}\right)&\\ +3g_{\mu\nu}w^{\rho}\nabla_{\rho}\lambda-6w_{(\mu}\nabla_{\nu)}\lambda+g_{\mu\nu}\Box\lambda-\nabla_{\mu}\nabla_{\nu}\lambda,& \quad (9)\end{aligned}$$

in which

$$f_Q\equiv\frac{\partial f(Q,T)}{\partial Q},\qquad f_T\equiv\frac{\partial f(Q,T)}{\partial T}. \quad (10)$$

Also, the definition of $T_{\mu\nu}$ and $\Theta_{\mu\nu}$ as

$$T_{\mu\nu}\equiv-\frac{2}{\sqrt{-g}}\frac{\delta(\sqrt{-g}L_m)}{\delta g^{\mu\nu}}, \quad (11)$$

$$\Theta_{\mu\nu}=g^{\alpha\beta}\frac{\delta T_{\alpha\beta}}{\delta g_{\mu\nu}}=g_{\mu\nu}L_m-2T_{\mu\nu}-2g^{\alpha\beta}\frac{\delta^2 L_m}{\delta g^{\mu\nu}\delta g^{\alpha\beta}}. \quad (12)$$

Here, the re-scaled energy-momentum tensor of the free Proca field is denoted by $S_{\mu\nu}$ and is defined as

$$S_{\mu\nu}=-\frac{1}{4}g_{\mu\nu}W_{\rho\sigma}W^{\rho\sigma}+W_{\mu\rho}W^{\rho}_{\nu}-\frac{1}{2}\tilde{m}^2 g_{\mu\nu}w_{\rho}w^{\rho}+\tilde{m}^2 w_{\mu}w_{\nu}, \quad (13)$$

and

$$W_{\mu\nu}=\nabla_{\nu}w_{\mu}-\nabla_{\mu}w_{\nu}. \quad (14)$$

It is also noted that the expression for the divergence of the matter energy-momentum tensor in the Weyl-type $f(Q,T)$ theory is given by [34]

$$\nabla^{\mu}T_{\mu\nu}=\frac{\kappa^2}{1+2\kappa^2 f_T}\left[2\nabla_{\nu}(f_T\mathcal{L}_m)-f_T\nabla_{\nu}T-2T_{\mu\nu}\nabla^{\mu}f_T\right].$$

III. SOLUTION OF THE FLRW MODEL

The standard Friedmann-Lemaitre-Robertson-Walker line element is taken into account in the present study and is written explicitly as

$$ds^2=-dt^2+a^2(t)\delta_{ij}dx^i dx^j, \quad (15)$$

where $a(t)$ is the cosmic scale factor.
The vector field w_{μ} is assumed to have the following form in the spatial symmetry: $w_{\mu}=[\psi(t),0,0,0]$ [34] implying $w^2=w_{\mu}w^{\mu}=-\psi^2(t)$, and $Q=-6w^2=6\psi^2(t)$.

The energy-momentum tensor for the perfect fluid is defined as:

$$T_{\mu\nu}=(\rho+p)\,u_{\mu}u_{\nu}+pg_{\mu\nu}, \quad (16)$$

where p and ρ are the pressure and the matter-energy density, respectively. The four-velocity vector u^{μ} is such that $u_{\mu}u^{\mu}=-1$. Thus implies $T^{\mu}_{\nu}=diag\,(-\rho,p,p,p)$, and $\Theta^{\mu}_{\nu}=\delta^{\mu}_{\nu}p-2T^{\mu}_{\nu}=diag\,(2\rho+p,-p,-p,-p)$.

The flat space constraint and the generalized Proca equation in the cosmological case can be represented as

$$\dot{\psi}=\dot{H}+\psi^2+2H^2-3H\psi, \quad (17)$$

$$\dot{\lambda}=\left(-\frac{1}{6}\tilde{m}^2-2\kappa^2 f_Q-2\lambda\right)\psi=-\frac{1}{6}\tilde{m}^2_{eff}\psi, \quad (18)$$

$$\partial_i\lambda=0. \quad (19)$$

From Eq (9) and using given metric (15) the obtained modified Friedmann equation is,

$$\begin{aligned}\frac{1}{2}\rho+\kappa^2 f_T\left(p+\rho\right)=\frac{\kappa^2}{2}f-\left(6\kappa^2 f_Q\,\psi^2+\frac{1}{4}\tilde{m}^2\psi^2\right)&\\ +3\lambda\left(H^2-\psi^2\right)+3\dot{\lambda}\left(H-\psi\right), \quad (20)&\end{aligned}$$

$$\begin{aligned}-\frac{1}{2}p=\frac{\kappa^2}{2}f+\frac{\tilde{m}^2\psi^2}{4}+\lambda\left(3H^2+3\psi^2+2\dot{H}\right)&\\ +\left(2H+3\psi\right)\dot{\lambda}+\ddot{\lambda}. \quad (21)&\end{aligned}$$

where ρ and p are the matter-energy density and the pressure, respectively. dot (.) represent the derivative with respect to time t.
We study the above Friedmann equation (20) and (21) for two type of $f(Q,T)$ models: (I) $f(Q,T)=\alpha Q+\frac{\beta}{6\kappa^2}T$ (linear) and (II) $f(Q,T)=\alpha Q^{m+1}+\frac{\beta}{6\kappa^2}T$ (nonlinear).

A. Model I :- $f(Q,T)=\alpha Q+\frac{\beta}{6\kappa^2}T$

For our investigation, we consider the linear functional form $f(Q,T)=\alpha Q+\frac{\beta}{6\kappa^2}T$, where α and β are model parameters. This particular functional form of $f(Q,T)$ is motivated in reference [34]. For certain choices of model parameters, this model is basically equivalent to ΛCDM model for certain redshift ranges.
Using this form and $\lambda=\kappa^2$ (for special case), we rewrite the field equations (20) and (21) as

$$-\left(\frac{\beta}{4}+\frac{1}{2}\right)\rho+\frac{\beta}{12}p=3\alpha\psi^2+\frac{M^2\psi^2}{4}+3\left(\psi^2-H^2\right), \quad (22)$$

$$\begin{aligned}-\left(\frac{\beta}{4}+\frac{1}{2}\right)p+\frac{\beta}{12}\rho=3\alpha\psi^2+\frac{M^2\psi^2}{4}&\\ +\left(3\psi^2+3H^2+2\dot{H}\right). \quad (23)&\end{aligned}$$

Where $M^2 = \tilde{m}^2/\kappa^2$, M represents the mass of the Weyl vector field and indicates the intensity of the Weyl geometry-matter coupling. In this situation, we've assumed that $M = 0.95$ [34]. To proceed further, we consider the relation of pressure and energy density as $p = \omega\rho$. Using the relation $\nabla_\lambda g_{\mu\nu} = -w_\lambda g_{\mu\nu}$ and $w_1 = \psi(t)$, we obtained $\psi(t) = -6H(t)$. Further simplifying Eq.(22) and (23), we obtained the first order differential equation as

$$A\,H(z) - B\,(1+z)\frac{dH(z)}{dz} = 0 \tag{24}$$

where $A = \frac{36\alpha+3M^2+35}{3\beta-\omega\beta+6} - \frac{36\alpha+3M^2+37}{6\omega-\beta+3\omega\beta}$ and $B = \frac{2}{9(2+\beta)\omega-3\beta}$.
The solution of the above differential equation is

$$H(z) = H_0(1+z)^{\mathcal{X}} \tag{25}$$

where

$$\mathcal{X} = \frac{3\omega(105+71\beta+36\alpha(3+2\beta))}{\beta(w-3)-6} + \frac{3\left(-111-108\alpha-73\beta-72\alpha\beta+3M^2(-1+\omega)(3+2\beta)\right)}{\beta(w-3)-6}$$

The deceleration parameter q is another important cosmological quantity and it is defined as (in terms of redshift z)

$$q(z) = -1 + (1+z)\frac{1}{H(z)}\frac{dH(z)}{dz} \tag{26}$$

After inserting Eq. (25) in (26), we obtained the deceleration parameter for our model I as

$$q(z) = -1 + \frac{3\left(\omega(36\alpha(2\beta+3)+71\beta+105)-111\right)}{\beta(\omega-3)-6} + \frac{3\left(-72\alpha\beta-108\alpha-73\beta+3(2\beta+3)M^2(\omega-1)\right)}{\beta(\omega-3)-6} \tag{27}$$

In the linear case, we found a power-law solution to the Friedmann equations. A fascinating answer to several unusual problems, including flatness and the horizon problem, is power-law cosmology. The literature has a strong justification for the power-law cosmology. Kumar [39] examined cosmic parameters using power law and data from Hz and SNe Ia. Statefinder analysis was used by Rani et al. [40] to analyze the power-law cosmology. In power-law solution scenario, the expression of the deceleration parameter is constant. However, due to the constant value of the deceleration parameter, it fails to offer redshift transition from deceleration to acceleration.

B. Model II :- $f(Q,T) = \alpha Q^{m+1} + \frac{\beta}{6\kappa^2}T$

For our investigation, we also consider the non-linear functional form $f(Q,T) = \alpha Q^{m+1} + \frac{\beta}{6\kappa^2}T$, where α, β and m are free model parameters. For certain choices of model parameters, this model is also equivalent to ΛCDM model for certain redshift ranges.
Using this non-linear functional form and $\lambda = \kappa^2$ (for special case), we rewrite the field equations (20) and (21) as

$$-\left(\frac{\beta}{4}+\frac{1}{2}\right)+\frac{\beta}{12}p = (6m+3)\,\alpha\,6^m\,\psi^{2m+2} + \frac{1}{4}M^2\psi^2 + 3(\psi^2-H^2) \tag{28}$$

$$-\left(\frac{\beta}{4}+\frac{1}{2}\right)p+\frac{\beta}{12}\rho = 3\,\alpha\,6^m\,\psi^{2m+2} + \frac{M^2\psi^2}{4} + \left(3\psi^2+3H^2+2\dot{H}\right). \tag{29}$$

Further simplifying Eq.(28) and (29), we obtained the first order differential equation as

$$A\,H^{2m+1}(z) + B\,H(z) + C\,(1+z)\,\frac{dH(z)}{dz} = 0 \tag{30}$$

where $A = \frac{36\alpha(2m+1)6^{3m+2}}{-3\beta+\beta w-6} - \frac{36\alpha 6^{3m+2}}{\beta-3\beta w-6w}$, $B = \frac{108M^2+1260}{-3\beta+\beta w-6} - \frac{108M^2+1332}{\beta-3\beta w-6w}$, and $C = \frac{24}{\beta-3\beta w-6w}$ are constants.

The solution of the above differential equation is

$$H(z) = -\frac{A}{B} + \left(H_0+\frac{A}{B}\right)(1+z)^{\frac{2\,m\,B}{C}} \tag{31}$$

After inserting Eq. (31) in (26), we obtained the deceleration parameter for model II as

$$q(z) = -1 + \frac{2\,m\,B\left(\frac{A}{B}+H_0\right)(z+1)^{\frac{2\,m\,B}{C}}}{C\left(\left(\frac{A}{B}+H_0\right)(z+1)^{\frac{2\,m\,B}{C}} - \frac{A}{B}\right)} \tag{32}$$

In the nonlinear case, we found a hybrid solution to the Friedmann equations. In this scenario, the expression of the deceleration parameter is non-constant. As a result, for this instance, we can offer a redshift transition from deceleration to acceleration.

IV. OBSERVATIONAL DATA, MCMC RESULTS, AND INFORMATION CRITERIA

The most favorable Weyl $f(Q,T)$ models are taken into consideration in this work, and they are evaluated using various combinations of observational data sets. We use the publically accessible *emcee* software, which is available at Ref. [41], to conduct an MCMC (Monte Carlo Markov Chain) analysis for each Weyl $f(Q,T)$ model and data set combination. By altering the parameters in a variety of conservative priors and examining the posteriors of the parameter space, the MCMC sampler constrains the model and cosmological parameters. As

a result, we obtain the one- and two-dimensional distributions for each parameter, with the one-dimensional distribution representing the posterior distribution of the parameter and the two-dimensional distribution showing the covariance between two different values.
In the present section, we analyze observational datasets that will be used in our research, as well as the statistical methods that will be applied. We will specifically employ data from Type Ia supernovae. Further, we propose several information criteria that provide information on the fit's quality.

Pantheon+ Sample

One of the most recent compilations of spectroscopically confirmed Type Ia supernovae (SNeIa), which we call $Pantheon^{+}$; this sample is a direct inheritor of the Pantheon analysis [42], which itself succeeded the Joint Light-curve Analysis. In terms of cosmology, the fundamental distinction between the $Pantheon^{+}$ study and the original Pantheon analysis is the inclusion of fresh data sets in the latter. The $Pantheon^{+}$ analysis includes 1701 SNIa samples, up from 1048 in the original Pantheon analysis. The 1701 light curves of 1550 unique Type Ia supernovae (SNe Ia) in the redshift range $0.001 < z < 2.26$ make up the $Pantheon^{+}$ dataset [43, 44]. The constraining power of SNeIa evolves manifest when employed as standard candles. This can be accomplished by using the distance modulus:

$$\mu_{th} = 5log\left(\frac{d_L(\mathbf{x},z)}{Mpc}\right) + 25, \tag{33}$$

where d_L is the luminosity distance and it can be written as

$$d_L(\mathbf{x},z) = c(1+z)\int_0^z \frac{dz'}{H(\mathbf{x},z')}. \tag{34}$$

For the Pantheon sample, the chi-squared function χ^2_{SN} is defined as

$$\chi^2_{SN} = \mu_{SN} C^{-1} \mu^T_{SN}, \tag{35}$$

where $\mu_{SN} = \mu_i - \mu_{th}(\theta_s, z_i)$ and $\mu_i = \mu_{B,i} - M$. The apparent maximum magnitude for redshift z_i is represented here by $\mu_{B,i}$. The hyper-parameter M measures uncertainties from many sources. It is utilized instead of free parameters space $(H_0, \alpha, \beta, \omega, \mathcal{M})$ and $(H_0, \alpha, \beta, m, \omega, \mathcal{M})$ in the view of the "BEAMS" with Bias Corrections method [45].

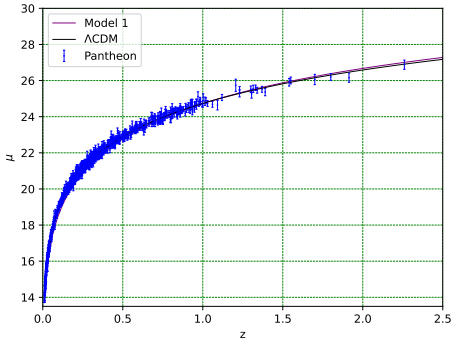


FIG. 1. The theoretical curve of distance modulus $\mu(z)$ of the model shown in blue line and ΛCDM model shown in black dotted line with $\Omega_{\rm m0} = 0.3$ and $\Omega_\Lambda = 0.7$, against $H(z)$ measurements are shown in blue dots with their corresponding error bars in magenta line.

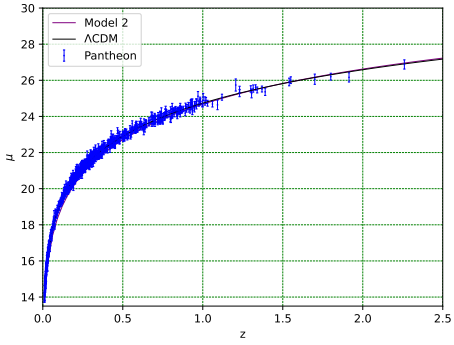


FIG. 2. The theoretical curve of distance modulus $\mu(z)$ of the model shown in blue line and ΛCDM model shown in black dotted line with $\Omega_{\rm m0} = 0.3$ and $\Omega_\Lambda = 0.7$, against $H(z)$ measurements are shown in blue dots with their corresponding error bars in magenta line.

MCMC Results Model I			
Model	Parameters	Priors	Best fit Value
ΛCDM Model	H_0	[50,100]	$69.854848^{+1.259100}_{-1.259100}$
Model I	H_0	[50,100]	$71.664375^{+0.797824}_{-0.797824}$
	α	[-2.,-1.]	$-1.069627^{+0.003345}_{-0.003345}$
	β	[0.2,0.8]	$0.502770^{+0.066665}_{-0.066665}$
	ω	[-1.2,-1.]	$-0.974603^{+0.358670}_{-0.358670}$
	$\mathcal{M}$	[-19.2334,0.0404]	$-19.272281^{+0.023579}_{-0.023579}$

TABLE I. Summary of the MCMC results using dataset.

MCMC Results of Model II			
Model	Parameters	Priors	Best fit Value
ΛCDM Model	H_0	[50,100]	$69.854848^{+1.259100}_{-1.259100}$
Model II	H_0	[50,100]	$71.804587^{+0.866627}_{-0.866627}$
	α	[-0.05,0.]	$-0.025867^{+0.016564}_{-0.016564}$
	β	[-1.6,-1.]	$-1.566355^{+0.020141}_{-0.020141}$
	m	[0.,0.05]	$0.026366^{+0.011292}_{-0.011292}$
	ω	[-0.4,0.]	$-0.184593^{+0.128431}_{-0.128431}$
	$\mathcal{M}$	[-19.2334,0.0404]	$-19.268359^{+0.024521}_{-0.024521}$

TABLE II. Summary of the MCMC results using dataset.

A. MCMC Results

We have presented the likelihood contours for the free parameters in our model, with $1-\sigma$ and $2-\sigma$ error, in Figs. 3 and 4, and shown the constrained values of these parameters at 68% confidence level in tables I and II. We have also compared our $f(Q,T)$ model with the ΛCDM model using the constrained values, and found that our model fits the observational data well with only marginal deviation from the ΛCDM model.

V. Om DIAGNOSTICS

In this study, we present a different approach that allows us to distinguish ΛCDM from other DE models without using the cosmic EOS directly [46]. The Om is geometrical diagnostics, and it is defined with the help of the Hubble parameter and redshift as

$$Om(z) = \frac{\left(\frac{H(z)}{H_0}\right)^2 - 1}{(1+z)^3 - 1} \tag{36}$$

where H_0 is the Hubble constant.
By observing the slope of $Om(z)$ trajectory, this diagnostic can be used to discriminate between various Dark energy models. The Dark energy behaves like a quintessence if the slope of $Om(z)$ trajectory is negative, whereas if the slope of $Om(z)$ trajectory is positive, the Dark energy behaves like a phantom. The zero slope of $Om(z)$ trajectory (means constant behavior of $Om(z)$) represents that Dark energy is a cosmological constant (ΛCDM). Fig. 5 clearly depicts this type of behavior. For our models, the evolutionary trajectory of $Om(z)$ shows a negative slope. That means our models show quintessence-like behavior.

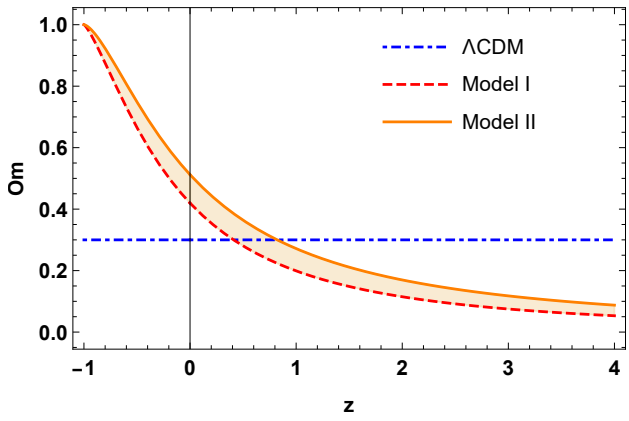


FIG. 5. The evolutionary trajectory of $Om(z)$ versus redshift z.

VI. INFORMATION CRITERIA

To analyze the sustainability of our model, we need to use one of the Information criteria (IC) such as the Akaike information criterion (AIC) [47], which is commonly used in model selection and given by [48–51] $\mathrm{AIC} = -2\ln(\mathcal{L}_{max}) + 2\kappa + \frac{2\kappa(\kappa+1)}{N-\kappa-1}$, where $\mathcal{L}_{max}$ is the maximum likelihood function, κ is the total number of model parameters, and N is the total number of data points used to fit the model. For large N, this formula reduces to the simpler expression $\mathrm{AIC} = -2\ln(\mathcal{L}_{max}) + 2\kappa$. The AIC can be used to compare the goodness-of-fit of different models, with the model having the lowest AIC being the most favored. The difference in AIC between two models is denoted by $\triangle\mathrm{AIC} = \mathrm{AIC}_{model} - \mathrm{AIC}_{min} = \triangle\chi^2_{min} + 2\triangle\kappa$, where $\triangle\chi^2_{min}$ is the difference in the minimum χ^2 values between the models and $\triangle\kappa$ is the difference in the number of parameters. Typically, $\triangle$AIC values in the range of $(0,2)$ are considered strongly supportive of a model, while values in the range of $(4,7)$ are weakly supportive. Values greater than 10 provide little or no support for a model.

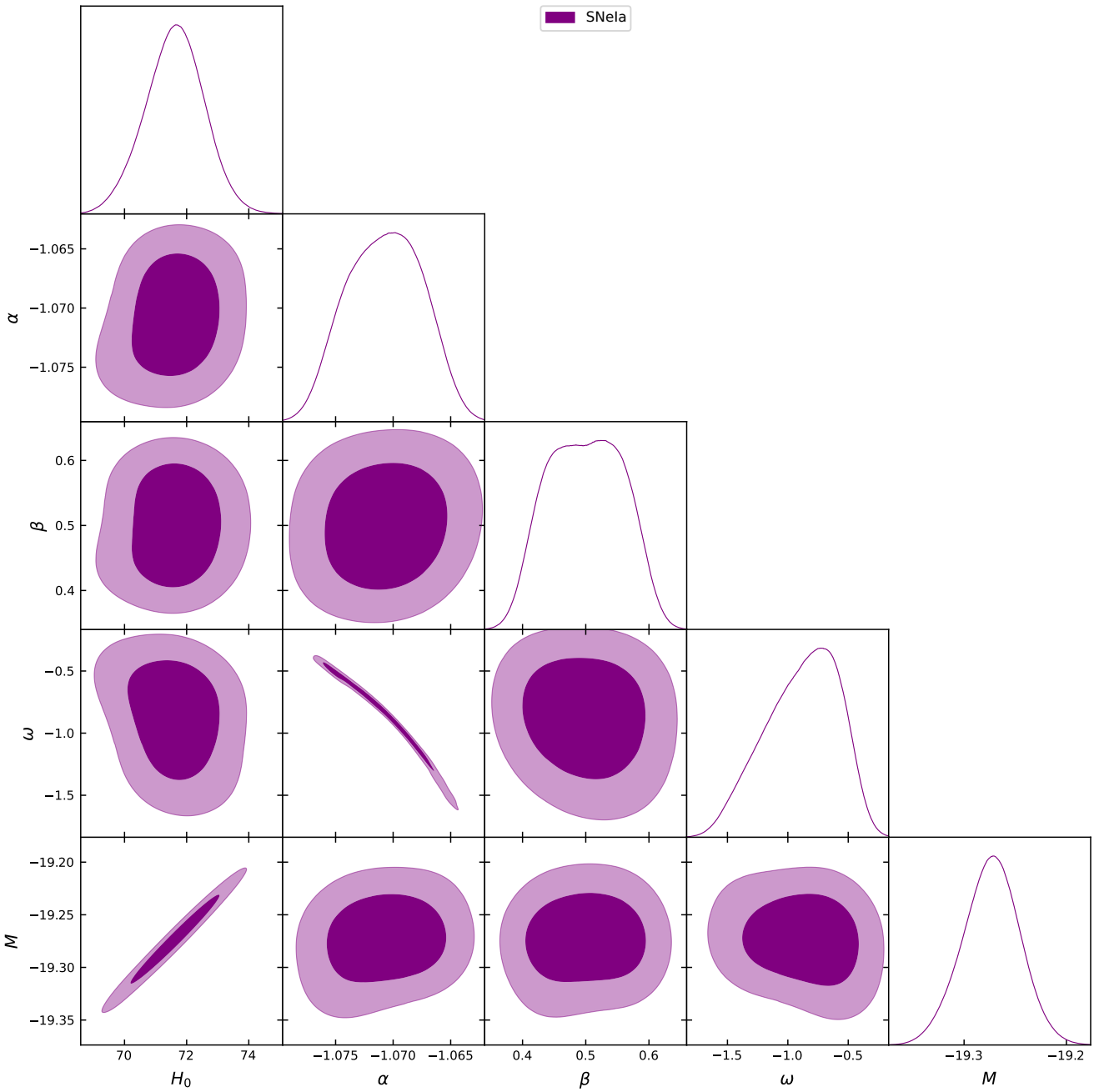


FIG. 3. The contour plot of free parameter space $(H_0, \alpha, \beta, \omega, \mathcal{M})$ for our model I with $1-\sigma$ and $2-\sigma$ errors obtained from the datasets.

Model	χ^2_{min}	χ^2_{red}	AIC	ΔAIC
ΛCDM Model	1100.89	0.982788	1107.84	0
Model I	1099.81	0.982230	1106.91	0.93367
Model II	1100.00	0.983378	1106.91	3.13595

TABLE III. Summary of the χ^2_{min}, χ^2_{red}, AIC and ΔAIC.

Model	$q(z=0)$	$\omega(z=0)$	$Om(z=0)$
ΛCDM Model	-0.535	-1	0.31
Model I	-0.37056	-0.974603	0.41963
Model II	-0.231809	-0.184593	0.51196

TABLE IV. The qualitative behavior of the models under consideration along with the ΛCDM model.

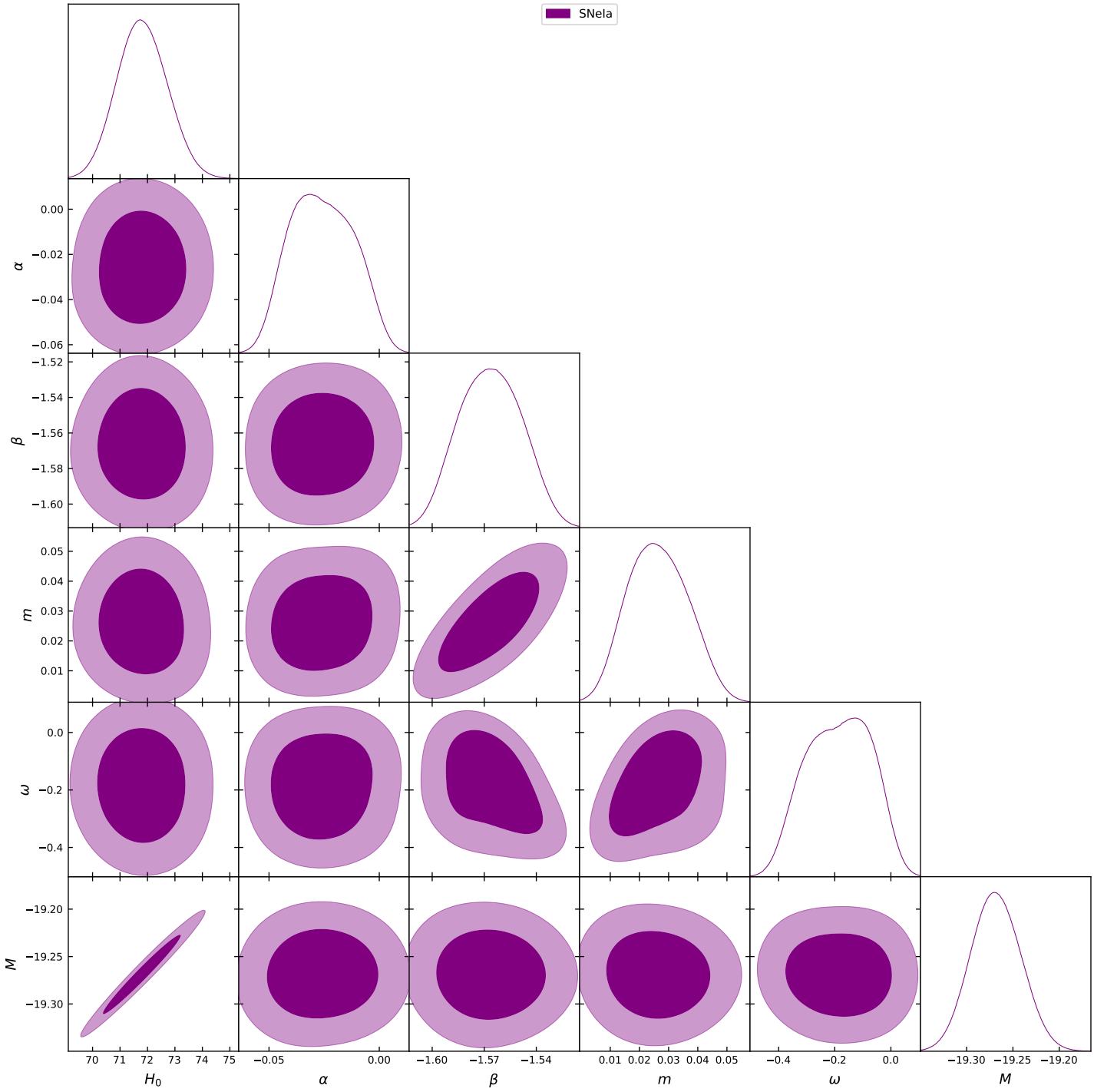


FIG. 4. The contour plot of free parameter space $(H_0, \alpha, \beta, m, \omega, \mathcal{M})$ for our model II with $1-\sigma$ and $2-\sigma$ errors obtained from the datasets.

VII. CONCLUSION

Explaining late-time acceleration is currently one of the biggest issues. To show some light on this issue, recently the Weyl-type $f(Q,T)$ theory of gravity has been proposed. In this theory, the non-metricity $Q_{\sigma\mu\nu}$ of the space-time is depicted in its standard Weyl form, and it is completely specified by a vector field w_μ.

In this work, we have used the latest observational data from the $SNIa$ $Pantheon^+$ sample in order to extract constraints on free parameter space in the framework of Weyl-type $f(Q,T)$ gravity. We know that the ΛCDM model is the most consistent model. It will be beneficial to compare our models with the ΛCDM model in order to examine how our Weyl $f(Q,T)$ models differ from the ΛCDM model in more detail. We use the Akaike Information Criteria (AIC) to compare the models to the standard ΛCDM, which takes into consideration both the goodness of fit (measured by χ^2_{min}) and the complexity of the model (defined by the number of parameters). In table III, we can see that the calculated values of χ^2_{min}, χ^2_{red}, AIC and ΔAIC. Our analysis revealed that the models under consideration are generally consistent with the ΛCDM model.

Due to the fact that different observational studies found varied values for H_0, the H_0-tension is a relatively new problem in modern cosmology. We can see the different values of H_0 in references [52–57]. Because of this problem, we intend to constrain the Hubble constant H_0 in the context of Weyl-type $f(Q,T)$ theory using the $Pantheon^+$ samples. For our MCMC analysis, the constrained values of H_0 as $H_0 = 71.664375^{+0.797824}_{-0.797824}$ kms^{-1} Mpc^{-1} and $H_0 = 71.804587^{+0.866627}_{-0.866627}$ kms^{-1} Mpc^{-1} for model I and model II, respectively.

As we know, some cosmological parameters, like equation-of-state and deceleration parameters, are crucial in defining the cosmic evolution of the universe. And it is well comprehended that the equation-of-state parameter implies a variety of fluid universe descriptions. With the help of the equation-of-state parameter, we can predict the present scenario of the universe by either quintessence ($-1 < \omega < -1/3$) or phantom ($\omega < -1$) behavior. For our MCMC analysis, we obtained the equation-of-state parameter values as $\omega = -0.974603^{+0.358670}_{-0.358670}$ and $\omega = -0.184593^{+0.128431}_{-0.128431}$ for model I and model II, respectively. One can see that the value of the EoS parameter of model I is well compatible with ΛCDM as compared to model II, and both models show the quintessence-like behavior of the universe. Further, we check the present value of deceleration parameter q_0 and it is obtained as $q_0 = -0.37056$ and $q_0 = -0.231809$ using the constrained values of free parameter for $Pantheon^+$ samples. The value of q_0 shows that our Weyl type $f(Q,T)$ models explain the present acceleration expansion of the universe. Further, we test our model using Om diagnostic and compare it to the ΛCDM model to determine its dark energy profile. The evolution trajectory of $Om(z)$ diagnostic with a negative slope is clearly visible in Fig. 5. This negative slope of trajectory shows that our model is in a quintessence phase.

In conclusion, our Weyl type $f(Q,T)$ models agree with observational data and could be a candidate for dark energy nature's description. Also, the statistical and cosmological point of view the Weyl $f(Q,T)$ model I (linear model) is more compatible with the ΛCDM model than Weyl $f(Q,T)$ model II (nonlinear model).

Data availability There are no new data associated with this article.

VIII. ACKNOWLEDGEMENTS

GNG acknowledges University Grants Commission (UGC), New Delhi, India for awarding Junior Research Fellowship (UGC-Ref. No.: 201610122060). PKS acknowledges the Science and Engineering Research Board, Department of Science and Technology, Government of India for financial support to carry out Research Project No.: CRG/2022/001847 and IUCAA, Pune, India for providing support through the visiting Associateship program.

[1] A. G. Riess, et al., The farthest known supernova: support for an accelerating universe and a glimpse of the epoch of deceleration, Astrophys. J. 560 (2001) 49–71. arXiv:astro-ph/0104455, doi:10.1086/322348.

[2] S. Perlmutter, M. S. Turner, M. White, Constraining dark energy with type ia supernovae and large-scale structure, Physical Review Letters 83 (4) (1999) 670.

[3] First year Wilkinson Microwave Anisotropy Probe (WMAP) observations: Preliminary maps and basic results, Astrophys. J. Suppl. 148 (2003) 1–27. arXiv:astro-ph/0302207, doi:10.1086/377253.

[4] First year Wilkinson Microwave Anisotropy Probe (WMAP) observations: The Angular power spectrum, Astrophys. J. Suppl. 148 (2003) 135. arXiv:astro-ph/0302217, doi:10.1086/377225.

[5] D. J. Eisenstein, I. Zehavi, D. W. Hogg, R. Scoccimarro, M. R. Blanton, R. C. Nichol, R. Scranton, H.-J. Seo, M. Tegmark, Z. Zheng, et al., Detection of the baryon acoustic peak in the large-scale correlation function of sdss luminous red galaxies, The Astrophysical Journal 633 (2) (2005) 560.

[6] T. Koivisto, D. F. Mota, Dark energy anisotropic stress and large scale structure formation, Physical Review D 73 (8) (2006) 083502.

[7] P. J. E. Peebles, B. Ratra, The cosmological constant and dark energy, Reviews of modern physics 75 (2) (2003)

559.
[8] V. Sahni, A. A. Starobinsky, The Case for a positive cosmological Lambda term, Int. J. Mod. Phys. D 9 (2000) 373–444. arXiv:astro-ph/9904398, doi:10.1142/S0218271800000542.
[9] H. A. Buchdahl, Non-linear lagrangians and cosmological theory, Monthly Notices of the Royal Astronomical Society 150 (1) (1970) 1–8.
[10] A. A. Starobinsky, Disappearing cosmological constant in f (r) gravity, JETP letters 86 (2007) 157–163.
[11] S. Capozziello, V. Cardone, H. Farajollahi, A. Ravanpak, Cosmography in f (t) gravity, Physical Review D 84 (4) (2011) 043527.
[12] T. Harko, F. S. Lobo, S. Nojiri, S. D. Odintsov, f (r, t) gravity, Physical Review D 84 (2) (2011) 024020.
[13] N. Goheer, R. Goswami, P. K. Dunsby, K. Ananda, Coexistence of matter dominated and accelerating solutions in f (g) gravity, Physical Review D 79 (12) (2009) 121301.
[14] E. Elizalde, R. Myrzakulov, V. V. Obukhov, D. Saez-Gomez, LambdaCDM epoch reconstruction from F(R,G) and modified Gauss-Bonnet gravities, Class. Quant. Grav. 27 (2010) 095007. arXiv:1001.3636, doi:10.1088/0264-9381/27/9/095007.
[15] J. M. Nester, H.-J. Yo, Symmetric teleparallel general relativity, arXiv preprint gr-qc/9809049 (1998).
[16] J. B. Jiménez, L. Heisenberg, T. Koivisto, Coincident general relativity, Physical Review D 98 (4) (2018) 044048.
[17] T. Harko, T. S. Koivisto, F. S. Lobo, G. J. Olmo, D. Rubiera-Garcia, Coupling matter in modified q gravity, Physical Review D 98 (8) (2018) 084043.
[18] S. Mandal, D. Wang, P. Sahoo, Cosmography in f (q) gravity, Physical Review D 102 (12) (2020) 124029.
[19] N. Frusciante, Signatures of f (q) gravity in cosmology, Physical Review D 103 (4) (2021) 044021.
[20] W. Khyllep, A. Paliathanasis, J. Dutta, Cosmological solutions and growth index of matter perturbations in f (q) gravity, Physical Review D 103 (10) (2021) 103521.
[21] I. Ayuso, R. Lazkoz, V. Salzano, Observational constraints on cosmological solutions of f (q) theories, Physical review d 103 (6) (2021) 063505.
[22] G. N. Gadbail, S. Mandal, P. Sahoo, Reconstruction of λcdm universe in f (q) gravity, Physics Letters B 835 (2022) 137509.
[23] S. Capozziello, R. D'Agostino, Model-independent reconstruction of f (q) non-metric gravity, Physics Letters B 832 (2022) 137229.
[24] W. Wang, H. Chen, T. Katsuragawa, Static and spherically symmetric solutions in f (q) gravity, Physical Review D 105 (2) (2022) 024060.
[25] Y. Xu, G. Li, T. Harko, S.-D. Liang, f (q, t) gravity, The European Physical Journal C 79 (2019) 1–19.
[26] S. Arora, S. K. J. Pacif, S. Bhattacharjee, P. K. Sahoo, $f(Q,T)$ gravity models with observational constraints, Phys. Dark Univ. 30 (2020) 100664. arXiv:2007.01703, doi:10.1016/j.dark.2020.100664.
[27] S. Arora, A. Parida, P. Sahoo, Constraining effective equation of state in f (q, t) gravity, The European Physical Journal C 81 (2021) 1–7.
[28] G. N. Gadbail, S. Arora, P. Sahoo, Generalized chaplygin gas and accelerating universe in f (q, t) gravity, Physics of the Dark Universe 37 (2022) 101074.
[29] S. Bhattacharjee, P. Sahoo, Baryogenesis in f (q, t) gravity, The European Physical Journal C 80 (3) (2020) 289.
[30] A. Nájera, A. Fajardo, Cosmological perturbation theory in f (q, t) gravity, Journal of Cosmology and Astroparticle Physics 2022 (03) (2022) 020.
[31] G. N. Gadbail, S. Arora, P. Sahoo, Reconstruction of f (q, t) lagrangian for various cosmological scenario, Physics Letters B (2023) 137710.
[32] M. Tayde, Z. Hassan, P. Sahoo, S. Gutti, Static spherically symmetric wormholes in gravity, Chinese Physics C 46 (11) (2022) 115101.
[33] M. Tayde, S. Ghosh, P. K. SAHOO, Non-exotic static spherically symmetric thin-shell wormhole solution in f(q,t) gravity, Chinese Physics C (2023).
[34] Y. Xu, T. Harko, S. Shahidi, S.-D. Liang, Weyl type f (q, t) gravity, and its cosmological implications, The European Physical Journal C 80 (5) (2020) 1–22.
[35] J.-Z. Yang, S. Shahidi, T. Harko, S.-D. Liang, Geodesic deviation, raychaudhuri equation, newtonian limit, and tidal forces in weyl-type f (q, t) gravity, The European Physical Journal C 81 (2021) 1–19.
[36] G. Gadbail, S. Arora, P. Sahoo, Power-law cosmology in weyl-type f (q, t) gravity, The European Physical Journal Plus 136 (10) (2021) 1040.
[37] G. N. Gadbail, S. Arora, P. Sahoo, Viscous cosmology in the weyl-type f (q, t) gravity, The European Physical Journal C 81 (12) (2021) 1088.
[38] H. Weyl, Gravitation und elektrizität', sitzungsberichte der preuÿ, Akad. Berlin, Math. Kl (1918) 465.
[39] Observational constraints on Hubble constant and deceleration parameter in power-law cosmology, Mon. Not. Roy. Astron. Soc. 422 (2012) 2532–2538. arXiv:1109.6924, doi:10.1111/j.1365-2966.2012.20810.x.
[40] J. Singh, S. Rani, Modified chaplygin gas cosmology with statefinder diagnostic in lyra geometry, Applied Mathematics and Computation 259 (2015) 187–197.
[41] C. Zhang, H. Zhang, S. Yuan, S. Liu, T.-J. Zhang, Y.-C. Sun, Four new observational h (z) data from luminous red galaxies in the sloan digital sky survey data release seven, Research in Astronomy and Astrophysics 14 (10) (2014) 1221.
[42] D. M. Scolnic, D. Jones, A. Rest, Y. Pan, R. Chornock, R. Foley, M. Huber, R. Kessler, G. Narayan, A. Riess, et al., The complete light-curve sample of spectroscopically confirmed sne ia from pan-starrs1 and cosmological constraints from the combined pantheon sample, The Astrophysical Journal 859 (2) (2018) 101.
[43] D. Brout, D. Scolnic, B. Popovic, A. G. Riess, A. Carr, J. Zuntz, R. Kessler, T. M. Davis, S. Hinton, D. Jones, et al., The pantheon+ analysis: cosmological constraints, The Astrophysical Journal 938 (2) (2022) 110.
[44] D. Scolnic, D. Brout, A. Carr, A. G. Riess, T. M. Davis, A. Dwomoh, D. O. Jones, N. Ali, P. Charvu, R. Chen, et al., The pantheon+ analysis: The full data set and light-curve release, The Astrophysical Journal 938 (2) (2022) 113.
[45] R. Kessler, D. Scolnic, Correcting type ia supernova distances for selection biases and contamination in photometrically identified samples, The Astrophysical Journal 836 (1) (2017) 56.
[46] V. Sahni, A. Shafieloo, A. A. Starobinsky, Two new diagnostics of dark energy, Physical Review D 78 (10) (2008) 103502.
[47] H. Akaike, A new look at the statistical model identification, IEEE transactions on automatic control 19 (6) (1974) 716–723.

[48] M. Li, X. Li, X. Zhang, Comparison of dark energy models: A perspective from the latest observational data, Science China Physics, Mechanics and Astronomy 53 (2010) 1631–1645.

[49] K. P. Burnham, D. R. Anderson, K. P. Huyvaert, Aic model selection and multimodel inference in behavioral ecology: some background, observations, and comparisons, Behavioral ecology and sociobiology 65 (2011) 23–35.

[50] K. P. Burnham, D. R. Anderson, Multimodel inference: understanding aic and bic in model selection, Sociological methods & research 33 (2) (2004) 261–304.

[51] A. R. Liddle, Information criteria for astrophysical model selection, Monthly Notices of the Royal Astronomical Society: Letters 377 (1) (2007) L74–L78.

[52] Scalar dark matter in the A4-based texture one-zero neutrino mass model within the inverse seesaw mechanism, PTEP 2021 (12) (2021) 123B01, [Erratum: PTEP 2022, 039301 (2022)]. arXiv:2102.03074, doi:10.1093/ptep/ptep130.

[53] J. Henning, J. Sayre, C. Reichardt, P. Ade, A. Anderson, J. Austermann, J. Beall, A. Bender, B. Benson, L. Bleem, et al., Measurements of the temperature and e-mode polarization of the cmb from 500 square degrees of sptpol data, The Astrophysical Journal 852 (2) (2018) 97.

[54] S. Aiola, E. Calabrese, L. Maurin, S. Naess, B. L. Schmitt, M. H. Abitbol, G. E. Addison, P. A. Ade, D. Alonso, M. Amiri, et al., The atacama cosmology telescope: Dr4 maps and cosmological parameters, Journal of Cosmology and Astroparticle Physics 2020 (12) (2020) 047.

[55] L. Balkenhol, D. Dutcher, P. Ade, Z. Ahmed, E. Anderes, A. Anderson, M. Archipley, J. Avva, K. Aylor, P. Barry, et al., Constraints on λ cdm extensions from the spt-3g 2018 e e and t e power spectra, Physical Review D 104 (8) (2021) 083509.

[56] L. Balkenhol, D. Dutcher, P. Ade, Z. Ahmed, E. Anderes, A. Anderson, M. Archipley, J. Avva, K. Aylor, P. Barry, et al., Constraints on λ cdm extensions from the spt-3g 2018 e e and t e power spectra, Physical Review D 104 (8) (2021) 083509.

[57] A. Bouali, H. Chaudhary, A. Mehrotra, S. Pacif, Model-independent study for a quintessence model of dark energy: Analysis and observational constraints, arXiv preprint arXiv:2304.02652 (2023).

Steerable Pyramid-based Multi-Scale Fusion Algorithm for Single Image Dehazing

Paulami Purkayastha
Department of Electronics and Communication Engineering
Delhi Technological University
Delhi, India
paulamipurkayastha@gmail.com

M. S. Choudhary
Department of Electronics and Communication Engineering
Delhi Technological University
Delhi, India
msc_1976@yahoo.com

Manjeet Kumar
Department of Electronics and Communication Engineering
Delhi Technological University
Delhi, India
manjeetchhillar@dtu.ac.in

2023 International Conference on Device Intelligence, Computing and Communication Technologies, (DICCT) | 978-1-6654-7491-7/23/$31.00 ©2023 IEEE | DOI: 10.1109/DICCT56244.2023.10110293

***Abstract*—Multi-Scale Fusion Technique employs different versions of the image to be dehazed to extract haze-relevant parameters that aid in image dehazing. The paper proposes a variant of the technique using a Steerable Pyramid has been proposed. The proposed method extracts steer-coefficient matrices from the original hazy image and incorporates them into the multi-scale fusion algorithm. The proposed technique aims to reduce the halo effect observed in image-dehazing applications and related works. Moreover, this paper aims at the quality improvement of the output image by the novel algorithm it proposes. Quantitative, as well as a visual display of results, using the I-HAZE dataset, give an accurate interpretation of the effectiveness of the proposed work.**

Keywords—Laplacian Pyramid, Steerable Pyramid, Gaussian Pyramid, Multi-Scale Fusion, Single Image Dehazing, MATLAB.

I. INTRODUCTION (*HEADING 1*)

Images captured in real life are often found to be, blurred, smokey or low in contrast. The noisy characteristic of such an image is called 'haze' in image processing terminology and the method to remove haze from images is called Image Dehazing. Atmospheric dust, pollution, water vapor, smog, low lighting and shaky photography are some causes of haze. A 'Clear Image' has harp object boundaries, good contrast and has been taken under good lighting conditions. Forensic photography, satellite imaging, remote sensing, record keeping, robotic vision, etc., are some of the areas that cannot function without a Clear Image. This fact along with the growing advancements in photo-editing, journaling and drones, make Image Dehazing a prime area for research. The vast research on Image dehazing can be categorized based on the 'dehazing process that is followed by the researcher. The flow chart of Figure 1 gives a brief idea about the different image dehazing approaches available in the literature. Under the aegis of image dehazing by Image Enhancement, the research area mainly focuses on improving the view of hidden objects in the image. The paper by B. Soni et al. [5], uses Contrast Limited Adaptive Histogram Equalization (CLAHE) method followed by an FIR Decomposition filter to dehaze hazy images. Another sub-branch of Image enhancement is the Retinex method employed in papers like [6] and [7], which make use of bio-inspired algorithms and fuzzy logic, respectively, in their modification of the Retinex method. The next category of Image Dehazing is dehazing by Restoration which is different from Image Enhancement, because, the latter does not require the researcher to know the exact degradations plaguing the image.

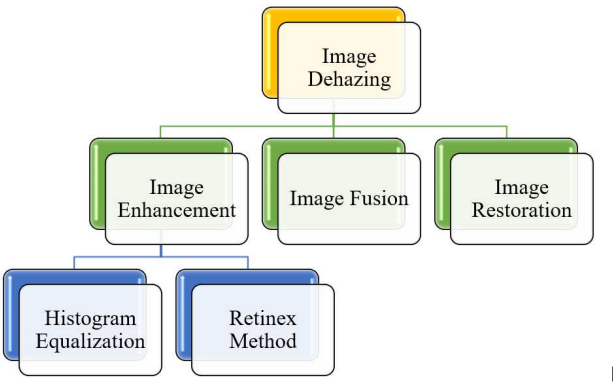


Figure 1: Classifying Dehazing Algorithms

Image Restoration in its fullest sense is a method that aims at re-doing or inverting the degradations performed on the image, that made it blurry in the first place. In a general sense, the Image Restoration method for Image Dehazing is a Restoration-Degradation model [8]. The paper by Kaiming He et al. [9], was a landmark in this category, since, the mainstream method of Dark Channel Prior (DCP) was first introduced in their paper. The method first finds a depth map corresponding to the non-sky patches in the image and then extracts a dark channel (DCP) from it. The dark channel defines the pixels that have abnormally low intensities and which form the transmission map. The papers by Tang et al. [10], explore haze-relevant characteristics of the hazy image and discover a multi-scale dark channel, hue-disparities, etc. and remove them to obtain a clear image. Image Restoration, however, mandates the use of a transmission map/ depth map/ image prior for image dehazing. Image Enhancement offers a significant advantage in this sense but, it is not efficient in case there are multiple images of the same scene or object just like in the case of the databases of Geographic Interphase System (GIS), where, there is a vast array of images of the same area from different angles and depth. Image Fusion then takes the lead because the method works by inculcating features from all available images of the scene/object under surveillance. Furthermore, in instances where images of a 'moving' object, like a human lung, growing cancer tumour, etc., are recorded, image fusion becomes necessary to combine all geometric transformations of the object to form a single master image.

The inspiration of this work is taken from Ancuti et al. [1] and Dalvi et al [2] and aims to modify the procedure by using a Steerable kernel. From the previous works in literature, it is observed that most works extract weight

Authorized licensed use limited to: DELHI TECHNICAL UNIV. Downloaded on May 04,2023 at 06:35:17 UTC from IEEE Xplore. Restrictions apply.

maps from the original input and then derive coefficient matrices from them. These matrices thus generated, provide the required multi-image scenario for image fusion [11-14]. The methodology proposed inculcates information from the original input along with the coefficients derived from weight maps as inputs to the fusion pyramid structure. This paper transmits the original image via a steerable pyramid [3] to obtain 'Steer Coefficients'. The coefficients are passed through a gaussian pyramid and correspondingly a matrix called a steer-gauss map is achieved. Additionally, Contrast-Enhancement and White balancing operations are performed on the input image to generate two corresponding weight maps. The weight maps and the steer-gauss map are used to generate a final weight map that acts as an input to the Laplacian pyramid. Finally, a fusion of the images as suggested by Ancuti et. al. [1] is performed to get the dehazed output. Therefore, this multi-scale fusion technique uses all three types of pyramid kernels and the coefficients from the unaltered image input, to compute the dehazed fusion image. The multi-scale fusion technique has been adopted because it helps in recovering hidden information from the original hazy image and is more efficient than the Image Enhancement and Restoration categories. Further, the steer coefficients derived from the hazy image prevent any loss of information that may arise while extracting contrast-enhanced and white-balanced coefficient matrices. The gaussian pyramid is a smoothing pyramid that removes the characteristic 'halo' observed around objects in the steer coefficient matrix. The Laplacian kernel is used to enhance the edges around the objects present in the image. In the proposed work, the Laplacian pyramid technique is used twice, once while computing corresponding weight maps of contrast-enhanced and white-balanced coefficient matrices and second, while generating the fused image. Further, normalization is performed before transmitting via the different kernels to avoid artefacts. The proposed technique is a per-pixel technique and thus does not need to estimate airlight (light reflected from nearby objects/secondary sources) for every region in the image. Moreover, since most techniques assume uniform airlight throughout the scene (which is not true in real-life), inaccurate results are a frequent occurrence. Hence, the proposed technique is said to maintain the originality of the scene through the airlight-free technique of fusion. This advantage stems from the fact that the proposed technique does not depend on Koschmeider's model for Image Dehazing. Also, the method proposed is efficient and independent because it derives all its weight maps from the single hazy image provided and does not need a transmission map for computations. The dataset I-Haze [4] is selected to test the algorithm proposed. The dehazed result has been compared with the previous methods in literature and performance metrics like PSNR, BRISQUE etc. are calculated and compared with previous related papers.

II. Related works

The fundamental research area for Image Fusion focuses on determining the best algorithm to combine the images and the best scale-space representation of the images. The common practice is to either combine multispectral images or form a single image for fusion to enhance the original image. First, two images are to be aligned so that the pixels are in corresponding positions. Next, the images are decomposed using frequency or wavelet transforms of choice. The High-High (H-H), High-Low (H-L), Low-High (L-H) and Low-Low (L-L) sub-bands are thus obtained at the coarsest level. Except for the low-low band, all other bands have non-positive values corresponding to the "salient features" of the image indicating the edges, troughs and lines. As a result, it is always better to integrate the greater absolute value out of the two for each pixel location and thus perform the fusion. Lastly, an inverse transform gives a dehazed image. The paper [11] uses specific maps to weigh the image and then creates a fusion using the resultant weights. Another paper by the same author takes the concept one step further by using the Multi-Scale Fusion technique that employs using more than one version of the original image. As given in [1], they compute three weighting maps containing weights of luminance, chromaticity, and saliency and then reduce irregularities. In the paper [12], the encoder captures input images, while the decoder captures outputs. The outputs are computed after passing the test image through the trained network. The constructed network has a fusion plan of finding specific inputs from the test hazy image. This is done by first White Balance, second Contrast Enhancing, and finally, Gamma Correction. Lastly, pixel-based confidence maps are computed to preserve good colour visibility. These papers list the importance of fusion in image dehazing applications. For underwater enhancements too, image fusion works well as shown in the paper [13]. For colour images, the FWT using the technique of the weight as suggested by [14] is efficient. It is noteworthy that the research on fusion pyramids for Image Dehazing started with the landmark paper by Andelson & Anderson et al [15] which introduced the pyramid methods to process images. Since then, many types and combinations of kernels have been explored for pyramids, of which, the most popular (used in [11] & [1]), is the gaussian kernel in which gaussian filters are used to smoothen the pixels as a step in pyramid generation stage. In this pyramid, blurring gives the next level, which is again blurred to form subsequent levels. This method ensures that each pixel corresponds to the local average of its neighbours in the lower level. The gaussian pyramid is nothing but a chain of down-sampling operations. The next type of kernel is the Laplacian kernel which is a slight modification of the gaussian kernel in the sense that here each level has a laplacian coefficient which equals the difference of levels in the gaussian pyramid. Though these definitions prove to be quite simple, however, the computations involved require an upscaling of the smaller image to allow subtraction between the two levels. The Laplacian pyramid is just a low-frequency vestigial of the gaussian pyramid. Both of the kernels defined above employ only one kernel at each subsequent step. The Steerable Pyramid method, suggested by Simoncelli et al. [3], is an advancement that employs a multi-scale pyramid having multiple directional orientations. In other words, it can be thought of as a band-pass filter bank which is an orientation-specific version of the Laplacian pyramid.

III. Background theory

Luminance is the directional intensity of light rays emitted from an object. In case of the presence of an external light

Authorized licensed use limited to: DELHI TECHNICAL UNIV. Downloaded on May 04,2023 at 06:35:17 UTC from IEEE Xplore. Restrictions apply.

TABLE I Quantitative analysis of the proposed method versus the results of Ancuti et al. [1].

Images	Ancuti et al.					Proposed Method				
	SSIM	PSNR	MSE	NIQE	BRISQUE	SSIM	PSNR	MSE	NIQE	BRISQUE
Teapot	0.3655	9.9760	0.1006	3.1032	28.1294	0.3604	10.2633	0.0941	2.9038	18.8559
Teddy	0.5238	11.4789	0.0711	3.9488	31.4826	0.5624	13.0917	0.0491	3.3473	22.8193
Telescope	0.4955	10.0528	0.0988	3.0803	30.7487	0.4136	9.7064	0.1070	3.0505	20.1761
Playroom	0.5684	10.7115	0.0849	3.7728	38.9794	0.5509	11.0553	0.0784	3.3548	30.7017

source, It is the light which gets reflected from the object or objects in the scene under consideration and enters the camera lens. The Image Degradation model or Atmospheric Scattering model relates the attenuation of luminance, through the atmosphere, with the degraded image. If $I(x)$ is the degraded image and $J(x)$ is its restored version, then, the Atmospheric scattering model gives the following equation;

$$I(x) = J(x)t(x) + A(1 - t(x)) \quad (1)$$

Where $t(x)$ stands for 'direct transmission' and 'A' is the Airlight of the scene.

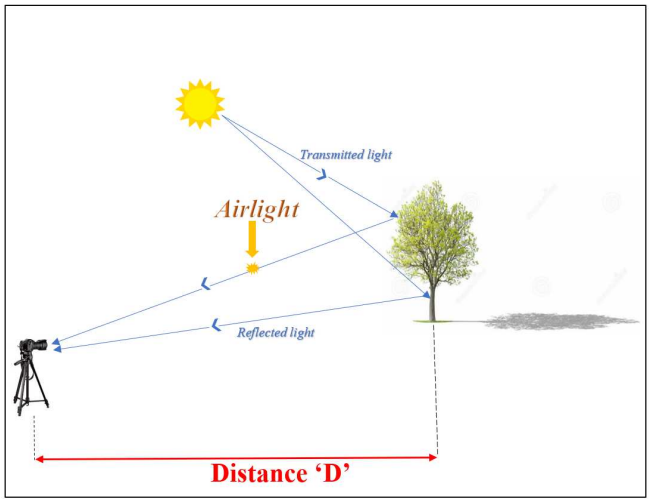


Figure 2: Atmospheric Scattering Model

The 'direct transmission can be defined with the help of the atmospheric scattering coefficient (β), which is a parameter governing the amount of scattering suffered by the rays reflected by the object.

$$t(x) = e^{\beta d} \quad (2)$$

Where d(x) is denoted by 'D' in Figure 2. The other parameters used can be visualized in the adjoined Figure 2.

IV. FUSION-BASED DEHAZING

A. Derived Inputs

1) White Balanced Image: In real life, on a camera-clicked picture, the unnatural shade of colour overlaying the real colours is pretty evident. This tone of colour is not visible to the naked eye because the brain generally compensates for this unnaturalistic phenomenon. However, for the camera-taken pictures, the employed technique is called white balancing.

2) Contrast Enhanced Image: Contrast enhancement has been employed in this paper in order to search for any hidden details in structure or texture of the hazy image.

B. Weight Maps

1) Weight Map from Gaussian and Steerable Pyramid: A Steerable pyramid structure [16] is multi-scale, translation invariant and self-inverting in nature. In other words, it can be used for multiple representations of the same image and the coefficients obtained in between the process, are of the same size as the original image.

ALGORITHM 1: ALGORITHM TO CONSTRUCT WHITE BALANCED IMAGE

Input: RGB Components of Hazy Image; $\{Im = [R\ G\ B]\}$
Output: White Balanced RGB Components; $\{Im_{wb} = [R_w\ G_w\ B_w]\}$
Step 1: Compute the average of RGB components (Ravg)
  for (R ϵ Im (: ,:, 1); G ϵ Im (: ,:, 2); B ϵ Im (:,:,3))
    Ravg = Avg (R)
    Gavg = Avg (G)
    Bavg = Avg (B)
  end
Step 2: Compute Gray Value (GV)
  while (*Im_avg = [Ravg Gavg Bavg]*)
  do: $GV = sum \frac{Im_{avg}}{size(Im_{avg}, 2)}$
  end
Step 3: Compute Scale Value (SV)
  $sv = \frac{GV}{Im_{avg}}$
Step 4: White Balanced RGB Components [Rw Gw Bw]
  while (SV ϵ $[sv_R\ sv_G\ sv_B]$)
  do: *Rw = SV{1} * R*
    *Gw = SV{2} * G*
    *Bw = SV{3} * B*
  end

ALGORITHM 2: ALGORITHM TO CONSTRUCT CONTRAST-ENHANCED IMAGE

Input: RGB Components of Hazy Image; $\{Im = [R\ G\ B]\}$
Output: Contrast-Enhanced RGB Components; $\{Im_{ce} = [R_{ce}\ G_{ce}\ B_{ce}]\}$
Step 1: Compute Luminance (L)
  for (R ϵ Im (:,:, 1); G ϵ Im (: ,:, 2); B ϵ Im (:,:,3))
    $L_R = 0.299 \times R$
    $L_G = 0.587 \times G$
    $L_B = 0.114 \times B$
  end
Step 2: Determine Colour Balancing Constant (*Gamma*)
  while $(L = [L_R\ L_G\ L_B])$
    $g = 2(0.5 + Avg(L))$ // *Gamma is a constant denoted by g*
  end
Step 3: Compute Contrast Enhanced RGB components
  for (R ϵ Im (:,:, 1); G ϵ Im (: ,:, 2); B ϵ Im (:,:,3))
    $R_{ce} = g(R - Avg(L))$
    $G_{ce} = g(G - Avg(L))$
    $B_{ce} = g(B - Avg(L))$
  end

This is because the projections of the steerable filters and that of the basis functions are identical [17]. The image is first filtered through steerable kernels. Kernels are matrices that are concatenated to form filters (Figure 3). The image is thus split into a highpass component and other residuals.

Authorized licensed use limited to: DELHI TECHNICAL UNIV. Downloaded on May 04,2023 at 06:35:17 UTC from IEEE Xplore. Restrictions apply.

TABLE II Quantitative analysis of the results of Dalvi et al. [2] versus the proposed method.

Images	Dalvi et al.					Proposed Method				
	SSIM	PSNR	MSE	NIQE	BRISQUE	SSIM	PSNR	MSE	NIQE	BRISQUE
Teapot	0.4930	13.3204	0.0466	3.1529	26.3851	0.3604	10.2633	0.0941	2.9038	18.855
Teddy	0.6562	14.0054	0.0398	4.3730	33.1575	0.5624	13.0917	0.0491	3.3473	22.819
Telescope	0.4945	7.6992	0.1699	3.4884	33.3251	0.4136	9.7064	0.1070	3.0505	20.176
Playroom	0.6559	13.3241	0.0455	3.6719	39.8957	0.5509	11.0553	0.0784	3.3548	30.701

The residuals are passed through the next steerable kernel to obtain lower passbands and subbands oriented in different projections in space. The subbands are called basis functions and recursive splitting of the lower passband, forms the rest of the pyramid. The property of steerability in the kernels gives the ability of orientation tuning however, the recursion technique employed to build the pyramid, constraints scale tuning ability. To overcome this issue, frequency domain construction [18] is preferred and has been employed for this work.

In this work, the fourth subband matrix has been transmitted via the gaussian pyramid to create the corresponding weight map called a steer-gauss map. Since this weight map has been directly derived from the hazy input image, it aids in filling in information gaps during the formation of the final dehazed image.

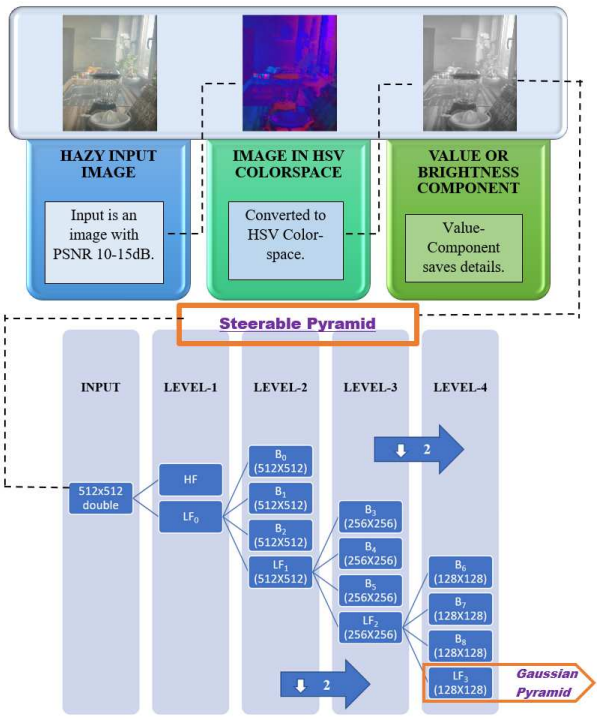


Figure 3: Flowchart: Steerable Pyramid

2) Weight Maps from Derived Inputs: The Laplacian pyramid is used to process the derived inputs to get contrast-enhanced and white-balanced weight maps (Figure 4). The Laplacian pyramid becomes an essential part of the process. Passing through the Laplacian pyramid sharpens the image by re-discovering hidden edges of the object without disturbing white balance or contrast. This excellent method has also been employed by Ancuti et al. [1] and has been reused as a part of the proposed method.

C. Multi-Scale Fusion

The fusion operation is performed by pixel-wise multiplication of the weight maps obtained as a result of the Gaussian and Laplacian pyramids. An important point to note is that the decomposition level or the number of layers for both the Laplacian and Gaussian pyramids must be the same for proper fusion. Also, the weight maps which are to be fused must remain at the same sizes. Successively, the multiplication operation in a bottom-up manner combines the different weight maps derived during processing [1]. The last step is to sum the final outputs of all the layers to create the dehazed image.

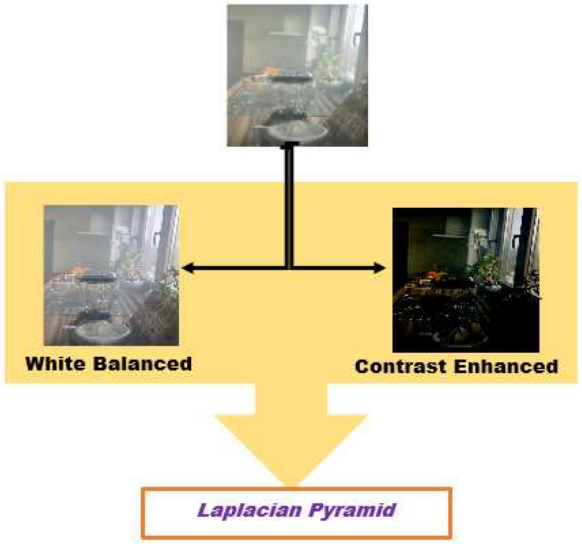


Figure 4: Processing Weight Maps

V. RESULT AND DISCUSSION

The significant difference between Ancuti et al [1], Dalvi et al. [2] and the proposed work is the use of a lowpass coefficient matrix of the original image. The coefficient matrices are derived from the steerable pyramid and are then fed to the gaussian pyramid as input. The visual results are compared with related works [1], [2] using the I-HAZE [4] dataset for validation. This paper presents the dehazed results of four images from [4] namely, Teapot (I-HAZE:09), Teddy (I-HAZE:19), Telescope (I-HAZE:01) and Playroom (I-HAZE:35). The Steerable pyramid employed in this paper decomposes the image into 5 levels using one high and four low pass filters. It is observed that

Authorized licensed use limited to: DELHI TECHNICAL UNIV. Downloaded on May 04,2023 at 06:35:17 UTC from IEEE Xplore. Restrictions apply.



Figure 5: Comparing visual dehazed results of 4 test images for [1], [2] and the proposed method.

the proposed work is independent of the level of decomposition selected [17]. Hence, based on visual observations, the fourth level of decomposition has been selected for this work. Some major regions of notice are the images' background and the picture's bottom. In the dehazed image presented in Figure 5, it is noticed that no information has been lost to dehazing and the background and foreground are clearly visible unlike the results of methods [1] and [2]. Moreover, the halo effect is significantly reduced in the background which is a major problem in Telescope and Playroom Images. The results are compared and tabulated in below Figure 6. Some other parameters like SSIM, PSNR etc. are summarized in Table 1.

In Table I, the SSIM [19] for the proposed work does not vary significantly from the related work. Since the haze has been removed, the values of SSIM are quite low for both images. The improvement in PSNR [20] values indicate good quality result, with the exception being the Telescope image, as seen in the third row of Table I. Likewise, MSE [21] values are compared for both methods and expectedly, the Telescope image proves to be an exception. A reduction in MSE values is observed in the results of the proposal as compared to traditional methods. The performance metrics computed before are with the original hazy image taken as a reference. Two other parameters have been listed to encompass the non-reference image quality metrics, NIQE [22] and BRISQUE [23]. The lower values of both NIQE and BRISQUE indicate the good quality result of the proposed method. An important point to notice is that even when the Telescope image is considered an exception with reference to its greater SSIM, PSNR and MSE values, visual

Authorized licensed use limited to: DELHI TECHNICAL UNIV. Downloaded on May 04,2023 at 06:35:17 UTC from IEEE Xplore. Restrictions apply.

results tend to differ. Therefore, supporting the visual observation, the NIQE and BRISQUE results prove enhancement in quality of dehazed output than the previous related works. On comparing the proposed method with that devised by Dalvi et al. [2], all the images show a decrease in SSIM values. The good SSIM value can be credited to the excellent method proposed by [2]. Moreover, it is observed the proposed method shows improvement neither in the PSNR values nor in the error estimates by the MSE method except for the case of the Telescope image. In spite of the poor performance, the visual results are better for the proposed method as compared to [2] and this fact is proved by the significant reduction in values of NIQE and BRISQUE techniques for all images used in validation.

VI. Conclusion

Herein, a new Multi-scale, Multi-pyramid Fusion based strategy has been proposed for image dehazing. The method employs a Steerable Pyramid to extract information from the LF sub-band of the input image and discards the noisy high-frequency band. This method aids in saving vital information to reconstruct the dehazed image. The use of the Laplacian pyramid has been retained from previous related works to transfer the edges identified. Moreover, the fusion strategy in the proposed work, uses the method of products to retain all information. The steerable coefficient matrices prevent hallow formation in the background and retains the colors of the foreground. The proposed method has been validated by the images from dataset I-HAZE and the performance metrics SSIM, PSNR, NIQE, etc. have been extracted. The visual and quantitative results show the superiority of the algorithm presented.

References

[1] C. O. Ancuti and C. Ancuti, " "Single Image Dehazing by Multi-Scale Fusion,"," *IEEE Transactions on Image Processing, ,* vol. 22, no. 8, pp. 3271-3282, 2013.

[2] Vleeschouwer, "I-HAZE: a dehazing benchmark with real hazy and haze-free indoor images," in *NTIRE 2018 CVPR workshop*, 2018.

[3] B. Soni, Foggy Image Enhancement Using Improved Histogram Equalization and Guided Filter, 2022, pp. 443-452.

[4] Z. Yao, "The Retinex-based image dehazing using a particle swarm optimization method," *Multimedia Tools and Applications.,* 2021.

[5] K. Tang, "Investigating Haze-relevant Features in A Learning Framework," in *IEEE Conference on Computer Vision and Pattern Recognition*, 2014.

[6] W. Wang, "Recent Advances in Image dehazing," *IEEE/CAA Journal of Automatica Sinica,* vol. 4, pp. 410-436, 2017.

[7] C. A. a. P. B. C. O. Ancuti, " "Effective single image dehazing by fusion,," in *IEEE International Conference on Image Processing*, 2010.

[8] MathWorks-Documentation Team, "Naturalness Image Quality Evaluator (NIQE) No-Reference Image Quality Score," MathWorks, [Online]. Available: https://in.mathworks.com/help/images/ref/niqe.html. [Accessed 27 October 2022].

[9] MathWorks Documentation Team, "Blind/Referenceless Image Spatial Quality Evaluator (BRISQUE) no reference image quality score," MathWorks, [Online]. Available: https://in.mathworks.com/help/images/ref/brisque.html?s_tid=doc_ta. [Accessed 27 October 2022].

[10] Wikipedia, "Mean Squared Error," Wikipedia, The Free Encyclopedia, 2022 August 22. [Online]. Available: https://en.wikipedia.org/w/index.php?title=Mean_squared_error&oldid=1105990031. [Accessed 27 October 2022].

[11] Wikipedia, "Peak Signal-to-Noise Ratio," Wikipedia, The Free Encyclopedia, 2022 August 22. [Online]. Available: https://en.wikipedia.org/w/index.php?title=Peak_signal-to-noise_ratio&oldid=1105990972. [Accessed 27 October 2022].

[12] Wkipedia, "Structural Similarity," Wkipedia, The Free Encyclopedia, 16 September 2022. [Online]. Available: https://en.wikipedia.org/w/index.php?title=Structural_similarity&oldid=1110646665. [Accessed 27 October 2022].

[13] Freeman and Simonicelli, "The Steerable Pyramid: A Flexible Architecture for Multi-Scale Derivative Computation.," in *IEEE Second International Conference on Image Processing*, Washington DC, 1995.

[14] Freeman and E. P. Simoncelli. [Online]. Available: https://pyrtools.readthedocs.io/en/latest/tutorials/tutorial3.html.

[15] H. Zhang, X. Liu, Z. T. Huang and Y. F. Ji, "Single image dehazing based on fast wavelet transform with weighted image fusion," in *IEEE International Conference on Image Processing*, Paris, France, 2014.

[16] Dalvi, Shah, Shetty and Vanmali, "Improved weight map guided single image dehazing," in *IJERT-IEEE*, 2016.

[17] K. He, "Single image haze removal using dark channel prior," in *IEEE Conference on Computer Vision and Pattern Recognition,*, 2009.

[18] Nam and G. Pyo, "New Fuzzy-Based Retinex Method for the Illumination Normalization of Face Recognition.," *International Journal of Advanced Robotic Systems,* 2012.

[19] Ogden, E. Andelson, C. Anderson, J. Bergen and P. Burt, "Pyramid methods in image processing," *Radio Corporation of America (Engineer),* vol. 29, no. 6, 1984.

[20] S. Fang, R. Deng, Y. Cao and C. L. Fang, "Effective single underwater image enhancement by fusion," *Journal of Computational and Applied Mathematics,* vol. 8, no. 4, pp. 904-911, 2013.

[21] Simoncelli, "The steerable pyramid: A flexible architecture for multi-scale derivative computation," in *International Conference on Image Processing*, 1995.

[22] Z. Liu and K. Tsukada, "Image Fusion by using Steerable Pyramid," *Pattern Recognitioon Letters, Elsevier,* vol. 22, no. 9, pp. 929-939, 2001.

[23] W. Ren, L. Ma, J. Zhang, J. Pan, X. Cao, W. Liu and Y. Ming-Hsuan, "Gated Fusion Network for Single Image Dehazing," in *Proceedings of the IEEE Conference on Computer Vision and Pattern Recognition (CVPR)*, 2018.

Authorized licensed use limited to: DELHI TECHNICAL UNIV. Downloaded on May 04,2023 at 06:35:17 UTC from IEEE Xplore. Restrictions apply.

2023 6th International Conference on Information Systems and Computer Networks (ISCON)
GLA University, Mathura, India. Mar 3-4, 2023

2023 6th International Conference on Information Systems and Computer Networks (ISCON) | 979-8-3503-4696-1/23/$31.00 ©2023 IEEE | DOI: 10.1109/ISCON57294.2023.10112094

Stilbostemin C as a Potential Candidate for Therapeutic Targeting of Rab3b Protein in Countering Alzheimers

Sanya Madaan
Molecular Neuroscience and Functional Genomics Laboratory, Dept. of Biotechnology Delhi Technological University
Delhi – 110042, India
sanyamadaan34.sm@gmail.com

Pravir Kumar*
Molecular Neuroscience and Functional Genomics Laboratory, Dept. of Biotechnology Delhi Technological University
Delhi – 110042, India
pravirkumar@dtu.ac.in

***Abstract*— Alzheimer's disease (AD), the most common form of dementia, affects more than 20 million individuals globally. One of the main mechanisms driving the emergence of neurodegenerative illnesses, including AD, is dysfunction in neuronal autophagy. Autophagy is the only route for organelle turnover in cells and is crucial for breaking down aggregated and normal proteins, especially in stressful or injured situations[1]. The endocannabinoid system, the mTOR pathway, neuroinflammation, and the metabolism of Aβ and tau protein are all important aspects of autophagy that may all work together to mediate its impact on AD[2]. As a result, drugs that target autophagy may lead to the development of novel therapeutic strategies for the treatment of AD. Tau protein tangles inside of cells and amyloid-β containing neuritic plaques are two features of Alzheimer's disease (AD). This kind of pathology demonstrates unequivocally that AD compromises the systems of neuronal housekeeping and protein quality regulation. Growing data suggest that autophagosome-lysosomal degradation can be hindered, which could interfere with the processing of Aβ plaques and cause AD pathogenesis. The GEO datasets provide publicly available gene expression and clinical data on AD patients to study the prognosis of patient death rates and thereby identify AD biomarkers. In this study, we used the GDC data portal to analyze linked genes with clinical data to determine the most significant AD genes using functional enrichment analysis and protein-protein interaction (PPI). In order to distinguish the genes with different expression levels between the mutant and normal groups, we identified differential expression genes (DEGs). RAB3B, a member of the small GTP-binding protein RAB family that is involved in cell autophagy, is being used. There are several potential mechanisms that could inhibit the function of the RAB3B protein interactome and thus impair autophagy and promote AD pathology. Furthermore, we used the GDC Data Portal to estimate their significance in AD. A natural substance called Stilbostemin C might be evaluated as a therapy option. For a better understanding of the interactions between the bioactive substances and the RAB3B protein, molecular docking research was performed. According to the molecular docking analysis, Stilbostemin C has a stronger affinity for RAB3B. The ADME/T study also revealed the potential of Stilbostemin C for further research.**

Keywords*— *Alzheimer's, Datasets, Differential expression genes, Biomarkers, RAB3B protein, Stilbostemin C

I. INTRODUCTION

As the world's population ages, Alzheimer's disease (AD), the most common neurological condition affecting the elderly, will have an adverse societal and economic impact. AD is hypothesized to be caused by a number of pathogenic mechanisms, including tau phosphorylation, neuroinflammation, neurotransmitter dysregulation, and oxidative stress. It is characterised by the development of neurofibrillary tangles (NFTs) made of tau protein and senile plaques, which are largely made of amyloid β (Aβ), as well as a progressive and irreversible loss of cognitive function[3].

The metabolism of Aβ is dysregulated in AD patient's brains, which causes Aβ to build up and aggregate. Autophagy has a significant impact on how the Aβ and tau proteins are metabolized. Organelles and proteins are destroyed during autophagy, a lysosome-dependent, homeostatic process, and then recycled into energy. The accumulation of harmful proteins in the AD brain is therefore thought to be caused by autophagy which is dysfunctional[4].

Too much or too little autophagic activity in neurons impairs their homeostasis and survival rate, resulting in neurodegeneration. Moreover, neurons feature intercellular connection structures like axons, dendrites, and synapses that need the reciprocal transport of proteins, organelles, and autophagosomes over significant distances from the soma. Neurodegeneration is caused by defects in autophagy, which disrupt intercellular communication[5]. Due to its historically known involvement in hunger and other mitigating harsh circumstances including oxidative damage and organelle damage, autophagy is widely regarded as a pro-survival activity.

In numerous neurodegenerative illnesses, a significant buildup of autophagic vacuoles, including autophagosomes or autolysosomes, has been seen in the affected brain region. However, the precise involvement of autophagy in each neurodegenerative illness is still unknown. Sustained autophagy activation, disturbance of the balance between autophagosome production and lysosomal fusion, and impairment of lysosomal components are thought to contribute to nervous system degeneration, as neurons are more prone to protein mis-regulation due to their postmitotic condition[6].

In doing so, we hope to alter the autophagy pathway that ultimately results in Alzheimer's disease. A subset of the Ras superfamily are the low-molecular-weight GTPases known as Rab proteins. By tethering/docking vesicles to their appropriate compartments, Rab GTPases function as molecular switches that alternate between GTP-bound active and GDP-bound inactive forms to regulate vesicle transit to the proper destinations[7].

Authorized licensed use limited to: DELHI TECHNICAL UNIV. Downloaded on May 11,2023 at 10:10:43 UTC from IEEE Xplore. Restrictions apply.

Small GTP-binding protein RAB3B, a member of the RAB family that has been linked to drug resistance and cell autophagy, has been described as a key oncogene in a number of malignancies and neurodegenerative illnesses.

To stop the buildup of amyloid Aβ plaques, we will target the rab3b gene, which is implicated in autophagy.

II. Materials and Methods

A. Data set

The microarray gene expression datasets used in this investigation were obtained from the NCBI-GEO (https://www.ncbi.nlm.nih.gov/gds) database maintained by the National Centre for Biotechnology Information. For these results, we used 31 different microarrays to examine the gene expression in nine healthy controls and 22 AD patients of differing severity. The expression of each gene was then compared across all 31 subjects, independent of illness, to Mini-Mental Status Examination (MMSE) and neurofibrillary tangle (NFT) scores. The results of these studies showed a substantial transcriptional response including thousands of genes that were significantly linked with AD indicators. Only control and participants with early-stage AD were included in the correlation of several hundred of these genes with AD markers. The selection criteria were |log(foldchange)| > 2 and P 0.01 for DEGs.

B. Functional Enrichment Analysis

All of the DEGs that were shared by the microarray AD datasets were subjected to the pathway and GO analyses using the web-based gene set enrichment analysis (GSEA) tool EnrichR (https://maayanlab.cloud/Enrichr/). The biological process (BP) Gene Ontology (GO) was employed as an annotation source in this research, and its threshold was set at P 0.05. The analysis of KEGG pathway enrichment was declared statistically significant at the highest p-value of 0.05. do not revise any of the current designations.

C. Protein-Protein Interactions (PPI) Network Analysis

The web-based visualization tool STRING (https://string-db.org/) was used to create a protein-protein interactions (PPI) network of the common DEGs. The PPI network is a database that offers correlations between proteins' physical and functional properties.

D. Data Collection For Molecular Docking

A web-based open-source project called COCONUT (Collection of Open Natural Products) is used to store, search for, and analyze natural products (https://coconut.naturalproducts.net/). 31 natural compounds with anti-inflammatory capabilities and the well-known natural chemical Huperzine A were used as standards for reference when identifying natural products as a treatment for AD. We downloaded the SDF structures of these medicines from PubChem. For molecular docking, the RAB3B gene was chosen, and the PDB structure was obtained. RAB3B was ready to use Discovery Studio to perform docking. Using Discovery Studio, 40 ligands were translated into mol2 format. After the ligands and proteins were ready, SwissDock was used to execute docking.

E. ADMET Analysis

SwissADME which is a web-based tool allowed us to predict ADME parameters for drug discovery (http://www.swissadme.ch/). The Canonical SMILES were taken from PubChem and the virtual physicochemical properties of all fifty ligands are analyzed using the Swiss ADME tools, including water-solubility, lipophilicity, pharmacokinetics, and drug-likeness parameters.

III. RESULTS

A. Differently Expressed Genes (DEGs)

The two selected microarray datasets were analysed by comparing normal samples with AD cases. We identified 31 genes.

B. Functional Enrichment Analysis

The biological process (BP) GO and KEGG pathway structural enrichment investigation was conducted utilising 31 DEGs to demonstrate the molecular pathways and functions related to AD. The picture displays a bar graph of KEGG pathways linked to AD and the central nervous system.

TABLE I. KEGG Human Pathway

Term	Overlap	P-value	Adjusted P-value	Old P-value	Old Adjusted P-value	Odds Ratio	Combined Score	Genes
Cell adhesion molecules	2/148	0.018127	0.257672	0	0	10.44573	41.89082	NRXN1; SELE
Calcium signalling pathway	2/240	0.044179	0.257672	0	0	6.378151	19.89669	CAMK1G; GRIN1
African trypanosomiasis	Jan-37	0.05056	0.257672	0	0	20.51029	61.21495	SELE
Primary immunodeficiency	Jan-38	0.051892	0.257672	0	0	19.95495	59.03873	RFXAP
Cocaine addiction	Jan-49	0.066422	0.257672	0	0	15.37346	41.68871	GRIN1
Malaria	Jan-50	0.067732	0.257672	0	0	15.05896	40.54171	SELE
Neuroactive ligand-receptor interaction	2/341	0.081967	0.257672	0	0	4.454958	11.14381	TAC1; GRIN1
Steroid hormone biosynthesis	Jan-61	0.082028	0.257672	0	0	12.29136	30.73698	SRD5A1
Long-term potentiation	Jan-67	0.089736	0.257672	0	0	11.17059	26.93099	GRIN1
Amyotrophic lateral sclerosis	2/364	0.091619	0.257672	0	0	4.167021	9.959667	NUP93; GRIN1
TNF signaling pathway	1/112	0.145592	0.260474	0	0	6.62696	12.76979	SELE
Huntington disease	1/306	0.350793	0.367498	0	0	2.388221	2.5018	GRIN1
Alzheimer disease	1/369	0.406537	0.415991	0	0	1.973027	1.775885	GRIN1
Pathways of neurodegeneration	1/475	0.490071	0.490071	0	0	1.523519	1.086583	GRIN1

Authorized licensed use limited to: DELHI TECHNICAL UNIV. Downloaded on May 11,2023 at 10:10:43 UTC from IEEE Xplore. Restrictions apply.

TABLE II. GO MOLECULAR FUNCTION

Term	Overlap	P-value	Adjusted P-value	Old P-value	Old Adjusted P-value	Odds Ratio	Combined Score	Genes
GDP binding (GO:0019003)	Jan-67	0.089736	0.162024	0	0	11.17059	26.93099	RAB3B
ligand-gated cation channel activity (GO:0099094)	Jan-80	0.106224	0.180764	0	0	9.326301	20.91147	GRIN1
amyloid-beta binding (GO:0001540)	Jan-80	0.106224	0.180764	0	0	9.326301	20.91147	GRIN1
calcium channel activity (GO:0005262)	Jan-84	0.111239	0.180764	0	0	8.875056	19.49027	GRIN1
ion channel activity (GO:0005216)	Jan-84	0.111239	0.180764	0	0	8.875056	19.49027	GRIN1
voltage-gated cation channel activity (GO:0022843)	Jan-97	0.127351	0.194363	0	0	7.66821	15.80269	GRIN1
cysteine-type peptidase activity (GO:0008234)	Jan-98	0.128579	0.194363	0	0	7.588774	15.56619	USP9Y
cation channel activity (GO:0005261)	Jan-98	0.128579	0.194363	0	0	7.588774	15.56619	GRIN1
cysteine-type endopeptidase activity (GO:0004197)	1/105	0.137126	0.199825	0	0	7.075499	14.05799	USP9Y
thiol-dependent deubiquitinase (GO:0004843)	1/106	0.13834	0.199825	0	0	7.00776	13.86161	USP9Y
deubiquitinase activity (GO:0101005)	1/112	0.145592	0.203015	0	0	6.62696	12.76979	USP9Y
GTPase binding (GO:0051020)	1/201	0.246492	0.320439	0	0	3.661481	5.12764	BICD2
guanyl ribonucleotide binding (GO:0032561)	1/214	0.260232	0.327905	0	0	3.43575	4.625147	RAB3B

C. PPI Network Analysis

By contrasting normal samples with AD cases, the two chosen microarray datasets were examined. We discovered 31 genes.

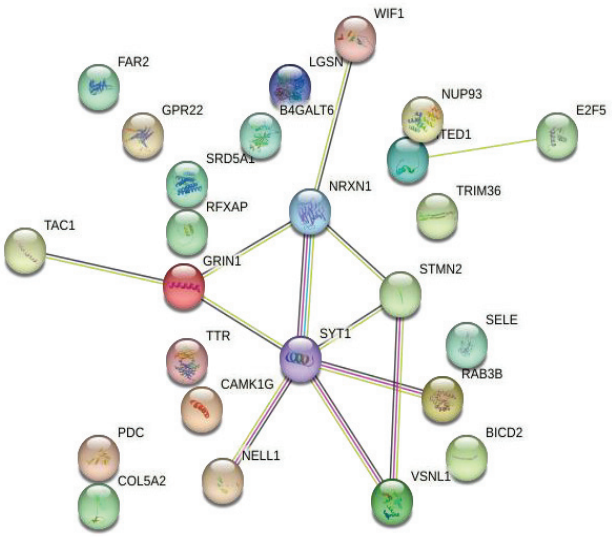


Fig. 1. The PPI network of 31 genes

D. Molecular Docking Result

SwissDock was used in studying the natural compounds with interactions of RAB3B protein. Out of 40 natural compounds docked, 6 compounds met the required parameters binding energy less than - 7.12 Kcal/mol (energy of standard compound). Out of these six, Stilbostemin C has the most negative binding energy which suggests it has the best binding affinity with the protein[8].

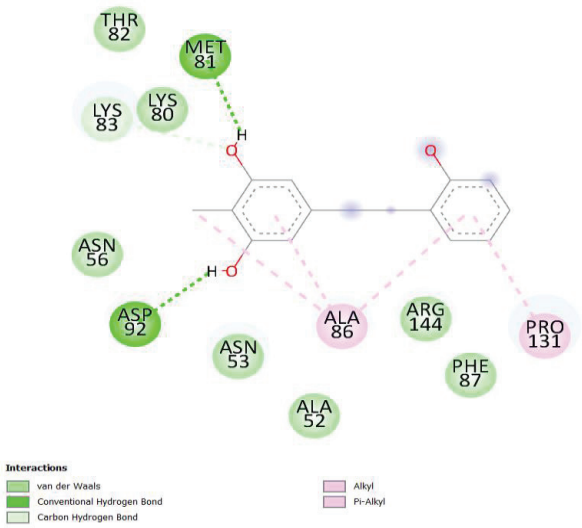


Fig. 2. Structure of Stilbostemin C

Authorized licensed use limited to: DELHI TECHNICAL UNIV. Downloaded on May 11,2023 at 10:10:43 UTC from IEEE Xplore. Restrictions apply.

E. Admet Analysis

ADMET analysis was performed using SwissADME and Stilbostemin C was found to have high GI absorption capacity and BBB permeant. Lipinski rule is one of the most popular parameters used to evaluate the drug-likeness of small molecules. With a bioavailability score of 0.55 and 0 violations, Stilbostemin C satisfies with Lipski rule's drug-likeness standards for bioavailable drugs

TABLE III. TABLE MOLECULAR DOCKING AND ADME/T ANALYSIS

Name	Cluster	Element	FullFitness (kcal/mol)	Estimated ΔG (kcal/mol	GI absorption	Lipinski	BBB permeant	Log Kp (skin permeation)
HuperzineA (Standard)	0	0	-5215	-7.12	High	Yes; 0 violation	Yes	-7.77 cm/s
Dipeptidyl peptidase I (DPPI) \	38	1	-5166	-5.31	High	Yes; 0 violation	Yes	-5.66 cm/s
Helenalin	12	0	-5210	-7.19	high	Yes; 0 violation	Yes	-7.47 cm/s
Spiramine U	0	0	-5013	-6.98	High	Yes; 0 violation	Yes	-6.97 cm/s
Glaucocalyxin A	11	0	-5199	-7.36	High	Yes; 0 violation	Yes	-7.10 cm/s
Stilbostemin c	0	0	-5253	-6.88	High	Yes; 0 violation	Yes	-5.35 cm/s
Ribaliprenylene	0	0	-5198	-7.63	High	Yes; 0 violation	Yes	-5.99 cm/s
Jerantinine E	0	3	-5195	-7.21	High	Yes; 0 violation	Yes	-6.44 cm/s
Toddaliopsin A	16	0	-5172	-7.18	High	Yes; 0 violation	Yes	-5.99 cm/s

IV. CONCLUSION

A highly controlled, universal, and conserved eukaryotic transportation mechanism called autophagy transports cytoplasmic cargo to lysosomes for degradation. Autophagy contributes significantly to Aβ production by influencing β - and γ-secretases and controlling APP recycling. When autophagy is impaired, tau and Aβ protein clearance is reduced, and their accumulation is accelerated. The clearing of soluble and aggregated Aβ and tau proteins is improved by the induction of autophagy. As a result, regulating autophagy-lysosome protein degradation is becoming a key therapeutic focus for AD. In contrast to this approach, in this study, 31 different microarrays were used to examine the gene expression of 22 AD patients and nine healthy controls with varying degrees of the disease. Out of 31, it was discovered that the RAB3B gene is connected to the autophagy lysosomal pathway in the build-up of aberrant proteins that cause Alzheimer's disease. RAB3B may serve as a reliable prognostic indicator for controlled autophagy. Stilbostemin C may be an effective Alzheimer's drug, based on the molecular docking of the RAB3B genes with 40 natural compounds. Following the Lipinski rule, having BBB that permeates, and being more drug-like are all conclusions drawn from the ADMET study of Stilbostemin C.

ACKNOWLEDGMENT

We express our gratitude to Delhi Technological University's senior administration for their continuous support and direction.

REFERENCES

[1] W. Zhang et al., “MRTF-A-mediated protection against amyloid-β-induced neuronal injury correlates with restoring autophagy via miR-1273g-3p/mTOR axis in Alzheimer models.,” Aging, vol. 14, no. 10, pp. 4305–4325, May 2022, doi: 10.18632/aging.203883.

[2] C. Wang, X. Zhang, Z. Teng, T. Zhang, and Y. Li, “Downregulation of PI3K/Akt/mTOR signaling pathway in curcumin-induced autophagy in APP/PS1 double transgenic mice,” Eur J Pharmacol, vol. 740, pp. 312–320, Oct. 2014, doi: 10.1016/j.ejphar.2014.06.051.

[3] X. Xu et al., “Metformin activates chaperone-mediated autophagy and improves disease pathologies in an Alzheimer disease mouse model,” Protein Cell, vol. 12, no. 10, pp. 769–787, Oct. 2021, doi: 10.1007/s13238-021-00858-3.

[4] J. Dou, P. Su, C. Xu, Z. Wen, Z. Mao, and W. Li, “Targeting Hsc70-based autophagy to eliminate amyloid β oligomers,” Biochem Biophys Res Commun, vol. 524, no. 4, pp. 923–928, Apr. 2020, doi: 10.1016/j.bbrc.2020.02.016.

[5] D. Türei et al., “Autophagy Regulatory Network — A systems-level bioinformatics resource for studying the mechanism and regulation of autophagy,” Autophagy, vol. 11, no. 1, pp. 155–165, Jan. 2015, doi: 10.4161/15548627.2014.994346.

[6] P. A. Parcon et al., “Apolipoprotein E4 inhibits autophagy gene products through direct, specific binding to CLEAR motifs,” Alzheimer’s & Dementia, vol. 14, no. 2, pp. 230–242, Feb. 2018, doi: 10.1016/j.jalz.2017.07.754.

[7] C. Lin, Y. Chen, F. Zhang, B. Liu, C. Xie, and Y. Song, “Encoding gene RAB3B exists in linear chromosomal and circular extrachromosomal DNA and contributes to cisplatin resistance of hypopharyngeal squamous cell carcinoma via inducing autophagy,” Cell Death Dis, vol. 13, no. 2, p. 171, Feb. 2022, doi: 10.1038/s41419-022-04627-w.

[8] G. Bitencourt-Ferreira and W. F. de Azevedo, “Docking with SwissDock.,” Methods Mol Biol, vol. 2053, pp. 189–202, 2019, doi: 10.1007/978-1-4939-9752-7_12.

Authorized licensed use limited to: DELHI TECHNICAL UNIV. Downloaded on May 11,2023 at 10:10:43 UTC from IEEE Xplore. Restrictions apply.

Eur. Phys. J. Plus (2023) 138:460
https://doi.org/10.1140/epjp/s13360-023-04110-1

THE EUROPEAN PHYSICAL JOURNAL PLUS

Regular Article

Study of SXR and HXR transitions with intensity spectra of W LXIX

Richa Paijwar[1], **Rinku Sharma**[1,a], **Alok Kumar Singh Jha**[2]

[1] Department of Applied Physics, Delhi Technological University, Delhi 110042, India
[2] School of Physical Sciences, Jawaharlal Nehru University, Delhi 110067, India

Received: 15 December 2022 / Accepted: 15 May 2023
© The Author(s), under exclusive licence to Società Italiana di Fisica and Springer-Verlag GmbH Germany, part of Springer Nature 2023

Abstract We present complete spectroscopic data and a detailed theoretical investigation of C-like W (WLXIX) based on the fully relativistic multi-configuration Dirac–Fock (MCDF) method. We included quantum electrodynamics (QED) corrections due to vacuum polarization, and self-energy effects and Breit correction due to the exchange of virtual photons between two electrons are fully considered in our calculations. For the lowest 205 fine structure levels, we have provided the energy levels and radiative data for multiple transitions such as electric dipole (E1), electric quadrupole (E2), magnetic dipole (M1), and magnetic quadrupole (M2) and identified soft X-ray transitions (SXR) and hard X-ray (HXR) transitions from highly excited states to ground state have been predicted. The credibility and authenticity of our furnished results and related calculations have also been performed using another independent fully relativistic configuration interaction program (Flexible Atomic Code) based on self-consistent Dirac–Fock–Slater iteration method. A reasonably good agreement is found between our two independent atomic structure calculations. We also compared our computed energies with experimental energy levels compiled by NIST and other available theoretical data in the literature, and there are a few minor differences discussed. We have studied the intensity spectra for transitions decaying to ground state for W LXIX. We expect that our newly reported atomic and radiative data of C-like W will help identify and analyze spectral lines obtained from various diagnoses of solar, fusion plasma research and astrophysical exploration.

1 Introduction

Carbon-like isoelectronic sequence has always been a trending and challenging element for experimentalists and theoretical researchers because of their high abundance in the universe [1]. Neutral carbon lines are prominent in both stellar and interstellar spectra, as reported in the literature [2]. Purely, data pertaining to the adjacent C-like ionization stage are essential for understanding various chemical diagnostics and astrophysical processes. However, due to the complexity of six-electron systems, calculating C-like sequences remains a challenge for theorists to calculate atomic properties ab initio to high precision. Thus, researchers must analyze the spectroscopic parameters of the carbon isoelectronic sequence. Few works using various theoretical methodologies and experimental techniques with advanced instruments have been published on C-like ions as communicated in the literature over the last decades, which is limited to only few energy levels. To encapsulate, more systematic and extensive studies are required to provide reliable spectroscopic data for C like W.

1.1 Experimental work on C-like ions

The visible and UV spectra of the symbiotic nova RR Telescopii by Young et al. [3] were utilized to determine the reference wavelengths for many forbidden as well as intercombination transitions of ions between + 1 and + 6 of elements C, N, O, Ne, Na, Mg, Al, Si, P, S, Cl, Ar, K, and Ca, and the wavelengths were used to determine the new energy values for such levels within the ions. In the energy (wavelength) range of 398 eV (31.15) to 450 eV (27.55), high-resolution K-shell photoionization cross sections for the C-like atomic nitrogen ion (N +) have been reported by Mosnier et al. [4]. At the Shanghai Electron Beam Ion Trap, Chen et al. [5] have experimented with studying the resonant energies for KLL dielectronic recombination of He-, Li-, Be-, B-, C-, N-, among O-like xenon ions. Chen et al. also measured the resonant energies at an average uncertainty level of 0.03 percent and were compared with the calculation findings with the help of relativistic configuration interaction (RCI) theory, multiconfiguration Dirac–Fock (MCDF) theory as well as relativistic many-body perturbation theory (RMBPT). Feldman et al. [6] have identified the high-temperature (at $T_e = 3 \times 10^6$ K) of Ne, Na, Mg, Ar, K, Ca, Ti, Cr, Mn, Fe, Co, and also for Ni lines that were detected in the specified region such as 500 to 1600 Å for spectral range of Solar Ultraviolet Measurements of Emitted Radiation (SUMER); SUMER is spectrometer on the Solar and Heliospheric Observatory (SOHO) which obtained spectra from a high-temperature region above

[a] e-mail: rinkusharma@dtu.ac.in (corresponding author)

Published online: 25 May 2023

the west limb in the solar corona. At the SOLEIL synchrotron radiation facility, Bizau et al. [7] have provided detailed measurements of absolute cross sections for single photoionization, double K-shell photoionization of C-like O2 + , and Ni-like O^+ ions in the range between 526 and 620 eV photon energy, using the ion-photon merged beam method. Dere et al. [8] have upgraded the modeling of satellite lines in X-ray wavelengths explicitly with the aid of Version 9 (IDL as well as Python) and include autoionization also with dielectronic recombination phenomena in the determination of level populations for selected members of the lithium (Li) isoelectronic sequence as well as Fe XVIII to Fe XXIII. Using monochromatic x rays approximately 6.6 keV at the PETRA III synchrotron photon source, Rudolph et al. [9] have studied photoabsorption based on the primary K_α transitions of highly charged ions between He-like and F-like (Fe^{24+}–Fe^{17+}). Edlen et al. [10] have concluded the experimental data on the energy structure of the low ($n = 2$) configurations in 3 to 9 electron systems and also studied Z-dependence of the differences among observed and theoretical levels in the carbon isoelectronic sequence for configurations $2s^22p^2$, $2s2p^3$ and $2p^{4\cdot}$ Liao et al. [11] have analyzed 36 Chandra High Energy Transmission Grating data of K transitions of neutral along with low-ionized metal (like oxygen, neon, and magnesium) to find and evaluate ISM absorption lines on sight lines for 11 low-mass X-ray binaries. McCarthy et al. [12] have identified the 43 spectral emission lines ranging from F-like to Li-like sulfur ions in the wavelength range of 17.5–50 nm in spectra produced following tracer injection into plasmas generated in a magnetically confined plasma device, using stellarator TJ-II. For C-like Mg^{6+}, it is forming Mg^{5+} as well as B-like Mg^{7+} forming Mg^{6+}. Lestinskyet al. [13] have measured electron–ion recombination; experiments were performed at the TSR heavy-ion storage ring in Heidelberg, Germany, utilizing a merged electron–ion beam setup. The extreme-ultraviolet (EUV) spectra of highly charged ions Kr XXI–Kr XXXIV produced in an electron beam ion trap(EBIT) were observed and analyzed by Podpaly et al. [14], by using collisional radiative modeling; the magnetic dipole transition inside the ground configuration $3s^23p$ was demonstrated. With the help of an electron cyclotron resonance ion source, Trabert et al. [15] have measured the lifetime of the system Ne^{4+} at the TSR heavy ion storage ring, where the magnetic dipole decay channel becomes dominant.

1.2 Theoretical work on C-like ions

Wang et al. [16] have explored the detailed description of systematic calculations of energy levels and transition rates of C-like ions with $13 \leq Z \leq 36$ by applying many-body perturbation theory (MBPT). Zheng et al. [17] have studied the ionization potential of excited states in C-like sequences systematically using the weakest bound electron potential model theory and the idea of iso-spectrum-level series. Using the CIV3, K.M. Aggarwal et al. [18] have evaluated the oscillator strengths for transitions in C-like F IV and Ar XIII ions. Sansonetti et al. [19] have provided the handbook of basic atomic spectroscopic data. Rodrigues et al.[20] have analyzed the atomic binding energies between lithium (3 electrons) and dubnium (105 electrons) isoelectronic series using Dirac–Fock approximation. They have also calculated the total atomic energies of ground state configurations. Fawcett et al.[21] have provided the wavelengths as well as classifications of emission lines due to $2s^22p^n - 2s2p^{n+1}$, $2s2p^n - 2p^{n+1}$ transitions up to $Z \leq 28$. Chen et al. [22] have calculated the energies with radiative transitions as well as the radial expectation values of the $1s^22s^22p^2\ ^3P$ ground state and the $1s^22s2p^3\ ^5S$, ^1D, ^3S highly excited states of C and O^{2+}. Naze et al. [23] have reported the energy levels along with specific mass shift parameters and electronic densities at the nucleus by using relativistic configuration interaction (RCI) calculations for various states like the beryllium, boron, and carbon as nitrogen isoelectronic sequences. For the $\Delta n = 0$ transitions from $n = 2$ in C-like ions with nuclear charge numbers Z in the range $9 \leq Z \leq 54$, relativistic distorted-wave collision intensities have been predicted by Zhang et al. [24]. For the 185 $\Delta n = 0$ transitions from $n = 2$, Zhang et al. [25] have estimated the 67 C-like ions with nuclear charge numbers Z in $26 \leq Z \leq 92$, using relativistic distorted-wave collision strengths. Gu et al. [26] have determined the level energies of $1s^2\ 2l^q$ ($1 \leq q \leq 8$) states for ions with $Z \leq 60$ by using both a combined CI and MBPT technique. Ray et al. [27] have studied the high-stripped carbon-like ions in radiative transitions using the time-dependent Coupled Hartree–Fock (TDCHF) method. By using fully relativistic codes (GRASP2K), Sang et al. [28] have studied the energy levels, hyperfine structure, and the 2 s-2p radiative transition technique of C-like Fe, Co. For elements having atomic numbers $55 \leq Z \leq 95$, Shpatakovskaya et al. [29] have calculated data on the ionization potential of ions in the ground state with the number of electrons $N_e \leq 46$. Further, Fisher et al. [30] have calculated the transitions for C-like sequence using the Multi Configuration Hartree–Fock (MCHF) approach and Breit–Pauli Corrections. Furthermore, Fisher et al. [31] have also reported energy levels and lifetimes as well as transition probabilities of transitions between calculated levels for Be to Ne-like sequences. Recently, Palmeri et al. [32] have computed the impacts of the plasma environment on the ionization potentials (IPs) and K-thresholds utilized in the modeling of K lines for all ions related to the isonuclear sequences of abundant elements apart from O and Fe, notably C, Si, Ca, Cr, as well as Ni. Jönsson et al. [33] have discussed atomic data with many applications, including plasma diagnostics with interpreting the spectra of distant astronomical objects, and showed how large-scale simulations can produce spectroscopically accurate transition energies, transition rates with estimated uncertainty of a few percent for a wide range of ions using fully relativistic MCDF approaches. The soft X-ray emission lines of highly charged sulfur ions (S vii–S xv) in the range of 30–80A^o have been studied by Li et al. [34], and with the help of updated excitation data from the R-matrix technique, a collisional radiative model was also created to estimate line emissivities of S-ions.

1.3 Available data on C-like W

C-like W has already been the subject of some theoretical calculations and experimental measurements using various experimental techniques and theoretical methods. Tu et al. [35] have used a fast electron beam-energy scanning approach to study the photorecombination of highly charged tungsten (W)-ions at the Shanghai electron beam ion trap. By using dielectronic recombination (DR), Tu et al. [36] have also reported the studies of the KLL dielectronic recombination (DR) resonance strengths for He-, Li-, Be-, B-, C-, N-, as well as O-like tungsten ions, with the help of calculation and experiment, were estimated by using a flexible atomic coding (FAC). Using the Dirac–Fock method, for 54 tungsten ions in the W^{6+}–W^{71+} range, radiative recombination and photoionization cross sections, radiative recombination, and radiated power loss rate coefficients have been done by Trzhaskovskaya et al. [37]. By using the MCDF technique, Liu et al. [38] have computed the energy levels, oscillator strengths, transition rates and wavelengths, and also lifetimes for $2s^2 2p^2\ ^3P_1$and $2s^2 2p^2\ ^3P_2$ along with $2s2p^3\ ^5S_2$ levels of ions in the C-like sequence (nuclear charges up to $Z = 7$–92). Beiersdorfer et al. [39] have explained the high-Z ionization balance accurately by applying critical ingredients for characterizing and assessing the energy balance of high-temperature plasmas. The wavelengths and emissivities vs. temperature of the most vital spectral lines expected to be emitted by W ions at EUV longer than 45 nm were determined by Feldman et al. [40]. In order to predict electron binding energies that have been scaled based on experimental results, Kramida et al. [41] used the Hartree–Fock method to compute the ionization energies of multiply charged tungsten ions from W^{2+} to W^{71+}. Huang et al. analyzed the ground-state ionization potentials (IP) for Li through Ne isoelectronic sequences with $Z = 37$–82 using the MCDF method [42]. Safronova et al. [43] have investigated the relativistic energy of atomic systems using quantum electrodynamic (QED) perturbation theory. Carlson et al. [44] have studied multiply charged ions by computing IP up to $Z = 103$ and have also produced the IP for neutral atoms by performing calculations based on a basic spherical shell solution. However, the majority of the literature only covers a few levels of W LXIX, indicating scarcity in consistent and accurate atomic data for this ion. Our main aim in this paper is to present the energies for higher excited state energy levels, as well as radiative data for multipole transitions (E1, E2, M1 & M2) for WLXIX.

2 Theoretical method

2.1 MCDF method

For the study of highly charged carbon like tungsten ion considered in this paper, a completely relativistic MCDF approach refined by Norrington and previously established by Grant et al. [45] to perform these large-scale computations. The inclusion of LSJ names for the levels/configurations in addition to the standard jj nomenclature of the relativistic codes is a particularly helpful feature of this edition. Contributions from Breit interactions are included, along with QED corrections such as vacuum polarization as well as self-energy, which are often incorporated as a first-order perturbation correction. These relativistic effects must be considered, particularly for high Z ions, because the nuclear potential energy is very strong and the velocity of inner electrons is fast. The theoretical basis of our current computation method has already been extensively addressed in some publications and can be found here [46]. To evaluate radial wave functions during self-consistent field (SCF) operation, We chose extended average level (EAL), which minimizes the weighted trace of the Hamiltonian matrix.

By diagonalizing the relativistic Hamiltonian H, the energy levels of an atomic ion with N electrons are obtained as

$$H = \sum_{i=1}^{N} H_D(i) + \sum_{i<j}^{N} \frac{1}{r_{ij}}, \tag{1}$$

In Eq. (1), the single electron Dirac Hamiltonian is $H_D(i)$. An atomic state function (ASF) estimates the particular wave function of an atomic state for an N electron atom or ion system.

The configuration state functions (CFSs) are antisymmetrized linear combinations of relativistic orbital products, which are defined as follows:

$$\emptyset_{nkm} = \frac{1}{r}\begin{pmatrix} P_{nk}(r) & \chi_{km}(\theta,\emptyset,\sigma) \\ -i\,Q_{nk}(r) & \chi_{-km}(\theta,\emptyset,\sigma) \end{pmatrix} \tag{2}$$

where the relativistic angular quantum number denotes k.P_{nk} is component radial wave functions and $Q_{nk}(r)$ small component radial wave functions in Eq. (2). Spinor spherical harmonic is $\chi_{-km}(\hat{r})$.

The N electronic configuration state function (CSF) of the ASF is a linear combination, and it is written as:

$$\Psi(\gamma P J) = \sum_{i=1}^{N} c_i \emptyset(\gamma_i P J) \tag{3}$$

The configuration, along with the angular coupling tree, signifies as γ_i. Final angular quantum number is J, P is parity. The expansion coefficients are denoted by the c_i, which is obtained by diagonalizing the Dirac–Coulomb–Hamiltonian in Eq. (3).

2.2 Flexible atomic code

We also performed computations using the FAC approach to verify the correctness of our findings. Gu created FAC at Stanford University [47]. FAC is performed to a self-consistent Dirac Slater iteration on a fictitious mean configuration to derive local central potential [46]. The advantage of FAC is that it is incredibly efficient to run, as well as this code is also included as fully relativistic. In FAC, there is a difference between these two fully relativistic codes in calculations, the local central field is used, and the MCDF conducts energy minimization for a particular set of states. Nuclear charge and electron–electron interaction both contribute to the local potential employed in the FAC. Below is a listing of the nuclear potential:

$$V^N = \begin{cases} \frac{Z}{2}\left(\frac{r}{R_N}\right)\left[3 - \left(\frac{r}{R_N}\right)^2\right], & r \le R_N \\ Z, & r > R_N \end{cases} \tag{4}$$

where the radius of the nucleus is denoted by R_N in Eq. (4).

As a result, Table 1 also includes the findings (FAC) obtained with the same CI as with GRASP.

2.3 Computational procedure

In order to obtain accurate results for W^{68+} (C-like tungsten) as we have chosen the following method:

Firstly, we have provided ground state configuration, i.e., $1s^22s^22p^2$ and considered configurations as $1s^22s^12p^23l(l = 0–2)$,$1s^22s^12p^24l(l = 0–3)$,$1s^22s^12p^25l(l = 0–4)$,$1s^22s^12p^26l(l = 0–4)$ and $1s^22s^22p^13l(l = 0–2)$, $1s^22s^22p^14l(0–3)$, $1s^22s^22p^15l(0–4)$, $1s^22s^22p^16l(l = 0–4)$ by taking single electron excitation from 2s and 2p orbitals.

In other step, we have included configuration like $1s^22p^4$,$1s^22p^33l(l = 0–2)$,$1s^22p^34l(l = 0–3)$,$1s^22p^35l(0–4)$,$1s^22p^36l(0–4)$ from 2s orbital by considering double electron excitation.

3 Results and discussions

3.1 Energy levels

The lowest 205 fine structure levels are listed in this study, belonging to the configurations $1s^22s^22p^2$, $1s^22s^12p^3$, $1s^22p^4$ from GRASP and FAC both in Table 1. We used 54 combinations in our computations, namely $1s^22s^12p^23l(l = 0–2)$,$1s^22s^12p^24l(l = 0–3)$,$1s^22s^12p^25l(l = 0–4)$,$1s^22s^12p^26l(l = 0–4)$ as well as $1s^22p^33l(l = 0–2)$, $1s^22p^34l(l = 0–3)$, $1s^22p^35l(l = 0–4)$, $1s^22p^36l(l = 0–4)$ and $1s^22s^22p^13l(l = 0–2)$, $1s^22s^22p^14l(0–3)$, $1s^22s^22p^15l(0–4)$, $1s^22s^22p^16l(l = 0–4)$.

From Table 1, we observed that contribution of QED is less than Breit. So in the case of W LXIX, QED effects are less significant. We have compared our calculated data from GRASP and FAC with NIST [48] and the maximum discrepancy of GRASP and FAC results with results compiled by NIST is 0.42%, respectively. The percentage difference between GRASP and FAC is displayed in Table 1 under the column of "ΔE".

$$\Delta E = \frac{|E_{\mathrm{FAC}} - E_{\mathrm{GRASP}}|}{E_{\mathrm{FAC}}} \times 100\% \tag{5}$$

The maximum value of ΔE is 0.42%. This shows that our results from their two independent calculations for most levels are in reasonable agreement and verify that our results are accurate. The small variations in some levels between GRASP and FAC energies are mostly due to different computations of electron wave functions for radial orbitals with recoupling methods of angular parts.

3.2 Radiative data

For the E1, M1, E2, and M2 transitions, connection between the transition rates and oscillator strength (f_{ij}) along with line strength (S_{ij}) can be described as:

$$\text{for } E1 \text{ transitions} : A_{ji} = \frac{2.0261 \times 10^{18}}{\omega_j \lambda_{ji}^3} S_{ij} \text{ and } f_{ij} = \frac{303.75}{\lambda_{ji}\omega_i} S_{ij}, \tag{6}$$

$$\text{for } M1 \text{ transitions} : A_{ji} = \frac{2.6974 \times 10^{13}}{\omega_j \lambda_{ji}^3} S_{ij} \text{ and } f_{ij} = \frac{4.044 \times 10^{-3}}{\lambda_{ji}\omega_i} S_{ij}, \tag{7}$$

$$\text{for } E2 \text{ transitions} : A_{ji} = \frac{1.1199 \times 10^{18}}{w_j \lambda_{ji}^5} S_{ij} \text{ and } f_{ij} = \frac{167.89}{\lambda_{ji}^3\omega_i} S_{ij}, \tag{8}$$

Table 1 Energies (in Ryd.) of lowest 205 fine structure levels of W LXIX

Levels	Configurations	Parity	MCDF				FAC	NIST	ΔE
			Zero-order	Breit	QED	Total			
1	$2s^2 2p^2 (^3P_2)^3P_0$	Even	000.00	–	–	000.0000	000.0000	000.00	–
2	$2s^2 2p^2 (^3P_2)^3P_1$	Even	105.1250	− 1.5700	0.1260	103.6821	103.7865		
3	$2s^2 2p^2 (^1D_2)^1D_2$	Even	107.0863	− 2.1800	0.1260	105.0345	105.1361	105.08	0.100
4	$2s^1 2p^3 (^2P_1)^3S_1$	Odd	128.0918	− 0.6050	− 1.2000	126.2834	126.0415		
5	$2s^1 2p^3 (^2P_1)^1P_1$	Odd	134.3963	− 0.3690	− 1.2000	132.8238	132.5726	132.44	0.187
6	$2s^2 2p^2 (^3P_2)^3P_2$	Even	213.6133	− 3.3400	0.2320	210.5102	210.7195		
7	$2s^2 2p^2 (^1S_0)^1S_0$	Even	217.6028	− 2.6600	0.2310	215.1751	215.3811		
8	$2s^1 2p^3 (^4S_3)^5S_2$	Odd	230.8832	− 1.9700	− 1.0800	227.8351	227.7146		
9	$2s^1 2p^3 (^2D_3)^3D_3$	Odd	235.1278	− 2.9100	− 1.0800	231.1403	231.0105		
10	$2s^1 2p^3 (^2P_1)^3P_0$	Odd	238.3523	− 1.4600	− 1.0800	235.8156	235.6887		
11	$2s^1 2p^3 (^4S_3)^3S_1$	Odd	240.4511	− 1.8800	− 1.0800	237.4951	237.3575		
12	$2s^1 2p^3 (^2P_1)^3P_1$	Odd	241.4010	− 1.8200	− 1.0800	238.5081	238.0410		
13	$2s^1 2p^3 (^2D_3)^1D_2$	Odd	241.7216	− 2.4600	− 1.0800	238.1790	238.3713		
14	$2p^4 (^3P_2)^3P_2$	Even	265.3201	− 0.8380	− 2.3900	262.0943	261.6043		
15	$2p^4 (^1S_0)^1S_0$	Odd	269.5109	− 0.1440	− 2.3900	266.9799	266.4868		
16	$2s^1 2p^3 (^2D_3)^3D_2$	Odd	343.6099	− 3.4700	− 0.9520	339.1892	339.1791		
17	$2s^1 2p^3 (^2D_3)^3D_1$	Odd	349.8123	− 3.2600	− 0.9520	345.5953	345.5759		
18	$2p^4 (^3P_2)^3P_1$	Even	371.2252	− 1.9700	− 2.2800	366.9760	366.6109		
19	$2p^4 (^1D_2)^1D_2$	Even	373.1988	− 2.5700	− 2.2800	368.3496	367.9819		
20	$2p^4 (^3P_2)^3P_0$	Even	481.3380	− 3.2700	− 2.1600	475.9136	475.6745		
21	$2s^2 2p^1 3s^1 (^2S_1)^3P_0$	Odd	766.8732	− 2.5400	0.3080	764.6434	764.8544		
22	$2s^2 2p^1 3s^1 (^2S_1)^3P_1$	Odd	767.2421	− 2.6400	0.3120	764.9127	765.1279		
23	$2s^2 2p^1 3s^1 (^2P_1)^3D_1$	Even	773.6478	− 2.2900	− 0.0578	771.3004	771.4046		
24	$2s^2 2p^1 3s^1 (^2P_1)^1S_0$	Even	777.0314	− 2.0500	− 0.0626	774.9180	775.0496		
25	$2s^2 2p^1 3s^1 (^2S_1)^5P_1$	Even	787.4731	− 1.1600	− 1.0100	785.3054	785.2092		
26	$2s^2 2p^1 3s^1 (^2S_1)^3P_0$	Even	790.2751	− 1.0200	− 1.0100	788.2447	788.1378		
27	$2s^2 2p^1 3p^1 (^2P_1)^5D_0$	Odd	794.6412	− 0.6170	− 1.3800	792.6463	792.3879		
28	$2s^2 2p^1 3p^1 (^2P_1)^5D_1$	Odd	794.7796	− 0.8130	− 1.3800	792.5866	792.4441		
29	$2s^2 2p^1 3p^1 (^2P_1)^3P_1$	Even	806.3343	− 2.5700	− 0.0261	803.7407	803.7880		
30	$2s^2 2p^1 3p^1 (^2P_1)^3D_2$	Even	806.4141	− 2.7400	− 0.0196	803.6553	803.8709		
31	$2s^2 2p^1 3d^1 (^2D_1)^3F_2$	Odd	811.2927	− 2.7700	− 0.0719	808.4549	808.5099		
34	$2s^2 2p^1 3d^1 (^2D_1)^3D_3$	Odd	820.9356	− 2.9900	− 0.0716	817.8766	817.9344		
35	$2s^1 2p^2 3d^1 (^2P_1)^5P_2$	Odd	827.0909	− 1.2200	− 1.3200	824.5490	824.3632		
36	$2s^1 2p^2 3p^1 (^2P_1)^3D_1$	Odd	827.4841	− 1.2000	− 1.3500	824.9395	824.7543		
37	$2s^1 2p^2 3d^1 (^2D_1)^5F_1$	Even	831.8005	− 1.1200	− 1.4000	829.2818	829.0161		
38	$2s^1 2p^2 3p^1 (^2D_1)^3D_2$	Even	832.4294	− 1.3000	− 1.4000	829.7243	829.4624		
39	$2s^1 2p^2 3p^1 (^2D_1)^3D_3$	Even	841.0644	− 1.5300	− 1.4000	838.1382	837.8820		
40	$2s^1 2p^2 3p^1 (^2D_1)^3F_2$	Even	842.2457	− 1.3900	− 1.4000	839.4554	839.2033		
41	$2s^2 2p^1 3s^1 (^2S_1)^3P_2$	Odd	875.5322	− 4.1200	0.4090	871.8239	872.1006		
42	$2s^2 2p^1 3s^1 (^2S_1)^1P_1$	Odd	876.1694	− 4.0800	0.4110	872.4989	872.7872		
43	$2s^2 2p^1 3p^1 (^2P_1)^3S_1$	Even	883.4646	− 3.6300	0.0277	879.8598	880.0395		
44	$2s^2 2p^1 3p^1 (^2P_1)^1D_2$	Even	883.7755	− 3.8000	0.0295	880.0019	880.1853		
45	$2s^1 2p^2 3s^1 (^2D_1)^5P_2$	Even	890.1976	− 2.7800	− 0.8800	886.5383	886.5125		
46	$2s^1 2p^2 3s^1 (^2S_1)^3P_1$	Even	892.2823	− 2.7200	− 0.8750	888.6838	888.6661		
47	$2s^1 2p^2 3s^1 (^2S_1)^3D_3$	Even	893.9534	− 3.6100	− 0.8850	889.4627	889.4257		

Table 1 continued

Levels	Configurations	Parity	MCDF				FAC	NIST	ΔE
			Zero-order	Breit	QED	Total			
48	$2s^1 2p^2 3s^1(^2S_1)^3D_2$	Even	895.7740	− 3.4400	− 0.8870	891.4508	891.4182		
49	$2s^1 2p^2 3p^1(^2P_1)^5D_1$	Odd	897.0121	− 2.2900	− 1.2600	893.4594	893.3276		
50	$2s^1 2p^2 3p^1(^2P_1)^5D_2$	Odd	898.0991	− 2.5700	− 1.2600	894.2745	894.1451		
51	$2s^1 2p^2 3s^1(^2S_1)^1S_0$	Even	899.1447	− 2.7300	− 0.8840	895.5352	895.4848		
52	$2s^1 2p^2 3s^1(^2S_1)^1P_1$	Even	899.4471	− 2.9300	− 0.8830	895.6355	895.5854		
53	$2s^1 2p^2 3s^1(^2S_1)^3D_1$	Even	899.8117	− 2.8300	− 0.8920	896.0925	896.0348		
54	$2s^1 2p^2 3s^1(^2S_1)^1D_2$	Even	900.3707	− 3.1500	− 0.8850	896.3391	896.2856		
55	$2s^1 2p^2 3p^1(^2P_1)^1F_3$	Odd	901.2262	− 3.3700	− 1.2600	896.5961	896.4544		
56	$2s^1 2p^2 3p^1(^2P_1)^3P_2$	Odd	903.6575	− 2.8500	− 1.2500	899.5491	899.4290		
57	$2s^1 2p^2 3p^1(^2P_1)^3P_0$	Odd	905.5283	− 2.3600	− 1.2600	901.9161	901.7459		
58	$2s^1 2p^2 3p^1(^2P_1)^3D_1$	Odd	905.7809	− 2.5300	− 1.2600	901.9970	901.8282		
59	$2s^1 2p^2 3p^1(^2P_1)^5F_2$	Odd	906.3338	− 2.8800	− 1.2600	902.2008	902.0357		
60	$2s^1 2p^2 3p^1(^2P_1)^3D_1$	Odd	909.5769	− 2.4600	− 1.2600	905.8639	905.7204		
61	$2s^2 2p^1 3p^1(^2P_1)^1P_1$	Even	913.7990	− 4.1600	0.0730	909.7153	909.8593		
62	$2s^2 2p^1 3p^1(^2P_1)^3D_3$	Even	913.8117	− 4.2200	0.0759	909.6684	909.9052		
63	$2s^2 2p^1 3p^1(^2P_1)^3P_2$	Even	916.0398	− 4.1100	0.0747	912.0012	912.2132		
64	$2s^2 2p^1 3p^1(^2P_1)^1S_0$	Even	917.8013	− 3.8400	0.0748	914.0325	914.2500		
67	$2s^2 2p^1 3d^1(^2D_1)^3F_3$	Odd	921.4414	− 4.4700	0.0239	916.9992	917.1242		
72	$2s^2 2p^1 3d^1(^2D_1)^3F_4$	Odd	927.9074	− 4.4400	− 0.0059	923.4658	923.5886		
74	$2s^1 2p^2 3p^1(^2S_1)^5D_3$	Odd	928.4912	− 3.0100	− 1.2000	924.2820	924.3268		
76	$2s^1 2p^2 3p^1(^2P_1)^3S_1$	Odd	929.3757	− 2.9300	− 1.2100	925.2343	925.1989		
77	$2s^2 2p^1 3d^1(^2D_1)^1F_3$	Odd	930.2472	− 4.3100	− 0.0108	925.9291	925.8950		
78	$2s^1 2p^2 3p^1(^2P_1)^3D_2$	Odd	930.6172	− 2.8700	− 1.1900	926.5587	926.4441		
80	$2s^1 2p^2 3p^1(^2P_1)^3P_0$	Odd	931.5094	− 2.7400	− 1.2200	927.5527	927.4490		
81	$2s^1 2p^2 3p^1(^2P_1)^3F_4$	Odd	932.5244	− 3.7400	− 1.1900	927.5935	927.4788		
82	$2s^1 2p^2 3p^1(^2P_1)^3P_2$	Odd	933.3612	− 3.4600	− 1.2300	928.6734	928.5452		
83	$2s^1 2p^2 3p^1(^2P_1)^3D_3$	Odd	934.3641	− 3.5900	− 1.2100	929.5634	929.4517		
84	$2s^1 2p^2 3p^1(^2P_1)^1P_1$	Odd	934.4165	− 3.3500	− 1.2300	929.8361	929.7048		
85	$2s^1 2p^2 3d^1(^2D_1)^5D_0$	Even	934.7393	− 2.5000	− 1.2700	930.9683	930.4441		
86	$2s^1 2p^2 3d^1(^2D_1)^5F_2$	Even	934.7480	− 2.8500	− 1.2800	930.6249	930.6587		
87	$2s^1 2p^2 3d^1(^2D_1)^5D_1$	Even	934.8193	− 2.7000	− 1.2800	930.8394	930.7867		
88	$2s^1 2p^2 3d^1(^2D_1)^5F_3$	Even	935.7611	− 3.1100	− 1.2700	931.3739	931.1948		
89	$2s^1 2p^2 3p^1(^2P_1)^3D_2$	Odd	937.5835	− 2.7900	− 1.2300	933.5663	933.4182		
90	$2s^1 2p^2 3p^1(^2P_1)^3D_3$	Odd	938.2886	− 3.3000	− 1.2200	933.7667	933.6258		
91	$2s^1 2p^2 3p^1(^2P_1)^3P_0$	Odd	938.9291	− 2.9300	− 1.2200	934.7800	933.6303		
92	$2s^1 2p^2 3d^1(^2D_1)^3G_4$	Odd	938.9540	− 3.8600	− 1.2700	933.8193	934.2529		
93	$2s^1 2p^2 3p^1(^2P_1)^3P_1$	Odd	939.0947	− 2.7800	− 1.2200	935.0931	934.6437		
94	$2s^1 2p^2 3p^1(^2P_1)^3D_2$	Odd	939.3890	− 3.1400	− 1.2200	935.0230	934.8795		
95	$2s^1 2p^2 3d^1(^2D_1)^3F_3$	Even	939.4025	− 3.6800	− 1.2800	934.4462	934.8816		
96	$2s^1 2p^2 3p^1(^2P_1)^3P_1$	Odd	939.7655	− 2.9400	− 1.2200	935.6063	934.9480		
97	$2s^1 2p^2 3d^1(^2D_1)^3D_2$	Even	939.9472	− 3.5800	− 1.2800	935.0831	935.4731		
98	$2s^1 2p^2 3d^1(^2D_1)^3S_1$	Even	940.4750	− 3.4000	− 1.2900	935.7866	935.5754		
99	$2s^1 2p^2 3d^1(^2D_1)^5F_4$	Even	942.5321	− 3.1400	− 1.2700	938.1181	937.9424		
100	$2s^1 2p^2 3d^1(^2D_1)^3F_2$	Even	942.9346	− 3.0400	− 1.2800	938.6185	938.4080		
101	$2s^1 2p^2 3d^1(^2D_1)^1P_1$	Even	943.2990	− 2.7900	− 1.2800	939.2371	938.9979		

Table 1 continued

Levels	Configurations	Parity	MCDF				FAC	NIST	ΔE
			Zero-order	Breit	QED	Total			
102	$2s^1 2p^2 3d^1(^2D_1)^3G_3$	Even	943.8354	− 3.3500	− 1.2800	939.2124	939.0223		
103	$2s^1 2p^2 3d^1(^2D_1)^3P_2$	Even	944.4245	− 3.0000	− 1.2800	940.1475	939.9640		
104	$2s^1 2p^2 3d^1(^2D_1)^3F_3$	Even	944.8424	− 3.1200	− 1.2800	940.4453	940.2711		
105	$2s^1 2p^2 3d^1(^2D_1)^3D_1$	Even	945.2310	− 3.1900	− 1.2800	940.7642	940.5477		
106	$2s^1 2p^2 3d^1(^2D_1)^3F_2$	Even	945.6718	− 3.2400	− 1.2800	941.1555	940.9344		
107	$2s^1 2p^2 3d^1(^2D_1)^3P_0$	Even	946.2912	− 3.2700	− 1.2800	941.7494	940.9345		
108	$2s^1 2p^2 3d^1(^2D_1)^3G_5$	Even	946.3724	− 3.9700	− 1.2700	941.1244	941.5295		
109	$2s^1 2p^2 3d^1(^2D_1)^3D_1$	Even	946.4190	− 2.9700	− 1.2800	942.1702	941.9896		
110	$2s^1 2p^2 3d^1(^2D_1)^3D_3$	Even	948.0844	− 3.8000	− 1.2800	943.0085	942.8191		
111	$2s^1 2p^2 3d^1(^2D_1)^3F_4$	Even	948.5545	− 3.9200	− 1.2700	943.3587	943.1707		
112	$2s^1 2p^2 3d^1(^2D_1)^1D_2$	Even	948.7602	− 3.6500	− 1.2800	943.8327	943.6444		
113	$2s^1 2p^2 3d^1(^2D_1)^1P_1$	Even	949.5789	− 3.5500	− 1.2900	944.7408	944.5573		
114	$2s^1 2p^2 3d^1(^2D_1)^3P_0$	Even	950.0805	− 3.5400	− 1.2800	945.2568	945.0689		
115	$2s^1 2p^2 3d^1(^2D_1)^3D_3$	Even	951.6991	− 3.0700	− 1.2900	947.3400	947.1256		
116	$2s^1 2p^2 3d^1(^2D_1)^1G_4$	Even	952.5710	− 3.5000	− 1.2700	947.8005	947.5881		
117	$2s^1 2p^2 3d^1(^2D_1)^3P_2$	Even	953.1490	− 3.0800	− 1.2800	948.7920	948.5732		
118	$2s^1 2p^2 3d^1(^2D_1)^3P_1$	Even	953.5145	− 3.3300	− 1.2800	948.9078	948.6674		
119	$2s^1 2p^2 3d^1(^2D_1)^1F_3$	Even	953.5743	− 3.4200	− 1.2800	948.8775	948.6941		
120	$2s^1 2p^2 3d^1(^2D_1)^1D_2$	Even	953.7540	− 3.3200	− 1.2800	949.1555	948.9443		
135	$2s^1 2p^2 3s^1(^2S_1)^3S_1$	Even	1008.0785	− 3.8800	− 0.7640	1003.4329	997.2035		
136	$2s^1 2p^2 3p^1(^2P_1)^5S_2$	Odd	1008.8319	− 4.1700	− 1.1300	1003.5279	1003.4857		
137	$2s^1 2p^2 3s^1(^2P_1)^3P_1$	Even	1009.1799	− 4.3900	− 0.7650	1004.0203	1003.4545		
138	$2s^1 2p^2 3p^1(^2P_1)^3D_3$	Odd	1009.3157	− 4.4800	− 1.1400	1003.6982	1003.6596		
140	$2s^1 2p^2 3s^1(^2P_1)^1S_0$	Even	1010.4418	− 3.7600	− 0.7710	1005.9127	1005.9406		
141	$2s^1 2p^2 3p^1(^2P_1)^3P_0$	Odd	1016.2367	− 3.4100	− 1.1300	1011.6967	1011.6165		
142	$2s^1 2p^2 3p^1(^2P_1)^1P_1$	Odd	1016.4457	− 3.5900	− 1.1400	1011.7235	1011.6425		
143	$2s^1 2p^2 3p^1(^2P_1)^3S_1$	Odd	1016.8529	− 3.9900	− 1.1400	1011.7234	1011.6466		
144	$2s^1 2p^2 3p^1(^2P_1)^1D_2$	Odd	1017.1280	− 4.1200	− 1.1400	1011.8656	1011.7902		
160	$2s^1 2p^2 3p^1(^2P_1)^5D_4$	Odd	1038.7119	− 4.8000	− 1.1000	1032.8143	1032.7823		
161	$2s^1 2p^2 3p^1(^2P_1)^5p_3$	Odd	1038.9763	− 4.7600	− 1.1100	1033.1097	1033.0764		
162	$2s^1 2p^2 3p^1(^2P_1)^3S_1$	Odd	1039.8126	− 4.6700	− 1.1100	1034.0310	1033.9965		
164	$2s^1 2p^2 3p^1(^2P_1)^1D_2$	Odd	1042.1182	− 4.5600	− 1.1100	1036.4523	1036.4296		
165	$2s^1 2p^2 3d^1(^2D_1)^5D_2$	Even	1045.9349	− 4.6100	− 1.1600	1040.1730	1040.0710		
166	$2s^1 2p^2 3d^1(^2D_1)^5P_1$	Even	1046.2290	− 4.6200	− 1.1600	1040.4486	1040.2062		
167	$2s^1 2p^2 3d^1(^2D_1)^5D_3$	Even	1046.3764	− 4.9200	− 1.1500	1040.3030	1040.3475		
168	$2s^1 2p^2 3p^1(^2P_1)^3P_0$	Odd	1046.6112	− 4.4400	− 1.1000	1041.0698	1041.0023		
169	$2s^1 2p^2 3p^1(^2P_1)^3P_2$	Odd	1046.6798	− 4.0300	− 1.1000	1041.5541	1041.3518		
170	$2s^1 2p^2 3d^1(^2D_1)^3F_4$	Even	1046.8238	− 5.1500	− 1.1500	1040.5224	1041.4319		
171	$2s^1 2p^2 3p^1(^2P_1)^3F_3$	Odd	1047.0493	− 4.5300	− 1.1000	1041.4186	1041.4909		
172	$2s^1 2p^2 3p^1(^2P_1)^3P_1$	Odd	1047.2941	− 3.9200	− 1.1100	1042.2701	1042.2077		
173	$2s^1 2p^2 3p^1(^2P_1)^3P_2$	Odd	1047.9115	− 4.3000	− 1.1000	1042.5093	1042.4572		
176	$2s^1 2p^2 3p^1(^2P_1)^1P_1$	Odd	1050.2740	− 4.2400	− 1.1000	1044.9320	1044.8855		
179	$2s^1 2p^2 3d^1(^2D_1)^5F_5$	Even	1052.7334	− 5.0800	− 1.1500	1046.4993	1046.4047		
180	$2s^1 2p^2 3d^1(^2D_1)^3D_1$	Even	1052.8860	− 4.2100	− 1.1600	1047.5168	1046.7224		
181	$2s^1 2p^2 3d^1(^2D_1)^5D_4$	Even	1052.9446	− 4.9800	− 1.1500	1046.8154	1047.1493		

Table 1 continued

Levels	Configurations	Parity	MCDF				FAC	NIST	ΔE
			Zero-order	Breit	QED	Total			
182	$2s^1 2p^2 3d^1 (^2D_1)^3P_0$	Even	1053.0203	− 4.6000	− 1.1600	1047.2636	1047.3858		
184	$2s^1 2p^2 3d^1 (^2D_1)^1D_2$	Even	1053.6966	− 4.2800	− 1.1500	1048.2668	1048.0897		
186	$2s^1 2p^2 3d^1 (^2D_1)^3F_3$	Even	1054.1322	− 4.7600	− 1.1500	1048.2162	1048.1402		
187	$2s^1 2p^2 3d^1 (^2D_1)^3D_2$	Even	1054.5487	− 4.5700	− 1.1500	1048.8318	1048.7026		
188	$2s^1 2p^2 3d^1 (^2D_1)^3D_1$	Even	1054.6264	− 4.2700	− 1.1500	1049.2007	1049.0660		
191	$2s^1 2p^2 3d^1 (^2D_1)^3P_1$	Even	1055.6024	− 4.7100	− 1.1600	1049.7363	1049.6381		
192	$2s^1 2p^2 3d^1 (^2D_1)^3D_3$	Even	1055.8620	− 4.8700	− 1.1500	1049.8432	1049.7409		
197	$2s^1 2p^2 3d^1 (^2D_1)^3P_0$	Even	1056.4228	− 4.7300	− 1.1500	1050.5422	1050.4381		
198	$2s^1 2p^2 3d^1 (^2D_1)^3P_2$	Even	1056.6277	− 4.7700	− 1.1600	1050.7030	1050.6059		
202	$2s^1 2p^2 3d^1 (^2D_1)^3F_4$	Even	1061.2064	− 4.7000	− 1.1800	1055.3224	1055.4316		
203	$2s^1 2p^2 3d^1 (^2D_1)^1F_3$	Even	1061.7963	− 4.6200	− 1.1800	1055.9993	1055.8786		
205	$2s^1 2p^2 3d^1 (^2D_1)^3P_1$	Even	1062.7499	− 4.6000	− 1.1700	1056.9767	1057.8510		

Table 2 Radiative data for E1 transitions in W LXIX

S. no	Transition		λ_{ji} (in Å)	A_{ji} (in s^{-1})	f_{ij}	S_{ij} (in a.u.)
	Lower level (*i*)	Upper level (*j*)				
1	1	5	6.861	1.2654E+13	2.6787E−01	6.0503E−03
2	1	11	3.837	7.3749E+10	4.8833E−04	6.1685E−06
3	1	12	3.821	4.7639E+09	3.1277E−05	3.9341E−07
4	1	17	2.637	2.3222E+06	7.2617E−09	6.3036E−11
5	1	22	1.191	5.4283E+13	3.4650E−02	1.3590E−04
6	1	28	1.150	5.5629E+14	3.3074E−01	1.2519E−03
7	1	36	1.105	5.3901E+14	2.9582E−01	1.0758E−03
8	1	42	1.044	9.7912E+09	4.8037E−06	1.6517E−08
9	1	49	1.020	6.1057E+07	2.8566E−08	9.5919E−11
10	1	58	1.010	9.3914E+10	4.3111E−05	1.4339E−07
11	1	60	1.006	1.5102E+11	6.8734E−05	2.2763E−07
12	1	76	0.985	5.3554E+10	2.3365E−05	7.5758E−08
13	1	84	0.980	9.3519E+10	4.0398E−05	1.3034E−07
14	1	93	0.975	5.4388E+11	2.3231E−04	7.4530E−07
15	1	96	0.974	3.7956E+11	1.6194E−04	5.1926E−07
16	1	142	0.901	1.1571E+07	4.2220E−09	1.2519E−11
17	1	143	0.901	1.2218E+07	4.4580E−09	1.3219E−11
18	1	162	0.881	3.6772E+06	1.2845E−09	3.7265E−12
19	1	172	0.874	1.1952E+08	4.1091E−08	1.1827E−10
20	1	176	0.872	4.2104E+06	1.4402E−09	4.1348E−12
21	1	178	0.869	7.5240E+14	2.5552E−01	7.3098E−04

$$\text{for } M1 \text{ transitions} : A_{ji} = \frac{1.4910 \times 10^{13}}{\omega_j \lambda_{ji}^5} S_{ij} \text{ and } f_{ij} = \frac{2.236 \times 10^{-3}}{\lambda_{ji}^3 \omega_i} S_{ij}. \quad (9)$$

In equations from (6) to (9), λ_{ji} is $_{\text{the}}$ transition wavelength, w_j and w_i are upper and lower-level statistical weights. In Tables 2, 3, 4, 5, we have found 11 E1, 11 E2, 11 M1, and 11 M2 SXR transitions and 10 E1, 13 E2, 14 M1, and 19 M2 HXR transitions from the higher excited states to the ground state. Our presented radiative data for W LXIX are reliable and can be used further to identify spectral lines observed experimentally. In Fig. 1, we plotted multipole transition intensities decaying to ground state relative to the intensity of strong E1 transition 1–28 for W LXIX. From the intensity spectra of W LXIX, we found that all transitions have negligible intensity w.r.t to the intensity 1–28 transition except two E1 transitions, 1–178 and 1–36. The intensity of 1–36 E1 SXR transition is near 1–28, while the intensity of 1–178 E1 HXR transition is approximately double that of 1–28.

Table 3 Radiative data for E2 transitions in W LXIX

S. no	Transition		λ_{ji} (in Å)	A_{ji} (in s^{-1})	f_{ij}	S_{ij} (in a.u.)
	Lower level (i)	Upper level (j)				
1	1	3	8.676	9.0584E+07	5.1110E−06	1.9880E−05
2	1	6	4.329	4.8014E+02	6.7444E−12	3.2586E−12
3	1	14	3.477	1.5565E+07	1.4104E−07	3.5309E−08
4	1	19	2.474	3.1626E+03	1.4509E−11	1.3085E−12
5	1	30	1.134	1.4419E+12	1.3896E−03	1.2067E−05
6	1	38	1.098	5.9544E+12	5.3838E−03	4.2481E−05
7	1	40	1.086	1.3181E+13	1.1644E−02	8.8716E−05
8	1	44	1.036	8.4462E+07	6.7891E−08	4.4902E−10
9	1	45	1.028	2.5440E+07	2.0149E−08	1.3033E−10
10	1	48	1.022	3.0530E+08	2.3914E−07	1.5215E−09
11	1	54	1.017	1.0709E+09	8.2967E−07	5.1927E−09
12	1	63	0.999	2.6674E+08	1.9963E−07	1.1861E−09
13	1	86	0.979	2.9477E+04	2.1186E−11	1.1848E−13
14	1	97	0.975	1.0644E+09	7.5776E−07	4.1772E−09
15	1	100	0.971	1.1910E+10	8.4148E−06	4.5865E−08
16	1	103	0.969	6.9707E+09	4.9091E−06	2.6627E−08
17	1	106	0.968	8.1675E+09	5.7397E−06	3.1032E−08
18	1	112	0.966	1.3508E+09	9.4390E−07	5.0600E−09
19	1	117	0.960	2.7568E+10	1.9062E−05	1.0059E−07
20	1	120	0.960	6.7771E+09	4.6826E−06	2.4682E−08
21	1	165	0.876	1.6077E+05	9.2494E−11	3.7043E−13
22	1	184	0.869	1.9507E+07	1.1050E−08	4.3237E−11
23	1	187	0.869	4.1261E+07	2.3348E−08	9.1209E−11
24	1	198	0.867	1.6551E+07	9.3320E−09	3.6261E−11

Table 4 Radiative data for M1 transitions in W LXIX

S. no	Transitions		λ_{ji} (in Å)	A_{ji} (in s^{-1})	f_{ij}	S_{ij} (in a.u.)
	Lower level (i)	Upper level (j)				
1	1	2	8.789	1.7134E+10	5.9529E−04	1.2937E+00
2	1	18	2.483	3.4166E+04	9.4751E−11	5.8179E−08
3	1	23	1.182	1.4928E+09	9.3721E−07	2.7380E−04
4	1	25	1.160	4.8103E+09	2.9132E−06	8.3588E−04
5	1	29	1.134	2.9054E+10	1.6797E−05	4.7091E−03
6	1	37	1.099	7.4861E+08	4.0656E−07	1.1047E−04
7	1	43	1.036	1.2476E+07	6.0189E−09	1.5414E−06
8	1	46	1.025	4.0817E+06	1.9303E−09	4.8943E−07
9	1	52	1.018	2.3281E+07	1.0839E−08	2.7271E−06
10	1	53	1.017	5.3152E+07	2.4722E−08	6.2166E−06
11	1	61	1.002	3.5186E+06	1.5879E−09	3.9332E−07
12	1	87	0.979	1.3489E+06	5.8145E−10	1.4075E−07
13	1	98	0.974	4.2293E+06	1.8038E−09	4.3434E−07
14	1	101	0.970	1.6625E+06	7.0383E−10	1.6885E−07
15	1	105	0.969	8.2739E+04	3.4916E−11	8.3629E−09
16	1	109	0.967	9.7185E+04	4.0889E−11	9.7791E−09
17	1	113	0.965	6.8788E+05	2.8784E−10	6.8653E−08
18	1	118	0.960	7.7561E+05	3.2171E−10	7.6394E−08
19	1	135	0.908	2.3479E+03	8.7091E−13	1.9557E−10
20	1	137	0.908	1.3042E+02	4.8319E−14	1.0844E−11
21	1	166	0.876	1.4297E+02	4.9324E−14	1.0682E−11
22	1	180	0.870	4.1393E+03	1.4089E−12	3.0306E−10
23	1	188	0.869	2.0767E+03	7.0458E−13	1.5132E−10
24	1	191	0.868	3.9625E+04	1.3430E−11	2.8828E−09
25	1	205	0.862	1.3071E+04	4.3697E−12	9.3155E−10

Table 5 Radiative data for M2 transitions in W LXIX

S. no	Transition		λ_{ji} (in Å)	A_{ji} (in s^{-1})	f_{ij}	S_{ij} (in a.u.)
	Lower level (*i*)	Upper level (*j*)				
1	1	4	7.216	1.4866E+07	5.8026E−07	9.7537E−02
2	1	8	4.000	4.1941E+05	5.0294E−09	1.4396E−04
3	1	13	3.826	3.4074E+05	3.7388E−09	9.3671E−05
4	1	16	2.687	1.6275E+03	8.8054E−12	7.6385E−08
5	1	31	1.127	3.6011E+09	3.4295E−06	2.1971E−03
6	1	33	1.115	5.0921E+10	4.7423E−05	2.9378E−02
7	1	35	1.105	2.5055E+10	2.2940E−05	1.3852E−02
8	1	41	1.045	1.4425E+04	1.1814E−11	6.0350E−09
9	1	50	1.019	1.2719E+06	9.9000E−10	4.6861E−07
10	1	56	1.013	1.1477E+07	8.8288E−09	4.1059E−06
11	1	59	1.010	3.3542E+06	2.5651E−09	1.1825E−06
12	1	65	0.994	2.0481E+05	1.5182E−10	6.6785E−08
13	1	66	0.993	4.1171E+06	3.0455E−09	1.3355E−06
14	1	75	0.986	4.2403E+07	3.0886E−08	1.3234E−05
15	1	78	0.984	6.3950E+04	4.6368E−11	1.9732E−08
16	1	82	0.981	1.4512E+06	1.0474E−09	4.4272E−07
17	1	89	0.976	3.7450E+07	2.6748E−08	1.1128E−05
18	1	94	0.975	2.1231E+07	1.5117E−08	6.2599E−06
19	1	125	0.949	3.3600E+06	2.2665E−09	8.6549E−07
20	1	130	0.940	1.7160E+08	1.1360E−07	4.2178E−05
21	1	136	0.908	4.6777E+02	2.8913E−13	9.6847E−11
22	1	144	0.901	6.6448E+03	4.0397E−12	1.3200E−09
23	1	145	0.892	7.0367E+02	4.2010E−13	1.3358E−10
24	1	148	0.890	1.7217E+04	1.0229E−11	3.2285E−09
25	1	164	0.879	2.9454E+02	1.7067E−13	5.1892E−11
26	1	169	0.875	1.8511E+04	1.0621E−11	3.1821E−09
27	1	173	0.874	1.5186E+01	8.6975E−15	2.5986E−12
29	1	177	0.869	2.1425E+09	1.2142E−06	3.5705E−04
30	1	189	0.866	2.6775E+10	1.5063E−05	4.3814E−03

In Fig. 2, we have demonstrated the discrepancy between length and velocity oscillator strengths for C-like W. Length gauge as well as velocity gauge discrepancies is analyzed for the result of C-like W. Line strengths can be divided into three parts for E1 transitions (a) $S < 0.001$ a.u., (b) $0.001 < S < 0.002$ a.u., and (c) $S > 0.005$ a.u. In these regions, as can be seen, our logarithmic ratio of oscillator strengths has a maximum value of around 1.07. In the majority of transitions, this ratio is quite close to zero; 19 transitions have oscillator strengths ratios that are not equal to zero, as can also be seen. 0.001 a.u. of line strengths lies below, whereas 2 transitions are between 0.001 and 0.002 a.u. and 1 transition lie in the region 0.004—0.005 a.u. line strengths which have zero ratio of oscillator strength. For C-like W, this clearly represents that the terms of length form along with velocity form, or in both gauges, oscillator strengths are nearly equivalent. Again, for E2 transitions in Fig. 3, line strengths are categories into three zones. (a) $S < 0.0002$ a.u., (b) $0.0004 < S < 0.0006$ a.u., and (c) $S > 0.0010$ a.u.. As can be seen, our maximum logarithmic oscillator strength ratio is 0.58, and for the majority of transitions, this ratio is quite close to zero. Additionally, we can observe that for 10 transitions, the ratio of oscillator strengths is not the same as zero and line strengths of 0.0002 a.u. lie below, whereas 1 transitions lie between 0.0004 and 0.0006 a.u. and 1 transition is located in the range of 0.0008 to 0.0010 a.u. line strength resulting in a zero oscillator strength ratio.

We have shown $\log10(S_n/S_{n+1})$ against line strength (S_n) for n = 5 for the E1, E2 transitions and M1, M2 transitions for C-like W in Figs. 4, 5, 6, and 7. The maximum value of the logarithmic ratio $\log10(S_5/S_6)$ of line strengths for C-like W is 3.88×10^{-2} for E1 and 1.83×10^{-1} for E2, as shown in Figs. 4 and 5 (Tables 2 and 3). Moreover, this ratio is close to zero for C-like W. From Figs. 6 and 7 for M1 and M2 transitions, as can be observed, the maximum values of the logarithmic ratio $\log10(S_5/S_6)$ for M1 and M2 are 1.54×10^{-1} and 2.10×10^{-1}, respectively (Table 4 and 5).

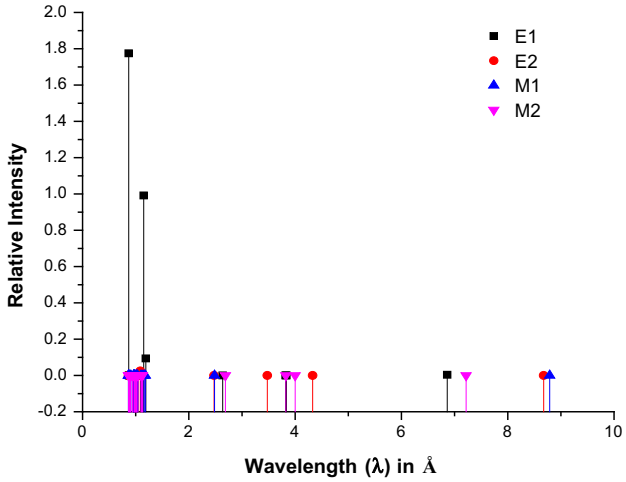


Fig. 1 Relative intensity for W LXIX

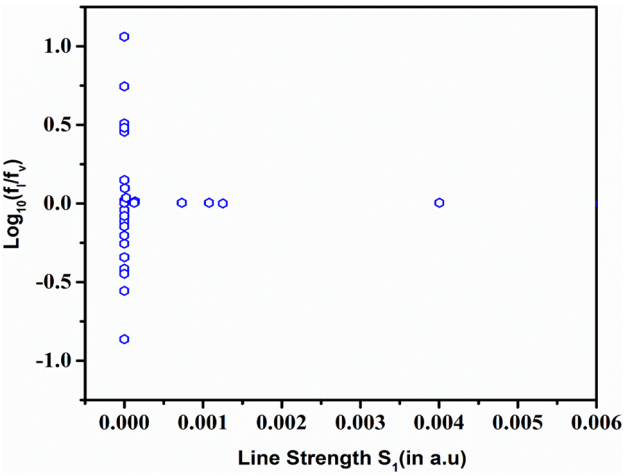


Fig. 2 Comparisons between the velocity form (f_v) and the length form (f_l) of oscillator strengths for $E1$ transition of C-like W

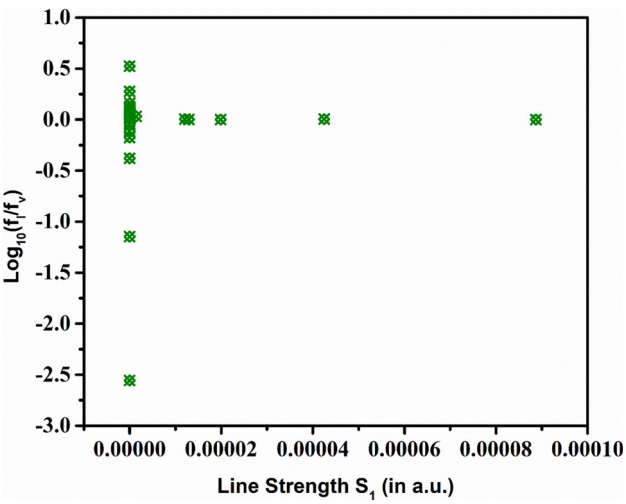


Fig. 3 Comparisons between the velocity form (f_v) and the length form (f_l) of oscillator strengths for $E2$ transition of C-like W

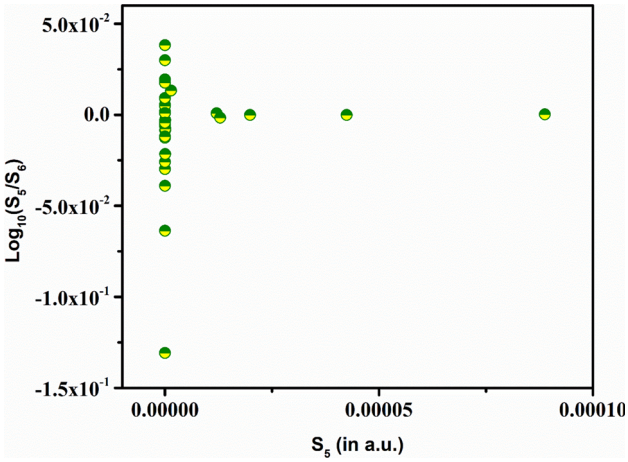


Fig. 4 Line strength (S_n) against log10(S_n/S_{n+1}) for $n = 5$ for $E1$ transitions of C-like W

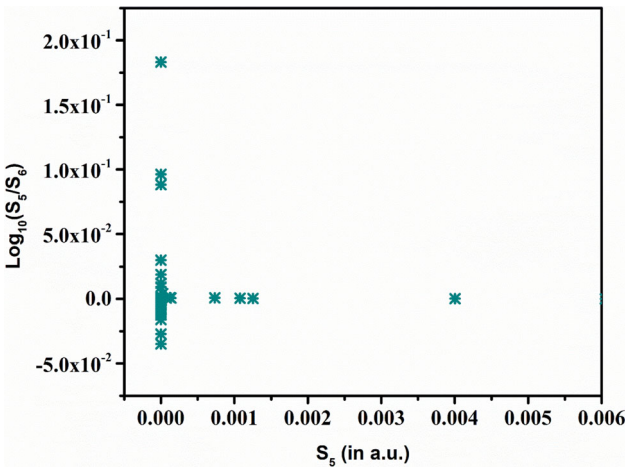


Fig. 5 Line strength (S_n) against log10(S_n/S_{n+1}) for $n = 5$ for $E2$ transitions of C-like W

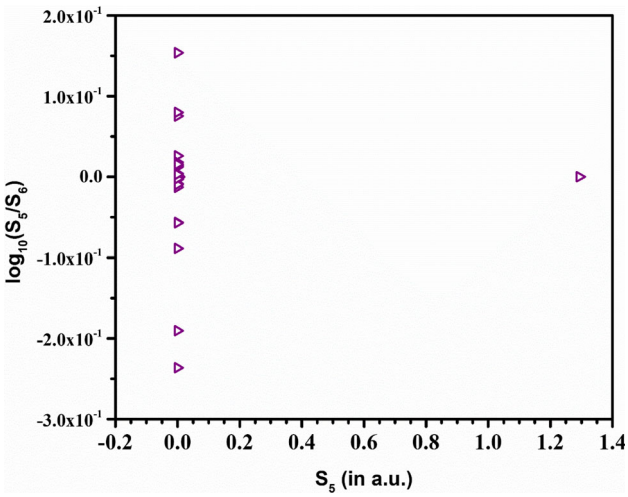


Fig. 6 Line strength (S_n) against log10(S_n/S_{n+1}) for $n = 5$ for $M1$ transitions of C-like W

4 Conclusion

The energy levels as well as radiative data for the transitions of E1, E2, M1, and M2 among the lowest level 205 fine structure levels for C-like W are reported in this work. In the calculations, two separate codes, GRASP and FAC, are used and the outcomes of both

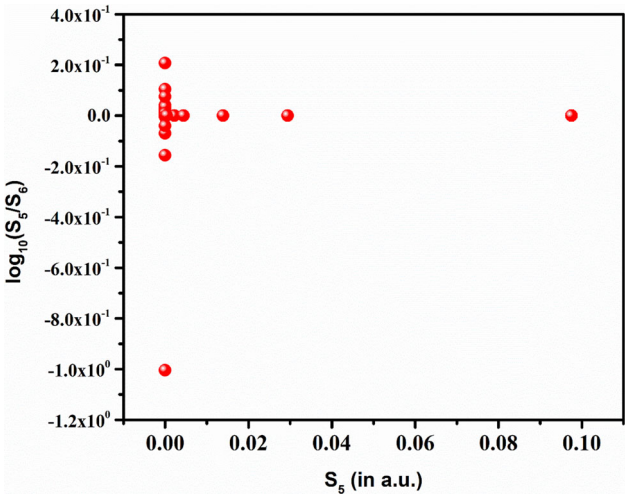


Fig. 7 Line strength (S_n) against $\log10(S_n/S_{n+1})$ for $n = 5$ for $M2$ transitions of C-like W

codes are compared. The discrepancy between our GRASP energies and current theoretical and experimental data in the literature is explained thoroughly. We believe our findings are extensive and new and will be beneficial in identifying and studying fusion plasmas, astrophysical and diagnosis of solar and fusion plasmas that require appropriate atomic data for the analysis.

Acknowledgements We appreciate the support and better facilities provided by Delhi Technological University.

Data Availability Statement This manuscript has associated data in a data repository. [Authors' comment: The data used to support the findings of this study are included within the article and are cited at relevant places within the text as references.]

References

1. G. Tachiev, C.F. Fischer, Breit-Pauli energy levels and transition rates for the carbonlike sequence. Can. J. Phys. **79**, 955–976 (2001). https://doi.org/10.1139/cjp-79-7-955
2. A. Al-Modlej, R.A.B. Alraddadi, N.B. Nessib, Energy levels and oscillator strengths for carbon isoelectronic sequence from C I to Ne V. Eur. Phys. J. Plus. (2018). https://doi.org/10.1140/epjp/i2018-12192-9
3. P.R. Young, U. Feldman, A. Lobel, Forbidden and intercombination lines of RR Telescopii: wavelength measurements and energy levels. Astrophys. J. Suppl. Ser. (2011). https://doi.org/10.1088/0067-0049/196/2/23
4. J.P. Mosnier, E.T. Kennedy, J.M. Bizau, D. Cubaynes, S. Guilbaud, C. Blancard, B.M. McLaughlin, Photoionization cross-sections of carbon-like n+ near the k-edge (390–440 ev). Atoms **9**, 1–18 (2021). https://doi.org/10.3390/atoms9020027
5. W.D. Chen, J. Xiao, Y. Shen, Y.Q. Fu, F.C. Meng, C.Y. Chen, B.H. Zhang, Y.J. Tang, R. Hutton, Y. Zou, Precise studies on resonant energies of the first intershell (KLL) dielectronic recombination processes for He- up to O-like xenon. Phys. Plasmas. (2008). https://doi.org/10.1063/1.2967486
6. U. Feldman, W. Curdt, E. Landi, K. Wilhelm, Identification of spectral lines in the 500–1600 a wavelength range of highly ionized Ne, Na, Mg, Ar, K, Ca, Ti, Cr, Mn, Fe Co, and Ni emitted by flares (T e ≥ 3 x 10 6 K) and their potential use in plasma diagnostics. Astrophys. J. **544**, 508–521 (2000). https://doi.org/10.1086/317203
7. J.M. Bizau, D. Cubaynes, S. Guilbaud, M.M. Alshorman, M.F. Gharaibeh, I.Q. Ababneh, C. Blancard, B.M. McLaughlin, K -shell photoionization of O^+ and O^{2+} ions: experiment and theory. Phys. Rev. A At. Mol. Opt. Phys. **92**, 1–14 (2015). https://doi.org/10.1103/PhysRevA.92.023401
8. K.P. Dere, G. Del Zanna, P.R. Young, E. Landi, R.S. Sutherland, CHIANTI—an atomic database for emission lines. XV. version 9, improvements for the X-ray satellite lines. Astrophys. J. Suppl. Ser. **241**, 22 (2019). https://doi.org/10.3847/1538-4365/ab05cf
9. J.K. Rudolph, S. Bernitt, S.W. Epp, R. Steinbrügge, C. Beilmann, G.V. Brown, S. Eberle, A. Graf, Z. Harman, N. Hell, M. Leutenegger, A. Müller, K. Schlage, H.C. Wille, H. Yavaş, J. Ullrich, J.R.C. López-Urrutia, X-ray resonant photoexcitation: linewidths and energies of Kα transitions in highly charged Fe ions. Phys. Rev. Lett. **111**, 1–6 (2013). https://doi.org/10.1103/PhysRevLett.111.103002
10. B. Edlé, Comparison of theoretical and experimental level values of the $n = 2$ configurations in the nitrogen isoelectronic sequence. Phys. Scr. **30**, 125–145 (1984). https://doi.org/10.1088/0031-8949/30/2/007
11. J.Y. Liao, S.N. Zhang, Y. Yao, Wavelength measurements of k transitions of oxygen, neon, and magnesium with X-ray absorption lines. Astrophys. J. (2013). https://doi.org/10.1088/0004-637X/774/2/116
12. K.J. McCarthy, N. Tamura, S.K. Combs, R. Garcia, J.H. Sánchez, M. Navarro, N. Panadero, I. Pastor, A. Soleto, Identification of S VIII through S XIV emission lines between 17.5 and 50 nm in a magnetically confined plasma. Phys. Scr. (2018). https://doi.org/10.1088/1402-4896/aaa22c
13. M. Lestinsky, N.R. Badnell, D. Bernhardt, D. Bing, M. Grieser, M. Hahn, J. Hoffmann, B. Jordon-Thaden, C. Krantz, O. Novotný, D.A. Orlov, R. Repnow, A. Shornikov, A. Müller, S. Schippers, A. Wolf, D.W. Savin, Electron-ion recombination of Mg^{6+} forming Mg^{5+} and of Mg^{7+} forming Mg^{6+}: laboratory measurements and theoretical calculations. Astrophys. J. (2012). https://doi.org/10.1088/0004-637X/758/1/40
14. Y.A. Podpaly, J.D. Gillaspy, J. Reader, Y. Ralchenko, EUV measurements of Kr XXI-Kr XXXIV and the effect of a magnetic-dipole line on allowed transitions. J. Phys. B At. Mol. Opt. Phys. (2014). https://doi.org/10.1088/0953-4075/47/9/095702
15. E. Träbert, M. Grieser, R. Hahn, C. Krantz, R. Repnow, A. Wolf, M1 and E2 decay-dependent lifetime of the lowest 1S 0 level in C-like ions up to Ne^{4+} measured at a heavy-ion storage ring. New J. Phys. (2012). https://doi.org/10.1088/1367-2630/14/2/023061
16. K. Wang, D.F. Li, H.T. Liu, X.Y. Han, B. Duan, C.Y. Li, J.G. Li, X.L. Guo, C.Y. Chen, J. Yan, Systematic calculations of energy levels and transition rates of C-like Ions with Z = 13–36. Astrophys. J. Suppl. Ser. **215**, 1–14 (2015). https://doi.org/10.1088/0067-0049/215/2/26

17. N.W. Zheng, T. Wang, Systematical study on the ionization potential of excited states in carbon-like sequence. Chem. Phys. Lett. **376**, 557–565 (2003). https://doi.org/10.1016/S0009-2614(03)01021-2
18. K.M. Aggarwal, F.P. Keenan, A.Z. Msezane, Oscillator strengths for transitions in C-like ions between K XIV and MN XX. Astron. Astrophys. **401**, 377–383 (2003). https://doi.org/10.1051/0004-6361:20030117
19. J.E. Sansonetti, W.C. Martin, Handbook of basic atomic spectroscopic data. J. Phys. Chem. Ref. Data. **34**, 1559–2259 (2005). https://doi.org/10.1063/1.1800011
20. G.C. Rodrigues, P. Indelicato, J.P. Santos, P. Patté, F. Parente, Systematic calculation of total atomic energies of ground state configurations. At. Data Nucl. Data Tables. **86**, 117–233 (2004). https://doi.org/10.1016/j.adt.2003.11.005
21. B.C. Fawcett, Wavelengths and classifications of emission energy levels for the above isoelectronic. Science **164**, 135–164 (1975). https://doi.org/10.1103/PhysRevA.88.042504
22. C. Chen, Energies, radial expectation values, hyperfine structures of the ground state and highly excited states for C and O^{2+}. Int. J. Mod. Phys. B. (2020). https://doi.org/10.1142/S0217979220501970
23. C. Nazé, S. Verdebout, P. Rynkun, G. Gaigalas, M. Godefroid, P. Jönsson, Isotope shifts in beryllium-, boron-, carbon-, and nitrogen-like ions from relativistic configuration interaction calculations. At. Data Nucl. Data Tables. **100**, 1197–1249 (2014). https://doi.org/10.1016/j.adt.2014.02.004
24. H.L. Zhang, C.J. Fontes, Relativistic distorted-wave collision strengths and oscillator strengths for the 185 $\Delta n = 0$ transitions with $n = 2$ in C-like ions with $9 \leq Z \leq 54$. At. Data Nucl. Data Tables. **63**, 275–314 (1996). https://doi.org/10.1006/adnd.1996.0014
25. H.L. Zhang, C.J. Fontes, Relativistic distorted-wave collision strengths and oscillator strengths for the 185 $\Delta n = 0$ transitions with $n = 2$ in the 67 C-like ions with $26 \leq Z \leq 92$. At. Data Nucl. Data Tables. **101**, 41–142 (2015). https://doi.org/10.1016/j.adt.2014.08.001
26. M.F. Gu, Energies of 1s22lq ($1 \leq q \leq 8$) states for $Z \leq 60$ with a combined configuration interaction and many-body perturbation theory approach. At. Data Nucl. Data Tables. **89**, 267–293 (2005). https://doi.org/10.1016/j.adt.2005.02.004
27. D. Ray, P.K. Mukherjee, Radiative transitions in highly-stripped carbon-like ions. Phys. Scr. **51**, 81 (1995). https://doi.org/10.1088/0031-8949/51/1/013
28. C.C. Sang, Z.B. Chen, Y. Sun, X.Z. Shen, F. Hu, J. Ma, X.L. Wang, Hyperfine structure and 2s–2p transition in C-like Fe, Co and Ni. J. Electron. Spectros. Relat. Phenom. **230**, 26–32 (2019). https://doi.org/10.1016/j.elspec.2018.11.001
29. G.V. Shpatakovskaya, Patterns of the ionization potentials of multicharged ions of heavy elements. JETP Lett. **114**, 737–741 (2021). https://doi.org/10.1134/S0021364021240073
30. C.F. Fischer, H.P. Saha, Multiconfiguration hartree-fock results with breit-pauli corrections for transitions in the carbon sequence. Phys. Scr. **32**, 181–194 (1985). https://doi.org/10.1088/0031-8949/32/3/004
31. C.F. Fischer, G. Tachiev, Breit-Pauli energy levels, lifetimes, and transition probabilities for the beryllium-like to neon-like sequences. At. Data Nucl. Data Tables. **87**, 1–184 (2004). https://doi.org/10.1016/j.adt.2004.02.001
32. P. Palmeri, P. Quinet, C. Mendoza, M.A. Bautista, J. García, M.C. Witthoeft, T.R. Kallman, Atomic decay data for modeling K lines of iron peak and light odd-Z elements. Astron. Astrophys. **543**, 1–9 (2012). https://doi.org/10.1051/0004-6361/201219438
33. P. Jönsson, G. Gaigalas, P. Rynkun, L. Radžiute, J. Ekman, S. Gustafsson, H. Hartman, K. Wang, M. Godefroid, C.F. Fischer, I. Grant, T. Brage, G. Del Zanna, Multiconfiguration dirac-hartree-fock calculations with spectroscopic accuracy: applications to astrophysics. Atoms **5**, 1–24 (2017). https://doi.org/10.3390/atoms5020016
34. F. Li, G.Y. Liang, G. Zhao, Soft X-ray emission lines of S VII-S XIV in procyon. Astrophys. J. (2013). https://doi.org/10.1088/0004-637X/762/1/53
35. B. Tu, J. Xiao, K. Yao, X. Wang, Y. Shen, Y. Yang, D. Lu, L. Huang, C. Zhen, Y. Fu, B. Wei, R. Hutton, Y. Zou, Photorecombination studies of highly charged tungsten ions at Shanghai EBIT. J. Phys. Conf. Ser. (2017). https://doi.org/10.1088/1742-6596/875/2/012003
36. B. Tu, J. Xiao, Y. Shen, Y. Yang, D. Lu, T.H. Xu, W.X. Li, C.Y. Chen, Y. Fu, B. Wei, C. Zheng, L.Y. Huang, R. Hutton, X. Wang, K. Yao, Y. Zou, B.H. Zhang, Y.J. Tang, KLL dielectronic recombination resonant strengths of He-like up to O-like tungsten ions. Phys. Plasmas. (2016). https://doi.org/10.1063/1.4948420
37. M.B. Trzhaskovskaya, V.K. Nikulin, Radiative recombination and photoionization data for tungsten ions. Electron structure of ions in plasmas. Atoms **3**, 86–119 (2015). https://doi.org/10.3390/atoms3020086
38. H. Liu, G. Jiang, F. Hu, C.K. Wang, Z.B. Wang, J.M. Yang, Intercombination transitions of the carbon-like isoelectronic sequence. Chin. Phys. B. (2013). https://doi.org/10.1088/1674-1056/22/7/073202
39. P. Beiersdorfer, M.J. May, J.H. Scofield, S.B. Hansen, Atomic physics and ionization balance of high-Z Ions: critical ingredients for characterizing and understanding high-temperature plasmas. High Energy Density Phys. **8**, 271–283 (2012). https://doi.org/10.1016/j.hedp.2012.03.003
40. U. Feldman, J.F. Seely, E. Landi, Y. Ralchenko, Bright EUV lines emitted by highly ionized tungsten ions as diagnostic indicators of the tungsten transport in ITER core plasmas (Te > 7 keV). Nucl. Fusion. (2008). https://doi.org/10.1088/0029-5515/48/4/045004
41. A.E. Kramida, J. Reader, Ionization energies of tungsten ions: $W2^{+}$ through $W71^{+}$. At. Data Nucl. Data Tables. **92**, 457–479 (2006). https://doi.org/10.1016/j.adt.2006.03.002
42. J. Huang, G. Jiang, Q. Zhao, Ground-state ionization potentials for lithium through neon isoelectronic sequences with $Z = 37$–82. Chin. Phys. Lett. **23**, 69–72 (2006). https://doi.org/10.1088/0256-307X/23/1/021
43. U.I. Safronova, Z.B. Rudzikas, Perturbation theory for the relativistic energy of atomic systems. J. Phys. B At. Mol. Phys. **9**, 1989–2001 (1976). https://doi.org/10.1088/0022-3700/9/12/011
44. T.A. Carlson, C.W. Nestor, N. Wasserman, J.D. Mcdowell, Calculated ionization potentials for multiply charged ions. At. Data Nucl. Data Tables. **2**, 63–99 (1970). https://doi.org/10.1016/S0092-640X(70)80005-5
45. I.P. Grant, B.J. McKenzie, P.H. Norrington, D.F. Mayers, N.C. Pyper, An atomic multiconfigurational Dirac-Fock package. Comput. Phys. Commun. **21**, 207–231 (1980). https://doi.org/10.1016/0010-4655(80)90041-7
46. R. Sharma, R. Paijwar, Spectroscopic study of EUV and SXR spectral lines with partition function and level population of W LVI. Can. J. Phys. **99**, 657–669 (2021). https://doi.org/10.1139/cjp-2020-0497
47. M.F. Gu, The flexible atomic code. Can. J. Phys. **86**, 675–689 (2008). https://doi.org/10.1139/p07-197
48. A. Kramida, Yu. Ralchenko, J. Reader, and NIST ASD Team, https://physics.-nist.gov/asd for NIST Atomic Spectra Database (ver. 5.6.1) (2019).

Springer Nature or its licensor (e.g. a society or other partner) holds exclusive rights to this article under a publishing agreement with the author(s) or other rightsholder(s); author self-archiving of the accepted manuscript version of this article is solely governed by the terms of such publishing agreement and applicable law.

e-ISSN: 2582-5208
International Research Journal of Modernization in Engineering Technology and Science
(Peer-Reviewed, Open Access, Fully Refereed International Journal)
Volume:05/Issue:05/May-2023 Impact Factor- 7.868 www.irjmets.com

SUSPENSION GEOMETRY OPTIMISATION FOR OFF-ROAD VEHICLES USING ARTIFICIAL NEURAL NETWORK AND PARTICLE SWARM OPTIMISATION

Satwik Dudeja*1, Satwik Gupta*2, Shaswat Garg*3

*1,2,3Department of Mechanical Engineering, Delhi Technological University, New Delhi, India,
DOI : https://www.doi.org/10.56726/IRJMETS39315

ABSTRACT

This research paper investigates how to forecast wheel alignment angles and optimize double wishbone suspension geometry for off-road vehicles. The suspension three-dimensional points are analysed using a Particle Swarm Optimisation (PSO) to obtain preferred values for wheel alignment angles. To accurately predict these angles at all bump angles, an Artificial Neural Network is employed. The results indicate that the camber, toe, caster, and kingpin have a lower deviation from optimum values, compared to our previous study. For an ATV's optimal performance in bumps and droops, all four angles must be within their specific ranges, and PSO optimises the population by moving candidate chromosomes in the search space with the help of mathematical functions like Rosenbrock or StyblinskiTang over the chromosome's velocity and acceleration. Using Lotus Suspension Analysis software, the findings are verified, resulting in the best possible wheel alignment.

Keywords - Particle Swarm Optimisation, Artificial Neural Network, Double Wishbone, Suspension, Toe, Camber, Kingpin, Castor, off-road Vehicle, Optimization

I. INTRODUCTION

Optimizing the wheel alignment angles of an All-Terrain Vehicle's suspension system, such as the Camber, Toe, Castor, and Kingpin, is essential to improve vehicle dynamics and reduce tire wear over time. Traditional methods to determine these angles rely on iterative testing and analysis, which can be time-consuming and inefficient. Recently, machine learning techniques such as artificial neural networks (ANN) have been used to predict these angles accurately, which helps automate the suspension design process. Additionally, optimization techniques such as genetic algorithms (GA) and particle swarm optimization (PSO) have been used to arrive at optimal suspension configurations.

In this research, we propose the use of an ANN to accurately predict the wheel-alignment angles and PSO to optimize them. This approach eliminates the need for Lotus Analysis Software, making the process of creating optimal suspension geometries more efficient. An ANN is a machine learning model inspired by the structure and function of biological neural networks, capable of learning complex relationships between inputs and outputs. By training the ANN with data from suspension simulations, we can predict the wheel alignment angles accurately. PSO is a population-based optimization technique that iteratively updates the positions of particles, each of which represents a possible solution to the optimization problem. By setting multiple objectives and using a fitness function for parent selection, we can arrive at a suspension configuration that meets our design goals.

This research builds on previous work that has used optimization techniques such as GA to optimize suspension systems. For example, Habibi et al. [1] used GA to minimize the caster, toe, and camber of a McPherson strut system. Similarly, Alkhatib et al. [2] optimized a 1DOF vibration oscillator and linear quarter car suspension model using GA. Sancibrian et al. [3] developed GA to optimize a double wishbone suspension system, focusing on camber and toe. Goga et al. [4] optimized damping and stiffness coefficients of a passive suspension system using evolutionary computation techniques. Mitra et al. [5] modeled a 4-DOF system to analyze driver comfort and optimized sprung and unsprung mass, spring and tire stiffness, and damping coefficients using GA. Nariman et al. [6] optimized a 5 DOF vehicle vibration model using a multi-objective uniform-diversity GA. Finally, El Demerdash et al. [8] optimized the passive suspension system of a military armored vehicle, including the driver's seat. Using our previous research [9] as base, we focused on improving the accuracy of our learning models and also improve the quality of the evolutionary computation algorithm. Thus, in this work we employed Artificial Neural Networks (ANN) to predict the properties of the suspension model and replaced Genetic Algorithm with Particle Swarm Optimization (PSO) to generate offspring's.

e-ISSN: 2582-5208
International Research Journal of Modernization in Engineering Technology and Science
(Peer-Reviewed, Open Access, Fully Refereed International Journal)
Volume:05/Issue:05/May-2023 Impact Factor- 7.868 www.irjmets.com

II. DOUBLE WISHBONE SUSPENSION SYSTEM

A suspension system is a crucial component in a vehicle that plays a significant role in ensuring a smooth ride by countering surface irregularities. The suspension system connects the wheels to the vehicle and has three primary objectives, namely maintaining maximum surface contact, improving vehicle handling, and maximizing driver comfort [10]. There are two types of suspension systems, dependent and independent. Dependent suspension systems experience movement of one wheel that affects the other, while in independent suspension systems, the movement of one wheel is not impacted by the other. Off-road vehicles typically use independent suspension systems in the front due to the high number of surface abnormalities encountered. The double wishbone suspension system is an independent suspension system that utilizes two wishbone-shaped control arms that connect the knuckle and the vehicle's chassis. It is a preferred front suspension geometry for off-road vehicles as it is adjustable, simple to manufacture and cost-effective. In this research, we have focused on the double A-Arm design and have proposed a geometry design optimization algorithm that analyses the suspension geometries in Lotus Suspension Software.



Figure 1. Double A Arm Suspension Geometry

DATASET PREPARATION

The research utilized data from 189 different suspension designs created on the Lotus Suspension Analysis software, including the best ones produced by the Genetic Algorithm. The data was processed to extract all relevant coordinates, specifically the eight points for the arms and tie rod, as well as the mounting positions of the arms on the chassis, the inner tie rod point, and the connection between the upright and the tie rod and arms. The instantaneous axis, which determines the camber change rate, roll center information, and steering characteristics, is formed by the line of intersection of the planes created by the lower and upper front pivot, rear pivot, and outer ball joint points. The position of the tie rod, including its length and instantaneous center, is also important for controlling bump steer. The dataset consists of 24 features for the coordinates of the points and an additional feature for the bump value to predict the four alignment angles (camber, toe, caster, and kingpin) for 189 suspension iterations at 14 different bump values. This creates a final dataset of 2646×29. Outliers were detected during exploratory data analysis, and were removed during data cleaning. The training, validation, and testing data splits were created with a ratio of 70:15:15.

Table 1. Dataset Parameters

Property	Value
Input parameters	25
Response Parameters	4
Rows	189×14
Dimension	2646×29

e-ISSN: 2582-5208
International Research Journal of Modernization in Engineering Technology and Science
(Peer-Reviewed, Open Access, Fully Refereed International Journal)
Volume:05/Issue:05/May-2023 Impact Factor- 7.868 www.irjmets.com

Table 2. Geometry Point Labels For Figure 2

Index	Point
1	Upper Wishbone Rear Pivot
2	Upper Wishbone Front Pivot
3	Lower Wishbone Front Pivot
4	Lower Wishbone Rear Pivot
5	Upper Wishbone Outer Ball Joint
6	Lower Wishbone Outer Ball Joint
7	Outer Track Rod Ball Joint
8	Inner Track Rod Ball Joint

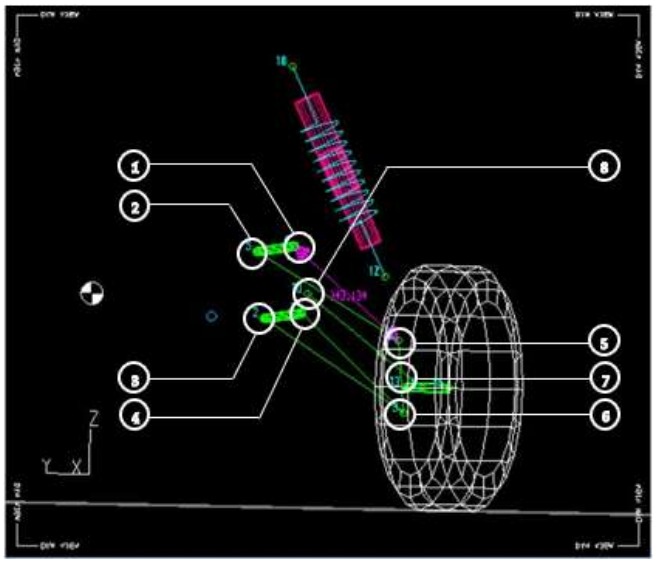


Figure 2. Geometry Points in a Quarter Car Model

III. ARTIFICIAL NEURAL NETWORK

Artificial neural networks (ANN) [11] are a class of machine learning algorithms that are inspired by the structure and function of biological neural networks. ANNs consist of interconnected processing nodes that receive inputs, perform calculations, and generate outputs. The structure of an ANN is defined by the number and arrangement of the nodes, as well as the connections between them.

The equations used in the neural network model are as follows:

- The output of a node in the hidden layer is calculated as follows:

$$z = Wx + b$$

where z is the weighted sum of the inputs x, W is the weight matrix, and b is the bias vector.

- The activation function for the hidden layer is the rectified linear unit (ReLU) function, defined as follows:

$$f(z) = max(0, z)$$

- The output of a node in the output layer is calculated as follows:

$$y = Vh + c$$

where y is the predicted output, h is the output of the hidden layer, V is the weight matrix, and c is the bias vector.

For our suspension geometry prediction problem, we used a feedforward neural network with a single hidden layer. The network takes the suspension coordinates along with bump value as inputs. The output layer consisted of four nodes corresponding to the predicted values of these variables. The hidden layer consisted of 10 nodes with a rectified linear activation function.

e-ISSN: 2582-5208
International Research Journal of Modernization in Engineering Technology and Science
(Peer-Reviewed, Open Access, Fully Refereed International Journal)
Volume:05/Issue:05/May-2023 Impact Factor- 7.868 www.irjmets.com

The neural network was trained using a backpropagation algorithm with mean squared error as the loss function. The training dataset was split into 75% for training and 25% for validation. We used the MATLAB Neural Network Toolbox to implement the neural network.

To evaluate the performance of the neural network, we used the R-squared (R2) coefficient of determination, which measures the proportion of variance in the data that is explained by the model. We also calculated the root-mean-square error (RMSE) as a measure of the prediction error.

Table 3. Regression Model Parameters

Algorithm	Testing R2 score	Training R2 score
KNNR	0.793	0.908
Decision Tree	0.711	0.863
ELM	0.88	0.908
RBF	0.46	0.469
ANN	**0.987**	**0.994**
GPR	0.981	0.979

The performance of the neural network was compared to other machine learning algorithms such as Gaussian process regression, K-nearest neighbours' regression, decision tree regression, extreme learning machine, radial basis function network, and artificial neural network. The comparison was based on the R2 score for each algorithm.

The final neural network model had an R2 score of 0.995 for camber, 0.987 for toe, 0.997 for caster, and 0.997 for kingpin, indicating excellent predictive accuracy. The RMSE values were 0.002 for camber, 0.007 for toe, 0.002 for caster, and 0.002 for kingpin.

Overall, the use of artificial neural networks proved to be an effective approach for predicting the suspension geometry parameters with high accuracy.

IV. PARTICLE SWARM OPTIMISATION

Particle Swarm Optimization (PSO) [12] is a population-based optimization algorithm inspired by the social behaviour of bird flocks and fish schools. In PSO, a swarm of particles moves through a multi-dimensional search space, looking for the optimal solution. Each particle represents a candidate solution and its position in the search space represents the set of solution variables.

The algorithm begins with an initial population of particles, which are randomly distributed across the search space. Each particle's movement is governed by its position and velocity vectors. The position vector represents the particle's current location in the search space and the velocity vector represents the direction and magnitude of its movement.

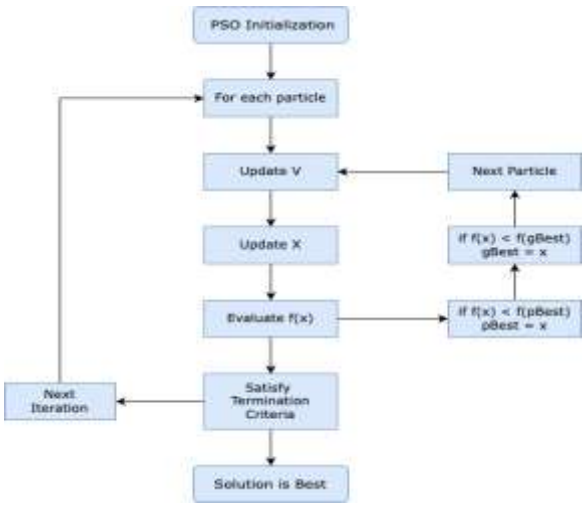


Figure 3. PSO Algorithm Structure

e-ISSN: 2582-5208
International Research Journal of Modernization in Engineering Technology and Science
(Peer-Reviewed, Open Access, Fully Refereed International Journal)
Volume:05/Issue:05/May-2023 Impact Factor- 7.868 www.irjmets.com

At each iteration, particles evaluate their fitness based on an objective function that measures how close they are to the optimal solution. The value determines the quality of a particle's position in the search space. The swarm then updates the position and velocity vectors of each particle based on the best position that it has encountered so far, as well as the best position that any particle in the swarm has encountered so far.

PSO is based on two main components: the social component and the cognitive component. The social component represents the swarm behaviour, and the cognitive component represents the personal experience of each particle. These two components interact to guide the swarm towards the optimal solution.

The social component of PSO is represented by the global best position, which is the best solution found by any particle in the swarm. The cognitive component is represented by the personal best position, which is the best solution found by an individual particle.

In our suspension geometry optimization problem, we aim to minimize bump steer and reduce camber gain, while ensuring that the predicted values of camber, toe, kingpin, and castor angle are within the desired range. The objective function for this problem can be defined as follows:

$$f = w1 * abs(bump_steering - desired_bump_steering) + w2 * abs(camber_gain - desired_camber_gain) + w3 * abs(toe_change - desired_toe_change)$$

where $bump_steering$, $camber_gain$, and toe_change represent the corresponding suspension parameters, and $desired_bump_steering$, $desired_camber_gain$, and $desired_toe_change$ are the desired values for these parameters. The weights $w1$, $w2$, and $w3$ can be adjusted to reflect the relative importance of each parameter in the optimization process. The objective of PSO is to find the set of suspension geometry parameters that minimize the objective function.

The position of a particle in the search space is represented by a vector $x = [x_1, x_2, \dots, x_n]$, where x_i represents the value of the i-th suspension geometry parameter. The velocity of a particle is represented by a vector $v = [v_1, v_2, \dots, v_n]$, where v_i represents the velocity of the i-th parameter.

The position and velocity of each particle are updated based on the following equations:

$$v_i(t+1) = w * v_i(t) + c_1 * r_1 * (p_i - x_i(t)) + c_2 * r_2 * (pg - x_i(t)) x_i(t+1) = x_i(t) + v_i(t+1)$$

where t represents the current iteration, w is the inertia weight, c_1 and c_2 are the cognitive and social learning factors, respectively, p_i is the personal best position of the particle, pg is the global best position of the swarm, and r_1 and r_2 are random values between 0 and 1.

The inertia weight w controls the balance between the global and local search capabilities of the swarm. It determines the impact of the particle's previous velocity on its current velocity. A high inertia weight favours global exploration, while a low inertia weight favours local exploitation.

The cognitive and social learning factors control the impact of the particle's personal experience and the swarm's collective experience on its movement. A high cognitive learning factor favours local exploitation, while a high social learning factor favours global exploration.

V. RESULTS

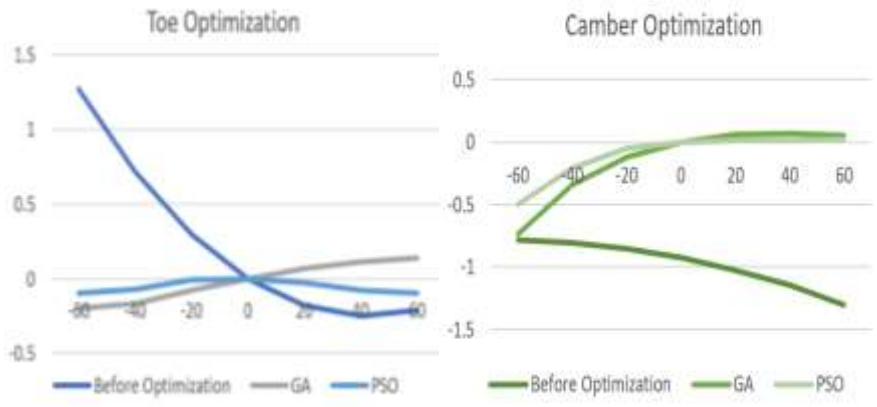


Figure 4. Optimized Geometry Camber and Toe variation

e-ISSN: 2582-5208
International Research Journal of Modernization in Engineering Technology and Science
(Peer-Reviewed, Open Access, Fully Refereed International Journal)
Volume:05/Issue:05/May-2023 Impact Factor- 7.868 www.irjmets.com

The goal of developing an optimization algorithm for double wishbone suspension systems has been achieved by combining Particle Swarm Optimization (PSO) with Artificial Neural Networks (ANN). The optimization process was automated to minimize the camber and toe angles of the wheel during jounce and rebound between 200- and -60-mm. The castor and kingpin angles were also optimized. Using an ANN with R2 scores up to 0.997 improved predictions of these angles significantly. The results show that the PSO-ANN algorithm outperforms the Genetic Algorithm (GA) with Regression, achieving a better geometry optimization. .

Table 4. Acceptable Values For Steering Parameters

Parameter	Range
Kingpin Angle	3 to 8°
Castor Angle	4 to 9°
Toe Angle	-1 to +1°
Camber Angle	-2 to +2°

Table 5. Comparison Of Geometries Before And After Optimization

Conditions	*Toe*	*Camber*
Before Optimization (Initial Population)	At static position = 0 deg. At full bump = -20.36 deg. At full droop = 7.88 deg	At static position = -1.58 deg. At full bump = -5.03 deg. At full droop = -0.66 deg
	At static position = 0 deg. At full bump = 3.51 deg. At full droop = 1.27 deg	At static position = -0.092 deg. At full bump = -3.67 deg. At full droop = -0.79 deg
	At static position = 0 deg. At full bump = -2.15 deg. At full droop = -1.81 deg	At static position = 0 deg. At full bump = -2.94 deg. At full droop = 0.18 deg
	At static position = 0 deg. At full bump = -16.17 deg. At full droop = -48.95 deg	At static position = 0 deg. At full bump = 17.77 deg. At full droop = -1.52 deg
	At static position = 0 deg. At full bump = 4.02 deg. At full droop = 0.62 deg	At static position = 0 deg. At full bump = -1.83 deg. At full droop = 0.051 deg
After Optimization	At static position = 0 deg. At full bump = -0.2 deg. At full droop = -0.1 deg	At static position = 0 deg. At full bump = -0.6 deg. At full droop = -0.5 deg

Table V. shows the variation of camber and toe before and after optimization, indicating a significant reduction in both angles. The optimized suspension geometry exhibits minimal bump steer, resulting in better grip and maximum contact with the ground. Figure 4. shoes that the performance of the PSO-ANN optimized suspension was validated using Lotus Suspension, where the camber and toe values were found to be close to the ideal value of zero throughout the suspension travel. These values are considerably closer to 0 for all latitudes, as compared to GA which wasn't as optimal in extreme cases, show in Figure 4.

Thus, the PSO-ANN algorithm offers a more effective and efficient method for optimizing double wishbone suspension systems, providing a significant improvement in suspension performance and handling.

VI. CONCLUSION

In conclusion, the present study demonstrated the effectiveness of using particle swarm optimization (PSO) and artificial neural network (ANN) for optimizing the suspension geometry of all-terrain vehicles. The proposed PSO-ANN algorithm was found to outperform the traditional genetic algorithm (GA) with regression approach in terms of achieving near-optimal wheel alignment values for extreme bump and droop conditions.

The optimized suspension geometry design resulted in near-zero values for both camber and toe, and castor and kingpin angles were within their respective desired ranges, for all tested bump and droop values. The obtained steering parameters were validated using Lotus Suspension, and it was found that the optimized geometry produced near-ideal camber and toe values throughout the travel, resulting in maximum grip and negligible bump steer.

The proposed PSO-ANN approach can be an effective tool for automating the suspension geometry design process for all-terrain vehicles, and can potentially lead to improved vehicle performance on all types of terrain. Further research can be conducted to investigate the feasibility and effectiveness of this approach for other types of vehicles and suspension systems.

VII. REFERENCES

[1] Habibi, H., Shirazi, K. H., & Shishesaz, M. (2008). Roll steer minimization of McPherson-strut suspension system using genetic algorithm method. Mechanism and Machine Theory, 43(1), 57–67.

[2] Alkhatib, R., Nakhaie Jazar, G., & Golnaraghi, M. (2004). Optimal design of passive linear suspension using genetic algorithm. Journal of Sound and Vibration, 275(3–5), 665–691.

[3] Sancibrian, R., Garcia, P., Viadero, F., Fernandez, A., & De-Juan, A. (2010). Kinematic design of double-wishbone suspension systems using a multiobjective optimisation approach. Vehicle System Dynamics, 48(7), 793–813.

[4] Goga, V., & Kľúčik, M. (2012). Optimization of Vehicle Suspension Parameters with use of Evolutionary Computation. Procedia Engineering, 48, 174–179.

[5] Mitra, A. C., Desai, G. J., Patwardhan, S. R., Shirke, P. H., Kurne, W. M., & Banerjee, N. (2016). Optimization of Passive Vehicle Suspension System by Genetic Algorithm. Procedia Engineering, 144, 1158–1166.

[6] Nariman-Zadeh, N., Salehpour, M., Jamali, A., & Haghgoo, E. (2010). Pareto optimization of a five-degree of freedom vehicle vibration model using a multi-objective uniform-diversity genetic algorithm (MUGA). Engineering Applications of Artificial Intelligence, 23(4), 543–551.

[7] Khan, S., Horoub, M. M., Shafiq, S., Ali, S., & Bhatti, U. N. (2019). Optimization of Vehicle Suspension System Using Genetic Algorithm. 2019 IEEE 10th International Conference on Mechanical and Aerospace Engineering (ICMAE). Published.

[8] El Demerdash, S. M., Kamel, H., Mohsen, M., & Sharaf, A. M. (2018b). Optimal design of passive suspension system of a 6 × 6 multi-wheeled all-terrain vehicle using genetic algorithm. International Journal of Heavy Vehicle Systems, 25(3/4), 508.

[9] Garg, S., Dudeja, S., Gupta, S., & Rastogi, V. (2022, July). Optimization of a Double Wishbone Suspension Geometry for Off-road Vehicles using Genetic Algorithm and Machine Learning. In 2022 13th International Conference on Mechanical and Aerospace Engineering (ICMAE) (pp. 472-477). IEEE.

[10] Metz, D. L., Milliken, W. F., & Milliken, D. L. (1997). Race Car Vehicle Dynamics Workbook [R-146]. Society of Automotive Engineers.

[11] Yegnanarayana, B. (2009). Artificial neural networks. PHI Learning Pvt. Ltd..

[12] Kennedy, J., & Eberhart, R. (1995, November). Particle swarm optimization. In Proceedings of ICNN'95-international conference on neural networks (Vol. 4, pp. 1942-1948). IEEE.

J. Inst. Eng. India Ser. B
https://doi.org/10.1007/s40031-023-00893-0

ORIGINAL CONTRIBUTION

Third Harmonic Injected Nearest Level Control of Nine-Level Grid-Tied PV-CHB Converter

Sanjay Upreti[1] · **Bhim Singh**[2] · **Narendra Kumar**[3]

Received: 18 April 2022 / Accepted: 28 April 2023
© The Institution of Engineers (India) 2023

Abstract This paper presents the power quality analysis of nine-level three-phase cascaded H-Bridge (CHB) inverter with third harmonic injected nearest level modulation (THI-NLM). The inclusion of THI with NLM provides multiple benefits. Due to the involvement of THI, the magnitude of the fundamental component is increased in CHB output voltage and also enhances the power quality by mitigation of harmonics. The NLM technique provides fundamental switching, less switching losses and good dynamic performance with the less complexity in comparison with popular multi-carrier-based modulation techniques. Modeling of nine-level CHB converter is done with voltage and current equations for understanding the working and operation. THI-NLM controlled multilevel converter feeds the solar power with enhanced efficiency and power regulation is achieved in closed loop by robust DQ control. System is simulated in MATLAB, and its dynamic performance is tested in varying solar photovoltaic environment. Harmonic analysis is conducted for NLM and THI-NLM at various solar irradiances. Obtained results in simulation are tested with real-time simulator OP5700.

Keywords CHB inverter · Nearest level modulation · Third harmonic injection · Power quality

✉ Sanjay Upreti
supreti223@gmail.com

[1] Department of Electrical Engineering, Bhagwan Parshuram Institute of Technology, Rohini, New Delhi 110089, India

[2] Department of Electrical Engineering, Indian Institute of Technology, Hauzh Khas, New Delhi, Delhi 110016, India

[3] Department of Electrical Engineering, Delhi Technological University, New Delhi, Delhi 110042, India

Introduction

Renewable energy resources, i.e., Solar photovoltaic (PV), wind, are gaining more and more importance due to environmental issues [1–3]. However, there are many technical and economic challenges in the harvesting of renewable energy, non-uniform availability of the energy and maximum energy extraction management are major technical issues. The higher capital cost of renewable energy than traditional energy is the major economic challenge. Solar PV among the renewable energy sources is the most popular as solar irradiation is available almost everywhere, and the scale of power generation can vary from a few watts to several megawatts.

Multilevel inverters (MLIs) have attracted increased attention in solar PV applications of high voltage [4–6]. The high voltage level in MLI is achieved by the addition of low voltage DC sources. The number of output voltage levels of MLI increases with the number of DC sources, which makes output voltage near to sinusoidal waveform. The main advantage of the multilevel converter is lower output total harmonic distortion (THD) than traditional two-level converters besides low THD multilevel converters are formed by low voltage rating switches as multiple voltage levels are achieved by connecting low voltage DC sources in series. The most common topologies of multilevel converters are neutral point clamped (NPC), flying capacitor (FC) and cascaded H-Bridge (CHB) [7–9]. The CHB converter is a preferred configuration due to its modular structure and simple control. Several modulation techniques for generation of switching sequence have been developed and implemented for closed-loop harmonics analysis of converter voltage [10, 11]. The rise in number of output voltage levels of a MLI increases the complexity of switching sequence implementation in real-time. Sinusoidal pulse width modulation (SPWM) is the most common technique of switching sequence generation for the MLI, which is very

Published online: 25 May 2023

easy to implement [12]. The drawbacks of triangular carrier-based classical modulation techniques are that harmonics are introduced around the higher switching frequency and difficult implementation as the number of levels of MLI increases. Space vector modulation (SVM) is well suited for MLI due to its ability to reduce common-mode voltage [13–15]. The algorithms of SVM involves three steps: selection of nearest three vectors (NVTs) of the reference voltage, computing the dwell times for its nearest vectors, and switching sequence of the selected vectors. These steps make SVM difficult to implement [16]. High frequency modulation methods are excellent in achieving high-quality output; however, switching losses are more in these techniques [17–19]. The nearest level modulation (NLM) method is independent of triangular carrier wave as it computes the switching state and duty cycle directly from the reference signal [20–22]. It is simple and easy to implement for the large number of voltage levels. The NLM has advantage of very low switching frequency that increases the inverter efficiency due to low switching loss. Third harmonic injection is well-known technique for 3-phase two-level converters [23, 24]. Reference signal/wave in all above techniques is sinusoidal that results in poor utilization of DC-link voltage. The modification of reference signal by injection of one-six third harmonic that increases the inverter voltage by 15% without over modulation. In this paper, the nine-level CHB-MLI is operated by using the nearest level modulation technique and the reference signal is injected with a third harmonic. Performance of MLI is analyzed for power quality in terms of THD and its static and dynamic performance are analyzed in varying solar irradiation.

System Configuration

The proposed solar photovoltaic (SPV) is a single stage conversion system as depicted in Fig. 1, which is formed by a series connection of four H-bridge inverter cells. Each H-Bridge inverter cell is powered by a similar solar array of with V_{PV} of 95 V and output of each inverter cell takes three voltage levels + V_{PV}, 0 and -V_{PV} depending on switching states of four switches. Phase voltages of four power cells are given as follows:

$$V_{con1} = V_P V_1 (S_{a1} - S_{a4}) = D_1 V_{PV1} \tag{1}$$

$$V_{con2} = V_{PV2}(S_{a5} - S_{a8}) = D_2 V_{PV2} \tag{2}$$

$$V_{con3} = V_{PV3}(S_{a9} - S_{12}) = D_3 V_{PV3} \tag{3}$$

$$V_{con4} = V_{PV4}(S_{a13} - S_{a16}) = D_4 V_{PV4} \tag{4}$$

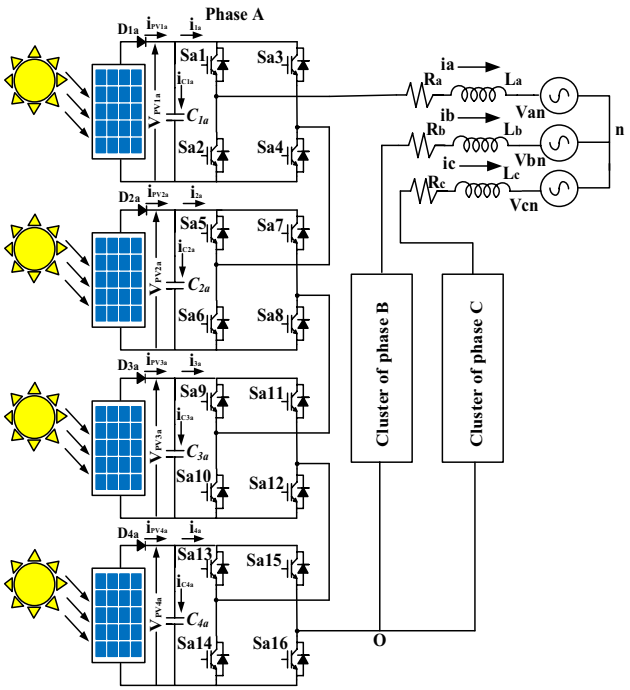


Fig. 1 Nine-level CHB-PV system

Here, $V_{con1\text{-}4}$, $V_{PV1\text{-}4}$ are voltage output of H-bridge inverter and PV arrays of power cell 1–4, respectively. $S_{a1\text{-}a16}$ are switching states, which is 1 and 0 for ON and OFF position, respectively. D1-4 is discrete function having the values − 1,0 or + 1 depending up on the switching position of $S_{a1\text{-}a16}$. Dynamic response of the system can be represented as follows:

$$C_{1a}\frac{dV_{PV1}}{dt} = i_{PV1a} - i_{1a} \tag{5}$$

$$C_{2a}\frac{dV_{PV2}}{dt} = i_{PV2a} - i_{2a} \tag{6}$$

$$C_{3a}\frac{dV_{PV3}}{dt} = i_{PV3a} - i_{3a} \tag{7}$$

$$C_{4a}\frac{dV_{PV4}}{dt} = i_{PV4a} - i_{4a} \tag{8}$$

Switching sequence of sixteen switches for nine-level voltage output in the phase is shown in Table 1. Each solar PV array is provided with a maximum power point tracker (MPPT) controller, which ensures the maximum energy extraction from solar irradiation. The inverter output is connected to the grid through the inductive filter.

Table 1 Switching states for CHB-PV converter

S. No	Operating switches	V_{out} (V)
1	S_{a1}, S_{a4}, S_{a6}, S_{a8}, S_{a10}, S_{a12}, S_{a14}, S_{a16}	$+V_{pv}$
2	S_{a1}, S_{a4}, S_{a5}, S_{a8}, S_{a10}, S_{a12}, S_{a14}, S_{a16}	$+2V_{pv}$
3	S_{a1}, S_{a4}, S_{a5}, S_{a8}, S_{a9}, S_{a12}, S_{a14}, S_{a16}	$+3V_{pv}$
4	S_{a1}, S_{a4}, S_{a5}, S_{a8}, S_{a9}, S_{a12}, S_{a13}, S_{a16}	$+4V_{pv}$
5	S_{a2}, S_{a4}, S_{a6}, S_{a8}, S_{a10}, S_{a12}, S_{a14}, S_{a16}	0
6	S_{a2}, S_{a3}, S_{a6}, S_{a8}, S_{a10}, S_{a12}, S_{a14}, S_{a16}	$-V_{pv}$
7	S_{a2}, S_{a3}, S_{a5s}, S_{a8}, S_{a10}, S_{a12}, S_{a14}, S_{a16}	$-2V_{pv}$
8	S_{a2}, S_{a3}, S_{a5s}, S_{a8}, S_{a9}, S_{a12}, S_{a14}, S_{a16}	$-3V_{pv}$
9	S_{a2}, S_{a3}, S_{a5s}, S_{a8}, S_{a9}, S_{a12}, S_{a13}, S_{a16}	$-4V_{pv}$

Adopted Control Scheme

The control scheme of the nine-level CHB-PV system comprises of THI integrated NLM modulation and grid-tied power controller. It is explained in detail in the subsequent sub-sections.

Concept of Third Harmonic Injection

The sinusoidal pulse width signals are obtained from the closed-loop *dq* controller as (M_a, M_b, M_c). These have a 120° phase shift, and the equations are given as follows:

$$M_a = V_{an}\mathrm{Sin}(\theta_{an}) \tag{9}$$

$$M_b = V_{an}\mathrm{Sin}(\theta_{an} - 120°) \tag{10}$$

$$M_c = V_{an}\mathrm{Sin}(\theta_{an} - 240°) \tag{11}$$

Here, Ma-c is modulating signals, V_{an} and θ_{an} are grid voltage and phasor position of phase 'a'. The third harmonic three-phase modulating signals are generated for closed-loop THI control. The equations for each phase THI are given as follows:

$$U_{THIa} = A_{THI}\mathrm{Sin}(\theta_{an}) + \mathrm{Sin}(3\theta_{an}) \tag{12}$$

$$U_{THIb} = A_{THI}\mathrm{Sin}(\theta_{an}) + \mathrm{Sin}(3(\theta_{an} - 120°)) \tag{13}$$

$$U_{THIc} = A_{THI}\mathrm{Sin}(\theta_{an}) + \mathrm{Sin}(3(\theta_{an} - 240°)) \tag{14}$$

where $U_{THIa\text{-}c}$ is the third harmonic modulating signals, which are fed to nearest level algorithm.

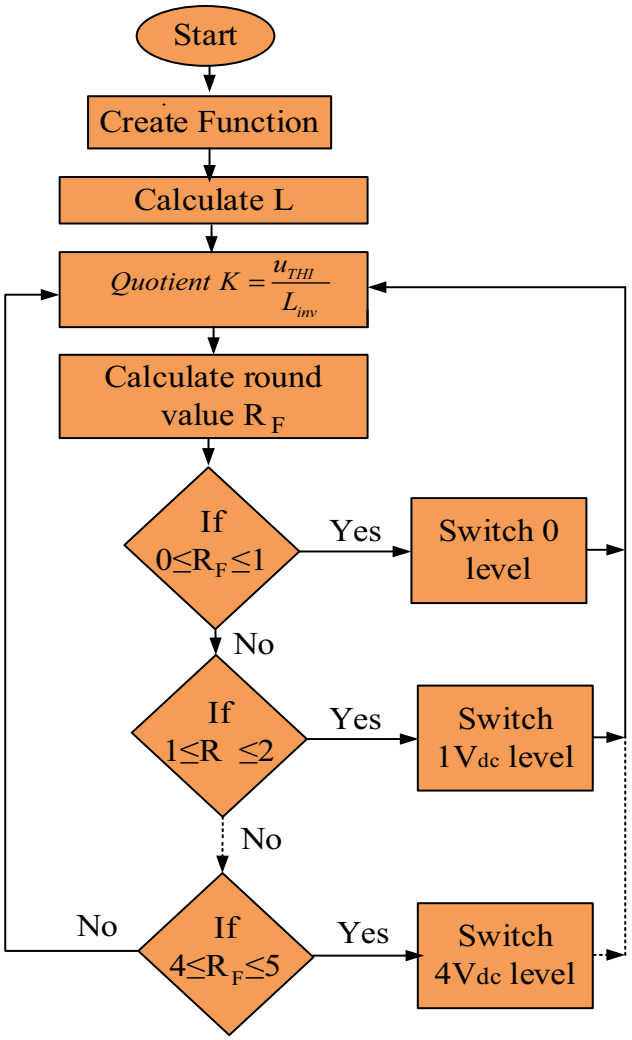


Fig. 2 Algorithm for NLM Switching

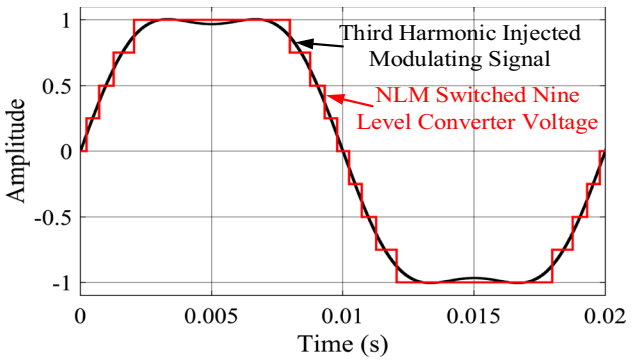


Fig. 3 THI Modulating signal and converter output voltage

THI Modulated Nearest Level Switching

Figs 2, 3 show the flowchart of third harmonic injected NLM and its simulated waveforms. The function is created to take 3-phase third harmonic signals as an input, which is given as follows;

$$y_{a-c} = u_{\mathrm{THI}}(a,\ b,\ c) \tag{15}$$

where y is output variable and u_{THI} as an input. The inverse function of NLM is given as follows

$$L_{\mathrm{inv}} = \frac{1}{N_p} \tag{16}$$

where N_p is the number of positive steps. The quotient is calculated as the ratio of THI signals and inverse function, which is given as follows:

$$K = \frac{u_{\mathrm{THI}}}{L_{\mathrm{inv}}} \tag{17}$$

The quotient K yields nearest integer to have round function R_F, which is as follows.

$$R_F = \mathrm{round}\ (K) \tag{18}$$

The R_F is compared with the level ranges of inverter output voltage and switch combination as given in Table 1 are turned ON at fundamental frequency.

Grid-Tied Power Controller

Fig. 4(a) depicts the voltage and current control of converter. The DC-link capacitor between PV array and converter is charged by the power from the PV array injects pulsating power to the grid by discharging. The power push-up to the grid causes the voltage ripple on the dc-link capacitor. The power balance control maintains the balance between PV power and power injected to the grid. In this control, average of all measured DC-link voltage $V_{dcact-ave}$ is compared with the average of all twelve MPPT controllers reference voltage $V_{ref-ave,}$ which generates the current reference I_{dref} through controller PI_1.The current control consists of comparison of direct and quadrature axes currents I_d, I_q, I_{dref} and $I_{qref,}$ respectively. The direct and quadrature reference voltages are obtained by following equations:

$$V_{\mathrm{dref}} = K_p(I_d - I_{\mathrm{dref}}) + K_1 \int (I_d - I_{\mathrm{dref}})\mathrm{d}t - \omega L_f I_q + V_d \tag{19}$$

$$V_{\mathrm{qref}} = K_p(I_q - I_{\mathrm{qref}}) + K_1 \int (I_q - I_{\mathrm{qref}})\mathrm{d}t + \omega L_f I_d + V_q \tag{20}$$

where V_{dref} and V_{qref} are direct and quadrature voltages obtained from Park transformation of grid voltages V_{gabc}. Inverse Park or DQ-ABC transformation gives the modulation signal M_{abc}. Fig. 4(b) shows the single stage control with MPPT block, which senses actual PV current and voltages. The output of MPPT block provides reference voltage. The error signal is generated from difference of reference and actual voltage as e_{1_a}. Similarly, the errors for other MPPTs are obtained and minimized with average PI_1 voltage regulator. Fig. 5 shows THI-NLM-based switching pulse generation.

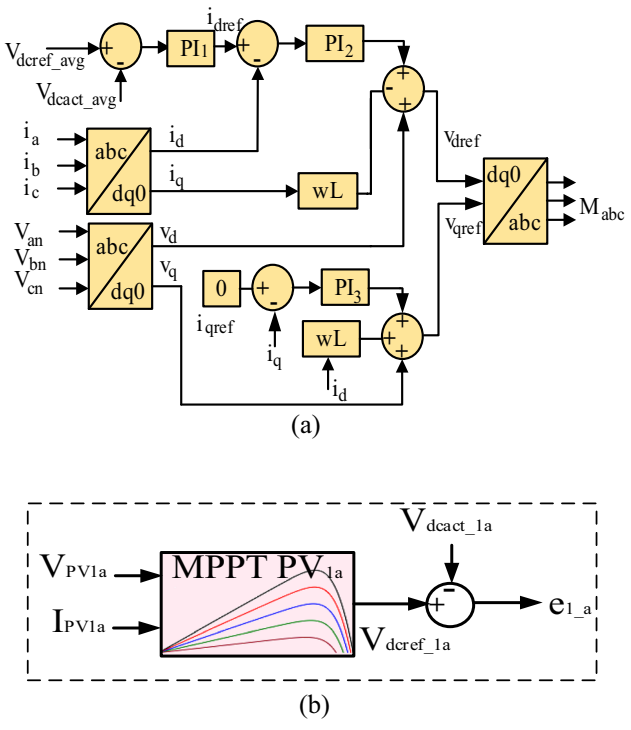


Fig. 4 Grid Controller **a** close-loop 3-phase control **b** single stage MPPT control for solar array with voltage V_{PV1a}

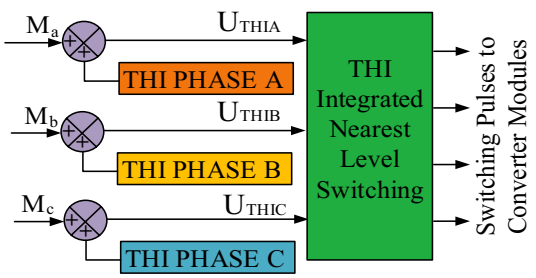


Fig. 5 Switching Pulse generation from THI-NLM

Results and Discussion

Overall system is modeled in MATLAB tool, and harmonic analysis with THI modulated NLM is done, and performance is compared with level shifted multi-carrier modulation technique. The detailed comparison with respect to THD of converter voltage is conducted. The system dynamics are covered for fixed and variable solar irradiances. The steady-state performance of this nine-level CHB-PV system is studied at 1000 W/m^2 solar irradiation, and it is shown in the different sub-sections of Fig. 6(a). Sub-section (A) shows that power of each phase P_g(kW) is balanced and equal to 24.43 kW. In (B), total PV power (P_{PV}) of 75.55 kW is transferred in the grid at 97% conversion efficiency. In (C), Pg of 73.28 kW is shown, (D) shows the three-phase sinusoidal grid voltages, (E) shows the grid current in three phases, (F) shows the inverter output phase voltage V_{conp}, (G) shows the converter line voltage $V_{conl,}$ and sub-section (H) shows the THI modulating signal.

The dynamic response of the system with the varying solar irradiation is presented in Figs. 6(b)-(c). When solar radiation falls to 600 W/m^2, the solar power P_{PV} and grid power P_G are also reduced proportionally as shown in sub-section (B) and (C) of Fig. 6(b), respectively. Sub-section (A) shows that grid power per phase remains equally distributed, and (D) shows the three-phase grid voltages, which remain balanced in the dynamic environment. Sub-section (E) shows that grid current reduces 60% of the rated value; (F), (G) and (H) show the converter phase, line voltage and modulating signal, respectively, which remain balanced and maintain 120° phase difference among one-another.

Similarly, Fig. 6(c) shows the observations for all sub-sections with excellent dynamic response for rise in irradiance from 60% to rated power. A balanced power is fed in the grid with magnitude of 73.28 kW. The variation of converter voltage is also shown with dynamic behavior of solar irradiance. The converter levels are perfect in rise/fall scenario of irradiance.

Harmonics Assessment

Table 2 discusses the harmonic magnitudes of nine-level CHB-PV system by application of nearest level and multi-carrier modulation with sinusoidal and THI sinusoidal modulating signal. For different solar irradiations, the harmonic assessment is done. The adopted modulation shows better performance in THD and higher fundamental voltage component. The sub-headings here represent the harmonics assessment with the two modulation techniques (with and without THI).

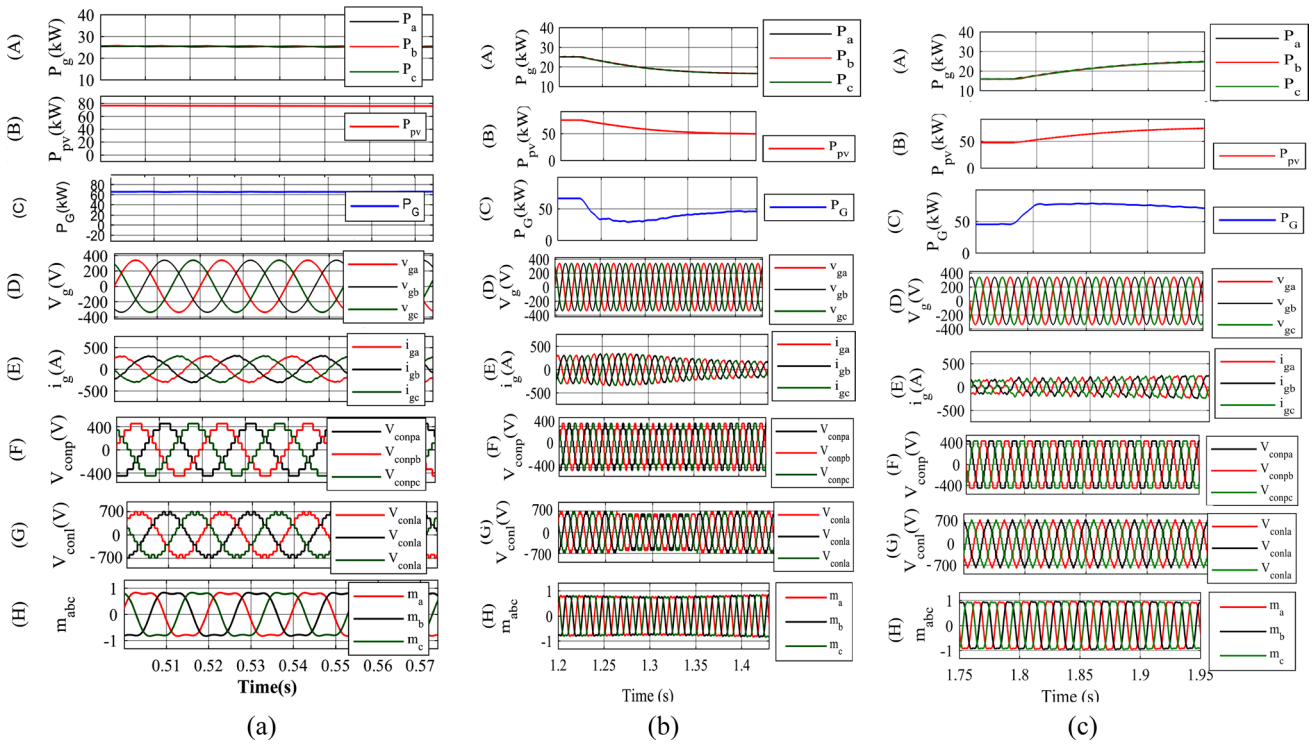


Fig. 6 Recorded set of results **a** steady-state **b** fall of irradiance **c** rise of irradiance

Table 2 THI-NLM-based detailed harmonics comparison

Modulation schemes	Modulating signal	1000W/m^2		900W/m^2		800W/m^2		700W/m^2		600W/m^2	
		THD (V_{conl}) (%)	THD (V_{conp}) (%)	THD (V_{conl}) (%)	THD (V_{conp}) (%)	THD (V_{conl}) (%)	THD (V_{conp}) (%)	THD (V_{conl}) (%)	THD (V_{conp}) (%)	THD (V_{conl}) (%)	THD (V_{conp}) (%)
Nearest level	THI	5.53	16.16	8.08	19.55	7.27	15.84	6.43	17.82	10.78	28.01
	Sinusoidal	7.63	9.37	10.05	12.55	10.81	11.55	10.87	14.14	11.94	16.72
Multi-carrier	THI	7.48	19.89	7.87	22.93	9.40	20.01	10.85	25.23	12.86	27.84
	Sinusoidal	8.28	13.46	8.62	16.78	10.58	17.41	12.11	24.41	13.35	27.84

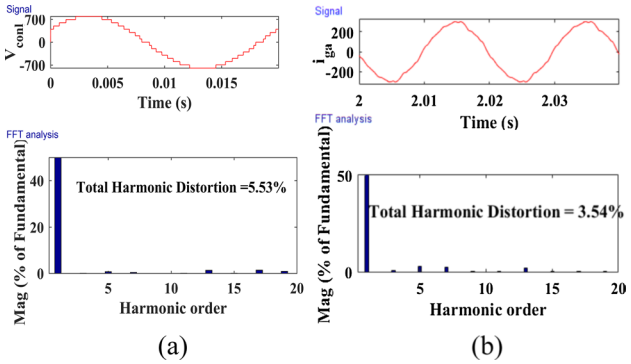


Fig. 7 Simulated THD of **a** multilevel output **b** phase current

Analysis with Nearest Level

Table 2 shows harmonics of NLM-based converter voltage. In NLM with THI injection, the converter voltage THD is 5.53% (Line) & 16.16% (Phase) at 1000W/m^2. The THD increases to 10.78% and 28.01% for line and phase voltages, respectively, at 600W/m^2. The THD performance of NLM with sinusoidal reference signal is 7.63% (Line), 9.37% (Phase) and 11.94% (Line), 16.72% (Phase) at 1000 and 600W/m^2 of solar irradiation, respectively. It shows that the NLM with third harmonic injected signal has lower THD.

Analysis with Multi-Carrier

The THD in multi-carrier modulation technique ranges from 7.48–12.86% in line voltage and 19.89–27.84% in phase voltage when the reference signal is THI sinusoidal. The THD for sinusoidal reference signal varies from 8.28–13.35% for line voltage and 13.46–27.84% for phase voltage.

The nearest level with THI reference signal delivers lowest THD in line voltages, and this technique is implemented in the control of solar CHB-PV system. The line voltage THD of 5.53% is shown in Fig. 7(a), and fundamental component of voltage is enhanced. Grid current has THD of 3.54%, which is shown in Fig. 7(b) meeting the IEEE 519 standard.

Real-Time Implementation

The system performance is validated by the real-time simulator OPAL-RT. In real-time simulation, system runs with physical clock and validates the system performance in real-time. Figs. 8–11 depict the steady-state and dynamic response results from the real-time OPAL-RT. Fig 8(a) shows the converter, grid voltage, grid and solar PV power. Fig 8(b) shows, 17 level converter line voltages which are 120° displaced from each other. Fig 8(c) shows

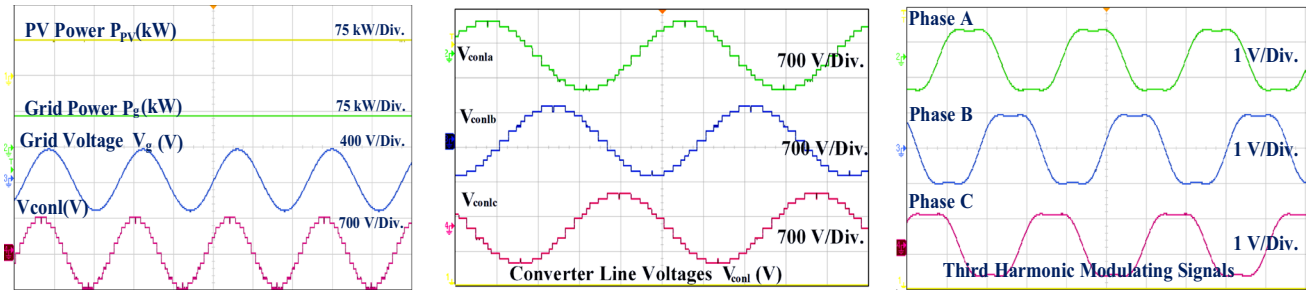


Fig. 8 Real-time recorded performance-I **a** at 1000 W/m^2 **b** Staircase Line Voltages **c** Modulating signals

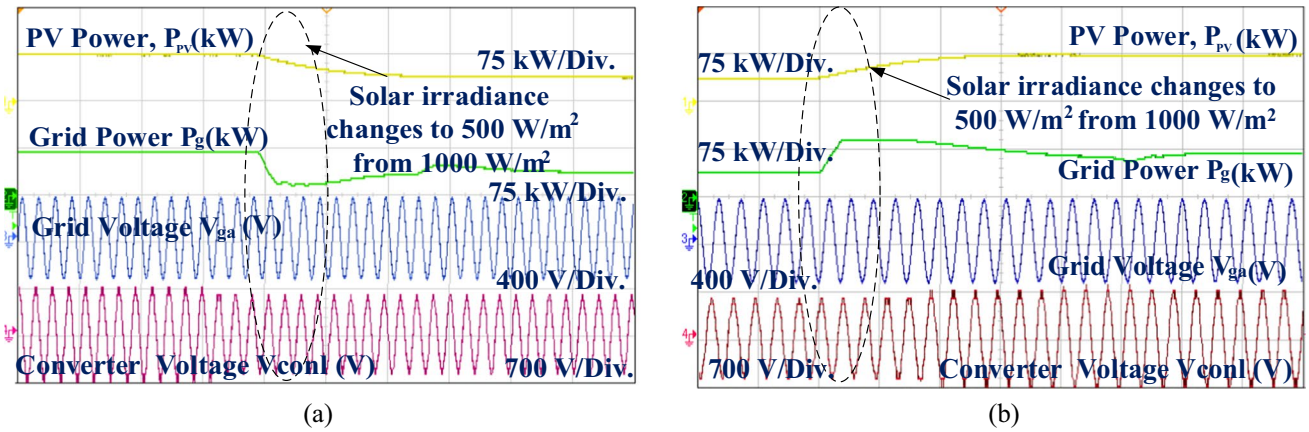


Fig. 9 Real-time recorded performance-II **a** Fall in solar power **b** Rise in solar power

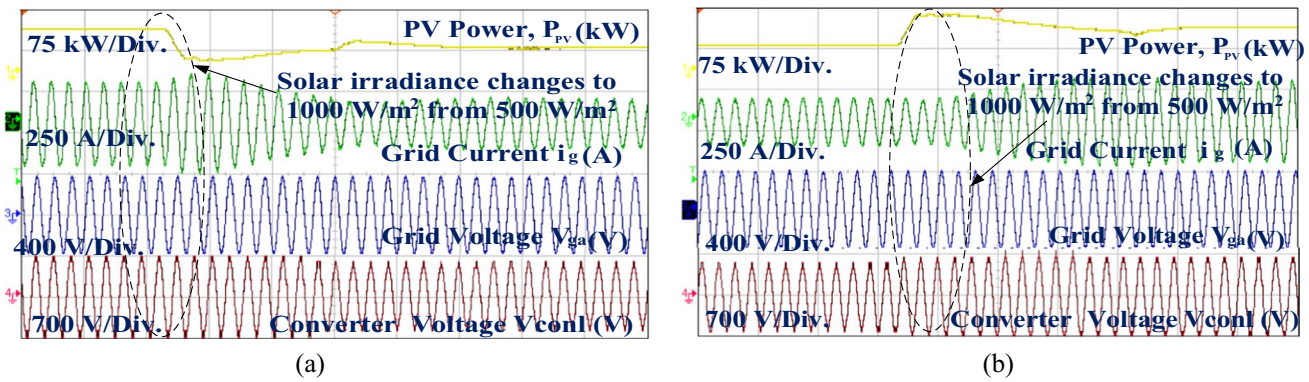


Fig. 10 Real-time recorded performance-III **a** Fall in grid current **b** Rise in grid current

the third harmonic injected modulating signals of three phases of the converter, which are compared with nearest level algorithm to generate the switching sequence. Fig. 9(a)-(b) shows the response with rise and fall of the solar irradiation. PV system settles with 50% power transfer to the grid when solar irradiation falls to 50% and vice-versa. Fig. 10(a)-(b) shows the dynamics of grid current which settles at the 50% of the value at 1000 W/m^2 when solar irradiation falls by 50%, and grid voltage remains same. Fig. 11(a)-(b) shows the harmonic performance of voltage THD of 5.53%, while grid current has THD of 2.78%. Obtained real-time results validate the system performance of third harmonic injected nearest level-based PV system.

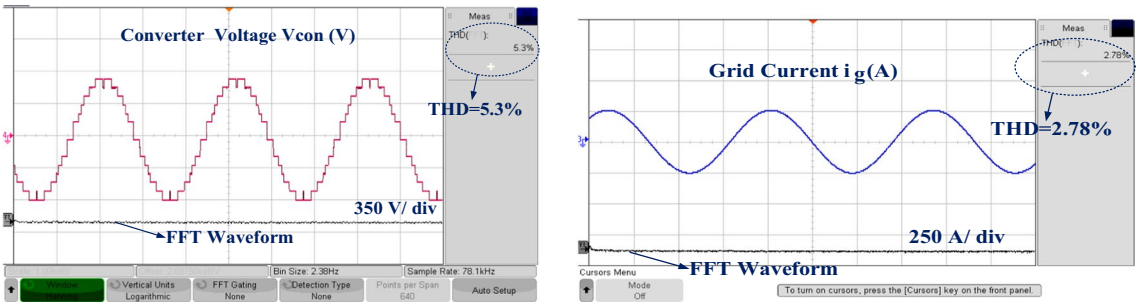


Fig. 11 Real-time THD **a** converter waveform **b** phase current of grid

Table 3 Selection of injection level (IL)

IL	THI multi-carrier		THI-NLM	
	THD (%)	V_F (V)	THD (%)	V_F (V)
1/3	8.20	743.8	6.50	746.0
1/4	7.68	756.4	5.99	756.8
1/5	7.56	753.6	5.75	764.6
1/6	7.48	758.7	5.53	766.7
1/7	7.56	755.7	5.59	760.0
1/8	7.62	752.3	5.65	755.0
1/9	7.72	748.3	5.65	755.0
1/10	7.82	748.9	5.95	750.0

Table 3 shows the manual approach for selection of third harmonic injection level (IL), which fits best for improved harmonic performance. It is simple and feasible approach as compared to optimization algorithms. The analysis shows that injection level of 1/6 at rated power condition has minimum THD. For multi-carrier, THI method minimum THD is 7.48% and for THI-NLM, the THD reduces to 5.53%. For injection levels greater and less than 1/6, the harmonic performance is not promising for proper operation of multilevel converter. The fundamental component of converter line voltage is highest for the injection level of 1/6. For multi-carrier, THI method fundamental voltage component is 758.7 V and for THI-NLM, it is found as 766.7 V. Therefore, the increase in fundamental voltage signifies the better DC bus utilization. The DC bus utilization for injection level of 1/3 is lowest in both multi-carrier and THI-NLM. For the THI multi-carrier, the magnitude of fundamental voltage component is 743.8 V and 746.0 V for THI-NLM. Moreover, it is evident that THI-NLM performs better than multi-carrier THI.

Conclusion

A new integrated control with third harmonic injection and nearest level modulation is implemented for closed-loop control of CHB-based solar photovoltaic system. CHB modules with twelve PV arrays have fed the solar power in the grid. The detailed modeling, discussion of third harmonic injection and comparative analysis of harmonics are done for the presented work. Obtained results are tested in MATLAB simulation and real-time, which successfully validate the effectiveness of the THI-NLM integrated control. This NLM-THI modulation-based closed-loop controller has shown the good dynamic response, and power is perfectly tracked with changes in irradiation. The power quality of grid current is under the IEEE-519 standard (<5%) with NLM-based switching. This method has given a new improved solution toward feeding the power in the multilevel converter interfaced grid with enhanced power quality.

Acknowledgements The authors are grateful to Department of Science and Technology (DST), Govt. of India to provide research grant: RP03195 in Electrical Department at IIT, Delhi. The authors also acknowledge RESCUES Project: RP02979 and "SERB National Science Chair Fellowship" for providing research funds.

Funding The authors are grateful to Department of Science and Technology (DST), Govt. of India to provide research grant: RP03195 in Electrical Department at IIT, Delhi. The authors also acknowledge "SERB National Science Chair Fellowship" for providing research funds.

Declarations

Conflict of interest The authors declare that there are no competing interests.

Appendix

$V_{pv} = 95.00$ V, $I_{pv} = 66.21$ A, $P_{pv} = 75.55$ kW, $R = 0.05$ Ω, $L = 1.0$ mH, $V_g = 415$ V, $C = 10{,}000$ μF, $Ts = 10$ μS, $f_s = 50$ Hz, PI_{dc}: $k_{pdc} = 1.05$, $k_{idc} = 0.001$, PR_{ac}: $k_{pm} = 0.0008$, $k_{im} = 0.0001$.

References

1. A.K. Singh, R. Raushan, R.K. Mandal, M.W. Ahmad, A new single-source nine-level quadruple boost inverter (NQBI) for PV application. IEEE Access **10**, 36246–36253 (2022)
2. M. Talha, S.R.S. Raihan, N.A. Rahim, M.N. Akhtar, O.M. Butt, M.M. Hussain, Multi-functional PV inverter with low voltage ride-through and constant power output. IEEE Access **10**, 29567–29588 (2022)
3. M.H. Mondol, S.P. Biswas, M.A. Rahman, M.R. Islam, A.M. Mahfuz-Ur-Rahman, K.M. Muttaqi, A new hybrid multilevel inverter topology with level shifted multicarrier PWM technique for harvesting renewable energy. IEEE Trans. Ind. Appl. **58**(2), 2574–2585 (2022)
4. D. Solatialkaran, K.G. Khajeh, F. Zare, Output filter design for grid-tied cascaded multi-level inverters based on novel mathematical expressions. IEEE Access **8**, 62505–62516 (2020)
5. R. Barzegarkhoo, Y.P. Siwakoti, F. Blaabjerg, A new switched-capacitor five-level inverter suitable for transformerless grid-connected applications. IEEE Trans. Power Electron. **35**(8), 8140–8153 (2020)
6. S. Ahmad, S.H. Johari, A. Ahmad, M.F.M.A. Halim, Grid connected multilevel inverters for PV application, in *2015 IEEE Conference on Energy Conversion (CENCON)*, (2015), pp. 181–186
7. Y.P. Siwakoti, A. Palanisamy, A. Mahajan, S. Liese, T. Long, F. Blaabjerg, Analysis and design of a novel six-switch five-level active boost neutral point clamped inverter. IEEE Trans Ind. Electron. **67**(12), 10485–10496 (2020)
8. M.J. Sathik, N. Sandeep, F. Blaabjerg, High gain active neutral point clamped seven-level self-voltage balancing inverter. IEEE Trans. Circuits Syst. II Express Briefs **67**(11), 2567–2571 (2020)
9. N. Vosoughi, S.H. Hosseini, M. Sabahi, A new transformer-less five-level grid-tied inverter for photovoltaic applications. IEEE Trans. on Energy Convers. **35**(1), 106–118 (2020)
10. P. Hamedani, C. Garcia, J. Rodriguez, Analytical calculation of harmonics and harmonic losses in five-phase carrier-based PWM voltage source inverters. IEEE Access **10**, 37330–37344 (2022)
11. X. Guo, X. Wang, C. Wang, Z. Lu, C. Hua, F. Blaabjerg, Improved modulation strategy for singe-phase cascaded H-bridge multilevel inverter. IEEE Trans. Power Electron. **37**(3), 2470–2474 (2022)
12. J. Pribadi, D.D. Le, D.-C. Lee, Novel control scheme for five-level hybrid flying-capacitor inverters without DC-link balancing circuits. IEEE Trans. Power Electron. **37**(7), 8133–8145 (2022)
13. Q. Yan, L. Xiao, H. Chen, X. Yuan, H. Xu, R. Zhao, An analytical discontinuous space-vector PWM for three-level inverters with unbalanced DC-link voltages. IEEE Trans. Power Electron. **37**(7), 7718–7728 (2022)
14. A. Lewicki, C.I. Odeh, D. Kondratenko, M. Morawiec, Hybridized space-vector pulsewidth modulation for multiphase two-level voltage source inverter. IEEE Trans. Power Electron. **37**(7), 7663–7674 (2022)
15. L. Vancini, M. Mengoni, G. Rizzoli, L. Zarri, A. Tani, Voltage balancing of the DC-link capacitors in three-level T-type multiphase inverters. IEEE Trans. Power Electron. **37**(6), 6450–6461 (2022)
16. X. Xu, Z. Zheng, K. Wang, B. Yang, Y. Li, A carrier-based common-mode voltage elimination method for back-to-back three-level NPC converters. IEEE Trans. Power Electron. **37**(3), 3040–3052 (2022)
17. Z. Xu, X. Zheng, T. Lin, J. Yao, A. Ioinovici, Switched-capacitor multi-level inverter with equal distribution of the capacitors discharging phases. Chin. J. Electr. Eng. **6**(4), 42–52 (2020)
18. H. Makhamreh, M. Sleiman, O. Kükrer, K. Al-Haddad, Lyapunov-based model predictive control of a PUC7 grid-connected multilevel inverter. IEEE Trans. Ind. Electron. **66**(9), 7012–7021 (2019)
19. S. Jain, V. Sonti, A highly efficient and reliable inverter configuration based cascaded multilevel inverter for PV systems. IEEE Trans. Ind. Electron. **64**(4), 2865–2875 (2017)
20. S.K. Yadav, N. Mishra, B. Singh, S. Padmanaban, F. Blaabjerg, Scott-tied magnetically linked solar multilevel converter in varying environmental conditions. IEEE J. Emerg. Sel. Top. Ind. Electron. **3**(3), 559–571 (2022)
21. N. Mishra, S.K. Yadav, B. Singh, S. Padmanaban, F. Blaabjerg, Binary-quintuple progression based 12-switch 25-level converter with nearest level modulation technique for grid-tied and standalone applications. IEEE Trans. Ind. Appl. **57**(3), 3214–3223 (2021)
22. S.K. Yadav, N. Mishra, B. Singh, Optimal third harmonic injection based nearest level control of large-scale solar photovoltaic multilevel converter. Energy Convers. Econ. **3**(2), 61–71 (2022)
23. S. Albatran, A.R.A. Khalaileh, A.S. Allabadi, Minimizing total harmonic distortion of a two-level voltage source inverter using optimal third harmonic injection. IEEE Trans. Power Electron. **35**(3), 3287–3297 (2020)
24. S.K. Chattopadhyay, C. Chakraborty, Third harmonic injected binary hybrid multilevel inverter for grid connected photovoltaic system, in *2011 IEEE International Symposium on Industrial Electronics*, (2011), pp. 1154–1159

Publisher's Note Springer Nature remains neutral with regard to jurisdictional claims in published maps and institutional affiliations.

Springer Nature or its licensor (e.g. a society or other partner) holds exclusive rights to this article under a publishing agreement with the author(s) or other rightsholder(s); author self-archiving of the accepted manuscript version of this article is solely governed by the terms of such publishing agreement and applicable law.

2023 IEEE 8th International Conference for Convergence in Technology (I2CT)
Pune, India. Apr 7-9, 2023

TransFAS: Transformer-based network for Face Anti-Spoofing using Token Guided Inspection

1st Dipra Chaudhry
Department of Information Technology
Delhi Technological University
Delhi, India
diprachaudhry18@gmail.com

2nd Harshit Goel
Department of Information Technology
Delhi Technological University
Delhi, India
harshitgoel413@gmail.com

3rd Dr Bindu Verma
Department of Information Technology
Delhi Technological University
Delhi, India
binduverma@dtu.ac.in

2023 IEEE 8th International Conference for Convergence in Technology (I2CT) | 979-8-3503-3401-2/23/$31.00 ©2023 IEEE | DOI: 10.1109/I2CT57861.2023.10126455

***Abstract*—Face IDs are becoming the most acceptable modality used for authentication purposes in many recognition systems. This makes it crucial for the recognition and authentication systems to carry out a spoof detection operation before performing facial recognition. The Face Anti-Spoofing (FAS) systems handle the task of identifying fakes. Traditionally, Convolutional Neural Networks (CNNs) have been used to detect spoofs. But, CNNs have certain limitations. One such limitation is that they are not very efficient in extracting the relative placement of different objects. In this paper, we propose a novel TransFAS system. It is based on Video Vision Transformer (VVT). The system takes a bunch of frames at a time and then extracts tokens from them. These tokens are flattened and then loaded with positional information to store the relative placement of each entity in a token. These embedded tokens are passed on to the Transformer Encoder. In the transformer encoder, work is done in different layers. Its final output is a prediction of whether the input sample is live or spoof (print attack, replay attack or 3D Mask attack). Our model is trained on Replay-Attack and 3DMAD datasets. Results show that our model performs better than most of the existing models.**

***Index Terms*—Face Anti-Spoofing, Self-Attention, Tokens, Video Vision Transformer**

I. Introduction

The use of biometric systems is increasing at a rapid rate. Multiple methods of authentication are used in Biometric Systems. These include fingerprint scanning, iris recognition, facial identification and voice recognition. Face ID is gradually replacing the other authentication modes because it is a quick and user-friendly way of identity verification. All that the user has to do is to present his face in front of the camera. The Biometric system matches the input face with its existing database. If a match is found; the user is granted access to the system; otherwise not. Since the Face IDs are unique, it appears that Biometric Systems based on facial recognition would be highly secure and reliable. However, this is not the case. Cyber criminals have designed multiple types of attacks to deceive the authentication systems. These attacks include print, replay, 3D mask or makeup attacks. Printed copies or digital photographs of a legitimate user are used to carry out a print attack. These are then presented in front of the biometric camera to gain unauthorized access. Replay attacks involve using a digital device like a phone, laptop or tablet. The attacker plays pre-recorded videos of the authentic user using any one of these devices to fool the biometric system. A more advanced type of attack is the 3D mask or makeup attack – wherein the attacker wears a mask or does makeup to look like a bona fide user.

Many times, the biometric systems fail to identify an illegitimate user. Fake images are posed in front of the recognition system by a malicious user to gain illicit access to the system. Hence, they are highly susceptible to Presentation Attacks. This makes it highly important to integrate FAS mechanisms into the authentication system. FAS systems use a varying range of criteria to detect fake faces. One of the earliest methods to counter static attacks (like print attacks) used eye-blinking cues. Gradually with the emergence of more advanced attacks like print attacks with eye regions cut or replay attacks, eye blinking cues became insignificant. More recently, mask and makeup attacks are also becoming common. All this is making it challenging for FAS to detect these attacks. Fig. 1 shows live and attack images. The live and spoof samples are similar in appearance. Multiple approaches have been proposed to detect spoofs. Some of the earliest ones include r-ppg [1], Feature-based CNN [2]–[7], Depth-based CNN [6], [8], hand crafted features. Many popular methods make use of CNNs for identifying spoofs. Vision transformers (ViTs) are gradually replacing CNNs in image classification tasks. They are inspired by transformers and have similar architecture. They incorporate an attention mechanism module and work on patches. Transformers can achieve the same performance as CNNs with lesser computation time. ViTs perform exceptionally well and outperform CNNs when trained on large datasets. This transformer-based image classification technique can be extended to videos as well.

We propose the TransFAS model, which has many advantages over the existing CNN models:

1. Identifies subtle facial movements: As more advanced attacks are coming up, it is becoming tough for the FAS models to detect spoofs. Our model follows a patch-based strategy. This makes it possible to pick the slightest facial movements.

2. Uses attention mechanisms: CNN-based models are not very efficient in capturing long-range dependencies in frames. To overcome this, transformers make use of attention mechanisms. They help extract important regions by dividing large

Authorized licensed use limited to: DELHI TECHNICAL UNIV. Downloaded on May 29,2023 at 05:52:58 UTC from IEEE Xplore. Restrictions apply.

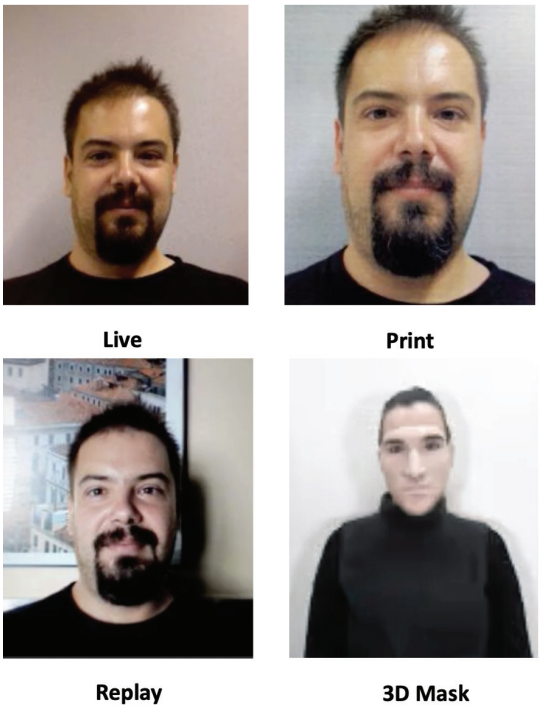


Fig. 1. Shows live, print attack, replay attack and 3D mask attack samples.

frames into multiple small tokens. The critical information captured in these tokens distinguishes live samples from spoofs.

3. Needs lesser number of layers: To achieve similar results, lesser number of layers are needed in the case of transformers. This reduces their computation time as compared to CNNs. There are three types of layers in a transformer. These include Multi-Head Self Attention Layer (MSA), Multi-Layer Perceptron (MLP) and Layer Normalization (LN). Each of these layers has a particular function. The MSA layer computes the token's linear projection, which uses attention mechanisms and gives the output to the next layer. An MLP classification layer is added after the MSA layer. LN is used for normalization. The last MLP layer is responsible for classifying the input sample.

The major contributions of this work are as follows:

- We propose a novel VVT-based approach for FAS.
- We study the embedded tokens in a video in our Anti-Spoofing model.
- We achieve better than the state-of-the-art performance on the diversified dataset.

The rest of the paper is structured as follows: In section 2, we survey the existing FAS models. In section 3, we explain the architecture and working of VVT. In section 4, we discuss the datasets used and analyze the performance of our model. In section 5, we examine the possible future improvisations followed by the conclusion.

II. Literature Survey

In this section, we study the evolution of different FAS techniques in the past few years. In our research, we categorize all the existing FAS models into four classes. These include:

1) **Traditional FAS techniques:** Eye blinking [9] cues were the criteria used by the earliest FAS models to detect print attacks. Such approaches failed in case of print attacks with eye regions cut and replay attacks. Hence, more advanced methods were needed to pick such attacks. Raden Budiarto Hadiprakoso et al. [10]. detected liveness cues using lip movements. Some works focused on characteristics like LBP [11], [12], and DOG [13] to distinguish between live and spoof images. One problem with them is that they are susceptible to illumination changes. Hence, they are not very dependable. Zinelabidine Boulkenafet et al. [14] worked on Color Texture Analysis. This field was further explored by Raden Budiarto Hadiprakoso [9], who studied Color Spaces using HSV. YCbCr texture analysis was done by Zinelabidine Boulkenafet et al. [15]. Bofan Lin et al. [1] exploited the r-ppg difference between the live and spoof because spoof samples do not have the r-ppg details present in the live ones. Spoof traces, which included color distortion, Moire pattern and 3D mask edge were used by Yaojie Liu et al. [16] in their model. The model separated the spoof traces from the live parts of the image and then learned discriminating cues from them. Zitong Yu et al. conducted pixel-wise studies [17], which used the concept of pyramid supervision to capture key details from the input samples.
2) **CNN-based methods:** CNNs are known to perform well on image and video classification tasks. A vanilla CNN [2] approach was implemented by Jianwei Yang et al. to categorize samples into live and spoof classes. Z. Xu et al. [3] clubbed LSTM and CNN in one model to incorporate the advantages of both. In their LSTM-CNN architecture, the CNN component is responsible for feature extraction, while the LSTM component relates multiple input frames. The model is trained on a video dataset. The model makes a single prediction by studying all the input video frames. L. Li et al. [4] and K. Patel et al. [5] used pre-trained CNN models (CaffeNet and GoogLeNet respectively) and fine-tuned them to distinguish live and spoof samples. A combination of patch and depth CNNs [6] was suggested by Yousef Atoum et al. Depth maps were made using depth CNN. While the texture-based analysis was done on local patches by Patch CNN. Rui Shao et al. [7] proposed the technique of deep dynamic textures. These textures were learned from input samples which were then used to extract facial movements by CNN.
3) **Depth-based techniques:** Many depth estimation strategies have been used in anti-spoofing models in the last few years. M. Parisa Beham et al. [8] proposed a three-step method in their paper. The first step involved

Authorized licensed use limited to: DELHI TECHNICAL UNIV. Downloaded on May 29,2023 at 05:52:58 UTC from IEEE Xplore. Restrictions apply.

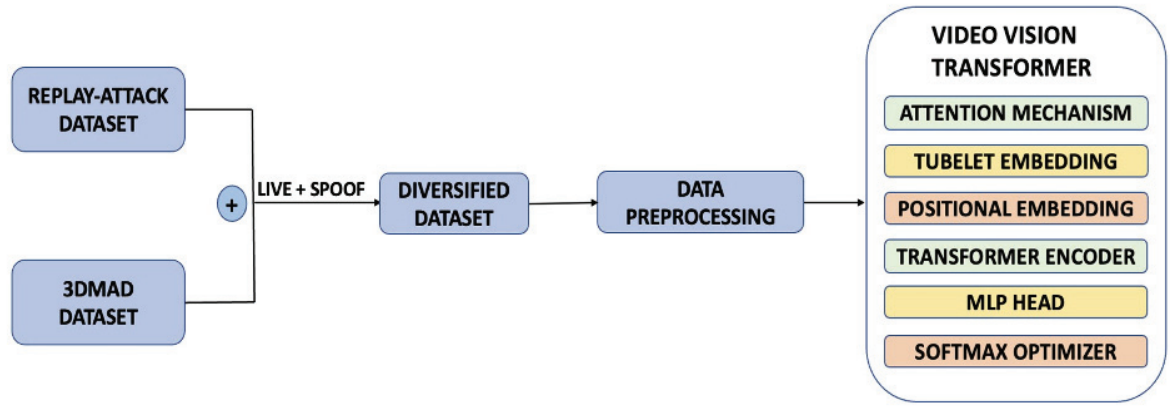


Fig. 2. Framework of TransFAS.

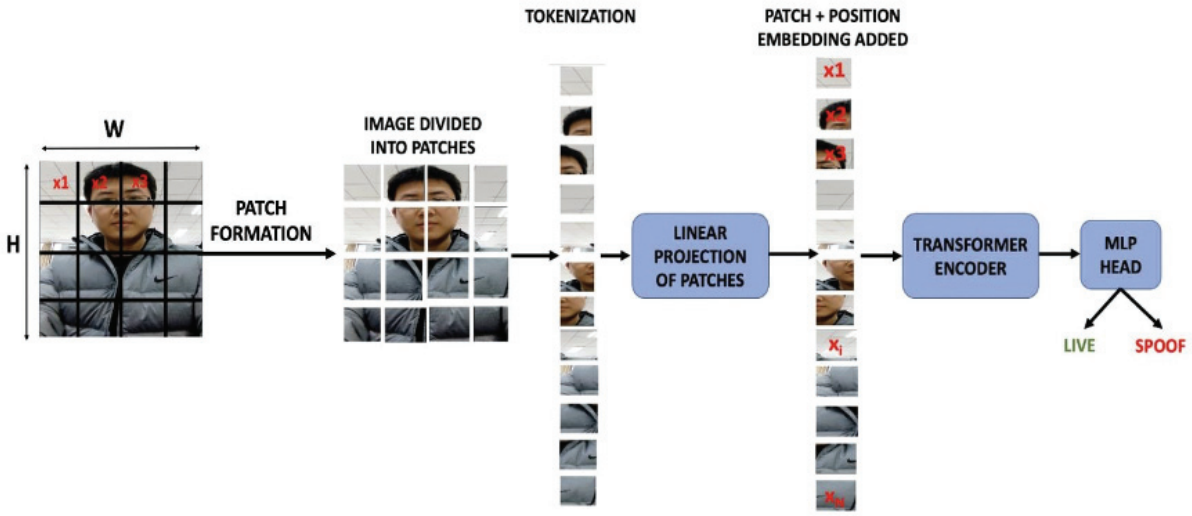


Fig. 3. Working of ViT.

generating a defocused depth image from the input frames. This depth map was used to learn the Gradient Binary Patterns. At last, a Sparse Representation Classifier (SRC) was used to classify samples as live ones or spoofs. Depth CNN proposed by Yousef Atoum et al. [6] made depth estimations to identify spoofs. One limitation of depth-based CNN is that they sometimes do not give zero depth or a black monochrome depth map for print and replay attacks. Hence, depth estimation should not be the only factor distinguishing between live and spoof images.

4) **Other methods:** Every surface reflects light differently. This property was manipulated by Kudzaishe Mhou et al. [18]. Their model used light reflection patterns, color moments and Local Binary Pattern features to detect spoofs. Yaojie Liu et al. [19] proposed a Deep Tree Network and followed an unsupervised approach to group input samples. Each of the 13 types of spoof attacks were further divided into subgroups. Zhuo Wang et al. implemented a Shuffled Style Assembly Network (SSAN) [20] to make the FAS model generalizable. Style and content features were separated in the SSAN model. Different combinations could be generated by randomly selecting style and content features and grouping them. To make a generalizable model, domain-specific features had to be suppressed. A contrastive learning technique was followed to achieve this.

III. Methodology

In this section, we explain the architecture and implementation of TransFAS. The model is trained and evaluated on Replay-Attack and 3DMAD datasets. All the data is pre-processed and then passed to the VVT component of TransFAS. In the pre-processing stage, videos are broken down into frames. A total of 96 key frames are extracted from each video. These are then resized to (56,56). The VVT consists of 6 modules as shown in Fig. 2.

Our model uses a spatio-temporal attention mechanism to mark important regions in the input. Tokens are extracted

Authorized licensed use limited to: DELHI TECHNICAL UNIV. Downloaded on May 29,2023 at 05:52:58 UTC from IEEE Xplore. Restrictions apply.

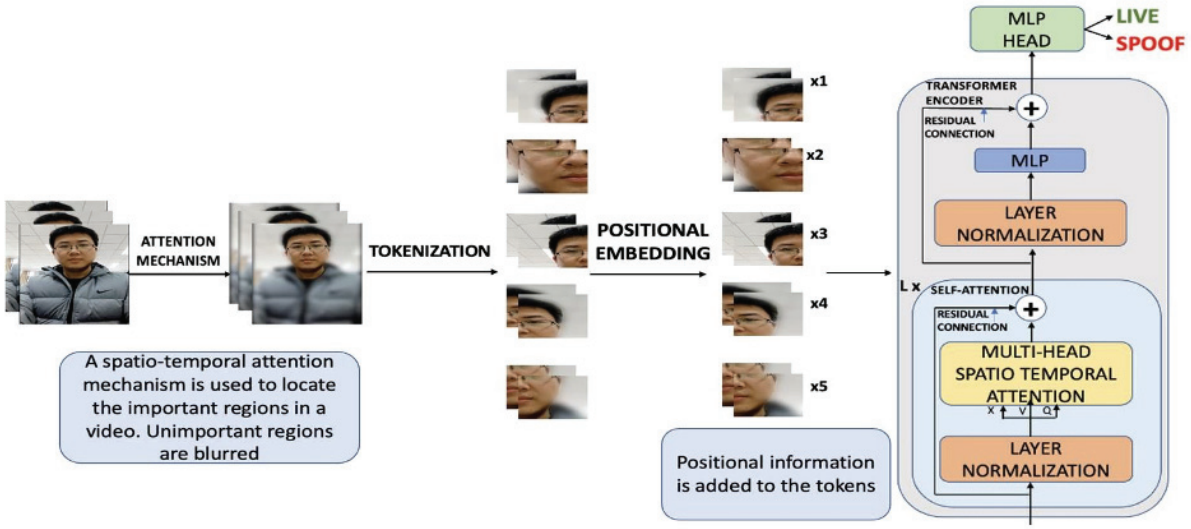


Fig. 4. Architecture of VVT.

from the input video using the Tubelet Embedding function. Subsequently, their linear projection is obtained. Positional information is added to the tokens. The transformer uses this information to learn the relative positioning of different tokens. The tokens are then flattened and passed to the Transformer Encoder. In the end, an MLP head or an optional softmax layer makes the final prediction about the input video.

A. Basics of Vision Transformer

A Vision Transformer uses the concept of a standard transformer and behaves like an image classifier. Fig. 3 demonstrates the working of ViT. An image of resolution (H, W) having C number of channels is the input to the ViT. This input can be represented as x $\in \mathrm{R}^{(H \times W \times C)}$. This is divided into 2-dimensional patches, which can be represented as x_p $\in \mathrm{R}^{N \times (P.P.C)}$. This process of generating patches is referred to as the tokenization of the input. Square patches are extracted from the input images.
The number of patches extracted from an input image can be calculated by using the below formula:

$$N = \frac{H \times W}{P^2} \tag{1}$$

For a patch of resolution (P,P), the tokenization process can be expressed as follows:

$$x_{in} = \{x_1, x_2 \ldots\ldots x_N\} \tag{2}$$

Where x_{in} is the input image and x_i is the positional encoding of the i^{th} patch.

The patches are flattened, and their linear projection is obtained. Following this, a position embedding represented by p $\in \mathrm{R}^{N \times d}$ (where d represents the token dimensionality) is appended to each patch. All the placement-related information of each patch is stored in this embedding and is used later to improve the classification results. These embedded patches are then sent to the Transformer Encoder. It consists of encoder blocks, each of which has the following layers:

- Multi-Headed Self Attention (MSA)
- Layer Normalization (LN)
- Multi-Layer Perceptron (MLP) block

An attention mechanism called MSA is applied to the linear projection of the patches. LN is added to normalize the data. After this, a classification network called MLP is appended. A softmax optimizer sometimes follows this and it gives a final prediction.

B. Video Vision Transformer

A video is a bunch of frames, snapped at different time instants keeping the time interval between each snap the same. ViTs have been performing well for image classification tasks, so this paper extends the same technique to video data. Applying ViT to video data is known as VVT. Input video comprises many frames, of which the first frame is broken down into square patches of size $(P \times P)$. A projection of this patch on all frames is obtained. These projections are then combined. The projections are patches of the subsequent frames. These patches have the same projection on the x-y plane. So, they only differ in the z coordinate, which represents time. A collection of these patches is called a token. Fig. 4 explains the architecture of VVT.
VVT uses tubelet embedding to extract tokens from the input. Once positional information is appended to these, they are flattened and sent to the Transformer Encoder. The encoder uses MSA as its attention module. It is a spatio-temporal attention mechanism that fuses spatial attention mechanism with temporal attention mechanism to incorporate the advantages of both. A spatio- temporal attention map is constructed from the input. This helps in efficiently picking the key tokens. The MSA layer is followed by an LN. It is used for normalization purposes. At last, an MLP layer is added. It is

Authorized licensed use limited to: DELHI TECHNICAL UNIV. Downloaded on May 29,2023 at 05:52:58 UTC from IEEE Xplore. Restrictions apply.

TABLE I
SHOWS THE DIVISION OF VIDEOS INTO TRAIN AND TEST FOLDERS

DATASETS	TRAIN				TEST			
	LIVE	PRINT	REPLAY	3D MASK	LIVE	PRINT	REPLAY	3D MASK
REPLAY-ATTACK	240	160	640	0	60	40	160	0
3DMAD	136	0	0	68	34	0	0	17
TOTAL	376	160	640	68	94	40	160	17

a classification network. The last MLP layer, called the MLP head, is responsible for making the classification.

1) Input to the transformer: The videos input to TransFAS have a duration of 8-9 seconds and a frame rate of 30 fps. 96 key frames are extracted from them. Each of these frames have a dimension of $1920 \times 1080 \times 3$ $(Height \times Width \times Channels)$. To reduce computation, the pre-processing stage resizes the frames to $(56 \times 56 \times 3)$.These resized frames become the input to the transformer.

2) Tubelet Embedding: The purpose of tubelet embedding is to retain temporal information of the input video. Tubes are extracted from the input videos. A tube consists of multiple patches having the same x-y projection but captured at different time instants. This process is also called the tokenization of a video. Tokens of dimension $(t \times h \times w)$ can be represented in the following way:
z $\in \mathrm{R}^{t \times h \times w \times d}$(d is the token dimensionality)

3) Positional Embedding: Positional Embeddings hold the position-related information of each token. In this work, we add 1D positional embedding information to each token, as using 2D positional embedding information is not beneficial in our case. Once the tokens are loaded with this positional information, they are reshaped to $R^{N \times d}$ (where N is the positional embedding and d is the token dimensionality). These reshaped tokens, represented by z, become input to the transformer encoder.

4) Encoder: It comprises a chain of blocks known as encoder blocks or layers. Embedded tokens are the input to the encoder. Since the encoder blocks form a chain-like structure, the output of one block becomes the input for the next. The spatio-temporal attention mechanism is used by the encoder. Layer normalization is done in the encoder block. After this, an MLP block is added, which is responsible for making a prediction. An optional softmax optimizer layer can be added at the end of the final MLP block.

IV. EXPERIMENTAL SETUP

A. Dataset

The performance of TransFAS is evaluated using Replay-Attack, 3DMAD and diversified dataset.

1) Replay-attack dataset: The Replay-attack dataset [12] has a total of 1300 video clips. Each video has a duration of 9 seconds. Multiple videos of 50 subjects are recorded to create the dataset. 300 live samples, 200 print samples and 800 replay attack samples are present in this dataset. The dataset includes two categories in replay attacks: mobile-based and tablet-based attacks (called High-Definition attacks). 2 methods are used to record videos: Fixed and Hand-held method. In the fixed method, the recording device is set on a stand. While in the Hand-held technique, the attacker holds the recording device in his hands. The dataset has ten different attacking modes. Four different types of mobile attacks, four high-resolution attacks from iPad and tablet and two types of print attacks are present in these ten modes.

2) 3DMAD dataset: The 3DMAD dataset [21] comprises 255 video clips. 170 of these videos are live samples and 85 are 3D mask attacks videos. Each video is of 9 seconds. Videos of 17 clients are recorded in three sessions. Each session has five videos per client. Sessions 1 and 2 have live samples, whereas session 3 has videos of 3D mask attacks.

3) Diversified Dataset: The Replay-Attack lacks 3D Mask attack videos. On the other hand, the 3DMAD dataset only has live and mask attack samples. So, our model combines both these datasets, and a diversified dataset is thus created. The diversified dataset has the following samples:

- Live samples
- Print attack samples
- Replay attack samples
- 3D mask attack samples

B. System configuration and Evaluation metrics

The VVT that we implement has a learning rate of 0.0001, along with a weight decay of 0.00001. We use a batch size of 216. Our system extracts 96 frames from each video. These frames are then resized to (56,56). The number of heads used by MSA is 16. The number of encoder blocks is set to 32. The projection dimension used is 128. The model's performance is accessed using the standard metrics established by ISO/IEC 30107-3:2023(en) [22]:

$$APCER = \frac{FN}{(FN + TP)} \tag{3}$$

$$BPCER = \frac{FP}{(FP + TN)} \tag{4}$$

$$ACER = \frac{APCER + BPCER}{2} \tag{5}$$

$$Accuracy = \frac{(TN + TP)}{(TN + FN + TP + FP)} \tag{6}$$

Authorized licensed use limited to: DELHI TECHNICAL UNIV. Downloaded on May 29,2023 at 05:52:58 UTC from IEEE Xplore. Restrictions apply.

$$Recall = \frac{TP}{(TP + FN)} \tag{7}$$

$$Precision = \frac{TP}{(TP + FP)} \tag{8}$$

TABLE II
EVALUATING TRANSFAS'S PERFORMANCE ON SIX DIFFERENT METRICS.

PERFORMANCE METRICS	VALUE
APCER	0.050
BPCER	0.175
ACER	0.112
ACCURACY	90.01%
RECALL	0.94
PRECISION	0.91

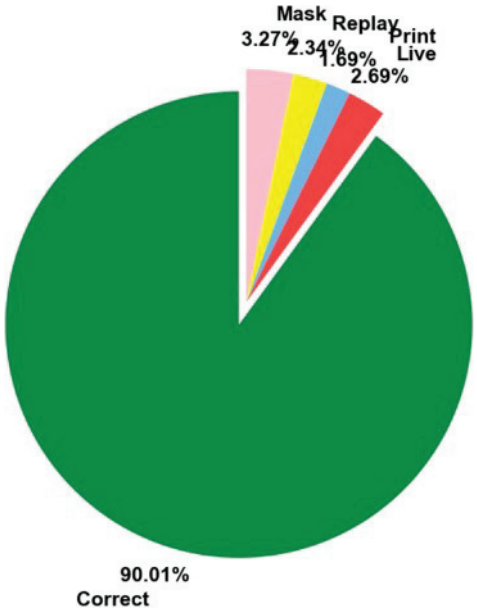


Fig. 5. Shows the accuracy of TransFAS. All non-green colours represent the misclassification percentage of each class.

Table II shows the performance of TransFAS on the six metrics explained above. The pie chart in Figure 5 depicts the accuracy of our model. 90.01% of total samples are correctly predicted. The remaining 9.99% of the samples are misclassified. 3.27% of the total samples which belonged to the mask attack class were misclassified into other classes. Of all the samples, 2.34% which were replay attacks, were misidentified. Similarly, the misclassification percentage was 1.69% for print attacks and 2.69% for live samples.

C. Experimental Comparison

In this section, we test our model on two different datasets and then compare the results with the existing models.

i) Performance on the Replay-Attack dataset: ACER metric is used to compare our model with the existing ones.

TABLE III
ACER COMPARISON OF DIFFERENT FAS MODELS TRAINED ON REPLAY-ATTACK DATASET.

S.No.	MODEL	ACER(%)
1.	**TransFAS(Our Model)**	**0.63**
2.	Patch-Depth Fusion [6]	0.79
3.	Multi-Scale [2]	2.14
4.	Depth-based CNN [6]	3.78
5.	Patch-based CNN [6]	4.44
6.	Fine-tuned VGG-Face [4]	8.4

ii) Performance on the 3DMAD dataset: We evaluate our model on the six metrics discussed previously. The results are shown in table IV.

TABLE IV
PERFORMANCE OF TRANSFAS ON 3DMAD DATASET.

PERFORMANCE METRICS	VALUE
APCER	0.050
BPCER	0.175
ACER	0.112
ACCURACY	86.67%
RECALL	0.949
PRECISION	0.914

V. CONCLUSION

This paper proposes a novel VVT-based anti-spoofing model called TransFAS. The performance of our model proves the importance of using attention mechanisms and a patch-based approach for classifying spoof and live samples. We are able to achieve a substantial reduction in the values of ACER, APCER and BPCER compared to the existing models when tested on Replay-Attack and 3DMAD datasets. The performance is assessed on multiple metrics, as shown in table II. From the results, we can conclude that transformers work better than CNN-based models for anti-spoofing tasks. The accuracy distribution of our model on the Diversified dataset is shown in Fig. 5. The model has been trained and tested on the Replay-Attack dataset and the 3DMAD dataset. In the future, larger datasets can be used to train the model. Data augmentation techniques like GANs or VGPNNs can be used to increase the dataset.

ACKNOWLEDGMENT

This research is based upon work supported by the Information Technology Department of Delhi Technological University, New Delhi, India. The model has been tested on two datasets: Replay-Attack dataset [12] and 3DMAD dataset [21] by Idiap Research Institute, Switzerland.

Authorized licensed use limited to: DELHI TECHNICAL UNIV. Downloaded on May 29,2023 at 05:52:58 UTC from IEEE Xplore. Restrictions apply.

REFERENCES

[1] B. Lin, X. Li, Z. Yu, and G. Zhao, "Face liveness detection by rppg features and contextual patch-based cnn," in *Proceedings of the 2019 3rd international conference on biometric engineering and applications*, pp. 61–68, 2019.

[2] J. Yang, Z. Lei, and S. Z. Li, "Learn convolutional neural network for face anti-spoofing," *arXiv preprint arXiv:1408.5601*, 2014.

[3] Z. Xu, S. Li, and W. Deng, "Learning temporal features using lstm-cnn architecture for face anti-spoofing," in *2015 3rd IAPR asian conference on pattern recognition (ACPR)*, pp. 141–145, IEEE, 2015.

[4] L. Li, X. Feng, Z. Boulkenafet, Z. Xia, M. Li, and A. Hadid, "An original face anti-spoofing approach using partial convolutional neural network," in *2016 Sixth International Conference on Image Processing Theory, Tools and Applications (IPTA)*, pp. 1–6, IEEE, 2016.

[5] K. Patel, H. Han, and A. K. Jain, "Cross-database face antispoofing with robust feature representation," in *Biometric Recognition: 11th Chinese Conference, CCBR 2016, Chengdu, China, October 14-16, 2016, Proceedings 11*, pp. 611–619, Springer, 2016.

[6] Y. Atoum, Y. Liu, A. Jourabloo, and X. Liu, "Face anti-spoofing using patch and depth-based cnns," in *2017 IEEE International Joint Conference on Biometrics (IJCB)*, pp. 319–328, IEEE, 2017.

[7] R. Shao, X. Lan, and P. C. Yuen, "Joint discriminative learning of deep dynamic textures for 3d mask face anti-spoofing," *IEEE Transactions on Information Forensics and Security*, vol. 14, no. 4, pp. 923–938, 2018.

[8] M. P. Beham, S. M. Roomi, and D. Dharmalakshmi, "Face spoofing detection based on depthmap and gradient binary pattern," *International Journal of Applied Engineering Research*, vol. 9, no. 21, p. 2014.

[9] R. B. Hadiprakoso, "Face anti-spoofing method with blinking eye and hsv texture analysis," in *IOP Conference Series: Materials Science and Engineering*, vol. 1007, p. 012034, IOP Publishing, 2020.

[10] R. B. Hadiprakoso, H. Setiawan, *et al.*, "Face anti-spoofing using cnn classifier & face liveness detection," in *2020 3rd International Conference on Information and Communications Technology (ICOIACT)*, pp. 143–147, IEEE, 2020.

[11] W. Zhang and S. Xiang, "Face anti-spoofing detection based on dwt-lbp-dct features," *Signal Processing: Image Communication*, vol. 89, p. 115990, 2020.

[12] I. Chingovska, A. Anjos, and S. Marcel, "On the effectiveness of local binary patterns in face anti-spoofing," in *2012 BIOSIG-proceedings of the international conference of biometrics special interest group (BIOSIG)*, pp. 1–7, IEEE, 2012.

[13] X. Tan, Y. Li, J. Liu, and L. Jiang, "Face liveness detection from a single image with sparse low rank bilinear discriminative model.," *ECCV (6)*, vol. 6316, pp. 504–517, 2010.

[14] Z. Boulkenafet, J. Komulainen, and A. Hadid, "Face spoofing detection using colour texture analysis," *IEEE Transactions on Information Forensics and Security*, vol. 11, no. 8, pp. 1818–1830, 2016.

[15] Z. Boulkenafet, J. Komulainen, and A. Hadid, "Face antispoofing using speeded-up robust features and fisher vector encoding," *IEEE Signal Processing Letters*, vol. 24, no. 2, pp. 141–145, 2016.

[16] Y. Liu and X. Liu, "Physics-guided spoof trace disentanglement for generic face anti-spoofing," *arXiv preprint arXiv:2012.05185*, 2020.

[17] Z. Yu, X. Li, J. Shi, Z. Xia, and G. Zhao, "Revisiting pixel-wise supervision for face anti-spoofing," *IEEE Transactions on Biometrics, Behavior, and Identity Science*, vol. 3, no. 3, pp. 285–295, 2021.

[18] K. Mhou, D. van der Haar, and W. S. Leung, "Face spoof detection using light reflection in moderate to low lighting," in *2017 2nd Asia-Pacific Conference on Intelligent Robot Systems (ACIRS)*, pp. 47–52, IEEE, 2017.

[19] Y. Liu, J. Stehouwer, A. Jourabloo, and X. Liu, "Deep tree learning for zero-shot face anti-spoofing," in *Proceedings of the IEEE/CVF Conference on Computer Vision and Pattern Recognition*, pp. 4680–4689, 2019.

[20] Z. Wang, Z. Wang, Z. Yu, W. Deng, J. Li, T. Gao, and Z. Wang, "Domain generalization via shuffled style assembly for face anti-spoofing," in *Proceedings of the IEEE/CVF Conference on Computer Vision and Pattern Recognition*, pp. 4123–4133, 2022.

[21] N. Erdogmus and S. Marcel, "Spoofing in 2d face recognition with 3d masks and anti-spoofing with kinect," in *2013 IEEE sixth international conference on biometrics: theory, applications and systems (BTAS)*, pp. 1–6, IEEE, 2013.

[22] I. Standard, "Information technology–biometric presentation attack detection–part 3: testing and reporting," *International Organization for Standardization: Geneva, Switzerland*, 2017.

Authorized licensed use limited to: DELHI TECHNICAL UNIV. Downloaded on May 29,2023 at 05:52:58 UTC from IEEE Xplore. Restrictions apply.

2023 IEEE 8th International Conference for Convergence in Technology (I2CT)
Pune, India. Apr 7-9, 2023

Transfer Learning Approach to Multilabel Biomedical Literature Classification using Transformer Models

Pahalage Dona Thushari
Department of Software Engineering
Delhi Technological University
New Delhi, India
pahalagedonathushari_2k19se155@dtu.ac.in

Sakina Niazi
Department of Software Engineering
Delhi Technological University
New Delhi, India
sakinaniazi_2k19se107@dtu.ac.in

Shweta Meena
Department of Software Engineering
Delhi Technological University
New Delhi, India
shwetameena@dtu.ac.in

2023 IEEE 8th International Conference for Convergence in Technology (I2CT) | 979-8-3503-3401-2/23/$31.00 ©2023 IEEE | DOI: 10.1109/I2CT57861.2023.10126262

***Abstract* - The recently developed transformer models have a significant influence on Natural Language Processing (NLP) research. Transformer-based models have attained innovative results on numerous NLP benchmarks in linguistics. Researchers have also investigated transformer models for a variety of applications in the biomedical field. To facilitate information classification, this work aims to thoroughly investigate four state-of-the-art transformer-based models (BERT, Roberta, SciBERT, and ClinicalBERT). Large language model training, however, requires a lot of time and processing resources. As a result, pre-trained language models like BERT are advantageous because they (1) offer cutting-edge performance, (2) The knowledge gained can be used to do several tasks, such as categorization, and (3) free up practitioners from having to gather enough resources (including the hardware, data and time) to train models. However, pre-trained models possibly will perform poorly in some domains since they are generic. Here, we inspect the case of multilabel classification for biomedical Literature, which is a domain that has received relatively minor attention in the literature assessing pre-trained language models. Based on our study, using SciBERT as the baseline model gave the best results compared to the rest of the models with an 89.35% micro F1 score. In the context of classifying Biomedical Literature, domain-specific pre-trained models tend to perform better compared to generic models.**

Keywords—Transformers, Biomedical Literature, Bidirectional Encoder Representations, Multilabel Biomedical Text Classification, Feed Forward Neural Networks

I. INTRODUCTION

One of the most quickly evolving research technologies is Artificial Intelligence (AI), which has gained a lot of funding recently. Private AI investment in the medical sector has exceeded USD. 13.8 billion, which is 4.5 times above in 2019 [1]. Given the exponential expansion of both the biomedical, and scientific literature, and clinical data, more robust but exact computational approaches are needed to assign disease-specific texts effectively and extract insightful information from the biomedical literature.

Additionally, classifying different forms of biomedical textual data, for instance, clinical notes or biomedical publications is not effective enough in using classical approaches. NLP is therefore regarded as a link that enables computers to comprehend, process, and examine human linguistics. The significance of NLP as a tool for enhancing human-generated information comprehension follows naturally from the fact that data is context-dependent. Data is more meaningful when it is understood in its context, which simplifies text analysis and mining. Because they aid in the analysis of a lot of unstructured, low-quality material and the finding of significant insights, NLP approaches are thus widely used for this purpose.

Classification of texts is further divided into Multinomial (multi-class) and multilabel classification. Every textual document linked with a multiclass classification task has a single label or in other words, labels are mutually exclusive. For example, binary classification is one of the utmost popular multiclass classifications when there are only two classes available. A text document may be given two or more labels for multi-label text classification. For instance, publications in PubMed are routinely given a dozen pertinent Medical Subject Headings (MeSH) terms as part of the indexing process. Multilabel text classification is usually measured to be more difficult than multinomial classification since each text document can be given an arbitrary number of labels [2].

In this study, we use Bidirectional Error Reduction Technique (BERT) models that have already been trained to optimize a multilayer perceptron. In this work we present a multilayer perceptron combined with pre-trained BERT models, also known as Bidirectional Encoder Representations, to build a multilabel classification model. We have used ClinicalBERT, Sci-BERT, RoBERTa, and BERT-based models to compare the performances of the generic models (RoBERTa and BERT) versus domain-specific ones.

In writings about biomedicine Due to the wide range of possible applications and the relationships between such entities, each textual document can be given two or more labels. Therefore, it has become difficult for practitioners and scholars to annotate the pertinent literature [3]. Numerous computational techniques have been suggested to resolve this conundrum. However, a lot of these techniques have just fair accuracy or efficiency, and they've only had sporadic real-world success. Working with massive text volumes, however, makes creating unique models for each task more difficult. We have suggested a Feed-Forward Neural Network (FFNN) based classifier to address this issue. It will use transformer models and transfer learning curated to help diverse domain-specific tasks.

Although multilabel text classification models have been proposed in the past, most of these efforts have concentrated on employing already-existing deep learning or machine learning architectures. Such architectures were developed with the objective of producing general-purpose classification models that excel in small text datasets. Our work has two areas of focus:

Authorized licensed use limited to: DELHI TECHNICAL UNIV. Downloaded on May 29,2023 at 05:45:24 UTC from IEEE Xplore. Restrictions apply.

1. We offer a strategy that enables combining neural network classification models to learn from automated state-of-the-art language models like transformers to address specialized challenges like classifying clinical literature as well as other NLP issues in healthcare.
2. Additionally, we also hope to evaluate whether the generic models can adapt in accordance with the problem domain.

The rest of this paper is organized as follows. Section II consists of the literature survey of the related work and Section III discusses the research methodology respectively. Section IV indicates the results of the study, and the conclusion and future work will be discussed in section V.

II. Literature Survey

A substantial number of biomedical publications are released with the rapid advances of technology leading to new discoveries. Discovering pertinent and relevant information in a large pool of literature has also become a challenging task. As a result, biomedical discovery today heavily relies on automated literature mining, particularly natural language processing (NLP), to help researchers quickly access unique information [4]. Manual curation and interpretation are significantly hampered by the quick expansion of the biological literature [5].

The medical sector has greatly advanced in research solutions over the past few decades, particularly during the Covid-19 era. The majority of these procedures were based on cutting-edge technologies at the time. There are multiple works that are published focusing on solving multilabel text classification of biomedical texts using traditional methods. These methods range from employing KNN models [6], convolutional neural networks [7] [8], and hybridized shallow neural networks [9], to ensemble learning [10]. In addition to innovations in design, multilabel text classification systems have seen improvements in areas including optimization, regularization, activation functions, and data augmentation. Another work focuses on using multiple linear regression modeling techniques to enhance classification by combining neighbor-based and feature-based similarity scores [11].

There is significant work done to improve the performance of baseline transformer models to help with biomedical literature-related tasks. Hebbar S. and Xie Y. proposed CovidBERT to extract biomedical relationships based on BERT to Identify unique relationships between various biomedical Entities using the transformer architecture to train on Covid-19 literature [12]. Another study introduced the BLURB benchmark (Biomedical Language Understanding & Reasoning Benchmark) [13] in order to gain a noteworthy gain over the pretraining of general-domain language models for biomedical textual data. An earlier study introduced LITMC-BERT, a transformer-based multi-label biomedical literature classification model that uses a shared BERT backbone to capture label-specific features and the correlations between label pairs [14].

The database on COVID-19 literature consisting of more than 2,00,000 articles has been published on LitCovid enabling free access to millions of users from around the world. One of the mentioned primary curated responsibilities is to provide annotations to articles which is a challenging task to perform manually [15]. Several procedures [16] [17] [18] have already been proposed to automate the manual annotating process. Given the novelty of the LitCovid dataset, our work aims to explore whether it can support such models using a transfer learning approach to classify biomedical literature. In addition to annotation, a number of methods have been proposed to categorize those annotated texts in the field of biomedical literature using Litcovid Data [19] [20]. Another study focused on pre-training a biomedical BERT-based model called Bioformer [21] which achieved the best results in the LitCovid track [15]. Another study that was done covered the bag-of-concepts method of text classification [22]. BioBERT, which is a domain-focused model that has been pre-trained using sizable biomedical text corpora, was presented by Lee, Jinhyuk, et al. [23].

Since transformer-based applications in the domain of biological literature have gained the focus of the public consensus, our study seeks to employ pre-trained transformer models to aid biological multilabel classification problems by proposing a general pipeline using multi-layer perceptions. Another goal of our work is to compare the effectiveness of the most advanced domain-specific transformers with those that are more prevailing.

III. Research Methodology

Exploring transformer-based models for multilabel classification using both pre-trained generic and customized models is the aim of this project to make it easier to conduct a Covid literature classification and perform other NLP tasks. In order to extract different kinds of biomedical concepts, we thoroughly investigated four broadly used transformer models, BERT [24], RoBERTa [25], ClinicalBERT [26], and SciBERT [27]. The classification operation is then carried out by feeding the outputs into a multilayer neural network with a sigmoid function. Due to the usage of pre-trained transformer models, transfer learning can be used to train the LitCovid data. We employ the AdamW [28] optimizer, which separates the optimization step from weight decay. This makes it possible to optimize the weight decay and learning rate independently.

A. Dataset

To address automation of topic annotation for COVID-19 literature, the LitCovid dataset was developed, and it is curated for the multi-label document classification task, which comprises 34, 000 unique entries and gives one or more labels for each item. 24, 960, 6,239, and 2,500 articles from the LitCovid dataset serve as the training, testing, and development sets, respectively. Treatment, Prevention, Diagnosis, Transmission, Mechanism, Case Report, and Epidemic Forecasting are the seven topic labels used in LitCovid. These subjects have proven successful for data retrieval and are applied in a variety of downstream biomedical applications. For curators and researchers worldwide, automated topic prediction in such scientific publications would be a welcome advancement. Fig. 1 shows the correlation between the labels.

Authorized licensed use limited to: DELHI TECHNICAL UNIV. Downloaded on May 29,2023 at 05:45:24 UTC from IEEE Xplore. Restrictions apply.

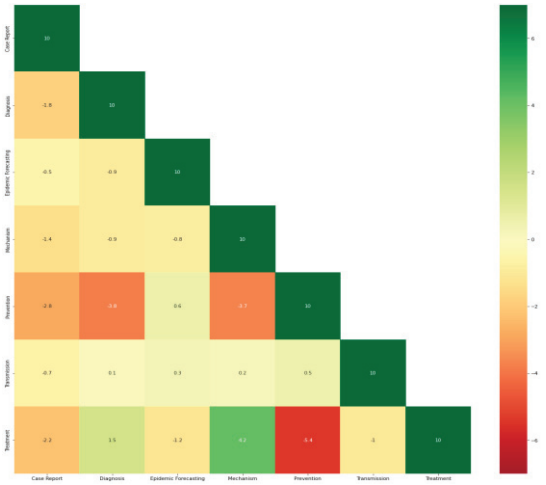


Fig. 1. Correlation between each label

Additionally, we examine the application of optimizing BERT and RoBERTa models in the biomedical literature to see whether these cutting-edge techniques are reliable for undertaking tasks that are specialized to a given domain, like multi-label classification. Stop words, special symbols, words with numbers, and duplicate entries, were removed and the Title and abstracts were combined under preprocessing tasks. To facilitate the pretraining process, we employed LitCovid training and development sets and considered random subsamples of the data to create 7,000, 3,743, and 2,496 instances in each training, testing, and validation set, respectively. Fig. 2 displays the percentages of each set.

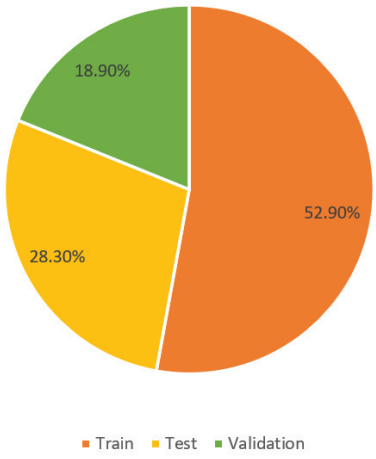


Fig. 2. Train, Test, Validation percentage

B. Transformer Models

Transformer-based models learn contextual representations at the sub-token level by breaking words into sub-tokens using a variety of word segmentation methods. We created a model architecture to employ the pre-trained model along with a multilayer Neural Network to merge each transformer-based model with our classification model. The BERT and BERT-variant models that were used have a fine-tuning layer on top of the pre-trained BERT that is made up of one fully connected layer with four units and an activation function. The specifications of each model are as follows:

- BERT [19]: BERT (Bidirectional Encoder Representations from Transformers) is a pre-trained deep learning model which can be tailored for specific categorization tasks. BERT models have a reputation for being able to grasp the context of the words in a text, making them the perfect choice for text categorization problems.
- RoBERTa [20]: RoBERTa (Robustly Optimized BERT Pre-training Approach) is a reimplementation of BERT that makes slight embedding adjustments and some changes to the major hyperparameters. Another significant distinction between RoBERTa and BERT is that the latter was developed utilizing a more efficient training method and a considerably larger dataset.
- SciBERT [21]: Built on BERT and then trained using a sizable corpus of scientific material, SciBERT is a pre-trained linguistic model. It is a compact language model that has demonstrated performance on par with larger BERT-based models.
- ClinicalBERT [22]: As the name suggests, ClinicalBERT learns in-depth clinical text representations using BERT. These representations can reveal clinical insights (such as illness forecasts), identify connections between interventions and results, or summarize corpora.

C. Model Architecture

On the grounds of our classification model, we experimented with the four transformers and compared the results on the test set. A common set of data is used to optimize all hyperparameters for training all four classifiers. The model hyperparameters reported in Table 1 were all selected based on their best performance on the validation dataset.

TABLE I. HYPERPARAMETERS

S.no	Hyperparameter	Value
1	MAX_LEN	256
2	TRAIN_BATCH_SIZE	8
3	VALID_BATCH_SIZE	8
4	EPOCHS	5
5	LEARNING_RATE	1e-05
6	THRESHOLD	0.5

To perform the classification task, we added one FFNN layer to each transformer model which is an artificial neural network model which does not comprise looping nodes. Since the input is sent forward, this type of neural architecture is also referred to as a multi-layer neural network. The input nodes of the FFNN will receive embedded data throughout the

Authorized licensed use limited to: DELHI TECHNICAL UNIV. Downloaded on May 29,2023 at 05:45:24 UTC from IEEE Xplore. Restrictions apply.

classification process, which travels through hidden layers and produces labels as the output. Here, the output layer's activation function is a SoftMax function, which is used to forecast a multinomial probability distribution. The model architecture is represented in fig. 3.

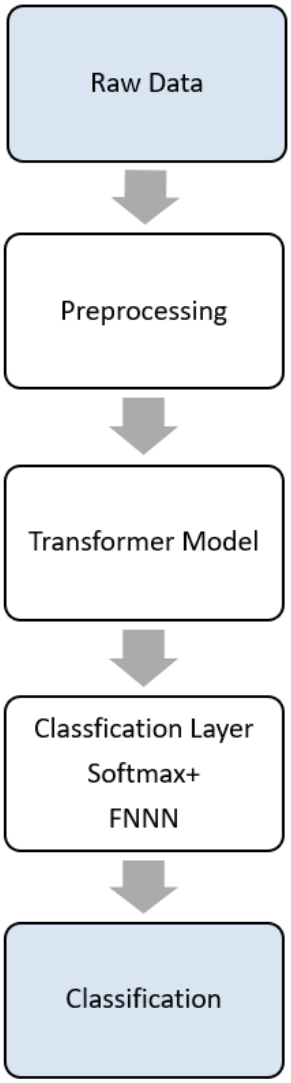


Fig. 3. Model Architecture

IV. RESULTS

We trained the model for 5 iterations and used a batch size of 8 per iteration Our input data, which is discussed in Chapter III, is used to train, and assess the model. The sigmoid function threshold for the FFNN is set at 0.5, and the learning rate is 10-5. For the purpose of assessing our suggested model, we use Precision, Recall, and F1-Score as measures. Precision is defined as the ratio of true positives to the total number of predicted positives. The recall is the ratio of true positives to the actual number of positives. We can obtain the harmonic mean of these measures using the F1 Score that takes precision and recall into account. As the assessment criterion, we employed the macro and micro averages of the precision, recall, and F1 measures. To assess the performance more broadly, we used representative indicators from both the macro and micro averages. We specifically computed macro- and micro-averages for precision, recall, and F1-score for label-based metrics. In contrast to the micro-average, which computes the weighted average based on the number of examples, the macro-average computes the arithmetic average by treating all topics equally regardless of the number of occurrences per class. Therefore, the Micro-average returns the average considering proportion for the respective labels in the dataset, whereas the Macro average shows the performance of the individual categories. The formulas of precision (P), recall (R), F1 score, Macro-P, Micro-P, Macro-R, Micro-R, Macro-F1, and Micro-F1 are as follows:

$$Precision = \frac{True\ Positives}{True\ Positives + False\ Positives} \quad (1)$$

$$Recall = \frac{True\ Positives}{True\ Positives + False\ Negatives} \quad (2)$$

$$F1\ Score = \frac{2 \times Precision \times Recall}{Precision + Recall} \quad (3)$$

$$MacroP = \frac{\Sigma_{n=1}^{N} P_n}{N} \quad (4)$$

$$MicroP = \frac{\Sigma_{n=1}^{N} TP_n}{\Sigma_{n=1}^{N} TP_n + \Sigma_{n=1}^{N} FP_n} \quad (5)$$

$$MacroR = \frac{\Sigma_{n=1}^{N} R_n}{N} \quad (6)$$

$$MicroR = \frac{\Sigma_{n=1}^{N} TR_n}{\Sigma_{n=1}^{N} TR_n + \Sigma_{n=1}^{N} FR_n} \quad (7)$$

$$MacroF1 = \frac{\Sigma_{n=1}^{N} F1_n}{N} \quad (8)$$

$$MicroF1 = \frac{2 \times MicroP \times MicroR}{MicroP + MicroP} \quad (9)$$

where N is the number of categories.

The precision, recall, and f1-scores obtained on each label are shown in Table II. This makes it easier for us to assess how well our model performs for each class. Table III displays the model's overall performance. With an F1-score of 0.89, we observed that the SciBERT model had the best performance. We observe that in the context of classifying Biomedical Literature, domain-specific models performed marginally better than generic models. To further illustrate the breakdown of correctly and incorrectly classified, the confusion matrix of each model is depicted in Fig.4.

TABLE II. LABEL-WISE MODEL PERFORMANCE

Model	Micro			Macro		
	Precision	Recall	F1-score	Precision	Recall	F1-score
BERT	0.8902	0.8607	0.8752	0.8632	0.7862	0.8193
RoBERTa	0.8628	0.8903	0.8763	0.8131	0.8264	0.8174
Sci-BERT	0.8965	0.8907	0.8936	0.8430	0.8163	0.8257
Clinical-BERT	0.8855	0.8514	0.8681	0.8416	0.7725	0.7915

Authorized licensed use limited to: DELHI TECHNICAL UNIV. Downloaded on May 29,2023 at 05:45:24 UTC from IEEE Xplore. Restrictions apply.

TABLE III. OVERALL MODEL PERFORMANCE

Model	BERT			RoBERTa		
Label	**Precision**	**Recall**	**F1-score**	**Precision**	**Recall**	**F1-score**
Case report	0.8858	0.8920	0.8889	0.9242	0.8502	0.8857
Diagnosis	0.8947	0.8226	0.8571	0.8531	0.8742	0.8635
Epidemic forecasting	0.8736	0.6552	0.7488	0.7778	0.6638	0.7163
Mechanism	0.8578	0.8220	0.8395	0.8135	0.8777	0.8444
Prevention	0.9115	0.9308	0.9211	0.9237	0.9358	0.9297
Transmission	0.7273	0.5063	0.5970	0.5350	0.6772	0.8846
Treatment	0.8915	0.8745	0.8829	0.8643	0.9059	0.8846
Model	**SciBERT**			**Clinical-BERT**		
Label	**Precision**	**Recall**	**F1-score**	**Precision**	**Recall**	**F1-score**
Case report	0.9444	0.8718	0.9067	0.8624	0.8955	0.8786
Diagnosis	0.8752	0.8653	0.8702	0.8676	0.8527	0.8601
Epidemic forecasting	0.6628	0.7500	0.7037	0.6720	0.7241	0.6971
Mechanism	0.8504	0.8923	0.8709	0.8439	0.8622	0.8530
Prevention	0.9505	0.9397	0.9451	0.9040	0.9383	0.9208
Transmission	0.7273	0.4898	0.5854	0.8125	0.3291	0.4685
Treatment	0.8915	0.8745	0.8829	0.8643	0.9059	0.8846

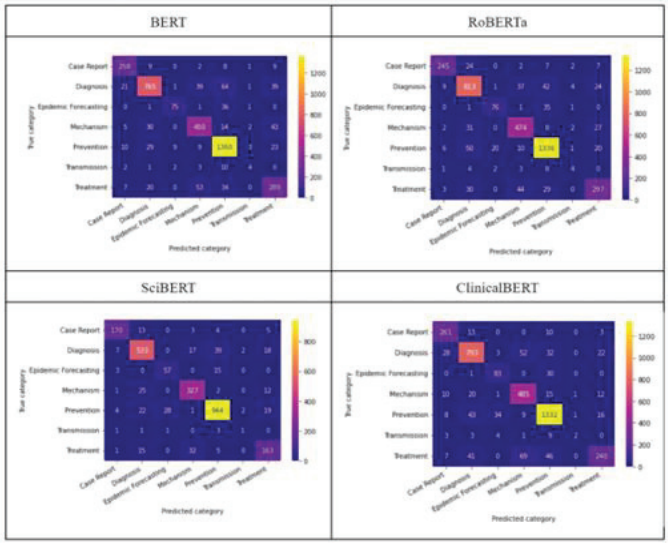


Fig. 4. Confusion matrix of BERT, RoBERTa, SciBERT, and ClinicalBERT models

The main significance of this study lies in the following areas. To first filter pertinent correlations from the biomedical literature, we built a generalized multilabel classification model utilizing transformer models as a baseline model. These classifiers may decrease the time required for manual assessment of those extracted associations when used in a procedure for expert review. Second, we examined and discovered hyperparameter values that enhance the models' overall performance. To compare the effectiveness of each baseline model with our classification model, common hyperparameter values were employed. The thresholds on precision, recall, or F1 score for classification models would determine the degree of effort reduction.

We addressed two research questions: (1) Would the use of generic transformer models as the baseline model improve classification performance in the biomedical literature, and (2) Would a classifier constructed from labeled datasets for the same domain be generalizable to similar data classification?

V. CONCLUSION & FUTURE WORK

Through our study, we have successfully used transfer learning to develop a multilabel classifier to categorize relevant biomedical literature. We sourced our training data, from the LitCovid Dataset. We used four pre-trained transformer models as baseline models separately for our classification pipeline to generate the classifier and evaluate the performance. Using four transformer models with identical hyperparameters and fine tweaking, we have also weighted how the model will perform for comparison. However, the models can be improved to give better results by using an independent set of hyperparameters for fine-tuning each model. Here we have proposed a general model which can be used in the future to aid the automation of multilabel classifications for various domains. In this study, modern transformer models, such as ClinicalBERT, SciBERT, BERT, and RoBERTa were put to test. We demonstrate how transformer-based models are more stable and require fewer annotated data. Moreover, our classification model performed noticeably better than older conventional methods, making it more suited for automation. In the future, work can be extended to automate the dissemination of information through research by deploying and testing such a multilabel classifier on online applications and mobile applications.

ACKNOWLEDGMENT

We would like to thank Delhi Technological University and all the faculty members for providing us with the facilities and platform required to finish our project work as well as the editorial board members for their valuable inputs.

REFERENCES

[1] Zhang, Daniel & Mishra, Saurabh & Brynjolfsson, Erik & Etchemendy, John & Ganguli, Deep & Grosz, Barbara & Lyons, Terah & Manyika, James & Niebles, Juan & Sellitto, Michael & Shoham, Yoav & Clark, Jack & Perrault, Raymond. (2021). The AI Index 2021 Annual Report.

[2] Jingcheng Du, Qingyu Chen, Yifan Peng, Yang Xiang, Cui Tao, Zhiyong Lu, ML-Net: multi-label classification of biomedical texts with deep neural networks, Journal of the American Medical Informatics Association, Volume 26, Issue 11, November 2019, Pages 1279–1285, https://doi.org/10.1093/jamia/ocz085.

Authorized licensed use limited to: DELHI TECHNICAL UNIV. Downloaded on May 29,2023 at 05:45:24 UTC from IEEE Xplore. Restrictions apply.

[3] Simon, Christian & Davidsen, Kristian & Hansen, Christina & Seymour, Emily & Barnkob, Mike & Olsen, Lars. (2019). BioReader: A text mining tool for performing classification of biomedical literature. BMC Bioinformatics. 19. 10.1186/s12859-019-2607-x.

[4] Alam, Tanvir & Schmeier, Sebastian. (2021). Deep Learning in Biomedical Text Mining: Contributions and Challenges. 10.1007/978-3-030-67303-1_14.

[5] Z. Chen and J. Peng, "Learning Label Independence and Relevance for Multi-Label Biomedical Text Classification," 2022 IEEE International Conference on Systems, Man, and Cybernetics (SMC), Prague, Czech Republic, 2022, pp. 2776-2781, doi: 10.1109/SMC53654.2022.9945404.

[6] Dramé, K., Mougin, F. & Diallo, G. Large scale biomedical texts classification: a KNN and an ESA-based approaches. J Biomed Semant 7, 40 (2016). https://doi.org/10.1186/s13326-016-0073-1.

[7] Yan, Yan & xu, Yin & Yang, Chun & Li, Sujian & Zhang, Bo-Wen. (2018). Biomedical literature classification with a CNNs-based hybrid learning network. PLOS ONE. 13. e0197933. 10.1371/journal.pone.0197933.

[8] M. A. Parwez, M. Abulaish and Jahiruddin, "Multi-Label Classification of Microblogging Texts Using Convolution Neural Network," in IEEE Access, vol. 7, pp. 68678-68691, 2019, doi: 10.1109/ACCESS.2019.2919494.

[9] Xain, Mini & Khan, Muhammad Usman & Mehmood, Faiza & Asim, Muhammad & Mahmood, Waqar. (2021). GHS-NET A Generic Hybridized Shallow Neural Network for Multi-Label Biomedical Text Classification. Journal of Biomedical Informatics. 116. 103699. 10.1016/j.jbi.2021.103699.

[10] Jinghang Gu, Emmanuele Chersoni, Xing Wang, Chu-Ren Huang, Longhua Qian, Guodong Zhou, LitCovid ensemble learning for COVID-19 multi-label classification, Database, Volume 2022, 2022, baac103, https://doi.org/10.1093/database/baac103

[11] P. Wang, R. Ge, X. Xiao, M. Zhou and F. Zhou, "hMuLab: A Biomedical Hybrid MUlti-LABel Classifier Based on Multiple Linear Regression," in IEEE/ACM Transactions on Computational Biology and Bioinformatics, vol. 14, no. 5, pp. 1173-1180, 1 Sept.-Oct. 2017, doi: 10.1109/TCBB.2016.2603507.

[12] Hebbar S. and Xie Y. (2021) CovidBERT-biomedical Relation Extraction for Covid-19. Proceedings of FLAIRS-34, 34.

[13] Gu, Y., Tinn, R., Cheng, H., Lucas, M., Usuyama, N., Liu, X., Naumann, T., Gao, J., & Poon, H. (2020). Domain-Specific Language Model Pretraining for Biomedical Natural Language Processing. ArXiv. https://doi.org/10.1145/3458754

[14] Q. Chen, J. Du, A. Allot and Z. Lu, "LitMC-BERT: Transformer-Based Multi-Label Classification of Biomedical Literature With An Application on COVID-19 Literature Curation," in IEEE/ACM Transactions on Computational Biology and Bioinformatics, vol. 19, no. 5, pp. 2584-2595, 1 Sept.-Oct. 2022, doi: 10.1109/TCBB.2022.3173562.

[15] Qingyu Chen, Alexis Allot, Robert Leaman, Rezarta Islamaj, Jingcheng Du, Li Fang, Kai Wang, Shuo Xu, Yuefu Zhang, Parsa Bagherzadeh, Sabine Bergler, Aakash Bhatnagar, Nidhir Bhavsar, Yung-Chun Chang, Sheng-Jie Lin, Wentai Tang, Hongtong Zhang, Ilija Tavchioski, Senja Pollak, Shubo Tian, Jinfeng Zhang, Yulia Otmakhova, Antonio Jimeno Yepes, Hang Dong, Honghan Wu, Richard Dufour, Yanis Labrak, Niladri Chatterjee, Kushagri Tandon, Fréjus A A Laleye, Loïc Rakotoson, Emmanuele Chersoni, Jinghang Gu, Annemarie Friedrich, Subhash Chandra Pujari, Mariia Chizhikova, Naveen Sivadasan, Saipradeep VG, Zhiyong Lu, Multi-label classification for biomedical literature: an overview of the BioCreative VII LitCovid Track for COVID-19 literature topic annotations, Database, Volume 2022, 2022, baac069, https://doi.org/10.1093/database/baac069.

[16] Lee, J., Yoon, W., Kim, S., Kim, D., Kim, S., So, C. H., & Kang, J. (2019). BioBERT: A pre-trained biomedical language representation model for biomedical text mining. ArXiv. https://doi.org/10.1093/bioinformatics/btz682.

[17] Joulin, A., Grave, E., Bojanowski, P., Douze, M., Jégou, H., & Mikolov, T. (2016). FastText.zip: Compressing text classification models. ArXiv. https://doi.org/10.48550/arXiv.1612.03651

[18] Rakotoson, L., Letaillieur, C., Massip, S., & Laleye, F. (2021). BagBERT: BERT-based bagging-stacking for multi-topic classification. ArXiv. https://doi.org/10.48550/arXiv.2111.05808.

[19] Gully A Burns, Xiangci Li, Nanyun Peng, Building deep learning models for evidence classification from the open access biomedical literature, Database, Volume 2019, 2019, baz034, https://doi.org/10.1093/database/baz034

[20] Jinghang Gu, Emmanuele Chersoni, Xing Wang, Chu-Ren Huang, Longhua Qian, Guodong Zhou, LitCovid ensemble learning for COVID-19 multi-label classification, Database, Volume 2022, 2022, baac103, https://doi.org/10.1093/database/baac103.

[21] Fang, L., & Wang, K. (2021, November). Team Bioformer at BioCreative VII LitCovid Track: Multic-label topic classification for COVID-19 literature with a compact BERT model. In Proceedings of the seventh BioCreative challenge evaluation workshop (pp. 272-274).

[22] Marcos Antonio Mouriño García, Roberto Pérez Rodríguez and Luis E. Anido Rifón. Biomedical literature classification using encyclopedic knowledge: a Wikipedia-based bag-of-concepts approach. PeerJ. Vol. 3. DOI: 10.7717/peerj.1279

[23] Lee, J., Yoon, W., Kim, S., Kim, D., Kim, S., So, C. H., & Kang, J. (2019). BioBERT: A pre-trained biomedical language representation model for biomedical text mining. ArXiv. https://doi.org/10.1093/bioinformatics/btz682

[24] Devlin, J., Chang, M., Lee, K., & Toutanova, K. (2018). BERT: Pre-training of Deep Bidirectional Transformers for Language Understanding. ArXiv. https://doi.org/10.48550/arXiv.1810.04805

[25] Liu, Y., Ott, M., Goyal, N., Du, J., Joshi, M., Chen, D., Levy, O., Lewis, M., Zettlemoyer, L., & Stoyanov, V. (2019). RoBERTa: A Robustly Optimized BERT Pretraining Approach. ArXiv. https://doi.org/10.48550/arXiv.1907.11692.

[26] Iz Beltagy, Kyle Lo, and Arman Cohan. 2019. SciBERT: A Pretrained Language Model for Scientific Text. In Proceedings of the 2019 Conference on Empirical Methods in Natural Language Processing and the 9th International Joint Conference on Natural Language Processing (EMNLP-IJCNLP), pages 3615–3620, Hong Kong, China. Association for Computational Linguistics.

[27] Alsentzer, E., Murphy, J. R., Boag, W., Weng, W., Jin, D., Naumann, T., & McDermott, M. B. (2019). Publicly Available Clinical BERT Embeddings. ArXiv. https://doi.org/10.48550/arXiv.1904.03323

[28] Loshchilov, Ilya, and Hutter, Frank. "Decoupled Weight Decay Regularization."arXiv,2017, https://doi.org/10.48550/arXiv.1711.05101.

Authorized licensed use limited to: DELHI TECHNICAL UNIV. Downloaded on May 29,2023 at 05:45:24 UTC from IEEE Xplore. Restrictions apply.

Journal of Computational Electronics
https://doi.org/10.1007/s10825-023-02030-y

Transition metal induced-magnetization in zigzag SiCNTs

Anurag Chauhan[1] · **Kapil Sharma**[1] · **Sudhanshu Choudhary**[2]

Received: 29 September 2022 / Accepted: 16 March 2023
© The Author(s), under exclusive licence to Springer Science+Business Media, LLC, part of Springer Nature 2023

Abstract
In this paper, we report the induced magnetization in metallic and semiconducting SiCNTs on the adsorption of transition metals. The resultant adsorbed SiCNTs structures showed half-metal-ferromagnetic and ferromagnetic behaviour verifying the induced magnetization. The spin-density of states and bandstructure have also been studied, confirming the induced magnetic behaviour. The strength of the induced ferromagnetic behaviour is varied with the various transition metals and is then related to the calculated magnetic moment in the adsorbed structure. The Cr adsorbed (8,0) SiCNT indicated strong half- metal-ferromagnetic behaviour with a magnetic moment of 5.4 μ_B. Only Cu-adsorbed (6,0) metallic SiCNT showed ferromagnetic behaviour among all the simulated structures indicating the impact of transition metal on the SiCNT structures. These promising results will be helpful in designing of devices like spin-valves, MTJs, and MRAMs in the field of spintronics.

Keywords Silicon carbide nanotube · Ferromagnetism · Density functional theory · Adsorption · Transition metals · Magnetic moment

1 Introduction

In the last 2 decades, carbon nanotubes have opened a new world of possibilities for researchers and the semiconductor industry. They are considered as one of the promising candidates for designing of nanodevices like nanosensors due to their high stability, unique electronic and mechanical properties and high frequency response [1, 2].

The successful synthesis of the Boron-Nitride nanotube showed that nanotubes synthesized from other materials are also feasible [3, 4]. Later, silicon carbide nanotubes were also reported to be grown using the self-assembling technique [5]. These nanostructures showed very different and unique properties compared to their bulk forms due to their small size and tubular structure. The nanotubes could behave metallic or semiconducting based on their chirality and diameter dimensions. Compared to carbon nanotubes (CNTs), silicon carbide nanotubes (SiCNTs) are more suitable in the electronics industry field due to their unique physical and electronic properties. Therefore, SiCNTs are more suitable for higher power, temperature, and frequency operations [6–9].The studies report that the nature of SiCNTs depends on the value of (n, m), where n and m are the chirality vectors. The (n, 0) nanotubes are identified as zigzag nanotubes, whereas (n, n) nanotubes are identified as armchair nanotubes. It also states that (n, 0) i,e., zigzag SiCNTs for n = (7,9) are semiconducting in nature, and their bandgap increases with the value of the chiral vector n, whereas they are metallic for $n \leq 6$ [10, 11]. For the case of (n, n), i.e., armchair nanotubes, SiCNTs are metallic for n = 5 and 6 but semiconducting in the range n = (7,10) with their bandgap decreasing with an increasing value of n. Due to these properties of SiCNTs, they make a very suitable material to be used as the channel in developing spintronic devices [12, 13].

Spintronic devices find their applications in designing of programmable logic elements, magnetic sensors, Magnetic Tunnel Junctions (MTJ) and magnetic random-access memory (MRAM). While choosing an electrode material for designing of spintronic device, half- metallicity is the most important characteristic. Materials possessing half metallicity are highly selective to the spin orientation of the electron and hence are used as electrode material in the designing of

✉ Anurag Chauhan
anuragchauhan@dtu.ac.in

Kapil Sharma
kapil@ieee.org

Sudhanshu Choudhary
sudhanshu.choudhary@und.edu

[1] Delhi Technological University, New Delhi, India

[2] University of North Dakota, Grand Forks, ND, USA

Published online: 17 May 2023

MTJs. The efficiency of an MTJ is decided by its property to allow/ block electron of a particular spin (up/ down). A very high (~ 100%) TMR was reported for an MTJ designed with CrO_2 as half metallic electrodes and SiCNT as channel [12].

SiCNT in intrinsic form is non- magnetic in nature. For the SiCNT to be used in spin-dependent transport, it is highly desired that the SiCNT should itself be made spin-polarized. It has been implemented for the CNTs by either doping the nanotube with transition metals or adsorption of transition metals on the surface of the CNTs [14]. Recent studies have demonstrated that the electrical properties and the conductivity of the CNTs can be manipulated by the adsorption of transition metals on their surface. It will use the hybrid structure in the field of spintronics, generation of magnetic sensors and biosensors [15]. A very recent study has reported that the semiconducting CNT can behave as half-metal ferromagnetic (HMF) or Ferromagnetic (FM) on adsorption of transition metals [16–18].

Therefore, it would be interesting to study the impact of the adsorption of transition metals on the surface of SiCNTs. Here, we have investigated the zigzag SiCNT (4,0) which are metallic and SiCNT (8,0) which are semiconducting in their pristine forms. Their electronic properties have been verified by calculating their bandstructures and spin-DOS and confirming the results with the already existing literature. The magnetic properties of the adsorbed structures have also been analyzed by calculating their magnetic moments.

2 Computational details

The transfer of electric charge from the transition metal to the SiCNT occurs due to the reciprocal effect, due to which SiCNT exhibits changed magnetic properties. In zigzag SiCNT, the ratio of Si: C ratio is fixed at 1:1, and the Si–C bond length is set at 1.78 Å. The changes in the magnetic properties of both (4,0) SiCNT and (8,0) SiCNT are studied by adsorbing transition metals on their surface. One atom of the transition metal to be adsorbed (Ti, Cr, Fe, Co, Cu, Zr, Mo and Ag) is placed near the surface of the (4,0) SiCNT and (8,0) SiCNT, and the resulting geometry is relaxed till the forces on each atom have been reduced to not more than 0.05 eV/Å.

The spin-polarized Density of States (spin-DOS) has been plotted for both the metallic (4,0) SiCNT as well as semiconducting (8,0) SiCNT based on density functional theory using the Atomistix simulation Toolkit [2, 19–21]. Spin-polarized generalized gradient approximation (SGGA) has been used for providing the exchange–correlation energy using numerical LCAO basis sets (linear combination of atomic orbitals). The threshold energy of 130 Rydberg has been specified with k point sampling of (1,1,100) along x, y and z directions, respectively. The band structure calculations have also been carried out to verify the results obtained from the spin-DOS analysis. The calculations have been done for all the adsorbed structures for both metallic (4,0) SiCNT as well as semiconducting (8,0) SiCNT. The sampling set has been set to (1,1,3) along the x, y and z directions, respectively, with the Brillouin zone set to G, Z, Y.

According to the energy distribution interpretation, the Density of States (DOS) provides the number of available states between energy E and $E + dE$ can be given as:

$$DOS(E) = \frac{\Delta n}{\Delta E \times L} = \frac{1}{\sqrt{2}\pi A}\left(E - \frac{E_g}{2}\right)^{-\frac{1}{2}} \tag{1}$$

where $DOS(E)$ represents the density of states at a given energy level E,E_g is the energy gap, $A = at$ is the Taylor expansion coefficient, and L is the length of SiCNT.

Also, the carrier concentration of the material at a given energy E can be found using the density function and the probability density function as:

$$n(E) = \int DOS(E)f(E)dE \tag{2}$$

To ensure the feasibility of transition metals on the surface of SiCNT, adsorption energy can be calculated as:

$$E_{ads} = E_{structure} - [E_{TM} + E_{SiCNT}] \tag{3}$$

where E_{ads} is the energy of adsorption, $E_{structure}$ is the total energy of the optimized structure after adsorption of transition metal on the surface of SiCNT, E_{SiCNT} is the total energy of the intrinsic SiCNT and E_{TM} is the total energy of one transition metal. Also, a larger negative value of E_{ads} means a more stable structure and the process is thermodynamically exothermic [22].

3 Results and discussions

Figure 1a shows the relaxed geometry of the pristine (4,0) SiCNT which is very similar to the (4,0) CNT [16]. The geometry has been constructued by substituting half of the carbon (C) atoms in a dimer of (4,0) CNT with silicon (Si) atoms. The geometry was then optimized so that the resulting structure was stable and could be used for further analysis. The bandstructure and spin-density of states for pristine (4,0) SiCNT are plotted as shown in Fig. 2a. It can be observed that the pristine (4,0) SiCNT is metallic as it has no bandgaps with bands crossing the Fermi level. It can be observed from its spin-DOS shown in Fig. 2a that both spin-states (spin-up and spin-down) are present at the Fermi level for (4,0) SiCNT. But its calculated zero magnetic moment as shown in Table 1 preserves its non-magnetic nature. These

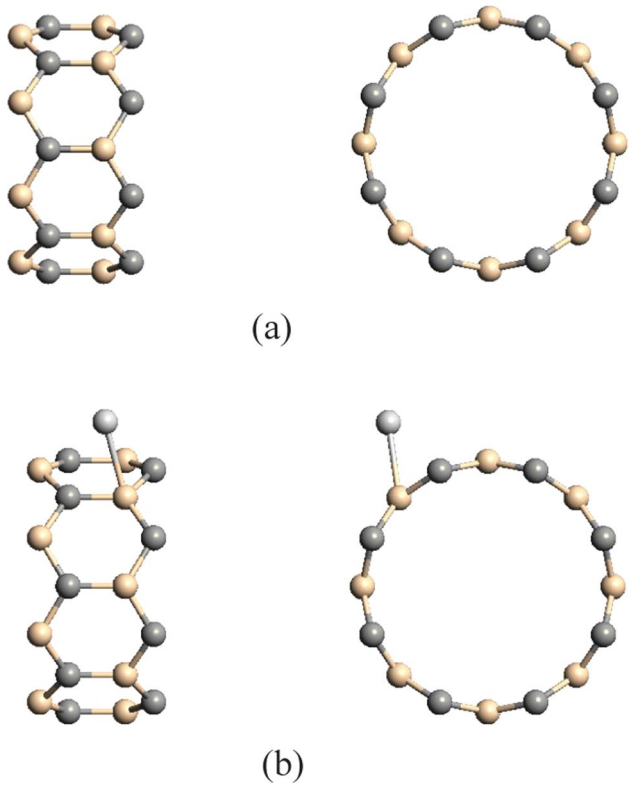


Fig. 1 **a** Semiconducting (8,0) SiCNT **b** Ag atom adsorbed (8,0) SiCNT

results conclude that pristine (4,0) SiCNT is a non- magnetic metal which is consistent with the already existing research [10].

To understand the effect of adsorption, it is necessary to investigate the electronics and magnetic characteristics of the adsorbed structures. To investigate this, the transition metals were kept near to the surface of pristine SiCNT and overall structure was relaxed. The relaxed structure of Ag-adsorbed (8,0) semiconducting SiCNT can be seen in Fig. 1b. Similarly other transition metals were also adsorbed individually on the pristine (4,0) SiCNT and (8,0) SiCNTs. The resulting structures were then relaxed to optimize them. To ensure the feasibility of different transition metals on the surface of SiCNT, the adsorption energy of the structure was calculated. The adsorption energy of all the structures came out to be negative which means that the structure is stable, and the adsorption was instantaneous. A larger negative value of adsorption energy means stronger adsorption between the transition metal and the SiCNT.

The bandstructure and spin-DOS of the Ag-adsorbed zigzag (4,0) SiCNT shown in Fig. 2b shows its metallic nature. In addition, it also preserves its non-magnetic behaviour as the magnetic moment remains insignificant (see Table 1) even though its spin- DOS shows conduction states in both spin-up and spin-down channels. However, the magnetic

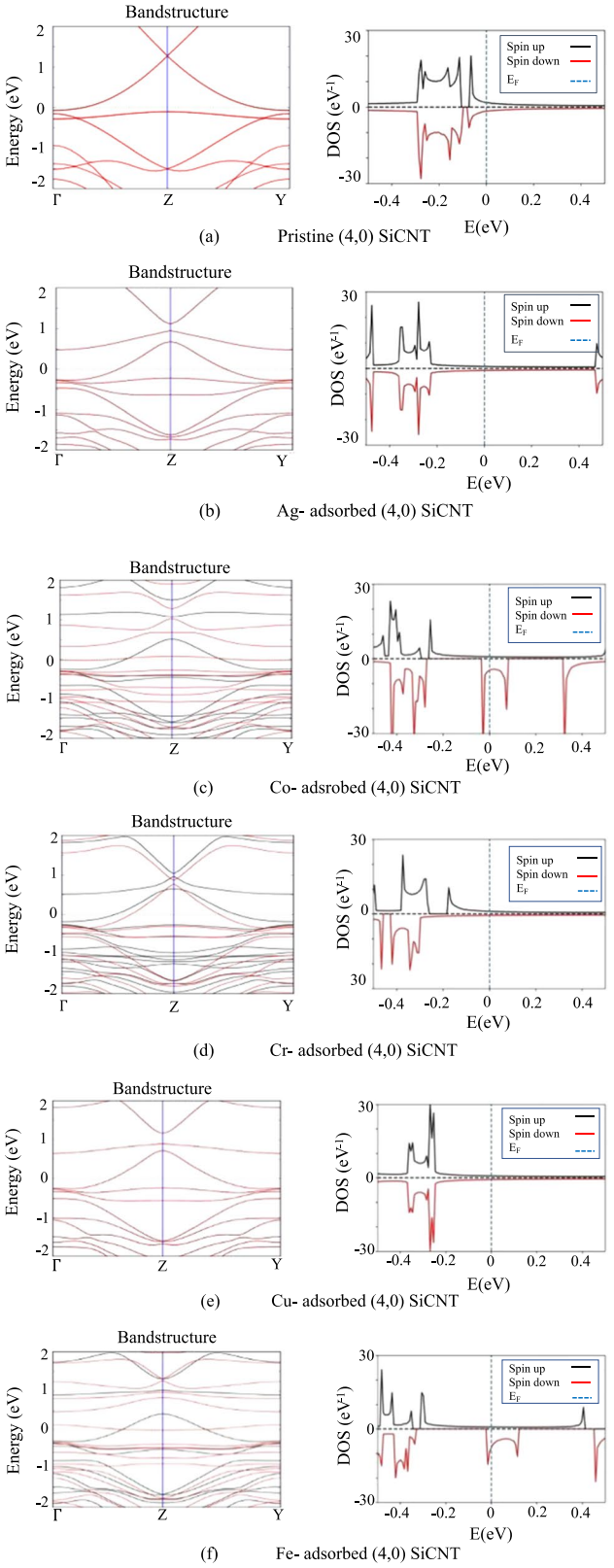


Fig. 2 Bandstructure and spin-DOS of **a** pristine (4,0) SiCNT **b** Ag-adsorbed (4,0) SiCNT **c** Co-adsorbed (4,0) SiCNT **d** Cr-adsorbed (4,0) SiCNT **e** Cu-adsorbed (4,0) SiCNT **f** Fe-adsorbed (4,0) SiCNT **g** Mo-adsorbed (4,0) SiCNT **h** Ti-adsorbed (4,0) SiCNT **i** Zr-adsorbed (4,0) SiCNT

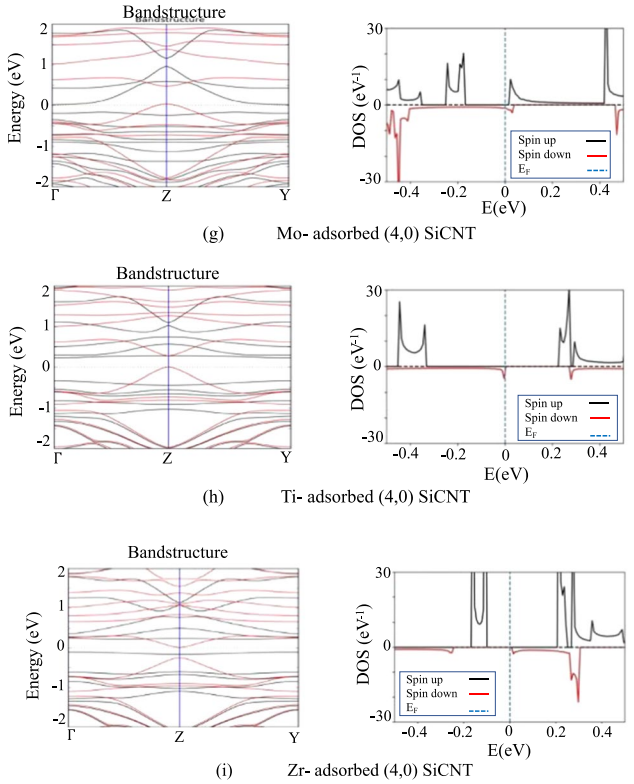


Fig. 2 (continued)

moment rises to significant levels when zigzag (4,0) SiCNT is adsorbed with Co. The zero bandgap at the Fermi level can be observed from its bandstructure in Fig. 2c. Also, majority of the conduction states for the Co-adsorbed structures are available in only the spin-down direction and negligible states are available in the spin-down channel in comparison to the spin-up states. This shows its Half-Metallic-Ferromagnetic (HMF) nature. The HMF materials have this unique characteristic that they allow electrons of a particular spin (up/down) to conduct while blocking the electron having the opposite spin (down/up). This unique property of HMF allows their use in novel fields like spintronics for the fabrication of novel devices like spin valves and magnetic tunnel junctions (MTJs). The significant magnetic moment of ~ 2 μ_B for Co-adsorbed (4,0) SiCNT confirm its magnetic behaviour (see Table 1). Similar induction of HMF behaviour can be observed in Fe, Mo and Ti-adsorbed where most of the conduction is allowed in the spin-down states and no/negligible conduction is allowed in the spin-up states (see Fig. 2f, g and h). Their significant magnetic moments of ~ 3, 4 and 2 μ_B respectively exhibit the change of nature to magnetic as compared with the non-magnetic nature of pristine (4,0) SiCNT (see Table 1). The Cr- adsorbed (4,0) SiCNT also shows half metallicity as it allows conduction only in the spin-up channels and blocks the conduction of spin-down electrons (see Fig. 2d). Its significant magnetic moment of 4.8 μ_B reflects its magnetic nature (see Table 1).

From the spin- DOS of Cu-adsorbed (4,0) SiCNT shown in Fig. 2e, it can be observed that only Cu-adsorbed (4,0) SiCNT structure shows ferromagnetic behaviour as it has conducting states in both spin-up and spin-down channels. It also has a significant magnetic moment of ~ 4.8 μ_B (see Table 1). As shown in Table 1, the Zr-adsorbed (4,0) SiCNT, inspite of significant magnetic moment is non- magnetic in nature since it does not have any conduction states at the Fermi level which can be observed from its spin- DOS as shown in Fig. 2i.

The bandstructure of all the transition metal adsorbed (4,0) SiCNT structures shows zero bandgap at the Fermi level indicating the metallic nature of all the adsorbed structures. The magnetic nature in the adsorbed structures is attributed to its significant magnetic moment availability of conducting states in its spin- up and spin- down channels.

Table 1 Magnetic Properties of (4,0) SiCNT after adsorption of TM

Simulated structure	Spin-up	Spin-down	Magnetic moment per atom (μ_B)	Magnetic behaviour
Pristine (4,0) SiCNT	Passed	Passed	NIL	Non-magnetic
Ag adsorbed SiCNT	Passed	Passed	0	Non-magnetic
Co adsorbed SiCNT	Not passed	Passed	+2.1	HMF
Cr adsorbed SiCNT	Passed	Not passed	+4.8	HMF
Cu adsorbed SiCNT	Passed	Passed	+4.8	FM
Fe adsorbed SiCNT	Not passed	Passed	+3.2	HMF
Mo adsorbed SiCNT	Not passed	Passed	+4.2	HMF
Ti adsorbed SiCNT	Not passed	Passed	+2.1	HMF
Zr adsorbed SiCNT	Not passed	Not passed	+1.8	Non- Magnetic

The calculated magnetic moment in the TM-adsorbed (4,0) SiCNT results primarily due to the unpaired electrons present in the d- orbital of the transition metals. The carbon and silicon atoms have negligible contribution to the overall magnetic moments of the adsorbed structures, which is verified by the obtained zero magnetic moment of the pristine (4,0) SiCNT. The resulting structures result into the metallic/ half metallic is due to the transfer of charge from the transition metal to the carbon/ silicon atoms on which it is adsorbed. Therefore, the results suggest that the adsorption of transition metals on the pristine (4,0) SiCNT can transform its non-magnetic nature into FM/ HMF nature.

The (8,0) SiCNT is a semiconductor [23, 24] and the same can be observed from the bandstructure and the DOS of Fig. 3a. The bandstructure plot shows a significant energy gap at the Fermi level signifying its semiconducting nature. Non- availability of conducting states in either channel (spin- up/ spin- down) at the Fermi level in the spin DOS verifies its semiconducting nature. The Table 2 shows that pristine zigzag (8,0) SiCNT has zero magnetic moment. This verifies that (8,0) SiCNT in pristine form is non- magnetic.

When (8,0) SiCNT is adsorbed with Ag- atom, its semiconducting nature changes to metallic as its bandstructure shows zero bandgap at the Fermi level (see Fig. 3b). Although it has conducting states in both spin-up and spin-down channels but it preserves its non- magnetic nature due to negligible magnetic moment (see Table 2). However, when Co atom is adsorbed on (8,0) SiCNT, it remains semiconducting as its bandstructure in Fig. 3c shows a finite energy gap at the Fermi level. Also, its spin -DOS shown in Fig. 3c has no available conducting states which makes it non- magnetic. Table 2 shows a negative magnetic moment for Co- adsorbed (8,0) SiCNT which is primarily due to the unpaired d- orbital electron of the Co atom, but as no conducting states as visible from the spin-DOS in Fig. 3c, it remains non- magnetic. Similar non-magnetic behaviour can be seen in Fig. 3f and g for Fe-adsorbed and Mo-adsorbed (8,0) SiCNT structures. They have significant magnetic moments of 2 μ_B and 4 μ_B respectively. This magnetic moment is mainly contributed by the transition Fe and Mo atoms respectively, but it has no impact on the magnetic nature of the adsorbed structure as no conducting states in either spin-up or spin-down channels are available as shown in Fig. 3f and g.

However, Cr-adsorbed (8,0) SiCNT structure is able to change its non-magnetic behaviour to magnetic. It exhibits the highest magnetic moment of 5.47869 μ_B, which is the highest among all the (8,0) SiCNT simulated structures (see Table 2). Its spin- DOS shown in Fig. 3d allows conduction in the spin-down channel (see Fig. 3d) while simultaneously blocking the spin- down channel, making it an HMF material. Similarly, the Cu- adsorbed (8,0) SiCNT also results in an HMF material which allows

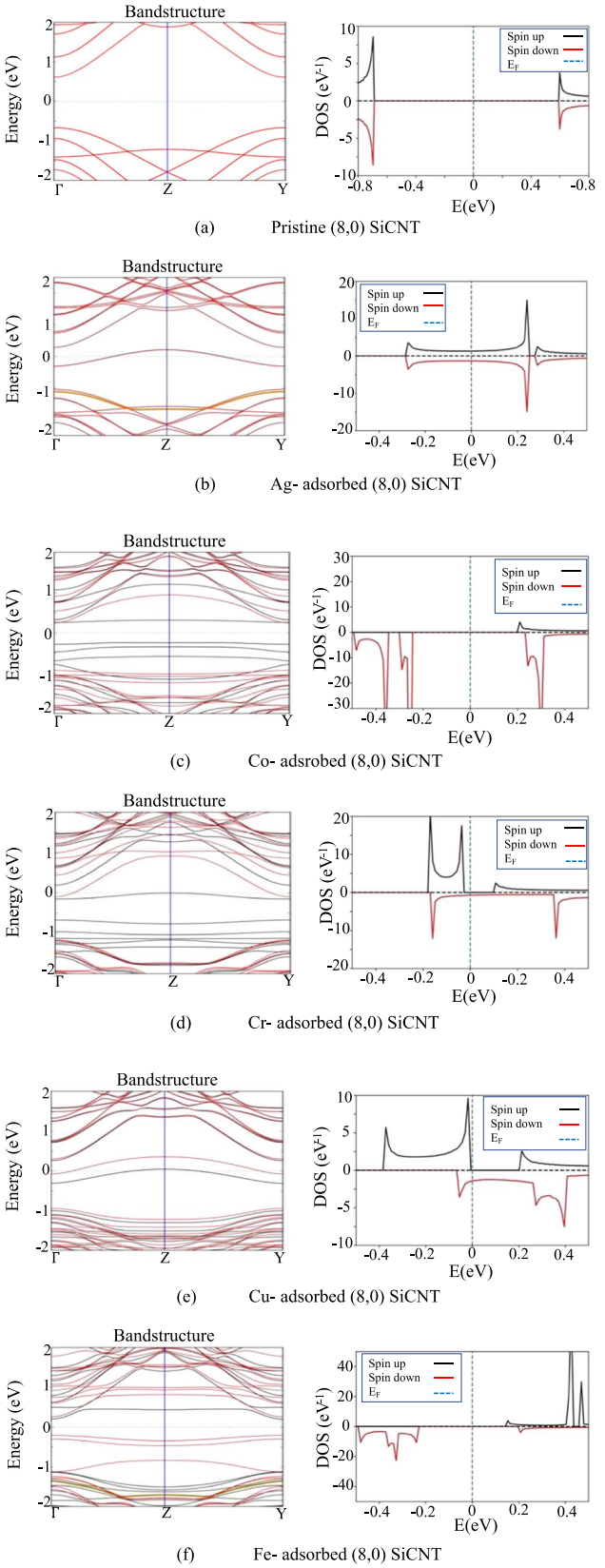


Fig. 3 Bandstructure and DOS of **a** pristine (8,0) SiCNT **b** Ag-adsorbed (8,0) SiCNT **c** Co-adsorbed (8,0) SiCNT **d** Cr-adsorbed (8,0) SiCNT **e** Cu-adsorbed (8,0) SiCNT **f** Fe-adsorbed (8,0) SiCNT **g** Mo-adsorbed (8,0) SiCNT **h** Ti-adsorbed (8,0) SiCNT **i** Zr-adsorbed (8,0) SiCNT

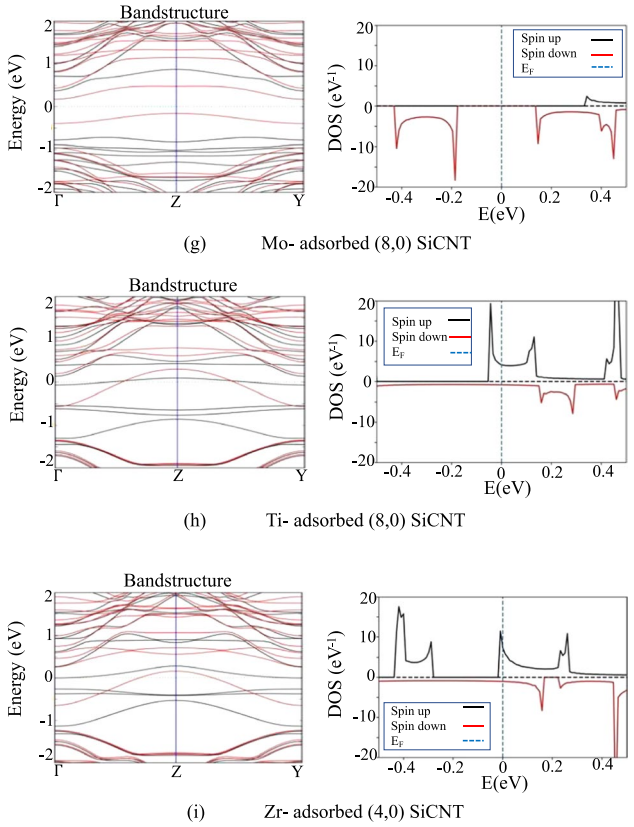


Fig. 3 (continued)

conduction in the spin-down channel as shown in Fig. 3e. Its magnetic nature can also be verified by its non-zero magnetic moment of 0.4 μ_B. The simulated Ti- adsorbed and Zr- adsorbed (8,0) SiCNT structures also result in magnetic structures. Their spin-DOS and bandstructure can be seen in Fig. 3h and i respectively. Their spin-DOS shows that conducting is allowed in only spin-up channel whereas negligible conduction can be observed in spin-down channels. Ti- on adsorption produces a strong magnetic moment of 3.1 μ_B in the adsorbed structure. Zr- adsorbed (8,0) SiCNT exhibited a strong magnetic nature with calculated magnetic moment of 2.5 μ_B as seen in Table 2. These strong magnetic moments along with spin-DOS showing conduction in only spin-up channel confirms the transformation of non- magnetic SiCNT to HMF structures on adsorption of Ti and Zr.

4 Conclusion

The DFT simulations are performed based on the first principles study to analyze the induced magnetic behaviour of TM when adsorbed on metallic zigzag (4,0) SiCNT and semiconducting zigzag (8,0) SiCNT. The SiCNTs, otherwise non-magnetic, showed a strong FM and HMF nature when adsorbed with transition metals, suggesting their capability to induce magnetization in non-magnetic materials, both metallic and semiconducting zigzag SiCNTS. The (4,0) SiCNT, when adsorbed with Co, Cr, Fe, Mo and Ti, exhibited the HMF nature. The (8,0) SiCNT, which is semiconducting, when adsorbed with Cr, Cu, Ti and Zr, is also found to exhibit an HMF nature. The results also showed that Cr and Ti are able to transform both metallic and semiconducting zigzag SiCNTs into HMF and are promising candidates for inducing magnetization in both metallic as well as semiconducting zigzag SiCNT structures. The FM and HMF materials are the most used materials for constructing the electrodes in spin-based devices. Thus, the TM-adsorbed SiCNTs can play a significant role in designing magnetic devices like magnetic storage devices, MTJs, and spin valves for applications in the field of spintronics.

Table 2 Magnetic Properties of (8,0) SiCNT after adsorption of TM

Simulated structure	Spin-up	Spin-down	Magnetic moment per atom (μ_B)	Magnetic behaviour
Pristine (8,0) SiCNT	Not passed	Not passed	NIL	Non-magnetic
Ag adsorbed SiCNT	Passed	Passed	NIL	Non-magnetic
Co adsorbed SiCNT	Not passed	Not passed	−1.0	Non-magnetic
Cr adsorbed SiCNT	Not passed	Passed	+5.4	HMF
Cu adsorbed SiCNT	Not passed	Passed	+0.4	HMF
Fe adsorbed SiCNT	Not passed	Not passed	+2.0	Non-magnetic
Mo adsorbed SiCNT	Not passed	Not passed	+4.0	Non-magnetic
Ti adsorbed SiCNT	Passed	Passed	+3.1	HMF
Zr adsorbed SiCNT	Passed	Passed	+2.5	HMF

Author contributions All authors contributed to the study, conception and design. Material preparation, data collection and analysis were performed by Anurag Chauhan. The first draft of the manuscript was written by Anurag Chauhan, and all authors commented on previous versions of the manuscript. All authors read and approved the final manuscript.

Funding No funding was received to conduct this study.

Availability of data and material Not applicable.

Code availability Not applicable.

Declarations

Conflicts of interest The authors declare they have no conflict of interest.

Consent to participate Not applicable.

Ethics approval This article does not contain any studies with human participants or animals performed by any of the authors.

References

1. Iijima, S.: (1991) Synthesis of carbon nanotubes. Nature **354**, 56–58. References—Scientific Research Publishing. https://www.scirp.org/(S(i43dyn45teexjx455qlt3d2q))/reference/ReferencesPapers.aspx?ReferenceID=1241661. Accessed Dec. 28, 2021
2. Barla, P., Joshi, V.K., Bhat, S.: Spintronic devices: a promising alternative to CMOS devices. J. Comput. Electron. **20**(2), 805–837 (2021). https://doi.org/10.1007/S10825-020-01648-6
3. Loiseau, A., Willaime, F., Demoncy, N., Hug, G., Pascard, H.: Boron nitride nanotubes with reduced numbers of layers synthesized by arc discharge. Phys. Rev. Lett. **76**(25), 4737 (1996). https://doi.org/10.1103/PhysRevLett.76.4737
4. Chopra, N.G., et al.: Boron nitride nanotubes. Science 1979 **269**(5226), 966–967 (1995). https://doi.org/10.1126/SCIENCE.269.5226.966
5. Yan, B., Zhou, G., Wu, J., Duan, W., Gu, B.L.: Bonding modes and electronic properties of single-crystalline silicon nanotubes. Phys. Rev. B Condens. Matter. Mater. Phys. (2006). https://doi.org/10.1103/PHYSREVB.73.155432
6. Behzad, S., Moradian, R., Chegel, R.: Structural and electronic properties of silicon carbide nanotubes. pp 1860–1869 (2012). https://doi.org/10.1166/jctn.2012.2597
7. Zhao, M., Xia, Y., Li, F., Zhang, R.Q., Lee, S.T.: Strain energy and electronic structures of silicon carbide nanotubes: density functional calculations. Phys. Rev. B Condens. Matter Mater. Phys. **71**(8), 1–6 (2005). https://doi.org/10.1103/PhysRevB.71.085312
8. Menon, M., Richter, E., Mavrandonakis, A., Froudakis, G., Andriotis, A.N.: Structure and stability of SiC nanotubes. Phys. Rev. B Condens. Matter Mater. Phys. **69**(11), 45–48 (2004). https://doi.org/10.1103/PhysRevB.69.115322
9. Peng, B., Annamalai, M., Mothes, S., Schröter, M.: Device design and optimization of CNTFETs for high-frequency applications. J. Comput. Electron. **20**(6), 2492–2500 (2021). https://doi.org/10.1007/S10825-021-01805-5/FIGURES/9
10. Larina, E.V., Chmyrev, V.I., Skorikov, V.M., D'yachkov, P.N., Makaev, D.V.: Band structure of silicon carbide nanotubes. Inorg. Mater. **44**(8):823–834 (2008). https://doi.org/10.1134/S0020168508080086.
11. Choudhary, S., Qureshi, S.: Theoretical study on effect of radial and axial deformation on electron transport properties in a semiconducting Si–C nanotube. **35**(5):713–718 (2012)
12. Choudhary, S., Chauhan, A.: First-principles study of spin transport in CrO_2–SiCNT–CrO_2 magnetic tunnel junction. J. Comput. Electron. (2015). https://doi.org/10.1007/s10825-015-0725-x
13. Saini, M., Choudhary, S.: Understanding the spin transport in H_2O-adsorbed CNT-based magnetic tunnel junction. J. Supercond. Nov. Magn. **32**(4), 925–929 (2018). https://doi.org/10.1007/S10948-018-4783-8
14. Yang, C.-K., Zhao, J., Lu, J.P.: Magnetism of transition-metal/carbon-nanotube hybrid structures. (2003). https://doi.org/10.1103/PhysRevLett.90.257203.
15. Meshginqalam, B., Alaei, S.: Transition metals adsorption and conductivity modification in carbon nanotubes: analytical modeling and DFT study. Adsorption **24**(6), 575–583 (2018). https://doi.org/10.1007/S10450-018-9964-Z
16. Choudhary, S., Singh, N., Ranjan, P.: Journal of magnetism and magnetic materials induced magnetization in armchair and zigzag CNTs on adsorbing transition metals. J. Magn. Magn. Mater. **538**(July), 168287 (2021). https://doi.org/10.1016/j.jmmm.2021.168287
17. Yang, C.K., Zhao, J., Lu, J.P.: Magnetism of transition-metal/carbon-nanotube hybrid structures. Phys. Rev. Lett. **90**(25), 4 (2003). https://doi.org/10.1103/PHYSREVLETT.90.257203/FIGURES/4/MEDIUM
18. Yang, C.-K., Zhao, J., Lu, J.P.: Complete spin polarization for a carbon nanotube with an adsorbed atomic transition-metal chain. Letters **4**, 561–563 (2004). https://doi.org/10.1021/nl035104x
19. Cui, H., Zhang, G., Zhang, X., Tang, J.: Rh-doped $MoSe_2$ as a toxic gas scavenger: a first-principles study. Nanoscale Adv. **1**(2), 772–780 (2019). https://doi.org/10.1039/C8NA00233A
20. Srivastava, A., Jain, S.K., Khare, P.S.: Ab-initio study of structural, electronic, and transport properties of zigzag GaP nanotubes. J. Mol. Model (2014). https://doi.org/10.1007/S00894-014-2171-2
21. Chauhan, A., Maahich, A., Pal, J.: First-principles calculations of the electronic and optical properties of $WS_{e2}/Cd_{0.9}Zn_{0.1}Te$ van der Waals heterostructure. J. Comput. Electron. **20**(1), 13–20 (2021). https://doi.org/10.1007/s10825-021-01659-x
22. Bahamon, D., Khalil, M., Belabbes, A., Alwahedi, Y., Vega, L.F., Polychronopoulou, K.: A DFT study of the adsorption energy and electronic interactions of the SO2 molecule on a CoP hydrotreating catalyst. RSC Adv. **11**(5), 2947–2957 (2021). https://doi.org/10.1039/C9RA10634K
23. Lei, T., Pochorovski, I., Bao, Z.: Separation of semiconducting carbon nanotubes for flexible and stretchable electronics using polymer removable method. Acc. Chem. Res. **50**(4), 1096–1104 (2017). https://doi.org/10.1021/ACS.ACCOUNTS.7B00062
24. Du, T., Getty, S.A., Cobas, E., Fuhrer, M.S.: Extraordinary mobility in semiconducting carbon nanotubes. (2004) https://doi.org/10.1021/nl034841q.

Publisher's Note Springer Nature remains neutral with regard to jurisdictional claims in published maps and institutional affiliations.

Springer Nature or its licensor (e.g. a society or other partner) holds exclusive rights to this article under a publishing agreement with the author(s) or other rightsholder(s); author self-archiving of the accepted manuscript version of this article is solely governed by the terms of such publishing agreement and applicable law.

e-ISSN: 2582-5208
International Research Journal of Modernization in Engineering Technology and Science
(Peer-Reviewed, Open Access, Fully Refereed International Journal)
Volume:05/Issue:05/May-2023 Impact Factor- 7.868 www.irjmets.com

TRIBOLOGICAL ANALYSIS OF NANOPARTICLES IN LUBRICANTS USING FOUR BALL TESTER

Shaurya Tarun*1, Siamjoyful Keishing*2, Subhash Sharma*3

*1,2,3Delhi Technological University, Mechanical Engineering Department, Delhi Technological University, Delhi, India

DOI : https://www.doi.org/10.56726/IRJMETS39666

ABSTRACT

Lubricants are essential for keeping internal combustion engine parts lubricated and extending the engine's useful life. For its application, lubricating oils' load carrying capacity is a crucial factor. This study measures the coefficient of friction of 20W40 engine oil with various nanoparticles using the Four-Ball testing method. The tribological characteristics of the formed oil were assessed by a four ball tester during tests that were conducted in accordance with conventional test procedures. For 30 minutes, the spinning ball is rotated at 1,200 rpm at 75 °C. As per ASTM D 4172 B, the coefficient of friction was assessed.

Keywords: Nano particles, nano fluids, four ball testing machine, 20W/40SW engine oil

I. INTRODUCTION

A lubricant is an additive, generally organic, that is used to lessen the friction between moving surfaces, which, in turn, lessens the heat produced when the surfaces move. Additionally, it might be used for force transmission, the transportation of foreign particles, or the heating or cooling of surfaces. Lubricants are substances that are applied to machine parts to reduce friction and lengthen their service lives. They are often liquids, but they can also be solids or semi-solids.

- Properties of Lubricants
- A high boiling point and low freezing point (in order to say liquid within a wide range of temperature)
- A high viscosity index
- Thermal stability
- Hydraulic stability
- Corrosion prevention
- A high resistance to oxidation
- Four Ball Tribometer:

The four ball testing machine is frequently used to assess the tribological characteristics of lubricating oil, such as wear prevention, severe pressure, and shear stability. Under typical operating conditions, the device can be used to assess the coefficient of friction, anti-wear, and load carrying ability of lubricating oils. Four balls make up this device: one on top and three at the bottom that are clamped together. The test lubricating oil is contained in a ball pot with the bottom three balls clamped together and pressed up against the test ball. The bottom three balls press against the top ball, which is then manipulated to rotate at the proper pace. In general, these devices have rubbing test specimens that are subjected to quantifiable loads that can change. Speeds, test specimen shape, load and temperature ranges, and test materials are all different between the testing equipment. The lubricating oils are chosen with a variety of operational parameters in mind, including temperature rise, operating load, typical working temperature, extreme conditions, etc. the evaluated oils' wear scar diameter with the use of an image collection equipment.

II. METHODOLOGY

Preparation of Nanofluids:

Servo engine oil 20W/40SW was used as the base oil and different types of nano particle like Al2O3,TiO2, SiO2, CuO, ZnO (0.05% weight each) were blended together using magnetic blender for a duration of 30 minute each, at 75 oC and 1200rpm.

e-ISSN: 2582-5208
International Research Journal of Modernization in Engineering Technology and Science
(Peer-Reviewed, Open Access, Fully Refereed International Journal)
Volume:05/Issue:05/May-2023 Impact Factor- 7.868 www.irjmets.com



FIG 1: Magnetic Blender



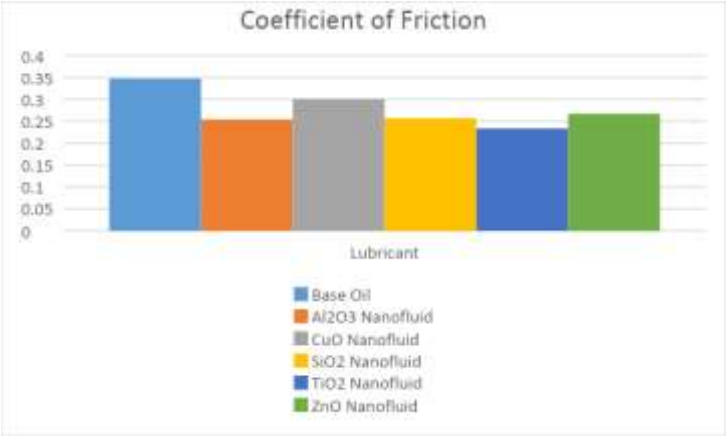
FIG 2: Analytical Balancer

Experiment and Procedure:

The experiment is carried out in ASTM-D4172 machine mainly called as the four ball tester(TR-30 series). After the preparation of the nanofluids a little amount of it is poured into the 3 ball disc holder and then it is allowed to process through the chamber where the performance test for friciton is measured the required output are directly shown to us through computer, load of 4 kg is used for the experiment which give a normal load of about 400N.

III. RESULTS AND DISCUSSION

The data for the calculation of coefficient of friction were taken using four ball tester and measured using winducom 2008. The tests provide a chance of using nanofluids as an alternate source of lubricant oil.



e-ISSN: 2582-5208
International Research Journal of Modernization in Engineering Technology and Science
(Peer-Reviewed, Open Access, Fully Refereed International Journal)
Volume:05/Issue:05/May-2023 Impact Factor- 7.868 www.irjmets.com

From these data we can conclude that the coefficient of friction of SiO2 nanofluid is less than the other experimented nanofluids but due to higher thermal conductivity of Al2O3-CuO, it is considered to be the optimal solution as a nano additive.

IV. CONCLUSION

From this experiment we can conclude that the value of coefficient of friction for SiO2 is the least among the nanoparticles but it has lower thermal conductivity when compared to Al2O3 Hence we selected Al2O3 for hybridization. Experiment on Hybrid of Al2O3/CuO was done and we came to the conclusion that the coefficient of friction of a hybrid nanofluid give better COF compared to individual nanofluids, the wear resistance also increases because of lower COF, The thermal conductivity of a hybrid nanofluid also increase as compared to individual nanofluid .

V. REFERENCES

[1] Tuan Ngo, Vi Hoang, Sinh Hoang, "Research on Applying Nano Cutting Oils in Spur Gear Hobbing Process" World Journal of Engineering and Technology, Vol.5 No.2, May 2017 DOI: 10.4236/wjet.2017.5.2023

[2] Muzammil S. Khan, Mahendra Singh Sisodia, Shubham Gupta, M. Feroskhan, S.Kannan,Karunamurthy Krishnasamy, "Measurement of tribological properties of Cu and Ag blended coconut oil nanofluid for metal cutting" hool of Mechanical and Building Sciences, VIT Chennai, Tamilnadu, India, 2019.

[3] Hu, E. Z., Xu, Y., Hu, K. H. & Hu, X. G. Tribological properties of 3 types of MoS2 additives in different base greases. Lubrication Science. 29, 541–555 (2017)

[4] Y. Wang, C. Li, Y. Zhang, B. Li, M. Yang, X. Zhang, S. Guo, G. Liu, M. Zhai, Comparative evaluation of the lubricating properties of vegetable-oil-based nanofluids between frictional test and grinding experiment, Journal of Manufacturing Processes, vol. 26, pp. 94-104, 2017, DOI: 10.1016/j.jmapro.2017.02.001

[5] A.K. Sharma, A.K. Tiwari, A.R. Dixit, R.K. Singh, M. Singh, Novel use of alumina/graphene hybrid nanoparticle additives for improved tribological properties of lubricant in turning operation, Tribology International, vol. 119, pp. 99-111, 2018, DOI: 10.1016/j.triboint.2017.10.036

2023 10th International Conference on Signal Processing and Integrated Networks (SPIN) | 978-1-6654-9099-3/23/$31.00 ©2023 IEEE | DOI: 10.1109/SPIN57001.2023.10116564

Tunable LSPR in Asymmetric Plasmonic Bowtie Nanostructures

Kirti Dalal
Department of Electronics and Communication Engineering
Delhi Technological University
Delhi, India
kirtidalal_2k20phdec03@dtu.ac.in

Yashna Sharma
Department of Electronics and Communication Engineering
Delhi Technological University
Delhi, India
yashnasharma@dtu.ac.in

***Abstract*—Asymmetrical plasmonic bowtie nanostructures on a silica substrate are presented in this paper. The electromagnetic enhancement achieved at the centric vicinity of the asymmetric nano-bowtie is numerically modelled using the Finite Difference Time Domain (FDTD). The effects of the degree of asymmetry in terms of the flared angle and the length of the nano-bowtie, the effect of the angle of incident light, and the effect of periodic and aperiodic configurations of these nanostructures are extensively analysed to study the tunability of the localized surface plasmon resonance (LSPR) wavelength over the visible and near infrared wavelength ranges. These nanostructures can be employed for numerous plasmonic applications like biomedical sensing, fluorescence microscopy, and surface enhanced Raman spectroscopy (SERS).**

***Keywords*—Nanostructures, Plasmonics, Finite Difference Time Domain, Asymmetric nano-bowtie**

I. Introduction

Plasmonics is a promising field of nano-optics which offers the capability to couple light at nanoscale and leads to the development of ultrafast as well as ultrasmall nanophotonic devices [1-3]. Plasmonics involves the investigation of resonant interactions between light and free electrons at the metal and dielectric interface [4]. It typically utilizes the principle of surface plasmon polaritons (SPPs) [5] or localized surface plasmon resonance (LSPR) [6]. SPPs are the coherent electron oscillations that travel with the electromagnetic wave along the metal-dielectric interface [7]. On the other side, LSPR results from the confinement of surface plasmons in the nanoparticles at sub-wavelength scale [8].

Plasmonic nanostructures can be designed with different kind of geometries such as – nanospheres [9], nanorods [10], nanodiscs [11], nanocubes [12], nanorings [13], nanoholes [14], nanocylinders [15], and others. One of the most widely employed geometry is a nano-bowtie because of its ability to couple the electromagnetic (EM) field at the centre of its two triangles [16-18]. Asymmetry in the two triangles of the plasmonic nano-bowtie is often explored to achieve enhanced performance [19-22]. In this work, we have proposed asymmetric plasmonic bowtie nanostructures (Fig. 1) to study the tunability of the LSPR wavelength over the visible and near infrared wavelength range by manipulating the degree of asymmetry in its geometric parameters. These nanostructures can be employed for various plasmonic applications including – sensors for chemicals or bioanalytes, surface enhanced Raman spectroscopy (SERS), and nanophotonic devices such as switches and modulators for communications – among many others. Table I shows a comparison of the proposed work with the previously published works in terms to tunable LSPR range as the figure of merit. This work consists of gold triangular nano-bowties on a silicon dioxide substrate as depicted in Fig. 1. Plasmonic properties of these asymmetric bowtie nanostructures are a strong function of its geometric parameters like the length of the nano-bowtie, the thickness of the nano-bowtie, the flared angle of the nano-bowtie, and the gap between the two triangles of the nano-bowtie. The plasmonic properties further depend on the material used for the nano-bowtie and the substrate, the angle of incident light, as well as the configuration of the nano-bowtie relative to the incident light. In this work, we used Finite Difference Time Domain (FDTD) modelling to provide an extensive analysis of the effect of asymmetry in terms of the flared angle and the length of the nano-bowtie on the electromagnetic behaviour of the proposed nanostructures. We also show the effect of angle of incident light on the LSPR wavelength for the proposed nanostructure. Moreover, a comparison between the electromagnetic behaviour for the periodic and aperiodic configurations of the proposed asymmetric plasmonic bowtie nanostructures is also carried out.

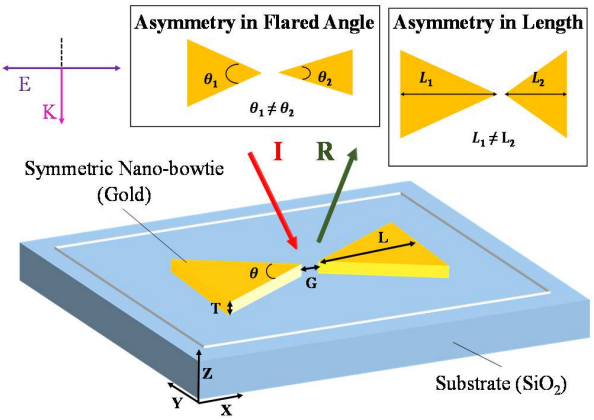


Fig. 1. Schematic of plasmonic bowtie nanostructure on glass substrate with length 'L', height 'T', flared angle 'θ', and gap 'G'. Inset 1 shows the asymmetry in the flared angle when the flared angles of the two triangles of the nano-bowtie are not same, i.e., $\theta_1 \neq \theta_2$. Inset 2 shows the asymmetry in length when the lengths of the two triangles of the nano-bowtie are not same, i.e., $L_1 \neq L_2$. The red arrow marks the incident light and the green arrow marks the reflected light. The electric-field vector and propagation constant for the incident light are denoted by 'E' and 'K', respectively.

TABLE I. Comparison Of This Work With Previous Works

Ref. No.	Description of nanostructure	Tunable LSPR range
Huang et al., 2019 [23]	Core-shell spiky nanoparticles	150 nm (650 nm to 800 nm)
Wang et al., 2019 [24]	Waveguide with two rectangular cavities	176 nm (585 nm to 761 nm)
Liu et al., 2020 [25]	Nanospheres / nanoshells / nanoflowers / nanostars	142 nm (551 nm to 693 nm)
Yamada et al., 2022 [26]	Nanoholes with edge structure	279 nm (785 nm to 1064 nm)
This work	Asymmetric plasmonic bowtie nanostructure	205 nm (730 nm to 935 nm)

978-1-6654-9099-3/23/$31.00 ©2023 IEEE

Authorized licensed use limited to: DELHI TECHNICAL UNIV. Downloaded on May 15,2023 at 09:57:22 UTC from IEEE Xplore. Restrictions apply.

II. Numerical Methods

We used 3D FDTD modelling to execute the numerical simulations with the help of a commercial Lumerical Inc. FDTD Solver software. A total field scatter field (TFSF) source for aperiodic simulations and a plane wave source for periodic simulations were employed to illuminate the nanostructures. The source with an incident electric field of 1 V/m was taken to be linearly polarized in the X-direction as shown by the electric-field vector (E) in Fig. 1. The light was incident from Z-direction as shown in Fig. 1. After carefully doing the convergence tests, a uniform mesh size of 1 nm was chosen over all the three directions. For aperiodic simulations, perfectly matched layer (PML) boundaries were employed in every directions of the nanostructure. For periodic simulations, periodic boundaries were employed in the X and Y directions and PML boundaries were employed in the Z direction. The materials for the bowtie nanostructures and the substrate were chosen as gold (Au) and silicon dioxide (SiO_2), respectively. The dielectric constants of both these materials were taken in accordance with the Lorentz-Drude model [27].

III. Results And Discussion

The asymmetric plasmonic bowtie nanostructures consisting of gold triangular nano-bowties on silica substrate are numerically simulated using 3D-FDTD method. The excitation of localized surface plasmons takes place when the linearly polarized light falls at the asymmetric plasmonic bowtie nanostructures. These localized surface plasmons get coupled to the surface plasmons travelling along the interface between the gold nano-bowtie and the silica substrate. The coupling leads to the development of highly confined EM hotspots at the centre of the plasmonic nano-bowtie. The thickness (T) of the asymmetric plasmonic bowtie nanostructures is considered as 50 nm. The gap (G) in between the two triangles of the nano-bowtie is kept constant as 5 nm. The vertices of the nano-bowtie are designed with a 2 nm rounding radius in order to assure fabrication feasibility of the proposed nanostructures. The parameters like the flared angle and the length of the nano-bowtie are being varied because at the time of fabrication all these parameters are very important. For example, making nano-bowties with small flared angle is very difficult using conventional lithography processes but flared angles which are larger can be easily fabricated. Further, the effect of aperiodic and periodic configuration is shown so that a comparison can be done between an array form of the nanostructure and a non-array form of the nanostructure. Moreover, the effect of angle of incident light is also shown to justify the fact that the asymmetric plasmonic bowtie nanostructure is not only limited to angled incidence as in conventional LSPR setups but can also be employed with normal incidence without the need of having a prism coupling or a Kretschmann configuration integrated with it. Hence, it is a free-standing nanostructure which can also be operated at normal as well as oblique angle of incident light.

A. Effect of periodic and aperiodic configurations

The effect of the periodic and aperiodic configurations on the electromagnetic enhancement for symmetric bowties (SBT) with flared angles $\theta_1 = \theta_2 = 30$ degree, SBT with flared angles $\theta_1 = \theta_2 = 60$ degree and asymmetric bowties (ASBT) with flared angles $\theta_1 = 60$ degree and $\theta_2 = 30$ degree is shown in Fig. 2. It can be seen from Fig. 2(a) that for aperiodic configuration there are two minor LSPR peaks at 620 nm and720 nm wavelengths and one major LSPR peak with high E - field enhancement at 895 nm wavelength for SBT with 30 degree flared angle. For SBT with 60 degree flared angle, the E-field enhancement is reduced resulting in one minor LSPR peak at 650 nm wavelength and one major LSPR peak at 840 nm wavelength. However, for ASBT with 60 degree and 30 degree flared angles, there is a high E-field enhancement at LSPR peak of 870 nm wavelength. From Fig. 2(b) it can be observed that the E-field enhancement for periodic configuration decreases significantly in comparison to the aperiodic configuration shown in Fig. 2(a). The periodicity (p), i.e., the distance between the two subsequent plasmonic nano-bowties, is take as 30 nm. Further, maximum E-field enhancement for SBT with 30 degree flared angle is achieved at 900 nm. This LSPR peak is slightly blue-shifted to 830 nm wavelength for SBT with 60 degree flared angle. However, highest E-field enhancement is achieved in the case of ASBT with 60 degree and 30 degree flared angles in comparison to the SBTs. The major LSPR peak is achieved at 865 nm wavelength for the ASBT nanostructure.

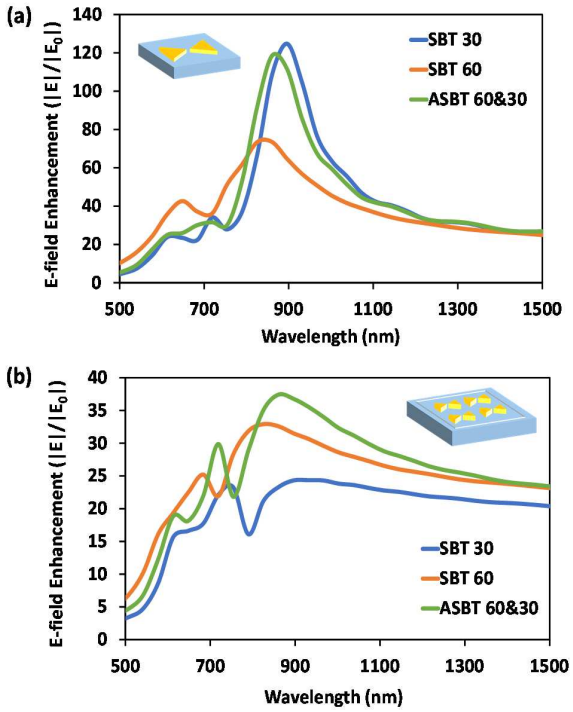


Fig. 2. Effect of (a) aperiodic and (b) periodic configurations on the electromagnetic enhancement for symmetric bowties (SBT) with flared angles $\theta_1 = \theta_2 = 30$ degree, SBT with flared angles $\theta_1 = \theta_2 = 60$ degree and asymmetric bowties (ASBT) with flared angles $\theta_1 = 60$ degree and $\theta_2 = 30$ degree. The length (L) of the nano-bowties is 100 nm. The periodicity (p) for the periodic configuration is 30 nm.

B. Effect of flared angle asymmetricity

The effect on the electromagnetic enhancement for asymmetry in the flared angle of the asymmetric plasmonic bowtie nanostructures with different ratios is shown in Fig. 3. For this analysis, the length and the height of the nano-bowtie are taken as 100 nm and 50 nm, respectively. The flared angle of one of the triangles of the nano-bowtie is considered constant as 60 degree and the flared angle of the other triangle of the nano-bowtie is reduced in steps of 15 degree. It can be observed from Fig. 3 that the E-field enhancement for SBT nanostructure (i.e., ratio of 1:1 where both the flared angles are 60 degree) is comparatively less than the ASBT nanostructures with different flared angles. The LSPR peak achieved for SBT nanostructure with ratio of 1:1 is at 840 nm.

Authorized licensed use limited to: DELHI TECHNICAL UNIV. Downloaded on May 15,2023 at 09:57:22 UTC from IEEE Xplore. Restrictions apply.

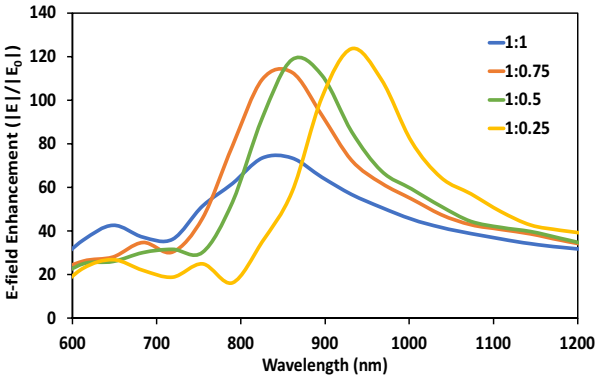


Fig. 3. Effect on the electromagnetic enhancement for asymmetricity with different ratios of the flared angle of the asymmetric plasmonic bowtie nanostructures. The length (L) of the nano-bowties is 100 nm. The ratio 1:1 is for the symmetric flared angles of $\theta_1 = \theta_2 = 60$ degree. The ratio 1:0.75 is for the asymmetric flared angles of $\theta_1 = 60$ degree and $\theta_2 = 45$ degree. The ratio 1:0.5 is for the asymmetric flared angles of $\theta_1 = 60$ degree and $\theta_2 = 30$ degree. The ratio 1:0.25 is for the asymmetric flared angles of $\theta_1 = 60$ degree and $\theta_2 = 15$ degree.

The LSPR peak achieved for ASBT nanostructure with ratio 1:0.75 and flared angles of $\theta_1 = 60$ degree and $\theta_2 = 45$ degree is at 845 nm. The LSPR peak achieved for ASBT nanostructure with ratio 1:0.5 and flared angles of $\theta_1 = 60$ degree and $\theta_2 = 30$ degree is at 870 nm. The LSPR peak achieved for ASBT nanostructure with ratio 1:0.25 and flared angles of $\theta_1 = 60$ degree and $\theta_2 = 15$ degree is at 935 nm. Hence, it can be concluded that there is a constant red-shift of LSPR wavelength as the asymmetricity in the flared angles is increased.

C. Effect of length asymmetricity

The effect on the electromagnetic enhancement for asymmetricity in the length of the asymmetric plasmonic bowtie nanostructures with different ratios is shown in Fig. 4. For this analysis, the height and the flared angle of the nano-bowtie are taken as 50 nm and 60 degree, respectively. The length of one of the triangles of the nano-bowtie is fixed as 100 nm and the length of the other triangle of the nano-bowtie is reduced in steps of 25 nm. It can be seen from Fig. 4 that the E-field enhancement for SBT nanostructure (i.e., ratio of 1:1 where both the lengths are 100 nm) is comparatively more than the ASBT nanostructures with different flared angles. The LSPR peak achieved for SBT nanostructure with ratio 1:1 is at 840 nm. The LSPR peak achieved for ASBT nanostructure with ratio 1:0.75 and lengths of $L_1 = 100$ nm and $L_2 = 75$ nm is at 800 nm. The LSPR peak achieved for ASBT nanostructure with ratio 1:0.5 and lengths of $L_1 = 100$ nm and $L_2 = 50$ nm is at 770 nm. The LSPR peak achieved for ASBT nanostructure with ratio 1:0.25 and lengths of $L_1 = 100$ nm and $L_2 = 25$ nm is at 730 nm. Hence, it can be concluded that there is a constant blue-shift of LSPR wavelength as the asymmetricity in the lengths is increased.

D. Effect of angle of incident light

The effect of the angle of incident light on the asymmetric plasmonic bowtie nanostructures is shown in Fig. 5. The E-field enhancement for ASBT nanostructure with the flared angles of $\theta_1 = 60$ degree and $\theta_2 = 30$ degree is shown in Fig. 5(a) for 0 degree and 30 degree angle of incident light with respect to the propagation constant vector (K). It can be seen from Fig. 5(a) that the LSPR peaks for the both the angles of incident light are at the same wavelengths. The comparison of E-field enhancement for SBT nanostructures and ASBT nanostructure under 30 degree angle of incident light is shown in Fig. 5(b). It can be seen that the angle of incident light has very minute effect on the plasmonic nanostructures. Thus, the proposed plasmonic nanostructures can be employed for normal as well as oblique angle of incident light.

Tunable LSPR refers to shift in the LSPR peaks from one plasmon resonance wavelength to another plasmon resonance wavelength. The shifting of LSPR peaks or tunability of LSPR offers a vast range of wavelengths over which electromagnetic enhancement in the sub - 10 nm gap (i.e., the gap between the

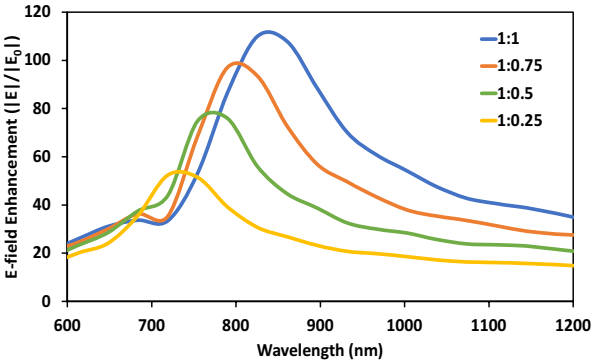


Fig. 4. Effect on the electromagnetic enhancement for asymmetricity with different ratios of the length of the asymmetric plasmonic bowtie nanostructures. The flared angle (θ) of the nano-bowties is 60 degree. The ratio 1:1 is for the symmetric lengths of $L_1 = L_2 = 100$ nm. The ratio 1:0.75 is for the asymmetric lengths of $L_1 = 100$ nm and $L_2 = 75$ nm. The ratio 1:0.5 is for the asymmetric lengths of $L_1 = 100$ nm and $L_2 = 50$ nm. The ratio 1:0.25 is for the asymmetric lengths of $L_1 = 100$ nm and $L_2 = 25$ nm.

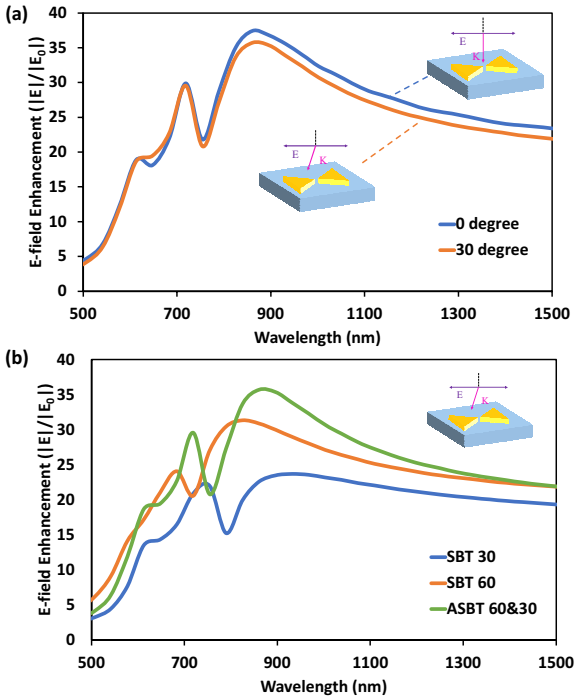


Fig. 5. (a) Effect of angle of incident light on electromagnetic enhancement of the asymmetric plasmonic bowtie nanostructures with flared angles $\theta_1 = 60$ degree and $\theta_2 = 30$ degree. (b) Electromagnetic enhancement achieved with 30 degree of incidence angle for SBT with flared angles $\theta_1 = \theta_2 = 30$ degree, SBT with flared angles $\theta_1 = \theta_2 = 60$ degree and ASBT with flared angles $\theta_1 = 60$ degree and $\theta_2 = 30$ degree. The length (L) of the asymmetric plasmonic bowtie nanostructures in all the above cases is 100 nm. The periodicity (p) is 30 nm.

Authorized licensed use limited to: DELHI TECHNICAL UNIV. Downloaded on May 15,2023 at 09:57:22 UTC from IEEE Xplore. Restrictions apply.

two triangles of the nano-bowtie) can be achieved. This enhancement in EM field can be exploited to detect traces of analytes even up to picomolar concentration. The tunability of LSPR can be clearly seen from Figs. 3 and 4, where asymmetry is introduced in terms of the flared angle and the length of the nano-bowtie, respectively. As it can be seen that when asymmetricity in the flared angle is increased from 1:1 to 1:0.75 to 1:0.5 to 1:0.25, the plasmon resonance wavelength changes from 840 nm to 845 nm to 870 nm to 935 nm. Further, when asymmetricity in the length is increased from 1:1 to 1:0.75 to 1:0.5 to 1:0.25, the plasmon resonance wavelength changes from 840 nm to 800 nm to 770 nm to 730 nm. Hence, the 840 nm plasmon resonance wavelength can be tuned across 730 nm to 935 nm, leading to tunable LSPR range of 205 nm for the proposed nanostructures.

IV. Conclusions

We hereby summarize that the asymmetric plasmonic bowtie nanostructures consisting of gold triangular nano-bowties on silicon dioxide substrate demonstrate tunability of the LSPR wavelength over the visible and near infrared spectral range. The E-field enhancement in these plasmonic nanostructures strongly depends on the geometrical parameters of the nano-bowtie like the length of the nano-bowtie and the flared angle of the nano-bowtie. Hence, the values of such significant parameters must be chosen properly to achieve desired operational wavelength range for the application of these plasmonic nanostructures.

References

[1] S. A. Maier, Plasmonics: Fundamentals and applications, Springer, New York, USA, 2007. ISBN: 9780387331508. DOI: https://doi.org/10.1007/0-387-37825-1

[2] A. Maradudin, J. R. Sambles, and W. L. Barnes, Modern plasmonics, Elsevier Science, 2014. ISBN: 9780444595263.

[3] E. Ozbay, "Plasmonics: Merging photonics and electronics at nanoscale dimensions", Science, vol. 311, no. 5758, pp. 189-193, 2006. DOI: https://doi.org/10.1126/science.1114849

[4] J. A. Schuller, E. S. Barnard, W. Cai, Y. C. Jun, J. S. White, and M. L. Brongersma, "Plasmonics for extreme light concentration and manipulation", Nature Materials, vol. 9, no. 3, pp. 193-204, 2010. DOI: https://doi.org/10.1038/nmat2630

[5] J. M. Pitarke, V. M. Silkin, E. V. Chulkov, and P. M. Echenique, "Theory of surface plasmons and surface-plasmon polaritons" Reports on Progress in Physics, vol. 70, no. 1, 2006. DOI: https://doi.org/10.1088/0034-4885/70/1/R01

[6] E. Hutter and J. H. Fendler, "Exploitation of localized surface plasmon resonance", Advanced Materials, vol. 16, no. 19, pp. 1685-1706, 2004. DOI: https://doi.org/10.1002/adma.200400271

[7] V. G. Achanta, "Surface waves at metal-dielectric interfaces: Material science perspective", Reviews in Physics, vol. 5, pp. 100041, 2020. DOI: https://doi.org/10.1016/j.revip.2020.100041

[8] S. Lv, Y. Du, F. Wu, Y. Cai, and T. Zhou, "Review on LSPR assisted photocatalysis: effects of physical fields and opportunities in multifield decoupling", Nanoscale Advances, vol. 4, pp. 2608-2631, 2022. DOI: https://doi.org/10.1039/D2NA00140C

[9] X. Gong, J. Tang, Y. Ji, B. Wu, H. Wu, and A. Liu, "Adjustable plasmonic optical properties of hollow gold nanospheres monolayers and LSPR-dependent surface-enhanced Raman scattering of hollow gold nanosphere/graphene oxide hybrids", RSC Advances, vol. 5, pp. 42653-42662, 2015. DOI: https://doi.org/10.1039/C5RA08057F

[10] C. D. Chen, S. F. Cheng, L. K. Chau, and C. R. C. Wang, "Sensing capability of the localized surface plasmon resonance of gold nanorods", Biosensors and Bioelectronics, vol. 22, no. 6, pp. 926-32, 2007. DOI: https://doi.org/10.1016/j.bios.2006.03.021

[11] K. Dalal and Y. Sharma, "Broadband plasmonic switches based on nanodisc-dimers with progressively increasing diameters on a plasmonic film with a VO_2 spacer", Optics Communications, vol. 530, pp. 129121, 2023. DOI: https://doi.org/10.1016/j.optcom.2022.129121

[12] L. Zhang, J. Zhang, F. Wang, J. Shen, Y. Zhang, L. Wu, X. Lu, L. Wang, Q. Fan, and W. Huang, "An Au@Ag nanocube based plasmonic nano-sensor for rapid detection of sulfide ions with high sensitivity", RSC Advances, vol. 8, pp. 5792-5796, 2018. DOI: DOI https://doi.org/10.1039/C7RA12779K

[13] M. M. Abbasi, S. Darbari, and M. K. Moravvej-Farshi, "Tunable plasmonic force switch based on graphene nano-ring resonator for nanomanipulation", Optics Express, vol. 27, no. 19, pp. 26648-26660, 2019. DOI: https://doi.org/10.1364/OE.27.026648

[14] M. Vala, C. T. Ertsgaard, N. J. Wittenberg, and S. H. Oh, "Plasmonic sensing on symmetric nanohole arrays supporting high-Q hybrid modes and reflection geometry", ACS Sensors, vol. 4, no. 12, pp. 3265-3274, 2019. DOI: https://doi.org/10.1021/acssensors.9b01780

[15] S. Murai, M. Saito, Y. Kawachiya, S. Ishii, T. Nakanishi, and K. Tanaka, "Temperature sensing of a plasmonic nanocylinder array by a polymer film containing chameleon complex", Journal of the Optical Society of America B, vol. 36, no. 7, pp. E15-E20, 2019. DOI: https://doi.org/10.1364/JOSAB.36.000E15

[16] M. A. Butt, N. L. Kazanskiy, and S. N. Khonina, "Highly sensitive refractive index sensor based on plasmonic bow tie configuration", Photonic Sensors, vol. 10, pp. 223-232, 2020. DOI: https://doi.org/10.1007/s13320-020-0588-z

[17] B. Wang, S. C. Singh, H. Lu, and C. Guo, "Design of aluminum bowtie nanoantenna array with geometrical control to tune LSPR from UV to Near-IR for optical sensing", Plasmonics, vol. 15, pp. 609-621, 2019. DOI: https://doi.org/10.1007/s11468-019-01071-z

[18] A. Das, K. Kumar, and A. Dhawan, "Periodic arrays of plasmonic crossed-bowtie nanostructures interspaced with plasmonic nanocrosses for highly sensitive LSPR based chemical and biological sensing", RSC Advances, vol. 11, pp. 8096-8106, 2021. DOI: https://doi.org/10.1039/D0RA09012C

[19] K. Dalal and Y. Sharma, "Tunable plasmon resonance in asymmetric plasmonic cross-bowtie nanostructures", 2022 IEEE International Conference on Nanoelectronics, Nanophotonics, Nanomaterials, Nanobioscience & Nanotechnology (5NANO), pp. 1-3, 2022. DOI: https://doi.org/10.1109/5NANO53044.2022.9828941

[20] V. P. Pena, R. A. Alves, and M. N. Cia, "From symmetric to asymmetric bowtie nanoantennas: electrostatic conformal mapping perspective", Nanophotonics, vol. 9, no. 5, pp. 1177-1187, 2020. DOI: https://doi.org/10.1515/nanoph-2019-0488

[21] W. Wei, X. Yan, B. Shen, and X. Zhang, "Plasmon-induced tansparency in an asymmetric bowtie structure", Nanoscale Research Letters, vol. 14, pp. 246, 2019. DOI: https://doi.org/10.1186/s11671-019-3081-0

[22] Y. Y. Yang, Y. L. Zhang, F. Jin, X. Z. Dong, X. M. Duan, Z. S. Zhao, "Steering the optical response with asymmetric bowtie 2-color controllers in the visible and near infrared range", Optics Communications, vol. 284, no. 13, pp. 3474-3478, 2011. DOI: https://doi.org/10.1016/j.optcom.2011.03.043

[23] Z. Huang, G. Meng, X. Hu, Q. Pan, D. Huo, H. Zhou, Y. Ke, and N. Wu, "Plasmon-tunable Au@Ag core-shell spiky nanoparticles for surface-enhanced Raman scattering", Nano Research, vol. 12, pp. 449-455, 2019. DOI: https://doi.org/10.1007/s12274-018-2238-y

[24] Q. Wang, Z. Ouyang, Y. Sun, M. Lin, and Q. Liu, "Linearly tunable fano resonance modes in a plasmonic nanostructure with a waveguide loaded with two rectangular cavities coupled by a circular cavity", Nanomaterials, vol. 9, no. 5, pp. 678, 2019. DOI: https://doi.org/10.3390/nano9050678

[25] Y. Liu, N. Lyu, V. K. Rajendran, J. Piper, A. Rodger, and Y. Wang, "Sensitive and direct DNA mutation detection by surface-enhanced raman spectroscopy using rational designed and tunable plasmonic nanostructures", Analytical Chemistry, vol. 92, no. 8, pp. 5708-5716, 2020. DOI: https://doi.org/10.1021/acs.analchem.9b04183

[26] H. Yamada, D. Kawasaki, K. Sueyoshi, H. Hisamoto, and T. Endo, "Wavelength-tunable dual-band edge plasmon mode based on gold edge-hole plasmonic nanostructure", Results in Physics, vol. 37, pp. 105541, 2022. DOI: https://doi.org/10.1016/j.rinp.2022.105541

[27] Y. Sharma and A. Dhawan, "Active near-field plasmonic switches based on Sierpinski-fractal nanoantennas on VO_2 films", Journal of Optics, vol. 24, no. 6, pp. 065001, 2022. DOI: https://doi.org/10.1088/2040-8986/ac6208

Authorized licensed use limited to: DELHI TECHNICAL UNIV. Downloaded on May 15,2023 at 09:57:22 UTC from IEEE Xplore. Restrictions apply.

2023 6th International Conference on Information Systems and Computer Networks (ISCON)
GLA University, Mathura, India. Mar 3-4, 2023

Underwater Image Enhancement using Convolutional Block Attention Module

Nishant Singh
Computer Science and Engineering Department
Delhi Technological University
Delhi, India
singhnishant88@gmail.com

Aruna Bhat
Computer Science and Engineering Department
Delhi Technological University
Delhi, India
arunabhat@dtu.ac.in

2023 6th International Conference on Information Systems and Computer Networks (ISCON) | 979-8-3503-4696-1/23/$31.00 ©2023 IEEE | DOI: 10.1109/ISCON57294.2023.10111974

***Abstract*— Underwater images include poor contrast, fuzzy features, and colour distortion due to light scattering, refraction and absorption by unwanted dust particles in water. This research demonstrates that assigning the appropriate receptive field size context depending on the traversal scope of the color channel can result in a significant performance boost for the objective of underwater image enhancement. It's critical to reduce non-uniform multiple contextual elements, and also boost the model's representational potential. So to dynamically modify the learnt multi-contextual characteristics, we included an attentive skip method. The suggested framework is improved via pixel wise and feature based cost functions. Experiments and comparisons with existing deep learning models and conventional approaches validate the framework for underwater image enhancement. The proposed framework is superior according to comparison results.**

Keywords—Image processing; deep learning; Underwater Image Enhancement; Convolution Block Attention Module (CBAM;, Underwater Image Enhancement Benchmark (UIEB)

I. INTRODUCTION

The ocean is rich in numerous resources. Humans, however, have not adequately investigated and used it, particularly in the undersea environment. Underwater image processing is critical in underwater tasks performed by humans or underwater robots, such as underwater archaeology, device protection, environmental monitoring, item recognition, and search and retrieve. Underwater optical images have inferior quality due to suspended particles and light attenuation in water, with drawbacks such as color distortion, poor contrast and hazy features. Also the capturing mechanism of images in underwater is far varying from the normal environment due to the differences in the medium and the capturing mechanism. As a result, in order to gain additional underwater information, the deteriorated underwater photos must be enhanced and restored.

Classic strategies for improving underwater images contain equalization of histogram, transformation of wavelet, and the Retinex algorithm [1]. Whereas, each of these models has its own disadvantages. For example, Histogram equalization may result in image detail loss and in excess of enhancement. The wavelet transform's efficacy in analyzing images taken in shallow seas is restricted. In the event of a substantial brightness difference, the halo effect must be handled with the Retinex algorithm. For example, in [2], two or three of these augmentation strategies are used to eliminate such drawbacks.

An image based system is required to restore underwater images. Chiang and Chen [3] suggest a representational system. The essential to applying this module is estimating the transmission map as well as the overall light conditions. Many scholars have been working on the estimate of these parameters in recent years. In general, there are two sorts of studies: one is the priori driven techniques and other one is the data driven approaches.

Prior driven techniques to image enhancement take out the transmission map and the ambient light surroundings using a variety of priors or expectation. The Dark Channel Prior (DCP) approach [4] is a common method. However, because red light absorbs so fast in the underwater environment, the DCP rules are frequently broken, producing in an imbalance across the three channels. Drews et al. [5] presented an Underwater Dark Channel Prior (UDCP) technique to alter the DCP method, which only employs the blue and green channels to compute the dark channel.

Galdran et al. [6] developed the Red Channel Prior (RCP), which generates a reliable transmission diagram based on the link between red channel attenuation and the DCP. However, because of the loss in dependability, such improvements only yield a slight gain in the precision of transmission map estimate. Carlevaris-Bianco et al. [7] suggested a novel prior that calculates the depth of the scene using attenuation difference based on the observation that the red channel attenuates more quickly than the green and blue channels.

However, because these priors rely on color information, the transmission of elements with green or blue hue is underestimated. However, if the ambient lighting is significantly brighter than the image, such a technique can fail because the majority of the pixels will reflect to the same location, making distinguishing the haze lines impossible.

Deep learning, a data-driven strategy, is becoming increasingly prominent in digital image processing. Deep learning based approaches focus on understanding the correlation between images that allows the method to keep away from estimation mistakes caused by erroneous priors. Convolutional Neural Network (CNN) is a characteristic deep learning technology that has been widely applied to underwater image processing. Initial applications, such as [8], are mostly focused on estimating transmission in images. These CNN-based algorithms are trained using a synthetic data set to attenuate transmission and provide more refined recovered images than traditional approaches. Further applications, such as [9], address both transmission and ambient light. However, because these approaches are based on the premise that three channels have the similar transmission, they only partially address the issue of

Authorized licensed use limited to: DELHI TECHNICAL UNIV. Downloaded on May 11,2023 at 10:12:55 UTC from IEEE Xplore. Restrictions apply.

dispersion. Although image contrast has been enhanced, color divergence cannot be addressed effectively.

Wang et al. [10] first estimated the blue channel using the T-network and A-network, and then calculated the red and green channels using the connection between the channels to recover underwater images. It is well understood that the success of data-driven approaches is heavily dependent on the integrity of training data. Underwater images for training are often created by synthesis, either without color variation (e.g., [8]) or with color variation (e.g., [9]). However, because of the complexity of the underwater atmosphere, the color variation of underwater images comprises diverse blue or green tones. Li et al. [11] employed Generative Adversarial Networks (GAN) to generate underwater damaged images to increase the quality of the synthetic data set. While comparing to genuine underwater images, the recovered underwater images are not as real.

The remaining sections of the paper are described as follows: Section II displays the methods used in the proposed technique and the dataset; Section III gives the image processing results and related discussion; and Section IV is the conclusion.

II. PROPOSED WORK

A. *Proposed Algorithm*

Convolutional Block Attention Module (CBAM) is a basic however successful attention module for feed forward convolutional neural networks (CNN). Provided an intermediary feature map, the module dedus attention maps into two distinct domains, channel attention module and spatial attention module, and after that multiplies the attention maps by the input feature map for dynamic feature refinement. Since Convolutional block attention module is a compact as well as a generalized method, it can even be smoothly incorporated into any Convolution layer with low overheads and is trainable end-to-end alongside base CNNs.

Before delving into the specifics of CBAM, let's first examine the module's overall structure as shown in Fig. 1. CBAM is designed by two consecutive sub modules; one is the Channel Attention Module (CAM) and second is the Spatial Attention Module (SAM) that is used in that sequence. According to the research, CBAM is used at each convolutional layer in dense networks to generate consecutive "Refined Feature Maps" out from "Input Intermediate Feature Maps."

SAM and CAM are perhaps the most commonly used in Computer Vision, particularly when discussing convolutional layers. The input to any convolutional layer is a tensor, and the output is also a tensor. This tensor is defined by three dimensions: first is the height represented by h within each feature map, second is the width represented by w within each feature map, and third is for overall number of channels, tensor depth or feature maps represented by c. This is why the measurements of the input are commonly denoted as (c h w). The extracted features are basically the piece of a cube-shaped tensor, layered together. The overall count of convolution filters employed in that layer determines the c dimension value.

The domain space enclosed by each feature map is referred to as spatial. On the feature map, spatial attention indicates the attention mechanism/attention mask, or a single cross-sectional segment of the tensor. For example, as shown in Fig. 2 below, the item of focus is a bird; therefore Spatial Attention will build a mask that enhances the characteristics that distinguish that bird. By improving these channels with the help of Spatial Attention, we increase the contribution to the succeeding convolutional layers, which improves the model's performance.

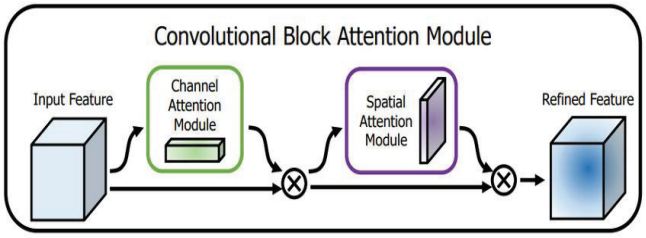


Fig. 1. Layout of Convolutional Block Attention Module

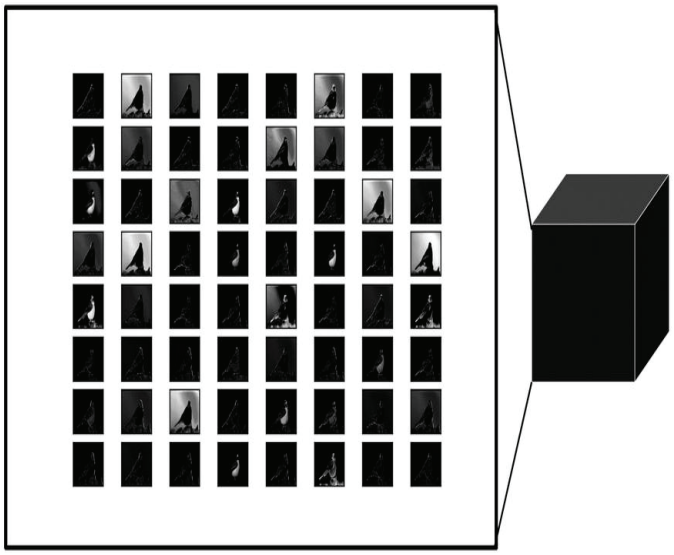


Fig. 2. Feature Maps representation as a Tensor

As previously stated, channels are effectively feature maps layered in a tensor, with each cross sectional segment being a feature map with the dimension of (h x w). Typically, the trainable weights that comprise the filters in convolutional layers learn relatively tiny values (zero), resulting in comparable feature maps, with many seeming to be clones of one another. Despite their identical appearance, these filters are incredibly beneficial in understanding distinct sorts of characteristics.

While some are designed to teach horizontal and vertical edges, whereas some are more generic and teach a specific texture in an image. The channel attention simply offers a weight for every channel, improving those specific channels that support the most to knowledge and then improves overall system execution.

Fig. 3 represents our proposed work which has been divided into four major parts. In first part we are taking the input corrupted underwater image than separated channel wise and find out the multiple contextual features. We obtain the multiple contextual features with the help of parametric ReLU layers and batch normalization. In second part the input is the multiple contextual features and then we find the output in the form of color specific distortion residuals.

Authorized licensed use limited to: DELHI TECHNICAL UNIV. Downloaded on May 11,2023 at 10:12:55 UTC from IEEE Xplore. Restrictions apply.

These color specific distortion residuals are further adaptively developed by using Convolution Block Attenuation Module (CBAM). In third part the input is the color specific distortion residual and the output is the overall color correction residuals. In fourth part we are taking overall color correction as an input and generate the improved underwater image as an output. This improved underwater image is obtained by applying reconstruction module with the help of de-convolution layer after that attentive residual block and in last by again de-convolution layer.

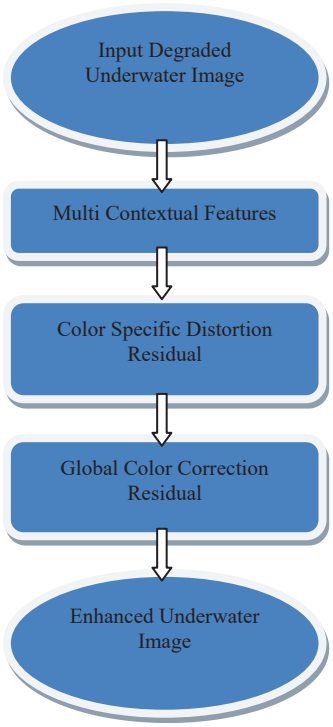


Fig. 3. Flow Chart of Proposed Work

B. *Datasets*

We used the freely accessible underwater image enhancement benchmark dataset (UIEB) [12]. We used this datasets for the enhancement problem, which contain the pair underwater images of size 256 * 256. The testing dataset is composed of 510 similar pairs of images. The UIEB dataset includes 890 related images. Following [12], an arbitrary selection of 800 images is chosen as to train the dataset, while the remaining 90 images are used as the testing dataset. Given the memory restriction, we downsized the training images to 512 * 512. We also used the UIEB Challenge dataset, which comprises of 50 deteriorated images with no ground truth references.

III. Result Comparison

To provide a more comprehensive evaluation of the proposed approach, non reference image quality and reference image quality measurements have been included.

We are providing both the quantitative and qualitative result analysis. Quantitative results have been presented in Table I and Table II. Table I indicates that the suggested model beat the already proposed research works on practically all image quality measures used.

While in MSE, PSNR, SSIM & UISM the suggested approach improved by 14.7%, 5.68%, 3.75%, and 0.71%, respectively. In the instance of underwater image improvement, the suggested model has likewise obtained dominance on 5 out of 7 image quality measures.

TABLE I. RESULTS EVALUATION ON UIEB DATASETS

Methods	PSNR	SSIM	MSE	UIQM	UISM	UIConM	UCIQE
GAN	24.44	0.78	0.38	2.85	6.82	0.77	0.58
UGAN-P	24.41	0.78	0.38	2.91	6.81	0.77	0.59
Funie-GAN	24.22	0.77	0.39	2.95	6.88	0.82	0.59
Funie-GAN-UP	23.65	0.75	0.62	2.92	6.84	0.77	0.58
SESR	25.65	0.78	0.36	3.07	7.05	0.76	0.57
Our Method	26.63	0.81	0.31	3.02	7.05	0.75	0.56

TABLE II. RESULTS EVALUATION ON UIEB CHALLENGE TEST SET

Methods	PSNR	SSIM	MSE	UIQM
GAN	15.85	0.55	1.72	1.27
GAN-P	17.88	0.62	1.35	1.15
Funie-GAN	15.31	0.58	1.91	1.11
Funie-GAN-UP	15.85	0.55	1.75	0.92
SESR	19.11	0.78	0.79	0.98
Our Method	20.35	0.81	0.62	2.11

In Fig. 4, we also show a comprehensive analysis of the current work to existing approaches. Fig. 4 shows that the previous approaches GAN and GAN-P suffer from color under and over-saturation in improved images. While Funie-GAN and Funie-GAN-UP approaches recover damaged images very slightly, the suggested method produces very good visually appealing improved underwater images.

In this we also displayed the qualitative findings from the Challenge test set of UIEB dataset. It is clear that the suggested works improved outcomes more effectively preserve the water's bluish hue than the present ones do as shown in Fig. 5.

Table II represents the quantitative outcome of the Challenge set. It is clear that our suggested approach has significantly improved upon the evaluation of the most underwater image enhancement models. It could be due to adaptive utilization in residual learning and wavelength-specific receptive field widths of the kernels allocated to each color channel.

IV. Conclusion

This paper suggested a revolutionary underwater image enhancing deep learning based approach. We demonstrated how a multi contextual formulation of this kind supports in the knowledge of the many global and local exposure of every channel of the underwater images. Additionally, the suggested

technique performs noticeably better by using a block attention mechanism that adaptively refines the learnt features. We have demonstrated the superiority of the suggested method over the best-published studies currently in use across several benchmark datasets.

Authorized licensed use limited to: DELHI TECHNICAL UNIV. Downloaded on May 11,2023 at 10:12:55 UTC from IEEE Xplore. Restrictions apply.

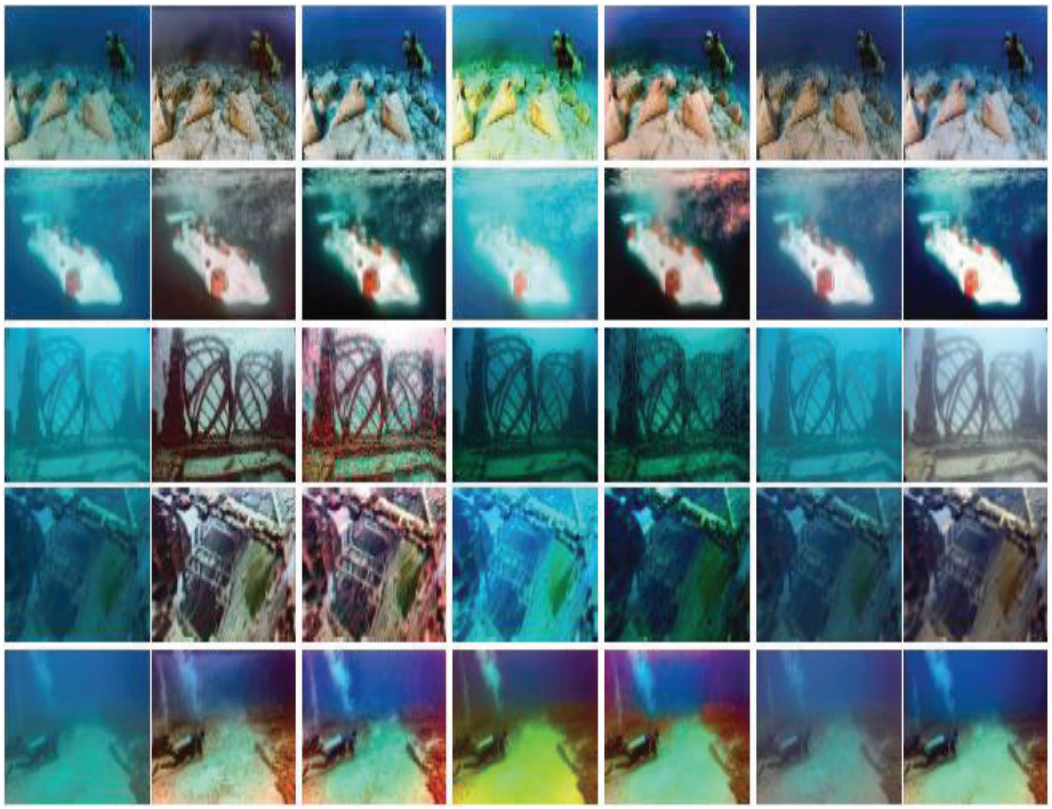


Fig. 4. Quality Comparison on UIEB Dataset of Underwater Image Enhancement



Fig. 5. Quality Comparison on UIEB Challenge test set of Underwater Image Enhancement

REFERENCES

[1] A. Bindhu and O. U. Maheswari, "Color corrected single scale retinex based haze removal and color correction for underwater images," Color Research and Application, vol. 45, pp. 1084-1903, 2020.

[2] A.S.A Ghani, "Image contrast enhancement using an integration of recursive-overlapped contrast limited adaptive histogram specification and dual-image wavelet fusion for the high visibility of deep underwater image," Ocean Engginering, pp, 224–238, 2018.

[3] J. Y. Chiang and Y. C. Chen, "Underwater Image Enhancement by Wavelength Compensation and Dehazing," IEEE Transaction Image Process, vol. 21, pp. 1756–1769, 2012.

[4] K. He, J. Sun and X. Tang, "Single image haze removal using dark channel prior," IEEE Transactions on Pattern Analysis and Machine Intelligence, vol. 33, pp. 2341–2353, 2011.

[5] P. L. Drews, E. R. Nascimento, S. S. C. Botelho and M. F. M. Campos, "Underwater Depth Estimation and Image Restoration Based on Single Images," IEEE Computer Graphics and Application, vol. 36, pp. 24–35, 2016.

[6] A. Galdran, D. Pardo, A. Picón and A. Gila, "Automatic Red-Channel underwater image restoration," Journal of Vision Communication and Image Representation, vol. 26, pp. 132–145, 2015.

[7] N. Carlevaris-Bianco, A. Mohan and R. M. Eustice, "Initial results in underwater single image dehazing," In Proceedings of the IEEE Conference on OCEANS, vol. 27, 2010, pp. 1–8.

[8] W. Ren, S. Liu, H. Zhang, J. Pan, X. Cao and M. H. Yang, "Single Image Dehazing via Multiscale Convolutional Neural Networks," In European Conference on Computer Vision, 2016, pp. 154–169.

[9] Y. S. Shin, Y. G. Cho, G. Pandey and A. Kim, "Estimation of ambient light and transmission map with common convolutional architecture," In Proceedings of the IEEE Conference on OCEANS, 2016, pp. 1–7.

[10] K. Wang, Y. Hu, J. Chen, X. Wu, X. Zhao and Y. Li, "Underwater Image Restoration Based on a Parallel Convolutional Neural Network," Remote Sensing, vol. 11, no. 13, pp. 1591, 2019.

Authorized licensed use limited to: DELHI TECHNICAL UNIV. Downloaded on May 11,2023 at 10:12:55 UTC from IEEE Xplore. Restrictions apply.

[11] Li, J.; Skinner, K.A.; Eustice, R.M.; Johnson-Roberson, M.WaterGAN: Unsupervised Generative Network to Enable Real-Time Color Correction of Monocular Underwater Images. IEEE Robotics and Automation. Letters, vol. 3, pp. 387–394, 2018.

[12] L. Chongyi, G. Chunle, R. Wenqi, C. Runmin, H. Junhui, K. Sam and T. Dacheng, "An Underwater Image Enhancement Benchmark Dataset and Beyond," IEEE Transactions on Image Processing, vol. 29, pp. 4376–4389, 2020.

Authorized licensed use limited to: DELHI TECHNICAL UNIV. Downloaded on May 11,2023 at 10:12:55 UTC from IEEE Xplore. Restrictions apply.

2023 10th International Conference on Signal Processing and Integrated Networks (SPIN) | 978-1-6654-9099-3/23/$31.00 ©2023 IEEE | DOI: 10.1109/SPIN57001.2023.10116627

Underwater Image Restoration Using Color Correction and Empirical Mode Decomposition

Amarendra Kumar Mishra
Electronics and Communication Engineering
Delhi Technological University
Delhi, India
amarendra_2k18dce502@dtu.ac.in

Mahipal Singh Choudhry
Electronics and Communication Engineering
Delhi Technological University
Delhi, India
mschoudhry@dtu.ac.in

Manjeet Kumar
Electronics and Communication Engineering
Delhi Technological University
Delhi, India manjeetchhillar@gmail.com

***Abstract*: Underwater imaging plays a significant role in discovering assets in the ocean. Underwater images are not visible due to the presence of noise and artifacts in the sea. The author proposed a technique to resolve this problem. In this article, the degraded underwater image applies to empirical mode decomposition after color correction to enhance the image. The suggested approach is compared to the existing state-of-the-art method. The picture has been taken from the UIEB data set for qualitative and quantitative analysis. Compared to traditional procedures, the suggested method produces superior enhanced images with improved visual quality.**

Keywords-Underwater image, EMD, IMFs, color correction.

I. INTRODUCTION

The Underwater images have a significant research area these days to uncover the underwater for sea bottom exploration and navigation. Due to extensive ocean floor investigation for studying coral reefs, fish recognition, historical heritage site assessment, and other related operations, underwater image processing has received widespread acceptance and interest among scholars[1]. In such situations, vision is crucial. Underwater photography yields fuzzy results. This fuzziness is caused by the medium's turbidity, scattered particles, and limited visibility range. Artificial light is used to increase this visibility range, but it also produces forward and backward scattering, along with color attenuation, which leads to low-contrast picture. Aside from that, the red color component suffers the most significant attenuation due to the longest wavelength, resulting in poor red composition in underwater images [2].

II. EXISTING WORK

In There are numerous approaches proposed in the literature to improve the visibility of underwater images[3][4][5]. Image dehazing approaches are widely categorized into single and several picture-based solutions. Numerous picture-based method employ many pictures of the similar scene taken from various perceptions [6][7]. In [8], haze reduction is achieved using depth evidence from the scene. However, due to its unusual structure, this method's usefulness for Underwater Image Processing (UIP) is limited. When the reference image is not available, the images can be dehazed from single haze images. Technical publications in the literature demonstrate the technique's popularity, usability, and viability.

R. Tan resolves this issue by enhancing the direct transmission's local disparity [9]. Based on the independent component analysis, R. Fattal proposed dehazing [10]. Dark channel prior (DCP) [11] is the most promising among these technique. This conventional method is based on finding the lowest pixel intensity value among the three-color channels in a small region called a patch. The smallest pixel value should be lies in the whole patch. Due to the enhancement of the transmission map by soft matting, this method requires extensive computational work**.** This constraint is solved with the use of guided filtering [12]. The guided filter is just a smoothing operator that preserves the edges.

The wavelength correction and picture denoising approach provided the best results for underwater image processing [13]. Nevertheless, this method is based on pre-calculated scattering coefficient values. In a realistic scenario, it is different and depends on the structure of the water body, temperature, season, and other relevant factors. Consequently, this algorithm's potential for general use is constrained. The other two notable works in the haze removal field are dehazing based on contextual regularization and boundary restriction [14] and dehazing based on color attenuation prior [15]. In this paper image is processed through color correction and empirical mode decomposition to enhance the degraded picture. The final image compared with the existing conventional technique, visually and statistically. The result shows that it is one of the best-suggested techniques.

In our proposed method, image restoration is carried out using the color correction and empirical mode decomposition. The main contribution of the authors are as follows:

- The authors made color correction before change RGB to HSV color space to correct the color cast of the degraded underwater image.
- Empirical mode decomposition algorithm is applied to decompose the image into intrinsic mode function.
- The authors have applied the iteration process on IMF. Finally, we concatenate all components of color space to obtained an enhanced image.

978-1-6654-9099-3/23/$31.00 ©2023 IEEE

Authorized licensed use limited to: DELHI TECHNICAL UNIV. Downloaded on May 15,2023 at 09:53:29 UTC from IEEE Xplore. Restrictions apply.

- Using the suggested technique, high-quality visual images have been derived out of raw underwater images lit under different light intensities.

III. METHODOLOGY

In this section, the author provides suggested methods for image restoration. The process will be created to increase contrast while preserving the brightness of the original image. The degraded image has been taken from underwater image enhancement benchmark data set. The proposed technique depends on the image restoration method, which contains the following different key factors: converting RGB to HSV color space, color correction, empirical mode decomposition, adding all the IMF with assigned weight, and finally, convert HSV color space to RGB. All these steps are demonstrated below:

A. Color Correction

To restore the color distortion of the original image, color correction is applied to the deteriorated input image. A linear mapping model based on a Gaussian distribution is used for color correction. Firstly, the maximum and minimum value of the original image I is calculated for each channel. Mathematically it is given by:

$$I^c_{max} = I^c_{mean} + \alpha I^c_{var}$$
$$I^c_{min} = I^c_{mean} - \alpha I^c_{var} \qquad (1)$$

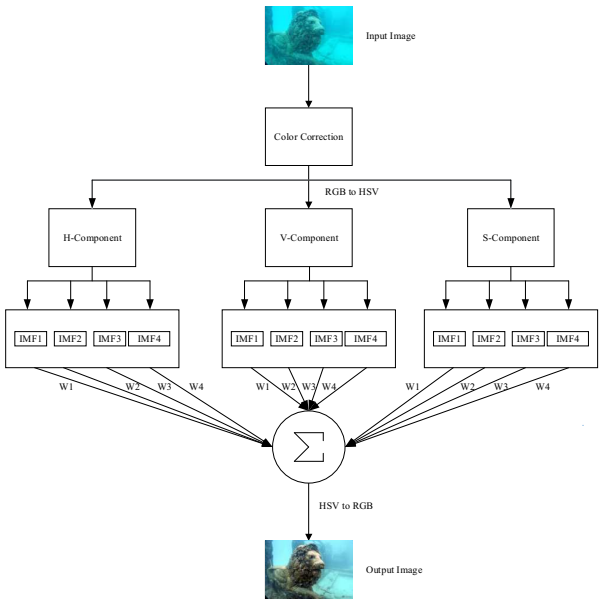


Fig.1 Schematic flow diagram of the suggested method.

Here, I^c_{mean} and I^c_{var} denote the mean value and standard deviation of the image in each channel, respectively and $c \in \{r, g, b\}$. α denotes the controlling parameters of the picture, which control the dynamic range of a picture. In our experiments, it is set to $\boldsymbol{\alpha = 2.4}$. Finally, color corrected image $\boldsymbol{I^c_{cc}}$ is obtained as:

$$I^c_{cc} = \frac{I^c - I^c_{min}}{I^c_{max} + I^c_{min}}; \qquad (2)$$

B. Empirical Mode Decomposition

Huang [16] suggested empirical mode decomposition as a flexible technique for time-frequency image pixel data analysis. Intrinsic Mode Functions (IMFs) are generated using the non-parametric data-driven analytic tool. EMD is used to analyze non-linear non-stationary signals. [17][18][19]. This technique decomposes the signal without leaving the time domain into Intrinsic Mode Functions (IMF). We also get a residue signal in addition to the IMFs. The higher-order IMFs capture the slower oscillating signal types. Whereas the lower-order IMFs catch faster oscillating signal patterns[20].

The obtained IMF and original signal are orthogonal to each other. The valid IMFs must satisfy the following criterion:

- There are only one maxima present between zero crossings is permitted for an IMF.
- The mean value of envelope defined by local maxima and the local minima must be zero at any point in the envelope which is created by image pixel data.

An IMFs are calculated using a very simple shifting technique. The original image pixel data is sifted until the subsequent pixel data sequence is fixed. The process is iterative and proceeds as follows:

(a) First, let's make an assumption, color corrected $input_{m,n}(i,j) = I^c_{cc}(i,j)$ where $I^c_{cc}(i,j)$ represent the color-corrected picture. The variable, m=1,2,3….., M represent total intended number of IMFs, and $k = 1,2,3,4 \ldots\ldots N$ is the amount of iterations required to produce one IMF.

(b) Then, all local maxima generated by 2-D envelope and local minima generated by 2-D envelope in the input are interpolated using a 2-D cubic spline. Then generating the upper envelope $E_1(i,j)$ and lower envelope $E_2(i,j)$.

(c) The mean envelope $E(i,j)$ is evaluated by mathematically $E(i,j) = \left(\frac{(E_1(i,j)+E_2(i,j))}{2}\right)$

(d) From the input signal, $input_{m,n}(i,j)$, the mean envelope $E(i,j)$ is subtracted. Mathematically it is defined as, $s_{m,n}(i,j) = input_{m,n}(i,j) - E(i,j)$.

(e) There are stopping criterion (α), which is required to evaluate and show How many iterations are needed. It is assessed by $\alpha = \frac{\sum_{i=1}^{P}\sum_{j=1}^{Q}|E(i,j)|}{P \times Q}$, where P and Q represent the average envelope's dimensions $E(i,j)$. Now the defined condition less than the specific value i.e., $\alpha < \gamma$ for a specific $k = K$ where γ is the specific threshold, then $s_{m,n}(i,j)$ is the m^{th} IMF, i.e., $IMF(i,j) = s_{m,n}(i,j)$. If the condition is not met by the stopping criterion, i.e., $\alpha > \gamma$ then the input

Authorized licensed use limited to: DELHI TECHNICAL UNIV. Downloaded on May 15,2023 at 09:53:29 UTC from IEEE Xplore. Restrictions apply.

$input_{m,n}(i,j)$, used to begin the following loop, and then steps (a)-(e) are repeated.

(f) If the m^{th} IMF i.e. imf_m is properly obtained, the residual signal is then determined as follows: $\mathcal{R}_m(i,j) = input_{m1}(i,j) - IMF_m(i,j)$.

(g) The residue $\mathcal{R}_m(i,j)$ is used as an input image to determine the subsequent IMF, and steps (a)-(f) are repetitive again. In the above-suggested algorithm, we obtain M IMFs and the final residue $\mathcal{R}_M(i,j)$. The final image of this algorithm is the summation of all the IMF's and residue, and it is represented mathematically as $I(i,j) = \mathcal{R}_M(i,j) + \sum_{m=1}^{M} IMF_m(i,j)$.

(h) The outcome demonstrates that the higher-order IMFs lack spatial properties and have low-frequency characteristics. The lower-order IMFs will provide a more detailed view of the overall spatial structure of the image.

$$S(x,y) = \sum_{l=1}^{L} \mathrm{W}_l \times IMF^R + \mathrm{W}_l \times IMF^G + \mathrm{W}_l \times IMF^B \quad (3)$$

Where $S(x,y)$ denotes the output modified picture, and W_l Represent the weight of l^{th} IMF. In this experiment, we have taken four IMF and corresponding four weight W_1, W_2, W_3, and W_4 respectively. The numerical value of weight is taken as 0.15, 0.3, 0.25, and 0.2, respectively.

IV. Results and Discussion

The suggested technique is implemented in MATLAB2019b, used on a 64-bit Windows 10 platform with intel(R) core(TM) i5-8265U @1.60GHz and 8.0GB RAM. The proposed technique is compared to the existing conventional technique, which are also implemented on the same platform. The author analyses the qualitative and quantitative analysis separately.

A. Qualititative Analysis

In this experiment, images have been taken of size 900 × 900 pixel value. The output image of existing methods such as MSRCR [21], HUWIE [22], RB [23], RED [24], WSCT [25], and the proposed technique has been shown in figure 2. The proposed method shows-pleasant visual results compared to other techniques. Method RED [24] does not preserve the naturalness of the image because it produces a brighter image. In MSRCR [21] approach, the red component is dominant, as shown in figure 2.

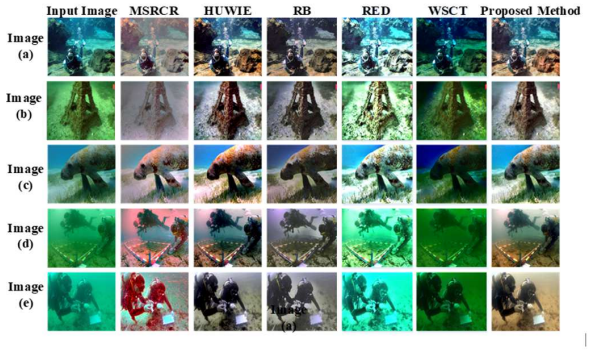


Fig. 2 Shows the output image of the suggested technique and existing method.

B. Quantitative Analysis

Apart from Qualitative analysis, the author also does quantitative analysis for the superiority of the proposed technique. The author evaluates two parameters, i.e., PCQI [26] and SSIM [27], of five images shown in Table.1 and Table.2, respectively. The numerical value of the parameters of five images in the case of the proposed method is better than the existing technique. It is also represented by a box plot shown in figure.3 and figure.4.

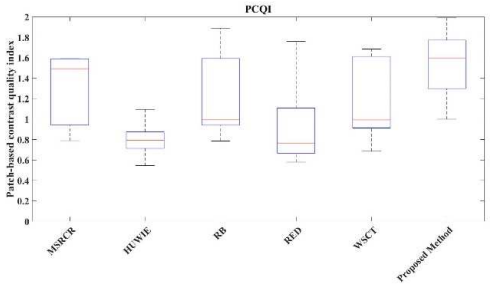


Fig. 3 Shows a box plot of the PCQI of the proposed method and the existing method.

The value of PCQI of the suggested technique is better than the existing method, as shown in figure.3. it's range lies between 0.99 to 1.99. This indicates that the numerical value of different images does not deviate much more. But the deviation is more in this case, such as MSRCR and WSCT.

TABLE. 1
PCQI of different method for different images.

	Image-a	Image-b	Image-c	Image-d	Image-e
MSRCR	1.588863	1.492424	1.590777	0.991324	0.788415
HUWIE	1.094639	0.801381	0.793299	0.770594	0.545680
RB	1.888685	0.991376	1.492853	0.992954	0.786136
RED	1.759761	0.765160	0.696051	0.578665	0.889791
WSCT	1.684909	1.589482	0.992408	0.989215	0.685477
Proposed method	1.989586	1.598216	1.698654	1.396892	0.998578

Authorized licensed use limited to: DELHI TECHNICAL UNIV. Downloaded on May 15,2023 at 09:53:29 UTC from IEEE Xplore. Restrictions apply.

TABLE. 2
SSIM of different method for different images.

	Image-a	Image-b	Image-c	Image-d	Image-e
MSRCR	0.205604	0.711564	0.267446	0.809693	0.322002
HUWIE	0.769216	0.747598	0.854777	0.656513	0.796444
RB	0.773201	0.868750	0.865479	0.896953	0.839533
RED	0.621134	0.734560	0.605537	0.766041	0.594070
WSCT	0.560599	0.707621	0.730281	0.126331	0.616235
Proposed method	0.778321	0.877456	0.886271	0.907513	0.858351

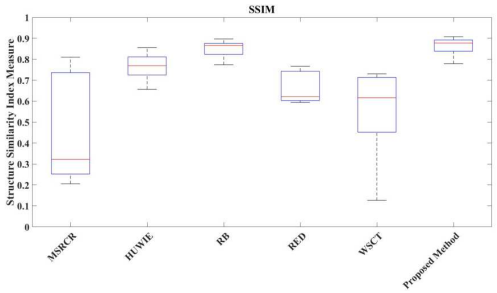


Fig. 4 Shows a box plot of the SSIM of the proposed method and the existing method.
Table 2

V. CONCLUSION

A novel technique is proposed in this article to restore underwater images. A color correction is applied to the degraded underwater picture. Convert these RGB color space images into HSV color space. The HSV color-corrected image is used as input for EMD algorithm. We have taken the first four intrinsic mode functions of empirical mode decomposition of the color-corrected image. Then take the summation of all the components with weight. Finally, we convert HSV color space into RGB to obtain an modified picture. The suggested technique is compared with the existing conventional method. The suggested technique shows superior visual quality compared to other conventional methods.

REFERENCES

[1] A. K. Mishra, M. S. Choudhry, and M. Kumar, "Underwater image enhancement using multiscale decomposition and gamma correction," *Multimed. Tools Appl.*, pp. 1–19, 2022.

[2] J. S. Jaffe, "Computer modeling and the design of optimal underwater imaging systems," *IEEE J. Ocean. Eng.*, vol. 15, no. 2, pp. 101–111, 1990.

[3] S. Bazeille, I. Quidu, L. Jaulin, and J.-P. Malkasse, "Automatic underwater image pre-processing," in *CMM'06*, 2006, p. xx.

[4] C. J. Prabhakar and P. U. Kumar, "An image based technique for enhancement of underwater images," *arXiv Prepr. arXiv1212.0291*, 2012.

[5] M. S. Hitam, E. A. Awalludin, W. N. J. H. W. Yussof, and Z. Bachok, "Mixture contrast limited adaptive histogram equalization for underwater image enhancement," in *2013 International conference on computer applications technology (ICCAT)*, 2013, pp. 1–5.

[6] Y. Y. Schechner, S. G. Narasimhan, and S. K. Nayar, "Instant dehazing of images using polarization," in *Proceedings of the 2001 IEEE Computer Society Conference on Computer Vision and Pattern Recognition. CVPR 2001*, 2001, vol. 1, pp. I–I.

[7] S. G. Narasimhan and S. K. Nayar, "Contrast restoration of weather degraded images," *IEEE Trans. Pattern Anal. Mach. Intell.*, vol. 25, no. 6, pp. 713–724, 2003.

[8] S. G. Narasimhan and S. K. Nayar, "Interactive (de) weathering of an image using physical models," in *IEEE Workshop on color and photometric Methods in computer Vision*, 2003, vol. 6, no. 6.4, p. 1.

[9] R. T. Tan, "Visibility in bad weather from a single image," in *2008 IEEE conference on computer vision and pattern recognition*, 2008, pp. 1–8.

[10] R. Fattal, "Single image dehazing," *ACM Trans. Graph.*, vol. 27, no. 3, pp. 1–9, 2008.

[11] K. He, J. Sun, and X. Tang, "Single image haze removal using dark channel prior," *IEEE Trans. Pattern Anal. Mach. Intell.*, vol. 33, no. 12, pp. 2341–2353, 2010.

[12] K. He, J. Sun, and X. Tang, "Guided image filtering," *IEEE Trans. Pattern Anal. Mach. Intell.*, vol. 35, no. 6, pp. 1397–1409, 2012.

[13] J. Y. Chiang and Y.-C. Chen, "Underwater image enhancement by wavelength compensation and dehazing," *IEEE Trans. image Process.*, vol. 21, no. 4, pp. 1756–1769, 2011.

[14] G. Meng, Y. Wang, J. Duan, S. Xiang, and C. Pan, "Efficient image dehazing with boundary constraint and contextual regularization," in *Proceedings of the IEEE international conference on computer vision*, 2013, pp. 617–624.

[15] Q. Zhu, J. Mai, and L. Shao, "A fast single image haze removal algorithm using color attenuation prior," *IEEE Trans. image Process.*, vol. 24, no. 11, pp. 3522–3533, 2015.

[16] N. E. Huang *et al.*, "The empirical mode decomposition and the Hilbert spectrum for non-linear and non-stationary time series analysis," *Proc. R. Soc. London. Ser. A Math. Phys. Eng. Sci.*, vol. 454, no. 1971, pp. 903–995, 1998.

[17] R. Fontugne, J. Ortiz, D. Culler, and H. Esaki, "Empirical mode decomposition for intrinsic-relationship extraction in large sensor deployments," in *Workshop on Internet of Things Applications, IoT-App*, 2012, vol. 12.

[18] D. M. Klionski, N. I. Oreshko, V. V Geppener, and A. V Vasiljev, "Applications of empirical mode decomposition for processing non-stationary signals," *Pattern Recognit. image Anal.*, vol. 18, no. 3, pp. 390–399, 2008.

[19] S. Majumdar and A. K. Mishra, "Empirical mode decomposition with wavelet transform based analytic signal for power quality assessment," *Int. J. Electron. Commun. Eng.*, vol. 12, no. 4, pp. 329–334, 2018.

[20] H. Hariharan, A. Gribok, M. A. Abidi, and A. Koschan, "Image fusion and enhancement via empirical mode decomposition," *J. Pattern Recognit. Res.*, vol. 1, no. 1, pp. 16–32, 2006.

[21] S. Parthasarathy and P. Sankaran, "An automated multi scale Retinex with color restoration for image enhancement," *2012 Natl. Conf. Commun. NCC 2012*, 2012, doi: 10.1109/NCC.2012.6176791.

[22] X. Li, G. Hou, L. Tan, and W. Liu, "A hybrid framework for underwater image enhancement," *IEEE Access*, vol. 8, pp. 197448–197462, 2020.

[23] X. Fu, P. Zhuang, Y. Huang, Y. Liao, X.-P. Zhang, and X. Ding, "A retinex-based enhancing approach for single underwater image," in *2014 IEEE International Conference on Image Processing (ICIP)*, 2014, pp. 4572–4576.

[25] C. Li, J. Guo, and C. Guo, "Emerging from water: Underwater image color correction based on weakly supervised color transfer," *IEEE Signal Process. Lett.*, vol. 25, no. 3, pp. 323–327, 2018.

[26] S. Wang, K. Ma, H. Yeganeh, Z. Wang, and W. Lin, "A patch-structure representation method for quality assessment of contrast changed images," *IEEE Signal Process. Lett.*, vol. 22, no. 12, pp. 2387–2390, 2015.

[27] Z. Wang, A. C. Bovik, H. R. Sheikh, and E. P. Simoncelli, "Image quality assessment: from error visibility to structural similarity," *IEEE Trans. image Process.*, vol. 13, no. 4, pp. 600–612, 2004

Authorized licensed use limited to: DELHI TECHNICAL UNIV. Downloaded on May 15,2023 at 09:53:29 UTC from IEEE Xplore. Restrictions apply.

Circuits, Systems, and Signal Processing
https://doi.org/10.1007/s00034-023-02397-0

Variation-Tolerant Sense Amplifier Using Decoupling Transistors for Enhanced SRAM Read Performance

Ayush Dahiya[1] · **Poornima Mittal**[1] · **Rajesh Rohilla**[1]

Received: 19 November 2022 / Revised: 30 April 2023 / Accepted: 2 May 2023
© The Author(s), under exclusive licence to Springer Science+Business Media, LLC, part of Springer Nature 2023

Abstract
A decoupled inverter pair sense amplifier (DIPSA) is proposed for improved sensing in differential SRAM. The DIPSA is designed at 45-nm technology node with a decreased sensing delay of 31.44% and 28.44% over the conventional latch-type sense amplifier (CLSA) and current-latched SA with an NMOS footswitch (CSANF) at 1.1 V, respectively. The performance of DIPSA is validated using delay and power consumption comparison with prior SA designs across a set of supply voltages. Monte Carlo simulation for 3σ deviation yields a reliable design with no read failures and mean delay of 488.81 ps across the 1k data points with a deviation of 54.87 ps. The threshold voltage variation contribution to process variation is considered for these calculations. The sizing of the decoupling transistors is discussed and its impact on the delay and power of DIPSA shown. The performance of existing voltage and current sense amplifiers is compared to DIPSA.

Keywords Low-voltage SRAM · Sensing delay · Sense amplifier · SRAM sensing · Transient analysis · Variation-tolerant circuits

1 Introduction

The SRAM forms a dominant part of most modern computational systems-on-chip (SoCs). The SRAM component covers larger area compared to the logic circuits in

✉ Poornima Mittal
poornimamittal@dtu.ac.in

Ayush Dahiya
ayushdahiya010@gmail.com

Rajesh Rohilla
rajesh@dce.ac.in

[1] Department of Electronics and Communication Engineering, Delhi Technological University, Delhi 110042, India

Published online: 23 May 2023

the system. The ever-evolving system requirements of the artificial intelligence (AI)-based accelerators or internet-of-things (IoT) devices require real-time computations, which have to be accounted for by the memory. Thus, a clear impact on the continued performance of the whole system in terms of reliability, delay, power consumption, cost and area occupied by the chip can be seen due to the SRAM architecture deployed for the requisite application [7]. The SRAM design requirements are stringent and a direct approach towards the selection of the bit cell 6T, 7T [13–15], 9T [9], etc., and the peripheral and assist circuitry in the form of write driver, column multiplexer [8], address decoder and sense amplifier (SA) is necessary.

The Sense amplifier is critical in terms of the read operation of the SRAM as it senses small differential signals on large capacitive bit lines although single-ended SAs have also been adopted [16]. The sense amplifiers can be broadly classified into four categories, namely voltage, current, charge-transfer SAs and advanced SAs. The voltage SAs [4, 17, 21] are widely used for their simplicity and reliability during operation, and most are designed around the cross-coupled inverter pair. The current-mode SAs overcome the need for larger differential bit line voltage by using current conveyor [18] and clamped bit-line technique to find a trade-off between speed and power. The charge transfer SAs [6] are less sensitive to bit-line capacitances but with an overhead of intermediate voltage and control signals. The transistor mismatch introduced due to scaling of the technology node is overcome by utilizing advanced SAs like redundancy SA [20] and multi-sized SA [19], which have an increased power consumption while decreasing SA offset.

In this paper, we propose a decoupled inverter pair sense amplifier (DIPSA) with differential sensing for a read delay improvement without a large power consumption penalty across design parameter variations. Section 2 consists of the existing SAs with their operation being highlighted. The working and design consideration for the DIPSA are discussed in Sect. 3. Section 4 consists of performance comparison of all the existing voltage and current SAs with DIPSA across supply voltage. Section 5 concludes the paper.

2 Existing Sense Amplifier Architectures

The cross-coupled inverter latch with strong positive feedback is the central component in the voltage sense amplifiers. The large capacitive bit line associated with larger cell arrays can be countered by using pass transistors. The decoupled latch-type sense amplifier (DLSA) [21] in Fig. 1a uses two bidirectional pass transistors, namely M5 and M6. These transistors act to decouple the bit lines leading to faster sensing and lower power consumption as the large capacitive bit lines are no longer driven by the cross-coupled inverters. Before the read phase, the bit lines are precharged to V_{DD} by the PMOS transistors; M8–M10 are operated by the precharge voltage (VPC). The double-tail sense amplifier (DTSA) [17] depicted in Fig. 1b is a two-tail sensing strategy with one tail focused on the input (BL and BLB) and the other on the cross-coupled inverter-based latch. The precharge phase (CLK=0) in the operation of DTSA charges the nodes Di+ and Di- of the PMOS transistors M8 and M9 to V_{DD}. This results in the M5 and M6 transistors causing the output nodes (SAO) to be pulled

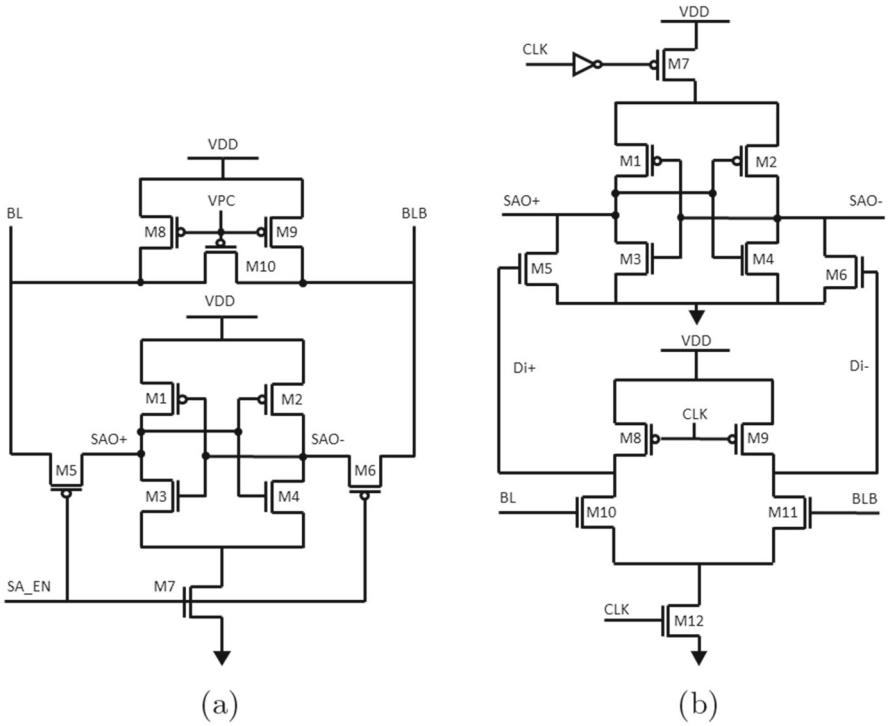


Fig. 1 Circuit schematics for voltage SAs **a** decoupled latch-type SA **b** double-tail SA

to ground. As the CLK goes high, the M7 and M12 transistors are both turned ON, which causes the Di voltages to monotonically decrease at the rate proportional to the ratio of current through M12 and capacitances at Di nodes. This gives rise to an input-dependent voltage difference ΔVDi. This ΔVDi is then passed to the cross-coupled inverter pair, which regenerates the voltage difference when the SAO nodes can no longer be clamped to GND by M5 and M6. Therefore, DTSA provides good isolation between the input and output due to M5 and M6 and is also conducive to operation at lower supply voltages.

The current-mode sense amplifiers are widely utilized for higher speed and larger SRAM designs as these are independent of the differential voltage present on the bit lines. Figure 2 a depicts the hybrid current-mode sense amplifier (HCSA) [22] where the equal sized cross-coupled PMOS transistors; M10–M13 constitute a current transport mechanism [18]. It is a flip-flop configuration but can be termed as a current conveyor [2, 3, 10] as it has low input resistance with unity gain transfer characteristic. The HCSA can be thought of as a conventional clamped SA together with a current conveyor.

The read operation for HCSA is as follows: M7 is turned on by making precharge voltage (VPC) high, which leads to a differential current signal appearing at the bit lines BL and BLB. This differential current signal passes through the source terminals of the NMOS devices M3 and M4, which leads to generation of a small voltage signal

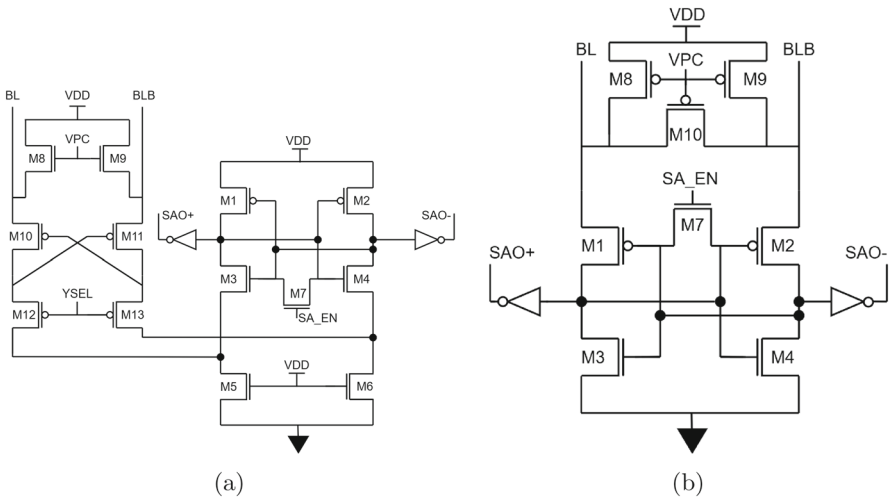


Fig. 2 Circuit schematics for current SAs **a** hybrid current SA **b** modified clamped SA

at their drains. The cross-coupled latch then amplifies this small differential voltage to a larger voltage swing. The design shown in Fig. 2b is the modified clamped sense amplifier (MCSA) [3]. The structure of the SA is comprised of the inverter latch and an equalizing transistor M7 with M8–M10 forming the precharge circuit. The two-stage read operation works as follows: initially bit lines are equalized by switching SA_EN high to turn on M7. During the sensing stage, SA_EN is turned off, M1–M4 form a traditional inverter pair, which amplifies the differential current flowing through the drains of transistors M3 and M4 to give rise to a voltage difference across the output nodes of the SA.

3 Proposed Decoupled Inverter Pair Sense Amplifier

3.1 Structure and Operation of DIPSA

In this section, we propose a decoupled inverter pair sense amplifier (DIPSA) whose schematic is shown in Fig. 3 a. The circuit is designed with the PMOS transistors; M1–M3 act as the precharge circuit for the bit lines turned on by VPC. The conventional cross-coupled latch is formed by the two inverters M4, M8 and M5, M9. The additional PMOS devices M6 and M7 act as decoupling switches in the cross-coupled inverter latch and are activated turning SA_EN OFF. The addition of CMOS inverters at the outputs of the SA provides better isolation for the internal SA nodes while providing faster rail-to-rail voltage swing, at the expense of leakage. The sense amplifier's operation can be divided into two stages: precharge and sense signal amplification. To begin read operation for the memory, the bit lines BL and BLB precharge to V_{DD} via the transistors M1–M3. The PMOS devices M6 and M7 are turned off for precharge stage (SA_EN = V_{DD}). The precharge stage concludes with M6 and M7 turning on

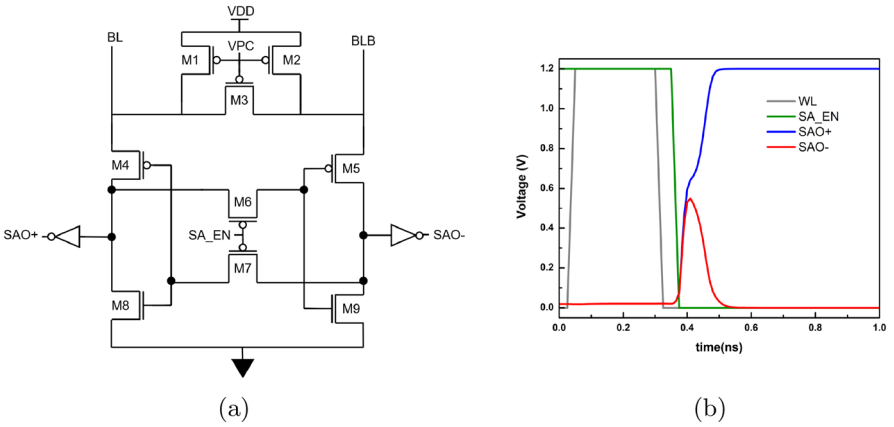


Fig. 3 **a** Circuit schematic **b** Transient response of the DIPSA at V_{DD} = 1.2 V and C_{BL} = 50 fF for PMOS transistors M6 and M7 sized with W/L = 300 nm/45 nm

which creates the cross-coupled inverter pair formed by PMOS devices; M4, M5 and NMOS devices; M8, M9.

These devices then act as a high-gain positive feedback amplifier similar to the working of clamped SA. This positive feedback leads to generation of a differential current across drains of M8 and M9, which is followed by the differential voltage at the output nodes SAO+ and SAO-. The differential voltage at the output nodes rapidly pulls SAO+ low and SAO- high for a positive differential current. The transient response of the DIPSA at V_{DD} = 1.2 V and bit line capacitance being 50 fF is shown in Fig. 3b. The word line (WL) of 6T SRAM cell (to turn ON the testbench) and SA_EN are the timing control signals used for operating the DIPSA and determining its transient response. A low SA_EN signal turns the SA in ON mode and thus leads to the bit lines; BL and BLB pulled apart to the full swing digital output signal. The transient response is used to derive the delay of the sense amplifier, which for all calculations is assumed to be the difference in time between the 50% (half of the maximum value) point on the rising edge of WL and the 50% point of the difference between outputs SAO+ and SAO- [24]. The power consumption is calculated for the time period between rising edge of WL and the rising edge of precharge signal for the next read operation. The power consumption calculations include the bit cell being read as well as the precharge circuit used.

3.2 Optimal Sizing for Decoupling Transistors

The inclusion of M6 and M7 in the design of DIPSA serves to decouple the inverters in the latch before the SA is enabled. These transistors and their sizing have an immense impact on the SAs performance. Figure 4a shows the read delay variation for different widths of the PMOS devices M6 and M7 for the given set of supply voltage variations. The delay is lowest for supply voltage of 1.2 V. The delay increases as voltage supply is decreased to 0.8 V. The widths of the PMOS transistors have a negligible effect on

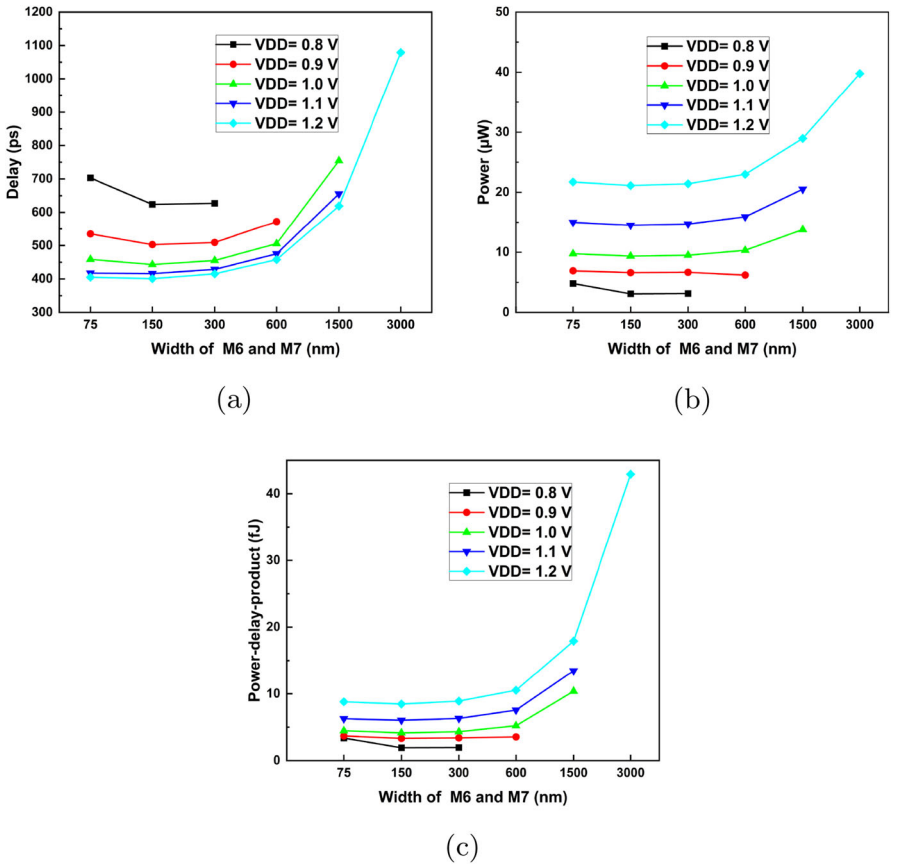


Fig. 4 **a** Delay **b** Power consumption **c** Power-delay-product of DIPSA as a function of the width of PMOS devices M6 and M7 for different supply voltages

the delay for widths less than 500 nm. The width increasing beyond 500 nm causes a steep increase at almost all supply variations. The power consumption is directly correlated to the increase in the decoupling transistors' width as is evident in Fig. 4b where $V_{DD} = 0.8$ V achieves the smallest power consumption. The increasing width of decoupling transistors also has an adverse effect on the read operation with the value stored in the bit cell being flipped. The delay and power consumption calculations are therefore omitted for the widths that cause erroneous data to be read from the bit cell in Fig. 4.

Figure 4c shows the power-delay product (PDP) for the different widths of PMOS decoupling transistors. The trade-off between decrease in delay and power consumption can be made on the basis of PDP variations. The decoupling PMOS devices (M6 and M7) with widths of 300 nm are selected for the design so as to achieve a smaller delay and also maintaining lower power consumption and being able to operate at each of the supply voltage without the read data being false. The transistors M4, M5 are sized to W/L = 90 nm/45 nm with M8, M9 sized to W/L = 45 nm/45 nm. The

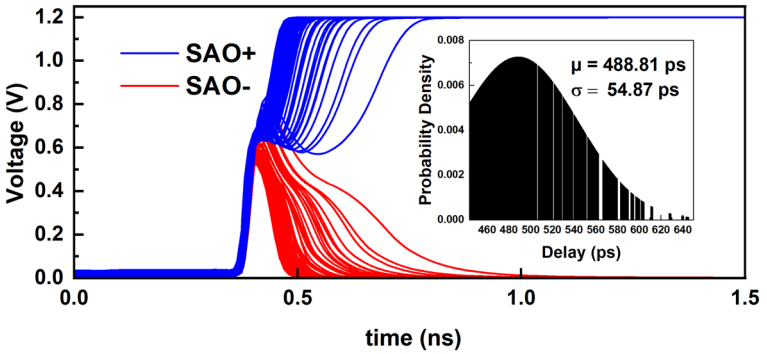


Fig. 5 Transient response and delay distribution (inset) of DIPSA for 1k Monte Carlo simulations at V_{DD} = 1.2 V and C_{BL} = 50 fF

precharge circuit comprising of M1–M3 are sized to larger W/L = 3000 nm/45 nm. The larger M6, M7 width also improves the performance of the DIPSA for process variation tolerance.

3.3 Variability Tolerance in DIPSA Design

The effect of process variation on the DIPSA is analyzed using Monte Carlo simulations for 1k data points. The transient response for the SA at V_{DD} = 1.2 V and C_{BL} = 50 fF is depicted in Fig. 5. The transient response thus depicted showcases that there are no false reads or read failure incurred during DIPSA operation. The number of failures calculated from the Monte Carlo simulations for DIPSA is thus zero. CMOS parameter variations can be categorized into front-end and back-end variations with majority contributor to the front-end random variations being threshold voltage (V_{TH}) variation. Random dopant fluctuations (RDF) dictate transistor parameter inconsistency. RDF is due to the variation in dopant atoms in the transistor channel, and the number of dopant atoms decreases to around ten atoms at 16 nm from a few tens at 45 nm [5]. A read failure might occur due to V_{TH} variations, which is defined as the read output going to zero instead of V_{DD} for a read "1" operation. The threshold voltage variation is assumed to be a Gaussian distribution with 3σ variations around the mean μ.

The reliability of a SA is calculated based on lowest read failures. The symmetry of most differential ended SAs is of critical importance for a reliable read operation in SRAMs. The Monte Carlo simulations are widely used in memory design and are run for parameter variations to check whether the results are in a desired range. The process variation tolerance of SA is important to characterize its performance so that we can account for transistor mismatch and improve our SA architecture design scaling. The distribution of read delay shown in Fig. 5 (inset) is derived through the MC simulations with a mean delay of 488.81 ps across V_{TH} variations and standard deviation of 54.87 ps. This shows only a 24.74% difference between the best- and worst-case delay values for DIPSA.

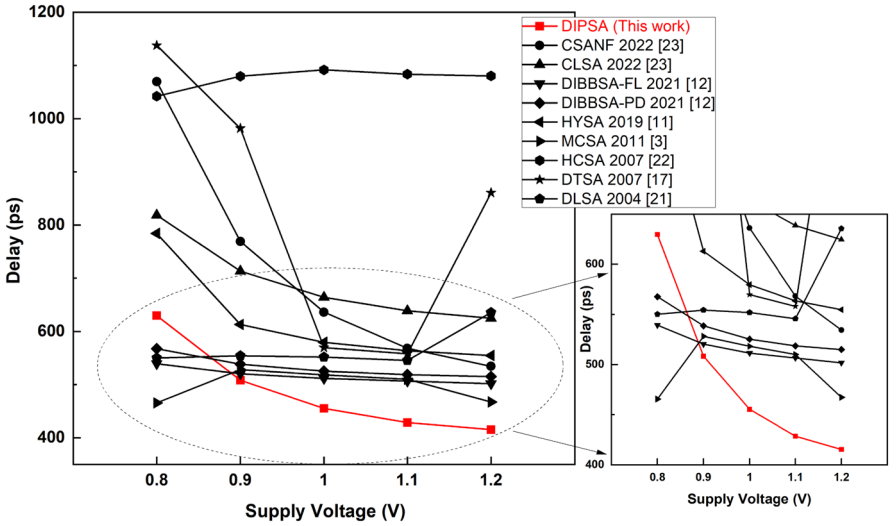


Fig. 6 Delay comparison of all SAs as a function of the supply voltage (C_{BL} = 50 fF)

4 Performance Comparison of DIPSA with Existing SA Topologies

The comparative analysis of all the previously presented sense amplifier architectures is presented in this section with all the SAs being designed using predictive technology model (PTM) [1] at 45-nm technology node. A uniform sizing was employed to bring all the different SAs to a common platform in order to perform an objective analysis at different supply voltages. The previously reported SAs [3, 11, 12, 17, 21–23] have pass transistors sized with W/L = 3000 nm/ 45 nm and the rest all of them being W/L = 75 nm/ 45 nm. The delay, power consumption of all the SAs together with DIPSA have been simulated for supply voltage variations. A widely used performance metric for SA is a power consumption and delay product defined as power-delay product (PDP). The lower PDP values demonstrates a higher overall performance. The timing and control signal employed for simulations across all designs are taken in the exact order as given in their corresponding literature with the same word line (WL) and sense amplifier enable (SA_EN) timings. The simulation testbench employed to calculate the simulation values is similar to the one used in [24] with 6T SRAM bit cell. The bit line capacitance (C_{BL}) is modelled using the π-3 model to be equivalent to larger cell arrays and is assumed to be equal to 50 fF for all the SA designs simulated.

4.1 Sensing Performance

The conventional voltage and current-mode sense amplifiers are simulated together with state-of-the-art calibration-based SA architectures [11, 12, 23] across all supply voltages considered. The proposed DIPSA has the lowest delay as shown in Fig. 6 at nearly all the supply voltages except for V_{DD} = 0.8 V. The best- and worst-case delay numbers across the supply voltages for DIPSA are just 197.45 ps apart. The delay of

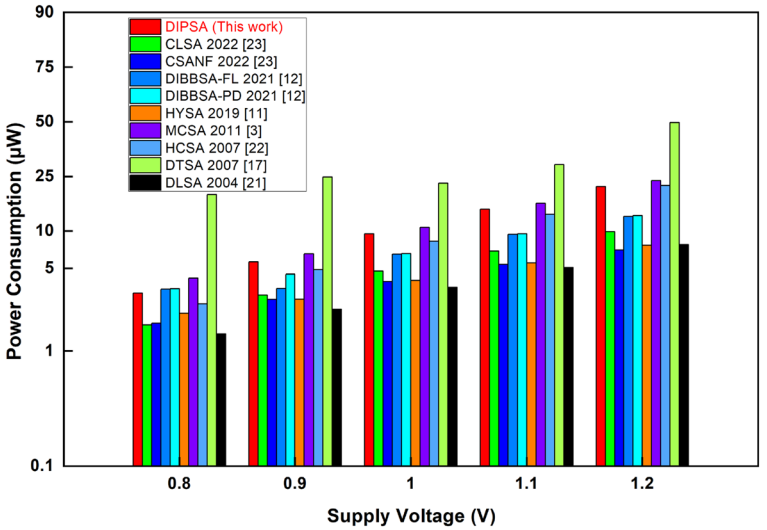


Fig. 7 Power consumption comparison of all SAs as a function of the supply voltage (C_{BL} = 50 fF)

DIPSA compared to DTSA and HCSA is 51.738% and 61.55% faster. Amongst the current-mode SAs compared, only HCSA has delay consistently larger than 1 ns across all the supply voltages applied. The most consistent delay is depicted by DIBBSA-FL [12] with a deviation of 13.20 ps, while CSANF [23] shows the worst deviation with 194.54 ps for the given supply voltages. The voltage SA designs compared above are all simulated for a bit line capacitance modelled by 50 fF. The DIPSA performs the best at higher supply voltages with a steady increase in delay as the supply voltage scales to lower values while having the one of the smallest area amongst all the SAs discussed.

4.2 Power Consumption

The power consumption of DIPSA is also on the lower end of the scale when compared with other SAs. This is depicted in Fig. 7. The power consumption increases for all SA as supply voltage increases, which is to be expected as power is proportional to the supply voltage as well as the current through the SA. The power consumption of DTSA is consistently the highest among all the SA designs discussed. The inclusion of more control signals also leads to more power being consumed. The CLSA [23], CSANF and DLSA are designed to make the bit line capacitance charge and discharge smaller, which allows for lower power consumption. The presence of precharged bit lines is a significant power contributor in SA design. The DIPSA consistently has lower power consumption compared to DTSA and MCSA. However, DIPSA is not the most power-efficient SA design. There is always a trade-off in sensing delay and power consumption during SA design. The PDP of all the SAs is shown in Fig. 8 with the bit line capacitance (C_{BL}) being assumed to be 50 fF. The DTSA has the highest PDP with an average of 23.56 fJ for the set of supply voltages. The conventional latch-type

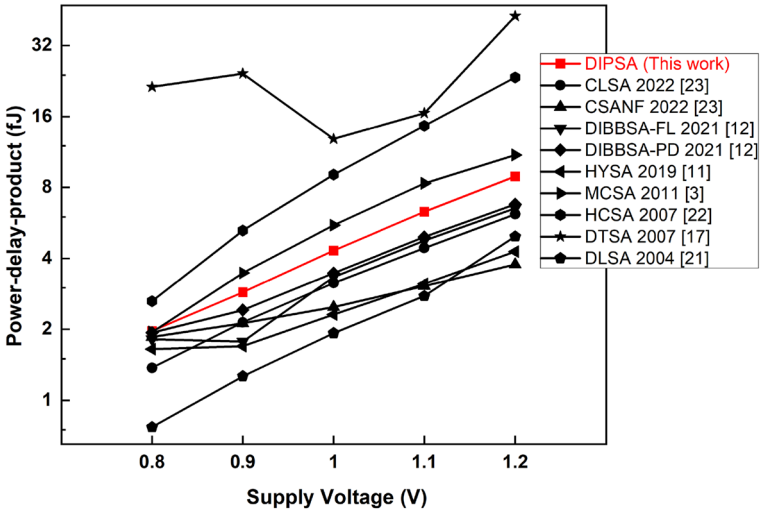


Fig. 8 Power-delay-product comparison of all SAs as a function of the supply voltage (C_{BL} = 50 fF)

Table 1 Comparison of performance summary of DIPSA with state-of-the-art SA designs at 1 V supply voltage

SA Design	Delay (ps)	Avg. Power (μW)	PDP (fJ)	No. of transistors
HYSA 2019 [11]	579.5894	3.9823	2.3081	11T
DIBBSA-FL 2021 [12]	511.4790	6.5198	3.3347	10T
DIBBSA-PD 2021 [12]	525.3752	6.5993	3.4671	12T
CLSA 2022 [23]	664.0057	4.7347	3.1439	15T
CSANF 2022 [23]	636.1495	3.9038	2.4834	15T
DIPSA	**455.2523**	**9.488**	**4.3194**	**9T**

SA-based designs like DLSA and HYSA have the best PDP when compared to other designs. The DIPSA can be used for faster applications albeit at the cost of a slightly larger power consumption while occupying the least area due to its lowest transistor count amongst state-of-the-art designs as shown in Table 1.

5 Conclusion

A decoupling inverter pair sense amplifier (DIPSA) with improved robustness against process variation and improved read performance is presented in this work. A performance analysis of the architectures and techniques of previously presented SAs was done at 45-nm technology node. A uniform sizing for the transistors across designs together with symmetrical timing control scheme was employed to equalize the sense amplifiers for transient simulations. The performance analysis consists

of using power consumption and delay as evaluation metrics for a set of supply voltages. The DIPSA shows a 18% and 31% delay improvement over the DIBBSA-FL and HYSA, respectively, at V_{DD} = 1.1 V. The reliability of DIPSA has been shown using Monte Carlo Simulations to account for process variations. The calculated sensing delay for threshold voltage variation has a difference of 125.3 ps across best- and worst-case delay.

Funding Not applicable

Data Availability My manuscript has no associated data

Declarations

Conflict of interest Not applicable

Code Availability Not applicable

References

1. Arizona State University NI, Group M (2008) Predictive Technology Models. http://ptm.asu.edu/latest.html
2. A.T. Do, Z.H. Kong, K.S. Yeo, Hybrid-mode SRAM sense amplifiers: new approach on transistor sizing. IEEE Trans. Circuits Syst. II Exp. Br. **55**(10), 986–990 (2008)
3. A.T. Do, Z.H. Kong, K.S. Yeo et al., Design and sensitivity analysis of a new current-mode sense amplifier for low-power SRAM. IEEE Trans. Very Large Scale Integr. Syst. (VLSI) **19**(2), 196–204 (2011)
4. D. Dutt, P. Mittal, B. Rawat et al., Design and performance analysis of high-performance low power voltage mode sense amplifier for static RAM. Adv. Electr. Electron. Eng. **20**(3), 285–293 (2022)
5. C. Hernández, A. Roca, J. Flich et al., Characterizing the impact of process variation on 45 nm NoC-based CMPs. J. Parallel Distrib. Comput. **71**(5), 651–663 (2011)
6. W. Marble, K. Kotani, C. Petrie, Practical charge-transfer amplifier design architectures for low-power flash A/D converters. IEEE Trans. Circuits Syst. I Regul. Pap. **51**(11), 2157–2164 (2004)
7. J.K. Mishra, B.B. Upadhyay, P.K. Misra et al., Design and analysis of SRAM cell using body bias controller for low power applications. Circuits Syst. Signal Process. **40**(5), 2135–2158 (2021)
8. P. Mittal, B. Rawat, N. Kumar, Tetra-variate scrutiny of diverse multiplexer techniques for designing a barrel shifter for low power digital circuits. Microprocess. Microsyst. **90**, 104491 (2022)
9. M. Moghaddam, S. Timarchi, M.H. Moaiyeri et al., An ultra-low-power 9T SRAM cell based on threshold voltage techniques. Circuits, Syst., Signal Process. **35**, 1437–1455 (2016)
10. S. Pandey, S. Kumar, V. Bhatnagar et al., A low leakage substrate bias-assisted technique for low voltage dual bit-line SRAM. Comput. Electr. Eng. **102**, 108216 (2022)
11. D. Patel, A. Neale, D. Wright et al., Hybrid latch-type offset tolerant sense amplifier for low-voltage SRAMs. IEEE Trans. Circuits Syst. I: Regul. Pap. **66**(7), 2519–2532 (2019)
12. D. Patel, A. Neale, D. Wright et al., Body biased sense amplifier with auto-offset mitigation for low-voltage SRAMs. IEEE Trans. Circuits Syst. I Regul. Pap. **68**(8), 3265–3278 (2021)
13. B. Rawat, P. Mittal, A 32 nm single-ended single-port 7T static random access memory for low power utilization. Semicond. Sci. Technol. **36**(9), 095006 (2021)
14. B. Rawat, P. Mittal, A comprehensive analysis of different 7T SRAM topologies to design a 1R1W bit interleaving enabled and half select free cell for 32 nm technology node. in *Proceedings of the Royal Society A: Mathematical, Physical and Engineering Sciences* **478**(2259), 20210745 (2022)
15. B. Rawat, P. Mittal, A reliable and temperature variation tolerant 7T SRAM cell with single bitline configuration for low voltage application. Circuits Syst. Signal Process. **41**(5), 2779–2801 (2022)
16. B. Rawat, P. Mittal, A switching NMOS based single ended sense amplifier for high density SRAM applications. ACM Trans. Des. Autom. Electron. Syst. **28**(3), 1–14 (2023)

17. D. Schinkel, E. Mensink, E. Klumperink et al., A double-tail latch-type voltage sense amplifier with 18ps setup+ hold time, in *2007 IEEE international solid-state circuits conference*. (Digest of technical papers, IEEE, 2007), pp. 314–605
18. E. Seevinck, P.J. van Beers, H. Ontrop, Current-mode techniques for high-speed VLSI circuits with application to current sense amplifier for CMOS SRAM's. IEEE J. Solid-State Circuits **26**(4), 525–536 (1991)
19. V. Sharma, S. Cosemans, M. Ashouei et al., A 4.4 pJ/access 80 MHz, 128 kbit variability resilient SRAM with multi-sized sense amplifier redundancy. IEEE J. Solid-State Circuits **46**(10), 2416–2430 (2011)
20. N. Verma, A.P. Chandrakasan, A 65nm 8T sub-Vt SRAM employing sense-amplifier redundancy, in *2007 IEEE International Solid-State Circuits Conference*. (Digest of Technical Papers, IEEE, 2007), pp. 328–606
21. B. Wicht, T. Nirschl, D. Schmitt-Landsiedel, Yield and speed optimization of a latch-type voltage sense amplifier. IEEE J. Solid-State Circuits **39**(7), 1148–1158 (2004)
22. M. Wieckowski, S. Patil, M. Margala, Portless SRAM-A high-performance alternative to the 6T methodology. IEEE J. Solid-State Circuits **42**(11), 2600–2610 (2007)
23. Y. Zhao, J. Wang, Z. Tong et al., An offset cancellation technique for SRAM sense amplifier based on relation of the delay and offset. Microelectron. J. **128**, 105578 (2022)
24. J. Zhu, N. Bai, J. Wu, A review of sense amplifiers for static random access memory. IETE Tech. Rev. **30**(1), 72–81 (2013)

Publisher's Note Springer Nature remains neutral with regard to jurisdictional claims in published maps and institutional affiliations.

Springer Nature or its licensor (e.g. a society or other partner) holds exclusive rights to this article under a publishing agreement with the author(s) or other rightsholder(s); author self-archiving of the accepted manuscript version of this article is solely governed by the terms of such publishing agreement and applicable law.

Multimedia Tools and Applications
https://doi.org/10.1007/s11042-023-15219-x

Word spotting and character recognition of handwritten Hindi scripts by Integral Histogram of Oriented Displacement (IHOD) descriptor

Enock Osoro Omayio[1] · **Sreedevi Indu**[2] · **Jeebananda Panda**[2]

Received: 6 July 2022 / Revised: 3 October 2022 / Accepted: 30 March 2023
© The Author(s), under exclusive licence to Springer Science+Business Media, LLC, part of Springer Nature 2023

Abstract
This paper proposes efficient and robust segmentation-based word spotting and character recognition systems for offline handwritten Hindi scripts using a newly proposed shape descriptor called integral histogram of oriented displacement (IHOD). IHOD descriptor is easy to construct, has high discriminating power and minimizes intra-class variance while enhancing inter-class variance. IHOD descriptor has been used to train multilayer perceptron (MLP) to obtain MLP-based word spotting and character recognition models. The word spotting model has been evaluated with 3 datasets of handwritten Hindi word images whereas the character recognition model has been evaluated with 2 datasets of handwritten Hindi character images. The proposed word spotting technique attained a mean average precision of 0.9736 and best k-precision of 0.9758. The proposed character recognition technique achieved best recognition accuracy of 97.45%. Performance of the proposed word spotting technique has been compared with CNN-based state-of-art techniques like AlexNet, DenseNet, VGG and Inception. In this work also, a new dataset of segmented handwritten Hindi word images has been created for use in development and testing of word spotting systems. The dataset consists of 43,572 instances of words from 415 different writers.

Keywords Word spotting · Character recognition · Integral histogram of oriented displacement (IHOD) · Mean average precision (MAP) · k-precision(kPr)

✉ Enock Osoro Omayio
omayio2008@gmail.com

Sreedevi Indu
s.indu@dce.ac.in

Jeebananda Panda
jpanda@dce.ac.in

[1] Department of Electronics and Communication Engineering, Delhi Technological University, Delhi, India

[2] Department of Electronics and Communication Engineering, Delhi Technological University, India, Shahbad Daulatpur, Bawana Road, Delhi 110042, India

Published online: 05 May 2023

1 Introduction

Due to advancement of information and communication technology (ICT), huge number of documents have been scanned and stored in electronic forms as scans or digital images. Manual word search/retrieval from such large database of document images in digital forms is unfeasible, wearisome and prone to errors. This calls for an automated process. Word spotting and character recognition systems are solutions to the aforementioned challenges. In word spotting, a query is used to find other word images (candidate word images) of the same instance from a large database. The retrieved candidate word images are in a ranked list starting with most similar word and ends with least similar word image. A query can be a word image or a string. Features of a query word image are matched with features of candidate word images, and similarity scores computed using some matching techniques. Similarity scores are used to make a ranked list of candidate words of similar instance to the query. Similarity scores can be obtained using distance measures like Euclidean distance [19, 30], cosine similarity, normalization cross correlation [7], dynamic time warping [42]. The ranked list consists of words with same ASCII equivalent [42]. Word spotting is very useful in various document-related tasks like Postal tasks to read mail addresses [56], in banking sector to read cheques [56], and in historical documents [4] among many others. There is need for robust and efficient techniques for automatic indexing and retrieving of document images and especially the handwritten ones. The methods will minimize much reliance on OCR because it performs very well in scanned machine printed documents but not in handwritten documents. This is attributed to unstandardized and varying styles of handwriting among different authors.

In this work, segmentation-based technique using IHOD has been proposed for word spotting and character recognition for Hindi scripts. From literature, much work in word spotting and character recognition has been done for Latin/Roman scripts (both machine printed and handwritten forms) as compared to Hindi scripts. Classical Latin alphabets are widely used in many languages like English, Spanish, Germany, Dutch, Swedish, Portuguese, French and many African indigenous languages. There are quite a number of standard datasets of many languages employing Latin alphabets. Such datasets are publicly available for development and testing of word spotting systems, hence their advanced progress. But in the case of Hindi language, development of word spotting and character recognition systems is challenging due to scarcity of publicly available standard datasets. This is also compounded by the cursive nature of Hindi characters, character similarity, and variability of styles of writing among different writers [13]. The sources of within class variability are: (i) elongation of free stroke endpoints, (ii) hill and dale writing—a case where the general orientation of a handwritten word is at an angle to horizontal axis of the paper, (iii) unconstrained writing, (iv) variation of writing styles among different writers, and (v) connectedness and unconnectedness of constituent characters in a word for different writers.

1.1 Hindi language script

Hindi is a language most widely used in India. It is also used as an official language there. It is the third popular language used globally [35]. It is written using Devanagari script. Devanagari script also, forms the basis for other widely used Indic languages like Marathi, Sanskrit, and Sindhi among others. Devanagari consists of 36 base characters/consonants, 12 vowels, and 10 digits. Tables 1, 2 and 3 show the Devanagari numerals, vowels, and base consonants respectively. Besides base characters or consonants, compound characters

Table 1 Devanagari numerals

Hindi Label	Label
०	0
१	1
२	2
३	3
४	4
५	5
६	6
७	7
८	8
९	9

are formed by combining base characters. A compound character has a more complex structure than base character. A detailed description on this Devanagari script can be found in a survey by Jayadevan et al. [23].

In this work, word spotting and character recognition techniques are proposed for handwritten Hindi scripts. The proposed systems use integral histogram of oriented displacement (IHOD) shape descriptor constructed from segmented word and character images. IHOD is used to describe text strokes of scanned document word or character images at local and global levels. To construct IHOD, word/character image is sub-divided into square cells of fixed dimension. For every cell, displacements of foreground pixels from cell centre are computed. Also computed for each cell are orientation angles of foreground pixels with respect to the cell centre. The orientation angles are quantized into bins of equal angle width. For each foreground pixel, the length of its displacement is a vote in its corresponding angle/bin in histogram of oriented angles (quantized into bins). The histograms are concatenated to form IHOD. Construction of IHOD descriptor is explained in detail in Section 3.4. IHOD descriptor is used to train multilayer perceptron (MLP) classifier to obtain word spotting and character recognition models. From experiments done, the proposed method performs very well in word spotting and character recognition tasks in handwritten Hindi script images. This work has been inspired by Gowayyed et al. [18] who used histogram of oriented displacement

Table 2 Devanagari vowels

Hindi Label	Label
अ	a
आ	aa
इ	i
ई	ee
उ	u
ऊ	oo
ए	ae
ऐ	ai
ओ	o
औ	au
अं	an
अः	ah

Table 3 Devanagari consonants

Hindi Label	Label
क	ka
ख	kha
ग	ga
घ	gha
ङ	kna
च	cha
छ	chha
ज	ja
झ	jha
ञ	yna
ट	ta
ठ	tha
ड	da
ढ	dha
ण	ana
त	taa
थ	thaa
द	daa
ध	dhaa
न	na
प	pa
फ	pha
ब	ba
भ	dha
म	ma
य	ya
र	ra
ल	la
व	va
श	motosaw
ष	petchiryosaw
स	patalosaw
ह	ha
क्ष	ksha
त्र	tra
ज्ञ	gya

(HOD) as a 2D trajectory descriptor to represent 3D motion of human body joints. In their work, length of displacement of a body joint between two successive time steps and in a given direction, is a vote in orientation angles histogram. They used HOD to give temporal behaviour of human joints. The proposed IHOD descriptor differs from HOD in three major ways: (i) IHOD is constructed using all foreground pixels from entire word/character image whereas HOD is constructed from pixels of interest points (body joints), (ii) IHOD consists of 3 levels of concatenation whereas HOD has only 1 concatenation step, and (iii) IHOD has both local and global information whereas HOD has local information only. More differences

are explained in Section 3.4.2(e). The contributions made by this paper are: (a) new shape descriptor called IHOD with high discriminating power is proposed, (b) new method for slant correction referred to as local centred-slant correction method is proposed, and (c) construction of a new dataset of segmented handwritten Hindi word images. For the remaining part of this paper, section two covers related word spotting and character recognition techniques that have been reported in literature, section three explains the proposed word spotting and character recognition techniques, section four discusses the results, and section five is conclusion.

2 Literature Survey

2.1 Classification of word spotting techniques

Word spotting techniques are classified based on three main criteria: (i) learning free versus learning based, (ii) segmentation free versus segmentation based, and (iii) script-dedicated. In learning free versus learning based criteria, word spotting is carried out using either learning based or learning free methods. In learning free methods, no training is required. Learning free word spotting methods employ QBE (query by example) or QBS (query by string) modes. For QBE approach, a query is a word image that is used to search instances of similar words from a database of candidate word images. In QBE mode, features of query word and candidate word images are compared and similarity scores computed. Candidate words with similarity scores above a set threshold are included in the list of similar words [44]. The list of similar words is ranked on the basis of similarity scores obtained. QBE approach is feasible for low scale word spotting applications. In QBS approach, a string (mostly machine printed) is used. QBS approach is used mostly where large amounts of document images are involved. Examples of learning free based word spotting systems that have been developed are by Khursid et al. [25] and Papandreou et al. [39]. Learning free methods do not rely on models, are simple to carry out, and do not depend on prior knowledge on trained data. Their down side is their low performance compared to learning-based methods [43]. For learning-based word spotting methods, a trained model is used. The model is trained using statistical learning methods which in turn is used to score and rank candidate word images. This method uses classifiers like neural networks [58], HMM (hidden markov model) [15], SVM (support vector machine) [6]. The merit of learning-based word spotting approaches is their higher performance as compared with learning free methods. However, they require huge labelled training data, and have low performance with small data. In segmentation-based word spotting techniques, document images are first segmented to individual words, followed by feature extraction from individual word images. The extracted features are then compared with features of query word image after which similarity matching is carried out. Similarity scores obtained are used to output a ranked list of most likely similar words. Segmentation-based methods perform well for machine printed and good quality documents. However, with challenging task of segmentation, the performance decreases in cases of handwritten and degraded document images. Segmentation-based word spotting systems include those by Bhardwaj et al. [7] and Srihari et al. [57]. Segmentation free word spotting methods do not need segmentation of a document to individual words during word spotting operation. A query word scans all over the whole document, where in every step, similarity scoring is performed with text in overlapped region. Candidate words that score above a set threshold are selected as most likely similar words and a ranked list is obtained [44]. These methods perform better than

segmentation-based methods. However, their speed may be low as they may scan areas with no candidate words. Examples of segmentation free methods are those of Shaw et al. [49], Shaw et al. [48], and Amanatiadis et al. [2].

Script-dedicated word spotting techniques are script dependent. The script nature can be writing nature (machine printed or hand written), number of writers (single author or multi-author), and language (single language or multi-language). Language-dedicated word spotting methods are informed by differences in character structure across natural languages.

2.1.1 Related work on handwritten Hindi word spotting

Bhaldwaj et al. [7] used moment-based features in their segmentation-based word spotting system. In their work, moment features are extracted from words and indexed. The indexed features were matched with those of query word using cosine similarity scores and high-ranking candidate words obtained. Srihari et al. [57] used word shape method for word spotting in Devanagari and Arabic scripts. A number of word spotting methods of good performances have been reported in literature. Example is Lu et al. [30] whose method was based on word shape coding, Shekhar and Jawahar [50] who used SIFT (scale invariant feature transform) and bag of visual words as features for word spotting in Bangla scripts. Shape descriptor method by Hassan et al. [19] has been used for word spotting in Hindi and Bangla document images where precision of 87% is reported. A word spotting system using convolution neural network (CNN) has been developed by Sudholt and Fink [58]. In their proposed system, training is done using a representation of pyramidal histogram of characters. The system has good performance. Zhang et al. [63] used segmentation free technique to carry out word spotting for Bangla handwritten document images. Key points of word images were represented by Heat Kernel signature (HKS) features. A zoning-based word spotting technique has been proposed in which only the middle zone is used. Better performance is reported when tested on Bangla and Devanagari scripts. However, the proposed method may not work well especially for Indic words with similar or same middle zone but different upper and lower zones. In the word spotting work by Zagoris et al. [62], key points based on local gradient vectors and orientations have been used as features. The method does not take into consideration variations among similar words due to slanting and varying character sizes. In addition, slant and skew correction are not performed. Zonal features have been used by Roy et al. [45] in partial-based word spotting in documents of Indic languages like Bangla and Devanagari. In this method, image word is divided into horizontal layers (or zones) and features for every zone extracted. These zonal features are used in similarity matching to find similar instances of the same word. Though Roy et al. [45] reports that zoning-based word spotting methods performs better than word spotting based on full word images, others in their word spotting works hold a different view, like Fischer et al. [15] who reports that techniques that do not carry out zoning/sub-segmentation of word image performs better. For example, word spotting approach by Zagoris et al. [63], which is based on full word images, it is reported to perform very well. Another zone-wise segmentation word spotting technique is that of Bhunia et al. [9]. In this technique, text line is used instead of a word and only features from middle zone are used. A better performance compared to word-based zone-based techniques is reported. Roy et al. [46] used dynamic shape coding descriptor for word spotting in Indic and Latin scripts.

Amanatiadis et al. [2] used key points for word spotting done using mobile devices. Their method is segmentation free and training free. Good accuracy and fast retrieval speed

are reported. Omayio et al. [33] developed an MLP-based model for word spotting. The model was obtained by training MLP classifier using integral histogram of oriented displacement (IHOD) features that extracted from binarized word images and consisting of local and global information. Good performance is reported.

Sapkal et al. [47] employed CNN-based Siamese network for key-word spotting of historical documents. The other works in word spotting employing CNN-based approaches include those of Sushma and Sharada [59] who used Autoencoder for word spotting with Devanagari historical handwritten manuscripts. Also, Giotis et al. [17] used a combination of spatial transformer and adversarial networks for word spotting. Singh and Ahmed [54] used model-based technique to extract word strings from images consisting of text and non-text components. Kumar et al. [29] proposed a probability-based method for classifying unstructured string or text to either positive, negative, or neutral polarity.

2.2 Classification of character recognition techniques

In character recognition system, models are developed by training suitable classifiers with features extracted from characters. On the basis of features, character recognition systems (CRS) can be grouped to two broad classes: (i) those using hand crafted features, and (ii) those with automated feature extraction. For Devanagari CRS using hand crafted features, the commonly used features are Moment invariants [41], Gradient [36, 37], structural [5], Fourier descriptors [40], and chain code [11] among others. Details of features used for character recognition can be found in surveys by Trier et al. [61] and Dongre and Mankar [12]. These features are used to train a suitable classifier to be used as a model for character recognition. In Devanagari/Hindi character recognition, classifiers that are often used are modified quadratic discriminant function (MQDF), SVM, compound MQDF (CMQDF), k-nearest neighbour (KNN), mirror image learning (MIL), subspace method (SM), multilayer perceptron (MLP), and Euclidean distance (ED). They are discussed in detail in a survey by Pal et al. [36]. The Devanagari/Hindi CRS employing automated feature extraction is mainly based on deep convolution neural network (DCNN) where convolution and pooling layers and kernels automate feature extraction process. The DCNN extracts and learns features that enable it to map the input to output classes.

2.2.1 Related handwritten Hindi character recognition work

Aneja and Aneja [3] employed transfer learning for recognition of handwritten Devanagari characters. The pre-trained convolution networks (CovNets) that were tuned are AlexNet [28], DenseNet 121 [20], VGG [52], and Inception [60]. Aneja and Aneja [3] reports that Inception V3 posted best performance of 99% accuracy. Performances for other pre-trained models are: AlexNet (98%), DenseNet (90%), and VGG (99%). Their implementation is computationally expensive. Madhuri and Purwar [31] used HOG (histogram of oriented gradients) descriptor with SVM and MLP to develop a model for Devanagari handwritten character recognition, where 96.8% accuracy is reported. Sonawane and Shelke [55] used transfer learning with AlexNet CovNet to develop a model for recognition of 22 handwritten Devanagari consonants. The dataset used consists of 16,870 samples. Test accuracy obtained is 95.46%. A layer-wise based DCNN has been proposed by Jangid and Srivastava [22] for Devanagari handwritten character recognition. Information Sharing Devanagari character (ISIDCHAR) dataset is used. Recognition accuracy obtained is 98%. Sing [53] used HOG features to train artificial neural network (ANN) to obtain a model for

Devanagari handwritten character recognition. Data set used has 62 classes (52 characters and 10 numerals). Accuracy obtained is 97.06%. Iamsa-at and Horata [21] also used HOG descriptors where 80% recognition accuracy is reported.

Gharde et al. [16] used invariant moments for Devanagari handwritten character and numerals recognition. Accuracies reported are 94.56% and 99.48% for vowels and numerals respectively. Acharya et al. [1] developed a deep CNN-based character recognition system for Devanagari handwritten characters. The data set used consists of base consonants and numerals. Accuracy of 98.47% is reported. Pant et al. [38] used structural features to develop a character recognition model with Radial Basis Function (RBF) and MLP classifiers. Recognition accuracies obtained are 80.25%, 86.04%, and 94.44% for consonants, vowels and numerals respectively. Bhattaacharya and Chaudhuri [8] used wavelet features to train MLP for recognition of Devanagari handwritten numerals. Dataset used consists of 22,556 samples. Accuracy reported is 99.04%. Pal et al. [37] proposed offline handwritten Hindi character recognition system by combining SVM and MQDF. Gradient and curvature features were used. The data set used has 36,172 samples. Recognition accuracy obtained is 94.24%. Arora et al. [5] used structural properties and distance-based technique for recognition of handwritten Devanagari characters. Data set used has 5,000 samples. Recognition accuracy reported is 89.12%.

In most hand written Devanagari character recognition systems, the sizes of data used range from 2,000 to 50,000 samples. Majority of data sets used are not publicly available for comparison with other recognition techniques. Recognition accuracies obtained from various character recognition systems proposed range from 80–99.56% and can be found in a survey by Jayadevan et al. [23].

2.3 Problem statement

Much progress has been achieved on word spotting in English scripts [26, 42] as compared to Hindi scripts. As of early 2020, there is minimal progress in word spotting and character recognition for handwritten Hindi scripts. This is partly attributed to lack of enough standard handwritten Hindi datasets. Therefore, much effort is needed in developing word spotting and character recognition systems for handwritten Hindi scripts. In addition, most of the existing word spotting and character recognition techniques for Hindi scripts have the challenge of low performance and high computational cost especially for CNN-based techniques. The proposed work is out to address such challenges using a new IHOD shape descriptor which has high discriminating powers.

3 Methodology

The proposed methods for handwritten Hindi word spotting (HHWS) and handwritten Hindi character recognition (HHCR) have four main steps: pre-processing, word segmentation, IHOD feature extraction, and training. Figures 1 and 2 shows frameworks of the proposed HHWS and HHCR techniques respectively. The main component in the design of HHWS and HHCR systems is extraction of IHOD features which are used in training phase. Each system takes input query word/character image, pre-processes the word/character image, extracts IHOD features, and then trains a multilayer perceptron (MLP) classifier. After training, MLP-based HHWS and HHCR models are obtained, which are used to respectively find similar words and characters from respective databases.

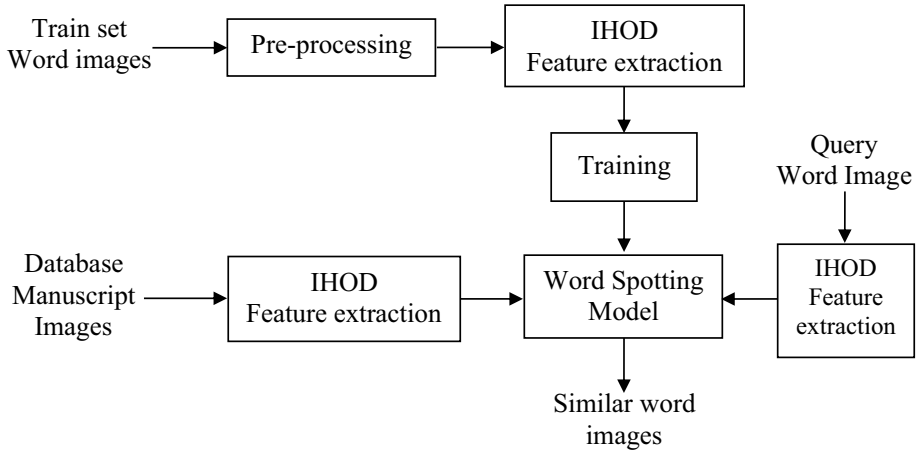


Fig. 1 Handwritten Hindi word spotting (HHWS) framework where IHOD denotes integral histogram of oriented displacement

3.1 Pre-processing

Many of the document images have various forms of degradations like poor contrast and noise. Pre-processing is needed for proper feature extraction. In the proposed techniques, word and character images are the inputs to HHWS and HHCR systems respectively. If the input is a colour image, it is first converted to gray scale image. Mean filter masks are used for noise filtering. The query word/character image is then binarized using Otsu method [34] such that foreground (text region) is 1 and background (non-text region) is 0.

3.2 Word image segmentation

For HHWS system, document images are segmented to obtain individual words. Segmentation is done using component tracing and association (CTA) method by Omayio et al. [32]. The CTA method works well by riding on high connectedness of Hindi words. For HHCR system, a rectangular region enclosing foreground only is obtained.

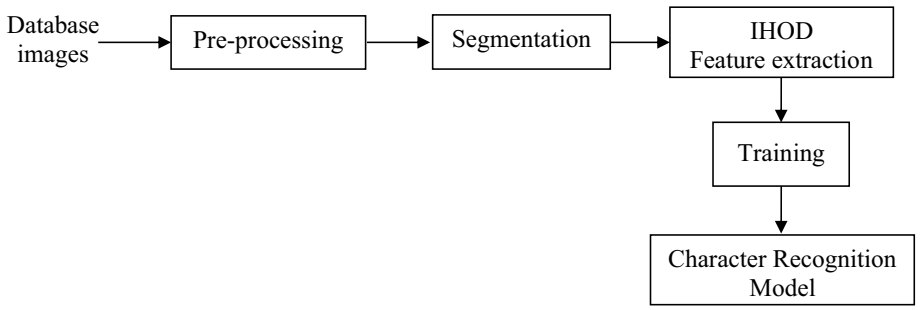


Fig. 2 Handwritten Hindi character recognition (HHCR) framework where IHOD denotes integral histogram of oriented displacement

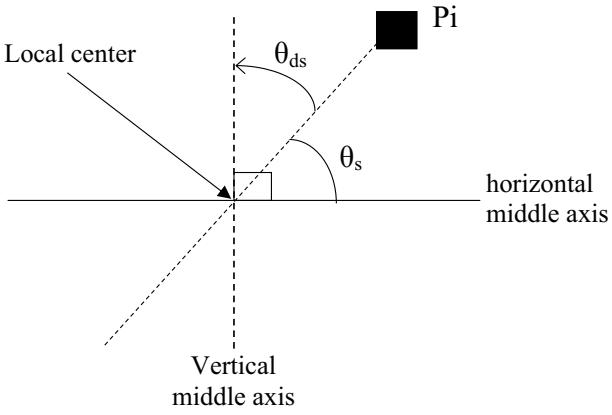


Fig. 3 Local centered-slant correction where θ_s is slant angle and θ_{ds} is de-slanting angle

3.3 Normalization

Skew and slantness of segmented words and characters are detected and corrected accordingly. Skew of a word/character image is the angle formed by horizontal axis of a word/character image and horizontal axis of the document image. Skew correction is performed to align text orientation with its axes. Projection profile is used as explained in the procedure below.

(i) A word/character image is rotated about its center in the range -50° to 50° in angle steps of 1°.
(ii) In each angle step, obtain horizontal projection profile.
(iii) The angle (θ_{sk}) for which horizontal projection profile has highest peak is the skew of the word/character.
(iv) Perform skew correction by rotating the word/character image by angle equivalent to skew angle but in opposite direction, that is $-\theta_{sk}$.

Slant is the orientation of vertical strokes of a word/character with respect to horizontal axis of the word/character. Projection profile is used for slant correction as explained below.

(i) A word/character image is rotated about its center in the range -50° to 50° in angle steps of 1°.
(ii) In each angle step, obtain vertical projection profile.
(iii) The angle (θ_{ds}) for which vertical projection profile has highest peak is the de-slant angle. Slanting angle (θ_s) is obtained by subtracting θ_{ds} from 90.
(iv) Perform slant correction using local centered-slant correction approach. θ_{ds} is used as global de-slant correction angle.

Local centered-slant correction A foreground (text) pixel is rotated at an angle $-\theta_{ds}$ about a local center. The local center is such that it is at the intersection of horizontal middle axis and vertical middle axis of text word/character as shown in Fig. 3. The acute angle formed by the line connecting foreground pixel and local center, and horizontal middle axis is slant angle (θ_s) as shown in Fig. 3. This slant correction ensures preservation of stroke size of word/character images.



Fig. 4 Normalization of word images by local centered-slant correction method. Left column are un-normalized word images and right column are respective normalized and binarized word images

After normalization, morphological dilation and erosion are performed to fill any resulting gaps. Figure 4 shows normalized word/character images obtained by local centered-slant correction method.

3.4 IHOD feature extraction

In this section, a 2D shape descriptor called integral histogram of oriented displacement (IHOD) is explained. IHOD is a combination of 2 histograms of oriented displacement that describe text strokes at both local and global levels as will be explained. Displacement is computed as a distance between foreground pixels and local (cell) or global centres. For local displacements, the word/character image is sub-divided into cells of fixed width and height dimensions. For global displacements, the image is not sub-divided into rectangular cells. Displacement of foreground pixels (in each cell or entire image) from their respective centres are described by histogram of directions between them (foreground pixels) and the centres. The first step in the construction of IHOD descriptor is standardization of word/character image.

3.4.1 Word/character image standardization

For word spotting task, word images (I(x,y)) are resized to standard image ($I_f(x,y)$) of dimensions 45×135 that is 45 rows (height) by 135 columns (width). For character recognition task, each character image is resized to standard dimension of 30×30 pixels. Standardization of word/character image dimensions is given by pseudo Eq. 1. This will ensure uniform size of extracted features.

$$I_f(x, y) = Resize(I(x, y), dim) \tag{1}$$

where $dim = (135, 45)$ for word images and $dim = (30, 30)$ for character images, is resizing dimension.

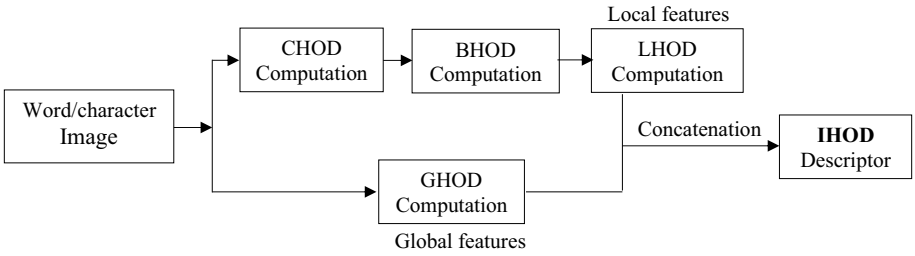


Fig. 5 Framework for construction of IHOD shape descriptor

3.4.2 IHOD computation

There are 5 steps in construction of IHOD descriptor: (a) computation of cell histogram of oriented displacement (CHOD), (b) block histogram of oriented displacement (BHOD), (c) local histogram of oriented displacement (LHOD), (d) global histogram of oriented displacement (GHOD), and (e) computation of IHOD by concatenation of LHOD and GHOD as illustrated in Fig. 5. The steps are explained in sections that follow.

(a) **Computing cell histogram of oriented displacement (CHOD)**

To compute CHOD features for a word/character image, first, the standardized word/character image $I_f(x,y)$ is thinned (skeletonised) to obtain thinned binary word/character image $I_t(x,y)$ whose strokes are one pixel thick. $I_t(x,y)$ is then divided into cells of dimension $m \times m$ as shown in Fig. 6a, where $m = 15$. Figure 6b shows the cell with cell center, C(x,y), and foreground pixels $p1(x_1,y_1)$ and $p2(x_2,y_2)$.

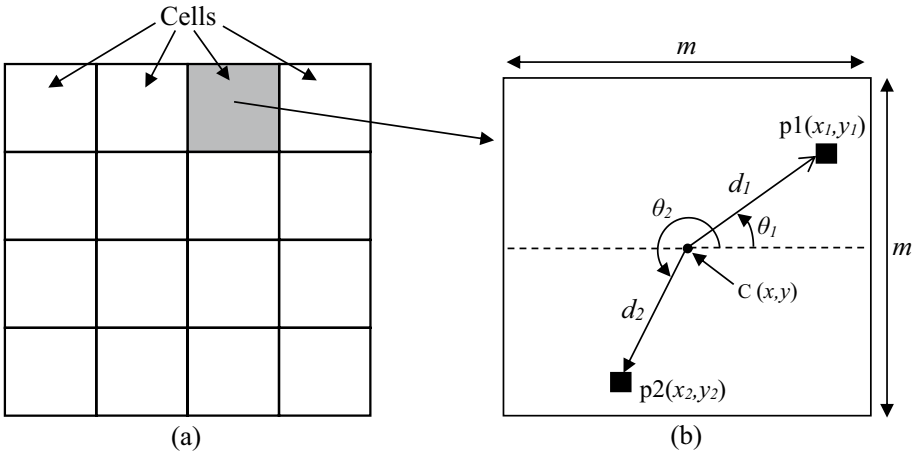


Fig. 6 CHOD computation: (**a**) is a thinned word/character image $I_t(x,y)$ divided into $m \times m$ cells, and (**b**) is a $m \times m$ cell containing sample foreground pixels p1 and p2. d_1 and d_2 are, respectively, displacements of foreground pixels p1 and p2 from cell center C(x,y) whereas θ_1 and θ_2 are respectively orientations of p1 and p2 with respect to C(x,y)

For a foreground/object pixel $P_i(x_i,y_i)$ within the cell, its displacement (d_i) from the cell center (x,y) is obtained using Eq. 2.

$$d_i = \sqrt{(x_i - x)^2 + (y_i - y)^2} \tag{2}$$

Orientations (θ_i) of a foreground pixel ($Pi(x_i,y_i)$) with respect to cell center (C(x,y)) is calculated using Eq. 3.

$$\theta_i(x_i, y_i) = \arctan\left(\frac{y_i - y}{x_i - x}\right) \tag{3}$$

Orientations are measured in counter clockwise direction from right-going horizontal axis whose origin is cell center, C(x,y) as shown in Fig. 6b. θ_i ranges between 0 and 360 degrees. Orientation angles are then quantized into bins each of bin width of 20 degrees. Thus 18 bins are used. Therefore, each foreground pixel in a cell is described by displacement d from cell center and orientation angle θ (or bin). Bin index (bin_i) is the quotient obtained from division of θ_i by bin width (20 degrees). For $\theta = 360^o$ the bin index is 17. For each cell, a 1D cell descriptor vector is obtained by voting process. In a particular cell, votes are a function of displacement (d_i) of foreground pixels from the cell center of their respective cells. That is, votes are displacement magnitudes. Each bin index receives votes of corresponding displacements which are then summed up. Votes for bins are represented as a histogram which is the cell histogram of oriented displacement (CHOD), whose length is 18**.** CHOD describes foreground pixels (portion of strokes) within a cell of a word/character image. Bin width of 20 degrees is used because it was experimentally found to be the optimum width at which shape descriptor obtained leads to best performing word spotting and character recognition models.

(b) **Computing block histogram of oriented displacement (BHOD)**

To compute BHOD, adjacent cells are joined together to form overlapping blocks of 2×2 cells such that the dimension of each block is $2m \times 2m$ where m is a cell dimension fixed at 15 pixels as explained in Section 4.3. Thus, dimension of each block is 30×30 pixels. CHOD of cells in a block are concatenated in left–right, top-down order to form a single block descriptor vector referred to as block histogram of displacement (BHOD), of length 72. This is the first level-concatenation. This 1st level concatenation is for 2 purposes: (i) helps to minimize intra-class variation resulting mainly from variation of handwriting styles in different writers, and (ii) enhances discriminative powers of the final descriptor. BHOD is then normalized by L2 Euclidean norm as given in Eq. 4.

$$\mathrm{BHOD}_{norm} = \frac{\mathrm{BHOD}}{\sqrt{\|\mathrm{BHOD}\|^2 + \varepsilon}} \tag{4}$$

where ε is a small positive regularization number which prevents division by zero. It is so small that it will not change the computed result.

(iii) **Computation of local histogram of oriented displacement (LHOD)**

LHOD is obtained by concatenating BHOD_{norm} descriptors resulting from the whole word/character image, in left–right, top-down order into a single descriptor vector. This is the 2nd level concatenation which is global in scope.

(iv) **Computation of global histogram of oriented displacement (GHOD)**

The process of computing GHOD is the same as that of CHOD in Section 3.4.2(a), taking the entire word/character image as a cell. Thus, the centre used is image centre (*w/2, h/2*) where *w* is width and *h* is height of word/character image. Displacements and orientation angles of foreground (text stroke) pixels are calculated with respect to global image centre (w/2, h/2) and then voted to their respective angle bins. The length of GHOD vector obtained is 18 which is equal to number of bins used.

(e) **Computation of Integral Histogram of Oriented Displacement (IHOD)**

IHOD is obtained by concatenating LHOD and GHOD vectors. This is the 3rd and final level concatenation resulting to formation of one combined shape descriptor, IHOD. IHOD descriptor is integral in that, it captures both local and global shape information of text strokes, thus enhancing its discriminating power. IHOD descriptor is used in training MLP classifier for word spotting and character recognition tasks. IHOD descriptor differs from HOD descriptor used by Gowayyed et al. [17] in various ways: (i) IHOD captures both local and global information while HOD captures local information only, (ii) IHOD is computed using all foreground pixels while HOD is computed using human body joints (interest points) only, (iii) in IHOD, displacement is centroid distance from foreground pixels to a fixed cell centroid while for HOD, displacement is distance moved by body joint between 2 consecutive time steps, (iv) IHOD describes shape of text strokes while HOD describe temporal behaviour of body joint motion, (v) IHOD is constructed by 3-level concatenation of CHOD, BHOD, LHOD, and GHOD descriptors whereas HOD is constructed by 1-level concatenation of orientation angle histograms of human body joints, and (vi) IHOD is spatial whereas HOD is spatio-temporal.

Pseudocode for computing IHOD

(1) *For* $0<i<n$, *do:* # where i & n are pixel index and number of pixels in a cell respectively

- Compute d_i (Eq. 2)
- Compute θ_i (Eq. 3)
- Compute $bin_i = int(\theta_i/20)$
- $bin_i \leftarrow d_i$
- $CHOD = \{bin_0, bin_1, ..., bin_{17}\}$

(2) $BHOD = Concatenate\ (CHOD_0, CHOD_1, CHOD_2, CHOD_3)$
Where $CHOD_i$ *are of adjacent* 2×2 *cells arranged in left–right and top-down order.*

(3) $LHOD = Concatenate\ (BHOD_{00}, ..., BHOD_{0k}, BHOD_{10}, ..., BHOD_{1k}, ..., BHOD_{m0}, ..., BHOD_{m-1,k-1})$
Where k is number of blocks (2×2 *cells) in a row and m is number of blocks in a column.*

(4) *For* $0<j<N$, *do: # Where j is pixel index in entire image and N is total number of pixels.*

- Compute d_i (Eq. 2)
- Compute θ_i (Eq. 3)
- Compute $bin_i = int(\theta_i/20)$
- $bin_i \leftarrow d_i$
- $GHOD = \{bin_0, bin_1, ..., bin_{17}\}$

(5) $IHOD = Concatenate(LHOD, GHOD)$

3.4.3 IHOD vector size

For a word/character image of height h and width w, $cell_dim = m \times m$, $block_dim = 2m \times 2m$, the number of blocks in horizontal axis (B_H) and vertical axis (B_V) is given by Eqs. 5 and 6 respectively.

$$B_H = \frac{w - 2 * m}{s} + 1 \tag{5}$$

$$B_V = \frac{h - 2 * m}{s} + 1 \tag{6}$$

where s is stride and $m = 15$ is cell dimension fixed as explained in Section 4.1.1. Stride equal to cell dimension (m) is used. The length of LHOD descriptor is given by Eq. 7.

$$LHOD_{size} = 72 * B_H * B_V \tag{7}$$

Since GHOD size is 18 as explained in Section 3.4.2(d), length of IHOD vector is given by Eq. 8.

$$IHOD_{size} = LHOD_{size} + GHOD_{size} = 72 * B_H * B_V + 18 \tag{8}$$

For a word image of size 45×135, $m = 15$, and $s = 15$ pixels, IHOD size is 1170. For a character image of dimensions 30×30, IHOD size is 90.

3.5 Dataset preparation

A dataset of handwritten Hindi word images was created for evaluating the proposed word spotting technique. It consists of 43,572 samples (words) from 415 different writers, with lexicon size of 630 words. Word length ranges from 1–10 characters. The ages of writers range from 12–50 years. 20 template documents with machine printed Hindi paragraphs were prepared and given to writers who copied the same content using their pens of choice in free space provided. The free space provided unconstrained conditions for obtaining natural and real handwriting styles. Each writer copied at most 2 documents. The handwritten scripts were scanned with HP Scanjet G2410 scanner with a resolution of 300 dots per inch (dpi). A scanned sample of template and handwritten scripts are shown in Fig. 7. The handwritten sections are cropped and stored as colour (RGB) images. The handwritten document images are manually segmented into words. Figure 8 shows samples of segmented word images. The segmented word images are split to train (35,870 images), validation (2,779 images) and test (4923 images) sets. The merit of our data set is that it is prepared from many writers. Therefore, it is good in performance evaluation of word spotting systems in multi-writer environment. The dataset created is named DTU-HW-Hindi.

3.6 Data augmentation

Since robust machine learning-based models need a lot of training data, data augmentation is used to supplement the already provided data. Data augmentation is the manipulation of real data provided using some techniques so as to generate another data. The generated data and real data have many similarities. The augmented data together with

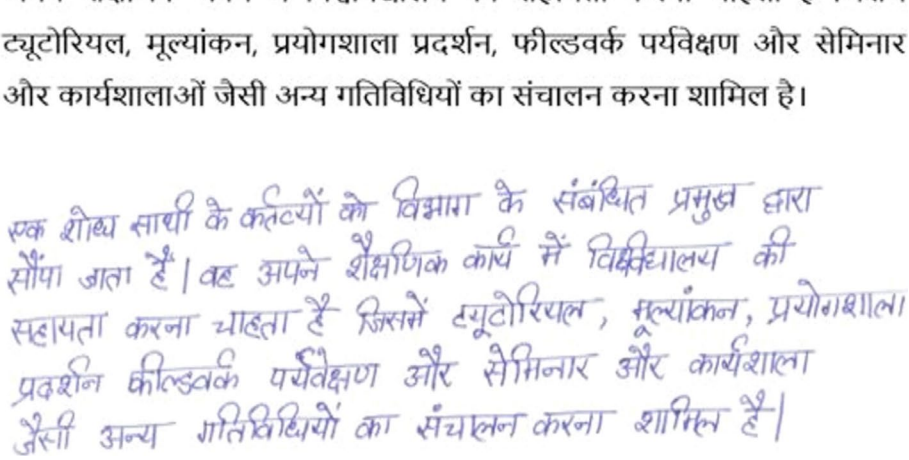


Fig. 7 Sample of scanned template content at the top and unconstrained handwritten form at bottom

real data help to reduce over-fitting and hence enhance robustness of the trained models. In our case, the augmented techniques used are affine transformation and elastic distortion [51]. In affine transformation, the approaches used are full and partial shearing, and scaling. In partial shearing, only half of the word image is subjected to shearing. After augmentation, a data set is increased 10–15 times. Figure 9 shows sample of augmented word images.

3.7 Model Development

IHOD descriptors were used to train MLP classifier to obtain HHWS and HHCR models. Python 3.6 was used together with Keras module. Keras sequential model was used where

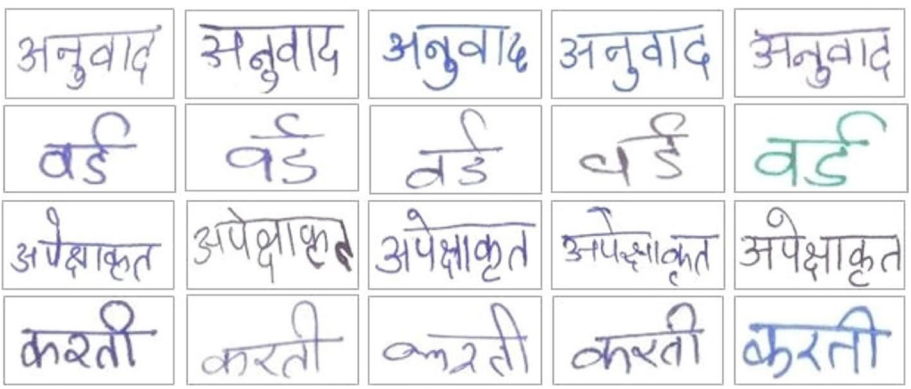


Fig. 8 Segmented word images, where each row consists of word images of same instances

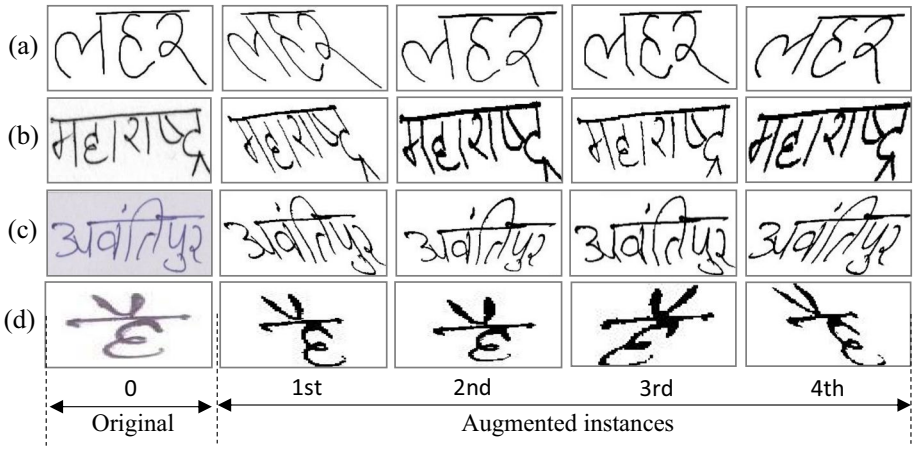


Fig. 9 Augmented images where column 0 consists of original images and columns 1–4 have respective augmented instances. Original image in row (**a**) is from RoyB dataset [45], rows (**b**-**c**) are from IIIT-HW-DEV dataset [14], and row (**d**) is from the created dataset (DTU-HW-Hindi)

it is constructed by linearly stacking fully connected layers [24]. Training was done using a core i5 8th generation HP laptop with 1 TB HDD, 8 GB RAM, and 1.8 GHz clock frequency. Figure 10 shows architecture of a fully connected MLP network consisting of 3 layers that was trained to obtain HHCR and HHWS models. For the MLP network trained to obtain HHWS model, input layer (layer 1) has 4,096 units, layer 2 has 2,048 units, and third layer 3 (output layer) has *k* units where k is number of classes. In layers 1 and 2, activation function used is ReLU (Rectified linear unit) and for layer 3 (output layer), softmax is activation function used. Optimizer used is adaptive moment (Adam). The loss function used is categorical cross-entropy which is suitable for multiple classification tasks, given by Eq. 9. Drop out of 30% was used as regularization to reduce effect of overfitting. Batch training was done with 15 epochs and batch size of 64 samples. For the MLP network trained to obtain HHCR

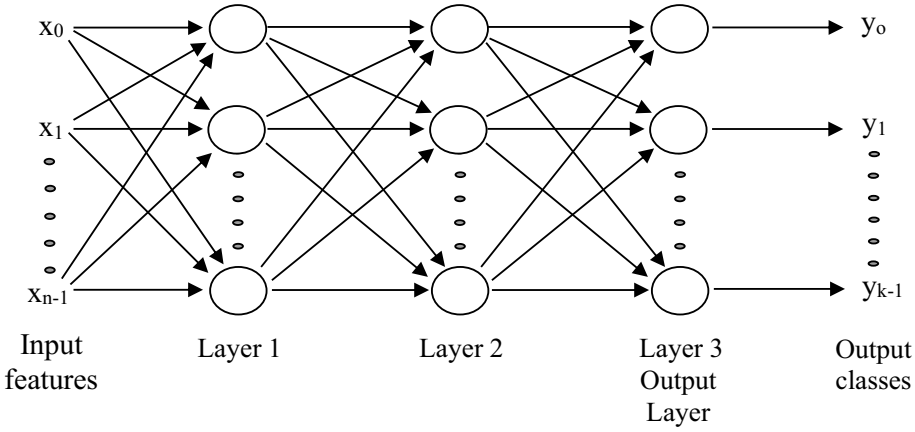


Fig. 10 Fully connected MLP network used to develop word spotting and character recognition models, where *n* is the input feature size, *and k* is the number of output classes

model, layer 1 has 256 units, layer 2 has 128 units, and layer 3 has units equivalent to number character classes. Optimizer, dropout rates, loss functions, epochs, and batch size are the same as that of the MLP architecture used to develop HHWS model as explained before.

$$Loss = -\sum_{i=1}^{k} t_i log y_i \tag{9}$$

where i is index of input training sample, k is number of classes, t is actual output label, and y is predicted output of the network.

The novelty of the proposed technique is as follows: (i) the IHOD shape descriptor used has high discriminating power thus explaining the high performance of the proposed technique. This is due to the descriptor capturing both local and global information of word and character strokes. Local information is obtained from local (cell and block)-based computation of histogram of oriented displacement (LHOD features) whereas global information is obtained from global-based computation of histogram of oriented displacement (GHOD features). (ii) IHOD features are easy to compute. (iii) The proposed technique has low computational cost. In computation of IHOD features, the only calculations involved are those of angles, local/global oriented displacements, and voting by bin-wise accumulation of length of displacements. (iv) During model development, only a 3-layer fully connected MLP network is used which is less computational and need fewer training epochs compared to CNN-based techniques which need high number of training epochs. This makes the proposed technique memory efficient. Due to this, the proposed technique can be used with stand-alone digital devices like mobile phones, personal digital assistant (PDA) and give appreciable performance.

4 Results and Discussion

4.1 Evaluation Datasets

The proposed HHWS technique has been evaluated on three datasets: (i) DTU-HW-Hindi data set which was created as afore-explained in Section 3.5, (ii) IIIT-HW-DEV dataset [14], and (iii) RoyDB Devanagari dataset [45]. DTU-HW-Hindi consists of total of 43,572 instances from a lexicon of 630 segmented word images. It is written by 415 different writers. It is divided into training set (35,870 images), validation set (2,779 images), and testing set (4,923 images). IIIT-HW-DEV dataset [14] has 95,381 instances of words written by 12 different writers. The data set has 9540 unique words. It is divided into 3 sets: train (70%), validation (15%), and testing (15%) sets. RoyDB Devanagari dataset [45] consists of 16,128 instances of handwritten Hindi word images. There are 1,957 unique words in the dataset. It is divided into train set (10,667 samples), validation set (1,872 samples), and testing set (3,589 samples).

The IHOD-based HHCR technique for character recognition is evaluated with 2 datasets: AcharyaPG-DHCD [1] and PantPJ-DHCD [38]. AcharyaPG-DHCD [1] dataset consists of 92,000 character samples from 46 classes (36 for consonants and 10 for digits). Each class has 2,000 samples. It is divided into train set of 78,200 samples (85%) and test set of 13,500 samples (15%). In each class, 1,700 samples are used for training while 300 samples are used for testing. PantPJ-DHCD [38] dataset consists of 12,912 character samples with 58 classes (36 for consonants, 12 for vowels, and 10 for numerals). Consonants

have 205 samples per class, vowels have 221 samples per class, and numerals have 288 samples per class.

4.2 Evaluation metrics

Evaluation metrics used in evaluating performance of HHWS technique are k-precision (kPr) and mean average precision (MAP), whereas mean accuracy (MA) metric is used in evaluation of the proposed IHOD-based HHCR technique.

4.2.1 k-precision (kPr)

This is the proportion of relevant words/items retrieved in top k retrieved words/items. It is obtained using Eq. 10.

$$kPr = \frac{k_o}{k} \tag{10}$$

where k_o is the number of relevant words in top k retrieved words.

4.2.2 Mean average precision (MAP)

MAP is the average precision in increasing retrieving rank (size). It is obtained using Eq. 11 [62]

$$MAP = \frac{\sum_{k=1}^{j} (kPr \times rel(k))}{No.\ of\ relevant\ words} \tag{11}$$

where j is the number of similar word images retrieved and $rel(k)$ is given by Eq. 12

$$rel(k) = \begin{cases} 1 & if\ word\ at\ rank\ k\ is\ relevant \\ 0 & if\ word\ at\ rank\ k\ is\ not\ relevant \end{cases} \tag{12}$$

MAP is a good retrieval performance metric for retrieving systems [10] since it shows the retrieval size which the word spotting system can handle well. MAP and kPr metrics range from 0–1 and the larger the values, the better the word spotting system.

4.2.3 Mean Accuracy (MA)

This is the average recognition accuracy of characters obtained with cross validation approach explained as follows: The evaluation data set for HHCR (Section 4.1) is first divided into N disjoint sub-sets of equal size. During training, one sub-set is reserved for testing while the rest are used for model development. Recognition accuracy of thedeveloped model is computed using the test sub-set. The same is repeated with a different sub-set as a testing set until all sub-sets are used as testing sets. That is, N models are obtained with different sub-sets as testing set. Average recognition accuracy of all recognition accuracies due to different models is obtained. This average recognition accuracy is mean accuracy (MA), given by Eq. 13.

$$Mean - Accuracy = \frac{1}{N} \sum_{i=1}^{N} \frac{r_i}{R_i} \tag{13}$$

Table 4 Performance of the proposed word spotting technique for various cell dimensions ($m \times m$) used during IHOD feature extraction for k-precision (kPr) and mean average precision (MAP) evaluation metrics

m	9	11	13	**15**	17	19	21	23
kPr	0.7713	7887	0.8475	**0.97588**	0.8671	0.8498	0.8423	0.8151
MAP	0.7435	0.7611	0.7971	**0.9736**	0.8411	0.8250	0.8151	0.7891

Bold entries denote the cell dimension (15 × 15 pixels) for which performance is optimum

where N is number of folds, i is fold index, r is number of relevant characters, and R is total number of characters.

4.3 Evaluation of handwritten Hindi Word spotting (HHWS) model

In evaluating the proposed HHWS technique, query by example (QBE) method was used to search instances of similar words from a database of candidate word images. The proposed technique is evaluated with the three afore-mentioned data sets (Section 4.1): DTU-HW-Hindi, IIIT-HW-DEV [14], and RoyDB Devanagari [45] datasets. First, performance of the proposed HHWS technique for word spotting is evaluated when different cell sizes are used during feature extraction (discussed in Section 3.4).

Table 4 and Fig. 11 shows evaluation scores of kPr and MAP metrics for the proposed word spotting technique for various cell sizes (ranging from 9–23 pixels) used during IHOD feature extraction (section 3.4). It can be seen that performance of the proposed word spotting system increases with increase in cell size to maximum when cell size is 15 pixels, beyond which the performance starts to fall gradually. When cell sizes of above 15 pixels are used during feature extraction, much useful information is lost due to lumping together of large foreground regions. This makes the obtained IHOD descriptor having reduced discriminating power. This in turn leads to less efficient models being obtained, thus reduced performance. When cell size used in features extraction is less than 15 pixels, many redundant features are obtained that lead to increased feature dimension. This causes network complexity, hence less efficient model obtained during training. The most efficient

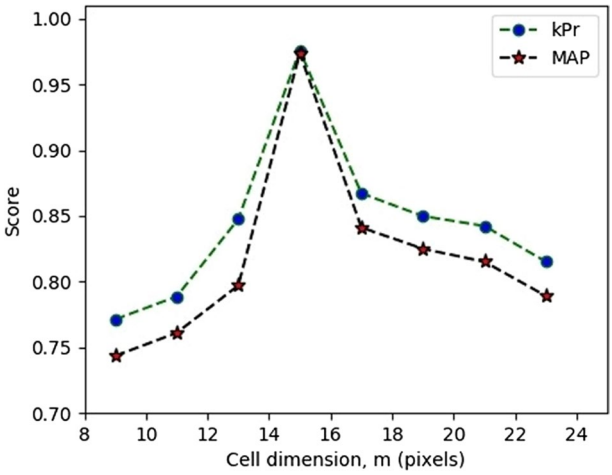


Fig. 11 Word spotting model performance plot for various cell sizes used during IHOD feature extraction, where kPr is k-precision, MAP is mean average precision, and m is cell dimension in pixels

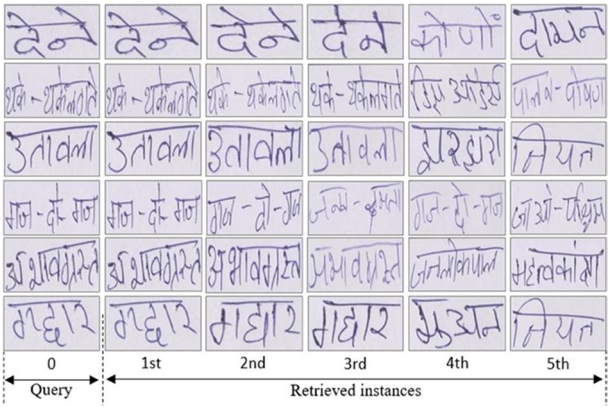


Fig. 12 Retrieved word images of IIIT-HW-DEV dataset [14], using developed word spotting model where column 0 consists of query images and columns 1–5 has retrieved instances in descending order of scores

model is obtained when cell sizes of dimensions (width and height) of 15 pixels are used during feature extraction (Section 3.4), when feature redundancy is at minimum.

In evaluating the proposed HHWS technique with IIIT-HW-DEV dataset [14], query images used are from test set. It was noted that all unique words from query set (test set) have frequency of 3 and below except one word image with frequency of 4. Therefore, when computing kPr and MAP metrics, 3 retrievals were used. Figure 12 shows samples of retrieved instances of respective query images for IIIT-HW-DEV dataset [14]. It can be seen from Fig. 12 that the top 3 retrieved instances are similar to the query word image whereas 4th and 5th retrieved instances are not. This is because almost all query word images have frequency of 3 and below as noted before. Also, the first (column 1st) retrieved word instance is the query word itself since it is from the test set.

Table 5 shows comparative performance of the proposed method on IIIT-HW-DEV [14], and RoyDB [45] Devanagari datasets. Performance scores for end2end network are obtained from a paper by Dutta et al. [13].

From Table 5, it can be seen that MAP and k-precision metrics for the proposed word spotting technique are very high. For IIIT-HW-DEV dataset [14], performance of the proposed technique compares very well with that of End2End Network [27] technique. Though End2End Network [27] performs better than the proposed technique by a very small margin, it is computationally expensive and relies exclusively on GPU. In our case, developing the word spotting model with IIIT-HW-DEV dataset [27] was done using a laptop as noted before. Model development in the proposed HHWS took 30 min, for 15 epochs. That is 2 min per epoch which is compatible and usable with a variety of portable digital devices which have relatively low memory and computation capacity compared to GPU. For RoyDB dataset [45], the proposed method has the best performance. HHWS model development with RoyDB dataset [45] took 4 min for 15 epochs translating to about

Table 5 Word spotting performance comparison with IIIT-HW-DEV [14] and RoyDB [45] datasets

Technique	IIIT-HW-DEV [14]		RoyDB [45]	
	kPr	MAP	kPr	MAP
End2End Network [27]	-	0.6387	-	0.9439
HMM-based method [45]	-	-	0.9495	-
Proposed	0.6426	0.6195	0.9631	0.9613

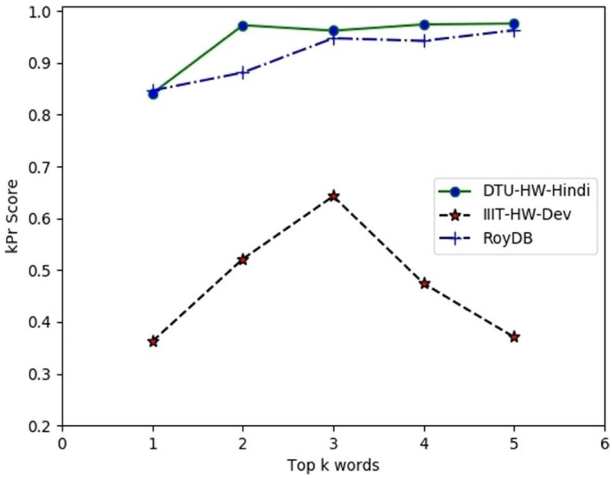


Fig. 13 Precision of proposed HHWS technique on k top words retrieved for DTU-HW-Hindi, IIIT-HW-DEV [14], and RoyDB [45] datasets

16 s per epoch. This shows that the proposed method is computationally less expensive and with appreciable performance. For RoyDB dataset [45], it can be noted that kPr and MAP scores are higher than those for IIIT-HW-DEV dataset [14]. This is because IIIT-HW-DEV dataset [14] has larger lexicon size (9,540) as compared to RoyDB dataset [45] with lexicon size of 1,957 words. As the lexicon increases, there are many classes whose handwritten structure are similar, hence higher chances of misclassification.

Figures 13 and 14 respectively show k-precision and MAP scores of the proposed HHWS technique for different top k words retrieved for DTU-HW-Hindi (section 3.5), IIIT-HW-DEV [14] and RoyDB [45] datasets. From Figs. 13 and 14, it can be seen that for DTU-HW-Hindi (Section 3.5) and RoyDB [45], kPr and MAP scores for HHWS method increase as the number of top words retrieved increases up to the best scores peaking at 5 top words retrieved. The scores peak at 5 top words because this is the average number of words per class for test sets of both DTU-HW-Hindi and RoyDB [45] datasets. For IIIT-HW-DEV dataset [14], the performance of HHWS method peaks at 3 top words (see Figs. 13 and 14)

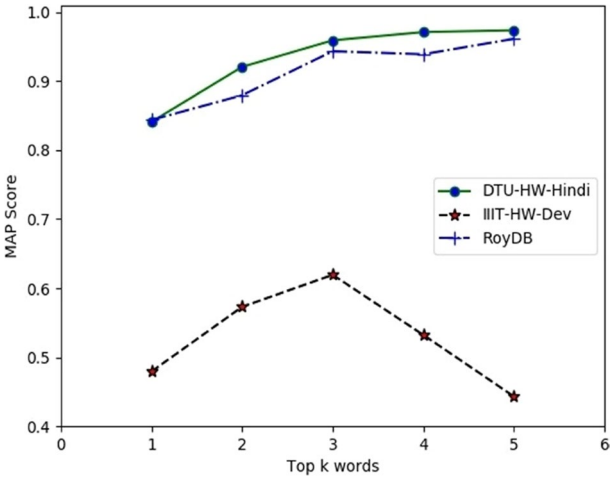


Fig. 14 MAP of the proposed HHWS technique on k top words retrieved for DTU-HW-Hindi, IIIT-HW-DEV [14], and RoyDB [45] datasets

Table 6 Comparative performance of the proposed character recognition technique for AcharyaPG-DHCD dataset [1]

Technique	Cons (%)	Num (%)	Cons + Num (%)	Time/epoch (min)
AlexNet [28]	-	-	98	2.2
DenseNet 121 [20]	-	-	89	5.3
DenseNet 201 [20]	-	-	90	7.6
VGG 11 [52]	-	-	99	5.7
VGG 16 [52]	-	-	98	8.8
VGG 19 [52]	-	-	98	9.9
Inception V3 [60]	-	-	99	16.3
DCNN-based [1]	-	-	98.47	-
Proposed	96.78	99.55	95.45	1.4

*Cons = Consonants, Num = Numerals

beyond which it starts to decrease. As mentioned before, this is because class size of test set of IIIT-HW-DEV dataset [14] is 3 words and below except for one class (word) having a frequency of 4. Therefore, when the number of top words retrieved is beyond 3, dissimilar instances are included which accounts for the decreased scores of kPr and MAP metrics.

4.4 Evaluation of handwritten Hindi character recognition (HHCR) technique

The proposed IHOD-based HHCR technique is evaluated with AcharyaPG-DHCD [1] and PantPJ-DHCD [38] datasets (described in Section 4.1). In Table 6, performance (recognition accuracy) of the proposed HHCR technique is compared with other techniques for AcharyaPG-DHCD [1] dataset. Performances of tuned AlexNet [28], DenseNet [20], VGG [52], and Inception [60] CovNets were obtained from work by Aneja and Aneja [3]. The tuned CNN-based models were trained in 15 epochs which is the same as in the proposed IHOD-based HHCR technique. These CNN-based architectures were implemented by a GPU.

From Table 6, it is seen that Inception V3 [60] tops in terms of recognition accuracy with 99% followed by VGG (99%) [52] and AlexNet (98%) [28] in that order. This is because they ride on good pre-learned features before further training with dataset of characters. DCNN-based [1] technique also has good character recognition accuracy of 98.47% due to efficient features learnt by convolution layers. The proposed method (with recognition accuracy of 95.45%) is outperformed by all others except DenseNet [20] (having 89%). However, the proposed method compares very well with other better performing CNN-based methods given that the range from the best performing techniques is less than 3%. Despite good performances of the other CNN-based methods, they are computationally complex due to many trainable parameters in their respective architectures, a reason they are implemented with GPU. Thus, they are not feasible with standalone devices like personal digital assistants (PDA) or ordinary desktop personal computers which have relatively low computation capability. The proposed HHCR is less computationally expensive compared to other CNN-based methods, hence is feasible with standalone devices like personal digital assistants (PDA) or ordinary desktop personal computers. In terms of speed (execution time), the proposed HHCR technique is the fastest with 1.4 min per epoch whereas Inception V3 [60] is the slowest with 16.3 min per epoch. The proposed HHCR method performs better on individual numeral (96.78%) and consonant (99.55%) sets than

Table 7 Performance of the proposed character recognition technique for PantPJ-DHCD [38] dataset

Technique	Cons (%)	Vow (%)	Num (%)	Cons + Num + Vow (%)	Time/epoch (sec)
MLP-RBFNet [38]	80.25	86.04	94.44	-	-
Proposed	92.84	94.08	98.41	94.15	8

*Cons = Consonants, Vow = Vowels, Num = Numerals

when combined (95.45%). This is because individual sets (consonants and numerals) have high between class variance and very low within class variance. When the sets are combined, within class variance increases since structures of some handwritten characters from different classes look similar. Example of such different characters with similar handwritten forms are ३ (3) and ङ (kna), ३ (3) and उ (da), २ (2) and र (ra) (see Tables 1 and 3) among others as also noted by Aneja and Aneja [3].

Table 7 shows performance (recognition accuracy) of the proposed HHCR technique for PantPJ-DHCD [38] dataset. HHCR model was developed by training MLP classifier (Section 3.7) in 15 epochs with this data set. The proposed method outperformed MLP-RBFNet [38] technique in individual sets of consonants, vowels and numerals by relatively big range. This can be attributed to less complex and high discriminating power of IHOD descriptor used to develop HHCR model. MLP-RBFNet [38] method is complex with likeliness of redundant features being extracted which leads to relatively less efficient model being obtained, thus outperformed by the proposed HHCR method. When the consonants, vowels and numerals sets are combined, performance of the proposed technique drops by a small margin of less than 4%. This is due to increase in cases of within class variance and more cases of between classes similarity. The proposed method is less computational as it takes an average of 8 s per epoch for a laptop with specifications mentioned in Section 3.7. This shows that the proposed method is very efficient.

5 Conclusion

Efficient segmentation-based offline word spotting and character recognition techniques for hand written Hindi document scripts have been proposed. The methods use a newly proposed shape descriptor called integral histogram of oriented displacement (IHOD) to train MLP classifier to obtain handwritten Hindi word spotting (HHWS) and handwritten Hindi character recognition (HHCR) models. IHOD is obtained by concatenating local and global histograms of oriented displacements. Local histogram of oriented displacement is obtained from oriented displacement between foreground pixels and local (cell) centers whereas global histogram of oriented displacement is obtained from oriented displacement between foreground pixels and global (character/word image) center. IHOD shape descriptor is used to describe foreground(text) pixels at word/character level. The descriptor is scale invariant and has very good discriminative properties since it incorporates both local and global information about text/character strokes. The IHOD-based HHWS technique takes input query word image to search for similar instances from a given database of handwritten word images. The proposed IHOD-based HHWS technique was evaluated with 3 datasets: DTU-HW-Hindi (data set created), IIIT-HW-DEV [14], and RoyDB Devanagari [45] datasets. The best scores obtained are 0.9758 and 0.9736 for k-precision

and mean average precision respectively. The IHOD-based HHCR technique was evaluated with AcharyaPG-DHCD [1] and PantPJ-DHCD [38] datasets of handwritten Hindi characters attaining best performance of 97.45% in recognition accuracy. Also, DTU-HW-Hindi dataset has been created. The dataset consists of 43,572 segmented handwritten Hindi word images from 415 writers.

In the proposed HHWS and HHCR techniques, IHOD shape descriptor has a small proportion of global information (via GHOD) compared to that of local information (via LHOD). For future work, we plan to device ways of increasing global information in IHOD descriptor so as to enhance its application suitability. We will also include zone-wise HOD information, that is, HOD computed at segmented zone levels. The zones can be horizontally or vertically oriented. The proposed IHOD descriptor will also be extended to word spotting and character recognition of non-Hindi scripts.

Declarations

Data availability The dataset generated and analyzed during the current study is available from the corresponding author on request.

Conflict of Interest The authors declare that they have no conflict of interest.

References

1. Acharya A, Pant AK, Gyawali PK (2015) Deep Learning Based Large Scale Handwritten Devanagari Character Recognition. In Proceedings of the 9th International Conference on Software, Knowledge, Information Management and Applications, IEEE pp 121–126
2. Amanatiadis A, Zagoris K, Pratikakis I (2021) Word Spotting as a Service for Handwritten Documents. IEEE International Conference on Consumer Electronics (ICCE), Las Vegas, NV, USA. https://doi.org/10.1109/ICCE50685.2021.9427583
3. Aneja N, Aneja S (2019) Transfer Learning using CNN for Handwritten Devanagari Character Recognition. 1st International Conference on Advances in Information Technology pp 293–296
4. Antonacopoulos A, Downton A (2007) Special issue on the analysis of historical documents. IJDAR 9(2):75–77. https://doi.org/10.1007/s10032-007-0045-1
5. Arora S, Bhatcharjee D, Nasipuri M, Malik L (2007) A two stage classification approach for handwritten Devanagari characters. In: International conference on computational intelligence and multimedia applications (ICCIMA). IEEE, Sivakasi, pp 399–403. https://doi.org/10.1109/ICCIMA.2007.254
6. Arora S, Bhattacharjee D, Nasipuri M, Malik L, Kundu M, Basu DK (2020) Performance comparison of SVM and ANN for handwritten Devnagari character recognition. Int J Comput Sci Issues 7(3) (6):18–26
7. Bhardwaj A, Jose D, Govindaraju V (2008) Script Independent Word Spotting in Multilingual Documents. International Joint Conference on Natural Language Processing
8. Bhattacharya U, Chaudhuri BB (2009) Handwritten numeral databases of Indian scripts and multistage recognition of mixed numerals. IEEE Trans Pattern Anal Mach Intell 31(3):444–457. https://doi.org/10.1109/TPAMI.2008.88
9. Bhunia AK, Roy PP, Sain A, Pal U (2020) Zone-based keyword spotting in Bangla and Devanagari documents. Multimed Tools Appl. https://doi.org/10.1007/s11042-019-08442-y
10. Chatzichristofis SA, Zagoris K, Arampatzis A (2011) The trec files: the (ground) truth is out there. 34th international ACM SIGIR conference on Research and development in Information, ser. SIGIR '11. New York, NY, USA: ACM pp 1289–1290
11. Deshpande PS, Malik L, Arora S (2008) Fine classification & recognition of hand written Devnagari characters with regular expressions & minimum edit distance method. J Comput 3(5):11–17. https://doi.org/10.4304/jcp.3.5.11-17
12. Dongre VJ, Mankar VH (2010) A Review of Research on Devnagari Character Recognition (0975 – 8887). Int J Comput Appl 12(2):8–15

13. Dutta K, Krishnan P, Mathew M, Jawahar CV (2018) Towards spotting and recognition of handwritten words in Indic scripts. In: 16th IEEE International Conference on Frontiers in Handwriting Recognition (ICFHR), Niagara Falls, NY. https://doi.org/10.1109/ICFHR-2018.2018.00015
14. Dutta K, Krishnan P, Mathew M, Jawahar CV (2018b) Offline Handwriting Recognition on Devanagari using a new Benchmark Dataset. 13th IAPR International Workshop on Document Analysis Systems (DAS), IEEE pp 25–30
15. Fischer A, Keller A, Frinken V, Bunke H (2012) Lexicon-free handwritten word spotting using character HMMs. Pattern Recogn Lett 33(7):934–942. https://doi.org/10.1016/j.patrec.2011.09.009
16. Gharde SS, Ramteke RJ, Kotkar VA, Bage DD (2016) Handwritten Devanagari Numeral and Vowel Recognition using Invariant Moments. International Conference on Global Trends in Signal Processing, Information Computing and Communication pp 255–260
17. Giotis, AP, Sfikas, G, Nikou, C (2022) Adversarial deep features for weakly supervised document image keyword spotting. IEEE 14th Image, Video, and Multidimensional Signal Processing Workshop (IVMSP), Nafplio, Greece. https://doi.org/10.1109/IVMSP54334.2022.9816250
18. Gowayyed MA, Torki M, Hussein ME, El-Saban M (2013) Histogram of Oriented Displacements (HOD): Describing Trajectories of Human Joints for Action Recognition. Proceedings of the Twenty-Third International Joint Conference on Artificial Intelligence pp 1351–1357
19. Hassan E, Chaudhury S, Gopal M (2013) Word shape descriptor-based document image indexing: anew DBH-based approach. Int J Doc Anal Recognit 16:227–246. https://doi.org/10.1007/s10032-012-0187-7
20. Huang G, Liu Z, Maaten L, Weinberger KQ (2017) Densely connected convolutional networks. In: IEEE conference on computer vision and pattern recognition (CVPR), Honolulu, pp 2261–2269. https://doi.org/10.1109/CVPR.2017.243
21. Iamsa-at S, Horata P (2013) Handwritten Character Recognition Using Histograms of Oriented Gradient Features in Deep Learning of Artificial Neural Network. International Conference on IT Convergence and Security (ICITCS), IEEE pp 1–5
22. Jangid M, Srivastava S (2018) Handwritten Devanagari character recognition using layer-wise training of deep convolutional neural networks and adaptive gradient methods. J Imaging 4(2):41–54. https://doi.org/10.3390/jimaging4020041
23. Jayadevan R, Kolhe SR, Patil PM, Pal U (2011) Offline recognition of Devanagari script: a survey. IEEE Trans Syst Man Cybern Part C Appl Rev 41(6):782–796. https://doi.org/10.1109/TSMCC.2010.2095841
24. Keras documentation: Getting started with the Keras Sequential model. https://keras.io/getting-started/sequential-model-guide/. Accessed 20 Oct 2021
25. Khurshid K, Faure C, Vincent N (2012) Word spotting in historical printed documents using shape and sequence comparisons. Pattern Recogn 45(7):2598–2609
26. Kolz A, Alspector J, Augusteijn M, Carlson R, Popescu GV (2000) A line-oriented approach to word spotting in handwritten documents. Pattern Anal Appl 3(2):153–168
27. Krishnan P, Dutta K, Jawahar CV (2018) Word spotting and recognition using deep embedding. 13th IAPR International Workshop on Document Analysis Systems (DAS), IEEE
28. Krizhevsky A (2014) One weird trick for parallelizing convolutional neural networks. ArXiv, abs/14045997. Accessed 11 Apr 2023
29. Kumar SS, Ahmed ST, Bai N, Vınutha BA (2019) Type of Supervised Text Classification System for Unstructured Text Comments using Probability Theory Technique. Int J Recent Technol Eng (IJRTE) 8(10):860–867. https://doi.org/10.35940/ijrte.B1158.0982S1019
30. Lu S, Li L, Tan CL, Member S (2008) Document Image Retrieval through Word Shape Coding. IEEE Trans Pattern Anal Mach Intell 30(11):1913–1918
31. Madhuri Y, Purwar RK (2018) Hindi handwritten character recognition using oriented gradients and Hu- geometric moments. J Electron Imaging 27(5):051216. https://doi.org/10.1117/1.JEI.27.5.051216
32. Omayio EO, Indu S, Panda J (2022) Word Segmentation by Component Tracing and Association (CTA) Technique. J Eng Res. https://doi.org/10.36909/jer.15207
33. Omayio, EO, Indu, S, Panda, J (2021) Word spotting of handwritten Hindi scripts by circular histogram of oriented displacement (CHOD) features. 4th Biennial International Conference on Nascent Technologies in Engineering 2021, held at Fr. C. Rodrigues Institute of Technology, Vashi, Navi Mumbai, India
34. Otsu N (1979) A threshold selection method from grey level histogram. IEEE Trans Syst Man Cybern 9(1):62–66. https://doi.org/10.1109/TSMC.1979.4310076
35. Pal U, Chaudhuri BB (2004) Indian script character recognition: a survey. Pattern Recogn 37:1887–1899. https://doi.org/10.1016/j.patcog.2004.02.003
36. Pal U, Wakabayashi T, Kimura F (2009) Comparative study of Devanagari handwritten character recognition using different features and classifiers. In: IEEE 10th international conference on

document analysis and recognition, Barcelona, pp 1111–1115. https://doi.org/10.1109/ICDAR.2009.244
37. Pal U, Sharma N, Wakabayashi T, Kimura F (2007) Off-line handwritten character recognition of Devnagari script. In: 9th IEEE international conference on document analysis and recognition (ICDAR), Curitiba, pp 496–500. https://doi.org/10.1109/ICDAR.2007.4378759
38. Pant AK, Panday SP, Joshi SR (2012) Off-line Nepali handwritten character recognition using Multilayer Perceptron and Radial Basis Function neural networks. In Proceedings of 2012 Third Asian Himalayas International Conference on Internet, IEEE pp 1–5
39. Papandreou A, Gatos B, Louloudis G (2014) An adaptive zoning technique for efficient word retrieval using dynamic time warping. Proceedings of the First International Conference on Digital Access to Textual Cultural Heritage (DATeCH) pp 147–152
40. Rajput GG, Mali SM (2010) Fourier descriptor based isolated Marathi handwritten numeral recognition. Int J Comput Appl 3(4):9–13
41. Ramteke RJ, Mehrotra SC (2006) Feature extraction based on moment invariants for handwriting recognition. In Proc IEEE Conf Cybern Intell Syst pp 1–6
42. Rath TM, Manmatha R (2003) Word image matching using dynamic time warping. In: 2003 IEEE computer society conference on computer vision and pattern recognition, vol 2, Madison, p II. https://doi.org/10.1109/CVPR.2003.1211511
43. Retsinas G, Louloudis G, Gatos SN, B (2019) Efficient Learning-Free Keyword Spotting. IEEE Trans Pattern Anal Mach Intell 41(7):1587–1600
44. Roy PP, Rayar F, Ramel JY (2015) Word spotting in historical documents using primitive code book and dynamic programming. Image Vis Comput 44:15–28
45. Roy PP, Bhunia AK, Das A, Dey P, Pal U (2016) HMM-based Indic handwritten word recognition using zone segmentation. Pattern Recogn 60:1057–1075. https://doi.org/10.1016/j.patcog.2016.04.012
46. Roy PP, Bhunia AK, Bhattacharyya A, Pal U (2019) Word searching in scene image and video frame in multi-script scenario using dynamic shape coding. Multimed Tools Appl 78:7767–7801. https://doi.org/10.1007/s11042-018-6484-5
47. Sapkal, A, Chhavi, Sharma, S, Kumar, P, Yadav, S (2021) Keyword spotting in historical document collections without segmentation using the Siamese Network. International Conference on Innovative Computing, Intelligent Communication and Smart Electrical Systems (ICSES), https://doi.org/10.1109/ICSES52305.2021.9633920
48. Shaw B, Parui SK, Shridhar M (2008) Offline handwritten Devanagari word recognition: a holistic approach based on directional chain code feature and HMM. In: 2008 IEEE international conference on information technology, Bhubaneswar, pp 203–208. https://doi.org/10.1109/ICIT.2008.33
49. Shaw B, Bhattacharya U, Parui SK (2014) Combination of features for efficient recognition of offline handwritten Devanagari words. In: 14th IEEE international conference on Frontiers in handwriting recognition (ICFHR), Hersonissos, Greece, pp 240–245. https://doi.org/10.1109/ICFHR.2014.48
50. Shekhar R, Jawahar CV (2012) Word Image Retrieval using Bag of Visual Words. In: 10th IAPR International Workshop on Document Analysis Systems, IEEE, Gold Coast, pp 297–301. https://doi.org/10.1109/DAS.2012.96
51. Simard PY, Steinkraus D, Platt JC (2003) Best practices for convolutional neural networks applied to visual document analysis. In: 7th international conference on document analysis and recognition. Edinburgh, pp 958–963. https://doi.org/10.1109/ICDAR.2003.1227801
52. Simonyan K, Zisserman A (2015) Very deep convolutional networks for large-scale image recognition. In: 3rd international conference on learning representations. ICLR 2015, San Diego CoRR, abs/1409.1556
53. Singh N (2018) An efficient approach for handwritten Devanagari character recognition based on artificial neural network. In: 5th international conference on signal processing and integrated networks. IEEE, Noida, pp 894–897. https://doi.org/10.1109/SPIN.2018.8474282
54. Singh KD, Ahmed ST (2020) Systematic linear word string recognition and evaluation technique. In: 2020 international conference on communication and signal processing (ICCSP). IEEE, Chennai, pp 0545–0548. https://doi.org/10.1109/ICCSP48568.2020.9182044
55. Sonawane PK, Shelke S (2018) Handwritten Devanagari Character Classification using Deep Learning. International Conference on Information, Communication, Engineering and Technology (ICICET), IEEE, Pune India pp 1–4
56. Srihari SN, Huang C, Srinivasan H (2005) A search engine for handwritten documents. Document Recognition and Retrieval pp 66–75

57. Srihari SN, Srinivasan H, Huang C, Shetty S (2006) Spotting words in Latin, Devanagari and Arabic scripts. Vivek: Indian J Artif Intell 6(3):2–9
58. Sudholt S, Fink GA (2016) PHOCNet: A deep convolutional neural network for word spotting in handwritten documents. Proceedings of the 15th Int. Conf. Frontiers in Handwriting Recognition (ICFHR), Shenzhen, China, pp 277–282
59. Sushma SN, Sharada B (2022) A Convolutional Autoencoder based Keyword Spotting in Historical Handwritten Devanagari Documents. Int Conf Inventive Comput Technol (ICICT). https://doi.org/10.1109/ICICT54344.2022.9850900
60. Szegedy C, Vanhoucke V, Ioffe S, Shlens J, Wojna Z (2016) Rethinking the inception architecture for computer vision. In: 2016 IEEE conference on computer vision and pattern recognition (CVPR), Las Vegas, pp 2818–2826. https://doi.org/10.1109/CVPR.2016.308
61. Trier D, Jain AK, Taxt T (1996) Feature Extraction Method for Character Recognition - A Survey. Pattern Recogn 29(4):641–662
62. Zagoris K, Pratikakis I, Gatos B (2014) Segmentation-based historical handwritten word spotting using document-specific local features. In: 14th international conference on Frontiers in handwriting recognition. IEEE, Hersonissos, pp 9–14. https://doi.org/10.1109/ICFHR.2014.10
63. Zhang X, Pal U, Tan CL (2014) Segmentation-free keyword spotting for Bangla handwritten documents. In: 2014 14th international conference on Frontiers in handwriting recognition. IEEE, Hersonissos, pp 381–386. https://doi.org/10.1109/ICFHR.2014.70

Publisher's note Springer Nature remains neutral with regard to jurisdictional claims in published maps and institutional affiliations.

Springer Nature or its licensor (e.g. a society or other partner) holds exclusive rights to this article under a publishing agreement with the author(s) or other rightsholder(s); author self-archiving of the accepted manuscript version of this article is solely governed by the terms of such publishing agreement and applicable law.